

**Eighteenth Symposium on**

**NAVAL HYDRODYNAMICS**

**Ship Motions**

**Ship Hydrodynamics**

**Experimental Techniques**

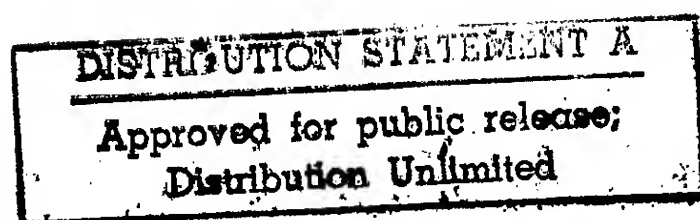
**Free-Surface Aspects**

**Wave/Wake Dynamics**

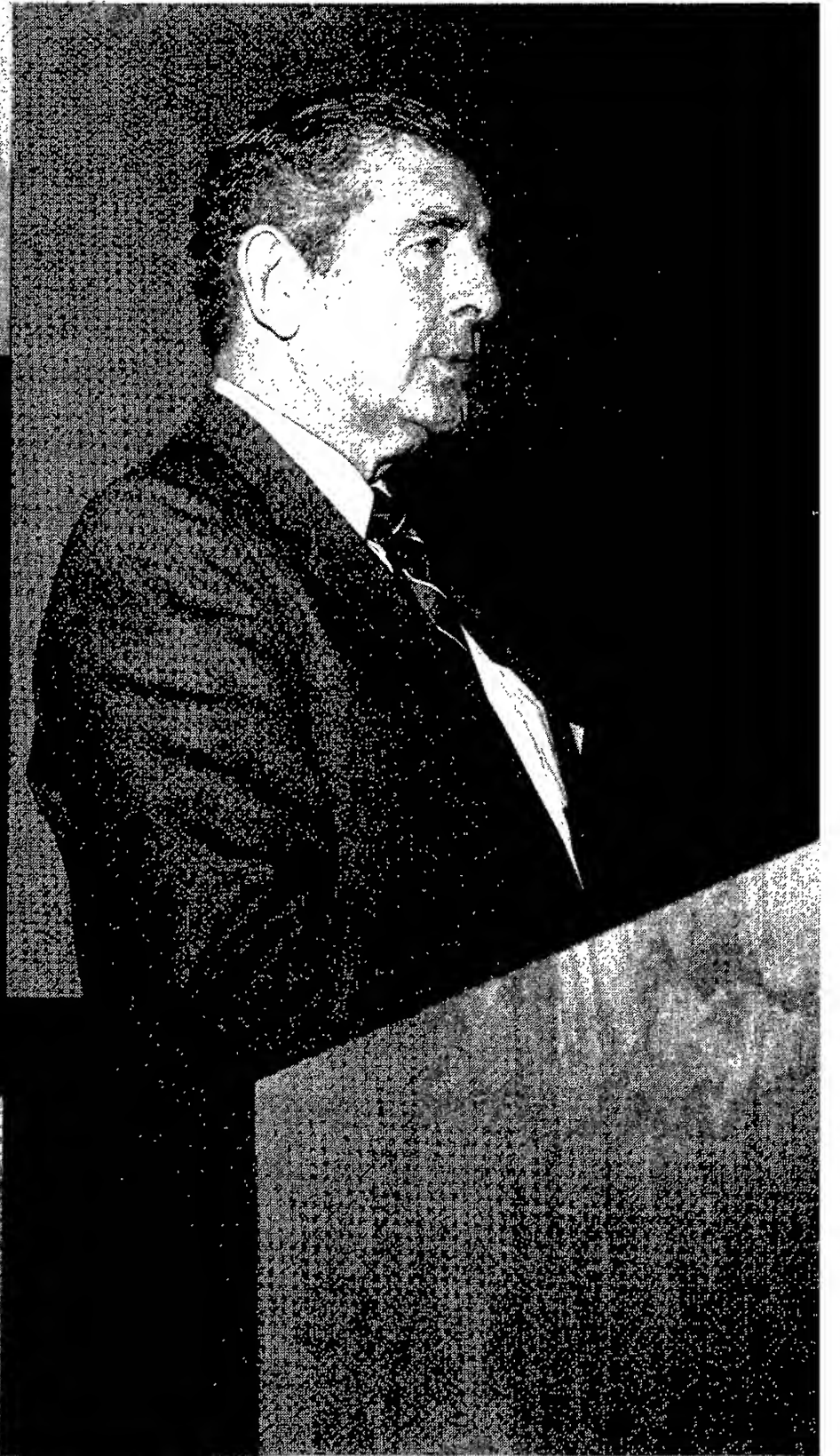
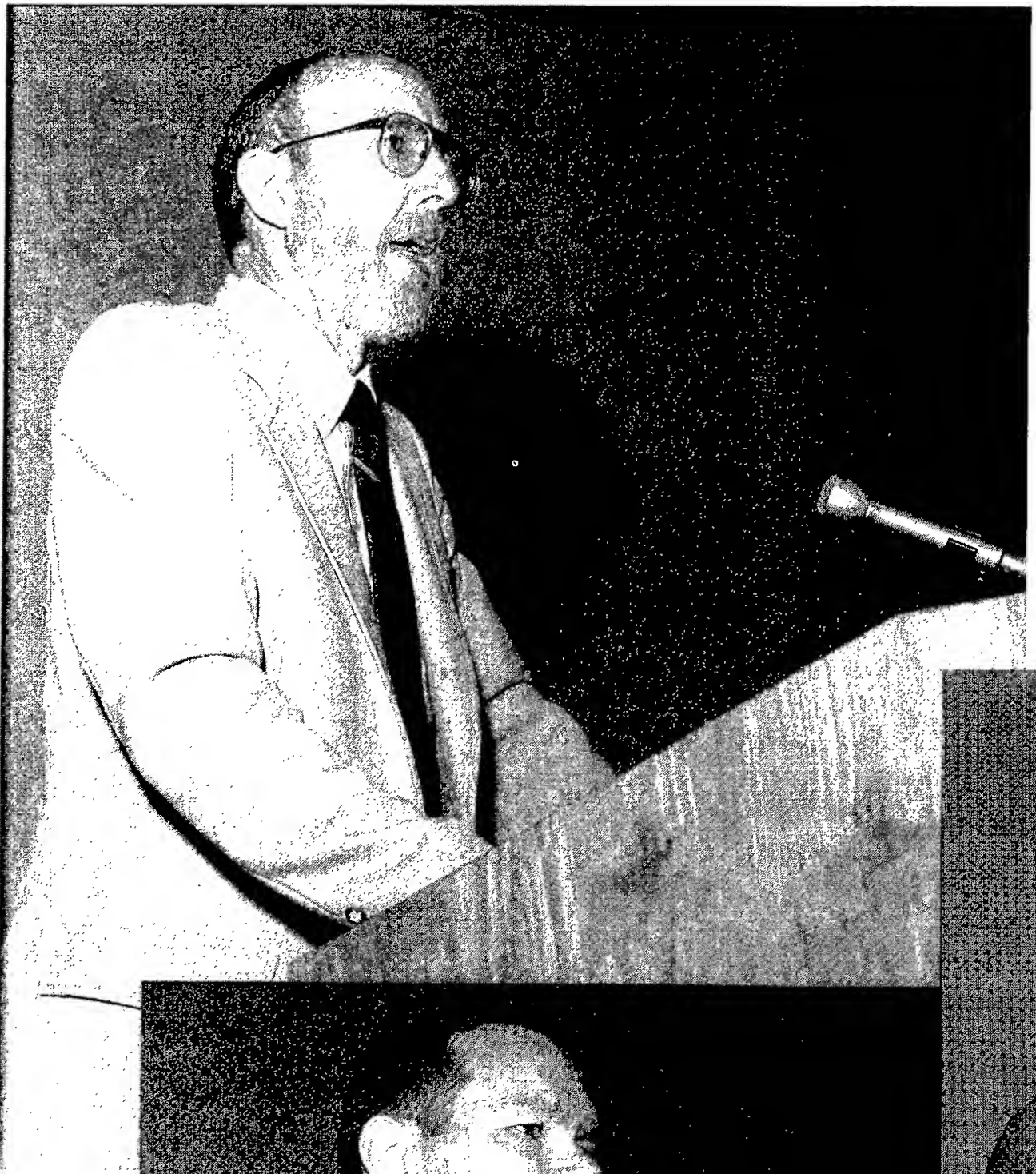
**Propeller/Hull/Appendage Interactions**

**Viscous Effects**

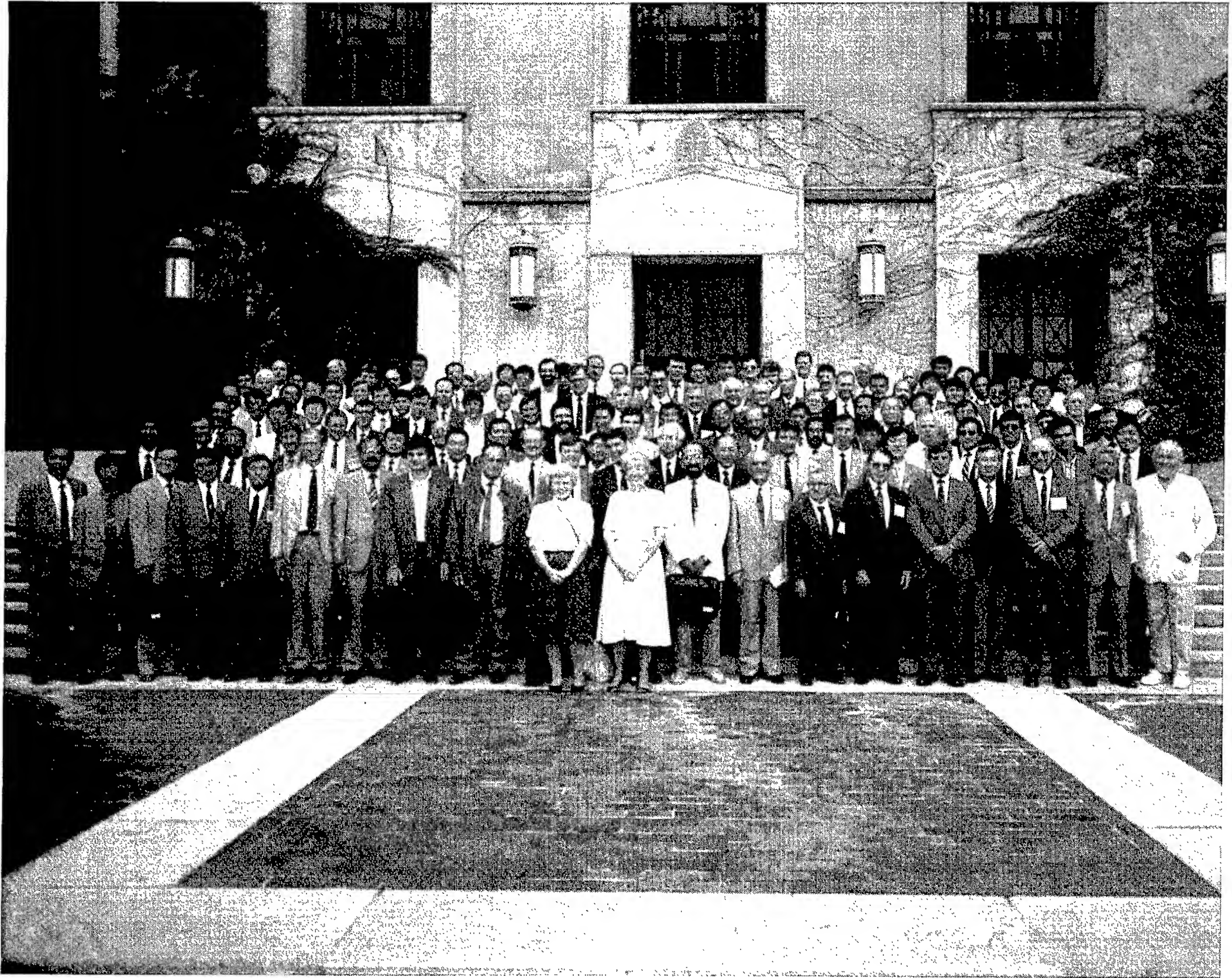
DTIC QUALITY INSPECTED 4



19970924 049







**Eighteenth Symposium on  
NAVAL HYDRODYNAMICS**

**Ship Motions  
Ship Hydrodynamics  
Experimental Techniques  
Free-Surface Aspects  
Wave/Wake Dynamics  
Propeller/Hull/Appendage Interactions  
Viscous Effects**

sponsored jointly by

**Office of Naval Research**

**The University of Michigan, Ann Arbor**

**Naval Studies Board  
Commission on Physical Sciences, Mathematics,  
and Applications  
National Research Council**

**NATIONAL ACADEMY PRESS  
Washington, D.C. 1991**

NOTICE: The project that is the subject of this report was approved by the Governing Board of the National Research Council, whose members are drawn from the councils of the National Academy of Sciences, the National Academy of Engineering, and the Institute of Medicine. The members of the committee responsible for the report were chosen for their special competences and with regard for appropriate balance.

This report has been reviewed by a group other than the authors according to procedures approved by a Report Review Committee consisting of members of the National Academy of Sciences, the National Academy of Engineering, and the Institute of Medicine.

The National Academy of Sciences is a private, nonprofit, self-perpetuating society of distinguished scholars engaged in scientific and engineering research, dedicated to the furtherance of science and technology and to their use for the general welfare. Upon the authority of the charter granted to it by the Congress in 1863, the Academy has a mandate that requires it to advise the federal government on scientific and technical matters. Dr. Frank Press is president of the National Academy of Sciences.

The National Academy of Engineering was established in 1964, under the charter of the National Academy of Sciences, as a parallel organization of outstanding engineers. It is autonomous in its administration and in the selection of its members, sharing with the National Academy of Sciences the responsibility for advising the federal government. The National Academy of Engineering also sponsors engineering programs aimed at meeting national needs, encourages education and research, and recognizes the superior achievements of engineers. Dr. Robert M. White is president of the National Academy of Engineering.

The Institute of Medicine was established in 1970 by the National Academy of Sciences to secure the services of eminent members of appropriate professions in the examination of policy matters pertaining to the health of the public. The Institute acts under the responsibility given to the National Academy of Sciences by its congressional charter to be an adviser to the federal government and, upon its own initiative, to identify issues of medical care, research, and education. Dr. Samuel O. Thier is president of the Institute of Medicine.

The National Research Council was organized by the National Academy of Sciences in 1916 to associate the broad community of science and technology with the Academy's purposes of furthering knowledge and advising the federal government. Functioning in accordance with general policies determined by the Academy, the Council has become the principal operating agency of both the National Academy of Sciences and the National Academy of Engineering in providing services to the government, the public, and the scientific and engineering communities. The Council is administered jointly by both Academies and the Institute of Medicine. Dr. Frank Press and Dr. Robert M. White are chairman and vice chairman, respectively, of the National Research Council.

This work related to Department of Navy Contract N00014-87-C-0018 issued by the Office of Naval Research under contract authority NR 201-124. However, the content does not necessarily reflect the position or the policy of the Department of the Navy or the government, and no official endorsement should be inferred.

The United States Government has at least a royalty-free, nonexclusive, and irrevocable license throughout the world for government purposes to publish, translate, reproduce, deliver, perform, and dispose of all or any of this work, and to authorize others so to do.

Partial support for the publication of these proceedings was provided by the Office of Naval Research of the Department of the Navy. The content does not necessarily reflect the position or the policy of the Navy, the U.S. Government, or the National Research Council, and no endorsement should be inferred. In the interest of timely publication, the individual authors' papers are presented here as received and with minimal editorial attention.

Library of Congress Catalog Card No. 91-62359  
International Standard Book Number 0-309-04575-4

Copies available from:  
National Academy Press  
2101 Constitution Avenue  
Washington, D.C. 20418

S413

Printed in the United States of America



## Naval Studies Board

Robert J. Hermann (Chair), United Technologies Corporation  
George F. Carrier, Harvard University  
Seymour J. Deitchman, Institute for Defense Analyses  
John F. Egan, Lockheed Electronic Systems Group  
Ivan A. Getting, Los Angeles, California  
Ralph R. Goodman, University of Southern Mississippi  
Willis M. Hawkins, Lockheed Corporation  
David W. Hyde, Science Applications International Corporation  
Sherra E. Kerns, Vanderbilt University  
Ray L. Leadabrand, Leadabrand and Associates  
John D. Lindl, Lawrence Livermore National Laboratory  
Chester M. McKinney, Applied Research Laboratories, University of Texas (Austin)  
William J. Moran, Los Altos, California  
George A. Paulikas, The Aerospace Corporation  
Alan Powell, University of Houston  
Robert C. Spindel, Applied Physics Laboratory, University of Washington  
J. Pace VanDevender, Sandia National Laboratories  
Vincent Vitto, Lincoln Laboratories, Massachusetts Institute of Technology  
George M. Whitesides, Harvard University

## Navy Liaison Representatives

Frank E. Shoup III, Office of the Chief of Naval Operations  
Ronald N. Kostoff, Office of Naval Research

## Staff

Lee M. Hunt, Staff Director

## Commission on Physical Sciences, Mathematics, and Applications

Norman Hackerman (Chair), Robert A. Welch Foundation  
Peter J. Bickel, University of California at Berkeley  
George F. Carrier, Harvard University  
Herbert D. Doan, The Dow Chemical Company (retired)  
Dean E. Eastman, IBM, T.J. Watson Research Center  
Marye Anne Fox, University of Texas  
Phillip A. Griffiths, Duke University  
Neal F. Lane, Rice University  
Robert W. Lucky, AT&T Bell Laboratories  
Christopher F. McKee, University of California at Berkeley  
Richard S. Nicholson, American Association for the Advancement of Science  
Jeremiah P. Ostriker, Princeton University Observatory  
Alan Schriesheim, Argonne National Laboratory  
Roy F. Schwitters, Superconducting Super Collider Laboratory  
Kenneth G. Wilson, Ohio State University

Norman Metzger, Executive Director

## FOREWORD

The Eighteenth Symposium on Naval Hydrodynamics was held in Ann Arbor, Michigan, on August 19-24, 1990. This international symposium was jointly sponsored by the Office of Naval Research (Fluid Dynamics Program), the National Research Council (Naval Studies Board), and the University of Michigan (Department of Naval Architecture and Marine Engineering). This biennial symposium promotes the exchange of technical developments in naval research of common interest to all the countries of the world. The forum encourages both formal and informal discussion of the presented papers, and the occasion provides opportunity for direct communication between international peers.

Nearly 200 participants from some 20 countries attended the symposium, representing a mixture of experience and expertise from newly graduated students to scientists of established international repute. Fifty papers were presented in seven topical areas covered by the symposium: ship motions, ship hydrodynamics, experimental techniques, free-surface aspects, wave/wake dynamics, propeller/hull/appendage interactions, and viscous effects. These topics were chosen for this particular meeting because of recent advances that have been made in these areas. Examples of significant advances presented in the papers are the solution of nonlinear equations for ship motions and ship hydrodynamics, the small-scale dynamics of cavitation inception, development and implementation of

multipoint, free-surface measurements, modeling of solitons in Kelvin wakes, reconnection phenomena for vortex interactions with the free surface, Navier-Stokes solutions for propellers, and the inclusion of the hull boundary layer in predictions of hull flows. This brief list illustrates the quality and timeliness of the symposium for naval hydrodynamics.

The success of this symposium is the result of hard work on the part of many people. There was, of course, the Organizing and Paper Selection Committee: Dr. Edwin Rood and Mr. James Fein (Office of Naval Research), Mr. Lee Hunt (National Research Council), Prof. Robert Beck and Prof. Armin Troesch (University of Michigan), Dr. Gerard van Oortmerssen (MARIN), Dr. William Morgan and Mr. Justin McCarthy (David Taylor Research Center). The contribution of this committee was certainly the cornerstone for the success of the symposium. However, the administrative preparation and execution would not have been possible without the support of Ms. Elizabeth Lucks and Mrs. Susan Campbell of the Naval Studies Board of the National Research Council, and Ms. Virginia Konz and Ms. Lisa Payton and the rest of the staff of the Department of Naval Architecture and Marine Engineering at the University of Michigan. Appreciation is extended to the Towing Tank staff at the University of Michigan for the informative demonstration of their unique research capabilities.

Edwin P. Rood  
Office of Naval Research

## CONTENTS

<b>Opening Remarks</b> RADM William C. Miller, USN Chief of Naval Research	1
<b>Session I - Ship Motions</b>	
<b>Prediction of Radiation Forces on a Catamaran at High Froude Number</b> M. Ohkusu Kyushu University, Japan O.M. Faltinsen Norwegian Institute of Technology, Norway	5
<b>Ship Motions by a Three-Dimensional Rankine Panel Method</b> D. Nakos, P. Sclavounos Massachusetts Institute of Technology, USA	21
<b>Numerical Solutions for Large-Amplitude Ship Motions in the Time Domain</b> W.-M. Lin Science Applications International Corporation, USA D. Yue Massachusetts Institute of Technology, USA	41
<b>A Coupled Time and Frequency Approach for Nonlinear Wave Radiation</b> P. Ferrant Laboratoire d'Hydrodynamique Navale, France	67
<b>Nonlinear and Linear Motions of a Rectangular Barge in a Perfect Fluid</b> R. Cointe <sup>1</sup> , P. Geyer <sup>2</sup> , B. King <sup>1</sup> , B. Molin <sup>2</sup> , M. Tramon <sup>2</sup> <sup>1</sup> Bassin d'Essais des Carenes, France, <sup>2</sup> Institut Français du Pétrole, France	85
<b>Session II - Ship Motions</b>	
<b>A Numerical Research of Nonlinear Body-Wave Interactions</b> Z. Zhou, M. Gu China Ship Scientific Research Center, China	103
<b>The Influence of a Slowly Oscillating Movement on the Velocity Potential</b> C. van der Stoep, A.J. Hermans Delft University of Technology, The Netherlands	119
<b>Rolling of Biased Ships in Quartering Seas</b> N. Sanchez University of Texas at San Antonio, USA A. Nayfeh Virginia Polytechnic Institute and State University, USA	133
<b>A Stochastic Analysis of Nonlinear Rolling in a Narrow Band Sea</b> A. Francescutto, R. Nabergoj University of Trieste, Italy	141
<b>Effect of Viscous Damping on the Response of Floating Bodies</b> M. Downie <sup>1</sup> , J. Graham <sup>2</sup> , X. Zheng <sup>1</sup> <sup>1</sup> University of Newcastle upon Tyne, United Kingdom <sup>2</sup> Imperial College of London, United Kingdom	149
<b>Nonlinear Motions and Whipping Loads of High-Speed Crafts in Head Sea</b> S.-K. Chou, F.-C. Chiu, Y.-J. Lee National Taiwan University, China	157



### Session III - Ship Hydrodynamics

<b>Nonlinear Free Surface Waves Due to a Ship Moving Near the Critical Speed in a Shallow Water</b>	173
H.-S. Choi, K.J. Bai, J.-W. Kim, I.-H. Cho Seoul National University, Korea	
<b>Numerical Simulation of Ship Waves and Some Discussions on Bow Wave Breaking &amp; Viscous Interactions of Stern Wave</b>	191
K.-H. Mori, S.-H. Kwag, Y. Doi Hiroshima University, Japan	
<b>Analysis of Transom Stern Flows</b>	207
A. Reed, J. Telste David Taylor Research Center, USA	
C. Scragg Science Applications International Corporation, USA	
<b>A Boundary Integral Approach in Primitive Variables for Free Surface Flows</b>	221
C. Casciola I.N.S.E.A.N., Italy	
R. Piva Universita di Roma, Italy	
<b>Numerical Appraisal of the New Slender Ship Formulation in Steady Motion</b>	239
H. Maruo University of California, Santa Barbara, USA	
W.-S. Song Shanghai Jiao Tong University, China	
<b>Numerical Solution of the "Dawson" Free-Surface Problem Using Havelock Singularities</b>	259
C. Scragg, J. Talcott Science Applications International Corporation, USA	
<b>Free-Surface Effects on a Yawed Surface-Piercing Plate</b>	273
H. Maniar, J.N. Newman, H. Xu Massachusetts Institute of Technology, USA	

### Session IV - Experimental Techniques

<b>Wave Devouring Propulsion Sea Trial</b>	287
Y. Terao Tokai University, Japan	
H. Isshiki Hitachi Zosen Corporation, Japan	
<b>Numerical and Experimental Analysis of Propeller Wake by Using a Surface Panel Method and a 3-Component LDV</b>	297
T. Hoshino Mitsubishi Heavy Industries, Ltd., Japan	
<b>Cavity Thickness on Rotating Propeller Blades - Measurements by Two Laser Beams</b>	319
H.D. Stinzing VWS, Berlin Model Basin, Germany	
<b>The Dynamics and Acoustics of Travelling Bubble Cavitation</b>	331
S. Ceccio, C. Brennen California Institute of Technology, USA	
<b>Nonintrusive, Multiple-Point Measurements of Water Surface Slope, Elevation and Velocity</b>	349
G. Meadows <sup>1</sup> , D. Lyzenga <sup>2</sup> , R. Beck <sup>1</sup> , J. Lyden <sup>2</sup> , <sup>1</sup> The University of Michigan, USA <sup>2</sup> Environmental Research Institute of Michigan, USA	

<b>Turbulence Measurements in a Submerged Jet Near a Free Surface</b>	361
D. Anthony, W. Willmarth, K. Madnia, L. Bernal	
The University of Michigan, USA	

#### Session V - Free Surface Aspects

<b>Adequacy of Free Surface Conditions for the Wave Resistance Problem</b>	375
H. Raven	
Maritime Research Institute Netherlands, The Netherlands	
<b>The Dispersion of Large-Amplitude Gravity Waves in Deep Water</b>	397
W. Webster	
University of California, Berkeley, USA	
D.-Y. Kim	
Wageningen, The Netherlands	
<b>Three-Dimensional, Unsteady Computations of Nonlinear Waves Caused by Underwater Disturbances</b>	417
Y. Cao, W. Schultz, R. Beck	
The University of Michigan, USA	
<b>A Numerical Solution Method for Three-Dimensional Nonlinear Free Surface Problems</b>	427
C.-G. Kang, I.-Y. Gong	
Ship Research Station, KIMM, Korea	
<b>Nonlinear Ship Waves</b>	439
Y.-H. Kim	
David Taylor Research Center, USA	
T. Lucas	
University of North Carolina-Charlotte, USA	
<b>A Model for the Generation and Evolution of an Inner-Angle Soliton in a Kelvin Wake</b>	453
R. Hall, S. Buchsbaum	
Science Applications International Corporation, USA	
<b>Near-Field Nonlinearities and Short Far-Field Ship Waves</b>	465
F. Noblesse, D. Hendrix	
David Taylor Research Center, USA	

#### Session VI - Wave/Wake Dynamics

<b>Vortex Ring Interaction with a Free Surface</b>	479
M. Song, N. Kachman, J. Kwon, L. Bernal, G. Tryggvason	
The University of Michigan, USA	
<b>Submerged Vortex Pair Influence on Ambient Free Surface Waves</b>	491
S. Fish	
David Taylor Research Center, USA	
C. von Kerczek	
University of Maryland, USA	
<b>Scarred and Striated Signature of a Vortex Pair on the Free Surface</b>	503
T. Sarpkaya, P.B. Suthon	
Naval Postgraduate School, USA	
<b>Measurement and Computations of Vortex Pair Interaction with a Clean or Contaminated Free Surface</b>	521
A. Hirs, G. Tryggvason, J. Abdollahi-Alibeik, W. Willmarth	
The University of Michigan, USA	
<b>Hydrodynamics of Ship Wake Surfactant Films</b>	533
R. Peltzer <sup>1</sup> , J.H. Milgram <sup>2</sup> , R. Skop <sup>3</sup> , J. Kaiser <sup>1</sup> , O. Griffin <sup>1</sup> , W. Barger <sup>1</sup>	
<sup>1</sup> Naval Research Laboratory, USA,	
<sup>2</sup> Massachusetts Institute of Technology, USA,	
<sup>3</sup> University of Miami, USA	

**Three-Dimensional Instability Modes of the Wake Far Behind a Ship** 553  
 G. Triantafyllou  
 Massachusetts Institute of Technology, USA

**Ship Internal Waves in a Shallow Thermocline: The Supersonic Case** 567  
 M. Tulin  
 University of California, Santa Barbara, USA  
 T. Miloh  
 Tel Aviv University, Israel

#### Session VII - Propeller/Hull/Appendage Interactions

**On the Optimization, Including Viscosity Effects, of Ship Screw Propellers with Optional End Plates** 585  
 K. de Jong  
 University of Groningen, The Netherlands

**Steady and Unsteady Characteristics of a Propeller Operating in a Non-Uniform Wake: Comparisons Between Theory and Experiments** 607  
 F. Genoux, R. Baubeau  
 Bassin d'Essais des Carènes, France  
 A. Bruere, M. DuPont  
 Office National des Etudes et Recherches Aéropatiales, France

**Navier-Stokes Analysis of Turbulent Boundary Layer and Wake for Two-Dimensional Lifting Bodies** 633  
 P. Nguyen, J. Gorski  
 David Taylor Research Center, USA

**A Three-Dimensional Theory for the Design Problem of Propeller Ducts in a Shear Flow** 645  
 J. Falcao de Campos  
 Maritime Research Institute Netherlands, The Netherlands

**A Potential Based Panel Method for the Unsteady Flow Around Open and Ducted Propellers** 667  
 S. Kinnas, C.-Y. Hsin, D. Keenan  
 Massachusetts Institute of Technology, USA

**A Navier-Stokes Solution of Hull-Ring Wing-Thruster Interaction** 687  
 C.-I. Yang  
 David Taylor Research Center, USA  
 P. Hartwich, P. Sundaram  
 NASA Langley Research Center, USA

#### Session VIII - Viscous Effects

**An Interactive Approach for Calculating Ship Boundary Layers and Wakes for Nonzero Froude Number** 699  
 Y. Tahara, F. Stern  
 Iowa Institute of Hydraulic Research, The University of Iowa, USA  
 B. Rosen  
 South Bay Simulations Inc., USA

**Viscous Flow Past a Ship in a Cross Current** 721  
 V.C. Patel, S. Ju, J.M. Lew  
 Iowa Institute of Hydraulic Research, The University of Iowa, USA

**A Numerical Study of Three-Dimensional Viscous Interactions of Vortices with a Free Surface** 727  
 D. Dommermuth  
 Science Applications International Corporation, USA  
 D. Yue  
 Massachusetts Institute of Technology, USA



<b>On the Numerical Solution of the Total Ship Resistance Problem under a Predetermined Free Surface</b>	789
G. Tzabiras, T. Loukakis, G. Garofallidis National Technical University of Athens, Greece	
<b>The Calculations of Fluid Actions on Arbitrary Shaped Submerged Bodies Using Viscous Boundary Elements</b>	801
W. Price, M. Tan Brunel University, United Kingdom	
<b>The Flow Past a Wing-Body Junction - An Experimental Evaluation of Turbulence Models</b>	815
W. Devenport, R. Simpson Virginia Polytechnic Institute and State University, USA	
<b>Symposium Attendees</b>	829

## OPENING REMARKS

Rear Admiral William C. Miller, USN  
Chief of Naval Research

Ladies and gentlemen, officials and faculty of the University of Michigan, and distinguished colleagues from the international naval hydrodynamics community, I wish you a good morning.

As Chief of Naval Research, as steward of the Navy's science and technology development, and as a former sailor and commanding officer in several classes of naval ships, I have a particular interest in naval hydrodynamics. Accordingly, it is my great pleasure to welcome you to this symposium dedicated to the advancement of the science and technology of naval hydrodynamics.

The symposium is unique; it is the only professional gathering dedicated specifically to scientific understanding and technology of hydrodynamics in support of marine applications. Among you are the most prominent hydrodynamicists of the world. I am confident you will find the papers to be presented here uniformly excellent. Their selection proved a difficult task, given the number of quality papers submitted.

This is the eighteenth symposium since the series was inaugurated in 1956. Each symposium in the series has been sponsored by the Office of Naval Research, the National Research Council, and a host institution. This year, we express our gratitude to our gracious host, the University of Michigan.

The site for these symposia rotates between the United States and other countries, and over the years, seven different nations have hosted your meeting. This week, in keeping with the international flavor of this symposium, authors from 10 countries will be presenting 51 papers—very strong evidence that the scientific communities are coming together to solve common hydrodynamics problems.

The world is dramatically different today than when we began the series in 1956. We were then at the height of the cold war; now we are joined in a fervent hope that that period of international tension is nearing an end. Changes that would have seemed unthinkable only a few months ago are continuing to occur almost daily. Old barriers are falling; new challenges arising. Defense capabilities and requirements are being scrutinized in the light of new global realities. There is no question in my mind that the decade of the 1990s will exhibit a different international military presence than the decade that preceded it, and with those changes comes a corresponding adjustment to the distribution and focus of research and development activity.

Political realignments and military changes notwithstanding, geography alone tells us that the United States will remain a maritime nation with economic and defense imperatives closely tied to free and unimpeded access to the sea lines of communication in order to pursue peaceful commerce. Also unchanged is the need of a maritime nation such as ours to pursue a broad program of science to better understand and utilize the seas that surround it.

Joseph Conrad, that great chronicler of sea lore, once said,

*The sea never changes, and its works, for all the talk of man,  
are wrapped in mystery.*

The sea probably has not changed much since Conrad penned those words, but advances in science and technology and development of new tools have helped to lift some of the mysteries associated with the seagoing trades.

This is particularly true in naval hydrodynamics. With the emerging capability to understand and predict such complex processes as unsteady ship hydrodynamics, brought about by application of

supercomputers in both physical and numerical experiments, the field is ready for new and significant scientific breakthroughs to lead to improved propulsive efficiency, reduced ship motion, and more accurate tracking. For many problems in hydrodynamics, however, the level of understanding sufficient to drive technology application remains years away and, in Conrad's words, still "are wrapped in mystery."

It is the nature of scientific discovery that results frequently are a long time coming and often not clearly foreseen. Therefore, the Office of Naval Research has adopted the strategy of preserving our investment in fundamental research in the field of naval hydrodynamics, selecting the best intellects and the best ideas, while expressing our confidence that this long-term investment will pay valuable dividends.

The University of Michigan's selection to be host this year reflects this investment philosophy, partly in recognition of university's work in free-surface hydrodynamics, funded by the University Research Initiative of the U.S. Department of Defense. Under this program, the Office of Naval Research provided financial support to the University of Michigan to pursue aggressive investigation into improving the state of knowledge of ship wakes. This initiative has been in place for four years now and has provided the means for developing and fielding a unique instrumentation system to quantify hydrodynamic features observed in both surface and subsurface wakes. Several papers to be presented at this symposium describe this instrumentation and associated research findings. In addition, a tour of facilities dedicated to this effort will be conducted tomorrow morning; it promises to be an eye opener for any who may have lingering doubts regarding whether there is significant science left to be pursued in the field of naval hydrodynamics.

As this audience certainly appreciates, understanding the physical mechanisms present in ship wakes can have major influence on naval operations. In fact, the very title of this symposium proclaims its naval orientation. Certainly, knowledge of unsteady nonlinear ship motions is an elusive goal that may be in sight with new advances—such as prediction of "chaotic" ship motion and unsteady ship wake-propulsion interaction. These advances should have an impact on commercial shipping as well as military operations, responding to the shared needs of all maritime nations.

It is in the spirit of pushing back the frontiers in basic understanding of naval hydrodynamics that this symposium retains its preeminence. Papers are presented, discussions—oftentimes quite lively—are entertained, and professional and personal contacts are made or renewed, all with the intent of fostering open information exchange among scientific professionals. We anticipate that the result will be a focusing of efforts and minimization of unwarranted duplication, leading to achievement of shared objectives within the limited resources available.

The papers to be presented cover seven topics: ship motions; ship hydrodynamics; experimental techniques; free-surface aspects; wave/wake dynamics; propeller/hull/appendage interactions; and viscous effects. I have been assured by the selection committee that they are uniformly excellent and will add to our pride in once again sponsoring this symposium. I trust that you too will enjoy them and will take home with you that sense of professional excitement and interaction you came here to enjoy.

Thank you for your attention. You all have my personal best wishes for a most productive symposium.

**Session I**  
**Ship Motions**



# Prediction of Radiation Forces on a Catamaran at High Froude Number

M. Ohkusu (Kyushu University, Japan)

O.M. Faltinsen (Norwegian Institute of Technology, Norway)

## ABSTRACT

Practical approach is investigated to predict three dimensional hydrodynamic interaction between two hulls of a catamaran oscillating and running at forward speed. Chapman's approach is tried to solve the boundary value problem for the unsteady velocity potential around twin hulls' section contour with retaining all the terms of the full linear free surface condition including forward speed effect. Results show that predicted hydrodynamic forces agree generally well at high Froude number with the measured on a model ship and interaction between twin hulls is certainly weak at this high speed.

## INTRODUCTION

It may be a practical approach to generalize strip theories to predict motions of a catamaran advancing in waves. Strip theories are certainly the most successful theories for practical purpose of predicting wave induced motions of ships at moderate forward speed.

For applying strip theories two hulls of the catamaran are considered to be close to each other. Two dimensional theory is used to evaluate flow around the contour of two sections oscillating on the free surface. Experiments tell, however, that hydrodynamic interaction effects between two hulls are not so strong as expected from ship's lengthwise summation of the 2D effects (Ohkusu(1971)). This is more so for higher forward speed. If we assume two hulls are located away from each other, theories to be applied must not be strip theories any more. We need a practical theory to take into account correctly three dimensionality of hydrodynamic interaction between two hulls of the catamaran.

Strip theories account for the effect of forward speed in a simple way. The linear free surface condition including forward speed term is simplified such that the unsteady waves generated by the body motions propagate only in the breadthwise directions of the ship. A more complicated wave system must be considered if the three dimensionality of the flow has to be considered.

Three dimensional panel method at forward speed will be one alternative for this purpose. But even with recent progress in computational schemes of the Green function (Ohkusu and Iwashita(1989)), it can not be so practical as strip theories because of long computational time. Besides we have no valid approach to treat with a line singularity appearing at the intersection of the surface piercing body and the free surface.

Chapman's approach (Chapman(1976)) is a simplified, but still satisfying the full linear free surface condition, high speed theory for a vertical surface-piercing flat plate in unsteady yaw and sway motion. Daoud's theory (Daoud(1975)) for analyzing stationary flow around the bow of the ship is also a theory retaining all the terms of the linear free surface condition in the region close to the body and solving essentially 2D problem around section's contour. Ogilvie's description (Ogilvie (1977)) on these theories is full of insight into hydrodynamics and very informative. Furthermore one of the present author (Faltinsen(1983)) presented a theory for solving diffraction problem at the bow of the ship along a similar line. All those are attractive ideas in the point that the  $x$ -derivatives in the free surface condition is completely retained and still numerical work is almost on two dimensional problem. Recent comprehensive analysis by Yeung and Kim (1985)

Makoto Ohkusu, Research Institute for Applied Mechanics, Kyushu Univ., Fukuoka, Japan  
Odd M. Faltinsen, Norwegian Institute of Technology, Trondheim, Norway.

gives more analytical foundation for Chapman's approach.

We present in the main text an application of Chapman-Daoud-Faltinsen's approach for computing hydrodynamic forces on the catamaran. First we investigate the far-field effect of unsteady bow flow caused by heave and pitch motions of the ship. Then we describe a set of assumptions leading to the full linear free surface condition retaining the  $x$  derivatives in the near-field. Numerical solutions of the 2D boundary problems for the velocity potentials near the body is a version of Daoud's approach. Finally we compare computed and measured added mass and damping of a catamaran at high Froude number and present wave elevation generated by the ship motion between two hulls of a catamaran as well as in the far-field.

### FAR-FIELD SOLUTION

Velocity potential describing the flow around an oscillating ship at forward speed is expressed in the form of

$$\phi = Ux + \phi_s(x, y, z) + \phi_r(x, y, z)e^{i\omega t} \quad (1)$$

where the  $x$ -axis directs astern from the origin at FP, the  $z$  axis vertically upward and the  $xy$  plane coincides with the calm water surface (Fig.1).  $U$  is steady ambient flow velocity in the direction of the  $x$ -axis (or the ship's speed),  $L$  the ship length,  $\omega$  circular frequency of motion.  $\phi_s$  is the steady part of the potential and  $\phi_r$  the unsteady part.

We start with a simple expression of the solution of  $\phi_r$  valid in the far-field of the ship's hull. The solution  $\phi_r$  satisfying the full linear free surface condition

$$(i\omega + U \frac{\partial}{\partial x})^2 \phi_r + g \frac{\partial \phi_r}{\partial z} = 0 \quad \text{on } z = 0 \quad (2)$$

is expressed at  $x, y = O(1)$  by the velocity potential of a line source  $\sigma(x)e^{i\omega t}$  distributed on the longitudinal axis of the ship hull since we are concerned with the symmetrical flow field. A Fourier transform type of expression is given by

$$\begin{aligned} \phi_r(x, y, z) = & -\frac{1}{\pi} \int_{-\infty}^{\infty} dk e^{ikx} \sigma^*(k) \\ & \times \lim_{\mu \rightarrow 0} \int_{-\infty}^{\infty} \frac{d\ell \exp[i\ell y + z\sqrt{R^2 + \ell^2}]}{\sqrt{R^2 + \ell^2} - (\omega + Uk - i\mu)^2/g} \end{aligned} \quad (3)$$

where

$$\sigma^*(k) = \int_0^L \sigma(x) e^{-ikx} dx \quad (4)$$

We assume high frequency of motions  $\omega = O(\varepsilon^{-1/2})$  just as in Ogilvie and Tuck (1969) and we may proceed along their line. In Ogilvie and Tuck's analysis this integral is assumed to include only the contribution from up to  $|k| = o(1)$  (in their notation  $|k| = o(\varepsilon^{-1/2})$ ), because  $\sigma^*(k)$  drops off rapidly enough with large  $|k|$ . Reason of this is very smooth variation of  $\sigma(x)$  everywhere in  $x$ . When we assume flow variables vary steeply over the bow region, for instance, the  $x$ -derivative of  $\sigma$  is of the order of  $O(\varepsilon^{-1/2}\sigma)$  over the region close to the bow, then  $\sigma^*(k)$  does not drop off so rapidly. With this assumption we extend the integral intervals at least until  $|k| = O(\varepsilon^{-1/2})$  is included (In Ogilvie and Tuck's notation this corresponds to  $|k| = O(\varepsilon^{-1})$ ). Then we obtain from equation (3)

$$\begin{aligned} \phi_r = & - \int_{-O(\varepsilon^{-1/2})}^{k_2} dk \frac{2i\sigma^*(\omega/Uk)(1+k)(\omega/U)}{\sqrt{(1+k)^4 - (k/\tau)^2}} \\ & \times \exp[ik(\omega/U)x + i\nu y \sqrt{(1+k)^4 - (k/\tau)^2} \\ & \quad + \nu z(1+k)^2] \\ & - \int_{k_1}^{k_2} dk \frac{2\sigma^*(\omega/Uk)(1+k)^2(\omega/U)}{(k/\tau)^2 - (1+k)^4} \\ & \times \exp[ik(\omega/U)x - \nu y \sqrt{(k/\tau)^2 - (1+k)^4} \\ & \quad + \nu z(1+k)^2] \\ & - \int_{k_1}^{O(\varepsilon^{-1/2})} dk \frac{-2i\sigma^*(\omega/Uk)(1+k)^2(\omega/U)}{\sqrt{(1+k)^4 - (k/\tau)^2}} \\ & \times \exp[ik(\omega/U)x - i\nu y \sqrt{(1+k)^4 - (k/\tau)^2} \\ & \quad + \nu z(1+k)^2] \\ & + O(\varepsilon) \end{aligned} \quad (5)$$

where

$$\begin{aligned} k_{1,2} = & -1 - (1/2\tau \mp \sqrt{1/\tau + 1/4\tau^2}) \\ \tau = & \omega U/g, \quad \nu = \omega^2/g \end{aligned} \quad (6)$$

The method of stationary phase (Erdelyi (1956)) can be applied to evaluating the integrals because we are many wave lengths away from the sources at  $\omega/U = O(\varepsilon^{-1/2})$  and  $\nu = O(\varepsilon^{-1})$ . Let

assume  $(x - \xi) \gg y$  in this equation, then one stationary point exists within the interval of each integral, as far as the 1st and 3rd terms of equation (5) are concerned. For large  $\tau$  stationary points  $\kappa_1$  for the 3rd and  $\kappa_2$  for the 1st integral are approximately

$$\kappa_{1,2} \simeq -1 \pm \frac{(x - \xi)}{2\tau y} \quad (7)$$

Dominant part of the righthand side of equation (5) is then evaluated as follows.

$$\begin{aligned} \phi_r \sim & -2 \int_0^x \sigma(\xi) d\xi \\ & \times \left\{ i \frac{\sqrt{\pi K_0}}{\sqrt{y}} \exp \left[ -i \frac{\omega}{U} (x - \xi) - \frac{i}{4} \frac{K_0 (x - \xi)^2}{y} \right. \right. \\ & \quad \left. \left. + \frac{1}{4} \frac{K_0 (x - \xi)^2 z}{y^2} - i \frac{\pi}{4} \right] \right. \\ & - i \frac{\sqrt{\pi K_0}}{\sqrt{y}} \exp \left[ -i \frac{\omega}{U} (x - \xi) + \frac{i}{4} \frac{K_0 (x - \xi)^2}{y} \right. \\ & \quad \left. \left. + \frac{1}{4} \frac{K_0 (x - \xi)^2 z}{y^2} + i \frac{\pi}{4} \right] \right. \\ & + \frac{\sqrt{2\pi|k_1|}(\omega/U)}{(\tau + 1/4)^{1/4}} \frac{1}{\sqrt{|x - \xi|}} \exp \left[ i k_1 \frac{\omega}{U} (x - \xi) \right] \\ & \left. + \frac{\sqrt{2\pi|k_2|}(\omega/U)}{(\tau + 1/4)^{1/4}} \frac{1}{\sqrt{|x - \xi|}} \exp \left[ i k_2 \frac{\omega}{U} (x - \xi) \right] \right\} \quad (8) \end{aligned}$$

where  $K_0 = g/U^2$ . The last two terms of this equation come from the singularities at end points  $k = k_1$  and  $k_2$  of the interval (Erdelyi (1957)) and are higher order than the first two.  $z$  dependence in the last two terms is ignored because  $\exp(\omega z/U)$  is  $1 + O(\varepsilon^{1/2})$ .

If  $x$  is away from the bow region such as  $x = O(1)$  and  $\sigma(x)$  varies smoothly there, we can once again apply the stationary phase method to evaluate the parts of the integrals (8) from  $\xi = O(\varepsilon^{1/2})$  to  $x$ . We obtain

$$\begin{aligned} \phi_r \sim & -2 \int_0^{O(\varepsilon^{1/2})} \sigma(\xi) d\xi \\ & \times \left\{ i \frac{\sqrt{\pi K_0}}{\sqrt{y}} \exp \left[ -i \frac{\omega}{U} (x - \xi) - \frac{i}{4} \frac{K_0 (x - \xi)^2}{y} \right. \right. \\ & \quad \left. \left. + \frac{1}{4} \frac{K_0 (x - \xi)^2 z}{y^2} + i \frac{\pi}{4} \right] \right. \\ & - i \frac{\sqrt{\pi K_0}}{\sqrt{y}} \exp \left[ -i \frac{\omega}{U} (x - \xi) + \frac{i}{4} \frac{K_0 (x - \xi)^2}{y} \right. \\ & \quad \left. \left. + \frac{1}{4} \frac{K_0 (x - \xi)^2 z}{y^2} - i \frac{\pi}{4} \right] \right. \\ & + \frac{\sqrt{2\pi|k_1|}(\omega/U)}{(\tau + 1/4)^{1/4}} \frac{1}{\sqrt{|x - \xi|}} \exp \left[ i k_1 \frac{\omega}{U} (x - \xi) \right] \\ & + \frac{\sqrt{2\pi|k_2|}(\omega/U)}{(\tau + 1/4)^{1/4}} \frac{1}{\sqrt{|x - \xi|}} \exp \left[ i k_2 \frac{\omega}{U} (x - \xi) \right] \\ & + 4\pi i \sigma(x - 2\tau y) \exp(-i\nu y + \nu z) \\ & - 4\pi \frac{\sqrt{2}}{(\tau + 1/4)^{1/4}} \sigma(x) \exp(-i \frac{\pi}{4}) \quad (9) \end{aligned}$$

These expressions will provide some idea of the near field solutions whose approximations away from the hull will be obtained by letting  $y \rightarrow \varepsilon$ . The first and second terms of equation (8) representing the divergent waves are dominant and one can not neglect the  $x$ -derivatives of the flow variables in the free surface condition. Far behind the bow region where  $\sigma$  must vary smoothly, the fifth term of equation (9) that represents the 2D term dominant in the strip theory (Ogilvie and Tuck (1969)) appear. The fifth term is rewritten as

$$\sim 4\pi i [\sigma(x) - 2\tau y \sigma'(x)] \exp(-i\nu y + \nu z)$$

This argument suggests that the divergent waves approximation (the first and second terms of equation (8)) will be a good approximation of the far field effect in some region near the hull even over the ship length and it includes waves appearing in the strip theory far behind the bow region.

Effect of the transverse waves might be taken into account approximately as follows. They satisfy the free surface condition far behind the bow region and satisfy the body boundary condition because of the approximately zero normal velocity on section contours. These terms will exert

pressure of the second order on sections behind the bow region.

## FORMULATION OF THE SOLUTION

Our general assumptions are:

$$n_1 = O(\varepsilon), \quad n_{2,3} = O(1), \quad \omega = O(\varepsilon^{-\frac{1}{2}}) \quad (10)$$

$$\frac{\partial f}{\partial y, z} = O(f\varepsilon^{-1}), \quad \phi_r = O(\delta) \quad (11)$$

where  $n_{1,2,3}$  are the  $x, y$  and  $z$  components of a unit normal vector to the wetted part of the hull surface whose positive direction is into the fluid.  $\varepsilon$  is the slenderness ratio of the hull geometry and  $\delta$  characterize smallness of the oscillatory motions' amplitude.  $f$  is any flow variable caused by the body in some region near the hull.

The unsteady part of flow  $\phi_r$  is rather straightforwardly linearized based on  $\delta$  that is generally independent of the hull geometry. The steady flow  $\phi_s$  and its interaction with the unsteady part are related closely to the hull geometry and their linearization is strongly dependent on flow characteristics we assume. We have two alternatives in order to retain  $U\partial/\partial x$  term in the free surface condition:

- (i)  $U = O(\varepsilon^{-1/2})$ ,  $\partial f/\partial x = O(1)$
- (ii)  $U = O(1)$ ,  $\partial f/\partial x = O(\varepsilon^{-1/2})$ .

(i) gives  $\phi_s = O(\varepsilon^{3/2})$  and steady wave elevation  $\zeta_s = O(\varepsilon)$ . The result is that we can not transfer the free surface condition to  $z = 0$  because of  $\zeta_s \partial \phi_s / \partial z = O(1)$ ; the free surface condition for  $\phi_s$  becomes non-linear.

(ii) may be justified with some assumptions on the flow characteristics close to the bow as mentioned in the previous section. Recently Faltinsen and Zhao (1990) employed another alternative  $n_1 = O(\varepsilon^{1/2})$  to analyze the same problem. With this assumption, however, we once again end up with a non-linear free surface condition for the steady flow  $\phi_s$ . In this context  $\phi_r$  has to satisfy the free surface condition not on  $z = 0$  but on the steady free surface displaced finitely from  $z = 0$ .

Assume (ii) as well as (10) and (11), then we obtain  $\phi_s = O(\varepsilon^2)$ ,  $\zeta_s = O(\varepsilon^{3/2})$  with which we have no trouble to linearize the free surface condition for  $\phi_s$ . If we retain the lowest order terms

with respect to  $\varepsilon$  and  $\delta$ , then we reach to the following linearized free surface conditions presenting weak interaction between the steady and unsteady flows.

$$(i\omega + U \frac{\partial}{\partial x})^2 \phi_r + g \frac{\partial \phi_r}{\partial z} = 0 \quad \text{on } z = 0 \quad (12)$$

$$U^2 \frac{\partial^2 \phi_s}{\partial x^2} + g \frac{\partial \phi_s}{\partial z} = 0 \quad \text{on } z = 0 \quad (13)$$

Terms we omitted in the derivation of those free surface conditions are  $\varepsilon^{1/2}$  higher in the order of magnitude.

The velocity potentials must satisfy

$$\frac{\partial^2 \phi_{s,r}}{\partial y^2} + \frac{\partial^2 \phi_{s,r}}{\partial z^2} = 0 \quad (14)$$

in the fluid domain.

Body boundary conditions to be satisfied on the mean oscillating position are:

$$\frac{\partial \phi_s}{\partial N} = -Un_1 \quad (15)$$

$$\frac{\partial \phi_{rj}}{\partial N} = i\omega n_j + m_j \quad (j = 3, 5) \quad (16)$$

where  $\phi_{rj}$  is  $\phi_r$  for the  $j$  mode of motion of unit amplitude.  $j = 3$  and  $5$  correspond to heaving and pitching motions of the ship respectively and

$$\begin{aligned} n_5 &= -(x - L/2)n_3 \\ m_3 &= -\frac{\partial}{\partial N} \frac{\partial \phi_s}{\partial z} \\ m_5 &= -Un_3 - (x - L/2)m_3 \end{aligned} \quad (17)$$

The body boundary conditions (16) contain two different order terms. The terms with  $m_j$  are certainly of  $\varepsilon^{1/2}$  higher order than the first terms on the right hand side. The  $m_j$  terms arise because the steady flow satisfies the body boundary conditions on the mean oscillatory position and not the instantaneous position of the ship. In principle similar terms should be present in the free surface condition. However they have been neglected in our analysis. Inclusion of the  $m_j$  terms in the body boundary conditions (16) is inconsistent and most of our results are with only

the lowest order terms retained in (16). Some of results in which we keep even the  $m_j$  terms inconsistently will be presented.

Chapman (1975) presented a simplified high-speed theory satisfying the full linear free surface condition in the near field for a surface piercing flat plate in yaw and sway motion problems. We apply a generalized and linearized version of his idea to solve the boundary problems (12), (13), (14), (15) and (16). In details we follow the approaches proposed by Ogilvie (1977) and Daoud (1975) in analyzing bow flow for the wave resistance problem. This method is economical in the computational effort because one identical scheme can be applied for both the steady and the unsteady problems.

It is convenient in the analysis to define new potentials

$$\psi_r(x, y, z) = e^{i(\omega/U)x} \phi_r(x, y, z) \quad (18)$$

Without any simplification the boundary value problems for both  $\phi_s$  and  $\psi_r$  then become the similar problems with the only difference in the body boundary conditions. For brevity we do not state the boundary value problems for  $\phi_s$  hereafter.

$$\frac{\partial^2 \psi_r}{\partial y^2} + \frac{\partial^2 \psi_r}{\partial z^2} = 0 \quad (19)$$

$$U^2 \frac{\partial^2 \psi_r}{\partial x^2} + g \frac{\partial \psi_r}{\partial z} = 0 \quad \text{on } z = 0 \quad (20)$$

$$\frac{\partial \psi_r}{\partial N} = \begin{cases} e^{i(\omega/U)x} \left[ i\omega n_3 - U \frac{\partial}{\partial N} \frac{\partial \phi_s}{\partial z} \right] & \text{for } j = 3 \\ e^{i(\omega/U)x} \left[ -i\omega n_3 (x - L/2) + U(-n_3 + (x - L/2) \frac{\partial}{\partial N} \frac{\partial \phi_s}{\partial z}) \right] & \text{for } j = 5 \end{cases} \quad (21)$$

on the body surface below  $z = 0$ .

We set starting condition on  $\psi_r$  and  $\partial \psi_r / \partial x$  at  $x=0$ . We assume the velocity potential and the

free surface elevation equal to zero at  $x \leq 0$ . Reason of this assumption is that no upstream waves are generated far in front of the bow because we are concerned with the case of  $\tau \gg 1/4$ . We assume here simply

$$\psi_r = 0, \quad \frac{\partial \psi_r}{\partial x} = 0 \quad \text{at } x \leq 0 \quad (22)$$

We will now introduce an expression for the solution  $\psi_r$  as suggested by Ogilvie (1977).

$$\begin{aligned} \psi_r = & \int_{L(x)+R(x)} d\ell \Sigma_r(x; \eta, \zeta) \log \frac{r}{r'} \\ & - 4\sqrt{K_0} \int_0^x d\xi \int_{L(\xi)+R(\xi)} d\ell \Sigma_r(\xi; \eta(\xi), \zeta(\xi)) \\ & \times \int_0^\infty d\omega \exp[\omega^2(z + \zeta(\xi))] \cos \omega^2(y - \eta(\xi)) \\ & \times \sin \sqrt{K_0} \omega(x - \xi) \end{aligned} \quad (23)$$

where

$$r, r' = \sqrt{(y - \eta)^2 + (z \mp \zeta)^2}$$

$L(x)$  and  $R(x)$  are the contours of the catamaran's left and right sections at  $x$  (we ignore the contribution from  $L(x)$  for a single hull ship). We assumed in this formulation that each demihull of the catamaran locates in the near field of each other.

Equation (23) implies that  $\psi_r$  at  $x$  is represented by the potential caused by a distribution  $\Sigma_r$  of impulsive sources on that section contours and the effect of source distributions at all sections upstream of  $x$ . One may use Daoud's expression (1975) for the velocity potential instead of equation (23). He distributed sources and normal dipoles based on more systematic derivation. But we can transform his expression into that of only the source distribution without difficulty by considering another boundary value problem on the flow interior the body. So there is no reason that the expression (23) is not appropriate.

Contribution from the line singularities at the intersection of the body and the free surfaces is considered to be of higher order for slender hull form based on Daoud's argument (1975). We remark that if we had to include really this term, one more condition such as the least singularities



of flow in addition to the body boundary condition should be imposed in order to determine the strength of this line singularities. We do not know what condition is physically correct.

The last term of equation (23) is the complicated triple integral including the unknown  $\Sigma_r$  in its integrand. But this term gives the effect only from the sections upstream of the section and does not depend on the source density at  $\xi = x$  where the integral equation is to be solved, because of the term  $\sin \sqrt{K_0} \omega(x - \xi)$ .

Starting from  $x=0$ , we can solve this equation step by step. Details of numerical computations are described in the following section.

When we let  $y \rightarrow \infty$  on the equation (23), a far field approximation of the near field solution is to be obtained as follows.

$$\begin{aligned} \phi_r &= e^{-i(\omega/U)x} \psi_r \\ &\sim + \int_0^x d\xi S(\xi; \kappa) \sqrt{\frac{\pi K_0}{y}} \\ &\quad \times \exp\left[-i\left(\frac{\omega}{U}\right)x - \frac{i}{4} \frac{K_0(x - \xi)^2}{y} \right. \\ &\quad \left. + \frac{1}{4} \frac{K_0(x - \xi)^2 z}{y^2} \right] \\ &+ i \int_0^x d\xi S(\xi; \kappa) \sqrt{\frac{\pi K_0}{y}} \\ &\quad \times \exp\left[-i\left(\frac{\omega}{U}\right)x + \frac{i}{4} \frac{K_0(x - \xi)^2}{y} \right. \\ &\quad \left. + \frac{1}{4} \frac{K_0(x - \xi)^2 z}{y^2} \right] \end{aligned} \quad (24)$$

where

$$\kappa = \frac{1}{4} \frac{K_0(x - \xi)^2}{y^2} \quad (25)$$

This leads to

$$\begin{aligned} S(\xi; \kappa) &= \int_{R(\xi)} d\ell \Sigma_r(\xi; \eta, \zeta) e^{\kappa z} \cos \kappa(y - \eta) \\ &\sim \int_{R(\xi)} d\ell \Sigma_r(\xi; \eta, \zeta) \quad \text{for } y \rightarrow \infty \end{aligned} \quad (26)$$

Comparison of expressions (8) and (24) suggests that  $\sigma(x)$  describing the far field solution is determined from  $\Sigma(x)$  by the following relation.

$$\sigma(x) = \exp\left[-i\left(\frac{\omega}{U}\right)x - i\frac{\pi}{4}\right] \int_{R(x)} d\ell \Sigma_r(x; \eta, \zeta) \quad (27)$$

Dynamic pressure  $P e^{i\omega t}$  linear to the amplitude of motion  $\delta$  will be derived by Bernoulli's formula as follows.

$$\begin{aligned} P &= -\rho \delta \exp(-i\omega/Ux) U \frac{\partial}{\partial x} \psi_r \\ &\quad - \rho \delta \exp(-i\omega/Ux) \left[ \frac{\partial \psi_r}{\partial y} \frac{\partial \phi_s}{\partial y} + \frac{\partial \psi_r}{\partial z} \frac{\partial \phi_s}{\partial z} \right] \end{aligned} \quad (28)$$

In this equation we did not include the static pressure component induced on the hull surface by the displacement of the body in the non-uniform steady pressure field. This component will be measured independently of the dynamic pressure in our experiments.

Once again there are different order terms in the right hand side of equation (28). The lowest of them is the first line. The second line is  $\epsilon^{1/2}$  higher order than the first and should not be included in the computation of forces on the body, while we include this terms in some cases. In our computation an identical scheme is employed to solve the unsteady problem as well as the steady problem and  $\phi_s$  is always available when  $\psi_r$  is calculated. Inclusion of the second term in the computation of the forces does not need more computational effort.

Pressure integrated on the body surface gives the forces  $F_j$  ( $j = 3, 5$ ) on the ship.

$$F_j = - \int_0^L d\xi \int_{L(\xi)+R(\xi)} P n_j ds \quad (29)$$

## NUMERICAL COMPUTATION

The source density must be determined such that the body boundary condition (21) is satisfied. We rewrite the second term of equation (23) into the discrete source density form: we divide each section contour of the catamaran into  $M$  pieces of segments on each of which the density is assumed constant  $\Sigma_r(x; j)$ . After integrating analytically the constant source density on each segment, the normal derivative is taken. Then we have an integral equation

$$\begin{aligned} \frac{\partial \psi_r}{\partial N} = & -\frac{\partial}{\partial N} \int_{L(x)+R(x)} d\ell \Sigma_r(x; \eta, \zeta) \log \frac{r}{r'} \\ & - \frac{\pi K_0}{\pi K_0} \int_0^x d\xi \sum_{j=1}^{2N} \Sigma_r(\xi; j) \\ & \times \text{Re}[-(n_y + in_z) \exp(-i\alpha_j) \\ & \times \left( \frac{w(Z_{j+1})}{\sqrt{|z + \zeta_{j+1}| + i(y - \eta)}} \right. \\ & \quad \left. - \frac{w(Z_j)}{\sqrt{|z + \zeta_j| - i(y - \eta_j)}} \right) \\ & \quad + (n_y - in_z) \exp(i\alpha_j) \\ & \times \left( \frac{w(\bar{Z}_{j+1})}{\sqrt{|z + \zeta_{j+1}| - i(y - \eta_{j+1})}} \right. \\ & \quad \left. - \frac{w(\bar{Z}_j)}{\sqrt{|z + \zeta_j| - i(y - \eta_j)}} \right)] \end{aligned} \quad (30)$$

where  $(\eta_j, \zeta_j)$  and  $(\eta_{j+1}, \zeta_{j+1})$  are the coordinates of the end points of the  $j$ -th segment,  $\text{Re}$  denotes the real part and

$$Z_j = \frac{1}{2} \frac{\sqrt{K_0}(x - \xi)}{\sqrt{|z + \zeta_j| + i(y - \eta_j)}} \quad (31)$$

$$\alpha_j = \tan^{-1} \frac{\eta_{j+1} - \eta_j}{\zeta_{j+1} - \zeta_j} \quad (32)$$

where  $\bar{Z}_j$  is the complex conjugate of  $Z_j$ .  $w(z)$  is Error function for complex arguments defined as

$$w(z) = e^{z^2} \text{erfc}(-iz) \quad (33)$$

In the derivation of (30) we assumed wall sided hull form and the segment closest to the free surface is vertical. This leads to

$$\frac{w(Z_j)}{\sqrt{(z + \zeta_j) \pm (y - \eta)}} \sim \left( \frac{1}{\sqrt{|y - \eta|}} \right), z, \zeta_j = 0 \quad (34)$$

This singularity may not cause serious problem in solving the integral equation (30) numerically. Efficient program to compute  $w(z)$  at accuracy of 12 digits is available (Iwashita and Ohkusu (1989)) in which several different expressions, continued fractions, asymptotic expansions and finite series approximations, are combined the most efficient way.

$m_j$ , that we need to compute when we retain the second order terms in the body boundary conditions will not be so seriously singular close to the free surface, provided the hull form is wall sided. It is not difficult to show

$$\frac{\partial \phi_s}{\partial z} = O(1), \quad z \frac{\partial^2 \phi_s}{\partial y \partial z} = O(1) \quad (35)$$

Wave elevation  $\zeta_r$  in the region near to the hull surface is computed with numerical  $x$ -derivatives of the solution  $\psi_r$  on  $z = 0$ .

$$\begin{aligned} \zeta_r = & -\frac{1}{g} (i\omega + U \frac{\partial}{\partial x}) [\exp(-i \frac{\omega}{U} x) \psi_r]_{z=0} \\ \sim & -\frac{1}{g} \exp(-i \frac{\omega}{U} x) \frac{\psi_r(x + \Delta x) - \psi_r(x)}{\Delta x} \end{aligned} \quad (36)$$

Both hulls of a catamaran are considered to be within the near field of each other, the source density on both contours must be symmetrical with respect to  $xz$  plane. Each section contour is divided into a number of segments on which the source strength is assumed constant and the integral equation (30) is solved such that the boundary condition is satisfied on the midpoint of each segment. This implies that upstream effect represented by the second term of (30) is evaluated on the midpoint.

The ship length is divided too into a number of strips with thickness of  $\Delta x$ . Assuming the source is concentrated at the center of  $\Delta x$  we step the integral equation (30) to next section. Of course only the sources located upstream have effect on the current section; the sources from 0 to  $x - \Delta x$  have the effects.

We tested our method using only the impulsive sources against results of Daoud (1975) and Faltinsen (1983) on stationary waves around a wedge. Daoud solved the integral equation on the velocity potential on the contour of each section instead of the source strength. Faltinsen expressed the velocity potential around a section with the fundamental sources distributed on the free surface as well as on the section contour. The conditions are imposed on the free surface, on the contour and at infinity. He solved the integral equation on the velocity potential and step the free surface condition to next section with using the dynamic and the kinematic free surface conditions.

Wave elevations around a wedge for a half angle 7.5 degree are compared in Fig.2. Results of our method agree well with their results.

In our method magnitude of  $\Delta x$  will have essential effect on the accuracy of results because we employ the concentrated sources in the  $x$ -wise and we are assuming fast variation of the solution in the  $x$  direction. Added mass coefficient for heave and added moment of inertia for pitch of a hull form (one of twin hulls of a catamaran model later described) were computed with increasing the number of strips  $N$  from 20 up to 60 as shown in Figs.3 and 4. Results of computation without  $m_j$  seem to converge consistently and  $N = 20$  gives accurate enough results, while results with  $m_j$ , added moment of inertia in particular, are slow in convergence. This may be due to the smallness of  $A_{55}$  value vulnerable to singularity in  $m_j$  close to the intersection of the section contours and the free surface. We need a smaller segment size there to have more consistent results.

Hydrodynamic forces computed with the present method for a mathematical hull form with semi-circle section contour and water plane form  $y = (0.3/L)x(L - x)$  are compared with those computed by Newman's unified theory (Newman (1978)) in Figs. 5 to 8. Results are obtained with ignoring the terms including  $\phi_s$  in the body boundary condition (21) and retaining only the first term in the pressure (28). Actually in pitch mode the term  $-Un_3$  in (21) is retained, though it is of higher order. In order to evaluate the first term of (28) we need to differentiate numerically  $\phi_r$  in the  $x$  direction just like in equation (36).

Unified theory's results we have shown here are too without  $m_j$ . The present method and unified theory predict hydrodynamic forces al-

most similar in magnitude, while agreement is not consistent. Damping of pitch computed by the present method is much smaller in lower frequency. We need experiments to decide which is better in such a high Froude number region.

We did forced heave and pitch motion test for a catamaran whose demihull has a form shown in Fig.9. Length of the model is 1m, the breadth 0.086m, the draft 0.043m and the distance between the centers of both hulls 0.30m. Heave or pitch of appropriate magnitude was given on the towed model with other motions suppressed. Measured force record was analyzed into several terms of harmonics. Length of records measured after stationary state is reached is averagely 10 cycles of motion.

In-phase force measured contain the force that would act when the ship were displaced from the original position at  $\omega = 0$ . Here we measured it by giving some displacement to the model towed on calm water. Assuming magnitude of this force is approximately linear to amount of the displacement, we get a spring constant as illustrated in Fig.14. This component was excluded from the measured in-phase forces to obtain added mass. In the frame work of the present theory, however, difference of this component at non-forward speed and at forward speed in the non-uniform steady flow field must be considered to be of the second order.

Results of experiments are plotted in Figs.10 to 13. A few of black circles depicted in Fig.11 have dash mark. At these points noise level was so high with reasons we do not know at present (magnitude of higher harmonics was as large as 50 percent of the fundamental one) that we are not confident of their accuracy.

Computed hydrodynamic force with the present method are shown in those figures. Results depicted as without  $m_j$ , which were obtained with ignoring consistently the effects of  $\phi_s$  in equations (16) and (28), predict well the measured ones at high Froude number 0.5 to 0.89. One reason of a little discrepancy will be that the analysis is not valid at the ends of the ship. In the case of transom stern like our model we expect that the flow leaves the stern tangentially in the downstream direction so that there is atmospheric pressure at the last section. This means that the sum of the added mass forces and hydrostatic restoring force on the last section is zero. The same is true with the damping force on the last section. In our analysis the hydrodynamic

behaviour at the last section is dependent on the upstream effect. There is no effect from downstream. This means we have no information that there should be atmospheric pressure at the last section. The consequence is a wrong prediction of hydrodynamic forces at the last section. Inclusion of the interaction with steady flow at high Froude number ( with  $m_j$  ) does not seem to improve the correlation between the predicted and the measured.

Wave elevation between two hulls of a catamaran will cause occurrence of impact pressure on the bridge structure connecting two hulls of a catamaran. We need a practical prediction method of it. It is well known that strip theory in which we consider two hulls are in the near field of each other predicts too strong interaction between them (Ohkusu (1971)) and the prediction of wave elevation is not realistic. Figs.15 and 16 are examples of wave elevation computed by the present method. They are for the cases of pitch motion at  $Fn = 0.5$  and  $Fn = 0.89$  with  $\omega^2 L/g = 20$ . The far left of Figs.15 and 16 is the midpoint of the distance between two hulls. It is clear that wave elevation is almost symmetrical around each hull. This implies that there is almost no interaction of two hulls if we are close to the hull. Wave elevation in these examples is certainly high at  $Fn = 0.5$  than at  $Fn = 0.89$ .

We can compute the velocity potential and wave elevation in the far-field generated with a line source  $\sigma(x)$  determined by equation (27). Information on the wave field will make it possible to evaluate added resistance of high speed ships in waves. Damping is also computed from energy flux in the far field. A line doublet as well as a line source will be required to describe correctly the wave field around a catamaran. Considering low interaction effect between two hulls in the near field, two line sources distributed on both hulls may be enough to give wave elevation correctly.

Short wave components of the waves generated by a point source will be dominant at high speed and at position close to the source. Actually waves by a point source vary dreadfully, while waves by a line source does not because of integration of the effects from all sources on a line. But realizing this smoothing effect correctly on numerical computation requires very accurate evaluation of wave elevation generated by each source. New scheme to evaluate the Green function for ship motion at forward speed proposed by one of the present author (Ohkusu and Iwashita

(1989)) will be useful for this purpose.

We computed  $\Sigma_r$  by solving the integral equation at 20 strips along the ship length and then interpolated  $\sigma$  at 200 positions. Effects from 200 point sources are summed to represent the effect of a line source. Figs.17 and 18 are computed examples of the wave elevation at  $t = 0$  for the heaving model. Divergent waves are remarkable and transverse waves are not seen until far behind the ship at such a high speed. If this information is compared with the measured wave pattern, it will provide strong data to investigate if our theory is really accurate.

## CONCLUDING REMARKS

Chapman-Doud-Faltinsen's approach was applied for predicting radiation forces of heave and pitch of a catamaran at high forward speed. The dominant far-field effects caused by a ship are the diverging waves close to the hull where we assumed large variation in the flow variables.

Computed added mass and damping are compared fairly well with the measured on forced heave and pitch motion experiment. However results obtained with the steady flow terms in the body boundary conditions and in the pressure equation taken into consideration, though it is inconsistent in our analysis, do not show better correlation.

It may be concluded that our approach in predicting various factors, hydrodynamic forces and wave elevations etc., associated with seakeeping of a catamaran at high speed seems to be promising from practical view point. But we need careful study with more computational and experimental examples before reaching definite conclusions.

## ACKNOWLEDGEMENT

This study was initiated during the first author's stay at the Norwegian Institute of Technology with support of Royal Norwegian Council for Scientific and Industrial Research (NTNF) and Scandinavia Sasakawa Foundation.

## REFERENCES

- (1)Chapman, R.B.(1976). Free Surface Effects for Yawed Surface-Piercing Plate. J.Ship Research 20
- (2)Daoud, N. (1975). Potential Flow Near to a Fine Ship's Bow, Rep. No.177, Dep. Nav. Archt. Marine Eng., Univ. of Michigan.
- (3)Erdélyi, A. (1956). Asymptotic Expansions, Dover Publications, New York.
- (4)Faltinsen, O.(1983). Bow Flow and Added Resistance of Slender Ships at High Froude Number and Low Wave Lengths. J. Ship Research 27
- (5)Faltinsen, O. and Zhao, R. (1990) . Numerical Predictions of a Ship Motion at High Forward Speed, the Meeting on the Dynamics of Ships, the Royal Society of London .
- (6)Iwashita, H. and Ohkusu, M. (1989). Hydrodynamic Forces on a Ship Moving with Forward Speed in Waves, Vol.166, J. Society Naval Architects of Japan
- (7)Newman, J.N.(1978). The theory of Ship Motions, Advance in Applied Mechanics, Vol.18, Academic Press.
- (8)Ogilvie, T.F. (1977). Singular-Perturbation Problems in Ship Hydrodynamics, Advances in Applied Mechanics, Vol.17, Academic Press, New York
- (9)Ogilvie, T. F. and Tuck, E.O. (1969). A Rational Strip Theory for Ship Motions, Part 1, Rep. No.013, Dep. Nav. Archit. Marine Eng. Univ. of Michigan
- (10)Ohkusu, M. and Iwashita, H. (1989). Evaluation of the Green Function for Ship Motions at Forward Speed and Application to Radiation and Diffraction Problems, 4th International Workshop on Water Waves and Floating Bodies, Norway
- (11)Ohkusu, M. (1971) On the Motion of Twin Hull Ship in Waves, Vol.129 J. Society Naval Architects of Japan
- (12)Yeung, R.W. and Kim, S.H. (1985) A New Development in the Theory of Oscillating and Translating Slender Ships, 15th Symposium of Naval Hydrodynamics

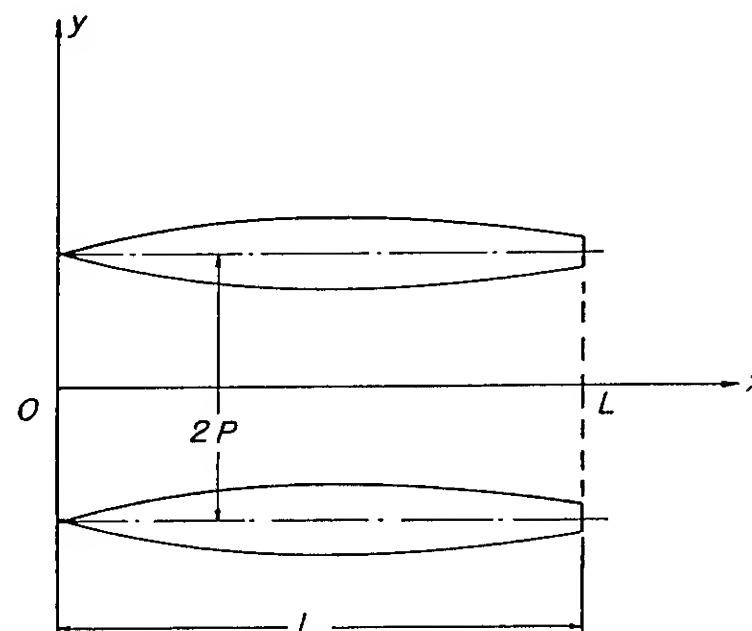


Fig.1 Coordinate System

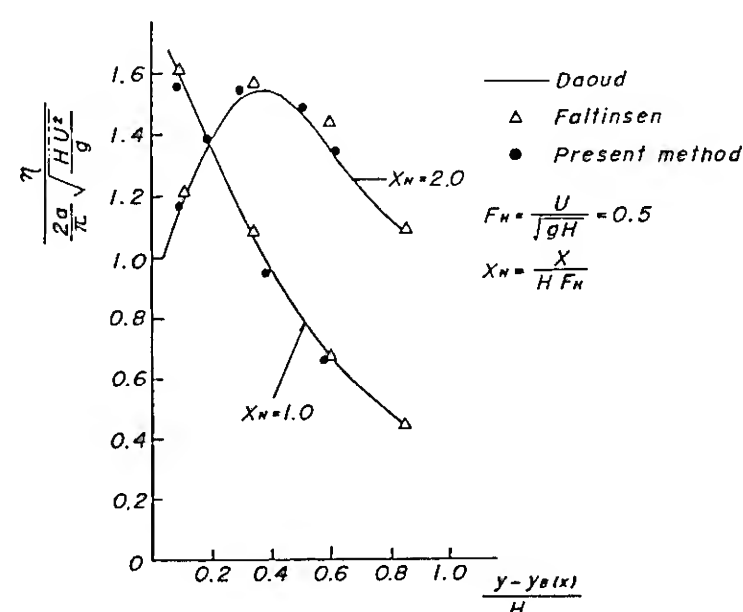


Fig.2 Waves around a Wedge

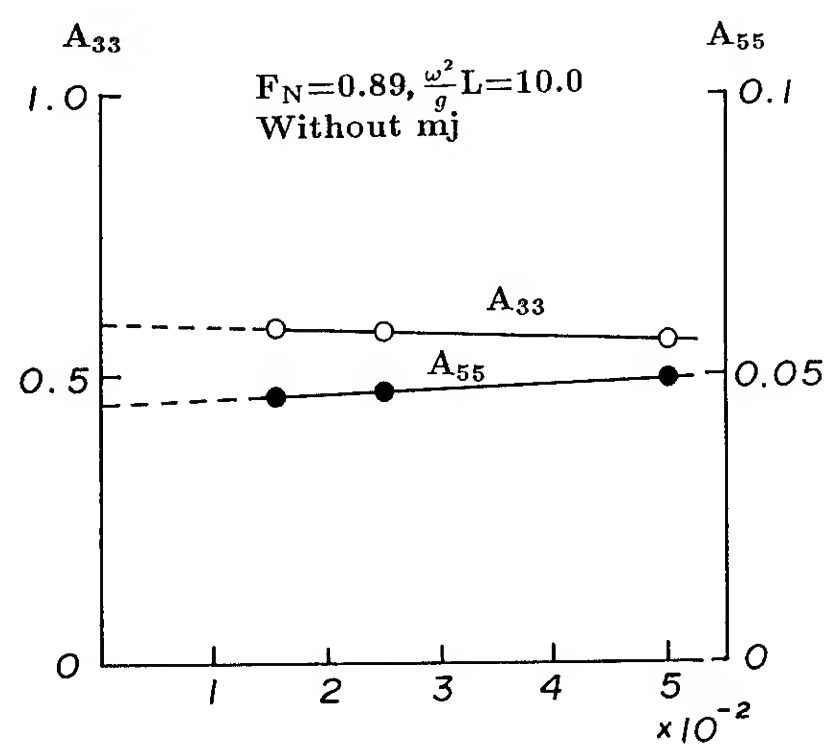


Fig.3 Convergence with Increase of Number of Strips

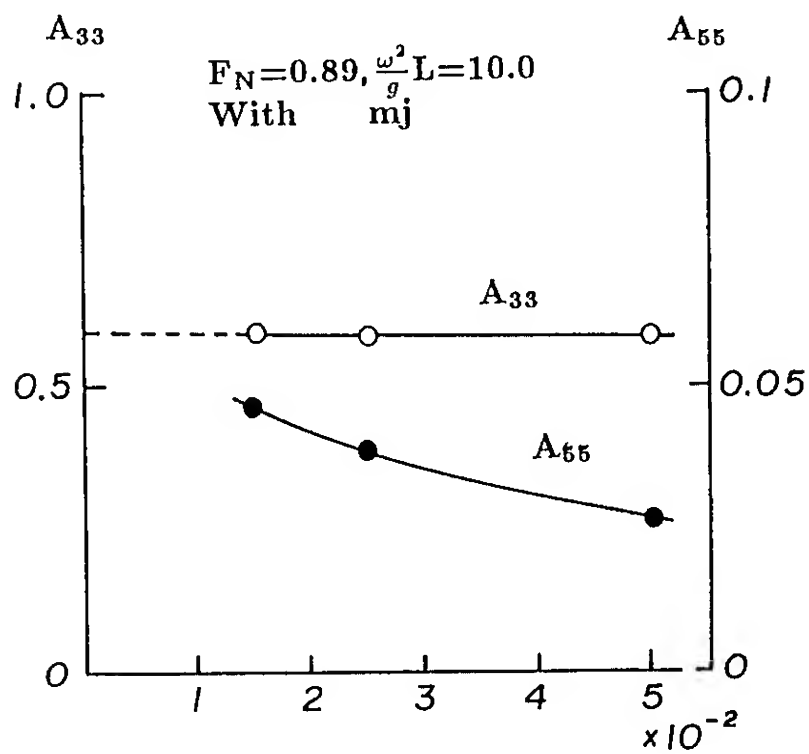


Fig.4 Convergence with Increase of Number of Strips

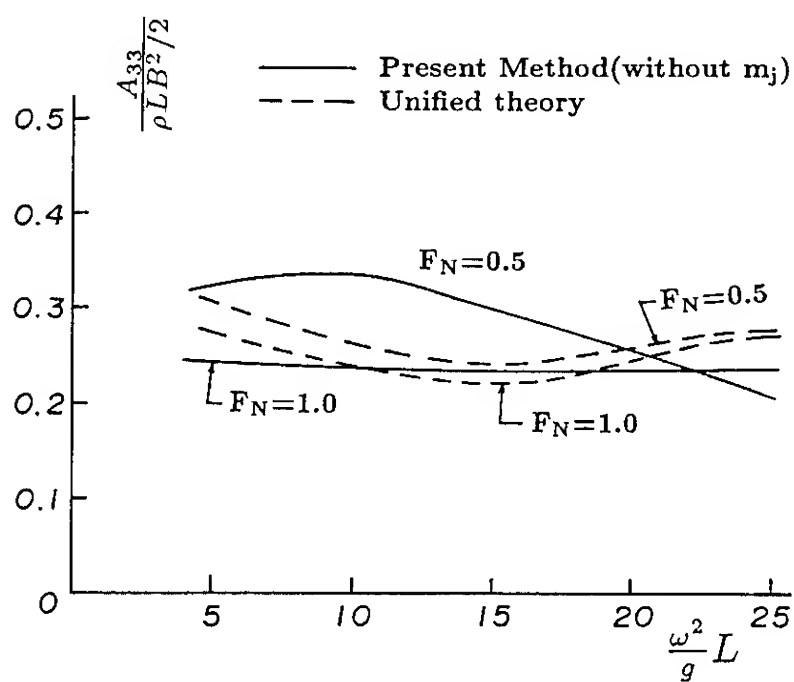


Fig.5 Added Mass (Heaving) of a Single Hull Ship

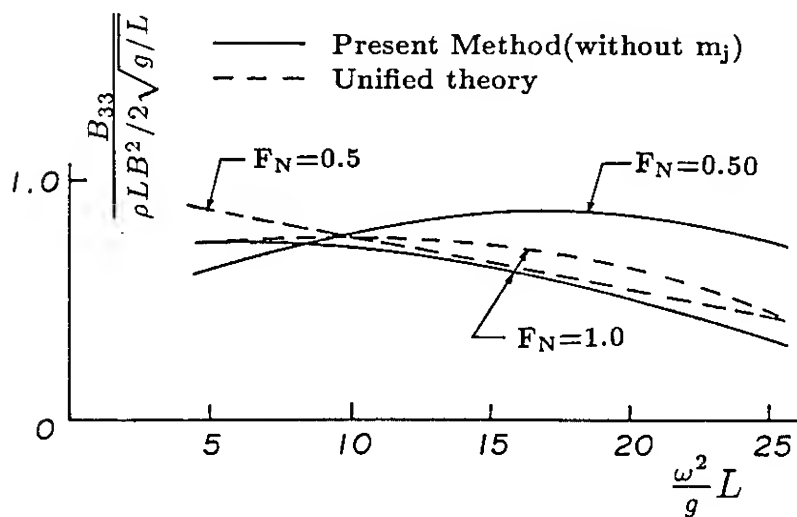


Fig.6 Damping (Heaving) of a Single Hull Ship

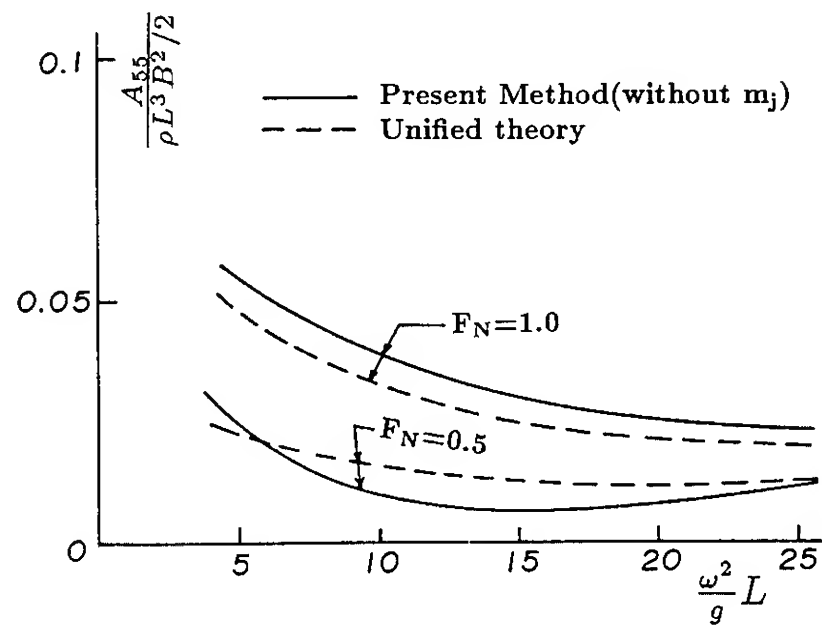


Fig.7 Added Mt. of Inertia (Pitching) of a Single Hull Ship

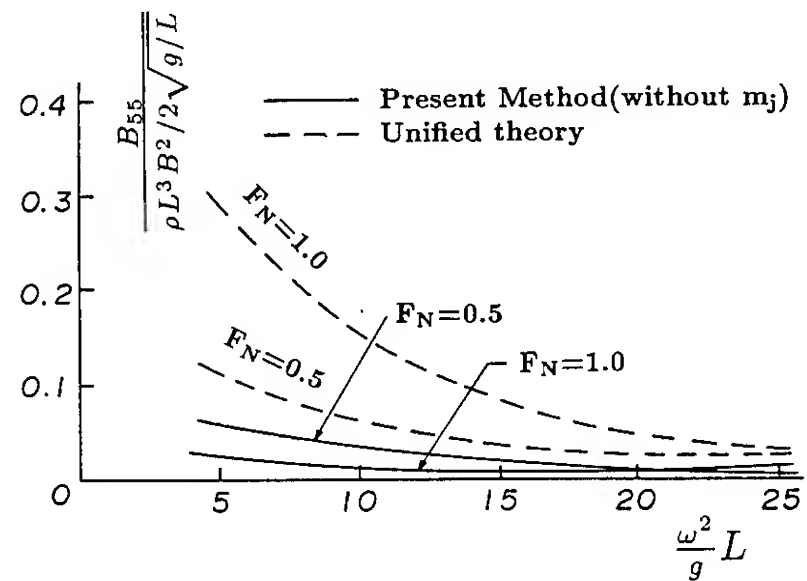


Fig.8 Damping (Pitching) of a Single Hull Ship

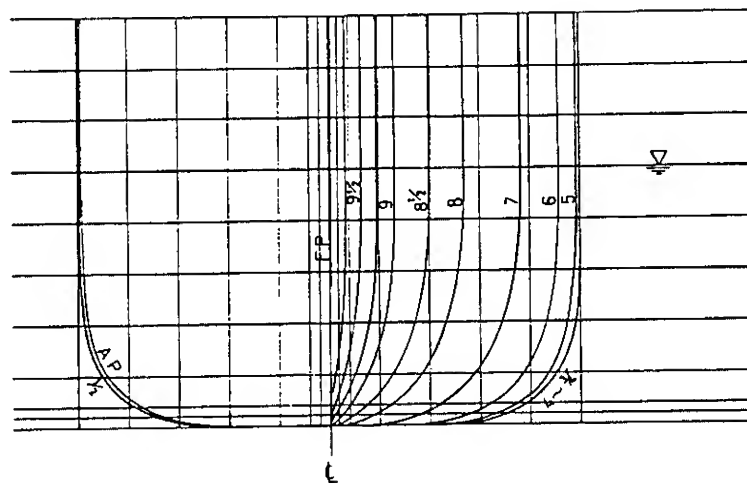


Fig.9 Body Plan of a Catamaran



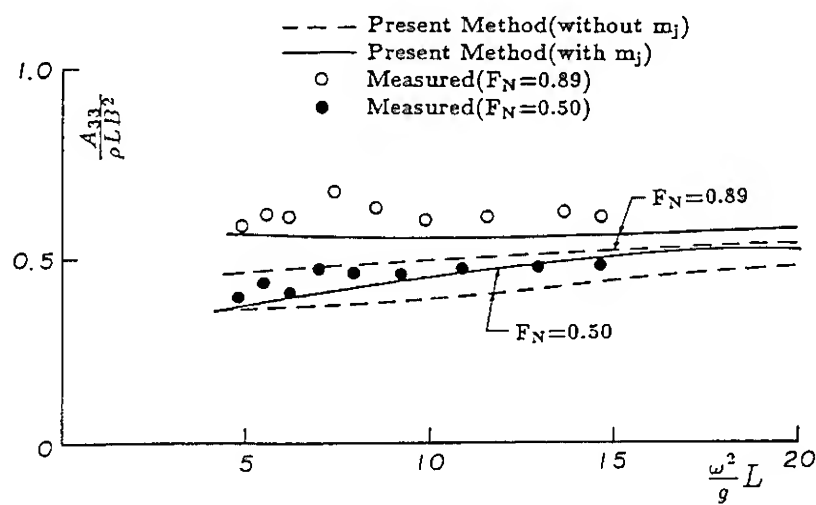


Fig.10 Added Mass (Heaving) of a Catamaran

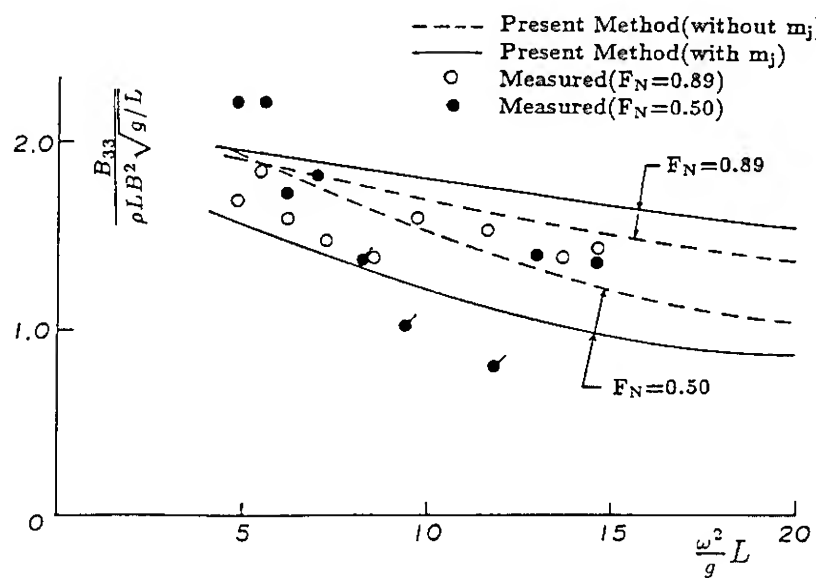


Fig.11 Damping (Heaving) of a Catamaran

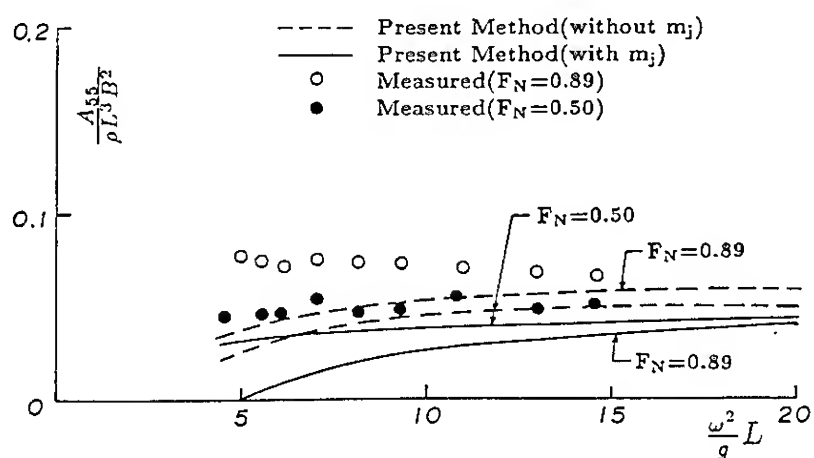


Fig.12 Added Mt. of Inertia (Pitching) of a Catamaran

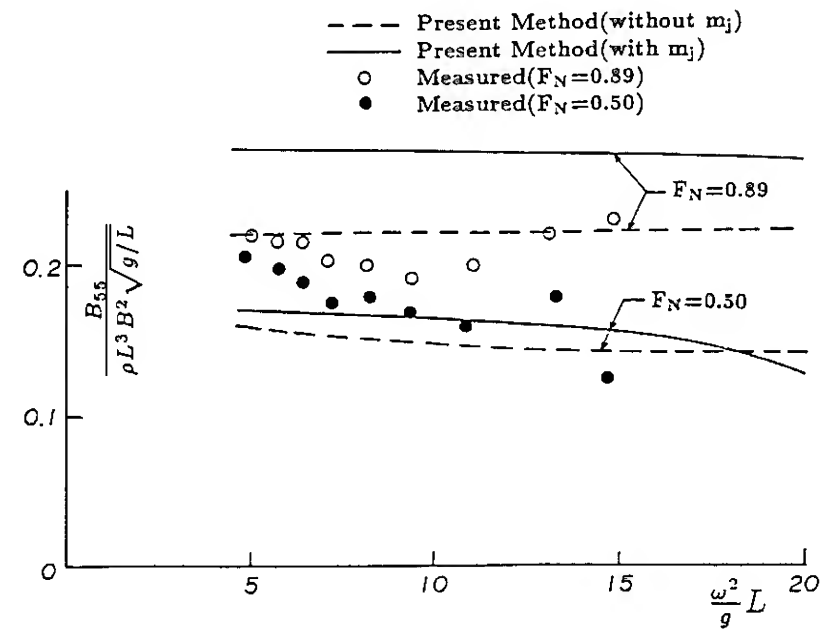


Fig.13 Damping (Pitching) of a Catamaran

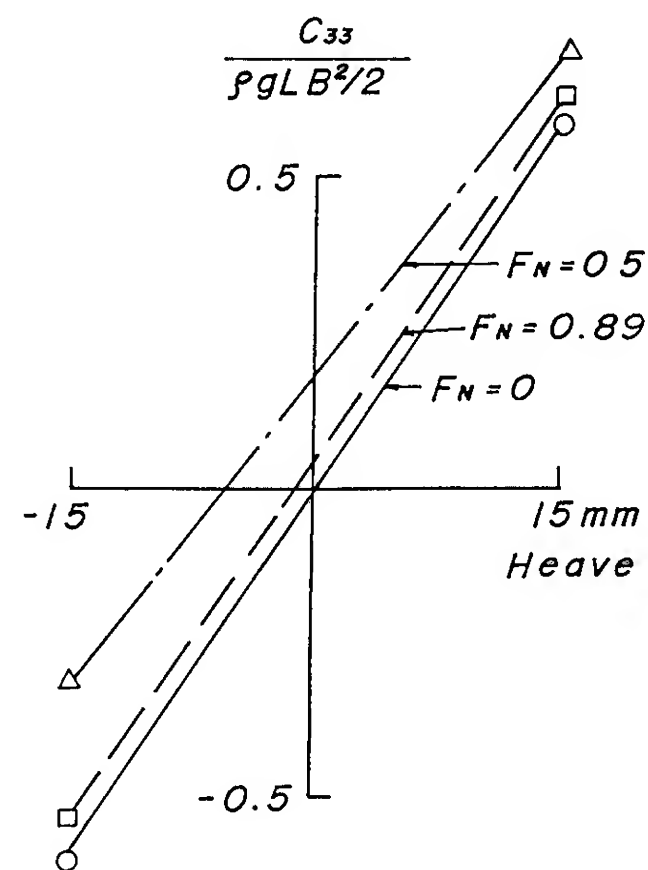


Fig.14a Variation of Restoring Force (Heave)

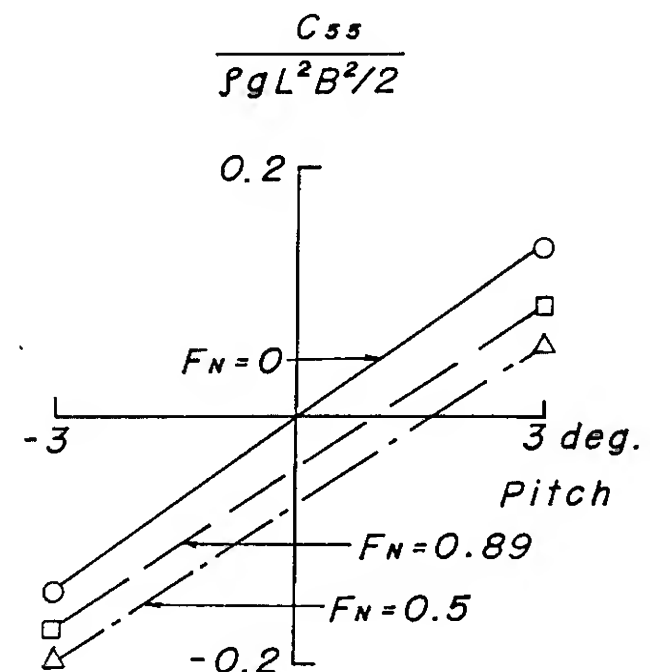


Fig.14b Variation of Restoring Force (Pitch)

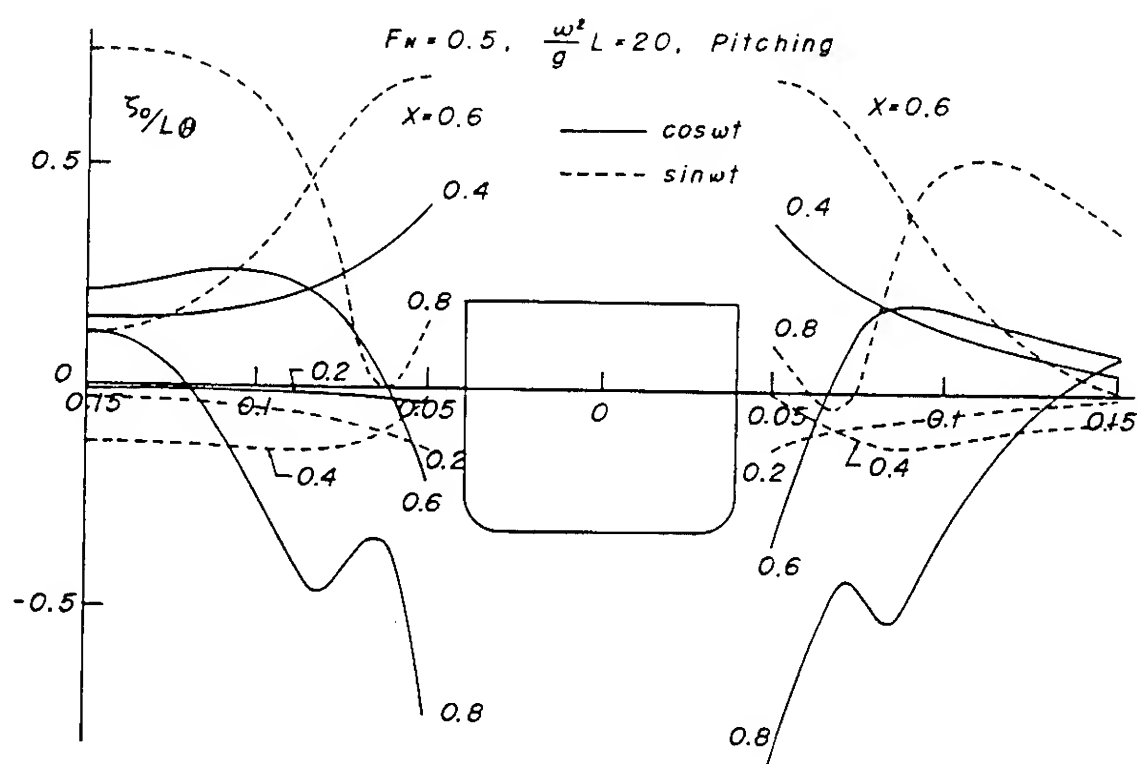


Fig.15 Wave Elevation

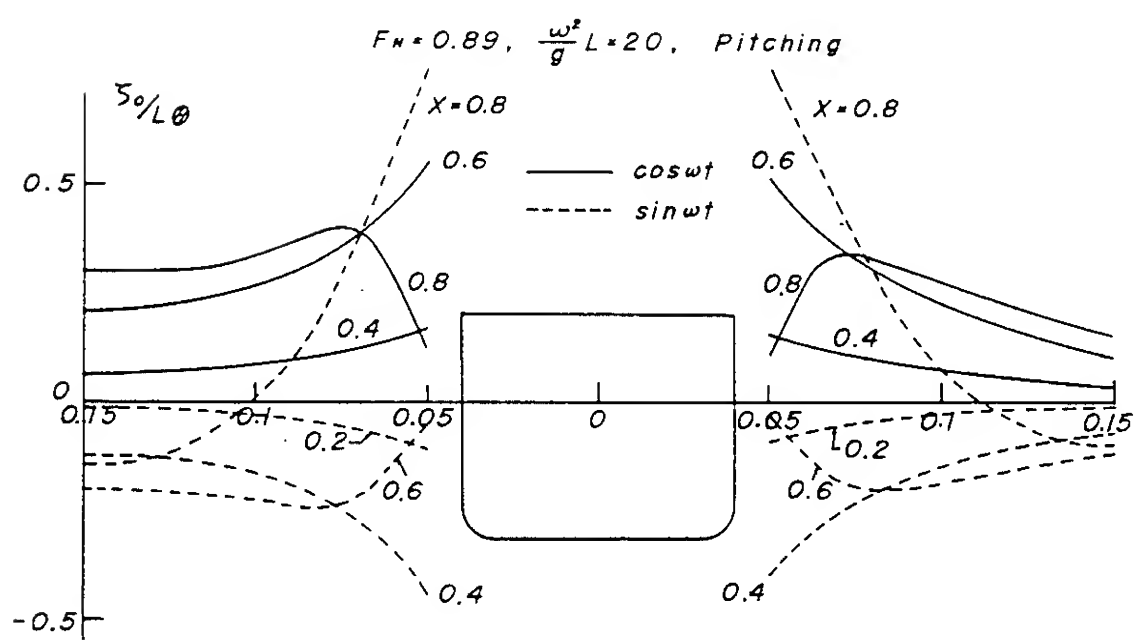


Fig.16 Wave Elevation

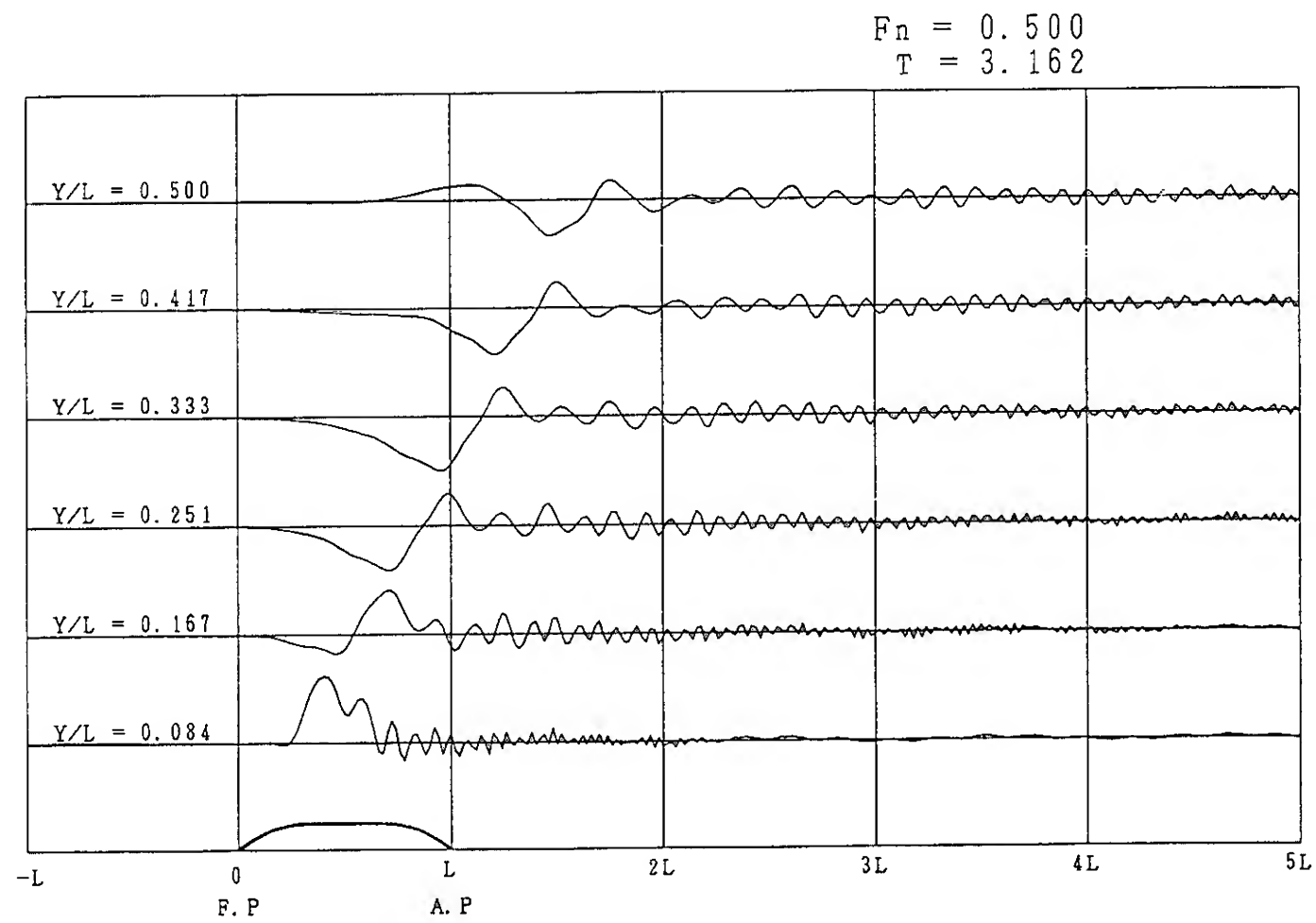


Fig.17 Wave Elevation in the Far Field

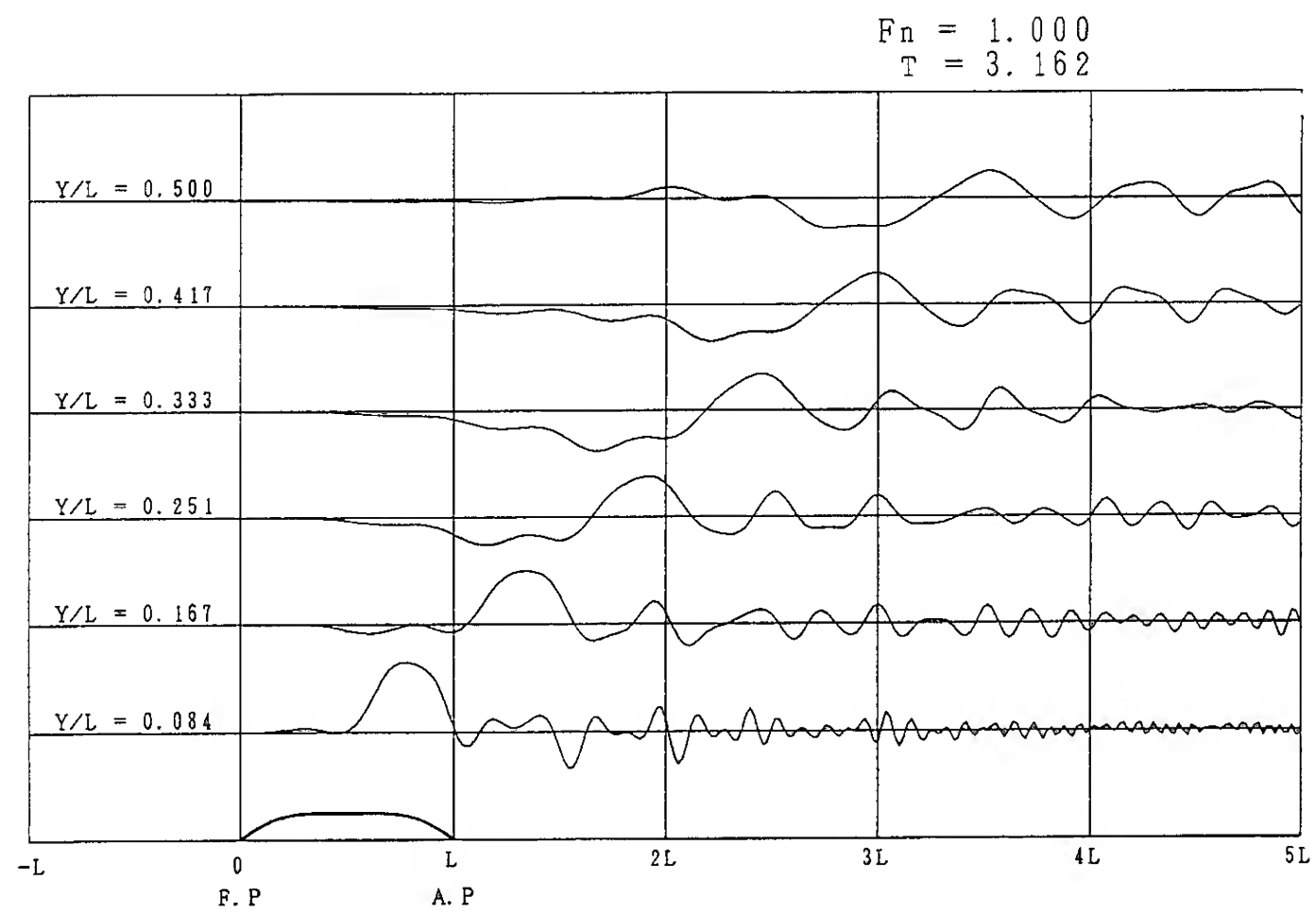


Fig.18 Wave Elevation in the Far Field

## DISCUSSION

Ronald W. Yeung  
University of California at Berkeley, USA

The approach taken here is one already taken up by Yeung & Kim (1981, 3rd Numerical Ship Hydrodynamic Conference) for a single body. The present calculations have qualitative features, in terms of agreement with expt., not so different from the above work which the authors are apparently unaware of. Indeed, our experience, as I recall, was that the terms associated with the change in waterline width need to be accounted for. In our calculations of those days, the  $m_j$  terms involving the steady-state body potential was not included, but improvement over strip approximation was evident. The numerical approximation over the artificial time variables ( $x-\xi$ ) is particularly important when ( $x-\xi$ ) is large and ( $y-\eta$ ) is small. Accuracy and precision can be achieved if the  $\xi$  variable is integrated analytically. The procedure is described in more detail in Yeung (1982, J.Engng.Math). The role played by the transverse waves was analysed in Ref [12] but I suspect they are not important as the Froude numbers being considered here.

## AUTHORS' REPLY

I appreciate Prof. Yeung for attracting our attention to his extensive works done before. I understand the terms associated with the change in waterline width indicates a line integral on the intersection of the free surface and the body surface. This term is of higher order in our analysis, that is, of the same order as  $m_j$ . Our results do not show any essential difference from the results obtained with solving the near field problem by distributing the fundamental sources on the free surface as well as the body surface. This seems to show that inclusion of the line integral has the secondary effect on the results.

# Ship Motions by a Three-Dimensional Rankine Panel Method

D. Nakos, P. Slavounos (Massachusetts Institute of Technology, USA)

## ABSTRACT

A Rankine Panel Method is presented for the solution of the complete three-dimensional steady and time-harmonic potential flows past ships advancing with a forward velocity. A new free-surface condition is derived, based on linearization about the double-body flow and valid uniformly from low to high Froude numbers.

Computations of the steady ship wave patterns reveal significant detail in the Kelvin wake a significant distance downstream of the ship, permitted by the cubic order and zero numerical damping of the panel method. The wave pattern appears to be sensitive to the selection of the free-surface condition only for full ship forms.

The heave and pitch hydrodynamic coefficients, exciting forces and motions of a Wigley and a Series-60 hull have been evaluated in head waves over a wide range of frequencies and speeds. A robust treatment is proposed of the  $m$ -terms which are found to be critical importance for the accurate solution of the problem. In all cases the agreement with experiments is very satisfactory indicating a significant improvement over strip theory, particularly in the cross-coupling and diagonal pitch damping coefficients.

## 1. INTRODUCTION

Theoretical methods for the prediction of the seakeeping of ships have evolved in three phases over the past 40 years. The first phase involved the development of strip theory, and was followed by a series of developments in slender-body theory which formulated rationally the ship motion problem and produced several refinements of strip theory. The advent of powerful computers in the early 80's allowed the transition into the third and current phase of seakeeping research which aims at the numerical solution of the three-dimensional problem. This paper presents our progress in that direction.

The pioneering work of Korvin-Kroukovsky (1955) stimulated a number of studies on the strip method which led to the theory of Salvesen, Tuck and Faltinsen (1970). Its popularity to date arises from its satisfactory performance in the prediction of the motions of conventional ships and its computational simplicity. Well documented are however its limitations in the prediction of the derived responses,

structural wave loads and in general the seakeeping characteristics of ships advancing at high Froude numbers [e.g. O'Dea and Jones (1983)].

The 60's and 70's witnessed several analytical studies aiming to extend the slender-body theory of aerodynamics to the seakeeping of slender ships. The rational justification of strip theory, as a method valid at high frequencies and moderate Froude numbers, was presented by Ogilvie and Tuck (1969). This theory was extended to the diffraction problem by Faltinsen (1971) and was further refined by Maruo and Sasaki (1974). The high-frequency restriction in earlier slender-ship theories was removed by the unified theory framework presented by Newman (1978). Its extension to the diffraction problem was derived by Slavounos (1984) and applied to the seakeeping of ships by Newman and Slavounos (1980) and Slavounos (1984). Subsequent slender-ship studies by Kim and Yeung (1984) and Nestegard (1986), accounted directly for convective forward-speed wave effects near the ship hull and represented the transition to numerical studies aiming at the solution of the three-dimensional ship-motion problem.

By the mid-80's, the performance of slender-body theory for the seakeeping problem could only be validated from experimental measurements. Moreover, it had become evident that end-effects at high Froude numbers cannot be modelled accurately by slender-body approximations and the need for a numerical solution of the complete three-dimensional had emerged. Early efforts towards this goal by Chang (1977), Inglis and Price (1981) and Guevel and Bougis (1982) were not conclusive because the significant computational effort necessary for the evaluation of the time-harmonic forward-speed Green function limited the total number of panels used on the ship surface. More recently, King, Beck and Magee (1988) circumvented this difficulty by solving the same problem in the time domain, therefore making use of the zero-speed transient Green function which is easier to evaluate.

The last decade witnessed the growing popularity of Rankine Panel Methods for the solution of the steady potential flow past ships. The success of the early work of Gadd (1976) and Dawson (1977) motivated several analogous studies which concentrated upon the prediction of the Kelvin wake and evaluation of the wave resistance. The principal advantages of the method are twofold - the Rankine singularity is simple to treat computationally and the distribution of panels over the free surface allows the enforcement of more general free-surface conditions with vari-

able coefficients. A drawback of Rankine-panel methods is that they require about twice as many panels as methods based on the distribution of wave singularities over the ship surface alone. The resulting computational overhead is associated with the solution of the resulting matrix equation, but may not be significant if an out-of-core iterative solution method is available.

This paper outlines the solution of the three-dimensional time-harmonic ship motion problem by a Rankine Panel Method. For the steady problem, the theory for the analysis of the properties for such numerical schemes was introduced by Piers (1983) and generalized by Sclavounos and Nakos (1988). The extension of this numerical analysis to the time-harmonic problem is presented in Nakos and Sclavounos (1990). In this reference the convergence properties of a new quadratic-spline scheme are derived, which has been found to be accurate and robust for the solution of both steady and time-harmonic free-surface flows in three dimensions. This scheme is applied in this paper to the solution of the time-harmonic radiation/diffraction potential flows around realistic ship hulls and the evaluation of the hydrodynamic forces and motions in regular head waves.

A new three-dimensional free-surface condition is derived, using the double-body flow as the base disturbance due to the forward translation of the ship. This is shown to be valid uniformly from low to high Froude numbers and over the entire frequency range. Known low-Froude-number conditions for the steady problem, as well as the Neumann-Kelvin condition, are obtained as special cases. The ship-hull condition includes the  $m$ -terms which are evaluated from the solution of the three-dimensional double-body flow. An important property of the solution scheme is that the evaluation of the double gradients of the double-body flow is circumvented by an application of Stokes theorem.

Computations are presented of the steady wave patterns trailing a fine Wigley model and a fuller Series-60 hull. The cubic order and zero numerical damping of the free-surface discretization allows the prediction of significant detail of the Kelvin wake at a large distance downstream of the ship. A comparison of the wave patterns obtained from the Neumann-Kelvin and the more general double body free-surface conditions reveals good agreement for the Wigley hull, while evident differences appear in the respective Series-60 wakes.

Predictions of the heave and pitch added-mass and damping coefficients and exciting forces are found to be in very good agreement with experimental measurements both for the Wigley and the Series-60 hull. The contribution of the complete  $m$ -terms is found to be important, particularly in the cross-coupling coefficients. The validity of a more general set of Timman-Newman relations is observed and conjectured in connection with free-surface conditions based on the double-body flow.

The heave and pitch motion amplitudes and phases predicted by the present method are found in very good agreement with experiments and present an improvement over strip theory.

## 2. THE BOUNDARY VALUE PROBLEM

Define a Cartesian coordinate system  $\vec{x} = (x, y, z)$  fixed on the ship which translates with a constant speed  $U$ . The positive  $x$ -direction points upstream and the positive  $z$ -axis upwards. The boundary-value problem will be expressed relative to this translating coordinate system, therefore the flow at infinity is a uniform stream and the ship hull velocity is due to its oscillatory displacement from its mean position.

The fluid is assumed incompressible and inviscid and the flow irrotational, governed by a potential function  $\Psi(\vec{x}, t)$  which satisfies the Laplace equation in the fluid domain

$$\nabla^2 \Psi(\vec{x}, t) = 0. \quad (2.1)$$

Over the wetted portion of the ship hull ( $B$ ), the component of the fluid velocity normal to ( $B$ ) is equal to the corresponding component of the ship velocity  $\vec{V}_B$ , or

$$\frac{\partial \Psi}{\partial n}(\vec{x}, t) = (\vec{V}_B \cdot \vec{n})(\vec{x}, t), \quad (2.2)$$

where the unit vector  $\vec{n}$  points out of the fluid domain.

The fluid domain is also bounded by the free surface, defined by its elevation  $z = \zeta(x, y, t)$  and subject to the kinematic boundary condition,

$$\left( \frac{\partial}{\partial t} + \nabla \Psi \cdot \nabla \right) [z - \zeta(x, y, t)] = 0 \quad \text{on} \quad z = \zeta(x, y, t). \quad (2.3)$$

The vanishing of the pressure on the free surface combined with Bernoulli's equation, leads to the dynamic free surface condition

$$\zeta(x, y, t) = -\frac{1}{g} \left( \Psi_t + \frac{1}{2} \nabla \Psi \cdot \nabla \Psi - \frac{1}{2} U^2 \right)_{z=\zeta}. \quad (2.4)$$

The elimination of  $\zeta$  from (2.3) and (2.4) leads to

$$\Psi_{tt} + 2 \nabla \Psi \cdot \nabla \Psi_t + \frac{1}{2} \nabla \Psi \cdot \nabla (\nabla \Psi \cdot \nabla \Psi) + g \Psi_z = 0 \quad \text{on} \quad z = \zeta. \quad (2.5)$$

If the fluid domain is otherwise unbounded, the additional condition must be imposed that at finite times the flow velocity at infinity tends to that of the undisturbed stream.

### Linearization of the free surface condition

Physical intuition suggests that linearization of the preceding boundary value problem is justified when the disturbance of the uniform incoming stream due to the ship is in some sense small. Small disturbances may be justified by geometrical slenderness, slow forward translation, or a combination of the above. Full-shaped ships typically advance at low speed and cause a small steady wave disturbance. Fine-shaped ships, on the other hand, often advance at high Froude numbers. Yet the steady disturbances they generate, is small if their geometry is sufficiently thin or slender. Linearization may therefore be justified both at low and high Froude numbers  $F$ , as long as it is tied to the hull slenderness  $\epsilon$ . Linearization of the unsteady flow is also supported by the assumption of a small ambient wave amplitude.

The linearized free surface condition derived next is uniformly valid between these two limits, and its validity is



heuristically justified if the parameter  $\epsilon F^2$  is sufficiently small. The details of the derivation outlined below are given in Nakos (1990). The total flow field  $\Psi(\vec{x}, t)$  is decomposed into a basis flow  $\Phi(\vec{x})$ , assumed to be of  $O(1)$ , the steady wave flow  $\phi(\vec{x})$ , and the unsteady wave flow  $\psi(\vec{x}, t)$

$$\Psi(\vec{x}, t) = \Phi(\vec{x}) + \phi(\vec{x}) + \psi(\vec{x}, t) \quad (2.6)$$

The double-body flow is chosen as the basis flow, a selection primarily motivated by the body boundary condition as well as the simplifications it allows in the ensuing analysis. Thus,  $\Phi$  is subject to the rigid wall condition :

$$\Phi_z = 0, \quad \text{on } z = 0 \quad (2.7)$$

The wave disturbances  $\phi$  and  $\psi$  are superposed upon the double-body flow and are taken to be small relative to the  $\Phi$ . Linearization of (2.4-5), correct to leading order in  $\phi$  and  $\psi$ , leads to the conditions :

$$\left\{ \begin{array}{l} \nabla \Phi \cdot \nabla (\nabla \Phi \cdot \nabla \phi) + \frac{1}{2} \nabla (\nabla \Phi \cdot \nabla \Phi) \cdot \nabla \phi + g \phi_z - \\ - \Phi_{zz} (\nabla \Phi \cdot \nabla \phi) = -\frac{1}{2} \nabla (\nabla \Phi \cdot \nabla \Phi) \cdot \nabla \Phi - \\ - \frac{1}{2} (U^2 - \nabla \Phi \cdot \nabla \Phi) \Phi_{zz}, \quad \text{on } z = 0 \\ \zeta(x, y) = -\frac{1}{g} \left( \frac{1}{2} \nabla \Phi \cdot \nabla \Phi - \frac{1}{2} U^2 + \nabla \Phi \cdot \nabla \phi \right)_{z=0} \end{array} \right\} \quad (2.8)$$

$$\left\{ \begin{array}{l} \psi_{tt} + 2 \nabla \Phi \cdot \nabla \psi_t + \nabla \Phi \cdot \nabla (\nabla \Phi \cdot \nabla \psi) \\ + \frac{1}{2} \nabla (\nabla \Phi \cdot \nabla \Phi) \cdot \nabla \psi + g \psi_z - \\ - \Phi_{zz} (\psi_t + \nabla \Phi \cdot \nabla \psi) = 0, \quad \text{on } z = 0 \\ \zeta(x, y, t) = -\frac{1}{g} (\psi_t + \nabla \Phi \cdot \nabla \psi)_{z=0} \end{array} \right\} \quad (2.9)$$

for the steady and unsteady flows, respectively.

For slender/thin ships with  $\epsilon$  small, and for Froude numbers of  $O(1)$ , the uniform incident stream  $-Ux$  may be used as the basis flow. In this case, (2.8-9) reduce to the well-known Neumann-Kelvin conditions. In the opposite limit of bluff ships with  $\epsilon$  of  $O(1)$  advancing at low Froude numbers, (2.8-9) reduce to the conditions of slow-ship theory. The condition (2.8) contains all terms present in Dawson's (1977) condition, and it is closest to the one proposed by Eggers (1981). This property may explain the fact that, even though Dawson's and Egger's conditions have been derived as low Froude number approximations, they have been found to perform satisfactorily over a wider range of forward speeds.

#### Linearization of the body boundary condition

The linearization of the ship hull boundary condition may also be derived from the decomposition (2.6). By definition, the velocity potential of the double-body flow is

subject to

$$\frac{\partial \Phi}{\partial n} = 0, \quad \text{on } (\bar{B}) \quad (2.10)$$

Consequently, the steady wave flow also satisfies the homogeneous condition

$$\frac{\partial \phi}{\partial n} = 0, \quad \text{on } (\bar{B}), \quad (2.11)$$

leaving the right-hand-side of (2.8) as the only forcing of the steady wave problem.

The unsteady forcing due to the oscillatory motion of the vessel is accounted for by the unsteady wave flow  $\psi$ . If  $\vec{a}$  is the oscillatory displacement vector measured from the mean position of the vessel  $(\bar{B})$ , it follows by substituting of (2.6) in (2.2) that

$$\frac{\partial \psi}{\partial n} = \frac{\partial \vec{a}}{\partial t} \cdot \vec{n} - \nabla (\Phi + \phi) \cdot \vec{n}, \quad \text{on } (B) \quad (2.12)$$

Assuming that the magnitude of the displacement vector  $\vec{a}$  is small and comparable to the ambient wave amplitude, the boundary condition (2.12) may be linearized about the mean position of the hull surface [Timman and Newman(1962)],

$$\frac{\partial \psi}{\partial n} = \frac{\partial \vec{a}}{\partial t} \cdot \vec{n} - [(\vec{a} \cdot \nabla) \nabla \Phi + (\nabla \Phi \cdot \nabla) \vec{a}] \cdot \vec{n}, \quad \text{on } (\bar{B}) \quad (2.13)$$

The last term in (2.13) accounts for the interaction between the steady and unsteady disturbances in a manner consistent with the assumptions underlying the derivation of the free-surface conditions (2.8). An alternative form of (2.13) may be derived in terms of the rigid-body global displacements  $(\xi_1, \xi_2, \xi_3)$  and rotations  $(\xi_4, \xi_5, \xi_6)$ , along the axes  $(x, y, z)$  respectively,

$$\frac{\partial \psi}{\partial n} = \sum_{j=1}^6 \left( \frac{\partial \xi_j}{\partial t} n_j + \xi_j m_j \right), \quad \text{on } (\bar{B}), \quad (2.14)$$

where  $m_j, j = 1, \dots, 6$ , denote the so-called *m-terms* [Ogilvie and Tuck (1969)].

If the basis flow is approximated by the uniform stream the only non-zero *m-terms* are  $m_5 = Un_3$  and  $m_6 = -Un_2$ , which merely account for the 'angle of attack effect' due to yaw and pitch. This approximation of the *m-terms* has been employed in most previous studies of the ship motion problem, consistently with the linearization steps leading to the Neumann-Kelvin free surface boundary condition. The performance of this linearization in practice will be the subject of numerical experiments presented in section 7.

#### Frequency domain formulation of the unsteady problem

The unsteady excitation is due to an incident monochromatic wave train. The frequency of the incident wave, as viewed from the stationary frame is  $\omega_0$ , while in the translating frame of reference  $\vec{x}$ , the incident wave arrives at

the frequency of encounter  $\omega$ . If  $\beta$  is the angle between the phase velocity of the incident wave and the forward velocity of the ship,  $\omega$  is given by

$$\omega = |\omega_0 - U \frac{\omega_0^2}{g} \cos \beta| \quad (2.15)$$

In the frame  $\vec{x}$ , the velocity potential of the incident wave of unit amplitude, in deep water, is given by the real part of the complex potential  $\varphi_0$ :

$$\varphi_0(\vec{x}, t) = i \frac{g}{\omega_0} e^{\frac{\omega_0^2}{g}(z - ix \cos \beta - iy \sin \beta)} e^{i\omega t} \quad (2.16)$$

The linearity of the Boundary Value Problem that governs the physical system, along with the form of the body boundary condition (2.14), suggest the decomposition of the wave flow as follows,

$$\psi(\vec{x}, t) = \Re \left\{ e^{i\omega t} \left[ A(\varphi_0 + \varphi_7) + \sum_{j=1}^6 \xi_j \varphi_j \right] \right\} \quad (2.17)$$

where  $A$  is the amplitude of the incoming wave train,  $\varphi_7$  is the complex diffraction potential, and  $\varphi_j$ ,  $j = 1, \dots, 6$ , are the complex radiation potentials due to the harmonic oscillation of the ship in each of the six rigid-body degrees of freedom, at frequency  $\omega$  and with unit amplitude.

Upon substitution of the linear decomposition into (2.9), the free surface conditions for  $\varphi_j$ ,  $j = 1, \dots, 7$ , are derived. It is important to point out that the free surface condition for the diffraction problem is inhomogeneous, the forcing arising from the interaction of the incoming wave train with the double-body flow. In the limit of slender/thin ships, where the uniform stream may be taken as the basis flow, this inhomogeneity vanishes.

### 3. THE HYDRODYNAMIC FORCES

Given the solution of the potential flow problem formulated in the preceding section, the hydrodynamic pressure follows from Bernoulli's equation. Of particular interest, in practice, is the pressure distribution on the ship wetted surface and resultant forces and moments necessary for the determination of the ship motions.

The pressure on the hull is given by

$$p = -\rho \left[ \Psi_t + \frac{1}{2} \nabla \Psi \cdot \nabla \Psi - \frac{1}{2} U^2 + gz \right]_{\vec{x} \in (B)} \quad (3.1)$$

The unsteady portion of (3.1), correct to leading order in  $\psi$ , may be expressed as follows:

$$p = -\rho (\psi_t + \nabla \Phi \cdot \nabla \psi)_{\vec{x} \in (\bar{B})} - \rho \left[ (\vec{a} \cdot \nabla) \left( \frac{1}{2} \nabla \Phi \cdot \nabla \Phi + gz \right) \right]_{\vec{x} \in (\bar{B})} \quad (3.2)$$

Under the assumption of small monochromatic motions at the frequency of encounter  $\omega$ , the components of the unsteady force  $\vec{F} = (F_1, F_2, F_3)$  and moment  $\vec{M} = (F_4, F_5, F_6)$  acting on the ship, accept the familiar decomposition

$$F_i(t) = \Re \left\{ e^{i\omega t} \left[ AX_i + \sum_{j=1}^6 \xi_j (\omega^2 a_{ij} i\omega b_{ij} - c_{ij}) \right] \right\} \quad (3.4)$$

where,

$$X_i = -\rho \Re \left\{ \iint_{(\bar{B})} [i\omega(\varphi_0 + \varphi_7) + \nabla \Phi \cdot \nabla(\varphi_0 + \varphi_7)] n_i ds \right\}$$

$$a_{ij} = -\frac{\rho}{\omega^2} \Re \left\{ \iint_{(\bar{B})} (i\omega \varphi_j + \nabla \Phi \cdot \nabla \varphi_j) n_i ds \right\}$$

$$b_{ij} = \frac{\rho}{\omega} \Im \left\{ \iint_{(\bar{B})} (i\omega \varphi_j + \nabla \Phi \cdot \nabla \varphi_j) n_i ds \right\} \quad (3.5)$$

$$c_{ij} = \rho \iint_{(\bar{B})} (\vec{a} \cdot \nabla) \left( \frac{1}{2} \nabla \Phi \cdot \nabla \Phi + gz \right) n_i ds,$$

for  $i, j = 1, \dots, 6$ .

The exciting forces  $X_i$  and the added mass and damping coefficients,  $a_{ij}$  and  $b_{ij}$  are therefore functions of the forward speed and the frequency of oscillation  $\omega$ . The restoring coefficients  $c_{ij}$ , on the other hand, include the classical hydrostatic contribution augmented by a dynamic term due to the gradients of the double-body flow. The latter contribution depends linearly upon the deflection of the ship surface from its mean position and quadratically on the ship speed. It is therefore expected to be substantial at high Froude numbers.

The equations governing the time-harmonic responses of the ship follow from Newton's law. Using the definitions (3.5) of the forces acting on the hull, the familiar six-degree of freedom system of equations is obtained

$$\sum_{j=1}^6 [-\omega^2 (m_{ij} + a_{ij}) + i\omega b_{ij} + c_{ij}] \xi_j = X_i, \quad i = 1, \dots, 6, \quad (3.6)$$

where  $m_{ij}$  is the ship inertia matrix,  $\xi_j$  the complex amplitudes of the oscillatory ship displacements, and the restoring coefficients  $c_{ij}$  are modified to include the moments in pitch and roll due to the corresponding displacement of the center of gravity.

### 4. THE INTEGRAL FORMULATION

Green's second identity is applied for the unknown potentials,  $\Phi$ ,  $\phi$  or  $\varphi_j$ ,  $j = 1, \dots, 7$ , using the Rankine source potential,

$$G(\vec{x}; \vec{x}') = \frac{1}{2\pi} \frac{1}{|\vec{x} - \vec{x}'|} \quad (4.1)$$

as the Green function. The fluid domain is bounded by the hull surface  $(\bar{B})$ , the free surface  $(FS)$  and a cylindrical 'control' surface  $(S_\infty)$ . The resulting integral equation takes the form

$$\begin{aligned} \phi(\vec{x}) - \iint_{(FS)} \frac{\partial \phi(\vec{x}')}{\partial z'} G(\vec{x}; \vec{x}') d\vec{x}' + \iint_{(FS) \cup (\bar{B})} \phi(\vec{x}') \frac{\partial G(\vec{x}; \vec{x}')}{\partial n'} d\vec{x}' \\ = \iint_{(\bar{B})} \frac{\partial \phi(\vec{x}')}{\partial n'} G(\vec{x}; \vec{x}') d\vec{x}' \quad , \quad \vec{x} \in (FS) \cup (\bar{B}) \quad . \quad (4.2) \end{aligned}$$

where  $\phi$  stands for any of the potentials  $\Phi, \phi, \varphi_j$ ,  $j = 1, \dots, 7$ , introduced in the preceding sections. The surface integrals over the control surface  $(S_\infty)$  can be shown to vanish in the limit as  $(S_\infty)$  is removed to infinity with  $|\vec{x}|$  kept finite.

The derivatives of  $\Phi, \phi$  and  $\varphi_j$  normal to the ship surface  $(\bar{B})$  are known. The corresponding vertical derivative on the free surface  $(FS)$  is replaced by the appropriate combination of the value and tangential convective derivatives, according to the corresponding free surface condition.

Of particular interest is the treatment of the integral over the ship hull which accounts for the  $m$ -terms in the boundary condition (2.14). This is of the form :

$$\iint_{(\bar{B})} m_j G(\vec{x}; \vec{x}') d\vec{x}' \quad , \quad j = 1, \dots, 6 \quad . \quad (4.3)$$

The evaluation of the  $m$ -terms in (4.3) requires the computation of second order derivatives of the double-body potential  $\Phi$  on the ship hull. When it comes to the evaluation of gradients of the solution potential, low-order panel methods are known to be sensitive to discretization error, unless their implementation and panel distribution is carefully selected. The evaluation of double gradients of the solution are known to introduce serious difficulties, as illustrated by Nestegard (1984) and Zhao and Faltinsen (1989).

Here, an alternative expression for the evaluation of the integral (4.3) is derived by an application of Stokes' theorem. Given that the basis flow  $\Phi$  satisfies a zero flux condition on the ship hull and the  $z = 0$  plane, it follows that, for  $j = 1, \dots, 6$ ,

$$\iint_{(\bar{B})} m_j G(\vec{x}; \vec{x}') d\vec{x}' = - \iint_{(\bar{B})} [\nabla \Phi(\vec{x}') \cdot \nabla_{\vec{x}'} G(\vec{x}; \vec{x}')] n_j d\vec{x}' \quad (4.4)$$

The right-hand side of (4.4) involves only first derivatives of  $\Phi$  on the hull, consequently it is clearly superior from the computational standpoint.

The integral equation (4.2) will not accept unique solutions unless a radiation condition is imposed enforcing no waves upstream. In practice the solution domain of (4.2) on the  $z = 0$  plane will be truncated at a rectangular boundary located at some distance from the ship where appropriate 'end conditions' will be imposed enforcing the radiation condition. Due to the convective nature of the flow, the condition at the upstream boundary is the most critical and takes the form

$$\left( i\omega - U \frac{\partial}{\partial x} \right) \phi = \left( i\omega - U \frac{\partial}{\partial x} \right)^2 \phi = 0, \quad (4.5)$$

where  $\phi$  stands for either the steady or the unsteady wave disturbance. The origin and physical interpretation of these

two upstream conditions are discussed in detail in Sclavouno and Nakos (1988) for a two-dimensional steady flow, and are extended to time-harmonic flows in Nakos (1990). It is shown that both are necessary in order to ensure physically meaningful numerical solutions of the steady and unsteady problems. For  $\tau = \omega U/g > 1/4$  no wave disturbance is present upstream of the ship and the conditions (4.5) can be shown to enforce this property of the flow. For  $\tau < 1/4$  and with increasing Froude numbers, the amplitude of the waves upstream of the ship decreases relative to that of the trailing wave pattern and conditions (4.5) perform well if the truncation boundary is sufficiently removed from the ship. No conditions are necessary on the transverse and downstream truncation boundaries.

## 5. THE NUMERICAL SOLUTION ALGORITHM

The solution of integral equation (4.2) for the steady and unsteady flows is obtained using a Panel Method. The systematic methodology for the study of the numerical properties of Rankine Panel Methods for free surface flows developed in Sclavounos and Nakos (1988) led to the design of a bi-quadratic spline-collocation scheme of cubic order, zero numerical dissipation and capable to enforce accurately the radiation condition (4.5).

The boundary domain - including the ship hull and the free surface solution domain - is discretized by a collection of plane quadrilateral panels [see Figure 1]. The unknown velocity potential is approximated by the linear superposition of bi-quadratic spline basis functions  $B(\vec{x})$ , as follows

$$\phi(\vec{x}) \simeq \sum_j a_j B_j(\vec{x}) \quad , \quad (5.1)$$

where  $B_j$  is the basis function centered at the  $j$ 'th panel and  $a_j$  is the corresponding spline coefficient. By collocating the integral equation (4.2) at the panel centroids and enforcing the upstream condition (4.5), the discrete formulation follows in the form of a system of simultaneous linear equations for the coefficients  $a_j$ . The relation (5.1) provides a  $C^1$ -continuous representation of the velocity potential and may be differentiated to give the velocity field on the domain boundaries. The free surface elevation and hydrodynamic pressure are evaluated using the relations (2.8-9) and (3.1-2), respectively.

The error and stability analysis of the bi-quadratic spline scheme is presented in Nakos and Sclavounos (1990). It is based on the introduction of a discrete dispersion relation governing the wave propagation over the discretized free surface. Comparison of the continuous and discrete dispersion relations allows the rational definition of the consistency, order and stability properties of the numerical solution scheme. It is shown that the numerical dispersion is of  $O(h^3)$  where  $h$  is the typical panel size and that no numerical dissipation is present. Both are valuable properties for the computation of ship wave patterns which are not substantially distorted, damped or amplified by the numerical algorithm.

Essential for the performance of the method is a stability condition restricting the choice of the grid Froude number,  $F_h = U/\sqrt{gh_x}$  relative the panel aspect ratio,  $\alpha = h_x/h_y$ , where  $h_x, h_y$  are the panel dimensions in the streamwise

and transverse directions, respectively. This condition, derived and discussed in detail in Nakos and Sclavounos (1990), establishes 'stable' domains on the  $(F_h, \alpha)$  plane with boundaries dependent on the frequency of oscillation.

For a given a Froude number, a stable discretization for the highest frequency of oscillation is stable for all lowest frequencies. Therefore, no regridding of the ship hull and free surface is necessary for the solution of the time harmonic problem over a range of frequencies. The resulting complex linear system is solved by an accelerated block Gauss-Siedel iterative scheme which makes extensive use of out-of-core storage therefore permitting the use of discretizations with several thousand panels.

Experimental verification of the convergence of the solution algorithm has been established by comparing computations of 'elementary' flows around singularities and thin-struts with analytical solutions [Nakos and Sclavounos (1990) and Nakos (1990)]. The convergence of the hydrodynamic added-mass and damping coefficients is discussed in Section 7.

## 6. STEADY AND UNSTEADY SHIP WAVE PATTERNS

The forward-speed ship wave problems formulated in Section 2 have been solved for two hull forms using the numerical algorithm outlined in the preceding section. This section presents converged computations of the steady and time harmonic wave patterns around a Wigley and a Series-60 hull.

The Wigley model has parabolic sections and waterlines, a length-to-beam ratio  $L/B = 10$  and beam-to-draft ratio  $B/T = 1.6$ . The grid used for the solution of the steady problem consists of  $40 \times 10$  panels on half the hull, providing adequate resolution of the geometry, while the panels on the free surface are aligned with those on the hull and have a typical aspect ratio is  $\alpha = h_x/h_y = 1$ . The grid Froude number is  $F_h \approx 6.3 \cdot F$ , allowing an adequate resolution of the steady wave flow for Froude numbers as low as  $F = 0.20$  [see Nakos (1990)]. The free surface domain is truncated at a distance  $x_{up} = 0.2L$  upstream of the bow and one ship length downstream of the stern. The truncation in the transverse direction is selected at  $y_{out} = 0.75L$ , so that the entire wave sector is included in the computational domain. The total number of panels in the grid is 2020.

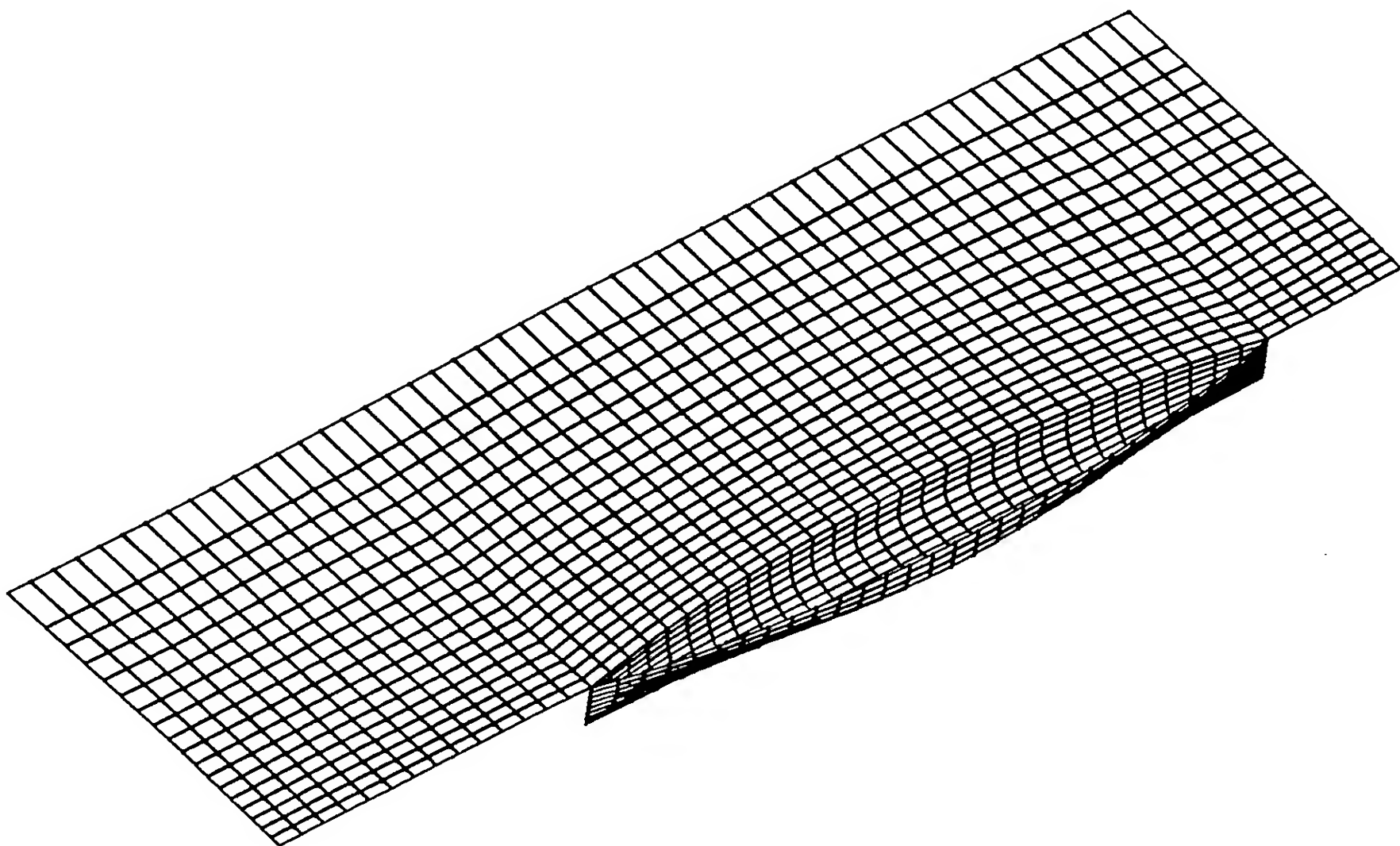


Figure 1 : Discretization of the free surface and the hull for a modified Wigley model, using 1110 panels on half the configuration.

Figure 2 shows contour plots of the wave patterns resulting from the steady forward translation of the Wigley model at  $F = 0.25, 0.35, 0.40$ . Predictions based on both the Neumann-Kelvin and the double-body linearizations are presented. Due to the slenderness of this Wigley model, the two wave fields agree well even at high speeds. Small differences are visible along the diverging portion of the wave system which originates from the stern, where the Neumann-Kelvin solution tends to generate steeper waves, particularly along the caustic. The opposite appears to be true in the 'bow wave system'. For all Froude numbers, the calculated wavelengths are not affected significantly by

the selected linearization.

The second ship tested is the Series-60- $C_b = 0.6$  hull which is significantly fuller than the Wigley model, with length-to-beam and beam-to-draft ratios  $L/B = 7.5$  and  $B/T = 2.5$ , respectively. The principal characteristics of the grid used for the computations are the same to those employed for the Wigley model.

Figure 3 illustrates the wave patterns around the Series-60 model for  $F = 0.20, 0.25, 0.35$ , respectively. At low speeds ( $F < 0.30$ ) the amplitude of the generated waves are comparable – if not smaller – than the ones computed

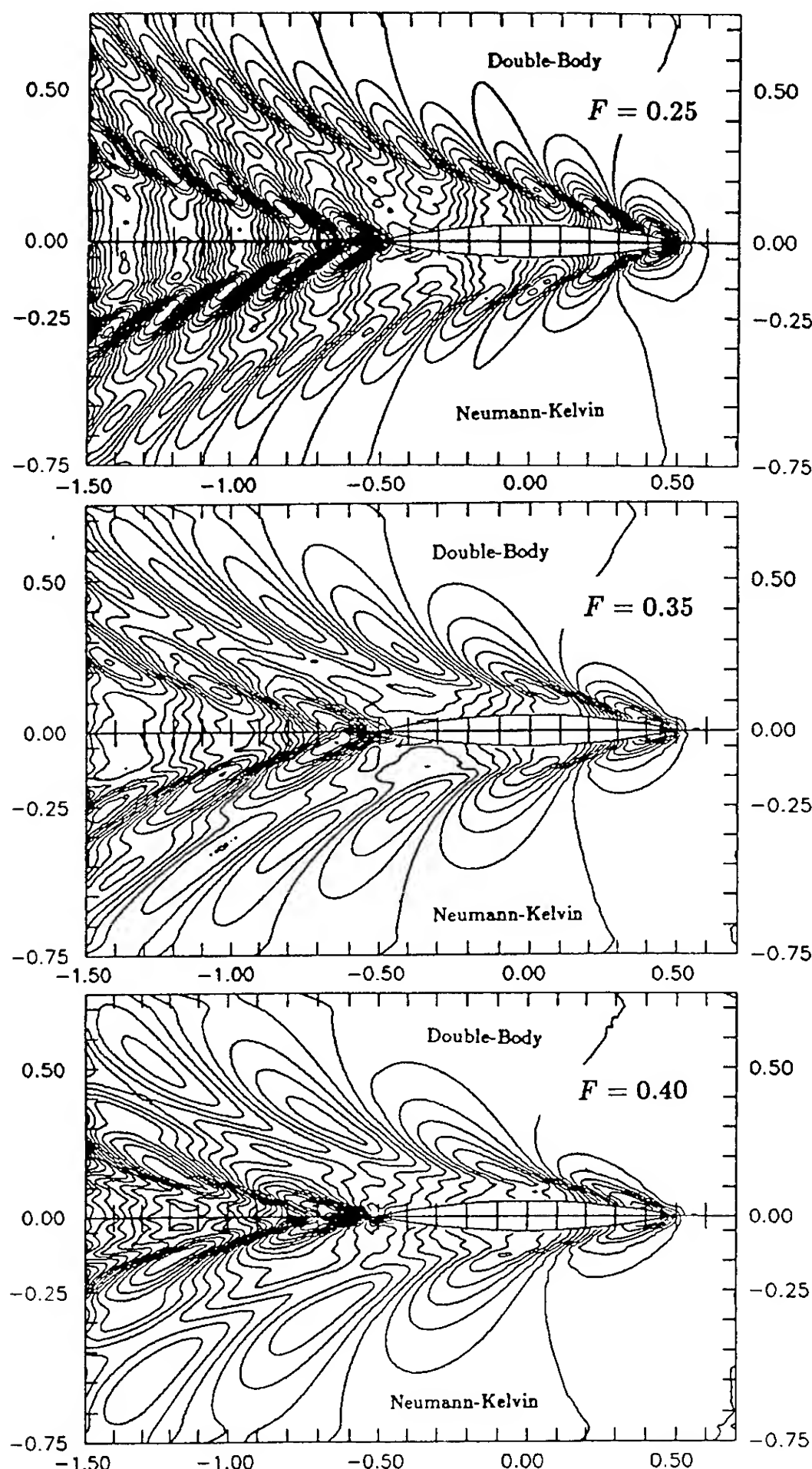


Figure 2 : Contour plots of the steady wave patterns due to the parabolic Wigley model advancing at Froude numbers  $F = 0.25, 0.35, 0.40$ .



around the Wigley model, despite the increase in the 'fullness' of the hull shape. For the Wigley model the bow- and stern-wave systems are well formed while the corresponding wave pattern around the Series-60 hull appears to be more 'confused'.

Differences between the steady wave pattern computations from the Neumann-Kelvin and double-body linearizations are here clearly noticeable. Again, significant discrepancies occur along the diverging portion of the stern-wave system, where the Neumann-Kelvin solution shows larger amplitudes and shorter wavelengths. Moreover, the caustic

lines originating from the bow and stern appear at a larger angle in the solution based on the double-body linearization. The differences between the two solutions become more pronounced as the speed increases, resulting in quite different wave patterns at  $F=0.35$  (see Figure 3c).

Figure 4 is a snapshot of the time-harmonic wave pattern around a modified Wigley model translating at  $F = 0.2$  and oscillating in heave at frequencies  $\omega\sqrt{L/g} = 3$  and  $\omega\sqrt{L/g} = 5$ . The grid used for this flow field has the same density as that in Figure 1. Both frequencies are over-critical ( $\tau = \omega U/g > 0.25$ ), thus two wave systems appear

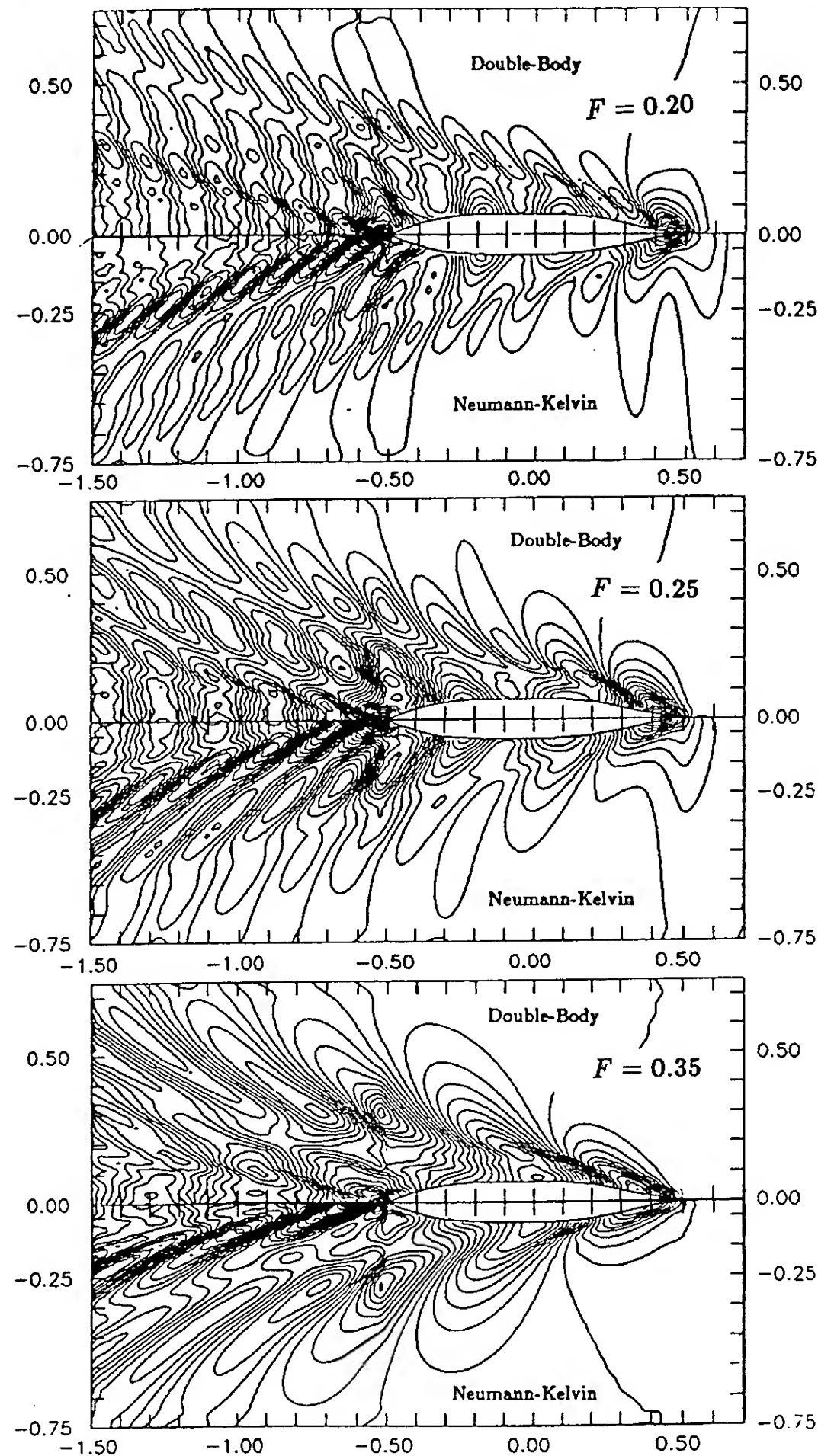


Figure 3 : Contour plots of the steady wave patterns due to the Series-60- $c_b=0.6$  vessel advancing at Froude numbers  $F=0.20, 0.25, 0.35$ .



downstream. At  $F = 0.3$ , the time-harmonic wave fields around the modified Wigley model are illustrated in Figure 5 and are obtained from the same grid as for  $F = 0.2$ . For this larger Froude number, the wavelengths appearing in Figure 5 are larger than their counterparts of Figure 4, although the general structure of the wave field is similar.

Figure 6 illustrates the wave patterns around the Series-60- $C_b = 0.7$  hull advancing at  $F = 0.2$  and heaving at frequencies  $\omega\sqrt{L/g} = 3$  and  $\omega\sqrt{L/g} = 4$ . Relative to the corresponding patterns generated by the Wigley hull, the diverging wave system originating from the stern is more pronounced and is attributed to the more three-dimensional shape of the Series-60 geometry. In all cases the steady wave pattern has been removed.

Certain common features of these three-dimensional time harmonic wave patterns are worth emphasizing. The shortest wavelength scales are associated with the transverse wave system which appears downstream of the stern and

propagates in the streamwise direction. Along the ship length, on the other hand, the wave field is dominated by relatively long divergent waves which propagate in the transverse direction and tend to become more two dimensional as the frequency increases. This character of the time harmonic wave pattern therefore appears to support the assumptions of slender-body theory. Near the ship hull the wave disturbance is convected primarily in the transverse direction and becomes more focused as the frequency increases. Its variation in the lengthwise direction is gradual since cancellation effects appear to significantly reduce the amplitude of the short transverse waves which are clearly visible downstream of the stern.

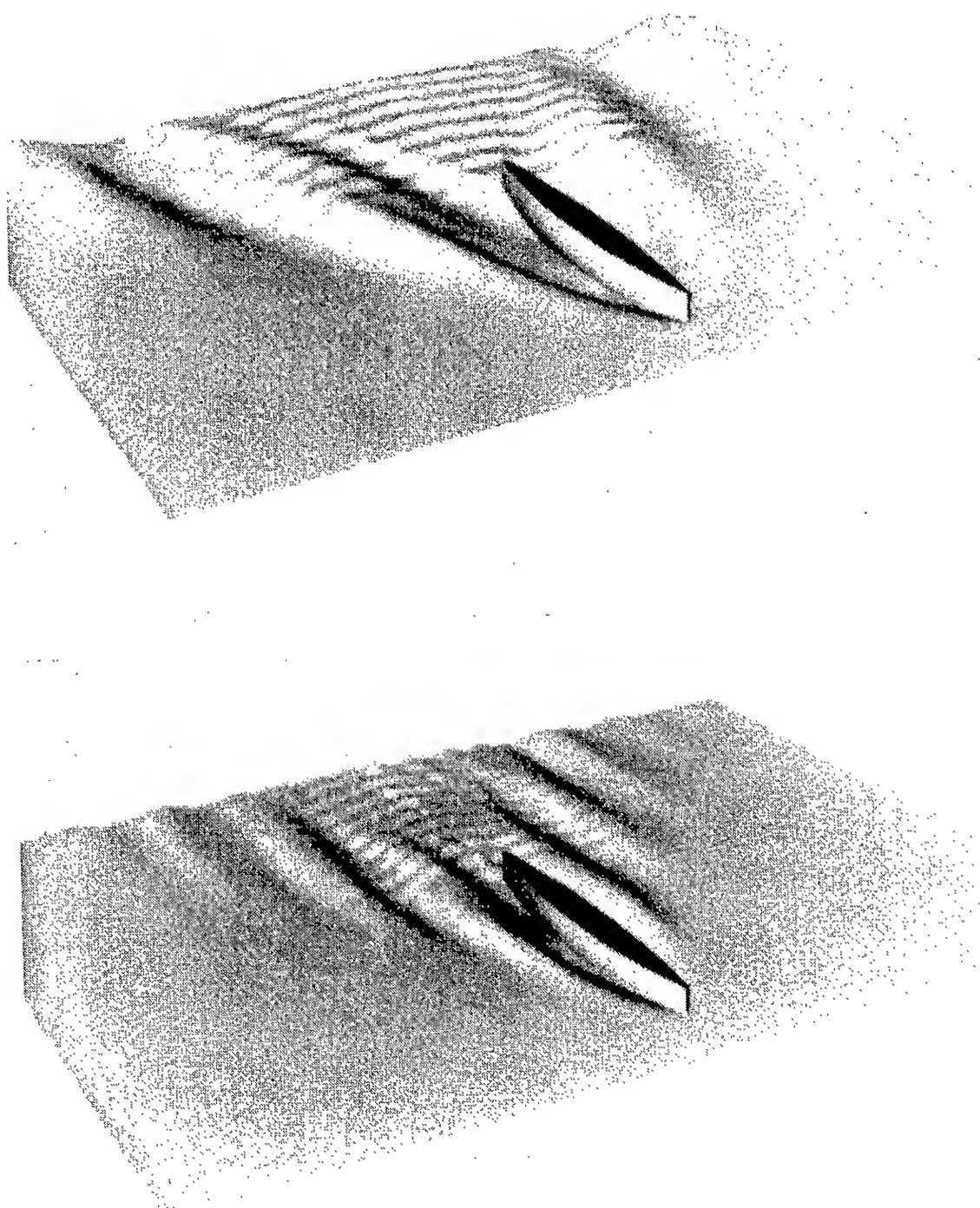


**Figure 4 :** Snapshots of the time-harmonic wave patterns due to a modified Wigley model advancing at  $F = 0.20$  while oscillating in heave at frequencies  $\omega\sqrt{L/g} = 3.0, 5.0$ .

## 7. HYDRODYNAMIC FORCES AND MOTIONS IN HEAD WAVES

The unsteady hydrodynamic pressure on the hull is evaluated from expression (3.2). The restoring component of the pressure which depends on the ship displacement and the gradients of the steady flow has been neglected since it been found to be small for the ship hulls and Froude numbers considered below. The gradients of the steady and time-harmonic potentials are obtained from the formal differentiation of the spline representation of the velocity potential (5.1). Integration of the pressure over the hull according to expressions (3.5), allows the determination of the added-mass, damping coefficients and exciting forces from expressions (3.5), and Response Amplitude Operators from the solution of the linear system (3.6). Only the coupled heave and pitch modes of motion in head waves are considered in this paper.

In order to establish the convergence of the solution algorithm, a systematic study of the effect of grid density on the computations of the hydrodynamic coefficients was carried out for a modified Wigley model with  $L/B = 10$  and  $B/T = 1.6$ . The time-harmonic wave flow was solved at a Froude number  $F = 0.3$  for several frequencies of oscillation in the range of practical interest  $\omega\sqrt{L/g} \in [2.5, 5.0]$ .

The free surface domain was truncated at a distance  $0.25L$  upstream of the bow,  $0.5L$  downstream of the stern and  $L$  in the transverse direction. Four different grids were considered, resulting in a systematic increase of the discretization density on both the free surface and the hull. These grids use 20, 30, 40 and 50 panels along the length of the hull, respectively, while for all of them the aspect ratio of the free surface panels is equal to 1.

Computations of the heave and pitch added-mass and damping coefficients obtained from these grids, are illustrated in Figure 7. The convergence rate is very satisfactory and

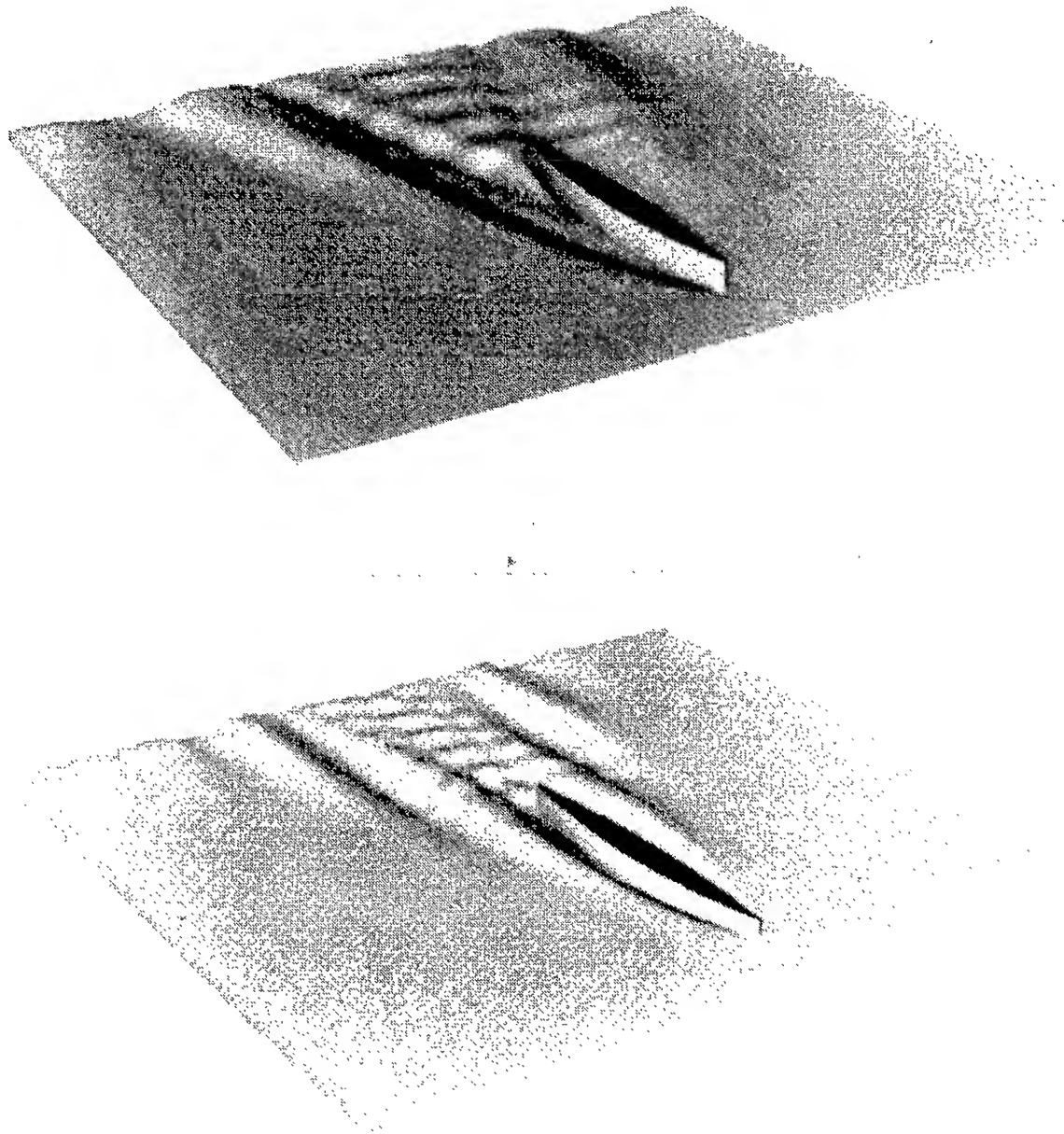


Figure 5 : Snapshots of the time-harmonic wave patterns due to a modified Wigley model advancing at  $F = 0.30$  while oscillating in heave at frequencies  $\omega\sqrt{L/g} = 3.0, 5.0$ .

appears not to depend strongly on the frequency.

Having established the convergence of the numerical algorithm, the hydrodynamic coefficients and ship motions are next compared to experimental measurements and strip theory. A systematic set of experiments for a modified Wigley hull were recently conducted by Gerritsma(1986). The diagonal heave and pitch added-mass and damping coefficients at  $F = 0.3$  are illustrated in Figure 8. The experimental measurements are compared to strip theory and the present method. The solid line, hereafter denoting results from SWAN (ShipWaveANalysis), is based on the double-body free-surface condition (2.9) and the complete treatment of the  $m$ -terms. The Neumann-Kelvin curve is obtained from the solution of the linearized problem using the present Rankine panel method and is obtained by approximating the steady flow by the uniform stream  $-Ux$  both in the free-surface and body boundary conditions.

The agreement between SWAN and experiments is quite satisfactory and represents an improvement over strip theory. For the diagonal coefficients, SWAN and the Neumann Kelvin problem are in good qualitative and quantitative agreement.

Significant differences between the three theoretical predictions occur in the heave and pitch cross-coupling coefficients illustrated in Figure 9. These coefficients are known to be sensitive to end-effects, therefore their accurate prediction requires the complete treatment of the  $m$ -terms which attain large values near the ship ends. This is confirmed by the very good agreement between SWAN and the experimental measurements. In spite of its three-dimensional character, the departure of the Neumann Kelvin solution from the experiments is mainly attributed to the incomplete treatment of the  $m$ -terms.

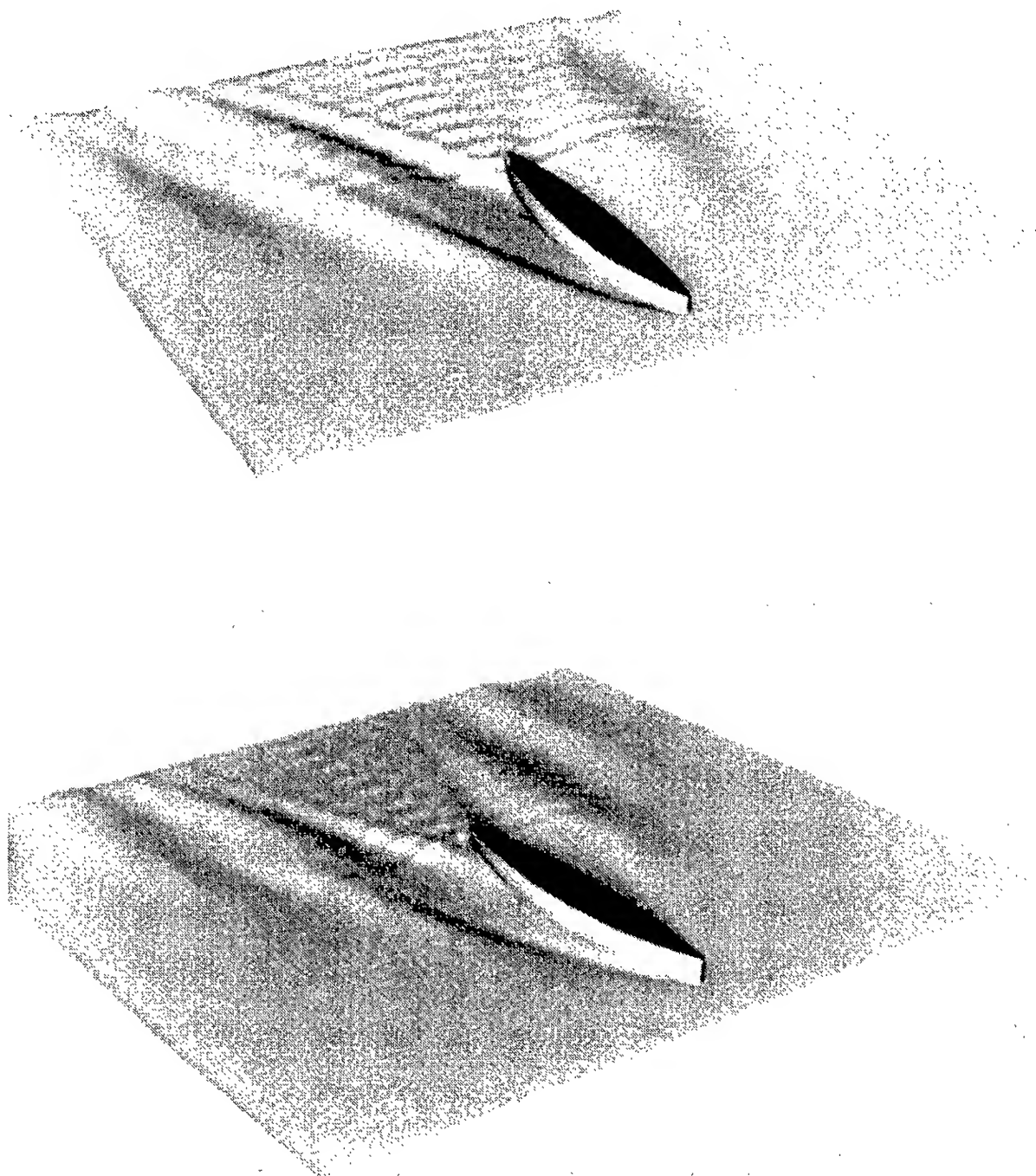


**Figure 6 :** Snapshots of the time-harmonic wave patterns due to the Series-60- $c_b = 0.7$  vessel advancing at  $F=0.20$  while oscillating in heave at frequencies  $\omega\sqrt{L/g}=3.0, 4.0$ .

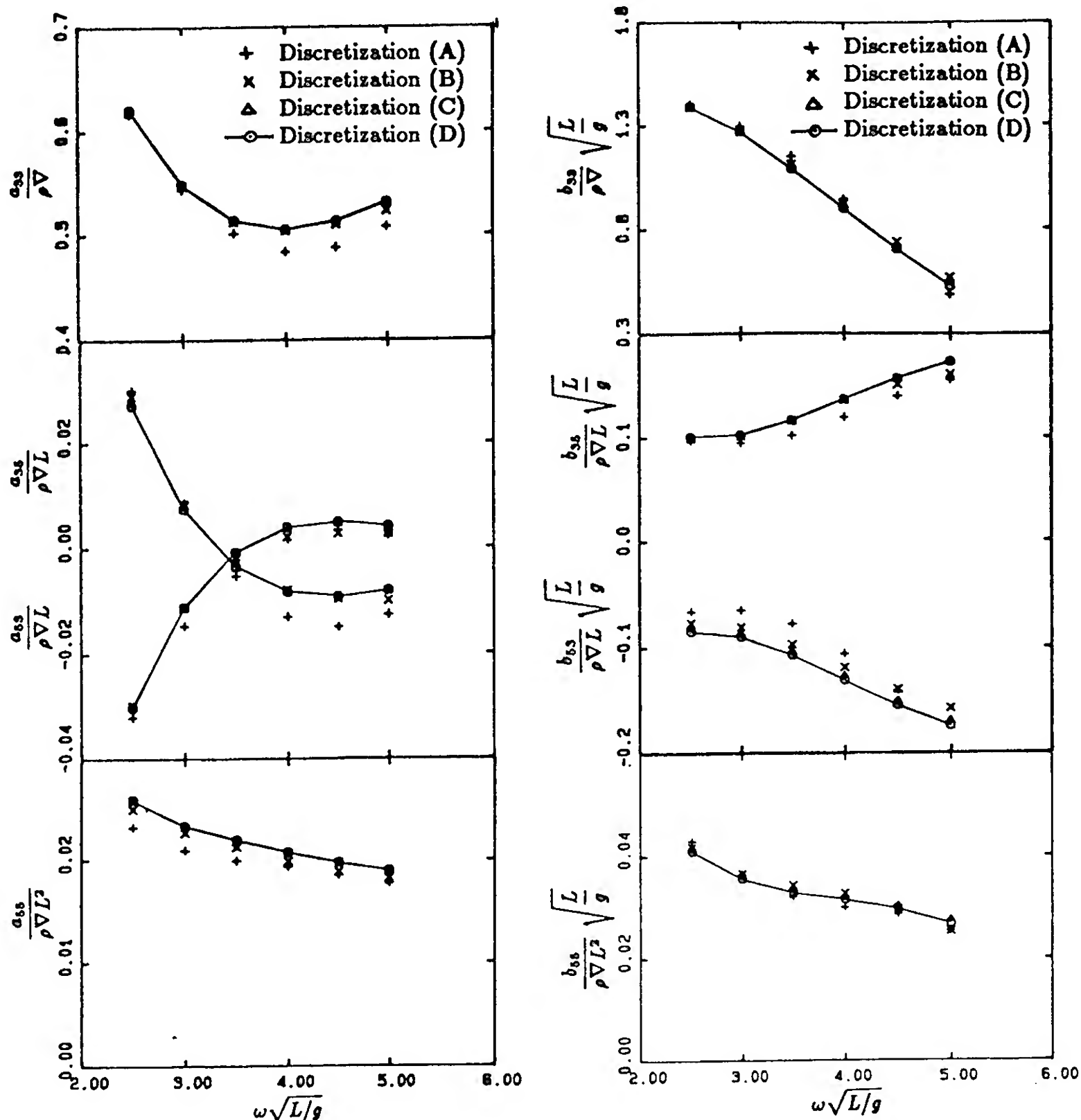


Figure 7 : Numerical convergence study for the heave and pitch hydrodynamic coefficients of a modified Wigley model advancing at  $F = 0.3$ .

Of interest is also the observed symmetry of the experimental measurements and the SWAN predictions of the cross-coupling coefficients. The modified Wigley hull is symmetric fore and aft and a generalization of the Timman-Newman symmetry relations appears to hold. The original Timman-Newman relations were shown to be exact for submerged vessels and the Neumann-Kelvin free-surface condition. It is here conjectured that they are also exactly valid for surface piercing vessels when the free-surface condition is based on the double-body flow. No proof has yet been attempted using the condition (2.9).

Figure 10 compares experimental measurements with the strip-theory and SWAN and predictions for the heave and pitch exciting-force and motion modulus and phase. The pitch radius of gyration of the modified Wigley hull is  $k_y = 0.25L$ , and the center of gravity is taken at  $x = y = z = 0$ . The agreement of SWAN with the experiments is in all cases very satisfactory. The strip-theory predictions have been obtained from the MIT 5-D Ship Motion program which is regarded a standard strip-theory code. The discrepancy between the strip-theory and experimental heave and pitch resonant frequencies, is attributed to the poor prediction of the  $b_{55}$  and the cross-coupling coefficients by strip theory (Figures 8 and 9).

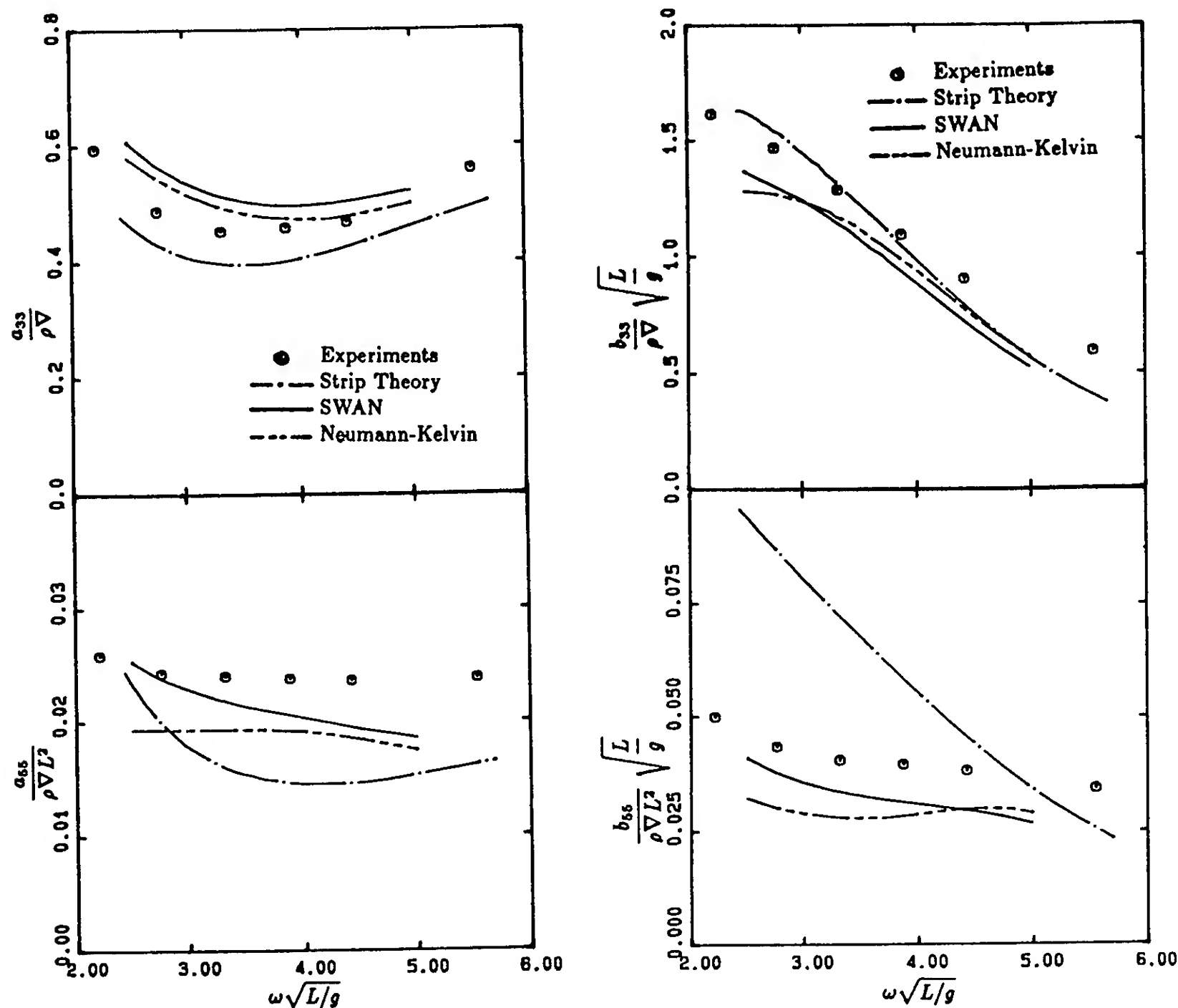


Figure 8 : Diagonal hydrodynamic coefficients in heave and pitch for a modified Wigley model advancing at Froude number  $F=0.3$ .

Figures 11 and 12 compare experiments with the strip theory and SWAN predictions of the heave and pitch added-mass and damping coefficients of the Series-60- $C_b = 0.7$  model, advancing at Froude number  $F=0.2$ . The experimental data are due to Gerritsma, Beukelman and Glansdorp (1974). The performance of SWAN is in all cases very satisfactory, offering a significant improvement over strip theory.

Due to the fore-aft asymmetry of the Series-60 model, the Timman-Newman relations for the cross-coupling coefficients do not hold. It is interesting, however, to notice that the curves corresponding to  $a_{35}$  and  $b_{35}$  are very close

to being mirror images of the those corresponding to  $a_{53}$  and  $a_{53}$ , respectively about a non-zero value. In strip theory, for example, it may be shown easily that  $a_{35} - a_{53}$  and  $b_{35} - b_{53}$  are symmetric about the corresponding coefficients at zero forward speed ( $F=0$ ), but no such proof is yet available in three dimensions.

The Series-60 heave and pitch motion amplitude and phase are shown in Figure 13. The agreement between theory and experiments is again satisfactory for both strip-theory and SWAN, with a slight detuning of the strip-theory predictions again attributed to its discrepancies with experiments in the cross-coupling coefficients and  $b_{55}$ .

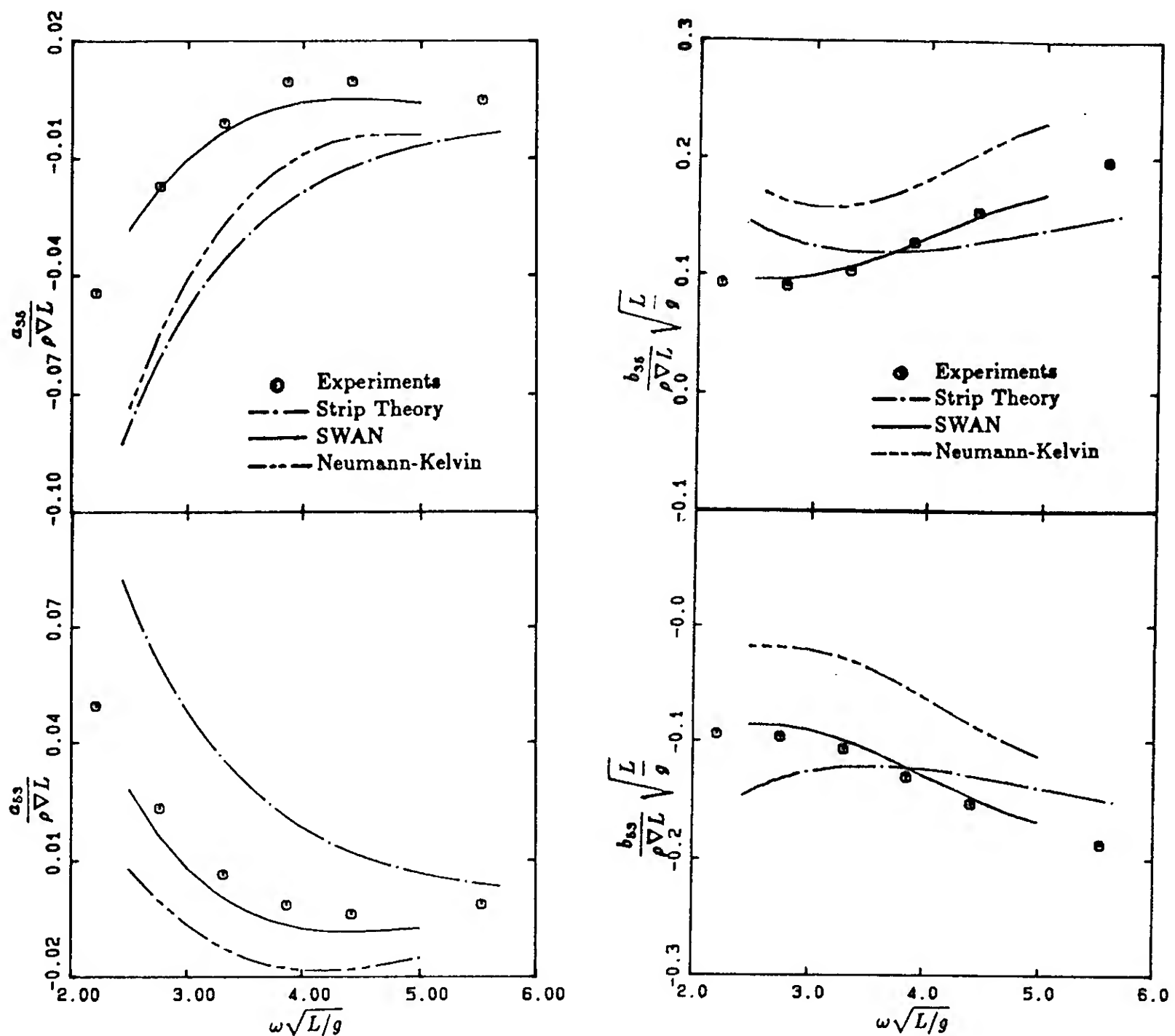


Figure 9 : Cross-coupling hydrodynamic coefficients between heave and pitch for a modified Wigley model advancing at Froude number  $F=0.3$ .

## 8. CONCLUSIONS AND FUTURE WORK

A new three-dimensional Rankine Panel Method method, referred to as SWAN, has been developed for the solution of the complete three-dimensional steady and time-harmonic ship-motion problem. Its principal attributes are:

- The use of a new free-surface condition based on the double-body flow and valid uniformly from low to high Froude numbers.
- The complete and accurate treatment of the  $m$ -terms.
- A high-order non-dissipative numerical algorithm for the enforcement of the free-surface and radiation conditions.



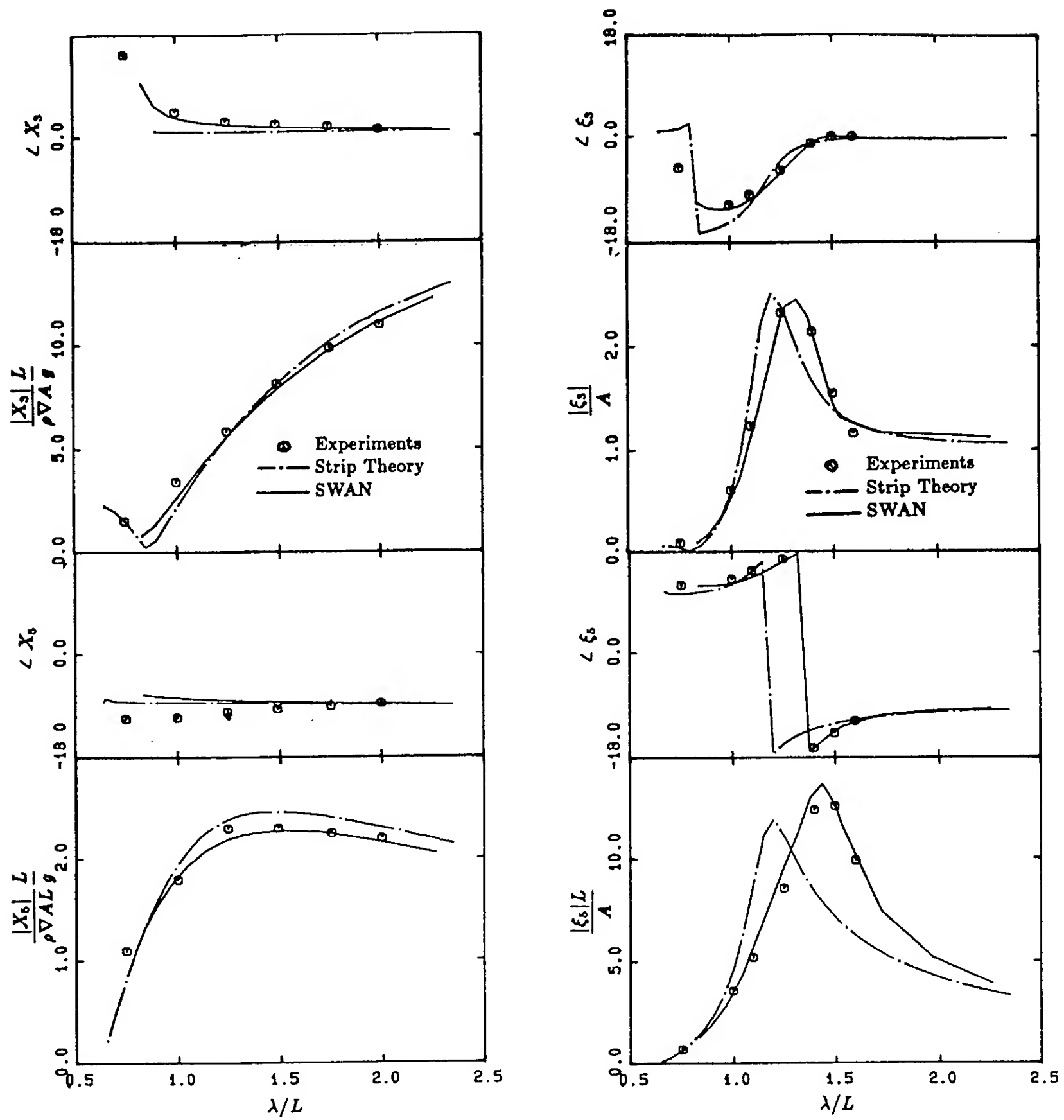


Figure 10 : Heave and pitch exciting forces and motions of a modified Wigley model advancing at Froude number  $F=0.3$  through regular head waves.

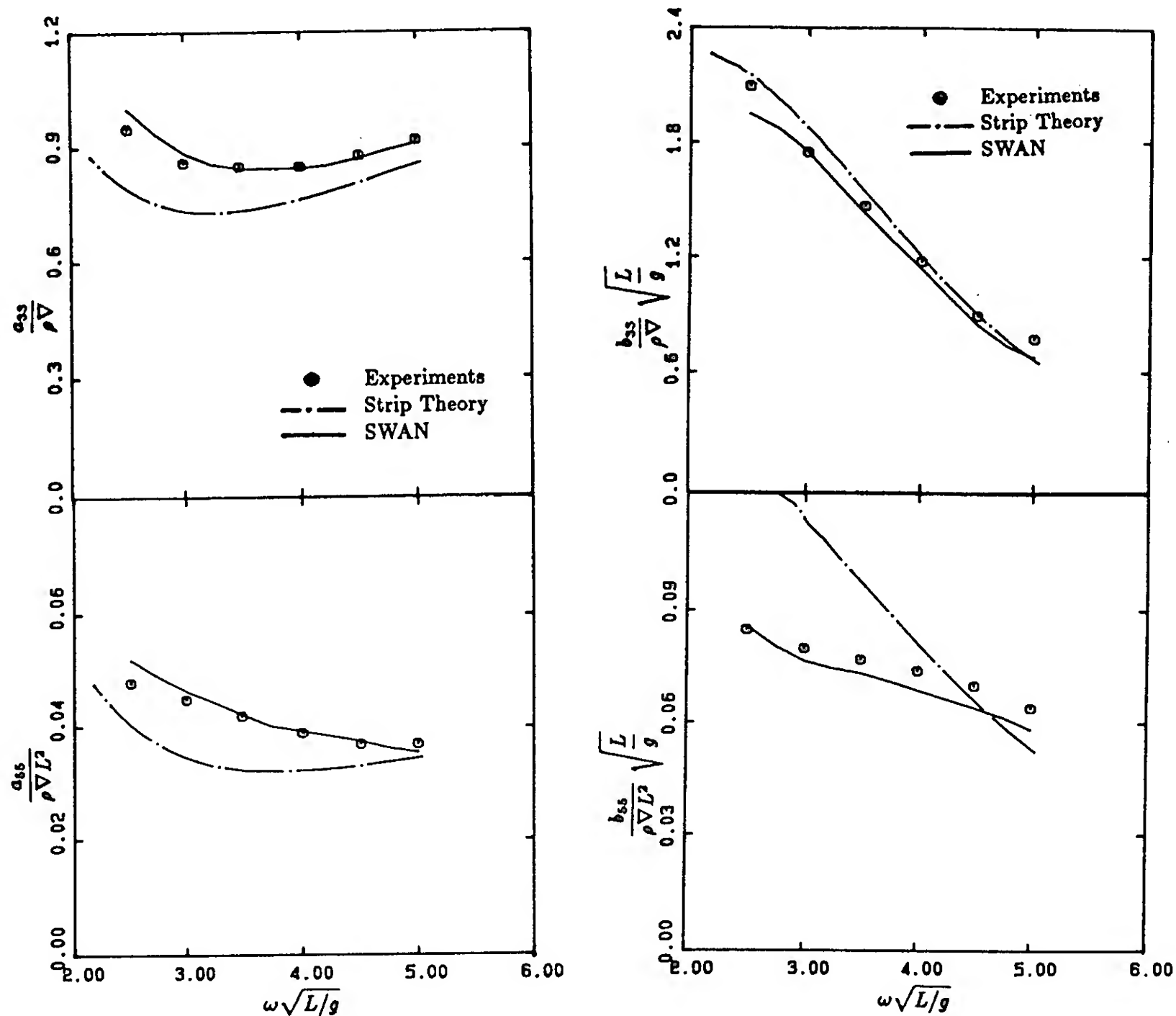


Figure 11 : Diagonal hydrodynamic coefficients in heave and pitch for the Series-60- $c_b=0.7$  vessel advancing at Froude number  $F=0.2$ .

Computations of steady and time-harmonic ship wave patterns illustrate the capability of the method to resolve considerable detail in the wave disturbance and at a significant downstream of the ship.

Predictions of the heave and pitch added-mass, damping coefficients, exciting forces and motions of a Wigley and the Series-60 hull are found to be in very good agreement with experiments and present a significant improvement over strip theory. A complete treatment of the  $m$ -terms

has been developed and found to be essential for the accurate prediction of the cross-coupling coefficients and ship motions.

In summary, all important features of the three-dimensional time-harmonic flow around the ship appear to be well predicted by the present method. This will permit the accurate prediction of the hydrodynamic pressure distribution, wave loads, derived responses and added-resistance by direct use of the velocity potential and its gradients on the ship hull and the free surface.

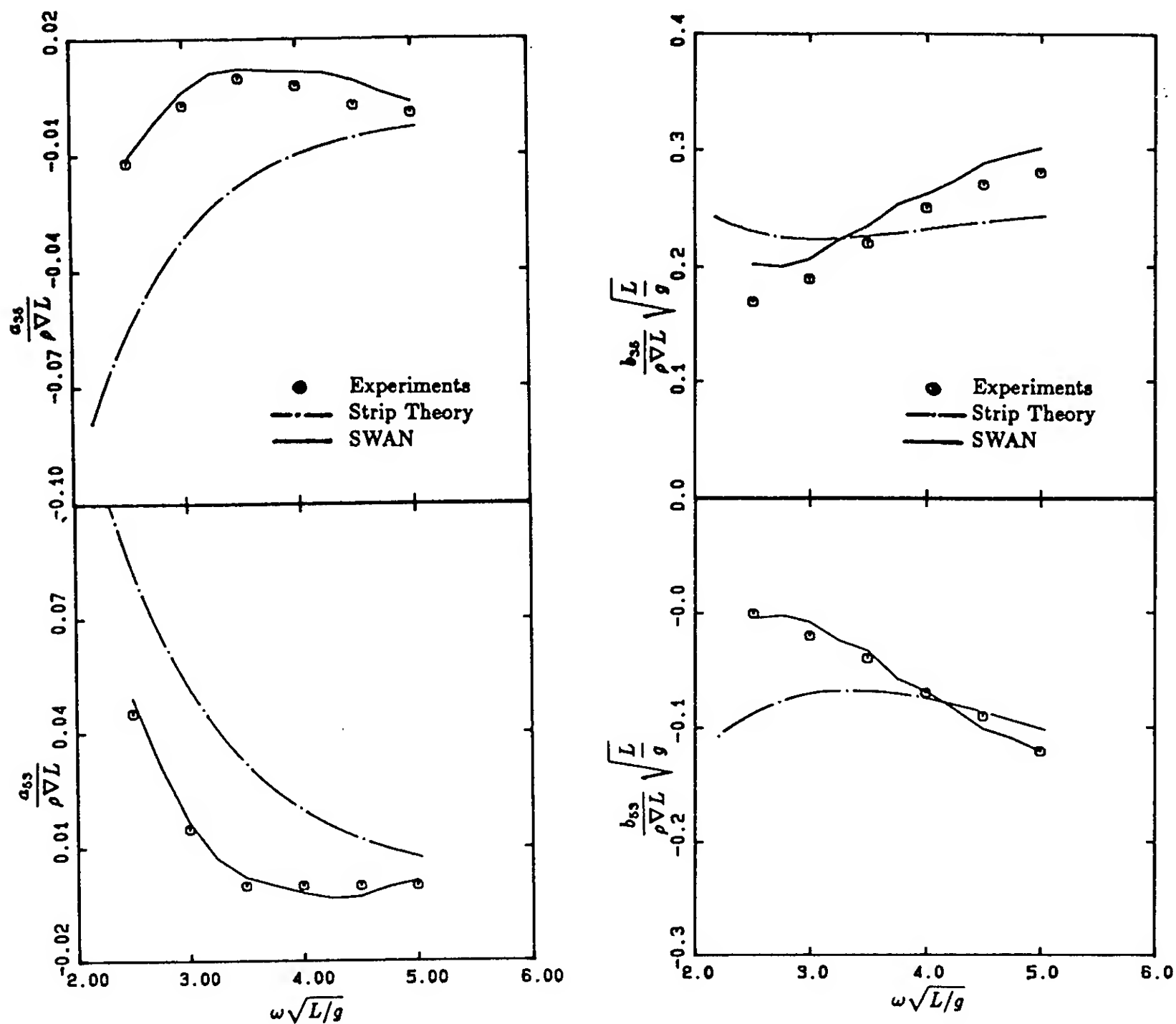


Figure 12 : Cross-coupling hydrodynamic coefficients between heave and pitch for the Series-60- $c_b=0.7$  vessel advancing at Froude number  $F=0.2$ .

Future research towards the further development of the present rankine panel method in the steady problem, will concentrate upon the determination of the ship wave spectrum from the available numerical data over the discretized portion of the free surface. This information is useful for the characterization of ships from their Kelvin wake and the accurate and robust evaluation of the wave resistance. The proper implementation of the present numerical scheme to hull forms with significant flare will also be studied in both the steady and time-harmonic problems.

The application is also planned of the same method to the prediction of the seakeeping properties of unconventional ship forms (e.g. SWATH ships and SES's) the hydrodynamic analysis of which is particularly amenable by the present three-dimensional panel method.

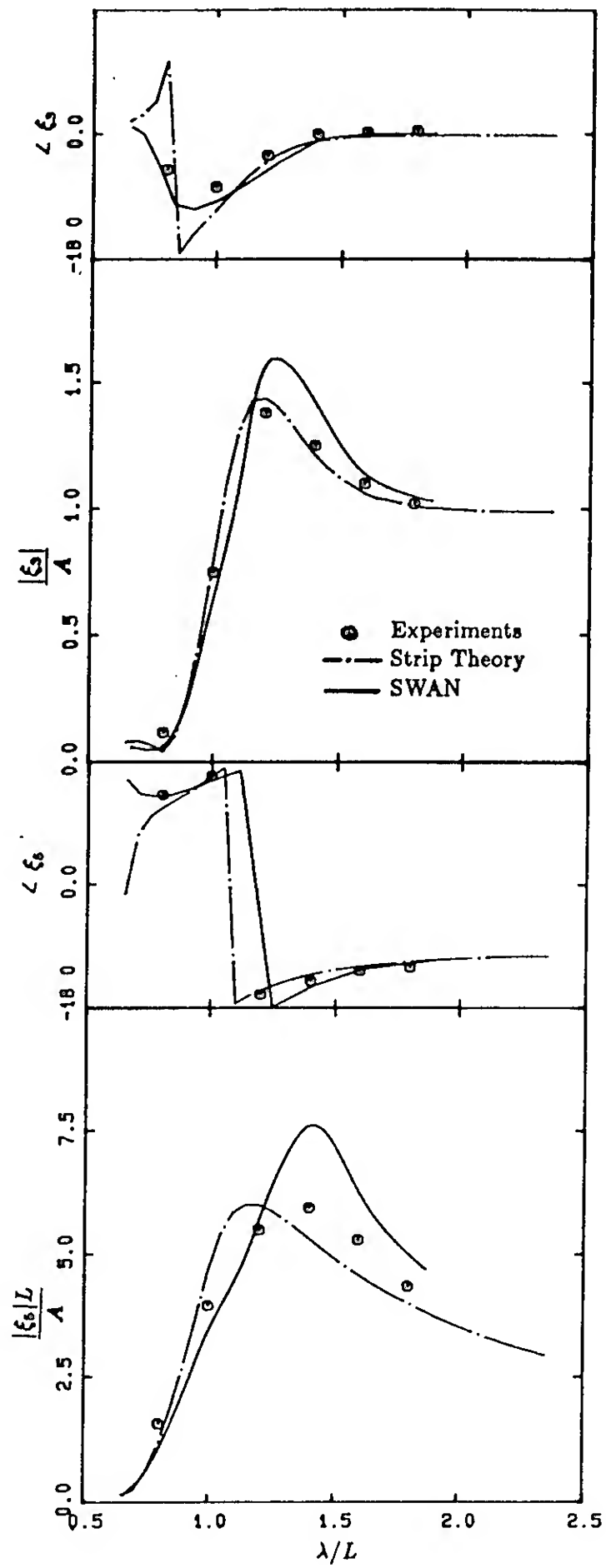


Figure 13 : Heave and pitch motions of the Series-60- $c_b=0.7$  vessel advancing at Froude number  $F=0.2$  through regular head waves.

## 9. ACKNOWLEDGEMENTS

This research has been supported by the Applied Hydromechanics Research Program administered by the Office of Naval Research and the David Taylor Research Center (Contract: N00167-86-K-0010) and by A. S. Veritas Research of Norway. The majority of the computations reported in this paper were carried out on the National Science Foundation Pittsburgh YMP Cray under the Grant OCE880003P. This award is greatly appreciated. We are also indebted to the Computer Aided Design Laboratory of the Department of Ocean Engineering at MIT for their assistance in the preparation of the time-harmonic ship wave patterns on their IRIS Workstation.

## REFERENCES

- Chang, M.-S., 1977, 'Computations of three-dimensional ship motions with forward speed', 2nd International Conference on Numerical Ship Hydrodynamics, USA.
- Dawson, C. W., 1977, 'A practical computer method for solving ship-wave problems', 2nd International Conference on Numerical Ship Hydrodynamics, USA.
- Eggers, K., 1981, 'Non-Kelvin Dispersive Waves around Non-Slender Ships', *Schiffstechnik*, Bd. 28.
- Faltinsen, O., 1971, 'Wave Forces on a Restrained Ship in Head-Sea Waves', Ph.D. Thesis, University of Michigan, USA.
- Gadd, G. E., 1976, 'A method of computing the flow and surface wave pattern around full forms', *Trans. Roy. Asst. Nav. Archit.*, Vol. 113, pg. 207.
- Gerritsma, J., 1986, 'Measurements of Hydrodynamic Forces and Motions for a modified Wigley Model', (unpublished).
- Gerritsma, J., Beukelman, W., and Glansdorp, C. C., 1974, 'The effects of beam on the hydrodynamic characteristics of ship hulls', 10th Symposium on Naval Hydrodynamics, USA.
- Guevel, P., and Bougis, J., 1982, 'Ship Motions with Forward Speed in Infinite Depth', *International Shipbuilding Progress*, No. 29, pp. 103-117.
- Inglis, R. B., and Price, W. G., 1981, 'A Three-Dimensional Ship Motion Theory - Comparison between Theoretical Predictions and Experimental Data of Hydrodynamic Coefficients with Forward Speed', *Transactions of the Royal Institution on Naval Architects*, Vol. 124, pp. 141-157.
- King, B. K., Beck, R. F., and Magee, A. R., 1988, 'Seakeeping Calculations with Forward Speed Using Time-Domain Analysis', 17th Symposium on Naval Hydrodynamics, The Netherlands.
- Korvin-Kroukovsky, B. V., 1955, 'Investigation of ship motions in regular waves', *Soc. Nav. Archit. Mar. Eng., Trans.* 63, pp. 386-435.
- Maruo, H., and Sasaki, N., 1974, 'On the Wave Pressure Acting on the Surface of an Elongated Body Fixed in Head Seas', *Journal of the Society of Naval Architects of Japan*, Vol. 136, pp. 34-42.
- Nakos, D. E., 1990, 'Ship Wave Patterns and Motions by a Three-Dimensional Rankine Panel Method', Ph.D. Thesis, Mass. Inst. of Technology, USA.
- Nakos, D. E., and Slavounos, P. D., 1990, 'Steady and Unsteady Ship Wave Patterns', *Journal of Fluid Mechanics*, Vol 215, pp. 265-288.
- Nestegard, A., 1984, 'End effects in the forward speed radiation problem for ships', Ph.D. Thesis, Mass. Inst. of Technology, USA.
- Newman, J. N., 1978, 'The theory of ship motions', *Advances in Applied Mechanics*, Vol. 18, pp. 221-283.
- Newman, J. N., and Slavounos, P. D., 1980, 'The Unified Theory of Ship Motions', 13th Symposium on Naval Hydrodynamics, Japan.
- O'Dea, J. F., and Jones, H. D., 1983, 'Absolute and relative motion measurements on a model of a high-speed container ship', Proceedings of the 20th ATTC, USA.
- Ogilvie, T. F., and Tuck, E. O., 1969, 'A rational Strip Theory for Ship Motions - Part 1', Report No. 013, Dept. of Naval Architecture and Marine Engineering, Univ. of Michigan, USA.
- Piers, W. J., 1983, 'Discretization schemes for the modelling of water surface effects in first-order panel methods for hydrodynamic applications', NLR report TR-83-093L, The Netherlands.
- Salvesen, N., Tuck, E. O., and Faltinsen, O., 1970, 'Ship motions and wave loads', *Soc. Nav. Archit. Mar. Eng., Trans* 78, pp. 250-287.
- Slavounos, P. D., 1984a, 'The Diffraction of Free-Surface Waves by a Slender Ship', *Journal of Ship Research*, Vol. 28, No. 1, pp. 29-47.
- Slavounos, P. D., 1984b, 'The unified slender-body theory : Ship motions in waves' 15th Symposium on Naval Hydrodynamics, Germany.
- Slavounos, P. D., and Nakos, D. E., 1988, 'Stability analysis of panel methods for free surface flows with forward speed', 17th Symposium on Naval Hydrodynamics, The Netherlands.
- Timman, R., and Newman, J. N., 1962, 'The coupled damping coefficients of symmetric ships', *Journal of Ship Research*, Vol. 5, No. 4, pp. 34-55.
- Yeung, R. W., and Kim, S. H., 1984, 'A New Development in the Theory of Oscillating and Translating Slender Ships', 15th Symposium on Naval Hydrodynamics, Germany.
- Zhao, R., and Faltinsen, O., 1989, 'A discussion of the m-terms in the wave-current-body interaction problem', 3rd International Workshop on Water Waves and Floating Bodies, Norway.

## DISCUSSION

William R. McCreight  
David Taylor Research Center, USA

Your predictions of added mass and damping for the Series 60 hull are better than those for the Wigley hull, yet the motion predictions are not as good. Could you describe the accuracy on the Series 60 exciting-force computations, which are not shown. If this does not account for the discrepancy, what do you believe is the cause of this?

## AUTHORS' REPLY

In response to Dr. McCreight's question we want to state that the calculation of the heave/pitch exciting forces typically compare very well with corresponding experimental data. Discrepancies between the numerical and experimental results for the motions of the Series-60 may be partly attributed to the speed dependent portion of the restoring force, which was not included in the presented calculations. Additional differences may also arise due to ambiguities about the appropriate values for the pitch moment of inertia and the vertical position of the center of gravity, as well as about the location of the point about which the heave/pitch motions are referenced.

## DISCUSSION

Hoyte Raven  
Maritime Research Institute Netherlands, The Netherlands

This paper is very interesting for me, in particular, as it addresses some points studied in my paper. I have a question on the steady wave resistance. You found differences in the remote wave pattern between the Kelvin and the show-ship condition. These may, however, be due to subtle changes in interference between wave components. Did you find any substantial difference in wave resistance? Secondly, as you noticed your free surface condition is intermediate in form between those of Dawson and Eggers, 1979. I have implemented your FSC in our code to make the same comparisons as in my paper, and found that the result was also intermediate for the Series 60  $C_b=0.60$  model: the predicted  $R_w$  is 6-8% lower than with Dawson's condition, while Eggers is 20% lower. For a full hull form, again the resistance is lower than Dawson, but better behaved than Egger's condition. Ref. Raven, H.C., "Adequacy of Free Surface Conditions for the Wave Resistance Problem," this volume.

## AUTHORS' REPLY

We would like to thank Dr. Raven for implementing and testing the free surface condition proposed in this paper. The differences of the wave patterns, as predicted by different free surface linearization models are indeed reflected on the corresponding wave resistance calculations. We strongly believe, however, that "numerical" evaluation of the relative performance of different linearization models is still clouded due to the delicate nature of the underlying calculations. The robustness of each scheme ought to be established individually before comparison arguments can be stated. We are currently working towards this direction by employing the conservation of momentum as the self-consistency criterion ([1]).

[1] Nakos, D.E., 1991, "Transverse Wave Cut Analysis by a Rankine Panel Method," 6th Int. Workshop on Water Waves and Floating Bodies, Woods Hole, MA, USA.



# Numerical Solutions for Large-Amplitude Ship Motions in the Time Domain

W.-M. Lin (Science Applications International Corporation, USA)

D. Yue (Massachusetts Institute of Technology, USA)

## ABSTRACT

A three-dimensional time domain approach is used to study the large-amplitude motions and loads of a ship in a seaway. In this approach, the exact body boundary condition is satisfied on the instantaneous wetted surface of the moving body while the free-surface boundary conditions are linearized. The problem is solved using a transient free-surface Green function source distribution on the submerged hull.

Extensive results are presented which validate and demonstrate the efficacy of the method. These results include linear and large-amplitude motion coefficients and diffraction forces with and without forward speed, calm-water resistance and added-resistance with waves and motions, the large-amplitude motion history of a ship advancing in an irregular seaway, as well as load distributions on the changing submerged hull. Most of the large-amplitude results we obtained are new and illustrate the importance of nonlinear effects associated with the changing wetted hull. Of special significance are the dramatic changes of the added mass, the steady resistance, and sinkage and trim forces as the motion amplitudes increase.

The present method is a major step forward in the development of design and prediction tools for ship motions and loads, and represents a significant milestone towards a *fully*-nonlinear capability in the foreseeable future.

## 1 INTRODUCTION

The accurate prediction of wave-induced motions and hydrodynamic loads is of crucial importance in ship design. In addition to concerns such as

efficiency and comfort, severe motions can limit operability and affect safety, while extreme loads may lead to structural failure. Thus the general problem of a moving body interacting with waves has been pursued actively since at least the time of Froude (1868) and Michell (1898).

Traditionally, the problem is linearized and formulated in the frequency domain, by assuming the motions to be small and time harmonic, and the resulting boundary-value problem is solved using a singularity distribution on the mean body boundary. For zero speed problems, this approach is quite successful and has become a standard tool for the design of large offshore structures (*e.g.*, Korsmeyer, *et al*, 1988). In the presence of forward speed, the so-called Neumann-Kelvin problem is significantly more difficult due primarily to the complexity of the corresponding Green function. Thus, despite several earlier attempts (*e.g.*, Chang, 1977; Inglis & Price, 1981; Guevel & Bougis, 1982), a truly satisfactory numerical solution is as yet unavailable. A promising variation due to Gadd (1976) and Dawson (1977) is the use of Rankine sources on the body surface as well as a portion of the free surface on which more general quasi-linearized free-surface conditions can be specified. Such approaches have been developed actively in the past 5 or 6 years (*e.g.*, Chang & Dean, 1986; Xia, 1986; Larsson, 1987; Boppe, *et al*, 1987; Jensen, *et al*, 1988; Letcher, *et al*, 1989; Bertram, 1990; Nakos & Sclavounos, 1990), with increasingly encouraging results. In all of these methods, however, the free surface and body geometry remain fixed in the undisturbed positions, and geometric nonlinearities are not included.

An alternative to the frequency-domain approach is to formulate the time-domain initial-value problem (*cf.*, Finkelstein, 1957; Cummins, 1962). The

requisite time-dependent Green function which satisfies the linearized free-surface boundary condition is simpler than the corresponding ones in the frequency domain, yet is capable of describing arbitrary (large-amplitude) motions when the proper free-surface memory effects are included. While linearized and even fully nonlinear time-domain results have been available for problems in two dimensions (or with vertical axisymmetry) for some time, developments for three-dimensional problems have been relatively recent. Such work include Korsmeyer (1988) for the linearized radiation problem without forward speed, and Liapis (1986), Beck & Liapis (1987), King (1987), King et al. (1988) for the general linearized problem with constant forward speed. For submerged bodies, results for linearized free surface but large body motions have been obtained by Ferrant (1988) and recently by Beck & Magee (1990). We remark that for *linearized* (small-amplitude) motions with zero or constant forward speed, these time-domain solutions are formally related to the frequency-domain results via Fourier transforms.

In this paper, we extend the time-domain approach to arbitrary large-amplitude motions of a surface-piercing body in a seaway. The exact body boundary condition is applied on the instantaneous submerged hull surface while a linearized free-surface condition is used. This approximation can be justified in principle upon the assumptions of small incident wave slopes and slenderness of the body geometry in the directions of the (large-amplitude) motions. The practical utility of this approach must, in the final analysis, be demonstrated by the validity and accuracy of its predictions. This is the focus of much of the present work.

In a boundary-element approach, the submerged body surface at each time step is divided into a number of panels over which linearized transient free-surface sources are distributed. In contrast to earlier work, the problem is formulated in a coordinate system fixed in space. This is clearly necessary for the case of *arbitrary* large-amplitude motions and excursions which is the primary objective of the present code. Under this formulation, a general and concise waterline integral term can be derived to account for arbitrary translations and distortions of the body waterplane, and the diffraction problem can be included straightforwardly by adding the incident wave contribution to the body boundary condition. For gen-

eral nonlinear calculations, the position and orientation of the body is updated (by solving the equations of motion or as prescribed) and the underwater body surface is repanelized at each time step. Since the body boundary condition is satisfied on the exact instantaneous hull, the so called "*m-term*" effects associated with forward speed (Ogilvie & Tuck, 1969) are automatically and *exactly* included. For the special case of constant forward speed and small oscillatory motions (the linearized seakeeping problem), the traditional linearization (and decoupling) of the latter is, however, less explicit in the earth-fixed (time-domain) formulation. For these linear forward-speed calculations, the quadratic terms are included in the force calculations to account for the forward-speed couplings but the *m*-terms are otherwise neglected in the body boundary conditions.

Linear and large-amplitude computational results are presented for a floating sphere, two Wigley hulls, and the Series 60 ( $C_B = 0.7$ ) hull undergoing free or captive motions and with or without forward speed or incident seas. The program is applicable for general six-degree-of-freedom motions (without lift) but we restrict ourselves to vertical plane motions in head seas in this paper. For the linear problems without forward speed, (time) impulse response functions are computed from which the requisite motion coefficients are obtained via Fourier transforms. For the nonlinear cases and for problems with forward speed, the bodies are started from rest and computations typically continued until steady states (limit cycles) are achieved. Where available, the results are compared with other time- and frequency-domain calculations and experimental data. In all cases, the importance of the nonlinear effects due to geometry variation is identified.

## 2 MATHEMATICAL FORMULATION

We consider a general three-dimensional body floating on a free surface and undergoing arbitrary six-degree-of-freedom motion in the presence of incident waves. An earth-fixed Cartesian coordinate system is chosen with the  $x$ - $y$  plane coincident with the quiescent free surface, and  $z$  is positive upward. The fluid is assumed to be homogeneous, incompressible, inviscid and its motion irrotational. Surface tension is not included and the water depth is infinite.

The fluid motions can be described by a velocity potential

$$\Phi_T(\vec{x}, t) = \Phi_I(\vec{x}, t) + \Phi(\vec{x}, t), \quad (1)$$

where  $\Phi_I$  is the incident wave potential,  $\Phi = \Phi_T - \Phi_I$  the total disturbance potential,  $t$  is time, and  $\vec{x}$  is the position vector. In the fluid domain  $\mathcal{V}(t)$ ,  $\Phi$  satisfies Laplace's equation

$$\nabla^2 \Phi = 0. \quad (2)$$

On the mean free surface  $\mathcal{F}(t)$ , we impose the linearized condition

$$\Phi_{tt} + g\Phi_z = 0 \quad \text{on } \mathcal{F}(t), \quad t > 0, \quad (3)$$

where  $g$  is the acceleration due to gravity. On the *instantaneous* body boundary  $\mathcal{B}(t)$ , we require no normal flux:

$$\frac{\partial \Phi}{\partial n} = V_n - \frac{\partial \Phi_I}{\partial n} \quad \text{on } \mathcal{B}(t), \quad t > 0, \quad (4)$$

where the unit normal vector to the body  $\vec{n}$  is positive out of the fluid and  $V_n$  is the instantaneous body velocity in the normal direction. For finite time, the conditions at infinity,  $\mathcal{S}_\infty$ , are

$$\Phi, \Phi_t \rightarrow 0 \quad \text{on } \mathcal{S}_\infty, \quad t > 0, \quad (5)$$

and the initial conditions at  $t = 0$  are

$$\Phi = \Phi_t = 0 \quad \text{on } \mathcal{F}(t), \quad t = 0. \quad (6)$$

We introduce the transient free-surface Green function for a step-function source below the free surface (see, *e.g.*, Stoker, 1957):

$$G(P, t; Q, \tau) = G^0 + G^f = \frac{1}{r} - \frac{1}{r'} + 2 \int_0^\infty [1 - \cos(\sqrt{gk}(t - \tau))] e^{k(z+\zeta)} J_0(kR) dk$$

for  $P \neq Q, t \geq \tau$ , (7)

where  $P = (x, y, z)$  and  $Q = (\xi, \eta, \zeta)$  are the source and field points,  $r = |P - Q|$ ,  $r' = |P - Q'|$ ,  $Q' = (\xi, \eta, -\zeta)$ ,  $R^2 = (x - \xi)^2 + (y - \eta)^2$ ,  $G^0 = 1/r - 1/r'$  is the Rankine part of the Green function,  $G^f = G - G^0$  is the free-surface memory part, and  $J_0$  Bessel function of order zero. Eq. (7) satisfies the following initial-boundary-value problem:

$$\begin{aligned} \nabla^2 G &= 0 & \text{in } \mathcal{V}(t), & \quad t > \tau \\ G_{tt} + gG_z &= 0 & \text{on } \mathcal{F}(t), & \quad t > \tau \\ G, G_t &\rightarrow 0 & \text{for } t > \tau \\ G = G_t &= 0 & \text{on } \mathcal{F}(t), & \quad t = \tau. \end{aligned}$$

Note that  $G_\tau^0 = 0$ , so that

$$G_\tau = G_\tau^f = -2 \int_0^\infty \sqrt{gk} \sin(\sqrt{gk}(t - \tau)) e^{k(z+\zeta)} J_0(kR) dk. \quad (8)$$

To obtain a boundary integral formulation for  $\Phi$ , we apply Green's identity to  $\Phi(Q, \tau)$  and  $G_\tau(P, t; Q, \tau)$  in a fluid domain  $\bar{\mathcal{V}}(\tau)$  bounded by  $\bar{\mathcal{F}}(\tau)$ ,  $\bar{\mathcal{B}}(\tau)$ ,  $\mathcal{S}_\infty$ , and a small surface  $\mathcal{S}_P$  excluding point  $P$ :

$$\begin{aligned} & \iiint_{\bar{\mathcal{V}}(\tau)} (\Phi \nabla_Q^2 G_\tau - G_\tau \nabla_Q^2 \Phi) dV \\ &= \iint_{\mathcal{S}_\infty + \bar{\mathcal{F}}(\tau) + \bar{\mathcal{B}}(\tau) + \mathcal{S}_P} (\Phi G_{\tau n_Q} - G_\tau \Phi_{n_Q}) dS, \quad (9) \end{aligned}$$

where  $\bar{\mathcal{V}}(\tau)$ ,  $\bar{\mathcal{F}}(\tau)$ ,  $\bar{\mathcal{B}}(\tau)$  are respectively  $\mathcal{V}(\tau)$ ,  $\mathcal{F}(\tau)$ ,  $\mathcal{B}(\tau)$  with the exclusion of possible point  $P$ .

The left-hand side of (9) and the integrals over  $\mathcal{S}_\infty$  and  $\mathcal{S}_P$  on the right-hand side are all zero. Integrating the resulting equation with respect to  $\tau$  from 0 to  $t$ , we obtain

$$\int_0^t d\tau \iint_{\bar{\mathcal{F}}(\tau) + \bar{\mathcal{B}}(\tau)} (\Phi G_{\tau n_Q} - G_\tau \Phi_{n_Q}) dS = 0. \quad (10)$$

To eliminate the integral over  $\bar{\mathcal{F}}(\tau)$ , it is necessary to exchange the time and surface integrals involving  $\bar{\mathcal{F}}(\tau)$ . It should be noted that  $\bar{\mathcal{F}}(\tau)$  is time-dependent in the earth-fixed coordinate system. Applying the linearized free-surface condition (3) and the transport theorem we obtain finally.

$$\begin{aligned} & \iint_{\bar{\mathcal{F}}(\tau)} (\Phi G_{\tau n_Q} - G_\tau \Phi_{n_Q}) dS \\ &= -\frac{1}{g} \left\{ \frac{\partial}{\partial \tau} \iint_{\bar{\mathcal{F}}(\tau)} (\Phi G_{\tau\tau} - G_\tau \Phi_\tau) dS \right. \\ & \quad \left. - \int_{\bar{\Gamma}(\tau)} (\Phi G_{\tau\tau} - G_\tau \Phi_\tau) V_N dL \right\}, \quad (11) \end{aligned}$$

where  $\bar{\Gamma}(\tau)$  is the instantaneous intersection of the body with the free surface (excluding possible point  $P$ ),  $\vec{N}$  the unit normal to  $\bar{\Gamma}(\tau)$  on the free surface, positive out of the fluid domain, and  $V_N$  the normal velocity of  $\bar{\Gamma}(\tau)$  in the  $\vec{N}$  direction.

Combining (10) and (11) and applying the free surface condition on  $G$  and the initial conditions on  $\Phi$ , we obtain

$$\iint_{\bar{\mathcal{F}}(t)} \Phi G_\zeta^0 dS + \int_0^t d\tau \iint_{\bar{\mathcal{B}}(\tau)} (\Phi G_{\tau n_Q} - G_\tau \Phi_{n_Q}) dS$$

$$+ \frac{1}{g} \int_0^t d\tau \int_{\bar{\Gamma}(\tau)} (\Phi G_{\tau\tau} - G_{\tau} \Phi_{\tau}) V_N dL = 0. \quad (12)$$

The integral over the free surface  $\bar{\mathcal{F}}(\tau)$  can now be eliminated by applying Green's identity again to  $\Phi(Q, t)$  and  $G^0$  in  $\bar{V}(t)$  and combining the result with (12). Finally, we have for  $P$  on  $B(t)$ :

$$\begin{aligned} 2\pi\Phi(P, t) + \iint_{B(t)} (\Phi G_{n_Q}^0 - \Phi_{n_Q} G^0) dS \\ = \int_0^t d\tau \left\{ \iint_{B(\tau)} (\Phi G_{\tau n_Q}^f - \Phi_{n_Q} G_{\tau}^f) dS \right. \\ \left. + \frac{1}{g} \int_{\Gamma(\tau)} (\Phi G_{\tau\tau}^f - \Phi_{\tau} G_{\tau}^f) V_N dL \right\}. \quad (13) \end{aligned}$$

The overhead bars on the integration surfaces are dropped since the integration over  $S_P$  on these surfaces gives no contribution. The waterline memory integral over  $\Gamma(\tau)$  in (13) is the general form for arbitrary large motions in the earth-fixed coordinate system. For a submerged body, this term vanishes. For the special case of horizontal planar motions only, this integral reduces to a similar term formulated in a body-fixed coordinate system given by Liapis (1986).

For large-amplitude problems, the evaluation of the tangential velocities on the body is of critical importance, and, in the absence of lift, a source formulation is preferred. To obtain the equation for the source distribution, we formulate the interior problem governed by an equation similar to (13), which upon combining with (13) yields

$$\begin{aligned} \Phi(P, t) = -\frac{1}{4\pi} \left\{ \iint_{B(t)} (\sigma G^0 dS + \int_0^t d\tau \right. \\ \left. \left[ \iint_{B(\tau)} \sigma G_t^f dS - \frac{1}{g} \int_{\Gamma(\tau)} \sigma G_t^f V_N V_n dL \right] \right\} \quad (14) \end{aligned}$$

where  $\sigma(Q, \tau)$  is the source strength at point  $Q$  at time  $\tau$ , and  $V_N$  and  $V_n$  are related by  $V_N = V_n / \bar{N} \cdot \bar{n}$ .

Finally, we apply the body boundary condition for  $P$  on  $B(t)$  to obtain:

$$\begin{aligned} \frac{\partial \Phi}{\partial n_P} = V_n(P, t) - \nabla \Phi_I(P, t) \cdot \bar{n}_P \\ = -\frac{1}{4\pi} \left\{ \iint_{B(t)} \sigma G_{n_P}^0 dS + \int_0^t d\tau \right. \\ \left. + \left[ \iint_{B(\tau)} \sigma G_{n_P t}^f dS - \frac{1}{g} \int_{\Gamma(\tau)} \sigma G_{n_P t}^f V_N V_n dL \right] \right\}. \quad (15) \end{aligned}$$

Eq.(15) can be solved for the unknown  $\sigma(P, t)$  given  $B(t)$ ,  $V_n(t)$ ,  $\Phi_I(t)$ , and  $\sigma(P, \tau)$  and  $B(\tau)$  for  $0 \leq \tau < t$ . Once the source strength is found,  $\Phi$  is evaluated by (14), and the velocity on the body,  $\nabla \Phi$ , is obtained using a vector form of (15).

The total pressure is given by Bernoulli's equation,

$$p = -\rho \left( \frac{\partial \Phi_T}{\partial t} + \frac{1}{2} |\nabla \Phi_T|^2 + gz \right), \quad (16)$$

and the force on the body is obtained by integrating (16) over the instantaneous submerged hull  $B(t)$ .

The formulation for the *general* arbitrary motions problem is thus complete. For linear (small motions) problems without forward speed, the body boundary condition is linearized by applying (15) on the mean body position  $B_0$  (the waterline term is absent) and the quadratic term is neglected in integrating (16) on  $B_0$  for the forces. For the linearized problem with forward speed (the linear sea-keeping problem) in the present earth-fixed coordinate system, the quadratic contributions are included in the pressure integration (Eqs. 16 and 19) to account for forward-speed effects, but the body boundary condition (15) on  $B_0$  is otherwise not further expanded. The formulation is thus neither strictly linearized (in terms of the motion amplitudes) nor consistent (in that the associated  $m$ -terms are not included). This is a consequence of the fact that a formal decomposition of the problem in terms of the steady forward-speed disturbance and the (small) oscillatory disturbance is no longer straightforward in the earth-fixed time-domain system. (In this system, the forward speed is in fact a *large-amplitude* motion.) A more convenient formulation for the linearized constant forward speed problem is, of course, to adopt a coordinate system translating with the ship (*cf.*, Liapis & Beck, 1985).

### 3 NUMERICAL METHOD

#### 3.1 Solution of the Integral Equation

A panel method is used for the solution of the integral equation (15). The body surface  $B(t)$  is divided into  $N(t)$  quadrilateral elements over which the source strength is assumed constant. Non-planar quadrilaterals are mapped to planar elements by fitting to the corner points in a least-squares sense (Hess & Smith, 1964). Similarly, the

body waterline  $\Gamma(t)$  is divided into  $N_W(t)$  straight line segments on which the source strength  $\sigma^*$  is assumed to be the same as that of the adjacent body panel. The equation is satisfied at collocation points corresponding to null points of the panels. A forward Euler scheme with constant time step,  $\Delta t$ , is used to integrate forward in time and the convolution integral is computed using a trapezoidal rule.

The discretized form of (15) is given by:

$$\begin{aligned} & \sum_{j=1}^{N^M} \sigma_j^M \iint_{S_j} G_{n_P}^0(P_i, Q_j; 0) dS \\ &= -4\pi \left[ \vec{V}(P_i, t) - \nabla \Phi_I(P_i, t) \right] \cdot \vec{n}_{P_i} \\ & - \Delta t \sum_{m=0}^{M-1} \epsilon_m \left[ \sum_{j=1}^{N^m} \sigma_j^m \iint_{S_j} G_{n_P}^f(P_i, Q_j; t - \tau) dS \right. \\ & \quad \left. - \sum_{k=1}^{N_W^m} \sigma_k^{*m} \int_{\Gamma_k} G_{n_P}^f(P_i, Q_k; t - \tau) V_{Nk} V_{nk} dL \right] \\ & \quad \text{for } i = 1, 2, \dots, N^M. \quad (17) \end{aligned}$$

In the above,  $M$  and  $m$  are the indices for  $t$  and  $\tau$  respectively where  $t = M\Delta t$  and  $\tau = m\Delta t$ ;  $i, j$  are respectively the panel indices for collocation points  $P$  and field points  $Q$  ( $k$  is the index for the waterline field points); and  $\epsilon_0 = 1/2$  and  $\epsilon_m = 1$  for  $m > 0$ . Note that the convolution summation ends at  $m = M - 1$  due to a property of  $G^f$ .

Eq. (17) is in the form of a system of linear equations:

$$\sum_{j=1}^{N^M} A_{ij} \sigma_j^M = B_i \quad i = 1, 2, \dots, N^M, \quad (18)$$

which can be solved for the unknown panel source strengths,  $\sigma_j^M$ , by standard means.

### 3.2 Evaluation of the Free Surface Transient Green Function

The integrals involving the Rankine part of the Green function  $G^0$  are evaluated using a method similar to Hess & Smith (1964). Special efforts have been made to completely vectorize these evaluations, resulting typically in several factors of savings on vector processors.

The numerically more time consuming task is the evaluation of the memory term  $G^f$  and its derivatives which, because of the convolution integrals, must be evaluated a large number of times. There has been much effort in recent years to develop efficient and accurate numerical methods for calculating  $G^f$  and its derivatives, including Newman (1985, 1990), Liapis & Beck (1985), and Magee & Beck (1989). The present approach is an improvement upon the method given in Newman (1985). The domain for  $G^f$  is divided into a number of regions wherein, depending on the arguments, ascending series, asymptotic series or a combination of these and two-dimensional economized (Chebyshev) polynomial approximations are utilized. The final results are maintained to a minimax accuracy of 6D for  $G^f$  and 5D for its first and second derivatives. The entire procedure is completely vectorized and the average computing time required for the evaluation of  $G^f$  and its two first and two second derivatives is  $O(1-3)$  microseconds on a Cray-Y/MP depending on the relative frequency of evaluations in the different regions. Details can be found in Lin & Yue (1990).

The numerical integration of  $G^f$  and its derivatives over the quadrilateral panels is performed using two-dimensional Gauss-Legendre quadrature after mapping the general quadrilaterals into unit squares. A similar one-dimensional quadrature is used for the waterline elements.

### 3.3 Implementation & Force Evaluation

The present method is general for arbitrary large-amplitude six-degree-of-freedom motions which in general requires the modelling of a changing underwater body geometry. Depending on the type and amplitude of the motions, different numerical treatments are required:

1. *Linear motions with zero or constant forward speed* — In this case, the underwater geometry does not change with time and the matrix  $A_{ij}$  in (18), which represents the Rankine influences and depends only on the *relative* distances between  $P_i$  and  $Q_j$ , is constant. Thus,  $A_{ij}$  needs to be evaluated and inverted only once at the beginning of the computations. Furthermore, since  $G^f$  and its derivatives depend only on  $|P_i - Q_j|$  and  $t - \tau$ , for zero or constant horizontal velocity, the previous values of  $G_f$  can be reused at each time step.



Thus only one new set of evaluations for  $G^f$  and its derivatives is necessary at a new time step, and the rest can be obtained from previous calculations. The main differences between zero and constant forward speed problems are the absence of the waterline contribution in the former, and the need to include quadratic terms in the force evaluation to account for forward-speed cross-coupling contributions in the latter.

2. *Linear motions with arbitrary horizontal excursions* — The body moves with variable speed on a straight course or perform arbitrary excursions in the horizontal plane. In this case, the underwater body geometry still does not change in time and  $A_{ij}$  needs to be evaluated and inverted only once. However, the fixed relationships of  $|P_i - Q_j|$  and  $t - \tau$  between time steps no longer exist and evaluations of  $G^f$  and its derivatives have to be done for different  $\tau$ 's at every time step. This increases the computational burden significantly.
3. *Arbitrary large-amplitude motions* — In this case, the underwater body geometry changes with time, and both  $A_{ij}$  and all values of  $G^f$  and its derivatives must be reevaluated at each time step.

For large-amplitude motions, a robust geometry processing capability is essential and an automatic repanelizer was developed for this task. The original input geometry must now include the above-mean-waterline portion. At each time step, the underwater geometry is represented by a number of vertical strips with each strip having a fixed number of panels along its girth. As the body moves, its new location and orientation is updated in the global coordinate system and the new waterline is found from the intersection with the mean free surface. The underwater portion of each strip is then repanelized using a spline curve fitting. For simplicity, the number of panels in each strip is kept the same but any particular vertical strip may be eliminated completely if it is out of the water.

The force evaluation follows from integration of (16) over the instantaneous or mean submerged hull for the nonlinear and linearized problems respectively. The quadratic terms are included in the nonlinear and forward-speed calculations and are evaluated directly given the normal and tangential

velocities on the body. The calculation of  $\partial\Phi_T/\partial t$  is separated into two parts:  $\partial\Phi_I/\partial t$  is given from the incident waves, and  $\partial\Phi/\partial t$  is evaluated by

$$\left(\frac{\partial\Phi}{\partial t}\right)_i^m = \left(\frac{\Phi_i^m - \Phi_i^{m-1}}{\Delta t}\right) - V_i^m \cdot \nabla\Phi_i^m, \quad (19)$$

where  $V_i^m$ , the 'grid' velocity at point  $P_i$ , is equal to  $(P_i^m - P_i^{m-1})/\Delta t$  for the nonlinear problem, and is simply the forward speed,  $U$ , in the linearized forward-speed problem. We remark that because of repanelization for the nonlinear problems, the control points  $P_i$  in general do not represent the same global points or the same body points. When the number of panels changes between time steps, (19) can not be used in a straightforward manner and special care must be taken. This is not considered in the present code.

## 4 RESULTS

Numerical computations were performed for linearized radiation and diffraction problems; large-amplitude forced motions and free motions of a floating body with and without forward speed and the presence of ambient waves; as well as wave resistance and added resistance problems. For simplicity we limit ourselves to heave/pitch motions in head seas although the present code is capable of *general* six degree-of-freedom motions (without lift). A sphere, two Wigley hull forms, and the Series 60 ( $C_B=0.7$ ) hull were used for this study.

The first Wigley form was used by Gerritsma (1988) in his seakeeping experiments and has a beam-to-length ratio  $2b/L=0.1$ , and draft-to-length ratio  $H/L=0.0625$ . This is designated as the " $W_{SK}$ " hull hereafter. The half beam  $y$  is given by:

$$\frac{y}{b} = (1-X)(1-Z)(1+0.2X) + Z(1-Z^4)(1-X)^4$$

where  $X \equiv (2x/L)^2$  and  $Z \equiv (z/H)^2$ . The other Wigley hull is commonly used for wave resistance studies which we designate the " $W_{RT}$ " hull. This hull has  $2b/L=0.1$ , and  $H/L=0.0625$  with half beam given by  $y/b=(1-X)(1-Z)$ .

For convenience, unless otherwise noted, all quantities in the following are nondimensionalized by fluid density  $\rho$ , gravitational acceleration  $g$ , and body length  $L$  (or radius  $a$  for the sphere). The panel numbers,  $N$ , indicated are always for *half*



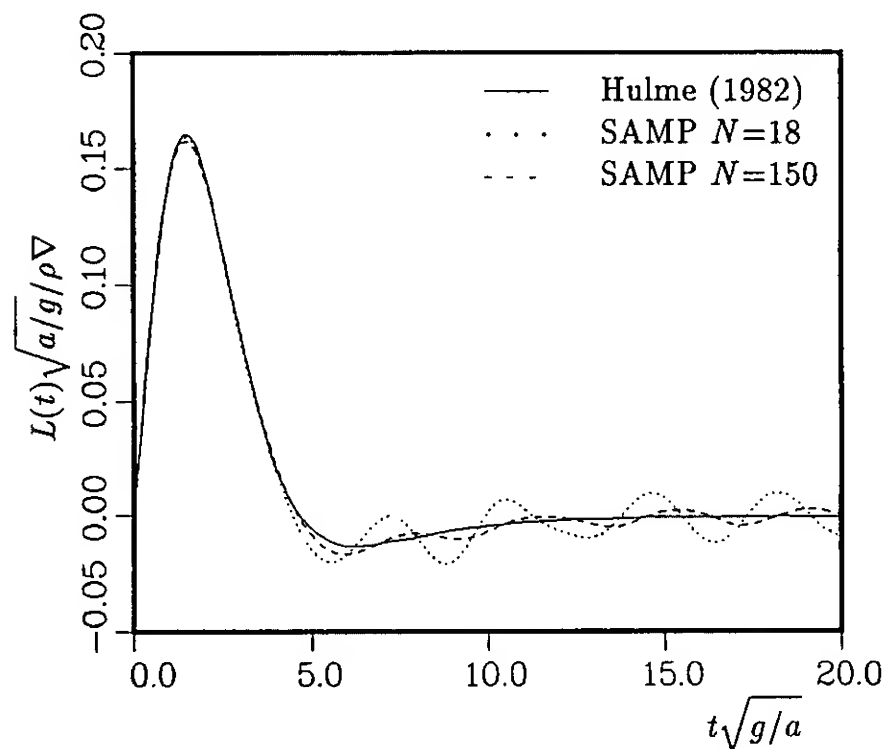


Fig. 1: Impulse response function for the heave force on a hemisphere,  $\nabla \equiv 2\pi a^3/3$ .

of the (submerged) body. The present computational results are referred to as SAMP (Small Amplitude Motion Program) when the linear option (fixed underwater geometry) is used, and as LAMP (Large Amplitude Motion Program) when the large-amplitude capability with changing submerged geometry is employed. Where available, numerical calculations from the linearized time-domain method developed at the University of Michigan (Magee & Beck, 1988) are included and denoted as "Michigan". Strip theory results are based on Salvesen, Tuck & Faltinsen (1970). Those used in Secs. 4.1 and 4.2 are taken from Magee & Beck (1988).

#### 4.1 Linear Radiation Problem

Fig. (1) shows the impulse-response function,  $L(t)$ , for the heave force on a hemisphere, radius  $a$ , as a function of time, obtained using SAMP with  $\Delta t=0.05$ . Here  $L(t)$  is defined as

$$L(t) = \rho \iint_{B_0} \Phi_t n_z dS, \quad (20)$$

for an impulse (delta function) acceleration at  $t=0$ . The curve for Hulme (1982) is obtained from Fourier transform of his analytic frequency-domain results. The time-domain results show the characteristic oscillations at larger times which are caused by the presence of irregular frequencies of the interior problem (Adachi & Ohmatsu, 1982). Note that the amplitudes of these spurious oscillations decrease as the number of panels is increased.

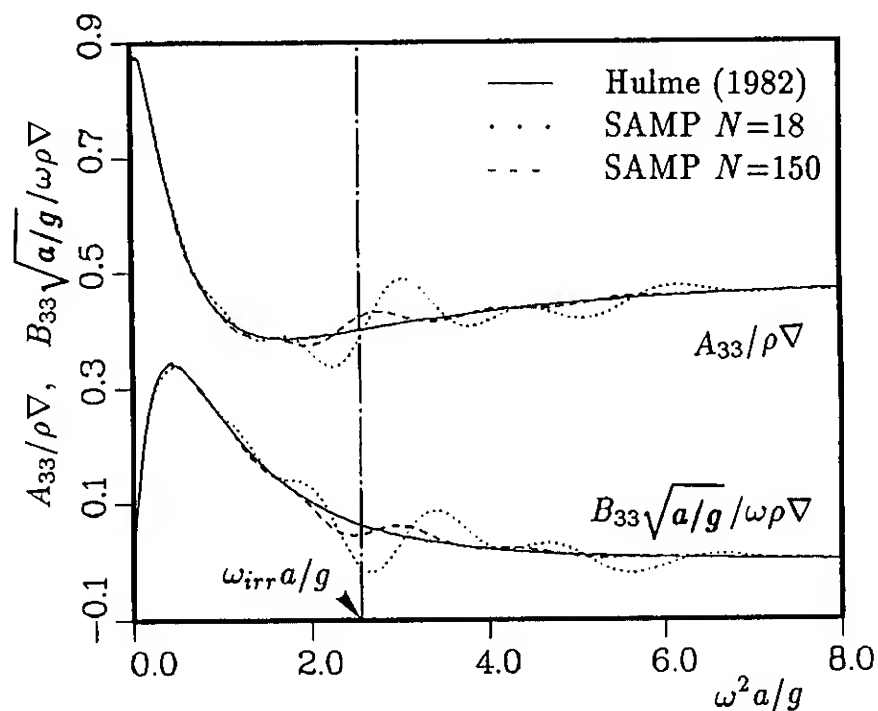
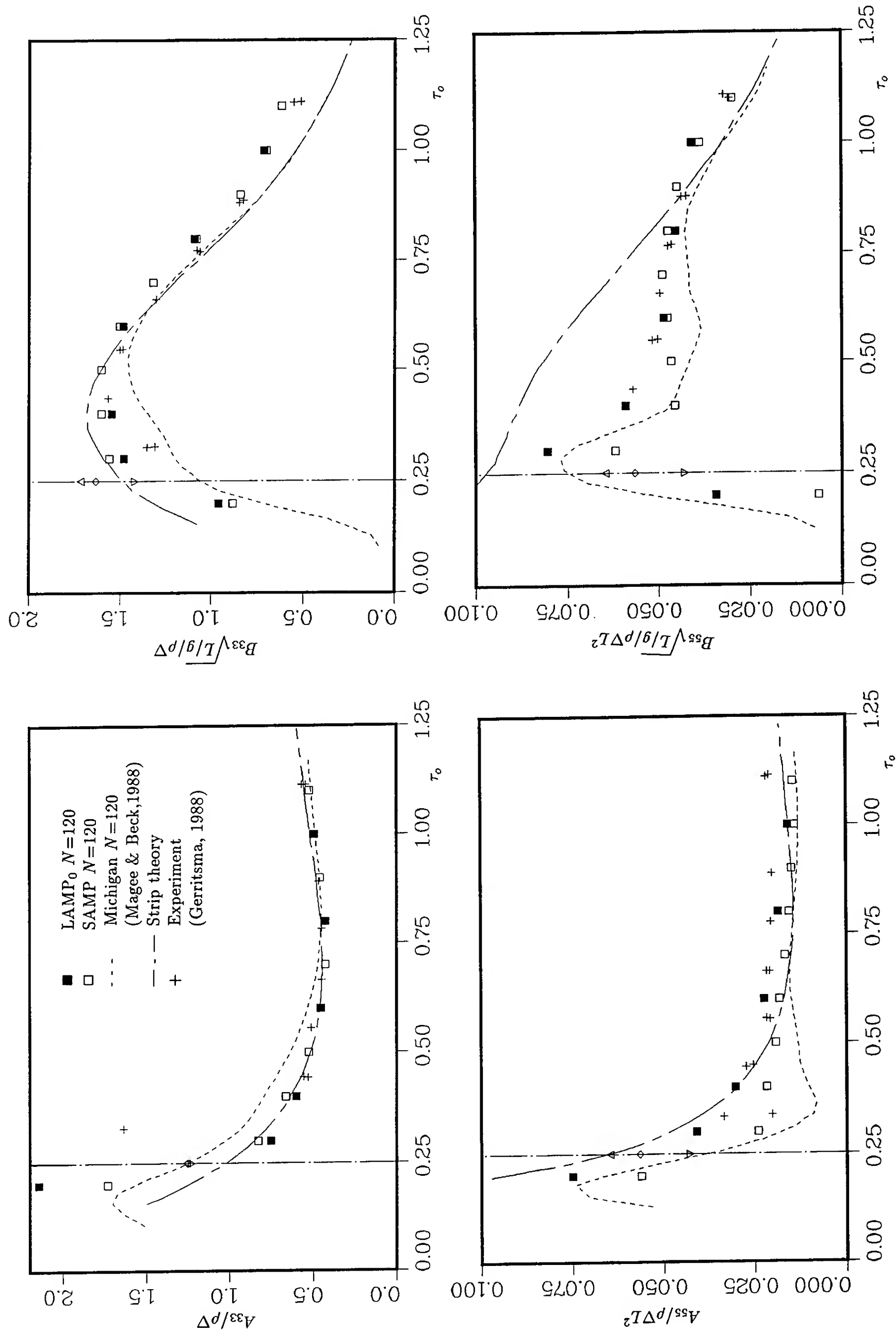


Fig. 2: Heave added-mass and damping coefficients for a hemisphere.

The added mass and damping coefficients are related to the cosine and sine transforms respectively of the impulse-response function. These are shown in Fig. (2) as compared to the frequency-domain result of Hulme (1982). For illustration the location of the lowest irregular frequency ( $\omega_{irr}^2 a/g \approx 2.56$ , Hulme, 1983) is also indicated. It is seen that the oscillations in Fig. (1) are directed related to the irregular behavior near  $\omega_{irr}$ , although the singular nature is not fully captured because of the finite-time truncation of  $L(t)$  (at  $t=20$  in this case). We note again the smaller and more confined oscillations for larger  $N$ .

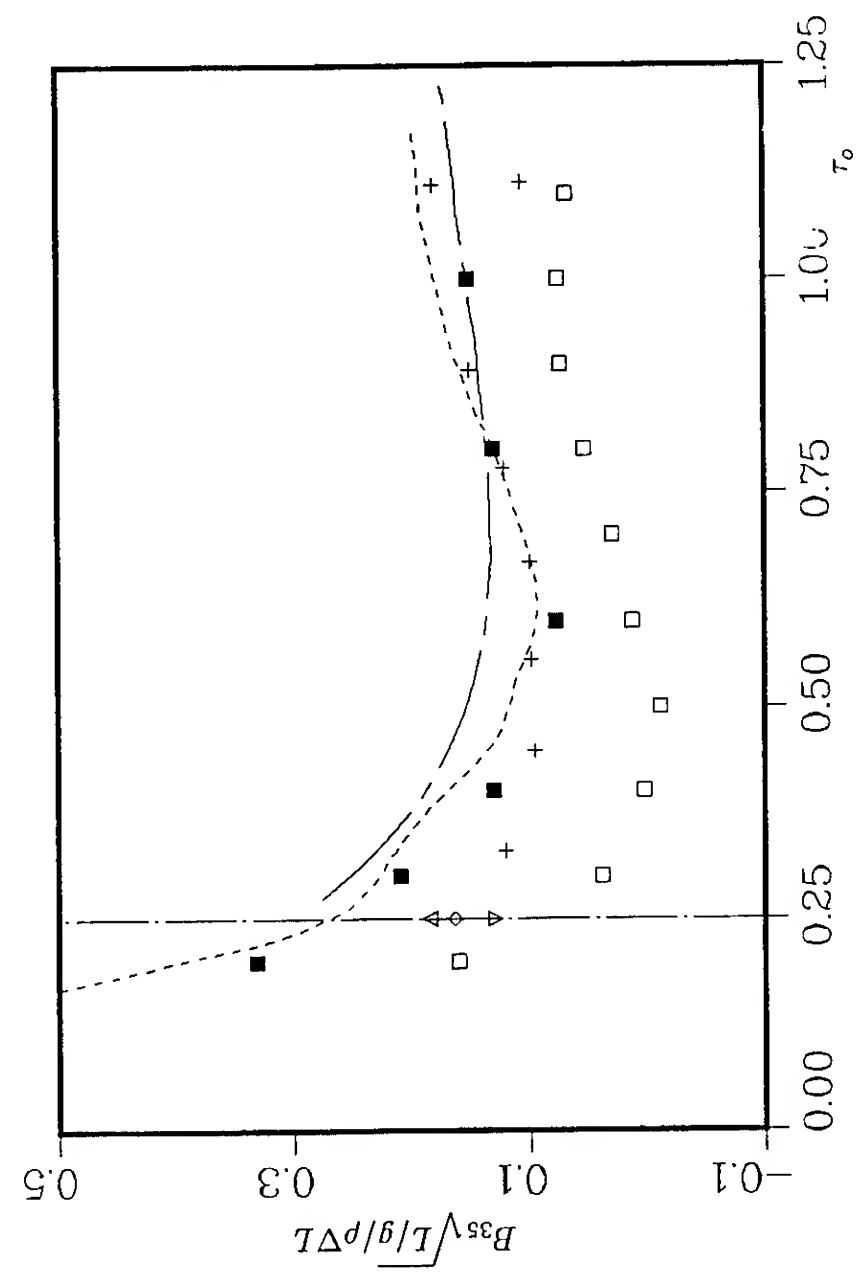
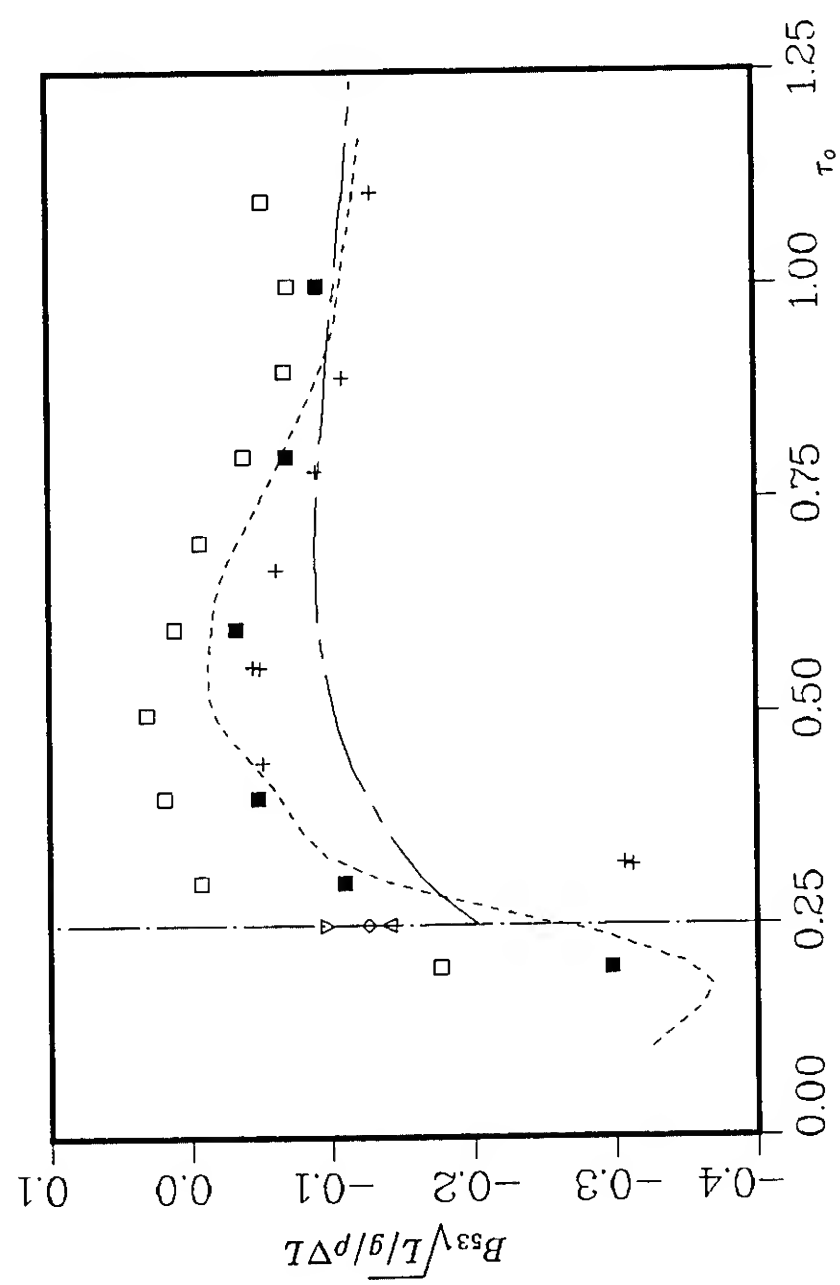
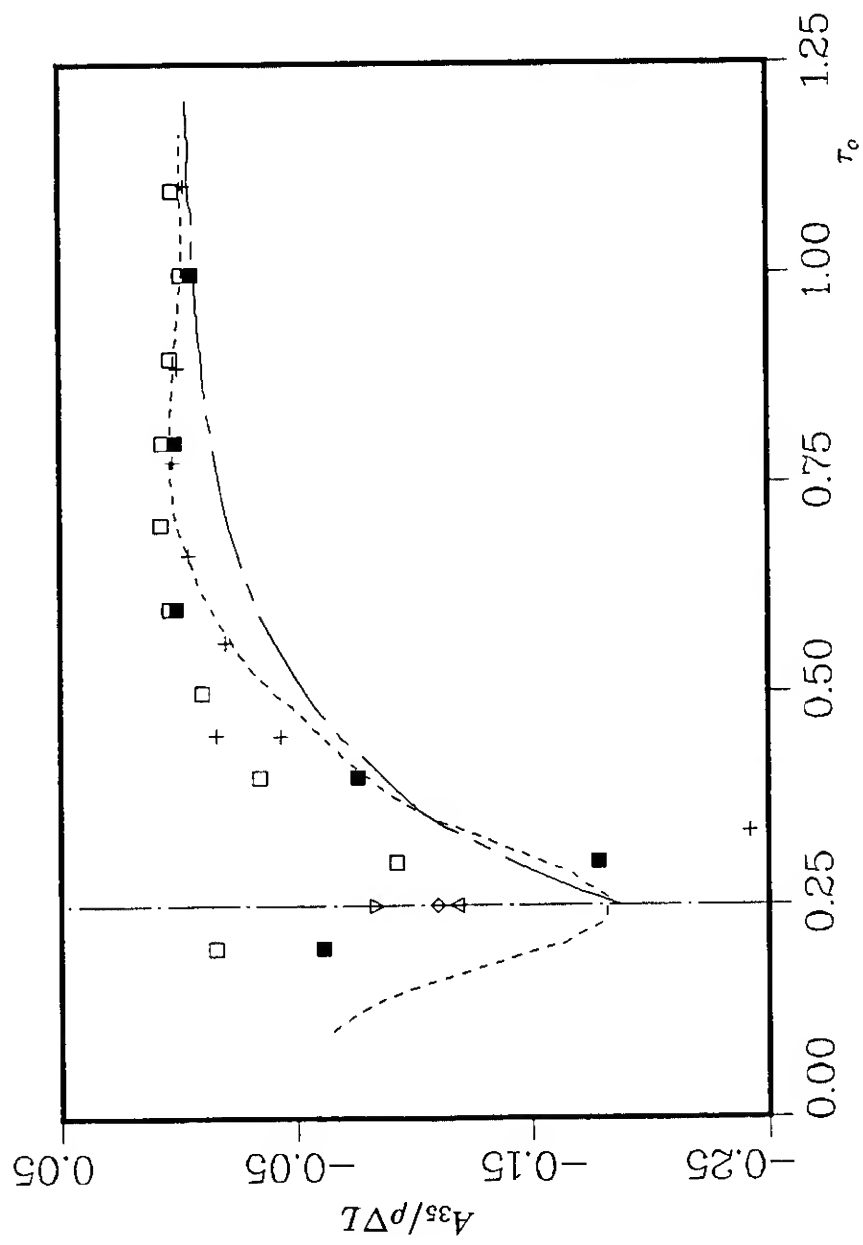
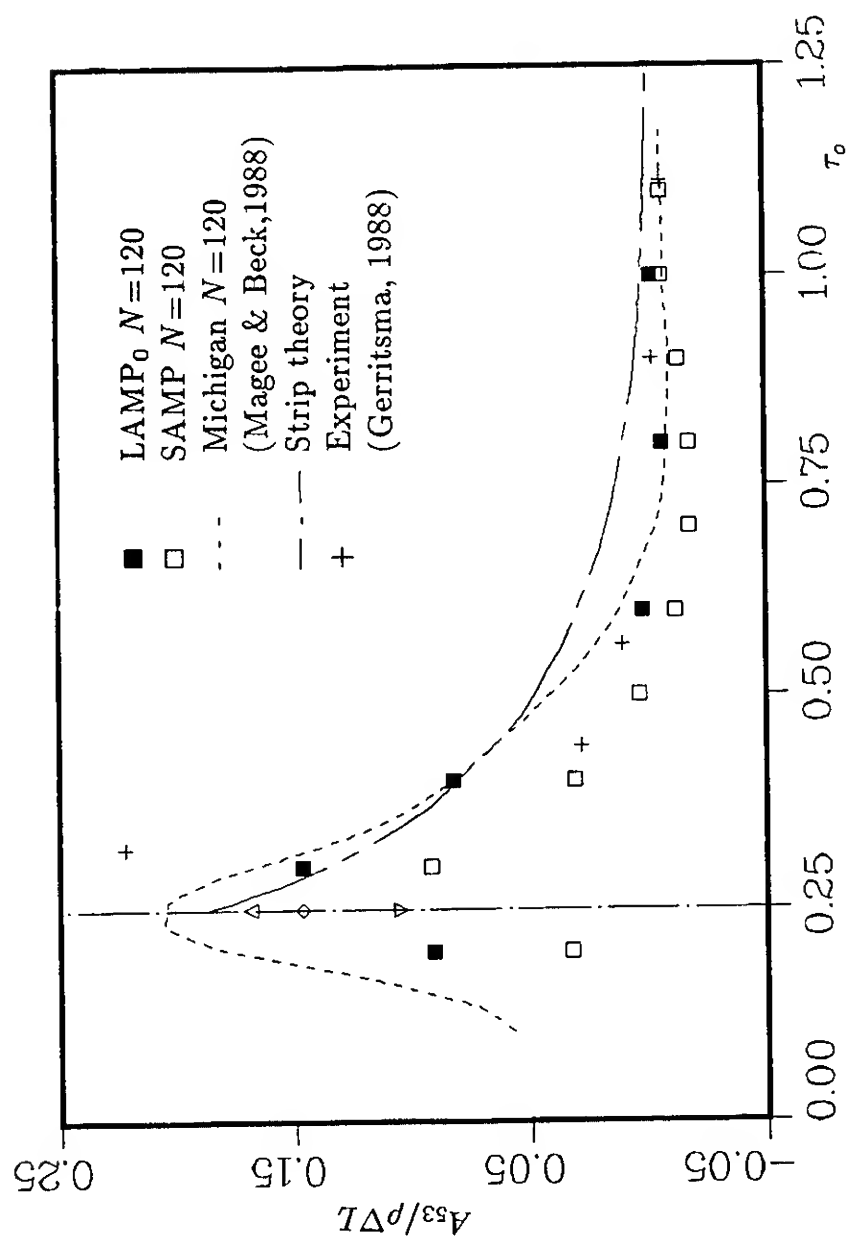
For radiation problems with forward speed, a forced oscillatory motion is superimposed on a step-function jump of the forward velocity to the prescribed value. The force coefficients are then obtained from Fourier transforms of the SAMP force time histories after steady state is reached. In the presence of forward speed, quadratic contributions must be retained in the present space-fixed formulation and the impulse-response function is not generally useful. This computational inefficiency for the special case of linearized sea-keeping is the main (in fact only) disadvantage of the space-fixed formulation.

Figs. (3,4) show the heave and pitch diagonal and off-diagonal added-mass and damping coefficients of the  $W_{SK}$  hull at Froude number  $F_n \equiv U/\sqrt{gL}=0.2$ . The SAMP calculations use  $N=120$  and  $\Delta t=0.1$ . These results are considered to have converged in that selected calculations (not shown)



Figs. 3: Diagonal heave and pitch added-mass and damping coefficients of a  $W_{5K}$  hull at  $F_n=0.2$ .

For values at  $\tau_0 = 1/4$ , ( $\nabla, \diamond, \Delta$ ): SAMP  $N=120$ ,  $T_{cut}=(10,20,40)$



Figs. 4: Off-diagonal heave and pitch added-mass and damping coefficients of a  $W_{SK}$  hull at  $F_n=0.2$ .

For values at  $\tau_0 = 1/4$ , ( $\nabla, \diamond, \Delta$ ): SAMP  $N=120$ ,  $T_{cut}=(10,20,40)$

using  $N=200$  and  $\Delta t=0.05$  show changes of less than 1% in the force coefficients. As pointed out earlier, the SAMP calculations do not contain the contributions of the  $m$ -terms while the general LAMP computations do. To gauge the importance of these effects, we include in the figures the small-amplitude limits of the large-amplitude LAMP results (see Sec.4.5). These values are obtained from extrapolations of the small finite-amplitude LAMP results to zero amplitude and are denoted hereafter as  $LAMP_0$ . From Figs.(18), it is seen that LAMP approaches the  $LAMP_0$  limit very smoothly so that the estimates are reliable.

For the diagonal coefficients (Fig.3), the  $LAMP_0$  and SAMP results are both reasonably satisfactory although the  $m$ -term effects appear to play an appreciable role as the relative frequency,  $\tau_o \equiv U\omega/g$ , decreases and especially for the pitch coefficients. On the other hand, the Michigan results (which include  $m$ -terms) using the same  $N$  show unexplained deviations for intermediate values of  $\tau_o$ . Not surprisingly, strip theory performs better for larger  $\tau_o$  but appears to be affected significantly only for  $B_{55}$  at lower frequencies.

The results are much more interesting for the off-diagonal coefficients. For the added-mass terms  $A_{35}$  and  $A_{53}$ , the SAMP calculations compare well to measured data. When effects of the  $m$ -term are included, the deviations of  $LAMP_0$  from SAMP are primarily at lower frequencies but the comparison to experiments is otherwise not improved. For the damping terms  $B_{35}$  and  $B_{53}$ , the SAMP results are inadequate, showing a large somewhat constant shift, and indicate that the  $m$ -term effects may play an important role for these coefficients. Indeed, when the  $m$ -term effects are included, the  $LAMP_0$  and Michigan results are both reasonably close to experimental measurements.

In summary, we see that the SAMP results are satisfactory for the off-diagonal added mass coefficients, and generally acceptable for the diagonal coefficients. Taken together, the  $LAMP_0$  predictions provide overall good agreement with experiments and are clearly superior. By comparing SAMP and  $LAMP_0$  results, the effect of the  $m$ -terms is quantified and shown to be important for pitch-related coefficients at lower frequencies and especially for the off-diagonal damping terms. It is noteworthy that since LAMP uses a linearized free-surface condition, the present results suggest that nonlinear free-surface terms such as those that

may be included in Dawson-type codes (e.g., Nakos & Sclavounos, 1990) may otherwise not be as important in the prediction of the motion coefficients.

A well-known theoretical difficulty of the linear seakeeping problem is the singularity at the critical relative frequency  $\tau_o = 1/4$  (e.g., Dagan & Miloh, 1980). Physically, this may be explained by the simple fact that at  $\tau_o = 1/4$  the group velocity of the waves generated by the oscillatory motion matches the ship speed  $U$  and resonance occurs. In the frequency domain, the linearized result is unbounded while in the time-domain the resonance is manifest as a slow unbounded growth of the solution with time.

While actual predictions at the critical frequency may not be contemplated in the context of linearized theory, it is useful to be able to avoid the undesirable growing solution in *general* time-dependent simulations. An obvious idea (also suggested by Beck & Magee, 1990) is to simply truncate the duration of the memory effect convolution terms in (15) by requiring  $t - \tau \leq T_{cut}$ , say. This is illustrated in Fig. (5) which shows the time history of the vertical force on a  $W_{SK}$  hull starting from rest with a heaving frequency of  $\omega=1.25$  and a forward speed corresponding to  $\tau_o = 1/4$  ( $F_n=0.2$ ). When the memory effect is not limited, the force grows slowly without reaching steady-state. When we set  $T_{cut}=10$ , however, steady-state is quickly reached resembling the results at non-critical  $\tau_o$ 's. We point out that because of the relatively slow growth and the effective truncation of  $T_{cut}$  by the total duration of the simulation, the problem of the critical frequency may not pose a severe limitation in practice for general (not critically forced) time-domain applications. The motion coefficients obtained from SAMP calculations using different values of  $T_{cut}$  are presented as separate symbols on the  $\tau_o = 1/4$  vertical in Figs. (3,4). We caution that these results should not be considered as 'predictions' at the critical frequency despite the fact that they are now finite and appear to give a roughly continuous trend.

## 4.2 Linear Diffraction Problem

The presence of incident waves,  $\Phi_I(\vec{x}, t)$ , can be included into the governing equation (15) in a straightforward manner. In practice, this is introduced instantaneously at  $t=0$  and the diffraction effects evaluated after the transients vanish typi-

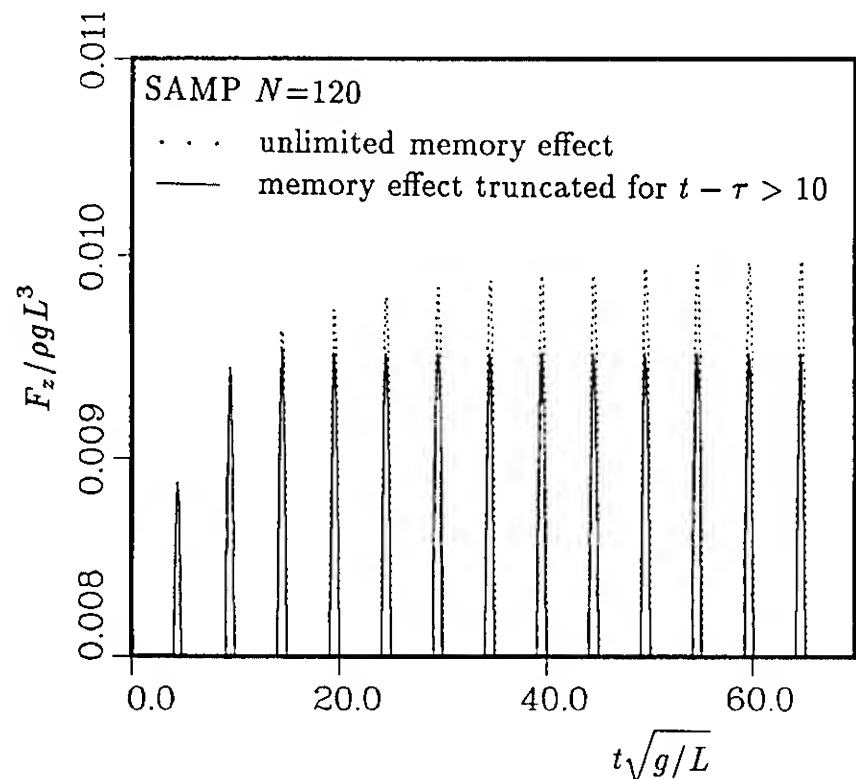


Fig. 5: Peaks of the heave force history for a  $W_{SK}$  hull at  $F_n=0.2$ ,  $\tau_o=1/4$ .

cally in a very short time. In the case of no forward speed, the linear diffraction problem is validated for a floating hemisphere. The SAMP results are indistinguishable from the earlier computations of Cohen (1986) and King (1987) and the comparisons are not shown here.

Figs. (6) shows the amplitude and phase of the wave exciting forces on a  $W_{SK}$  hull moving with forward speed,  $F_n=0.2$ , in head seas. For the SAMP results,  $N=120$  and 30 time steps per incident wave period is used. The comparisons to the time-domain results of Michigan, strip theory and experiments are overall satisfactory. The Michigan calculations underpredict the secondary hump at high frequency although both of the 3D time-domain calculations show better correlations to the experiments than strip theory.

For a more realistic and complicated geometry, we consider the Series 60 ( $C_B=0.7$ ) hull form for which extensive experimental data are available. Figs. (7) show a complete set of results for  $F_n=0.2$  in head seas. The SAMP results with  $N=180$  and 250 have clearly converged (30 time steps per incident wave period are found to be more than adequate) and compare very well with experimental data. Not surprisingly, strip theory results are generally acceptable compared to SAMP predictions at higher frequencies. On the other hand, the Michigan results do not indicate convergence and appear to underpredict the amplitudes especially at the higher frequency second hump.

### 4.3 Large-Amplitude Motions at Zero Speed

As a first example, we study the large-amplitude heaving of a (complete) sphere. The sphere is initially semi-submerged with its center at the origin and a forced heaving motion with  $z(t) = -A_h \sin \omega t$  is imposed at  $t=0$ . We set  $\omega=1$  and use  $N=150$  and  $\omega \Delta t = 2\pi/30$ . As pointed out earlier, at each time step, the submerged portion of the sphere is repanelized, the Rankine influence matrix reevaluated and solved, and the memory terms recalculated from  $\tau=0$  to  $\tau=t$ .

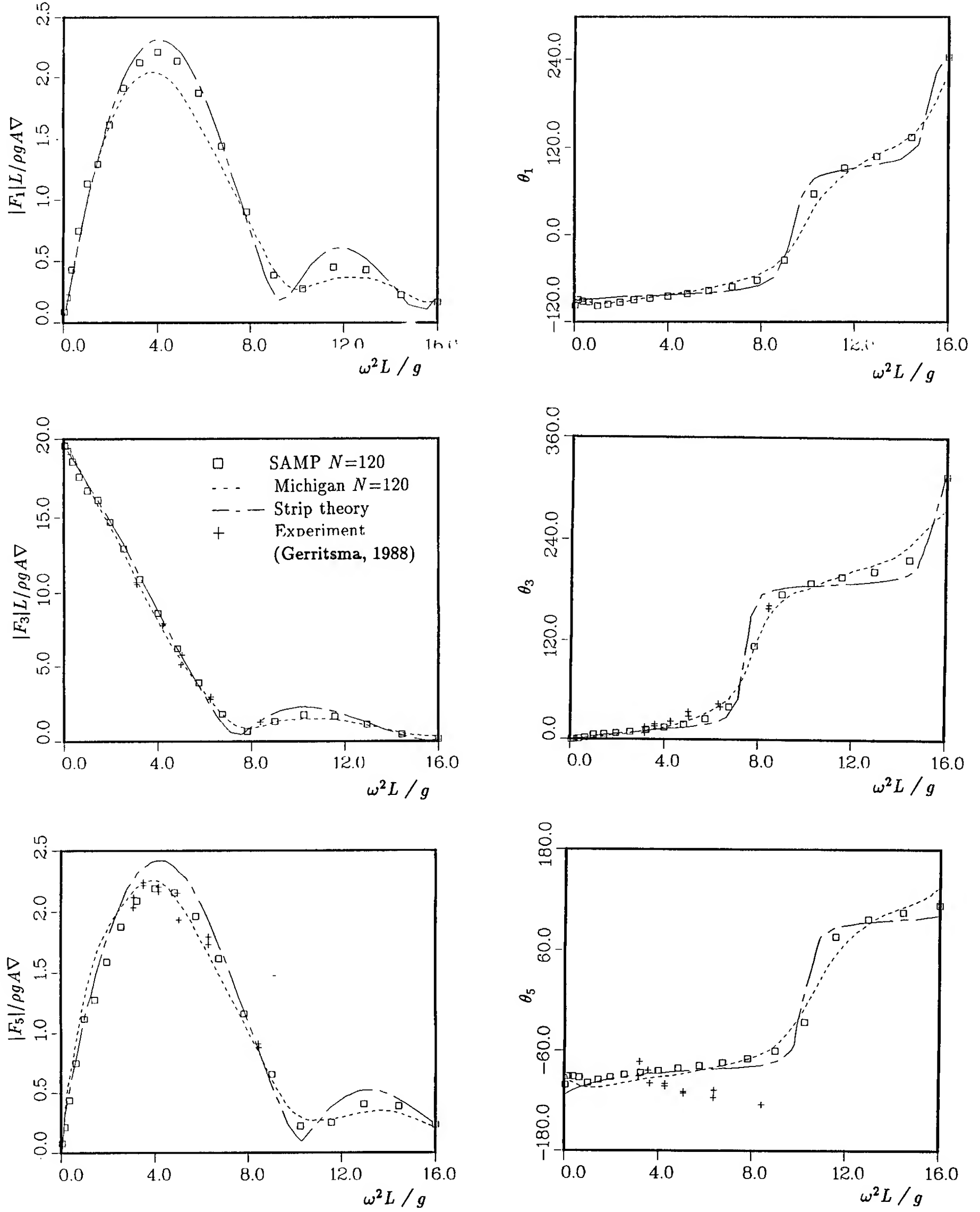
Fig. (8) shows the different components of the vertical force on the sphere as a function of time for the case of  $A_h/a=0.5$ . Steady-state (limit cycle) is rapidly reached (within one period) for all the components. For this geometry, the hydrostatic force is a large part of the total. The inertia ( $-\partial\Phi/\partial t$ ) term shows distinct higher-harmonic components while the quadratic ( $-|\nabla\Phi|^2/2$ ) component is primarily at the second harmonic, as expected. Surprisingly, these higher harmonic contributions appear to cancel closely so that the *total* force oscillates primarily at forcing frequency together with a negative (suction) steady component.

To validate the large-amplitude capability of LAMP, systematic convergence tests were performed for this case. A typical example is Fig. (9) which shows the hydrodynamic force history ( $F_{HD}$ ) for varying  $N$  and  $\omega \Delta t$  for  $A_h/a=0.5$ . The results are indistinguishable indicating that  $N=150$  and  $\omega \Delta t = 2\pi/30$  are more than adequate.

Fig. (10) shows the time history of the vertical hydrodynamic forces on the sphere for different  $A_h/a$ . As expected, the nonlinear curves approach the linear one as  $A_h/a$  decreases. For larger heaving amplitudes, the peaks become sharper and higher, while the troughs become shallower. The nonlinear effect, however, is relatively small even when the heaving amplitude is 50% of the radius. This was found also in earlier *fully*-nonlinear simulations for heaving axisymmetric bodies (Lin, *et al*, 1984; Dommermuth & Yue, 1986).

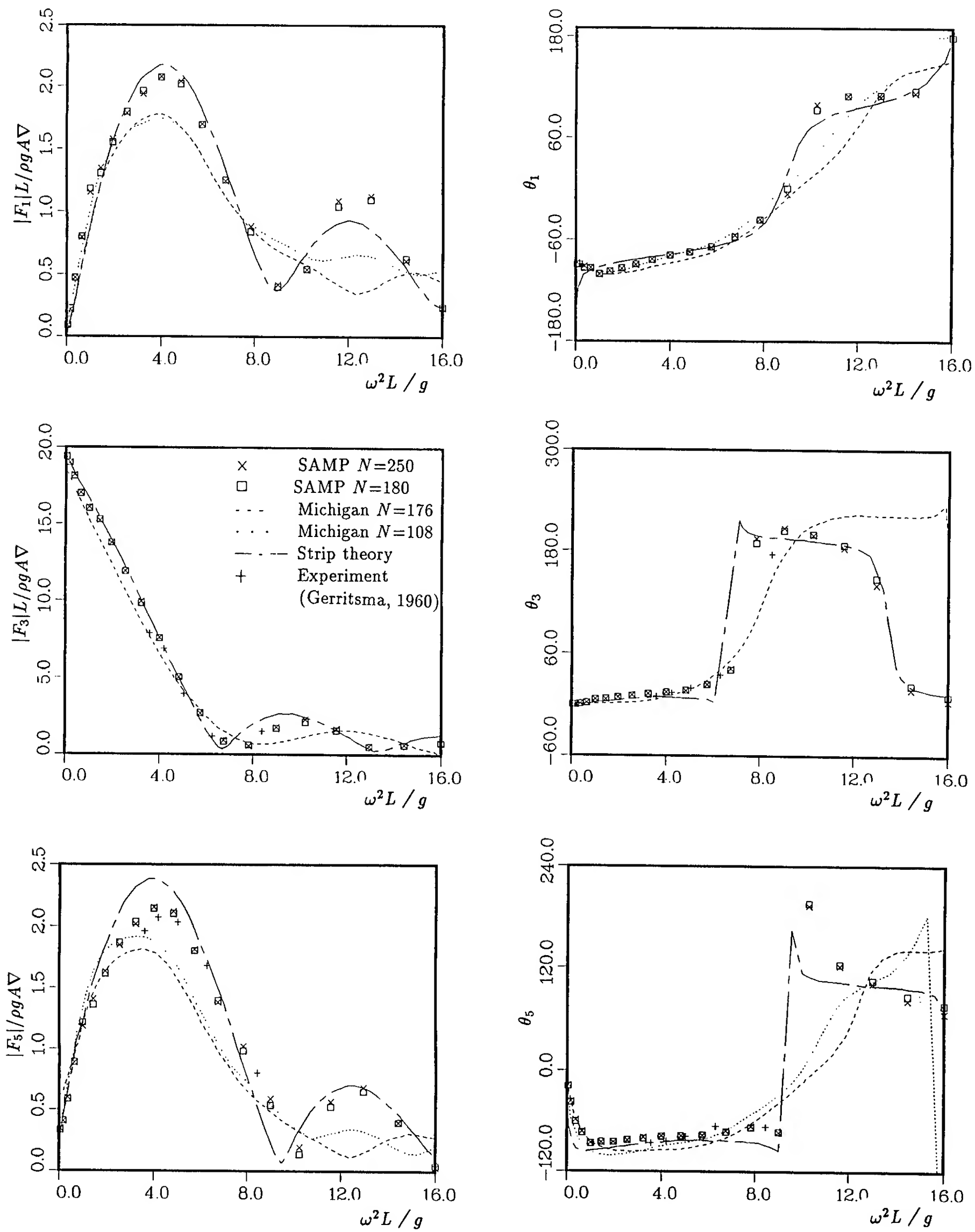
A detailed analysis of the frequency components of the force can be obtained from Fourier transform of the steady-state (limit-cycle) time history. For convenience, we define the frequency components of the vertical force:

$$F_z(t) = \Re \left[ f_0 + f_1 e^{i\omega t} + f_2 e^{i2\omega t} + \dots \right].$$



Figs. 6: Magnitude and phase of the wave exciting forces on a  $W_{SK}$  hull at  $F_n=0.2$ .





Figs. 7: Magnitude and phase of the wave exciting forces on a Series 60 ( $C_B=0.7$ ) hull at  $F_n=0.2$ .

Table 1: Frequency component amplitudes of the vertical force on a sphere undergoing large-amplitude heaving motion,  $A_h/a=0.5$ .

$A_h/a$	$f_0/\rho g \pi a A_h^2$	$ f_1 /\rho g \pi a^2 A_h$		$ f_2 /\rho g \pi a A_h^2$
	dynamic	dynamic	total	dynamic
linear	—	0.3351	0.7427	—
0.125	-0.0085	0.3331	0.7328	0.1813
0.250	-0.0105	0.3285	0.7269	0.1779
0.375	-0.0129	0.3229	0.7161	0.1771
0.500	-0.0144	0.3129	0.7010	0.1758
0.625	-0.0182	0.3026	0.6834	0.1748

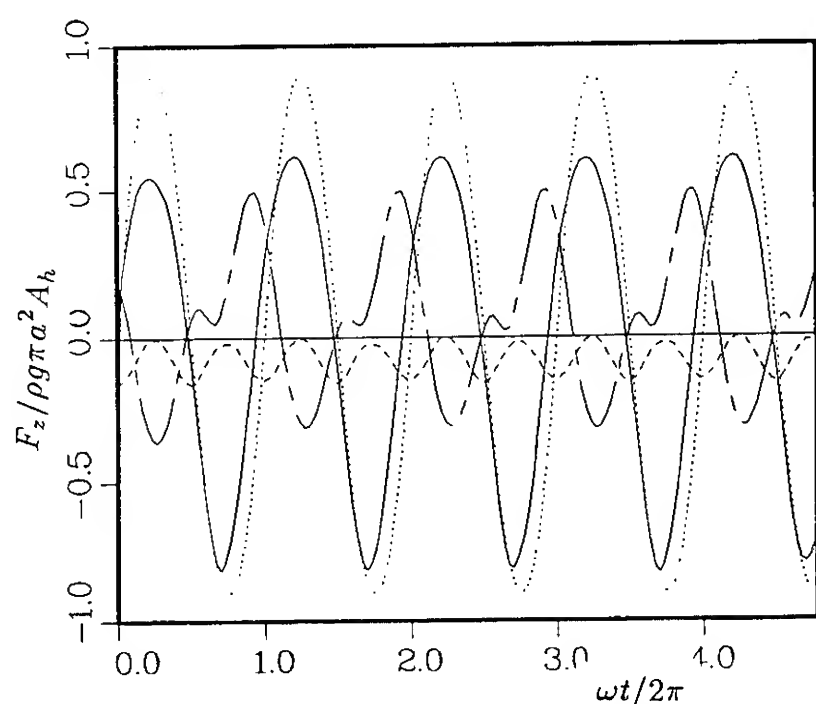


Fig. 8: Components of the vertical force on a sphere undergoing large-amplitude heaving motion ( $A_h/a=0.5$ ). — total;  $\cdots$  hydrostatic;  $---$  inertia ( $-\partial\Phi/\partial t$ );  $- \cdot -$  quadratic ( $-|\nabla\Phi|^2/2$ ).

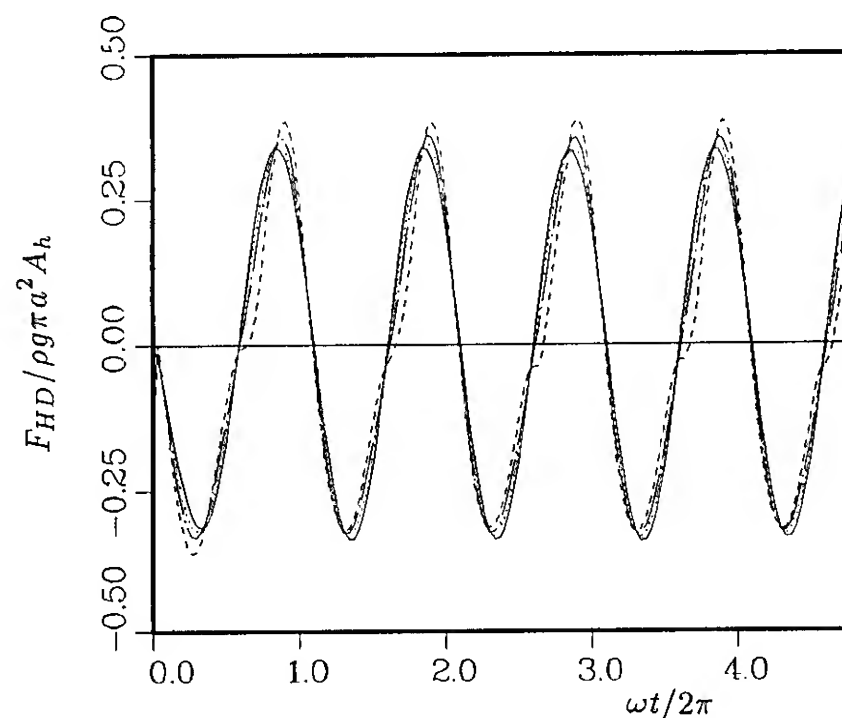


Fig. 10: Hydrodynamic vertical force on a sphere undergoing large-amplitude heaving motion. — linear;  $\cdots$   $A_h/a=0.125$ ;  $- \cdot -$   $A_h/a=0.25$ ;  $---$   $A_h/a=0.5$ .

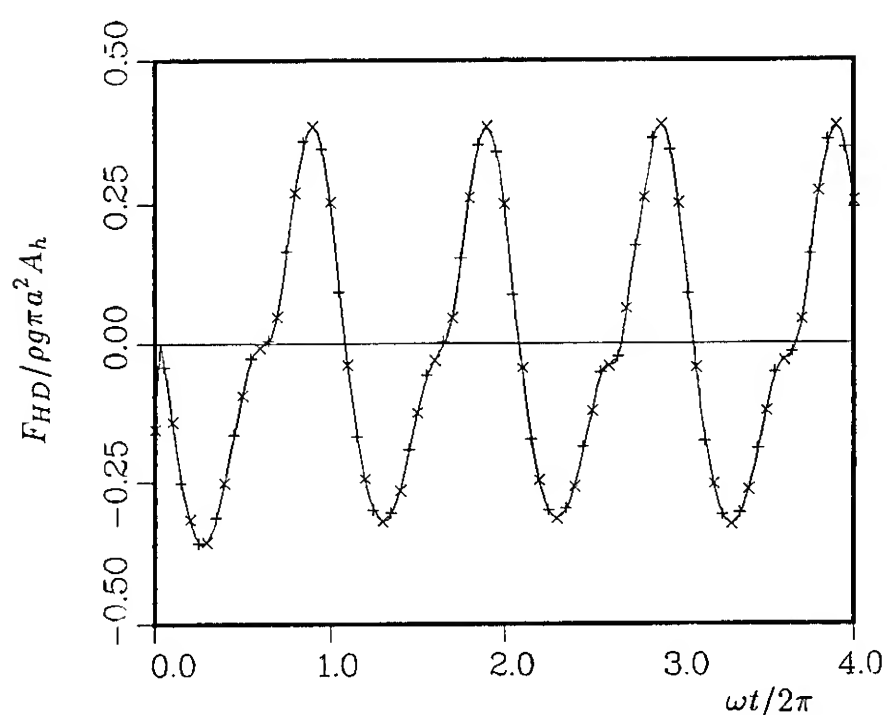


Fig. 9: Convergence of the hydrodynamic force on a sphere undergoing large-amplitude heaving motion ( $A_h/a=0.5$ ). —  $N=150$ ,  $\omega\Delta t=2\pi/30$ ; +  $N=150$ ,  $\omega\Delta t=2\pi/40$ ;  $\times$  :  $N=200$ ,  $\omega\Delta t=2\pi/30$ .

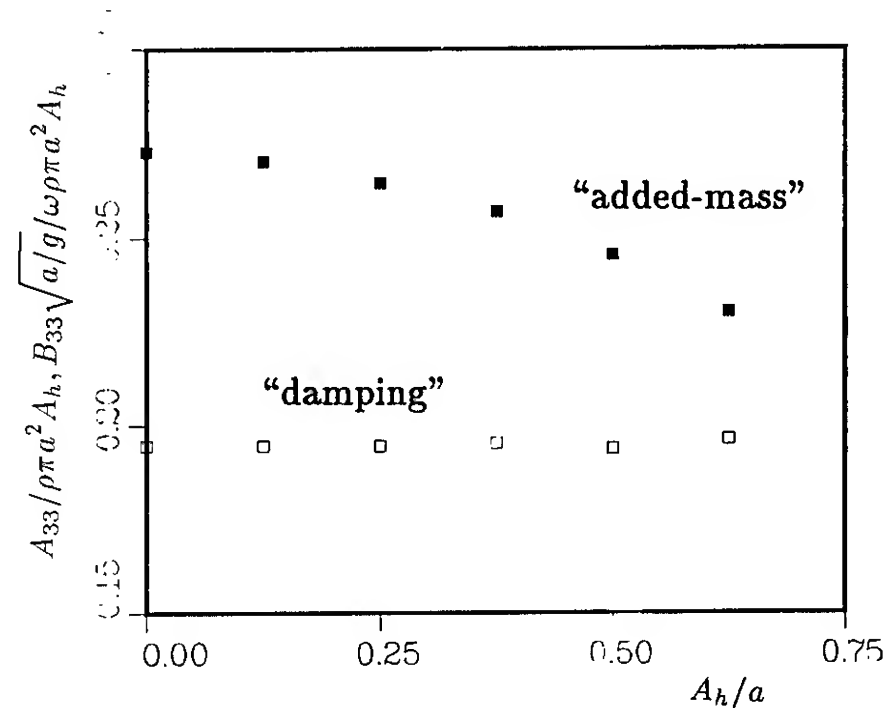


Fig. 11: Excitation frequency components of the limit-cycle hydrodynamic vertical force on a sphere undergoing large-amplitude heaving motion ( $\omega=1.0$ ).  $\blacksquare$  in-phase with acceleration (“added-mass”);  $\square$  out-of-phase with acceleration (“damping”) coefficients using LAMP  $N=150$ .

These are given in appropriately normalized form in Table 1 for the hydrodynamic as well as the total force for different  $A_h/a$ . The hydrostatic force is given analytically by:

$$F_{HS}(t) = \rho g \pi a^3 \left[ \frac{2}{3} + \frac{z(t)}{a} - \frac{1}{3} \left( \frac{z(t)}{a} \right)^3 \right],$$

which contains both linear and nonlinear first-harmonic and nonlinear third-harmonic components. The mean (steady) hydrodynamic suction force,  $f_0$ , is caused primarily by an approximately 180° phase shift between the heaving and wave motions. Interestingly, its amplitude increases more than quadratically with  $A_h/a$ . For the reaction at forcing frequency,  $f_1$ , the large-amplitude results match the linear limit smoothly for small  $A_h/a$  but increases slower than linearly with  $A_h/a$  as the amplitude increases. For the hydrodynamic second-harmonic (double-frequency) component, the normalized amplitude  $|f_2|/A_h^2$  remains nearly constant for the heaving amplitudes considered.

Fig. (11) plots as a function of  $A_h/a$ , the normalized components of  $f_1$  in phase and out of phase with the acceleration. These quantities can be considered the large-amplitude “added-mass” and “damping” coefficients respectively as they would be in the linearized limit. Here, the “added-mass” coefficient shows a clear decreasing trend as heave amplitude increases. This is a new result and has important implications to the overall dynamics of the body. On the other hand, the “damping” coefficient remains almost constant over the range of heaving amplitudes. This behavior of the wave damping term may be partly a result of the linearized free surface condition used in the present approach. We caution, however, that the dependencies of the motion coefficients on amplitude can, in general, be sensitive to the forcing frequency (Ferrant, 1988).

The linearization of the free surface conditions cannot in principle be justified as the motion amplitudes become very large. For many body geometries and motions, however, the nonlinear effects associated with the geometry alone play a predominant role so that the neglect of free-surface nonlinearities may be acceptable. This was indicated, for example, by many of the fully-nonlinear simulations of Dommermuth & Yue (1986).

#### 4.4 Steady Forward Speed Without Motions — The Wave Resistance Problem

The idea that the steady-state limit of the time-domain approach may be useful for the steady resistance problem (and thereby circumventing the difficulties of the Neumann-Kelvin formulation) was one of the motivations for its development. In any event, it certainly seems valuable to validate the method for the case of steady forward speed without motions as a basis for general motion applications with forward speed. Despite the above, the resistance prediction for ship hulls using a time-domain calculation does not appear to have been systematically performed before.

As an illustration, we show in Fig. (12) the horizontal force (wave resistance) coefficient,  $C_x$ , as a function of time for the ‘resistance’ Wigley hull,  $W_{RT}$ . The body is started abruptly from rest to a constant forward speed corresponding to  $F_n=0.3$ . The resistance coefficient is defined as  $C_x = F_x / \frac{1}{2} \rho U^2 S$ , where  $S$  is the (mean) wetted surface area of the hull. For the SAMP calculation,  $N=168$  and  $\Delta t = 2\pi/40$  are used. The  $C_x$  curve shows sharp initial transients which settle rapidly to a decaying oscillation of period  $T \approx T_0 \equiv 8\pi U/g$  around a constant mean value. The period and rate of decay of this oscillatory behavior is consistent with the asymptotic result given by Wehausen (1964). (These qualitative features can in fact be deduced by considering the group velocity and dispersion of the ‘start-up’ transient.)

To obtain a prediction of the steady wave resistance, we average the large-time value of  $C_x$  over a period of  $T_0$  (Dommermuth & Yue, 1988). The SAMP predictions are compared with ITTC experimental data (McCarthy, 1985) as well as steady calculations based on a Dawson-type program (Letcher, et al., 1989) hereafter designated as SLAW. The SLAW results use a total of 240 panels on the body and 1380 panels on the free surface (assuming port-starboard symmetry). The comparison between SAMP and SLAW predictions is remarkably good although both results slightly over-predict the wave resistance given by the band of experimental measurements.

In a similar manner, the steady sinkage force and pitch moment can be estimated from the vertical force and pitch moment time histories. These are shown in Figs. (13,14) respectively and again compared to SLAW calculations. The comparison for

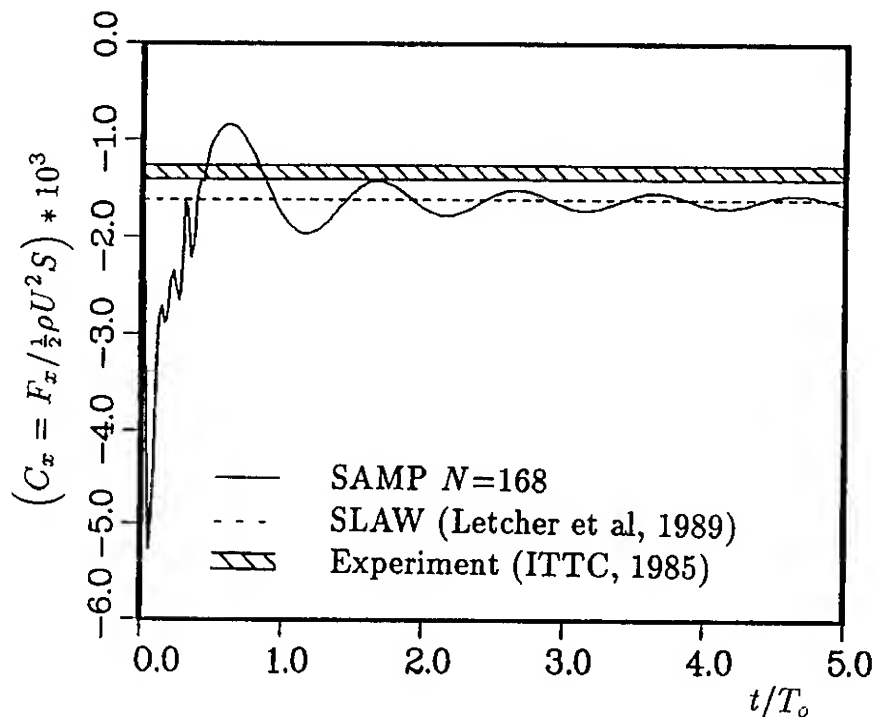


Fig. 12: Horizontal force time history for a  $W_{RT}$  hull moving at  $F_n=0.3$ .

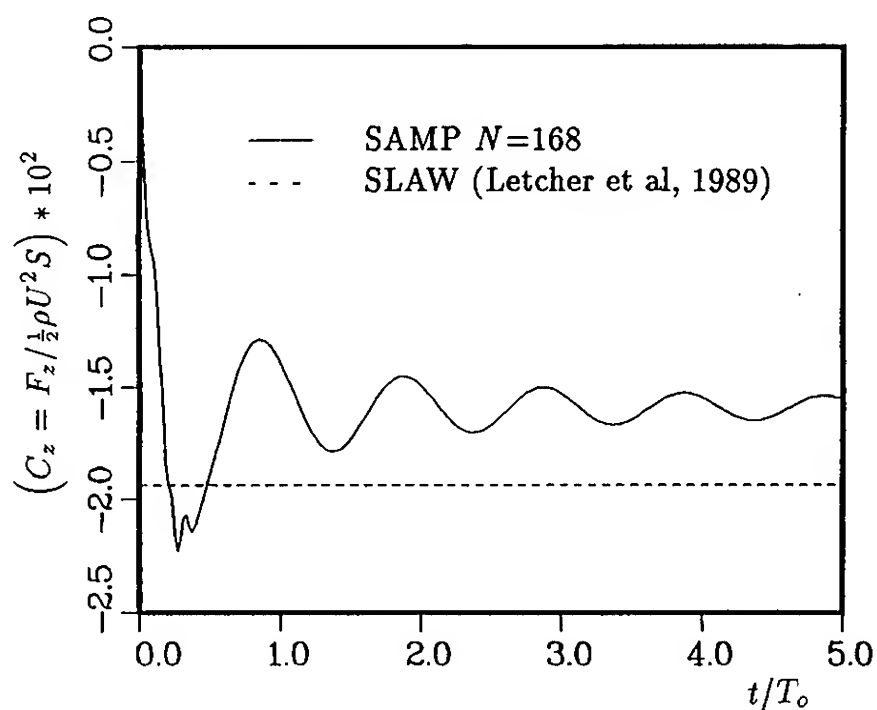


Fig. 13: Vertical force time history for a  $W_{RT}$  hull moving at  $F_n=0.3$ .

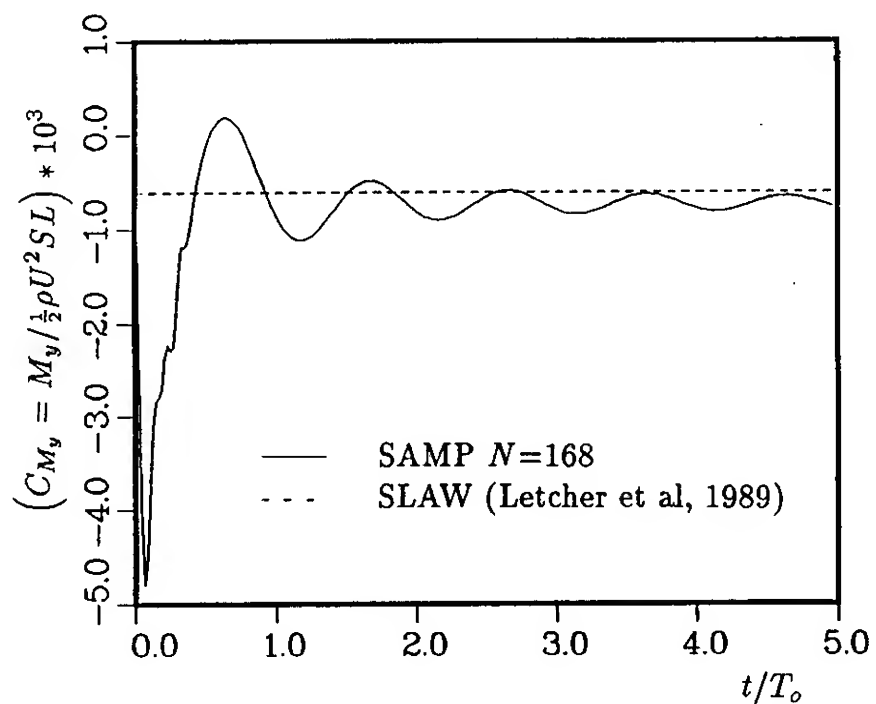


Fig. 14: Pitch moment time history for a  $W_{RT}$  hull moving at  $F_n=0.3$ .

the pitch moment is very good while the two results differ by about 15% for the steady vertical force.

To evaluate the dependence of SAMP predictions on panel size and time steps, systematic convergence tests were performed for different numbers of panels and time steps for  $F_n=0.3$  and 0.4. These results are summarized in Tables 2 and 3. Three different grid distributions — uniform, cosine and ‘geometric’ spacing — are considered in the longitudinal direction while the girth-wise grid sizes are kept constant. The so-called ‘geometric’ spacing is based on the criterion that the projection of each panel on the  $y$ - $z$  plane be constant. For the parabolic  $W_{RT}$  hull, this corresponds to a square root grid distribution in the longitudinal direction. From the tables, some indication of convergence is observed, although a definite trend is still difficult to obtain. This suggests that possibly larger numbers of panels may be required for more accurate predictions at these Froude numbers. Comparing the three grid distributions, the geometric grids seem to give the best and most consistent results. For the calculations in this and later sections, a geometric grid with  $N=168$  ( $28 \times 6$ ) and  $\Delta t=2\pi/40$  was used.

To obtain a complete resistance curve, the calculation of Fig. (12) was repeated for Froude numbers ranging from 0.2 to 0.45. The final results are shown in Fig. (15) together with the ITTC experimental data. The overall comparison is quite satisfactory.

Finally, we evaluate the possible effect of the start-up velocity profile on the steady-state force predictions. For illustration, three velocity profiles were considered with  $V(t)=0$  for  $t < 0$ ,  $V(t) = U$  for  $t > T_1$ , and for  $0 < t < T_1$ : (i) impulsive start,  $V(t) = U$ ; (ii) ramp start,  $V(t) = Ut/T_1$ ; and (iii) cosine-function start,  $V(t) = U[1 - \cos(\pi t/2T_1)]/2$ . Fig. (16) shows the horizontal force time histories for these three cases with  $T_1/T_0=0.6$ . The initial transients and the phases of the later oscillations differ appreciably between (i) and (ii),(iii) but the same steady-state value is reached. As expected, the smoother ramp and cosine-function profiles produce smaller transient and  $T_0$  oscillations (associated with milder start-up disturbances) and are preferred for practical resistance predictions using SAMP.

Table 2: Wave resistance coefficients  $C_x \times 10^3$  of the  $W_{RT}$  hull at  $F_n=0.3$  as a function of grid size and distribution.

$\Delta t/2\pi$	uniform grid			cosine grid			geometric grid		
	20x6	28x6	36x6	20x6	28x6	36x6	20x6	28x6	36x6
1/20	2.53	2.84	1.70	2.82	1.99	1.48	1.20	1.48	2.50
1/30	2.50	1.37	1.58	1.82	1.87	0.94	1.57	1.62	1.60
1/40	1.68	2.79	1.26	1.22	1.84	1.78	1.29	1.64	1.75

Table 3: Wave resistance coefficients  $C_x \times 10^3$  of the  $W_{RT}$  hull at  $F_n=0.4$  as a function of grid size and distribution.

$\Delta t/2\pi$	uniform grid			cosine grid			geometric grid		
	20x6	28x6	36x6	20x6	28x6	36x6	20x6	28x6	36x6
1/20	1.32	1.56	1.53	1.43	1.62	1.71	1.42	1.68	2.07
1/30	0.33	2.50	1.96	1.68	1.98	2.12	2.24	2.07	1.94
1/40	4.22	1.24	2.24	1.61	2.33	2.10	2.05	2.15	2.09

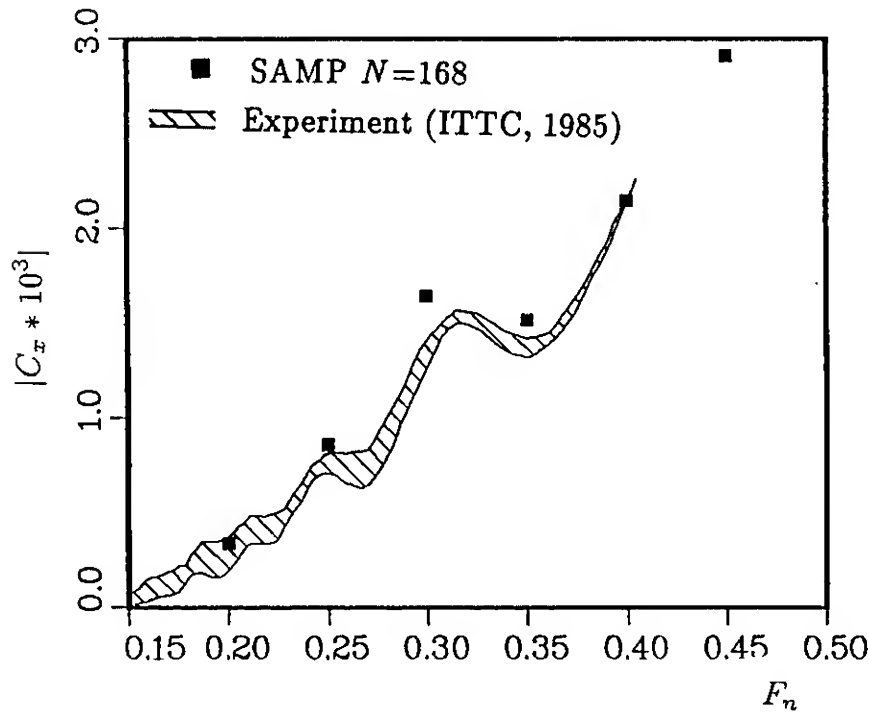


Fig. 15: Wave resistance coefficient for the  $W_{RT}$  hull as a function of Froude number.

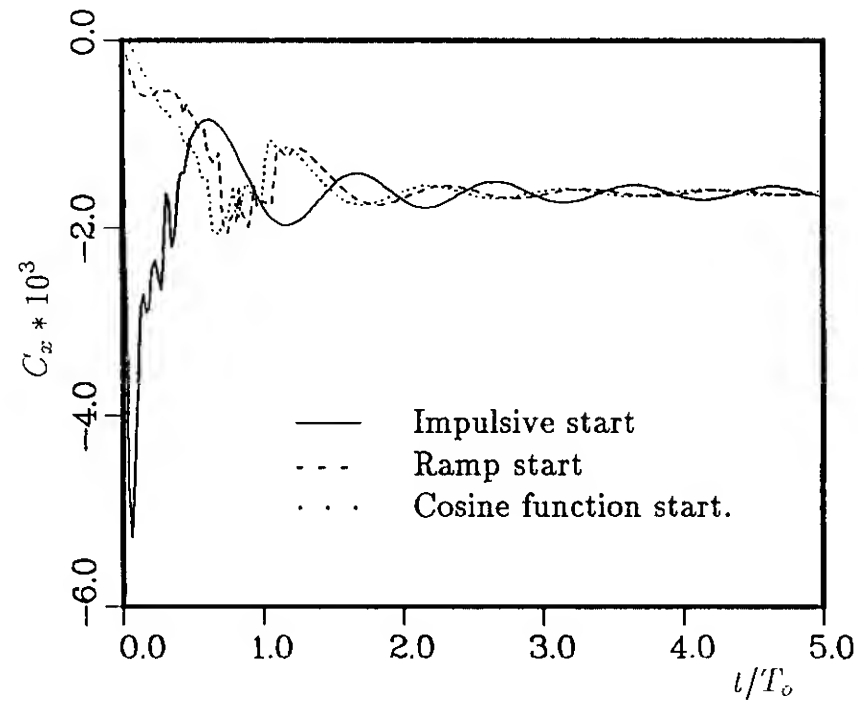


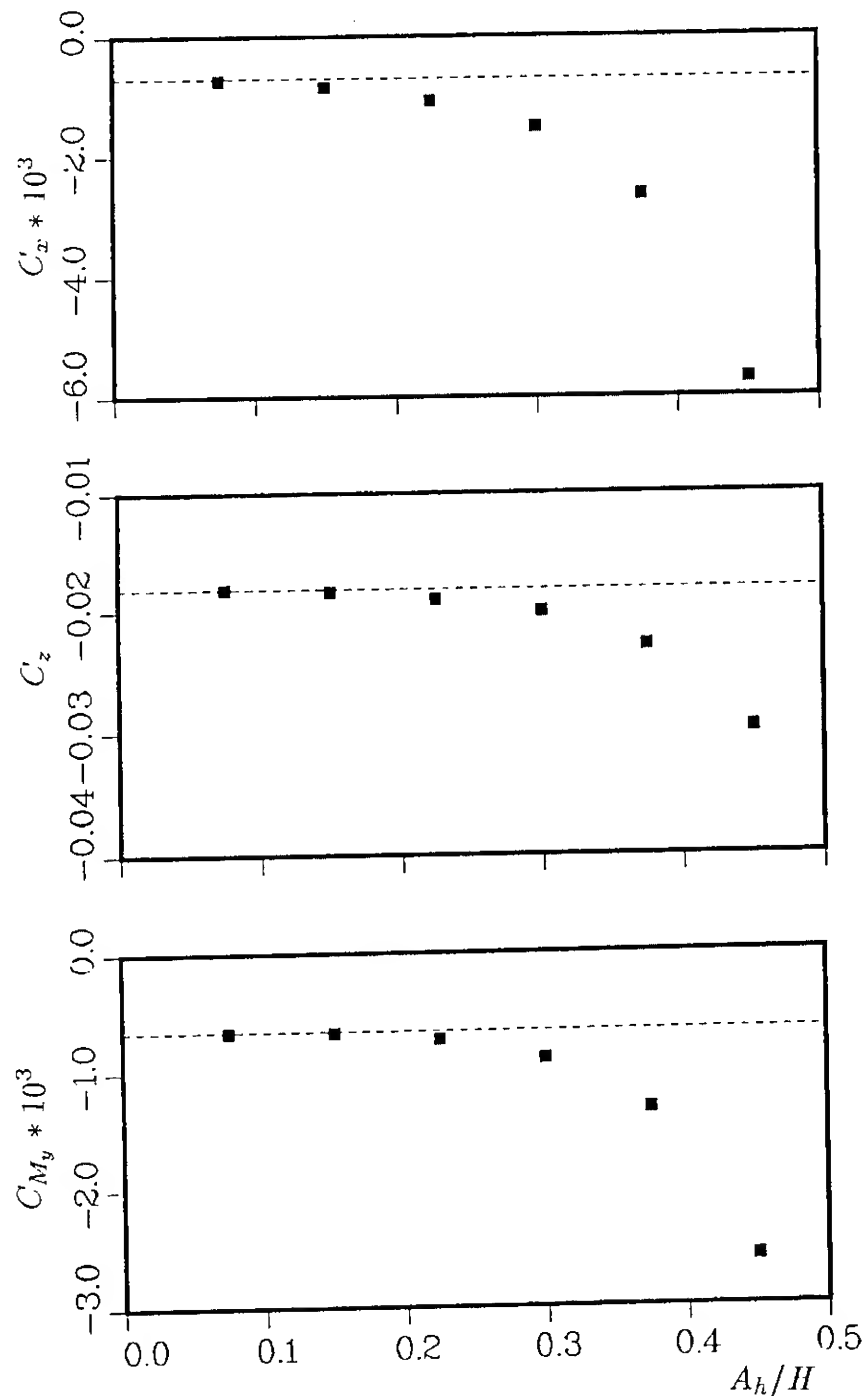
Fig. 16: Horizontal force time history for a  $W_{RT}$  hull moving at  $F_n=0.3$  using different start-up velocity profiles ( $T_1/T_0=0.6$ ).

#### 4.5 Large-Amplitude Motions with Forward Speed

A main objective of this work is to evaluate and quantify the importance of large-amplitude motions on seakeeping characteristics. While the change of such relevant quantities as added mass (and hence natural frequencies and response ampli-

tudes) due to large-amplitude motions can be expected on physical grounds, and has been reported in experiments (e.g., O'Dea & Troesch, 1987), the precise magnitudes or even dependencies are as yet not well known.

To address this problem, the LAMP program was applied to the large-amplitude forced heav-



Figs. 17: Steady surge, heave and pitch forces and moment on a heaving (frequency  $\omega=1.0$ , amplitude  $A_h$ )  $W_{RT}$  hull moving with constant forward speed ( $F_n=0.2$ ). ■ : LAMP ( $N=160$ ); - - - : 'calm-water' ( $A_h=0$ ) value obtained with SAMP.

ing of a  $W_{RT}$  hull moving with constant forward speed. Specifically we chose a Froude number  $F_n=0.2$ , a heaving frequency  $\omega=1.0$ , and considered a range of heaving amplitudes corresponding to  $A_h/H \sim 7.5 - 45\%$  where  $H$  is the draft. Figs.(17) show the added resistance, added sinkage and added trim forces as a function of the heave amplitude. For contrast, the 'calm-water' values (cf. Sec.4.4) are also indicated. For small  $A_h/H$ , the results are close to the calm-water values as expected and the approach to this limit is very smooth. As the amplitude increases, however, the

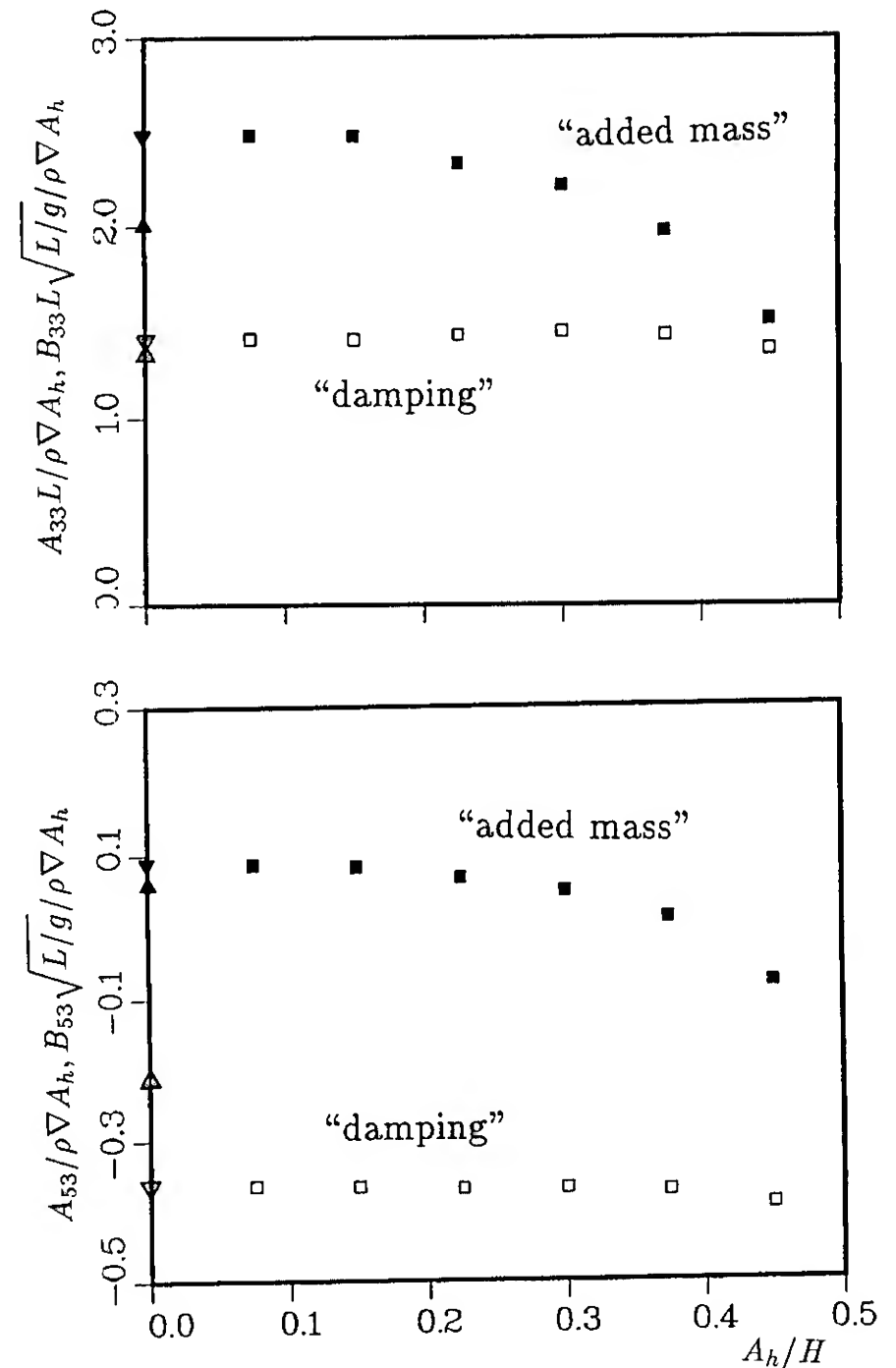


Fig. 18: Excitation frequency components of the limit-cycle forces and moment on a heaving ( $\omega=1.0$ , amplitude  $A_h$ )  $W_{RT}$  hull moving with constant forward speed ( $F_n=0.2$ ). ■ in phase with acceleration ("added-mass"); □ out-of-phase with acceleration ("damping") coefficients using LAMP ( $N=160$ ). Also indicated are ▼, ▽ : small-amplitude limits (LAMP<sub>0</sub>); and ▲, △ : SAMP added mass and damping coefficients.

added resistance increases rapidly and is as much as  $O(5)$  or more times the calm-water value for the larger amplitudes considered. The picture is similar for the mean vertical force and moments but somewhat less dramatic.

By analysing the limit-cycle force and moment histories for the frequency components at the forcing frequency that are in phase and out of phase respectively with the acceleration, the so-called large-amplitude "added-mass" and "damping" coefficients with forward speed can again be identified (cf. Sec.4.3). These diagonal and off-diagonal



seakeeping coefficients are shown in Figs.(18) as a function of  $A_h/H$ . For small amplitudes, the approaches to the linear (zero amplitude) limits are very smooth allowing accurate extrapolation for the linearized LAMP<sub>0</sub> estimates. As noted in Figs.(3,4), this small-amplitude limit of LAMP differs from the linearized SAMP prediction (also shown in Figs.18) because of the absence of the effect of the  $m$ -terms in the latter.

As in the case for the heaving sphere with no forward speed (Figs.11), the large-amplitude added mass shows a clear dependence on the amplitude and decreases appreciably as  $A_h$  increases. As an illustration, when the heave amplitude is  $\sim 40\%$  of the draft,  $A_{33}$  has decreased to about 60% of the small-amplitude value. For the present  $W_{RT}$  hull, the waterplane area changes very little with heave amplitude and consequently the relevant heave natural frequency would increase by  $\sim 20\%$  compared to the linear value in this case. This may explain some of the "unexpected" dependencies of the response amplitude functions on forcing amplitude observed in experiments. As with the sphere with no forward speed, the LAMP damping coefficients here are less sensitive to heave amplitude probably due to the fact that nonlinear radiation mechanisms are absent in the present approximation.

#### 4.6 Motions of a Floating Body and Unsteady Loads

With the ability to determine the relevant hydrodynamic forces at any given instant, the complete six degree-of-freedom motion history of the body can be obtained by a direct integration of the dynamical equations. Thus LAMP can be employed to study general time-dependent motions such as in the case of a ship advancing in an irregular seaway. Indeed, one of the important applications is the study of *episodic* events involving large loads and motions in the time domain.

To validate the motions solver, we consider first the decaying motions of a freely-floating sphere released from rest with a given initial vertical displacement. As a test, we integrate the problem directly in time, although for the linearized problem the solution can be obtained by a Laplace transform involving the force impulse-response function of Fig. (1) (Liapis, 1986). Consistent with the open time quadrature formula of (17), we employ an ex-

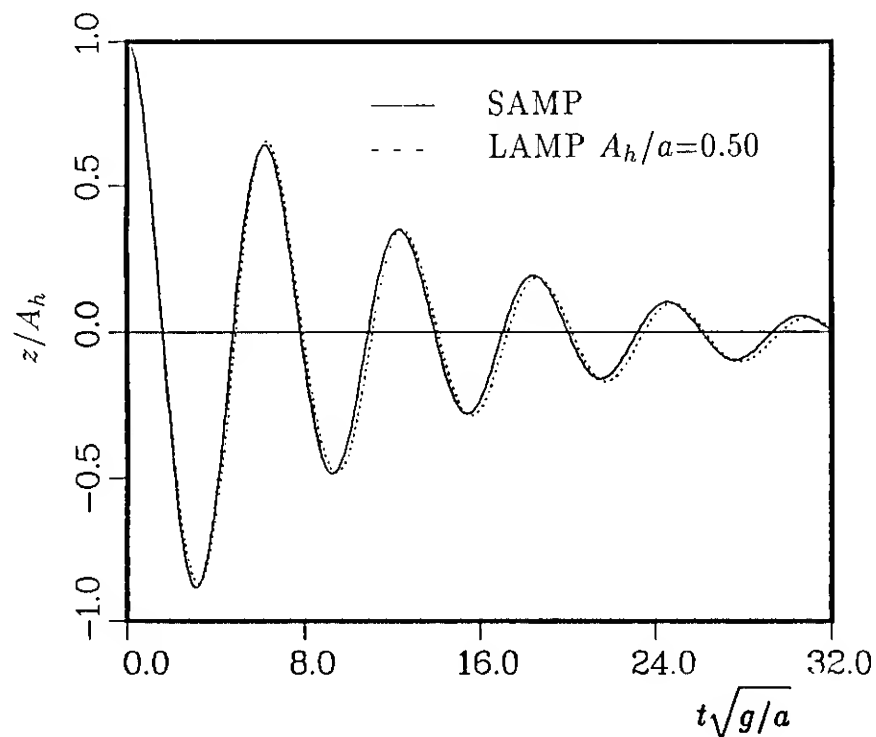


Fig. 19: Vertical displacement history of a floating hemisphere released from rest with an initial height  $A_h$ .

plicit multi-step scheme for the motion time integration.

First, SAMP computations were performed and compared to the linearized calculations and small-amplitude experiments of Liapis (1986). The results are indistinguishable and very close to the measurements and are not shown. Fig. (19) shows the SAMP and LAMP (for initial amplitude  $A_h/a=0.5$ ) results with  $N=150$  and  $\Delta t=0.1$ . The difference in the (normalized) amplitudes is small but it is of interest to note that the LAMP oscillation periods are longer than the linearized values by about 5%. This is caused by the competing effects of added-mass decrease due to large-amplitude motions (*cf.* Fig. (11)) which tends to decrease the period, and the reduction in the average waterplane area (and hence the hydrostatic force) which tends to increase the period of oscillation. In this case, the latter effect is greater and consequently an increase in natural period is observed. This again underscores the importance of nonlinear geometry effects.

An interesting application of the motion program is to reexamine the calm-water resistance problem of Sec.4.4 but this time allowing the body to freely sink and trim until steady-state values are reached. Starting from rest, the ship is held to a constant forward speed but is otherwise free to heave and pitch. In the large-amplitude simulation, the underwater geometry is allowed to change as steady-

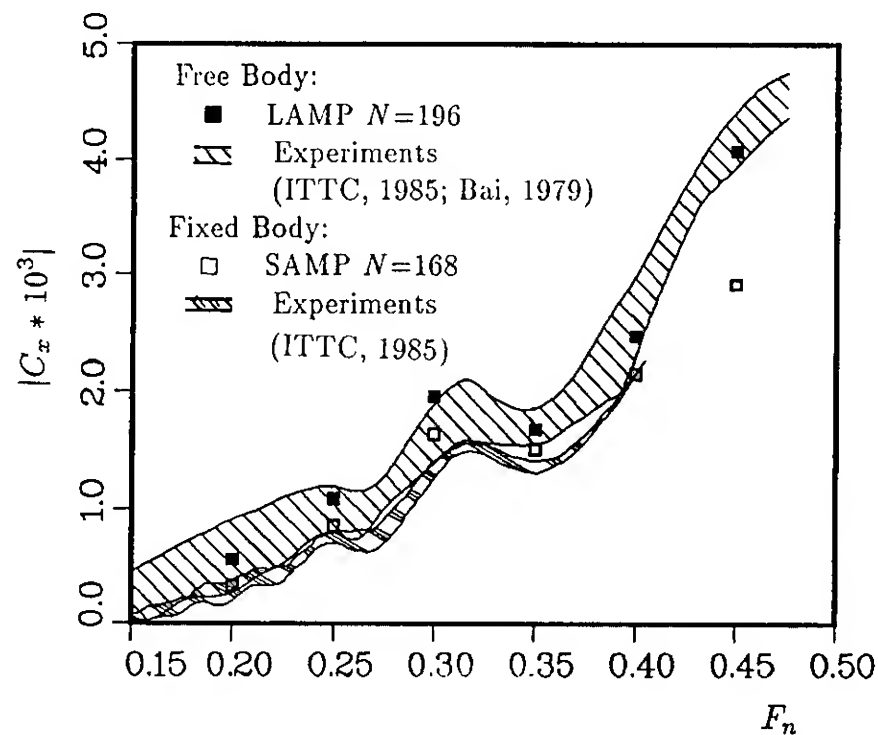


Fig. 20: Wave resistance coefficient for the  $W_{RT}$  hull as a function of Froude number.

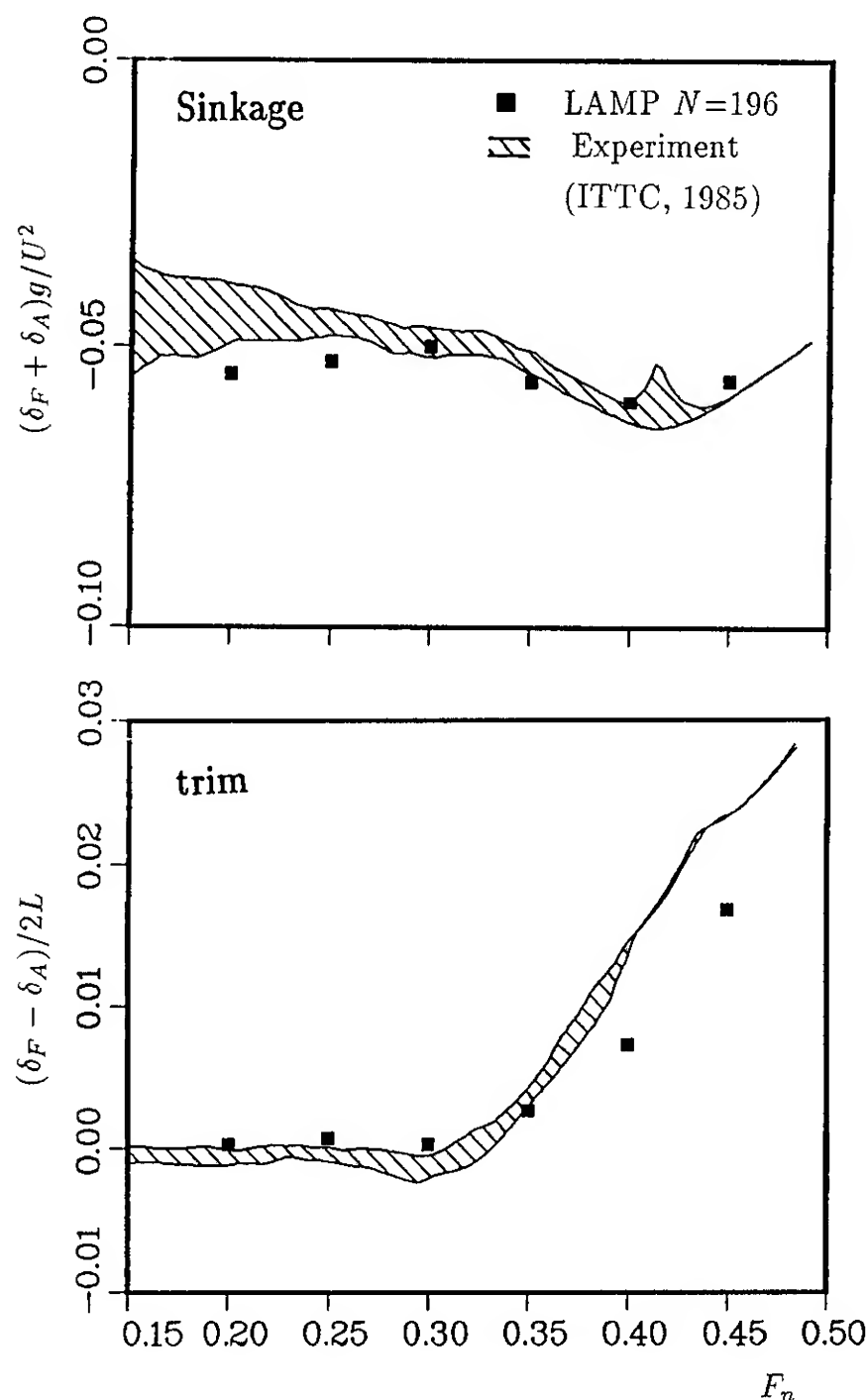


Fig. 21: Sinkage (a) and trim (b) of the  $W_{RT}$  hull as a function of Froude number.  $\delta_A \equiv$  draft at  $AP$ ,  $\delta_F \equiv$  draft at  $FP$ . Positive trim means bow up.

state is attained by an equilibrium between hydrostatic forces of the final geometry and the steady vertical force and pitch moment.

Fig. (20) shows the free sinkage and trim wave resistance of the  $W_{RT}$  hull as compared to corresponding experimental measurements as well as the fixed body resistance results of Fig. (15). The present LAMP calculations use  $\Delta t = 2\pi/40$  and  $N=196$  ( $28 \times 7$ ) where an extra horizontal row of panels is added to the grid of Fig. (15) to model the extra draft due to sinkage. From the figure, the increase in wave resistance due to sinkage and trim is clearly predicted. Comparisons between the LAMP results and experiments are excellent.

The comparison for sinkage and trim is shown in Figs. (21). The LAMP predictions are again satisfactory both in the magnitude and the forward speed dependence. The results are somewhat better for the sinkage and show a slight underprediction of the trim at higher speeds. Since sinkage is the main reason for the resistance increase, the under-prediction of trim at high  $F_n$  does not affect the resistance prediction significantly.

Finally, we applied LAMP to study free vertical-plane motions of a ship advancing in irregular head seas. A time record of the free surface was constructed using a two-parameter Pierson-Moskowitz spectrum with a significant wave height  $H_{1/3}=10$  feet and a modal period  $T_m=12$  seconds with low and high frequency cutoffs at 0.1 and 4.25 rad/sec respectively.

A 400 foot long  $W_{RT}$  hull with constant forward speed corresponding to  $F_n=0.2$  was first chosen. Figure (22) shows the time history of the incident wave elevation at the ship center of gravity, along with the pitch and heave displacements from LAMP calculations ( $N=160$ ,  $\Delta t=0.3526$  seconds). For contrast, strip theory predictions obtained by superposition of the linear frequency-domain responses at the component incident frequencies are also included. To be consistent with the strip theory program used here, the LAMP calculations include the hydrostatic (and Froude-Krylov) forces only up to the mean waterline. To remove the effects of starting transients, the LAMP simulation has been started from rest at  $t=-10$  seconds.

As can be seen in Fig. (22), the differences between LAMP and strip theory are small for the pitch displacement, with the exception of apparent memory (transient) effects around  $10 < t < 60$  and

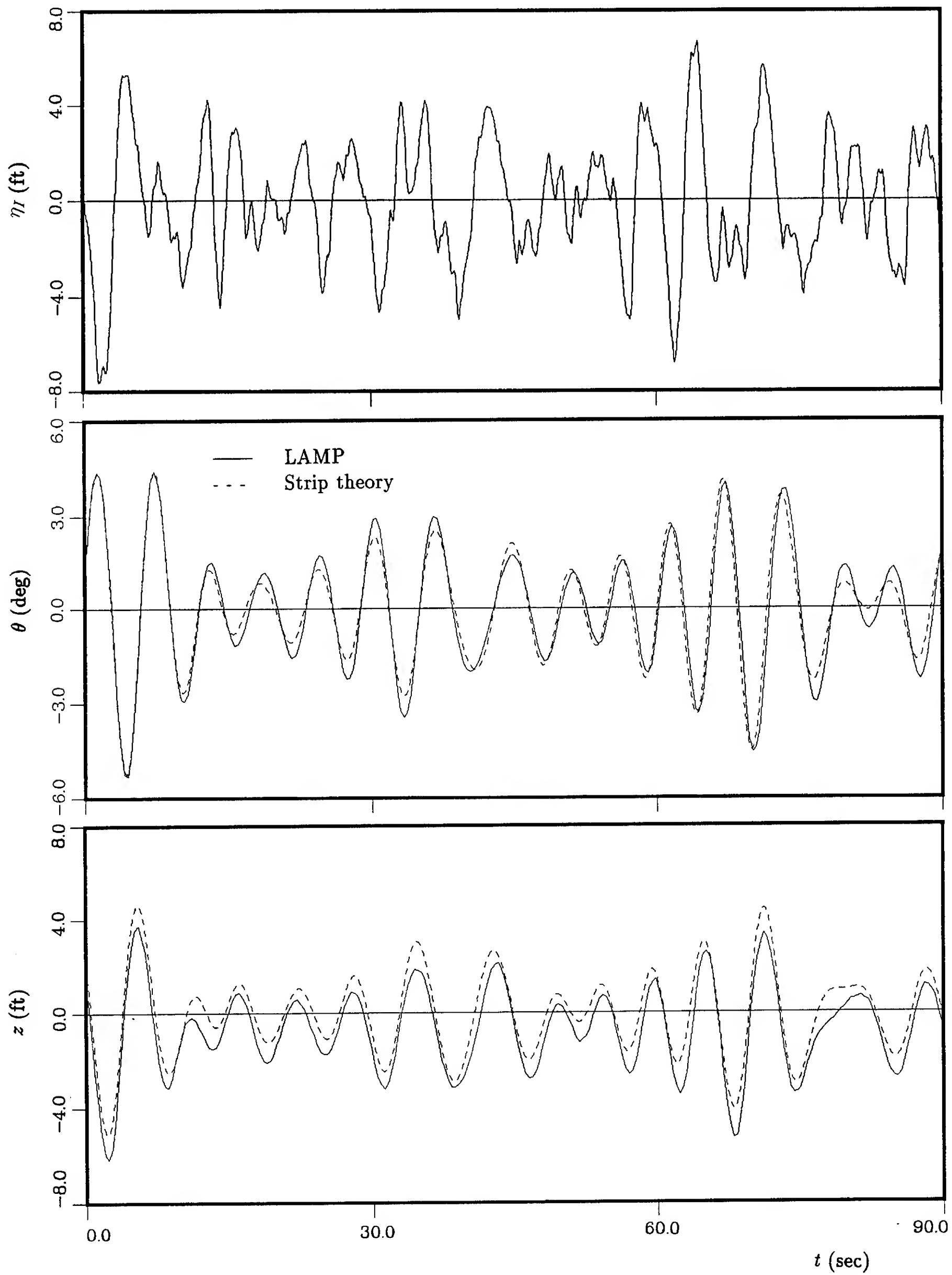


Fig. 22: Incident wave elevation ( $\eta_I$ ) at the ship's center of gravity, pitch angle ( $\theta$ ), and heave displacement ( $z$ ) of a  $W_{RT}$  hull at  $F_n=0.2$  in irregular head seas.

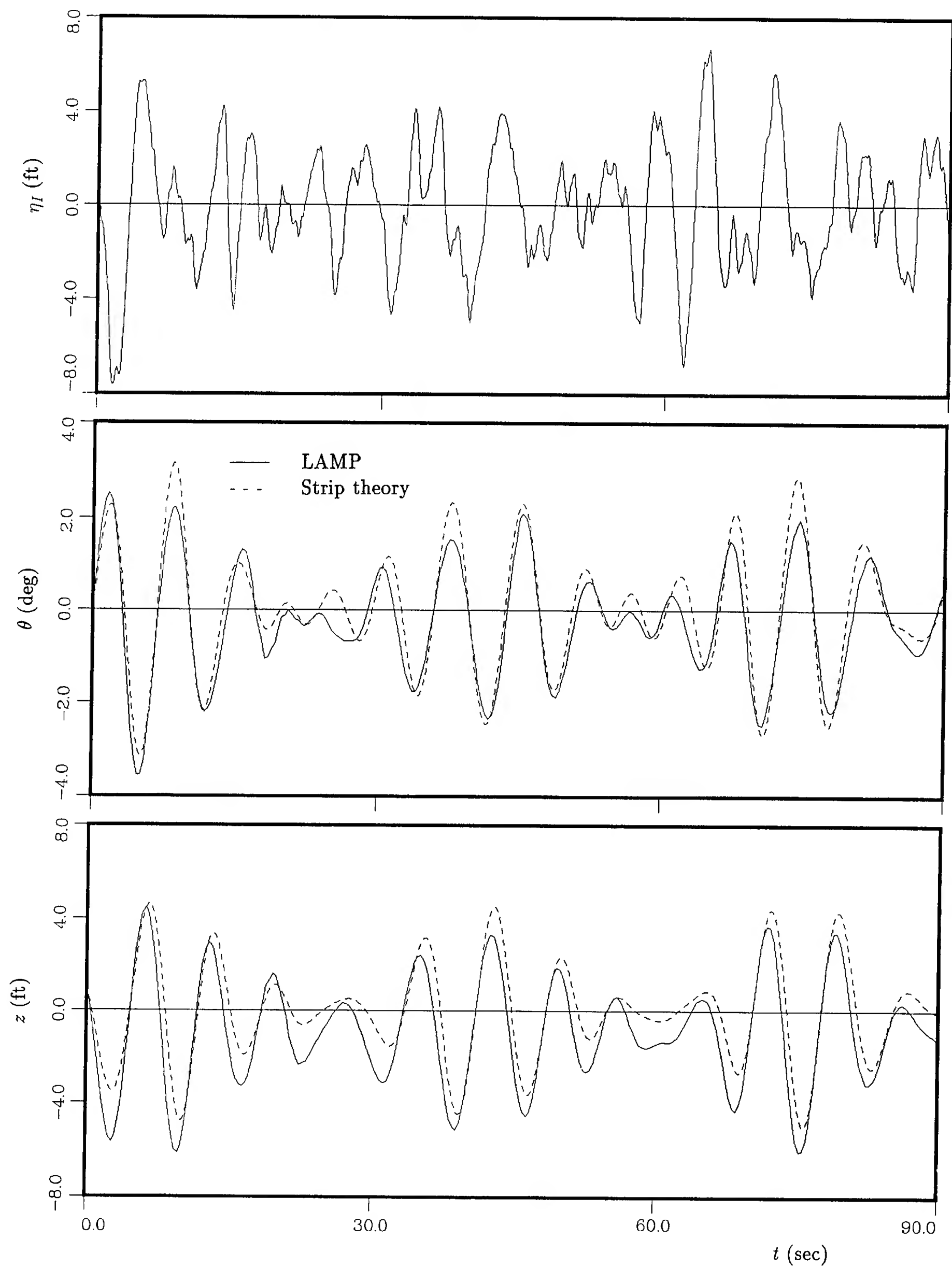


Fig. 23: Incident wave elevation ( $\eta_I$ ) at the ship's center of gravity, pitch angle ( $\theta$ ), and heave displacement ( $z$ ) of a Series 60 ( $C_B=0.70$ ) hull at  $F_n=0.2$  in irregular head seas.

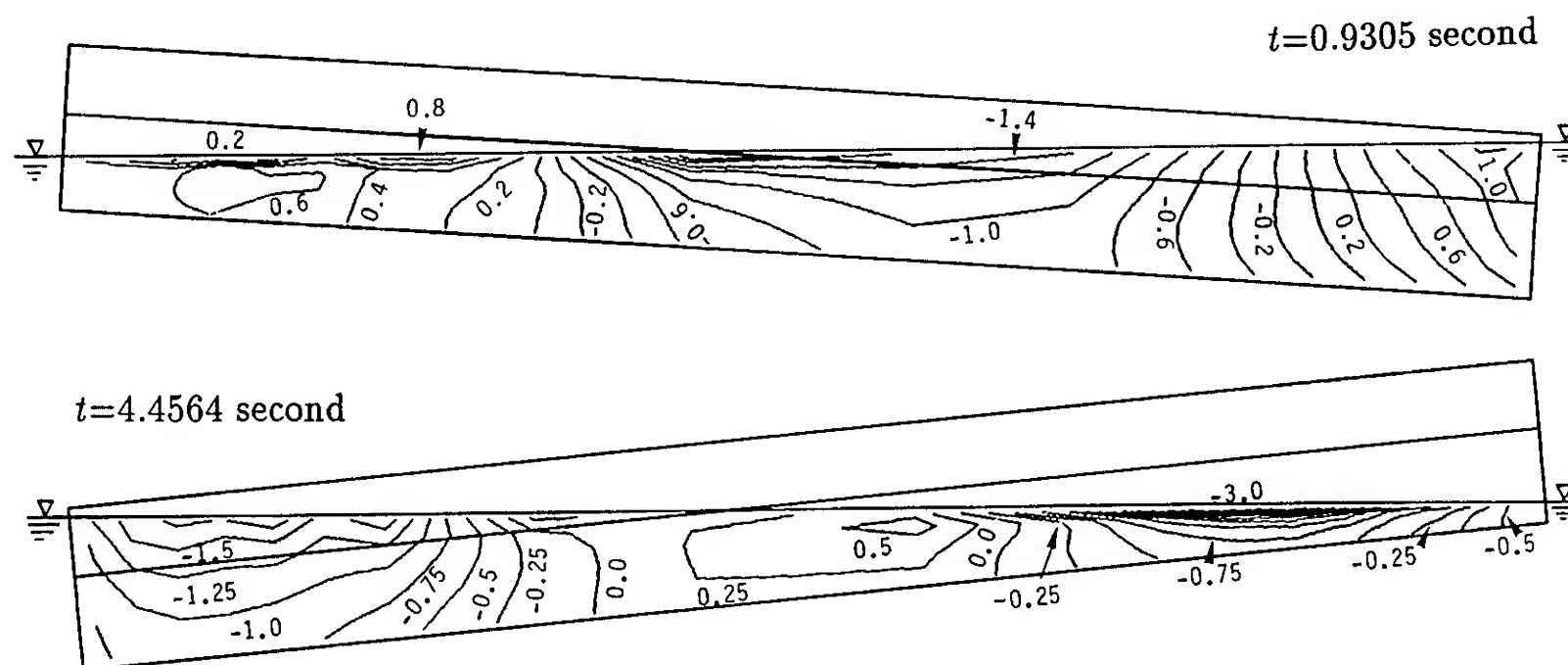


Fig. 24: Non-dimensional dynamic pressure distribution on a  $W_{RT}$  hull at two time instances.

$80 < t < 90$ . The same is true for the heave displacement except for a nearly constant downward shift of the nonlinear result. This is caused by the steady sinkage force associated with forward speed which is present in LAMP but absent in the strip theory (from Fig. 21, this is estimated at about 0.53 feet for a 400 foot hull). Overall, the relative good performance of the strip theory is not unexpected for the mathematical  $W_{RT}$  hull (with relatively small geometry changes near the water line) and for head seas.

For a more realistic geometry, we show in Fig. (23) the corresponding case for a 400 foot long Series 60 ( $C_B=0.7$ ) hull at  $F_n=0.2$ . In this case, strip theory overpredicts the pitch motion significantly, in some instances by over 50% (e.g., near  $t=75$  sec). For the heave displacement, there are appreciable underpredictions of the troughs in addition to the absence of the steady downward sinkage. These deficiencies of strip theory for the more complicated Series 60 hull are consistent with the observations of Frank & Salvesen (1970).

As a final illustration, we display the pressure distribution on the hull as output from LAMP. Fig. (24) shows the dynamic pressure distribution on the  $W_{RT}$  hull at  $t=0.9305$  and 4.4564 seconds respectively corresponding to the case in Fig. (22). Note that the pressures are given on the actual submerged surface. The complete unsteady loads on the ship hull can now be obtained from the pressure distribution and motion histories.

## 5 CONCLUSIONS

A time-domain method, LAMP (Large-Amplitude Motion Program), was developed for the general large-amplitude motions of a three-dimensional surface-piercing body in a seaway. The body boundary condition is satisfied exactly on the instantaneous underwater body surface while a linearized free-surface condition is used.

To validate the approach and evaluate its accuracy, the method was applied extensively to obtain linearized motion coefficients for a number of different geometries with or without forward speed. The results include added-mass and damping coefficients, wave exciting forces and steady wave resistance, sinkage and trim forces and moments. These are compared to experimental measurements and existing linear time- and frequency-domain calculations. The comparisons are overall satisfactory for all the results and show that LAMP is equal or superior to any of the existing computational methods in terms of accuracy.

The main feature and purpose of LAMP, however, is for general nonlinear large-amplitude motions. To illustrate its effectiveness, we apply LAMP to study the large-amplitude forced heaving of a (complete) floating sphere; the large vertical-plane motions and the free sinkage and trim of a Wigley hull moving with constant forward speed; and the general time-dependent large-amplitude motions of a Series-60 ship advancing in an irregular seaway.

Some of the main findings are the importance of (added) steady (and higher-harmonic) components, and the modifications of the first-harmonic (excitation frequency) motion coefficients. In the first case, the presence of large-amplitude heaving motions is shown to result in significant increases of the wave resistance and steady sinkage and trim forces. In the latter, the nonlinear "added-mass" is found to decrease markedly with increasing heave amplitude. The consequent reduction of inertia and increase in natural frequency may have important implications to the motion dynamics of the ship. This may also explain some of the experimentally observed dependencies on amplitude of normalized motion response functions. When applied to general time-dependent motions in irregular waves, LAMP demonstrates the importance of transient (memory) and nonlinear geometry effects especially for realistic ship geometries where strip theory is found to be inadequate. The road is now laid for nonlinear simulations of extreme episodic events and complete load and motion predictions.

The current version of LAMP is fully vectorized for high-speed vector processors. For a nonlinear (large-amplitude) simulation using  $O(150-200)$  unknowns on the body and a similar number of time steps, the typical CPU time on a single Cray Y-MP processor is  $O(1-2)$  hours. Further code optimization may reduce this requirement by a small factor. For applications involving significantly larger number of unknowns and time steps, the time domain formulation may be particularly suited for parallel algorithms on multiple processors.

## Acknowledgement

This research was sponsored by the Office of Naval Research, the U.S. Coast Guard, and the Defense Advanced Research Projects Agency. We are grateful to Cray Research, Inc., for the use of their Cray Y-MP/832 supercomputer. Some computations were also performed on the NSF Pittsburgh Supercomputer Center Cray Y-MP. We thank M. Meinhold and K. Weems for valuable technical and graphical help.

## REFERENCES

- Adachi, H. & Ohmatsu, S. (1979), "On the influence of irregular frequencies in the integral equation solutions of the time dependent free surface problems" *J. Eng. Math.*, **16**: 97-119.
- Bai, K.J. (1979), "Overview of results," *Proc. of the Workshop on Ship Wave-Resistance Computation*, DTNSRDC, USA.
- Beck, R.F. & Liapis, S.J. (1987), "Transient motion of floating bodies at zero forward speed" *J. Ship Res.*, **31**: 164-176.
- Beck, R.F. & Magee, A. (1990), "Time-domain analysis for predicting ship motions," *Proc. IUTAM Symp., Dynamics of Marine Vehicles & Structures in Waves*, London.
- Bertram, V. (1990), "A Rankine source approach to forward speed diffraction problems," *Proc. 5th Intl. Workshop on Water Waves and Floating Bodies*, Manchester.
- Boppe, C. W., Rosen, B. S., & Laiosa, J. P. (1987), "Stars and Stripes 87: Computational flow simulations for hydrodynamic design," *8th Chesapeake Sailing Yacht Symposium (SNAME)*, pp. 123-146.
- Chang, M.S. (1977), "Computation of three-dimensional ship motions with forward speed," *Proc. 2nd Intl. Conf. Num. Ship Hydro.*, UC Berkeley, California.
- Chang, B. & Dean, J.S. (1986), "User's manual for the XYZ Free Surface Program," Report No. DTNSRDC-86/029.
- Cohen, S.B. (1986), "A time-domain approach to three-dimensional free-surface hydrodynamic interaction in narrow basins," Ph.D. Thesis, U. Michigan, Ann Arbor, Michigan.
- Cummins, W.E. (1962), "The impulsive response function and ship motions" *Schiffstechnik*, **9**: 124-135.
- Dagan, G. & Miloh, T. (1980), "Flow past oscillating bodies at resonant frequency," *Proc. 13th Symp. Naval Hydro.*, Tokyo, Japan, 355-373.
- Dawson, C.W. (1977), "A practical computer method for solving ship-wave problems," *Symp. 2nd Intl. Conf. Num. Ship Hydro.*, UC Berkeley, California.
- Dawson, C.W. (1979), "Calculations with the XYZ Free Surface Program for five ship models," *Proc. Workshop Ship Wave-Resistance Computations*, DTRC.
- Dommermuth, D.G. & Yue, D.K.P. (1988), "The nonlinear three-dimensional waves generated by a moving surface disturbance," *Proc. 17th Symp. Naval Hydro.*, The Hague, The Netherlands.
- Dommermuth, D.G. & Yue, D.K.P. (1986), "Study of nonlinear axisymmetric body-wave interactions," *Proc. 16th Symp. Naval Hydro.*, UC Berkeley, California.
- Ferrant, P. (1988), "Radiation d'ondes de gravité par les déplacements de grande amplitude d'un corps immergé: comparaison des approches fréquentielle et instationnaire," thèse de Doctorat, Université de Nantes.
- Finkelstein, A. (1957), "The initial value problem for transient water waves" *Comm. Pure App. Math.*, **10**.
- Frank, W. & Salvesen, N. (1970), "The Frank close-



- fit ship-motion computer program," DTNSRDC Report No. 3289.
- Froude, W. (1868), "Observations and suggestions on the subject of determining by experiment the resistance of ships," *The Papers of William Froude*: 120-127.
- Gadd, G.E. (1976), "A method for computing the flow and surface wave pattern around full forms," *Trans. Roy. Inst. Naval Arch.*, 113: 207.
- Gerritsma, J. (1960), "Ship Motions in Longitudinal Waves," *Intl. Shipbuilding Progress*, 66: 42-95.
- Gerritsma, J. (1988), "Motions, wave loads and added resistance in waves of two Wigley hull forms," Rep. No. 804, Technical University of Delft, Netherlands.
- Guevel, P. & Bougis, J. (1982), "Ship motions with forward speed in infinite depth," *Intl. Shipbuilding Progress*, 29: 103-117.
- Hess, J.L. & Smith, A.M.O (1964), "Calculation of non-lifting potential flow about arbitrary three-dimensional bodies," *J. Ship Res.*, 8: 22-24.
- Hulme, A. (1982), "The wave forces acting on a floating hemisphere undergoing forced periodic oscillations," *J. Fluid Mech.*, 121: 443-463.
- Hulme, A. (1983), "A ring-source/integral equation method for the calculation of hydrodynamic forces executed on floating bodies of revolution," *J. Fluid Mech.*, 128: 387-412.
- Inglis, R.B. & Price, W.G. (1981), "A three-dimensional ship motion theory — comparison between theoretical prediction and experimental data of the hydrodynamic coefficients with forward speed," *Trans. Roy. Inst. Naval Arch.*, 124: 141-157.
- Jensen, G., Soeding, H. & Mi, Z.X. (1988), "Rankine source methods for numerical solutions of the steady wave resistance problem," *Proc. 17th Symp. Naval Hydro.*, The Hague, The Netherlands.
- King, B.W. (1987), "Time-domain analysis of wave exciting forces on ships and bodies," Report No. 306, Dept. Naval Arch. Marine Eng., U. Michigan, Ann Arbor, Michigan.
- King, B.W., Beck, R.F. & Magee, A.R. (1988), "Seakeeping calculations with forward speed using time domain analysis," *Proc. 17th Symp. Naval Hydro.*, The Hague, Netherlands.
- Korsmeyer, F.T. (1988), "The first and second order transient free-surface wave radiation problems," Ph.D Thesis, Dept. Ocean Eng., MIT, Cambridge, Massachusetts.
- Korsmeyer, F.T., Lee, C.-H., Newman, J.N. & Sclavounos, P.D. (1988), "The analysis of wave effects on tension leg platforms," *Proc. Intl. Conf. Offshore Mech. & Arctic Eng.*, Houston, Texas.
- Larsson, L. (1987), "Numerical predictions of the flow and resistance components of sailing yachts," *Proc. Conf. Yachting Tech.*, U. W. Australia, Australia.
- Letcher, J.S., Weems, K.M., Oliver, J.C., Shook, D.M. & Salvesen, N. (1989), "SLAW: Ship Lift and Wave Code, theory, implementation, and numerical results," SAIC Report 89/1196.
- Liapis, S.J. & Beck, R.F. (1985), "Seakeeping computations using time-domain analysis," *Proc. 4th Intl. Conf. Num. Ship Hydro.*, National Academy of Sciences, Washington, D.C., 34-54.
- Liapis, S.J. (1986), "Time-domain analysis of ship motions," Report No. 302, Dept. Naval Arch. Marine Eng., U. Michigan, Ann Arbor, Michigan.
- Lin, W.M., Newman, J.N. & Yue, D.K.P. (1984), "Non-linear forced motions of floating bodies," *Proc. 15th Symp. Naval Hydro.*, Hamburg, West Germany
- Lin, W.M. & Yue, D.K.P. (1990), "LAMP — Large Amplitude Motion Program," SAIC report (in preparation).
- Magee, A.R. & Beck, R.F. (1988), "Compendium of ship motion calculations using linear time-domain analysis," Report No. 310, Dept. Naval Arch. Marine Eng., U. Michigan, Ann Arbor, Michigan.
- Magee, A.R. & Beck, R.F. (1989), "Vectorized computation of the time-domain Green function," *Proc. 4th Intl. Workshop on Water Waves & Floating Bodies*, Oystese, Norway, 139-144.
- McCarthy, J.H. (1985), "Collected experimental resistance component and flow data for three surface ship model hulls," Report No. DTNSRDC-85/011.
- Michell, J.H. (1898), "The wave resistance of a ship," *Phil. Mag.*, 45: 106-123.
- Nakos, D.E. & Sclavounos, P.D. (1990), "Ship motions by a three-dimensional rankine panel method," *18th Symp. Naval Hydro.*, Ann Arbor, Michigan.
- Newman, J.N. (1985), "The evaluation of free-surface Green functions," *Proc. 4th Intl. Conf. Num. Ship Hydro.*, National Academy of Sciences, Washington, D.C.
- Newman, J.N. (1990), "The approximation of free-surface Green functions," *Proc. Fritz Ursell Retirement Meeting*, London.
- O'Dea, J. & Troesch, A.W. (1987), "Comparative seakeeping model experiments," *Proc. ATTC*.
- Ogilvie, T.F. & Tuck, E.O. (1969), "A rational strip theory for ship motions — part I," Report No. 013, Dept. Naval Arch. Marine Eng., U. Michigan, Ann Arbor, Michigan.
- Salvesen, N., Tuck, E.O. & Faltinsen, O. (1970), "Ship motions and sea loads," *Trans. Soc. Naval Arch. Marine Eng.*, 78: 250-287.
- Stoker, J.J. (1957), "Water Waves," *Pure and App. Math.*, Volume IV.
- Wehausen, J.V. (1964), "Effect of the initial acceleration upon the wave resistance of ship models," *J. Ship Res.*, 7: 38-50.
- Xia, F. (1986), "Numerical calculations of ship flows, with special emphasis on the free-surface potential flow," Dissertation, Chalmers U., Goteborg, Sweden.

## DISCUSSION

Pierre Ferrant  
Sirehna S.A., France

I would like to make a comment on your results about the heaving sphere. I do not completely agree with your analysis of the behaviour of the damping coefficient which you show to remain constant when amplitude is varied. My own results show that at least for a submerged body, the nonlinear phenomena associated to the body boundary condition are very frequency-sensitive. In fact, when dealing with oscillatory motions, even in the time domain, one cannot ignore the importance of frequency and this parameter must be varied before drawing conclusions. I would therefore be very interested if you could give result for the surface-piercing heaving sphere at lower frequencies, say about  $\omega \sqrt{R/g} = 0.4$ .

## AUTHORS' REPLY

We have preliminary results for the heaving (surface-piercing) sphere for normalized frequencies ranging from  $\omega \sim 0.4$  to  $\sim 3$  and amplitudes ranging from  $A_h/a \sim 0$  to  $\sim 0.5$  or higher. In contrast to your results for the submerged sphere, the damping coefficient remains relatively independent of amplitude for lower frequencies ( $\omega < \sim 1$ ) and shows some sensitivity only for intermediate frequencies. The precise mechanisms for these dependencies (an amplitude and frequency) are as yet not completely understood.

The following table lists the results for the frequency  $\omega = 0.4$  you suggested. For comparison, the data for Fig. (1) at  $\omega = 1.0$ , as well as  $\omega = 1.5$  and  $3.0$  are also included. Again, we note that these results are only preliminary.

Normalized damping coefficients for a (surface-piercing) heaving sphere.

$A_h/a$	$\omega=0.4$	$\omega=1.0$	$\omega=1.5$	$\omega=3.0$
0.125	0.036	0.195	0.151	0.314
0.250	0.036	0.195	0.154	0.312
0.375	0.035	0.195	0.170	0.312
0.500	0.035	0.194	0.185	0.316

# A Coupled Time and Frequency Approach for Nonlinear Wave Radiation

P. Ferrant (Laboratoire d'Hydrodynamique Navale, France)

## ABSTRACT

In this paper we report on computations using a semi nonlinear time domain formulation for the three-dimensional wave radiation problem with a free surface. The body boundary condition is applied at the actual time-dependent body surface, and the free surface conditions are linearized. An initial value problem is solved for the potential on the moving body, using a boundary elements method. The method allows the hydrodynamic forces on bodies of arbitrary geometry undergoing large amplitude forced motions in six degrees of freedom to be determined, as well as the unsteady wave field generated by the body motions.

Two different applications are presented. The first one refers to the problem of a sphere undergoing large amplitude periodic motions below the free surface. A thorough parametrical study (amplitude - frequency) has been completed in this first case, and the influence of the body nonlinearity is clearly highlighted both on the hydrodynamic forces and on the structure of the radiated wave field, which is investigated using specific frequency domain Green functions associated to the body-nonlinear problem. Some results on a submerged spheroid starting from rest with a constant velocity parallel to the free surface are also presented, as an unsteady approach to the wave resistance problem.

## INTRODUCTION

Time domain modelization of free-surface hydrodynamics is all but a new subject. Some time before the publication of the commonly quoted paper by Finkelstein (1957) on the time-domain Green function, Brard (1948) gave the expression of the time depending free-surface potential generated by a submerged source of arbitrary path and strength. The formulation of the integral equations of the linearized wave-body interaction problem in the time domain has been presented by many authors, including Stoker (1957) and Wehausen (1967), the latter with a clear presentation of the connection between frequency and time domain solutions for fully linearized problems.

With the increasing power of computers, practical numerical solutions of linearized time domain formulations have become available, starting with 2D problems with for example Adachi & Ohmatsu (1980) or Yeung (1982) with boundary elements methods (BEM). Jami (1982) solved the 2D problem using a mixed formulation associating finite elements and integral representation, and formulated the solution of the 3D problem, giving practical expressions for

the computation of the 3D time domain Green function. Newman (1985-a) solved the problem of the impulsive heaving motion of a floating cylinder, using time depending ring sources. Some time later, the 3D problem was solved numerically, both for forced and free motions of a floating sphere by Jami & Pot (1985), whereas Liapis (1985) presented the first results of a time-domain BEM formulation for the radiation problem with forward speed. Specific algorithms for the computation of the 3D time domain Green function were given. Newman (1985-b) presented his own algorithms for the Green function computation. The solution of the forward speed problem was extended to diffraction by King & al (1988).

The accurate numerical schemes for the computation of the time-domain Green function, developed at that time, were a prerequisite for the reliable solution of the time domain wave body interaction problem, and besides academic applications, computations on realistic bodies such as Tlp's became possible and demonstrated the interest of time domain methods for industrial applications, compared with more conventional frequency domain methods (Korsmeyer & al 1988). Nevertheless, the Cpu requirements of the model, mainly due to Green function evaluations, restricted the use of the corresponding codes to vector computers, with Cpu times much higher than for linear frequency domain analysis, on equivalent cases. A considerable speed-up was obtained by Ferrant (1988-a), using a tabulation-interpolation procedure for the evaluation of the time-domain Green function in infinite depth. The power of the method was demonstrated on the linear time domain analysis of the ISSC Tlp, discretized by 1200 panels. The results were obtained on a scalar computer (Vax8700) with moderate Cpu times.

Besides its interest for linear time-domain analysis, the tabulation-interpolation procedure puts Cpu requirements at a sufficiently low level to allow the so-called body-nonlinear problem to be solved in the time domain. In such a formulation, a linearized free surface condition is maintained, but the body boundary condition is applied at the exact time-dependent body surface. This leads to an integral formulation very similar to the fully linearized one, except for a line integral appearing in certain cases for surface-piercing bodies. The additional difficulty mainly lies in the numerical implementation, for the Green function terms in the convolution integrals have to be entirely recomputed at each time step, due to the changing position of the body surface on which the integral equations are solved. This results in  $O(Nt^2)$  Cpu times, where  $Nt$  is the number of time steps, to be compared with  $O(Nt)$  when the body boundary condition is linearized.

(1) now with SIREHNA SA, 2 quai de la Jonelière. 44300 NANTES-FRANCE.

A first experience on the solution of the body-nonlinear problem in the frequency domain was reported in Clément & Ferrant (1987), where partial results were given on a submerged sphere with forced heaving motion. Although results were successfully compared with the experiments of Dassonville (1987), the formulation was very heavy and the resulting code was not considered to be fully reliable, due to problems of convergence of the influence coefficients at large amplitude. Furthermore, the extension of the formulation to arbitrary motions was not possible. The only alternative was to solve the problem in the time-domain, but intensive computations with the basic code based on conventional schemes for the Green function were practically impossible, with about 12 Cpu hours on a Vax 8700 to reach steady-state with sufficiently fine time and space discretizations. This was in fact our main motivation for the development of the tabulation-interpolation procedure for the evaluation of the time-domain Green function. With simple arrangements in the convolution computations leading to  $O(Nt)$  Cpu times, the resulting code is considerably faster, and a typical run on the heaving sphere as presented in this paper requires now about 10 minutes.

Intensive runs of the program being possible, a complete parametrical study (amplitude-frequency) in the case of a submerged heaving sphere has been undercome, the results of which are presented in this paper. Time-depending forces and wave elevation, as well as the results of the harmonic analysis of steady-state are given for various values of the amplitude, over the whole significant frequency range. A method for the fast analysis of the steady-state radiated wave field, based on frequency domain Green functions for the body-nonlinear problem is also presented.

A few additional results are given on the time domain approach of the wave resistance problem, in order to demonstrate the versatility of the time-domain body nonlinear formulation, which is basically able to cope with any free-surface linear problem.

## TIME DOMAIN FORMULATION

### Basic Assumptions

The fluid domain  $D(t)$  is bounded by a free surface  $Sf(t)$ , the body surface  $Sb(t)$ , and is unbounded in horizontal directions. The fluid depth is infinite. A fixed coordinate system is chosen so that the  $z$ -axis points upwards, and the origin lies in the mean free surface. An ideal fluid is assumed, with irrotational flow, so that the fluid velocity derives from a potential satisfying Laplace's equation:

$$\Delta\Phi(x,y,z,t) = 0 \text{ in } D(t) \quad (1)$$

$$U(x,y,z,t) = \nabla\Phi(x,y,z,t) \text{ in } D(t) \quad (2)$$

The body boundary condition is applied at the actual time depending body surface, while the perturbation at the free surface is assumed to remain sufficiently small for a linearized condition to be valid, so that:

$$\frac{\partial\Phi}{\partial n} = \mathbf{V} \cdot \mathbf{n} \text{ on } Sb(t) \quad (3)$$

and:

$$\frac{\partial^2\Phi}{\partial t^2} + g \frac{\partial\Phi}{\partial z} = 0 \text{ on } Sf(z=0) \quad (4)$$

with:

- $\mathbf{n}$  unit normal on  $Sb(t)$  pointing out of the fluid domain  $D(t)$
- $\mathbf{V}$  local velocity of the body surface

Additionally, the fluid velocity must vanish at spatial infinity:

$$\nabla\Phi(x,y,z,t) \longrightarrow 0 \text{ for } (x^2+y^2) \longrightarrow \infty \text{ or } z \longrightarrow -\infty \quad (5)$$

and the fluid is supposed to be initially at rest:

$$\Phi, \Phi_t = 0 \text{ for } t = 0 \quad (6)$$

### Integral Equation

The fluid problem being now completely defined, various integro-differential representations of the solution may be derived, either for the potential on the moving body (distribution of sources and normal dipoles), or for the source density on the body (sources only), using Green's theorem and the threedimensional time domain Green function  $G(M,P,t)$  (see Appendix 1). In the first case, we obtain after some transformations the following integral equation to be solved for the velocity potential  $\Phi(M,t)$  on the moving body surface:

$$\begin{aligned} \frac{\Omega(M)}{4\pi} \Phi(M,t) - \iint_{Sb(t)} \Phi(P,t) \frac{\partial}{\partial n_P} G_o(M,P) dS_P \\ = - \iint_{Sb(t)} G_o(M,P) \frac{\partial}{\partial n_P} \Phi(P) dS_P \end{aligned} \quad (7)$$

$$\begin{aligned} + \int_0^t d\tau \iint_{Sb(\tau)} [\Phi(P,\tau) \frac{\partial}{\partial n_P} F(P(\tau),M(t),t-\tau) - F(P,M,t-\tau) \frac{\partial}{\partial n_P} \Phi(P,\tau)] dS_P \\ + \frac{1}{g} \int_0^t d\tau \int_{Cb(\tau)} [\Phi(P,\tau) \frac{\partial}{\partial \tau} F(P(\tau),M(t),t-\tau) - F(P,M,t-\tau) \frac{\partial}{\partial \tau} \Phi(P,\tau)] (\mathbf{n} \wedge d\mathbf{l}) \cdot \mathbf{V} \mathbf{c}(P,\tau) \end{aligned}$$

where  $Cb(t)$  is the the closed line defined by the intersection between the instantaneous body surface  $Sb(t)$  and the  $X$ - $Y$  plane,  $\mathbf{V} \mathbf{c}$  is the velocity of a point on  $Cb$  and  $\Omega(M)$  is the solid angle under which the fluid domain  $D(t)$  is seen from  $M$ .  $G_o$  and  $F$  (see Appendix 1) are defined by:

$$G(M,P,t) = G_o(M,P) \cdot \delta(t) + H(t) \cdot F(M,P,t) \quad (8)$$

The actual occurrence of the line integral in (7) is governed by  $\mathbf{V} \mathbf{c}$ . For example, this term is zero for the linearized problem without forward speed (see e.g. Ferrant

1988), where  $C_b$  is time invariant. In the applications presented in this paper, the body is fully submerged, and the line integral obviously vanishes.

#### Hydrodynamic Forces.

The unsteady hydrodynamic pressure (without hydrostatics) in the fluid domain is given by:

$$\frac{p(M,t)}{\rho} = -\frac{\partial \Phi(M,t)}{\partial t} - \frac{1}{2} |\nabla \Phi(M,t)|^2 \quad (9)$$

It is more convenient for the present study to introduce the total derivative of the potential on the body, yielding for  $M$  on  $S_b(t)$ :

$$\frac{p(M,t)}{\rho} = -\frac{D}{Dt}[\Phi(M,t)] - \frac{1}{2} |\nabla \Phi(M,t)|^2 + \mathbf{V} \cdot \nabla \Phi \quad (10)$$

The first term in the right hand side of (10) is directly obtained by finite-differencing in time the potential on the body. The two other terms require the computation of the fluid velocity on the body. The method used for this computation depends on the space discretization scheme and will be discussed when describing the numerics.

Force computations follows by simply integrating (10) over the discretized body surface.

#### Free Surface Elevation

According to the linearized condition (4), the free surface elevation is given by linearized Bernoulli's equation:

$$\eta(M,t) = -\frac{1}{g} \frac{\partial \Phi(M,t)}{\partial t} \quad (11)$$

$\eta$  may be computed by finite differencing in time the velocity potential at the free surface, or directly from an integral representation of  $\Phi_t$  which for a submerged body (no line integral) and  $M$  on the free surface shrinks to:

$$\begin{aligned} \frac{\partial}{\partial t} \Phi(M,t) = \\ = \int_0^t d\tau \iint_{S_b(\tau)} [F_t(P,M,t-\tau) \frac{\partial}{\partial n_P} \Phi(P,\tau) - \Phi(P,\tau) \frac{\partial}{\partial n_P} F_t(P,M,t-\tau)] dS_P \end{aligned} \quad (12)$$

#### STEADY-STATE COMPONENTS FOR PERIODIC FORCED MOTIONS

In the body-nonlinear problem of the forced oscillations of a submerged body about a fixed mean position, the influence of the body boundary condition nonlinearity on forces and free-surface elevation is investigated.

First, the time depending forces on the body are straightforwardly computed from (10), after solution of the transient integral problem. These forces tend rapidly to a

periodic steady-state which is Fourier-analyzed for a quantification of nonlinearities.

On the contrary, the transient wave field, if computed at some distance from the body to eliminate near field components, needs a long simulation to reach the periodic steady-state, mainly because of the low group velocity of the higher harmonics. This point offers an opportunity to use special Green functions already developed for the solution of the body-nonlinear problem in the frequency domain (Clément & Ferrant 1985, 1987). These Green functions are shortly described in appendix 2. Thus, for a direct and economical computation of the steady state wave field, we first extract the harmonic components of the singularity distribution on the moving body, obtained from the time-domain solution after a few cycles of motion. That is, for example in the case of sources only and periodic forced motion:

$$\begin{aligned} \sigma(M,t) \longrightarrow \sum_{n=0}^{\infty} \sigma_n^*(M) \cos n\omega t + \sigma_n^{**}(M) \sin n\omega t \\ \text{for } M \text{ on } S_b(t) \text{ and } t \longrightarrow \infty \end{aligned} \quad (13)$$

The steady-state potential in the fluid is then obtained from:

$$\Phi_s(P,t) = \sum_{n=0}^{\infty} \iint_{S_b} [\sigma_n^*(M) G_{1n}(M,P,t) + \sigma_n^{**}(M) G_{2n}(M,P,t)] dS_M \quad (14)$$

and the corresponding free-surface elevation, for  $P$  on the free-surface:

$$\eta_s(P,t) = \frac{-1}{g} \sum_{n=0}^{\infty} \iint_{S_b} [\sigma_n^*(M) \frac{\partial}{\partial t} G_{1n}(M,P,t) + \sigma_n^{**}(M) \frac{\partial}{\partial t} G_{2n}(M,P,t)] dS_M \quad (15)$$

For harmonic heave motion, the expressions of  $G_{in}$  are simplified, and for fixed points  $P$  on the free-surface, the harmonic components of  $\Phi_s$  and  $\eta_s$  are directly calculated by eliminating the time variable from the expressions of  $G_{in}$  (A2.10), (A2.11).

When only the far field is to be computed, which is sufficient to study the structure of the radiated wave field (amplitudes of harmonics, dispersion of energy on the components of  $\eta$ ), asymptotic expressions of  $G_{in}$  are used. Again, the computation is drastically simplified in the present case of the heave motion,  $G_{in}$  reducing to the very simple expressions (A2.12), (A2.13). No numerical integration, but only computations of modified Bessel functions are involved.

#### NUMERICAL IMPLEMENTATION

The major part of the numerical results given in this paper have been obtained using a first version of the computer code completed in 1988. In this version, a very classical discretization scheme is used. The body surface is discretized into plane polygonal panels over which



singularity distributions are assumed to be constant. The impulsive part of the Green function ( $G_0$ ) is integrated analytically over the panels, and the memory part  $F$  is integrated using a variable order Gaussian quadrature. Numerical tests have proved that, at least for submerged bodies, one single point of integration per panel is sufficient for a good accuracy, the local flow being dominated by the singular part of  $G_0$ . Thus, wave terms are treated as monopoles situated at panel centroids, which greatly reduces computational requirements. Note that such a mixed procedure for the space integration of a Green function as also been proved to be a valuable compromise for the solution of the steady wave resistance problem (Doctors & Beck, 1987). The time variable is discretized into constant time steps and the convolutions integrals are evaluated using a trapezoidal rule.

At each time step the convolution terms at the right-hand side of the linear system of equations are actualized by computing and assembling the corresponding wave terms, and a new kernel is obtained by computing the motion-dependent part of  $G_0$ . The linear system is then solved using a standard Gauss solver. Faster solvers are obviously available, but in fact the computing time is dominated by the evaluation of the convolution terms.

Actually, two integral equations are solved at each time step. First a mixed distribution of sources and dipoles is used for a direct computation of the potential on the body. Then the integral equation for sources only is solved, and the result is used for the computation of the fluid velocity at panels centroids. Although increasing the computer time, the method allows the fluid velocities, and thus the full hydrodynamic pressure to be obtained without having to calculate the second spatial derivatives of the Green function.

At the end of the simulation, the different terms in the hydrodynamic pressure are computed at panels centroids.  $\Phi_t$  is obtained by finite differencing the time depending potential, and the quadratic terms are computed from the previously computed fluid velocity. Forces are then obtained by integrating the pressure which is assumed to be constant on each panel. The time depending wave elevation at prescribed points is also available. For simplicity, this computation is based on the source solution.

In the case of a periodic forced motion, the solution of the time-domain problem is followed by the computation of the harmonic components of the steady state part of the response. For reasons initially related to an economical computation of the convolution terms, the time step is adjusted to obtain an integer number of steps per period, and the harmonics can be accurately computed by simple trapezoidal rule over one single period, typically the last, in order to provide the best approximation of the steady state. The harmonic analysis is applied first to the time depending forces, and then to the source solution. The latter results are used for the computation of the steady-state periodic wave field using the Gij functions described in appendix. In consistency with the method used for the solution of the time-depending problem, this computation is based on a monopole approximation of the source distribution on the body. In the case of the heave motion, the computation of the harmonic components of the far field wave system is straightforward and of negligible CPU cost.

At last, for a quantification of the influence of the body boundary condition nonlinearity, the linear solution is systematically computed for comparison.

## REDUCTION OF COMPUTING TIME

Apart from the use of frequency domain Green functions, the numerical implementation as described in the preceding paragraph is very classical. In fact, the main difficulty is related to the extensive Cpu and mass storage requirements of the body-nonlinear time-domain formulation. These requirements may be lowered first by accelerating the Green function computations, and secondly by reducing the number of Green function computations necessary to the evaluation of the convolutions. These two points have been addressed in the present study.

### Tabulation-Interpolation of the Green Function

The well-known time domain Green function for a source of impulsive strength in infinite depth is given in Appendix, with the following notation:

$$G(M, P, t) = \delta(t) \cdot G_0(M, P) + H(t) \cdot F(M, P, t) \quad (16)$$

The memory part  $F$  of that Green function can be easily put under the following form:

$$F(M, P, t) = -\frac{g^{1/2} r^{3/2}}{2\pi} \int_0^\infty \sin(\lambda^{1/2} \beta) J_0[\beta(1-\mu)^{1/2}] e^{-\lambda\mu} \lambda^{1/2} d\lambda \quad (17)$$

or:

$$F(M, P, t) = g^{1/2} r^{3/2} \hat{F}(\mu, \beta) \quad (18)$$

$$\text{with } \mu = -(z+z')/r' \text{ and } \beta = t(g/r')^{1/2}.$$

The first parameter is linked to the relative positions of points  $M$  and  $P$ , and varies from 0 to 1., whereas  $\mu$  is an essentially positive time parameter.

Thus, the only non-trivial terms to be evaluated during the computation of the convolution integrals are reduced to the bivariate function  $F$  and its first derivatives.

This fact can be exploited for deriving a very fast procedure for the evaluation of the wave terms. This procedure, based on very simple principles, has been already described in Ferrant (1988). The 2D domain described by  $\mu$  and  $\beta$  is truncated at a large value  $\beta_{\max}$ , and the remaining bounded domain is mapped by a discrete set of equispaced points for which  $F$  and its first derivatives are computed by numerical schemes very similar to the ones described by Newman(1985) or King & al (1988). This computations are performed once for all, and the results are stored on permanent disk files. When a simulation has to be performed, the resulting evaluations of the memory part of the Green function are based on linear bivariate interpolations of the stored data. Note that the content of the file is read once for all at the beginning of the simulation, so that no disk access is necessary during the time-stepping procedure. The tabulated part of the  $(\mu, \beta)$  domain is sufficiently extended to allow the use of simple large-time asymptotic expressions when  $\beta > \beta_{\max}$ . In a very thin layer near  $\mu=0$  where the function presents large oscillations, the precision of the interpolation may be insufficient and we simply return to the original numerical schemes. However,



for the forced motions of a submerged body about a fixed mean position, computations never occur in this part of the domain and the interpolation is used throughout the simulation. The use of a regular tabulation grid allows for a very quick search in the tables, and the resulting code is very fast: less than 30  $\mu$ s are necessary for one evaluation of the Green function and its first space derivatives, on a Vax 8700 computer, from and back to physical variables. This is about the time needed for one evaluation of the sine function. The grid is composed of 200x1200 points in the rectangular domain defined by  $0 \leq \mu \leq 1$ , and  $0 \leq \beta \leq 30$ . For the Green function and its gradient, 3 tables have to be stored, resulting in about 720Kwords or 2.9 Mbytes on a 32 bit computer. Note that we do not pretend to have an optimized set of tabulation parameters. Such an optimization could be necessary to reduce memory requirements for a given accuracy, but the present size of the tabulation files is not a problem on the computer we use.

When the problem to be treated leads to large horizontal displacements, as it happens with forward speed, a substantial number of computations may occur near  $\mu = 0$ , and a special scheme is needed to maintain both precision and low Cpu in this portion of the computational domain.

Such a refined procedure has been subsequently derived by Magee & Beck (1989), exploiting an analytical approximation of the Green function in the vicinity of the  $\mu=0$  axis, and a higher order interpolation scheme for the remaining part of the Green function on various subdomains. Although more precise for a given number of tabulated points, their method is certainly a bit less efficient in terms of computing time, but comparisons are delicate between runs on scalar and vector computers. The use of an analytical approximation is a very clever idea for reducing the oscillations of the function near  $\mu = 0$ , and we intend to adopt a similar scheme, but in our opinion, bilinear interpolation should be preferred for the interpolation of the remaining smooth function, whenever a very high precision is not necessary. We are not sure that the precision of  $10^{-8}$  obtained by Magee & Beck is necessary when the overall accuracy of the computations is dominated by space & time discretization errors. A precision of about  $10^{-5}$ , easily obtained by a simple bilinear interpolation method in the major part of the computational domain is certainly sufficient for most applications.

#### Reduction of the Number of Green Function Evaluations

Basically, during one run of the program,  $N_p^2(N_t-1)$  computations of the Green function are required at time step  $It$  for the evaluation of the convolution. This results in a total of  $N_p^2 N_t(N_t-1)$  computations for a simulation over  $N_t$  time steps, if  $N_p$  is the number of panels. A crude method for reducing this number is to truncate the convolution integrals, considering that the influence of the past history of the solution tends to zero for large time delays. However, such an approach is not safe, for it is very difficult to estimate the influence of the truncation on the final results.

In many particular problems of forced motions, an adequate choice of the time step allows a substantial reduction of the number of Green function evaluations without affecting the numerical results. The idea is as follows:

The Green function terms to be computed in the convolution depend essentially on  $MP$  and  $t-\tau$ , where  $M(t)$  is

a point on the body at time  $t$  (field point),  $P(\tau)$  is the position of a point on the body at time  $\tau$  (source point), and  $t-\tau$  is the time delay. The idea is to adjust the time step  $\Delta t$ , i.e. the positions of the body at times  $i\Delta t$  to reduce the number of combinations of  $MP$  and  $t-\tau$  to be considered in the computation of the discretized convolution.

For clarity, let us illustrate the procedure on the case of forced motions of period  $T$  about a fixed mean position, for which the appropriate choice is  $\Delta t = T/N_{per}$ . Consider the discretized convolution to be computed at time step  $it$ ,  $it \geq N_{per}$ . The Green function terms to be evaluated may be schematically written  $G[MP(it, it), (it-it)\Delta t]$ , with  $it \leq it$ . For  $it \geq N_{per}$ , we have obviously:

$$G[MP(it, it), (it-it)\Delta t] = G[MP(it-N_{per}, it-N_{per}), (it-N_{per})-(it-N_{per})\Delta t] \quad (19)$$

The term at the right-hand side has already been necessary for the computation of the convolution at time step  $it-N_{per}$ , and thus has already been computed and stored. Thus the only new terms to be computed correspond to the influence at time step  $it$  of the  $N_{per}$  time steps of the first period. The total number of  $N_p \times N_p$  sets of terms to be computed is now:

$$N_{call} = \frac{N_t(N_t-1)}{2} \quad \text{for } N_t < N_{per} \quad (20)$$

$$N_{call} = \frac{N_{per}(N_{per}-1)}{2} + (N_t - N_{per})N_{per} \quad (21)$$

$$= N_t N_{per} - \frac{N_{per}(N_{per}-1)}{2} \quad \text{for } N_t \geq N_{per}$$

The resulting total number of Green function evaluations is now a linear function of the number of time steps, as opposed to the quadratic behaviour obtained when  $\Delta t$  is arbitrary. The ratio of reduction, after a few periods of simulation is approximately:

$$G \approx \frac{N_t}{2N_{per}} = \frac{N_T}{2} \quad (22)$$

where  $N_T$  is the number of simulated periods. For the computations presented in this paper, 4 to 8 periods are simulated, and the Green function computations are reduced by a factor 2 to 4 using this artifice.

The procedure that we have illustrated in the case of periodic motions is also applicable when a constant forward speed is superimposed to the oscillations. In the case of a smooth starting of duration  $N_{start}$ , the gain is lower, but a linear law is maintained:

$$N_{call} = N_t \cdot (N_{per} + N_{start}) - \frac{(N_{per} + N_{start})(N_{per} + N_{start} + 1)}{2} \quad (23)$$

For problems with constant forward speed without superimposed oscillations (unsteady approach of the wave resistance problem), simulations with an abrupt start lead to the same number of computation as for a linear code. If a smooth start is chosen,  $N_{call}$  is given by (23), with  $N_{per} = 0$ . In this case, the introduction of a smooth start of duration  $N_{start}$  multiplies the number of Green function evaluations by the factor  $N_{start}$ .

## NUMERICAL RESULTS

### Submerged Heaving Sphere

We give in this section the results obtained on the problem of a submerged heaving sphere, with a mean depth of submergence equal to the diameter ( $Z_0/R = 2$ , Figure 1). Starting from rest, the body is given a purely harmonic motion, with frequency  $\omega$ .

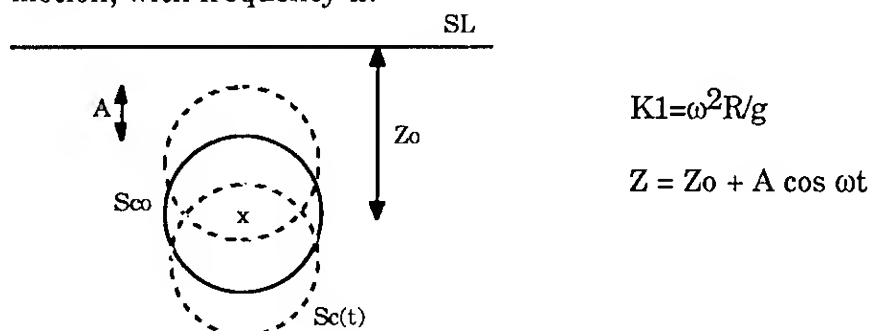


Figure 1

### Time Domain Results

We first give in figures 2 to 9 a sample of the unsteady (vertical) force signals computed from the time domain formulation. The results of the fully linearized formulation (dashed line) have been systematically computed for comparison with the body-nonlinear formulation. The difference of the two results is also plotted.

Results are given for two values of the amplitude,  $A/R = 0.50$  and  $A/R = 0.70$ , and four values of the fundamental wavenumber  $K_1 = \omega^2 R/g = 0.1, 0.25, 0.50, 2.0$ . A periodic steady-state is very rapidly obtained, and a significant influence of the body boundary condition nonlinearity is observed, mainly for  $K_1 = 0.25$ , the difference between the two results being weaker at low and high frequency. This difference mainly appears in the form of higher harmonics in the response, the fundamental being apparently not much modified. At high and low frequency, the superharmonics tend to be in phase with the fundamental. The analysis will be easier on the harmonic components of the steady state response, given in a following section.

Then, in figures 10 to 17, for the same two values of the amplitude, and for  $K_1 = 0.2, 0.4, 0.7, 1.0$ , we give the transient wave elevation computed at a distance  $20R$  from the sphere. Again, the linearized solution in dashed line is given for comparison. At low frequency, the influence of the nonlinearity is much stronger than on forces, but the difference between linear and body-nonlinear solutions tends to zero at high frequency, at least for the smaller amplitude,  $A/R = 0.50$ . For  $A/R = 0.7$  and  $K_1 = 1.0$ , a small second harmonic component remains sensible. At low frequency, the influence of the body boundary condition nonlinearity is already very sensible for a moderate amplitude, as demonstrated by figure 18 giving the wave elevations for  $A/R = 0.30$ . For such an amplitude, a linear analysis is commonly considered to give correct results. The present results prove that at least for wave generation, a linear analysis is inadequate, the body nonlinearity having a very strong influence on the structure of the radiated wave field.

This phenomenon, already highlighted using a frequency domain analysis of the problem by Clément & Ferrant (1987), has been fully confirmed by the experiments of Dassonville (1987). Comparisons were made over a wide frequency range, but we simply give in figure 19 a comparison between experiments and time domain body-nonlinear analysis for  $A/R = 0.50$ , and  $K_1 = 0.28$ , i.e. in the vicinity of the maximum nonlinear behaviour given by the numerical model. Due to experimental constraints, the distance from the sphere is here equal to  $16.5R$ . A small difference in the starting transients is observed, due to the imposed smooth start of the experimental apparatus. During the steady-state part of the response, the wave elevation is slightly overestimated by the numerical model, but harmonic content as well as phases are perfectly recovered. At large time, the comparison is not significant, the experiments being affected by tank wall reflexions.

### Harmonic Components

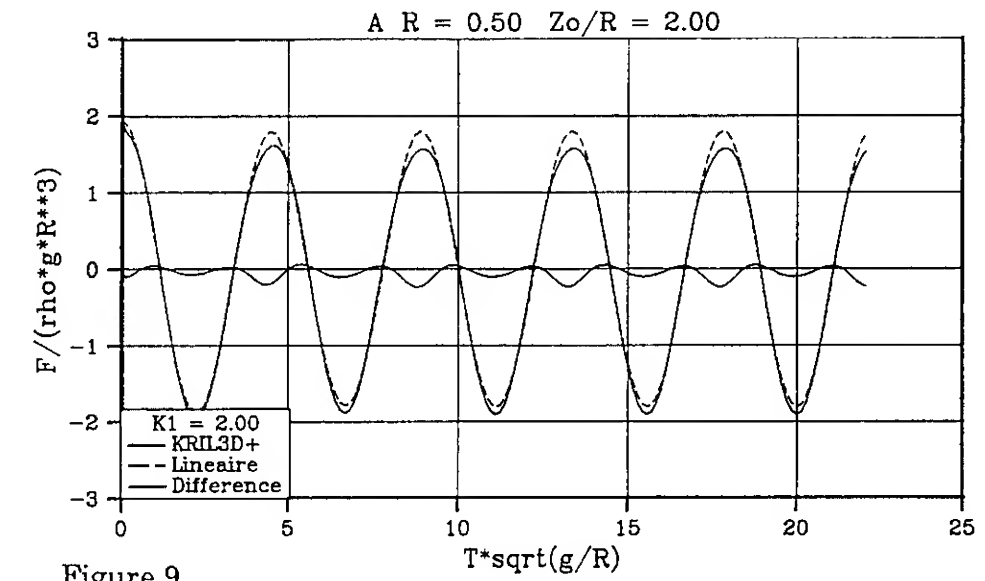
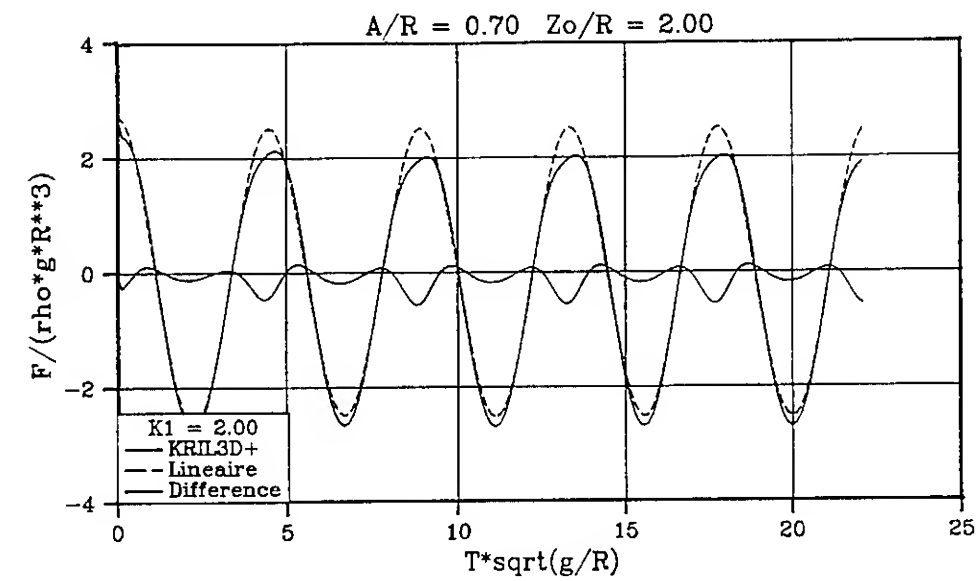
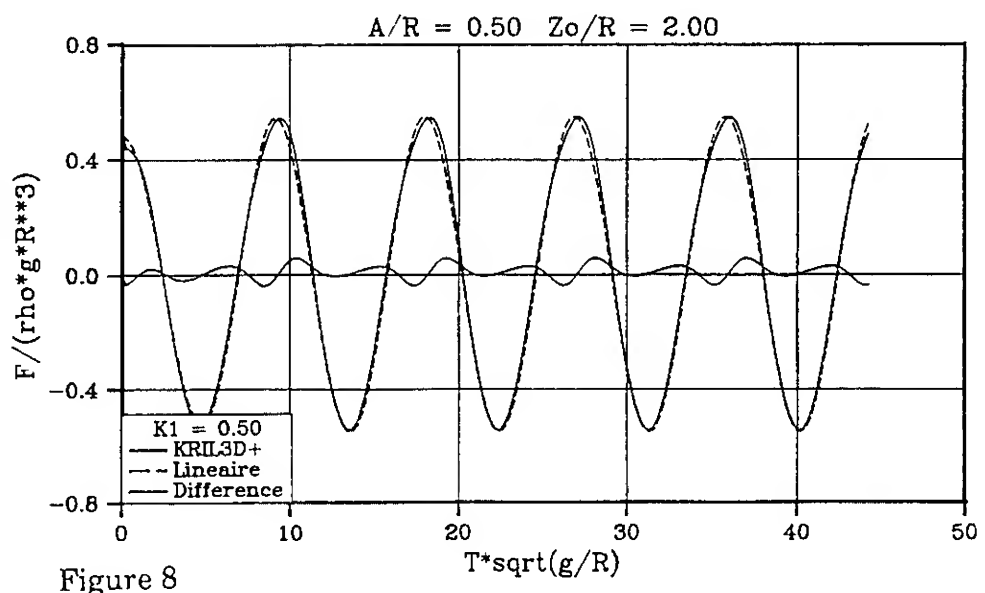
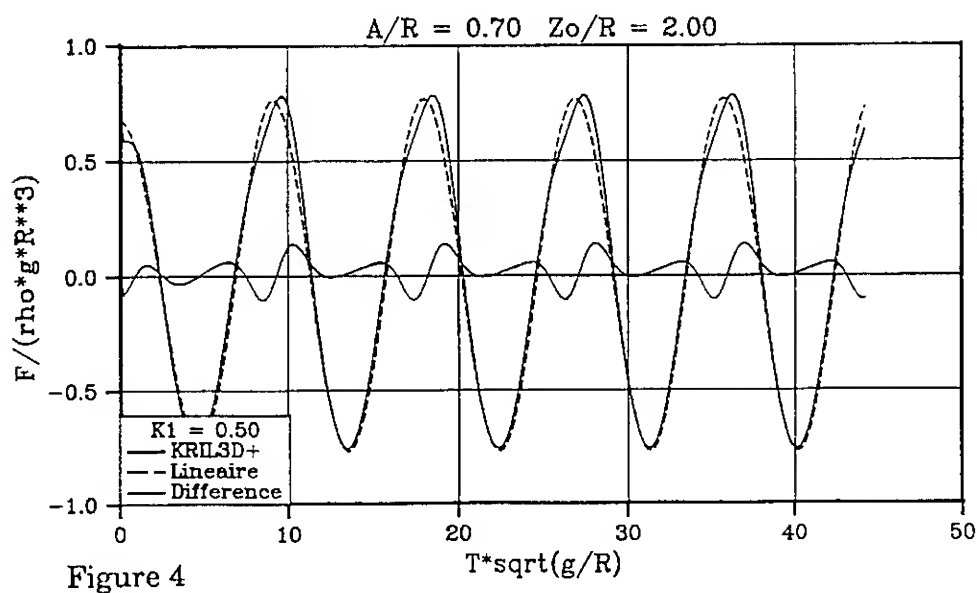
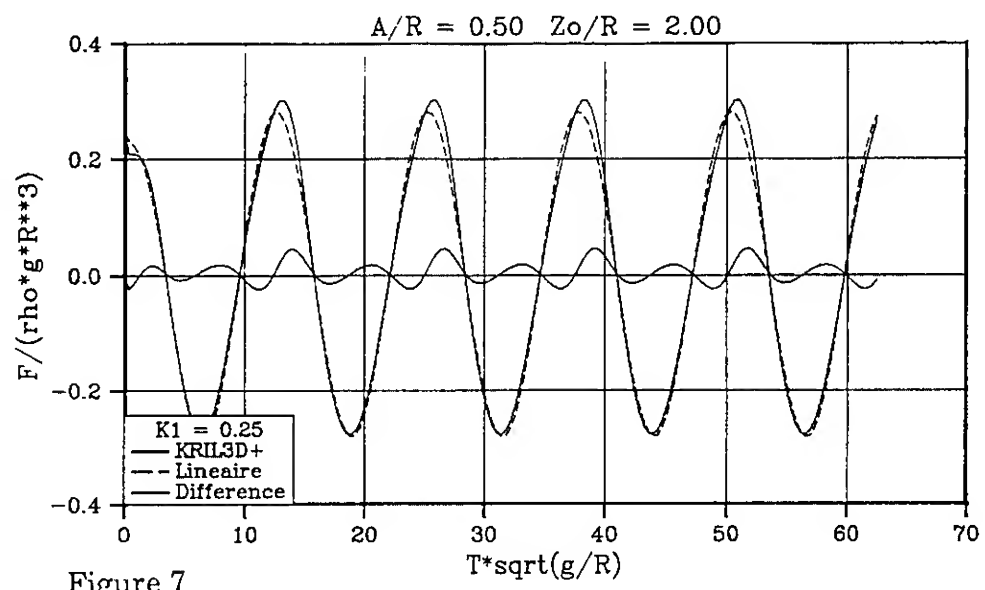
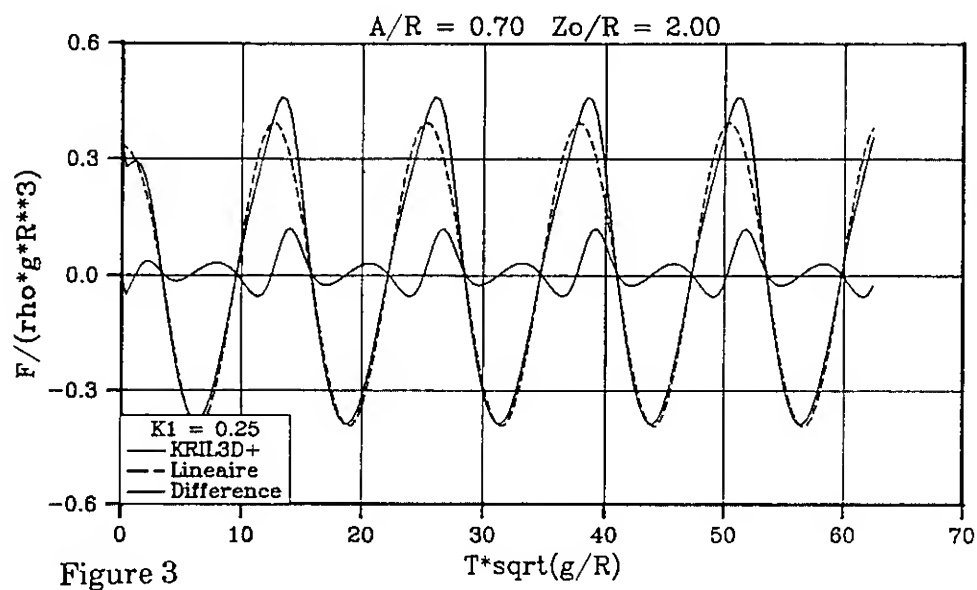
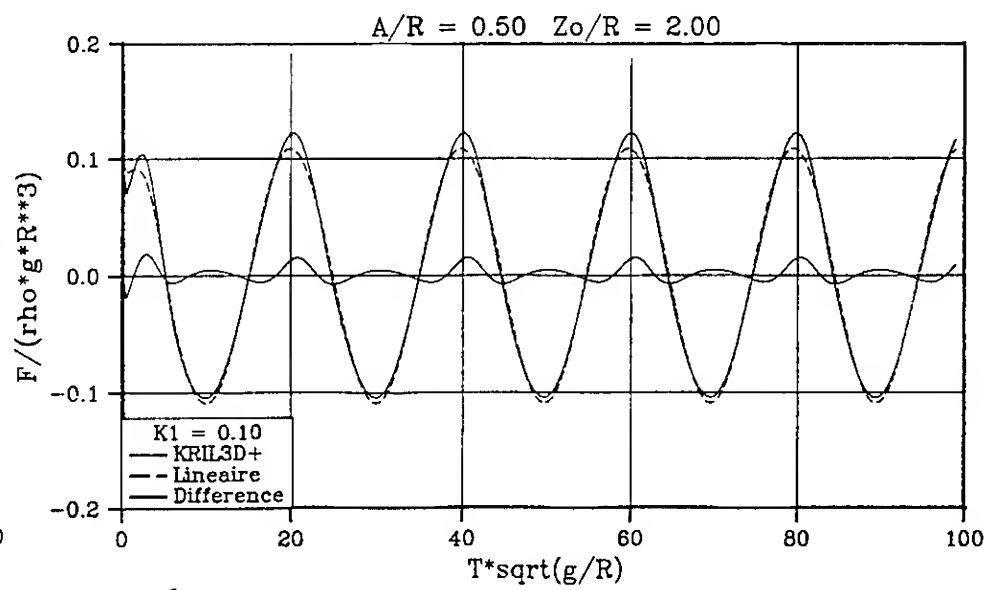
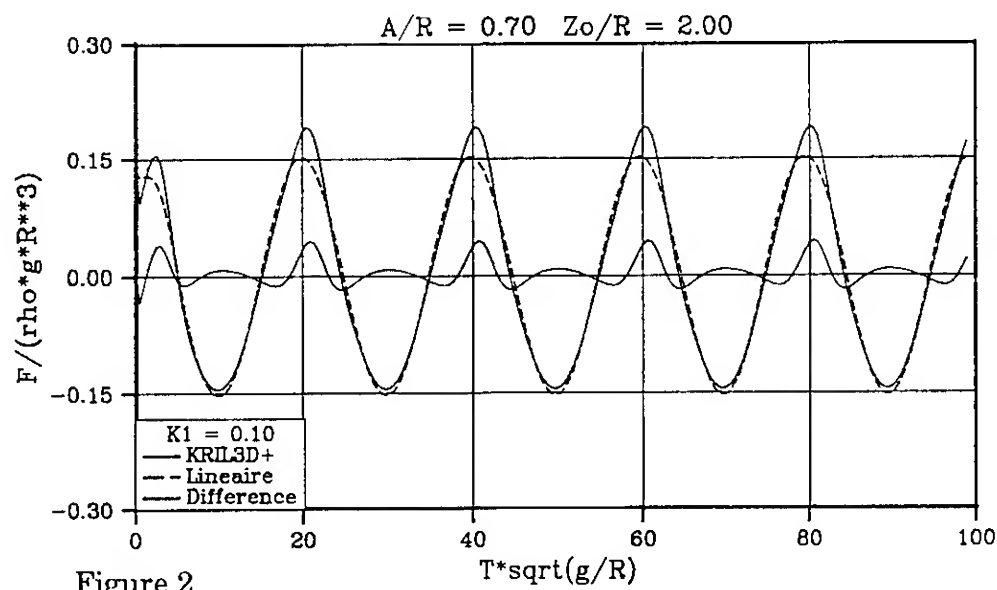
Concerning the hydrodynamic forces exerted on the moving body, the harmonic analysis is performed after obtention of the steady-state, and the results are given under the form:

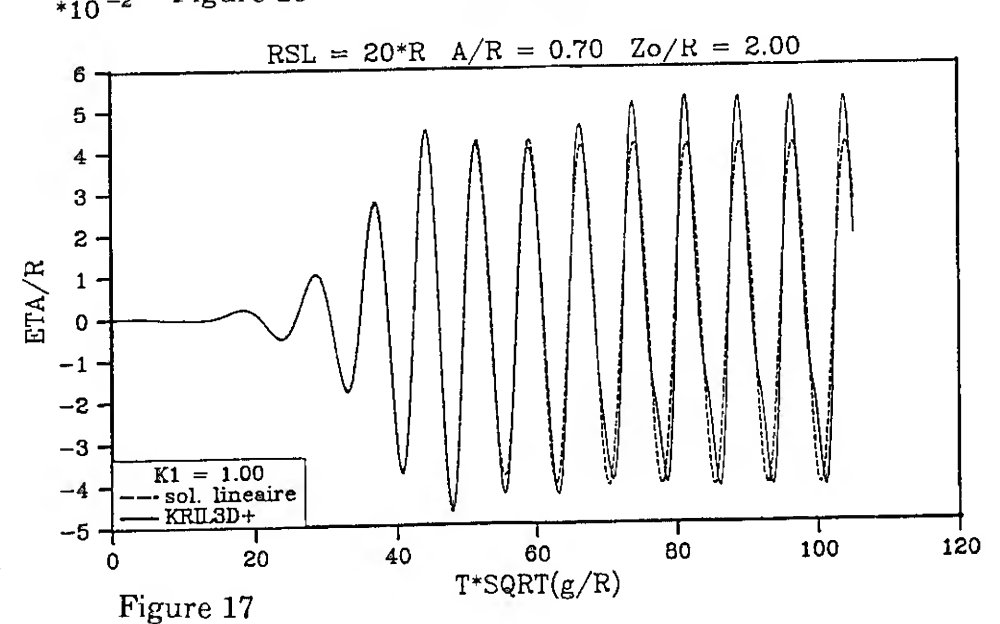
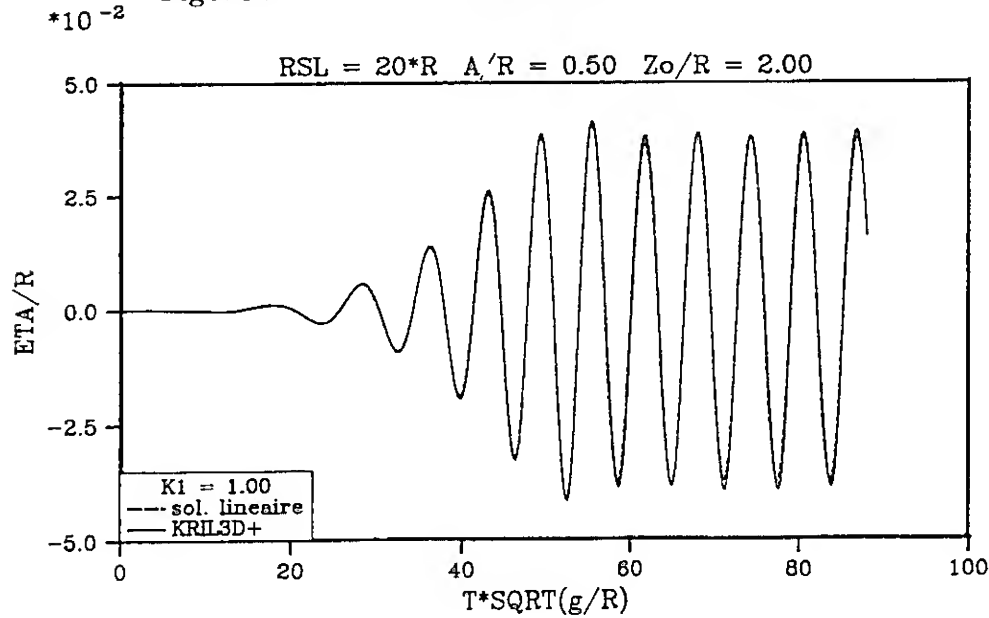
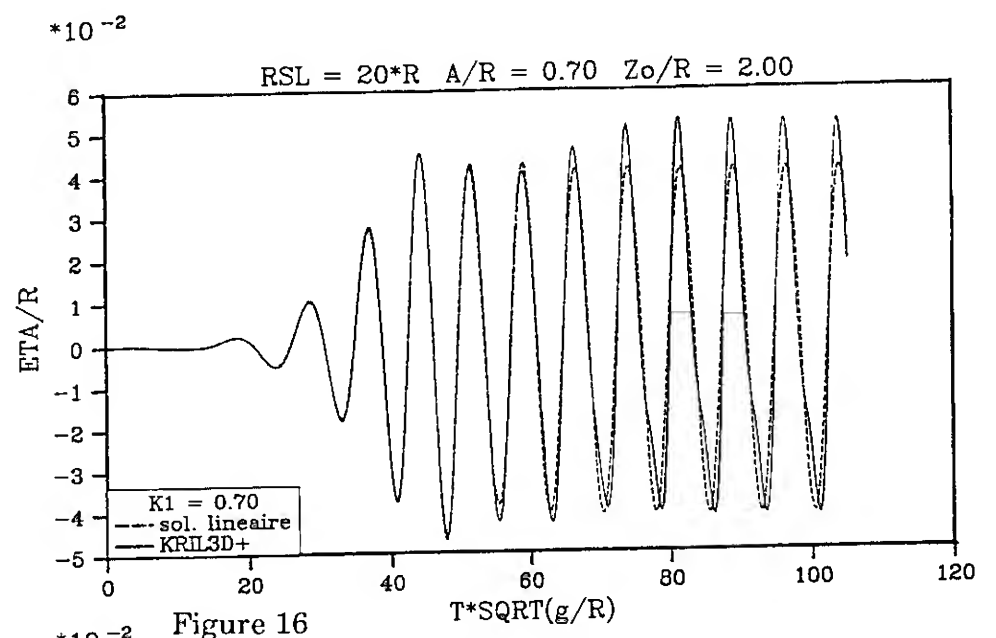
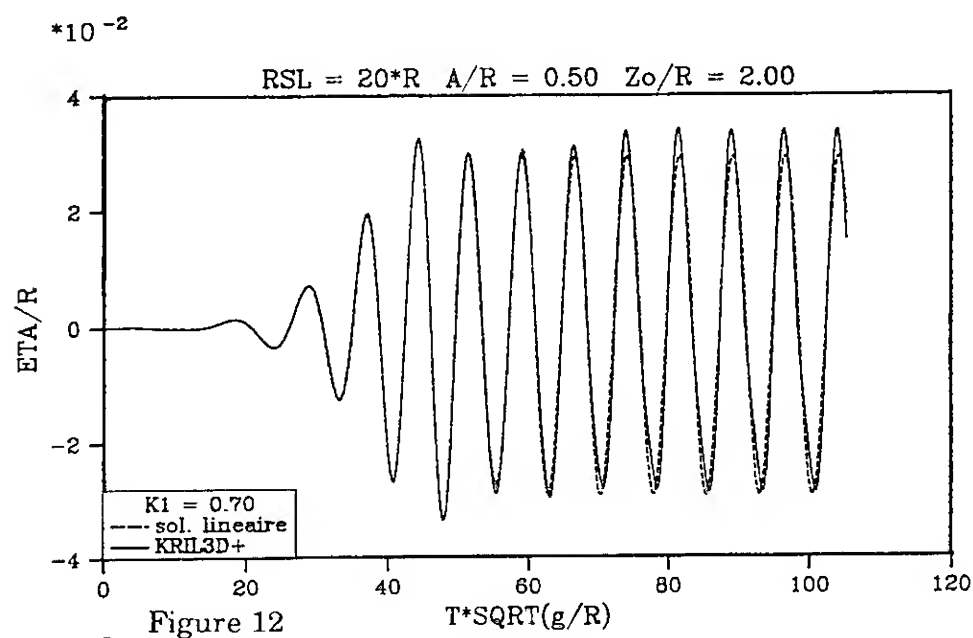
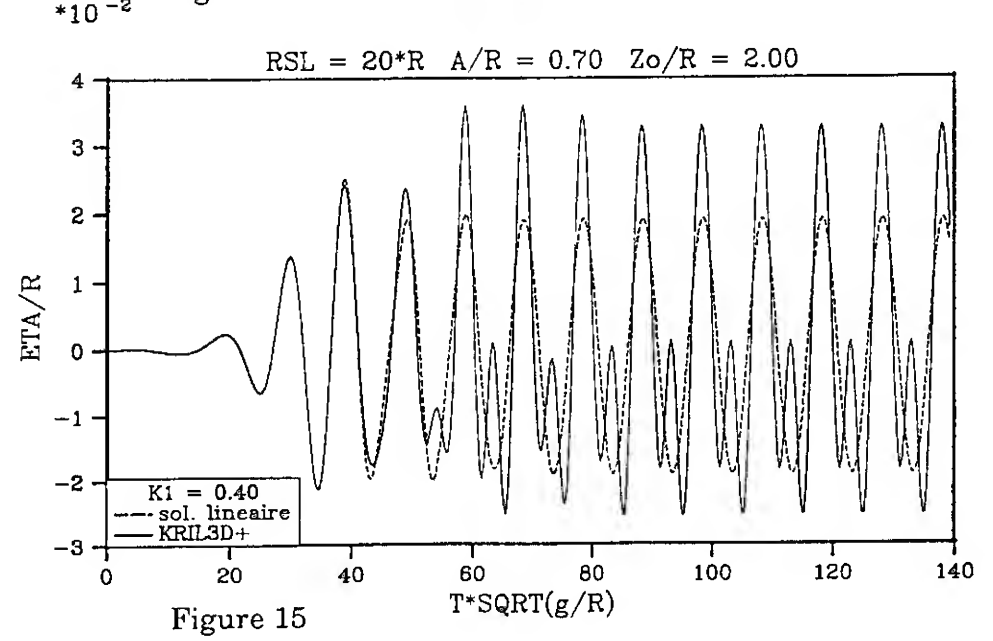
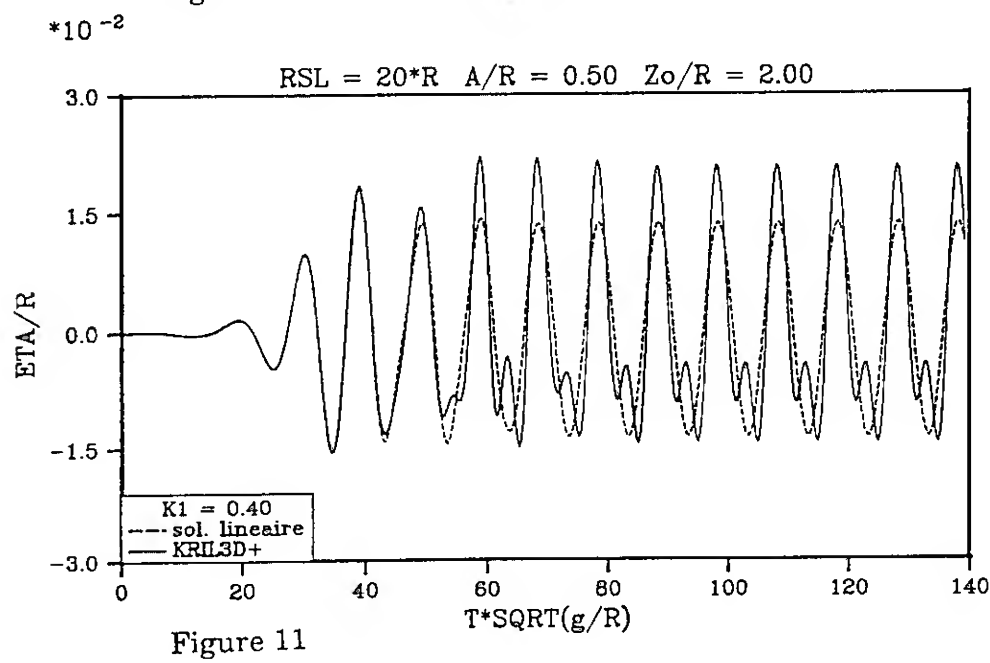
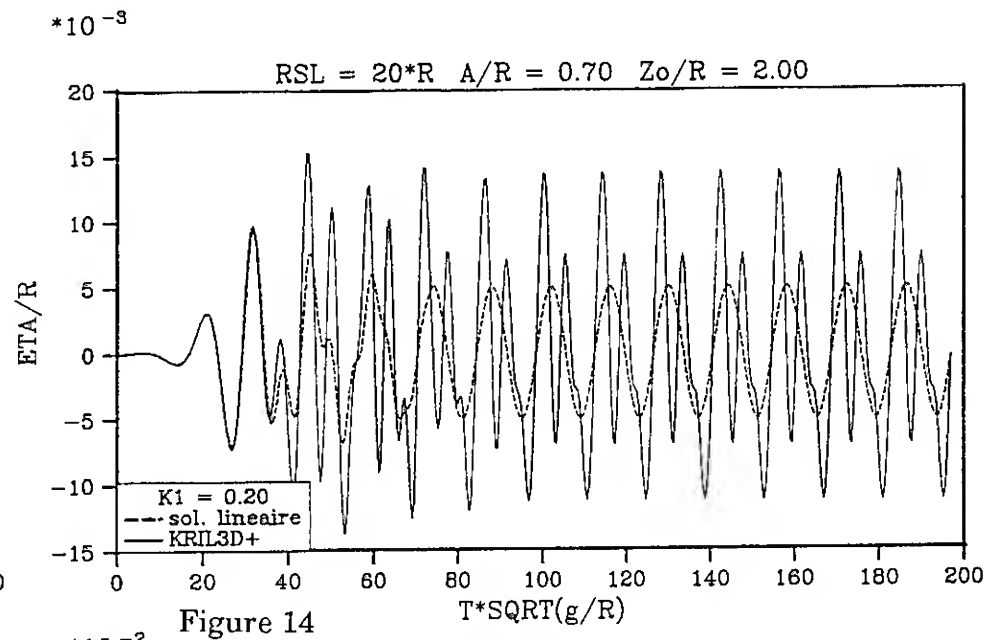
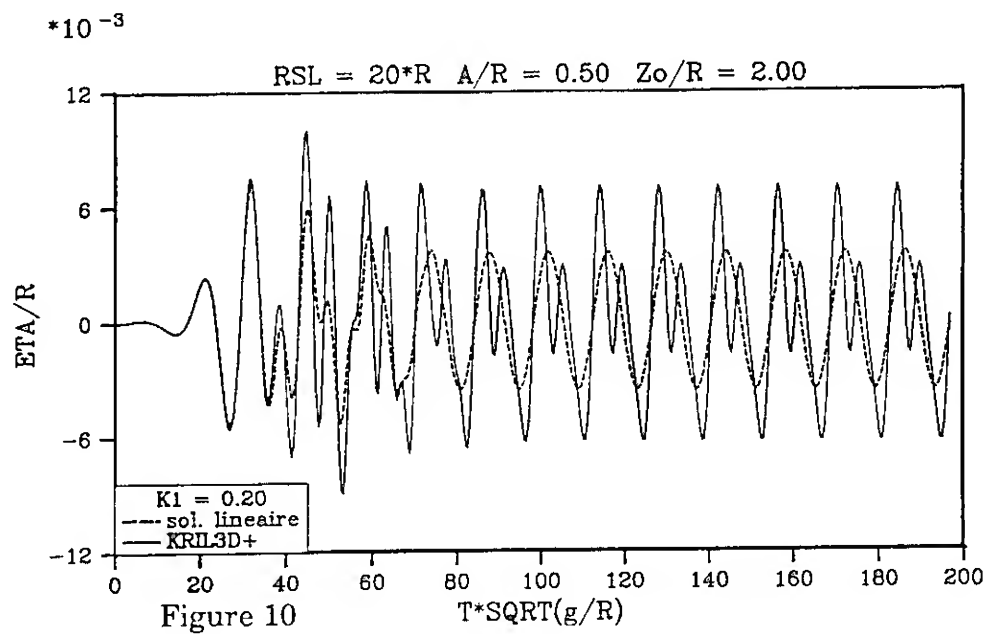
$$F(t) = \frac{1}{\rho g K_1 R^2 A} \sum_{n=0}^{\infty} F_n^* \cos n\omega t + F_n^{**} \sin n\omega t \quad (24)$$

Full results may be found in table 1, where the harmonic components of the vertical force on the sphere, from the constant term to the fifth harmonic, are given for three values of the amplitude, over the whole frequency range of interest, together with the purely harmonic frequency domain linear results. A part of these results is graphically represented in figures 20 to 27, for the two largest amplitudes, and up to the fourth harmonic. The results being scaled in the usual manner of frequency domain analysis, the first harmonic components tend to the usual linear added mass and damping coefficients when the amplitude tends to zero. In figures 22 and 23, the linear hydrodynamic coefficients are plotted together with the first harmonic components of the body-nonlinear results. The stronger relative difference lies in the damping coefficient, especially between 0.2 and 0.9, in the ascending part of the curve.

At low and high frequency,  $F^{**}$  components tend to zero. At high frequency,  $F^*$  components tend to a constant. This behaviour cannot be observed at low frequency, the frequency range being insufficient. These observations agree with the asymptotic analysis of the problem, which gives predominant added mass effects at low and high frequency, where the steady-state flow is in phase with the body motion.

The steady-state far-field wave elevation harmonic components are computed from equation (15), after an harmonic analysis of the singularity distribution on the body. This procedure avoids the computation of the transient wave field, and is of negligible Cpu cost. The results are given in the form of the distribution of the total radiated energy over the different harmonics of the wave field, in figures 28 and 29, for  $A/R = 0.50$  and  $A/R = 0.70$ , as a function of frequency. The very strong deviation from the





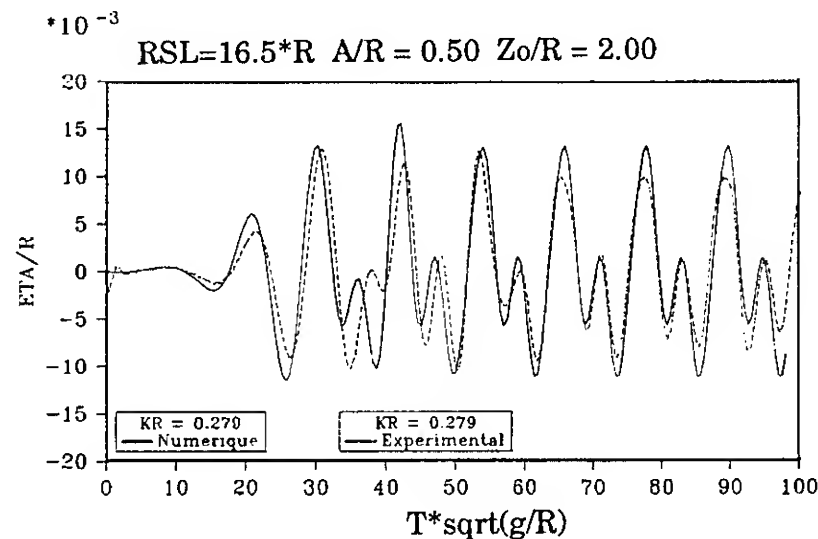
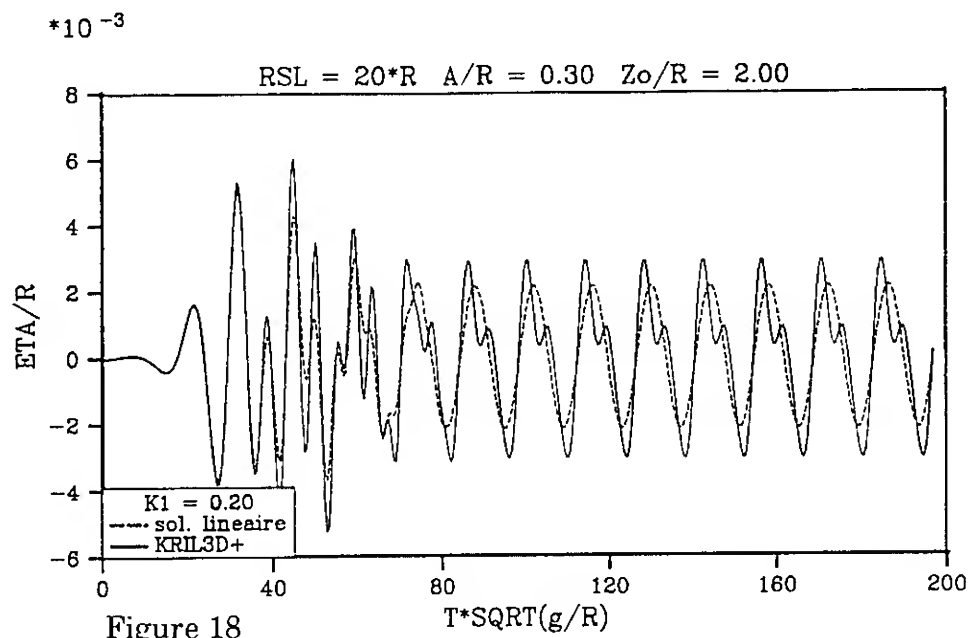


Figure 19

linear analysis already observed on time domain results is confirmed, with a maximum about  $\omega \cdot \sqrt{R/g} = 0.2$  ( $K_1 = 0.4$ ) where for  $A/R = 0.50$  only 60% of the total energy input by the moving body is recovered on the first harmonic of the wave field. This phenomenon appears approximately in the same frequency range as the maximum deviation from linear results of the damping coefficient  $F1^{**}$ . For confirmation, we give in figures 30 and 31 the damping coefficient computed from the body nonlinear formulation, together with linear results. The difference is also plotted, as a function of frequency.

Results on the sphere have been obtained with a discretization of 200 panels on the entire body.

#### Time Domain Wave Resistance of a Submerged Ellipsoid.

Results are now given on the problem of a submerged ellipsoid of beam/length ratio  $B/L = 0.2$ , and submergence  $Zo/L = 0.16$ . Two different discretizations are used, with respectively 60 and 168 panels on the half-body, and the simulations were run over 150 time steps. Starting from rest, the body is abruptly given a constant velocity in the positive X direction, parallel to the free surface. We give in figures 32 to 34 the transient horizontal force on the body, for three values of the Froude number,  $Fr = 0.4, 0.45, 0.5$ . After some oscillations, the force tends to a constant, which actually is the wave resistance of the body. We give in table 2 the  $C_w$  wave resistance coefficient estimated from the ultimate value of the transient force, compared with the results of a conventional Neumann-Kelvin wave resistance code (Delhommeau 1987), obtained with a 192 panels discretization. The results of a semi-analytical formulation, deduced from curves given in Farell (1973), are also presented. With the finest discretization,  $N_{pan}=168$ , the agreement between time-domain analysis and steady-state results is correct. The influence of the time-step has not been investigated. A smaller time step would certainly lead to a better agreement, especially for larger Froude numbers.

Fr	Cw (time domain)		Cw (N-K)	Cw (Farell)
	(Np=60)	(Np=168)	(Np=192)	
0.40	0.01226	0.01267	0.01175	0.01320
0.45	0.01592	0.01667	0.01734	0.01713
0.50	0.01619	0.01671	0.01775	0.01822

Table 2

Note that the oscillations are greater for smaller Froude numbers. At  $Fr = 0.8$  (figure 35), only a small

overshoot is observed during the transients, a constant resistance being very rapidly obtained.

Similar results on the transient approach of the wave resistance problem have already been published by Jami & G  lebart (1987), and more recently by Magee & Beck (1990), with comments on the oscillatory behaviour of the time depending wave resistance and its connection with the critical parameter  $\tau = 0.25$  of the forward speed seakeeping problem. Present computations simply intend to demonstrate the versatility of the body-nonlinear time domain formulation.

#### CONCLUSION

A systematic attention on computational efficiency has led to a time domain body-nonlinear code with Cpu requirements sufficiently low for intensive computations to become possible, as demonstrated on the problem of the heaving sphere. Strong nonlinear effects, both on forces and wave field, already detected using a frequency domain approach (Cl  ment & Ferrant 1987) have been confirmed and their validity extended to the whole frequency range and to larger amplitudes. Furthermore, the time domain formulation can cope with arbitrary motions and is absolutely robust. Future computations will be undertaken with a refined version of the code based on a linear representation of the velocity potential on the body.

Other researchers are also working on the time domain body-nonlinear problem, and for example a considerable experience has been gained on the time domain seakeeping problem with forward speed by Professor Beck's team. The variety of possible applications will certainly motivate many interesting studies in the future. The extension to finite depth depends on the development of fast algorithms for the computation of the corresponding Green function, on which preliminary results have been obtained by Newman (1990).



# Harmonic Components

			F <sub>0</sub>	F <sub>1*</sub>	F <sub>1**</sub>	F <sub>2*</sub>	F <sub>2**</sub>	F <sub>3*</sub>	F <sub>3**</sub>	F <sub>4*</sub>	F <sub>4**</sub>	F <sub>5*</sub>	F <sub>5**</sub>
K1= 0.025 OM= 0.158	A=0.00     A=0.30   0.0104   A=0.50   0.0194   A=0.70   0.0324		2.1290	0.0003									
			2.1356	0.0003	0.0364	0.0005	0.0081	0.0004	0.0014	0.0002	0.0002	0.0001	
			2.1489	0.0003	0.0668	0.0009	0.0249	0.0013	0.0075	0.0012	0.0019	0.0007	
			2.1739	0.0004	0.1093	0.0015	0.0575	0.0031	0.0248	0.0044	0.0090	0.0040	
K1= 0.050 OM= 0.224	A=0.00     A=0.30   0.0125   A=0.50   0.0237   A=0.70   0.0411		2.1478	0.0020									
			2.1568	0.0022	0.0524	0.0052	0.0129	0.0037	0.0021	0.0013	0.0002	0.0003	
			2.1752	0.0026	0.0973	0.0100	0.0399	0.0118	0.0109	0.0073	0.0019	0.0028	
			2.2115	0.0039	0.1631	0.0182	0.0936	0.0306	0.0353	0.0270	0.0074	0.0149	
K1= 0.100 OM= 0.316	A=0.00     A=0.30   0.0157   A=0.50   0.0305   A=0.70   0.0554		2.1807	0.0130									
			2.1941	0.0156	0.0749	0.0372	0.0122	0.0158	0.0008	0.0031	-0.0001	0.0004	
			2.2222	0.0217	0.1383	0.0717	0.0366	0.0497	0.0033	0.0164	-0.0011	0.0036	
			2.2782	0.0364	0.2281	0.1292	0.0788	0.1209	0.0052	0.0549	-0.0084	0.0156	
K1= 0.200 OM= 0.447	A=0.00     A=0.30   0.0223   A=0.50   0.0433   A=0.70   0.0770		2.2319	0.0711									
			2.2465	0.0857	0.0354	0.1062	-0.0029	0.0187	-0.0016	0.0021	-0.0002	0.0001	
			2.2757	0.1159	0.0606	0.1948	-0.0107	0.0565	-0.0084	0.0102	-0.0021	0.0007	
			2.3286	0.1747	0.0853	0.3186	-0.0325	0.1254	-0.0293	0.0286	-0.0096	0.0010	
K1= 0.300 OM= 0.548	A=0.00     A=0.30   0.0281   A=0.50   0.0512   A=0.70   0.0829		2.2533	0.1624									
			2.2587	0.1830	-0.0267	0.1026	-0.0085	0.0153	-0.0015	0.0010	-0.0002	0.0000	
			2.2696	0.2234	-0.0490	0.1857	-0.0266	0.0447	-0.0079	0.0048	-0.0014	0.0000	
			2.2888	0.2950	-0.0821	0.2939	-0.0624	0.0933	-0.0247	0.0118	-0.0054	-0.0012	
K1= 0.400 OM= 0.632	A=0.00     A=0.30   0.0310   A=0.50   0.0530   A=0.70   0.0781		2.2287	0.2570									
			2.2263	0.2744	-0.0512	0.0701	-0.0123	0.0115	-0.0014	0.0009	-0.0001	0.0000	
			2.2219	0.3084	-0.0927	0.1287	-0.0363	0.0336	-0.0068	0.0040	-0.0008	0.0000	
			2.2147	0.3675	-0.1477	0.2060	-0.0780	0.0699	-0.0196	0.0101	-0.0030	-0.0004	
K1= 0.500 OM= 0.707	A=0.00     A=0.30   0.0305   A=0.50   0.0500   A=0.70   0.0686		2.1567	0.3296									
			2.1520	0.3411	-0.0489	0.0444	-0.0127	0.0062	-0.0013	0.0005	-0.0001	0.0000	
			2.1422	0.3640	-0.0906	0.0823	-0.0373	0.0188	-0.0060	0.0027	-0.0004	0.0001	
			2.1240	0.4046	-0.1471	0.1334	-0.0788	0.0410	-0.0166	0.0076	-0.0011	0.0006	
K1= 0.600 OM= 0.775	A=0.00     A=0.30   0.0269   A=0.50   0.0435   A=0.70   0.0576		2.0784	0.3730									
			2.0750	0.3805	-0.0397	0.0350	-0.0115	0.0030	-0.0013	0.0003	-0.0001	0.0000	
			2.0666	0.3957	-0.0753	0.0633	-0.0343	0.0095	-0.0063	0.0018	-0.0005	0.0003	
			2.0486	0.4227	-0.1257	0.1002	-0.0737	0.0224	-0.0177	0.0061	-0.0016	0.0015	
K1= 0.700 OM= 0.837	A=0.00     A=0.30   0.0208   A=0.50   0.0337   A=0.70   0.0444		1.9976	0.3865									
			1.9959	0.3925	-0.0332	0.0347	-0.0096	0.0014	-0.0012	0.0001	-0.0001	0.0000	
			1.9905	0.4041	-0.0631	0.0604	-0.0291	0.0045	-0.0061	0.0009	-0.0006	0.0003	
			1.9769	0.4241	-0.1062	0.0912	-0.0639	0.0114	-0.0177	0.0038	-0.0023	0.0017	
K1= 0.800 OM= 0.894	A=0.00     A=0.30   0.0131   A=0.50   0.0215   A=0.70   0.0287		1.9247	0.3763									
			1.9238	0.3821	-0.0314	0.0376	-0.0080	0.0009	-0.0011	0.0000	-0.0001	0.0000	
			1.9204	0.3930	-0.0583	0.0642	-0.0242	0.0029	-0.0055	0.0002	-0.0007	0.0002	
			1.9106	0.4107	-0.0958	0.0938	-0.0539	0.0070	-0.0167	0.0017	-0.0029	0.0015	
K1= 1.000 OM= 1.000	A=0.00     A=0.30   -0.0034   A=0.50   -0.0052   A=0.70   -0.0066		1.8190	0.3148									
			1.8168	0.3214	-0.0370	0.0420	-0.0062	0.0017	-0.0009	-0.0001	-0.0001	0.0000	
			1.8121	0.3333	-0.0650	0.0717	-0.0185	0.0046	-0.0043	-0.0002	-0.0007	0.0001	
			1.8033	0.3520	-0.0991	0.1040	-0.0408	0.0090	-0.0135	-0.0001	-0.0032	0.0008	
K1= 1.200 OM= 1.095	A=0.00     A=0.30   -0.0172   A=0.50   -0.0285   A=0.70   -0.0391		1.7659	0.2361									
			1.7604	0.2429	-0.0460	0.0403	-0.0060	0.0026	-0.0007	0.0000	-0.0001	0.0000	
			1.7505	0.2553	-0.0795	0.0697	-0.0175	0.0072	-0.0036	0.0001	-0.0006	0.0000	
			1.7356	0.2749	-0.1172	0.1033	-0.0370	0.0145	-0.0110	0.0004	-0.0028	0.0003	
K1= 1.400 OM= 1.183	A=0.00     A=0.30   -0.0264   A=0.50   -0.0445   A=0.70   -0.0630		1.7503	0.1648									
			1.7415	0.1711	-0.0531	0.0342	-0.0065	0.0029	-0.0007	0.0001	-0.0001	0.0000	
			1.7257	0.1826	-0.0918	0.0602	-0.0187	0.0085	-0.0033	0.0006	-0.0005	0.0000	
			1.7023	0.2012	-0.1352	0.0917	-0.0385	0.0179	-0.0099	0.0017	-0.0024	0.0003	
K1= 1.600 OM= 1.265	A=0.00     A=0.30   -0.0312   A=0.50   -0.0535   A=0.70   -0.0775		1.7563	0.1092									
			1.7449	0.1145	-0.0568	0.0266	-0.0071	0.0028	-0.0007	0.0002	-0.0001	0.0000	
			1.7244	0.1245	-0.0990	0.0477	-0.0204	0.0084	-0.0034	0.0009	-0.0005	0.0001	
			1.6933	0.1407	-0.1475	0.0748	-0.0419	0.0183	-0.0099	0.0027	-0.0022	0.0005	
K1= 1.800 OM= 1.342	A=0.00     A=0.30   -0.0327   A=0.50   -0.0570   A=0.70   -0.0843		1.7723	0.0694									
			1.7594	0.0737	-0.0576	0.0194	-0.0075	0.0024	-0.0003	0.0002	-0.0001	0.0000	
			1.7357	0.0818	-0.1015	0.0355	-0.0218	0.0073	-0.0036	0.0010	-0.0005	0.0002	
			1.6989	0.0951	-0.1533	0.0573	-0.0450	0.0165	-0.0104	0.0032	-0.0021	0.0006	
K1= 2.000 OM= 1.414	A=0.00     A=0.30   -0.0323   A=0.50   -0.0568   A=0.70   -0.0856		1.7914	0.0427									
			1.7777	0.0460	-0.0565	0.0134	-0.0077	0.0019	-0.0008	0.0002	-0.0001	0.0000	
			1.7524	0.0522	-0.1005	0.0252	-0.0225	0.0058	-0.0038	0.0009	-0.0005	0.0002	
			1.7121	0.0626	-0.1539	0.0419	-0.0471	0.0137	-0.0111	0.0031	-0.0022	0.0007	
K1= 2.500 OM= 1.581	A=0.00     A=0.30   -0.0279   A=0.50   -0.0500   A=0.70   -0.0778		1.8333	0.0110									
			1.8202	0.0125	-0.0508	0.0045	-0.0075	0.0007	-0.0008	0.0000	-0.0001	0.0000	
			1.7950	0.0153	-0.0918	0.0091	-0.0223	0.0026	-0.0041	0.0005	-0.0006	0.0001	
			1.7533	0.0201	-0.1443	0.0165	-0.0481	0.0068	-0.0121	0.0020	-0.0025	0.0006	
K1= 3.000 OM= 1.732	A=0.00     A=0.30   -0.0236   A=0.50   -0.0426   A=0.70   -0.0674		1.8603	0.0021									
			1.8487	0.0026	-0.0454	0.0011	-0.0070	0.0001	-0.0008	-0.0001	-0.0001	-0.0001	
			1.8261	0.0037	-0.0826	0.0024	-0.0211	0.0008	-0.0040	0.0001	-0.0006	0.0000	
			1.7875	0.0056	-0.1316	0.0055	-0.0462	0.0026	-0.0121	0.0008	-0.0026	0.0002	

Table 1



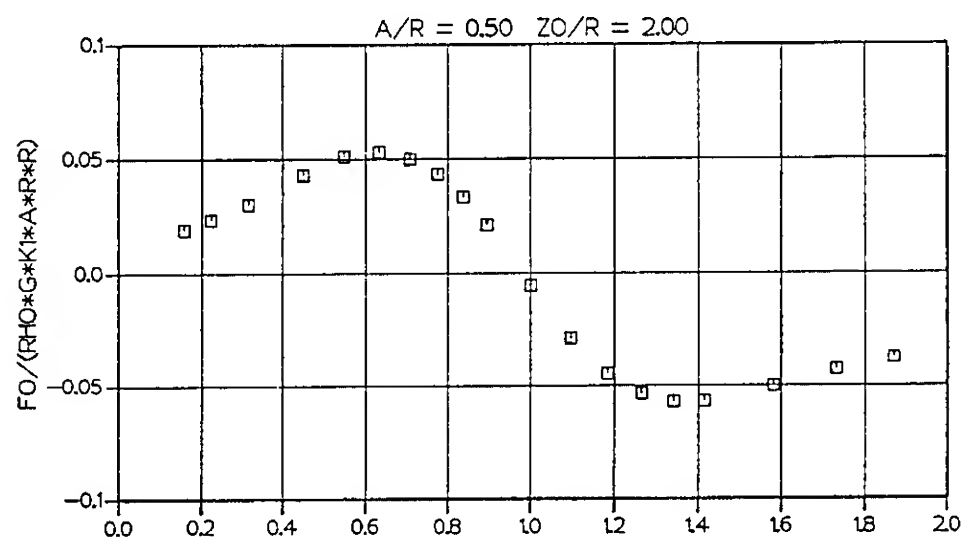


Figure 20

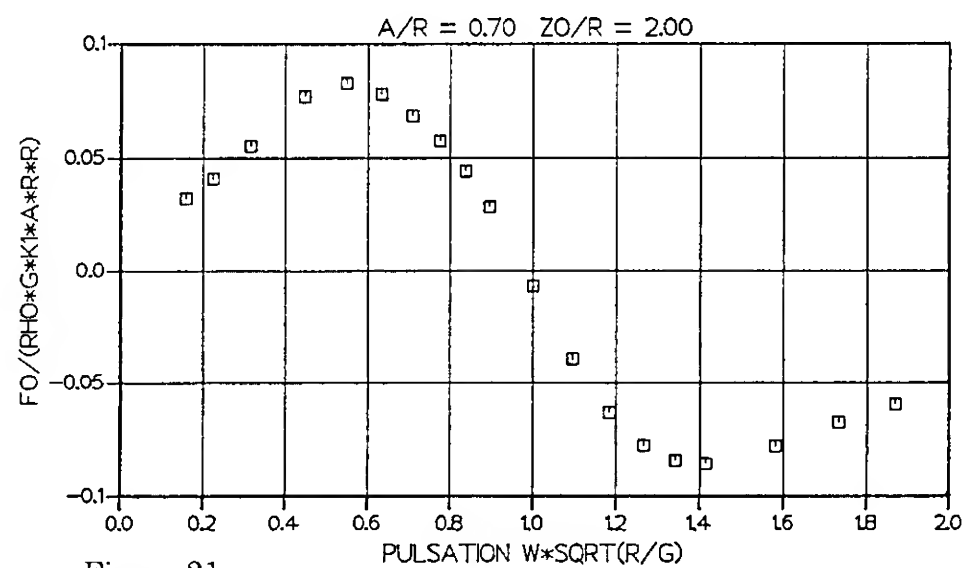


Figure 21

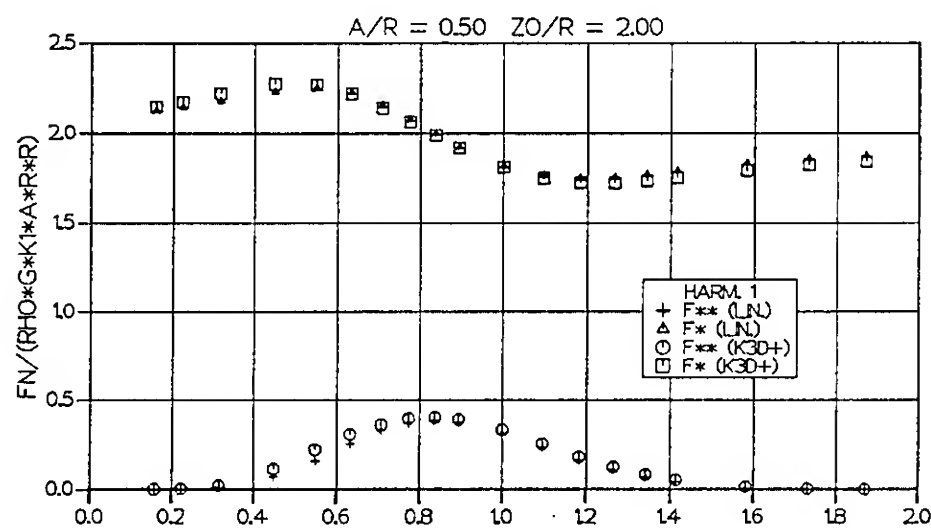


Figure 22

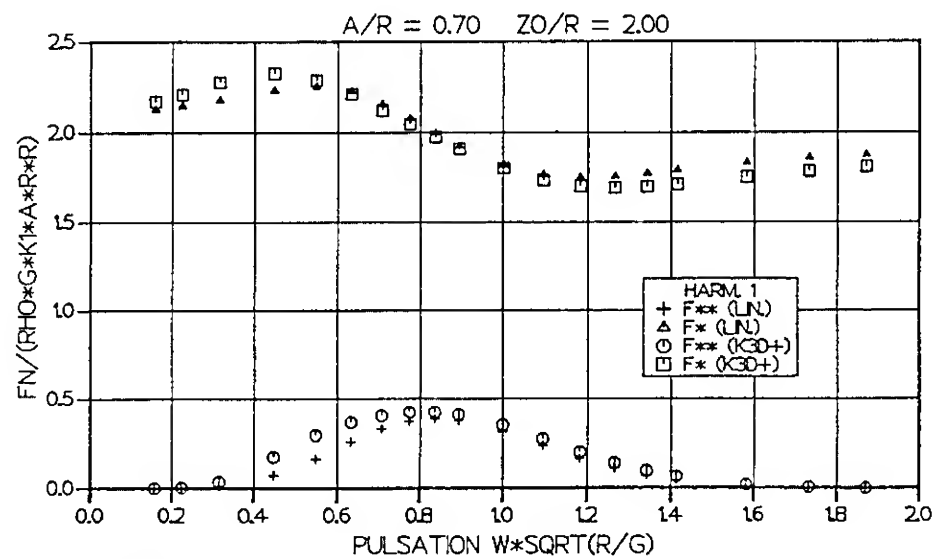


Figure 23

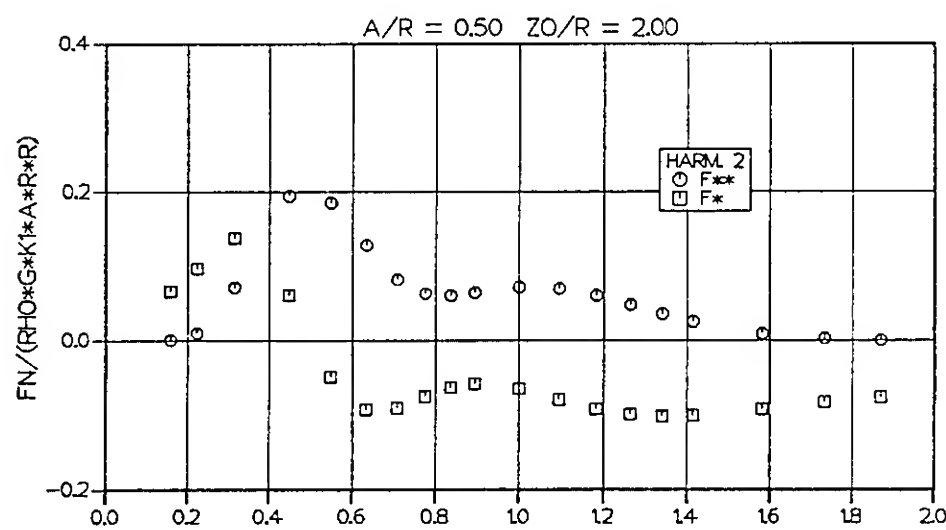


Figure 24

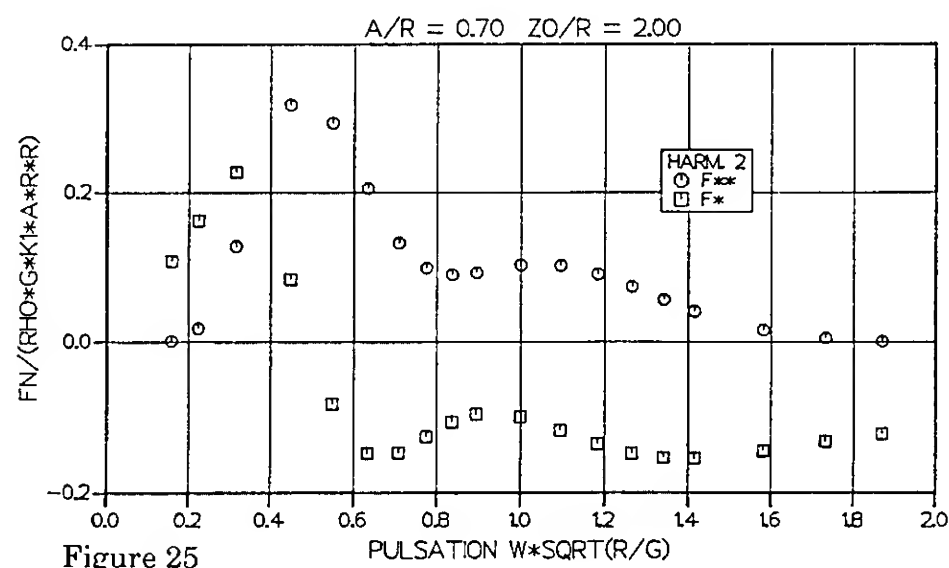


Figure 25

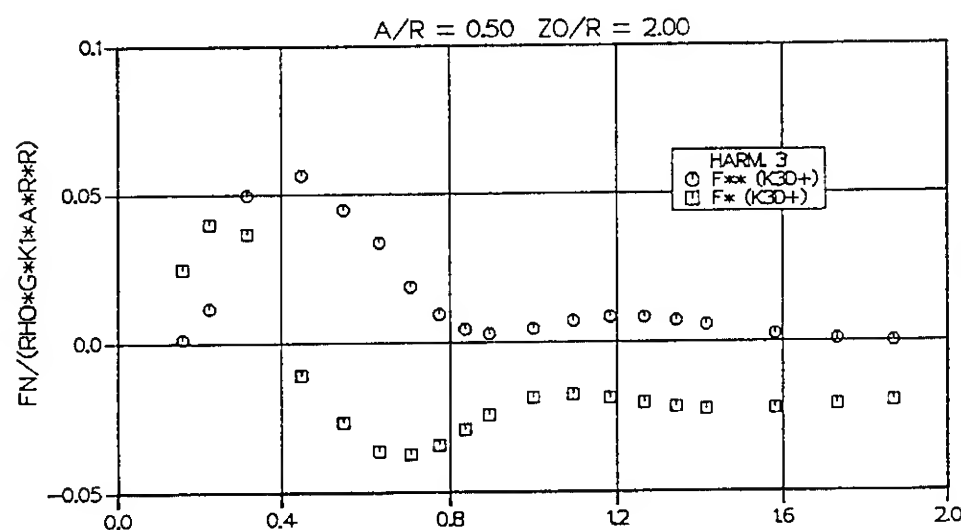


Figure 26

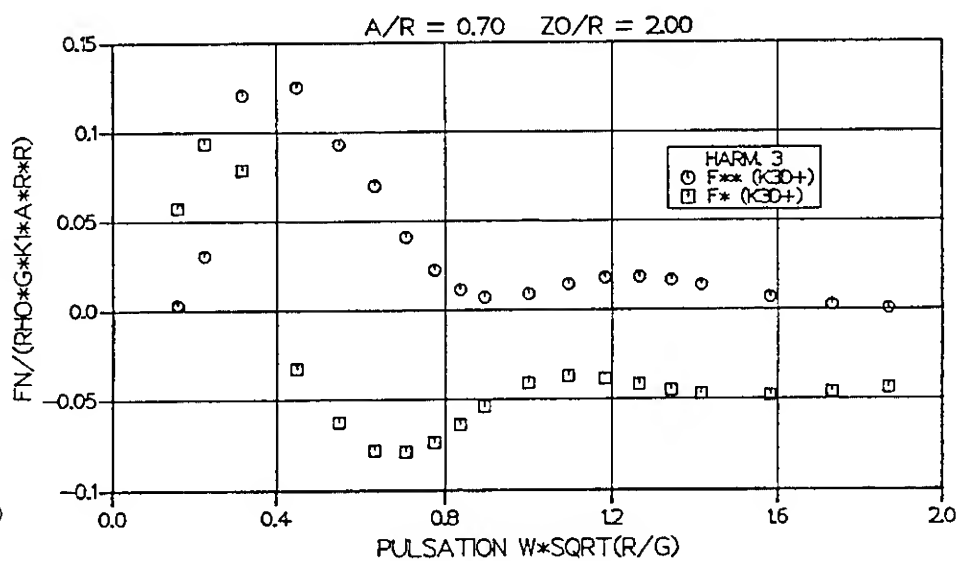


Figure 27

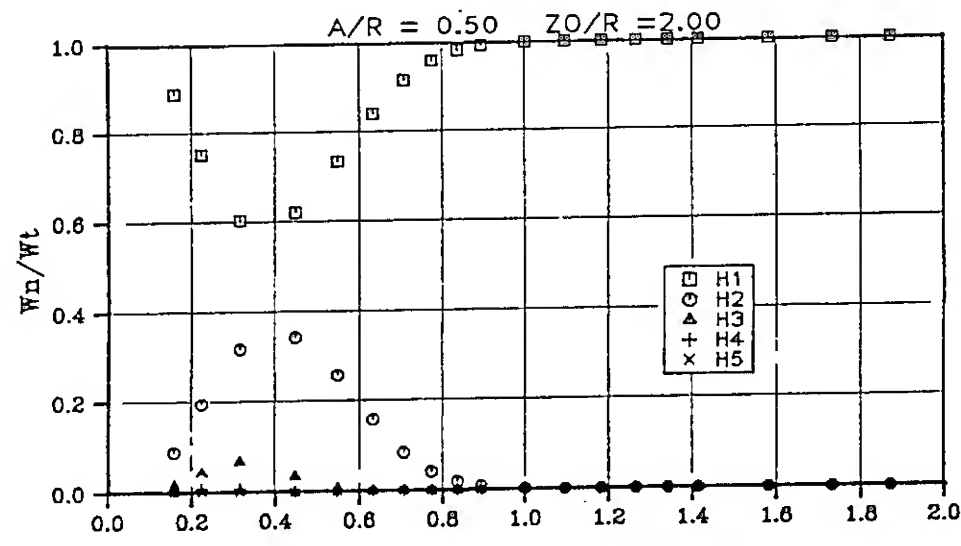
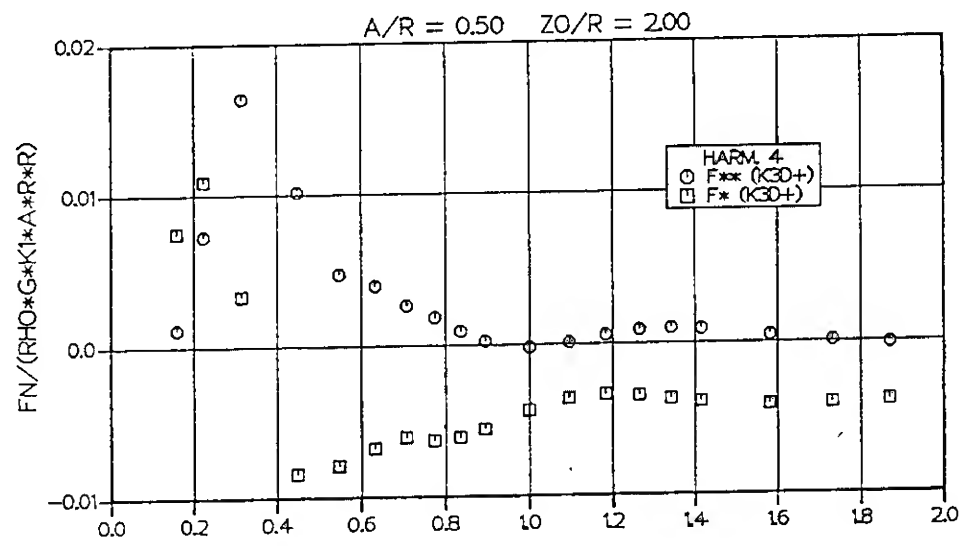


Figure 28

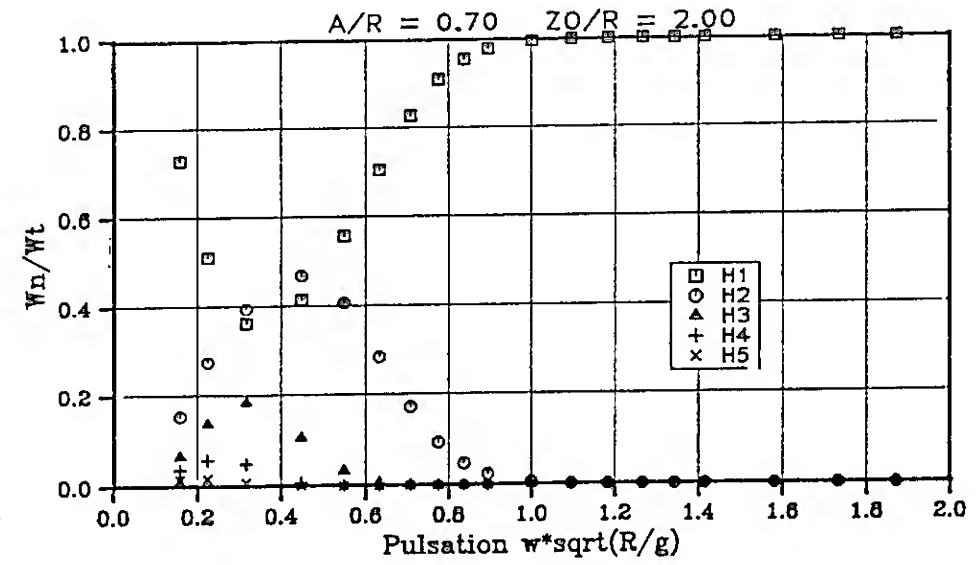
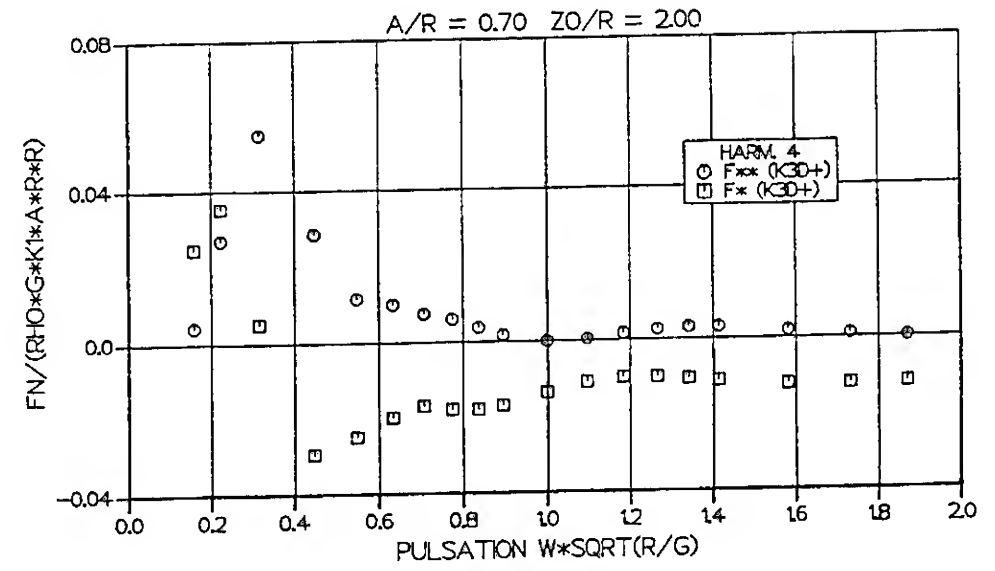


Figure 29

WAVE ENERGY DISPERSION

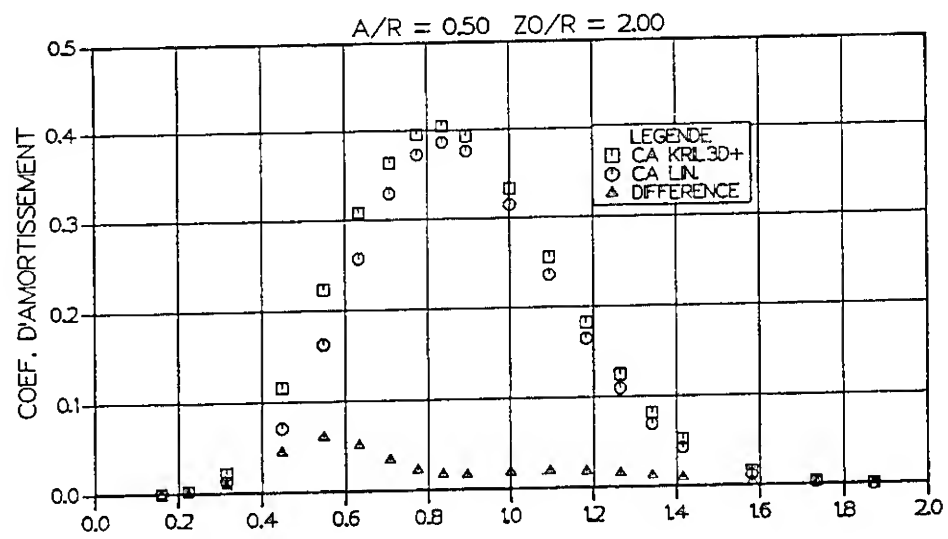


Figure 30

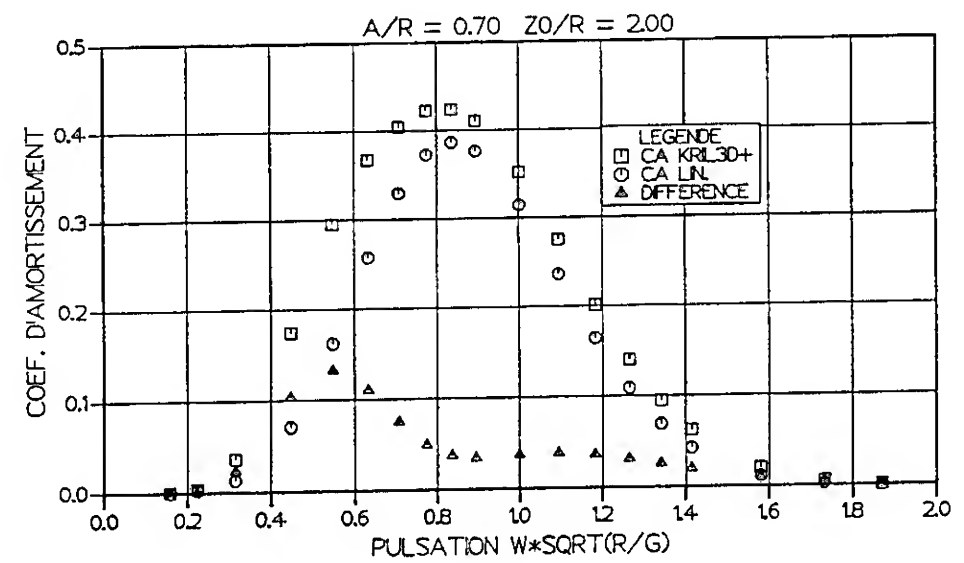


Figure 31

DAMPING COEFFICIENT

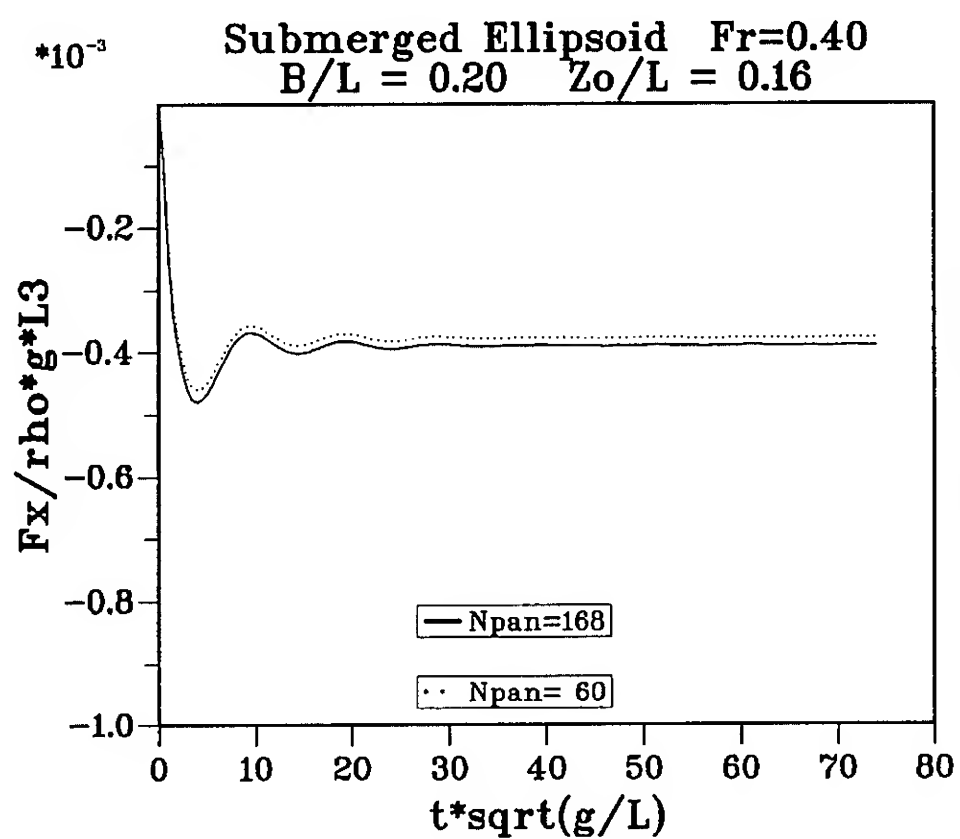


Figure 32

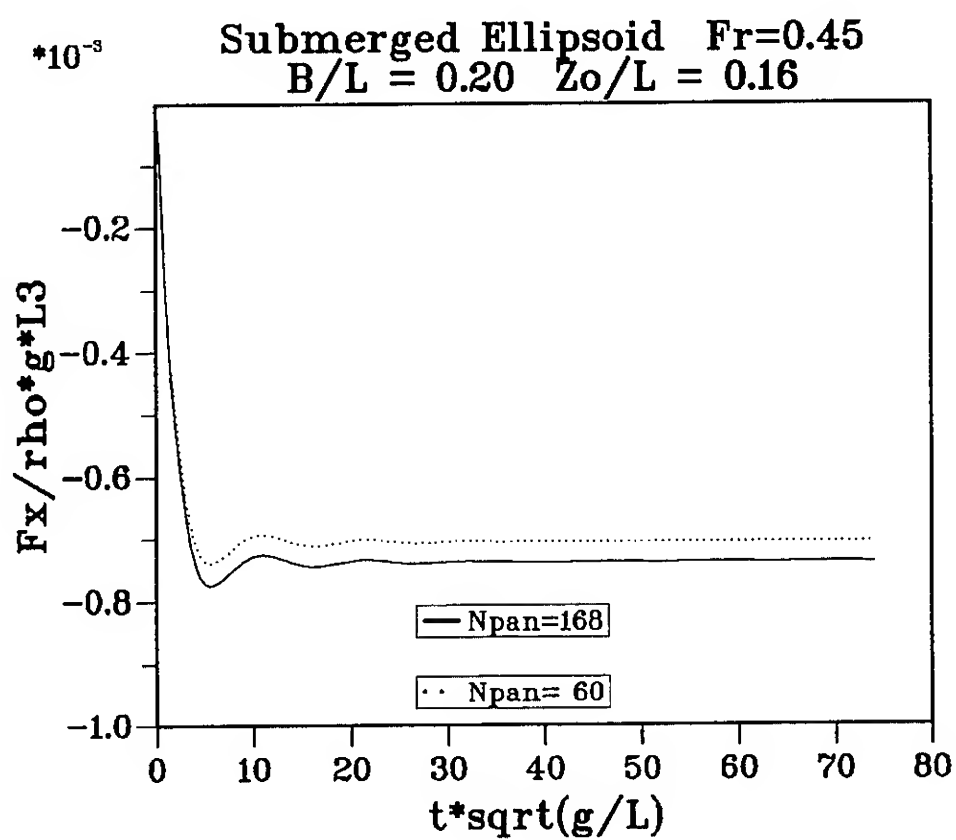


Figure 33

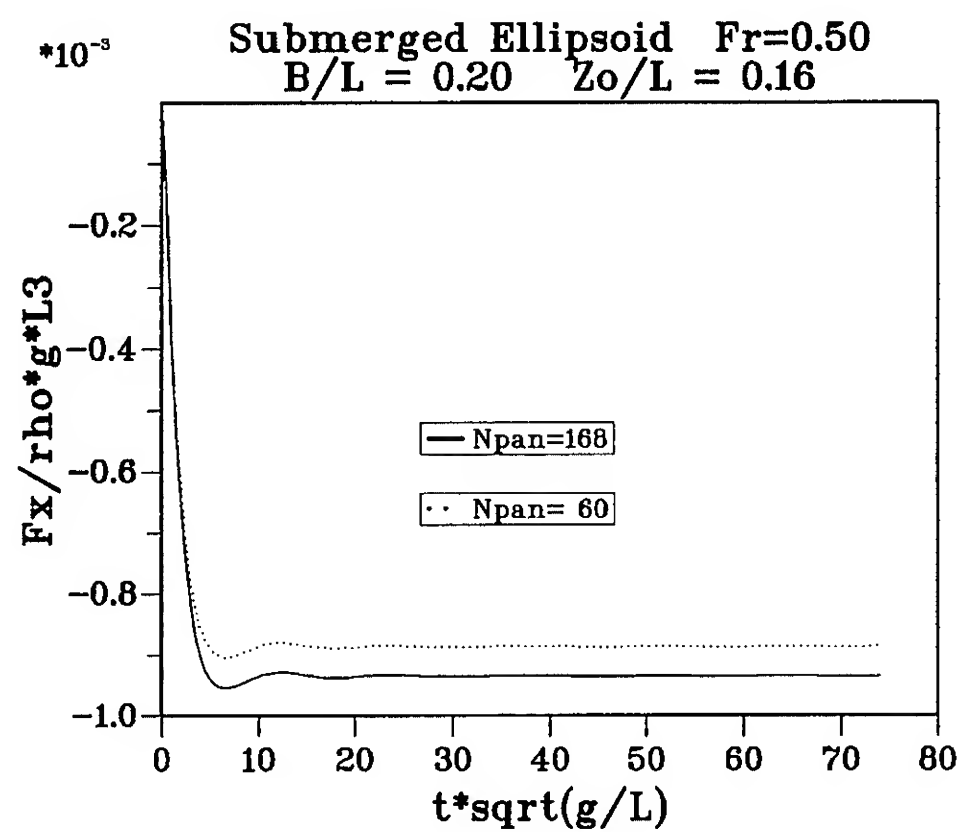


Figure 34

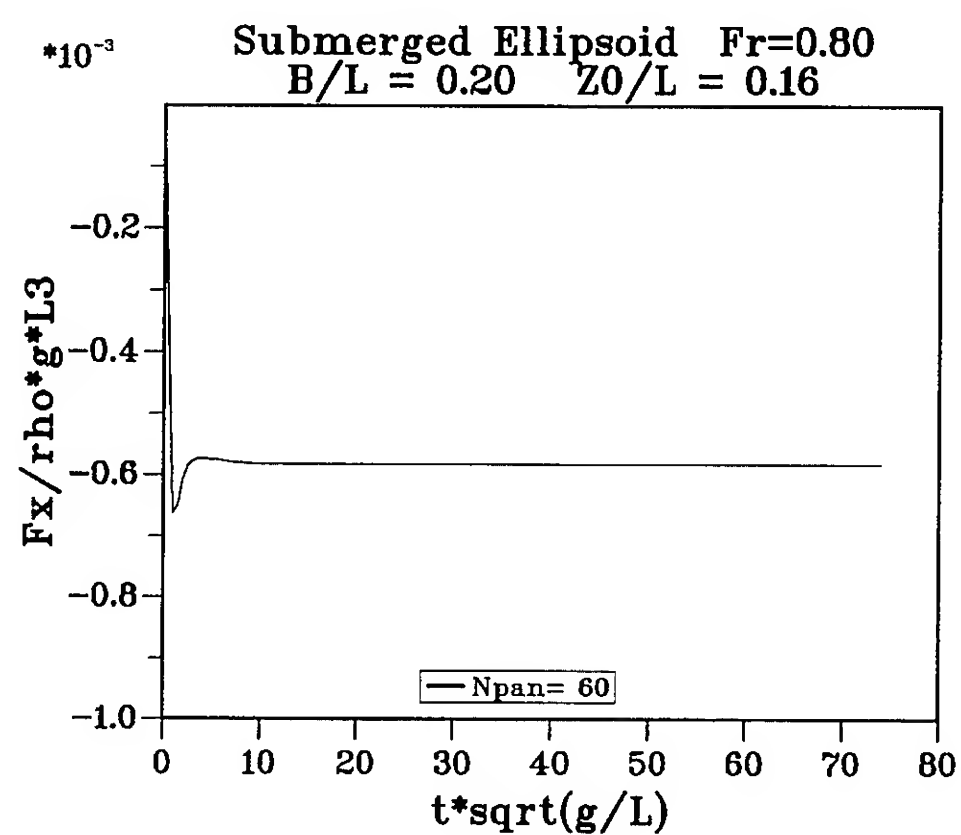


Figure 35

## REFERENCES:

- Abramowitz M., Stegun I.A., "Handbook of mathematical functions". Dover Publications, New York, 1965.
- Adachi H., Ohmatsu S., "On the time-dependent potential and its application to wave problems". Proc. 13th ONR Symposium on Naval Hydrodynamics. Tokyo, 1980.
- Brard. R., "Introduction à l'étude théorique du tangage en marche" Bulletin de l'ATMA, 1948.
- Clément A., Ferrant P., "Free surface potential of a pulsating singularity in harmonic heave motion". Proc. Fourth Int. Conf. on Num. Ship Hydrodynamics. Washington, 1985.
- Clément. A., Ferrant. P., "Superharmonic waves generated by the large amplitude motion of a submerged body". IUTAM Symposium on Nonlinear Waves. Tokyo, 1987.
- Dassonville B., "Etude expérimentale des effets non-linéaires du mouvement de grande amplitude d'un corps faiblement immergé", thèse de Docteur-Ingénieur. Université de Nantes, 1987.
- Delhommeau G., "Les problèmes de diffraction-radiation et de résistance de vagues: Résolution numérique par la méthode des singularités". Thèse de Doctorat ès Sciences, Nantes, 1987.
- Doctors L.J., Beck R.F., "Convergence properties of the Neumann-Kelvin problem for a submerged body". Journal of Ship Research, Vol. 31, n° 4, pp. 227-234, 1987.
- Farell C., "On the wave resistance of a submerged spheroid". Journal of Ship Research, Vol. 17, n° 1, pp. 1-11, 1973.
- Ferrant P., "An fast computational method for transient 3D wave-body interactions". Proc. Int. Conference on Computer Modelling in Ocean Engineering. Balkema Publishers, 1988.
- Ferrant P., "Radiation d'ondes de gravité par les déplacements de grande amplitude d'un corps immergé: Comparaison des approches fréquentielle et instationnaire", thèse de Doctorat, Université de Nantes, 1988.
- Finkelstein A.B., "The initial value problem for transient water waves". Comm. on Pure and Applied Maths., vol. 10, pp 511-522, 1957.
- Gradshteyn I.S., Ryzhyk I.W., "Tables of integrals, series and products", Academic Press, New York, 1965.
- Jami A., "Etude théorique et numérique de phénomènes transitoires en hydrodynamique navale." thèse de Doctorat ès Sciences. ENSTA, 1982.
- Jami A., Gélebart L., "Une approche transitoire des mouvements de translation de corps immergés". Premières Journées de l'Hydrodynamique, Nantes, 1987.
- Jami A., Pot G., "Finite element solution for the transient flow past a freely floating body". Proc. Fourth Int. Conf. on Num. Ship Hydrodynamics. Washington, 1985.
- King B.K., Beck R.F., Magee A.R., "Seakeeping calculations with forward speed using time-domain analysis". Proc. 17th ONR Symposium on Naval Hydrodynamics. The Hague, 1988.
- Korsmeyer F.T., Lee C.H., Newman J.N., Sclavounos P.D., "The analysis of wave effects on tension-leg platforms". OMAE Conference. Houston, 1988.
- Liapis S., Beck R.F., "Seakeeping computation using time domain analysis". Proc. Fourth Int. Conf. on Num. Ship Hydrodynamics. Washington, 1985.
- Magee A.R., Beck R.F., "Vectorized computation of the time-domain Green function". Fourth Int. Workshop on Water Waves and Floating Bodies. Oystesee, Norway, 1989.
- Magee A.R., Beck R.F., "Time domain analysis for predicting ship motions". Iutam Symposium. London, 1990.
- Newman J.N., "Transient axisymmetric motion of a floating cylinder". J.F.M., Vol. 157, pp. 17-33, 1985.
- Newman J.N., "The evaluation of free surface Green functions". Proc. Fourth Int. Conf. on Num. Ship Hydrodynamics. Washington, 1985.
- Newman J.N., "The approximation of free-surface Green functions". F. Ursell Retirement Meeting, Manchester, 1990.
- Pot G., "Etude theorique et numérique des mouvements libres de corps flottants ou immergés. Extension au cas des grands mouvements de corps immergés". Thèse de Docteur-Ingénieur, ENSTA, 1986.
- Stoker J.J., "Water Waves", Interscience Publishers, New York, 1957.
- Webster W.C., "The flow about arbitrary, three-dimensional smooth bodies". Journal of Ship Research, Vol. 19, n° 4, pp. 206-218, 1975.
- Wehausen J.V., Laitone E.V., "Surface Waves" in *Handbuch der Physik*, Springer Verlag Ed., Berlin, 1960.
- Yeung R.W., "The transient heaving motion of floating cylinders". Journal of Engineering Mathematics, Vol. 16, pp. 97-119, 1982.

## APPENDIX 1

### INTEGRAL REPRESENTATION OF THE VELOCITY POTENTIAL

#### 1. Green function

Let us first introduce the three-dimensional Green function for a point source of impulsive strength:

$$G(M, P, t) = \delta(t) \cdot G_0(M, P) + H(t) \cdot F(M, P, t) \quad (A1.1)$$

with the notations:

$$G_0(M, P) = -\frac{1}{4\pi r} + \frac{1}{4\pi r'} \quad (A1.2)$$

$$F(M, P, t) = -\frac{1}{2\pi} \int_0^\infty (gk)^{1/2} \sin[(gk)^{1/2} t] J_0(kR) e^{k(z+z')} dk \quad (A1.3)$$

$$\begin{aligned} M &= (x, y, z) \\ P &= (x', y', z') \\ r &= [(x-x')^2 + (y-y')^2 + (z-z')^2]^{1/2} \\ r' &= [(x-x')^2 + (y-y')^2 + (z+z')^2]^{1/2} \\ R &= [(x-x')^2 + (y-y')^2]^{1/2} \end{aligned}$$

and where  $\delta(t)$  and  $H(t)$  are respectively Dirac's delta function and Heaviside's step function.

$G$  is the potential induced at point  $P$  by a point source of strength  $\delta(t)$  located at point  $M$ , and can be shown to have the following properties:

$$\Delta G(M, P, t) = \delta(r) \cdot \delta(t) \quad (A1.4)$$

$$\frac{\delta^2 G(M, P, t)}{\delta t^2} + g \frac{\delta G(M, P, t)}{\delta z'} = 0 \quad \text{for } P \in S_1 (z'=0) \quad (A1.5)$$

$$G(M, P, 0) = G_t(M, P, 0) = 0 \quad (A1.6)$$

$$G(M, P, t) = G(P, M, t) \quad (A1.7)$$

$$G = O(r^{-2}); \nabla G = O(r^{-3}) \quad \text{when } r \rightarrow +\infty \quad (A1.8)$$

#### 2. Green's identity

Applying Green's identity in the fluid domain at time  $\tau$  to  $\Phi(P, \tau)$  and to  $G(M(t), P(\tau), t-\tau)$  yields:

$$\iiint_{D(\tau)} [\Phi(P, \tau) \Delta G(M(t), P(\tau), t-\tau) - \Delta \Phi(P, \tau) G(M(t), P(\tau), t-\tau)] dV_P = \quad (A1.9)$$

$$\iint_{S(\tau)} [\Phi(P, \tau) \frac{\partial}{\partial n(P)} G(M, P, t-\tau) - \frac{\partial}{\partial n(P)} \Phi(P, \tau) G(M, P, t-\tau)] dS_P$$

with  $S(\tau) = S_b(\tau) + S_f(\tau) + S_\infty$

Left side of equation (A1.9) is a Stieltjes integral which can be reduced accounting for (A1.4) and (1), to give:

$$\delta(t-\tau) \cdot \frac{\Omega(M)}{4\pi} \Phi(M, \tau) = \quad (A1.10)$$

$$\iint_{S(\tau)} [\Phi(P, \tau) \frac{\partial}{\partial n(P)} G(M, P, t-\tau) - \frac{\partial}{\partial n(P)} \Phi(P, \tau) G(M, P, t-\tau)] dS_P$$

where  $\Omega(M)$  is the solid angle under which  $D$  is seen from  $M$ , when  $M$  is in  $D$  or  $S$ . (1.10) is then integrated with respect to  $\tau$  from 0 to  $t$ , giving, due to the fundamental property of  $\delta$ :

$$\frac{\Omega(M)}{4\pi} \Phi(M, t) = \quad (A1.11)$$

$$\int_0^t d\tau \iint_{S(\tau)} [\Phi(P, \tau) \frac{\partial}{\partial n_P} G(M, P, t-\tau) - \frac{\partial}{\partial n_P} \Phi(P, \tau) G(M, P, t-\tau)] dS_P$$

$\Phi$  being bounded at infinity (finite energy), and accounting for (A1.8), the integral over  $S_\infty$  in the right hand side of last equation vanishes. Next step is to transform the integral over  $S_f$ :

$$I_{Sf} = \int_0^t d\tau \iint_{Sf(\tau)} [\Phi(P, \tau) \frac{\partial}{\partial n_P} G(M, P, t-\tau) - \frac{\partial}{\partial n_P} \Phi(P, \tau) G(M, P, t-\tau)] dS_P \quad (A1.12)$$

On  $S_f$ ,  $\Phi$  and  $G$  both satisfy the linearized free surface condition, so that:

$$\Phi_n(M, P, \tau) = -\frac{1}{g} \Phi_{\tau\tau}(M, P, \tau) \quad (A1.13)$$

$$G_n(M, P, t-\tau) = -\frac{1}{g} G_{\tau\tau}(M, P, t-\tau)$$

and:

$$\begin{aligned} I_{Sf} &= -\frac{1}{g} \int_0^t d\tau \iint_{Sf(\tau)} [\Phi G_{\tau\tau} - G \Phi_{\tau\tau}] dS_P \\ &= -\frac{1}{g} \int_0^t d\tau \iint_{Sf(\tau)} [\Phi G_\tau - G \Phi_\tau]_\tau dS_P \end{aligned} \quad (A1.14)$$

then, introducing the total derivative in  $\tau$  of the integral over  $S_f$ :

$$\begin{aligned} \frac{D}{D\tau} \iint_{Sf(\tau)} [\Phi G_\tau - G \Phi_\tau] dS &= \iint_{Sf(\tau)} [\Phi G_\tau - G \Phi_\tau]_\tau dS \\ &+ \oint_{Cb(\tau)} [\Phi G_\tau - G \Phi_\tau] (n \wedge dl) \cdot Vc \end{aligned} \quad (A1.15)$$

where  $C_b$  is the curve defined by the intersection of the instantaneous body surface  $S_b$  and the free surface  $z=0$  and  $Vc$  is the velocity of a point on  $C_b$ , we may write for  $I_{Sf}$ :

$$I_{sf} = \quad (A1.16)$$

$$\frac{-1}{g} \int_0^t d\tau \frac{D}{D\tau} \iint_{S_f(\tau)} [\Phi(P(\tau), \tau) G_\tau(M, P, t-\tau) - G(M, P, t-\tau) \Phi_\tau(P, \tau)] dS_P$$

$$+ \frac{1}{g} \int_0^t d\tau \oint_{Cb(\tau)} [\Phi(P(\tau), \tau) F_\tau(M(t), P(\tau), t-\tau) - F\Phi_\tau] (n_p \wedge dl_p) \cdot Vc(P)$$

The first term is zero, due to the initial conditions for  $G$  and  $\Phi$ , and gathering terms, we finally obtain the following integral representation of the velocity potential in the fluid domain  $D(t)$ , in terms of a mixed distribution of sources and normal dipoles on  $S_b$ . (Go terms in the integral over  $S_b$  have been extracted accounting for the integral property of  $\delta(t)$ , and eliminated from the line integral, for  $G_0$  is identically zero at the free surface)

$$\frac{\Omega(M)}{4\pi} \Phi(M, t) = \quad (A1.17)$$

$$\iint_{S_b(t)} [\Phi(P, t) \frac{\partial}{\partial n_P} G_0(M, P) - G_0(M, P) \frac{\partial}{\partial n_P} \Phi(P, t)] dS_P$$

$$+ \int_0^t d\tau \iint_{S_b(\tau)} [\Phi(P, \tau) \frac{\partial}{\partial n(P)} F(M, P, t-\tau) - \frac{\partial}{\partial n(P)} \Phi(P, \tau) F(M, P, t-\tau)] dS_P$$

$$+ \frac{1}{g} \int_0^t d\tau \oint_{Cb(\tau)} [\Phi(P(\tau), \tau) F_\tau(M(t), P(\tau), t-\tau) - F\Phi_\tau] (n_p \wedge dl_p) \cdot Vc(P)$$

When  $M$  is on  $S_b$ ,  $\Omega(M) = 2\pi$  (if the normal is continuous in  $M$ ) and (A1.17) gives the integral equation to be solved for  $\Phi$  on  $S_b$ , considering  $\partial\Phi/\partial n$  to be known (forced motions). After solution, (A1.17) may be used to compute  $\Phi$  everywhere else in the fluid domain  $D$ , where  $\Omega(M) = 4\pi$ . When the body is fully submerged or when  $Cb$  is time invariant, the line integral in (A1.17) simply vanishes.

At last, note that the solution may also be represented by a distribution of sources only. The derivation of the corresponding integral representation follows comparable steps and, for brevity, will not be given.

## APPENDIX 2

### FREQUENCY DOMAIN GREEN FUNCTIONS FOR THE BODY-NONLINEAR PROBLEM

We are interested here in the steady-state periodic free-surface potential generated by a submerged point source following an arbitrary periodic motion of frequency  $\omega$ , with a source strength of frequency  $p\omega$ ,  $p \geq 0$ , i.e. solution of the following problem:

$$\Delta G_{ip}(M(t), P, t) = \delta(r(t)) \cdot \begin{matrix} \cos p\omega t & (i=1) \\ \sin p\omega t & (i=2) \end{matrix} \quad (A2.1)$$

$$\frac{\partial^2 G_{ip}}{\partial x^2} + g \frac{\partial G_{ip}}{\partial z'} = 0 \quad \text{for } z' = 0 \quad (A2.2)$$

$$\nabla G_{ip} \longrightarrow 0 \quad \text{for } r \longrightarrow \infty \quad (A2.3)$$

$$+ \text{radiation condition} \quad (A2.4)$$

for  $M(t) = [x(t), y(t), z(t)]$  prescribed motion of frequency  $\omega$   
 $P = [x', y', z']$  fixed point

$$r(t) = [(x(t)-x')^2 + (y(t)-y')^2 + (z(t)-z')^2]^{1/2} \quad (A2.5)$$

An exhaustive study of the solutions of this problem may be found in Ferrant (1988), where these Green functions were initially developed for the solution of the body-nonlinear problem in the frequency domain. Only the results liable to be useful for the present paper will be repeated in this appendix.

#### 1. General case - Arbitrary periodic motion

The preceding problem may be solved using different methods (Fourier transform, time asymptotic limit of unsteady solution,...), the details of which being given in Ferrant (1988). Although involving some tedious algebra, the results may be expressed in a very concise form, involving the frequency domain Green function for a fixed point source. In the general case of an arbitrary periodic motion,  $G_{1p}$  and  $G_{2p}$  are given by:

$$G_{1p}(M(t), P, t) = \frac{1}{2\pi} \int_0^{2\pi} \cos p\tau [G_{\omega 0}(0, M(\tau/\omega), P) \quad (A2.6)$$

$$+ 2 \operatorname{Re} \sum_{l=1}^{\infty} G_{\omega 0}(l\omega, M(\tau/\omega), P) e^{-il(\omega\tau - t)}] d\tau$$

$$G_{2p}(M(t), P, t) = \frac{1}{2\pi} \int_0^{2\pi} \sin p\tau [G_{\omega 0}(0, M(\tau/\omega), P) \quad (A2.7)$$

$$+ 2 \operatorname{Re} \sum_{l=1}^{\infty} G_{\omega 0}(l\omega, M(\tau/\omega), P) e^{-il(\omega\tau - t)}] d\tau$$

where  $G_{\omega 0}(\omega, M, P)$  is the complex Green function for the frequency domain diffraction-radiation problem.  $G_{\omega 0}(0, M, P)$  is the zero frequency limit of this function, i.e. for infinite depth:

$$G_{\omega 0}(0, M, P) = -\frac{1}{4\pi r} - \frac{1}{4\pi r'} \quad (A2.8)$$



*Nota:* Although initially derived for the infinite depth case, expressions (A2.6), (A2.7) can be easily shown to hold for finite depth too, provided the finite depth diffraction-radiation Green function is substituted to  $G_{\omega 0}$ .

## 2. Sine heave motion

### 2.1 Basic formulations

Explicit forms of the body-nonlinear frequency domain Green functions may be derived by first imposing the analytic form of the source path, and then introducing appropriate formulations of  $G_{\omega 0}$  (Near-Field, Haskind, ...). In the case of a time-harmonic heaving motion, we have:

$$M(t) = (x_0, y_0, z_0 + a \cos \omega t) \quad (A2.9)$$

Then, substituting for example the Near-Field formulation of  $G_{\omega 0}$  in (A2.6), (A2.7), we get, after some transformations:

$$G_{1p}[M(t), P, t] = -\frac{\cos p\omega t}{4\pi} \cdot \left[ \frac{1}{r(t)} + \frac{1}{r'(t)} \right] \quad (A2.10)$$

$$- \sum_{n=1}^{\infty} \left\{ \frac{2k_n}{\pi^3} \int_0^{\pi} \cos p\tau \cdot \cos n\tau R_e \left\{ \int_0^{\pi/2} e^{\zeta_n(\tau/\omega)} E_1[\zeta_n(\tau/\omega)] d\theta \right\} d\tau \cdot \cos n\omega t \right.$$

$$\left. + \frac{k_n}{2} e^{k_n(z_0+z')} [I_{p+n}(ak_n) + I_{p-n}(ak_n)] \cdot [H_0(k_n R) \cos n\omega t - J_0(k_n R) \sin n\omega t] \right\}$$

and:

$$G_{2p}[M(t), P, t] = -\frac{\sin p\omega t}{4\pi} \cdot \left[ \frac{1}{r(t)} + \frac{1}{r'(t)} \right] \quad (A2.11)$$

$$- \sum_{n=1}^{\infty} \left\{ \frac{2k_n}{\pi^3} \int_0^{\pi} \sin p\tau \cdot \sin n\tau R_e \left\{ \int_0^{\pi/2} e^{\zeta_n(\tau/\omega)} E_1[\zeta_n(\tau/\omega)] d\theta \right\} d\tau \cdot \sin n\omega t \right.$$

$$\left. + \frac{k_n}{2} e^{k_n(z_0+z')} [I_{p-n}(ak_n) - I_{p+n}(ak_n)] \cdot [H_0(k_n R) \sin n\omega t + J_0(k_n R) \cos n\omega t] \right\}$$

where  $H_0$  and  $J_0$  are respectively the Struve and Bessel functions of order 0,  $I_p$  is the modified Bessel function of order  $p$ ,  $E_1$  is the exponential-integral function, and :

$$k_n = (n\omega)^2/g$$

$$R = [(x_0 - x')^2 + (y_0 - y')^2]^{1/2}$$

$$\zeta_n(t) = k_n [z(t) + z' + j R \cos \theta]$$

$$j^2 = -1$$

These expressions are mostly appropriate for the computation of  $G_{ip}$  when  $R$  is small. For larger radial distances, formulations based on the modified Haskind form of  $G_{\omega 0}$  are to be preferred; see details in Ferrant (1988).

### 2.2 Far-field behaviour

Accounting for the asymptotic behaviour of the special functions  $H_0$ ,  $J_0$  and  $E_1$ , the following far-field

expressions for  $G_{ip}$  are easily derived, for a source motion being given by (A2.9):

$$G_{1p}(M(t), P, t) = \quad (A2.12)$$

$$\sum_{n=1}^{\infty} \left( \frac{k_n}{2\pi R} \right)^{1/2} e^{k_n(z_0+z')} [I_{p+n}(ak_n) + I_{p-n}(ak_n)] \cdot \sin(k_n R - n\omega t - \pi/4)$$

$$+ o(R^{-1}) \quad \text{for } R \longrightarrow \infty$$

and:

$$G_{2p}(M(t), P, t) = \quad (A2.13)$$

$$\sum_{n=1}^{\infty} \left( \frac{k_n}{2\pi R} \right)^{1/2} e^{k_n(z_0+z')} [I_{p-n}(ak_n) - I_{p+n}(ak_n)] \cdot \cos(k_n R - n\omega t - \pi/4)$$

$$+ o(R^{-1}) \quad \text{for } R \longrightarrow \infty$$

As can be deduced from these expressions, the far-field is a superposition of regular circular waves of velocities  $C_n = g/n\omega$ ,  $1 \leq n \leq \infty$ , the amplitudes of the harmonics being explicitly given by the coefficients in front of the sine functions, involving modified Bessel functions of arguments  $ak_n$ .

# Nonlinear and Linear Motions of a Rectangular Barge in a Perfect Fluid

R. Cointe<sup>1</sup>, P. Geyer<sup>2</sup>, B. King<sup>1</sup>, B. Molin<sup>2</sup>, M. Tramoni<sup>2</sup>

(<sup>1</sup>Bassin d'Essais des Carènes, France),

(<sup>2</sup>Institut Français du Pétrole, France)

## 1 Abstract

The motion of a rectangular barge in beam seas is studied within the framework of potential flow theory.

A simulation technique based on the Mixed Eulerian-Lagrangian method is described. It allows the simulation of the flow and the resulting barge motions to be performed with either linear or fully nonlinear boundary conditions on the hull and on the free surface. Efficient artificial boundary conditions are implemented that allow nonlinear and linear simulations to be performed over a large number of wave periods. Results from linear frequency domain theories are recovered and nonlinear phenomena are presented.

## 2 Introduction

Numerical models based on linear potential theory have proved themselves to be efficient tools to predict the seakeeping behavior of floating structures. As a matter of fact, very often they have been found to perform surprisingly well given all the limitations of the theoretical framework (small motion, small wave steepness, no viscous effects).

A known exception is the roll motion of ships and barges at or near resonance, where diffraction-radiation codes are known to overpredict the response. Addition of a supplementary damping (accounting for the vortex shedding at the bilge corners) to the motion equa-

tion usually notably improves the prediction. For barges however, it has been argued that the nonlinearity of the exciting forces (due to the large variations of the wetted part of the hull) should also be taken into account (e.g. see Denise [1]). The relative importance of these two factors (viscous damping and nonlinear excitation) has led to some controversy.

In past years some attempts have been made at modeling the vortex shedding from the bilge corners within linear potential flow models. Excellent agreement has been reported with available experimental data [2], [3].

This success seems to rule out the possibility of the nonlinearity of the potential loading playing an important role [4]. It is our feeling however that the published numerical and experimental results are too scarce to entitle any general conclusions to be drawn. Obviously, many parameters such as the shape of the bilge corners (sharp or rounded), the beam over draft ratio, the amount of potential damping present at resonance, etc., are to play a role. (We are currently performing extensive experiments to forge our own religion, by varying all these parameters). It seems therefore to be of interest to quantify the amount of nonlinearity present in the excitation forces, and this is the aim of the numerical technique described in the present paper.

To investigate this problem we make use of a time domain numerical model, Sindbad, based on the so-called Mixed Eulerian-Lagrangian method, which simulates a two-

dimensional wavetank. Sindbad has been validated on such problems as sloshing in tanks, wave generation by piston type wave makers, and wave diffraction over submerged cylinders, [5], [6], [7]. Two difficulties had to be solved in order to extend its capabilities to the wave response of a freely floating body :

- a means must be devised so that the waves reflected by the body do not reflect again on the wavemaker and pollute the incident waves. In wave basins this problem is avoided by locating the body far enough from the wave maker, so that a steady state can be reached prior to contamination of the incident waves. In the numerical model it is necessary to restrict the length of the tank in order to limit the size of the problem;

- the hydrodynamic loading on the hull needs to be calculated carefully in such a way to permit a simultaneous integration of the body motion equations.

Section 3 is devoted to a short description of the model and to the way these two problems have been solved.

Even though Sindbad can be run to solve both the nonlinear and linear problems, it was felt that a proper assessment of the validity of its results required some confrontation with more traditional linear frequency domain models. Comparisons have been made with two such models, one based on matching of eigenfunction expansions of the potential in the three sub-domains limited by a rectangular barge (left, right, and underneath), and the other on a Rankine source distribution on the hull and free surface. Both models are briefly described in section 4.

The last part of the paper (section 5) is devoted to the presentation of some numerical results. First the linear option of Sindbad is checked by recovering, once a steady state has been reached, the frequency domain results to a satisfactory accuracy. Results from nonlinear simulations are then presented for the diffraction problem (fixed barge) and for the diffraction-radiation problem.

### 3 Nonlinear and Linear Transient Solutions

#### 3.1 Introduction

Since the work of Longuet-Higgins and Cokelet [8] that pioneered the Mixed Eulerian-Lagrangian method (MEL), this method has been widely used for the simulation of two-dimensional free-surface flows; numerous implementations exist. Many authors have been interested in the description of steep waves and the MEL has proven very successful in describing the flow up to overturning, see for instance [9]. Vinje and Brevig [10] first modelled waves interacting with rigid obstacles, either fixed, in forced motion, or in free motion. This problem has since been addressed by several authors (e.g. [11], [12], [13], [14]). The motions of a rectangular barge have been studied using an implementation of the MEL at St John's [15]. However, many of these studies were somewhat qualitative and it appears that little attention has been given to the validation of the resulting codes by proper comparisons with other theories and experiments. For instance, if computations of the free motion of floating bodies have been performed, systematic comparisons with results from linear theory are almost nonexistent. In our opinion, it is now time to validate the MEL and to use it to provide quantitative results.

An implementation of the MEL at the Institut Français du Pétrole, and in cooperation with DGA, led to the development of the code **Sindbad** (for **S**imulation **n**umérique d'un **b**assin de **h**oule). Developments concerning this code are presently under way at both organisms. Its application to the simulation of two-dimensional flows in the presence of a submerged or surface-piercing body in forced motion has been described elsewhere in some detail (e.g., [5], [7]).

In the next sections attention will focus on the new developments that have been necessary to deal with a freely floating body of arbitrary shape. First some indications concerning the principle of the simulation will be given.

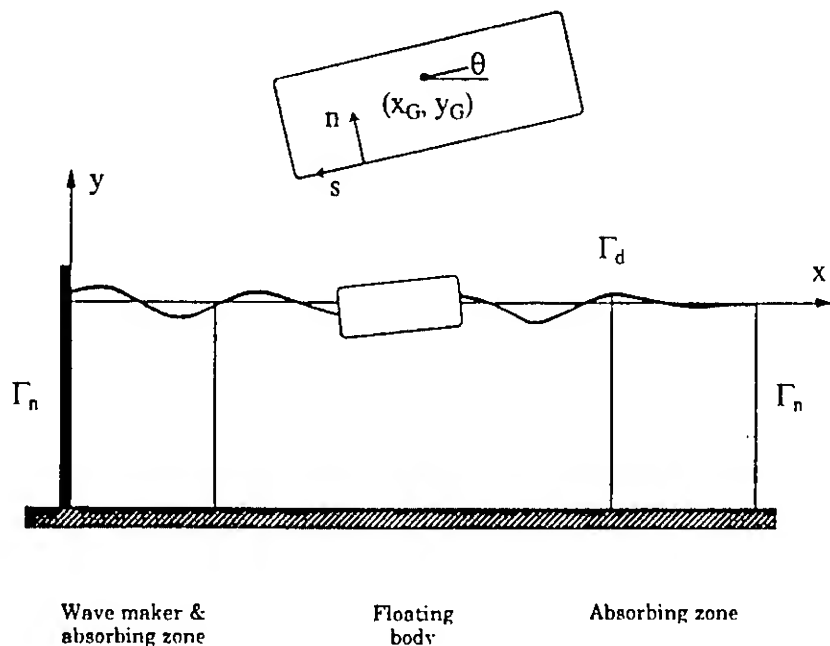


Figure 1: Sindbad wave basin geometry

### 3.2 Outline of the Method

The main idea of the numerical procedure is to choose markers initially at the free surface and to follow them in their motion.

We use a coordinate system  $(x, y)$ . The  $x$ -axis coincides with the reference position of the free surface and the  $y$ -axis is oriented vertically upwards — see figure 1 for geometric definitions. The fluid is assumed to be incompressible and the flow irrotational so that the velocity field  $\vec{v}$  is given by:

$$\vec{v} = \vec{\nabla} \phi, \quad (1)$$

with:

$$\Delta \phi = 0. \quad (2)$$

The computation is performed in a bounded domain. Along rigid boundaries ( $\vec{x} \in \Gamma_n(t)$ ), the normal velocity in the fluid is equal to the normal velocity of the boundary: a Neumann boundary condition.

Along the free surface, we use Bernoulli's equation and the fact that the free surface is a material surface. The corresponding equations are written for a marker  $\vec{x}$  on the free surface ( $\vec{x} \in \Gamma_d(t)$ ) and the associated value of the potential,  $\phi(\vec{x})$ . This yields<sup>1</sup>:

$$\frac{D\phi}{Dt} = -y - \left(\frac{1}{2} - \zeta\right) \phi_s^2 + \frac{1}{2} \phi_n^2 - p + c(t) \quad (3)$$

<sup>1</sup>For the sake of simplicity, we use units such that the acceleration of gravity,  $g$ , the specific mass of water,  $\rho$ , and the depth of the tank,  $h$ , are equal to 1.

$$\frac{D\vec{x}}{Dt} = \zeta \phi_s \vec{s} + \phi_n \vec{n}, \quad (4)$$

where  $D$  is used to indicate a material derivative,  $\vec{s}$  and  $\vec{n}$  are vectors tangent and normal to the free surface, respectively, and  $\zeta$  is an arbitrary constant. This constant specifies the tangential motion of the markers:  $\zeta = 1$  identifies markers as particles while  $\zeta = 0$  yields a zero tangential motion of the markers. This last choice allows a current to be simulated in the tank. For the applications discussed here,  $\zeta = 1$ .

The pressure is assumed constant along the free surface; it can thus be included in the function of time  $c(t)$ . With an appropriate choice of the velocity potential, this function can be taken equal to zero.

The kinematic constraint  $\Delta \phi = 0$ , associated with the boundary condition on  $\Gamma_n$ , permits the free surface boundary conditions (3)-(4) to be expressed as an evolution equation for  $(\phi, \vec{x})$ . This stems from the fact that if, at a given instant  $t$ ,  $\phi$  is known along  $\Gamma_d(t)$  and  $\phi_n$  is known along  $\Gamma_n(t)$ , then  $\phi_n$  can be computed along the free surface and the right-hand sides of (3)-(4) can be evaluated. These equations can be solved numerically using standard time-stepping procedures, such as a fourth-order Runge-Kutta algorithm.

The main numerical task is to solve for the harmonic function  $\phi$  at each time-step knowing  $\phi$  along  $\Gamma_d(t)$  and  $\phi_n$  along  $\Gamma_n(t)$ . We use the integral equation:

$$\begin{aligned} & -\theta(P) \phi(P) + \int_{\Gamma_d + \Gamma_n} \phi(Q) G_n(P, Q) ds_Q \\ & = \int_{\Gamma_d + \Gamma_n} \phi_n(Q) G(P, Q) ds_Q, \end{aligned} \quad (5)$$

where  $P$  is a point on the boundary,  $G$  is the simple source Green function,  $\theta(P)$  the angle between two tangents of the boundary at  $P$  (equal to  $\pi$  for a smooth curve) and  $s$  a curvilinear abscissa along  $\Gamma$ . Equation (5) is discretized using a standard collocation method. The boundary of the domain is approximated by segments and  $\phi$  and  $\phi_n$  are assumed to vary linearly along each segment. This allows an analytical integration of the Green function, its normal derivative and their products by the

curvilinear abscissa so that the calculation of the matrix elements is rather simple and vectorizes well.

Special care has to be taken at corners of the fluid boundary and more particularly at the intersections between the free surface and a piercing body. The numerical treatment that is used there is based on a local asymptotic analysis in the *weakly nonlinear regime* that corresponds to a small acceleration (relative to gravity) of the body. This numerical treatment is discussed in more details in [6] and [7].

### 3.3 Wave Generation and Absorption

#### 3.3.1 Generalities

We are interested in computing the motions of a floating body in the open ocean, submitted to a given incident wave field, over several wave periods. Since the boundary of the entire fluid domain has to be discretized, artificial boundaries must be introduced. For the numerical procedure to be efficient, the fluid domain should be as small as possible. It is therefore necessary to generate the incident waves and to avoid their reflection on the artificial boundaries introduced. Difficulties in reaching a steady-state, even for waves of small steepness, probably explain why comparisons with linear results have not been more systematically performed.

When the steady-state linear solution is computed, an incident wave is prescribed and a radiation condition is written that transmitted and reflected waves must satisfy. Writing a proper radiation condition for the second-order problem has long been a matter of controversy. For the transient problem, the proper behavior at infinity can be accounted for by using a proper elementary solution, the Green function. This approach requires a convolution in time and is only possible if the problem is linear (at least in an outer domain extending to infinity).

In the absence of any mathematically satisfying answer yielding perfectly transparent boundary conditions, we have chosen a pragmatic solution similar to that used for an ex-

periment in a tank. This approach does not involve any hypothesis concerning the steepness of the outgoing waves. Waves are generated by a piston-type wavemaker and the tank is closed at the other end by a vertical wall. Two damping zones, one at each end of the tank, are used for the absorption of the parasitic waves that are generated in the tank — see figure 1. This is equivalent to having an absorbing beach at one end and an absorbing wavemaker at the other end.

#### 3.3.2 Absorbing beach

This absorbing beach is a damping zone, similar to that used in [16]. In this zone, the free surface boundary conditions are modified by adding a damping term. We write:

$$\frac{D\phi}{Dt} = -y - \left(\frac{1}{2} - \zeta\right) \phi_s^2 + \frac{1}{2} \phi_n^2 - \nu(x_e) (\phi - \phi_e) \quad (6)$$

$$\frac{D\vec{x}}{Dt} = \zeta \phi_s \vec{s} + \phi_n \vec{n} - \nu(x_e) (\vec{x} - \vec{x}_e), \quad (7)$$

where the subscript  $e$  corresponds to the reference configuration for the fluid (here, the fluid at rest).

The principle of this damping zone is to absorb the incident wave energy before it can reach the wall. It may be seen intuitively that, if the absorption is too weak, part of the incident wave energy will reach the wall and be reflected. Inversely, if the absorption is too strong, part of the energy will be reflected by the damping zone itself.

The choice of the damping coefficient  $\nu(x)$  is crucial to its efficiency. This coefficient is equal to zero except in the damping zone ( $x_0 \leq x \leq x_1$ ). In this zone it is chosen to be continuous and continuously differentiable, and is “tuned” to a characteristic wave frequency  $\omega$  and a characteristic wave number  $k$ :

$$\nu(x) = \alpha \omega \left[ \frac{k}{2\pi} (x - x_0) \right]^2 \quad (8)$$

$$x_0 \leq x \leq x_1 = x_0 + \frac{2\pi \beta}{k},$$

where  $\alpha$  and  $\beta$  are dimensionless parameters.

### 3.3.3 Absorbing Wavemaker

The absorbing beach allows long simulations to be performed in the numerical tank when the generation and the propagation of surface waves are the only concerns. A difficulty appears for the simulation of the free motions of a body in the tank. Waves are partly reflected by the body and then reflected back by the wavemaker. In a real tank, this problem is overcome by locating the tested body sufficiently far from the wavemaker. For the numerical tank, this would imply too large a number of discretization points. It is therefore crucial to develop a method to avoid this reflection on the wavemaker.

The method that has been developed is similar to that used for the absorbing beach: the energy corresponding to the reflected wave has to be damped before it can reach the wavemaker. This reflected wave is defined as the difference between the actual wave and the incident wave, i.e. the wave that would exist in the absence of the body. The damping term is thus applied to the difference between the solution at time  $t$  and the solution that would be obtained at time  $t$  without the body.

This solution can either be computed numerically (by running the code for calibration without the body) or, if the steepness of the incident wave is sufficiently small, quasi-analytically by computing the linear solution. This last method appears to be easy to implement, cheap to run, and surprisingly efficient to use, even for moderate steepnesses. In fact, it is not even necessary to compute the transient linear solution; the steady state solution is used (damping being only applied once a steady state is reached in the damping zone).

In equation (8), values of  $\alpha$  and  $\beta$  equal to 1 are appropriate for the absorption of a wave train of wave frequency  $\omega$  and wave number  $k$  — see figure 2 where the reflection coefficient (ratio of the reflected wave amplitude to the incident wave amplitude) is plotted as a function of the wave number for these values of  $\alpha$  and  $\beta$  and for the linear computation. The computation is performed for a tank length equal to 5 wave lengths with 200 nodes on the free sur-

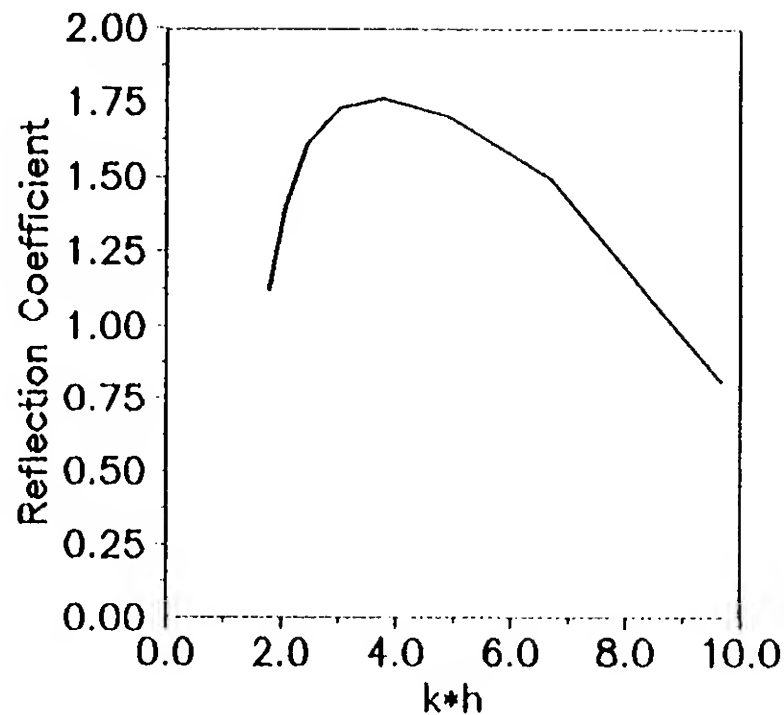


Figure 2: Reflection coefficient vs. wave number

face and 10 on each wall. The wave elevation is analyzed near the middle of the tank over 10 periods after the 15th. Note that the reflection coefficient is always less than 2%, showing the excellent performance of the absorbing zone. Even though systematic tests have not yet been performed (they are underway for bichromatic waves), it seems that a damping zone of given characteristics absorbs reasonably well over a rather large range of frequencies.

### 3.4 Free Motions of a Body

Sindbad was first devised to study the flow around a body which is fixed or in forced motion. For a freely floating body, the body boundary conditions are not known a priori. In this case it is necessary to solve the equations governing the body motion and those governing the motion of the fluid in parallel.

The body motion is specified by the three degrees of freedom  $x_G$ ,  $y_G$ , and  $\theta$  that give the position of the center of mass and the angle between an axis linked to the body and a fixed axis (see figure 1).

Let  $M$  be the mass of the floating body and  $I$  the moment of inertia relative to the center of mass. The equations of motion for the body can then be written as:

$$M \ddot{x}_G = F_x \quad (9)$$

$$M \ddot{y}_G = F_y \quad (10)$$

$$I \ddot{\theta} = \mathcal{M}. \quad (11)$$



This equation can also be written using matrix notations as:

$$M \ddot{\vec{x}}_G = \vec{F}. \quad (12)$$

External forces applied to the body,  $\vec{F}$ , are written as the sum of hydrodynamic forces and other external forces. No distinction is made between hydrodynamic and hydrostatic forces because, in the nonlinear case, there is no obvious way to distinguish them. For instance, if hydrostatic forces are defined as those resulting from the integration of the hydrostatic pressure over the wetted part of the body, they are seen to depend on the dynamics of the flow through the variation of the position of the waterline. Hydrodynamic forces are obtained by integrating the pressure over the body. This pressure is obtained from Bernoulli's equation:

$$p = -\phi_t - \frac{1}{2} \vec{\nabla} \phi \cdot \vec{\nabla} \phi - \gamma. \quad (13)$$

The potential  $\phi$  is the solution of the Laplace equation together with the free surface boundary conditions and the kinematic boundary condition on the body:

$$\phi_n = \vec{v} \cdot \vec{n}, \quad (14)$$

where  $\vec{v}$  is the velocity of a point moving with the body. The pressure over the body depends on the body dynamics through this boundary condition.

At a given instant  $t$ , we assume that  $\vec{x}_G$  and  $\dot{\vec{x}}_G$  are known as well as the position of the free surface and the value of the potential along it. The velocity of a point  $\vec{\alpha} = (\alpha, \beta)$  linked to the body is easily computed:

$$\dot{\alpha} = \dot{x}_G - (\beta - y_G) \dot{\theta} \quad (15)$$

$$\dot{\beta} = \dot{y}_G + (\alpha - x_G) \dot{\theta} \quad (16)$$

The kinematic boundary condition along the body boundary can thus be written. As seen previously, the velocity of the markers along the free surface and the time derivative of the velocity potential associated to these markers can then be computed.

In order to proceed with the numerical time-stepping, it is necessary to compute the

acceleration of the body. To determine the acceleration of the body, the forces acting on the body may be computed and equation (12) can be solved.

For the force determination, the potential  $\phi$  and  $\phi_t$  are required for the Bernoulli equation. The simplest method for determining  $\phi_t$  on the body boundary is by a finite difference scheme in time, using the result of the previous time step. The material derivative may be calculated following the body from which  $\phi_t$  may be determined.

This approach is quite satisfactory for the calculation of forces on fixed bodies or bodies with prescribed motions. However, it appears to be inadequate for the time stepping of the free motion equations. Most time-stepping procedures treat each time step as a new initial-value problem and a dependence on the past via a finite difference is not permitted.

Since  $\phi_t$  is harmonic in the fluid domain, it has to satisfy an integral equation similar to (5):

$$\begin{aligned} & -\theta(P) \phi_t(P) + \int_{\Gamma_d + \Gamma_n} \phi_t(Q) G_n(P, Q) ds_Q \\ & = \int_{\Gamma_d + \Gamma_n} \phi_{tn}(Q) G(P, Q) ds_Q. \end{aligned} \quad (17)$$

where  $\phi_{tn}$  designates the normal component of the gradient of  $\phi_t$  along the body boundary, i.e.  $(\vec{\nabla} \phi_t) \cdot \vec{n}$ . The value of  $\phi_t$  may be determined much more accurately by solving this integral equation. This approach is similar to what was done in [10] for the problem in  $\phi$ - $\psi$ .

At a point  $\vec{\alpha}$  linked to the body, it can be shown [6] that:

$$\begin{aligned} \phi_{tn} &= \ddot{\vec{\alpha}} \cdot \vec{n} + \dot{\theta} (\dot{\vec{\alpha}} \cdot \vec{s} - \phi_s) \\ &\quad - \left( \frac{1}{R} \phi_s + \phi_{sn} \right) \dot{\vec{\alpha}} \cdot \vec{s} \\ &\quad + \left( \phi_{ss} - \frac{1}{R} \phi_n \right) \dot{\vec{\alpha}} \cdot \vec{n}, \end{aligned} \quad (18)$$

where  $s$  is a curvilinear abscissa along the body (oriented as shown on figure 1). The radius of curvature  $R$  is taken positive when the center of curvature is inside the body. Tangential derivatives of the potential appear in this expression because, in potential flow theory, the no-slip condition is not enforced.

In equation (18), the velocity  $\dot{\vec{\alpha}}$  is given by equations (15) and (16). The acceleration  $\ddot{\vec{\alpha}}$  is given by:

$$\ddot{\alpha} = \ddot{x}_G - (\beta - y_G) \ddot{\theta} - (\alpha - x_G) \dot{\theta}^2 \quad (19)$$

$$\ddot{\beta} = \ddot{y}_G + (\alpha - x_G) \ddot{\theta} - (\beta - y_G) \dot{\theta}^2. \quad (20)$$

As a consequence of these equations,  $\phi_{tn}$  depends linearly on  $\ddot{\vec{x}}_G$ . As a result, hydrodynamic forces applied to the body at a given instant  $t$  can finally be written as:

$$\vec{F}_h = \mathbf{M}' \ddot{\vec{x}}_G + \vec{F}_0. \quad (21)$$

The vector  $\vec{F}_0$  corresponds to the forces applied to the body when its acceleration is equal to zero. The matrix  $\mathbf{M}'$  is similar to an added mass matrix. Its coefficients can be evaluated by computing the forces corresponding to a unit acceleration of each degree of freedom.

It should be noted that in order to estimate the right hand side of (18), it is necessary to compute the derivatives of  $\phi$  and  $\phi_n$  with respect to the curvilinear abscissa  $s$ . These derivatives are computed numerically using finite differences.

By combining the equation of motion for the body (12) with the result for the fluid forces (21) the acceleration of the body,  $\ddot{\vec{x}}_G$  may be determined. The evolution equation for the free surface variables  $(\phi, \vec{x})$  is replaced by an evolution equation for  $(\phi, \vec{x}, \ddot{\vec{x}}_G, \dot{\vec{x}}_G)$ . The same time-stepping procedure is used for the six degrees of freedom corresponding to the rigid body motion and for those corresponding to the free surface.

### 3.5 Linear Version of the Code

Mainly for validation purposes, it was deemed necessary to develop a linear version of the code. This linear version differs from the nonlinear version only by the boundary conditions that are used; linear boundary conditions are written on the mean position of the boundaries. Since the geometry of the computational domain stays the same as time proceeds, it is only necessary to compute and invert the matrix corresponding to the boundary integral equation once. Only the right hand side has to be computed at each time step. As a result, the

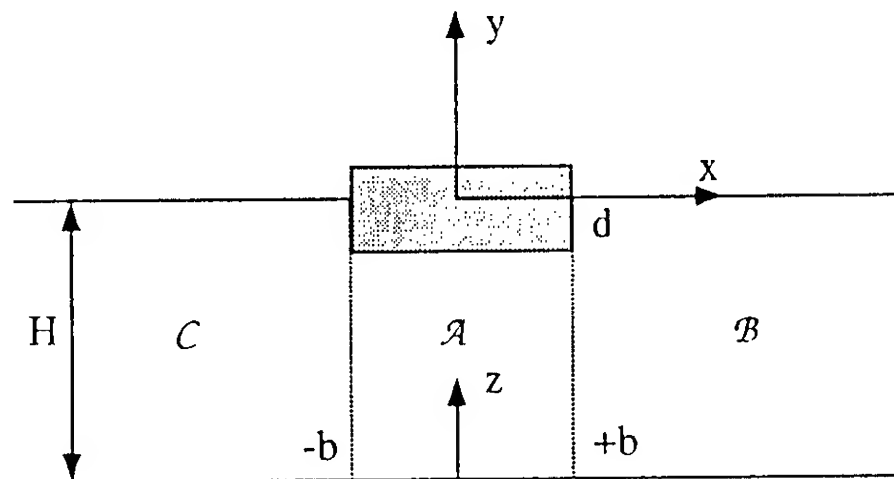


Figure 3: Geometric definitions for the eigen-function expansion

computational cost of the linear computation is an order of magnitude smaller than that of the nonlinear computation.

For free motions, a linear stiffness matrix is computed from the body geometry. The corresponding linear hydrostatic force is added to the linear hydrodynamic force computed at each time-step.

It is also possible to account for some nonlinear effects at little additional computational cost. For instance, nonlinear hydrostatic forces (corresponding to the mean or instantaneous free surface position) or nonlinear hydrodynamic forces (obtained by keeping the  $\vec{\nabla}\phi \cdot \vec{\nabla}\phi$  term in Bernoulli's equation) can be accounted for. At the present stage, our main purpose was to compare the fully linear and the fully nonlinear solutions. It is obvious, however, that once some understanding of the phenomena will be gained, it might be appropriate to use a partially nonlinear code that would be much less expensive to run than the fully nonlinear one.

## 4 Linear Frequency-domain Computations

### 4.1 Eigen-function Expansions

This method takes advantage of the geometry of the fluid domain which, for a rectangular barge, consists of three rectangular sub-domains: underneath the barge (domain A),

right of the barge (B) and left (C) — see figure 3. It has already been applied to the same problem, see for instance Mei and Black [17]. (Our matching procedure differs somewhat from their's, and is inspired from Garrett [18]).

The total velocity potential is written in the classical form:

$$\phi = \Re \left\{ \left[ \varphi_I + \varphi_D + \sum_{j=1}^3 -i\omega x_j \varphi_{Rj} \right] e^{-i\omega t} \right\}, \quad (22)$$

where  $x_1 = x_G$ ,  $x_2 = y_G$  and  $x_3 = \theta$ .

The diffraction potential  $\varphi_D$  and radiation potentials  $\varphi_{Rj}$  admit the following decompositions:

• Domain B:

$$\begin{aligned} \varphi_B = & b_0 \frac{\cosh k_0 z}{\cosh k_0 H} e^{ik_0(x-b)} \\ & + \sum_{n=1}^{\infty} b_n \cos k_n z e^{-k_n(x-b)} \end{aligned} \quad (23)$$

• Domain C:

$$\begin{aligned} \varphi_C = & c_0 \frac{\cosh k_0 z}{\cosh k_0 H} e^{-ik_0(x+b)} \\ & + \sum_{n=1}^{\infty} c_n \cos k_n z e^{k_n(x+b)} \end{aligned} \quad (24)$$

where  $k_0, k_n$  are the roots of the equation :  $\omega^2 = gk_0 \tanh k_0 H = -gk_n \tan k_n H$

• Domain A:

$$\begin{aligned} \varphi_A (+\varphi_I) = & \varphi_P + a_{01} + a_{02} \frac{x}{b} \\ & + \sum_{n=1}^{\infty} a_{n1} \frac{\cosh \lambda_n x}{\cosh \lambda_n b} \cos \lambda_n z \\ & + \sum_{n=1}^{\infty} a_{n2} \frac{\sinh \lambda_n x}{\sinh \lambda_n b} \cos \lambda_n z \end{aligned} \quad (25)$$

where  $\lambda_n = n\pi/h$  and  $\varphi_P$  is a particular solution which is zero for the diffraction and sway radiation potentials, and is equal to  $(z^2 - x^2)/2h$  for heave and to  $(x/2h)(x^2/3 - z^2)$  for roll.

In the previous expressions  $H$  is the total waterdepth,  $b$  the half-width of the barge,  $z = y + H$ , and  $h = H - d$  the waterdepth underneath the barge,  $d$  being the draft.

The coefficients  $a_{n1}, a_{n2}, b_n, c_n$  are determined by truncating the infinite series at some finite orders  $N_a, N_b = N_c$ , and equating the potential expansions and their  $x$  derivatives at  $x = b$  and  $x = -b$ . Considering, for instance, the diffraction problem, equating  $\varphi_B + \varphi_I$  and  $\varphi_A$  in  $x = b$  yields, after taking advantage of the orthogonality of the  $\cos \lambda_n z$  functions over  $[0, h]$  by integrating in  $z$ :

$$\vec{A}_1 + \vec{A}_2 = \mathcal{A} \vec{B} + \vec{R}_1 \quad (26)$$

where  $\vec{A}_i = {}^T(a_{0i}, \dots, a_{N_{ai}})$ ,  $\vec{B} = {}^T(b_0, \dots, b_{N_b})$ , and  $\mathcal{A}$  is a  $N_a \cdot N_b$  matrix.

Similarly equating  $\varphi_C + \varphi_I$  and  $\varphi_A$  at  $x = -b$  yields :

$$\vec{A}_1 - \vec{A}_2 = \mathcal{A} \vec{C} + \vec{R}_1 e^{-2ik_0 b} \quad (27)$$

Similar considerations on the  $x$  derivatives in  $x = b$  and  $x = -b$ , combined with integrations in  $z$  over  $[0, H]$ , yield :

$$\vec{B} = \mathcal{B} (T_1 \vec{A}_1 + T_2 \vec{A}_2) + \vec{R}_2 \quad (28)$$

$$\vec{C} = \mathcal{B} (T_1 \vec{A}_1 - T_2 \vec{A}_2) - \vec{R}_2 e^{-2ik_0 b} \quad (29)$$

where  $\mathcal{B}$  is a  $N_b \cdot N_a$  matrix, and  $T_1, T_2$  are two diagonal matrices.

Some manipulation of these 4 vectorial equations yields the final system in  $\vec{B} + \vec{C}$  and  $\vec{B} - \vec{C}$  :

$$\begin{aligned} [I - \mathcal{B} T_1 \mathcal{A}](\vec{B} + \vec{C}) = & \\ \mathcal{B} T_1 \vec{R}_1 (1 + e^{-2ik_0 b}) + \vec{R}_2 (1 - e^{-2ik_0 b}) & \end{aligned} \quad (30)$$

$$\begin{aligned} [I - \mathcal{B} T_2 \mathcal{A}](\vec{B} - \vec{C}) = & \\ \mathcal{B} T_2 \vec{R}_1 (1 - e^{-2ik_0 b}) + \vec{R}_2 (1 + e^{-2ik_0 b}) & \end{aligned} \quad (31)$$

The resolution of this system yields truncated series expansions for the potentials in each domain and allows the hydrodynamic coefficients and the diffraction forces to be computed.

## 4.2 Linear Integral-equation

The radiation and diffraction potentials are found by the solution of an integral equation

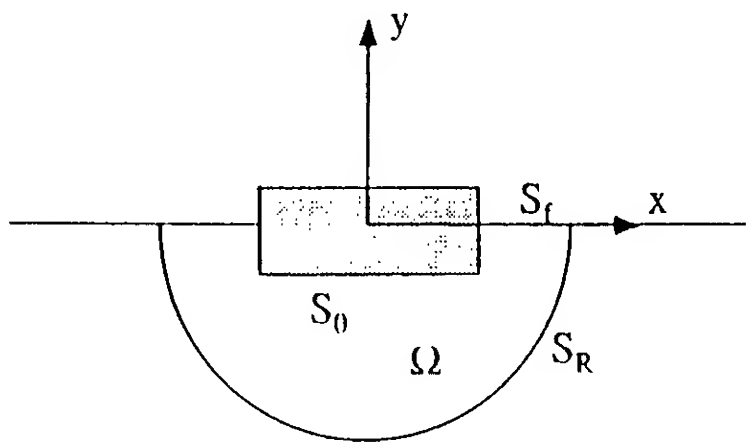


Figure 4: Geometric definitions for the linear integral equation

resulting from the application of Green's third identity. The approach used follows that of Nestegard and Sclavounos [19], where a closed domain  $\Omega$  is used for the problem solution; the radiation condition is satisfied by matching with the multipole solution of Ursell [20]. The approach is free of irregular frequencies and is useful for careful calculation of linear hydrodynamic properties. The integral equation for an unknown potential  $\varphi_D$  or  $\varphi_{Rj}$  takes the form:

$$\begin{aligned} -\pi \varphi(P) &+ \int_{S_0} ds \varphi \frac{\partial G}{\partial n} \\ &+ \int_{S_f} ds \varphi \left( \frac{\partial G}{\partial z} - \kappa G \right) \\ &+ \int_{S_R} ds \left( \varphi \frac{\partial G}{\partial n} - G \frac{\partial \varphi}{\partial n} \right) \\ &= \int_{S_0} ds \frac{\partial \varphi}{\partial n} G \end{aligned} \quad (32)$$

where the Green function is a simple source:

$$G = \log(r_{PQ}),$$

and  $S_0$  is the body boundary,  $S_f$  the free surface and  $S_R$  an artificial boundary of circular shape — see figure 4.

The normal derivative of  $\varphi$  is known along  $S_0$ . The normal derivative on the surface  $S_R$  is eliminated by the coupling with the multipole solution. This coupling is accomplished by enforcing continuity of the potential and its normal derivative across the circular contour. It

may be shown that:

$$BA^{-1}\varphi = \frac{\partial \varphi}{\partial n} \quad (33)$$

where the operator  $BA^{-1}$  can be expressed in terms of the multipoles [19]. By substitution of the operator  $BA^{-1}$  equation for the normal derivative of the potential on  $S_R$  into (32), an integral equation for the unknown potential  $\varphi$  is obtained. The discretization is implemented using  $N_B$ ,  $N_F$  and  $N_R$  segments on  $S_0$ ,  $S_f$  and  $S_R$ , respectively. The multipole series appearing in the operator  $BA^{-1}$  is truncated and  $N_R$  terms are retained.

## 5 Numerical Results

### 5.1 Parameters for the Numerical Computations

We are mainly interested in assessing the capability of the time domain simulation to deal with the prediction of the seakeeping behavior of a barge. We will therefore only present results for a particular configuration, show that the linear frequency domain results can be recovered, and present some nonlinear simulations performed over a large number of wave periods (about 40). Model tests for different configurations are presently under way and systematic comparisons between computations and experiments will be reported later.

For the numerical computations presented here, two geometries were considered: a rectangular barge with sharp corners and a rectangular barge with rounded corners. In either case, the draft is equal to 6 m, the beam to 30 m and the center of gravity is located 4.45 m above the undisturbed free surface. The inertia of the barge (relative to the center of mass) is equal to  $2.18 \cdot 10^6$  kg.m. This value of the inertia was chosen in order to have a natural period in roll close to 8 s in the sharp corners case. The barge with rounded corners has a bilge radius equal to 1.5 m and its natural period in roll is close to 7.5 s.

Both the transient computation and the eigen-function expansion are performed in finite depth. In order to avoid finite depth effects, a depth of 150 m was used. The linear

integral-equation method is performed in infinite depth.

To account for some viscous damping and to avoid very long transient phenomena in the unsteady computation, a linear damping coefficient equal to  $5 \cdot 10^5 \text{ kg.m.s}^{-1}$  (and corresponding to less than 2.5% of critical damping) was added to the equations of motion. Since a non-zero horizontal drift force is expected for the nonlinear computation, a linear restraint in sway was also added. The corresponding stiffness is equal to  $5 \cdot 10^5 \text{ Nm}^{-2}$  and the damping coefficient is equal to  $5 \cdot 10^3 \text{ kg.s}^{-1}\text{m}^{-1}$ . This leads to a natural period in sway larger than five times the natural period in roll.

## 5.2 Linear Computation

The linear version of Sindbad was used to compute the transient response of a rectangular barge submitted to an incident regular wave. Computations were performed for a fixed barge (diffraction problem) and for a freely floating barge (diffraction-radiation problem) restrained in sway.

Figure 5 shows the moment about the center of gravity as a function of time for the diffraction problem and for a barge with rounded corners. The wave period is equal to 8 s and the length of the tank is equal to 600 m (for a depth of 150 m). 200 nodes are used on the free surface and 80 on the barge. We use 40 time steps per period. A steady state is rapidly reached, showing the efficiency of the damping zones. Note that the steady state moment is very small (in fact, the linear transfer function for this moment shows that it becomes equal to zero around 8 s).

Figure 6 shows convergence results for the diffraction moment about the center of gravity for the two barges with and without rounded corners. For the transient computation and the linear integral-equation method, this moment is plotted as a function of the total number of panels on the barge. For the eigen-function expansion method, it is plotted as a number of terms in the series (with  $N_a = N_b = N_c$ ). Note that for the rectangular barge, the convergence is rather slow: about 150 panels are

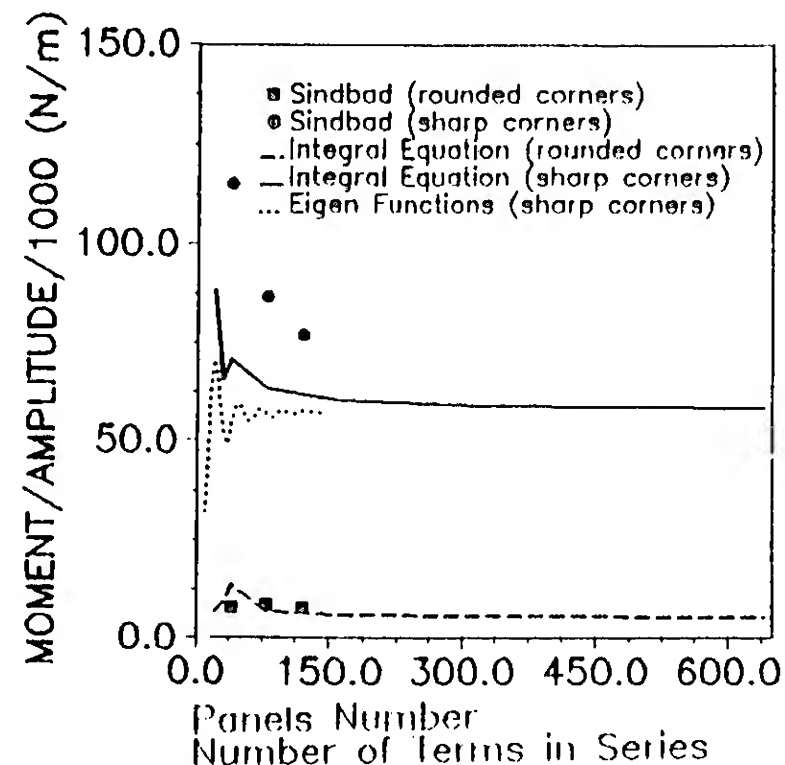


Figure 6: Convergence curve for the moment

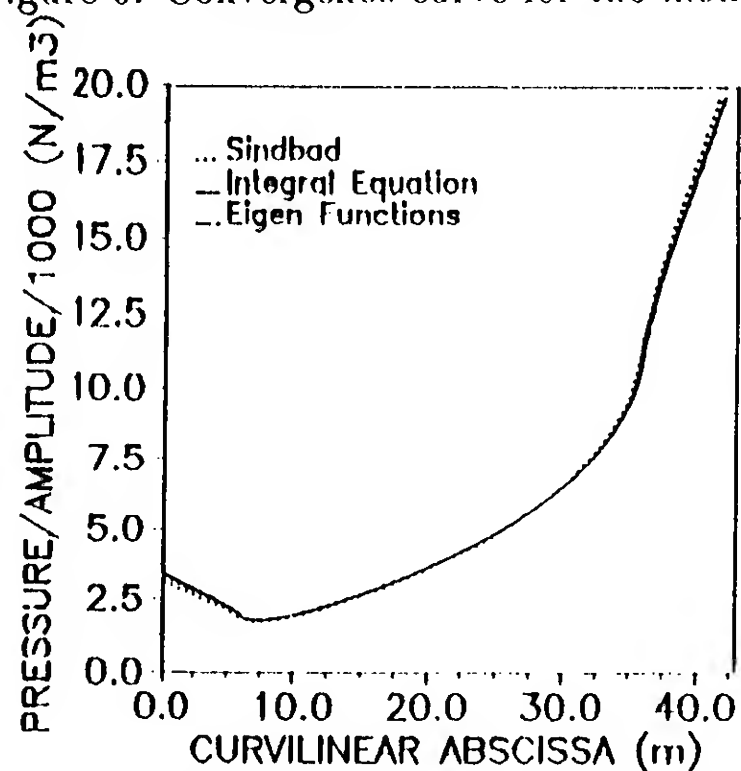


Figure 7: Dynamic pressure along the barge

needed for the integral-equation method<sup>2</sup>. The very poor convergence of the results from the transient simulation for the barge with sharp corners probably stems from the pressure integration that assumes the normal to be continuous.

Figure 7 shows a comparison of the amplitude of the pressure variation in the sharp corner case as a function of the curvilinear abscissa along the barge. The results from the transient simulation are obtained through a Fourier analysis of the calculated transient pressure. Note that, even though only 80 nodes are used on the barge, an excellent agreement is obtained with the frequency domain results. This confirms the accuracy of the simulation technique.

<sup>2</sup>For the radiation problem, it was suggested in [19] to use a value of  $N_B \simeq 20$ .

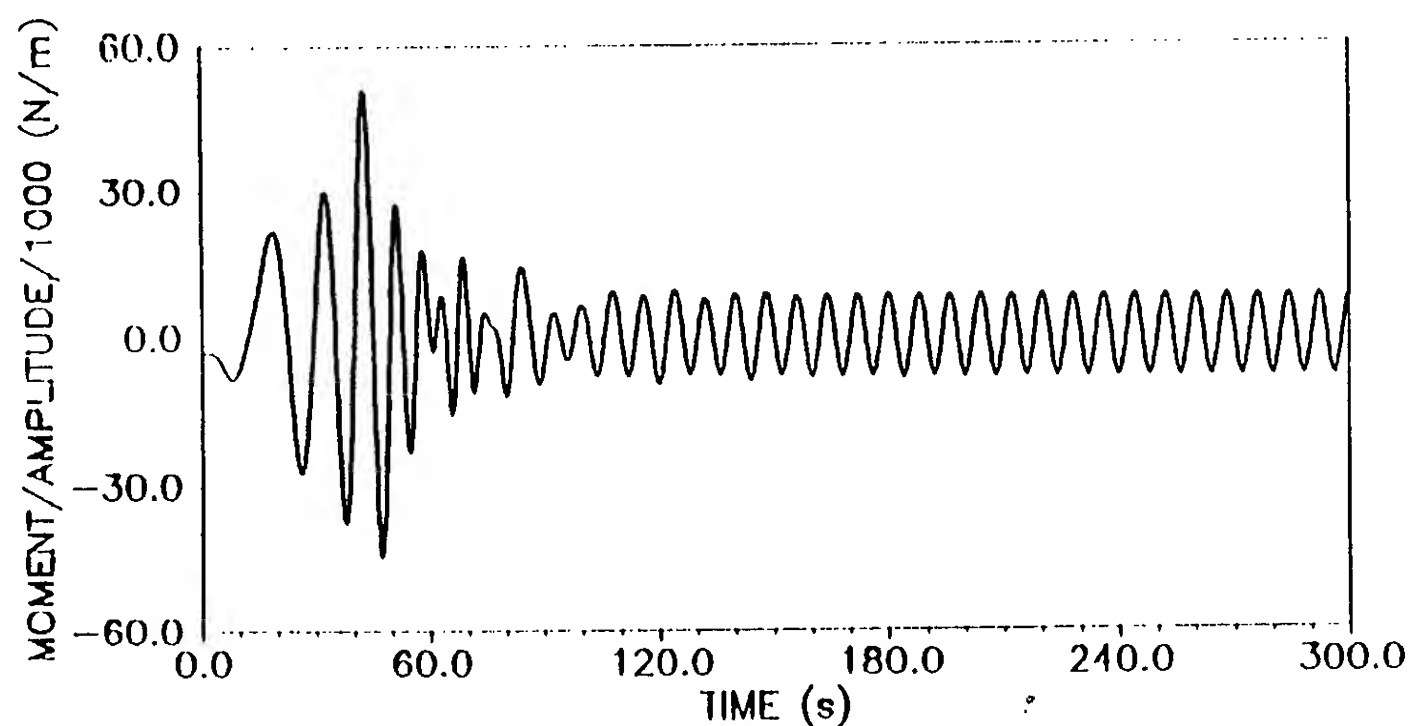


Figure 5: Moment vs. time (linear simulation)

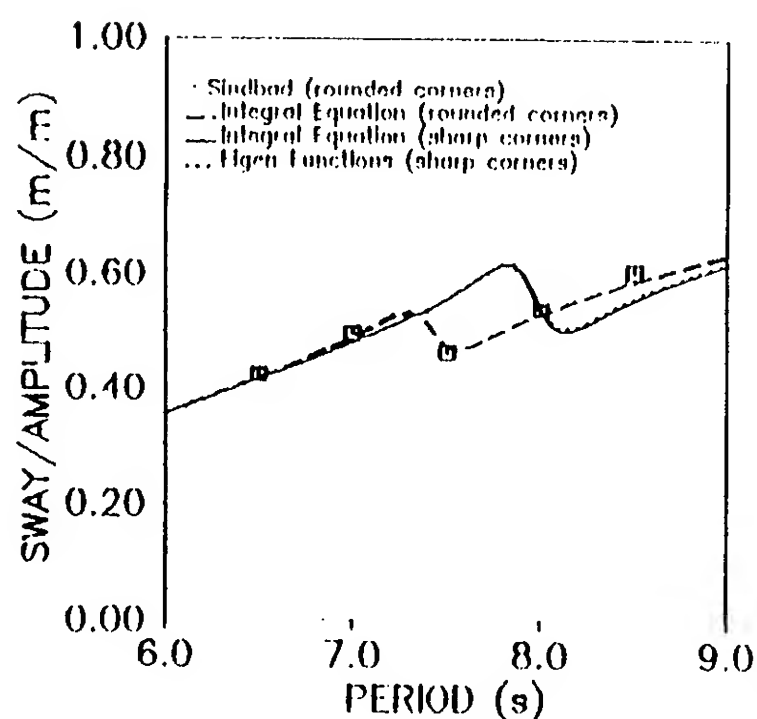


Figure 8: Sway transfer function

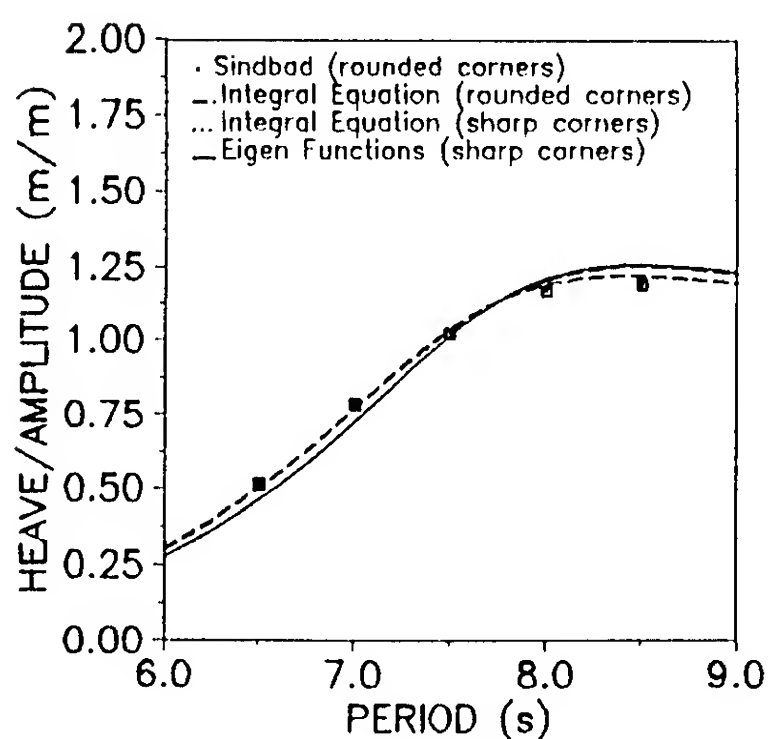


Figure 9: Heave transfer function

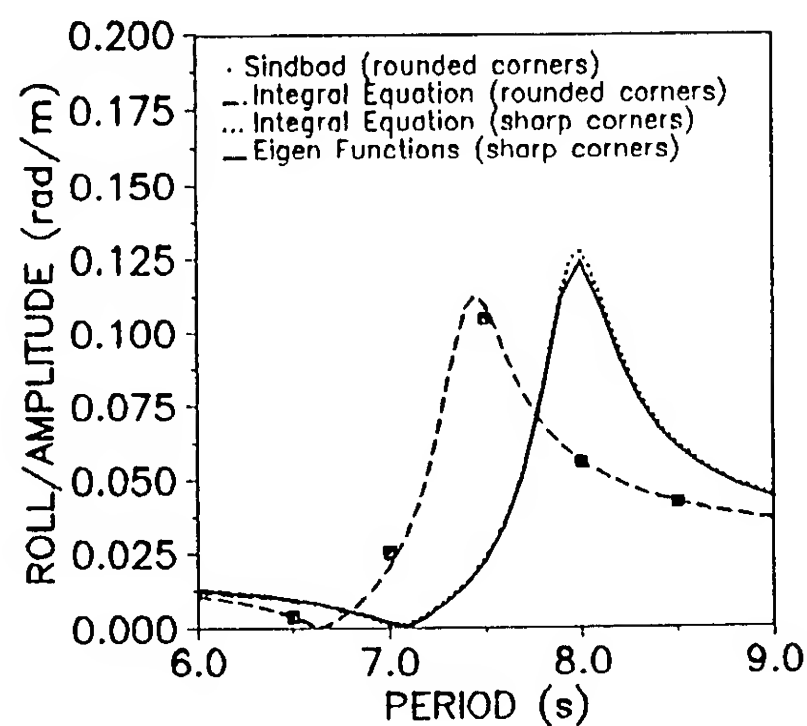


Figure 10: Roll transfer function

Figures 8 to 10 show the sway, heave, and roll transfer functions for the barge with rounded corners. The transient simulation is performed with 200 nodes on the free surface and 80 on the barge. The length of the tank is approximately equal to 6 wave lengths and the barge is located at midtank. Forty time steps per period were used. A good agreement is obtained between the transient simulation and the frequency-domain result. The coupling between the motion of the fluid and that of the barge is properly modeled.

### 5.3 Nonlinear Motions of a Rectangular Barge

The same computations as before have been performed using the fully nonlinear version of



Sindbad. Due to difficulties related to the sharp corners<sup>3</sup>, only the rectangular barge with rounded corners will be considered here.

Figure 11 shows the moment about the center of gravity as a function of time for the diffraction problem, the incident wave amplitude being equal to 2 m (the wave period is still equal to 8 s and the same discretization as in the linear case is used). As in the linear case, a steady state is reached rapidly. However, nonlinear effects are very strong and the presence of higher harmonics is obvious. A Fourier analysis of the signal reveals that even the amplitude of the first harmonic is not well predicted by linear theory and that the second harmonic is twice as large in magnitude.

Figure 12 and 13 show the sway and roll displacements ( $x_G$  and  $\theta$ ) as a function of time for a floating barge restrained in sway. The wave period is equal to 7.5 s (corresponding to the resonance) and the wave amplitude is equal to 1 m. The same discretization as in the linear case is used. A graphical representation of the free-surface profiles during the simulation is shown in figure 14. There are much less higher harmonics than in the diffraction case, the body presumably acting as a "filter". The response amplitude in roll is significantly modified, indicating that the nonlinear potential flow effects are important.

## 6 Conclusion

A simulation technique based on the Mixed Eulerian-Lagrangian method has been described. It allows the simulation of the flow and the resulting barge motions to be performed with either linear or fully nonlinear boundary conditions on the hull and on the free surface. Efficient artificial boundary conditions have been implemented that allow long simulations of diffraction-radiation problems.

Linear frequency domain results have been recovered using the linear version of the code.

<sup>3</sup>As shown before, the convergence is very poor for the barge with sharp corners. Note moreover that the singularity for the complex potential is expected to be in  $z^{2/3}$  yielding an infinite pressure due to the  $\vec{\nabla}\phi \cdot \vec{\nabla}\phi$  term.

Comparisons have been performed not only for global quantities, such as transfer functions, but also for local quantities, such as pressures. This linear version appears to be well validated.

Nonlinear simulations have been performed, lasting for a large number of wave periods. Even though these nonlinear results are difficult to validate, the accuracy of the linear version of the code gives some confidence concerning the validity of the model.

## References

- [1] Denise, J.P., 1983, "On the Roll Motion of Barges," TRINA, Vol. 125.
- [2] Standing, R.G., Cozens, P.D., and Downie, M.J., 1988, "Prediction of Roll Damping and Response of Ships and Barges, Based on the Discrete Vortex method," Proc. Int. Conf. on Computer Modelling in Ocean Eng., Venice.
- [3] Downie, M.J., Graham, J.M.R., and Zheng, X., 1990, "The Influence of Viscous Effects on the Motion of a Body Floating in Waves," Proc. Ninth Int. Conf. Offshore Mech. and Arctic Eng., Houston.
- [4] Robinson, R.W., and Stoddart, A.W., 1987, "An Engineering Assessment of the Role of Non-linearities in Transportation Barge Roll Response," TRINA, pp. 65-79.
- [5] Cointe, R., Molin, B., and Nays, P., 1988, "Nonlinear and Second-order Transient Waves in a Rectangular Tank," BOSS'88, Trondheim.
- [6] Cointe, R., 1989, "Quelques Aspects de la Simulation Numérique d'un Canal à Houle," Thèse de Doctorat de l'Ecole Nationale des Ponts et Chaussées, Paris (in French).
- [7] Cointe, R., 1990, "Numerical Simulation of a Wavetank," *Engineering Analysis with Boundary Elements*, special issue on "Nonlinear Wave Analysis", to appear.
- [8] Longuet-Higgins, M.S., and Cokelet, E.D., 1976, "The Deformation of Steep Surface

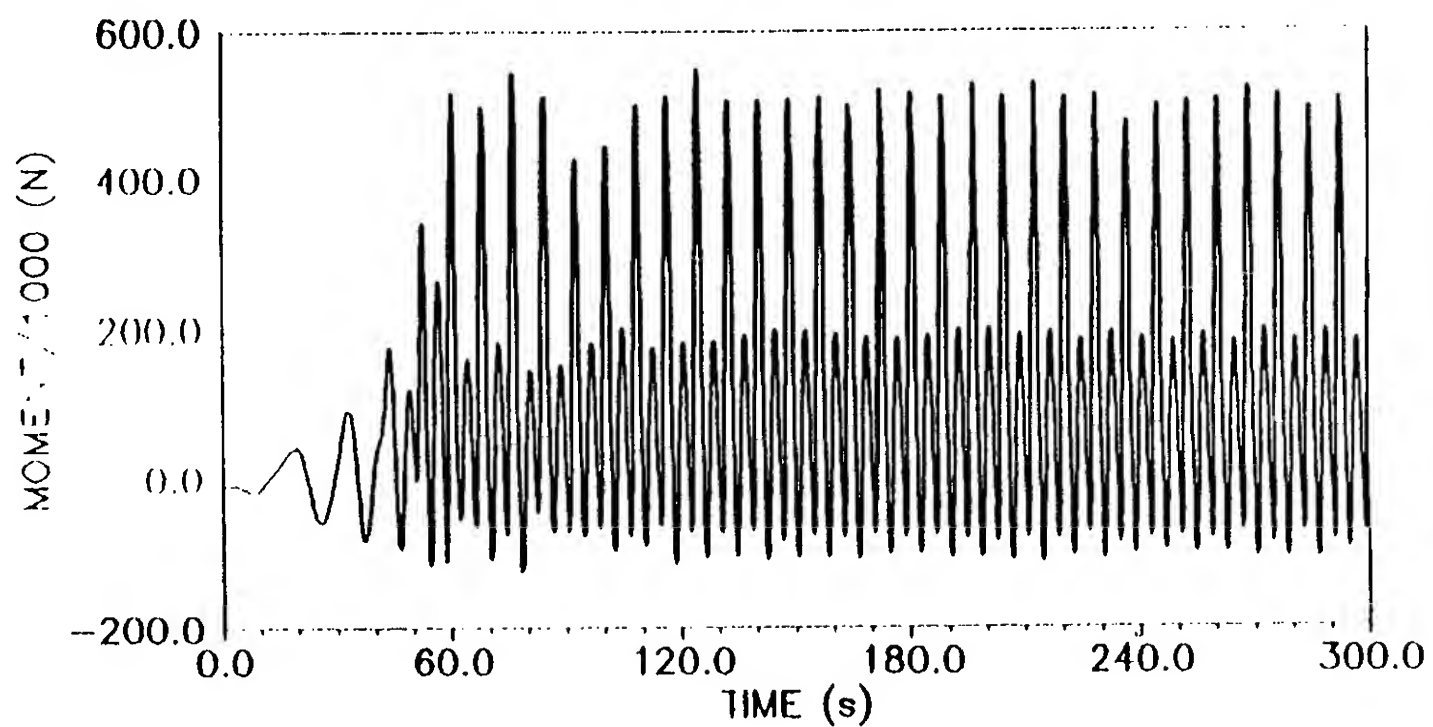


Figure 11: Moment vs. time (nonlinear simulation)

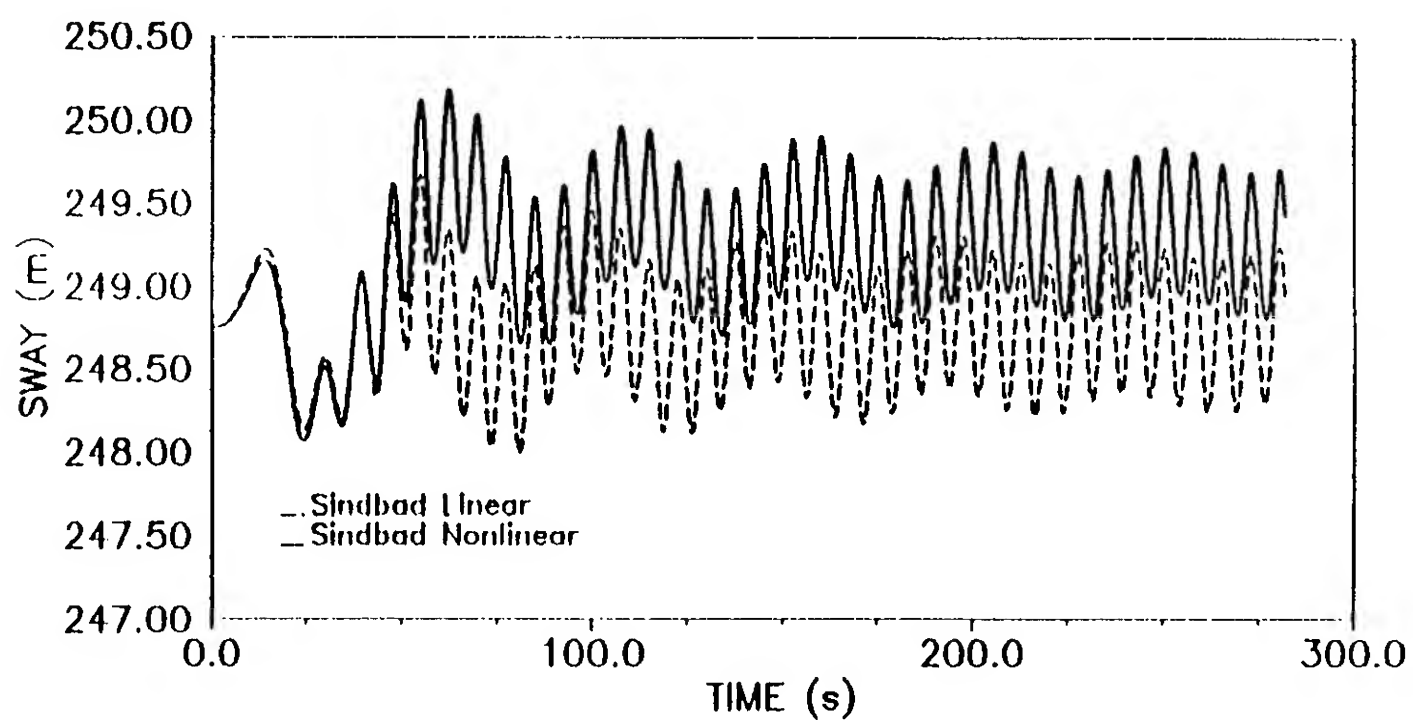


Figure 12: Sway vs. time

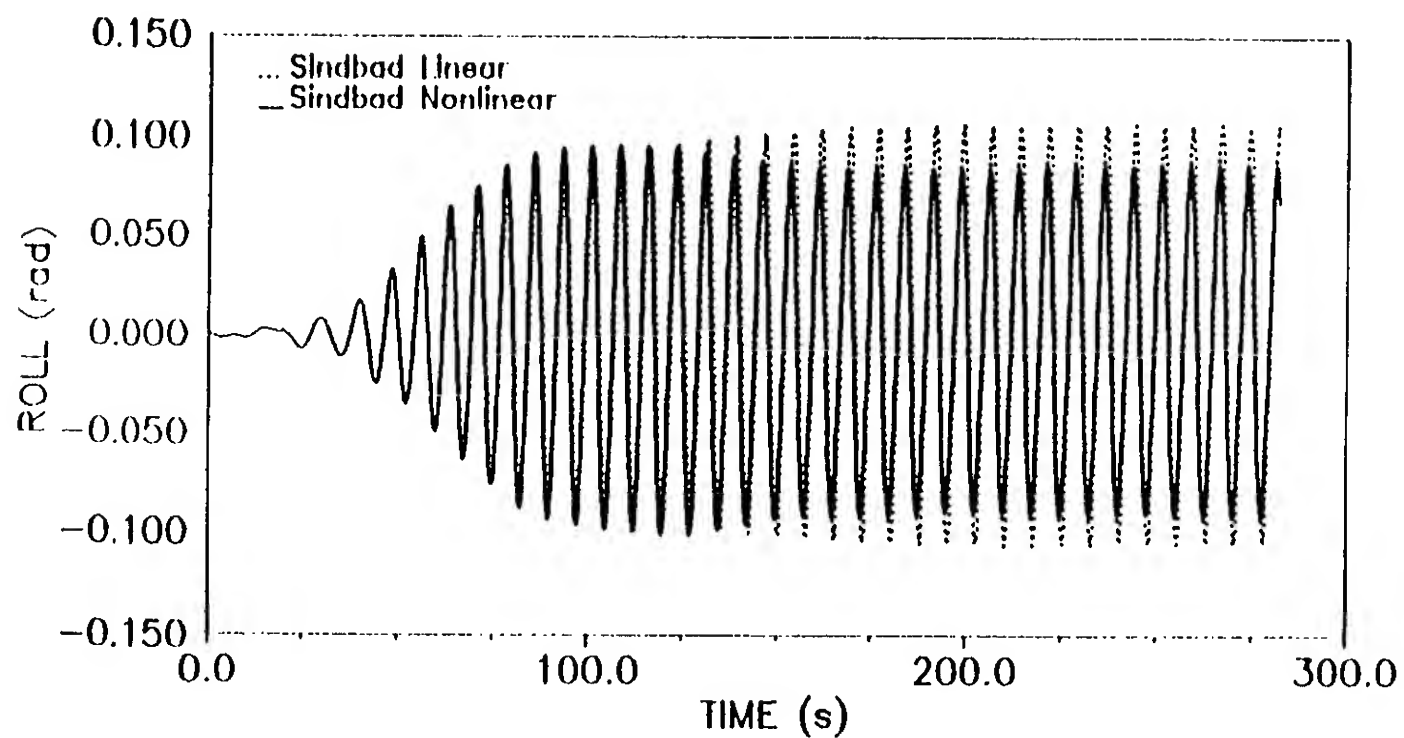


Figure 13: Roll vs. time

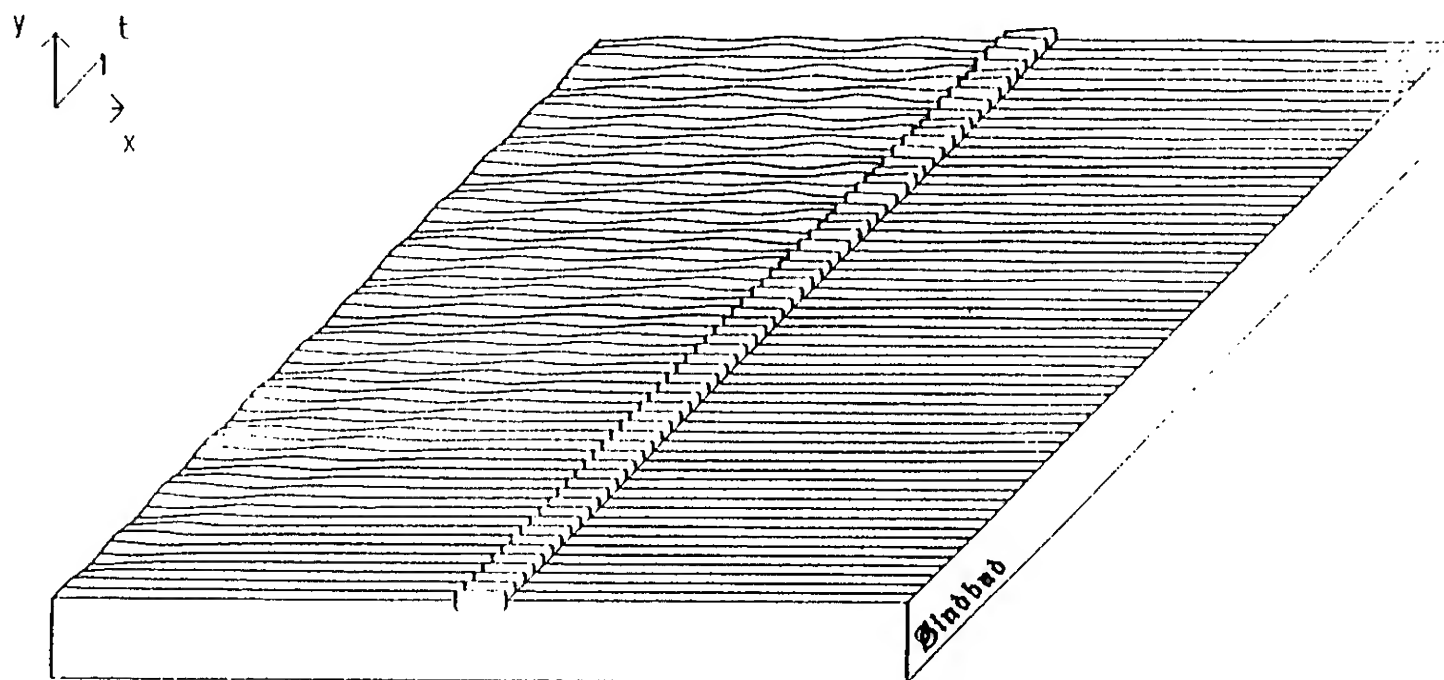


Figure 14: Free-surface profiles

- Waves on Water. I. A Numerical Method of Computation," *Proc. R. Soc. London*, Vol. A 364, pp. 1-26.
- [9] Peregrine, H.D., 1990, "Computation of Breaking Waves," *Water Wave Kinematics*, Kluwer Academic Publishers, pp. 475-490.
- [10] Vinje, T., and Brevig, P., 1981, "Nonlinear, Two-dimensional Ship Motions," Norwegian Institute of Technology, Report R-112.81.
- [11] Faltinsen, O.M., 1977, "Numerical Solutions of Transient Nonlinear Free Surface Motion Outside or Inside Moving Bodies," 2nd International Conference on Numerical Ship Hydrodynamics, Berkeley, pp. 347-357.
- [12] Lin, W.M., 1984, "Nonlinear Motion of the Free Surface near a Moving Body," Ph.D. Dissertation, MIT, Cambridge, Mass.
- [13] Dommermuth, D.G., 1987, "Numerical Methods for Solving Nonlinear Water-wave Problems in the Time Domain," Ph.D. Dissertation, MIT.
- [14] Hwang, J.H., Kim, Y.J., and Kim, S.Y., 1988, "Nonlinear Hydrodynamic Forces Due to Two dimensional Forced Oscillation," Proceedings, IUTAM Symposium on Nonlinear Water Waves (Tokyo), Springer-Verlag, pp. 231-238.
- [15] Sen, D., Pawlowski, J.S., Lever, J. and Hinchey, M.J., 1989, "Two-dimensional Numerical Modelling of Large Motions of Floating Bodies in Waves", Fifth International Conference on Numerical Ship Hydrodynamics, Hiroshima, pp.351-373.
- [16] Baker, G.R., Meiron, D.I., and Orszag, A., 1981, "Applications of a Generalized Vortex Method to Nonlinear Free-Surface Flows," Third International Conference on Numerical Ship Hydrodynamics, Paris, pp. 179-191.
- [17] Mei, C.C. and Black, J.L., 1969, "Scattering of Surface Waves by Rectangular Obstacles in Waters of Finite Depth", *Journal of Fluid Mechanics*, Vol.38, part 3, pp. 499-511.
- [18] Garrett, C.J.R., 1971, "Wave Forces on a Circular Dock", *Journal of Fluid Mechanics*, Vol. 46, pp. 129-139.
- [19] Nestegard, A., and Sclavounos, P.D., 1984, "A Numerical Solution of Two-Dimensional Deep Water Wave-Body Problems," *Journal of Ship Research*, Vol. 28, pp. 48-54.
- [20] Ursell, F., 1949, "On the Heaving Motion of A Circular Cylinder on the Surface of a Fluid," *Quarterly Journal of Mechanics and Applied Mathematics*, Vol. 2, pp. 218-231.

## DISCUSSION

J. Nicholas Newman  
Massachusetts Institute of Technology, USA

This type of complete fully-nonlinear analysis seems to show very different results for the roll response compared to the simplified (hydrostatic) analyses described in the papers by Sanchez and Nayfeh or Francescutto and Nabergoj. Perhaps this is due to the large beam-draft ratio of this barge and its large damping? If so, it would be very interesting to apply the Sindbad program to a vessel with smaller roll damping.

## AUTHORS' REPLY

The question of Prof. Newman is very interesting but we fear that we cannot give a satisfactory answer at this stage of our study. Our motivation for performing fully nonlinear simulations of the roll motion of barges certainly stems from our desire to get a better understanding of nonlinear phenomena involved. In particular, we would like to use such simulations to assess the validity of models using different levels of approximation. In this paper, however, we describe the method that has been devised to perform the simulation and we insist on the procedure that is used to validate it. We understand that is somehow frustrating to discuss more the tool than its results, but we strongly feel that nonlinear simulations can only be useful if carefully validated.

The result we presented is for a barge having a large beam to draft ratio, a very small radiation damping and an important roll-sway coupling. It does not seem obvious to us why, in this particular case, it should be very different from that of a simplified analysis, as long as the roll-sway coupling is properly accounted for. The fully nonlinear computation is still quite time consuming (it took several hours on an Alliant FX80 for the example shown) and it cannot be used for a systematic investigation in the phase plane. It is our feeling that intermediate models might be better suited to check if the analyses performed on a simple single degree of freedom system apply to real situations.

We are currently performing experiments and we will use the Sindbad program, as well as more less sophisticated simplified models, to make comparisons. We shall report the results in the future and we hope that we will then be able to answer this question more satisfactorily.

## DISCUSSION

Ronald W. Yeung  
University of California at Berkeley, USA

I find it puzzling how you could eliminate the reflected waves in the upstream zone by applying the damping layer to  $(\phi - \phi_i)$ ,  $\phi_i$  being the incident wave potential. The difficulty, as I see it, is that the reflected wave from the body does not occupy the same fluid domain as the incident waves since the problem is nonlinear. You must have made additional assumptions in applying this procedure. Perhaps you can clarify this point.

## AUTHORS' REPLY

We thank Prof. Yeung for his question that will allow us to clarify some points concerning the absorption mechanism we use. The method we propose is based on physical considerations rather than on a rigorous mathematical analysis. As a consequence, it is not clear to us what is meant by "additional assumptions." We substitute the original problem with another problem with different boundary conditions. As for a real tank with an absorbing beach or an absorbing wavemaker, the only way to assess the efficiency of the method is to perform tests to quantify the reflection.

As pointed out by Prof. Yeung, the reflected wave does not occupy the same fluid domain as the incident wave. The definition of the reflected wave that we give is therefore difficult to interpret is one refers to the Eulerian velocity potential in the fluid domain. However, as we use a Lagrangian specification for the time-stepping procedure, there is no ambiguity for the implementation of the method; we refer to the potentials attached to a marker labeled by its abscissa  $x_c$  along the reference position of the free surface (that coincides with the x-axis). Similarly, the damping coefficient  $v(x_c)$  is that attached to the same marker.

**Session II**  
**Ship Motions**

# A Numerical Research of Nonlinear Body-Wave Interactions

Z. Zhou, M. Gu (China Ship Scientific Research Center, China)

## ABSTRACT

This paper presents numerical research results of nonlinear body-wave interactions. The body-wave interaction is treated as a transient problem with known initial conditions. The development of the flow can be obtained by a time-stepping procedure, in which the velocity potential of the flow at any instant is obtained by utilizing a source density distribution on all boundary surfaces. The Orlanski's method is used to implement the boundary condition at the open boundary. The position of intersection points are determined by a direct method.

The contents of this paper are: (1) A study of the nonlinear radiation problem of a floating body; (2) A study of nonlinear wave diffraction problem around large structures; (3) Interaction of nonlinear waves with a free floating body; (4) An attempt in generating a numerical wave tank. Pretty good agreement is met between the numerical results and the analytical solution.

## NOMENCLATURE

a	cylinder radius
d	still water depth
$F_k$	six components of force/moment acting on the body.
g	the acceleration due to gravity
H	incident wave height
$I_x, I_y, I_z$	moment of inertia about x, y and z axes
K	wave number
$\bar{K}$	wave number of the wave envelope
m	mass of the body
N	number of elements on $S_b + S_c + S_d + S_f$
$N_b, N_c$	number of elements on $S_b, S_c$
$N_d, N_f$	number of elements on $S_d, S_f$
$S_b$	wetted body surface
$S_c$	outer boundary or control surface
$S_d$	bottom surface
$S_f$	free surface
$Z_g$	vertical position of the body centre
$\eta$	wave elevation
$\rho$	fluid density
$\phi$	total wave potential

Zhenquan Zhou and Maoxiang Gu,

China Ship Scientific Research Center, P.O. Box 116, Wuxi 214082, Jiangsu, China

$\phi_0$	velocity potential of incident waves
$\phi_s$	scattered wave potential

## I. INTRODUCTION

The interactions between large floating structures and the sea wave are generally predicted on the basis of linear ship motion theories, which are formally valid for small-amplitude sinusoidal waves. For nonlinear wave forces, the methods which have been applied so successfully to the linear predictions are no longer available. Therefore much attention has been paid to perturbations involving second order potential in the past few years. However, when the wave is very steep and the nonlinear effects more serious, it may not be appropriate to consider only second order forces.

An alternative approach to the nonlinear body-wave interaction problem has been adopted by Isaacson [1], in his model, the nonlinear wave-body interaction is solved numerically by a time stepping procedure. In this field, Lin, Newman and Yue [2] have presented a method of matching the finite computational domain to a linear outer solution for the transient heaving motion of an axisymmetric cylinder. Liu and Yang [3] have presented the study results for nonlinear three-dimensional but axisymmetric free-surface problems using a mixed Eulerian-Lagrangian scheme.

The main difficulties in simulating fully three-dimensional nonlinear interactions between a free-surface and a body are as follows: (1) The treatment of the body and free-surface interface. A confluence of boundary conditions exists at the line of intersection of the free-surface and the body surface. As a result, the panel solution exhibits a singularity at points on that line, which is the one of the main causes of divergence. (2) The selection of suitable outer boundary condition or radiation condition. The outer boundary in a numerical model is a control surface surrounding the body and waves which reflect the requirement at the far field in guaranteeing for the uniqueness of solution. To accomplish this the outer boundary condition



is made to fulfil the function of allowing all the outgoing radiated and scattered waves to pass through without any reflections into the inner wave field. (3) Stability of the free surface. In the case of nonlinear waves the wave slope is large, which is conducive to unsteadiness, and hence disrupt the computational effort to reach a steady state solution. (4) The interaction of the body motion and wave motion. For each time step, it is necessary to re-determine the relative positions of the body and the wave, which in turn needs high computational accuracy.

It is realized from the very beginning that in dealing with nonlinear computations of body-wave problems, the method adopted at the present state-of-the-art depends on the target aimed for investigation, if it were the local phenomenon such as the nature of singularity at the body-wave intersection and of wave breaking and/or spray formation were aimed at, then full attention should be paid to the treatment of the local singularity. However, if it were the global forces and moments acting on the body that is aimed at, then the method should adopt a pragmatic treatment of local singularities, which paying attention to the rest of the problems to keep the computational treatment robust and efficient. The method outlined in the present paper follows the latter philosophy. In the present method, the body wave interaction is treated as a transient problem. The development of the flow is obtained by a time stepping procedure, the velocity potential is obtained by utilizing a panel method, in which simple source are distributed over all boundary surfaces, including the free surface, the immersed surface of the body and the bottom surface. Plane quadrilateral surface elements are used to approximate those surfaces, and the physical variables are assumed to be constant at each element. The center of each element is used as the pivotal point. The integral equation for the source density is replaced by a set of algebraic equations. When this set of equations are solved, velocities at and off the surfaces are obtained.

The contents of this paper are:

(1) A study of the nonlinear radiation problem of a floating body. (2) A study of the nonlinear wave diffraction problem around large structures. (3) Interactions of nonlinear waves with a free floating body. (4) An attempt in generating a 3-D numerical wave tank.

## 2. MATHEMATICAL FORMULATION

As in Fig.1, an arbitrary body is shown floating at the free surface and moving in large amplitude in waves.

Let  $x, y, z$  from a cartesian coordinate system as indicated in Fig.1, with  $x$  measured in the direction of incident wave propagation and  $z$  measured upwards from the still water level. The fluid motion is described by a velocity potential  $\phi$  which satisfies the Lap-

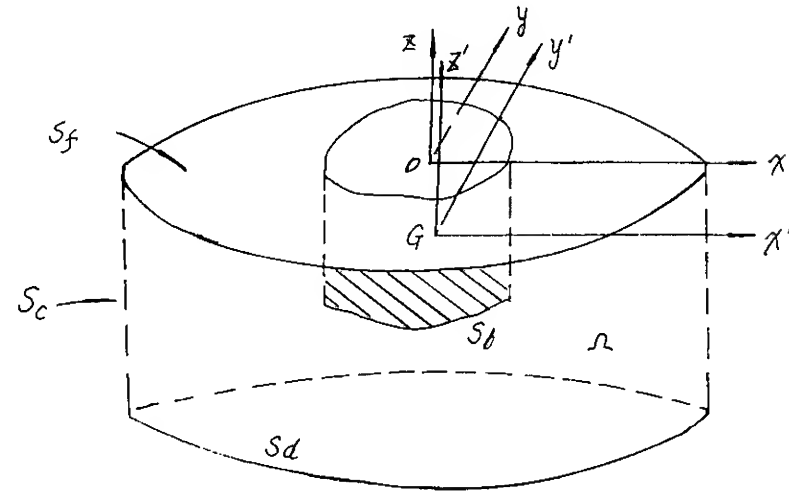


Fig.1 Coordinates systems

lace's equation within the fluid domain,

$$\nabla^2 \phi(x, y, z, t) = 0 \quad (1)$$

the boundary conditions are as follow:

$$\frac{\partial \phi}{\partial n}(x, y, z, t) = \vec{v} \cdot \vec{n} \quad \text{on } S_b \quad (2)$$

$$\frac{\partial \phi}{\partial z} = \frac{\partial \eta}{\partial t} + \frac{\partial \phi}{\partial x} \frac{\partial \eta}{\partial x} + \frac{\partial \phi}{\partial y} \frac{\partial \eta}{\partial y} \quad \text{on } S_f \quad (3)$$

$$\frac{\partial \phi}{\partial t} + g\eta + \frac{1}{2}(\nabla \phi \cdot \nabla \phi) = 0 \quad \text{on } S_f \quad (4)$$

$$\frac{\partial \phi}{\partial n}(x, y, z, t) = 0 \quad \text{at } z = -d \quad (5)$$

$\phi$  also satisfies a suitable radiation condition to be discussed later and a proper initial condition.

In order to solve nonlinear interaction of the Body and wave, The development of the flow is obtained by a time stepping procedure, with the velocity potential field at any one instant obtained by a panel source method.

In this method,  $\phi$  is represented as the velocity potential of the field point which is evaluated by

$$\phi(x, y, z) = \iint_{\partial \Omega} \sigma(q) \frac{1}{r(p, q)} ds \quad (6)$$

where  $r(p, q)$  is the distance between the points  $p$  and  $q$ . The normal derivative of the integral in (6) at  $p$  of the surface  $\partial \Omega$  is

$$V_n = -[2\pi\sigma(p) + \vec{n}(p) \cdot \iint_{\partial \Omega} \sigma(q) \frac{\vec{r}(p, q)}{r^3(p, q)} ds] \quad (7)$$

where the unit vector  $n$  is normal to the body surface and pointing outwards into the fluid.

In order to make the computer program extensible to arbitrary bodies of 3 dimensions, the surface  $S_b, S_c, S_f$  are divided into finite number of elements. Assuming that the source

density is taken as constant over each element, the potential at p of Eq. (6) may be written in a discretized form as:

$$\phi_i = \sum_{j=1}^N \phi_{ij} \sigma_j \quad i=1,2,\dots,N \quad (8)$$

where

$$\phi_{ij} = \iint_{S_j} \frac{d\xi d\eta}{[(x-\xi)^2 + (y-\eta)^2 + z^2]^{\frac{3}{2}}} \quad (9)$$

The normal induced velocity is then

$$V_{n_i} = \sum_{j=1}^N K_{ij} \sigma_j \quad i=1,2,\dots,N \quad (10)$$

where

$$K_{ij} = \begin{cases} -2\pi & i=j \\ -\vec{n}_i \cdot \iint_{S_j} \frac{\vec{r}}{r^3} ds & i \neq j \end{cases} \quad (11)$$

In conducting the time stepping procedure, the boundary conditions at each time interval  $t+\Delta t$  are established in explicit forms containing quantities at times  $\Delta t$  and  $t-\Delta t$  which are known from previous iterations, e.g:

$$\begin{aligned} \left(\frac{\partial \phi}{\partial n}\right)_{t+\Delta t}^d &= F^d(\phi_t, \phi_{t-\Delta t}, \left.\frac{\partial \phi}{\partial n}\right|_t, \left.\frac{\partial \phi}{\partial n}\right|_{t-\Delta t}) \text{ on } S_d \\ (\phi)_{t+\Delta t}^c &= F^c(\phi_t, \phi_{t-\Delta t}, \left.\frac{\partial \phi}{\partial n}\right|_t, \left.\frac{\partial \phi}{\partial n}\right|_{t-\Delta t}) \text{ on } S_c \\ (\phi)_{t+\Delta t}^f &= F^f(\phi_t, \phi_{t-\Delta t}, \left.\frac{\partial \phi}{\partial n}\right|_t, \left.\frac{\partial \phi}{\partial n}\right|_{t-\Delta t}) \text{ on } S_f \\ \left(\frac{\partial \phi}{\partial n}\right)_{t+\Delta t}^b &= F^b(\phi_t, \phi_{t-\Delta t}, \left.\frac{\partial \phi}{\partial n}\right|_t, \left.\frac{\partial \phi}{\partial n}\right|_{t-\Delta t}) \text{ on } S_b \end{aligned} \quad (12)$$

Taking into account of (8) and (10) above, and the boundary conditions (12), a set of surface integrals on source density  $\sigma(t+\Delta t)$  may be up-dated to the advanced time interval  $t+\Delta t$ , thus:

$$\sum_{j=1}^N M_{ij} \sigma(x,y,z,t+\Delta t) = G_{i,t+\Delta t} \quad i=1,2,\dots,N \quad (13)$$

in which, the matrix of coefficients are

$$M_{ij} = \begin{cases} K_{ij} & i=1,2,\dots,N_d \\ \phi_{ij} & i=N_d+1,\dots,N_d+N_c+N_f \\ K_{ij} & i=N_d+N_c+N_f+1,\dots,N \end{cases} \quad (14)$$

and,

$$G_i = \begin{cases} \left(\frac{\partial \phi}{\partial n}\right)_{i,t+\Delta t}^d & i=1,2,\dots,N_d \\ (\phi)_{i,t+\Delta t}^c & i=N_d+1,\dots,N_d+N_c \\ (\phi)_{i,t+\Delta t}^f & i=N_d+N_c+1,\dots,N_d+N_c+N_f \\ \left(\frac{\partial \phi}{\partial n}\right)_{i,t+\Delta t}^b & i=N_d+N_c+N_f+1,\dots,N \end{cases} \quad (15)$$

the velocity of a point in the field may be expressed as

$$\vec{V}_i = \sum_{j=1}^N (C_{ijx} \vec{e}_1 + C_{ijy} \vec{e}_2 + C_{ijz} \vec{e}_3) \sigma_j \quad (16)$$

Whenever the velocity potential  $\phi$  and the velocity  $\vec{V}$  as well as the body motions are known at time  $t$ , the quantities of these variables at the advanced time interval  $t+\Delta t$  may be evaluated according to the following process. Update the wave elevation over the free surface  $S_f$  at time  $t+\Delta t$ ; according to the motion of the body, determining the new position of the body, which modifies the immersed body surface at interval  $t+\Delta t$  under the new free surface  $S_f(t+\Delta t)$ ; in the new fluid domain  $\Omega(t+\Delta t)$ , re-calculate the coefficient matrix  $M_{ij}$ , and update the matrix of boundary conditions  $G_{i,t+\Delta t}$ ; finally find the solution of source density  $\sigma(t+\Delta t)$  at the interval  $t+\Delta t$  from (13). The pressure  $p$  over the body surface is obtained by the unsteady Bernoulli's equation:

$$P = -\rho [gz + \phi_t + \frac{1}{2} \nabla \phi \cdot \nabla \phi] \quad (17)$$

The force components  $F_k$  may be calculated as appropriate integrations of pressure

$$F_k = - \iint_{S_b} p n_k dS \quad (18)$$

where subscript  $K=1,2,\dots,6$  and  $F_k$  correspond to forces in, and moments about  $x,y,z$  direction respectively.

### 3. THE NONLINEAR RADIATION PROBLEM OF A FLOATING BODY

#### 3.1 Formulation

As indicated in Fig.1, consider the forced heaving motion of an arbitrary floating body on the free surface, a Lagrangian's description is used, the kinematic and dynamic boundary conditions (3),(4) are rewritten as:

$$\frac{Dx}{Dt} = \frac{\partial \phi}{\partial x}; \quad \frac{Dy}{Dt} = \frac{\partial \phi}{\partial y}; \quad \frac{Dz}{Dt} = \frac{\partial \phi}{\partial z}; \quad (19)$$

$$\frac{D\phi}{Dt} = \frac{1}{2} \nabla \phi \cdot \nabla \phi - g\eta$$

The above free-surface conditions are discretized by an explicit time-step scheme as follows:

$$\begin{aligned} x_p(t+\Delta t) &= x_p(t) + \frac{1}{2} \Delta t \{ 3 \left(\frac{\partial \phi}{\partial x}\right)_t - \left(\frac{\partial \phi}{\partial x}\right)_{t-\Delta t} \}_p \\ y_p(t+\Delta t) &= y_p(t) + \frac{1}{2} \Delta t \{ 3 \left(\frac{\partial \phi}{\partial y}\right)_t - \left(\frac{\partial \phi}{\partial y}\right)_{t-\Delta t} \}_p \\ z_p(t+\Delta t) &= z_p(t) + \frac{1}{2} \Delta t \{ 3 \left(\frac{\partial \phi}{\partial z}\right)_t - \left(\frac{\partial \phi}{\partial z}\right)_{t-\Delta t} \}_p \end{aligned} \quad (20)$$

On the pivotal point, the potential is:

$$\phi_j(t+\Delta t) = \phi_j(t) + \frac{1}{2} \Delta t \{ 3 \left(\frac{1}{2} \nabla \phi \cdot \nabla \phi - g\eta\right)_t - \left(\frac{1}{2} \nabla \phi \cdot \nabla \phi - g\eta\right)_{t-\Delta t} \} \quad (21)$$

Let the body be surrounded by a vertical control surface  $S_c$ . Within the immediate vicinity of  $S_c$ , the scattered wave element may be approximated as a plane wave, propagating outwards with celerity along a direction  $\vec{T}$ . Assuming that the scattered wave near the outer

boundary satisfies the Orlanski's [4] condition, one have

$$\frac{\partial \phi}{\partial t} + C_R(t) \frac{\partial \phi}{\partial r} = 0 \quad (22)$$

where  $C_R$  is the phase velocity for potential function. Let  $R$  denote the intersection point of the free surface and the outer boundary, and point  $R-1$  a neighbouring point  $\Delta R$  distant from point  $R$  along the radial direction, the phase velocity  $C_R$  is then obtained from  $\phi$  of the free-surface as:

$$C_R^t = \frac{-\phi_{R-1}^t + \phi_{R-1}^{t-2}}{2\Delta t(V_r)_{R-1}^{t-1}} \quad (23)$$

Considering that the scattered wave should be outgoing waves,  $C_R \geq 0$ . In practical computations, the limits on  $C_R$  may be set as [4]

$$C_R(t) = \begin{cases} \frac{\Delta R}{\Delta t} & \text{if } \bar{C}_R \geq \frac{\Delta R}{\Delta t} \\ \bar{C}_R(t) & \text{if } 0 \leq \bar{C}_R < \frac{\Delta R}{\Delta t} \\ 0 & \text{if } \bar{C}_R < 0 \end{cases} \quad (24)$$

where  $\bar{C}_R(t)$  is obtained from Eq. (23). The solution of the radiation problem may be obtained from (13), together with the boundary conditions listed in (19)-(24).

### 3.2 The Panelling of The Instantaneous Wetted Surface Near The Free Surface.

At intersection line of the body and the free-surface a confluence of boundary condition exists. As a result, the solution exhibits a singularity at the line. To accommodate this, we determine the position of intersection points by a direct method. From a physical point of view, the fluid particle may not penetrate into the body, it may only slide along the body surface. Therefore, in the numerical model, the vertical position of the intersection point is obtained by interpolation along the radius form wave elevations. The horizontal positions  $(x, y)$  of the intersection point may be obtained by setting their absolute increments as zero. Another advantage of this method is in using the centre point of the panel as the pivotal point, this avoiding singularity at the intersection point of the body and the free surface.

At the intersection of the freesurface and the outer boundary, the vertical position of the intersection point is determined by allowing it to be the same as the wave elevation calculated at the outer boundary surface.

For each time step, the immersed body surface changes in accordance to the motion of the body and of the wave surface. There are several configurations which the panel on the body may be intersected by the free surface  $\eta(t)$ . Fig.2.

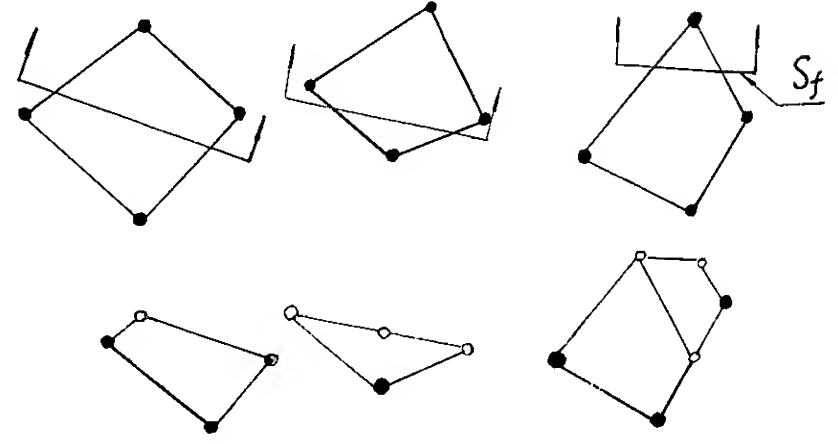


Fig. 2: Nodal points on the intersected body panel.

Let  $(x_1, y_1, z_1)$  and  $(x_2, y_2, z_2)$  be two nodes on a panel line, which are located under and above the wave surface  $\eta(t)$  respectively, thus, the new node on the wave surface  $\eta(t)$  is:

$$\begin{aligned} z_0 &= \eta(t) \\ y_0 &= y_1 + (y_2 - y_1) \frac{z_1 - \eta(t)}{z_1 - z_2} \\ x_0 &= x_1 + (x_2 - x_1) \frac{z_1 - \eta(t)}{z_1 - z_2} \end{aligned} \quad (25)$$

### 3.3 Numerical Examples of Large Amplitude Radiation Problems and Discussion

In this section, results are presented for the case of forced heaving motion of a floating truncated vertical circular cylinder of radius  $a$  and mean draft  $a/2$ . The length, time and mass units are so chosen that the radius  $a$ , gravity  $g$  and density  $\rho$  all equal unity. The vertical velocity of the body is prescribed to be

$$V(t) = H \omega \sin \omega t \quad (26)$$

with the body draft

$$h(t) = -\frac{1}{2} - H \cos \omega t \quad (27)$$

The total number of panels is 232, with  $N_d=26$ ,  $N_c=48$ ,  $N_f=84$ ,  $N_b=74$ .

Let the radius of outer boundary be  $R=5.0$ , amplitude be  $H=0.05$ , frequency  $\omega=\frac{1}{2}\pi$ , time increment be  $\Delta t=0.1$ , and water depth be  $d=4$ ,  $T=24$ , i.e. a total of 6 periods.

The comparison between Lin's results[2] and our results for the above problem is shown in Fig. 3, it seems agreement is good.

#### 3.3.1 The Effect of Different Radiation Conditions Adopted for The Nonlinear Radiation Solution.

Two groups of computations are carried out to investigate the effect of different radia-

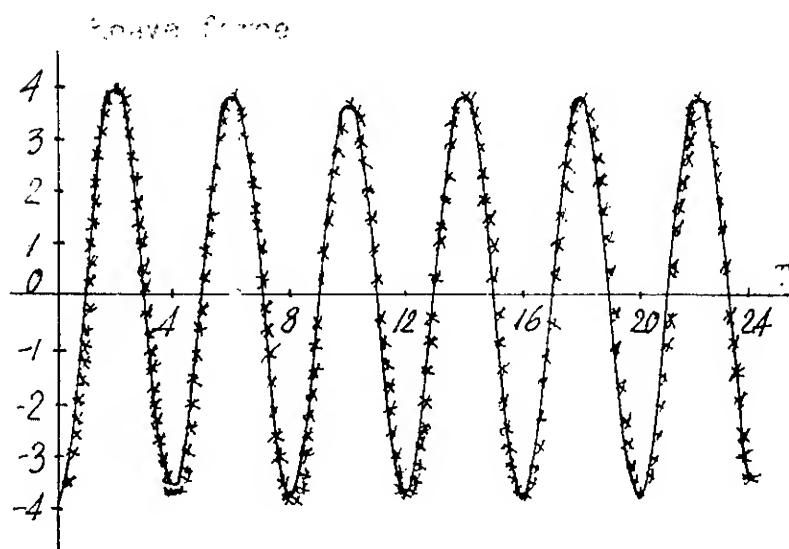


Fig.3 Comparison of heave force history  
— present result; \*\*\* Lin's result [2].

tion conditions. Here, the time interval  $T=16.0$ . In group A, radiation condition as proposed by Isaacson[1] is adopted.

$$\phi = 0, \quad \frac{\partial \phi}{\partial n} = 0 \quad (28)$$

In group B, the radiation condition of Eq. (22) is adopted.

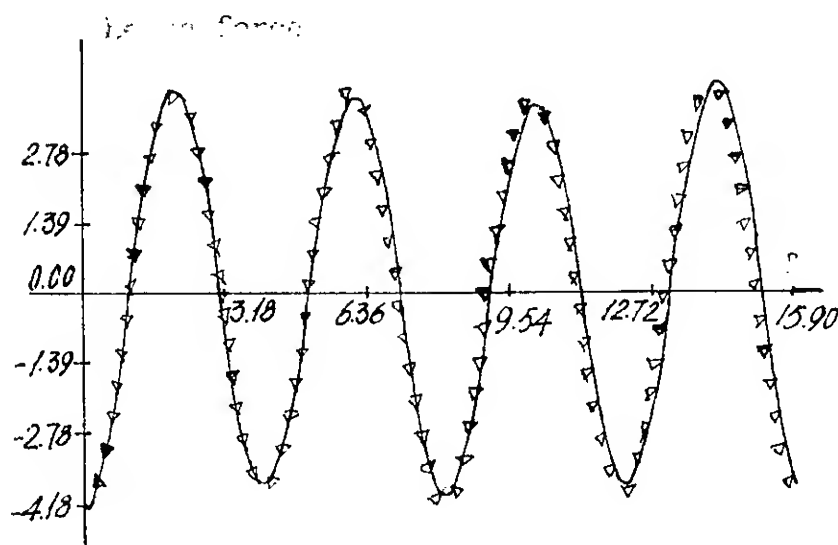


Fig. 4: Comparison of heave force for different radiation conditions.  $\nabla \nabla \nabla$  group A; — group B.

A comparison of vertical force acting on the cylinder in both cases is shown in Fig.4. In the first one and half period, the result of group A is consistent with that of group B. But as the time increases, there begins a difference between them; the period of group A becomes gradually less than that of group B. This phenomenon arises from the reflection of scattered waves in group A. At the beginning, the scattered waves did not reach the outer boundary  $S_c$ , therefore results of the two groups are consistent. When the scattered waves reach the boundary  $S_c$ , in the case of group A the condition of (28) induces a ingoing

reflection of the scattered waves. It is the interference of the scattered waves that causes the change in the period of the wave forces.

### 3.3.2 The Effect of Changing The Distance of The Outer Boundary Surface from The Origin.

A comparison of three groups of calculation using different radii of the outer boundary surface are carried out to investigate the effect of changing distances of outer boundary surface. Here (a)  $R=5.0$ , (b)  $R=8.0$ , (c)  $R=10.0$ . Fig. 5 shows the time history of wave elevation at an intersection point of the body and free surface. Here, the result of  $R=8.0$  is consistent with that of  $R=10.0$ , but the result for  $R=5.0$  is different. For the first cycle, (a) is consistent with (b) and (c), but difference of amplitude appear when time interval increases.

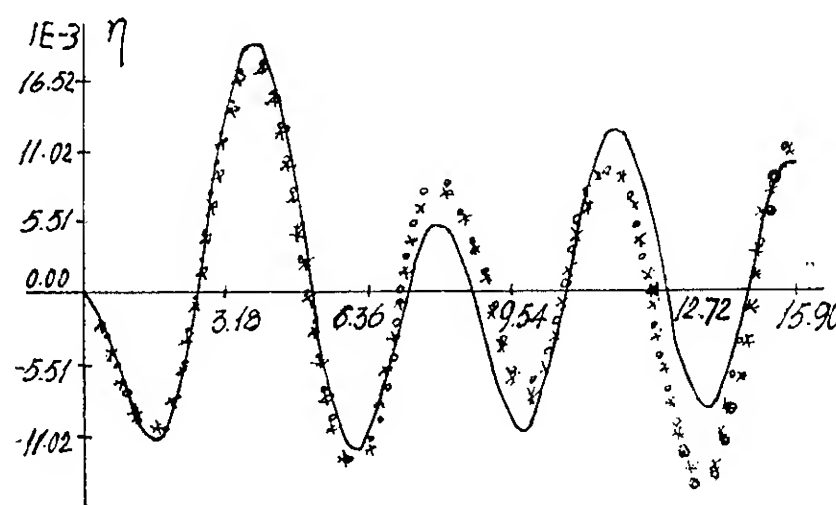


Fig. 5 History of an intersection point. --- group a; \*\*\* group b; o o o group c.

The free surface profiles in the radial direction corresponding to groups (a), (b), (c), for  $t=6.0, 8.0, 14.4$  are shown in Fig. 6-8. For  $t=6.0$ , groups (a), (b) and (c) are consistent. For  $t=8.0$ , a slight reflection causes the difference between group (a) and group (b), (c). For  $t=14.4$ , inconsistencies developed even between  $R=8$ , and  $R=10$ . Near the body surface, the wave profiles are consistent, but near the boundary  $S_c$  they are different. Fig. 9 is the pressure on the bottom center panel. Fig. 10 is the vertical forces acting on the cylinder of group (a), (b), (c). It is shown that by changing the distance of  $S_c$  from the origin little effect is introduced as far as the hydrodynamic forces are concerned. From the above comparisons a conclusive remark may be drawn: For the Orlanski's condition, changing the radius of the outer boundary causes little influence to the wave force but may have a large influence to the wave profiles. For computational stability it is advisable that the outer boundary surface be placed at a distance sufficiently far from the body.

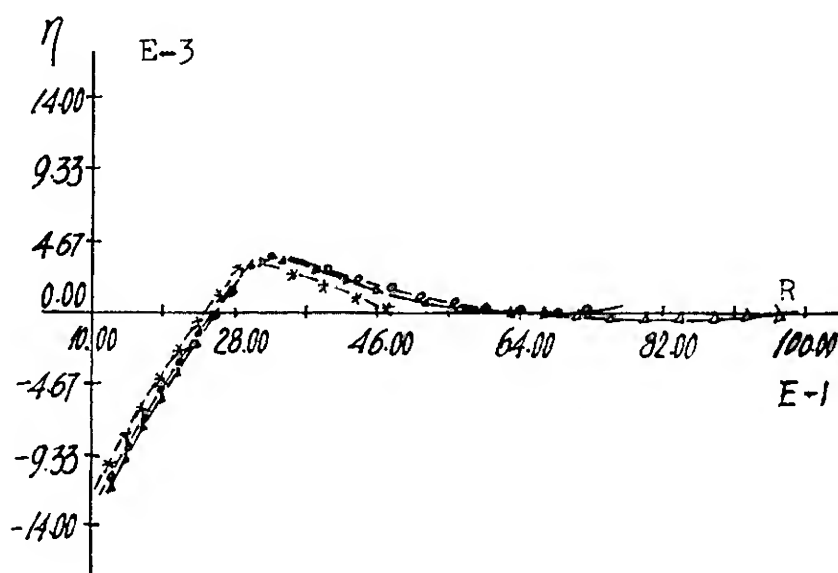


Fig. 6 Free surface profiles ( $t=6$ )  
 -\*-group a; -o-group b; -Δ-group c.

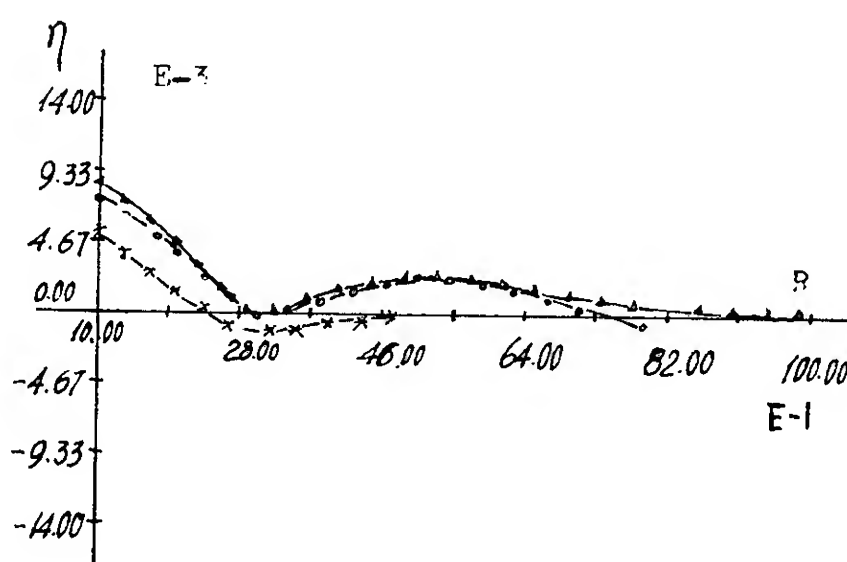


Fig. 7 Free surface profiles ( $t=8.0$ ).  
 -\*-group a; -o-group b; -Δ-group c.

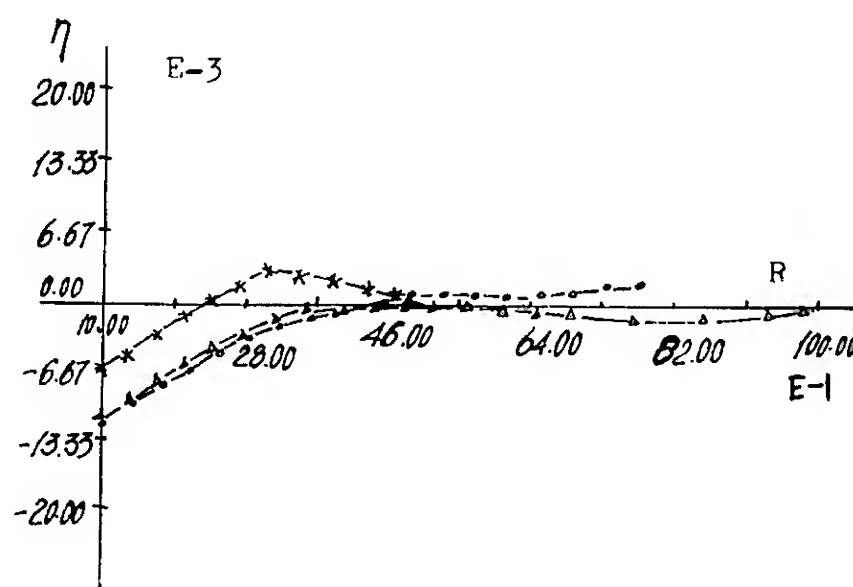


Fig. 8 Free surface profiles ( $t=14.4$ )  
 -\*-group a; -o-group b; -Δ-group c.

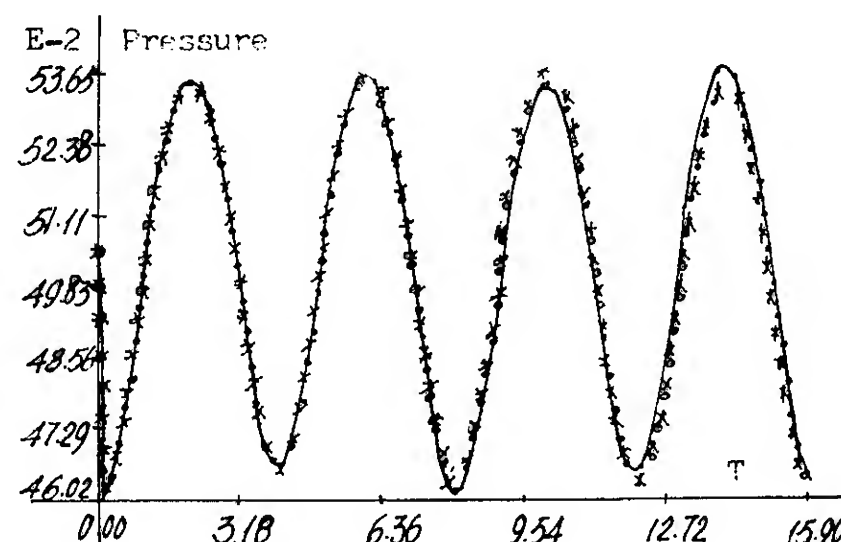


Fig. 9 Pressure on the central element  
 \*\*\* group a; o o o group b,  
 — group c.

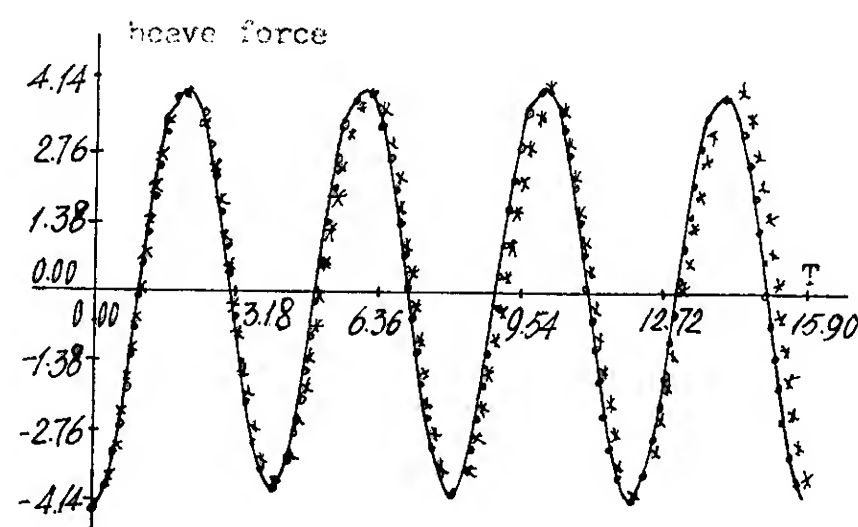


Fig. 10 Heave forces for different radii.  
 \*\*\*\*\* group a;  
 o o o group b; — group c.

### 3.3.3 The Effect of Changing the Amplitude of Body's Oscillation.

Generally, large-amplitude motions result in nonlinear phenomena. Four cases of large amplitude forced heaving motions are investigated in which  $R=8.0$ ,  $\omega=\frac{1}{2}\pi$ ,  $d=4.0$ ,  $T=16.0$ ,  $t=0.1$  and in case (a)  $H=0.05$ ,  $\delta_a=H/h=10\%$ ,  $h$  is the mean draft. (b)  $H=0.10$ ,  $\delta_b=20\%$ , (c)  $H=0.15$ ,  $\delta_c=30\%$ . (d)  $H=0.25$ ,  $\delta_d=50\%$ . Fig. 11-14 show the radial free surface profiles for the above four cases. With increasing amplitude, the wave profiles change drastically as steeper waves appear and greater amount of wave energy are transported outwards. Fig. 15 shows wave surface profiles of four cases of  $H$  (at  $t=9.0$ ) respectively. In each figure, configuration and phase of wave profiles for these four cases are the same, but the greater the oscillation amplitude, the steeper the wave and the stronger the non-linearity.

Fig.16 is the time history of a body wave surface intersection point which is the same as the wave elevation on the body surface. It is shown that a larger wave motion appears for a larger body oscillation amplitude, but the period and trend are the same. In the case of the larger amplitudes, there appears more asymmetry in the curves which easily results in instability of the numerical process. Fig.17 shows the pressure acting on the bottom centre panel. A distortion at the peak of the pressure history as a result of strong nonlinearity appears when the oscillation amplitude becomes too large, while a drop in pressure appears in the very beginning. Since the body starts to rise from rest and form its initially displaced position at the bottom of the stroke. The comparison of the vertical hydrodynamic force acting on the body in Fig. 18 shows little change for the four cases considered.

It is shown that the variations in the radial free surface profiles and in the local pressures are much more serious than in its vertical forces for different amplitudes of oscillation. Thus the nonlinear effect should be considered when dealing with a local strength problem involving integration of local pressures.

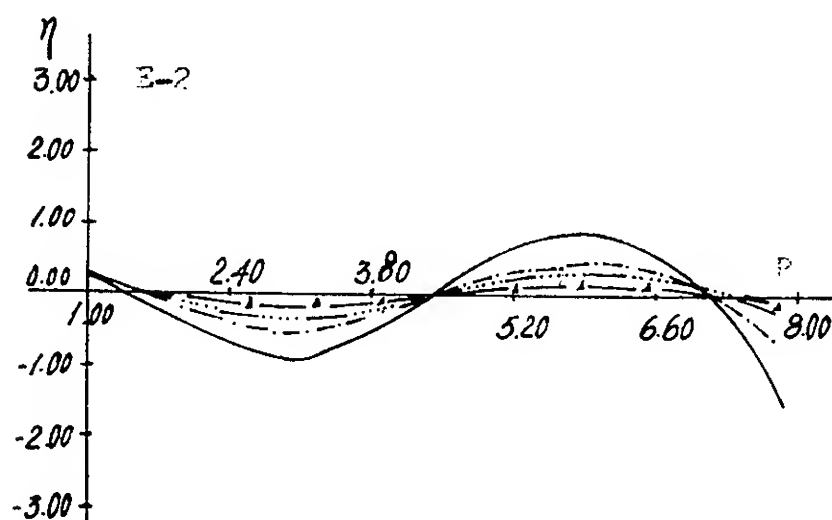


Fig. 15 Wave surface profiles for different amplitudes ( $t=9.0$ ). — $\Delta$ — case a; -...- case b; -.- case c; — case d.

#### 4. NONLINEAR WAVE DIFFRACTION AROUND LARGE STRUCTURES

##### 4.1 Formulation

In approach to the diffraction problem, the wave diffraction is treated as a transient problem with known initial conditions corresponding to still water in the immediate vicinity of the structure, and with a prescribed incident wave form approaching from  $x=-\infty$  and propagating past the structure, Fig. 19.

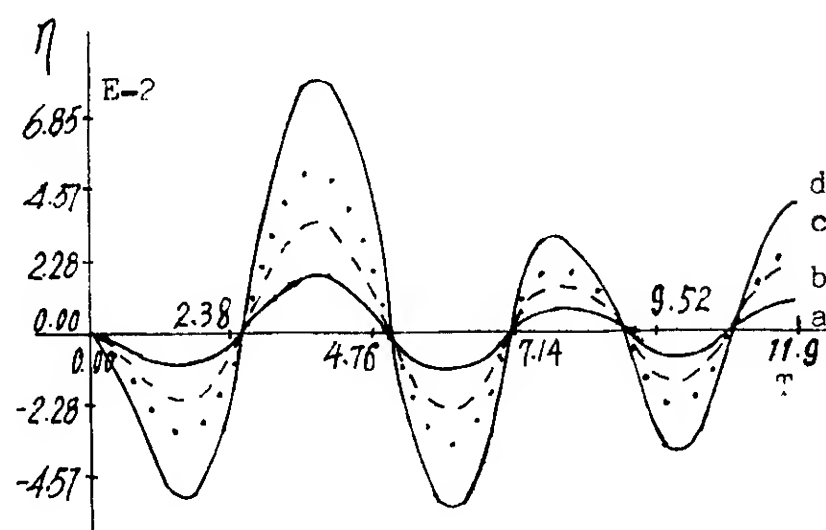


Fig.16 History of an intersection point for different amplitudes.

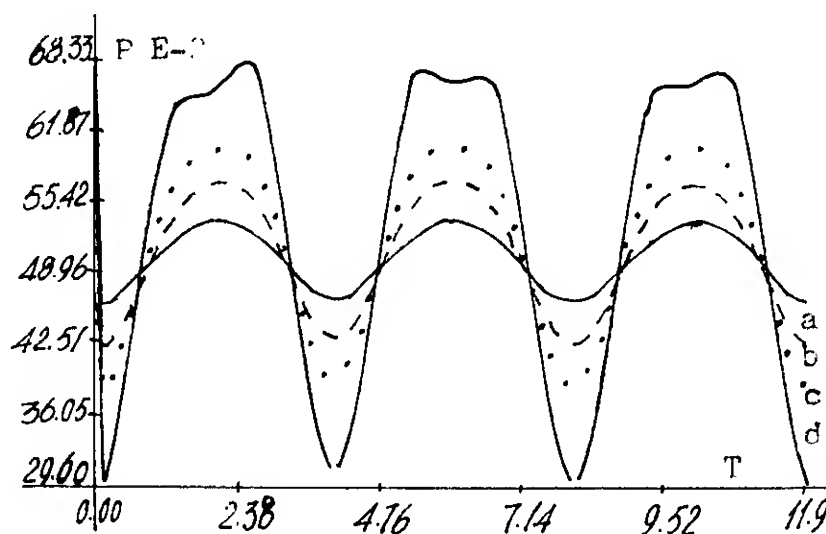


Fig.17 Pressure on the bottom central panel.

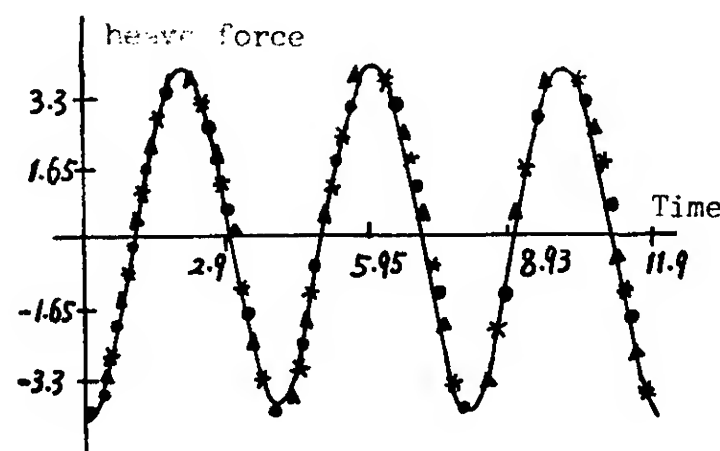


Fig.18 Heave Forces for different amplitudes. — case a;  $\circ \circ \circ$  case b;  $\Delta \Delta \Delta$  case c;  $* * *$  case d.



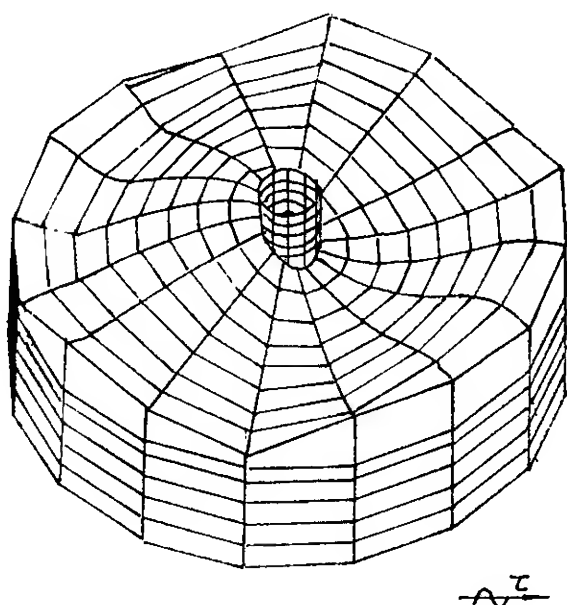


Fig. 19 An isometric view of body-wave interaction.  $H_2/d=1/3$ ,  $t=1.3$ .

When incident waves exist, Lagrangian free surface conditions of the form (19) may easily lead to interpenetration of the wave surface panel and the body surface. In order to avoid the difficulty of shaping and rearranging the free surface panel, a set of Eulerian free-surface conditions is proposed here.

$$\left. \begin{aligned} \frac{\partial \phi}{\partial n} - \frac{\partial \eta}{\partial t} n_z &= 0 \\ \frac{\partial \phi}{\partial t} + g\eta + \frac{1}{2}(\nabla \phi)^2 &= 0 \end{aligned} \right\} \quad (29)$$

For the outer boundary condition provided that it is lying at a suitable distance from the body, then in the beginning period when the scattered waves are still in the inner domain, the outer boundary condition may be written as the Isaacson's version, i.e.

$$\frac{\partial \phi}{\partial n} = \frac{\partial \phi_0}{\partial n} \quad \phi = \phi_0 \quad (30)$$

However, when  $T \geq T_c$ , where  $T_c$  is the time when the scattered waves travelling at its group velocity begin to meet the outer boundary, the Orlandi's condition is adopted:

$$\frac{\partial \phi_s}{\partial t} + c_\phi \left( K_r \frac{\partial \phi_s}{\partial r} + K_\theta \frac{\partial \phi_s}{\partial \theta} \right) = 0 \quad (31)$$

$$\begin{aligned} K_r &= \alpha \cdot \frac{\partial \phi_s}{\partial r} / \sqrt{\left( \frac{\partial \phi_s}{\partial r} \right)^2 + \left( \frac{\partial \phi_s}{\partial \theta} \right)^2} \\ K_\theta &= \alpha \cdot \frac{\partial \phi_s}{\partial \theta} / \sqrt{\left( \frac{\partial \phi_s}{\partial r} \right)^2 + \left( \frac{\partial \phi_s}{\partial \theta} \right)^2} \end{aligned} \quad (32)$$

Here

$$\alpha = \begin{cases} 1 & \text{if } \frac{\partial \phi_s}{\partial r} \geq 0 \\ -1 & \text{if } \frac{\partial \phi_s}{\partial r} < 0 \end{cases} \quad (33)$$

It is assumed here that the scattered wave potential

$$\phi_s = \phi - \phi_0 \quad (34)$$

It must be mentioned that a note of mathematical inconsistency occurs here as for nonlinear wave dynamics, the principle of superposition is not strictly applicable.

For the initial condition, as there is initially no incident wave motion immediately adjacent to the body, so the scattered potential is initially zero.

In our numerical procedure, the corner point  $\eta_0$  of the wave surface panel is determined by the area average of its four surrounding panels, let  $\eta, s$  represent wave elevation and area respectively, then

$$\eta_0 = \frac{\sqrt{S_A} \cdot \eta_d + \sqrt{S_B} \cdot \eta_c + \sqrt{S_C} \cdot \eta_b + \sqrt{S_D} \cdot \eta_a}{\sqrt{S_A} + \sqrt{S_B} + \sqrt{S_C} + \sqrt{S_D}} \quad (35)$$

For each time step, the adjusted wave surface will truncate a part of the body panels near the free-surface. If the remaining part of the body panel becomes smaller than  $\epsilon$ , a predetermined number, then it is deleted from the body surface to avoid divergence.

## 4.2 Numerical Examples

A computer program which incorporates the method described above has been used to generate results for a few specific situations in order to establish the practical viability of the method used. Suitable comparisons with available results may be made only for relatively few restricted cases for which known diffraction solutions are available.[1].

### 4.2.1 The Diffraction of Small Amplitude Waves Past A Vertical Circular Cylinder

A surface-piercing vertical cylinder is subjected to a linear incident wave. Here,  $d/a=2$ ,  $H/a=0.1$ ,  $Ka=1.5$ ,  $\bar{k}/k=0.5$ .

Fig. 20 shows a) the incident wave elevation at  $x=0$ , b) the time history of the horizontal force acting on the cylinder. The results obtained from our program is shown in dotted lines, the predicted force variation agrees with that given in [1].

The program has also been tested for the case of a surface piercing vertical cylinder subjected to a prescribed solitary wave form given by

$$\eta = H \text{sech}^2[K(x_s - Ct)] \quad (36)$$

where  $K = \sqrt{3H/4d^3}$ ,  $x_s = x + a + 3.0/K$ , and  $d/a=0.5$ ,  $H/d=0.1$ .

Comparison of results with closed-form solutions given by Isaacson [1] is presented in Fig. 21. The solid line indicates the closed-form solution given by Isaacson, the broken line is the numerical results calculated by Isaacson's model [1], and the dotted line is the numerical result calculated by the present model. Results evaluated by this report serves to highlight the fact that the outer boundary condition presented in this section is capable of allowing the outgoing scattered waves to pass through effectively with little reflection inwards. It also enables the

computation of wave forces to run on for a sufficient duration of time so that the wave motion is fully established at the vicinity of the body.

#### 4.2.2 The Diffraction of Large Amplitude Shallow Water Waves

Results are presented for a circular dock fixed at the free surface subjected to a large amplitude shallow water wave. let  $d/a=1.5$ ,

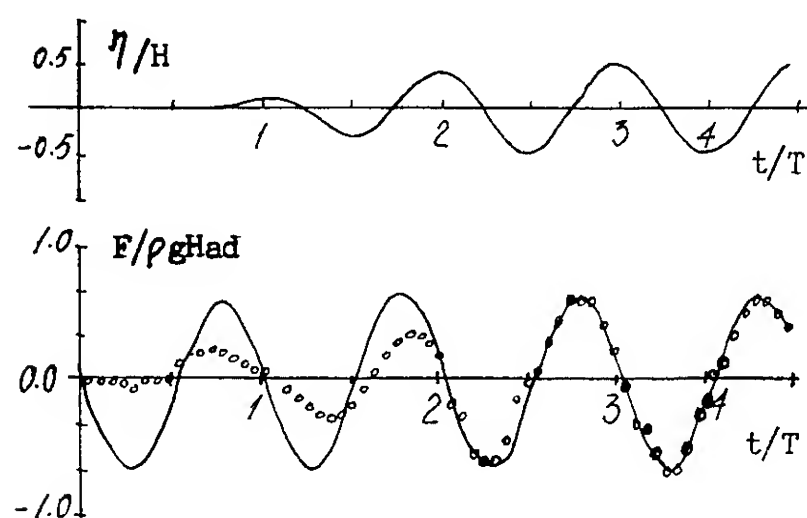


Fig. 20: a) The incident wave elevation at  $X=0$ . b) History of horizontal wave force. --- closed-form solution [1]; o o o present results.

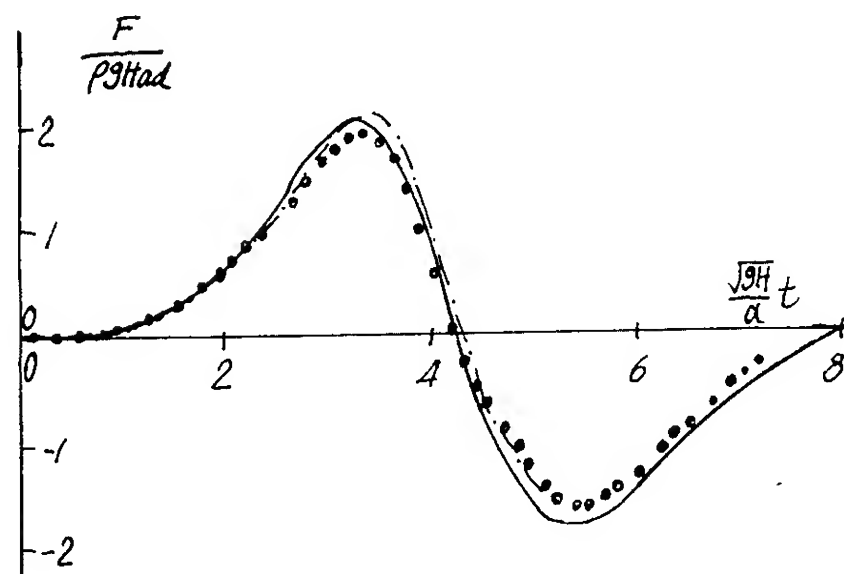


Fig. 21: Horizontal wave force. — closed-form solution[1]; --- numerical results[1]; o o o present results.

$h/a=0.5$ ,  $d/gT^2=0.018$ , and  $H_1/d=1/4$ ,  $H_2/d=1/3$ , where  $h$  is the draft of the dock,  $T$  is the wave period,  $H_1$ ,  $H_2$  are wave heights.

Fig. 22 shows a) the incident wave elevation at  $x=0$ , b) comparison of horizontal forces for cases of two wave heights. The dot-chain line represents the result predicted by linear wave theory [5]. The broken line and

the solid line represent results given by the present theory for  $H/d=1/4$  and  $1/3$  respectively. There is a  $90^\circ$  phase difference between the wave force and the incident wave form. The maximum force coefficient occurring at  $t/T=0.488$  are respectively 15% and 21% greater than that of the linear-theory prediction.

The total wave profiles occurring for diffraction around the fixed dock are presented in Fig. 23. It is noticeable that the steepness is large. In Fig. 23, it is seen that the incident waves diffract around the body, and propagate past the body, comparing the wave crests at two sides of the body, a little delay of the phase may be noticed found. It shows that the wave behind the body may come from diffraction of the wave in front of the body.

Since the wave is obstructed by the body, the wave elevation in front of the body swells up to a value, much higher than that behind the body. As a result, a pressure difference is formed and a periodic wave force is generated.

Fig. 19 is an isometric view of the body-wave interaction showing the mechanism of diffraction with  $H/d=1/3$ ,  $t=1.3$ .

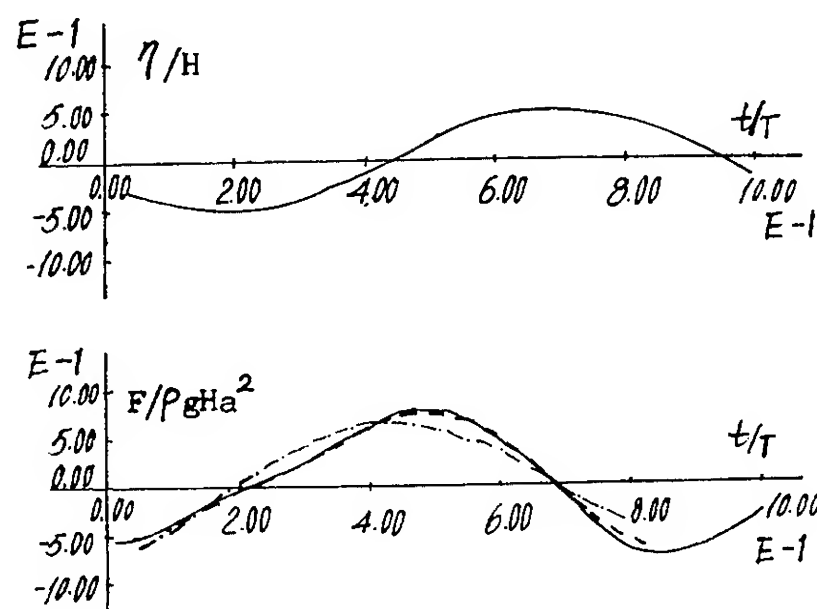


Fig. 22: a) Incident wave elevation at  $X=0$ . b) Horizontal wave forces. --- linear diffraction solution[5]; ---  $H_1/d=1/4$ ; —  $H_2/d=1/3$ .

## 5. INTERACTIONS OF NONLINEAR SURFACE WAVE WITH A FREELY FLOATING BODY

### 5.1 Formulation

In order to consider the effects of three dimensional nonlinear interactions between wave and body, the boundary conditions on the immersed body surface are expressed in terms of velocity  $U_k$  ( $k=1,2,\dots,6$ ) which are the six velocity components in the moving co-ordinate system fixed to the body. Thus

$$\frac{\partial \phi}{\partial n} = \sum_{k=1}^6 n_k u_k \quad (37)$$

The six values of  $U_k$  may be determined from the dynamical equations of motion:

$$\begin{aligned}
F_1' &= m(\dot{u}_1 + u_5 u_3 - u_6 u_2) \\
F_2' &= m(\dot{u}_2 + u_6 u_1 - u_4 u_3) \\
F_3' &= m(\dot{u}_3 + u_4 u_2 - u_5 u_1) \\
F_4' &= I_x \dot{u}_4 - (I_y - I_z) u_5 u_6 \\
F_5' &= I_y \dot{u}_5 - (I_z - I_x) u_6 u_4 \\
F_6' &= I_z \dot{u}_6 - (I_x - I_y) u_4 u_5
\end{aligned} \quad (38)$$

or simply, (38) may be expressed as

$$F_k' = m_k \dot{u}_k + f_k \quad (39)$$

Here the external force  $F_k'$  may be grouped into the following subgroups

$$F_k' = F_{Ak}' + F_{Bk}' + F_{Ck}' \quad (40)$$

where  $F_{Ak}'$  denotes the fluid dynamic forces and moments of potential nature,  $F_{Bk}'$  is that due to gravity of the body and  $F_{Ck}'$  that due to external mooring forces or viscous damping forces.

The fluid dynamic force components are:

$$F_{Ak}' = -\rho \sum_{j=1}^{N_b} n_{kj} \Delta S_j \left[ g z + \frac{\partial \phi}{\partial t} - \vec{v}_e \cdot \vec{v}_{+1/2} (\nabla \phi)^2 \right] \quad (41)$$

substituting (41) into (39), we have

$$\begin{aligned}
m_k \dot{u}_k + \rho \sum_{j=1}^{N_b} \frac{\partial \phi}{\partial t} n_{kj} \Delta S_j = \\
- \rho \sum_{j=1}^{N_b} \{ n_{kj} \Delta S_j [ g z - \vec{v}_e \cdot \nabla \phi + \frac{1}{2} (\nabla \phi)^2 ] \}_j \\
- f_k + F_{Bk}' + F_{Ck}'
\end{aligned} \quad (42)$$

In the coordinate system fixed to the body center G,  $n_{kj} \Delta S_j$  do not vary with time for the time step considered, thus, (42) may be written as

$$\frac{\partial H_k}{\partial t}(t) = h_k(t) \quad (43)$$

and for the next time step  $t + \Delta t$ .

$$H_k(t + \Delta t) = H_k(t) + \frac{1}{2} \Delta t \{ 3h_k(t) - h_k(t - \Delta t) \} \quad (44)$$

where

$$H_k(t) = m_k u_k + \rho \sum_{j=1}^{N_b} \phi_j n_{kj} \Delta S_j \quad (45)$$

$$\begin{aligned}
h_k = - \rho \sum_{j=1}^{N_b} \{ n_{kj} \Delta S_j [ g z - \vec{v}_e \cdot \nabla \phi + \frac{1}{2} (\nabla \phi)^2 ] \}_j \\
- f_k + F_{Bk}' + F_{Ck}'
\end{aligned} \quad (46)$$

$\vec{v}_e$  is the velocity at the point considered on the body.

$$\vec{V}_e = \vec{V}_g + \vec{\omega} \times \vec{r} \quad (47)$$

$\vec{V}_g$  is the velocity of the center G,  $\vec{r}$  is the position vector relative to the origin G.

The term  $-n_{kj} \Delta S_j \vec{v}_e \cdot \nabla \phi$  is different from the term  $d[n_{kj} \Delta S_j] / dt$  in Isaacson's expression

[5] which was neglected in his numerical computations.

Finally, substituting  $U_k$  in (45) into the body boundary condition (37), the body surface equation may be rewritten as:

$$\sum_{j=1}^N (K_{ij} - A_{ij}) \sigma_j = \sum_{k=1}^6 n_{ki} H_k / m_k \quad i=1, 2, \dots, N \quad (48)$$

where

$$A_{ij} = - \sum_{l=1}^{N_b} \phi_{ljk} \sum_{k=1}^6 \frac{\rho}{m_k} n_{kl} n_{ki} \Delta S_l \quad (49)$$

## 5.2 Numerical Results

As an illustration of the method, results are presented for the case of a large freely floating circular dock at the free-surface subjected to a given shallow water wave of large amplitude. Let  $d/a=1.5$ ,  $h/a=0.5$ ,  $d/gT=0.0136$ ,  $H_1/d=1/4$ ,  $H_2/d=1/3$ . Initially,  $Z_g/h=-1/4$ , and  $m_4/\rho a^5=0.47$ . Here, a circular cylindrical surface is adopted as the outer boundary, the radius of which is  $R/a=9.0$ .

In Fig. 24 is shown a) the incident wave elevation at the centre of the dock ( $x=0$ ), b) the heave motion of the centre of the dock G. From Fig. 24 it is seen that the heave motion is essentially in phase with the incident wave motion at G, which means that the static restoring force terms still play the dominant part. The heave motion under  $H_1$  and  $H_2$  are not the same. This is a result of nonlinear action, because in linear theory, they should be same non-dimensionally.

The horizontal wave force variation in the case of  $H/a=1/4$  is shown in Fig. 25. There is a  $90^\circ$  lag in the phase between the force and the waves which occurs also in the linear theory.

The heave motion profiles of a free floating dock in the incident waves are presented in Fig. 26. Under the excitation of incident waves, the dock moves in heave motion, but with different degrees of phase lag. In the case of the large amplitude waves, a case of  $180^\circ$  difference in phase may occur, which brings the crest of heave motion to correspond with the trough of the wave and vice versa. When this occurs, shipping of green water and slamming may occur.

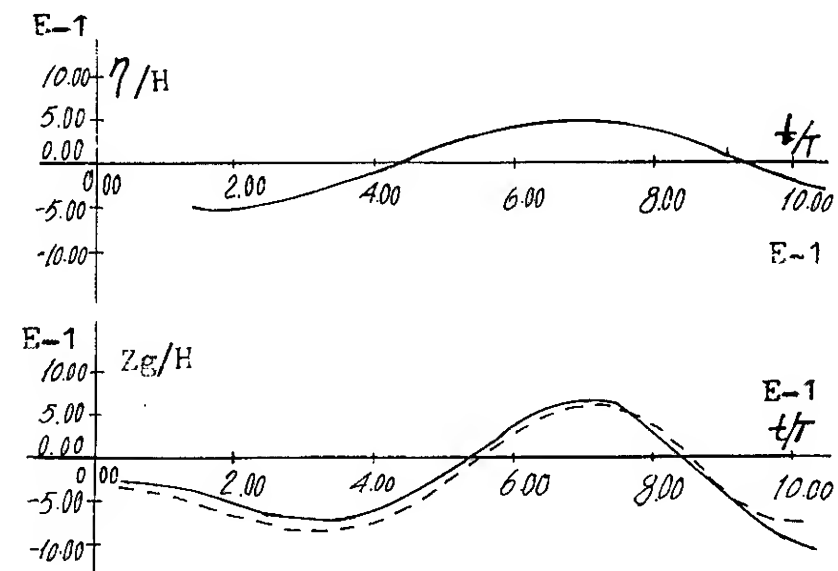


Fig. 24: a) Incident wave elevation at  $X=0$ . b) Heave variation for a floating dock. ---  $H_1/d=1/4$ ; —  $H_2/d=1/3$ .

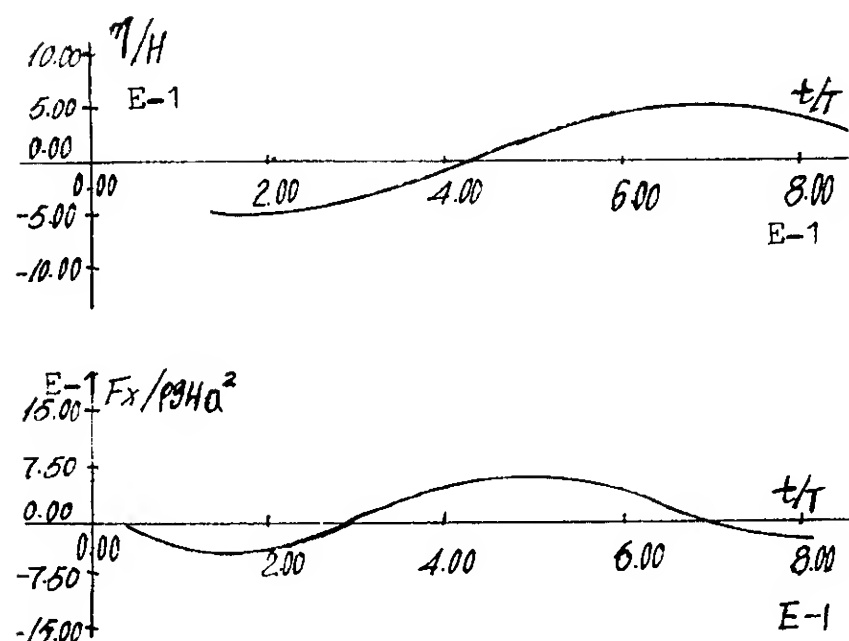


Fig. 25: a) Incident wave elevation at  $X=0$ . b) Horizontal wave force.  $H/d=1/4$ .

#### 6. AN ATTEMPT TO SIMULATE A NUMERICAL WAVE TANK

A numerical model is constructed for a cylindrical wavemaker operating in a seakeeping tank of finite depth but of infinite dimensions. Attention is focussed on numerically simulating the nonlinear waves with a wave front and acting on another body in a numerical seakeeping tank. The first step is to generate numerically the waves simulating 3-D nonlinear waves generated by a wavemaker. The second step is to simulate the tank experiment by requiring these numerical waves with a wave front to act on computational models of large offshore structures or ships. The attempt to justify the prediction of nonlinear wave force on an offshore structure numerically is a realistic proposition.

For illustration, the results of simulating the diffraction experiment of a large floating dock fixed on the free surface and subjected to an approaching nonlinear wave with a wave front generated by a cylindrical wave maker numerically are presented.

The computational model is as Fig. 27. The cylindrical wavemaker is a circular floating dock operating in a forced heave mode, the instantaneous draft of which is expressed as

$$h(t) = -DF + H \sin \omega t \quad (50)$$

where the velocity of its centre  $G$  is accordingly:

$$V_g(t) = H \omega \cdot \cos \omega t \quad (51)$$

Here,  $DF/a=1.0$ ,  $H/a=0.2$ ,  $d/a=4.0$ ,  $\omega = \pi$ . The generated wave time history  $\phi(t)$  and wave potential history  $\eta(t)$  at a point  $p$  ( $x/a=-0.8$ ,  $y/a=0$ ) are shown in Fig. 28. The numerically generated wave along  $x$  direction is a propagating wave with a front, which when acted on

a fixed dock would easily satisfy the initial condition as required by the present paper, viz. at  $t=0$  there is no incident wave immediately adjacent to the fixed dock.

The history of horizontal wave force due to diffraction by the fixed dock is shown in Fig. 29. Here,  $d/a=1.5$ . A maximum horizontal force coefficient of  $F/pgha^2 = 0.65$  seems reasonable compared to Fig. 22.

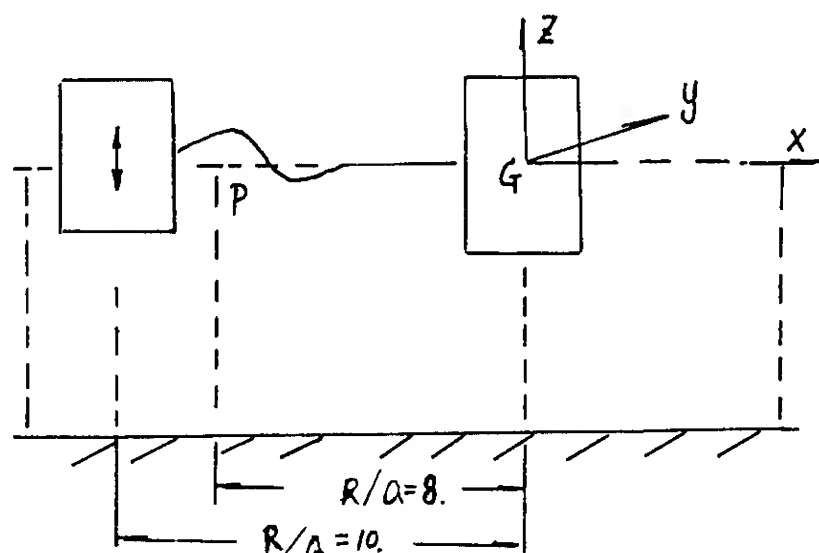


Fig. 27: Computational model of a numerical tank.

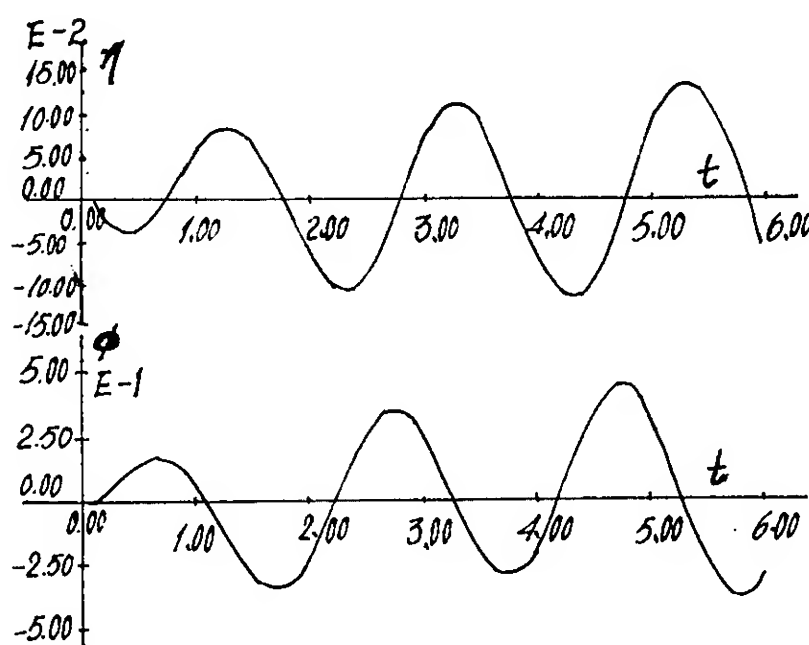


Fig. 28: a) The generated numerical wave; b) The generated wave potential.

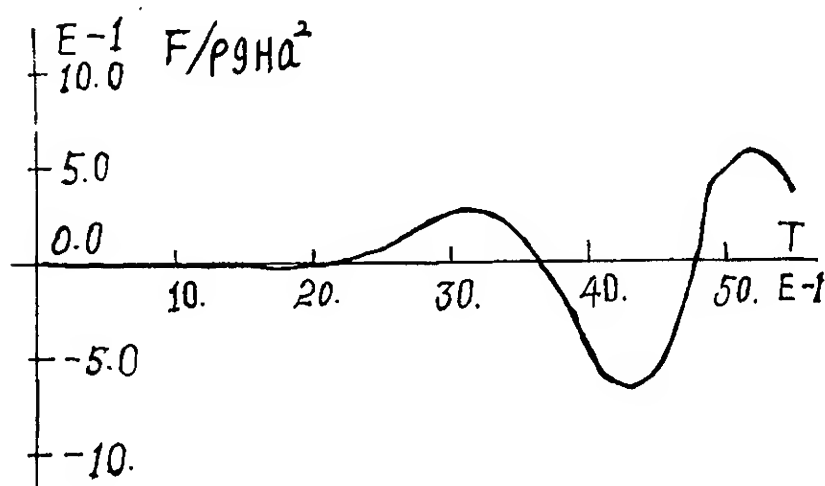


Fig. 29: Horizontal wave force.

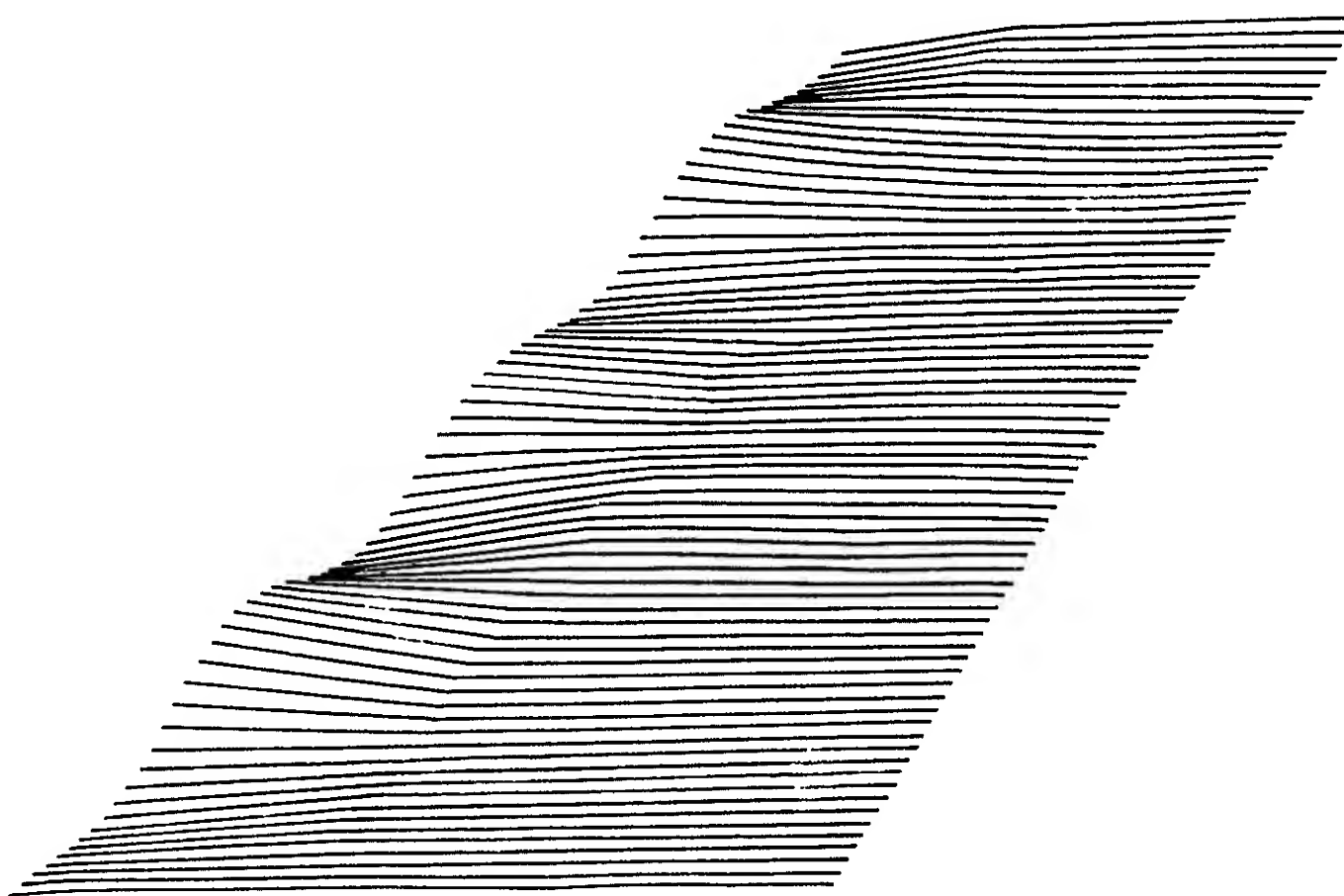


Fig. 11 Nonlinear radial free surface profiles, case a, amplitude  $H=0.05$ ,  $\delta=10\%$   
 $(1 < r < 8, t=0.1, 0.3, \dots)$

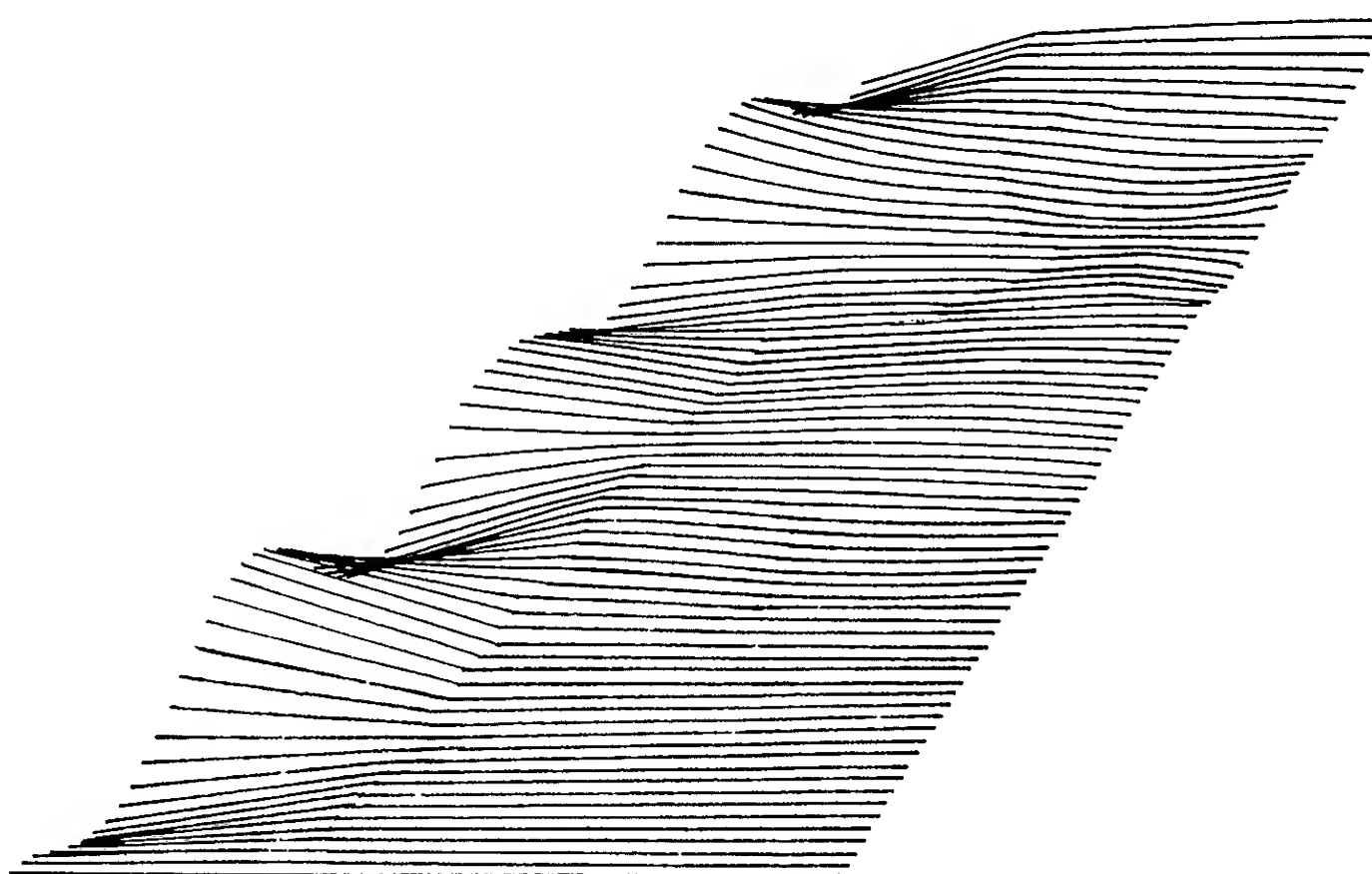


Fig. 12 Nonlinear radial free surface profiles, case b, amplitude  $H=0.1$ ,  $\delta=20\%$   
 $(1 < r < 8, t=0.1, 0.3, \dots)$

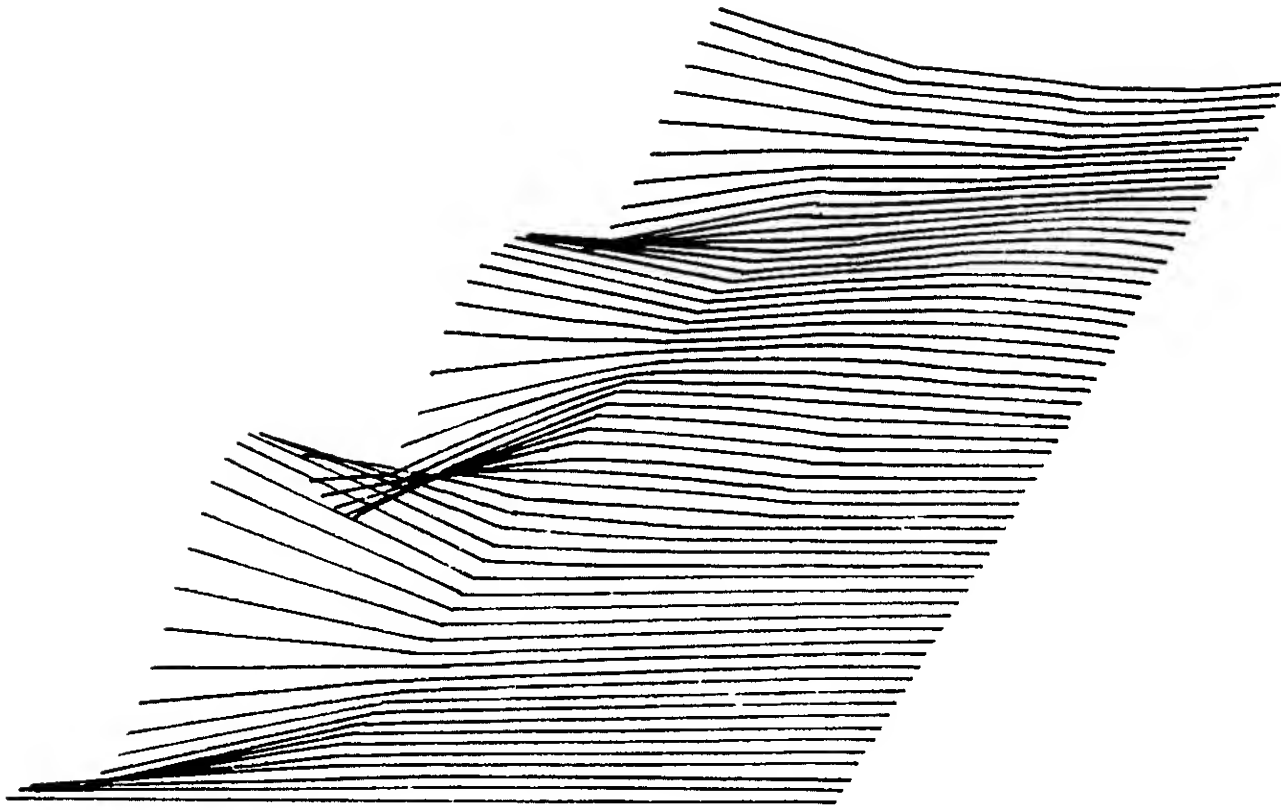


Fig. 13 Nonlinear radial free surface profiles, case c, amplitude  $H=0.15$ ,  $\delta=30\%$   
( $1 < r < 8$ ,  $t=0.1, 0.3, \dots$ )

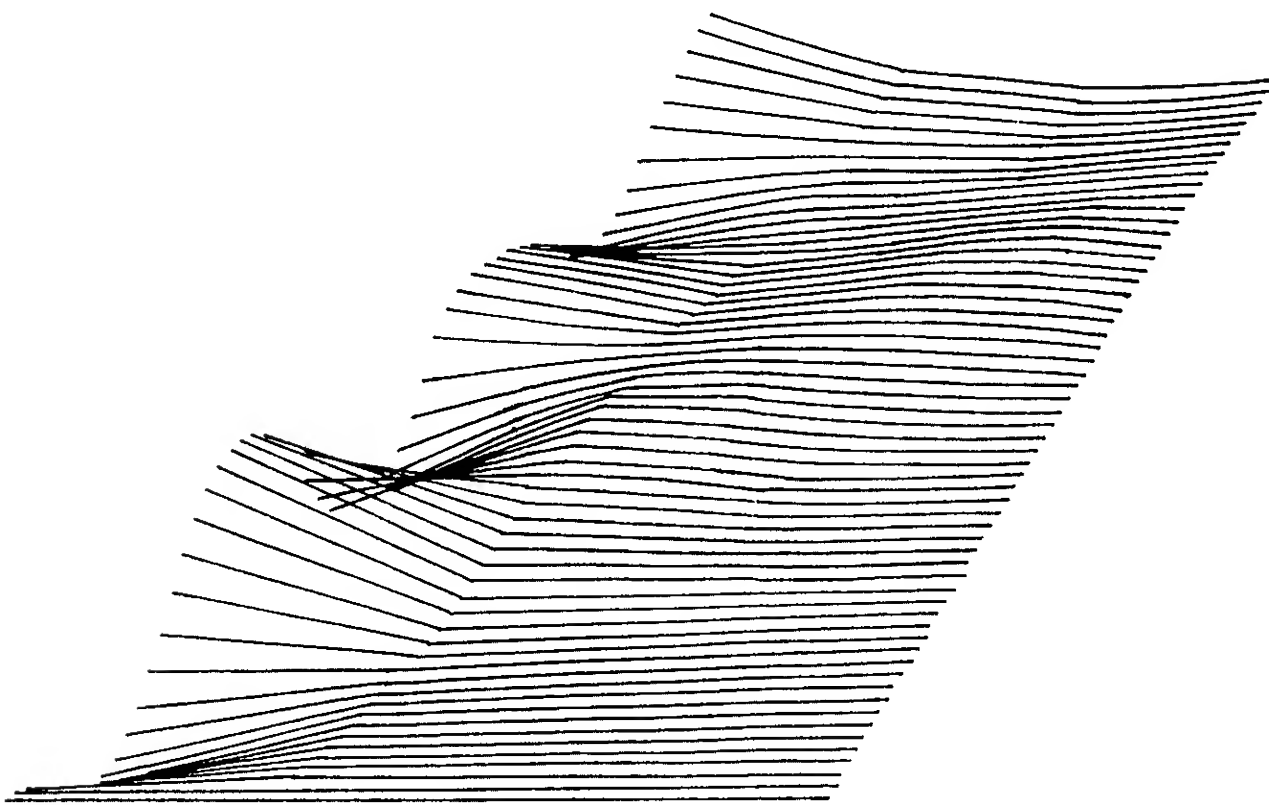


Fig. 14 Nonlinear radial free surface profiles, cases d, amplitude  $H=0.25$ ,  $\delta=50\%$   
( $1 < r < 8$ ,  $t=0.1, 0.3, \dots$ )



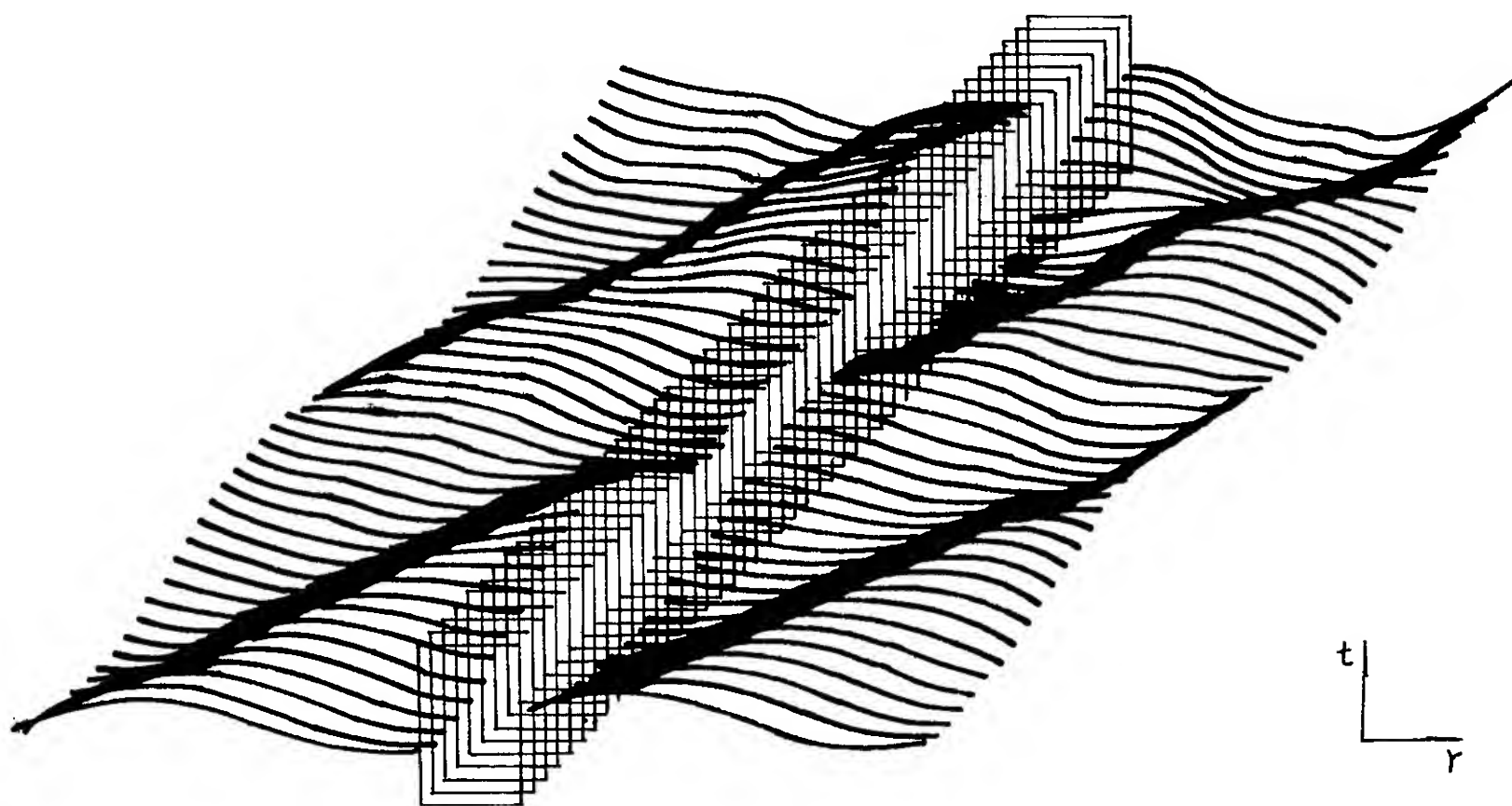


Fig. 23 The wave profiles occurring for diffraction around a fixed dock.  $H/d=1/4$   
 $(-9.0 < r < 9.0, t=0.1, 0.2, 0.3, \dots)$

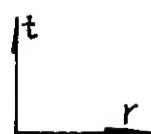


Fig. 26 Heave motion of a floating dock in the incident waves.  $H/d=1/3$   
 $(-9.0 < r < 9.0, t=0.1, 0.2, 0.3, \dots)$

## 7. CONCLUSION

A numerical study of body-wave interaction as an approach to 3-D nonlinear seakeeping problems has been attempted. For illustration, several numerical examples are presented to demonstrate the influences of the change of different parameters, several interesting remarks may be drawn.

(1) Regarding the treatment of the outer boundary condition, although Orlanski's equation is adopted as an open boundary condition, the position of the outer boundary still counts. It results in a more serious influence on the wave surface profiles than on the forces. Therefore for different engineering problems, a different radius of outer boundary may be adopted.

(2) Generally there is a difference between the results predicted from nonlinear theory and that from linear theory. Sometimes although this difference is not large from a global point of view, it may exhibit significant differences at local areas.

(3) The blockage due to a large fixed body to the wave will cause local swell up. The principal zone of influence may be restricted to a small zone adjacent the body. If the zones are a little further from the body, the wave motions are mainly incoming waves. This phenomena may allow us to treat the body-wave interaction by matching the nonlinear solution in an inner domain near the body with a linear solution in the outer domain.

(4) An unfavorable phasing of wave and body motion is demonstrated in which shipping of green water or slamming may occur, especially in the case of large amplitude motions.

(5) An effort to simulate a numerical wave tank of infinite horizontal dimensions by a novel idea of a heaving cylinder is attempted, and validated by computation that such waves with a wave front may be brought upon an offshore structure with proper initial conditions and numerically treated to yield nonlinear wave forces of the right order.

(6) Difficulties associated with the intersection points of the body and the wave-surface has been pragmatically resolved by the interpolation on the free-surface and avoiding the singularity at the intersection point. This may not be justified for the local phenomena, but may be applicable for global force evaluations.

## REFERENCE

- [1] Isaacson, M de St. Q., "Nonlinear Wave Forces on Large Offshore Structures", Coastal/Ocean Engineering Report, University of British Columbia, 1981.
- [2] Lin, V. -M., Newman, J.M. and Yue, D.K., "Nonlinear Forced Motions of Floating Bodies", Proc. 15th ONR/SNH, Hamburg, Sept. 2-7, 1984.
- [3] Liu, Y.Z. and Yang, C., "Nonlinear Radiation Problem of An Axisymmetric Cylinder", Advances in Hydrodynamics, China. Vol.2, NO.1, 1987.

[4] Orlanski, L., "A Simple Boundary Condition For Unbounded Hyperbolic Flows", J. Computational Physics, 21, 1976.

[5] Isaacson, M. de St. Q., "Nonlinear wave Effects on Fixed and Floating Bodies", J. Fluid Mech., Vol.20: pp 267-281, 1982.

## DISCUSSION

T. Francis Ogilvie  
Massachusetts Institute of Technology, USA

You use the Orlanski condition for closure of the computational domain. This is a condition for hyperbolic systems. Please explain how you are able to use it in the water-wave problem, which is elliptical.

## AUTHORS' REPLY

Orlanski's condition is a numerical condition on the open boundary. So far, the availability of Orlanski's condition cannot be proved in mathematics, however, it is useful in numerical computation.

## DISCUSSION

Choung M. Lee  
Pohang Institute of Science and Technology, Korea

We always find difficulty in determining the point of intersection of the free surface on a body under motion. It is mentioned in your paper the free-surface intersection was obtained by interpolation of the free-surface to the body. Would it not violate the kinematic body boundary condition at the intersection point? Since your attempt is to obtain an exact solution for nonlinear body-wave interaction, the problem of finding the intersecting point should be addressed more clearly.

## AUTHORS' REPLY

As mentioned in the first section of this paper, the singularity of intersection point is a local problem. In our paper, we adopt a pragmatic treatment to local singularity. We have tested many methods for treating the intersection points in 3-D problem, the direct interpolation method may be the best one in these methods from our numerical test; it keeps the computation robust and efficient.

# The Influence of a Slowly Oscillating Movement on the Velocity Potential

C. van der Stoep, A.J. Hermans  
(Delft University of Technology, The Netherlands)

## Abstract

The central problem in this paper will be the determination and calculation of the influence of a slowly oscillating movement on the velocity potential. This is for instance important when you want to calculate the *dynamic swell-up* and the *added resistance* of a sailing ship. Two boundary integral equations for the velocity potential are derived to solve the steady and the insteedy problem. It will be shown that the potential can be represented as a area source singularity distribution over the ship hull and a source line distribution on the ship waterline. The equations that have been obtained in this way can be solved using an iterative scheme. First and second order solutions of the equations have been obtained.

## Nomenclature.

B	Beam at midship
$\Sigma$	Wetted surface area at rest
U	Ship speed
$C_B$	Ship block coefficient
g	Gravitational acceleration
p	Pressure
$\eta(\underline{x})$	Wave elevation along hull
$\eta_0$	steady wave elevation
$\eta_1$	unsteady wave elevation
$z_a$	Oscillator amplitude
L	Length at water line
H	Draft at midship
x,y,z	coordinate system moving with velocity U
x	in forward direction
z	vertically upward
$\underline{n}$	unit vector normal to $\Sigma$ in outward direction
$F_n$	Froude number( $U/\sqrt{gL}$ )
G	Green function
F.S.	Free Surface
$\bar{\phi}$	steady wave potential
$\tilde{\phi}$	unsteady wave potential
$\Phi$	total potential
$\underline{a}$	motion vector
$\omega$	frequency of motion
$\gamma$	dipole strength
$\sigma$	source strength
$T_n$	Chebychev polynomial of order n
$J_n, K_n, Y_n$	Bessel functions

## 1 Introduction

The estimation of a ship speed and power was usually based on still water performance. Assuming a potential flow the stationary problem of calculating the ship wave resistance is described by the Laplace equation and the conditions on the ship hull and the free surface. Numerous computer programs have been written to tackle this problem.

In order to be able to predict ship performance in seaway it is also desirable to be able to calculate the instationary problem of a sailing ship. For example a ship sailing in waves or an oscillating vessel. In preliminary design studies the use of a fast computer algorithm could help to assist the traditional model testing methods. The central problem in this paper will be the calculation of the added resistance and the dynamic swell-up of a ship when it is slowly oscillating. Dynamic swell-up is the effect of water being pushed up around a bow higher than can be accounted for by considering heaving, pitching and incident wave alone (see also figure 1.1). The swell-up is given by the quotient of  $\eta_0$ (amplitude of relative motion) and  $z_a$ (oscillator amplitude).

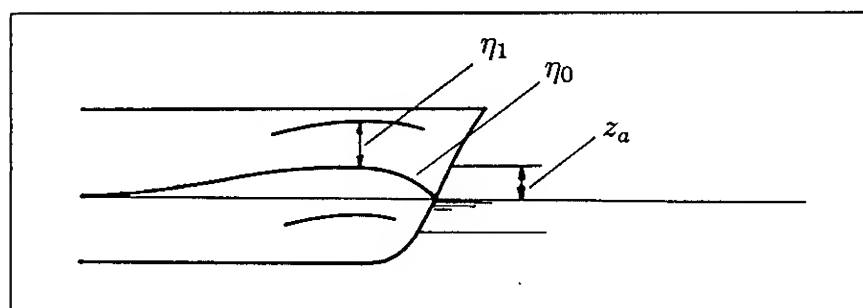


Figure 1.1: The dynamic 'swell-up'.

Some work in this area has been done by Blok ([1]) and Tasaki ([2]). Tasaki was the first to introduce the term swell-up and on the basis of experiments obtained some sort of empirical formula for the calculation of the dynamic swell-up, when the wave frequency, ship speed and ship block coefficient  $C_B$  are between some give limits.

The problem will be divided into several subproblems:

- The treatment of the free surface condition.
- The treatment of the body boundary condition.

- The numerical treatment of the associated Green function.
- The numerical solution of the resultant integral equation.
- The calculation of the added resistance.

Every subproblem will be dealt with in this paper. The research is carried out in cooperation with MARIN.

## 2 Mathematical formulation

### 2.1 Introduction

We consider an object moving horizontally with forward speed  $U$  in an infinitely extended fluid. Viewed from an inertial frame  $(x, y, z)$  attached to the ship, there is an incident stream of velocity  $U$  in the positive direction. The formulation will be done in a Cartesian coordinate system moving with the object. With the  $x$  coordinate in forward direction and the  $z$  coordinate vertically upward.

The free surface elevation  $\eta$  will be given by:

$$z = \eta(x, y) \quad (2.1)$$

The total velocity potential  $\Phi_{total}$  can be split in a *steady* and an *unsteady* part:

$$\Phi_{total}(x, y, z, t) = \underbrace{Ux + \bar{\phi}(x, y, z)}_{steady} + \underbrace{\tilde{\phi}(x, y, z, t)}_{unsteady} \quad (2.2)$$

We are especially interested in the influence of the steady part  $\bar{\phi}$  on the unsteady part  $\tilde{\phi}$ .

$\Phi_{total}$  has to satisfy the following three conditions:

$$\Delta \Phi_{total} = 0 \quad \text{outside the object, } z \leq \eta(x, y) \quad (2.3)$$

At the free surface  $\eta(x, y)$  we have the dynamic and the kinematic boundary conditions:

$$\begin{cases} \frac{\partial \Phi}{\partial t} + \frac{1}{2} \left( \frac{\partial \Phi}{\partial x}^2 + \frac{\partial \Phi}{\partial y}^2 + \frac{\partial \Phi}{\partial z}^2 \right) + gz = 0 & \text{at } z = \eta \\ \frac{\partial \Phi}{\partial z} - \frac{\partial \eta}{\partial t} - \frac{\partial \Phi}{\partial x} \cdot \frac{\partial \eta}{\partial x} - \frac{\partial \Phi}{\partial y} \cdot \frac{\partial \eta}{\partial y} = 0 & \text{at } z = \eta \end{cases} \quad (2.4)$$

and a boundary condition on the ship hull:

$$\frac{\partial \Phi}{\partial n} = V_n, \quad \text{at } \Sigma \quad (2.5)$$

The main difficulty in this problem is to find a solution of the Laplace equation using boundary conditions at a free surface which is still unknown. Various attempts to solve this problem have been done by Brandsma ([3] + [4]), Baba [5], Sakamoto [6], Hermans [7] and many others. Most of them are using some sort of expansion in a small parameter usually the small ship velocity or some sort of ship slenderness parameter.

To derive an approximating solution of the problem we continue by linearizing the free surface condition (2.4) (as will be done in the next section) and the body boundary condition (2.5).

### 2.2 Linearizing the free surface condition

The free surface condition consists of two parts:

The dynamic boundary condition:

$$\frac{\partial \Phi}{\partial t} + \frac{1}{2} \nabla \Phi \cdot \nabla \Phi + gz = \frac{1}{2} U^2 \quad \text{at } z = \eta(x, y) \quad (2.6)$$

and the kinematic boundary condition:

$$\frac{\partial \Phi}{\partial z} - \frac{\partial \eta}{\partial t} - \frac{\partial \Phi}{\partial x} \cdot \frac{\partial \eta}{\partial x} - \frac{\partial \Phi}{\partial y} \cdot \frac{\partial \eta}{\partial y} = 0 \quad \text{at } z = \eta(x, y) \quad (2.7)$$

One way of dealing with this problem could be neglecting the higher order terms in  $\Phi$ . Then equation (2.7) leads to:

$$\frac{\partial \Phi}{\partial z} = \frac{\partial \eta}{\partial t} \quad (2.8)$$

and the linearized free surface height will be given by:

$$\eta = -\frac{1}{g} \frac{\partial \Phi}{\partial t} \quad (2.9)$$

combining equations (2.8) and (2.9) leads to the well known free surface condition:

$$\frac{\partial^2 \Phi}{\partial t^2} + g \frac{\partial \Phi}{\partial z} = 0 \quad \text{at } z = 0 \quad (2.10)$$

In this paper we will obtain an asymptotic solution for the free surface condition. Let  $|\epsilon| \ll 1$  and expand the free surface elevation around a 'known' solution  $\eta = \eta_0$ :

$$\eta = \eta_0 + \epsilon \eta_1 + \dots \quad (2.11)$$

Denote the total velocity potential by  $\Phi_{total}$ , and split this total potential in a steady and an unsteady part as follows:

$$\Phi_{total}(x, y, z, t) = Ux + \bar{\phi}(x, y, z) + \epsilon \tilde{\phi}(x, y, z, t) \quad (2.12)$$

All the terms in the free surface condition (2.6) and (2.7) have to be expanded. This leads to the following free surface condition:

For the first order problem (the steady state solution):

$$\boxed{\bar{\phi}_z + \frac{1}{2g} \nabla(Ux + \bar{\phi}) \cdot \nabla[\nabla(Ux + \bar{\phi}) \cdot \nabla(Ux + \bar{\phi})] = 0} \quad \text{at } z = \eta_0 \quad (2.13)$$

and for the second order problem (the unsteady state solution):

$$\boxed{\begin{aligned} &g(\tilde{\phi}_z - \tilde{\phi}_x \eta_{0x} - \tilde{\phi}_y \eta_{0y} - \tilde{\phi}_{zz}(\tilde{\phi}_t + \nabla(Ux + \bar{\phi}) \cdot \nabla \tilde{\phi}) + \\ &2\nabla(Ux + \bar{\phi}) \cdot \nabla \tilde{\phi}_t + \nabla(Ux + \bar{\phi}) \cdot \nabla[\nabla(Ux + \bar{\phi}) \cdot \nabla \tilde{\phi}] + \\ &\tilde{\phi}_{tt} = 0 \end{aligned}} \quad \text{at } z = \eta_0 \quad (2.14)$$

### 2.3 The body boundary condition

The body boundary condition for the stationary potential reads as:

$$\frac{\partial \Phi}{\partial n} = V_n \quad \text{at the body } \Sigma \quad (2.15)$$

or equivalently:

$$\vec{n} \cdot \nabla(Ux + \bar{\phi}) = 0 \quad \text{at } \Sigma \quad (2.16)$$

And now the calculation for the instationary part (see also for instance Timman [8] et al.). The displacement of the ship hull is given by:

$$\underline{x} - \underline{x}' = \epsilon \underline{\alpha}(x, t) \quad (2.17)$$

where  $\underline{x}$  denotes the coordinate system moving with velocity  $U$ , and  $\underline{x}'$  denotes the coordinate system fixed to the ship. The body boundary condition states that: *at the momentary position of the hull, the normal velocity of the fluid is equal to the normal velocity of the hull.* Expansion of  $\Phi$  round the rest position with a small parameter  $\epsilon \underline{\alpha}$  yields:

$$\Phi_{\text{momentary}} = \Phi_{\text{total}} + \epsilon \underline{\alpha} \cdot \nabla \Phi_{\text{total}} \quad (2.18)$$

so for the body boundary condition this leads to:

$$\vec{n} \cdot \nabla(\Phi_{\text{total}} + \epsilon \underline{\alpha} \cdot \nabla \Phi_{\text{total}}) = \epsilon \vec{n} \cdot \frac{\partial \underline{\alpha}}{\partial t} \quad (2.19)$$

combining equation (2.16) and (2.19) leads to:

$$\frac{\partial \tilde{\phi}}{\partial n} = \vec{n} \cdot \left( \frac{\partial \underline{\alpha}}{\partial t} - \nabla(\underline{\alpha} \cdot \nabla(Ux + \bar{\phi})) \right) \quad (2.20)$$

now using the assumption of  $\underline{\alpha}(\underline{x}, t)$  and  $\tilde{\phi}(\underline{x}, t)$  to be oscillatory:

$$\begin{aligned} \underline{\alpha}(\underline{x}, t) &= \underline{\alpha}(\underline{x}) \cdot e^{-i\omega t} \\ \tilde{\phi}(\underline{x}, t) &= \hat{\phi}(\underline{x}) \cdot e^{-i\omega t} \end{aligned} \quad (2.21)$$

this finally leads to the following body boundary condition:

$$\frac{\partial \hat{\phi}}{\partial n} = -\vec{n} \cdot (i\omega \underline{\alpha} + \nabla(\underline{\alpha} \cdot \nabla(Ux + \bar{\phi}))) \quad (2.22)$$

and free surface condition (2.14):

$$-\omega^2 \hat{\phi} - 2i\omega U \hat{\phi}_x + U^2 \hat{\phi}_{xx} + g \hat{\phi}_z = \mathcal{L}(U; \bar{\phi}) \{ \hat{\phi} \} \quad \text{at } z = \eta_0 \quad (2.23)$$

where  $\mathcal{L}(U; \bar{\phi})$  denotes a linear differential operator acting on  $\hat{\phi}$ .

## 3 The leading equations

### 3.1 Calculation of the singularity distributions

Introduction of a Green's function  $G$  and application of Green's theorem to the domain as can be seen in figure 3.1. The function  $G$  has to fulfill the following condition:

$$-\omega^2 G + 2i\omega U G_\xi + U^2 G_{\xi\xi} + g G_\zeta \quad \text{at } \zeta = 0 \quad (3.1)$$

with the function  $G$  written as:

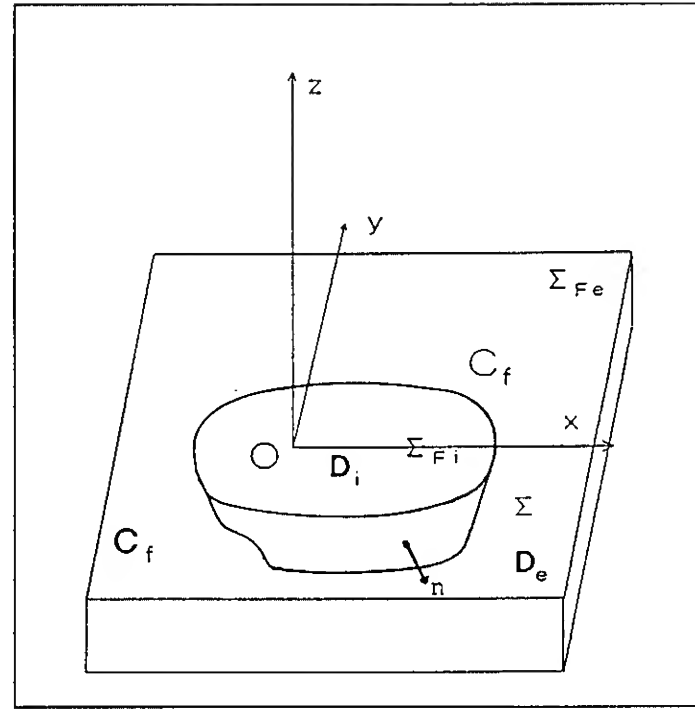


Figure 3.1: The mathematical domain.

$$G = \left( -\frac{1}{r} + \frac{1}{r_1} - \Psi(\underline{x}, \underline{\xi}; U) \right) \quad (3.2)$$

In the same way as Brard [9] we consider the following integral formulations:

$$I_E = \iint_{\Sigma_{F_e} + \Sigma_e + \Gamma} \left( \phi_e \frac{\partial G}{\partial n_e} - G \frac{\partial \phi_e}{\partial n_e} \right) dS \quad (3.3)$$

and

$$I_I = \iint_{\Sigma_{F_i} + \Sigma_i} \left( \phi_i \frac{\partial G}{\partial n_i} - G \frac{\partial \phi_i}{\partial n_i} \right) dS \quad (3.4)$$

then the following is valid:

$$I_E = \begin{cases} 4\pi \phi_e & x \in D_e \\ 0 & x \in D_i \end{cases} \quad (3.5)$$

$$I_I = \begin{cases} 4\pi \phi_i & x \in D_i \\ 0 & x \in D_e \end{cases} \quad (3.6)$$

At  $\Sigma_{F_i}$  and  $\Sigma_{F_e}$  the following equations (2.23) and (3.1) are valid:

$$\frac{\partial \phi}{\partial n} = \frac{1}{g} \{ \mathcal{L}(\phi) + \omega^2 \phi + 2i\omega U \frac{\partial \phi}{\partial x} - U^2 \frac{\partial^2 \phi}{\partial x^2} \} \quad (3.7)$$

$$\frac{\partial G}{\partial n} = \frac{1}{g} \{ \omega^2 G - 2i\omega U \frac{\partial G}{\partial x} - U^2 \frac{\partial^2 G}{\partial x^2} \} \quad (3.8)$$

Combining equations (3.7) and (3.8) leads for equation (3.3) to:

$$\begin{aligned} \left( \phi_e \frac{\partial G}{\partial n_e} - G \frac{\partial \phi_e}{\partial n_e} \right) &= \frac{\omega^2}{g} \phi_e G - \frac{2i\omega}{g} U \phi_e \frac{\partial G}{\partial x} \\ &\quad - \frac{U^2}{g} \phi_e \frac{\partial^2 G}{\partial x^2} - \frac{1}{g} \mathcal{L}(\phi) G \end{aligned}$$



$$\begin{aligned}
& - \frac{\omega^2}{g} \phi_e G - \frac{2i\omega}{g} U \frac{\partial \phi_e}{\partial x} G \\
& + \frac{U^2}{g} \frac{\partial^2 \phi_e}{\partial x^2} G \quad (3.9)
\end{aligned}$$

regrouping the expressions at the right hand side of equation (3.9) leads to the following formulation:

$$- \frac{2i\omega}{g} U \frac{\partial(\phi_e G)}{\partial x} + \frac{U^2}{g} \frac{\partial(\frac{\partial \phi_e}{\partial x} G - \phi_e \frac{\partial G}{\partial x})}{\partial x} - \frac{1}{g} \mathcal{L}(\phi_e) G \quad (3.10)$$

and almost the same for equation (3.4). The  $\Sigma_{F_e}$  part of equation (3.3) leads to:

$$\begin{aligned}
\iint_{\Sigma_{F_e}} (\phi_e \frac{\partial G}{\partial n_e} - G \frac{\partial \phi_e}{\partial n_e}) dS &= - \int_{C^\infty - C_f} \frac{2i\omega}{g} U \phi_e G dy \\
& - \int_{C^\infty - C_f} \frac{U^2}{g} (\frac{\partial \phi_e}{\partial x} G - \phi_e \frac{\partial G}{\partial x}) dy \\
& - \frac{1}{g} \iint_{\Sigma_{F_e}} \mathcal{L}(\phi_e) G dS \quad (3.11)
\end{aligned}$$

and for the  $\Sigma_{F_i}$  part:

$$\begin{aligned}
\iint_{\Sigma_{F_i}} (\phi_i \frac{\partial G}{\partial n_i} - G \frac{\partial \phi_i}{\partial n_i}) dS &= \int_{C_F} \frac{U^2}{g} (\frac{\partial \phi_i}{\partial x} G - \phi_i \frac{\partial G}{\partial x}) dy \\
& - \int_{C_f} \frac{2i\omega}{g} U \phi_i G dy \quad (3.12)
\end{aligned}$$

adding equations (3.11) and (3.12) results in (with  $\frac{\partial}{\partial n_i} = -\frac{\partial}{\partial n_e} = \frac{\partial}{\partial n}$ ):

$$\begin{aligned}
I_e + I_i &= \int_{\Sigma} (\frac{\partial \phi_e}{\partial n} - \frac{\partial \phi_i}{\partial n} G dS + \frac{2i\omega}{g} U \int_{C_f} (\phi_e - \phi_i) G dy \\
& + \frac{U^2}{g} \int_{C_f} (\frac{\partial \phi_i}{\partial x} - \frac{\partial \phi_e}{\partial x}) G dy + \frac{U^2}{g} \int_{C_f} (\phi_e - \phi_i) \frac{\partial G}{\partial x} dy \\
& - \iint_{\Sigma_{F_e}} \mathcal{L}(\phi_e) G dS - \frac{1}{g} \iint_{\Sigma_{F_i}} \mathcal{L}(\phi_i) G dS \\
& + \int_{\Sigma} (\phi_i - \phi_e) \frac{\partial G}{\partial n} dS \quad (3.13)
\end{aligned}$$

The source and vortex distribution are defined as:

$$\begin{aligned}
\gamma &= \phi_e - \phi_i \\
\sigma &= \frac{\partial \phi_i}{\partial n} - \frac{\partial \phi_e}{\partial n} \quad (3.14)
\end{aligned}$$

equation (3.13) will now transform into:

$$\begin{aligned}
& - \int_{\Sigma} \gamma(\xi) \frac{\partial G(x, \xi)}{\partial n} dS_\xi - \int_{\Sigma} \sigma(\xi) G(x, \xi) dS_\xi \\
& + \frac{2i\omega}{g} U \int_{C_f} \gamma(\xi) G(x, \xi) d\eta + \frac{U^2}{g} \int_{C_f} \gamma(\xi) \frac{\partial G(x, \xi)}{\partial x} d\eta
\end{aligned}$$

$$\begin{aligned}
& + \frac{U^2}{g} \int_{C_f} (-\alpha_t \frac{\partial \gamma}{\partial t} - \alpha_T \frac{\partial \gamma}{\partial T} + \alpha_n \sigma(\xi) G(x, \xi) d\eta \\
& - \frac{1}{g} \iint_{F.S.} \mathcal{L}(\phi) G(x, \xi) dS_\xi = 4\pi\phi(\underline{x}) \quad (3.15)
\end{aligned}$$

with:

$$\begin{aligned}
\alpha_t &= \cos(Ox, t) \\
\alpha_T &= \cos(Ox, T) \\
\alpha_n &= \cos(Ox, n) \quad (3.16)
\end{aligned}$$

with a choice of  $\gamma(\xi) \equiv 0$  the following expression will be obtained:

$$\begin{aligned}
4\pi\tilde{\phi}(\underline{x}) &= - \int_{\Sigma} \sigma(\xi) G(x, \xi) dS_\xi + \frac{U^2}{g} \int_{C_f} \alpha_n \sigma(\xi) G(x, \xi) d\eta \\
& + \frac{1}{g} \iint_{F.S.} \mathcal{L}(\hat{\phi}) G(x, \xi) dS_\xi \quad (3.17)
\end{aligned}$$

using the body boundary condition (2.22) we may obtain a description of the potential function  $\hat{\phi}$  by means of a source distribution of the following form:

$$\begin{aligned}
& - 4\pi\tilde{n} \cdot (i\omega\alpha + \nabla(\alpha \cdot \nabla(Ux + \bar{\phi}))) = -2\pi\sigma(x) \\
& - \int_{\Sigma} \sigma(\xi) \frac{\partial G(x, \xi)}{\partial n_x} dS_\xi + \frac{U^2}{g} \int_{C_f} \alpha_n \sigma(\xi) \frac{\partial G(x, \xi)}{\partial n_x} d\eta \\
& - \frac{1}{g} \iint_{F.S.} \mathcal{L}(\hat{\phi}) \frac{\partial G(x, \xi)}{\partial n_x} dS_\xi \quad (3.18)
\end{aligned}$$

**Remark:**

We consider the following potential  $\Phi$ :

$$\Phi = \iint_{\Sigma} \frac{\sigma}{r} dS \quad (3.19)$$

the following is valid (Kellogg [10]): if the density  $\sigma$  of the distribution on  $\Sigma$  is continuous at  $x$ , the normal derivative of the potential  $\Phi$  approaches limits as  $X$  approaches  $x$  along the normal to  $\Sigma$  at  $x$  from either side.

These limits are:

$$(\frac{\partial \Phi}{\partial n})_+ = -2\pi\sigma(x) + \iint_{\Sigma} \sigma(\xi) \frac{\partial 1/r}{\partial n} dS_\xi \quad (3.20)$$

$$(\frac{\partial \Phi}{\partial n})_- = +2\pi\sigma(x) + \iint_{\Sigma} \sigma(\xi) \frac{\partial 1/r}{\partial n} dS_\xi \quad (3.21)$$

So when using the  $\frac{1}{R}$  sources the resulting equations looks like:

$$+ 2\pi\sigma(x) - \iint_{\Sigma} \sigma \frac{\partial G(x, \xi)}{\partial n_x} dS_\xi + \dots = V_n \quad (3.22)$$

and when the  $-\frac{1}{R}$  sources are used (as in Brard [9]) the resulting equation transforms into:

$$-2\pi\sigma(x) - \iint_{\Sigma} \sigma \frac{\partial G(x, \xi)}{\partial n_x} dS_{\xi} + \dots = V_n \quad (3.23)$$

### 3.2 Calculation of source strength and potential function

We will use an expansion of  $\sigma$ ,  $\hat{\phi}$  and  $G$  in the small parameter  $\omega$ :

$$\begin{aligned} \sigma(\underline{x}) &= \sigma_0(\underline{x}) + \omega\sigma_1(\underline{x}) + \dots \\ \hat{\phi}(\underline{x}) &= \hat{\phi}_0(\underline{x}) + \omega\hat{\phi}_1(\underline{x}) + \dots \\ G(\underline{x}, \underline{\xi}) &= G_0(\underline{x}, \underline{\xi}) + \omega G_1(\underline{x}, \underline{\xi}) + \dots \end{aligned} \quad (3.24)$$

substitution of these expansions in equations (3.17) and (3.18) leads for the first order problem to:

$$\begin{aligned} -4\pi\underline{n} \cdot \nabla(\underline{\alpha} \cdot \nabla(U\underline{x} + \bar{\phi})) &= -2\pi\sigma_0(\underline{x}) \\ - \iint_{\Sigma} \sigma_0(\xi) \frac{\partial G_0(x, \xi)}{\partial n_x} dS_{\xi} + \frac{U^2}{g} \int_{C_f} \alpha_n \sigma_0(\xi) \frac{\partial G_0(x, \xi)}{\partial n_x} d\eta \\ - \frac{1}{g} \iint_{F.S.} \mathcal{L}_0(\hat{\phi}) \frac{\partial G_0(x, \xi)}{\partial n_x} dS_{\xi} \end{aligned} \quad (3.25)$$

and  $\hat{\phi}_0$  is given by:

$$\begin{aligned} -4\pi\hat{\phi}_0(\underline{x}) &= \\ - \iint_{\Sigma} \sigma_0(\xi) G_0(x, \xi) dS_{\xi} + \frac{U^2}{g} \int_{C_f} \alpha_n \sigma_0(\xi) G_0(x, \xi) d\eta \\ + \frac{1}{g} \iint_{F.S.} \mathcal{L}_0(\hat{\phi}) G_0(x, \xi) dS_{\xi} \end{aligned} \quad (3.26)$$

and for order  $\omega$ :

$$\begin{aligned} -4\pi\sigma_1(x) - \iint_{\Sigma} \sigma_1(\xi) \frac{\partial G_0(x, \xi)}{\partial n_x} dS_{\xi} + \frac{U^2}{g} \int_{C_f} \sigma_1(\xi) \frac{\partial G_0(x, \xi)}{\partial n_x} d\eta = \\ -4\pi\underline{n} \cdot i\underline{\alpha} + \iint_{\Sigma} \sigma_0(\xi) \frac{\partial \Psi_1(x, \xi)}{\partial n_x} dS_{\xi} - \frac{U^2}{g} \int_{C_f} \alpha_n \sigma_0(\xi) \frac{\partial \Psi_1(x, \xi)}{\partial n_x} d\eta \\ + \frac{1}{g} \iint_{F.S.} (\mathcal{L}_1(\hat{\phi}_0) + \mathcal{L}_0(\hat{\phi}_1) \frac{\partial G_0(x, \xi)}{\partial n_x} + \mathcal{L}_0(\hat{\phi}_0) \frac{\partial \Psi_1(x, \xi)}{\partial n_x}) dS_{\xi} \end{aligned} \quad (3.27)$$

and  $\hat{\phi}_1$  is given by:

$$\begin{aligned} -4\pi\hat{\phi}_1(\underline{x}) &= \\ - \iint_{\Sigma} (\sigma_0(\xi) \Psi_1(x, \xi) + \sigma_1(\xi) G_0(x, \xi)) dS_{\xi} \\ + \frac{U^2}{g} \int_{C_f} \alpha_n (\sigma_0(\xi) \Psi_1(x, \xi) + \sigma_1(\xi) G_0(x, \xi)) d\eta \\ - \frac{1}{g} \iint_{F.S.} (\mathcal{L}_0 + \mathcal{L}_1) G_0(x, \xi) + \mathcal{L}_0(\hat{\phi}_0) \Psi_1(x, \xi) dS_{\xi} \end{aligned} \quad (3.28)$$

### 3.3 The incorporation of the body boundary condition

The right hand side of equation (2.22) contains a vector  $\underline{\alpha}^k$ :

$$\underline{\alpha}^k(\underline{x}, t) = \begin{cases} \underline{\alpha}_k(t) i_k & k = 1, 2, 3 \\ \underline{\alpha}_k(t) (i_k \times \underline{x}) & k = 4, 5, 6 \end{cases} \quad (3.29)$$

here  $\underline{\alpha}_k(t)$  is the deflection in translational motion for  $k = 1, 2, 3$  and for  $k = 4, 5, 6$ ,  $\underline{\alpha}_k(t)$  represents rotation angles about the  $x_{k-3}$ -axis. So for example for  $k=1$  (surge) this looks like:

$$\frac{\partial \phi}{\partial n} = -i\omega n_1 - n_1 \bar{\phi}_{xx} - n_2 \bar{\phi}_{xy} - n_3 \bar{\phi}_{xz} \quad (3.30)$$

when  $\bar{\phi} \ll 1$  then the expansion (3.24) will start with leading order  $\omega$  ( $\sigma = \omega\sigma_1 + \omega^2\sigma_2 + \dots$ ) and then equation (3.25) will transform into:

$$-2\pi\sigma_1 - \iint_{\Sigma} (\sigma_1 \frac{\partial G_0}{\partial n} + \underbrace{\sigma_0}_{=0} \frac{\partial G_1}{\partial n}) + \dots = -n_1 \quad (3.31)$$

when  $\bar{\phi} = \mathcal{O}(1)$  then the expansion will start with leading order zero and equation (3.25) will look like:

$$-2\pi\sigma_0 - \iint_{\Sigma} \sigma_0 \frac{\partial G_0}{\partial n} + \dots = -n_1 \bar{\phi}_{xx} - n_2 \bar{\phi}_{xy} - n_3 \bar{\phi}_{xz} \quad (3.32)$$

it should also be noted that for the calculation of the *steady* wave potential  $\bar{\phi}$  the *same* matrix equation (3.25) as for the *unsteady* potential  $\hat{\phi}$  can be used! But of course the right hand side for  $\phi_n$  now looks like:

$$\frac{\partial \phi}{\partial n} = -n_1 U \quad (3.33)$$

### 3.4 Solution of the integral equation.

The solutions obtained by the singularity distributions are two *coupled* integral equations. Equations (3.25) and (3.26) will be solved using an iterative scheme. In this scheme use has been made of the numerical evaluation of the wave resistance Green function as done by Newman ([11] + [12]).

The numerical solution of equation (3.25) and (3.26) is carried out using a finite element method. The wetted body  $\Sigma$  is divided into  $N$  triangular panels and integration is done using a piecewise constant variation of the source strength  $\sigma(\xi)$ .

$$\iint_{\Sigma} = \sum_{j=1}^N \left( \iint_{e_j} \sigma(\xi) \frac{\partial G(\underline{x}, \underline{\xi})}{\partial n_x} dS_{\xi} \right) \quad (3.34)$$

In this way a set of  $N$  linear equations for the  $N$  source strengths  $\sigma_j$  is obtained. The Green function contains a  $1/R$ -term. The integration of these  $1/R$ -terms is carried out by a subroutine developed at MARIN [13] using analytical expressions of those integrals in order to avoid large errors from numerical integration for points close to the panel.

## 4 The Green's function

### 4.1 Behavior of the Green's function.

In Wehausen and Laitone [14] the Green's function of an oscillating source is given:

$$G(\underline{x}, \underline{\xi}; U) = -\frac{1}{r} + \frac{1}{r_1} - \Psi(\underline{x}, \underline{\xi}; U) \quad (4.1)$$

with the function  $\Psi$  given by:

$$\begin{aligned} \Psi(\underline{x}, \underline{\xi}; U) &= \frac{2g}{\pi} \int_0^{\frac{1}{2}\pi} \int_{L_1} F(\theta, k) d\theta dk \\ &+ \frac{2g}{\pi} \int_{\frac{1}{2}\pi}^{\pi} \int_{L_2} F(\theta, k) d\theta dk \end{aligned} \quad (4.2)$$

where  $F(\theta, k)$  is given by:

$$F(\theta, k) = \frac{k e^{k(z+\zeta+i(x-\xi)\cos\theta)} \cos(k(y-\eta)\sin\theta)}{gk - (\omega + kU\cos\theta)^2} \quad (4.3)$$

the paths  $L_1$  and  $L_2$  are given in figure 4.1.  
with  $k_1 - k_4$  the poles of  $F(\theta, k)$ :

$$\sqrt{gk_1} = \frac{1 - \sqrt{1 - 4\tau \cos\theta}}{2\tau \cos\theta} \omega \quad \theta \in (0, \frac{\pi}{2}) \quad (4.4)$$

$$\sqrt{gk_2} = \frac{1 + \sqrt{1 - 4\tau \cos\theta}}{2\tau \cos\theta} \omega \quad \theta \in (0, \frac{\pi}{2}) \quad (4.5)$$

$$\sqrt{gk_3} = \frac{1 - \sqrt{1 - 4\tau \cos\theta}}{2\tau \cos\theta} \omega \quad \theta \in (\frac{\pi}{2}, \pi) \quad (4.6)$$

$$\sqrt{gk_4} = -\frac{1 + \sqrt{1 - 4\tau \cos\theta}}{2\tau \cos\theta} \omega \quad \theta \in (\frac{\pi}{2}, \pi) \quad (4.7)$$

with  $\tau = \frac{U\omega}{g}$ , so  $\tau \ll 1$  this leads to:

$$\sqrt{gk_1} = \sqrt{gk_3} \simeq \omega + \mathcal{O}(\omega^2) \quad (4.8)$$

$$\sqrt{gk_2} = -\sqrt{gk_4} \simeq \frac{g}{U \cos\theta} + \omega + \mathcal{O}(\omega^2) \quad (4.9)$$

when for instance  $U \rightarrow 0$  then  $k_2$  and  $k_4$  will go to  $\infty$  and the paths  $L_1$  and  $L_2$  will coincide with there poles located at  $k_1 = k_3 = \omega^2/g$ . see also figure 4.2.

and when  $\omega \rightarrow 0$  the poles  $k_1$  and  $k_2$  will move to the origin and the paths  $L_1$  and  $L_2$  will look like as can be seen in figure 4.3.

However this is not correct, when  $\omega \rightarrow 0$  a factor  $k$  can be removed from the function  $F(\theta, k)$  and looks like this:

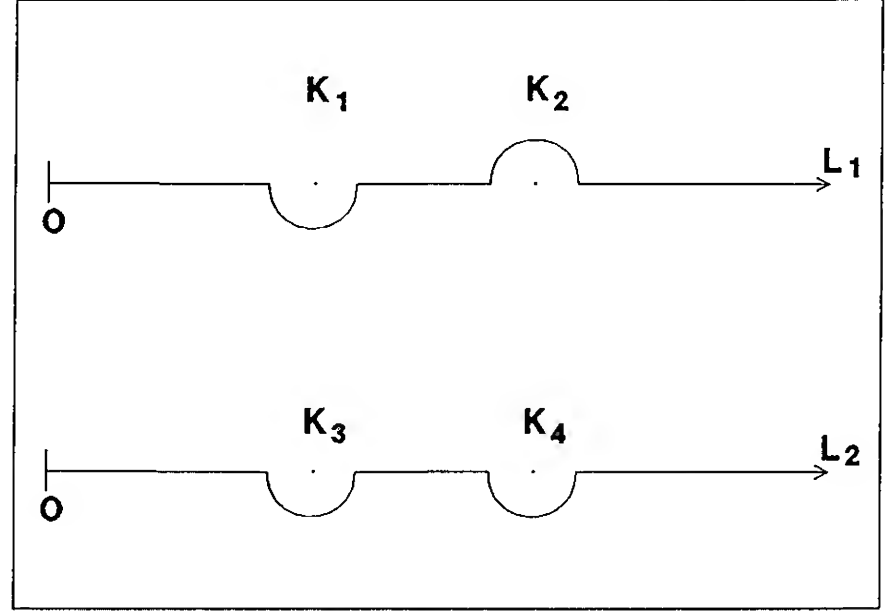


Figure 4.1: The contours  $L_1$  and  $L_2$ .

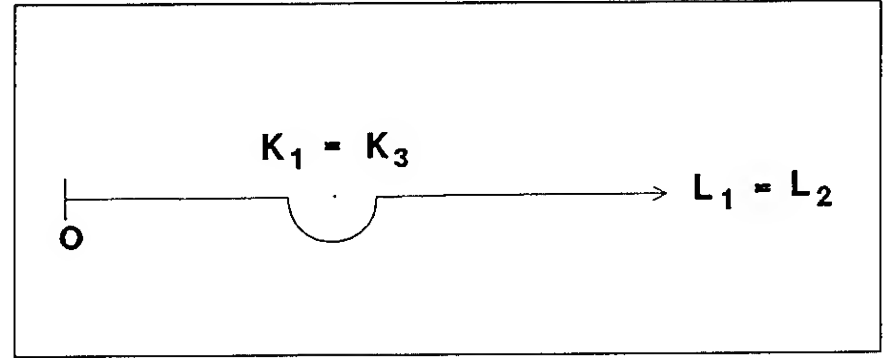


Figure 4.2: The location of the poles when  $U \rightarrow 0$ .

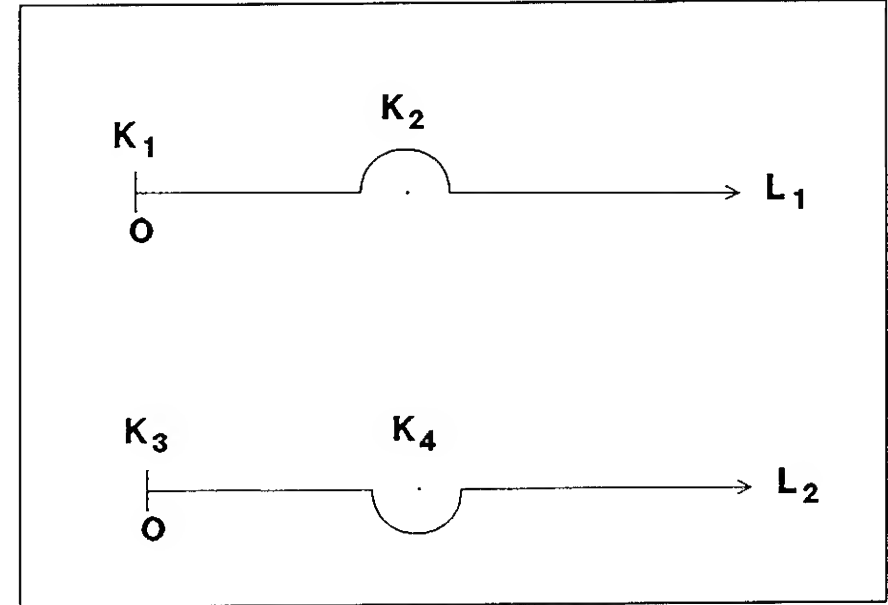


Figure 4.3: The location of the poles when  $\omega \rightarrow 0$ .

$$F_{\omega=0}(\theta, k) = \frac{e^{k(z+\zeta+i(x-\xi)\cos\theta)} \cos(k(y-\eta)\sin\theta)}{g - kU^2 \cos^2\theta} \quad (4.10)$$

with only one pole, located at  $k_2 = k_4 = \frac{g}{U^2 \cos^2\theta}$ .

## 4.2 Calculation of the Green function.

Newman ([11]+ [12]) has written two papers in the Journal of Ship research about the evaluation of the wave resistance Green function: one of the calculation of the double integral and one for the calculation of the single integral on the centerplane. The Green function is written in the following form (see Wehausen and Laitone [14]):

$$G = \frac{1}{R_0} - \frac{1}{R} - \frac{4}{\pi} \int_0^{\frac{1}{2}\pi} \int_0^{\infty} \frac{e^{-kz} \cos(kx \cos \theta) \cos(ky \sin \theta)}{k \cos^2 \theta - 1} dk d\theta - 4 \int_0^{\frac{1}{2}\pi} e^{-z \sec^2 \theta} \sin(x \sec \theta) \cos(y \sec^2 \theta \sin \theta) \sec^2 \theta d\theta \quad (4.11)$$

The quantities are defined as can be seen in figure 4.4.

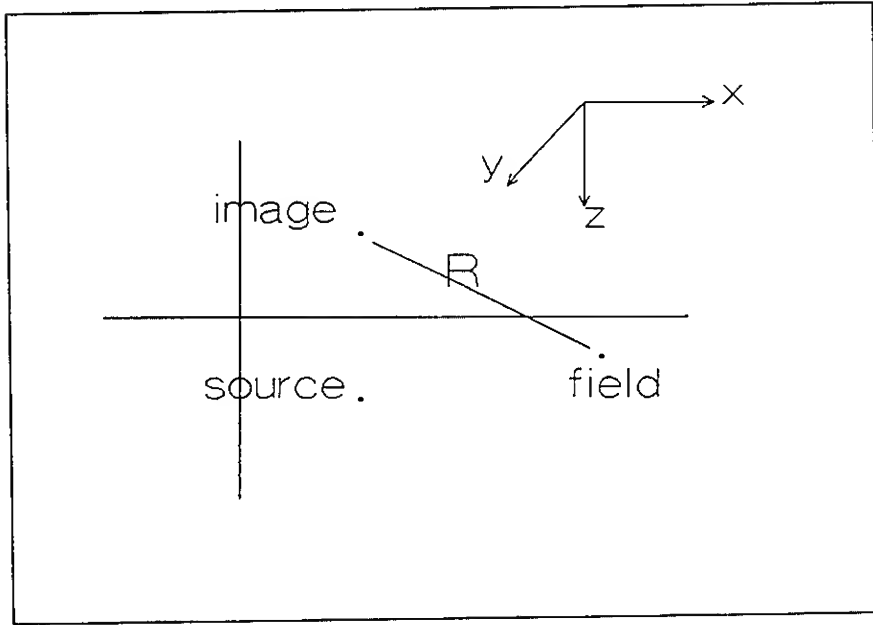


Figure 4.4: Location of field-, source- and image point.

with  $R = \sqrt{x^2 + y^2 + z^2}$ .

As has been done by Newman this integral can be split in a *Double* and a *Single* integral as follows:

$$Double = \frac{2}{\pi} \int_{-\frac{1}{2}\pi}^{+\frac{1}{2}\pi} \int_0^{\infty} \cos \psi \frac{e^{-kz + ik|x| \sec \psi + ky \tan \psi}}{k - \cos^2 \psi + i\epsilon} dk d\psi \quad (4.12)$$

$$Single = 4iH(-x) \int_{-\frac{1}{2}\pi}^{+\frac{1}{2}\pi} \sec^2 \theta e^{-z \sec^2 \theta + ix \sec \theta + iy \sec^2 \theta \sin \theta} d\theta \quad (4.13)$$

### 4.2.1 Double integral

The double integral as given by equation (4.12) will be approximated by Chebychev polynomials as done by Newman. In order to approximate a function  $f$  of one variable  $x$  in the normalized range  $[-1, +1]$  the Chebychev polynomial of order  $n$  is defined by:

$$T_n(x) = \cos(n \arccos x) \quad -1 \leq x \leq +1 \quad (4.14)$$

so the function  $f(x)$  is approximated by:

$$f(x) = \sum_{m=0}^N c_m T_m(x) \quad (4.15)$$

The coefficients  $c_m$  can be found according to:

$$c_m = \frac{\epsilon_m}{N} \sum_{n=0}^N {}'' f(x_n) T_m(x_n) \quad (4.16)$$

with  $\epsilon_0 = 1, \epsilon_m = 2$ , the double prime indicates that the first and the last terms in this summation are multiplied by  $\frac{1}{2}$ . The coordinates  $x_n$  are given by:

$$x_n = \cos\left(\frac{n\pi}{N}\right) \quad (4.17)$$

(see Fox and Parker [15])

For the 3D-case the situation is completely equivalent. In equation (4.12) logarithmic singularities are present when  $R = 0$ . These singularities must be subtracted and approximated first in order to improve convergence of the approximation. The final approximation is given by:

$$D \simeq S + \sum_{i=0}^{16} \sum_{j=0}^{16} \sum_{k=0}^8 C_{ijk} T_i[f(R)] T_j\left(-1 + \frac{4}{\pi}\theta\right) T_{2k}\left(\frac{2}{\pi}\alpha\right) \quad (4.18)$$

The function  $f(R)$  is defined so as to transform the interval  $(0, \infty)$  into  $(-1, +1)$  see figure 4.5.

$\alpha$  and  $\theta$  are defined as:

$$\begin{aligned} x &= R \sin \theta \\ z + iy &= R \cos \theta e^{i\alpha} = \rho e^{i\alpha} \end{aligned} \quad (4.19)$$

$T_i$ ,  $T_j$  and  $T_{2k}$  are Chebychev polynomials.  $S$  is the logarithmic part of the double integral. The Chebychev coefficients  $C_{ijk}$  are calculated and tabulated by Newman. Also the differentiated Green function has to be evaluated, which contains terms like  $\partial G(x, \xi)/\partial n_x$  (see equation (3.25) and

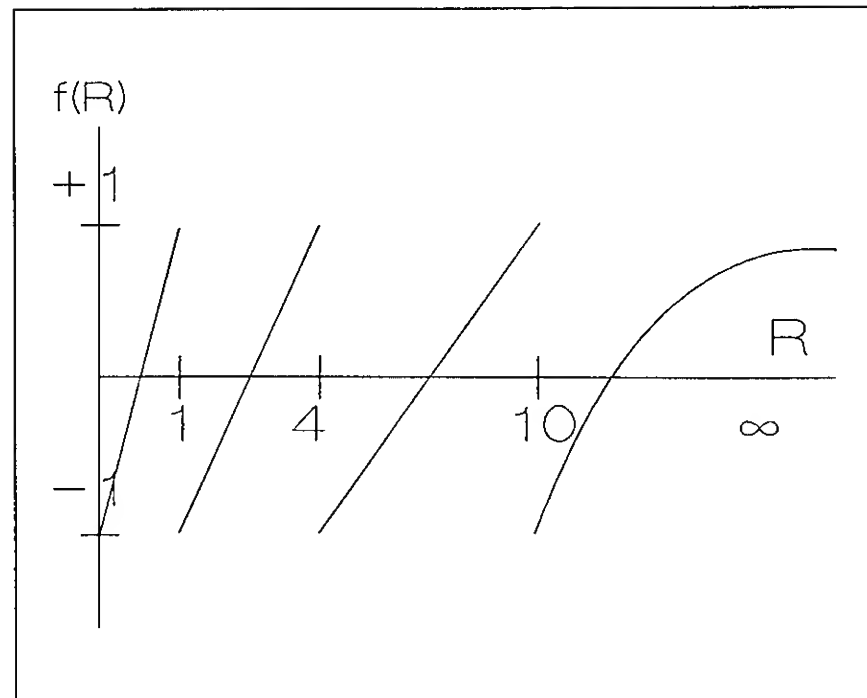


Figure 4.5: The transformation function  $f(R)$ .

(3.27)). Each part of the expansion (4.18) has to be differentiated and evaluated analytically. The following terms have to be evaluated:

$$\frac{\partial D}{\partial x} = A \cdot \frac{\partial D}{\partial \alpha} \quad (4.20)$$

with the transformation matrix A given by:

$$A = \begin{pmatrix} \frac{\partial \theta}{\partial x} & \frac{\partial \alpha}{\partial x} & \frac{\partial R}{\partial x} \\ \frac{\partial \theta}{\partial y} & \frac{\partial \alpha}{\partial y} & \frac{\partial R}{\partial y} \\ \frac{\partial \theta}{\partial z} & \frac{\partial \alpha}{\partial z} & \frac{\partial R}{\partial z} \end{pmatrix} \quad (4.21)$$

and also for the singular part S. For example the next figure 4.6 is obtained. The singular character is well shown here.

#### 4.2.2 Single integral

The single integral as given by equation (4.13) is evaluated by Newman at the *centerplane*, i.e. a special case where the source and field point are in the same longitudinal plane. This is especially important when analyzing *thin ships*. The

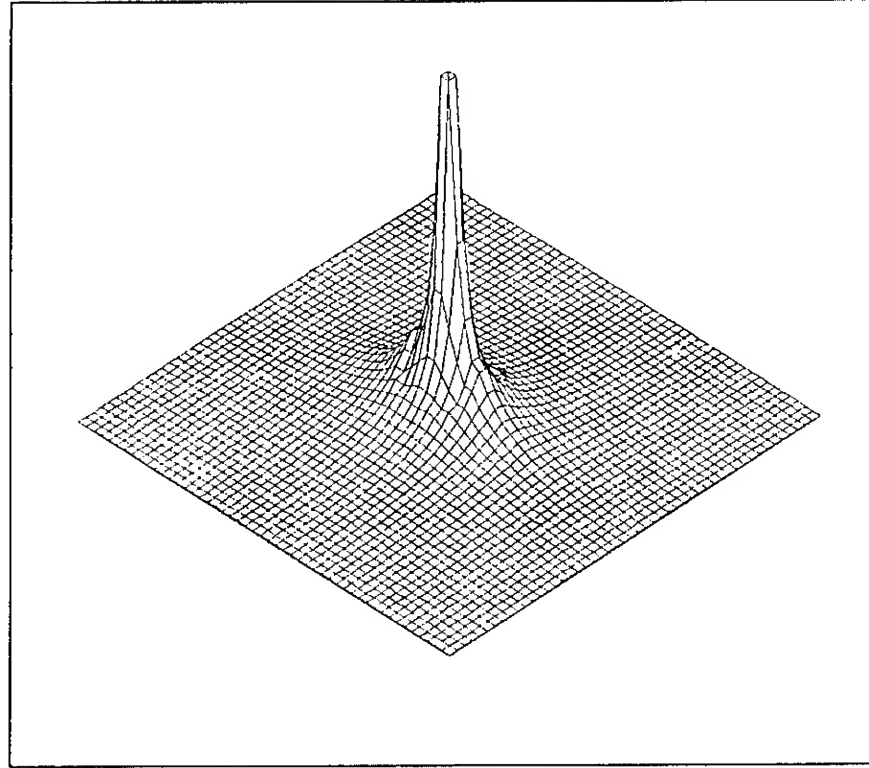


Figure 4.6: Function plot of the Double integral.

case  $y \neq 0$  will be dealt with later. For instance with the use of Padé approximations. The centerplane integral looks like this:

$$S(x, y, z)|_{y=0} = -8H(-x) \int_0^{\frac{1}{2}\pi} \sec^2 \theta e^{-z \sec^2 \theta} \sin(x \sec \theta) d\theta \quad (4.22)$$

In each of the different x-z regions (see figure 4.7), the integral will be approximated differently.

**region A:** (small z) an expansion involving differentiated Bessel functions of the second kind:

$$S \simeq \frac{1}{\sqrt{z}} F(\xi) - \sum_{n=0}^{\infty} \frac{1}{n!} z^n \frac{d^{2n}}{dx^{2n}} \left[ \frac{\pi}{2} Y_1(x) + \frac{1}{x} \right] \quad (4.23)$$

where  $Y_1(x)$  denotes the Bessel function of the second kind,  $\xi$  equals  $\frac{1}{2} \frac{x}{\sqrt{z}}$  and  $F(\xi)$  Dawson's integral:

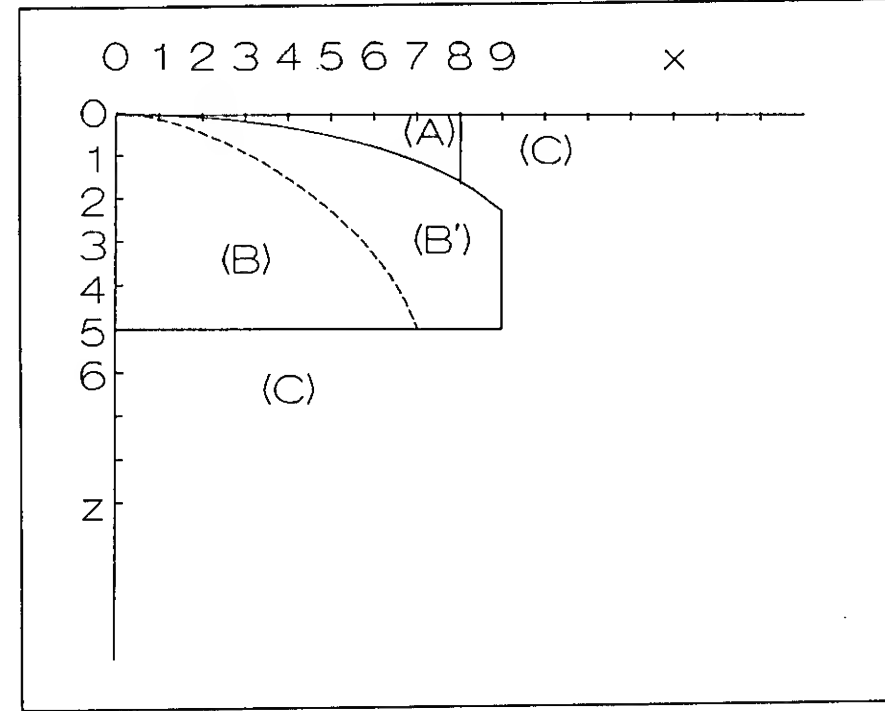


Figure 4.7: Domains for the approximation of the single integral.

$$F(x) = e^{-x^2} \int_0^x e^{t^2} dt \quad 0 \leq x < \infty \quad (4.24)$$

**region B:** an expansion in Neumann series, products of Bessel functions of the first kind and modified Bessel functions of the second kind:

$$S = \frac{1}{2} e^{-\frac{1}{2}z} \sum_{n=0}^{\infty} (-1)^n J_{2n+1}(x) \left[ K_n\left(\frac{1}{2}z\right) + K_{n+1}\left(\frac{1}{2}z\right) \right] \quad (4.25)$$

where  $J_n(x)$  denotes the Bessel function of the first kind and  $K_n(z)$  the modified Bessel function of the second kind.

**Region C:** large distances from the origin, steepest-descent expansion. The final expansion looks like this:

$$S \simeq -\frac{1}{2} i e^{h(0)+i\delta} \sum_{n=0}^{\infty} (2n+1) B_n \left(\frac{2}{\rho}\right)^{n+\frac{1}{2}} (\beta + i\alpha)^n \Gamma\left(n + \frac{1}{2}\right) \quad (4.26)$$

where only the coefficient  $B_n$  has to be evaluated. For all the expansions in the different domains (A)-(C) the differentiated Green's function has to be evaluated. An example for the Green function can be seen in figure 4.8. The wave character is well observed here.

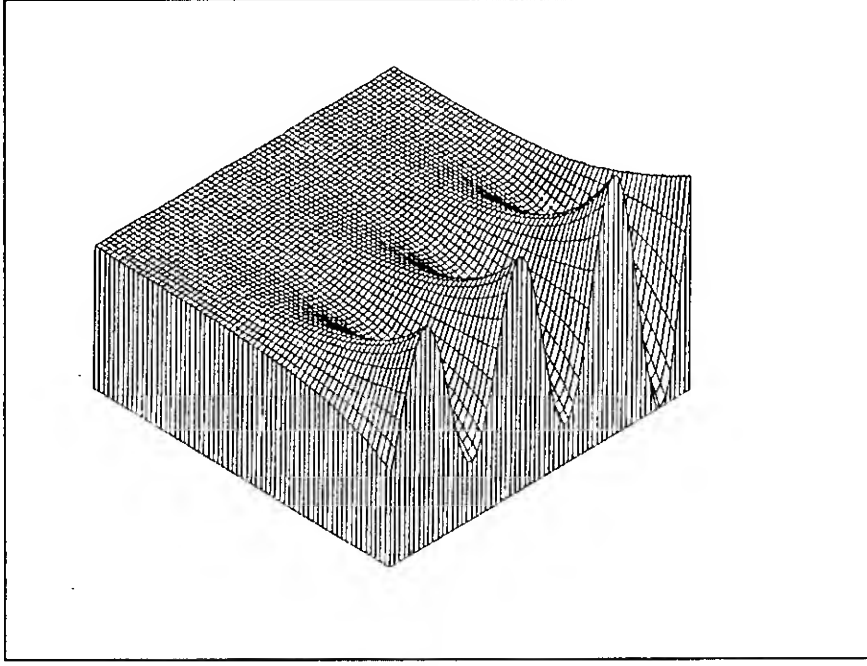


Figure 4.8: The Single integral at  $y \equiv 0$ .

## 5 Padé Approximations.

### 5.1 Introduction

The basis for the Padé approximation technique is the *formal Taylor series expansion*. From this basis a Padé approximation can be found. It is also possible for a Taylor expansion to be divergent and the Padé expansion to be convergent and also vice versa. For instance the Taylor expansion of the exponential function:

$$e^x = \sum_{n=0}^{\infty} \frac{x^n}{n!} = 1 + x + \frac{1}{2}x^2 + \frac{1}{6}x^3 + \dots \quad r_c = \infty \quad (5.1)$$

and for instance the Euler function:

$$E(x) = \int_0^{\infty} \frac{e^{-t}}{1+xt} dt = 1 - x + 2x^2 - 6x^3 + \dots \quad r_c = 0 \quad (5.2)$$

The idea of Padé expansion is to approximate the function by a rational function of the following form:

**Definition:** (see Baker [16]+[17]) We denote the L,M Padé approximant of  $f(x)$  by:

$$[L/M] = \frac{P_L(x)}{Q_M(x)} \quad (5.3)$$

where  $P_L(x)$  is a polynomial of degree at most L and  $Q_M(x)$  is a polynomial of degree at most M. The formal power series of  $f(x)$  reads as:

$$f(x) = \sum_{i=0}^{\infty} a_i x^i \quad (5.4)$$

When we require:

$$f(x) - [L/M] = \mathcal{O}(x^{L+M+1}) \quad (5.5)$$

Then the coefficients of  $P_L$  and  $Q_M$  can be found according to the following scheme (Baker):

$$\begin{array}{rclcl} a_0 & & & & = p_0 \\ a_1 & + & a_0 q_1 & & = p_1 \\ a_2 & + & a_1 q_1 & + & a_0 q_2 & = p_2 \\ \vdots & & & & \vdots \\ a_l & + & a_{l-1} q_1 & + & \dots & + a_0 q_l & = p_l \\ a_{l+1} & + & a_l q_1 & + & \dots & + a_{l-m+1} q_m & = 0 \\ \vdots & & & & \vdots \\ a_{l+m} & + & a_{l+m-1} q_1 & + & \dots & + a_l q_m & = 0 \end{array} \quad (5.6)$$

$$a_n \equiv 0 \quad n < 0$$

$$q_1 = 1$$

$$q_j \equiv 0 \quad j > M$$

for instance the  $[1/1]$  approximant for  $e^x$  reads as:

$$e^x \simeq \frac{2+x}{2-x} \quad (5.7)$$

inevitable a pole occurs at  $x = 2$ . So the Padé approximants seems worse here.

The Euler function evaluated at  $x = 1$  is wildly oscillating (when using Taylor expansion). The answer however for  $E(1)$  is known:  $E(1) \simeq 0.5963$ . The Taylor expansion never reaches this value. The Padé approximants however do. The  $[2/2]$  approximant reads as:

$$[2/2](x) = \frac{1+5x+2x^2}{1+6x+6x^2} \quad (5.8)$$

So  $E(1) \simeq 0.6154$ , only *five* Taylor terms have been used to get this accuracy. The Taylor expansion leads to the result:

$$Taylor_5(1) = 20. \quad (5.9)$$

The  $[6/6](x)$  approximant is even better:  $E(1) \simeq 0.5968$ . So Padé approximant could lead to valuable results when Taylor expansion fails (see also van Gemert [18]). In the next paragraph use will be made of this when evaluating the single integral at  $y \neq 0$ .

### 5.2 Padé approximations in the single integral

The single integral to be approximated is given by equation (4.13) repeated here:

$$Single = 4iH(-x) \int_{-\frac{1}{2}\pi}^{+\frac{1}{2}\pi} \sec^2 \theta e^{-z \sec^2 \theta + ix \sec \theta + i|y| \sec^2 \theta \sin \theta} d\theta \quad (5.10)$$

the real part will be used:

$$-8H(-x) \int_0^{\frac{1}{2}\pi} \sec^2 \theta e^{-z \sec^2 \theta} \sin(x \sec \theta) \cos(y \sec^2 \theta \sin \theta) d\theta \quad (5.11)$$

wich will be denoted by:

$$-8H(-x) f(x, y, z) \quad (5.12)$$



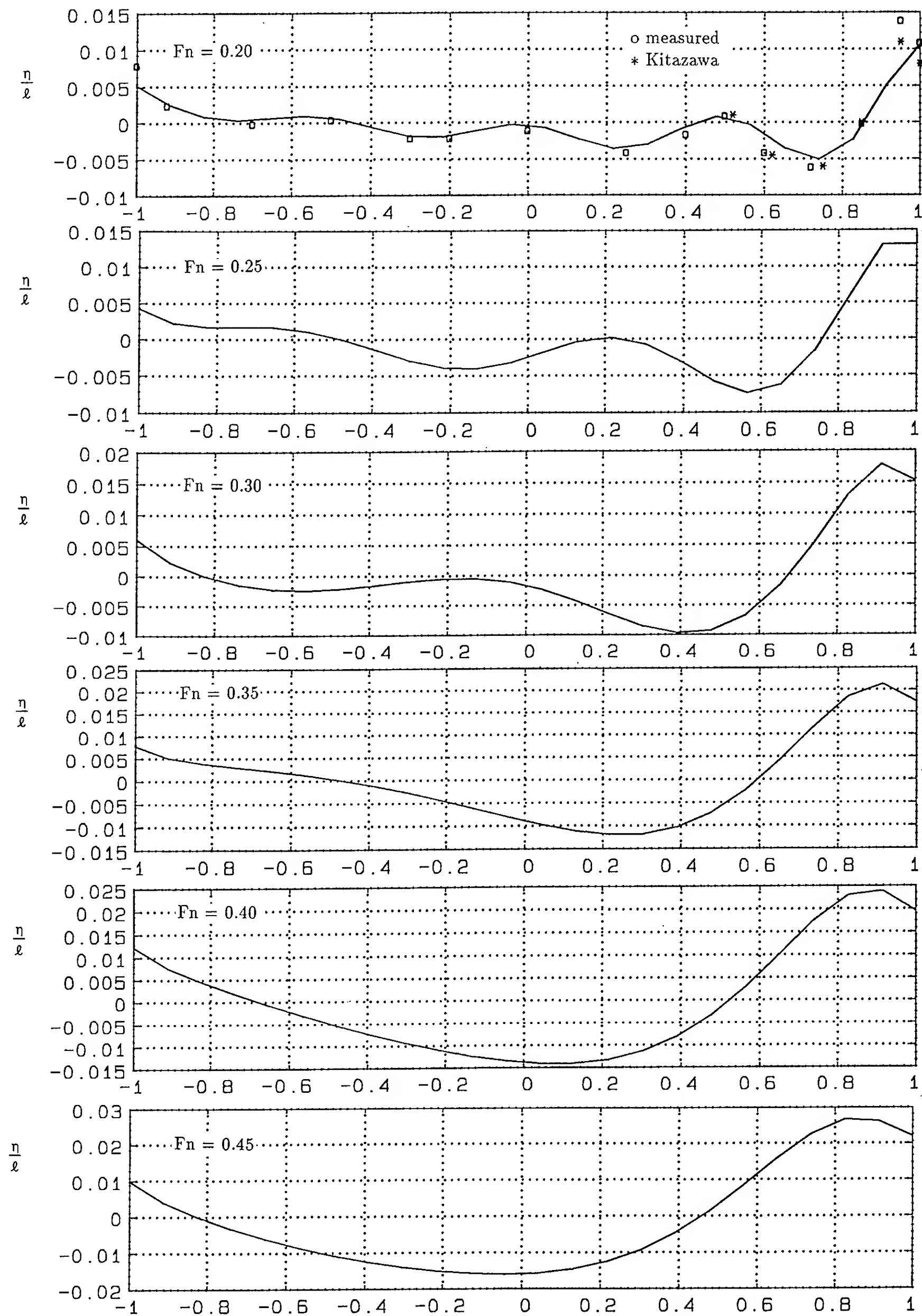


Figure 6.3: Hull side wave profiles of WIGLEY.

changing of variable to  $s = \sec \theta$  leads to:

$$f(x, y, z) = \int_1^\infty \frac{se^{-zs^2}}{\sqrt{s^2 - 1}} \sin(sx) \cos(ys\sqrt{s^2 - 1}) ds \quad (5.13)$$

Taylor expansion of  $f(x, y, z)$  leads to:

$$\begin{aligned} f(x, y, z) &= f(x, 0, z)|_{y=0} + y \frac{\partial f(x, y, z)}{\partial y} \Big|_{y=0} \\ &+ \frac{1}{2} y^2 \frac{\partial^2 f(x, y, z)}{\partial y^2} \Big|_{y=0} + \dots \end{aligned} \quad (5.14)$$

applying this to (5.13) leads to:

$$\begin{aligned} f(x, y, z) &= \int_1^\infty \frac{se^{-zs^2}}{\sqrt{s^2 - 1}} \sin(sx) ds \\ &- \frac{1}{2} y^2 \int_1^\infty s^3 \sqrt{s^2 - 1} e^{-zs^2} \sin(sx) ds + \mathcal{O}(y^4) \end{aligned} \quad (5.15)$$

This is the formal Taylor series expansion. Numerical investigation reveals the fact that this series is not converging very well. Perhaps Padé approximation could lead to valuable results. Numerical experiments give raise to the following table (see table 1):

$(x, y, z)$	$f(x, y, z)$	Taylor	Padé[2/2]	Padé[0/4]
(.1,.1,.1)	.30124	.5179	.3019	.3031
(.1,.5,.1)	.0053	$2.7 \cdot 10^2$	.0073	-.0018
(.1,.9,.1)	.0029	$1.1 \cdot 10^5$	.006	-.00012
(.1,.9,.9)	.00252	.0044	.00254	.00255
(.5,.1,.9)	.2132	.2132	.2132	.2132
(.5,.9,.5)	.1608	2.11	.168	.177

Table 1: comparison between different approximation techniques.

So in some cases Padé approximation leads to better results.

## 6 Computational results.

### 6.1 Wave profiles of Wigley Hull.

Some examples for a parabolic Wigley Hull (Shearer [19]) will be calculated. The Wigley Hull is a mathematically defined form (see figure 6.1):

$$\begin{aligned} y &= \frac{B}{2} \left[ 1 - \left( \frac{2x}{L} \right)^2 \right] \left[ 1 - \left( \frac{z}{H} \right)^2 \right] \\ \text{with } -\frac{L}{2} &\leq x \leq \frac{L}{2}, -H \leq z \leq 0 \\ \frac{B}{L} &= 0.1 \quad \frac{H}{L} = 0.0625 \end{aligned} \quad (6.1)$$

As has been noted before, the calculation of the steady and the unsteady wave potential can be done using the same matrix kernel.

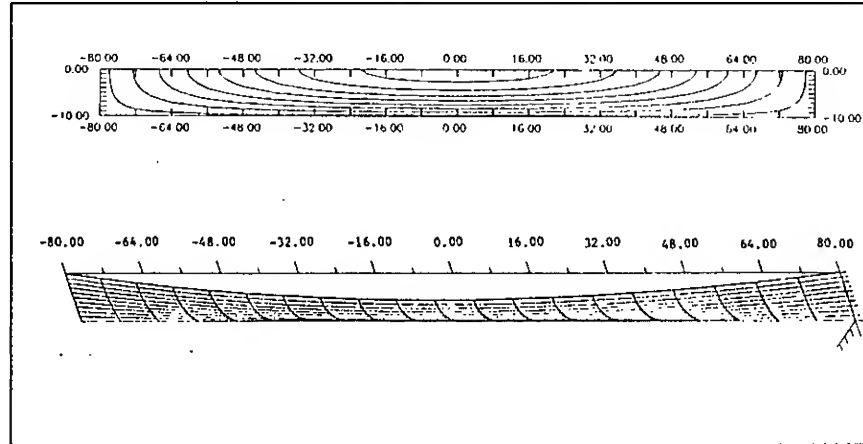


Figure 6.1: one side of Wigley Hull.

For the steady wave potential  $\bar{\phi}$ , matrix equation (3.25) together with the right hand side (3.33) have been used. The solution of this matrix equation is the source strength  $\sigma(\xi)$ . Now using equation (3.26) the potential  $\bar{\phi}$  can be calculated. A first order approximation for the wave height  $\eta(\underline{x})$  can be found using the following:

$$\eta(\underline{x}) = -\frac{U}{g} \bar{\phi}_x(x, y, 0) \quad (6.2)$$

The potential  $\bar{\phi}$  and the source strength  $\sigma$  are known (have been calculated). The wave height or equivalently  $\bar{\phi}_x$  can be calculated using approximately the same formulas as Kellogg ((3.20) and (3.21)):

$$\begin{aligned} \frac{\partial \phi}{\partial x} &= \frac{1}{2} \sigma(x) n_1 + \int \int_{\Sigma} \sigma(\xi) \frac{\partial G}{\partial x} dS_{\xi} \\ \frac{\partial \phi}{\partial y} &= \frac{1}{2} \sigma(x) n_2 + \int \int_{\Sigma} \sigma(\xi) \frac{\partial G}{\partial y} dS_{\xi} \\ \frac{\partial \phi}{\partial z} &= \frac{1}{2} \sigma(x) n_3 + \int \int_{\Sigma} \sigma(\xi) \frac{\partial G}{\partial z} dS_{\xi} \end{aligned} \quad (6.3)$$

The differentiated Green functions  $\partial G / \partial x_i$  are known because they have also been used in order to calculate matrix equation (3.25). So when setting up the computer program a data set with the  $\partial G / \partial x_i$  must be preserved. Now the wave heights can be calculated easily.

For a series of Froude numbers (0.20 - 0.45) the steady wave potential  $\bar{\phi}$  of a Wigley Hull have been calculated as can be seen in figure 6.3. The results have been compared with the measured and calculated values of Kitazawa and Kajitani [20]. In our calculations a grid size of 24 x 8 has been used, so discrepancies could be also due to this relatively large grid size. Especially near the bow this could lead to substantial errors. See for instance figure 6.2. These calculations have been performed on a 48 x 8 grid. The values near the bow agree more with the measured values. Starting from the bow the wave height first increases a little and then decreases rapidly as can be seen from the measurements and can also be observed in figure 6.2.

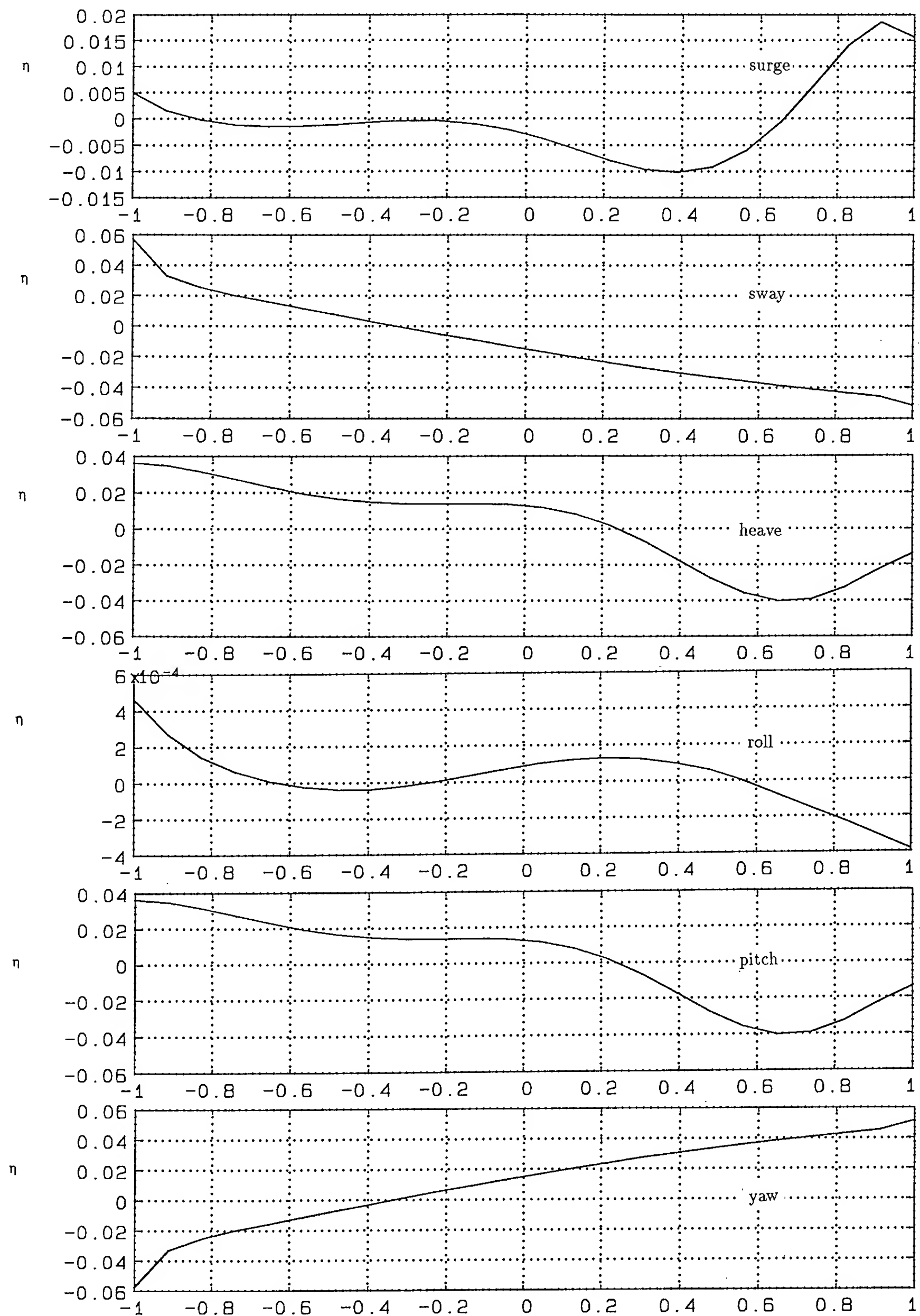


Figure 6.6: Wave heights for the unsteady motion ( $Fn = 0.31$ ).

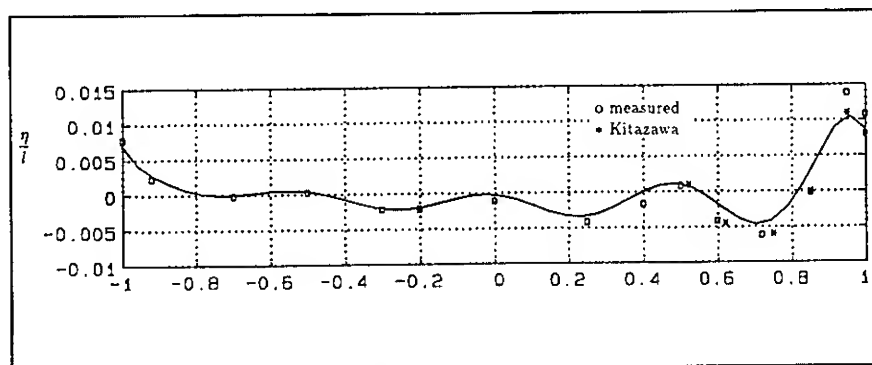


Figure 6.2: Wave profile on a 48 x 8 grid ( $F_n = 0.20$ ).

It can also be observed that only near the ship bow the wave height changes substantially when decreasing the grid size. So local grid refinement near the ship bow will lead to more accurate results.

For a specific value for the Froude number ( $F_n = 0.348$ ), the calculation can be compared with values calculated by Tsutsumi [21] and Dawson [22] as can be seen in figure 6.4. In all our calculations the wetted body  $\Sigma$  is divided into *triangular* panels. This has been done such that to obtain a symmetrical grid with respect to the  $y \equiv 0$  plane. In order to test the grid-independence of the algorithm, the symmetry with respect to this  $y \equiv 0$  plane has been removed. Results of this can be observed in figure 6.5. The algorithm seem to be relatively grid-independent.

For the unsteady motion  $\tilde{\phi}$  the water heights for the six different types of motion have been calculated using the same matrix equation (3.25) as for the unsteady motion  $\tilde{\phi}$  but now with different right hand sides (for instance equation (3.30)). see figure 6.6.

For this figure the following right hand sides for the unsteady wave motion  $\tilde{\phi}$  have been used:

$$\begin{aligned} \text{surge} : -\omega n_1 \quad \text{roll} : \omega(zn_2 - yn_3) \\ \text{sway} : -\omega n_2 \quad \text{pitch} : -Un_3 \\ \text{heave} : -\omega n_3 \quad \text{yaw} : Un_2 \end{aligned} \quad (6.4)$$

Of course as mentioned in the paragraph dealing with the incorporation of the body boundary condition, these right hand sides are not complete. For instance when  $\tilde{\phi} = \mathcal{O}(1)$  the right hand side for surge looks like:

$$-n_1 \tilde{\phi}_{xx} - n_2 \tilde{\phi}_{xy} - n_3 \tilde{\phi}_{xz} \quad (6.5)$$

But already some interesting features of the unsteady wave character or the dynamic swell-up factor can be observed here. In these figures there is a sway-yaw and a pitch-heave correspondence. This can also be seen from the right hand side of equation (6.4). But a different order for the magnitude: sway  $\mathcal{O}(\omega)$  and yaw  $\mathcal{O}(U)$  is evident.

## 6.2 Added Resistance.

Once all the characteristic quantities are known, the pressure can be determined from Bernoulli's equations. (added) Resistance can be calculated directly by integration of first and second order pressure, or by means of conservation of momentum, derived in a similar way as done by Huijsmans [23].

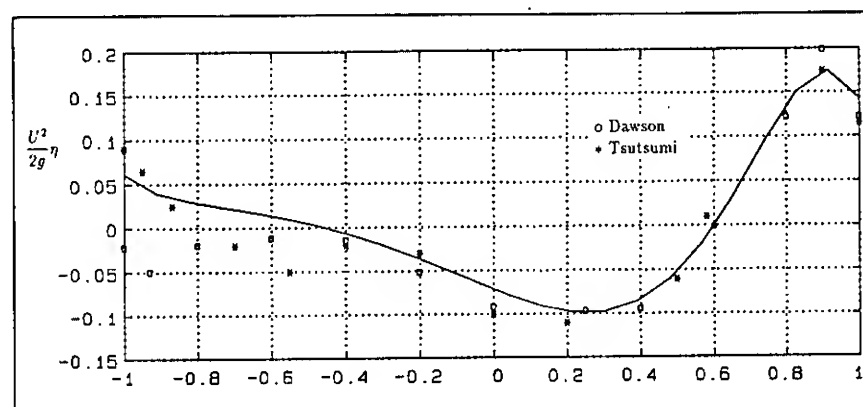


Figure 6.4: Wigley Hull - Wave Profiles for  $F_n = 0.348$

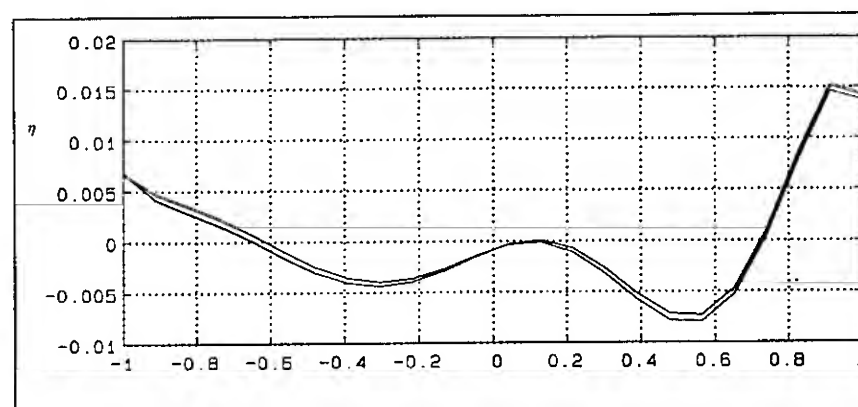


Figure 6.5: Grid independence of the algorithm ( $F_n=0.266$ ).

## 7 Concluding remarks.

We presented an asymptotic method for the calculation of the influence of a slowly oscillating movement on the velocity potential. Especially the steady~unsteady wave interaction is important. The free surface condition for the unsteady wave component was derived and the body boundary condition. The potential function, source strength and Green function are expanded in the small parameter  $\omega$ . A first order approximation for the unsteady wave have been obtained using calculation that only involves the evaluation of the steady wave Green function. This Green function must also be used when calculating the steady state characteristics. Future plans involve the calculation of (added) resistance in the computer program as well. Also at the Ship Hydromechanics Laboratory at the Delft University of Technology some model tests will be performed. So the calculated results can be compared with these test.

## Acknowledgments

The author wishes to thank R.H.M. Huijsmans and H.C. Raven of MARIN for their valuable comments.

## References

- [1] Blok, J.J. and Huisman, J., 'Relative motions and swell-up for a frigate bow.' *The Royal Institution of Naval Architects* (1983).
- [2] Tasaki, R., 'On shipment of water in head waves', *10th ITTC*. London, (1963).
- [3] Brandsma, F.J., Hermans, A.J., 'A quasi linear free surface condition in slow ship theory,' *Schiffstechnik* 32 Heft 2 pp. 25-41.
- [4] Brandsma, F.J., *Low froude number expansions for the wave pattern and the wave resistance of general ship forms*. Phd. Thesis. Delft (1987).
- [5] Baba, E., 'Wave resistance of ships in low speed.' *Mitsubishi Technical Bulletin* 109 (1976).
- [6] Sakamoto, T. and Baba, E., 'Minimization of resistance of slowly moving full hull forms in short waves.' (1985).
- [7] Hermans, A.J. and Huijsmans, R.H.M., 'The effect of moderate speed on the motion of floating bodies.', *Schiffstechnik*, 34 (1987).
- [8] Timman, R., Hermans, A.J. and Hsiao, G.C., *Water Waves and Ship Hydrodynamics*. Delft University Press (1985).
- [9] Brard, R., 'The representation of a given ship form by singularity distributions when the boundary condition on the free surface is linearized.' *Journal of Ship Research*, 16 (1972) 79-92.
- [10] Kellogg, O.D., *Foundations of Potential Theory*, Springer Verlag, Berlin (1929).
- [11] Newman, J.N., 'Evaluation of the wave-resistance Green function: Part 1 - The double integral.' *Journal of Ship Research*, 31 (1987) 79-90.
- [12] Newman, J.N., 'Evaluation of the wave-resistance Green function: Part 2 - The single integral on the centerplane.' *Journal of Ship Research*, 31 (1987) 145-150.
- [13] Dercksen, A., 'Panel integration of 1/R-function for nearby locations.' *MARIN report no. 50831-1-RF*, Wageningen (1988)
- [14] Wehausen, J.V. and Laitone, E.V., 'Surface waves', *Handbook of Physics* (1960).
- [15] Fox, L. and Parker, I.B., Chebychev polynomials in numerical analysis. *Oxford University Press U.K.* (1970)
- [16] Baker, G.A. jr., *Essentials of Padé approximants*, Academic Press, New York (1975).
- [17] Baker, G.A. jr. and Graves-Morris, P., *Padé approximants, part I & II*, *Encycl. of Mathematics* (1981).
- [18] van Gemert, P.H., A linearized surface condition in low speed hydrodynamics. *Delft University of Technology* (1988)
- [19] Shearer, J.R. and Cross, J.J., 'The experimental determination of the components of ship resistance for a mathematical model', *Transactions of the Royal Institution of Naval Architects*, vol.107 London, pp 459-473 (1965).
- [20] Kitazawa, T. and Kajitani, H., 'Computations of wave resistance by the low speed theory imposing accurate hull surface condition', *Proc. Workshop on Ship Wave-Resistance Comp.*, Bethesda, Maryland (1979) 288-305.
- [21] Tsutsumi, T., 'Calculation of the wave resistance of ships by the numerical solution of Neumann-Kelvin problem', *Proc. Workshop on Ship Wave-Resistance Comp.*, Bethesda, Maryland (1979) 162-201.
- [22] Dawson, C.W., 'Calculations with the XYZ free surface program for five ship models', *Proc. Workshop on Ship Wave-Resistance Comp.*, Bethesda, Maryland (1979) 232-255.
- [23] Huijsmans, R.H.M. and Hermans, A.J., 'The effect of the steady perturbation potential on the motions of a ship sailing in random seas', *5th Int. Conf. on Numerical Ship Hydrodynamics*, Hiroshima (1989).
- [24] Jensen, G., Mi, Z.X. and Söding, H., 'Rankine source methods for numerical solutions of the steady wave resistance problem', *Proc. 16th Symp. on Naval Hydrodynamics.*, Berkeley (1986).

## DISCUSSION

J. Nicholas Newman  
Massachusetts Institute of Technology, USA

It is very interesting to see this expansion about the  $\omega=0$  solution, complementing the studies at Delft where  $\Omega=0$  is the basis. But here the applications are less obvious. Added resistance is mentioned by the authors, but it is generally negligible for small  $\omega$ . Perhaps seakeeping problems in following or quartering seas are more appropriate applications?

## AUTHORS' REPLY

We would like to thank Professor Newman for this discussion; it will give us the opportunity to clarify this. The problem is not only the calculation of the added resistance, which can indeed be called small for small  $\omega$  (but will be calculated just as well), but also the determination of the dynamic swell-up. This swell-up is shown to be an important factor—for instance, when looking at the phenomenon of shipping of "green water". About your last remark, seakeeping problems in, for instance, following seas, is also an interesting thing to investigate. But when the incoming waves catch up with the ship, this ship is actually "riding" on a wave. A highly unstable situation occurs which cannot be considered by us thus far.

# Rolling of Biased Ships in Quartering Seas

N. Sanchez

(University of Texas at San Antonio, USA)

A. Nayfeh

(Virginia Polytechnic Institute and State University, USA)

## ABSTRACT

The equation governing the nonlinear rolling of a biased ship in quartering seas can be reduced to a nonlinear ordinary-differential equation with parametric and external excitations. The solutions of this equation are analyzed by performing analog-computer simulations to locate bifurcation points in a two-dimensional parameter space consisting of the waveslope and encounter frequency. The predicted instabilities for various levels of the parametric excitation are summarized in bifurcation diagrams that display the stable regions and the instabilities that take the ship into "dangerous" responses.

## INTRODUCTION

In the study of the roll motion of a vessel it is common to have an equation of motion with time-varying coefficients, which arise from time-dependent restoring moments due to the ship's position on the wave (1,2) or to changes in the displacement volume resulting from coupling with other modes (3). These time-varying coefficients constitute what is known as parametric excitations (4). A considerable number of roll studies (e.g., 1-3, 5-10) analyzed the influence of these excitations on the stability of a ship in the presence of resonances, which can lead to capsizing under rather mild sea conditions (9,10).

In previous work (9,10), we applied an analytical-numerical procedure to characterize the stability of the steady-state response of a ship when a parameter is slowly varied. Using this procedure, we analyzed the stability of an approximate analytical solution by using Floquet theory and elementary concepts of bifurcation theory. In (10), we have shown that a ship model under a purely parametric excitation, which is the case of rolling in longitudinal waves in the absence of heeling moments and pitch-roll coupling, displays self-similar behavior near the resonances. Instabilities can lead to capsizing through two scenarios: one evolving from a large oscillation through the disappearance of a chaotic attractor (crises) and a second, potentially more dangerous, developing from a small oscillation through a sudden tangent instability. Similar behaviors occur for excitation frequencies near the linear natural frequency, twice the natural frequency, and the

superharmonic frequencies (at higher excitation levels). In (9), we treated the behavior of the same ship model under an external excitation; that is, the case of rolling in beam seas. In this case we have also found a qualitatively similar behavior in the neighborhood of the primary resonance. These results are in agreement with the conjecture of Parlitz and Lauterborn (11) that this behavior represents a manifestation of some fundamental physical structure and should be observed in the neighborhood of every resonance of the system if the excitation amplitude is sufficiently large.

Wellicome (7) and Feat and Jones (2), among others, considered a second-order equation with parametric and external excitations. It models the rolling motion of a ship in (a) beam seas when the coupling with heave or the Smith effect is included or (b) longitudinal waves when bias is included. One of the important features of the nonlinear motions observed in these studies (2) is the difference in stability characteristics between ships with positive and negative bias angles, which confirms the experimental observations of Wright and Marshfield (12).

In this work we expand the above studies by analyzing the nonlinear rolling response of a biased ship to both parametric and external excitations. Our aim is to gain general understanding of the dynamics by identifying the instabilities that appear when a parameter is slowly varied and characterize the locus of these instabilities in a parameter space of physical significance. Results are presented for a broad portion of the amplitude and frequency of the external excitation, keeping the level of the parametric excitation fixed.

Following Wright and Marshfield (12) and Feat and Jones (2), we derive the equation of motion as a function of the relative motion of the ship and the wave. We let  $\phi$  be the absolute roll angle and  $\theta$  be the relative roll angle with respect to the local waveslope  $\alpha$ . Applying Newton's second law, we find that the equation of motion can be written as

$$(I + \delta I)\ddot{\theta} + D(\dot{\theta}) + K(\theta, \tau) = B - I\ddot{\alpha} \quad (1a)$$

$$\theta = \phi - \alpha \quad (1b)$$

where the overdots represent derivatives with respect to the time  $\tau$ ,  $I$  is the roll moment of inertia,  $\delta I$  is the added moment of inertia, which is assumed to be constant (12), and  $B$  is a constant bias moment, which might be due to a steady wind, or a shift in cargo, or water or ice on deck. The righting moment  $K(\theta, \tau)$  has



an explicit time dependence, which might come from two sources (2): the position of the ship on the wave or variations in the displacement volume due to heave coupling. We are mostly interested in the latter effect; however, consideration of the first effect only changes the numerical values of the coefficients. The righting-moment function is approximated as (5,12)

$$K(\theta, t) = \omega_0^2 [\theta + \alpha_3 \theta^3 + \alpha_5 \theta^5 + h \theta \cos(\hat{\Omega} \tau)] \quad (2)$$

where  $\omega_0$  is the linear undamped natural frequency of the ship, the odd polynomial fits the ship's righting moment curve, and the parametric term represents heave - roll coupling expressed by the coefficient

$$h = \frac{K_{\theta z} a_z}{2\omega_0^2} \quad (3)$$

Here,  $K_{\theta z}$  is the magnitude of the coupling coefficient and  $a_z$  is the amplitude of the heaving motion, which is assumed to be harmonic with frequency  $\hat{\Omega}$ . The damping moment  $D(\dot{\theta})$  is expressed as

$$D(\dot{\theta}) = 2\hat{\mu}\dot{\theta} + \hat{\mu}_3\dot{\theta}^3 \quad (4)$$

Assuming that the wavelength of the wave is large compared with the ship's beam, we can write the waveslope of a regular beam sea as a harmonic function  $\alpha = \alpha_m \cos \hat{\Omega} t$ , where  $\alpha_m$  is the maximum waveslope. Using (1b)-(4), we rewrite (1a) as

$$\begin{aligned} \ddot{\theta} + 2\hat{\mu}\dot{\theta} + \hat{\mu}_3\dot{\theta}^3 + \omega_0^2 [\theta + \alpha_3 \theta^3 + \alpha_5 \theta^5 + h \theta \cos(\hat{\Omega} \tau)] \\ = \omega_0^2 [\theta_s + \alpha_3 \theta_s^3 + \alpha_5 \theta_s^5] + \frac{\alpha_m \hat{\Omega}^2}{I + \delta I} \cos(\hat{\Omega} \tau + \gamma) \end{aligned} \quad (5)$$

where  $\gamma$  represents a phase angle between the wave and heave motions and  $\theta_s$  is the bias angle produced by the moment  $B$ .

To simplify the governing equation, we introduce the time scaling  $t = \omega_0 \tau$ , which transforms (5) into

$$\begin{aligned} \ddot{\theta} + 2\mu\dot{\theta} + \mu_3\dot{\theta}^3 + \theta + \alpha_3 \theta^3 + \alpha_5 \theta^5 + h \theta \cos(\Omega t) \\ = \theta_s + \alpha_3 \theta_s^3 + \alpha_5 \theta_s^5 + \hat{f}_1 \cos(\Omega t) - f_2 \sin(\Omega t) \end{aligned} \quad (6)$$

where the overdot represents the derivative with respect to  $t$ ,

$$\hat{f}_1 = \frac{\alpha_m \hat{\Omega}^2}{(I + \delta I)} \cos \gamma \quad (7)$$

and

$$f_2 = \frac{\alpha_m \hat{\Omega}^2}{(I + \delta I)} \sin \gamma \quad (8)$$

Using the transformation

$$\theta = \theta_s + u \quad (9)$$

we rewrite (6) as

$$\begin{aligned} \ddot{u} + 2\mu\dot{u} + \mu_3\dot{u}^3 + u + b_1 u + b_2 u^2 + b_3 u^3 \\ + b_4 u^4 + b_5 u^5 + h u \cos(\Omega t) = f_1 \cos(\Omega t) - f_2 \sin(\Omega t) \end{aligned} \quad (10)$$

where

$$\begin{aligned} b_1 = 3\alpha_3 \theta_s^2 + 5\alpha_5 \theta_s^4, \quad b_2 = 3\alpha_3 \theta_s + 10\alpha_5 \theta_s^3, \quad b_3 = \alpha_3 + 10\alpha_5 \theta_s^2 \\ b_4 = 5\alpha_5 \theta_s, \quad b_5 = \alpha_5 \end{aligned}$$

and

$$f_1 = \hat{f}_1 - h \theta_s \quad (11)$$

Equation (10) is general and can model the roll motion of biased and unbiased ships in a variety of regular sea conditions, including beam seas, head or following seas, and quartering seas. The cases treated in the two previous publications (9,10) are particular forms of this equation. When  $\gamma = 0$  and  $h = 0$ , (10) models the rolling of a biased or an unbiased ship in beam seas, depending on whether  $\theta_s$  is zero or nonzero. Similarly, when  $\alpha_m = 0$  and  $\theta_s = 0$ , (10) models the rolling motion of a biased or an unbiased ship in head or following seas. The natural frequency has been scaled to unity to make the results applicable to a wide number of cases. Because of the generality of the cases covered, we have a large number of excitation parameters to consider, namely,  $\Omega$ ,  $\gamma$ ,  $h$ ,  $\theta_s$ , and  $\alpha_m$ . Because our goal is to study the effect of the parametric amplitude  $h$ , we study primarily the stability boundaries in the  $\alpha_m$ - $\Omega$  parameter space at a set level of  $h$ . The phase angle  $\gamma$  is set equal to zero because this angle produces large amplitudes near  $\Omega = 1$ . The bias angle is taken to be either +6 or -6 degrees. The combined effect of the external and parametric terms complements the results previously shown (9,10) for the cases of a purely parametric or external excitation.

## BIFURCATION DIAGRAM

The results obtained by using an analog-computer simulation of (5) for  $\gamma = 0$ ,  $\theta_s = 0^\circ$ ,  $h = 0.3$ , and the other coefficients as given in Table 1 are shown in the bifurcation diagram in Figure 1. In this diagram, we present the bifurcations of three basic attractors which are stable near  $\Omega = 1$  and  $\Omega = 2$ . Figure 2 shows the phase portraits of the two attractors at  $\Omega = 0.856$  and  $\alpha_m = 0.048$ . The small attractor loses its stability when the parameters are varied across  $S_1$ , which is the locus of saddle-node bifurcations that produce a jump to another attractor. If the crossing occurs for values of  $\alpha_m > I_2$ , the ship capsizes. For crossings with values of  $\alpha_m < I_2$ , the jump is to the large attractor in Figure 2. The curve  $S_2$  is the locus of saddle-node bifurcations that produce a jump from the large to the small attractor. The large attractor also undergoes a period-doubling sequence to chaos in the region between  $P_1$  and  $J_1$ . Figure 3 shows phase diagrams and power spectra of various attractors at selected locations in this region. In the dotted region all initial conditions lead to capsize. When  $J_1$  is crossed the chaotic attractor loses stability and the ships capsizes or its response jumps to the small attractor, depending on whether the crossing occurs above or below  $I_1$ . The large attractor in Figure 2 also loses stability near  $\Omega = 2$ . Between  $P_3$  and  $P_4$  this limit cycle is unstable. When  $P_3$  is crossed from left to right the attractor undergoes a period-doubling bifurcation and a jump to the subharmonic response is observed. When  $P_4$  is crossed from right to left another period-doubling bifurcation is observed. Therefore, the period-one response is unstable in the region between  $P_3$  and  $P_4$ .

The third attractor represented in the bifurcation diagram in Figure 1 is the subharmonic response near  $\Omega = 2$ , which is stable in the region between  $P_4$  and  $J_2$ . Figure 4 shows selected attractors in this region: (a) shows the period-one response, (b) shows the subharmonic resonant response obtained after crossing  $P_4$  from right to left, (c) and (d) show quantitative changes in the subharmonic response, (e) shows the subharmonic response after a period-doubling bifurcation across  $P_2$ , and (f) shows a chaotic attractor to the right of  $J_2$ .

Figure 5 shows the bifurcation diagram obtained from an analog-computer simulation of (5) when the parameters are set at  $\gamma = 0$ ,  $\theta_s = +6^\circ$ , and  $h = 0.3$ . In this case the dotted region is much larger than that for the case of an unbiased ship. The region of stability of the subharmonic response shrank and the period-one and subharmonic responses only coexist in a narrow region between  $\Omega = 1.5$  and 2.0. The curves  $S_1$  and  $S_2$  represent saddle-node bifurcations of the large and small attractors of the period-one resonant response, which produce jumps in the corresponding attractors. Figure 6 shows the two attractors for  $\Omega = 0.768$  and  $\alpha_m = 0.217$ . In Figure 5,  $S_1$  represents a jump from the large to the small attractor;  $S_2$  represents a jump in the small attractor, which takes the system to the large attractor if  $\alpha_m$  is below the black dot or to capsize if it is above this point; and  $P_1$  represents period-doubling bifurcations, leading to either chaos in the portion of the curve enclosed by  $E_1$  or directly to an instability in the rest of the curve. The instability results in either capsize when  $\alpha_m$  is above the black dot on  $P_1$  or a jump to the subharmonic attractor when it is below  $P_1$ . Figure 7 shows the coexisting attractors of the period-one and subharmonic responses at  $\Omega = 1.758$  and  $\alpha_m = 0.046$ . The curve  $E_1$  in Figure 5 represents the point of capsize. For values of  $\Omega$  below the black dot on  $E_1$ , a period-doubling sequence to chaos such as the one shown in Figure 8 is observed. For crossings of  $E_1$  between the black dot and the point of merge with  $P_1$ , a saddle-node bifurcation is observed, making the period-2T solution unstable and capsizing takes place.

Figure 5 also shows that the stability region of the subharmonic response is narrower than that in Figure 1. Crossing  $P_3$  from right to left causes the period-one response to lose stability and the subharmonic becomes stable. When  $P_2$  is crossed, the system undergoes a sequence of period-doubling bifurcations leading to chaos, which disappears when  $E_2$  is reached, causing the ship to capsize. Figure 9 shows selected phase portraits of the above changes in the solution: (a) shows the period-one response, (b) and (c) show the subharmonic response after crossing  $P_3$ , (d) shows a period-doubling in the subharmonic after crossing  $P_2$ , and (e) shows a second period doubling in the subharmonic response.

Figure 10 shows the bifurcation diagram obtained from an analog-computer simulation of (5) when the parameters are set equal to:  $\gamma = 0$ ,  $\theta_s = -6^\circ$ , and  $h = 0.3$ . Figure 11 shows the attractors of the primary resonance. Across curve  $S$  in Figure 10, the small attractor undergoes a saddle-node bifurcation that produces capsizing. Across  $P_1$  the large attractor undergoes period-doubling bifurcations. In the portion of  $P_1$  enclosed by  $E_1$  a sequence of period-doubling bifurcations culminating in chaos is observed, in the rest of the curve capsizing occurs after the first period-doubling bifurcation. The large attractor also

undergoes period-doubling bifurcations across  $P_4$ . The subharmonic response undergoes period-doubling bifurcations across  $P_2$  and  $P_3$ . Capsizing is observed after crossing  $P_2$  and  $E_2$ . Figure 12 shows the coexisting attractors that are found between  $P_2$  and  $P_4$ .

## CONCLUSIONS

The present results show that the dynamics of a positively biased ship is different from that of a negatively biased ship, which confirms the experimental observations of Wright and Marshfield (12). However, it is difficult to conclude which of the two cases is more stable because the stability depends on the region of the parameter space under consideration. Nevertheless, it is clear that the motion is very sensitive to bias and the region where capsizing is observed grows considerably and appear to be bigger for positively biased ships. We have also found the bifurcation diagram to be sensitive to changes in the phase angle  $\gamma$ . The most interesting feature is the major qualitative changes that the bifurcation diagrams undergo as the bias angle changes. This clearly suggests the need for a complete analysis before a particular design can be considered safe to operate.

## ACKNOWLEDGEMENT

This work was supported by the Office of Naval Research under Contract Nos. N00014-83-K-0184/NR 4322753 and N00014-90-J-1149.

## REFERENCES

1. Kerwin, J. E., "Notes on Rolling in Longitudinal Waves," *International Shipbuilding Progress*, Vol 2, 1955, pp. 597-614.
2. Feat, G. and Jones, D., "Parametric Excitation and the Stability of a Ship Subjected to a Steady Heeling Moment," *International Shipbuilding Progress*, Vol. 28, 1984, pp. 263-267.
3. Paulling, J. R. and Rosenberg, R. M., "On Unstable Ship Motions Resulting from Nonlinear Coupling," *Journal of Ship Research*, Vol. 3, 1959, pp. 36-46.
4. Nayfeh, A. H. and Mook, D. T., *Nonlinear Oscillations*, Wiley-Interscience, New York, 1979.
5. Blocki, W., "Ship Safety in Connection with Parametric Resonance of the Roll," *International Shipbuilding Progress*, Vol. 27, 1980, pp. 36-53.
6. Abicht, W., "On Capsizing of Ships in Regular and Irregular Seas," *Proceedings of the International Conference on Stability of Ships and Ocean Vehicles*, Glasgow, 1975.
7. Wellicome, J. F., "An Analytical Study of the Mechanism of Capsizing," *Proceedings of the International Conference on Stability of Ships and Ocean Vehicles*, Glasgow, 1975.

8. Skomedal, N. G., "Parametric Excitation of Roll Motion and its Influence on Stability," Second International Conference on Stability of Ships and Ocean Vehicles, SIII-3a, October 1982.
9. Nayfeh, A. H. and Sanchez, N. E., "Stability and Complicated Responses of Ships in Regular Beam Seas," to appear, **International Shipbuilding Progress**, 1990.
10. Sanchez, N. E., and Nayfeh, A. H., "Nonlinear Rolling Motions of Ships in Longitudinal Waves," to appear, **International Shipbuilding Progress**, 1990.
11. Parlitz, U. and Lauterborn, W., "Superstructure in the Bifurcation Set of the Duffing Equation," **Physics Letters**, Vol. 107A, 1985, pp. 351-355.
12. Wright, J. H. G. and Marshfield, W. B., "Ship Roll Response and Capsize Behavior in Beam Seas," **Transactions Royal Institution of Naval Architects**, Vol. 122, 1980, pp. 129-147.
13. Nayfeh, A. H., **Introduction to Perturbation Techniques**, Wiley-Interscience, New York, 1981.
14. Bergé, P., Pomeau, Y. and Vidal, C., **Order Within Chaos**, Wiley-Interscience, New York, 1984.

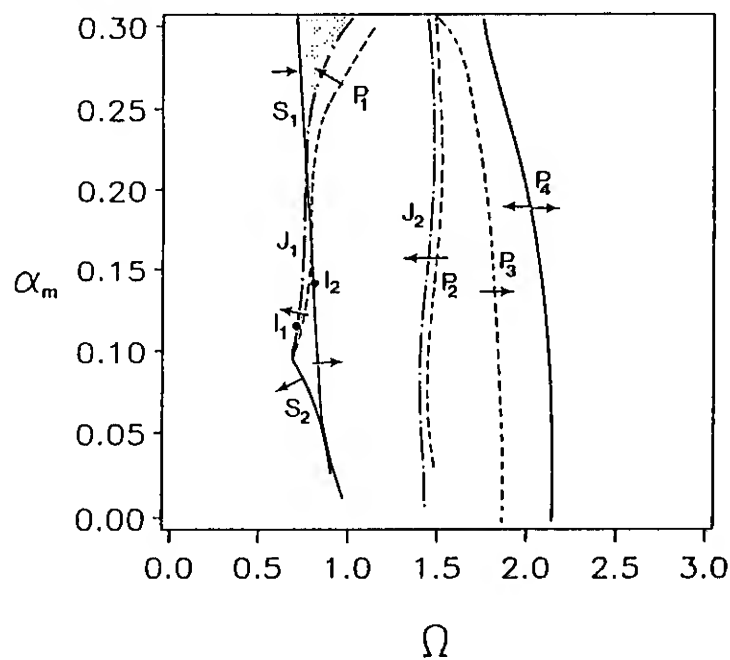


**Figure 1.** Bifurcation diagram from analog-computer simulations of equation (5) for  $\gamma = 0$ ,  $\theta_s = 0^\circ$ , and  $h = 0.3$ .

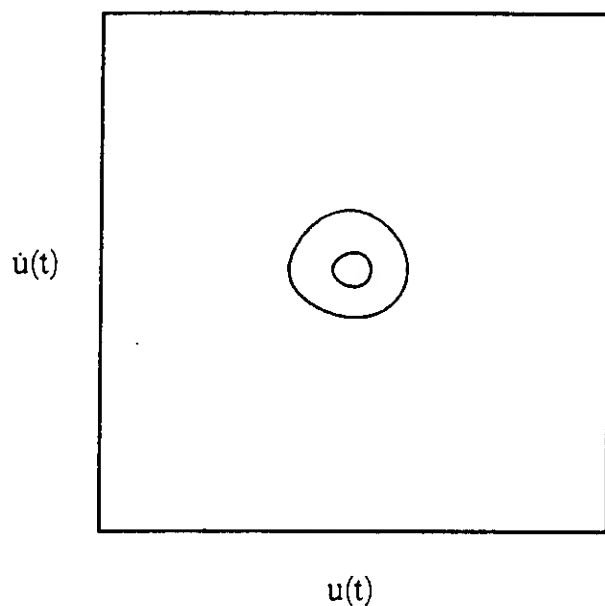


**Figure 2.** Phase portraits of coexisting attractors at  $\Omega = 0.856$  and  $\alpha_m = 0.048$ . Both attractors correspond to primary resonance.

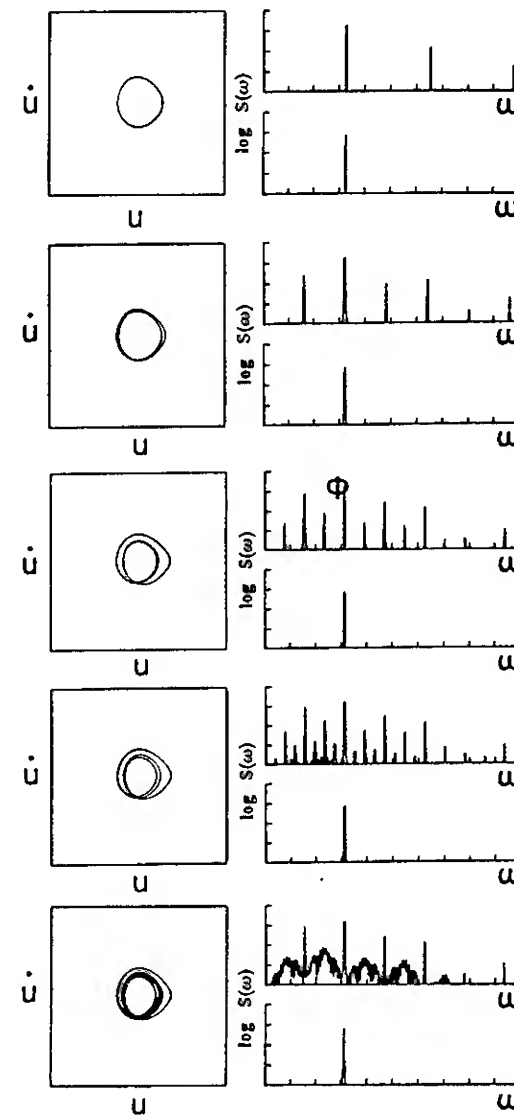


**Figure 3.** Phase portraits and power spectra of the attractor and the excitation at selected locations near the primary resonance : (a) T-periodic solution for  $\Omega = 0.983$  and  $\alpha_m = 0.258$ , (b) 2T-periodic solution for  $\Omega = 0.966$  and  $\alpha_m = 0.268$ , (c) 4T-periodic solution for  $\Omega = 0.942$  and  $\alpha_m = 0.282$ , (d) 8T-periodic solution for  $\Omega = 0.939$  and  $\alpha_m = 0.284$ , and (e) chaotic attractor for  $\Omega = 0.937$  and  $\alpha_m = 0.285$ .

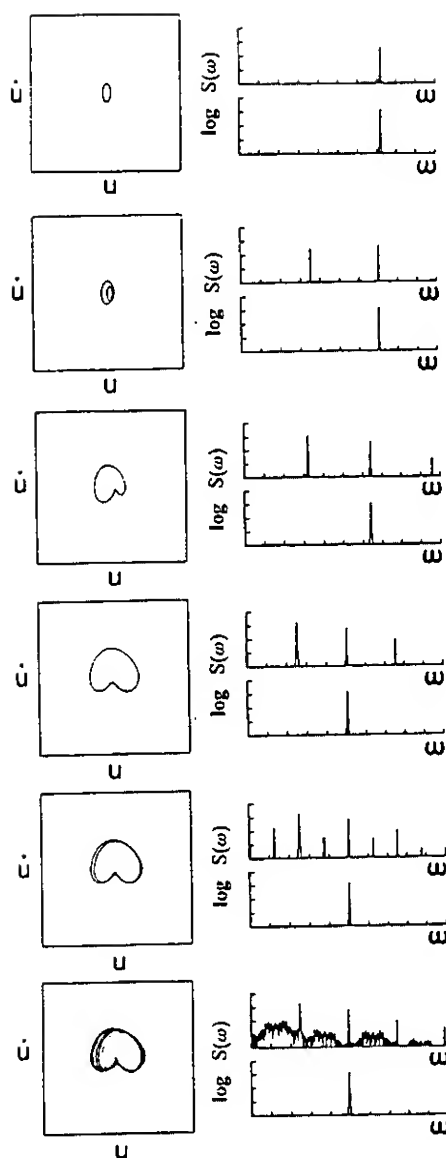


**Figure 4.** Phase portraits and power spectra of the attractor and the excitation at selected locations near the subharmonic resonance : (a) primary response for  $\Omega = 2.158$  and  $\alpha_m = 0.107$ , (b) subharmonic response for  $\Omega = 2.102$  and  $\alpha_m = 0.113$ , (c) subharmonic response for  $\Omega = 1.920$  and  $\alpha_m = 0.136$ , (d) subharmonic response for  $\Omega = 1.514$  and  $\alpha_m = 0.218$ , (e) 2T-periodic subharmonic response for  $\Omega = 1.505$  and  $\alpha_m = 0.221$ , and (f) chaotic attractor in the subharmonic response for  $\Omega = 1.480$  and  $\alpha_m = 0.228$ ,

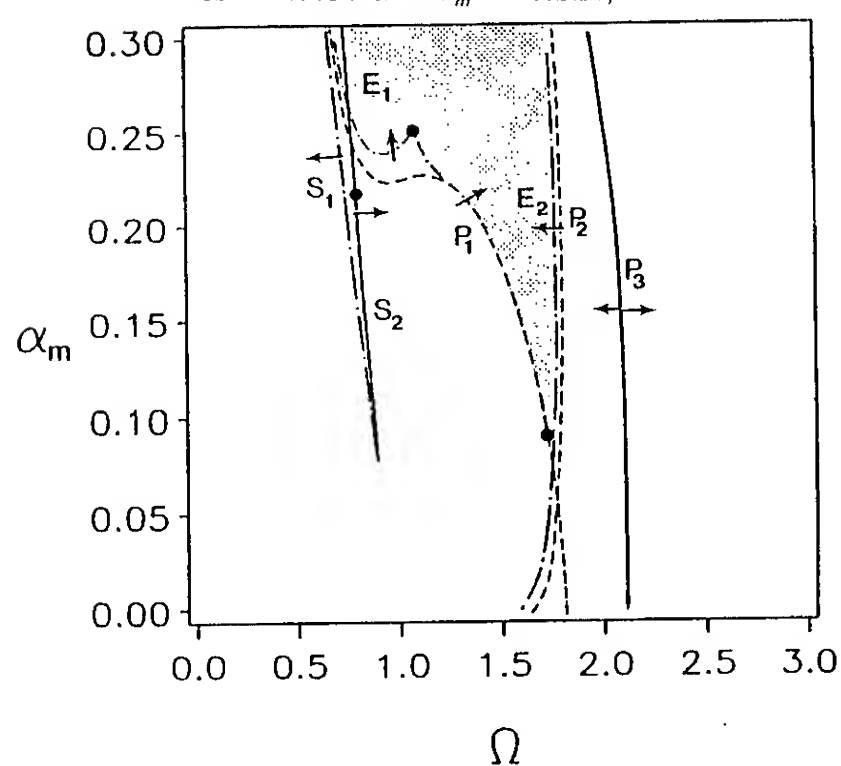


**Figure 5.** Bifurcation diagram from analog-computer simulations of equation (5) for  $\gamma = 0$ ,  $\theta_s = +6^\circ$ , and  $h = 0.3$

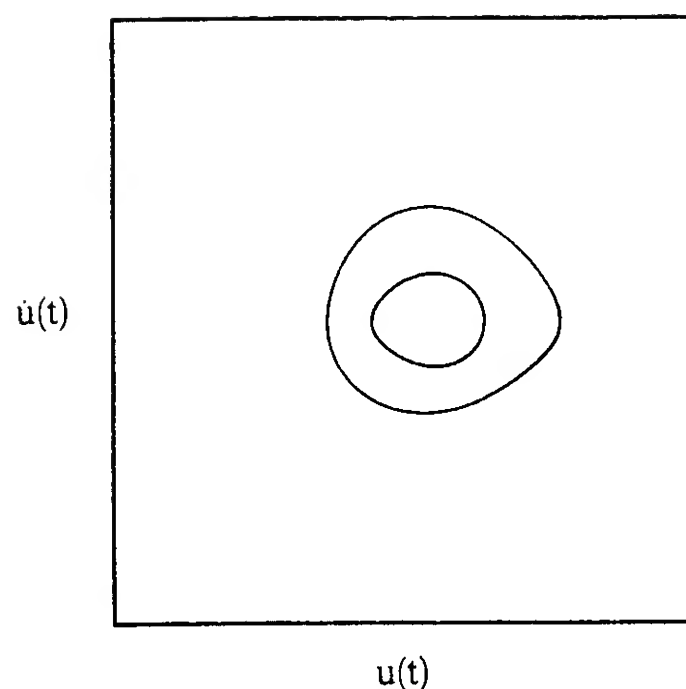


**Figure 6.** Coexisting attractors near the primary resonance for  $\Omega = 0.768$  and  $\alpha_m = 0.217$ .

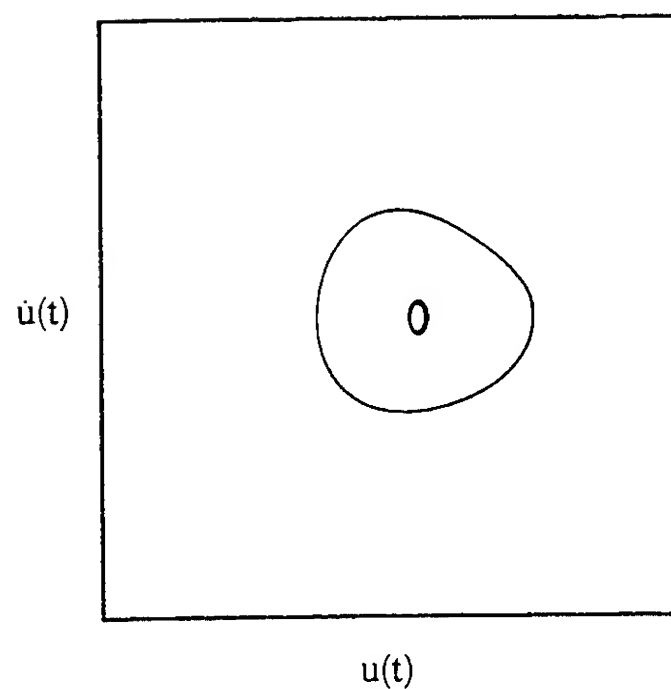


**Figure 7.** Coexisting attractors near the subharmonic resonance for  $\Omega = 1.758$  and  $\alpha_m = 0.046$ .

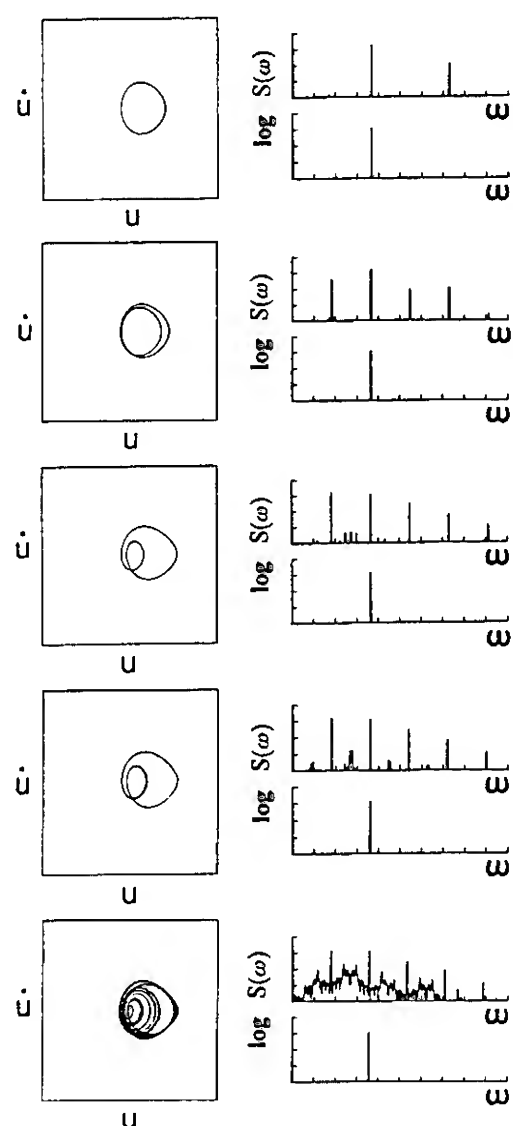


**Figure 8.** Phase portraits and power spectra of the response and the excitation near the primary resonance : (a) T-periodic response for  $\Omega = 1.098$  and  $\alpha_m = 0.228$ , (b) 2T-periodic response for  $\Omega = 1.098$  and  $\alpha_m = 0.231$ , (c) 2T-periodic response for  $\Omega = 1.098$  and  $\alpha_m = 0.245$ , (d) appearance of broad-band frequency content in the 2T-periodic response for  $\Omega = 1.093$  and  $\alpha_m = 0.248$ , and (e) chaotic attractor for  $\Omega = 1.067$  and  $\alpha_m = 0.249$ .

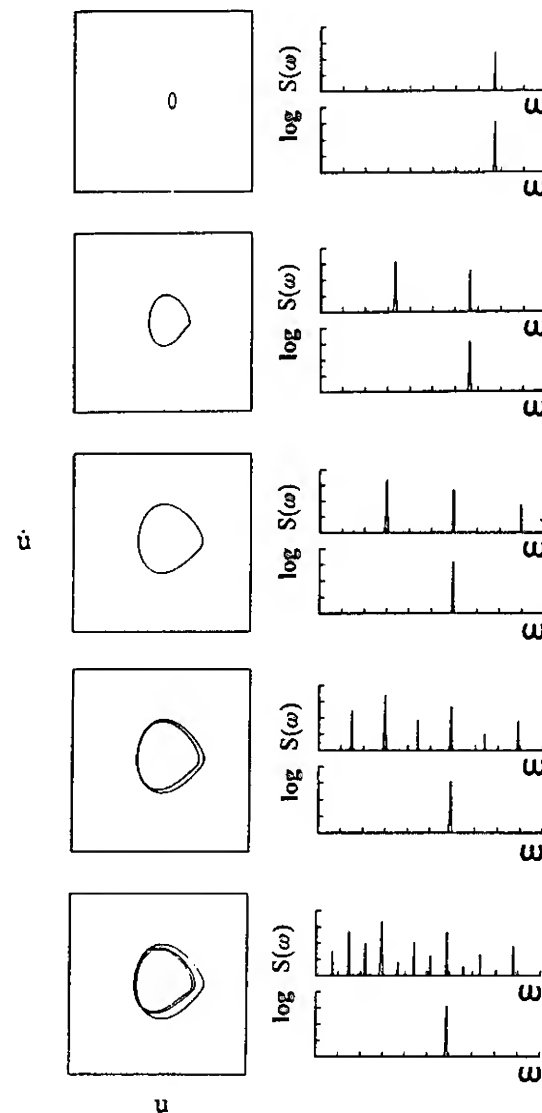


**Figure 9.** Phase portrait and power spectra of the response and the excitation near the subharmonic resonance : (a) primary response for  $\Omega = 2.319$  and  $\alpha_m = 0.058$ , (b) subharmonic response for  $\Omega = 1.997$  and  $\alpha_m = 0.078$ , (c) subharmonic response for  $\Omega = 1.794$  and  $\alpha_m = 0.097$ , (d) 2T-periodic attractor of the subharmonic response for  $\Omega = 1.780$  and  $\alpha_m = 0.099$ , (e) 4T-periodic attractor of the subharmonic response for  $\Omega = 1.763$  and  $\alpha_m = 0.100$ .

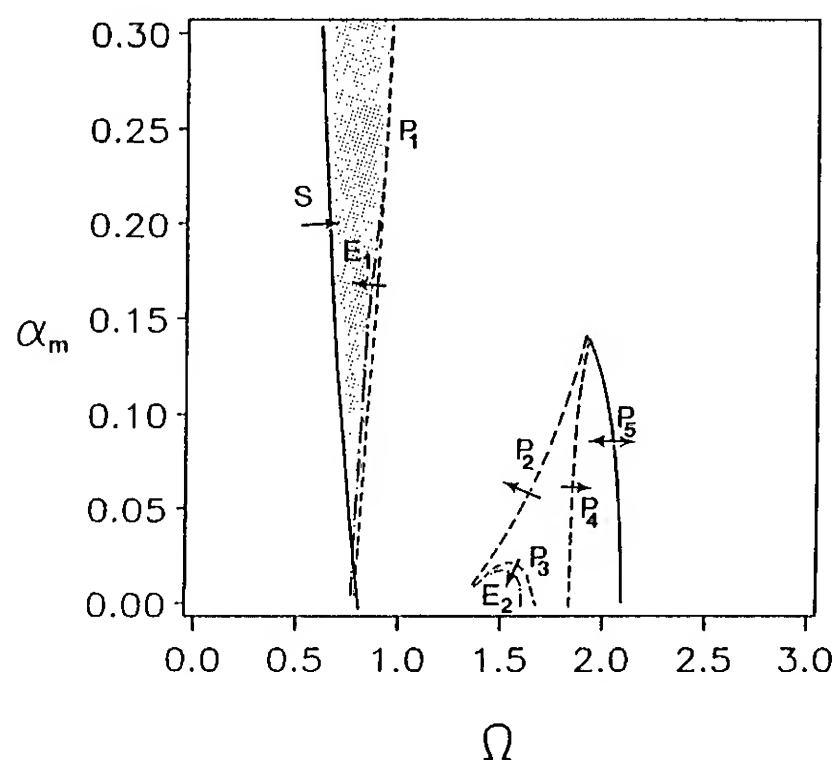


**Figure 10.** Bifurcation diagram from analog-computer simulations of equation (5) for  $\gamma = 0$ ,  $\theta_s = -6^\circ$ , and  $h = 0.3$ .

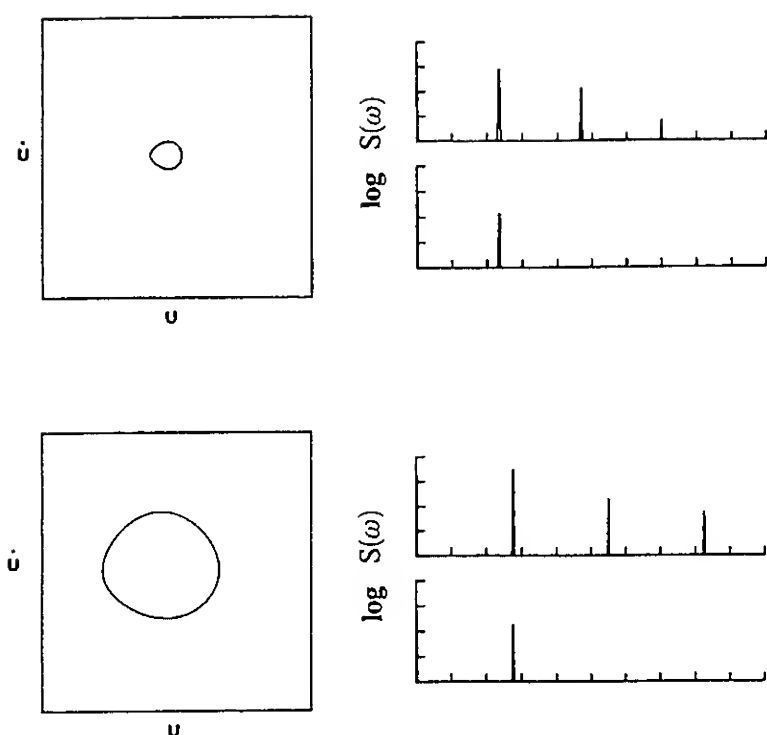


**Figure 11.** Phase portraits of the attractors near the primary resonance and the power spectra of the response and excitation for  $\Omega = 0.702$  and  $\alpha_m = 0.063$  and  $\Omega = 0.827$  and  $\alpha_m = 0.057$ .

Table 1. Coefficients of ship model considered.

$I$	$K$	$\omega_0$	$\mu$	$\mu_3$	$\frac{\alpha_3}{\omega_0^2}$	$\frac{\alpha_5}{\omega_0^2}$	$\delta I$
$mK^2$	110.mm	5.278	0.086	0.108	-1.402	0.271	0.25I

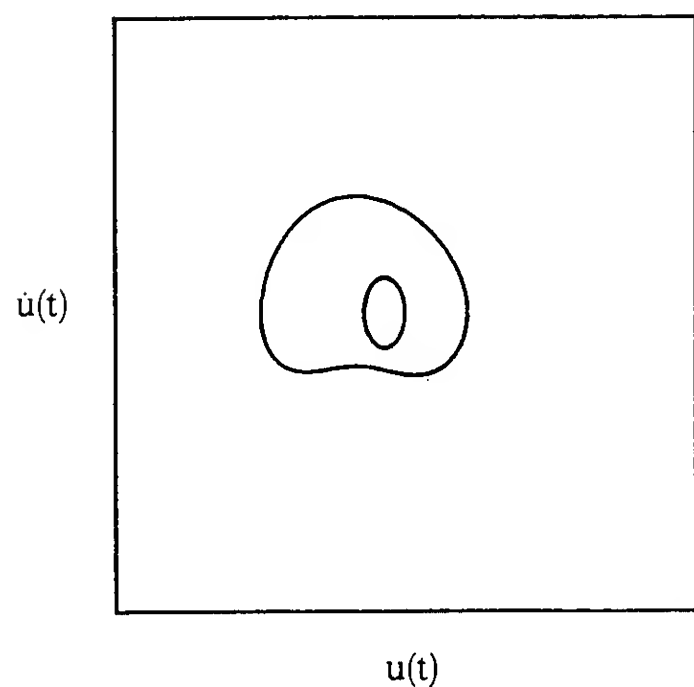


**Figure 12.** Coexisting attractors near the subharmonic resonance for  $\Omega = 1.698$  and  $\alpha_m = 0.061$ .



## DISCUSSION

Alberto Francescutto  
University of Trieste, Italy

First, I would congratulate the authors for this very interesting paper indicating the possibility of new terrible possibilities in the already complicated behaviour of a ship in longitudinal or quartering seas. The author, in his presentation, mentions the possibility of jumps, involving the oscillation amplitude, taking place sharply in time. In my experience, this sharpness indicates always a few cycles of the oscillation. Would the author comment on this point? Finally, it seems that the consideration of the angle between the wave train and ship's heading has been neglected in the construction of the equation of motion (5). This, in fact, would include an explicit external excitation also in the limiting case of pure longitudinal sea.

## AUTHORS' REPLY

Dr. Francescutto's first question has to do with the time it takes an unstable solution to grow from a given initial position to the point of capsize. The process may involve a fraction of a cycle to many cycles of oscillation, depending on the initial conditions and the scenario through which the vessel capsizes. In the case of capsize through saddle-node bifurcations, the capsize time may be very short. On the other hand, in the case of capsize through period-doubling bifurcations and chaos, the capsize time may be very long. In reference to the consideration of the angle between the wavetrain and the ship's longitudinal axis, we agree that it is not explicitly shown in equation (5). However, the governing equation is general and can treat arbitrary orientations by properly adjusting the excitation parameters in equation (10).

## DISCUSSION

Hongbo Xü  
Massachusetts Institute of Technology, USA (China)

You have shown that the nonlinear analysis is a very useful tool of studying the ship motion. When this one-degree freedom system (rolling of a ship in quartering seas) bifurcates, the magnitude of the ship motion undergoes a jump. There must be energy exchanges between the ship and waves or energy transfer between the potential component and kinetic component. I think it is important to identify the energy-sharing mechanism in order to understand the dynamics of the system. Perhaps you also have this kind of results to show us?

## AUTHORS' REPLY

Dr. Xü's question addresses the energy transfer mechanism between the wave and boat, as well as the exchange between the potential and kinetic energies. Understanding of these fundamental mechanisms is of primary importance as Dr. Xü points out. The basic mechanism is the adjustment of the phasing between the vessel motion and the wave.

## DISCUSSION

Hang S. Choi  
Seoul National University, Korea

The equation you have used seems very complicated; duffing oscillator for righting moment and Van der Pol oscillator for damping. In addition to these, the biased initial position is introduced as a control parameter. However, the resulting motion of this complex system depends strongly on the initial condition of the motion. Would you comment how the initial condition can be determined in your mathematical model?

## AUTHORS' REPLY

Dr. Choi's question addresses an important aspect of the mathematical model. The solution to the differential equation governing the oscillation of the vessel depends on the initial conditions in the form of position and velocity. Furthermore, there might be many possible solutions to the differential equation, depending on the initial conditions. This is exactly the essence of the basin of attraction shown in the paper. Each set of initial conditions, as an independent variable, is located on the phase plane and the solution reached from that point is determined. Therefore, the motion is strongly dependent on the initial conditions.

In summary, the initial conditions are independent variables which must be specified for the particular situation. To assess the stability of the vessel, we have to determine the solution for any physically meaningful set of initial conditions in phase space. This generates the domain of attraction of all possible solutions. From this information, we need to determine which solutions pose risk and use the analysis to evaluate the seaworthiness of the vessel under consideration.

# **A Stochastic Analysis of Nonlinear Rolling in a Narrow Band Sea**

A. Francescutto and R. Nabergoj (University of Trieste, Italy)

## **ABSTRACT**

The extensive analysis carried out in last years on the nonlinear rolling of a ship, through the use of different versions of perturbation methods, allowed many researchers to discover some very peculiar features of this motion. In a deterministic beam sea, it appeared the possibility of resonances different from synchronism, in particular subharmonic oscillations in both the upright and heeled conditions. Moreover, the resonance peaks as a function of tuning ratio are bent, mainly as a consequence of righting arm nonlinearity, so that in a suitable range of frequencies the oscillation can have three steady states of very different amplitude.

Later on, the possibility of successive bifurcations to chaotic behaviour was detected and it is actually widely and deeply studied. This "deterministic chaos" is in fashion and is very interesting in principle; on the other hand it is still related to the appearance of a strictly monochromatic sea, which is a possibility that can be hardly realized in a real seaway.

At the other extremum, stochastic nonlinear rolling was treated mainly as a process with sufficiently broad band to have no possibility of jump phenomena and no research was carried out taking the bandwidth as a parameter. To clarify this puzzling aspect, the nonlinear model introduced in previous work with the excitation represented by white noise filtered through a linear filter was studied in detail. The filter was allowed to vary centerpeak and bandwidth of the excitation. A representation as a sum of two sinusoidal processes with Gaussian slowly varying amplitudes was introduced. This description is particularly suitable for description of narrow band processes. The system of differential equations rolling motion plus filter, was solved by means of the perturbation method of multiple scales. Several curves roll variance/tuning ratio were obtained varying the bandwidth for an excitation variance corresponding to a moderate sea. The results indicate that, provided the bandwidth of the

excitation is not greater than a sharp JONSWAP spectrum, at least in the considered cases, the main resonance exhibits the same characteristic features shown in the deterministic, i.e. multivaluedness and jump possibility. This similarity is related to the fact that narrow bandwidth means high autocorrelation.

The perturbation method allows to obtain simplified equations giving the maximum roll variance as a function of the excitation variance.

These results are confirmed through the envelope analysis of a preliminary stochastic time-domain numerical simulation. The curve giving the probability density as a function of the variance of the motion, appears, in fact bimodal. Finally, the region of the first subharmonic has been analysed giving the response curves for the roll variance of the subharmonic component and the excitation variance threshold for its onset.

## **INTRODUCTION**

The connection between large amplitude rolling and capsizing is not very clear. In principle, the large amplitude rolling motion of a ship can be a stable motion, provided it be included in some stability boundary. In practice, the ship is a very complicate system, so that many dramatic scenarios can appear once large amplitude rolling is in some way originated. The reasons of these practical differencies can be summarized as depending on:

- wrong operation of the ship. This is for example the case when the rudder is released in the attempt to recover from an excessive heeling in manoeuvring, non properly adjusted antirolling tanks are employed to reduce excessive rolling, a route change is adopted to avoid the beam or quartering action of wave trains;
- structural failure with consequent opening of holes in the hull and flooding of some compartment;
- effect of additional heeling moments due to water loading on deck and through the deck openings caused by the large amplitude rolling or

shifting of cargo due to the large rolling accelerations. This last phenomenon can in turn give rise to a positive feedback with final capsizing or originate a structural failure;

- and of course, the concurrency of more than one of this phenomena. The analysis of casualties at sea reveals that this is often what happens when a ship is lost.

Actually, it is not very simple to quantify the relative importance of these consequences of large amplitude rolling. On the other hand, neither the probability of large amplitude rolling has been stated in a satisfactory way. This paper is thus devoted to a first analysis of this problem.

In previous papers [1-4], it has been shown that large amplitude rolling can be a consequence of a jump between the antiresonant state and the resonant one, or between non resonant and subharmonic states, due to the strong deviation from linearity of the rolling motion. This originates the possibility of bifurcations that can be effective as a consequence of some change in the parameters in the case of a deterministic excitation, and due to the very nature of the oscillation when a narrow band stochastic excitation is considered.

The phenomenon is not very fast, but quite difficult to forecast, inasmuch its occurrence is not related to some dramatic change in the excitation statistics. Moreover, the amplitude differences can be dramatic also in presence of non very intense excitation. Therefore, it appears of interest a parametric research to find the probability of its occurrence. To this end, the probability density function of the response levels should be computed by means of approximate analytical methods in the following three cases of interest:

- bifurcation between the anti- and the resonant oscillation in the main resonance region in stochastic beam sea;
- bifurcation between non resonant and subharmonic in the first subharmonic region in stochastic beam sea;
- bifurcation between zero amplitude (or negligible one) and parametric subharmonic rolling in stochastic following or quartering sea.

As a consequence of the possibility of bifurcations, the probability density functions (pdf) can be bimodal functions for some values of the parameters. This allows an evaluation of the probabilities of the considered different oscillation states, and in particular of the probability of the onset of large amplitude rolling.

In this paper, we will devote our attention to ship rolling in a beam sea, with particular regard to the possibilities offered by the bifurcations in the regions of synchronism and of the main subharmonic. The analysis is limited to the obtaining of the frequency response curves in terms of roll variance in synchronism and to the frequency response and excitation threshold in the case of subharmonic.

## NARROW BAND EXCITATION

The inclining moment due to the action of the sea waves, is usually represented by means of the introduction of the energy spectrum of the sea. Extensive campaigns of measurements allowed to obtain a statistical description of the different regions of the world. From these tables, some standard descriptions have been obtained, as the ITTC and ISSC standard spectra, and successive corrections and integrations. These spectra are usually considered to be sufficiently narrow band to allow a simplified statistical treatment, and at the same time sufficiently broad band with respect to the system transfer function to allow a simplified treatment of the response [5,6]. In addition, hypotheses such as Gaussianity, stationarity and ergodicity are often assumed to further simplify the analysis. For a detailed discussion of these problems see Ref. [7]. Actually, this procedure is a satisfying one when quasi-linear and non extreme phenomena are analysed. If we devote our attention to ship rolling, this is unfortunately not true, since it is a highly nonlinear, large amplitude motion, that can lead to extreme phenomena such as capsizing. It is not the scope of this paper to investigate in detail the connection between large amplitude rolling and capsizing. We will assume that large amplitude rolling is in itself an extremely interesting topic and we devote our attention to some conditions, non sufficiently investigated until now, that can lead to large amplitude rolling.

As shown in previous papers [1-4] in the deterministic domain, the rolling motion, due to its inherently high degree of non linearity, can exhibit peculiar phenomena leading to non expected large amplitude oscillations, also in weak to moderate seas. This is due to the appearance of different steady states of oscillation corresponding to the same excitation intensity and the consequent possibility of bifurcation with jumps among these different states. In the deterministic approach, the problem is an initial value problem, so that the phase plane, or the Van der Pol plane are divided in different regions, called domains of attraction, each leading to one of the steady state solutions. Neglecting the appearance of chaotic behaviour, that seems not playing a dramatic role, the jump is thus only possible when there is a change in the parameters defining the system or the excitation, such as cargo shifting, water on deck, wind gusts, change of heading.

The build-up of a jump is not an immediate process, requiring a few cycles of the excitation to be completed. In a very broad band stochastic excitation case, it is thus very unlikely to occur due to the very poor correlation among successive cycles. Actually this only means that its probability is very low, i.e. it is a 'rare event'.

On the other hand, ITTC spectrum is only an average one, so that its parameters are subject to statistical uncertainty. Moreover, a peak magnification factor has been suggested for the description of North Atlantic. With this correction,

one gets the quite sharp JONSWAP spectrum.

The description of the sea action through the spectrum, is a short term description, valid for the well developed sea. It does not exclude the possibility of appearance of narrow and very narrow spectra in particular conditions, as for example crossing channels or in port regions or in the developing zone, or simply as a statistical fluctuation of broader spectra.

In this case, there could be sufficient correlation among cycles of the excitation to allow for the jump between different amplitude states, without the need of any change in the system parameters.

The spectrum of the sea excitation  $f$  will be described through a simple linear filter of the type:

$$S_f = \gamma \omega_0^2 S_0 / [(\omega_f^2 - \omega^2)^2 + \omega^2 \gamma^2] \quad (1)$$

shaping Gaussian white noise  $W$  of level  $S_0$ . The excitation is zero mean and has variance  $\sigma_f^2 = \pi S_0$ . It is suited to describe narrow band excitation, as in the limit for  $\gamma \rightarrow 0$  it reduces to the sinusoidal excitation

$$f = e_w \cos \omega_f t, \quad (2)$$

with  $e_w^2 = 2\sigma_f^2$ , whose spectrum is represented by  $\pi S_0 \delta(\omega)$ .

In the following, the perturbation method of the multiple scales will be adopted. For this, it is convenient to represent the narrow band process  $f$  in the Stratonovich form [8]:

$$f(t) = F_c(t) \cos \omega_f t + F_s(t) \sin \omega_f t$$

where  $F_c$  and  $F_s$  are slowly varying independent Gaussian processes represented by the equations:

$$\frac{dF_c}{dt} = \left(\frac{\gamma}{2}\right)^{1/2} W_c - \left(\frac{\gamma}{2}\right) F_c$$

$$\frac{dF_s}{dt} = \left(\frac{\gamma}{2}\right)^{1/2} W_s - \left(\frac{\gamma}{2}\right) F_s$$

where  $W_c$  and  $W_s$  are independent Gaussian white noise processes with the same spectrum level of  $W$ . For further details see Ref. [9,10].

Actual values of the spectrum level  $S_0$ , bandwidth parameter  $\gamma$  and centerpeak frequency  $\omega_f$  can be obtained through a nonlinear fitting of the spectra to be approximated.

This procedure applied to normalized standard wave height spectra  $S_{\zeta\zeta}$  using IMSL library routine RNLIN, provided the following values [11]:

- ITTC

$$S_0 = .35 \quad \omega_f = 1.16 \quad \gamma = .50$$

- JONSWAP with sharpness magnification factor equal to 7 (maximum value)

$$S_0 = .13 \quad \omega_f = 1.01 \quad \gamma = .14$$

The transformation of wave heights into inclining moments actually broadens a little the spectrum. In any case, it appears that, also in the frame of standard spectra, there is the possibility of effectively narrow band spectra, in the sense of giving rise to jumps in rolling.

In the following, a value for  $\sigma_f$  will be used so as to give an excitation intensity corresponding to  $e_w = .2$ , a value used in previous calculations in the deterministic domain. This value represents a sinusoidal wave with effective wave slope well below the limit for breaking waves. The bandwidth factor  $\gamma$  will be varied as a parameter.

## THE EQUATION OF MOTION

In the light of the preceding discussion, the rolling motion in beam sea will be represented by the following nondimensional nonlinear differential equation:

$$\frac{d^2x}{dt^2} + (2\mu + \delta_1 x^2) \frac{dx}{dt} + \delta_2 \left(\frac{dx}{dt}\right)^3 + \omega_0^2 x + \alpha_3 x^3 = f(t) \quad (3)$$

We do not discuss here the meaning of the different terms, that can be found in Ref. [1].

The excitation  $f$  is represented by the expression (2) in the deterministic case, whereas in the stochastic it is represented by the solution of the following differential equation:

$$\frac{d^2f}{dt^2} + \gamma \frac{df}{dt} + \omega_f^2 f = \gamma^{1/2} \omega_f W \quad (4)$$

As mentioned, an approximate solution in terms of the variance  $\sigma^2$  of the motion will be obtained in the synchronism region  $\omega_f \approx \omega_0$  and in that of the main subharmonic  $\omega_f \approx 3\omega_0$ .

To get some insight into the nature of the solutions, attention was preliminarily focussed on a form of Eq. 3 containing the minimum of nonlinearities, i.e. only the righting arm one. In these conditions, the rolling motion is described by an equation of the Duffing type. This is tied to the fact that, in the deterministic approach, it is this nonlinearity that is responsible of the presence of bifurcations, whereas the damping moment nonlinearities play an important role in determining the maximum values that can be reached by the oscillation amplitude.

Once obtained a solution valid in the stochastic narrow band case, the deterministic sinusoidal solution can be recovered by means of the following positions:

$$\gamma = 0$$

$$\sigma^2 = \frac{C^2}{2} \quad (5)$$

$$\sigma_f^2 = \frac{e_w^2}{2}$$

$$\sigma_Q^2 = \frac{Q^2}{2}$$

being  $C$  the amplitude of the nonlinear response in resonance and  $Q$  the amplitude of the linear response out of resonance, both in the deterministic case

Only the results relative to the application of the method of multiple scales [12] will be reported.

### SYNCHRONISM REGION

The rolling motion in the region of synchronism is statistically governed by the following equation:

$$\frac{9}{4}\alpha_3^2\sigma^6 + 3\alpha_3(\omega_0^2 - \omega_f^2)\sigma^4 + [(\omega_0^2 - \omega_f^2)^2 + (2\mu\omega_f)^2(1 + \gamma/2\mu)^2]\sigma^2 = (1 + \gamma/2\mu)\sigma_f^2 \quad (6)$$

that, using the positions represented by Eq's 5, reduces to:

$$\frac{9}{16}\alpha_3^2C^6 + \frac{3}{2}\alpha_3(\omega_0^2 - \omega_f^2)C^4 + [(\omega_0^2 - \omega_f^2)^2 + (2\mu\omega_f)^2]C^2 = e_w^2 \quad (7)$$

in the sinusoidal case. Eq. 7 agrees with previous results [1].

Eq. 6 represents a very important result inasmuch as it allows a relatively simple calculation of the frequency response curve in presence of stochastic excitation. Due to the particular way through which it was obtained, its validity is limited to the narrow band case.

In Fig. 1 and Fig. 2, the response curves given by Eq. 6 are reported as a function of tuning ratio centerpeak frequency/natural frequency of small amplitude oscillations  $\omega_0$  for different values of the bandwidth parameter including the limiting case of sinusoidal excitation.

Fig. 1 represents a typical case of modern containership, whereas Fig. 2 refer to a more traditional case [13].

As one can see, the possibility of bifurcation is preserved also in the stochastic case, provided that the bandwidth is sufficiently small. In particular, in the considered cases, the most sharp JONSWAP is not far from the higher limit of values of  $\gamma$  that gives multiple regime of oscillations.

In the sinusoidal case, in the frequency region where three states are possible, only the two extreme represent stable oscillations and the bifurcation involves them. In the stochastic case,

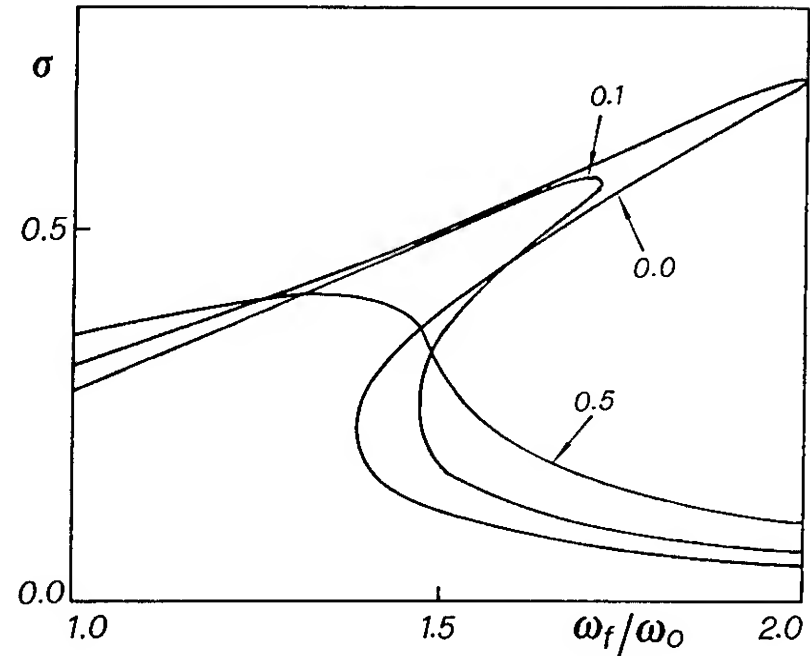


Fig. 1 Roll variance  $\sigma$  as a function of tuning ratio  $\omega_f/\omega_0$ . The following values have been used for the parameters:  $\alpha_3=4.0$ ,  $\mu=.05$ ,  $\sigma_f=.1414$  ( $e_w=.2$ ). The number on the curves indicates the value of  $\gamma$ .

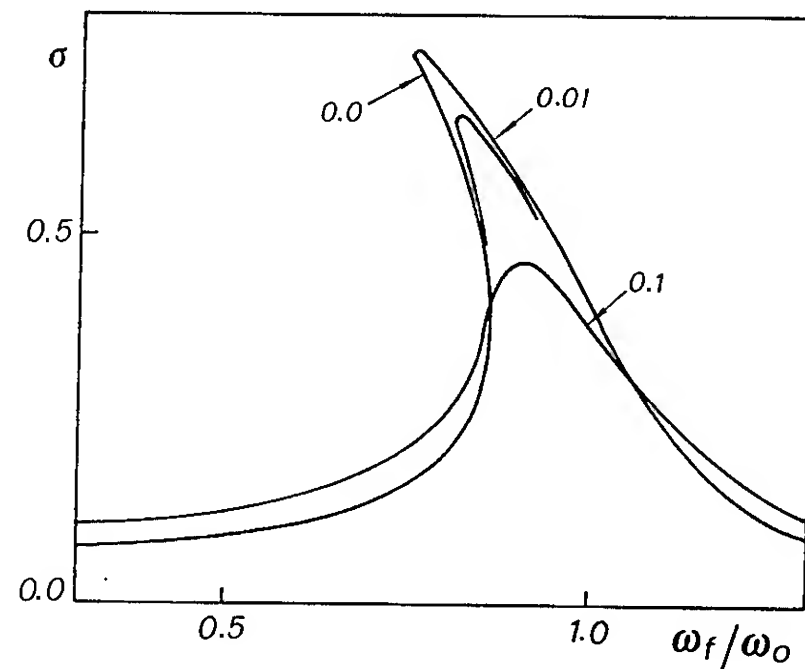


Fig. 2 Roll variance  $\sigma$  as a function of tuning ratio  $\omega_f/\omega_0$ . The following values have been used for the parameters:  $\alpha_3=-0.5$ ,  $\mu=.05$ ,  $\sigma_f=.1414$  ( $e_w=.2$ ). The number on the curves indicates the value of  $\gamma$ .

the concept of stability of an oscillation state loses part of its meaning. Actually, in the frequency region where three levels of variance are possible, the roll variance oscillates, having local maxima of probability in correspondence to the two extreme values. This is intrinsically connected with the nature of the stochastic excitation [14].

Neglecting the contribution of the nonlinear term, the solution far from resonances is obtained as:



$$\sigma_Q^2 = (1 + \gamma/2\mu) \sigma_f^2 / [(\omega_0^2 - \omega_f^2)^2 + (2\mu\omega_f)^2(1 + \gamma/2\mu)^2] \approx \sigma_f^2 / (\omega_0^2 - \omega_f^2)^2 \quad (8)$$

A perturbative analysis on Eq. 6, considering  $\omega_0 + \omega_f \approx 2\omega_0$  gives a second degree algebraic equation on the variable  $\Delta\omega = \omega_f - \omega_0$ . The reality condition of the solution gives a simple formula relating the maximum value of the roll variance  $\sigma_m^2$  to the excitation variance:

$$\sigma_m^2 = \sigma_f^2 / 4\mu^2\omega_0^2(1 + \gamma/2\mu)$$

that reduces to the sinusoidal expression:

$$C_m^2 = e_w^2 / 4\mu^2\omega_0^2$$

These expressions correspond to a linear approach and thus generally they are not sufficiently reliable.

A corresponding analysis conducted on the complete nonlinear rolling Eq. 3, allowed us to obtain the general equation for the roll variance in the implicit form:

$$\sigma_f^2 = \frac{\mu_{eq}}{1 + \gamma/2\mu_{eq}} [(\omega_0^2 - \omega_f^2)^2 - \frac{3}{2}\alpha_3\sigma^2 + (2\omega_0\mu_{eq})^2(1 + \gamma/2\mu_{eq})^2]\sigma^2$$

with

$$\mu_{eq} = \mu + \frac{1}{4}\sigma^2 \quad \delta_{eq} = (\delta_1 + 3\omega_0^2\delta_2)$$

A perturbation on this equation gives the implicit equation for the maximum roll variances:

$$(2\omega_0)^2[\mu^2(1 + \gamma/2\mu_{eq})\sigma_m^2 + \frac{1}{2}\mu(1 + \gamma/2\mu_{eq})\delta_{eq}\sigma_m^4 + \frac{1}{16}\delta_{eq}^2\sigma_m^6] = \sigma_f^2 \quad (9)$$

the corresponding sinusoidal expression proved good in the forecasting of the maximum roll amplitude in synchronism [15]. Here, the predictions are, of course, of a statistical nature, but sufficient for many practical scopes. When a bifurcation is possible, Eq. 9 refers to the highest variance level, irrespectively of its actual probability of occurrence..

### SUBHARMONIC SOLUTION

In the frequency region  $\omega_f \approx 3\omega_0$  the non resonant solution given by Eq. 8 is generally stable. Nevertheless, the analysis conducted in the sinusoidal case, indicated that there is the possibility of excitation of a resonant oscillation with frequency  $\omega_f/3 \approx \omega_0$ . The application of the

method of multiple scales permitted to obtain an equation describing the variance  $\sigma_s^2$  of the resonant part of the solution, i.e. the amplitude of the subharmonic component that has to be added, in some way, to the non resonant component of variance  $\sigma_Q^2$ . Here, only the results relative to the Duffing case will be presented. The analysis of the full Eq. 3 is actually in progress.

As a consequence of the stability of the non resonant component, we have the following possibilities:

$$\sigma_s^2 = 0$$

or

$$\frac{9}{4}\alpha_3^2\sigma_s^4 + [3\alpha_3Q_n - \frac{9}{4}\alpha_3^2(1 + \gamma/6\mu)\sigma_Q^2]\sigma_s^2 + [Q_n^2 + \frac{4}{9}\omega_f^2\mu^2(1 + \gamma/6\mu)^2] = 0 \quad (10)$$

with

$$Q_n = \omega_0^2 - \omega_f^2/9 + 3\alpha_3\sigma_Q^2$$

Eq. (10) is a second degree algebraic equation in the variable  $\sigma_s^2$ . The reality condition

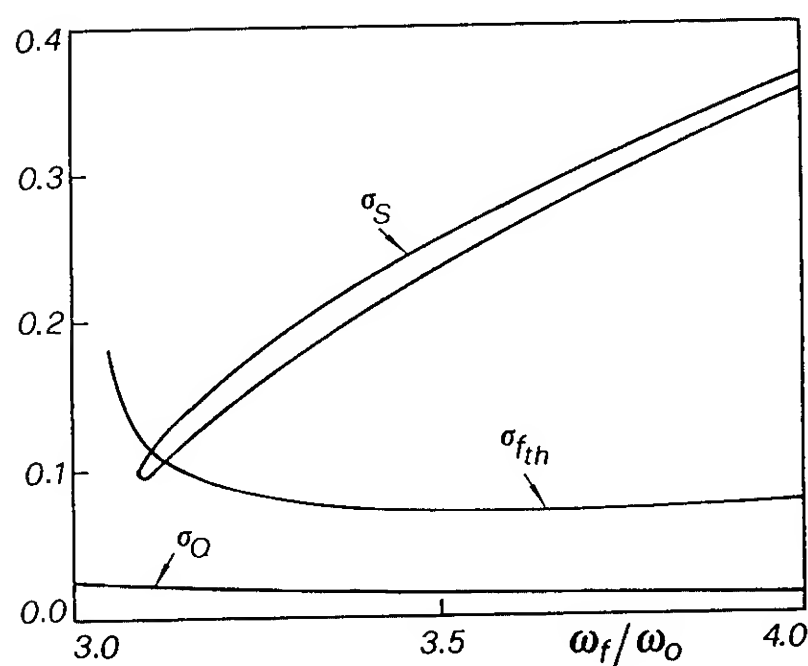


Fig. 3 Variance  $\sigma_s$  of the subharmonic component, excitation threshold  $\sigma_{fth}$  for subharmonic oscillation onset and variance  $\sigma_Q$  of the out of resonance component as a function of tuning ratio  $\omega_f/\omega_0$ . The following values have been used for the parameters:  $\alpha_3=4.0$ ,  $\mu=.005$ ,  $\sigma_f=.1414$ ,  $\gamma=.01$ .



for the solution gives the threshold value  $\sigma_{fth}^2$  of the excitation variance for the onset of a subharmonic component of the oscillation:

$$\sigma_{fth}^2 = -\frac{4}{3\alpha_3}(1+\gamma/2\mu) [(\omega_0^2-\omega_f^2)^2 + (2\mu\omega_f)^2(1+\gamma/2\mu)^2] \left\{ \omega_0^2-\omega_f^2/9 + \frac{\alpha_3}{|\alpha_3|} [(\omega_0^2-\omega_f^2/9)^2 - \frac{4}{9}\omega_f^2\mu^2(1+\gamma/6\mu)(7-\gamma/6\mu)]^{1/2} \right\} / (7-\gamma/6\mu)$$

This expression also reduces to the previous one [1] in the sinusoidal limit.

In Fig. 3 and Fig. 4, the values of  $\sigma_s$ ,  $\sigma_Q$ , and  $\sigma_{fth}$  are reported as a function of centerpeak

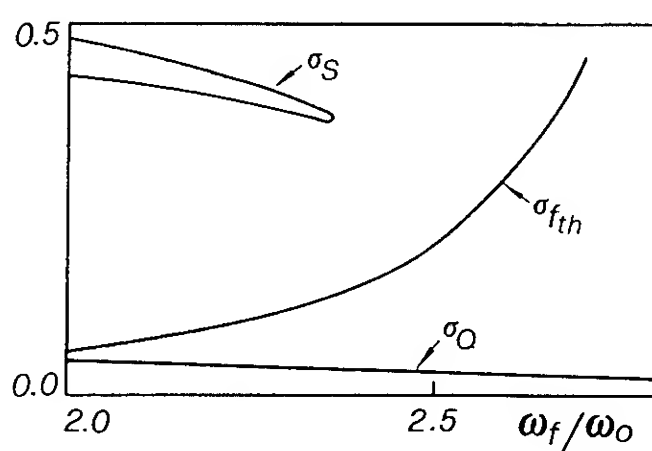


Fig. 4 Variance  $\sigma_s$  of the subharmonic component, excitation threshold  $\sigma_{fth}$  for subharmonic oscillation onset and variance  $\sigma_Q$  of the out of resonance component as a function of tuning ratio  $\omega_f/\omega_0$ . The following values have been used for the parameters:  $\alpha_3=-1.75$ ,  $\mu=.005$ ,  $\sigma_f=.1414$ ,  $\gamma=.01$ .

frequency of the excitation. As one can see, the excitation of a subharmonic component is a phenomenon possible also in the stochastic case. The required bandwidth is in general quite narrow and the roll damping quite low, so reducing the probability of occurrence.

#### NUMERICAL SIMULATION AND CONCLUSIONS

Numerical time domain simulation in the stochastic excitation case is not, in general, an easy task. This is due to a lot of complications arising in the realization of a true stochastic time series for the excitation as explained in [7]. In addition, is not clear what happens of the domains of attraction that define the set of initial conditions

that lead to a particular steady state solution. On the other hand, in the limit of narrow band the system has to recover the sinusoidal features.

Looking forward to the possibility of presenting a more complete numerical picture of the behaviour of this nonlinear system in stochastic domain in next future [14], we report here only some conclusions obtained from preliminary calculations.

Time domain simulation of Eq. 3 with the forcing term given by the following expression [16]:

$$f(t) = \left(\frac{2\sigma_f^2}{N}\right)^{1/2} \sum_{k=1}^N \cos(\omega_k t + \phi_k)$$

This gives a pseudorandom signal when the  $\omega_k$  are chosen independently from a random population with a pdf of the same form of the spectrum of  $f$  and the phases  $\phi_k$  are independent and uniformly distributed in  $(0, 2\pi)$ .

A time domain solution was obtained in the synchronism region where multiple regime was indicated. A statistical analysis on the time series indicated a bimodal pdf.

These results confirm that jump possibility is likely to occur in the domain of parameters indicated by approximate perturbative solutions. The probability of the highest state depends on the tuning ratio, decreasing as this increasingly deviates from the synchronism condition.

#### ACKNOWLEDGEMENTS

The authors would express their gratitude to Prof. H. G. Davies for the interesting discussion on narrow band processes during his visit in Trieste.

#### REFERENCES

- [1] Cardo, A., Francescutto, A., Nabergoj, R., "Ultraharmonics and Subharmonics in the Rolling Motion of a Ship: Steady-State Solution", *International Shipbuilding Progress*, Vol. 28, 1981, pp. 234-251.
- [2] Cardo, A., Francescutto, A., Nabergoj, R., "Deterministic Nonlinear Rolling: A Critical Review", *Bulletin de l'Association Technique Maritime et Aéronautique*, Vol. 85, 1985, pp. 119-141.
- [3] Cardo, A., Francescutto, A., Nabergoj, R., "Transient Nonlinear Rolling: The Domains of Attraction", *Proceedings 14th Scientific and Methodological Seminar on Ship Hydrodynamics*, Varna, Vol. 2, 1985, pp. 23-29.
- [4] Francescutto, A., "Jump phenomena in Nonlinear Rolling in a Stochastic Beam Sea", *Bulletin de l'Association Technique Maritime et Aéronautique*, Vol. 88, 1988, pp. 504-524.
- [5] Roberts, J. B., "A Stochastic Theory for Nonlinear Ship Rolling in Irregular Seas", *Journal of Ship Research*, Vol. 26, 1982, pp. 229-245.
- [6] Cardo, A., Francescutto, A., Nabergoj, R.,

"Stochastic Nonlinear Rolling: Which Approach?", Bulletin de l'Association Technique Maritime et Aéronautique, Vol. 87, 1987, pp. 491-505.

[7] Francescutto, A., "On the Nonlinear Motions of Ships and Structure in Narrow Band Sea", Proceedings of the IUTAM Symposium on Dynamics of Marine Vehicles and Structures in Waves, London 1990

[8] Stratonovich, R. L., Topics in the Theory of Random Noise, Vol. I, Gordon and Breach, New York, 1963.

[9] Rajan, S., Davies, H. G., "Multiple Time Scaling of the Response of a Duffing Oscillator to Narrow-Band Random Excitation", Journal of Sound and Vibration, Vol. 123, 1988, pp. 497-506.

[10] Davies, H., G., Rajan, S., "Random Superharmonic and Subharmonic Response: Multiple Time Scaling of a Duffing Oscillator", Journal of Sound and Vibration, Vol. 126, 1988, pp. 195-208.

[11] Francescutto, A., Cardo, A., Contento, G., "On the Representation of Sea Spectra Through Linear Filters" (in Italian), University of Trieste, Institute of Naval Architecture, Technical Report N. 67, 1988.

[12] Nayfeh, A. H., Mook, D. T., Nonlinear Oscillations, Wiley-Interscience, New York, 1979.

[13] Cardo, A., Francescutto, A., Nabergoj, R., "The Excitation Threshold and the Onset of Subharmonic Oscillations in Nonlinear Rolling", International Shipbuilding Progress, Vol. 32, 1985, pp. 210-214.

[14] Francescutto, A., "On the Probability of Large Amplitude Rolling and Capsizing as a Consequence of Bifurcations", Accepted for presentation at the 10th International Conference on Offshore Mechanics and Arctic Engineering 'OMAE', Stavanger, June 1991.

[15] Cardo, A., Francescutto, A., Nabergoj, R., "Nonlinear Rolling in Regular Sea", International Shipbuilding Progress, Vol. 31, 1984, pp. 3-7.

[16] Shinozuka, M., "Simulation of Multivariate and Multidimensional Random Processes", Journal of Acoustical Society of America, Vol. 49, 1971, pp. 357-367.

## DISCUSSION

Ali H. Nayfeh

Virginia Polytechnic Institute and State University, USA

How realistic are the results presented in Figures 1 and 3 for the case of a hardening-type righting arm? What are the assumptions underlying the derivation of eqs. (6), (7), (8), (9), and (10)? Are they the same as those used by Davis and Rajan? How different are your results from their results? What are the limitations of the method?

## AUTHORS' REPLY

The validity of the procedure adopted to get the perturbative approximate solutions is implicitly proved by the goodness of the comparison with the results of a numerical simulation (see [14] for more details). As regards the meaning of considering the case with hardening stiffness ( $\alpha_3 > 0$ ), we can deserve the following. A research on a consistent specimen of ships in a variety of loading conditions [17], indicated that the validity of a model of righting arm with  $\alpha_3 > 0$  can extend to quite large amplitude inclinations ( $30^\circ - 40^\circ$ ) especially for modern container ship forms. This is sufficient to assess the importance of the inclusion of this case in a true nonlinear seakeeping context, as far as rolling motion is considered. Capsizing, instead, is generally too a complicated phenomenon to be explained by means of relatively simplified models like those considered. On the other hand, when large amplitude rolling is generated, it is likely to think that additional mechanisms can deteriorate the stability qualities of the ship, leading to capsize as indicated in the introduction (see also ref. [14]). Additional references [17] Cardo, A., Francescutto, A., Nabergoj, R., "The Excitation Threshold and the Onset of Subharmonic Oscillations in Abulinear Rolling", International Shipbuilding Progress, Vol. 32, 1985, pp. 210-214.

## DISCUSSION

Odd Faltinsen

Norwegian Institute of Technology, Norway

Is the frequency dependence of hydrodynamic coefficients included in the model?

## AUTHORS' REPLY

Actually, the frequency dependence of the hydrodynamic coefficients is not included in the model. This is not due only to the obvious overcomplications involved, but to the necessity of a better clarification of the exact meaning of frequency in presence of a stochastic excitation with the possibility of multiple regime of oscillation and of the techniques for transferring this frequency dependence when doing time domain simulation with nonlinear models. On the other hand, in a full nonlinear approach, it is not very easy to separate added mass and damping contributions.

# Effect of Viscous Damping on the Response of Floating Bodies

M. Downie<sup>1</sup>, J. Graham<sup>2</sup>, X. Zheng<sup>1</sup>

(<sup>1</sup>University of Newcastle upon Tyne, United Kingdom)

(<sup>2</sup>Imperial College of London, United Kingdom)

## ABSTRACT.

The prediction of hydrodynamic damping due to vortex shedding on a three-dimensional body in waves is discussed. A method of matching precalculated results for separated oscillatory flow past an isolated edge at each vortex shedding region of the outer potential flow field of the body in waves has been extended to three-dimensional floating bodies by two different methods. In the first method the pressure field due to a local separated flow computed by a discrete vortex method, is applied at all vortex shedding edges of the hull. In the second method the effect of vortex shedding at an edge is represented directly in the frequency domain panel method by special edge panels. A dipole density on each of these edge panels is evaluated by making a comparison between the far field effect of the panel and the far field of the appropriate separated vortex flow modelled by the vortex method.

## NOTATION.

A,B,C,M	added mass, damping, restoring and mass coefficient matrices
$F_V$	vortex force
$H_j$	body motions = $\eta_j e^{-i\omega t}$
Kc	Keulegan-Carpenter number = $2\pi U/\omega L_B$
L	matching length scale
$L_B, L_V$	body and vortex length scales
l	barge beam
$l_{VP}$	vortex panel length
q	velocity amplitude
s	surface distance
U	velocity scale
z	complex coordinate in cross-sectional plane = $x + iy$
$\Gamma$	vortex strength (circulation)
$\delta$	internal edge angle
$\zeta$	complex coordinate in the transformed plane
$\mu$	dipole strength
$\rho$	density
$\sigma$	source density
$\Phi$	velocity potential, sum of component potentials $\phi_j e^{-i\omega t}$ , $j=1...6$ , for surge, sway, heave, roll pitch, and yaw.
$\omega$	frequency of motion

## INTRODUCTION.

Prediction of the forces and responses induced by waves on floating bodies is usually based on linear potential flow theory (1), which is quite adequate for the prediction of many types of response. The damping arising from linear potential flow is associated with the waves that radiate out from the body. However certain types of motion for which the first order radiation damping is fairly small are not well predicted. In these cases non-linear effects must be included in the analysis. The most important non-linearities may be accounted for by second order potential flow effects and separation. Both of these are significant for example in low frequency sway motion. In the present paper we are concerned with incorporating separation effects alone into a linear potential method. This is found to greatly improve the prediction of, in particular, roll motions of many types of floating body. The effect of neglecting separation is conspicuously evident in the case of roll, particularly near resonance, when the response can be greatly overpredicted by linear theory (2), see figure 1.

In engineering applications of linear potential theory it is usual practice to incorporate empirical coefficients into the calculation to represent the effects of viscous damping. Good agreement between predicted and experimental results can be obtained for most standard hull sections. The results of the semi-empirical method (3) to predict wave and viscous damping are also shown in figure 1. However prediction of the damping for non-standard hull shapes is more difficult. Other semi-empirical methods include experimental determination of the individual components of the roll damping (4), use of the concept of crossflow drag on a barge hull and its appendages (5), and work described in references (6 - 10). In the case of a barge or ship hull the dominant non-linear component at roll resonance is due to viscous, i.e. separation, effects. These effects, often described by the general term 'viscous damping' are primarily due to vortex shedding from the hull and its appendages. A two-dimensional model incorporating theoretically the effect of separation has been developed for barge roll (6). This model used a local solution of separated flow past an oscillating edge which was representative of the bilge of the hull and its relative motion. This local flow field was computed

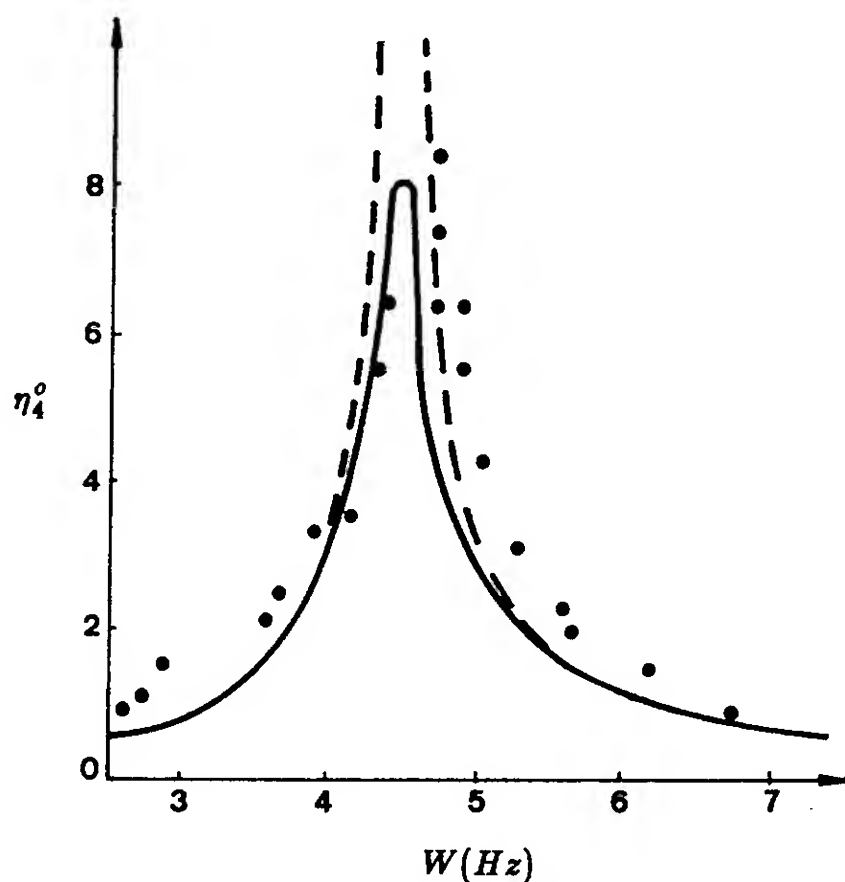


Fig. 1. Roll amplitude against frequency for a rectangular cylinder in beam waves (Salvesen *et al.*<sup>(2)</sup>).—, wave and viscous damping; - - -, wave damping only; •, experiment.

as a universal semi-infinite edge flow dependant only on the edge angle (typically  $90^\circ$ ) and was then applied by a matching process to the flow field around the hull. The method used to compute the flow field was the discrete vortex method (11) which gives good flow and force predictions for vortex shedding from sharp edges in oscillatory flow. The flows induced on floating bodies are essentially high Reynolds number and oscillatory. In many cases separation is fixed by the geometry of the body. Flows of this nature have a strong vortex structure that is easily modelled by the discrete vortex method. Numerical solution of the Navier-Stokes equations by finite differences or elements could also be used but is generally more expensive because unless a very fine grid is used these methods do not capture the thin shear layers in the flow field. The discrete vortex method provides a time domain solution for the separated flow. The Kutta-Joukowski condition is used in the inviscid case to specify the strength of vorticity shed from the edges. Later refinements of the method have shown that rounded edges, bilge keels and viscous effects can also be incorporated successfully, (12).

Since prediction of the response of a floating body requires a large range of input amplitudes, directions and frequencies to be computed, for practical use it is essential to have a method which minimises the computer time for each case. The use of a matched inner flow field as above provides this economy since the separated flow need only be calculated once for all edge sections of the body having the same included angle. This 'inner' flow is then matched to the 'outer' linearised potential flow at the bilge or salient region of separation so that one time consuming vortex calculation can be used to provide results

for a complete range of motions for any given body. The outer flowfield associated with the incident wave field and general motion of the body is solved with a full boundary integral method. Since this method is based on inviscid potential flow theory which cannot model flow separation, the flow field is singular along the lengths of bilges and other shedding edges. In the case of a three-dimensional body in a general incident wave field a quasi-two-dimensional assumption is made for the vortex shedding locally. The outer flow field is fully three-dimensional but it is assumed that the separated flow is generated within a formation region sufficiently close to the edge on the scale of the body that it may be considered to be locally two-dimensional. Hence the inner separated flow field is matched on a strip theory basis. This approach is justified at long continuous edges but clearly breaks down at those points where sudden changes in geometry occur. The method also assumes that the flows associated with different edges do not interact and also that the wave making effects of the vortices are insignificant. The first assumption is justified for sufficiently small amplitudes of motion, although the results of the method are in reasonable agreement with measured data up to moderately large roll angles. The second assumption is less certain, see for example (13). It should be noted here that the entire method is theoretically based and does not require the input of any empirical data. Also the linearised free surface boundary condition is applied so that the method is not limited to the low frequency approximation.

The separated flow field induced by oscillatory flow past an edge commonly consists of pairs of vortices, one pair shed during each flow cycle. These vortices are of alternate sign and often form a closely coupled pair moving away from the edge under their mutually induced velocity fields. Other modes of shedding also occur. A single vortex may convect along a surface under the induced velocity field of its image and for rounded edges two vortex pairs may be shed per cycle, (12).

This method which matches the vortex calculations to the outer flow past a general body has been described in detail in (14). The main feature is that the singularity at each edge in the potential flow past the body cross-section is evaluated by applying a conformal transformation to the section which opens the perimeter out into a straight line, figure 2. The force induced by the vortex shedding on the body is calculated from an integral over this transformed cross-section. This procedure is reasonably straightforward to implement for simple hull shapes but becomes complicated and difficult to specify for many other types of floating structure. For this reason an alternative approach which is the subject of this paper has been developed.

In the new method the effect of vortex shedding at an edge of the body is modelled directly in the potential flow calculation by dipole panels representing the vortices along each edge. The dipole panels satisfy the free surface boundary condition and may also be considered as representing the force induced by vortex

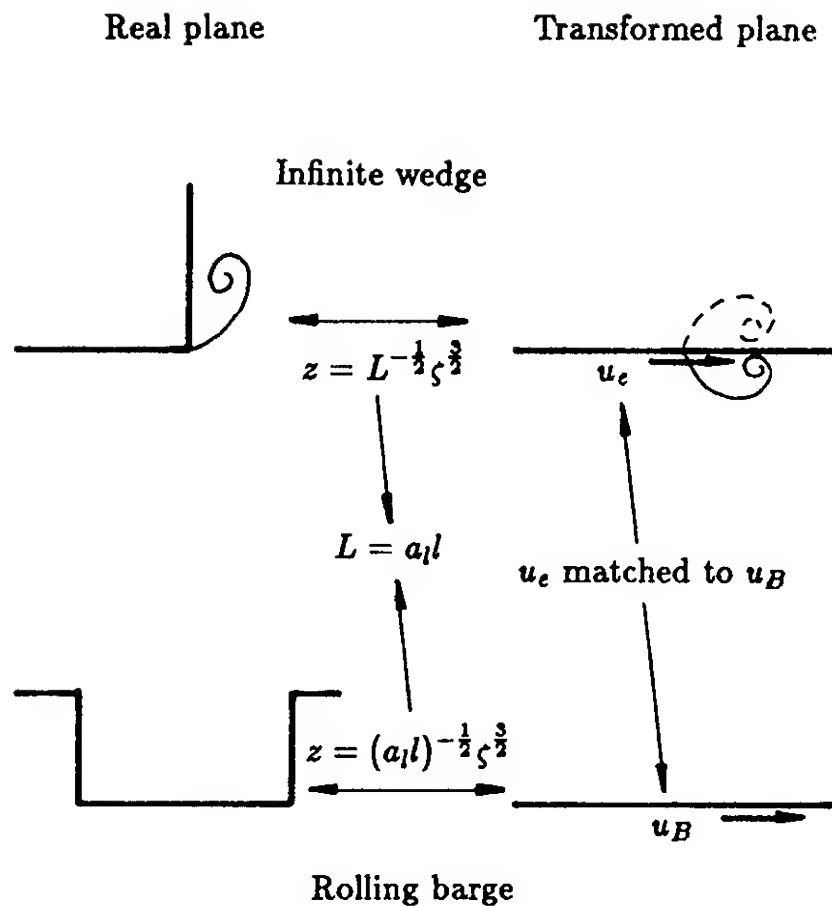


Fig. 2. Matching the local and exterior flows.

shedding at an edge. Because of the convenience of working in the frequency domain, as with the matching method, the non-linear vortex force is Fourier analysed into a fundamental component at the input frequency and harmonics which are all considerably smaller (10% or less) than the fundamental. It is therefore justifiable to neglect them when primary motions such as roll resonance are being considered. However the same would not necessarily be true where second order potential effects are important such as in low frequency response to waves. The dipole panels are therefore evaluated in the same way as the body surface singularity panels in terms of a complex amplitude at the input frequency. The length of the panels however depends on the amplitude of the motion or waves and is calculated by considering the separation condition at the edge.

#### COMPUTATION OF THE FLOW FIELD.

Oscillatory flow about a body may be characterised by the Keulegan-Carpenter number,  $Kc$ . At small  $Kc$  the maximum displacement of the fluid particles in the undisturbed flow is small in comparison with the scale of the body. Thus vortices may only move away from its edges under the influence of the velocity field of other vortices shed from those same edges, and hence the shedding from any one edge may become independent of the shedding from other edges. In these circumstances, the local flow becomes analogous to the local flow about an infinite wedge. The discrete vortex analysis of shedding from an isolated edge (11) carried out for a series of infinite wedges of varying internal angle showed that the complex force due to vortex shedding could be related to the vortex strengths and positions by

$$F_V = -i\rho \frac{d}{dt} \left\{ \sum \Gamma_j (\zeta_j - \zeta_j^I) \right\} \\ = 1/2 \rho U^2 L Kc^{(2\delta-\pi)/(3\pi-2\delta)} \Psi(t) \quad (1)$$

where  $\Psi$  is a dimensionless time-dependent force function which can be Fourier analysed into a fundamental and higher harmonics of the input frequency and  $U$  and  $L$  are length scales defined in the matching process.

#### Body Surface Panels.

The flow field is described by a velocity potential which satisfies Laplace's equation. For each wave frequency the total potential may be written in terms of the separate potentials for the undisturbed incident wave, the wave scattered by the body considered to be fixed and rigid, and the waves radiated by the body in its six degrees of freedom, where it is understood that the real part only of the potential is considered :

$$\Phi = \phi_0 e^{-i\omega t} + \sum_{j=1}^6 \phi_j H_j + \phi_7 e^{-i\omega t} \quad (2)$$

The potential satisfies the linearised free surface condition

$$-\omega^2 \phi_j + g \delta\phi/\delta y = 0, \quad j = 0 \dots 7, \quad y = 0 \quad (3)$$

where  $y$  is the vertical axis. A radiation condition, and a normal velocity condition on the body and sea bed are also satisfied. In the new method the potentials were represented by a mixture of sources and dipoles:

$$\phi_j(q') = 1/4\pi \int_B \left\{ \sigma_j(q) G(q',q) - 2 \phi_j(q) \frac{dG(q',q)}{dn} \right\} ds \\ j = 1 \dots 7 \quad (4)$$

The integral is over the points  $q$  lying on the wetted surface of the body  $B$  with normal  $n$ .  $\sigma(q)$  are the source densities and  $G(q',q)$  are suitable Green's functions (15). The potentials are evaluated by solving the boundary integral equations on the surface of the body numerically (16). The equations of motion of a freely floating body can conveniently be expressed as:

$$\sum_k \left\{ -\omega^2 (M_{jk} + A_{jk}) - i\omega B_{jk} + C_{jk} \right\} \eta_k = f_j \quad (5)$$

The force coefficients and the exciting forces  $f_j$  can be calculated from the linearised form of the Bernoulli's equation using the potentials given by the boundary integral method.

#### Vortex (Dipole) Panels.

We assume that the body has a number of well defined edges from which vortex shedding will take place. Cases where separation is taking place from a moderately curved continuous



surface will not be considered in this analysis. Then the solution for the above potential flow will have the local behaviour:

$$\Phi \sim s^{\pi/(2\pi-\delta)} \quad (6)$$

where  $\delta$  is the included angle of the edge and  $s$  is the surface distance measured perpendicularly to the edge. For simplicity we will now consider the case of a body for which all the edges are right angles so that  $\delta = \pi/2$ . Hence the surface speed in the vicinity of the edge is

$$q = c |s|^{-1/3} + O(1) \text{ terms} \quad (7)$$

where  $c$  can be evaluated from the two adjacent panels (1 and 2) as:

$$c = 2/3 (\Phi_2 - \Phi_1) / (|s_2|^{2/3} + |s_1|^{2/3}) \quad (8)$$

The viscous flow response to this singularity in  $q$  is for separation to occur resulting in the shedding of vortex pairs from the edge each flow cycle.

As in eqn.(1) vortex shedding of this type has been shown (17) to exert a force on the body in two-dimensional flow:

$$F_V = -i\rho \frac{d}{dt} \left\{ \sum \Gamma_j (\zeta_j - \zeta_j^I) \right\} \quad (9)$$

where  $\Gamma_j$  is the circulation of each shed vortex and  $\zeta_j$  is its location in a plane obtained by applying the local Schwartz-Christoffel transformation,

$$z = k \zeta^{2-\delta/\pi} \quad (10)$$

in the plane  $z = x + iy$  normal to the edge and local to it, figure 2.  $\zeta_j^I$  is the image of  $\zeta_j$  in the plane surface which is the transformed body surface in the  $\zeta$  plane.

The complex potential in the  $\zeta$  plane in the vicinity of the edge due to this array of shed vortices is

$$W = i/2\pi \sum \Gamma_j \left\{ \log(\zeta - \zeta_j) - \log(\zeta - \zeta_j^I) \right\} \quad (11)$$

We now make the assumption, as in the previous matching method (17), that the amplitude of the body motion or of the incident waves is sufficiently small for the vortex shedding to be considered as a local phenomenon at each edge. That is the length scale  $L_v$  associated with the vortex shedding (for example the typical distance of the centre of a vortex from the edge when it detaches and a new vortex starts to form) is much smaller than the typical length scale of the body cross-section  $L_B$ . This is a formal restriction, but having made it, the method will be used practically for amplitudes as large as can be justified by the results.

With this assumption the complex potential  $W$  takes the form, at large distances  $\zeta$  from the edge:

$$W \rightarrow -(i/2\pi\zeta) \sum \Gamma_j (\zeta_j - \zeta_j^I) \quad (12)$$

for  $L_v^{2/3} \ll \zeta \ll L_B^{2/3}$

This is the potential of a vortex dipole of strength:

$$\mu = - \sum \Gamma_j (\zeta_j - \zeta_j^I) \quad (13)$$

located at the edge  $\zeta = 0$ .

The shed vortices are therefore modelled by a dipole panel in the physical plane whose potential at large distances in the transformed  $\zeta$  plane including the effect of its image is equal to that of eqn.(13). It is convenient in the present panel method to represent the dipole by a piecewise constant distribution of source dipole density aligned in the direction normal to the panel surface, and hence to the vortex dipole direction, with the panel lying along the external bisector of the edge angle. This dipole may also be considered through eqns. (9) and (13) as being proportional to the impulse  $\int F_V dt$  exerted by the vortex shedding at the edge. Because of this the total dipole strength may be obtained directly from the vortex force computations in the form of eqn. (1). However the length of the vortex panels remains as an apparently disposable parameter in the numerical method. Since the intention is to derive a method which can be applied in the frequency domain, the dipole density is taken to be proportional to the component of the impulse at the fundamental frequency, which as discussed earlier is the dominant part. The length of the panel is kept constant through the flow cycle. The length can be assigned in a number of ways and it is not yet clear which is optimal. It could, for example, be made equal to the characteristic distance  $L_v$  of the vortices from the edge during the formation process. This is not always easy to specify and in the results described here the length is prescribed instead by requiring the Kutta-Joukowski separation condition to be satisfied in the mean sense over the flow cycle at each edge. Hence we obtain for a right angle edge, after some algebra, the source dipole density  $\mu'$  length  $l_{vp}$  given by:

$$\mu' = X^2 (b_1 \cos \omega t - a_1 \sin \omega t) / 4\omega l_{vp}^{2/3} \quad (14)$$

and

$$l_{vp} = \{ X (a_1^2 + b_1^2)^{1/2} / 4\pi\omega \}^{3/4} \quad (15)$$

where  $X = 3/2 |c|$ ,  $c$  being defined in eqn.(8) in terms of the potential  $\Phi$  on panels either side of the edge.  $a_1$  and  $b_1$  are the Fourier coefficients of the fundamental component of the vortex force



FV, defined by:

$$a_1 = \frac{\omega}{\pi} \int_0^{2\pi} F_V \cos \omega t \, dt \quad \text{and}$$

$$b_1 = \frac{\omega}{\pi} \int_0^{2\pi} F_V \sin \omega t \, dt \quad (16)$$

Having specified each vortex panel in this way in terms of the attached flow potential on the adjacent panels to each segment of an assumed shedding edge, the surface potential calculation is repeated with the vortex effect incorporated. The pressure field can then be computed from Bernoulli's equation over the panels on the surface of the body only, ie. excluding the vortex panels.

## RESULTS.

Both methods have been tested for cases of barges for which the hulls take the simple form of boxes with plane rectangular sides and right angle edges. Experimental data containing sufficient information to compute these cases however are scarce. Three cases have been studied, the first and second being cases of barge response in beam seas and the third a forced roll case. The first case was a barge with a beam to draught ratio of 10.0 and a length to beam ratio of approximately 3.3. Experimental data was obtained for a model of the barge, at scale 1:30, with rounded bilge corners with radius of curvature equal to 18% of the draught. The results (18) for roll in beam seas are compared with computed predictions using the first (matching) method in figure 3. In the second case study (8), a barge with a beam to draught ratio of 7.6 and a length to beam ratio of 3.0 was used. Experimental results for both sharp-edged and rounded bilge corners were obtained. The rounded ones had a radius of curvature of 38% of the draught. The damping was significantly reduced when the bilge corners were rounded. These experimental results and those computed by the first method for the sharp-edged case are shown in figure 4. In the third case results of a forced roll experiment (19) on a barge of beam to draught of 21.0 are compared with the computed results of the second numerical method. The experiment was on a barge spanning the test section of a tank whereas the computation was for a barge of the same beam to draught ratio and a length to beam of 6.14. The results for the damping coefficients for different wave amplitudes are shown in figure 5 and for the added mass in figure 6

## DISCUSSION.

The vortex force for each degree of freedom is predicted to have components in phase with the velocity and with the acceleration of the body. Therefore, the method accounts for viscous contributions to both the damping and added mass terms, including the effects of cross-coupling. In

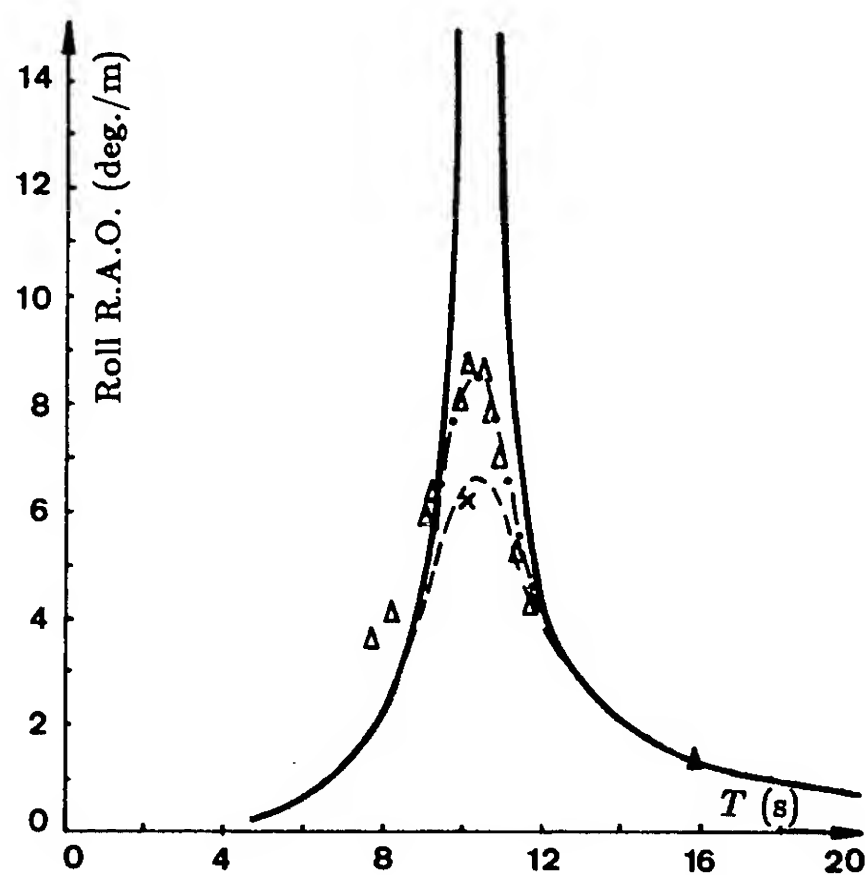


Fig. 3. Case study 1; Roll RAO against wave period. —, wave damping only; viscous damping included, — • —,  $H_w = 3$  m, — — —,  $H_w = 5$  m; experiment, —△—,  $H_w = 3$  m, — × —,  $H_w = 5$  m.

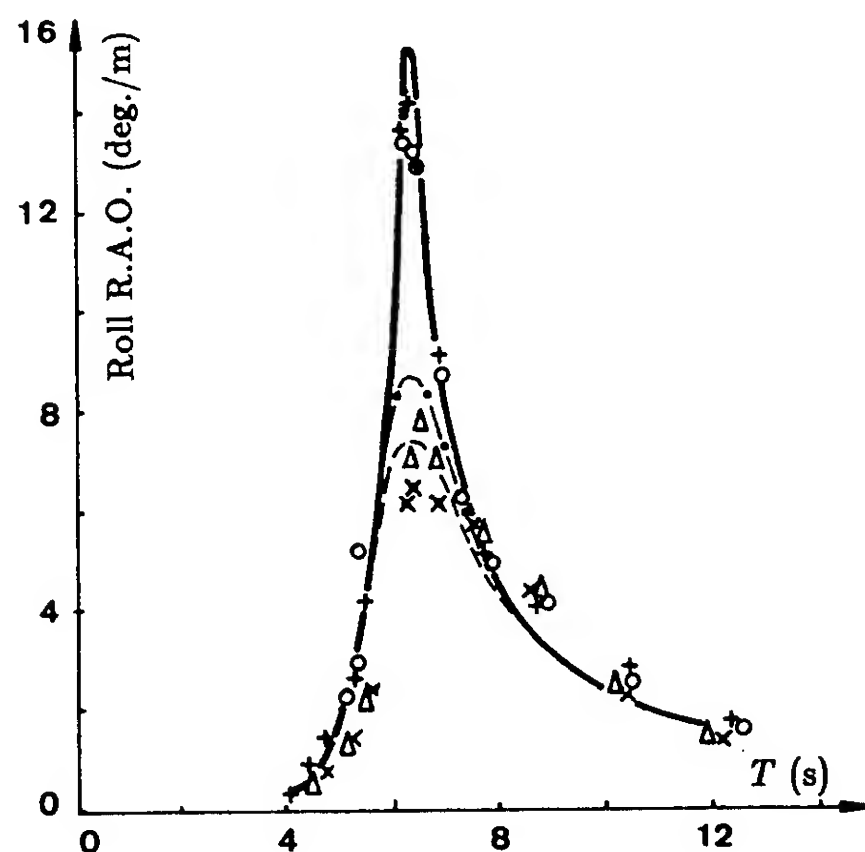


Fig. 4. Case study 2; Roll RAO against wave period in beam seas. —, wave damping only; viscous damping included, — • —,  $H_w = 0.90$  m, — — —,  $H_w = 1.74$  m; experiment, sharp edged bilges, —△—,  $H_w = 0.90$  m, — × —,  $H_w = 1.74$  m. round edged bilges, —○—,  $H_w = 0.90$  m, — + —,  $H_w = 1.74$  m.

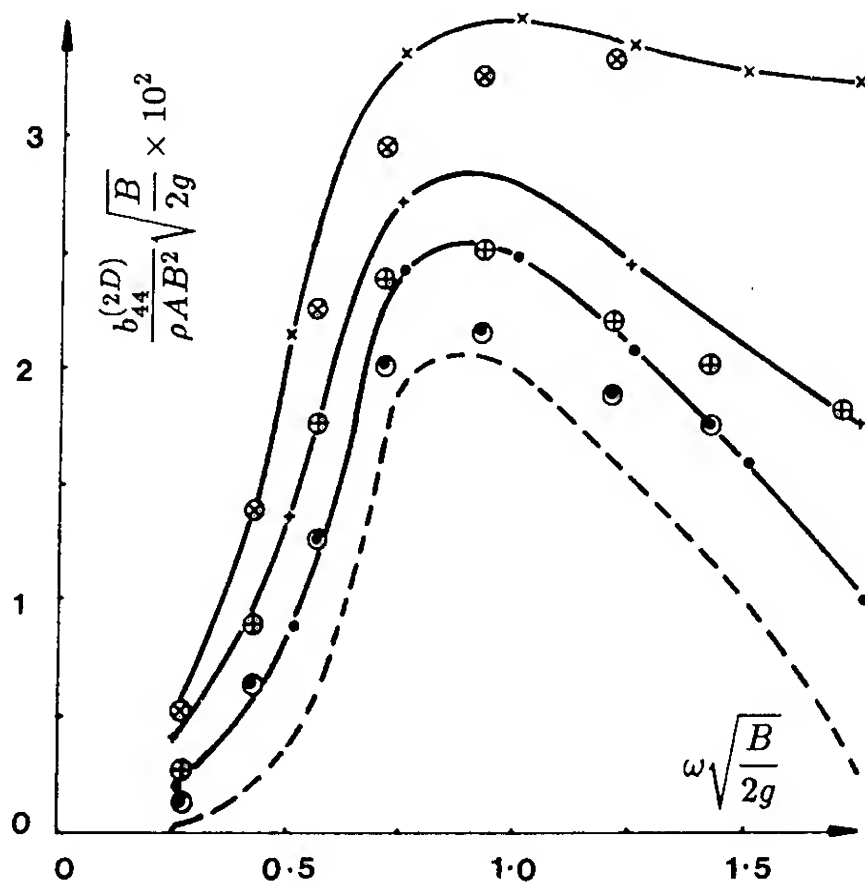


Fig. 5. Forced roll damping coefficient against frequency of motion. - - - wave damping only; viscous damping included, - • -,  $\hat{\theta} = 0.05$  rad., - + -,  $\hat{\theta} = 0.10$  rad., - × -,  $\hat{\theta} = 0.20$  rad.; experiment,  $\odot$ ,  $\hat{\theta} = 0.05$  rad.,  $\oplus$ ,  $\hat{\theta} = 0.10$  rad.,  $\otimes$ ,  $\hat{\theta} = 0.20$  rad.

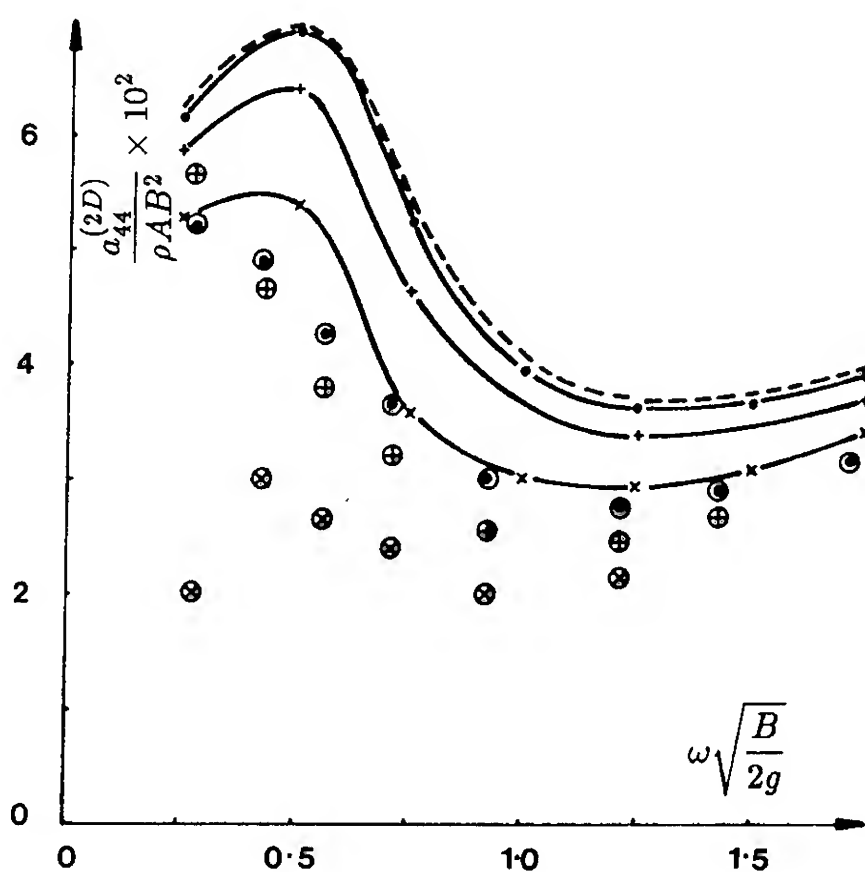


Fig. 6. Forced roll added mass moment of inertia against frequency of motion. - - - potential flow only; viscous effects included, - • -,  $\hat{\theta} = 0.05$  rad., - + -,  $\hat{\theta} = 0.10$  rad., - × -,  $\hat{\theta} = 0.20$  rad.; experiment,  $\odot$ ,  $\hat{\theta} = 0.05$  rad.,  $\oplus$ ,  $\hat{\theta} = 0.10$  rad.,  $\otimes$ ,  $\hat{\theta} = 0.20$  rad.

the first roll response case the results of the first method show good agreement between the predicted and measured roll responses through the resonance region. In reality the computed results are slightly on the high side because the model barge had rounded edges. This is evident in figure 4, where the model barge for the second roll response case was fitted alternately with rounded and sharp edges. However, both figures show a dramatic improvement in the prediction of roll when viscous effects are included in the calculation in comparison with the predictions of potential theory alone. Both sets of results also show that the non-linear dependence of the roll amplitude on the wave height is well predicted. The fact that the vortex forces are critically dependent on the relative velocity of the fluid in the immediate vicinity of the shedding edges, being very sensitive to the position of the roll centre and the barge geometry has been demonstrated before (6). For the first barge, which has a relatively high centre of gravity and less rounded bilge corners, the potential flow calculation greatly overpredicts the roll response. For the second barge, with its centre of gravity approximately at the level of the mean free surface and with well rounded bilges, the potential flow calculation gives results which are in quite good agreement with experiment. In this case the effects of vortex shedding from a rounded edge are small and a relatively large roll amplitude is obtained. However when this barge was fitted with sharp-edged bilges, vortex shedding became important and the response at resonance was considerably reduced to a value in reasonable agreement with the theory including vortex shedding effects and much lower than that predicted by potential theory alone. The assumptions made about the location of the roll centre when using forced roll data are therefore very important.

Figure 5 shows the comparison of damping and figure 6. the added mass for forced roll predicted by the second (vortex panel) method compared with experimental data (19). This data is for a rectangular barge of finite length. The potential theory result without vortex damping is shown calculated by the present three-dimensional potential panel method. The agreement between the predicted and measured damping coefficients is very good when the vortex panels are incorporated in the computation. The added mass is less well predicted. Disagreement here is somewhat unexpected because the vortex force contributes relatively a considerably smaller part to the overall added mass than it does to the damping. Any discrepancy would therefore be expected to be more clearly apparent in the damping rather than added mass coefficients. However Vugts has commented (19) that in this particular experiment it was difficult to measure the added mass very accurately. It should also be emphasised that the computation was carried out for a three-dimensional barge, but without computing vortex effects from the edges around the two ends, whereas the experiment was for a barge which spanned the test tank. The vortex damping is likely to be less effected by this difference than the added mass.

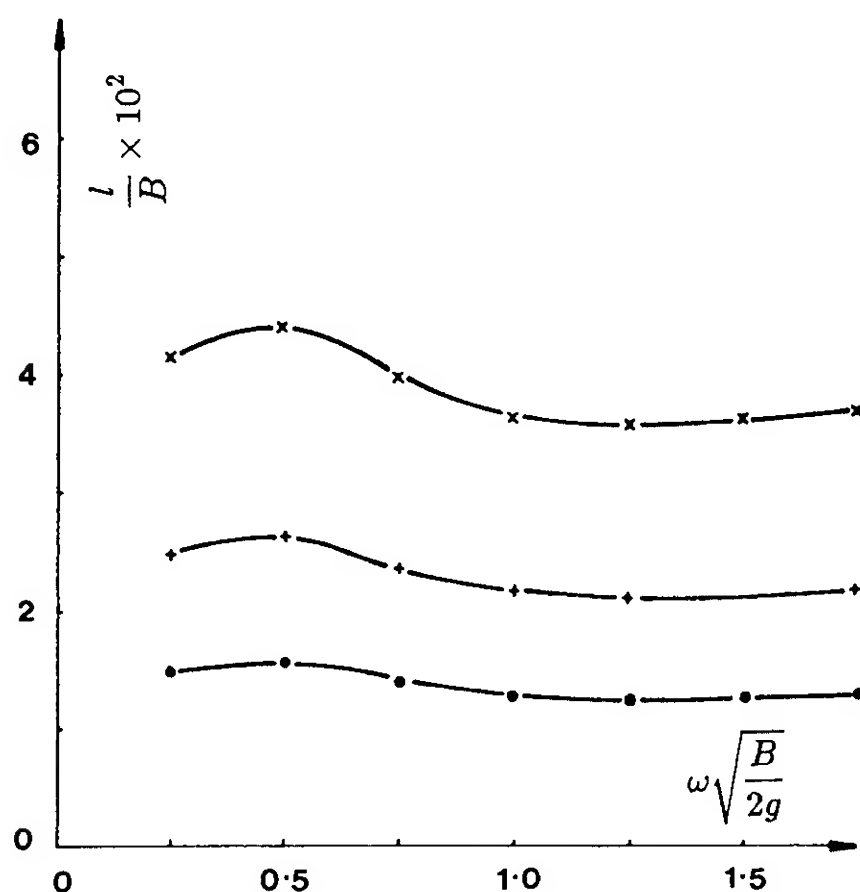


Fig. 7. Vortex/dipole panel length against frequency. — • —,  $\hat{\theta} = 0.05$  rad., — + —,  $\hat{\theta} = 0.10$  rad., — × —,  $\hat{\theta} = 0.20$  rad.

Results for three different forced roll amplitudes have been plotted and it is apparent that the vortex panel method does predict the increase in hydrodynamic damping with amplitude quite accurately. Figure 7 shows how the vortex panel length  $l_{vp}$  varies with frequency and amplitude. The fact that the length changes very little with frequency is not unexpected since it is only the effect of the free surface condition which will cause such a change. The variation of  $l_{vp}$  with amplitude is approximately proportional to (amplitude)<sup>3/4</sup> which would be expected from the variation of the vortex length scale  $L_v$ , (17).

## CONCLUSIONS.

It has been shown that the motions of a sharp-edged rectangular body floating freely in waves are well predicted by the first ( matching ) method. The results suggest that the non-linearities in response are largely due to vortex shedding from the body. The second ( vortex panel ) method has been used to predict damping of a barge due to forced roll and the results are similarly in good agreement with the measured data. The second method is the easier to set up and apply to general shapes of floating body and is therefore being developed into a full motion program.

## ACKNOWLEDGMENTS.

The authors gratefully acknowledge the financial support of the SERC through the Marine Technology Directorate Ltd.

## REFERENCES.

1. Newman, J.N. Marine Hydrodynamics. MIT Press, 1977.
2. Salveson, N, Tuck, E.O. and Faltinsen, O.M. 'Ship motions and sea loads.' Trans. SNAME, 78, 1970, p421.
3. Tanaka, N. 'A study on bilge keels. (Part 4. On the eddy making resistance to the rolling of a ship's hull). J. Soc. Nav. Arch. Japan 109, 1981, p205.
4. Ikeda, Y., Himeno, Y. and Tanaka, N. 'A prediction method for ship roll damping'. Dept. Nav. Arch., Univ. of Osaka Prefecture, Rep., 1978, p00405.
5. Kaplan P., Jiang C.-W. and Bentson J. 'Hydrodynamic analysis of barge platform systems in waves'. RINA. Spring Meeting, Paper No. 8, 1982
6. Bearman P.W., Downie M.J. and Graham J.M.R. 'Calculation method for separated flows with application to oscillatory flow past cylinders and the roll damping of barges'. Proc. 14th Symp. Naval Hydrodynamics, Ann Arbor, Michigan, 1982
7. Denise J.P. 'On the roll motion of barges', RINA Paper W10, 1982
8. Brown D.T., Eatock-Taylor R. and Patel M.H. 'Barge motions in random seas - a comparison of theory and experiment'. J. Fluid Mech. 129, 1983, p385.
9. Barge Motion Research Project. Noble Denton and Associates Ltd, London, 1978
10. DeBord F., Purl J., Mlady J., Wisch D. and Zahn P. 'Measurement of full scale barge motions and comparisons with model test and mathematical model predictions'. Trans. SNAME 95, 1987, p319.
11. Graham J.M.R. 'The forces on sharp-edged cylinders in oscillatory flow at low Keulegan-Carpenter numbers'. J. Fluid Mech., 97, 1, 1980, p331.
12. Braathen A. and Faltinsen O.M. 'Interaction between shed vorticity, free surface waves and forced roll motion of a two-dimensional floating body'. Fluid Dynamics Research, 3, 1988, p190.
13. Cozens P.D. 'Numerical modelling of the roll damping of ships due to vortex shedding'. PhD. Thesis, Univ. of London, 1987.
14. Downie M.J., Graham J.M.R. and Zheng X. 'The influence of viscous effects on the motion of a body floating in waves'. Proc. OMAE. Conf., Houston, Texas, 1990
15. John F. 'On the motion of floating bodies, Part II'. Commun. Pure Appl. Maths., 3, 1980, p45.
16. Zheng X. 'Prediction of motion and wave loads of mono- and twin-hulled ships in waves'. PhD. Thesis, Univ. of Glasgow, 1988.
17. Downie M.J., Bearman P.W. and Graham J.M.R. 'Effect of vortex shedding on the coupled roll response of bodies in waves'. J. Fluid Mech. 189, 1988, p243.
18. Standing R.G. Private communication, 1984.
19. Vugts J.H. 'The hydrodynamic coefficients for swaying, heaving and rolling cylinders in a free surface'. Netherlands Ship Res. Centre, TNO, Rept. 112S, 1970

## DISCUSSION

Choung M. Lee  
Pohang Institute of Science and Technology, Korea

It is a very interesting work to simulate the bilge vortices by doublet distribution. It may work very well for the zero-speed case; however, when the body has a forward speed, the bilge keel acting as a low-aspect ratio wing might have quite different types of vortex sheddings. How would you approach such a problem?

## AUTHORS' REPLY

We agree that the vortex shedding is different in the case of a body undergoing the combined motion of roll and forward speed, since the vorticity is now convected along the hull surface as well as away from it. Work is in progress to extend the model to this case and we hope to be able to report further on it at a future date.

## DISCUSSION

Targut Sarpkaya  
Naval Postgraduate School, USA

It will be appreciated if the authors would comment on the similarities and the fundamental differences in the boundary conditions of the physical experiments and the numerical simulations? What is the actual motion of the barge model in the experiments. Thank you.

## AUTHORS' REPLY

The calculations were carried out for two basic flow configurations. The first was a barge freely floating in beam waves, and the second was a barge undergoing forced roll in otherwise quiescent water. In both cases the potential flow part of the calculation was for a three dimensional barge. The matched edge technique has been applied to both cases, the forced roll calculations being reported in a previous paper. The viscous edge panel technique has so far been applied to the case of forced roll only. The results of the calculations were compared with experimental results, in the first case, obtained using a model barge floating in waves, and in the second case, with two dimensional results obtained with a rectangular section spanning a channel and undergoing forced roll.

There are of course some important differences between the computed and experimental flows, particularly in the case of forced roll. The computations have assumed perfectly two dimensional flow. In the freely floating case there will be some end effects which are not accounted for by the theory. Similarly, in the case of forced roll, the vortex shedding in the experiment will be affected by the presence of the end walls and will not be entirely two dimensional. Also, in both cases, the vortices approaching the free surface may be subject to strong three dimensional instabilities. Nevertheless we believe that the results are reasonably representative of the major effects of vortex shedding in the flow regimes considered and demonstrate a considerable improvement on those obtained using potential flow theory alone.

# Nonlinear Motions and Whipping Loads of High-Speed Crafts in Head Sea

S.-K. Chou, F.-C. Chiu, Y.-J. Lee (National Taiwan University, China)

## ABSTRACT

In this paper, the nonlinear motions and wave loads including whipping effects of high-speed crafts traveling in head sea are investigated theoretically and experimentally. The analysis is performed on an existing large-sized high-speed craft, following a modified nonlinear strip method and treating the ship's hull as an elastic beam from the view-point of hydroelasticity. The ship's hull is regarded as an Euler beam or Timoshenko beam and the structural response is represented by modal superposition method and finite element method, separately. The elastic backbone model testing technique is adopted to carry out the experiments for measuring vertical bending moments acting on ship's hull. Through the comparison with experimental results, the validity of the present calculation method is confirmed, and through serial calculations, the influence of structural rigidities on wave loads are also clarified.

## INTRODUCTION

Ship motions and wave loads of a displacement type ship in small amplitude waves can be estimated satisfactorily by the linear strip theory<sup>1-3</sup>. Dynamic behaviors of a displacement type ship suffered serious slamming in rough seas can be investigated by a nonlinear strip theory developed by Yamamoto, Fujino, and Fukasawa<sup>4</sup>, taking account of nonlinearities caused by hydrodynamic impact, the ship hull's shape and configurations. However, when a high-speed craft travels even in the moderate sea condition, nonlinear characteristics of ship motions and wave loads get significant because of high-speed traveling in waves. Several years ago, Chiu, one of the authors, and Fujino<sup>5-6</sup> developed a practical method, which is in principal based on the conventional Ordinary Strip Method synthesis but modified to be able to evaluate nonlinear hydrodynamic impact forces as well as dynamic lift in waves, for calculating vertical motions and wave loads of a high-speed craft which travels in regular head sea, and its validity was verified by comparing the computed motion and wave loads

with experimental results performed by using a ship model of hard chine type as well as a ship model of round bilge type. Recently, it was confirmed further that this method also can be applied even to estimated vertical motions of fishing vessels in head sea with accuracy enough for practical use<sup>7</sup>.

In the studies on nonlinear motions and wave loads of a high-speed craft mentioned at the above, the ship's hull is treated as a rigid body. However, in general, the size of high-speed craft has increased significantly<sup>8-10</sup>, and the occurrence of not only local damage due to serious slamming, but also whole structural damage caused by the subsequent whipping of the hull should be possible in case of a high-speed craft of large size. Hence, it becomes important to investigate the influence of hydro-elastic interactions on the structural responses of a large-sized high-speed craft in waves<sup>11-12</sup>.

In this paper, the authors investigate the nonlinear characteristics of ship motions and whipping loads of high-speed crafts theoretically and experimentally. The analysis is performed on an existing large-sized high-speed craft, following the above-stated modified nonlinear strip method basically, but extended to treat the ship's hull as an elastic beam, from the view-point of hydroelasticity. That is to say, the ship's hull is regarded as an Euler beam or Timoshenko beam and the structural response is represented by modal superposition method and finite element method, separately. The experiments are carried out by using an elastic backbone model. In order to generate pronounced whipping loads acting on model, rigidity of the elastic backbone is selected more flexible than that should be scaled down directly from the actual ship. Comparing the results of serial calculations of different structural representation methods with results obtained in elastic backbone model experiments, the influence of wave length, wave height and advance speed on wave loads are discussed. Furthermore, the influence of hull vibration, which is related to flexural rigidity and shear rigidity of hull structure, are also examined.



## 2. THEORY

In the previous formulation of nonlinear vertical rigid-body-motions of high-speed crafts running in head sea, nonlinearities of hydrodynamic forces acting on the ship hull are assumed to be exclusively due to the time-variation of submerged portion of the hull. This approach is followed basically in this paper, except the ship hull's girder is discretized into Timoshenko beam for considering both bending and shear deformation, and the formulation of finite element method is used to take both low frequency and high frequency vibration into consideration. The formulation of the present method is highly similar to that described in detail in the references<sup>5,6,7</sup>. Therefore, for convenience sake, the basic concept of the method will be subsequently described briefly.

### 2.1 Coordinate System and Incident Wave

The coordinate systems and the sign convention of translational and angular displacements used hereafter are shown in Fig.1. A space-fixed Cartesian coordinate system  $O-XYZ$  is introduced so that the  $X-Y$  plane coincides with the still water surface and the  $Z$ -axis directs downward. The ship advances in the negative  $X$  direction at a constant speed  $V$ . Another coordinate system  $o-xyz$  is ship-fixed with origin  $o$  located at the center of gravity of the ship and the  $x$ -axis parallel to the base line of the ship.

$\tau_i$  is the initial trim, and  $\tau_s$  and  $\zeta_s$  are the increments of trim and sinkage due to steady running in calm water respectively, while  $\theta$  and  $\zeta$  denote the variation of pitch angle and heave displacement in waves respectively. The counter clockwise rotation around the  $y$ -axis and downward heave displacement are regarded as positive.

The incident wave  $\zeta_w$  is described as

$$\zeta_w = \zeta_a \cos(\kappa x \cdot \cos \tau + \kappa y \cdot \sin \tau + \omega_e t)$$

in the ship-fixed coordinate system. For small  $\tau$ , the wave profile can be approximated by

$$\zeta_w = \zeta_a \cos(\kappa x + \omega_e t), \quad \text{and the sub-wave profile}$$

can be similarly approximated by

$$\zeta_c = \zeta_a \frac{\cosh \kappa(h - z_d)}{\cosh \kappa h} \cdot \cos(\kappa x + \omega_e t)$$

where  $\zeta_a$  is the wave amplitude,  $\kappa$  is the wave number,  $h$  is the water depth,  $\omega_e$  is the encounter frequency defined by  $\omega_e = \omega + \kappa V$  and  $\omega$  the wave frequency.  $z_d$  is the instantaneous draft at section  $x$  and expressed by

$$z_d = d - x \cdot \tan(\tau_s + \theta) + (\zeta_s + \zeta + w_v - \zeta_w) / \cos \tau \quad (1)$$

where  $d$  is the sectional draft of the ship without forward speed in calm water

$\tau$  is defined as  $\tau = \tau_i + \tau_s + \theta$

$w_v$  is the displacement induced by elastic vibration.

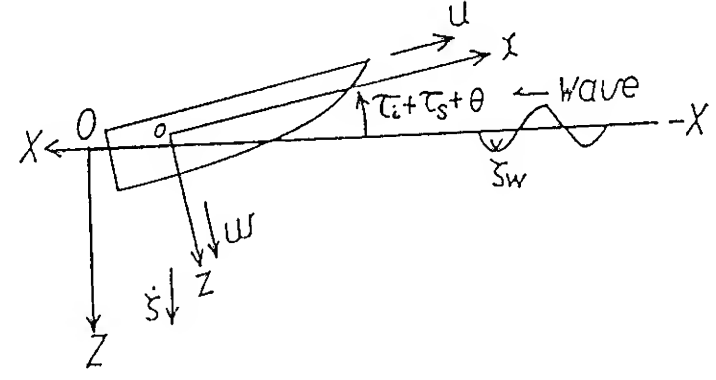


Fig.1 Coordinate system

### 2.2 Sectional External Forces

The velocity of wave particles relative to the ship's hull can be divided into two components,  $U_r$  and  $V_r$ , which are parallel to  $x$ - and  $z$ -axes respectively. By assumption of orbital velocity component of wave particle in  $X$ -direction is negligible and high order term dropped.  $U_r$  and  $V_r$  are approximately expressed by

$$U_r = -V \cos \tau \quad (2)$$

$$V_r = (\zeta_e - \zeta) \cos \tau_i + x \theta - V \sin \tau - \frac{d}{dt} w_v$$

Meanwhile, the two components of relative velocity for a ship running in calm water are expressed by

$$U_0 = -V \cdot \cos(\tau_i + \tau_s) \quad (3)$$

$$V_0 = -V \cdot \sin(\tau_i + \tau_s)$$

In deriving the hydrodynamic forces, the state of steady running in calm water is considered as the initial reference condition. From this point, the  $z$ -direction relative velocity  $V_r$  is expressed as follows

$$V_r = (V_r - V_0) + V_0 \quad (4)$$

$$= (\zeta_e - \zeta) \cos \tau + x \theta - \frac{d}{dt} w_v - V \{ \sin \tau - \sin(\tau_i + \tau_s) \} - V \sin(\tau_i + \tau_s)$$

thus  $V_r$  is separated into one steady term  $V_0$  associated with running in calm water and the remaining oscillatory term  $V_r - V_0$  due to waves.

#### 2.2.1 Sectional Force due to Change of Fluid Momentum

Denoting the heave added mass of a transverse section located at  $x$  for oscillatory motion with  $\rho S_z(x, t)$ , and the sectional heave added mass for steady running in wave and in calm water with  $\rho S_z^*(x, t)$  and  $\rho S_{z0}^*(x)$ , respectively, then the sectional hydrodynamic force due to the time variation of fluid momentum, when a ship is traveling in waves, can be described as follows



$$f_m = \frac{d}{dt} \{ \rho S_z(x, t) (V_r - V_0) + \rho S_z^*(x, t) V_0 - \rho S_{z0}^*(x) V_0 \} \quad (5)$$

In equation (5),  $\rho S_z(x, t)$  and  $\rho S_z^*(x, t)$  are both evaluated by the instantaneous submerged portion of the ship section while running in waves. The last term  $\rho S_{z0}^*$  is evaluated by the submerged portion of the ship section while running in calm water.

The operator  $\frac{d}{dt}$  can be expressed as

$$\frac{d}{dt} = \frac{\partial}{\partial t} + U_r \frac{\partial}{\partial x} \sim \frac{\partial}{\partial t} + V \cos \tau \frac{\partial}{\partial x}, \text{ thus the sectional force}$$

due to change of fluid momentum can be decomposed into the following five components

$$f_m = f_{ma} + f_{mj} + f_{mj}^* + f_{imp} + f_{imp}^* \quad (6)$$

where

$$\begin{aligned} f_{ma} &= \rho S_z(x, t) \frac{d}{dt} V_r \\ f_{mj} &= -V \cos \tau \frac{\partial \rho S_z(x, t)}{\partial x} \cdot (V_r - V_0) \\ f_{mj}^* &= -V \cos \tau \left( \frac{\partial \rho S_{z0}(x, t)}{\partial x} - \frac{\partial \rho S_{z0}^*(x)}{\partial x} \right) \cdot V_0 \\ f_{imp} &= \frac{\partial \rho S_z(x, t)}{\partial x} \cdot (V_r - V_0) \\ f_{imp}^* &= \frac{\partial \rho S_z^*(x, t)}{\partial x} \cdot V_0 \end{aligned} \quad (7)$$

The physical meaning of each term in the r.h.s of equation (6) are as follows

- $f_{ma}$ : sectional hydrodynamic inertia force
- $f_{mj}$ : hydrodynamic force due to longitudinal variation of sectional heave added mass associated with vertical oscillatory velocity
- $f_{mj}^*$ : hydrodynamic force due to longitudinal variation of sectional heave added mass associated with vertical steady velocity component of constant forward speed.
- $f_{imp}$ : sectional impact force due to time variation of sectional heave added mass associated with the vertical oscillatory velocity
- $f_{imp}^*$ : sectional impact force due to time variation of sectional heave added mass associated with vertical steady velocity of constant forward speed.

### 2.2.2 Sectional Damping Force

In a similar manner, the sectional damping force  $f_r$  is expressed as follows

$$f_r = \rho N_z(x, t) (V_r - V_0) + \rho N_z^*(x, t) V_0 - \rho N_{z0}^*(x) V_0 \quad (8)$$

where the sectional heave damping coefficient  $\rho N_z(x, t)$ ,  $\rho N_z^*(x, t)$  and  $\rho N_{z0}^*(x)$  have the physical meanings analogous to those of sectional heave added mass  $\rho S_z(x, t)$ ,  $\rho S_z^*(x, t)$  and  $\rho S_{z0}^*(x)$ , respectively.

### 2.2.3 Restoring Force and Froude-Krylov Force

The sum of sectional restoring force and Froude-Krylov force can be approximately expressed as follows

$$f_s = -\rho g \{ A(x, t) - A_0(x) \} \cos \tau \quad (9)$$

where  $\rho$  is the fluid density and  $g$  is gravitational acceleration  $A_0$  is the sectional area of the portion under the undisturbed still water surface and  $A(x, t)$  represents the sectional area of the portion under the undisturbed effective incident wave surface by considering Smith Correction.

The sectional external force in total is obtained by summing the force components stated above, ie.

$$f_z = f_m + f_r + f_s \quad (10)$$

### 2.3 Equation of Motion

The displacement and rotation angle of a ship's section, which includes the vibration component as well as the rigid-body-motion component, are denoted by  $w$  and  $\phi$ , respectively. Then the bending strain  $\epsilon_x$  and shear strain  $\gamma$  can be expressed by

$$\begin{aligned} \epsilon_x &= -z \frac{\partial \phi}{\partial x} \\ \gamma &= \frac{\partial w}{\partial x} - \phi \end{aligned} \quad (11)$$

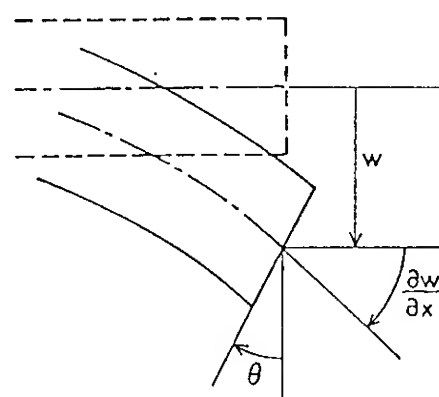


Fig.2 Displacement representation

The kinetic energy  $T$ , strain energy  $V$ , and work done by external forces  $W$  can be described as follow

$$T = \frac{1}{2} \int \mu \left( \frac{\partial w}{\partial t} \right)^2 dx \quad (12-1)$$

Where  $\mu$  denotes the sectional mass of ship's hull

$$V = V_b + V_s \quad (12-2)$$

where  $V_b$ , denotes the strain energy due to bending deformation, is expressed by

$$V_b = \frac{1}{2} \int EI \left( \frac{\partial \phi}{\partial x} \right)^2 dx \quad (12-3)$$

$V_s$ , denotes the strain energy due to shear deformation, is expressed by

$$V_s = -\frac{1}{2} \int GA_w \left( \frac{\partial w}{\partial x} - \phi \right)^2 dx \quad (12-4)$$

EI and  $GA_w$  are sectional flexural rigidity and shear rigidity, respectively

$$W = -\frac{1}{2} \int f_z w dx \quad (12-5)$$

In this manner, variational approach can be introduced to derive the Hamilton's Principle

$$\delta(T - V + W) - \delta D = 0 \quad (13)$$

where  $D$  denotes the dissipation function and  $\delta D$  is described by

$$\delta D = \eta_b \cdot \delta V_b + \eta_s \cdot \delta V_s \Big|_{\phi=\dot{\phi}, w=\dot{w}} \quad (13-1)$$

where  $\eta_b$  and  $\eta_s$  are the structural damping coefficients corresponding to bending and shear deformation, respectively.

The total displacement of a ship's section,  $w$ , can be expressed by a linear combination of  $N$  coordinate functions  $W_j$  as follows

$$w = \sum_{j=1}^N W_j(x) \cdot q_j(t) \quad (14)$$

where  $q_j$ 's are the generalized coordinates, and  $j=1,2$  denote the rigid body motions corresponding to heave and pitch,  $j \geq 3$  are related to vibration components.

### 2.3.1 Modal Superposition Method Formulation

For modal superposition analysis, the mode shape functions  $w_j$  are obtained by Myklestad's<sup>13</sup> method for a free-free Euler beam, the first 4 mode shape functions corresponding to vibration deformation,  $j=3-6$  are illustrated in Figure 3.

Equations of motion derived from Equation (13) by applying Galerkin method can be expressed in matrix form as follows

$$[M_{ij}] \{\ddot{q}_j\} + [C_{ij}] \{\dot{q}_j\} + [K_{ij}] \{q_j\} = \{f_i\} \quad (15)$$

where the assumption  $\phi = \frac{\partial w}{\partial x}$  is used and detailed expression of generalized mass, damping and stiffness matrices,  $[M]$ ,  $[C]$ ,  $[K]$  and generalized force function  $\{f\}$  are summarized in the Appendix A.

### 2.3.2 Finite Element Method Formulation

In finite element method, the generalized coordinates  $q_j$ 's correspond to nodal displacements.

The vibration components of  $w$  and  $\phi$ , denoted by  $w_v$  and  $\theta_v$ , can be approximated in terms of  $\{q_v\}$ , ie.

$$\begin{Bmatrix} w_v \\ \theta_v \end{Bmatrix} \Big|_{x=x_j-x_{j+1}} = [N] \{q_v\}_j \quad (16)$$

$\{q_v\}$ , the degrees of freedom at node point

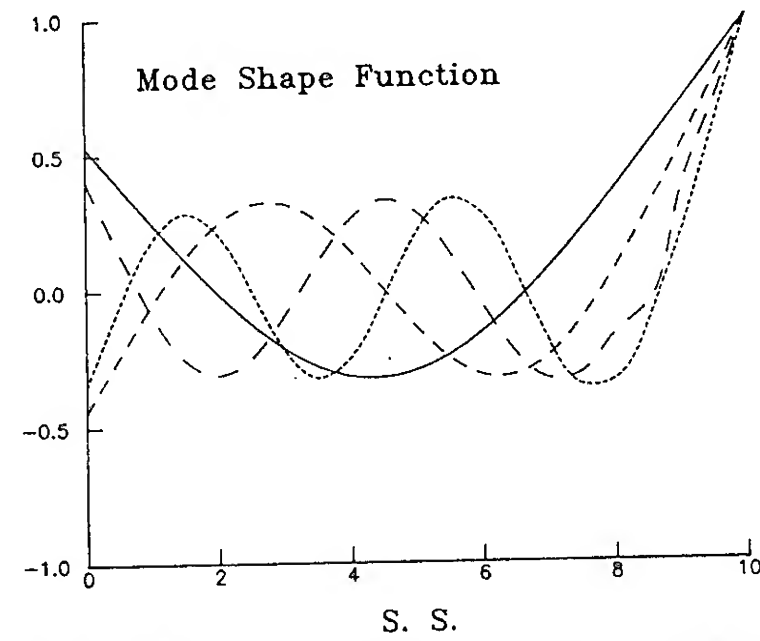


Fig.3 Mode shape functions of 3rd-6th mode

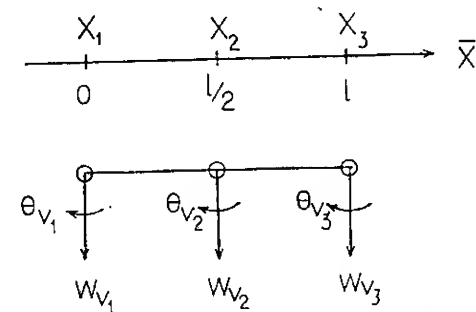


Fig.4 Degree of freedom in element

within the  $j$ -th element, are

$$\{q_v\}_j = \begin{Bmatrix} q_{wv} \\ q_{\theta v} \end{Bmatrix}_j \quad (16-1)$$

and the corresponding interpolation functions  $[N]$  are set to be quadratic forms

$$[N] = \begin{Bmatrix} N_v \\ N_\theta \end{Bmatrix} \quad (16-2)$$

where

$$\{q_{wv}\}_j = \begin{Bmatrix} w_{v1} \\ w_{v2} \\ w_{v3} \end{Bmatrix}_j \quad (16-3) \quad \{q_{\theta v}\}_j = \begin{Bmatrix} \theta_{v1} \\ \theta_{v2} \\ \theta_{v3} \end{Bmatrix}_j \quad (16-4)$$

$$[N_v] = [1-3\xi+2\xi^2 \quad 4\xi-4\xi^2 \quad -\xi+2\xi^2 \quad 0 \quad 0 \quad 0] \quad (16-5)$$

$$[N_\theta] = [0 \quad 0 \quad 0 \quad 1-3\xi+2\xi^2 \quad 4\xi-4\xi^2 \quad -\xi+2\xi^2] \quad (16-6)$$

$$\xi = \frac{x-x_j}{x_{j+1}-x_j} = \frac{\bar{x}}{l_j} \quad (16-7)$$

The resultant equations of motion in terms of total degrees of freedom combined by different elements can be expressed similarly in following matrix form:

$$[M^*] \{\ddot{q}\} + [C^*] \{\dot{q}\} + [K^*] \{q\} = \{f^*\} \quad (17)$$

The detailed expressions of various elements included in the coefficient matrices  $[M^*]$ ,  $[C^*]$ ,  $[K^*]$ , and force vector  $\{f^*\}$  are summarized in the Appendix B.

### 3. NUMERICAL SOLUTION

The numerical values of instantaneous sectional hydrodynamic coefficients are required for various sections of the ship to calculate the dynamic responses of a ship in waves.

The evaluations for these coefficients are performed under the following assumptions:

(1) The sectional hydrodynamic coefficients for heave motion in the  $z$ -direction are assumed to be equivalent to those in the  $Z$ -direction.

(2) The sectional hydrodynamic coefficients corresponding to oscillatory motion are evaluated at encounter frequency  $\omega_e$  for the part due to rigid body motion, and those at infinite frequency are used for the part due to vibration.

(3) The sectional hydrodynamic coefficients corresponding to steady forward velocity are evaluated at infinite frequency under the high-speed condition.

(4) The sectional hydrodynamic coefficients are evaluated for the instantaneous submerged portion under the undisturbed wave surface.

The nonlinearities of hydrodynamic forces related to the time-varying sectional hydrodynamic coefficients and hydrodynamic impact forces are treated in such a manner as described subsequently.

The sectional hydrodynamic coefficients at several different prescribed drafts of a section are computed by Frank close-fit method<sup>14</sup> for each transverse section. Those hydrodynamic coefficients for different drafts are expressed by a polynomial of  $n$ -th order as a function of the instantaneous sectional draft. Making use of such a polynomial expression, the sectional hydrodynamic coefficients are evaluated at each time step during numerical integration of equations of vertical motion.

If some section is clear of water at a certain time step, then during the following re-entry stage, water surface pile-up is considered according to Wagner's wedge impact theory<sup>15</sup> that is to say, the instantaneous draft is assumed to be  $\pi/2$  times of that under undisturbed wave surface. This consideration will be disregarded when the pile-up water surface cross over the chine. Furthermore, it is assumed that the hydrodynamic impact force is able to be disregarded when the ship section is detaching from the water. The validity of this assumption is confirmed by the results of the forced oscillation test performed by Yamamoto, Fujino and Ohtsubo<sup>16</sup>. The bottom impact and flare impact are evaluated with different schemes of computing the rate of change of the added mass.

The structural damping coefficient  $\eta_b$  and  $\eta_s$  are set to be of same value and can be expressed by

$$\eta_b = \eta_s = \frac{\delta_2}{\pi \omega_{2v}} \quad (18)$$

where  $\omega_{2v}$  is the natural frequency of 2-node vibration and  $\delta$  is the corresponding logarithmic decrement.

For the numerical integration of the equations of motion, Newmark- $\beta$  method with  $\beta=1/4$  is

used, and the discrete time increment  $\Delta t$  adopted for time integration is  $1/500$  of the encounter period.

From the view point of the stability of numerical integration, the encountered wave amplitude grows up gradually to steady state during the calculation and the dynamic responses are recorded only after stationary state motion is reached.

Wave loads can be estimated either by the integration of  $f_z - \mu \frac{\partial^2 W}{\partial X^2}$  along the ship's length or by the evaluation from differential formula in terms of  $W$ , the discrepancy between these two methods is insignificant and the former method gives more consistent results. Hence, the calculation results presented in this paper are all obtained by applying the integration evaluation, exclusively.

### 4. EXPERIMENTS AND NUMERICAL PREDICTION

#### 4.1 Elastic Backbone Model

In order to investigate the sectional wave loads along the ship's length and verify the validity of the numerical prediction method described in the previous sections, elastic backbone model testing technique<sup>11,17</sup> has been selected for experiments. A model in scale 1:14.5 of an existing 44.5 meter high-speed craft of hard chine type is used. The principal particulars and body plan are shown in Table 1 and Figure 5, respectively. At square station 1 to 8, the model made of wood, is divided into 9 segments which are connected with a backbone composed of 2 aluminum alloy (6063) beams as shown in Figure 6. The bending and shear rigid-

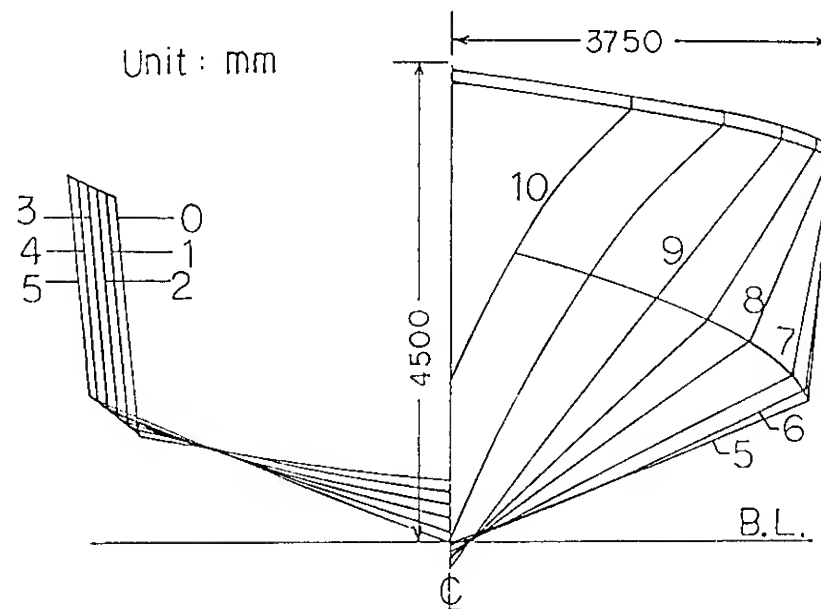


Fig.5 Body plan of Boat-4450

Length Overall	L	44.50 m
Breadth (☐)	B	7.50 m
Depth (☐)	D	3.50 m
Draft (☐)	d	1.58 m
Displacement	W	220.0 ton
Longitudinal Position of C.G.	LCG	2.05 m aft ☐
Longitudinal Gyradius	Yk	27.1 %L

Table 1 Principal particulars of Boat-4450

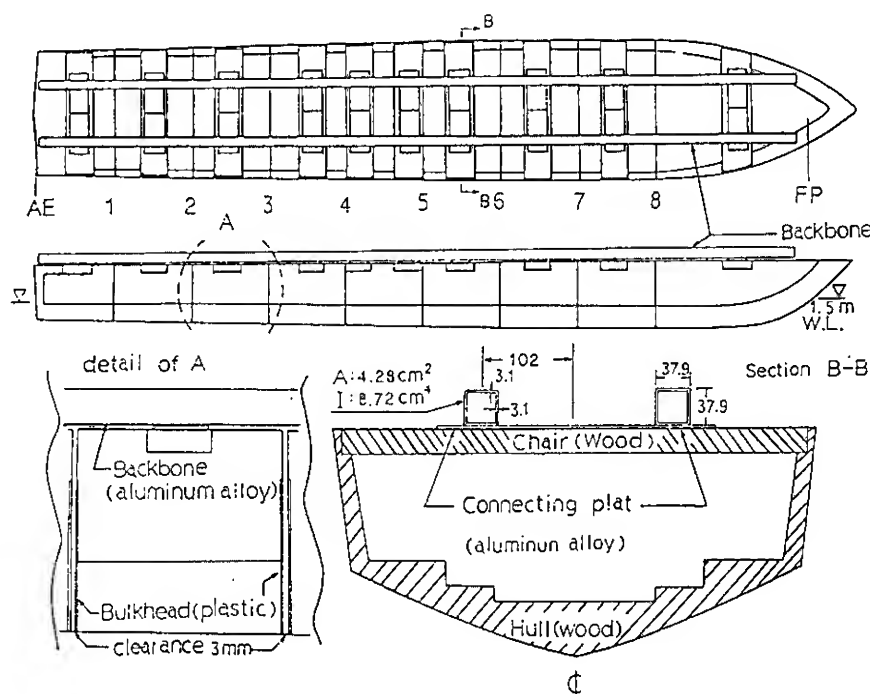


Fig.6 Structure of the elastic backbone model

ities of backbone are not on scale exactly. Namely, in order to generate pronounced whipping vibration easily, a more flexible backbone of lower bending rigidity is selected and shear rigidity is restricted by sectional geometry of the aluminum alloy beams. The structural rigidity and the weight distribution in full scale of the backbone model are shown in Figure 7. As a result, the bending and shear rigidities in full scale of the backbone model used in experiments are nearly equivalent to one-third and twenty times, respectively, of those of an actual ship which is made of steel.

The natural frequency of 2-node vibration  $\omega_{2v}$  and the logarithmic decrement  $\delta_2$ , obtained from impulsive response of the backbone model at floating condition, are 34.0 rad/sec (i.e. 5.4 Hz), and 0.102, respectively. These values are used to determine structure damping coefficient  $\eta$  by equation (18). Vertical bending moments are measured through bridged 4 strain gages on the upper and lower faces of the two aluminum alloy beams. Wave loads at square station 1 to 8 are measured. Static calibration on the relation between moment and strain outputs were carried out for the condition without hull segments. As a result, strain to moment ratio obtained is  $16.8 \times 10^{-8}/\text{kg}\cdot\text{m}$ . Furthermore, the heave and pitch motions are picked up by potentiometers at the center of gravity (here after called C.G.) of the model. Two accelerometers are set up at the C.G and square station 9.5 to pick-up the vertical acceleration at C.G and bow acceleration, respectively.

As mentioned previously, the trim and sinkage of a ship running in calm water should be known in advance for computing the ship response in waves. Therefore, the towing tests were carried out in calm water to measure the trim and sinkage, of which the results are shown in Figure 8.

#### 4.2 Experimental Conditions

Refer to the conclusions obtained through previous experiments on a similar elastic backbone model<sup>12</sup>, the present investigation was carried out on the following experimental conditions in head sea that may expect to

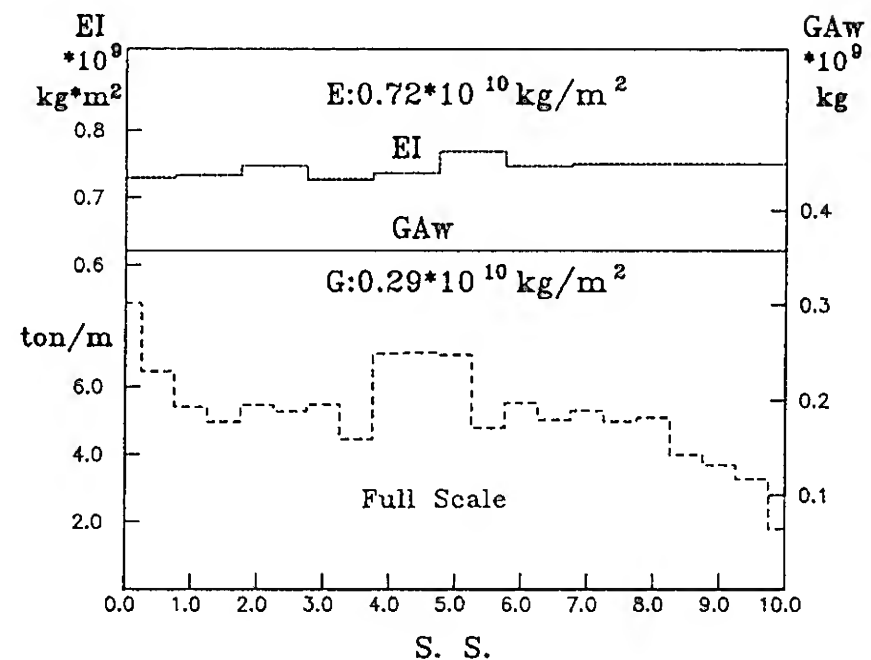


Fig.7 Rigidity and weight distribution of backbone model in full scale

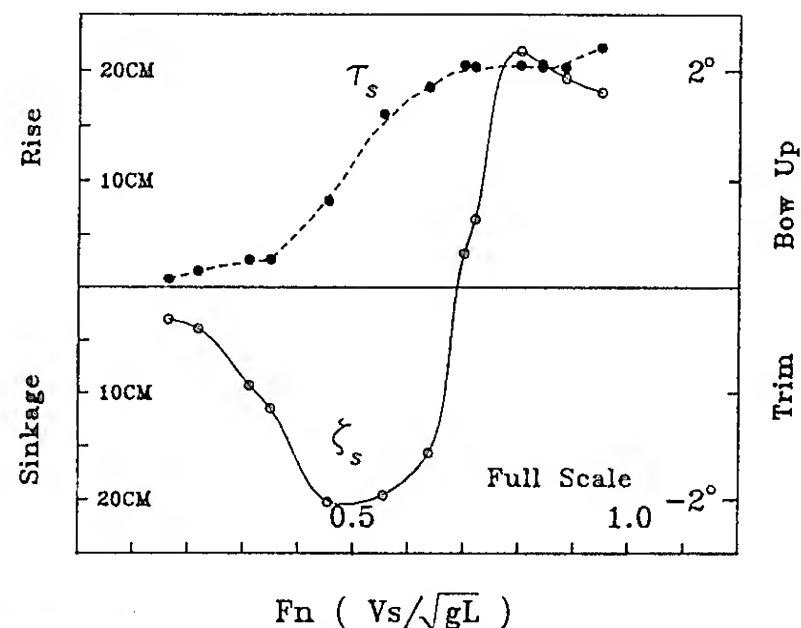


Fig.8 Running trim and sinkage in still water

exhibit pronounced nonlinear motions and suffer severe wave loads.

$$\begin{aligned} \lambda/L &= 1.125, 1.5, 1.7 \text{ for } F_n=0.35 \\ \lambda/L &= 1.125, 1.5, 1.7, 2.0 \text{ for } F_n=0.70 \\ \lambda/L &= 1.5, 1.7, 2.0 \text{ for } F_n=1.0 \end{aligned}$$

$H_w/\lambda$  is kept about 1/40 and 1/50, where,  $\lambda/L$ ,  $F_n$  and  $H_w/\lambda$  denote wave length to ship length ratio, Froude number in length and wave height to wave length ratio, respectively. Furthermore, in order to investigate the effects of forward speeds, another 5 different forward speed conditions are performed for the selected wave condition of  $\lambda/L=1.5$  and  $H_w/\lambda=1/40$ .

#### 4.3 Numerical Prediction

In this paper, two kinds of nonlinear calculations are performed as described subsequently.

(a) Modal superposition calculation (called "MODE-n")

The structure response is represented by modal superposition method in which the ship hull girder is assumed to be an Euler beam and mode shape functions used are obtained from Myklestad's method. The number  $n$  of mode shape functions taken in calculation is 6 in general, (that is, two rigid-body-motions and 4 vibrati-

on modes) while in some comparison cases, 4 mode shape functions calculation (called "MODE-4") and even only the first two rigid-body-motions mode shape functions calculation (hence called "RIGID") are also performed.

(b) Finite element calculation (called "F.E.M." or "EULER")

In this kind of calculation, if Timoshenko beam element formulation is used to evaluate the dynamic response of the ship hull's structure, the notation "F.E.M." is adopted. The calculation in terms of Euler beam element formulation by neglecting the shear deformation is called "EULER" for distinction.

## 5. COMPARISON BETWEEN NUMERICAL PREDICTION AND EXPERIMENTAL RESULTS

Figures 9 to 18 illustrate the nondimensionalized peak-to-peak bending moment distribution along the ship's length under various wave and speed conditions. In Figures 9 to 11, the experimental results for the case of  $F_n=0.35$  which may be considered as a typical speed of "non-planning" condition are shown together with the results predicted by the two kinds of numerical computations, namely, "MODE-6" and "F.E.M.". Both of the predicted values by modal superposition calculation "MODE-6" and finite element calculation "F.E.M." agree well with the experimental results. In the cases of  $F_n=0.70$  and  $1.0$  which may be considered as a typical speed of "semi-planning" and "planning" condition respectively, shown in Figures 12 to 18, the predicted values by "MODE-6" are satisfactory, except for the cases of relatively short waves, in which it tends to underestimate the wave loads acting on the fore-bodies. Nevertheless, the discrepancy in fore-bodies is improved significantly by the "F.E.M." calculation. As seen in these figures, it can be said that both of "MODE-6" and "F.E.M." calculations give reasonable results, and the agreement between the predicted responses and experimental results seems satisfactory enough for the practical point of view.

Figure 19 illustrates the forward speed dependence of bending moments at various square stations 4 to 7 in the selected wave condition of  $\lambda/L=1.5$  and  $H_w/\lambda=1/40$ . In Figures 19(a) and Figure 19(b), the nondimensionalized peak to peak bending moments obtained from experiments are plotted together with predicted results by "MODE-6" and "F.E.M." calculations, respectively. As shown in these figure, the discrepancy in the trend between the "Mode-6" prediction and the measured responses tends to be significant in the speed range of  $F_n=0.70$  to  $1.0$ . However, the predicted values obtained by "F.E.M." calculation and experimental results show qualitatively similar trends in full speed range, and their agreement in values is also remarkable.

In order to manifest the validity of the present nonlinear prediction of responses, the time histories of bending moments at square station 1 to 8 as well as C.G. acceleration and bow acceleration obtained by "F.E.M." calculation are shown together with the measured ones

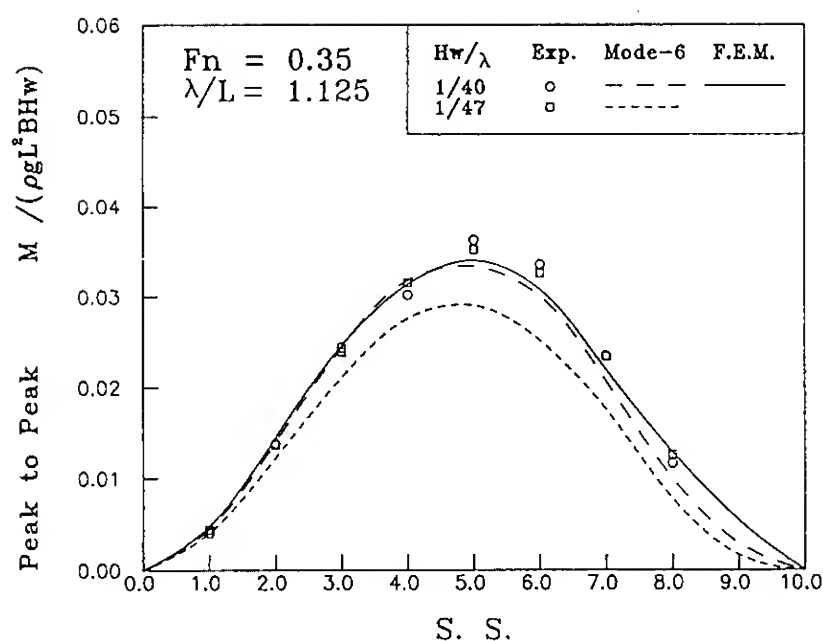


Fig.9 Longitudinal distribution of vertical bending moment ( $F_n=0.35, \lambda/L=1.125$ )

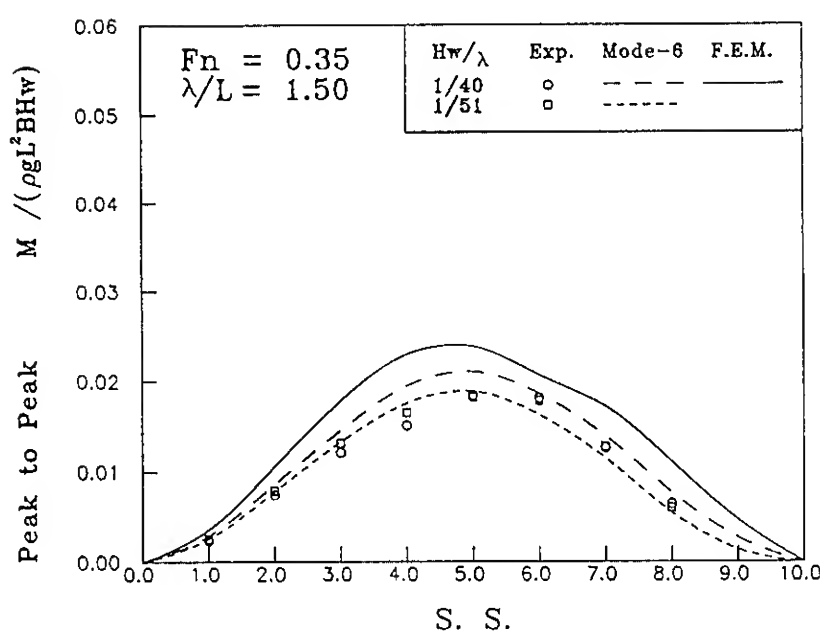


Fig.10 Longitudinal distribution of vertical bending moment ( $F_n=0.35, \lambda/L=1.5$ )

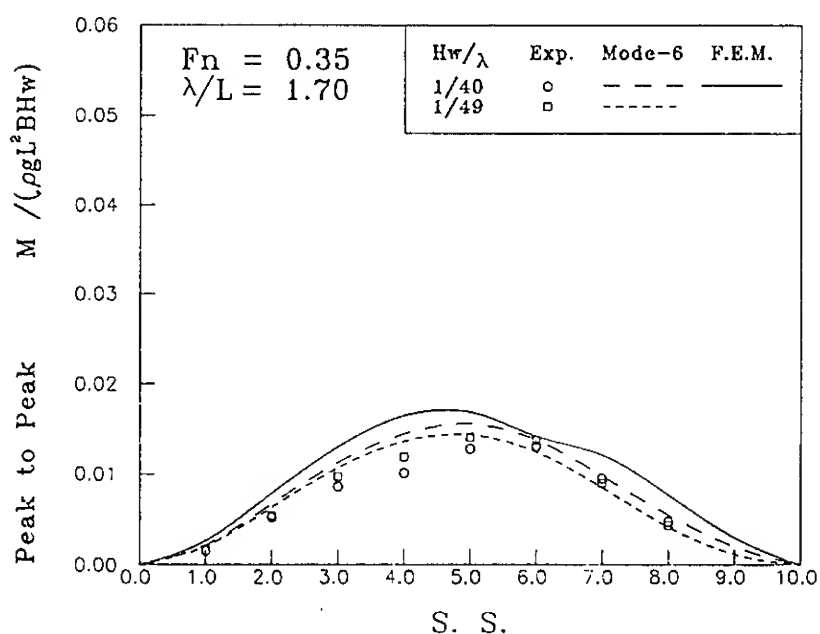


Fig.11 Longitudinal distribution of vertical bending moment ( $F_n=0.35, \lambda/L=1.7$ )

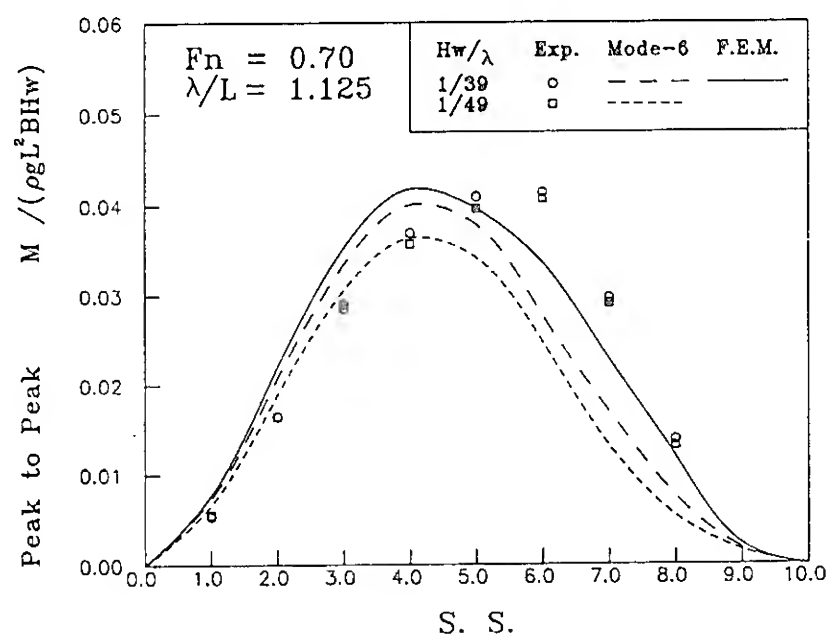


Fig.12 Longitudinal distribution of vertical bending moment ( $F_n=0.70, \lambda/L=1.125$ )

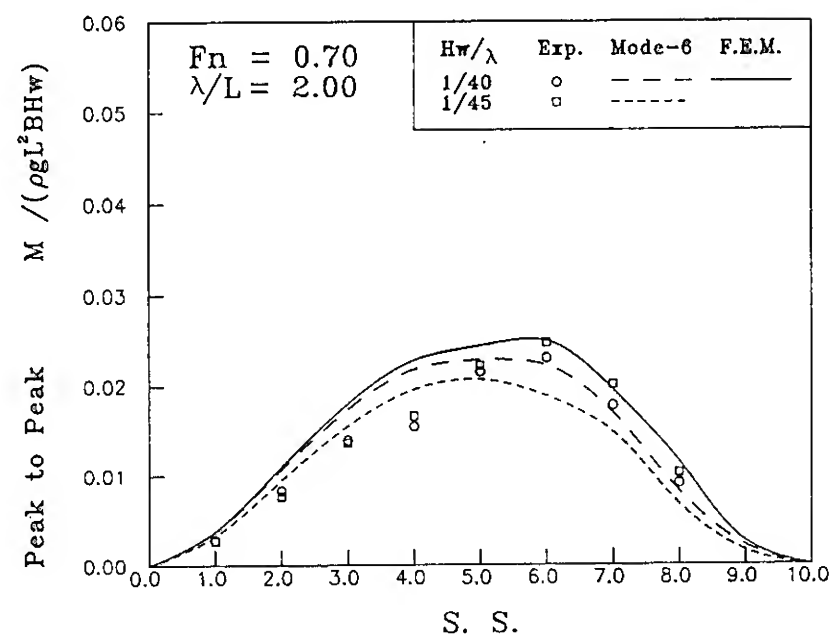


Fig.15 Longitudinal distribution of vertical bending moment ( $F_n=0.70, \lambda/L=2.0$ )

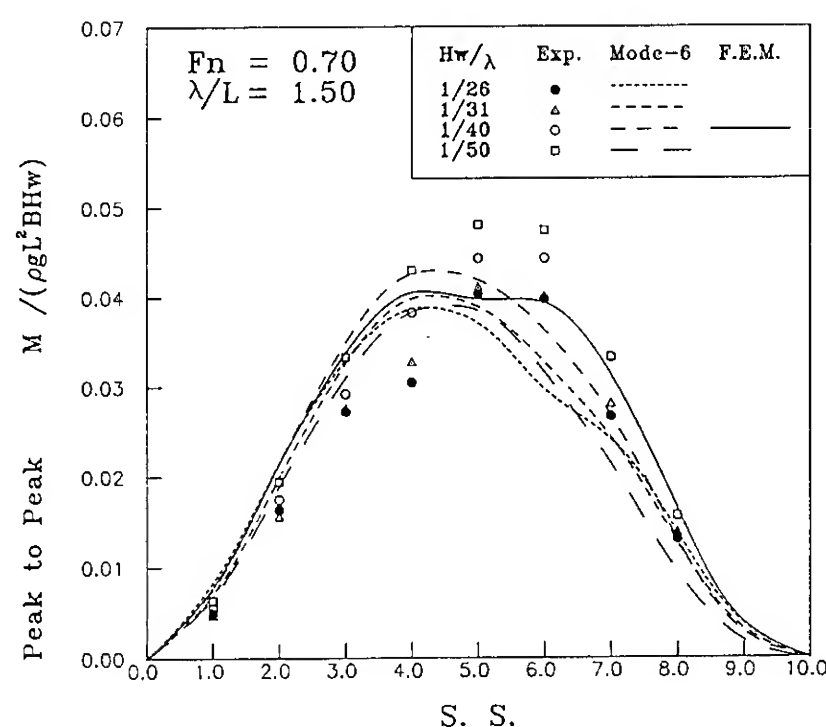


Fig.13 Longitudinal distribution of vertical bending moment ( $F_n=0.70, \lambda/L=1.5$ )

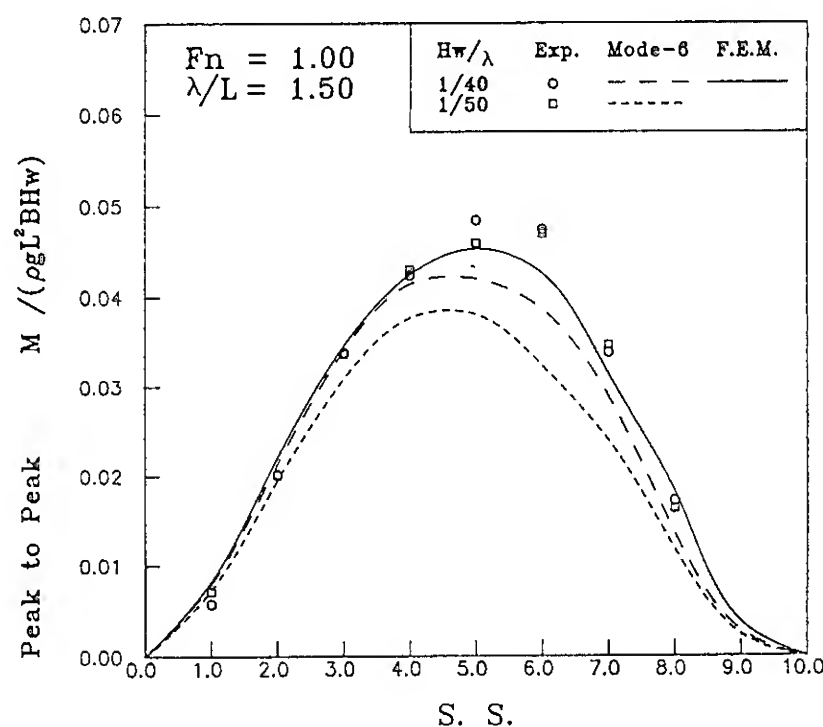


Fig.16 Longitudinal distribution of vertical bending moment ( $F_n=1.0, \lambda/L=1.5$ )

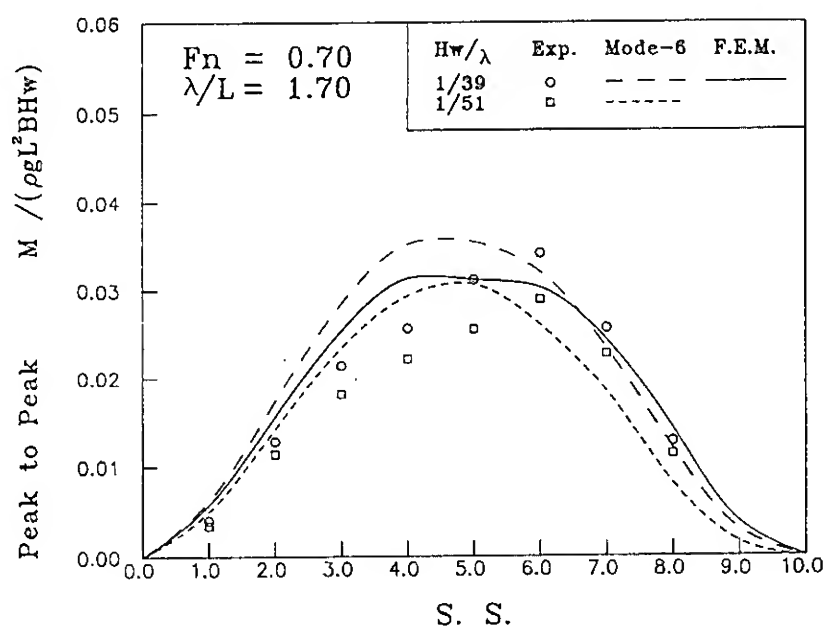


Fig.14 Longitudinal distribution of vertical bending moment ( $F_n=0.70, \lambda/L=1.7$ )

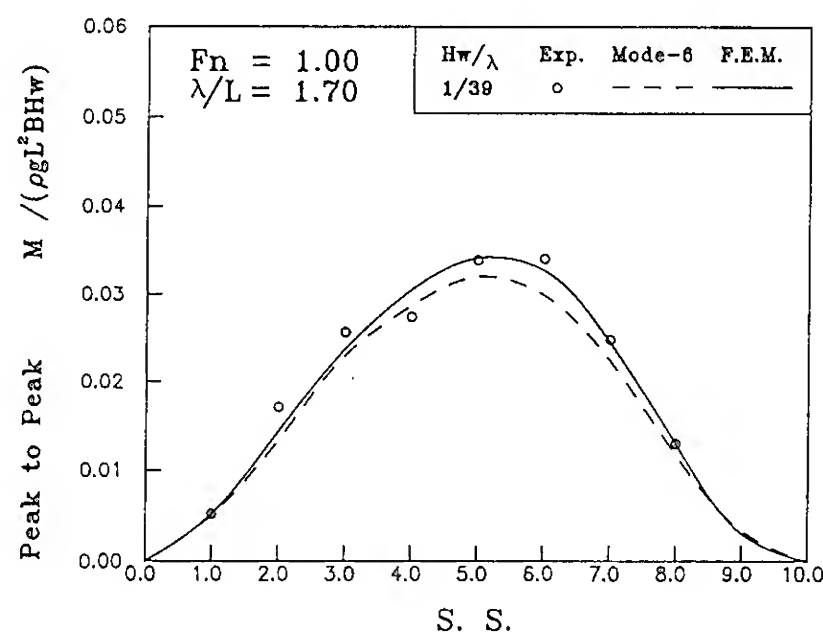


Fig.17 Longitudinal distribution of vertical bending moment ( $F_n=1.0, \lambda/L=1.7$ )



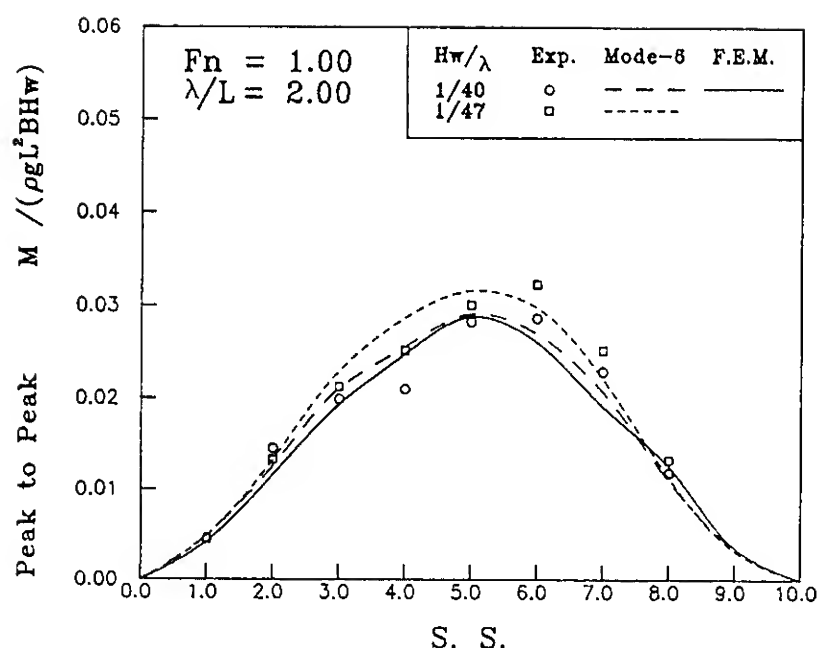


Fig. 18 Longitudinal distribution of vertical bending moment ( $F_n=1.0, \lambda/L=2.0$ )

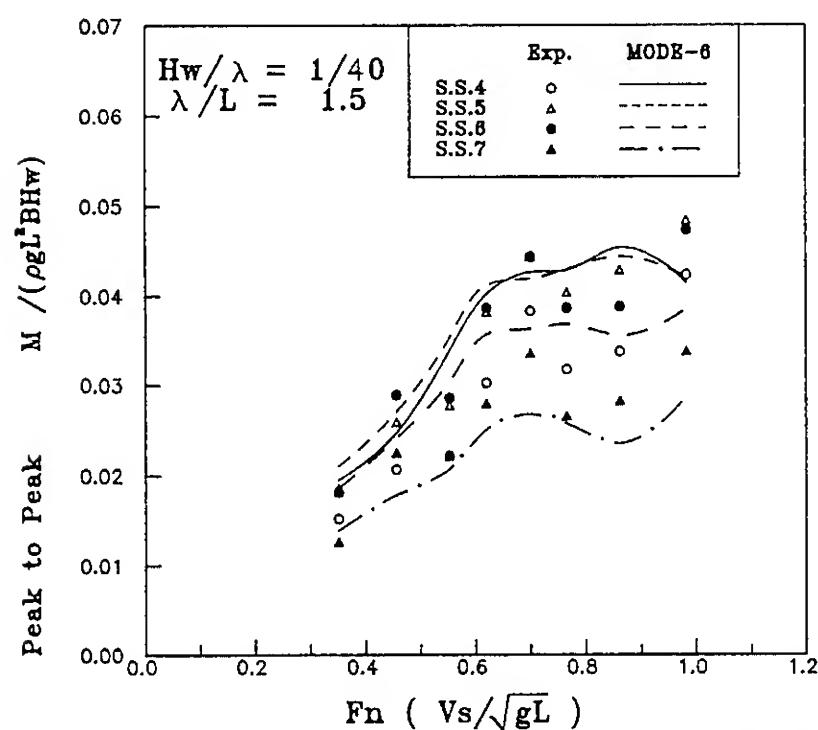


Fig. 19(a) Effect of ship speed on vertical bending moment ("MODE-6" calculation)

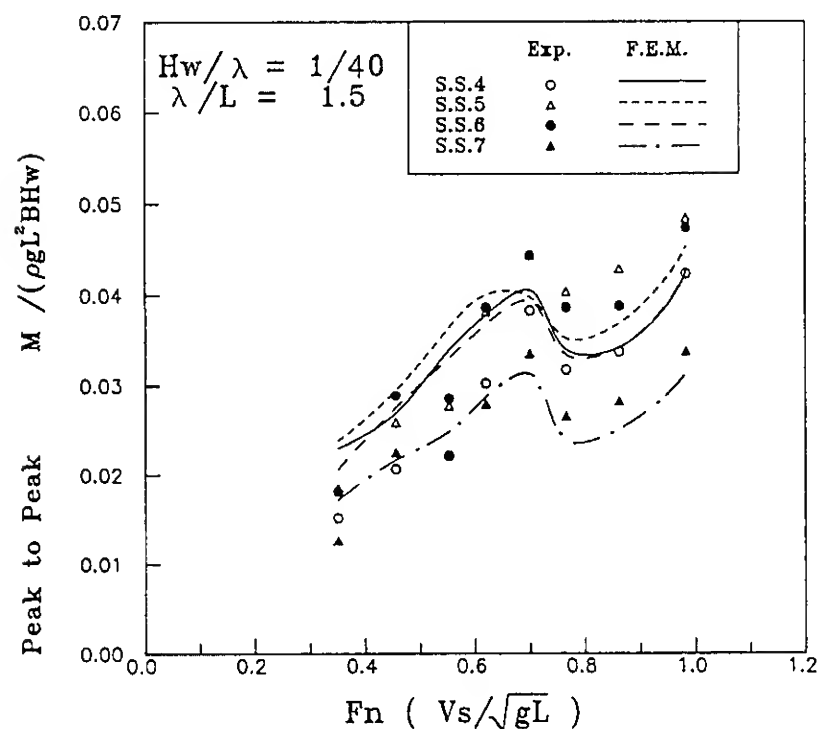


Fig. 19(b) Effect of ship speed on vertical bending moment ("F.E.M." calculation)

in both cases of  $F_n=0.70$  and  $1.0$  in Figures 20 and 21, respectively.

Although, the time histories of bending moments obtained by "F.E.M." calculation show slight difference of shape at hogging condition, from that obtained by measurements, as seen in Figures 20(a) and 21(a), the predicted time histories of bending moments and accelerations agree qualitatively well with the measured ones. The plausible reason of the discrepancy in time histories at hogging condition, in which the bow sections emerge from the water surface, between the predicted and the measured bending moments is that the incoming wave surface is assumed to be undisturbed even when the ship travels in waves at a high speed, namely, the effects of spray while planning occurred are not taken into consideration.

## 6. EFFECTS OF STRUCTURAL RIGIDITIES

As clarified in the previous sections, it can be said that vertical wave loads, in which whipping loads are included, acting on a high-speed craft traveling in head sea, can be predicted by the present "F.E.M." calculations with accuracy enough for the practical use.

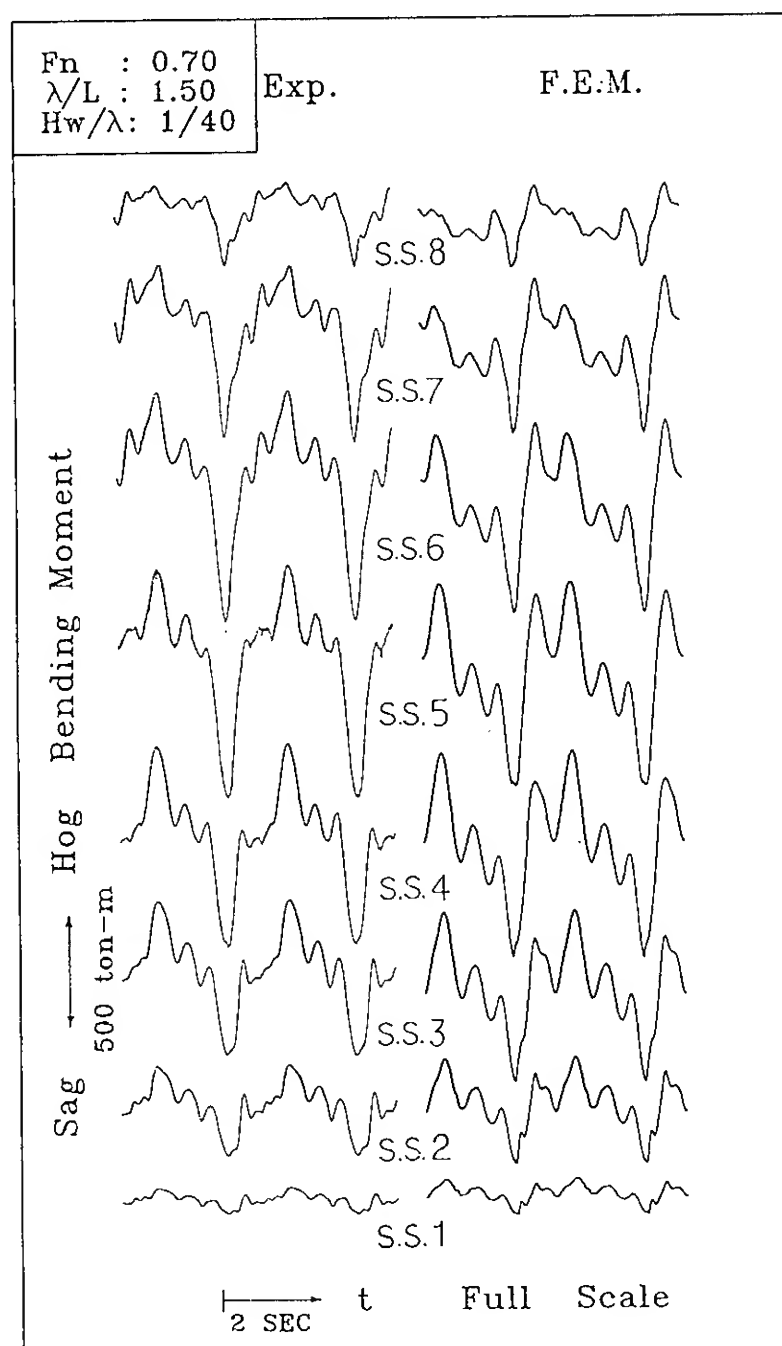


Fig. 20(a) Time histories of bending moment by experiment and calculation ( $F_n=0.7, \lambda/L=1.5, H_w/\lambda=1/40$ )

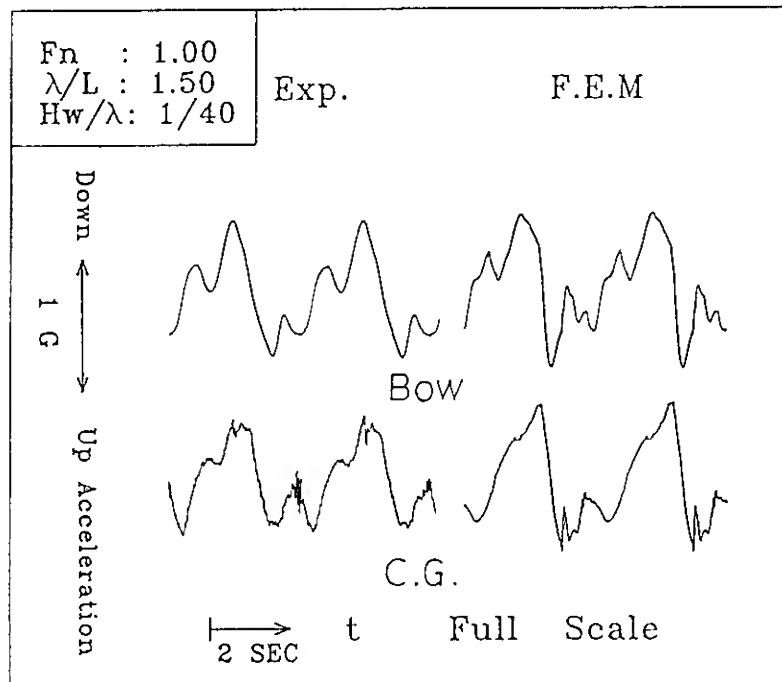


Fig.20(b) Time histories of bow acceleration and acceleration at C.G.  
( $F_n=0.7, \lambda/L=1.5, H_w/\lambda=1/40$ )

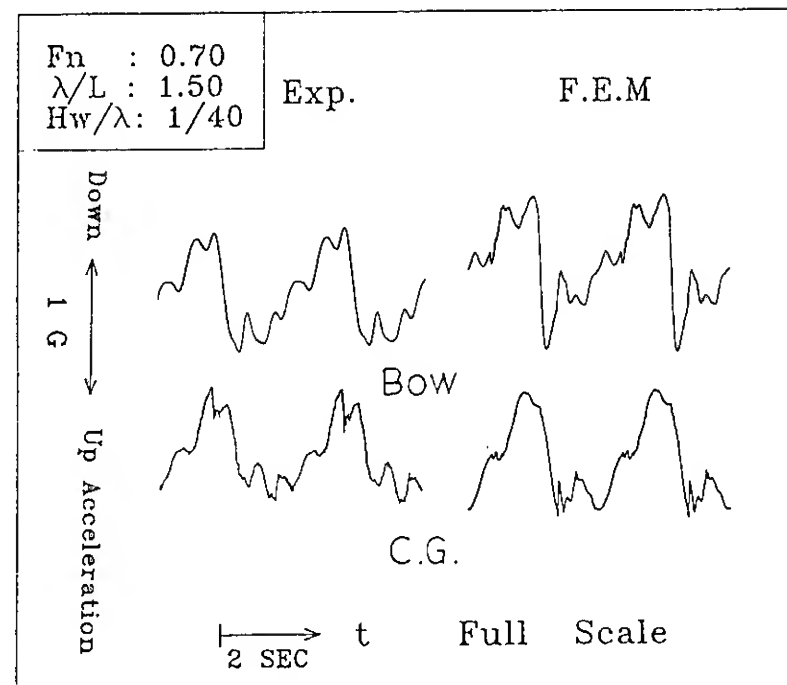


Fig.21(b) Time histories of bow acceleration and acceleration at C.G.  
( $F_n=1.0, \lambda/L=1.5, H_w/\lambda=1/40$ )

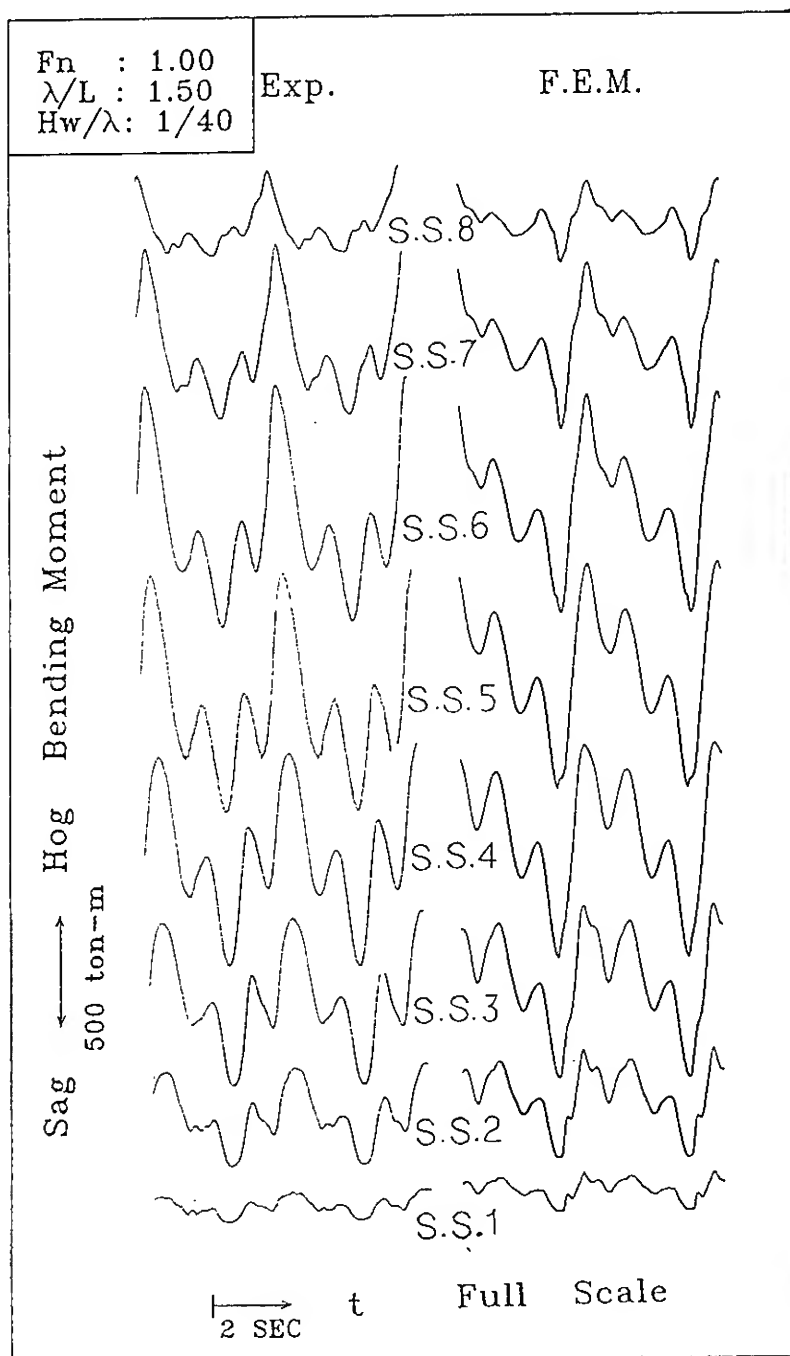


Fig.21(a) Time histories of bending moment by experiment and calculation  
( $F_n=1.0, \lambda/L=1.5, H_w/\lambda=1/40$ )

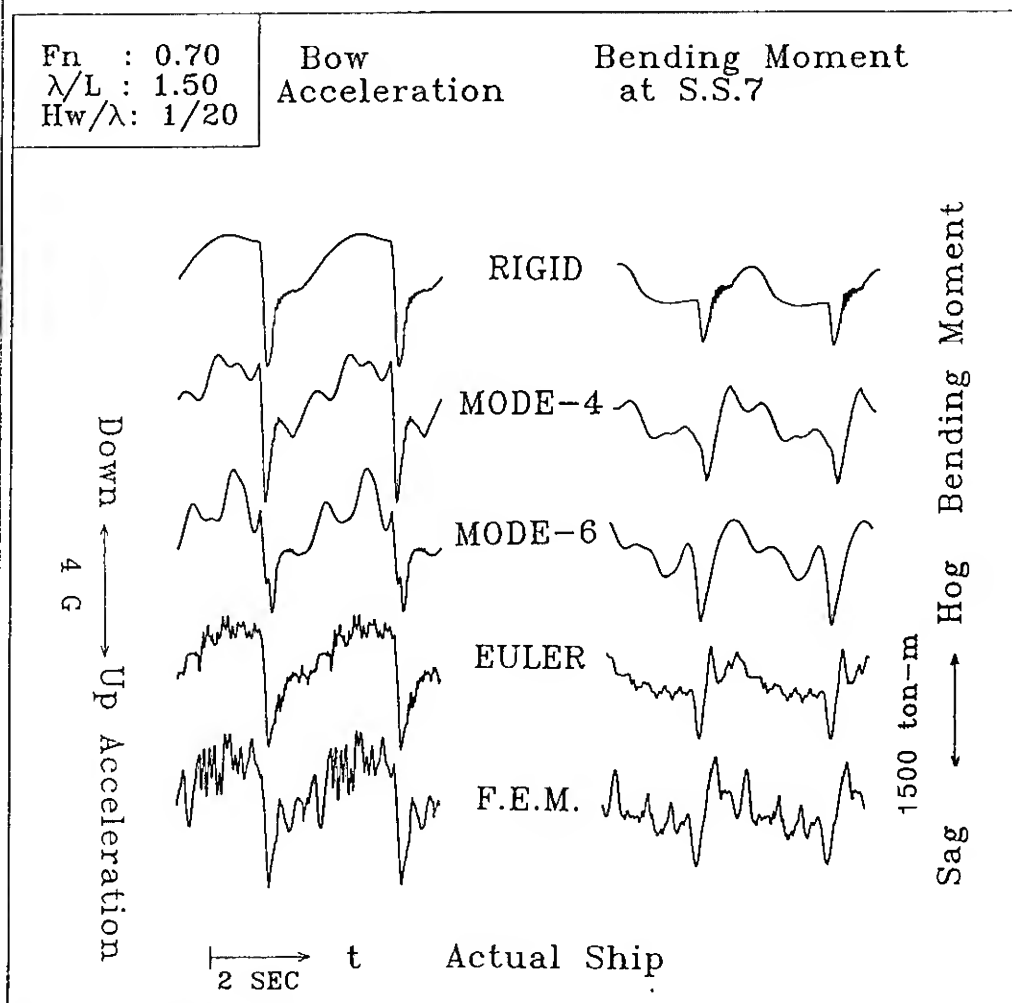


Fig.22 Time histories of acceleration at C.G. and bending moment at S.S.7 by various calculations  
( $F_n=0.7, \lambda/L=1.5, H_w/\lambda=1/20$ )

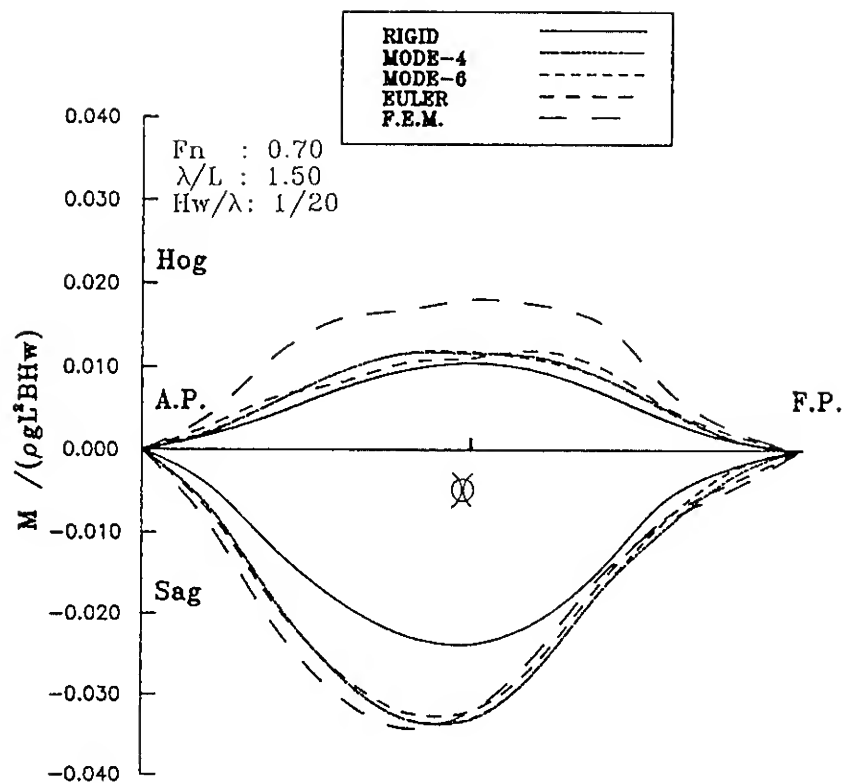


Fig.23 Longitudinal distribution of vertical bending moment by various calculations (Fn=0.7, λ/L=1.5, Hw/λ=1/20)

In this section, various kinds of calculation stated in section 4.3 are applied on the actual high speed craft to investigate the effects of structural rigidities on wave loads. In order to illustrate the effects more clearly, the computation performed at a severe wave condition of  $\lambda/L=1.5$  and  $Hw/\lambda=1/20$  with forward speed of  $Fn=0.70$ , are shown in Figures 22 and 23. Figure 22 shows the time histories of bow acceleration and bending moments at square station 7, and Figure 23 shows the nondimensionalized bending moment peak values distribution along ship's length obtained by various calculations. It can be seen in these figures, by comparing with "EULER" calculation, the "RIGID" calculation, in which structural rigidities are considered to be infinite and no vibration can be recognized, may underestimate the sagging moment significantly. Furthermore, by comparing with "F.E.M." calculation, the "EULER" calculation, in which shear rigidity is assumed to be infinite and no shear deformation can be recognized, may underestimate the hogging moment remarkably. Therefore, the "F.E.M." calculation by treating ship hull's girder as an Timoshenko beam seems to be necessary for predicting the wave loads acting on it at severe condition.

Furthermore, in order to illustrate the rigidities' dependence of wave loads, "F.E.M." calculation is applied on the actual high speed craft with variations of flexural rigidity and shear rigidity separately, at the same conditions which is stated above, namely,  $\lambda/L=1.5$  and  $Hw/\lambda=1/20$  with forward speed of  $Fn=0.70$ . Figure 24 shows the flexural rigidity's dependence of nondimensionalized bending moment peak values at square stations 5, 7 and 8, while the shear rigidity is kept to be original value of the actual ship. It can be seen in this figure, decreasing the flexural rigidity may reduce the

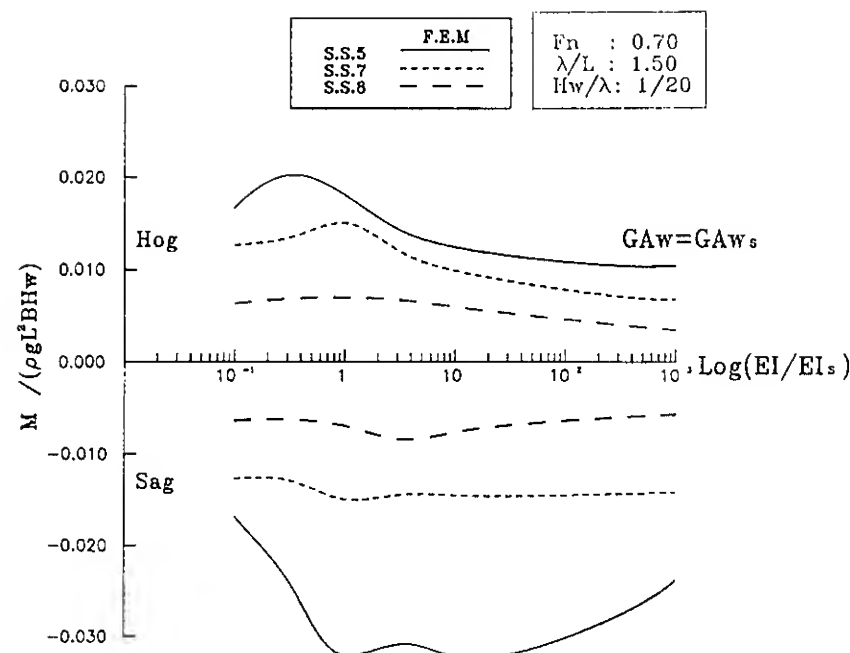


Fig.24 Effect of flexural rigidity on vertical bending moment (Fn=0.7, λ/L=1.5, Hw/λ=1/20)

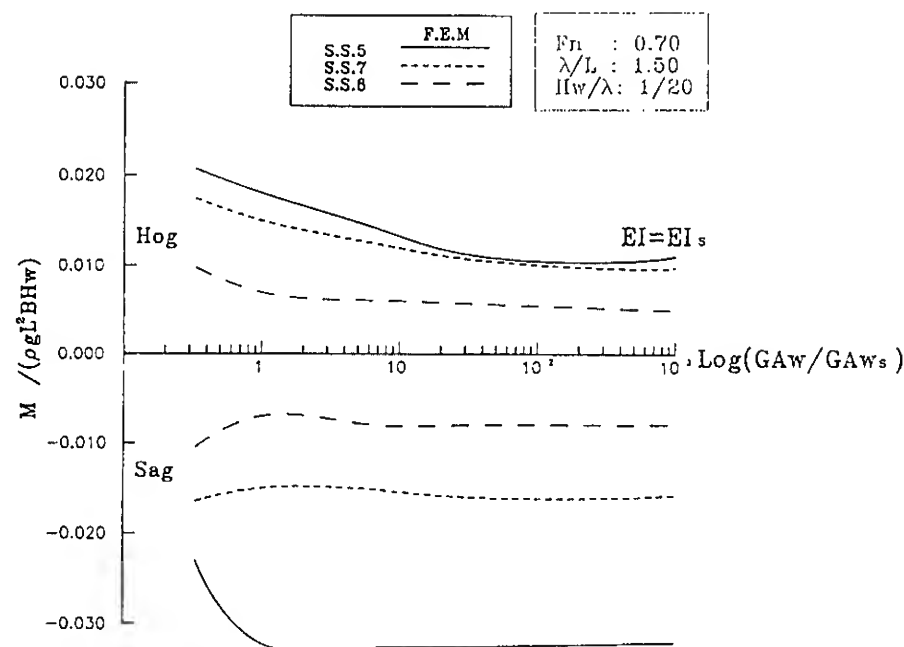


Fig.25 Effect of shear rigidity on vertical bending moment (Fn=0.7, λ/L=1.5, Hw/λ=1/20)

sagging moment acting on midship section significantly. Similarly, Figure 25 shows the shear rigidity's dependence of nondimensionalized bending moment peak values at square stations 5, 7 and 8, while the flexural rigidity is kept to be original value of the actual ship. It can be seen in this figure that although decreasing the shear rigidity may reduce sagging moment of midship remarkably, the hogging moment of midship may be increased, and the sagging as well as hogging moments acting at sections of fore-bodies may be increased significantly. However, it can be said that for the prediction of wave loads acting on the actual high-speed craft, neglecting shear deformation may underestimate the hogging moment, but has no significant effects on sagging moment.

## CONCLUSIONS

From the present investigation into nonlinear motions of large-sized high-speed craft in head sea and whipping effects included wave loads acting on it, the following conclusions may be drawn:

(1) Through the comparison between numerical prediction and elastic backbone model testing results, the present "F.E.M." calculation method, which is principally based on a modified nonlinear strip method, and following the Timoshenko beam element formulation, can be applied to estimate nonlinear motions and wave loads including whipping effects of a high-speed craft in head sea with accuracy enough for the practical point of view.

(2) Through serial calculations of different structural representation methods, the influences of neglecting the effects of vibration related to flexural deformation or shear deformation on the accuracy for predicting the vertical wave loads of a high speed craft can be summarized as follows:

(i) The prediction, which neglecting the effects of vibration related to flexural deformation, may underestimate the sagging moments along the ship's length significantly.

(ii) The prediction, which neglecting the effects of vibration related to shear deformation, may underestimate the hogging moments along the ship's length significantly.

(3) Through serial calculations on various structural rigidity of hull's structure on vertical wave loads acting on a high-speed craft can be summarized as follows:

(i) By decreasing the flexural rigidity, the sagging moment at mid-ship section which depends on impact strongly is reduced.

(ii) By decreasing the shear rigidity, sagging moment at mid-ship section is reduced significantly, but at the same time, the hogging moment of mid-ship section and the sagging as well as hogging moments of forward ship's sections may be increased.

## ACKNOWLEDGEMENTS

The financial support from the National Science Council of Republic of China under the grant NSC-77-0403-E002-08 is gratefully acknowledged. The authors wish to acknowledge the encouragement and the helpful discussions of Prof. M. Fujino, University of Tokyo. They also would like to express their cordial thanks to Mr. C.H. Li of the National Taiwan University for his cooperation in carrying out the experiments. The computation was carried out by CDC CYBER 2.3 in the computer center, National Taiwan University.

## REFERENCES

1. Krovin-Kroukovsky, B.V., "Investigation of Ship Motions in Regular Waves" Trans., Society of Naval Architects and Marine Engineers, Vol.63 (1955)

2. Tasai, F. and Takagi, M., "A Theory on Ship Dynamic Responses in Regular Waves and its Prediction Method", The 1st Symposium on Seakeeping, Society of Naval Architects of Japan (1969) (in Japanese)

3. Salvesen, N., E.O. Tuck and Faltinson, O., "Ship Motions and Sea Loads", Trans., Society of Naval Architects and Marine Engineers, Vol.78 (1970)

4. Yamamoto, Y., Fujino M. and Fukasawa, T., "Motion and Longitudinal Strength of a Ship in Head Sea and Effects of Nonlinearities (1st, 2nd, 3rd Reports)", Journ. Society of Naval Architects of Japan, Vol.143(1978), Vol.144 (1978), Vol.145(1979) (in Japanese)

5. Fujino, M. and Chiu, F.C., "Vertical motions of high-speed Boats in Head Sea and Wave Loads", Journ. Society of Naval Architects of Japan, Vol.154(1983) (in Japanese)

6. Chiu, F.C. and Fujino, M., "Nonlinear Prediction of Vertical Motions and Wave Loads of High-speed Crafts in Head Sea", International Shipbuilding Progress, Vol.36, No.406 (1989)

7. Chiu, F.C. and Fujino, M., "Nonlinear Prediction of Vertical Motions of a Fishing Vessel in Head Sea", Journal of Ship Research, (to be published, Accepted: July, 1989)

8. Kaneko Y. and Baba, E., Structural Design of Large Aluminium Alloy High-speed Craft, London, Royal Institution of Naval Architects (1982)

9. Kaneko Y., Takanashi, T. and Kihara, K., "A Proposal for Design Load on Structural Hull Girder and Bottom Structure of Large High-speed Craft (1st, 2nd Reports)", Trans., West-Japan Society of Naval Architects, Vol.70 (1985), Vol.72 (1986) (in Japanese)

10. Wang C.T., etc, "Model Test on the 4450-Boat", NTU-INA Tech. Rept.213, Institute of Naval Architecture, National Taiwan University (1985)

11. Kanedo, Y. and Takahashi, T., "Comparison between Nonlinear Strip Theory and Model Experiment on Wave Bending Moment Acting on a Semi-displacement Type High-speed Craft", Trans. West-Japan Society of Naval Architects, Vol.71 (1986) (in Japanese)

12. Chiu, F.C., Lee, Y.J. and Chou, S.K., "A Consideration on Vertical Wave Loads Acting on a Large-sized High-speed Craft", Journ., Society of Naval Architects of Japan, Vol.163 (1988)

13. Frank, W. and Salvesen, N., "The Frank Close-fit Ship Motion Computer Program", NSRDC Report No. 3289 (1970)

14. Wagner, H., "Über Stoss-und Greitvorgänge an der Oberfläche von Flüssigkeiten", Z.A.M.M., Band 12, Heft 4 (1932)

15. Yamamoto, Y., Fujino, M., and Ohtsubo, H., "Slamming and Whipping of Ships among Rough Seas", Numerical Analysis of the Dynamics of Ship Structures, EUR0MECH 122, ATMA, Paris (1979)

16. Bishop, R.E.D., "Myklestad's Method for Non-uniform Vibration Beam", The Engineer, Dec. 14 (1956)

17. Takahashi, T., and Kaneko, Y., "Experimental Study on Wave Loads Acting on a Semi-displacement Type High-speed Craft by Means of Elastic Backbone Model", High-speed Surface Craft Conference '83, London (1983)

## 7. CONCLUSIONS

From the present investigation into nonlinear motions of large-sized high-speed craft in head sea and whipping effects included wave loads acting on it, the following conclusions may be drawn:

(1) Through the comparison between numerical prediction and elastic backbone model testing results, the present "F.E.M." calculation method, which is principally based on a modified nonlinear strip method, and following the Timoshenko beam element formulation, can be applied to estimate nonlinear motions and wave loads including whipping effects of a high-speed craft in head sea with accuracy enough for the practical point of view.

(2) Through serial calculations of different structural representation methods, the influences of neglecting the effects of vibration related to flexural deformation or shear deformation on the accuracy for predicting the vertical wave loads of a high speed craft can be summarized as follows:

(i) The predication, which neglecting the effects of vibration related to flexural deformation, may underestimate the sagging moments along the ship's length significantly.

(ii) The prediction, which neglecting the effects of vibration related to shear deformation, may underestimate the hogging moments along the ship's length significantly.

(3) Through serial calculations on various structural rigidity of hull's structure on vertical wave loads acting on a high-speed craft can be summarized as follows:

(i) By decreasing the flexural rigidity, the sagging moment at mid-ship section which depends on impact strongly is reduced.

(ii) By decreasing the shear rigidity, sagging moment at mid-ship section is reduced significantly, but at the same time, the hogging moment of mid-ship section and the sagging as well as hogging moments of forward ship's sections may be increased.

## ACKNOWLEDGEMENTS

The financial support from the National Science Council of Republic of China under the grant NSC-77-0403-E002-08 is gratefully acknowledged. The authors wish to acknowledge the encouragement and the helpful discussions of Prof. M. Fujino, University of Tokyo. They also would like to express their cordial thanks to Mr. C.H. Li of the National Taiwan University for his cooperation in carrying out the experiments. The computation was carried out by CDC CYBER 2.3 in the computer center, National Taiwan University.

## REFERENCES

1. Krovin-Kroukovsky, B.V., "Investigation of Ship Motions in Regular Waves" Trans., Society of Naval Architects and Marine Engineers, Vol.63 (1955)

2. Tasai, F. and Takagi, M., "A Theory on Ship Dynamic Responses in Regular Waves and its Prediction Method", The 1st Symposium on Seakeeping, Society of naval Architects of Japan (1969) (in Japanese)

3. Salvesen, N., E.O. Tuck and Faltinson, O., "Ship Motions and Sea Loads", Trans., Society of Naval Architects and Marine Engineers, Vol.78 (1970)

4. Yamamoto, Y., Fujino M. and Fukasawa, T., "Motion and Longitudinal Strength of a Ship in Head Sea and Effects of Nonlinearities (1st, 2nd, 3rd Reports)", Journ. Society of Naval Architects of Japan, Vol.143(1978), Vol.144 (1978), Vol.145(1979) (in Japanese)

5. Fujino, M. and Chiu, F.C., "Vertical motions of high-speed Boats in Head Sea and Wave Loads", Journ. Society of Naval Architects of Japan, Vol.154(1983) (in Japanese)

6. Chiu, F.C. and Fujino, M., "Nonlinear Prediction of Vertical Motions and Wave Loads of High-speed Crafts in Head Sea", International Shipbuilding Progress, Vol.36, No.406 (1989)

7. Chiu, F.C. and Fujino, M., "Nonlinear Prediction of Vertical Motions of a Fishing Vessel in Head Sea", Journal of Ship Research, (to be published, Accepted: July, 1989)

8. Kaneko Y. and Baba, E., Structural Design of Large Aluminium Alloy High-speed Craft, London, Royal Institution of Naval Architects (1982)

9. Kaneko Y., Takanashi, T. and Kihara, K., "A Proposal for Design Load on Structural Hull Girder and Bottom Structure of Large High-speed Craft (1st, 2nd Reports)", Trans., West-Japan Society of Naval Architects, Vol.70 (1985), Vol.72 (1986) (in Japanese)

10. Wang C.T., etc, "Model Test on the 4450-Boat", NTU-INA Tech. Rept.213, Institute of Naval Architecture, National Taiwan University (1985)

11. Kanedo, Y. and Takahashi, T., "Comparison between Nonlinear Strip Theory and Model Experiment on Wave Bending Moment Acting on a Semi-displacement Type High-speed Craft", Trans. West-Japan Society of Naval Architects, Vol.71 (1986) (in Japanese)

12. Chiu, F.C., Lee, Y.J. and Chou, S.K., "A Consideration on Vertical Wave Loads Acting on a Large-sized High-speed Craft", Journ., Society of Naval Architects of Japan, Vol.163 (1988)

13. Frank, W. and Salvesen, N., "The Frank Close-fit Ship Motion Computer Program", NSRDC Report No. 3289 (1970)

14. Wagner, H., "Uber Stoss-und Greitvorgnge an der Oberflache von Flussigkeiten", Z.A.M.M., Band 12, Heft 4 (1932)

15. Yamamoto, Y., Fujino, M., and Ohtsubo, H., "Slamming and Whipping of Ships among Rough Seas", Numerical Analysis of the Dynamics of Ship Structures, EUROMECH 122, ATMA, Paris (1979)

16. Bishop, R.E.D., "Myklestad's Method for Non-uniform Vibration Beam", The Engineer, Dec. 14 (1956)

17. Takahashi, T., and Kaneko, Y., "Experimental Study on Wave Loads Acting on a Semi-displacement Type High-speed Craft by Means of Elastic Backbone Model", High-speed Surface Craft Conference '83, London (1983)

# APPENDIX A

$$M_{ij} = \int (\mu + \rho S_{zj}) W_i W_j dx \quad (19)$$

$$C_{ij} = \int \eta_i EI W_i'' W_j'' dx + \int \left( -\frac{\partial \rho S_{zi}}{\partial t} + \rho N_{zj} \right) W_i W_j dx \\ + V \cos \tau \int \rho S_{zj} (W_i' W_j - W_i W_j') dx \\ - V \cos \tau [\rho S_{zj} W_i W_j]_A^F \quad (20)$$

$$K_{ij} = \int EI W_i'' W_j'' dx - V \cos \tau \int \left( \frac{\partial \rho S_{zi}}{\partial t} + \rho N_{zj} \right) W_i W_j' dx \\ - V^2 \cos^2 \tau \int \rho S_{zj} W_i' W_j' dx \\ + V^2 \cos^2 \tau [\rho S_{zj} W_i W_j']_A^F \quad (21)$$

$$f_i = \cos \tau \left\{ \rho S_z \frac{\partial \xi_e}{\partial t} W_i dx + V \cos \tau \int \rho S_z \xi_e W_i dx \right. \\ \left. + \int \left( \frac{\partial \rho S_z}{\partial t} + \rho N_z \right) \xi_e W_i dx - V \cos \tau [\rho S_z \xi_e W_i]_A^F \right. \\ \left. - \rho g f (A - A_0) W_i dx \right\} \\ - V \sin(\tau_i + \tau_s) \left\{ V \cos \tau \int (\rho S_z^* - \rho S_{z0}^*) W_i' dx \right. \\ \left. + \int (\rho N_z^* - \rho N_{z0}^* + \frac{\partial \rho S_z^*}{\partial t}) W_i dx - V \cos \tau (\rho S_z^* - \rho S_{z0}^*) W_i \right\}_A^F \quad (22)$$

# APPENDIX B

The elemental coefficient matrices  $[M^*]_j$ ,  $[C^*]_j$ ,  $[K^*]_j$  and force vector  $\{f^*\}_j$  associated with  $j$ -th element are given by

$$[M^*]_j = (\mu + \rho S_z)_j \int_0^{l_j} [N_w]^T [N_w] d\xi \quad (23)$$

$$[K^*]_j = (EI)_j \int_0^{l_j} [N_\theta']^T [N_\theta'] d\xi \\ + (GA_w)_j \int_0^{l_j} ([N_\theta] - [N_w'])^T ([N_\theta] - [N_w']) d\xi \\ - V \cos \tau \left\{ \left( \frac{\partial \rho S_z}{\partial t} + \rho N_z \right)_j \int_0^{l_j} [N_w]^T [N_w'] d\xi \right. \\ \left. + V \cos \tau (\rho S_z)_j \left( \int_0^{l_j} [N_w']^T [N_w'] d\xi - [N_w]^T [N_w'] \Big|_0^{l_j} \right) \right\} \quad (24)$$

$$[C^*]_j = (\eta_b EI)_j \int_0^{l_j} [N_\theta']^T [N_\theta'] d\xi \\ + (\eta_s GA_w)_j \int_0^{l_j} ([N_\theta] - [N_w'])^T ([N_\theta] - [N_w']) d\xi \\ + \left( \frac{\partial \rho S_z}{\partial t} + \rho N_z \right)_j \int_0^{l_j} [N_w]^T [N_w] d\xi \\ + (V \cos \tau \rho S_z)_j \cdot \left\{ \int_0^{l_j} ([N_w']^T [N_w] - [N_w]^T [N_w']) d\xi \right. \\ \left. - [N_w]^T [N_w] \Big|_0^{l_j} \right\} \quad (25)$$

$$\{f^*\}_j = \cos \tau \left\{ \left[ \rho S_z \frac{\partial \xi_e}{\partial t} + \left( \frac{\partial \rho S_z}{\partial t} + \rho N_z \right) \xi_e - \rho g (A - A_0) \right. \right. \\ \left. - V \sin(\tau_i + \tau_s) \left( \frac{\partial \rho S_z^*}{\partial t} + \rho N_z^* - \rho N_{z0}^* \right) \right]_j \cdot \int_0^{l_j} [N_w]^T d\xi \\ \left. + V \cos \tau [\rho S_z \xi_e - V \sin(\tau_i + \tau_s) (\rho N_z^* - \rho N_{z0}^*)]_j \cdot \right. \\ \left. \left( \int_0^{l_j} [N_w']^T d\xi - [N_w]^T \Big|_0^{l_j} \right) \right\} \quad (26)$$

and the global coefficient matrices are obtained as assembly of the above element matrices by making use of nodal points correspondence.



**Session III**  
**Ship Hydrodynamics**

# Nonlinear Free Surface Waves Due to a Ship Moving Near the Critical Speed in a Shallow Water

H.-S. Choi, K.J. Bai, J.-W. Kim, I.-H. Cho  
(Seoul National University, Korea)

## ABSTRACT

This paper describes two methods of solution to the nonlinear free-surface waves generated by a ship moving steadily with a transcritical speed in a shallow water. As a mathematical model, a nonlinear initial/boundary-value problem is formulated within the scope of potential theory. One method is based on matched asymptotic expansion techniques and the Kadomtsev - Petviashvili equation is obtained as the leading-order solution for a slender ship. The other one is based on classical Hamilton's principle and the finite element method is implemented for numerical calculations. In order to examine the effect of the tank width on the wave field and resulting hydrodynamic forces, computations are made systematically for the Series 60 ship model with  $C_b = 0.8$  by these two different methods. For wider tanks, the pressure distribution on the free surface, equivalent to the ship model, is treated. The results obtained by two different methods are compared each other and with experimental measurements available. Also discussed are the appearance of stem waves at the tank wall and the evolution of the crestline of diverging waves in a wide tank.

## NOMENCLATURE

$A$	: typical wave amplitude
$C_b$	: block coefficient of ship
$D$	: fluid domain
$F_h$	: waterdepth-based Froude number
$g$	: gravitational acceleration
$h$	: water depth
$J$	: functional
$L$	: Lagrangian or ship's half length
$N$	: total number of nodes
$N_F$	: total number of free surface nodes
$N_i$	: trial function basis
$\vec{n}(n_x, n_y, n_z)$	: outward unit normal vector

$p$	: pressure
$q$	: source strength
$S(x)$	: longitudinal distribution of cross sectional area of ship
$S_B$	: blockage coefficient
$S_F$	: free surface
$\tilde{S}_F$	: projection of $S_F$
$S_m$	: maximum cross sectional area of ship
$S_o$	: ship surface
$t$	: time
$t^*$	: final time
$T_g$	: generation period between first two solitons
$U$	: ship's speed
$W$	: tank's half width
$x, y, z$	: rectangular coordinates
$x_c$	: $x$ -location of the crestline at $y = 0$
$\alpha$	: speed parameter or upwinding parameter
$\beta$	: blockage index
$\delta$	: slenderness parameter or variational operator
$\epsilon$	: nonlinear parameter
$\zeta$	: surface elevation
$\eta$	: tank width parameter
$\mu$	: dispersion parameter
$\rho$	: water density

## INTRODUCTION

A free-surface flow of an ideal fluid caused by a ship translating with a constant speed near the shallow water celerity is described by an initial/ boundary value problem governed by the Laplace equation with the free surface as a part of solution.

In the past, problems of this type were normally treated after the boundary conditions on the unknown free-surface had been linearized. Recently, however, there are growing interests in solving the

Hang S. Choi, Kwang J. Bai, Jang W. Kim, Il H. Cho  
Department of Naval Architecture, Seoul National University, Kwanak-Ku, Seoul 151-742, Korea

nonlinear free-surface problems more exactly. In some cases, it is of vital importance since linearized solutions fail to predict experimentally-identified phenomena. One example is the generation of upstream-advancing solitons by moving disturbances in shallow water. A comprehensive explanation on the physics involved is given by Wu [1].

There is a line of investigations on this nonlinear free-surface problem based on shallow water approximations which result in a variety of theories such as the Korteweg - de Vries (KdV), Kadomtsev - Petviashvili (KP), Boussinesq equations and the Green - Nagdhi formulation (GN) ; Many references in this area can be found in Ertekin and Qian [2]. To name few, Mei and Choi [3], Katsis and Akylas [4], Wu and Wu [5] and Ertekin, Webster & Wehausen [6] considered three-dimensional problems. There is another line of approach based on a numerical method as finite difference or finite element methods. Bai, Kim & Kim [7] were the first who applied the finite element method to a 3-dimensional nonlinear shallow water wave problem.

In the present paper, we concern with theoretical and numerical methods for solving a nonlinear three-dimensional free-surface flow problem in a shallow water. Specifically, a ship moving near the critical speed is treated to numerically simulate the experimental condition in the towing tank. It is formulated as an initial/boundary value problem within the scope of potential theory. As the solution procedure for the nonlinear problem, two different methods are described herein. In the first method, the given problem is reduced to a homogeneous KP equation with flux conditions on the boundaries. The ship is simplified to an equivalent slender body. Then the KP equation is numerically solved in the two-dimensional horizontal free-surface plane by an explicit finite difference scheme. In the second method, the original problem is replaced by an equivalent variational problem based on Hamilton's principle applied to water waves derived by Miles [8]. Then the variational functional defined as an integral in the unknown three-dimensional fluid domain is solved numerically by the finite element method. The variational functional used here is basically the same as the well-known Luke's variational principle [9]. However, the present functional is more advantageous in numerical computations compared to Luke's principle.

Recently, these two methods have been successfully applied to the generation and emission of solitons in the upstream and complicated waves in the downstream due to a moving ship in shallow water [7,10]. In these papers, however, no systematic investigations on the effect of the side walls have been undertaken. In the present study, it is our intention to clarify the effect of the width of the

side walls on the wave response and hydrodynamic forces. Thus the numerical results of the free surface elevations, hydrodynamic forces (*i.e.* wave resistance, lift and trimming moment) acting on a ship obtained from the both methods are presented and compared partially with the experimental findings of Ertekin [11]. The formation and development of stem waves is illustrated, when the generated waves are reflected at the tank wall. Also discussed are the evolutions of the crestline of diverging waves in a quite wide tank.

## INITIAL/BOUNDARY-VALUE FORMULATION

We consider a ship advancing steadily with a transcritical speed  $U$  along the centerline of a shallow tank. A rectangular Cartesian coordinate system moving with the ship's speed  $U$  is used, in which the  $x$ -axis coincides with the longitudinal axis of the ship and the  $z=0$  plane is the undisturbed free surface. The ship directs toward the negative  $x$ -axis and the positive  $z$ -axis points upward (see Fig.1). Under the usual assumptions in potential theory, fluid motions are expressed in terms of a velocity potential,  $\phi(x, y, z, t)$ , which is the solution of the Laplace equation

$$\nabla^2 \phi = 0 \quad -h \leq z \leq \zeta \quad (1)$$

in the fluid domain  $D$ , where  $h$  and  $\zeta$  are the water depth and the free-surface elevation, respectively. The kinematic condition is imposed on the ship surface  $S_0$

$$\phi_n = -Un_x, \quad (2)$$

where  $\vec{n} = (n_x, n_y, n_z)$  denotes the outward unit normal vector on  $S_0$ . No net flux condition also holds at the tank bottom and side walls

$$\phi_z = 0 \quad z = -h, \quad (3)$$

$$\phi_y = 0 \quad y = \pm W. \quad (4)$$

The kinematic and dynamic boundary conditions on the free surface  $S_F$  must be satisfied

$$\phi_z = \zeta_t + (U + \phi_x)\zeta_x + \phi_y\zeta_y, \quad (5)$$

$$g\zeta + \phi_t + U\phi_x + \frac{1}{2} |\nabla \phi|^2 + \frac{p}{\rho} = 0, \quad (6)$$

where  $g$  is referred to the gravity constant,  $\rho$  to the fluid density, and  $p = p(x, y, t)$  to the pressure, which is taken zero when the pressure distribution on  $S_F$  is absent.

By assuming that the fluid is initially at rest, the initial condition may be given as

$$\phi = \phi_t = 0 \quad \text{at } t = 0, \quad (7)$$

and the radiation condition yields to

$$\phi \rightarrow 0 \quad \text{as } x^2 + y^2 \rightarrow \infty. \quad (8)$$

It is to note that a modified radiation condition is utilized in computations for the downstream boundary.

## METHODS OF SOLUTION

Since the concept of the two methods employed here is quite different by their nature, a brief description on each method is necessary. We begin with the theoretical part, then the numerical part follows.

### Matched Asymptotic Expansion Technique

In order to analyze the above nonlinear problem, further assumptions and limitations are required. The first step is to introduce appropriate smallness parameters, with respect to which the expressions given in the previous section are to be perturbed. Hereby we define two small parameters

$$\epsilon = A/h, \quad \mu = h/L \quad (9)$$

and assume  $\epsilon = \mu^2$ , where  $A$  and  $2L$  mean the typical wave amplitude and the ship length, respectively. It corresponds to the Ursell number of order of unity, which implies that the nonlinearity and the dispersion are both important to the leading-order solution, *i.e.* we are dealing with a weakly nonlinear dispersive wave system. However, it may not be a serious restriction because the above assumption seems to be valid in a wide range of Ursell numbers as shown by Lee, Yates & Wu [12]. Since we are interested in the ship's speed in the neighborhood of the critical Froude number, it is expanded as follows:

$$F_h^2 = 1 - 2\alpha\mu^2 \quad \text{with } \alpha = O(1). \quad (10)$$

In order to include the lateral dispersion as well as the longitudinal dispersion, we have to choose a wide tank in comparison with the ship length

$$W/L = 1/\mu\eta \quad \text{with } \eta = O(1). \quad (11)$$

It is in general recognized that the governing parameter of the problem is the blockage coefficient, which is simply the area ratio of the midship to the tank cross-section. As pointed out by Mei [13], the order of magnitude of the blockage coefficient must be  $O(\mu^4)$

$$S_B = S_m/2Wh = O(\mu^4), \quad (12)$$

where  $S_m$  is the maximum cross-sectional area of a ship. If we assume the ship to be slender, of which the characteristic transverse dimension is denoted by  $R_o$ , then the slenderness parameter becomes

$$\delta = R_o/L = O(\mu^2). \quad (13)$$

It indicates that the nonlinearity arises directly from the disturbance caused by a slender ship.

As a result, we have four characteristic lengths in this problem; water depth ( $h$ ), tank width ( $2W$ ), ship's length ( $2L$ ) and transverse length ( $R_o$ ), which have vastly different scales each other.

$$h/L = O(\mu), \quad W/L = O(\mu^{-1}), \quad R_o/L = O(\mu^2). \quad (14)$$

To accommodate these in our analysis in a consistent manner, it is adequate to divide the fluid domain into three regions; near the ship, far from the ship and an intermediate region therebetween. The procedure of the derivation has been reported in detail in [10]. Hence we cite here only the results.

In the far field, the geometry of the tank affects the propagation of waves, but the generation mechanism of the waves is not known. The wave field is described by a homogeneous two-dimensional KdV or KP equation [14]

$$\zeta_\tau = \alpha\zeta_x + \frac{3}{2}\zeta\zeta_x + \frac{1}{6}\zeta_{xxx} + \frac{1}{2}\eta^2 \int_{-\infty}^x \zeta_{yy} dx. \quad (15)$$

It shows a balanced interplay between the nonlinear and the two-dimensional dispersion. It is a three-dimensional counterpart of the KdV equation, because it contains the lateral dispersion as well as the longitudinal dispersion. In the above, the variables are made dimensionless by

$$x = Lx', \quad y = Wy', \quad \zeta = A\zeta', \quad t = \frac{L}{\mu^2\sqrt{gh}}\tau. \quad (16)$$

For the sake of brevity, the primes are dropped hereafter.

In the near field, *i.e.* in the flow region closely around the ship, the kinematic boundary condition on the ship surface should be invoked. For a slender body, Eq.(2) can be replaced by

$$\phi_n \cong (U + \phi_x)R_x[1 + (R_\theta/R)^2]^{-1/2}, \quad (17)$$

where the normal derivative on the ship surface is approximated by that on its transverse plane. Here  $R_\theta$  stands for the circumferential derivative of the cross section. The presence of a ship and its motion can be represented by source distributions. By applying the law of mass conservation to a fluid domain surrounded by the ship surface, the free surface and a control surface located far away from the ship, but still within the near field, the source strength is readily determined

$$q = \frac{2}{\eta}\beta S_x(x) \quad \text{with } \beta = -\frac{S_B}{\mu^4}, \quad (18)$$

where  $S(x)$  is the longitudinal distribution of the cross sectional area of ship.

In the intermediate region, solutions of the far and the near fields are matched. As a result, the boundary condition for  $\zeta_y$  at  $y = 0$  turns out to be

$$\zeta_y(x, 0, \tau) = -\frac{1}{\eta^2} \beta S_{xx}(x). \quad (19)$$

And we have the leading-order hydrodynamic pressure

$$p = \mu^2 \rho g h \zeta + O(\mu^3). \quad (20)$$

The wave response can be computed by the KP equation given in Eq.(15) with the boundary conditions given in Eq.(4) and Eq.(19). The hydrodynamic forces and moment can be estimated based on the slender body approximation [3]. To do it, a simple explicit finite difference scheme is implemented for the KP equation, in which forward differences are chosen for time derivatives and central differences for spatial derivatives. But at the wall and the centerline of the tank, one-sided differences are used in order to incorporate with boundary conditions. Unidirectional Sommerfeld-type radiation conditions are imposed on both open boundaries. Nevertheless, a relatively large computation domain ahead of the ship is provided to avoid numerically reflected waves from the open boundary. Then the computation domain is gradually enlarged in both directions as the computation proceeds. Based on numerical experience, the grid size and time increment are chosen as

$$\Delta x = 0.1, \Delta \tau = 0.00002$$

and  $\Delta y$  is so taken as the ratio of  $\Delta x/\Delta y$  remains unity in the physical plane for better resolution of dispersion.

The Series 60 with  $C_b = 0.8$  is numerically modelled in terms of the longitudinal distribution of its cross-sectional area. However, the portion of both ends has been slightly modified by a parabolic distribution in order to satisfy the slender body assumption.

### Finite Element Method

The finite element method has been successfully applied to nonlinear water-wave problems, for example, Washizu et al.[15], Ikegawa [16], Nakayama & Washizu [17], Washizu & Nakayama [18], Betts & Assaat [19], Bai, Kim & Kim [7] (hereafter referred to as BKK), Bai, Kim & Lee [20], Bai, Kim & Lee [21] and Kim & Bai [22]. The finite element method is based on Luke's variational principle in [16]-[19]. However, in the present paper, the variational functional given in Miles [8] is used as the basis of the finite element computations. This variational form is simply a direct application of the classical Hamil-

ton's principle to the nonlinear water-wave problem. For the problem at hand we can define the functional  $J$  and the Lagrangian  $L$  as follows:

$$J = \int_0^{t^*} L dt, \quad (21)$$

$$L = \int_{\bar{S}_F} \bar{\phi} (\zeta_t + U \zeta_x) dS - U \int_{S_0} n_x \phi dS - \frac{1}{2} \int_D |\nabla \phi|^2 dV - \frac{g}{2} \int_{\bar{S}_F} \zeta^2 dS - \frac{1}{\rho} \int_{\bar{S}_F} p \zeta dS, \quad (22)$$

where  $\bar{S}_F$  is the projection of  $S_F$  on the  $Oxy$  plane and  $t^*$  is the final time.  $\bar{\phi}$  denotes the velocity potential on the free surface, i.e.  $\bar{\phi}(x, y, t) = \phi(x, y, \zeta, t)$ .

By taking the variations on  $J$  with respect to the unknown functions,  $\zeta$  and  $\phi$ , we obtain

$$\delta J_\zeta = \int_{\bar{S}_F} \{ (\bar{\phi} \delta \zeta)_{t=t^*} - (\bar{\phi} \delta \zeta)_{t=0} \} dS - \int_0^{t^*} \int_{\bar{S}_F} (\phi_t + U \phi_x + \frac{1}{2} |\nabla \phi|^2 + gz + \frac{p}{\rho})_{z=\zeta} \delta \zeta dS dt, \quad (23)$$

$$\delta J_\phi = \int_0^{t^*} dt \left[ \int_{\bar{S}_F} \left( \zeta_t + U \zeta_x - \frac{1}{n_x} \phi_n \right)_{z=\zeta} \delta \bar{\phi} dS - \int_{S_0} (\phi_n + U n_x) \delta \phi dS + \int_D \nabla^2 \phi \delta \phi dV \right]. \quad (24)$$

Here  $\delta J = \delta J_\zeta + \delta J_\phi$ . Equation (23) shows that the dynamic free-surface boundary condition is recovered from the stationary condition on  $J$  for the variation of  $\zeta$  at each time step. The wave elevations at  $t = 0$  and  $t^*$  are supposed to be specified as the constraints. Equation (24) shows that the kinematic condition on  $S_F$  and the governing equation in the fluid domain are recovered from the stationary condition on  $J$  for the variation of  $\phi$ .

In the numerical procedure for the application of the finite element method, we discretize the fluid domain into a number of finite elements. Then we approximate  $\phi$  in  $N$ -dimensional function space whose basis is continuous in  $D$ . We denote the basis of this trial space by  $\{N_i\}_{i=1, \dots, N}$ . It is convenient to introduce another set of basis function, denoted by  $\{M_k\}_{k=1, \dots, N_F}$ , which is defined only on the free surface. By the introduction of these basis functions, one can represent  $\phi$ ,  $\bar{\phi}$  and  $\zeta$  as

$$\phi(x, y, z, t) = \phi_i(t) N_i(x, y, z; \zeta), \quad (25)$$

$$\bar{\phi}(x, y, t) = \bar{\phi}_k(t) M_k(x, y), \quad (26)$$

$$\zeta(x, y, t) = \zeta_k(t) M_k(x, y), \quad (27)$$

where

$$M_k(x, y) = N_{i_k}(x, y, z; \zeta)|_{z=\zeta}, \quad (28)$$

$$k = 1, \dots, N_F.$$

Here  $N_F$  is the total number of nodes on  $S_F$  and  $i_k$  is the nodal number of the basis function  $N_i$ , of which the node coincides with that of the free-surface node  $k$ . Summation conventions for the repeated indices are used here. It should be noted that the basis function  $\{N_i\}_{i=1, \dots, N}$  is dependent on the free-surface shape  $z = \zeta(x, y, t)$  but its restriction on  $S_F$  is the function of  $(x, y)$  and independent of  $\zeta$ . This special property of  $\{M_k\}_{k=1, \dots, N_F}$  is maintained here since new nodal points in  $D$  are shifted only along the  $z$ -axis at each time step.

Once the trial function is represented by using the above basis function, the Lagrangian  $L$  can be written as

$$L = \bar{\phi}_k T_{kl} \frac{d}{dt} \zeta_l + U \bar{\phi}_k C_{kl} \zeta_l \quad (29)$$

$$- \frac{1}{2} \phi_i K_{ij} \phi_j - f_i \phi_i$$

$$- \frac{1}{2} \zeta_k P_{kl} \zeta_l - p_l \zeta_l,$$

where

$$T_{kl} = \int_{S_F} M_k M_l dS,$$

$$C_{kl} = \int_{S_F} M_k \frac{\partial M_l}{\partial x} dS,$$

$$K_{ij} = \int_D \nabla N_i \cdot \nabla N_j dV,$$

$$P_{kl} = g \int_{S_F} M_k M_l dS,$$

$$f_i = U \int_{S_0} n_x N_i dS,$$

$$p_k = \frac{1}{\rho} \int_{S_F} p(x, y, t) M_k dS.$$

The tensors  $K_{ij}$ ,  $P_{kl}$  are the kinetic and potential energy tensors and  $T_{kl}$  is the tensor obtained from the free-surface integral, which can be interpreted as a tensor related to the transfer rate between these two kinds of energy. It is of interest to note that in Eq.(29),  $P_{kl} = g T_{kl}$ . However,  $T_{kl}$  will be defined differently from this in the present computation by introducing the lumping scheme.

The stationary condition on  $J = \int L dt$  is equivalent to the following Euler-Lagrange equation

$$T_{kl} \frac{d}{dt} \bar{\phi}_l = - U C_{kl} \bar{\phi}_l \quad (30)$$

$$- \frac{1}{2} \phi_i \frac{\partial K_{ij}}{\partial \zeta_k} \phi_j - P_{kl} \zeta_l - p_k,$$

$$T_{kl} \frac{d}{dt} \zeta_l = - U C_{kl} \zeta_l \quad (31)$$

$$+ K_{i_k j} \phi_j + f_{i_k},$$

$$K_{ij} \phi_j = - f_i \quad \text{for } i \neq i_k. \quad (32)$$

Here Eq.(30) and Eq.(31) are the nonlinear ordinary differential equation for  $\{\zeta_k, \bar{\phi}_k\}_{k=1, \dots, N_F}$  and Eq.(32) is the algebraic equation for  $\{\phi_i\}_{i \neq i_k}$  which is the constraint for the above two equations. Here it should be noted that the second term on the right-hand side of Eq.(31) is computed by the volume integral as originally defined, whereas BKK used the surface integral reduced from the original volume integral. This change is made in the present work since the previous computation in BKK is found to be less accurate in the conservation of energy compared to the present scheme from our numerical test.

Eq.(30) through Eq.(32) are less advantageous in computations with respect to the numerical stability. To remedy this difficulty, we introduce the upwinding and local lumping schemes, which are often used in a wide class of computational fluid dynamics. Following these common steps, we obtain the final set of the reduced ordinary differential equations as follows:

$$\frac{d}{dt} \bar{\phi}_k = - U \tilde{T}_{km}^{-1} \tilde{C}_{ml} \bar{\phi}_l \quad (33)$$

$$- \tilde{T}_{km}^{-1} \left( \frac{1}{2} \phi_i \frac{\partial K_{ij}}{\partial \zeta_m} \phi_j + P_{ml} \zeta_l + p_m \right),$$

$$\frac{d}{dt} \zeta_k = - U \tilde{T}_{km}^{-1} \tilde{C}_{ml} \zeta_l \quad (34)$$

$$+ \tilde{T}_{km}^{-1} (K_{i_m j} \phi_j + f_{i_m}),$$



$$K_{ij}\phi_j = -f_i \quad \text{for } i \neq i_k, \quad (35)$$

where

$$\tilde{T}_{kl} = \int_{\bar{S}_F} \left( M_k + \frac{\alpha \Delta x}{2} \frac{\partial}{\partial x} M_k \right) M_l dS, \quad (36)$$

$$\tilde{C}_{kl} = \int_{\bar{S}_F} \left( M_k + \frac{\alpha \Delta x}{2} \frac{\partial}{\partial x} M_k \right) \frac{\partial}{\partial x} M_l dS, \quad (37)$$

$$\bar{T}_{kl} = \begin{cases} \sum_i T_{kl} & , k = 1; \\ 0 & , \text{otherwise.} \end{cases} \quad (38)$$

Here  $\alpha$  is the upwinding parameter as defined in Hughes & Brooks [23]. In Equations (33) and (34), a consistent upwinding scheme (also known as Petrov-Galerkin method) is employed as discussed in [23], whereas an inconsistent upwinding scheme was used in BKK. We leave out the detail procedures here since one can find them in BKK.

In the finite element computations, two numerical models are treated, *i.e.* a Series 60 ship model with block coefficient  $C_b=0.8$  and a pressure patch on the free surface equivalent to the above ship model. To simplify the finite-element grid generation, the Series 60 ship model is replaced by an vertical wall-sided ship which has the same cross-section area and the constant draft of the original model along the ship length. This means that the equivalent numerical ship model has rectangular cross section with a constant draft. The finite element subdivision under the ship's bottom is unchanged while the other finite element subdivision is changed at each time step to accomodate the new location of the free surface. An eight-node isoparametric element is used and the integration is carried out analytically along the vertical direction.

In the computations for the pressure patch on the free surface, a single finite element is taken along the depth with a higher-order polynomial basis function which satisfies the bottom condition. In this case the integration along the vertical direction is also carried out analytically. This is the so-called *p*-version while the former case is the *h*-version in the adaptive finite element method.

## NUMERICAL RESULTS & DISCUSSIONS

To simulate the tank tests [11], the Series 60 ship with  $C_b = 0.8$  is chosen as the numerical model. Its length, beam and draft are 1.52m, 0.23m and 0.075m respectively. The water depth is 0.15m. The tank widths are 1.22m, 2.44m, 4.88m. In addition to these, a much wider tank is considered to examine the effect of the tank width on the formation and propagation of upstream waves by the method based on the KP equation. But in the finite ele-

ment computations, an equivalent pressure patch is treated by increasing the width up to 480 times the water depth, since this is easier to compute than a ship model.

Throughout the computations, the motion is assumed to start with a prescribed constant speed as a step function. In presenting the two sets of computed results, we denote those obtained by the KP equation with a slender body approximation by KP, and those of the finite element method by FEM. The physical quantities with dimensions are shown as functions of the real time for the convenience to compare with the earlier experimental work [11]. Accordingly the wave resistance and the lift force are given in Newton and the moment in Newton-meter.

The numerical results of the forces and moment for the experimental condition with the tank width of 2.44 m are shown in Fig.2 through Fig.5. In these figures, the solid line corresponds to FEM, while the dotted line to KP, if not indicated otherwise. Fig.2a-2c display the time histories of the wave resistance for the depth Froude numbers  $F_h = 0.9$ , 1.0, and 1.1, respectively. For  $F_h = 0.9$ , the computed values by both methods coincide fairly well after 5 seconds. However, the discrepancies are considerable for  $F_h=1.0$  and 1.1. It is of interest to note that the magnitude of the oscillatory behavior becomes large in the case of FEM for  $F_h = 1.1$ . To investigate this rather large discrepancy, two different expressions for the pressure are used for the computation of forces and moment in FEM; the exact Bernoulli's equation and linearized Bernoulli's equation based on the linear shallow water approximation. These two sets of computations are given in Fig. 3a-3c, where the solid lines indicate the exact form and the dotted lines the linear approximation. These figures explain partly the source of the discrepancies observed in Fig. 2b and 2c, since the KP equation is an approximate solution to the problem. Furthermore, the ship has been assumed to be slender and only the leading-order pressure has been taken into account. It is to mention that the both methods give greater wave resistance than the experimental measurement in all the cases studied.

Fig. 4a-4c are the computed results of the lift force for  $F_h = 0.9$ , 1.0, and 1.1. Contrary to the wave resistance discussed above, the lift forces by FEM are consistently smaller than those by KP. FEM predicts a longer oscillatory period than KP. Presumably this is due to the difference in the dispersion in the two methods.

In the similar fashion, the moment with respect to the origin is illustrated in Fig.5a-5c. The moment estimated by KP is almost twice as large as that by FEM for  $F_h = 0.9$  in Fig 5a. The results of KP contain considerable oscillatory components, whereas those obtained by FEM are nearly constant

after 5 seconds.

The time histories of the forces and moment at the critical speed for the tank widths of 1.22m, 2.44m and 4.88m, denoted by 1, 2, 3 in this order, are depicted in Fig.6 through Fig.8. The wave resistance is given in Fig.6, and the lift force and moment are in Fig.7 and Fig.8, respectively. The results obtained by KP are indicated by (a) and FEM by (b) in these figures. As the tank width becomes larger, the wave resistance and the moment decrease and they seem to converge to some limit values. But the lift increases as the tank width increases.

The evolutions of the surface elevation evaluated at 90cm ahead of the bow (Gauge No. 3 in [11]) for the tank width of 2.44m are shown in Fig.9 a-c. The asterisk marks correspond to the experimental measurements, but the starting time is only of qualitative meaning due to the different nature of the initial conditions in the computations and the experiments. For the subcritical speed,  $F_h = 0.9$ , the measured profile looks closer to FEM, but the trend is opposed for  $F_h = 1.0$  and 1.1. Over the three speeds, the generation period of the upstream solitons is shorter in the results calculated by KP compared to those by FEM. It is observed that the mean water level is slightly higher in KP for  $F_h = 0.9$ .

In Table 1, the amplitude and propagation speed of the first soliton, and the generation period between first two solitons are listed together with the experimental measurements. Here the tank widths are indicated by the ratios to the ship length, namely  $W/L = 0.8, 1.6$  and  $3.2$  for  $2W = 1.22m, 2.44m$  and  $4.88m$ , respectively. The amplitude measured by experiments is the smallest among three for  $W/L = 0.8$ , but it is somewhat between the two computed results for  $W/L = 1.6$  and  $3.2$ . It is interesting to note that KP predicts consistently higher amplitudes for all cases. For the propagation speed, the overall behaviour is similar as in the amplitude. But there is no clear-cut trend in the case of the generation period. The period measured in the experiment is longer than the numerical predictions for  $F_h = 0.9$ , whereas the result obtained by FEM is the longest for  $F_h = 1.1$ .

Based on his systematic experiments, Ertekin [11] concluded that the characteristics of upstream-advancing solitons are determined primarily by the blockage coefficient and the detailed geometry of disturbances is of secondary importance. Recently Pedersen [24] and Ertekin & Qian [2] investigated the influence of parameters other than the blockage coefficient on the generation mechanism of solitons. Along this line, we carried out additional computations by KP for a slender ship with a parabolic distribution of cross sectional area ( $C_b = 0.667$ ) with

the same blockage coefficient as the Series 60 ship ( $C_b = 0.8$ ). The result for  $W/L = 1.6$  is given in Table 2. Comparing it to the corresponding result for the Series 60 ship in Table 1, we can recognize that the amplitude and the period have been remarkably changed. The amplitude is decreased by about 0.06 times the water depth and the period is increased by about 20% for all three speeds considered. We may conjecture that the hullform, which may be properly represented in terms of ship's block coefficient, plays a significant role on the generation of solitons.

Fig.10 and Fig.11 are the snapshots of wave contour around the ship in a tank of width 4.88m at the critical speed. Due to the different nondimensionalization, the time instances are slightly shifted in two figures. The solid lines represent a constant positive surface elevation and the dotted lines denote a negative surface level. Two adjacent lines differ the surface elevation by 0.04 times the water depth. The wave contours obtained by KP looks more complicated and upstream waves propagate faster than those obtained by FEM. It is partly due to the difference in the propagation speed, as shown in Table 1 (b). In these figures, we can observe the formation of stem waves at the wall, when the waves generated from the bow are reflected there. The stem waves are further developed, as time elapses. It suggests that the formation of straight crestlines is associated with the stem waves, which supports the conclusion made by Pedersen [24].

The perspective views of the wave fields for the above case are illustrated in Fig.12 for KP and Fig.13 for FEM, respectively. Cautions should be paid that the vertical displacement is exaggerated by 5 times compared to the horizontal scales. The upstream solitons and three-dimensional downstream waves are clearly shown.

Fig.14 shows the wave resistance computed by FEM by systematically increasing the tank width for the pressure patch. In this case the pressure distribution is specified to have the same blockage coefficient as the ship model in the earlier experimental condition. The pressure is assumed by a trapezoidal distribution in both  $x$ - and  $y$ - directions and constant along the length of the parallel middle body in the  $x$ -direction. The length of the pressure patch is taken to be same as the ship length. Along the  $y$ -axis the pressure distribution is assumed to be constant along 0.8 times the water depth and changes linearly to zero at the edges of the patch. The width of the patch is taken 2.4 times the water depth. The number indicated to the lines corresponds to the tank, whose width is consecutively doubled starting from  $2W = 1.22m$  upto 5. The line 6 is the case for the tank width of 72m.

The oscillatory component in the

wave resistance is pronounced for small tank width, whereas it becomes insignificant as the tank width becomes very large. However, the mean value of the wave resistance remains nearly constant after 5 seconds. It is to note that the values of wave resistance for the pressure patch are smaller than those for the ship (see Fig.6b).

For the above pressure patch, the computation domain is continuously enlarged up to  $2W/h = 480$ . The maximum tank width treated here may be regarded as a case of infinite width at that time. Because the tank width is kept sufficiently large by increasing it at every time step so that the disturbance near the side walls is not felt in the computations. Fig.15 is three-dimensional wave profile at  $Ut/h = 320$  obtained from FEM. It is to observe that two diverging waves have already advanced upstream.

The first crestline is plotted on a logarithmic scale in Fig.16, where  $x_c$  is referred to the  $x$  location of the crestline at the centerline of the tank. Although the slope in this scale varies slightly with time, it is approximately 0.5. It suggests that the crestline is almost a parabola, which was also discussed by Redekopp [25] and Lee & Grimshaw[26].

#### ACKNOWLEDGEMENTS

This work has been supported by the Korean Science & Engineering Foundation under the Non-linear Ship Hydrodynamics Program, Grant No. 87020703.

#### REFERENCES

- [1] Wu, T.Y., Generation of Upstream-Advancing Solitons by Moving Disturbances, *Journal of Fluid Mechanics*, Vol.184, 1987, pp.75-99.
- [2] Ertekin, R.C. and Qian, Z.-M., Numerical Grid Generation and Upstream Waves for Ships Moving in Restricted Waters, *Proceedings of the 5th International Conference on Numerical Ship Hydrodynamics*, 1989, pp.421-437.
- [3] Mei, C.C. and Choi, H.S., Forces on a Slender Ship Advancing Near the Critical Speed in a Wide Canal, *Journal of Fluid Mechanics*, Vol. 179, 1987, pp.59-76.
- [4] Katsis, C. and Akylas, T.R., On the Excitation of Long Nonlinear Water Waves by a Moving Pressure Distribution. Part 2: Three Dimensional Effects, *Journal of Fluid Mechanics*, Vol.177, 1987, pp.49-65.
- [5] Wu, D.-M. and Wu, T.Y., Precursor Solitons Generated by Three - Dimensional Disturbances Moving in a Channel, *Proceedings of IUTAM Symposium on Nonlinear Water Waves*, 1987, pp.69 -76.
- [6] Ertekin, R.C., Webster, W.C. and Wehausen, J.V., Waves Caused by a Moving Disturbance in a Shallow Channel of Finite Width, *Journal of Fluid Mechanics*, Vol.169, 1986, pp.275-292.
- [7] Bai, K.J., Kim, J.W. and Kim, Y.H., Numerical Computations for a Nonlinear Free Surface Flow Problem, *Proceedings of the 5th International Conference on Numerical Ship Hydrodynamics*, 1989 pp.403-420.
- [8] Miles, J.W., On Hamilton's Principle for surface waves, *J. Fluid Mech.*, 83, pp. 395-387.
- [9] Luke, J.C., A Variational Principle for a Fluid with a Free Surface, *Journal of Fluid Mechanics*, Vol.27, 1967, pp.395-397.
- [10] Choi, H.S. and Mei, C.C., Wave Resistance and Squat of a Slender Ship Moving Near the Critical Speed in Restricted Water, *Proceedings of the 5th International Conference on Numerical Ship Hydrodynamics*, 1989, pp.439-454.
- [11] Ertekin, R.C., Soliton Generation by Moving Disturbances in Shallow Water : Theory, Computation and Experiment, Ph.D. Thesis, University of California, Berkeley, 1984.
- [12] Lee, S.-J., Yates, G.T. and Wu, T.Y., Experiments and Analysis of Upstream - Advancing Solitary Waves Generated by Moving Disturbances , *Journal of Fluid Mechanics*, Vol.199, 1989, pp.569-593.
- [13] Mei, C.C., Radiation of Solitons by Slender Bodies Advancing in a Shallow Channel, *Journal of Fluid Mechanics*, Vol.162, 1986, pp.53-67.
- [14] Kadomtsev, B.B. and Petviashvili, V.I., On the Stability of Solitary Waves in Weakly Dispersive Media, *Soviet Physics - DOKLADY*, Vol.15, NO.6, 1970, pp.539-541.
- [15] Washizu, K., Nakayama, T. and Ikegawa, M., Application of Finite Element Method to Some Free Surface Fluid Problems, *Finite Elements in Water Resources*, Pentech Press, London, 1977, pp.4.247-4.246.
- [16] Ikegawa, M., Finite Element Analysis of Fluid Motion in a Container, *Finite Element Meth-*

ods in Flow Problems, UAH Press, Alabama, 1974, pp.737-738.

- [17] Nakayama, T. and Washizu, K., Nonlinear Analysis of Liquid Motion in a Container Subjected to Forced Pitching Oscillation, International Journal for Numerical Methods in Engineering, Vol.15, 1980, pp.1207-1220.
- [18] Washizu, K., Nakayama, T., Ikegawa, M., Tanaka, Y. and Adachi, T., Some Finite Element Techniques for the Analysis of Nonlinear Sloshing Problems, Finite Elements in Fluids Vol.5, John Wiley & Sons, 1984, pp.357-376.
- [19] Betts, P.L. and Assaat, M.I., Large-Amplitude Water Waves, Finite Elements in Fluids, Vol.4, John Wiley & Sons, 1982, pp.109-127.
- [20] Bai, K.J., Kim, J.W. and Lee, H.S., A Numerical Radiation Condition for Two Dimensional Steady Waves, Proc. Workshop on Nonlinear Mechanics, Korea Soc. Theoretical and Applied Mechanics, Seoul, Korea, 1990, pp.119-132.
- [21] Bai, K.J., Kim, J.W. and Lee, H.S., An Application of the Finite Element Method to a Nonlinear Free Surface Flow Problem, The

Second World Congress on Computational Mechanics, Stuttgart, Germany, 1990.

- [22] Kim, J.W. and Bai, K.J., A note on Hamilton's Principle for a Free Surface Flow Problem, Journal of Society of Naval Architects of Korea (in Korean), 1990, (in print).
- [23] Hughes, T. J. R. and Brooks, A. A Theoretical Framework for Petrov-Galerkin Methods with Discontinuous Weighting Functions: Application to the Streamline-Upwind Procedure, Finite Elements in Fluids, Vol. 4, John Wiley & Sons, 1982, pp. 47-65.
- [24] Pedersen, G., Three-Dimensional Wave Patterns Generated by Moving Disturbances at Transcritical Speeds, Journal of Fluid Mechanics, Vol.196, 1988, pp.39-63.
- [25] Redekopp, L.G., Similarity Solutions of Some Two-Space-Dimensional Nonlinear Wave Evolution Equations, Studies in Applied Mathematics, Vol.63, 1980, pp.185-207.
- [26] Lee, S.-J. and Grimshaw, H.J., Upstream-Advancing Waves Generated by Three-Dimensional Moving Disturbances, Physics of Fluid A2(2), 1990, pp.194-201.

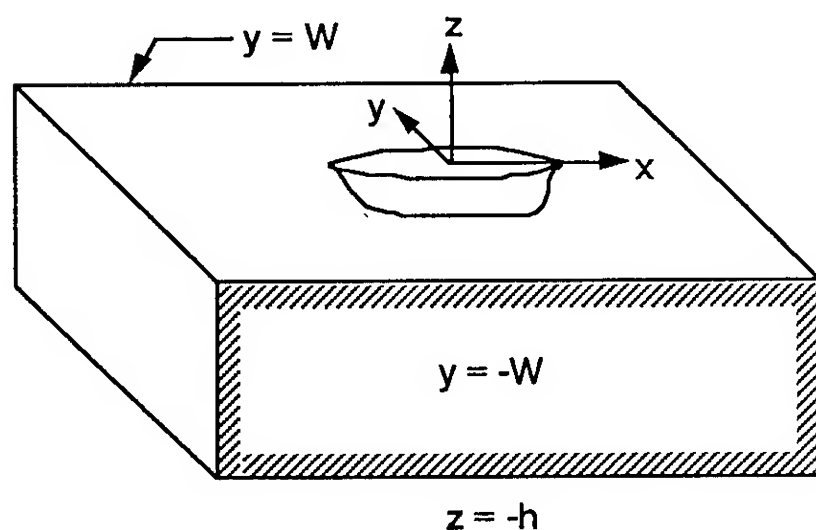
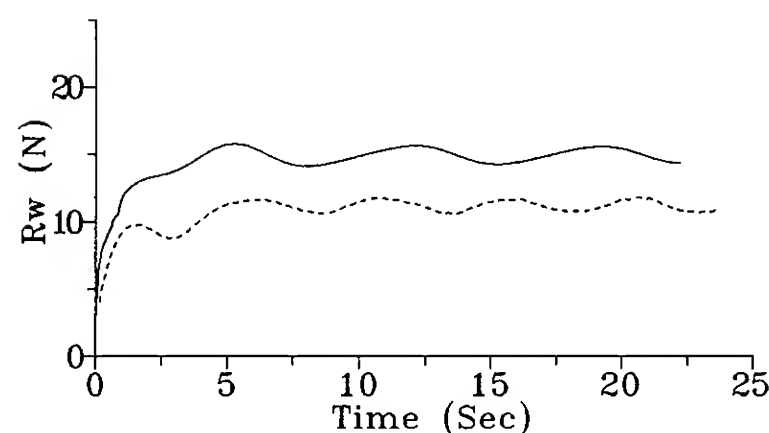
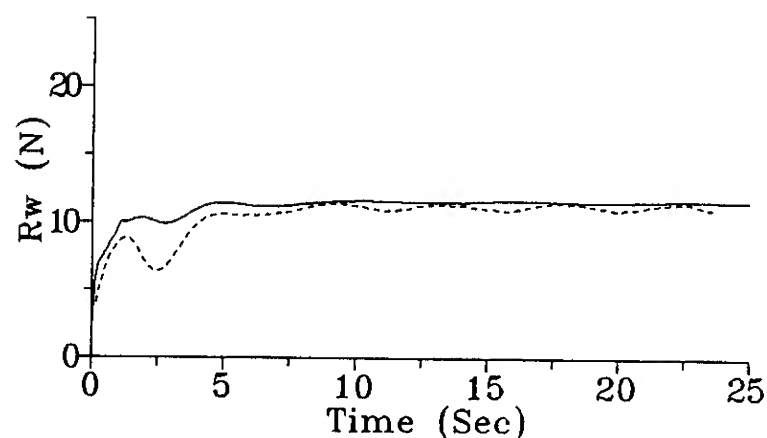


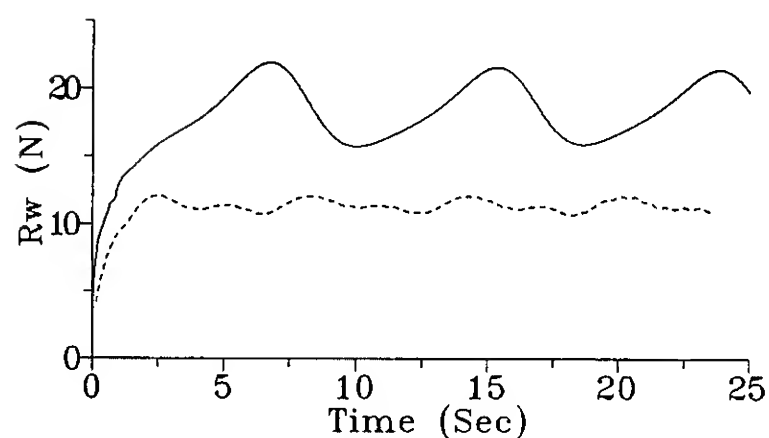
Fig.1 Definition Sketch



(b)  $F_h = 1.0$



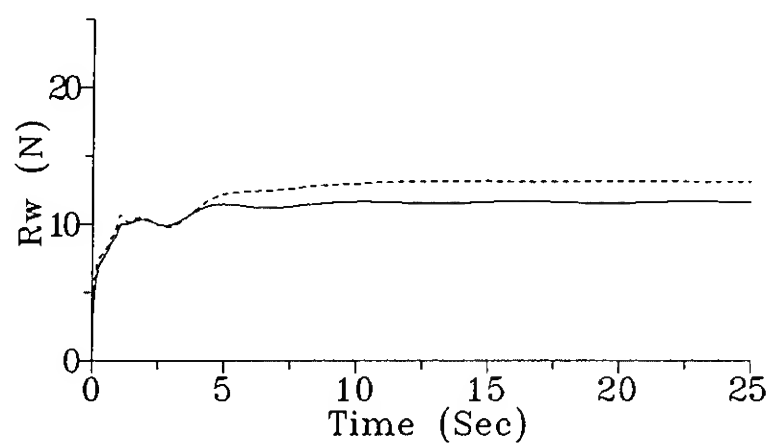
(a)  $F_h = 0.9$



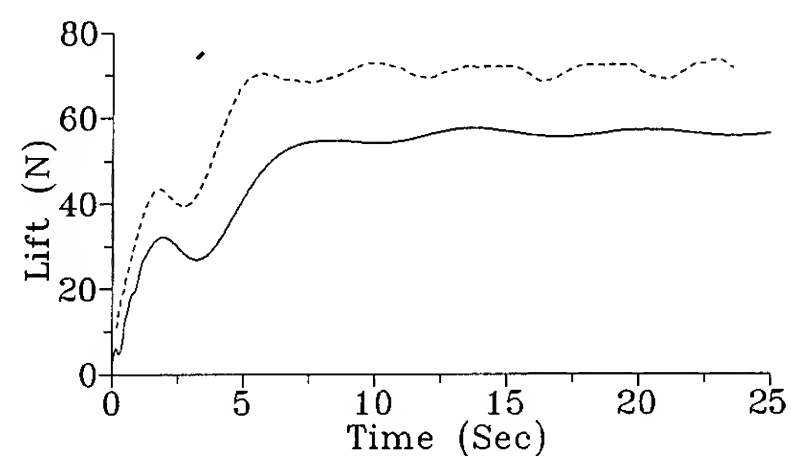
(c)  $F_h = 1.1$

Fig.2 Wave Resistance ( $2W = 2.44\text{m}$ )

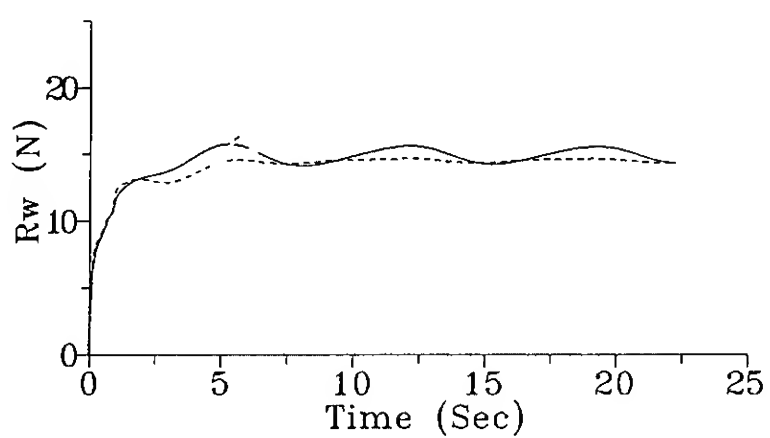
———— : FEM, - - - - - : KP



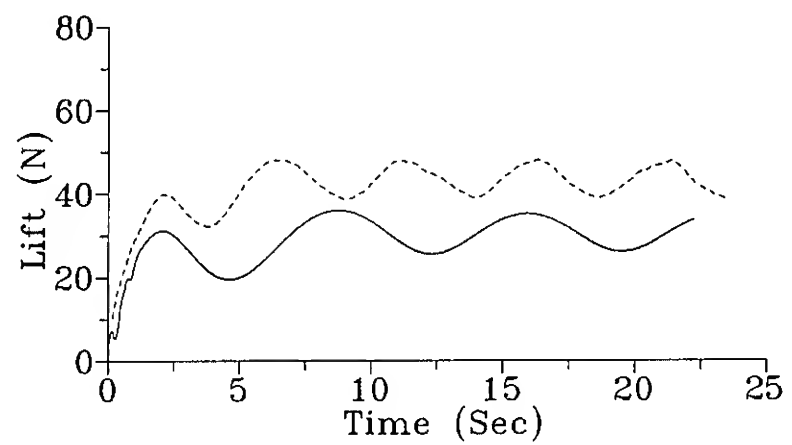
(a)  $F_h = 0.9$



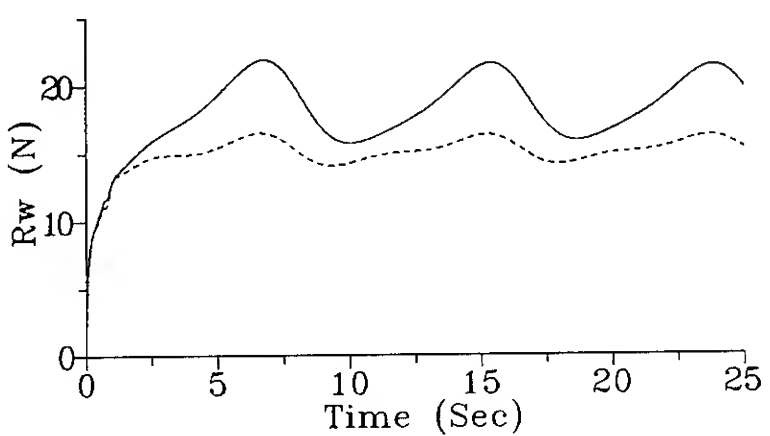
(a)  $F_h = 0.9$



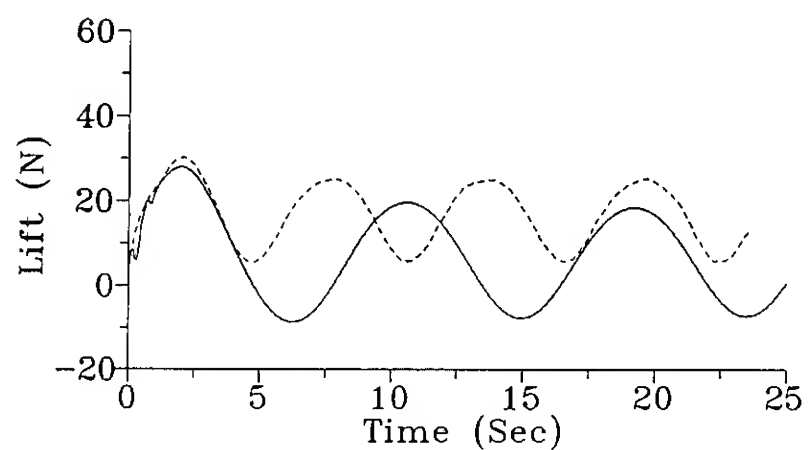
(b)  $F_h = 1.0$



(b)  $F_h = 1.0$



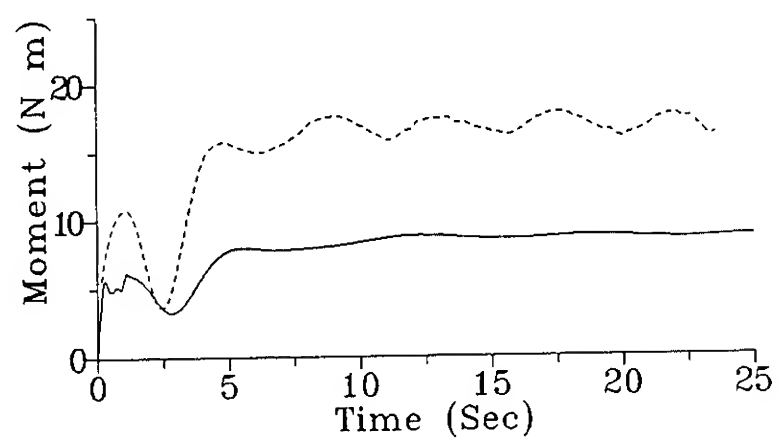
(c)  $F_h = 1.1$



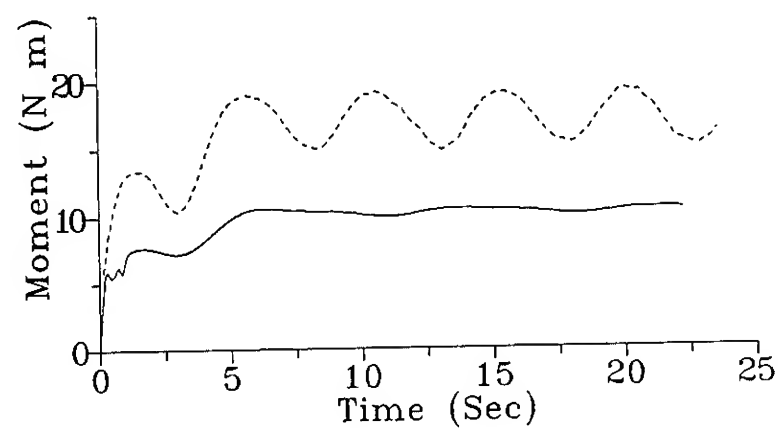
(c)  $F_h = 1.1$

Fig.3 Exact and Linear Approximate Wave Resistances by FEM ( $2W = 2.44m$ ).  
 — : Exact, - - - : Linear approximation

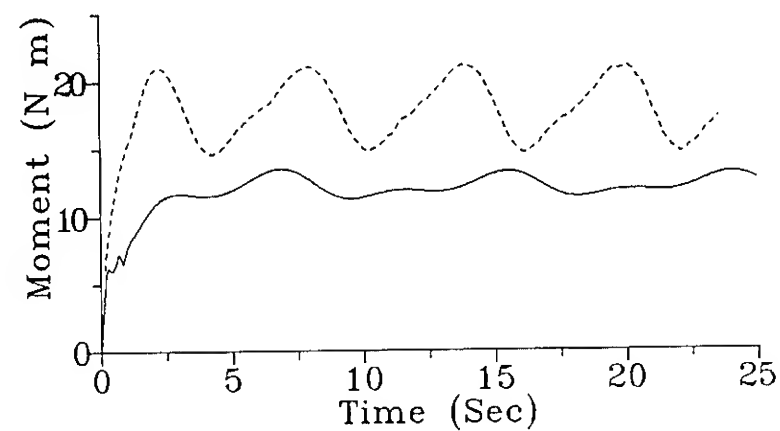
Fig.4 Lift Force ( $2W = 2.44m$ )  
 — : FEM, - - - : KP



(a)  $F_h = 0.9$

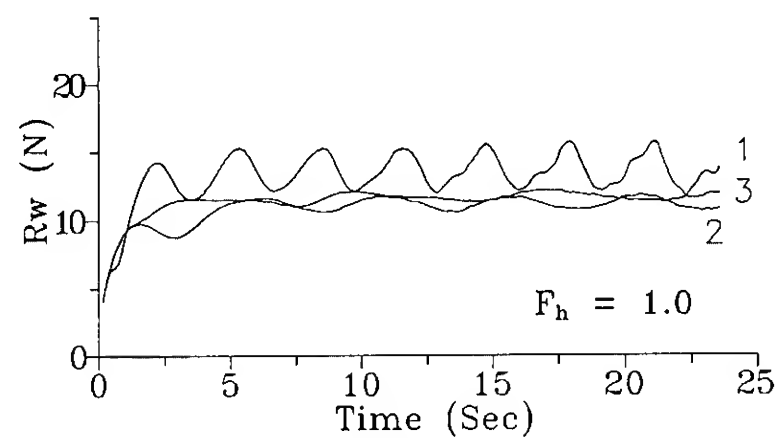


(b)  $F_h = 1.0$

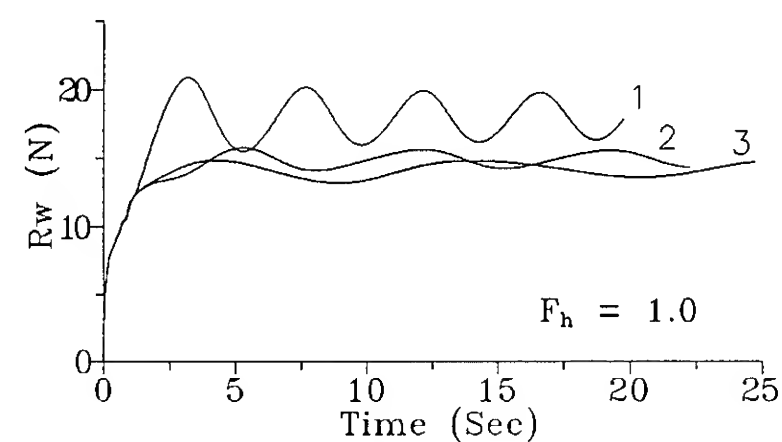


(c)  $F_h = 1.1$

Fig.5 Trimming Moment ( $2W = 2.44m$ )  
— : FEM, - - - : KP

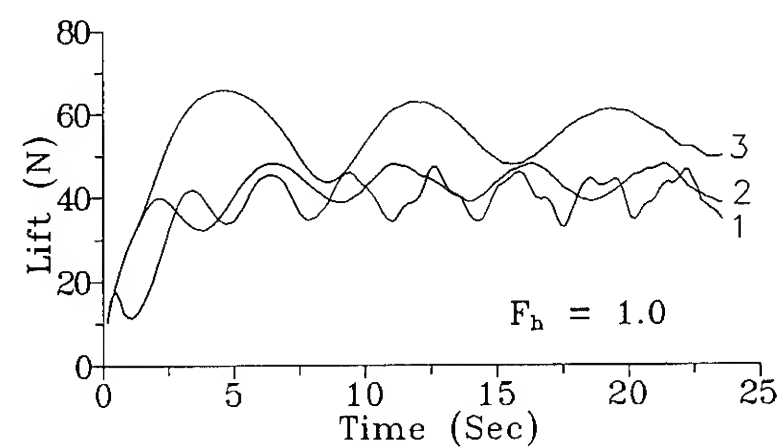


(a) KP

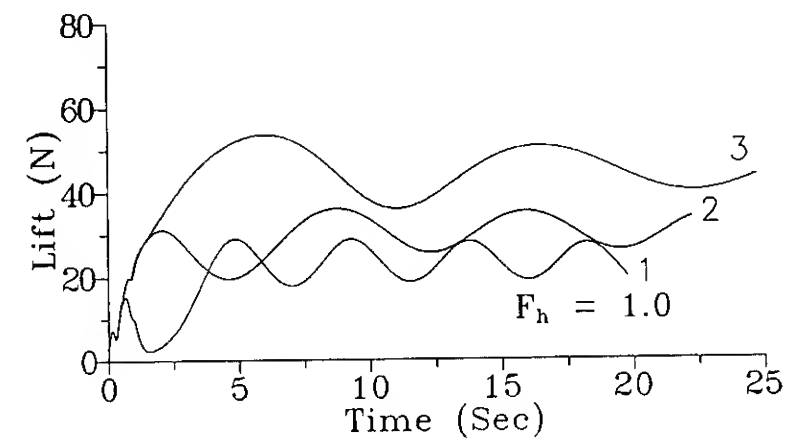


(b) FEM

Fig.6 Wave Resistances for Three Different Tank Widths ( 1 : 1.22m, 2 : 2.44m, 3 : 4.88m ) at the Critical Speed



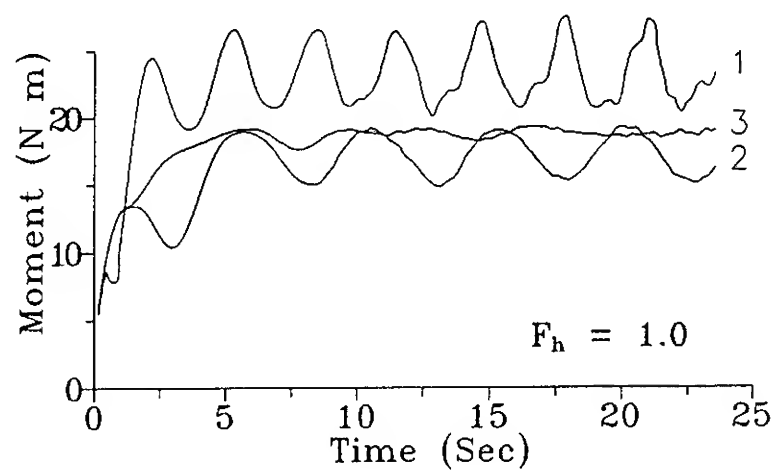
(a) KP



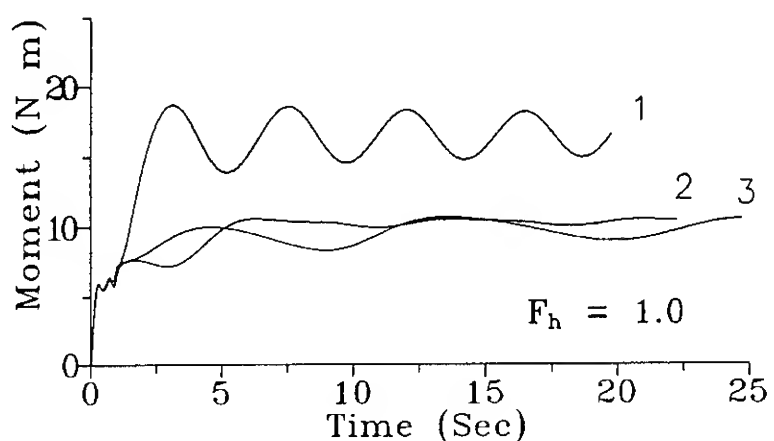
(b) FEM

Fig.7 Lift Forces for Three Different Tank Widths ( 1 : 1.22m, 2 : 2.44m, 3 : 4.88m ) at the Critical Speed



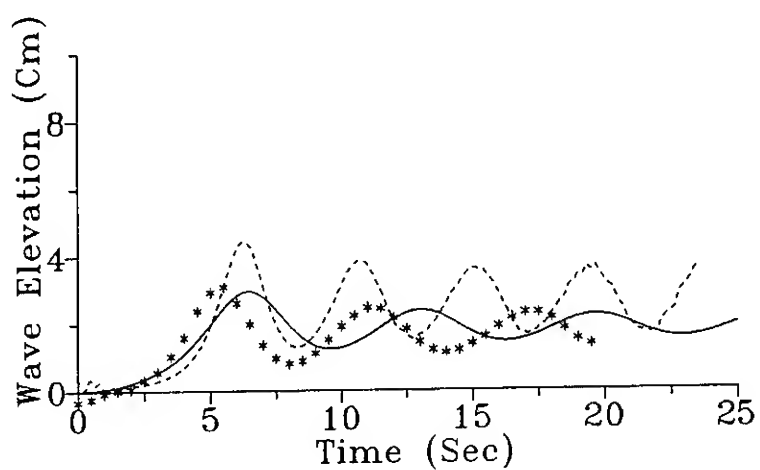


(a) KP

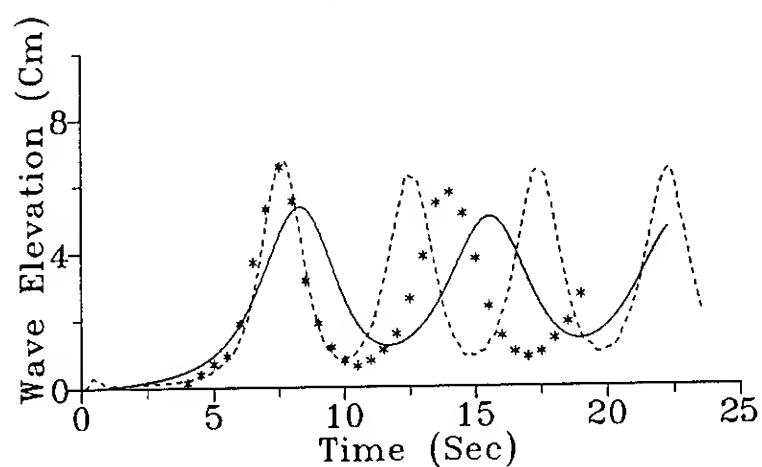


(b) FEM

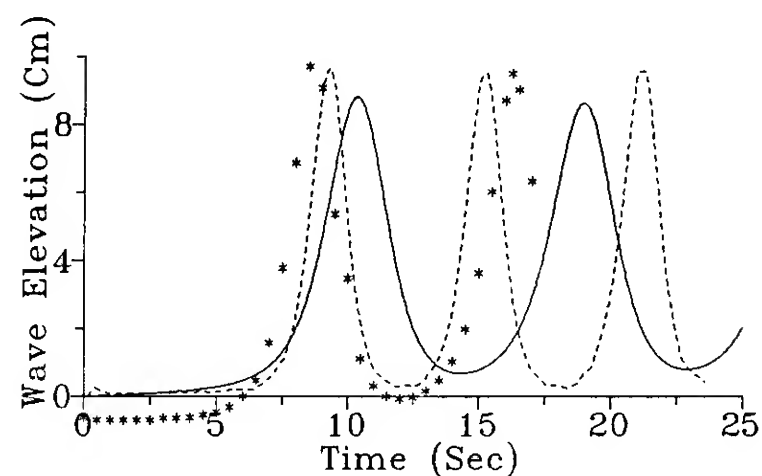
**Fig.8** Trimming Moment for Three Different Tank Widths ( 1 : 1.22m, 2 : 2.44m , 3 : 4.88m ) at the Critical Speed



(a)  $F_h = 0.9$

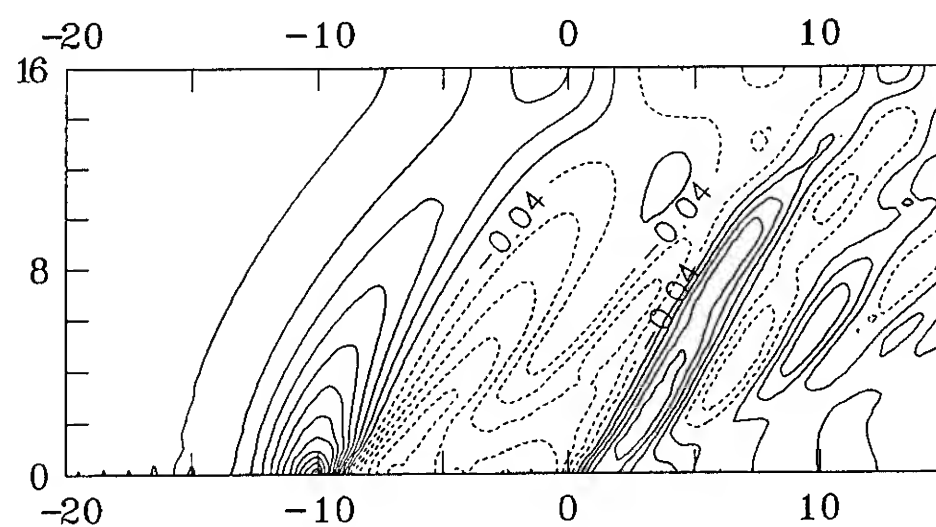


(b)  $F_h = 1.0$

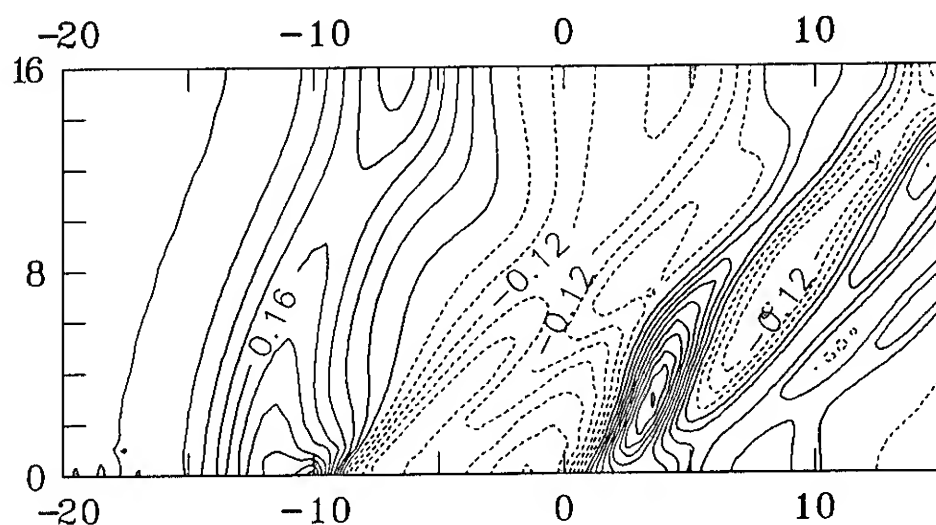


(c)  $F_h = 1.1$

**Fig.9** Free-Surface Elevation at the Gauge (90cm Ahead of the Bow) — : FEM, - - : KP, \*\*\*\*\* : EXP

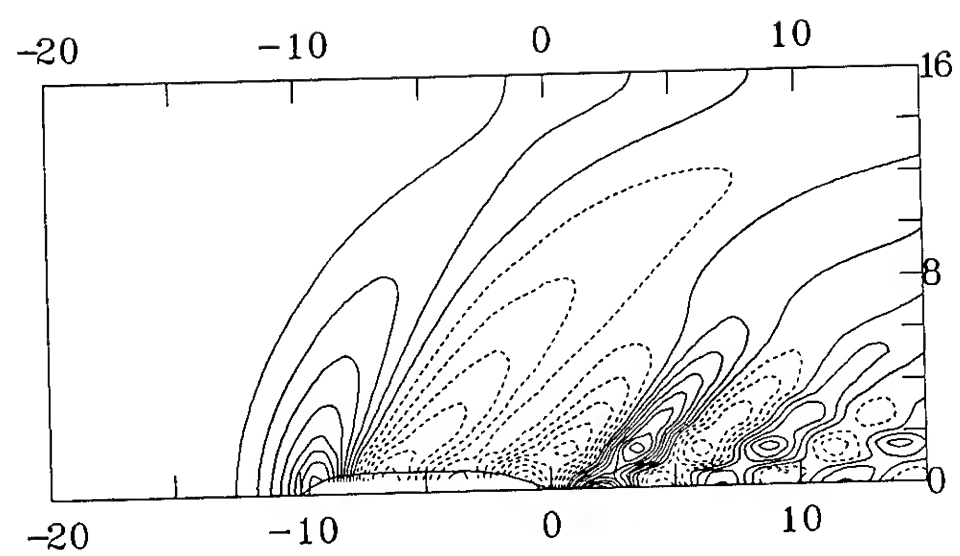


(a)  $U t/h = 19.65$

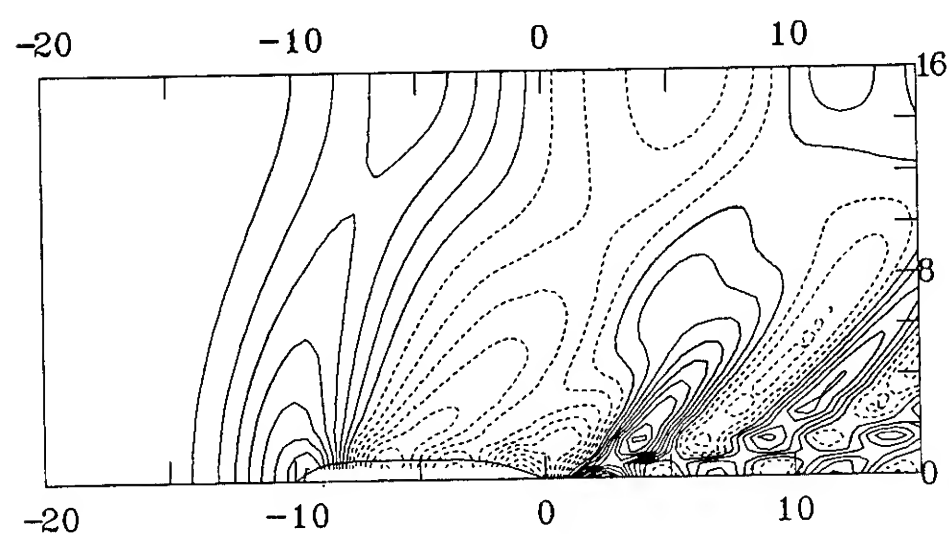


(b)  $U t/h = 39.3$

**Fig.10** Wave Contour at the Critical Speed (KP, 2W = 4.88m)

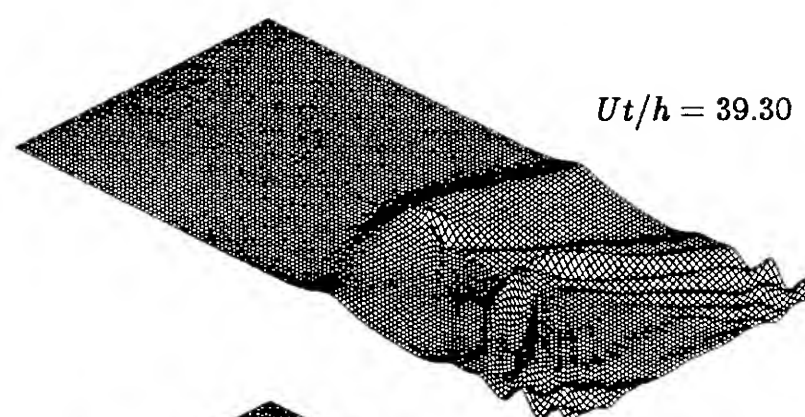


(a)  $Ut/h = 20.0$

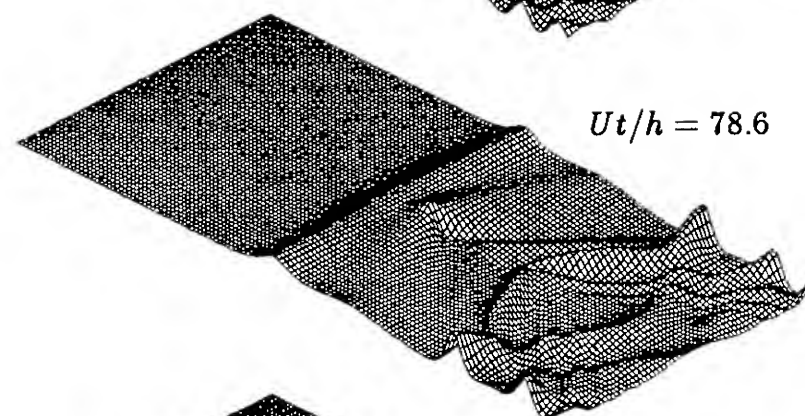


(b)  $Ut/h = 40.0$

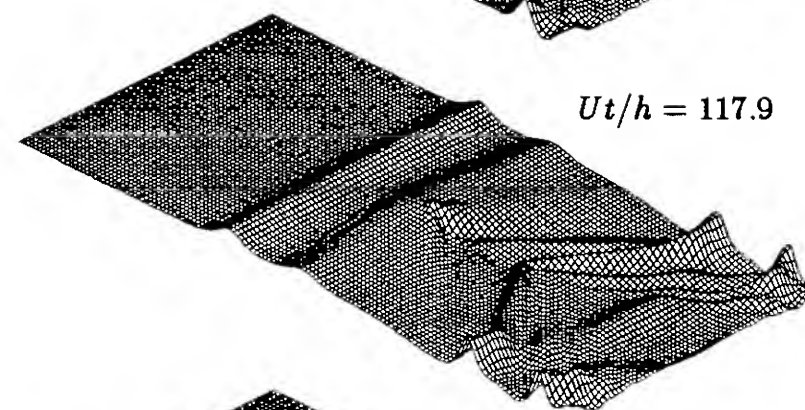
**Fig.11** Wave Contour at the Critical Speed (FEM,  $2W = 4.88\text{m}$ )



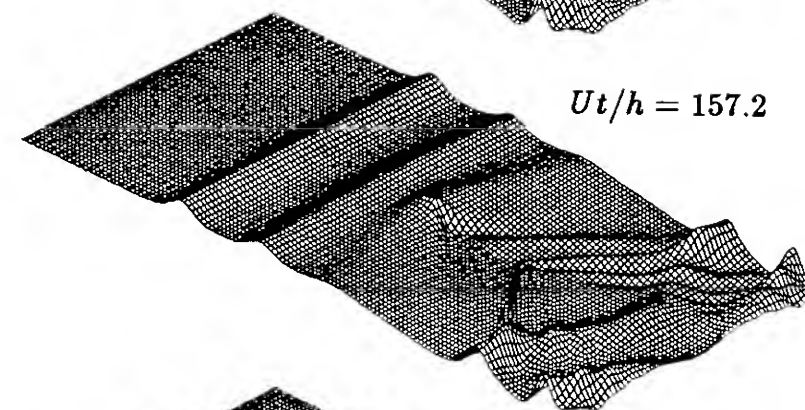
$Ut/h = 39.30$



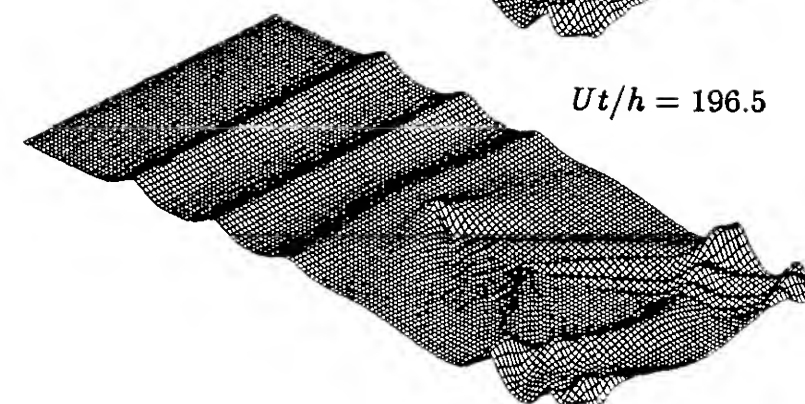
$Ut/h = 78.6$



$Ut/h = 117.9$



$Ut/h = 157.2$



$Ut/h = 196.5$

**Fig.12** Wave Evolution at the Critical Speed (KP,  $2W = 4.88\text{m}$ )

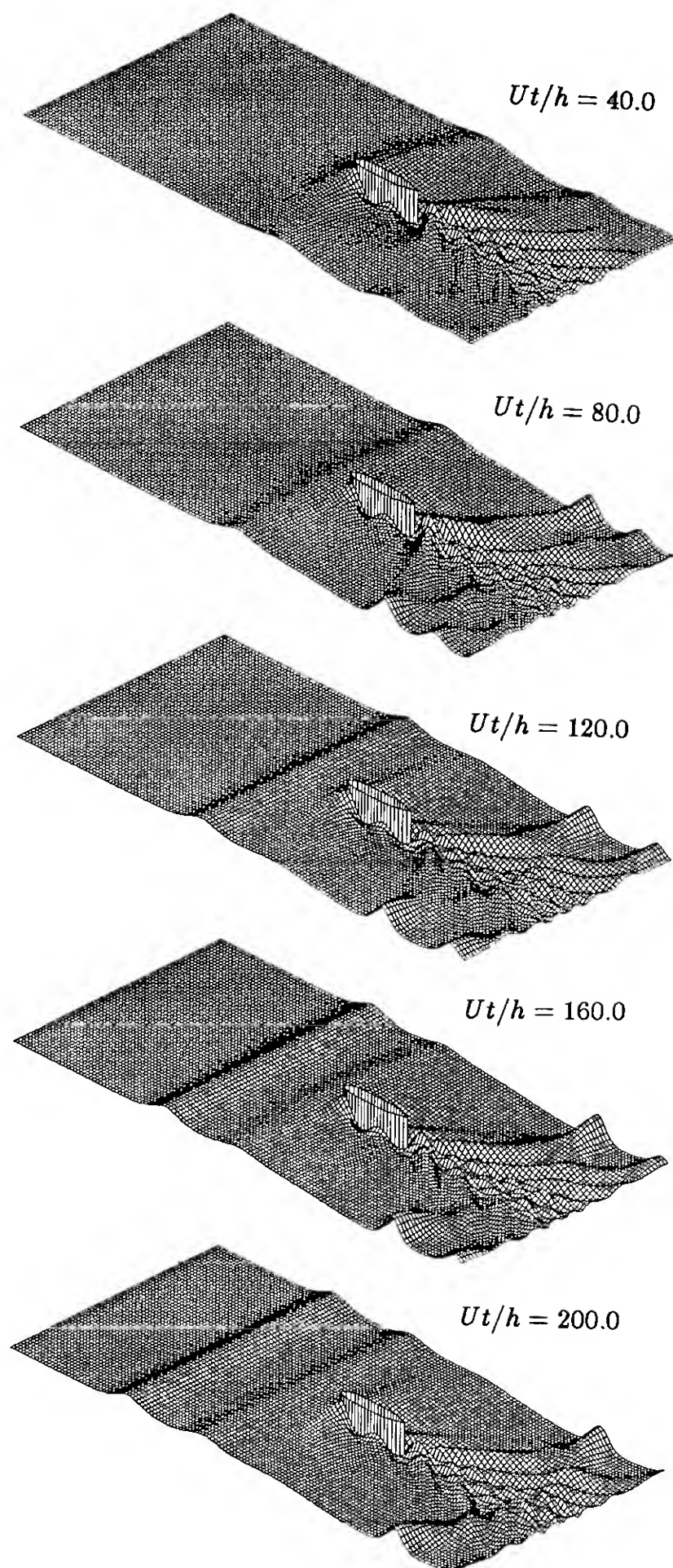


Fig.13 Wave Evolution at the Critical Speed (FEM,  $2W = 4.88\text{m}$ )

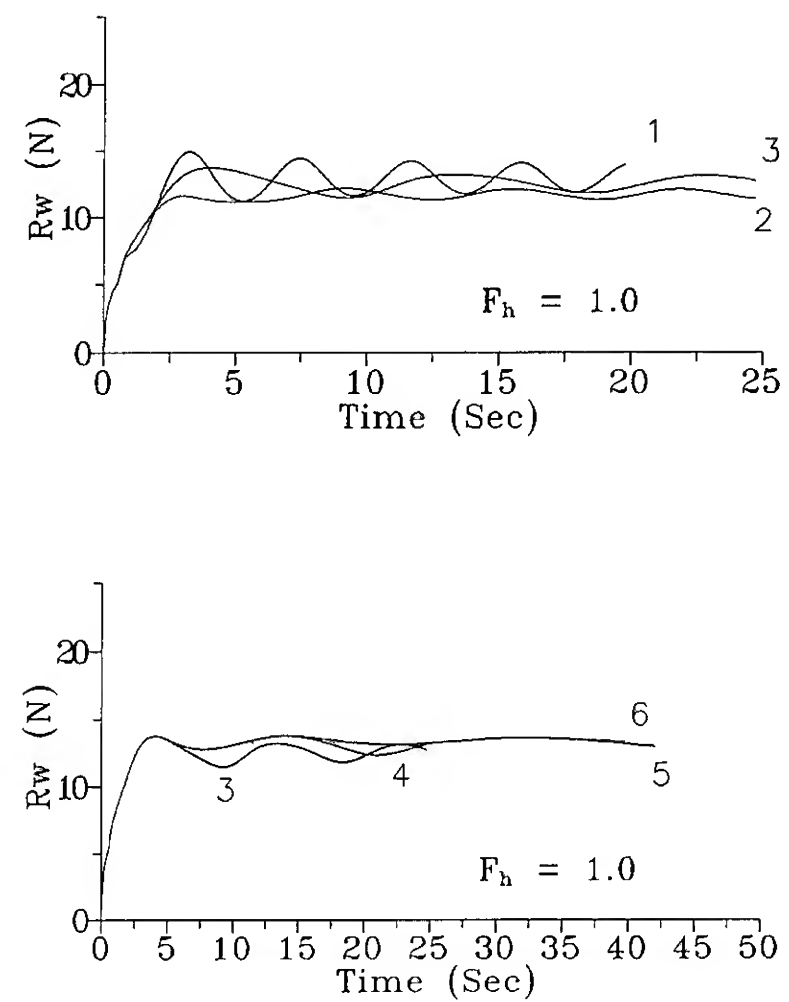


Fig.14 Wave Resistance for Various Tank Widths with Pressure Patch ( $F_h = 1.0$ )

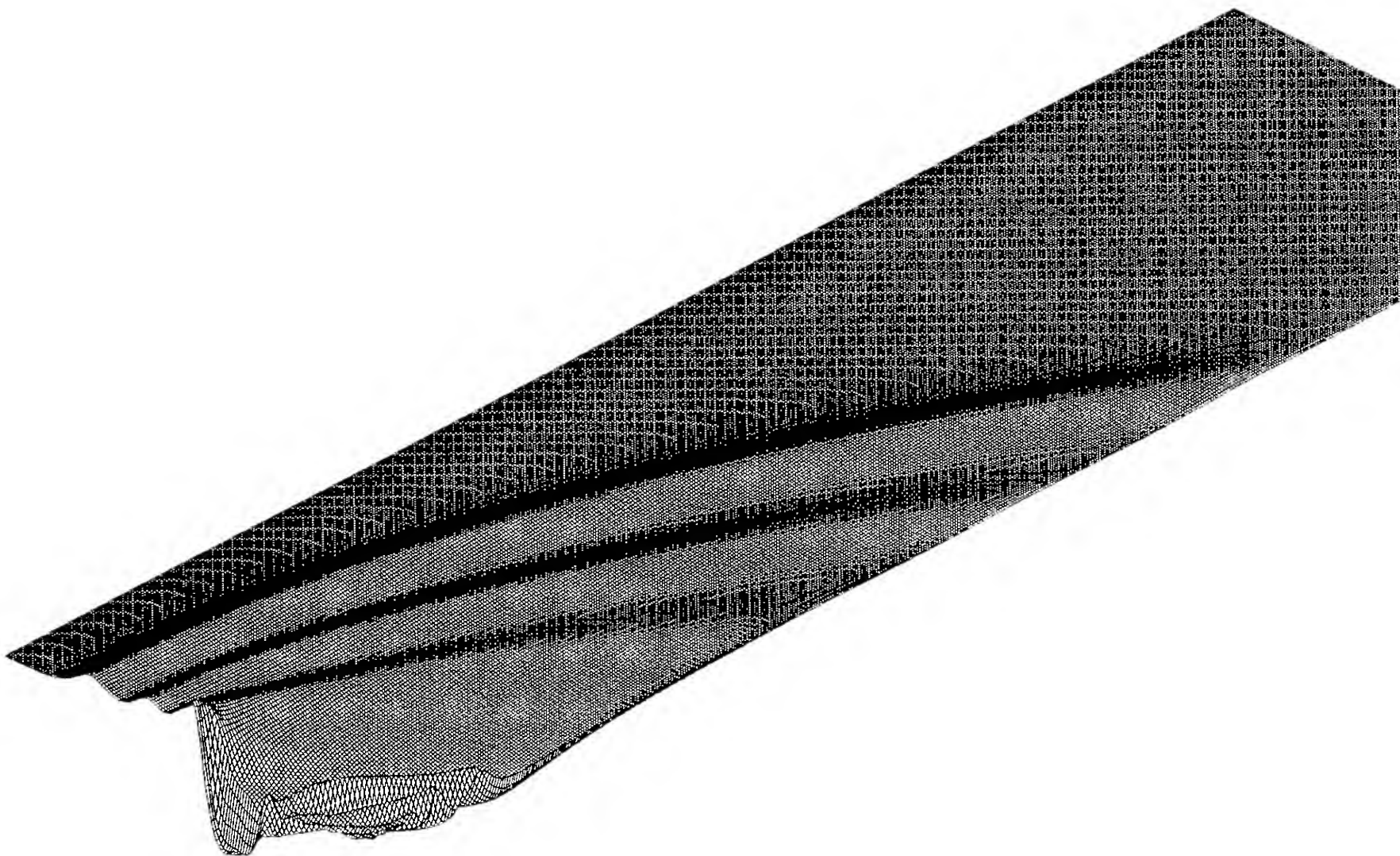


Fig.15 Wave Field for a Wide Tank ( $Ut/h = 320$ )

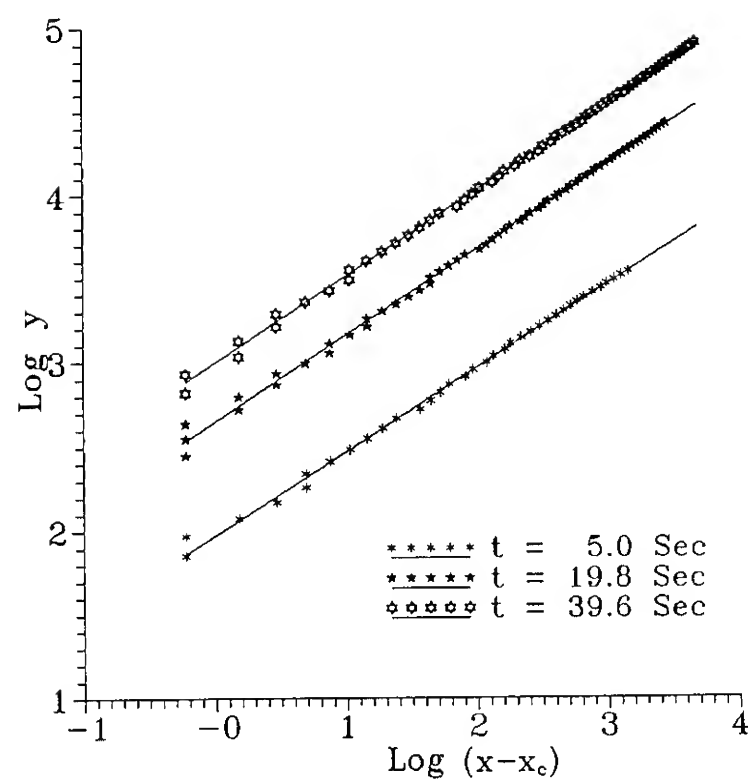


Fig.16 Plot of the Crestline of the First Upstream Diverging Wave

**Table 1** The Amplitude and Speed of the First Soliton, and the Generation Period Between First Two Solitons for Series 60 ( $C_b = 0.8$ )

(a) Amplitude

A/h		W/L=0.8	W/L=1.6	W/L=3.2
$F_h = 0.9$	KP	.480	.315	.202
	FEM	.384	.234	.134
	EXP	.367	.273	.143
$F_h = 1.0$	KP	.623	.445	.322
	FEM	.566	.397	.285
	EXP	.551	.438	.303
$F_h = 1.1$	KP	.785	.625	.490
	FEM	.686	.566	.475
	EXP	.608	.585	.480

**Table 2** The Amplitude and Speed of the First Soliton, and the Generation Period Between First Two Solitons for a Slender Ship ( $C_b = 0.667$ )

	A/h	$C/\sqrt{gh}$	$UT_g/h$
$F_h = 0.9$	.253	1.123	38.91
$F_h = 1.0$	.384	1.216	48.47
$F_h = 1.1$	.565	1.275	66.28

(b) Speed

$C/\sqrt{gh}$		W/L=0.8	W/L=1.6	W/L=3.2
$F_h = 0.9$	KP	1.218	1.155	1.078
	FEM	1.175	1.100	1.050
	EXP	1.170	1.100	1.060
$F_h = 1.0$	KP	1.293	1.216	1.153
	FEM	1.250	1.175	1.125
	EXP	1.240	1.190	1.130
$F_h = 1.1$	KP	1.367	1.304	1.227
	FEM	1.300	1.250	1.200
	EXP	1.280	1.260	1.210

(c) Generation Period

$UT_g/h$		W/L=0.8	W/L=1.6	W/L=3.2
$F_h = 0.9$	KP	20.04	31.83	41.26
	FEM	30.20	37.40	53.60
	EXP	32.70	48.10	65.10
$F_h = 1.0$	KP	24.89	39.29	60.26
	FEM	35.40	47.30	88.40
	EXP	37.80	49.80	85.20
$F_h = 1.1$	KP	33.14	54.75	90.78
	FEM	44.20	57.40	128.70
	EXP	39.00	50.11	103.60

## DISCUSSION

William C. Webster  
University of California at Berkeley, USA

In reference [6], we presented numerical results based on Green-Naghdi theory for the same problem. Did you compare your results with these computations?

## AUTHORS' REPLY

We are well aware of your excellent paper coauthored with Profs. Ertekin and Wehausen, where valuable numerical results are contained based on the Green-Haghdi directed-sheet model. We have already compared these results with ours based on the Finite Element Method and the KP equation in two separate papers, both presented at the 5th International Conference on Numerical Ship Hydrodynamics in references [7,10]. We did not include these comparisons here since we concentrated only on the effect of the tank width on the wave responses by using the two different methods.

## DISCUSSION

Theodore Y. Wu  
California Institute of Technology, USA

This paper, delivered lucidly by Prof. Hang Choi, is of basic interest and bears significance in that two theoretical models of quite different approach and of different orders in accuracy are here applied to provide results on this valuable comparative study. I hope the authors can clarify whether their FEM-method is indeed equivalent to the exact Euler flow model on theoretical basis, notwithstanding numerical errors.

Of particular interest would be a further exploration on the asymptotic behavior of these two models in two special limits: (i) as the body-length-to-channel width ratio tends to zero, (ii) as the velocity of forcing approaches the upper or the lower bound at which the upstream emission of solitary waves would evanesce. I would like to encourage the authors to continue their excellent efforts in these directions to cast new lights on this very interesting phenomenon.

## AUTHORS' REPLY

We highly appreciate the discussion raised by Prof. Wu. To the first question whether our FEM-method is equivalent to the exact Euler flow model on theoretical basis, we would like to stress that the basis of our FEM-method, i.e., the variational principle in our paper is equivalent to the exact inviscid irrotational flow with a free surface. In the procedure of the FEM-method, the unknown free surface is also represented as a part of solutions and solved numerically through iterative scheme. In this sense, the present FEM-method is equivalent to the exact potential flow model, except discretization of continuous functions.

Concerning with the comment on the case of laterally infinite tank, we tried to numerically follow the similarity solution of Redekopp [25]. But due to the limited computing capacity, we are able to show only an intermediate result which indicates the crestline of the first diverging waves being nearly a parabola.

Based on the present computations, it is hard to predict the upper and lower bounds of forcing speed at which the quasi-periodic emission of upstream-advancing solitons evanesces.

## DISCUSSION

John V. Wehausen  
University of California at Berkeley, USA

As I understand the authors, the calculations based upon the KP equations for a vertical strut just touching the bottom and with a profile determined by the section-curve of a Wigley hull or of Series 60,  $C_b = 0.80$ , whereas those based upon the Laplace equation are for a ship with the same overall dimensions as the latter hull but with an altered section-area curve appropriate to a wedge-shaped hull; the blockage coefficients are the same. One is tempted to conjecture that the differences in results may be due as much to the different geometries as to the different methods of computation. Table 2 may support this conjecture for the KP equations. Ertekin's (11) conclusion that blockage coefficient is the most important parameter in determining properties of the solitons was based upon experiments with only one hull shape. Later computations for struts, using T. Y. Wu's generalized Boussinesq equations, have shown also some dependence upon hull form. Would the authors care to comment?

By chance, calculations have been given in Ertekin, Qian and Wehausen (Engineering Science, Fluid Dynamics. A Symposium in Honor of T. Y. Wu. World Scientific Publishing Co., pp. 29-43, Table 1, line 1) for the same configuration as in Table 2, but only for  $F_h = 1.0$ . The generalized Boussinesq equations were used. The values obtained were  $A/h = 0.36$ ,  $c/(gh)^{1/2} = 1.14$ ,  $UT_g/h = 61$ . The agreement for the first two values is perhaps not unsatisfactory, but this does not seem to be true for the third. The discrepancies could be a result of numerical error or of the different equations used.

## AUTHORS' REPLY

Thank you very much for your nice comments. To the first comment, we agree with you. However, in the FEM computations we used not only the same length and draft but also the same sectional area with slightly reduced beam.

To the comments in the second paragraph, we also agree with you. The discrepancies in the numerical results by different methods are due to the differences in the numerical procedures as well as the governing equations.



# Numerical Simulation of Ship Waves and Some Discussions on Bow Wave Breaking & Viscous Interactions of Stern Wave

K.-H. Mori, S.-H. Kwag, Y. Doi (Hiroshima University, Japan)

## Abstract

Numerical calculations are carried out to simulate the free-surface flows around the Wigley model and S-103 Inuid model. The N-S equation is solved by a finite difference method where the body-fitted coordinate system, the wall function and the triple-grid system are invoked. The numerical scheme being examined for the scheme to be acceptable for discussions, the calculations are extended to the turbulent high-Reynolds number flows with the aid of the 0-equation model to discuss the Reynolds number dependency of the waves. The wave elevation at the Reynolds number of  $10^4$  is much less than that at  $10^6$  although the Froude number is the same. The numerical results are referred to predict the appearance of the sub-breaking waves around bow and stern. The prediction is qualitatively supported by the experimental observation. They are also applied to study precisely on the stern flow of S-103 as to which extensive experimental data are available. Although it is not yet made clear about the interaction between the separation and the stern wave generation, the effects of the bow wave on the developments of the boundary layer flows are concluded to be significant. The sub-breaking of the stern wave is also discussed.

## 1. Introduction

Free-surface flow around ship is one of the most complicated flows where various nonlinear phenomena exist such as wave breaking, viscous interactions, free-surface tension and so on. Not only for the practical hull form design but also for academic interests, it is important to make clear their flow mechanism. They are worthy to be studied more intensively.

There are pretty many experimental studies even about the wave break-

ing such as Duncan[1], Mori[2], Maruo[3], Groesenbaugh[4] and so on. In spite of their extensive experiments, however, the free-surface nonlinear phenomena still remain unclear. Theoretical investigations are also attempted to explain the phenomena or to provide a suitable model. Dagan[5], Tanaka[6] and Mori[7] applied the instability analysis to predict the breaking. Some models for breaking waves are proposed after experiments. There are few studies on the free-surface tension; Maruo[3].

The stern flows with the free-surface show also important phenomena in ship hydrodynamics. Although Doi[8] and Stern[9] studied extensively about them, very little are made clear. Despite the viscous interactions are essential there, theoretical approaches are so limited and most of the approaches are based on the simple flow models.

On the other hand, there are some researches by the direct numerical simulations such as Miyata[10], Groesenbaugh[4], Shin[11] and so on. They have tried to make clear the mechanism of the Navier-Stokes equations directly. Because the free-surface flows of our interests are strongly nonlinear and viscous effects are primary, the simulations by solving the Navier-Stokes equation can be a desirable tool for the study. They can provide any necessary data for the study once a calculation is carried out.

However, the important point is on whether their codes are accurate enough for such studies. It may be possible to draw misleading conclusions from the results calculated by an un-proved code. The use of an insufficient grid scheme is likely to bring forth misunderstanding for the phenomena. The assumptions of 2-dimensionality or laminar low Reynolds number flows are also possible sources for misunderstanding.

The present paper is a study along

the approach lastly mentioned; the wave breaking and the viscous interaction of the stern waves are studied by making use of the results of numerical simulations. The numerical scheme for the simulation is based on the MAC method where the body-fitted coordinates and the non-staggered grid system are used. The convection terms are presented by the third-order upstream differencings. The wall function is invoked to follow a steep velocity changes close to the hull in high Reynolds number flows. The turbulent stress terms are presented by a 0-equation model.

Bearing in mind the above-mentioned dangers, the computing code is validated first by carrying out various computations to be convinced with, although it may not be enough due to the limitation of the computer. The free-surface flows around the Wigley model at the Reynolds numbers of  $10^4$  and  $10^6$  are used for this purpose.

Although the theory is 2-dimensional, the results are used to predict the appearance of the sub-breaking waves. The viscous interaction of the stern waves is also discussed.

## 2. Numerical Simulation of Ship Waves

### 2.1 Basic Equation

Numerical simulations of 3-D free-surface flows are carried out by solving the N-S equation basically following to the MAC method. The velocity components  $u$ ,  $v$  and  $w$  at  $(n+1)$  time step are determined by

$$\begin{aligned} u^{n+1} &= (F^n - \phi_x^n) \Delta t \\ v^{n+1} &= (G^n - \phi_y^n) \Delta t \\ w^{n+1} &= (H^n - \phi_z^n) \Delta t \end{aligned} \quad (1)$$

where

$$\begin{aligned} F^n &= \frac{u^n}{\Delta t} + \left( \frac{1}{Re} + \nu_t \right) \nabla^2 u \\ &\quad - \left( u^n \frac{\partial u}{\partial x} + v^n \frac{\partial u}{\partial y} + w^n \frac{\partial u}{\partial z} \right) \\ &\quad - \frac{\partial}{\partial x} \left\{ \nu_t \left( 2 \frac{\partial u}{\partial x} \right) \right\} - \frac{\partial}{\partial y} \left\{ \nu_t \left( \frac{\partial u}{\partial y} + \frac{\partial v}{\partial x} \right) \right\} \\ &\quad - \frac{\partial}{\partial z} \left\{ \nu_t \left( \frac{\partial u}{\partial z} + \frac{\partial w}{\partial x} \right) \right\} \\ G^n &= \frac{v^n}{\Delta t} + \left( \frac{1}{Re} + \nu_t \right) \nabla^2 v \\ &\quad - \left( u^n \frac{\partial v}{\partial x} + v^n \frac{\partial v}{\partial y} + w^n \frac{\partial v}{\partial z} \right) \\ &\quad - \frac{\partial}{\partial x} \left\{ \nu_t \left( \frac{\partial u}{\partial y} + \frac{\partial v}{\partial x} \right) \right\} - \frac{\partial}{\partial y} \left\{ \nu_t \left( 2 \frac{\partial v}{\partial y} \right) \right\} \\ &\quad - \frac{\partial}{\partial z} \left\{ \nu_t \left( \frac{\partial v}{\partial z} + \frac{\partial w}{\partial y} \right) \right\} \end{aligned} \quad (2)$$

$$\begin{aligned} H^n &= \frac{w^n}{\Delta t} + \left( \frac{1}{Re} + \nu_t \right) \nabla^2 w \\ &\quad - \left( u^n \frac{\partial w}{\partial x} + v^n \frac{\partial w}{\partial y} + w^n \frac{\partial w}{\partial z} \right) \\ &\quad - \frac{\partial}{\partial x} \left\{ \nu_t \left( \frac{\partial u}{\partial z} + \frac{\partial w}{\partial x} \right) \right\} - \frac{\partial}{\partial y} \left\{ \nu_t \left( \frac{\partial v}{\partial z} + \frac{\partial w}{\partial y} \right) \right\} \\ &\quad - \frac{\partial}{\partial z} \left\{ \nu_t \left( 2 \frac{\partial w}{\partial z} \right) \right\} \end{aligned}$$

and

$$\phi^n = p + \frac{z}{Fn^2} \quad (3)$$

All the variables are on the cartesian coordinates system  $(x, y, z)$  where  $x$  is in the uniform flow direction,  $y$  in the lateral, and  $z$  in the vertical direction respectively;  $u, v$  and  $w$  are the velocity components in the  $x$ -,  $y$ -, and  $z$ -directions, respectively. They are normalized by the model overall length  $L$  and the uniform velocity  $U_0$ .

Subscripts denote the differentiations with respect to the referred variables and superscripts the values at the referred time-step. The term  $\Delta t$  stands for the time increment,  $p$  the pressure and  $\nu_t$  the eddy viscosity.  $Rn$  and  $Fn$  are Reynolds and Froude numbers respectively based on  $L$  and  $U_0$ , and

$$\nabla^2 = \frac{\partial^2}{\partial x^2} + \frac{\partial^2}{\partial y^2} + \frac{\partial^2}{\partial z^2} \quad (4)$$

Differentiating (1) with respect to  $x, y$  and  $z$ , we can have

$$\begin{aligned} \nabla^2 \phi &= F_x + G_y + H_z \\ &\quad - \left( u_x^{n+1} + v_y^{n+1} + w_z^{n+1} \right) / \Delta t \end{aligned} \quad (5)$$

The last term in (5) is expected to be zero to satisfy the continuity condition. (5) can be solved by the relaxation method. The new free-surface at the  $(n+1)$ th time-step is calculated by moving the marker particles by

$$\begin{aligned} x^{n+1} &= x^n + u^n \Delta t \\ y^{n+1} &= y^n + v^n \Delta t \\ z^{n+1} &= z^n + w^n \Delta t \end{aligned} \quad (6)$$

The oncoming flow is accelerated from zero to the given constant velocity. Third-order upstream differencing is used for the convection terms with the fourth-order truncation error, and for the central differencings, 4- or 5-point central differencings are used.

It is desirable to introduce numerical coordinate transformations which simplifies the computational domain in the transformed domain and facilitates applications of the bound-

ary conditions. In the present study, a numerically-generated, body-fitted coordinate system is used,

$$\begin{aligned}\xi &= \xi(x,y,z), \quad \eta = \eta(x,y,z) \\ \text{and } \zeta &= \zeta(x,y,z)\end{aligned}\quad (7)$$

It offers the advantages of generality and flexibility and, most importantly, transforms the computational domain into a simple rectangular region with equal grid spacing.

Through transformations, (1) can be written for the velocity component  $q$  as

$$\begin{aligned}q_t + U q_\xi + V q_\eta + W q_\zeta \\ = \left( \frac{1}{Re} + \nu_t \right) \nabla^2 q - K - REYSF(\xi, \eta, \zeta)\end{aligned}\quad (8)$$

where,  $U, V$  and  $W$  are the contravariant velocities and  $K$  is the pressure gradient. Their full expressions can be found in [12].  $REYSF(\xi, \eta, \zeta)$  represents the terms transformed from the last three terms on RHS of (2).

## 2.2 Triple-grid Method

It is common to use a single grid system for the whole computation whose minimum size is determined for the numerical diffusion to be less than that by viscosity. However, the grid size for the calculation of the free-surface elevation must be determined by a different scale, the minimum wave length[13]. In our simulation, three mesh systems are used whose sizes are different from each other depending on the characteristic of equations. We call it triple-grid method here. The first one is for the convective terms in the N-S equation, the second is for the Poisson equation, and the third is for the free-surface equation. The third grid system requires the finest one; a quarter of the first one in each direction. Because it is used only on the free-surface which is two-dimensional, the increment of the memory is modest. On the other hand, the second one can be coarser than the first one; here half of the first one is used. According to the results, the development of the free-surface elevation is strikingly improved. The CPU time and the memory size of the present computation are rather reduced owing to the use of coarse meshes of the second mesh system for the Poisson equation and the diffusion term.

## 2.3 Body Surface Condition

In the numerical solution for viscous flows, the no-slip condition for the solid surface is used by discretiz-

ing the region fine enough to the imposed condition. This method, however, requires a large number of grid points to resolve the large gradients in the near-wall region especially for the high Reynolds number flows. This is the main barrier in the high Reynolds number calculations. In view of the complexity involved in resolving the near-wall flow, it is preferable to employ a simpler wall-function approach for the velocity profile which can be valid for the velocity profile in the near wall region.

In the present study, the two-point wall-function approach is employed as by Chen and Patel[14]. The numerical solution is that the velocity at  $\eta=3$  ( $\eta=1$  is on the wall) is provided and the wall-friction velocity  $u_\tau$  is updated with some iterations by requiring this velocity to satisfy the law-of-wall equation. The iterative two-point wall-function approach for a three-dimensional flow means that it provides the updated boundary conditions for the numerical solution and the procedure is iterated until the solution converges.

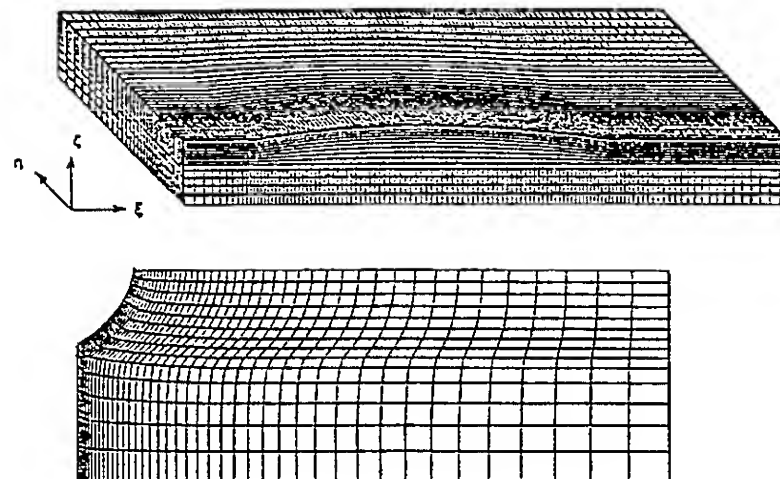


Fig.1 Perspective view of grid scheme

## 2.4 Computational Results and Discussions

Computations are performed for the flow fields around the Wigley model with free-surface at  $Rn=10^4$  and  $10^6$ . Fig.1 shows the perspective view of the grid scheme used. For the numerical stability and efficiency, the grid scheme near the hull is required to be orthogonal to it and the grid size should change smoothly. The grid number is  $74 \times 29 \times 19$ . During the computations, the location of grids between the free-surface and the bottom is redistributed proportionally to the free-surface elevation. By this scheme, it is expected that the free-surface con-

dition, i.e., the constant pressure condition can be directly applied without any interpolation. For the high Reynolds number flow, the two-layer algebraic Baldwin-Lomax model is used to make the eddy viscosity. The numerical results are compared with the experimental data [15].

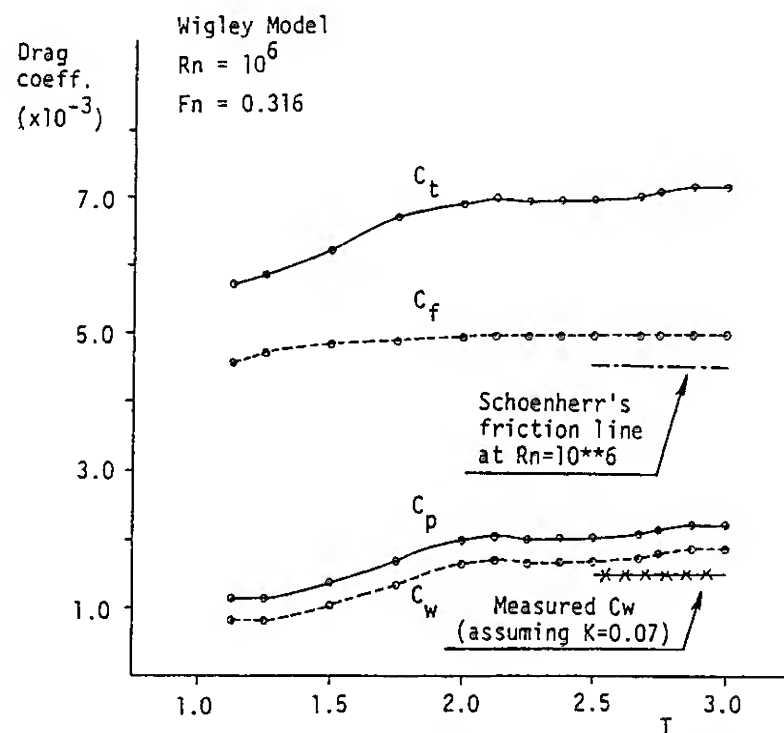


Fig.2 Time history of drag coefficients

In order to check the convergence of the computations, the wave patterns and drag coefficients of  $C_p$ ,  $C_f$  and  $C_w$  are compared along the marching time step as shown in Figs.2 and 3, where  $C_p$ ,  $C_f$  and  $C_w$  are the pressure, frictional and wave-making resistance coefficients respectively. Schoenherr friction line and the measured wave-making resistance coefficient are shown for comparison. Although the wave seems still developing further, it can be assumed to be converged at  $T=3.0$  where  $T$  is the non-dimensional time, which can be supported by the results shown in Fig.3. The calculated frictional resistance, which is directly derived by the difference of the velocities at the two points, is still larger than the Schoenherr.

Fig.4 shows the logarithmic plot of velocity at  $x/L=0.835$  in the format of the law-of-wall ( $q^+$  versus  $y^+$ ) using the friction velocity. Some plots are drawn at several points in the girth- and depth-wise directions; they are generally in good agreement.

Fig.5 shows the comparison of the velocity distributions near the wall between that obtained by making use of

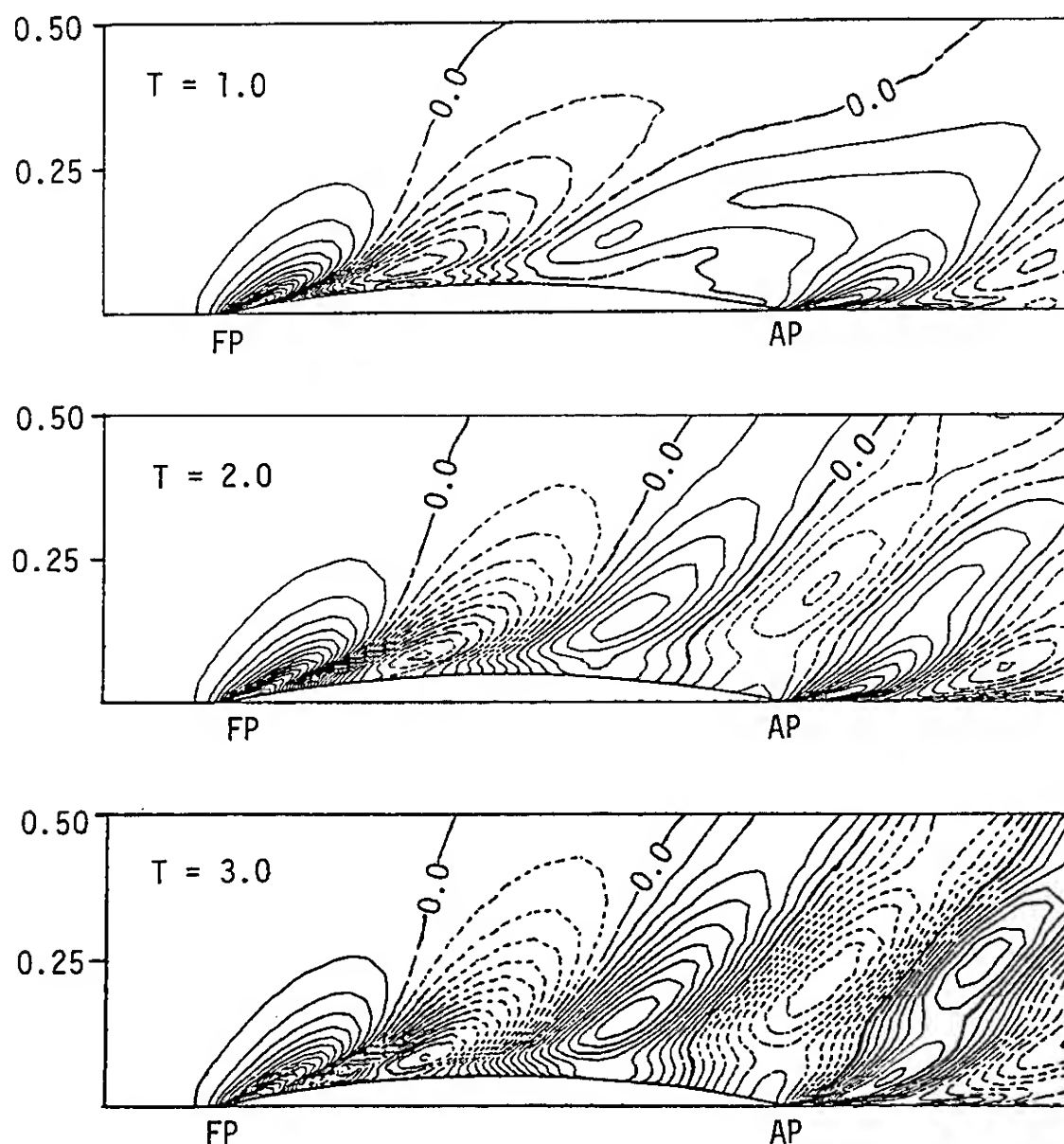


Fig.3  
Time history of wave patterns for Wigley at  $Rn=10^6$  and  $Fn=0.316$

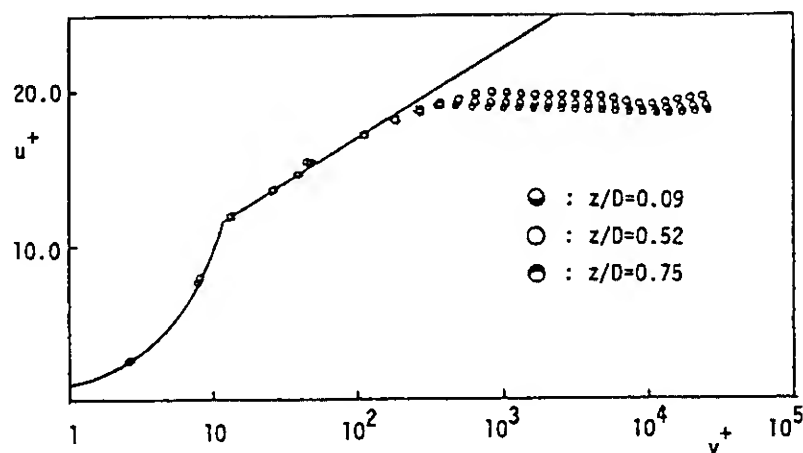


Fig.4 Log plot of velocity for Wigley model( $x/L=0.835$ )

the law-of-wall and directly. Because the expression by the wall-function is not valid any more for the separated flows, it is not applied in the stern 5% where the separation is suspected. There the scheme is switched into the direct method. We can see that the

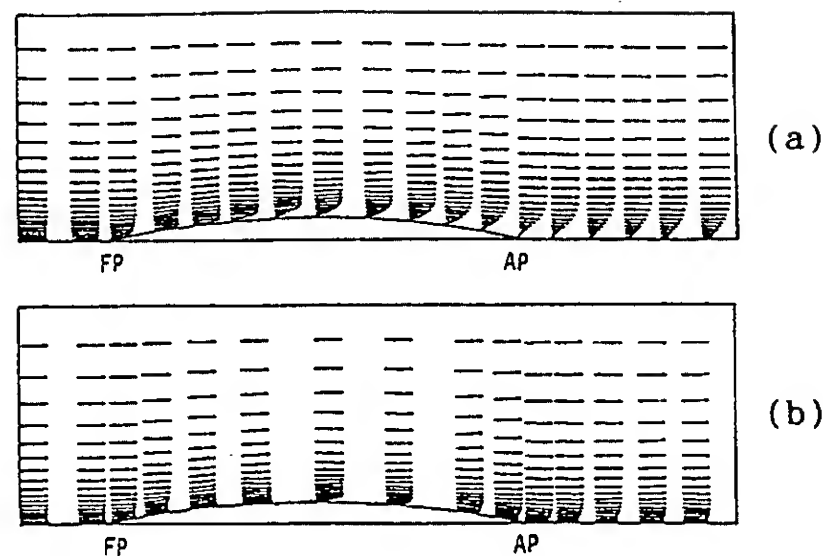


Fig.6 Velocity vectors on free-surface  
(a) Laminar flow at  $Rn=10^4$   
(b) Turbulent flow at  $Rn=10^6$

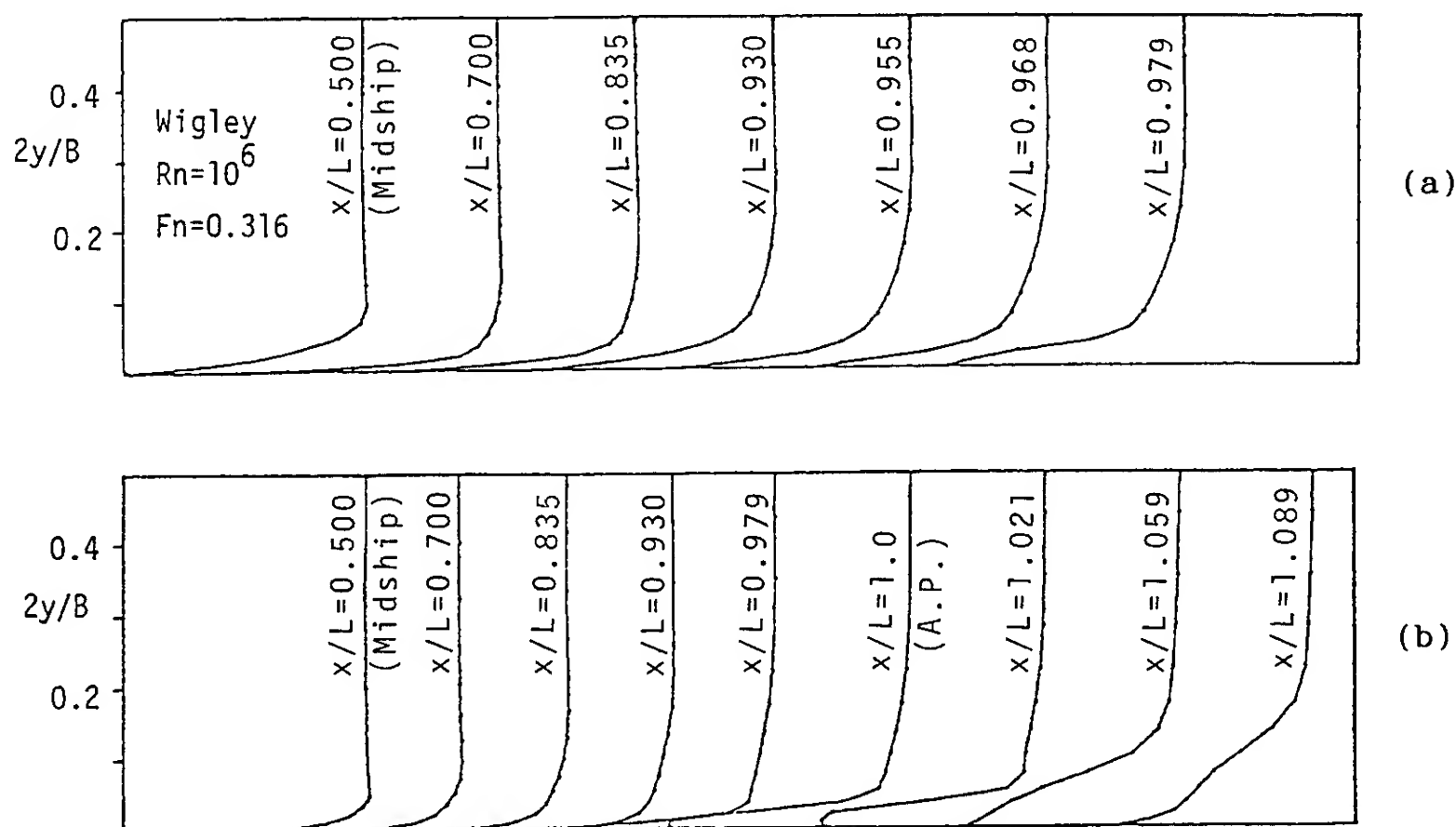


Fig.5 u-velocity distribution on free-surface  
(a) without wall function  
(b) with wall function

wall-function approach removes much of the dependency of the numerical solution on the location of the two mesh points and the steep velocity changes are well followed even by limited size of grid. The usual logarithmic law of the wall can be reasonably used in favorable pressure gradients.

Fig.6 shows the comparison of velocity vectors on free-surface between the two Reynolds numbers: the one

is  $10^4$  which is laminar flow while the other  $10^6$ , turbulent. The laminar flow is subject to separation in the stern region and wider boundary layer thickness, while the turbulent flow is to larger velocity gradient near the hull by which we can guess a larger wall-friction on the body surface. Fig.7 shows the comparison of the wave patterns at  $Rn=10^4$  and  $10^6$ . We can clearly see that the Reynolds number dependency



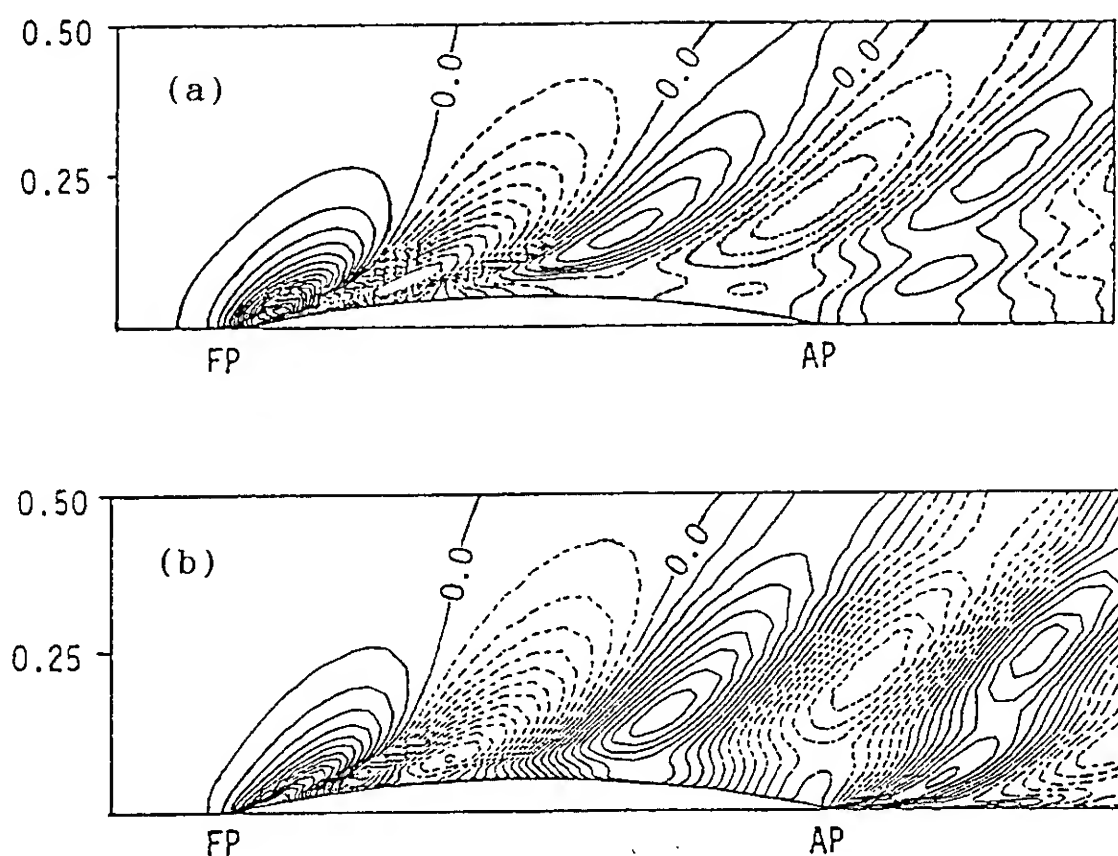


Fig.7  
Wave patterns of  
Wigley model at  $Fn=0.316$   
(a) Laminar flow at  $Rn=10^4$   
(Mesh size: 100x25x15)  
(b) Turbulent flow at  $Rn=10^6$   
(Mesh size: 70x25x15)

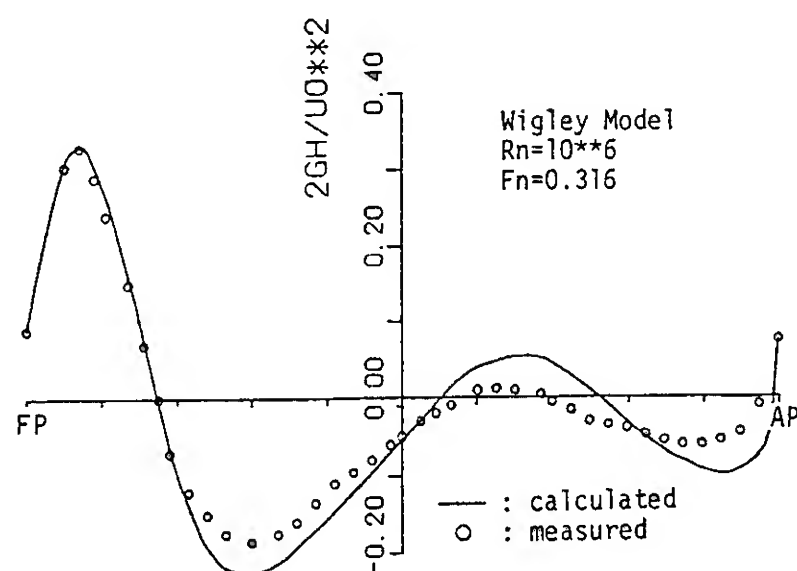


Fig.8 Wave profiles on hull surface

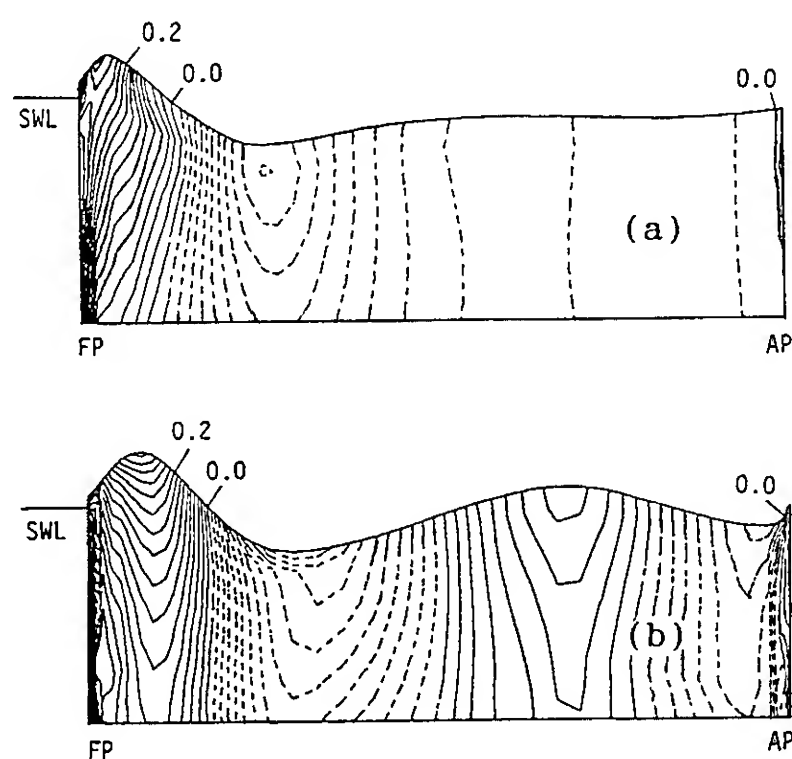


Fig.9 Pressure contour on Wigley  
hull surface at  $Fn=0.316$   
(a) Laminar flow at  $Rn=10^4$   
(b) Turbulent flow at  $Rn=10^6$

of the wave. It may confuse us that even the second wave crest differs much in height, for we usually expect the Reynolds number effect on wave is not so significant there.

Fig.8 shows the wave profile along the hull surface. The Reynolds number of the measurement is  $3.59 \times 10^6$ . It is well presented around the bow, but slight discrepancies are still observed in the aft half of the hull. Fig.9 shows the pressure contours on the hull surface at  $Rn=10^4$  and  $10^6$ . The pressure around the stern region is much recovered at  $10^6$  than the low Reynolds number flow. The pressure distribution on the hull surface shows some wiggles in appearance at the bow and stern parts due to the use of still coarse mesh. However, the wave height on free-surface, which means the pressure here, shows no serious wrinkles because finer grid is used there.

Fig.10 shows the comparison of wave patterns between the calculated and the measured. Although they can not be compared exactly due to difference of Reynolds number, we can say that the computed patterns are qualitatively reasonable for both the bow and stern waves.

Fig.11 shows the velocity vectors on the transverse section near A.P. in which the vortical motion can be observed around the keel. It seems not so easy to calculate the cross flows accurately at the stern part considering some aspects in the numerical point of views. First, the assumption of the symmetry or the steady flows should be pointed out. The unsteadiness and non-symmetry observed in experiment should be taken into account in numerical simulation. Of course the grid



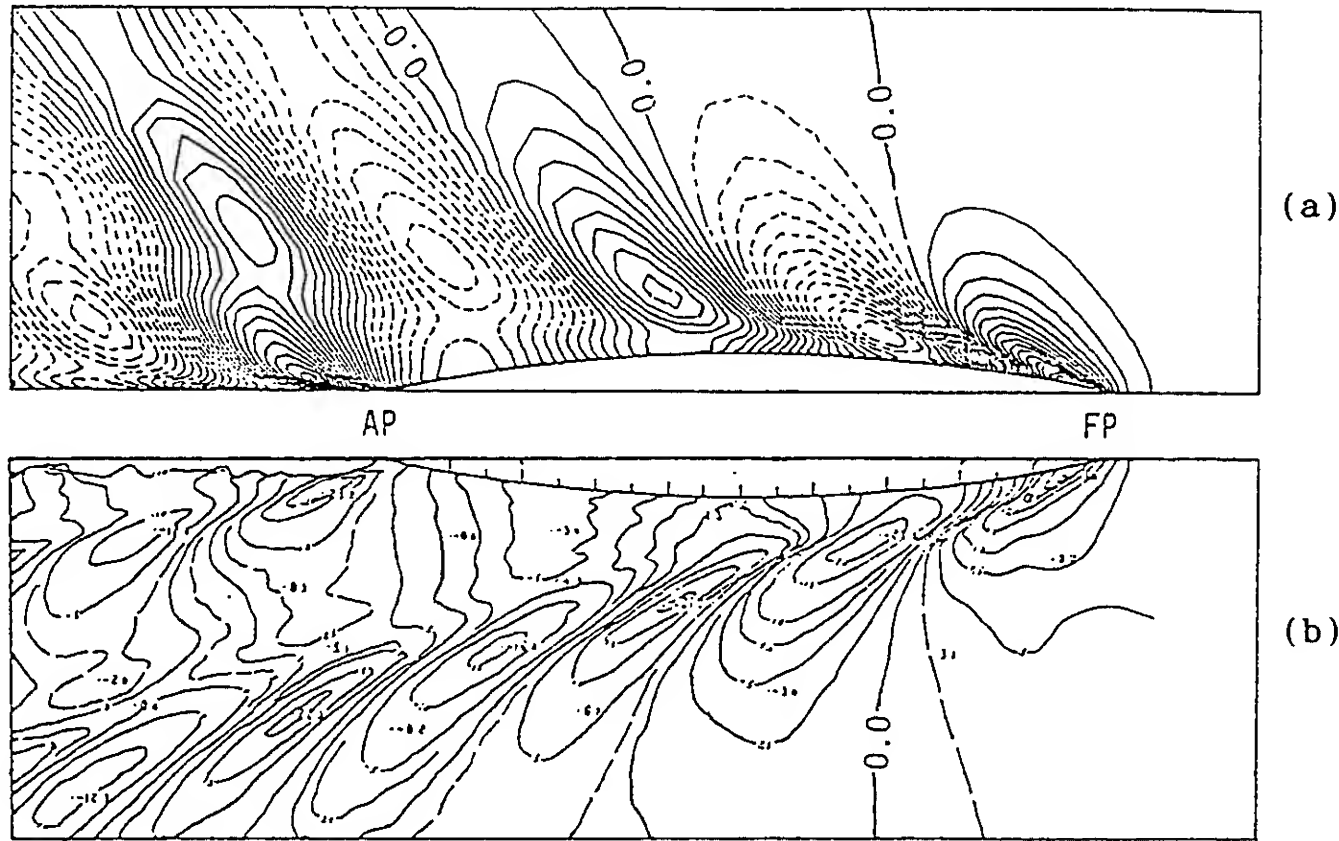


Fig.10 Comparison of wave patterns at  $Fn=0.289$   
 (a) Computed contour( $Rn=1 \times 10^6$ )  
 (b) Measured contour( $Rn=3 \times 10^6$ ) [15]

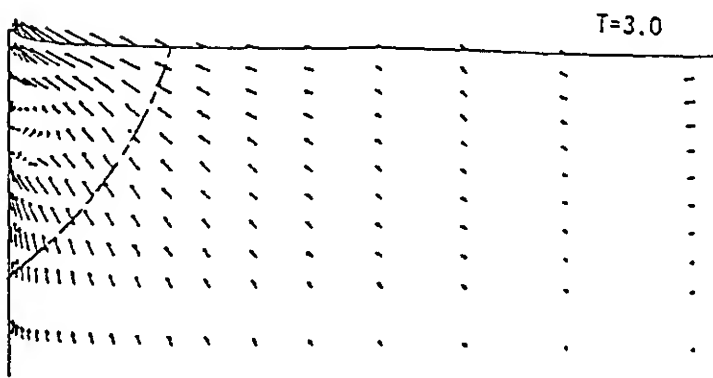


Fig.11 Velocity vectors of Wigley model( $Rn=10^6$ ,  $Fn=0.316$  and  $x/L=1.02$ )

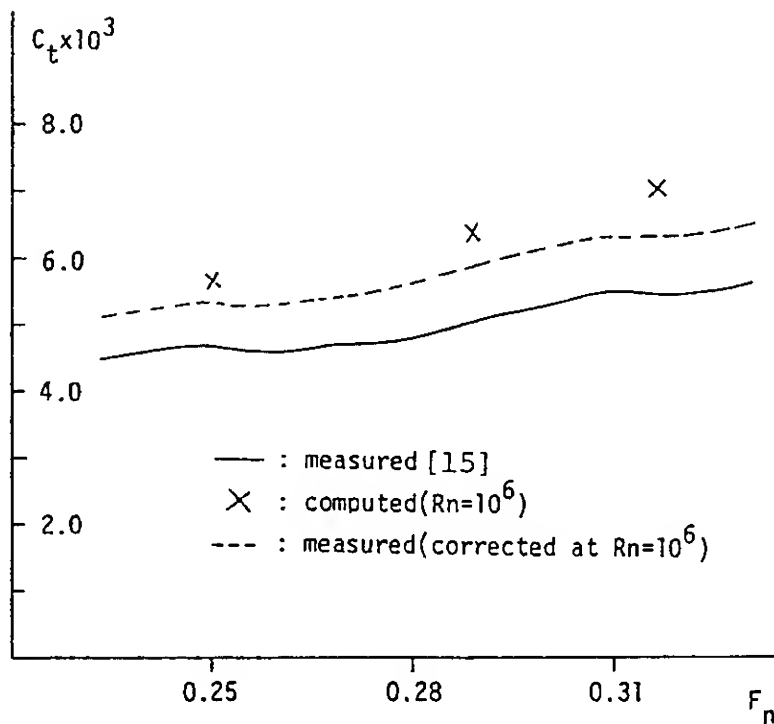


Fig.12 Comparison of total drag coefficients between the computed and measured.

used in the computing domain is still coarse and can be a reason of not being able to capture completely the details of the fluid motions.

In Fig.12, comparison is made for the total drag coefficients between the calculated at  $Rn=10^6$  and the measured. The Reynolds numbers of measurement are  $2.84 \times 10^6$ ,  $3.28 \times 10^6$  and  $3.59 \times 10^6$  for the corresponding Froude number of 0.25, 0.289 and 0.316, respectively. For the more direct comparisons, the measured results are corrected at the same Reynolds number of  $10^6$  by use of the Prandtl-Schlichting's friction formula. The computed drag is still greater than the experimental data; We can not mention the reason for the difference conclusively, but the accuracy of the velocity calculation close to the hull may not be enough which resulted in poor agreement in the frictional resistance. The computing time is abt. 90 hrs for one case by Apollo DN-10000 (abt.13 MFLOPS).

### 3. Detection of Sub-breaking Waves

#### 3.1 Appearing Condition of Sub-breaking Waves

Computed results are applied to detect the appearance of the appearing condition of sub-breaking waves around bow. The critical conditions for their appearance were studied in Mori[7]. There the breakings at their infant stage are concluded as a free-surface turbulent flow. The flow mechanism is

supposed that the surplus energy accumulated around the wave crest by the increment of the free-surface elevation is dissipated through the turbulence production and free-surface could eventually maintain itself without any overturnings or backward flows. An instability analysis for 2-dimensional flows provides a critical condition for their appearance;

$$\frac{M}{U_s} \frac{\partial M}{\partial s} - \frac{\partial U_s}{\partial s} - \frac{1}{n_z} \frac{\partial n_z}{\partial s} > 0 \quad (9)$$

where  $M$  is the circumferential force given by

$$M = (\kappa U_s^2 - n_z g) n_z \quad (10)$$

$s$  is the stream line coordinate along

the free-surface and  $h$  is its metric coefficient, while  $n$  is the normal;  $n_z$  the direction cosine of  $n$  to  $z$ .  $U_s$  is the velocity component of basic flow in the  $s$ -direction;  $\kappa$  is the curvature of the free-surface and  $g$  the gravity acceleration. Limiting ourselves to a narrow proximity to the wave crest, we assume  $n_z = 1$  and  $\partial/h \partial s \approx \partial/\partial x$ ; then (9) can be reduced approximately into

$$\frac{U_s^2}{M} \frac{\partial}{\partial x} \frac{M}{U_s} > 0 \quad (11)$$

where,

$$M = \kappa U_s^2 - g \quad (12)$$

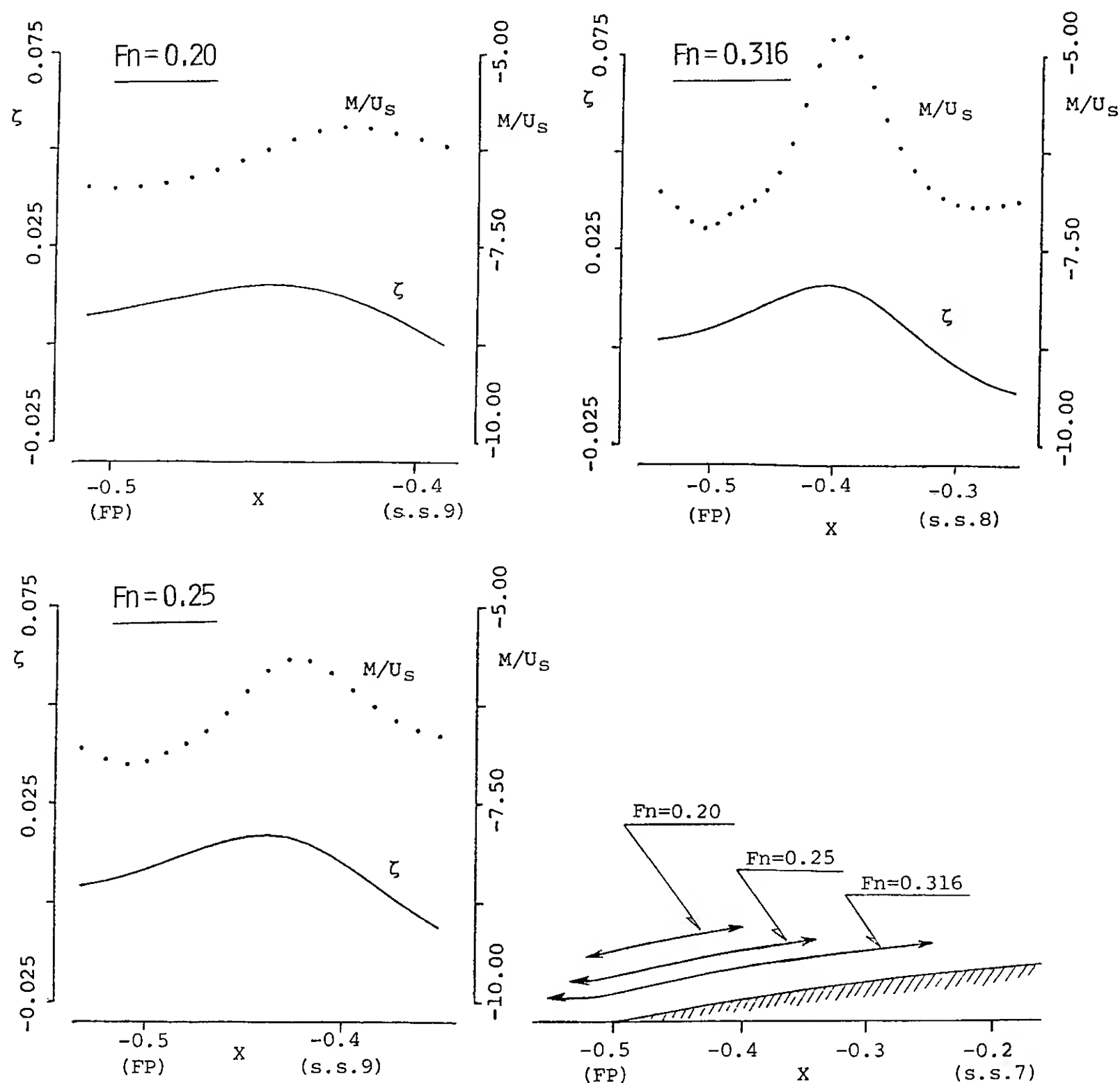


Fig.13 Variation of  $M/U_s$  and free-surface elevation and lines analyses for bow wave breaking.

Because  $M$  is always negative, the negative gradient of  $M/U_s$  to  $x$  suggests the possibilities for the free-surface flow to be unstable.

### 3.2 Numerical Application for Bow Waves

The appearing condition is numerically simulated to predict the ship wave sub-breakings by (11). Although the flow for the Wigley model is not 2-dimensional, 3-dimensionality may not be so strong that we can expect it is applicable without serious errors. Fig.13 shows the variations of  $M/U_s$  vs  $x$  around the first bow wave crest. The analyses are made at three speeds of  $Fn=0.20$ ,  $0.25$  and  $0.316$  along the curved lines indicated there;  $\zeta$  is the free-surface elevation.

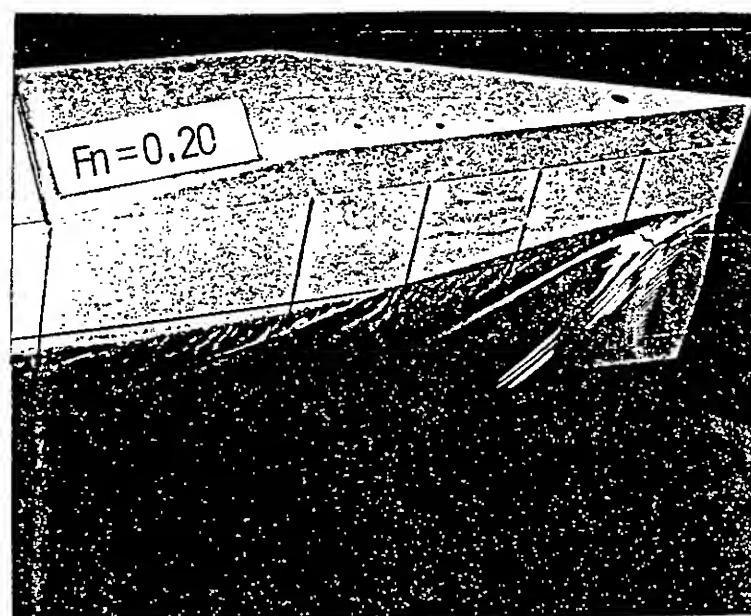
At  $Fn=0.20$ , no steep negative gradient is seen, but the gradients at  $Fn=0.25$  and  $0.316$  are significantly negative behind the wave crest. It may be suggested that the free-surface flows at  $Fn=0.25$  and  $0.316$  are likely to be unstable behind the wave crest while that at  $Fn=0.20$  is stable. Fig.14 shows the photographs of the free-surface flows taken at three corresponding Froude numbers. There can be seen wrinkle-like waves behind the diverging waves at  $Fn=0.25$  and  $0.316$ ; those at  $Fn=0.316$  are much more intensive than those at  $Fn=0.25$ . On the contrary, no such waves can be observed at  $Fn=0.20$ . This observation supports the instability analysis for the bow wave breaking.

### 4. Discussion on Stern Waves

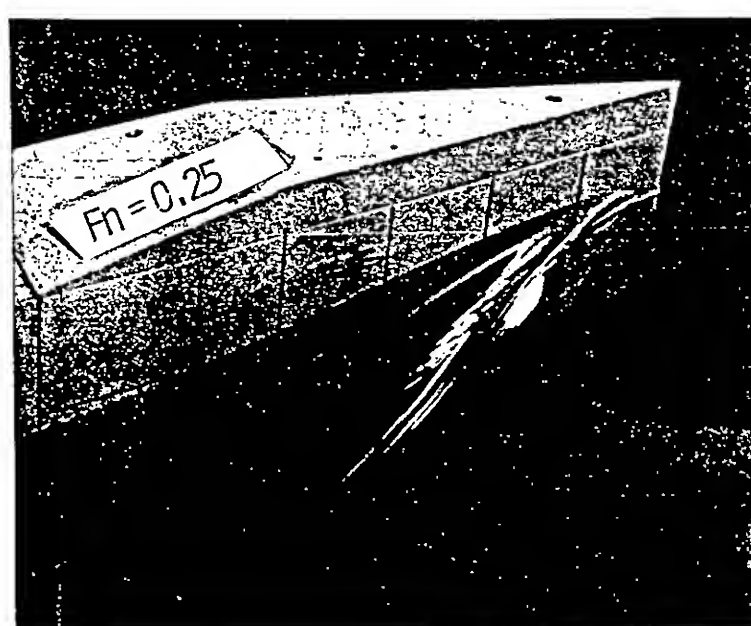
The stern wave of S-103 is studied to make clear the flow mechanism especially on the viscous interaction by referring the computed results. S-103 is an Inuid model with the beam/length ratio of  $0.09$  and extensive experiments have been carried out by Doi[8]. All the experimental data are referred from there.

#### 4.1 Computation for S-103 Model

Fig.15 is the computed wave contour at  $Fn=0.30$  and  $Rn=10^6$ . The result is that at the time  $T=4.0$ , when the convergence is well assured. The grid size is  $74 \times 29 \times 30$ ; computations are carried out on another finer grid scheme to find no significant difference in the resistance. The computing domain is  $-1.4 \leq x/l \leq 2.0$  and  $0.0 \leq y/l \leq 1.4$  which may not be enough especially to discuss the stern waves, where  $l$  is the half length of the model. However, the total grid number of  $64,380$  is the almost limit of the computer. The computing time is abt.



$Fn=0.20$



$Fn=0.25$



$Fn=0.316$

Fig.14 Photographs of wave profiles for Wigley model

240 hrs for a case by Apollo DN-10000 (abt.24 MFLOPS). All the computations are carried out at  $Rn=10^6$  and on the same grid scheme even if the Froude number differs.

Fig.16 shows the calculated and measured wave profiles along the hull surface at  $Fn=0.30$ . The computed

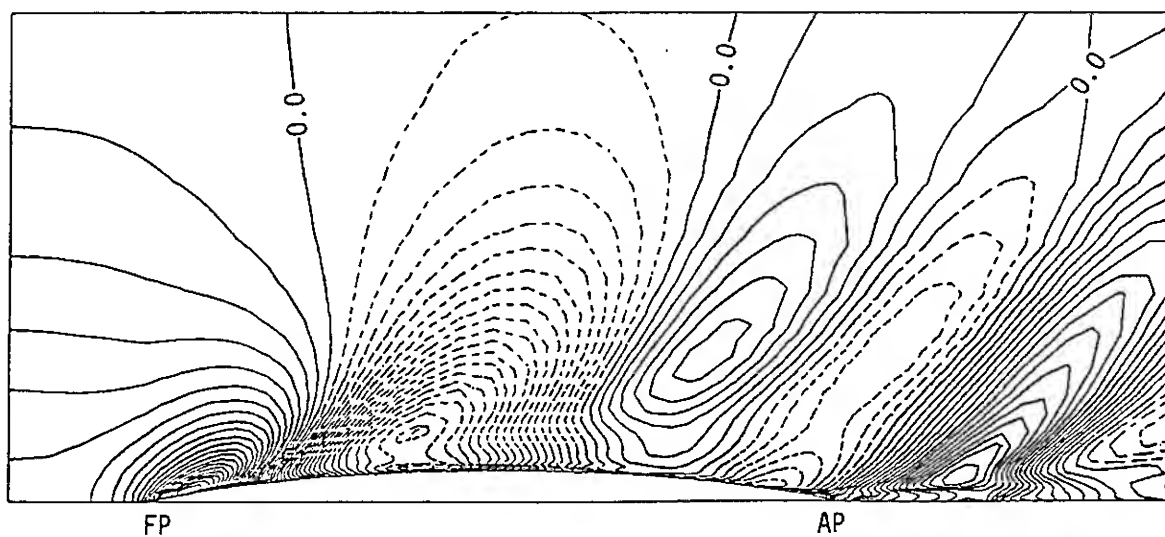


Fig.15

Wave pattern of S-103 at  $Fn=0.30$  and  $Rn=10^6$  (Contour interval is  $0.02 \times 2g\zeta/U_0^2$  and dotted lines show negative values)

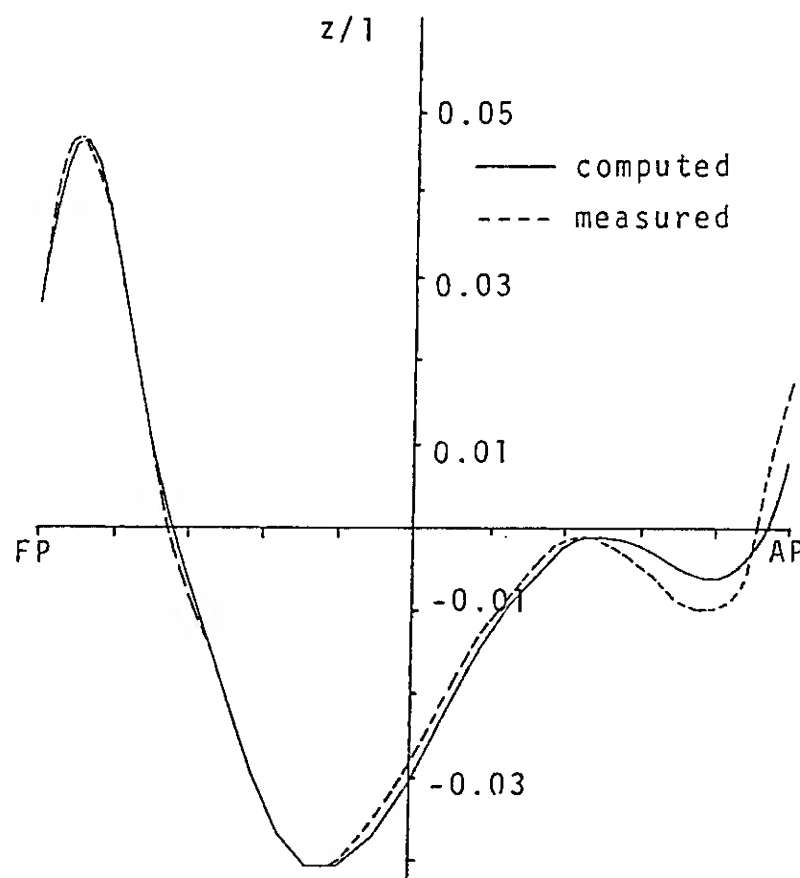


Fig.16 Comparison of wave profiles of S-103 model between the calculated and measured on hull surface at  $Fn=0.30$

profile shows a good agreement with the measured to conclude that the present numerical scheme works well and the results may endure for our purpose to discuss on the flow mechanism.

#### 4.2 Review of Experiments

Now let's refer the wave contours of S-103 from [8], shown in Fig.17. We can notice significant difference in the stern wave patterns although the Froude number changes modestly from 0.26 to 0.30; at  $Fn=0.27$  no significant stern wave is observed compared with those at  $Fn=0.26$  or 0.28. On the other hand, a wide "wake" zone is observed behind the hull at  $Fn=0.30$ . A careful observation of the "wake", as shown in

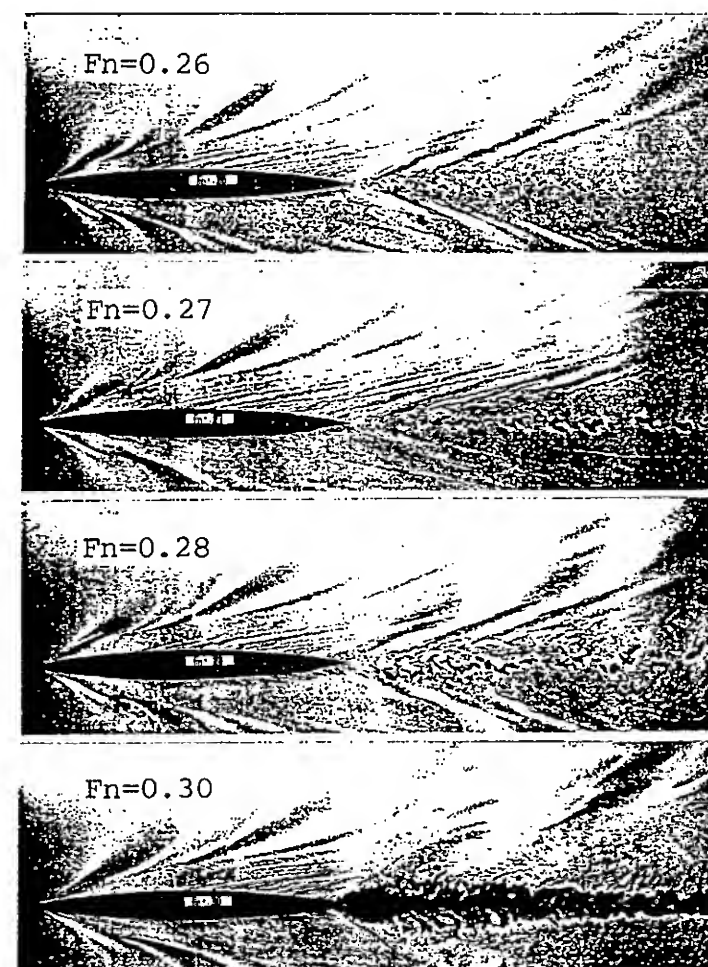


Fig.17 Wave patterns of S-103 at four different Froude numbers

Fig.18, tells us that the free-surface fluctuates intensively there. The free-surface of  $Fn=0.27$  is completely different where such free-surface fluctuation is not observed. This fluctuation of the free-surface is sub-breaking.

It is reported in Doi[8] that the starting points of the stern waves could be easily and definitely determined from the observed wave profiles along the hull at Froude numbers other than 0.27. This is because the wave profile at  $Fn=0.27$  is a little different from that at other speeds.

#### 4.3 Discussion on Viscous Interaction

Fig.19 shows the computed stern wave patterns at the three Froude num-

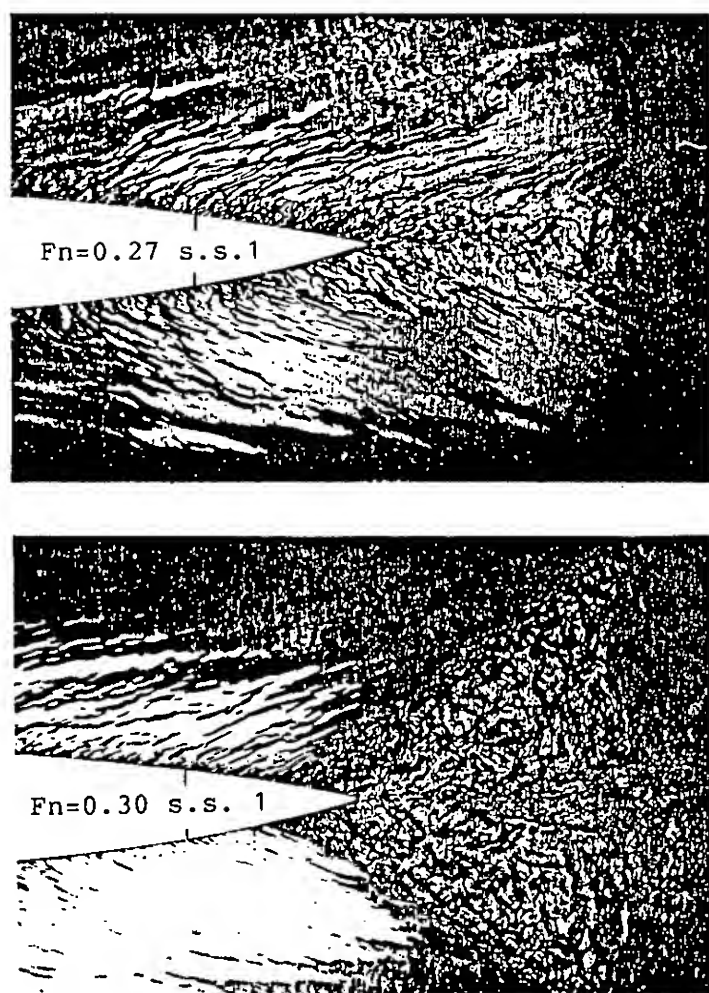
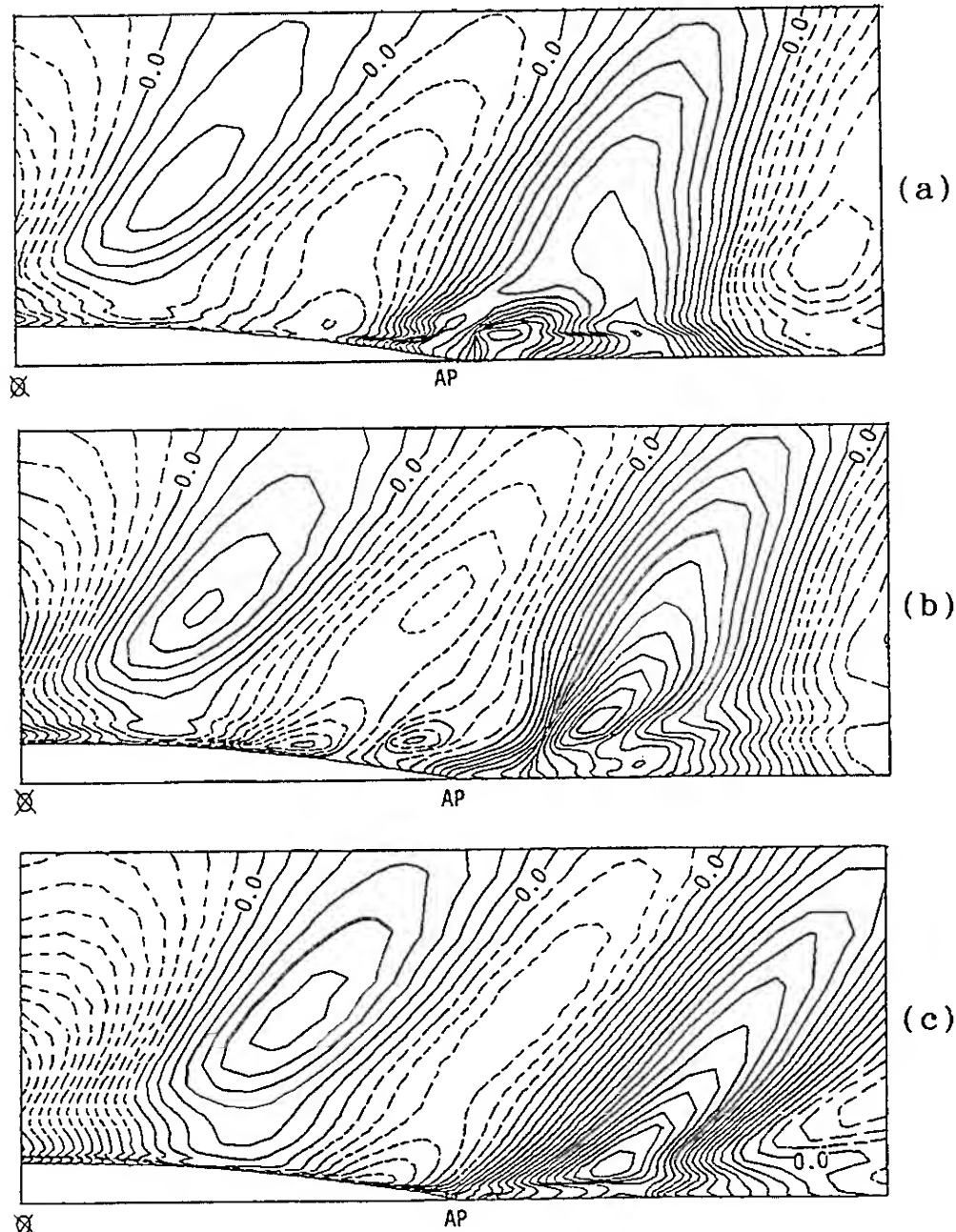


Fig.18 Stern wave pictures of S-103  
at  $Fn=0.27$  and  $0.30$

bers of  $0.27$ ,  $0.28$  and  $0.30$ . Comparing the first stern wave crests, we can see that the result of  $Fn=0.27$  looks different from the others; not so sharply developed. It differs from that of  $Fn=0.28$  although the difference in the speed is not so large. The stern wave crest of  $Fn=0.27$  is not clear. This may agree qualitatively with the observed. On the other hand, the crest of  $Fn=0.30$  is rather sharp and large.

The modest elevation of the stern wave at  $Fn=0.27$  may be much related to the development of the boundary layer and separation. Fig.20 shows the velocity profiles in the boundary layer around the stern and close to the free-surface. The separation of  $Fn=0.27$  takes place at more upstream position than that of  $Fn=0.30$ . This situation can be seen more clearly in the limiting streamlines shown in Fig.21. The separated region of  $Fn=0.27$  is significantly wider than that of  $0.30$ . The experiments by twin tufts show similar tendency; the separated region of  $Fn=0.30$  close to the free-surface is due to the free-surface sub-breaking which has been shown in Fig.18. It is quite natural that a dull pressure recovery by separation may bring forth

Fig.19  
Stern wave patterns  
of S-103 at  $Rn=10^6$   
(a)  $Fn=0.27$   
(b)  $Fn=0.28$   
(c)  $Fn=0.30$   
(Contour interval is  
 $0.02 \times 2g\zeta/U_0^2$  and  
dotted lines show  
negative values)





modest wave elevation. On the other hand, at  $Fn=0.30$ , separation region is so limited that a steep pressure gradient may generate strong waves.

Here we should remind that all the computations are carried out at the same Reynolds number of  $10^6$ . This means that the flow fields are exactly the same in the sense of the viscous effects. Then why such a difference in separation? The bow wave may be responsible; the phase of the bow wave can be a key factor for the separation. The wave contour lines change peculiarly in the boundary layer and wake at all the speeds. A careful observation of the free-surface, shown in Fig.18, suggests us complicated flows in the boundary layer, which may cor-

respond to the computed peculiar contour curves.

Fig.22 shows the velocity vectors at the two y-z sections. Compared between the two Froude numbers, it is obviously seen that the viscous region of  $Fn=0.27$  is much wider than that of  $Fn=0.30$ . A wider wake region made the stern wave elevation modest. The peculiar changes of the wave contour, pointed out in Fig.19, is assumed to appear in the viscous region.

#### 4.4 Detection of Sub-Breaking

Fig.23 shows the comparison of wave profiles and velocity vectors of  $Fn=0.30$  between the measured and the calculated. The measured free-surface fluctuates intensively around the crest (indicated by I there). This fluctuation corresponds to the sub-breaking seen in Fig.18. Because no special attention to the sub-breaking is paid in the calculation, the calculated free-surface is steady, of course. It should be pointed out that the measured wave crest is in upstream compared with the calculated. As seen Fig.18, the crest angle of  $Fn=0.30$  is much larger than the calculated. If we remind the good agreement in the wave profile along the hull surface, shown in Fig.16, we can say that the appearance of the free-surface fluctuation, i.e., sub-breaking makes the crest shift forward which is commonly observed in experiments.

The detection of the appearance of sub-breaking waves is made for the stern waves at  $Fn=0.27$  and  $0.30$ . The values of  $M/U_s$  are calculated along

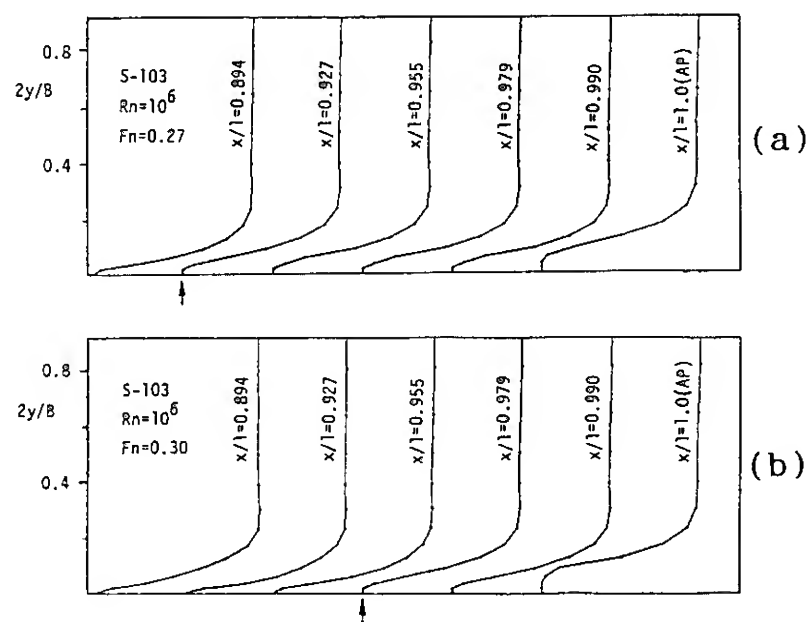


Fig.20 u-distribution for S-103 on free-surface  
(a)  $Fn=0.27$  (b)  $Fn=0.30$

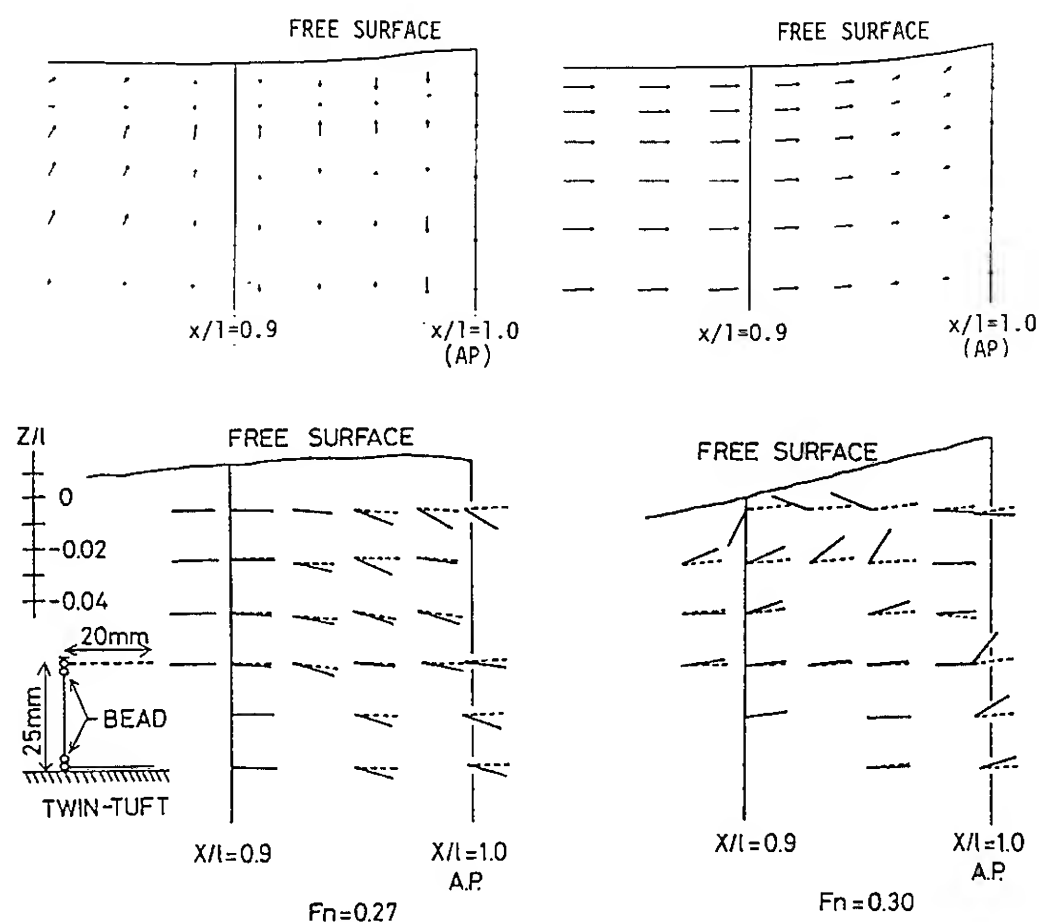


Fig.21  
Calculated (above)  
and observed (below)  
limiting streamlines  
at  $Fn=0.27$  and  $0.30$



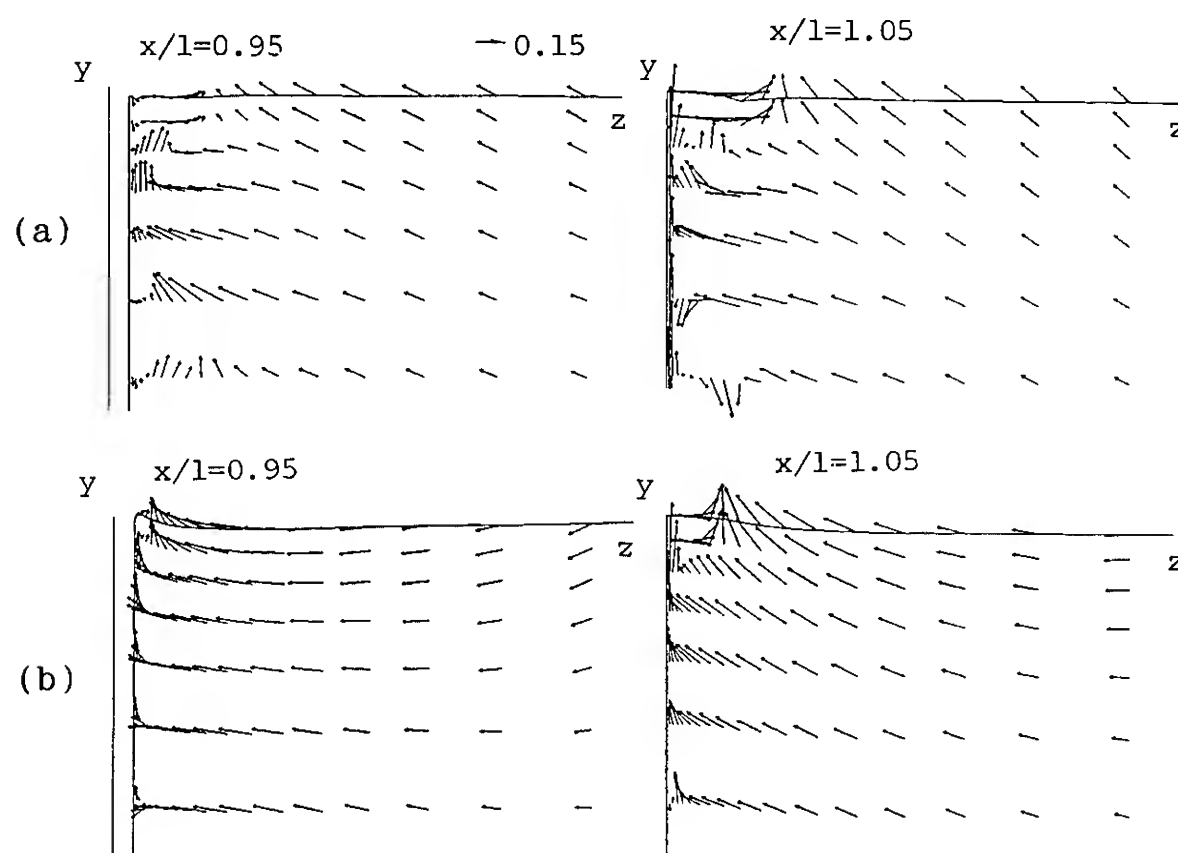


Fig.22  
Velocity vectors  
in y-z planes  
of S-103  
(a)  $Fn=0.27$   
(b)  $Fn=0.30$

$y/l=0.09$  which are shown in Fig.24. Similarly to Fig.13, the negative gradient of  $M/U_s$  to  $x$  suggests the occurrence of unstable free-surface flows. A steep negative gradient is seen in  $Fn=0.30$  but not so much in  $Fn=0.27$ . This means that the wave crest of  $Fn=0.30$  can be subject to sub-breaking but not at  $Fn=0.27$ .

We can point out that the bow wave affects much on the separation and eventually the stern wave generation appreciably. The appearance of sub-breaking waves makes the flow field completely different and it may be necessary to include them in the computation.

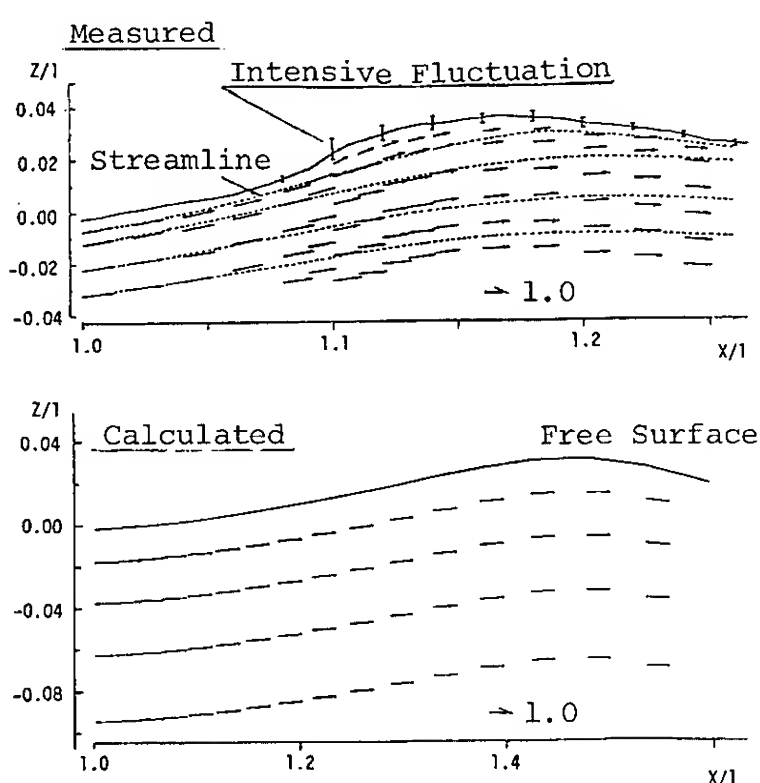


Fig.23 Wave profiles and velocity vectors on x-z plane at  $y/l=0.15$  for S-103

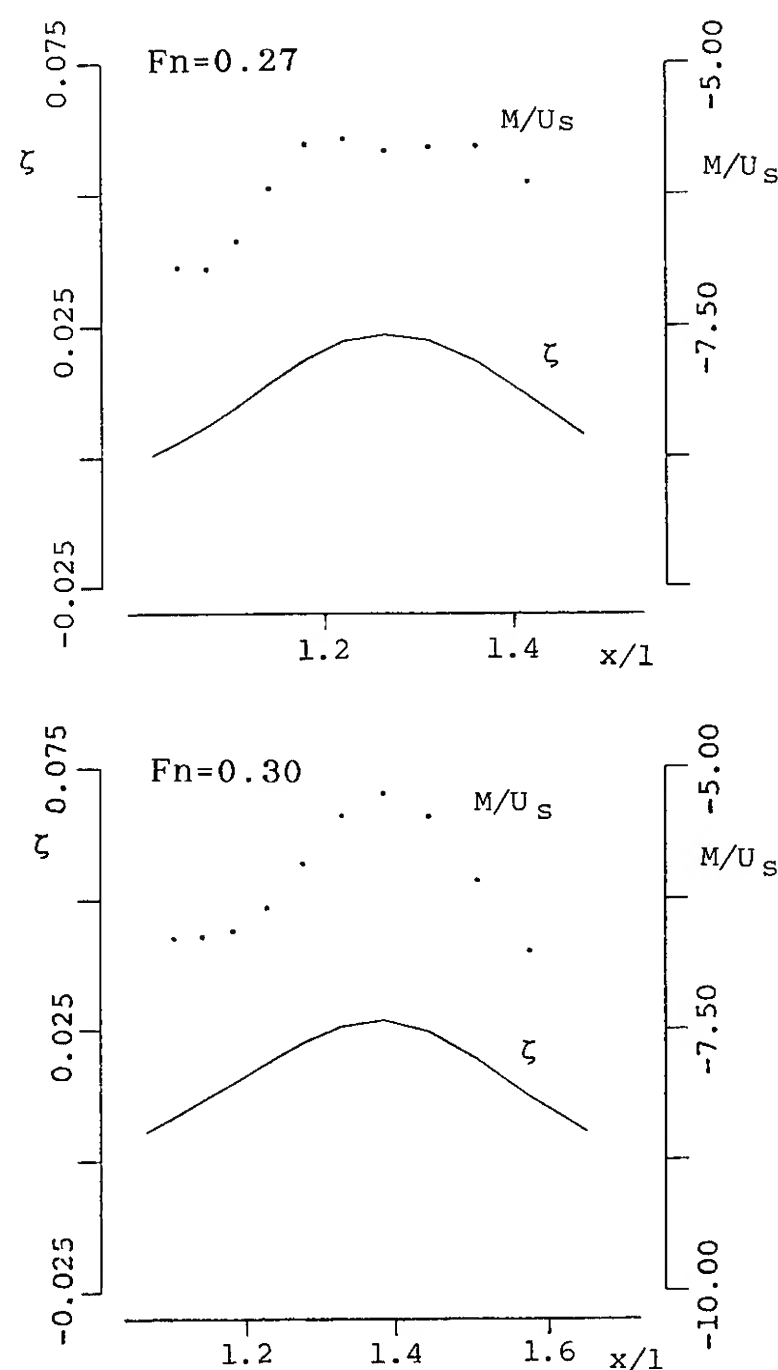


Fig.24 Variation of  $M/U_s$  and free-surface elevation and lines analyses for stern wave breaking of S-103

## 5. Concluding Remarks

A computational code is developed to simulate the high Reynolds number free-surface flows around ship by solving the full Navier-Stokes equation. After validating the scheme, it is applied for the studies on the Reynolds number effects, the detection of wave breaking and viscous interaction of the stern wave. Findings through the present study are summarized as follows.

(1) A numerical scheme is developed to simulate 3-D free-surface flows at high Reynolds number by which a steady-state solution can be obtained with monotonic convergency. The triple grid method is applied to get well-developed free-surface waves within a moderate computer's memory. The wall function is used to overcome still larger minimum grid spacing, which is confirmed to work well.

(2) The Reynolds number effects on waves are significant especially on the stern wave and pressure distribution in the aft part of the hull.

(3) The calculated resistance is greater than the measured. The estimation of the frictional resistance is still a source of over-estimation. The use of much finer grid is a possible improvement.

(4) The criterion for the appearance of sub-breaking waves works well, and the present numerical scheme can be applied to detect the occurrence of breaking waves of ships. The results are supported by the observation.

(5) The stern wave is much affected by the separation of the boundary layer flow which may be under the influence of the bow wave.

(6) The occurrence of sub-breaking changes the flow fields drastically, especially for the stern waves. It is important to introduce a model into the numerical calculation which is capable for the breaking.

All the calculations are carried out by Apollo DN-10000 Computer at N.A. & O.E. Dep't of Hiroshima University.

## Acknowledgments

The second author Mr. Kwag, who is now on leave from HMRI (Hyundai Maritime Research Institute, Korea), expresses appreciation to HMRI to allow him to make research at Hiroshima University.

## References

- [1] Duncan, J.H.: "The Breaking and Non-breaking Wave Resistance of a Two-dimensional Hydrofoil", Jour. Fluid Mech., Vol. 126, 1983
- [2] Mori, K., Doi, Y.: "Flow Characteristics of 2-Dimensional Sub-Breaking Waves, Turbulence Measurements and Flow Modeling", Hemisphere Pub. Co., 1985
- [3] Maruo, H., Ikehata, M.: "Some Discussions on the Free Surface Flow around the Bow", Proc. of 16th Symp. on Naval Hydro., 1986
- [4] Grosenbaugh, M.A., Yeung, R.W.: "Non-linear Bow Flows - An Experimental and Theoretical Investigation", Proc. of 17th Symp. on Naval Hydro., 1988
- [5] Dagan, G., Tulin, M.P.: "Two Dimensional Free-Surface Gravity Flow past Blunt Bodies", Jour. Fluid Mech., Vol. 51, Part 3, 1972
- [6] Tanaka, M., Dold, J.W., Peregrine, D.H.: "Instability and Breaking of a Solitary Wave", Jour. Fluid Mech., Vol. 185, 1987
- [7] Mori, K., Shin, M.S.: "Sub-Breaking Wave: Its Characteristics, Appearing Condition and Numerical Simulation", Proc. of 17th Symp. on Naval Hydro., 1989
- [8] Doi, Y., Kajitani, H., Miyata, H., Kuzumi, S.: "Characteristics of Stern Waves generated by Ships of Simple Hull Form (1st Report)", Jour. of Soc. of Naval Arch. of Japan, Vol. 150, 1981
- [9] Stern, F.: "Influence of Waves on the Boundary Layer of a Surface-Piercing Body", Proc. of 4th Int'l Conf. on Numerical Ship Hydro., 1985
- [10] Miyata, H., Kajitani, H., Shirai, M., Sato, T., Kuzumi, S., Kanai, M.: "Numerical and Experimental Analysis of Nonlinear Bow and Stern Waves of a Two-Dimensional Body (4th Report)", Jour. of Soc. of Naval Arch. of Japan, Vol. 157, 1985
- [11] Shin, M., Mori, K.: "On Turbulent Characteristics and Numerical Simulation of 2-Dimensional Sub-Breaking Waves", Jour. of Soc. of Naval Arch., Vol. 165, 1989
- [12] Kwag, S.H., Mori, K., Shin, M.: "Numerical Computation of 3-D Free Surface Flows by N-S Solver and Detection of Sub-breaking", Jour. of Soc. of Naval Arch. of Japan, Vol. 166, 1989
- [13] Xu, Q., Mori, K., Shin, M.: "Double-

Mesh Method for Efficient Finite-Difference Calculations", Jour. of the Soc. of Naval Arch. of Japan, Vol.166,1989

[14] Chen,H.C., Patel,V.C. : "Calculation of Trailing-Edge, Stern and Wake Flows by a Time-Marching Solution of the Partially-Parabolic Equations", IIHR Report, No.285,1985

[15] IHI,SRI,UT,YNU : "Cooperative Experiments on Wigley Parabolic Models in Japan", prepared for the ITTC Resistance Committee, 2nd edition, Dec.,1983

## DISCUSSION

Fred Stern  
The University of Iowa, USA

The authors' treatment of the free-surface boundary conditions is unclear. It appears that a MAC type method is implemented using a fixed grid that does not conform to the free surface since the terms necessary for a moving grid have not been included in the governing equations. A similar approach was presented by Hino at the 5th International Conference on Numerical Ship Hydrodynamics. Please explain the differences between the present approach and that of Hino. The grids used for each of the triple grids should be clearly stated. It appears from the results that the grid for the convective terms in the NS equations is much too coarse to accurately resolve the viscous flow, e.g., Fig. 4 indicates very few points within the boundary layer and virtually no resolution of the logarithmic and outer wake-like region of the boundary layer. The reliability of the discussions of the results is uncertain due to these issues.

## AUTHORS' REPLY

1. The free-surface boundary conditions consist of the pressure and kinematic ones. Here, the pressure condition can be directly applied because the uppermost moving grid at each time step corresponds always to the free-surface. The kinematic condition, the fluid particles on the free-surface keep staying on it, is used to determine the free-surface elevation at each time step in which the velocities  $u$ ,  $v$ , and  $w$  are extrapolated equally from the value at the lower grid points. The viscous condition, the tangential stress is zero on the free-surface, is not considered here.

2. In Hino's case, there are several grid points above the still water surface and the pressure boundary condition is applied at the intermediate point between grid points as used in the SUMMAC. But in our case, the pressure condition is directly applied without any interpolation. The time dependent term is, of course, taken into account when the grid is rearranged.

3. On the Triple Grid Method: We used three different schemes A, B, and C for the convective terms, the diffusion terms, and the free-surface condition respectively; A, B, and C are  $74 \times 29 \times 19$ ,  $37 \times 29 \times 19$ , and  $296 \times 116 \times 1$  in  $x$ ,  $y$ ,  $z$  directions. The point of the triple grid method is that the fourth order central difference scheme in the Poisson equation does not so much improve the accuracy even if finer grid is used, while, as you comment, the fine mesh system is necessary for the convective term. This is because the truncation errors which come from the dissipation terms, gradient of pressure and Poisson equation give little influence on the accuracy of the computations. The move of the free-surface particle to satisfy the kinematic free-surface condition requires fine grid.

4. Due to the limitation of computer, about 15 points are used around A.P. within boundary layer. It is the reason why we have introduced the wall function to compensate for the smaller number of grid points near the hull surface.

## DISCUSSION

Hoyte Raven  
Maritime Research Institute Netherlands, The Netherlands

When studying Reynolds number effects with a numerical method, one must be sure to have negligible numerical viscosity. This requires that the hull boundary layer is well resolved. How many grid points in normal direction did you use inside the boundary layer? It seems that your grid is not adapted to the boundary layer thickness and may therefore have no grid point at all inside the boundary layer near the bow.

## AUTHORS' REPLY

Thank you for your kind interest in our paper. Fifteen grid points are used within boundary layer around A.P. In CFD, the grid requirement is not easy to satisfy in case of calculating the boundary layer. Especially around the bow, the boundary layer thickness is so thin that it is very hard to catch the larger velocity gradient with two or three grids. In order to overcome that problem, we applied the empirical wall function approach to the scheme except for some stern region where the separation is suspected.

## DISCUSSION

Ronald W. Yeung  
University of California at Berkeley, USA

The instability criteria mentioned in the paper applies to, or was derived on the basis of, 2-D flow. I find it rather skeptical that it can be used for oblique waves along the side of the ship. Perhaps some additional justification is helpful.

## AUTHORS' REPLY

As the discussor pointed out, the criteria used here is that derived from 2-D instability analysis. Therefore, exactly speaking, it may not be applied to the 3-D ship waves. However, the obliqueness of the present case is so small that we expected to have some qualitative detection of sub-breaking; dependency of Froude number and so on. Through the present application, we have been much encouraged to provide a criteria based on 3-D analysis.

# Analysis of Transom Stern Flows

A. Reed, J. Telste (David Taylor Research Center, USA)  
C. Scragg (Science Applications International Corporation, USA)

## ABSTRACT

The boundary value problem for a transom stern ship at moderate and high Froude numbers is formulated and solved. The solution is obtained using lifting potential flow techniques, and involves satisfying a Kutta condition at the after edge of the hull. The full problem is linearized about the free stream velocity, and this linearized problem is solved using two different approaches. One method uses Havelock singularities, and the other uses Rankine singularities. Both of these approaches are applied to the solution for the flow about a high-speed transom stern ship, with encouraging results.

## NOMENCLATURE

$C$	Wave spectral function due to sources
$C_d$	Wave spectral function due normal dipoles
$C_R$	Residuary resistance coefficient, $C_R = R_R / \frac{1}{2} \rho S U^2$
$C_W$	Wave resistance coefficient, $C_W = R_W / \frac{1}{2} \rho S U^2$ , computed from wave spectral energy
$C'_W$	Wave resistance coefficient, computed by integrating predicted pressure over the surface of the hull
$C_{WP}$	Wave pattern resistance coefficient derived from measured wave pattern
$F_n$	Froude number, $F_n = U / \sqrt{gL}$
$g$	Gravitational acceleration
$G$	Green function
$i, j, k$	Unit vectors in the $x, y$ , and $z$ -directions, respectively
$k$	Wavenumber
$k_0$	Fundamental wavenumber, $k_0 = g / U^2$
$k_x, k'_x$	Longitudinal wavenumber
$k_y$	Lateral wavenumber
$L_{pan}$	Length of panel in the $x$ -direction
$L$	Length of ship
$\mathbf{n}$	Normal vector, taken into the fluid
$n_x, n_y, n_z$	Components of the normal vector, $\mathbf{n}$ , in the $x$ -, $y$ -, and $z$ -directions
N-K	Neumann-Kelvin
$r$	Distance from singular point to field point, $r = \sqrt{(x - \xi)^2 + (y - \eta)^2 + (z - \zeta)^2}$
$r'$	Distance from image of singular point to field point, $r' = \sqrt{(x - \xi)^2 + (y - \eta)^2 + (z + \zeta)^2}$
$s_i$	Surface of a panel on the hull, free surface, or wake

$S_B$	Ship hull surface (zero sinkage and trim)
$S_F$	Free surface (mean free-surface level)
$S_W$	Vortex wake surface
$u, v, w$	Perturbation velocity components in the $x$ -, $y$ -, and $z$ -directions
$U$	Ship speed; magnitude of free stream velocity in ship fixed coordinate system
$\mathbf{V}$	Total velocity vector
$V_n$	Component of the perturbation velocity in normal direction
$V_t$	Component of the perturbation velocity in tangential direction
$\mathbf{x}$	Vector coordinate of a field point, $(x, y, z)$
$x, y, z$	Coordinates of field point $\mathbf{x}$ in a right-handed ship fixed coordinate system, $x$ -axis forward, $y$ -axis to port, $z$ -axis upward
$x_t, y_t, z_t$	Coordinates of the perimeter of the transom
$Z$	Wave elevation
$\mu$	Dipole strength
$\xi$	Vector coordinate of a singular point, $(\xi, \eta, \zeta)$
$\xi, \eta, \zeta$	Coordinates of a singular point, $\xi$ , in the $x$ -, $y$ -, and $z$ -directions
$\rho$	Density of water
$\sigma$	Source strength
$\phi$	Perturbation velocity potential

## INTRODUCTION

Naval architects have been familiar with the use of transom sterns on high-speed displacement ships for well over 50 years. The concept of a transom stern applied to displacement ships appears to be an outgrowth of its use on planing craft where it has been applied since around the turn of the century. An understanding of when the use of transom sterns is most appropriate was developed in the years around the Second World War, when extensive systematic-series experiments were performed. In the more recent past, this knowledge concerning the proper application and design of transom sterns seems to have been lost. Modern naval ship designs have used larger and larger transoms while the maximum speed of ships has decreased and the size of ships has increased. Both of these factors should weigh against the use of transom sterns on modern naval vessels.

That the above statements are true is illustrated by the fact that model tests have shown that the resistance of modern naval ships such as the DD 963 is significantly

higher than it needs to be, due largely to the excessive transom area. In addition to the significantly elevated resistance of modern transom stern ships, these ships have significant wave breaking at the stern. This is manifest in two ways: first, by a large turbulent "rooster tail" aft of the transom, and second, by a large breaking transverse wave extending approximately one ship beam off to each side of the transom. Both of these features have a significant negative impact on the wake signatures of modern high-speed naval displacement ships.

While there has been substantial research in the field of wave resistance over the last twenty-five years, and while there has been substantial progress in the prediction of Kelvin wave flows (see for instance Lindenmuth *et al.* 1990), the treatment of transom stern flows has been largely neglected. As is obvious from the poor flow predictions in the region of the transom for Model 5415, given in Lindenmuth *et al.*, the Neuman-Kelvin and Dawson method solvers need major improvements if the flow about a transom stern is to be predicted adequately. However, there have been a few encouraging developments in this area; one of these, which may show a proper approach to this problem, will be discussed later.

At moderate and high speeds, the flow about transom stern ships is characterized by smooth separation of the stream lines at the transom. The manner in which the flow separates from the hull at the transom immediately suggests an analogy to the flow at the trailing edge of a lifting surface (see for example Newman 1977). In the extreme, for high Froude numbers, the problem becomes a planing problem. This limit provides some insight into the physics of the problem, and indicates some physical phenomena which must be modeled in order that a correct solution to the problem be obtained. At more moderate Froude numbers, the flow about a transom stern appears to have many analogies with the flow about a ventilated hydrofoil (again, see Newman 1977). This observation also provides insight into the proper solution to the transom stern flow problem.

Tulin and Hsu (1986) developed a model for high-speed slender ships with transom sterns. By making the assumption that both the beam and draft are small relative to the length, and examining the asymptotic limit as the Froude number approaches infinity, they were able to reduce the three-dimensional problem to a series of two-dimensional boundary value problems to be solved in the cross-flow plane. The problem solved at each cross section is similar to problems addressed in two-dimensional slender wing theory. On the free surface they employed a trailing vortex sheet in the wake of the hull to satisfy the free-surface boundary condition, which in their model was shown to be equivalent to the Kutta condition applied at the trailing edge of a wing. Perhaps the most significant result of their model was the existence of a drag force due to the presence of the trailing vortex sheet. This "stern-induced resistance" is equivalent to the induced drag associated with the shed vorticity in the analysis of three-dimensional lifting surfaces.

Tulin and Hsu calculated the magnitude of the stern-induced resistance for models from Series 64 and made comparisons with the residuary resistance measured at DTRC for a Froude number,  $F_n = U/\sqrt{gL}$ , of 1.49. The excellent agreement with the measured results suggests that, in the high speed limit where the wave resistance vanishes, the primary component of residuary resistance is induced drag due to vorticity shed from the transom. Furthermore, the

magnitude of the stern-induced resistance is quite large, of the same order as the wave resistance which occurs at moderate Froude numbers, and consequently any attempt to model the flow about transom stern ships at finite Froude numbers must include both the generation of free-surface waves and the effects of vorticity shed from the hull.

The trailing edge boundary condition which must be applied in the transom stern problem (actually the boundary condition must be applied on the hull surface just forward of the transom since the transom itself is assumed to be unwetted), is more restrictive than the Kutta condition applied in aerodynamics. In wing theory, we require that the flow at the trailing edge be tangent to the wing surface and that the pressure be continuous across the wake. For the transom stern problem, we require that the flow be tangent to the hull and that the pressure be equal to atmospheric pressure. This is equivalent to placing an additional boundary condition on the longitudinal component of the velocity, which can be satisfied by determining the appropriate longitudinal gradient of the dipole strength on the hull and/or by placing sources on the free surface aft of the transom. These sources aft of the transom would be equivalent to the sources which are used to model the cavity aft of a ventilated airfoil.

Cheng (1989) provides a solution to the transom stern problem in which he satisfies a similar set of boundary conditions at the transom. However, Cheng's solution uses only sources on the body boundary to satisfy the boundary value problem. Obviously, with such an approach the trailing vortex wake can not be modeled, nor can the body boundary condition and the transom boundary condition be satisfied at all points on the body simultaneously. Furthermore, in attempting to satisfy both a normal and a tangential flow boundary condition by varying only the distributed source strengths, the solution will be very sensitive to the tangential gradient of the source strengths, and consequently to panel size and location.

In the analysis of the flow about a surface-piercing strut operating at a small angle of attack, a direct application of the linearized Bernoulli equation along corresponding free-surface streamlines on the high and low pressure sides of the strut will lead to the conclusion that there can never exist a discontinuity in the free-surface elevation at the trailing edge of the strut. This result is, of course, inconsistent with observation. However, if one applies the full nonlinear Bernoulli equation to the same problem, it can be shown that on the two streamlines there will exist a difference in free-surface elevation at the trailing edge which is proportional to the longitudinal vorticity shed by the strut at the free surface. Interestingly, near the strut the perturbation velocities are small and the linearized free-surface equations remain an adequate approximation for the calculation of the flow about the body, including the vorticity distribution. Apparently, this is a situation in which the vorticity gives rise to nonlinear free-surface effects, but the presence of these nonlinear effects does not significantly affect the vorticity distribution. Similarly, the nonlinear wavebreaking which occurs in the wake of a transom stern ship is strongly dependent upon the vorticity shed from the transom, but the vorticity distribution at the stern is not greatly affected by the presence of downstream wavebreaking.

In this paper, we present a brief theoretical foundation for the transom stern boundary value problem. The full problem is linearized about the free stream velocity, and this



linearized problem is solved using two different approaches. One method uses Havelock singularities, and the other uses Rankine singularities. Both of these approaches are applied to the solution for the flow about a high-speed transom stern ship, at two Froude numbers.

### THEORETICAL FORMULATION

Consider a transom stern ship traveling at a comparatively high steady forward speed such that the flow separates cleanly from the hull at the transom. We assume that the fluid is inviscid and incompressible, and that the flow is irrotational everywhere except possibly along a sheet of trailing vorticity. We can then define a perturbation velocity potential  $\phi$  which satisfies Laplace's equation

$$\nabla^2 \phi = 0 \quad (1)$$

throughout the fluid domain. Using a ship-fixed coordinate system with the  $x$ -axis forward, the  $y$ -axis to port, and the  $z$ -axis upward, the velocity vector  $\mathbf{V}$  is related to the potential by

$$\begin{aligned} \mathbf{V} &= -U\mathbf{i} + \nabla\phi \\ &= (-U + u)\mathbf{i} + v\mathbf{j} + w\mathbf{k}, \end{aligned} \quad (2)$$

where  $U$  is the magnitude of the free-stream velocity, and  $u$ ,  $v$ , and  $w$  are the components of the perturbation velocity in the  $x$ -,  $y$ -, and  $z$ -directions, respectively.

While the free surface generally exhibits energetic wave breaking at some distance aft of the transom, it is assumed here that the effects of these breaking waves do not propagate upstream any significant distance. Therefore, there will exist a region aft of the ship and forward of the breaking stern waves over which the kinematic and dynamic free-surface boundary conditions are valid. Furthermore, if the effects of these breaking waves do not extend forward to the hull itself, then our solution in the region immediately surrounding the ship will be unaffected by an application of the kinematic and dynamic free-surface boundary conditions over the entire free surface. On the free surface  $Z$ , the non-linear kinematic boundary condition is written as

$$(-U + \phi_x)Z_x + \phi_y Z_y = \phi_z, \text{ on } z = Z(x, y). \quad (3)$$

The Bernoulli equation is applied on the free surface to give us the dynamic free-surface boundary condition,

$$gZ + \frac{1}{2}|\mathbf{V}|^2 = \frac{1}{2}U^2, \text{ on } z = Z(x, y). \quad (4)$$

It is assumed that both Equations (3) and (4) hold over the entire free surface, including the region directly astern of the transom. In addition, it is necessary to impose a radiation condition to ensure that the free-surface waves vanish upstream of the disturbance.

The boundary condition to be applied on the hull surface  $S_B$ , excluding the transom, is simply the zero normal flow condition

$$\mathbf{V} \cdot \mathbf{n} = 0, \text{ on } y = S_B(x, z; U), \quad (5)$$

where  $\mathbf{n}$  is the hull normal vector (directed into the fluid domain), and we note that the sunk and trimmed position of the hull surface depends upon the forward speed. It is assumed that the flow separates cleanly at the transom and

that the velocity vector at the trailing edge is tangent to the hull.

Since there can exist no discontinuities in the pressure within the fluid domain, the pressure on the hull just forward of the transom must be equal to the pressure on the free surface just aft of the transom. Therefore, we have an additional boundary condition to be applied on the hull surface at the transom:

$$\frac{1}{2}|\mathbf{V}|^2 = \frac{1}{2}U^2 - gz_t, \text{ on } y = S_B(x_t, z_t; U), \quad (6)$$

where  $x_t$  and  $z_t$  denote points at the intersection of the sunk and trimmed hull surface and the transom. Since Equation (5) requires that the normal flow on the hull be zero, Equation (6) can be viewed as a restriction upon the magnitude of the tangential component of the flow at the transom. We note since we are requiring that the pressure go to zero at the intersection of the hull surface with the transom, the present requirements are actually more restrictive than the Kutta condition applied at the trailing edge of an airfoil, for which we require only that the flow be finite and tangent to the foil, and that the pressure be continuous.

### Free-Stream Linearization

If we assume that the potential and its derivatives are small relative to the free-stream velocity  $U$ , we can replace the non-linear free-surface boundary conditions with their linearized counterparts. Combining Equations (3) and (4) to remove the explicit variable  $Z$ , and retaining only the first order terms in  $\phi$ , we can write the linearized free-surface boundary condition as

$$\phi_{xx} + k_0 \phi_z = 0, \text{ on } z = 0, \quad (7)$$

where  $k_0 = g/U^2$  is the fundamental wavenumber. The boundary condition is now applied on the position of the undisturbed free surface.

The hull boundary condition remains unchanged with the exception that it will now be applied at the position of the hull surface with zero sinkage and trim,  $S_B(x, z; U = 0)$ . Once the velocity potential has been determined, the sinkage force and the trim moment can be calculated and an improved estimate of the position on the hull surface  $S_B(x, z; U)$  can be used to solve the problem iteratively. However, for the validation cases presented in the following sections, the sinkage and trim were known from experimental measurements and the hull boundary condition could be applied at the sunk and trimmed position of the hull surface on the first iteration.

After dropping the non-linear terms, the pressure condition to be applied on the hull surface at the intersection with the transom, Equation (6), becomes simply

$$U\phi_x = gz_t, \text{ on } y = S_B(x_t, z_t; U). \quad (8)$$

The linearized problem addressed here is very similar to the Neumann-Kelvin (N-K) problem: the potential must satisfy Laplace's equation, Equation (1); throughout the fluid domain subject to a zero normal flow boundary condition, Equation (5); on the hull surface and subject to a linearized free-surface boundary condition, Equation (7). However, in the present problem we have the additional requirement that the pressure on the hull must go to zero at the stern, Equation (8). This additional independent



boundary condition, a restriction on the longitudinal component of the velocity which does not occur in the formulation of the Neumann-Kelvin problem for ships which do not have immersed transoms, indicates the need for additional unknowns in our numerical approach to the problem.

We solve this boundary-value problem by employing two different approaches, both of which are capable of modeling vortex sheets in the presence of the free surface. One approach uses Havelock sources and dipoles which are distributed over the hull surface and in the wake. The linearized free surface boundary condition is implicitly satisfied by the use of Havelock singularities, and therefore no singularities are required on the free surface. The other approach uses Rankine sources and dipoles which are distributed over the hull surface, the free surface, and in the wake. The details of the two approaches follow.

### Havelock Singularity Formulation

Our first approach to the numerical solution to this problem distributes Havelock singularities over the hull surface and along a trailing wake sheet. The hull surface and the wake sheet are divided into discrete panels comprised of coincident sources and normal dipoles of uniform singularity density. The Havelock singularity is a Green function for the problem which satisfies the linearized free-surface boundary condition on the mean free surface. The unknown singularity densities are determined by imposing the hull boundary conditions at the centroids of each panel.

There are several different methods for evaluating the potential  $\phi$  due to a distributed Havelock source of uniform density  $\sigma$ ,

$$\phi = \sigma \iint_{s_i} dS G(x, y, z; \xi, \eta, \zeta),$$

where  $G$  is the Havelock Green function and  $s_i$  is the panel surface. We use a form of the Green function which allows us to analytically calculate a wave spectral function by interchanging the order of integration:

$$G = -\frac{1}{r} + \frac{1}{r'} + \Re \left\{ \frac{2}{\pi} k_0 \int_{-\infty}^{\infty} dk_y \int_0^{\infty} dk_x \frac{e^{k(z+\zeta) + ik_x(x-\xi) + ik_y(y-\eta)}}{k_x^2 - k_0 k} - i \frac{k_0}{2} \int_{-\infty}^{\infty} dk_y \frac{\beta(k_y)}{k'_x} e^{k(z+\zeta) + ik'_x(x-\xi) + ik_y(y-\eta)} \right\}, \quad (9)$$

where

$$r = \sqrt{(x-\xi)^2 + (y-\eta)^2 + (z-\zeta)^2}, \quad (10)$$

$$r' = \sqrt{(x-\xi)^2 + (y-\eta)^2 + (z+\zeta)^2}$$

and

$$k = \sqrt{k_x^2 + k_y^2}.$$

The variables  $k_x$  and  $k_y$  are the longitudinal and lateral wave numbers of the free-surface waves, respectively. In the single integral, the longitudinal wave number is not an independent variable, and is related to  $k_y$  by

$$k'_x = \left[ \frac{1}{2} \left( k_0 + \sqrt{k_0^2 + 4k_y^2} \right) \right]^{1/2}.$$

The function  $\beta$  is given by

$$\beta = \frac{2 \left( k_0 + \sqrt{k_0^2 + 4k_y^2} \right)}{\sqrt{k_0^2 + 4k_y^2}}.$$

The first two terms in the Green function correspond to a Rankine source and its negative image above the free surface; their contributions to the potential are computed using standard techniques. The free-surface wave contributions to the potential are contained in the two integral terms of Equation (9). To compute these terms we first define a wave spectral function  $C(k_x, k_y)$ ,

$$C(k_x, k_y) = \iint_{s_i} dS e^{k\zeta - ik_x\xi - ik_y\eta}, \quad (11)$$

where the integration over the panel surface is performed analytically. The wave contribution to the potential can then be written as

$$\phi_w = \sigma \frac{2}{\pi} k_0 \int_{-\infty}^{\infty} dk_y \int_0^{\infty} dk_x C(k_x, k_y) \frac{e^{kz + ik_x x + ik_y y}}{k_x^2 - k_0 k} - \sigma i \frac{k_0}{2} \int_{-\infty}^{\infty} dk_y \frac{\beta}{k'_x} C(k'_x, k_y) e^{kz + ik'_x x + ik_y y},$$

where it is understood that we are taking the real part of the expression. In practice, all of the boundary conditions involve derivatives of the potential rather than the potential itself, but the spatial derivatives can be calculated simply by multiplying the spectral function by the appropriate wave number prior to the integration.

For a surface distribution of Havelock dipoles directed normal to the surface, the potential can be written as

$$\phi = \mu \iint_{s_i} dS \frac{\partial}{\partial n} G(x, y, z; \xi, \eta, \zeta),$$

where  $\mu$  is the dipole density. When we substitute the definition of the Green function [Equation (9)], into this expression, we find that the potential contains contributions from a Rankine dipole and its negative image above the free surface, and contributions from the wave terms. The wave spectral function for a Havelock dipole distribution,  $C_d(k_x, k_y)$ , can be analytically integrated over a flat panel, and is related to the wave spectral function for a Havelock source, Equation (11), by

$$C_d(k_x, k_y) = (n_z k - in_x k_x - in_y k_y) C(k_x, k_y),$$

where  $(n_x, n_y, n_z)$  are the components of the unit vector  $\mathbf{n}$ , normal to the dipole panel. The wave contributions to the potential can then be determined by integrating over  $k_x$  and  $k_y$ :

$$\phi_w = \mu \frac{2}{\pi} k_0 \int_{-\infty}^{\infty} dk_y \int_0^{\infty} dk_x C_d(k_x, k_y) \frac{e^{kz + ik_x x + ik_y y}}{k_x^2 - k_0 k} - \mu i \frac{k_0}{2} \int_{-\infty}^{\infty} dk_y \frac{\beta}{k'_x} C_d(k'_x, k_y) e^{kz + ik'_x x + ik_y y}.$$

Since both sources and dipoles are distributed over the panels on the hull surface, there exist two unknowns for each panel and we have some flexibility over the manner in which the singularity densities are to be determined. One could use a slender ship approximation to set the source densities *a priori*,

$$\sigma = Un_x/4\pi,$$

and then determine the dipole densities by imposing the hull boundary conditions at the centroid of each panel. Alternatively, the source strengths could be determined initially by solving the Neumann-Kelvin problem in the absence of the pressure condition, and then solving for the dipole strengths which satisfy both the zero normal flow condition and the pressure condition.

The zero pressure boundary condition, Equation (8), is highly dependent upon the tangential flow at the centroid of the last dipole panel on the hull surface. There exists a discontinuity in the tangential flow across a continuous distribution of surface dipoles which is proportional to the tangential gradient of the dipole strength. Unfortunately, this important term is lost when the continuous surface of the body is approximated by discrete panels of constant dipole strength. In order to include this term, we employ a finite differencing scheme for the panels immediately upstream and downstream of the last panel on the hull surface. If the pressure boundary condition is to be applied at the  $i$ th panel, we denote the immediate upstream panel as  $i+1$  and the adjoining wake panel as  $i-1$ . Then the tangential gradient over the  $i$ th panel can be approximated by

$$\Delta\mu_i = \frac{1}{2} \frac{(\mu_{i+1} - \mu_{i-1})}{L_{\text{pan}}},$$

where  $L_{\text{pan}}$  is the length of the  $i$ th panel. The tangential component of the perturbation velocity  $V_t$  due to this dipole gradient is

$$V_t = \pm 2\pi \Delta\mu_i,$$

where the negative sign corresponds to the outboard side of the panel and the positive sign corresponds to the inboard side. This tangential velocity must be added to the velocity calculated at the centroid of the uniform dipole panel only for those panels on which the zero pressure boundary condition is to be applied.

If we panel the wake with  $M$  dipole panels, and the hull with  $N$  panels on which are distributed both sources and dipoles, then the zero normal flow boundary conditions applied at the centroids of the  $N$  panels on the hull surface can be written as

$$\sum_j \mu_j V_{n_j}(x_i) = Un_{x_i} - \sum_j \sigma_j V_{n_j}(x_i), \quad i = 1, \dots, N,$$

where  $V_n$  is the normal component of the perturbation velocity. The additional  $M$  boundary conditions required are the zero pressure conditions applied at the centroids of the last  $M$  panels on the hull just forward of the trailing wake panels:

$$\begin{aligned} -2\pi \Delta\mu_i + \sum_j \mu_j u(x_i) \\ = \frac{g}{U} z_{t_i} - \sum_j \sigma_j u(x_i), \quad i = 1, \dots, M. \end{aligned}$$

The trailing wake sheets are extended straight aft from the transom for a distance of half a ship length. The effects of terminating the dipole sheets are therefore confined to a region well aft of the hull.

### Rankine Singularity Formulation

The Rankine singularity approach involves seeking the perturbation potential  $\phi$  of Equation (2) as the solution to the integral equation

$$\begin{aligned} 2\pi\phi = & \iint_{S_B} dS \phi \frac{\partial}{\partial n_\xi} \frac{1}{r} - \iint_{S_B} dS \frac{\partial \phi}{\partial n_\xi} \frac{1}{r} \\ & + \iint_{S_F} dS \phi \frac{\partial}{\partial n_\xi} \frac{1}{r} - \iint_{S_F} dS \frac{\partial \phi}{\partial n_\xi} \frac{1}{r} \\ & + \iint_{S_W} dS \mu \frac{\partial}{\partial n_\xi} \frac{1}{r}, \end{aligned} \quad (12)$$

obtained from Green's second identity. The field point may lie on the hull boundary  $S_B$  or the mean free-surface level  $S_F$ . The variable  $r$ , as it is in Equation (10), is the distance between the field point  $\mathbf{x}$  and the singular point  $\xi$ , and  $\mathbf{n}_\xi$  is the unit normal vector directed into the fluid domain. The hull surface is taken as the surface with either zero or known sinkage and trim. According to whether the field point  $\mathbf{x}$  is on  $S_B$  or  $S_F$ , one of the integrals involving  $\phi \partial/\partial n_\xi$  is a principal-value integral. The surface  $S_W$  represents a dipole sheet in the wake across which there is a jump  $\mu$  in the potential.

Using the integral equation as a basis of a solution technique, we panel the hull, a portion of the mean free-surface level near the hull, and the wake. The panels in the wake are grouped in longitudinal strips within which all the panels have the same normal dipole moment. Each of the panels is flat and is assumed to have constant source and normal dipole distribution. These approximations allow one to discretize the integral equation.

The integrals over the hull surface and the mean free-surface level involve  $\phi$  and its normal derivative. On both surfaces, the boundary conditions can be used to reduce the number of unknowns at a boundary. On the hull surface the normal derivative is given by the zero normal flow condition, Equation (5). On the mean free-surface level, the linearized free-surface boundary condition, Equation (7), can be used to express the unknown normal derivative in terms of longitudinal derivatives of  $\phi$ , i.e.  $\phi_{xx}$ . An upstream finite-differencing scheme involving the values of  $\phi$  at the centroids of free-surface panels is used to approximate  $\phi_{xx}$  at a point  $\mathbf{x}$  on the mean free-surface. Therefore, on the boundaries  $S_B$  and  $S_F$  only the function  $\phi$  at discrete points remains unknown.

Since free-surface panels are arranged in longitudinal strips with their centroids lying on curved lines, the finite-differencing scheme for determining  $\phi_{xx}$  must include panel centroids from several strips. In most cases an 11-point scheme is used: five points from the longitudinal strip of panels in which  $\mathbf{x}$  lies and three points from each of two adjacent strips. At the upstream ends of the strips of free-surface panels, we assume that  $\phi_x$  and  $\phi_{xx}$  are both zero (Sclavounos and Nakos 1988).

Aft of the transom, there are strips of free-surface panels that originate at the transom. On the panel closest to the transom,  $\phi_{xx}$  can be approximated from the transom depth and the hull shape. At the next panel downstream,

a differencing scheme involving  $\phi$  on that panel and  $\phi$ ,  $\phi_x$ , and  $\phi_{xx}$  on the panel nearest the transom is used. Approximations for  $\phi_x$  and  $\phi_{xx}$  on the free-surface panel nearest the transom are obtained from the linearized Bernoulli equation and the fact that the position of the free surface at the transom is known. In particular, we use Equation (8) and the partial derivative with respect to  $x$  of Equation (8). On the third panel downstream of the transom in these free-surface strips, a lower order upstream differencing scheme involving only  $\phi$  at panel centroids is used. For all other panels in these strips, the 11-point upstream differencing scheme is used.

On the transom, although it is unwetted, a boundary condition must be specified because we have formulated the boundary value problem in terms of an integral equation. That integral equation involves an integral over a closed boundary which includes the hull, the mean free-surface level, and possibly a vortex wake across which  $\phi$  may be discontinuous.

Several treatments of the transom boundary are possible. We may ignore the boundary—which is equivalent to specifying that both  $\phi$  and  $\phi_x$  vanish on the transom, a possible overspecification of boundary conditions. However, if the perturbation potential and its gradient are small, this approximation may not be bad. Another option is to treat panels on the transom in the same manner as other panels on the hull are treated. In this case,  $\phi_x$  on the transom is known and is set equal to  $Un_x$ . Without a surface of discontinuity extending downstream from the periphery of the transom, we should expect the flow to turn around the corner of the transom as it streams past the hull. The resulting calculated flow field will not satisfy the criterion that the fluid leaves the hull tangentially, and it will violate our linearization assumptions. Treating transom panels like other hull panels thus seems to require a lifting surface extending downstream. A third option is to set  $\phi_x$  equal to a value determined by Equation (8), the linearized Bernoulli equation. The three options are complicated by the fact that we have already decided to set  $\phi_x$  and  $\phi_{xx}$  at the free-surface panels immediately aft of the transom equal to those values required by Bernoulli's equation. Thus, for the sake of continuity in the boundary conditions, we choose the third option and set  $\phi_x$  equal to the value required by Equation (8).

There remains the task of determining  $\mu$ , the strength of the normal dipole moment on the trailing wake. Two options are readily apparent. We may, of course, set  $\mu$  to zero and thereby ignore the possibility or requirement of having a discontinuity of  $\phi$  in the wake. Otherwise, we are required to determine  $\mu$  from Bernoulli's equation. This is done by considering the linearized form given by Equation (8). For each wake strip, two points are chosen. One point is at the centroid of the hull panel nearest the transom. The other point is slightly aft of the transom on the side of the strip of dipole panels facing the fluid domain. A difference equation for  $\mu$  is obtained by discretizing Equation (8) using these two points.

Equation (12) is not the only integral equation that can be used to obtain  $\phi$ . We could replace  $1/r$  by  $1/r + 1/r'$  and obtain a second integral equation. The main difference is that in the first equation  $\phi$  is expressed in terms of dipoles and sources on the mean free-surface level, whereas in the second case only sources appear on the mean free-surface level.

We originally intended to use double-body linearization instead of free-stream linearization for the Rankine-source solution, but we encountered difficulties. In order to prevent the flow from turning the sharp corner formed by the transom, we used a wedge to extend the hull downstream for the double-body solution. There is no difficulty in obtaining such a solution. The non-zero Froude number solution, however, requires paneling on the entire free-surface near the hull, including the region aft of the transom. Normally, the double-body potential is itself differenced to build finite-difference coefficients so that the influence coefficients can be calculated. In order to proceed in this manner for the free-surface panels aft of the transom, the double-body potential was continued from the hull extension to the mean free-surface level by means of a Taylor series expansion. This was necessary because the fictitious potential inside the hull is identically zero. Once this was done, differencing of the analytically continued double-body potential was performed for first and second order derivatives in the mean free-surface level. Differencing for the first derivatives produced reasonable approximations. However, differencing for the second derivative resulted in large numerical errors.

A second and related issue with respect to linearization schemes is that the free-surface elevation computed from double-body linearization shows evidence of numerical instability, in that numerical noise seems to grow in the strips of free-surface panels in the downstream direction. This should be expected in view of the results of Slavounos and Nakos (1988). The fact that this numerical instability is not so pronounced in the free-surface linearization scheme was not expected.

The differencing schemes we used for double-body and free-stream linearization are not the same. The double-body differencing scheme involves centroids on the same free-surface strip because the free-surface paneling is determined so that the strips of free-surface panels are bounded by double-body streamlines. For free-stream linearization, the free-surface paneling cannot line up with the streamlines of the free-stream flow because free-surface paneling must conform to the shape of the hull and not penetrate into the hull. Thus the required differencing scheme is more complicated because it must include centroids of panels in several strips of panels. However, once it has been decided which centroids to include in the finite difference stencils, the finite-difference coefficients for approximating  $\phi_{xx}$  can be determined rather easily by eliminating truncation errors. A linear system of equations is set up to eliminate these errors up to fourth order. The method of singular value decomposition is used to obtain a set of differencing coefficients among the possible sets of differencing coefficients. For free-stream linearization at a particular Froude number, the coefficients of the derivatives of  $\phi$  in the free-surface boundary condition are known constants. This is not the case in double-body linearization, in which we are required to numerically approximate the coefficients of the derivatives of  $\phi$ , which introduces another source of error.

## PREDICTIONS

In order to validate the computational methods which have been developed based on the theory which was just discussed, predictions have been made for a high-speed transom stern model at two Froude numbers, 0.25 and 0.4136. The hull form examined for this study is that of DTRC Model 5415, which was studied as part of the Compar-

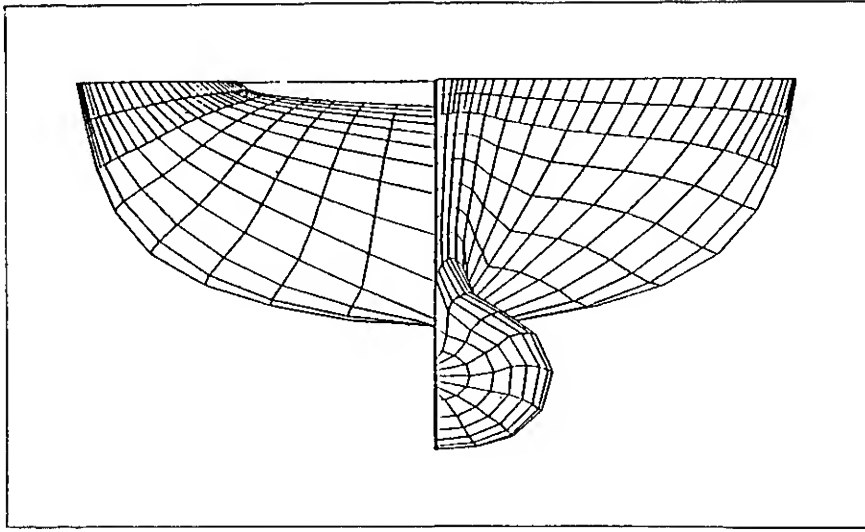


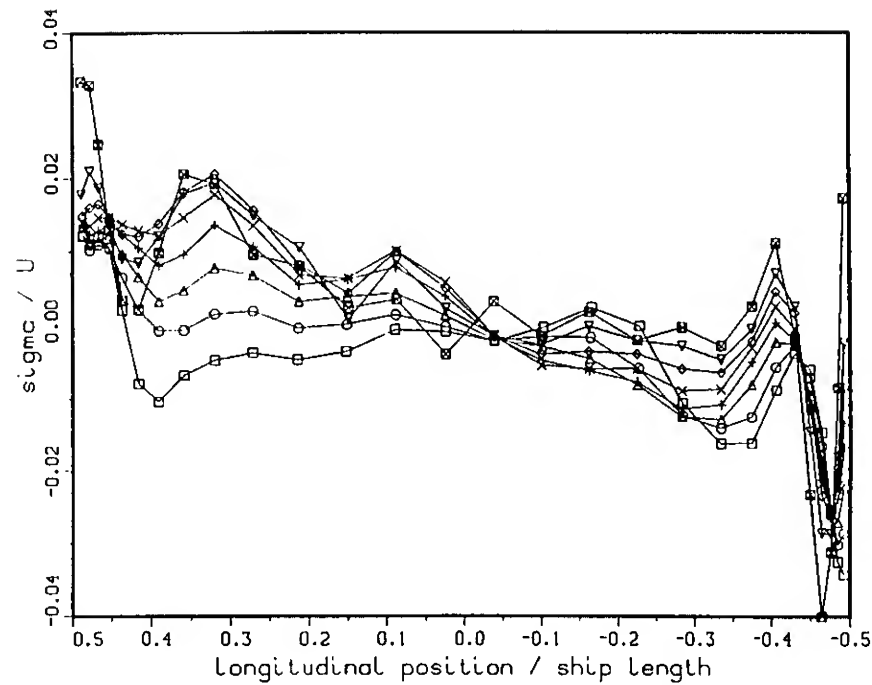
Fig 1—Panelization of high speed transom stern ship (DTRC Model 5415).

tive Study of Numerical Kelvin Wake Code Predictions, reported by Lindenmuth *et al.* (1990). A sample paneling of Model 5415 is shown in Fig. 1. On this model, Lindenmuth *et al.* reported a wave trough at the transom for  $F_n = 0.25$  and a crest at the transom for  $F_n = 0.4136$ .

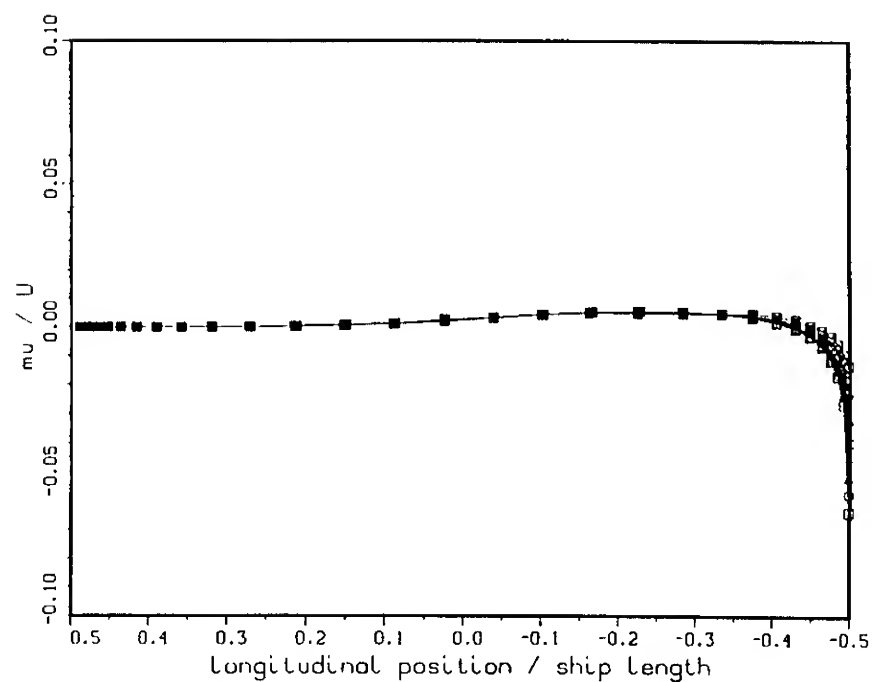
Because of concerns about violating linearization criteria, it was thought best to concentrate developmental efforts on the Havelock singularity code at the lower Froude number. The Rankine-source code requires paneling the mean free-surface level near the hull. Because the wavelengths associated with a lower Froude number are smaller, more paneling is required to resolve the same expanse of the free surface. More paneling requires more computer time and slower development time. Therefore, for the sake of efficiency, the development and modification of the Rankine singularity code were concentrated at the higher Froude number. For these reasons, the results in this section are presented in a somewhat inconsistent order. For the Havelock singularity method, results are presented first for the low Froude number and the major part of the results correspond to this Froude number. For the Rankine singularity method, the opposite is true; results are presented first for the higher Froude number, and then for the lower Froude number.

#### Havelock Singularity Results

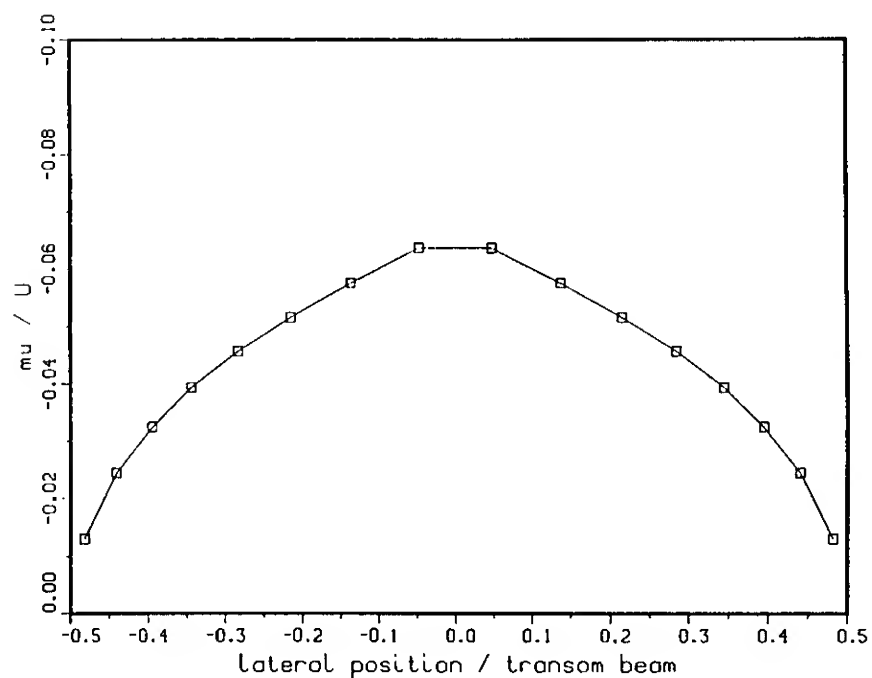
For the Havelock singularity calculations, Model 5415 was paneled at the measured sinkage and trim, with 320 panels on the hull and 8 trailing dipole panels in the wake. For the first test case, we set the source strengths using the slender-ship approximation, and solved for the dipole strengths. We found that the dipole strengths required to satisfy the zero normal flow condition on the hull were unrealistically large, and this approach has been abandoned. By starting with source strengths obtained from a N-K solution without any Kutta condition, we are in effect, using the sources to satisfy the normal flow condition, and using the dipoles to satisfy the tangential flow condition. This leads to a better behaved solution. The source strengths on the hull, from the N-K solution without a Kutta condition, for  $F_n = 0.25$ , are presented in Fig. 2a. Each curve in the figure corresponds to a row of panels on the hull (although the panels on the bulb are included in the solution, their source strengths are not plotted on this graph for reasons of clarity). These source strengths account for the interactions between the hull and the free-surface waves, but not for the zero pressure condition at the transom stern. The dipole



(a)—Source strengths on the hull.



(b)—Dipole strengths on the hull.



(c)—Dipole strengths across the wake.

Fig 2—Singularity strengths on the hull,  $F_n = 0.25$ . Each curve represents a row of panels at a different depth.

strengths required to satisfy the Kutta condition, Fig. 2b, are driven entirely by the zero pressure condition, in the sense that the dipole strengths would go to zero in the ab-

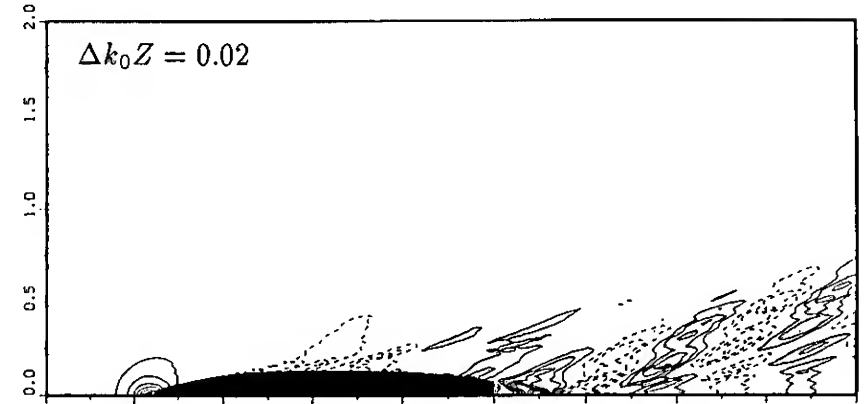


sence of this boundary condition. Apparently the effects of imposing the Kutta condition on the hull at the transom, as represented by the dipole distribution, do not extend very far forward of the transom. The dipole strengths are negligible over most of the length of the hull, but as the flow accelerates to satisfy the zero pressure condition, the dipole strengths drop quickly and smoothly to a minimum value at the transom. The dipole strengths are held constant on the trailing wake panels. The dipole distribution across the wake is shown in Fig. 2c. The similarities between this distribution and the spanwise distribution on an airfoil are striking. The significance of this trailing vorticity can be appreciated by noting that the magnitude of the dipole strengths is comparable to the strengths calculated on an airfoil of equal span, operating at a negative angle of attack of approximately five degrees. The sense of the vorticity will result in an upwelling flow on the centerline of the wake, and a diverging free-surface current across the wake, and may well be the physical mechanism responsible for such flows observed in the centerline wake region of transom stern ships.

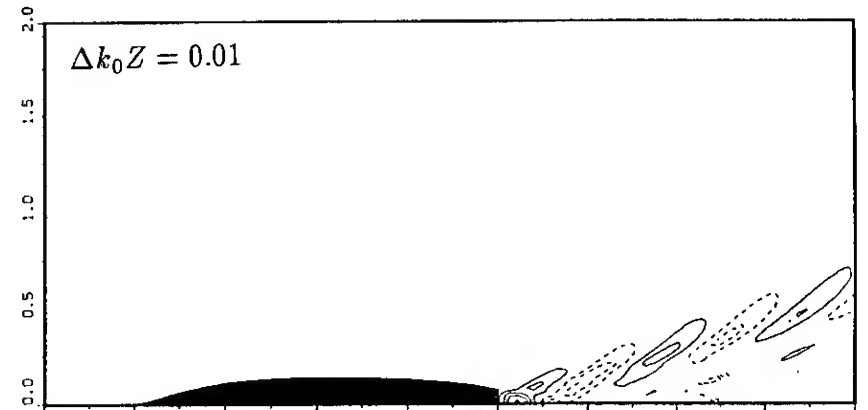
Contour plots of the contributions to the near-field wave elevations due to the sources alone and due to the dipoles alone are presented in Figs. 3a and 3b (note that the contour interval is reduced in Fig. 3b). The elevations have been non-dimensionalized by the fundamental wavenumber  $k_0$ . The changes in the wave field due to the dipoles are limited to a small region directly aft of the transom and a group of diverging waves which occur along a cusp line which originates near the stern. The total near-field wave elevations which result from the combined distribution of sources and dipoles on the hull are presented in Fig. 3c. The corresponding experimental results are shown in Fig. 3d. Including the Kutta condition at the transom leads to a solution which exhibits a very steep rise in the wave elevation aft of the transom, which will likely lead to wave breaking.

Wavecuts along  $y/L = 0.324$  are presented in Fig. 4. The measured wavecut is presented in Fig. 4a, while that predicted from a N-K solution without a Kutta condition is shown in Fig. 4b. In Fig. 4c we note that the transverse waves due to the dipoles are very small relative to those generated by the sources. The most significant far-field effect of the Kutta condition is the same group of diverging waves noted in the near-field contour plots. The combined wave fields are given in Fig. 4d. The inclusion of the dipoles results in a free-wave amplitude spectrum which is in good agreement with that obtained from the experimental wavecuts, Fig. 5. The predicted wave resistance,  $C_W$ , of 0.00042 compares well with the experimental wave pattern resistance,  $C_{WP}$ , of 0.00037.

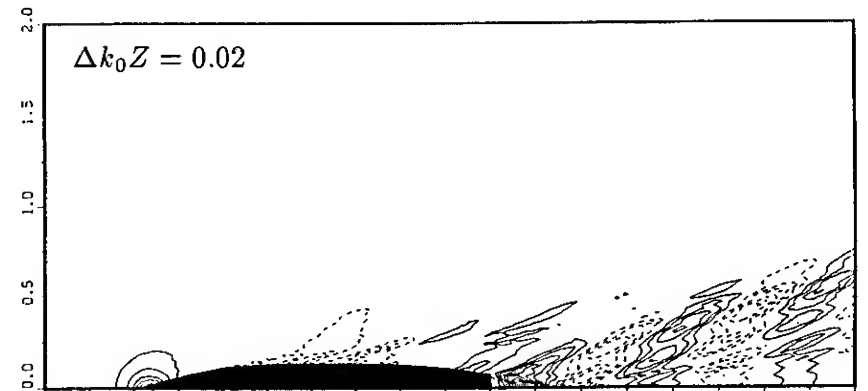
Fig. 6 presents contour plots of wave elevation for  $F_n = 0.4136$ . Fig. 6a presents the results for the combined distribution of sources and dipoles. The near-field waves generated by the dipoles alone are shown in Fig. 6b. The corresponding experimental results are shown in Fig. 6c. As before, the effects on the wave field of imposing the Kutta condition at the transom are relatively limited. The dipole distribution across the wake is shown in Fig. 7. The vorticity is somewhat stronger and has the same sense as before, leading to an upwelling along the centerline and a diverging flow across the wake. The measured wavecut along  $y/L = 0.324$  is presented in Fig. 8a. The predicted wavecut due to the combination of source and dipole panels is shown in Fig. 8b. Although the predictions are slightly higher than



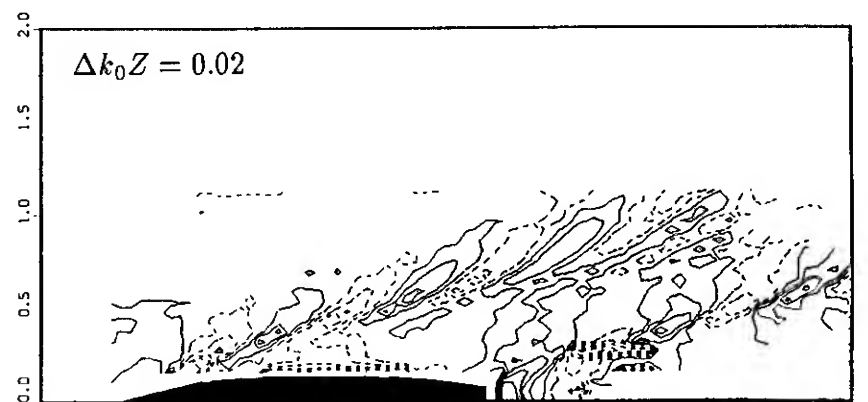
(a)—Due to Havelock sources alone.



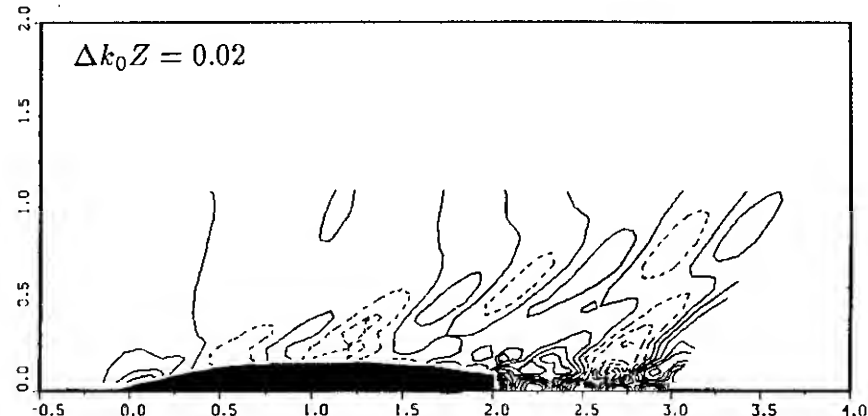
(b)—Due to Havelock dipoles alone.



(c)—Due to combination of Havelock sources and dipoles.

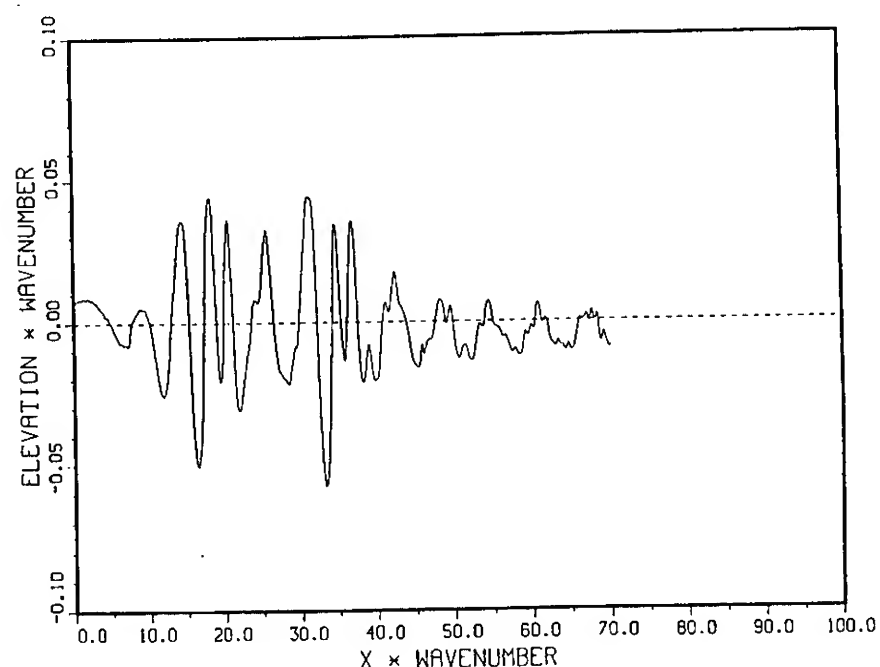


(d)—Measured. (from Lindenmuth *et al.* 1990)

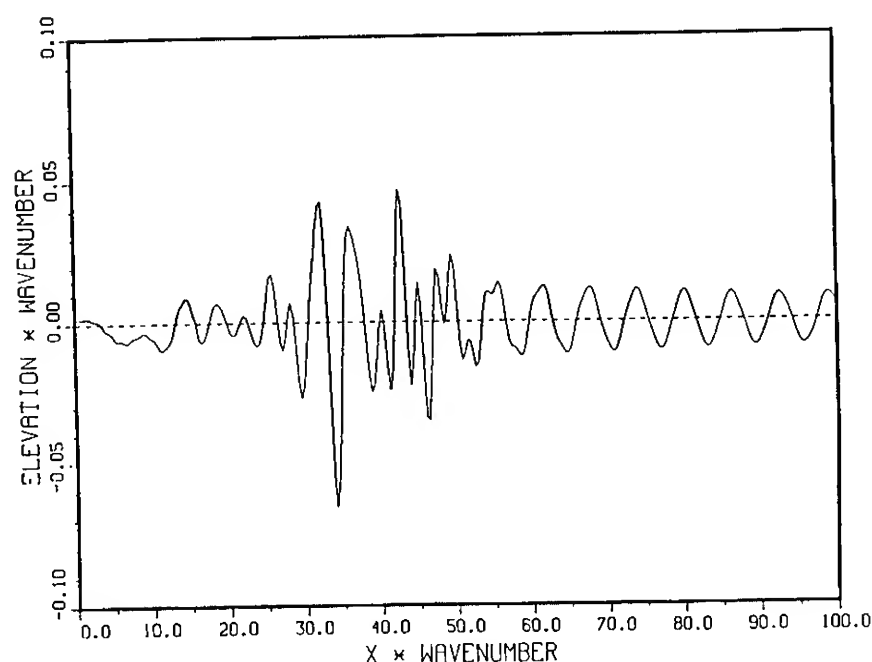


(e)—Due to Rankine singularities. (Transom panels, no wake panels)

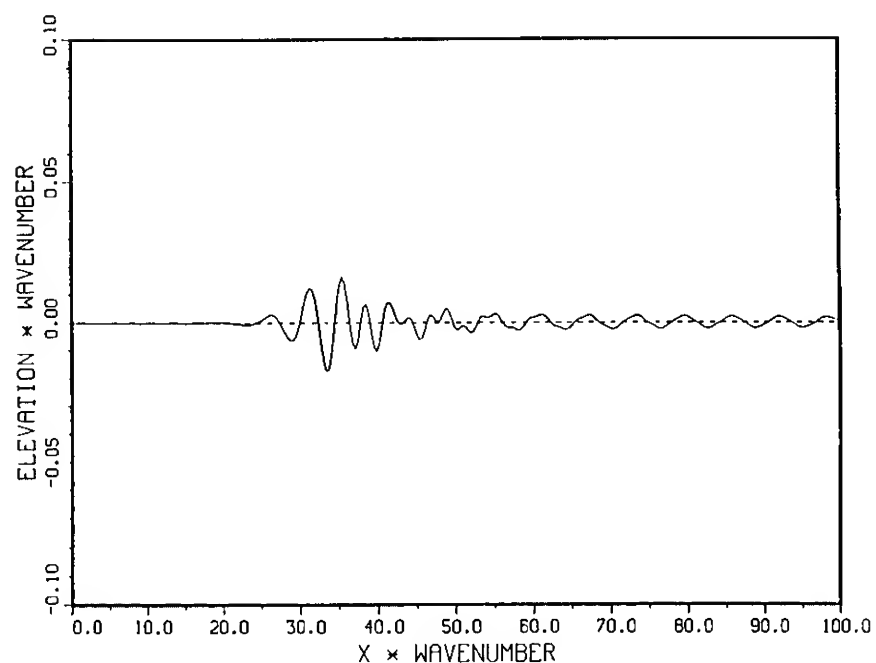
Fig 3—Non-dimensional near-field wave elevation contours for Model 5415 at  $F_n = 0.25$ .



(a)—Measured. (from Lindenmuth *et al.* 1990)



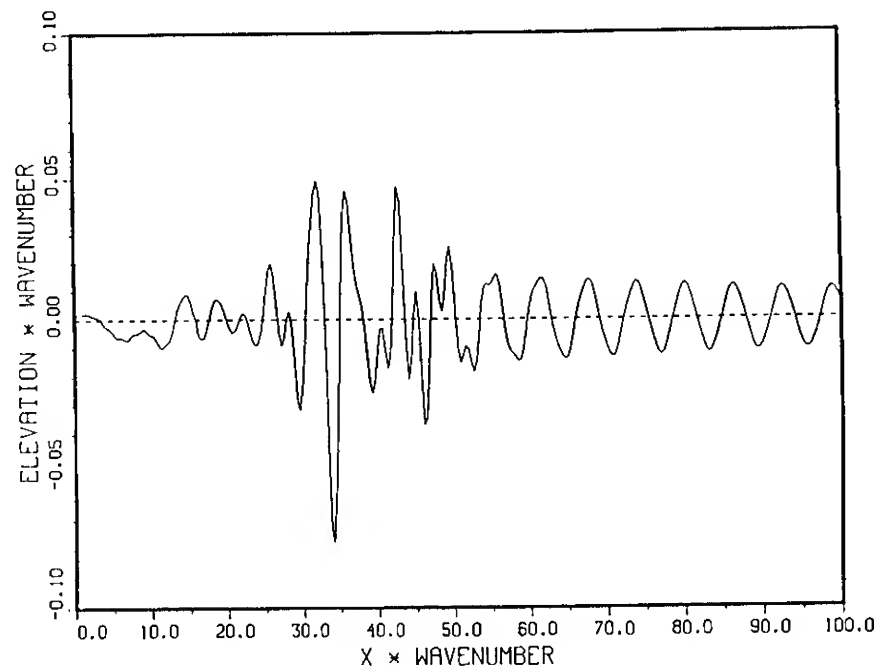
(b)—Due to Havelock sources alone.



(c)—Due to Havelock dipoles alone.

Fig 4—Wavecut at  $y/L = 0.324$  for Model 5415 at  $F_n = 0.25$ .

the data, the qualitative agreement between the measured and predicted far-field wave cuts is very good. The free-wave amplitude spectra are compared in Fig. 9.



(d)—Due to combination of Havelock sources & dipoles.

Fig 4 (Cont.)—Wavecut at  $y/L = 0.324$  for Model 5415 at  $F_n = 0.25$ .

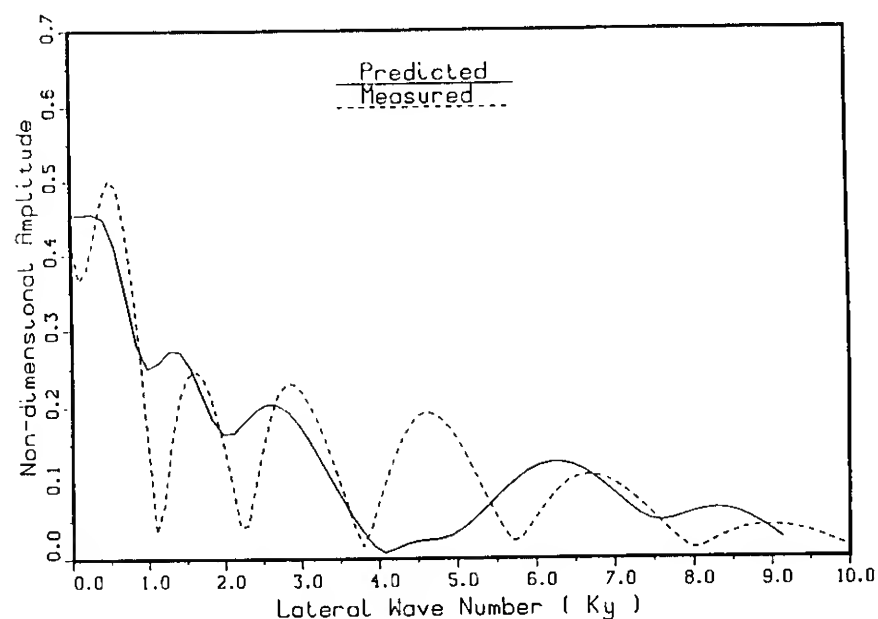


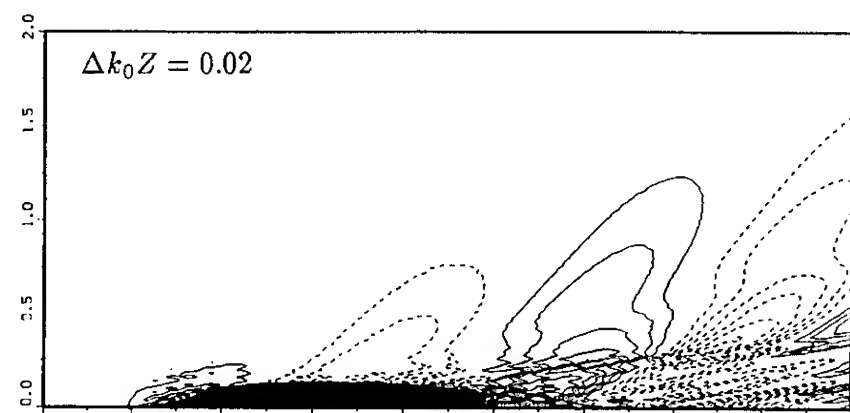
Fig 5—Comparison of measured (dashed line) and predicted (solid line) free-wave spectra for  $F_n = 0.25$ . (measured—from Lindenmuth *et al.* 1990)

#### Rankine Singularity Results

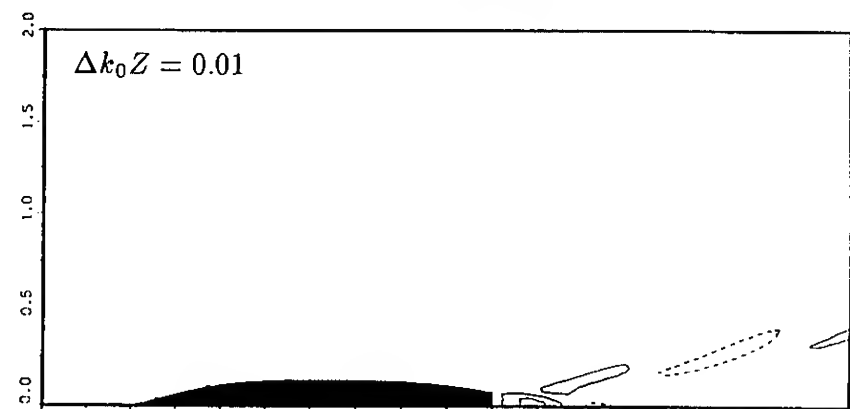
Since the flow configuration is assumed to be symmetric about the center plane of the ship, only half of the hull, free-surface, and wake are paneled. In either case the hull was paneled with 324 panels. The transom was paneled with 8 panels and the wake with 8 strips of panels. The free surface was paneled with 780 panels for the high Froude number case: 10 strips of 62 panels to the side and 8 strips of 20 panels aft of the stern. For the low Froude number case, more panels were deemed necessary because of the smaller wavelengths. Therefore the same expanse of the mean free-surface level was paneled in 10 strips of 80 panels to the side and with 8 strips of 23 panels aft of the stern. The paneling for the high Froude number case was allowed to be finer near the bow and stern whereas the paneling for the low Froude number case was nearly uniform in the longitudinal direction. Fig. 10 depicts the free-surface paneling for  $F_n = 0.4136$ ; the hull paneling is similar to that shown in Fig. 1.

Figs. 6d and 6e present contour plots of the wave elevation predicted using the Rankine source method for  $F_n = 0.4136$ . Fig. 6d corresponds to the case where wake panels

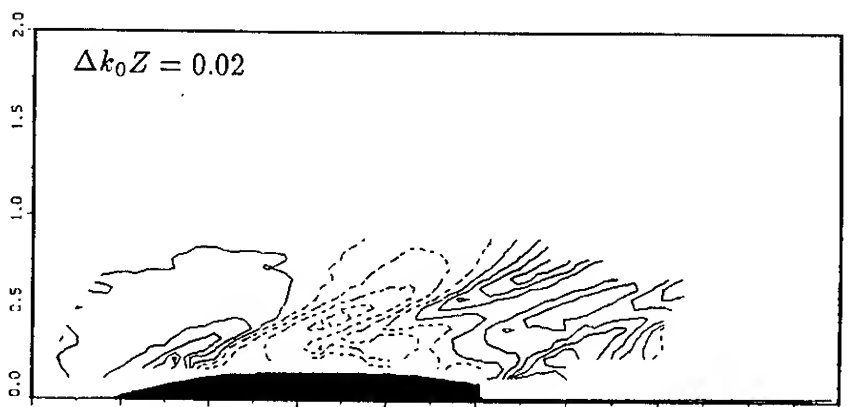




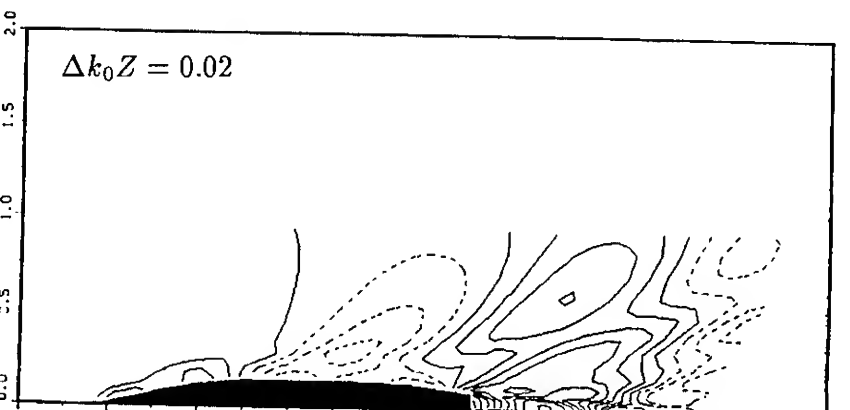
(a)—Due to combination of Havelock sources and dipoles.



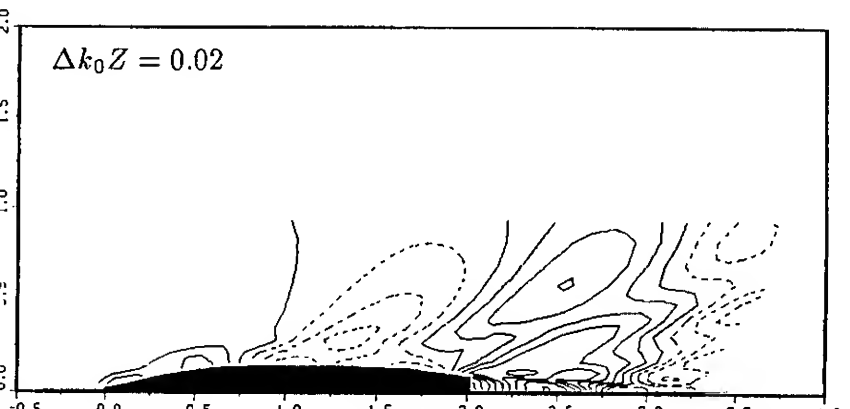
(b)—Due to Havelock dipoles alone.



(c)—Measured. (from Lindenmuth *et al.* 1990)



(d)—Due to Rankine singularities. (No transom panels, wake panels)



(e)—Due to Rankine singularities. (Transom panels, no wake panels)

Fig 6—Non-dimensional near-field wave elevation contours for Model 5415 at  $F_n = 0.4136$ .

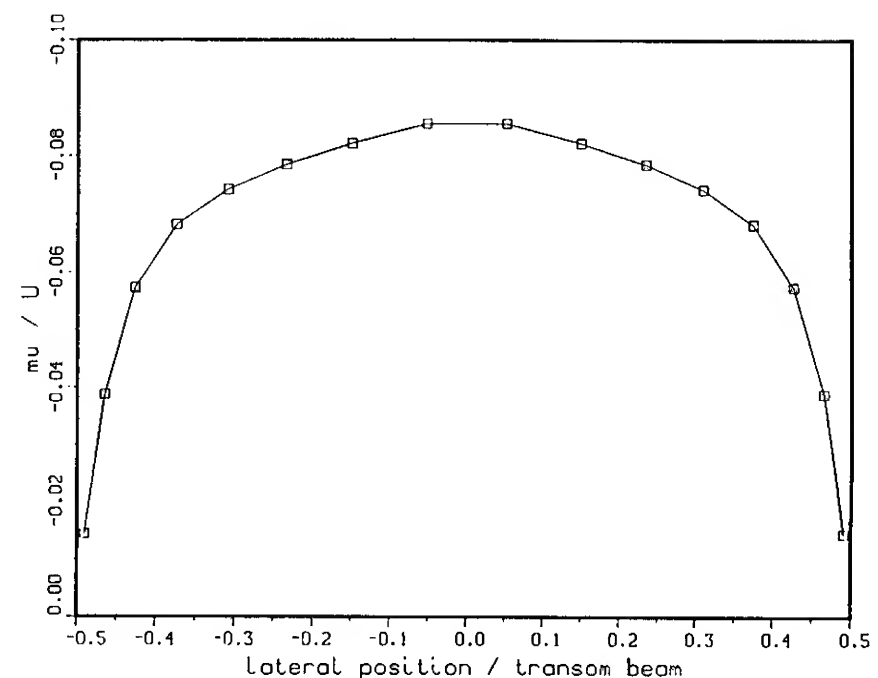
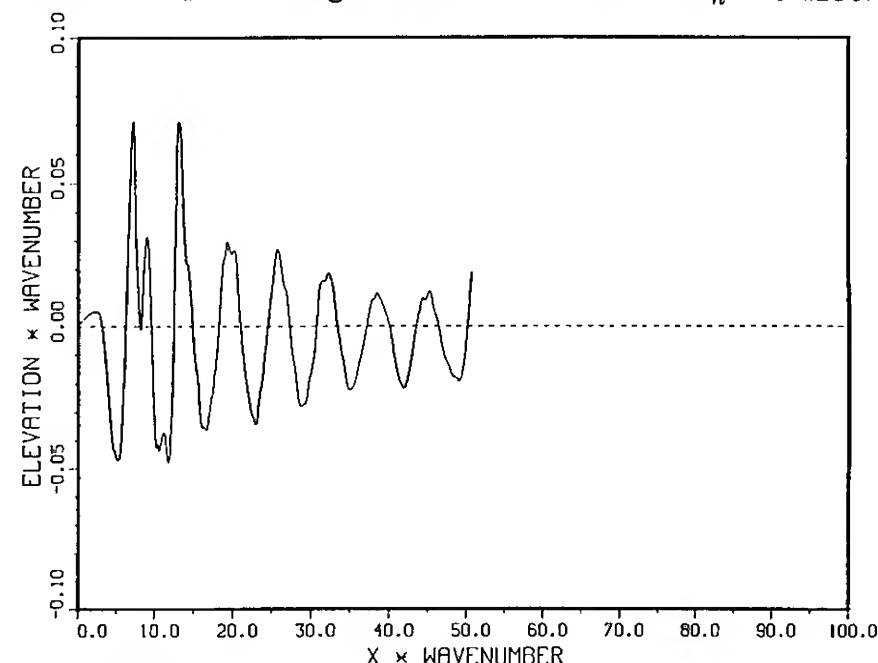
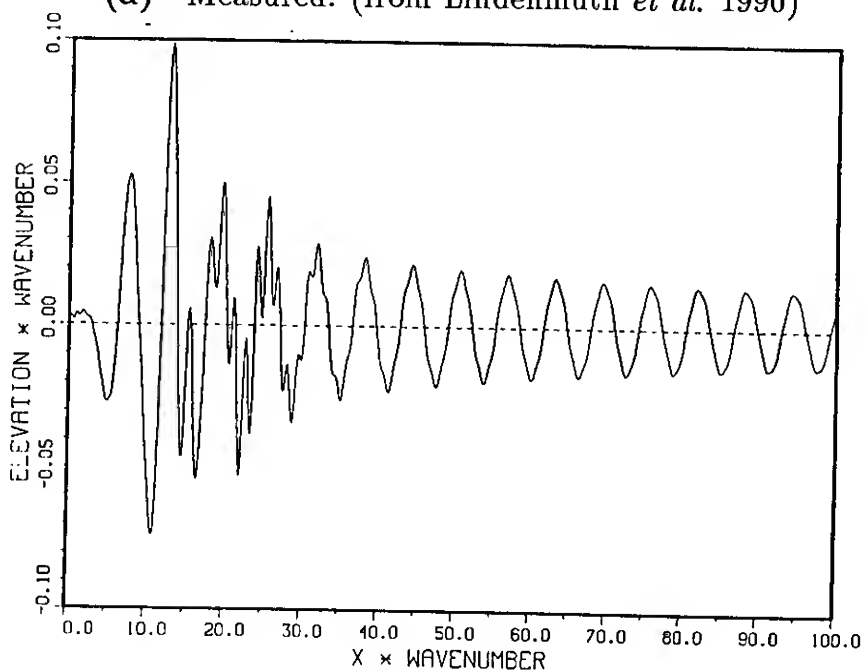


Fig 7—Dipole strengths across the wake for  $F_n = 0.4136$ .



(a)—Measured. (from Lindenmuth *et al.* 1990)



(b)—Predicted due to combination of sources and dipoles.

Fig 8—Wavecut at  $y/L = 0.324$  for Model 5415 at  $F_n = 0.4136$ .

are present and the panels on the transom are neglected. The normal dipole strengths of the wake panels were determined from the linearized Bernoulli equation. Fig. 6e corresponds to the case in which transom panels were included, but the normal dipole strengths in the wake were set to zero. There is very little difference between these two sets of results. A third attempt at finding a solution was made for which both the wake and the transom panels were

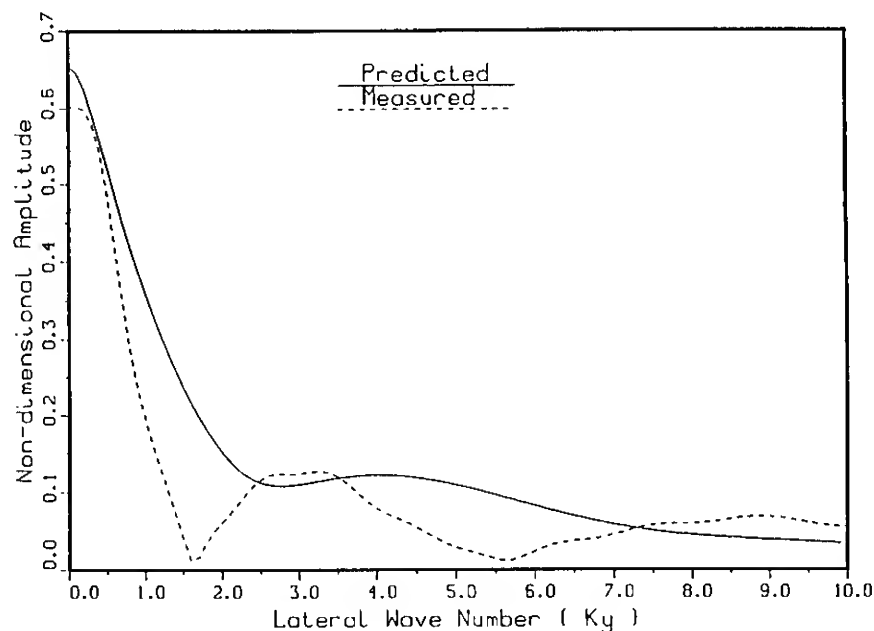


Fig 9—Comparison of measured (dashed line) and predicted (solid line) free-wave spectra for  $F_n = 0.4136$ . (measured—from Lindenmuth *et al.* 1990)

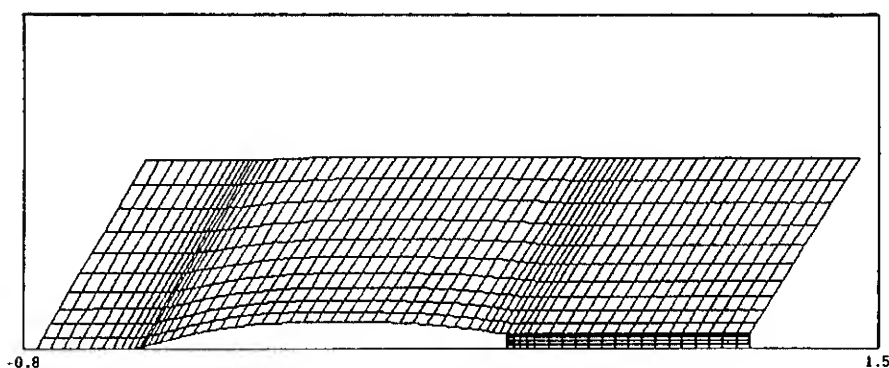
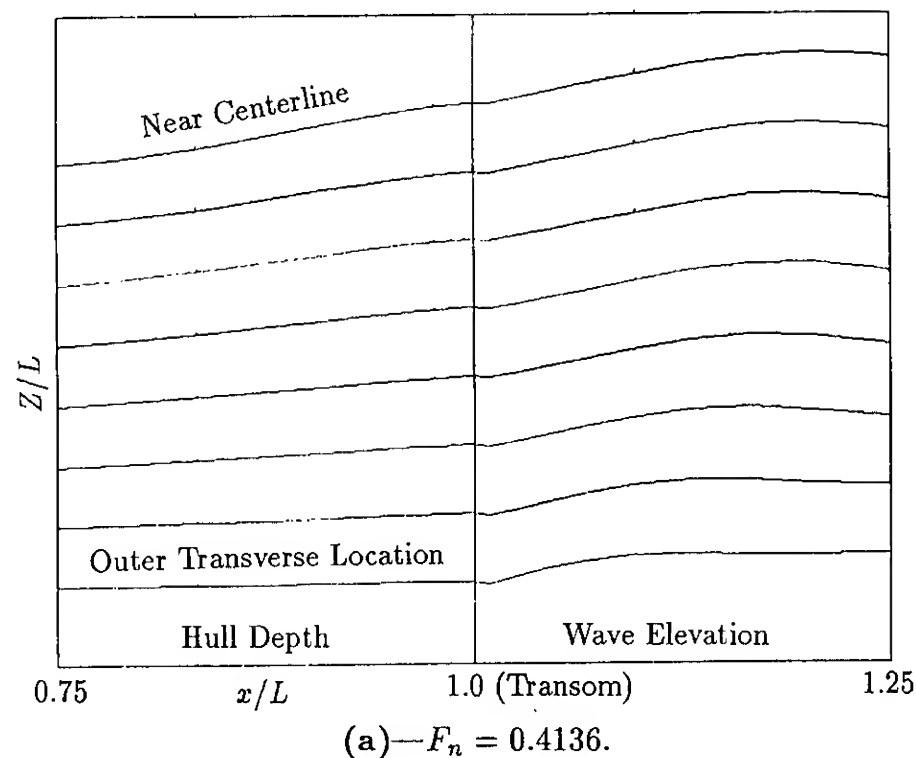


Fig 10—Free-surface panelization for  $F_n = 0.4136$ .

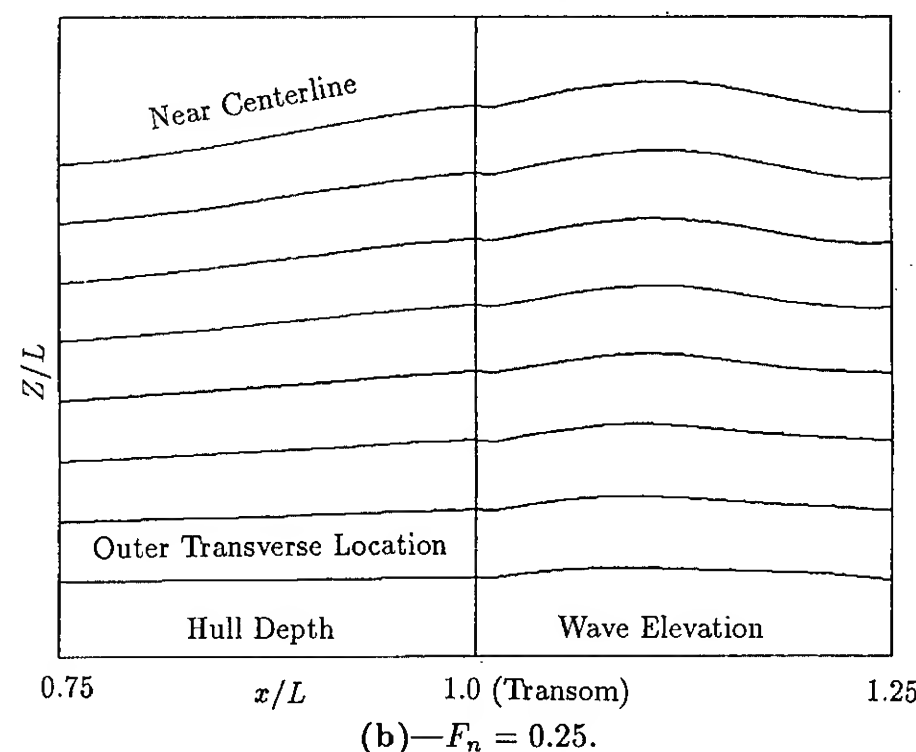
present. The third attempt failed because the resulting linear system of equations was too ill-conditioned to obtain a solution in 32-bit arithmetic. We are using direct solvers here because the iterative schemes we have been using do not converge for the problems being considered here.

Because of the presence of dipoles on the free surface, we are not able to separate the trailing vorticity due to the presence of the transom from that normally on the free surface. Therefore, there is no figure corresponding to Figs. 2c or 7.

Comparing the predicted wave elevations in Figs. 6d and 6e with the wave height obtained from experiments, Fig. 6c shows that the bow wave and the mid-ship trough are underpredicted. The discrepancy at the bow may be due to the paneling not being fine enough. In the stern area the predicted wave height does match the hull depth at the transom, as is indicated in Fig. 11a. This figure shows hull depth versus longitudinal position in the left half and predicted wave height versus longitudinal position in the right half. The hull depth and wave height are plotted for the eight longitudinal strips of panels on the main hull and the eight longitudinal strips of free-surface panels extending from the stern downstream. The wave height and the hull depth match at the stern. We may thus conclude that the pressure condition, Equation (8), is indeed satisfied. The predicted wave height rises from the transom depth to a peak of  $k_0 Z = 0.14$  before falling again. There are no experimental data in this area to determine the accuracy of these predictions. To the side and aft of the stern both the experimental data and the predictions show a wave height



(a)— $F_n = 0.4136$ .



(b)— $F_n = 0.25$ .

Fig 11—Hull depth and predicted wave height versus longitudinal position near the stern at eight transverse locations.

$k_0 Z = 0.08$ . A pressure integration over the portion of the hull beneath the mean free-surface level except for the transom was performed to obtain the wave resistance and induced drag as the force in the longitudinal direction,  $C'_W$ . The resulting value for  $C'_W$  was 0.00243, which is close to the  $C_{WP}$  of 0.0024.

Fig. 3e shows the predicted wave height contours for  $F_n = 0.25$ ; these results should be compared with the experimental measurements of Fig. 3d. The computations correspond to the case in which the transom has panels and there are no dipole panels in the wake. In this case the predicted results are not as good as at the higher Froude number because of the difficulty in resolving the finer details of the flow even with the finer free-surface paneling. In the stern area, Fig. 11b shows that the fluid leaves the hull tangentially just as it did for the higher Froude number case. This is a good indication that the atmospheric-pressure boundary condition on the hull at the transom is being satisfied. There are more data points from measurements for this case. The experimental data indicate a maximum wave height in the stern area of about  $k_0 Z = 0.10$

and a minimum wave height of about  $k_0 Z = -0.06$ . The predictions have a peak value of about  $k_0 Z = 0.14$  and a trough with depth of about  $k_0 Z = -0.10$ . In this case the wave resistance,  $C'_W$ , is predicted to be 0.00053, while the value from wave pattern analysis,  $C_{WP}$ , is 0.00037.

### CONCLUSIONS

The authors have developed two methods which are capable of modeling the flow about a ship with a transom stern, using vortex sheets to model the lift effects. Both methods implement a Kutta condition based on the fact that the pressure on the hull at the transom must be zero. This Kutta condition is used to determine the strength of trailing vorticity or the strengths of dipoles on the transom. The first method employs Havelock singularities which can be distributed over the hull surface and in the wake. The linearized free-surface boundary condition (obtained by free-stream linearization) is implicitly satisfied by the use of Havelock singularities, and therefore no singularities are required on the free surface. The second method employs Rankine singularities which can be distributed over the hull surface and in the wake. The technique requires that Rankine sources also be distributed over the free surface, and in this way a linearized free-surface boundary condition (linearization here is also about the uniform free stream) is satisfied. Computations based on the two methods have been compared with each other for flow about a high-speed transom stern ship (DTRC Model 5415). The results show encouraging agreement with one another and with experiments for the flow configurations considered.

The Havelock singularity method uses Havelock sources to satisfy the normal flow boundary conditions on the hull, and Havelock dipoles to satisfy tangential flow conditions. This leads to well-behaved solutions to the boundary-value problem. Imposing a zero pressure condition on the hull at the transom appears to have little effect upon the predicted far-field Kelvin wave. The effects in the near field are much more significant. The present results show a wave trough just behind the ship, and the wave elevation now matches the depth of the transom. There is a rapid rise to a wave peak immediately downstream of this trough. The waves generated by the Havelock dipole exhibit a distinct cusp line emanating from the corners of the transom. The predictions are consistent with observed wave fields generated by transom stern ships.

Perhaps more significant than the predicted wave field is the prediction of the vorticity shed by a transom stern ship. The flow is shown to accelerate toward the transom to satisfy the zero pressure condition; the result is an increase in the downward dynamic force on the hull. The shed vorticity is roughly equivalent to that shed by a hydrofoil with a span equal to the transom beam, operating as a negative angle of attack of approximately 5 degrees. The sense of the vorticity is such that there will be an upwelling flow on the centerline of the wake, and a diverging free surface current across the wake. Similar flow fields are frequently observed behind transom stern ships. To our knowledge, this is the first numerical result which offers an explanation for the source of this vorticity.

The Rankine singularity approach shows little difference in predicted wave resistance for two forms of problem formulation: first, when the transom is paneled and wake panels are absent and, secondly, when the wake is present and the transom is neglected. A third alternative corre-

sponding to paneling both the wake and the transom proved to be numerically ill conditioned. The ill conditioning very likely arises from the fact that the equations required to determine the strengths of the trailing vorticity essentially duplicate those set up to determine dipole strengths on the transom. At any rate, from the results we have seen, it seems best to neglect the wake panels altogether and to place dipole panels on the transom for this type of linearization.

When we attempted to formulate a Rankine singularity method based on a Dawson type double-body linearization, we had difficulties. To solve the double body problem, we extended the hull with a solid surface aft of the transom in order to obtain a double-body flow that did not turn a corner at the transom. We then attempted to apply a Dawson type free-surface condition on this extension of the transom which appeared not to work. Perhaps the solid hull extension should be replaced with a wake composed of a sheet of dipoles extending downstream from the perimeter of the transom to infinity.

We have found linear solutions to the problem of the steady flow about a transom stern hull form at realistic Froude numbers, using models which are capable of properly including the effects of shed vorticity. Obviously linear solutions are valid only forward of the region of energetic wave breaking which occurs in the wake downstream of the transom. However, this approach allows us to accurately calculate the flow field near the hull, including the free-surface wave elevations, the pressure on the hull, the shed vorticity and the stern-induced resistance. This transom stern analysis method should allow the design of transom sterns with lower resistance and lower wake signatures.

### ACKNOWLEDGMENTS

This work was supported by the Applied Hydromechanics Research program of the Applied Research Division of the Office of Naval Research, and administered by the David Taylor Research Center. The efforts of Suzanne Reed who edited the text and assembled the paper are greatly appreciated.

### REFERENCES

- Cheng, B. H. 1989. Computations of 3D Transom Stern Flows. *Proc. Fifth International Conference on Numerical Ship Hydrodynamics*, National Academy Press: Washington, DC, pp. 581-92.
- Lindenmuth, W. T., T. J. Ratcliffe and A. M. Reed. 1990. Comparative Accuracy of Numerical Kelvin Wake Code Predictions—"Wake-Off." DTRC Ship Hydromechanics Dept. R & D Report DTRC-90/010, 234+ix p.
- Sclavounos, P. D. and D. E. Nakos. 1988. Stability Analysis of Panel Methods for Free-Surface Flows with Forward Speed. *Proc. Seventeenth Symposium on Naval Hydrodynamics*, National Academy Press: Washington, DC, pp. 173-93.
- Newman, J. N. 1977. *Marine Hydrodynamics*. The MIT Press: Cambridge, MA, 402+xiii p.
- Tulin, M. P. and C. C. Hsu. 1986. Theory of High-Speed Displacement Ships with Transom Sterns. *J. Ship Res.*, 30(3):186-93.

## DISCUSSION

Hoyte Raven  
Maritime Research Institute Netherlands, The Netherlands

I have a few questions on this very interesting paper.

1. If no special treatment of the transom stern is applied, a free surface is predicted that intersects the transom at some point. Since one expects it to flow off the edge of the transom, one looks for modifications. But in a linearized method we generally do not care about the precise location of the intersection as its influence is of higher order. Is not, then, this method (though a very successful one) to incorporate in a linearized method something that in principle prohibits the linearization, viz. the presence of a sharp corner close to the free surface?
2. You point out the analogy with a Nutta condition. There is perhaps another analogy with free-streamline theory. This, however, predicts an infinite curvature of the separating streamline at the transom edge. Could such a behaviour fit into your method?
3. I was impressed by the fact that the Rankine singularity method with transom panels but without trailing wake panels was as good as that which incorporates the value. Does not this contradict the importance of trailing vorticity?

### AUTHORS' REPLY

1. This meeting is indeed an attempt to circumvent a difficulty in devising a linearization scheme. The objective is to find a basic flow from which the true flow deviates little. With a dipole sheet extending to downstream infinity from the edges of the transom, we are building into the basis flow the fact that fluid moves smoothly past the transom. The perturbation from the basis flow potential should then be small.
2. The method of free streamlines might be used to find a hull extension about which a double-body flow can be calculated. Flows corresponding to nonzero Froude numbers could be calculated based on linearizing the free-surface boundary conditions on the mean free-surface level outside the hull with its extension and on the surface of the extension.
3. We do not understand this seeming contradiction, but it may be that we can carry and are in fact carrying vorticity on the free surface. This matter needs to be studied more.

## DISCUSSION

Kazu-hiro Mori  
Hiroshima University, Japan

Although the linearized pressure condition (8) is consistent in your framework, it may not always provide non-jump in pressure. How was the resulted pressure there? Is the pressure condition satisfied?

### AUTHORS' REPLY

For the Havelock singularity method, the dipole strength in the wake is determined in such a way that the linearized zero-pressure condition (8) is satisfied. For the Rankine singularity method, the differencing scheme immediately aft of the stern is set up so that this condition is satisfied. Consequently, for either method, the pressure is zero at the intersection of the free surface with the hull. For the Rankine singularity method, this can be seen in Figs. 11a and 11b where the wave elevation aft of the stern has been calculated based on the linearized zero-pressure condition (8). The pressure based on the fully nonlinear Bernoulli equation has not been calculated.

## DISCUSSION

Dimitris Nakos  
Massachusetts Institute of Technology, USA

The approach followed in the paper appears to be able to "tune" linear and/or quasilinear numerical solutions of the steady ship wave problem behind a transom stern, so that they are in better correlation with reality. My question pertains to one of the most critical, and potentially most troublesome, assumptions behind the technique described in the paper...that is the positioning of the line across which separation occurs. In the case investigated by the authors, the loading condition of the vessel is such that part of the transom stern is submerged even in calm water, and the sharp edge of the transom appears as the safest alternative for "separation line." In many cases, however, the transom-like flow may be anticipated. Do the authors have any suggestions about the positioning of the separation line in such cases?

### AUTHORS' REPLY

The cases in question are nonlinear flows which we are not ready to handle. As a first approximation, one would not concern himself with the hull configuration above the level of the undisturbed free surface. When sinkage and trim is accounted for in subsequent calculations, it might be appropriate to also take into consideration this transom-like flow.

# **A Boundary Integral Approach in Primitive Variables for Free Surface Flows**

C. Casciola (I.N.S.E.A.N., Italy)  
R. Piva (Universita di Roma, Italy)

## **ABSTRACT**

The boundary integral formulation, very efficient for free surface potential flows, has been considered in the present paper for its possible extension to rotational flows either inviscid or viscous. We analyze first a general formulation for unsteady Navier Stokes equations in primitive variables, which reduces to a representation for the Euler equations in the limiting case of Reynolds infinity.

A first simplified model for rotational flows, obtained by decoupling kinematics and dynamics, reduces the integral equations to a known kinematical form whose mathematical and numerical properties have been studied. The dynamics equations to complete the model are obtained for the free surface and the wake. A simple and efficient scheme for the study of the non linear evolution of the wave system and its interaction with the body wake is presented. A steady state version for the calculation of the wave resistance is also reported. A second model has been proposed for the simulation of rotational separated regions, by coupling the integral equations in velocity with an integral equation for the vorticity at the body boundary. The same procedure may be extended to include the diffusion of the vorticity in the flowfield. The vortex shedding from a cylindrical body in unsteady motion is discussed, as a first application of the model.

## **INTRODUCTION**

One of the most successful approaches for the analysis of free surface flow problems is given by the boundary integral equation method. In particular, if the governing equations are linear, as it is for the potential flow approximation, this approach reduces by one the space dimensions of the computational domain. Moreover, it provides a description of the boundary conditions (which are usually non linear and unsteady) more accurate than any other compu-

tational model. As a matter of fact, the boundary integral equation method, together with some specific techniques introduced to linearize and discretize the kinematic and the dynamic boundary conditions at the free surface, leads to an extremely efficient computational methodology for the evaluation of the wave resistance and of the overall potential flow field, e.g. see [1].

However more realistic flows always contain regions of vorticity different from zero, which after being generated at the body wall, usually remains confined in a narrow region close to the body itself and its wake, provided the Reynolds number is sufficiently high. The relevance of the rotational flow may be enhanced by large separated regions about bluff bodies, by the interaction of the wake with the free surface or with other solid bodies (e.g. the propeller), or by a larger effect of the diffusion for moderate values of the Reynolds number.

In all these conditions, where either confined or large vortical regions appear, the inability to introduce the velocity potential prevents from using the very efficient model previously mentioned. In the former case (i.e. confined vortical regions) the overall picture of the flow field does not change much with respect to the potential one, so that the classical singular perturbation approach, that is a boundary layer-external solution interaction model, may give sufficiently accurate results. In the latter case (i.e. large vortical regions) any kind of external flow field correction becomes inefficient and the direct field discretization of the Navier Stokes equations (or a simplified version of them, e.g. parabolized) seems to be the only available approach for practical applications [2]. Anyhow in both cases we have to deal with more complicated techniques, which require a larger computational effort. In particular, extending the effect of viscosity to the entire flow field, we may even spoil from a numerical point of view the wave pattern simulation at the free surface, with respect to the much



simpler potential flow model.

It is reasonable at this point to try to answer the following questions: in which condition is it possible and convenient the extension of the boundary integral method to rotational flows? How large is the loss of efficiency due to the presence of non linear terms in the equations? In fact, these terms give rise to field integrals and cancelling one of the main advantages of the boundary integral formulation for potential flow (that is the only presence of boundary unknowns).

Purpose of this paper is to give some preliminary answers to these questions by illustrating a general boundary integral formulation for viscous flows in primitive variables (velocity components and pressure) which reduces to a representation for inviscid flows in the limiting case of Reynolds infinity. The theoretical analysis, developed by the authors in previous papers [3, 4, 5] and briefly summarized for the reader's convenience in Section 2, is successively applied to generate a set of computational models which are increasingly complicated as long as they become suitable to deal with flows presenting more relevant vortical regions.

A first group of models is obtained by decoupling the kinematics from the dynamics in the integral representation which holds in the limit of zero diffusion. By doing so, we recover the purely kinematical integral representation for the velocity vector, known as Poincaré formula, valid also for rotational flows [6]. The dynamical part of the equations, still in differential form, gives rise to auxiliary conditions for the free surface and for the wake. The generation of vorticity and its release from the body, in the classical case of sharp trailing edge, is assured by the enforcement of a "Kutta-type" condition, which accounts for the local viscous phenomena, as explained in details in Section 3. A further kinematical equation is required to account for the unknown position of the field discontinuity given by the free surface or by the wake.

The above assumptions provide a very simple and efficient model, able to analyze rotational unsteady flows and well equipped to treat the non linear free surface behaviour. Several computational results obtained by this method [3] are reported in Section 3. Also a steady state linearized version of the model which resembles, in terms of velocity, a classical potential flow model [1] largely used for the wave resistance calculation, is reported in Section 3, in order to show the versatility of the present approach and its capability to reproduce the most interesting positive features of the existing methods.

A further step in the direction of a complete simulation of the rotational flow, is attempted by including the diffusion phenomena, neglected in the previous group of models, as a first order effect acting over the inviscid solution. In fact, without introducing the

boundary layer equations, the viscous effects are recovered by the boundary integral formulation for the vorticity transport equation, given in Section 2. Assuming, as in the first order boundary layer theory, that the pressure does not change normally to the body wall, we combine its value from the inviscid solution is combined in order to obtain an integral equation in the wall vorticity. This procedure, described in Section 4, allows to detect, within the limits of the approximation, the separation point along the wall, hence the position and the intensity of the issuing vortex layers for the simulation of the rotational wake region.

Finally the boundary integral equations and the computational procedure for a complete model are briefly outlined in Section 5. By a complete model we mean a model in which dynamics and kinematics are fully coupled and the same viscous fundamental solutions together with the related integral representations are considered in the entire flow field. More specifically the concept of interacting external and internal solutions, which is typical of perturbation techniques, is not adopted here. The close relationship between this model and the previous ones may be of great help to overcome the numerical difficulties mainly due to the kernel of the integral equations, which becomes highly singular for increasing values of the Reynolds numbers. The numerical results concerning this model are still in progress and are going to be presented in a further paper.

## A GENERAL FORMULATION OF FLOW PROBLEMS IN TERMS OF BOUNDARY INTEGRAL EQUATIONS

The integral formulations of the Navier Stokes equations have been mainly used for studying the mathematical aspects of viscous flows. A detailed description of the method is given in the book of Ladyzhenskaya [8], where the integral representation for the steady state problem is also presented. More recently integral formulations have received new interest for the numerical simulation of viscous flows. In particular the authors investigated the flow about streamlined bodies when no massive separation occurs [9].

The analysis of the boundary integral equation given in full details in a previous paper [10], is briefly summarized here for completeness. Besides, an integral representation for the vorticity is proposed for its relevance to the solution procedure in the case of rotational separated flows.

### a. The velocity representation for viscous flows

We consider the case of the undisturbed fluid in uniform translation with constant velocity  $U_\infty$  with respect to the body frame of reference. The absolute



velocity is expressed as  $\mathbf{u} = \mathbf{u}_\infty + \mathbf{u}$ , where  $\mathbf{u}$  is a perturbation velocity. We also introduce a perturbation stagnation pressure  $P$

$$P = p + \frac{1}{2}\rho U^2 - p_\infty - \frac{1}{2}\rho U_\infty^2$$

so that at infinity  $P = 0$ . Introducing these quantities the governing equations become

$$\nabla \cdot \mathbf{u} = 0 \quad (1)$$

$$\mu \nabla^2 \mathbf{u} - \nabla P - \rho \frac{\partial \mathbf{u}}{\partial t} = \chi \quad (2)$$

where the right-hand side term  $\chi$  contains the nonlinear terms and the gravity force

$$\chi = -\rho \mathbf{u} \times \boldsymbol{\zeta} + \rho \mathbf{g}$$

Notice that with the above expression of the equations, the non linear terms, which give rise to a field integral, have to be accounted for only in the regions where the vorticity is not negligible.

The integral representation of the velocity as a solution of the system (1, 2) is given by [4]

$$\begin{aligned} u_k(x_*, t_*) = & \int_0^{t_*} \int_{\partial\Omega} (u_j t_j^{(k)} - t_j u_j^{(k)}) dS dt \\ & - \int_0^{t_*} \int_{\partial\Omega} \rho v_\sigma u_j u_j^{(k)} dS dt \\ & + \int_0^{t_*} \int_\Omega \chi_j u_j^{(k)} dV dt - \int_\Omega \rho u_j u_j^{(k)} dV dt \Big|_{t=0} \end{aligned} \quad (3)$$

where the stress vector  $\mathbf{t}$  is modified to include the dynamic pressure. As shown by (3) the field velocity is given in terms of surface as well as volume integrals. The first surface integral gives the effect of the boundary values of the velocity and the modified traction. The second surface integral gives the effect of the momentum flux due to the boundary motion. In free surface flows, this is a non linear contribution, because the boundary normal velocity component  $v_\sigma$  is strictly dependent on the fluid velocity field. This source of non linearity is localized on the free surface as in the case of potential flow. The first volume integral, related to the term  $\chi$ , accounts for the body force and for the vorticity effects in the fluid. This source of non linearity is within the field equations, and in particular is connected to the rotational flow region, which may be more or less confined, depending on the flow field. Finally the second volume integral gives the effect of the initial conditions. The fundamental solutions  $u_j^{(k)}$  and  $t_j^{(k)}$  are given by [4]

$$u_j^{(k)} = \delta_{jk} F - \frac{\partial^2 E}{\partial x_j \partial x_k} \quad (4)$$

$$p^{(k)} = -\frac{\partial G}{\partial x_k} \delta(t_* - t) \quad (5)$$

with

$$t_j^{(k)} = -p^{(k)} n_j + \mu \left( \frac{\partial u_j^{(k)}}{\partial x_i} + \frac{\partial u_i^{(k)}}{\partial x_j} \right) n_i$$

where for the two-dimensional case

$$\begin{aligned} G &= \frac{1}{2\pi} \ln r \\ F &= -\frac{1}{\rho} H(t_* - t) \frac{e^{-r^2/4\nu(t_* - t)}}{4\pi\nu(t_* - t)} \\ E &= -\frac{1}{4\pi\rho} E_1 \left( \frac{r^2}{4\nu(t_* - t)} \right) - G \\ \nabla^2 E &= F \end{aligned} \quad (6)$$

and  $E_1$  is the exponential integral.

#### b. The inviscid flow as limiting case

We consider now the limiting case of the previous theoretical formulation as the Reynolds number goes to infinity, i.e. as  $\nu$  goes to zero. In fact the parameter  $\nu t$  could be more appropriate as we can see from the expressions of the two functions  $F$  and  $E$  appearing in the fundamental solutions. We can easily see that their distributional limit is given by

$$\begin{aligned} F &= -\frac{1}{\rho} H(t_* - t) \delta(x_* - x) \\ E &= -\frac{1}{\rho} H(t_* - t) G(x_* - x) \end{aligned} \quad (7)$$

and the equation  $\nabla^2 E = F$  reduces to

$$\nabla^2 G = \delta(x_* - x)$$

Therefore the expressions of the fundamental solution become [5]

$$u_j^{(k)} = -\frac{H}{\rho} (t_* - t) \left( \delta_{ij} \frac{\partial^2 G}{\partial x_i \partial x_j} - \frac{\partial^2 G}{\partial x_j \partial x_k} \right) \quad (8)$$

$$t_j^{(k)} = \frac{\partial G}{\partial x_k} \delta(t_* - t) n_j \quad (9)$$

Combining them with (3) we obtain the representation valid for rotational inviscid flows, which in vector notation reads

$$\begin{aligned}
\mathbf{u}(x_*, t_*) = & \int_{\partial\Omega} (\mathbf{u} \cdot \mathbf{n}) \nabla G dS \\
& + \int_0^{t_*} \int_{\partial\Omega} \frac{P}{\rho} [(\mathbf{n} \cdot \nabla) \nabla G - n \nabla^2 G] dS dt \\
& - \int_0^{t_*} \int_{\partial\Omega} v_\sigma [(\mathbf{u} \cdot \nabla) \nabla G - \mathbf{u} \nabla^2 G] dS dt \\
& + \int_0^{t_*} \int_{\Omega} (\nabla_* \times \nabla_* G \times \chi) dV dt \\
& - \int_{\Omega} (\nabla_* \times \nabla_* G \times \mathbf{u}_0) dV
\end{aligned} \quad (10)$$

where the vector identity

$$(\mathbf{b} \cdot \nabla) \nabla G - \mathbf{b} \nabla^2 G = \nabla_* \times \nabla_* G \times \mathbf{b} \quad (11)$$

has been used in the expressions of the volume integrals, and  $\mathbf{u}_0$  is the initial velocity.

In order to keep the vector notation, when studying a two dimensional flow, we consider a cylindrical body in a three-dimensional space. In particular we assume a local set of orthonormal coordinates defined at each point of the boundary by the unit tangent vector  $\boldsymbol{\tau}$  (anti-clockwise), the unit normal vector  $\mathbf{n}$  (external to the fluid domain) in the cross section and  $\mathbf{k} = \boldsymbol{\tau} \times \mathbf{n}$ .

The integral representation (10) corresponds to the differential model for inviscid flows given by the Euler equations.

### c. Analysis of the boundary integral equation

The integral representation (3) for viscous flow gives, for  $x^*$  going to the boundary, an integral equation which is a constraint between the values assumed by the velocity and the traction at the boundary. In the limit a factor  $c$  ( $= \frac{1}{2}$  for smooth boundaries) appears at the left-hand side to account for the jump properties of the double layer kernel  $t_j^{(k)}$ . If either the velocity or the traction is assigned as boundary condition, we obtain an integral equation of first kind for the unknown traction or an integral equation of second kind for the unknown velocity respectively. Usually for free surface flows about submerged bodies we have a mixed-type boundary condition, that is the traction is assigned at the free surface and the velocity at the body wall. This exactly resembles the potential flow formulation that for the same physical case requires Neumann and Dirichlet boundary conditions for the body and the free surface, respectively.

At increasing values of the Reynolds number the kernel of the integral equation tends to become singular, in any of the described cases, as shown by the expressions (4) and (5) of the fundamental solution  $u_j^{(k)}$  and  $t_j^{(k)}$ . Actually, the functions  $F$  and  $E$  appearing in these expressions, become sharper and sharper as the kinematical viscosity goes to zero. The main difficulty in solving directly the integral equations for large Reynolds number flows is essentially related to the crucial behaviour of these functions rather than

to the presence of the volume integrals.

A deeper insight on the properties of these equations for large Reynolds numbers, is provided by the analysis of the limiting case of zero diffusion. It appears from (8) that the kernel  $u_j^{(k)}$  has a hypersingular behaviour when the collocation point approaches the boundary. It follows an interesting comparison with the viscous case, showing the computational difficulties to be expected asymptotically for increasing values of the Reynolds number.

In particular  $u_j^{(k)}$  is composed of two terms which are both singular. The first one is the well known hypersingular term which appears in the double layer representation of the velocity potential for the Neumann problem [11]. The second one is a Dirac delta function on the boundary itself. By combining the two terms together with a few vectorial identities and the Stokes theorem for a closed surface [11,12], the second surface integral may be re-expressed in the form

$$\int_{\partial\Omega} (\nabla \tilde{P} \times \mathbf{n}) \times \nabla G dS \quad (12)$$

which corresponds to a vortex layer of density  $\gamma = (\nabla \tilde{P} \times \mathbf{n})$  with  $\tilde{P} = \int_0^{t_*} \frac{P}{\rho} dt$ . Moreover the kernel does not show now the same singularity as in the original form.

By similar manipulation through known vectorial identities the third surface integral may be re-set in the form

$$\begin{aligned}
& \nabla_* \times \int_0^{t_*} \int_{\partial\Omega} 2v_\sigma (\nabla \times \mathbf{u}) G dS dt \\
& - \nabla_* \times \int_0^{t_*} \int_{\partial\Omega} v_\sigma (\mathbf{u} \times \nabla G) dS dt
\end{aligned} \quad (13)$$

which is not presenting particularly attractive features with respect to the original form. The volume integral containing the non linear convective term, through an integration by parts may be written as

$$\int_0^{t_*} \int_{\Omega} \nabla_* \times \nabla_* G \times \chi dV dt = \quad (14)$$

$$\nabla_* \times \int_{\Omega} G \times (\nabla \times \tilde{\chi}) dV - \nabla_* \times \int_{\partial\Omega} G \mathbf{n} \times \tilde{\chi} dS$$

with  $\tilde{\chi} = \int_0^{t_*} \chi dt$ .

By the same procedure, the volume integral containing the initial velocity term gives

$$\begin{aligned}
& - \int_{\Omega} (\nabla_* \times \nabla_* G \times \mathbf{u}_0) dV = \\
& - \nabla_* \times \int_{\Omega} G \zeta_0 dV + \nabla_* \times \int_{\partial\Omega} G \mathbf{n} \times \mathbf{u}_0 dS
\end{aligned} \quad (15)$$

Notice that in this form the initial term integral is not extended to the entire flow field, but it gives a

contribution only in the rotational region and along the boundary.

It is worth to notice that the representation (10) of the velocity vector, for  $x^*$  approaching the boundary, gives only one integral equation, when considering its normal projection. This fact is strictly related to the lower order of the corresponding differential equation for the inviscid case. Hence, only one integral constraint is expected among the two scalar quantities  $(\mathbf{u} \cdot \mathbf{n})$  and  $P$ , as the collocation point approaches the boundary. Namely, we obtain a Fredholm integral equation of second kind if  $P$  is assigned and a first kind Cauchy-type integral equation if the boundary condition prescribes the normal velocity component.

Also in this case, for the problem of the free surface flow about a submerged body we have a mixed-type boundary condition and the resulting system of discretized equations has to be carefully analyzed in order to determine the mathematical properties of the corresponding integral operator [3].

#### d. The integral representation for vorticity

In some of the models we are going to discuss in the next sections, we consider also the integral representation for vorticity in regions close to the body. Let us write the vorticity transport equation in the form

$$\nu \nabla^2 \zeta - \frac{\partial \zeta}{\partial t} = \nabla \times \chi \quad (16)$$

where the nonlinear terms are taken as a source at the right-hand side of the equation. The integral representation for the solution of (14) is given, in the case of a fixed fluid domain, by

$$\begin{aligned} \zeta(x_*, t_*) &= \int_0^{t_*} \int_{\partial\Omega} \nu \left( \zeta \frac{\partial F}{\partial n} - F \frac{\partial \zeta}{\partial n} \right) dS dt \\ &+ \int_0^{t_*} \int_{\Omega} (\nabla \times \chi) F dV dt - \int_{\Omega} \zeta_0 F dV \end{aligned} \quad (17)$$

where  $F$  is the fundamental solution of the diffusion equation given by (6) for the two-dimensional case. We notice that this representation is not independent from the representation (3) for velocity. Actually it can be obtained by performing the curl of (3) and by accounting also for the expression of the stress vector  $\mathbf{t}$  in terms of its normal and tangential components [15]

$$\mathbf{t} = -p\mathbf{n} + \mu \zeta \times \mathbf{n} \quad (18)$$

which is valid for a translating rigid body.

For the collocation point  $x^*$  approaching the boundary we obtain an integral equation which is a constraint between the values of  $\zeta$  and  $\frac{\partial \zeta}{\partial n}$  at the bound-

ary.

No simple boundary conditions are available for  $\zeta$  or  $\frac{\partial \zeta}{\partial n}$  and the latter is usually approximated by using the intensity of the vortex layer at the body boundary and by assuming a reasonable model for the diffusion of vorticity [13, 14]. For  $\frac{\partial \zeta}{\partial n}$  assigned as known boundary condition, a second kind integral equation for  $\zeta$  is obtained. The kernel  $\frac{\partial F}{\partial n}$  still presents some computational difficulties for large Reynolds numbers.

### THE DECOUPLING OF KINEMATICS AND DYNAMICS: A MODEL FOR ROTATIONAL INVISCID FLOWS

Let us consider the representation of velocity (10) combined with the new expressions (12) and (13) of the surface integrals, for the analysis of inviscid flow fields. The representation contains in its terms both the kinematical and the dynamical aspect of the physical model, as clearly shown by the two unknowns, namely the normal velocity and the stagnation pressure.

A coupled integral formulation like (10) allows for a straightforward enforcement of the boundary condition in terms of the boundary velocity and pressure. In addition their discretization does not imply any further difficulty as in the numerical models based on differential equations. Therefore a coupled integral formulation would be ideal for the simulation of free surface flow fields, where a particular attention has to be paid for a simple and accurate application of the boundary conditions. However, the presence of some computational difficulties (mainly related to the calculation of the surface integral (13) and the volume integral (14)) suggested to still follow the classical path of decoupling the kinematics from the dynamics, as successfully experienced by all the potential flow models.

#### a. The Poincaré formula for kinematics

A purely kinematical integral representation is obtained by eliminating the dynamical variables through a back substitution of the Euler equation and of the vorticity transport equation (in their differential form) into the integral representation (10) for inviscid flows.

For the sake of simplicity, we apply first the above procedure to a fluid domain fixed in time, so that the integrals which account for the free surface motion are dropped out. We will see later that their inclusion, is not going to modify the final result, although it complicates significantly the overall procedure. After introducing the new integral expressions (12), (14), (15) and combining with the vorticity transport equation for inviscid flow integrated in time

$$\zeta - \zeta_0 = -\nabla \times \tilde{\chi} \quad (19)$$

the integral representation (10) becomes

$$\begin{aligned} \mathbf{u}(x_*, t_*) &= \int_{\partial\Omega} (\nabla \tilde{P} \times \mathbf{n}) \times \nabla G dS \\ &+ \int_{\partial\Omega} (\mathbf{u} \cdot \mathbf{n}) \nabla G dS - \nabla_* \times \int_{\Omega} G \zeta dV \\ &+ \nabla_* \times \int_{\partial\Omega} G \mathbf{n} \times (\mathbf{u}_0 - \tilde{\chi}) dS \end{aligned} \quad (20)$$

Combining now the Euler equation integrated in time

$$(\mathbf{u} - \mathbf{u}_0) + \chi = -\nabla \tilde{P} \quad (21)$$

we obtain a kinematical representation for the velocity vector

$$\begin{aligned} \mathbf{u}(x_*, t_*) &= - \int_{\partial\Omega} (\mathbf{u} \times \mathbf{n}) \times \nabla G dS + \\ &+ \int_{\partial\Omega} (\mathbf{u} \cdot \mathbf{n}) \nabla G dS - \nabla_* \times \int_{\Omega} G \zeta dV \end{aligned} \quad (22)$$

where on the right-hand side both  $\mathbf{u}$  and  $\zeta$ , as function of time, are given for  $t = t_*$ . The velocity representation (22) is the well known Poincaré formula usually written as [6]

$$\begin{aligned} \mathbf{u}(x_*) &= \nabla_* \left[ \int_{\Omega} (\nabla \cdot \mathbf{u}) G dV - \int_{\partial\Omega} (\mathbf{u} \cdot \mathbf{n}) G dS \right] \\ &- \nabla_* \times \left[ \int_{\Omega} (\nabla \times \mathbf{u}) G dV + \int_{\partial\Omega} (\mathbf{u} \times \mathbf{n}) G dS \right] \end{aligned} \quad (23)$$

which is a velocity integral representation satisfying only the kinematical equations

$$\nabla \times \mathbf{u} = \zeta \quad \text{and} \quad \nabla \cdot \mathbf{u} = Q$$

In the present case  $Q$  is identically equal to zero.

Let us underline the fact that the splitting between kinematics and dynamics, inherent to the classical velocity potential formulation, is here recovered by recombining the Euler and the vorticity transport equations with the original coupled formulation. In order to verify the equivalence with the Poincaré formula also in the case of a moving boundary, as is the case for the free surface, it is more convenient to operate in a reverse way, that is to differentiate in time equation (22), accounting for the variation in time of part of the boundary  $\partial\Omega$ . A brief note on these calculations is reported in Appendix A.

Finally we deduce the boundary integral equations which follow from (22) by performing the tangential and the normal projections for the collocation point  $x^*$  approaching the boundary (assumed smooth)

$$\begin{aligned} \frac{1}{2} u_r^* + \int_{\partial\Omega} u_r \frac{\partial G}{\partial n^*} dS &= \\ &- \frac{\partial}{\partial \tau^*} \int_{\partial\Omega} u_n G dS + I_{\zeta r} \end{aligned} \quad (24)$$

$$\begin{aligned} \frac{1}{2} u_n^* + \int_{\partial\Omega} u_n \frac{\partial G}{\partial n^*} dS &= \\ &+ \frac{\partial}{\partial \tau^*} \int_{\partial\Omega} u_r G dS + I_{\zeta n} \end{aligned} \quad (25)$$

where  $I_{\zeta r}$  and  $I_{\zeta n}$  give the contribution of the volume integrals in the two projections, respectively.

Equation (24) is a second kind Fredholm equation for the unknown  $u_r$  or a first kind integral equation with a Cauchy type integral (the kernel  $\frac{\partial G}{\partial \tau^*}$  is singular) for the unknown  $u_n$ . The opposite is valid for equation (25). The two integral equations are completely equivalent in the sense that if you solve the first one, the solution will satisfy also the second one. The choice may depend on the assigned boundary condition and on the preference about the numerical technique to be used.

#### b. The dynamics of the free surface

For a solid wall the value of  $u_n$  is assigned and  $u_r$  is the unknown. Instead, for a free boundary  $u_n$  is the unknown, and the dynamical part of the model should provide the boundary value  $u_r$ . The procedure parallels exactly the one used for potential flows where  $\frac{\partial \phi}{\partial n}$  is the unknown and the values of the potential  $\phi$  are evaluated by means of the Bernoulli equation. In the case of rotational flows, the Euler equations must be used to relate the tangential velocity component to the pressure distribution assigned as boundary condition. Notice that the coupled representation (10) contains in it the pressure and no additional dynamic condition would be required.

We write the Euler equation for a point of the free surface, labeled by the Lagrangian variable  $\xi$ . The tangent projection of the Euler equation on the free surface at point  $\xi$  gives

$$\frac{D\mathbf{u}}{Dt} \cdot \boldsymbol{\tau} = -\frac{1}{\rho} \frac{\partial p}{\partial \tau} - g \frac{\partial \eta}{\partial \tau} \quad (26)$$

where  $\eta$  has the usual meaning of free surface elevation and  $\frac{\partial p}{\partial \tau}$  is equal to zero for the boundary condition of assigned constant pressure. The unit tangent vector  $\boldsymbol{\tau}$  at point  $\xi$  changes in time for the boundary motion. Therefore

$$\frac{D\mathbf{u}}{Dt} \cdot \boldsymbol{\tau} = \frac{D(\mathbf{u} \cdot \boldsymbol{\tau})}{Dt} - \mathbf{u} \frac{D\boldsymbol{\tau}}{Dt}$$

and, for  $\boldsymbol{\tau} \cdot \frac{D\boldsymbol{\tau}}{Dt}$  identically equal to zero, we finally obtain

$$\frac{Du_r}{Dt} = u_n n \cdot \frac{D\tau}{Dt} - g \frac{\partial \eta}{\partial \tau} \quad (27)$$

The non linear evolution equation (27) for the tangential velocity component gives at each time the required boundary value  $u_r$  for each of the two equations (24) and (25). We finally need to complete the formulation by means of a Lagrangian description in time of the fluid interface. Denoting by  $x_f(\xi, t)$  the position of the geometrical point, labeled by  $\xi$ , of the free surface the new interface geometry is determined by solving the initial value problem

$$\frac{dx_f}{dt} = u_f \quad x_f(\xi, 0) = x_0(\xi) \quad \xi \in D_\xi \quad (28)$$

where  $D_\xi$  is the set of values of the Lagrangian parameter  $\xi$  and  $u_f$  is assumed to coincide with the local fluid velocity  $u$ .

### c. The dynamics of the wake

The kinematical representation (22) expresses the field velocity as function of its boundary value and of the field vorticity both at the present time  $t_*$ . Hence, we have to determine the distribution of vorticity by adding a dynamic equation. For instance, the vorticity transport equation for incompressible inviscid flows in 2-D provides the very simple result of constant vorticity along the motion. We consider in this section the physical case of very large Reynolds number flows about streamlined bodies with sharp trailing edge, which do not experience any boundary layer separation [16]. We may simulate these conditions by the zero diffusion model with a vortical wake downstream of the body. These wakes (or free vortex sheets) are given by surfaces of discontinuity characterized by the fact that both pressure and normal fluid velocity are continuous across them, while the tangential components of velocity may admit a jump, that is a concentrated vorticity

$$\gamma k = [u] \times n \equiv [u_r] k \quad (29)$$

where  $[ ]$  is the symbol for the jump across the discontinuity surface. The volume integral  $I_\gamma$  appearing in (22), if the field vorticity is only concentrated on the wake, may be expressed as

$$I_\gamma = -\nabla_* \times \int_{\sigma_w} [u_r] G dS \quad (30)$$

where  $\sigma_w$  is the wake surface.

Similarly to what has been done for the free surface, we introduce a dynamic equation to study the evolution of  $[u_r]$ , which is given by [17].

$$\frac{D_w}{Dt} (J[u_r]) = 0 \quad (31)$$

where  $w$  is the velocity of a point  $\xi$  of the wake,  $\frac{D_w}{Dt}$  is the material derivative along the wake motion and  $J = \left| \frac{\partial x_w(\xi, t)}{\partial \xi} \right|$  is the Jacobian of the transformation  $x_w = \hat{x}_w(\xi, t)$  which gives at each time the position of the point  $\xi$  belonging to the wake. Equation (31) is equivalent to state that

$$\int_{\xi_1}^{\xi_2} J[u_r] d\xi = \text{const.} \quad (32)$$

along the motion, which has the physical meaning of conservation of concentrated vorticity for a portion ( $\xi_1 < \xi < \xi_2$ ) of the wake.

The initial value  $\gamma_{TE}$  of the vortex layer intensity at the trailing edge is taken to be the limit

$$\gamma_{TE} = \lim_{\substack{x_+ \rightarrow TE \\ x_- \rightarrow TE}} [u_r(x_+) + u_r(x_-)] \quad (33)$$

where  $x_\pm$  are points on the upper and lower side of the body and  $u_r(x_\pm)$  the corresponding tangential components of the velocity. In a sudden start the value of  $\gamma_{TE}$  decreases in time asymptotically to zero when the body reaches the steady state. The equation (31) plus the initial condition (33) is called a Kutta-type condition, because at steady state  $t$  satisfies the classical Kutta condition of zero vorticity at the trailing edge.

To describe the evolution of the geometrical configuration of the wake we adopt a Lagrangian model completely analogous to (28)

$$\frac{dx_w}{dt} = w \quad (28)$$

where  $w = (u_+ + u_-) / 2$ .

### d. Comparison with potential flow models

We describe now the solution procedure for the model consisting of the integral equations (24) or (25) plus the dynamics contribution for the free surface (eq. 27) and for the wake (eqs. (31) or (32)) to which the evolution equation (28) has to be added. A complete theoretical analysis for the solution of the two equations (24) and (25) has been recently performed [10] for the case of flow past bodies, that is for assigned normal velocity component on the boundary. The same would be for assigned tangential component all over the boundary. The contemporary presence of free surface and body complicates the analysis, because we have a mixed-type boundary condition, that is  $u_n$  assigned at the body wall and  $u_r$  at the free surface. Let us recall first the main findings of the previous analysis for the case of uniform boundary condition.

We consider here only the second kind Fredholm integral equation (i.e. the tangential component (24) for the unknown  $u_r$  or the normal component (25)



for the unknown  $u_n$ ). This formulation exactly corresponds to a Neumann internal problem for potential flow with a simple layer representation. A complete equivalence with regard to existence and uniqueness of the solution and compatibility conditions, holds. Namely, let us consider for instance equation (24), the compatibility condition for the right-hand side

$$\int_{\partial\Omega} \left[ -\frac{\partial}{\partial\tau^*} \int_{\partial\Omega} u_n G dS + I_{\zeta\tau} \right] dS^* = 0 \quad (34)$$

is identically satisfied, giving the existence of the solution, for any assigned normal velocity at the boundary and for any distribution of vorticity in the domain  $\Omega$  (notice that  $I_{\zeta}$  gives the velocity induced by the field vorticity whose circulation is identically zero being the vorticity only external to  $\partial\Omega$ ). Moreover, it is known from the potential theory that the solution is not unique and it may be expressed in the form

$$u_{\tau} = u_{\tau}^p + \alpha u_{\tau}^0 \quad (35)$$

where  $u_{\tau}^p$  is a particular solution and  $u_{\tau}^0$  is the eigen-solution, that satisfies the homogeneous equation for the Neumann problem. The solution for the homogeneous problem is given by the simple layer density for the related Robin potential, for which the property  $\int_{\partial\Omega} u_0 dS \neq 0$  holds.

By imposing the further condition of conservation of total vorticity, we find the circulation  $\Gamma$  around the body, as far as we know by (32) the vorticity issued at each time on the wake. Finally from the value of  $\Gamma$  we can find the constant  $\alpha$  appearing in (35) and determine uniquely the solution  $u_{\tau}$ .

As we said before, we do not need to consider here the singular integral equations of first kind which may require more sophisticated numerical techniques [12]. In fact, a mixed approach is used, that is we assume the normal component (25) to hold on the free surface and the tangential component (24) on the other boundaries. Although a deeper theoretical analysis would be required to study the mathematical properties of the corresponding integral operator, we experience a nice behaviour of the discretized equation from a numerical point of view.

The above illustrated solution procedure is simple enough to be comparable, for both theoretical and numerical aspects, to the classical one for potential flow. By the present procedure we may not only reproduce the results obtained by potential flow models, but also obtain an immediate extension to rotational inviscid flows, with vorticity confined in wakes or blubs. Moreover with regard to the free surface, the present model provides a very efficient unsteady technique to study the non linear evolution of the waves.

Few sample numerical results are reported. The

transient wave system due to the motion of a submerged circular cylinder, previously discussed in [3] is here reported as a test case for the accuracy of the model. The numerical results shown in Fig. 1, compare favourably with other classical results [18,19].

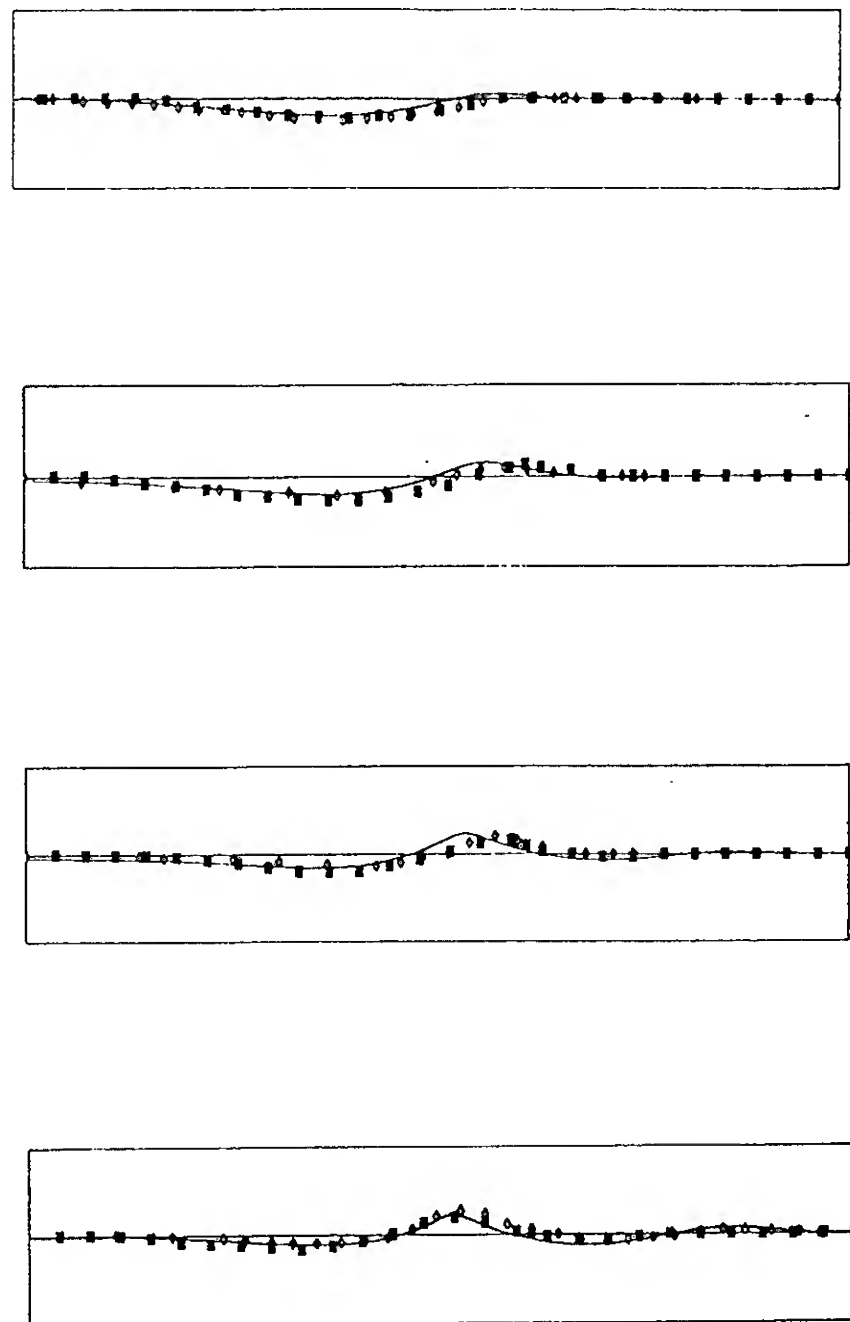


Figure 1: Free surface configurations after a sudden start of a submerged cylinder. Submergence  $h = 2$ ,  $Fr = .566$ ,  $D = 1$ ,  $t = 4.5, 6, 7.5, 9$ . — present solution,  $\diamond$  Ref. 18,  $\blacksquare$  Ref. 19

A more interesting case is given by the unsteady motion of a slightly submerged lifting airfoil. After a sudden start of the airfoil the vortex layer shedding from the sharp trailing edge, interacts with the free surface giving rise to a wave pattern which feels the influence of the wake vorticity. The airfoil at three different values of the angle of attack is shown in Fig. 2.



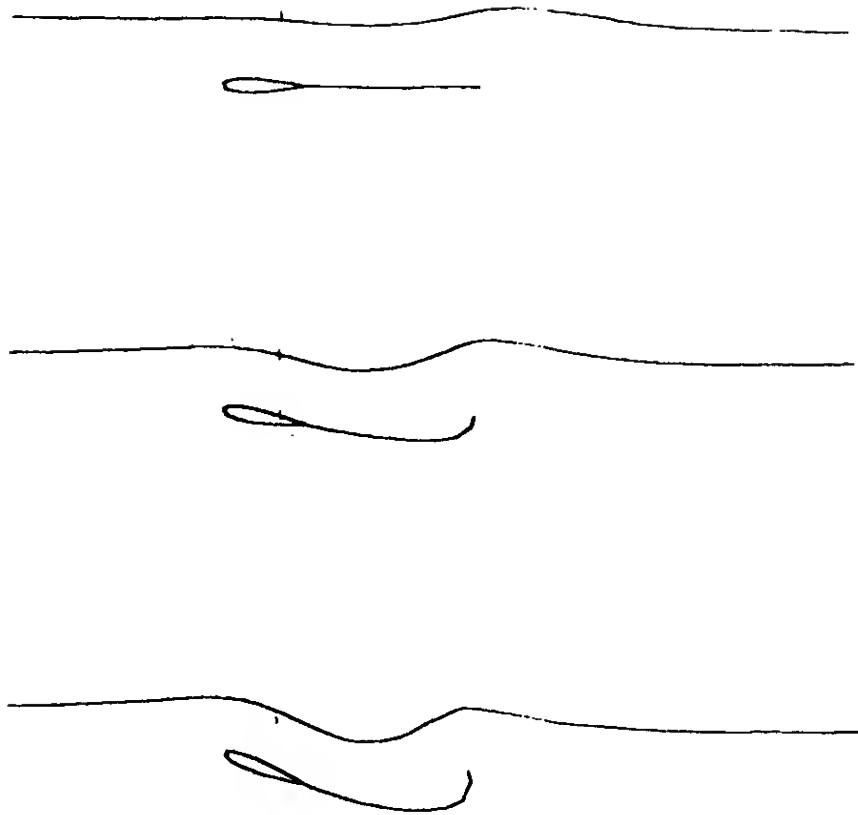


Figure 2: Free surface and wake configurations after a sudden start of a lifting airfoil. Submergence  $h = .75 * \text{chord}$ ,  $Fr = 1$  (with respect to the chord). Angle of attack  $0^\circ, 10^\circ, 20^\circ$ .  $t = 3$

#### e. A steady linearized free surface condition

To complete the comparison with potential flow models, we briefly discuss now the application to steady linearized boundary conditions at the free surface, frequently used for an efficient calculation of the wave resistance. Equation (27) which describes the dynamics of the free surface, for steady state and a zeroth order linearization reduces to

$$U_\infty \frac{\partial u_r}{\partial \tau} = -g \frac{\partial \eta}{\partial \tau} \quad (36)$$

considering that the unit tangent vector  $\tau$  in this approximation is constantly aligned with the undisturbed velocity  $U_\infty$ . The fluid interface motion given by the Lagrangian description (28) is here conveniently expressed through its linearized Eulerian form

$$U_\infty \frac{\partial \eta}{\partial \tau} = u_n \quad (37)$$

Combining (36) and (37) implies the well known Neumann-Kelvin condition

$$u_n = -\frac{U_\infty^2}{g} \frac{\partial u_r}{\partial \tau} \quad (38)$$

usually written in terms of the velocity potential. Introducing (38) into the right hand side integral of the equation (24) and integrating by parts we obtain

$$\frac{U_\infty^2}{g} \frac{\partial}{\partial \tau^*} \int_{\partial \Omega_f} \frac{\partial u_r}{\partial \tau} G dS = -\frac{U_\infty^2}{g} \frac{\partial}{\partial \tau^*} \int_{\partial \Omega_f} u_r \frac{\partial G}{\partial \tau} dS \quad (39)$$

with  $\partial \Omega = \partial \Omega_b + \partial \Omega_f$  where  $b$  and  $f$  stay for body and free surface respectively. Combining with (39), the integral equation (24) becomes

$$\frac{1}{2} u_r^* + \int_{\partial \Omega} u_r \frac{\partial G}{\partial n^*} dS + \frac{U_\infty^2}{g} \frac{\partial}{\partial \tau^*} \int_{\partial \Omega_f} u_r \frac{\partial G}{\partial \tau} dS = - \int_{\partial \Omega_b} u_n \frac{\partial G}{\partial \tau^*} dS + I_{\zeta, \tau} \quad (40)$$

This integral equation gives, for assigned normal velocity at the body boundary  $\partial \Omega_b$ , the tangential velocity component on the entire boundary  $\partial \Omega$ . Once  $u_r$  is known, we easily obtain the free surface elevation  $\eta$  by integrating equation (36). The tangential derivative of the free surface integral in (40) is discretized by the upwind finite difference scheme used in the potential flow model proposed by Dowson [1].

The steady linearized version of the present model exactly reproduces the numerical results obtained by the above mentioned potential model. For instance, the wave pattern generated by a submerged lifting airfoil is shown in Fig. 3, for a zero contribution of the term  $I_{\zeta, \tau}$ . However, the present technique may include some rotational effects relevant to steady state conditions.

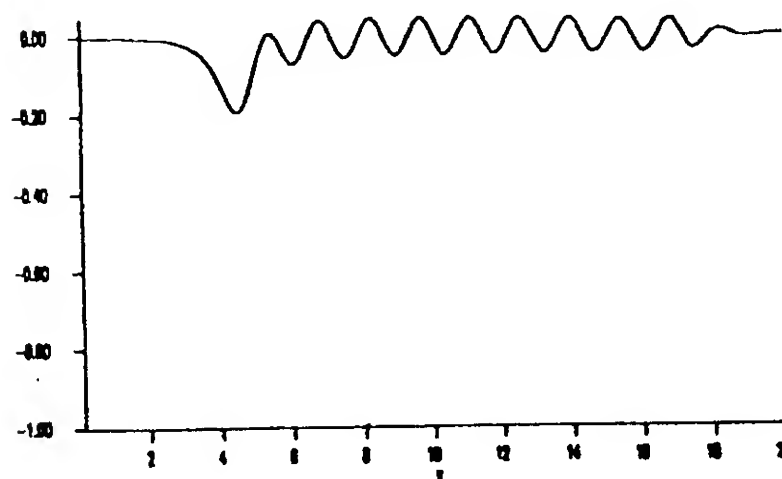


Figure 3: Wave elevation in a steady problem for a NACA0012 airfoil. Submergence  $h = 1 * \text{chord}$ ,  $Fr = .5$  (with respect to chord). Angle of attack  $10^\circ$ . Trailing edge position  $x = 4.5, y = -1$

# A VISCOUS-INVISCID INTERACTION MODEL FOR SEPARATED FLOWS

The model described in the previous section is appropriate for the simulation of inviscid rotational flows with either a field vorticity whose initial position and intensity are assigned or a vortex sheet issuing from a sharp trailing edge whose intensity is determined by a Kutta-type condition. Therefore, the vorticity generated at the body wall may be accounted for, always in the limit of Reynolds number going to infinity, but it is restricted to flows where no separation occurs. Actually, the diffusion phenomena were neglected everywhere in that model if we exclude, in a sense, the unsteady generation of the wake by the Kutta-type condition which provides the limiting behaviour of a viscous fluid. A further step in the direction of a complete simulation of rotational flows (i.e. with separated regions) is attempted by including an *internal* viscous solution which is going to modify the *external* inviscid solution. In fact, we do not introduce the boundary layer approximation, that would be inappropriate to the present aim, but we try to recover the viscosity effects in a more consistent way through a boundary integral formulation for the full vorticity transport equation, which is valid in principle in the entire flow field. However, as in the first order boundary layer theory, we introduce several drastic assumptions to simplify as much as possible the numerical solution of the boundary integral equation resulting from the representation (17) for  $\chi$ , approaching the boundary (assumed smooth)

$$\begin{aligned} \frac{1}{2}\zeta(x_*, t_*) &= \int_0^{t_*} \int_{\partial\Omega} \nu \left( \zeta \frac{\partial F}{\partial n} - F \frac{\partial \zeta}{\partial n} \right) dS dt \\ &+ \int_0^{t_*} \int_{\Omega} (\nabla \times \chi) F dV dt - \int_{\Omega} \zeta_0 F dV \end{aligned} \quad (41)$$

This is a Fredholm integral equation of the second kind if  $\frac{\partial \zeta}{\partial n}$  is assigned as boundary condition. From the differential Navier Stokes equation on the body boundary we obtain the general local identity which gives in the two-dimensional case, i.e. for  $\zeta = \zeta \mathbf{k}$ ,

$$\nabla p \times \mathbf{n} = -\mu(\nabla \times \zeta) \times \mathbf{n} = -\nu \frac{\partial \zeta}{\partial n} \mathbf{k} \quad (42)$$

In the framework of a first order theory we assume that the pressure doesn't change normally to the body wall within the viscous layer close to the body itself, and its value is given by the inviscid rotational model of Section 3. As a matter of fact, from that model we find  $u_r$ , and the pressure follows from the Euler equation at the wall

$$\frac{\partial p}{\partial r} = -\frac{\partial}{\partial r} \left( \frac{u_r^2}{2} \right) - \frac{\partial u_r}{\partial t} \quad (43)$$

It follows the boundary condition (42) for the normal derivative of vorticity. The two volume integrals of the non linear and the initial terms, appearing in eq. (41), are confined to very narrow layers (in the limit of  $Re \rightarrow \infty$  that we consider here) where the vorticity is different from zero. Consistently with this approximation, the fundamental solution  $F$  is taken constant across these layers. Hence, we may compute the integral across the layer of the non linear term

$$\nabla \times \chi = \nabla \times (u_r \zeta \mathbf{n} - u_n \zeta \tau),$$

$$\begin{aligned} \int (\nabla \times \chi) dn &= \mathbf{k} \int \left[ \frac{\partial}{\partial r} (u_r \zeta) \right. \\ &\quad \left. - \frac{\partial}{\partial n} (u_n \zeta) \right] dn \end{aligned}$$

In particular, for a layer close to the body boundary, whose thickness is  $\delta$ , taking into account that  $u_n \equiv 0$  at the body,  $\zeta \equiv 0$  at the outer edge of the layer and that within the layer  $\zeta = -\frac{\partial u_r}{\partial n}$  we have:

$$\int_0^\delta (\nabla \times \chi) dn = - \frac{\partial u_r^2/2}{\partial r} \Big|_\delta \mathbf{k} \quad (44)$$

Instead, for a wake of thickness  $2\delta$  with a jump  $[u_r] \equiv \gamma$  and a tangential velocity defined as  $w_r = \frac{u_r^+ + u_r^-}{2}$

$$\int_{-\delta}^\delta (\nabla \times \chi) dn = - \mathbf{k} \frac{\partial}{\partial r} \frac{u_r^2}{2} \Big|_{-\delta}^\delta = - \mathbf{k} \frac{\partial}{\partial r} (w_r \gamma) \quad (45)$$

By the same reasoning, we obtain respectively

$$\int_0^\delta \zeta_0 dn = -u_{r0}|_\delta \quad (46)$$

$$\int_{-\delta}^\delta \zeta_0 dn = -\gamma_0 \quad (47)$$

By combining the approximate values of the volume integrals (44), (45), (46), (47), with the integral equation (41), we have a relatively simple model to determine the value of the wall vorticity.

As a further crucial feature of the model, we place the separation point at the wall position where  $\zeta$  is changing its sign. A vortex layer is issuing from this separation point and its intensity is determined by a Kutta-type condition completely analogous to the one introduced in Section 3 for the wake at the sharp trailing edge of a streamlined body [20].

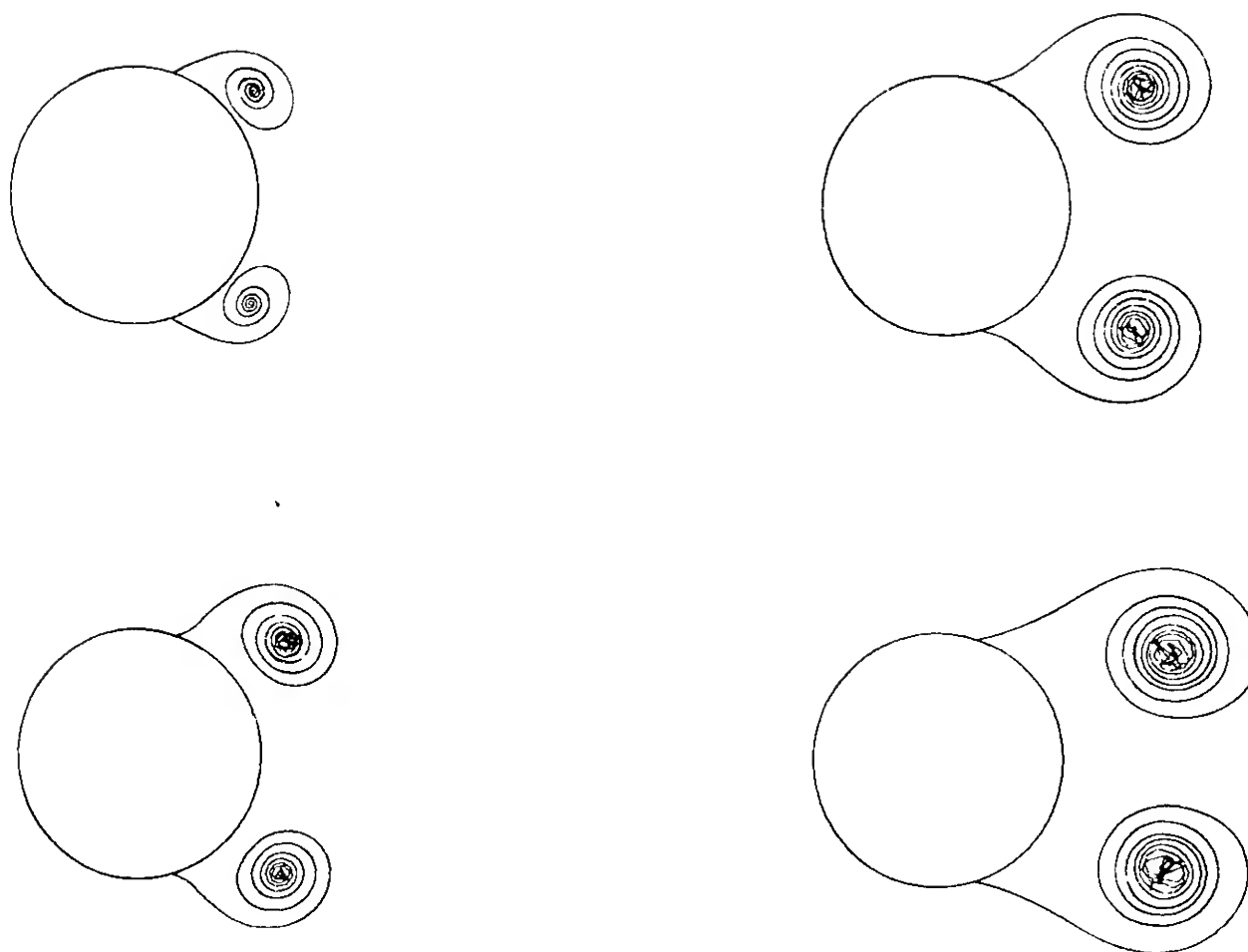


Figure 4: Wake evolution for flow past a cylinder. Separation point at fixed positions  $\alpha = \pm 108^\circ$ .  $t = 1, 2, 3, 4$

The numerical procedure alternates the solution of equations (24,25) for the *external* inviscid flow, with the solution of eq. (41) for the *internal* viscous layer. They are connected through the condition (42) which in a first order approximation relates the external pressure gradients with the generation of vorticity at the wall [21]. The simplifying hypothesis for the calculation of the volume integrals may be released to obtain better approximations.

The model has been applied to a cylindrical body. We didn't consider here the presence of the free surface to focus our attention on the generation scheme for the separated regions. In fact the model of generation still requires a deeper understanding and it seems reasonable to select a test case for which a large experience is available. Several computational models, using a Kutta-type condition for the calculation

of separated flows in the framework of vortex methods have been recently presented [23,24,25].

First we discuss some numerical results with two fixed separation points in symmetric position on the cylinder boundary ( $\alpha = \pm 108^\circ$  from the front stagnation point). A symmetric rear separated region, like the one shown in Fig. 4, is obtained if no perturbation is introduced in the solution procedure. By retarding of one time step the lower side of the cylinder with respect to the other, we introduce a large oscillation in the two vortex layers. By advancing in time, they assume a configuration (see the sequence in Fig. 5) which resembles the initial displacement of the vortices in the classical Karman street. For a more stable behaviour of the vortex layer we adopted a de-singularization technique [22] in order to eliminate the singularity of the kernel for  $\mathbf{x} \rightarrow \mathbf{x}^*$ .

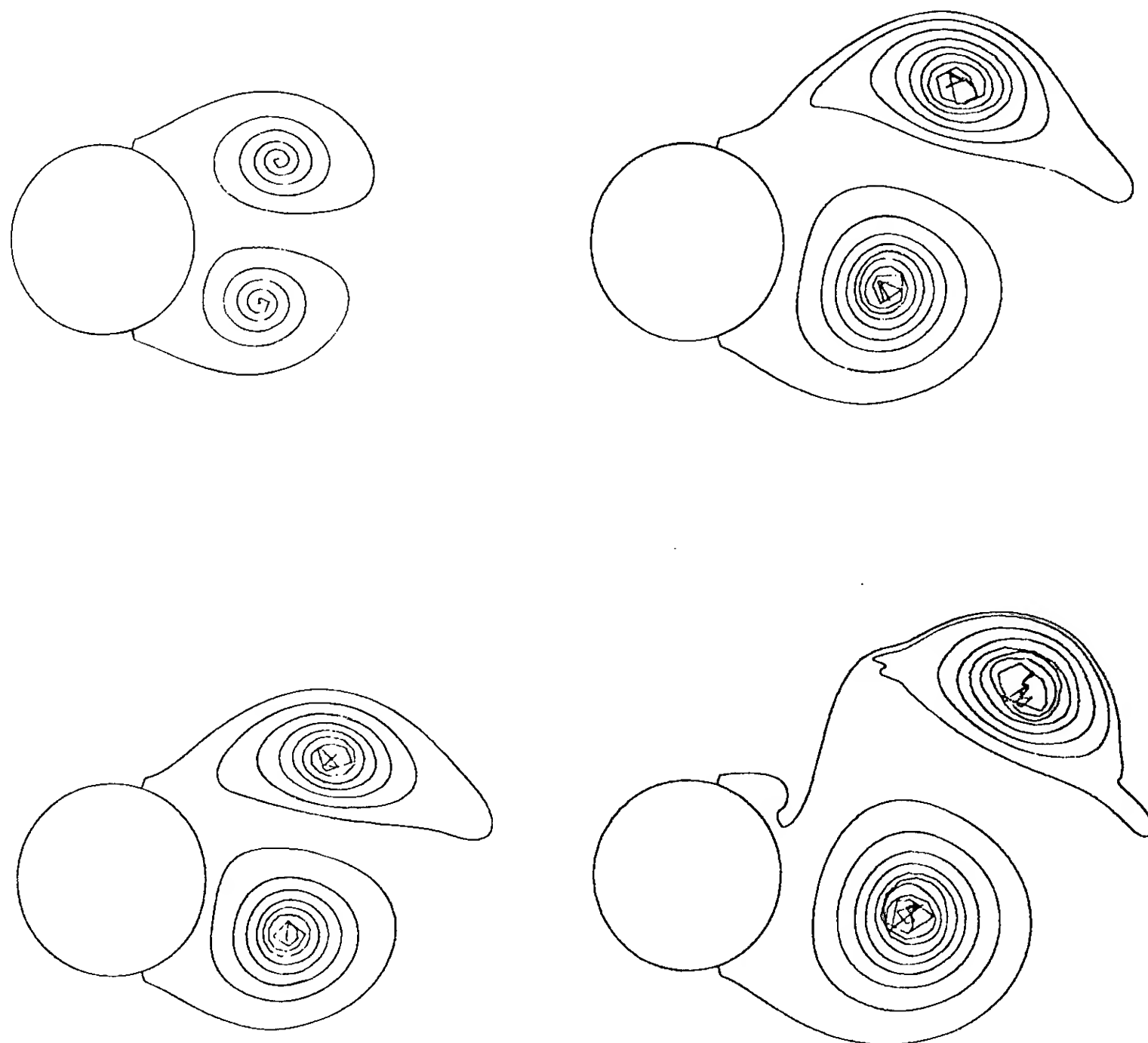


Figure 5: Wake evolution for flow past a cylinder with an initial perturbation. Separation points at fixed positions  $\alpha = \pm 108^\circ$ .  $t = 3, 5, 7, 8$

Finally the complete procedure including the interaction with the internal viscous solution, has been applied to the case of  $Re = 10^4$ . At each time step the Kutta-type condition is applied in a new position

corresponding to the zero value of vorticity which is determined from the solution of the integral equation (41). The sequence in Fig. 6 shows the motion of the separation points towards the rear part of the cylinder, starting from the initial position of  $90^\circ$ , which

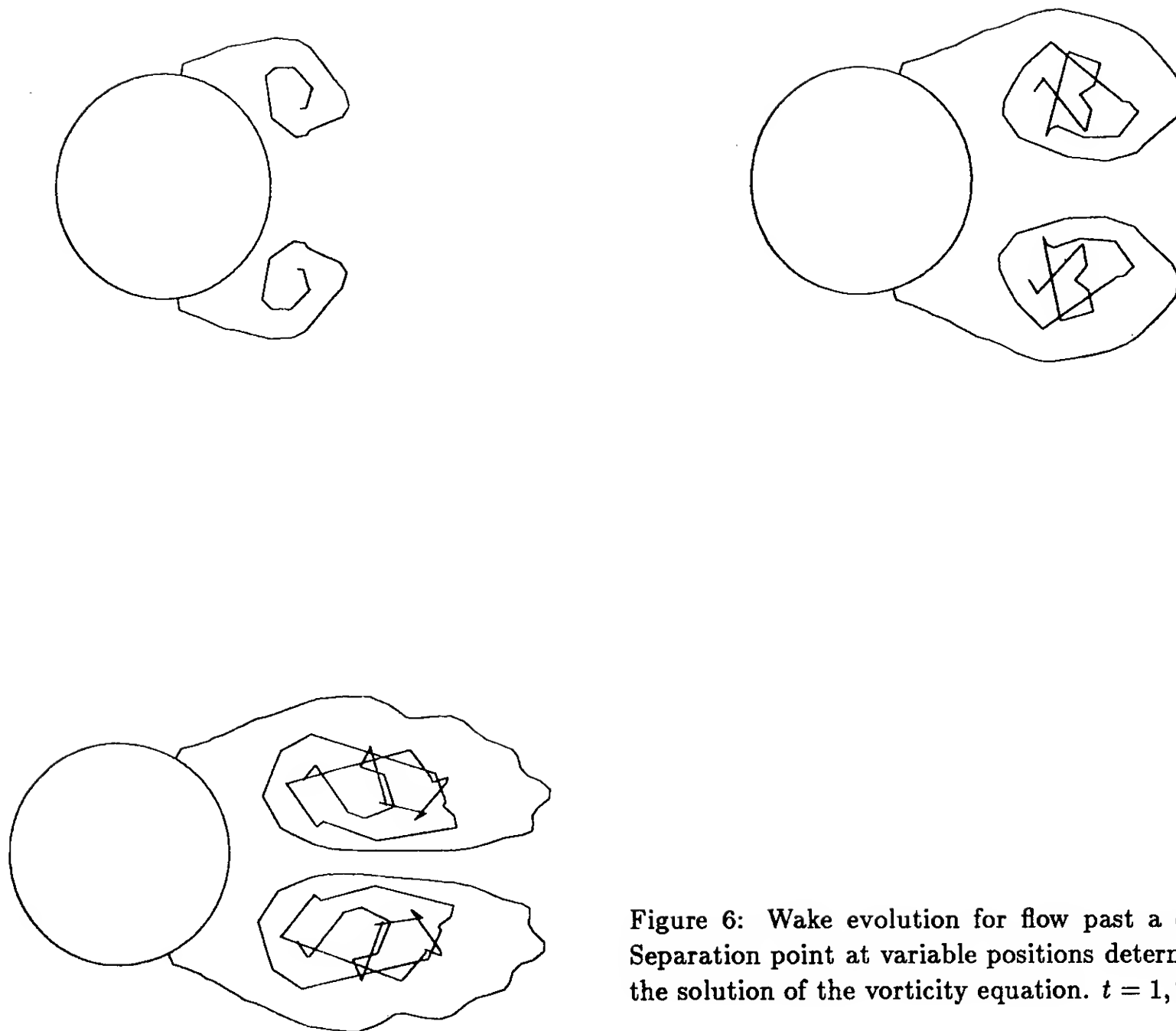


Figure 6: Wake evolution for flow past a cylinder. Separation point at variable positions determined by the solution of the vorticity equation.  $t = 1, 2, 3$

corresponds to zero tangential derivative of pressure (i.e. zero vorticity for no volume integrals in the first inviscid solution). The wiggles appearing in the wake configurations in the present case, are given to the motion of the separation point (i. e. the source of the vortex shedding) and not to a vortex layer instability. The convergence to a steady state solution is uncer-

tain in the sense that a steady state is almost reached, but is not maintained, as if it were an unstable solution. We don't have at the moment sufficient data to understand if this is just a numerical instability or it simulates the inherent physical instability present at those values of the Reynolds number.

## CONCLUDING REMARKS AND PERSPECTIVES

In the present paper we tried to answer several questions about the possibility and the convenience to extend boundary integral methods (usually very efficient for potential flows) to rotational free surface flows, either inviscid or viscous.

Starting from an integral formulation in primitive variables for unsteady viscous flows, we deduced a set of simplified models strictly connected, the one to the other, through their relevant mathematical structure. Actually the basic integral equations are very similar, so the experience may be transferred from simpler to increasingly complicated models.

The analysis of the limiting case for viscosity going to zero, has been of great help to understand the behaviour of the integral equation for tendentially singular kernels. The decoupling of kinematics and dynamics has been another crucial feature to reduce the integral representation to a form (the Poincaré formula) easy to be treated from a computational point of view. A further point to be stressed is the coupling of the original equations in primitive variables with the integral equation for vorticity, which leads to a more convenient approach for viscous flow solutions.

The theoretical analysis suggested a first model for the study of free surface flows with regions of assigned vorticity or vortex layers generated by the body motion. The resulting numerical procedure, efficient as the potential one, allows for an easy evaluation of several rotational effects.

A second more refined model, suitable for the investigation of separated flows with large rotational regions, was provided by the interaction with a *first order* viscous solution. The model implies a numerical procedure, which still requires a further analysis. However the numerical results are very promising in spite of the simplicity of the model.

The latter may be considered as a first step towards the fully coupled and fully viscous model which is the straightforward approach to study the generation of vorticity and the creation, through separation, of large vortical regions. The integral representation (3) for the velocity vector and the scalar version of the (41) for the vorticity (2D case) lead to boundary integral equations in the same unknowns if we account for the relations (18) and (42) valid at the body wall. A mixed procedure which solves alternatively the normal component of the first integral equation for the dynamic pressure and the second integral equation for the vorticity, is now in progress.

## REFERENCES

1. Dowson C.W., "A practical computing method for solving ship wave problem", 2nd Int. Conference Numerical Ship Hydrodynamics, Berkeley, 1977.
2. Miyata H., Sato T., and Baba N., "Difference Solution of a Viscous Flow with Free Surface Wave about an Advancing Ship", *J. Comput. Phys.*, no. 72, 1987, p. 393.
3. Casciola C.M., and Piva R., "A Boundary Integral Formulation for Free Surface Viscous and Inviscid Flows about Submerged Bodies", *Proceedings of the 5th International Conference on Numerical Ship Hydrodynamics*, Hiroshima (Japan), Sept. 25-29, 1989.
4. Piva R., and Morino L., "Vector Green's Function method for Unsteady Navier Stokes Equations", *Meccanica*, vol. 22, 1987, pp. 76-85.
5. Piva R., Graziani G., and Morino L., "Boundary Integral Equation Method for Unsteady Viscous and Inviscid Flows", *Advanced Boundary Element Methods*, Cruse T.A. (ed.), Springer Verlag, New York, USA, 1987.
6. Brard R., "Vortex theories for bodies moving in water", *Proceedings of 9th Symp. on Naval Hydrodynamics*, Brard R., and Castera A. (eds.), U.S. Gov. Printing Office, 1972, pp. 1187-1284.
7. Piva R., "The Boundary Integral Equation Method for Viscous and Inviscid Flows", *Proceedings ISCFD*, Oshima K. (ed.), Nagoya, Japan, 1989.
8. Ladyzhenskaja, O.A., *The Mathematical Theory of Viscous Incompressible Flows*, Gordon & Breach, New York, 1963.
9. Casciola C.M., Lancia M.R., and Piva R., "A General Approach to Unsteady Flows in Aerodynamics: Classical Results and Perspectives", *ISBEM 89*, East Hartford, USA, 1989, Springer Verlag, Berlin.
10. Bassanini P., Casciola C.M., Lancia M.R., and Piva R., "A boundary integral formulation for the kinetic field in aerodynamics. Part I: Mathematical analysis. Part II: Applications to Unsteady 2-D Flows", submitted to *European J. Mech., B/Fluids*, 1990.
11. Nedelec J.C., "Approximation des équations intégrales en mécanique et en physique", *Lecture Notes*, Centre de Mathématiques Appliquées, Ecole Polytechnique, Palaiseaux, France, 1977.



12. Hsiao G.C., "On boundary integral equations of the first kind", China-US Seminar on Boundary Integral Equations and Boundary Element Methods in Physics and Engineering, Jan. 1988, Xi'an, People's Republic of China.
13. Schmall R.A., and Kinney, R.B., "Numerical Study of Unsteady Viscous Flow Past a Lifting Plate", AIAA Journal, Vol. 12, 1974, pp. 1566-1673.
14. Wu J.C., "Numerical Boundary Conditions for Viscous Flow Problems", AIAA Journal, Vol. 14, 1976, pp. 1040-1049.
15. Berker R., "Integration des equations du Movement d'un Fluide Visqueux Incompressible", Encyclopedia of Physics, Flügge S. (ed.), Vol. VIII/2, 1963.
16. Morino L., "Helmoltz Decomposition Revisited: Vorticity Generation and Trailing Edge Condition", Computational Mechanics I.
17. Friedrichs K.O., Special Topics in Fluid Dynamics, Gordon & Breach, London, 1966.
18. Liu, P.L-F., and Liggett J.A., "Applications of the Boundary Element Method to Problems of Water Waves", Developments in Boundary Element Methods - 2, Banerjee P.K., and Shaw R.P., Applied Science publishers, London, 1982.
19. Haussling, H.J., and Coleman R.M., "Finite-Difference Computations Using Boundary Fitted Coordinate Systems for Free Surface Potential Flows Generated by Submerged Bodies", Proceedings of the 2nd Inter. Conference on Numerical Ship Hydrodynamics, Wehausen J.V., and Salvesen N. (eds.), 1977.
20. Sears, W.R., "Unsteady Motion to Airfoils and Boundary Layer Separation", AIAA Journal, Vol. 14, No. 2.
21. Lighthill, M.J., "Introduction. Boundary Layer Theory", Laminar Boundary Layers, L. Rosenhead (ed.), Oxford at the Clarendon Press, 1963, pp. 46-59.
22. Krasny, R., "Computation of vortex sheet roll-up in the Trefftz plane", Journal of Fluid Mechanics, Vol. 184, 1987, pp. 123-156.
23. Katz, J., "A discrete vortex method for the non steady separated flow over an airfoil", Journal of Fluid Mechanics, Vol. 102, 1981, pp. 315-328.
24. Kiya M., and Arie M., "A contribution to an inviscid vortex-shedding model for an inclined flat plate in uniform flow", Journal of Fluid Mechanics, Vol. 82, Part 2, 1977, pp. 223-240.
25. Sarpkaya T., "An inviscid model of two-dimensional vortex shedding for transient and asymptotically steady separated flow over an inclined plate", Journal of Fluid Mechanics, Vol. 68, Part 1, 1975, pp. 109-128.

## APPENDIX A

We remove here the assumption of fixed fluid domain, introduced in section 3a to simplify the calculations for the equivalence between the kinematical representation stemming from (10) and the Poincaré formula (23). Hence, we have to consider in (10) also the surface integral accounting for the motion of the free surface, neglected in section 3a. An easy way to prove this equivalence is to derive with respect to time the Poincaré formula. In particular the first surface integral in (23) perfectly coincides with the first in (10), therefore we focus our attention on the second surface integral

$$-\nabla_* \times \int_{\partial\Omega(t)} (\mathbf{u} \times \mathbf{n}) G dS = -\nabla_* \times \mathbf{k} \int_{\partial\Omega(t)} u_r G dS \quad (1A)$$

where now  $\partial\Omega$  is a function of time, described by the parametric equation  $\mathbf{x} = \mathbf{x}(\xi, t)$  with  $\xi \in D_\xi$ . The time derivative of this integral, expressed in terms of the Lagrangian parameter  $\xi$  is

$$\begin{aligned} \frac{d}{dt} \int_{\partial\Omega(t)} u_r G dS = \\ \frac{d}{dt} \int_{D_\xi} u_r [\mathbf{x}(\xi, t), t] G [\mathbf{x}(\xi, t), \mathbf{x}_*] J(\xi, t) d\xi = \\ \int_{D_\xi} \frac{d}{dt} (u_r J) G + u_r J \frac{d\mathbf{x}}{dt} \cdot \nabla G d\xi \quad (2A) \end{aligned}$$

where  $\frac{d}{dt}$  is a derivative for a given point  $\xi$  and  $J$  is the Jacobian of the transformation. We introduce in (2A) the following identities

$$\begin{aligned} \frac{d}{dt} (u_r J) &= \frac{D_w u_r}{Dt} J + u_r \frac{dJ}{dt} \\ &= J \left( \frac{D_w \mathbf{u}}{Dt} \cdot \boldsymbol{\tau} + \mathbf{u} \cdot \frac{d\boldsymbol{\tau}}{dt} \right) + u_r \frac{dJ}{dt} \quad (3A) \end{aligned}$$

where  $\frac{D_w}{Dt}$  is the total derivative following the free surface motion. Using the definition of  $J$

$$J = \left| \frac{\partial \mathbf{x}}{\partial \xi} \right|,$$

taking the time derivative of  $\frac{\partial \mathbf{x}}{\partial \xi} = \tau J$

$$\frac{d}{dt} \left( \frac{\partial \mathbf{x}}{\partial \xi} \right) = \frac{\partial \mathbf{w}}{\partial \xi} = \frac{d}{dt} (\tau J) = J \frac{d\tau}{dt} + \tau \frac{dJ}{dt},$$

its scalar product times  $\mathbf{u}$  divided by  $J$

$$\mathbf{u} \cdot \frac{d\tau}{dt} + u_r \frac{1}{J} \frac{dJ}{dt} = \mathbf{u} \cdot \frac{d\mathbf{w}}{d\tau}$$

and combining these results with the expression (3A) divided by  $J$ , leads to

$$\frac{1}{J} \frac{d}{dt} (u_r J) = \frac{D_w \mathbf{u}}{dt} \cdot \tau + \mathbf{u} \cdot \frac{\partial \mathbf{w}}{\partial \tau} \quad (4A)$$

The free surface velocity  $\mathbf{w}$  has the normal component  $w_n = u_n$ , while for the tangential component we may assume  $w_r = \frac{1}{2} u_r$ . The relationship between the material derivative and  $\frac{D_w}{dt}$  is

$$\frac{D \mathbf{u}}{dt} = \frac{D_w \mathbf{u}}{dt} + (u_r - w_r) \frac{\partial \mathbf{u}}{\partial \tau}$$

which combined with (4A) gives

$$\frac{1}{J} \frac{d}{dt} (u_r J) = \frac{D \mathbf{u}}{dt} \cdot \tau + \frac{\partial}{\partial \tau} \left( \frac{1}{2} u_n^2 \right) \quad (5A)$$

where the last term results after some tedious manipulation by

$$-\tau \cdot \frac{u_r}{2} \frac{\partial \mathbf{u}}{\partial \tau} + -\mathbf{u} \cdot \frac{\partial \mathbf{w}}{\partial \tau} = \frac{\partial}{\partial \tau} \left( \frac{1}{2} u_n^2 \right)$$

Now from the Euler equation

$$\tau \cdot \frac{D \mathbf{u}}{dt} = - \frac{\partial}{\partial \tau} \left( \frac{p}{\rho} + gz \right) \quad (6A)$$

from (5A) plus (6A) combined with (2A) we obtain

$$\begin{aligned} \int_{\partial \Omega(t)} \left[ - \frac{\partial}{\partial \tau} \left( \frac{p}{\rho} + gz - \frac{1}{2} u_n^2 \right) G \right] dS + \\ + \int_{\partial \Omega(t)} \left[ \frac{u_r^2}{2} \frac{\partial G}{\partial \tau} + u_r u_n \frac{\partial G}{\partial n} \right] dS \end{aligned} \quad (7A)$$

Integrating by parts the first integral and factorizing  $\frac{\partial G}{\partial \tau}$ , leads to

$$\int_{\partial \Omega(t)} \left[ \frac{\partial G}{\partial \tau} \left( \frac{p}{\rho} + gz - \frac{1}{2} u_n^2 + \frac{1}{2} u_r^2 \right) + u_r u_n \frac{\partial G}{\partial n} \right] dS \quad (8A)$$

which corresponds exactly to the term

$$\int_{\partial \Omega(t)} \left( \frac{P}{\rho} n_j u_j^k - \nu_\sigma u_j u_j^{(k)} \right) dS \quad (9A)$$

including the second and the third surface integrals of equation (10). Actually by introducing

$$\Pi_j = \frac{p}{\rho} n_j - \nu_\sigma u_j$$

and using the vector notations

$$\nabla_* \times \int_{\partial \Omega(t)} (\Pi \times \nabla G) \quad (10A)$$

where

$$\Pi \times \nabla G = \left( \Pi_r \frac{\partial G}{\partial n} - \Pi_n \frac{\partial G}{\partial \tau} \right) \mathbf{k}$$

with

$$\Pi_n = \frac{P}{\rho} - u_n^2 = \frac{p}{\rho} + \frac{u_r^2}{2} - \frac{u_n^2}{2} + gz$$

$$\Pi_r = -u_n u_r$$

by comparing we may verify the exact correspondence between (10A) and (1A)

In conclusion we see that the term (10A) which in the Euler equation is integrated in time, even in this case of moving boundary, perfectly coincides with the time derivative of the term (1A) of the Poincaré formula.

## DISCUSSION

Gerard Van Oortmerssen  
Marin Research Institute Netherlands, The Netherlands

The authors have given a rather fundamental analysis of free-surface flows and showed results of boundary integral computations for some basic cases involving simple geometries. Could you please elaborate on the perspective for applying these methods for more realistic cases of practical relevance.

### AUTHORS' REPLY

I'd like to thank Dr. Van Oortmerssen for his question which gives me the opportunity to discuss the perspectives of our work. We have presented in this paper several models for the analysis of vortical flows at different levels of complexity. In particular, the simplest one, for inviscid attached flows about bodies with a sharp trailing edge, may be directly used for applications in ship hydrodynamics. For instance, slightly submerged hydrofoils have been studied accounting properly for the nonlinear effects due both to the free surface and to the wake. The extension to the three-dimensional case has been completed from the theoretical point of view (see ref. 10) while its numerical application is still in progress.

On the other hand, more complex models for flows about bluff bodies still require a large amount of basic work, mainly about the vortex shedding modelling, so that the application to real problems is far ahead and presently the investigation is confined to two-dimensional test cases. In the framework of this application we have proposed two possible approaches. In the first one we considered the integral representation for the complete Navier-Stokes equations. A flow field simulation by this model would require a very large computational effort and only the simple case of two vortices is now under investigation. The second simplified approach is essentially based on the coupling of an external solution, obtained by the Poincaré identity, with an internal one for the detection of the separation point locations. Even for this model, a deep investigation is required to better understand its capability to represent the physical phenomenon and its range of applicability.

## DISCUSSION

Philippe G. Genoux  
Bassin d'Essais des Carènes, France

Is your solution able to simulate alternated vortices (Strouhal effects) in the case of a flow past a cylinder?

### AUTHORS' REPLY

In the present approach, the vorticity field is modeled by vortex sheets issuing from the separation points on the cylinder. We find that, after perturbing the system, the symmetric solution no longer exists and is replaced by a flow which shows the developments of alternate vortices. The solution is obtained with fixed (prescribed) separation points. Moreover, we found that under these conditions the flow doesn't evolve towards a periodic solution. Actually the strength of the vortex layer, still oscillating, decreases in time. This behavior may be explained by the fact that we keep the separation points fixed. In order to develop a procedure with moving separation points, we have introduced the interaction between the external and the internal solution. Presently we have an increasing oscillatory motion of the separation points; therefore, a comparison of the Strouhal number seems to be premature.

## DISCUSSION

J.M.R. Graham  
Imperial College of London, United Kingdom

Have the authors compared their prediction of the separation points on the circular cylinder in impulsively started flow with other published results? For example, the analysis of the onset of separation (Van Dommelen & Shen) and other similar work.

### AUTHORS' REPLY

As I said in the previous answers, the model we propose for vortex shedding after a bluff body is still under investigation and we obtained only some preliminary results. We don't consider however, the model suitable for studying the onset of separation at its very initial stage. Let me stress again the point that our purpose here is to devise a simplified model able to analyze recirculating or separated regions without solving the complete Navier Stokes equations. Presently, we are still in the stage to reproduce the physical phenomenon and to understand the essential features to be included in the model. From this point of view, we are very interested to consider the suggestions in the paper you mention.

# Numerical Appraisal of the New Slender Ship Formulation in Steady Motion

H. Maruo (University of California, Santa Barbara, USA)

W.-S. Song (Shanghai Jiao Tong University, China)

## ABSTRACT

A new formulation for the fluid motion around a slender ship is developed, on the basis of an asymptotic expression of the Kelvin-source around its track. The boundary value problem is expressed by an integral equation which is much more simplified than the solution of the Neumann-Kelvin approximation. In order to examine the validity of this theory, numerical computations are carried out with respect to the pressure distribution, wave pattern and wave resistance of several types of hull forms, i.e. the Wigley hull, a sailing yacht hull, and a Series 60 ( $C_B = 0.60$ ) hull. The results are compared with experimental data.

## 1. INTRODUCTION

The final goal of ship hydrodynamics is the theoretical determination of hydrodynamic forces acting on the ship hull within the accuracy of practical allowance. One of the most important in this respect is the computation of wave resistance in the steady forward motion. The pressure distribution over the hull surface becomes important when the boundary layer calculation is intended. Because of the complex geometry of the ship hull, the solution of fully or partially nonlinear boundary value problem by means of the computational approach of numerical simulation has not achieved the practical feasibility yet. The analytical solution, on the other hand, has to depend on the perturbation technique which leads to the linearization of the problem as the first approximation. It is well known, that the classical thin ship perturbation has not provided result which shows a satisfactory agreement with measured data. Several versions of linearized theory have been proposed, such as the Neumann Kelvin approximation (1). However most of them are rather inconsistent approach, lacking the rational basis in the sense of the perturbation analysis. The slender body theory is another possibility of rational approach of this problem. The first attempt of the application of the slender body theory to ships in steady forward motion appeared in 1962 - 1963 (2)(3)(4)(5). However the formul-

ation of the wave resistance by this theory was found quite unsatisfactory, because the values computed according to this theory showed a remarkable deviation from measured values, and the agreement was even poorer than the result of the classical Michell theory (6). No progress in this problem has been observed for as long as 20 years since that time. In 1982, one of the present authors developed a new approach to the slender ship in steady forward motion (7). The difference of this theory from the former theory lies in the treatment of the singularity which represents the body. The original formulation has followed the method of perturbation analysis, which is employed in the slender body in the unbounded fluid. Then it assumes that the slender body is represented by the source distribution along the longitudinal axis. The new theory, on the other hand, begins with the expansion of the Kelvin-source around its track. It is disclosed that it is not possible to represent the slender ship floating on the free surface by the source distribution along the longitudinal axis considered in the free surface.

The boundary value problem is expressed by an integral equation on the hull surface, because the singularity representing the hull must be distributed over the surface. Then the solution is more complex than the original slender body theory. However the solution of the integral equation is much more simplified than the solution in the Neumann-Kelvin approximation. The reason is first that the integral equation is of the Volterra type, so that the boundary value problem becomes parabolic. That means there is no contribution from the disturbance in the downstream to the boundary condition at the upstream section of the body. The marching procedure starting from the bow end is possible to solve the boundary value problem in each section. Secondly, the kernel function of the integral equation can be expressed by known functions, so that the high accuracy of the numerical work is achieved. An analytical method of solution by means of the conformal mapping has been intended, and several numerical results have been obtained in 1983. However it is found that the accuracy of the computation is not satis-

factory (8). Furthermore, the analytical method is not suitable for the numerical work, because the mapping of the transverse section to a unit circle needs much computer time. Then a numerical method of solution is developed. This method employs the source distribution to represent the hull, and the density of sources is determined numerically by the panel method. The program library is prepared for the computation of kernel functions. Three kinds of hull forms are employed for the numerical example. They are the Wigley hull, a sailing yacht hull, and the Series 60 ( $C_B = 0.60$ ) model. Items of the numerical work are the pressure distribution on the hull surface, wave resistance, the lateral force when moving obliquely, the wave profile alongside the hull, and the wave pattern around the hull. Some of the numerical results are compared with measured data.

## 2. LINEARIZATION OF THE VELOCITY POTENTIAL

It is assumed that the fluid is inviscid and incompressible, and the depth of water is infinite. Take the cartesian coordinate system with the origin on the undisturbed free surface,  $x$ - and  $y$ -axes on the horizontal plane, and  $z$ -axis directing vertically downwards. Consider a slender ship fixed in a uniform flow of velocity  $U$  in the direction of positive  $x$ . Assume the irrotational motion and write the velocity potential in the form like  $Ux + \phi$ . The field equation is the Laplace equation.

$$[L] \quad \nabla^2 \phi = 0 \quad (1)$$

The boundary condition on the hull surface is

$$[H] \quad \phi_n = -U \partial x / \partial n = -U n_x \quad (2)$$

where  $n$  is the normal drawn outwards on the hull surface, and  $\phi_n = \partial \phi / \partial n$ . The kinematic condition on the free surface at  $z = \zeta$  is

$$[K] \quad (U + \phi_x) \zeta_x + \phi_y \zeta_y - \phi_z = 0 \quad (3)$$

The dynamic condition on the free surface, that the pressure is constant, is

$$[D] \quad U \phi_x + \frac{1}{2}(\phi_x^2 + \phi_y^2 + \phi_z^2) - g \zeta = 0 \quad (4)$$

Since the depth of water is infinite,  $\phi_z = 0$  at  $z \rightarrow \infty$ , and  $\phi \rightarrow 0$  at  $x, y \rightarrow \pm \infty$ . One can eliminate  $\zeta$  between (3) and (4) such as

$$[F] \quad \left[ (U + \phi_x) \frac{\partial}{\partial x} + \phi_y \frac{\partial}{\partial y} + \phi_z \frac{\partial}{\partial z} \right] \left[ U \phi_x + \frac{1}{2}(\phi_x^2 + \phi_y^2 + \phi_z^2) - g \zeta \right] = 0 \quad (5)$$

In order to express the velocity potential of the fluid motion around the hull, we assume Green's function  $G(P, Q)$  with  $P = (x, y, z)$ ,  $Q = (x', y', z')$ , and apply Green's theorem in the  $x', y', z'$ -space bounded by the hull surface  $S$  below the still waterline, a large surface  $S_\infty$  surrounding  $S$  in the lower half space,

and the horizontal plane  $S_0$  between  $S$  and  $S_\infty$ .

$$\phi(P) = \frac{1}{4\pi} \iint_{S+S_\infty+S_0} \left[ \frac{\partial \phi(Q)}{\partial n_Q} G(P, Q) - \phi(Q) \frac{\partial G(P, Q)}{\partial n_Q} \right] dS_Q \quad (6)$$

We have assumed the analytic continuation of  $\phi$  to the entire space below the still water surface in the above equation. We will employ the Kelvin-source as Green's function, which satisfies the boundary condition,

$$U^2 \frac{\partial^2 G}{\partial x^2} - g \frac{\partial G}{\partial z} = 0 \quad (7)$$

on the horizontal plane  $z=0$ . If the surface  $S_\infty$  is taken at infinite distance, the integral on  $S$  vanishes. On the horizontal surface  $S_0$ , we have the relation derived from the free surface condition (5) such as

$$\frac{\partial \phi}{\partial z} \Big|_{z=0} = \frac{U^2}{g} \frac{\partial^2 \phi}{\partial x^2} \Big|_{z=0} + \frac{1}{g} \phi(x, y) \quad (8)$$

where

$$\begin{aligned} \phi(x, y) = & [2U(\phi_{xx} + \phi_y \phi_{xy} + \phi_z \phi_{xz}) + 2(\phi_x \phi_{xy} \phi_{yz} + \\ & + \phi_x \phi_{xz} \phi_{yz} + \phi_y \phi_{yz}^2 + \phi_{yy} \phi_y^2 + \phi_{zz} \phi_z^2)]_{z=\zeta} \\ & + \int_0^\zeta (U^2 \phi_{xx} - g \phi_{zz}) dz \end{aligned} \quad (9)$$

Making use of relations (7) (8) in the integral on  $S_0$ , and integrating by parts with respect to  $x'$ , we obtain

$$\begin{aligned} \phi(P) = & \frac{1}{4\pi} \iint_S \left[ \frac{\partial \phi(Q)}{\partial n_Q} G(P, Q) - \phi(Q) \frac{\partial G(P, Q)}{\partial n_Q} \right] dS_Q \\ & - \frac{U^2}{4\pi g} \int_{L_0} \left[ G(P, Q) \frac{\partial \phi(Q)}{\partial x'} - \phi(Q) \frac{\partial G(P, Q)}{\partial x'} \right]_{z'=0} dy' \\ & + \frac{1}{4\pi g} \iint_{S_0} \phi(x', y') G(P, Q) dx' dy' \end{aligned} \quad (10)$$

where  $L_0$  is the curve of intersection of the hull surface with the still water plane.

Now let us assume that the ship is very slender and the beam to length ratio is a small fraction  $\epsilon \ll 1$ . Then the slope of the hull surface to the longitudinal axis is small in the order of  $\epsilon$ , i.e.  $n_x = O(\epsilon)$ . From the hull boundary condition (2), we have

$$\phi_n = n_x \phi_x + n_y \phi_y + n_z \phi_z = U O(\epsilon) \quad (11)$$

where  $n_x, n_y, n_z$  are direction cosines of the outward normal to the hull surface. Because of the slender body,  $n_x = O(1)$ ,  $n_y = O(1)$ . If  $U = O(1)$ , we have  $\phi_x = O(\epsilon)$ ,  $\phi_y = O(\epsilon)$ . Since the hull surface area is regarded as  $O(\epsilon)$ , the first term on the right hand side of (10) is  $O(\epsilon^2)$ .  $\phi(x, y)$  is at most  $O(\epsilon^2)$  in the near field in the area of  $O(\epsilon)$  within  $S_\infty$ , so that the third term on the right hand side is at most  $O(\epsilon^3)$ . Omitting this term, we have

$$\begin{aligned} \phi(P) = & \frac{1}{4\pi} \iint_S \left[ \frac{\partial \phi(Q)}{\partial n_Q} G(P, Q) - \phi(Q) \frac{\partial G(P, Q)}{\partial n_Q} \right] dS_Q \\ & - \frac{U^2}{4\pi g} \int_{L_0} \left[ G(P, Q) \frac{\partial \phi(Q)}{\partial x'} - \phi(Q) \frac{\partial G(P, Q)}{\partial x'} \right]_{z=0} dy' \\ & \dots \dots \dots (12) \end{aligned}$$

Next assume a velocity potential  $\phi'$  in the lower half space, which is harmonic inside  $S$ , and satisfies the boundary conditions,

$$\begin{aligned} \phi' &= \phi & \text{on } S \\ \text{and} \end{aligned}$$

$$U^2 \frac{\partial^2 \phi'}{\partial x'^2} - g \frac{\partial \phi'}{\partial z} = 0 \quad \text{on } z=0$$

Applying Green's theorem to  $\phi'$  and  $G(P, Q)$  in the domain bounded by  $S$  and the plane  $z=0$ ,

$$\begin{aligned} 0 = & \frac{1}{4\pi} \iint_S \left[ \frac{\partial \phi'(Q)}{\partial n'} G(P, Q) - \phi'(Q) \frac{\partial G(P, Q)}{\partial n'} \right] dS_Q \\ & + \frac{U^2}{4\pi g} \int_{L_0} \left[ G(P, Q) \frac{\partial \phi'(Q)}{\partial x'} - \phi'(Q) \frac{\partial G(P, Q)}{\partial x'} \right]_{z'=0} dy' \\ & \dots \dots \dots (13) \end{aligned}$$

where  $n'$  is the normal of  $S$  drawn inwards. Adding (12) and (13), and putting

$$\sigma = \frac{1}{4\pi} \left( \frac{\partial \phi}{\partial n} + \frac{\partial \phi'}{\partial n'} \right) \quad (14)$$

we obtain

$$\begin{aligned} \phi = & \iint_S \sigma(Q) G(P, Q) dS + \frac{U^2}{g} \int_{L_0} \sigma(Q) G(P, Q) n_x \frac{dy'}{ds} ds \\ & \dots \dots \dots (15) \end{aligned}$$

This is the basic equation of the Neumann-Kelvin approximation. If the slender body is assumed,  $n_x$  and  $dy/ds$  are  $O(\epsilon)$ . Then the integral along the waterline  $L_0$  is  $O(\epsilon^3)$ , and can be omitted. In consequence, the velocity potential is given by

$$\phi = \iint_S \sigma(Q) G(P, Q) dS \quad \dots \dots \dots (16)$$

Thus the fluid motion around the hull is expressed by the distribution of Kelvin-sources over the hull surface. The Kelvin-source is given by the formula,

$$\begin{aligned} G(P, Q) &= G(x, y, z; x', y', z') \\ &= -\frac{1}{r} + \frac{1}{r'} + G'(\bar{x}, \bar{y}, \bar{z}) \end{aligned} \quad (17)$$

$$\begin{aligned} G'(\bar{x}, \bar{y}, \bar{z}) &= \\ &= \frac{K_0}{\pi} \int_{-\pi}^{\pi} d\theta \int_0^{\infty} \frac{\exp(-k\bar{z} + ik\bar{x}\cos\theta + ik\bar{y}\sin\theta)}{k\cos^2\theta - K_0} dk \end{aligned} \quad (18)$$

$$\begin{aligned} \text{where } r &= [(x-x')^2 + (y-y')^2 + (z-z')^2]^{\frac{1}{2}} \\ r' &= [(x-x')^2 + (y-y')^2 + (z+z')^2]^{\frac{1}{2}} \\ \bar{x} &= x-x', \quad \bar{y}=y-y', \quad \bar{z}=z+z', \quad K_0 = g/U^2. \end{aligned}$$

The integral with respect to  $k$  is taken along the real axis indented by a small semicircle in the lower side of the pole at  $k=K_0\sec^2\theta$ . Then the velocity potential is written in the form like

$$\phi = \phi_1 + \phi_2 \quad (19)$$

$$\phi_1 = -\iint_S \sigma(x', y', z') \left( \frac{1}{r} - \frac{1}{r'} \right) dS \quad (20)$$

$$\phi_2 = \iint_S \sigma(x', y', z') G'(\bar{x}, \bar{y}, \bar{z}) dS \quad (21)$$

### 3. ASYMPTOTIC EXPRESSION FOR THE KELVIN-SOURCE

Let us consider the asymptotic behavior of the Kelvin-source near the  $x$ -axis. In order to find out the asymptotic expression of  $G'(\bar{x}, \bar{y}, \bar{z})$ , we consider the following integral in the complex  $u$ -plane.

$$I_c = \int_C \frac{\exp[-u\bar{z} + iu(\bar{x}\cos\theta + \bar{y}\sin\theta)]}{u - K_0\sec^2\theta} du \quad (22)$$

along a closed circuit  $C$  composed of the positive real axis indented by a small semicircle in the lower side around the pole at  $u=K_0\sec^2\theta$ , and the positive or negative part of the imaginary axis together with a large quadrant arc connecting the ends of the axes. In the case of  $\bar{x}\cos\theta + \bar{y}\sin\theta > 0$ , the closed circuit is taken in the first quadrant. Since the pole is inside the contour, Cauchy's theorem gives

$$I_c = 2\pi i (\text{Residue at } u=K_0\sec^2\theta)$$

If the radius of the large circle tends to infinity, the integral along it vanishes, so that

$$\int_0^{\infty} + \int_{i\infty}^0 = 2\pi i \exp[-K_0\bar{z}\sec^2\theta + iK_0\sec^2\theta(\bar{x}\cos\theta + \bar{y}\sin\theta)]$$

and accordingly

$$\begin{aligned} & \text{Re} \int_0^{\infty} \frac{\exp[-u\bar{z} + iu(\bar{x}\cos\theta + \bar{y}\sin\theta)]}{u - K_0\sec^2\theta} du \\ &= \int_0^{\infty} \frac{t \cos t\bar{z} - K_0\sec^2\theta \sin t\bar{z}}{t^2 + K_0^2\sec^4\theta} e^{-t(\bar{x}\cos\theta + \bar{y}\sin\theta)} dt \\ & \quad - 2\pi e^{-K_0\bar{z}\sec^2\theta} \sin[K_0\sec^2\theta(\bar{x}\cos\theta + \bar{y}\sin\theta)] \end{aligned}$$

In the case of  $\bar{x}\cos\theta + \bar{y}\sin\theta < 0$  on the other hand, the closed circuit is taken in the fourth quadrant. Since the pole is outside the closed circuit, Cauchy's theorem gives  $I_c = 0$ , and we have the result,

$$\begin{aligned} & \text{Re} \int_0^{\infty} \frac{\exp[-u\bar{z} + iu(\bar{x}\cos\theta + \bar{y}\sin\theta)]}{u - K_0\sec^2\theta} du \\ &= \int_0^{\infty} \frac{t \cos t\bar{z} - K_0\sec^2\theta \sin t\bar{z}}{t^2 + K_0^2\sec^4\theta} e^{-t|\bar{x}\cos\theta + \bar{y}\sin\theta|} dt \end{aligned}$$



Therefore the function  $G'(\bar{x}, \bar{y}, \bar{z})$  is given by

$$G' = \frac{2K_0}{\pi} \int_{-\frac{1}{2}\pi}^{\frac{1}{2}\pi} \sec^2 \theta d\theta \int_0^\infty \frac{t \cos t \bar{z} - K_0 \sec^2 \theta \sin t \bar{z}}{t^2 + K_0^2 \sec^4 \theta} \times e^{-t|\bar{x} \cos \theta + \bar{y} \sin \theta|} dt - 4K_0 \int_{\theta_1}^{\frac{1}{2}\pi} e^{-K_0 \sec^2 \theta \bar{z}} \sin(K_0 \bar{x} \sec \theta) \cos(K_0 \bar{y} \sec \theta \tan \theta) \times \sec^2 \theta d\theta \quad (23)$$

where  $\theta_1$  is an angle between  $-\pi/2$  and  $\pi/2$  such that  $\tan \theta_1 = -\bar{x}/|\bar{y}|$ . The double integral is bounded, and expressed on the  $x$ -axis by known functions such as

$$\frac{1}{\pi} \int_{-\frac{1}{2}\pi}^{\frac{1}{2}\pi} \sec^2 \theta d\theta \int_0^\infty e^{-t|\bar{x}| \cos \theta} \frac{t dt}{t^2 + K_0^2 \sec^4 \theta} = \frac{1}{K_0 |\bar{x}|} + \frac{\pi}{2} [H_1(K_0 |\bar{x}|) - Y_1(K_0 |\bar{x}|) - \frac{1}{\pi}] \quad (24)$$

where  $H_1$  is the Struve function and  $Y_1$  is the Bessel function of the second kind (9). Next we consider the single integral of the second term on the right hand side of (23).

Changing the integration variable by  $\sec \theta = u$ ,

$$\int_{\theta_1}^{\pi} e^{-K_0 \bar{z} \sec^2 \theta} \sin(K_0 \bar{x} \sec \theta) \cos(K_0 \bar{y} \sec \theta \tan \theta) \times \sec^2 \theta d\theta = \left\{ \int_1^\infty + \int_1^{\sqrt{1+(\bar{x}/\bar{y})^2}} \right\} e^{-K_0 \bar{z} u^2} \sin(K_0 \bar{x} u) \cos(K_0 \bar{y} u \sqrt{u^2 - 1}) \times \frac{u}{\sqrt{u^2 - 1}} du \quad \text{when } \bar{x} > 0, \\ \int_1^\infty e^{-K_0 \bar{z} u^2} \sin(K_0 \bar{x} u) \cos(K_0 \bar{y} u \sqrt{u^2 - 1}) \frac{u}{\sqrt{u^2 - 1}} du \quad \text{when } \bar{x} < 0 \quad (25)$$

It has an essential singularity along  $x$ -axis. In order to isolate the singularity, let us consider the identity,

$$\int_1^\infty e^{-K_0 \bar{z} u^2} \sin(K_0 \bar{x} u) \cos(K_0 \bar{y} u \sqrt{u^2 - 1}) \frac{u}{\sqrt{u^2 - 1}} du = \int_0^\infty e^{-K_0 \bar{z} u^2} \sin(K_0 \bar{x} u) \cos(K_0 \bar{y} u^2) du - \int_0^1 e^{-K_0 \bar{z} u^2} \sin(K_0 \bar{x} u) \cos(K_0 \bar{y} u^2) du + \int_1^\infty e^{-K_0 \bar{z} u^2} \left[ \frac{u}{\sqrt{u^2 - 1}} \cos(K_0 \bar{y} u \sqrt{u^2 - 1}) - \cos(K_0 \bar{y} u^2) \right] \times \sin(K_0 \bar{x} u) du \quad (26)$$

The singularity is condensed in the first term on the right hand side. It is readily shown that the last integral is bounded and uniformly convergent on the  $x$ -axis.

$$\lim_{\substack{\bar{y} \rightarrow 0 \\ \bar{z} \rightarrow 0}} \int_1^\infty e^{-K_0 \bar{z} u^2} \left[ \frac{u}{\sqrt{u^2 - 1}} \cos(K_0 \bar{y} u \sqrt{u^2 - 1}) - \cos(K_0 \bar{y} u^2) \right] \times \sin(K_0 \bar{x} u) du = -\frac{1}{K_0 \bar{x}} \int_1^\infty \cos(K_0 \bar{x} u) \left( \frac{1}{\sqrt{u^2 - 1}} - \frac{1}{u} \right) du = -\frac{\pi}{2} Y_1(K_0 \bar{x}) - \cos(K_0 \bar{x}) / (K_0 \bar{x}) \quad (27)$$

The second integral is finite.

$$\lim_{\substack{\bar{y} \rightarrow 0 \\ \bar{z} \rightarrow 0}} \int_0^1 e^{-K_0 \bar{z} u^2} \sin(K_0 \bar{x} u) \cos(K_0 \bar{y} u) du = \frac{1 - \cos(K_0 \bar{x})}{K_0 \bar{x}} \quad \dots \quad (28)$$

Then the integral (25) is expressed asymptotically as

$$-\pi Y_1(K_0 \bar{x}) - \frac{2}{K_0 \bar{x}} + \frac{2}{\sqrt{K_0}} \int_0^\infty e^{-v^2 \bar{z}} \cos(v^2 \bar{y}) \sin(v \sqrt{K_0} \bar{x}) dv \quad \text{when } \bar{x} > 0, \\ = 0 \quad \text{when } \bar{x} < 0 \quad (29)$$

Summarizing the above results, the asymptotic expression for  $G(\bar{x}, \bar{y}, \bar{z})$  near the  $x$ -axis is given by

$$G(\bar{x}, \bar{y}, \bar{z}) \approx -8\sqrt{K_0} \int_0^\infty e^{-v^2 \bar{z}} \cos(v^2 \bar{y}) \sin(v \sqrt{K_0} \bar{x}) dv + \pi K_0 [H_1(K_0 \bar{x}) + 3Y_1(K_0 \bar{x})] + \frac{6}{x} - 2K_0 \quad \text{when } \bar{x} > 0 \quad (30)$$

$$\approx -\pi K_0 [H_1(K_0 \bar{x}) - Y_1(K_0 \bar{x})] + \frac{2}{x} - 2K_0 \quad \text{when } \bar{x} < 0 \quad (31)$$

The integral in (30) is expressed by the Fresnel function of complex argument such as

$$E(\bar{x}, \bar{y}, \bar{z}) = \int_0^\infty e^{-v^2 \bar{z}} \cos(v^2 \bar{y}) \sin(v \sqrt{K_0} \bar{x}) dv = -j m e^{-i K_0 \bar{x}^2 / 4Z} \sqrt{\frac{\pi}{2Z}} F[\bar{x} \sqrt{K_0} / (2\pi Z)] \quad (32)$$

where  $Z = y + iz$ , and

$$F(x) = C(x) + iS(x) = \int_0^x e^{i\pi u^2 / 2} du \quad (33)$$

#### 4. BOUNDARY VALUE PROBLEM FOR THE SLENDER SHIP

The velocity potential near the slender ship is simplified by the asymptotic expression of the Kelvin-source given in the preceding section. We have divided the velocity potential into two parts  $\phi_1$  and  $\phi_2$  in (19).  $\phi_1$  is expanded with respect to  $\varepsilon$ . Omitting higher order terms, it is expressed near the hull by

$$\phi_1 \approx \int_{C(x)} \sigma(x') \ln \frac{(y-y')^2 + (z-z')^2}{(y-y')^2 + (z+z')^2} ds \quad (34)$$

The expression for  $\phi_2$  near the hull is obtained from the expression (30) and (31).

$$\phi_2 = \int dx' \int_{C(x')} (x', y', z') G'(x-x', y-y', z+z') ds \quad (35)$$

where

$$G'(\bar{x}, \bar{y}, \bar{z}) = -4\sqrt{K_0} E(\bar{x}, \bar{y}, \bar{z}) (1 + \operatorname{sgn} \bar{x}) + \pi K_0 H_1(K_0 |\bar{x}|) + [\pi K_0 Y_1(K_0 |\bar{x}|) + 2/|\bar{x}|] \times (1 + 2\operatorname{sgn} \bar{x}) - 2K_0 \quad (36)$$

Then we can write

$$\phi_2 = -4\sqrt{K_0} \int (1 + \operatorname{sgn} \bar{x}) dx' \int_{C(x')} \sigma(x', y', z') \times E(\bar{x}, \bar{y}, \bar{z}) ds + \int H(\bar{x}) dx' \int_{C(x')} \sigma(x', y', z') ds \quad (37)$$

where

$$H(\bar{x}) = K_0 H_1(K_0 |\bar{x}|) + [\pi K_0 Y_1(K_0 |\bar{x}|) + 2/|\bar{x}|] \times (1 + 2\operatorname{sgn} \bar{x}) - 2K_0 \quad (38)$$

Let us consider first, the case that the longitudinal axis of the ship is along the  $x$ -axis. The ship is moving at zero drift angle, and the fluid motion is symmetric on both sides of the ship. The hull surface is given by the equation,

$$y = \pm f(x, z) \quad (39)$$

Then the boundary condition on the hull surface is written as

$$\frac{\partial \phi}{\partial n} = -U f_x / \sqrt{1 + f_x^2 + f_z^2} \quad (40)$$

Because of the slender body assumption  $f_x = O(\varepsilon)$ ,  $f_z = O(1)$ . Omitting terms of  $O(\varepsilon^2)$ , the direction cosine of the normal can be written as

$$\begin{aligned} n_x &\approx -f_x / \sqrt{1 + f_z^2} = v_x \\ n_y &\approx \pm 1 / \sqrt{1 + f_z^2} = v_y \\ n_z &\approx -f_z / \sqrt{1 + f_z^2} = v_z \end{aligned} \quad (41)$$

Then the hull surface condition is expressed as

$$\frac{\partial \phi}{\partial n} \approx \frac{\partial \phi}{\partial v} = -U v_x \quad (42)$$

where  $\partial/\partial v = v_y \partial/\partial y + v_z \partial/\partial z$ .

Taking the representation  $\phi = \phi_1 + \phi_2$ , we can write

$$\frac{\partial \phi_1}{\partial v} = -U v_x - \frac{\partial \phi_2}{\partial v} \quad (43)$$

When the ship is placed obliquely to the uniform flow, with a drift angle  $\alpha$ , the boundary condition on the hull surface becomes

$$\frac{\partial \phi}{\partial n} = -(U \cos \alpha n_x + U \sin \alpha n_y) \quad (44)$$

Then the velocity potential can be divided into the symmetric part  $\phi_s$  and the antisymmetric part  $\phi_a$  such as

$$\phi = \phi_s \cos \alpha + \phi_a \sin \alpha \quad (45)$$

If  $\alpha = O(\varepsilon)$ , the boundary condition on the hull surface for  $\phi_s$  is given by (42), and that for  $\phi_a$  is

$$\frac{\partial \phi_a}{\partial v} = -U v_y \quad (46)$$

From the definition of  $\phi_1, \phi_2$ ,

$$\begin{aligned} \frac{\partial \phi_1}{\partial v} &= 2\pi \sigma(x, y, z) \\ &+ \int_{C(x)} \frac{\partial}{\partial v} \left[ \ln \frac{(y-y')^2 + (z-z')^2}{(y-y')^2 + (z+z')^2} \right] \sigma(x', y', z') ds \end{aligned} \quad (47)$$

$$\frac{\partial \phi_2}{\partial v} = -8\sqrt{K_0} \int_{x_0}^x dx' \int_{C(x')} E_v(\bar{x}, \bar{y}, \bar{z}) \cdot \sigma(x', y', z') ds \quad (48)$$

where  $x=x_0$  gives the bow end, and

$$E_v(x, y, z) = v_y \frac{\partial E}{\partial y} + v_z \frac{\partial E}{\partial z} \quad (49)$$

Equations (47) (48) are substituted in (43), giving an integral equation for  $\sigma(x, y, z)$ . The expression (48) suggests that the integral equation with respect to  $x$  is of the Volterra type, so that the boundary value problem is parabolic. This fact facilitates the solution to a great extent. The integral of (48) is determined by the source density in cross sections upstream. Then  $\partial \phi_2 / \partial v$  is regarded as a known function at the section where the integral equation along the hull contour is solved. The solution begins at the bow end, and marches downstream.

#### 5. WAVE PATTERN AND WAVE RESISTANCE

The pressure on the hull is given by the Bernoulli equation.

$$\begin{aligned} P &= p - p_0 \\ &= \rho [-U(\cos \alpha \phi_x + \sin \alpha \phi_y) - \frac{1}{2}(\phi_y^2 + \phi_z^2) + gz] \end{aligned} \quad (50)$$

$\phi^2$  is omitted because of higher order compared with  $\phi^1$ ,  $\phi^2$ . The elevation of the free surface is obtained by

$$\zeta = -z$$

$$= -\frac{1}{g}[U(\cos\alpha\phi_x + \sin\alpha\phi_y) + \frac{1}{2}(\phi_y^2 + \phi_z^2)]_{z=0} \quad (51)$$

The quadratic term  $\phi_y^2 + \phi_z^2$  may be omitted in the formula for the wave pattern, but it is better to include in the pressure distribution below the waterline.

The wave resistance, the lateral force, and the yaw moment are calculated by the pressure integral.

$$F_x = -\iint_S P n_x dS \approx -\int dx \int_{C(x)} P v_x ds \quad (52)$$

$$F_y = -\iint_S P n_y dS \approx -\int dx \int_{C(x)} P v_y ds \quad (53)$$

$$M_z = \iint_S P(-n_x y + n_y x) dS \approx \int dx \int_{C(x)} P v_y ds \quad (54)$$

Substituting the expression for  $\phi$  in (50), the pressure distribution is determined. The free surface elevation, forces and moment are calculated therefrom. The velocity potential  $\phi_2$  includes a term which does not depend on  $z$ . It gives the pressure distribution irrespective of the depth. However the numerical example for pressure distribution indicates that better agreement with measured results is obtained by taking account of the attenuation of this term by depth of water. The draftwise variation is related to  $\partial G/\partial z$ . There is the relation by the free surface condition,

$$\frac{\partial G}{\partial z} = \frac{1}{K_0} \frac{\partial^2 G}{\partial x^2} \quad \text{at } z=0 \quad (55)$$

Therefore the variation of the kernel  $H(\bar{x})$ , defined by (38), is given by  $(z/K_0)\partial^2 H(\bar{x})/\partial \bar{x}^2$ . This problem appears when  $K_0 z$  is not small, or  $K_0 \bar{x}$  is large. Then the asymptotic expression for  $H(\bar{x})$  may be employed. At large  $K_0 \bar{x}$ , the asymptotic expression is determined by  $Y_1(K_0 \bar{x})$ , and we have the asymptotic relation

$$\partial^2 Y_1(K_0 \bar{x})/\partial \bar{x}^2 \approx -K_0^2 Y_1(K_0 \bar{x})$$

Therefore we can express the value of  $H(\bar{x})$  at depth  $z$  in the form like

$$(1 - K_0 z)H(\bar{x})$$

We make further simplification by taking the average of the attenuation factor through  $z$ . Then the factor  $1 - \frac{1}{2}K_0 z$  is multiplied to the corresponding term in the free surface elevation, and  $(1 - \frac{1}{2}K_0 z)^2$  is multiplied in the calculation of hydrodynamic forces.

## 6. NUMERICAL METHOD

The solution of the integral equation for the distribution of sources is calculated by means of the panel method. Since the hull is symmetric, one side of the hull surface under still waterline is divided in  $I \times J = M$  panel elements  $\Delta S_{ij}$ , with  $I$  divisions in  $x$  and  $J$  divisions in  $z$ . The source density is defined at the center of the panel, over which the density is assumed uniform.

The integral equation is discretized as

$$\sum_{k=1}^J \sigma(ij) L_{ij}(k) = -v_{xij} - \sum_{l=1}^{i-1} \sum_{k=1}^J \sigma(lk) M_{ij}(lk) \quad (j = 1, 2, \dots, J) \text{ for symmetric part} \quad (56)$$

$$\sum_{k=1}^J \sigma(ij) L_{ij}(k) = -v_{yij} - \sum_{l=1}^{i-1} \sum_{k=1}^J \sigma(lk) M_{ij}(lk) \quad (j = 1, 2, \dots, J) \text{ for antisymmetric part.} \quad (57)$$

$L_{ij}(k)$  and  $M_{ij}(lk)$  denote the normal velocity of  $\phi_1$  and  $\phi_2$  by unit source at the control point respectively. The left hand side is the source density which is to be determined. The summation on the right hand side is determined by the source density along the cross section upstream. It is regarded as a known quantity, because the solution is carried out from the foremost section and proceeds backwards.  $L_{ij}(k)$  is calculated analytically. The computation of the kernel matrix  $M_{ij}(lk)$  is more time-consuming.

$$M_{ij}(lk) = v_{yij} E_y(\bar{x}, \bar{y}, \bar{z}) + v_{zij} E_z(\bar{x}, \bar{y}, \bar{z}) \quad (58)$$

We have to calculate the derivatives of  $\phi_1$  and  $\phi_2$  for the determination of various quantities.  $\partial \phi_1/\partial x$  is replaced by the finite difference,

$$\frac{\partial \phi_1}{\partial x} = \frac{(\phi_1)_i - (\phi_1)_{i-1}}{\Delta x} \quad (59)$$

Analytical expressions are employed for other derivatives. The most time-consuming is the computation of  $E$ ,  $E_x$ ,  $E_y$ ,  $E_z$ . In order to facilitate this, the following transformation is employed. Consider the integrals

$$\left. \begin{aligned} ECC &= \int_0^\infty e^{-ct} \cos(2a^{\frac{1}{2}} t^{\frac{1}{2}}) \cos(bt) dt \\ ECS &= \int_0^\infty e^{-ct} \cos(2a^{\frac{1}{2}} t^{\frac{1}{2}}) \sin(bt) dt \\ QSC &= \int_0^\infty e^{-ct} t^{\frac{1}{2}} \sin(2a^{\frac{1}{2}} t^{\frac{1}{2}}) \cos(bt) dt \\ QSS &= \int_0^\infty e^{-ct} t^{\frac{1}{2}} \sin(2a^{\frac{1}{2}} t^{\frac{1}{2}}) \sin(bt) dt \\ EQC &= \int_0^\infty e^{-ct} t^{-\frac{1}{2}} \sin(2a^{\frac{1}{2}} t^{\frac{1}{2}}) \cos(bt) dt \\ EQS &= \int_0^\infty e^{-ct} t^{-\frac{1}{2}} \sin(2a^{\frac{1}{2}} t^{\frac{1}{2}}) \sin(bt) dt \end{aligned} \right\} \quad (60)$$

Put  $p = c + ib$ , and define

$$\left. \begin{aligned} A &= ECC - iECS = \int_0^\infty e^{-pt} \cos(2a^{\frac{1}{2}} t^{\frac{1}{2}}) dt \\ B &= QSC - iQSS = \int_0^\infty e^{-pt} t^{\frac{1}{2}} \sin(2a^{\frac{1}{2}} t^{\frac{1}{2}}) dt \\ C &= EQC - iEQS = \int_0^\infty e^{-pt} t^{-\frac{1}{2}} \sin(2a^{\frac{1}{2}} t^{\frac{1}{2}}) dt \end{aligned} \right\} \quad (61)$$

Then we have

$$\left. \begin{aligned} ECC &= \Re A, & ECS &= -\Im A \\ QSC &= \Re B, & QSS &= -\Im B \\ EQC &= \Re C, & EQS &= -\Im C \end{aligned} \right\} \quad (62)$$

Applying the Laplace transform,

$$A = p^{-1} + i\pi^{\frac{1}{2}} a^{\frac{1}{2}} p^{-3/2} e^{-a/p} \operatorname{erf}(ia^{\frac{1}{2}} p^{-\frac{1}{2}}) \quad (63)$$

$$B = a^{\frac{1}{2}} p^{-2} - i\pi^{\frac{1}{2}} p^{-5/2} (\frac{1}{2}p - a) e^{-a/p} \operatorname{erf}(ia^{\frac{1}{2}} p^{-\frac{1}{2}}) \quad (64)$$

$$C = -i\pi^{\frac{1}{2}} p^{-5/2} e^{-a/p} \operatorname{erf}(ia^{\frac{1}{2}} p^{-\frac{1}{2}}) \quad (65)$$

where  $\operatorname{erf}(Z)$  is the error function defined by

$$\operatorname{erf}(Z) = \frac{2}{\sqrt{\pi}} \operatorname{Erf}(Z) = \frac{2}{\sqrt{\pi}} \int_0^Z e^{-t^2} dt \quad (66)$$

There is the expansion for the error function about  $Z=0$  as

$$\operatorname{Erf}(Z) = \sum_{n=0}^{\infty} \frac{(-1)^n Z^{2n+1}}{n!(2n+1)} = e^{-Z^2} \sum_{n=0}^{\infty} \frac{2^n Z^{2n+1}}{(2n+1)!!} \quad (67)$$

where

$$(2n+1)!! = (2n+1)(2n-1)(2n-3)\dots\cdot 5\cdot 3\cdot 1$$

$$(-1)!! = 1$$

On the other hand, the error function has an asymptotic expansion at  $|Z| \rightarrow \infty$  such as

$$\operatorname{Erf}(Z) = \frac{\sqrt{\pi}}{2} - e^{-Z^2} \sum_{n=0}^{\infty} \frac{(-1)^n (2n-1)!!}{2^{n+1} Z^{2n+1}} \quad (68)$$

Now we put

$$\operatorname{Erf}(Z) = -e^{-Z^2} \sum_{n=0}^{N-1} \frac{(-1)^n (2n-1)!!}{2^{n+1} Z^{2n+1}} + \psi_N(Z) \quad (69)$$

The first term on the right hand side is the asymptotic expansion. If  $a_n$  denotes the  $n$ -th term of the asymptotic expansion, and  $\epsilon$  gives the accuracy, we have

$$\psi_N(Z) = \frac{\sqrt{\pi}}{2} \quad \text{for } |a_n| \leq \epsilon \quad (70)$$

$$\psi_N(Z) = \frac{(2N-1)!!}{2^N} \sum_{n=0}^{\infty} \frac{(-1)^{n-N} Z^{2n-2N+1}}{n!(2n-2N+1)} \quad \text{for } |a_n| > \epsilon \quad (71)$$

where  $N$  is the integral part of  $|Z^2|$ . When  $N=0$ , the first term of (69) becomes zero, and  $\operatorname{Erf}(Z) = \psi_0(Z)$ . Then (69) coincides with (67). If  $Z$  is pure imaginary,  $Z = iy$ ,

$$\operatorname{Erf}(iy) = \int_0^{iy} e^{-t^2} dt = i \int_0^y e^{-t^2} dt \quad (72)$$

Then it is pure imaginary. Put

$$\operatorname{Erf}(iy) = i \left[ e^{y^2} \sum_{n=0}^{N-1} \frac{(2n-1)!!}{2^{n+1} y^{2n+1}} \right] + \psi_N(iy) \quad (73)$$

$\psi_N(iy)$  is given by

$$\psi_N(iy) = 0 \quad \text{for } |a_n| \leq \epsilon \quad (74)$$

$$\psi_N(iy) = i \left[ \frac{(2N-1)!!}{2^N} \sum_{n=0}^{\infty} \frac{y^{2n-2N+1}}{n!(2n-2N+1)} \right] \quad \text{for } a_n > \epsilon \quad (75)$$

Sample calculations of the Fresnel integral, to which the existing program library is available, confirm excellent accuracy of the above method. Putting

$$a = K_0 \bar{x}^2/2, \quad b = \bar{y}, \quad C = \bar{z} > 0, \quad (76)$$

we obtain

$$\left. \begin{aligned} E_x(\bar{x}, \bar{y}, \bar{z}) &= \frac{1}{2} \sqrt{K_0} ECC = \frac{1}{2} \sqrt{K_0} \Re A \\ E_y(\bar{x}, \bar{y}, \bar{z}) &= -\frac{1}{2} QSS = \frac{1}{2} \Im B \\ E_z(\bar{x}, \bar{y}, \bar{z}) &= -\frac{1}{2} QSC = -\frac{1}{2} \Re B \\ E(\bar{x}, \bar{y}, \bar{z}) &= \frac{1}{2} EQC = \frac{1}{2} \Re C \end{aligned} \right\} \quad (77)$$

In order to check the computer time, the wave Pattern of a point source is calculated. The computation by means of the above expression takes 2.04sec.CPU by HITAC M-240H, while it takes 2min.-7sec.CPU, if  $E_x$  is calculated by Simpson's rule.

## 7. RESULTS OF THE WIGLEY HULL

The hull surface geometry is given by the equation

$$y = b[1 - (\frac{x}{\ell})^2][1 - (\frac{z}{d})^2] \quad (78)$$

where  $\ell = L/2$  is half length,  $b = B/2$  is half breadth, and  $d$  is the draft at still waterline. A model of dimensions  $L = 2.000\text{m}$ ,  $B = 0.200\text{m}$ ,  $d = 0.125\text{m}$  is employed for experiments in the towing tank of Yokohama National University.

The panel division for the numerical work is  $40(\text{length}) \times 10(\text{draft}) = 400$ , in equal intervals. The hull form with panel division is illustrated in Fig.1.

First of all, the source distribution over the hull surface is determined. A few sample results are illustrated in Figs.2,3. Comparison is made with the source distribution of the double model. Remarkable difference is observed near the free surface. This fact suggests the inadequacy of the original form of the slender ship theory, which employs the double body potential as the near field solution. Fig.4 shows the pressure distribution on the hull surface at Froude number 0.267. The result of computation is compared with measured results with 6m-model published by Namimatsu et al (10). Generally speaking, good agreement is observed between computed and measured results. Slight deviation at the stern region may be attributed to the boundary layer displacement effect.

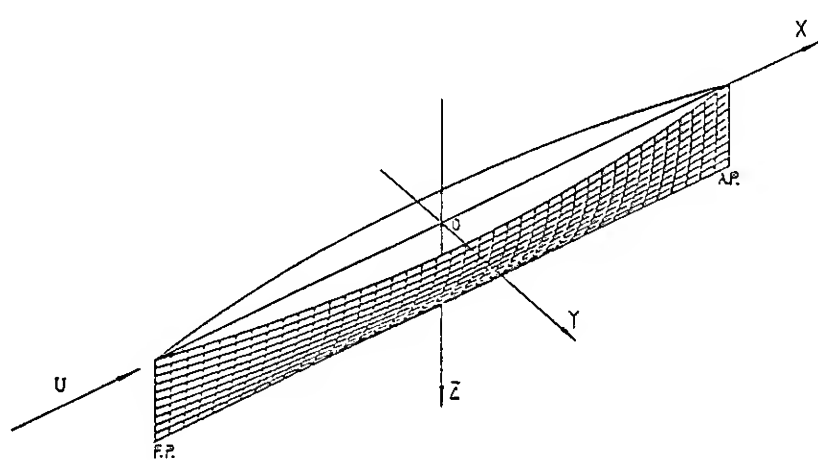


Fig. 1 Coordinate system (Wigley hull)

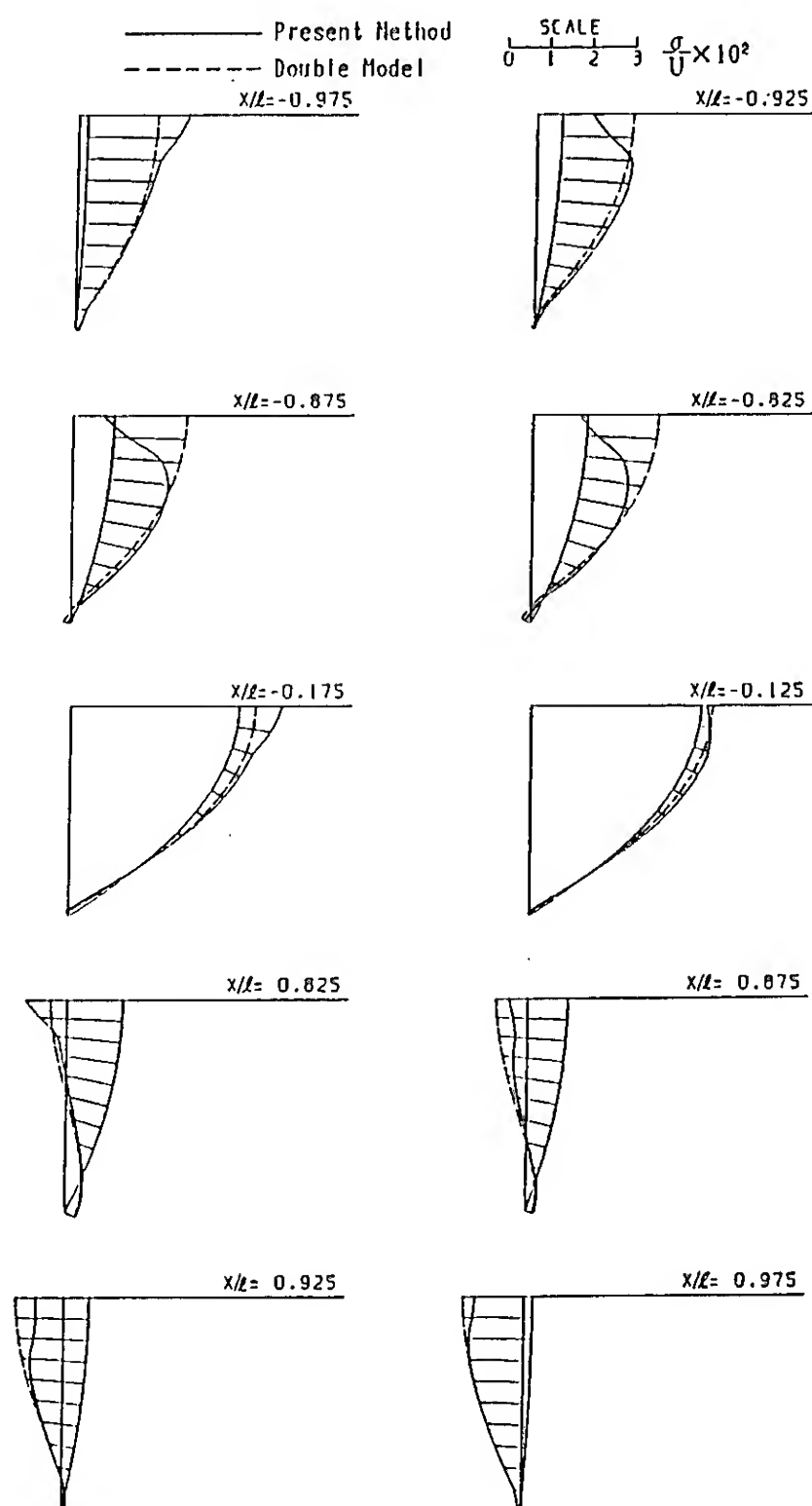


Fig. 2 Source distribution at each cross section  $F_n = 0.267$

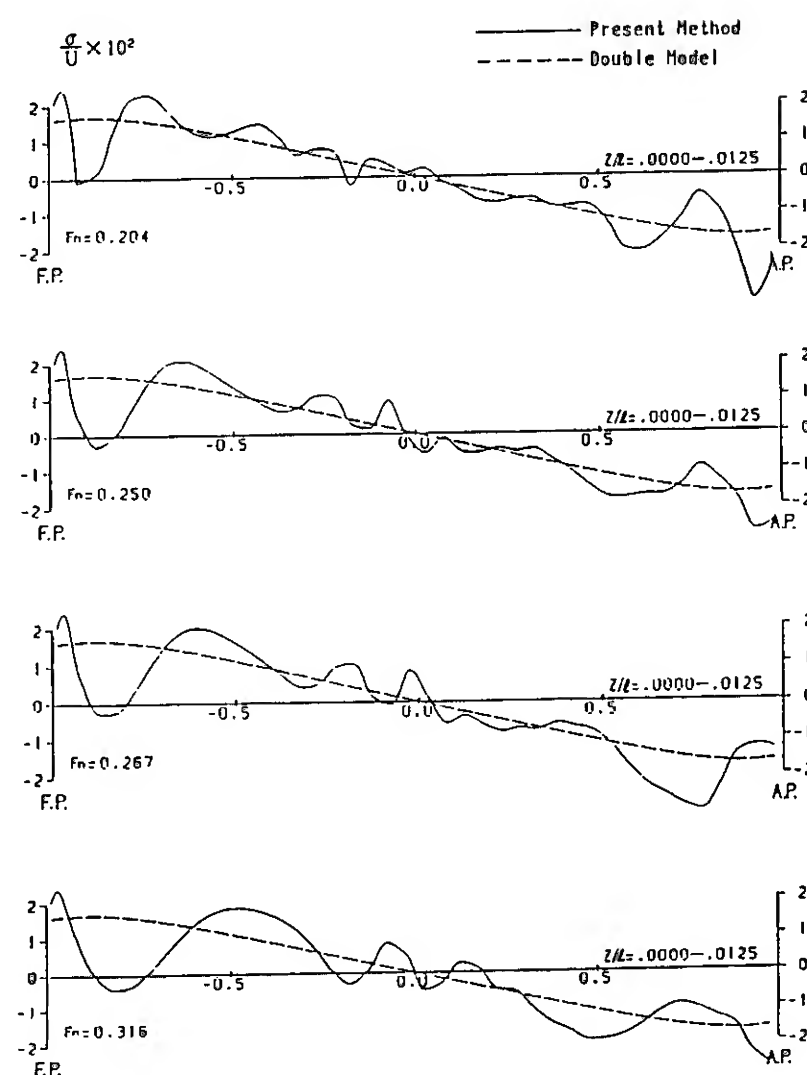


Fig. 3 Longitudinal distribution of sources at uppermost panels

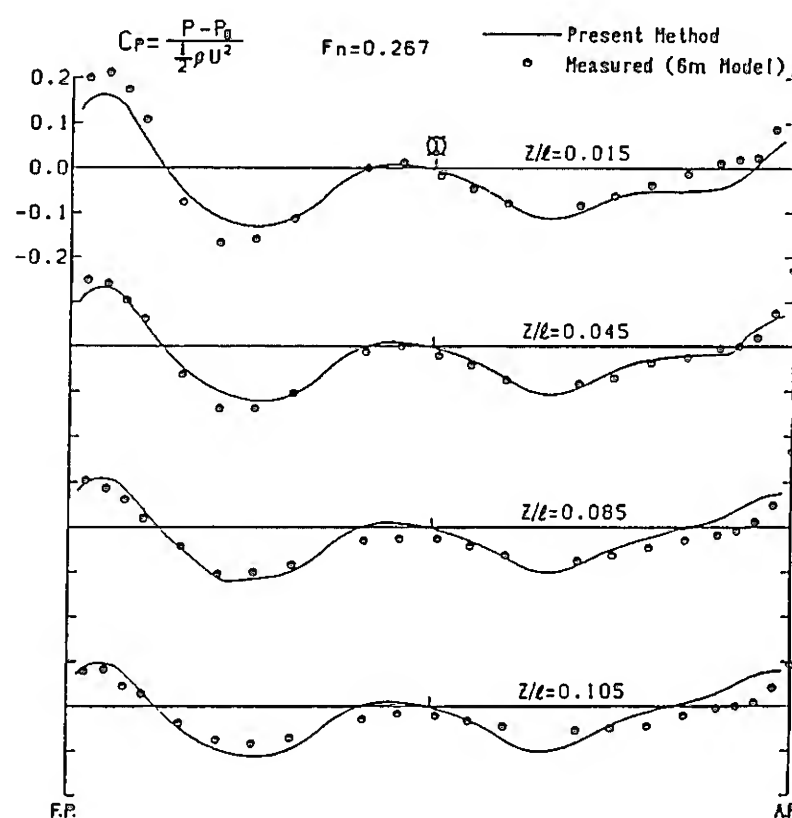


Fig. 4 Pressure distribution on the hull surface at  $F_n = 0.267$

Samples of computation of the wave profile alongside the model are illustrated in Fig.5. The result at Froude number 0.267 is compared with the experiment of 2m-model at YNU towing tank, and the result at Froude number 0.316 is compared with the measurement of 6m-model mentioned before. Slight discrepancies are observed at the wave trough. They may be attributed to the nonlinear effect because the phase of the wave is in good agreement. The computed wave pattern around the hull at Froude number 0.267 is illustrated in Fig.6, and the corresponding measurement is illustrated in Fig.7. Similar configurations in the crest and trough of waves are observed between computation and measurement. Fig.8 shows the result of computation of the wave resistance coefficient. The computed values given by white spots are compared with the values obtained by the longitudinal cut wave survey given by black spots. Good agreement in the position of humps and hollows is observed. The computed wave resistance is slightly higher than the wave-pattern resistance. It may be a common trend, that the wave-pattern resistance shows a little lower value. The dotted line gives the wave resistance obtained by the subtraction of viscous resistance defined by  $C_F(1+K)$ , where  $C_F$  is the Schoenherr friction coefficient and  $K = 0.15$ , the form factor, from the total resistance coefficient. This curve fits well with the computed values. The full line gives the Michell resistance, which shows a great deviation from the measurement.

Computations are also carried out with respect to the Wigley hull at finite drift angles,  $\alpha = 5^\circ, 10^\circ, 15^\circ, 20^\circ$ , as the example of the asymmetric flow. Fig.9 shows the computed wave profile alongside the model at  $\alpha = 10^\circ$ , Froude number 0.267. The result of measurement with 2m-model at Yokohama National University is also shown. Fairly good agreement except near the bow on the back side (leeway side), at which the leading edge separation may be present. The computed and measured wave pattern around the model is illustrated in Fig.10 and Fig.11 respectively. In spite of good agreement in the wave profile, some deviation is observed in the diverging wave pattern. It may be attributed to the distortion of the base flow due to the hull, while the computation does not take account of it.

Longitudinal and lateral components of the force and the moment about the vertical axis are given in Fig.12, Fig.13 and Fig.14 respectively. The nonlinearity of curves at large angle may be due to the inclusion of the term of velocity squared. There are no data available for comparison with measurement. The computation does not include the viscous force which must be present, though the flow separation at the leading edge is observed clearly. Therefore the computation under the condition of continuous flow of a perfect fluid may not hold in the actual condition.

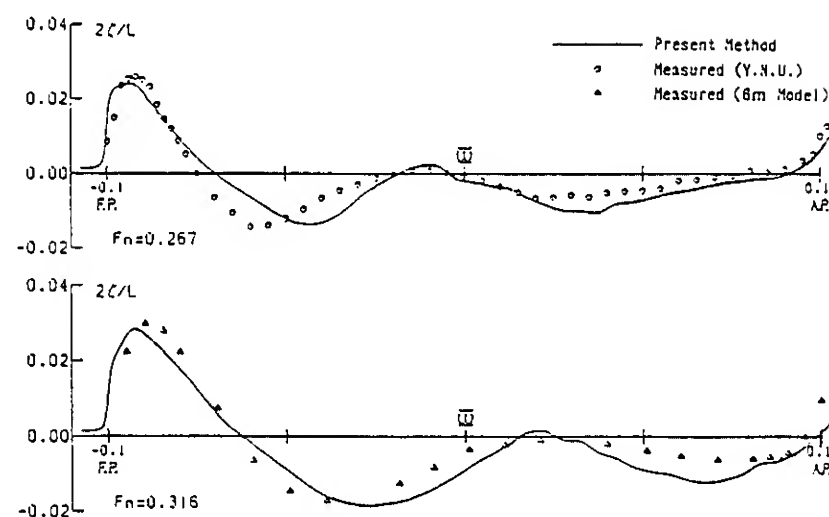


Fig. 5 Wave profile alongside the model at  $F_n = 0.267, 0.316$

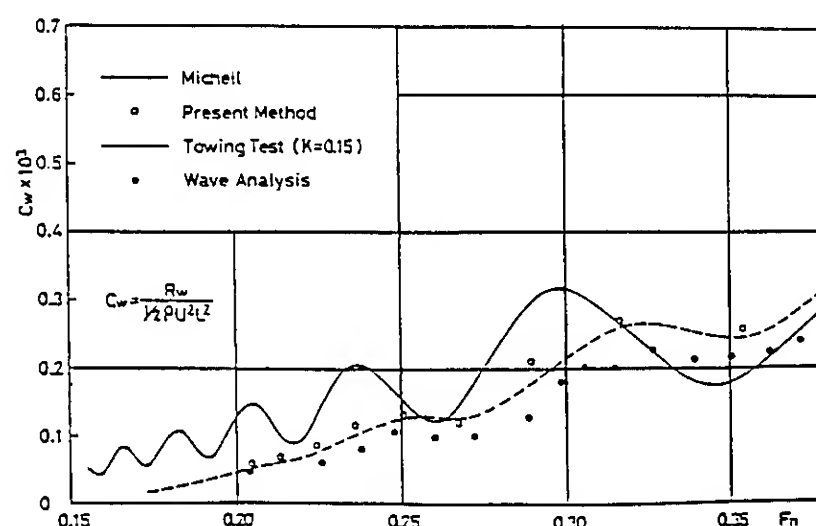


Fig.8 Wave resistance coefficient of Wigley hull

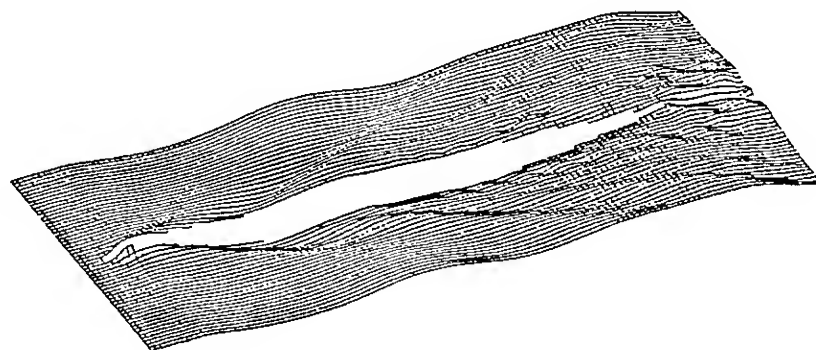


Fig. 6 Computed wave pattern at  $F = 0.267$

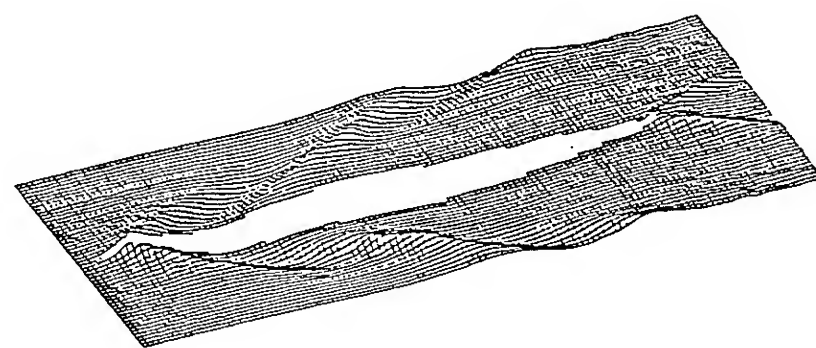


Fig. 7 Measured wave pattern at  $F_n = 0.267$



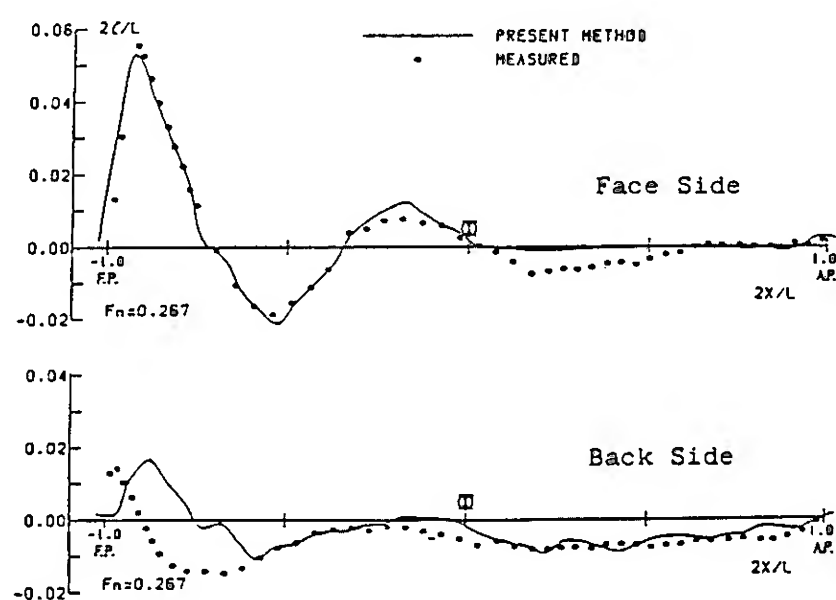


Fig. 9 Computed and measured wave profile alongside the hull  
 $\alpha = 10^\circ$ ,  $F_n = 0.267$

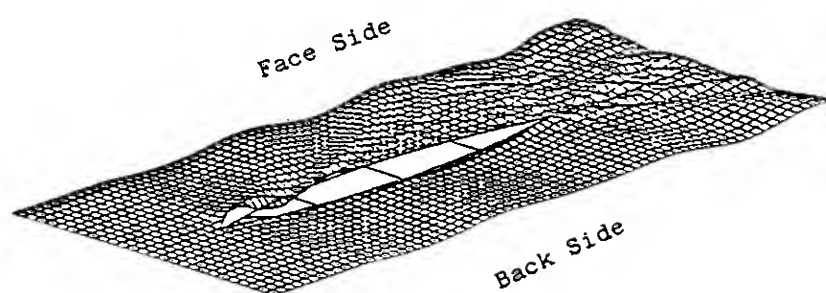


Fig. 10 Computed wave pattern  
 $\alpha = 10^\circ$ ,  $F_n = 0.267$

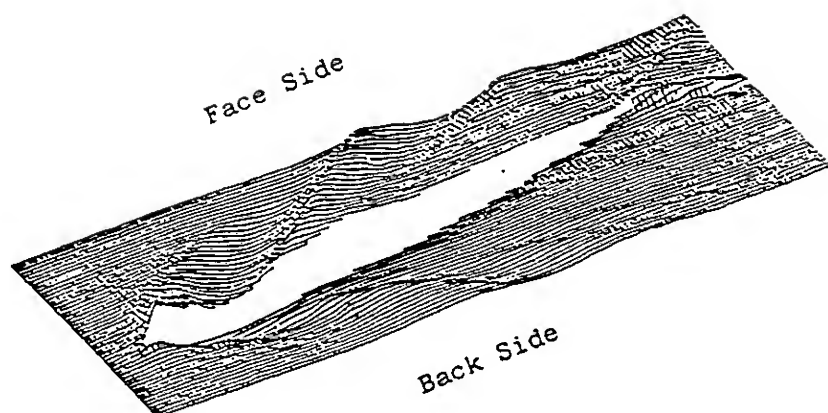


Fig. 11 Measured wave pattern  
 $\alpha = 10^\circ$ ,  $F_n = 0.267$

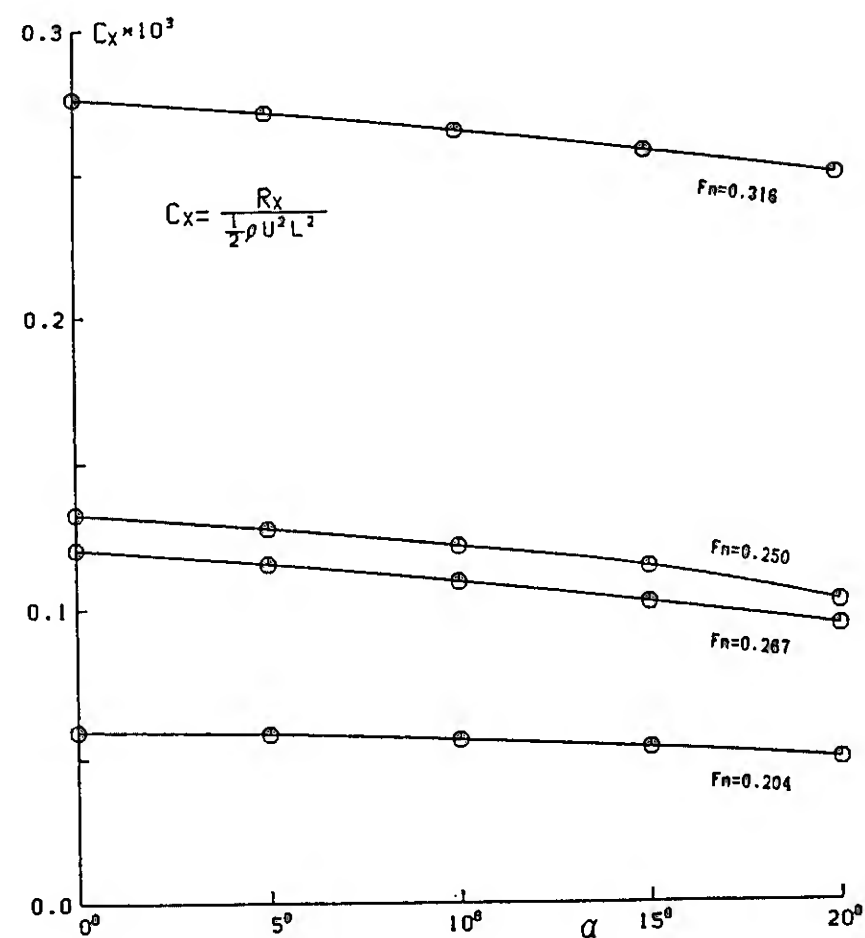


Fig. 12 Computed longitudinal force coefficient

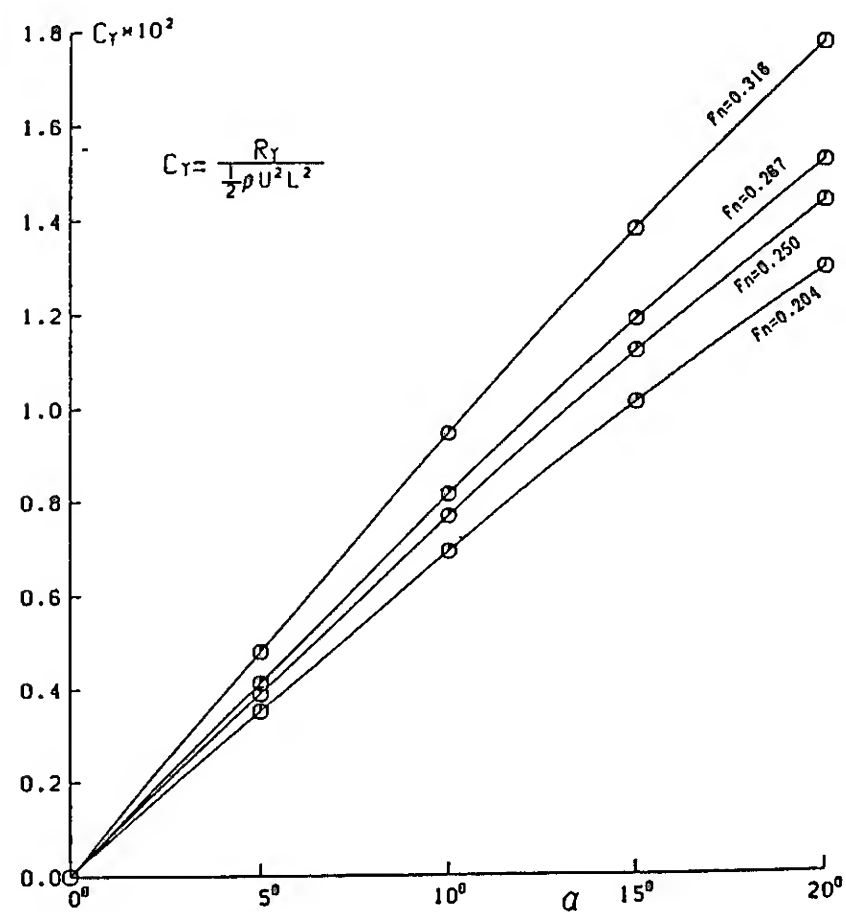
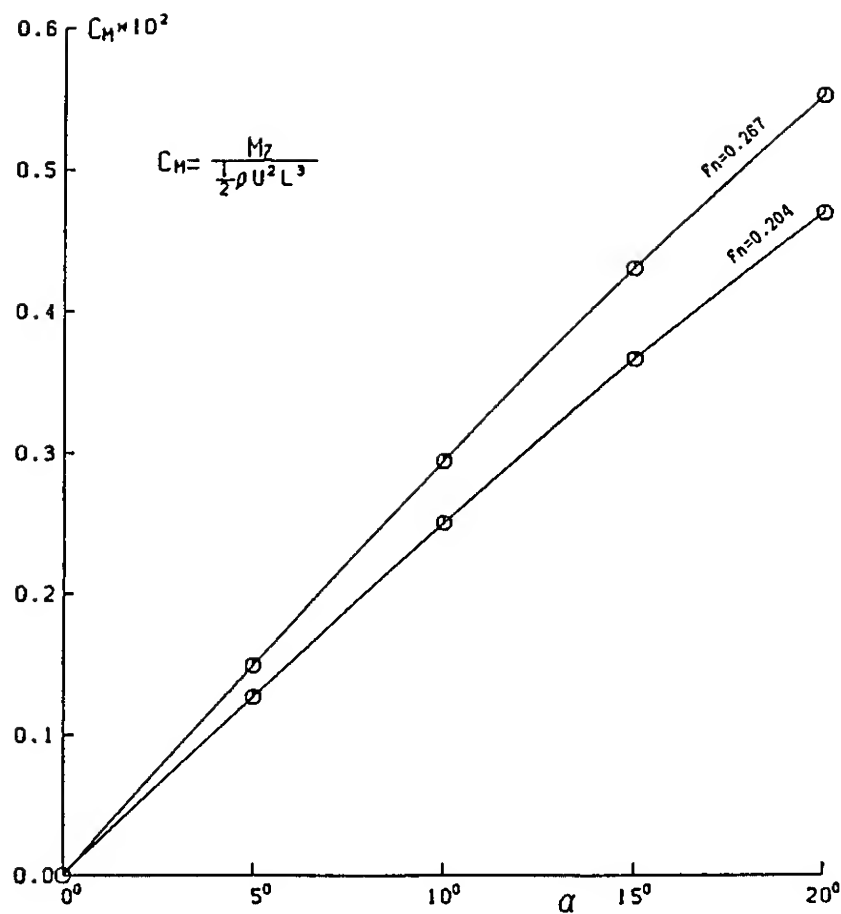


Fig. 13 Computed Lateral force coefficient



## 8. RESULTS OF THE SAILING YACHT HULL

The hull form has been designed by NCAC following the rule of 12 metre class yacht. The hull form with panel division is illustrated in Fig.15. The length is divided into 40 segments in equal intervals. The radial cut is employed in the draftwise division. The angle of the radial cut from the waterline is  $\alpha = 0^\circ, 8^\circ, 16^\circ, 24^\circ, 32^\circ, 40^\circ, 50^\circ, 70^\circ, 80^\circ, 90^\circ$ . The panel division on the solid keel is  $11 \times 8$ , but small panels are combined, resulting 70 panels. A model with a detachable solid keel and a rudder is made for towing tank experiment. The resistance test at zero drift angle is carried out at Yokohama National University tank. Experiments at the finite drift angle are conducted by Akishima Laboratory of Mitsui Shipbuilding Co.

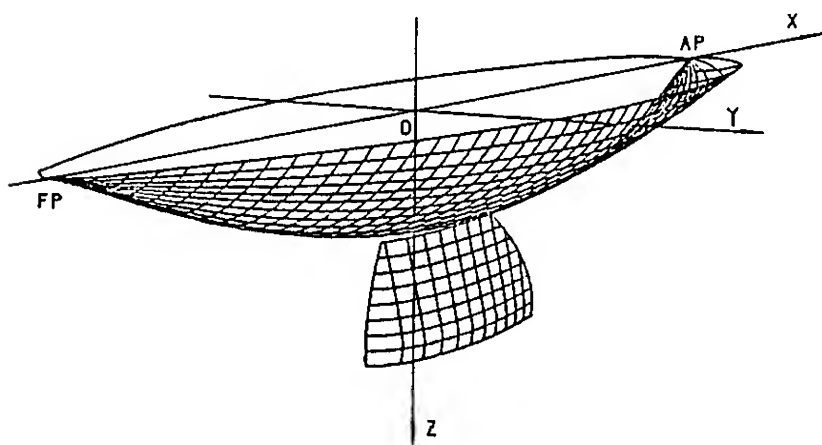
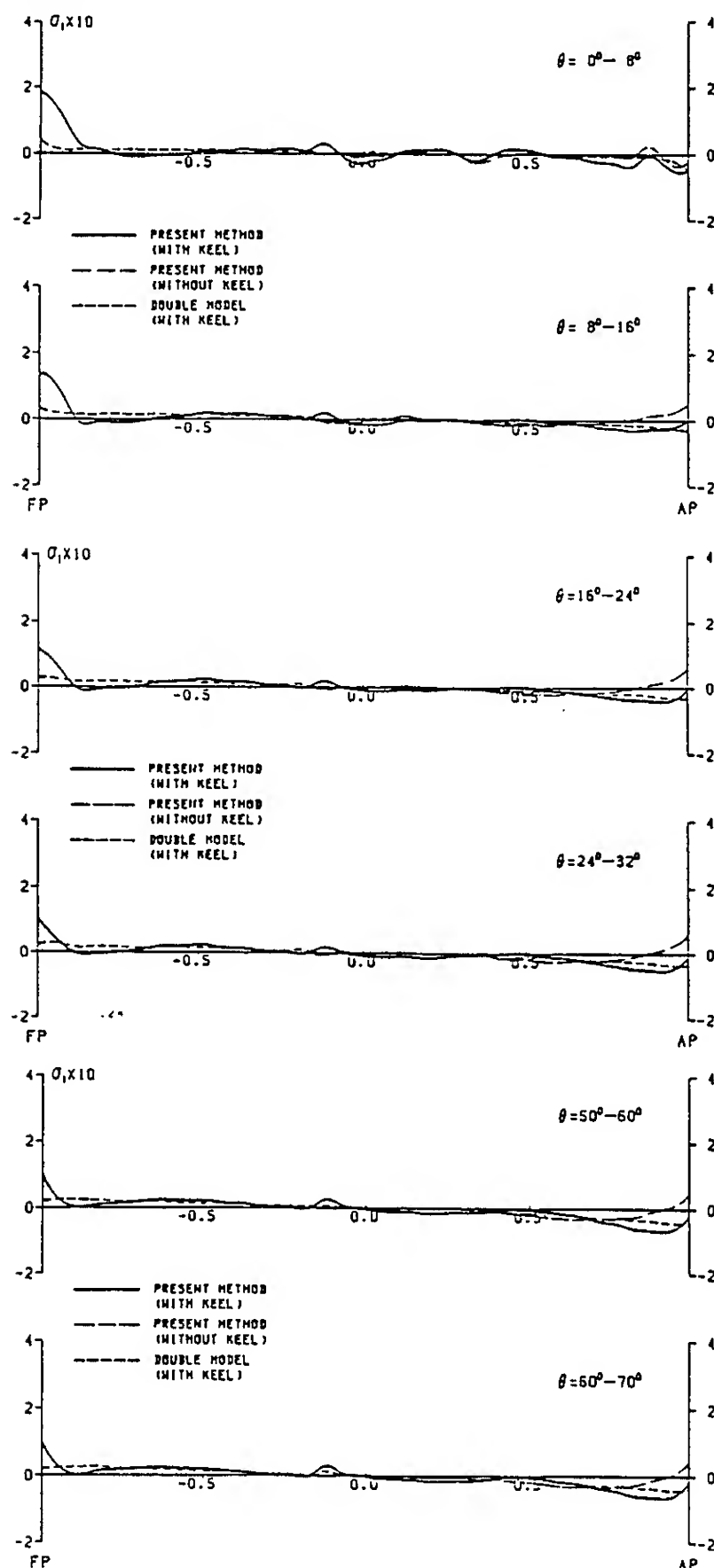


Fig. 15 Sailing yacht hull form

Fig.16 gives the longitudinal distribution of the symmetric part of sources on the canoe body with and without keel, and Fig.17 gives that of the antisymmetric part of sources at Froude number 0.269. A remarkable effect of the vertical keel to the source distribution on the canoe body at finite drift angle is observed. Fig.18 gives the wave profile alongside the hull, and Fig.19 illustrates the wave pattern around the hull by the wave contour, at the drift angle  $0^\circ, 4^\circ, 8^\circ$ , at Froude number 0.269. Because of small length to beam ratio and the flat stern, the wave pattern behind the stern becomes very complex. No measured data are available for comparison, but a particular feature of this hull form is observed in these figures.



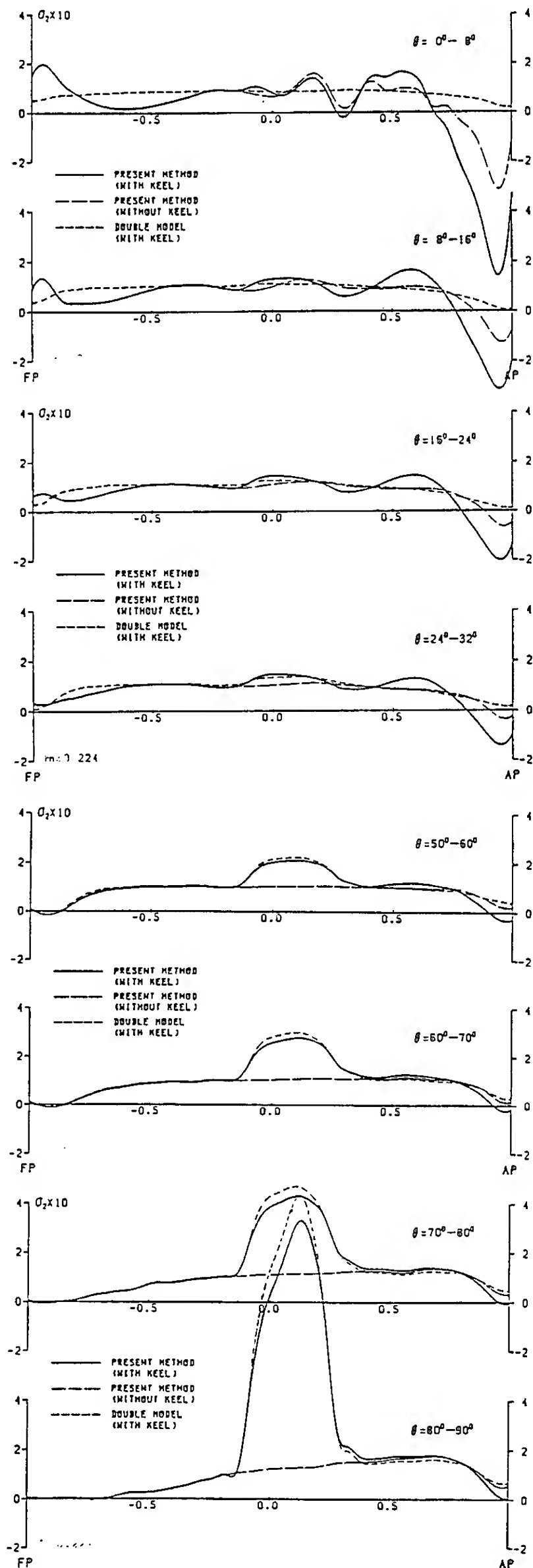


Fig. 17 Longitudinal distribution of antisymmetric part of sources  $F_n = 0.269$

Fig.20 shows the wave resistance coefficient of the canoe body without keel. Towing test results are given by the total resistance coefficient  $C_T$ , the residual resistance coefficient  $C_R$  based on the Schoenherr friction coefficient, and the wave resistance coefficient derived by the assumption of the form factor  $K = 0.29$ . The curve of residual resistance fits the computed values approximately. The deviation at higher Froude numbers may be attributed to the change of wetted hull geometry due to sinkage and trim, together with the bow wave elevation. Fig.21 shows the wave resistance coefficient of the hull with keel. The effect of the keel to the computed wave resistance is mainly due to the difference in the source distribution near the stern. The difference in  $C_T$  between results with and without keel is remarkable. The conventional method of the form factor for viscous resistance gives 0.54, which seems to be too large. The computed points are not parallel to the experimental curve. This deviation may be partly due to the change of trim, which is more remarkable than in the case without keel.

The axial and lateral forces when the model is moving at finite drift angle are calculated. The axial force coefficient  $C_x$  is shown in Figs.22,23. The computation does not include the induced drag of the solid keel. Therefore the difference between the results with and without keel is not remarkable. Experimental data obtained by the Akishima laboratory are shown in white spots. Since the model is free to heel and trim in the experiment, there is a considerable difference between experiment and computation. Then the comparison is only for reference.

The lateral force coefficient  $C_y$  is shown in Figs. 24, 25. The computation does not include the lift of the solid keel. In order to calculate the lift of the keel, the lifting surface computation such as the vortex lattice method is necessary. However the result of computation by the theory of large aspect ratio is added for simplicity. The result is shown in dotted lines. The measured data are shown by white spots. However comparison is difficult, because of the difference in conditions mentioned before. The computed yaw moment coefficient  $C_M$  is shown in Figs.26, 27. Different from the lateral force, difference between the moment with and without keel is remarkable. This means that the theory includes the moment of the keel. One may conclude from the above results, that the present theory is applicable to the wave resistance of the canoe body of the yacht, in spite of the small length to beam ratio, while other theories such as the vortex lattice computation is necessary for the prediction of hydrodynamic forces acting on the hull with vertical keel at finite drift angle.

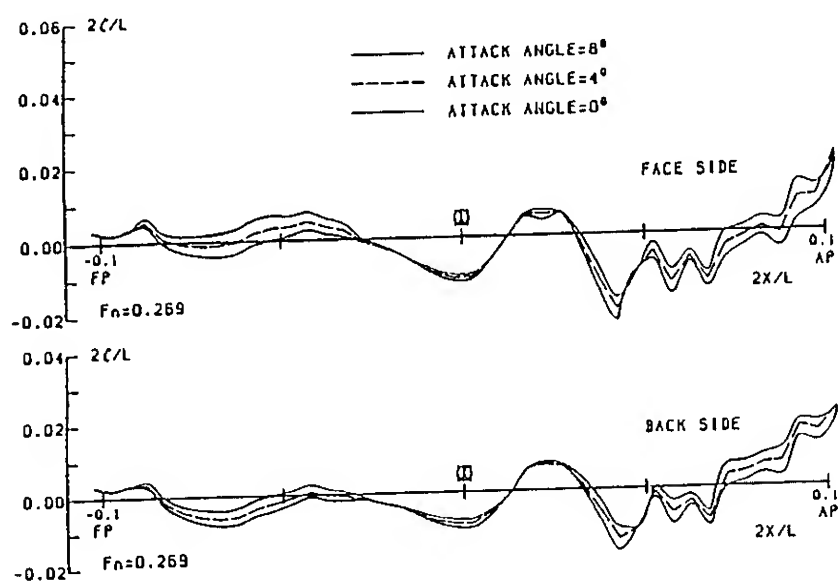


Fig. 18-a Computed wave profile  
alongside the hull  
without keel  $F_n = 0.269$

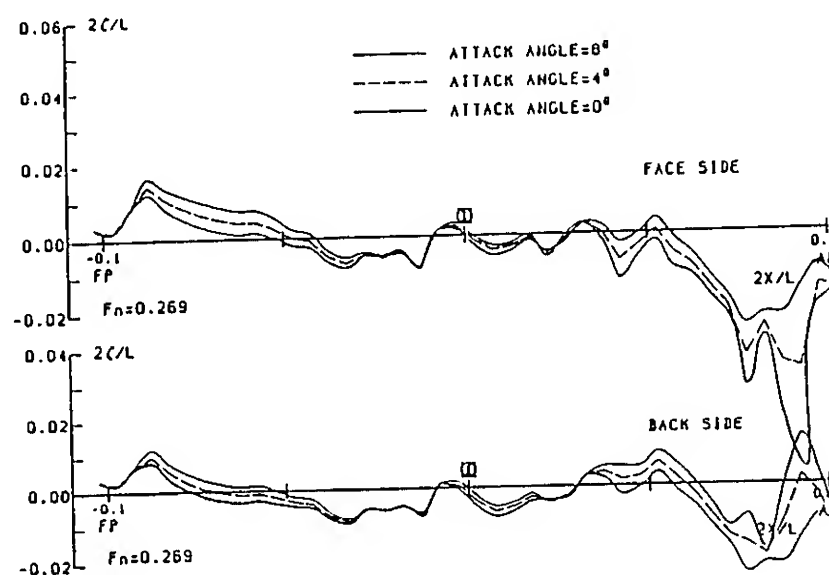


Fig. 18-b Computed wave profile  
alongside the hull  
with keel  $F_n = 0.269$

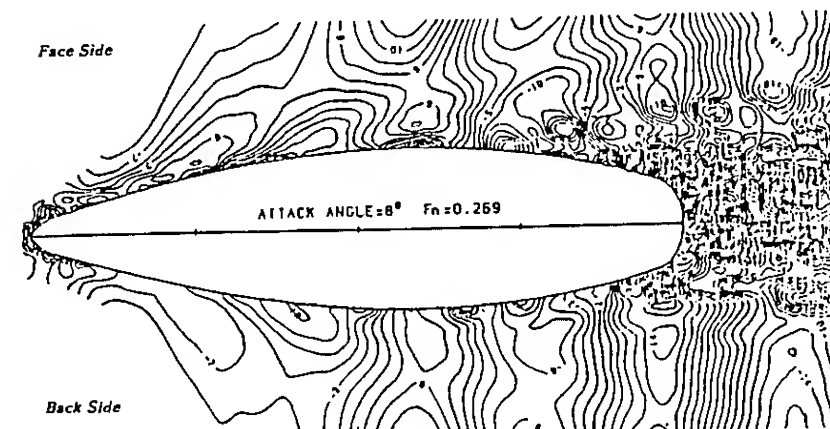
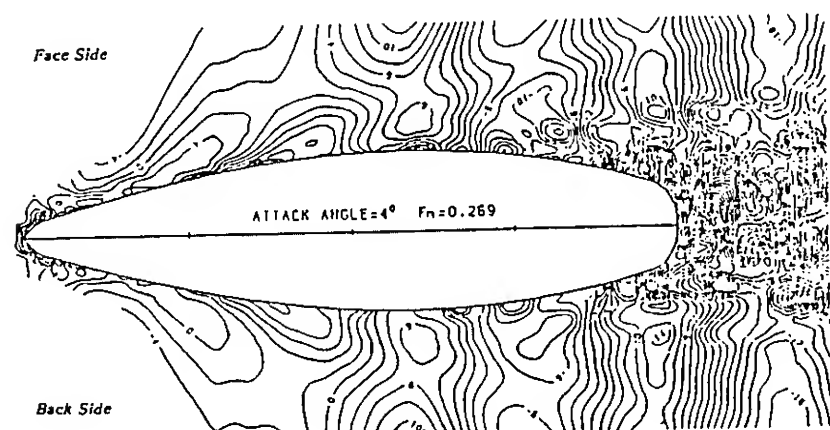
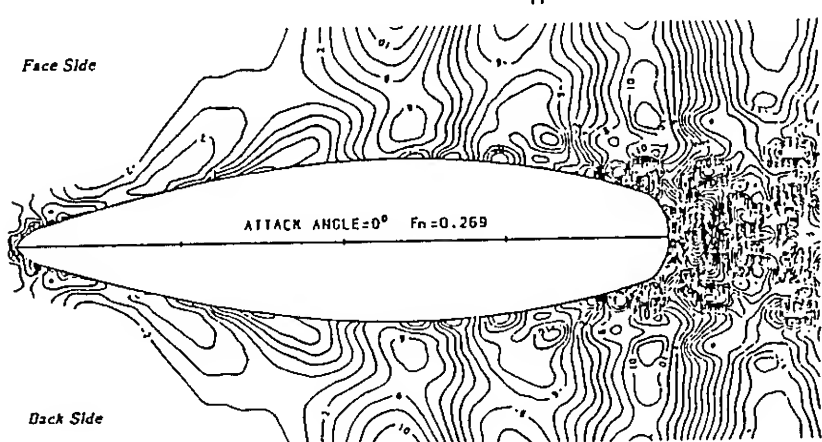


Fig. 19-a Computed wave contour  
without keel  $F_n = 0.269$

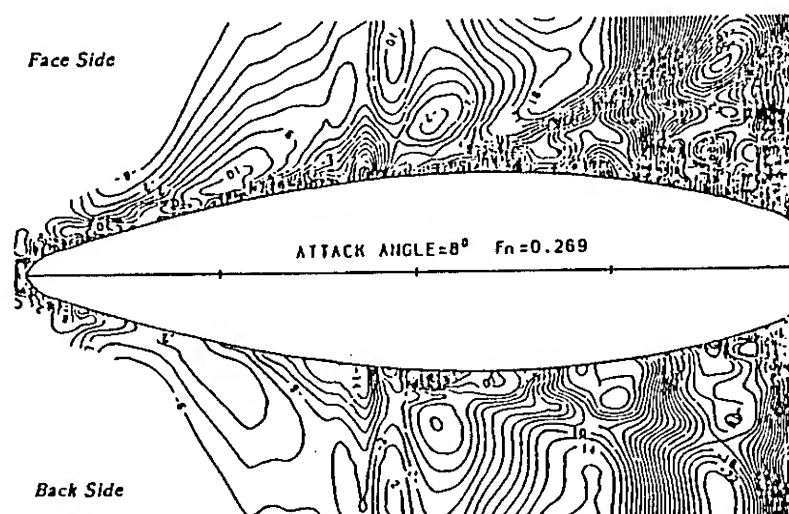
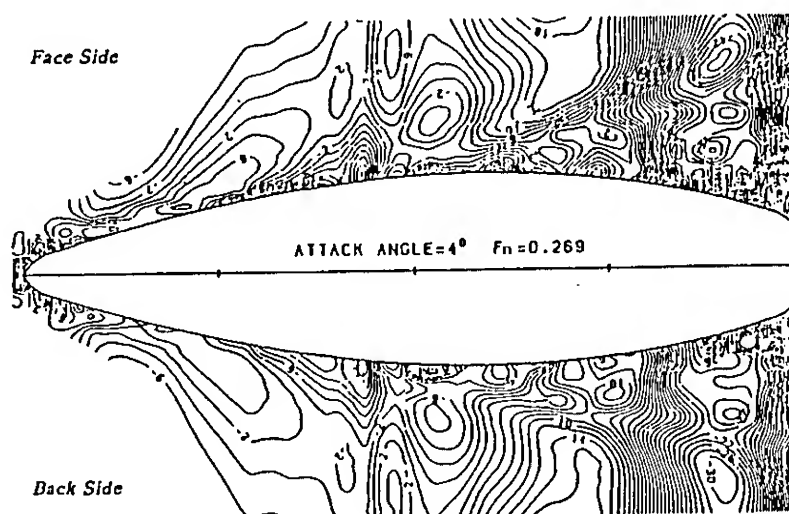
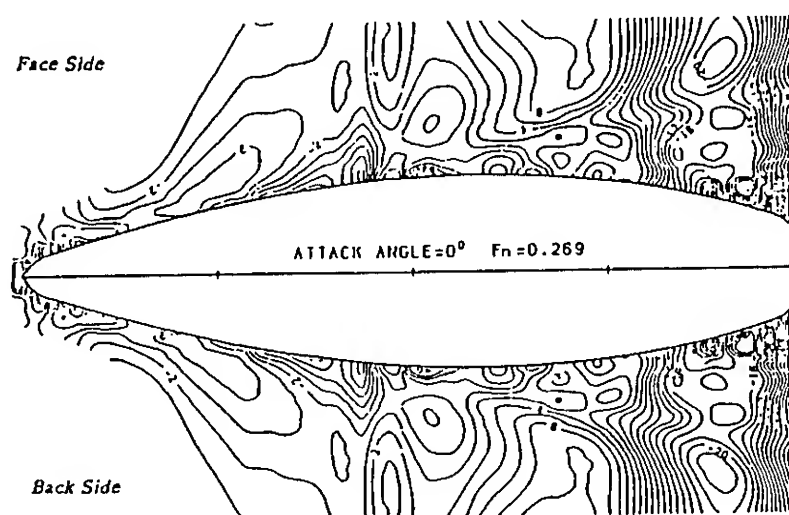


Fig. 19-b Computed wave contour  
with keel  $F_n = 0.269$

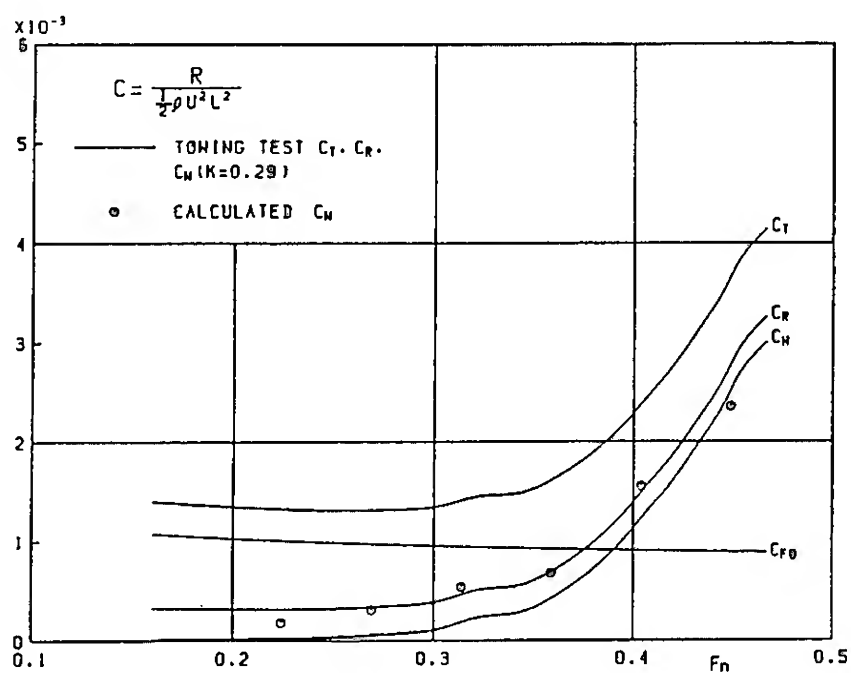


Fig. 20 Computed wave resistance coefficient compared with test results of yacht model without keel

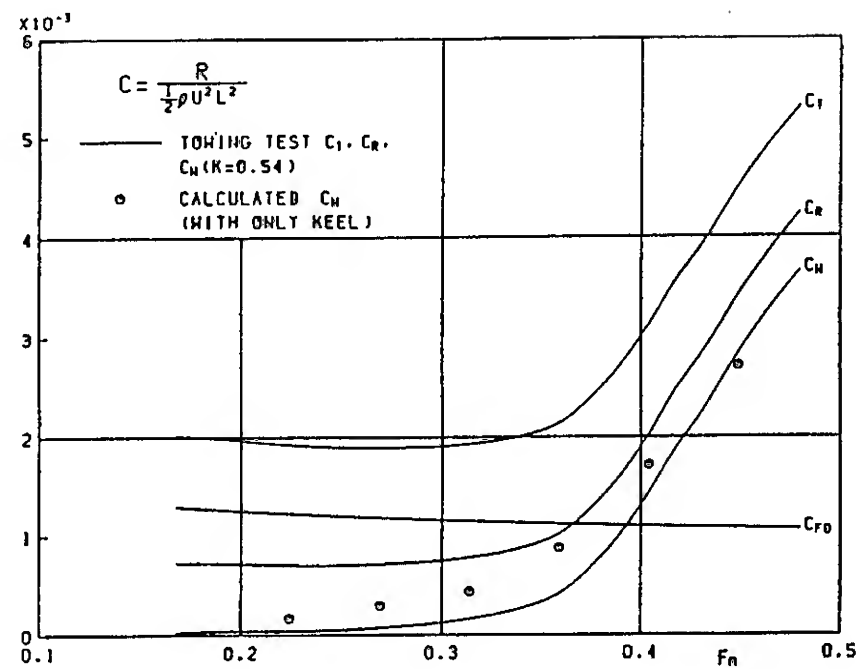


Fig. 21 Computed wave resistance coefficient compared with test results of yacht model with keel

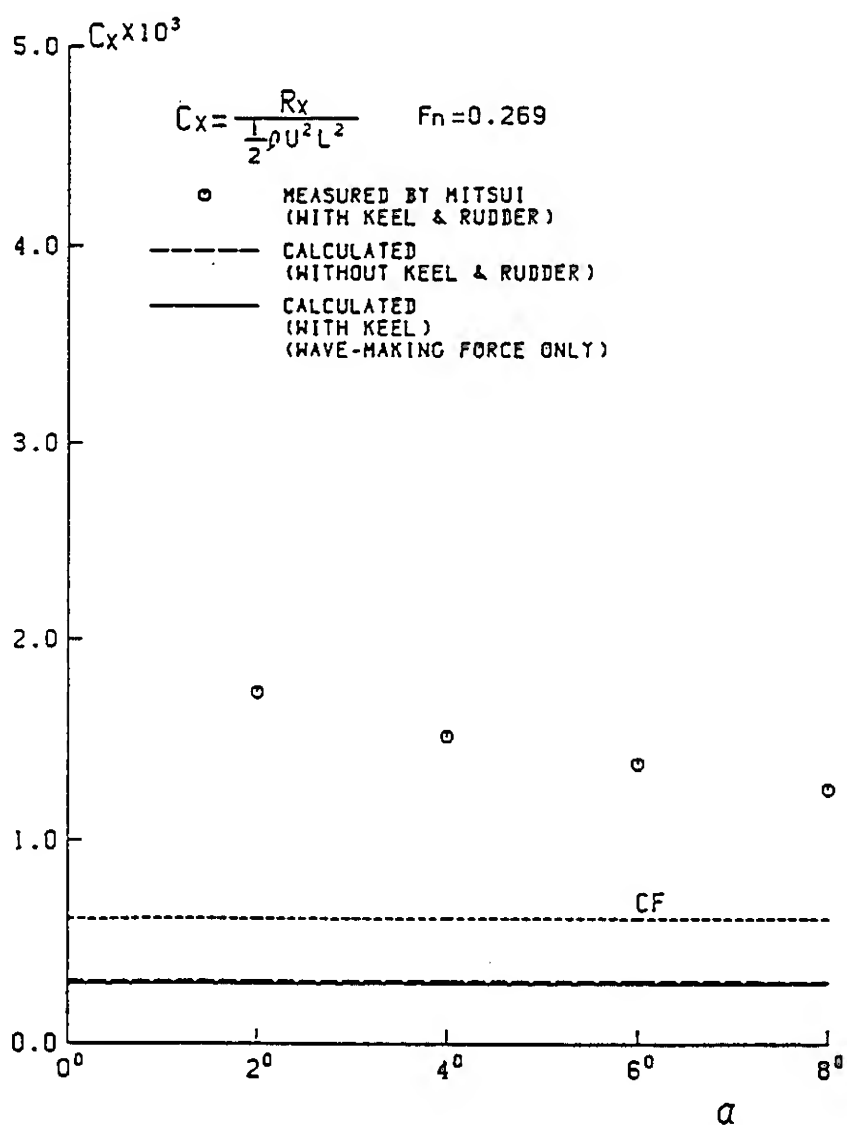


Fig. 21 Computed axial force coefficient of yacht model  $F_n = 0.269$

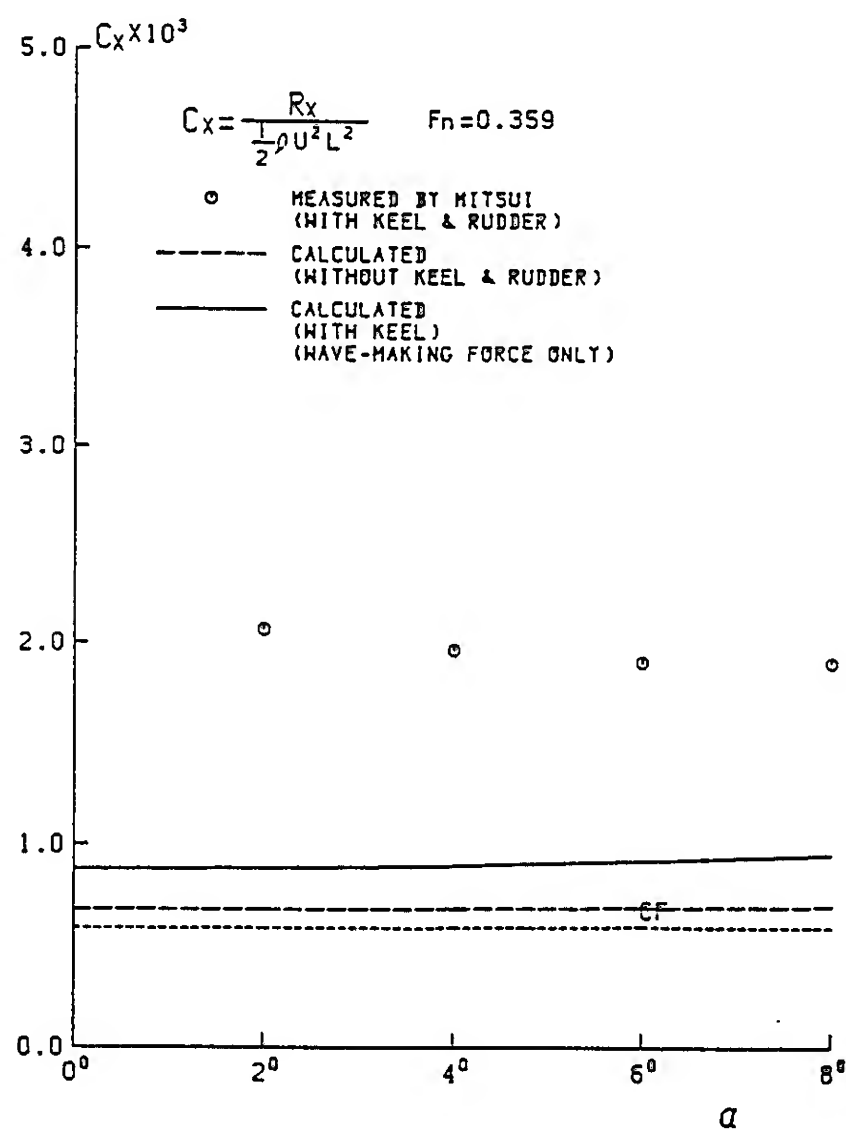


Fig. 23 Computed axial force coefficient of yacht model  $F_n = 0.359$

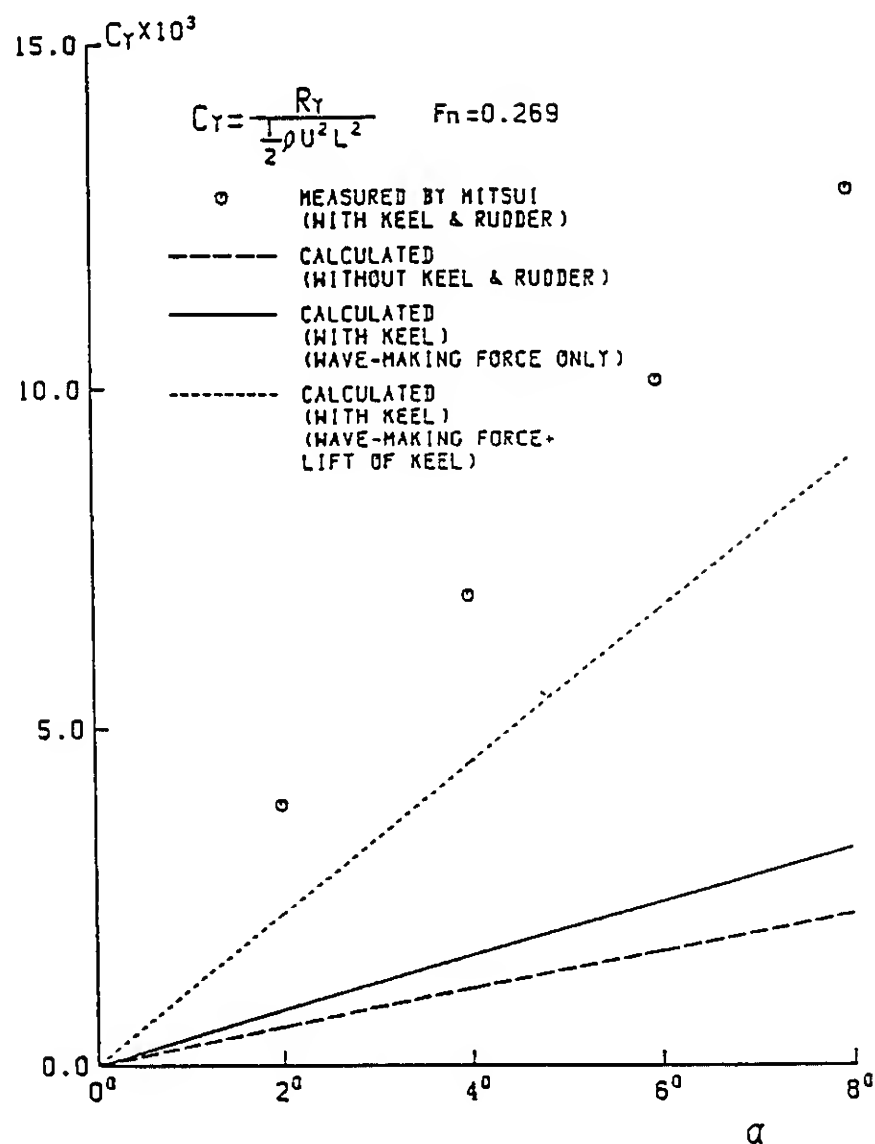


Fig. 24 Computed lateral force coefficient of yacht model  
 $F_n = 0.269$

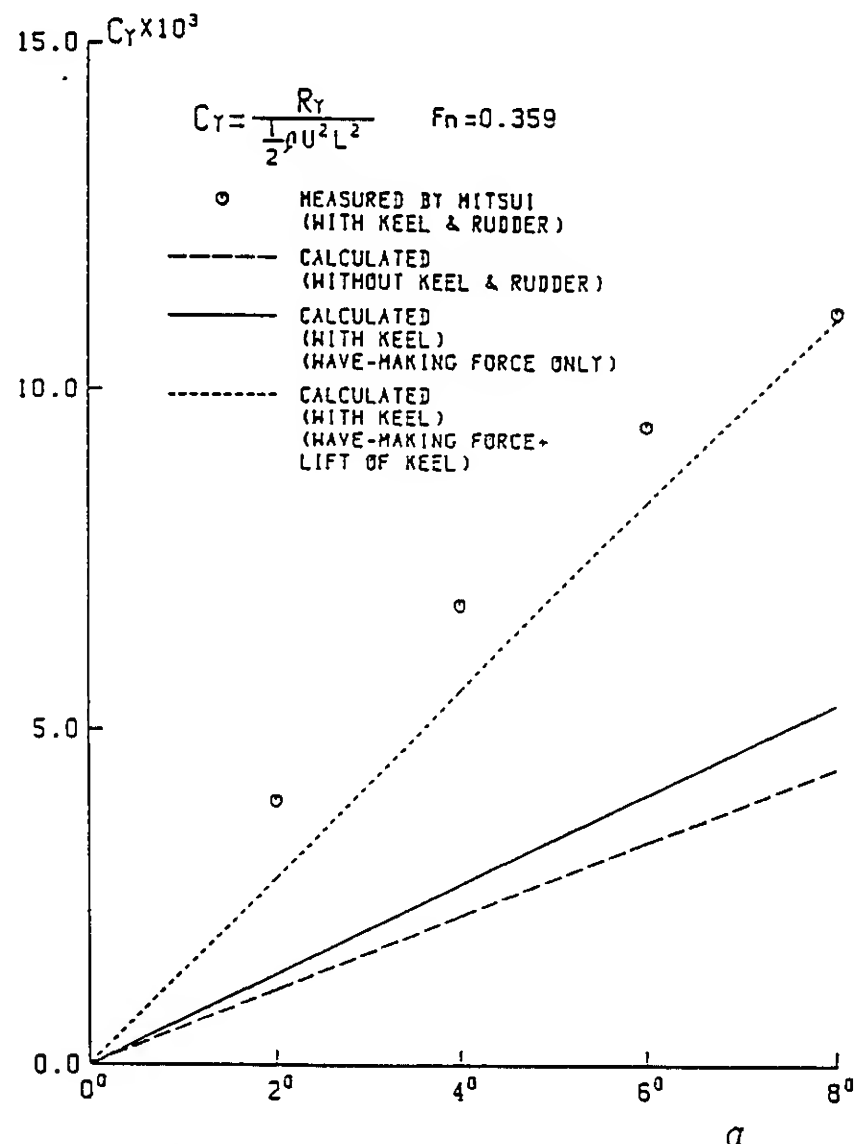


Fig. 25 Computed lateral force coefficient of yacht model  
 $F_n = 0.359$

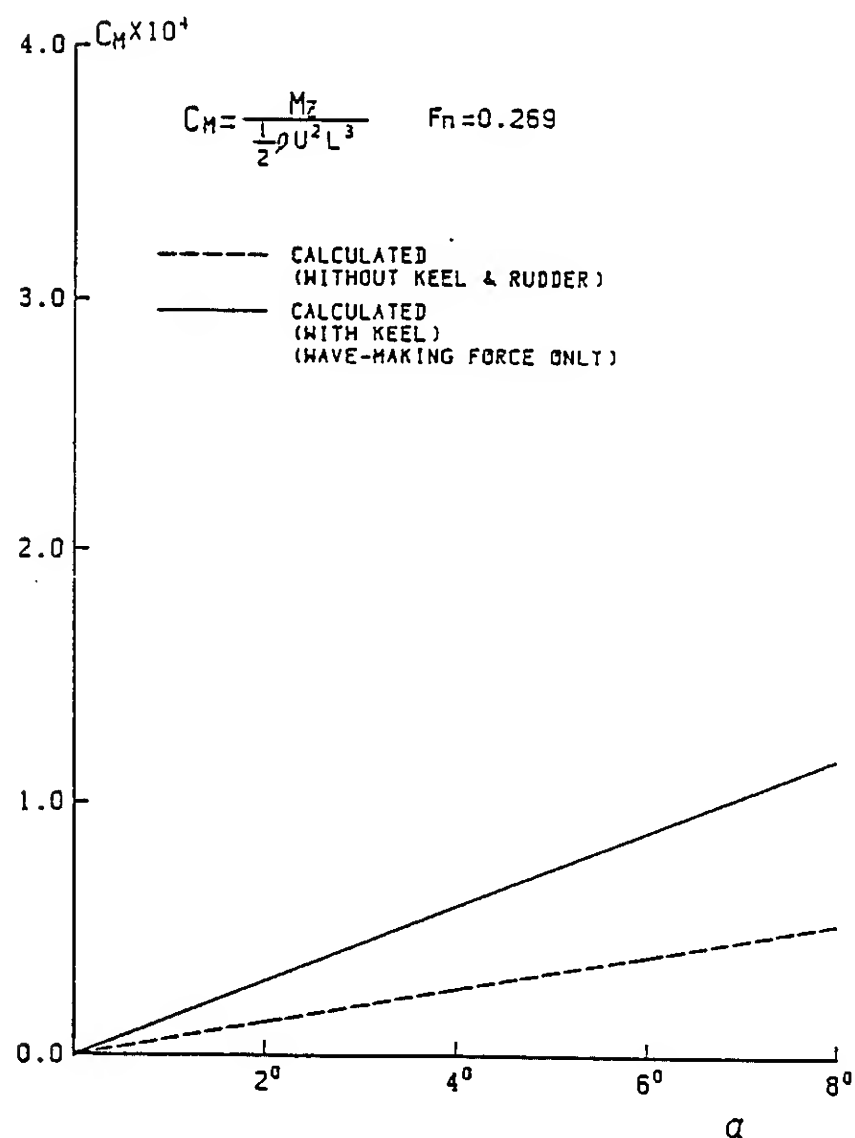


Fig. 26 Computed yaw moment coefficient of yacht model  
 $F_n = 0.269$

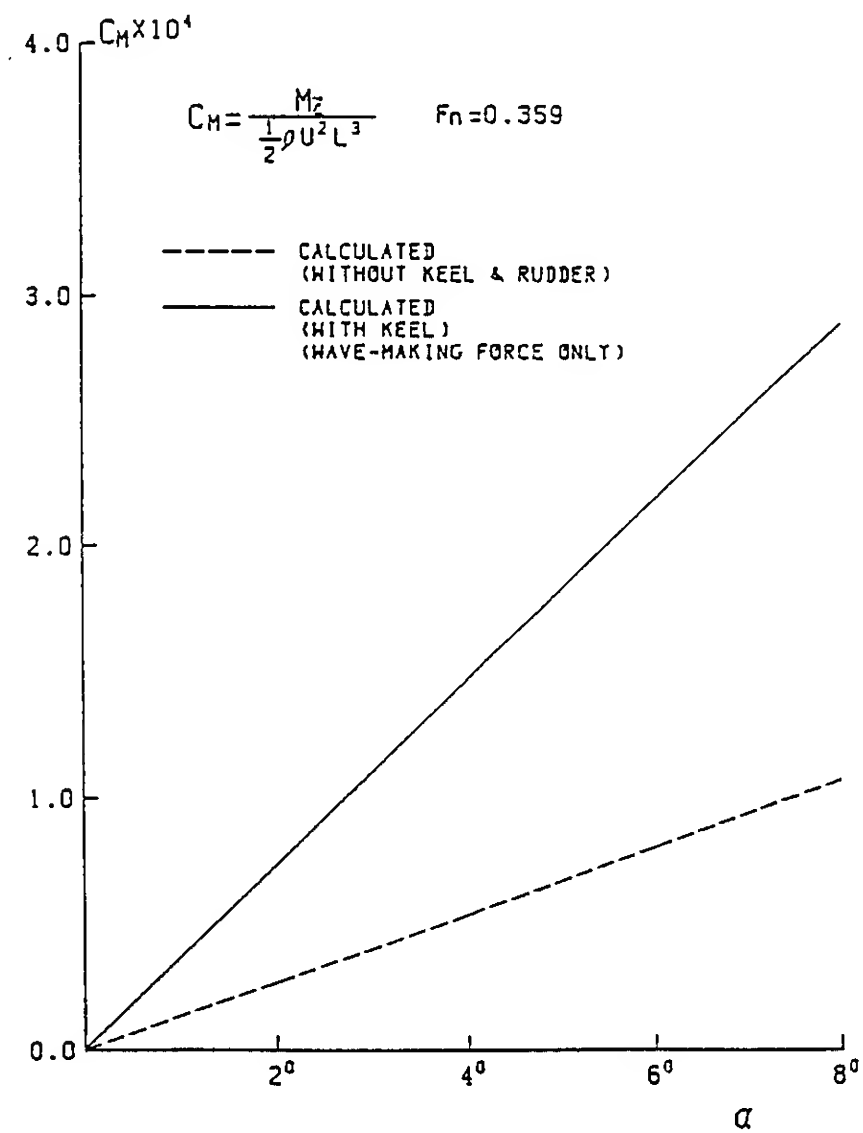


Fig. 27 Computed yaw moment coefficient of yacht model  
 $F_n = 0.359$



## 9. RESULTS OF SERIES 60 HULL

As an example of the conventional hull form, the well-known Series 60 model ( $C_B=0.60$ ) is employed for computation. The body plan is shown in Fig.28. The panel division is  $40(\text{length}) \times 8(\text{draft})$  in equal interval. The towing test of 3m-model is conducted at Yokohama national University tank. The wave profile alongside the model at Froude number 0.28, 0.30, 0.32, 0.34 are illustrated in Figs.29 ~ 32. Full lines give the measured results and dotted lines give the computation. Fairly good agreement between computed and measured wave profiles is observed throughout the results. The slight difference may be attributed to effects of the nonlinearity and the boundary layer displacement. The wave pattern around the model at Froude number 0.30 is illustrated by contour curves in Fig.33. Similarity between computed and measured wave patterns is observed.

In Fig.34, the computed wave resistance coefficient is compared with the residual resistance coefficient based on the Schoenherr friction coefficient and the wave pattern resistance by the longitudinal cut method. The computed value is slightly higher than the residual resistance. This may correspond to the tendency of lower wave height at the stern in the computed wave profile. Since the curvature of the hull surface at the stern is much higher than the case of other models, the number of panel division in this area may not be sufficient for good accuracy. The position of humps and hollows is in good agreement in theoretical and experimental curves.

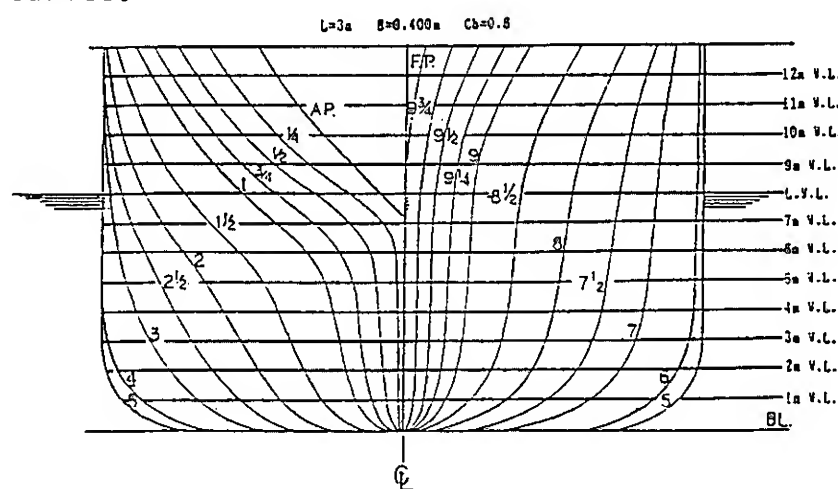


Fig. 28 Body plan of Series 60  
 $C_B = 0.60$

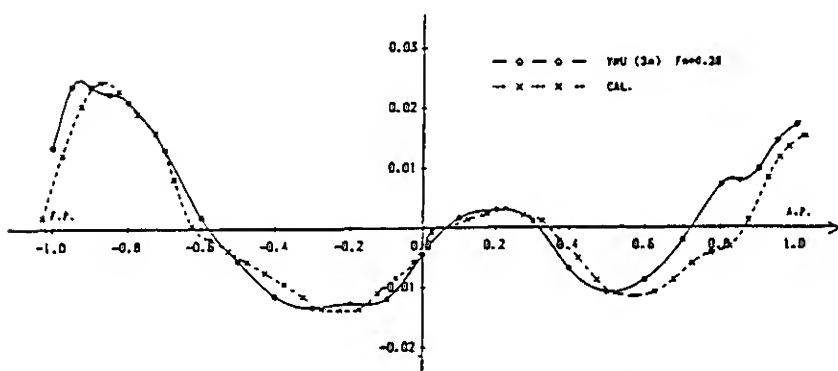


Fig. 29 Computed and measured wave profile  
alongside Series 60 model  
 $F_n = 0.28$

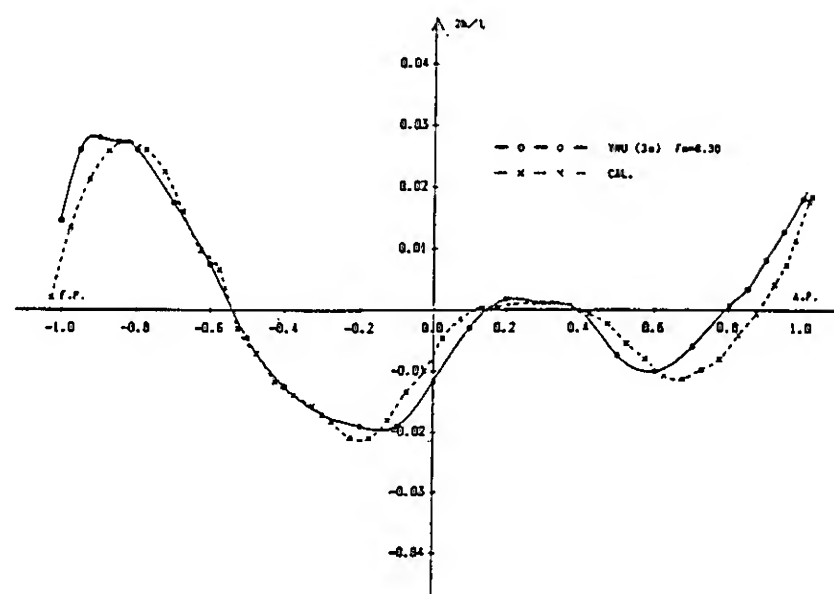


Fig. 30 Computed and measured wave profile  
alongside Series 60 model  
 $F_n = 0.30$

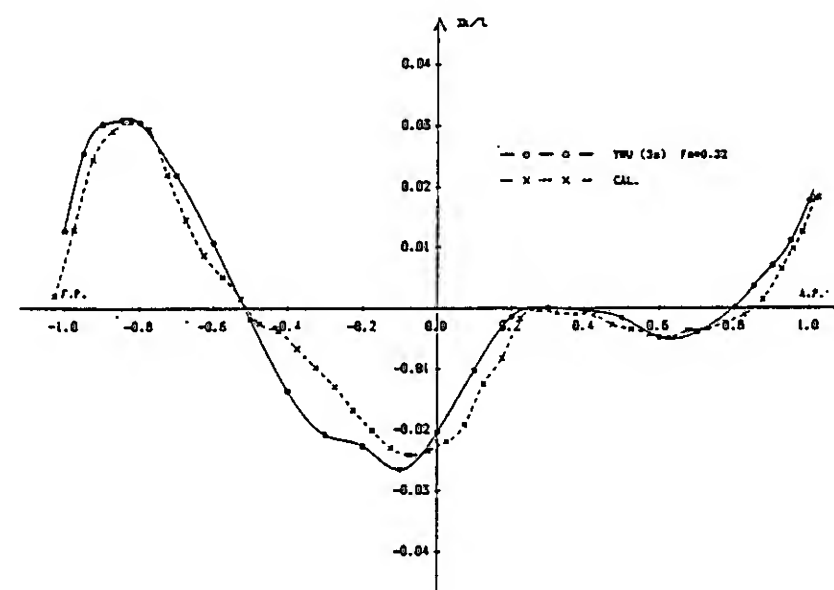


Fig. 31 Computed and measured wave profile  
alongside Series 60 model  
 $F_n = 0.32$

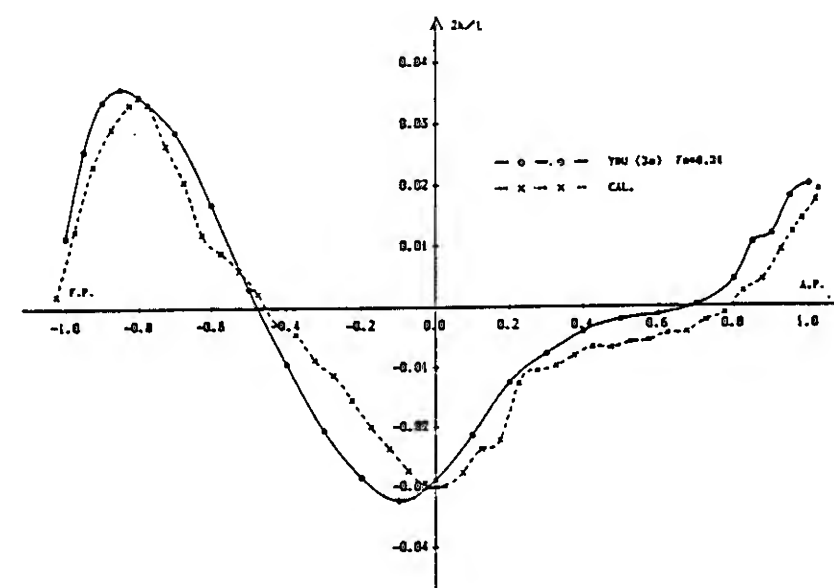


Fig. 32 Computed and measured wave profile  
alongside Series 60 model  
 $F_n = 0.34$

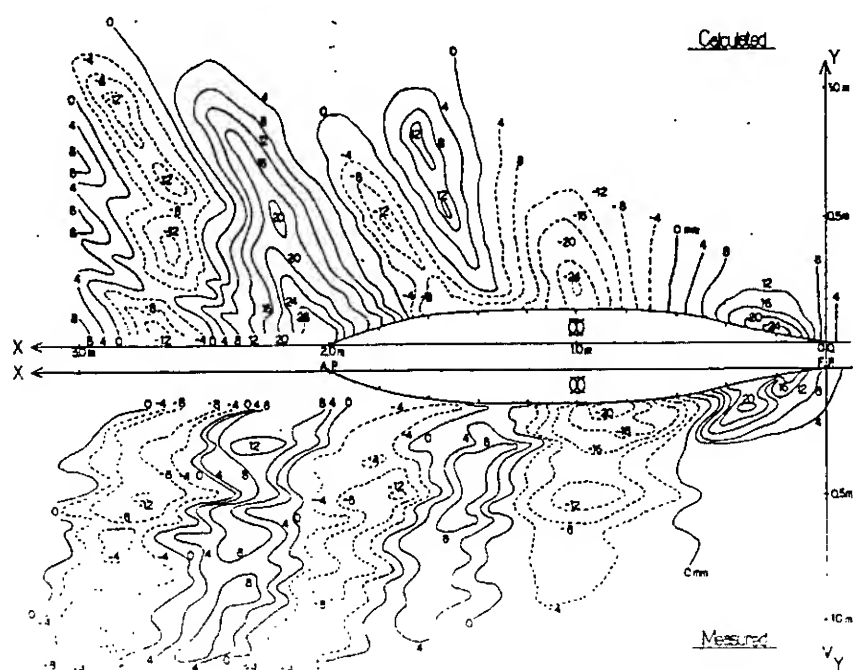


Fig. 33 Computed and measured wave contour of Series 60 model  $F_n = 0.30$

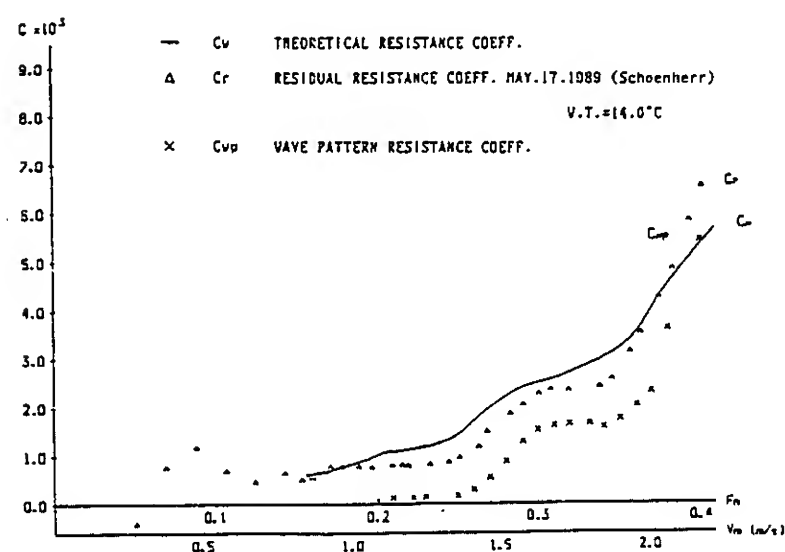


Fig. 34 Computed wave resistance coefficient compared with test results Series 60 model

## 10. CONCLUSIONS

The validity of the new slender ship formulation is examined by the computation of the wave pattern and wave resistance of the Wigley hull, the sailing yacht hull and the Series 60 model.

Satisfactory agreement is obtained in pressure distribution on the hull surface, the wave profile alongside the hull, and the wave resistance, between computed and measured values with respect to the Wigley hull. The computed wave resistance of the canoe body of the sailing yacht hull without keel shows good agreement with towing test results, in spite of small length to beam ratio. The effect of the solid keel is not fully accounted for by the present theory. The hydrodynamic forces, when the hull is at a finite drift angle, may be calculated

by the present theory supplemented by the lifting surface computation. Although a good agreement between the computed wave profile alongside the Series 60 hull and the measurement is obtained, a slight deviation is observed in the computed wave resistance from the towing test result. This fact may suggest that fine panel division is required for the prediction of wave resistance of conventional hull forms such as Series 60 model, because of the large curvature of the hull surface, especially at the stern area.

As the conclusion, the new formulation of slender ship approximation has achieved a remarkable improvement in the theoretical computation of the wave pattern and wave resistance. The result seems to confirm the usefulness of this theory in the prediction of hydrodynamic characteristics of practical hull forms in steady forward motion.

## ACKNOWLEDGMENTS

The authors express their thanks to Prof. M. Ikehata and staffs of Marine Hydrodynamic Laboratory of Yokohama National University for their cooperation in the experimental work. Their thanks are also to NCAC and the Akishima Laboratory of Mitsui Shipbuilding Co. for their generous permission for publishing the data concerning the sailing yacht hull.

It is noted that the numerical work has been carried out by the use of HITAC M28D computer of Yokohama National University Information Processing Center.

## REFERENCES

1. Brard, R., "The Representation of a Given Ship Form by Singularity Distributions when the Boundary Condition on the Free Surface is Linearized." *Journ. Ship Res.* Vol.16 (1972)
2. Vossers, G., "Some Applications of the Slender Body Theory in Ship Hydrodynamics." Thesis, Delft Technological University, (1962)
3. Maruo, H., "Calculation of the Wave Resistance of Ships, the Draught of which is as small as the Beam." *Journ. Soc. Naval Arch. Japan*, Vol.112 (1962)
4. Tuck, E.O., "The Steady Motion of a Slender Ship." Thesis, University of Cambridge, (1963)
5. Joosen, W.P.A., "Velocity Potential and Wave Resistance Arising from the Motion of a Slender Ship." *Internationnal Seminar on Theoretical Wave-Resistance*, Ann Arbor, (1963)
6. Lewison, G.R.G., "Determination of the Wave-Resistance of a Partly Immersed Axisymmetric Body." *International Seminar on Theoretical Wave-Resistance*, Ann Arbor (1963)

7. Maruo, H., "New Approach to the Theory of Slender Ships with Forward Velocity." Bulletin Faculty of Eng. Yokohama National University, Vol.31 (1982)
8. Maruo, H., Ikehata, M., "An Application of New Slender Ship Theory to Series 60,  $C_b = 0.60$ ." The Second Workshop on Ship Wave Resistance Computations, DTNSRDC Bethesda (1983)
9. Havelock, T.H., "Ship Waves: the Calculation of Wave Profiles." Proc. Royal Soc. A Vol. 135 (1932)
10. Namimatsu, M., Ogiwara, S., Tanaka, H., Hinatsu, M., Kajitani, H., "An Evaluation of Resistance Components on Wigley Geosim Models, 3. An analysis and Application of Hull surface Pressure Measurement." Journ. Kansai Soc. of Naval Architects, Japan, No.197 (1985)
- 11.<sup>1</sup> Maruo, H., Ikehata, M., Takizawa, Y., Masuya, T., "Computation of Ship Wave Pattern by the Slender Body Approximation." Journ. Soc. Naval Arch. Japan, Vol.154 (1983)
- 12.<sup>1</sup> Song, W.-S., Ikehata, M., Suzuki, K., "Computation of Wave Resistance and Ship Wave Pattern by the Slender Body Approximation." Journ. Kansai Soc. Naval Arch. Japan, No.209 (1988)
- 13.<sup>1</sup> Song, W.-S., "Wave-making Hydrodynamic Forces Acting on a Ship with Drift Angle and Wave Pattern in her Neighborhood." Journ. Kansai Soc. Naval Arch. Japan, No.211 (1989)
- 14.<sup>1</sup> Song, W.-S., Ikehata, M., Suzuki, K., "On Wave-making Hydrodynamic Forces and Wave Pattern of a Sailing Yacht." Journ. Soc. Naval Arch. Japan, Vol.166 (1989)
- 15.<sup>2</sup> Maruo, H., "Evolution of the Theory of Slender Ships." Ship Technology Research, Vol. 36, No.3 (1989)

<sup>1</sup> Results in this paper are in part reported in these articles.

<sup>2</sup> The theory is discussed from the perturbation point of view.

## DISCUSSION

Ronald Yeung  
University of California at Berkeley, USA

In spite of the nonlinear conditions stated in the beginning of section 2, it seems clear that the starting point of this work remains the same as the Neumann-Kelvin problem. This is evident from the representation, Eq. (12) of the paper. What followed from there is essentially an approximation to the N-K solution, and one should not expect the present calculations can do any better than the 3-D Neumann-Kelvin solution. In terms of the slender-body approximation carried out here, or in Prof. Maruo's 1982 work, I don't feel that it is rationally based, at least not completely. I will point out 2 objections. (1) The neglect of the line integral in Eq. (15) cannot be justified simply on the basis of traditional infinite-fluid slender-body theory. Sources on the free surface exert much stronger influence than submerged distribution. It is well established these days that the waterline integral in the N-K problem yields a significant contribution. This contribution is taken into account in the matched asymptotic theory of Yeung & Kim (1984, 15th ONR Symposium). This leads to the 2nd point. (2) In our work, which Prof. Maruo might not be aware of, we showed that the near field approximation, Eq. (25), of paper is more elaborate than an impulsive 2-D source and a function, say,  $F$ , that depends only on the axial distance 'x'. Using matched asymptotics, we showed that the transverse wave-field is contained in  $F(x,y,z)$ , with explicit expressions given in Yeung & Kim (1984). Prof. Maruo's  $F$ -function corresponds to setting  $y-z=0$  in ours. It is clear that your analysis eventually lead to a rather ad-hoc "fix" in the paragraph following Eq. (55). It appears this deficiency can be corrected in the manner that we have derived from the matched field. I don't think such development should be done as a matter of convenience, rather, it should be rationally based. I would like Prof. Maruo to comment on these two issues.

## AUTHORS' REPLY

The slender body theory is based on the rational perturbation analysis. The fundamental technique is the series expansion of the complete solution of the fully nonlinear boundary value problem, its existence being assumed, with respect to the slenderness ratio  $\epsilon$ , as a small perturbation parameter. The lowest order of the expansion gives the linearized solution, which is discussed in this paper. The rigorous derivation of the result by the perturbation technique is not employed in this paper, because it has been given in another literature. The general form of the linearized solution in the near field is given by the velocity potential of the form  $\phi = \Phi^{(2D)} + g(x)$  where  $\Phi^{(2D)}$  is the solution of the two-dimensional Laplace equation  $\Phi^{(2D)}_{yy} + \Phi^{(2D)}_{zz} = 0$  and satisfies the boundary conditions on the body surface and on the free surface.  $g(x)$  is a function of  $x$  only, which is determined by matching with the far field solution. Both of these functions are  $O(\epsilon^2)$ . It is readily proved that the line distribution of sources along the waterline  $L_0$  is  $O(\epsilon^3)$ , so that it must be deleted from the linearized scheme. The function  $F(x,y,z)$  referred in the discussion is derived from the linearized far field potential, which is not correct in the near field. In order to obtain the consistent approximation in the near field, one must expand it with respect to the transverse coordinates  $y, z$ , and detain only the term of the lowest order. It is reduced to the limit at  $y = z = 0$ , if the function is bounded. It corresponds to the function  $g(x)$ . It should be emphasized that the higher order terms with respect to  $\epsilon$  should not be detained, because they are subject to the nonlinear portion of the boundary conditions which is not taken into account in the theory. The present discussion is concerning the higher order terms only, and does not make sense accordingly. It seems that the argument presented by Prof. Yeung is nothing but the consequence of the lack of knowledge about the rational perturbation analysis of the complex nonlinear problem.

## DISCUSSION

Hongbo Xü  
Massachusetts Institute of Technology, USA (China)

Prof. Maruo, the results you have are impressive. My question is about the theoretical results for Wigley hull at an angle of attack. Have you compared the lateral force and yaw moment coefficients with experimental data? The angle of attack  $\alpha$  used in your computation appears to be rather large (up to  $20^\circ$ ). As we know, the stall angle for a wing is about  $12^\circ$  to  $15^\circ$ . It may be important to find the approximate range for  $\alpha$  in which the slender ship theory is valid.

## AUTHORS' REPLY

The example for the Wigley hull in finite drift angle is rather an academic aspect because the leading edge separation must be present by the form with a sharp edge, though the theory does not take account of it. Therefore, the forces and moment computed by the theory may not represent the actual value except at small angles, less than  $5^\circ$  say. However, the comparison of the wave profile shown in Fig. 9 indicates that the theory can predict the behavior of the free-surface flow fairly well, even at  $10^\circ$ , which is not so small.

## DISCUSSION

Kazu-hiro Mori  
Hiroshima University, Japan

You explained that your results agree with the measured "fairly well." I don't think so, but the agreement is strikingly well! In your introductory remarks, you disclosed your negative opinion to the direct numerical method. Although it takes much computing time, it has a potentiality; e.g., the viscosity can be taken into account. The methods may be complimentary. I hope you may not have such a negative opinion to the numerical method, for you are so influential.

## AUTHORS' REPLY

The computational fluid dynamics depends on the capacity of computers. It has achieved a great success in various fields in hydrodynamics, such as in compressible aerodynamics. Unfortunately, the present stage of the application of CFD to the free-surface flow around the hull does not seem to reach the level of feasibility as a useful tool to resolve problems in the practical field of shipbuilding. However, the recent progress of the computer capacity is remarkable, so that there is much prospect that CFD will become a powerful tool with practical feasibility in the field of the full form research in future. Please, never be afraid.

# Numerical Solution of the "Dawson" Free-Surface Problem Using Havelock Singularities

C. Scragg, J. Talcott (Science Applications International Corporation, USA)

## ABSTRACT

A method of solving the steady free-surface ship wave problem satisfying "Dawson's" double-body linearization of the free-surface boundary condition, which employs distributed Havelock singularities on both the hull surface and on the free surface is presented. The use of Havelock singularities, as opposed to Rankine singularities, allows the solution to be extended into the far-field without difficulties. The present technique combines the superior aspects of Rankine/Dawson methods in the calculation of near-field waves and the far-field superiority of the Havelock methods. Encouraging results are presented for two simple hull forms, a submerged body of revolution and a Wigley hull.

## NOMENCLATURE

$B$	Beam
$C(k_x, k_y)$	Wave spectral function
$C_w$	Wave resistance coefficient
$g$	Gravitational constant
$G$	Green function
$H$	Draft
$k$	Wave number
$k_x$	Longitudinal wave number
$k_y$	Lateral wave number
$k_0$	Characteristic wave number $= g/U^2$
$L$	Ship length
$\mathbf{n}$	Unit normal vector into the fluid
$p$	Pressure
$R_w$	Wave resistance
$S(x, y)$	Hull surface
$U$	Ship speed
$\mathbf{V}$	Fluid velocity vector
$(x, y, z)$	Ship-fixed coordinate system, with $x$ forward, $y$ to port, and $z$ upward
$Z(x, y)$	Free-surface elevation
$Z_0$	Double-body wave elevation
$\Phi$	Velocity potential
$\phi$	Double-body velocity potential
$\varphi$	Perturbation potential
$\rho$	Fluid density
$\sigma$	Havelock source density

## INTRODUCTION

In 1977, Dawson [1], introduced a method of linearizing the free-surface boundary condition using a perturbation about the zero-Froude number potential. Since then, there has been significant interest in utilizing zero-Froude number or "double-body" linearization schemes in the field of wave resistance and in the prediction of Kelvin waves. Although there are several different methods of linearizing the free-surface boundary conditions (see

Raven, [2]), we refer to this basic approach as Dawson's method even though we do not actually use the same version of the linearized free-surface equations given by Dawson in his pioneering work. Several researchers have developed computer codes which satisfy the exact hull boundary condition and Dawson's free-surface condition by distributing Rankine singularities over the ship's hull and on the free surface. During the 1988 Workshop on Kelvin Wake Computations (Lindenmuth, et al. [3]), it became apparent that the best of these Rankine/Dawson codes were capable of predicting quite accurately the wave elevations in the near-field region directly around the ship. However, these codes encountered difficulties in the prediction of the freely-radiating far-field Kelvin waves. The solutions exhibited excessive numerical wave damping and/or wave reflections off the computational boundaries.

Although Rankine singularities provide a convenient and efficient method for the calculation of the zero-Froude number problem, they actually introduce some numerical difficulties into the calculation of the Kelvin wave field. These difficulties are avoided by solving Dawson's problem with distributed Havelock singularities. Since Rankine sources are symmetrical, it is necessary to impose some sort of numerical radiation condition to prevent upstream radiating waves. This difficulty is not encountered when Havelock singularities are used since the Havelock singularity inherently satisfies the radiation condition. The use of Havelock singularities also eliminates problems associated with wave reflections off the computational boundaries. Since neither Rankine singularities nor Havelock singularities distributed over the hull surface alone can satisfy Dawson's free-surface boundary condition, it is also necessary to panelize some region of the free surface surrounding the hull. With Rankine singularities, wave reflections at the edge of the computational domain can create serious problems, usually solved by the introduction of some numerical damping scheme. But with Havelock singularities, there is no difficulty at the edge of the panelized region since Havelock singularities always satisfy the linearized free-surface boundary condition, and consequently the far-field waves always propagate away from the hull as linear Kelvin waves. At moderate distances from the hull, the zero-Froude number potential approaches the undisturbed free-stream potential, and consequently, Dawson's free-surface boundary condition limits to the linearized free-surface boundary condition satisfied by Havelock singularities. Therefore, with Havelock singularities distributed on the free surface, the singularity strength necessary to satisfy the Dawson free-surface boundary condition will smoothly approach zero as the double-body flow approaches the free-stream. The computational domain is defined quite naturally as the limited region of non-zero singularity strength directly around the hull. Furthermore, this computational domain in which free-surface panels are required, is determined by examining the zero-Froude number solution, eliminating the need for elaborate free-surface panelization schemes.



This approach leads to a solution which satisfies the same field equations and the same boundary conditions as the Rankine/Dawson codes, and therefore, the near-field solutions are the same. But since the use of Havelock singularities eliminates the numerical problems associated with Rankine singularities, this method leads to solutions which are also valid in the far-field.

## THEORY

Consider a ship moving with steady forward speed  $U$  in the presence of a free surface. We define a ship-fixed coordinate system with the positive  $x$ -axis in the direction of travel, the  $y$ -axis directed to port, and the  $z$ -axis vertically upward. The origin is located on the mean free surface. We assume that the fluid is incompressible and inviscid and that the flow is irrotational. Consequently, we can define a velocity potential  $\Phi$  which satisfies the Laplace equation throughout the fluid domain,

$$\nabla^2 \Phi = 0, \quad (1)$$

and is related to the fluid velocity vector  $\mathbf{V}$  by

$$\mathbf{V} = \nabla \Phi. \quad (2)$$

On the surface of the body  $S(x, z)$ , we require that the flow be tangential to the hull surface,

$$\nabla \Phi \cdot \mathbf{n} = 0, \text{ on } y = S(x, z), \quad (3)$$

where  $\mathbf{n}$  is a unit normal vector directed out of the hull.

On the free surface  $Z(x, y)$ , the velocity potential must satisfy the kinematic free-surface boundary condition,

$$\Phi_z = \Phi_x Z_x + \Phi_y Z_y, \text{ on } z = Z(x, y), \quad (4)$$

and the dynamic free-surface boundary condition,

$$gZ + \frac{1}{2} \nabla \Phi \cdot \nabla \Phi = \frac{1}{2} U^2, \text{ on } z = Z(x, y), \quad (5)$$

where  $g$  is the gravitational constant. In addition, we require that the disturbance created by the body must vanish at points infinitely far away, and we require that the far-field free-surface waves generated by the body may not radiate upstream of the ship.

The free-surface gradients  $Z_x$  and  $Z_y$  can be written in terms of the velocity potential by differentiating equation (5) with respect to  $x$  and  $y$ . Then by substituting the gradients into equation (4), we can write a single free-surface boundary condition which must be satisfied by the potential:

$$\frac{1}{2} (\nabla \Phi \cdot \nabla \Phi)_x \Phi_x + \frac{1}{2} (\nabla \Phi \cdot \nabla \Phi)_y \Phi_y + g \Phi_z = 0, \text{ on } z = Z(x, y). \quad (6)$$

The manner in which this non-linear free-surface boundary condition is linearized is what distinguishes the Dawson problem from the Neumann-Kelvin problem. In both problems, we seek a solution to the Laplace equation (1) which satisfies an exact hull boundary condition (2). In the Neumann-Kelvin problem we rewrite the potential as the sum of a free-stream potential and a perturbation potential  $\varphi'$ , and we assume that the perturbation potential is, in some sense, small relative to the free-stream potential,

$$\Phi = -Ux + \varphi'. \quad (7)$$

If we substitute equation (7) into the free-surface boundary condition (6), and retain only terms which are linear in  $\varphi'$ , then we obtain the linearized Kelvin free-surface boundary condition

$$\varphi'_{xx} + k_0 \varphi'_z = 0, \text{ on } z = 0, \quad (8)$$

where  $k_0$  is the characteristic wave number defined by

$$k_0 = \frac{g}{U^2}. \quad (9)$$

To show that the boundary condition can be applied at the position of the mean free surface, one can expand the potential in a Taylor series about  $z = 0$ , and assume that the free-surface elevation  $Z$  is of the same order as the perturbation potential.

In Dawson's approach to the problem, the potential is divided into a double-body potential  $\phi$  and a perturbation potential  $\varphi$ ,

$$\Phi = \phi + \varphi, \quad (10)$$

and it is assumed that the perturbation potential is small relative to the double-body potential  $\phi$ . The double-body potential corresponds to the limiting solution as the Froude number goes to zero (i.e.  $g \gg U$ ), for which case the free surface acts as a reflection plane. The double-body potential is a solution to the Laplace equation at all points outside of the body,

$$\nabla^2 \phi = 0, \quad (11)$$

and satisfies the exact hull boundary condition,

$$\mathbf{n} \cdot \nabla \phi = 0, \text{ on } y = S(x, z), \quad (12)$$

and a reflection boundary condition applied on the position of the undisturbed free surface,

$$\phi_z = 0, \text{ on } z = 0. \quad (13)$$

The double-body solution can be readily obtained by well-known panelization methods utilizing Rankine ( $1/R$ ) singularities, and it will be assumed throughout the remainder of this discussion that the double-body potential and its derivatives can be treated as known quantities.

The perturbation potential must be a solution to the Laplace equation throughout the fluid domain, and must satisfy the same hull boundary condition,

$$\mathbf{n} \cdot \nabla \varphi = 0, \text{ on } y = S(x, z). \quad (14)$$

To obtain the linearized free-surface boundary condition which must be satisfied by the perturbation potential, we substitute equation (10) into the free-surface boundary condition, equation (6), and retain only first order terms in  $\varphi$ ,

$$\begin{aligned} & \frac{1}{2} (\nabla \phi \cdot \nabla \phi)_x \varphi_x + (\nabla \phi \cdot \nabla \varphi)_x \phi_x + \frac{1}{2} (\nabla \phi \cdot \nabla \phi)_y \varphi_y \\ & + (\nabla \phi \cdot \nabla \varphi)_y \phi_y + g \varphi_z = -g \phi_z - \frac{1}{2} (\nabla \phi \cdot \nabla \phi)_x \phi_x \\ & - \frac{1}{2} (\nabla \phi \cdot \nabla \phi)_y \phi_y, \text{ on } z = Z(x, y). \end{aligned} \quad (15)$$

In order to apply the free-surface boundary condition at the position of the undisturbed free surface, it is necessary to expand equation (15) in a Taylor series about  $z = 0$ . By defining a wave elevation  $Z_0$  which depends only upon the double-body potential

$$Z_0 = \frac{1}{2g} (U^2 - \nabla \phi \cdot \nabla \phi), \quad (16)$$

and assuming that the wave elevation  $Z(x, y)$  is composed of  $Z_0$  plus additional terms which are of the order  $\varphi$ , we can obtain the linearized boundary condition to be satisfied on the mean free surface:

$$\begin{aligned} & (\phi_x)^2 \varphi_{xx} + 2(\phi_x \phi_y) \varphi_{xy} + (\phi_y)^2 \varphi_{yy} + 2(\phi_x \phi_{xx} + \phi_y \phi_{xy}) \varphi_x \\ & + 2(\phi_x \phi_{xy} + \phi_y \phi_{yy}) \varphi_y + g \varphi_z = -g Z_0 \phi_{zz} \\ & - (\phi_x \phi_{xx} + \phi_y \phi_{xy}) \phi_x - (\phi_x \phi_{xy} + \phi_y \phi_{yy}) \phi_y, \end{aligned} \quad (17)$$

where we have used the reflection condition,  $\phi_z = 0$ , to remove terms involving the vertical component of the double-body flow on  $z = 0$ .

It is important to note that since the double-body potential tends to the free-stream potential as we move away from the body, the Dawson free-surface boundary condition limits to



$$U^2 \varphi_{xx} + g \varphi_z = 0, \text{ as } \sqrt{x^2 + y^2} \rightarrow \infty. \quad (18)$$

This is identical to the linear Kelvin free-surface boundary condition written in equation (8). Consequently, the differences between the Dawson solution and the Neumann-Kelvin solution must be due to the differences between their respective free-surface boundary conditions, equations (17) and (8), which occur in a relatively limited region around the hull.

We propose to represent the double-body perturbation potential  $\varphi$  by a distribution of Havelock singularities on the hull surface and on the free surface in a region immediately surrounding the hull. At points farther away from the hull, where the Dawson free-surface condition tends to the Kelvin condition, the Havelock source strength necessary to satisfy the free-surface boundary condition goes to zero. In this approach it will be necessary to add the double-body potential  $\phi$ , which is represented by a distribution of Rankine singularities, to the perturbation potential  $\varphi$ , represented by Havelock singularities, in order to calculate the total flow field around the hull.

Alternatively, one could represent both the double-body potential and the perturbation potential by distributions of Havelock singularities on the hull and the free surface. In this approach, we seek the total potential  $\Phi$ , which must be a solution to the Laplace equation subject to the hull boundary condition (3). To obtain the linearized boundary condition which must be satisfied by  $\Phi$  on the mean free surface, we substitute equation (10) into equation (17):

$$\begin{aligned} &(\phi_x)^2 \Phi_{xx} + 2(\phi_x \phi_y) \Phi_{xy} + (\phi_y)^2 \Phi_{yy} + 2(\phi_x \phi_{xx} + \phi_y \phi_{xy}) \Phi_x \\ &+ 2(\phi_x \phi_{xy} + \phi_y \phi_{yy}) \Phi_y + g \Phi_z = -g Z_0 \phi_{zz} \\ &+ 2(\phi_x \phi_{xx} + \phi_y \phi_{xy}) \phi_x + 2(\phi_x \phi_{xy} + \phi_y \phi_{yy}) \phi_y. \end{aligned} \quad (19)$$

We note that this boundary condition is very similar to the linearized free-surface boundary condition which must be satisfied by the perturbation potential  $\varphi$ , equation (17), differing only in the coefficients of the last two terms on the right hand side. This approach, the solution to the total potential as represented by distributions of Havelock singularities, requires no fewer computations than the previous approach, since the double-body potential must still be solved as a "first step" to the problem. However, since the two sets of equations to be solved for the perturbation potential and for the total potential will involve identical influence matrices on the left hand side, and very similar expressions on the right hand side, one can solve both problems with little additional computational load. Obviously, the two methods should yield the same answers, but we decided to pursue both approaches so that we could investigate any numerical advantages of solving for the perturbation potential versus the total potential.

## NUMERICAL APPROACH

The typical numerical approach to solving this Dawson problem involves the distribution of Rankine singularities placed on panels covering the hull surface and some region of the free surface. Since Rankine singularities do not satisfy the linearized free-surface boundary condition, these solutions are limited to the computational domain over which the free surface has been panelized. The principle difference of the present approach is the use of Havelock singularities as opposed to Rankine singularities.

By distributing Havelock singularities over the hull surface and over the free surface in a near-field region immediately surrounding the vessel, we can obtain a potential solution which will satisfy the Dawson free-surface boundary condition and the radiation condition at all free-surface points. The use of the more complex Havelock singularities, as opposed to Rankine singularities, eliminates the difficulties associated with the use of a limited computational domain and allows us to extend the solution into the far-field without the wave attenuation created by the introduction of artificial damping. If we distribute  $N$  constant density

source panels over the hull surface and  $M$  panels over the undisturbed free surface, the perturbation potential can be written as

$$\begin{aligned} \varphi = & \sum_i^N \sigma_i \int_{s_i} ds G(x, y, z; \xi, \eta, \zeta) + \\ & \sum_i^M \sigma_i \int_{s_i} ds G(x, y, z; \xi, \eta, \zeta), \end{aligned} \quad (20)$$

where  $\sigma$  is the source density and  $G$  is the Havelock Green function given by (see Wehausen and Laitone [4]),

$$\begin{aligned} G = & -\frac{1}{R} + \frac{1}{R'} \\ & + \Re \left\{ \frac{2}{\pi} k_0 \int_{-\infty}^{\infty} dk_y \int_0^{\infty} dk_x \frac{e^{k(z+\zeta) + ik_x(x-\xi) + ik_y(y-\eta)}}{k_x^2 - k_0^2} \right. \\ & \left. - i \frac{k_0}{2} \int_{-\infty}^{\infty} dk_y \frac{\beta(k_y)}{k'_x} e^{k(z+\zeta) + ik'_x(x-\xi) + ik_y(y-\eta)} \right\} \end{aligned} \quad (21)$$

where

$$\begin{aligned} R &= \sqrt{(x-\xi)^2 + (y-\eta)^2 + (z-\zeta)^2}, \\ R' &= \sqrt{(x-\xi)^2 + (y-\eta)^2 + (z+\zeta)^2}, \end{aligned}$$

and

$$k = \sqrt{k_x^2 + k_y^2},$$

where  $k_x$  and  $k_y$  are the longitudinal and lateral wave numbers of the free-surface waves. In the single integral, the longitudinal wave number is not an independent variable, but is related to  $k_y$  by

$$k'_x = \left[ \frac{1}{2} \left( k_0 + \sqrt{k_0^2 + 4k_y^2} \right) \right]^{1/2}.$$

The function  $\beta(k_y)$  is given by

$$\beta = \frac{2 \left( k_0 + \sqrt{k_0^2 + 4k_y^2} \right)}{\sqrt{k_0^2 + 4k_y^2}}.$$

The unknown source densities are determined by applying the hull boundary condition, equation (14), at the centroid of each hull surface panel and applying the Dawson free-surface boundary condition, equation (17), at the centroid of each free-surface panel. Since the Havelock singularity automatically satisfies the Kelvin free-surface boundary condition, the source density required to satisfy the Dawson condition should smoothly tend toward zero at points away from the hull where the Dawson condition limits to the Kelvin condition. To evaluate the total potential  $\Phi$ , it is necessary to include a term corresponding to the free-stream velocity,

$$\begin{aligned} \Phi = & -Ux + \sum_i^N \sigma_i \int_{s_i} ds G(x, y, z; \xi, \eta, \zeta) \\ & + \sum_i^M \sigma_i \int_{s_i} ds G(x, y, z; \xi, \eta, \zeta). \end{aligned} \quad (22)$$

The source densities  $\sigma_i$  in equations (20) and (22) will of course be different due to the fact that they will be determined using different boundary conditions on the free surface, equations (17) and (19). We note the absence of the waterline integral which is necessary in the typical formulation of the Neumann-Kelvin problem where Havelock singularities are distributed only over the hull surface and along the intersection of the hull and the free surface. The waterline integral arises out of an application of Stokes Theorem to the integration over the free surface, reducing the surface integral to a contour integral. Since we have

retained the free-surface integration, no contour integral around the waterline occurs.

The first two terms in the Green function correspond to a Rankine source and its negative image above the free surface. These terms can be evaluated using standard techniques. The contribution to the potential due to free-surface waves is contained within the two integral terms in equation (21). To calculate this wave potential we first define a wave spectral function  $C(k_x, k_y)$  which can be evaluated analytically for a flat panel of uniform source density:

$$C(k_x, k_y) = \int_{s_i} ds e^{k\zeta - ik_x\xi - ik_y\eta}. \quad (23)$$

Then the contribution to the potential from the two integral terms in the Green function is

$$\begin{aligned} \varphi_w = & \sigma \frac{2}{\pi} k_0 \int_{-\infty}^{\infty} dk_y \int_0^{\infty} dk_x C(k_x, k_y) \frac{e^{kx + ik_x x + ik_y y}}{k_x^2 - k_0^2} \\ & - i \sigma \frac{k_0}{2} \int_{-\infty}^{\infty} dk_y \frac{\beta}{k'_x} C(k'_x, k_y) e^{kz + ik'_x x + ik_y y}. \end{aligned} \quad (24)$$

The boundary conditions on the hull and the free surface involve first and second derivatives of the potential which can be calculated by multiplying the spectral function by the appropriate wave number prior to performing the integration.

The calculation of the Kelvin waves generated by a discrete Havelock singularity at zero depth can be particularly troublesome. However, in the present formulation of the problem, the singularities are distributed uniformly over flat free-surface panels of finite dimensions. By first performing the spatial integration over the panel, we effectively filter out much of the high wave number content of the Havelock source and we can obtain well behaved spectral functions for an arbitrary panel, even one at zero depth. Some of the higher order derivatives of the potential which occur in the Dawson free-surface boundary condition can lead to an integrand which contains sufficient high wave-number content to present numerical difficulties. However, these high wave numbers correspond to waves which are not properly resolved by the free-surface panelization and which should be removed from the spectral function to prevent aliasing. In the results presented in the following sections, a cosine squared filter has been applied to the spectral functions with the filtering length set at twice the length of the free-surface panels. The spectral functions have been cut-off at half the panel dimension.

It is interesting to examine the limiting behavior of a distribution of Havelock singularities as both the depth of the panel and its collocation point go to zero. If the panel is located at an infinitesimal depth  $\epsilon < 0$ , then the collocation point should be interpreted as being located at the limit as the field point approaches the panel from below,  $z = \epsilon^-$ . The linearized free-surface boundary condition is actually satisfied on the other side of the panel, at  $z = 0$ , and there will exist a  $4\pi$  discontinuity in  $\varphi_z$  across the panel due to the first Rankine term in equation (21). Consequently, a free-surface distribution of Havelock singularities will not satisfy the Kelvin free-surface boundary condition at points located on the panel itself, although it will satisfy the boundary condition at all other points on the free surface. Therefore, on panels located at points away from the hull, where the Dawson free-surface condition approaches the Kelvin free-surface condition, the Havelock source density must go to zero, for otherwise the free-surface boundary condition could not be satisfied at the collocation point.

The  $N$  unknown source strengths on the hull surface panels and the  $M$  unknown source strengths on the free-surface panels are obtained by solving a set of independent linear equations composed of the  $N$  hull boundary conditions and the  $M$  free-surface boundary condition. Consequently, we have eliminated the finite differencing schemes usually employed in the solution to the Dawson problem.

## RESULTS - SUBMERGED BODY OF REVOLUTION

To investigate our numerical approach, we initially examined a fully submerged body, since this would avoid any difficulties associated with the intersection of the hull with the free surface. We chose the submerged prolate spheroid for which Neumann-Kelvin results have been presented by Doctors and Beck [5]. The ellipsoid of revolution can be defined by

$$r = \frac{1}{10} L \left[ 1 - (2x/L)^2 \right]^{1/2}, \quad (25)$$

where  $r$  is the radius of the body and  $L$  is the length. The hull centerline was located at a depth of  $z = 0.16L$ . The body was panelized with 240 panels on the half-body (symmetry about  $y = 0$  is assumed), using 8 rows of 30 panels with cosine spacing in the longitudinal direction. For this body of revolution, the hull surface can be panelized with flat quadrilaterals, and panel warpage is not an issue. The free surface was panelized using 240 square panels (on the half-space  $y > 0$ ) with dimensions of  $L/10$  on each side. The free-surface panels were arranged on a rectangular grid centered over the body, with 30 panels longitudinally and 8 panels laterally. The panelization of both the free surface and the submerged spheroid is shown in Figure 1. This panelization was chosen to cover the entire region of the free surface over which the double-body velocity magnitude differed from the free-stream by more than 1.0%. For this submerged body, the maximum difference between the double-body velocity magnitude and the free stream velocity is  $\approx 9\%$ . The magnitude of the double-body velocity on  $z = 0$  is plotted in Figure 2, where the solid lines represent 1% contours for which the magnitude is greater than the free-stream and the dashed lines represent contours less than the free-stream velocity. We expect that the Dawson free-surface condition differs from the Kelvin condition only over this limited region, and consequently, the Havelock singularity density should go to zero on the panels near the edges of our panelized domain.

### Approach I - Perturbation Potential

At a Froude number of 0.4, the solution of the perturbation potential,  $\varphi$ , resulted in the distribution of Havelock singularities on the free surface shown in Figure 3 (positive contours are shown as solid lines and negative contours are dashed). As expected, the source density is greatest near the body and goes smoothly to zero at the edges of the domain. The greatest source density which occurs on any edge panel is less than 2% of the peak value (-0.012), which occurs directly over the body. The corresponding Havelock singularity densities on the hull surface are shown in Figure 4. Each curve represents a row of panels at one circumferential angle on the body. The peak singularity densities found on the hull occur on the row of panels nearest the free surface, and are about twice the value of the peak free-surface sources. Contrast this singularity distribution with that obtained using our Neumann-Kelvin solution technique, Figure 5, which of course, does not have any singularities on the free surface. The Havelock/Dawson solution has peak singularity densities which are about one fourth of the peak values obtained in the Neumann-Kelvin solution, but more importantly, the Havelock/Dawson solution is significantly smoother, indicating that the geometric approximation of flat panels of constant source strength is more accurate for an equal number of hull surface panels. We also note that the Havelock/Dawson solution yields singularity densities which go smoothly to zero at both the bow and stern.

The near-field free-surface elevations are calculated from the perturbation potential using a linearized version of the Bernoulli equation which is consistent with the linearized Dawson free-surface boundary condition:

$$p = \frac{1}{2} \rho U^2 - \rho g z - \frac{1}{2} \rho \nabla \phi \cdot \nabla \phi - \rho \nabla \phi \cdot \nabla \varphi, \quad (26)$$

where  $p$  is the pressure and  $\rho$  is the density of the fluid. The free-surface elevation calculated over the panelized domain is presented in Figure 6 (non-dimensionalized by the characteristic wave number  $k_0$ ). As expected, the edges of the computational domain do not create any wave attenuation or reflections. The extension of this solution to the far-field is accomplished by using equation (23) to calculate the free-wave spectrum  $C(k'_x, k_y)$  associated with the Havelock singularities on both the hull and the free surface, and then calculating the far-field potential from the far-field limit of equation (24):

$$\varphi_w \approx -i k_0 \int_{-\infty}^{\infty} dk_y \frac{\beta}{k'_x} C(k'_x, k_y) e^{kz + i k'_x x + i k_y y}. \quad (27)$$

In Figure 7 is shown a comparison of the far-field Kelvin waves calculated from the Havelock/Dawson solution (solid line) and from the Neumann-Kelvin solution (dotted line). The similarity is remarkable. The components of the far-field waves generated by the singularities on the hull and on the free surface can be calculated separately, and this result is shown in Figure 8. Although the singularity strengths on the hull are twice as large as those on the free surface, the far-field waves generated by these singularities (solid line in Figure 8) are significantly smaller due to the exponential attenuation with depth.

#### Approach II - Total Potential

The second numerical approach we examined was the solution of the total potential  $\Phi$  by distributed Havelock singularities on the hull and free surface. The free-surface singularities obtained are shown in Figure 9. Again we see the rapid reduction in the singularity density as we move away from the body. At the outermost panels, the densities (less than 3% of the peak values) are similar in absolute value to those obtained in the previous approach, and may represent some measure of the numerical noise. The peak values (-0.007) are less and the distribution of Havelock singularities seems to be limited to an even smaller region than was observed in the solution to the perturbation potential. Unlike the perturbation potential, the singularities do not seem to go monotonically to zero as we move laterally away from the body, but exhibit a slight oscillatory behavior, suggesting that this approach may require a finer free-surface panelization. The singularity densities distributed over the hull surface are shown in Figure 10. Both the qualitative and quantitative similarities between these source densities and the corresponding Neumann-Kelvin results (Figure 5) are striking. The strong singularities at the bow and stern are an order of magnitude greater than the peak values found on the free-surface panels.

As before, the near-field free-surface elevations are calculated from a consistent linearized version of the Bernoulli equation. To obtain the pressure equation in terms of the total potential  $\Phi$  rather than the perturbation potential  $\varphi$ , we substitute equation (10) into equation (26), which leads to

$$p = \frac{1}{2} \rho U^2 - \rho g z + \frac{1}{2} \rho \nabla \phi \cdot \nabla \phi - \rho \nabla \phi \cdot \nabla \Phi. \quad (28)$$

The non-dimensional free-surface wave elevations are given in Figure 11. Although the wave heights obtained here are slightly higher than those obtained from the perturbation potential (Figure 6), the overall agreement is quite good. The far-field wave elevations obtained from the free-wave spectrum are compared to the Neumann-Kelvin results in Figure 12. The present results (solid line in Figure 12) are somewhat higher than those obtained from the perturbation solution (Figure 7) and consequently, the quantitative agreement with the Neumann-Kelvin results (dotted line) is not quite as good, although qualitatively, the results are similar. The contribution to the far-field waves from the hull surface singularities dominates the solution, as shown in Figure 13. The waves generated by singularities on the hull are shown by

the solid line and those generated by free-surface singularities are shown by the dotted line.

#### Wave Resistance Calculation

The wave resistance can be calculated either by integrating the linearized Bernoulli pressure, equation (26) or (28), over the hull surface, or by calculating the energy in the far-field Kelvin waves. Pressure integration is the standard technique employed in Dawson's method, while most Neumann-Kelvin solvers calculate the wave resistance from the energy in the free-wave spectrum. Using equation (23) to calculate the free-wave spectrum from the distribution of Havelock singularities on both the hull and free surface, we can obtain the wave resistance from

$$R_w = 2\pi \rho k_0^2 \int dk_y \beta |C(k'_x, k_y)|^2. \quad (29)$$

The non-dimensional wave resistance coefficient  $C_w$  is defined as

$$C_w = \frac{R_w}{\frac{1}{2} \rho S U^2}, \quad (30)$$

where  $S$  is the total wetted surface area of the hull. We will use  $C_d$  to designate the comparable resistance coefficient obtained from pressure integration. It is probably more reasonable to compare  $C_w$  with a drag coefficient obtained by integrating the full non-linear Bernoulli pressure over the hull surface rather than the linearized version contained in equations (26) and (28). The results obtained from the free-wave spectrum and from pressure integration over the hull are presented in Table I for both Havelock/Dawson approaches and compared with the Neumann-Kelvin result. The Neumann-Kelvin solution given by Doctors and Beck [5] is within 1% of the comparable result presented here.

Table I. Wave Resistance Coefficient for Submerged Body

	$C_d^{(1)}$	$C_d^{(2)}$	$C_w$
H/D Soln: $\varphi$	0.0132	0.0143	0.0150
H/D Soln: $\Phi$	0.0148	0.0162	0.0190
N-K Soln.	—	0.0124	0.0124

$C_d^{(1)}$ : Obtained by integrating the linearized Bernoulli pressure.

$C_d^{(2)}$ : Obtained by integrating the non-linear Bernoulli pressure.

$C_w$ : Obtained from free-wave spectrum.

The steep gradients found in the source densities directly over the body suggest that the solutions would benefit from the use of smaller panels in this region. The calculations were repeated using quarter size panels on an inboard region defined by  $-0.6 < x/L < 0.6$  and  $-0.2 < y/L < 0.2$ , with the outboard region using the larger panels shown in Figure 1. The solutions had more well defined singularity densities but the resulting wave-fields and wave resistances did not change significantly.

#### RESULTS - WIGLEY HULL

Our initial attempts to solve the Dawson problem using distributed Havelock singularities employed the submerged body described above. In this section we report on the results obtained when the same numerical approach was applied to a surface piercing body, specifically the Wigley hull form defined by

$$y = \frac{1}{2} B \left[ 1 - (2x/L)^2 \right] \left[ 1 - (z/H)^2 \right], \quad (31)$$

where  $B$  = beam =  $L/10$ , and  $H$  = draft =  $L/16$ . The panelized free surface, Figure 14, contains 300 square panels ( $L/10$  on each side) in the half-space  $y > 0$ . The hull surface panelization contained only 50 quadrilateral panels, each panel having a



length of  $L/10$  and a depth of  $H/5$ . This panelization is much coarser than we would usually use for a comparable Neumann-Kelvin solution, but we wanted to match panel size on the hull with adjoining free-surface panels. The fact that the hull surface panels are flat quadrilaterals means that there will exist some gaps between the panel edges.

The double body velocity magnitudes are shown in Figure 15. Due to the high length/beam ratio of the Wigley hull and the relatively large free-surface panels, the double-body velocity magnitudes calculated at the centers of the panels never differ from the free stream velocity magnitude by more than 3%. On the outermost panels, the double-body velocities are reduced by more than one order of magnitude. Consequently, we would not expect the Havelock/Dawson solution to differ significantly from the Neumann-Kelvin solution. The slight fore/aft asymmetry which can be seen in the contours is one effect of the gaps in the hull surface created by the use of flat quadrilateral panels.

The free-surface singularity distribution corresponding to the solution of the perturbation potential at a Froude number of 0.40 is shown in Figure 16. The singularity densities go smoothly to zero at a very short distance from the hull. Since the free-surface panelization does not seem to adequately resolve the distribution of singularities near the hull, it would appear that smaller panels distributed over a more limited free-surface domain would yield a better result for the same number of panels. The corresponding hull surface singularity distribution is given in Figure 17. Each of the 5 curves in the figure represents a row of panels at the same depth on the hull. The singularity densities are comparable in peak values to the densities on the free surface, although adjoining hull and free-surface panels can have quite different densities, as evidenced on panels near both the bow and stern. The densities on the free surface reach their peak values near the ends of the hull while the hull-surface singularities seem to be tending smoothly to zero at the ends. Comparing these singularities with the Neumann-Kelvin solution shown in Figure 18, we note that (like the similar comparison for the submerged hull) the Havelock/Dawson solution results in much smaller peak values and much smoother trends.

Calculated non-dimensionalized near-field free-surface elevations are given in Figure 19. As before, the computations are not affected by the edge of the panelized domain, and can be readily extended into the far-field. The far-field wave elevations are compared to the Neumann-Kelvin result in Figure 20, where the solid line represents the Havelock/Dawson result and the dotted line represents the Neumann-Kelvin result. There is more high wave number energy in the Neumann-Kelvin result, as evidenced by the steep diverging waves which occur at non-dimensional distances of  $-10$  to  $-12$ , but otherwise the results are quite similar. The generation of the far-field waves is dominated by the free-surface singularities, as can be seen in Figure 21.

For this particular case, the wave resistance coefficient obtained from the Havelock/Dawson solution  $C_w = 0.00204$  compares very well with the value obtained from the Neumann-Kelvin solution ( $C_w = 0.00212$ ). The drag coefficient obtained by integrating the linearized Bernoulli pressure is somewhat higher ( $C_d = 0.00258$ ) while the drag coefficient obtained from the full non-linear Bernoulli pressure is 0.00248. However, these results may not be too meaningful given the coarseness of the panelization on the hull surface.

The second approach to the Havelock/Dawson problem, solving for the total potential rather than the perturbation potential yielded a disappointing result. The free-surface singularities, Figure 22, did not tend smoothly to zero at the edges of the panelized domain, but exhibited regular oscillations as we moved laterally away from the stern. The singularity densities shown in the figure are quite small, one tenth the magnitude of the hull-surface singularities (which are quite similar to the Neumann-Kelvin singularities), but they generate a comparable wave field due to their free-surface location. In fact, the far-field wave elevations shown in Figure 23 show that a remarkable degree of cancellation will

occur between the waves generated by the free-surface singularities and the hull-surface singularities. We speculate that the solution is suffering from a loss in numerical accuracy caused by this cancellation. It would appear that this problem is unique to this particular approach. In the first approach, the solution for the perturbation potential, the free-surface waves are dominated by the singularities distributed over the free-surface panels, and the loss of accuracy does not occur.

## SUMMARY AND CONCLUSIONS

Our original objective in this effort was to develop a method of combining the superior near-field predictions of the Rankine/Dawson codes with the superior far-field predictions of the Havelock codes. We set out to demonstrate that the use of Havelock singularities distributed over the free surface as well as on the hull surface, rather than Rankine singularities, could result in a solution to the Dawson problem which was free of the wave reflections often caused by the boundaries of the computational domain and free of the wave attenuations introduced by numerical damping schemes. This Havelock/Dawson solution could be extended to an arbitrary distance in the far-field.

By examining two simple geometries, a submerged spheroid and a Wigley hull, we have demonstrated the feasibility of the method. The free-surface singularity densities go to zero at the outer edges of the panelized domain and both the near-field and far-field wave elevations are well behaved, with no evidence of wave reflections or artificial damping. The far-field wave elevations have been shown to be comparable to those obtained from a solution to the Neumann-Kelvin problem.

We have presented results obtained from two different numerical approaches. In the first approach, we solve for a perturbation potential represented by distributions of Havelock singularities, to which must be added a double-body potential which is obtained in the usual manner from distributions of Rankine singularities on the hull. In the second approach, we solve for the total potential represented by distributions of Havelock singularities. The two approaches should yield comparable results, but we found that with the first approach we did not experience the degree of numerical difficulties encountered with the second approach.

The singularity distributions obtained when solving for the perturbation potential were exceptionally well behaved. The peak values of the singularity densities were comparable on the hull and on the free surface, and were significantly smaller in peak value and noticeably smoother than the singularity distributions obtained from the Neumann-Kelvin solution. For the two simple geometries examined in this study, the hull-surface singularities tended toward zero at both the bow and the stern. The wave fields were dominated by the contributions from the free-surface singularities.

The second approach, solving for the total potential, yielded acceptable results only for the submerged body. For both the submerged spheroid and the Wigley hull, the hull-surface singularity distributions obtained were remarkably similar to those obtained with our Neumann-Kelvin solver. The free-surface singularity distributions were significantly smaller than the hull-surface distributions, but their location on the free surface resulted in wave fields which were comparable to those generated by the singularities on the hull. For the Wigley hull, it appeared that cancellation between the waves generated by the hull singularities and the free-surface singularities resulted in a loss of accuracy.

It has yet to be demonstrated that the Havelock/Dawson approach can reproduce, for realistic hull forms, the superior near-field results of the Rankine/Dawson methods which were reported by Lindenmuth et al. [3]. The only geometries investigated to date have been so simple that one would not expect significant differences between Neumann-Kelvin results and Rankine/Dawson results. However, these encouraging results indicate that the Havelock/Dawson method may well give us the ability

to combine the best aspects of both the Rankine/Dawson codes and the Havelock codes.

#### ACKNOWLEDGMENTS

This work was supported by the Applied Hydromechanics Research program of the Applied Research Division of the Office of Naval Research, and administered by the David Taylor Research Center.

#### REFERENCES

- [1] Dawson, C.W. "A Practical Computer Method for Solving Ship-Wave Problems". The Proceedings of the Second International Conference on Numerical Ship Hydrodynamics, Berkeley, California, 1977.
- [2] Raven, H.C. "Variations on a Theme by Dawson". Seventeenth Symposium on Naval Hydrodynamics, The Hague, The Netherlands, 1988.
- [3] Lindenmuth, W.T., T.J. Ratcliffe and A.M. Reed. Comparative Accuracy of Numerical Kelvin Wake Code Predictions - "Wake-Off". David Taylor Research Center Report DTRC/SHD-1260-01, May 1988.
- [4] Wehausen, J.V. and Laitone, E.V. Surface Waves. "Encyclopedia of Physics," Vol. IX. Springer-Verlag, Berlin, 1960.
- [5] Doctors, L.J. and Beck, R.F. "Convergence Properties of the Neumann-Kelvin Problem for a Submerged Body". Journal of Ship Research, Vol. 31, No. 4, December 1987.

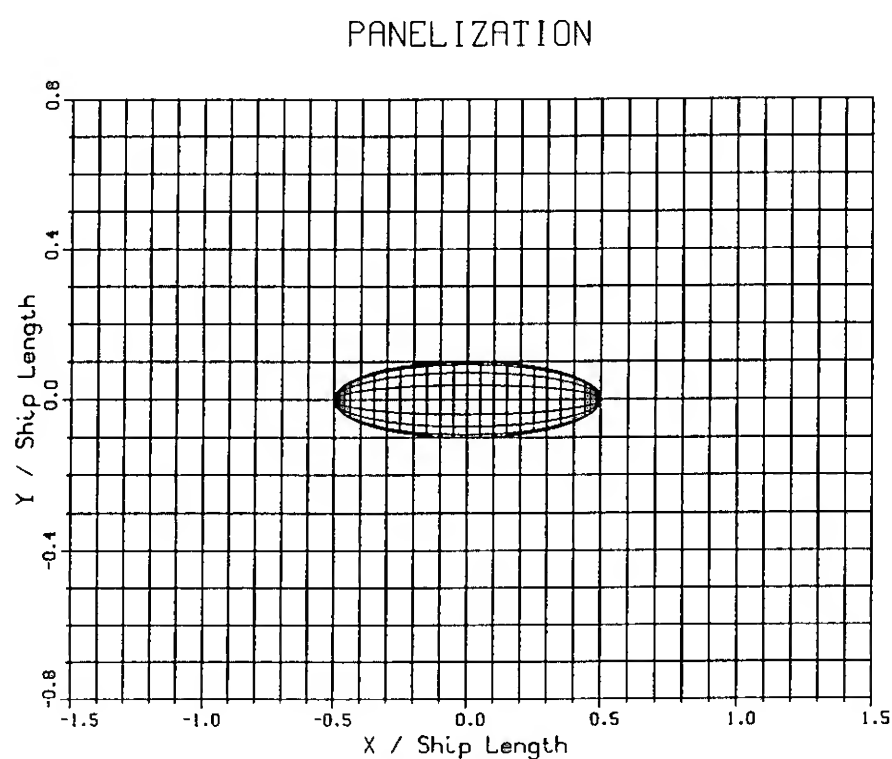


Figure 1. Hull panels on a submerged body of revolution and corresponding free-surface panels.

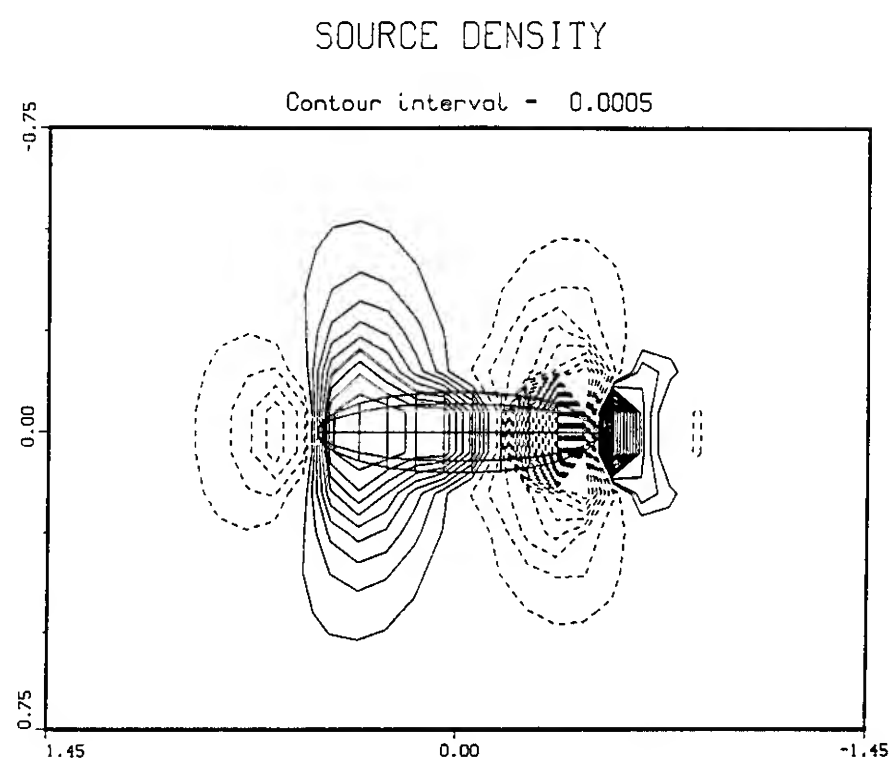


Figure 3. Source density on the free-surface resulting from a solution to the perturbation potential at  $F_n=0.40$ . Solid lines are positive contours, dashed lines are negative.

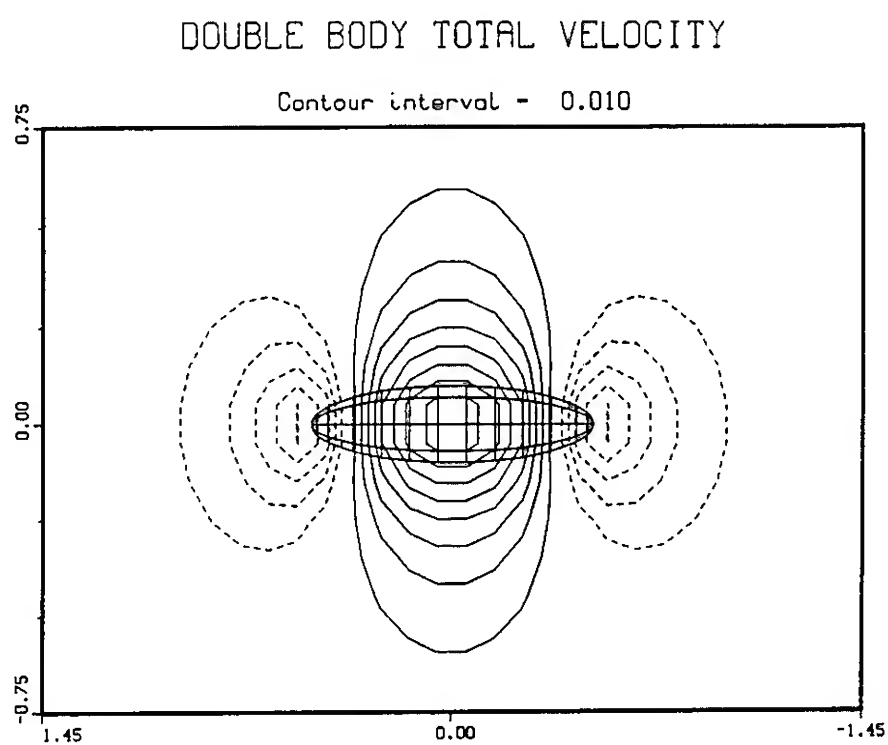


Figure 2. Double-body velocity magnitude on the free surface. Solid lines are contours greater than 1, dashed lines are less than 1.

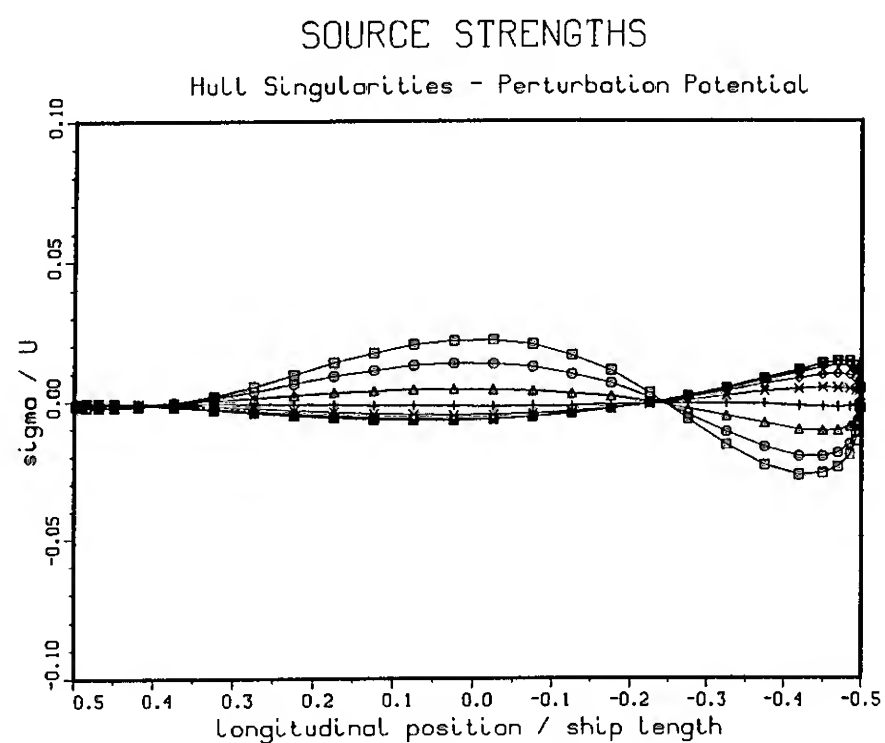


Figure 4. Source strengths on hull surface panels resulting from a solution to the perturbation potential. Each curve represents panels along one circumferential angle.



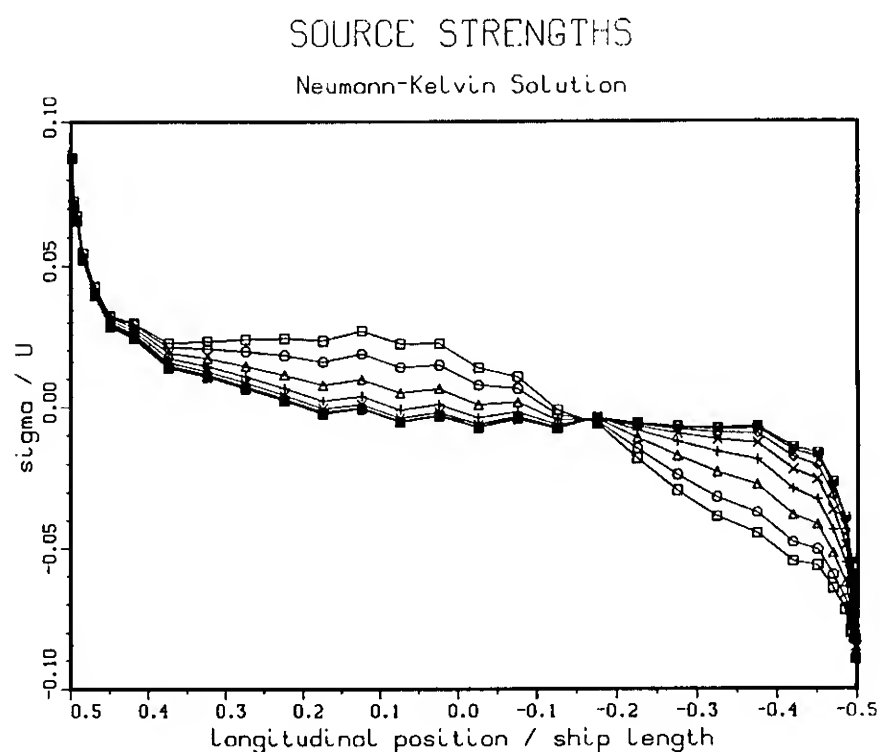


Figure 5. Source strengths on hull surface panels resulting from a solution to the Neumann-Kelvin problem at  $Fn=0.40$ .

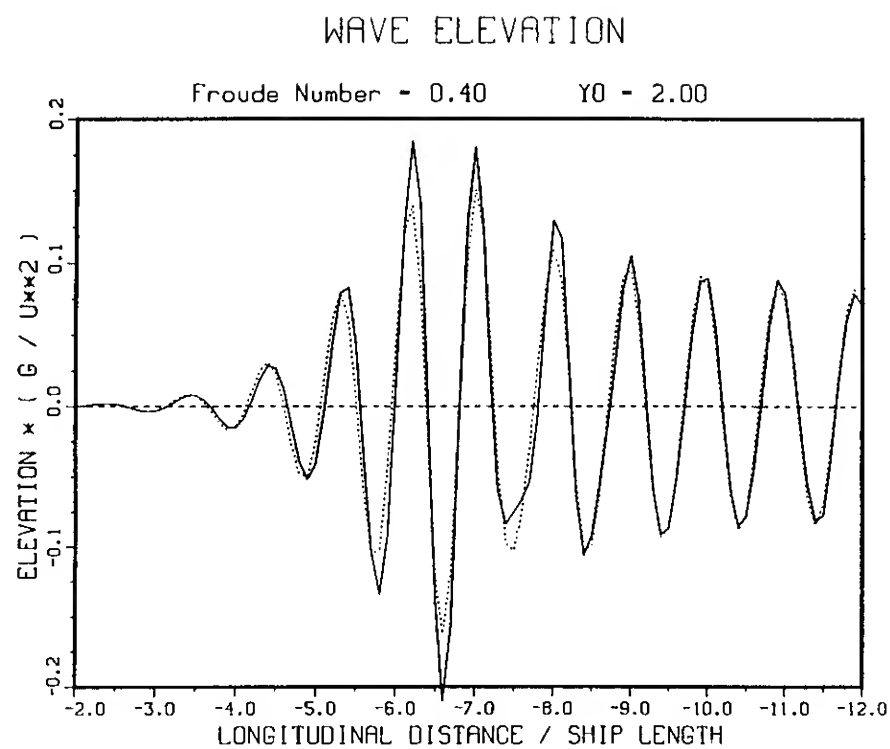


Figure 7. Comparison of far-field wave elevations obtained from the solution to the perturbation potential Dawson problem (solid line) and the Neumann-Kelvin problem (dashed line).

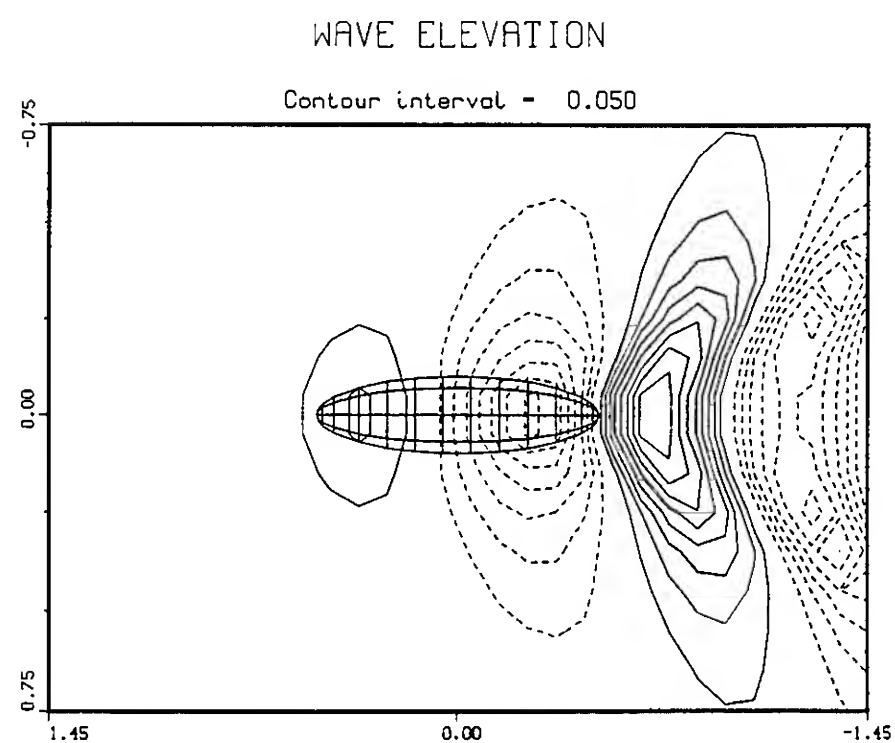


Figure 6. Free-surface elevations resulting from a solution to the perturbation potential at  $Fn=0.40$ . Solid lines are positive contours, dashed lines are negative.

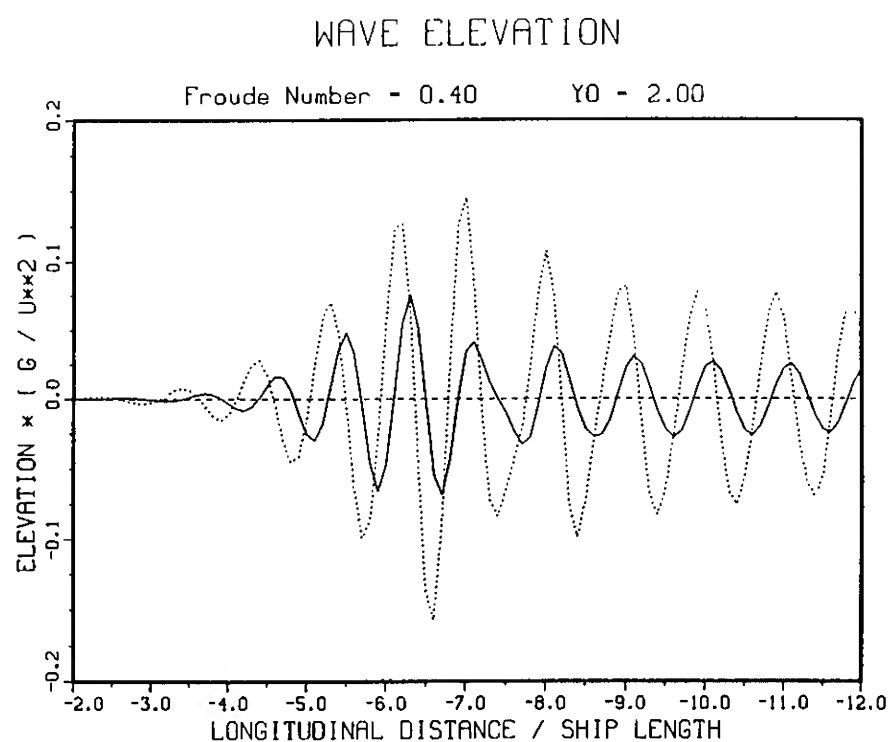


Figure 8. Contributions to the far-field wave elevations from the hull-surface panels (solid line) and from the free-surface panels (dashed line), corresponding to the solution to the perturbation potential.

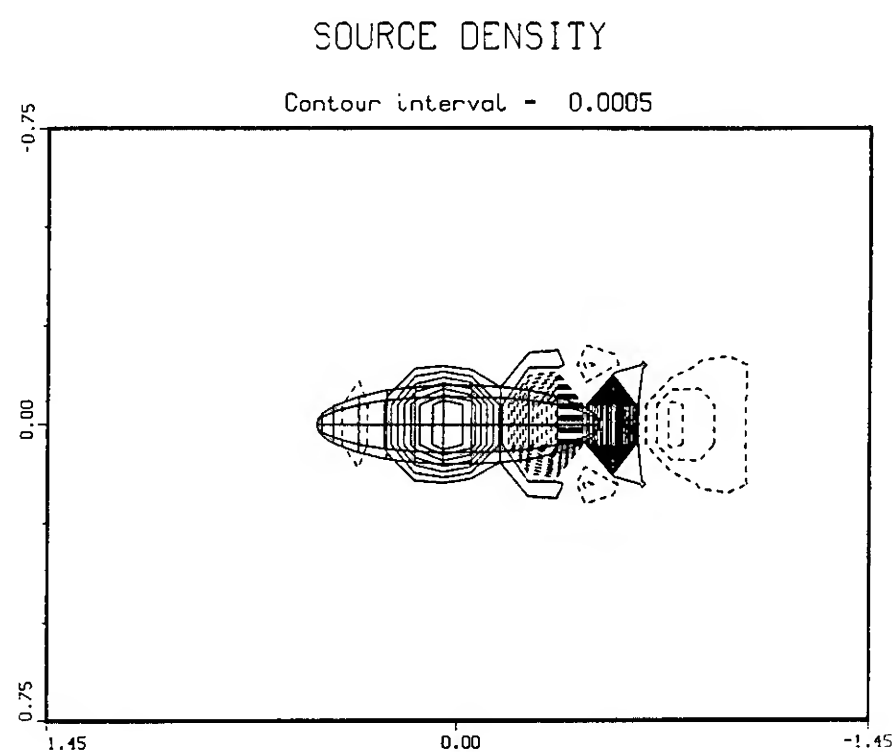


Figure 9. Source density on the free-surface resulting from a solution to the total potential at  $F_n=0.40$ .

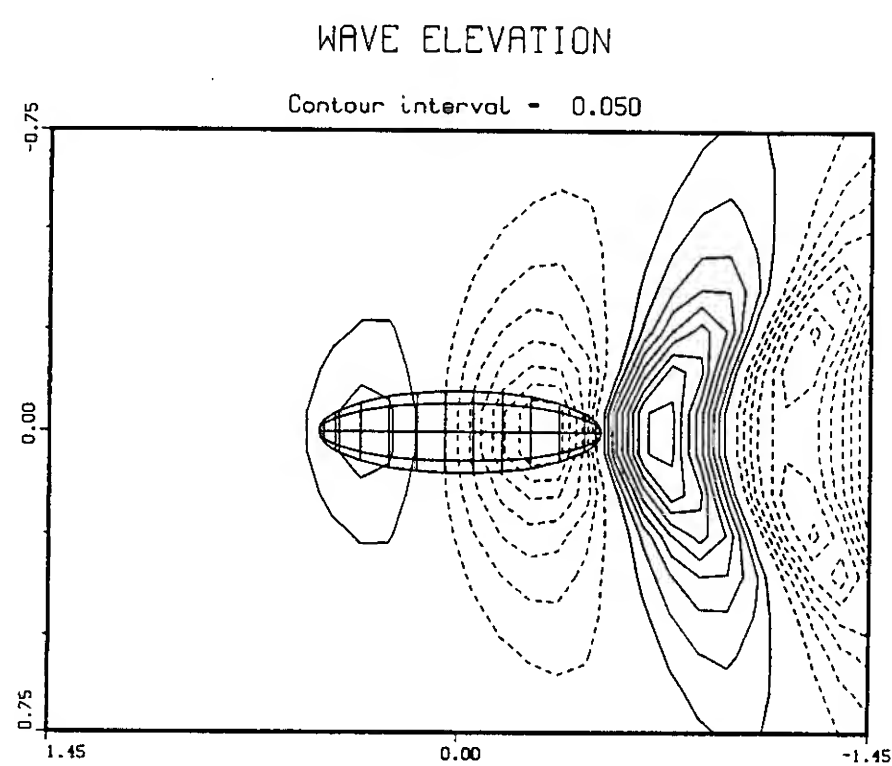


Figure 11. Free-surface elevations resulting from a solution to the total potential at  $F_n=0.40$ .

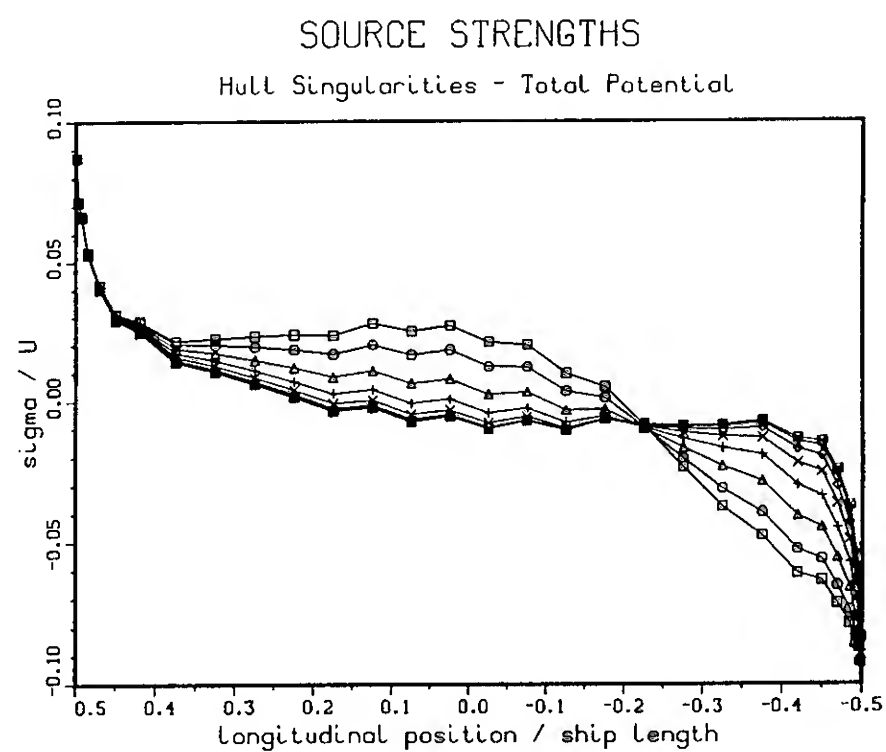


Figure 10. Source strengths on hull surface panels resulting from a solution to the perturbation potential at  $F_n=0.40$ .

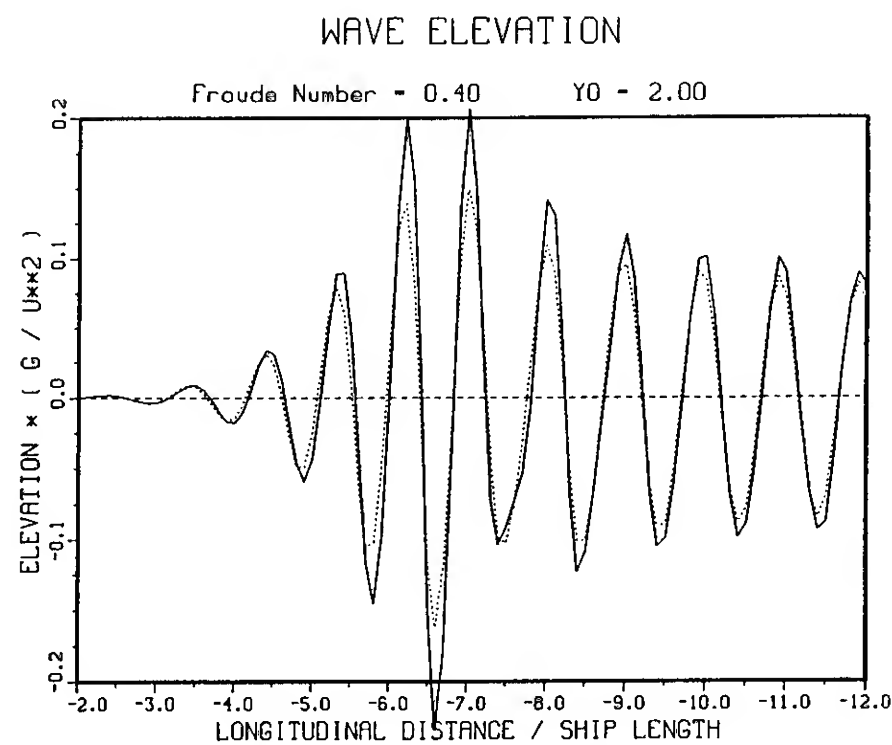


Figure 12. Comparison of far-field wave elevations obtained from the solution to the total potential Dawson problem (solid line) and the Neumann-Kelvin problem (dashed line).

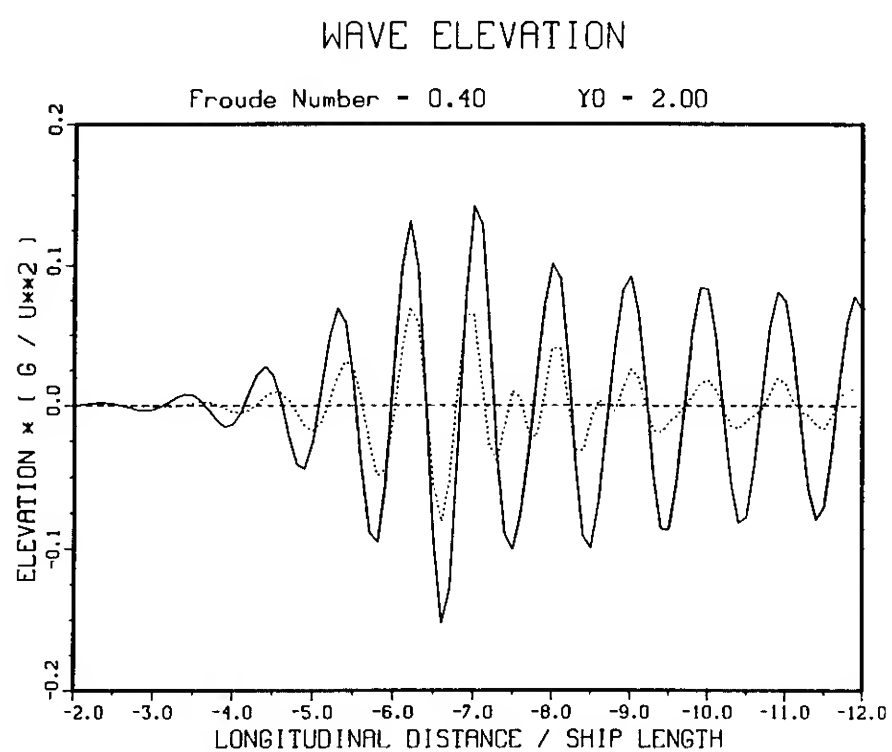


Figure 13. Contributions to the far-field wave elevations from the hull-surface panels (solid line) and from the free-surface panels (dashed line), corresponding to the solution to the total potential.

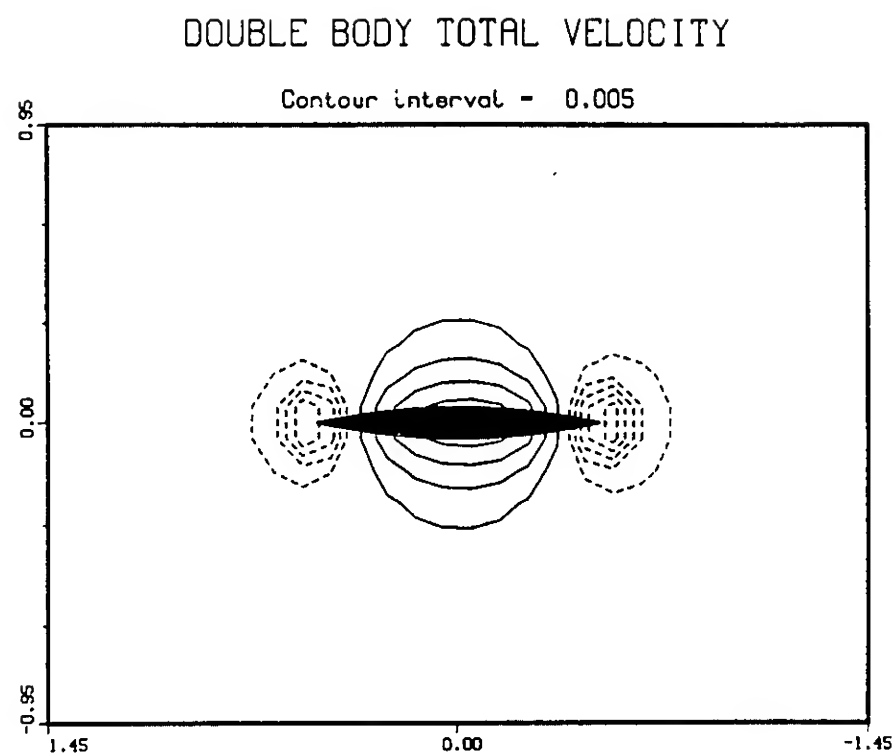


Figure 15. Double-body velocity magnitude on the free-surface for the Wigley hull.

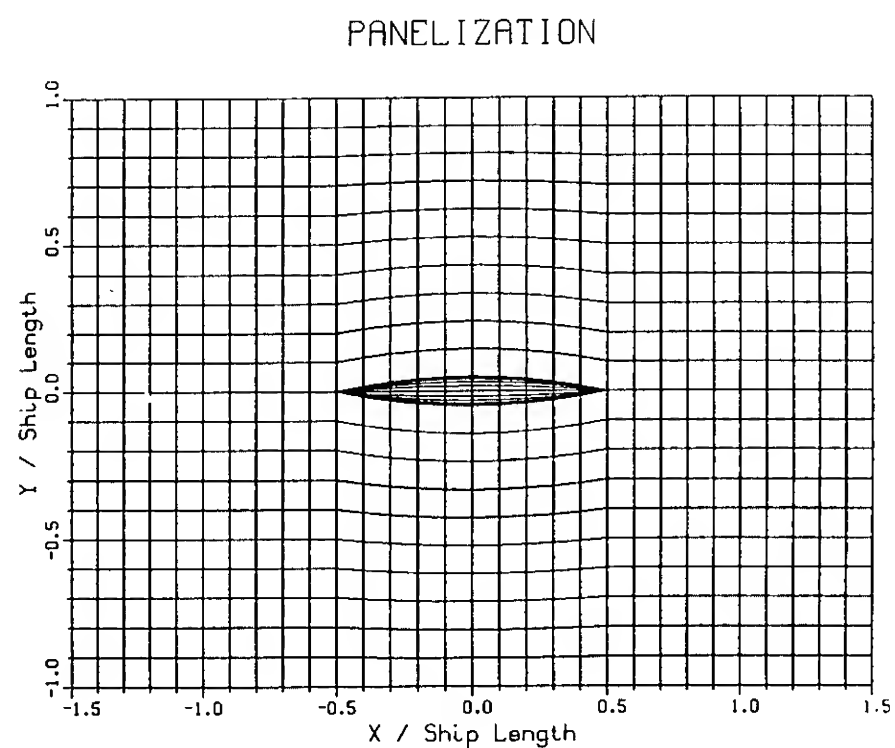


Figure 14. Hull panels on a Wigley hull and corresponding free-surface panels.

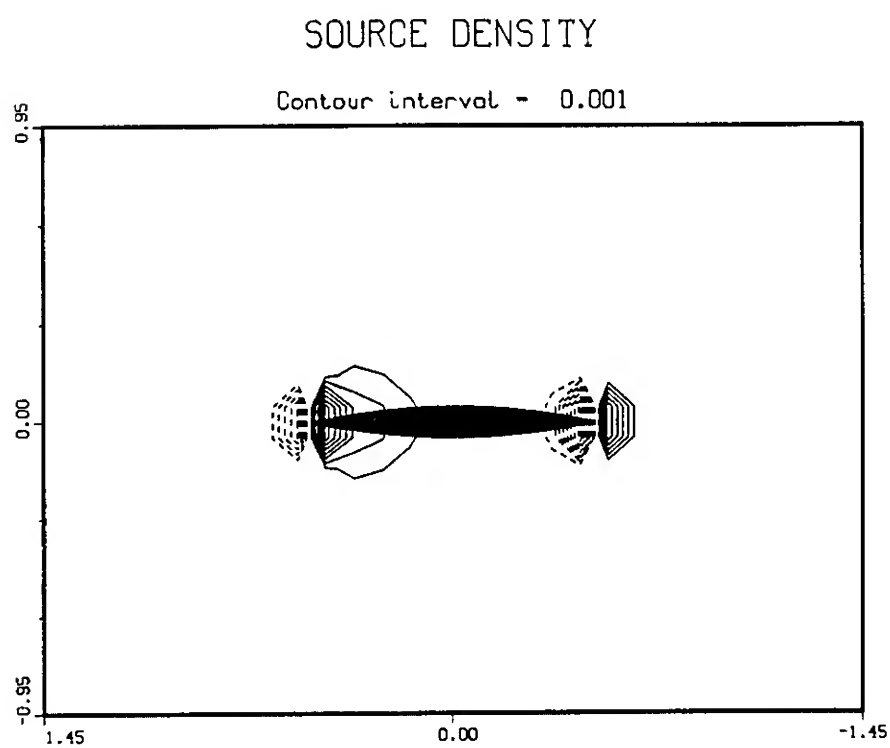


Figure 16. Source density on the free-surface resulting from a solution to the perturbation potential for the Wigley hull at  $Fn=0.40$ .

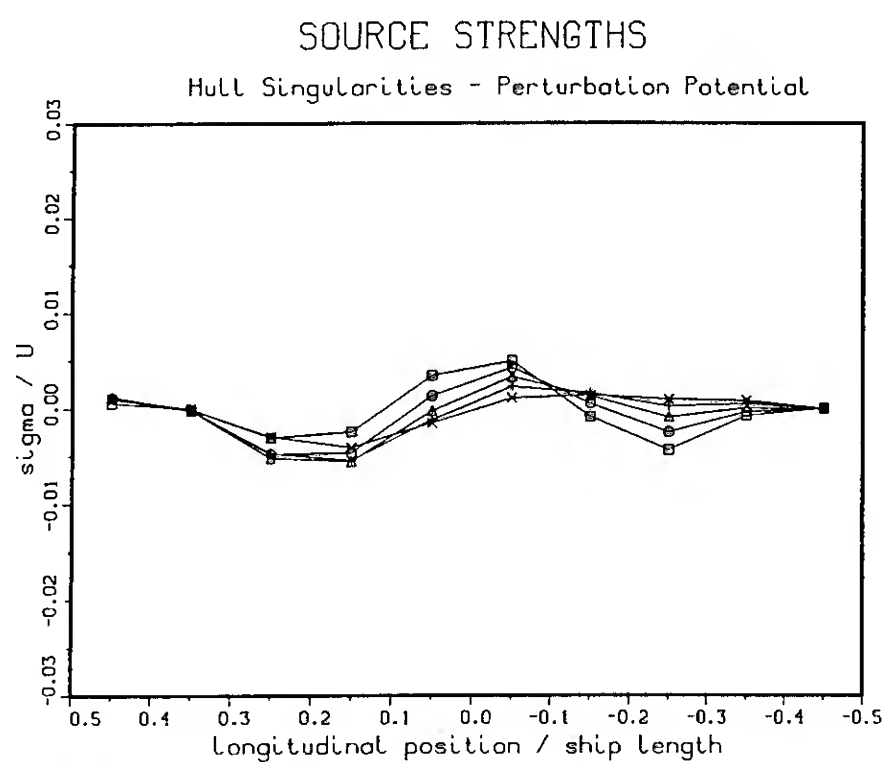


Figure 17. Source strengths on the hull-surface panels of Wigley hull resulting from a solution to the perturbation potential. Each curve represents a row of panels at a constant depth.

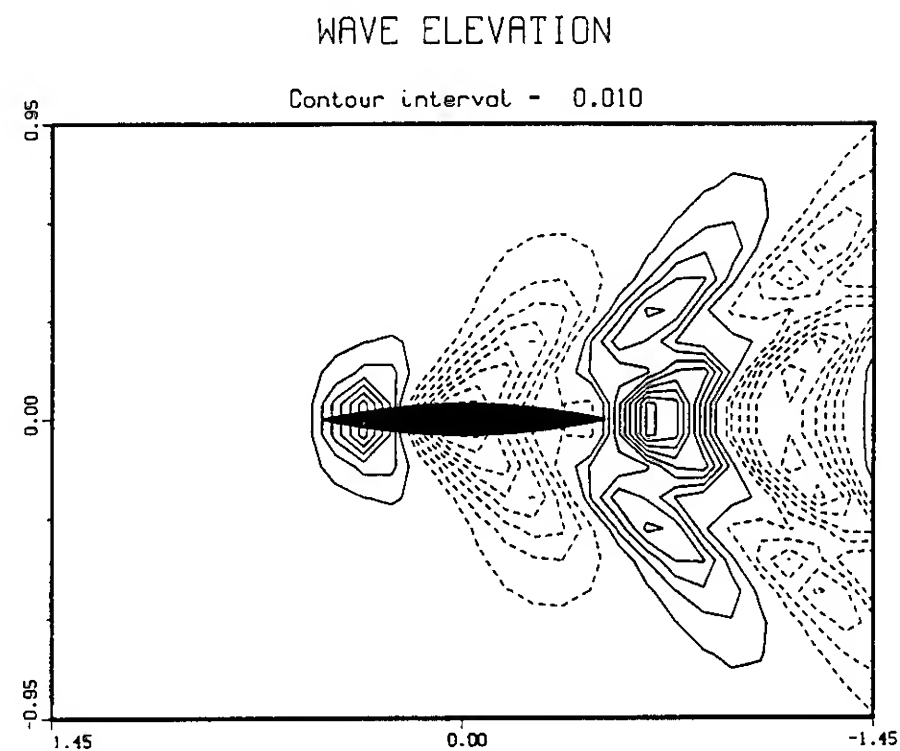


Figure 19. Free-surface elevations resulting from a solution to the perturbation potential for Wigley hull at  $Fn=0.40$ .

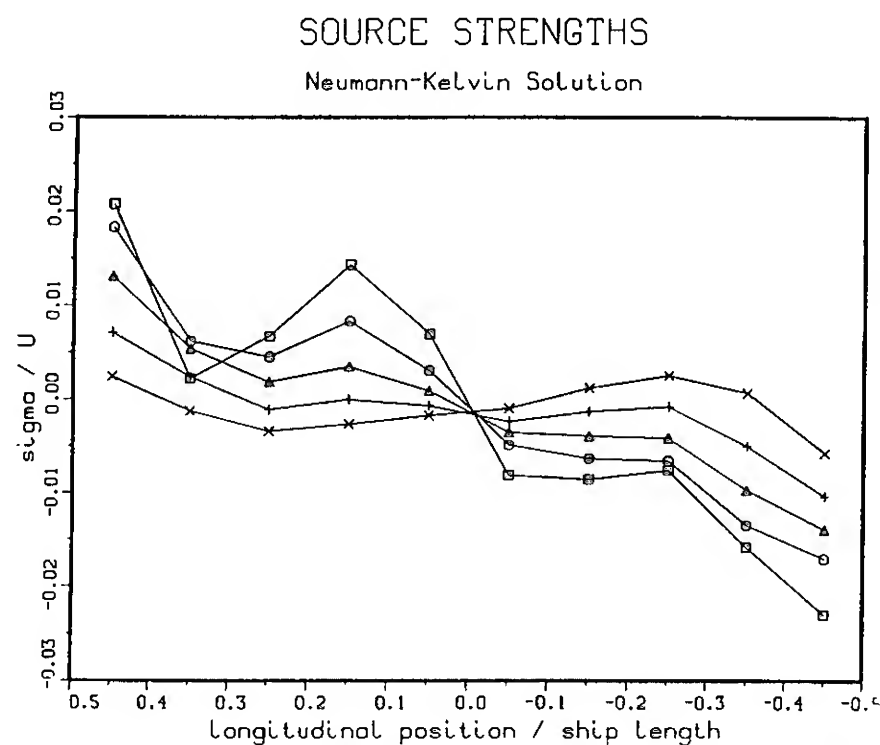


Figure 18. Source strengths on hull-surface panels of Wigley hull resulting from a solution to the Neumann-Kelvin problem at  $Fn=0.40$ .

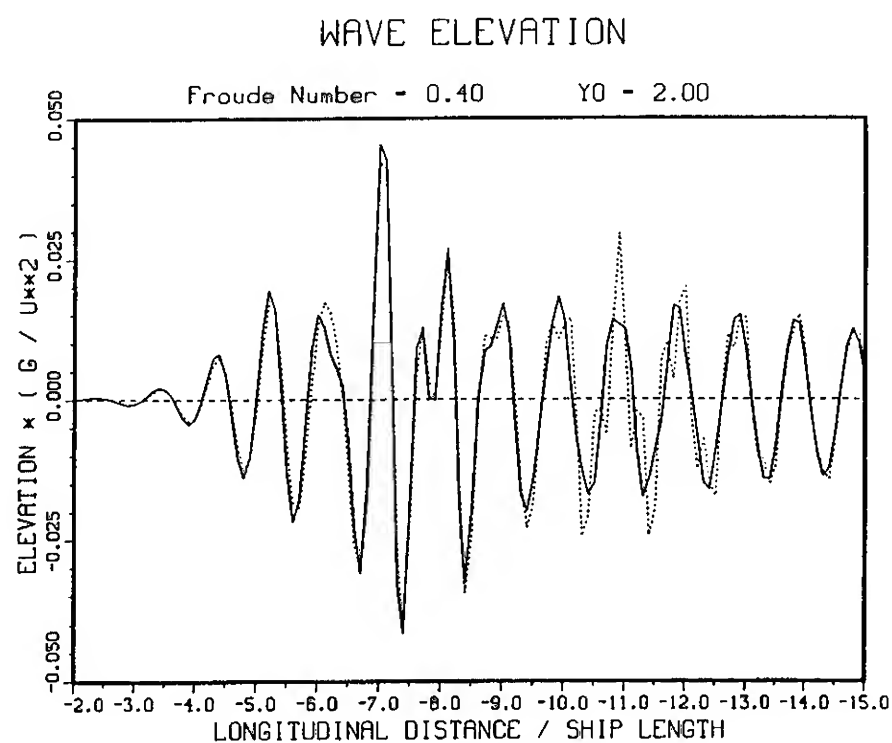


Figure 20. Comparison of far-field wave elevations obtained from the solution to the perturbation potential Dawson problem (solid line) and the Neumann-Kelvin problem (dashed line).

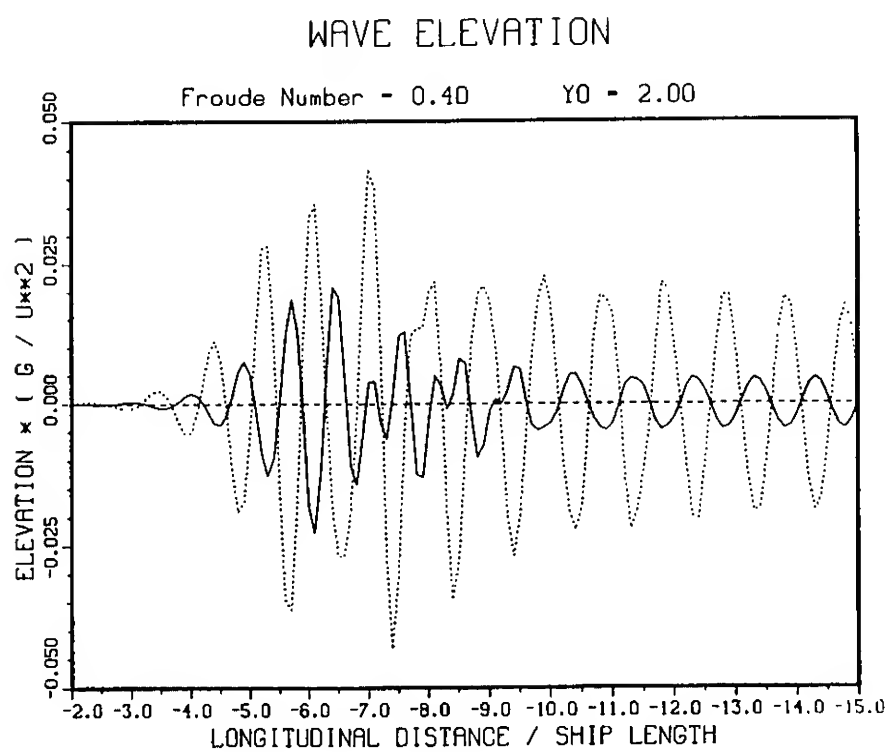


Figure 21. Contributions to the far-field wave elevations from the hull-surface panels (solid line) and from the free-surface panels (dashed line), corresponding to the solution to the perturbation potential.

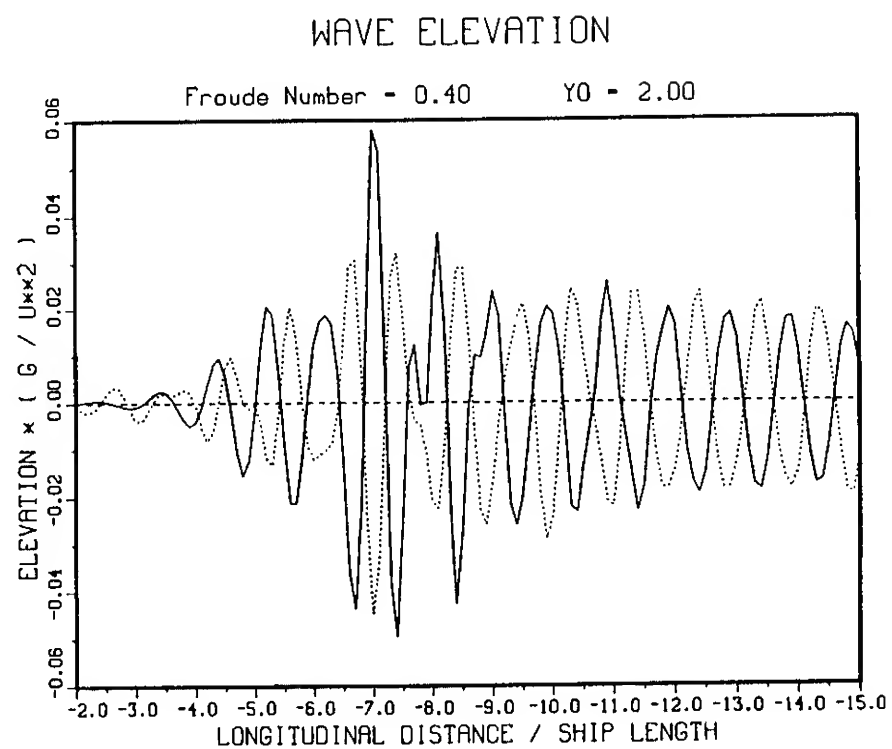


Figure 23. Contributions to the far-field wave elevations from the hull-surface panels (solid line) and from the free-surface panels (dashed line), corresponding to the solution to the total potential.

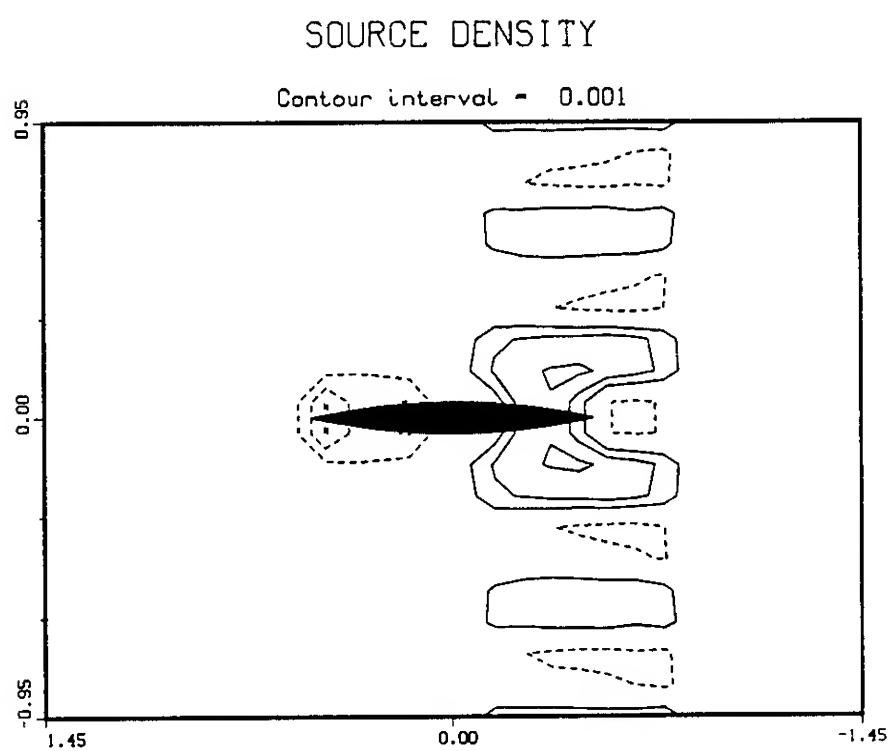


Figure 22. Source density on the free-surface resulting from a solution to the total potential for the Wigley hull at  $Fn=0.40$ .

# Free-Surface Effects on a Yawed Surface-Piercing Plate

H. Maniar, J.N. Newman, H. Xu  
(Massachusetts Institute of Technology, USA)

## ABSTRACT

Analytical and experimental results are presented for a thin vertical surface-piercing plate, moving in the plane of the free surface with constant velocity at a small angle of attack.

The analytical development is a generalization of linear thin-wing theory, using a normal dipole distribution on the plate and in the wake downstream of the trailing edge. A Kutta condition is imposed at the trailing edge. The linear free-surface boundary condition and far-field condition are satisfied by using for the dipole potential the transverse derivative of the classical ship-wave Green function for steady forward motion. Computations are performed for a rectangular planform with aspect ratio 0.5, and these are compared with experimental data. Results are presented for the integrated force and moment, distributed pressure, strength of the leading-edge singularity, and profile of the free surface alongside the plate.

Attention is focused on a local nonuniformity at the intersection of the free surface and trailing edge. The numerical solution is not convergent at this point, with the Kutta condition imposed. Experiments are made to study this region. These show that there is a jump in the free surface across the wake behind the trailing edge, contrary to the assumed boundary conditions, but this jump exists only above a critical Froude number. The jump is accompanied by a sharp transverse flow, contrary to the Kutta condition.

## 1. INTRODUCTION

The classical model of a thin ship was introduced in wave-resistance theory by J. H. Michell, to represent the steady forward motion of a ship hull with transverse symmetry. As in the analogous thickness problem of thin-wing theory, the solution can be constructed from a centerplane distribution of sources with local strength proportional to the longitudinal slope of the body. The thin-ship model has been used extensively for symmetric source-like applications including the analyses of wave resistance in calm water, and seakeeping in head seas.

Relatively little work has been devoted to the lifting problem, where a thin body is yawed or cambered. This problem combines the fields of lifting surfaces and ship waves. Following the analogous lifting problem of a thin wing, a centerplane distribution of transverse dipoles, or an equivalent combination of vortices, can be used to represent the velocity potential. The kinematic boundary condition on the plate yields an integral equation over this surface for the unknown dipole moment. As in the thin-wing formulation a Kutta condition is appropriate at the trailing edge, and trailing vortices (or dipoles of moment independent of  $x$ ) must be distributed in the wake to satisfy the condition of pressure continuity across this surface. But unlike the usual thin-wing analysis, the dipole potential must be generalized to satisfy the free-surface boundary condition; this substantially complicates the numerical analysis, and necessitates the development of special algorithms to achieve satisfactory results.

From the practical standpoint several applications require the solution of this problem. The most obvious are the yawed steady motion of a sailboat, which normally requires a side force to oppose the aerodynamic load on the sails. The same problem occurs in the yawed motion of a ship from the standpoint of maneuvering in calm water. Similar considerations apply to the struts on a hydrofoil vessel, and to the hulls of a SWATH or catamaran (which can experience lifting effects in straight motion without yaw due to the interactions between the hulls). In the unsteady generalization similar problems arise concerning the transverse modes of ship motions in waves. Finally, in an unlikely scenario which stimulated this investigation, the bow assembly of a ship was installed with the stem off-center, and questions arose subsequently concerning the hydrodynamic effects of this defect.

It is appropriate to idealize this class of problems by considering the linearized case of a flat plate with rectangular planform. In this case the integral equation for the dipole moment was derived by Newman [1], but lacking numerical results that work was never published. Subsequently in two independent studies Daoud [2] and Kern [3] attempted to obtain numerical results, but these efforts were not conclusive due to the limited computational resources of that time and the use of numerical integration



to evaluate the free-surface integral in the kernel. Analyses based on low-aspect-ratio approximations have been presented by Chapman [4] and others.

Several more general panel codes have been developed to represent the flow past a yacht hull, including the combined effects of the free surface and a transverse lift force. These codes, which are reviewed by Larsson [5], are effective as design tools but they are not sufficiently efficient and robust to study detailed aspects of the flow. Similarly, recent work by Ba *et al* [6] presents numerical and experimental results for several surface-piercing foils but the numerical procedure is not able to resolve details of the flow near the intersection with the free surface.

With the combined resources of supercomputers and special algorithms for the kernel, it seemed to us that a direct numerical solution of the integral equation might now be feasible, and would illuminate several features of the flow past a surface-piercing body.

One detail of the overall problem which relates directly to ship design is the strength of the leading-edge singularity, particularly where the bow intersects the free surface. Recent naval ships have been designed with a circular stem profile of negligible radius compared to the length scales of the hull. Thus a relatively small transverse flow component can induce separation, cavitation, or ventilation at the stem, and these effects can only be quantified by considering the global lifting problem. This was a primary motivation for initiating the present work, which includes specific results to address this issue, but as the investigation progressed our attention moved downstream to the trailing edge.

Observations of real flows just behind the trailing edge commonly reveal a sharp 'jump' in the free-surface elevation across the wake, as in the experiments of van den Brug *et al* [7]. This jump cannot be reconciled with the potential-flow boundary conditions since, if the pressure is constant on the free surface and continuous across the wake, the free-surface elevation must be continuous. The theoretical results described below are derived on this basis, but a pronounced nonuniformity exists in the solution near the intersection of the free surface and trailing edge.

To provide further insight into the trailing-edge flow experiments have been carried out to observe the elevation of the free surface along the sides of a thin uncambered strut, as a function of the Froude number and angle of attack. Two surprising results have emerged from these observations. First, it appears that the jump occurs only above a certain critical Froude number, and not more generally for all Froude numbers. (In [7] there is also a reference to two distinct regimes, depending on the Froude number.) Based on our experiments, and using the chord length to define the Froude number, the critical value is approximately 0.65. The magnitude of the jump increases with the Froude number beyond this point, and the jump appears to be linearly proportional to the angle of attack. The other surprise is that when the jump occurs there is a distinct transverse flow component, in contradiction to the Kutta condition. The vertical extent of this transverse flow is similar to the elevation of the jump.

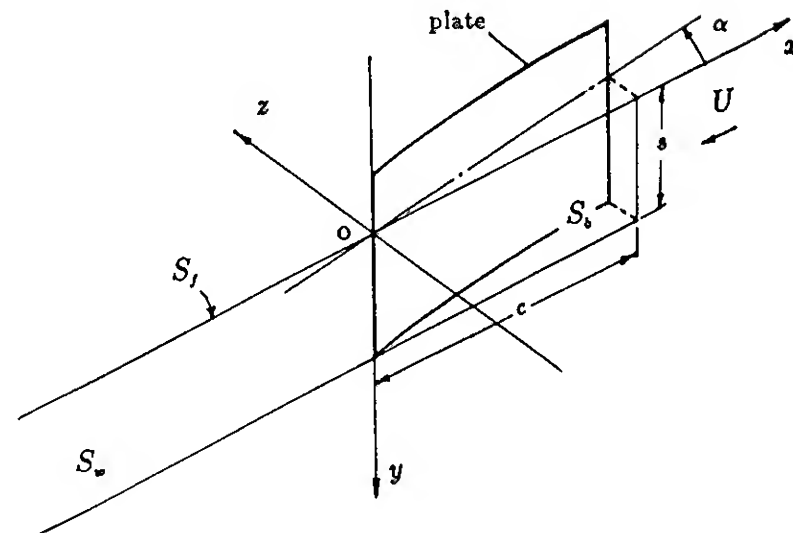


Figure 1. Definition sketch of the plate and coordinate system.

## 2. ANALYTICAL FORMULATION

We consider a vertical rectangular surface-piercing plate of zero thickness, moving with constant velocity  $U$  and a small angle of attack  $\alpha$ . The chord length is  $c$  and the draft (submerged span) is  $s$ . To simplify the presentation we assume that the plate is uncambered. Cartesian coordinates  $(x, y, z)$  are defined with the origin at the intersection of the trailing edge and the waterline, the  $x$ -axis in the direction of forward motion of the plate, and the  $y$ -axis positive downwards. The geometry of the plate and the coordinate system are shown in Figure 1.

Following the classical description of a planar lifting surface, the fluid is assumed to be inviscid, incompressible, and irrotational except for a thin sheet of trailing vorticity in the wake. The perturbation velocity field is represented as the gradient of a potential  $\phi$  which must satisfy the Laplace equation

$$\nabla^2 \phi = 0 \quad (1)$$

in the fluid domain.

Since the angle of attack is assumed small, the boundary conditions may be linearized on the free surface  $S_F$ , body surface  $S_B$ , and wake  $S_W$ . On  $S_F$  the kinematic and dynamic boundary conditions are combined in the form

$$\frac{\partial^2 \phi}{\partial x^2} - K \frac{\partial \phi}{\partial y} = 0 \quad \text{on } y = 0 \quad (2)$$

where  $K = g/U^2$  is the wave number of a plane progressive wave with the phase velocity  $U$  and  $g$  is the gravitational acceleration. Together with this boundary condition a radiation condition is imposed that the far-field waves are confined to a domain downstream of the body. On  $S_B$  the appropriate kinematic boundary condition may be written as

$$\frac{\partial \phi}{\partial z} = U \alpha \quad \text{on } z = 0 \quad (3)$$

The pressure in the fluid is given by the linearized Bernoulli equation

$$p - p_a = \rho U \frac{\partial \phi}{\partial x} + \rho g y \quad (4)$$

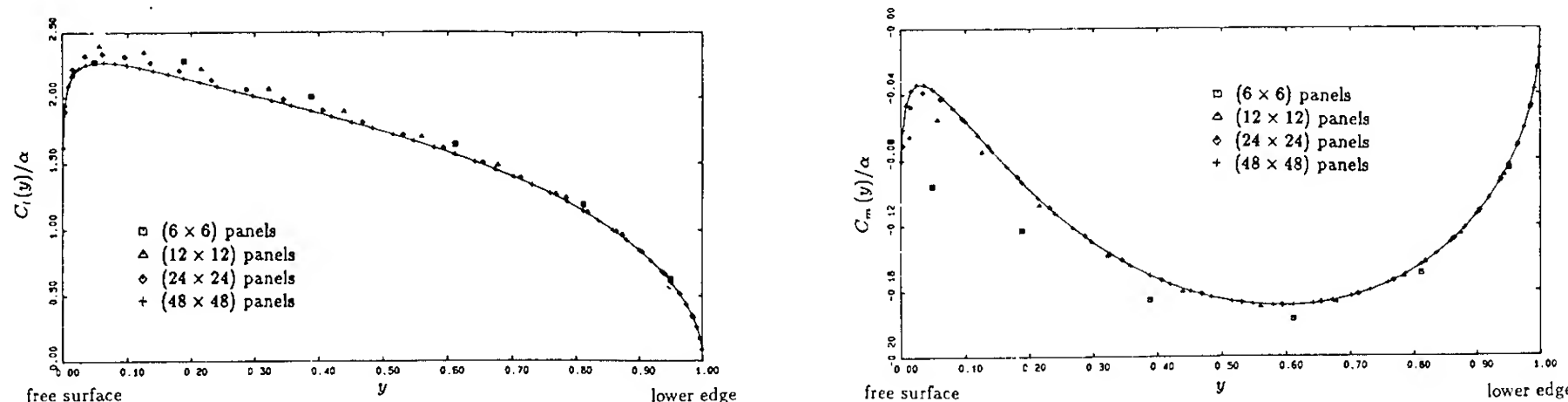


Figure 2. Results at a Froude number  $F = 0.8$  for the spanwise distribution of lift ( $C_l$ ) and moment ( $C_m$ ). Symbols denote different discretizations of  $S_b$  with the indicated numbers of panel segments in the chordwise and spanwise directions, respectively.

where  $p_a$  is the atmospheric pressure on free surface. Since the pressure must be continuous across the wake  $S_W$ , extending downstream from the trailing edge, it follows that

$$\frac{\partial}{\partial x}(\phi^+ - \phi^-) = 0 \quad (5)$$

where superscripts denote the limiting values on  $z \rightarrow 0 \pm$ .

In accordance with the Kutta condition the velocity is assumed to be finite and continuous at the trailing edge. Finally, for large depths beneath the free surface, the velocity is assumed to vanish.

From (4) the elevation of the free surface is given by

$$\eta_f = -\frac{U}{g} \frac{\partial \phi}{\partial x} \Big|_{y=0} \quad (6)$$

From (5) it follows that the free-surface elevation is continuous across the wake. Since the only inhomogeneous boundary condition (3) implies a solution  $\phi$  which is odd in  $z$ , the free-surface elevation will vanish everywhere on the  $x$ -axis except along the two sides of the plate, where this elevation will be equal in amplitude and opposite in sign.

Green's theorem can be used to reduce this boundary-value problem to an integral equation on  $S_B$ . For this purpose we first define the Green function

$$G(\mathbf{x}, \xi) = \frac{1}{r} - \frac{1}{r_0} + H(\mathbf{x}, \xi) \quad (7)$$

where  $\mathbf{x} = (x, y, z)$  is the field point,  $\xi = (\xi, \eta, \zeta)$  is the source point, and  $r$  and  $r_0$  are, respectively, the distances between the field point and the source point or its image above the free surface:

$$\begin{aligned} r &= [(x - \xi)^2 + (y - \eta)^2 + (z - \zeta)^2]^{1/2} \\ r_0 &= [(x - \xi)^2 + (y + \eta)^2 + (z - \zeta)^2]^{1/2}. \end{aligned} \quad (8)$$

The function  $H(\mathbf{x}, \xi)$  is harmonic in the fluid domain, and will be defined subsequently to satisfy the free-surface boundary condition and radiation condition.

If Green's theorem is applied to the control volume bounded by  $S_F$ ,  $S_B$ ,  $S_W$ , and a closure at infinity, the only nonvanishing contribution is from the normal dipoles on  $S_B \cup S_W$ . The result is

$$\phi(\mathbf{x}) = -\frac{1}{4\pi} \iint_{S_B^+ \cup S_W^+} [\phi(\xi, \eta, 0^+) - \phi(\xi, \eta, 0^-)] \frac{\partial G}{\partial n} d\xi d\eta \quad (9)$$

where  $S_B^+$  and  $S_W^+$  denote the side of  $S_B$  and  $S_W$  where  $z \rightarrow 0^+$ , and where  $\partial G / \partial n = \partial G / \partial z = -\partial G / \partial \zeta$ . Letting  $m(\xi, \eta) = \phi(\xi, \eta, 0^+) - \phi(\xi, \eta, 0^-)$ , equation (9) expresses the velocity potential in terms of a continuous normal dipole distribution over the lifting surface and its wake with the unknown moment  $m(\xi, \eta)$ . Differentiating both sides of this equation with respect to  $z$ , and imposing the boundary condition (3) on  $S_B$ , the resulting equation may be written as

$$\frac{1}{4\pi} \lim_{z \rightarrow 0} \frac{\partial}{\partial z} \iint_{S_B^+ \cup S_W^+} m(\xi, \eta) \frac{\partial G}{\partial \zeta} \Big|_{\zeta=0} d\xi d\eta = U\alpha \quad (10)$$

This is a Fredholm integral equation of the first kind, to be solved for the unknown function  $m(x, y)$ .

From the boundary condition (5) the unknown  $m(x, y)$  is independent of  $x$  on  $S_W$ ,

$$m(x, y) = m(0, y) \quad \text{for } -\infty < x \leq 0; \quad 0 \leq y \leq s \quad (11)$$

Thus the unknown function  $m$  is confined to the domain of the lifting surface  $S_B$ . Moreover, since the potential is continuous outside the surfaces  $S_B$  and  $S_W$ , the difference in the potential between the two sides must vanish at the leading edge and the lower edge of  $S_B$ . This gives the conditions

$$\begin{aligned} m(c, y) &= 0 & \text{for } 0 \leq y \leq s \\ m(x, s) &= 0 & \text{for } 0 \leq x \leq c \end{aligned} \quad (12)$$

However, no similar conditions can be applied on the waterline.

The Green function  $G$  is well known in ship-wave theory, and corresponds to the velocity potential of a sub-

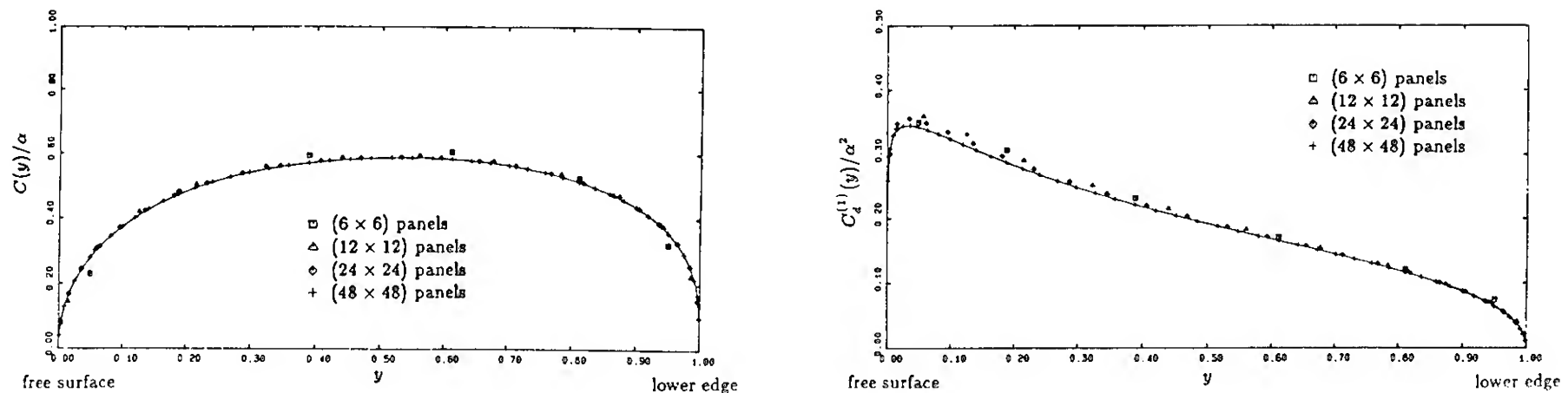


Figure 3. Spanwise distribution of the leading-edge singularity strength ( $C$ ) and drag coefficient ( $C_d$ ) for the same conditions described in Figure 2.

merged source moving with constant horizontal velocity beneath the free surface. The following form, as given by Newman [8], is convenient for numerical applications:

$$G(\mathbf{x}, \xi) = \frac{1}{r} - \frac{1}{r_0} + \text{Re} \left[ \lim_{\epsilon \rightarrow 0} \frac{2i}{\pi} \int_{-\pi/2}^{\pi/2} \cos \varphi d\varphi \int_0^\infty \frac{e^{-k(y+\eta) + ik|x-\xi| \sec \varphi + k(z-\zeta) \tan \varphi}}{k - K \cos^2 \varphi + i\epsilon} dk \right. \\ \left. + 4iH(\xi - x) \int_{-\pi/2}^{\pi/2} \sec^2 \vartheta \sin \vartheta e^{-K(y+\eta) \sec^2 \vartheta + iK(x-\xi) \sec \vartheta + iK|z-\zeta| d\vartheta} \right] \quad (13)$$

Here  $H(\xi - x)$  is the unit step function, equal to 1 if  $\xi > x$  and 0 otherwise. The double integral in (13) represents a symmetrical nonradiating disturbance, and the single integral accounts for the wave field downstream.

In the limits of zero or infinite Froude number the Green function reduces to  $(1/r \pm 1/r_0)$ , respectively. The solution of the integral equation (10) is then equivalent to that for the submerged plate plus its image above the free surface, in an otherwise unbounded fluid, where the angle of attack of the image is  $\pm\alpha$  respectively.

Except for the Rankine singularity  $1/r$ , which must be treated separately to account correctly for its limiting contribution on the boundary  $S_B^+$ , the kernel of the integral equation (10) can be evaluated from the second normal derivative of  $G$  on the centerplane  $z = 0$ . From Laplace's equation the corresponding tangential derivatives can be used instead. Thus the values of the integrals in (13) are only required on the centerplane, where special algorithms described by Newman [8,9] are applicable. Following this approach the double integral in (13) is replaced by polynomial approximations, and the single integral is replaced by a pair of complementary Neumann expansions. Corresponding analytic expressions have been derived for the second normal derivative of these integrals, and effective algorithms are described by Xü [10]. Using this approach the kernel in (10) can be evaluated without the computational burden of numerical integration and with uniform accuracy of the results.

The single integral in (13) contains an essential singularity along the  $x$ -axis, which corresponds physically to the short diverging waves with vanishing wavelength and unbounded amplitude downstream of a source in the free surface. Thus the limiting value of (13) is nonuniform for  $|z - \zeta| \rightarrow 0$ , but if  $z - \zeta = 0$  the value of the single integral is continuous as a function of the longitudinal and vertical coordinates. Thus when the source and field points are both restricted to the plane  $y = 0$  the single integral can be evaluated without fundamental difficulties. On the other hand, the second derivative of the Green function does amplify a logarithmic singular component of the double integral when  $r_0 \rightarrow 0$ . This singularity is weaker than the Rankine components  $1/r$  and  $1/r_0$ , but it may be responsible for the nonuniform features of the solution at the intersection of the plate with the free surface.

To obtain a numerical solution of the integral equation (10) the domain  $S_B^+$  is discretized in a similar manner to lifting-surface theory, generalizing the approach of Lan [11] with a nonuniform distribution of panels optimized to account for the square-root singularities at the leading edge and lower tip and for the more complicated behavior at the free surface. Further details regarding the analytic formulation and numerical analysis are given by Xü [10]. Standard algorithms [12] are used to evaluate the contribution from the Rankine singularities  $1/r$  and  $1/r_0$  as distributions with constant density over each panel. The remaining contribution from the free-surface integrals is evaluated by one-point quadrature at the control point of each panel. The boundary condition is satisfied by collo-

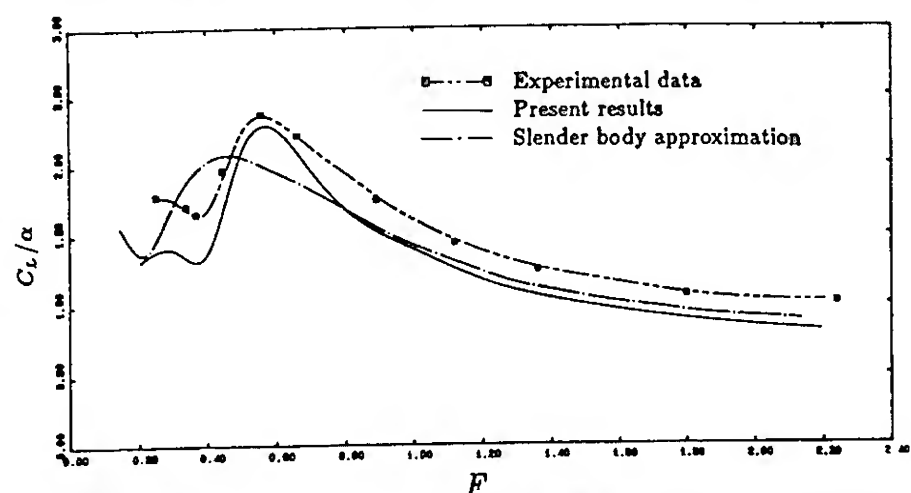


Figure 4. Comparison of the lateral-force coefficients at various Froude numbers. The experimental data is from van den Brug, et al (1971) and slender body approximation is due to Chapman (1976).

cation, leading to a system of  $N$  algebraic equations with the same number of unknowns. The contribution from the dipoles in the wake is evaluated by the same approach, with the wake discretized by rectangular panels and truncated at a sufficiently large distance downstream determined so that the results are not affected. This scheme has been validated in the zero-Froude-number limit by comparison with numerical results in the aerodynamic literature.

The theoretical results shown here are for an aspect ratio equal to 0.5. This value was selected to permit comparison with the experimental results of van den Brug [7]. Integrated quantities include the lift coefficient  $C_L$ , yaw moment  $C_M$  about the mid-chord point, drag coefficient  $C_D$ , and the thrust coefficient  $C_T$  from the leading-edge suction force. The lift force and yaw moment are evaluated directly by pressure integration over the discretized surface  $S_B$ . The leading-edge suction force is derived by assuming the square-root singularity of the nondimensional pressure coefficient

$$\Delta C_p = \frac{p^+ - p^-}{\frac{1}{2}\rho U^2} = \frac{2}{U} \cdot \frac{\partial m(x, y)}{\partial x} \quad (14)$$

to be of the form

$$\Delta C_p \simeq 2C(y)\sqrt{c}/\sqrt{c-x} \quad (15)$$

near the leading edge. After integrating both equations with respect to  $x$ ,

$$C(y) = \frac{1}{2U\sqrt{c}} \lim_{x \rightarrow c} \frac{m(x, y)}{\sqrt{c-x}} \quad (16)$$

This limit is extracted by Aitken's extrapolation algorithm, and the sectional leading-edge thrust coefficient is evaluated from the relation

$$C_t(y) = \frac{\pi}{2} C^2(y) \quad (17)$$

Finally, the drag coefficient is derived from the relation  $C_D = C_L \alpha - C_T$ . Note that  $C_D$  is the total drag coefficient including the sum of induced drag and wave drag. (Integration in the Trefftz plane is not practical due to the difficulties of evaluating the wave field far downstream.)

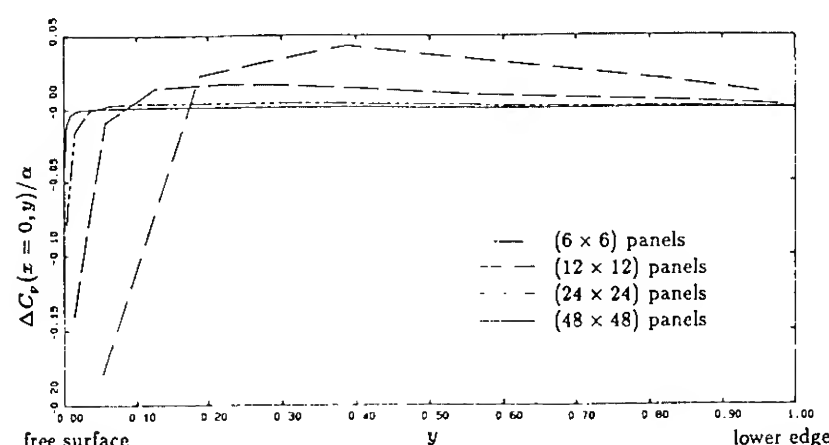


Figure 5. Spanwise distributions of pressure coefficients at the trailing edge for the same conditions described in Figure 2.

Tests of numerical convergence have been made by comparing the results based on discretizations with  $6 \times 6$ ,  $12 \times 12$ ,  $24 \times 24$ , and  $48 \times 48$  panels. Note that the latter computations involve a total of 2304 unknowns, and the solution of a linear system of equations with  $2304 \times 2304 = 5.3 \times 10^6$  coefficients to be evaluated from the derivatives of the Green function (13). Convergence to two significant figures is achieved for the integrated force coefficients with the  $24 \times 24 = 576$  discretization.

Most of the computations with less than 1000 panels were performed on a VAX-750 computer. Those for larger numbers of panels were performed on a Cray-YMP.

Results for the spanwise distribution of the lift and moment coefficients are shown in Figure 2. Figure 3 shows the spanwise distribution of the leading-edge singularity strength and drag coefficient. The leading-edge singularity vanishes at the free surface, since the pressure is constant on this surface. The other coefficients plotted in these two figures are all affected near the free surface by a local nonuniformity which manifests itself most strongly near the trailing edge, and is discussed further below.

Figure 4 compares the total lift and moment coefficients with the experimental data of van den Brug [7] and with the slender-body theory of Chapman [4]. The results appear to be satisfactory, with improved agreement from the present results compared to those of Chapman especially in the case of the moment.

Near the trailing edge the solution is not convergent, as indicated in Figure 5. Here the pressure coefficient is derived from L'Hospital's rule in terms of the second derivative of  $m$  with respect to the angular coordinate  $\theta$  defined by the relation  $\sin \theta = 2\sqrt{x(c-x)}/c$ . From the Kutta condition the pressure coefficient should vanish at the trailing edge, whereas the actual values computed in this manner are not precisely zero and the error appears to increase without limit as the free surface is approached from below.

The perspectives in Figure 6 show in a revealing manner the complete pressure distribution on  $S_B$  as a function of the Froude number. In the two limits of zero and infinity the result is well behaved near the trailing edge, and the same appears to be true for the Froude number  $F = 0.3$ , where the waves on the free surface are relatively short. However at  $F = 0.8$  a local nonuniformity is apparent at the intersection of the free surface and trailing edge. This nonuniformity is confined to a few panels adjacent to the intersection point; as the number of panels is increased, the domain of the nonuniformity is reduced.

To evaluate the free-surface profile along the intersection of the plate, the unknown  $m$  must be differentiated numerically with respect to the horizontal coordinate  $x$ , and extrapolated vertically from the uppermost collocation point to the free surface. The results are shown for various discretizations in Figure 7. For the case  $F = 0.3$  a finer discretization has been used longitudinally, to account for the shorter wavelength scale. Other results are shown later in conjunction with the experiments.

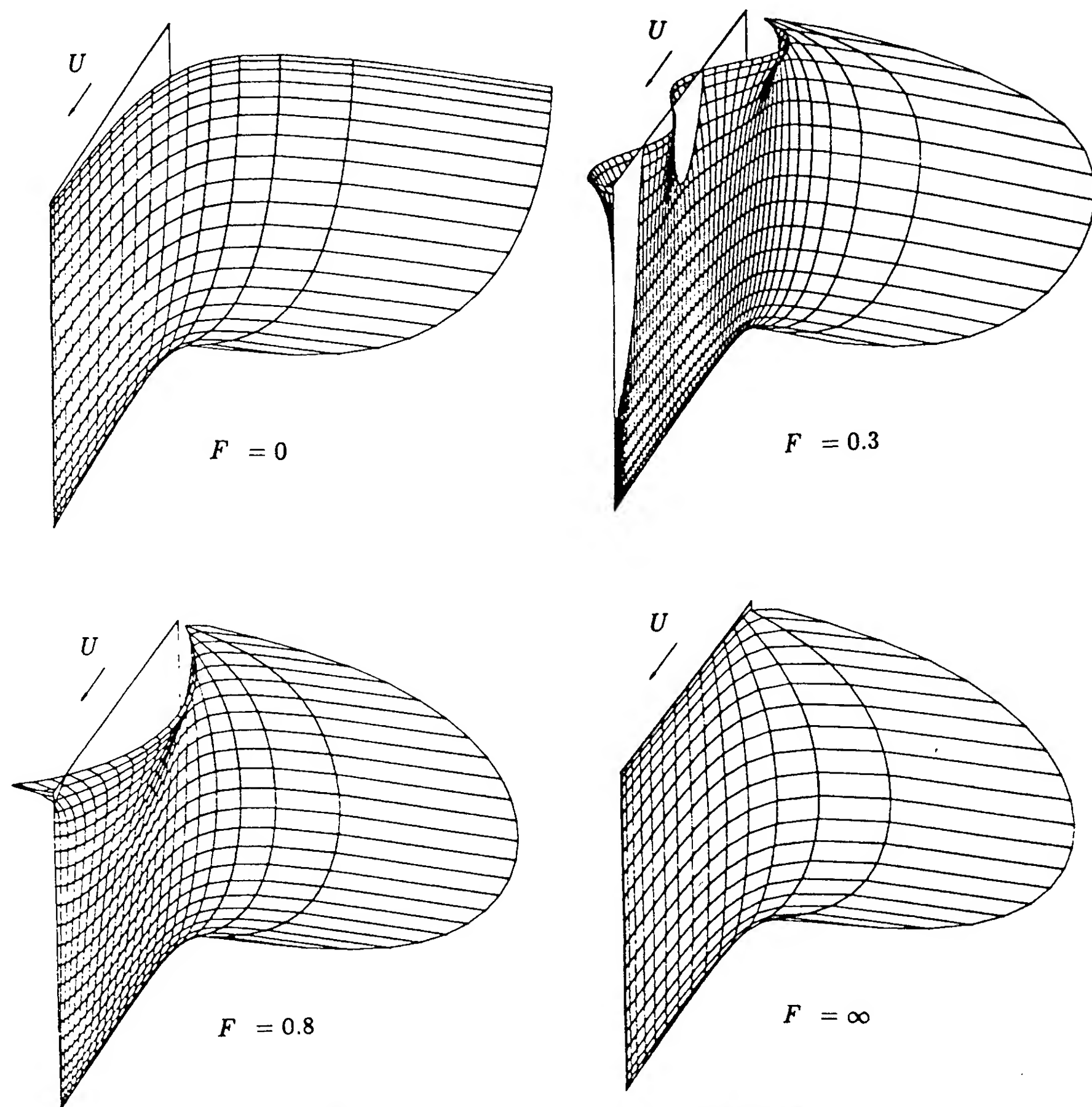


Figure 6. Normalized pressure distributions on the plate, at the indicated Froude numbers.

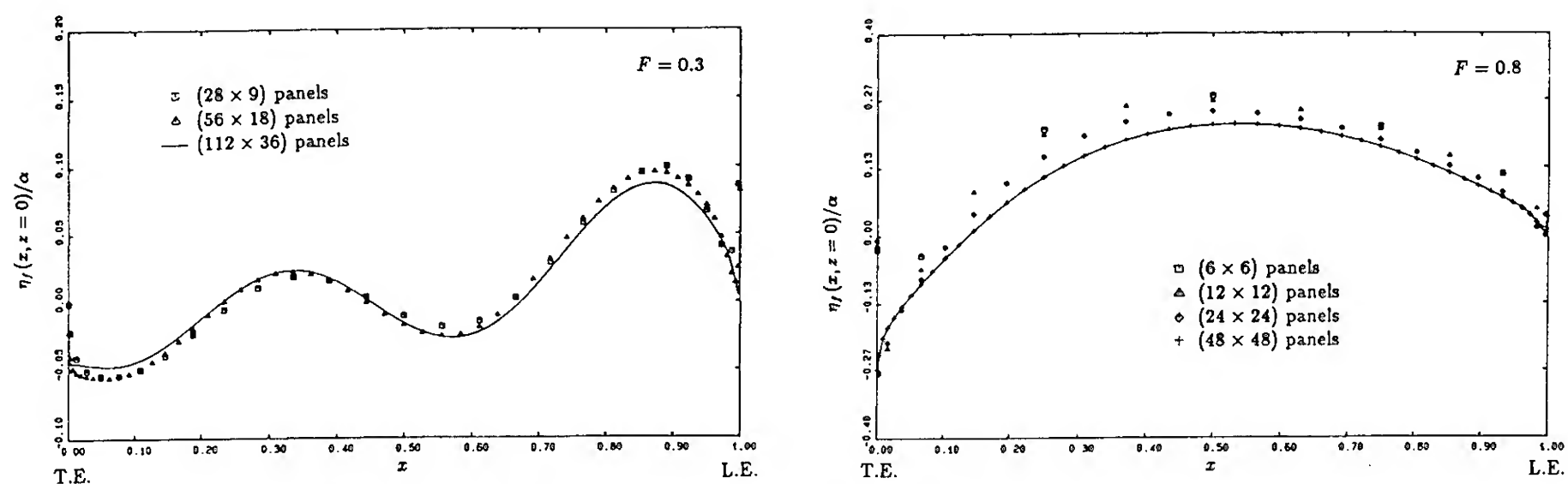


Figure 7. Free surface profile on the plate. Symbols denote different discretizations with the indicated numbers of panel segments in the chordwise and spanwise directions.



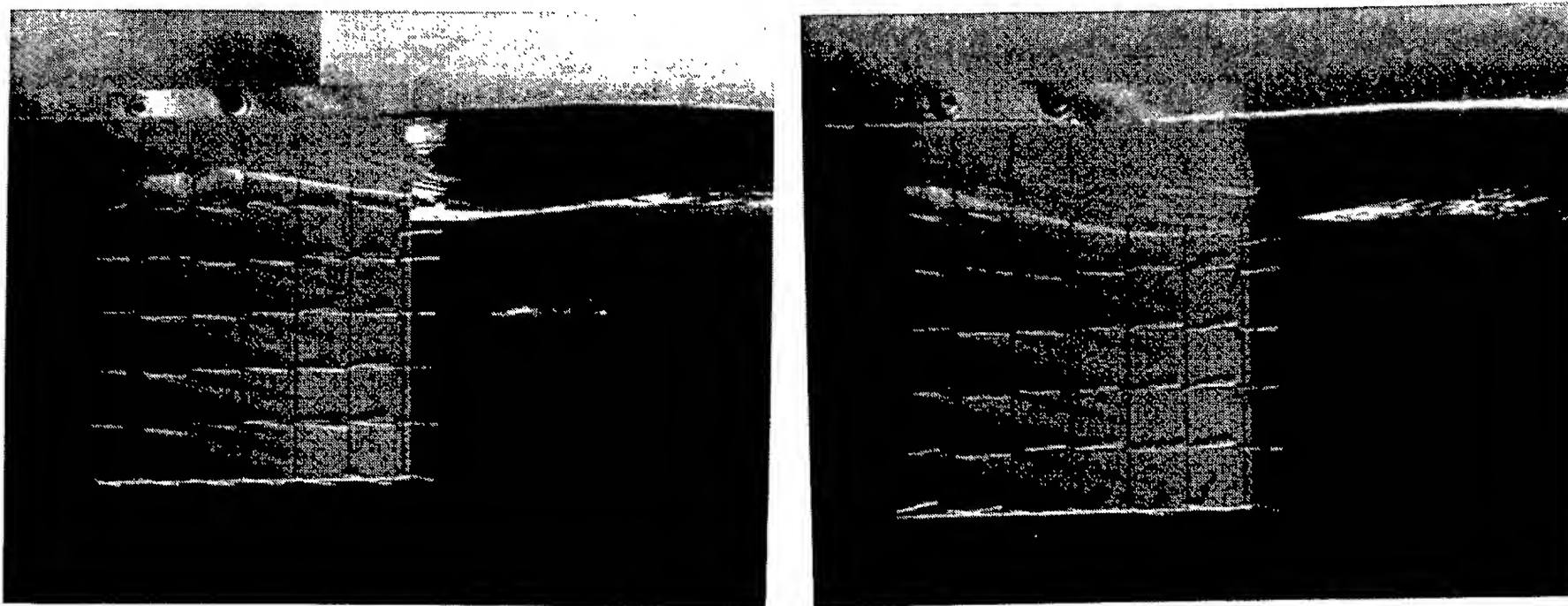


Figure 8. Side views of the experimental set-up and flow at an angle of attack  $\alpha = 6^\circ$  and Froude number  $F = 0.69$ , just above the critical Froude number. In the left figure the angle of attack is such that the view is from the pressure side, and in the right figure from the suction side. The jump is indicated in the left figure by the bright area extending downstream from the trailing edge. Grid spacing is one inch, and the height of the jump is about 0.4 inches.

### 3. EXPERIMENTS

Experiments have been carried out to observe the flow past a thin uncambered strut, mounted vertically and intersecting the free surface in the water tunnel of the MIT Marine Hydrodynamics Laboratory. This tunnel, which has a square cross section of 20 by 20 inches ( $0.51 \times 0.51$  meters), is normally used for tests of propellers and captive bodies without a free surface. By lowering the water level it is possible to perform tests with a free surface, and relatively uniform inflow conditions can be achieved with a level free surface if the depth Froude number is less than approximately 0.5. The present tests were conducted at a nominal depth of 14 inches (0.35m), and at velocities up to 3.2 feet per second (1 m/s). Large windows on the sides and bottom of the tunnel facilitate observations of the flow.

A suitable strut model with rectangular planform was constructed from aluminum plate, with chord 6.125 inches (156mm) and maximum thickness 0.25 inches (6mm). The profile was shaped to have an approximately parabolic leading-edge section, and a blunt trailing edge of thickness 0.04 inches (1mm). To facilitate observations a square grid with 1 inch spacing was established and threads were glued to the surface, as shown in Figure 8. The upper portion of the strut was attached to a vertical shaft which could be rotated to vary the angle of attack. The submerged span was adjusted by varying the elevation of the model and water depth, to obtain aspect ratios up to one.

The inflow velocity was measured with a laser Doppler anemometer (LDA). Some efforts were made to use the LDA to survey the region near the trailing edge, and it was possible to conclude in this manner that there was no substantial separation.

The principal measurements were visual and photographic observations of the free-surface elevation on the two sides of the strut, which could be resolved to an accuracy of about 1/16 inch (1.5mm). Near the leading edge a thin spray sheet makes it difficult to establish the free-

surface elevation, and no attempt was made to record data over the forward 30% of the chord. Measured values of the jump were based on the difference in elevation of the free surface on the two sides of the strut at the last grid line, 1/8 inch (3mm) upstream of the trailing edge.

In the following discussion results are given in nondimensional form based on the chord length, and the inflow velocity is defined by the corresponding Froude number, restricted to a maximum value of 0.8 due to the depth effect noted above. Except where otherwise noted the tests were conducted at an aspect ratio equal to one.

Initial observations revealed that there exists a critical Froude number  $F_c \approx 0.65$ . For  $F < F_c$  there is no observable jump, and the free surface is continuous across the wake downstream of the trailing edge. Conversely, a distinct jump exists if  $F > F_c$ . The height of the jump is nearly proportional to the angle of attack. Viewed from just below the plane of the free surface on the high-pressure side, as in the left photograph shown in Figure 8, the jump appears as a brightly illuminated triangular surface which extends 20-30% of the chord length downstream of the trailing edge. Viewed from the low-pressure side, as in the right photograph, the jump is apparent from the intersection point where the two sides of the jump cross and reverse their relative elevations in an oscillatory manner.

Figure 9 shows the corresponding view from below. Most of the threads at the trailing edge are oriented in the expected manner to accord with the Kutta condition of smooth tangential flow past the trailing edge, but the uppermost two threads are sharply deflected indicating a pronounced cross-flow near the free surface. The vertical extent of this cross-flow is comparable to the jump height, increasing in proportion to the angle of attack.

If the Froude number is increased gradually through the critical value  $F_c$ , it is apparent that the jump is related primarily to a change in the flow on the low-pressure side of the strut. Figure 10 illustrates this regime by showing



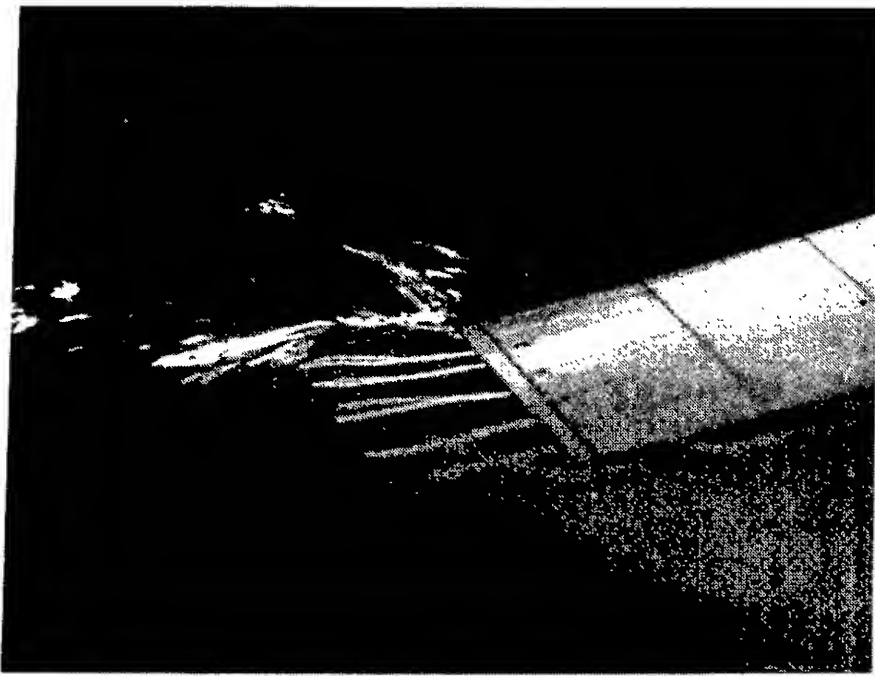


Figure 9. View from below in the same condition as Figure 8. Note the sharp deflection of the two uppermost threads at the trailing edge.

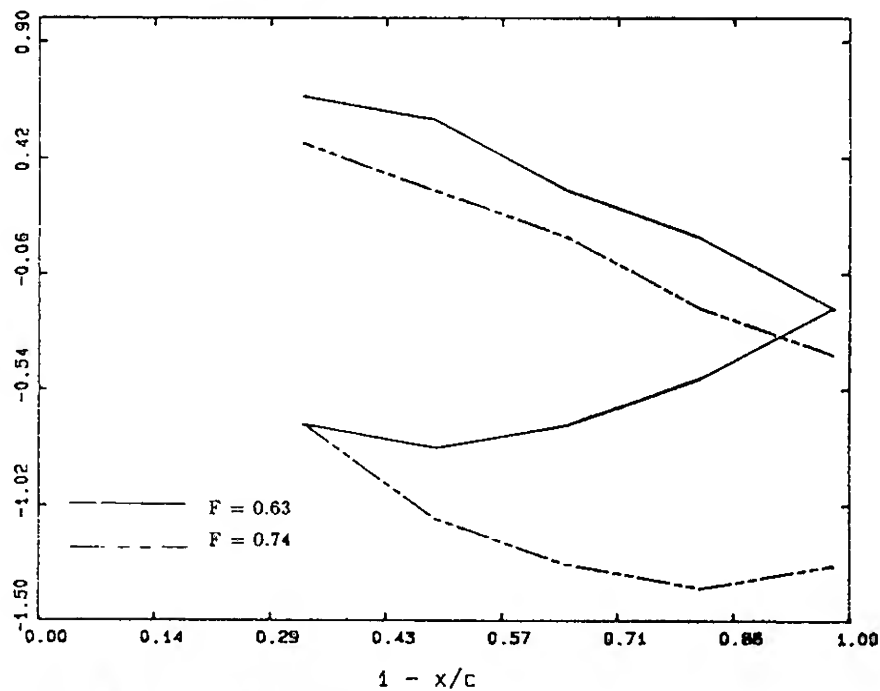


Figure 10. Free-surface profiles on the pressure (upper) and suction (lower) sides of the plate at subcritical (0.63) and supercritical (0.74) Froude numbers, at an angle of attack  $\alpha = 6^\circ$ . Elevation is normalized by the chord length and angle of attack.

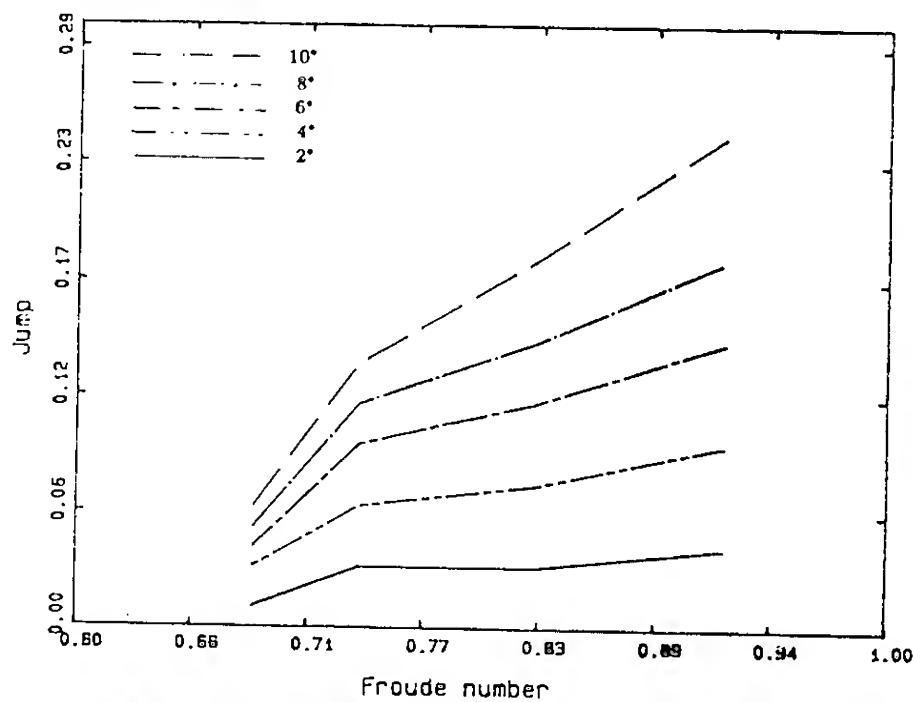


Figure 11. Normalized jump height versus Froude number for an aspect ratio 1.0. Height is normalized by the chord length.

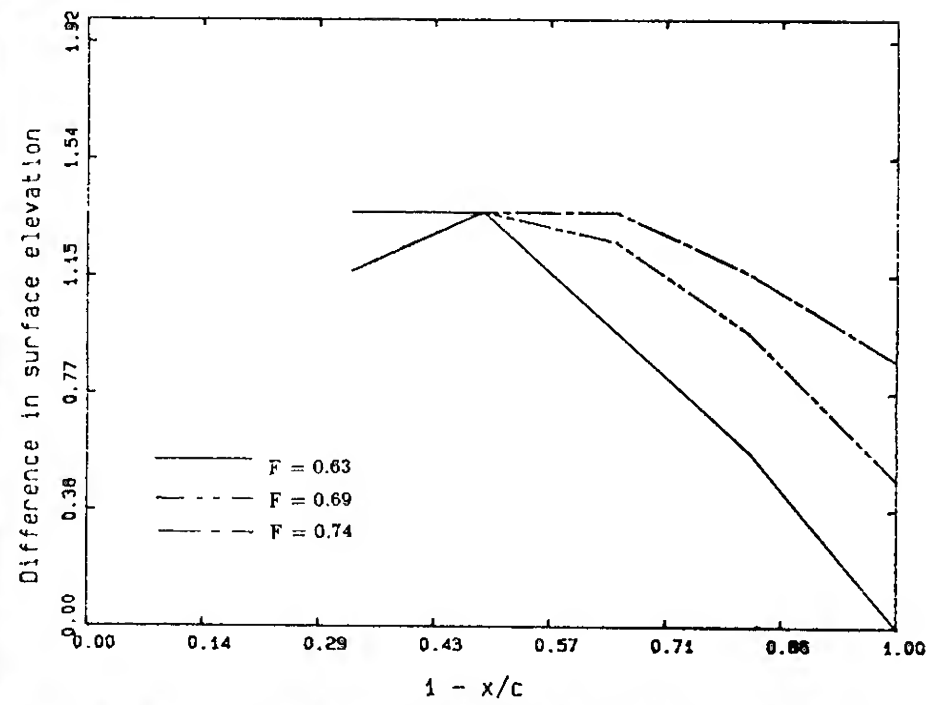


Figure 12. Difference in free-surface elevation between the two sides of the plate at the Froude numbers indicated, as a function of the chordwise position, aspect ratio 1.0, angle of attack  $6^\circ$ .

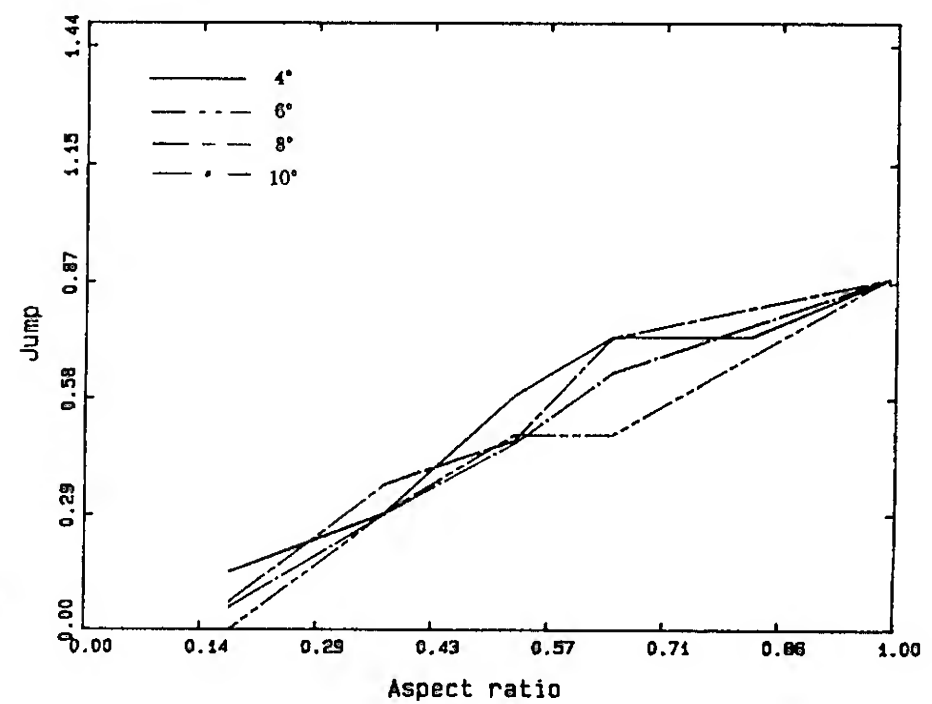


Figure 13. Effect of aspect ratio on the jump height. Froude number = 0.74.

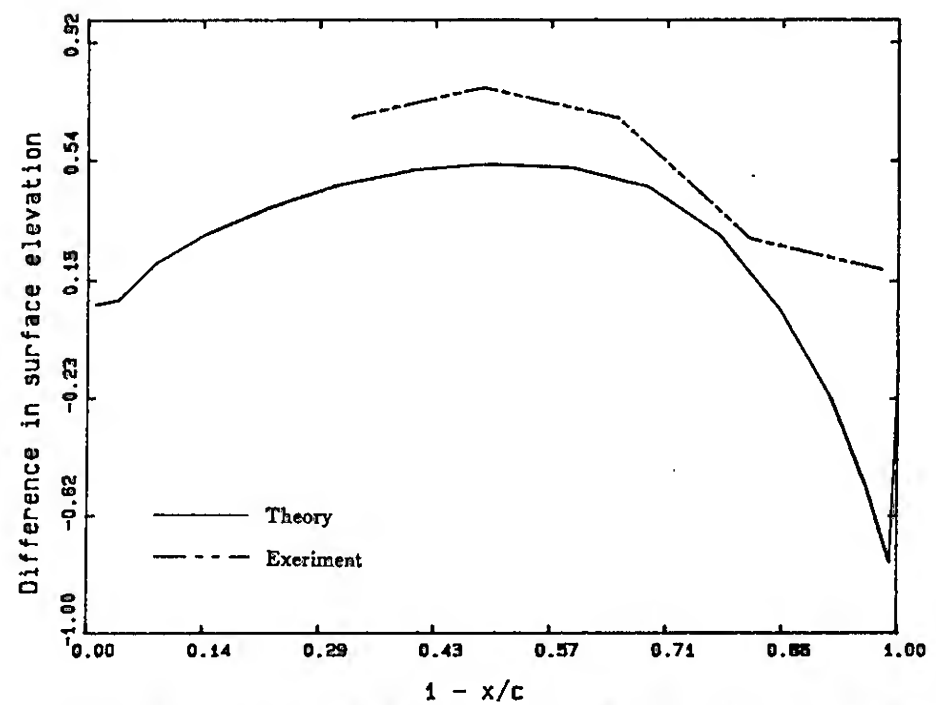


Figure 14. Comparison of computed and experimental free-surface elevation difference, aspect ratio 0.5, angle of attack  $6^\circ$ , Froude number 0.7.

separate free-surface profiles on the two sides of the strut at Froude numbers close to the critical value. The elevation of the free surface on the high-pressure side changes relatively slowly near  $F_c$ , but an abrupt shift occurs on the low-pressure side. For  $F < F_c$  there is a steep slope of the free surface on the low pressure side, with the elevation rising to meet the flow from the opposite side at the trailing edge. Above the critical Froude number this effort is abandoned, in favor of independent flows on the two sides with more gradual slopes.

Figure 11 shows the jump amplitude as a function of the Froude number. The tendency for the jump to vanish below a critical Froude number  $F_c$  is clear; the value of  $F_c$  appears to be close to 0.65.

The difference in elevation between the two sides of the strut for Froude numbers just below and above the critical value is shown in Figure 12. The difference is plotted here in order to remove the symmetric disturbance due to thickness. However for the supercritical case the nonsymmetric feature noted in connection with Figure 10 must be considered in attempting to distinguish between thickness and lifting effects.

In Figure 13 the effect of aspect ratio on the jump elevation is plotted, indicating a nearly linear proportionality. Thus the jump elevation is nearly proportional to the span or draft, for aspect ratios less than one.

In Figure 14, we compare the experimental and theoretical values of the free-surface elevation difference as a function of position along the chord, for an aspect ratio equal to 0.5. The theoretical curve shown is for  $F = 0.7$  whereas  $F = 0.69$  in the experiments. However other theoretical results are similar at  $F = 0.6$  and  $F = 0.8$ , hence the small difference in Froude numbers is not significant to this comparison. The results are similar up to a point about 20% of the chord upstream of the trailing edge, with the calculations based on the theory 20-30% less than the experiments. Closer to the trailing edge, however, the two results are dissimilar. The experimental difference associated with the jump remains positive, whereas the calculated difference changes sign before reverting to the forced value of zero at the trailing edge.

#### 4. CONCLUSIONS

For a vertical surface-piercing lifting surface we have demonstrated that convergent numerical results can be derived for most parameters of practical importance. These include the integrated force and moment coefficients, and their spanwise distributions. Also included are calculated values of the leading-edge singularity which can be used to predict the occurrence of ventilation, cavitation, or separation, and to design the stem radius of ships or surface-piercing struts on a rational basis to avoid these undesirable phenomena.

To obtain the present results special numerical techniques have been developed to evaluate the kernel of the integral equation, *i.e.* the second-derivative of the free-surface Green function, and the discretization of the lifting surface has been selected to improve the convergence rate.

To demonstrate numerical convergence up to 4032 panels have been used. This level of computation is only feasible by using a supercomputer, but reasonable engineering accuracy can be achieved with  $O(500)$  panels except for low Froude numbers where the wavelength is short.

The numerical solution breaks down locally at the intersection of the trailing edge with the free surface. At this point the pressure distribution is singular, and it is unclear if this is the result of the numerical differentiation and extrapolation required to derive this parameter, or if there is a more fundamental cause.

Special experiments have been conducted to study the flow near this singular point, and we find that a free-surface jump occurs when the Froude number exceeds a critical value  $F_c$ . For an aspect ratio of one  $F_c \simeq 0.65$ , based on the chord length. For aspect ratios in the range 0.25-1.0 the critical Froude number does not change significantly. For smaller values of the Froude number there is no evidence of a jump. In the supercritical regime where the jump occurs, a pronounced transverse velocity can be observed just behind the trailing edge, contrary to the Kutta condition.

The subcritical regime with no jump appears to be compatible with the classical view of a vertical trailing vortex sheet in the wake which intersects the free surface. The boundary conditions of constant pressure on the free surface and continuous pressure across the vortex sheet require the free-surface elevation to be continuous across the wake. Extending this argument, the kinematic boundary condition on the free surface implies continuity of the vertical velocity component across the wake, and hence vanishing of the trailing vorticity on the free surface. On this basis the slope of the spanwise lift distribution should vanish at the free surface, as in the simpler limiting case of zero Froude number where a simple image solution applies.

Our description of the supercritical regime is more speculative. If the jump is considered to be a vertical free surface, joined from below by the trailing vortex sheet, the pressure is continuous across the vortex sheet and hence the magnitude of the fluid velocity is the same on both sides of the sheet. This determines the velocity at the lower edge of the jump, and moving upward along the face of the jump the velocity is reduced to balance the hydrostatic pressure. A discontinuity in the vertical velocity component across the wake is accommodated by the different slopes of the free surface on the two sides of the jump, hence the trailing vorticity and slope of the spanwise lift distribution can be nonzero. The latter conditions must apply ultimately in the limit of infinite Froude number, where the negative image solution implies that the spanwise lift is zero (but its slope is nonzero) at the free surface.

A large negative pressure is required locally to offset the surface tension associated with the sharp curvature at the base of the jump, and this may explain the sharp cross flow just behind the trailing edge near the free surface.

There is no indication that the jump observed in experiments is related to the numerical instability in the same region, which is present for lower Froude numbers.

Moreover the numerical predictions of the free-surface elevation and pressure distribution near the free surface actually change sign just ahead of the trailing edge, increasing the longitudinal gradient in a manner precisely opposite to the experimental flow. Since the computations are dependent on numerical differentiation and extrapolation, it is impossible to be definitive on this point.

Further research is required to resolve these questions. We hope that independent experiments will be conducted to confirm and extend our observations, and to provide a more detailed velocity survey of the jump region. Further progress with the numerical analysis may also lead to a more robust algorithm for calculating the pressure coefficient and free-surface elevation near the trailing edge.

## 5. ACKNOWLEDGMENT

This work was supported by the Office of Naval Research, Contract N00014-88-K-0057. The computations with large numbers of panels were performed at the Pittsburgh Supercomputer Center. The experiments were conducted in the water tunnel of the MIT Marine Hydrodynamics Laboratory.

## 6. REFERENCES

1. Newman, J.N., "Derivation of the Integral Equation for a Rectangular Lifting Surface," unpublished manuscript, 1961.
2. Daoud, N., "Force and Moments on Asymmetric and Yawed Bodies on a Free Surface," Ph.D. Thesis, 1973, University of California, Berkeley.
3. Kern, E.C., "Wave Effects of a Free Surface Piercing Hydrofoil," Ph.D. Thesis, 1973, Massachusetts Institute of Technology.
4. Chapman, R.B., "Free Surface Effects for Yawed Surface Piercing Plates," *Journal of Ship Research*, Vol. 20, No. 3, 1976, pp 125-136.
5. Larsson, L., "Scientific Methods in Yacht Design," *Annual Review of Fluid Mechanics*, Vol. 22, 1990, pp 349-385.
6. Ba, M., Coirier, J., & Guilbaud, M., "Theoretical and Experimental Study of the Hydrodynamic Flow around Yawed Surface-Piercing Bodies," 2nd International Symposium on Performance Enhancement for Marine Applications, Newport, RI, 1990.
7. van den Brug, J.B., Beukelman, W., and Prins, G.J., "Hydrodynamic Forces on a Surface Piercing Flat Plate," Report No. 325, Shipbuilding Laboratory, Delft University of Technology, 1971.
8. Newman, J.N., "Evaluation of the Wave Resistance Green Function: Part 1. - The Double Integral," *Journal of Ship Research*, Vol. 31, No. 2, 1987, pp 79-90.
9. Newman, J.N., "Evaluation of the Wave Resistance Green Function: Part 2. - The Single Integral on the Centerplane," *Journal of Ship Research*, Vol. 31, No. 3, 1987, pp 145-150.
10. Xü, H., "Potential flow solution for a yawed surface-piercing plate," submitted for publication, 1989.
11. Lan, C.E., "A Quasi-Vortex-Lattice Method in Thin Wing Theory," *Journal of Aircraft*, Vol. 11, No. 9, 1974, pp 518-527.
12. Newman, J.N., "Distributions of Sources and Dipoles over a Quadrilateral Panel," *Journal of Engineering Mathematics* Vol. 20, 1986, pp 113-126.

## DISCUSSION

Arthur M. Reed  
David Taylor Research Center, USA

I have two questions concerning this paper: (1) Due to the small size of the experimental fail, could you please comment on the issue of scale effects (surface tension and Reynolds Number) with regard to the "classical froude" where a jump in the free surface at the trailing edge occurs; (2) In the case of SWATH ships, we see that there is a jump at the trailing edge for  $IF \sim 0.3 - 0.35$ , where the SWATH strut aspect ratio is  $0.10 - 0.15$  and the "angle of attack" of the strut is due to the flow induced by the opposite strut and the two hulls. Please comment on the effect of aspect ratio on critical  $IF$  and critical  $IF$  for SWATH ships.

## AUTHORS' REPLY

We only can speculate regarding the questions raised by Dr. Reed concerning the effects of surface tension, Reynolds number, and aspect ratio. Surface tension may be significant in balancing the pressure field, as noted in Section 4. However, we envisage no critical importance of this parameter with respect to the occurrence of a jump. A similar view applies to the Reynolds number.

The aspect ratio may be more important; for small values of this parameter the draft, rather than the length, may be the most significant length scale (despite our observations to the contrary in a relatively narrow range). In this event it would be expected that the critical Froude number for a swath strut (based on length) would be lower than the value we observe, by a factor approximately equal to the square root of the aspect ratio. The cause of the cross-flow should not affect the existence of the jump, and thus the observations noted by Dr. Reed appear to be consistent with our own.

We hope that other experimental observations will be made with thin lifting surfaces of larger dimensions to clarify these issues.

## DISCUSSION

Theodore Wu  
California Institute of Technology, USA

My sincere congratulations to Prof. Nick Newman and his coauthors for giving us such an interesting paper.

In respect to the surface-tension effects that may be involved in this problem, I would like to report a demonstration of flow instability (seemingly with a hysteresis) made a couple of decades ago by a colleague of mine, Taras Kicenuik. Starting with a surface-piercing strut at yaw to a uniform stream of water, held steadily without flow separation from the strut, a mere scratching of the water surface with a fine musical wire across any upstream station would at once lead to a rapid ventilation along the suction-side of the strut down to its lower tip, thus opening up a long and deep pocket of air ventilation, which can be readily closed up with some manual patching of the free surface. (I will try to find if any technical report has been issued on this experimental observation.)

## AUTHORS' REPLY

Professor Wu has recalled a closely-related experiment which illustrates the effect of hysteresis on ventilation. We assume that the Froude number and/or angle of attack in that work were substantially larger than in our own experiments. We saw no indication of ventilation in the indicated ranges of Froude number and angle of attack. We did not observe any signs of hysteresis with respect to the jump at the trailing edge, either in the context of changing the Froude number or the angle of attack, and when these parameters were fixed there were no indications of instability in the height of the jump at the trailing edge.

**Session IV**  
**Experimental Techniques**

# Wave Devouring Propulsion Sea Trial

Y. Terao (Tokai University, Japan)

H. Isshiki (Hitachi Zosen Corporation, Japan)

## ABSTRACT

The development of Wave Devouring Propulsion System and results of its sea trial are presented in this paper. WDP system is an idea not only for the ship propulsion system which converts wave energy directly into thrust but also the ship motion reduction system. This system consists of a ship hull and a hydrofoil installed at the bow. Improvement of the propulsive efficiency in waves and high seaworthiness is measured during the sea trial.

## NOMENCLATURE

a	wave amplitude.
B	ship breadth.
C	$C = \rho g \cdot H_w \cdot B / L$
g	gravitational acceleration.
H <sub>w</sub>	wave double amplitude.
	$H_w = 2a$
H <sub>w</sub>	significant wave height.
$1/3$	
K	wave number.
L	ship length.
R <sub>a</sub>	added resistance in waves.
R <sub>a</sub> ~	nondimensional added resistance.
	$R_{a\sim} = R_a / C$
$\Delta R$	resistance increase in waves.
	$\Delta R = R_a - T$
R~	nondimensional coefficient of resistance increase.
	$R_{\sim} = \Delta R / C$
T	thrust of foil.
T~	nondimensional thrust coefficient.
	$T_{\sim} = T / C$
T <sub>w</sub>	significant wave period.
	mass density of water.
$\theta_p$	pitch amplitude.
$\theta$ ~	nondimensional pitch amplitude.
	$\theta_{\sim} = \theta_p / (K \cdot a)$
$\lambda$	wave length.

Y. Terao: Dept. Naval Architecture, Tokai Univ.; 3-20-1, Orido Shimizu, Shizuoka 424, JAPAN  
H. Isshiki: Hitachi Zosen Corp.; 1 Sakurajima, Konohana-ku, Osaka 554, JAPAN

## 1. INTRODUCTION

It is well known that aquatic mammals, dolphins or whales, which propel themselves with their lunatic tails have high propulsive efficiency. Theoretical or experimental studies have already succeeded in explaining this oscillating hydrofoil propulsion system. The thrust generating mechanism of these propulsion system is quite simple. With forward speed and the combined motion of heaving and pitching of the fin produces relative fluid velocity which brings about an apparent inclined flow against the fin. Due to the Kutta-Joukowski lift theorem, lift force is generated perpendicularly to the flow. The mechanism of thrust generation is shown schematically in Fig. 1.

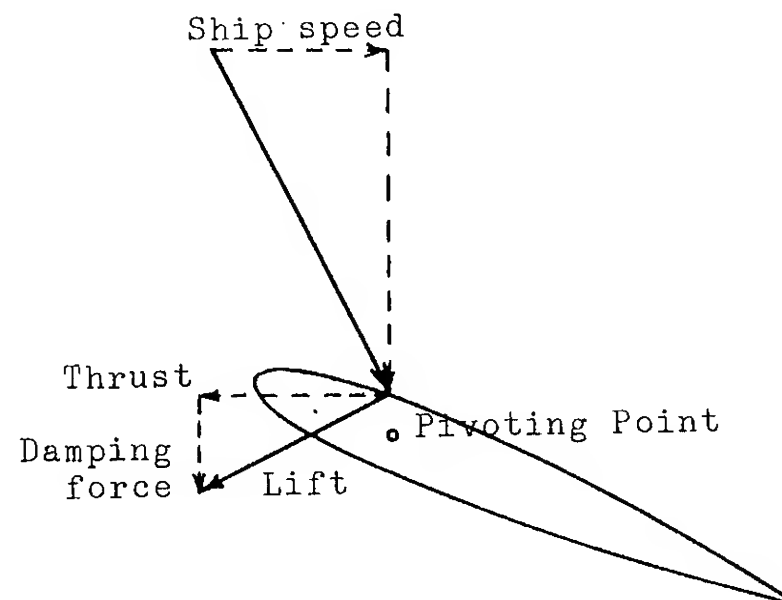


Fig. 1 Thrust generation of a fin in waves.

If we put a horizontal hydrofoil in the oscillating flow field, such as in waves, the relative flow acting on the hydrofoil causes thrust.

The wave devouring propulsion system (WDPS) consists of a ship hull and hydrofoil, which acts as a direct



wave energy to the thrust converter using these mechanisms. The hull is a collector of wave energy, and the motion of hydrofoil generates the thrust. The hydrofoil is installed in front of the ship's bow and the pitch motion of the hydrofoil is controlled under the sea.

The flow against the hydrofoil in waves is  $(U + u, v)$ .  $U$  is the ship's forward speed.  $u, v$  is the wave's vertical and horizontal velocity component plus relative hydrofoil motion due to ship motion and hydrofoil pitch motion in the waves. Thrust is generated as a horizontal component of lift( $L$ ), the magnitude of which is periodically increased or decreased but the thrust has a negative direction of  $U$ . Moreover, we must note the vertical direction of the lift which has an opposite direction to inflow velocity  $v$ . This means that the lift force creates pitch canceling moment, and thus, decreases the ship's pitch motion.

Now, the object of this study will be discussed. Our concern is the performance of the WDPS ship in waves. Therefore, two important subjects were expected.

First, the improvement of the propulsive efficiency of the ship using an oscillating hydrofoil, because the hydrofoil converts wave energy directly into thrust.

Second, the reduction of the ship motion in waves is expected.

Moreover, it is needed for WDPS ship production that the force acting on the hull and hydrofoil quantitatively through the sea trial.

Resistance increase of the ship in waves is well known phenomena for naval architects. This problem was studied theoretically or experimentally by many researchers. From the momentum theory, the resistance increase in waves has a physical explanation that the work done by the relative hull motion against the wave. Linear damping component is concerned with the wave making resistance which takes away the energy in the form of progressive waves. If the reduction of motion in waves was possible, we could expect the reduction of "resistance increase in waves". But if we consider it from such a view point that the reduction in motion reduces the increment of added resistance in waves, there are few studies. It seems that there is a field left not yet studied. It may be true that there is a limitation of the improvement in the total ship resistance in waves by normal hull design.

Furthermore, we can expect some thrust increase in waves due to the hydrofoil effect. For example, the ship proceeding in the North Pacific sea in the winter season was studied. It was observed that the wave length of about 100m has excessive wave power in this area, therefore, a ship with a length of less than 80m is desired for WDPS system. From the feasibility study of the thrust generation and the reduction of resistance increase in waves, we can expect the WDPS ship running in waves at 8 kt without any energy supply. Our approach, using a hydrofoil in the wave, might be the answer to improve the propulsive efficiency and advance seaworthiness of the ship.

Surprisingly enough, in 1985, H. Linden(1) already filed a British patent. He really built a 13-ft boat, named "Autonaut", equipped with two elastic fins both at bow and stern. According to the contemporary report, she could travel herself against the wind and waves at a speed from 3 to 4 Kt.

Regarding recent experimental studies of WDPS, which are concerned with direct wave energy to the thrust conversion, only Jakobsen(2) and the author(3),(4) have carried out experiments.

Abkowitz(5) reported on an anti-pitching fin using a model test. He used a pair of hydrofoils, total projected area of the hydrofoils is less than 7% of the ship waterline area, and the effectiveness of antipitching fin was confirmed. He also mentioned a significant improvement in speed in waves. He was concerned with the advancement of the lateral motion of the ship, therefore, did not discuss the thrust generation of the fin.

T.Y. Wu(6) first showed theoretically that wave energy can be converted into thrust and propulsive efficiency becomes more than one or even minus. He studied the two dimensional oscillating hydrofoil in waves.

Bessho(7) studied the restriction of the lateral ship motion using two fins one at the bow and stern. His group showed the possibility of ship with less heaving and pitching in waves.

Naitou and the author(8) succeeded in calculating the motion of a WDPS ship and the propulsive efficiency, especially the reduction in resistance increase in waves using OSM and the steady wing theory. The results will be discussed later.

## 2. WDPS SEA TRIAL PROJECT

WDPS sea trial project was planned using a 20-ton fishing vessel. Principal dimensions of the test ship, the foil dimensions and foil section are listed below. To know the thrust increase in waves, a larger hydrofoil area was selected compared with Abkowitz's experiment. The projected area of hydrofoil is 7.4% of the ship's waterline area.

### 2.1 TEST SHIP PRINCIPAL DIMENSIONS

Lpp	: 15.7 m
B	: 3.8 m
d	: 1.1 m
Displacement	: 19.9 ton
Speed	
Max	: 10 kt (2000 rpm)
Service	: 7.4kt (1500 rpm)

#### Hydrofoil Dimensions

Cord Length	: 1.05 m
Span	: 3.8 m
Depth	: 1.65 m
Section	: NACA0015

Center of the wing pitch motion is located at a quarter cord length aft from the wing leading edge.

General arrangement of WDPS ship, side view and top view are shown in Figs. 2 and 3.

### 2.2 THEORETICAL AND MODEL INVESTIGATIONS

Model testing and theoretical calculations are performed before the actual sea trial.

A 3.5 m model was tested in a tank in 1987, i.e. the hydrofoil cord length was  $L_{pp}/15$ , span is same as the ship breadth. The pivoting point of the hydrofoil is located at the quarter cord length of the hydrofoil span which is identical to the center of the steady lift force.

The thrust generation and resistance increase is calculated theoretically. The coefficients of ship motion was calculated by OSM, the hydrodynamics force acting on the hydrofoil is calculated using the quasi-steady theory including the three-dimensional effect. The resistance increase in waves is calculated using a simplified version of the Gerritsma(9) formula.

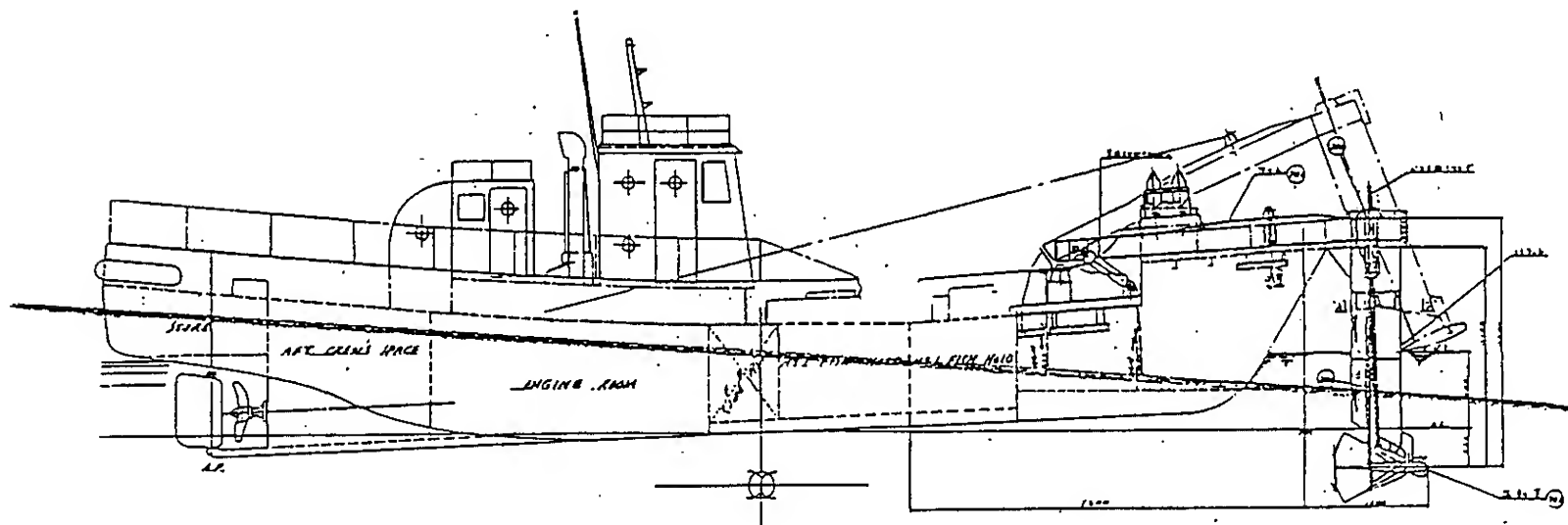


Fig. 2 Side view of WDPS ship.

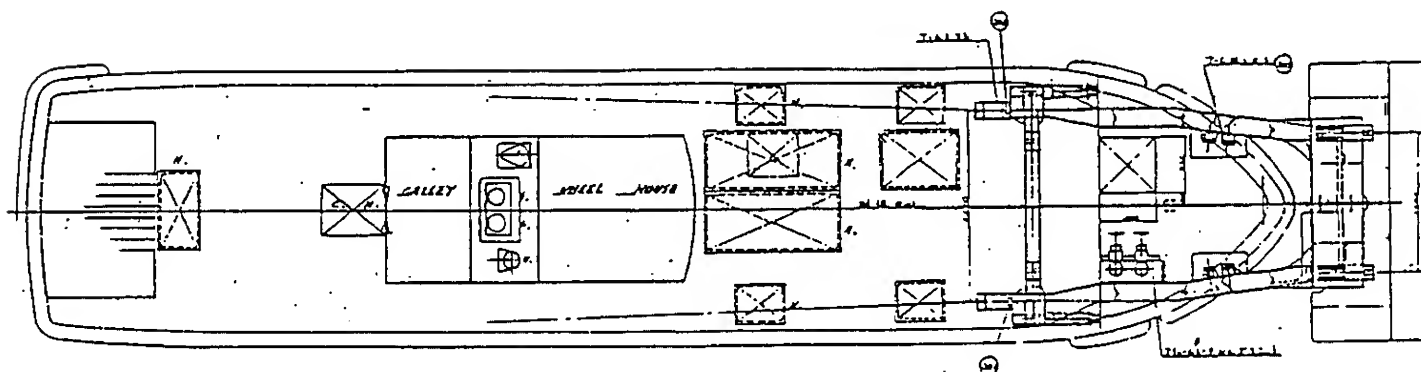


Fig. 3 Top view of WDPS ship.

Theoretical prediction and the results of model testing of the pitch motion, with and without hydrofoils shown in Fig.4.

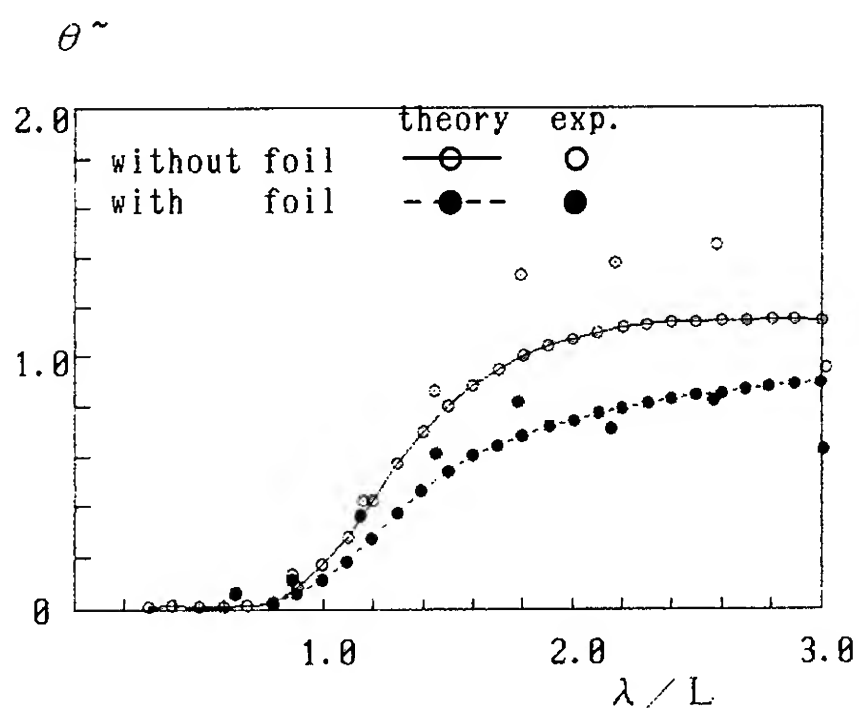


Fig. 4 Theoretical and model testing results of nondimensional pitch amplitude at a head sea condition ( $Fn=0.25$ ).

Up to 30% of the pitch reduction compared to the original ship is seen at the wave length to ship length ratio is greater than 1.6, so we can expect a pretty good pitch reduction effect, but compared to the reduction of model experiments, we had a much higher pitch reduction efficiency.

Figure 5 shows the theoretical results of the resistance increase in the head sea condition at  $Fn=0.25$ .

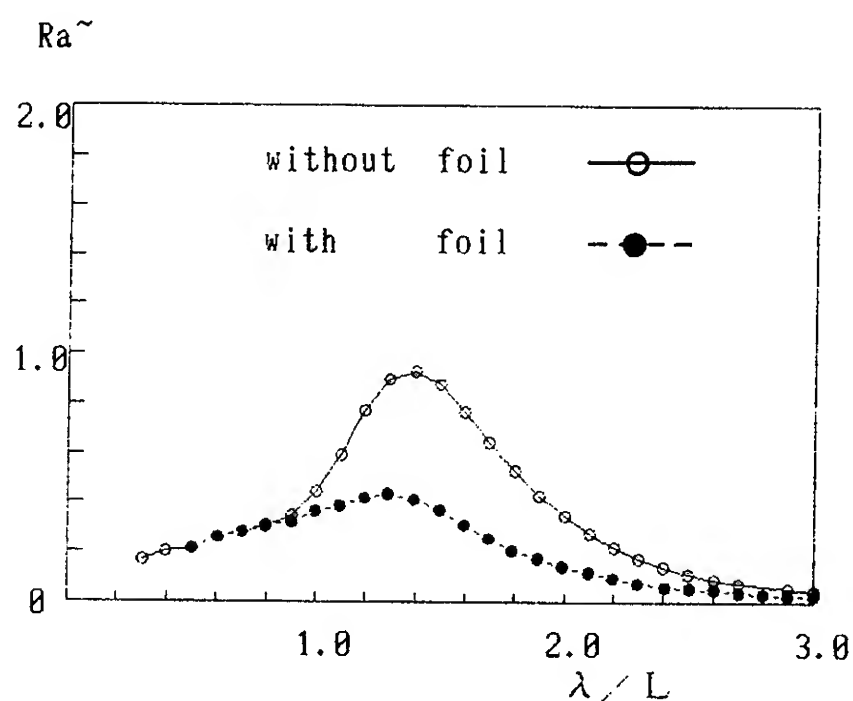


Fig. 5 Theoretical calculation of the resistance increase in head sea condition ( $Fn=0.25$ ).

This Figure shows the comparison of the coefficients of resistance increase with and without a hydrofoil at sea.

Figure 6 shows the thrust increase in waves. We can see that the reduction in the resistance increase in waves is due to the additive effects obtained by the direct effect and indirect effect. The direct effect is thrust generation due to the hydrofoil and the indirect effect is dependent on the reduction in ship motion which is also effectively affected by the existence of the hydrofoil.

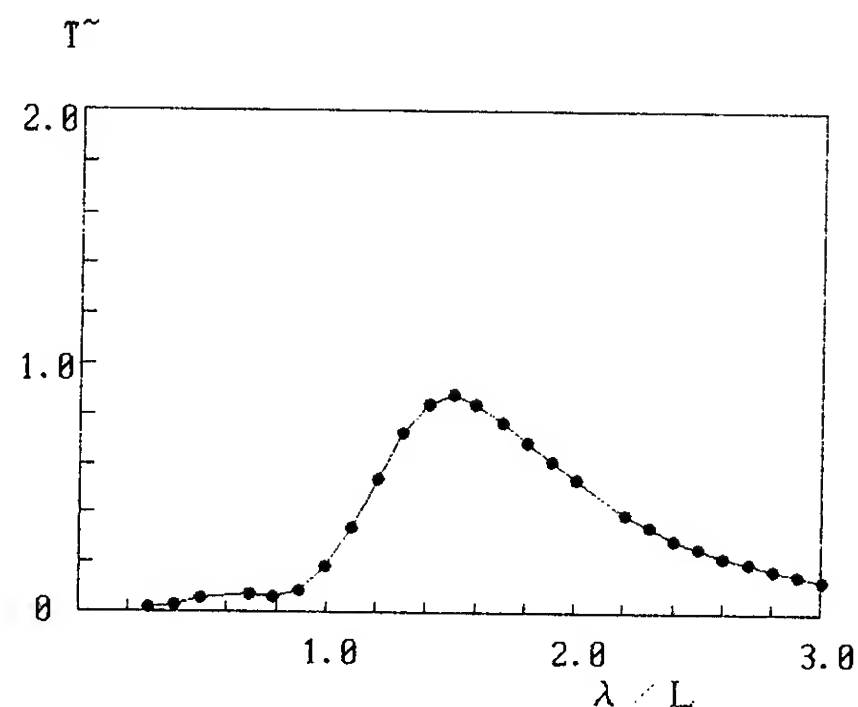


Fig. 6 Calculation of the thrust generation of a fin in head sea condition ( $Fn=0.25$ ).

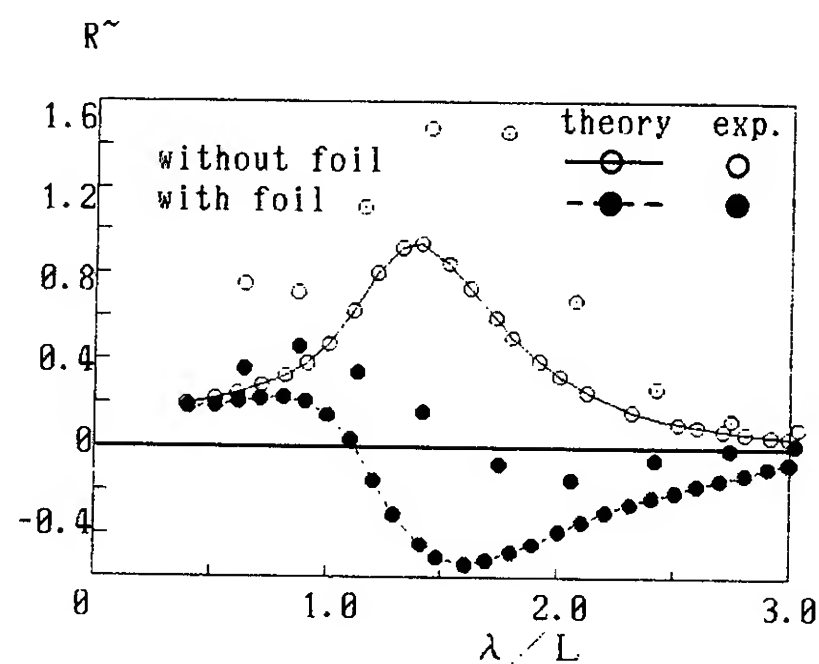


Fig. 7 The theoretical calculation of WDPs ship's resistance increase in head sea condition. ( $Fn=0.25$ )

Figure 7 shows the theoretical calculation of resistance increase in head seas. We can see a minus resistance increase at the results of WDPS ship in the wave length to ship length ratio greater than 1.1. This is total thrust gain from wave energy. If the hull resistance during a calm sea is less than the thrust gain from the waves, the WDPS ship can sail against waves without the need to use fuel for power.

The results of 3.5m model towing test during a head sea condition is also plotted. Towing speed was  $Fn=0.249$ . The difference between with hydrofoil (WDPS) and without hydrofoil is shown drastically. Frictional correction is not taken account. Theoretical prediction and tested results are in fairly good agreement with this figure.

WDPS ships at sea is shown in Fig.8 and 9. It is observed in Fig.8 that the rather tiger splash in front of the strut. This figure shows speed trial test using engine power and a foil. In Fig.9, we can see a foil and strut configurations which WDPS ship was equipped with.

### 3.WDPS SYSTEM DESIGN

Before the actual sea trial, a WDPS structural analysis and design are needed. Selected design wave height to length ratio is  $1/30$  and design wave length is  $1.6 L_{pp}$  of the ship.

Taking into the consideration of the actual sea trial using a rather small vessel, structural design was decided carefully to have enough strength. At the same time, reinforcement of hull structure are investigated.

During the tank test in 1987, we used the two bow hydrofoil system, left and right, which was moved independently using two servo motor. But in this actual sea trial, we selected one hydrofoil and the passive control system to simplify the experiment and keep safety of the mechanism at sea.

WDPS hydrofoil supporting system consists of two struts, a hydrofoil pitch spring system, and the struts up-down mechanism. The necessity to change the spring constant easily on board, variable spring constant system consists of a hydraulic pressure cylinder and an accumulator was selected. Changing the nitrogen gas pressure of the accumulator, we were able to use wide pitch spring constant.

Loading and equipment of the system, hull reinforcement of the testing ship were accomplished at Kanasashi Ship Yard. The ship used in the test was made of FRP and aged. The structure of the ship is of a monocoque type so that the fore deck shell scarcely supports the external force or weight of the testing apparatus. Therefore extra reinforcement of the support structures are needed in the bow section.

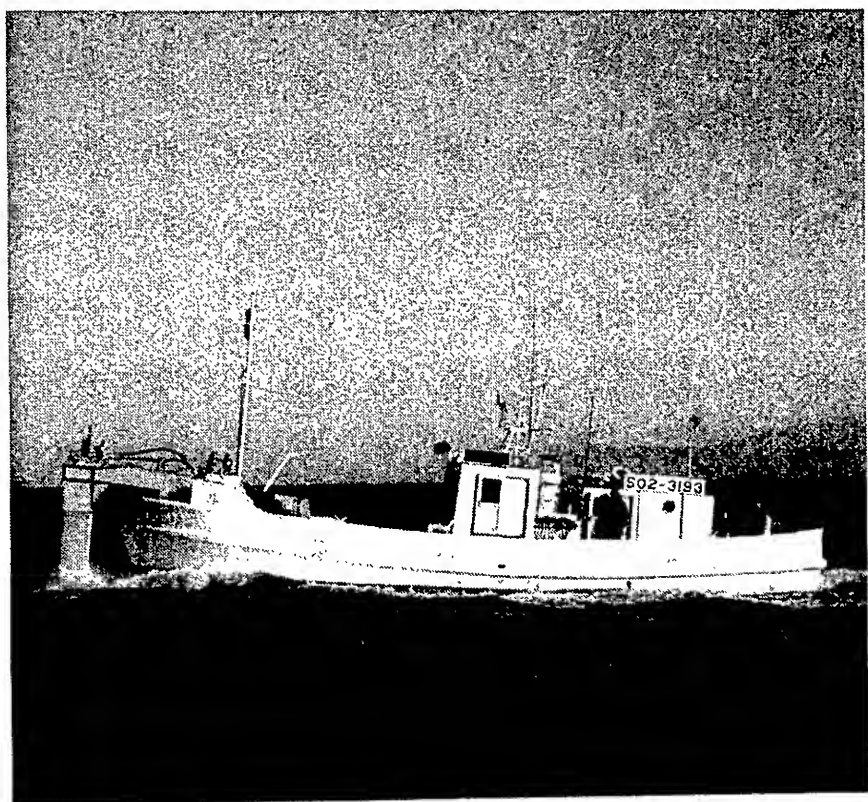


Fig. 8 WDPS ship speed trial (1500 rpm. at a heading sea condition).



Fig.9 WDPS ship raising a foil.

Support structures and equipment weighting up to about 6 tons, were installed at the bow, and more weight (3 ton) is needed at the stern to keep the even trim and to have enough GM height. During the experiments, we had a hard situation that the blue sea hit the hydrofoil when hydrofoil was hauled from sea but we had no damage to the hull, struts, hydrofoil or any of the instruments. So, we consider that the reinforcement and structural design were a success.

#### 4.RESULTS OF SEA TRIAL

The period of experiment was from December 12th,1988 to January 13th, 1989.

The measurement and testing plan is given below.

- (1) Efficiency of WDPS using as a sub-propulsion system.
- (2) Motion reduction effect of WDPS at sea.
- (3) Self propulsion test of WDPS in waves.
- (4) Force measurements acting on the hydrofoil and struts.

(1) and (2) measured the difference of the ship speed and motion, with and without a hydrofoil in the same sea condition at the same rotation of the propeller. Tidal or ship wake effects are canceled using a relative flow speed-meter.

(3) measured the forward speed of the ship using a WDPS without engine power.

(4) measured the force acting on the struts using strain gauges.

#### 4.1 APPARATUS OF SEA TRIAL

Suruga Bay ,offshore of Miho and Kunou was used as the test area. The items and apparatus used in the test are given below.

##### 4.1.1 TESTING APPARATUS

Relative Ship Speed  
: Relative Flow Meter  
Propeller Rotation  
: Optical Rotating Meter  
Ship Motion(6 degree of Freedom)  
: Rate Gyro  
Wave Height  
: Wave Prove (Drop type)  
Wind Direction and Speed  
: Wind Meter  
Stress of the WDPS arm  
: Strain Meter  
Pitch Angle of Foil  
: Linear Potentio Meter

An on board microcomputer was used for data sampling, and at the same time, data were recorded on a data recorder. Sampling program and analysis program were made for this fast sampling and analysis.

#### 4.2 SPEED TRIAL IN WAVES

A calibration test of the relative flow meter was carried out using the mile post of the Miho beach. The output of this flow speed data was adopted as the standard of the ship log speed. To know the basic propulsive performance of the ship, original condition without a fin, a speed trial was carried out on a day in which the sea was calm.

Results of speed trials are shown in Fig.10. This figure shows the speed reductions in a rather slow speed range, less than 1000 rpm, due to the frictional resistance increase by the existence of the hydrofoil and struts. However the high speed range (2000 rpm) there was no discrepancy between with and without hydrofoil results because the wave making resistance dominated at the higher speed range for the total resistance.

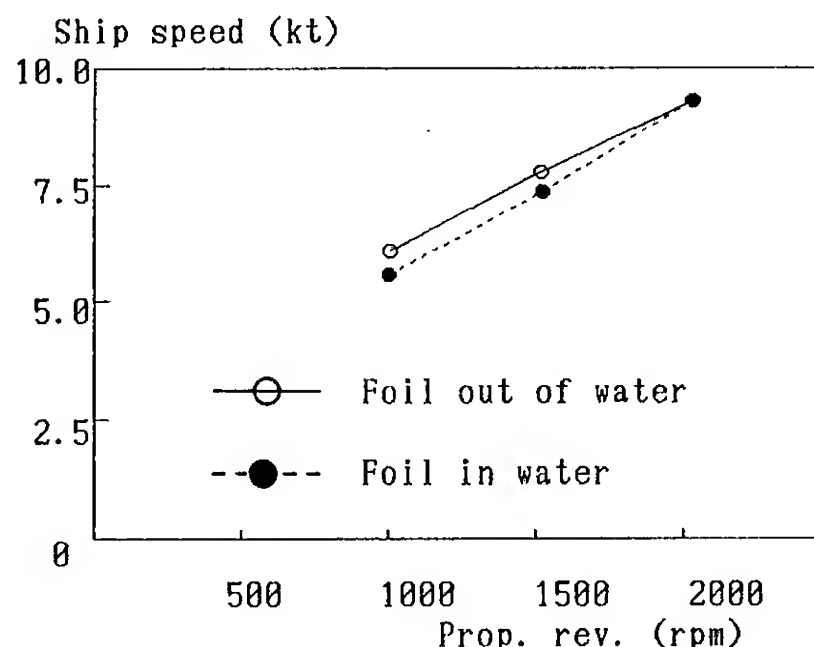


Fig.10 Ship speed trial in calm water.

It was normally observed that the operators of such small ships drive them at high cruising speeds. It may be considered that the weakness of the WDPS at rather the low speed range in a calm sea is not so serious.

Figure 11 and Table 1 show the results of the wave data. A significant wave height and mean wave period can be seen in Figs 12 and 13.



Table 1. Wave Statics Data (01/12/1989)

Elapsed time (min.)	RMS (m)	T max (sec.)	T 1/3 (sec.)	T mean (sec.)	Hw max (m)	Hw 1/3 (m)	Hw mean (m)
30	0.192	11.00	5.77	3.41	1.20	0.71	0.43
75	0.192	11.00	6.18	3.37	1.22	0.73	0.40
120	0.196	10.20	6.83	3.60	1.23	0.70	0.38

Along the coast of Miho and Kunou, it is known that the wave condition is not so severe even in the winter season. Also it is a one reason why we selected the WDPS test field, but during abnormally hot weather in the winter season, we scarcely had a proper wind and wave condition. You can see in Figs 12 and 13 that the wave is a wind wave, because the wave period is shorter and the length of waves are less than the ship length.

January 12th, 1989 we had a good wave condition. The direction of the incident waves and the swell were different all day but in the afternoon, wave height decreased and the swell subsided. Table 1 and Fig. 11 shows changes in the wave height.

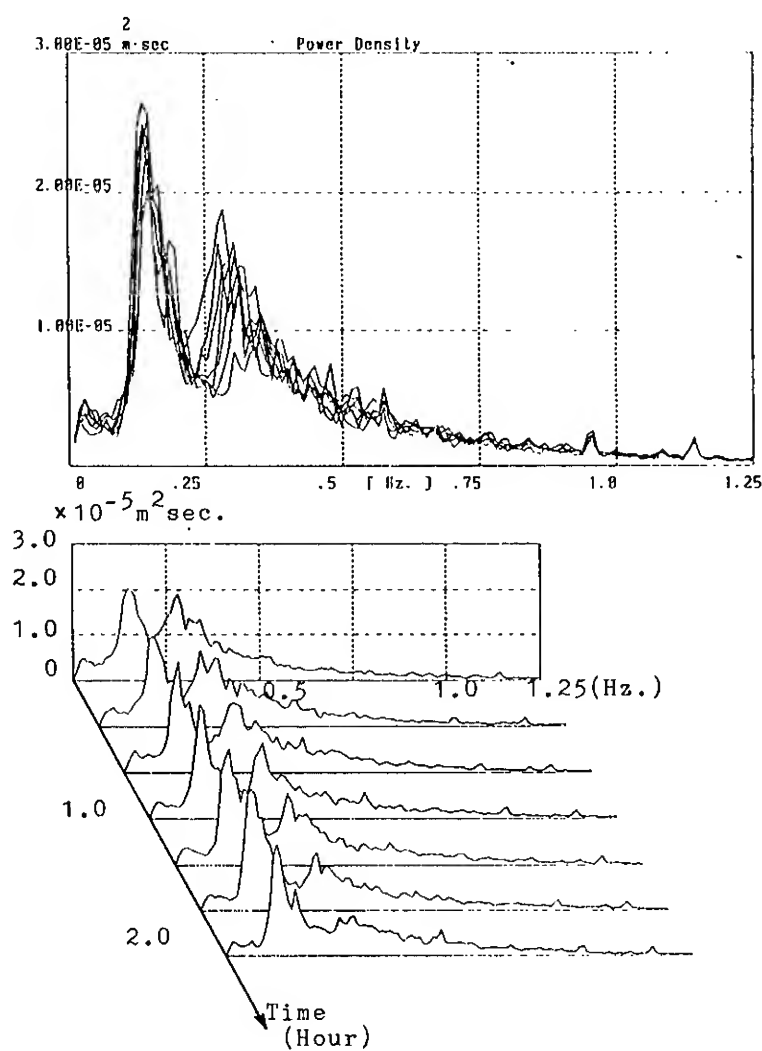


Fig.11 Example of wave power spectrum (01/12/1989).

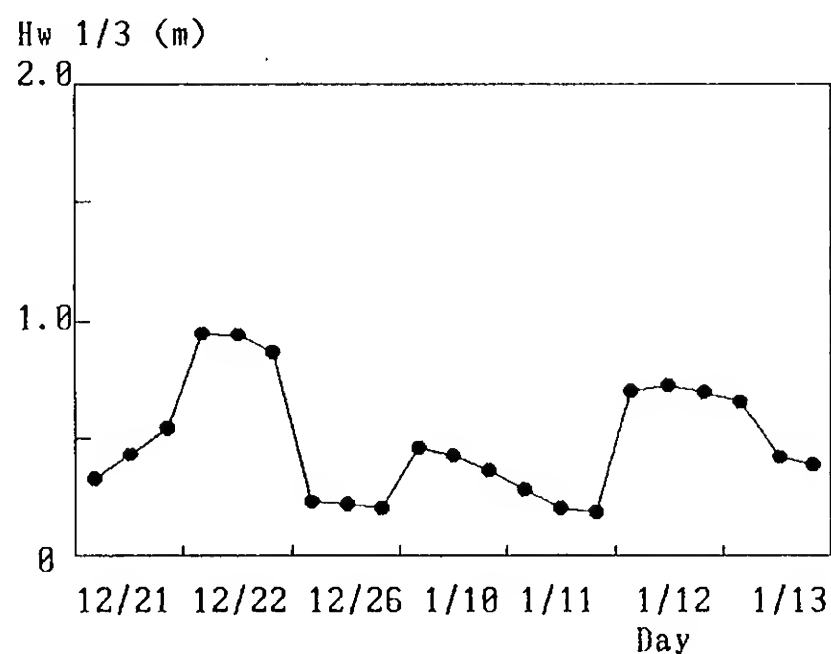


Fig.12 Significant wave height.

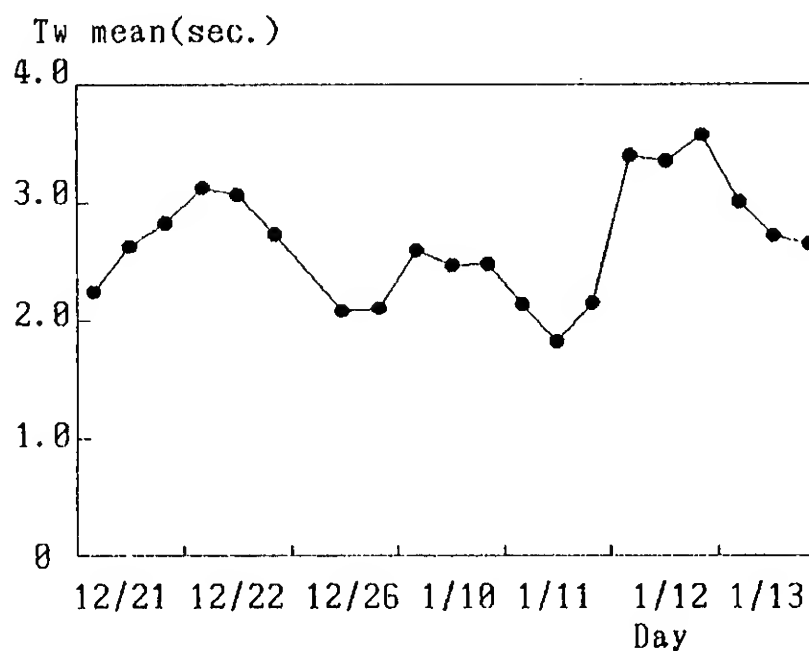


Fig.13 Mean wave period.



On this day, we had a speed of 2.5 kt in the head sea condition without using engine power. By the law of Froude, this speed corresponds to 5.6 kt with a ship length of 80 m. In North Pacific in the winter season, the wave condition was better than this case. It might be possible that the WDPS ship of a length of 80 m could cruise at a speed 8 kt.

The steering speed of this WDPS ship is 2.5 kt. Also it was observed in the unidirectional incident wave, the WDPS ship turns her bow to the incident waves.

With a hydrofoil in waves, the speed increase in the head sea is observed during the certain wave conditions. Each speed, with or without a hydrofoil in waves, are shown in Figs 13 and 14. The speed increase in waves, especially in the head sea, is thought as a propulsive efficiency increase in waves. We can see the wave length affecting the ship's advance speed in Fig. 7 and model testing results are also shown in Fig. 8. The wave condition strongly influenced the ship's speed and significant wave height ( $H_w 1/3$ ) and mean wave period ( $T_w$  mean) are shown in wave tables in Table 2 and 3.

Table 2. Wave Data (01/12/1989 Heading Sea)

Prop. (rpm)	$H_w 1/3$ (m)	$T_w$ mean (sec.)
0	0.965	3.12
1000	0.965	3.12
1500	0.955	3.06
2000	0.965	3.12

Table 3. Wave Data (01/12/1989 Following Sea)

Prop. (rpm)	$H_w 1/3$ (m)	$T_w$ mean (sec.)
0	0.965	3.12
1000	0.965	3.12
1500	0.955	3.06
2000	0.955	3.06

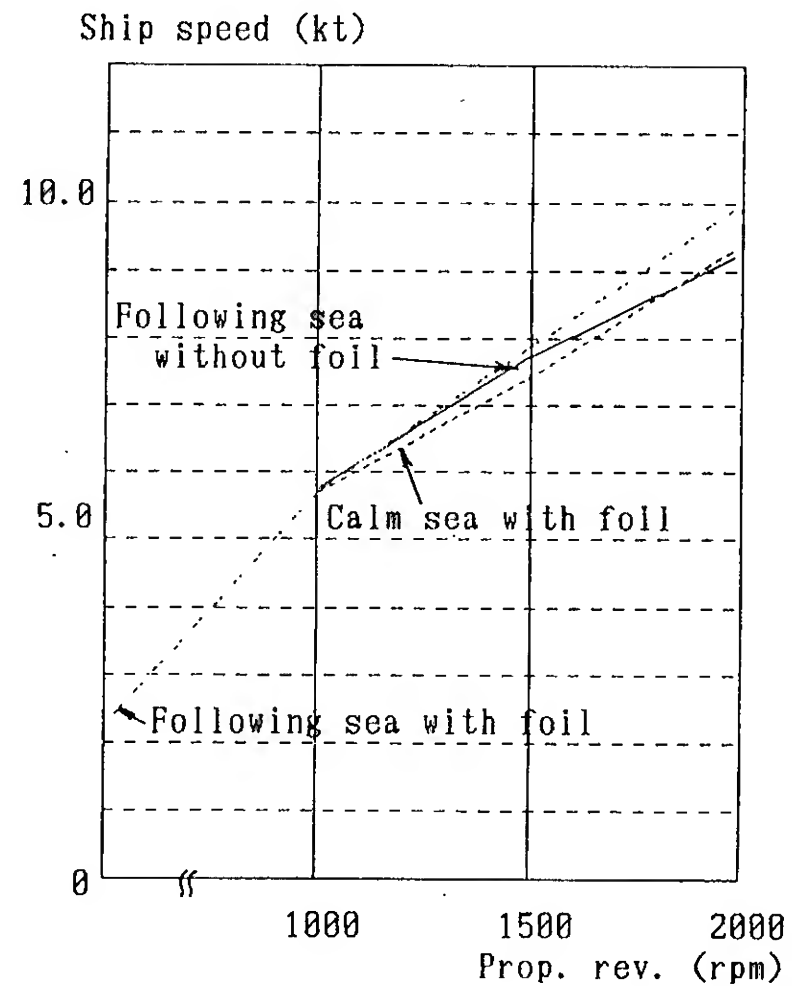


Fig.14 Results of speed trial in head sea condition.

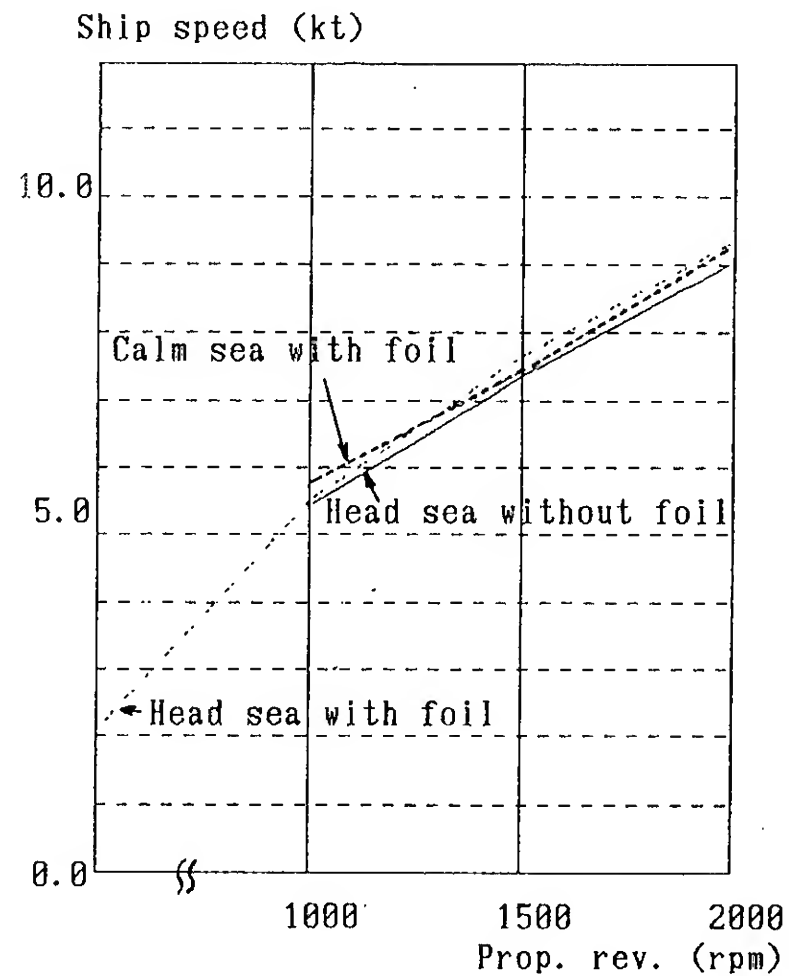


Fig.15 Results of speed trial in a following sea condition.

Sailing with a propeller rotation speed 1500 rpm, against the swell, a 7.7 kt forward speed could be obtained. This speed is equal to a calm sea condition without a hydrofoil. This data shows the possibility that the WDPS is useful as a sub-propulsor for the ship.

#### 4.3 SEAWORTHINESS OF WDPS SHIP

The motion reduction effect, especially pitch motion, is discussed here. From the theoretical analysis, it is expected that the pitch reduction effect is superior. Figure 15 shows the rate of the significant pitch amplitude, with hydrofoil data are divided by the without hydrofoil data. If the pitch motion of WDPS is less than the ordinary ship, then the plotted values become less than one. In this case, we have a 20 to 35% pitch reduction at the mean wave period is 1.75 to 2.7.

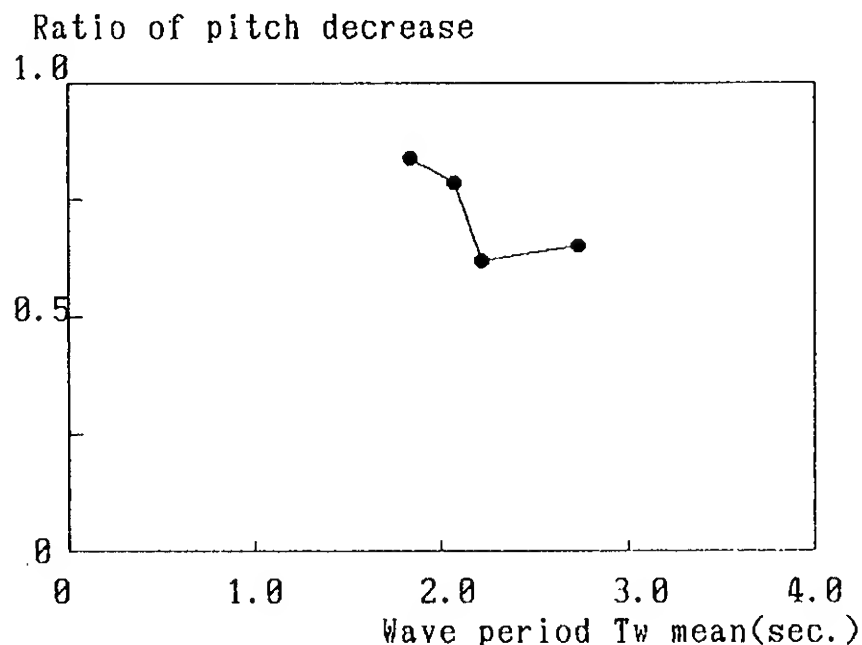


Fig.16 Results of pitch motion in a head sea condition.

Not only can we see the pitch reduction effect from this figure, but also the crews of the ship mentioned that she has less pitching motion in the rough sea than they had experienced.

At first, the crew would not sail WDPS ship during the rough sea condition even the bay area because they have no significance. However after the effectiveness of the hydrofoil was confirmed, they willingly tested the WDPS ship in heavy sea conditions where they had never sailed ordinary hydrofoil-less ship at the test speed range. We had a chance to compare the sailing test of her sister ship in the same rough sea at the same time. The sister ship could hardly sail together with the WDPS ship due to hard bow slamming of the waves.

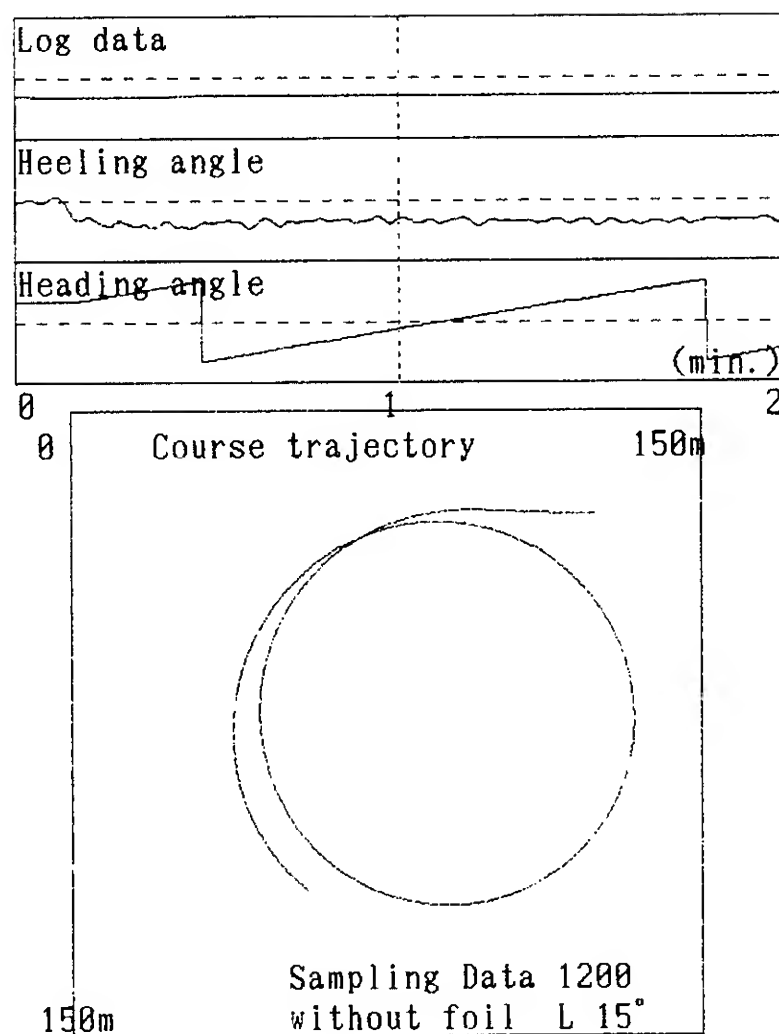


Fig.17 Turning trajectory of ship (without foil 1500rpm).

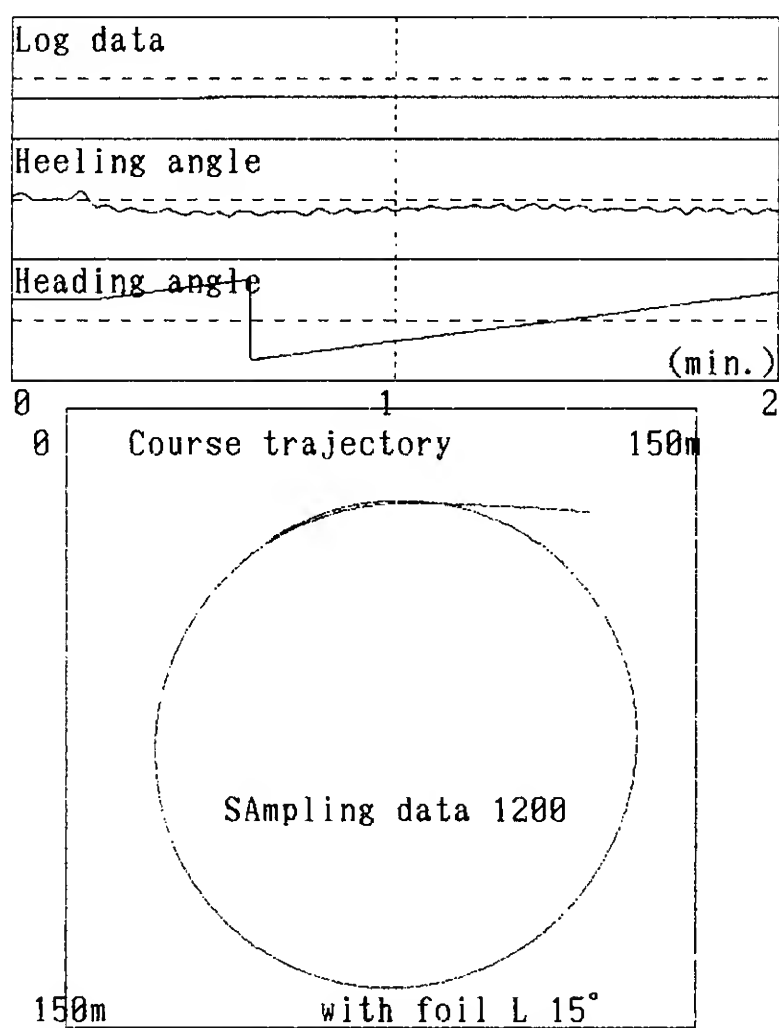


Fig.17 Turning trajectory of ship (with foil 1500 rpm).

It was not observed during the experiment which Abkowitz stated the horizontal hull vibration of the anti-pitching fin due to the hydrofoil impact.

The author consider that it is associated with the depth and projected area of the foil, which we adopted was deeper and larger area than the anti-pitching fin. The larger hydrofoil restricted the lateral motion of the ship fairly well and the phenomena of the foil penetration of the surface did not occur because of the deeper hydrofoil position.

#### 4.4 TURNING ABILITY OF WDPS SHIP

Figure 17 and 18 show the turning trajectory of the ship with a hydrofoil and without a hydrofoil in waves. It is apparent that the turning radius increased about 15% compared with the ordinary ship, but a lesser heeling angle was observed. This tendency was the same as a the calm sea turning test.

Considering the demerit of the increased turning radius, the merit of the increase of safety due to a lesser heeling angle especially in waves is more attractive in this ship.

#### 5. CONCLUSIONS

From our experiment of the wave devouring propulsion system at sea, following results were obtained

- a) Improvement of the ship propulsive performance in waves were observed.
- b) Reduction in motion, especially the pitch motion was observed.
- c) Vertical hull vibration due to the foil was not observed.

#### 6. ACKNOWLEDGEMENT

This work has been supported by the Japan Shipbuilding Industry Foundation.

The authors would like to thank the crew of Hokuto for their support during the experiment at sea.

#### REFERENCES

- (1)The Naval Architect(1973,Nov.)pp 239
- (2)Jakobsen,E.,2nd Int. Symp. on Waves & Tidal Energy , BHRA Fluid Engineering ,1981, pp.363-368
- (3)Terao,Y., "A Floating Structure Which Moves Toward the Waves," Journal of The Kansai Society of Naval Architects, No.184, Sept.,1984,pp.51-54.
- (4)Isshiki,H., Murakami,K., Terao,Y., "Utilization of Wave Energy into Propulsion of Ships (Wave Devouring Propulsion)," 15th Symp. Naval Hydrodynamics, 1985, pp.539-552
- (5)Abkowitz,M.A., "The Effect of Anti-pitching Fins on Ship Motions", Trans. of SNAME, vol.67, 1959, pp.210-252
- (6)Wu,T.Y., "Extraction of Flow Energy by Wing Oscillating in Waves", Journal of Ship Research (1972,Mar.) pp.66-78
- (7)Bessho,M., Kyojuka,Y., "On the Ship Motion Reduction by Antipitching Fins in Head Seas", 15th Symp. Naval Hydrodynamics, 1985, pp.109-118
- (8)Naitou,S., Isshiki,H., Fujimoto,K., "Thrust Generation of a Fin Attached to Ship in Waves", Journal of The Kansai Society of Naval Architects, No.202, Sep. 1986, pp.23-28.
- (9)J.Gerritsma,W.Beukelman, "Analysis of the Resistance Increase in Waves of a First Cargo Ship", International Shipbuilding Progress, Vol.19, No.217, Sept., 1972, pp.285-293.

# Numerical and Experimental Analysis of Propeller Wake by Using a Surface Panel Method and a 3-Component LDV

T. Hoshino (Mitsubishi Heavy Industries, Ltd., Japan)

## ABSTRACT

Hydrodynamic modeling of the trailing vortex wake of a propeller is one of the most important factors in developing a propeller theory. A variety of trailing vortex wake models have been proposed hitherto. However, details of geometrical features have not been known clearly. In the present study, flow fields around propeller are precisely measured in a cavitation tunnel using a 3-component Laser Doppler Velocimeter (LDV). Based on the experimental finding that the pitch of the tip vortices are smaller than that of the inboard trailing vortex sheets, the surface panel method with a deformed wake model of the trailing vortices is proposed. Then, the pressure distributions on the blade and the flow fields around propeller were calculated by the present surface panel method. A better agreement of pressure distributions near the hub is observed when the hub effect is considered in the calculations. It is shown that the calculated flow fields around propeller are in good agreement with the measured ones. Open-water characteristics of propeller calculated by the present method are also in good agreement with experimental data.

## NOMENCLATURE

$2\pi a(r)$	Pitch of blade section = $P(r)$	$n$	Normal coordinate for blade section
$B_{ij}$	Influence coefficient due to the $j$ -th source panel on blade and hub surfaces	$n$	Propeller rotational speed, [rps]
$c(r)$	Chord length	$\mathbf{n}$	Unit vector outward normal to surface
$C_{ij}$	Influence coefficient due to the $j$ -th doublet panel on blade and hub surfaces	$N$	Total number of blade and hub panels
$C_p(P_i)$	Pressure coefficient $= (p(P_i) - p_o) / \rho (V_A^2 + (r\Omega)^2) / 2$	$2N_c$	Number of chordwise blade panels
$D$	Propeller diameter	$N_R$	Number of radial blade panels
$e_1, e_2$	Local coordinates on panel	$O$	Propeller center
$J$	Advance coefficient = $V_A / (nD)$	$p(P_i)$	Pressure
$K$	Number of propeller blades	$p_o$	Static pressure at infinity
$K_T$	Thrust coefficient of propeller $= T / (\rho n^2 D^4)$	$P(r)$	Pitch of blade section
$K_Q$	Torque coefficient of propeller $= Q / (\rho n^2 D^5)$	$P_w(r)$	Pitch of trailing vortex sheet
$L$	Number of chordwise wake panels	$Q$	Propeller torque
		$r$	Radial coordinate from propeller axis $= \sqrt{y^2 + z^2}$
		$r_o$	Propeller radius = $D/2$
		$r_h$	Radius of propeller hub
		$r_{wh}$	Radius of hub vortex
		$r_{wT}$	Radius of ultimate wake
		$R(P, Q)$	Distance between field point $P$ and boundary point $Q$
		$R_{ijk}$	Distance between the $i$ -th control point and the $j$ -th integration point
		$s$	Chordwise coordinate for blade section
		$s_L(r)$	Chordwise coordinate of leading edge
		$S$	Boundary surface
		$S_j$	Surface of the $j$ -th panel
		$t_1, t_2$	Tangential coordinates on panel
		$T$	Propeller thrust
		$x, y, z$	Cartesian coordinates in the blade-fixed frame
		$x_R(r)$	Propeller rake
		$v$	Velocity
		$\mathbf{v}_t$	Perturbation velocity vector tangent to blade surface
		$V_A$	Speed of advance
		$\mathbf{V}_I$	Velocity vector of relative inflow
		$\mathbf{V}_t$	Total velocity vector tangent to blade surface
		$W_{ij}$	Influence coefficient due to the $j$ -th doublet strip on wake surface
		$\beta_G(r)$	Pitch angle of blade section
		$\beta_w(r)$	Pitch angle of trailing vortex sheet
		$\delta_{ij}$	Kronecker delta
		$\Delta S_i$	Area of the $i$ -th panel
		$\Delta \phi$	Potential jump across wake surface
		$\Delta \phi_j$	Discrete potential jump in the $j$ -th panel
		$\theta$	Angular coordinate from generator line of propeller = $\tan^{-1}(-y/z)$

Tetsuji Hoshino, Nagasaki Experimental Tank, Mitsubishi Heavy Industries, Ltd.  
3-48 Bunkyo Machi, Nagasaki 852, Japan

$\theta_k$	Angular coordinate of generator line of k-th blade = $2\pi(k-1)/K$
$\rho$	Fluid density
$\phi$	Perturbation velocity potential
$\phi_j$	Discrete potential in the j-th panel
$\Omega$	Angular velocity = $2\pi n$
$\nabla$	Gradient operator

#### Subscripts

$b\kappa$	Face and back sides of blade, respectively ( $\kappa=1$ ;face, $\kappa=2$ ;back )
B	Blade
D	Drag
H	Hub
i,j	Values on panels i,j, respectively
k	Value on k-th blade
P	Potential
Q	Value on boundary point Q
r, $\theta$	Radial and tangential components, respectively
TE	Value on trailing edge
w	Wake
x,y,z	Components in Cartesian coordinate, respectively
+	Upper surface
-	Lower surface
$\mu,\nu$	Values on corner points $\mu,\nu$ of panel, respectively

## 1. INTRODUCTION

In recent years, propellers with various blade geometries such as a highly skewed propeller have been fitted to ships in order to reduce the propeller induced vibration and noise, or to improve the propulsive performance of ship. A reliable numerical method is indispensable for the design and analysis of such propellers.

A number of propeller design and analysis methods based on lifting surface theories such as Vortex Lattice Method (VLM)[1] and Quasi-Continuous Method (QCM)[2] have been developed. However, the propeller lifting surface methods are essentially based on the thin wing theory. Therefore, they are insufficient to predict the pressure distribution on propeller blade, especially near the hub where the effect of blade thickness and hub would be dominant.

On the other hand, surface panel method has been remarkably advanced in the field of aerodynamics for the design and analysis of three-dimensional wing and bodies [3-12]. The surface panel method is one of the most advanced methods, because it allows precise representations of the complicated blade geometry of the propeller such as the highly skewed propeller. In the past few years, the surface panel method has been applied to marine propellers and also advanced turboprop problems [13-20]. In most of such propeller theories, however, the geometry of the trailing vortex wake of a propeller slipstream has been treated approximately because of the complexity of the slipstream.

Since the induced velocities on the blade due to the helical trailing vortex wake of a

propeller are much larger than those due to the trailing vortex wake of a wing, hydrodynamic modeling of the trailing vortex wake behind the propeller becomes important in developing propeller theories. In the past, the trailing vortex wake had been replaced by a prescribed helical surface with a constant pitch obtained from the undisturbed inflow or a constant hydrodynamic pitch calculated from the lifting line theory as described by Hanaoka [21]. In the actual propeller, the trailing vortices leave the trailing edge of the propeller blade and flow into the slipstream with the local velocity at that position. Therefore, the detailed knowledge of the velocity distributions of the propeller slipstream would be indispensable to establish the realistic model of the trailing vortex wake.

Due to the recent development of measuring technique with Laser Doppler Velocimeter(LDV), the measurements of time dependent flow fields around propeller have been reported by many researchers [22-27]. Based on the results of the flow field measurements, Kerwin and Lee [1] proposed a roll-up wake model which took into consideration the contraction of the slipstream and the roll-up of the trailing vortex sheets. However, the roll-up model in which the trailing vortices are assumed to be concentrated into a single hub vortex and a set of tip vortices at a certain distance behind the blade is considered to be too simplified. More realistic geometry of the trailing vortex wake behind propeller has to be taken into consideration.

In the present paper, a surface panel method is described for analyzing the flow fields around propeller operating in uniform flow at first. Green's identity is applied to obtain an integral equation with respect to the unknown potential strength over the surface of the propeller blades, hub and wake. Such method was firstly developed by Morino for general lifting bodies [6,7]. An improvement on Kutta condition is added to the Morino method. That is, the Kutta condition of equal pressure on the upper and lower surfaces at the trailing edge is applied in the present study.

Next, flow fields around propeller models operating in uniform flow are precisely measured in a cavitation tunnel using a 3-component LDV. Based on the measured velocity distributions of the propeller slipstream, a deformed wake model is proposed where the contraction of the slipstream and the variation of the pitch of the inboard helical trailing vortex sheets are taken into account.

Then, pressure distributions on the propeller blade and open-water characteristics calculated by the present method are compared with the experimental data. Further, flow fields around the propeller are calculated by the surface panel method and compared with those measured by the LDV.

## 2. FORMULATION OF PROPELLER PROBLEM

### 2.1 Coordinate Systems and Geometry of Propeller

We consider a propeller rotating clockwise with a constant angular velocity  $\Omega$  in an inviscid, incompressible, irrotational flow with a uniform axial speed  $V_A$  far upstream. The propeller consists of a finite number of axisymmetrically arranged blades of identical shape and a hub.

We define a Cartesian coordinate system  $O-xyz$  with origin  $O$  fixed at the center of the propeller, where  $x$  is measured along the downstream axis of rotation as shown in Fig.1. The  $z$ -axis coincides with generator line of the first blade and the  $y$ -axis completes right-handed coordinate system. A cylindrical coordinate system  $O-xr\theta$  is also introduced for convenience. Angular coordinate  $\theta$  is measured clockwise from the  $z$ -axis when viewed in the direction of positive  $x$ . Radial coordinate  $r$  is measured from the  $x$ -axis. Then, the Cartesian coordinate system  $O-xyz$  is transformed into the cylindrical coordinate system  $O-xr\theta$  by the relation

$$\begin{aligned} x &= x, \quad y = -r \cdot \sin \theta, \quad z = r \cdot \cos \theta, \\ \text{where} \\ r &= \sqrt{y^2 + z^2}, \quad \theta = \tan^{-1}(-y/z). \end{aligned} \quad (1)$$

Further, we introduce a helical coordinate system  $(r, s, n)$  with pitch  $2\pi a(r)$ . The  $s$ -axis is measured chordwise from leading to trailing edge of the blade section. The  $n$ -axis is measured normal to the  $s$ -axis from face to back side. Then, the cylindrical coordinate system  $O-xr\theta$  is related to the helical coordinate system  $(r, s, n)$  by

$$\begin{aligned} x &= [a(r) \cdot s - r \cdot n] / \sqrt{a(r)^2 + r^2} + x_R(r), \\ r &= r, \\ \theta &= [s + a(r) \cdot n / r] / \sqrt{a(r)^2 + r^2}, \end{aligned} \quad (2)$$

where  $x_R(r)$  is propeller rake defined by the  $x$  coordinate of generating line at radius  $r$ .

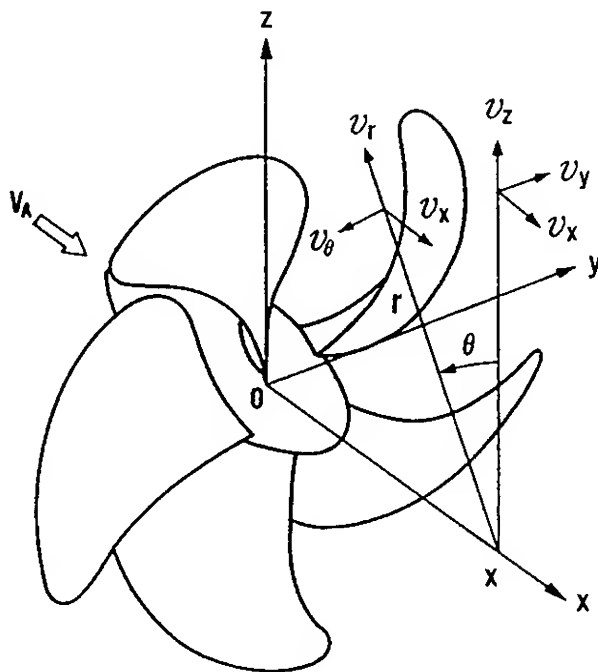


Fig.1 Coordinate systems of propeller

Blade section of propeller is usually defined in a way similar to that of a two-dimensional wing by the ordinates  $n_{bK}(r, s)$  of face and back sides along the chord where  $K = 1$  and  $2$  show the face and back sides, respectively. Then the coordinate of a point on the surface of the  $k$ -th blade can be expressed as

$$\left. \begin{aligned} x &= x_{bK}(r, s), \\ y &= -r \cdot \sin[\theta_{bK}(r, s) + \theta_k], \\ z &= r \cdot \cos[\theta_{bK}(r, s) + \theta_k], \end{aligned} \right\} \quad (3)$$

where

$$x_{bK}(r, s) = [a(r) \cdot s - r \cdot n_{bK}(r, s)] / \sqrt{a(r)^2 + r^2} + x_R(r),$$

$$\theta_{bK}(r, s) = [s + a(r) \cdot n_{bK}(r, s) / r] / \sqrt{a(r)^2 + r^2},$$

$$\theta_k = 2\pi(k-1)/K, \quad k = 1, 2, \dots, K,$$

$$K = \text{number of propeller blades.}$$

### 2.2 Velocity Potential and Boundary Condition

Under the assumption of potential flow, the flow field around a propeller is characterized by a perturbation velocity potential  $\phi$ , which satisfies Laplace's equation

$$\nabla^2 \phi = 0 \quad (4)$$

and vanishes at infinity. We consider a boundary surface  $S$ , which is composed of propeller blade surface  $S_B$ , hub surface  $S_H$  and wake surface  $S_w$ , and also unit outward normal vector  $\mathbf{n}$  to the surface  $S$ . Applying Green's identity, the perturbation potential at any field point  $P(x, y, z)$  can be written as a distribution of source and doublet over the boundary surface [6,7]:

$$\begin{aligned} 4\pi E \phi(P) &= \iint_S \phi(Q) \frac{\partial}{\partial n_Q} \left( \frac{1}{R(P, Q)} \right) dS \\ &\quad - \iint_S \frac{\partial \phi(Q)}{\partial n_Q} \cdot \frac{1}{R(P, Q)} dS \end{aligned} \quad (5)$$

where

$$E = \begin{cases} 0 & \text{for the point } P \text{ inside } S, \\ 1/2 & \text{for the point } P \text{ on } S, \\ 1 & \text{for the point } P \text{ outside } S. \end{cases}$$

and  $R(P, Q)$  is the distance from the field point  $P(x, y, z)$  to the boundary point  $Q(x', y', z')$  and  $\partial/\partial n_Q$  is the normal derivative to the boundary surface at the point  $Q$ .

Kinematic boundary condition is that the velocity normal to the blade surfaces  $S_B$  and the hub surface  $S_H$  should be zero. Using relative inflow velocity  $\mathbf{V}_I$ , the boundary condition with respect to a moving frame fixed on the propeller blade can be written as

$$\frac{\partial \phi}{\partial n_Q} = -\mathbf{V}_I \cdot \mathbf{n}_Q = -(\mathbf{V}_A + \Omega \times \mathbf{r}) \cdot \mathbf{n}_Q, \quad \text{on } S_B \text{ and } S_H, \quad (6)$$

where  $\mathbf{V}_A$  and  $\Omega$  are the advance and angular velocity vectors respectively and  $\mathbf{r}$  is the position vector of the point  $P$  on the boundary surface.



We assume that the wake surface  $S_w$  is infinitely thin and there is no flow and no pressure jump across the surface  $S_w$ , while the potential jump is allowed. The boundary condition on the wake surface  $S_w$  can be written as

$$\frac{\partial \phi_+}{\partial n_Q} = \frac{\partial \phi_-}{\partial n_Q}, \quad p_+ = p_- \quad \text{on } S_w, \quad (7)$$

where  $p_{\pm}$  are the pressures on the wake surface  $S_w$ , and subscripts  $+$  and  $-$  denote the upper and lower sides, respectively. For the steady propeller problem the potential jump  $\Delta\phi$  across the wake surface is constant along an arbitrary streamline in the wake and can be expressed as

$$\Delta\phi = \phi_+ - \phi_- \quad \text{on } S_w. \quad (8)$$

Considering Eqs.(6) through (8), the boundary integral equation (5) for the point  $P$  on the blade and hub surface reduces to

$$\begin{aligned} 2\pi\phi(P) - \iint_{S_B+S_H} \phi(Q) \frac{\partial}{\partial n_Q} \left( \frac{1}{R(P,Q)} \right) dS \\ - \iint_{S_w} \Delta\phi(Q') \frac{\partial}{\partial n_Q} \left( \frac{1}{R(P,Q')} \right) dS \\ = \iint_{S_B+S_H} (\mathbf{v}_I \cdot \mathbf{n}_Q) \frac{1}{R(P,Q)} dS \quad \text{on } S_B \text{ and } S_H. \end{aligned} \quad (9)$$

Here  $\iint$  denotes that Cauchy's principal value should be taken and  $Q'$  is any point on the wake surface  $S_w$ .

Eq.(9) is a Fredholm integral equation of second kind for the velocity potential  $\phi$  and can be solved uniquely. The resulting surface potential distribution can be differentiated to obtain velocities and pressures, which are integrated to yield the total forces and moments.

### 3. Numerical Procedure

#### 3.1 Discretization of Propeller Blade, Hub and Wake Surface

In order to obtain a numerical solution for the boundary integral equation (9), the surface of propeller blades, hub and wake is divided into a number of small elements. In the past application of the panel method to the propeller problem, planar quadrilateral panel has been used to approximate the surface. However, the elements representing the propeller blades must be nonplanar due to the helical blade surface, which results in gaps at the edge of the planar panel and therefore numerical errors. In order to yield a closed surface and avoid such numerical errors, the surface of the blades, hub and wake is approximated by a number of quadrilateral hyperboloidal panels in the present paper. This paneling is one of the important features of the present method.

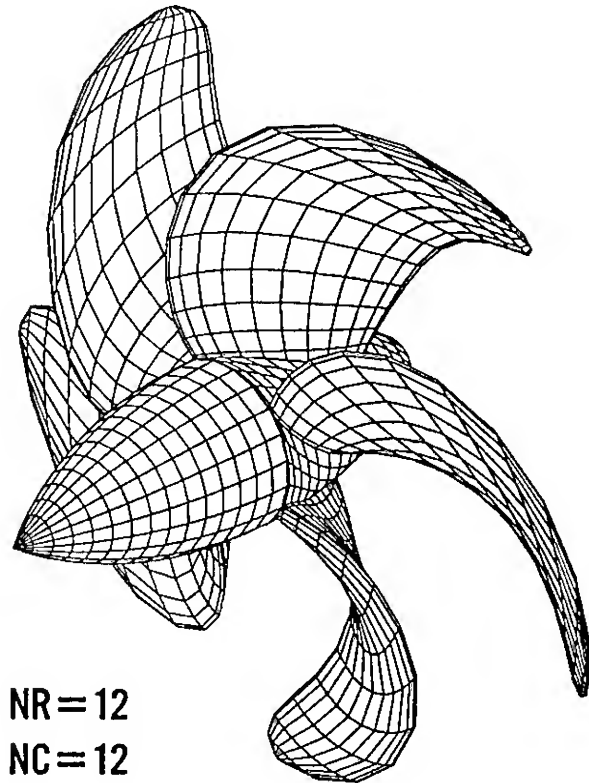
The discretization of a propeller is divided into three portions, i.e., the generation of blade panels, the generation of hub panels, and the generation of wake panels. We consider the discretization of a propeller blade at first. In the choice of the radial distribution of panel strips for a propeller blade, it should be noted that the better results could be obtained if the finer panel strip was used in the region of rapid variation of sectional properties. Therefore, we will use the cosine spacing which concentrates the panel strips at the hub and tip. If the radial interval from the hub  $r_h$  to the tip  $r_o$  is divided into  $N_R$  small panel strips, the radii of the corner points of each panel strip can be expressed as follows:

$$r_\mu = \frac{1}{2}(r_o + r_h) - \frac{1}{2}(r_o - r_h)\cos\alpha_\mu, \quad (10)$$

where

$$\alpha_\mu = \begin{cases} 0 & \text{for } \mu = 1, \\ \frac{(2\mu-1)\pi}{2(N_R+1)} & \text{for } \mu = 2, 3, \dots, N_R+1. \end{cases}$$

(Upstream View)



(Downstream View)

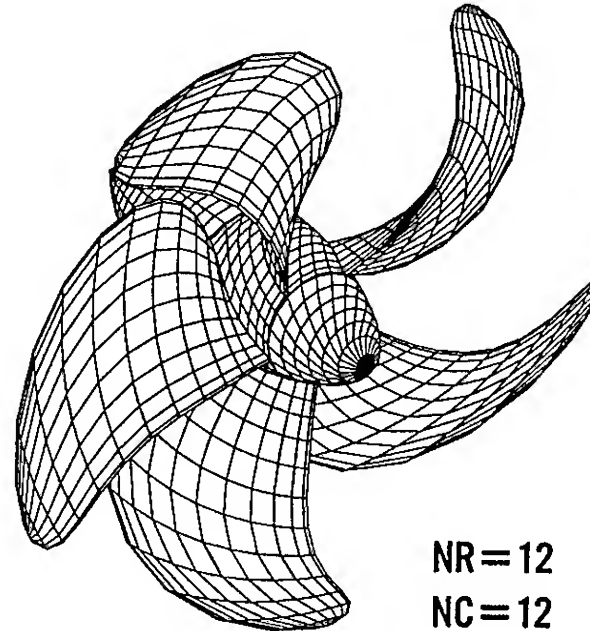


Fig.2 Panel arrangement for a highly skewed propeller

In the chordwise spacing of the blade panels, cosine spacing is considered to be the best. Therefore, the chordwise positions of the corner points of each panel are given by

$$s_{\mu v} = s_L(r_{\mu}) + \frac{c(r_{\mu})}{2}(1 - \cos \beta_v), \quad (11)$$

where

$s_L(r)$  = s-coordinate of the leading edge,

$c(r)$  = chord length of the blade,

$\beta_v = v\pi/N_C$ ,  $v = 0, 1, 2, \dots, N_C$ ,

$N_C$  = number of chordwise division.

This concentrates the panels at the leading and trailing edges, where greater resolution is required. A propeller blade surface is thus discretized into  $N_R \times 2N_C$  quadrilateral elements per each blade.

Propeller hub is considered to be an axisymmetric body on which the propeller blades are mounted. The blade panels adjacent to the hub surface are shortened or stretched to obtain the intersections with the hub surface. Then the axial positions of the hub panels meet with those of the blade panels at the intersections. The hub portion from the leading to the trailing edge is divided into some strips equally spaced in circumferential angle between the root blades. This generates the panels with helical pattern on the hub. The hub portion upstream of the leading edge of the blade is divided into straight panels with equal axial and circumferential spacings. On the other hand, the hub portion downstream of the trailing edge is helically divided with the pitch at the root of the propeller. An example of the panel arrangement on propeller blade and hub surface for a 5-bladed highly skewed propeller is shown in Fig.2.

Trailing vortex leaves the trailing edge of the blade and flows into the slipstream with the local velocity at that position. However, the wake surface is usually approximated by prescribed helical surface in order to avoid time consuming calculation of the slipstream velocities. In the present paper, the surface of the trailing vortex wake is determined based on the measured velocity distributions of the propeller slipstream. The wake surface is divided into  $N_R$  wake strips, which start from the trailing edges of the blade strips. Then, each wake strip is divided into  $L$  wake panels. The axial spacing of the wake panel is finer near the blade and gradually becomes coarser in the downstream. Details of the numerical modeling of the trailing vortex wake is shown in the following chapter.

### 3.2 Linear Algebraic Equations

As mentioned above, the blade and hub surface is divided into  $N$  small panels  $S_j$  and the wake surface is divided into  $N_R \times L$  small panels  $S_{\ell}$ . The values of the potential and  $(\mathbf{V}_I \cdot \mathbf{n}_Q)$  are assumed to be constant within each panel and equal to the values  $\phi_j$ ,  $\Delta\phi_j$  and  $(\mathbf{V}_I \cdot \mathbf{n}_j)$  at the centroid of the panel, respectively. Then, by satisfying Eq.(9) at

the centroid of each panel, one obtained a system of  $N$  linear algebraic equations as

$$\sum_{j=1}^N (\delta_{ij} - C_{ij}) \phi_j - \sum_{j=1}^{N_R} W_{ij} \Delta\phi_j = - \sum_{j=1}^N B_{ij} (\mathbf{V}_I \cdot \mathbf{n}_j) \quad (12)$$

for  $i = 1, 2, \dots, N$ .

Here  $\delta_{ij}$  is the Kronecker delta and  $C_{ij}$ ,  $W_{ij}$  and  $B_{ij}$  are influence coefficients defined by

$$\left. \begin{aligned} C_{ij} &= \sum_{k=1}^K \left[ \frac{1}{2\pi} \oint_{S_j} \frac{\partial}{\partial n_j} \left( \frac{1}{R_{ijk}} \right) dS_j \right], \\ W_{ij} &= \sum_{k=1}^K \sum_{\ell=1}^L \left[ \frac{1}{2\pi} \iint_{S_{\ell}} \frac{\partial}{\partial n_{\ell}} \left( \frac{1}{R_{i\ell k}} \right) dS_{\ell} \right], \\ B_{ij} &= \sum_{k=1}^K \left[ -\frac{1}{2\pi} \oint_{S_j} \left( \frac{1}{R_{ijk}} \right) dS_j \right], \end{aligned} \right\} \quad (13)$$

where  $R_{ijk}$  and  $R_{i\ell k}$  are the distances from the control point of the panel on the  $k$ -th blade and hub surfaces to the integration point on  $S_j$  and  $S_{\ell}$ .

The influence coefficients  $C_{ij}$  and  $B_{ij}$  are evaluated analytically in the near field [7]. On the other hand, they are approximated by a Taylor series expansion in the far field in order to save computation time. The coefficient  $W_{ij}$  are also calculated by using the expression for  $C_{ij}$ . Then, Eq.(12) can be solved numerically to yield the values of the unknown potential  $\phi_j$ .

The Kutta condition is applied to obtain the values of the unknown potential jump  $\Delta\phi_j$  on the wake surface. An equal pressure Kutta condition is introduced in the present study. A detailed formulation of the numerical Kutta condition is shown in APPENDIX.

### 3.3 Velocity and Pressure on the Surface

The velocity and pressure distributions on the blade and hub surfaces can be evaluated directly by taking the gradient of the influence coefficients for the velocity potential Eq.(13). However, it takes too much computation time because the influence coefficients for the induced velocity must be newly calculated. On the other hand, the velocity and pressure on the surface can be obtained also by differentiating the velocity potential over the body surface which is already known. This method takes much shorter computation time than the former but numerical differentiation is used to introduce some numerical errors.

In the present paper, the latter method is adopted to calculate the velocity and pressure distributions on the body surface. The numerical differentiation was conducted as follows [12]. The distributions of the velocity potential  $\phi$  are approximated by a quadratic equation passing through the potentials at the centroids of three adjacent panels as

$$\phi = at^2 + bt + c, \quad (14)$$

where  $t$  is the surface distance and  $a$ ,  $b$ , and  $c$  are the coefficients of the quadratic equation. Then, the derivatives of the potential

along the tangent directions  $t_1$  and  $t_2$  to the panel surface can be expressed as

$$\left. \begin{aligned} \phi_{t1} &\equiv \frac{\partial \phi}{\partial t_1} = 2a_1 t_1 + b_1, \\ \phi_{t2} &\equiv \frac{\partial \phi}{\partial t_2} = 2a_2 t_2 + b_2, \end{aligned} \right\} \quad (15)$$

respectively.

Next, we take the  $e_1$  axis in the direction of  $t_1$  and the  $e_2$  axis in the direction perpendicular to  $t_1$  in the plane composed of  $t_1$  and  $t_2$  as shown in Fig.3. Denoting the unit vectors in the directions of the  $e_1$ ,  $e_2$ , and  $t_2$  axis by  $e_1$ ,  $e_2$ , and  $t_2$ , respectively, the derivatives of the potential along the  $e_1$  and  $e_2$  axes can be expressed as

$$\left. \begin{aligned} \phi_{e1} &\equiv \frac{\partial \phi}{\partial e_1} = \phi_{t1}, \\ \phi_{e2} &\equiv \frac{\partial \phi}{\partial e_2} = \frac{\phi_{t2} - (t_2 \cdot e_1) \phi_{t1}}{(t_2 \cdot e_2)}. \end{aligned} \right\} \quad (16)$$

Then the perturbation velocity tangent to the body surface can be obtained by

$$v_t = \phi_{e1} e_1 + \phi_{e2} e_2, \quad (17)$$

Adding the tangential component of the relative inflow velocity  $V_I$ , we obtain the total velocity tangent to the body surface as

$$\begin{aligned} V_t &= V_I - (V_I \cdot n)n + v_t \\ &= [(V_I \cdot e_1) + \phi_{e1}]e_1 + [(V_I \cdot e_2) + \phi_{e2}]e_2, \end{aligned} \quad (18)$$

where

$$n = e_1 \times e_2.$$

The pressure on the body surface can be expressed by Bernoulli's equation as

$$p(P_i) = p_o + \frac{1}{2} \rho [ |V_I|^2 - |V_t|^2 ], \quad (19)$$

where

$p_o$  = static pressure at infinity,

$\rho$  = density of water.

The pressure is finally expressed in terms of the non-dimensional pressure coefficient  $C_p(P_i)$ , which is defined as

$$C_p(P_i) = \frac{p(P_i) - p_o}{\frac{1}{2} \rho W_o^2}, \quad (20)$$

where

$$W_o = \sqrt{V_A^2 + (r\Omega)^2}.$$

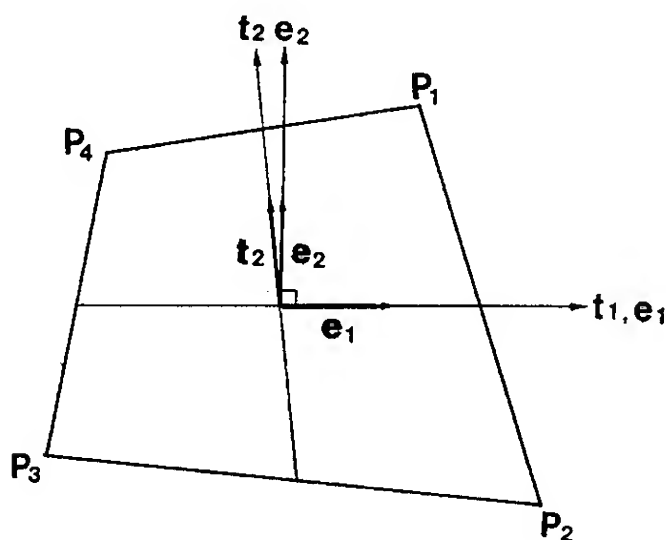


Fig.3 Local coordinate system on a panel

### 3.4 Field Point Velocity

The induced velocities at the field point  $P$  outside the closed surface  $S$  can be evaluated by taking the gradient of the velocity potential  $\phi$  as follows:

$$\begin{aligned} v(P) &= \nabla_P \phi(P) \\ &= \frac{1}{4\pi} \iint_{S_B + S_H} \phi(Q) \nabla_P \frac{\partial}{\partial n_Q} \left( \frac{1}{R(P, Q)} \right) dS \\ &\quad + \frac{1}{4\pi} \iint_{S_W} \Delta \phi(Q') \nabla_P \frac{\partial}{\partial n_{Q'}} \left( \frac{1}{R(P, Q')} \right) dS \\ &\quad + \frac{1}{4\pi} \iint_{S_B + S_H} (V_I \cdot n_Q) \nabla_P \left( \frac{1}{R(P, Q)} \right) dS. \end{aligned} \quad (21)$$

Then, Eq.(21) can be approximated by

$$v_i = \sum_{j=1}^N \phi_j \nabla_P C_{ij} + \sum_{j=1}^{N_R} \Delta \phi_j \nabla_P W_{ij} - \sum_{j=1}^N (V_I \cdot n_j) \nabla_P B_{ij}, \quad (22)$$

where

$$\left. \begin{aligned} \nabla_P C_{ij} &= \sum_{k=1}^K \left[ \frac{1}{4\pi} \iint_{S_j} \nabla_P \frac{\partial}{\partial n_j} \left( \frac{1}{R_{ijk}} \right) dS_j \right], \\ \nabla_P W_{ij} &= \sum_{k=1}^K \sum_{l=1}^L \left[ \frac{1}{4\pi} \iint_{S_{\ell}} \nabla_P \frac{\partial}{\partial n_{\ell}} \left( \frac{1}{R_{i\ell k}} \right) dS_{\ell} \right], \\ \nabla_P B_{ij} &= \sum_{k=1}^K \left[ \frac{1}{4\pi} \iint_{S_j} \nabla_P \left( \frac{1}{R_{ijk}} \right) dS_j \right]. \end{aligned} \right\} \quad (23)$$

Here, the influence coefficients  $\nabla_P C_{ij}$ ,  $\nabla_P B_{ij}$  and  $\nabla_P W_{ij}$  can be evaluated analytically in a manner similar to the determination of the influence coefficients for the potential [8].

### 3.5 Thrust and Torque of Propeller

The total forces and moments acting on a propeller can be obtained by integrating the pressures over the blade and hub surfaces. Denoting the components of the outward normal vector  $n_i$  by  $(n_{xi}, n_{yi}, n_{zi})$ , the potential components of the thrust  $T_p$  and torque  $Q_p$  of the propeller can be expressed as

$$\left. \begin{aligned} T_p &= K \sum_{i=1}^N p(P_i) n_{xi} \Delta S_i, \\ Q_p &= K \sum_{i=1}^N p(P_i) (n_{yi} z_i - n_{zi} y_i) \Delta S_i, \end{aligned} \right\} \quad (24)$$

where

$\Delta S_i$  = area of panel,

$(x_i, y_i, z_i)$  = coordinates of the point  $P_i$ .

With the skin friction coefficient  $C_f(P_i)$ , the viscous components of the thrust  $T_D$  and torque  $Q_D$  of the propeller can be written as

$$\begin{aligned} T_D &= \frac{1}{2} \rho K \sum_{i=1}^N C_f(P_i) V_{txi} |V_{ti}| \Delta S_i, \\ Q_D &= \frac{1}{2} \rho K \sum_{i=1}^N C_f(P_i) (V_{tzi} y_i - V_{tyi} z_i) |V_{ti}| \Delta S_i, \end{aligned} \quad (25)$$

where

$(V_{txi}, V_{tyi}, V_{tzi})$  = components of the tangential velocity  $V_{ti}$  at the point  $P_i$ .

Then we obtain the total thrust and torque of the propeller as

$$T = T_P + T_D, Q = Q_P + Q_D. \quad (26)$$

Finally, advance, thrust and torque coefficients are defined as

$$J = \frac{V_A}{nD}, K_T = \frac{T}{\rho n^2 D^4}, K_Q = \frac{Q}{\rho n^2 D^5}. \quad (27)$$

where

$n$  = propeller rotational speed,  
 $D$  = propeller diameter.

#### 4. MEASUREMENTS OF FLOW FIELD AROUND PROPELLER

##### 4.1 3-component LDV System

The LDV system used in the present study is a five beam, two-color, 3-component type with a 3-watt Argon-ion laser as shown in Fig.4. This LDV system allows simultaneous measurement of three components of time dependent velocities around a propeller [25].

In order to measure the time dependent velocity at the specified field point, one propeller revolution is divided into 256 angular positions and the velocity data are combined with the present angular positions of the propeller. In the present measurements, total of 5120 data are collected for each velocity component and rearranged according to each angular position. Then, mean values and standard deviations of the velocity are obtained at each blade angular position.

The water in the tunnel is filtered to  $10 \mu\text{m}$  particle size and then seeded with  $4 \mu\text{m}$  metallic coated particle which is best for the present 3-component LDV system because of its high reflection index and adequate size.

##### 4.2 Definition of Field Point Velocity

We define the velocity components in the  $x$ -,  $y$ - and  $z$ -axis directions of the flow around a propeller to be  $v_x$ ,  $v_y$ ,  $v_z$  as shown in Fig.1. Then, the velocity components in the  $r$ - and  $\theta$ -directions  $v_r$  and  $v_\theta$  can be expressed as:

Table 1 Principal particulars of propeller models

Propeller	A	B	C
Diameter of Propeller (mm)	250.0	250.0	250.0
Pitch Ratio at 0.7R	0.8000	1.0000	1.2000
Expanded Area Ratio	0.6500	0.6500	0.6500
Bass Ratio	0.1800	0.1800	0.1800
Number of Blades	5	5	5
Blade Thickness Fraction	0.0500	0.0500	0.0500
Rake Angle (deg.)	8.0	8.0	8.0

Table 2 Conditions for flow measurement by LDV

Propeller	Advance	Ratio, J
A	0.40, 0.56, 0.72	
B	0.50, 0.70, 0.90	
C	0.60, 0.84, 1.08	

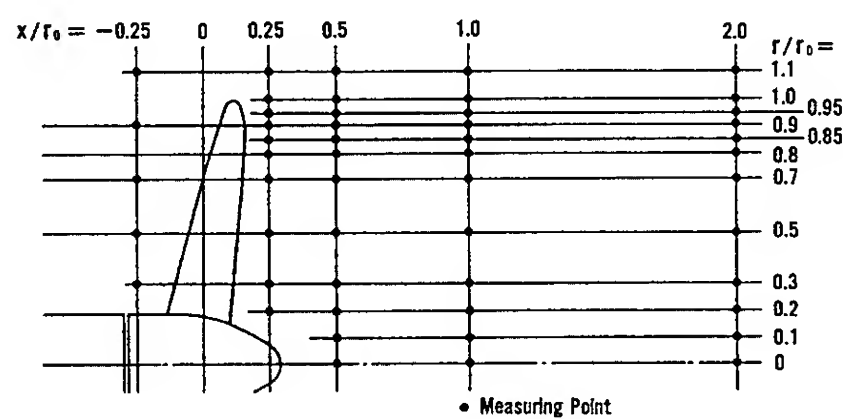


Fig.5 Measuring positions around propeller

$$\left. \begin{aligned} v_x &= v_x, \\ v_r &= -v_y \cdot \sin\theta + v_z \cdot \cos\theta, \\ v_\theta &= -v_y \cdot \cos\theta - v_z \cdot \sin\theta. \end{aligned} \right\} \quad (28)$$

If the velocity measurements were conducted in a vertical plane, the  $y$ -component  $v_y$  is identical but opposite in sign with the tangential component  $v_\theta$ , and the  $z$ -component  $v_z$  is identical with the radial component  $v_r$  as follows:

$$\left. \begin{aligned} v_x &= v_x, \\ v_r &= v_z, \\ v_\theta &= -v_y. \end{aligned} \right\} \quad (29)$$

In a uniform flow, the flow field around propeller is axisymmetrical and oscillating with the blade frequency. If the propeller rotates with a constant angular velocity, the time dependent velocity measurements at a certain radius correspond to the measurements at the same radius for many different angular positions of the measuring points at a fixed propeller position. Hence, the velocity measurements with respect to a certain propeller position give the instantaneous velocity distribution of the propeller at a certain time.

##### 4.3 Propeller Models and Measuring Conditions

Velocity measurements of the propeller slipstream were conducted in a uniform flow for three propeller models which are five-bladed and different in pitch. Principal particulars of propeller are shown in Table 1.

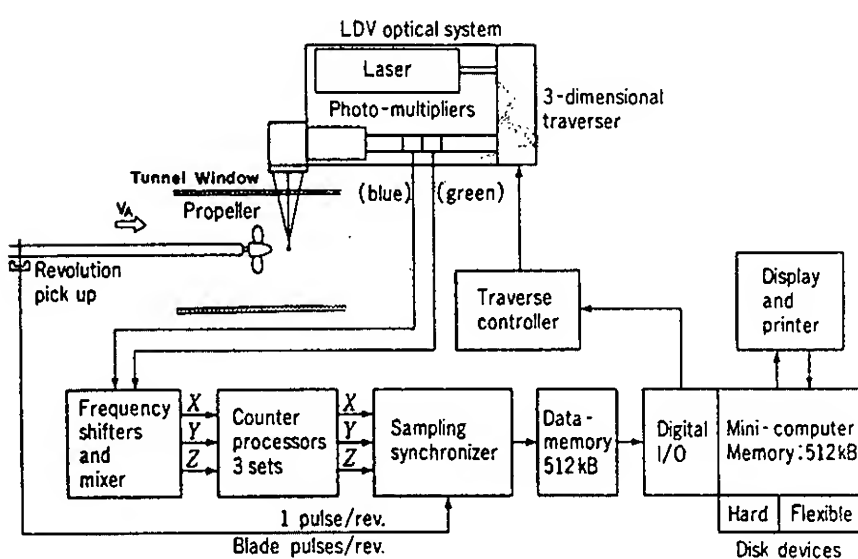


Fig.4 3-component LDV system

In the LDV-measurements, propeller rotational speed was kept constant of  $n=20$  rps and advance speed of the propeller  $V_A$  was changed to vary the advance coefficient  $J$ . Measuring conditions for each propeller are shown in Table 2. Measuring positions of the flow field around the propeller by LDV were taken upstream and downstream of the propeller as shown in Fig.5.

#### 4.4 Results of Measurements of Flow Field around Propeller

As an example of the results of the LDV measurements, circumferential variations of three components of the velocities around the propeller B at the advance coefficient of  $J=0.70$  are shown in Figs.6 - 8. It is shown that each velocity component is periodically fluctuating with the blade frequency.

Fig.6 shows the velocity fluctuations measured at various radial positions just upstream of the propeller ( $x/r_0=-0.25$ ). The variations of the axial and tangential velocities  $v_x, v_\theta$  are observed at inner radii.

Fig.7 shows the velocity fluctuations at axial position of  $x/r_0=0.25$  just behind the propeller. The sudden change of the radial velocity component shows the velocity jump across the trailing vortex sheet. The slope of the velocity jump of the radial component at inner radii ( $r/r_0 < 0.5$ ) is opposite to that at outer radii ( $r/r_0 > 0.8$ ). This shows that the strength of the trailing vortex changes its sign between the inner and outer radii.

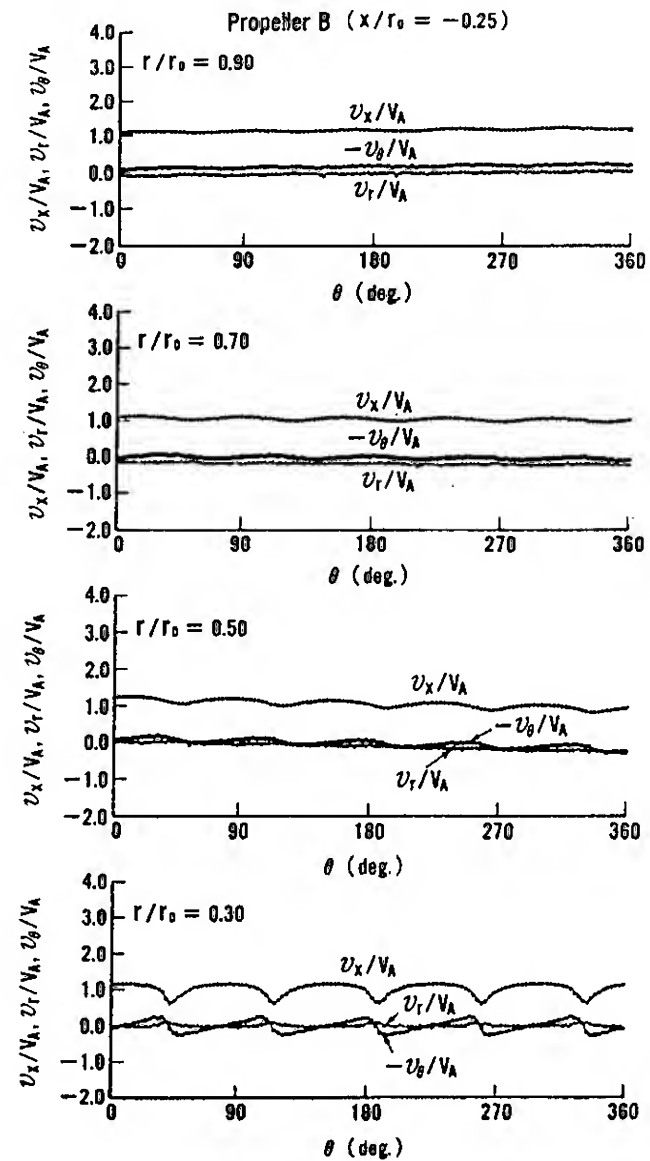


Fig.6 Circumferential variations of velocities upstream of propeller B ( $J=0.70, x/r_0=-0.25$ )

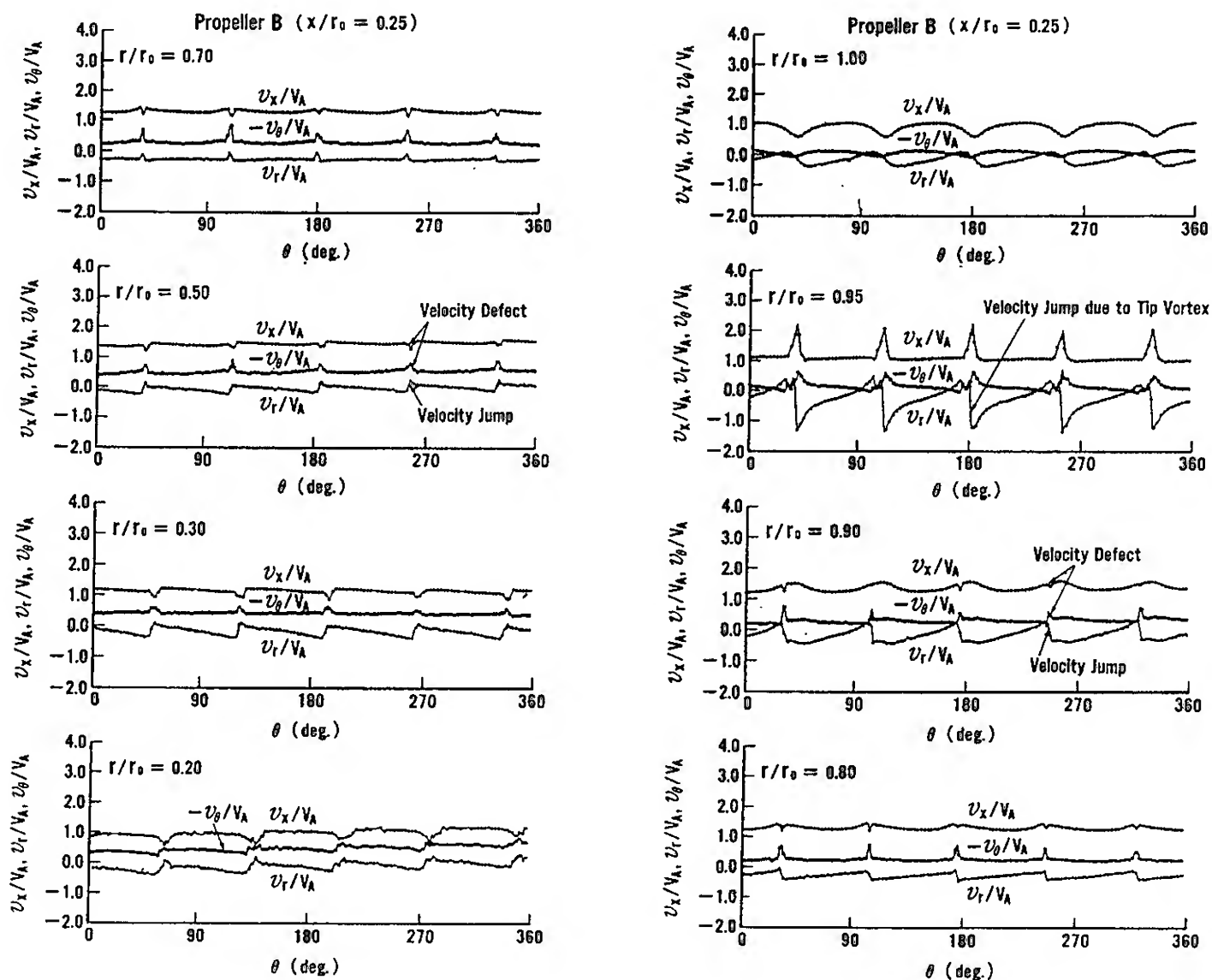


Fig.7 Circumferential variations of velocities downstream of propeller B ( $J=0.70, x/r_0=0.25$ )

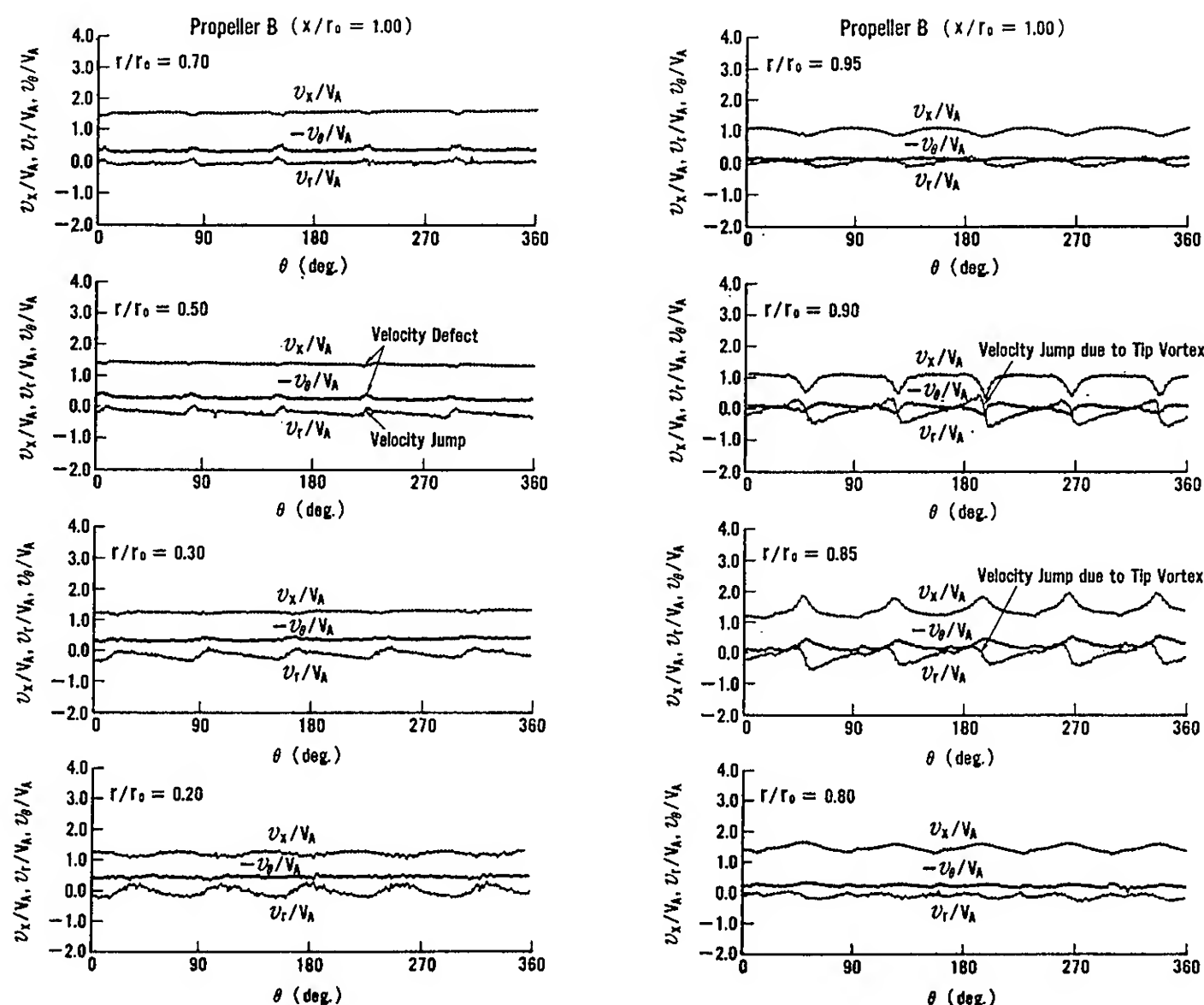


Fig.8 Circumferential variations of velocities downstream of propeller B (  $J=0.70$ ,  $x/r_0=1.00$  )

Further, this corresponds to the opposite slope of the radial circulation distribution at each radius. The strong variations in the radial velocity component at  $r/r_0=0.95$  seem to be due to strong tip vortices. Therefore, the tip vortices are considered to be located near this radius just behind the propeller. The velocity defects in the axial and tangential velocity components observed at the position where the velocity jump of radial component occurred correspond to the viscous wake of the boundary layer on the propeller blades.

Fig.8 shows the velocity fluctuations at axial position of  $x/r_0=1.00$  downstream of the propeller. Same tendency is observed on the axial, tangential and radial velocity components. The velocity defects in the axial and tangential components, however, become small. This shows the diffusion of the viscous wake of the blades. The trailing vortex sheets are still observed as the velocity jumps of radial component. The tip vortices are considered to be located between  $r/r_0=0.85$  and  $r/r_0=0.90$ , because the velocity change of axial component is opposite between those two radial positions. Same tendency was observed for the other operating conditions and the other propellers.

Velocity distributions around the propeller B at the advanced ratio of  $J=0.70$  are shown in Fig.9 as the form of the equi-velocity contour curves of axial component and the velocity vectors of cross components in a plan parallel to the propeller plane. This

figure is observed from the downstream side of the propeller. Since the propeller is right-handed, the tip vortices are rotating in the anti-clockwise direction as shown in Fig.9. Radial position of the center of the tip vortices moves from the blade tip to the inner radii along the downstream direction. This means the contraction of the slipstream. Trailing vortex sheets are also observed in these figures. Angular position of the tip vortex is larger than that of the trailing vortex sheet and the difference of the angular position is increasing along the downstream direction. This means that the pitch of the tip vortex is smaller than that of the trailing vortex sheet.

#### 4.5 Hydrodynamic Pitch

Using the circumferentially averaged axial and tangential velocities  $\bar{v}_x$ ,  $\bar{v}_\theta$ , hydrodynamic pitch angle of the trailing vortex sheets in the propeller slipstream can be calculated by

$$\beta_w = \tan^{-1} \left( \frac{\bar{v}_x}{r\bar{\Omega} + \bar{v}_\theta} \right). \quad (30)$$

where

$\bar{v}_x$  = mean axial velocity,

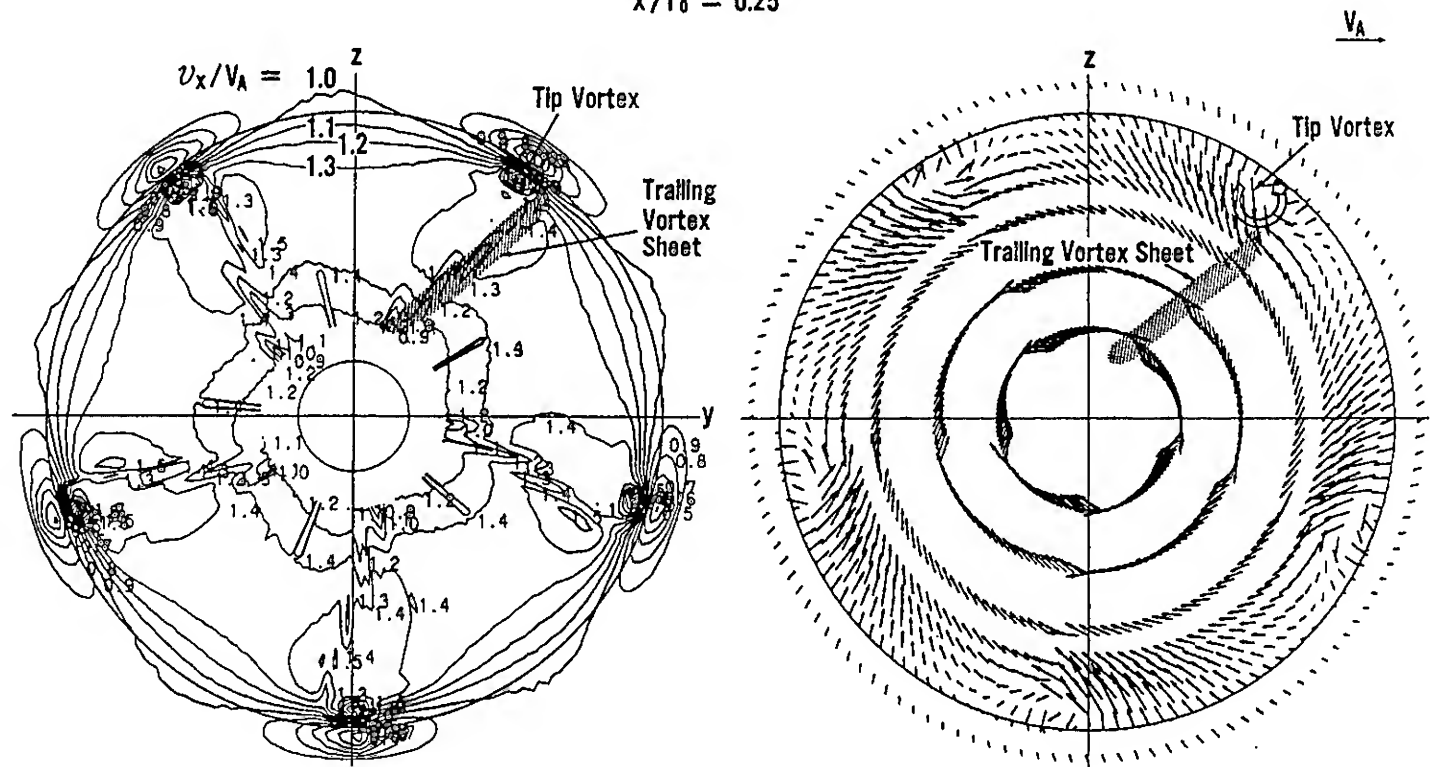
$\bar{v}_\theta$  = mean tangential velocity.

Radial distributions of the hydrodynamic pitch angle just behind the propeller for three kinds of propellers are shown in Fig.10, comparing with the geometrical pitch angles as follows :

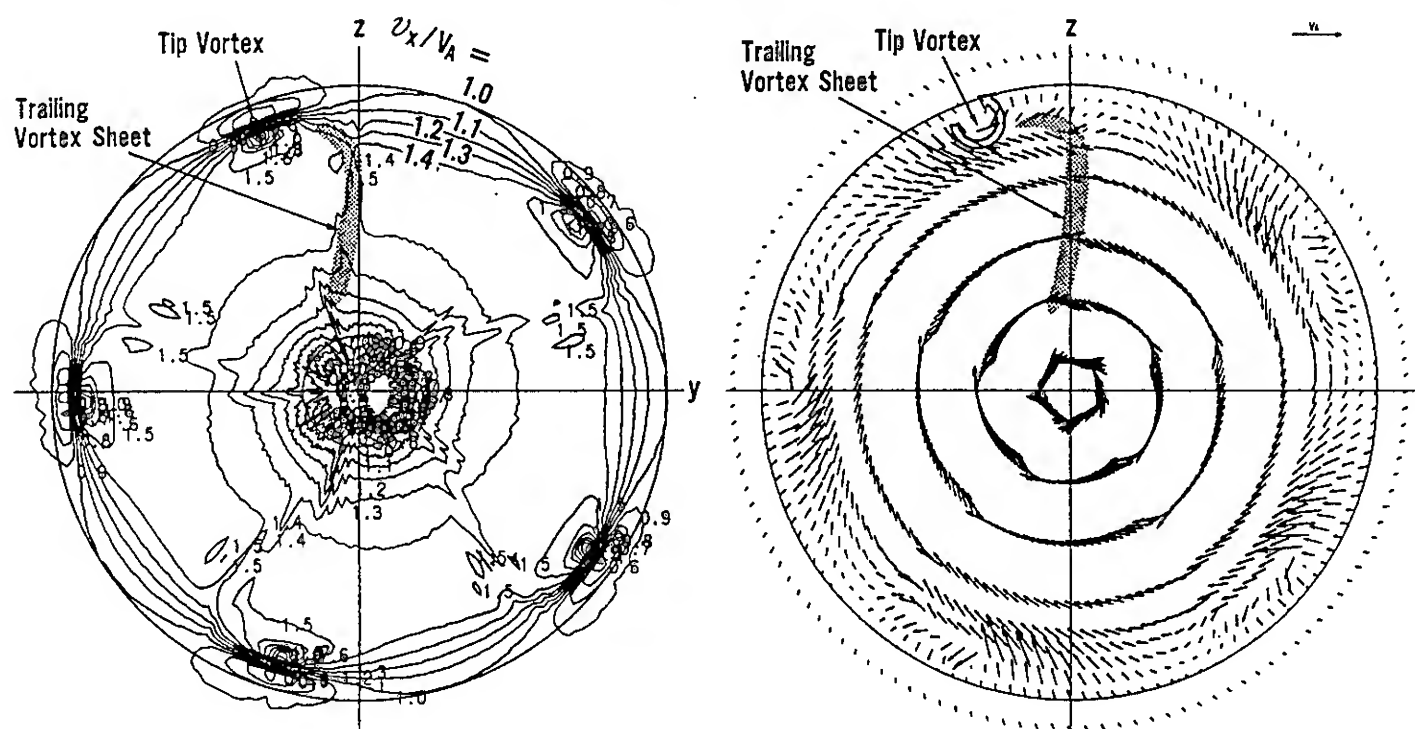


Propeller B

$x/r_0 = 0.25$



$x/r_0 = 0.50$



$x/r_0 = 1.00$

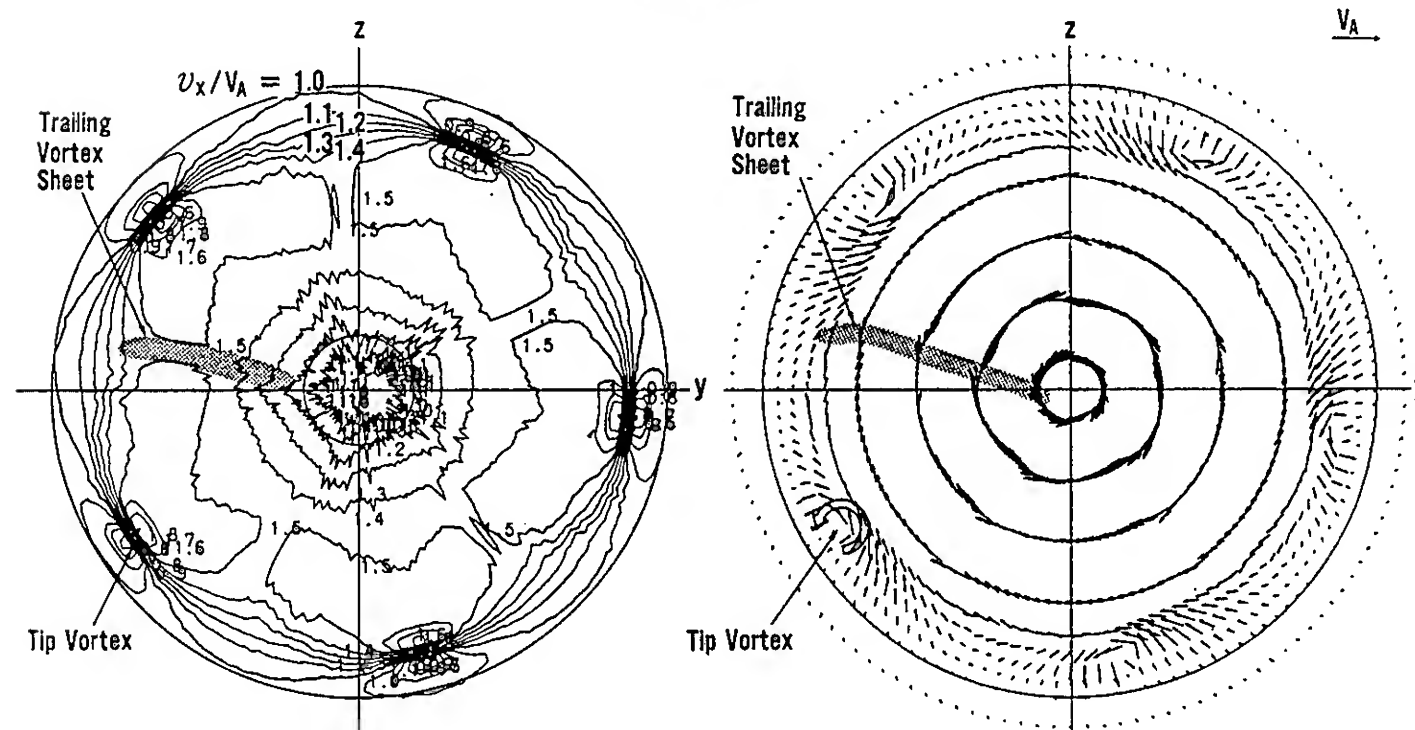


Fig.9-a Velocity distributions downstream of propeller B (  $J=0.70$  )

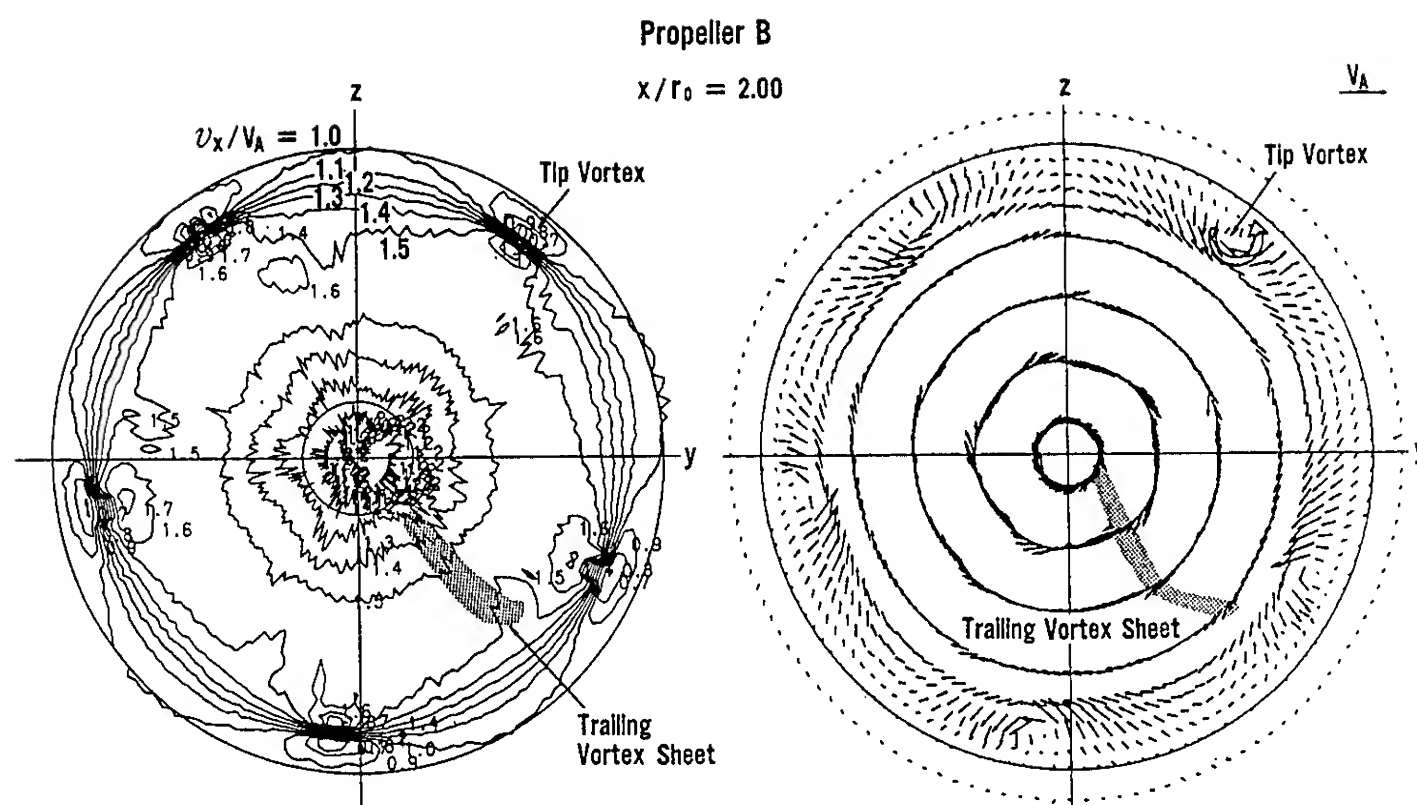


Fig.9-b Velocity distributions downstream of propeller B (  $J=0.70$  )

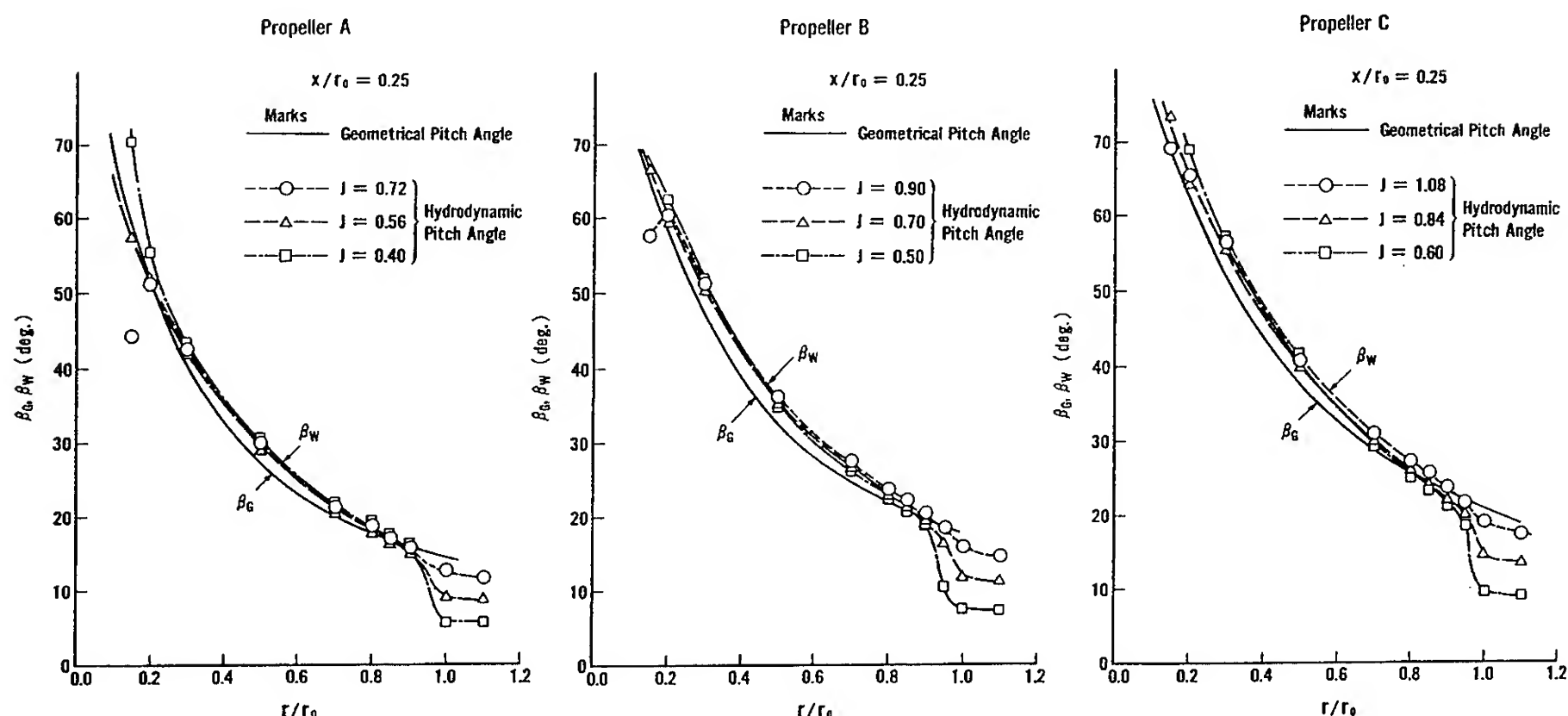


Fig.10 Comparison of radial distributions of hydrodynamic pitch angle of propeller slipstream ( Effect of propeller loading )

$$\beta_G = \tan^{-1} \left( \frac{P(r)}{2\pi r} \right), \quad (31)$$

where

$P(r)$  = geometrical pitch distribution.

In spite of difference of the operating condition of the propeller, the hydrodynamic pitch angles  $\beta_w$  are nearly constant and slightly larger than the geometrical pitch angles  $\beta_g$ . Same tendency is kept for the three propellers which are different in pitch. This is the reason why the geometrical pitch was introduced for the pitch of the ultimate trailing vortex wake in QCM [2].

The hydrodynamic pitch  $P_w(r)$  of the propeller slipstream can be obtained by

$$P_w(r) = 2\pi r \cdot \tan \beta_w. \quad (32)$$

An example of radial distributions of the hydrodynamic pitch of the slipstream is shown in Figs.11 - 13 for the propeller B. It is known that the hydrodynamic pitch increases as the distance from the propeller increases. Amount of increase in the hydrodynamic pitch becomes larger as the advance ratio decreases. This shows the tendency opposed to the conventional wake model, in which the hydrodynamic pitch of the slipstream had been assumed to be proportional to the advance coefficient [21]. Increase in the hydrodynamic pitch would be due to the contraction of the slipstream along the downstream direction. Pitch of the tip vortices is obtained from the axial variations of the angular positions of the center of the tip vortices and also plotted in Figs.11 - 13. Pitch of the tip vortices is considerably smaller than that of the inboard helical trailing vortex sheets.

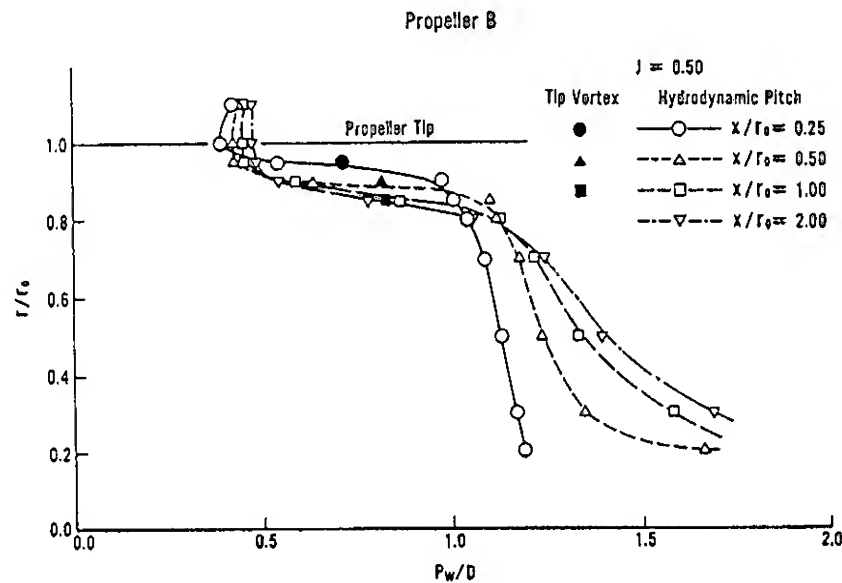


Fig.11 Variations of hydrodynamic pitch downstream of propeller B (  $J=0.50$  )

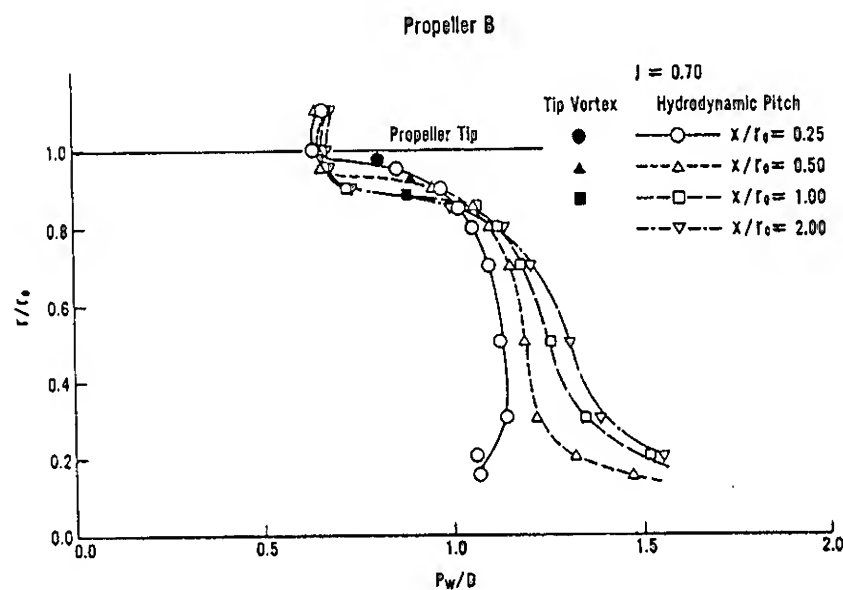


Fig.12 Variations of hydrodynamic pitch downstream of propeller B (  $J=0.70$  )

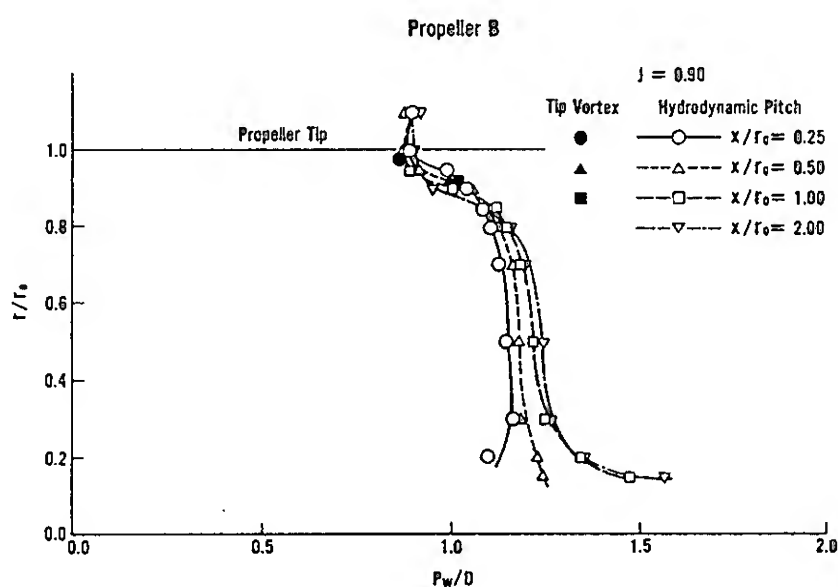


Fig.13 Variations of hydrodynamic pitch downstream of propeller B (  $J=0.90$  )

The present LDV-measurement shows that the helical trailing vortex sheets behind propeller are not always concentrated into a set of tip vortices and a single hub vortex as shown in Fig.14. The roll-up model of the trailing vortex sheets would be too simplified. In order to construct a more realistic model of the trailing vortex sheets, it is necessary to take into account the increase in pitch of the

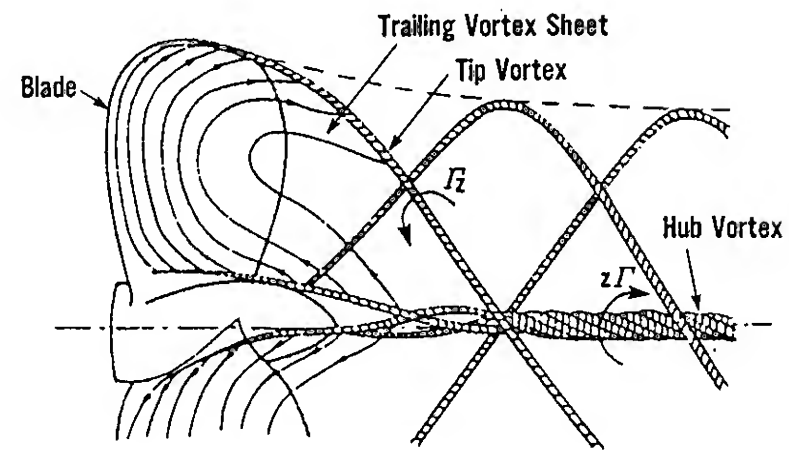


Fig.14 A model of vortex pattern of propeller ( from 16th ITTC report[28] )

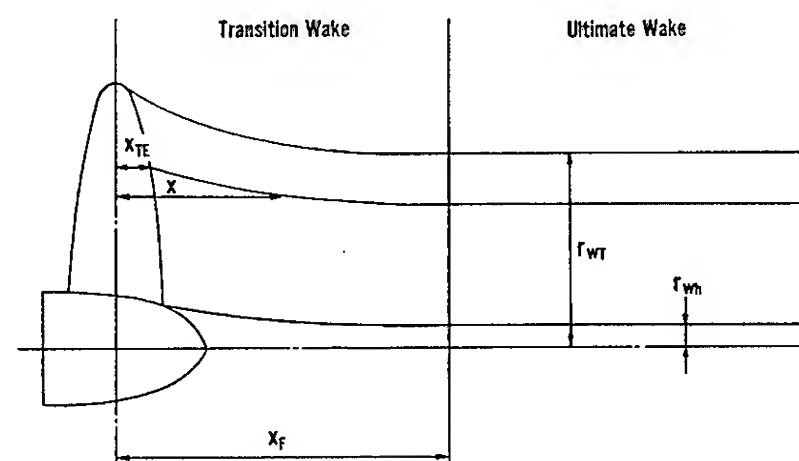


Fig.15 Model of propeller slipstream

inboard helical trailing vortex sheets and the decrease in pitch of the tip vortices near outer edge of the slipstream.

#### 4.6 Numerical Modeling of Trailing Vortex Sheet

A linear wake model of the trailing vortex sheets which was based on the geometrical pitch of blades and ignored the contraction of slipstream was used in the previous paper[20]. Based on the measured velocity distributions of the propeller slipstream, a new wake model of the helical trailing vortex sheets is considered. In the present study, the trailing vortex wake is divided into two parts, transition wake region and ultimate wake region as shown in Fig.15. Contraction and variations of pitch of the trailing vortex sheets are considered in the transition wake region. On the other hand, radial positions and pitch of the trailing vortex sheets are kept constant in the ultimate wake region.

Contraction of the propeller slipstream is considered at first. If the radial interval from the hub vortex radius  $r = r_{wh}$  to the tip vortex radius  $r = r_{wt}$  in the ultimate wake is divided into  $N_R$  small panel strips by the cosine spacing, the radii of each panel strip can be expressed as follows:

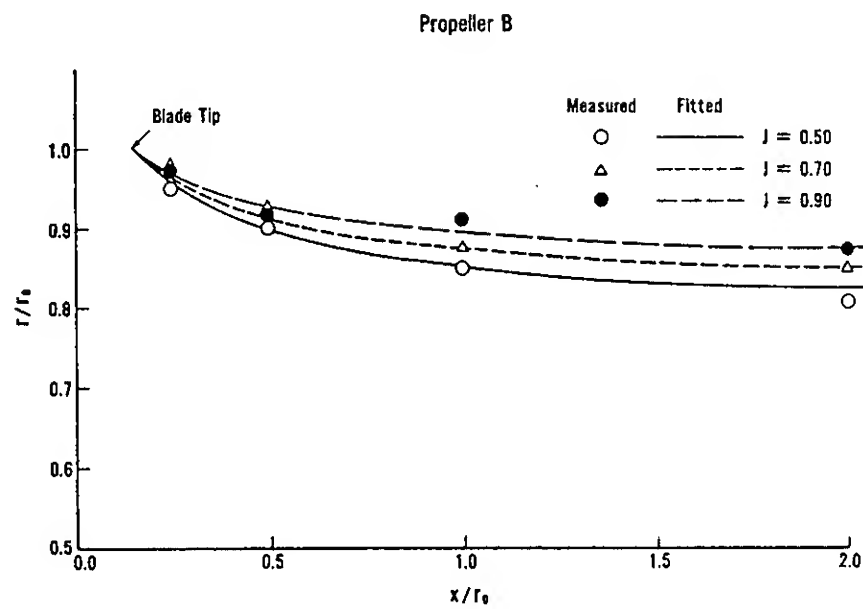


Fig.16 Comparison of contraction of slipstream

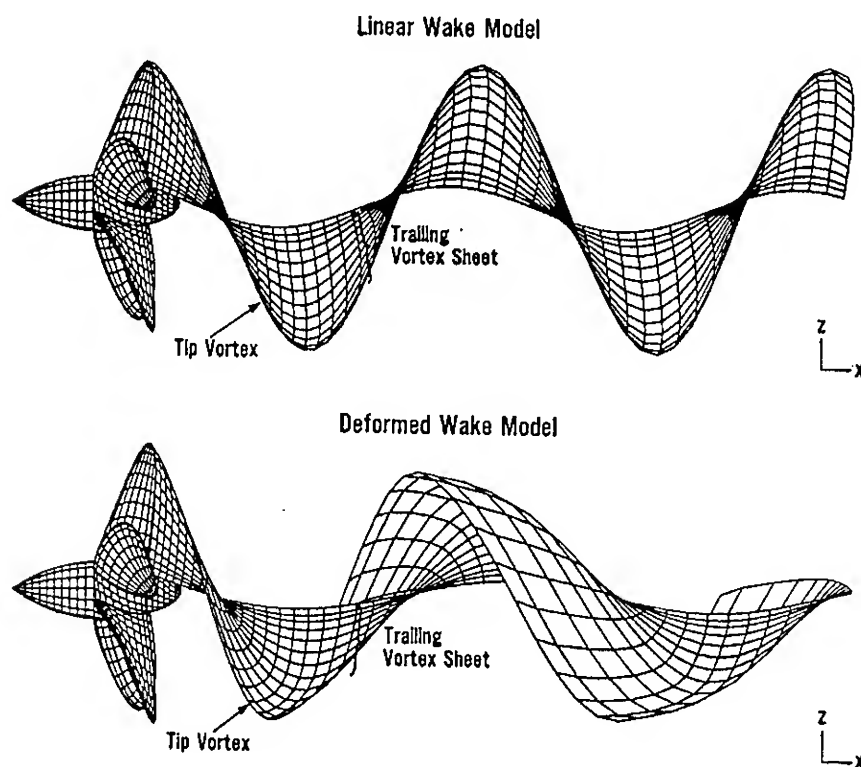


Fig.17 Comparison between linear and deformed wake models

$$r_{w\mu} = \frac{1}{2}(r_{wT} - r_{wh}) - \frac{1}{2}(r_{wT} - r_{wh}) \cos \alpha_{\mu}. \quad (33)$$

Radial positions of the trailing vortex sheet at the trailing edge of the propeller blade must coincide with those of the panel strips on the blade surface given by Eq.(10). Then variations of the radial positions of the trailing vortex panel strips in the transition wake region can be approximated by a polynomial expression as

$$r_{t\mu} = r_{\mu} - (r_{\mu} - r_{w\mu}) \cdot f_r(\xi). \quad (34)$$

where

$$f_r(\xi) = \sqrt{\xi} + 1.013\xi - 1.920\xi^2 + 1.228\xi^3 - 0.321\xi^4,$$

$$\xi = \frac{x - x_{TE}}{x_F - x_{TE}},$$

$x_{TE}$  = x-coordinate at the trailing edge of blade,

$x_F$  = x-coordinate of the point where the ultimate wake region starts.

Based on the measured results, the radius of the tip vortices in the ultimate wake region can be expressed as a function of slip ratio  $s$  as follows:

Table 3 Principal particulars of DTRC propeller models

Propeller Number	P.4679	P.4718
Diameter of Propeller	610	610
Pitch Ratio at 0.7R (mm)	1.572	0.888
Expanded Area Ratio	0.755	0.440
Bass Ratio	0.300	0.300
Number of Blades	3	3
Blade Thickness Fraction	0.099	0.069
Skew Angle (deg.)	51	25
Rake Angle (deg.)	0	0
Blade Section	NACA	NACA
Design Advance Coefficient	1.077	0.751

$$r_{wT}/r_0 = 0.887 - 0.125s, \quad (36)$$

where

$s$  = slip ratio =  $1 - J/p$ ,

$p$  = pitch ratio at 0.7 radius.

The radius of the hub vortex and the axial coordinate of the starting point of the ultimate wake are kept constant as

$$r_{wh}/r_0 = 0.1, \quad x_F/r_0 = 2.0. \quad (37)$$

Variations of the radial positions of the center of the tip vortices calculated by the above equations are shown in Fig.16, comparing with those obtained from the results of the flow measurements by LDV. It can be said that the contraction of the slipstream is approximated well by using the present formulae.

Variations of the pitch distributions in the transition and ultimate wake regions can be also expressed in the similar manner as the contraction of the propeller slipstream. The deformed wake model based on the measurements of the flow field around the propeller are compared with the conventional linear wake model in Fig.17. Large deformation of the tip vortices can be observed in the new wake model, which is similar to the wake model based on the measured wake pitch shown by Jessup [27].

## 5. NUMERICAL EXAMPLES

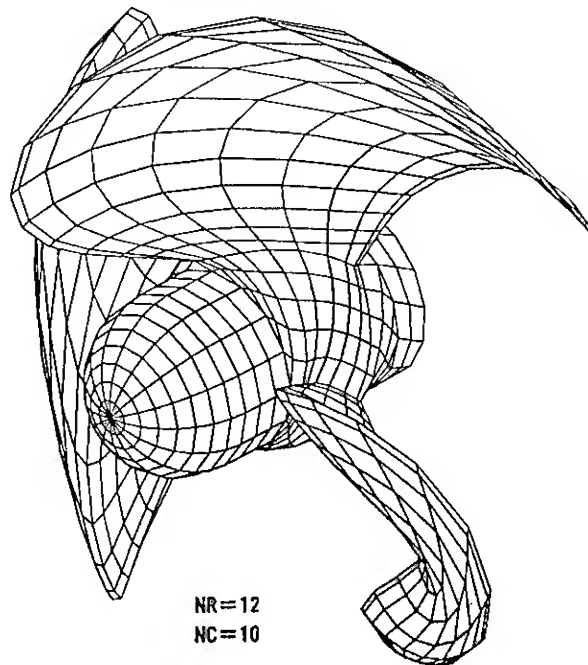
### 5.1 Pressure Distribution on Blade

In order to evaluate the accuracy and the applicability of the present panel method, David Taylor Research Center (DTRC) propeller models P.4718 and P.4679 were selected, since very precise measurements of blade surface pressure were conducted by Jessup[29,30]. Both propellers are three-bladed and different in skew. Principal particulars of the propellers are shown in Table 3.

#### 5.1.1 Effect of Iterative Kutta Condition

In the present calculation, the propeller blade surface was divided into 240 hyperboloidal quadrilateral panels per blade ( $N_R=12$ ,  $N_C=10$ ) and the hub surface was approximated by 155 panels per 1/3 sector for both propellers. Panel arrangements of the propellers are illustrated in Fig.18.

DTRC P.4679 (Upstream View)



DTRC P.4718 (Upstream View)

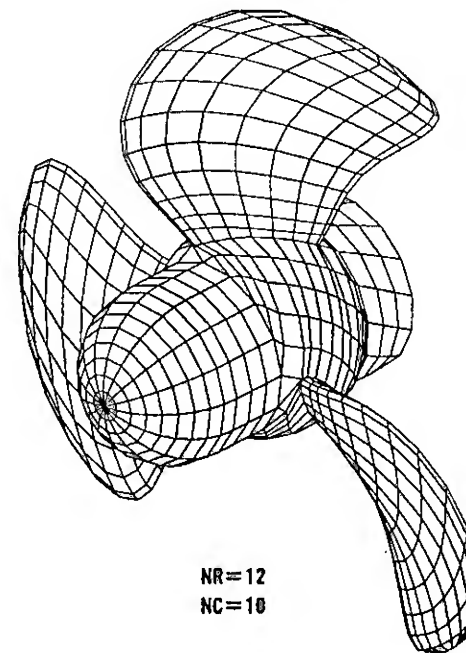


Fig.18 Panel arrangements for DTRC propeller models

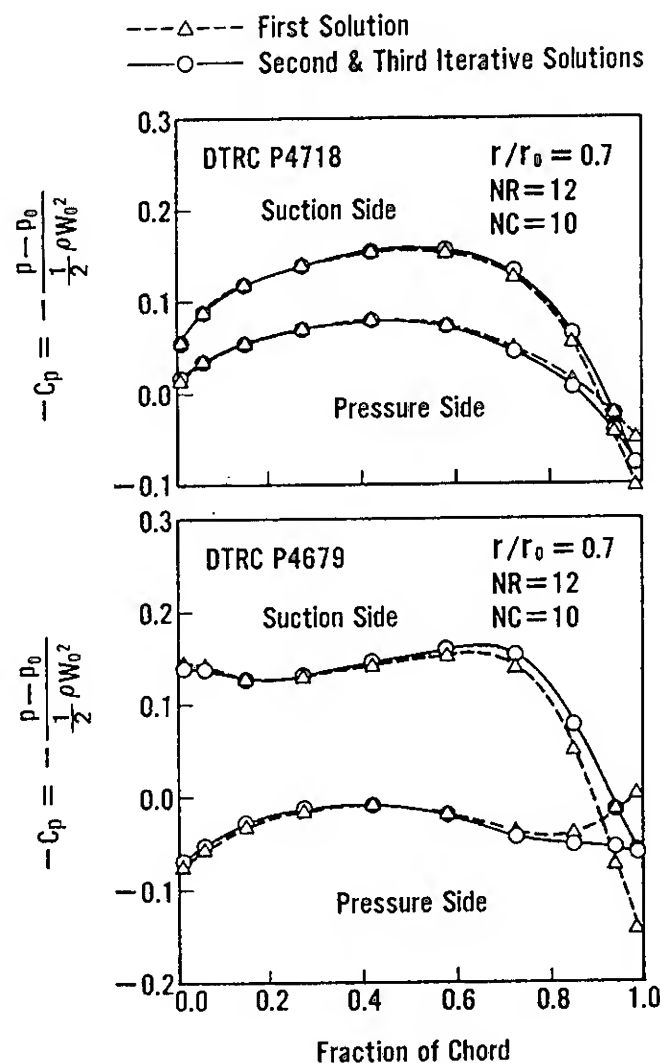


Fig.19 Comparison of chordwise pressure distributions at 0.7 radius ( effect of Kutta condition )

The chordwise pressure distributions on the blade at 0.7 radius were calculated at several steps of the iterative Kutta condition. Fig.19 shows comparison between the first, second and third solutions. The first solution which corresponds to the application of the Morino Kutta condition gives large discrepancy of the pressure on the upper and lower sides at the trailing edge, while the second and third solutions give almost equal pressure at the trailing edge by the application of the iterative Kutta condition. It can be pointed out that the convergence of the present iterative Kutta condition is very fast.

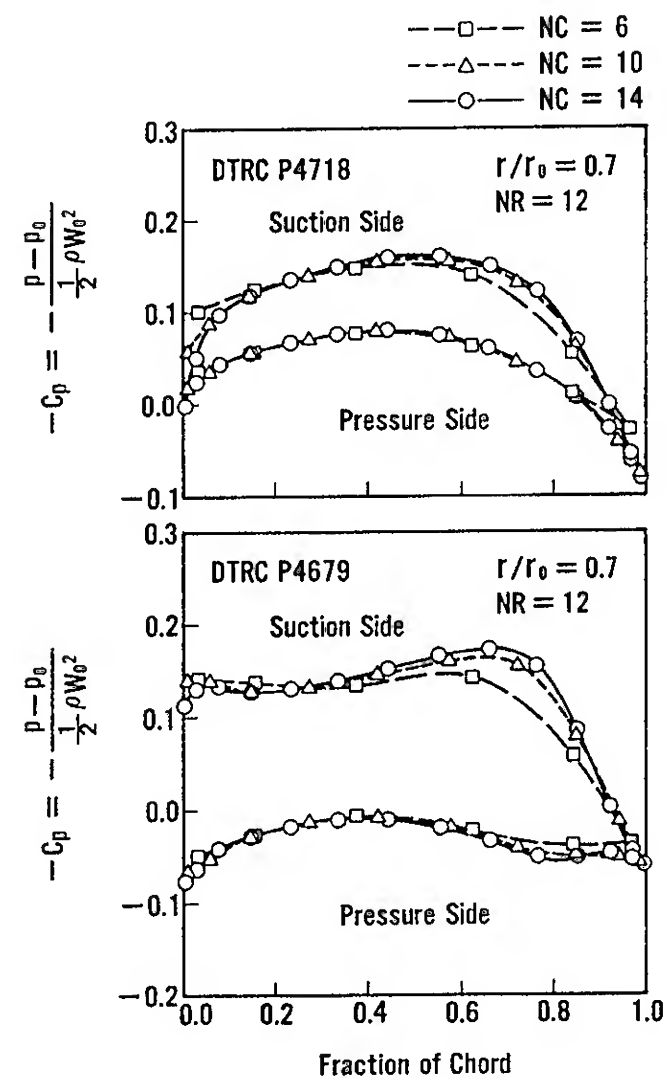


Fig.20 Comparison of chordwise pressure distributions at 0.7 radius ( effect of panel size )

### 5.1.2 Effect of Panel Size

Comparative calculations for three kinds of discretized models were conducted to investigate the effect of panel size. The propeller blade was replaced with 144 ( $N_C=6$ ), 240 ( $N_C=10$ ), and 336 ( $N_C=14$ ) panels per blade respectively and the hub was approximated by 125, 155, and 185 panels per 1/3 sector respectively.

The chordwise pressure distribution at 0.7 radius were also calculated and compared as shown in Fig.20. Results of  $N_C=6$  are fairly different from those of  $N_C=10$  and 14. There

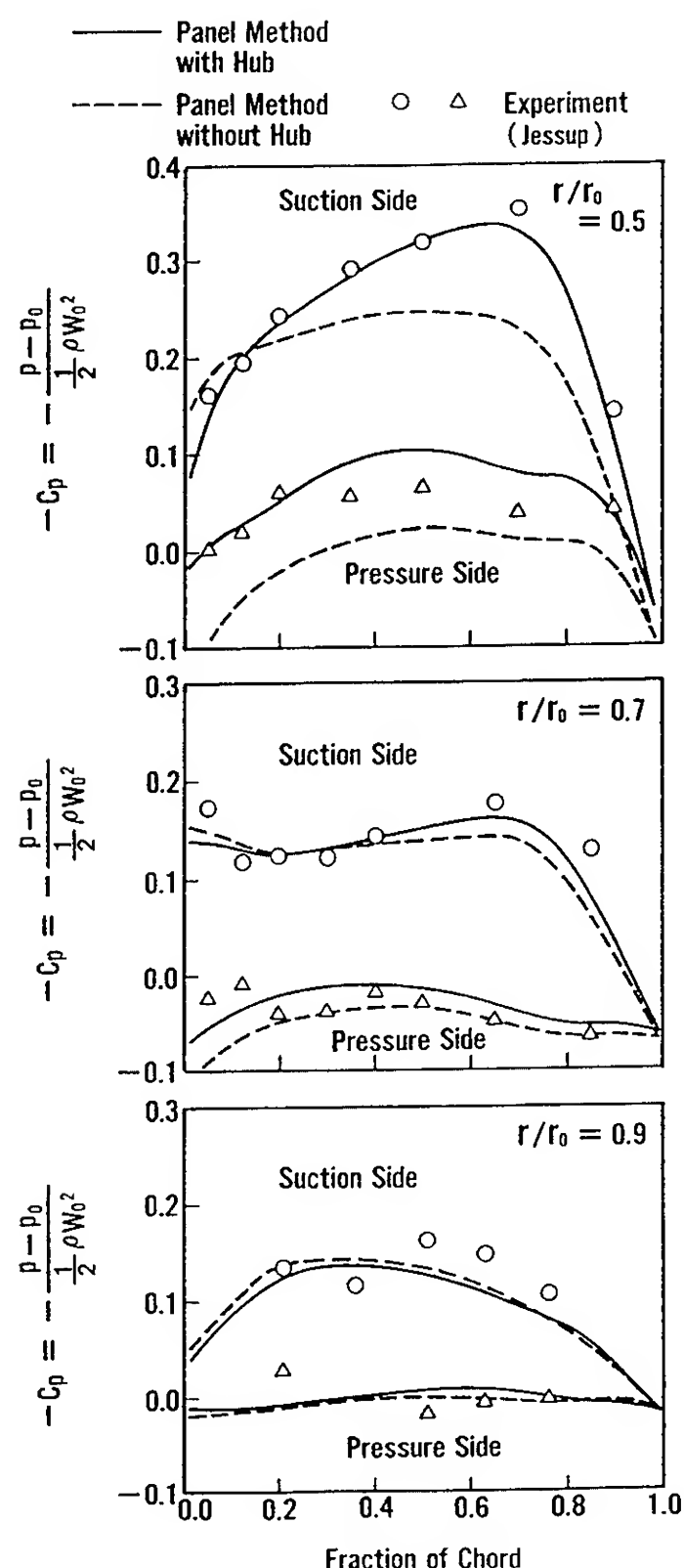


Fig.21 Comparison of chordwise pressure distributions with and without a hub for DTRC P4679

is, however, not so large discrepancy of the calculated pressure between the  $N_C=10$  and  $N_C=14$ , except at the leading edge.

### 5.1.3 Comparison with Experimental Data

The discretized models with 240 blade panels and 155 hub panels were used in the following comparison. The pressure distributions of the blades at 0.5, 0.7, and 0.9 radii were calculated with and without a hub to investigate the hub effect. In the case without the hub, end plate panels are attached to the inner blade panels in order to compose a closed surface. The calculated results were compared with experiments as shown in Figs.21 and 22. They show good agreement between the calculation with the hub and the experiments for the both propellers. On the other hand, the calculation without the hub underestimates the pressure especially at inner radii, where the hub effect is expected to be large.

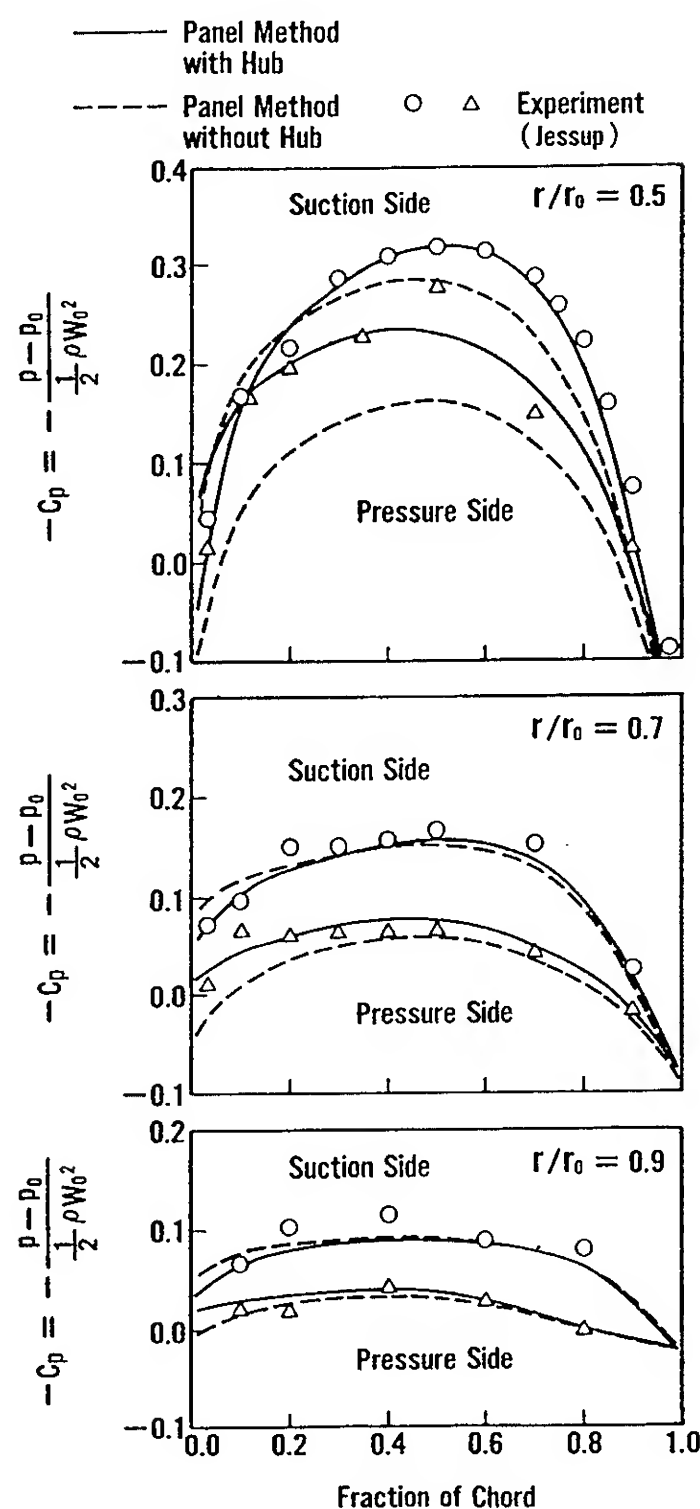


Fig.22 Comparison of chordwise pressure distributions with and without a hub for DTRC P4718

### 5.2 Field Point Velocity

In order to evaluate the accuracy of the present panel method, flow fields around propeller were calculated for both the linear wake and the deformed wake models and compared with the measurements by LDV. Each of the three propeller models A, B and C is replaced with 240 panels per blade ( $N_R=12$ ,  $N_C=10$ ) and 84 hub panels per 1/5 sector (3 rows).

Comparison of the two calculated velocity distributions with the measured ones in the upstream and downstream of the propeller B is shown in Figs.23 and 24 as the form of equi-velocity contour curves and shown in Fig.25 as the velocity vectors in a plane parallel to the propeller plane. Both calculation results of the axial velocity  $v_x$  agree well with the measurements in the upstream of the propeller. On the other hand, agreement between the calculations and the measurements of the velocities is better for the deformed wake model than for the linear wake model in the downstream of the propeller.



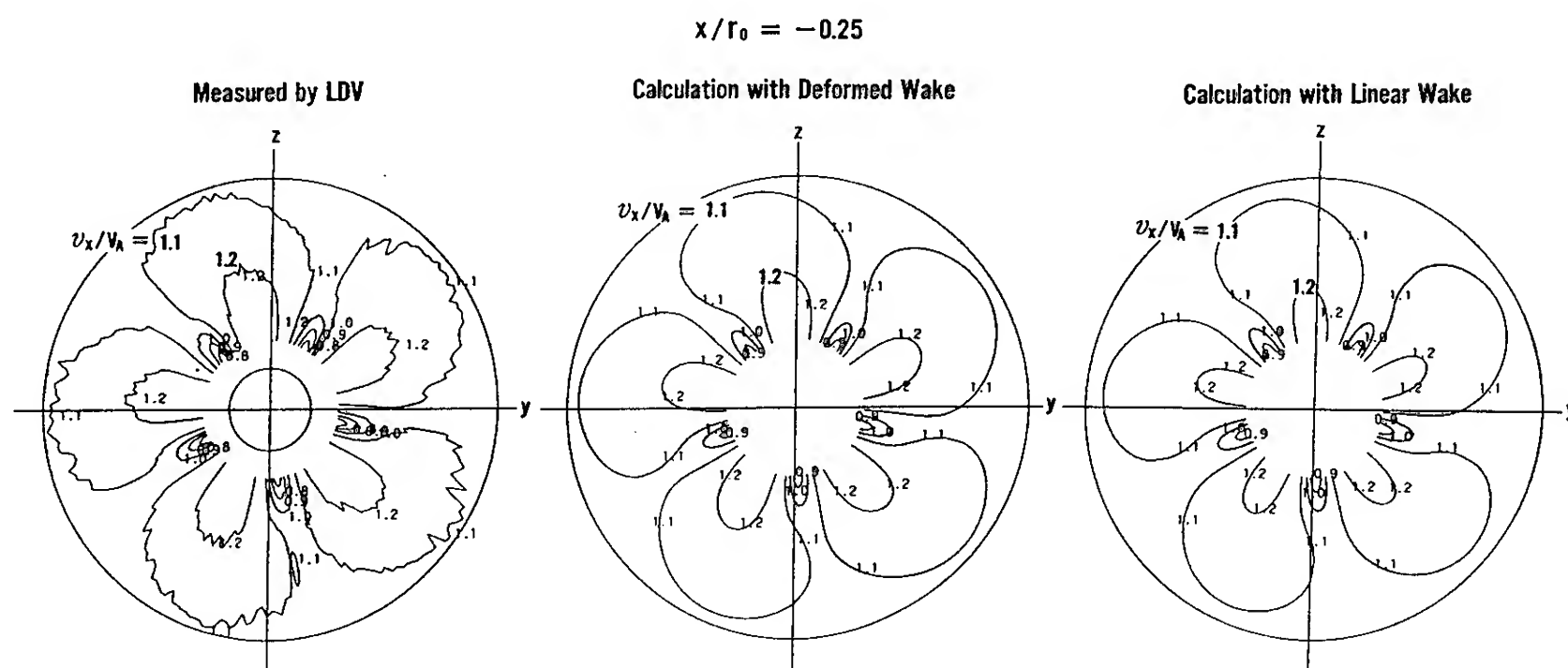


Fig.23 Comparison of axial components of velocities upstream of propeller B  
(  $J=0.70$ ,  $x/r = -0.25$  )

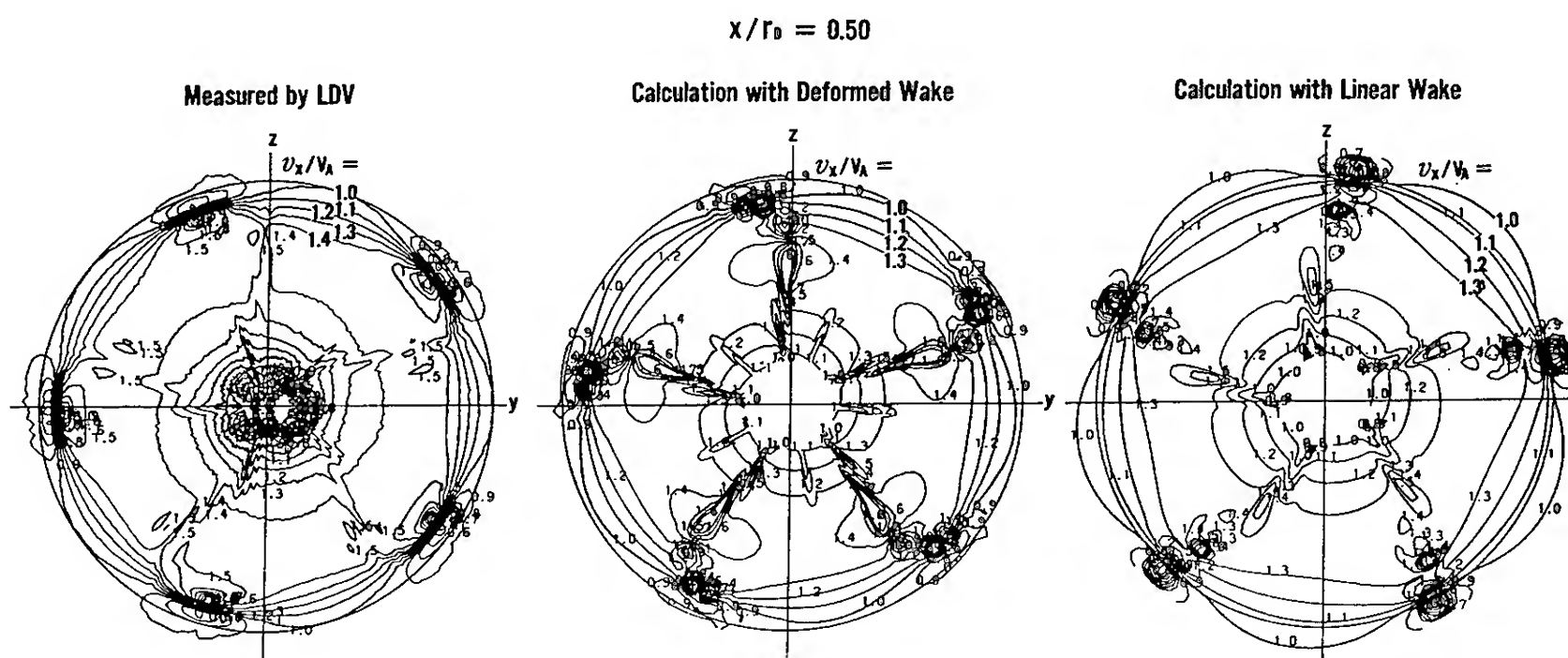


Fig.24 Comparison of axial components of velocities downstream of propeller B  
(  $J=0.70$ ,  $x/r = 0.50$  )

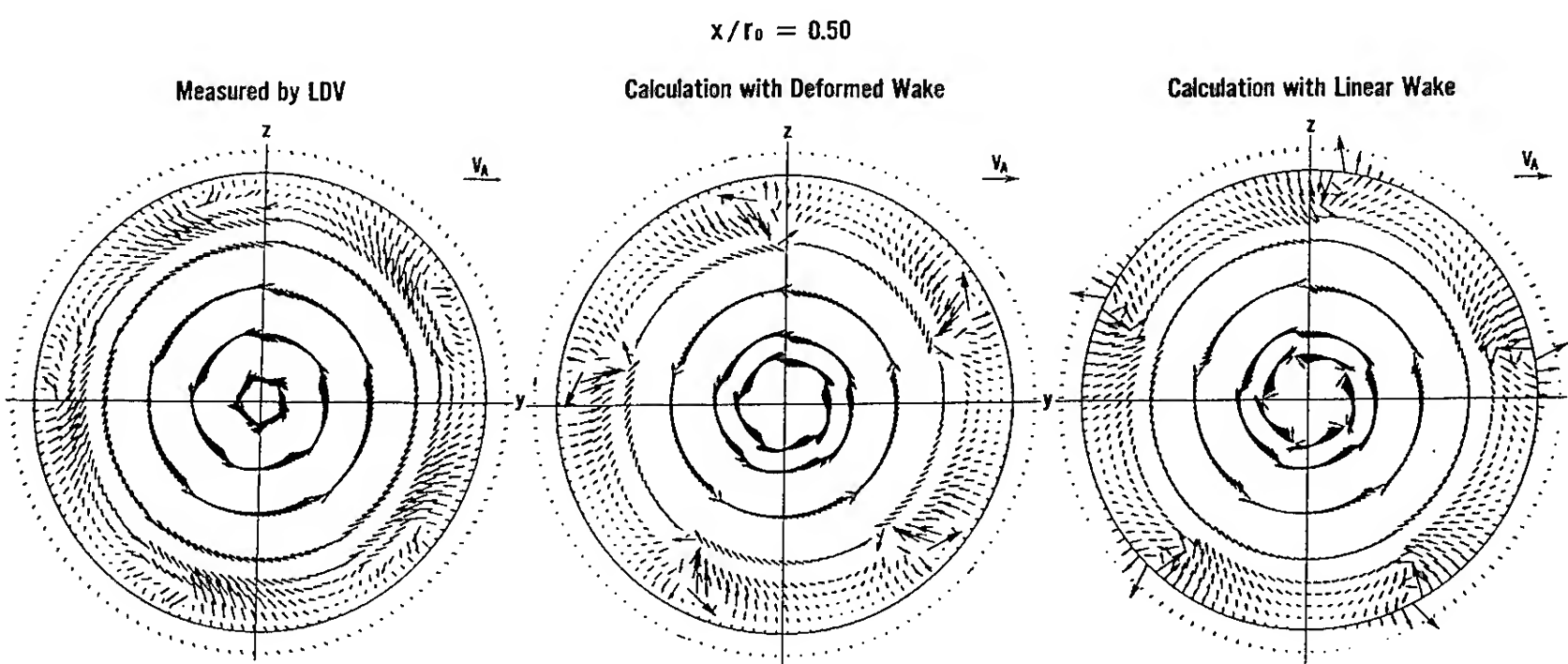


Fig.25 Comparison of cross components of velocities downstream of propeller B  
(  $J=0.70$ ,  $x/r = 0.50$  )

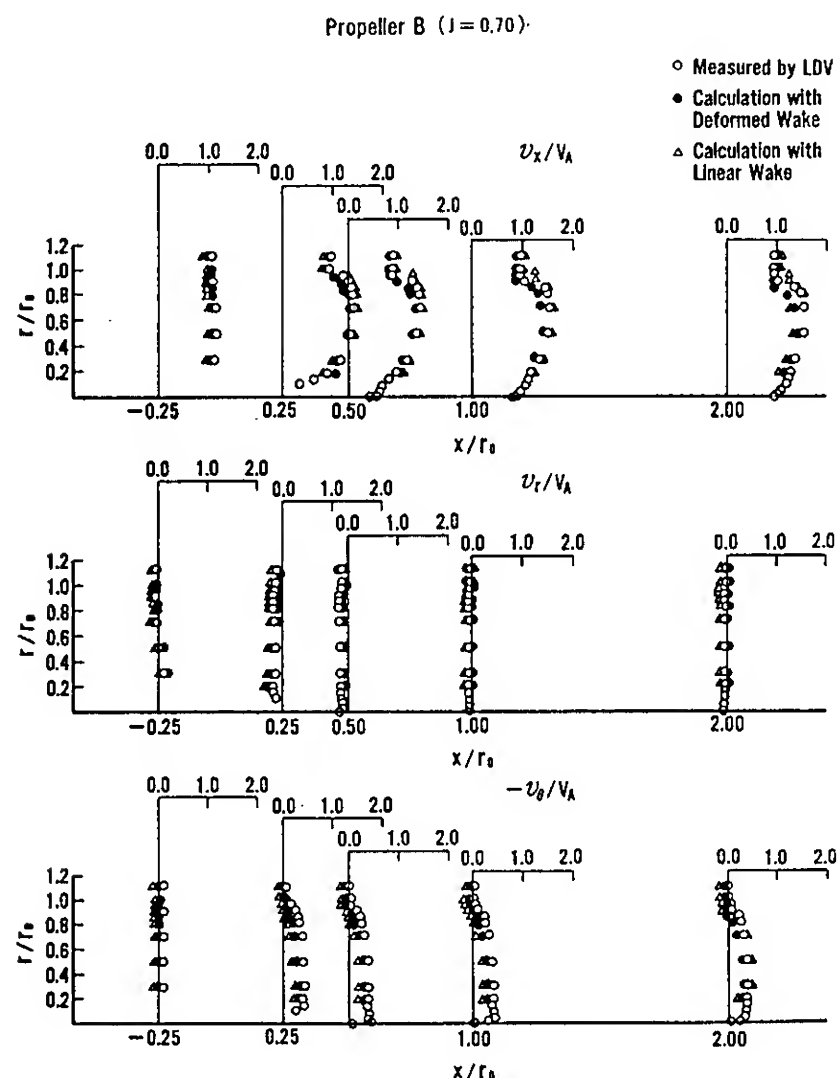


Fig.26 Comparison of circumferentially averaged velocities for propeller B

Radial distributions of the circumferentially averaged velocities calculated by the present method are compared with the measurements for the propeller model B. Calculated results using the linear wake model are also shown in Fig.26. The agreement between the calculations and the measurements is generally good. There is, however, disagreements in the axial velocities at outer radii for the calculations with the linear wake model. It can be said that close agreement between the calculations and the measurements is due to the consideration of both the contraction of the propeller slipstream and the variation of pitch of the trailing vortex sheets in the present calculation.

### 5.3 Open-Water Characteristics

The open-water characteristics of the three kinds of propellers calculated by the present panel method with the deformed wake model are shown in Figs.27 - 29, comparing with the experiments and the calculations by the previous panel method with the linear wake model [20]. The present panel method gives slightly lower values of thrust and torque than the previous panel method. This difference would be due to the effect of the contraction and the pitch variations of the trailing vortex sheets considered in the present panel method. It can be said that the open-water characteristics of propeller calculated by the present panel method with the deformed wake model are also in good agreement with the experimental data.

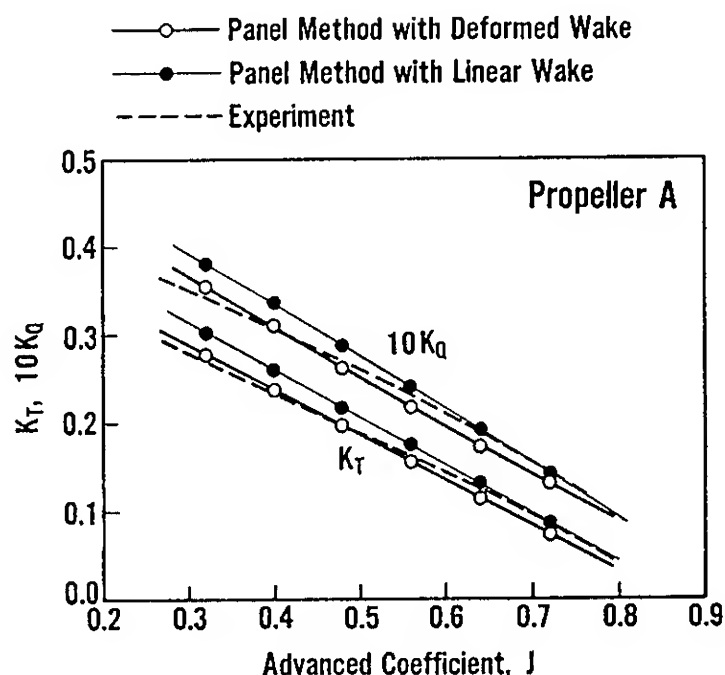


Fig.27 Comparison of open-water characteristics of propeller A

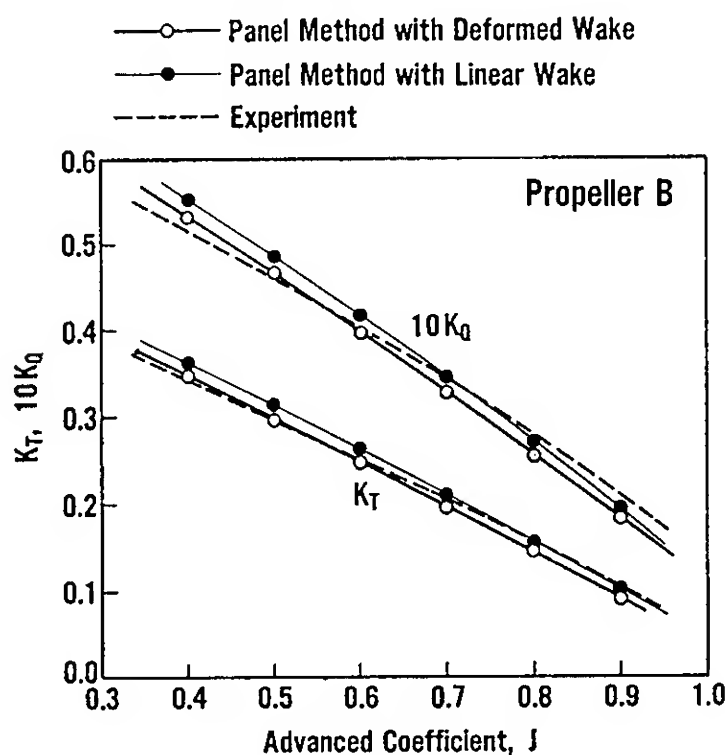


Fig.28 Comparison of open-water characteristics of propeller B

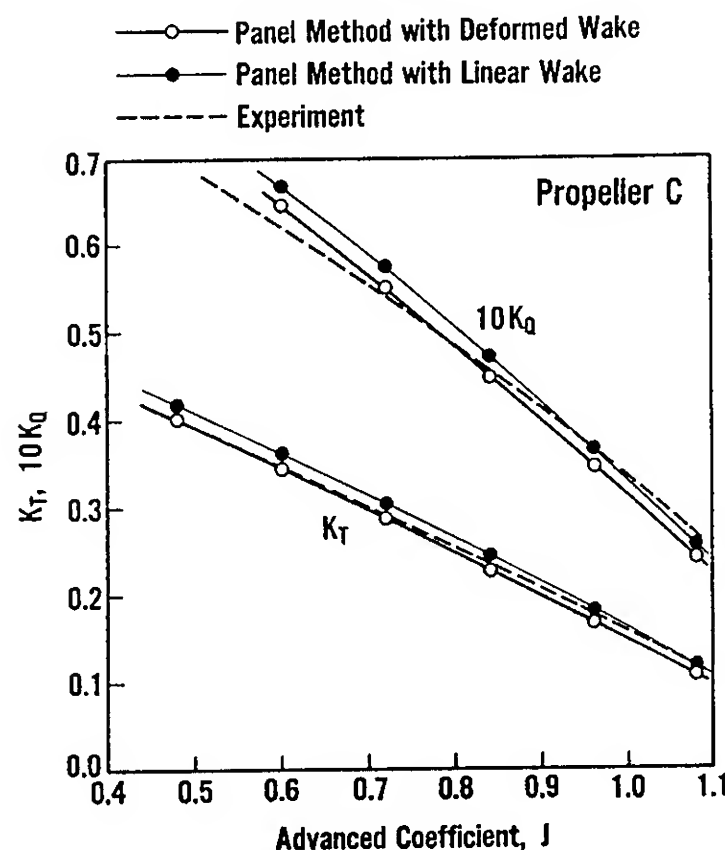


Fig.29 Comparison of open-water characteristics of propeller C

## 6. CONCLUDING REMARKS

A surface panel method to analyze the hydrodynamic properties of a propeller operating in a uniform flow was presented. Further, flow fields around three propeller models were investigated precisely by using a 3-component LDV. Based on the measured velocity distributions of the slipstream, a deformed wake model of the helical trailing vortex sheets behind propeller was proposed. Comparison of the calculations by the present panel method with the measurements led the following conclusions:

- (1) Convergence of the iterative Kutta condition used in the present method is remarkably fast.
- (2) The present panel method can predict blade pressure distributions precisely, especially at the inner radii where the thickness and hub effects are large.
- (3) Three-dimensional flow field around a propeller can be predicted by the present panel method with reasonable accuracy.
- (4) Open-water characteristics of propeller calculated by the present panel method with the deformed wake model are also in good agreement with experimental data.

## ACKNOWLEDGMENTS

The author would like to express his sincere gratitude to Professor Emeritus R. Yamazaki of Kyushu University for his initial motivation of the present work.

The present work could not have been accomplished without the cooperation of staff of the Nagasaki Experimental Tank of the Nagasaki Research and Development Center, Mitsubishi Heavy Industries, Ltd. The author feels very grateful to Dr. E. Baba, Manager of the Ship & Ocean Engineering Laboratory of the Nagasaki R & D Center, for his valuable guidance in preparing this paper.

## REFERENCES

1. Kerwin, J.E. and Lee, C.S., "Prediction of Steady and Unsteady Marine Propeller Performance by Numerical Lifting Surface Theory," Transactions SNAME, Vol.86, 1978, pp.218-253.
2. Hoshino, T. and Nakamura, N., "Propeller Design and Analysis Based on Numerical Lifting-Surface Calculations," Marine and Offshore Computer Applications, Springer-Verlag, Berlin, 1988, pp.549-574.
3. Rubbert, P.E., Saaris, G.R., et al., "A General Method for Determining the Aerodynamic Characteristics of Fan-in-Wing Configurations. Volume 1 Theory and Application," Technical Report No.67-61A, Dec. 1967, USAVLABS, Fort Eustis, Va.
4. Woodward, F.A., "Analysis and Design of Wing-Body Combinations at Subsonic and Supersonic Speeds," Journal of Aircraft, Vol.5, No.6, Nov.-Dec. 1968, pp.528-534.
5. Hess, J.L., "Calculation of Potential Flow About Arbitrary Three-Dimensional Lifting Bodies. Final Technical Report," Report MDC J5679-01, Oct. 1972, McDonnell Douglas Co., Long Beach, Calif.
6. Morino, L., "A General Theory of Unsteady Compressible Potential Aerodynamics," CR-2464, Dec. 1974, NASA.
7. Morino, L., Chen, L.-T. and Suciu, E.O., "Steady and Oscillatory Subsonic and Supersonic Aerodynamics around Complex Configurations," AIAA Journal, Vol.13, No.3, Mar. 1975, pp.368-374.
8. Suciu, E.O. and Morino, L., "A Nonlinear Finite-Element Analysis of Wings in Steady Incompressible Flows With Wake Roll-Up," AIAA Paper 76-64, 14th Aerospace Sciences Meeting, Washington, D.C., Jan. 1976.
9. Johnson, F.T., "A General Panel Method for the Analysis and Design of Arbitrary Configurations in Incompressible Flows," CR-3079, May 1980, NASA.
10. Suzuki, S. and Washizu, K., "Calculation of Wing-Body Pressures in Incompressible Flow Using Green's Function Method," Journal of Aircraft, Vol.17, No.5, May 1980, pp. 326-331.
11. Maskew, B., "Prediction of Subsonic Aerodynamic Characteristics: A Case for Low-Order Panel Methods," Journal of Aircraft, Vol.19, No.2, Feb. 1982, pp.157-163.
12. Yanagizawa, M., "Calculations for Aerodynamic Characteristics on a 3-D Lifting Body in Subsonic Flow Using Boundary Element Method," TR-835, Sept. 1984, National Aerospace Laboratory, Mitaka, Japan.
13. Ling, Z., Sasaki, Y. and Takahashi, M., "Analysis of Three-Dimensional Flow Around Marine Propeller by Direct Formulation of Boundary Element Method (1st Report: in Uniform Flow)," Journal of the Society of Naval Architects of Japan, Vol.157, June 1985, pp.85-97.
14. Hess, J.L. and Valarezo, W.O., "Calculation of Steady Flow About Propellers Using a Surface Panel Method," Journal of Propulsion and Power, Vol.1, No.6, Nov.-Dec. 1985, pp.470-476.
15. Feng, J. and Dong, S., "A Panel Method for the Prediction of Unsteady Hydrodynamic Performance of the Ducted Propeller with a Finite Number of Blades," Proceedings of the International Symposium on Propeller and Cavitation, Wuxi, Apr. 1986, pp.126-135.
16. Koyama, K., Kakugawa, A. and Okamoto, M., "Experimental Investigation of Flow Around a Marine Propeller and Application of Panel Method to the Propeller Theory," Proceedings of the 16th Symposium on Naval Hydrodynamics, Berkeley, Calif., July 1986, pp.289-311.
17. Chen, S.H. and Williams, M.H., "A Panel Method for Counter Rotating Propfans," AIAA-87-1890, AIAA/ASME/SAE/ASEE 23rd Joint Propulsion Conference, San Diego, Calif., June-July 1987.
18. Yang, C.-I. and Jessup, S.D., "Marine Propeller Analysis with Panel Method," AIAA-87-2063, AIAA/ASME/SAE/ASEE 23rd Joint Propulsion Conference, San Diego, Calif., June-July 1987.
19. Kerwin, J.E., Kinnas, S.A., Lee, J.T. and Shih, W.Z., "A Surface Panel Method for Hydrodynamic Analysis of Ducted Propellers," Transactions SNAME, Vol.95, 1987, pp.93-122.
20. Hoshino, T., "Hydrodynamic Analysis of Propeller in Steady Flow Using a Surface

- Panel Method," Journal of the Society of Naval Architects of Japan, Vol.165, June 1989, pp.55-70.
21. Hanaoka, T., "Fundamental Theory of a Screw Propeller ( Especially on Munk's Theorem and Lifting-Line Theory )," Report of Ship Research Institute, Vol.5, No.6, 1968, pp.1-41.
  22. Min, K.S., "Numerical and Experimental Methods for the Prediction of Field Point Velocities around Propeller Blades," Report 78-12, June 1978, Dept. of Ocean Engineering, MIT, Cambridge, Mass.
  23. Kobayashi, S., "Propeller Wake Survey by Laser-Doppler Velocimeter," Proceedings of the International Symposium on Application of Laser-Doppler Anemometry to Fluid Mechanics, Lisbon, 1982.
  24. Jessup, S.D., Schott, C., Jeffers, M. and Kobayashi, S., "Local Propeller Blade Flows in Uniform and Sheared Onset Flow Using LDV Techniques," Proceedings of the 15th Symposium on Naval Hydrodynamics, Hamburg, Germany, Sept. 1984, pp.221-237.
  25. Hoshino, T. and Oshima, A., "Measurement of Flow Field around Propeller by Using a 3-Component Laser Doppler Velocimeter (LDV)," Mitsubishi Technical Review, Vol.24, No.1, Feb. 1987, pp.46-53.
  26. Blaurock, J. and Iammers, G., "The Influence of Propeller Skew on the Velocity Field and Tip Vortex Shape in the Slipstream of Propeller," Proceedings of the SNAME Propellers '88 Symposium, Virginia Beach, Va., Sept. 1988.
  27. Jessup, S.D., "An Experimental Investigation of Viscous Aspects of Propeller Blade Flow," PhD Thesis, The School of Engineering and Architecture, The Catholic University of America, Washington, D.C., 1989.
  28. Report of Propeller Committee, Proceedings of the 16th ITTC, Leningrad, Sept. 1981, pp.61-128.
  29. Jessup, S.D., "Measurement of the Pressure Distribution on Two Model Propellers," DTNSRDC-82/035, July 1982, David Taylor Research Center, Bethesda, Md.
  30. Jessup, S.D., "Further Measurements of Model Propeller Pressure Distributions Using a Novel Technique," DTNSRDC-86/011, May 1986, David Taylor Research Center, Bethesda, Md.

## APPENDIX

### Equal Pressure Kutta Condition

The so-called Kutta condition is a physical condition that the velocity at the trailing edge of the blade should be finite. This physical Kutta condition cannot be applied directly to a general numerical procedure. Therefore, three forms of numerical Kutta condition for three-dimensional lifting bodies were proposed by Hess as follows (Ref.5, p.36):

- (a) A stream surface of the flow leaves the trailing edge with a direction that is known, or at least can be approximated.

- (b) As the trailing edge is approached, the surface pressures ( velocity magnitudes ) on the upper and lower surfaces have a common limit.
- (c) The source density at the trailing edge is zero.

Morino introduced an approximate Kutta condition that the strength of the doublet in the wake surface is equal to the difference in the value of the doublet strength of the upper and lower panels adjacent to the trailing edge[6, 7]. This can be expressed as

$$\Delta\phi = \Delta\phi_{TE}. \quad (38)$$

However, this form of the Kutta condition was found to contain a fundamental error when the free stream from the trailing edge had a cross flow component as pointed out by Kerwin et al. [19] and the present author [20]. Therefore, in the present study the Kutta condition (b) is employed, where the pressure is same at the two control points of the upper and lower panels adjacent to the trailing edge. The equal pressure Kutta condition becomes non-linear function with respect to the unknown potential  $\phi$  and cannot be solved directly. Ling et al. [13] introduced Simplex method to satisfy the equal pressure Kutta condition iteratively. However, that method takes many iterative calculations for obtaining a convergent solution in general. A Newton-Raphson iterative procedure is, therefore, adopted in the present method for faster convergence.

The equal pressure Kutta condition will be applied to determine the unknown  $\Delta\phi_j$  of the doublet strength in the wake surface. In the numerical calculation, the Kutta condition that the pressure difference at the control points on the upper and lower blade panels adjacent to the trailing edge should be zero can be expressed as

$$\Delta p_i = p_{+TE}(P_i) - p_{-TE}(P_i) = 0 \quad (39)$$

$$\text{for } i = 1, 2, \dots, N_R,$$

where subscript TE indicates the value at the control point of each panel adjacent to the trailing edge. If we define the derivative

$$A_{ij} = \frac{\partial(\Delta p_i)}{\partial(\Delta\phi_j)}, \quad (40)$$

Eq.(39) can be solved iteratively by solving the following sets of linear equations. Namely, using the values of  $\Delta\phi_j^{(m)}$  and  $\Delta p_i^{(m)}$  at the m-th step, the equation for the next step solution  $\Delta\phi_j^{(m+1)}$  can be derived from Eq.(40) as

$$\sum_{j=1}^{N_R} A_{ij} [\Delta\phi_j^{(m+1)} - \Delta\phi_j^{(m)}] = -\Delta p_i^{(m)} \quad (41)$$

for  $i = 1, 2, 3, \dots, N_R$ .

The above process is repeated until the value of the pressure difference  $\Delta p_i^{(m)}$  becomes zero within the desired accuracy. The initial guess of the solution  $\Delta\phi_j^{(1)}$  was obtained by applying the Morino Kutta condition given by Eq.(38).

## DISCUSSION

Jinzhang Feng  
Pennsylvania State University, USA (China)

1. Numerical prediction of a propeller wake is very difficult because it demands an adequate representation of the deformed wake vortex. With the experience the author has, would he comment on the feasibility of using an empirical model with a few open parameters, such as the one proposed in Eq. (33) to predict the flow field behind the propeller?

2. In both Figures 21 and 22, the hub effect on pressure distribution at sections  $r/r_0 > 0.5$  is larger than expected. Usually one would assume the hub effect is very much confined to  $r/r_0 < 0.5$  region and to a less extent. Is this because in his computation the author used a conical cap proceeding the propeller disk to close the hub?

## AUTHORS' REPLY

(1) The present empirical wake model was based on the LDV-measurements of slipstream for a few propellers and therefore applicability of the wake model would be limited. Further measurements and/or calculations of propeller slipstream for various propellers would be indispensable to construct more general wake model. (2) A conical cap proceeding the propeller was not only used in the calculations but also in the measurements of pressure distributions and the measurements were conducted under the same condition. The reason why the hub effect on the pressure distribution is larger than expected would be large hub to diameter ratio for the controllable pitch propeller.

## DISCUSSION

Gun iL Choi  
Hyundai Heavy Industries Co., Ltd, Korea

According to your expression the contraction of the propeller slipstream in the ultimate wake region is obtained as follows:

$$\begin{aligned} \text{for the case of neglecting slip ratio } r_{wT}/r_0 &= 0.887 \\ \text{for the case of } J = 0 \quad r_{wT}/r_0 &= 0.762 \end{aligned}$$

The above calculations indicate that the contraction of slipstream in the lightly loaded propeller will be more than 10% which is difficult to understand.

## AUTHORS' REPLY

In reply to the question by Mr. Choi, according to the momentum theory, the radius of propeller slipstream is expressed as follows:

$$\begin{aligned} r_{wT} &= 1.0 \quad \text{for the case of slip ratio} = 0.0 \\ r_{wT} &= 0.707 \quad \text{for the case of slip ratio} = 1.0 \end{aligned}$$

The above values are different from those obtained by Eq. (36) because of extreme off-design conditions of the propeller, however, the tip radius given by Eq. (36) is close to the measured one as shown in Fig. 16.

## DISCUSSION

William B. Morgan  
David Taylor Research Center, USA

The author draws the conclusion that his panel method with his deformed wake model is in good agreement with experimental data. However, the data given in Figs. 27 through 29 would indicate that there would be little improvement with the deformed wake model. Does the author have any comment? Also, the deformed wake model is apparently based on measurements. Did the author try to base the wake model on calculated deformed wake? It would appear that even a lifting line model could be used to calculate the deformed wake. Also, in Figure 16, how much did the contraction of the slipstream deviate from a momentum theory analysis?

## AUTHORS' REPLY

(1) The effect of wake model on the integrated values of pressure distribution over the surface such as thrust and torque of a propeller would be small but the flow fields around propeller especially in slipstream were greatly affected by wake model as shown in Figs. 23-25. Therefore, wake model would become important in solving the interaction problem between two propulsors such as counter-rotating propellers. (2) Amount of contraction or hydrodynamic pitch of slipstream in the ultimate wake region would be calculated by a momentum theory or a lifting-line theory. However, variations of the radial positions and the pitch distributions of the trailing vortices in the transition wake region would be too difficult to be estimated by numerical calculations only. Therefore, a deformed wake model based on LDV-measurement was proposed in the present paper.

## DISCUSSION

Wolfgang Faller  
Sulzer-Escher Wyss GmbH Ravensburg, Germany

On Fig. 24 of your paper you show calculated velocities in the tip vortex regions. Does your method provide pressure values in these regions also and/or have you compared these pressures to tip vortex cavitation data obtained from your experiments?

## AUTHORS' REPLY

I have never compared the calculated pressure with the results of observation of tip vortex cavitation because the present panel method could not calculate the pressure inside the tip vortex. Viscous effect would be dominant for the inception of tip vortex cavitation and therefore must be considered in the calculation method to estimate the tip vortex cavitation.



## DISCUSSION

Kuniharu Nakatake  
Kyushu University, Japan

I admire your elaborate experimental work and calculations. I have two questions: (1) Do you have any explanation about the smaller pitch of tip vortices? (2) Even your modified wake model does not express the hub vortex. Do you have any idea?

## AUTHORS' REPLY

(1) The smaller pitch of tip vortices would be due to the strong induced velocities by the strong tip vortices themselves. (2) A wake model including the hub vortex were considered, in which the hub vortex started from the end of hub surface as shown in Fig. A. However, propeller characteristics were not so affected by consideration of the hub vortex. Precise measurement of flow fields around a hub vortex would be indispensable to construct a more realistic hub vortex model.

## DISCUSSION

Shi-Tang Dong  
China Ship Scientific Research Center, China

Congratulate on author's excellent work. I would like to ask two questions: (1) You calculate the total forces acting on the propeller by integrating the pressure distribution on the blade surface. How do you ensure the accuracy in calculating the force acting on the nose region of the leading edge of the blade section especially at off design condition since the direction of surface normal changes rapidly and the shape is rather thin and sharp at the leading edge, and there exists pressure peak there at off-design condition? (2) Have you any special consideration in arranging the panels at the tip region for highly skewed propeller? Thank you.

## AUTHORS' REPLY

First of all, I would like to thank all discussers for their interest and their stimulating comments on my paper. In reply to the questions by Prof. Dong: (1) As Prof. Dong pointed out, the direction of surface normal and the surface pressure change rapidly at the leading edge. Therefore, the cosine spacing was adopted for the chordwise spacing of the blade panels, which concentrated the panels at the leading edge. Then the number of chordwise divisions  $N_c = 10$  or  $14$  was enough for calculating the force acting on the blade as shown in Fig. 22. (2) Twisting of the panel becomes large at the tip region especially for tip unloaded and highly skewed propeller. Therefore, the cosine spacing was also used for the radial spacing to concentrate the panels at the tip region.

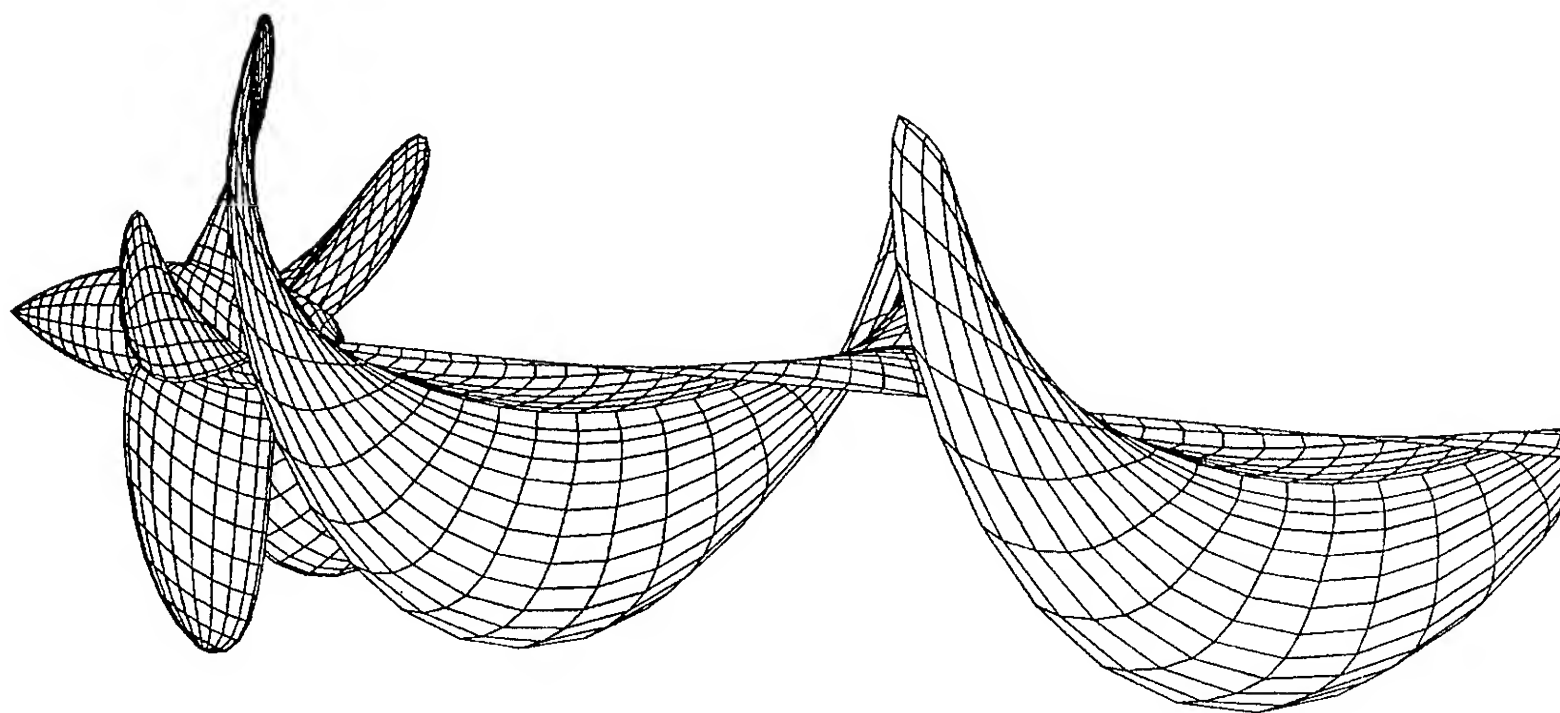


Fig.A New modeling of trailing vortex wake including hub vortex



# **Cavity Thickness on Rotating Propeller Blades - Measurements by Two Laser Beams**

H.D. Stinzing (VWS, Berlin Model Basin, Germany)

## **ABSTRACT**

A prediction of propeller-induced vibratory hull pressures needs computation of the cavity volume, which depends on blade geometry and operating conditions of the propeller. In order to verify or, if necessary, to improve the theoretical model developed by the Hamburg Ship Model Basin (HSVA), measurements of thickness and extension of the blade cavitation at two propeller models of different blade geometry were executed by a laser technique, and the results were compared with those following from computations.

Extensive preliminary studies for optimizing the laser technique were necessary in order to develop a precise and easily applicable method. The essential feature of the new procedure is the use of two laser beams of constant intensity intersecting at the surfaces of the cavity and of the propeller blades, resp.

## **INTRODUCTION**

As a result of the efforts to increase the delivered power of ship propellers, to build lighter hulls and to use propellers with larger diameters ship hull vibrations are an increasing problem. These vibrations are mainly caused by forces acting on the propeller. The non-uniform wake field of the ship results in periodically changing load of the propeller blades which affects the hull through the propeller shaft. In addition, the propeller produces pressure fluctuations which are transferred to the hull through the water.

An essential reason for the propeller-induced pressure fluctuations is the nonsteady propeller cavitation. The extension and the thickness of the cavity on a propeller blade vary according to the blade position and the

operating conditions of the propeller. These volume variations cause pressure fluctuations and thereby vibrations at the afterbody.

The prediction of such propeller-induced pressure fluctuations thus requires the calculation of the cavity volume. For this the Hamburg Ship Model Basin (HSVA) has developed a theoretical model that had to be confirmed and, if necessary, improved by measurements executed by the Berlin Model Basin (VWS).

The aim of the investigations discussed below was to provide a method to measure the cavity thickness on rotating propeller blades by using the advantages of laser light and to apply this technique to two different propeller models operated in the small cavitation tunnel of the VWS. The results had to be compared with calculations made by the HSVA.

## **MEASURING TECHNIQUES**

### **Basic Methods**

The simplest methods to "measure" the cavity thickness are visual observation or simple photographs taken at stroboscopic illumination of the propeller. Both provide useful information about the shape of the cavity, its thickness, however, can only be roughly estimated.

Slightly more accurate results are achieved by stereo-photogrammetry which gives the three-dimensional shape of the cavity. This technique, however, still may produce errors as high as 100 percent (1). Another disadvantage is the troublesome evaluation of stereo-photographs.

The pin-gauge method uses streamlined, scaled pins normally fixed to the blade surface (2). They allow an easy estimation of the cavity thickness. But great disadvantages of

Hanns-Dieter Stinzing, Versuchsanstalt fuer Wasserbau und Schiffbau  
Mueller-Breslau-Str. (Schleuseninsel), D-1000 Berlin 12, FR Germany

this method result from the disturbance of the flow around the blades and from cavitation that may be produced by the pins themselves.

The final breakthrough in cavity thickness measurement was achieved by the use of lasers utilizing the strong beaming and the high intensity of their light. The basic idea of this technique was to measure the distance between the light spots that appear where the laser beam hits the surfaces of the blade and the cavity, resp. To make those spots as small as possible the beam has to be pulsed like a stroboscope. These pulsations are generated by means of an acousto-optic or electro-optic modulator, triggered by the propeller shaft. In case of an acousto-optic modulator, which has the same effect as an optical grating, for the selection of the 1st order beam a pinhole has to be attached in front. By using an electro-optic modulator, which rotates the plane of polarization of the laser light, a polarizer is needed additionally.

If a single laser beam is used to measure the cavity thickness, a sight device is necessary to define the measuring direction (3). By means of this device a vertical virtual plane containing the measuring direction is selected, while the laser beam enters the tunnel horizontally. In order to hit the cavity where the measuring direction penetrates the cavity surface, the laser beam, which initially is positioned on the blade surface, has to be shifted parallel with the propeller shaft. The cavity thickness then follows from the shift with regard to the measuring direction and the blade geometry (Fig.1).

In the beginning of a measurement the laser beam, entering the tunnel horizontally and normally to the propeller shaft, is adjusted to the measuring point on the blade surface while the tunnel pressure is high, i.e. while the propeller is not cavitating. Then the measuring direction is defined by means of the sight device and the tunnel pressure is reduced according to the desired cavitation number. Finally the laser is shifted as far as the light spot, that is visible on the cavity surface, lies in the measuring direction.

In the past useful results were obtained by this method. That's why it served as a basis for the investigations within the scope of our project.

Another technique to measure the cavity thickness by means of laser light is to use two convergent and synchronously pulsed laser beams intersecting in a point. The beam intersection first is positioned in the

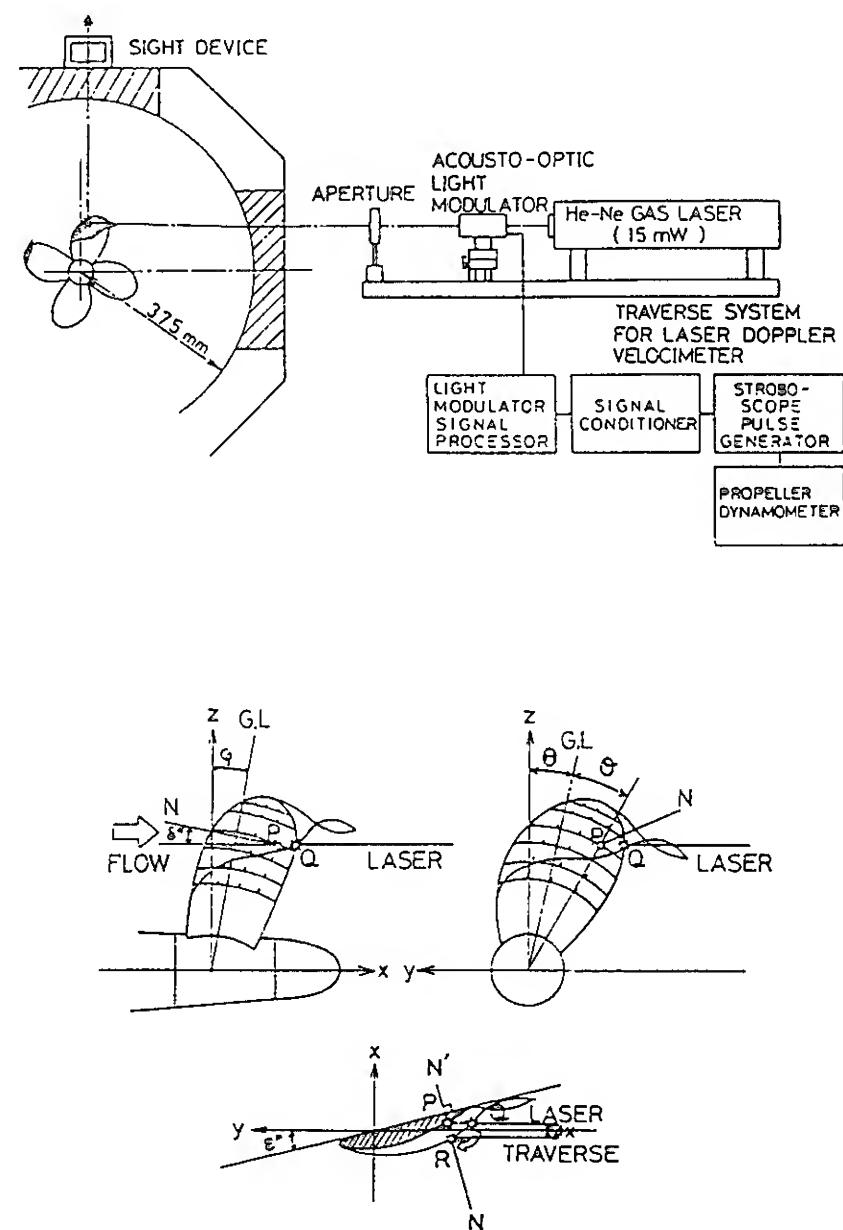


Fig.1 Cavity thickness measurement according to Ukon, Y. and Kurobe, Y. (3)

measuring point on the blade surface when the propeller is not cavitating. The cavity thickness there is then calculated from the distance of the two light spots observable on the cavity surface, when the propeller is cavitating. This method has been successfully applied on large ships (4).

#### Method Applied By The VWS

Due to the good results obtained with a single pulsed laser beam in Japan, that technique initially was selected to be used at VWS, too. To re-examine the measuring principle, the beam of a He-Ne laser of 5 mW power was electro-optically modulated using a Pockels-cell and a Glan-Taylor polarizer attached in front of it. All the components were mounted on an optical bench that was fixed to a tube stand. So the laser beam could be freely directed towards the propeller in the cavitation tunnel. The 250 V pulses required to control the Pockels-cell, were supplied by a special video amplifier that on his part was controlled by a pulse generator triggered by the propeller shaft. The

pulse generator could produce square-wave pulses of any duty factor.

Preliminary tests showed that not nearly all positions on the back of the propeller can be reached by a laser beam directed normally to the tunnel window. That is because of the limited height of the windows as well as the geometry of the propeller. That's why an inclined laser beam must be used in spite of a number of disadvantages: Since the tunnel window is not a coated optical glass but simple perspex, the reflection losses at the outer surface may be quite high. Moreover, the inclined beam is refracted in the window as well as in the tunnel water so that the direction in which it strikes the propeller is unknown. This means that the cavity thickness can no longer be calculated from the laser shift as described above, but has to be measured as the direct distance of the light spots, using a glass scale for instance. This technique is more complicated.

A further result of the preliminary tests was that, even at 90° angle of incidence, a laser power of only 5 mW is too low. Especially in the case of a smooth cavity surface it is difficult and over and above it often impossible to recognize the light spot generated by such a weak laser. In addition, since long light pulses are perceived as lines on the blade or the cavity surface the desired punctiform illumination requires very short pulses (approx. 50  $\mu$ s) which complicates the visual observation. Finally, the intensity losses in the tunnel water, mainly caused by air bubbles, have to be taken into account, too.

The results of the preliminary tests called for another measuring principle and in addition for the installation of a more powerful laser. Because of the considerably larger dimensions of the 35 mW He-Ne laser presently used in the VWS and the very restricted space on the portside of the VWS cavitation tunnel it became necessary to install the laser away and to transport its light to the measuring point through an optical fiber. That means that now, instead of the laser, only the much smaller and lighter fiber positioner had to be shifted. However, substantial losses in light intensity, mainly caused by the coupling into the optical fiber (monomode with a 3  $\mu$ m core), are disadvantageous.

The preliminary tests have shown that the laser beam always can be observed clearly and sharp-edged where it is crossed by the propeller blades and thus strikes the solid blade surface - provided that adequately

long light pulses are used. This led to the idea to use two permanent laser beams intersecting in one point, instead of a single pulsed beam, and to utilize the beam intersection, which in the interesting propeller regions always can be clearly seen, as a pointer tip. If this pointer tip is moved parallel with the propeller shaft from a position on the propeller blade to the cavity surface, the cavity thickness in this direction is obtained directly from that shift. The decisive advantage of this method is the existence of a defined measuring direction independent on the direction of the laser beams.

A precondition for the positioning of the beam intersection point is the visual fixation of the propeller by additional stroboscopic illumination. One can always adjust the intensity of the stroboscope flashes so that the laser light is not outshined, simply by adequate covering of the reflector.

Using a stroboscope has the further advantage that the complete three-dimensional shape of the cavity can be observed while it is measured. This is important especially when measurements have to be made in critical regions, namely near to the leading edge of the blade or under the bulge of the cavity close to the trailing edge or when bubbles complicate the observation of the cavity surface.

## MEASUREMENTS AND RESULTS

### Measurements

The measurements were performed with models of the six-bladed "Hongkong-Express" propeller (HSVA No. 2076, 211.11 mm diameter) and the five-bladed "Sydney-Express" propeller (HSVA No. 2054, 200.00 mm diameter). The axial velocities adjusted by means of sieves are shown in Figs. 2 and 3.

To define the measuring points the suction sides of the two measuring blades (in both cases blade No. 1) have been provided with rasters by polar coordinates consisting of circular arcs spaced in equidistances of 0.02 R (where R designates the propeller radius) and with radii every 2° (Fig. 4). This raster was definitely fixed by the point given by half the chord length of the 0.7 R arc. The radius going through this point was also used to define the blade position.

In order to obtain realistic measuring conditions for the models data of the ships served as a basis. These are the ship velocity  $v_s = 22.5$  kn, the rate of revolutions  $n = 92 \text{ min}^{-1}$  and the torque  $Q = 2,750 \text{ kNm}$  for the

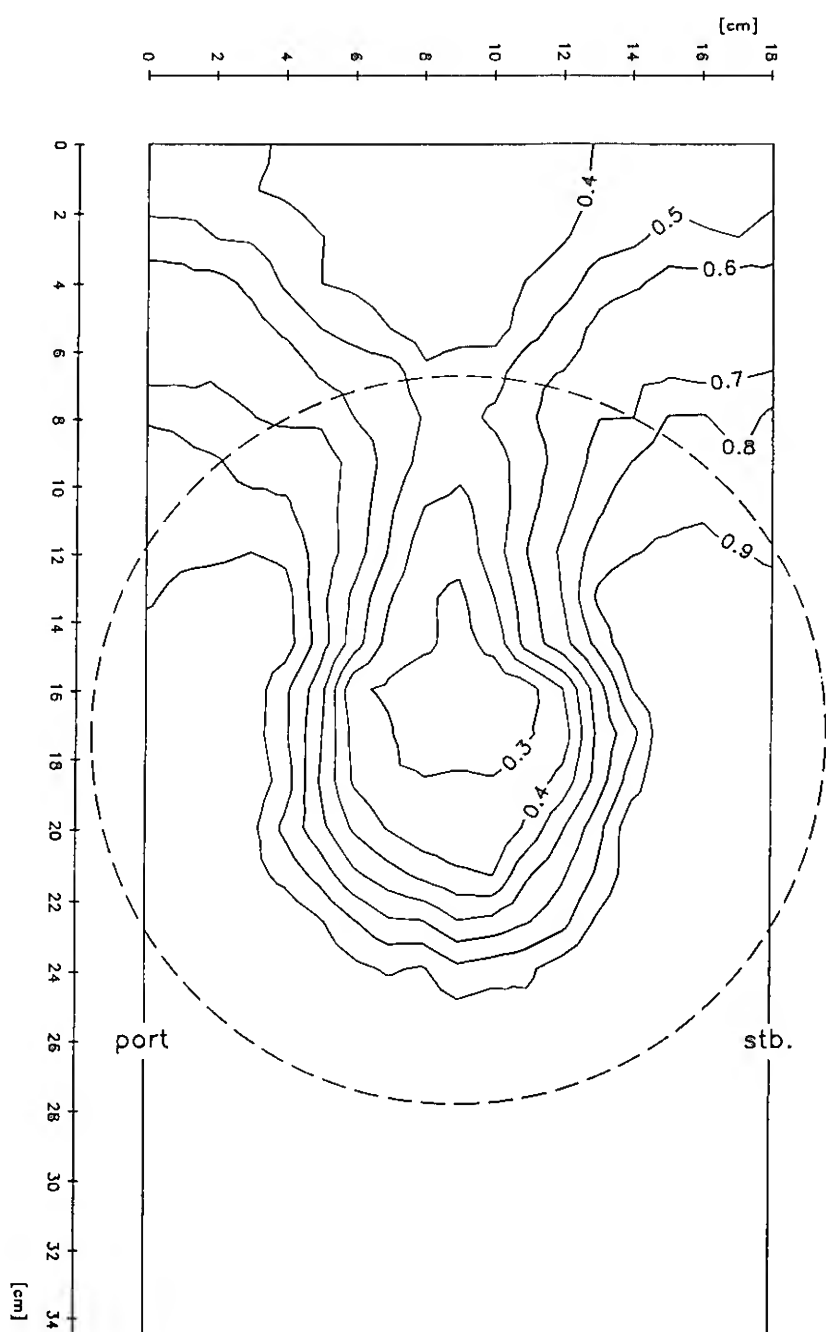


Fig.2 Axial inflow of propeller No. HSVA 2076

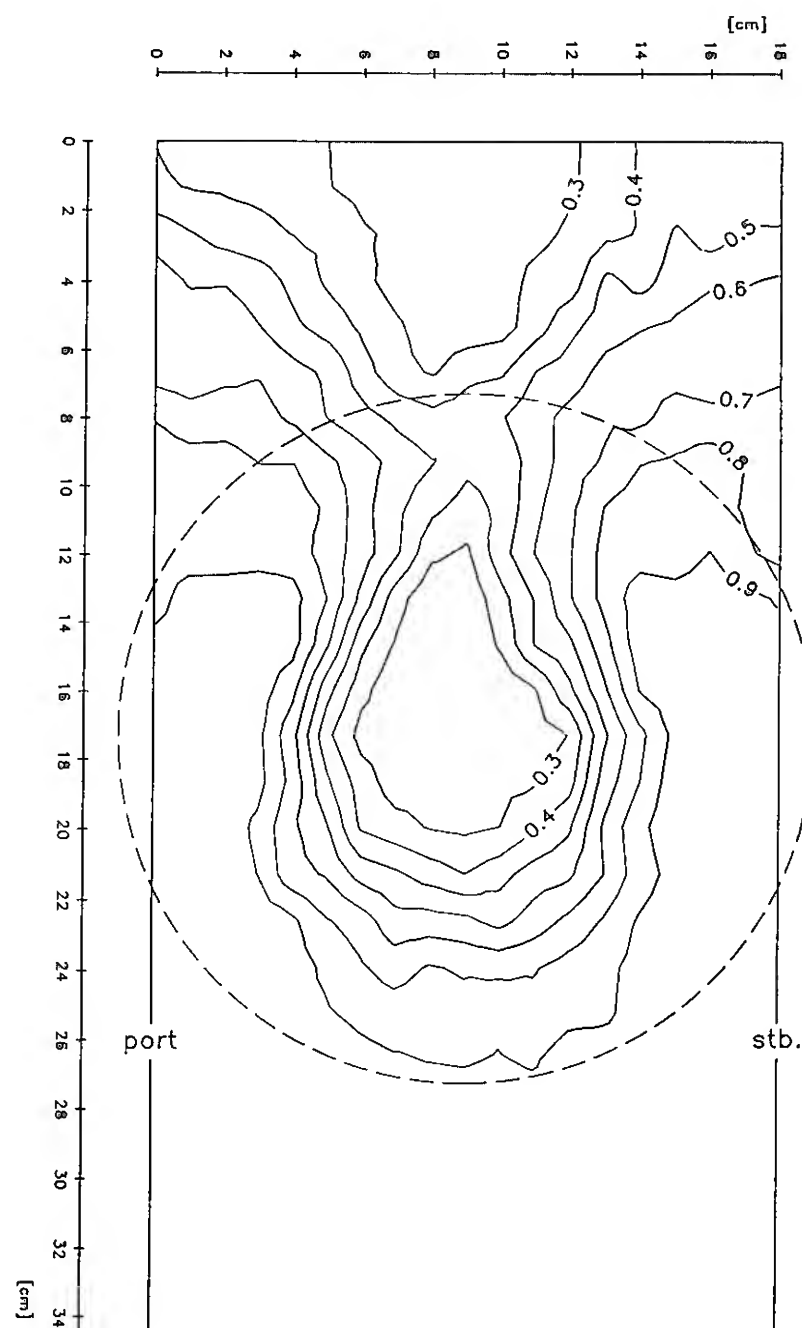


Fig.3 Axial inflow of propeller No. HSVA 2054

"Hongkong Express" and  $v_s = 22.0$  kn,  $n = 110$  min<sup>-1</sup> and  $Q = 2,000$  kNm for the "Sydney Express". These values give the torque coefficients  $K_Q = 0.045$  and  $K_Q = 0.035$ , resp., and from the open water diagrams result the thrust coefficients  $K_T = 0.250$  and  $K_T = 0.215$ , resp.

To define the cavitation numbers a depth of the propeller shafts of 7.0 m for the "Hongkong Express" and 6.7 m for the "Sydney Express" were assumed. Thus the propeller diameters of 7.6 m and 7.0 m, resp., and 1.0 m of height of the stern wave give the cavitation numbers  $\sigma_{0.8} = 0.340$  and  $\sigma_{0.8} = 0.280$ , resp., with regard to the highest position on 0.8 R.

The test setup is shown in Fig.5: The beam of the He-Ne laser (1) is coupled into a 10 m long optical fiber (3) with the aid of a fiber coupler (2). On the other end it is fed into simple LDA-optics (5) using a fiber positioner (4). The optical system, consisting of a beam splitter, a beam displacer and a front lens (focal length 600 mm), divides the entering laser beam into two convergent beams intersecting in one point. For posi-

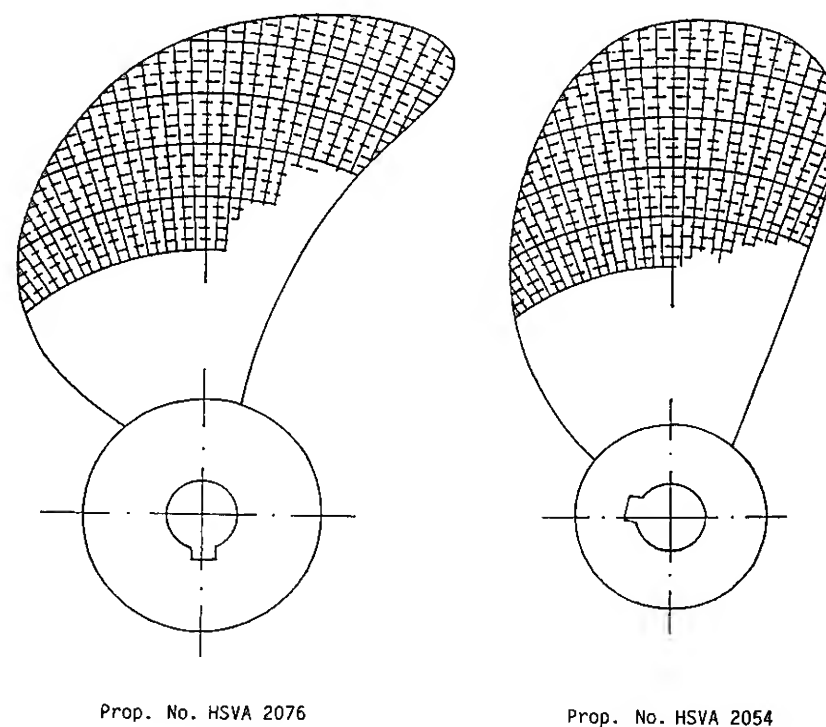


Fig.4 Polar-coordinate raster for measuring-point definition

tioning this intersection, fiber positioner and optics are fixed to two translation stages (7) with a rotary stage (8) between them. These stages

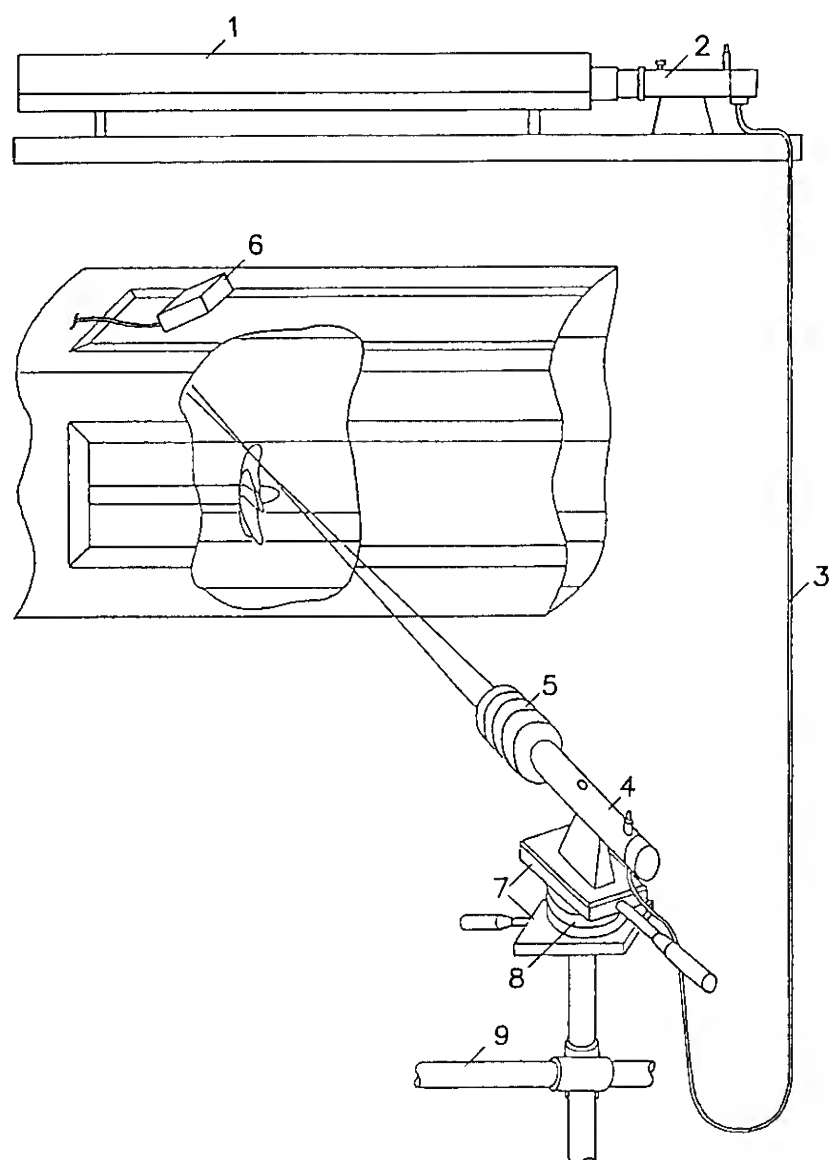


Fig.5 Test setup

- |                      |                       |
|----------------------|-----------------------|
| (1) He-Ne-laser      | (6) stroboscope lamp  |
| (2) fiber coupler    | (7) translation stage |
| (3) optical fiber    | (8) rotary stage      |
| (4) fiber positioner | (9) tube stand        |
| (5) LDA-optics       |                       |

are mounted on a manifoldly adjustable tube stand (9). The cavity thickness is measured with the lower translation stage which is aligned parallel with the propeller shaft. With the stroboscope lamp (6), triggered by the propeller shaft, the propeller is flashed in proper phase relation and thus visually fixed.

The tests were performed as shown in Fig.6: At first thrust and torque of the propeller are adjusted according to the coefficients  $K_T$  and  $K_Q$ , resp., by adjusting the flow velocity at a given propeller speed. Then the desired blade position is fixed by changing the stroboscope trigger adequately. After that the tunnel pressure is reduced according to the cavitation number, to examine the extension of the cavity. Subsequently the pressure is increased until the cavitation disappears, this being necessary for positioning the beam intersection in the measuring point on the blade surface using the rotary and the translation stages. For the same reason it is necessary to reduce the in-

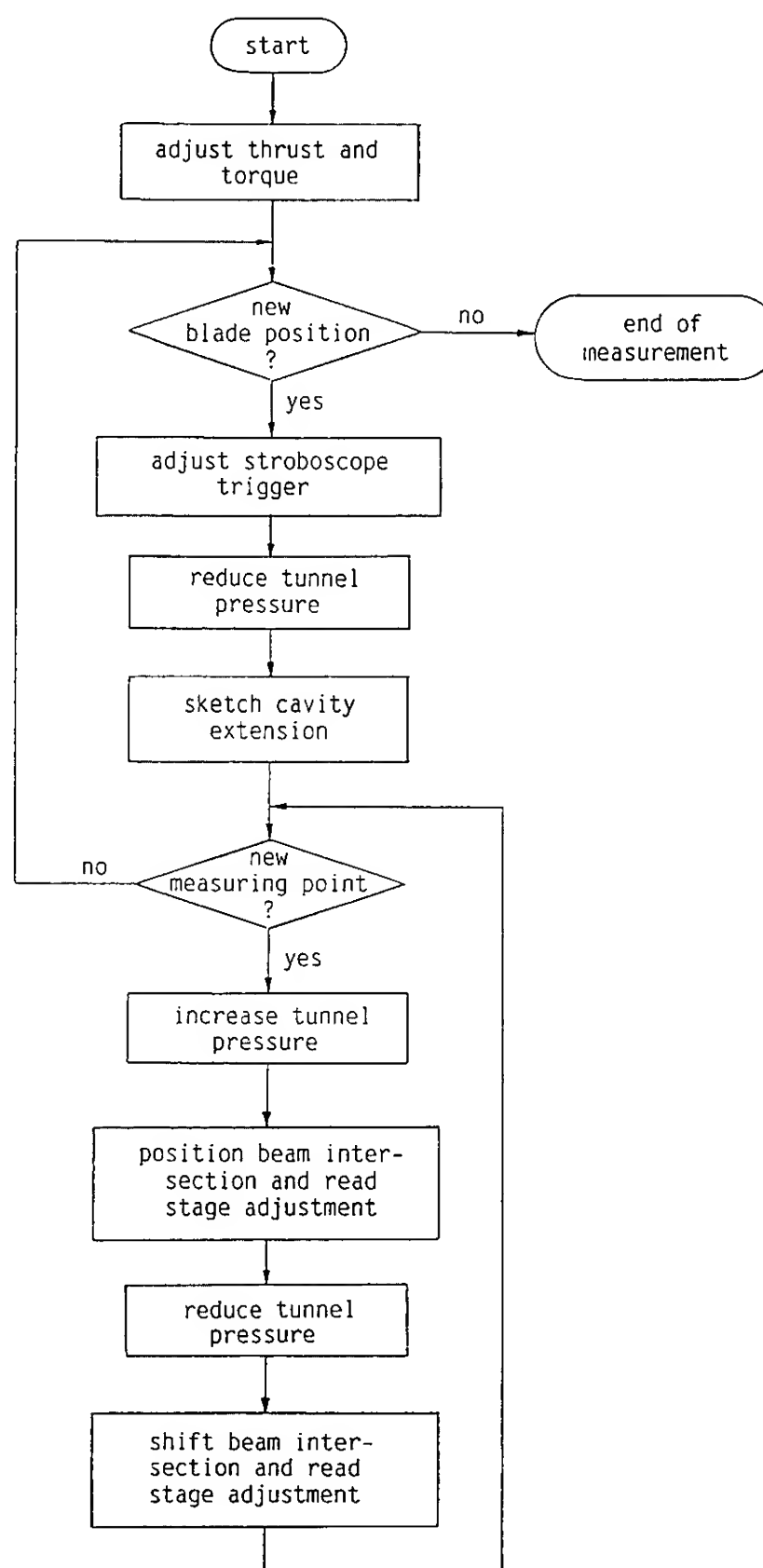


Fig.6 Schematic of test procedure

tensity of the laser light which expediently can be achieved by means of two rotating polarizing filters, inserted between fiber positioner and LDA-optics. Following the positioning, the light intensity is increased again and the adjustment of the lower translation stage is noted down. Finally the tunnel pressure is lowered again down to the required value to get cavitation and the beam intersection is shifted into the cavity surface with the aid of the lower stage. The adjustment of which is noted down again. The cavity thickness then follows directly from the beam shift.

According to this method, 330 points in 16 blade positions were measured on propeller HSVA No. 2076

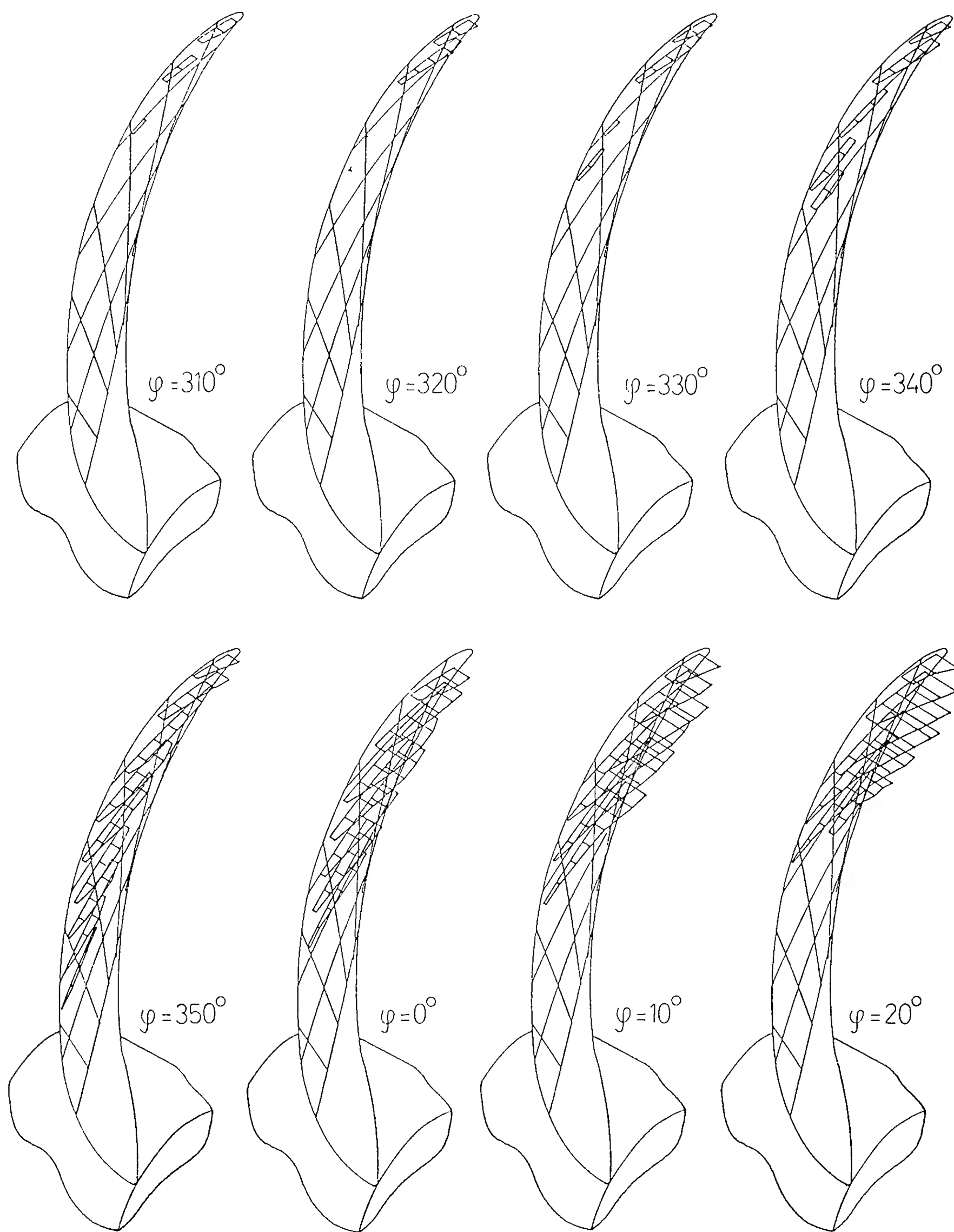


Fig.7 Measured cavity thicknesses of propeller No. HSVA 2076 (isometric representation)



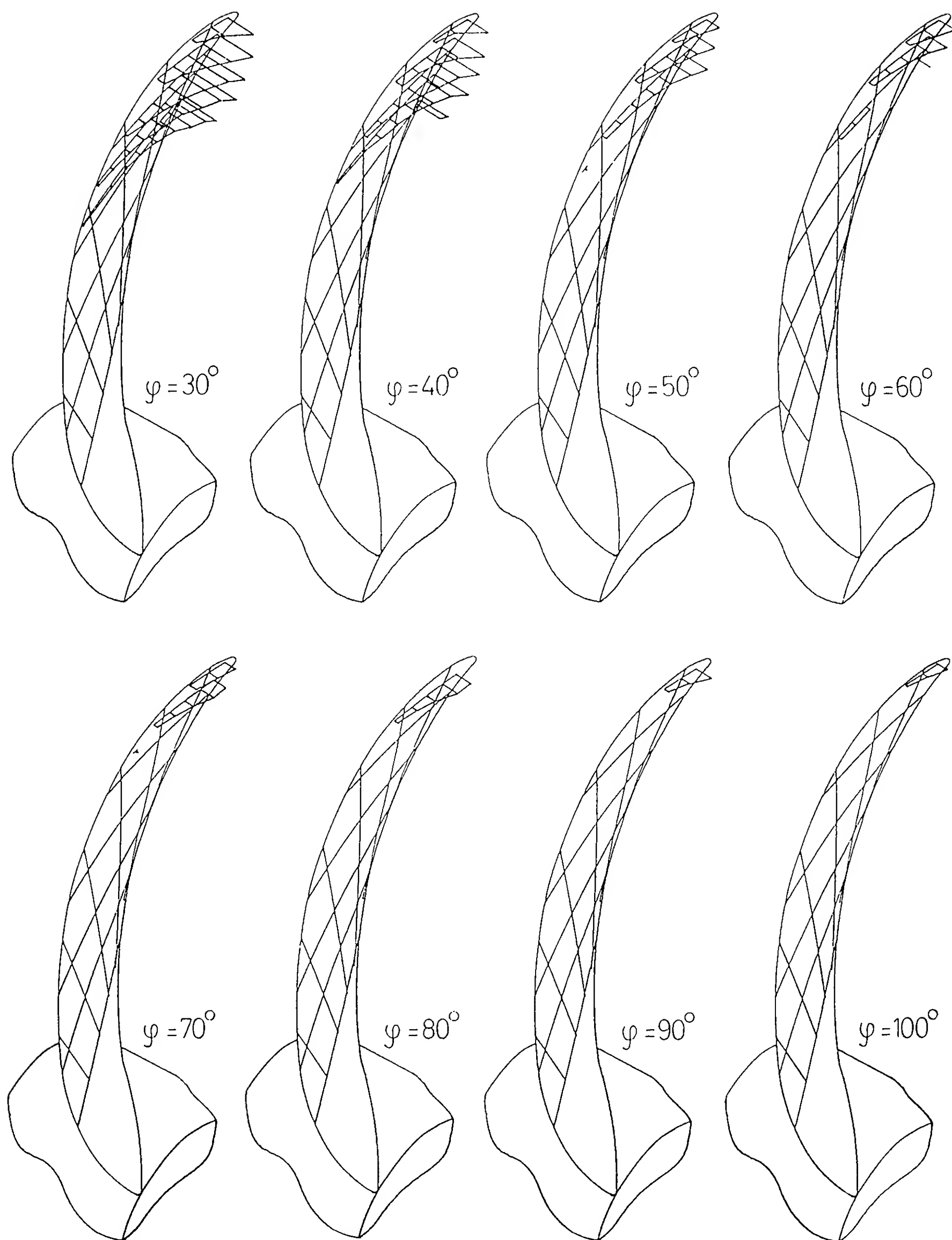


Fig.8 Measured cavity thicknesses of propeller No. HSVA 2076 (isometric representation)

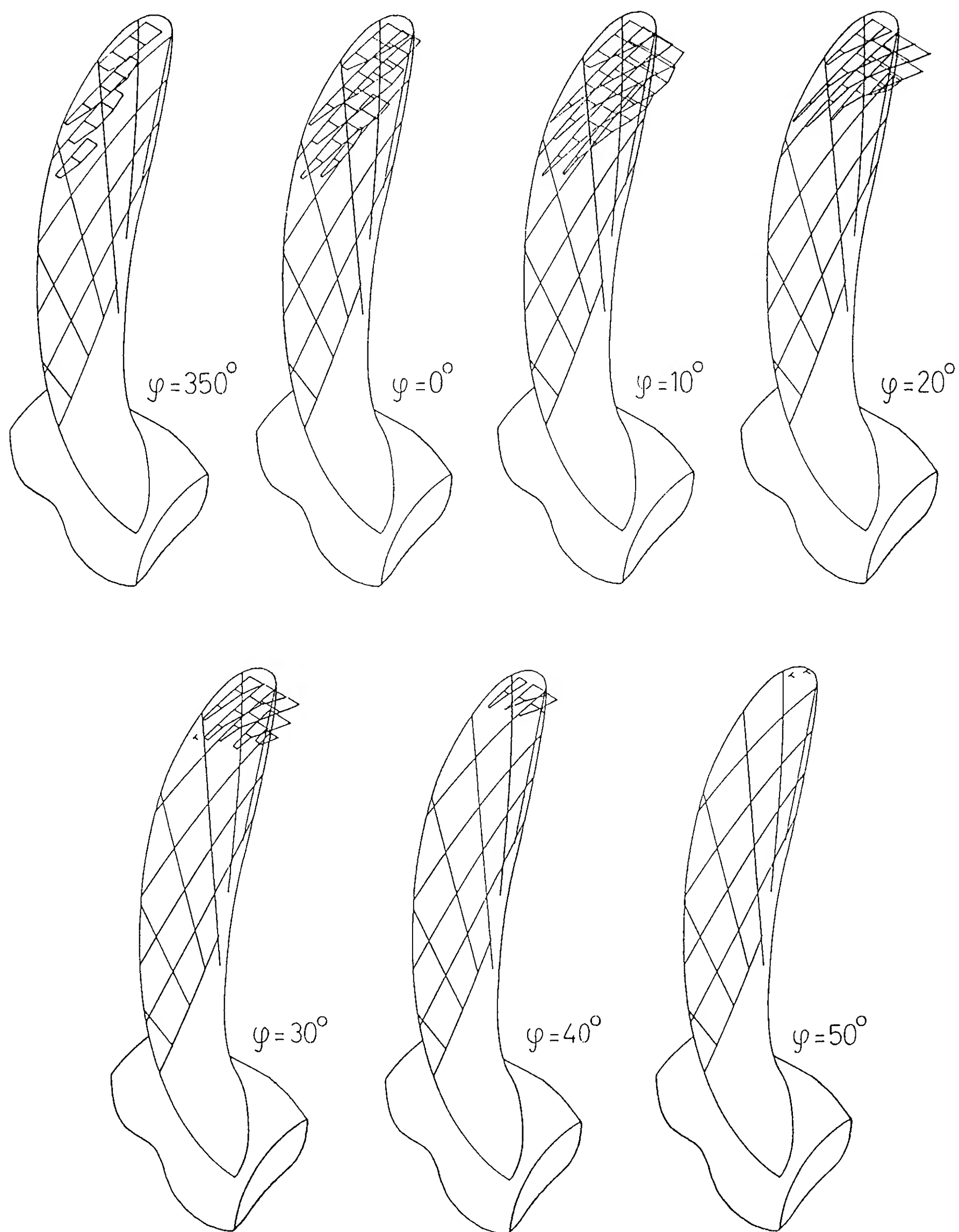


Fig.9 Measured cavity thicknesses of propeller No. HSVA 2054 (isometric representation)

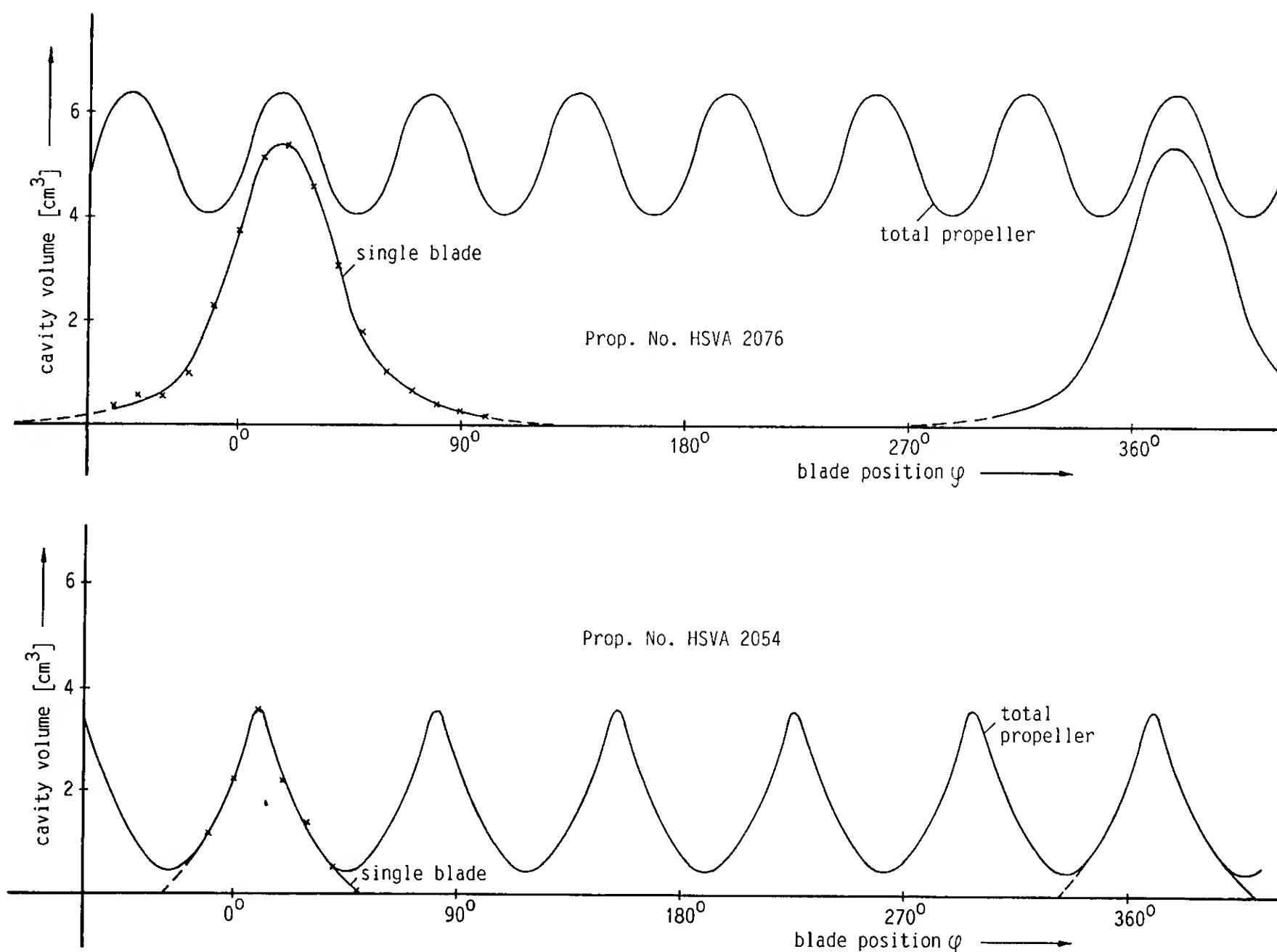


Fig.10 Cavity volume variation in the course of one revolution

and 139 points in 7 positions on propeller HSVA No. 2054.

#### Results

The measured cavity thicknesses are shown in Figs.7 to 9 in an isometric representation, which gives a good survey of the cavity geometry and its changes according to the blade position.

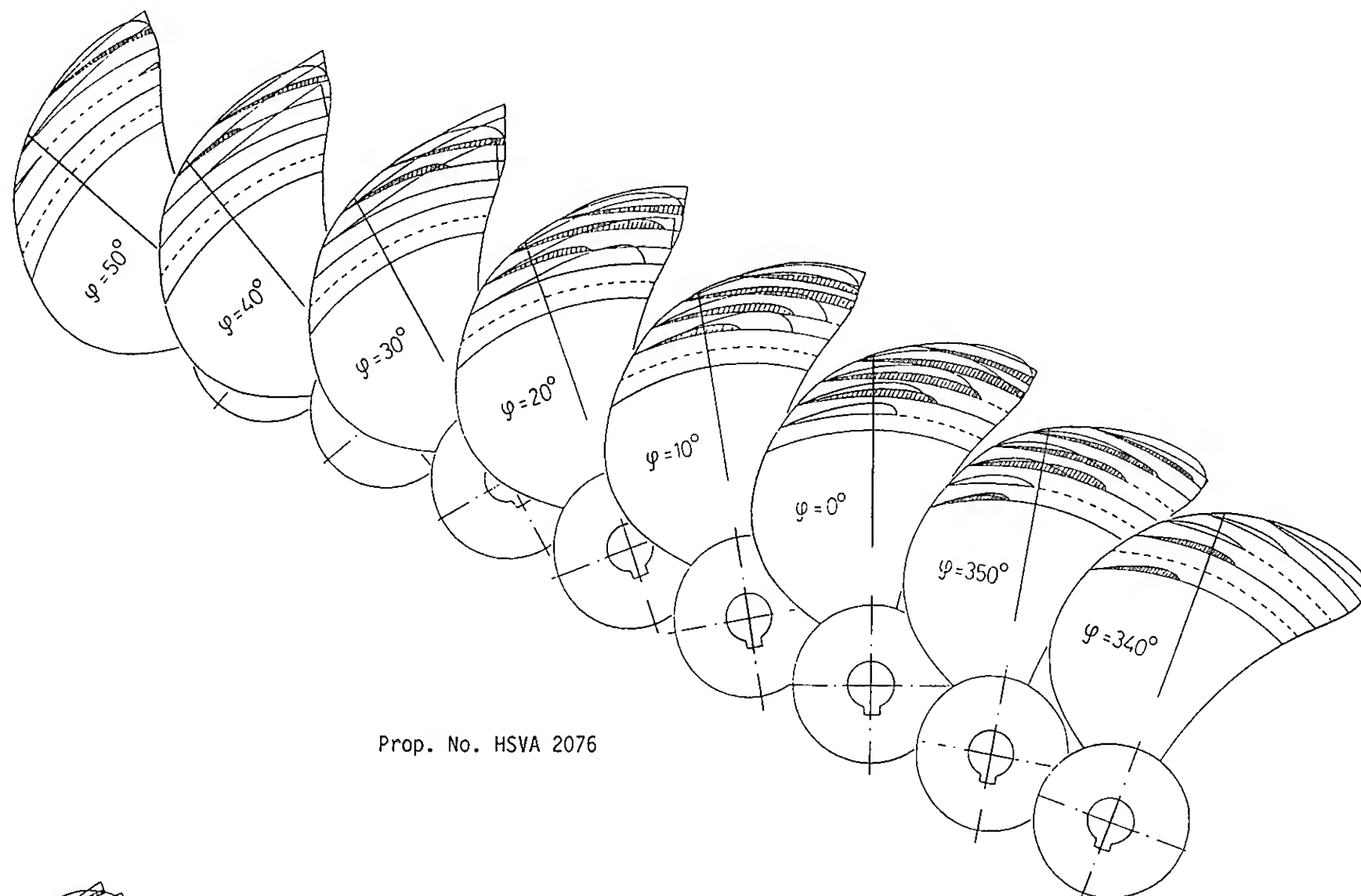
To facilitate the calculation of the cavity volume as a step function, the cavity thickness measured in direction of the propeller shaft has been converted to the direction normal to the blade surface. The required angles were determined experimentally by reflecting a laser beam at the blade surface.

The cavity volumes appearing on a single blade and on the complete propeller during one revolution are shown in Fig.10. It is conspicuous that the "Hongkong-Express" propeller produces a considerably greater cavity volume than the "Sydney-Express" propeller despite the higher cavitation number. But the resultant volume fluctuations are much smaller on the "Hongkong-

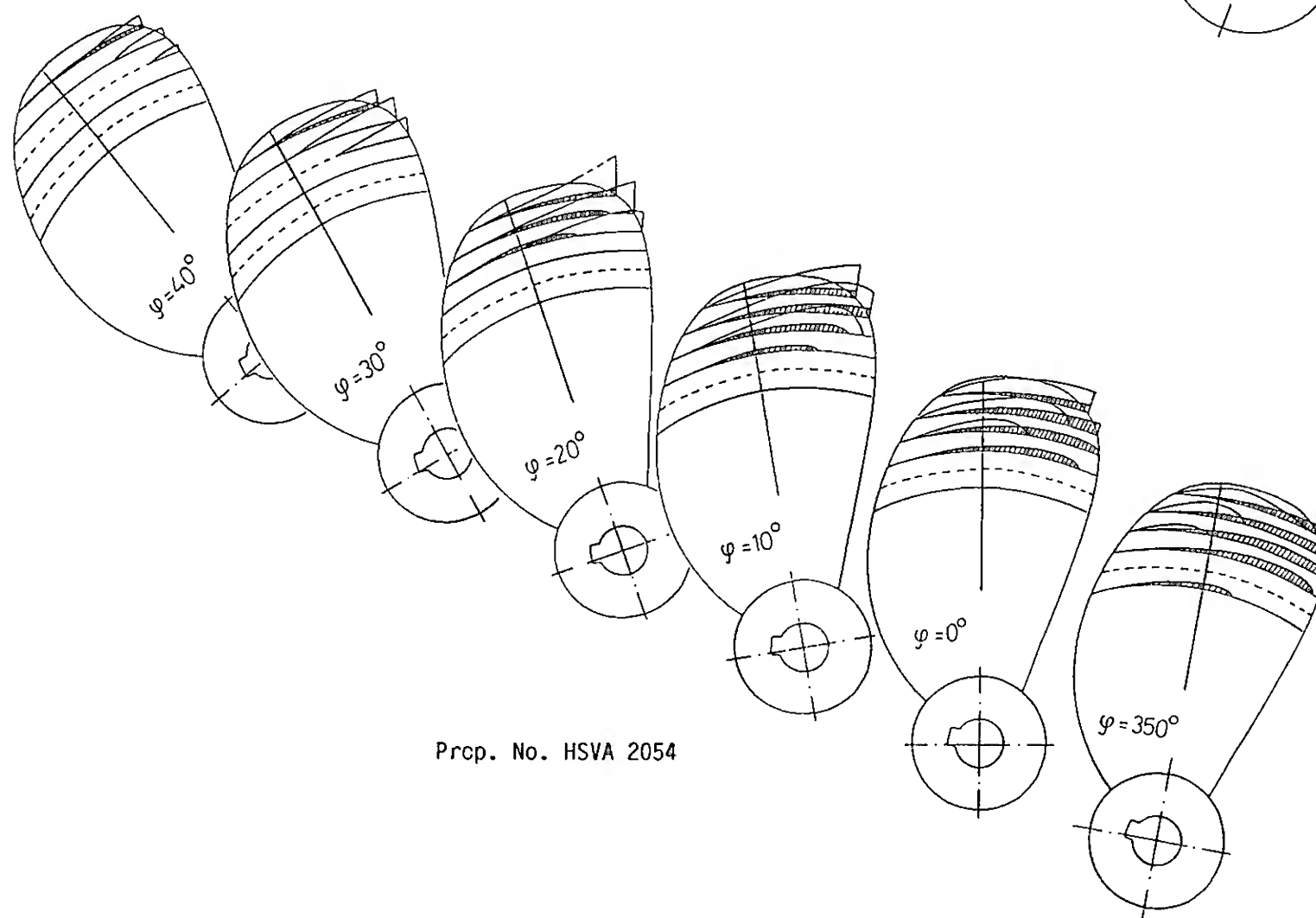
Express" than on the "Sydney-Express" propeller, which may be explained by the larger number of blades, the different blade geometry and especially the larger skew.

The calculations made by the HSVA differ considerably from the results of the VWS measurements as Fig.11 shows. This applies to the cavitation inception, the extension of the cavity and the cavity thickness likewise.

According to the calculations, on the "Hongkong-Express" propeller the cavitation incepts later and closer to the blade root and it disappears much quicker than is revealed by the measurements. Correspondingly, the differences in cavity extension may be quite large. At blade positions between  $\varphi=350^\circ$  and  $\varphi=0^\circ$ , measurements and calculations agree fairly well, but outside this range the calculated extensions are considerably smaller than the measured values. Such differences are inevitably connected with differences in cavity thickness. Similar values are only obtained for the blade position of  $\varphi=350^\circ$ . At the following positions the measured cavity thicknesses may exceed the results obtained



Prop. No. HSVA 2076



Prop. No. HSVA 2054

Fig.11 Measured and calculated (hatched) cavity thicknesses

by linear calculation by a factor of 5. The greatest differences in each case appear at the trailing edge of the propeller blade.

On the "Sydney-Express" propeller the calculated cavitation inception appears much earlier than the measured one, which is in contrast to the "Hongkong-Express" propeller. Accordingly, up to blade positions of  $\varphi=0^\circ$  and  $\varphi=10^\circ$  the calculated cavity extensions are larger than the measured ones. For subsequent positions the situation is vice versa. Furthermore it can be stated that the measured cavities are located closer to the tip region than the calculated ones.

Concerning the cavity thickness on the "Sydney-Express" propeller the smallest differences belong to blade positions near to  $\varphi=350^\circ$ . After that the measured values become considerably larger and again the greatest differences can be observed at the trailing edge.

One possible reason for the discrepancy between measurement and calculation results might have been the poor condition of the propellers. Especially the "Hongkong-Express" propeller, that is made of aluminum, has a lot of corrosion pits at the leading edge. Another reason may be that the cavity thickness depends on the concentration of the cavitation nuclei and macroscopic gas bubbles within the tunnel water, but these parameters have not been taken into account in the calculations.

However, to be able at least to estimate the effect of the gas bubbles on the measured cavity thicknesses, the number and size of the bubbles (relative values) were determined by a light scatter method at nearly all measurements and shown as histograms. In addition, at all tests the oxygen content of the tunnel water was measured by means of an electrode.

The histograms didn't give any significant differences in bubble-size spectra. According to visual observation one may also suppose that the propeller, working in a closed circuit, produces his own bubble spectrum. After a relatively short period of about one minute the same situation can be observed again and again. However, this does not exclude that different bubble spectra in fact result in different cavity thicknesses.

The oxygen measurements proved that the content of dissolved gas does not affect the cavity thickness. A test run over a whole day, constantly revealed the same thickness for a given position, while the oxygen content was greatly reduced by degasing. The accuracy of these thickness measurements was 0.1 to 0.2 mm. The same

can be assumed for most of the measurements performed. Only if the cavity is hard to be observed, or if measurements must be taken under the bulge of the cavity or if heavy fluctuations or bubbles complicate positioning on the cavity surface, the accuracy of measurement is smaller. In such cases it is estimated to be 0.5 mm.

## CONCLUSIONS

The striking advantage of the new method is its well-defined measuring direction. Its try-out with two propeller models has shown that it measures cavities fast and exactly. A Japanese report (5) received after closing the investigations described, seems to confirm the practicability of this technique.

The following task is to improve the theoretical model. In addition efforts should be made to modify the measuring technique so that the cavity outside the propeller blades, i.e. within the range of the tip vortex, can be measured, too. Finally a method has to be developed to vary and record size and number of the macroscopic gas bubbles of the tunnel water in order to clarify their effect on the propeller cavitation.

## REFERENCES

1. Sontvedt, T. and Frivold, H., "Low Frequency Variation of the Surface Shape of Tip Region Cavitation of Marine Propeller Blades and Corresponding Disturbances on Nearby Solid Boundaries", Proceedings of the 11th Symposium on Naval Hydrodynamics, London 1976, pp. 717-729.
2. Chiba, N., Sasajima, T., and Hoshino, T., "Prediction of Propeller-Induced Fluctuating Pressures and Correlation with Full Scale Data", Proceedings of the 13th Symposium on Naval Hydrodynamics, Tokyo 1980, pp. 89-103.
3. Ukon, Y. and Kurobe, Y., "Measurements of Cavity Thickness Distribution on Marine Propellers by Laser Scattering Technique", Report of Ship Research Institute, Vol. 19, No. 3, 1982, pp. 1-12.
4. Kodama, Y., Takei, Y., and A. Kakugawa, "Measurements of Cavity Thickness on a Full Scale Ship Using Lasers and a TV Camera", Papers of Ship Research Institute, No. 73, Dec. 1983.
5. N.N., "Twenty Years of Ship Research at IHI with the Ship Model Basin 1966-1986", Research Institute Ishikawajima-Harima Heavy Industries Co., Ltd., Anniversary Publication, Tokyo 1987.

## DISCUSSION

Jinzhong Feng  
Pennsylvania State University, USA (China)

Cavitation measuring is difficult. It is more so near the blade tip where the cavity bulb is usually fluctuating. The author, however, has measured the bulb thickness remarkably close to the blade tip as shown on Fig. 7 and Fig. 8. Is this because the author used time average to smooth out the fluctuation or because the propeller the author used in the test has a very little loading at the blade tip?

## AUTHORS' REPLY

The operating conditions of both the propeller models were derived from normal operating conditions of the full scale propellers (see values). So, their loads should have been normal, too. At these loads and the cavitation numbers mentioned, cavity fluctuations did not occur at the blade tip but at the blade root boundary of the cavity where its thickness was small. There, indeed, mean values were measured. But due to the thin cavity these values contribute only very little to the cavity volume, the quantity wanted.

## DISCUSSION

Spyros A. Kinnas  
Massachusetts Institute of Technology, USA

The paper offers valuable experimental information of unsteady cavity shapes, which can be used to validate existing analytical techniques. I would like to address the following two points though: (a) The technique used in the paper measures the cavity thickness only on the propeller blade. As it appears though from Figs. 7-9, the cavity seems to extend beyond the trailing edge of the blade. Is the volume of the cavity extending behind the trailing edge accounted for in the computation of the cavity volume? (b) The analytical method that is used appears to underpredict the cavity extend and volume substantially. A reference for this method would be nice to have been given. Is it a quasi-steady vs unsteady method and is it a stripwise 2-D method vs a completely 3-D method?

## AUTHORS' REPLY

Figs. 7-9 indicate that the cavities indeed extended beyond the trailing edges of the propeller blades. The technique described does not enable cavities to be measured outside the blades. So the specified cavity volumes only include the measured blade cavities. For the calculation of the cavity thicknesses, a quasi-steady and 2-D method was used. It is described in detail by K.-Y. Chao and H. Streckwall in "Kavitationsuntersuchungen, Druckschwankungsmessungen und Vibrationsbewertung an schnellen Containerschiffen hoher Leistung," HSVA-Rep. No. 1569, August 1989.



# The Dynamics and Acoustics of Travelling Bubble Cavitation

S. Ceccio, C. Brennen (California Institute of Technology, USA)

## ABSTRACT

Individual travelling cavitation bubbles generated on two axisymmetric headforms were detected using a surface electrode probe. The growth and collapse of the bubbles were studied photographically, and these observations are related to the pressure fields and viscous flow patterns associated with each headform. Measurements of the acoustic impulse generated by the bubble collapse are analyzed and found to correlate with the maximum volume of the bubble for each headform. These results are compared to the observed bubble dynamics and numerical solutions of the Rayleigh-Plesset equation. Finally, the cavitation nuclei flux was measured and predicted cavitation event rates and bubble maximum size distributions are compared with the measurements of these quantities.

## 1. INTRODUCTION

Though the dynamics and acoustics of travelling bubble cavitation have been extensively studied both experimentally and theoretically, the behavior of naturally occurring cavitation bubbles near surfaces has not been examined in great detail. It has been known for some time that cavitation bubbles generated near surfaces are usually not spherical (as often assumed in theory) but hemispherical caps (Knapp and Hollander (1948) and Parkin (1952)), and a cavitation bubble collapsing near a solid boundary may produce a microjet of fluid which has been speculated to cause surface cavitation damage (Benjamin and Ellis (1966), Plesset and Chapman (1970), Lauterborn and Bolle (1975), Kimoto (1987) and, for a review, Blake and Gibson (1987)). The complex shapes that travelling bubbles assume will clearly be influenced by macroscopic flow phenomena such as pressure gradients, boundary layers, separation, and turbulence. Researchers have attempted to study these effects by observing cavitation bubbles induced in a venturi (Kling and Hammit (1972)) or above a surface (Chahine et al. (1979), van der Meulen (1989)). Yet detailed, systematic studies of hydrodynamically-produced cavitation bubbles are almost non-existent. The random nature of naturally occurring cavitation is the primary reason why investigators have focused on integral measurements in their study of cavitating flows, leaving the detailed behavior of individual cavitation bubbles unexamined.

Analyses of cavitation noise have generally been based on the theoretical behavior of single, spherical bubbles following the work of Fitzpatrick and Strasberg (1956). From this data base, researchers have synthesized the acoustic emission from cavitating flows

with multiple events (Blake (1986)). Many experiments have attempted to extract the actual behavior of individual bubbles from the integral measurement of the noise produced by cavitation (Mellon (1956), Blake, Wolpert, and Geib (1977), Hamilton (1981), Hamilton, Thompson, and Billet (1982), and Marboe, Billet, and Thompson (1986)). Although trends are seen in the measured spectra which may be related to theoretical predictions, the difficulty of obtaining free field acoustic spectra in the confines of most water tunnels has always made interpretation of experimental spectra problematic.

Researchers have also attempted to treat cavitation as a stochastic process. The spectral emission of a cavitating flow will depend not only on the noise produced by single bubbles but also on the cavitation rate and event statistics (Morozov (1969) and Baiter (1986)). Furthermore, cavitation noise scaling like that suggested by Blake, Wolpert, and Geib (1977) will be significantly influenced by changes in the cavitation event rate. As the number of cavitation events increase, bubble interactions will affect individual bubble volume histories and their acoustic emission (e.g. Morch (1982), Arakeri and Shanmuganathan (1985), and d'Agostino, Brennen, and Acosta (1988)). Analyses of multiple bubble effects depend upon a knowledge of the nuclei distribution in the flow and the dynamics causing the nuclei to cavitate.

Yet, the effect of nuclei number distribution on the total cavitation process is poorly understood, and this is due largely to the difficulty of accurately measuring this quantity. In fact, most cavitation studies neglect to include any measure of the nuclei number distribution. As we shall demonstrate, the number and size distribution of cavitation bubbles, and the resulting noise emission, can vary substantially over the course of an experiment, even at a nominally fixed operating point. Although the mean cavitation event rate may be approximately determined by the acoustic pulse rate (Marboe, Billet, and Thompson (1986)), cavitation bubble size distributions have only been determined in very rough form (Baiter (1974) and Meyer, Billet, and Holl (1989)). Although knowledge of the cavitation rate and bubble size distribution is essential, no simple method has been found to count and measure cavitation bubbles.

The above observations indicate a need to study the dynamics and acoustic emission of individual cavitation bubbles. A method of detecting and measuring cavitation bubbles was needed, and this paper presents

data obtained through the use of a new electrical probe developed for this purpose. Using this new instrument experiments were performed to study individual cavitation events and their statistics in an attempt to address the above issues.

## 2. NOMENCLATURE

$A(R_O)$	streamtube capture area for given nuclei
$C_P$	pressure coefficient, $(P - P_0) / (\frac{1}{2}\rho U^2)$
$C_{PM}$	minimum pressure coefficient on body surface
$f$	frequency
$I$	measured acoustic impulse
$I^*$	dimensionless acoustic impulse
$N(R_O)$	free stream nuclei distribution
$Pr_O(R_M)$	max. bubble volume distribution associated with nuclei of size $R_O$
$Pr(R_M)$	maximum bubble volume distribution
$P_A$	acoustic pressure
$P_O$	freestream pressure
$P_V$	water vapor pressure
$r$	acoustic path length
$R(t)$	calculated bubble radius
$R_C$	critical nuclei radius
$R_B$	headform radius at $C_{PM}$
$R_H$	headform radius
$R_L$	bubble radius along trajectory
$R_M$	cavitation bubble maximum radius
$R_{MR}$	cavitation bubble maximum reduced radius
$R_O$	nuclei radius
$Re$	Reynolds number, $UD/\nu$
$S$	water surface tension
$S_P$	acoustic pressure spectral coefficients
$t$	time
$t_1, t_2$	integration limits for experimental impulse
$T$	acoustic pulse duration
$T^*$	calculated dimensionless pulse duration
$U$	free stream velocity
$V(t)$	calculated bubble volume
$We$	Weber number, $\rho U^2 R_H / S$
$\alpha$	constant, pulse width relationship
$\beta$	constant, nuclei stability relationship
$\kappa$	headform radius of curvature at $C_{PM}$
$\nu$	water viscosity
$\rho$	water density
$\sigma$	cavitation number, $(P - P_V) / (\frac{1}{2}\rho U^2)$
$\sigma_i$	bubble cavitation inception index
$\sigma_{ac}$	attached cavity formation index
$\Theta$	cavitation event rate

## 3. EXPERIMENTAL SETUP

The experiments were conducted in the Caltech Low Turbulence Water Tunnel (LTWT); a full description of the facility is presented by Gates (1977). For all experiments, the test section free stream velocity was set and the tunnel static pressure lowered until the desired cavitation number was reached. The operating air content was generally between 6–8 ppm, and the tunnel water was well filtered. The free stream nuclei number distribution of the upstream fluid was measured using in-line pulsed holography. A detailed description of the holographic system is presented by Katz (1981).

Two axisymmetric headforms were used in the present experiments. The first was a Schiebe headform with an ultimate diameter of 5.08 cm. (Gates et al (1979)); the second, which has a modified ellipsoidal shape with a diameter of 5.59 cm, is known as the

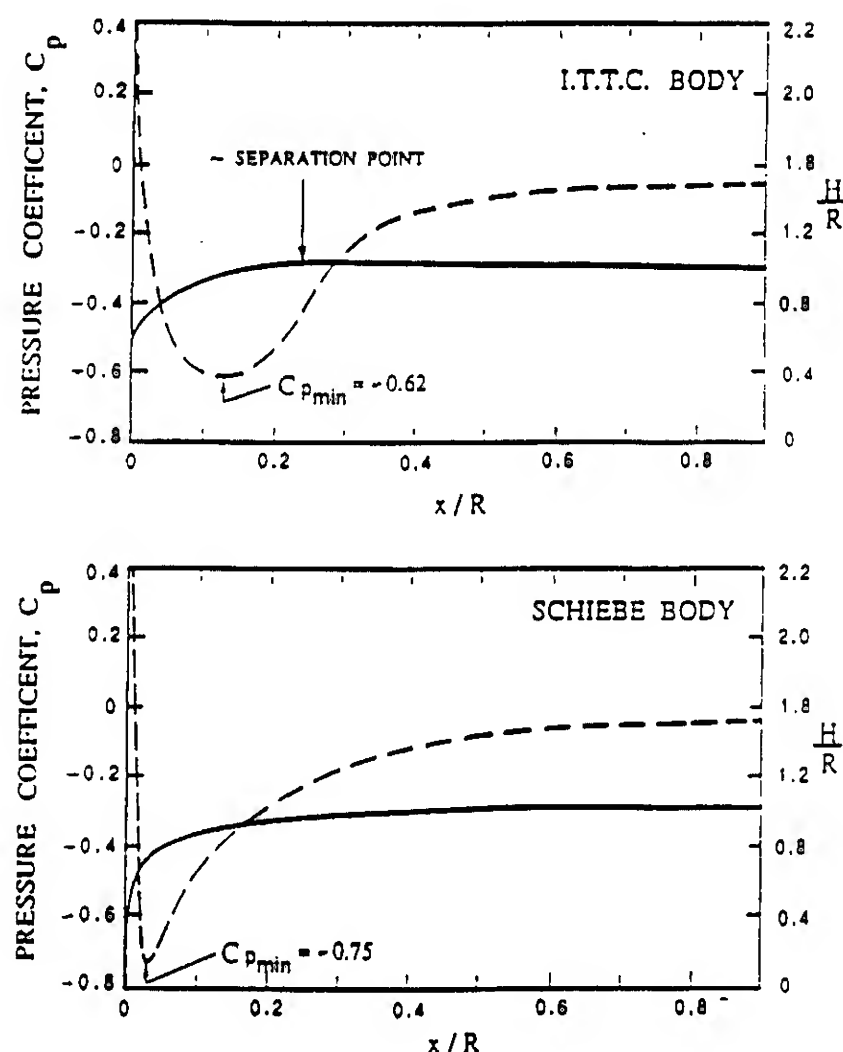


Figure 1. Surface pressure distributions and profiles of the I.T.T.C. body and the Schiebe body.

I.T.T.C. headform (Lindgren and Johnsson (1966)). Surface pressure distributions for the Schiebe body (Gates et al (1979)) and the I.T.T.C. headform (Hoyt (1966)) are available in the literature. The headform contours and surface pressure distributions are presented in Figure 1.

The headforms were fabricated out of lucite, a material whose acoustic impedance is a fair match to that of water. The hollow interior of both bodies was filled with water in which a hydrophone was placed. The hydrophone, an ITC-1042, has a relatively flat response out to 80 kHz. Except for ultralow frequencies ( $\ll 1$  Hz), the hydrophone signal was not filtered. All acoustic signals were digitized at a sampling rate of 1 MHz. Because of the relatively good acoustic impedance match between lucite and water, the interior hydrophone allows the noise generated by the cavitation bubbles to reach the hydrophone relatively undistorted; reflected acoustic signals from other parts of the water tunnel only make their appearance after the important initial signal has been recorded.

In addition to the hydrophone, each headform was provided with novel equipment developed from instrumentation which had previously been used to measure volume fractions in multiphase flows (Bernier (1981)). This instrumentation consisted of a series of electrodes arrayed on the headform surface which were used to detect and measure individual cavitation bubbles. A pattern of alternating electric potentials is applied to the electrodes and the electric current from each is monitored. When a bubble passes over one of the electrodes the impedance of the local conducting medium is altered, causing a change in the current from the electrode. This change, which is detected and recorded, permits the position and volume of the bubble to be monitored.

One specific electrode geometry consisted of patches arrayed in the flow direction to cover the major extent of the cavitating region. Another consisted of electrodes which encircled the entire circumference of the headform in the region of maximum bubble growth. These two electrode geometries were used for different purposes. Signals from the patch electrodes indicated cavitation at a specific location on the headform, and, by electronically triggering flash photography, simultaneous plan and profile photographs of individual bubbles could be taken at a prescribed moment in the bubble history. Thus, a whole series of bubbles could be inspected at the same point in their trajectory. Furthermore, by simultaneously recording the acoustic signal from the hydrophone, one could correlate the noise with the geometry of the bubbles.

The circular geometry was used to detect the occurrence of every cavitation bubble at a particular location on the headform. This position was chosen to be near the location of maximum bubble volume, and for relatively moderate event rates only one bubble would occur over the electrode at any given time. Because almost all the cavitation bubbles maintain the same distance above the electrodes (this will be discussed below), the output of the circular electrode system is directly proportional to the area covered by the bubble, and the peak of the signal is proportional to the major diameter of the bubble base. This system was calibrated photographically and found to be quite linear. The volume of the bubbles was then determined from a measure of the base diameter using a functional relationship derived through the photographic study of many individual bubbles (Ceccio (1990)). Two kinds of experiments were performed with the circular electrode system. The first involved the measurement of event statistics and bubble maximum size distributions. In the second, the acoustic emission of individual cavitation bubbles was analyzed and the result correlated with the bubble maximum volume.

#### 4. OBSERVATIONS OF SINGLE CAVITATION BUBBLES

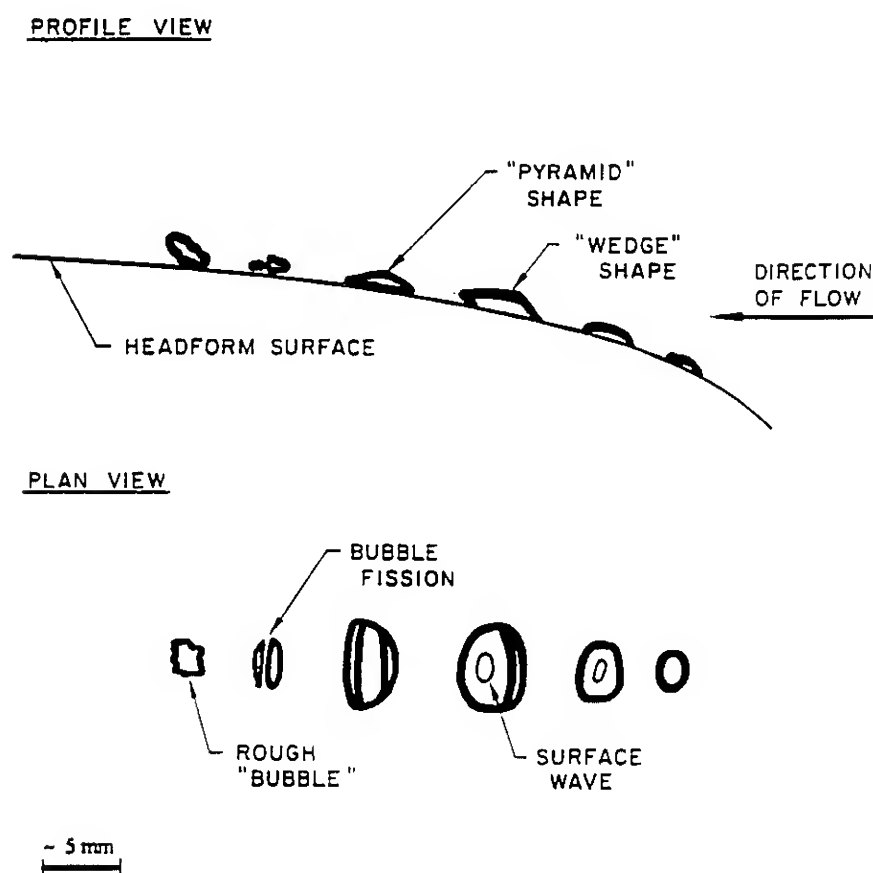


Figure 2. Schematic diagram of typical bubble evolution on the Schiebe headform.

Cavitation bubbles were observed on both the Schiebe and I.T.T.C. headforms over a range of cavitation numbers. The cavitation number was varied between the traveling bubble cavitation inception value,  $\sigma_i$ , and the value at which attached cavitation occurred,  $\sigma_{ac}$ . The inception index on both bodies was strongly dependent on the ambient nuclei number distribution (Ooi (1981)). Inception occurred on the Schiebe body at cavitation numbers as high as  $\sigma_i = 0.65$ , and on the I.T.T.C. body at  $\sigma_i = 0.58$  for tunnel water of 6–7 ppm air content. However on both bodies the inception index was reduced to about  $\sigma_i = 0.50$  immediately after deaeration. Any definition of the bubble cavitation inception index must therefore be associated with a particular free stream nuclei number distribution. The attached cavitation formation index for the Schiebe body was  $\sigma_{ac} = 0.40$  and for the I.T.T.C. body  $\sigma_{ac} = 0.41$ . These values were almost constant over the fairly narrow range of Reynolds numbers of the experiments ( $Re = 4.4 \times 10^5 - 4.8 \times 10^5$ ).

Before detailing the results from each headform, one observation can be made for both geometries. For a given tunnel velocity and cavitation number, the maximum bubble volumes were quite uniform. Although the incoming nuclei diameter ranged over almost three orders of magnitude, the maximum cavitation bubble volume varied over only one order of magnitude. The reason for this is given below.

For both headforms, the growth phase of the nuclei was very similar to that described in the original observations of Knapp and Hollander (1948) and Ellis (1952). For most of their evolution, the bubbles take on a hemispherical or "cap" shape and move extremely close to the headform surface; only very occasionally would quasi-spherical bubbles be observed at a distance above the surface. Small waves could be observed on the bubble surface in many instances. As the bubbles reach their maximum volume they become somewhat elongated in the direction normal to their motion while their thickness normal to the surface remains relatively constant. At this point, the difference in the flows around the two bodies begins to cause differences in the bubble dynamics.

The Schiebe body was designed to suppress laminar separation in the region of cavitation (Schiebe (1972)). It possesses a sharp pressure drop with a minimum pressure coefficient of -0.75 (Figure 1). Figure 2 represents a schematic of the typical bubble evolution, and Figure 3 consists of a series of photographs of bubbles at various stages during this process. After the bubble has reached its maximum volume, it begins to lose its cap-like shape and becomes elongated progressing into a pyramid-like shape; the bubble thickness normal to the headform surface consistently decreases after reaching its maximum. The bubble then collapses rapidly and develops an elongated shape. The elongation of the bubble and the formation of tubes is probably due to rotation of the bubbles caused by the shear in the boundary layer. As the bubble collapses it may fission into two or three tubes of collapsing vapor, and the residual gas in these tubes may cause a rebound to produce a rough bubble or group of bubbles after collapse.

The I.T.T.C. headform has a relatively smooth pressure drop with a minimum pressure coefficient of -0.62. A distinguishing feature of this headform is that, unlike the Schiebe body, it possess a laminar

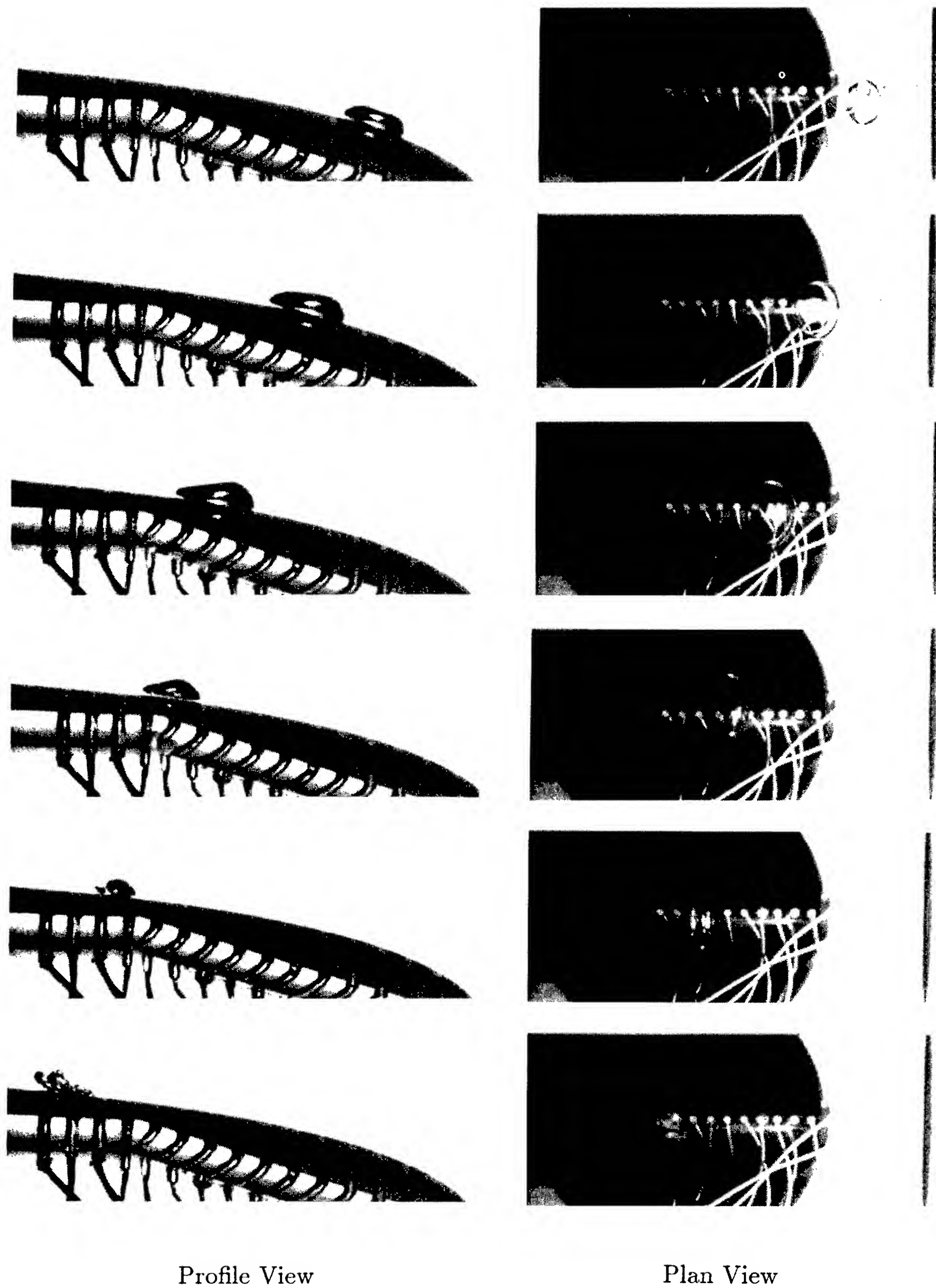


**Figure 3.** Series of photographs detailing typical bubble evolution on the Schiebe headform,  $U = 9m/s$  and  $\sigma = 0.45$ .



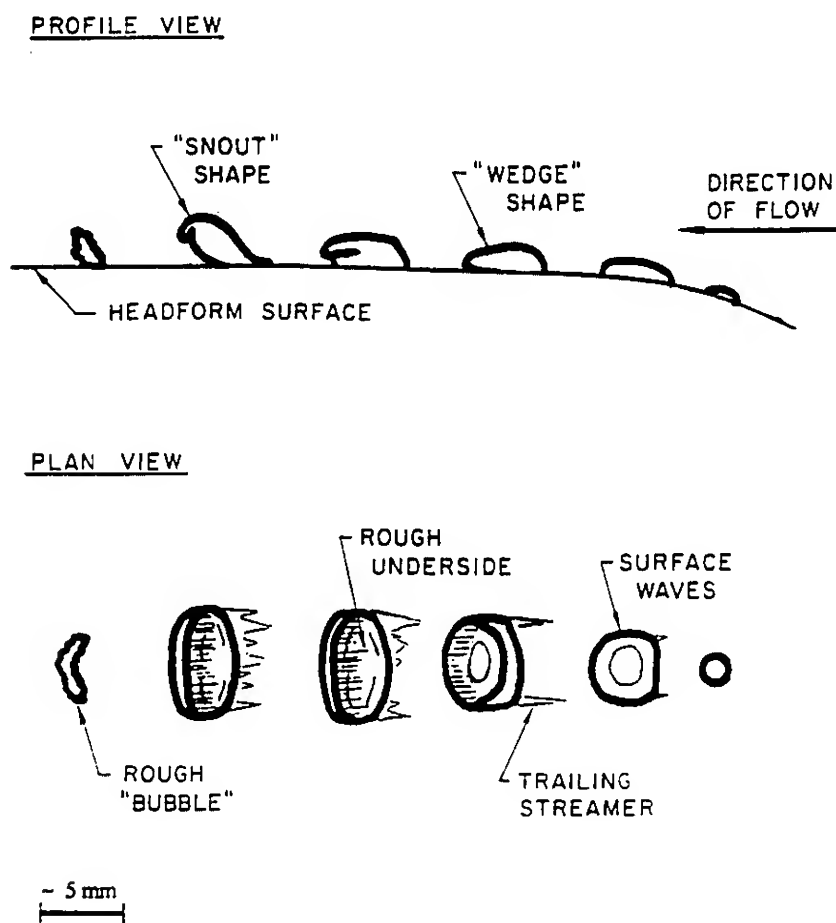


Figure 4. Schematic diagram of typical bubble evolution on the I.T.T.C. headform.

separation region (Figure 1). Figure 4 is a schematic of the typical bubble evolution, and Figure 5 presents a series of photographs of bubbles at various stages of this development. The bubble has a cap-like shape until it reaches its maximum volume where it then becomes further elongated evolving into the wedge-like shape. However, unlike the bubbles on the Schiebe body, the cavity starts to lift off the surface and begins to roll up into a snout-like shape. This may be due to recirculating flow associated with the separation region or the stretching of the bubble in the velocity gradient. As it collapses, the "snout" continues to roll up into a vapor tube eventually collapsing to produce a rough bubble after collapse.

On both the Schiebe and I.T.T.C. headforms, the rough bubble or group of bubbles which is formed after collapse is sheared by the surface flow and usually disperses into smaller bubbles on the order of  $50\mu m$ , although a second collapse and rebound is not uncommon. The mean lifetime of a bubble depends upon the tunnel velocity, cavitation number, and initial nuclei size, but, for most of the observed bubbles on both headforms, it is approximately 3ms.

The laminar separation on the I.T.T.C. body has been carefully studied in the context of its effect on attached cavitation (Arakeri and Acosta (1973)). Clearly, the separated flow also influences bubble cavitation for cavitation bubbles were observed riding over the separation "bubble". As seen in Figures 4 and 5, the underside of the bubbles become roughened as they pass over the region of turbulent reattachment. These local flow disturbance seem to shear vapor off the underside of the bubble, leaving a trail of much smaller bubbles. This phenomenon was not observed on the Schiebe body.

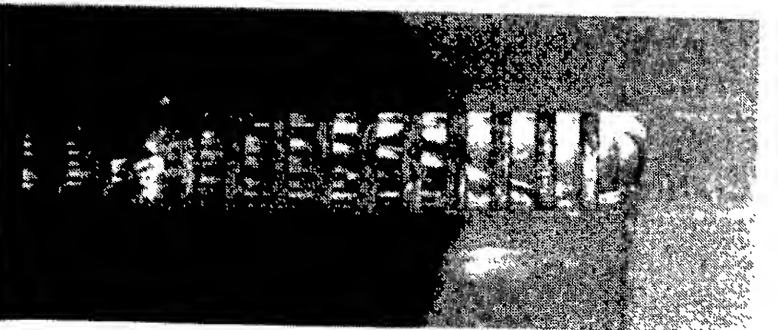
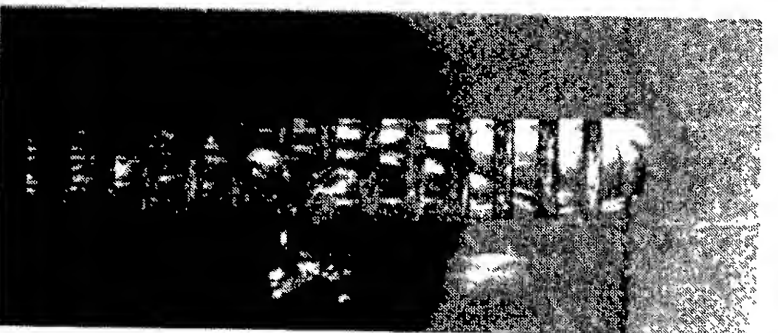
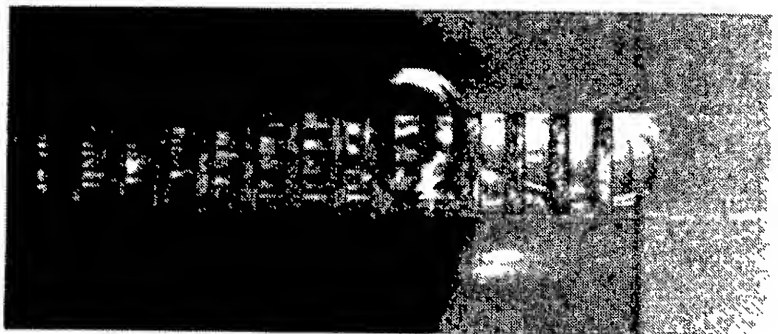
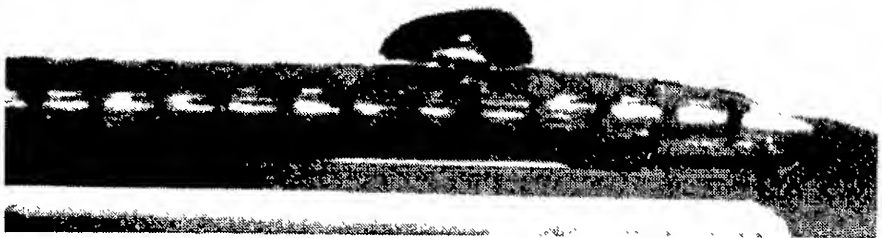
Furthermore, some bubbles were seen to cause local attached cavitation. When the operating cavitation number was close to the attached cavity formation index, trailing "streamers" were often observed down-

stream of the cavitation bubble (Figure 6). These streamers were generally associated with the larger bubbles on the I.T.T.C. body (and occasionally on the Schiebe body) and were seen to develop gradually at the location of the laminar separation point (Arakeri and Acosta (1973)). As the bubble is swept downstream, the streamers continue to grow, and in many cases persist even after the bubble has collapsed. Why these bubbles cause the attached cavitation streamers at the lateral extremities of the bubble is unclear. This phenomena has also been observed with travelling bubble cavitation on hydrofoils (van der Meulen (1980), and Rood (1989)). The process could be considered an inception mechanism for attached cavities.

The classic observations of Knapp and Hollander (1949) may be compared those of this study. Both experiments revealed that bubbles travelling near surfaces are cap shaped, and the gross characteristics of growth and collapse are similar. However, the pressure distribution on the ogive of Knapp and Hollander generated a long and steady growth, and the bubbles often retained a quasi-spherical shape even near the final stages of collapse. These bubbles would often rebound many times maintaining their quasi-spherical shape after each collapse. The bubbles observed in this study usually rebounded only once and lost most of their coherent shape after the first collapse. This difference may be explained by noting that the water tunnel facility used by Knapp and Hollander was not equipped with any deaeration system, and extremely bubbly flows were used to increase the odds of photographing a cavitation event. Consequently, the cavitating nuclei observed by Knapp and Hollander were large, containing more undissolved gas. Increasing the amount of residual gas reduces the violence of the bubble collapse making coherent rebounds possible. On the other hand, the nuclei populations of the present study were quite small, and the cavitation bubbles observed were almost entirely vaporous. Such bubbles collapse violently and therefore coherent rebounds are less likely.

Photographs of bubbles presented by Ellis (1952) show many of the features in the present study. Principally, bubbles formed close to the headform also progressed from a cap shape to a wedge shape before collapse, although the collapse mechanism is difficult to distinguish in Ellis' silhouette images. He observed that the bubble surface profile approximately coincided with lines of constant pressure for bubbles near the point of maximum volume. This accounts for the wedge shape of the bubble. Examination of the isobaric lines computed for flow around the Schiebe body (Schiebe (1972)) also show the bubbles observed in this study are being shaped by the pressure gradients close to the surface.

Returning to the present study, the collapse mechanisms for bubbles on both headforms were discerned through the study of many photographs. A composite mechanism is presented in Figure 7 for the Schiebe body with sample photographs in Figure 8. For the I.T.T.C. body similar results are included in Figures 9 and 10. Previous researchers have noted the generation of a liquid microjet in bubbles collapsing near a solid surface (Lauterborn and Bolle (1975) and Kimoto (1987), for example), and this microjet is often identified as the main cause of cavitation erosion damage. Although many photographs were taken during the present investigation, a reentrant microjet was



Profile View

Plan View

**Figure 5.** Series of photographs detailing typical bubble evolution on the I.T.T.C. headform,  $U = 8.7\text{m/s}$  and  $\sigma = 0.45$ .



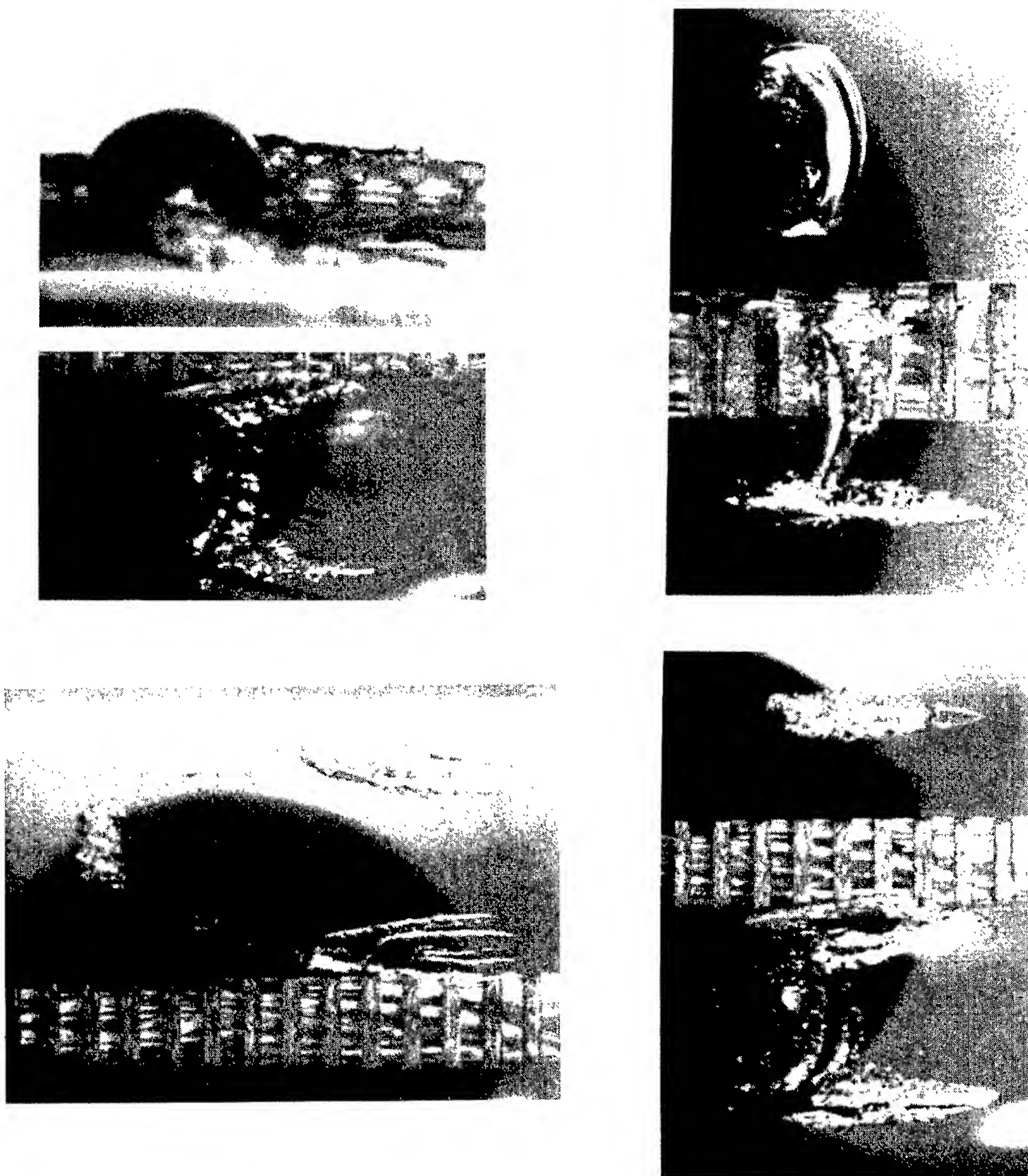


**Figure 6.** Series of photographs detailing bubbles with tails the I.T.T.C. headform,  $U = 9\text{m/s}$  and  $\sigma = 0.42$ .

not observed in any of the present photographs of bubble collapse, although the jet may have occurred too rapidly to be detected. The observed bubbles lack the compact geometry we might expect to be associated with coherent microjet formation.

## 5. MEASUREMENT OF THE ACOUSTIC EMISSION OF SINGLE CAVITATION BUBBLES

The detailed relationship between the collapse mechanism of hydrodynamic cavitation bubbles and the resulting noise generation is not completely clear, but some features are suggested by the present work. First, as other investigators have concluded (for example Harrison (1952) and Chahine, Courbiere, and Garnaud (1979)), the majority of the noise is generated by the violence of the first collapse; the growth phase contributed no measurable noise signal. The rebound produces a rough bubble which may also collapse to produce a second noise pulse of lesser magnitude. However, noise was not necessarily generated by every bubble collapse. Smaller bubbles would often collapse without an acoustic pulse, and larger bubbles would sometimes produce a muted collapse.

Figure 11 presents two examples of the initial noise pulse generated by the collapse of a bubble on the I.T.T.C. headform. The first pulse has only one peak, but the second trace is an example of a multiple peak event. Multiple peaks suggest bubble fission prior to collapse, and the photographs presented in the previous section reveal that many bubbles have undergone fission.

Although some researchers have used the peak acoustic pressure to characterize cavitation noise intensity (e.g. Van der Meulen (1989)), in this study the magnitude of acoustic pulses will be characterized by the acoustic impulse defined as

$$I = \int_{t_1}^{t_2} P_A dt \quad (1)$$

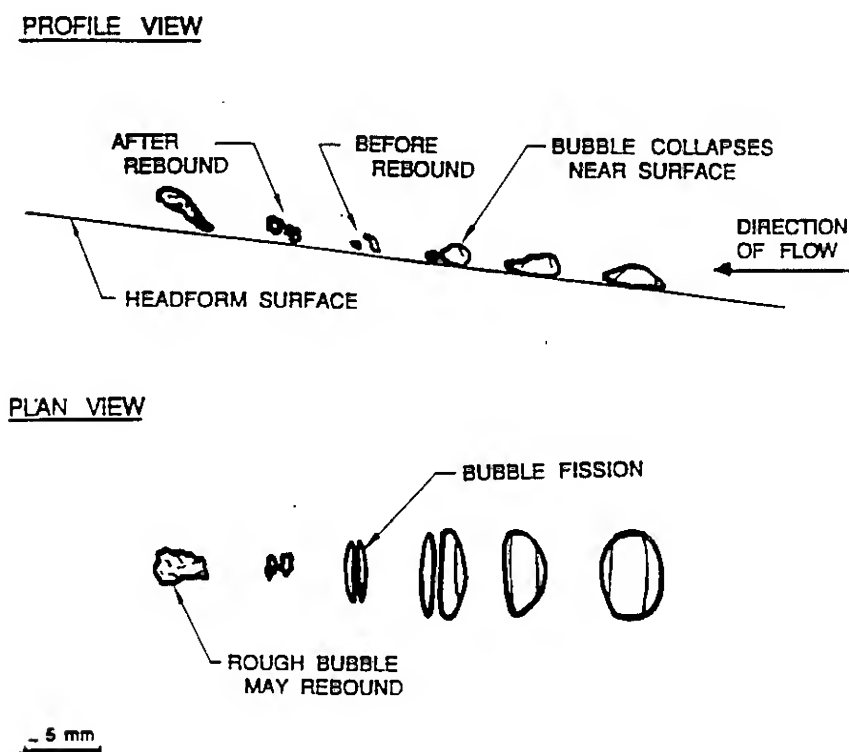


Figure 7. Schematic diagram of typical bubble collapse mechanism on the Schiebe headform.

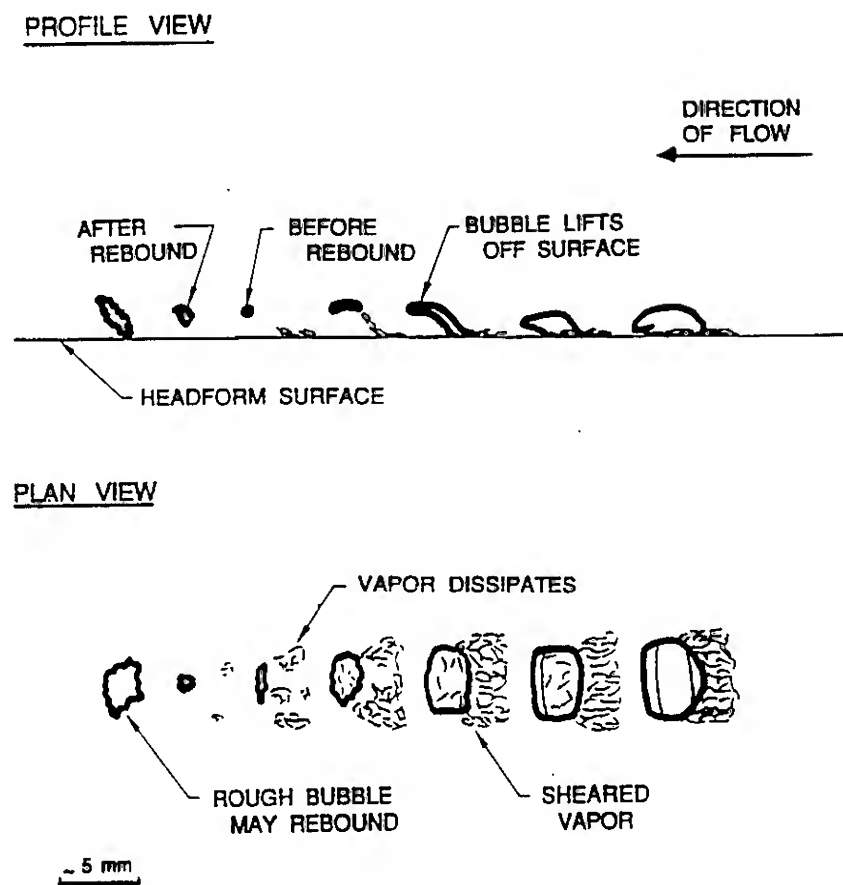


Figure 9. Schematic diagram of typical bubble collapse mechanism on the I.T.T.C. headform.

The times  $t_1$  and  $t_2$  were chosen to exclude the shallow pressure rise before collapse and the reverberation produced after the collapse. Experimentally measured impulses for the Schiebe body at a tunnel velocity of  $U = 9m/s$  and cavitation numbers of  $\sigma = 0.55$  and  $\sigma = 0.42$  are presented in Figure 12 and 13. The data all appear to lie below an envelope which passes through the origin. The existence of this well-defined impulse envelope suggests that a collapsing bubble can generate, for a certain maximum volume, a specific impulse if it collapses in some particular but unknown

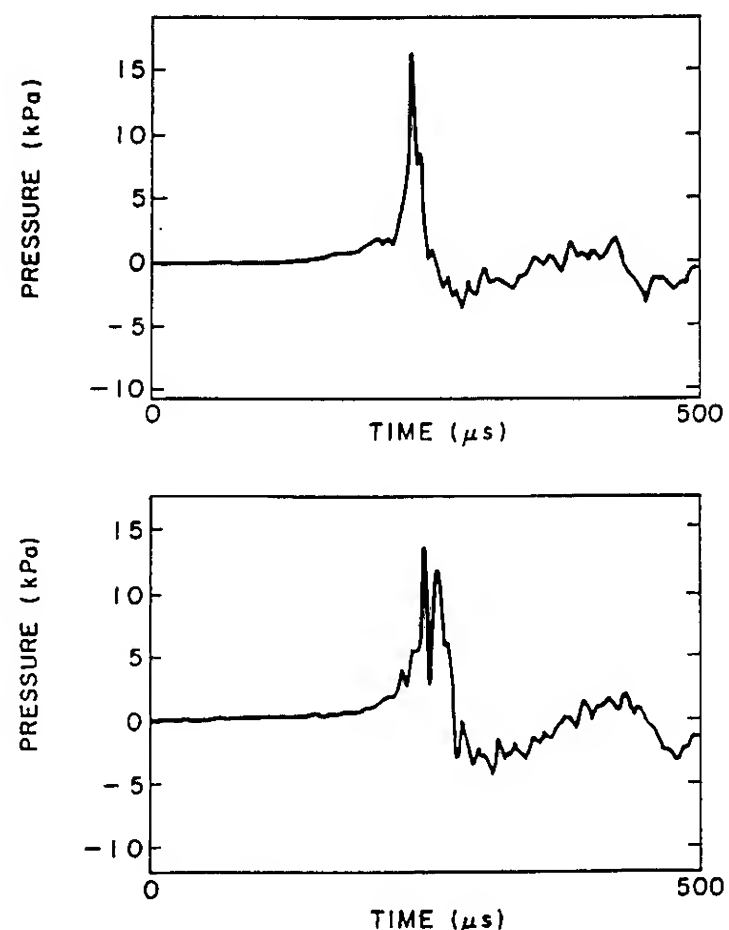
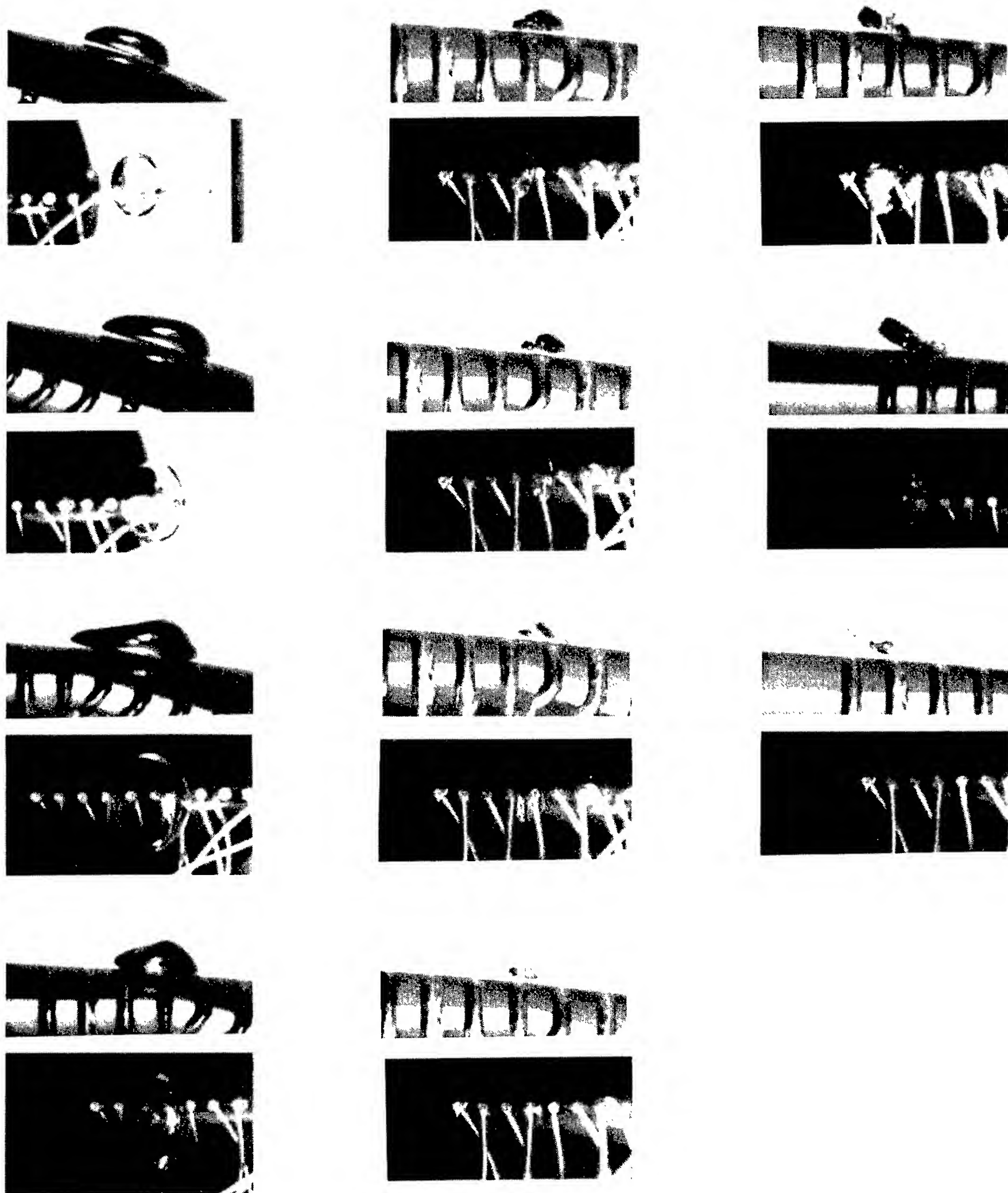


Figure 11. Two examples of typical cavitation initial noise pulses. The bubbles were generated on the I.T.T.C. headform at  $\sigma = 0.45$  and  $U = 8.7m/s$ .



**Figure 8.** Series of photographs detailing typical bubble collapse mechanism on the Schiebe headform,  $U = 9m/s$  and  $\sigma = 0.45$ .



Figure 10. Series of photographs detailing typical bubble collapse mechanism on the I.T.T.C. headform,  $U = 8.7m/s$  and  $\sigma = 0.45$ .



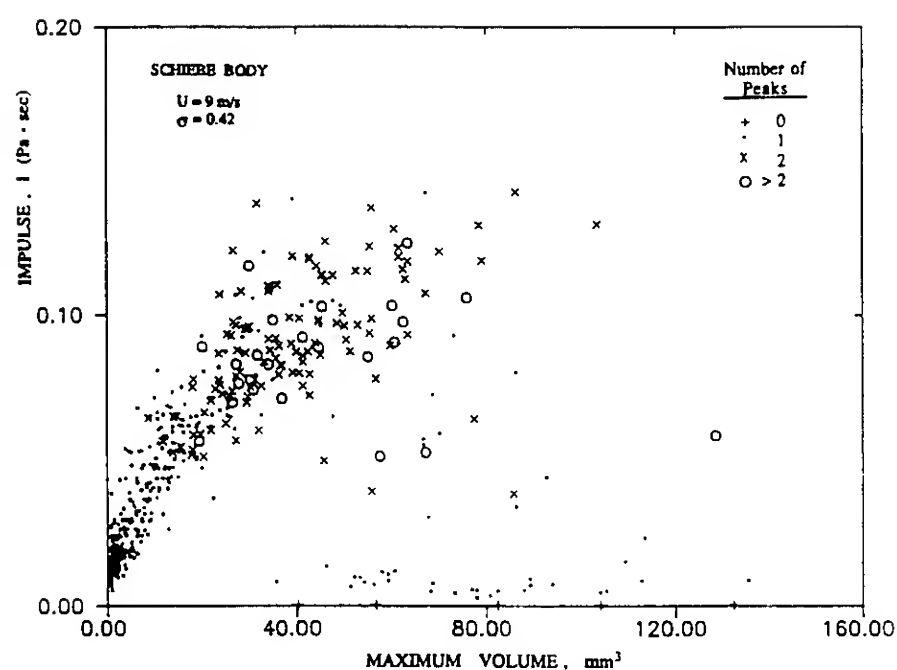


Figure 12. Acoustic impulse plotted against the maximum bubble volume for the Schiebe body at  $U = 9 \text{ m/s}$  and  $\sigma = 0.42$ .

way. It can, however, produce less than this maximum impulse if it collapses in other ways.

The different symbols represent the different number of acoustic peaks which are generated upon collapse. As shown in Figure 12, the probability that a collapse will produce multiple peaks increases for larger bubbles. Yet, even as the number of peaks increases, the impulse often reaches its maximum possible value implying that, in some collapse mechanisms, fission does not decrease the total stored energy available to produce noise. Other large bubbles collapse to produce almost no acoustic impulse. The production of noise upon collapse is the result of violent changes in bubble volume near the point of minimum bubble volume, but larger bubbles may be sheared apart and dissipate thus losing their organized shape and preventing a coherent and concentrated collapse. Furthermore, larger bubbles may contain more contaminant gas (as a result of dissolution) and this would cushion the collapse and reduce the acoustic emission.

At higher cavitation numbers such as that of Figure 13 the number of larger bubbles is reduced, and most bubbles collapse to produce only one acoustic pulse. However, a large number of very small bubbles will collapse and produce no significant impulse, and these cases are represented by the "0" symbols. Mute events are generally not examples of "pseudo-cavitation" as observed by Dreyer (1987) but distinct cavitation events with a near-silent collapse mechanism.

The general trends in the data for the Schiebe body are also evident in the results from the I.T.T.C. headform. Significantly, however, the average acoustic impulse is about three times larger than that of the Schiebe body. This will be discussed further below. Furthermore, as the cavitation number is lowered to near the attached cavitation inception index of the I.T.T.C. body, the impulse data changes significantly. Figure 14 presents an example of data from the I.T.T.C. body taken at a tunnel velocity of  $U = 8.7 \text{ m/s}$  and a cavitation number of  $\sigma = 0.42$  at near the attached cavitation formation index. The impulses generated by smaller bubbles are much more uncertain, and, for many larger bubbles, no significant impulse is generated. Since these larger bubbles gen-

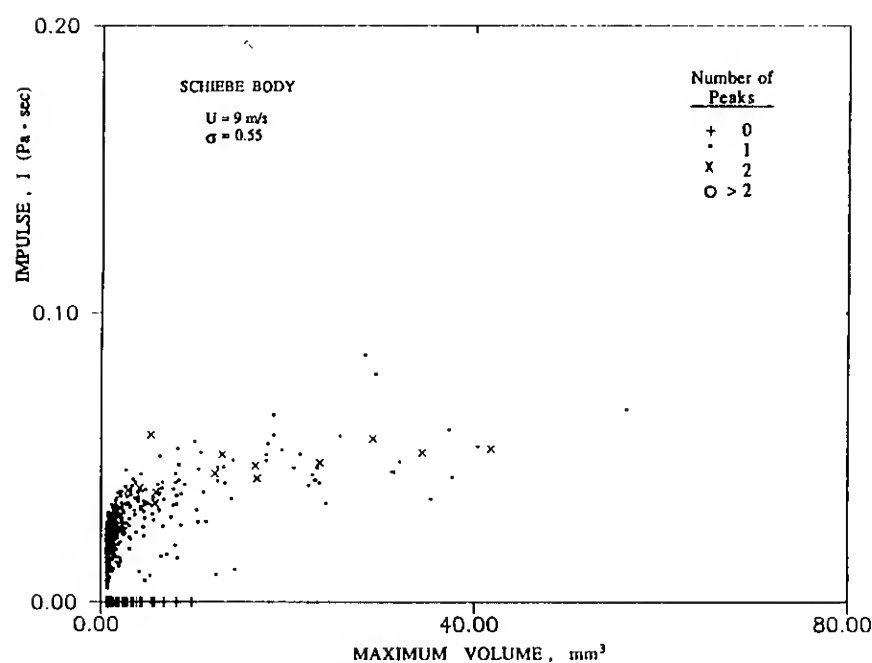


Figure 13. Acoustic impulse plotted against the maximum bubble volume for the Schiebe body at  $U = 9 \text{ m/s}$  and  $\sigma = 0.55$ .

erally have trailing streamers, it would seem that the streamers interfere with the collapse in a way which decreases or eliminates the noise.

The average number of peaks for a given average diameter is plotted in Figure 15 for both headforms. For smaller bubbles, the average is less than unity, reflecting the influence of muted bubbles, and for larger bubbles, multiple peaking produces an average above unity. For the case of the I.T.T.C. body, however, the muting effect of the trailing streamers causes a reduction in the average number of peaks for the data set with the largest average volume. This data set occurs at the lowest cavitation number, near the attached cavitation inception point.

## 6. COMPARISON WITH ANALYTICAL RESULTS

In order to place the above experimental results in some analytical perspective, calculations were made of the bubble sizes and acoustic impulses predicted by integration of the Rayleigh-Plesset equation starting

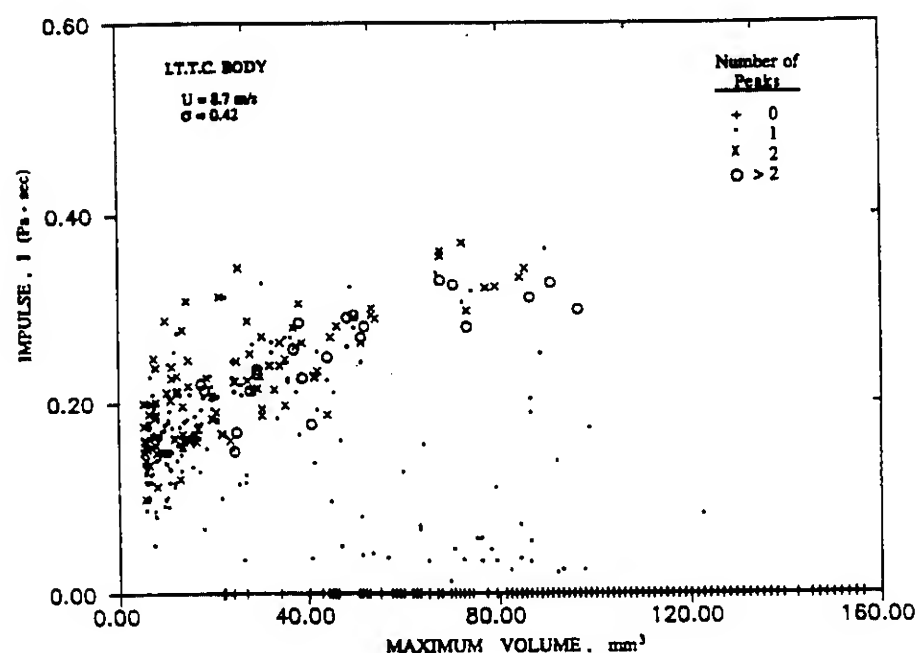


Figure 14. Acoustic impulse plotted against the maximum bubble volume for the I.T.T.C. body at  $U = 8.7 \text{ m/s}$  and  $\sigma = 0.42$ .

with various sizes of freestream nuclei. The known surface pressure distributions for both headforms were employed to construct the pressure-time history which a nucleus would experience while passing near the headform. No slip between the bubble and the liquid and a small offset from the stagnation streamline are assumed. Calculations were performed with various free stream velocities, cavitation numbers, and offsets from the stagnation streamline. Figure 16 provides an example of the dependence of the maximum bubble radius on the original nucleus size for the I.T.T.C. headform and various cavitation numbers. Note that nuclei below a certain size (which depends on the cavitation number) hardly grow at all and would therefore not contribute visible cavitation bubbles. This critical size is predicted by the stability analysis of Johnsson and Hsieh (1966) and Flynn (1964). Bubbles below the critical size grow quasistatically, whereas larger bubbles grow explosively. A bubble is critically unstable if

$$\frac{R_L}{R_H} > \frac{8}{3} \frac{S}{\rho R_H U^2} \frac{1}{(-\sigma - C_{PM})} \quad (2)$$

where  $C_{PM}$  is the minimum pressure coefficient (-0.62 for the I.T.T.C. headform) and  $R_L$  is the local bubble size. The computations show that so long as the bubble remains stable, then  $R_L$  is somewhere in the range  $R_O < R_L < 2R_O$  for the common circumstances of interest here. Consequently, the critical nucleus size  $R_C$  is given by

$$R_C > \frac{8}{3} \frac{\beta S}{\rho U^2} \frac{1}{(-\sigma - C_{PM})} \quad (3)$$

where  $\beta$  is a constant. The results of this simple expression are presented in Figure 17 along with data on the critical nucleus size obtained from the Rayleigh-Plesset solutions. The qualitative agreement is excellent and suggests a value of  $\beta$  slightly greater than 0.5. Note that the higher the velocity,  $U$ , the smaller the critical size, and therefore the larger the number of nuclei that will be involved in cavitation.

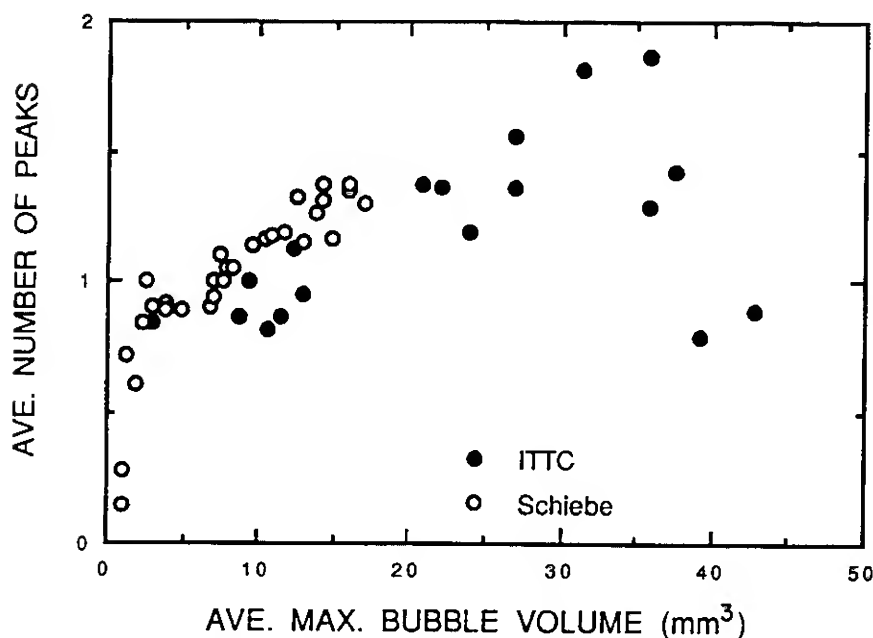


Figure 15. Average number of peaks as a function of average maximum bubble volume for bubbles generated on the Schiebe body and the I.T.T.C. body.

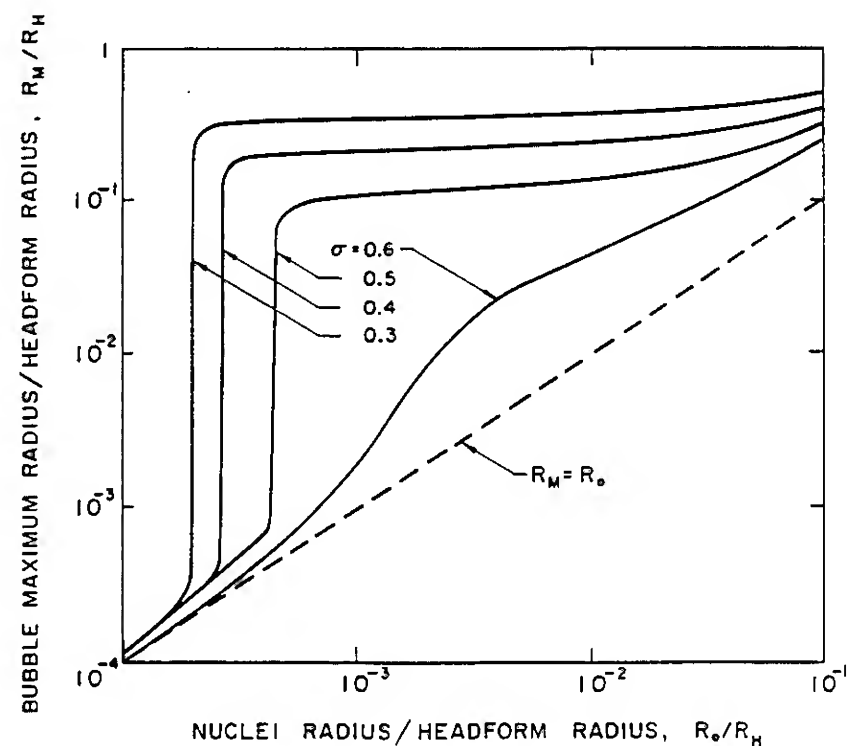


Figure 16. Numerical calculation of the bubble maximum radius as a function of nucleus radius for nuclei passing near the I.T.T.C. headform.

The other feature of Figure 16 which is important to note is that virtually all nuclei greater than the critical nucleus size grow to approximately the same maximum size. The asymptotic growth rate of an unstable cavitating bubble is a function only of the pressure and not the initial nucleus size. Consequently, the maximum size achieved will be approximately independent of the nucleus size. This accounts for the uniformity of cavitation bubbles observed experimentally. Similar calculations were performed for nuclei experiencing the Schiebe body pressure distribution, and the results were qualitatively similar to those of the I.T.T.C. body.

The above calculations yield the volume-time history for a cavitating bubble, and the acoustic pressure generated by the bubble may be approximately given by

$$P_A(r, t) = \frac{\rho}{4\pi r} \frac{d^2 V}{dt^2} \quad (4)$$

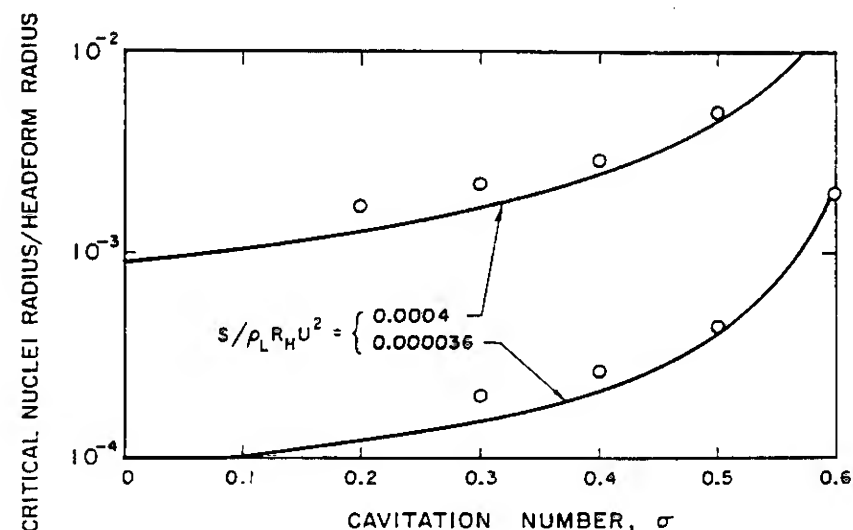
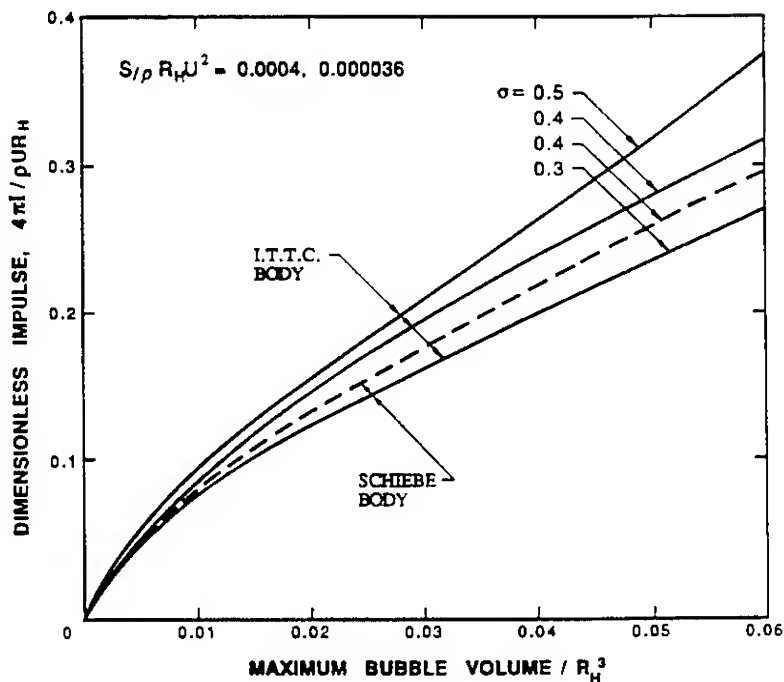


Figure 17. Critical nuclei radius as a function of flow parameters for nuclei passing near the I.T.T.C. headform.





**Figure 18.** Numerical calculation of the acoustic impulse as a function of the maximum bubble volume for bubbles generated on the Schiebe body and the I.T.T.C. body.

were  $V(t)$  is the bubble volume,  $\rho$  is the fluid density, and  $r$  is the distance from the center of the bubble. This relationship is valid in the acoustic far-field and for subsonic wall velocities. The acoustic impulses,  $I$ , were calculated from the definition (1) where  $t_1$  and  $t_2$  were taken to be the times when  $d^2V/dt^2 = 0$  before and after the first collapse.

For those nuclei which become unstable and explosively cavitate the non-dimensional impulse,  $I^*$ , is defined as

$$I^* = \frac{4\pi I}{\rho R_H U} \quad (5)$$

where we have assumed  $r = R_H$  since this is the location of the hydrophone in the experiments. The impulse  $I^*$  is plotted in Figure 18 against the maximum volume of the bubbles non-dimensionalized by  $R_H^3$ . A number of investigators (i.e. Fitzpatrick and Strasberg (1956) and Hamilton et.al. (1982)) have suggested that the magnitude of the acoustic signal should be related to the maximum size of the bubble, and this is born out in Figure 18 where the data for a range of cavitation numbers and two Weber numbers,  $We$ , are contained within a fairly narrow envelope.

The median line was converted to dimensional values and is plotted in Figure 19 where it is compared with data sets from the Schiebe and I.T.T.C. experiments. It is striking to note that the envelope of the maximum impulse from the experiments is within a factor of two of the Rayleigh- Plesset calculation for the I.T.T.C. body and within a factor of six for the Schiebe body. This suggests that, despite the departure from the spherical shape during collapse, the incompressible Rayleigh-Plesset solutions correctly predict the order of magnitude of the noise impulse generated by individual bubbles.

It is not surprising that the predicted impulse is greater than the experimental value. In fact, the theoretical impulse may be considered the maximum

impulse possible for a given bubble volume since a spherically symmetric collapse is probably the most efficient noise producing mechanism. The difference between the measured impulses and the theoretical impulse is an indication of the inefficiency of the actual collapse mechanism. Furthermore the average impulses are closer to the theoretically predicted values for the I.T.T.C. body than for Schiebe body, and this is consistent with the photographic evidence that the I.T.T.C. collapse mechanism is more compact than that on the Schiebe body.

The duration of the impulse (as opposed to the magnitude) is much better understood. Here, the duration is defined as  $T = t_1 - t_2$ . This time is simply related to the total collapse time derived by Rayleigh (1917) which is used by many authors (e.g. Blake, Wolpert, and Geib (1977) and Arakeri and Shanmuganathan (1985)). Like the collapse time, it will be approximated by

$$T^* = \alpha \frac{R_M}{U} \left( \frac{2}{\sigma} \right)^{1/2} \quad (6)$$

where  $\alpha$  is some constant of order unity. It follows that the dimensionless impulse duration  $T^* = TU/R_H$  should be primarily a function of  $R_M/R_H$ , and this is confirmed by the results of the Rayleigh-Plesset solutions shown in Figure 20. Also plotted are typical experimental data from the Schiebe body. Note that the calculated results lie within a narrow envelope for a range of cavitation numbers and that the slope of the narrow envelope is close to unity. The experimental data is about one third the predicted magnitude. Note, however, that the definitions of  $t_1$  and  $t_2$  are somewhat arbitrary.

Figure 21 presents spectra of the noise measured in the experiments. A series of individual acoustic pulses were recorded at a particular velocity and cavitation number. The resulting spectra were averaged to produce the composite spectra in the figure; the

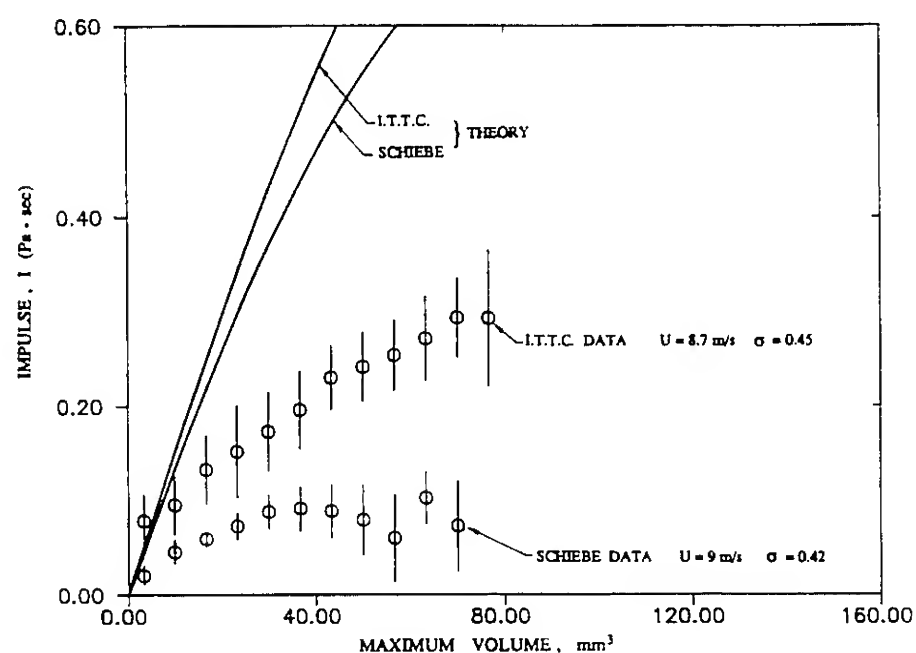


**Figure 19.** Comparison of theoretically predicted and experimentally measured acoustic impulse as a function of the maximum bubble volume for bubbles generated on the Schiebe body and I.T.T.C. body. Experimental data for  $\sigma = 0.45$  and  $U = 9m/s$  for the Schiebe body and  $U = 8.7m/s$  for the I.T.T.C. body.

signals were not altered to remove the effects of tunnel reverberation. Such a composite spectrum will be equivalent to the spectrum derived from a measurement of a long series of cavitation noise pulses, provided the cavitation events occur randomly (Morozov (1969)). The measured spectral shape varies little with cavitation number; only the overall spectral magnitude changes. A decrease of approximately  $-12\text{dB/decade}$  is noted until about  $100\text{kHz}$  where a sharp falloff occurs. This cut-off frequency corresponds to the frequency response limit of the hydrophone.

Asymptotic analyses of the Rayleigh-Plesset equation (Blake (1986)) predict a spectral shape of  $f^{-2/5}$  for frequencies in the range of  $10\text{kHz}$  to  $100\text{kHz}$ . The experimental spectrum has a shape of approximately  $f^{-3/5}$  which is similar but not identical to the predicted trend. Hamilton (1981), on the other hand, observed an almost completely flat spectrum in this range based on his integral measurement of bubble cavitation noise. The high frequency roll-off associated with fluid compressibility was not observed below  $100\text{kHz}$ , and this is consistent with the observations of Hamilton (1981) and Barker (1975).

## 7. OBSERVATIONS OF CAVITATION EVENT RATES AND BUBBLE MAXIMUM SIZE DISTRIBUTIONS

Experiments were performed to measure the cavitation event rate and bubble maximum size distribution on both headforms along with the freestream nuclei number distribution. Furthermore, an analytical model was derived to study the relationship between the nuclei flux and the resulting cavitation statistics.

The cavitation event rate and bubble maximum size distribution were measured for several thousand events at various operating conditions, and examples of these measurements for the Schiebe headform are given in Figure 22. Note that the bubble maximum sizes are presented as reduced radii. The reduced bubble radius is the radius of a sphere of volume equal to the measured bubble volume. Although the four bubble size distributions presented are all at the same cavitation number and tunnel velocity, their event rates and size distributions are quite different. Since the

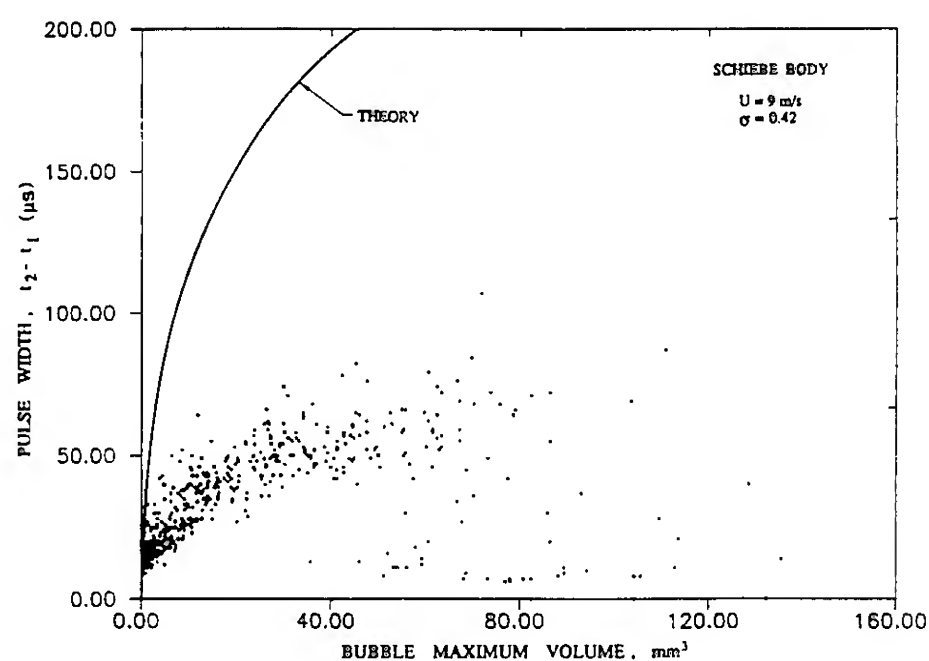


Figure 20. Comparison of theoretically predicted and experimentally measured pulse width as a function of the maximum bubble volume for bubbles on the Schiebe body at  $U = 9\text{m/s}$  and  $\sigma = 0.45$ .

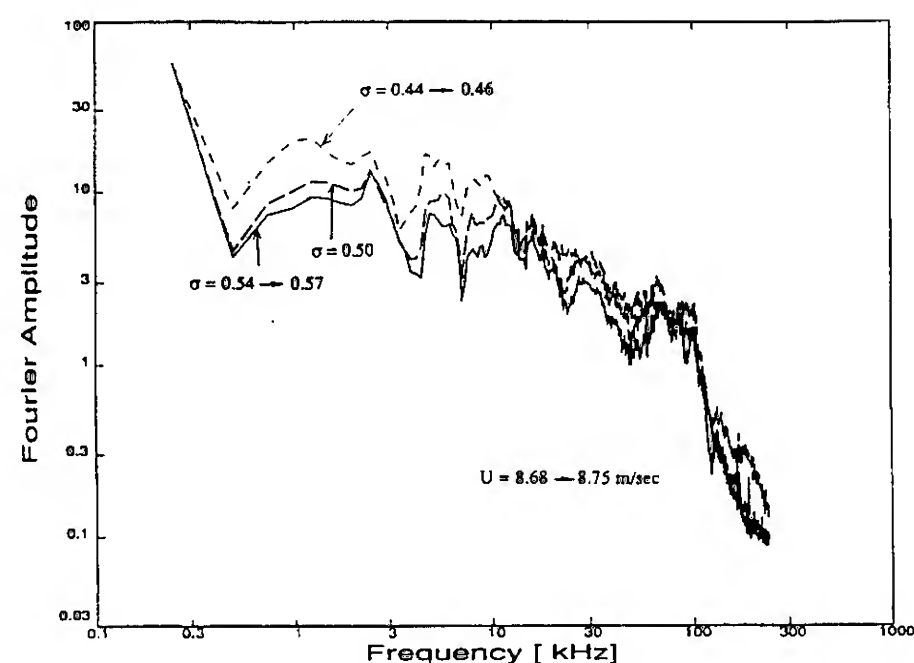


Figure 21. Averaged acoustic spectra derived from acoustic pulses generated by bubbles on the Schiebe body at average  $U = 8.7\text{m/s}$  and  $\sigma = 0.45, 0.50$ , and  $0.56\text{m/s}$ .

cavitation bubble maximum volume distribution is directly related to the incoming nuclei number distribution these results clearly indicate that the nuclei number distribution can be quite different for the same tunnel operating conditions. Weak control of the number of nuclei was affected through deaeration and nuclei injection. But, as Figure 22 indicates, the nuclei number distribution is a highly variable factor which influences travelling bubble cavitation and cavitation noise. The time between cavitation events was Poisson distributed, as would be expected for randomly distributed nuclei. Consequently, the total noise spectra produced by these flows should be equivalent to the composite spectra presented in Figure 21.

A relationship between the nuclei flux and the resulting cavitation event rate and bubble maximum size distribution can be developed as follows. Whether a nucleus cavitates or not is strongly determined by the local minimum pressure it experiences. On the surface of the headform, this pressure is given by the minimum pressure coefficient. On streamlines above

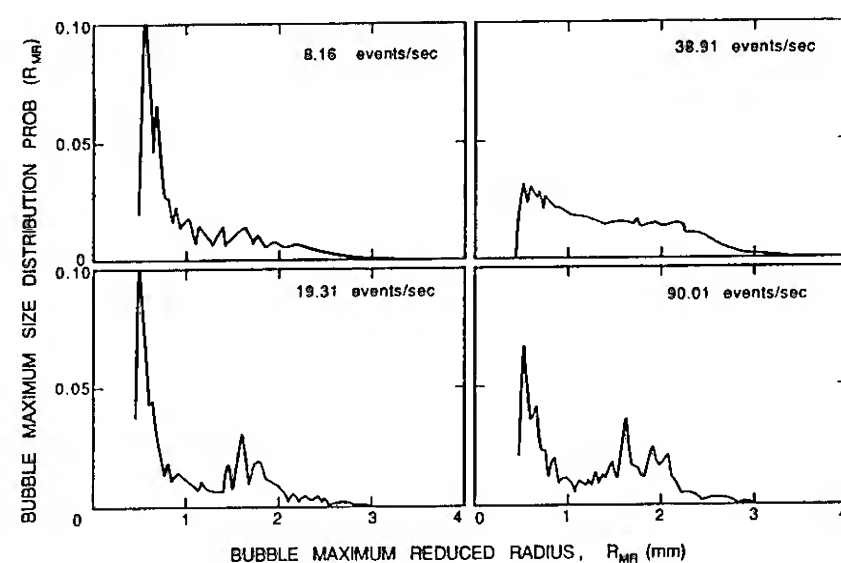


Figure 22. Example of four bubble maximum size distributions for a particular free stream velocity and cavitation number for cavitation on the Schiebe body.

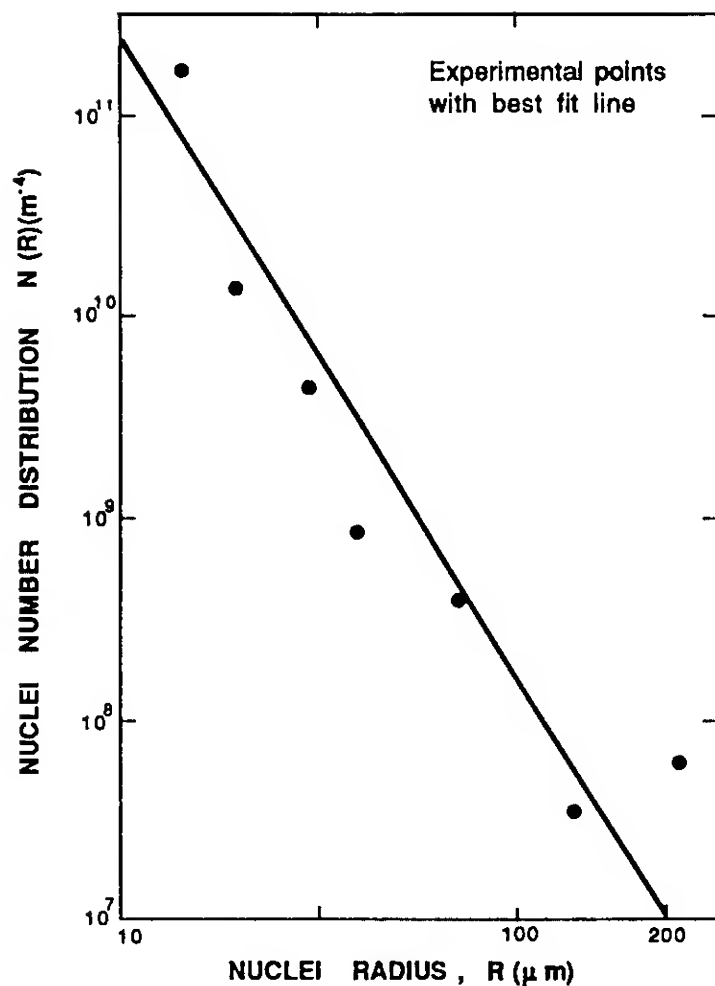


Figure 23. Example measurement of the free stream nuclei number distribution,  $U = 9\text{ m/s}$  and  $\sigma = 0.45$ .

the body surface, the fluid pressure may still be low enough to cause a nucleus to cavitate provided that the minimum pressure it experiences is below the critical pressure, derived from Equation (3). An incoming streamtube may therefore be defined for a nucleus of specific size such that the nucleus will always encounter a pressure low enough to cause it to cavitate during its flow around the body. The fluid capture area of this streamtube will be a function of the nuclei radius,  $R_O$ , the free stream cavitation number, and the flow geometry. By assuming that the pressure gradient normal to the surface corresponds to the centrifugal pressure gradient caused by the radius of curvature,  $\kappa$ , of the surface at the minimum pressure point, and by assuming no slip between the nuclei and the fluid, the following expression for the nuclei capture area,  $A(R_O)$ , may be readily obtained (Ceccio (1990)):

$$A(R_O) = \frac{R_B \kappa \pi}{\sqrt{1 - C_{PM}}} (-\sigma - C_{PM}) \left(1 - \frac{R_C}{R_O}\right) \quad (7)$$

where  $R_O$  is the original nuclei radius,  $R_B$  is the headform radius at the point of minimum pressure, and  $R_C$  is the minimum cavitable nucleus given by Equation (3). Equation (7) may be rewritten as

$$A(R_O) = A_V \left(1 - \frac{R_C}{R_O}\right) \quad (8)$$

where  $A_V$  is the capture area enclosing all streamlines which involve pressures less than vapor pressure; note that  $A_V$  is a function only of the flow geometry and free stream conditions. Finally, the to-

tal flux of cavitable nuclei or total cavitation event rate,  $\Theta$ , is

$$\Theta = \int_{R_C}^{\infty} A(R_O) N(R_O) U dR_O \quad (9)$$

where  $N(R_O)$  is the free stream nuclei number distribution.

Now consider the distribution of bubble maximum sizes which this process will produce. This distribution is the result of different nuclei trajectories and sizes. Cavitating nuclei travelling on streamlines farther away from the headform will not grow to the same maximum volume as those travelling near the surface. Consequently, a flux of uniform nuclei,  $R_O$ , will yield a probability distribution of bubble maximum sizes,  $R_M$ , denoted by  $Pr_O(R_M)$ . Because of the slight dependence of bubble maximum size upon nucleus size,  $Pr_O$  is a function of  $R_O$ . A flux of nuclei represented by the nuclei number distribution,  $N(R_O)$ , will therefore produce a distribution of maximum bubble sizes,  $Pr$ , given by

$$Pr(R_O) = \frac{1}{\Theta} \int_{R_C}^{\infty} Pr_O A(R_O) N(R_O) U dR_O \quad (10)$$

If no relationship existed between nuclei size and the maximum bubble size,  $Pr$  would be independent of the nuclei number distribution; changes in  $N(R_O)$  would merely change the total event rate. The experimental data indicate, however, that the bubble maximum size distributions are influenced by the nuclei number distribution. The varying event rates reported in Figure 22 indicate different nuclei populations, and each example is accompanied by a unique bubble size distribution. The small influence of nuclei size upon the maximum bubble size will ultimately have a significant influence upon the bubble maximum size distribution.

We shall now compare the measured cavitation event rates and bubble maximum size distributions with the predicted quantities based on holographically-determined free stream nuclei number distributions. The nuclei populations were measured at the same time that the cavitation statistics were recorded, and the smallest nucleus which could be detected with certainty was approximately  $20\mu\text{m}$  in diameter. An example nuclei distribution is presented in Figure 23. Table 1 presents the measured event rates and the predicted event rates based on Equations (7) and (9). The measured event rates fall within the range of the predicted values, with the uncertainty in the predicted event rates resulting from uncertainty in the measured

PREDICTED $\Theta$ (events/sec)	MEASURED $\Theta$ (events/sec)
$128 \pm 25$	156
$164 \pm 25$	147
$147 \pm 25$	162

Table 1. Comparison of measured and predicted cavitation event rates for cavitation generated on the I.T.T.C. body at  $U = 9\text{ m/s}$  and  $\sigma = 0.45$ .

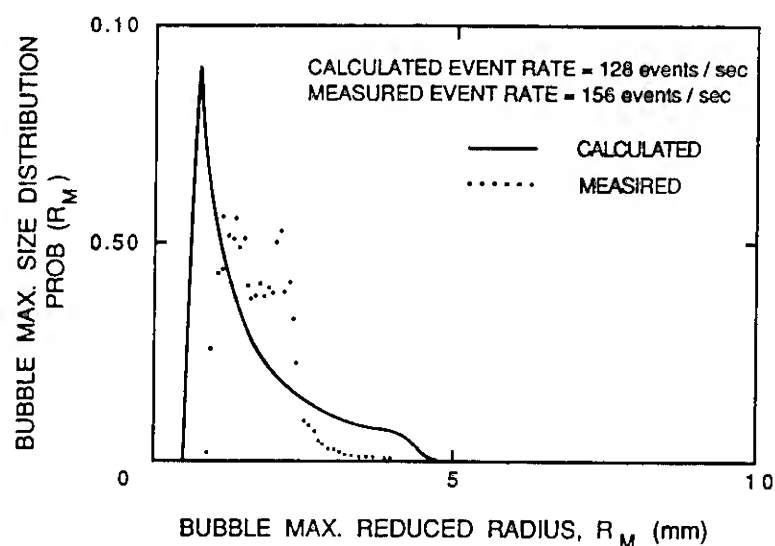


Figure 24. Calculated and measured event rate and bubble maximum size distribution for cavitation on the I.T.T.C. headform at  $U = 9\text{ m/s}$  and  $\sigma = 0.45$ .

nuclei number distributions. The close match between the predicted and measured event rates indicates that the nucleus stability criteria from Equation (3) adequately models the actual cavitation process. The minimum cavitable nucleus for this flow is calculated to be approximately  $20\mu\text{m}$  in radius, and the measured nuclei number distribution indicate that most of the cavitating nuclei are in the range 20 to  $100\mu\text{m}$ . The success of the model suggests that the quantities  $Av$  and  $R_C$  may be used to adequately characterize the nuclei capture area for flows over more complicated bodies.

The calculated bubble maximum volume distributions, however, depart substantially from the measured size distribution in terms of its details. Figure 24 presents a measured bubble maximum size distribution along with the predicted distribution based on Equations (7), (9), and (10), the results of Figure 16, and the measured free stream nuclei distribution. The calculated size distribution departs substantially from the measured distribution in its details. The predicted bubble size range is about twice the observed size range, and the number of larger bubbles predicted is much smaller than the observed percentage. These discrepancies may be the result of several phenomena. First, the maximum size achieved by a nucleus subjected to a specific pressure history may not be adequately predicted by the Rayleigh-Plesset equation since bubble growth may be limited by the positive pressure gradients above the headform surface. Once the bubble has grown sufficiently, the mean pressure on the bubble surface will be larger than the surface pressure used in the Rayleigh-Plesset calculation, reducing the driving force for bubble growth. Furthermore, the experimental bubble maximum size distributions often show several maxima which were repeatable for nominally fixed operating conditions. These distributions cannot be simulated with simple, smooth nuclei distributions with several well defined peaks. It seems likely that these maxima are the result of a complicated nuclei number distribution. Such detail could not be ascertained using the current holographic nuclei distribution methodology; its existence was only revealed by the electrode system which permits very large quantities of data on bubble size distributions.

## 8. CONCLUSION

Although theories of individual bubble cavitation abound, this study demonstrates that a great deal may still be learned through the observation of naturally occurring cavitation bubbles, especially bub-

bles formed in flows near surfaces. Cavitation bubbles are significantly affected by the viscous flow near surfaces, and this in turn effects their noise production and possibly their damage potential. Yet, numerical integration of the Rayleigh-Plesset provided a reasonable base for comparison with the experimentally measured data. The relationship between the nuclei flux and the resulting cavitation was successfully predicted based upon simple parameters derived from the non-cavitating flow around the body, although estimation of the bubble maximum size distribution was more difficult.

By combining the results of this study, cavitation noise may systematically be synthesized. Analysis of cavitation event statistics and size distributions can relate the freestream nuclei distribution to the cavitation process. And, once the number and size of the cavitation events are known, the total noise emission may be estimated based on the single bubble measurements. The results presented here are useful for the case of limited cavitation, but multiple bubble effects must be included to characterize flows in which the bubbles interact with one another. The importance of the nuclei number distribution as a parameter in cavitation studies cannot be overemphasized, although simple and accurate methods are still needed to measure this quantity with speed, ease, and precision.

## ACKNOWLEDGEMENTS

The authors would like to thank Professor Allan Acosta for his advice and considerations. We would also like to acknowledge the assistance of Sanjay Kumar and Douglas Hart. This work was supported by the Office of Naval Research under contract number N-00014-85-K-0397.

## REFERENCES

- Arakeri, V. H. and Acosta, A. J. 1973. Viscous Effects in the Inception of Cavitation on Axisymmetric Bodies. *ASME Journal of Fluids Engineering*, Vol. 95, pp. 519-527.
- Arakeri, V. H. and Shangumanathan, V. 1985. On the Evidence for the Effect of Bubble Interference on Cavitation Noise. *Journal of Fluid Mechanics*, Vol. 159, pp. 131-150.
- Baiter, H. J. 1974. Aspects of Cavitation Noise. Symposium on High Powered Propulsion of Ships, Wageningen, The Netherlands, Publication No. 490, pp. 1-39.
- Baiter, H. J. 1986. On Different Notions of Cavitation Noise and What They Imply. International Symp. on Cavitation and Multiphase Flow Noise, ASME FED Vol. 45, pp. 107-118.
- Barker, S. J. 1975. Measurement of Radiated Noise is the Caltech High-Speed Water Tunnel-Part II: Radiated Noise from Cavitating Hydrofoils. Guggenheim Aeronautics Laboratory, California Institute of Technology Report.
- Benjamin, T. B. and Ellis, A. T. 1966. The Collapse of Cavitation Bubbles and the Pressures Thereby Produced Against Solid Boundaries. *Philosophical Transactions of the Royal Society of London*, Vol. 260, pp. 221-240.
- Bernier, J. N. 1981. Unsteady Two-Phase Flow Instrumentation and Measurement. Rep. E200.4, California Institute of Technology, Division of Engineering and Applied Science.



- Blake, J. R. and Gibson, D. C. 1987. Cavitation Bubbles Near Boundaries. *Ann. Rev. Fluid Mechanics*, Vol. 19, pp. 99-123.
- Blake, W. K., Wolpert, M. J. and Geib, F. E. 1977. Cavitation Noise and Inception as Influenced by Boundary Layer Development on a Hydrofoil. *Journal of Fluid Mechanics*, Vol. 80, pp. 617-640.
- Blake, W. K. 1986. *Mechanics of Flow Induced Sound and Vibration*. Volume 1, Chapter 6, Introduction to Bubble Dynamics and Cavitation, Academic Press, pp. 370-425.
- Ceccio, S. L. 1990. Observations of the Dynamics and Acoustics of Travelling Bubble Cavitation, Rep. E249.11, California Institute of Technology, Division of Engineering and Applied Science.
- Chahine, G. L., Courbiere, P. and Garnaud, P. 1979. Correlation Between Noise and Dynamics of Cavitation Bubbles. *Sixth Conference on Fluid Machinery*, Budapest, Vol. 1, pp. 200-209.
- d'Agostino, L., Brennen, C. E. and Acosta, A. J. 1988. Linearized Dynamics of Two-Dimensional Bubbles and Cavitating Flows Over Slender Surfaces. *Journal of Fluid Mechanics*, Vol. 199, pp. 155-176.
- Dreyer, J. J. 1987. Free Stream Microbubble Effects on Travelling Bubble Cavitation Inception on the Schiebe Headform. ARL/PSU Technical Memorandum 87-205.
- Ellis, A. T. 1952. Observations on Cavitation Bubble Collapse. Rep. 21-12, California Institute of Technology, Hydrodynamics Lab.
- Fitzpatrick, H. M. and Stasberg, M. 1956. Hydrodynamic Sources of Sound. *First Symposium on Naval Hydrodynamics*, Washington, D. C., pp. 241-280.
- Flynn, H. G. 1964. *Physics of Acoustic Cavitation in Liquids*. Physical Acoustics, editor W. P. Mason, Academic Press.
- Gates, E. M. 1977. The Influence of Freestream Turbulence, Freestream Nuclei Populations, and Drag Reducing Polymer on Cavitation Inception on Two Axisymmetric Bodies. Rep. E182-2, California Institute of Technology, Division of Engineering and Applied Science.
- Gates, E. M., Billet, M. L., Katz, J., Ooi, K. K., Holl, W. and Acosta, A. J. 1979. Cavitation Inception and Nuclei Distribution - Joint ARL-CIT Experiments. Rep. E244-1, California Institute of Technology, Division of Engineering and Applied Science.
- Hamilton, M. F. 1981. Travelling Bubble Cavitation and Resulting Noise. *Appl. Res. Lab., Penn. State, Tech. Mem. TM 81-76*.
- Hamilton, M. F., Thompson, D. E. and Billet, M. L. 1982. An Experimental Study of Travelling Bubble Cavitation and Noise. *ASME International Symposium on Cavitation Noise*, pp. 25-33.
- Harrison, M. 1952. An Experimental Study of Single Bubble Cavitation Noise. *Journal of the Acoustical Society of America*, Vol. 28, pp. 776-782.
- Hoyt, J. W. 1966. Wall Effect on I.T.T.C. Standard Head Shape Pressure Distribution. Contribution to 11th International Towing Tank Conference.
- Johnsson, V. E. and Hsieh, T. 1966. The Influence of Gas Nuclei on Cavitation Inception. *Proc. Sixth Symposium on Naval Hydrodynamics*, Washington D. C.
- Katz, J. 1981. Cavitation Inception in Separated Flows. Rep. E183-5, California Institute of Technology, Division of Engineering and Applied Science.
- Kling, C. L. and Hammitt, F. G. 1972. A Photographic Study of Spark Induced Cavitation Bubble Collapse. *A.S.M.E. Journal of Basic Engineering*, Vol. 94, pp. 825-833.
- Knapp, R. T. and Hollander, A. 1948. Laboratory Investigations of the Mechanisms of Cavitation. *Trans. ASME*, July 1948, p. 419.
- Kimoto, H. 1987. An Experimental Evaluation of the Effects of a Water Microjet and a Shock Wave by a local Pressure Sensor. *International Symposium on Cavitation Research Facilities and Techniques*, ASME FED Vol. 57, pp. 217-224.
- Lauterborn, W. and Bolle, H. 1975. Experimental Investigation of Cavitation-Bubble Collapse in the Neighborhood of a Solid Boundary. *Journal of Fluid Mechanics*, Vol. 72, pp. 391-399.
- Lindgren, H. and Johnsson, C. A. 1966. Cavitation Inception on Headforms: I.T.T.C. Comparative Experiments. *Eleventh International Towing Tank Conference Proceedings*, Tokyo.
- Marboe, M. L., Billet, M. L. and Thompson, D. E. 1986. Some Aspects of Travelling Bubble Cavitation and Noise. *International Symp. on Cavitation and Multiphase Flow Noise*, ASME FED Vol. 45, pp. 119-126.
- Mellon, R. H. 1956. An Experimental Study of the Collapse of a Spherical Cavity in Water. *Journal Acoustic Society of America*, Vol. 28, pp. 447-454.
- Meyer, R. S., Billet, M. L. and Holl, J. W. 1989. Free Stream Nuclei and Cavitation. *International Symp. on Cavitation Inception*, ASME FED Vol. 89, pp. 55-62.
- Morch, K. A. 1982. Energy Consideration on the Collapse of Cavity Clusters. *Applied Scientific Research*, Vol. 38, p. 313.
- Morozov, V. P. 1969. Cavitation Noise as a Train of Sound Pulses Generated at Random Times. *Soviet Physics-Acoustics*, Vol. 14, pp. 361-365.
- Ooi, K. K. 1981. Scale Effects on Cavitation Inception in Submerged Jets. Rep. E183-6, California Institute of Technology, Division of Engineering and Applied Science.
- Parkin, B. R. 1952. Scale Effects in Cavitating Flow. Ph.D. Thesis, California Institute of Technology.
- Plesset, M. S. and Chapman, R. B. 1970. Collapse of an Initially Spherical Vapor Cavity in the Neighborhood of a Solid Boundary. Rep. 85-49, California Institute of Technology, Division of Engineering and Applied Science.

- Rood, E. P. 1989. Mechanisms of Cavitation Inception. International Symp. on Cavitation Inception, ASME FED Vol. 89, pp. 1-22.
- Schiebe, F. R. 1972. Measurement of the Cavitation Susceptibility of Water Using Standard Bodies. Rep. No. 118, St. Anthony Falls Hydraulic Laboratory, University of Minnesota.
- Van der Meulen, J. H. J. 1980. Boundary Layer and Cavitation Studies of NACA 16-012 and NACA 4412 Hydrofoils. Thirteenth Symposium on Naval Hydrodynamics, Tokyo.
- Van der Meulen, J. H. J. and van Renesse, R. L. 1989. The Collapse of Bubbles in a Flow Near a Boundary. Seventeenth Symposium on Naval Hydrodynamics, The Hague.

## DISCUSSION

William B. Morgan  
David Taylor Research Center, USA

This paper presents a very interesting investigation of cavitation acoustics and the authors are congratulated for such a fine and thorough piece of work. I have one question concerning Fig. 19. This figure shows a significant difference between the acoustic impulses from the "I.T.T.C." headform and the "Schiebe" headform. Do the authors feel this difference is due to the difference in the way the bubbles collapse relative to the headform or do you think there would be an actual difference in the radiated noise?

## AUTHORS' REPLY

The authors would like to thank Dr. Morgan for pointing out this phenomena. The significant difference in the average acoustic impulse measured for the two headforms prompted the authors to investigate several factors which could explain the difference. Care was taken to accurately measure the true bubble maximum volume, since bubbles on the I.T.T.C. body were often larger than those on the Schiebe body. Yet, bubbles of equal maximum volume on the two headforms were found to produce significantly different impulses. In fact, a listener standing near the tunnel could easily detect the difference in the acoustic emission between the two headforms. Consequently, the authors have concluded that different acoustic impulses generated by bubbles of equal maximum volume result from the significant difference in the bubble collapse mechanisms, in turn influences the radiated noise.



# Nonintrusive, Multiple-Point Measurements of Water Surface Slope, Elevation and Velocity

G. Meadows<sup>1</sup>, D. Lyzenga<sup>2</sup>, R. Beck<sup>1</sup>, J. Lyden<sup>2</sup>,

(<sup>1</sup>The University of Michigan, USA)

(<sup>2</sup>Environmental Research Institute of Michigan, USA)

## ABSTRACT

This paper describes the Hydrodynamic Monitoring Facility (HMF), an instrument designed to measure slope, elevation, and velocity simultaneously at an array of spatial locations over an area of the water surface. The instrument was designed to provide quantitative measurements used in the study of ship wake phenomena. The HMF is comprised of three separate systems: an optical wave slope measurement system which uses a Helium-Neon (HeNe) laser source and a wave height/surface velocity measurement system which uses a CO<sub>2</sub> laser. These systems and the results of an initial experiment will be discussed in detail.

The experiment utilized a subsurface air bubble source and a surface wind wave source, in conjunction with the HMF, to investigate the effects of short wave propagation on a spatially variable current. A multi-frequency Doppler radar system was employed to concurrently investigate the interaction of active microwave energy with the surface buoyant driven flow.

## INTRODUCTION

Many of the hydrodynamic problems presently of interest to the Navy have not traditionally been investigated by ship hydrodynamicists. The purpose of the Program in Ship Hydrodynamics (PSH) is to bring together an interdisciplinary research team to investigate selected aspects of these non-traditional problems. Because many of the hydrodynamic aspects of the remote sensing (both acoustic and non-acoustic) of ships are not well understood, an increase in fundamental knowledge related to this area has been chosen as the primary goal of the PSH.

Much is still unknown and there is a lack of consensus concerning the physics of the remote sensing of ship wakes by Synthetic Aperture Radar (SAR). Therefore, a major task of the PSH has been to obtain fundamental experimental measurements in the controlled environment of the towing tank. Calibrated radar scatterometers, contributed by the Environmental Research Institute of Michigan (ERIM), have been mounted over the towing tank and the return signals are correlated with high resolution fluid surface measurements in order to determine backscattering mechanisms of the moving surface. This complete instrument suite, we believe, is unique in the world.

The surface fluid flow in the wake of a self-propelled body is a manifestation of the flow below the surface. The flow in the wake is extremely complex, being a combination of turbulent shear flows, coherent vortex flows, free surface waves, internal waves and bubble flows with complex interactions among the various components.

The inaugural experimental use of the Hydrodynamic Monitoring Facility (HMF) has been to provide a detailed set of tow tank measurements of large coherent vortical structures (with axes oriented parallel to the free surface) (Figure 1). These flows are modeled after the observed diverging surface flow field in the wake of surface ships producing a persistent, dark centerline wake in SAR images (Figure 2). The modeled flow fields are buoyancy driven, with bubbles playing a significant role in the observed persistence of the vortical structure. Surface velocity, two-dimensional wave slope and height data were obtained by the HMF along with calibrated Doppler radar scatterometer data over the surface, wave/current interaction region of these flows.

## INSTRUMENTATION

To make substantial progress in the understanding of the hydrodynamic mechanisms which allow ship generated disturbances to be remotely sensed, experimental measurements which can correlate the hydrodynamic properties of the flow field with the electromagnetic properties of the sensing field are necessary. To make these types of measurements, specialized facilities had to be developed. To achieve this goal, the Hydrodynamic Monitoring Facility was developed under Navy University Research Initiative (URI) sponsorship.

The experimental study of the surface perturbations associated with the natural wind stressed ocean have led to

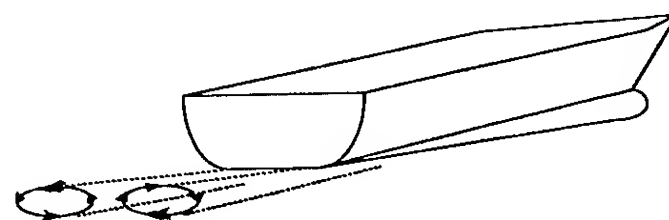


Figure 1. Depiction of diverging surface current flow field generated by the passage of a high speed surface ship.

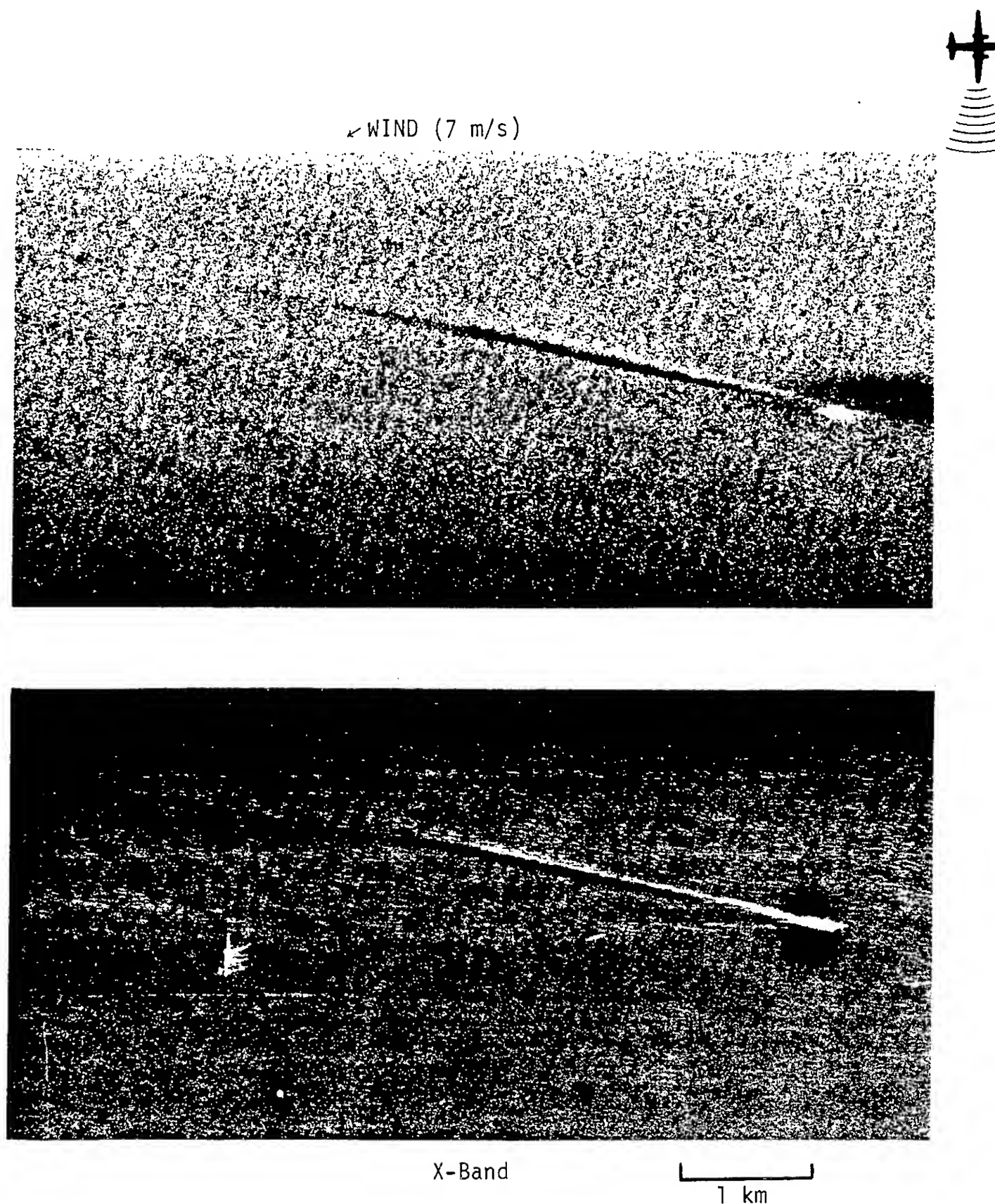


Figure 2. Simultaneously obtained L- and X-band optical SAR imagery of a dark centerline wake feature.

many novel observational techniques to determine the sea state. The method of optical observation was quantified in the classical work of Cox and Monk [1] in which they related the distribution of brightness of the sun glitter to the statistics of the sea surface slope distribution. This basic analysis has been the underpinning of nearly all modern work on optical and microwave scattering of larger scale waves. However, the influence of the smaller waves, particularly, in the study of microwave scattering has led to the use of more complete scattering calculations. Recent studies, which have relied on a deterministic approach based on knowledge of the true surface morphology where the microwave scattering occurred, have been very successful in quantifying the scattering process.

The problem in the vicinity of a moving ship is more complex than in the open ocean where only history and

wind create the sea, but the success of the deterministic approach is compelling. To fully describe the "sea" surface implies that the morphology of the fluid surface and the associated velocity field are known in sufficient detail to compute the scattering properties and other signatures which are desired.

This constraint has led to the development of an instrument system, the HMF, which provides a spatial description of the surface wave height, slope and velocity fields in two-dimensions. Furthermore, the HMF provides this two-dimensional characterization in a temporal period which is short compared to the wave periods of interest. A detailed description of the surface wave slope, height and velocity sensing systems will follow.

## Surface-Slope - Laser Refraction

The use of reflected and refracted laser light to profile the instantaneous surface of a fluid medium has been described by Chang and Wagner [2], using methods closely related to those described by Cox and Munk [1]. The reflection technique relies on the fact that when a narrow beam of light crosses a dielectric boundary, such as the water surface, a fraction of that light, about two percent for vertical incidence, is reflected symmetrically about the surface normal. Thus, if the reflected beam is monitored by observing its intersection with a screen during a scan of the laser beam across the water surface one gains knowledge of the surface slope at all points along the laser scan. This technique was employed by Kwoh and Lake [3] to define a two-dimensional wave distribution in water where microwave scattering observations were being taken.

The reflected laser measurement of the wave surface is extremely sensitive to the slope of the surface, being reflected at twice the surface normal angle. In regions where the surface slope is large, such as the near wake, the reflection technique may in fact be too sensitive. The use of a refracted ray from an underwater source reduces the sensitivity to about 0.34 of the angle of the wave normal, thus allowing much larger wave slopes to be monitored. This technique was used by Kwoh and Lake but with the origin of the laser located above the water rather than below as we have employed here. The refraction method was shown to be particularly suitable for determining the structure of the wake where the surface is more structured and varies rapidly in time and space and was adopted for the HMF. A schematic representation of the fluid slope sensor system is provided in Figure 3.

In this method, the laser beam is incident sequentially in time and space with different angles of incidence from below the water surface. The refracted beam is detected instantaneously by a position detector on an imaging screen above the water. The scanning range on the water surface is approximately 1 meter by 1 meter. This area is determined by the desired size of the imaging screen above

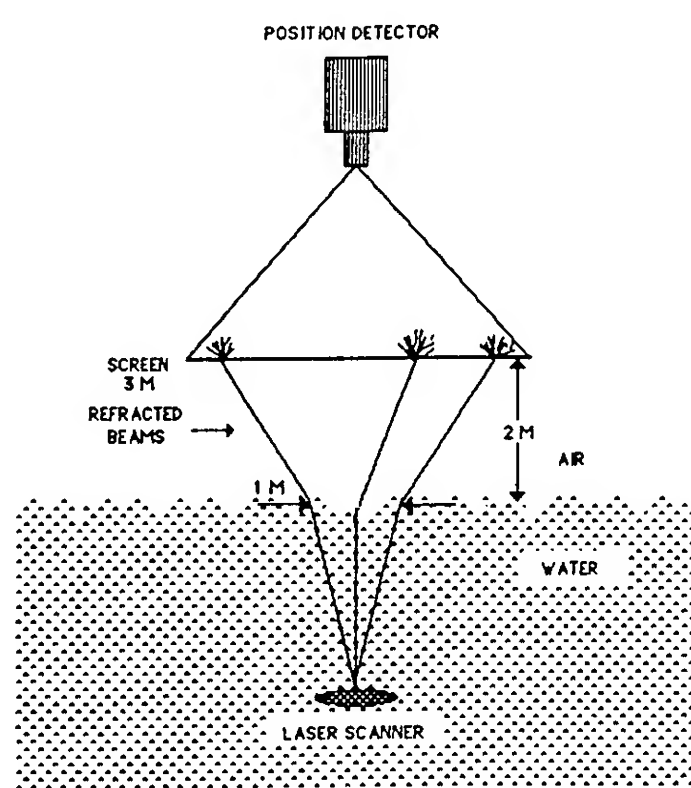


Figure 3. Schematic representation of two-dimensional fluid slope measurement system.

the water surface, the laser intensity and the slope of the wave surface. To reconstruct a wave surface, the water surface area of interest is scanned in a user selected pattern with  $M$  by  $N$  points. The number of scanning points on the surface depends on the required accuracy of the reconstructed surface. The scanning of the laser beam and its detection are synchronous and fast enough to insure that the positions of the laser beam at the initial time and subsequent times are independent and unambiguous events. A detailed description of the analysis procedure and free surface reconstruction is provided in Wu and Meadows (1990).

## Surface Wave Height and Velocity Observations - Tracking of Laser Induced "Warm Spots"

The surface wave height and velocity of the water behind a ship or in the laboratory behind a model are of great importance in defining the wake characteristics. It is imperative to observe the height and velocity fields with spatial and temporal scales that match those of the waves of interest. These high resolution requirements and the desire to measure precisely on the free surface rule out many of the conventional techniques of velocity measurement. We have adopted a thermal tracer technique as our method of choice for the HMF.

A pattern of distributed thermal perturbations or "warm spots" are created using a modulated  $\text{CO}_2$  infrared laser, (lasing at  $10.6 \mu$ ) and a pointing system. These perturbations are then tracked using stereo infrared thermal scanners. The surface height and velocity fields are determined from the displacement of these perturbations between successive infrared image frames. The distribution of spots are user selectable in linear patterns providing velocity profiles, in structured patterns which will yield two-dimensional vorticity and divergence, or in other specific arrays which will depend upon the information desired. At the present time warm spots of 5mm diameter are placed on the water surface at a maximum rate of 40/sec utilizing a 10 watt  $\text{CO}_2$  laser. The water surface is warmed  $+0.75^\circ\text{C}$  above ambient which produces a 0.75 sec persistence time in the thermal imagers. Data is recorded in standard video format at 30 full frames per second and is analyzed as Lagrangian trajectories of tagged particles. A schematic representation of this surface wave height and velocity sensing system is provided in Figure 4.

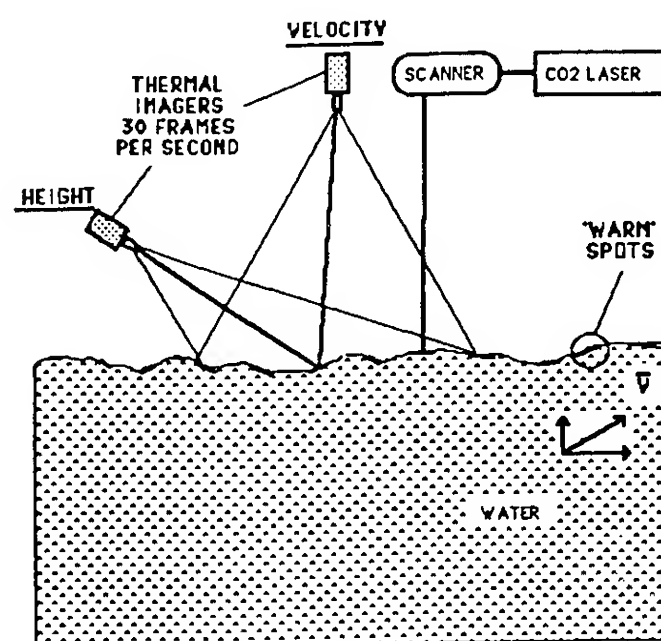


Figure 4. Schematic representation of two-dimensional surface velocity and height system.

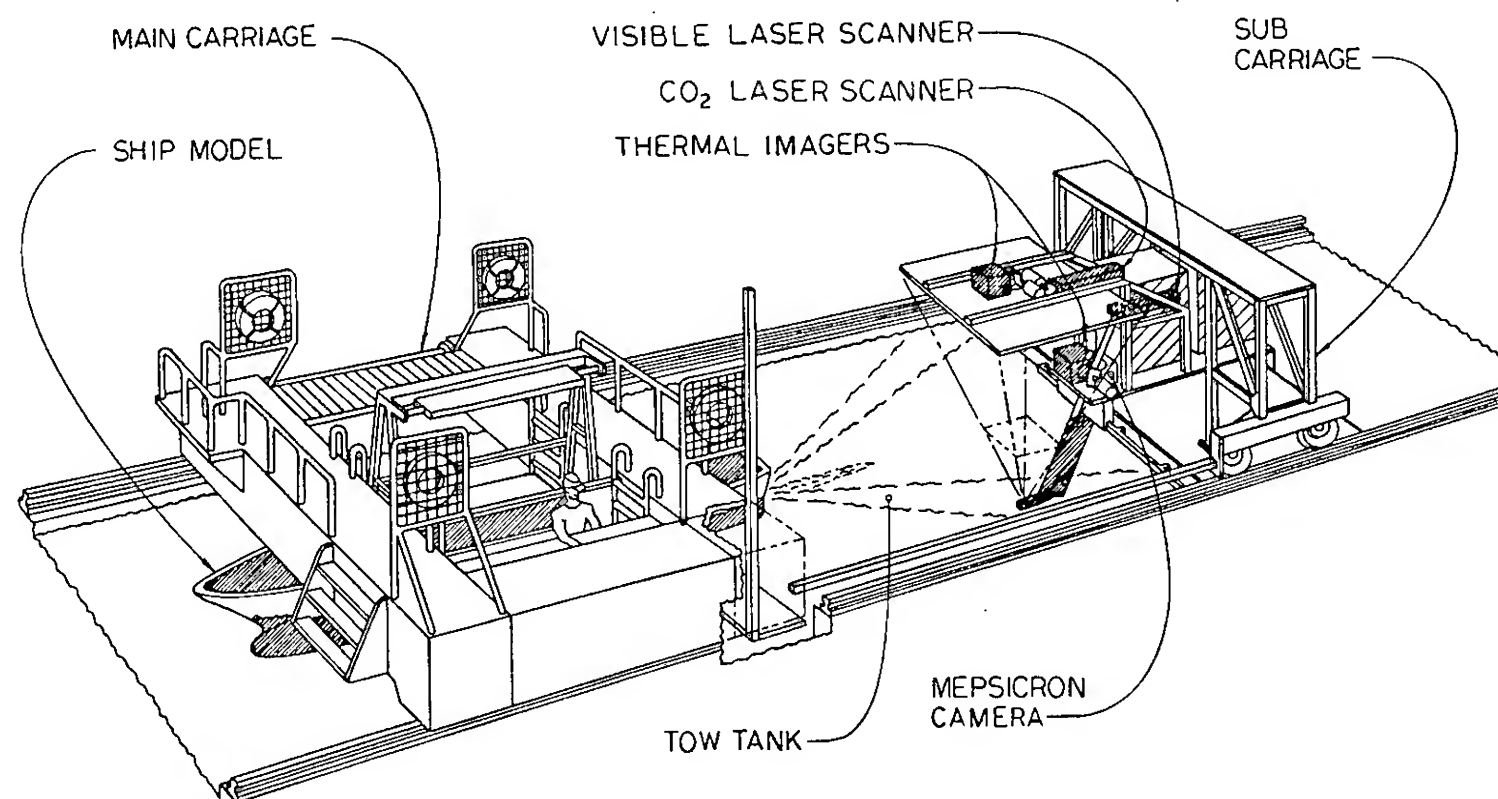


Figure 5. Hydrodynamic Monitoring Facility configuration in the Ship Hydrodynamics Laboratory.

The entire HMF sensing system is mounted on a subcarriage which is towed at selected distances behind the main carriage which suspends the ship model. The HMF field of view is also free to traverse in the cross tank direction to provide spatial views of various sections of the downstream wake. A schematic of the entire system arrangement is provided in Figure 5. In addition, as a result of the initial testing and inaugural experimentation, the demonstrated and design capabilities of the HMF are provided in Table 1.

#### ERIM Calibrated Doppler Scatterometer

The radar used in this experiment is a modification of a previously constructed dual-polarized system operating at C-band (4.8 GHz) and X-band (9.6 GHz). The original device consisted of a transmit antenna fed by a frequency-modulated r.f. source, and a pair of orthogonally-polarized receive antennas whose outputs were mixed with a portion of the transmitted signal and recorded on analog tape. This device was modified by splitting the signal from one of the receive antennas and adding a 90-degree phase shift in order to sample the in-phase (I) and quadrature (Q) components of the received signal. These I and Q channels were simultaneously sampled, digitized, read into memory, and subsequently recorded on floppy disks.

The Doppler spectrum of the radar return was obtained by assigning the I and Q components of the received signal to the real and imaginary parts of a complex number, and

Fourier transforming the resulting time series over a set of 256 samples. The data presented in this paper were sampled at a rate of 100 complex samples per second and thus cover the frequency range from -50 to +50 Hz. Each spectrum shown represents an average 10 data segments of 2.56 seconds duration each. Data were collected at both C-band and X-band, and with both vertical and horizontal polarization; however, only the C-band vertically-polarized measurements are discussed in this paper.

The range of parameters observed by this combined instrumentation effort is summarized in Table 2. Wave making and ancillary data collection capabilities of the Ship Hydrodynamics Laboratory have been extensively upgraded to accommodate the experimental opportunities brought about by the development of the HMF.

#### INITIAL EXPERIMENT: BUOYANCY MAINTAINED VORTICES IN THE SURFACE SHIP WAKE

The inaugural experiments utilizing the HMF in the Ship Hydrodynamics Laboratory at The University of Michigan as part of the URI funded Program in Ship Hydrodynamics, have sought to elucidate the effects of bubbles in maintaining the flow patterns in surface ship wakes.

Bubble clouds have been observed in the wakes of ships at depths of several tens of meters. These bubbles presumably originate from cavitation, entrainment at the



	Proposed Capabilities (acceptable)	Demonstrated Capabilities As of May 1990 Slope (visible)	Height, Velocity (I.R. System)
Scan:.....	100 x 100 (10 x 10)	81 x 81	10 x 5
Time:.....	0.1 s	0.1 s	1.0 s
Scan Area:.....	1 x 1 m (.4 x .4 m)	0.5 m diam	25 x 18 cm
Height Resolution:.....	1 mm (2 mm)	---	(~4 mm)
Maximum Height:.....	15 cm	---	??
Slope Resolution:.....	0.2	0.5 ° typical	---
Maximum Slope:.....	35	~21°	---
Velocity Resolution:.....	1 mm/s	---	5.4 cm/Persistence frames
Maximum Velocity:.....	100 cm/s	---	300 cm/s
Spot Size:.....	1 mm 2 mm	1.5 mm	10 mm
Spot to Spot Centers:.....	2 to 10 mm (5 to 10 mm)	2 mm	10 mm

Table 1. Hydrodynamic Monitoring Facility design and demonstrated capabilities

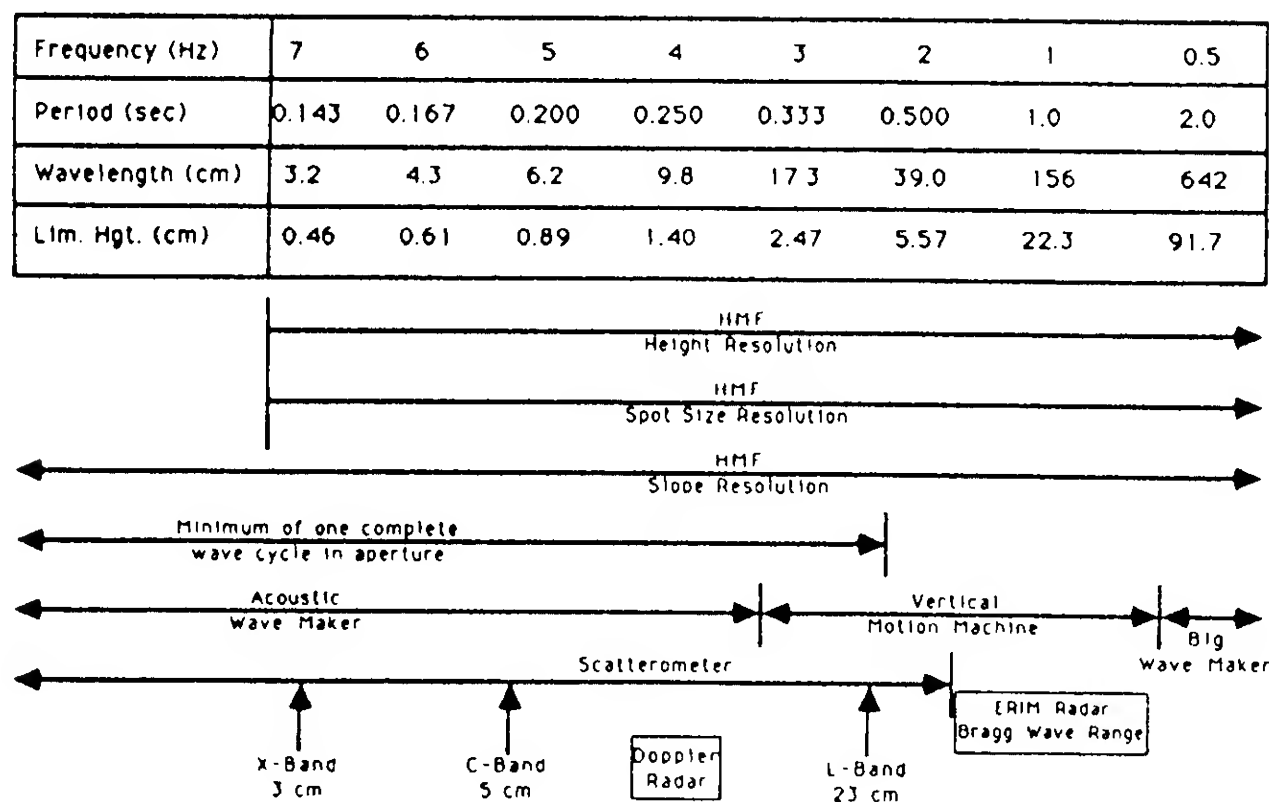


Table 2. Summary of range of experimental conditions achievable by the Hydrodynamics Monitoring Facility.

surface, and possibly other sources. The buoyancy flux associated with the bubble clouds may contribute substantially to the maintenance of an upwelling region which in turn leads to the persistence of the dark centerline wake observed in radar images.

#### Hydrodynamic Measurements

A laboratory wave tank experiment was devised to quantify the role of these buoyancy driven flows. A pair of counter rotating vortices are generated near the free surface, with vortex diameters on the order of two meters. This vortex pair produces diverging surface currents to simulate the centerline wake region of a large displacement vessel traveling in the cross-tank direction. Measurements of surface velocity, wave height, slope and radar cross-section are made across the interaction region. This series of measurements have been made both with, and without, externally generated waves present on the surface. The experimental configuration is depicted in Figure 6.

The objectives of this initial set of experiments was to investigate the interaction of short waves with spatially variable current similar to that produced by passage of a large displacement ship. In addition, the role of buoyancy driven flows in the maintenance and persistence of this portion of the centerline wake is evaluated. The measurements included a characterization of the free surface (its two-dimensional slope, wave height, and velocity distributions) as well as the radar cross-section and Doppler spectrum variations across this region of interaction.

The HMF was configured to provide two-dimensional surface wave slope information on a 50 x 50 points grid at 1 cm spacing with a two-dimensional frame completed every 0.06 seconds or 16.65 Hz. The infrared system for surface wave height and velocity was configured for this initial experiment in an array of 25 x 1 grid points at 2.5 cm spacing. The complete frame was sampled every 0.82 seconds or at a rate of 1.21 Hz. For this initial experiment, the purpose was to consider variations in surface roughness as a result of wave/current interactions for direct comparison with radar measurements. The selection of a 25 x 1 scan in the IR system precludes the direct determination of wave height. However, since the absolute elevation of the water surface is known within the

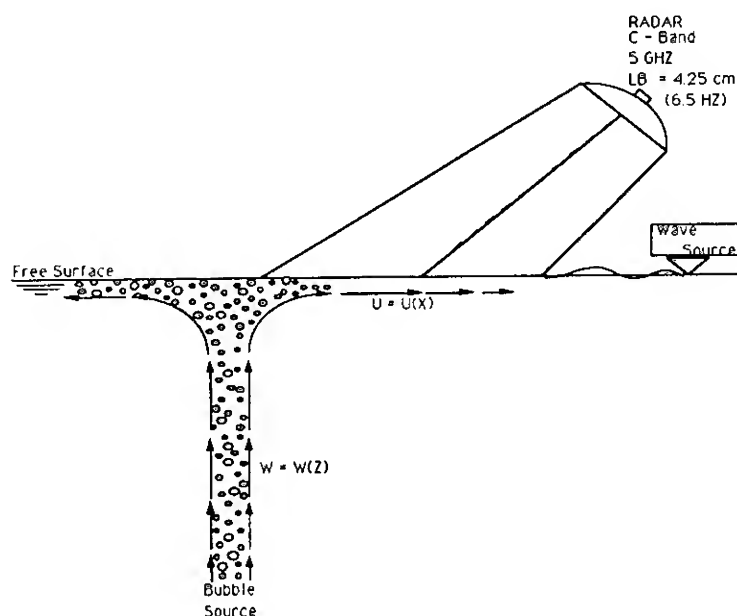


Figure 6. Experimental configuration for buoyancy driven vortex flow.

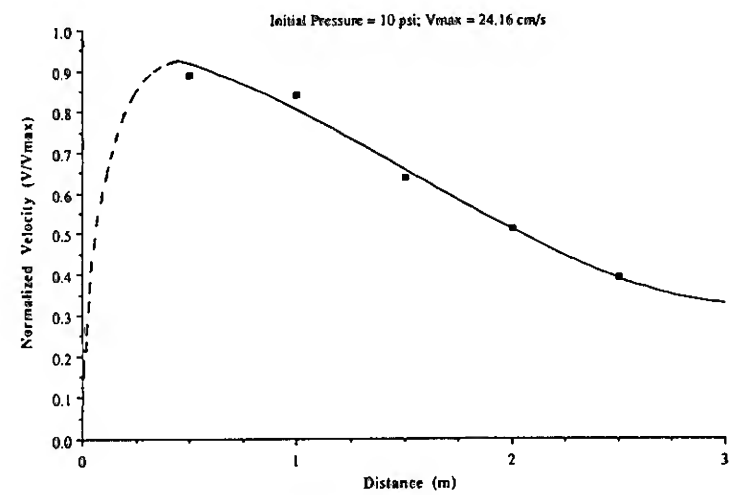


Figure 7. Mean surface velocity resulting from buoyancy driven subsurface vortex.

frame, the two-dimensional wave height distribution can be obtained from an integration of the two-dimensional slope data.

The buoyancy flux required to initiate the large scale vortical flow was provided by a linear bubble generator located approximately 1 meter below the water surface. The bubble volume in the rising column of fluid directly above the linear bubble generator was approximately 6% of the total water column. Averaging over the total volume of the vortical flow, (which has a width of approximately 6 meters in the along-tank direction) results in a void fraction of approximately  $1 \times 10^{-6}$ . This void fraction is consistent with open ocean measurements of high near surface bubble densities.

The average surface flow resulting from this experimental configuration is presented in Figure 7. Maximum divergent surface velocities of approximately 24 cm/sec were obtained near the bubble curtain which spatially decays to approximately 40% of the initial value at a distance of 3 meters from the bubble generator. Careful selection and maintenance of air pressure at the bubble generator produced extremely repeatable surface flow conditions.

The rate of decay in the surface velocity field was measured under two test conditions. In the first set of experiments the initial bubble void fraction was instantaneously reduced to zero at time  $t = 0$  seconds. The rate of decay of the coherent structures resulting from the buoyancy flow was then measured with the HMF through time. The time rate of decay of the maximum velocity is presented in Figure 8 for these conditions.

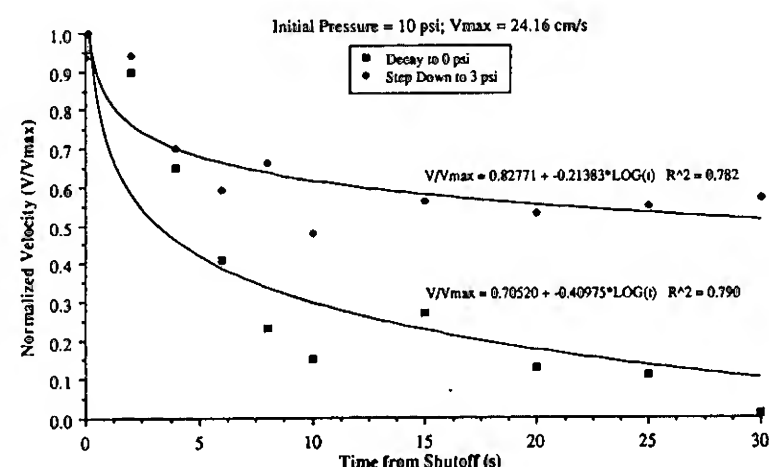


Figure 8. Time rate of decay of the maximum surface velocity for vortex decay with and without bubble buoyancy flux.



Similarly a second set of experiments was conducted with the same initial void fraction in buoyancy flux, however, at time  $t = 0$  the bubble density was reduced to 1% of the original volume (void fraction  $1.7 \times 10^{-7}$ ). The purpose of this second set of experiments was to simulate role of a small buoyancy flux consistent with that observed in the late wake of a surface ship in maintaining divergent surface currents in the centerline wake region. The rate of decay produced by the reduced buoyancy flux is presented in the upper curve of Figure 8.

It is apparent that a substantial reduction in the rate of decay of these large scale coherent structures is produced by just a small buoyancy flux in the central region. The implication of this set of observations is that bubbles produced by the passage of surface ship wake appear to play a substantial role in the maintenance of diverging surface currents and the persistence of centerline wake, very far downstream of high speed vessels.

To investigate the effect that these persistent and sustained diverging surface currents have on the anticipated radar return for the centerline portion of the wake, wind generated waves produced by a near surface fan were propagated across the spatially varying current pattern. Presented in Figures 9 (a) through (c) are plots of the along-tank wave slope spectra recorded by the HMF at positions 1/2 meter upwind of the centerline of the diverging current, 1 meter and 3 meters downstream, respectively, plotted as a function of the along-tank wave number. The corresponding radar backscattering measurements are described in the following section.

#### Radar Measurements

A series of calibrated Doppler scatterometer measurements was made to investigate the variations in radar backscatter caused by the wave/current interactions across the diverging surface currents, both in the absence of wind and in the presence of a wind-generated wave field. Three sets of measurements were made using the experimental setup shown in Figure 6. For this operating configuration the radar footprint was approximately 50 cm in diameter consistent with the chosen geometry of the HMF.

The first set of measurements was conducted with the bubble source in operation but without the fan. The purpose of this set of measurements was to quantify the surface roughness generated directly by the bubbles, or by the bubble-induced turbulence. The second set of measurements was made with the fan on but without the bubble source. The purpose of this set of measurements was to characterize the surface wave field generated by the fan. Finally, a set of measurements was made with both the fan and the bubbler in operation, in order to determine the effect of the bubble-generated currents on the incident wave field.

An example output from the first set of measurements (with only the bubble source in operation) is shown in Figure 10. During this set of measurements, the surface wave height was much smaller than the radar wavelength and thus, the backscatter is expected to be quite well predicted by a simple Bragg scattering model (e.g., Wright, [5]). The observed C-band Doppler spectra tend to confirm this, being dominated in most cases by peaks corresponding to approaching and receding Bragg waves. The wavenumber of these Bragg waves is given by the equation

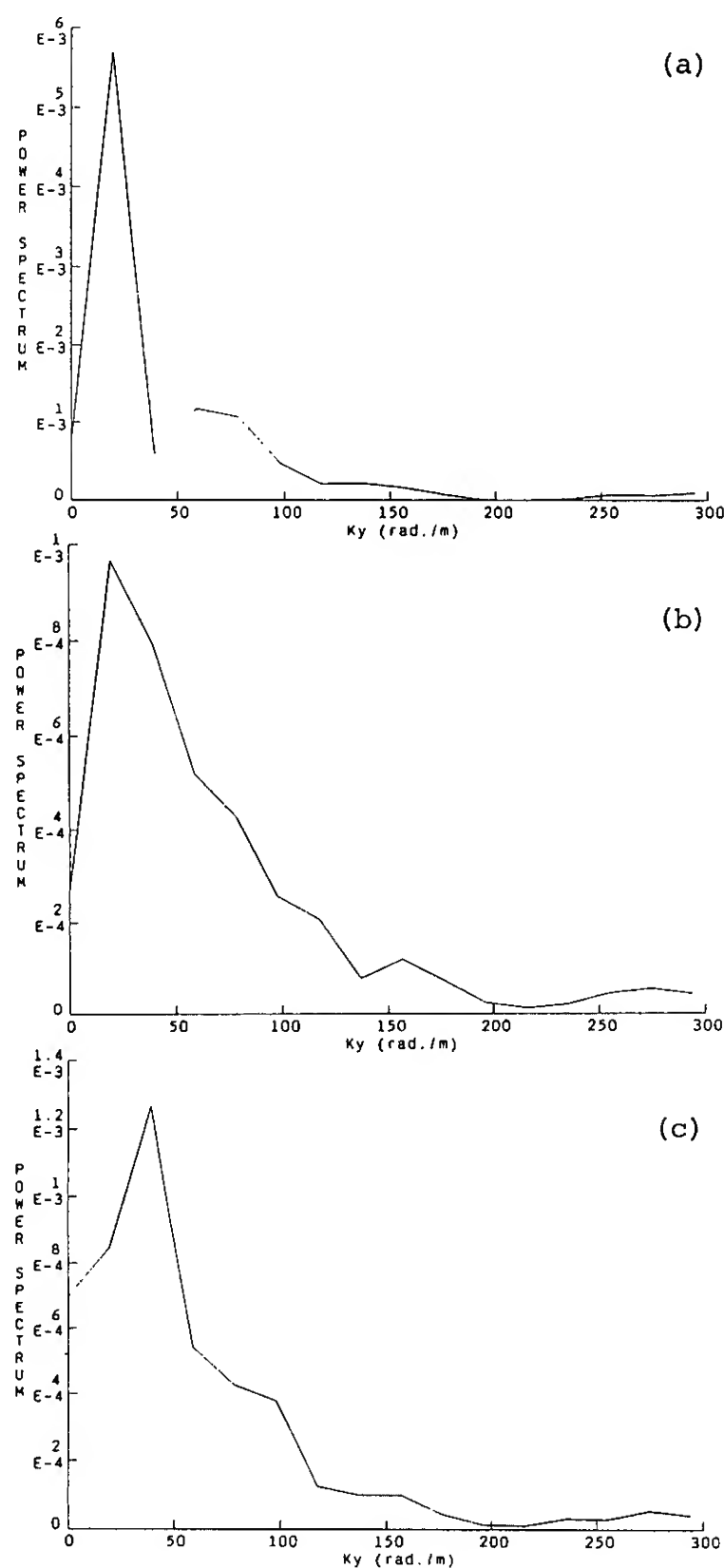


Figure 9. Wave slope spectra across wave/current interaction regions.

- (a) 1/2 meter upwind of centerline
- (b) 1 meter downstream
- (c) 3 meters downstream

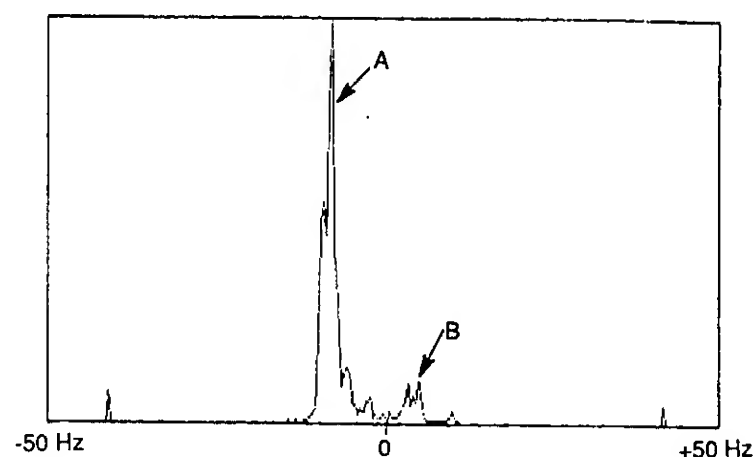


Figure 10. Doppler spectrum measured 3 meters from bubble source. Arrow "A" indicates primary Bragg peak at -8.2 Hz and "B" indicates secondary Bragg peak at +4.9 Hz.

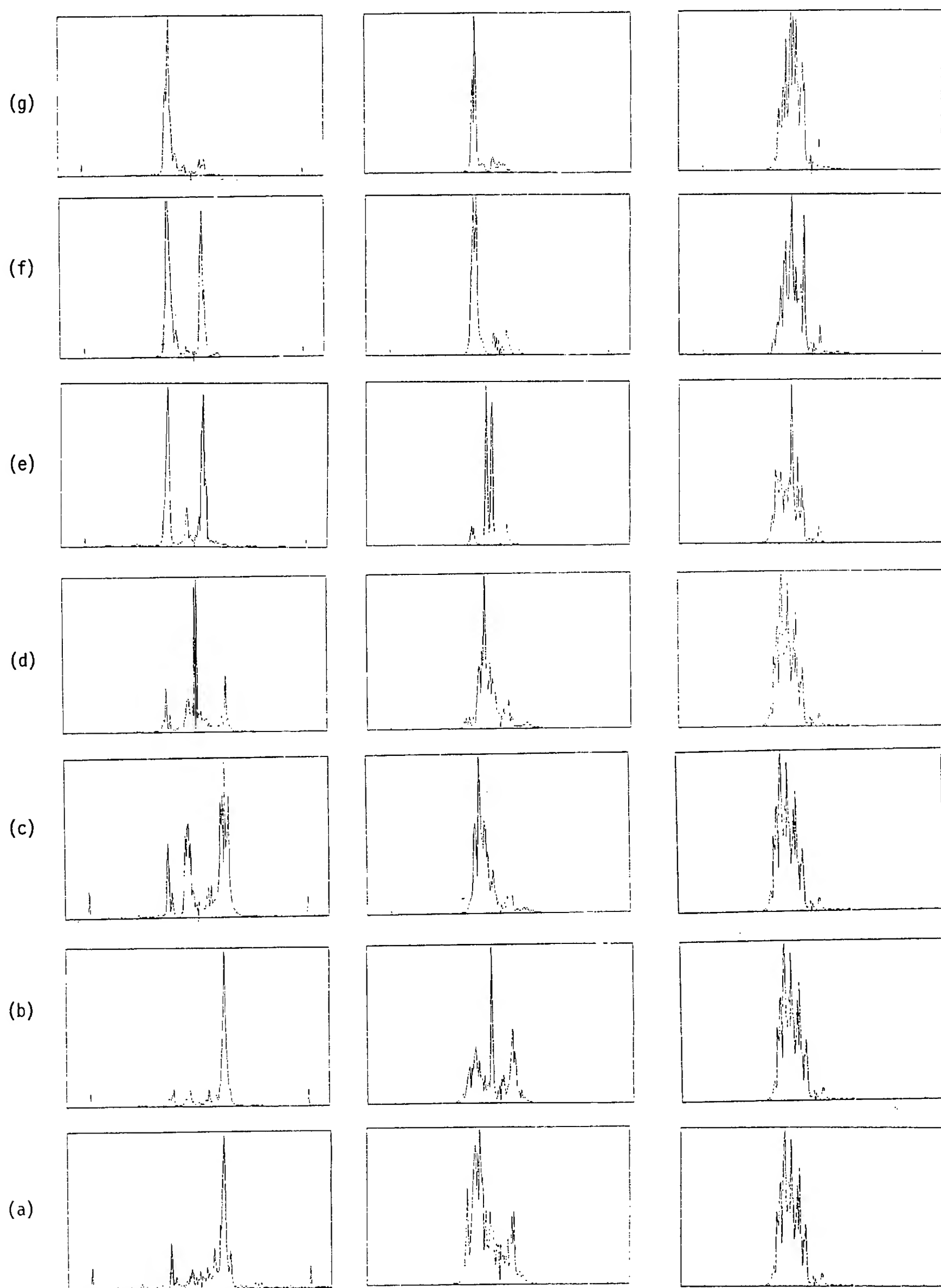


Figure 11. Measured C-band doppler spectra for bubble source only (left column), bubble source and fan-generated waves (center column), and with fan only (right column). Rows correspond to down range positions in intervals of 1 meter, with row (d) centered on the bubble source.

$$k_B = 2 k_o \sin \theta$$

where  $k_o = 2\pi / (6.2\text{cm})$  is the electromagnetic wavenumber and  $\theta = 45^\circ$  is the angle of incidence. This yields a wavelength  $\lambda_B = 4.4\text{cm}$  for these waves. In still water, the Doppler shift of the radar return equals the intrinsic frequency of these waves, or  $f_B = \pm 6.5\text{Hz}$ . In a current having a component  $u$  in the plane of incidence, the Doppler shift equals the apparent frequency of the waves, or

$$f_D = f_B + u/\lambda_B.$$

The spectrum shown in Figure 10, which was collected 3 meters downrange from the bubble source is dominated by a single peak corresponding to the receding Bragg wave, as would be expected for waves generated near the bubble source. A smaller peak corresponding to an approaching set of Bragg waves is also shown. The average Doppler shift for these two sets of waves is  $-1.6\text{ Hz}$ , which implies a surface current of  $7.2\text{ cm/sec}$  away from the bubble source.

The Doppler spectra observed at seven downrange locations relative to the bubble source are shown in Figure 11. The spectrum shown in Figure 10 is reproduced in the upper left corner of Figure 11, and the other spectra observed during the first set of measurements are shown below this one in the first column. The spectra observed with both the fan and the bubble source in operation are shown in the middle column, and the spectra obtained with the fan in the same relative position but with the bubbler off are shown in the right-hand column.

The Doppler spectra in the second and third rows of the first column in Figure 11 show two peaks of approximately equal amplitude, corresponding to the receding and approaching Bragg waves. The mechanism for the generation of the approaching Bragg waves is not clear, but the amplitude of such waves would be expected to increase due to their interaction with the surface currents in this region. The average Doppler shifts for these data sets are  $-3.4\text{ Hz}$  and  $-3.3\text{ Hz}$ , implying currents of  $15\text{ cm/sec}$  and  $14.5\text{ cm/sec}$ , respectively.

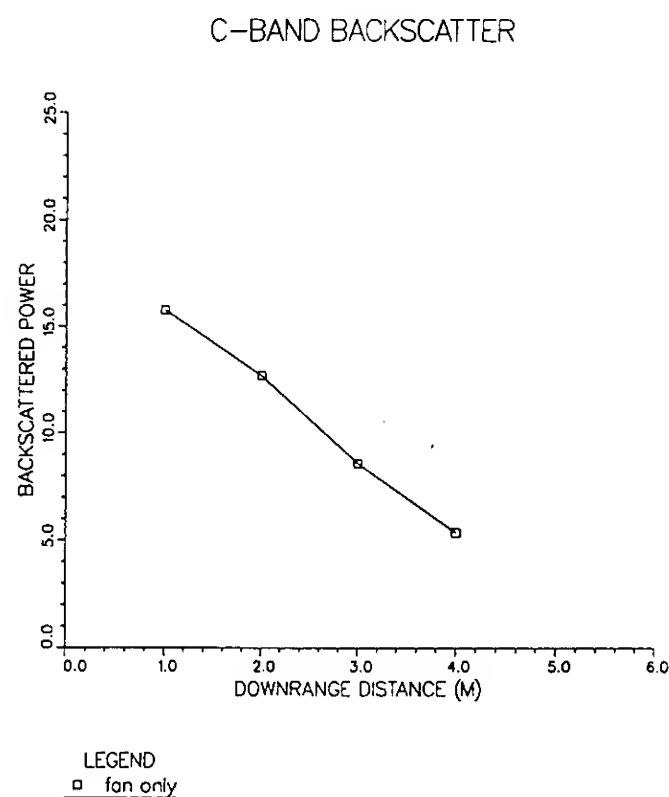


Figure 12. Backscattered power due to fan generated waves versus distance from fan.

The spectrum in Figure 11(d), on the left, which was collected with the radar footprint approximately centered on the bubble source, is rather complicated but nearly symmetric, indicating a zero mean surface current. The peak on the left may be due to a set of receding Bragg waves on the far side of the radar footprint which are Doppler shifted by a current of approximately  $19.6\text{ cm/s}$  away from the center, while the peak on the right is due to the corresponding set of approaching Bragg waves on the near side of the footprint. The two central peaks may be due to waves which are made nearly stationary by the current near the bubble source.

Figures 11(c), (b), and (a) show dominant peaks corresponding to the approaching Bragg waves generated near the bubble source and smaller peaks corresponding to the receding Bragg waves. The average Doppler shifts are  $3.2\text{ Hz}$ ,  $2.8\text{ Hz}$ , and  $2.7\text{ Hz}$ , corresponding to currents of  $14\text{ cm/s}$ ,  $12.3\text{ cm/s}$  and  $11.9\text{ cm/s}$ , respectively, away from the bubble source. Another peak appearing at about  $11\text{ Hz}$  in each of these spectra is not accounted for, but a set of peaks appears at the same frequency in the X-band data collected during the same time interval, indicating the possibility of external interference.

The second set of runs was made at a series of distances away from the fan, with the bubble source turned off. The resulting Doppler spectra are shown in the right-hand column of Figure 11. These spectra are much broader and are centered at roughly  $-8\text{ Hz}$ . The broadening of the spectra is due to the presence of much higher amplitude and longer wavelength waves. The energy is mostly confined to negative Doppler frequencies, corresponding to receding waves, as expected since the fan was blowing away from the radar. The Doppler spectrum appears to be centered at the Bragg peak with an additional shift due to a surface drift current of about  $6\text{--}8\text{ cm/s}$ . The received power (i.e., the integral of the Doppler spectrum) is plotted versus distance from the fan in Figure 12 and shows an approximately linear falloff over this region.

The set of measurements shown in the middle column of Figure 11 was made with both the fan and the bubble source turned on. The fan was directed toward the bubble source and was sufficiently far away so that waves were

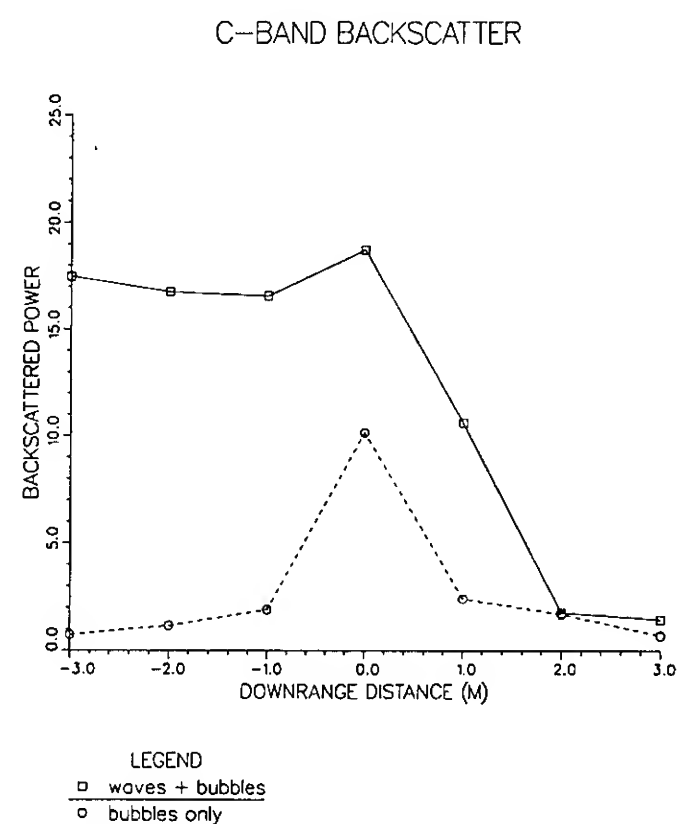


Figure 13. Backscattered power versus distance from bubble source, with and without fan-generated waves present.

generated only on the near side of the bubble source. The spectra for the downwind side (at the top of Figure 11) are almost identical to those collected with the fan off (left column) indicating that most of the fan-generated waves have been attenuated by the bubble-induced current. Approaching the upwind side, the spectra become more complicated but show a gradual transition toward the broad spectra observed in the fan-only case (right column).

The total received power for the left and center columns versus distance is plotted in Figure 13. The received power with the fan off peaks at the position of the bubble source, as expected. With the fan on, the received power peaks slightly at the center and then falls off rapidly on the downwind side.

The received power for the bubble-only case was subtracted from the power for the combined measurement to estimate the contribution from waves generated by the fan which have propagated through the current, and the results are shown in Figure 14. For the two points furthest downwind, this contribution is on the order of a few percent of the backscattered power in the absence of the bubble-induced current.

## DISCUSSION OF RESULTS

A comparison of the results of the radar and HMF measurements with the predictions of wave-current interaction theory can be made by applying the wave action conservation principle and assuming that the backscatter is proportional to the wave spectral density at the Bragg wavenumber. Neglecting relaxation effects, the action conservation principle (e.g., Phillips, [6]) states that for a continuous spectrum of waves, the action spectral density for a given wave group remains constant, i.e.,

$$N(k_1) = N(k_2)$$

where  $k_1$  and  $k_2$  are the wavenumbers for the wave group at any two locations in the current pattern. These wavenumbers are related through the kinematic conservation equation, which can be written as

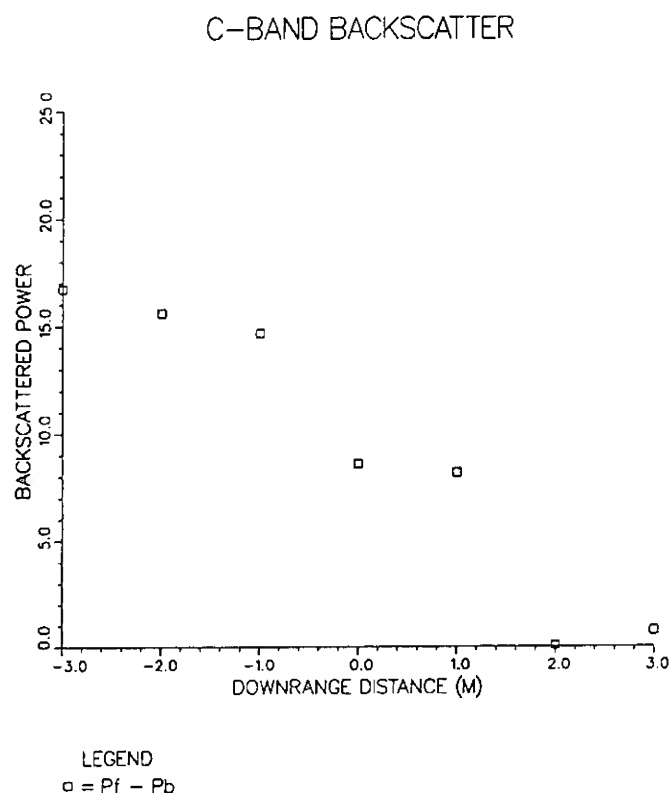


Figure 14. Backscattered power due to wind waves interacting with bubble-generated current.

$$\omega_1 + k_1 u_1 = \omega_2 + k_2 u_2$$

where  $\omega$  is the intrinsic frequency corresponding to the wavenumber  $k$ . The currents at the positions corresponding to Figures 9 (a) through (c), were approximately -10 cm/s, respectively. Applying the kinematic conservative equation, the wavenumber for the left-hand peak in Figure 9(a) (i.e., 20 rad/m, 32 cm wavelength) is reduced by approximately a factor of two (64 cm wavelength) at the location of Figure 9(b). This wavenumber is not resolved by the chosen viewing aperture of the HMF and, therefore, does not appear in Figure 9(b). The second peak in Figure 9(a), however, appears to track through the other two measurements, specifically, a wavenumber of 80 rad/m (8 cm wavelength) in Figure 9(a) translated into 25 rad/m (25 cm wavelength) in Figure 9(b) and 32 rad/m (20 cm wavelength) in Figure 9(c). For comparison with the radar measurements, we have chosen  $u_2 = 7$  cm/s as the surface current at the downwind endpoint and  $k_2 = 1.4$  rad/cm as the Bragg wavenumber, the apparent frequency of this wave is 50 rad/sec. The corresponding wavenumber at the location where  $u_1 = -7$  cm/s would be  $k_1 = 3.0$  rad/cm. Assuming that the incident wave action spectrum falls off as  $k^{-4.5}$ , the Bragg wave spectral density at the end point is then a factor of  $(1.4/3.0)^{4.5} = 0.03$  smaller than that at the wave source, which is in reasonable agreement with the observed reduction in backscatter.

The significance of this apparent agreement is encouraging in view of the simplifying assumptions made in these calculations, notably the neglect of wave dissipation effects and the use of a simple Bragg scattering model. The calculations and the observations both illustrate the large reduction in backscatter caused by the injection of bubbles and indicate that the interaction of waves with the mean surface current induced by the bubbles is mainly responsible for this reduction. The turbulent fluctuation of this current may increase the damping effect, but does not appear to be necessary to explain the observations.

## ACKNOWLEDGEMENTS

This work was supported under the Program in Ship Hydrodynamics at The University of Michigan, funded by the University Research Initiative of the Office of Naval Research, Contract No. N000184-86-K-0684.

## REFERENCES

1. Cox, C. and Munk, W., "Measurement of the Roughness of the Sea Surface from Photographs of Sun's Glitter," *J. Opt. Soc.*, Vol. 44, 1954, p. 838.
2. Chang, J.H. and Wagner, R., "Measurement of Capillary Waves," *Conference on Atmospheric and Oceanic Waves and Stability*, American Meteorological Society, 1976.
3. Kwok, D.S.W. and Lake, B.M., "Laboratory Study of Microwave Backscattering from Water Waves, Part I: Short Gravity Waves without Wind," *IEEE Journal of Oceanic Engineering*, Vol. OE-9, No. 5, Dec. 1984, pp. 291-307.
4. Wu, Z. and Meadows, G., "2-D Surface Reconstruction of Water Waves," *OCEANS 90*, IEEE Oceanic Engineering Society, in press.

5. Wright, J.W., "A New Model for Sea Clutter," IEEE Trans. Antennas Propogat., Vol. AP-16, 1968, pp. 217-223.
6. Phillips, O.M., The Dynamics of the Upper Ocean, 2nd Ed., Cambridge University Press, 1980, 336 p.

# Turbulence Measurements in a Submerged Jet Near a Free Surface

D. Anthony, W. Willmarth, K. Madnia, L. Bernal  
(The University of Michigan, USA)

## ABSTRACT

The results of two experimental investigations on the flow structure of a circular jet issuing beneath a free surface are presented. The mean flow scaling was determined from velocity measurements made with a hot-film anemometer. The free surface is shown to decrease the decay rate of the maximum velocity in comparison to a free jet. The similarity scaling of the flow is discussed based on a simple model. The mean flow and all components of the Reynolds stress tensor were measured with a three-component LDV system. Measurements beneath a clean free surface show that the mean flow spreads laterally in a shallow surface current, and the turbulent velocity fluctuations become anisotropic as the surface is approached. Flow visualization reveals that the surface current contains fluid structures ejected from the jet, and the current is suppressed with the addition of surface active agents.

## NOMENCLATURE

$c$	Similarity constant.
$c_1$	Similarity constant.
$d$	Jet exit diameter.
$h$	Jet centerline depth.
$h_m$	Maximum velocity depth from the free surface.
$J_o$	Jet momentum flux.
$L$	Half velocity width.
$u$	Streamwise velocity component.
$v$	Horizontal velocity component.
$w$	Vertical velocity component.
$x$	Streamwise coordinate, positive downstream.
$x_o$	Streamwise location of virtual origin.
$y$	Horizontal coordinate, positive for right-handed coordinate system.
$z$	Vertical coordinate, positive upward.
$\rho_o$	Water density.
$c$	(subscript) Jet centerline.
$e$	(subscript) Jet exit.
$m$	(subscript) Profile maximum.

$s$	(subscript) Surface.
$y$	(subscript) Half velocity width measured in $y$ direction.
$z$	(subscript) Half velocity width measured in $z$ direction.

Capital letters are used for mean quantities, primes to denote RMS fluctuations, and overlines to indicate Reynolds stresses, e.g.,  $U$ ,  $w'$ ,  $\overline{uv}$ .

## INTRODUCTION

Synthetic Aperture Radar (SAR) images of ship wakes have generated a great deal of interest in the interaction of turbulent shear flows with a free surface. These images show a dark band along the track of the ship believed to be related, either directly or indirectly, to the interaction of turbulence in the wake with the free surface. The study of a turbulent jet beneath a free surface was undertaken to gain some insight on the interaction of turbulent shear flows with the free surface.

The surface signature of a submerged turbulent jet was documented by Bernal and Madnia (1988). They found that the large scale structures in the jet cause surface deformations and the generation of surface waves as they interact with the free surface. Farther downstream, in the region of interaction of the turbulence in the jet with the free surface, persistent surface dimples are observed associated with vortex lines terminating at the free surface. This phenomenon has been studied in detail by Bernal and Kwon (1989) and Kwon (1989) for the case of a vortex ring interacting with a free surface.

In this investigation we consider the interaction of a submerged jet with the free surface. The flow geometry and coordinates system used is shown schematically in Figure 1. Here we focus on the velocity field beneath the surface. We discuss first the similarity scaling of the mean velocity profiles based on velocity measurements obtained with a hot-film anemometer at several jet



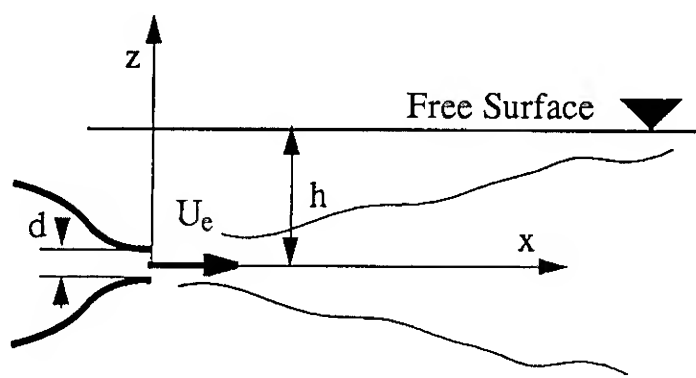


Figure 1. Schematic diagram of the flow geometry

depths. In the second part of the paper the results of measurements of the mean flow and turbulence stresses are presented. These measurements were obtained with a three-component Laser Doppler Velocimeter.

### SCALING OF THE FREE SURFACE JET

Rajaratnam and Humphries (1984) studied the mean flow characteristics of free surface jets when the free surface is located at the edge of the jet nozzle. In their investigation they did not study the free surface motion caused by the jet/free-surface interaction. However they reported a reduction of the mean velocity near the surface at high Froude numbers which was attributed to surface wave generation. Self-similarity was found for the mean velocity profiles. Rajaratnam and Humphries (1984) and more recently Ramberg *et al.* (1989) have studied two-dimensional free-surface jets. Ramberg *et al.* noted the pervasive effects of jet confinement in their tank. These confinement effects have been studied by Kotsovinos (1976, 1978). These effects can lead to breakdown of the similarity scaling laws because of the momentum flux associated with the entrained fluid.

### Experimental Apparatus

The scaling experiments were conducted in a water tank facility consisting of a free surface tank and a jet tank. The free surface tank was made of glass and was 76.2 cm wide, 76.2 cm high and 167.6 cm long. The jet flow was generated by a jet tank located inside the free surface tank. The jet issues from a circular orifice 0.64 cm in diameter located on the side of the tank. A circular-arc-shaped nozzle with radius 1.27 cm provides a smooth transition from the side wall of the tank to the jet exit plane. For the data discussed here the exit velocity was 200 cm/s which gives a Reynolds number of 12,700.

Velocity data were obtained using a constant temperature hot film anemometer. A standard TSI quartz coated cylindrical sensor was used in the measurements. The sensor length was 0.51 mm and the diameter 25  $\mu\text{m}$ . The sensor axis was positioned perpendicular to the flow direction and parallel to the free surface. The hot film was operated at the overheat ratio of 1.09. The output of the anemometer was DC shifted and amplified using a Tektronix AM501 operational amplifier wired as a differential amplifier with a gain of 2.6. The output of the differential amplifier was digitized using a Lecroy 8210 Transient Digitizer. Typical sampling rates used were between 200-800 Hz. The digitized output was then stored on permanent files using an IBM CS9000 computer. Additional details on the facility and instrumentation can be found in Madnia (1989).

### Scaling

A simple model is proposed based on dimensional reasoning and similarity concepts which describes the scaling in the far field of the free surface jet. In this model we consider the momentum flux of the jet  $J_o$  as well as the momentum flux of an image jet above the surface as shown schematically in Figure 2. Thus the free surface is assumed to be a plane of symmetry for the flow. It is further assumed that the dominant length scale is  $h$ , the distance from the jet centerline to the free surface. The jet exit diameter plays an indirect role through its effect on the jet momentum  $J_o$ .

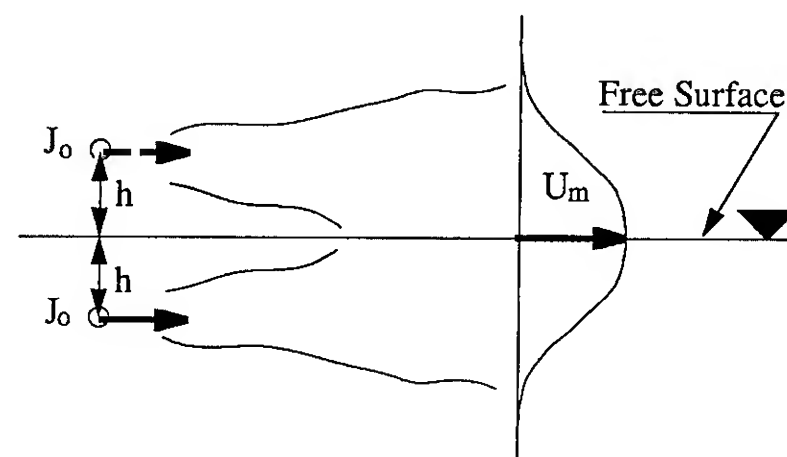


Figure 2. Far field scaling of the free surface jet

The similarity scaling in the far field of the turbulent axisymmetric jet has been discussed by several authors (e.g., Rajaratnam 1976). If the jet momentum flux is constant, the linear growth of length scales with downstream distance implies that sufficiently far downstream compared to the jet exit diameter the mean centerline velocity,  $U_m$ , can be written as:

$$\sqrt{\frac{J_o}{\rho_o}} \frac{1}{U_m} \sim c x$$

where  $\rho_o$  is the fluid density and  $c$  is a constant. It follows that for the free surface jet at sufficiently large distance compared to the jet depth  $h$ , the maximum velocity  $U_m$  is given by

$$\sqrt{\frac{2J_o}{\rho_o}} \frac{1}{U_m} = c (x - x_o)$$

where  $2J_o$  is used instead of  $J_o$  to account for the momentum of the image jet above the surface. The constant  $c$  should be the same as for the free jet while the location of the virtual origin  $x_o$  depends on the geometry of the jet and consequently can not be expected to be the same as for the free jet.

In order to verify this scaling arguments, the equation for the free surface jet can be written in terms of the jet exit parameters as follows

$$\frac{U_e d}{U_m h} = \frac{c_1}{\sqrt{2}} \left( \frac{x}{h} - \frac{x_o}{h} \right);$$

where we have used the relation  $J_o \sim \rho_o (U_e d)^2$ . The same analysis applied to the free jet gives,

$$\frac{U_e}{U_m} = c_1 \left( \frac{x}{d} - \frac{x_o}{d} \right).$$

Thus, the constant  $c_1$  can be determined from free jet data, which gives  $c_1 = 0.162$  (Madnia, 1989). It should be noted that in order for the constant  $c_1$  to have the same value for a free jet as for a free surface jet it is required that the selfsimilar velocity profiles in both of these flows have the same shape.

These arguments are based on the assumption that  $J_o$  is a constant independent of  $x$ . As discussed by Kotsovinos (1976,1978) this fails to account for the momentum flux of the entrained fluid which tends to reduce the momentum flux as the flow evolves downstream. Also in the free-surface jet problem, surface waves generated at the interaction will carry momentum away from the jet which will result in a lower effective value of  $J_o$ . Another important effect is the presence of surface active agents which may contribute to a reduced momentum flux.

In summary, the similarity arguments presented above suggests that: (i) the proper velocity scale for the free-surface jet is  $U_e d/h$ ; (ii) the proper length scale for the interaction is  $h$ , the depth of the jet; and (iii) the maximum mean velocity approaches the free surface with downstream distance.

## Results and Discussion

Figure 3 is a plot of  $U_e d/U_m h$  as a function of  $x/h$  for free-surface jet data obtained at several values of  $h/d$ . It is apparent that the proposed similarity scaling results in good collapse of the data throughout the interaction. Yet the slope of the data is somewhat smaller than the expected value of  $c_1/\sqrt{2}=0.115$ . It is only when the values at  $x/h=24$  and 32 are used to determine the slope that there is good agreement of the measured slope 0.114 with the calculated value.

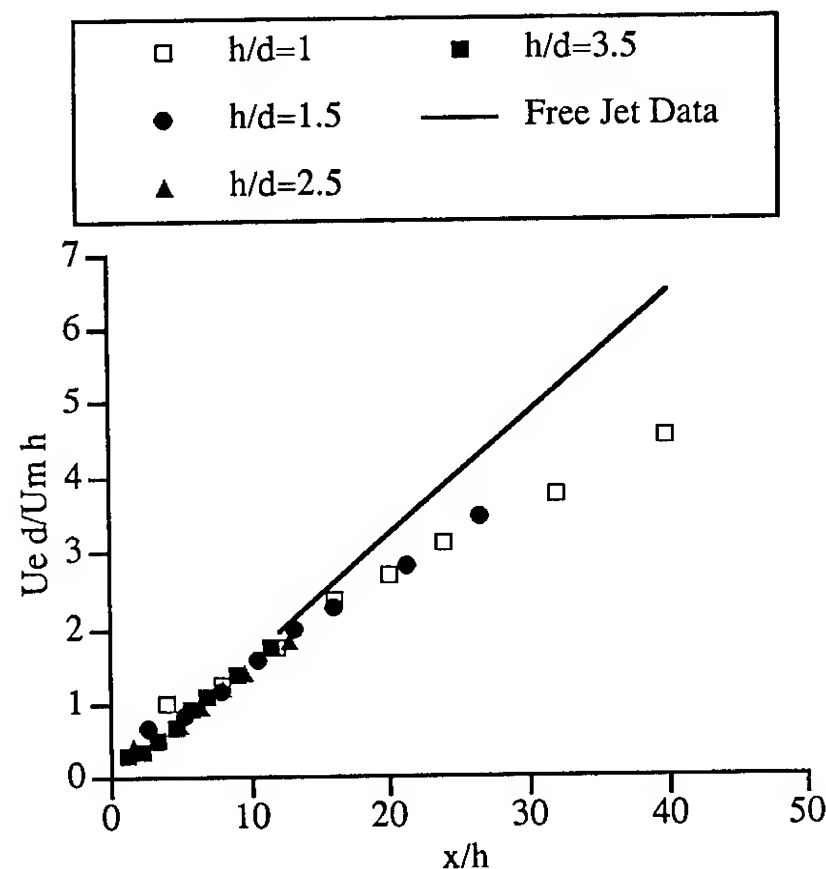


Figure 3. Decay of maximum mean velocity.

The collapse of the data in Figure 3 throughout the interaction region suggests that velocity profiles measured at the same value of  $x/h$  for different  $h/d$  should collapse on a single similarity curve. Similarity profiles for various values of  $x/h$  are presented in Figures 4 and 5. In each figure, plot (a) presents the similarity profiles in the direction normal to the free surface and plot (b) presents the profiles parallel to the free surface. For a normalized distance of  $x/h \approx 12$ , Figure 4(a) shows a significant reduction of the mean velocity close to the free surface (the free surface is located at  $z/L_z \approx 1$ ). The mean velocity profiles at  $x/h=24$  and 32 are given in Figure 5. The profile in the direction perpendicular to the surface at  $x/h=24$ , Figure 5(a), shows that the maximum velocity occurs away from the surface. At  $x/h=32$  the maximum occurs closer to the free surface. It is apparent that only downstream of  $x/h=32$  do the similarity profiles of the free surface jet resemble those of a free jet. We expect that the far field slope  $c_1/\sqrt{2}$  can only be obtained downstream of this location.

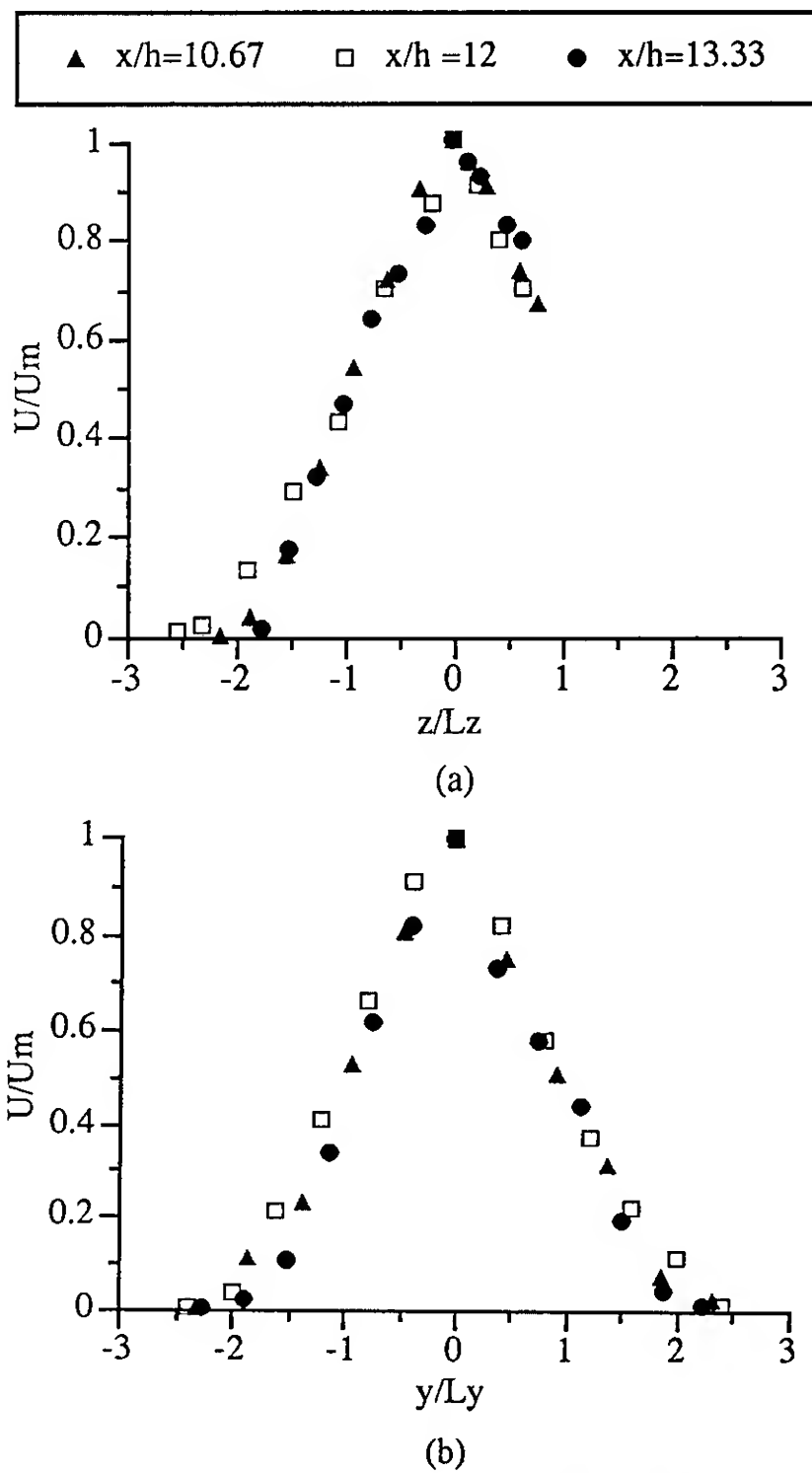


Figure 4. Mean velocity similarity profiles.  $U_e=200$  cm/s,  $x/h = 10.67, 12, 13.3$ . (a) Profiles perpendicular to the surface. (b) Profiles parallel to the surface.

The growth rate of the mean velocity profiles was characterized by the half velocity widths  $L_y$  and  $L_z$  in the directions parallel and perpendicular to the free surface. These half velocity widths were determined with reference to the location of the maximum velocity in the profile. The similarity argument suggests that in the far field the maximum velocity should be found on the free surface, i.e.  $h_m \sim 0$ , and also  $L_y \sim L_z$ . Thus, in the far field  $L_y \sim L_z + h_m$ , where  $L_z + h_m$  is a measure of the thickness of the high momentum region on the vertical symmetry plane. The normalized widths  $L_y/h$  and  $(L_z + h_m)/h$  are plotted in Figure 6 as a function of  $x/h$  for all values of  $h/d$ . These results show that the high momentum region is deeper than it is wide throughout the interaction region. The asymmetry persists for large

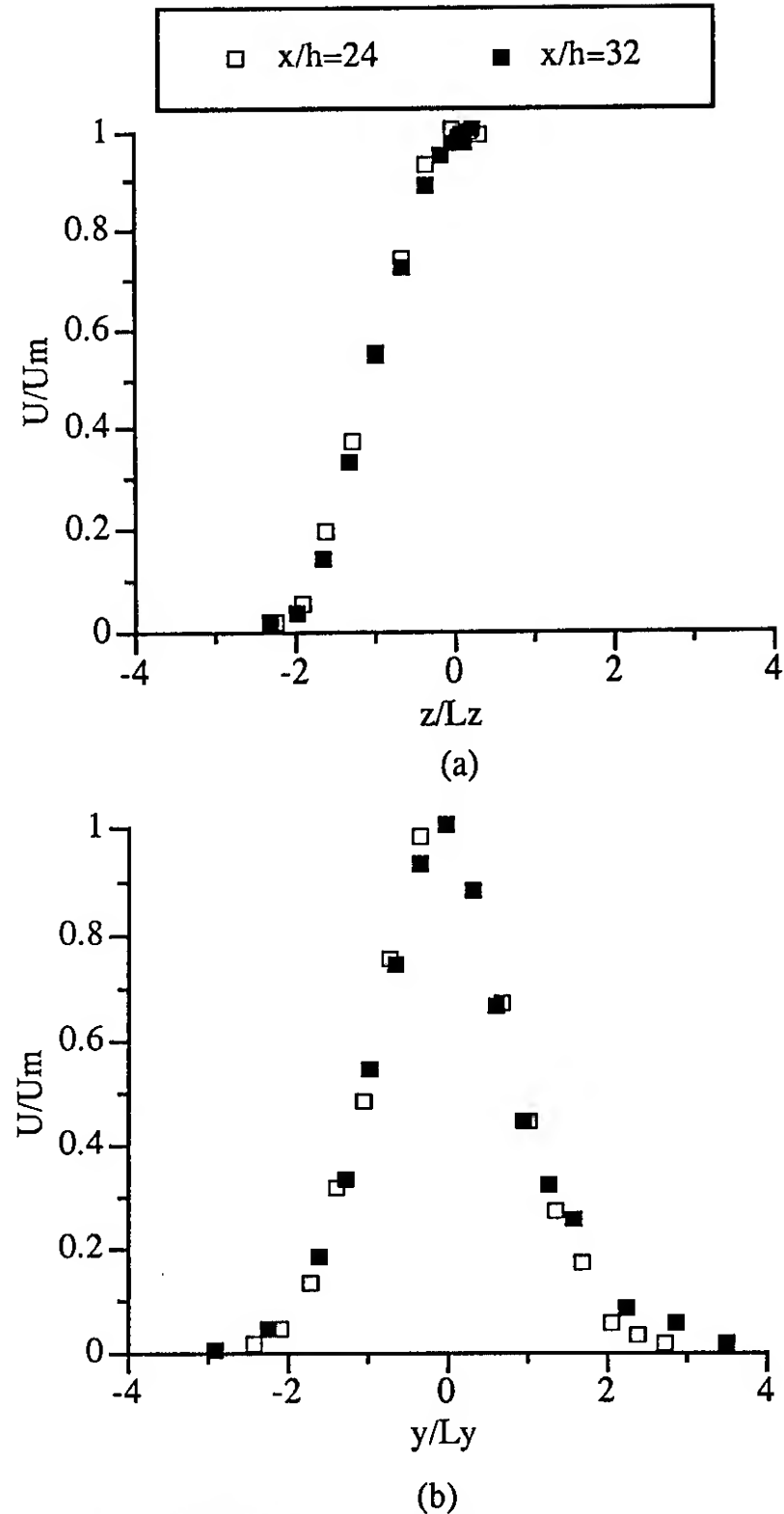


Figure 5. Mean velocity similarity profiles.  $U_e=200$  cm/s,  $x/h = 24, 32$ . (a) Profiles perpendicular to the surface. (b) Profiles parallel to the surface.

distances downstream. Only for  $x/h \approx 32$  the values of  $L_y$  and  $L_z + h_m$  begin to converge toward each other as is expected in the far field. Both  $L_y/h$  and  $(L_z + h_m)/h$  grow almost linearly with  $x$ . The slope of these lines, 0.078, is in good agreement with the results for a free jet. This result is not consistent with reported measurements in free surface jets by Rajaratnam and Humphries (1984).

The downstream evolution of the normalized mean surface velocity along the jet centerline, measured at a distance of approximately 2 mm below the surface, is shown in Figure 7. The mean surface velocity is very small for  $x/h \leq 5$ . The mean surface velocity reaches a maximum at  $x/h \approx 11$  and decreases downstream of this point. The solid line in this plot is a least squares curve fit through the normalized maximum mean velocity data

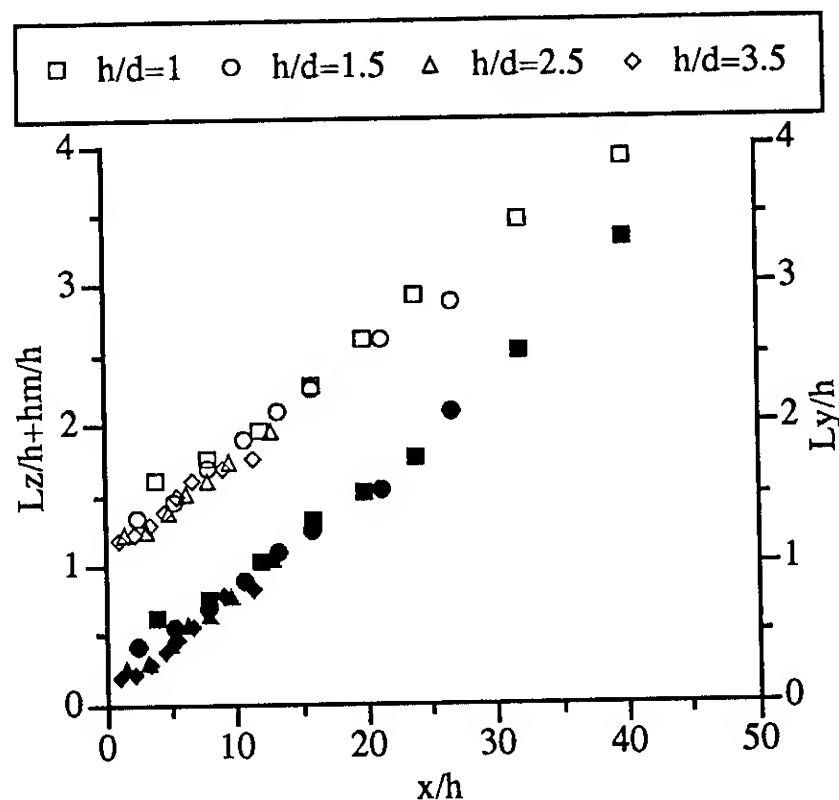


Figure 6. Evolution of half velocity width. Solid symbols,  $Ly/h$ ; open symbols  $Lz/h+hm/h$ .

presented in Figure 3. From Figure 7 it can be seen that the surface velocity approaches the maximum mean velocity in the profile for large values of  $x/h$ . It appears that the rate of decay of surface velocity is much slower than its initial rate of increase in the axial direction. This can have a significant effect in the dynamics of surface waves in this region. It is interesting to note that the location of the maximum velocity,  $x/h=11$ , is downstream of the location of maximum surface activity as determined by surface curvature measurements,  $x/h \sim 5$  to  $10$  (Madnia, 1989).

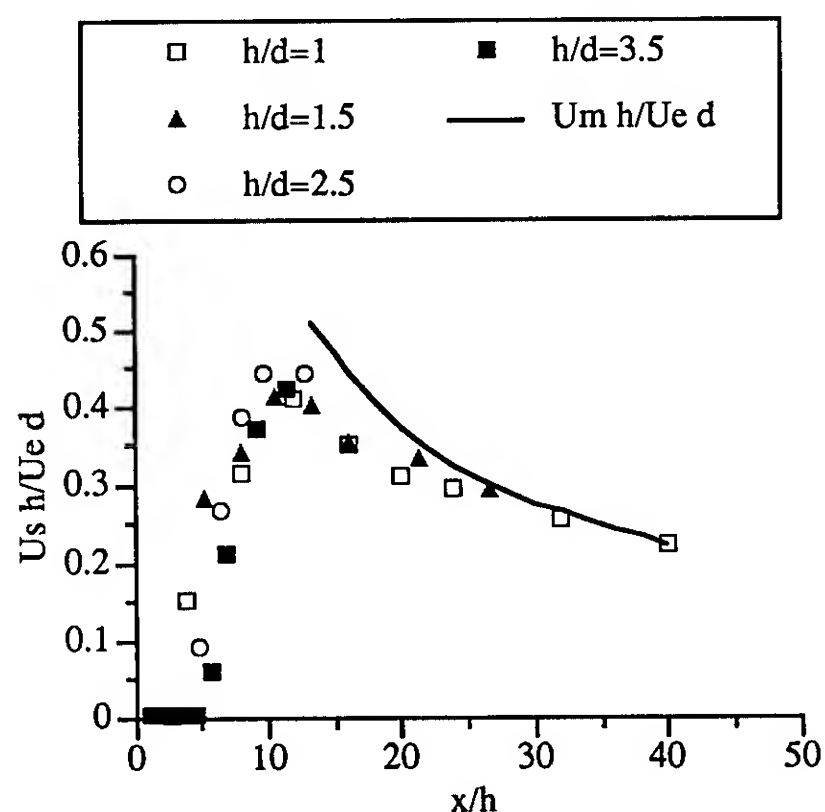


Figure 7. Evolution of mean velocity near the surface.

## TURBULENCE MEASUREMENTS

### Experimental Apparatus

Measurements of jet turbulence beneath a free surface were made using a three-component, underwater Laser Doppler Velocimeter (LDV) designed for wake measurements in a towing tank. The LDV used the three strongest lines, 514.5 nm (green), 488.0 nm (blue), and 476.5 nm (violet), of an Argon ion laser in a three-color, six-beam configuration. The green and blue beam pairs determined the velocity components in a plane, and the violet beams determined the component perpendicular to this plane (Figure 8). The LDV used optical fibers to carry the transmitted beams to two watertight optical probes and to carry backscattered light from the probes to the photodetectors. The submerged probes were mounted oppositely in a cylindrical housing, and a pair of underwater mirrors folded the six beams to a crossing approximately 1.25 m from the housing axis. The measurement volume diameters were approximately .020 cm on all three components, and frequency shifting using Bragg cells was employed to allow discrimination of reversed flow of any component. The Doppler bursts

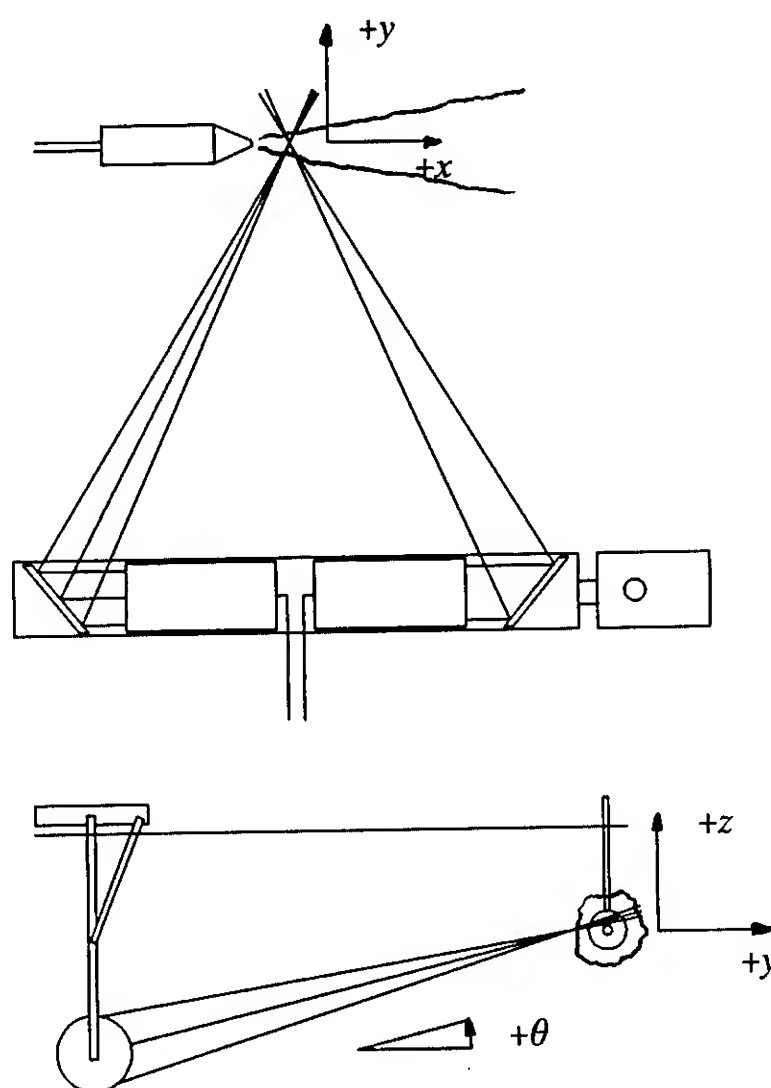


Figure 8. Plan and side views of the three-component LDV and jet nozzle. The LDV translates perpendicular to the jet and rotates about its own axis; the jet nozzle translates on its axis.

were processed using counter-type processors, and the burst information from all three processors was tested for simultaneity or was rejected. The data were stored on an IBM PC. See Willmarth (1987) for a more complete description of the LDV design.

The LDV was operated in a 2400-gallon small towing tank facility at the University of Michigan. The LDV probe was suspended from a carriage that allowed translation in one direction. A stepping motor attached to the underwater housing allowed the LDV to be rotated about its axis.

The jet itself consisted of a brass nozzle attached to a pair of concentric PVC cylinders; within the cylinders were screens and honeycomb for turbulence management. The jet was suspended from the facility's towing carriage and was moved axially to provide the third axis of positioning. This 'free' jet arrangement allowed entrainment from all directions, in contrast to that used for the scaling measurements of Part I where the jet issued from a wall that spanned the facility. The jet exit diameter was .635 cm, and the jet exit velocity was 200 cm/s. Figure 8 shows the LDV probe, the jet, and the coordinate system.

The water in the towing facility was continuously circulated and filtered when not taking measurements, so as to maintain a uniform temperature throughout the tank. A submersible pump drew from the towing tank, and the jet discharged back into the tank; in this manner, seeding uniformity between jet and ambient fluid could be assured. Titanium dioxide was added to the water to seed the fluid with scattering particles prior to taking measurements.

## Results and Discussion

Three-component LDV measurements of the flow velocity in a submerged turbulent jet at depths of 60 and 2 diameters were made to quantify the behavior of turbulence beneath a free surface. The jet Reynolds number based on exit velocity and jet diameter was approximately 12,700. The data were obtained using a simultaneity window set equal to the time required for a scattering particle travelling with the measured mean speed to traverse the diameter of the measurement volume. Data rates tended to be low, around 30 Hz near the jet centerline and less than 10 Hz at the jet edges. For the data reported here, at least 1000 individual measurements were recorded at each location; this number was chosen based on the appearance of the velocity histograms for each component. Ensemble averages were corrected for particle arrival bias using the reciprocal of the magnitude of the instantaneous velocity vector (McLaughlin and Tiederman, 1973) to weight the individual measurements.

Measurements of the flowfield of a deep jet ( $h/d \approx 60$ ) were made as a baseline from which to compare measurements made in a shallow jet ( $h/d = 2$ ) beneath a free surface. The streamwise velocity component on the jet centerline is shown in Figure 9, plotted so as to reveal its inverse dependence on  $x$ , as expected from similarity considerations. The measured slope of this line gives  $U_c/U_e \approx 6.3/(x/d)$ , in agreement with that reported elsewhere, e.g. Rajaratnam (1976). However, at 32 diameters downstream, the flow can still not be considered fully developed, in the sense that the turbulence quantities become self-similar. Wygnanski and Fiedler (1969) have shown that the turbulence

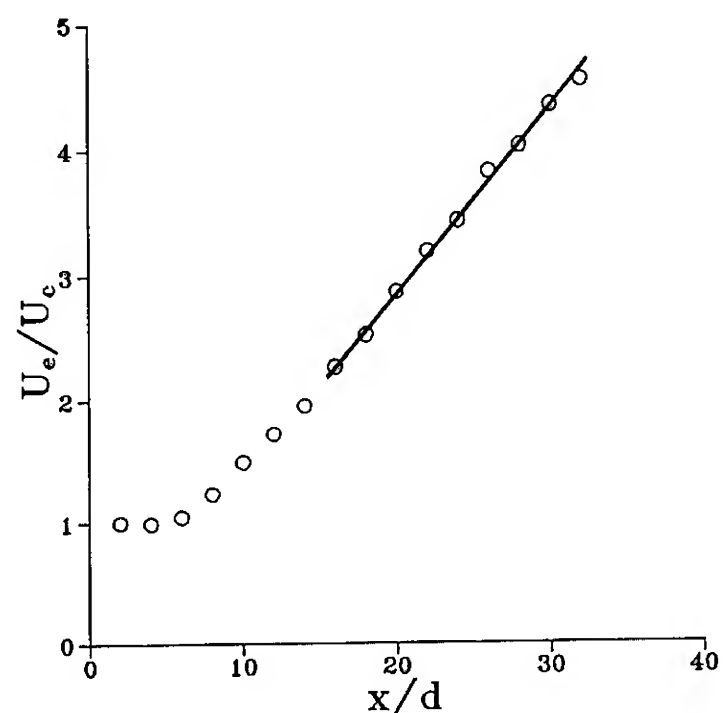


Figure 9. Variation of jet centerline velocity with downstream distance,  $h/d \approx 60$ . Scaling determined from straight line segment shown.

quantities in an axisymmetric jet do not become self-preserving until about 80 diameters downstream.

Profiles of mean velocity, RMS turbulent fluctuations, and Reynolds stresses were measured at downstream stations of 16, 24, and 32 diameters. Shown in Figs. 10a-d are profiles at  $x/d = 32$  for varying  $z$  at  $y = 0$ ; corresponding profiles for varying  $y$  at  $z = 0$ , though not shown, are in excellent agreement and serve to verify that the jet is indeed axisymmetric. The profiles are plotted using similarity variables, normalizing the vertical coordinate  $z$  by the downstream distance  $x$  and the velocity components by  $U_e$ , the mean velocity on the jet centerline. The vertical mean velocity component  $W$ , shown in Fig. 10b, shows outward flow near the jet centerline, and inward flow (entrainment) at the jet edges. This behavior is expected to differ when the jet discharges near a free surface, because of the restrictions the boundary places on the vertical growth of the jet and on the entrainment



of fluid into the jet from above. The RMS turbulent fluctuations (Fig. 10c) show the horizontal and vertical fluctuations  $v'$  and  $w'$  to have the same magnitude, while the magnitude of the streamwise fluctuations  $u'$  is somewhat greater. By symmetry, the cross-stream mean velocity  $V$  (Fig. 10b) and the Reynolds stresses  $\overline{uv}$  and  $\overline{vw}$  (Fig. 10d) should be zero; to within the limits of experimental error, these terms are effectively zero.

Shallow jet data ( $h/d=2$ ) were obtained at  $x/d=32$ , for the same Reynolds number, and are presented in Figs. 11a–d. The same similarity variables are used so that direct comparison between Figs. 10 and 11 is possible. Comparison of the streamwise mean velocity profiles (Figs. 10a and 11a) reveals that the location of maximum mean velocity approaches the surface, in agreement with the scaling results of Part I above. Fig. 11b shows a profile of the vertical mean velocity; near the jet centerline, the flow is again outward, and well below the centerline, the flow is entraining inward. The flowfield above the jet centerline shows the effects of the free surface, driving the vertical mean velocity to zero as it is approached. The RMS turbulent fluctuations, Fig. 11c, reveal a distinctive behavior as the surface is approached: The fluctuations normal to the free surface are significantly diminished, while those parallel to the surface are enhanced. The Reynolds stresses are plotted in Fig. 11d, showing that the principal stress  $\overline{uw}$  diminishes to zero as the surface is approached.

Measurements of turbulence beneath a free surface in inherently two-dimensional flows such as the channel flows reported by Komori, et. al. (1982) and Rashidi and Banerjee (1988), and the plane surface jet flow reported by Ramberg, et. al. (1989) have previously shown that the turbulent fluctuations become anisotropic beneath a free surface. Beneath a shear-free plane surface as is appropriate to the image model outlined above, the vertical velocity and vertical fluctuations must go to zero as a consequence of the plane boundary. However, the interaction of the jet with a free surface shows considerable surface activity, including the generation of surface waves, and the vertical fluctuations need not go to zero as the surface is approached. Recent research investigating the dynamics of vortex rings at a free surface (Bernal and Kwon, 1989) revealed a process of vortex reconnection to the free surface. The vortex lines comprising the rings were found to disconnect and become attached to the surface, resulting in open vortex lines beginning and terminating at the free surface. We suggest that the physical mechanism acting to redistribute the turbulent energy from the vertical to lateral fluctuations is a process whereby vortex filaments in turbulence become attached to the free surface.

Lateral velocity profiles were taken between the jet centerline  $z=0$  and the free surface  $z=h$ , again at  $x/d=32$ . Those points nearest the free surface were within 1 mm of the undisturbed surface and were as close to the surface as was possible without the measurement volume being interrupted by surface deformations. Though not shown, these data reveal a significant increase in the jet width as the surface is approached. The flow is inward at the jet edges on and just above the jet centerline, corresponding to entrainment, but is outward in a thin layer just beneath the surface that extends laterally to several jet widths from the jet centerline. We refer to this thin layer as the surface current.

To investigate this surface current, the LDV was operated without requiring simultaneity among the three components; this allows determination of the mean velocities, but sacrifices the turbulence quantities in favor of a higher data acquisition rate. The data shown in Figs. 12a–d are averages of at least 2000 individual measurements per channel at each location, and are not corrected for bias. Shown are vector plots of the mean velocity components  $V$  and  $W$  at various downstream stations. At  $x/d=16$ , the data show the beginnings of the surface current in the data taken at the surface, but not in that taken below it. Proceeding downstream to 24 and 32 diameters, the current is seen to develop, growing significantly wider than the turbulent jet flow beneath it, but remaining confined to a shallow layer just beneath the surface. At 48 diameters downstream, the surface current dominates the flowfield, the velocity components throughout the jet having diminished with increasing distance downstream.

Near the jet centerline, the mean flow has a component outward (as the jet grows wider downstream), and well below the jet centerline, the flow is inward as ambient fluid is entrained. In the current layer, a strong outward flow causes the entraining flow below it to be turned outward. One might attribute such turning to the action of a streamwise vortex lying just outboard of the jet, as the flowfield is suggestive of a vortex pair lying just beneath and parallel to the free surface. A similar flow pattern appears in wake data taken behind surface ships, and this pattern is sometimes attributed to the action of large streamwise vortices shed from the stern or bilges of the ship. In the case of the jet, stretching of ring-like or helical vortical structure within the jet could yield streamwise structure in the mean. Far from the free surface, there should be no preferred azimuthal position for these structures, but in close proximity to the surface, a stable configuration of streamwise vorticity could develop. This feature might be characteristic of the interaction between a three-dimensional turbulent shear flow and a free surface.



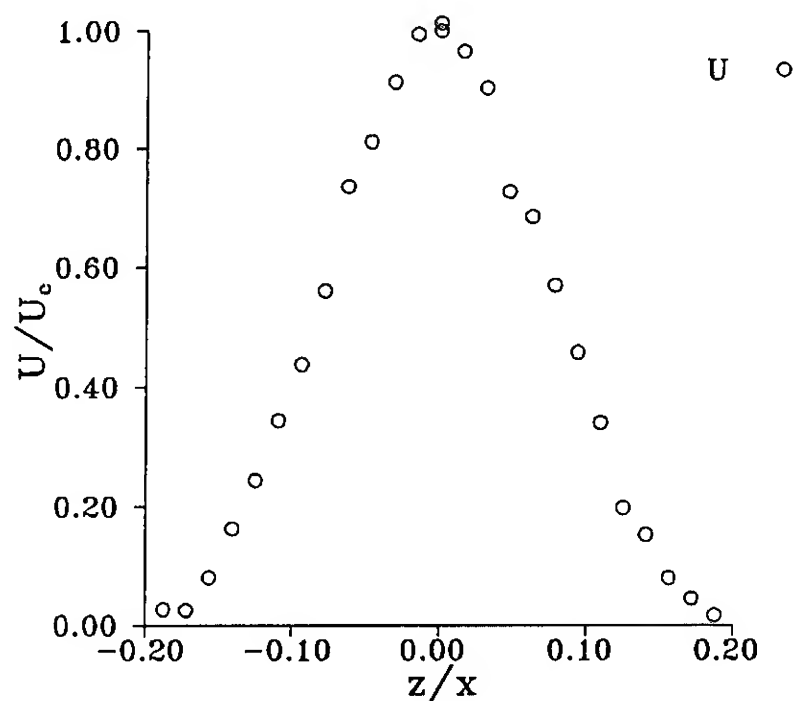


Figure 10a. Profile of streamwise mean velocity component,  $x/d=32$ ,  $h/d=60$ .

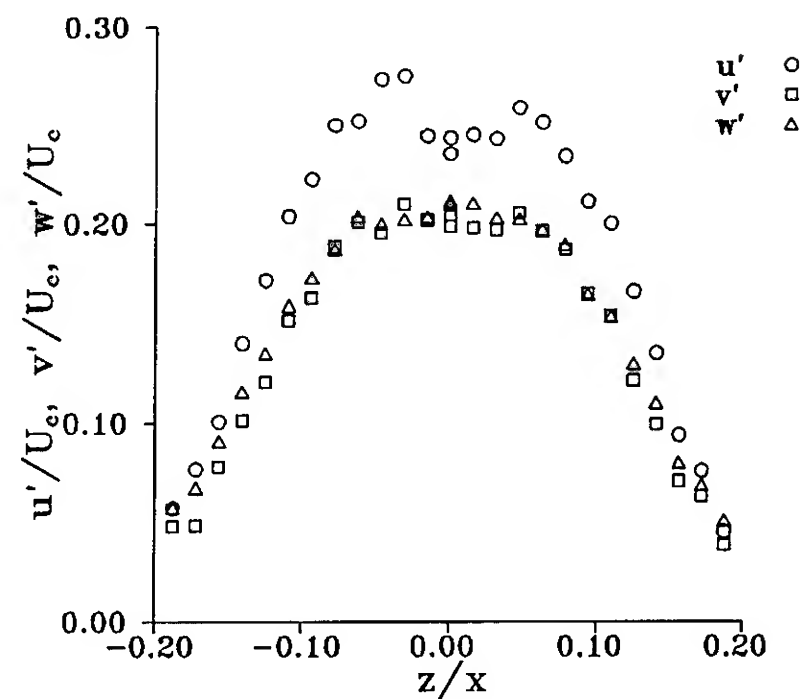


Figure 10c. Profiles of RMS turbulent fluctuations,  $x/d=32$ ,  $h/d=60$ .

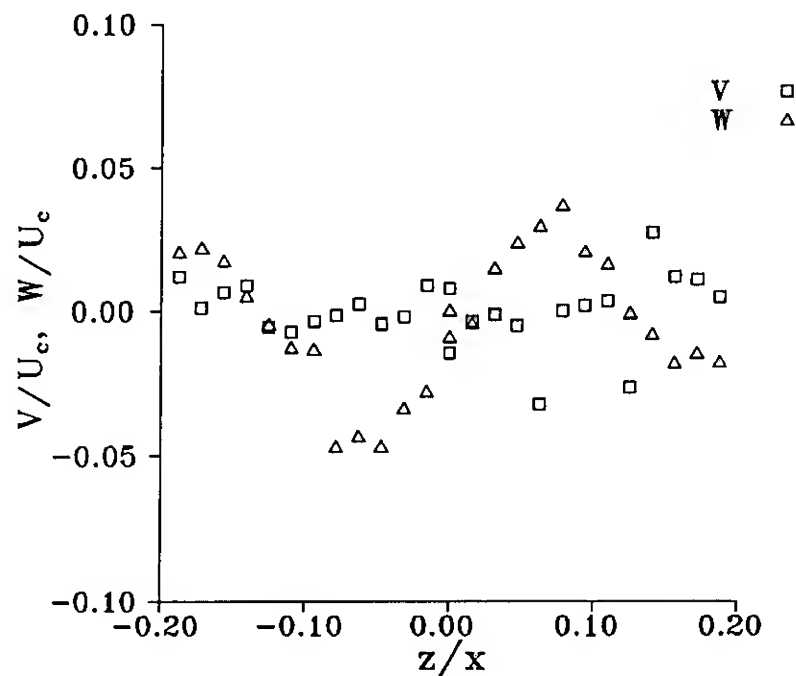


Figure 10b. Profiles of horizontal and vertical mean velocity components,  $x/d=32$ ,  $h/d=60$ .

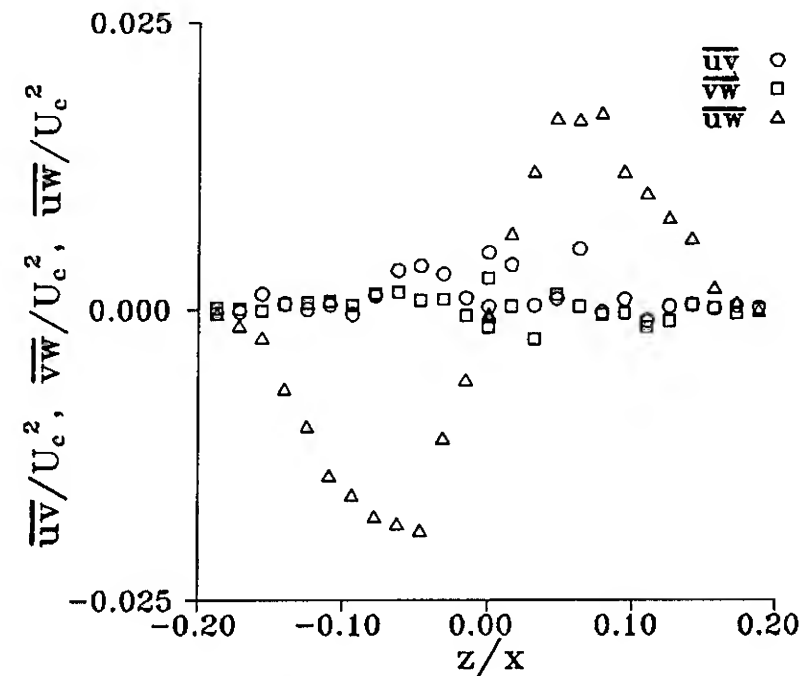


Figure 10d. Profiles of Reynolds stresses,  $x/d=32$ ,  $h/d=60$ .

The surface current does not obviously follow from the considerations of Part I for a shallow submerged jet merging with its image above the surface, although the concept of image vorticity is essential to understanding the surface current. To understand the origin of the surface current, flow visualization using laser-induced fluorescence (LIF) was used. A small amount (3 ppm) of fluorescein dye was added to the reservoir supplying the jet, and a cross-stream plane ( $x/d=32$ ), normal to the free surface and the axis of the

jet, was illuminated with a laser light sheet. The boundary of the jet was observed to be very uneven and unsteady, appearing to emit puffs of dyed, vortical fluid in random directions; these puffs initially propagated outward and away from the jet. The puffs that were emitted downward slowed rapidly and were rarely observed to propagate far from the jet boundary. However, those that were ejected near the surface, having little downward velocity, were observed to

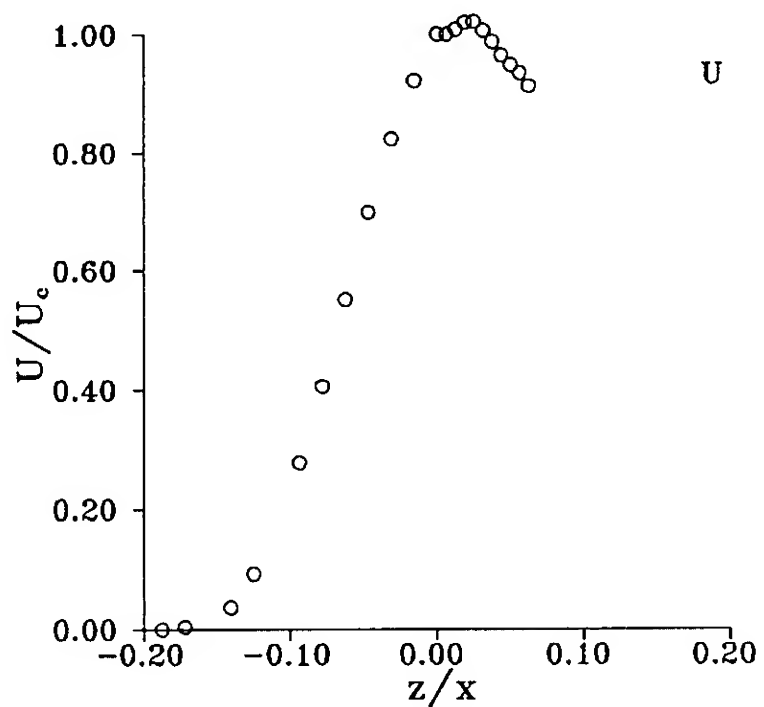


Figure 11a. Profile of streamwise mean velocity component,  $x/d=32$ ,  $h/d=2$ .

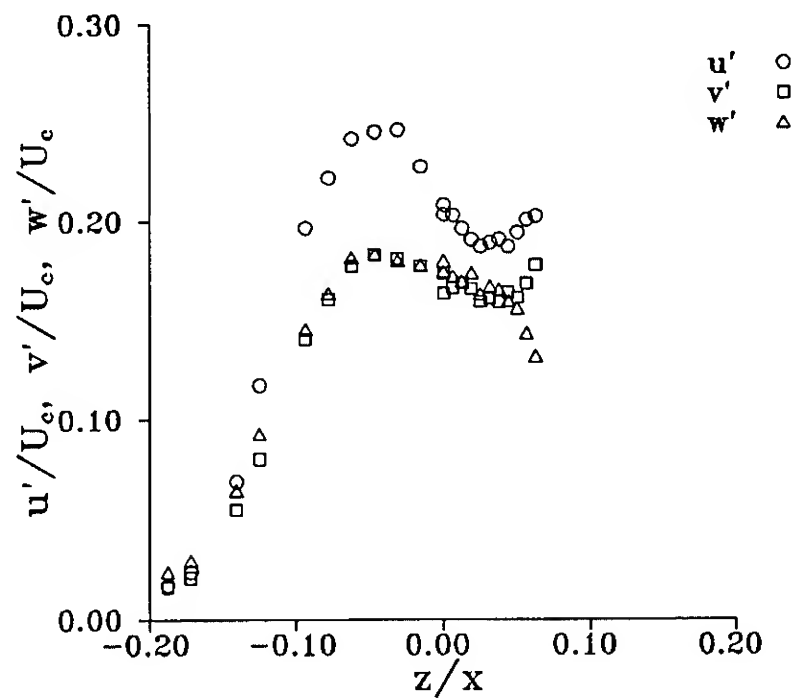


Figure 11c. Profiles of RMS turbulent fluctuations,  $x/d=32$ ,  $h/d=2$ .

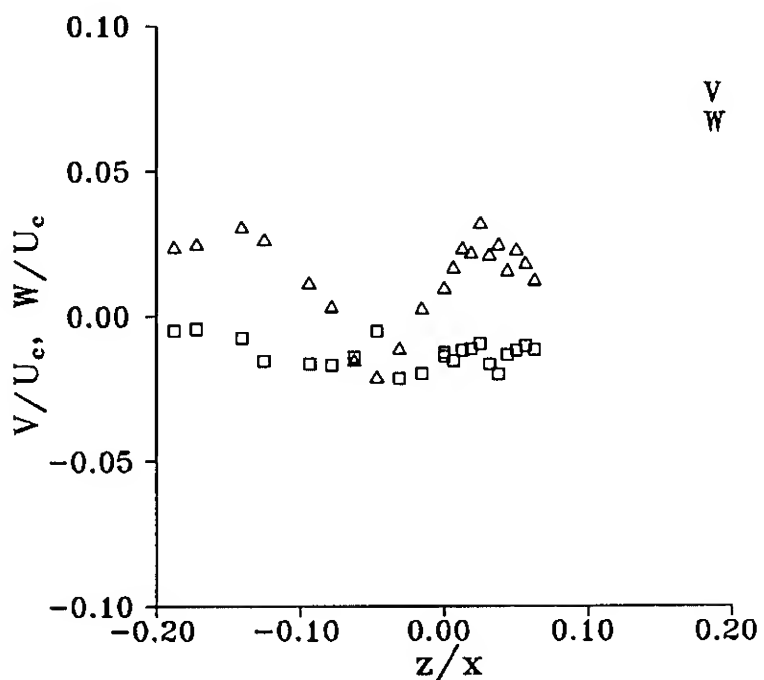


Figure 11b. Profiles of horizontal and vertical mean velocity components,  $x/d=32$ ,  $h/d=2$ .

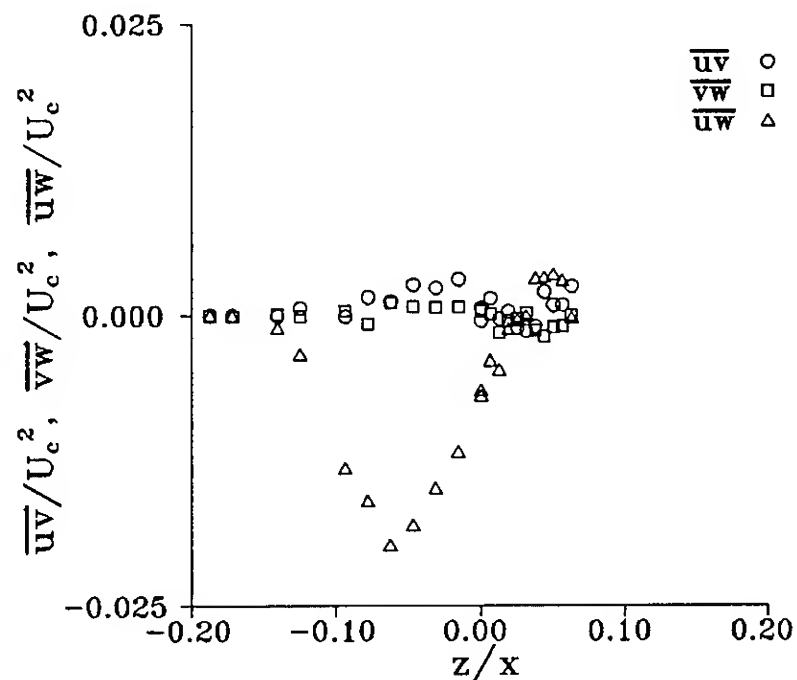


Figure 11d. Profiles of Reynolds stresses,  $x/d=32$ ,  $h/d=2$ .

continue to propagate parallel to the surface away from the jet boundary. These emissions persisted to several jet half-widths from the boundary in a thin layer just below the surface. The average of many such emissions and their subsequent propagation outward gives rise to a mean outward flow which is observed as a surface current.

Using a horizontal light sheet, planes parallel to the surface were illuminated. With the sheet just beneath the surface, a plan view of the surface current was obtained. The layer appears to originate near  $x/d=16$  for a jet depth  $h/d=2$ . The current layer shows puffs of dyed fluid ejected from the jet propagating outward at an angle of about 35 degrees to the jet axis, whereas the jet flow itself spreads at about 12 degrees.

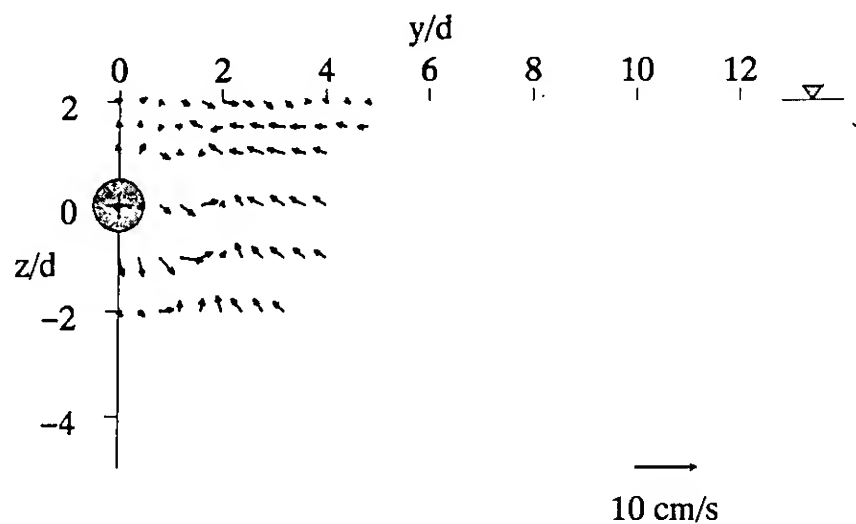


Figure 12a. Vector plot of horizontal and vertical mean velocity components,  $x/d=16$ ,  $h/d=2$ . Shaded circle shows jet nozzle, shaded triangle shows location of free surface.

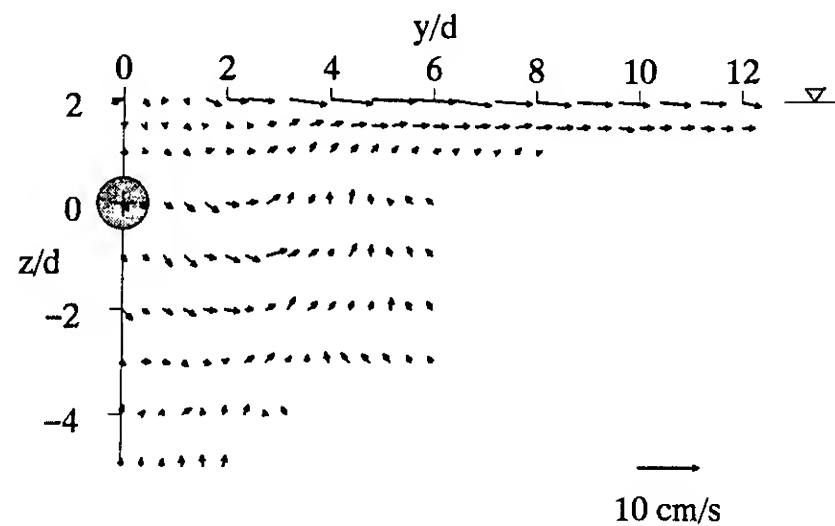


Figure 12c. Vector plot of horizontal and vertical mean velocity components,  $x/d=32$ ,  $h/d=2$ .

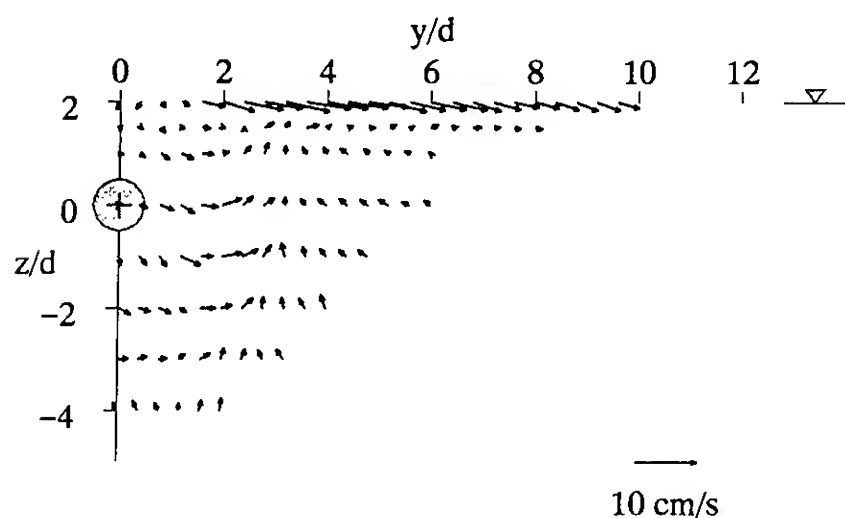


Figure 12b. Vector plot of horizontal and vertical mean velocity components,  $x/d=24$ ,  $h/d=2$ .

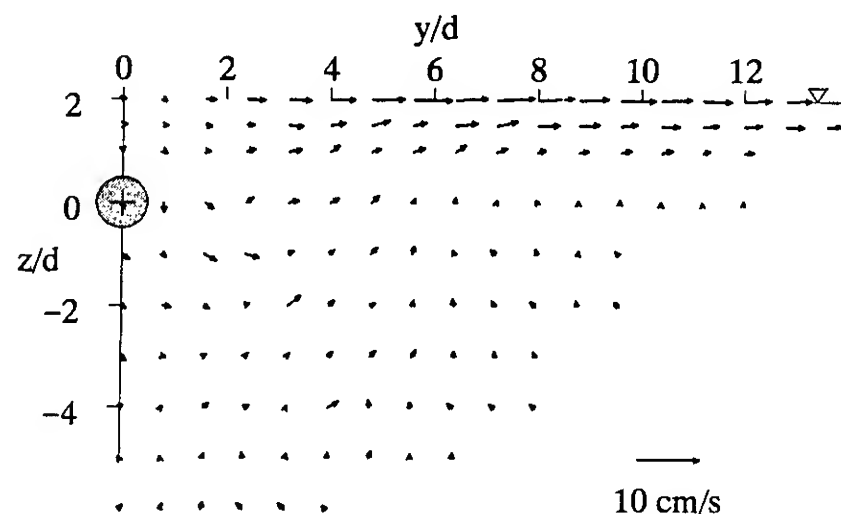


Figure 12d. Vector plot of horizontal and vertical mean velocity components,  $x/d=48$ ,  $h/d=2$ .

The ejected structures remained relatively coherent, and high concentrations of dye in the ejected fluid suggest that turbulent mixing is greatly reduced within the layer. Illuminating a plane through the jet centerline,  $z=0$ , reveals characteristic deep jet behavior up to approximately 24 diameters, at which distance the structures emitted in the surface layer have grown in scale sufficiently to intercept the sheet from above, well outboard of the 12 degree jet boundary. In a plane beneath the jet,  $z/d=-1$ , the only evidence of the layer comes from the few structures large enough to reach the light sheet.

Although we have not directly measured the vorticity, the fact that the surface puffs continue to propagate away from their origin near the jet boundary indicates that they consist of vortical fluid. The dye concentration of the fluid carried with the surface puffs indicates that this fluid has not mixed with the surrounding (non-dyed) fluid as the puffs propagate outward along the surface.

The recent work of Bernal, et. al. (1989) and Hirs (1990) in determining the behavior of a vortex pair

beneath a free surface revealed the importance of surface-active agents in determining the vortex trajectories and the generation of secondary vorticity beneath surfaces contaminated with such agents. Discrete vortices travelling toward a free surface propagate outward beneath the surface when the surface is relatively free of surfactant, but rebound from the surface when surfactant is present. The rebounding is caused when secondary vorticity of opposite sign to the primary vortices is generated beneath a surfactant covered surface. Oleyl alcohol, an insoluble surface-active agent for which the constitutive relation between surface pressure and concentration is known, was added to the free surface, and the LIF flow visualizations were repeated. The surface current did not form, and vortical ejections from the jet, emitted near and parallel to the free surface, were confined laterally through interaction with secondary vorticity generated beneath the surfactant layer.

#### Acknowledgements

This work is supported at the University of Michigan by the Office of Naval Research University Research Initiative Program in Ship Hydrodynamics, Contract Number N000184-86-K-0684 and at the David Taylor Research Center by the ONR Surface Ship Wake Consortium, Contract Number N0001490-WX-22034.

#### References

- Bernal, L. P. and Kwon, J. T., (1989), "Vortex Ring Dynamics at a Free Surface," Physics of Fluids A, Vol. 1, No. 3, pp. 449-451.
- Bernal, L. P., Hirs, A., Kwon, J. T., and Willmarth, W. W., (1989), "On the Interaction of Vortex Rings and Pairs with a Free Surface for Varying Amounts of Surface Active Agent," Physics of Fluids A, Vol. 1, No. 12, pp. 2001-2004.
- Hirs, A., (1990), "An Experimental Investigation of Vortex Pair Interaction with a Clean or Contaminated Free Surface," Ph.D. Thesis, The University of Michigan, Ann Arbor, MI.
- Komori, S., Ueda, H., Ogino, F., and Mizushima, T., (1982), "Turbulence Structure and Transport Mechanism at the Free Surface in an Open Channel Flow," International Journal of Heat and Mass Transfer, Vol. 25, No. 4, pp. 513-521.
- Kotsovinos, N.E. (1976), "A note on the spreading rate and virtual origin of a plane turbulent jet", J. Fluid Mech., Vol. 77, 305-311
- Kotsovinos, N.E. (1978), "A note on the conservation of the axial momentum of a turbulent jet", J. Fluid Mech., Vol. 87, 55-63.
- Kwon, J.T. (1989) "Experimental study of vortex ring interaction with a free surface", Ph.D. Thesis, University of Michigan.
- Madnia, K. (1989) "Interaction of a turbulent round jet with the free surface," PhD Thesis, The University of Michigan.
- McLaughlin, D. K. and Tiederman, W. G., (1973), "Biasing Correction for Individual Realization of Laser Anemometer Measurements in Turbulent Flows," Physics of Fluids, Vol. 16, No. 12, pp. 2082-2088.
- Rajaratnam, N., (1976), Turbulent Jets, Elsevier Scientific Publishing Co., New York, NY.
- Rajaratnam, N. and Humphries, J.A., (1984) "Turbulent Non-Buoyant Surface Jets," Journal of Hydraulic Research, Vol. 22, No. 2, pp. 103-115
- Ramberg, S. E., Swann, T. F., and Plesnia, M. W., (1989), "Turbulence Near a Free Surface in a Plane Jet," NRL memorandum Report 6367, Naval Research Laboratory, Washington, DC.
- Rashidi, M. and Banerjee, S., (1988), "Turbulence Structure in Free-Surface Channel Flows," Physics of Fluids, Vol. 31, No. 9, pp. 2491-2503.
- Willmarth, W. W., (1987), "Design of Three Component Fiber Optic Laser Doppler Anemometer for Wake Measurements in a Towing Tank," Proceedings of the International Towing Tank Conference.
- Wynanski, I. and Fiedler, H., (1969), "Some Measurements in the Self-Preserving Jet," Journal of Fluid Mechanics, Vol. 38, Part 3, pp. 577-612.

## DISCUSSION

John P. McHugh  
The University of New Hampshire, USA

Did you notice any pattern on the free surface near the jet? Were there any distinct streamwise or transverse waves visible?

## AUTHORS' REPLY

Under the conditions investigated, the interaction of the jet flow with the free surface led to the generation of surface waves near the jet centerline. These waves, generated continually and apparently at random by the large-scale structures in the jet flow, were observed to coalesce and to propagate in a direction almost perpendicular to the jet axis. Measurements of the wavelength and wavespeed from shadowgraph images of the free surface showed the waves to be gravity-capillary waves of wavelengths between 1 and 4 cm, travelling with approximately the minimum wavespeed, 23 cm/s, attainable on deep water having a clean free surface.

**Session V**  
**Free Surface Aspects**



# Adequacy of Free Surface Conditions for the Wave Resistance Problem

H. Raven (Maritime Research Institute Netherlands, The Netherlands)

## ABSTRACT

This paper compares three different linearized free surface conditions for steady potential flow around a ship, viz. the Kelvin condition and the slow-ship conditions of Dawson and of Eggers. All are implemented in a Rankine-source method of the type proposed by Dawson. The comparisons concern the predicted wave resistance and wave patterns, the magnitude of the nonlinear terms neglected in the FSC, and the remaining errors in the dynamic and kinematic conditions at the predicted free surface. Rather substantial errors are found for all linearized methods. Dawson's condition does not perform any better than the Kelvin condition except for full hull forms. The occasional prediction of a negative wave resistance for full ships is explained in terms of an energy flux through the free surface. The condition of Eggers, though theoretically preferable, is found to lead to non-convergence of the basic perturbation expansion near the bow in one of the cases and so to give worse results than Dawson's.

## NOMENCLATURE

D	downstream plane up to $y=\eta$
$D_0$	downstream plane up to $y=0$
E	energy flux
$F_n$	Froude number
FS	free surface $y=\eta$
$FS_0$	undisturbed free surface $y=0$
g	gravity acceleration
$l_T$	intersection of plane D with free surface
n	normal vector
$\bar{n}_x$	longitudinal component of n
p	pressure
$R_w$	wave resistance
$R_{wf}$	wave resistance according to (7)
$R_{wp}$	wave resistance according to (9)
U	ship speed
$V_n$	normal velocity component of control surface
x,y,z	Cartesian coordinate system; x astern, y upward, z to port; origin at $\frac{1}{2}L$ unless stated otherwise

$\eta$	linearized wave elevation
$\eta_r$	double-body wave elevation (23)
$\eta_r$	$\eta - \eta_r$
$\bar{\eta}$	wave elevation including nonlinear terms (18,25)
$\eta^*$	wave elevation including nonlinear and transfer terms (19,26,28)
$\rho$	fluid density
$\phi$	total velocity potential
$\Phi$	double-body potential
$\phi'$	$\phi - \Phi$

## 1. INTRODUCTION

One of the oldest and most extensively studied problems in ship hydrodynamics is the determination of the wave pattern and wave resistance of a ship sailing in still water. This is partly related with its visible importance for the efficiency of a ship and the fact that it is the primary quantity derived from towing tank tests; but also the rather obvious formulation of an appropriate mathematical model for the potential flow with free surface boundary conditions has played a role. Particularly in the sixties and seventies much work has been done to simplify this basic model to a method, simple and yet accurate enough in practical applications. The most important result of all this activity was probably the formulation of the slow-ship theory, based on linearization with respect to the flow about the hull at zero Froude number, i.e. the "double-body flow". At the Second International Conference on Numerical Ship Hydrodynamics two papers applying this condition, by Baba [1] and by Dawson [2], attracted much attention due to the realism of the predictions shown. Additionally Dawson's method raised much interest owing to its very original and apparently straight-forward implementation differing substantially from current methods of that time.

Since then, Dawson's method or a very similar one has been implemented by many others. One member of this family is our program DAWSON, which follows the same basic procedure but differs in several details from

H.C. Raven, MARIN, P.O. Box 28, 6700 AA Wageningen, The Netherlands

the original method. More about it can be found in [3]. This program is being used extensively as a design tool at MARIN, giving detailed information on the pressure and streamline direction on the hull, the wave pattern, the resistance and other forces, etc. With careful interpretation this allows to optimize a design before model tests are being performed. As a matter of fact this has led to a few quite successful designs. It appears that in some respects the ideal role of Numerical Ship Hydrodynamics integrated in the design procedure is being approached here already.

Still, in practical applications to current ship forms certain problems and doubts on the reliability of the predictions may arise. In studying these it appears that some aspects of slow-ship theory have not yet been settled entirely. The principle of Dawson's method is generally taken for granted, as is illustrated by the fact that even the algebraic mistake [3] in the derivation of the free surface condition is copied without comment in most papers! Current work on wave resistance calculations is mostly concerned either with further extensions of Dawson's method to new applications, or with methods solving the nonlinear problem, and does not address the basics of the methods so widely used now.

In a certain sense this paper makes a plea for a renewed critical look at the wave resistance calculation methods. It questions the assumed superiority of the slow-ship condition by showing that for a large class of ships the predictions are nothing better than if the Kelvin condition is used instead. The paradoxical occurrence of negative wave resistance predictions, perhaps more widely known but ignored, is studied in Section 3. The validity of the linearization assumptions is investigated by estimating the nonlinear terms and by directly evaluating the velocity field at the predicted free surface. Some of the conclusions motivate and direct the development of a method to satisfy the nonlinear boundary conditions; Section 6 briefly discusses the prospects for such work.

## 2. WAVE RESISTANCE PREDICTIONS

### 2.1. Background

The mathematical model pertinent to calculation of the wave pattern and wave resistance of a ship is that of a potential flow subject to kinematic and dynamic free surface conditions (FSC's). Solving this problem in its exact form is quite complicated, not only owing to the nonlinearity of the dynamic condition but also since both conditions must be applied at the unknown free surface. The general approach is therefore to linearize the FSC. This linearization can be performed with respect to either the undisturbed uniform flow

or the double-body flow. In the former case, the Kelvin FSC is obtained:

$$Fn^2 \phi_{xx} + \phi_y = 0 \quad (1)$$

which, if combined with the exact form of the hull boundary condition gives rise to a "Neumann-Kelvin" problem. The other approach results in the slow-ship FSC, which can e.g. have the form chosen by Dawson:

$$Fn^2 \left\{ \frac{1}{2} \left( \phi_x \frac{\partial}{\partial x} + \phi_z \frac{\partial}{\partial z} \right) (\phi_x^2 + \phi_z^2) + \left( \phi_x \frac{\partial}{\partial x} + \phi_z \frac{\partial}{\partial z} \right) (\phi_x \phi_x + \phi_z \phi_z - \phi_x^2 - \phi_z^2) + \phi_y \right\} = 0 \quad (2)$$

where  $\Phi$  is the double-body potential and  $\phi$  is the total potential. Present methods also impose that the perturbation potential  $\phi' = \phi - \Phi$  satisfies the exact hull boundary condition.

Since the appearance of the slow-ship FSC this has become by far the most popular boundary condition in wave resistance calculation methods. Its assumed superiority is probably based to a great extent on the results of the First Workshop on Ship Wave Resistance Calculations in 1979 [4]. Here many different methods were applied to common test cases, viz. the Wigley hull, an Inuid form, the Series 60 block 60 hull, a fast naval vessel and a tanker model. For all these cases Dawson's predictions were consistent and acceptably close to the experimental values. On the other hand, Fig. 1 illustrates the results of methods solving the Neumann-Kelvin problem. The only conclusion to be drawn from this figure is that large numerical errors must be present in most of them, since solutions of the same problem predict resistances differing by a factor of 2 in some cases. The magnitude of these errors forbids all conclusions on the relative merits of the free surface conditions used, and the results are certainly no reason to do away with the Neumann-Kelvin approach! Still this is what happened: from about 1980 onwards, the majority of the effort in the wave resistance field concerned Dawson's method including the FSC (2). It seems that the motivation for the general preference for the slow-ship condition is not very sound.

Actually a comparison of predictions by Neumann-Kelvin methods and slow-ship methods is only allowed if one is very careful on the point of numerical accuracy. This is because these two classes of methods use an entirely different approach and contain therefore numerical errors of a different origin. Neumann-Kelvin methods generally exploit the known form of the Green function for the problem. So-called Kelvin source panels are distributed over the hull and along the water-

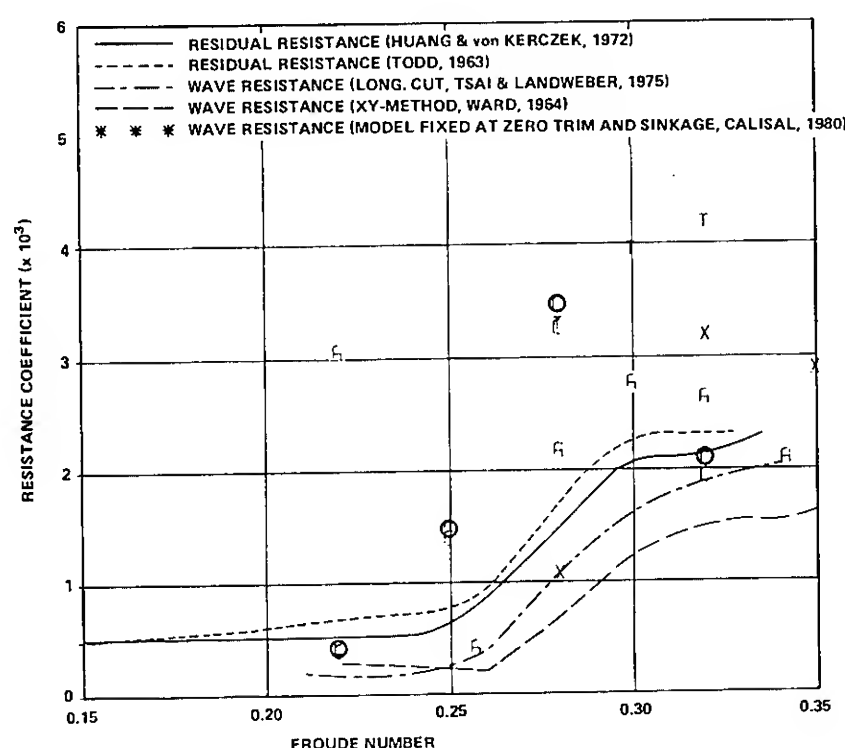


Fig. 1 Wave resistance coefficient for Series 60 model. Symbols indicate results of various Neumann-Kelvin methods [4]

line; the potential induced by these panels automatically satisfies the Kelvin free surface condition. Numerical errors are present in the hull panelling, the treatment of the singularities of the Green function, the numerical integrations over the panels and the waterline integral.

On the other hand, most slow-ship methods use a distribution of Rankine sources on both the hull and a part of the free surface surrounding the hull. Discretization errors are made in the panelling of both surfaces, but also in the difference scheme used to implement the velocity derivatives in the free surface condition. Additionally, the truncation of the free surface domain and the "numerical" imposition of the radiation condition may introduce errors.

However, a fairer comparison of different FSC's is possible. The flexibility of Dawson's numerical implementation allows to treat all sorts of linearized FSC's in basically the same way. Instead of using Kelvin sources to solve the Neumann-Kelvin problem, we now use a distribution of Rankine sources on the hull and a part of the free surface for both FSC's; and the velocity derivative is implemented by a difference scheme. Actually, the only change needed in the program DAWSON is to replace the double-body flow terms in the free surface condition by a uniform flow, as appears from the formulations given above.

Due to the very similar implementations of the FSC's the numerical errors will now be of comparable magnitude; and using the current experience on the required discretization we can make sure that these errors have little influence on the predictions. It is true that

near the stagnation points, in the limit for zero panel size, numerical errors could locally again dominate the comparison due to singular behaviour. But in practice these singularities are always "discretized away". Thus the comparison tells us how important the double-body flow contribution to the FSC is for practical discretizations, which have been checked to be adequate.

## 2.2. Results

This methodology has been applied to a number of ships. First the standard test cases were attempted. For the Wigley hull, a discretization with  $20 \times 6$  hull panels and  $10 \times 38$  free surface panels was used in the calculation for  $Fn=0.40$ . As expected in view of the near-uniformity of the double-body flow for this slender hull, the difference between the Neumann-Kelvin and Dawson resistance predictions amounted to only 1%.

A more realistic test case is the Series 60, block 60 hull.  $24 \times 20$  hull panels and  $10 \times 128$  free surface panels were used. Fig. 2 displays the predicted resistance curves, compared with some of the experimental data. Here again the differences between both methods are negligible, except perhaps above  $Fn=0.32$ . This contradicts the results of the Workshop mentioned before, where the Neumann-Kelvin predictions were, on the average, substantially higher. Which FSC is more accurate cannot be deduced from comparison with experimental data, not only because of the small differences but also due to the disappointing scatter of all available measurements.

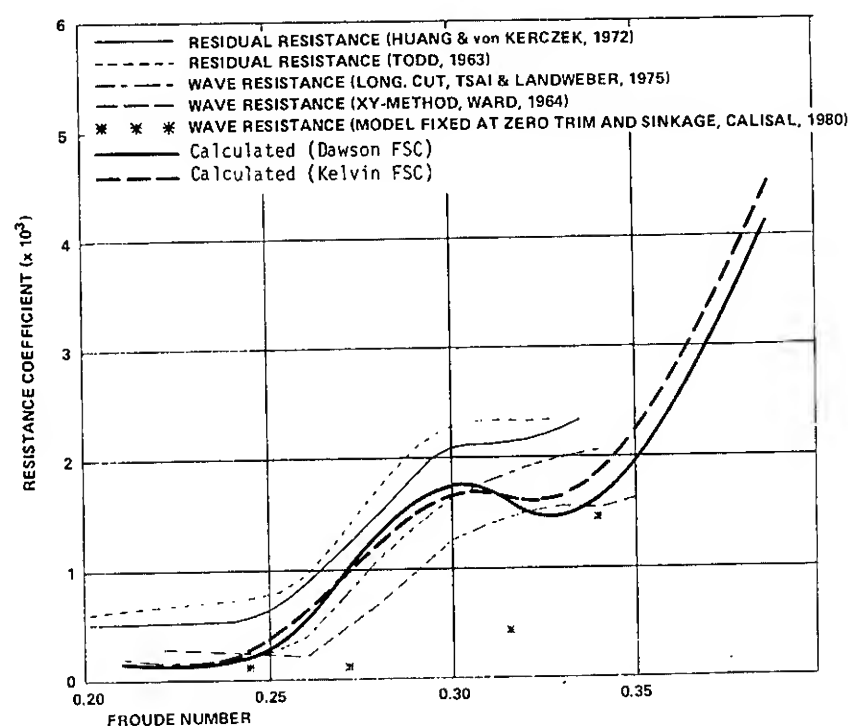


Fig. 2 Wave resistance coefficient for Series 60 model, predicted with Kelvin and Dawson's FSC

Fig. 3 compares the predicted wave profiles for both methods. Both are in close agreement with each other and with the data. Generally, Dawson's FSC leads to a small forward shift of the bow wave and a somewhat more pointed wave shape. The largest differences are found aft of the ship's stern: The Neumann-Kelvin predictions often have a substantially larger wave amplitude here. This can probably be explained by the damping effect of the base flow acceleration in the slow-ship FSC.

The same sort of comparison has been made for several practical cases. The fact that there is remarkably little difference between the Dawson and Kelvin predictions is a recurrent feature for all ships with a block coefficient up to about 0.60 or 0.70. This is in marked contrast with the general conviction! Since in commercial projects the present use of the predicted wave resistance values is generally qualitative or comparative rather than quantitative, we can safely state that the Kelvin FSC performs just as well as the slow-ship FSC.

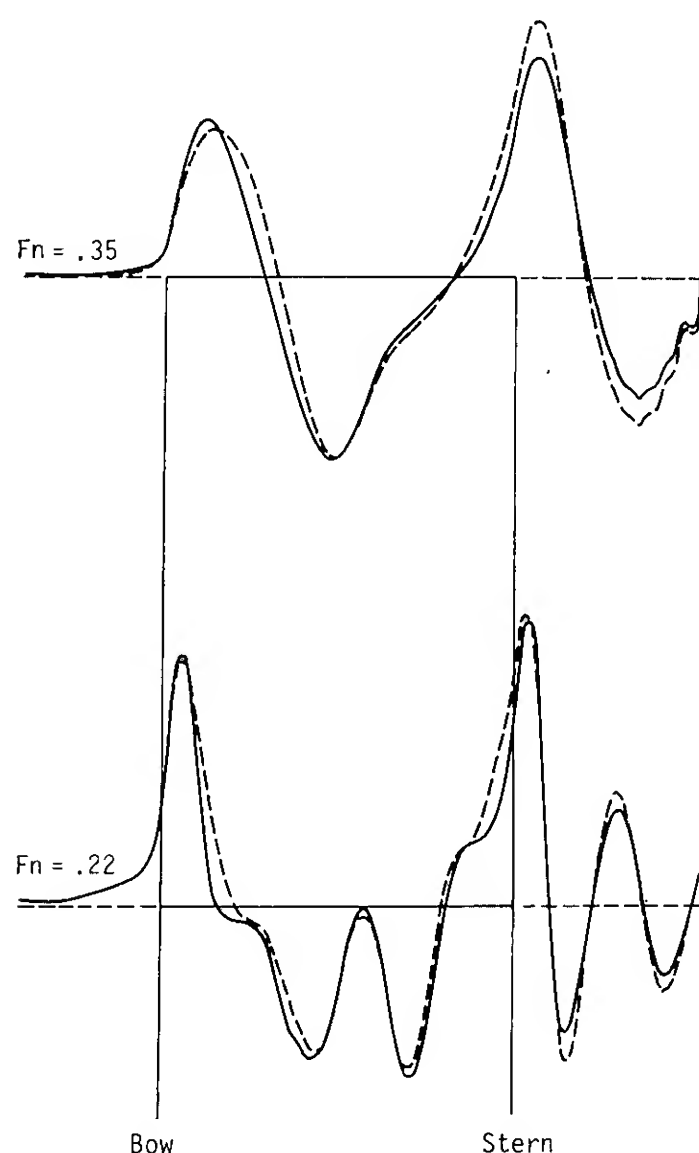


Fig. 3 Wave profiles along the hull predicted with Kelvin and Dawson's FSC; Series 60,  $Fn = .35$  and  $Fn = .22$

— Dawson  
- - - Kelvin

There are, however, exceptions. Since the difference between both FSC's increases with the nonuniformity of the double-body flow, there will be a limit on the hull fullness for which the above statement is valid. Fig. 4 shows what happens for very full hull forms, in this case a 55000 tdw tanker with a block coefficient of 0.82. At higher speeds (in excess of the service speed) both predictions are similar (though not identical) again, but for decreasing speed quite substantial differences appear. The Kelvin FSC still yields a large resistance far exceeding the experimental value, while the slow-ship FSC predicts a rapid decrease of the resistance. Even so the predicted wave patterns are very much alike (Fig. 5) and give no indication of such drastic resistance differences. Again Dawson's condition typically results in a forward shift of the bow wave. Due to the large curvature of the waterlines of such full hull forms this brings about a large resistance difference, concentrated at the forebody.

For the same ship at ballast draught the resistance predicted using Dawson's condition is in good agreement with the experimental data, while the Kelvin resistance exceeds this by a factor of 3. At full draught the Kelvin result is 4 times as high as the experimental result at the service speed, ..... but Dawson's condition yields a negative resistance! This physically unacceptable behaviour has been found for several slow, full-formed ships.

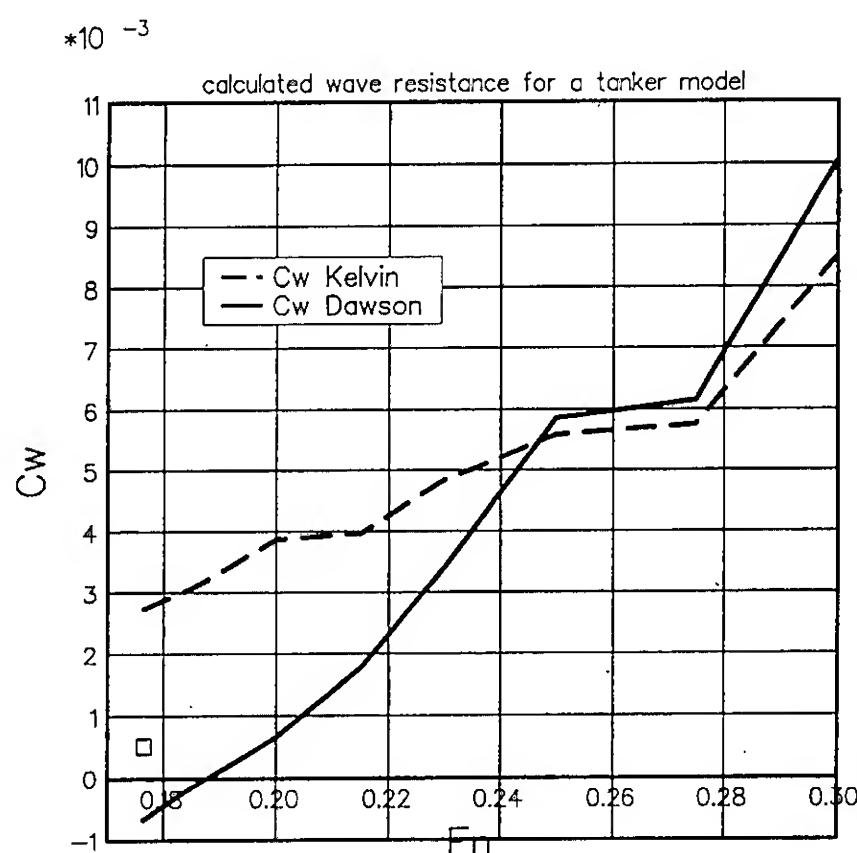


Fig. 4 Calculated wave resistance for a tanker model

□ Experiment

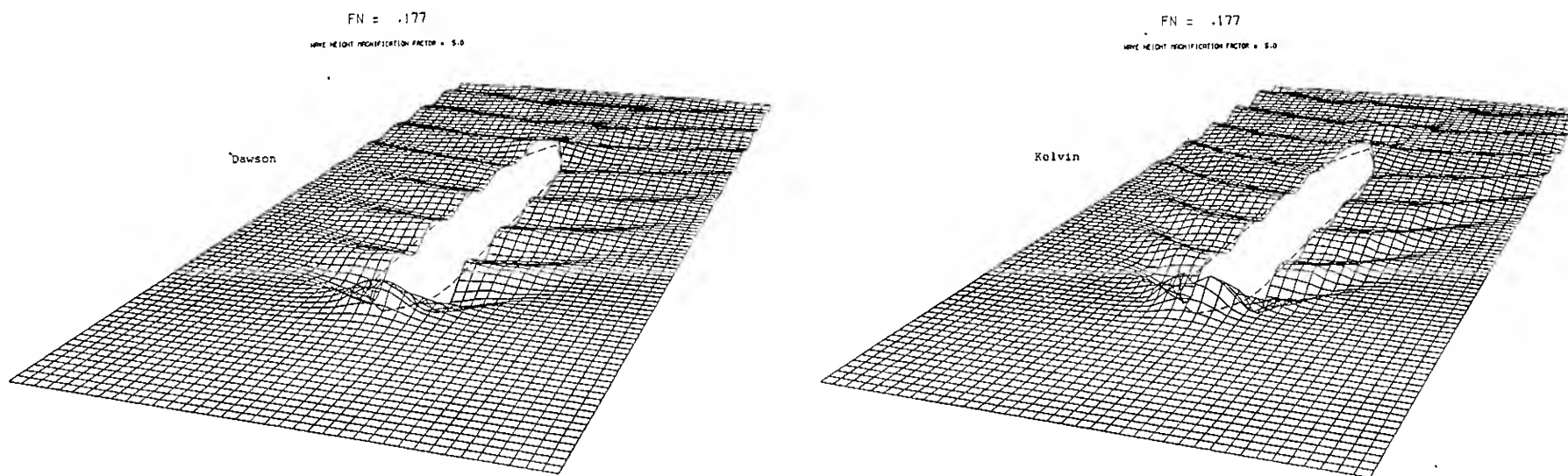


Fig. 5a Calculated wave patterns of tanker model, with Dawson's (left) and Kelvin's FSC (right), at  $Fn = 0.177$  (service speed)

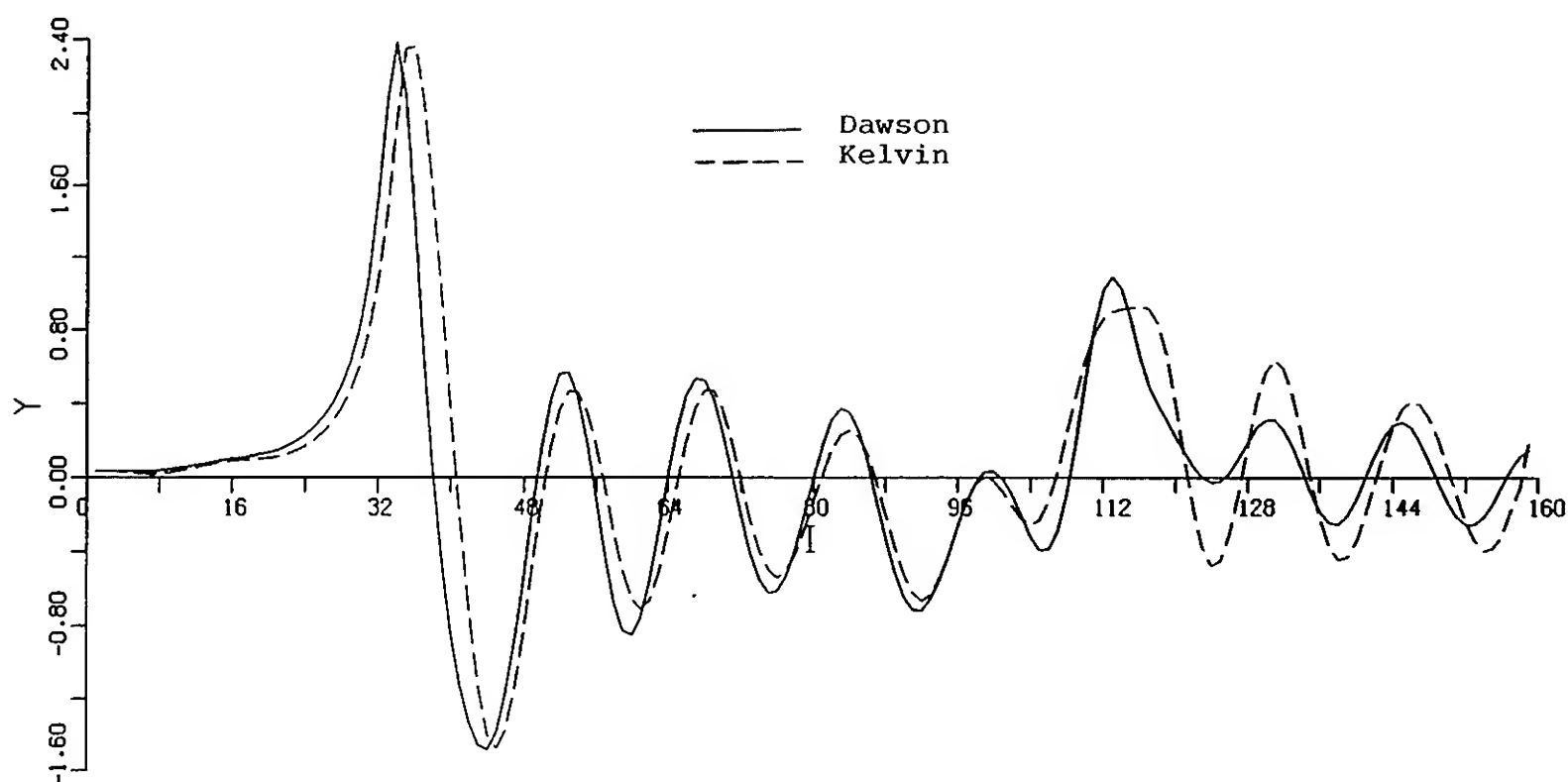


Fig. 5b Calculated wave profiles along the hull

Summarizing the results of these comparisons, for a large class of ships there is no reason to prefer Dawson's FSC to the Kelvin FSC; for practical discretizations the double-body flow effect is of minor importance. In extreme cases however, appreciable differences in resistance may occur, but none of the FSC's gives an accurate and reliable result.

The next section first tries to resolve the mystery of negative wave resistance. Then, we shall assess the adequacy of the FSC's by other means.

### 3. THE PARADOX OF NEGATIVE WAVE RESISTANCE

#### 3.1. General

The fact that a negative value of the wave resistance is sometimes predicted by Dawson's method is known to more people that

apply this method to real commercial ship hull forms. Generally this phenomenon is attributed to an insufficient resolution of the large pressure gradients on the hull. As a matter of fact we often find large differences in the pressure on adjacent panels, and the simple pressure integration over the hull could well be numerically inaccurate.

The accuracy of the pressure integration and of alternative formulations of the resistance based on Lagally's law has been discussed in [3]. It has been shown there that, provided the pressure integration is corrected for the zero-Froude number pressure integral, these formulations are all of about the same level of accuracy, determined by the accuracy with which the hull boundary condition is satisfied and so by the density of the hull panel distribution. Therefore, for the present test case the hull panelling has been



refined, from 545 to 1090, and then to 1415 panels on one half of the hull. Table 1 shows that this does reduce the zero-Froude number pressure integral (which has the exact value zero due to d'Alemberts paradox). However, the wave resistance (according to all three expressions) converges to a negative value! Similarly, increasing the free surface panel density did not give any substantial change in the predicted wave resistance. Therefore, contrary to the general belief discretization errors can probably be rejected as cause for the negative resistance, at least in some of the case investigated.

A negative value of the wave resistance in the presence of a physically realistic wave pattern radiated by the ship as shown in Fig. 5 is, of course, paradoxical. Apparently such a wave pattern need not have the correct energy budget. The wave pattern represents radiation of wave energy; since this energy travels with the group velocity which in harmonic deep-water waves is half the phase speed, it lags behind the wave crest propagation, hence it must be supplied at the wave origin, i.e. at the ship. But a negative resistance means that instead the ship extracts energy from the waves. A steady flow can only exist if some other source of energy is present.

### 3.2. Energy Conservation

To investigate what the source of energy can be we consider the energy fluxes through the boundaries of a control volume surrounding the hull and moving with the hull, in a stationary frame of reference (Fig. 6). We define the x-axis to point astern, the y-axis vertically upward with  $y=0$  at the undisturbed water level.

As derived in [5] the general expression for the energy flux through a surface, expressed in a general unsteady potential  $\Phi$ , is:

$$\dot{E} = - \iint \{ \rho \Phi_t (\Phi_n - V_n) - p \cdot V_n \} dS \quad (3)$$

where  $V_n$  is the velocity of the surface itself in the normal direction, and the energy flux is defined positive in the sense consistent with that of the normal. For a steady flow,  $\Phi_t = U \phi_x$ , where now  $\nabla \phi$  is the disturbance of the uniform flow and  $U$  the ship speed.

The energy fluxes out of the control volume then become:

through the hull surface:

$$\dot{E}_H = -U \iint p \cdot n_x \cdot dS = -U \cdot R_w \quad (4)$$

(where  $n$  is the inward normal on the hull);

through the upstream plane:

$$\dot{E}_U = -U \iint_U \rho g y \, dS \quad (5)$$

through the downstream plane:

$$\dot{E}_D = +U \iint_D \rho g y \, dS - \frac{1}{2} \rho U \iint_D (\phi_x^2 - \phi_y^2 - \phi_z^2) dS \quad (6)$$

where the lateral and upstream boundaries (but not the downstream plane) have been assumed to recede to infinity. It is noted that no energy flux is present through the free surface, since the pressure is equal to zero and  $\phi_n = V_n$ , for exact satisfaction of the free surface conditions.

Table 1 Calculated resistances for tanker model,  $Fn = 0.1765$

A) influence of hull panel density; Dawson's FSC.

Number of hull panels per side	545	1090	1415
Zero-Fn pressure integral	.00071	.00042	.00020
Wave resist. pressure integration	-.00082	-.00068	-.00067
Wave resist. Lagally integr. over FS	-.00054	-.00048	-.00047
Wave resist. Lagally integr. over hull	-.00068	-.00054	-.00052

B) influence of free surface condition; 1090 hull panels.

Free surface condition	Kelvin	Dawson	Eggers
Wave resist. pressure integration	.00270	-.00068	-.00158
Wave resist. Lagally integr. over FS	.00282	-.00048	-.00146
Wave resist. Lagally integr. over hull	.00288	-.00054	-.00156
Waterline integral (10)	.00062	.00054	.00015



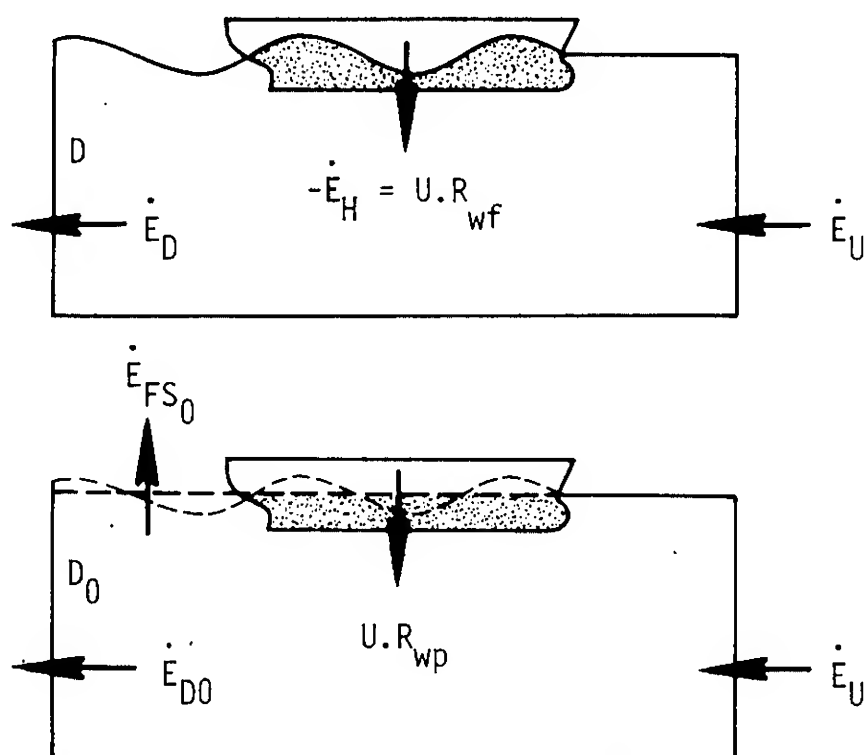


Fig. 6 Control volumes for energy balance;  
above: exact case;  
below: linearized case

Conservation of energy then requires that

$$R_{wf} = \frac{1}{2} \rho \iint_D (-\phi_x^2 + \phi_y^2 + \phi_z^2) dS + \frac{1}{2} \rho g \int_{l_T} \eta^2 dz \quad (7)$$

The first integral is over a transverse plane astern of the hull and the second one along its intersection  $l_T$  with the free surface; the latter line integral basically takes into account the contribution of the potential energy, as it stems from the  $\rho g y$  term in the pressure. This is a well-known result that is the basis of wave-pattern analysis methods.

However, the derivation may not be entirely relevant to our calculations. The linearized FSC is imposed on the undisturbed free surface, not on the actual wave surface. The fluid domain considered thus extends only to  $y=0$ , and so should our control volume. Therefore we now redefine the control volume by taking not the exact free surface as its upper boundary but the  $y=0$  plane.

The energy fluxes must then be slightly modified. An energy flux through the undisturbed free surface may now be present, according to the general expression (3):

$$\dot{E}_{FS0} = - \iint_{FS0} \rho \phi_x \phi_y dS \quad (8)$$

It is important to note that here no FSC has been substituted yet.

Energy conservation now demands that

$$R_{wp} = \frac{1}{2} \rho \iint_{D_0} (-\phi_x^2 + \phi_y^2 + \phi_z^2) dS + \frac{1}{2} \rho \iint_{FS0} \phi_x \phi_y dS \quad (9)$$

It is noted in passing that the energy supply through the hull surface, and thereby the resistance found, now only concerns the  $y < 0$  part of the hull. This introduces a difference that can be approximated by:

$$\Delta R_W = + \frac{1}{2} \rho g \int_{WL} \eta^2 n_x d\ell \quad (10)$$

However, this waterline integral is often ignored, following Dawson [4], since it generally does not improve the results; its magnitude for the present case is included in Table 1 and found to be not negligible, but not affecting the conclusions on the negative resistance either. Similarly the integral over the downstream plane extends only to  $y=0$ .

In any case,  $R_{wf}$  may be considered as the resistance that is physically associated with the generation of the wave pattern that is predicted in the far field, since (7) has been derived without making any simplification of the boundary conditions. On the other hand, the pressure integration over the hull in our linearized calculation need not be equal to  $R_{wf}$  because of the simplifications of the FSC and the different control volume, but it will give a result in agreement with  $R_{wp}$ . Therefore, the origin of the paradox, being a contradiction of the calculation and our physical insight, must be sought in the difference between both expressions.

Substitution of the potential of a free harmonic wave in  $R_{wf}$  shows that the wave resistance so obtained is positive definite, in agreement with our physical observation of the radiated wave pattern. Also its value is independent of the position of the aft plane, since in harmonic waves there is a constant horizontal energy transport and a pure exchange between kinetic and potential energy. In expression (9) however, the horizontal energy flux is not constant: the potential energy is absent as the control volume extends now only to  $y=0$ , and it thus cannot compensate the variations of the kinetic energy flux. But still the resistance from (9) is independent of  $x$ , since for harmonic waves the variations of the kinetic energy flux are now compensated by the flux through the undisturbed free surface, the integral over  $FS0$ .

More generally, we can evaluate (9) by substituting the Kelvin condition:

$$\phi_y = U\eta_x; \quad \eta = -\frac{U\phi'_x}{g};$$

$$\begin{aligned} -\rho \iint_{FS_0} \phi'_x \phi_y dS &= +\rho g \iint \eta \eta_x dS = \\ &= \frac{1}{2}\rho g \int_{\ell_T} \eta^2 dz + \frac{1}{2}\rho g \int_{WL} \eta^2 n_x d\ell \end{aligned} \quad (11)$$

where  $n$  is now the inward normal on the waterline. So  $R_{wp}$  and  $R_{wf}$  are equal to leading order, except for a waterline integral which is of opposite sign to (10); this difference in sign has been called "Gadd's paradoxon" and is dealt with in [6]. Apart from this, if the Kelvin condition is imposed (7) and (9) give the same result at least asymptotically; so the pressure integration over the hull in our linear problem, which satisfies (9), is equal to the resistance deduced from the far-field wave pattern corresponding to (7), hence it is positive and independent of  $x$  if a system of harmonic waves is present at the aft plane. Again the energy flux through  $FS_0$  just takes into account the variations of the potential energy. It appears that this correspondence relies on the precise relation between the velocity components at the free surface and the wave elevation, so on the FSC.

However, for free surface conditions other than Kelvin's this equality may be lost. E.g. for the slow-ship condition we find from (9):

$$\begin{aligned} R_{wp} &= \frac{1}{2}\rho \iint_{D_0} (-\phi_x^2 + \phi_y^2 + \phi_z^2) dS + \\ &\quad - \rho \iint_{FS_0} \phi_x (\phi_x \eta_x + \phi_z \eta_z + \phi'_x \eta_{rx} + \\ &\quad + \phi'_z \eta_{rz}) dS \end{aligned} \quad (12)$$

which does not correspond with  $R_{wf}$  generally. If a realistic system of waves is present behind the ship, (7) will again give a positive resistance. But  $R_{wp}$  may be different as part of the wave energy may have been supplied through  $FS_0$  instead of by the ship. The intuitively expected correspondence between a radiated wave pattern and a resistance acting on the hull is thus not verified for all FSC's. In the extreme case the pressure integration over the hull can give a negative resistance: the ship rides on waves generated by the free surface condition, in this case governed by the double-body flow nonuniformity.

In order to obtain a more realistic wave resistance prediction for such extreme cases, two approaches now suggest themselves. Since  $R_{wf}$  seems to have the desired property of positive definiteness, we could try to deduce the resistance from the far-field wave pat-

tern. Otherwise, we could perhaps modify the FSC so as to eliminate the excess energy flux through the free surface.

### 3.3. Far-Field Resistance Calculation

Evaluation of (7) is not a straightforward matter in a Rankine-source method, since it requires to calculate the velocities in a dense grid of field points in a transverse plane astern of the ship. The integral over  $D_0$  thus found must then be supplemented by the line integral and a contribution of the difference  $D-D_0$ . An alternative would be to apply one of the formula's used in wave pattern analysis methods, which are based on (7).

Before undertaking such a study we better first consider its chance of success. Since we want to get a resistance independent of the  $x$ -position of the transverse plane, this plane should be located outside the region where there is still an excess energy flux through the free surface. We know that for vanishing double-body flow disturbance the slow-ship condition boils down to the Kelvin condition, for which we have shown the absence of leading-order energy flux. Therefore we must choose the downstream plane far enough from the hull to avoid the double-body flow disturbance. In practice a logical choice would be a position at or beyond the aft edge of the free surface panel distribution.

However, since no singularities are located aft of this plane, d'Alembert's paradox is valid for the 'body' generated by the collection of sources on the double body and free surface: the momentum flux through the transverse plane will be always zero! The wave resistance is an internal force inside this virtual body and is compensated by an opposite force exerted by the hull on the free surface panels.

Therefore the integral over  $D_0$  is zero, and

$$R_{wp} = -\rho \iint_{FS_0} \phi_x \phi_y dS \quad (13)$$

which is precisely the expression obtained from Lagally's law. Similarly the first term of (7) is dominated by this effect and loses the properties it has in harmonic waves; thus  $R_{wf}$  cannot be supposed to be positive definite and independent of  $x$  any more. This must be caused by the truncation of the free surface domain locally distorting the potential field corresponding with harmonic waves.

$R_w$  (1) will only give a reliable result if the free surface panelling is continued a large distance beyond the aft plane  $D$ , which means a considerable extra expense in computer time.

In view of their relation with (7) and the assumptions on the potential field, the same is likely to be true for wave pattern analysis methods. Besides, these could be subject to errors caused by the inherent damping of the numerical approximation. The experiences of Maisonneuve [7] with such a resistance evaluation do show that this is not a good alternative for the pressure integration.

### 3.4. Energy Flux Through The Free Surface

Another, more fundamental remedy for the occurrence of a negative wave resistance could be to modify the FSC so as to eliminate the excess energy flux through the free surface. Whatever the FSC imposed this energy flux into the fluid domain can be written as

$$-\dot{E}_{FS} = \iint_{FS} (\rho U \phi_x \Delta V_n - U \cdot \Delta p \cdot \eta_x) dS \quad (14)$$

where the integration is over the predicted wave surface,  $\Delta V_n$  is the remaining normal velocity and  $\Delta p$  the pressure prevailing there. To eliminate the energy flux at every point of the free surface both  $\Delta V_n$  and  $\Delta p$  should be zero, so we have to satisfy the exact non-linear FSC's; the best that can be achieved in a linearized method is a reduction of the energy flux to higher order in the perturbation parameter.

For the slow-ship condition this parameter is the square of the Froude number  $Fn$ . Since the resistance coefficient is supposed to be of  $O(Fn^4)$ ,  $dE/dt$  should be  $O(Fn^6)$ .  $\phi_x$  and  $\eta_x$  contain the double-body disturbances which are  $O(1)$ , hence both  $\Delta V_n$  and  $\Delta p$  must be  $O(Fn^6)$ . Now Dawson's FSC does contain terms up to  $O(Fn^4)$  and ought to satisfy this requirement; but as has been pointed out in [3] and will be shown in the next section, Dawson's FSC is inconsistent due to the absence of terms incorporating the transfer of the velocities from the actual to the undisturbed free surface. Including these terms,  $\eta_x \phi_{yy} + \eta'_{yy}$ , yields an FSC that can be written as:

$$Fn^2 \left\{ \frac{1}{2} \left( \phi_{xx} + \phi_{zz} + \phi_x \frac{\partial}{\partial x} + \phi_z \frac{\partial}{\partial z} \right) (\phi_x^2 + \phi_z^2) + \left( \phi_{xx} + \phi_{zz} + \phi_x \frac{\partial}{\partial x} + \phi_z \frac{\partial}{\partial z} \right) (\phi_x \phi_x + \phi_z \phi_z + \phi_x^2 - \phi_z^2) \right\} + \phi_y = 0 \quad (15)$$

This in fact reduces  $\Delta V_n$  and  $\Delta p$  to  $O(Fn^6)$  and thus should suit our purpose.

Now this is exactly what has been derived in a different way by Eggers [8], in a paper that seems to have been given little attention. From the analogous requirement that the far-field resistance found from a slow-ship calculation should be invariant to leading order for the choice of control volume, he

derived this same FSC (15). Although in his paper this is suggested to form an additional proof of the correctness of the order assumptions made in the linearization, the above consideration shows that actually it is subject to these same assumptions.

Therefore, Eggers's FSC does provide equality of  $R_{wf}$  and  $R_{wp}$  up to higher order in  $Fn$ , just like the Kelvin condition does up to higher order in the wave steepness. This could solve the problem of negative wave resistances. The FSC (15) has therefore been implemented in our program and applied to a few cases. For the Wigley hull the predicted resistance differed by 3% from the Dawson prediction, and the wave profile was almost identical. For the Series 60 model the resistance curve is included in Fig. 7 and turns out to be similar in shape but consistently lower than those obtained with the two other FSC's.

Surprisingly however, the predicted  $R_w$  for the tanker form (Table 1) is even more negative than that found with Dawson's FSC. The wave profile along the hull is hardly different; the wave pattern (Fig. 8) shows a remarkable reduction of the Kelvin angle, but is otherwise similar to Dawson's. These results suggest that only more energy has been supplied through FS. Moreover, the resistance curve goes down for increasing speed, and at somewhat higher speeds flow reversal at the free surface is predicted! The results were found to be extremely sensitive to details of the implementation. It thus seems that for large double-body flow disturbances this FSC is not adequate, notwithstanding its theoretical consistency. An explanation of this will be given in Section 5.

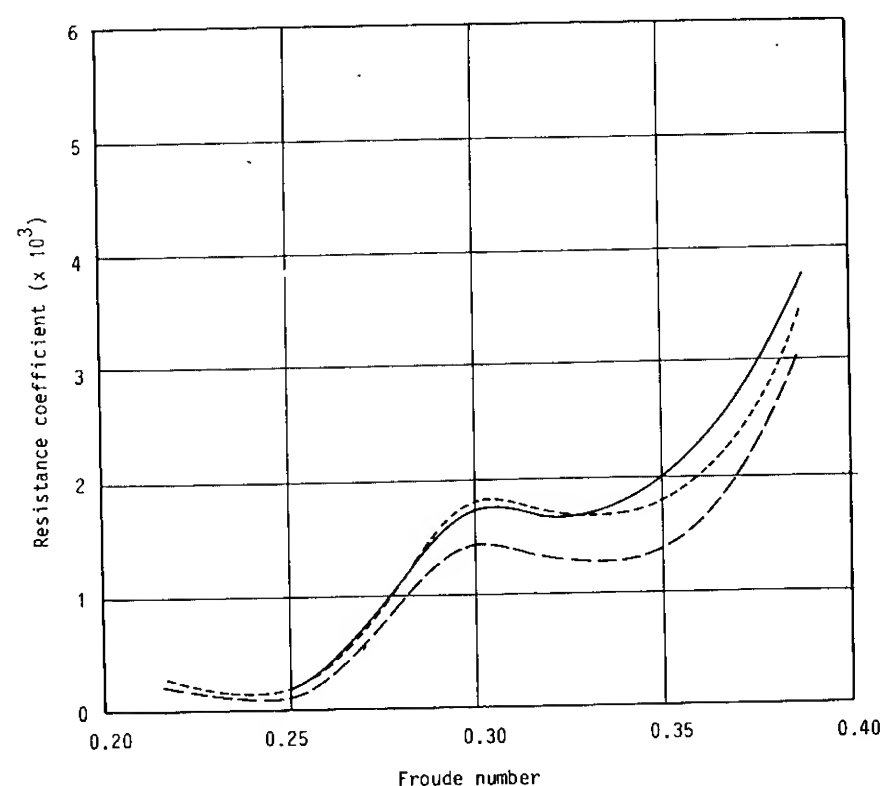


Fig. 7 Predicted wave resistance coefficient using Kelvin, Dawson's and Eggers's FSC

— Kelvin  
 ---- Dawson  
 - - - Eggers

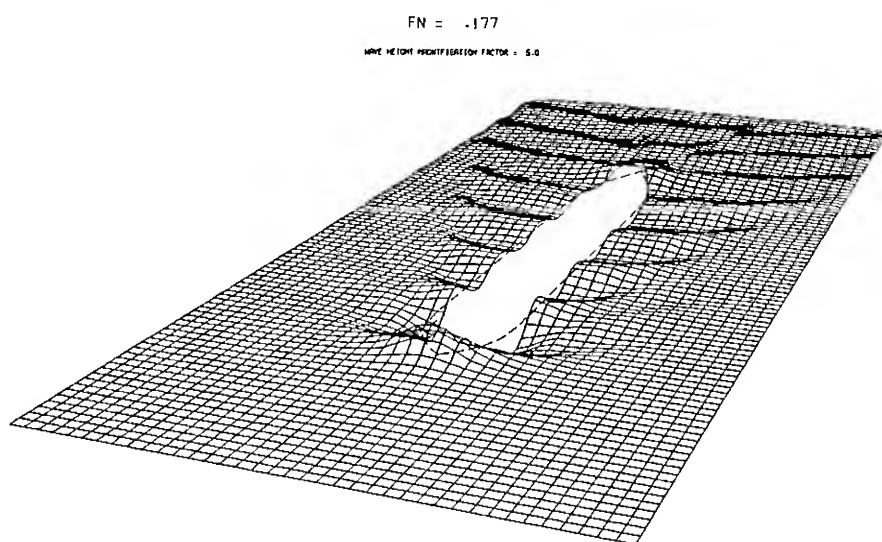


Fig. 8 Calculated wave pattern for tanker model, with FSC of Eggers

### 3.5. Summary

Summarizing some of the findings of this section, the paradoxical occurrence of negative wave resistance in the presence of a plausible radiated wave pattern can be explained by the possibility of an energy flux through the undisturbed free surface differing from the amount needed to represent the potential energy variations. This energy flux can be expressed in the remaining normal velocity and pressure at the calculated free surface. Reduction to higher order of both quantities leads to the FSC derived by Eggers. Although this gives reasonable predictions for slender ships, for the tanker hull an erroneous flow field is sometimes obtained and the resistance is again negative. Therefore the higher order contributions to the energy flux are probably significant here. The next section attempts to shed some light on the magnitude and origin of these higher order terms in general.

## 4. HIGHER-ORDER TERMS

### 4.1. Approach

In the derivation of the linearized free surface conditions several linear and nonlinear terms have been dropped based on the fact that they are of higher order in the perturbation parameter adopted. Now the notion of higher order just means that these terms become insignificant asymptotically for a vanishing value of the parameter; no information is available a priori on the actual magnitude of these terms in practical cases. Therefore the range of applicability of a linearized method can in general only be determined in practice.

It is clear, however, that agreement with experimental data is not a very suitable yardstick for the accuracy of wave resistance calculations and has therefore not been used in Section 2. The residual resistance is often

affected by uncertainty on the viscous resistance, and wave pattern measurement techniques give results consistently lower than the residual resistance and with a considerable amount of scatter. Therefore a method to assess the magnitude of the neglected terms directly could give a much better idea of the adequacy of FSC's. In addition it might provide directions for setting up a method to solve the exact nonlinear problem.

Evaluation of the nonlinear terms would in principle be possible from velocity measurements at a very dense grid of points near the free surface; but no such measurements seem to be available. A better way would be to compute these terms from solutions of the nonlinear problem; but these exist only for unrealistic test cases, or in the form of numerical solutions of insufficient accuracy.

For these reasons another approach has been chosen here: to evaluate the nonlinear terms 'a posteriori', from the flow field calculated by a linear method. Of course this technique does have its own restrictions: How the predictions would change if the nonlinear terms were included in the FSC is not clear; nor is there any certainty on how the terms themselves would change in magnitude. Additionally, the singular behaviour at the stagnation points will cause some of the higher-order contributions to blow up. Hence also the comparison of the higher-order terms is limited to practical discretizations, although, as we have found, within fairly wide margins: approaching the stagnation points magnifies the relative magnitude of the nonlinear terms but does not immediately affect the comparison of FSC's.

### 4.2. Derivation Of Higher-Order FSC's

To define the neglected terms we must first of all expand the FSC's to higher order. The combination of the kinematic and dynamic free surface conditions that is actually imposed demands that the flow at the undisturbed free surface has a direction parallel to the isobar planes. Only afterwards the free surface elevation is retrieved by using the dynamic condition. In view of this, in the following I have chosen the approach to start from the kinematic condition and to derive the higher order terms in it.

Now the prime difficulty here is that the exact FSC should be applied at  $y=\eta$ , not at the undisturbed free surface  $y=0$ . To derive the error in the FSC would require the calculated velocity field at  $y=\eta$ ; but this cannot be evaluated since for  $\eta>0$ , the singularities generating the flow lie inside the fluid domain. Therefore we have to resort to Taylor expansions to express flow quantities at  $y=\eta$  in those at  $y=0$ . But precisely the validity of these expansions has been a point of debate in the derivation of the slow-ship FSC. The wave

elevation including the double-body contribution is  $O(Fn^2)$ ; it has been argued that the perturbation  $\phi'$  has a wavy character with wave number  $O(Fn^{-2})$ , so all terms in the Taylor expansion for the transfer would be of the same order; neither the analytic continuation of the flow field, nor the truncation of the expansions would then be permitted. We have, however, adopted the basic order assumptions of Eggers [8] as discussed in [3] and consequently ignored the possible order reduction by differentiation.

The nonlinear terms can be formulated consistently, including only the contributions of next-higher order, or inconsistently in an attempt to approximate the exact FSC as closely as possible. There is a quantitative difference between both forms but the conclusions are the same for most cases.

The best estimate of the wave elevation is that which includes the nonlinear terms and the transfer terms; it is noted  $\eta^*$  below. For the Kelvin condition, the perturbation parameter is the wave steepness  $\varepsilon = \frac{||\eta||}{Fn^2}$ . The velocities at  $y=\eta$  are:

$$\phi'_x = (\phi'_x)_{y=0} + \eta \phi'_{xy} + O(\varepsilon^3), \text{ etc.} \quad (16)$$

Substituting this into the dynamic FSC gives the following expressions for the wave height  $\eta$ :

linear:

$$\eta = -Fn^2 \phi'_x + O(\varepsilon^2) \quad (17)$$

nonlinear:

$$\bar{\eta} = \eta - \frac{1}{2} Fn^2 (\phi'^2_x + \phi'^2_y + \phi'^2_z) + O(\varepsilon^2) \quad (18)$$

including transfer:

$$\eta^* = \bar{\eta} - Fn^2 \eta \phi'_{xy} + O(\varepsilon^3) \quad (19)$$

The consistent decomposition of the kinematic FSC is then:

$$\begin{aligned} \phi_y = & \underbrace{\eta_x}_{\text{term 1}} + \underbrace{(\phi'_x \eta_x + \phi'_z \eta_z)}_{\text{term 3}} + \underbrace{(\bar{\eta}_x - \eta_x)}_{\text{term 4}} + \\ & \underbrace{(\eta^*_x - \bar{\eta}_x)}_{\text{term 5}} - \underbrace{\eta \phi'_{yy}}_{\text{term 6}} + O(\varepsilon^3) \end{aligned} \quad (20)$$

while an inconsistent form is:

$$\eta^* = \bar{\eta} - Fn^2 \eta (\phi_x \phi_{xy} + \phi_y \phi_{yy} + \phi_z \phi_{yz}) \quad (21)$$

$$\begin{aligned} \phi_y = & \underbrace{\eta_x}_{\text{term 1}} + \underbrace{(\phi'_x \eta_x + \phi'_z \eta_z)}_{\text{term 3}} + \underbrace{\left(\phi_x \frac{\partial}{\partial x} + \phi_z \frac{\partial}{\partial z}\right)(\bar{\eta} - \eta)}_{\text{term 4}} + \\ & \underbrace{\left(\phi_x \frac{\partial}{\partial x} + \phi_z \frac{\partial}{\partial z}\right)(\eta^* - \bar{\eta})}_{\text{term 5}} + \\ & \underbrace{\eta^* (\phi_{xy} \eta^*_x + \phi_{yz} \eta^*_z - \phi_{yy})}_{\text{term 6}} \end{aligned} \quad (22)$$

For the consistent form of the slow-ship FSC the wave height expressions are:

double-body:

$$\eta_r = \frac{1}{2} Fn^2 (1 - \phi_x^2 - \phi_z^2) \quad (23)$$

linear:

$$\eta = \frac{1}{2} Fn^2 (1 - \phi_x^2 - \phi_z^2 - 2\phi_x \phi'_x - 2\phi_z \phi'_z) \quad (24)$$

nonlinear:

$$\bar{\eta} = \eta - \frac{1}{2} Fn^2 (\phi'^2_x + \phi'^2_y + \phi'^2_z) \quad (25)$$

including transfer:

$$\begin{aligned} \eta^* = & \bar{\eta} - Fn^2 \left\{ \eta_r^2 (\phi_x \phi_{xyy} + \phi_z \phi_{zyy} - \phi_{yy}^2) + \right. \\ & \left. + \eta_r (\phi_x \phi'_{xy} + \phi_z \phi'_{zy} - \phi_{yy} \phi'_y) \right\} + O(Fn^8) \end{aligned} \quad (26)$$

The resulting expression for the FSC is getting excessively complicated. The higher-order terms now contain third derivatives of the double-body potential. These are rather hard to calculate and quite susceptible to numerical oscillations. A simplified form was therefore derived by dropping the transfer terms associated with the double-body potential. This is not entirely a matter of convenience; as shown in Fig. 9 the extension of the double-body flow field above the undisturbed waterplane, based on its assumed symmetry, only reduces the accuracy of the approximation for hulls with strongly flared sections at the waterline. With this simplification the consistent form becomes:

$$\begin{aligned} \phi_y = & \underbrace{\phi_x \eta_x}_{\text{term 1}} + \underbrace{\phi_z \eta_z}_{\text{term 2}} + \underbrace{\phi'_x \eta_{rx} + \phi'_z \eta_{rz}}_{\text{term 2}} + \\ & \underbrace{\phi'_x \eta'_x + \phi'_z \eta'_z}_{\text{term 3}} + \underbrace{\left(\phi_x \frac{\partial}{\partial x} + \phi_z \frac{\partial}{\partial z}\right)(\bar{\eta} - \eta)}_{\text{term 4}} + \\ & \underbrace{\left(\phi_x \frac{\partial}{\partial x} + \phi_z \frac{\partial}{\partial z}\right)(\eta^* - \bar{\eta})}_{\text{term 5}} + \\ & \underbrace{\eta_r (\eta_{rx} \phi'_{xy} + \eta_{rz} \phi'_{yz})}_{\text{term 6}} - \frac{1}{2} \eta_r^2 \phi'_{yyy} + \\ & - \eta' \phi'_{yy} - \underbrace{\eta_r \phi'_{yy}}_{\text{term 7}} + O(Fn^8) \end{aligned} \quad (27)$$



where

$$\eta^* = \eta - Fn^2 \eta_r (\phi_x \phi'_{xy} + \phi_z \phi'_{yz}) \quad (28)$$

and the inconsistent form is identical to (22).

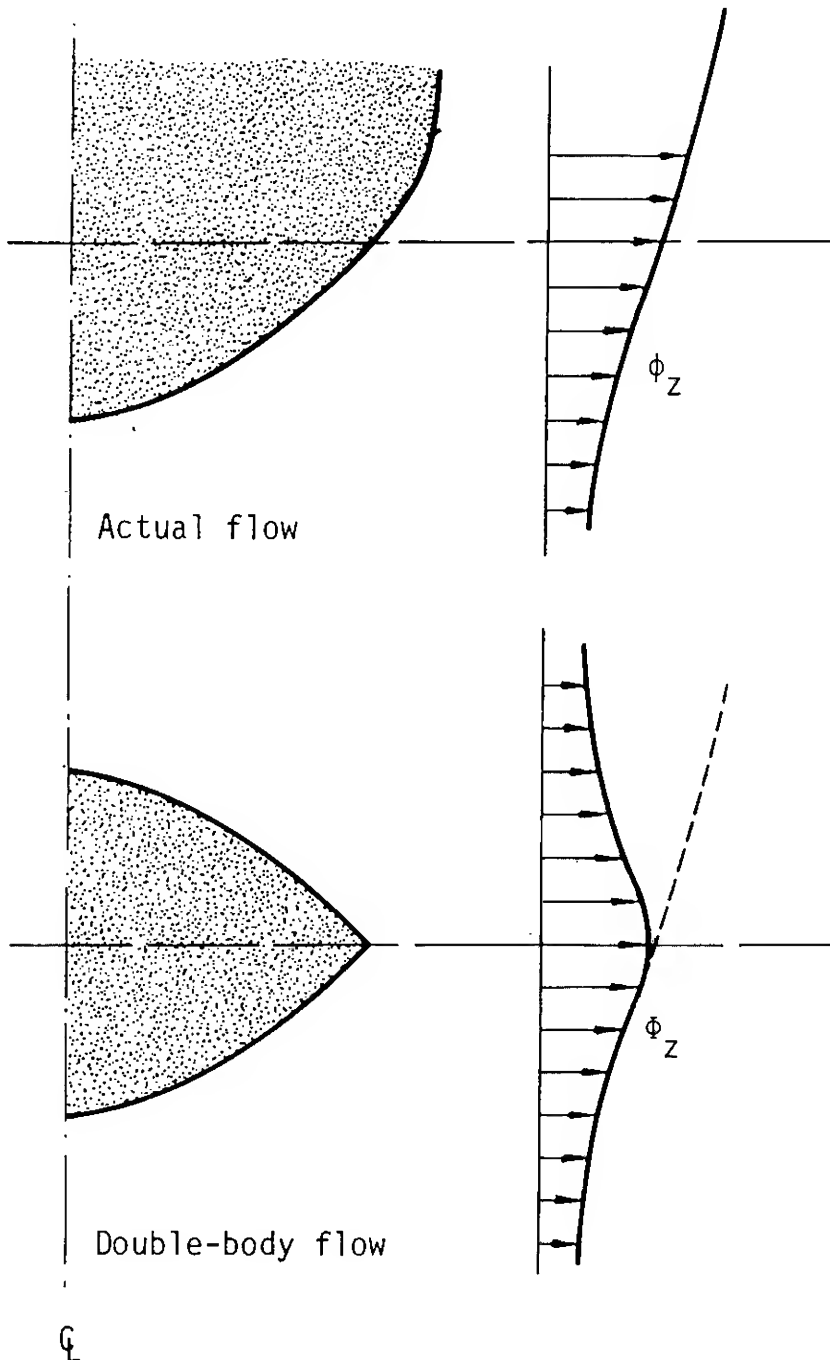


Fig. 9 Transfer terms for double-body flow may reduce the accuracy

In all above expressions, the notation of the terms is as follows. Terms 1 and 2 are linear and are included in the linearized FSC. Terms 5 and 6 result from the transfer of the FSC to the undisturbed free surface, while terms 3 and 4 are the other nonlinear contributions to the FSC. Term 7 is a linear transfer term for the vertical velocity. If, here, we would not neglect the terms connected with the double-body flow transfer, its form would be

$$-\eta_r \phi'_{yy} - \eta \phi_{yy} = O(Fn^2) \quad (29)$$

which we shall denote by 'term 8' in the following. This is the transfer term alluded to in the previous section; it is neglected in Dawson's FSC but is present in that of Eggers.

It may be noted that for the double-body flow replaced by a uniform flow, the inconsistent expressions become equal, but the consistent ones (19,20) and (27,28) do not for term 5 and  $\eta^*$ .

#### 4.3. Results

Evaluating all these terms was restricted mainly to the Wigley hull, the Series 60 block .60 model and the tanker form dealt with before. For clearness of presentation we shall sum up the main conclusions drawn, grouped under the test case concerned.

The figures illustrating these results are set up as follows: the quantity plotted is indicated in the caption; as all terms are contributions to the vertical velocity, they are non-dimensionalized by the ship speed and compared with either the vertical velocity itself or the dominant contribution to it (term 1), as indicated. The abscissa is the panel number on the longitudinal strip of free surface panels along the hull and the centre line. The panel lengths are uniform. The locations of bow (left) and stern(right) need no further indication.

##### 1. Series 60 block .60 at $Fn = 0.35$ and $0.22$

\* Of the linear terms included in the FSC, only term 1 is significant (Fig. 10). Only at bow and stern term 2 may give a modest contribution, but due to the considerable phase shift between  $\eta$  and  $\eta_r$  this contribution is often of the wrong sign. Probably term 2 could well be deleted from the FSC but computationally this gives no simplification at all.

\* The linear term 8 neglected in Dawson's FSC is generally larger than term 2 and is mostly concentrated at the bow (Fig. 10). For the Series 60 hull its maximum contribution is about 20%, at  $Fn=0.35$ . Including this term reduces the wave resistance by 20% in this case.

\* The nonlinear terms (i.e. the error in the linearized FSC) are dominated by the transfer terms. The effect of imposing the FSC at the correct location is often far more important than to include all squares and cross-products.

\* The sum of the higher-order terms is shown in Figs. 11 and 12 for two Froude numbers. It appears that at  $Fn=0.35$  it is of quite substantial magnitude, locally as large as the linear terms. That still the predictions are acceptable must be due to some sort of



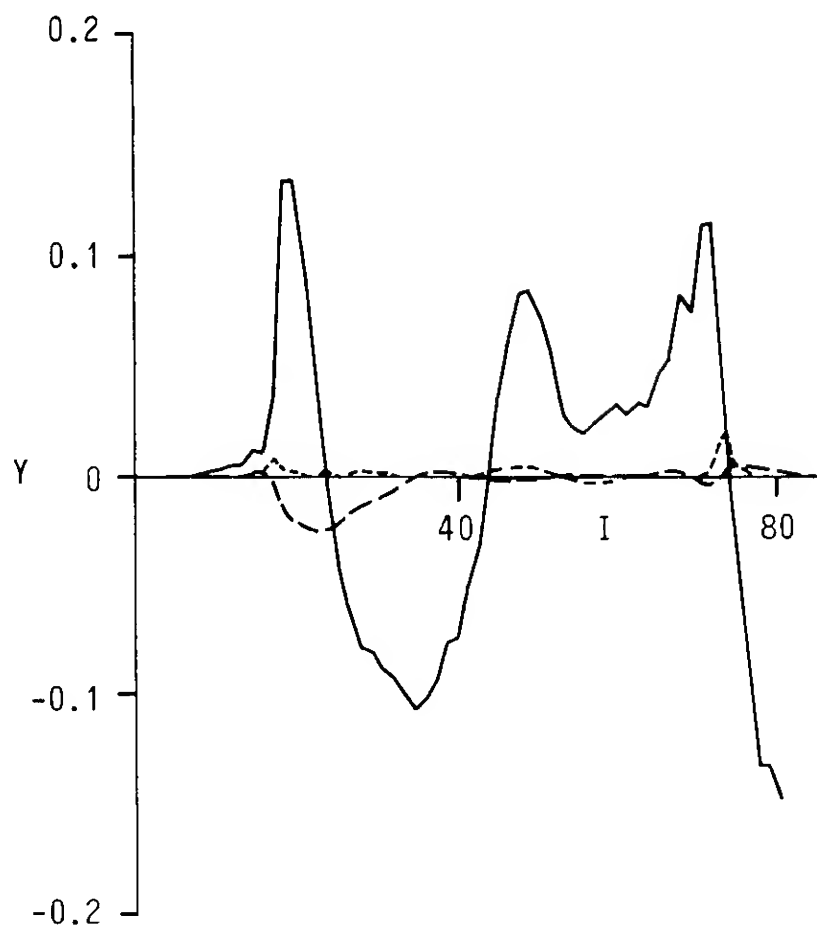


Fig. 10 Linear terms in free surface condition; Dawson's FSC, Series 60,  $Fn = .35$

— Term 1  
 - - - Term 2  
 - · - Term 8

error cancelling, or to the fact that the evaluation a posteriori is too pessimistic. At  $Fn=0.22$  all methods have fairly small error terms, confirming that linearization is adequate in this case.

\* The sum of the neglected terms (terms 3 to 8 for Kelvin and Dawson, 3 to 6 for Eggers), which indicates the adequacy of the linearized FSC, is of comparable magnitude for all FSC's; all are oscillating with similar amplitude and mean value. No significant improvement for the slow-ship conditions is observed.

\* Eggers's FSC gives results closely corresponding with those of Dawson's; although term 8 is now included in the FSC, the sum of neglected terms is not substantially less than for Dawson's FSC, since term 8 has a much smaller wave number than the other terms; therefore the mean value of the error is changed but the result is not visibly improved in general.

## 2. Tanker model, $Fn = 0.1765$

Similar conclusions were drawn for this test case, except for the following:

\* The nonlinear terms for the slow-ship FSC's are of moderate magnitude here, so the linearization is not particularly inadmissible (Fig. 13).

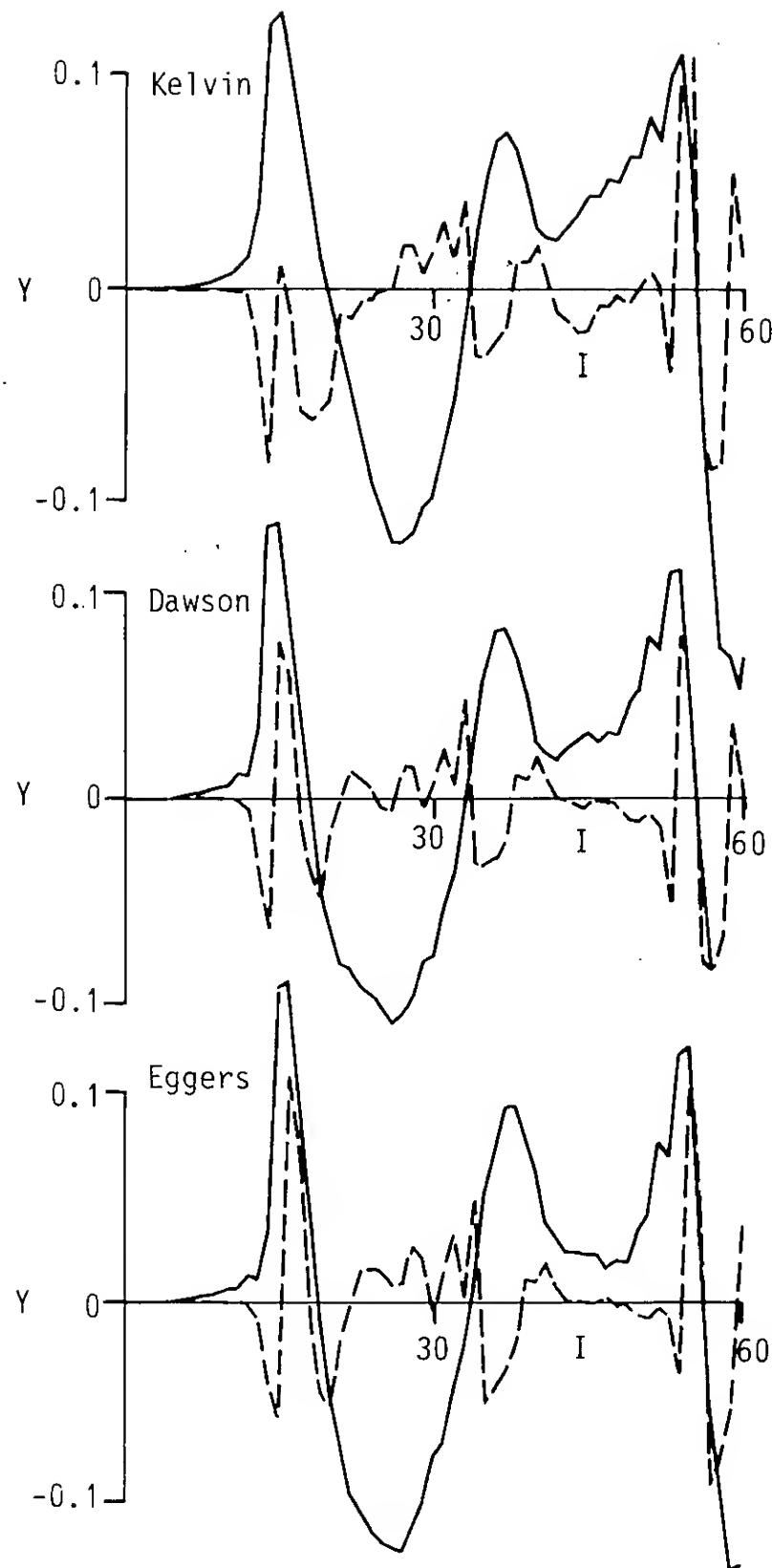


Fig. 11 Nonlinear terms in free surface conditions; Series 60,  $Fn = .35$

— Term 1  
 - - - Terms 3 + 4 + 5 + 6

\* The transfer term 8 is now quite large at the bow, about 70% of the vertical velocity (Fig. 14). It is understandable that this causes the substantial difference between the predictions using Dawson's and Eggers's condition.

\* The nonlinear terms are significantly larger for the Kelvin FSC than for both slow-ship FSC's now (Fig. 13).

\* The sum of the neglected terms is somewhat larger for Dawson's FSC than for that of Eggers in this case, which is entirely due to term 8.

We thus conclude that for the Series 60 model even from this evaluation of the non-linear terms no advantage for the slow-ship condition over the Kelvin condition can be observed. Only for very full hulls the slow-ship condition is again more appropriate than Kelvins condition for practical free surface discretizations. The large differences in neglected terms are largely in agreement with the wide spread in the predictions for the tanker case; but the slightly greater accuracy of the linearization underlying Eggers's condition is not reflected in a better resistance prediction. Further study of this is therefore needed and will be performed in the next section.

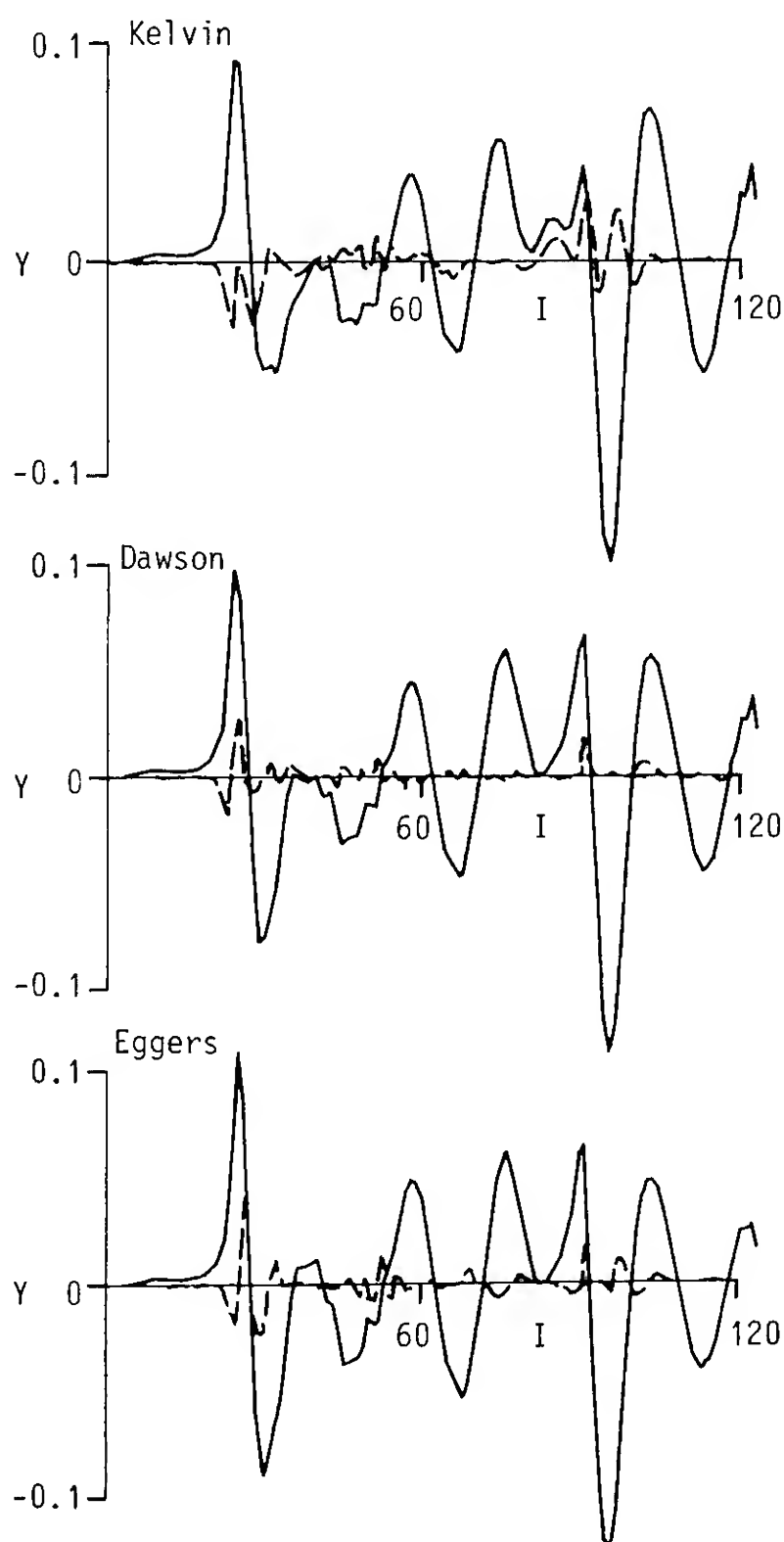


Fig. 12 Nonlinear terms in free surface conditions; Series 60,  $Fn = .22$

— Term 1  
 --- Terms 3 + 4 + 5 + 6

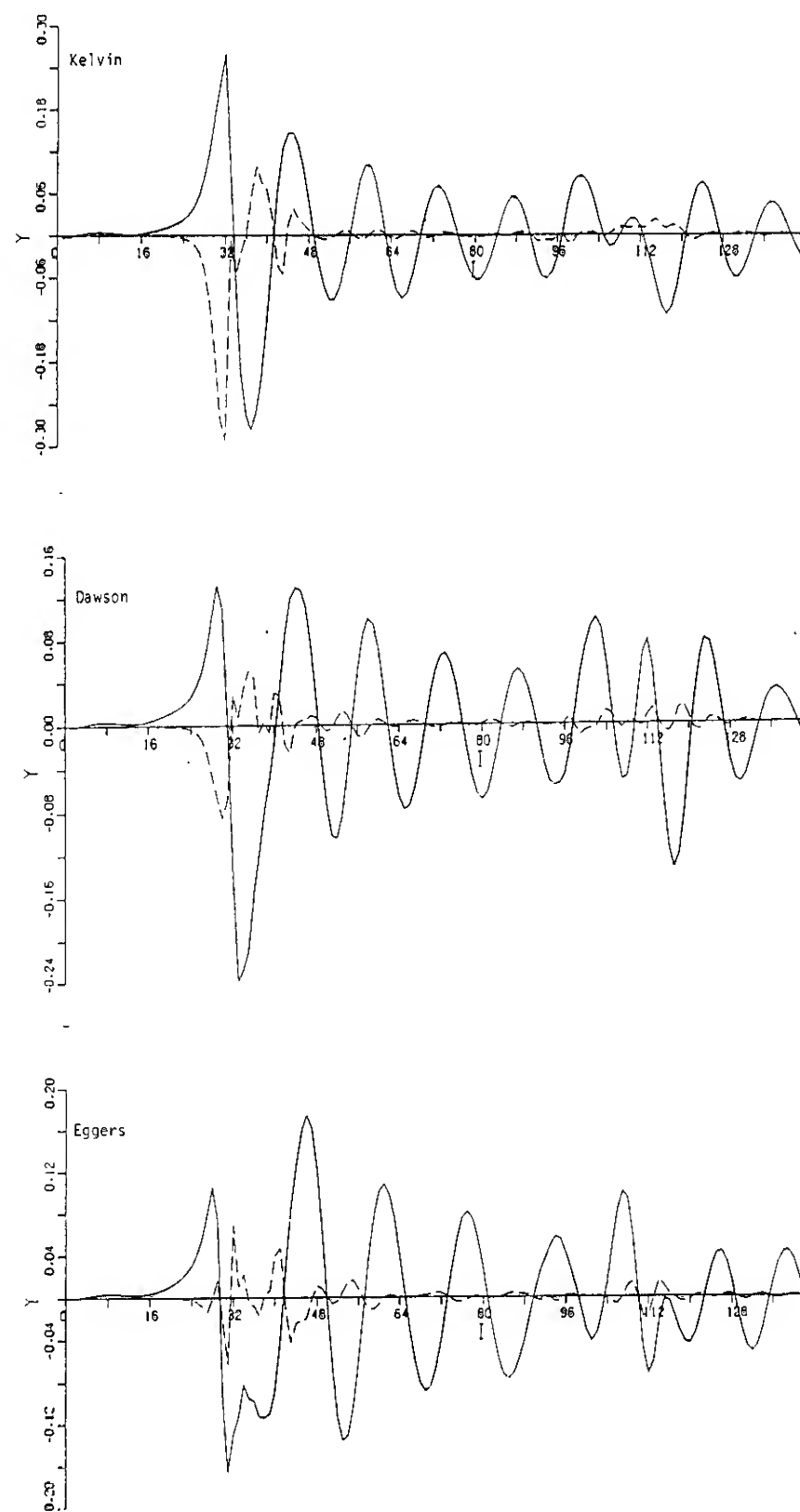


Fig. 13 Terms neglected in FSC; terms 3 to 6 for Kelvin and Eggers, terms 3 to 8 for Dawson; Tanker model,  $Fn = 0.1765$

— V  
 --- Sum of neglected terms

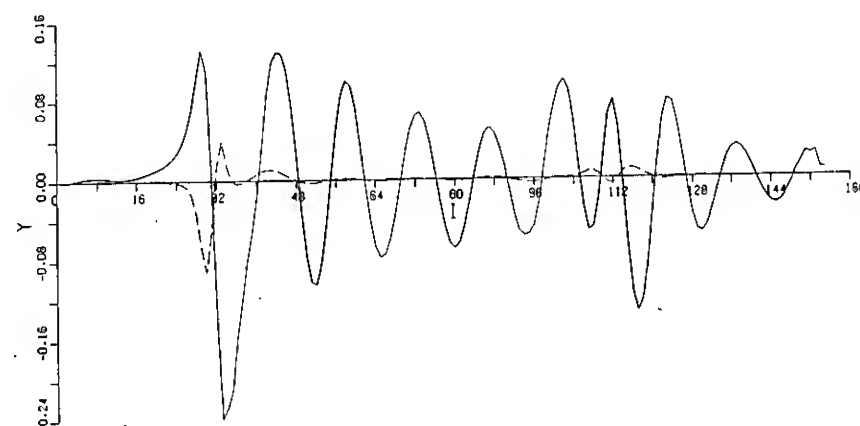


Fig. 14 Importance of linear transfer term; Dawson's FSC, Tanker model,  $Fn = .1765$

— V  
 --- Term 8

In general it was found that at least for the more severely nonlinear cases the Taylor expansions do not converge as quickly as one might hope, as testified by considerable differences between consistent and inconsistent formulations of some of the nonlinear contributions. Thus any method solving a nonlinear problem must apply the FSC right at the actual free surface, otherwise the most important nonlinear effects are missed or poorly represented. This is a fact not properly recognised in some of the methods proposed up to now [9,10]. Another fact learnt from this exercise is the appearance of double and triple wave numbers in the higher-order terms as could be foreseen from the theory. Accordingly a nonlinear calculation only makes sense if the discretization is fine enough to resolve their contributions!

## 5. DIRECT EVALUATION AT THE FREE SURFACE

Our doubts on the validity and accuracy of the Taylor expansions partly apply as well to the calculation of nonlinear terms performed here. The dominance of the transfer, the difference between consistent and inconsistent forms and the oscillatory character of the higher derivatives of the calculated velocities make the comparison somewhat unsafe. Therefore another approach has been developed.

As mentioned above, a direct evaluation of the velocity field at the actual free surface is prohibited in the usual method by the singularities inside the fluid domain. This can be avoided by generating the flow field by singularities not on the undisturbed free surface, but above it at a distance sufficient to keep clear of the highest waves. In the course of another study such a method had been developed. Source panels are located above the undisturbed free surface at a fixed distance, while the collocation points where the FSC is satisfied remain on the undisturbed free surface. Once the solution has been obtained, it is an easy matter to compute the velocities generated by these sources in points on the calculated free surface. From these, the residual errors in the exact kinematic and dynamic FSC can be found.

For the same test cases we then draw the following conclusions;

1. Series 60 block .60 model,  $Fn = 0.35$  and  $0.22$

\* There are significant differences between the velocities on the undisturbed free surface and those on the actual free surface, particularly for the vertical velocity. Including the transfer terms from Taylor expansions makes the tangential velocities fairly accurate except at the stern wave; but the difference in vertical velocity is not well represented by the consistent term 8 (Fig. 15).

\* The remaining errors in the dynamic FSC are represented by the difference between the "linearized" and the "exact" wave elevation (Fig. 16), and provide little surprise. The Kelvin linearization consistently gives slightly larger errors.  $\eta$ , the wave height approximation employed in the previous section, appears to be almost exact in this case.

\* The error in the kinematic condition (Figs. 17 and 18) is generally more important than that in the dynamic FSC. In the case considered the advantage of Dawson's condition compared with Kelvin's is now slightly more pronounced than with the method of Section 4. The error at the bow for  $Fn=0.35$  is 55% of the vertical velocity for Kelvin and 30% for Dawson. At lower  $Fn$  the difference is reduced.

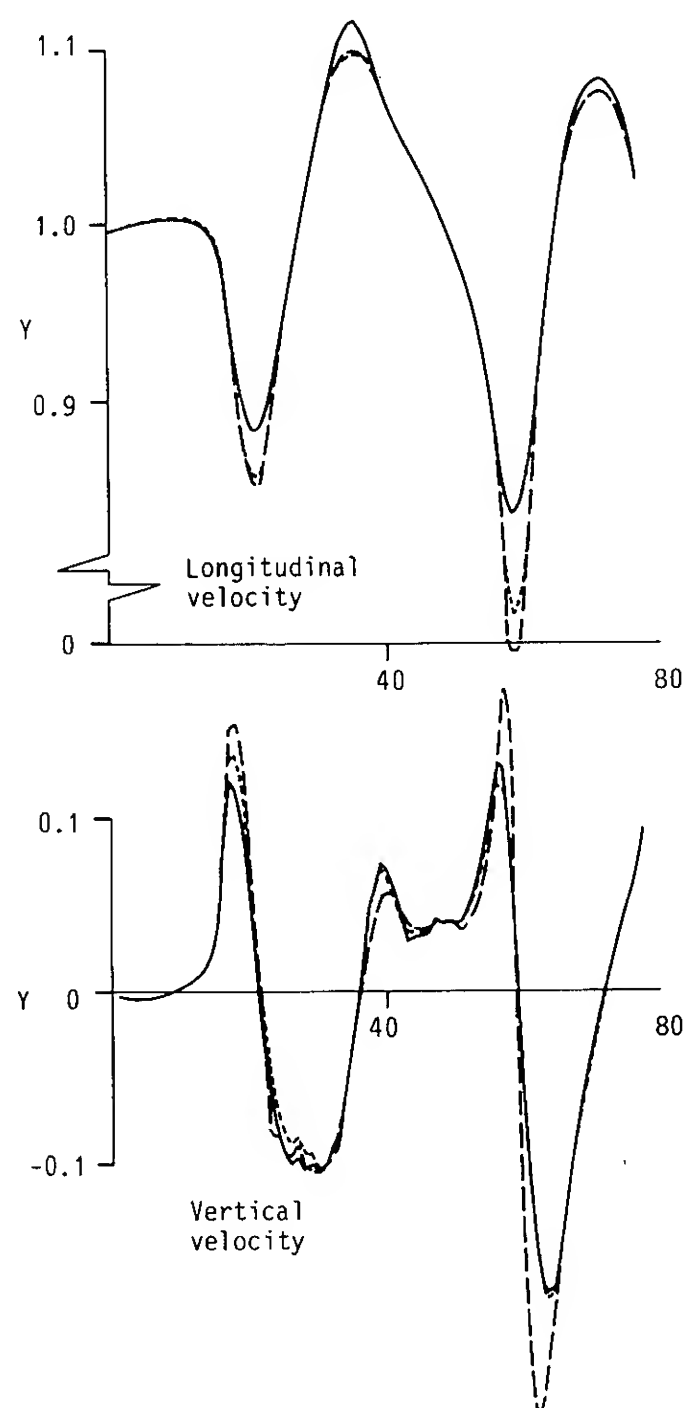


Fig. 15 Velocities at undisturbed free surface, with transfer term and evaluated at actual free surface; Dawson's FSC, Series 60,  $Fn = .35$

—  $U, V$  ( $y = 0$ )  
 ----  $U^*, V^*$  (including transfer)  
 - - -  $U_{ex}, V_{ex}$  ( $y = \eta$ )

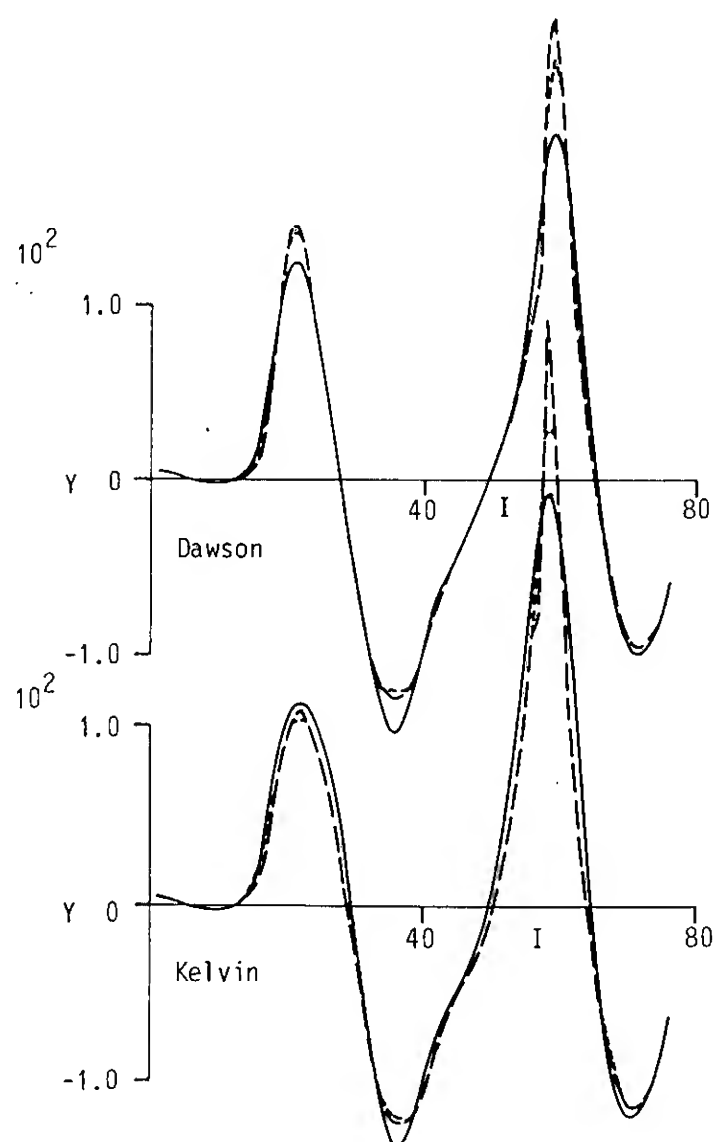


Fig. 16 Wave profile along the hull, and error in dynamic free surface condition; Series 60,  $Fn = .35$

—  $\eta_{lin}$  (linearized)  
 - - -  $\eta^*$  (including transfer)  
 - · -  $\eta_{ex}$  (evaluated at  $y = \eta_{lin}$ )

\* The FSC of Eggers leads to slightly smaller errors than that of Dawson at both speeds.

\* It was verified that the evaluation of the nonlinear terms as made in the previous section was qualitatively right and indicative of the accuracy of the FSC, although unduly oscillatory.

Thus we find that in this evaluation the advantage of slow-ship linearization is rather more pronounced. The reduction of the errors for decreasing  $Fn$  is slow. Although term 8 does not quite well approximate the transfer effect, including it seems to increase the accuracy somewhat.

## 2. Tanker model, $Fn = 0.1765$

Some remarkable conclusions could be drawn from these calculations.

\* Again the error in the dynamic condition is quite small for the slow-ship approach, and well represented by the transfer terms ( $\eta$ ). The Kelvin linearization again leads to a somewhat larger error in  $\eta$ .

\* The error in the kinematic condition (Fig. 19) is very much larger for the Kelvin FSC than for Dawson's FSC, and amounts to 0.33 times the ship speed, which is 1.57 times the vertical velocity ahead of the bow. For Dawson's condition it is 0.152 times the ship speed. This agrees with the bad wave resistance prediction obtained with the Neumann-Kelvin method.

\* The same error with Eggers's condition has sharp positive and negative peaks near the bow, of +0.178 and -0.192 times the ship speed, so this method is now suddenly worse than Dawson's, which matches its bad resistance prediction.

\* This large and irregular error is explained by the excessive transfer effect on  $v$  and, in particular,  $u$  (Figs. 20 and 21). There are extreme differences between the velocities on  $y=0$  or those including transfer terms and those evaluated on the free surface, if the condition of Eggers is used. Even the error in  $v$  including term 8 (i.e. including part of the transfer effect) is larger than the error in  $v$  (without any transfer correction) with Dawson's FSC.

\* A negative  $u$ , i.e. flow reversal, was found at the free surface just ahead of the bow.

The explanation of this lies just in the fact that the transfer term 8 is included in the FSC. The FSC can then be written as (15), and the coefficient of  $\phi_{xx}$  is  $\frac{3}{2} \phi_x^2 - \frac{1}{2}$  which is zero for  $\phi_x = \sqrt{\frac{1}{3}} = 0.577$ . In the present case  $\phi_x = 0.658$ , and the coefficient is quite small. As a result, an excessive value of  $\phi_{xx}$  is not controlled by the FSC. Now

$$v_{ex} - v = \eta \phi_{yy} + \frac{1}{2} \eta^2 \phi_{yyy} + \dots = \text{term 8} + \eta' \phi'_{yy} + \frac{1}{2} \eta^2 \phi_{yyy} + \dots \quad (30)$$

$$u_{ex} - u = \eta \phi_{xy} + \frac{1}{2} \eta^2 \phi_{xyy} + \dots \quad (31)$$

which shows that exactly the consistent inclusion of transfer effects increases the higher order contributions to the transfer, to the extent of invalidating the FSC.

This is, therefore the explanation for the unrealistic results obtained with Eggers's free surface condition for full hull forms, in contrast with its theoretical preferability and acceptable results for less extreme cases.

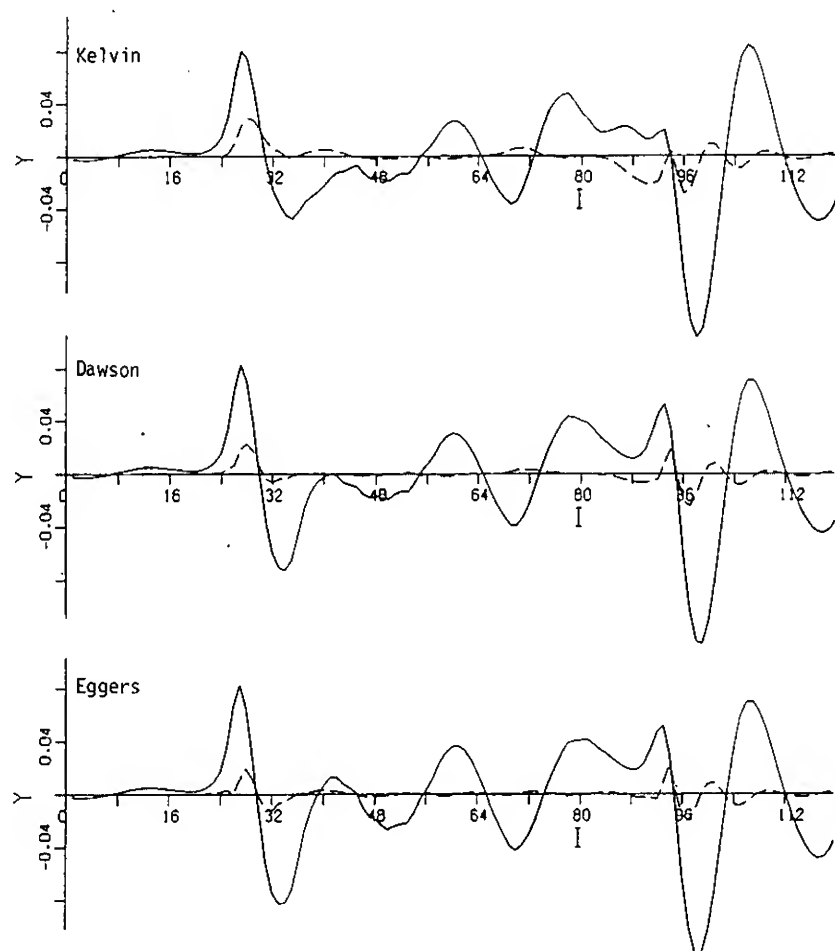


Fig. 17 Error in kinematic free surface condition, evaluated at predicted free surface; Series 60,  $Fn = .22$

— V  
- - -  $\Delta V$

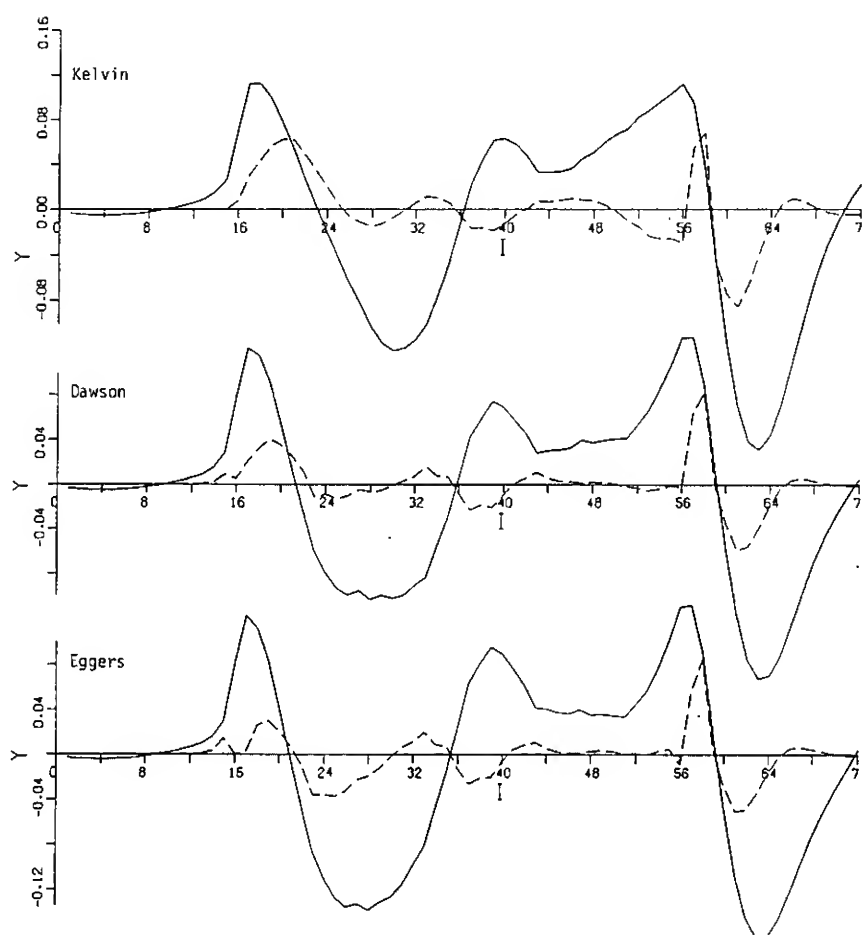


Fig. 18 Error in kinematic free surface condition, evaluated at predicted free surface; Series 60,  $Fn = .35$

— V  
- - -  $\Delta V$

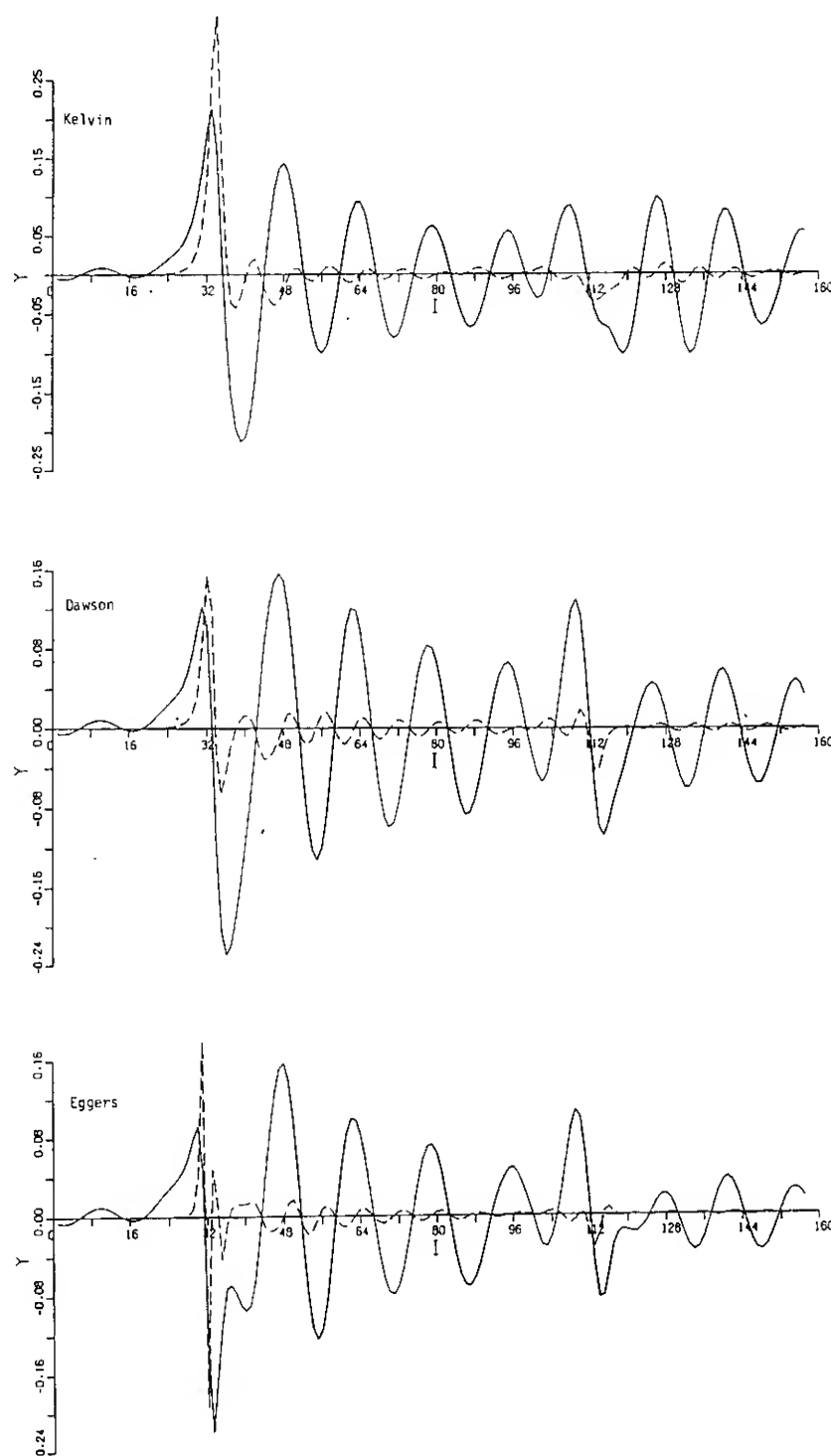


Fig. 19 Error in kinematic free surface condition, evaluated at predicted free surface; Tanker model,  $Fn = .1756$

It is fair to point out here that the possible vanishing of the coefficient of  $\phi_{xx}$  has already been given due attention<sup>xx</sup> before. Brandsma and Hermans [11] thought this fact a reason not to trust the order assumptions underlying the Taylor expansions for the transfer and proposed an alternative with imposition of the FSC on the double-body wave surface. Eggers [6,12] interpreted the change of sign of the coefficient near the bow as a change of character of the mathematical problem and tried to explain this in physical terms.

But the vanishing coefficient is an artefact of the Taylor expansion used for transferring the boundary condition; and as shown here, this expansion tends to diverge if the coefficient vanishes. Therefore I believe that no physical interpretation may be given to the change of sign, and that it simply imposes a bound on the hull fullness for which this free surface condition is applicable (and perhaps even theoretically preferable).

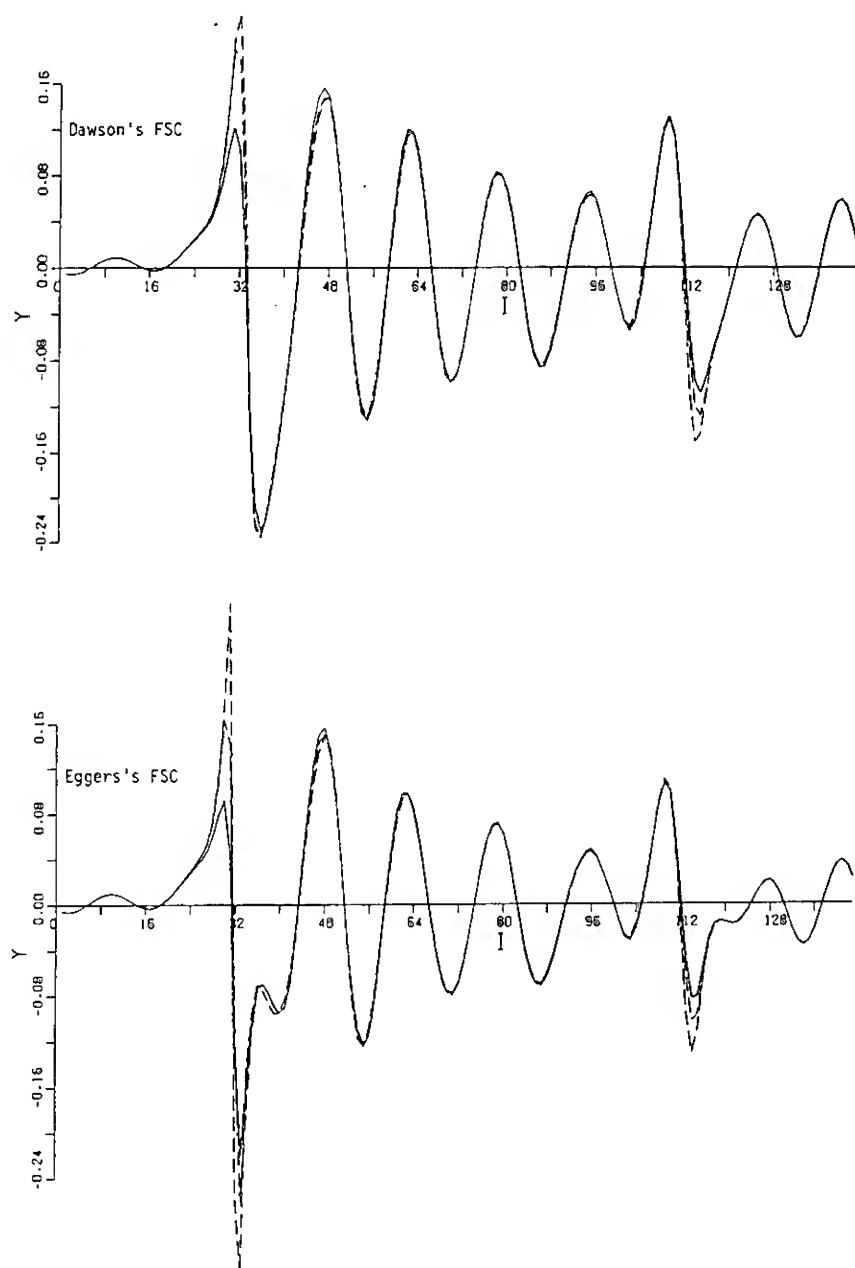


Fig. 20 Vertical velocities, at undisturbed free surface, with transfer term and evaluated at actual free surface; Tanker model,  $Fn = .1765$

———  $V$  ( $y = 0$ )  
 - - - -  $V^*$  (including transfer)  
 - · - ·  $V_{ex}$  ( $y = \eta$ )

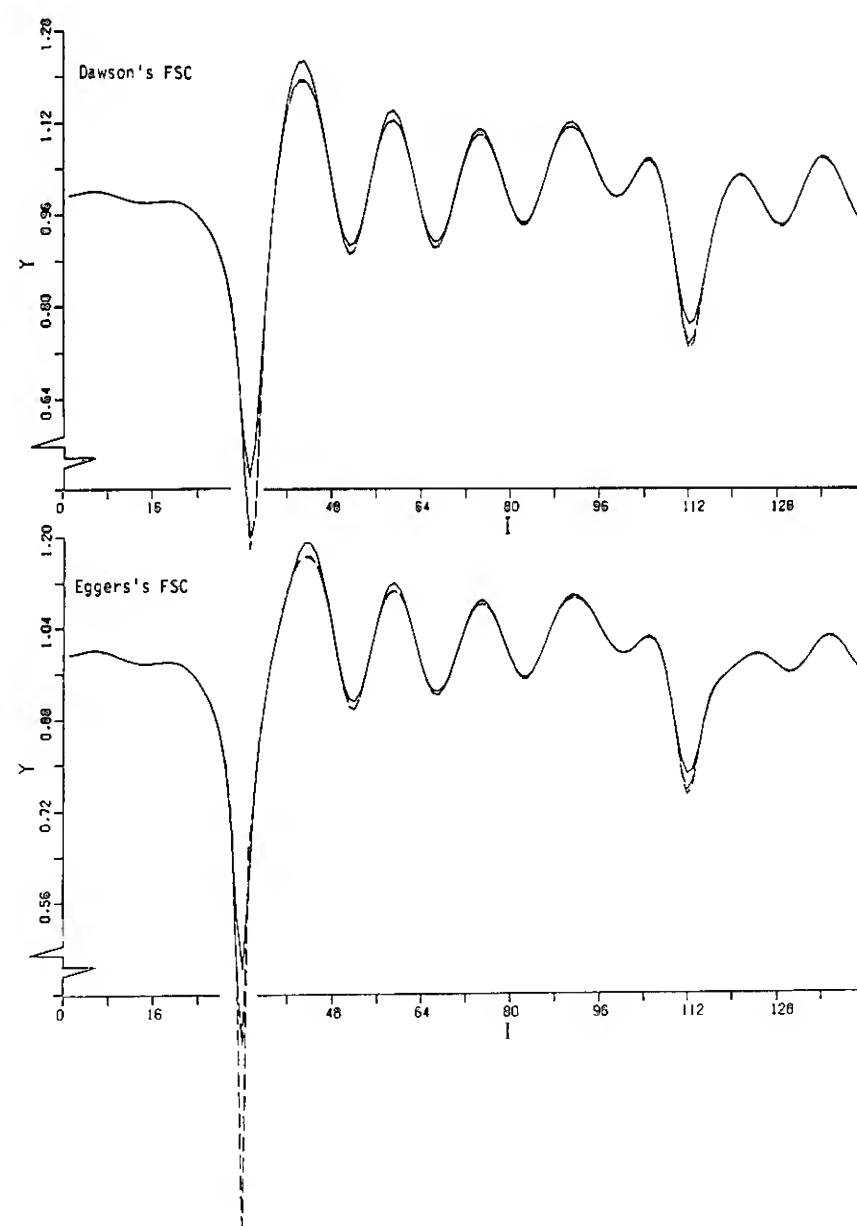


Fig. 21 Horizontal velocities, at undisturbed free surface, with transfer term and evaluated at actual free surface; Tanker model,  $Fn = .1765$

———  $U$  ( $y = 0$ )  
 - - - -  $U^*$  (including transfer)  
 - · - ·  $U_{ex}$  ( $y = \eta$ )

## 6. PROSPECTS FOR SOLUTION OF THE NONLINEAR PROBLEM

To my knowledge only very little information of this kind on the adequacy of linearized free surface conditions has been published up to now. Although the consistency of the FSC of Eggers, as opposed to that of Dawson, is well-known, it seems as if nobody had tried yet what results the modification has. The first results published here seem already to cast an entirely new light upon this issue. This suggests that there is still much more work to do on linearized methods.

On the other hand, all the studies reported in this paper at best add to our insight but give no indication on how current methods can be improved: the widely used FSC of Dawson has turned out to be not markedly superior for most ships, but to be a fairly

reliable choice throughout the range of practical hull forms. Even the occurrence of negative wave resistances could not be cured within the framework of linearized methods. From the practical point of view, therefore, this study contributes nothing at all.

Although one may thus disagree on the question whether or not the linearized methods are well enough established to make the step towards a nonlinear method, it is true that computationally current methods require only little effort, and the present computer capacity allows commercial use of far more complicated programs. Moreover, a nonlinear method could well resolve some of the problems met with current methods. The negative resistance predictions dealt with in Section 3 will be eliminated by solving the exact problem with sufficient numerical accuracy.



Additionally, the magnitude of the nonlinear terms, even in cases where the predictions are generally realistic, asks for a method that includes these terms just for reasons of reliability of the predictions.

Furthermore, certain physical effects, known to be important and sometimes forming the main difference between variations of a design, are entirely eliminated by the linearization. Examples of this are:

- Slightly or partly submerged bulbous bows; the phenomena occurring in the vicinity of the bow are strongly nonlinear and cannot well be represented by a linear approach. In addition, the increased submergence due to the sinkage and the bow wave elevation substantially alters the effect of the bulb, a phenomenon poorly represented in a linear calculation.
- The flow off a very flat stern, as often found on ferry hulls. In this case the waterline shape changes considerably due to the wave elevation; the experience is that linearized methods overpredict the stern wave height.
- The gradual transition from the flow off a stern with flat sections to the flow off a transom stern; in a linearized approach both regimes are reasonably well representable, but one has to choose beforehand which one is more appropriate. This is not a very satisfactory approach.

Hence there are several practical incentives to develop a nonlinear method even though there may still be more work to be done on linearized methods. Such a development has therefore recently been undertaken at MARIN.

Abandoning the linearizations adds several complications to the problem. The following aspects should in principle be taken into account:

- The free surface condition should be applied at the actual free surface; this is probably the dominant effect, as concluded from Section 4.
- The hull boundary condition must be applied on the actual wetted surface, instead of on the surface below the undisturbed waterline.
- All nonlinear terms (squares and cross products of disturbances) should be included.
- The dynamic trim and sinkage of the hull should be taken into account.

Without restricting oneself from the outset to a direct extension of current linearized methods one has a wide variety of methods to choose from. In the first place, the nonlinear steady problem could be solved either by iteration or by a transient approach. Both methods have already been proposed. The iterative approach may have a greater efficiency if successful, but meets problems in the convergence. Secondly, in each

time step or iteration the Laplace equation for the velocity potential has to be solved (provided that the potential flow model is retained). Here again several alternatives are possible. Panel or boundary integral methods appear to be the most popular choice.

Whatever the choices made, it is clear that any advance compared with linearized methods is only possible if the utmost care is taken in the numerical solution. The fact that the nonlinear terms generally have higher wave number already illustrates this necessity. But also the behaviour near the hull/free surface intersection could be far more difficult to deal with than in a linearized method. All these aspects deserve separate studies. In any case most of the nonlinear solutions published up to now are, in my opinion, not more accurate than linear solutions of state-of-the-art numerical accuracy.

Even if this can all be solved satisfactorily, the theory remains limited to potential flows, without any viscous or wave-breaking effects. This could prohibit convergence of the solution in the limit of zero discretization spacing near the waterline, and additional methods to deal with this region might become necessary.

Nevertheless I believe that the development of a method to solve the problem of potential flow with nonlinear free surface boundary conditions is the best next step for further enhancing the role of Computational Fluid Dynamics in the optimization of the wave-making characteristics of ships.

## 7. CONCLUSIONS

This paper has provided more detailed information on the adequacy of linearized free surface conditions for the wave resistance problem. All of them were implemented in a Rankine-source method of the type proposed by Dawson. In particular the Neumann-Kelvin formulation and two free surface conditions from the slow-ship theory, that of Dawson and of Eggers, have been compared. These comparisons concerned the wave resistance and wave profile predictions, the magnitude of the terms neglected in the FSC, and the remaining errors in the dynamic and kinematic FSC at the predicted free surface. The main conclusions are summarized below.

1. For practical discretizations Dawson's FSC gives results not significantly different from solutions of the Neumann-Kelvin problem, for all ships with a block coefficient not exceeding about 0.60 or 0.70. Also from the magnitude of the terms neglected in the linearization no significant advantage for Dawson's condition is found. This is at variance with the general preference for the slow-ship approach.

2. For full hull forms the Kelvin FSC predicts a resistance far exceeding the experimental value. On the other hand, both slow-ship FSC's predict, paradoxically, a negative wave resistance while the predicted wave pattern is physically plausible. The magnitude of the neglected terms is much larger for the Kelvin FSC than for Dawson's FSC here.
3. The use of a linearized free surface condition imposed on the undisturbed free surface changes the energy balance in such a way that a negative resistance is not ruled out. Wave energy can locally be supplied through the free surface which has no counterpart in a wave resistance acting on the hull.
4. If the linearized free surface condition is consistently formulated, the possible negative contribution from the free surface energy flux is reduced to a higher order in the perturbation parameter than the wave resistance itself. This is true for the Kelvin condition and for that of Eggers, but not for Dawson's FSC due to the absence of transfer terms.
5. The FSC of Eggers yields a resistance consistently lower than Dawson's, for the Series 60 model. For the tanker model however, an even more strongly negative resistance and an erroneous flow field were obtained. The cause of this was found to be the near-vanishing of the coefficient of  $\phi_{xx}$  in the FSC near the bow; thus an excessive value of  $\phi_{xx}$  is not controlled by the FSC. As a result the Taylor expansion underlying the linearization locally does not converge, and the reduction of the energy flux to higher order does not prevent a negative resistance here.
6. The transfer term neglected in Dawson's FSC and included in that of Eggers was found to be of substantial magnitude even for the Series 60 hull.
7. The magnitude of the neglected terms in the FSC and of the errors in the exact FSC at the predicted free surface has turned out to be quite significant even if fair resistance predictions are obtained. E.g. for the Series 60 model at  $Fn=0.35$ , the error in the vertical velocity using Dawson's FSC amounted to 30%.
8. Although more work would be needed to make the foundations of linearized methods sounder, part of the problems and uncertainties might be eliminated by solving the exact nonlinear problem. In this respect the present study has shown the importance of imposing the FSC at the actual free surface and the higher resolution required for accurately incorporating nonlinear effects.

## REFERENCES

1. Baba, E. and Hara, M., "Numerical Evaluation of a Wave-Resistance Theory for Slow Ships," Proceedings of the Second Int. Conf. on Numerical Ship Hydrodynamics, Berkeley, 1977, pp. 17-29.
2. Dawson, C.W., "A Practical Computer Method for Solving Ship-Wave Problems," Proceedings of the Second Int. Conf. on Numerical Ship Hydrodynamics, Berkeley, 1977, pp. 30-38.
3. Raven, H.C., "Variations on a Theme by Dawson," Proceedings of the 17th Symposium on Naval Hydrodynamics, The Hague, Netherlands, 1988, pp. 151-172.
4. Proceedings of the Workshop on Ship Wave Computations, DTNSRDC, Bethesda, Md., USA, 1979.
5. Wehausen, J.V., and Laitone, E.V., "Surface Waves," Encyclopaedia of Physics, Vol. IX, Springer Verlag, 1960, pp. 446-778.
6. Eggers, K., "A Method for Assessing Numerical Solutions to a Neumann-Kelvin Problem," Proceedings of the Workshop on Ship Wave-Resistance Computations, Supplementary Papers, DTNSRDC, Bethesda, Md., USA, 1979, pp. 526-527.
7. Maisonneuve, J.J., "Résolution du Problème de la Résistance de Vagues des Navires par une Méthode de Singularités de Rankine," Thesis, ENSM, Nantes 1989.
8. Eggers, K., "On the Dispersion Relation and Exponential Variation of Wave Components Satisfying the Slow-Ship Differential Equation on the Undisturbed Free Surface," Research Report 1979, Study on Local Nonlinear Effect in Ship Waves, pp. 43-62. See also: Schiffstechnik Bd. 28, 1981, pp. 223-252.
9. Maruo, H., and Ogiwara, S., "A Method of Computation for Steady Ship Waves with Nonlinear Free Surface Conditions," Proceedings of the 4th Int. Conf. on Numerical Ship Hydrodynamics, Washington D.C., 1985, pp. 218-230.
10. Musker, A.J., "A Panel Method for Predicting Ship Wave Resistance," Proceedings of the 17th Symposium on Naval Hydrodynamics, The Hague, Netherlands, 1988, pp. 143-150.
11. Brandsma, F., and Hermans, A.J., "A Quasi-Linear Free Surface Condition in Slow-Ship Theory," Schiffstechnik, Bd. 32, 1985, pp. 25-41.
12. Eggers, K., "A Comment on Free Surface Conditions for Slow Ship Theory and Ray Tracing," Schiffstechnik, Bd. 32, 1985, pp. 42-47.

## DISCUSSION

Paul D. Sclavounos  
Massachusetts Institute of Technology, USA

I would like to congratulate Dr. Raven for yet another thorough study on the effect of the free-surface linearization upon the evaluation of the ship wave resistance. Having read the article, I would like to offer a conjecture on why the wave resistance from pressure might be negative and invite the author to discuss it. The potential flow near the ship bow and stern, subject to either the Neumann-Kelvin or a double-body condition, most likely develops a singular behavior associated with the finite entry angle of the waterline or from the singularity of gradients of the double body flow at its stagnation point. This singular behavior may be sufficiently strong that a localized contribution to the resistance may arise from the waterline due to a local singularity of the hydrodynamic pressure. This contribution would be directly analogous to the leading-edge suction force in linearized hydrofoil theory, which cannot be captured by direct pressure integration over the mean chord position. Should such a singularity exist and be of sufficient strength, it will contribute to an  $O(1)$  component to the resistance arising from the waterline, which cannot be accounted for by integrating the pressure over the mean position of the ship hull. This effect, if it exists, may shed more light into the occurrence of negative wave resistance reported by the author.

## AUTHORS' REPLY

This is a good point; the possible occurrence of singularities at the stagnation points should indeed be a matter of concern. However, in my opinion, the comparison with a leading-edge singularity is not entirely valid. At a zero-thickness leading-edge, a finite force contribution arises by the pressure going to minus infinity, while in the present case a positive resistance contribution could only arise from a positive pressure which, however, is bounded by the stagnation pressure. The latter seems to be numerically fairly well-resolved here. Furthermore, it seems reasonable to assume any force contribution from the waterline to have a vertical extent scaling with the wave length or stagnation height. It can then be expected to be similar to the waterline integral (10), which turns out not to eliminate the negative resistance in all cases. Hence, a localized force contribution is expected to be at least of  $O(Fn^4)$ , and to be already approximately included in the present results.

A more probable effect of the singularity seems to me the occurrence of a localized energy flux through the free-surface. This, too, may contribute to the wave generation without being found in the pressure integration. Recently, I have calculated this energy flux for the tanker model according to Eq. (14). Its distribution has a large spike quite close to the bow, strongly suggesting the presence of a singularity. For the FSC of Eggers, the spike occurs at the point where the coefficient of  $\phi_{xx}$  vanishes; for the other FSCs it is found slightly further aft. This spike almost entirely determines the total energy influx, which, if expressed as a contribution to the wave resistance coefficient, is of the same order of magnitude as the pressure integral but may be severely grid-dependent. The localized energy flux through the free-surface due to this singularity thus largely explains both the large differences between the three FSCs and the large negative resistance values even if the energy flux is formally of higher order. These results therefore support the explanation given in my paper but stress the possible role of singularities at the bow in this respect.

## DISCUSSION

J. Nicholas Newman  
Massachusetts Institute of Technology, USA

One thought is prompted by the case shown in Figure 4 where, for the lowest Froude number, the Kelvin free-surface condition overestimates the wave resistance whereas the Dawson condition yields a negative value. Obviously the average of these two would be an improvement! This suggestion is not entirely facetious. It is common in perturbation solutions to find higher-order approximations oscillating about the correct result and diverging to an increasing extent. An example is the high-aspect-ratio lifting surface (lifting-line) theory as described by Van Dyke and reproduced in Figure 5.22 of my book. If this analogy has any relevance, it implies that we should look for a different asymptotic approximation about the zero-Froude-number limit and construct a composite approximation in the manner described by Van Dyke. I admire the spirit of this paper and look forward to further contributions from the author.

## AUTHORS' REPLY

Thank you for pointing out this interesting analogy. Although the Kelvin condition and the slow-ship FSC are based on different perturbation parameters, one could loosely regard slow-ship theory as an approximation to higher order in flow nonuniformity (so, in some slenderness parameter). Some of my results in fact suggest that for increasing nonuniformity it diverges (or rather, it produces unrealistic results) more quickly than the Neumann-Kelvin approach. In the case of lifting line theory, the similar behavior indicates that systematic expansions to higher order will not bring us any further, and a different basic approach is needed to get a higher accuracy. It appears to me that a strict analogy would imply here that we should construct a different approximation about the limit for zero flow nonuniformity rather than for zero Froude number. Alternatively, the present behavior might indeed suggest the need to revise the zero-Froude-number limit. Some possibilities for this have been proposed in the past but seem not to have been pursued.

# The Dispersion of Large-Amplitude Gravity Waves in Deep Water

W. Webster (University of California, Berkeley, USA)

D.-Y. Kim (Wageningen, The Netherlands)

**Abstract:** The Green-Naghdi (GN) theory of fluid sheets is used to analyze large amplitude, deep water waves in the time domain. Level III theory is used to simulate a train of steep regular waves and a random wave record corresponding to steep seas measured during hurricane Camille. An analysis of the simulated random wave record shows that the linear dispersion assumed for referring a random wave train from one point in space to another does not result in conservative estimates of two important quantities used in design: the crest elevation and particle velocity under the crest.

## 1. Introduction

The focus of this paper is on the behavior of large amplitude water waves in deep water, with a particular emphasis on the implications of this behavior for the engineering analysis of the motions of and loads acting on ships and offshore platforms. For the problems of greatest concern here the waves are of a length scale comparable to the horizontal dimensions of the ship or platform. For such waves it is common (and reasonable) to neglect both surface tension and viscosity, and we shall do so here. During the last few decades significant advances have taken place in the understanding of these water waves in both deep and shallow water, and there is a very large literature on this research. We will not attempt an exhaustive review this research here since our interest is a fairly narrow one.

Much of the research into deep water waves and their applications to design can be divided into two principal and almost mutually exclusive thrusts: the description of the kinematics and the stability of regular, two-dimensional waves of large amplitude (up to and including breaking), and the description and measurement of random wave systems using analyses which rely on superposition and linearity.

This split has its counterpart in the design office. A typical problem in design is to determine the adequacy of a structure under consideration to withstand the forces imposed by the largest waves it will encounter in its lifetime (the so-called "survival" problem). This problem can be thought of as composed of two parts: a description of the wave situations (in the absence of the structure) which would lead to the survival conditions, and estimation of loads and motions which result from the interaction of these waves with the structure. The focus here is on the first part, the description of the wave system, although it is recognized that the second part is probably the more difficult of the two.

This problem is at once nonlinear and random, since the waves which lead to the survival conditions are likely to be breaking, or nearly breaking, local storm waves. This design problem causes a dilemma for the engineer, since he often must choose between an analysis of his structure based on the impingement of a single, regular, large-amplitude wave (the design wave approach) or an analysis based on the impingement of a random wave system of superposed linear wave components (the spectral approach).

We note that the use of the spectral approach for the estimation of the motions in more moderate seas where linear superposition is probably not a bad assumption (the so-called "operational" problem) has become almost universally accepted, since the use of linear, random-wave analysis does have several advantages. Its use brings with it the powerful theoretical bases of time series analysis and stochastic process theory. These provide a rational framework for the estimation of the reliability and operability of the structure. Further, since the wave components in the spectral decomposition are linear, one can treat with almost equal ease both the fre-

<sup>1</sup> Department of Naval Architecture & Offshore Engineering, University of California, Berkeley, CA 94707

<sup>2</sup> Currently: Department of Naval Architecture, Seoul National University, Kwanak-Gu, Seoul, Korea



quency domain and time domain problems.

Both approaches to the more severe survival problem have advantages and disadvantages. The loads used in the design wave approach reflect the sharpening of the crests and the flattening of the troughs due to nonlinear effects, and these effects, in particular, often have significant consequences on the wave loads on offshore platforms and on the shipping of green water on the deck of surface ships. The use of a design wave does yield a deterministic load system which is relatively easy to incorporate into a design analysis. For this purpose, it is common to use fifth or higher-order Stokes wave approximations or, more recently, the results of stream function expansions (Dean, 1974, Chaplin, 1980). The methods used to determine these nonlinear waves make use of approaches which can neither be extended to three dimensions nor be generalized to arbitrary time-domain calculations in which a representation of steep, random wave systems can be made. Kinematic descriptions of regular deep water waves (assuming one can ignore viscosity and surface tension) are known to great accuracy (Schwartz, 1974; Fenton, 1988). It is not difficult to formulate a second-order or higher-order perturbation approximations for non-linear waves in the time domain, but they have been little exploited, if at all, in the design process.

The random and three-dimensional character (short-crestedness) of a measured real storm wave system is captured by the usual spectral analysis approach. Time series analysis allows identification of the spectral composition of the wave surface elevation at the point of measurement, and allows identification of some of the directional character of the seaway if many such points of measurement are made close by concurrently. When the spectral representation of the water surface is known, the prediction of the pressures and velocities at and under the free surface at the reference location is usually made by associating the Fourier components of the wave surface with linear (Airy) wave components. This superposition is only valid if the original wave system is of a height and character which is consistent with linearization of the free surface boundary condition. Such an assumption becomes ever more questionable as the waves become steeper and approach breaking. There are a number of approaches whereby the interpretation of the spectral decomposition is modified to improve the prediction of the pressure and velocity fields corresponding to the free surface description. We shall discuss one of these due to Wheeler (1969) in a subsequent section of this paper.

The prediction of the pressures and velocities at locations remote from the reference location requires, in addition, an estimate of the dispersion of the waves. If one supposes the superposition of Airy waves, then each component travels at a different speed which is uniquely related to its own frequency. Thus, the phasing of these components at the remote location is different from that at the reference location. However, it is known from the study of nonlinear regular waves that steeper waves of the same length travel faster than their less steep counterparts. One can therefore anticipate that there will be a nonlinear interaction between the component waves which will affect their wave speed. For instance, consider the case where one analyzes the motions of a large ship in head seas and prescribes the wave time history at one point on the ship, say amidships. In order to perform this calculation, it is necessary to predict the wave environment over the whole length of the ship at each instant in time. Since the length of typical large ships is in the order of 400' to 1000' or more, small differences in the estimated dispersion of shorter waves may cause significant discrepancies between the wave time history at the bow and at the stern. Further, since the discrepancy at the bow is of the opposite sense from that at the stern (relative to a reference point amidships), these discrepancies may become especially important for pitch or yaw motions which reflect the difference in forces bow and stern.

Although linear ship motions analysis can be considered state-of-the-art, nonlinear motions analysis is not. In particular, much of the thrust in recent years in nonlinear ship motions has revolved about the slow drift problem where second-order forces and waves are taken into account. These endeavors are extremely complex and the prospect of accomplishing in the near future an analysis correct to, say, the third order is not bright. What is troublesome with this state of affairs is the fact that the second-order wave problem predicts the same wave celerity as the linear problem and has many of the dispersion characteristics of Airy theory. The third-order solution is the lowest order perturbation theory which predicts an increase in celerity of regular waves with steepness similar to that observed in nature and interactions between waves which lead to "phase-locking".

In conclusion, it is fair to say that neither design approach to the survival loading (design wave or spectral decomposition) is wholly satisfactory. It is the purpose of this paper to explore the substantial gap which exists between these two design approaches by presenting a different model for the behavior of large-amplitude deep water waves in the time domain. It is of particu-

lar interest to use this model to investigate the dispersion of a random wave system from one location to another so that some insight into the omissions of current linear and second-order theories can be obtained. The foundation for this development is the Green-Naghdi theory of fluid sheets (hereafter referred to simply as GN theory) and, in particular, the extension of this theory to deep water waves (Green & Naghdi, 1986 & 1987). This study could also have been performed using other nonlinear formulations, but GN theory was chosen since it is particularly efficient computationally.

Following the introduction of the GN governing equations for level III theory below, the remainder of the paper will consist of two parts: (a) validation of the theory using known results of steep regular waves, and (b) use of the time-domain solution of these equations to simulate a steep, random seaway.

## 2. GN level III theory of deep water waves

GN theory is a model for three-dimensional fluid flow which, since it involves one fewer independent space variable than three-dimensional space, is called a fluid *sheet* model. The basis of this model is rather different from traditional models derived from potential theory using perturbation methods or from the specialized methods often introduced to compute with high accuracy the characteristics of regular, two-dimensional water waves. When viscosity and surface tension are ignored and the fluid flow is assumed to be irrotational, the field equation (Laplace's equation) is linear. The only nonlinearities are found in the boundary conditions on the free surface. The treatment of the field equation and nonlinear boundary conditions by perturbation methods and GN theory are the antithesis of one another.

In the perturbation method, the field equation is retained exactly and the boundary conditions are approximated; in GN theory the field equation is approximated and the full boundary conditions are retained. However, it is not our purpose here to give a detailed discussion of the consequences of these different approaches. The reader is referred to Green & Naghdi (1986, 1987) for a precise exposition of GN approach to water waves, and to Webster & Shields, (1990) for an overview and commentary on the method.

Since perturbation parameters or scales are not used in its development, the limits of applicability of GN theory are implicit and must be determined by physical or numerical experiment. For the problem of steep water waves we choose GN level III theory, as defined in Webster & Shields (1990). Although this theory is com-

plex, this level theory was necessary for the treatment of even a narrow-banded spectrum.

We introduce a coordinate system Oxyz, with the Oz axis oriented vertically up and the Oxy plane horizontal and corresponding to the undisturbed free surface. In the GN theory used here, the vertical dependence (i.e., the dependence on  $z$ ) of the kinematics of the fluid flow is restricted. That is, we introduce a set of functions  $\lambda_n(z)$  which will serve as a basis for the vertical dependence. These functions play the same rôle that "shape functions" play in finite element analysis. We assume that the fluid velocity,  $\mathbf{v}(x,y,z;t) = (u,v,w)$  can be approximated with three of these basis functions (for level III). Thus,

$$\mathbf{v}(x,y,z;t) = \sum_{n=1}^3 \mathbf{v}_n(x,y;t) \lambda_n(z), \quad (1)$$

where  $\mathbf{v}_n = (u_n, v_n, w_n)$  are vector coefficients associated with the function  $\lambda_n$ . Following Green and Naghdi (1986), we select basis functions given by

$$\lambda_n(z) = z^{(n-1)} e^{az}, \quad n = 1, 2, 3 \quad (2)$$

where  $a$  is a constant, the choice of which will be discussed below. The exponential factor,  $\lambda_1 = e^{az}$  was selected since it has the same form as the  $z$  dependence found in the Airy wave solution. The other terms in the basis can be regarded as systematic variations of the Airy wave velocity pattern.

The kinematic assumption (1) is inserted into the equations for conservation of mass, conservation of momentum (Euler's equations), and the kinematic boundary condition on the free surface,  $z = \beta(x,y;t)$ . It is possible to satisfy all of these equations identically except for conservation of momentum, which is satisfied only approximately. Euler's equations are multiplied by  $\lambda_1, \lambda_2, \lambda_3$  and integrated with respect to  $z$ . The result is a set of three vector equations which reflect conservation of momentum in a weighted average sense. These together with exact statements of conservation of mass and the kinematic boundary conditions are the evolution equations for this model of the flow. The final evolution equations can be expressed in rather compact general form (equations 3.4, 3.8 & 3.11, respectively, in Webster & Shields (1990)) but these equations will not be repeated here. The determination of the evolution equations in terms of derivatives of the primary variables requires a prodigious amount of algebraic manipulation. This manipulation is, however, not difficult if one uses any of the new symbolic processors now available. (A program called *Mathematica*<sup>TM</sup> was used for this manipulation).



The final set of four evolution equations for unsteady two-dimensional flow is presented in Appendix A. The components of the vertical components of the  $\mathbf{v}_n$  ( $w_1, w_2, w_3$ ) have been eliminated, as have the so-called "integrated pressures"  $p_1, p_2$  and  $p_3$ . The pressure on the free surface,  $\hat{p}$ , is taken to be zero. The remaining four variables are the free surface elevation,  $\beta(x, t)$ , and the three horizontal components of the  $\mathbf{v}_n$ :  $u_1(x, t)$ ,  $u_2(x, t)$  and  $u_3(x, t)$ . These evolution equations will be used for all of the nonlinear computations in this paper.

### 3. Large-amplitude waves of permanent form

In this paper we use the GN level III theory for time domain calculations of the dispersion of random waves. The authors know of no high accuracy calculations of these wave systems to compare with. Since this theory is a new one, it seems prudent to first compare the characteristics of large amplitude regular waves predicted by this theory with known very accurate results for these waves.

To determine waves of permanent form, the transformation  $\partial/\partial t \rightarrow u_0 \partial/\partial x$  is applied to the evolution equations in Appendix A (these equations are Galilean invariant). The equations now only depend on the primary variables  $\beta$ ,  $u_1$ ,  $u_2$  and  $u_3$  and their derivatives with respect to  $x$ . The problem of determining a wave of permanent form of a given length and elevation at the crest can be posed as a two-point boundary value problem over a domain equal to the half-length of the wave, with a symmetry condition imposed at both ends of the domain and an elevation condition at the crest imposed at one end of the domain. In addition, global conditions stipulating that the flow is irrotational on the average and the mean water depth is zero need to be applied. A procedure based on Thomas' method described by Ertekin (1984) and generalized by Shields (1986) was used to find these solutions. For the comparisons below, the  $x$  domain was discretized into 200 equally-spaced intervals (201 nodes) for one wave length. Central difference formulas were used throughout.

Several characteristics of these waves are obvious candidates for comparison. These include: wave celerity, wave profile and velocity profile. The parameters which are of importance here are wave steepness, wave length and the constant,  $a$ , which appears in the basis functions (2). As mentioned in the previous section, this constant governs the exponential decay of the velocities in depth. A value of  $a$  equal to the wave number,  $k = 2\pi/\lambda$ , where  $\lambda$  is the wave length, produces the same decay with  $z$  as predicted by Airy wave theory and this choice yields the best

comparison with finite regular waves. We introduce the notion of "bandwidth", the ability of GN theory to predict waves of wave numbers which are different from  $a$ . We anticipate that there will be a range of wave numbers  $k_1 \leq a \leq k_2$  for which the theory will produce satisfactory results. Accurate, high-order stream function results computed by Sobey (1989) are used for the comparisons below.

#### a. Wave celerity.

The celerity, or phase velocity of the wave, is the speed,  $u_0$ , of the coordinate system necessary to yield a time invariant wave form. Figure 1 shows the ratio of the celerity of infinitesimal waves predicted by various levels of GN theory to the celerity of Airy waves. It is seen that the bandwidth of GN level I for a relative celerity error of, say, 2% is very narrow, that of GN level II is broader and that of GN level III is broader still. Since the focus of this paper is a random wave train, it seemed appropriate to choose the theory with the broadest bandwidth and therefore GN level III was selected primarily on this basis.

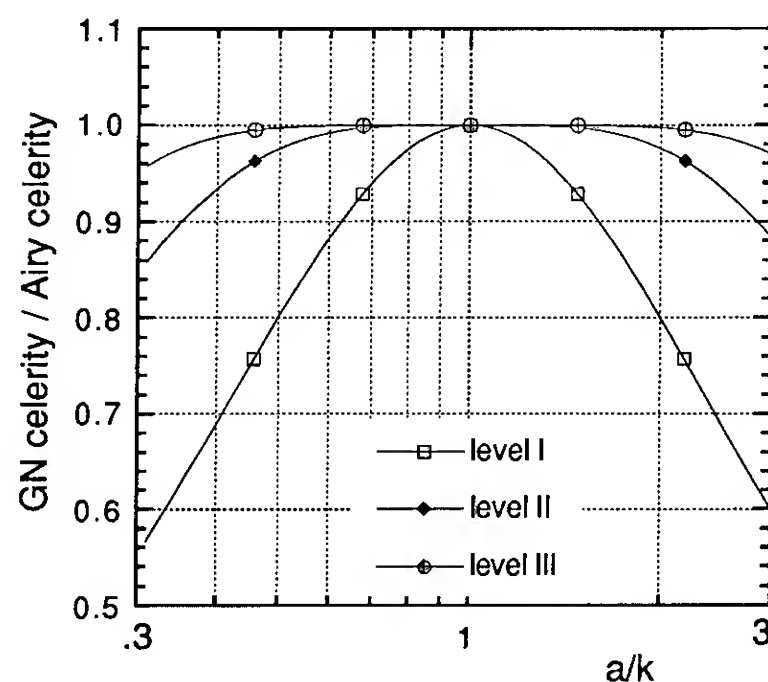


Figure 1. The ratio of celerity of infinitesimal waves predicted by various levels of GN theory to that predicted by Airy wave theory.

It is well known that the celerity of a regular wave depends on its steepness. Figure 2 shows the results of GN level III theory for waves of various steepness for the special situation where  $k \equiv a$ . The error between the GN results (the line) and the stream function results (the black squares) is much smaller than 1% and cannot be detected on this figure. For values of  $k$  different from  $a$ , Figure 3 shows the error in celerity as a function of steepness. It is seen that for values of  $2.25 > a/k > 0.5$ , the celerity error is within 1% for all values of steepness less than 0.12 (breaking waves correspond to a steepness of

about 0.14). That is, the celerity error is less than 1% for waves of one-half of the length of the wave for which  $k \equiv a$  to waves which are well over twice the length of the wave for which  $k \equiv a$ ). For waves of lower steepness the bandwidth is somewhat larger, but the bandwidth is, of course, always smaller than that for infinitesimal waves.

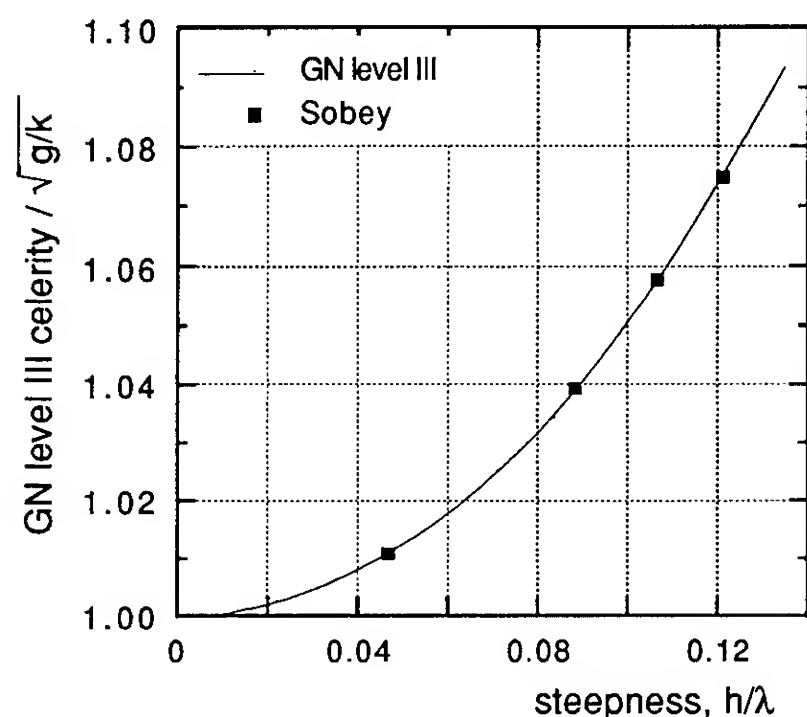


Figure 2. The variation of celerity with steepness for GN level III theory for  $a/k = 1.0$  (curve) and for numerically accurate results (black squares).

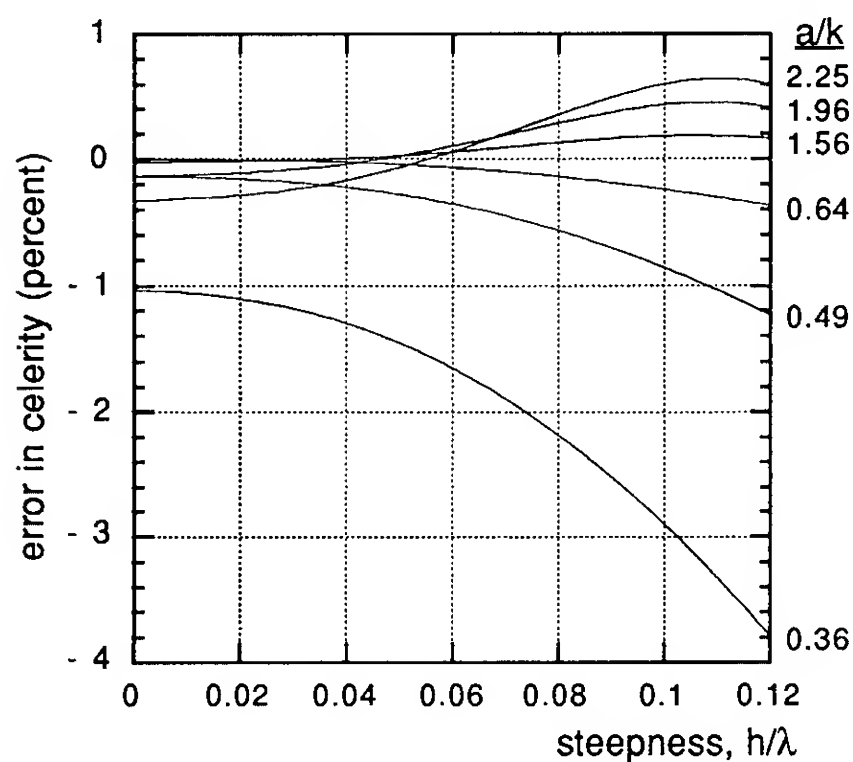


Figure 3. Error in prediction of the celerity of regular waves by GN level III theory as a function of steepness for  $a/k \neq 1$ .

#### b. Wave profile.

Figure 4 shows the wave profiles computed for waves of various elevations at the crest for the case  $k \equiv a$ . These profile shapes deviate less than one line width from high accuracy profiles (the deviation is much less than 1% of the wave

height). For wave of small wave height the elevation varies almost sinusoidally in  $x$ . As the wave steepens, the crest becomes sharper and the trough flattens. Figure 5 shows the profiles for waves of steepness 0.106 predicted for various values of  $a/k$ . It is seen that even for this very steep wave, the variation in profiles is very little for the range of  $a/k$  between 0.5 and 2.0.

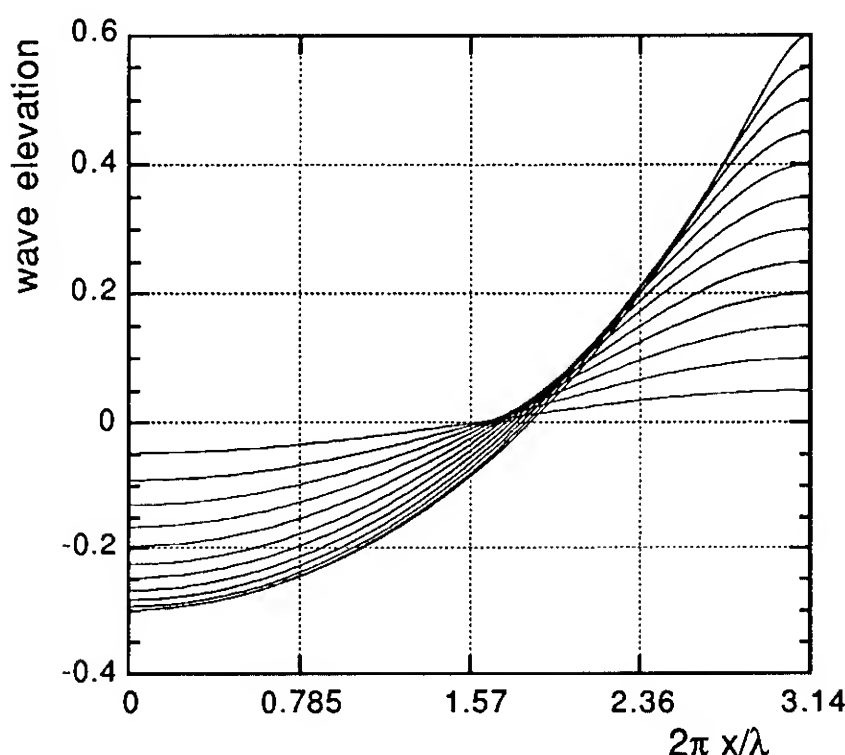


Figure 4. Wave profiles predicted by GN level III theory for regular waves of various crest heights for  $a/k = 1$ .

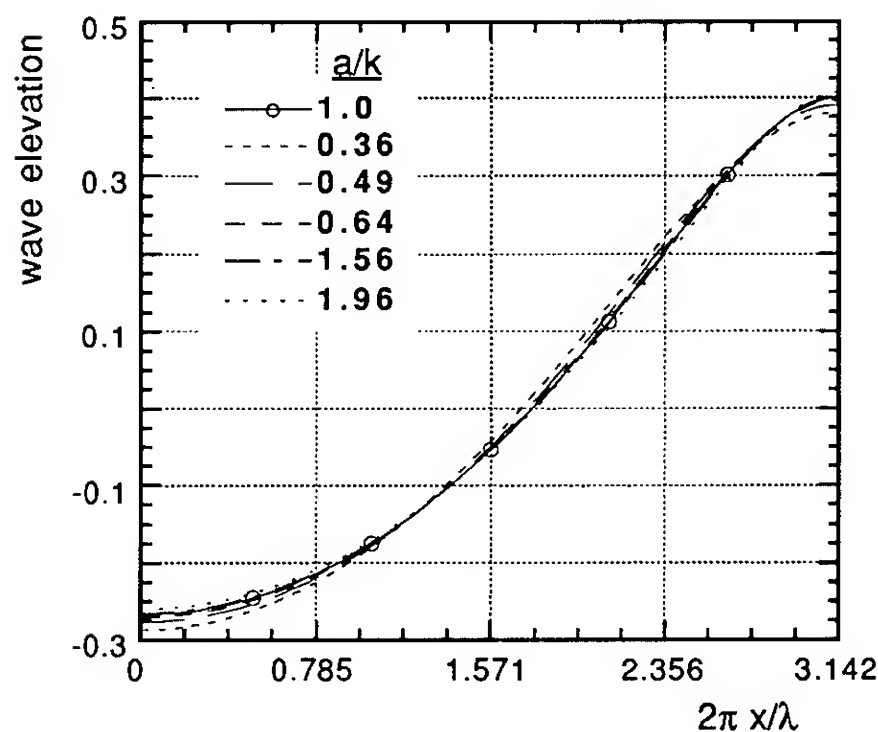


Figure 5. Profile of waves of steepness 0.106 predicted by GN level III theory for various values of  $a/k$ .

#### c. Particle velocity

From the point of view of design of many offshore platforms, the horizontal particle velocity under the crest of the wave is probably the most important. It is this characteristic of the flow which causes the most significant loads on

fixed (jacketed) platforms. Once again, the horizontal velocity under the crest of even very steep waves is predicted with much less than a 1% error if  $k \equiv a$ . For  $k \neq a$  deviations occur. Figure 6 shows the variation with  $z$  of the horizontal velocity under the crest for a wave of steepness 0.106. The velocity is non-dimensionalized with the Airy celerity. Curves for various values of  $a/k$  are shown, where the value for  $a/k = 1$  is coincident with numerically accurate results. The water surface at the crest of this wave is at a non-dimensional value of  $2\pi z/\lambda = 0.403$ , and the undisturbed water level corresponds to a value of  $z = 0$ . Also shown on this figure is the horizontal particle velocity prediction from Airy wave theory.

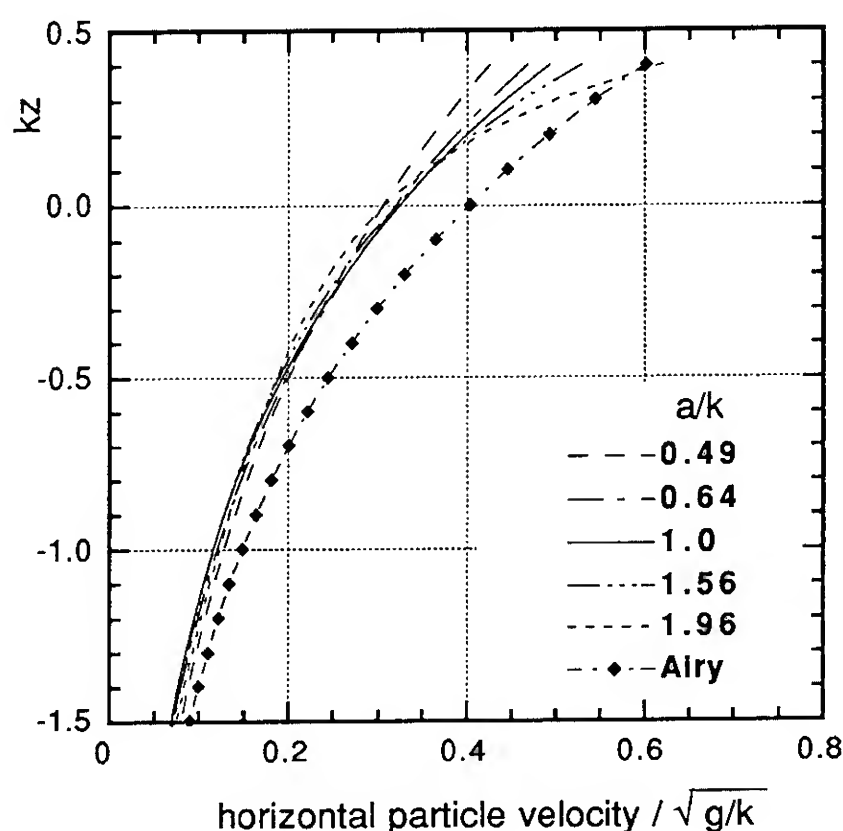


Figure 6. Variation of horizontal particle velocity under the crest of a wave of steepness 0.106 as a function of non-dimensional altitude.

It is seen that Airy wave theory uniformly over-predicts the horizontal particle velocity under the crest for all  $z$ . In general, the prediction of the GN level III theory is good, except very near the crest. If  $0.64 \leq a/k \leq 1.56$  the error is everywhere less than 5% of the numerically exact result. For  $a/k = 1.96$  the error is 25% at the water surface but becomes less than 5% for values of  $2\pi z/\lambda \leq 0.25$ ; for  $a/k = 0.49$  the error is 14% at the water surface but does not drop to less than 5% unless  $2\pi z/\lambda \leq 0$ .

Separate investigations were also made at different values of steepness and at different locations along the wave. At the crest at a steepness of 12%, the error for  $0.64 \leq a/k \leq 1.56$  increased slightly to 6%; that for  $a/k = 0.49$  and 1.96 increased to 20% and 35%, respectively. Beneath the trough much smaller particle velocity errors were observed for all values of  $a/k$  discussed here

and, thus, it appears that the crest is the most critical location.

#### d. Summary of regular wave comparisons.

The bandwidth for particle velocity error is much narrower than for either wave celerity error or for wave profile error. Let us denote the wave length for which  $a/k = 1$  by  $\lambda_0$ . The above comparisons indicate that as long as  $2/3 \lambda_0 \leq \lambda \leq 3/2 \lambda_0$ , we can anticipate errors of less than 1% for celerity or wave profile and less than 6% for horizontal particle velocities for a steepness up to 12%. These limitations imply that the GN level III theory may be a good model for a steep, narrow-banded seaway.

#### 4. Time domain results

Two different wave situations were investigated using the time domain version of the Green-Naghdi level III equations in Appendix A. The evolution equations are second-order in time and third order in space. At each instant the time derivatives (on the left-hand side of each equation in Appendix A) can be found as a solution to a two-point boundary value problem. Since this is an initial-value problem starting from an initially quiescent condition, the global conditions for irrotationality or for mean water level used for determining waves of permanent form need not be applied here.

The difference formulation for the two-point boundary value problem is the same Thomas' algorithm used for the waves of permanent form. Integration in time is performed using a modified Euler method. Both integrations in space and time are second-order accurate and variations in both time and space steps were made to assure that convergence was adequate (less than 1% error).

One of the particular advantages of GN theory in general is that it yields differential equations in the horizontal coordinates. Since the computational effort required to solve the two-point boundary value problem grows linearly with the computational domain, the overall time integration retains this property. In this sense, the GN theory allows one to compute larger spatial domains than, say, boundary element methods where the effort typically grows with at least the square of the size of the number of nodes.

The left-hand boundary for both problems below was considered to be a "wave-maker" where values of  $\beta(x_w, t)$ ,  $u_1(x_w, t)$ ,  $u_2(x_w, t)$  and  $u_3(x_w, t)$  were prescribed ( $x_w$  is the  $x$  location of the wavemaker). In general, the values of the three  $u$ 's are not known *a priori* for the nonlinear wave system. We used the values obtained from a

linear solution of the GN level III equations to relate these quantities to  $\beta$ . The local disturbance caused by the not quite correct values of the three  $u$ 's appeared to die out quickly (as it does with a real wave-maker in a wave tank). In order to avoid any initial disturbances, a cosine-squared ramp was provided at the start of the wave-maker. The ramp was applied only to the first full cycle of the wave maker.

A simple Sommerfeld boundary condition was imposed on the right-hand boundary for both examples and this condition was based on the assumption that all waves have a celerity equal to that of infinitesimal waves of length  $\lambda_0$ . In practice, little reflection was observed, but in both examples the right-hand boundary was taken far enough away to minimize any possible adverse consequences from reflections.

#### a. The generation of regular waves.

In order to assure that the time domain integration scheme and the wave-maker were performing correctly, a set of regular waves was generated. Although the internal calculations were all performed non-dimensionally, the results are reported dimensionally, corresponding to typical ocean wave scales. The computational domain consisted of 1300 space steps of 12.28' and the time steps were 0.2 sec. The waves had a wave length of 809' and final height of 70' (corresponding to steepness of 8.65%). Figure 7

shows a snapshot of the wave elevation profile 160 seconds after the start-up of the wave-maker. Since the wave packet had not progressed past 6000', the remainder of the computational domain is not shown. This figure shows that the eldest two waves (the rightmost two waves) are somewhat distorted, and that the train of noticeably steep, but regular waves follows.

Figure 8 shows the wave elevation time history as seen by an observer 644' from the wave maker. This observer sees almost twice as many waves as seen in the surface elevation view because the group velocity is much less than the celerity (a manifestation of dispersion). A very short time after the time of figure 7, the leading wave of this packet became quite steep and reached a breaking condition. Local snapshots of this process at 2 second intervals are shown in Figure 9. The solution algorithm breaks down when the wave reaches breaking conditions and the computation can not continue.

It was not clear, at first, whether the breaking wave at the front of the group was real or simply an artifact of either the start-up of the wave maker or of the GN theory. Longuet-Higgins (1974) demonstrated, both theoretically and experimentally, that the leading wave in a packet of generated waves will steepen. Further, his experiments showed that the leading wave can break if the generated waves were steep enough to begin with. Unfortunately, his linear

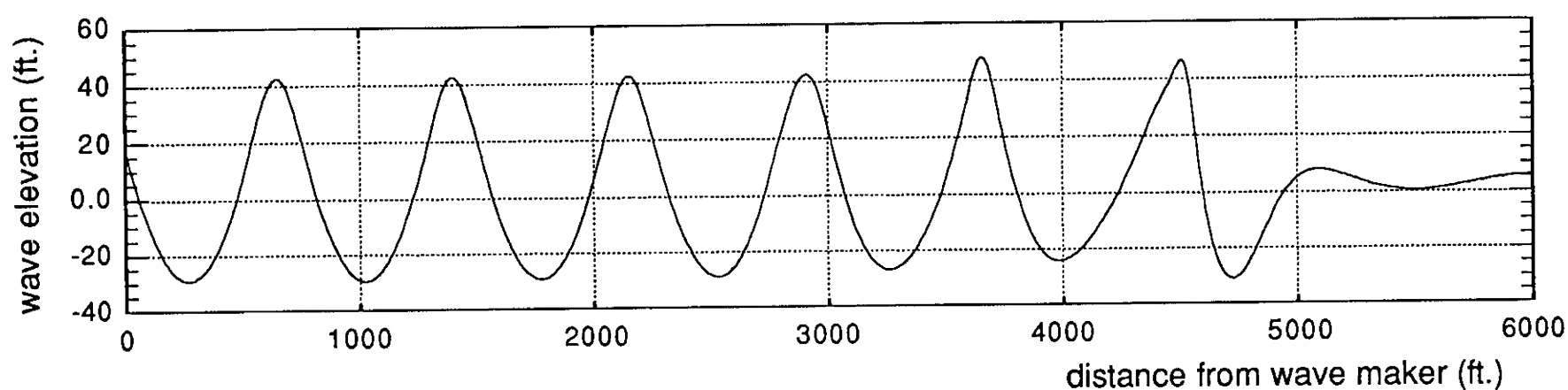


Figure 7. Wave surface elevation at time = 160 seconds after initiation of wavemaker (regular waves of length = 809' and height = 70')

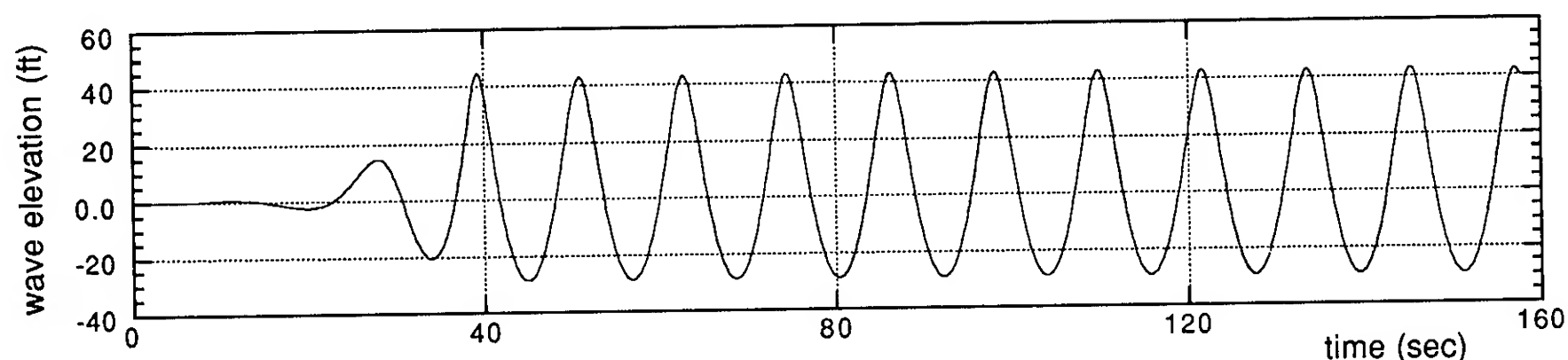


Figure 8. Wave elevation time history at a point 644' away from wavemaker.

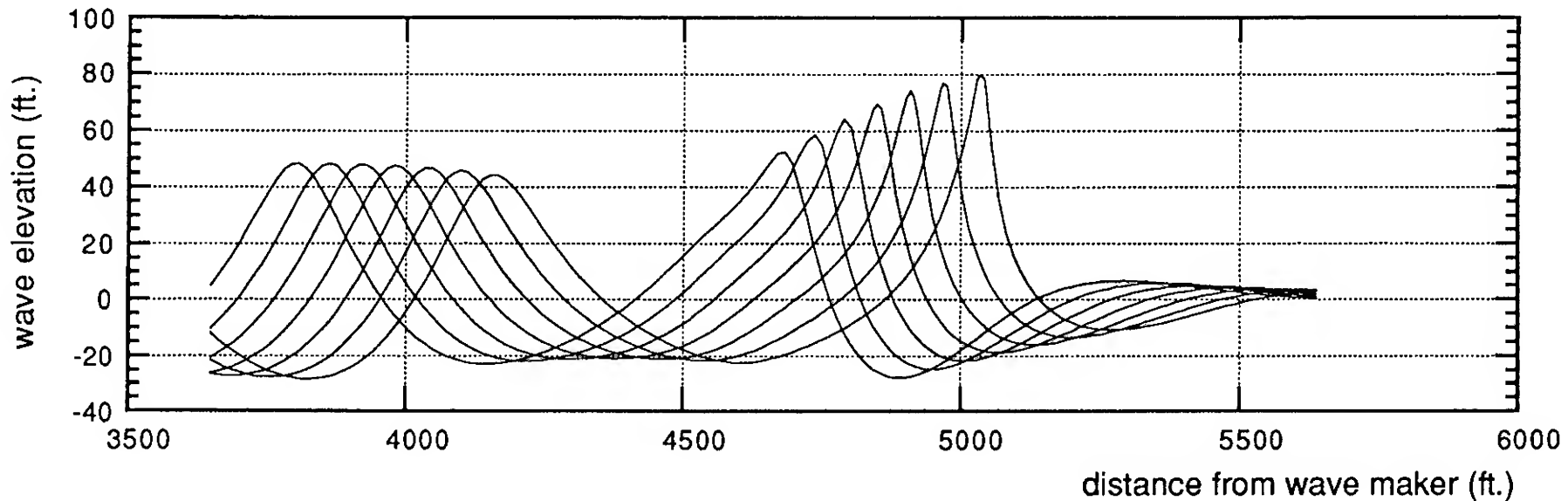


Figure 9. Details of breaking wave at leading edge of wave packet.

analysis was unable to predict such an occurrence. In order to investigate this further, we attempted to duplicate the simulated wave situation in the Ship Model Towing Tank at U.C. Berkeley. To our surprise, we found that we were unable to make a train waves at this steepness *without* the wave in the front of the group breaking after about 12-14 wave maker cycles (that is with 6 or 7 waves in the tank). The breaking occurred even when the wave maker was turned on very smoothly over three wave cycles.

#### b. Steep random waves.

In order to investigate the dispersion of random waves, a numerical experiment was conducted. An existing measurement of steep waves, recorded during Hurricane Camille in the Gulf of Mexico, August 16-17, 1969 was used as a foundation for this experiment. The particular record covered 512 seconds in real time with two measurements per second. Although this record was taken in a water depth of 325 ft (which corresponds to a depth at which shallow water effects are just beginning to be perceived), it was felt that this sample was a good representative of the survival conditions one might encounter.

The waves were simulated in exactly same fashion as the regular waves in a. above were. However, it was desired to generate a wave system like that from Hurricane Camille at a given reference point removed some distance from the wave-maker. The coordinate system was chosen so that this reference point was  $x = 0$ . A finite, untruncated Fourier transform of the record was determined,

$$\beta(t) = \sum_{n=0}^{\frac{1}{2}n_{\max}} a_n \sin \omega_n t + b_n \cos \omega_n t, \quad (3)$$

where

$$\omega_n = \frac{2\pi n}{\delta t n_{\max}},$$

$\delta t$  is the time interval between data points,  
 $n_{\max}$  is the number of data points in the record.

Using linear dispersion (Airy theory), the record (3) was referred to a new location  $x_w$ , assuming that the waves are two-dimensional and progressing in the positive  $x$  direction, yielding

$$\beta(t) = \sum_{n=0}^{\frac{1}{2}n_{\max}} a_n \sin \phi(t) + b_n \cos \phi(t), \quad (4)$$

where the phase  $\phi(t) = \omega_n \left( t - \frac{\omega_n x_w}{g} \right)$

For the numerical experiment described below,  $x_w$  was taken to be -644' (i.e. 644' up weather from the point  $x = 0$ ). This new record was used to drive the wave maker. Three wave probes were "mounted" in the computational domain, at  $x = 0$ ,  $x = 400$  and  $x = 800$ '. The distance between the probe at the reference point at  $x = 0$  and that at  $x = 400$ ' is comparable to the length of a typical offshore platform; the distance between the reference point at  $x = 0$  and that at  $x = 800$ ' is comparable to the length of a typical large ship. The constant  $a$  was selected to correspond to waves for which  $\lambda_0 = 809$ ' (i.e.  $a = 2\pi/809$ ) and the computation was run for the same 512 seconds of the original record with temporal steps of 0.2 sec. and 1300 spatial steps of 12.28'.

Figure 10 shows a comparison of the wave elevation measured at the probe at  $x = 0$  and the original Hurricane Camille record. In general the two traces compare very well except near  $t = 130$  and  $t = 450$ . The computed wave elevation history is smoother than the original record presumably because the bandwidth of the GN level III theory is limited. We do note however, that most of the waves do lie within the wave length range of 500' to 1200' corresponding to the range



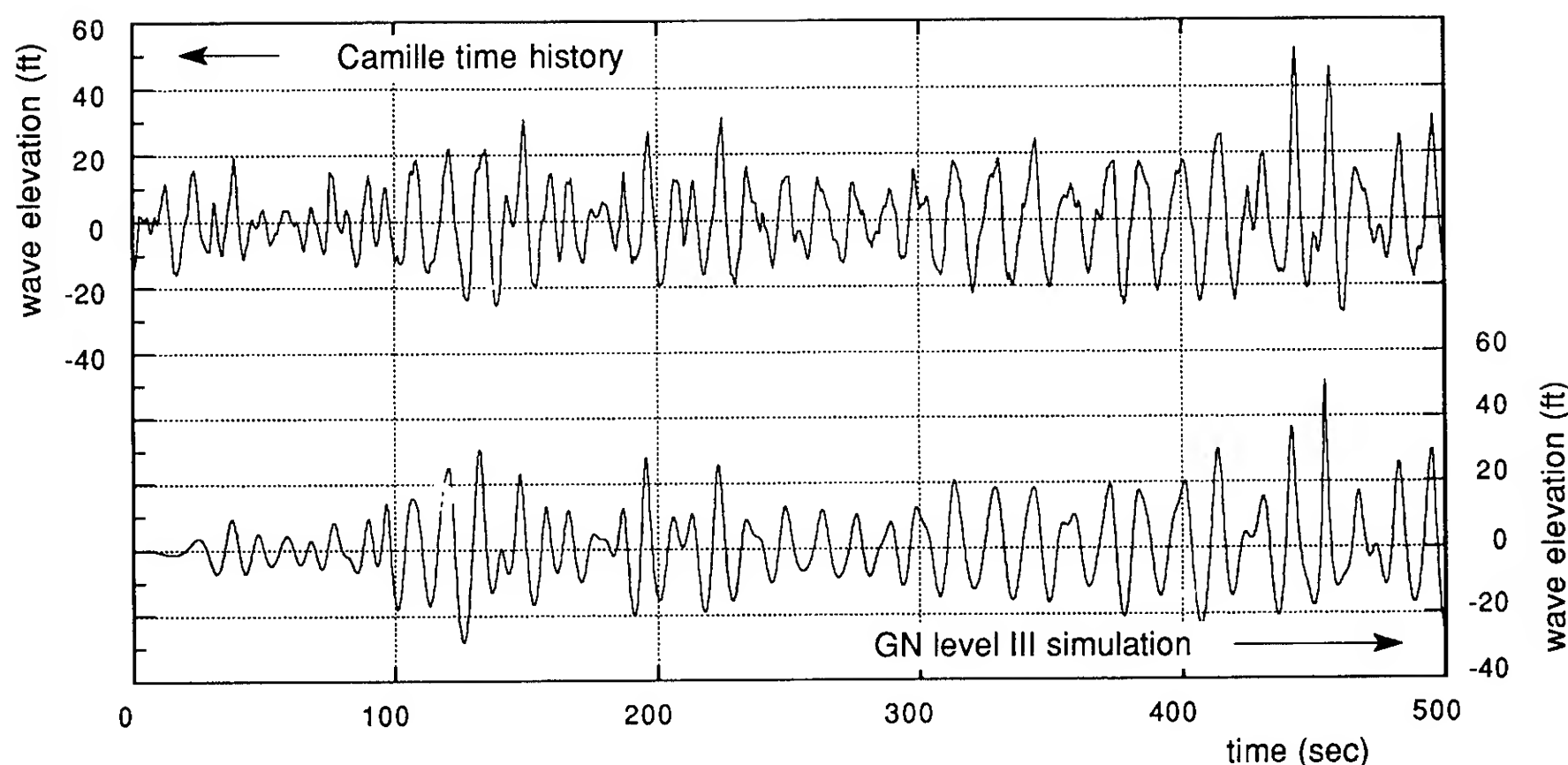


Figure 10. Comparison of GN level III simulation at  $x = 0$  with recorded Camille time history

$2/3 \lambda_0 \leq \lambda \leq 3/2 \lambda_0$  for which the GN level III theory yields uniformly excellent results. The useful part of the wave elevation records at the three probes cover a somewhat smaller time interval than the original Camille record because of the time it takes for waves to progress from the wavemaker to the probes.

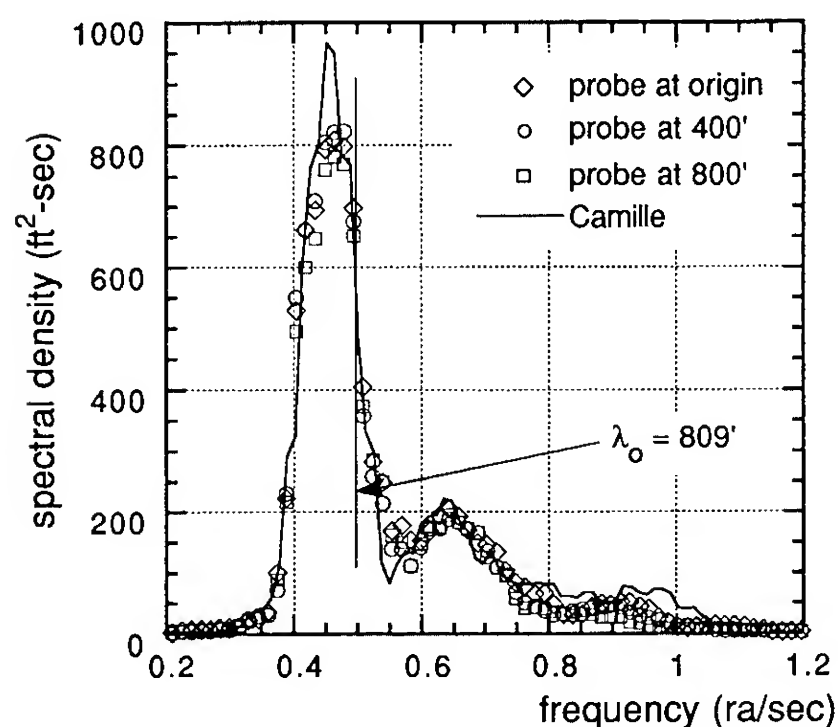


Figure 11. Spectrum of the original Camille record and that measured at the three wave probes.

Finite Fourier transforms of these records were also made and spectra formed. Figure 11 shows the spectrum of the original record, as well as the spectra of the time histories recorded at the three probes. These spectra have been smoothed using a seven-point moving average.

All four spectra are very nearly the same except the original Camille spectrum has a peak at a wave frequency of about 0.45 rad/sec which does not occur in the simulated record. The three spectra from the wave probes can be considered identical.

Several additional simulations were performed using the same input record but with input to the wavemaker multiplied by a factor. The simulation with a factor of 1.2 (i.e., the input was 20% larger) produced waves which were almost breaking. Larger factors produced waves which did break and in these cases it was not possible to complete the simulation.

The spectra of the time histories of the three wave probes were all about equal for the 20% larger simulation and all were almost exactly 44% larger than the corresponding spectra for the original simulation, as one would anticipate. The actual wave profiles, although quite similar in form, were measurably more "peaked" near the highest waves. In the discussion below we will use both the simulation using the original wavemaker input (labelled 100% Camille input) and that resulting from the 20% larger input (labelled 120% Camille input).

The time histories of the wave elevation at  $x = 0$  are now parts of a consistent description in time and space of nonlinear wave systems, and these descriptions afford an opportunity for assessing of the effects of nonlinear dispersion. Let us suppose that the time history recorded at the numerical wave probe at  $x = 0$  is a realistic



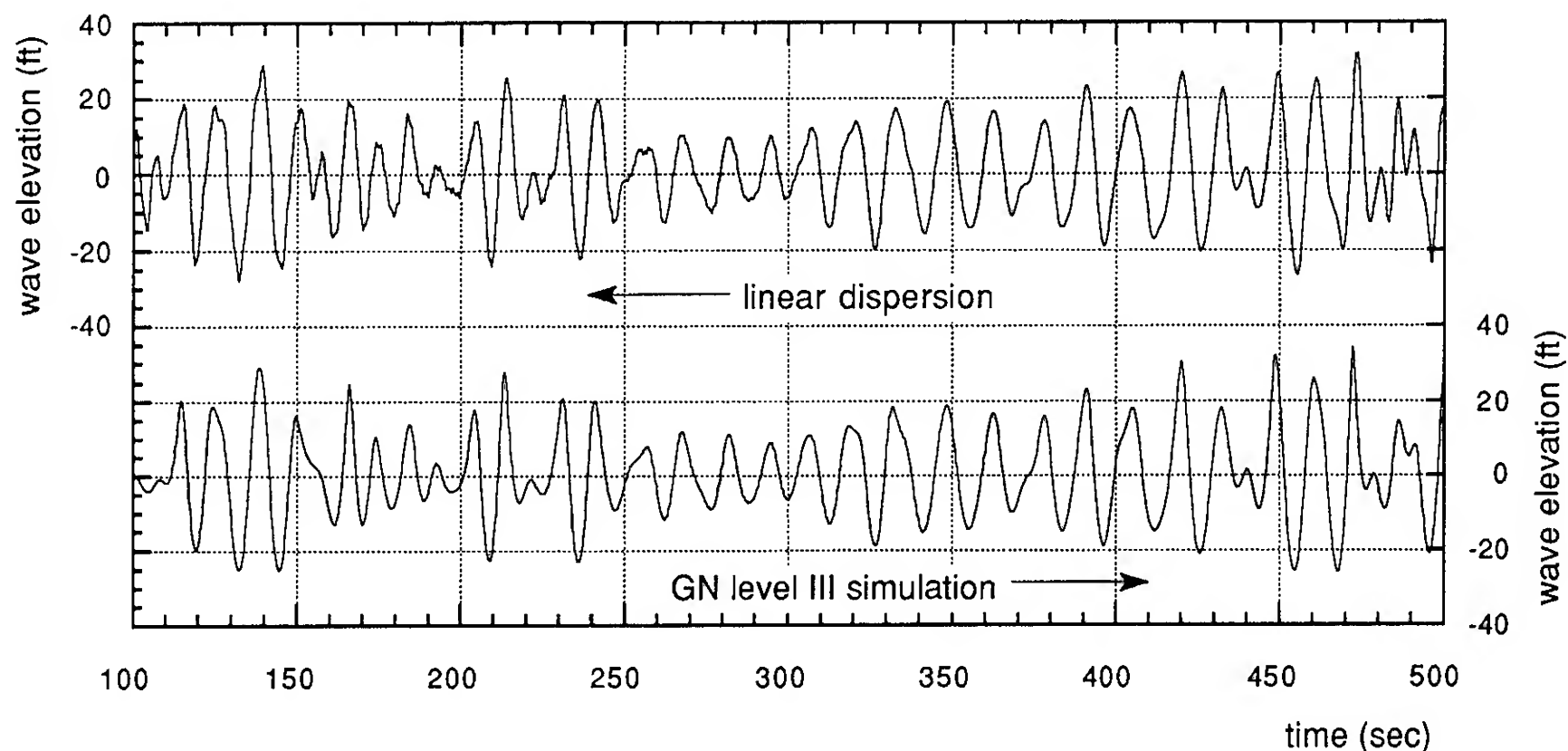


Figure 12. Comparison of waves at  $x = 400'$  predicted by GN level III and by linear dispersion from  $x = 0'$  (100% Camille input).

record of a possible realization of a storm wave system (its closeness to the measured Hurricane Camille record lends credibility to this supposition). This time history will be taken as a reference time history. The time histories of wave elevation at the probes at  $x = 400'$  and  $800'$  recorded in the simulations are part of a nonlinear wave system, but can also be estimated from the reference time history at  $x = 0'$  using finite Fourier transforms and linear dispersion (as was done in (3) and (4) above). Such a process is spectrum-preserving and therefore these estimated time histories at the other two probes will have exactly the same spectrum as the simulated time history at  $x = 0'$ . However, the spectra of the simulated time histories at the  $x = 0'$ ,  $400'$  and  $800'$  are all sensibly the same (see Figure 10). Thus, the two sets of time histories: the nonlinear GN level III simulation, and that derived by linear dispersion will have essentially the same spectra at each probe. In other words, each represents a different realization of the same spectrum.

The comparison between the time histories at the two alternate probe locations is essentially a comparison between linear dispersion and nonlinear dispersion. Figure 12. shows a comparison of the time histories at  $x = 400'$  for the original wavemaker input (100% Camille input). It is clear that the character of both wave systems is more similar than the comparison between the simulation and the original Camille record, but upon close examination one finds the trace from nonlinear dispersion shows sharper peaks and flatter troughs than that from the linear dispersion.

The relation between linear and nonlinear dispersion can be perhaps more clearly seen in Figure 13. The top three graphs in this figure show the results of matching the elevations of the individual crests and troughs from the record produced by the nonlinear dispersion simulation and that from the linear dispersion. The values resulting from each are plotted along a different axis.

For the probe at  $x = 0'$  there is a perfect correlation between the crest and trough elevations derived from the time history and those derived from the finite Fourier transform, since the transform was determined using the whole wave time history at this point and no terms were thrown away.

The two time histories at the probes at  $x = 400'$  and  $800'$  were not identical and, in some cases, were not geometrically similar. Thus, identifying the corresponding crests and troughs was sometimes ambiguous and scatter occurred. For these two probes, the points show a significant deviation from the  $45^\circ$  line which would indicate perfect correlation. It is seen that, in comparison with the nonlinear dispersion simulation, the linear dispersion results show smaller crest heights and larger trough depths. This discrepancy is worse for the probe at  $x = 800'$  than for that at  $x = 400'$ .

What is important in design of many ships and platforms is the *combination* of the maximum wave elevation at the crest and the horizontal particle velocity at the crest. For the superposition of waves given by (3), Airy theory predicts

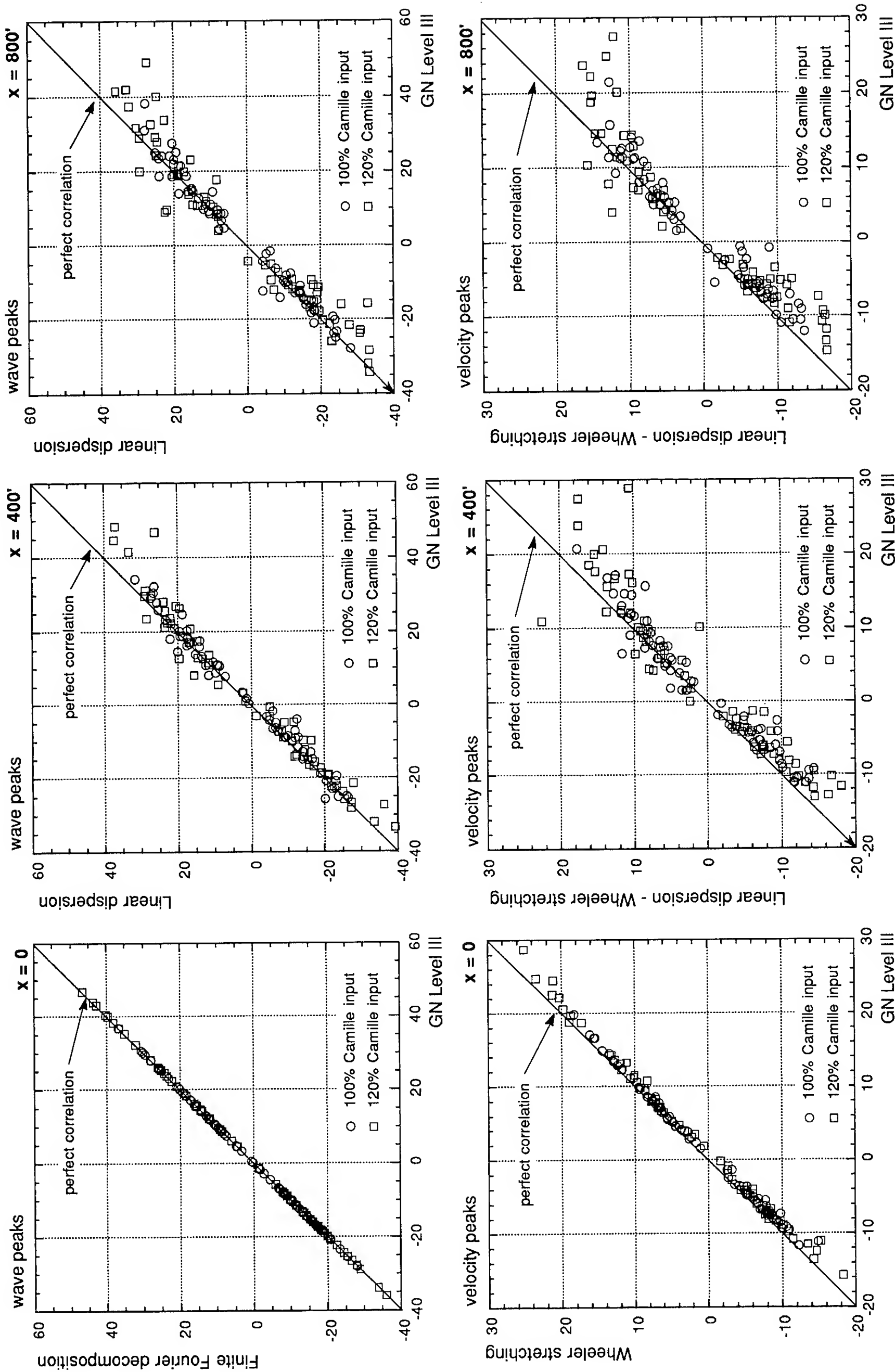


Figure 13. Correlations of the GN level III simulations and the results of linear dispersion at  $x = 0'$ ,  $400'$  and  $800'$ . (Figures at the top are for wave elevation extrema; those at the bottom are for horizontal particle velocity  $10'$  below the free surface).

the horizontal particle velocity,  $\tilde{u}(x,z,t)$ , in the waves to be

$$\tilde{u}(x,z,t) = \sum_{n=0}^{\frac{1}{2}n_{\max}} \omega_n e^{\left(\frac{\omega_n^2 z}{g}\right)} (a_n \sin \omega_n t + b_n \cos \omega_n t) \quad (5)$$

Referring again to Figure 6, it is clear that Airy theory yields particle velocities which are much too high. It is typical in many offshore applications to use an approximation called "Wheeler stretching" (Wheeler, 1969). In this approach, the exponential decay factor in (5) is modified, yielding

$$\bar{u}(x,z,t) = \sum_{n=0}^{\frac{1}{2}n_{\max}} \omega_n e^{\left(\frac{\omega_n^2 z'}{g}\right)} (a_n \sin \omega_n t + b_n \cos \omega_n t), \quad (6)$$

where  $z' = z - \beta(x,t)$ . That is, the value of  $z$  used in the exponential decay measures the *relative* distance below the free surface rather than the absolute distance below the undisturbed free surface level.

The bottom graphs in Figure 13 are correlation plots showing particle velocities both under the crest and under the troughs. It relates the corresponding peaks in the horizontal particle velocity at a distance 10' below the free surface at  $x = 0'$  computed by using the GN level III model, (1), and that determined using the finite Fourier sum (3) and Wheeler stretching (6). The sum in (6) is unrealistically dominated by the large number of high-frequency components in the finite Fourier decomposition when the exponential decay factor is unity, as it is when  $z \equiv \beta$  (i.e.,  $z' = 0$ ). The effect of these high frequency components is unimportant for very small values of  $z' \neq 0$  and thus a value of  $z' = -10'$  was selected. The correlation between the prediction of horizontal particle velocity at  $x = 0'$  from GN level III theory and Wheeler stretching is very good under the crest (positive velocities) and only slightly less good under the troughs (negative velocities). A significant deviation occurs only for the very highest waves and the deviation remains no more than about 5%.

Although we do not show the results here, finite Fourier decompositions and estimates of the particle velocities using Wheeler stretching were performed for the GN level III time histories recorded at the other two wave probes. This information was used to develop correlation diagrams similar to the bottom graph in Figure 13. These correlations were almost identical in

character to the left-hand bottom graph in Figure 13. As a result, we conclude that if the time history of the wave elevation is known at the point of interest, Wheeler stretching is a very good estimator of the peak velocities beneath the crest of a wave and a good estimator for the velocities beneath the trough of the wave.

Let us now investigate the situation when the wave elevation history is not known at the point of interest and must be determined by linear dispersion. The middle and right graphs on the bottom of Figures 13 are correlation diagrams resulting from comparing the horizontal particle velocity at the probes at  $x = 400'$  and  $800'$ . The GN level III prediction is based on (1) using the values of  $u_1, u_2, u_3$  and  $\beta$  determined at these locations by the nonlinear simulation; the spectral method prediction is based on the Fourier decomposition (3), linear dispersion (4) and Wheeler stretching (6). It is obvious that the comparison at the probe at  $x = 400'$  is significantly poorer than that at  $x = 0'$ , and that at  $x = 800'$  is poorer still. In particular, GN theory predicted particle velocities under many of the crests in excess of 30 fps, whereas the linear dispersion result did not predict any velocities this large.

When viewed as a whole, the graphs in Figure 13 show that the relationship between horizontal particle velocity discrepancy and the wave crest and trough discrepancy is nearly constant. That is, when the wave crest and trough predictions are good, the horizontal particle velocity predictions are good; when the wave crest and trough predictions are poor, the particle velocities are corresponding poor. It appears therefore that linear dispersion is the weak link in the prediction process rather than the Wheeler stretching.

Perhaps a more instructive view of the difference between linear dispersion can be gleaned from a comparison of the wave elevation profiles. Figure 14a shows snapshots of the wave elevation computed using linear dispersion for  $x = -400'$  to  $x = 2000'$  at 2 second intervals from  $t = 442$  to  $t = 462$  seconds. Figure 14b shows the same set of snapshots for the simulated waves using GN level III. Both sets correspond to the 120% Camille input to the wavemaker and by construction, both sets of records have exactly the same time histories at  $x = 0'$ . The linear dispersion record shows many small wiggles which are the result of the high frequency terms in the 2100 terms of the finite Fourier sum. In general these effects are localized near  $x = 0$ .

A cursory glance shows that the two sets of snapshots are similar, but a significant difference occurs between  $t = 454$  and  $t = 460$ . The GN level III simulation predicts a large, nearly breaking wave crest which persists for about 6

seconds and has a maximum elevation of 65' above the undisturbed free surface. This wave was the highest crest obtained by the simulation. The corresponding wave for the linear dispersion case is never more than 50' high and lacks the coherence of the simulated wave. The difference appears to be that the Airy wave components are not "phase-locked" and can not remain together for any length of time.

## 5. Conclusions

A nonlinear fluid sheet model for predicting the dispersion of random wave systems in the time domain was introduced and compared with known results for steep waves of permanent form. It was found that the particular model used here, Green-Naghdi level III, compared extremely well with the results for wave celerity and wave profile for a wide range of steepness and over a fairly broad bandwidth of wave lengths. The comparison with wave particle velocities was good over a fairly narrow, but useful, bandwidth of wave lengths.

The GN level III model was used to predict the generation of regular waves and it was found (and confirmed by laboratory experiment) that the leading edge of a packet of relatively steep waves always appears to break before very many waves are created.

This nonlinear model was also used to model a real steep wave record, that measured during Hurricane Camille in 1969. The purpose of this study was to investigate the effects of nonlinear dispersion. These results can be summarized as follows: linear dispersion leads to *under-prediction* of both the wave elevation and the wave particle velocities at a point remote from a location where the wave elevation history is known. This under-prediction may represent a significant lack of conservatism in the use of the spectral method for design to withstand survival conditions.

The time histories at all probes either recorded from the nonlinear simulation or from linear dispersion from the probe at  $x = 0$  all had spectra which were sensibly the same. That is, all were acceptable realizations of the same spectrum. Yet those time histories of either wave elevation or particle velocity resulting from linear dispersion did not compare well with those which resulted from nonlinear dispersion. Thus, we can further conclude that not all realizations of a spectrum correspond to realistic wave systems, if the waves high enough to lead to significant nonlinear effects.

## Acknowledgement

This research was in part sponsored by the Office of Naval Research, United States Navy, under contract N00014-88-K-0002 with the University of California, Berkeley.

## References

- Chaplin, J. R. (1980). Developments of stream function wave theory. Coastal Engineering, Vol. 3, pp. 179-205.
- Dean, R. G. (1974), Evaluation and development of water wave theories for engineering application. U. S. Army Coastal Engineering Research Center, Report SR-1 (two volumes).
- Ertekin, R. C. (1984). Soliton generation by moving disturbances in shallow water. Ph.D. Thesis, Univ. of Calif. Berkeley. v + 352 pp.
- Fenton, J. D. (1988). The numerical solution of steady water wave problems. Comput. Geosci., Vol 14, pp. 357-368.
- Green, A. E. and Naghdi, P. M. (1986). A nonlinear theory of water waves for finite and infinite depths. Philos. Trans. Roy. Soc. London Ser. A, Vol. 320, pp. 37-70.
- Green, A. E. and Naghdi, P. M. (1987). Further developments in a nonlinear theory of water waves for finite and infinite depths. Philos. Trans. Roy. Soc. London Ser. A, Vol. 324, pp. 47-72.
- Longuet-Higgins, M. S. (1974), Breaking waves - in deep or shallow water. 10th Symposium on Naval Hydrodynamics, MIT, pp. 597-605.
- Schwartz, L. W. (1974) Computer extension and analytic continuation of Stokes' expansion for gravity waves. J. Fluid Mech. Vol. 62, pp. 553-578.
- Shields, J. J. (1986). A direct theory for waves approaching a beach. Ph.D. Thesis, Univ. of Calif. Berkeley. v + 137 p.
- Sobey, R. J. (1989). Variations on Fourier wave theory. International Journal for Numerical Methods in Fluid Mechanics, Vol. 9, pp.1453-1467.
- Webster, W. C. & Shields, J. J. (1990). Applications of high-level, Green-Naghdi theory to fluid flow problems. IUTAM Symposium on Marine Dynamics, Brunel University, London (in press).
- Wheeler, J. D. (1969). Method for calculating forces produced by irregular waves. Off-shore Technology Conference, Houston, Texas, OTC 1006.

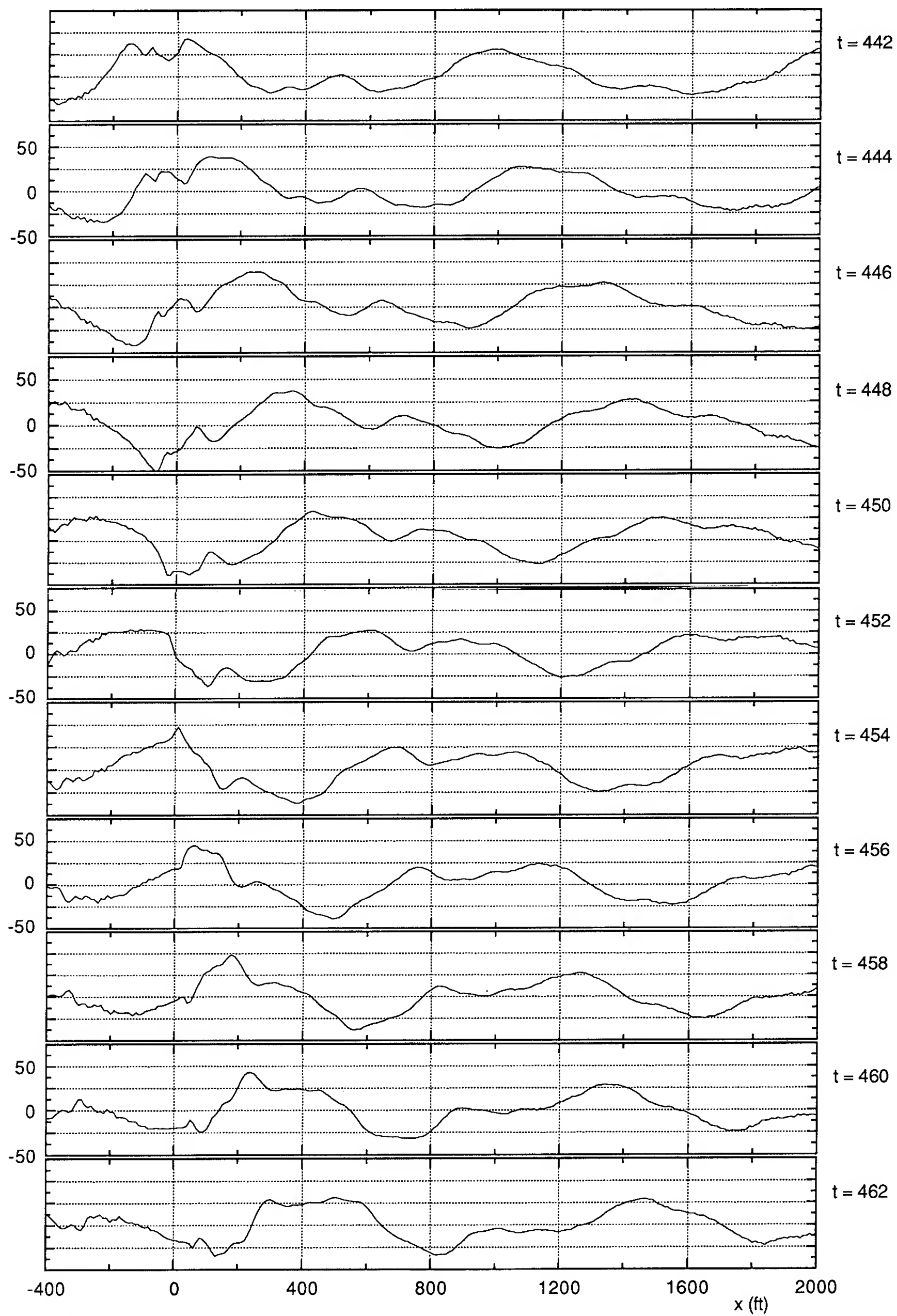


Figure 14a. Wave profiles predicted by superposition of Airy waves and linear dispersion.



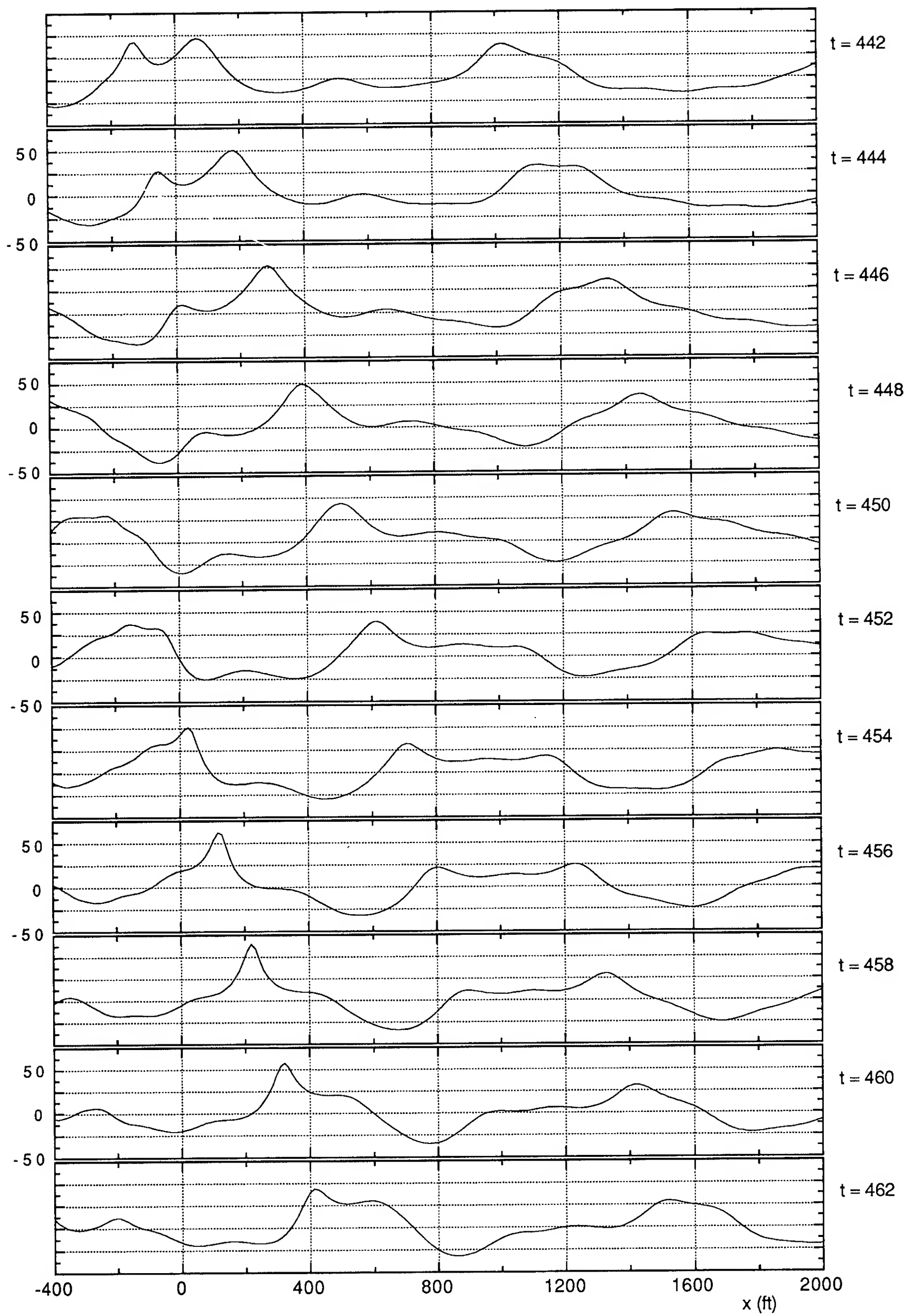


Figure 14b. Wave profiles predicted by GN Level III theory.



# Appendix A. Green-Naghdi Level III Evolution Equations for Deep Water Waves

equation 1:

$$-\frac{a^3 \frac{\partial \beta}{\partial t}}{e a \beta} = a^2 \frac{\partial u_1}{\partial x} + a(-1 + a\beta) \frac{\partial u_2}{\partial x} + a \frac{\partial \beta}{\partial x} (a^2 u_1 + a a \beta u_2 + (a\beta)^2 u_3) - (-2 + 2 a \beta - (a\beta)^2) \frac{\partial u_3}{\partial x}$$

equation 2:

$$\begin{aligned} \frac{81 a^2}{4 e a \beta} \left\{ 2 a^4 \frac{\partial u_1}{\partial t} - 4 a^3 \frac{\partial \beta}{\partial x} \frac{\partial^3 u_1}{\partial t \partial x^2} - 2 a^2 \frac{\partial^3 u_1}{\partial t \partial x^2} + a^3 (-1 + 2 a \beta) \frac{\partial u_2}{\partial t} - 4 a^2 (-1 + a \beta) \frac{\partial \beta}{\partial x} \frac{\partial^2 u_2}{\partial t \partial x} - a^2 (-1 + 2 a \beta - 2 (a \beta)^2) \frac{\partial u_3}{\partial t} \right. \\ \left. + 4 a (-2 + 2 a \beta - (a \beta)^2) \frac{\partial \beta}{\partial x} \frac{\partial^2 u_3}{\partial t \partial x} + (-7 + 6 a \beta - 2 (a \beta)^2) \frac{\partial^3 u_3}{\partial t \partial x^2} \right\} = - \left\{ \frac{81 a^6 g}{e^3 a \beta} \frac{\partial \beta}{\partial x} + 81 a^5 \frac{\partial \beta}{\partial x} \frac{\partial u_1^2}{\partial x} + 27 a^4 \frac{\partial u_1}{\partial x} \frac{\partial^2 u_1}{\partial x^2} + 9 a^3 (-1 + 3 a \beta) \frac{\partial u_1}{\partial x} \frac{\partial^2 u_2}{\partial x^2} \right. \\ \left. + 81 a^4 (-1 + 2 a \beta) \frac{\partial \beta}{\partial x} \frac{\partial u_1}{\partial x} \frac{\partial u_2}{\partial x} + 9 a^3 (-4 + 3 a \beta) \frac{\partial^2 u_1}{\partial x^2} \frac{\partial u_2}{\partial x} - 81 a^3 (a \beta - (a \beta)^2) \frac{\partial \beta}{\partial x} \frac{\partial u_2^2}{\partial x} - 3 a^2 (-5 + 15 a \beta - 9 (a \beta)^2) \frac{\partial u_2}{\partial x} \frac{\partial^2 u_2}{\partial x^2} - 3 a^2 (-26 + 24 a \beta - 9 (a \beta)^2) \frac{\partial^2 u_1}{\partial x^2} \frac{\partial u_3}{\partial x} \right. \\ \left. - 9 a^4 \frac{\partial u_1}{\partial x} (3 a u_2 + 2 (-1 + 3 a \beta) u_3) - 3 a^2 \frac{\partial^3 u_1}{\partial x^3} [9 a^2 u_1 + 3 a (-1 + 3 a \beta) u_2 - (-2 + 6 a \beta - 9 (a \beta)^2) u_3] + 3 a^3 \frac{\partial u_2}{\partial x} (9 a^2 u_1 + 9 a u_2 + (-8 + 24 a \beta - 9 (a \beta)^2) u_3) \right. \\ \left. - 81 a^3 \frac{\partial \beta}{\partial x} \frac{\partial^2 u_1}{\partial x^2} (a^2 u_1 + a a \beta u_2 + (a \beta)^2 u_3) - 81 a^2 \frac{\partial \beta}{\partial x} \frac{\partial^2 u_2}{\partial x^2} [a^2 (-1 + a \beta) u_1 - a (a \beta - (a \beta)^2) u_2 - ((a \beta)^2 - (a \beta)^3) u_3] - 162 a^3 (-1 + a \beta - (a \beta)^2) \frac{\partial \beta}{\partial x} \frac{\partial u_1}{\partial x} \frac{\partial u_3}{\partial x} \right. \\ \left. - 3 a \frac{\partial^3 u_2}{\partial x^3} [3 a^2 (-4 + 3 a \beta) u_1 - a (-5 + 15 a \beta - 9 (a \beta)^2) u_2 + (-4 + 12 a \beta - 18 (a \beta)^2 + 9 (a \beta)^3) u_3] + 3 a (-4 + 12 a \beta - 18 (a \beta)^2 + 9 (a \beta)^3) \frac{\partial u_2}{\partial x} \frac{\partial^2 u_3}{\partial x^2} \right. \\ \left. + 81 a^2 (2 a \beta - 3 (a \beta)^2 + 2 (a \beta)^3) \frac{\partial \beta}{\partial x} \frac{\partial u_2}{\partial x} \frac{\partial u_3}{\partial x} + 9 a (-4 + 12 a \beta - 9 (a \beta)^2 + 3 (a \beta)^3) \frac{\partial^2 u_2}{\partial x^2} \frac{\partial u_3}{\partial x} - (-32 + 96 a \beta - 144 (a \beta)^2 + 90 (a \beta)^3 - 27 (a \beta)^4) \frac{\partial u_3}{\partial x} \frac{\partial^2 u_3}{\partial x^2} \right. \\ \left. + 3 a^2 [6 a^2 (-4 + 3 a \beta) u_1 - a (16 + 6 a \beta - 9 (a \beta)^2) u_2 - 2 (-8 + 24 a \beta - 9 (a \beta)^2) u_3] \frac{\partial u_3}{\partial x} + 81 a (2 (a \beta)^2 - 2 (a \beta)^3 + (a \beta)^4) \frac{\partial \beta}{\partial x} \frac{\partial u_3^2}{\partial x} \right. \\ \left. - 3 a^2 (-2 + 6 a \beta - 9 (a \beta)^2) \frac{\partial u_1}{\partial x} \frac{\partial^2 u_3}{\partial x^2} + 81 a \frac{\partial \beta}{\partial x} [a^2 (-2 + 2 a \beta - (a \beta)^2) u_1 - a (2 a \beta - 2 (a \beta)^2 + (a \beta)^3) u_2 - (2 (a \beta)^2 - 2 (a \beta)^3 + (a \beta)^4) u_3] \frac{\partial^2 u_3}{\partial x^2} \right. \\ \left. + [3 a^2 (-26 + 24 a \beta - 9 (a \beta)^2) u_1 - 9 a (-4 + 12 a \beta - 9 (a \beta)^2 + 3 (a \beta)^3) u_2 + (-32 + 96 a \beta - 144 (a \beta)^2 + 90 (a \beta)^3 - 27 (a \beta)^4) u_3] \frac{\partial^3 u_3}{\partial x^3} \right\} \end{aligned}$$

equation 3:

$$\begin{aligned}
& \frac{243 a^2}{8 e a \beta} \left\{ 2 a^4 (-1 + 2 a \beta) \frac{\partial u_1}{\partial t} - 8 a^3 (-1 + a \beta) \frac{\partial \beta}{\partial x} \frac{\partial^3 u_1}{\partial t \partial x^2} - 2 a^2 (-3 + 2 a \beta) \frac{\partial^3 u_1}{\partial t \partial x^2} - 2 a^3 (-1 + 2 a \beta - 2 (a \beta)^2) \frac{\partial u_2}{\partial t} + 8 a^2 (-1 + 2 a \beta - (a \beta)^2) \frac{\partial \beta}{\partial x} \frac{\partial^2 u_2}{\partial t \partial x} \right. \\
& + 2 a (-5 + 6 a \beta - 2 (a \beta)^2) \frac{\partial^3 u_2}{\partial t \partial x^2} + a^2 (-3 + 6 a \beta - 6 (a \beta)^2 + 4 (a \beta)^3) \frac{\partial u_3}{\partial t} - 8 a (-2 + 4 a \beta - 3 (a \beta)^2 + (a \beta)^3) \frac{\partial \beta}{\partial x} \frac{\partial^2 u_3}{\partial t \partial x} - (-25 + 34 a \beta - 18 (a \beta)^2 + 4 (a \beta)^3) \frac{\partial^3 u_3}{\partial t \partial x^2} \Big\} \\
& = - \left\{ 243 a^5 (-1 + a \beta) \frac{\partial \beta}{\partial x} \frac{\partial u_1^2}{\partial x} + 27 a^4 (-4 + 3 a \beta) \frac{\partial u_1}{\partial x} \frac{\partial^2 u_1}{\partial x^2} - 243 a^4 (-1 + 3 a \beta - 2 (a \beta)^2) \frac{\partial \beta}{\partial x} \frac{\partial u_1}{\partial x} \frac{\partial u_2}{\partial x} - 9 a^3 (-17 + 24 a \beta - 9 (a \beta)^2) \frac{\partial^2 u_1}{\partial x^2} \frac{\partial u_2}{\partial x} \right. \\
& - 9 a^4 \frac{\partial u_1}{\partial x} \left[ 3 a (-1 + 3 a \beta) u_2 - 2 (-2 + 6 a \beta - 9 (a \beta)^2) u_3 \right] - 243 a^3 \frac{\partial \beta}{\partial x} \frac{\partial^2 u_1}{\partial x^2} \left[ a^2 (-1 + a \beta) u_1 - a (a \beta - (a \beta)^2) u_2 - (a \beta)^2 - (a \beta)^3 \right] u_3 \Big] \\
& + 27 a^3 \frac{\partial u_2}{\partial x} \left[ a^2 (-1 + 3 a \beta) u_1 + a (-1 + 3 a \beta) u_2 - (-2 + 6 a \beta - 9 (a \beta)^2 + 3 (a \beta)^3) u_3 \right] + 486 a^3 (-1 + 2 a \beta - 2 (a \beta)^2 + (a \beta)^3) \frac{\partial \beta}{\partial x} \frac{\partial u_1}{\partial x} \frac{\partial u_3}{\partial x} \\
& - 9 a^2 \frac{\partial^3 u_1}{\partial x^3} \left[ 3 a^2 (-4 + 3 a \beta) u_1 - a (-5 + 15 a \beta - 9 (a \beta)^2) u_2 + (-4 + 12 a \beta - 18 (a \beta)^2 + 9 (a \beta)^3) u_3 \right] + 9 a^2 (-38 + 60 a \beta - 36 (a \beta)^2 + 9 (a \beta)^3) \frac{\partial^2 u_1}{\partial x^2} \frac{\partial u_3}{\partial x} \\
& + 3 a \frac{\partial^3 u_2}{\partial x^3} \left[ 3 a^2 (-17 + 24 a \beta - 9 (a \beta)^2) u_1 - 27 a (-1 + 3 a \beta - 3 (a \beta)^2 + (a \beta)^3) u_2 + (-26 + 78 a \beta - 117 (a \beta)^2 + 90 (a \beta)^3 - 27 (a \beta)^4) u_3 \right] \\
& + 243 a^2 \frac{\partial \beta}{\partial x} \frac{\partial^2 u_2}{\partial x^2} \left[ a^2 (-1 + 2 a \beta - (a \beta)^2) u_1 - a (a \beta - 2 (a \beta)^2 + (a \beta)^3) u_2 - (a \beta)^2 - 2 (a \beta)^3 + (a \beta)^4 \right] u_3 - 243 a^2 (2 a \beta - 5 (a \beta)^2 + 5 (a \beta)^3 - 2 (a \beta)^4) \frac{\partial \beta}{\partial x} \frac{\partial u_2}{\partial x} \frac{\partial u_3}{\partial x} \\
& - 9 a^2 \left[ 2 a^2 (-5 + 15 a \beta - 9 (a \beta)^2) u_1 + a (-4 + 12 a \beta + 9 (a \beta)^2 - 9 (a \beta)^3) u_2 - 6 (-2 + 6 a \beta - 9 (a \beta)^2 + 3 (a \beta)^3) u_3 \right] \frac{\partial u_3}{\partial x} + 243 a^3 (a \beta - 2 (a \beta)^2 + (a \beta)^3) \frac{\partial \beta}{\partial x} \frac{\partial u_2^2}{\partial x} \\
& - 243 a (2 (a \beta)^2 - 4 (a \beta)^3 + 3 (a \beta)^4 - (a \beta)^5) \frac{\partial \beta}{\partial x} \frac{\partial u_3^2}{\partial x} + 9 a^2 (-4 + 12 a \beta - 18 (a \beta)^2 + 9 (a \beta)^3) \frac{\partial u_1}{\partial x} \frac{\partial^2 u_3}{\partial x^2} - 3 a (-26 + 78 a \beta - 117 (a \beta)^2 + 90 (a \beta)^3 - 27 (a \beta)^4) \frac{\partial u_2}{\partial x} \frac{\partial^2 u_3}{\partial x^2} \\
& - 243 a \frac{\partial \beta}{\partial x} \left[ a^2 (-2 + 4 a \beta - 3 (a \beta)^2 + (a \beta)^3) u_1 - a (2 a \beta - 4 (a \beta)^2 + 3 (a \beta)^3 - (a \beta)^4) u_2 - (2 (a \beta)^2 - 4 (a \beta)^3 + 3 (a \beta)^4 - (a \beta)^5) u_3 \right] \frac{\partial^2 u_3}{\partial x^2} + \frac{243 a^6}{e^3 a \beta} (-1 + a \beta) \frac{\partial \beta}{\partial x} \\
& + (-220 + 660 a \beta - 990 (a \beta)^2 + 828 (a \beta)^3 - 378 (a \beta)^4 + 81 (a \beta)^5) \frac{\partial u_3}{\partial x} \frac{\partial^2 u_3}{\partial x^2} - 3 a (-68 + 204 a \beta - 225 (a \beta)^2 + 117 (a \beta)^3 - 27 (a \beta)^4) \frac{\partial^2 u_2}{\partial x^2} \frac{\partial u_3}{\partial x}
\end{aligned}$$

$$\begin{aligned}
& -9a^3 \left( -5 + 15a\beta - 9(a\beta)^2 \right) \frac{\partial u_1}{\partial x} \frac{\partial^2 u_2}{\partial x^2} + 81a^2 \left( -1 + 3a\beta - 3(a\beta)^2 + (a\beta)^3 \right) \frac{\partial u_2}{\partial x} \frac{\partial^2 u_2}{\partial x^2} - \left[ 9a^2 \left( -38 + 60a\beta - 36(a\beta)^2 + 9(a\beta)^3 \right) u_1 \right. \\
& \left. - 3a \left( -68 + 204a\beta - 225(a\beta)^2 + 117(a\beta)^3 - 27(a\beta)^4 \right) u_2 + \left( -220 + 660a\beta - 990(a\beta)^2 + 828(a\beta)^3 - 378(a\beta)^4 + 81(a\beta)^5 \right) u_3 \right] \frac{\partial^3 u_3}{\partial x^3} \Bigg\} \\
& \text{equation 4:} \\
& -\frac{243a^2}{8e\alpha\beta} \left\{ 2a^4 \left( -1 + 2a\beta - 2(a\beta)^2 \right) \frac{\partial u_1}{\partial t} - 8a^3 \left( -2 + 2a\beta - (a\beta)^2 \right) \frac{\partial \beta}{\partial x} \frac{\partial^3 u_1}{\partial t \partial x^2} - 2a^2 \left( -7 + 6a\beta - 2(a\beta)^2 \right) \frac{\partial^3 u_1}{\partial t \partial x^2} - a^3 \left( -3 + 6a\beta - 6(a\beta)^2 + 4(a\beta)^3 \right) \frac{\partial u_2}{\partial t} \right. \\
& + 8a^2 \left( -2 + 4a\beta - 3(a\beta)^2 + (a\beta)^3 \right) \frac{\partial \beta}{\partial x} \frac{\partial^2 u_2}{\partial t \partial x} + a \left( -25 + 34a\beta - 18(a\beta)^2 + 4(a\beta)^3 \right) \frac{\partial^3 u_2}{\partial t \partial x^2} + 2a^2 \left( -3 + 6a\beta - 6(a\beta)^2 + 4(a\beta)^3 - 2(a\beta)^4 \right) \frac{\partial u_3}{\partial t} \\
& - 8a \left( -4 + 8a\beta - 8(a\beta)^2 + 4(a\beta)^3 - (a\beta)^4 \right) \frac{\partial \beta}{\partial x} \frac{\partial^2 u_3}{\partial t \partial x} - 2 \left( -33 + 50a\beta - 34(a\beta)^2 + 12(a\beta)^3 - 2(a\beta)^4 \right) \frac{\partial^3 u_3}{\partial t \partial x^2} \Bigg\} = -243a^4 \left( -2 + 6a\beta - 5(a\beta)^2 + 2(a\beta)^3 \right) \frac{\partial \beta}{\partial x} \frac{\partial u_1}{\partial x} \frac{\partial u_2}{\partial x} \\
& + 3a^2 \left( -68 + 204a\beta - 225(a\beta)^2 + 117(a\beta)^3 - 27(a\beta)^4 \right) \frac{\partial u_2}{\partial x} \frac{\partial^2 u_2}{\partial x^2} - 9a^4 \frac{\partial u_1}{\partial x} \left[ a \left( -2 + 6a\beta - 9(a\beta)^2 \right) u_2 - 2 \left( -2 + 6a\beta - 9(a\beta)^2 + 9(a\beta)^3 \right) u_3 \right] \\
& - 3a^2 \frac{\partial^3 u_1}{\partial x^3} \left[ 3a^2 \left( -26 + 24a\beta - 9(a\beta)^2 \right) u_1 - 9a \left( -4 + 12a\beta - 9(a\beta)^2 + 3(a\beta)^3 \right) u_2 + \left( -32 + 96a\beta - 144(a\beta)^2 + 90(a\beta)^3 - 27(a\beta)^4 \right) u_3 \right] \\
& + 3a^3 \frac{\partial u_2}{\partial x} \left[ 3a^2 \left( -2 + 6a\beta - 9(a\beta)^2 \right) u_1 + 3a \left( -2 + 6a\beta - 9(a\beta)^2 \right) u_2 - \left( -20 + 60a\beta - 90(a\beta)^2 + 90(a\beta)^3 - 27(a\beta)^4 \right) u_3 \right] + 9a^4 \left( -26 + 24a\beta - 9(a\beta)^2 \right) \frac{\partial u_1}{\partial x} \frac{\partial^2 u_1}{\partial x^2} \\
& - 243a^3 \frac{\partial \beta}{\partial x} \frac{\partial^2 u_1}{\partial x^2} \left[ a^2 \left( -2 + 2a\beta - (a\beta)^2 \right) u_1 - a \left( 2a\beta - 2(a\beta)^2 + (a\beta)^3 \right) u_2 - \left( 2(a\beta)^2 - 2(a\beta)^3 + (a\beta)^4 \right) u_3 \right] - 9a^3 \left( -38 + 60a\beta - 36(a\beta)^2 + 9(a\beta)^3 \right) \frac{\partial^2 u_1}{\partial x^2} \frac{\partial u_2}{\partial x} \\
& + 243a^2 \frac{\partial \beta}{\partial x} \frac{\partial^2 u_2}{\partial x^2} \left[ a^2 \left( -2 + 4a\beta - 3(a\beta)^2 + (a\beta)^3 \right) u_1 - a \left( 2a\beta - 4(a\beta)^2 + 3(a\beta)^3 - (a\beta)^4 \right) u_2 - \left( 2(a\beta)^2 - 4(a\beta)^3 + 3(a\beta)^4 - (a\beta)^5 \right) u_3 \right] \\
& + 243a^3 \left( 2a\beta - 4(a\beta)^2 + 3(a\beta)^3 - (a\beta)^4 \right) \frac{\partial \beta}{\partial x} \frac{\partial u_2}{\partial x} + a \frac{\partial^3 u_2}{\partial x^3} \left[ 9a^2 \left( -38 + 60a\beta - 36(a\beta)^2 + 9(a\beta)^3 \right) u_1 - 3a \left( -68 + 204a\beta - 225(a\beta)^2 + 117(a\beta)^3 - 27(a\beta)^4 \right) u_2 \right. \\
& \left. + \left( -220 + 660a\beta - 990(a\beta)^2 + 828(a\beta)^3 - 378(a\beta)^4 + 81(a\beta)^5 \right) u_3 \right] - 243a^2 \left( 4a\beta - 10(a\beta)^2 + 12(a\beta)^3 - 7(a\beta)^4 + 2(a\beta)^5 \right) \frac{\partial \beta}{\partial x} \frac{\partial u_2}{\partial x} \frac{\partial u_3}{\partial x}
\end{aligned}$$

$$\begin{aligned}
& + 486 a^3 (-2 + 4 a \beta - 5 (a \beta)^2 + 3 (a \beta)^3 - (a \beta)^4) \frac{\partial \beta}{\partial x} \frac{\partial u_1}{\partial x} \frac{\partial u_3}{\partial x} + 3 a^2 (-260 + 456 a \beta - 360 (a \beta)^2 + 144 (a \beta)^3 - 27 (a \beta)^4) \frac{\partial^2 u_1}{\partial x^2} \frac{\partial u_3}{\partial x} + \frac{243 a^6}{e^3 a \beta} (-2 + 2 a \beta - (a \beta)^2) \frac{\partial \beta}{\partial x} \\
& - a (-532 + 1596 a \beta - 1908 (a \beta)^2 + 1260 (a \beta)^3 - 459 (a \beta)^4 + 81 (a \beta)^5) \frac{\partial^2 u_2}{\partial x^2} \frac{\partial u_3}{\partial x} + 3 a^2 (-32 + 96 a \beta - 144 (a \beta)^2 + 90 (a \beta)^3 - 27 (a \beta)^4) \frac{\partial u_1}{\partial x} \frac{\partial^2 u_3}{\partial x^2} \\
& - 27 a^3 (-4 + 12 a \beta - 9 (a \beta)^2 + 3 (a \beta)^3) \frac{\partial u_1}{\partial x} \frac{\partial^2 u_2}{\partial x^2} - 3 a^2 \left[ 6 a^2 (-4 + 12 a \beta - 18 (a \beta)^2 + 9 (a \beta)^3) u_1 + a (-4 + 12 a \beta - 18 (a \beta)^2 - 36 (a \beta)^3 + 27 (a \beta)^4) u_2 \right. \\
& \left. - 2 (-20 + 60 a \beta - 90 (a \beta)^2 + 90 (a \beta)^3 - 27 (a \beta)^4) u_3 \right] \frac{\partial u_3}{\partial x} - 243 a \left( 4 (a \beta)^2 - 8 (a \beta)^3 + 8 (a \beta)^4 - 4 (a \beta)^5 + (a \beta)^6 \right) \frac{\partial \beta}{\partial x} \frac{\partial u_3}{\partial x} + 243 a^5 (-2 + 2 a \beta - (a \beta)^2) \frac{\partial \beta}{\partial x} \frac{\partial u_1^2}{\partial x} \\
& - a (-220 + 660 a \beta - 990 (a \beta)^2 + 828 (a \beta)^3 - 378 (a \beta)^4 + 81 (a \beta)^5) \frac{\partial u_2}{\partial x} \frac{\partial^2 u_3}{\partial x^2} + 81 (-8 + 24 a \beta - 36 (a \beta)^2 + 32 (a \beta)^3 - 18 (a \beta)^4 + 6 (a \beta)^5 - (a \beta)^6) \frac{\partial u_3}{\partial x} \frac{\partial^2 u_3}{\partial x^2} \\
& - 243 a \frac{\partial \beta}{\partial x} \left[ a^2 (-4 + 8 a \beta - 8 (a \beta)^2 + 4 (a \beta)^3 - (a \beta)^4) u_1 - a (4 a \beta - 8 (a \beta)^2 + 8 (a \beta)^3 - 4 (a \beta)^4 + (a \beta)^5) u_2 - (4 (a \beta)^2 - 8 (a \beta)^3 + 8 (a \beta)^4 - 4 (a \beta)^5 + (a \beta)^6) u_3 \right] \frac{\partial^2 u_3}{\partial x^2} \\
& - \left[ 3 a^2 (-260 + 456 a \beta - 360 (a \beta)^2 + 144 (a \beta)^3 - 27 (a \beta)^4) u_1 - a (-532 + 1596 a \beta - 1908 (a \beta)^2 + 1260 (a \beta)^3 - 459 (a \beta)^4 + 81 (a \beta)^5) u_2 + \right. \\
& \left. 81 (-8 + 24 a \beta - 36 (a \beta)^2 + 32 (a \beta)^3 - 18 (a \beta)^4 + 6 (a \beta)^5 - (a \beta)^6) u_3 \right] \frac{\partial^3 u_3}{\partial x^3}
\end{aligned}$$

## DISCUSSION

Krish Thiagarajan  
University of Michigan, USA

The authors have prescribed a certain velocity distribution at the wave-maker position in their numerical wavetank. They also claim that disturbances caused due to this specified distribution are localized and die out quickly with horizontal distance. This claim may not be entirely true. Satisfying the no-flow condition on the wave-maker surface had been a known problem. Existing second order wave generator theories (Ref[1] reviews some of them.) indicate the existence of a second order free wave of frequency twice the fundamental wave frequency generated by the wave maker. This free wave is parasitic in nature as it travels along with the wave of interest, i.e., it does not die out. My own experiments have confirmed this (Ref[1]). The above discussion, while pertaining to a physical tank, may also be applicable to a numerical wave tank.

Ref.[1]: Thiagarajan, K. "An Experimental Study on Higher Order Waves and Hydrodynamic Loading on Vertical Surface Piercing Cylinders," M.Eng. Thesis, Faculty of Engineering, Memorial University of Newfoundland, St. John's, Canada, 1989

# Three-Dimensional, Unsteady Computations of Nonlinear Waves Caused by Underwater Disturbances

Y. Cao, W. Schultz, R. Beck (The University of Michigan, USA)

## Abstract

Three-dimensional unsteady nonlinear waves generated by underwater disturbances (such as a moving source-sink pair or a moving body) are modeled using a mixed Eulerian-Lagrangian time marching procedure combined with a desingularized boundary integral method. The waves computed by the present method are compared with those for linear theory to find the nonlinear effects. The wave resistance, lift, moment and the pressure distributions on the body are also calculated. We find that the wave patterns of a spheroid and a relevant simple source-sink pair disturbance are very similar as long as the disturbances are not too close to the free surface.

## 1 Nomenclature

$C_D$	drag coefficient
$C_L$	lift coefficient
$C_M$	moment coefficient
$C_p$	pressure coefficient
$D$	diameter of spheroid
$D_m$	local mesh size
$F_r$	Froude number
$\vec{F}$	hydrodynamic force acting on body
$\vec{M}$	hydrodynamic moment acting on body
$h$	submerged depth of disturbance
$\vec{i}, \vec{j}, \vec{k}$	unit vectors
$L$	length of major axis of spheroid
$L_d$	desingularization distance
$l_d$	factor of desingularization
$\vec{M}$	moment acting on body
$N^b$	node number on spheroid
$N_\theta^b$	number of elements on spheroid in $\theta$ direction
$N_x^b$	number of elements on spheroid in $x$ direction
$N^f$	node number on free surface
$N_x^f$	node number on free surface in $x$ direction
$N_y^f$	node number on free surface in $y$ direction
$\vec{n}$	outward normal of body surface into fluid
$p$	pressure
$\vec{r}$	position vector from center of body
$S$	area of spheroid surface
$S_b$	body boundary
$S_f$	free-surface boundary
$S_b'$	singular surface inside body
$S_f'$	singular surface above free surface

$t$	time
$\vec{V}$	velocity of body surface
$V(t)$	velocity of disturbance
$\vec{x}$	field point
$\vec{x}_f$	position vector of free surface = $(x_f, y_f, z_f)$
$\vec{x}_b$	point on body
$\vec{x}_s$	singular point of fundamental solution
$\alpha$	desingularization exponent
$\beta$	startup inverse time constant
$\lambda$	wave length of 2-D linear wave
$\eta$	wave elevation
$\sigma(t)$	strength of source-sink disturbance
$\sigma_o$	steady value of $\sigma(t)$
$\sigma_f$	strength of source distribution above free surface
$\sigma_b$	strength of source distribution inside body
$\phi$	velocity potential
$\Omega$	fluid domain

## 2 Introduction

Since Longuet-Higgins and Cokelet<sup>1</sup> first developed the mixed Eulerian-Lagrangian method for two-dimensional surface waves on water, variations of this method have been used for a variety of nonlinear free surface problems in two dimensions (Baker,<sup>2</sup> Vinje and Brevig,<sup>3</sup> etc). The methods require at each time step: 1) solve a boundary value problem in an Eulerian frame and 2) update the free surface points (which construct the free surface) by integrating the nonlinear kinematic and dynamic free surface boundary conditions with respect to time. More recently, the method has been used for three-dimensional nonlinear wave problems. Dommermuth and Yue<sup>4</sup> used this method to solve several axisymmetric problems. Extensions to fully three-dimensional nonlinear unsteady waves are given in Dommermuth and Yue<sup>5</sup> using a spectral expansion procedure that is limited to periodic problems without bodies. Jensen, Mi and Söding<sup>6</sup> solved the steady nonlinear ship wave problem by using a simple source distribution above the free surface. Cao, Schultz and Beck<sup>7</sup> used the time marching procedure for a preliminary study of the three-dimensional nonlinear wave pattern caused by a simple disturbance (a source-sink pair) moving under the free surface.

To make the time marching procedure practical, it is important to have an effective solution method for the bound-



ary value problem since it requires most of the computation time. A boundary integral method is powerful because it reduces the computational domain by one dimension. In conventional boundary integral formulations, singularities of the fundamental solution are placed on the domain boundary. When singularities of the fundamental solution are placed away from the boundary and outside the domain of the problem, a desingularized boundary integral equation is obtained.

The first use of a desingularized method is the classical work by Von Kármán<sup>8</sup> for the flow about axisymmetric bodies using an axial source distribution. The strength of the source distribution is determined by the kinematic boundary condition on the body surface. Kupradze<sup>9</sup> proposes locating the boundary nodes on an auxiliary boundary outside the problem domain. Heise<sup>10</sup> studies some numerical properties of integral equations in which the singular points are on an auxiliary boundary outside the solution domain for plane elastostatic problems. Han and Olson<sup>11</sup> and Johnston and Fairweather<sup>12</sup> use an adaptive method in which the singularities are located outside the domain and allowed to move as part of the solution process. This adaptive method requires considerably fewer singularities than the number of boundary nodes, but it results in a system of nonlinear algebraic equations for both the strength and the location of the singularities. For unsteady nonlinear waves, Schultz and Hong<sup>13</sup> use the desingularization technique in two dimensions. McIver and Peregrine<sup>14,15</sup> show that a two-dimensional overturning wave can be well modeled by only a few singularities outside the flow domain with desingularization. Webster<sup>16</sup> uses a triangular mesh of a simple source distribution inside the surface of arbitrary, three-dimensional smooth bodies and improves the accuracy of solution. Cao, Schultz and Beck<sup>7,17</sup> compute the unsteady waves caused by a simple source-sink pair using a source distribution above the free surface as in the steady nonlinear computations of Jensen, Mi and Söding<sup>6</sup>.

In the following sections, we describe the problem formulation in section 3 and a more detailed discussion on the desingularized boundary integral method in section 4. Finally we present the results of the computations for the waves caused by a simple disturbance moving below a free surface with forward speed and the results for a fully submerged spheroid moving below a free surface.

### 3 Problem Formulation

For an irrotational, incompressible flow in an ideal fluid, the Laplace equation is the governing equation for the velocity potential  $\phi$ :

$$\Delta\phi = 0 \quad (\text{in } \Omega). \quad (1)$$

The boundary conditions are:

$$\frac{D\phi}{Dt} = -z_f + \frac{1}{2} \nabla\phi \cdot \nabla\phi \quad (\text{on } S_f), \quad (2)$$

$$\frac{D\vec{x}_f}{Dt} = \nabla\phi \quad (\text{on } S_f), \quad (3)$$

$$\frac{\partial\phi}{\partial n} = \vec{V} \cdot \vec{n} \quad (\text{on } S_b), \quad (4)$$

$$\nabla\phi \rightarrow 0 \quad (\text{as } \vec{x} \rightarrow \infty), \quad (5)$$

where  $\Omega$  is the fluid domain. Equations (2) and (3) are the dynamic and kinematic conditions on the free surface  $S_f$  in Lagrangian form. Here,  $\vec{x}_f = (x_f, y_f, z_f)$  is the position vector of a fluid particle on the free surface,  $\frac{D}{Dt}$  is the substantial derivative following the fluid particle,  $\vec{n}$  is the unit normal vector of the body surface pointing into the fluid.  $\frac{\partial}{\partial n}$  is the normal derivative on  $S_b$ , and  $\vec{V}$  is the velocity of the body surface, which we assume is given. The quantities are nondimensionalized by setting the gravitational acceleration, the fluid density and an appropriate length scale equal to unity.

For the unsteady problem, initial conditions are required. Here, we study the flows generated by disturbances starting from rest. Therefore, at  $t = 0$ , we require that  $\phi \equiv 0$  and the free surface elevation  $\eta \equiv 0$ . The coordinate system is shown in Fig. 1.

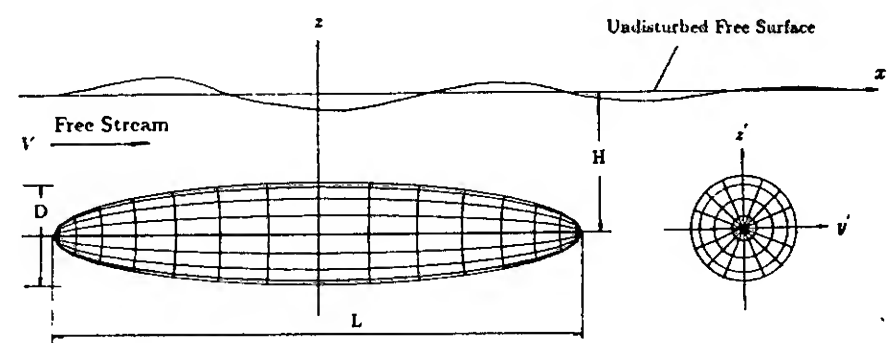


Fig. 1 Problem definition and coordinate system

### 4 Solution Procedure

The initial boundary value problem (1-5) and the associated initial conditions are solved by the mixed Eulerian-Lagrangian method. In this method, the following boundary value problem with a Dirichlet condition on the free surface and a Neumann condition on the body surface is solved in the Eulerian frame at each time step:

$$\Delta\phi = 0 \quad (\text{in } \Omega), \quad (6)$$

$$\phi = \phi_o \quad (\text{on } S_f), \quad (7)$$

$$\frac{\partial\phi}{\partial n} = \vec{V} \cdot \vec{n} \quad (\text{on } S_b), \quad (8)$$

$$\nabla\phi \rightarrow 0 \quad (\text{as } \vec{x} \rightarrow \infty), \quad (9)$$

where  $\phi_o$  and  $S_f$  are known from the previous time step. After solving the boundary value problem, the velocities of the fluid particles constructing the free surface can be calculated and the free surface conditions (2) and (3) can be integrated with respect to time following the fluid particles to update their potentials and positions which serve as the boundary conditions at the next time step. This procedure is repeated as time goes.

There are many methods to solve (6-9). The method we use is the desingularized boundary integral method. Similar to conventional boundary integral methods, it reformulates the boundary value problem into a boundary integral equation. The difference is that the desingularized method separates the integration and control surfaces, resulting in nonsingular integrals. There are two versions of the method: direct and indirect. In the direct method, the integral equation is obtained from Green's second identity evaluated on a surface (control surface) somewhere outside the problem domain and the integration surface is the problem boundary. In the indirect method, the solution is constructed by integrating a distribution of some fundamental solutions over a surface (integration surface) outside the problem domain. The integral equation for the distribution is obtained by satisfying the boundary conditions on the problem boundary (control surface).

The effectiveness and accuracy of desingularized boundary integral methods have been examined by Schultz and Hong<sup>13</sup> for two-dimensional problems, Webster<sup>16</sup> for three-dimensional steady flows, and Cao, Schultz and Beck<sup>7,17</sup> for three-dimensional unsteady waves caused by simple underwater disturbances. The following are advantages of the desingularized boundary integral method:

- More accurate solutions may be obtained by a desingularized boundary integral method for a given truncation.
- The kernels are nonsingular, so special care is not required to integrate the singular contribution. Simple numerical quadrature greatly reduces the computational effort by avoiding transcendental functions.
- Fewer nodes may be required since simple quadrature eases the restrictions of a flat panel.
- There is more flexibility since higher-order Green functions or fundamental solutions can be more easily incorporated.

The indirect desingularized boundary integral method has two more advantages when compared to the direct one:

- Integrals can be replaced by a summation if the desingularization distance is sufficiently large. This makes the computation even simpler.
- The indirect method may result in smaller errors due to truncation of an infinite boundary.

Desingularization also causes some difficulties associated with uniqueness and completeness. However, if the singular point is located away from the boundary a distance proportional to the local mesh size, the singular point will get closer to the surface as the mesh becomes finer. In the limit, the desingularized formulation becomes identical to the singular formulation.<sup>7</sup>

Because of its advantages, we use the indirect desingularized method. We construct the solution using a source distribution on a surface ( $S'_f$ ) above the free surface and a source distribution on a surface ( $S'_b$ ) inside the body surface:

$$\phi(\vec{x}) = \int \int_{S'_f} \sigma_f(\vec{x}_s) \frac{1}{|\vec{x} - \vec{x}_s|} dS' + \int \int_{S'_b} \sigma_b(\vec{x}_s) \frac{1}{|\vec{x} - \vec{x}_s|} dS'. \quad (10)$$

By applying the boundary conditions, (7) and (8), we obtain a boundary integral equation for the unknown strength of the singularities,  $\sigma_f(\vec{x}_s)$  and  $\sigma_b(\vec{x}_s)$ ,

$$\int \int_{S'_f} \sigma_f(\vec{x}_s) \frac{1}{|\vec{x}_f - \vec{x}_s|} dS' + \int \int_{S'_b} \sigma_b(\vec{x}_s) \frac{1}{|\vec{x}_f - \vec{x}_s|} dS' = \phi_o(\vec{x}_f) \quad (\text{on } S_f) \quad (11)$$

and

$$\int \int_{S'_f} \sigma_f(\vec{x}_s) \frac{\partial}{\partial n} \left( \frac{1}{|\vec{x}_b - \vec{x}_s|} \right) dS' + \int \int_{S'_b} \sigma_b(\vec{x}_s) \frac{\partial}{\partial n} \left( \frac{1}{|\vec{x}_b - \vec{x}_s|} \right) dS' = \vec{V} \cdot \vec{n} \quad (\text{on } S_b), \quad (12)$$

where  $\vec{x}_s$  is the integration point on surfaces  $S'_f$  and  $S'_b$ ,  $\vec{x}_f$  is the control point on  $S_f$ , and  $\vec{x}_b$  is the control point on  $S_b$ .

After  $\sigma_f(\vec{x}_s)$  and  $\sigma_b(\vec{x}_s)$  are determined, the fluid particle velocities on the free surface can be calculated. Then the time marching procedure integrates the free surface boundary conditions.

The pressure on the body surface is evaluated using the Bernoulli equation:

$$-p = \frac{\partial \phi}{\partial t} + \frac{1}{2} |\nabla \phi|^2 + z = \frac{d\phi}{dt} + \left( \frac{1}{2} \nabla \phi - \vec{V} \right) \cdot \nabla \phi + z, \quad (13)$$

where  $\frac{d\phi}{dt} = \left( \frac{\partial}{\partial t} + \vec{V} \cdot \nabla \right) \phi$  is the substantial derivative of the potential at fixed points on the body surface. The second form is more useful when following points fixed on the body moving with velocity  $\vec{V}$ .

The forces and the moments on the body are calculated by integrating the pressure over the body surface:

$$\vec{F} = \int \int_{S_b} -p \vec{n} ds, \quad (14)$$

and

$$\vec{M} = \int \int_{S_b} -p (\vec{r} \times \vec{n}) ds. \quad (15)$$

where  $\vec{r}$  is the position vector of the body surface point to a reference point (usually the center of the body).

## 5 Numerical Implementation

In the results presented in this paper, the submerged disturbance (either a simple source-sink pair or a spheroid) moves in the  $-x$  direction smoothly starting from rest to a final speed. The strength of the source-sink pair is also smoothly increased from zero to a final value.

The free surface conditions (2) and (3) are in the fixed coordinate system. This has an advantage since no spatial derivatives are required on the free surface which helps reduce numerical reflection from the truncated boundary.

For large time simulations, the computational window moves with the disturbance. At certain time steps, some fluid particles are ignored downstream and new particles with zero values of potential and elevation are added upstream. The initial free surface grid (at  $t = 0$ ) is equally spaced in the  $x$  direction and the spacing is increased algebraically in the  $y$  direction. The moving computational window makes it difficult to have a non-uniform grid in the  $x$  direction with finer spacing near the disturbance.

Collocation is used to satisfy the boundary conditions on the surface grid. The solutions are constructed by replacing the integrals over surfaces  $S_f'$  and  $S_b'$  in (10) by isolated sources on the surfaces. The sources are placed approximately perpendicular from the node points on the boundaries at a distance  $L_d$  determined by

$$L_d = l_d(D_m)^\alpha \quad (16)$$

where  $l_d$  is a parameter that reflects how far the integral equation is desingularized,  $D_m$  is the nondimensional local mesh size (we choose  $D_m$  as the square root of the average of the areas of the four elements around the node point) and  $\alpha$  is a parameter associated with the convergence of the mesh refinement. An appropriate  $\alpha$  lies between 0 and 1 to ensure the convergence of the mesh refinement and the uniqueness and completeness properties of the solution of the integral equation. We have examined the influence of  $l_d$  for two problems: 1) a simple potential problem in which a dipole is below a  $\phi = 0$  infinite flat plane and 2) a preliminary study of the nonlinear waves by a simple source-sink disturbance. It was found that good solutions could be obtained for  $1 < l_d < 3$  and the solutions are not sensitive to the variation of  $l_d$  in this region. More detailed discussion on the selection of  $\alpha$  and  $l_d$  can be found in Cao, Schultz and Beck<sup>7</sup>. We found that  $l_d = 1$  is "optimal" in consideration of the condition of the resulting algebraic system. This value is therefore used in the present computations for the free surface desingularization.

For the example with the submerged body, the mesh size on the free surface is usually larger than that on the body by about 10 times and the differences among the influence matrix coefficients are large, so that the resulting system for  $\sigma_f$  and  $\sigma_b$  is likely to be poorly conditioned. To avoid this, we split the system into two, one for  $\sigma_f$  and the other for  $\sigma_b$  which are alternately solved using LU decomposition for each subsystem. Each set of equations is much better behaved and more accurate solutions can be expected. Another advantage of splitting is that the coefficient matrix for  $\sigma_b$  does not change with time and needs only to be inverted once for the entire time simulation. The matrix for  $\sigma_f$  does not change during the iteration between the body and the free surface and only needs to be inverted once for the current instant of time. Of course, the matrix for  $\sigma_f$  changes at next instant of time. In contrast, the source-sink pair disturbance has fewer unknowns and can be solved very efficiently with a GMRES minimization procedure.<sup>7</sup>

The pressure on the body is evaluated at the node points. The substantial derivative of the potential  $\frac{d\phi}{dt}$  in (13) is calculated using a four-point forward difference scheme. A fourth-order Runge-Kutta-Fehlberg method is used in the nonlinear

free surface integration. An initial time increment is set, but is modified by the Runge-Kutta-Fehlberg subroutine where appropriate.

## 6 Results

### 6.1 Numerical aspects

In the two examples presented in this section, the disturbance velocity is given by  $V(t) = F_r(1 - e^{-\beta t})$  in the  $-x$  direction, where  $F_r$  is the Froude number. For the source-sink disturbance, the strength of the source and sink is given by  $\sigma(t) = \sigma_0(1 - e^{-\beta t})$ . The problems are assumed to possess symmetry about the  $xz$  plane.

The free surface is discretized using  $N_x^f$  nodes and  $N_y^f$  nodes in the  $x$  and  $y$  directions, respectively, to form  $N^f = N_x^f \times N_y^f$  free surface nodes. For the body problem, the spheroid used by Doctors and Beck<sup>18</sup> is chosen. The diameter-to-length ratio  $D/L$  is 0.2. The basic grid on the surface is shown in Fig. 1. The grid lines are spaced uniformly in the circumferential direction. The grid lines have a cosine spacing in the longitudinal direction. The body has a grid with  $N_x^b$  elements in  $x$  direction and  $N_\theta^b$  elements in the circumferential direction, resulting in  $N^b = (N_x^b - 1) \times (N_\theta^b + 1) + 2$  body nodes including the two end points. To improve the computational far-field behavior, we add negative images of the disturbance singularities.<sup>7</sup>

The pressure is integrated over the body in (14) and (15) using Simpson's rule first in the circumferential direction and then the longitudinal direction. The usual hydrodynamic coefficients ( $C_D$ ,  $C_L$  and  $C_M$ ) are obtained by multiplying  $\vec{F} \cdot \vec{i}$ ,  $\vec{F} \cdot \vec{k}$  and  $\vec{M} \cdot \vec{j}$  by  $2/(SF_r^2)$ , where  $S$  is the area of the spheroid surface. The pressure coefficient,  $C_p$ , is defined as  $2p/F_r^2$ .

We require the ratio of the element size in  $x$  direction to the wave length to be less than 1/10 to resolve the waves. The nondimensional wave length  $\lambda$  is estimated by  $\lambda = 2\pi F_r^2$  using two-dimensional linear theory.

### 6.2 Waves generated by a source-sink pair moving below a free surface

In this example, the length scale is chosen to make the depth of the submerged disturbance unity. The distance between the source and sink is chosen to be 0.1. The Froude number based on depth is unity. The midpoint between the source and sink is initially located at point (5, 0, -1). The grid on  $S_f$  at  $t = 0$  has  $41 \times 16$  node points within  $0 \leq x \leq 20$  and  $0 \leq y \leq 7.5$ . The spacing increases by 10 percent in the  $y$  direction. The initial time increment in the time marching is 0.2.

The potential  $\phi$  is expressed as a sum of 1) the source-sink disturbance pair at the distance  $h$  below the undisturbed free surface, 2) the image disturbance above the undisturbed free surface, and 3) a sum of  $N^f$  sources of unknown strength in an array a distance  $L_d$  above the disturbed free surface using (16).

The method is first applied to the waves generated by a sufficiently small disturbance such that linear wave theory is a good approximation. The results of the present method using fully nonlinear free surface conditions are compared to an "exact" solution computed from a time-dependent Green function for a Kelvin wave source that satisfies the linearized free surface condition.<sup>19</sup> Fig. 2 shows the comparison of the wave elevation along the symmetry plane at  $t = 10$  computed by the present method to that computed by the linear calculation for a weak disturbance ( $\sigma_0 = 0.05$ ). The nonlinear and linear results agree very well. Independent compu-

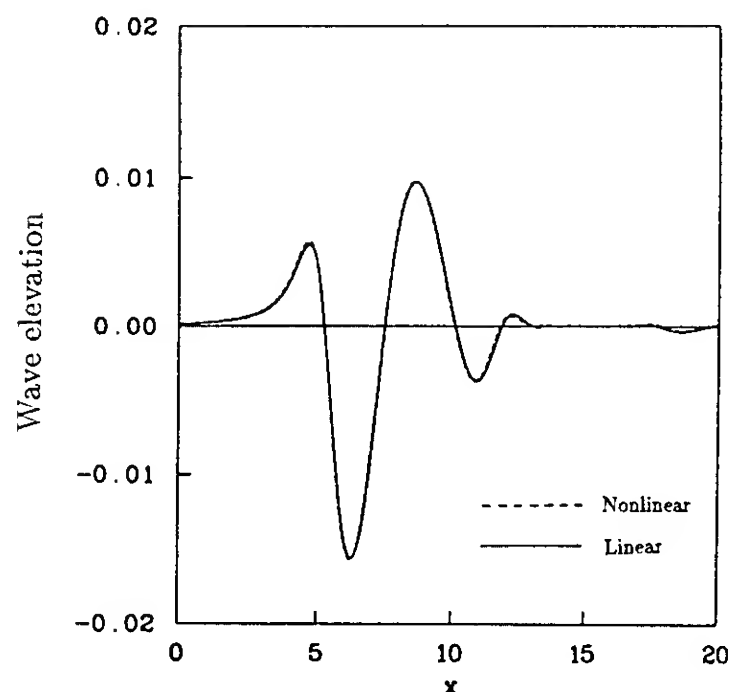


Fig. 2 Wave profiles along  $y = 0$  (weak disturbance)

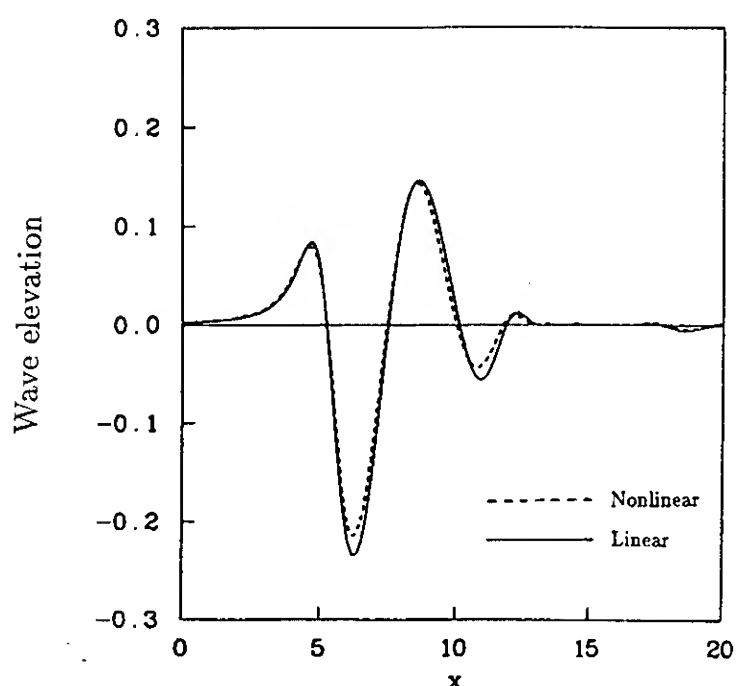


Fig. 3 Wave profiles along  $y = 0$  (strong disturbance)

tations using: a) a smaller computational domain (with the same mesh spacing within  $0 \leq x \leq 15$  and  $0 \leq y \leq 7.5$ ), b) finer mesh grids ( $81 \times 16$  and  $41 \times 31$  with the same computational domain), and c) doubling the time increment, result in negligible difference for the nonlinear calculation. This indicates that even for the small disturbance example studied here, the differences in Fig. 2 are primarily due to nonlinear

effects. Fig. 3 shows the results for a stronger disturbance ( $\sigma_0 = 0.75$ ), showing the larger nonlinear effects of the free surface conditions, especially at the troughs.

### 6.3 Waves generated by a spheroid moving below a free surface

In this example, the length scale is chosen to make the length of the spheroid  $L$  unity. The center of the spheroid is initially located at  $(2, 0, -h)$ , again with a moving computational window. On the free surface, we use  $61 \times 16$  nodes within  $0 \leq x \leq 7.5$  and  $0 \leq y \leq 1.875$ . The spacing in the  $y$  direction increases by 10 percent for each row of nodes further from the centerline. For comparisons to the results presented in Doctors and Beck,<sup>18</sup> we use the same submergence depths of the spheroid ( $h/L = 0.16$  and  $0.245$ ).

The potential  $\phi$  is expressed as 1) a sum of  $N^b$  sources of unknown strength inside the body, 2) the image of 1) above the undisturbed free surface, and 3) a sum of  $N^f$  sources of unknown strength above the disturbed free surface. The desingularization distances of the sources above  $S_f$  are given by (16). To represent the body, the singularities (except at the bow and stern) were distributed on a spheroid of smaller minor axis inside the body. After some preliminary calculations, the ratio of the minor axes of the two spheroids was fixed at 0.3 in our calculations.

Fig. 4 shows a three-dimensional view and contour lines of the wave pattern caused by the spheroid for  $h/L = 0.245$  and  $F_r = 0.6$  at  $t = 25$ . A smooth startup ( $\beta = 2$ ) and  $N_x^b = 2N_\theta^b = 16$  are used. We compare the waves produced by the spheroid and those made by the relevant simple source-sink pair disturbance in Fig. 4 and Fig. 5. The strength of the pair and the distance between the source and sink are determined to give a Rankine oval having the same length and midsectional area as the spheroid moving in an infinite fluid. The comparison becomes meaningless if the disturbance is too close to the free surface because the simple source-sink no longer represents the body well. The same depth of submergence, location of the center and motion of the disturbance as those for the spheroid are used for a direct comparison. Comparison of Fig. 4 and Fig. 5 shows that the wave patterns of the spheroid and the relevant source-sink are very similar except that the spheroid generates steeper waves near the stern.

Fig. 6 shows the drag, lift and moment acting on the spheroid as a function of time. As seen, the solution is close to the steady state after the body has moved 10 to 15 body lengths. Fig. 7 shows an influence of the two different startups of the body ( $\beta = 2$  and  $\infty$ ) on the hydrodynamic forces. Although both eventually merge to the same values, the body experiences very different forces during the transition. We notice that the body experiences a negative drag for a short time soon after an impulsive startup.

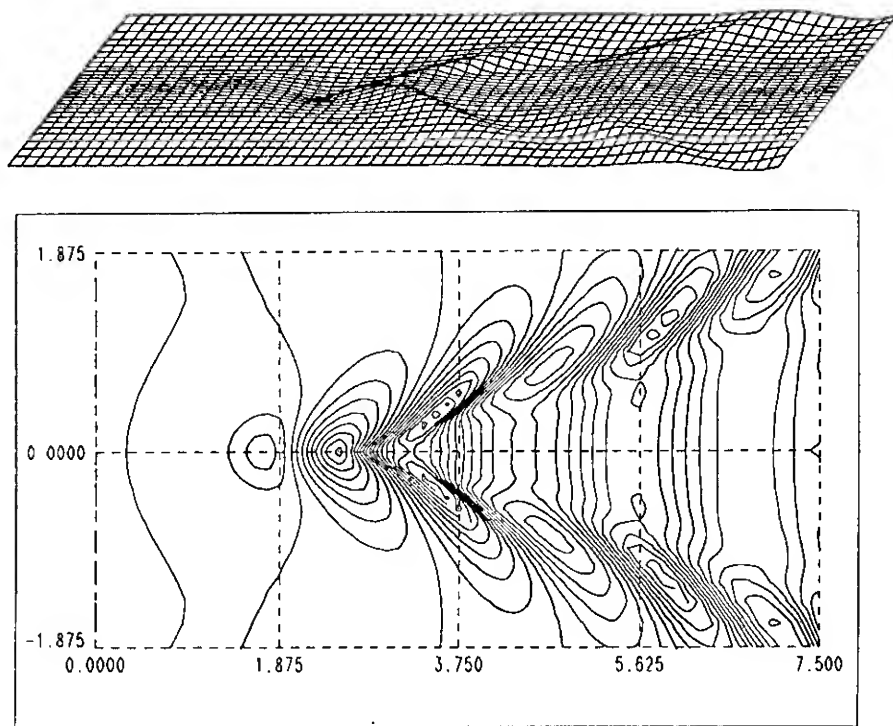


Fig. 4 Wave pattern (by spheroid)  
(elevation contours are 0.02 apart)

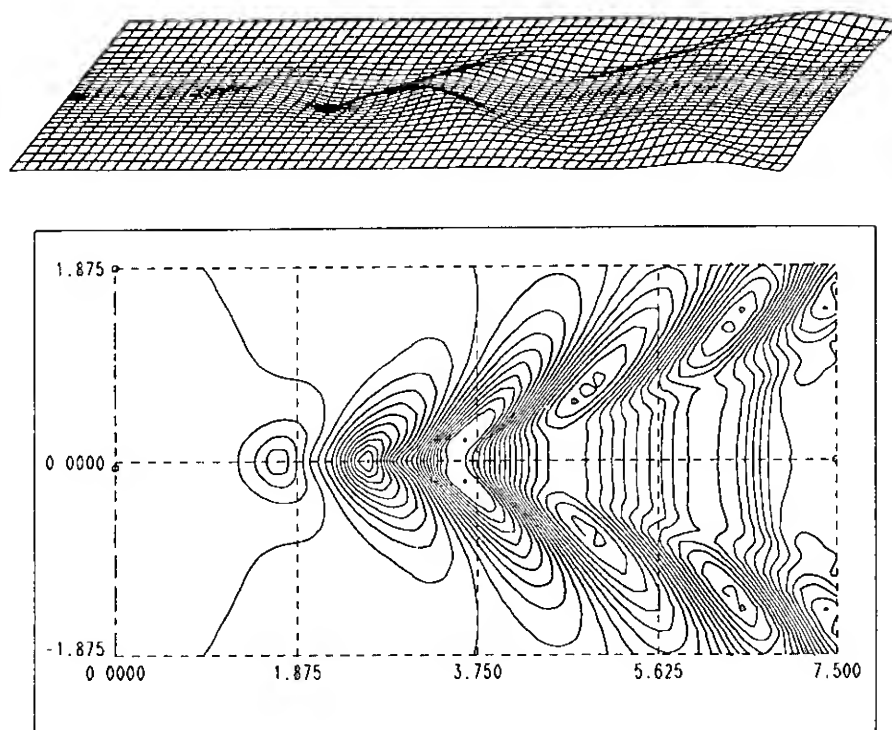


Fig. 5 Wave pattern (by source-sink pair)  
(elevation contours are 0.02 apart)

Fig. 8 compares the pressure on the spheroid using the present method and the Neumann-Kelvin calculation at  $t = 25$  for the same conditions as those for Fig. 4. The comparison is made for the pressure along the body centerlines of the top, bottom and side. In the Neumann-Kelvin calculation, the body surface is divided into flat panels with distributions of constant source strength. The strengths are determined by satisfying the body boundary condition at the centers of the panels. The pressure is calculated at the center points. The pressure elsewhere is obtained by interpolation. The differences between the linear and the nonlinear results are noticeable.

Fig. 9 shows the convergence of the drag, lift and moment on the body as a function of node number  $N^b$  using  $N_x^b = 2N_\theta^b = 8, 12, 16$  and 20. For all these cases, the free surface grid ( $61 \times 16$ ) adequately resolves the waves.

The comparison of the hydrodynamic coefficients to linear theories at different Froude numbers is shown in Fig. 10. Our results for  $h/L = 0.245$  (solid triangles) compare well with linear calculations. Our computations used a finer free surface grid ( $71 \times 16$ ) for the smaller Froude numbers to resolve the waves. For  $h/L = 0.16$ , the body is too close to the free surface. For all attempted Froude numbers, the free surface is sucked down and touches the body surface which in turn stops the computation. The linear calculations are not affected by this because the free surface boundary conditions

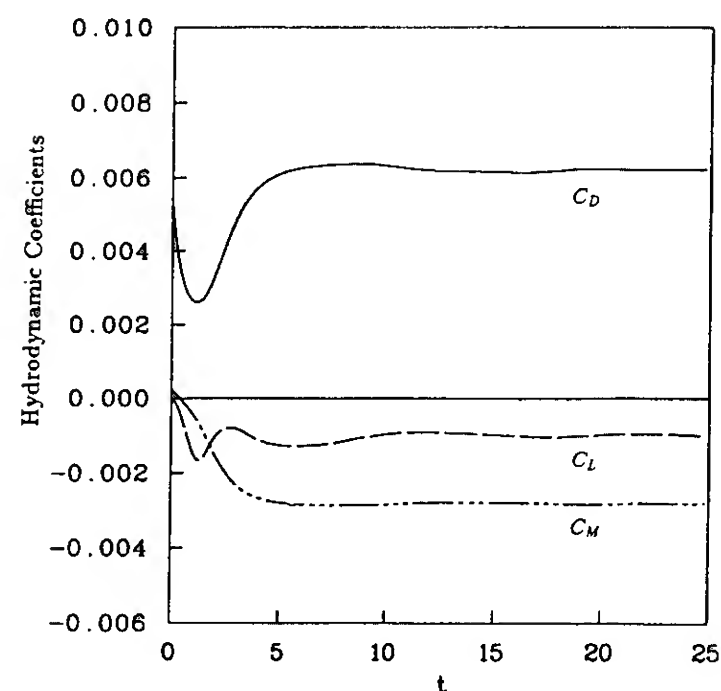


Fig. 6 Hydrodynamic coefficients vs. time

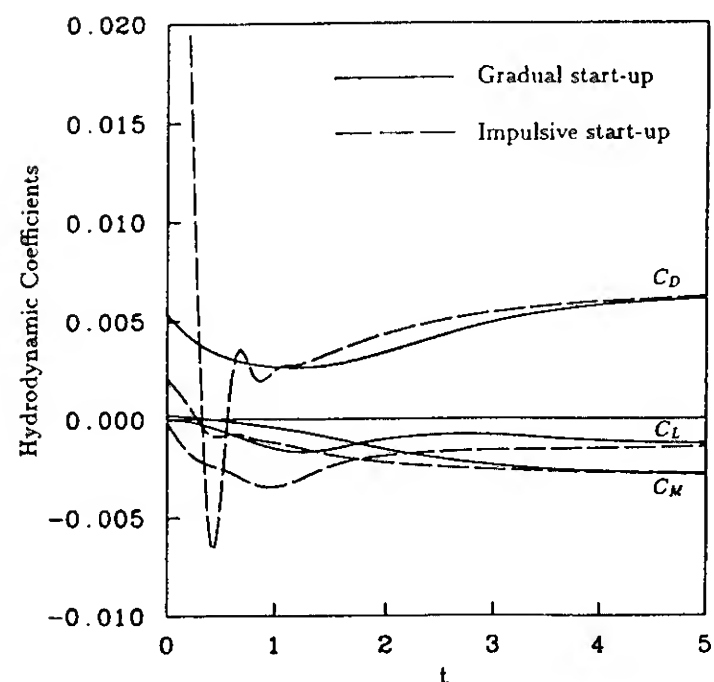


Fig. 7 Influence of the start-up of the spheroid



are satisfied at  $z = 0$ . (Note: To compare to Doctors and Beck<sup>18</sup>, the moments for this figure are taken about the vertical projection of the spheroid center onto the undisturbed free surface. The moments shown in the other figures are taken about the centroid of the spheroid).

The computations were carried out on a Cray Y-MP. The results shown in Fig. 4 took approximately 4.3 CPU seconds to solve the boundary value problem (6-9) which required

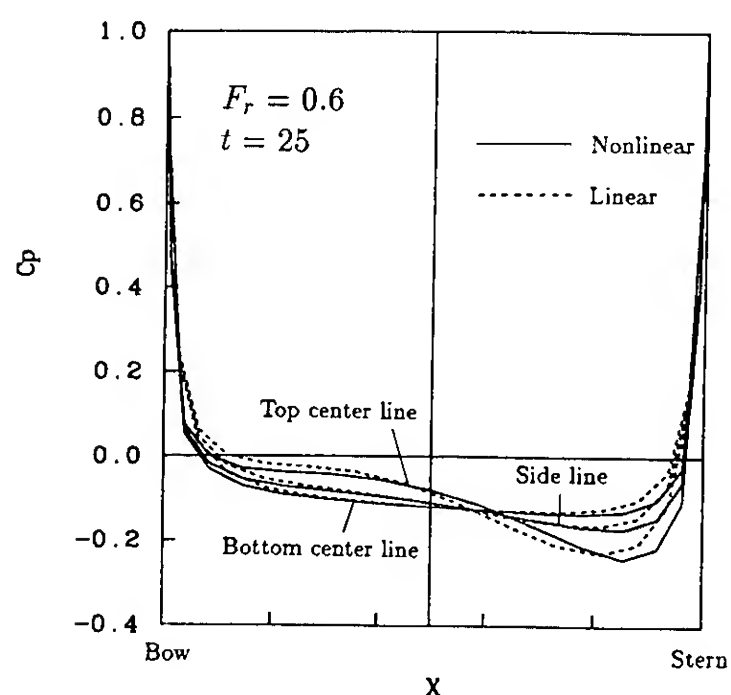


Fig. 8 Comparison of the pressure on the spheroid

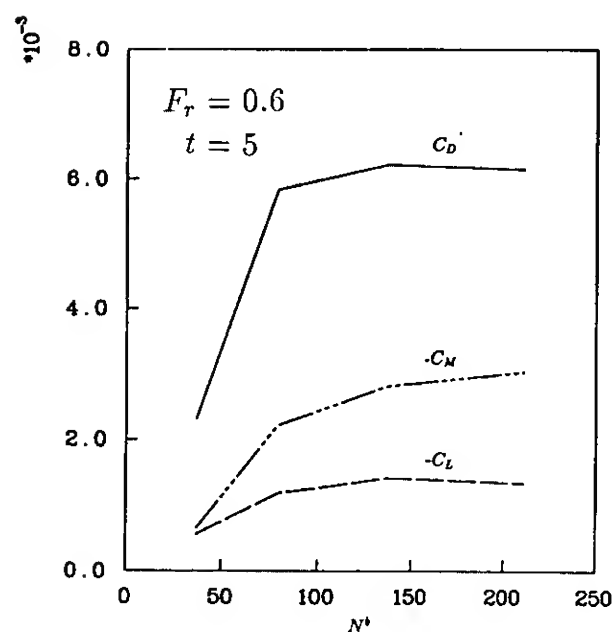


Fig. 9 Sensitivity of body mesh

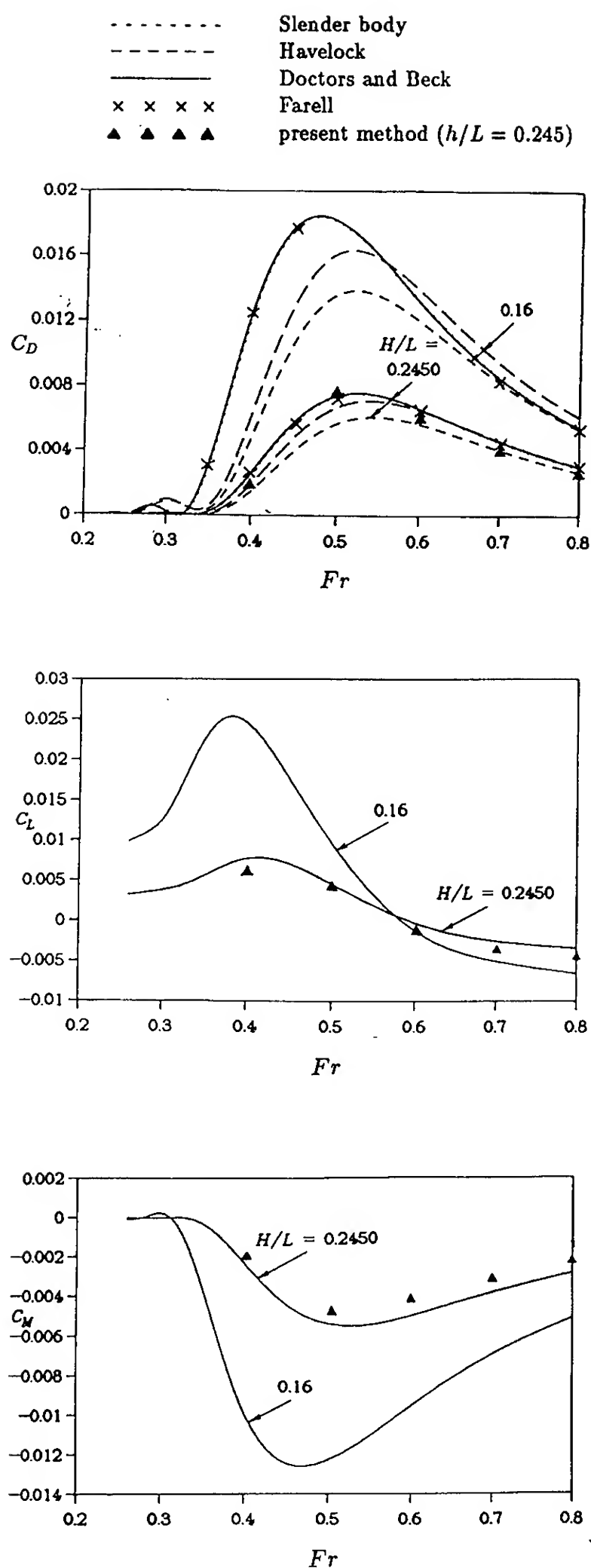


Fig. 10 Comparison of hydrodynamic coefficients (modified from Doctors & Beck)



solving each subsystem approximately 5 times. About 10 percent of this time was required for matrix setup. The CPU for the entire time simulation was 45 minutes. The computations for the simple disturbance in Fig. 5 took approximately 3.9 CPU seconds to solve (6-9) and 40 minutes for the entire time simulation. The difference in the CPU time for the two computations is small because the splitting procedure for the body problem only requires the additional evaluation of multiple right-hand sides.

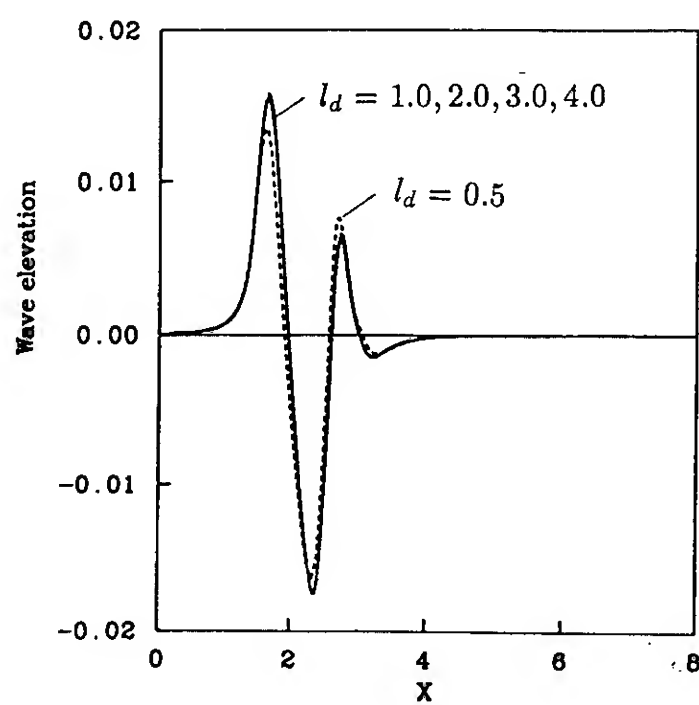


Fig. 11 Effect of desingularization factor  $l_d$

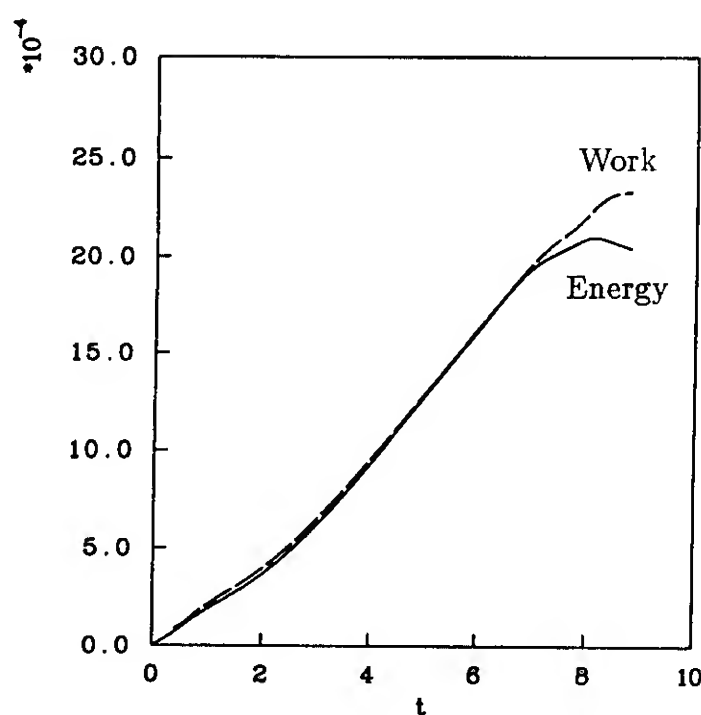


Fig. 12 Balance of wave energy and work done by spheroid

A faster iterative matrix solver can be used effectively in the simple disturbance example.<sup>7</sup> About one-fifth of the CPU time was required using the General Minimal Residual Algorithm (GMRES) as compared to using LU decomposition. Although GMRES could be used for the spheroid example, it would require special preconditioning. We tried solving the entire system for the spheroid example using both LU decomposition and GMRES without preconditioning. The LU algorithm gave inaccurate solutions while GMRES did not converge.

Fig. 11 shows the effect on the wave computations of five different values of desingularization ( $l_d = 0.5, 1.0, 2.0, 3.0$  and  $4.0$ ). The results are not significantly affected except for  $l_d = 0.5$ , which is too small for the integration by the summation (or equivalently one point Gauss quadrature).

We also performed an energy conservation check for a fixed control volume bounded by the free surface, the body surface, a horizontal bottom and four vertical surfaces representing the truncated far-field boundaries. The body starts to move from rest at the center of the control volume. The energy of the fluid in the control volume and the work done by the body are shown in Fig. 12. The energy and the work balance each other well for  $t < 6$  before the waves and the body reach the truncated boundary. Since the energy flux is neglected, agreement is not to be expected after the body or the waves reach the boundary.

## 7 Conclusions

Desingularization performs well for fully nonlinear free surface problems without surface piercing bodies. Desingularization is not dispersive nor dissipative. Similar to those methods requiring free surface discretization, our method favors high Froude numbers since fewer nodes are required to resolve the waves. Iteration between the free surface and the body surface conditions is required. The waves produced by the spheroid and the relevant source-sink disturbance are similar if they are sufficiently submerged. This indicates that a simple disturbance (with a much simpler iterative procedure and fewer unknowns) can be used if the surface waves are the main interest.

## Acknowledgment

This work is supported under the Program in Ship Hydrodynamics at The University of Michigan, funded by The University Research Initiative of the Office of Naval Research, Contract Number N000184-86-K-0684. Computations were made in part using a CRAY Grant at the University Research and Development Program of the San Diego Supercomputer Center. We acknowledge A. Magee for the linear calculation of pressure shown in Fig. 8.

## References

1. Longuet-Higgins M.S., and Cokelet, C.D., "The Deformation of Steep Surface Waves on Water: I. A Numerical Method of Computation," *Proc. R. Soc. London*, **A350**, 1-26 (1976).

2. Baker, G.R., Meiron, D.I., and Orszag, S.A., "Generalized Vortex Methods for Free Surface Flow Problems," *J. Fluid Mech.*, **123**, 477-501 (1982).
3. Vinje, T., and Brevig, P., "Nonlinear Ship Motions," *Proc. of 3rd Int. Conf. on Numerical Ship Hydrodynamics*, Paris (1981).
4. Dommermuth, D.G., and Yue, D.K.P., "Numerical Simulations of Nonlinear Axisymmetric Flows with a Free Surface," *J. Fluid Mech.*, **178**, 195-219 (1987).
5. Dommermuth, D.G., and Yue, D.K.P., "The Nonlinear Three-dimensional Waves Generated by a Moving Surface Disturbance," *Proc. of 17th Symposium of Naval Hydrodynamics*, The Hague (1988).
6. Jensen, G., Mi, Z.X., and Söding, H., "Rankine Source Methods for Numerical Solutions of the Steady Wave Resistance Problem," *Proc. of 16th Symposium on Naval Hydrodynamics*, University of California, Berkeley (1986).
7. Cao, Y., Schultz, W.W., and Beck, R. F., "Three-Dimensional Desingularized Boundary Integral Methods for Potential Problems," to appear in *Int. J. Num. Meth. Fluids* (1990).
8. Von Kármán, T., "Calculation of Pressure Distribution on Airship Hulls," NACA Technical Memorandum No. 574 (1930).
9. Kupradze, V., "On the Approximate Solution of Problems in Mathematical Physics," *Russ. Math. Surveys*, **22**, 59-107 (1967).
10. Heise, U., "Numerical Properties of Integral Equations in Which the Given Boundary Values and the Solutions Are Defined on Different Curves," *Comput. Struct.*, **8**, 199-205 (1978).
11. Han, P.S., and Olson, M.D., "An Adaptive Boundary Element Method," *Inter. J. Num. Meth. in Engin.*, **24**, 1187-1202 (1987).
12. Johnston, R.L., and Fairweather, G., "The Method of Fundamental Solutions for Problems in Potential Flow," *Appl. Math. Modeling*, **8**, 265-270 (1984).
13. Schultz, W.W., and Hong, S.W., "Solution of Potential Problems Using an Overdetermined Complex Boundary Integral Method," *J. Comp. Phys.*, **84**, 414-440 (1989).
14. McIver, P., and Peregrine, D.H., "Motion of a Free Surface and Its Representation by Singularities," Report AM-81-12, Bristol University (1981).
15. McIver, P., and Peregrine, D.H., "The Computation of Unsteady and Steady Free Surface Motions Using a Small Number of Singularities in the Exterior Flow Field," Report AM-81-13, Bristol University (1981).
16. Webster, W.C., "The Flow About Arbitrary, Three-Dimensional Smooth Bodies," *J. Ship Research*, **19**, 206-218 (1975).
17. Schultz, W.W., Cao, Y., and Beck, R.F., "Three-Dimensional Nonlinear Wave Computation by Desingularized Boundary Integral Method," *5th International Workshop on Water Waves and Floating Bodies*, Manchester (1990).
18. Doctors, L.J., and Beck, R.F., "Convergence Properties of the Neumann-Kelvin Problem for a Submerged Body," *J. Ship Research*, **31**, 227-234 (1987).
19. King, B., Beck, R.F., and Magee, A., "Seakeeping Calculations with Forward Speed Using Time-Domain Analysis," *Proc. of 17th Symposium of Naval Hydrodynamics*, The Hague (1988).

# A Numerical Solution Method for Three-Dimensional Nonlinear Free Surface Problems

C.-G. Kang, I.-Y. Gong (Ship Research Station, KIMM, Korea)

## ABSTRACT

The nonlinear hydrodynamics of a three-dimensional body beneath the free surface is solved in the time domain by a semi-Lagrangian method. The boundary value problem is solved by using the boundary integral method. The geometries of the body and the free surface are represented by the curved panels. The surfaces are discretized into the small surface elements using a bi-cubic B-spline algorithm. The boundary values of  $\phi$  and  $\frac{\partial \phi}{\partial n}$  are assumed to be bilinear on the subdivided surface. The singular part proportional to  $\frac{1}{R}$  are subtracted off and are integrated analytically in the calculation of the induced potential by singularities.

The far field flow away from the body is represented by a dipole at the origin of the coordinate system. The Runge-Kutta 4-th order algorithm is employed in the time stepping scheme. The three-dimensional form of the integral equation and the boundary conditions for the time derivative of the potential is derived. By using these formulas, the free surface shape and the equations of motion are calculated simultaneously. The free surface shape and the forces acting on a body oscillating sinusoidally with large amplitude are calculated and compared with published results. Nonlinear effects on a body near the free surface are investigated.

## 1. INTRODUCTION

The free surface effects are considered in the design of submerged bodies operating near free surface. The linearized theories were developed during many decades. Recently the nonlinear free surface problem is solved in the time domain by the semi-Lagrangian method

Longuet-Higgins and Cokelet (1976) presented a mixed Eulerian-Lagrangian method for following the time-history of space-periodic irrotational sur-

face waves. The only independent variables at the beginning of each time step were the coordinates and velocity potential of marked particles on the free surface. At each time-step an integral equation was solved for the new normal component of velocity. This method was applied to a free, steady wave of finite amplitude, and was found to give excellent agreement with calculations based on Stokes's series. It was then extended to unsteady waves, produced by initially applying an asymmetric distribution of pressure to a symmetric, progressive wave. The results showed the freely running wave then steepened and overturned.

Using a technique similar to that of Longuet-Higgins and Cokelet (1976), Faltinsen (1977) solved a nonlinear two dimensional free surface problem including a harmonically oscillating body. The body intersected the free surface and was constrained to move in the vertical direction. The numerical calculations were reduced by representing the flow far away from the body as a dipole located at the center of the body. A formula to calculate the exact force on the body was presented. It was only necessary to know the velocity potential on the positions of the free surface and the wetted body surface.

A numerical method for the time simulation of the nonlinear motions of two dimensional surface-piercing bodies of arbitrary shapes in water of finite depth was presented by Vinje & Brevig (1981). Periodicity in space was assumed. At each time step, Cauchy's integral theorem was applied to calculate the complex potential and its time derivative along the boundary. The solution was stepped forward in time by integrating the exact kinematic and dynamic free-surface boundary conditions as well as the equation of motion for the body. They solved the problem of capsizing in beam seas, caused by extreme waves.

Two-dimensional nonlinear free surface problems by a dipole (vortex and source) distribution method were solved by Baker, et al. (1982). The resulting Fredholm integral equation of the second kind was solved by iteration which reduced storage

and computing time. Applications to breaking water waves over finite-bottom topography and interacting triads of surface and interfacial waves were given.

The semi-Lagrangian method was extended to vertically axisymmetric free surface flows by Dommermuth & Yue (1986). Since they solved the finite depth problem, a far field closure was implemented by matching the linearized solution outside a radiation boundary. The intersection line between the body and free surface was treated by extending Lin's (1984) method.

The nonlinear hydrodynamics of an axisymmetric body beneath the free surface in the time domain were solved by Kang & Troesch (1988). The free surface shape and the forces acting on a sphere oscillating sinusoidally with large amplitude are calculated and compared with published results. The far field flow away from the body is represented by a dipole at the origin of the coordinate system similar to Faltinsen (1977). This is only valid until waves arrive. Waves generated by the numerical error at the truncation boundary are not observed.

In this paper, the method used for axisymmetric flows by Kang and Troesch (1988) is extended to three-dimensional free surface flows. The free surface shape and the forces acting on a three-dimensional body moving forward and oscillating sinusoidally with large amplitude are calculated and compared with published results. When the body motion is unknown, the time derivative of the potential on the body is needed for the time simulation. In two dimensions, Vinje & Brevig (1982) derived the integral equation and the boundary conditions for the time derivative of the potential and stream function. However their formulas may not be extended to three-dimensional problems. The three-dimensional form is derived in this work. By using these formulas, the free surface shape and the equations of motion are calculated simultaneously. The Runge-Kutta 4-th order algorithm is employed in the time stepping scheme (See Appendix 1).

Numerical calculations are performed for the following cases:

- (a) A body oscillating vertically near the free surface
- (b) A body oscillating horizontally near the free surface.

## 2. MATHEMATICAL FORMULATION

Consider an ideal fluid below the surface given by  $F(\underline{x}, t) = 0$ , where  $\underline{x}(x, y, z)$  is a right-handed coordinate system with  $z$  positive upwards and the

origin located at the mean free surface. The fluid is assumed to be inviscid and incompressible and the flow is assumed to be irrotational. The fluid domain is bounded with the following surfaces, the free surface,  $S_F$ , the body,  $S_B$ , and the surfaces at infinity,  $S_\infty$  (Fig. 1). The surfaces, taken as a whole, will be denoted as  $S$ . The governing equation and the boundary conditions are as follows (Longuet-Higgins & Cokelet (1976) and Dommermuth & Yue (1986)):

Laplace equation :

$$\nabla^2 \phi = 0 \quad \text{in the fluid domain} \quad (1)$$

Kinematic free surface condition :

$$\frac{D\underline{x}}{Dt} = \nabla \phi \quad \text{on} \quad F(\underline{x}, t) = 0 \quad (2)$$

Dynamic free surface condition

$$\frac{D\phi}{Dt} = -gz + \frac{1}{2} \nabla \phi \cdot \nabla \phi \quad \text{on} \quad F(\underline{x}, t) = 0 \quad (3)$$

Body boundary condition :

$$\nabla \phi \cdot \underline{n}(\underline{x}, t) = \underline{V} \cdot \underline{n} \quad \text{on} \quad B(\underline{x}, t) = 0 \quad (4)$$

Radiation condition :

$$\phi \rightarrow 0 \quad \text{as} \quad |\underline{x}| \rightarrow \infty, t < \infty \quad (5)$$

where  $\frac{D}{Dt} (= \frac{\partial}{\partial t} + \nabla \phi \cdot \nabla)$  is the substantial derivative,  $F(\underline{x}, t) = 0$  is the function representing the free surface geometry at time  $t$ ,  $\underline{V}$  includes both translational and rotational velocities, and  $B(\underline{x}, t) = 0$  is the function representing the body surface geometry at time  $t$ .

The Green function,  $G(\underline{x}; \underline{y})$ , satisfies the following equation.

$$\nabla^2 G(\underline{x}; \underline{y}) = -\delta(\underline{x} - \underline{y}) \quad (6)$$

where  $\underline{x}$  is the vector to the field point,  $\underline{y}$  is the vector to the source point, and  $\delta(\underline{x} - \underline{y})$  is the Dirac delta function. Through the application of Green's second identity in the fluid domain, the potential is given as

$$\alpha(\underline{x}, t) \phi(\underline{x}, t) = \iint_S \left[ \frac{\partial \phi}{\partial n} - \phi \frac{\partial}{\partial n} \right] G dS \quad (7)$$

where  $\alpha$  is an included solid angle at  $\underline{x}$ . In this problem,  $\alpha$  is  $2\pi$  on the surface.

The Green function that satisfies Eq. (6) is

$$G(\underline{x}, \underline{y}) = \frac{1}{R} = \frac{1}{|\underline{x} - \underline{y}|} \quad (8)$$

where  $\underline{x}$  is the position vector of a field point and  $\underline{y}$  is that of a source point.

The solution of Eq. (3) gives the potential  $\phi$  on the free surface  $F(\underline{x}, t) = 0$ . Also  $\phi_n$  on the body is known from the body boundary condition, Eq. (4). The normal and tangential velocities on the free surface are needed to solve Eq. (3). The normal velocity on the free surface is a solution of Eq. (7). Details to calculate the tangential velocity is given in the section 3. Consequently, a Fredholm integral equation of the second kind on the body and of the first kind at the free surface may be solved.

#### Far Field Condition

The far field condition is important in the nonlinear free surface problem. It can be resolved by using periodic boundary conditions if the physical problem has spatial periodicity (Longuet-Higgins & Cokelet, 1976). Faltinsen (1977) and Kang (1988) assumed that the behavior of the potential is like that of a dipole at the origin of the coordinate system.

A far field closure by matching the nonlinear computational solution to a general linear solution of transient outgoing radiated waves was used by Dommermuth & Yue (1986). This method is mathematically complete.

A numerical radiation condition was posed so as no waves reflected from the truncated surface (Yang & Liu (1989)). They found that the usual one-dimensional Sommerfeld condition gave reasonable results for an axisymmetric cylinder heaving in the still water. Also it was extended to 2-D case for the cylinder swaying in the still water.

In this work, the far field closure similar to that used by Faltinsen (1977) and Kang (1988) is posed. It is simple and it works well until waves arrive at the truncation boundary.

At the far field, the velocity potential,  $\phi$ , and the wave elevation,  $\eta$ , are small from the radiation condition, Eq. (5). For example,

$$\phi(z = \eta) = \phi(z = 0) + \eta \frac{\partial \phi}{\partial z}(z = 0) + \text{H.O.T.} \quad (9)$$

Assuming the behavior of the potential,  $\phi$ , is like that of a dipole at the origin of the coordinate system, it follows that as  $r \rightarrow \infty$

$$\begin{aligned} \phi(z = 0) &= 0 \\ \frac{\partial \phi}{\partial z}(z = 0) &\sim \frac{1}{r^3} \\ \eta &= \int_0^t \frac{\partial \phi}{\partial z}(z = 0) dt \sim \int_0^t \frac{1}{r^3} dt \end{aligned} \quad (10)$$

$$\phi(z = \eta) \sim \eta \frac{\partial \phi}{\partial z}(z = 0) \sim \frac{1}{r^6}$$

where  $r$  is  $\sqrt{x^2 + y^2}$ . This is only valid until waves arrive at the truncation boundary.

If we take a large value of  $r$ , the potential  $\phi$  on the free surface must be relatively small to the vertical velocity  $\frac{\partial \phi}{\partial z}$ . Therefore the effect of the potential at the far field can be neglected. The far field condition is approximately satisfied by including the effect of the vertical velocity  $\frac{\partial \phi}{\partial z}$  at the far field.

### 3. NUMERICAL IMPLEMENTATION

The body surface and the free surface are discretized into the small surface elements  $\Delta S_{ij}$  using a bicubic B-spline algorithm (Barsky & Greenberg (1980)). The surfaces  $\Delta S_{ij}(x, y, z)$  can be represented by the parameters,  $u$  and  $v$ . Thus

$$\begin{aligned} x_{ij}(u, v) &= \sum_{s=-2}^1 \sum_{t=-2}^1 b_s(u) V_{i+s, j+t}^x b_t(v) \\ y_{ij}(u, v) &= \sum_{s=-2}^1 \sum_{t=-2}^1 b_s(u) V_{i+s, j+t}^y b_t(v) \\ z_{ij}(u, v) &= \sum_{s=-2}^1 \sum_{t=-2}^1 b_s(u) V_{i+s, j+t}^z b_t(v) \end{aligned} \quad (11)$$

$$\text{for } 0 \leq u \leq 1 \text{ and } 0 \leq v \leq 1$$

where  $b_s(u)$  and  $b_t(v)$  are the uniform cubic B-spline basis functions and  $V_{ij}$  are vertices (See Appendix 2). This allows the curved panels.

The end condition should be imposed to get a complete B-spline approximation. There are several methods to impose end conditions according to the geometrical characteristics (Barsky(1982)). The derivative of B-spline interpolation at the end is set to get the tangent of the given geometry if the tangent is known. If the tangent is not known, the derivative at the end is set to be the slope between two vertices at the end obtained by using B-spline algorithm.

The boundary values of  $\phi$  and  $\frac{\partial \phi}{\partial n}$  are assumed to be bilinear on the subdivided surface  $\Delta S_{ij}$  as shown below.

$$\begin{aligned} \phi &= a_0 + a_1 u + a_2 v + a_3 uv \\ \frac{\partial \phi}{\partial n} &= b_0 + b_1 u + b_2 v + b_3 uv \end{aligned} \quad (12)$$

for  $0 \leq u \leq 1$  and  $0 \leq v \leq 1$

To evaluate the integrals over the segments the two point Gaussian Quadrature formula (Ferziger

(1981), Abramowitz & Stegun (1964)) is used when the field point is not a corner of the pannel. In Eq. (7),  $G_n$  is not singular but  $G$  has  $(\frac{1}{R})$  type singularity in the transformed  $u - v$  domain as the field point approaches the source point. The singularity is integrable and can be integrated by numerical quadrature. But since an accurate integration of the singularity requires a higher order quadrature formula, the method following Ferziger (1981) and Dommermuth & Yue (1986) can be used. The integral can be factored into the sum of the  $(\frac{1}{R})$  type singular part which is integrable analytically and the non-singular part which requires numerical quadrature (Ferziger(1981)).

#### Removal of $(\frac{1}{R})$ type singularity

In Eq. (7),  $G$  has  $(\frac{1}{R})$  type singularity as the field point approaches the source point. The  $(\frac{1}{R})$  type singularity is integrable in the surface integration.

$$I = \iint_{\Delta S_{ij}} \phi_n \frac{1}{R} dS \quad (13)$$

First, consider the induced potential at  $(f_{00}, g_{00}, h_{00})$ , which is one of the corners of panel, by the source panel  $\Delta S_{ij}$ . Eq. (11) can alternatively be represented by the following equations :

$$\begin{aligned} x' &= \sum_{i=0}^3 \sum_{j=0}^3 f_{ij} u^i v^j \\ y' &= \sum_{i=0}^3 \sum_{j=0}^3 g_{ij} u^i v^j \\ z' &= \sum_{i=0}^3 \sum_{j=0}^3 h_{ij} u^i v^j \end{aligned} \quad (14)$$

By using Eqs.(14) and (40),  $dS$  and  $R$  can be transformed and expanded into Taylor's series about  $u = 0, v = 0$  as follows :

$$\begin{aligned} dS &= |J| du dv \\ &= \sqrt{EG - F^2} du dv \\ &= \left\{ \left[ \left( \frac{\partial x'}{\partial u} \right)^2 + \left( \frac{\partial y'}{\partial u} \right)^2 + \left( \frac{\partial z'}{\partial u} \right)^2 \right] \right. \\ &\quad \times \left[ \left( \frac{\partial x'}{\partial v} \right)^2 + \left( \frac{\partial y'}{\partial v} \right)^2 + \left( \frac{\partial z'}{\partial v} \right)^2 \right] \\ &\quad \left. - \left( \frac{\partial x'}{\partial u} \frac{\partial x'}{\partial v} + \frac{\partial y'}{\partial u} \frac{\partial y'}{\partial v} + \frac{\partial z'}{\partial u} \frac{\partial z'}{\partial v} \right)^2 \right\}^{1/2} du dv \\ &= [J_0 + H.O.T.] du dv \end{aligned} \quad (15)$$

where

$$J_0 = \left\{ (f_{10}g_{01} - f_{01}g_{10})^2 + (g_{10}h_{01} - g_{01}h_{10})^2 \right.$$

$$\left. + (h_{10}f_{01} - h_{01}f_{10})^2 \right\}^{1/2} \quad (16)$$

and

$$\begin{aligned} R &= \left\{ (x - x')^2 + (y - y')^2 + (z - z')^2 \right\}^{1/2} \\ &= \left\{ (-f_{10}u - f_{01}v \dots)^2 + (-g_{10}u - g_{01}v \dots)^2 \right. \\ &\quad \left. + (-h_{10}u - h_{01}v \dots)^2 \right\}^{1/2} \\ &= \sqrt{Au^2 + Buv + Cv^2} + H.O.T. \end{aligned} \quad (17)$$

where

$$\begin{aligned} A &= f_{10}^2 + g_{10}^2 + h_{10}^2 \\ B &= 2(f_{10}f_{01} + g_{10}g_{01} + h_{10}h_{01}) \\ C &= f_{01}^2 + g_{01}^2 + h_{01}^2 \end{aligned} \quad (18)$$

The integral,  $I$ , can be divided into two parts. One of them includes singular part in the integrand and the other does not include singular part. After some manipulations of Eq. (13) by using Eqs. (14)-(18), the first integral  $I_1$  becomes

$$I_1 = b_0 J_0 \int_0^1 \int_0^1 \frac{du dv}{(Au^2 + Buv + Cv^2)^{1/2}}. \quad (19)$$

The integral,  $I_1$ , can be evaluated in closed form as follows (Gradsteyn & Ryzhik (1980), Forbes(1989)):

$$\begin{aligned} I_1 &= b_0 J_0 \left[ \frac{1}{\sqrt{A}} \ln \left( 2A + B + 2\sqrt{A(A+B+C)} \right) \right. \\ &\quad - \frac{1}{\sqrt{A}} \ln \left( B + 2\sqrt{AC} \right) \\ &\quad + \frac{1}{\sqrt{C}} \ln \left( 2C + B + 2\sqrt{C(A+B+C)} \right) \\ &\quad \left. - \frac{1}{\sqrt{C}} \ln \left( B + 2\sqrt{AC} \right) \right] \end{aligned} \quad (20)$$

The second one can be described as follows :

$$\begin{aligned} I_2 &= \int_0^1 \int_0^1 \left[ \frac{(b_0 + b_1 u + b_2 v + b_3 uv) J}{R} \right. \\ &\quad \left. - \frac{b_0 J_0}{\sqrt{Au^2 + Buv + Cv^2}} \right] du dv \end{aligned} \quad (21)$$

The integrand of the integral,  $I_2$ , does not have the  $(\frac{1}{R})$  type singularity near  $u = 0$  and  $v = 0$ . Thus  $I_2$  can be obtained accurately even by the two point Gaussian Quadrature. Similarly, the integral (13) can be obtained at the rest corners ( $u = 0, v = 1$ ), ( $u = 1, v = 0$ ), and ( $u = 1, v = 1$ ).

To get the tangential velocity, the velocity potential  $\phi$  on the surfaces can be represented by the bicubic B-spline (See Appendix 2). Even if this representation is inconsistent with Eq. (12), it gives smooth variation of the tangential velocity on the surface.

The derivatives  $\phi_u$  and  $\phi_v$  are obtained by differentiating the potential with respect to  $u$  and



$v$  respectively. Generally, the tangential vector  $\underline{t}_u$  ( $f_u, g_u, h_u$ ) along  $u$ -axis is not perpendicular to the vector  $\underline{t}_v$  ( $f_v, g_v, h_v$ ) along  $v$ -axis. Therefore Gram-Schmidt orthogonalization is needed to get the orthogonal tangential vectors on the surface.

#### 4. CALCULATION OF THE TIME DERIVATIVE OF POTENTIAL

For the time simulation,  $\frac{\partial \phi}{\partial t}$  should be known to calculate the forces and moments acting on the body. In two dimensions Vinje & Brevig(1982) derived an integral equation and boundary condition for  $\frac{\partial \phi}{\partial t}$  by using the  $\phi$  and  $\psi$  formulation. However their results can not be extended to the three-dimensional case. Since  $\frac{\partial}{\partial n}(\frac{\partial \phi}{\partial t})$  can not be calculated by using the given motion, a boundary value problem for  $\frac{\delta \phi}{dt}$ , the time derivative of the potential in body fixed coordinates, is derived as follows:

$$\begin{aligned} \frac{\delta}{dt}(\frac{\partial \phi}{\partial n}) &= \underline{n} \cdot \frac{\delta}{dt} \nabla \phi + \nabla \phi \cdot \frac{\delta \underline{n}}{dt} \\ &= \underline{n} \cdot [\frac{\partial}{\partial t} \nabla \phi + (\underline{V} \cdot \nabla) \nabla \phi] + \nabla \phi \cdot (\underline{\omega} \times \underline{n}) \\ &= \underline{n} \cdot [\nabla \frac{\partial \phi}{\partial t} + \nabla(\underline{V} \cdot \nabla \phi) + \underline{\omega} \times \nabla \phi] + \nabla \phi \cdot (\underline{\omega} \times \underline{n}) \\ &= \frac{\partial}{\partial n}(\frac{\delta \phi}{dt}) \end{aligned} \quad (22)$$

which can be expressed as

$$\frac{\partial}{\partial n}(\frac{\delta \phi}{dt}) = \underline{n} \cdot (\frac{\partial \underline{V}_T}{\partial t} + \underline{\omega} \times \underline{r} - \underline{\omega} \times \underline{V}_T) \quad (23)$$

Following the nomenclature of Vinje & Brevig (1982), the operator  $\frac{\delta}{dt}$  is  $(\frac{\partial}{\partial t} + \underline{V} \cdot \nabla)$ ,  $\underline{V} = \underline{V}_T + \underline{\omega} \times \underline{r}$ ,  $\underline{V}_T$  is the translational velocity of the center of mass of the body,  $\underline{r}$  is the position vector to the boundary from the center of mass of the body, and  $\underline{\omega}$  is the angular velocity vector of the body. Eq. (23) is useful in that most quantities of interest are expressed in the body coordinate system rather than a fixed, inertial one.

Since  $\underline{V} \cdot \nabla \phi$  satisfies Laplace equation, the time derivative of the potential,  $\frac{\delta \phi}{dt}$ , can be calculated by using Green's theorem. The limiting behavior of  $\underline{V} \cdot \nabla \phi$  at  $r \rightarrow \infty$  can also be checked, or

$$\underline{V} \cdot \nabla \phi = O(r \frac{\phi}{r}) = O(\phi) \quad \text{as } r \rightarrow \infty \quad (24)$$

Applying Green's theorem for  $\frac{\delta \phi}{dt}$  instead of  $\phi$  in Eqs. (1), (6), and (7), the following equation can be obtained:

$$\alpha \frac{\delta \phi}{dt} = \int_S [\frac{\partial}{\partial n}(\frac{\delta \phi}{dt}) - (\frac{\delta \phi}{dt}) \frac{\partial}{\partial n}] G dS \quad (25)$$

R.H.S. of Eq. (23) may be represented as follows :

$$\underline{n} \cdot (\frac{\partial \underline{V}_T}{\partial t} + \underline{\omega} \times \underline{r} - \underline{\omega} \times \underline{V}_T) = \sum_{i=1}^6 a_i n_i \quad (26)$$

where  $\underline{n} = (n_1, n_2, n_3)$  and  $\underline{r} \times \underline{n} = (n_4, n_5, n_6)$ .

The time derivative of the potential,  $\frac{\delta \phi}{dt}$ , can be decomposed as follows:

$$\frac{\delta \phi}{dt} = \sum_{i=1}^6 a_i \frac{\delta \phi_i}{dt} + \frac{\delta \phi_7}{dt} \quad (27)$$

The auxiliary terms,  $\frac{\delta \phi_i}{dt}$  and  $\frac{\delta \phi_7}{dt}$ , are solutions of the following boundary value problems:

$$\begin{aligned} \frac{\partial}{\partial n}(\frac{\delta \phi_i}{dt}) &= n_i \quad \text{and} \quad \frac{\partial}{\partial n}(\frac{\delta \phi_7}{dt}) = 0 \\ &\text{on } B(\underline{x}, t) = 0 \end{aligned} \quad (28)$$

and

$$\begin{aligned} \frac{\delta \phi_i}{dt} &= 0 \quad \text{and} \quad \frac{\delta \phi_7}{dt} = \underline{V} \cdot \nabla \phi - \frac{1}{2} \nabla \phi \cdot \nabla \phi - gz \\ &\text{on } F(\underline{x}, t) = 0 \end{aligned} \quad (29)$$

The time derivative of the potential on the free surface,  $\frac{\delta \phi_7}{dt}$ , is calculated by using solutions of the integral equation, Eq. (7).

#### 5. THE PRESSURES AND FORCES

Once the time derivative of the potential is known, the pressures are found by applying Bernoulli's equation. Bernoulli's equation is derived for the variables relative to an inertial coordinate system. However, it is convenient for the purpose of solving the boundary value problem to use body fixed coordinates. Under these circumstances, spatial differentiation is invariant with coordinate transformation, but temporal differentiation is not. Bernoulli's equation can be expressed as

$$\begin{aligned} \frac{p}{\rho} &= -\frac{\partial \phi}{\partial t} - \frac{1}{2} \nabla \phi \cdot \nabla \phi - gz \\ &= -\frac{\delta \phi}{dt} + \underline{V} \cdot \nabla \phi - \frac{1}{2} \nabla \phi \cdot \nabla \phi - gz. \end{aligned} \quad (30)$$

The term  $\frac{\delta \phi}{dt}$  in the above equation is calculated by Eq. (27). With the pressure known, the force and moment become

$$\begin{aligned} \underline{F} &= m \underline{\dot{V}} \\ &= \int_S p \underline{n} dS - mg \underline{k} \end{aligned}$$

$$= -\rho \iint_S \underline{n} \left( \frac{\delta\phi}{dt} - \underline{V} \cdot \nabla\phi + \frac{1}{2} \nabla\phi \cdot \nabla\phi + gz \right) dS - mg \underline{k} \quad (31)$$

$$\underline{M} = \iint_S \underline{r} \times \underline{n} dS.$$

For three-dimensional bodies the force and moment are rearranged as follows :

$$\begin{aligned} \underline{F} &= \underline{F}_1 + \underline{F}_2 + (\rho g \nabla - mg) \underline{k} \\ \underline{M} &= \underline{M}_1 + \underline{M}_2 \end{aligned} \quad (32)$$

where  $\nabla$  in Eq. (32) is the displaced volume of the sphere,

$$\begin{aligned} \underline{F}_1 &= -\rho \iint_{S_B} \underline{n} \frac{\delta\phi}{dt} dS, \\ \underline{F}_2 &= -\rho \iint_{S_B} \underline{n} \left( \underline{V} \cdot \nabla\phi - \frac{1}{2} \nabla\phi \cdot \nabla\phi \right) dS, \\ \underline{M}_1 &= -\rho \iint_{S_B} \underline{r} \times \underline{n} \frac{\delta\phi}{dt} dS, \text{ and} \\ \underline{M}_2 &= -\rho \iint_{S_B} \underline{r} \times \underline{n} \left( \underline{V} \cdot \nabla\phi - \frac{1}{2} \nabla\phi \cdot \nabla\phi \right) dS. \end{aligned} \quad (33)$$

## 6. NUMERICAL CALCULATION

### Heave motion

To demonstrate the usefulness of the technique shown in the previous section, the force acting on a sphere oscillating beneath the free surface is determined. The motion of a sphere is given by  $z = -h + a \cos \omega t$  for  $t$  greater than zero. Initially the potential and wave elevation at the free surface are zero.

The number of elements on the body is 200 and that on the free surface is  $40 \times 40$ . The truncation boundary is the position from the origin of the coordinate system where waves reaches in four periods of the body motion ( $-16 \leq x/R \leq 16$ ,  $-16 \leq y/R \leq 16$ ). So, it depends on the group velocity of wave. Even spacing is used on the body and free surface. The typical time interval is approximately 0.05 period of motion for the time simulation of the sphere.

The mean depth of immersion for the center of the sphere,  $h$ , is  $h/R=2.0$ . The time history of the force acting on the oscillating sphere with a large ratio of motion amplitude,  $a$ , to radius,  $R$ , ( $a/R=0.5$ ) was calculated and is compared with the results of the axisymmetric free surface problem (Kang & Troesch (1988)) in Fig. 2. They show good agreement. In the reference[13], the calculation results

for the sphere oscillating vertically with small amplitude showed good agreement with those given by Ferrant(1987). This means the 3-D algorithm in this paper works well.

In Fig. 3, the time history of force components which consist of  $F_1$  and  $F_2$  is shown. The forces are nondimensionalized by  $\rho g K a R^3$ , where  $K$  is a wave number,  $\omega^2/g$ , and  $g$  is the gravitational constant and the time  $t$  is nondimensionalized by  $\sqrt{R/g}$ . The harmonic distributions of the total force are shown in Table 1. The second order amplitude of the force is 6.5% of the first order one. And the mean force is 1.5% of the first order. Fig. 4 shows the three dimensional wave profiles at four different times. All the wave profiles are exaggerated by factor 50 in  $z$ -direction. In the figures  $T$  is a period of the motion.

### Surge motion

The surge motion of the sphere is given by  $x = a \cos \omega t$  for  $t$  greater than zero. The mean depth of immersion for the center of the sphere is  $h/R = 2.0$ . The amplitudes of the motion is  $a/R = 0.5$ . The nondimensionalized wave number,  $KR$ , is equal to 1.0.

The time histories of the forces acting on the sphere are shown in Fig. 5-6. The harmonic distributions of the horizontal and vertical forces are given in Table 2. The three dimensional wave profiles at 4 different times are shown in Fig. 7.

In case of surge motion, the first order surge force is dominant unlike the heave motion. However nonlinear effects appear only in the vertical force. The first order vertical force is negligible, but the mean and second order vertical forces are not. The mean vertical force is important for a submerged body to keep a constant depth.

### Advancing motion

Saw-tooth instability is not observed in the computation of the oscillatory motions. But it seems to be inevitable and break down the numerical time stepping in case of advancing sphere. It may be due to short waves generated by the body. The length of short waves is less than the mesh size in this computation. The numerical error does not die out but was accumulated continuously. Eventually the numerical scheme breaks down. Thus a simple numerical filtering scheme are tried to avoid break down, but still does not work well. Fig. 8 shows the wave profile before breakdown.

All the calculations were carried out on CRAY2S and each solution time was approximately 50000 seconds.

## 7. CONCLUSION

In this paper the nonlinear hydrodynamics of a three-dimensional body beneath the free surface is solved in the time domain. The free surface shape and forces acting on a sphere oscillating sinusoidally with large amplitude are calculated and compared with published results. The far field flow away from the body is represented by a three dimensional dipole at the origin of the coordinate system. This is only valid until waves arrive at the truncation boundary. Any numerical instability is not observed in the computation of the oscillatory motions. The integral equation and boundary conditions to calculate the time derivative of the potential on the body are derived. By using these formulas, the free surface shape and forces are calculated simultaneously. A Runge-Kutta 4-th order scheme is employed in the solution method. Nonlinear effects on the oscillating body submerged in infinite water depth are studied.

## ACKNOWLEDGMENT

This work was supported by the Basic Research Program, contract ED469 of the Korea Research Institute of Ships and Ocean Engineering (KRISO). Acknowledgement is also given to the Ministry of Science and Technology of Korea (MOST). The authors should appreciate Dr. Choung Mook Lee for his encouragements.

## REFERENCES

- [1] Abramowitz, M. & Stegun, I.A. , Handbook of Mathematical Functions, Government Printing Office, Washington, 1964.
- [2] Baker, G.R., Meiron, D.I. & Orsag, S.A. , "Generalized Vortex Methods for Free-Surface Flow Problems," Journal of Fluid Mechanics, 123, pp477-501, 1982 .
- [3] Barsky, B.A. & Greenberg, D.P. , "Determining a Set of B-Spline Control Vertices to Generate an Interpolating Surface," Computer Graphics and Image Process 14, pp203-226, 1980.
- [4] Barsky, B.A. , "End Conditions and Boundary Conditions for Uniform B-Spline Curve and Surface Representations," Computers in Industry 3, pp. 17-29, 1982.
- [5] Dommermuth, D.G. & Yue, D.K.P. 1986 , "Study of Nonlinear Axisymmetric Body-Wave Interactions," In Proc. 16th Symp.on Naval Hydrodynamics, Berkeley.
- [6] Dommermuth, D.G. , "Numerical Methods for Solving Nonlinear Water-Wave Problems in the Time Domain," Ph.D. Thesis, MIT, 1987.
- [7] Faltinsen, O.M. , "Numerical Solution of Transient Nonlinear Free-Surface Motion Outside or Inside Moving Bodies," Proc. 2nd Intl. Conf. on Num. Ship Hydro., U.C. Berkeley, 1977.
- [8] Ferrant, P. , "Sphere immergee en mouvement de pilonnement de grande amplitude," Premiers Journees De L'hydrodynamique, Nantes, 1987.
- [9] Ferziger, J.H. , Numerical Methods for Engineering Application, John Wiley and Sons, Inc., 1981.
- [10] Forbes, L.K. , "An Algorithm for 3-Dimensional Free-Surface Problems in Hydrodynamics," Journal of Computational Physics 82, pp.330-347, 1989.
- [11] Gradshteyn, I.S. and Ryzhik, I.M. , Table of Integrals, Series, and Products, Academic Press, 1980.
- [12] Kang, C.-G. , "Bow Flare Slamming and Nonlinear Free Surface-Body Interaction in the Time Domain," Ph.D. Thesis, Univ. of Michigan, 1988.
- [13] Kang, C.-G. & Troesch, A.W. , "Nonlinear Interaction between Axisymmetric Bodies and The Free Surface-Body in Water of Infinite Depth," Proc. the Seminar on Ship Hydrodynamics to honor Prof. J.H.Hwang, Seoul, Korea, 1988.
- [14] Kaplan, W. , Advanced Mathematics for Engineers, Addison-Wesley Publishing Co.
- [15] Lin, W.M. , "Nonlinear Motion of the Free Surface near a Moving Body," Ph.D. Thesis, M.I.T., Dept. of Ocean Engineering, 1984.
- [16] Lin, W.M., Newman, J.N. & Yue, D.K.P. , "Nonlinear Forced Motions of Floating Bodies," Proc. 15th Symp. on Naval Hydro., Hamburg, 1984.
- [17] Longuet-Higgins, M.S. & Cokelet, E.D. , "The Deformation of Steep Surface Waves on Water, I. A Numerical Method of Computation," Proc. R. Soc. Lond. A., 350, pp1-26, 1976
- [18] Newman, J.N. , "Transient Axisymmetric Motion of a Floating Cylinder," J. Fluid Mech., 157, pp17-33, 1985.
- [19] Vinje, T. & Brevig, P. , "Nonlinear Ship Motions," Proc. 3rd Intl. Conf. on Numerical Ship Hydrodynamics, Paris, 1981.
- [20] Vinje, T. & Brevig, P. , "Nonlinear, Two Dimensional Ship Motions," Seminar on the Norwegian Ships in Rough Seas (SIS) Project, 1982.
- [21] Yang, C. & Liu, Y.Z. , "Time-Domain Calculation of the Nonlinear Hydrodynamics of Wave-Body Interaction," 5 th Intl. Conf. on Num. Ship

Table 1 Harmonic Distributions of the Total Force for Heave Motion  
( $a/R=0.5, h/R=2.0, KR=1.0$ )

Heave Force	$F/\rho g K a R^3$	
I-TH	COS	SIN
0	-0.2850707E-01	0.0000000E+00
1	0.1843049E+01	0.2665849E+00
2	-0.1033978E+00	0.6141333E-01
3	0.6449880E-01	0.8355246E-02
4	-0.5114811E-02	-0.1019468E-01
5	0.2418429E-01	0.2957444E-02

Table 2 Harmonic Distribution of the Total Force for Surge Motion  
( $a/R=0.5, h/R=2.0, KR=1.0$ )

Surge Force	$F/\rho g K a R^3$	
I-TH	COS	SIN
0	-0.1308621E-02	0.0000000E+00
1	0.1927655E+01	0.1237885E+00
2	0.2138726E-03	-0.1002954E-02
3	0.3005543E-01	0.1583521E-02
4	-0.1381397E-04	-0.4408678E-03
5	0.2590462E-01	-0.4266882E-03

Heave Force	$F/\rho g K a R^3$	
I-TH	COS	SIN
0	-0.1274143E-01	0.0000000E+00
1	-0.4001656E-03	0.4211906E-04
2	0.2037149E-01	0.2325045E-01
3	-0.3133378E-03	0.8355940E-04
4	-0.3846344E-03	-0.2575103E-03
5	-0.2204935E-03	0.9557988E-04

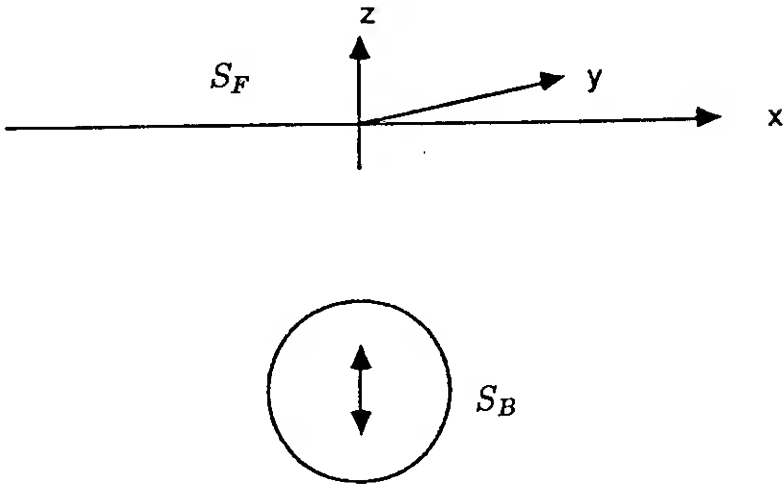


Fig. 1 Coordinate System

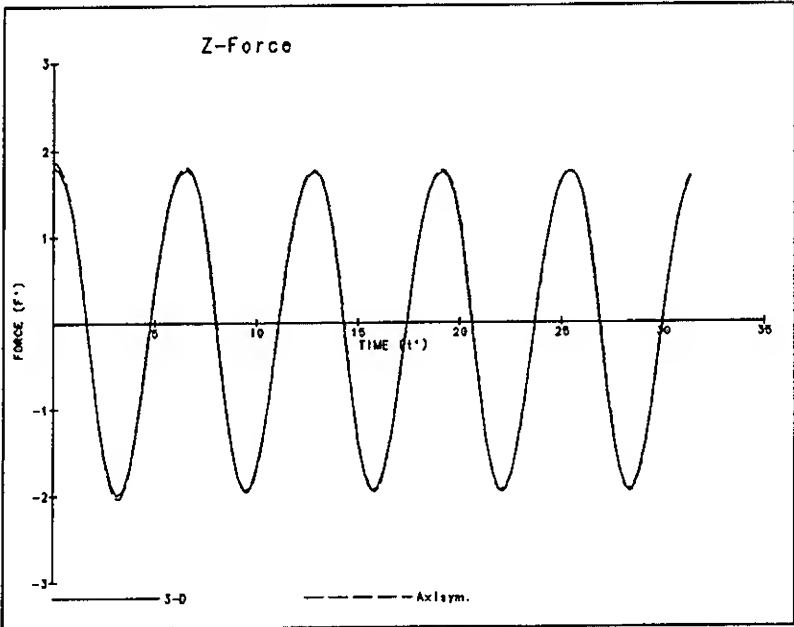


Fig. 2 Comparison of Heave Force Acting on the Sphere by 3-D and Axisymmetric Solutions ( $a/R=0.5, h/R=2.0, KR=1.0$ )

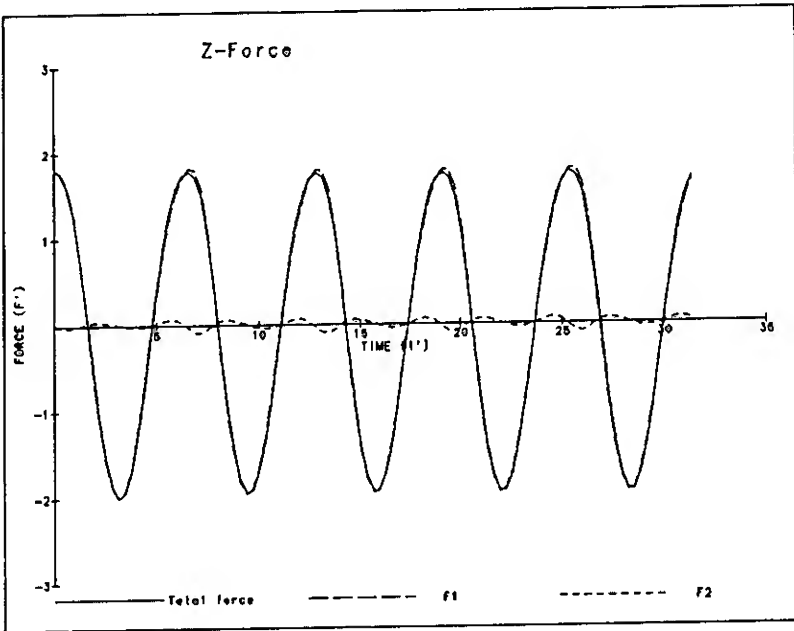


Fig. 3 Time History of the Heave Force Components Acting on the Heaving Sphere ( $a/R=0.5, h/R=2.0, KR=1.0$ )

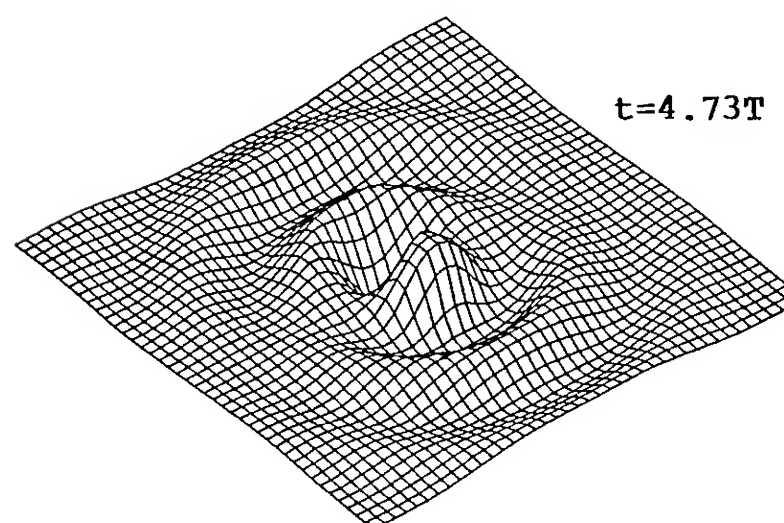
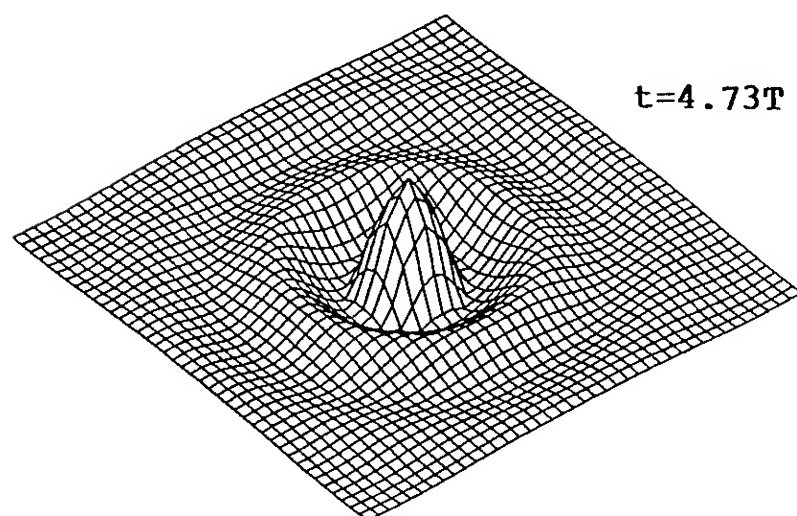
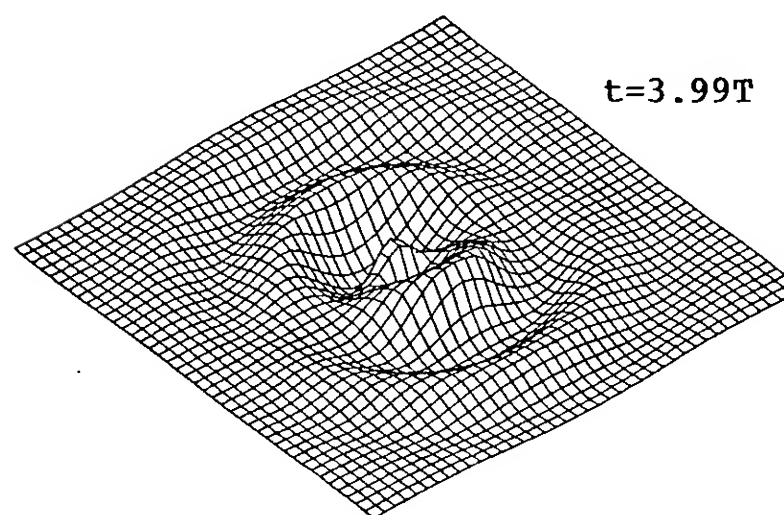
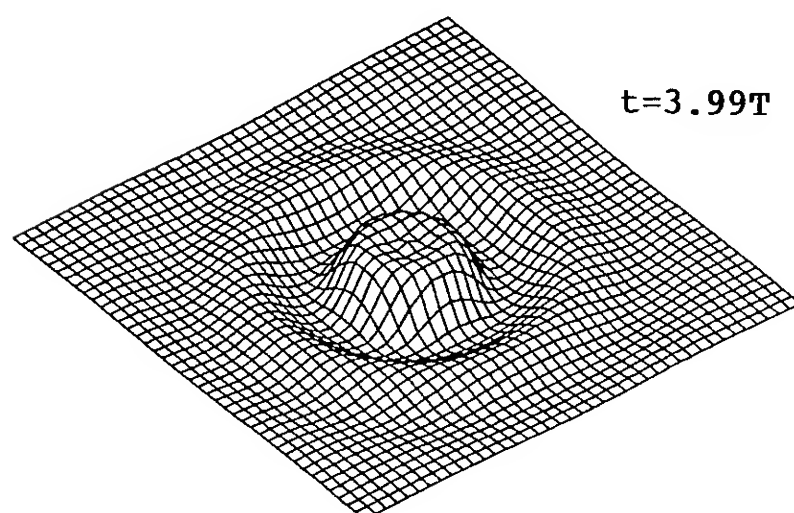
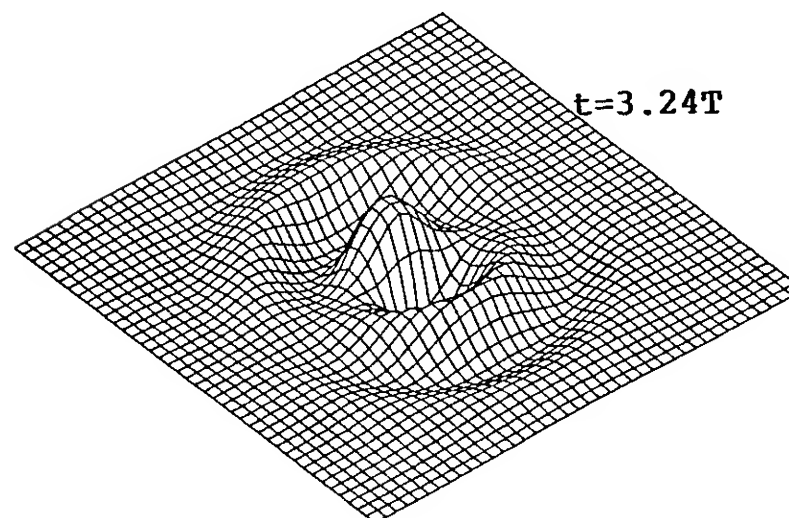
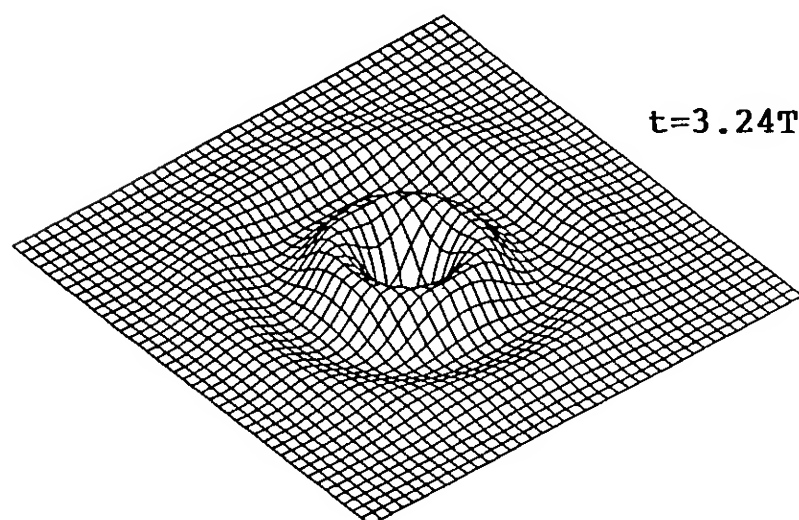
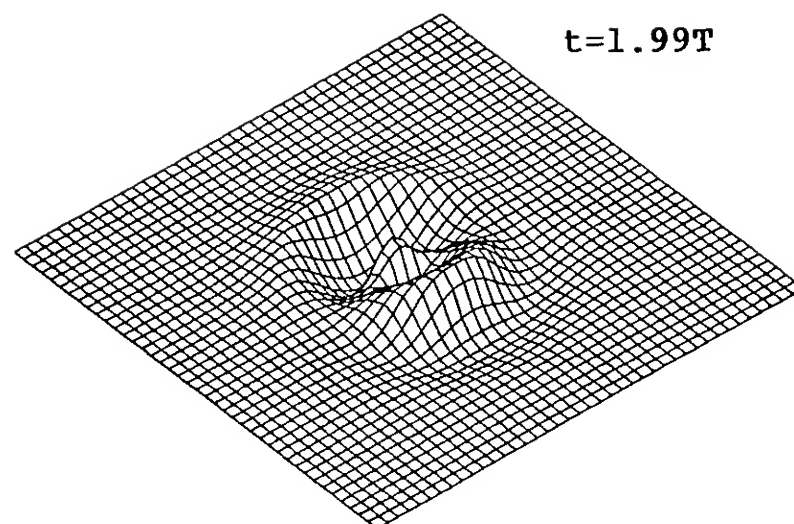
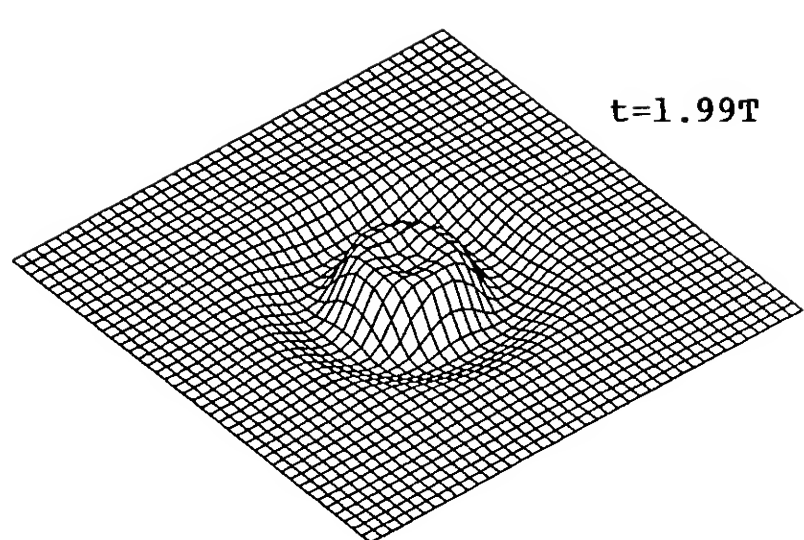


Fig. 4 Wave Profiles for Heave Motion  
( $a/R=0.5$ ,  $h/R=2.0$ ,  $KR=1.0$ )

Fig. 7 Wave Profiles for Surge Motion  
( $a/R=0.5$ ,  $h/R=2.0$ ,  $KR=1.0$ )



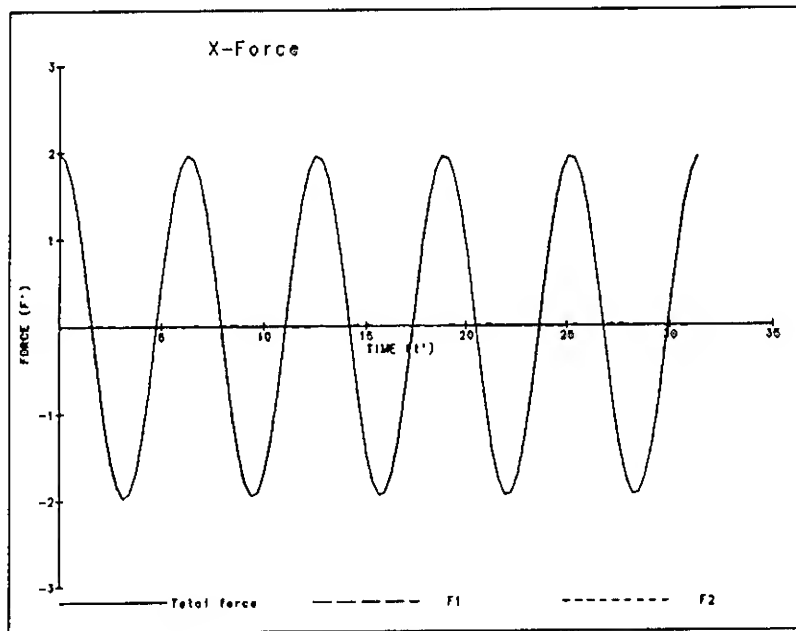


Fig. 5 Time History of the Surge Force Components Acting on the Surging Sphere ( $a/R=0.5$ ,  $h/R=2.0$ ,  $KR=1.0$ )

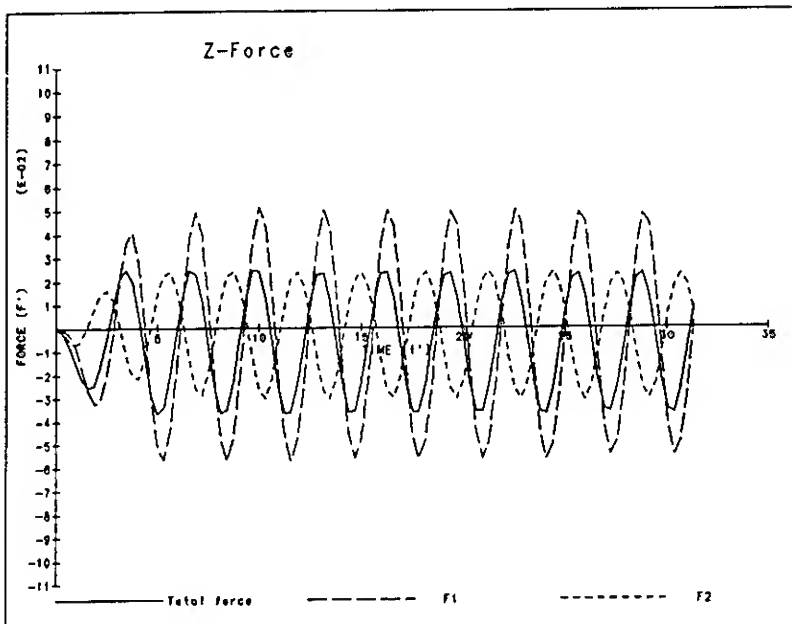


Fig. 6 Time History of the Heave Force Components Acting on the Surging Sphere ( $a/R=0.5$ ,  $h/R=2.0$ ,  $KR=1.0$ )

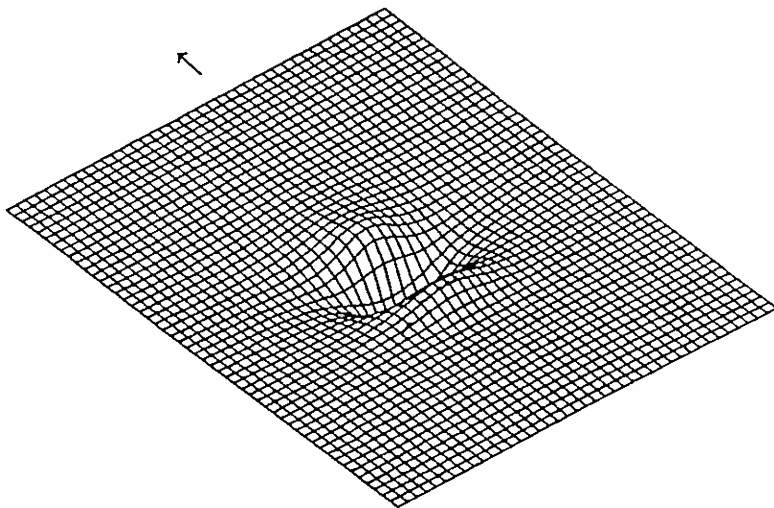


Fig. 8 Wave Profile Generated by an Advancing Sphere ( $U = 2.557m/sec$  for  $2.557 < t$ ,  $U = t$  for  $0 < t < 2.557$ ,  $h/R = 2.0$ ,  $t = 3.6sec$ )

## Appendix 1. The 4th order Runge-Kutta method [9]

When  $y' = f(x, y)$  is nonlinear, this can be solved by Runge-Kutta methods. The most commonly used Runge-Kutta methods are fourth order accurate and there are a number of these. The best known such method (sometimes called the fourth order Runge-Kutta method) is

$$y_{n+1/2}^* = y_n + \frac{h}{2} f(x_n, y_n)$$

(Euler predictor - half step)

$$y_{n+1/2}^{**} = y_n + \frac{h}{2} f(x_{n+1/2}, y_{n+1/2}^*)$$

(Backward Euler corrector - half step)

$$y_{n+1}^{***} = y_n + h f(x_{n+1/2}, y_{n+1/2}^{**}) \quad (34)$$

(Midpoint rule predictor - full step)

$$y_{n+1} = y_n + \frac{h}{6} [f(x_n, y_n) + 2f(x_{n+1/2}, y_{n+1/2}^*) + 2f(x_{n+1/2}, y_{n+1/2}^{**}) + f(x_{n+1}, y_{n+1}^{***})]$$

(Simpson's rule corrector - full step)

Looking at this method one can see that derivation of such methods is not an easy task. An analysis of it for the general case is also difficult. It is not too difficult to analyze, however, when applied to  $y' = \alpha y$ . We find that

$$y_{n+1} = \left( 1 + \alpha h + \frac{(\alpha h)^2}{2} + \frac{(\alpha h)^3}{6} + \frac{(\alpha h)^4}{24} \right) y_n \quad (35)$$

so that the method is indeed fourth order accurate and the error is of order  $(\alpha h)^5/120$ . It is interesting to note that the steps that comprise this method are of order one, one, two, and four, respectively, and the method has inherited the accuracy of the final corrector.

## Appendix 2. Parametric Uniform B-spline Surface Representation [3]



A B-spline surface is defined in a piecewise manner, where each piece is a segment of the surface called a surface patch. The entire surface is a mosaic of these patches sewn together with appropriate continuity (Fig. 9). A bicubic B-spline surface consists of patches which are cubic in each of the two parametric directions and it is everywhere continuous along with its first and second derivative vectors, in both directions. This continuity constraint reduces to requiring continuity of the first and second parametric derivative vectors across the borders of adjacent patches. The B-spline surface is defined by, but does not interpolate, a set of points called control vertices. These control vertices form a two-dimensional array. Although the vertices actually exist in three-dimensional  $x-y-z$  space, they are organized as a two-dimensional graph. Each vertex is either an interior vertex or a boundary vertex. This notion can be formalized quite elegantly by drawing on graph theory. The set of control vertices can be considered as a graph  $V, E$  whose vertices form the set

$$V = \{V_{ij} \mid i = 0, \dots, m; j = 0, \dots, n\}$$

and with the set of edges

$$E = \{(V_{ij}, V_{i,j+1}) \mid i = 0, \dots, m-1; j = 0, \dots, n\} \\ \cup \{(V_{ij}, V_{i+1,j}) \mid i = 0, \dots, m-1; j = 0, \dots, n\}$$

The interior vertices are the vertices  $V_{ij}$ , where  $1 \leq i \leq m-1$  and  $1 \leq j \leq n-1$ , and the boundary vertices are  $V_{0j}, j = 0, \dots, n-1$ ,  $V_{in}, i = 0, \dots, m-1$ ,  $V_{mj}, j = 1, \dots, n$ , and  $V_{i0}, i = 1, \dots, m$ . To emphasize this graph-theoretic interpretation, the term control graph to describe the set of control vertices is chosen (Fig. 10). A major advantage of the B-spline formulation is that it is a local representation. A bicubic B-spline surface patch is controlled by 16 control vertices and is unaffected by all other control vertices.

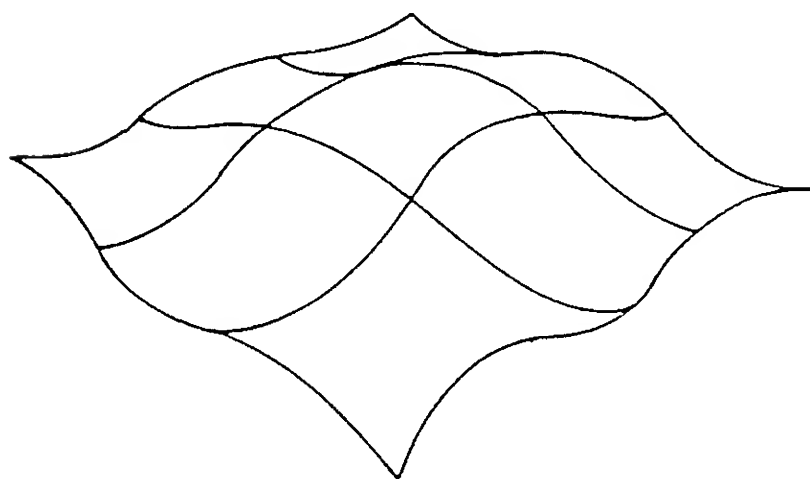


Fig. 9 A B-Spline Surface is a Mosaic of Surface Patches.

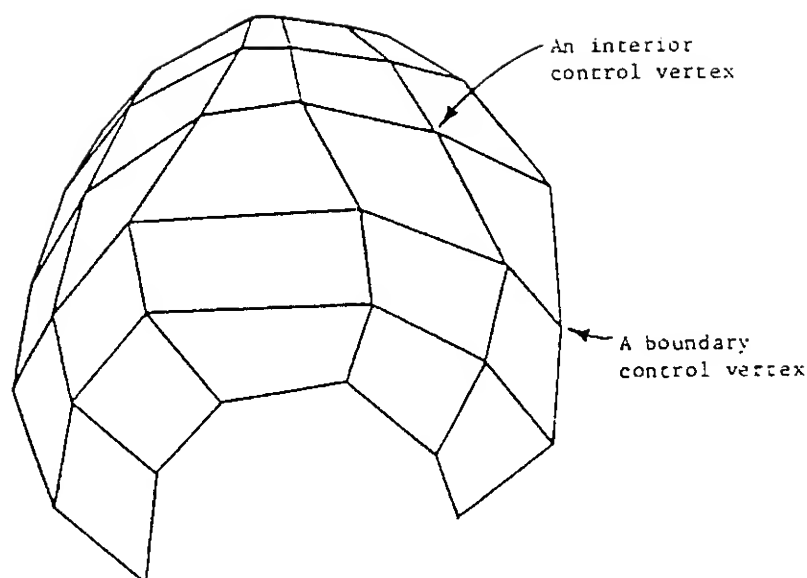


Fig. 10 A B-Spline Control Graph

Conversely, a given control vertex exerts influence over only 16 surface patches and has no effect on the remaining patches. This means that the effects of moving a control vertex are limited to 16 patches. A point on the  $(i, j)$  th uniform bicubic B-spline surface patch is a weighted average of the 16 vertices  $V_{i+r, j+s}$ ,  $r = -2, -1, 0, 1$  and  $s = -2, -1, 0, 1$ . The mathematical formulation for the patch  $Q_{ij}(u, v)$  is then

$$Q_{ij}(u, v) = \sum_{r=-2}^1 \sum_{s=-2}^1 bb_{rs}(u, v) V_{i+r, j+s} \\ \text{for } 0 \leq u, v \leq 1 \quad (36)$$

The set of bivariate uniform basis functions is the tensor product of the set of univariate uniform basis functions. That is,

$$bb_{rs}(u, v) = b_r(u) b_s(v) \\ \text{for } r = -2, -1, 0, 1, \text{ and } s = -2, -1, 0, 1 \quad (37)$$

Thus, the formulation for the patch  $Q_{ij}(u, v)$  can be rewritten as

$$Q_{ij}(u, v) = \sum_{r=-2}^1 \sum_{s=-2}^1 b_r(u) V_{i+r, j+s} b_s(v) \\ \text{for } 0 \leq u, v \leq 1 \quad (38)$$

The univariate uniform cubic B-spline basis functions are graphed in Fig. 11, and can be written in matrix form as

$$[b_{-2}(u) \ b_{-1}(u) \ b_0(u) \ b_1(u)]$$

$$= [u^3 u^2 u^1] 1/6 \begin{bmatrix} -1 & 3 & -3 & 1 \\ 3 & -6 & 3 & 0 \\ -3 & 0 & 3 & 0 \\ 1 & 4 & 1 & 0 \end{bmatrix} \quad (39)$$

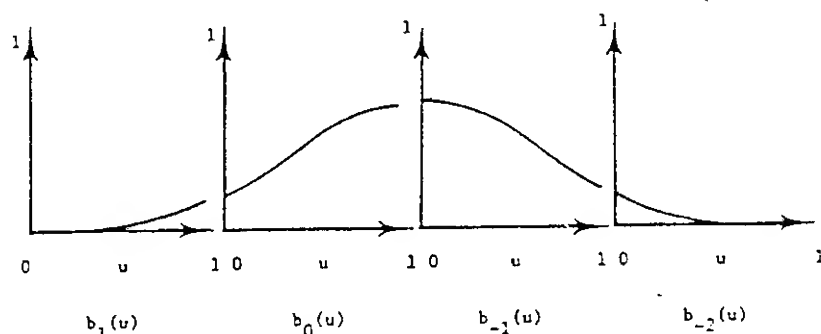


Fig. 11 Graphs of the Univariate Uniform Cubic B-Spline Basis Functions

### Appendix 3 Calculation of the Surface Integral and the Normal Vector

The surface integral can be calculated as follows (Kaplan, 1981) :

$$\begin{aligned} & \iint_S H(x, y, z) \, d\sigma \\ &= \iint_{S_{uv}} H[f(u, v), g(u, v), h(u, v)] \sqrt{EG - F^2} \, du \, dv \end{aligned} \quad (40)$$

where

$$\begin{aligned} x &= f(u, v), \quad y = g(u, v), \quad z = h(u, v) \\ \underline{P}_1 &= x_u \underline{i} + y_u \underline{j} + z_u \underline{k} \\ \underline{P}_2 &= x_v \underline{i} + y_v \underline{j} + z_v \underline{k} \\ E &= |\underline{P}_1|^2 = \left(\frac{\partial x}{\partial u}\right)^2 + \left(\frac{\partial y}{\partial u}\right)^2 + \left(\frac{\partial z}{\partial u}\right)^2 \\ F &= \underline{P}_1 \cdot \underline{P}_2 = \frac{\partial x}{\partial u} \frac{\partial x}{\partial v} + \frac{\partial y}{\partial u} \frac{\partial y}{\partial v} + \frac{\partial z}{\partial u} \frac{\partial z}{\partial v} \\ G &= |\underline{P}_2|^2 = \left(\frac{\partial x}{\partial v}\right)^2 + \left(\frac{\partial y}{\partial v}\right)^2 + \left(\frac{\partial z}{\partial v}\right)^2 \end{aligned}$$

The normal vector on the surface S is calculated by using the following formula.

$$\underline{n} = \frac{\underline{P}_1 \times \underline{P}_2}{|\underline{P}_1 \times \underline{P}_2|} \quad (41)$$

### DISCUSSION

Tor Vinje  
Norwegian Contractors, Norway

It seems to me that you have treated the computation of the forces in a way that is much more complicated than necessary. The splitting up of the  $\partial\phi/\partial t$  values, according to Vinje & Breirg, does not make sense for forced motion. In this case it can be computed by means of a central difference scheme at a later stage. If you, on the other hand, are dealing with problems where the dynamic equations of motion of the body have to be integrated in time, you have to split the forces (and  $\partial\phi/\partial t$ ) in the way you did. This is due to the occurrence of numerical instability if you apply, for instance, backward differences in time to compute  $\partial\phi/\partial t$ , and thus the forces acting on the body.

### AUTHORS' REPLY

Even if the calculation examples in this paper are restricted to the forced motion, this motion can be directly applied to the problems where the body motion is unknown. The calculation method of the forces in this paper is not much complicated because the integral equation for the potential (7) has the same influence coefficients that the integral equation for the time derivative of the potential (25). Also, this method gives more accurate results for the calculation of the forces than a central difference scheme.

### DISCUSSION

Pierre Ferrant  
Sirehna, S.A., France

Your computations were run only for  $\omega = 1.0$ . According to my computations on the submerged heaving sphere,  $\omega = 1.0$  is a local minimum for the higher harmonic terms in the force. Furthermore, this frequency is too high to make higher harmonics appear in the wave field, and your result for the wave field is purely harmonic and certainly very close to the result of a fully linearized model, as demonstrated in my paper presented in this conference. For this geometry and for heaving motion, major nonlinear effects appear especially low frequency, say about  $\omega = 0.4$ . Future runs of your code should be situated in this frequency range in order to obtain significant nonlinear body-wave interaction.

### AUTHORS' REPLY

I agree with you. I have some experiences for the computation on a submerged heaving sphere by using the axisymmetric code (13). The nonlinear effects appear strongly at low frequencies and small submerged depth (21). Reference: (21) Kang, C.-G, "Nonlinear Free Surface Flows for an Axisymmetric Submerged Body," submitted to *J. of the Society of Naval Architects of Korea*.

## Nonlinear Ship Waves

Y.-H. Kim (David Taylor Research Center, USA)  
T. Lucas (University of North Carolina-Charlotte, USA)

### ABSTRACT

A boundary element method is presented for solving a nonlinear free surface flow problem for a ship moving a constant speed on a calm sea. The method of solution is based on distribution of simple Rankine type( $1/r$ ) singularities on the body and on the true location of the free surface, which must be obtained by iteration. The key is the iterative algorithm for determining the free surface and wave resistance using a new one parameter family of upstream finite difference methods. A verification of numerical modeling is made using Wigley hull and validity of computer program is examined carefully by comparing the details of wave profiles and wave-making resistance with Series 60,  $C_B=0.60$  model.

### INTRODUCTION

Many of problems facing engineers involve such difficulties as a nonlinear governing equation and nonlinear boundary conditions at known or unknown boundaries. The determination of surface ship waves is a nonlinear problem wherein the governing equation is linear but there is a nonlinear free surface condition imposed at an unknown boundary. In practice the solution is approximated using numerical techniques, analytical techniques and combinations of both. Foremost among the analytical techniques is the systematic method of perturbations in terms of a small parameter.

In the past, problems of this type were generally treated after the boundary condition on the free surface was linearized. Limited studies on nonlinear boundary conditions have been conducted for simplified two-dimensional cases. With the recent advent of supercomputers and numerous new techniques in computational fluid dynamics there is growing interest in solving the three-dimensional nonlinear free surface problems by various schemes. Dommermuth and Yue[1] reported their study on the nonlinear three-dimensional gravity waves created by a moving surface pressure distribution using a higher-order spectral method. During the 5th International Conference on Numerical Ship Hydrodynamic a significant amount of work was been reported on this subject including Jensen[2], Musker[3], and Bai[4]. SSPA's series of reports by Xia[5], Ni[6], and Kim[7] also deal with this topic.

Many different numerical schemes have been proposed. The method proposed here is a boundary element method with Rankine type source as the kernel function. The drawback to this approach is, as well known, the necessity of proper numerical implementation of the radiation condition required since the potential flow model contains no viscosity. The upstream finite difference operator first introduced by Dawson[8] successfully satisfies the radiation condition by producing an inherent local damping of the free surface waves by upwinding. Since then numerous researchers have tried to improve Dawson's method and to extend it to the nonlinear free surface problem. SWIFT (Ship Wave Inviscid Flow Theory) is a computer code developed by the authors and S.H. Kim[9] based on the linearized free surface condition. SWIFT uses a higher order panel method with either constant or linearly varying singularity strength distribution across a curved panel. The stability and accuracy of the computational results have been examined and found to be quite robust.

In the present paper the SWIFT approach is extended to the nonlinear free surface problem and, though developed independently, is very similar to Ni[6] and Kim[7] of SSPA. The convergence of the method has been major focal point among researchers who have been working on the nonlinear problems. Xia[5] experienced severe convergence problems during iteration. Ni[6] used a higher order method and test results were converged if an under relaxation coefficient was used to modify the wave elevation and velocity distribution for the next iteration. Kim[7] obtained convergent solutions successfully by satisfying the kinematic and dynamic boundary conditions simultaneously without a relaxation factor. They all used the three point finite difference operator instead of Dawson's four point operator. Musker[3] extensively studied stability and accuracy of a nonlinear code, and experienced the usual difficulties in convergence with the four point scheme. In this paper we introduce a new one parameter family of four point schemes which can give an arbitrarily large damping. The four point method of Dawson[8] and three point method of Xia[5] are special cases of this approach. We have experienced greatly enhanced stability for all tested ship hullforms over a broad range of speeds. Wigley mathematical hull is used to verify the numerical modeling of the problem. The measured wave profiles and wave-making resistance of Series60,  $C_B=0.60$  are used to validate the developed computer program.

## MATHEMATICAL FORMULATION

We consider a ship which moves in the positive  $x$ -direction with constant forward speed  $U_0$  in Figure 1. Let  $Oxyz$  be a Cartesian coordinate system with  $Oz$  opposing the direction of gravity and  $z=0$  coincides the undisturbed free surface, the positive  $x$ -axis in the direction of the ship's forward velocity. The fluid is assumed to be inviscid and incompressible and its motion is irrotational such that the velocity field of the fluid  $\bar{v}$  can be defined as

$$\bar{v}(x, y, z) = \nabla\phi(x, y, z) \quad (1)$$

where  $\phi(x, y, z)$  is the velocity potential and satisfies the Laplace equation

$$\nabla^2\phi = 0 \quad (2)$$

in the fluid domain  $D$  and the boundary condition

$$\phi_n = U_{0n} \quad (3)$$

on the body surface  $S_0$  where  $n=(n_x, n_y, n_z)$  denotes the outward unit normal vector on the boundary.

On the free surface  $z = \zeta(x, y)$ , where  $\zeta$  is the free surface elevation, the kinematic boundary condition and dynamic boundary conditions can be given respectively as

$$\phi_x \zeta_x + \phi_y \zeta_y - \phi_z = 0 \quad (4)$$

$$g\zeta + \frac{1}{2}(\nabla\phi \cdot \nabla\phi - U_0^2) = 0 \quad (5)$$

where  $g$  denotes the gravitational acceleration. Combining both dynamic and kinematic conditions Eqs. (4) and (5) becomes

$$\nabla\phi \cdot \nabla \left[ \frac{1}{2}(\nabla\phi)^2 \right] + g\phi_z = 0 \quad (6)$$

Finally, energy consideration requires that velocity potential approaches the uniform onset flow potential and that there be no waves far upstream of the ship, and that waves always travel downstream.

The problem described in equations (1) thru (5) is nonlinear, since the free surface boundary conditions (4) and (5) themselves are nonlinear and should be satisfied on the true free surface which is unknown and should be obtained as a part of solution. In their exact form the problem is difficult to solve. In order to be able to treat the problem, the equations are approximated by ones which are more tractable.

Following linearizations are similar to Ni[6] and Kim[7]. First we define

$$D_1(\sigma, \zeta) = \phi_x \zeta_x + \phi_y \zeta_y - \phi_z$$

$$D_2(\sigma, \zeta) = g\zeta + \frac{1}{2}(\nabla\phi \cdot \nabla\phi - U_0^2)$$

We denote  $\phi^0$  and  $\zeta^0$  the velocity potential and the wave profiles, respectively, obtained from the previous step and introduce two small parameters  $\delta\sigma$  and  $\delta\zeta$  with

respect to the previous solution. Take Taylor series expansion of  $D_1(\sigma, \zeta)$  and discard higher order terms greater than  $\delta\sigma$  and  $\delta\zeta$ , then the kinematic free surface condition becomes

$$\begin{aligned} D_1(\sigma, \zeta) &\approx D_1(\sigma^0, \zeta^0) + \frac{\partial}{\partial\sigma} D_1(\sigma, \zeta^0) \delta\sigma + \frac{\partial}{\partial\zeta} D_1(\sigma^0, \zeta) \delta\zeta \\ &= \phi_x^0 \zeta_x^0 + \phi_y^0 \zeta_y^0 - \phi_z^0 \\ &\quad + \delta\phi_x \zeta_x^0 + \delta\phi_y \zeta_y^0 - \delta\phi_z^0 \\ &\quad + \phi_x^0 \delta\zeta_x + \phi_y^0 \delta\zeta_y + (\phi_{xz}^0 \zeta_x^0 + \phi_{yz}^0 \zeta_y^0 - \phi_{zz}^0) \delta\zeta \end{aligned} \quad (7)$$

We redefine a new velocity potential  $\phi = \phi^0 + \delta\phi$  and the linearized kinematic boundary condition can be expressed as follows:

$$\begin{aligned} D_1(\sigma, \zeta) &\approx \phi_x \zeta_x + \phi_y \zeta_y - \phi_z \\ &\quad + \phi_x^0 \delta\zeta_x + \phi_y^0 \delta\zeta_y + (\phi_{xz}^0 \zeta_x^0 + \phi_{yz}^0 \zeta_y^0 - \phi_{zz}^0) \delta\zeta = 0 \end{aligned} \quad (8)$$

Similarly the dynamic boundary condition can be linearized as follows;

$$\begin{aligned} D_2(\sigma, \zeta) &\approx \delta\zeta \left( 1 + \frac{1}{g} (\phi_x^0 \phi_{xz}^0 + \phi_y^0 \phi_{yz}^0 + \phi_z^0 \phi_{zz}^0) \right) + \zeta^0 \\ &\quad - \frac{1}{2g} \left\{ U_0^2 + \phi_x^{0^2} + \phi_y^{0^2} + \phi_z^{0^2} - 2(\phi_x^0 \phi_x + \phi_y^0 \phi_y + \phi_z^0 \phi_z) \right\} = 0 \end{aligned} \quad (9)$$

Now the new linearized boundary value problem is formulated. The singularity distribution and wave profile are continuously updated until the solution converges and satisfies original Eqs. (4) and (5). Once the singularity strength distributions are determined, the wave resistance can be computed by

$$R_w = \iint_{S_0} p n_x ds \quad (10)$$

where  $S_0$  is the wetted ship hull surface and the fluid pressure  $p$  is given by the Bernoulli equation

$$p = -\frac{\rho}{2} [(\nabla\phi)^2 - U_0^2] - \rho g z \quad (11)$$

## NUMERICAL SCHEME

The method used here is a boundary element method in which simple Rankine sources are distributed across each panel. The boundary-value problem formulated above then reduces to a determination of an unknown singularity distribution over the boundary surface of the fluid domain. Once the singularity distribution is determined, the hydrodynamic quantities of interest, the velocity and the pressure, are also determined.

The present method uses a panel scheme to achieve a numerical solution to the problem of Eqs. (1) thru (9). Panel schemes proceed by first dividing the boundary surface into panels. Source distributions ( $\sigma$ ) are assigned to each panel. These distributions are expressed in terms of unknown singularity parameters  $\lambda_j$  associated with the panel and neighboring panels. A finite set of control points (equal in number to the number of singularity parameters) is selected at which the boundary conditions are imposed.

The construction of each network requires numerical development in these areas: A. Surface geometry definition; B. Singularity strength definition; and C. Control point selection and boundary condition specification. Essential features of the computational scheme in each of these areas are as follows

A. Geometry input for a network is assumed to be a grid of corner point coordinates partitioning the network surface into panels. Panel surface is obtained by fitting a paraboloid to corner points in an immediate neighborhood by the method of least squares.

B. Discrete values of singularity strength at certain points on each network are assigned as singularity parameters. Singularity splines are constructed for each network by fitting a linear distribution on each panel of the network by the method of least squares.

C. Certain standard points on each network are assigned as control points. These points include panel center points as well as network edge points. Boundary conditions involving the specification of potential or velocity are applied at panel center points for the purpose of controlling local properties of the flow.

#### Curved Panel Approximation

We use curved panels to patch the ship and free surface. Let  $S$  be a true surface element bounded by four corner points  $P_1, P_2, P_3$ , and  $P_4$  as shown in Fig. 2. We assume that  $S$  may be represented in the approximate form

$$\zeta(\xi, \eta) = \zeta_0 + \zeta_\xi \xi + \zeta_\eta \eta + \frac{1}{2} \zeta_{\xi\xi} \xi^2 + \zeta_{\xi\eta} \xi \eta + \frac{1}{2} \zeta_{\eta\eta} \eta^2 \quad (12)$$

where  $(\xi, \eta, \zeta)$  are orthogonal coordinates local to  $S$ . The six coefficients  $(\zeta_0, \zeta_\xi, \zeta_\eta, \zeta_{\xi\xi}, \zeta_{\xi\eta}, \zeta_{\eta\eta})$  are obtained by requiring that the approximate surface given by Eq. (12) pass through its four corner points exactly and through its neighboring points approximately in a least square sense. That is, for each panel the expression

$$R = \frac{1}{2} \sum_k W_k (\zeta(\xi_k, \eta_k) - \zeta_k)^2 \quad (13)$$

is minimized with respect to the six unknown coefficients appearing in Eq. (12). The summation in Eq. (13) ranges over the  $N$  neighboring grid points. The choice of the  $N$  points and the weight  $W_k$  has been made in an attempt to minimize any irregularities that may appear in the paraboloid approximation on the true surface. In the present formulation  $N=16$  and  $W_k=1$  or  $10^8$  are used depending on the location of the panel in the surface panel network. Here we used the term network to represent the collection of quadrilaterals.

The choice of these features is required by the

argument given by Hess[10] that certain computing methods which use flat panels do not obtain increased accuracy over the basic zero order method (constant source on flat panels) even though they use higher order source distributions. For purposes of computational efficiency Eq. (12) can be reduced by an appropriate coordinate transformation to the canonical form

$$\zeta = a\xi^2 + b\eta^2 \quad (\xi, \eta) \in \Sigma \quad (14)$$

where  $\Sigma$  is the quadrilateral formed by the projection of the corner points on the  $(\xi, \eta)$  plane. In the case of flat panel,  $a$  and  $b$  are both zero.

#### Singularity Strength Definition

The true singularity distribution will be approximated by a truncated Taylor's series on each panel. Such a representation is valid on any interior part of the network providing the paneling there is sufficiently fine. We will consider a linearly varying singularity distribution on source panels. There may be an advantages in using even higher order distribution, but as pointed out by Hess[10], it would be necessary to consider a higher order panel geometry definition for the sake of consistency. Specifically, we assume that the singularity strength  $\sigma$  at a point  $(\xi, \eta, \zeta)$  on a panel  $S$  is given by

$$\sigma(\xi, \eta) = \sigma_0 + \sigma_\xi \xi + \sigma_\eta \eta \quad (15)$$

The coefficients in Eq. (15) are determined by using a method of weighted least squares over the panel and up to eight of its neighboring panels. This method requires that the form of Eq. (15) gives exactly the singularity value at its centroid and approximate values in the least square sense at centroids of the neighboring panels.

#### Induced Velocity Potential

The velocity potential at  $P=(x, y, z)$  induced by a singularity distribution on  $S$  is given by

$$\phi = -\frac{1}{4\pi} \iint \frac{\sigma}{r} ds \quad (16)$$

where  $r = \{ (\xi-x)^2 + (\eta-y)^2 + (\zeta-z)^2 \}^{1/2}$  and  $\sigma$  is given in Eq. (15). We are now in a position to evaluate the integral Eq. (16) using the relations of Eqs. (13), (14), and (15). The  $\phi$  can be expanded in closed form by using a combination of closed form calculations and recursive relationships. Details are fully included in Johnson[11] and Kim et al.[9]. Derivatives of velocity component along  $z$ -direction in Eqs. (8) and (9) are new and their final closed forms are summarized in the Appendix.

#### METHOD OF SOLUTION

As usual we discretize the fluid boundary into a finite number of panels. Because of symmetry, half of the ship as well as the free surface domain is used as an input. A typical free surface domain is truncated at a half ship length ( $L=2.0$ ) ahead of the ship and is extended more than one ship length aft of the ship and a half ship length or more to the side. Since the convective term in the free surface condition involves  $x$  and  $y$  directional derivatives,



we use an algebraically generated waterline-fitted coordinate system, independent of the double model streamline coordinate, to create the panel network. As shown in Fig. 3 the transverse lines are straight and vertical to the center line of the ship. Our numerical experiments indicate that the solution becomes more stable and accurate when the aspect ratio of the free surface panel away from the ship closes to unity. The same finding was discussed by Musker(1989).

During iteration, the panels are rearranged such that the projection on the horizontal plane  $z=0$  is unchanged, i.e,  $x$  and  $y$  coordinates are fixed and the  $z$ -coordinate is allowed to move up and down. The method of solution requires that the linearized free surface conditions (8) and (9) are satisfied for a given  $\phi^0$  and  $\zeta^0$  which were obtained from the previous step. The iteration starts from the solution which satisfies the well-known linearized free surface condition. In each iteration the free surface panels as well as body surface panels are adjusted according to the newly computed wavy surface and boundary conditions are applied to the updated boundaries. The iteration continues until the solution satisfies the exact free surface conditions. In practice, we provide a certain convergence criteria in the computation that requires the iteration to continue until the residual error satisfies the provided tolerance. This part will be discussed more extensively with numerical results later.

#### One Parameter Family of Advection Methods to Enhance Convergence

In this section we derive a *one parameter family of advection methods* to enhance convergence for the nonlinear free surface problem. A number of researchers have been concerned with the question of convergence of various forms of the nonlinear method. Xia had severe convergence problems with his approach and recommended the three point finite difference operator instead of Dawson's more accurate four point operator. Ni and Kim have developed more powerful methods. Recently Musker has completed a detailed stability and accuracy test of a nonlinear code, and experienced the usual difficulties in convergence with the four point method. Musker used two approaches to enhance convergence: he used a spline scheme involving four upwind points and he elevated the free surface panels. His nonlinear iterations, unlike those of Ni and Kim, are all on the flat surface.

In this paper we introduce a new one parameter family of four point advection schemes which can give an arbitrarily large damping. The four point method of Dawson and the three point method are special cases of this approach, and without the use of elevation of the panels (which we have not examined) we have experienced greatly enhanced stability. We recommend the inclusion of this technique into existing codes. For most programs this would require only a minor modification of a few lines of code, as will be seen below.

The four point method is:

$$\text{Slope}_i = -(A_4 f_i + B_4 f_{i-1} + C_4 f_{i-2} + D_4 f_{i-3}) \quad (17)$$

where for an uniform mesh spacing of size  $l$ ,  $A_4 = 1.667l^{-1}$ ,  $B_4 = -2.5l^{-1}$ ,  $C_4 = l^{-1}$ ,  $D_4 = -0.167l^{-1}$ . The related three point scheme is of the form

$$\text{Slope}_i = -(A_3 f_i + B_3 f_{i-1} + C_3 f_{i-2}) \quad (18)$$

where for an uniform mesh spacing of size  $l$ ,  $A_3 = 1.5l^{-1}$ ,

$B_3 = -2.0l^{-1}$ ,  $C_3 = 0.5l^{-1}$ . In considering all possible four point schemes for approximating  $f'$  one might like to require that they be exact for quadratics. These three restrictions on a formula of the type

$$\text{Slope}_i = -(A_N f_i + B_N f_{i-1} + C_N f_{i-2} + D_N f_{i-3}) \quad (19)$$

leave only one degree of freedom and since both the three point and four point methods satisfy a quadratic exactly, the general derivation of this general family is very simple:

$$\begin{aligned} A_N &= (1 - Q_{mul}) A_4 + Q_{mul} A_3 \\ B_N &= (1 - Q_{mul}) B_4 + Q_{mul} B_3 \\ C_N &= (1 - Q_{mul}) C_4 + Q_{mul} C_3 \\ D_N &= (1 - Q_{mul}) D_4 \end{aligned} \quad (20)$$

where  $Q_{mul}$  is a parameter to be chosen greater than or equal to zero. The case  $Q_{mul} = 0$  gives the familiar four point formula while  $Q_{mul} = 1$  returns the more stable three point formula. We have found that  $Q_{mul} = 1$  is often fine for lower speeds but for higher speeds  $Q_{mul} = 3$  (or even sometimes  $Q_{mul} = 5$ ) eliminates most of the problems with convergence for reasonably regular computational grids and with little loss of accuracy.

To analyze the effect of the one parameter method, and to get some feel for the meaning of the parameter  $Q_{mul}$ , it is instructive to examine the coefficient of  $f_i'''$  which is the leading term in the Taylor expansion of the error for both the three point and four point formula. (Recall that the basis of the four point formula was not that the  $f_i'''$  term was eliminated but rather that the  $f_i''''$  term was required to have a zero coefficient.) Here we will take an uniform spacing of size  $l$ . The coefficient of  $f_i'''$  in the three point method is of the magnitude  $l^2/3$  while in the four point method it is  $l^2/6$ , leading again to the well known conclusion that the superior damping of the three point method will frequently enhance convergence over that of the four point method, an important finding of Xia for example. Thus the one parameter  $Q_{mul}$  method has a coefficient for  $f_i'''$  of the magnitude

$$l^2((1 - Q_{mul})/6 + Q_{mul}/3) = l^2(1 + Q_{mul})/6$$

giving again  $l^2/6$  and  $l^2/3$  for  $Q_{mul} = 0$  or 1 as before. When denser meshes are used, or for large speeds where  $f'''$  may be smaller, the use of larger values of  $Q_{mul}$  such as  $Q_{mul} = 3$  or 5 gives the (larger) coefficients of  $f_i'''$  of magnitude  $2/3l^2$  or  $l^2$  giving in these cases twice or triple the damping of the 3 point method.

We now examine briefly the spline scheme considered by Musker, which for an uniform mesh has the form (refer to (20)) with  $A_4 = 1.555l^{-1}$ ,  $B_4 = -2.177l^{-1}$ ,  $C_4 = 0.689l^{-1}$ ,  $D_4 = -0.0667l^{-1}$ . This method does not quite make the quadratic term zero, so is not included in the above family, but it is very close with a value of  $Q_{mul}$  of about 0.6. Thus it has much of the improved stability associated with the three point scheme, giving a coefficient of  $f'''$  of the magnitude  $0.27l^2$ , closer to the  $0.33l^2$  of the 3 point method than the  $0.166l^2$  of the 4 point method. Thus we would be led to conjecture that the 3 point scheme would be more stable than the spline scheme, at negligible loss of accuracy.

#### RESULT AND DISCUSSION

To facilitate comparisons, the following non-dimensionalization has been made:



$$C_W(\text{wave-making resistance}) = R_w / (1/2 \rho U^2 S)$$

$$\zeta(\text{wave profile}) = \zeta / (L/2)$$

$$= \zeta / (U^2 / (2g)) \quad (\text{used in Figures})$$

Although the higher order panel method gives better results, we used linearly varying source strength distribution across curved panel for the ship hull and constant source strength across flat panel for free surface during computation because of the following reasons:

(1) The higher order panel method requires a much longer computing time, normally 3 or 4 times longer with the same number of panels.

(2) The finite difference scheme used for the convective terms in the free surface condition requires such small panel sizes that the advantages of higher order panel scheme cannot be fully utilized over the free surface domain.

Numerical experiments have indicated that the differences in results are negligible between using higher order panel and flat panel on the free surface domain. On the other hand, a Neumann condition imposed on the hull surface does not require any numerical differentiation and the higher order panel method gives better results than flat panel result with even fewer panels. Furthermore, the wave-making resistance is small quantity and to get this quantity accurately the integration of the pressure distribution over the entire wetted hull surface has to be carried out precisely. It is therefore required that the pressure distribution as well as panel surface be precisely approximated.

#### Qmul Test with Wigley Hull

Wigley parabolic hull was used to verify the proposed one parameter family of advection methods. The following computational conditions were used:

Wigley model	L=2.0, L/B=10.0, D/B=0.625 Bow = +1.0, Stern = -1.0
Computation domain (SSPA recommended)	x= -2.0, +2.0 y= -0.75
Number of panels	132 on ship (23 Stax7Wls) 400 on free surface (41x11)
Froude numbers	0.316, 0.408
Qmul's	0, 1, 3, 5
Computer	Cray X-MP/24

We used the computational domain that Xia[5] and other SSPA reports recommended and also matched the panels on the ship hull and free surface. We selected higher Froude numbers because several researchers have experienced convergence problems particularly at higher speeds. Table 1 shows the computed wave making resistance using four different Qmul's: 0, 1, 3, and 5. The solutions diverged when Qmul = 0 and 1, and converged when Qmul=3 and 5. The experimental values of wave-making resistance coefficients were reported at the 17th ITTC[12] and  $C_W$  ranges between  $1.7 \times 10^{-3}$  and  $2.3 \times 10^{-3}$  at  $Fn=0.408$ . Qmul=0 is the four point scheme and the solution diverged after 2 iterations. At Qmul=1, the three point scheme, the solution diverged after 5 iterations. Qmul=3 required only 4 iterations and Qmul=5 required just 2 iterations to get a converged solution. The magnitude of the wave making resistance is slightly smaller than that of Qmul=3. It is likely that the larger damping by using Qmul=5 caused the difference.

Table 1 Qmul Test  
(Wigley Hull at  $F_N = 0.408$ )

$$C_W(\text{Experiment}) = 2.0$$

$$C_W \times 10^3$$

Qmul	linear	1st Iter	2nd Iter	3rd Iter	4th Iter	5th Iter	Non-linear
0	2.248	1.562	1.863	Divrg			
1	2.304	1.890	2.067	1.683	1.726	1.899	Divrg
3	2.317	2.009	1.976	1.982	1.978	1.978	Convrg
5	2.231	1.965	1.939	1.939	1.940	1.940	Convrg

The two small parameters  $\delta\sigma$  and  $\delta\zeta$  used when linearizing the free surface conditions were continuously monitored during the computation. In Table 2 Error, the summation of the square root of  $\delta\zeta$  squared terms, is tabulated at each iteration for different Qmul's and in Table 3, that of  $\delta\sigma$ . At Qmul=1, Error oscillates during the iterations until the solution diverges. With Qmul=3 or 5, the magnitude of Error decreases steadily as the iteration continues. In practice, the convergence rate after several iterations is rather slow so we assumed the solution to be converged when the ratio of the current Error to the first iteration Error is smaller than 1% for both  $\delta\sigma$  and  $\delta\zeta$ .

Table 2  $\delta\zeta$  Convergence Test  
(Wigley Hull at  $F_N = 0.408$ )

$$\text{error1} = \sum_{i=1}^N \sqrt{(\delta\zeta_i)^2}, \quad N = 400$$

$$\text{error1} \times 10^2$$

Qmul	1st Iter	2nd Iter	3rd Iter	4th Iter	5th Iter	Non-linear
0	8.248	4.550	152.5	Divrg		
1	4.199	4.493	5.488	2.683	4.975	Divrg
3	2.955	1.857	0.507	0.333	0.036	Convrg
5	2.859	0.695	0.298	0.033		Convrg

Table 3  $\delta\sigma$  Convergence Test  
(Wigley Hull at  $F_N = 0.408$ )

$$\text{error2} = \sum_{i=1}^N \sqrt{(\delta\sigma_i)^2}, \quad N = 400$$

Qmul	1st Iter	2nd Iter	3rd Iter	4th Iter	5th Iter	Non-linear
0	1.10	1.30	Divrg			
1	0.62	1.10	1.00	0.58	0.84	Divrg
3	0.43	0.09	0.062	0.017	0.009	Convrg
5	0.42	0.10	0.012	0.006	0.001	Convrg

Fig. 4 depicts the wave profiles at the hull surface during iterations including the wave profile obtained from the linearized free surface conditions. As the iteration progresses the bow wave grows and the first trough becomes deeper with the phase shifting slightly towards the bow. Only insignificant differences are observed after during the iterations. Figure 5 shows the wave profile comparisons between the experimental, linear and nonlinear computations. The nonlinear solution is now much closer to the experimental.

Series60,  $C_B=0.60$

The Series60 with block coefficient 0.60 has extensive model experimental results, including wave profiles and wave-pattern resistance. Experimental values used here were determined by Kim and Jenkins[13]. Experimental data only for model fixed were considered in comparisons. Wave profiles were marked at every station along hull with a grease pencil during the run and were read after each run. Wave resistances were obtained from longitudinal wave profile measurements. The following computational conditions are used:

Series60 model	L=2.0, L/B=7.5, D/B=0.4 Model is fixed Bow = +1.0, Stern=-1.0
Computation domain	x = (-3.5, 2.0) y = (-1.5, 0.0)
Number of panels	192 on ship(25 Sta x 9WLs) 696 on free surface(59 x 13)
Froude numbers	0.22,0.25,0.28,0.30,0.32,0.35
Computer	Cray X-MP/24

Figure 6 shows the comparison of wave profiles along the hull between computed and measured. The wave profiles obtained from linearized free surface condition are also plotted together. The nonlinear solution significantly improves the wave profiles, in particular, at the bow and the first trough and after that the difference between linear and nonlinear results seems insignificant.  $Q_{mul} = 1$  is used for  $F_n = 0.22, 0.25$ , and  $0.28$ , and  $Q_{mul} = 3$  for  $F_n = 0.30, 0.32, 0.35$ .

Table 4. Wave Resistance Coefficient Comparison Series60, $C_B = 0.60$ (Model Fixed)						
(C <sub>w</sub> x10 <sup>3</sup> )						
F <sub>n</sub>	linear	1st Iter	2nd Iter	3rd Iter	4th Iter	Nonlin ear
0.22	0.369	0.278	0.271	0.268	0.266	0.255
0.25	0.664	0.398	0.357	0.354	0.355	0.354
0.28	1.581	1.123	1.049	1.043	1.043	1.045
0.30	2.144	1.548	1.474	1.467	1.460	1.460
0.32	1.815	1.401	1.333	1.350	1.354	1.357
0.35	2.148	1.886	1.800	1.816	1.828	1.836

Table 4. summarizes the wave-making resistance computation results at each iteration and in Figure 7 the linear and nonlinear results are compared with the experimental data. It is interesting to see that linear solution consistently predicts higher wave-making resistance throughout the Froude number range. Nonlinear results show very close agreement with the measured data. Even though all the runs converged successfully, at the lower Froude numbers 0.22 and 0.25 agreement on wave profiles as well as wavemaking resistance were rather poor. It is likely that the panel size may be too large at lower Froude number where wave length is shorter and is inadequate to resolve the flow phenomena accurately. At  $F_n=0.22$  the estimated characteristic wavelength is 0.608 which is less than 1/3 of the ship length. In usual practice between 10 and 12 points per wave length are considered to get acceptable numerical accuracy for wave making resistance. This means at least 33 evenly distributed panels along the ship hull have to be provided. No further attempt was made to increase the panel density at the lower Froude numbers, because it exceeds Cray X-MP memory restriction 3 million words. This particular run requires 2.6 million words computer memory(maximum usable capacity is 3 million+) and approximately 70 CPU seconds were used at each iteration.

As seen in Table 4. the most sizable improvement was made at the first iteration and in subsequent iterations improvement was small. In practice we may need one more iteration over the linear solution to have reasonable results. Convergence of the solution is always monitored carefully during computation. Table 5 shows one example.

Table 5. Convergent Test series60, $C_B=0.60$ at $F_n = 0.32$				
Iteration	error1	error2	source	C <sub>w</sub> x10 <sup>3</sup>
Linear	-	-	2.9383	1.815
1	0.9147	0.670	3.0646	1.401
2	0.1783	0.170	3.1157	1.333
3	0.0513	0.017	3.1411	1.350
4	0.0219	0.037	3.1521	1.354
5	0.0153	0.013	3.1521	1.357

Here error1 and error2 are defined in Tables 2 and 3 and

$$\text{source} = \sum_j^{NF} \sqrt{(\sigma_j^{i+1})^2}$$

NF is the total number of free surface control points. For example, if we average error1 by  $NF=696$ , average wave height increment  $\delta h^1$  at each free surface panel after the first iteration is 0.001314 and after the fifth iteration  $\delta \zeta^5$  becomes 0.000022 which are nondimensionalized by half of the ship length. If Series60 hull length is 200m,  $\delta \zeta^1=131.4\text{mm}$  becomes  $\delta \zeta^5=2.2\text{mm}$  after five iterations.

Fig. 8 shows two pairs of the contour plots using the locally developed visualization program WAVE[14]. The Froude number is 0.32. The nonlinear solution was obtained after 6 iterations. The first pair shows contours of the wave height and source strength distribution on the free

surface for the linear step, and the second pair for the nonlinear solution. The wave height is plotted for the positive y-plane and the source strength for the negative y-plane for convenience. 0.03 uniform spacing is used between contour lines for both plots. Solid lines indicate positive wave height and positive source strength, dotted lines negative wave height and negative source strength, and dashed lines zero. We observe the following: (1) the source strengths on the body toward the bow of the ship(not plotted here) are large and positive, but at the free surface near the bow a locally concentrated sink distribution is noticed, with a strong and wide source distribution following immediately downstream,, (2) at the stern there is only sink distribution on the ship surface and the free surface, (3) the humps and hollows of wave height are out of phase to those of source strength. Zeroes of wave height occurs near the mean of either source or sink distribution along x-axis.

## CONCLUSIONS

1. The introduction of a one parameter family of advection methods has significantly enhanced the convergence. This new scheme can control the magnitude of damping in the numerical solution, and proper choice of  $Q_{mul}$  may eliminate the numerical instabilities that several researchers have experienced when using either the three point or the four point method.

2. Contour plots similar to Fig.8 for example, are strongly recommended when studying such a complex numerical model. Using the contour plots we can more easily visualize the quality of computational results and choices of truncation regions and panel densities which often may be misjudged just looking the local flow characteristics such as the wave profile or streamline tracing along the ship hull or especially a scalar quantity such as wave resistance alone. We have found that numerical instability sometimes starts at the edge of a boundary with negligibly small magnitude, and it progressively grows and spreads as iteration continues.

3. The most significant improvement was made between the linear solution and the first iteration. It is suggested that at least for the first iteration an under relaxation coefficient either obtained from Eq. (22) or provided with small value such as 0.5 used by Ni[6] be used. For practical purposes, 2 to 3 iterations may be sufficient.

4. It now appears that the long search for programs to accurately estimate wave resistance is now drawing to a successful conclusion, and the next emphasis should be on the more difficult problems of simulating the wave height on the hull and more generally the wave heights on the free surface. Here the comparison with experimental results combined with flow visualization methods is essential.

## ACKNOWLEDGMENT

The first author was funded by the Applied Hydromechanics Research(AHR) Program supported by the Office of Naval Research and administered by David Taylor Research Center(DTRC).The second author was supported in part by an IPA grant from DTRC and super-computer grants from the National Science Foundation (Grant Number ECS 8515174) and the North Carolina Supercomputer Center. The authors express their gratitude to Dr. Wen-Chin Lin and Dr. Michael Wilson of DTRC for their valuable suggestions and encouragement during the

course of this work. The authors also thank Mr. Peter Chang and Mr. Steve Fisher for their kind support.

## REFERENCES

1. Dommermuth, D.G. and D.K.P. Yue, "The Nonlinear Three-Dimensional Waves Generated by a Moving Surface Disturbance," Proceedings of the 17th Symposium on Naval Hydrodynamics, the Hague, Netherlands, 1988
2. Jensen, G., V. Bertram, and H. Soding, "Ship Wave-Resistance Computation," Proceedings of Fifth International Conference on Numerical Ship Hydrodynamics, Hiroshima, Japan, Sept., 1989.
3. Musker, A.J., "Stability and Accuracy of a Non-Linear Model for the Wave Resistance Problem," Proceedings of Fifth International Conference on Numerical Ship Hydrodynamics, Hiroshima, Japan, Sept., 1989.
4. Bai, K.J., J.W. Kim, and Y.H. Kim, "Numerical Computations for a Nonlinear Free Surface Flow Problem," Proceedings of Fifth International Conference on Numerical Ship Hydrodynamics, Hiroshima, Japan, Sept., 1989.
5. Xia, F., "Numerical Calculations of Ship Flows, with Special Emphasis on the Free surface Potential Flow," Chalmers University of Technology, Goteborg, Sweden, 1986.
6. Ni, S.-Y., "Higher Order Panel Methods for Potential Flows with Linear or Non-linear Free Surface Boundary Condition," Chalmers University of Technology, Goteborg, 1987.
7. Kim, K.J., "Ship Flow Calculations and Resistance Minimization," Chalmers University of Technology, Goteborg, Sweden, 1989.
8. Dawson, C.W., "A Practical Computer Method for Solving Ship-Wave Problems," Proceedings of the 2nd International Conference on Numerical Ship Hydrodynamics, Berkeley, Calif., 1977.
9. Kim, Y.H., S.H. Kim, and T.R. Lucas, "Advanced Panel Method for Ship Wave Inviscid Flow Theory," DTRC-89/029, 1989.
10. Hess, J.L., "Consistent Velocity and Potential Expansions for Higher Order Surface Singularity Method," MDCJ 6911, pp.1-30, June, 1975.
11. Johnson, F.T., "A General Panel Method for the Analysis and Design of Arbitrary Configuration in Incompressible Flow," NASA Contract Rpt 3079, Boeing Com. Airplane Co., Seattle, 1980.
12. Norrbin, N.H.(editor), "The Proceedings of the 17th International Towing Tank Conference," SSPA, Goteborg, 1984

13. Kim, Y.H. and D. Jenkins, "Trim and Sinkage Effects on Wave Resistance with Series60,  $C_B=0.60$ ," DTNSRDC/SPD-1013-01, 1981.

14. Robinson, C.R., "Ship Wave Color Graphics Using DI-3000." Computer Science Senior Project, U. of North Carolina at Charlotte, 1986.

## APPENDIX

### Derivatives of Velocity Components in Z-direction

$$\phi_{xz} = \iint_{\Sigma} \frac{\sigma(\xi-x)(\zeta-z)}{r^5} \sec(\bar{\zeta} \cdot \bar{n}) d\xi d\eta \quad (21)$$

$$\phi_{yz} = \iint_{\Sigma} \frac{\sigma(\eta-y)(\zeta-z)}{r^5} \sec(\bar{\zeta} \cdot \bar{n}) d\xi d\eta \quad (22)$$

$$\phi_{yz} = \iint_{\Sigma} \frac{\sigma(\zeta-z)^2}{r^5} \sec(\bar{\zeta} \cdot \bar{n}) d\xi d\eta - \iint_{\Sigma} \frac{\sigma}{3r^3} \sec(\bar{\zeta} \cdot \bar{n}) d\xi d\eta \quad (23)$$

where  $\sigma(\xi, \eta)$  is given Eq.(15),  $r = \{(\xi-x)^2 + (\eta-y)^2 + (\zeta-z)^2\}^{1/2}$ , and  $\Sigma$  shown in Fig. 2.

We assume that surface panel is sufficiently fine that the term  $\sec(\bar{\zeta} \cdot \bar{n})$  becomes zero. After algebraic manipulation, the following expressions are obtained:

$$\phi_{xz} = \sigma_o K_{ox}(1,1) + \sigma_{\xi}(xK_{ox}(1,1) + K_{ox}(2,1)) + \sigma_{\eta}(yK_{ox}(1,1) + K_{ox}(1,2)) \quad (24)$$

$$\phi_{yz} = \sigma_o K_{oy}(1,1) + \sigma_{\xi}(xK_{oy}(1,1) + K_{oy}(2,1)) + \sigma_{\eta}(yK_{oy}(1,1) + K_{oy}(1,2)) \quad (25)$$

$$\phi_{zz} = \sigma_o K_{oz}(1,1) + \sigma_{\xi}(xK_{oz}(1,1) + K_{oz}(2,1)) + \sigma_{\eta}(yK_{oz}(1,1) + K_{oz}(1,2)) \quad (26)$$

where

$$\begin{aligned} K_{ox}(m,n) = & -hH(m+1,n,5) \\ & + a[ H(m+3,n,5) - 5h^2H(m+3,n,7) \\ & + 2xH(m+2,n,5) - 10xh^3H(m+2,n,7) ] \\ & + b[ H(m+1,n+2,5) - 5h^2H(m+1,n+2,7) \\ & + 2yH(m+1,n+1,5) - 10yh^2H(m+1,n+1,7) ] \\ & + c[ H(m+1,n,5) - 5h^2H(m+1,n,7) ] \end{aligned} \quad (27)$$

$$\begin{aligned} K_{oy}(m,n) = & -hH(m,n+1,5) \\ & + a[ H(m+2,n+1,5) - 5h^2H(m+2,n+1,7) \\ & + 2xH(m+1,n+1,5) - 10xh^2H(m+1,n+1,7) ] \\ & + b[ H(m,n+3,5) - 5h^2H(m,n+3,7) \\ & + 2yH(m,n+2,5) - 10yh^2H(m,n+2,7) ] \\ & + c[ H(m,n+1,5) - 5h^2H(m,n+1,7) ] \end{aligned} \quad (28)$$

$$\begin{aligned} K_{oz}(m,n) = & h^2H(m,n,5) \\ & - a[ 2hH(m+2,n,5) - 5h^3H(m+2,n,7) \\ & + 4hxH(m+1,n,5) - 10xh^3H(m+1,n,7) ] \\ & - b[ 2hH(m,n+2,5) - 5h^3H(m,n+2,7) \\ & + 4hyH(m,n+1,5) - 10yh^3H(m,n+1,7) ] \\ & - c[ 2hH(m,n,5) - 5h^3H(m,n,7) ] \end{aligned} \quad (29)$$

Here

$$c = ax^2 + by^2 - z_o$$

$$h = z - z_o$$

$$z_o = ax_o + by_o$$

$$H(m,n,k) = \iint \frac{(\xi-x)^{m-1}(\eta-y)^{n-1}}{\rho^k} d\xi d\eta$$

$$\rho = \{(\xi-x)^2 + (\eta-y)^2 + h\}^{1/2}$$

The  $H(m,n,k)$  integral has recursion relations and actual computation can be done very efficiently and accurately.

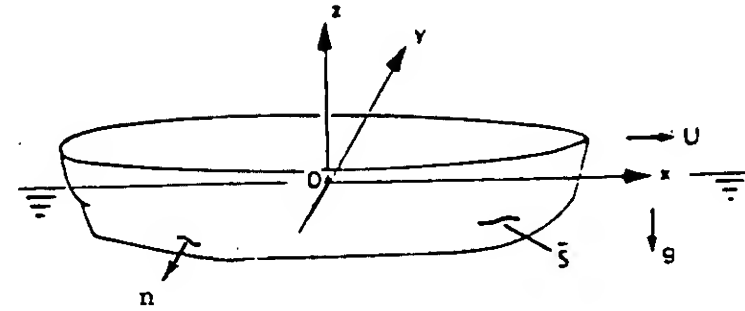


Fig. 1. Coordinate system.

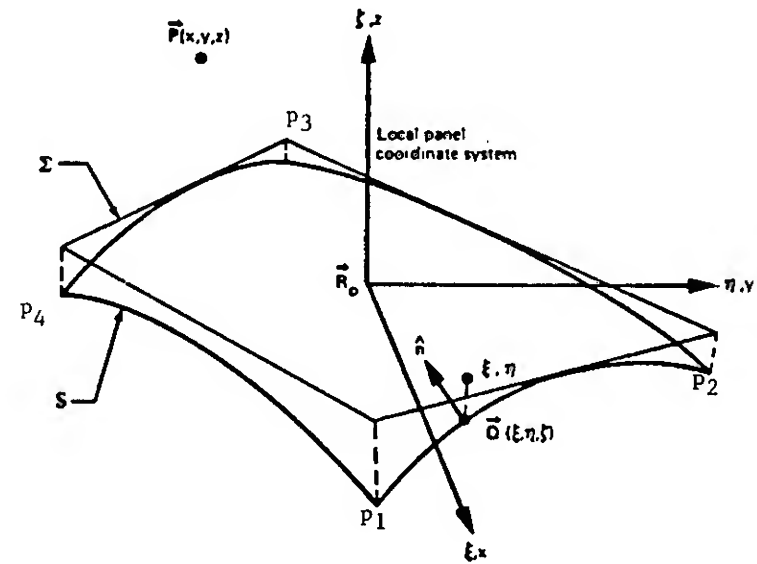


Fig. 2. Field point/panel geometry.

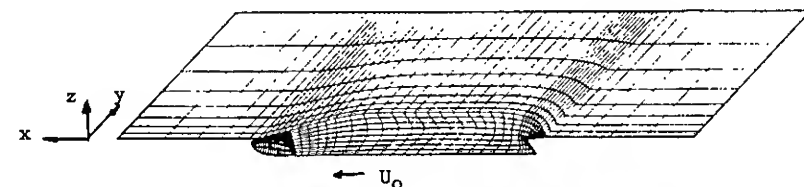


Figure 3. Typical Panel Arrangement

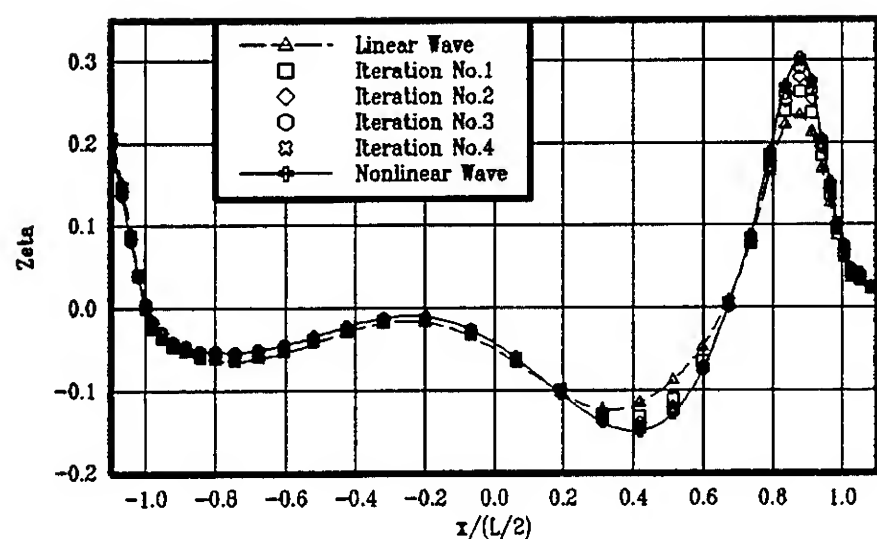


Fig. 4. Wave Profiles at Hull Surface  
Wigley Hull at  $F_n=0.316$

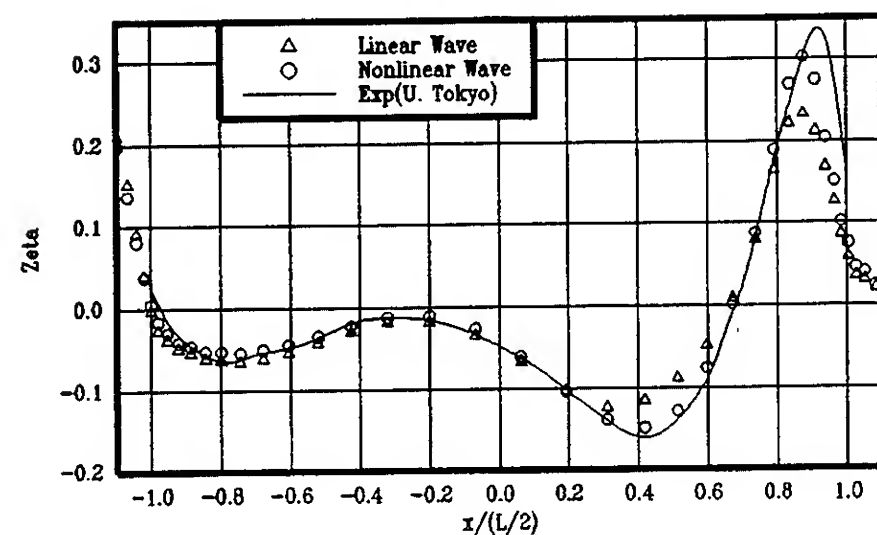


Fig. 5. Wave Profile Comparisons at Hull Surface  
Wigley Hull at  $F_n=0.32$

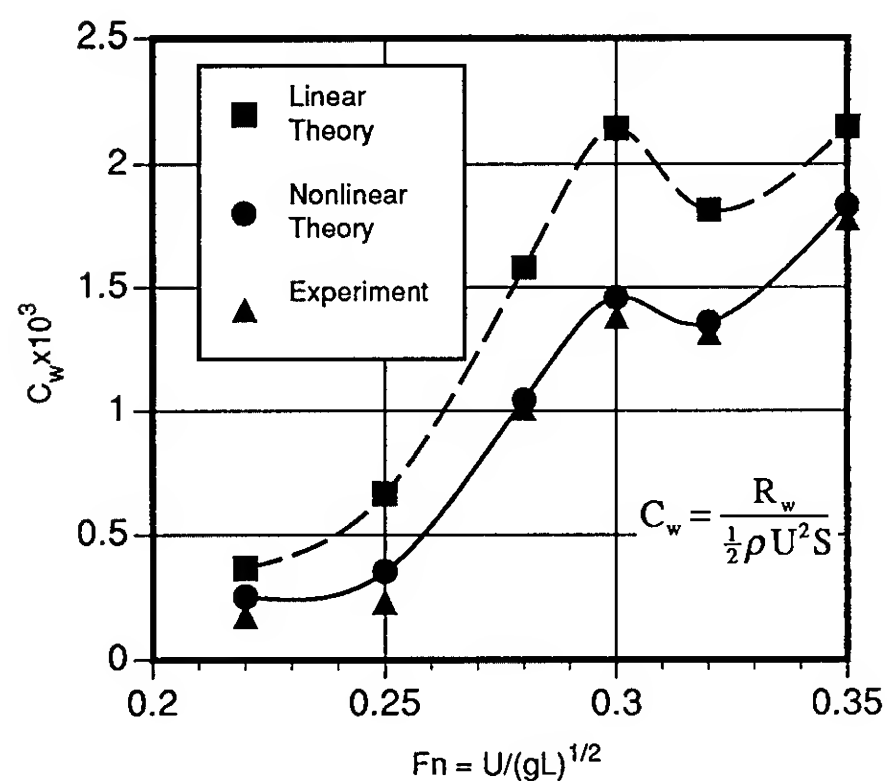
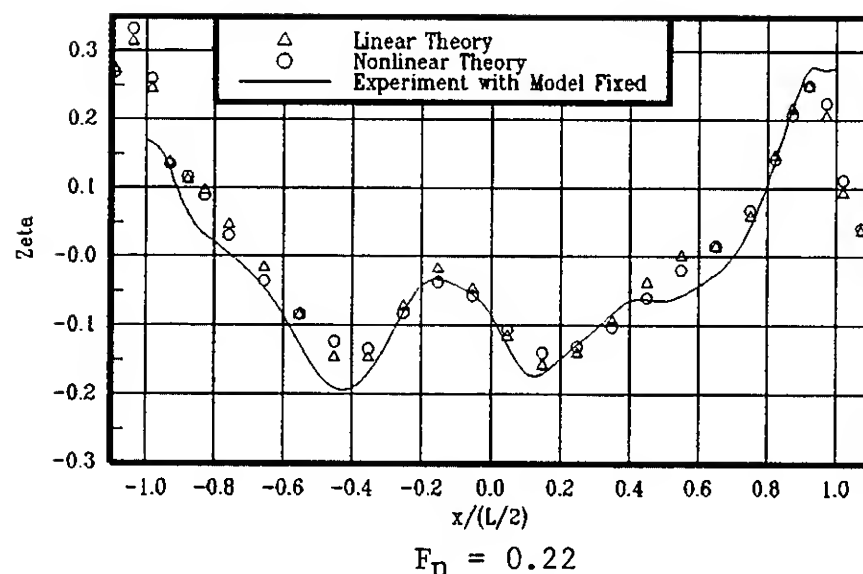
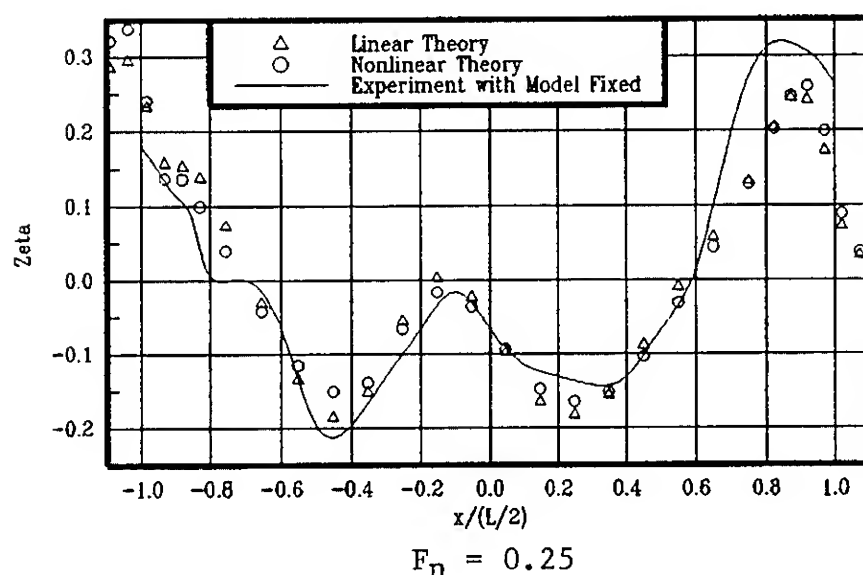


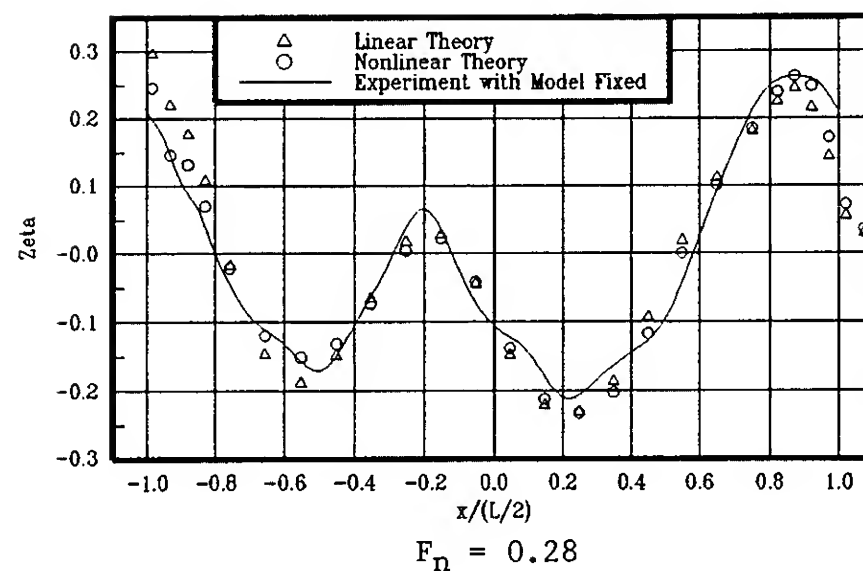
Fig. 6. Wave Making Resistance Comparisons  
Series60,  $C_p=0.60$



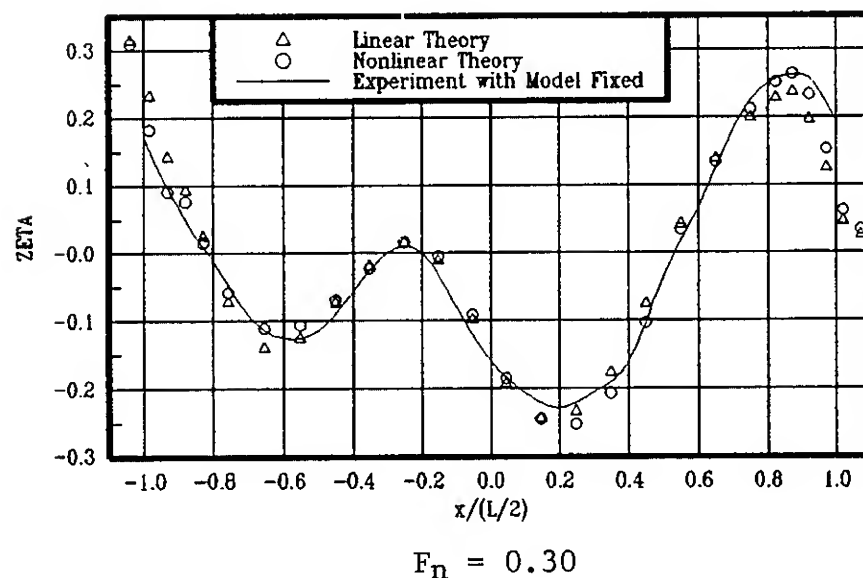
$F_n = 0.22$



$F_n = 0.25$



$F_n = 0.28$



$F_n = 0.30$



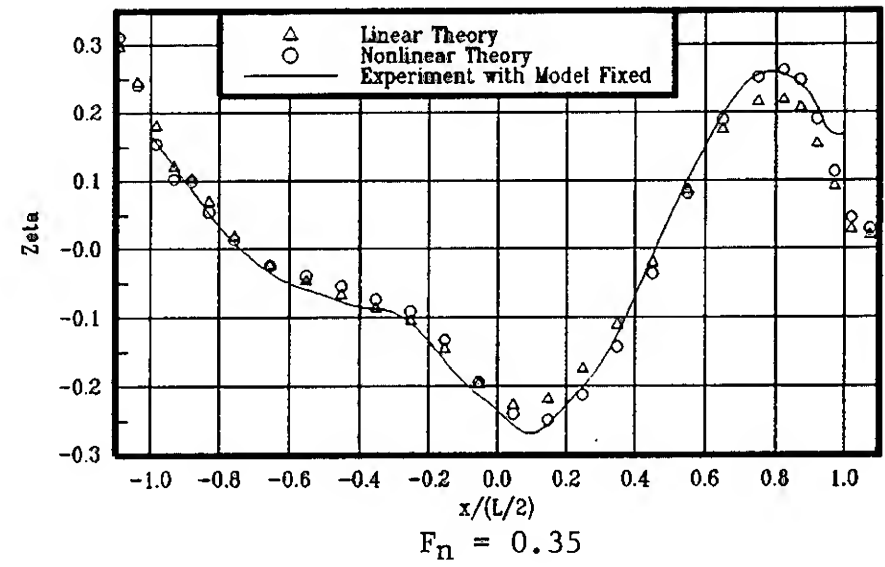
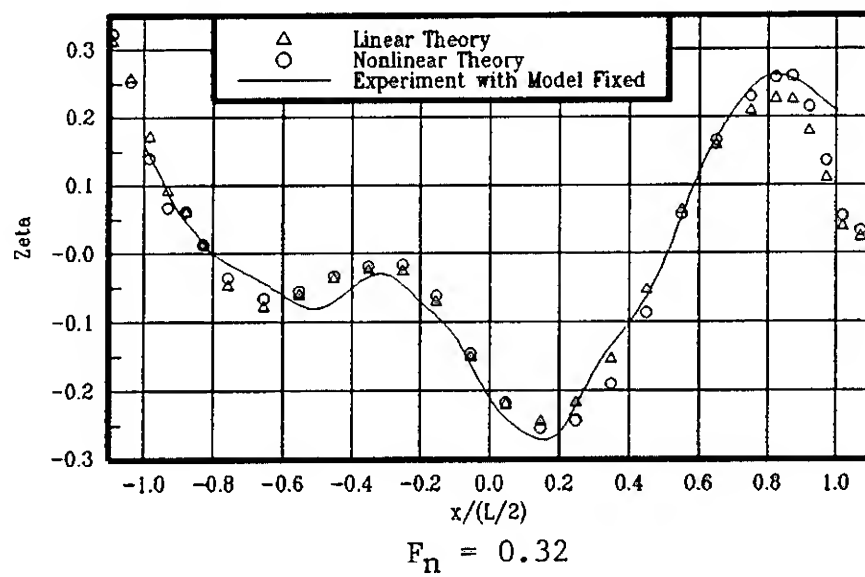


Figure 7. Wave Profile Comparisons at Hull Surface  
Series 60,  $C_B = 0.60$

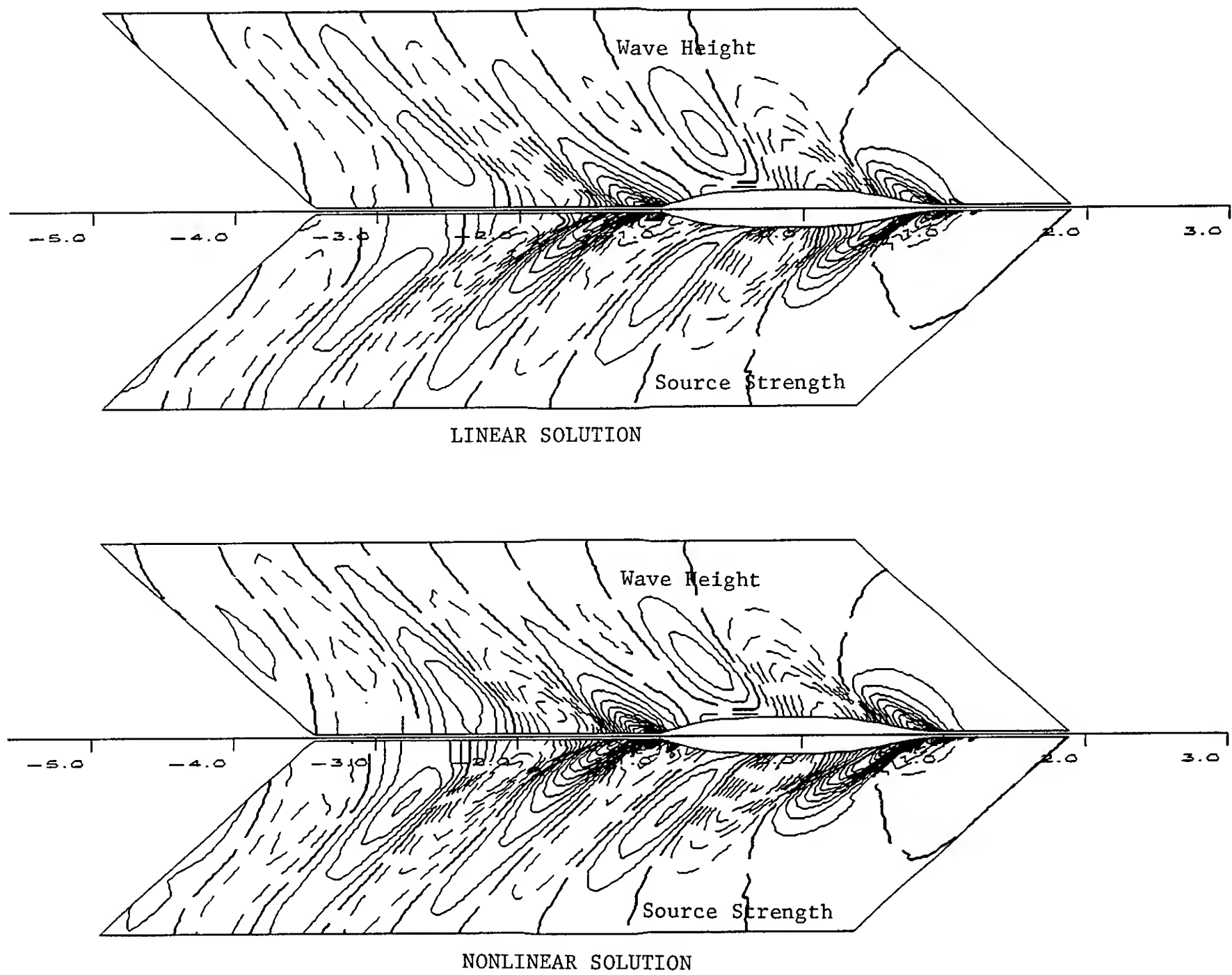


Figure 8. Contour Plots of Wave Height and Source Strength  
Series 60,  $C_B = 0.60$  at  $F_n = 0.32$



## DISCUSSION (SESSION V, PAPER 5)

John V. Wehausen  
University of California at Berkeley, USA

The agreement between the authors' "nonlinear" computations and measurement is impressive, but I wonder is one should not be suspicious of such good agreement. Since the computations are based on the irrotational flow of an inviscid fluid, shouldn't a measured wave resistance based upon residuary resistance, or even wave-pattern resistance, show at least some discrepancy with the computed resistance? The wave resistance is a rather sensitive test, for it is the difference between two large numbers and one expects to see some effect of viscosity in the stern region. I shall be curious to see the results for similar computations for Series 60,  $C_B = 0.80$ . I also have a question concerning the numerical procedure. "Convergence," or lack of it, appears to depend upon the choice of  $Q_{mul}$ , but  $Q_{mul} = 3$  or  $5$  both lead to convergence, but to different values. Which should I believe? and why? Even if they were identical, can one give an estimate of the difference between the obtained value and the solution to the exact problem (when  $1 \rightarrow 0$  in some fashion)?

## DISCUSSION

Ronald W. Yeung  
University of California at Berkeley, USA

Your results show remarkably good agreement in terms of wave resistance and wave/profile when compared with experimental data. Jensen and Söding (1988, Jahrbuch der Schiffbautechnische Gesellschaft) have also obtained similarly good agreement for the same formulation but using discrete sources. They also have very good conveyence in their iterative scheme. I was wondering if it will be possible for you to compare your results with theirs. To my recollection, their stern wave profiles do not have as good an agreement with experiments as yours. Of course, for an identical model, and identical mathematical problem, there should be only one set of correct results. For a blunt bow ship, Jensen & Söding had difficulty obtaining convergent and accurate results in the bow area. You may like to try a similar test with your code. I want to congratulate you and your colleagues, including Dr. S. H. Kim, for the successful development of this code.

## DISCUSSION

Hauime Maruo  
University of California, Santa Barbara, USA

The examples, which are employed in this paper, are Wigley hull and Series 60 hull. In these cases the effect of nonlinearity is comparatively small, and the advantage of the nonlinear computation may not be well demonstrated. The nonlinear effect is remarkable in the case of hull forms as was employed in the paper by Maruo & Ogihara (1985), for which the nonlinear computation is indispensable.

## DISCUSSION

Hoyte Raven  
Maritime Research Institute Netherlands, The Netherlands

Your method shows a very good convergence for the cases studied. However, this convergence depends on the numerical (artificial) damping caused by the difference scheme. This damping does not vanish upon convergence but remains present in the result. For the rather mild cases shown, its influence does not seem to be large, but for full hull forms the required value of  $Q_{mul}$  could be much higher and the damping could be more detrimental. Similarly, a reduction of the panel size is likely to ask for higher  $Q_{mul}$ . Therefore, I believe that other inherently more robust formulations of the iterative procedure remain something to be searched for. Could you comment on this?

## DISCUSSION

Kuniharu Nakatake  
Kyushu University, Japan

I congratulate you on your fine results. You tested a new family of upstream finite difference schemes in order to satisfy the radiation condition. As well known, the calculated results vary with choice of different scheme. I think it is not reasonable. We are using a phase-shift method which we call KU (Kyushu Univ) method.<sup>1</sup> The feature of this method is nonuse of difference scheme. According to our experience, it is applicable to very narrow computation domain. And a theoretical proof for it is to be presented by Dr. H. Seto (Mitsubishi Heavy Ind.) in Nov. 1990. I recommend you to test KU method too.

[1] J. Ando and K. Nakatake, Tran. of West-Japan Society of Naval Architects, Vol. 75, 1987.

## DISCUSSION

Dimitris Nakos  
Massachusetts Institute of Technology, USA

The design of iteration schemes, based on linearization about the previous solution step, is the most critical issue in numerical solutions of nonlinear steady ship waves. Such schemes are desired to be convergent within a few iterations, due to the large computational effort involved at each solution step. It is fair to state that the part of the wave flow which is expected to resist convergence is associated mostly with the diverging wave system. The authors have demonstrated effectively that excessive numerical damping is able to "filter out" all short diverging waves and consequently accelerate the convergence (see e.g. Figure 8). The question that arises is the following: Is it proper to disregard essential features of the flow in the name of numerical convergence, in particular, in light of the fact that the relatively long transverse waves are mostly unaffected by nonlinearities?

## AUTHORS' REPLY

We would like to express our thanks to all of the participants who have shown their interest in our paper, made comments, and expressed their critiques. Several questions have a common interest and we have grouped them without advance consent.

Reply to Professor Wehausen:

The experimental values of the wave-making resistance we used to make comparisons were obtained by the longitudinal wave profile measurement suggested by Eggers[1]. In his derivation the effect of the viscosity is neglected and the corresponding computer code has been reported by Reed[1]. Table A summarizes the linear, nonlinear and measured wave-making resistance for Series 60,  $C_B = 0.60$ . At the lower Froude number, the discrepancy between the measurement and the nonlinear solution is significant and even at the higher Froude number the difference is still noticeable.

Reply to Professors Wehausen, Maruo, Yeung, and Dr. Raven:

They have shown common interest in the nonlinear effects on a ship with blunt bow and large block coefficient. We have selected Series 60,  $C_B = 0.80$  which has a half entrance angle of 43 degrees as an additional test case. Figures A and B show the linear and nonlinear wave profiles together with a series of wave profiles obtained during each iteration for  $Fn = 0.20$  and  $0.25$  with  $Q_{mul} = 3$  and  $5$  respectively. No comparisons were made with measurements because of lack of availability. As Prof. Maruo pointed out, the nonlinear effects on Series 60,  $C_B = 0.80$  is more significant than those on Wigley hull or Series 60,  $C_B = 0.60$ . One noticeable difference observed between ships during the iteration is that for Series 60,  $C_B = 0.80$  the wave profile after the first iteration has the largest hump and hollow near bow region and from the second iteration the wave profiles oscillate within the linear and the first wave profile band until the solution converged. On the other hand, for Wigley hull or Series 60,  $C_B = 0.60$ , the wave profiles always progressively grow as the iteration number increases until the solution converged. For  $Fn = 0.30$ , we increased  $Q_{mul}$  from 5 to 7 to 9, but failed to get a converged solution. As the iterations continued, the wave amplitude grew continuously and after the third iteration the wave amplitude near the bow region exceeded the ship draft and the solution diverged. Without having measurements, it is difficult to evaluate the quality of our converged solutions for a fullform ship. Whether the  $Fn = 0.30$  case is beyond the capability of our code would require further study, but as the  $Q_{mul}$  method is very new, and has now been shown to converge nicely for lower Froude numbers even for this fullform ship, with further research we would anticipate convergence even at  $Fn = 0.30$ .

Reply to Prof. Yeung:

Dr. Jensen compares his wavemaking resistance computations with Ogiwara's experimental results which were conducted at free sinkage and trim conditions. Our code can be extended to handle the free sinkage and trim conditions. There are no plots on the wave profile in Jensen's paper.

Reply to Prof. Nakatake:

The phase shift and the shift of collocation point may be different terminology for the same approach. A shifting also introduces numerical damping and is algorithmically similar to the use of upstream finite difference formulae. We had earlier implemented the shift of the collocation method in our computer code and tested it. In our numerical experiments, we shifted the collocation points forward between 10% and 50% of the characteristic length of each panel. Our numerical results showed that the shifting apparently removed the oscillation of wave profiles, in particular near the bow region, but decreased the wave amplitude proportionally as we increased the shifting. According to our numerical experience, we haven't found significant advantages to applying the shifting logic to our code.

Reply to Prof. Wehausen, Dr. Nakos, and Dr. Raven:

It is well known that the panel method using a Rankine type singularity with an upstream finite difference scheme to satisfy the free surface and radiation conditions provides good results near the ship [4]. But because of an inherent local damping introduced by upwinding, the wave amplitudes attenuate significantly as they propagate and the results get poorer far downstream. Our aim was to develop a quality computer program which is practical for ship designers in the shipbuilding business. The linear codes of the past made many simplifications. We have provided an approach to solve the original nonlinear problem that eliminates these, and gives results that compare well with those of experiment, with a modest use of computer time. We haven't examined the relations between panel size, Froude numbers, and  $Q_{mul}$ s carefully at this point, however we will be considering these questions in the future. Your comments and critiques are very much appreciated.

#### References:

- [1] Eggers, K.W.H., "Über die Ermittlung des Wellenwiderstandes eines Schiffsmodells durch Analyse seines Wellensystem," I.II Schiffstechnik 9, pp. 79-84, 1962; Disk 85; 10, pp. 93-106, 1963.
- [2] Reed, A.M., "Documentation for a Series of Computer Programs for Analyzing Longitudinal Wave Cuts and Designing Bow Bulbs," DTNSRDC/SPD-0820-01, June, 1979.
- [3] Sclavounos, P.D. and D.E. Nakos, "Stability Analysis of Panel Methods for Free-Surface Flows with Forward Speed," Proc. 17th Symp. on Naval Hydrodynamics, The Hague, The Netherlands, 1988.
- [4] Lindenmuth, W.T., T.J. Ratcliffe, and A.M. Reed, "Comparative Accuracy of Numerical Kelvin Wake Code Prediction-'Wake-Off'," DTNCSHD-12601-01, May, 1988.

Table A Wave-Making Resistance Comparisons Series60, $C_B=0.60$ (Model Fixed)			
(C <sub>w</sub> x10 <sup>3</sup> )			
F <sub>n</sub>	Linear	Nonlinear	Experiment
0.22	0.369	0.255	0.176
0.25	0.664	0.354	0.230
0.28	1.581	1.045	1.011
0.30	2.144	1.460	1.375
0.32	1.815	1.357	1.316
0.35	2.148	1.836	1.780

Fig.A. Series60,  $C_B=0.80$  at  $F_n=0.200$

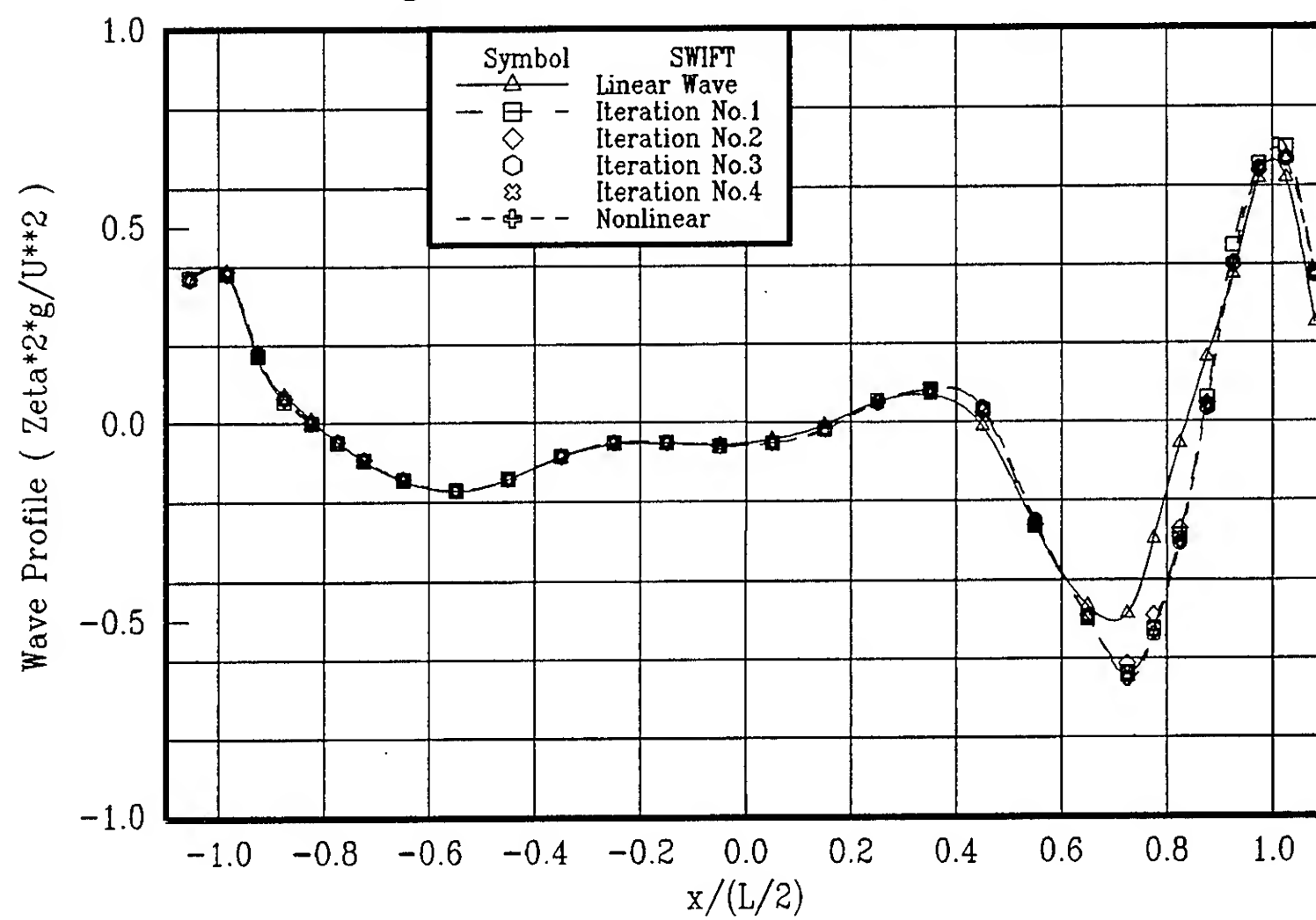
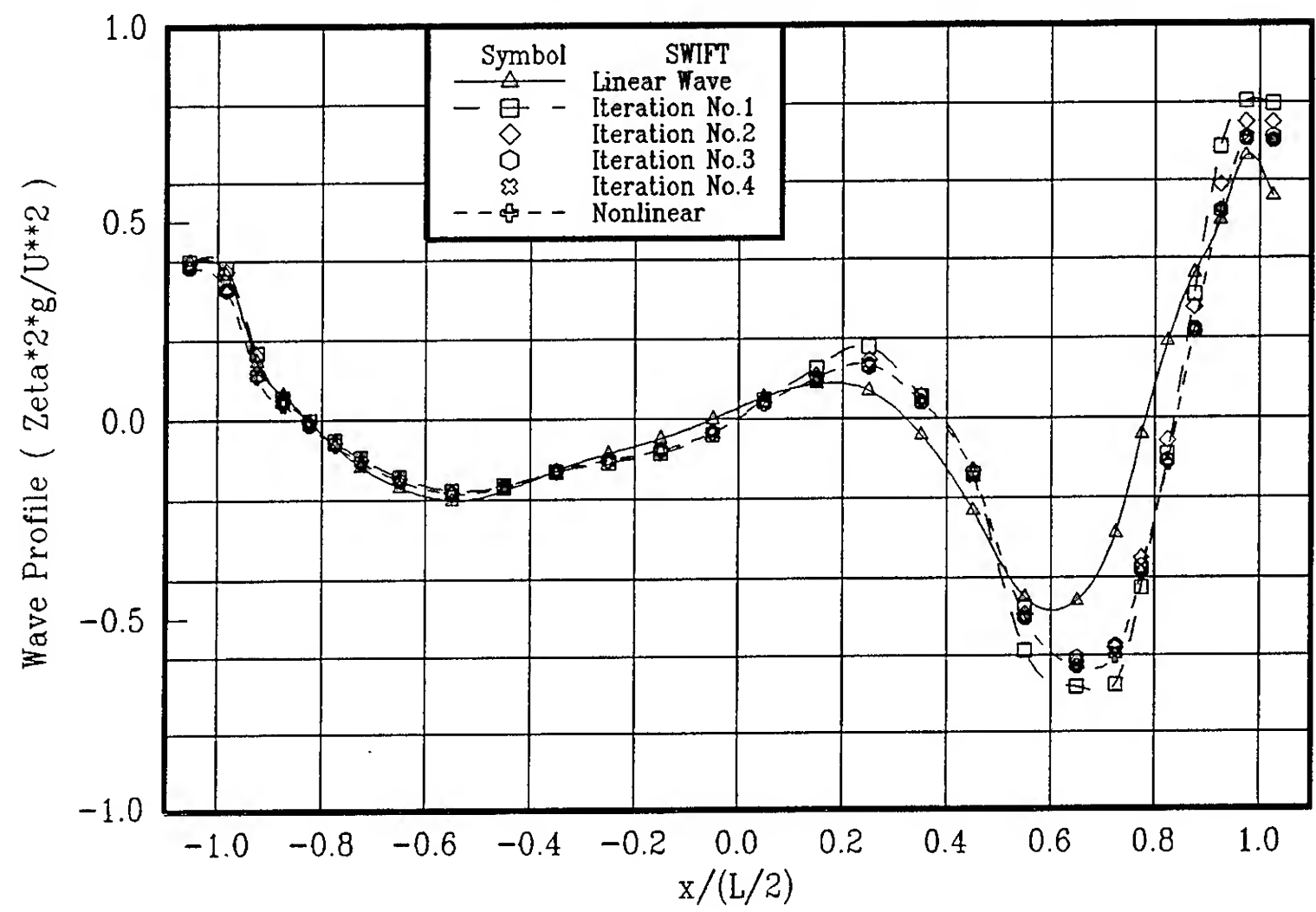


Fig.B. Series60, CB=0.80 at Fn=0.250



# **A Model for the Generation and Evolution of an Inner-Angle Soliton in a Kelvin Wake**

R. Hall, S. Buchsbaum

(Science Applications International Corporation, USA)

## **ABSTRACT**

We develop a simple model for the generation and evolution of an inner-angle soliton in a Kelvin wake. The generation is modeled as an interference maximum due to a source-sink pair and the evolution is modelled using the nonlinear Schrodinger equation. The model is used to explain the results of a recent experiment. Although some of the parameters in the model are fit to experimental data, the values of the parameters are physically reasonable, thus we conclude that the model captures the essential physics.

## **1. INTRODUCTION**

It has long been observed that rays appear inside the cusp line within the diverging portion of the Kelvin wake of a ship. The simplest explanation for these rays is an interference pattern due to the superposition of the wave fields generated by the bow and the stern. Interest in these rays has increased in recent years because they are a possible explanation for some of the long bright lines observed in imagery of ship wakes collected from space [1].

Since these rays can form as a result of an interference pattern, they will appear in any model for the Kelvin wake of a ship as long as that model is capable of calculating the far-field wake. If the wave amplitude in the ray is small, or if the Kelvin wake model uses a linearized form of the free surface

boundary condition, then each ray inside the cusp line diverges linearly as it propagates aft: the width increases linearly with distance aft and the amplitude decreases as the inverse of the square root of the distance aft (the cusp line, of course, diverges slower).

In a recent experiment [2,3], a ray in the Kelvin wake of a Coast Guard cutter was studied. Figures 1 and 2 show the near- and far-field wakes, respectively. The ship speed was 15 knots (the Froude number was 0.5) and the ray appeared at an angle of 10.9 degrees from the wake centerline, which is close to the angle predicted by the interference model discussed above. However, the far-field evolution of the ray was not consistent with linear theory. Although Figure 2 shows that the width of the ray increased somewhat over the first few ship lengths aft of the stern, by a few hundred meters aft the width did not increase and the ray was shown to be an oblique nonlinear solitary wave packet. Related theoretical work [4] on the nonlinear evolution of a wave packet showed similar behavior.

In this paper we will develop a simple physical model for the generation and evolution of the inner-angle ray observed in the experiment. In Section 2, the generation of the ray will be modeled using a simple linear theory in which the bow of the cutter is represented by a source and the stern is represented by a sink. In Section 3, the evolution of the ray into an oblique nonlinear solitary wave packet will be modeled using a two-



Figure 1. The near-field wake of the Coast Guard Cutter Point Brower. The ship speed is 15 knots. The lower photo shows the port side cusp line and soliton. The soliton intersects the lower left hand corner of the photo.



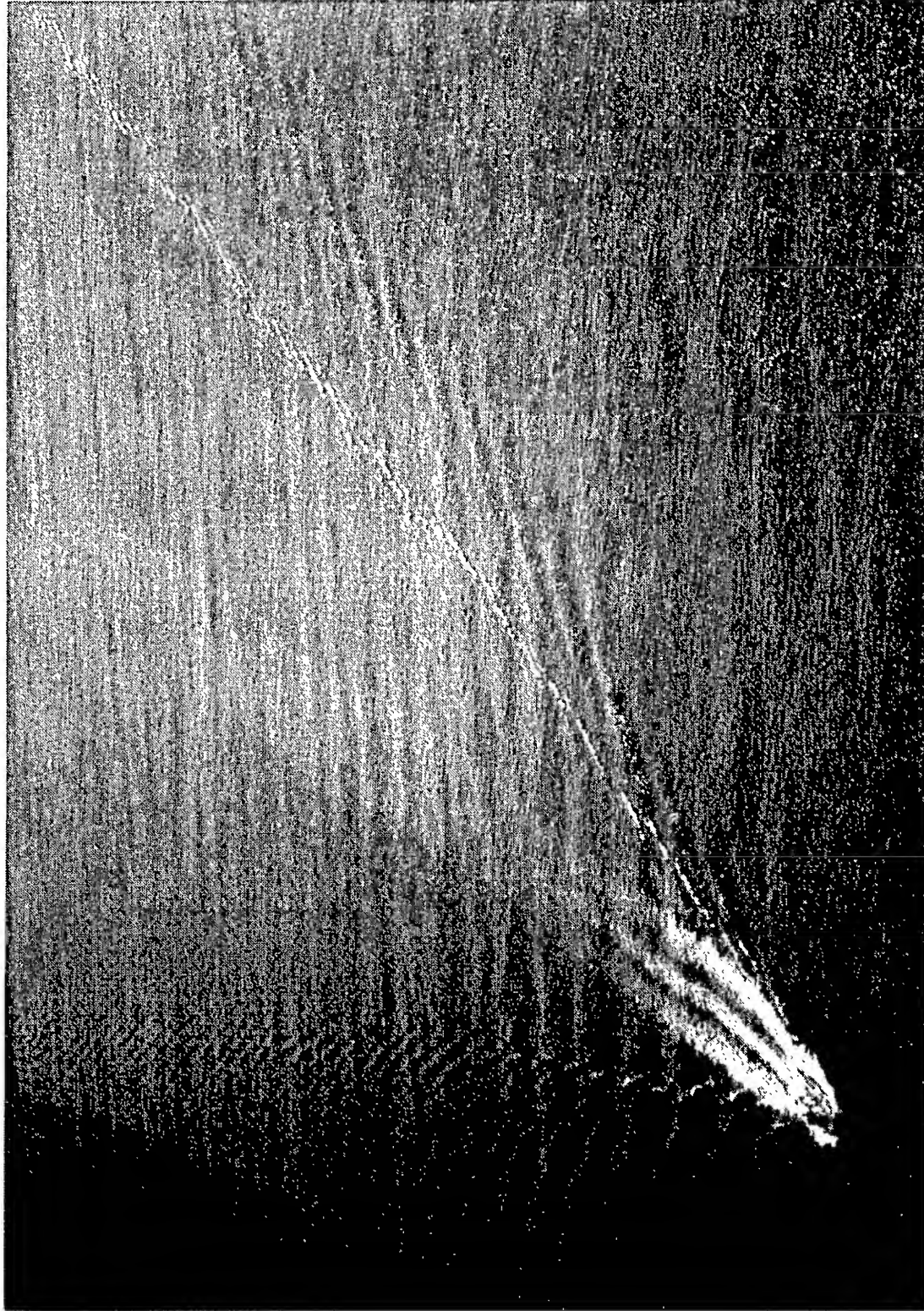


Figure 2. The far-field wake of the Coast Guard Cutter Point Brower. The ship speed is 15 knots. The image of the port side soliton is enhanced by sun glint. The port side cusp line appears outside the port side soliton. Note the wave breaking on the first few crests of both the port and starboard solitons.

dimensional nonlinear Schrodinger equation for the complex packet envelope. Compared to the current state-of-the-art in modeling the Kelvin wakes of ships, our model is crude, but it has the virtue of capturing the essential physics in a simple way. In the conclusions we will review the limitations of the model and will suggest future improvements.

Included in the Appendix is brief review of Kelvin wake kinematics, including the geometry of the interference rays generated by a source-sink pair, and a list of the parameters of the soliton observed in the experiment.

## 2. LINEAR THEORY

Our model for the generation of the ray consists of a source-sink pair in a potential flow with linearized free surface boundary conditions. The interior continuity equation is

$$\nabla^2 \Phi = S_B + S_S, \quad (1)$$

the linearized dynamic boundary conditions on  $z=0$  are

$$\Phi_t - U\Phi_x = -P - g\eta \quad (2)$$

and

$$P = 0, \quad (3)$$

and the linearized kinematic boundary condition on  $z=0$  is

$$\eta_t - U\eta_x = \Phi_z. \quad (4)$$

The coordinate system is fixed to the ship, which is moving with speed  $U$  in the positive  $x$  direction.  $y$  is positive to port and  $z$  is positive upward.  $\Phi$  is the velocity potential for the perturbation to the uniform oncoming flow,  $\eta$  is the free surface elevation relative to the mean ambient level  $z=0$ , and  $P$  is the surface pressure divided by the density. The source at the bow,  $S_B$ , and the sink at the

stern,  $S_S$ , are given by point singularities:

$$S_B = UA\delta(x-a)\delta(y)\delta(z-c) \quad (5)$$

and

$$S_S = -S_B, \text{ with } a \rightarrow -a. \quad (6)$$

The depth of the source is  $-c$  and the distance between the source and the sink is  $2a$ . Note that  $x=0$  is amidships; hereinafter, when we refer to distance aft, we mean distance aft of amidships, or  $-x$ . The volume flux emitted by the source is  $UA$ . In the limit that  $a \gg \sqrt{A}$ ,  $A$  is the cross-sectional area amidships of the region occupied by the fluid emitted from the source. Since the source is steady and the coordinate system is fixed to the ship, the solution of Equations (1)-(6) will be steady.

In the experiment discussed in [1], the ship was a Point Class Coast Guard cutter (Point Brower) and the ship speed was 15 knots. We obtain the required parameters for our model from Coast Guard Drawing No. 82(D) WPB-0700-1, "82 Foot Patrol Boat (Class D) Docking Plan." The forward and aft (at the stern) perpendiculars are defined using a draft of 5'-3" above the base of the propellor. The distance between them is 78' (23.8 meters), which is the waterline length for this draft. The cross-section nearest amidships shown in the plan is a bulkhead located 36' aft of the forward perpendicular. Using the 5'-3" waterline, this cross-section has a beam of 4.4 meters at the waterline, a draft of 1.0 meters above the bottom of the bare hull, and a cross-sectional area of 3.3 square meters below the waterline. We do not know the actual static waterline or the running sinkage and trim for the experiment.

For our model, we will use  $U=15$  knots and we will let  $A$  be 3.3 square meters, which is the submerged cross-sectional area at the 36' bulkhead. The depth of the source,  $-c$ , will be half the draft at the bulkhead, or 0.5 meters. We could let the distance between the source

and the sink,  $2a$ , be the 23.8 meter waterline length, but we chose a smaller value of 22.2 meters instead. This value is chosen so that the position of the ray in the model is fit to the observed position of the soliton in the experiment, as shown in the Appendix. It is reasonable that the value of  $2a$  be less than the waterline length because the wave generation regions lie between the forward and aft perpendiculars.

The solution of Equations (1)-(6) is given in terms of a superposition of two of the Green functions defined in Equation (7) of [5]. Figure 3a shows the surface elevation out to a distance of 400 meters aft. Only the far field portion of the solution, the portion given by Equation (7b) of [5], is shown. The first ray inside the cusp line is the ray that evolves into the soliton. The ray appears at an angle of 10.9 degrees from the wake centerline and the wave vector at the peak of the ray is  $(k_x, k_y) = (0.426, 1.01)m^{-1}$  (see the Appendix). Unfortunately, there are two problems with this solution. First, the wave slopes within the diverging portion of the Kelvin wake are unrealistically large. This can be seen more clearly in Figure 4, which shows the cross-track slope  $\eta_y$  at 100 meters aft. Second, two additional rays, which were not observed in the experiment, appear inside the first ray. Both of these problems can be corrected by replacing the point sources at the bow and stern with distributed sources. This is a reasonable modification of the model because the bow and stern regions are of finite extent. For convenience, we chose a Gaussian distribution in the horizontal plane,

$$S_B = \frac{UA}{2\pi\sigma^2} \exp\left\{-\frac{(x-a)^2 + y^2}{2\sigma^2}\right\} \delta(z-c) \quad (7)$$

and

$$S_S = -S_B, \text{ with } a \rightarrow -a, \quad (8)$$

because it reduces each spectral component in the solution by the simple factor

$$\exp(-\sigma^2 k^2 / 2), \quad (9)$$

where  $k$  is the horizontal wavenumber. Figure 3b shows the surface elevation for the solution of Equations (1)-(4), (7) and (8), with a value of 1.2 meters for  $\sigma$ . This particular value is chosen so that the amplitude of the soliton obtained in Section 2 agrees with the observations. The value is reasonable because it yields a value of 2.8 meters for the full width at half height of the Gaussian, which is consistent with the length scales in the bow and stern. Figure 4 shows the cross-track slope at 100 meters aft for this solution. Note that the values are now physically reasonable.

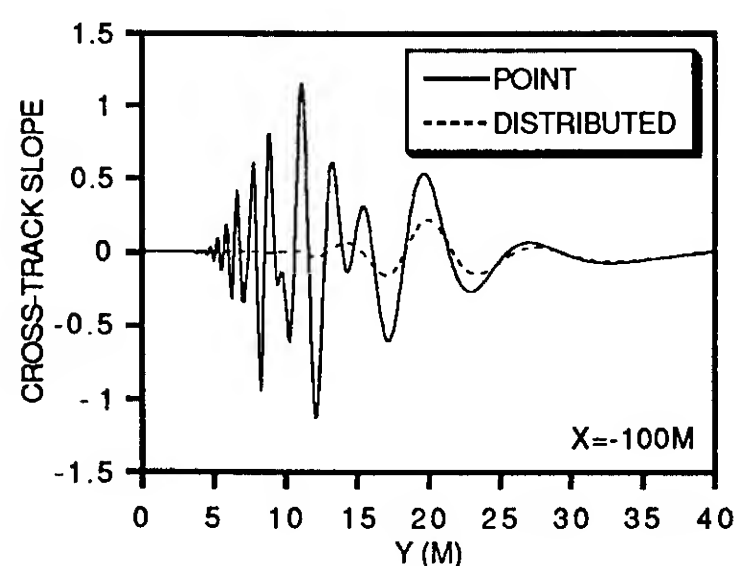
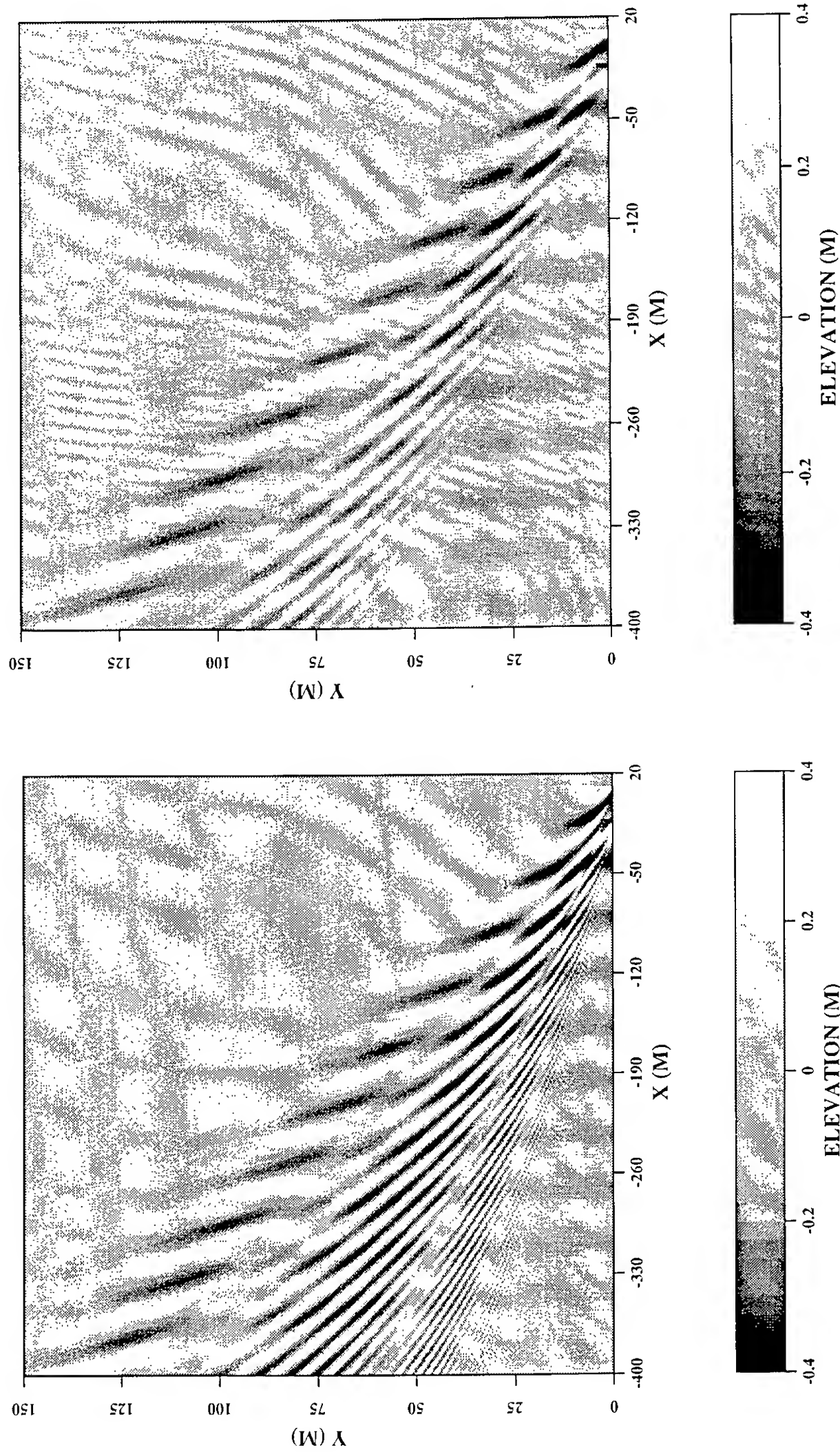


Figure 4. A comparison of the cross-track slope at 100m aft for the two types of sources.

### 3. NONLINEAR THEORY

We model the evolution of the ray into an oblique nonlinear solitary wave packet by using a time-dependent, two-dimensional nonlinear Schrodinger equation for the complex packet envelope. One procedure for doing this is to take the cross-track profile of the ray at a couple of ship lengths aft and



POINT SOURCE-SINK PAIR

DISTRIBUTED SOURCE-SINK PAIR

Figure 3a (left) and 3b (right). A comparison of the solutions of the source-sink pair generation model for point sources and distributed sources. Note that the y axis is expanded relative to the x axis. The first ray inside the cusp line is the ray that will evolve into the soliton when nonlinear effects are included. It intersects the left side of each figure near  $y=75\text{m}$ .



use it as an inflow boundary condition for the nonlinear Schrodinger equation. A second procedure, which is suitable when the generation model is linear, is to bandpass the source term for the narrow band of spectral components that generate the ray, and then include this narrow-band source term in the nonlinear Schrodinger equation. We adopt this second procedure.

We begin by returning to the generation model and separating the velocity potential  $\Phi$  into a double body term  $\phi_{DB}$  and a wave term  $\phi$

$$\Phi = \phi_{DB} + \phi. \quad (10)$$

The double-body flow satisfies the interior equation

$$\nabla^2 \phi_{DB} = S_B + S_S, \quad (11)$$

and the boundary conditions

$$\phi_{DBZ} = 0 \quad (12)$$

and

$$P_{DB} = U\phi_{DBx} \quad (13)$$

on  $z=0$ . The wave field satisfies the interior equation

$$\nabla^2 \phi = 0 \quad (14)$$

and the boundary conditions

$$\phi_t - U\phi_x = P_{DB} - g\eta \quad (15)$$

and

$$\eta_t - U\eta_x = \phi_z \quad (16)$$

on  $z=0$ . We solve Equations (11)-(13) for  $P_{DB}$  and bandpass the result so that it only contains the narrow band of spectral components  $\tilde{P}_{DB}$  that generate the ray.

The rigorous procedure for bandpassing  $P_{DB}$  involves finding the

wavevectors of the two nodes in the Kelvin wake that bound the ray, then using a top hat filter to pass all of the spectral components along the Kelvin wake dispersion curve in between these nodes. For simplicity, we adopt an alternate approximate procedure: we replace the top hat filter with a Gaussian filter, we approximate the spectrum of  $P_{DB}$  in the vicinity of the filter by a uniform value for the source and another uniform for the sink, and we set each uniform value equal the value at the spectral component corresponding to the peak of the ray. The resulting expression for  $\tilde{P}_{DB}$  is

$$\tilde{P}_{DB} = \text{Re} \left\{ H \exp \left[ i (k_x x + k_y y) \right] \right\}, \quad (17)$$

where

$$H = H_B + H_S, \quad (18)$$

$$H_B = -\frac{2i\omega}{k} U A \exp \left[ -\frac{\sigma^2 k^2}{2} - k|c| - i(k_x a) \right] F_B, \quad (19)$$

and

$$H_S = -H_B, \text{ with } a \rightarrow -a, \quad (20)$$

and where  $F_B$  is given by

$$F_B = \frac{\sigma_{k_x} \sigma_{k_y}}{2\pi} \exp \left[ -\frac{\sigma_{k_x}^2 (x-a)^2 + \sigma_{k_y}^2 y^2}{2} \right]. \quad (21)$$

$(k_x, k_y) = (0.426, 1.01)m^{-1}$  is the wavevector of the Kelvin wave at the peak of the ray, and  $k = 1.10m^{-1}$  and  $\omega = 3.28\text{rad/s}$  are the wavenumber and frequency, respectively (see the Appendix). We choose a value of  $\sigma_{k_y} = k_y/2$  for the standard deviation of the Gaussian filter in the  $k_y$  direction. This is the most important direction because it is roughly parallel to the

Kelvin wake dispersion curve in the  $(k_x, k_y)$  plane. This value of  $\sigma_k$  does a reasonable job of passing the spectral components that lie between the two nodes that bound the ray, as well as excluding the spectral components beyond the nodes (see the Appendix). The value of  $\sigma_k$  must be large enough to pass the spectral components that lie between the nodes. We let it equal  $\sigma_k$ , for convenience. Although this is a few times larger than necessary, the additional filter width is normal to the Kelvin wake dispersion curve and does not contribute to the far-field wake.

Assuming that the surface elevation has the narrow-band form

$$\tilde{\eta} = \text{Re} \left\{ B \exp[i(k_x x + k_y y)] \right\}, \quad (22)$$

we use standard procedures (see [6]) on Equations (14)-(17) to obtain the linear Schrodinger equation for the complex packet envelope:

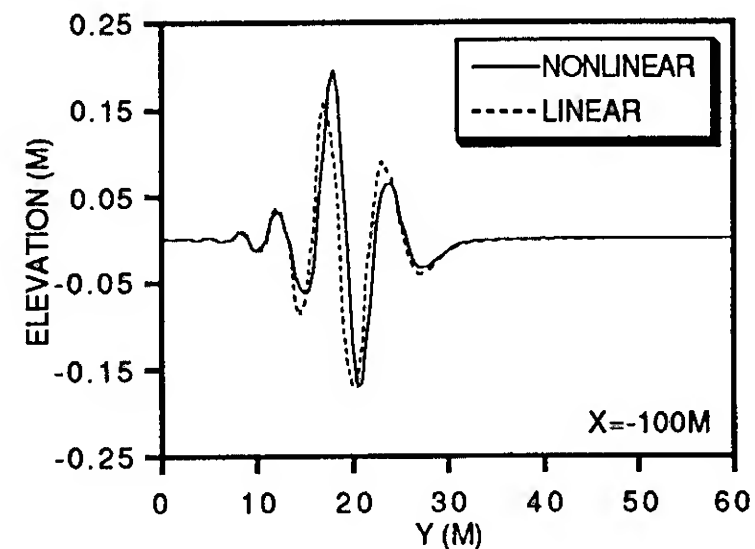
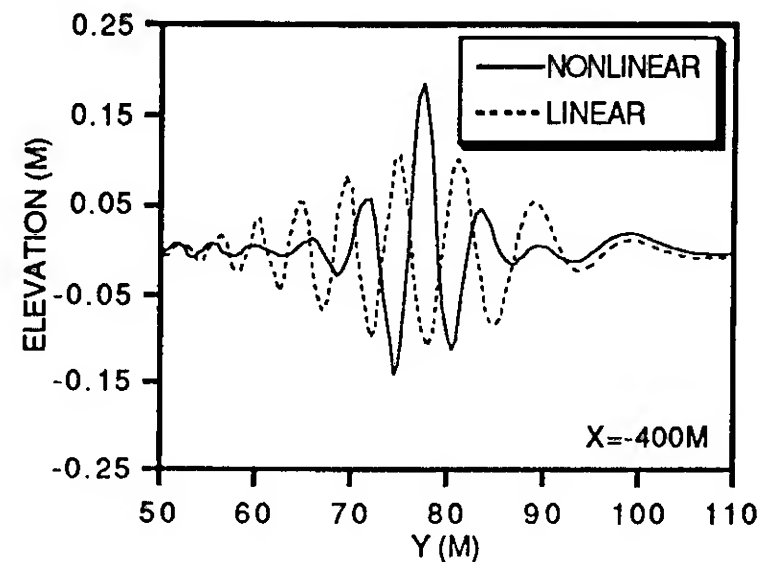
$$\begin{aligned} B_t - UB_x = & -\frac{g}{2\omega k} (k_x B_x + k_y B_y) \\ & + \frac{ig}{8\omega k^3} \left[ (2k_y^2 - k_x^2) B_{xx} \right. \\ & \left. - 6k_x k_y B_{xy} + (2k_x^2 - k_y^2) B_{yy} \right] \\ & + \frac{i\omega H}{2g}. \end{aligned} \quad (23)$$

The solution of this equation is shown in Figure 5a. We note that the ray in Figure 3b appears somewhat larger than the ray in Figure 5a only because the former ray is superimposed on the transverse wave (note the different gray scales in the figures). The actual wave amplitudes are comparable.

The nonlinear Schrodinger equation is obtained by using the nonlinear versions of Equations (15) and (16) in the derivation of Equation (23) (see [6]). The well-known result is to add the term

$$-\frac{i\omega k^2}{2} |B|^2 B \quad (24)$$

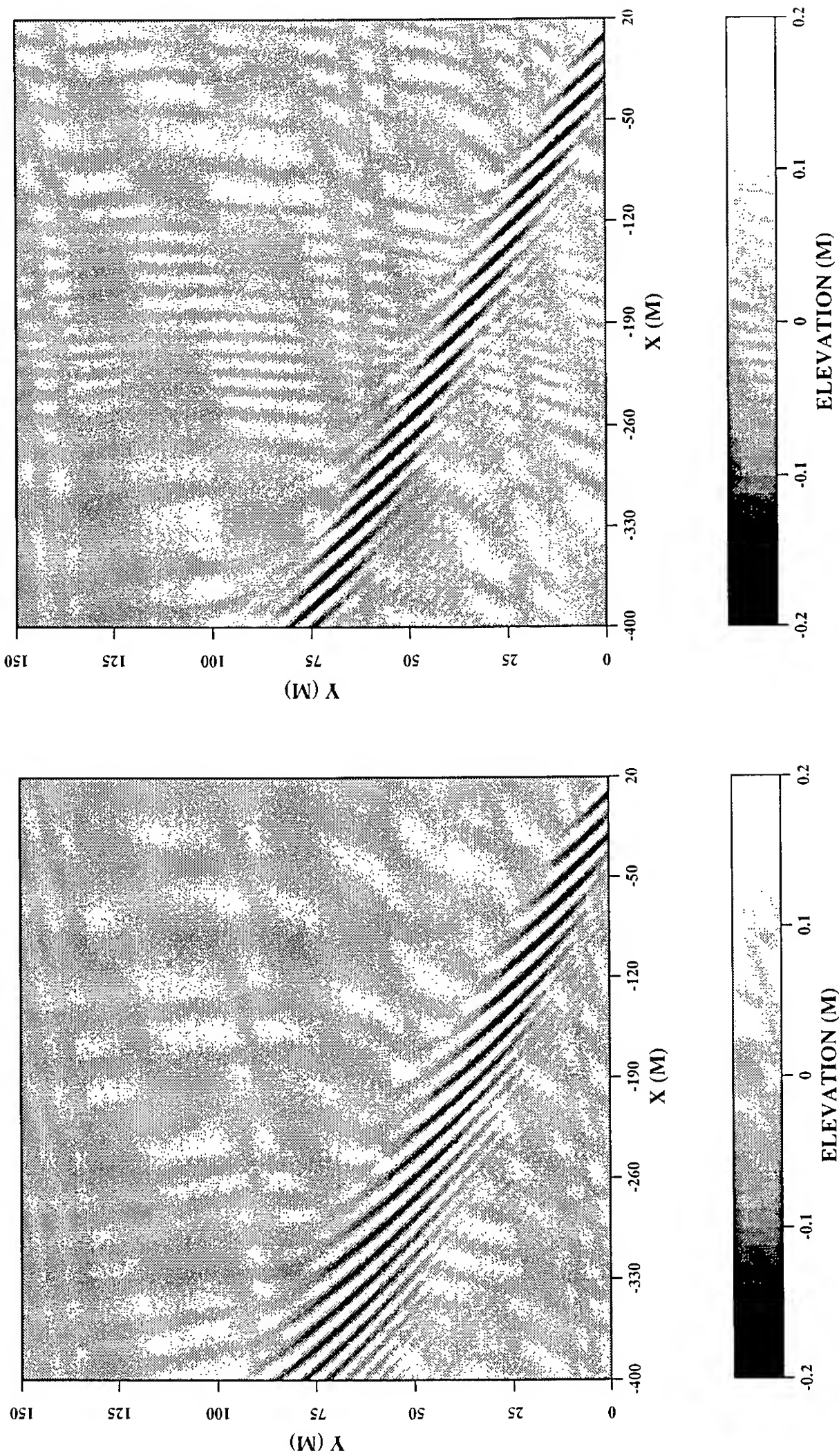
to the right hand side of Equation (23). This term represents the increase in the phase speed of the wave due to nonlinearity. The solution of Equation (23), with (24), is shown in Figure 5b. The nonlinear term arrests the dispersion of the ray yielding an oblique nonlinear solitary wave packet. Figures 6a and 6b compare the linear and nonlinear Schrodinger equation results at 100m and 400m aft, respectively.



Figures 6a (bottom) and 6b (top). A comparison of the solutions of the linear and nonlinear Schrodinger equations.

We note that we have performed additional calculations with the model





### LINEAR SCHRÖDINGER EQUATION

### NONLINEAR SCHRÖDINGER EQUATION

Figure 5a (left) and 5b (right). A comparison of the solutions of the linear and nonlinear Schrödinger equation evolution models. Nonlinear effects arrest the dispersion of the ray. Note that the axes in these figures are the same as in Figure 3, but the gray scales are different.

using reduced forcing. If the peak slope of the soliton just aft of the source-sink region drops to 0.1, then a soliton does not form by 400 m aft. The required conditions on the initial packet for soliton formation are discussed in [3].

#### 4. CONCLUSIONS

We have developed a simple model for the generation and evolution of the inner-angle ray observed in the experiment. The generation is modeled as an interference maximum due to a source-sink pair and the evolution is modelled using the nonlinear Schrodinger equation. Although some of the parameters in the model are fit to experimental data, the values of the parameters are physically reasonable, thus we conclude that the model captures the essential physics.

We have three recommendations for future research. First, the generation model should be improved using one of the state-of-the-art Kelvin wake models, with the objective of replacing our fit with a true prediction. This is particularly important at low Froude number, where there are a larger number of interference rays and a model with a detailed representation of the hull form and the near-field flow is essential. Second, the output from the generation model should be used as an inflow condition for the far-field equations, rather than using the double-body pressure forcing, as in our evolution model. The double-body pressure forcing is only suitable when the generation model is linear. Third, the far-field model should be upgraded to include a higher order expansion [6] or a fully-nonlinear equation. This will improve the approximation of the linear dispersion relation near the nodes and will add a nonlinear correction to the group velocity.

#### ACKNOWLEDGEMENTS

We thank Carl Scragg for the use of some of his linear Kelvin wake codes.

#### REFERENCES

1. Munk, W.H., Scully-Power, P., and Zachariasen, F., "Ships from space," Proceedings of the Royal Society of London, Series A, Vol. 412, 1987, pp. 231-254.
2. Brown, E.D., Buchsbaum, S.B., Hall, R.E., Penhune, J.P., Schmitt, K.F., Watson, K.M., and Wyatt, D.C., "Observations of a nonlinear solitary wave packet in the Kelvin wake of a ship," Journal of Fluid Mechanics, Vol. 204, 1989, pp. 263-293.
3. Buchsbaum, S.B., "Ship Wakes and Solitons," Ph D Thesis, University of California, San Diego, 1990.
4. Akylas, T.R., Kung, T.-J., and Hall, R.E., "Nonlinear Groups in Ship Wakes," Proceedings, 17th ONR Symposium on Naval Hydrodynamics, The Hague, the Netherlands, National Academy Press, Washington, D.C., 1988.
5. Noblesse, F., "Alternative integral representations for the Green function of the theory of ship wave resistance," Journal of Engineering Mathematics, Vol. 15, No. 4, 1981, pp. 241-265.
6. Dysthe, K.B., "Note on a modification to the nonlinear Schrodinger equation for application to deep water waves," Proceedings of the Royal Society of London, Series A, Vol. 369, 1979, pp. 105-114.

#### APPENDIX

In this appendix we review Kelvin wake geometry. The condition that a wave is steady with respect to the ship is

$$\frac{\omega}{k_x} = U, \quad (A1)$$

where the dispersion relation for the wave is

$$\omega = \sqrt{gk} > 0, \quad k = \sqrt{k_x^2 + k_y^2} > 0. \quad (A2)$$

The group velocity of the wave determines its position in the wake, given by the angle  $\alpha$  with respect to the wake centerline:

$$\tan \alpha = \frac{\partial \omega / \partial k_y}{U - \partial \omega / \partial k_x}. \quad (\text{A3})$$

The condition for an interference maximum in a source-sink pair model is

$$2ak_x = n\pi, \quad n \text{ odd}. \quad (\text{A4})$$

The condition for an interference minimum is Equation (A4) with  $n$  even.

The observed frequency of the soliton in the experiment was 3.28 rad/sec [2]. Using a ship speed of 15 knots (7.7 m/s), the above formula imply that  $(k_x, k_y) = (0.426, 1.01)m^{-1}$  and  $\alpha = 10.9$  deg. Equation (A4) then yields a value of  $2a = 22.2m$  for the distance between the source and sink that yields a ray at the observed angle. Using this distance, Equations (A4) and (A3) yield a value of 15.9 degrees and 8.3 degrees for the nodes on either side of the ray peak. The  $k_y$  wavenumbers of these nodes are  $0.393 m^{-1}$  and  $1.854 m^{-1}$ , respectively.

Based upon an average of 24 runs beyond 0.5 km aft [2], the spatial width of the feature was 8.9m (measured at  $1/e$  of the peak) and the peak wave amplitude was 15.1 cm (this was 1.1 times the theoretical soliton value calculated from the other parameters). An average of the runs at 0.5 km aft yielded a peak amplitude of 20 cm.

# Near-Field Nonlinearities and Short Far-Field Ship Waves

F. Noblesse, D. Hendrix (David Taylor Research Center, USA)

## ABSTRACT

The short divergent waves in the steady wave pattern of a ship are analyzed on the basis of a linear far-field flow representation and a nonlinear near-field flow approximation. More precisely, the far-field wave spectrum is determined in a simple and practical manner by means of a waterline-integral approximation obtained from a modified Neumann-Kelvin integral representation; and the nonlinear near-field flow along the ship waterline is determined via a nonlinear correction defined by a simple analytical expression. Numerical calculations for the Wigley hull predict short divergent waves too steep to exist in reality within a significant sector in the vicinity of the ship track. The predicted waves also exhibit a well-defined peak at an angle from the ship track equal to about  $1^\circ$  to  $2^\circ$ .

## INTRODUCTION

The ongoing search for explanations of the features displayed by remote-sensing images of ship wakes has prompted the formulation of various alternative theoretical hypotheses. One such hypothesis is that some features of ship wake radar images might be attributable to characteristics of the steady Kelvin wave pattern.

Efforts to determine whether the pattern of steady far-field waves generated by a ship does in fact exhibit any notable property capable of causing a corresponding identifiable feature in remote-sensing images have motivated a number of recent studies of the Kelvin wake, including Scragg [1], Barnell and Noblesse [2], Keramidas and Bauman [3], Milgram [4], and Trizna and Keramidas [5]. All these numerical studies are based upon a highly-simplified hydrodynamic model, namely the zeroth-order slender-ship approximation proposed in Noblesse [6]. It is shown in Baar [7], Andrew, Baar and Price [8], Lindenmuth, Ratcliffe and Reed [9], and Noblesse, Hendrix and Barnell [10] that the first-order slender-ship approximation provides fairly realistic predictions of the wave profile, the

near-field wave pattern and the long waves in the wave spectrum. However, the zeroth-order slender-ship approximation is a poor approximation to the Neumann-Kelvin theory in the short-wave limit, as is indicated by the numerical results depicted in Figure 2a in [10] and is confirmed by the results obtained further on in this study. The wave calculations reported in [1] through [5] therefore are unlikely to provide realistic representations of the short waves in the wave pattern of a ship.

Earlier numerical calculations of the wave spectrum or the wave pattern of a ship may be found in the literature, e.g. Sharma [11] and Tuck, Collins and Wells [12]. However, these calculations are also based upon a highly-simplified hydrodynamic model, namely the Michell thin-ship approximation. Similarly, the far-field wave calculations of Ursell [13] correspond to an elementary free-surface pressure singularity.

The steady wave pattern and wave spectrum of a ship thus have been relatively little studied, and are ill known. In particular, the asymptotic behavior of the wave-spectrum function in the short-wave limit is not known, and it is not known whether this asymptotic behavior might explain the common observation that the wake of a ship in the vicinity of the track exhibits no short divergent wave.

The short waves in the wave-spectrum function and the far-field wave pattern of a ship are examined in the present study within the context of a somewhat more realistic hydrodynamic model than the Michell thin-ship theory and the slender-ship approximation used in the previously mentioned numerical studies. More precisely, the theoretical framework adopted in the present study is that provided by the linearized Neumann-Kelvin flow representation. This theory defines, via well-known formulas, the steady wave pattern (and the wave resistance) of a ship in terms of the wave-spectrum function, which is defined in terms of the flow at the ship mean wetted-hull surface.

Accurate theoretical predictions of the steady wave spectrum of a ship therefore are necessary for obtaining reliable wave-signature (and wave-resistance) predictions.

However, accurate numerical calculations of the wave-spectrum function cannot readily be obtained because this function is defined as the sum of two integrals, namely a line integral around the ship mean waterline and a surface integral over the ship mean wetted-hull surface, which very nearly cancel out in the manner recently shown in Noblesse, Lin and Mellish [14]. Inaccuracies which inevitably occur in the numerical evaluation of the waterline and hull integrals cause imperfect cancellations between these two integrals and correspondingly large errors in their sum. The foregoing cancellation phenomenon and the resulting numerical inaccuracies are especially acute for the short waves in the wave spectrum.

A mathematical remedy to this fundamental numerical difficulty is presented in [14]. The remedy consists in an alternative mathematical expression for the wave-spectrum function. This alternative expression defines the wave spectrum as the sum of modified waterline and hull integrals. No significant cancellation occurs between these modified integrals, which are of the same order of magnitude as the wave-spectrum function defined as their sum. The large cancellations occurring between the waterline integral and the hull integral in the usual expression for the spectrum function thus are automatically and exactly accounted for, via a mathematical transformation, in the alternative new expression given in [14]. This new expression for the wave spectrum thus is considerably better suited than the usual expression for accurate numerical calculations, notably for the short waves in the spectrum.

Nevertheless, the integral representation for the wave spectrum given in [14] is not suitable for evaluating the very short divergent waves. For instance, the use of this (or indeed any similar) integral representation for the numerical calculation of ship waves with wavelength between 5 cm and 40 cm, corresponding to backscattering of the electromagnetic waves in typical systems used for remote sensing of ship wakes, would require an exceedingly large number of extremely small panels for representing the hull surface. In fact, such short waves can only be evaluated analytically, via a short-wave asymptotic approximation of the integral representation of the spectrum function given in [14].

Reliable predictions of the short waves in a ship wave spectrum are quite difficult to obtain because of the significant numerical difficulties mentioned in the foregoing, as well as for yet another reason. This second source of difficulties stems from the

fact that short far-field ship waves are closely related to the velocity distribution along the ship mean waterline, especially the fluid velocity at the ship bow and stern, as is shown further on in this study. However, existing near-field-flow calculation methods (so-called nonlinear methods included) are unable to provide realistic velocity predictions at a ship bow and stern because they cannot model the strongly nonlinear flow in the immediate vicinity of these points, as was recently shown in Noblesse, Hendrix and Kahn [15]. The nonlinear analytical/experimental and analytical/numerical velocity distributions along the mean waterline of the Wigley hull defined in [15] are used in the present study for predicting the short divergent waves generated by the Wigley hull.

#### FOURIER REPRESENTATION OF THE WAVE PATTERN

The wave potential  $\phi_w(\vec{\xi})$  at any point  $\vec{\xi} = (\xi, \eta, \zeta < 0)$  behind the stern of a ship advancing at constant speed in calm water can be defined in terms of a Fourier representation, as is well known. Specifically, (20) in [14] yields

$$\phi_w(\vec{\xi}) = (2/\pi) \int_0^\infty \exp(v^2 \zeta p^2) \cos(v^2 \eta p t) \operatorname{Im} \exp(iv^2 \xi p) K(t) dt, \quad (1)$$

where the wave potential  $\phi_w$  and the coordinates  $\xi, \eta, \zeta$  are nondimensional with respect to the ship length  $L$  and speed  $U$ , and  $v$  is the inverse of the Froude number  $F$ ; we thus have

$$v = 1/F \quad \text{with} \quad F = U/(gL)^{1/2}, \quad (2a,b)$$

where  $g$  is the acceleration of gravity. Furthermore,  $p$  in (1) is related to the Fourier variable  $t$  as follows:

$$p = (1+t^2)^{1/2}. \quad (3)$$

Finally the (nondimensional) function  $K(t)$  in (1) is the wave-spectrum function. The wave potential is defined by (1) in terms of a familiar Fourier superposition of elementary plane waves

propagating at angles  $\theta$  from the ship track (the  $x$ -axis) given by

$$\tan \theta = t. \quad (4)$$

The amplitudes of these elementary plane-wave components are essentially given by the spectrum function  $K(t)$ , which thus contains essential information directly relevant to a ship's signature (and wave resistance). This study is concerned with the numerical/analytical evaluation and the behavior of the spectrum function  $K(t)$  in the short-wave limit  $t \rightarrow \infty$  ( $\theta \rightarrow 90^\circ$ ).

It is convenient and useful to express the spectrum function  $K(t)$  as the sum of two terms as follows:

$$K(t) = K_0(t) + K_\phi(t), \quad (5)$$



where  $K_0$  represents the zeroth-order slender-ship approximation and  $K_\phi$  the Neumann-Kelvin correction term in the Neumann-Kelvin

approximation  $K_0 + K_\phi$ . More precisely, the spectrum function  $K_0 + K_\phi$  corresponds to the usual linearized Neumann-Kelvin approximation, in which the nonlinear terms in the free-surface boundary condition are neglected. These nonlinear terms result in an additional term in (5), defined by an integral over the mean free surface [6,14], which is ignored in this study. The slender-ship approximation  $K_0$  is defined explicitly in terms of the value of the Froude number and the hull shape, whereas the Neumann-Kelvin correction  $K_\phi$  also depends on the value of the tangential fluid velocity at the hull [14]. For a ship with port and starboard symmetry, as is considered here, the slender-ship approximation  $K_0$  and the Neumann-Kelvin correction  $K_\phi$  can be expressed in the form

$$K_0 = K_0^+ + K_0^-, \quad (6a)$$

$$K_\phi = K_\phi^+ + K_\phi^-, \quad (6b)$$

where the superscripts + and - correspond to the contributions of the port and starboard sides of the ship, respectively.

Modified mathematical expressions for the functions  $K_0$  and  $K_\phi$  are given in [14].

Approximate forms of these expressions valid in the short-wave limit are now given.

### THE WAVE SPECTRUM: APPROXIMATE INTEGRAL REPRESENTATION

The expression for the slender-ship approximation  $K_0$  defined by (30) in [14] involves the exponential function  $\exp(P^2 z)$ , where  $P^2$  is given by

$$P^2 = v^2 p^2 = (\sec^2 \theta) / F^2. \quad (7)$$

For negative values of the vertical coordinate  $z$ , the exponential function  $\exp(P^2 z)$  is negligibly small in the short-wave limit  $P^2 \rightarrow \infty$ . We then have

$$K_0^\pm \approx \int_w E_\pm (n_x^2 - u^2) t_y dl - i v^2 u \int_s \exp(P^2 z) E_\pm n_z da \quad (8)$$

as  $P^2 \rightarrow \infty$ .

The expression for the Neumann-Kelvin correction  $K_\phi$  defined by (73) and (74a,b) in [14] can likewise be approximated by restricting the integration over the hull surface  $h$  in (73) to the hull side  $s$ . We then have

$$K_\phi^\pm \approx \int_w E_\pm A_w^\pm dl \pm i v^2 \int_s \exp(P^2 z) E_\pm A_h^\pm da / |\vec{t} \times \vec{s}| \quad (9)$$

as  $P^2 \rightarrow \infty$ , where the amplitude functions  $A_w^\pm$  and  $A_h^\pm$  are defined as

$$A_w^\pm = (t_x \phi_t + s_x \phi_s) t_y \pm u(v - Cu) (\phi_t + \epsilon \phi_s), \quad (10a)$$

$$A_h^\pm = [(v - Cu) t_x \mp (u + Cv) t_y - i C t_z] (\phi_s + \epsilon \phi_t) - [(v - Cu) s_x \mp (u + Cv) s_y - i C s_z] (\phi_t + \epsilon \phi_s). \quad (10b)$$

The functions  $E_+$  and  $E_-$  in (8) and (9) are the trigonometric functions defined by (19) in [14], that is we have

$$E_\pm = \exp[-i P^2 (u x \pm v y)], \quad (11)$$

where  $u$  and  $v$  are given by

$$u = 1/p \quad \text{and} \quad v = t/p; \quad (12a,b)$$

It may then be seen from (3) that we have  $1 \geq u \geq 0$

and  $0 \leq v \leq 1$  for  $0 \leq t \leq \infty$ , with

$$u^2 + v^2 = 1. \quad (13)$$

Furthermore,  $w$  and  $s$  in (8) and (9) represent the positive halves of the mean waterline and of the mean wetted-hull side and  $dl$  and  $da$  the differential elements of arc length of  $w$  and area of  $s$ , respectively. Also,  $\vec{t} = (t_x, t_y, t_z)$  and  $\vec{s} = (s_x, s_y, s_z)$  are unit vectors tangent to the hull side along

curves which roughly correspond to waterlines

and framelines, respectively. The vectors  $\vec{t}$  and  $\vec{s}$

are roughly (but not necessarily exactly) orthogonal

and point toward the bow and the keel line,

respectively. At the mean free surface, the vector  $\vec{t}$

is tangent to the mean waterline  $w$  and we thus

have  $t_z = 0$ . The normal vector  $\vec{n} = (n_x, n_y, n_z)$  to

the hull side is defined by

$$\vec{n} = (\vec{t} \times \vec{s}) / |\vec{t} \times \vec{s}|.$$

The term  $\epsilon$  in (10a,b) is defined as

$$\epsilon = \vec{t} \cdot \vec{s}$$

and  $\phi_t$  and  $\phi_s$  represent the components of the

velocity vector  $\nabla \phi$  along the unit vectors  $\vec{t}$  and  $\vec{s}$

tangent to the hull side; we thus have

$$\nabla \phi \cdot \vec{n} = \phi_t \vec{t} + \phi_s \vec{s}, \quad \text{where the hull boundary condition } \partial \phi / \partial n = n_x \text{ was used. The components } \phi_t \text{ and } \phi_s \text{ of } \nabla \phi \text{ along the tangent vectors } \vec{t} \text{ and } \vec{s} \text{ and the velocities } \partial \phi / \partial t = \nabla \phi \cdot \vec{t} \text{ and } \partial \phi / \partial s = \nabla \phi \cdot \vec{s} \text{ are related as follows:}$$

$$\partial \phi / \partial t = \phi_t + \epsilon \phi_s, \quad (14a)$$

$$\partial \phi / \partial s = \phi_s + \epsilon \phi_t, \quad (14b)$$

$$\phi_t = (\partial \phi / \partial t - \epsilon \partial \phi / \partial s) / (1 - \epsilon^2), \quad (14c)$$

$$\phi_s = (\partial \phi / \partial s - \epsilon \partial \phi / \partial t) / (1 - \epsilon^2). \quad (14d)$$

Finally,  $C$  in (10b) is an arbitrary complex function

of  $t$ . Equations (9) and (10a,b) thus define a one-

parameter family of mathematically-equivalent

expressions for the Neumann-Kelvin correction

$K_\phi$ .

It may be seen from (30) and (73) in [14] that an

estimate of the error associated with the

approximate expressions (8) and (9) is provided by

the exponential function  $\exp(P^2 z)$  where  $z$  is taken

equal to the negative of the ship draft  $d$ . This error



estimate is smaller than a prescribed error  $\varepsilon$  for  $p \geq p_e$ , or equivalently for  $\theta \geq \theta_e = \sec^{-1}(p_e)$ , where  $p_e$  is given by  $p_e(F; \varepsilon, d) = F [\ln(1/\varepsilon)/d]^{1/2}$ . The values of  $p_e$  and  $\theta_e$  corresponding to values of the error  $\varepsilon$  and the ship draft  $d$  equal to 0.01 and 0.05, respectively, and to five values of the Froude number between 0.1 and 0.5 are listed in Table 1.

F	0.1	0.2	0.3	0.4	0.5
$p_e$	1	1.9	2.9	3.8	4.8
$\theta_e$	0	59°	70°	75°	78°

**Table 1.** Values of  $p_e$  and  $q_e$  for  $\varepsilon = 0.01$  and  $d = 0.05$ .

The exponential function  $\exp(P^2 z)$  in the integrands of the integrals over the hull side  $s$  in (8) and (9) decays rapidly with decreasing (negative) values of  $z$  if  $P^2 \gg 1$ , that is for small values of the Froude number and/or large values of  $t = \tan\theta$ . The major contributions to the hull-side integrals in (8) and (9) therefore stem from the upper part of the hull side  $s$  in the vicinity of the waterline  $w$ . These hull-side integrals can in fact be approximated by single (one-fold) integrals along the waterline. These waterline-integral approximations for the spectrum functions  $K_0$  and  $K_\phi$  are now given.

#### THE WAVE SPECTRUM: WATERLINE-INTEGRAL APPROXIMATION

The upper part of the hull side  $s$  can be defined by the following parametric equations:

$$x = \xi(l) + x_1(l)s + x_2(l)s^2/2 + \dots, \quad (15a)$$

$$y = \eta(l) + y_1(l)s + y_2(l)s^2/2 + \dots, \quad (15b)$$

$$-z = z_1(l)s + z_2(l)s^2/2 + \dots, \quad (15c)$$

where  $s \geq 0$  and the curve  $s = 0$  corresponds to the waterline  $w$ . The waterline is then defined by the parametric equations

$$x = \xi(l) \quad \text{and} \quad y = \eta(l), \quad (16a,b)$$

where  $l$  is the arc length along  $w$ . The previously-defined unit tangent vectors  $\vec{t}$  and  $\vec{s}$  to the hull side  $s$  are given by

$$\vec{t} = (t_x, t_y, t_z) = \partial \vec{x} / \partial l,$$

$$\vec{s} = (s_x, s_y, s_z) = \partial \vec{x} / \partial s.$$

In particular, at the waterline  $w$ , we have

$$(t_x, t_y, t_z) = (\xi', \eta', 0), \quad (17a)$$

$$(s_x, s_y, s_z) = (x_1, y_1, -z_1), \quad (17b)$$

where the notation  $(\cdot)'$  denotes differentiation with respect to the arc length  $l$  along  $w$ .

By using the foregoing representation of the upper hull side  $s$ , we can approximate the integrals on the hull side in (8) and (9) as integrals along the mean waterline  $w$ . Details of this short-wave

asymptotic approximation are given in Noblesse and Hendrix [16], where the following waterline-integral approximation to the spectrum function  $K(t)$  is obtained:

$$K \approx \int_w \{A_+ \exp[-iP^2(u\xi + v\eta)] + A_- \exp[-iP^2(u\xi - v\eta)]\} dl. \quad (18)$$

The amplitude functions  $A_\pm$  are defined as

$$A_\pm [-s_z + i(us_x \pm vs_y)] = A_0^\pm + S_\pm \phi_s + T_\pm \phi_t, \quad (19)$$

where  $A_0^\pm$  corresponds to the slender-ship approximation and is given by

$$A_0^\pm = -s_z t_y (n_x^2 - u^2) + i[t_y n_x^2 (us_x \pm vs_y) - s_y u^2 (ut_x \pm vt_y)]. \quad (20)$$

The terms  $S_\pm$  and  $T_\pm$  in (19) are defined as

$$S_\pm = -s_z [s_x t_y \pm uv(s_x t_x + s_y t_y)] - i[us_z^2 t_y - (ut_x \pm vt_y)(s_x s_y \pm uv)], \quad (21a)$$

$$T_\pm = (t_x t_y \pm uv)(-s_z \pm ivs_y) + iut_x(ut_x \pm vt_y)(us_y \pm vs_x). \quad (21b)$$

For sufficiently large values of  $p = \sec\theta$ , the Neumann-Kelvin approximation  $K$  thus is defined by the waterline-integral approximation (18), (19), (20), and (21a,b).

These equations provide a simple and practical basis for numerically evaluating the short divergent waves in the steady wave spectrum of a ship, given the value of the fluid velocity components  $\phi_s$  and  $\phi_t$  at the waterline, by dividing the waterline  $w$  into a large number of straight segments within which the amplitude functions  $A_\pm$  are assumed to vary linearly.

Figures 1a,b,c depict the real and imaginary parts of the Neumann-Kelvin approximation to the spectrum function  $K(t)$  for the Wigley hull at three values of the Froude number equal to 0.1, 0.25 and 0.4. The dashed-line curves in these figures correspond to the waterline-integral approximation (18) obtained in this study; the solid-line curves correspond to the exact mathematical expression for the Neumann-Kelvin approximation to the spectrum function given by (21), (22), (73) and (74a,b) in [14]. The velocity potential on the Wigley hull in these exact expressions, and at the waterline in the waterline-integral approximation (18) obtained in the present study, is taken as the (first-order) slender-ship potential defined in [6]. Figures 1a,b,c show that the waterline-integral approximation (18) does in fact become quite accurate for sufficiently large values of  $t = \tan\theta$ . The waterline-integral approximation (18) may then be used henceforth in this study. Figures 1a,b,c also show that the general numerical method based on the exact expressions for the wave-spectrum function given in [14] can provide reliable predictions if a sufficiently large number of panels is used for representing the ship hull form.

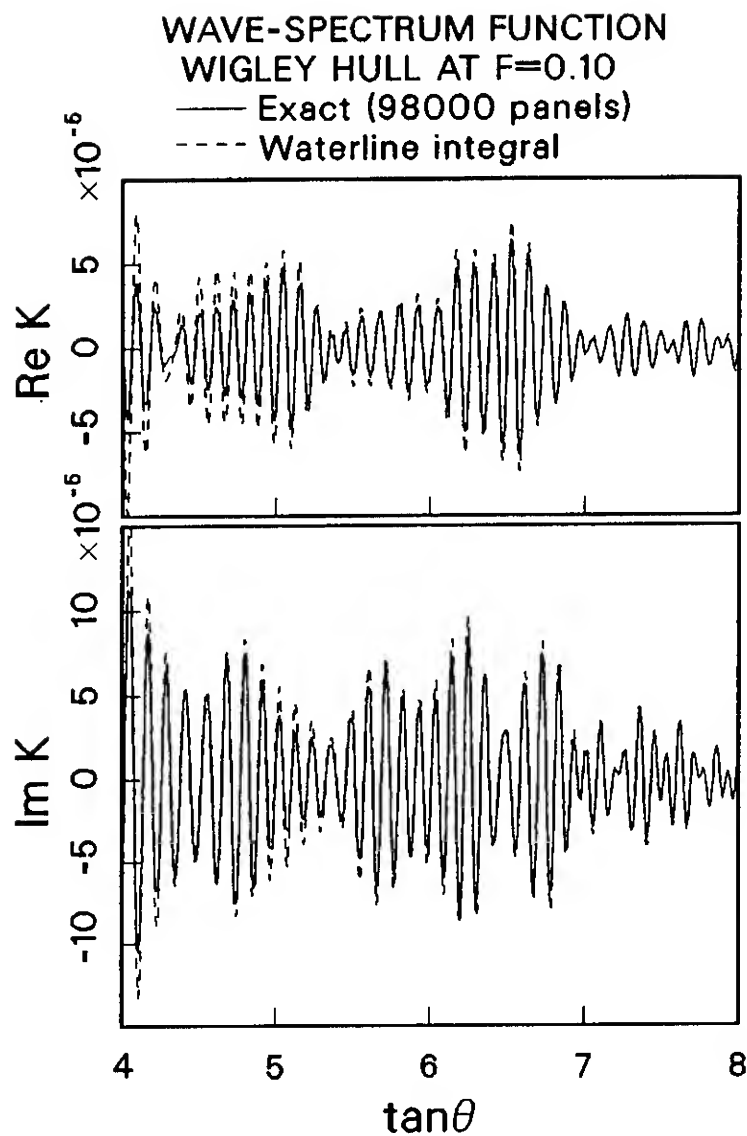


Fig. 1a. Real and imaginary parts of the wave-spectrum function  $k(\theta)$ .

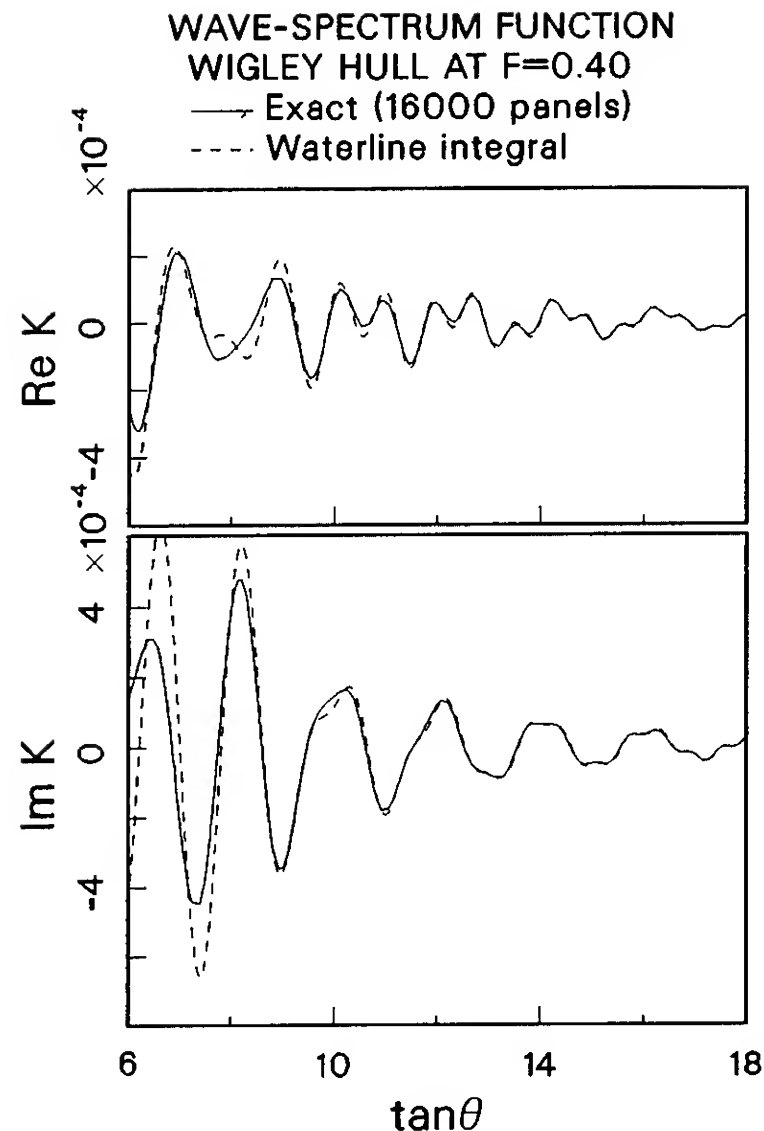


Fig. 1c. Real and imaginary parts of the wave-spectrum function  $k(\theta)$ .

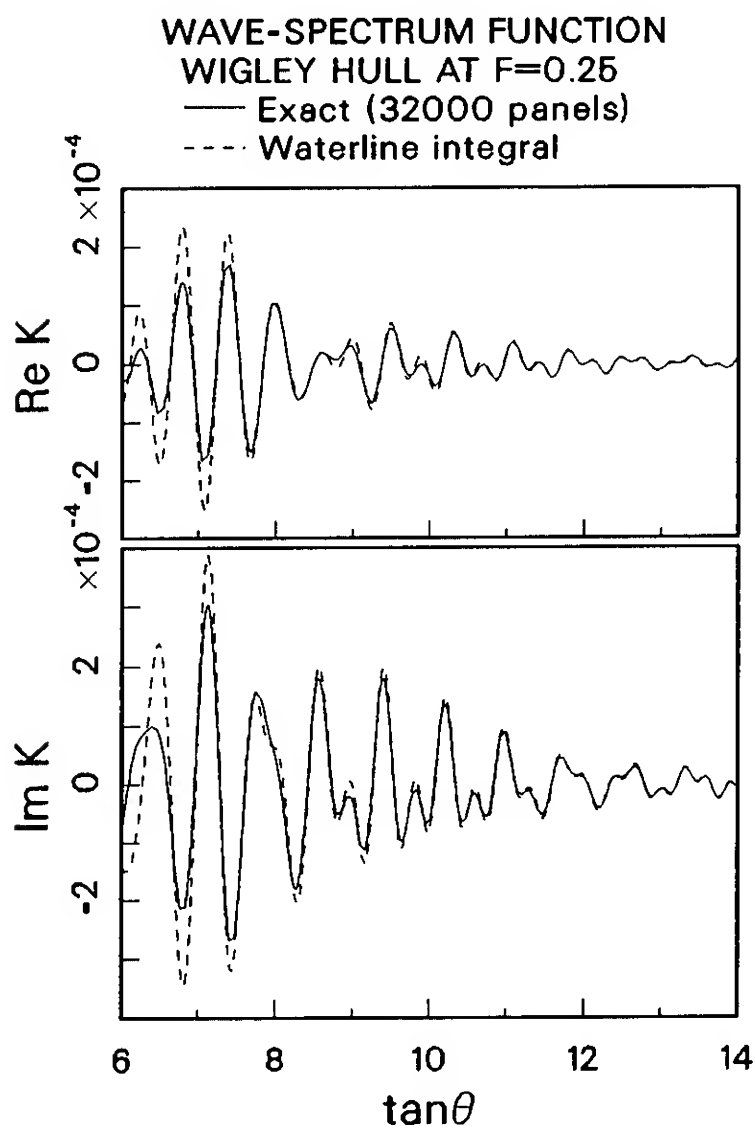


Fig. 1b. Real and imaginary parts of the wave-spectrum function  $k(\theta)$ .

#### THE WAVE SPECTRUM: STATIONARY-PHASE APPROXIMATION

An analytical approximation to the spectrum function  $K(t)$  can in principle be obtained by applying the method of stationary phase, since the trigonometric functions  $\exp[-iP^2(u\xi \pm v\eta)]$  in (18) oscillate rapidly for large values of  $P^2 = v^2 p^2 = (\sec^2 \theta)/F^2$ . This method shows that the major contributions to the waterline integral (18) stem from the end points of the integration range, that is the ship bow and stern, and the points where the phases of the trigonometric functions  $\exp[-iP^2(u\xi \pm v\eta)]$  are stationary. These points of stationary phase are defined by the conditions  $u d\xi \pm v d\eta = 0$ , which yield the relations

$$u t_x \pm v t_y = 0, \quad t_x = v, \quad t_y = \mp u. \quad (22a,b,c)$$

by virtue of (17a), (13), and the identity  $t_x^2 + t_y^2 = 1$ . By using (12a,b) and (13) in (22b,c) we may obtain

$$\tan \phi = t_y / t_x = \mp 1/t = \mp \cotan \theta,$$

where  $\phi$  is the angle between the x-axis and the unit tangent vector  $\vec{t}$  to the waterline. We thus have the relation

$$|\phi| = \pi/2 - \theta, \quad (23)$$

which shows that the very short divergent waves in the steady wave spectrum of a ship primarily stem from the central (midship) portion of the ship

where the waterline is almost parallel to the centerplane, as well as the ship bow and stern.

It is shown in [16] that application of the method of stationary phase to (18) fails to provide a simple, practically useful analytical approximation because the second terms in the asymptotic expansions for the contributions of both the end points (i.e., the ship bow and stern) and the points of stationary phase are of the same order of magnitude (in the limit  $t \rightarrow \infty$ ) as the first terms, and thus cannot be neglected. Unfortunately, the second terms in the asymptotic expansions are extremely complex. It can nevertheless be shown that we have

$$K \sim K_{B,S} + K_{\text{phase}},$$

where  $K_{B,S}$  and  $K_{\text{phase}}$  correspond to the contributions from the ship bow and stern and from the interior point(s) of stationary phase, respectively. Furthermore, we have

$$K_{B,S} \sim 1/t^3 \text{ and } K_{\text{phase}} \sim 1/t^4 \text{ as } t \rightarrow \infty. \quad (24)$$

### NEAR-FIELD FLOW AND NONLINEARITIES

The tangential velocity components  $\phi_s$  and  $\phi_t$  in (19) are merely taken equal to 0 in the zeroth-order slender-ship approximation to the spectrum function defined in [6]. More generally, the values of these velocity components at the mean waterline  $w$  may be predicted numerically using any near-field-flow calculation method, including the relatively simple first-order slender-ship approximation defined in [6], in the Neumann-Kelvin approximation to the spectrum function. However, it was already noted that existing near-field-flow calculation methods, including the so-called nonlinear methods, cannot provide accurate predictions of the velocity components  $\phi_s$  and  $\phi_t$  in the immediate vicinity of a ship bow and stern.

The velocity components  $\phi_s$  and  $\phi_t$  along the wave profile of a ship can be defined in terms of the nondimensional elevation  $e = Eg/U^2$  of the wave profile and its slope  $e_t = dE(L)/dL$  in the direction of the unit tangent vector  $\vec{t}$  to the mean waterline by means of analytical expressions given in [15]. More precisely, (27) and (23) in [15] define the velocities  $\partial\phi/\partial t = t_x \partial\phi/\partial x + t_y \partial\phi/\partial y$  and  $\partial\phi/\partial s = s_x \partial\phi/\partial x + s_y \partial\phi/\partial y + s_z \partial\phi/\partial z$  at the wave profile of a ship as follows:

$$\partial\phi/\partial t = t_x - (1-2e)^{1/2}/[1+(1+\mu^2)e_t^2]^{1/2}, \quad (25a)$$

$$\partial\phi/\partial s = s_x - [\varepsilon + (1+\mu^2)s_z e_t](1-2e)^{1/2}/[1+(1+\mu^2)e_t^2]^{1/2}, \quad (25b)$$

where  $\varepsilon$  and  $\mu^2$  are given by

$$\varepsilon = \vec{s} \cdot \vec{t} = s_x t_x + s_y t_y,$$

$$\mu^2 = n_z^2/(1-n_z^2) = (s_x t_y - s_y t_x)^2/s_z^2.$$

The tangential velocity components  $\phi_s$  and  $\phi_t$  can then be determined from the velocities  $\partial\phi/\partial s$  and

$\partial\phi/\partial t$  by means of (14c,d). The analytical expressions (25a,b) can be used in conjunction with either experimental measurements or numerical predictions of the wave profile, corrected at the bow and the stern in the manner specified by the nonlinear local solution given in [15].

In the special case of a wall-sided hull like the Wigley hull, we have  $\mu = 0$  since  $n_z = 0$  at the waterline, and  $\varepsilon = 0$  since we may choose the tangent vector  $\vec{s}$  to the hull at the waterline as  $\vec{s} = (0,0,-1)$ ; (25a,b) thus become

$$\partial\phi/\partial t = t_x - (1-2e)^{1/2}/(1+e_t^2)^{1/2}, \quad (26a)$$

$$\partial\phi/\partial s = e_t (1-2e)^{1/2}/(1+e_t^2)^{1/2}. \quad (26b)$$

It is shown in [15] that the steady wave profile at the ship bow must be tangent to the stem, and likewise at the stern. This tangency condition shows that we have  $e_t = -\infty$  at the bow and the stern of the Wigley hull. It then follows from (26a,b) that we have

$$\partial\phi/\partial t = t_x \approx 1, \quad (27a)$$

$$\partial\phi/\partial s = -(1-2e)^{1/2} \approx 1 \quad (27b)$$

at the bow and the stern of the Wigley hull.

The velocities  $\partial\phi/\partial t$  and  $\partial\phi/\partial s$  along the horizontal and vertical tangent vectors  $\vec{t} = (t_x, t_y, 0)$  and  $\vec{s} = (0,0,-1)$  to the Wigley hull at the waterline are depicted in Figs. 2a and 2b for a value of the Froude number equal to 0.25. The dashed-line curves in these two figures were determined using the nonlinear expression (26a,b) in which the wave-profile elevation  $e$  is taken as the experimental profile obtained at the University of Tokyo and corrected at the bow and stern in accordance with the previously mentioned tangency condition [15]. The solid-line curves in Fig. 2a correspond to numerical predictions obtained using the slender-ship approximation defined in [6]. Figure 2a shows that discrepancies between these linear numerical predictions and the corresponding nonlinear analytical/experimental predictions are quite large in the vicinity of the bow and the stern, where nonlinear effects indeed are important. The solid-line curves in Fig. 2b were obtained from the nonlinear expression (26a,b) in which the wave-profile elevation  $e$  is taken as the profile predicted numerically using the slender-ship approximation [6], corrected at the bow and stern in the manner specified in [15] and used also for determining the analytical/experimental dashed-line curves in Figs. 2a and 2b. Thus, both the solid-line curves in Fig. 2b and the dashed-line curves in Figs. 2a and 2b correspond to the nonlinear analytical expression (26a,b). The discrepancies between these nonlinear analytical/experimental and analytical/numerical predictions clearly are much smaller than the discrepancies corresponding to the linear numerical predictions shown as solid-line curves in Fig. 2a. The oscillations in the latter curves correspond to the divergent waves in the wave pattern. These

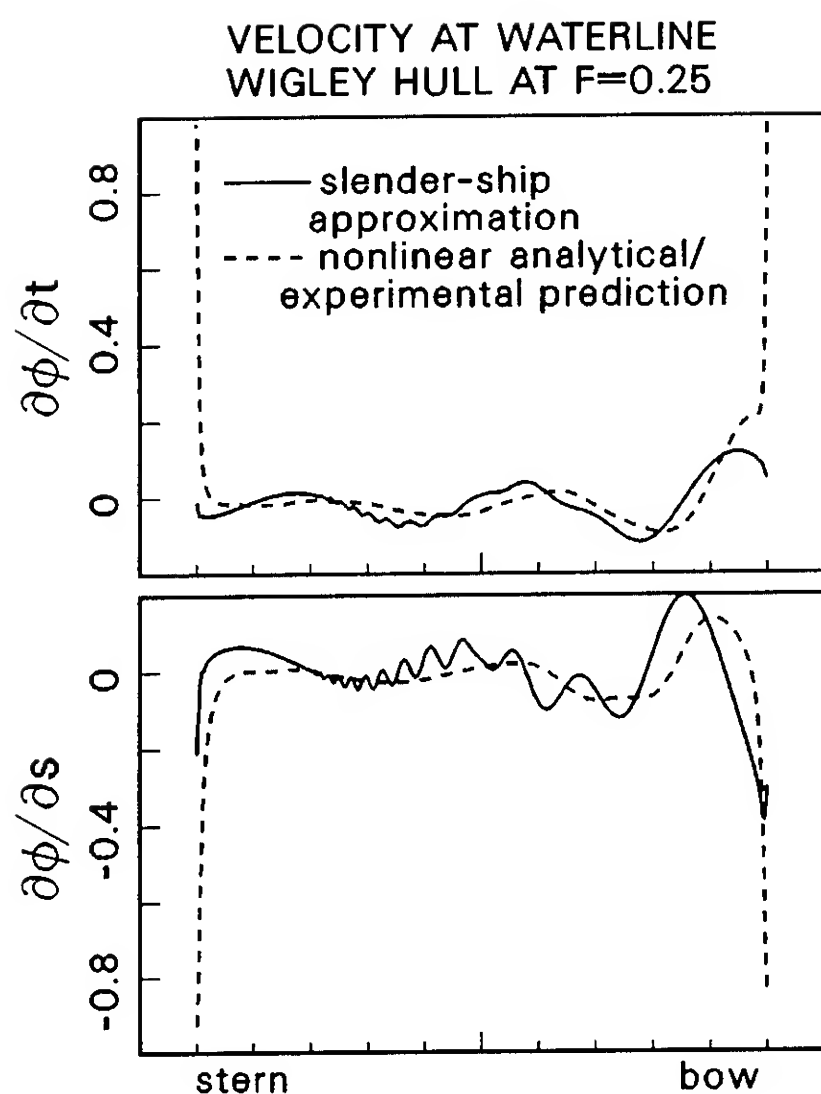


Fig. 2a. Velocity components  $\partial\phi/\partial t$  and  $\partial\phi/\partial s$ .

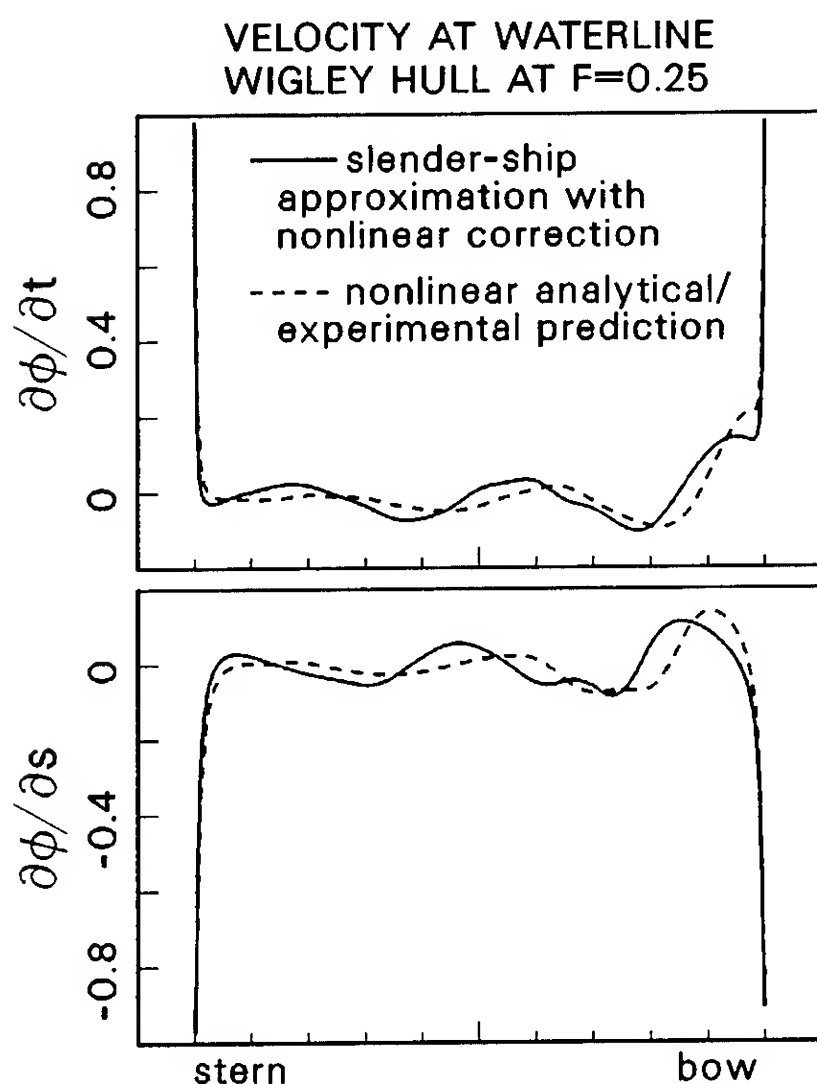


Fig. 2b. Velocity components  $\partial\phi/\partial t$  and  $\partial\phi/\partial s$ .

oscillations do not appear in the corresponding numerical predictions corrected for nonlinear effects depicted in Fig. 2b because the number of numerical data points used for defining the curves in this figure is fairly small (only 26 data points are used for both the experimental and the numerical results).

#### THE WAVE SPECTRUM CORRESPONDING TO FOUR NEAR-FIELD-FLOW APPROXIMATIONS

The modulus,  $|K|$ , of the wave-spectrum function  $K(t)$  of the Wigley hull is represented in Figs. 3a,b and 4a,b for values of  $t = \tan\theta$  in the range  $7 \leq t \leq 19$ , which approximately corresponds to values of  $\theta$  in the range  $82^\circ \leq \theta \leq 87^\circ$ . Figures 3a and 4a correspond to a value of the Froude number  $F$  equal to 0.25, while Figs. 3b and 4b correspond to  $F = 0.4$ .

The dashed-line curves in Figs. 3a and 3b correspond to the zeroth-order slender-ship approximation, so that the velocity components  $\phi_t$  and  $\phi_s$  in (19) are merely taken equal to 0. The solid-line curves in these two figures correspond to the Neumann-Kelvin approximation defined by (18), with the near-field velocity components  $\phi_t$  and  $\phi_s$  in (19) determined from the first-order slender-ship potential defined in [6]. The numerical results depicted in Figs. 3a,b show that the predictions corresponding to the Neumann-Kelvin approximation (first-order slender-ship approximation) are significantly larger than those corresponding to the zeroth-order slender-ship approximation. The latter approximation thus appears unlikely to provide realistic predictions of the short waves in the wave spectrum of a ship, as was already noted.

The predictions corresponding to the foregoing Neumann-Kelvin approximation are also depicted in Figs. 4a and 4b. These predictions correspond to the thick solid-line curves located much below the other two sets of curves represented in Figs. 4a and 4b. The latter two sets of curves correspond to the Neumann-Kelvin approximation defined by (18), with the near-field velocity components  $\phi_t$  and  $\phi_s$  in (19) determined from the nonlinear expression (26a,b). These two sets of curves thus correspond to nonlinear near-field-flow predictions, whereas the thick solid-line curves in Figs. 4a,b correspond to linear near-field-flow predictions. More precisely, the thin dashed-line and solid-line curves in Figs. 4a,b correspond to the nonlinear experimental and numerical, respectively, near-field-flow predictions depicted in Fig. 2b. It may be seen from Figs. 4a,b that discrepancies between these predictions of the wave spectrum corresponding to the nonlinear experimental and numerical near-field-flow predictions are relatively small, whereas the prediction of the wave spectrum corresponding to

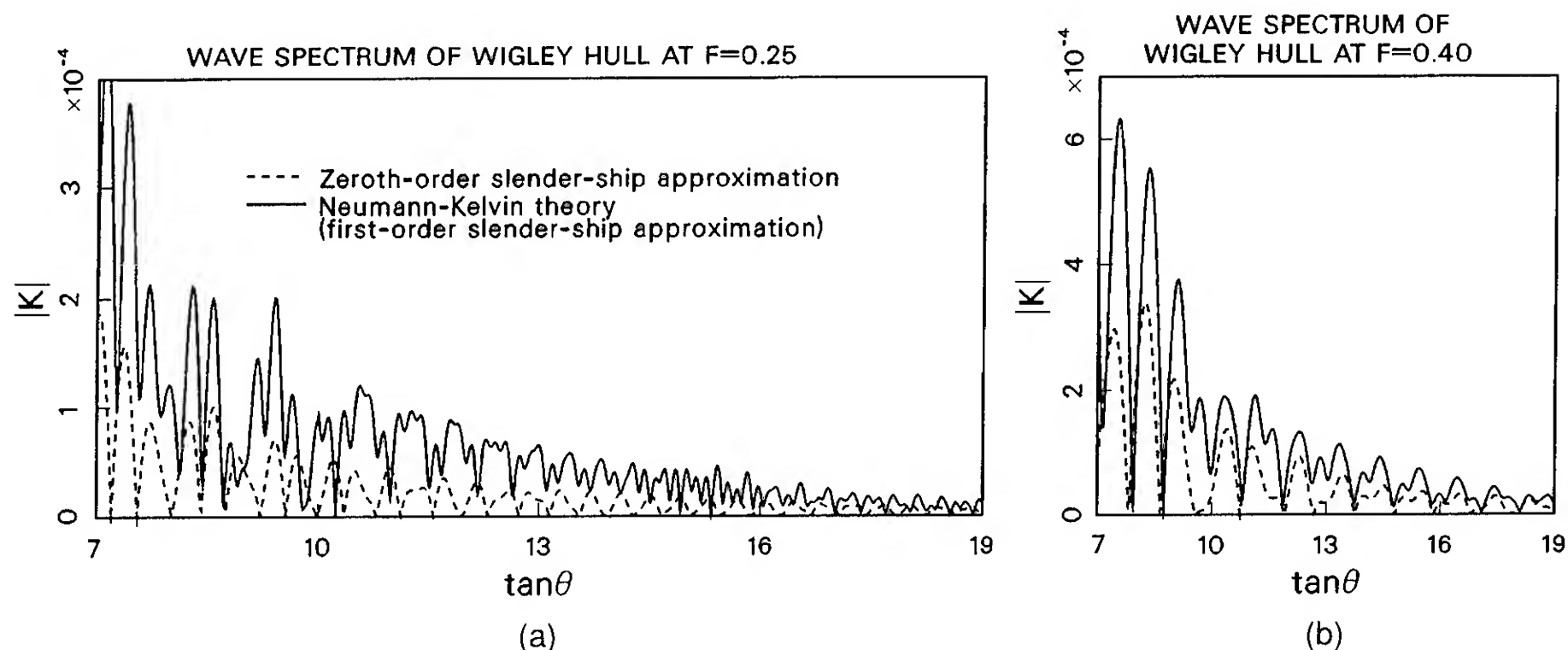


Fig. 3. Modulus of the wave spectrum function  $k(\theta)$ .

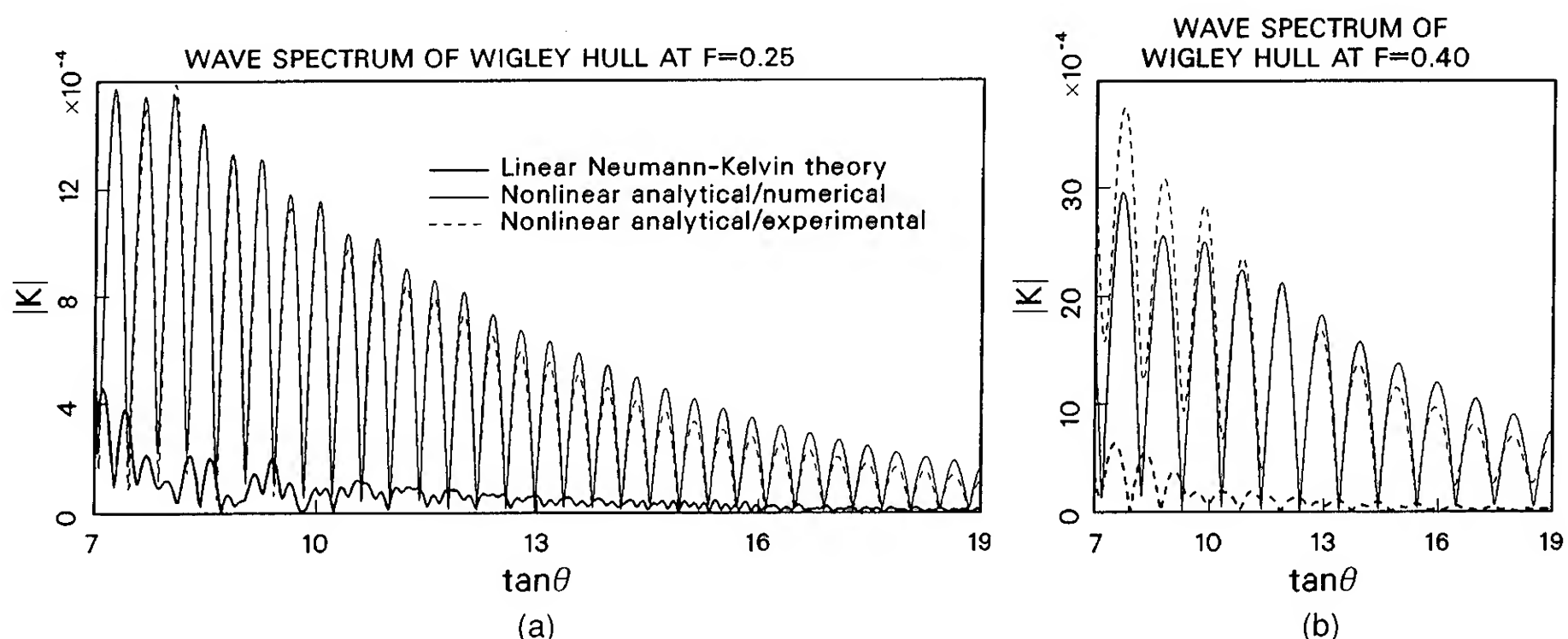


Fig. 4. Modulus of the wave spectrum function  $k(\theta)$ .

the linear near-field-flow calculations are much smaller. These numerical results indicate that the major contributions to the waterline integral (18) clearly stem from the ship bow and stern, and that the simple nonlinear correction of the linear numerical predictions of the wave-profile elevation presented in [15] and depicted in Fig. 2b thus can be used effectively for predicting the short-wave tail of the wave-spectrum function.

#### THE FAR-FIELD DIVERGENT WAVES

It is appropriate to analyze the far-field wave pattern of a ship in terms of the nondimensional far-field coordinates  $(x, y, z) = v^2(\xi, \eta, \zeta) = (X, Y, Z)g/U^2$ , where  $(X, Y, Z)$  are dimensional and  $(\xi, \eta, \zeta) = (X, Y, Z)/L$  are the nondimensional near-field coordinates used in (1), the nondimensional

potential  $\psi = v^2\phi = \Phi g/U^3$  and the wave-spectrum function  $k = v^2K$ . By using these far-field variables in (1) we may obtain the equivalent alternative expression

$$\pi\psi(x, y, z) = \text{Im} \int_0^\infty [E_+(t; x, y, z) + E_-(t; x, y, z)] k(t) dt, \quad (28)$$

where the functions  $E_\pm(t; x, y, z)$  are defined as

$$E_\pm(t; x, y, z) = \exp[zp^2 + i(x \pm yt)p]$$

with  $p$  given by (3).

The nondimensional free-surface elevation  $e(x, y) = Eg/U^2$ , where  $E$  is dimensional, is given by  $e = \partial\psi/\partial x$ , where the function  $\partial\psi/\partial x$  is evaluated at the mean free-surface plane  $z = 0$ .

By differentiating (28) we may obtain

$$\pi e(x, y) = \text{Re} [e_+(x, y) + e_-(x, y)], \quad (29)$$



where the functions  $e_{\pm}$  are defined as

$$e_{\pm}(x, y) = \int_0^{\infty} \exp[i x \theta_{\pm}(t; \sigma)] k(t) p \, dt; \quad (30)$$

the phase functions  $\theta_{\pm}(t; \sigma)$  in (30) are given by

$$\theta_{\pm}(t; \sigma) = (1 \mp \sigma t) p, \quad (31)$$

with  $\sigma$  defined as

$$\sigma = y/(-x) = \tan \alpha. \quad (32)$$

We have  $x < 0$  and we may assume  $y \geq 0$  since the wave pattern is symmetric about the ship track  $y = 0$ . We thus have  $\sigma \geq 0$  and  $0 \leq \alpha \leq \pi/2$ .

Asymptotic approximations, valid in the limit  $x \rightarrow -\infty$ , to the functions  $e_{\pm}$  defined by (30) and (31) can be obtained by using the method of stationary phase, as is well known. The phase  $\theta_{-}(t; \sigma) = (1 + \sigma t)p$  is monotonic increasing for  $t \geq 0$ . The phase  $\theta_{+}(t; \sigma) = (1 - \sigma t)p$  is monotonic decreasing for  $t \geq 0$  if  $\sigma > 1/2^{3/2}$ , whereas it is stationary at  $t = t_{-}(\sigma)$  and  $t = t_{+}(\sigma)$  if  $0 < \sigma < 1/2^{3/2}$ , as is shown in detail in [2]. It may then be seen from (30) and (31) that we have

$$\pi e(x, y) \approx \text{Re } e_{+}(x, y) \quad (33)$$

as  $x \rightarrow -\infty$  if  $0 < \sigma < 1/2^{3/2} \approx 0.35$ . The points of stationary phase  $t_{-}(\sigma)$  and  $t_{+}(\sigma)$  are defined by  $t_{\pm} = [1 \pm (1 - 8\sigma^2)^{1/2}]/(4\sigma)$  and correspond to the transverse and the divergent waves, respectively, in the wave pattern. Only the divergent waves are considered here.

Let the stationary-phase value  $t_{+}(\sigma)$  be denoted  $\tau(\sigma)$ , which may be expressed in the form

$$\tau = T/(2\sigma) \quad (34)$$

with the function  $T(\sigma)$  defined as

$$T = [1 + (1 - 8\sigma^2)^{1/2}]/2. \quad (35)$$

The corresponding value of  $p = (1 + t^2)^{1/2} = (1 + \tau^2)^{1/2}$  then is given by

$$p = P/(2\sigma) \quad (36)$$

with the function  $P(\sigma)$  defined as

$$P^2 = [1 + 4\sigma^2 + (1 - 8\sigma^2)^{1/2}]/2. \quad (37)$$

At the stationary point  $t = \tau(\sigma)$ , the phase function  $\theta_{+}(t; \sigma)$  defined by (31) takes the value  $\theta(\sigma)$  given by

$$\theta = Q/(4\sigma),$$

where the function  $Q(\sigma)$  is defined as

$$Q = P[3 - (1 - 8\sigma^2)^{1/2}]/2. \quad (38)$$

By using (32) in the foregoing expression for  $\theta$  we may then obtain

$$x\theta = -Qx^2/(4y). \quad (39)$$

By applying the method of stationary phase to the integral  $e_{+}$  defined by (30) we may then obtain

$$(\pi/2)^{1/2} (-x)^{1/2} (1 - 8\sigma^2)^{1/4} e \approx \text{Re } P^{3/2} [k/(2\sigma)^{3/2}] \exp[-i \{Qx^2/(4y) - \pi/4\}] \quad (40)$$

as  $x \rightarrow -\infty$  if  $0 < \sigma < 1/2^{3/2} \approx 0.35$ , where  $k$  represents the value of the wave-spectrum function  $k(t)$  at the

stationary point  $t = \tau(\sigma)$  defined by (34) and (35). It may readily be seen from (35), (37), and (38) that the functions  $T(\sigma)$ ,  $P(\sigma)$ , and  $Q(\sigma)$  are nearly equal to 1 for small values of  $\sigma = y/(-x)$ .

The asymptotic approximation (40) shows that the phase  $Qx^2/(4y) \approx x^2/(4y)$  of any divergent wave is nearly constant along a parabola having the  $y$ -axis as axis and the origin  $x = 0$ ,  $y = 0$  as vertex. The divergent waves in the steady far-field wave pattern of a ship thus consist of a family of such parabolas, as is well known. It may be seen from (40) that the amplitudes, a say, of these waves are given by

$$(-x)^{1/2} a = (2/\pi)^{1/2} P^{3/2} [|k|/(2\sigma)^{3/2}]/(1 - 8\sigma^2)^{1/4}. \quad (41)$$

The corresponding wavelengths,  $\lambda$  say, are given by  $\lambda = 2\pi/|\nabla Qx^2/(4y)|$ . We may then obtain

$$\lambda = 8\pi\sigma^2/P^2. \quad (42)$$

The steepness  $s = a/\lambda$  of the divergent wave defined by (41) and (42) thus is given by

$$(-x)^{1/2} s = (2\pi^3)^{-1/2} P^{7/2} [|k|/(2\sigma)^{7/2}]/(1 - 8\sigma^2)^{1/4}. \quad (43)$$

The angle  $\theta$  between the ship track and the direction of propagation of the divergent waves is defined by the relation  $\cotan \theta = 2(\tan \alpha)/T$ , as may readily be verified from (4), (32) and (34). The corresponding interior point(s) of stationary phase on the ship waterline is (are) defined by the condition  $|t_y| = 2\sigma/P$ , which readily follows from (22c), (12a) and (36), or by the alternative equivalent condition (23). In summary, we thus have

$$\lambda/(2\pi) = 8(\tan^2 \alpha)/[1 + (1 - 8\tan^2 \alpha)^{1/2} + 4\tan^2 \alpha], \quad (44a)$$

$$\cotan \theta = \tan |\phi| = 4(\tan \alpha)/[1 + (1 - 8\tan^2 \alpha)^{1/2}]. \quad (44b)$$

These equations define the wavelength  $\lambda$ , the wave propagation angle  $\theta$  and the waterline tangent angle  $|\phi|$  as functions of the ray angle  $\alpha$  in the wake. Equivalent simple expressions defining  $\lambda$ ,  $\theta$  and  $\alpha$  as functions of  $|\phi|$  can also be obtained from (44a,b). Specifically, we have

$$\lambda/(2\pi) = \sin^2 \phi, \quad \theta = \pi/2 - |\phi|, \quad (45a,b)$$

$$\tan \alpha = (\tan |\phi|)/(2 + \tan^2 \phi). \quad (45c)$$

The following equivalent expressions explicitly define  $\lambda$ ,  $|\phi|$  and  $\alpha$  in terms of  $\theta$ :

$$\lambda/(2\pi) = \cos^2 \theta, \quad |\phi| = \pi/2 - \theta, \quad (46a,b)$$

$$\tan \alpha = (\tan \theta)/(1 + 2\tan^2 \theta). \quad (46c)$$

Finally, the equivalent expressions

$$\sin |\phi| = [\lambda/(2\pi)]^{1/2}, \quad \tan \theta = (2\pi/\lambda - 1)^{1/2}, \quad (47a,b)$$

$$\tan \alpha = (2\pi/\lambda - 1)^{1/2}/(4\pi/\lambda - 1) \quad (47c)$$

explicitly define  $|\phi|$ ,  $\theta$  and  $\alpha$  in terms of  $\lambda$ .

By using (3) and (4) in (46a,b,c) we may obtain the following expressions for the values of the wavelength  $\lambda$ , the wave propagation angle  $\theta$ , the waterline tangent angle  $|\phi|$ , and the wake ray angle  $\alpha$  corresponding to a given value of  $p$ :



$$\lambda/(2\pi) = 1/p^2, \quad \cos\theta = \sin|\phi| = 1/p, \quad (48a,b)$$

$$\tan\alpha = (p^2-1)^{1/2}/(2p^2-1). \quad (48c)$$

In summary, the far-field pattern of divergent waves is defined by (40), and the waves' amplitude, wavelength, and steepness by (41), (42), and (43). These expressions involve the value of the wave-spectrum function  $k \equiv v^2 K$  at the stationary point  $t = \tau(\sigma)$  defined by (34) and (35). The corresponding values of  $p \equiv (1+t^2)^{1/2}$ , the wavelength  $\lambda$ , the wave propagation angle  $\theta$ , the wake ray angle  $\alpha$ , and the waterline angle  $|\phi|$  are related by (48a,b,c). A practical approximate expression for the spectrum function  $K(t)$  is given by the waterline approximation (18). This approximation is valid in the limit  $p \rightarrow \infty$ , although Figures 1a,b,c indicate that it may be used in practice for moderate values of  $p$ . The near-field flow-velocity components  $\phi_t$  and  $\phi_s$  at the mean waterline in (19) can be determined from the wave-profile elevation  $e$  by using the analytical expressions (25a,b) obtained in [15]. The foregoing expressions provide an approximate but complete theoretical basis for predicting the short waves in the steady wave spectrum of a ship.

Figure 5 depicts the steepness  $(-x)^{1/2}s$ , defined by (43), of the divergent waves in the steady wave pattern of the Wigley hull for values of the wave angle  $\alpha$  in the range  $0 < \alpha \leq 4^\circ$ , which approximately corresponds to values of  $t$  in the range  $7 \leq t < \infty$  for which the waterline approximation (18) was previously shown to provide fairly accurate predictions. The top and bottom parts of Figure 5 correspond to values of the Froude number  $F$  equal to 0.25 and 0.4, respectively. The solid-line and dashed-line curves in this figure correspond to the nonlinear near-field-flow predictions defined by (26a,b), where the wave-profile elevation  $e$  is determined from experimental measurements and numerical calculations, respectively, in the manner explained previously. These analytical/ experimental and analytical/numerical steepness predictions are in reasonable agreement with one another. Both predictions exhibit a fairly well-defined peak at values of  $\alpha$  approximately equal to  $1.9^\circ$  and  $1.4^\circ$  for  $F = 0.25$  and  $0.40$ , respectively. Let  $\sigma$  denote the value of  $(-x)^{1/2}s$ . We thus have  $s = \sigma/(-x)^{1/2} = \sigma F/(-X/L)^{1/2}$  since  $x = Xg/U^2$ . We then have  $s = F\sigma/10$  at a distance of 100 ship lengths behind the ship. It may be seen from Fig. 5 that the predicted peak values of the wave steepness at 100 ship lengths thus are approximately equal to 0.3 and 0.6 for  $F = 0.25$  and  $0.40$ , respectively. These predicted peak values are extremely large and the corresponding waves could not exist in reality.

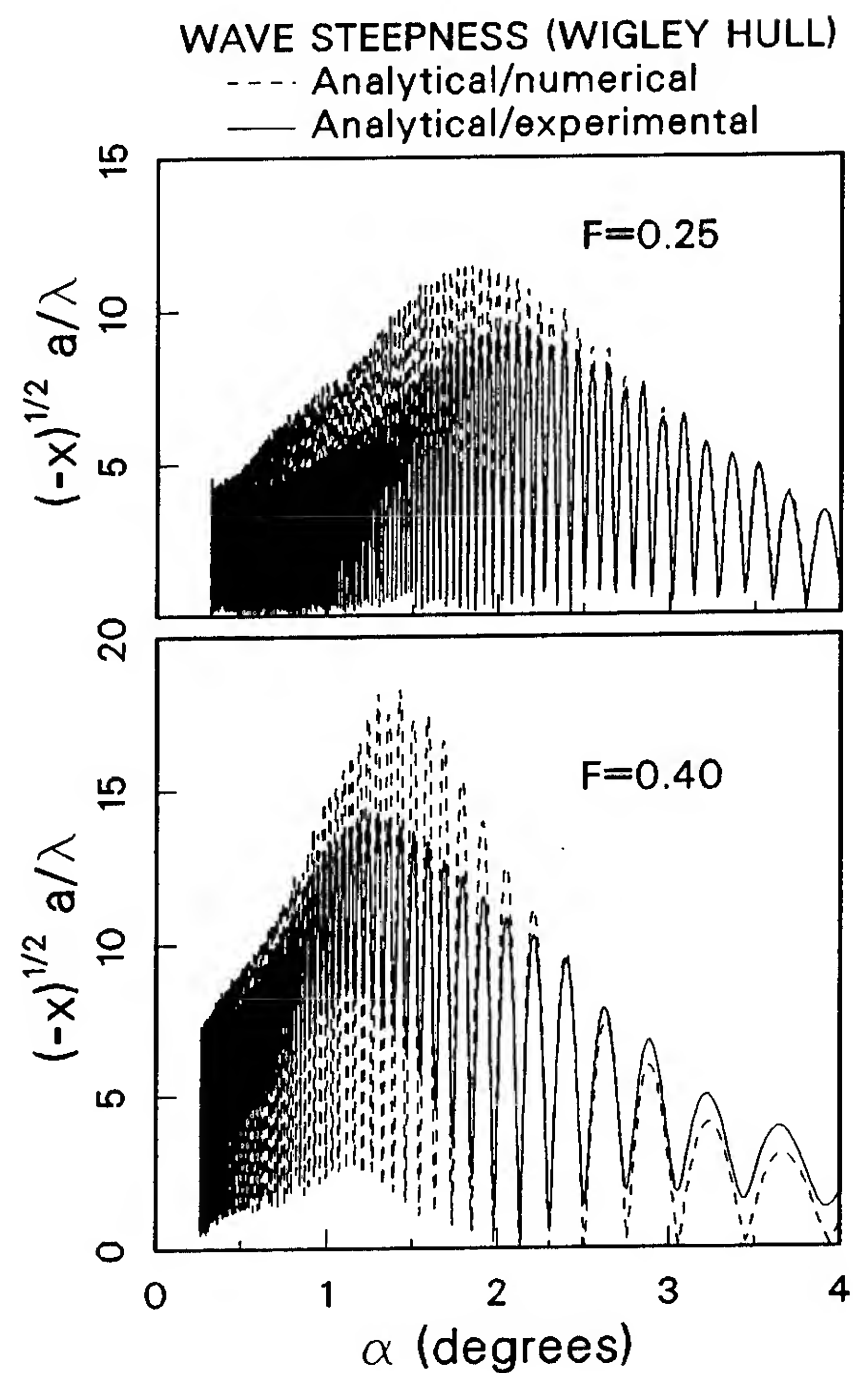


Fig. 5. Steepness of the short divergent waves.

## CONCLUSION

A simple practical analytical/numerical method for calculating the short divergent waves in the steady wave spectrum of a ship has been presented. The method is based on a waterline-integral approximation obtained from a modified Neumann-Kelvin integral representation of the wave-spectrum function. A comparison of numerical predictions obtained using the exact integral representation and the waterline-integral approximation showed excellent agreement for sufficiently short waves. This agreement demonstrates both the validity of the waterline-integral approximation and the robustness of the more general numerical method based on the exact integral representation. The waterline-integral approximation to the spectrum function shows that the short divergent waves in the wave pattern of a ship are defined in terms of the near-field flow along the ship waterline, and may indeed be regarded as an image of the flow along the ship waterline.

The foregoing linear far-field flow representation has been used in numerical experiments seeking to determine the sensitivity of the far-field waves to the near-field flow along the ship waterline. The simplest approximation is the trivial approximation corresponding to the zeroth-order slender-ship approximation, in which the disturbance potential is merely ignored. The next level of approximation for the near-field flow is that corresponding to the first-order slender-ship approximation. Significant discrepancies were found between the wave-spectrum predictions corresponding to these two near-field-flow approximations. The other two near-field-flow approximations were determined by applying a simple analytical expression defining the fluid velocity along the waterline in terms of the elevation of the wave profile, corrected at the bow and the stern according to the nonlinear local solution given in [15]; both wave profiles measured experimentally and predicted numerically using the slender-ship approximation were used. Discrepancies between the wave-spectrum predictions corresponding to the latter analytical/experimental and analytical/numerical near-field-flow approximations were found to be much smaller than the discrepancies between the wave-spectrum predictions corresponding to these nonlinear near-field-flow approximations, on one hand, and to the linear near-field flow prediction given by the slender-ship approximation on the other hand. This result indicates that the short divergent waves in the wave pattern of a ship stem mostly from the ship bow and stern; a result that is not surprising but points to the fundamental difficulty of predicting the short divergent waves since the flow at a ship bow and stern is strongly nonlinear and quite difficult to compute.

Numerical calculations for the Wigley hull showed that the steepness of the short divergent waves predicted on the basis of the foregoing linear far-field/nonlinear near-field flow analysis is too large for the waves to exist in reality within a sector of several degrees in the vicinity of the ship track. The wave steepness was also found to exhibit a well-defined peak at an angle of approximately  $1^\circ$  to  $2^\circ$  from the ship track. It is unclear whether or not these numerical predictions have real physical implications. On the one hand, the physically-unrealistic predicted wave steepness might be regarded as a theoretical indication for the common observation that the wake of a ship in the vicinity of the track does not contain divergent waves. On the other hand, these physically-unrealistic numerical predictions might be regarded as an indication that the assumptions of linear far-field waves and of steady nonlinear near-field flow underlying the mathematical model and the numerical results may not be correct. In particular, assumptions about the flow in the immediate

vicinity of the ship bow and stern clearly are crucial for the prediction of the short divergent waves in the wave pattern. Indeed, the present study underscores the need for a better understanding of the flow at a ship bow and stern.

It should be recognized that the assumptions underlying the short-wave analysis presented in this study are also adopted for numerical predictions of the longer waves in the steady wave pattern of a ship. In this respect, numerical experiments analogous to those performed in this study for the short divergent waves also seem useful for determining the sensitivity of the longer waves in the wave pattern to the assumptions used in the calculation of the near-field flow at a ship hull. Such numerical experiments will be presented in [16].

#### ACKNOWLEDGMENTS

This study was performed at the David Taylor Research Center with support from the Surface Ship Wake Signature Task, the Independent Research Program, and the Applied Hydrodynamics Research Program funded by the Office of Naval Research. The authors also wish to thank Dr. Robert Hall at SAIC and Dr. Patrick Purtell at DTRC for discussing the paper.

#### REFERENCES

1. Scragg, C.A., "A numerical investigation of the Kelvin wake generated by a destroyer hull form," Science Applications International, Report No. SAI-83/1216, 46 pp., 1983.
2. Barnell, A. and F. Noblesse, "Far-field features of the Kelvin wake," 16th Symposium on Naval Hydrodynamics, University of California, Berkeley, 1986.
3. Keramidas, G.A. and W.D. Bauman, "FFSW: a computer program for far-field ship wave calculations," Naval Research Laboratory, Report 6007, 80 pp., 1987.
4. Milgram, J.H., "Theory of radar backscatter from short waves generated by ships, with application to radar (SAR) imagery," Journal of Ship Research, Vol. 32, pp. 54-69, 1988.
5. Trizna, D.B. and G.A. Keramidas, "Calculated radar images of ship wakes from simulated wake hydrodynamic models," Naval Research Laboratory, Report 6203, 33 pp., 1989.
6. Noblesse, F., "A slender-ship theory of wave resistance," Journal of Ship Research, Vol. 27, pp. 13-33, 1983.
7. Baar, J.J.M., "A three-dimensional linear analysis of steady ship motion in deep water," Ph.D. thesis, Brunel University, U.K., 182 pp., 1986.

8. Andrew, R.N., J.J.M. Baar, and W.G. Price,  
"Prediction of ship wavemaking resistance  
and other steady flow parameters using  
Neumann-Kelvin theory," Transactions of  
the Royal Institution of Naval Architects,  
Vol. 130, pp. 119-129, 1988.
9. Lindenmuth, W.T., T.J. Ratcliffe and A.M.  
Reed, "Comparative accuracy of numerical  
Kelvin wake code predictions," David  
Taylor Research Center, Report  
DTRC/SHD-1260-01, 1988.
10. Noblesse, F., D. Hendrix and A. Barnell,  
"The slender-ship approximation:  
comparison between experimental data  
and numerical predictions," 2e Journees de  
l'Hydrodynamique, ENSM, Nantes,  
France, pp. 175-187, 1989.
11. Sharma, S.D., "Some results concerning  
the wavemaking of a thin ship," Journal of  
Ship Research, Vol. 13, pp. 72-81, 1969.
12. Tuck, E.O., J.I. Collins and W.H. Wells,  
"On ship wave patterns and their spectra,"  
Journal of Ship Research, Vol. 15, pp. 11-  
21, 1971.
12. Ursell, F. "On Kelvin's ship-wave  
pattern," Journal of Fluid Mechanics, Vol.  
8, pp. 418-431, 1960.
14. Noblesse, F., W.M. Lin and R. Mellish,  
"Alternative mathematical expressions for  
the steady wave spectrum of a ship,"  
Journal of Ship Research, in press.
15. Noblesse, F., D.M. Hendrix and L. Kahn,  
"Nonlinear local analysis of steady flow  
about a ship," Journal of Ship Research, to  
appear.
16. Noblesse, F. and D. Hendrix, "Steady near-  
field flow and far-field ship waves," in  
preparation.

**Session VI**  
**Wave/Wake Dynamics**

# Vortex Ring Interaction with a Free Surface

M. Song, N. Kachman, J. Kwon, L. Bernal, G. Tryggvason  
(The University of Michigan, USA)

## ABSTRACT

The results of numerical and experimental studies on the interaction of vortex rings with a free surface are presented. New results are reported on the interaction of a large vortex ring with a clean surface at normal incidence. The early stages of the interaction are well described by a simple axisymmetric vortex filament model. Transition to a fully three-dimensional state is observed at later stages of the interaction. Surface waves are generated at high Froude numbers by these three-dimensional motions. Results are also presented on the interaction of vortex rings with clean and contaminated free surfaces at inclined incidence. The phenomenon of vortex lines breaking and attachment to the free surface is documented. It is shown that small amounts of surface active agents greatly alter the interaction at inclined incidence. The effect differs depending on the local topology of the vortex lines. A Reynolds ridge and secondary vorticity generation are observed during the interaction with a contaminated surface.

## INTRODUCTION

The disturbance on a free surface created by a moving ship is composed of several superimposed and sometimes interacting phenomena. The most dramatic and best understood is the surface wave pattern generated, generally referred to as the Kelvin wake. Not only is the Kelvin wake the more visible mark left by the ship, it contributes also significantly to the drag of the ship, and is therefore of direct economic significance. Although it is, of course, well known that the ship also has a large viscous wake that is turbulent and can last for a long time, traditionally the turbulent wake has only been of interest as it directly relates to the drag of the ship, and in most such considerations the effect of the free surface can be neglected. Furthermore, for the purpose of drag estimation the focus is on the turbulent wake near the ship. It is only recently that the far wake of the ship has generated interest. The motivation is remote sensing technology. In

order to process the signal and to determine what is being detected, as well as to be able to reduce the detectability of ships, it is necessary to understand the detailed mechanisms of generation of surface signatures of ship wakes.

The surface signature of unsteady vortical motions below a free surface has recently been the subject of several investigations. Sarpkaya & Henderson<sup>1</sup> experimented with a delta wing moved below a free surface. The wing was set at a negative angle of attack, so that the trailing vortices moved upward to the free surface. As the vortices approached the surface a pair of long and narrow marks were observed on the free surface that appear to be directly related to the trailing vortices. These marks, called scars by Sarpkaya, are parallel to the direction of motion and moved outward with the vortices. The scars were accompanied by other features called "striations", perpendicular to the line of motion. A somewhat different setup, two-dimensional vortex pair was investigated by Willmarth *et al.*<sup>2</sup> and by Sarpkaya *et al.*<sup>3</sup> The surface signature of the pairs is similar to the trailing vortices, but the mean motion is now strictly two-dimensional. These experiments were motivated primarily by a desire to understand the surface signature of ship wakes, and the focus was mainly on the large scale motion.

Several numerical studies of this problem have followed the experimental work. These have mostly assumed an inviscid, two-dimensional motion. Tryggvason<sup>4</sup> presents a brief numerical study of surface deformation due to the roll-up of a submerged vortex sheet using a boundary integral/vortex method. Sarpkaya *et al.*<sup>3</sup> and Telste<sup>5</sup> use a similar technique to follow the motion of a vortex pair toward a free surface. A finite difference simulation of the point vortex problem have been reported by Marcus<sup>6</sup> who also discusses linearized aspects of the problem. More realistic vortex structure are used by Willmarth *et al.*<sup>2</sup> who simulate the formation of a vortex pair from an initially flat vortex sheet and the subsequent vortex motion and free surface deformation. A brief

comparison of experimental and computational results is contained in Reference 2. A thorough discussion of both vortex collision as well as the formation of vortices from a shear layer, and the resulting surface signature, is given by Yu and Tryggvason<sup>7</sup>, who simulated a large number of cases, and, in particular, explored the limits of high and low Froude numbers.

It should be noted that the signal from the ocean surface that is received by remote radar sensors is directly related to the presence of relatively short waves. It is therefore the surface roughness that is observed directly. Generally the large features of more interest such as changes in the ocean depth or currents and the wakes of ships can only be inferred through their modulation of the free surface roughness. For interpretation of these data it is therefore necessary to understand the interplay between the large and small scale features of the flow and their role in the generation of short surface waves. An example of such interplay is the relation between the scars and striations in the vortex wake problem studied by Sarpkaya and coworkers<sup>1,3</sup> and more recently by Hirs<sup>8</sup>. Also of primary interest in this regard is the role of smaller scale motions in the turbulent wake in the generation of short waves.

To examine the surface response to a turbulent subsurface flow Bernal and Madnia<sup>9</sup> studied a turbulent jet parallel to the surface located a few diameters from the surface. Near the jet exit, vortex rings are generated that produce some surface deformations and waves, but the most dramatic signature is produced when these vortex rings open and reconnect with the free surface. To explore this mechanism in more detail, Bernal and Kwon<sup>10</sup> and Kwon<sup>11</sup> experimented with a single ring moving parallel and at inclined incidence relative to the surface, respectively.

The above discussed investigations were not concerned with the effects of surface contaminants as such, but it appears that some of those results were influenced by the fact that a free surface is hardly ever hydrodynamically clean. Earlier, Davies<sup>12</sup> discussed the damping of turbulent eddies at a free surface, and Davies and Driscoll<sup>13</sup> experimented with ejecting pulses of colored water to a free surface, specifically addressing the rate of surface renewal and the effect of surface contamination. They found that the spreading of the colored water at the surface is reduced considerably for contaminated surfaces. However, their visualization technique did not allow for a clear explanation of the mechanism responsible for this behavior. Experiments on the collision of two-dimensional vortex pairs with a free surface were reported by Barker and Crow<sup>14</sup> whose main interest was in vortex collision with a rigid surface. The motivation for their experiments was the observed rebounding of aircraft trailing vortices from rigid surfaces. This rebounding of a vortex pair from a solid surface is due to the separation of the ground boundary layer and

subsequent formation of secondary vortices. Therefore it is not expected that rebounding will occur if the rigid surface is replaced by a stress free surface. However, Barker and Crow<sup>14</sup> observed rebounding in their free surface experiments, just as the rigid surface case, and suggested that this rebounding might be due to inviscid effects such as the deformation of the vortex cores. Saffman<sup>15</sup> refuted this suggestion, and showed that for inviscid flow and a flat boundary rebounding can not occur. He suggested that the behavior might be due to surface tension effects. Peace and Riley<sup>16</sup> performed numerical simulations of the Navier-Stokes equations for a two-dimensional vortex pair colliding with a flat no-slip and stress-free surface, and concluded that even for a stress-free boundary viscous effects could cause rebounding. However, even though their calculations clearly show rebounding, those are for rather low Reynolds numbers, and with increasing Reynolds number, the rebounding decreased significantly. Their results can therefore not explain the behavior in the Baker and Chow experiments, which were conducted at a much higher Reynolds number.

The explanation for rebounding from a free surface is clear from recent experiments by Bernal, Hirs, Kwon and Willmarth<sup>17</sup> who investigated the collision of both vortex rings and pairs with a free surface. They observed that the cleanness of the surface lead to considerable differences in the vortex motion itself. For very clean surfaces sufficiently weak vortices were deflected outward in a manner similar to what inviscid theory predicts (if the surface deforms some rebounding is predicted but most experiments have been conducted under conditions where surface deformation is minimal), but for contaminated surfaces the behavior was more like vortices encountering a rigid wall where secondary vorticity from the wall boundary layer is pulled away by the primary vortex that then rebounds as a result of its interaction with the wall vorticity. Detailed observations using Laser Induced Fluorescence (LIF) flow visualization lead Bernal *et al*<sup>17</sup> to conclude that the surface motion induced by the vortex generated an uneven distribution of contaminant that in turn caused shear stress at the surface, generating secondary vorticity. This vorticity rolls-up into a secondary vortex which results in the rebounding of the primary vortex. This generation and roll-up of secondary vorticity and its subsequent interaction with the primary vortex appears to be the leading effect of the surface contaminants.

Although rebound can usually be associated with viscous effects Dahm, Scheil and Tryggvason<sup>18</sup> have shown that a weak vortex colliding with a weak density interface can engulf a portion of the interface containing baroclinically generated vorticity which then causes the primary vortex to rebound in completely inviscid simulations. Yu and Tryggvason<sup>7</sup> also show that a deformable surface can lead to rebounding. However this occurs at much higher Froude number than in the experiments.



Observations of contaminated free surfaces have been reported on numerous occasions for over a century. One important phenomenon is the Reynolds ridge which appears on the boundary between the contaminated and clean surface regions when the surface flow is stopped by a barrier. This flow configuration develops when vortices collide with a free surface as shown by Hirs<sup>8</sup>. The upwelling generated by the vortices pushes the contaminated surface water to the side, thereby compressing the contaminated layer. The surface above the vortices is cleaner and is separated from the contaminated surface by a Reynolds ridge. For a Thorough discussion of the Reynolds ridge with historical perspective see Scott<sup>19</sup>. We should note that the occurrence of a Reynolds ridge, although often observed when separation takes place, is not directly related to the generation of secondary vortices. Indeed, a Reynolds ridge is easily generated in the absence of separation (see Scott<sup>19</sup>) and separation can take place without the formation of a Reynolds ridge.

In what follows an overview of recent results on the interaction of vortex rings with the free surface is presented. The flow geometry is shown schematically in Figure 1. Results on the interaction at normal incidence, Figure 1a, are presented first. Next the results of Kwon<sup>11</sup> for inclined incidence are briefly reviewed. Finally the results of recent experiments on the effect of surface contamination on the interaction at inclined incidence are presented and discussed.

## INTERACTION AT NORMAL INCIDENCE

The interaction of a vortex ring with the free surface at normal incidence is perhaps the simplest flow geometry involving the interaction of a vortical flow with the free surface. This type of interaction has been studied in detail in a recent experimental and numerical investigation by Song, Bernal and Tryggvason.<sup>20</sup> One objective of the investigation was to study the interaction at a scale substantially larger than previous experiments which were conducted in small water tank facilities.<sup>10,11</sup>

A large vortex ring generator with a nozzle exit diameter of 10 cm was used in this study. The general design and operating characteristics are similar to the smaller scale vortex ring generators.<sup>11</sup> The experiments were conducted in Tow Tank facility at the Hydrodynamics Laboratories of the University of Michigan. The water surface was cleaned by a continuous surface current. The current was interrupted and the flow motion allowed to dissipate before each vortex ring test. Because of these precautions the water surface is believed to have been free from contaminants on these tests.

Hot film velocity measurements along the axis of the flow were used to determine the vortex ring formation characteristics. The flow field during the interaction was

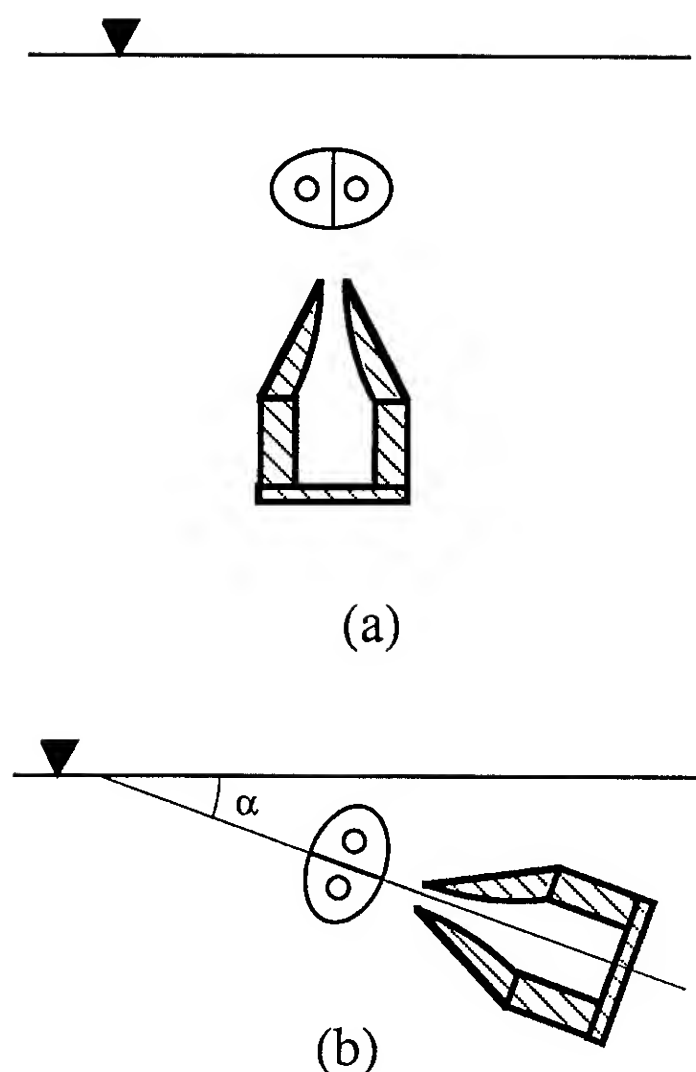


Figure 1. Schematic diagram of flow geometry. a) Normal incidence. b) Inclined incidence.

characterized by flow visualization of the underwater flow using the Hydrogen bubble technique and of the free surface using the shadowgraph technique. The surface signature during the interaction was also characterized by measurements of the free surface elevation using a capacitance probe.

The numerical simulations were conducted using a vortex/boundary-integral method. A single vortex filament with finite core size was found adequate for the objectives of the study. Comparison with experiments was made by adjusting the vortex ring circulation and core parameter to obtain the same circulation and initial propagation speed as in the tests. For additional details on the experimental setup and numerical simulations the reader is referred to Song et al.<sup>20</sup>

## Flow visualization

Typical flow visualization results of the interaction at normal incidence are shown in Figure 2. Figure 2a are visualizations of the surface deformation and underwater flow at a Froude number  $\Gamma/(gR^3)^{1/2} = 0.252$  where  $\Gamma$  is the circulation of the vortex ring,  $g$  is the gravitational acceleration and  $R$  is the radius of the ring before interaction. The corresponding Reynolds number was  $\Gamma/\nu=15,000$ . Figure 2b are similar visualizations at a

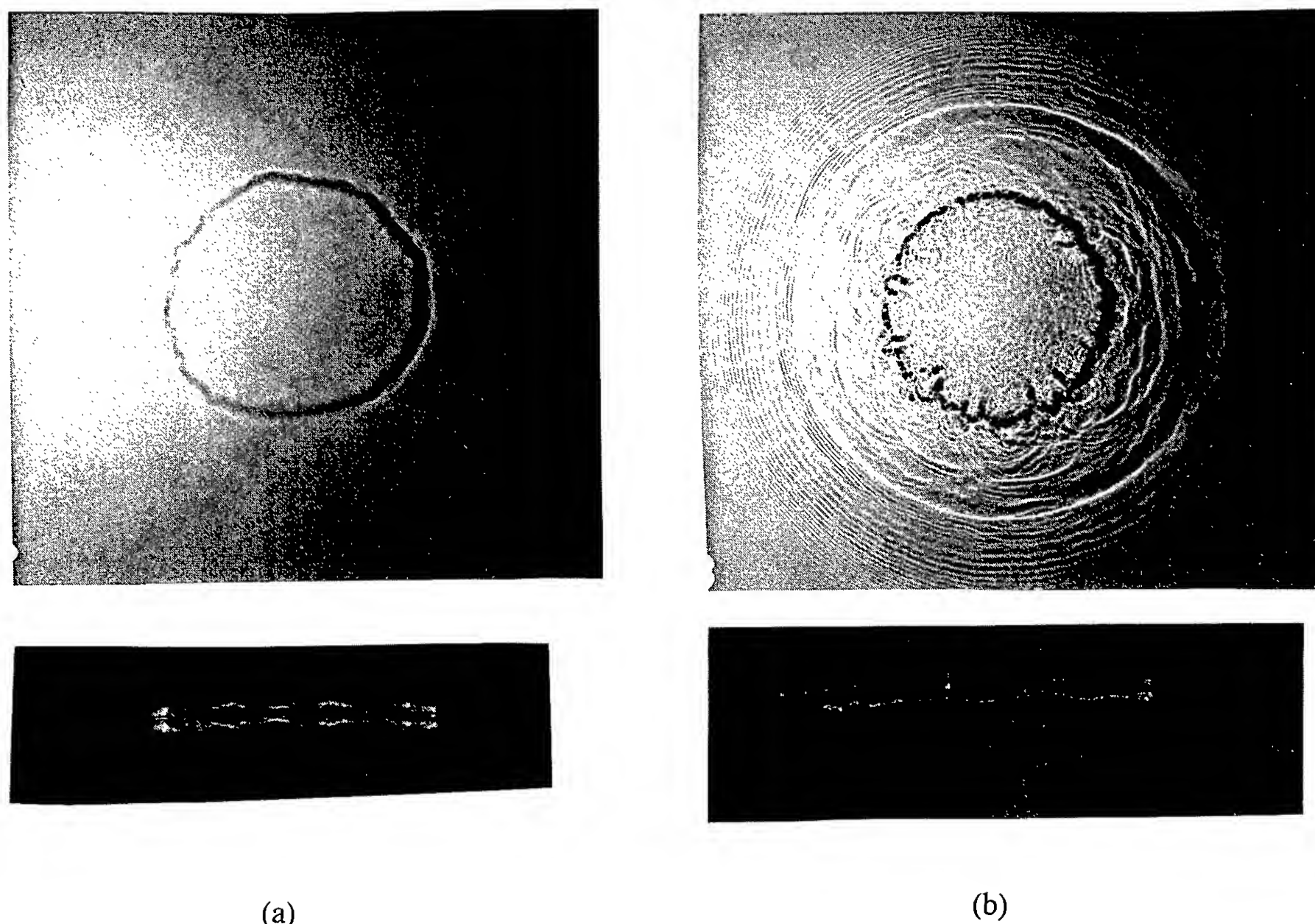


Figure 2. Flow visualization of the interaction of a vortex ring with a free surface at normal incidence. Top is a shadowgraph image of the surface, Bottom, underwater flow visualized by hydrogen bubbles. (a) Froude number 0.252. (b) Froude number 0.988.

Froude number of 0.988. The Reynolds number was 64,700. In both cases it is shown the shadowgraph image of the surface on top and the side view image obtained using the hydrogen bubble technique at the bottom. Both images were obtained on the same realization of the flow. The bubbles in the side view pictures tend to migrate towards the core of the vortices due to their low density. Note that on the side view the mirror image of the underwater flow is observed caused by total reflection of scattered light on the water surface.

The flow visualization results at low Froude number, Figure 2a, show a highly coherent axisymmetric surface pattern. The side view picture also shows a coherent axisymmetric core. The surface signature consists of a dark band bounded by two bright regions these features indicate a local depression of the surface. This surface depression is located above the vortex core and moves with it as it stretches outward due to the velocity field induced by the image vorticity above the surface. There were no surface waves generated during this process. At very low Froude number these features were observed during the entire interaction process.

Figure 2b shows flow visualization pictures at a higher Froude number as indicated. The shadowgraph visualization of the surface shows small scale three-dimensional structures superposed on an axisymmetric dark band associated with the core. Surface waves are generated by these small scale three-dimensional motions. These waves coalesce to form an axisymmetric wave front propagating away from the interaction region. The visualization of the core in the side view picture show small scale three-dimensional distortions of the core associated with the surface features. The development of the small scale three-dimensional features was found to occur rapidly, through an instability process. Before the instability the surface signature and general flow appearance was similar to the case shown in Figure 2a. After transition the flow features discussed in relation to Figure 2b appeared.

### Surface signature and subsurface flow

The measured and calculated trajectories of the vortex cores at a Froude number of 0.255 and 0.988 are shown in Figure 3. The measured and calculated results are in good agreement. There is no rebounding of the vortex core in the low Froude number case. This is expected since contaminants were not allowed to accumulate on the surface. At the larger Froude number the calculations show a small rebounding of the core. The measurements on the other hand are not accurate enough to confirm this result. An interesting observation shown by the data in Figure 3 is that the vortices attain a different final depth after the interaction for the two cases presented. Studies of many numerical simulations of the flow revealed that the final depth of the vortex core is controlled primarily by the core size parameter. For the cases shown in Figure 3 the core size parameter  $R/e$ , where  $e$  is the core radius, was 4.9 for the low Froude number case and 2.7 for the high Froude number case.

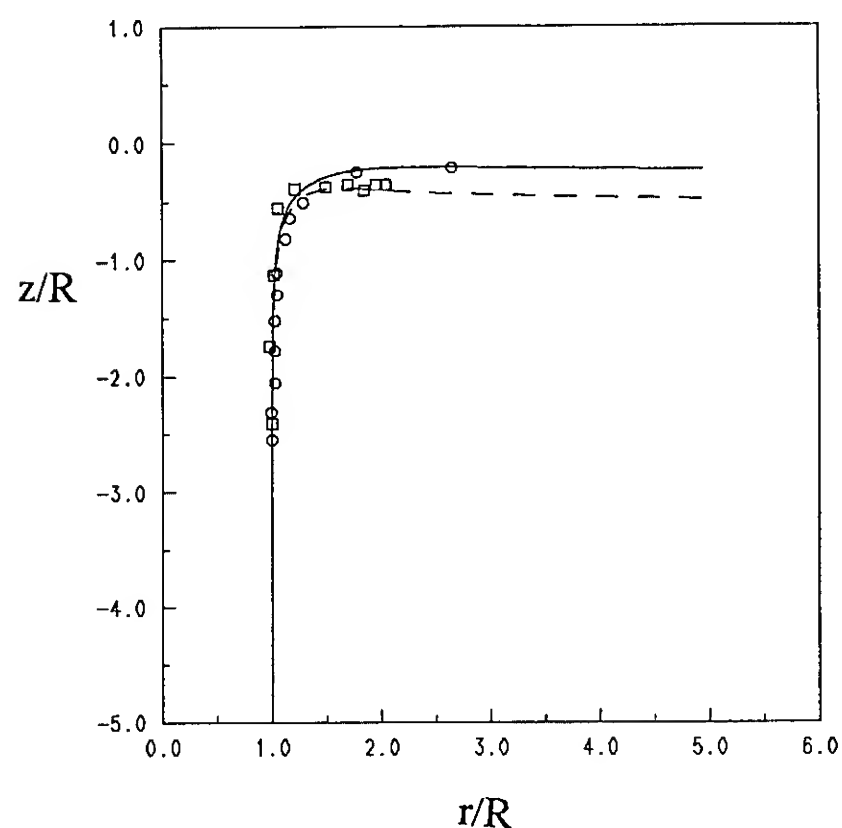


Figure 3. Vortex core trajectories for normal incidence. Froude number 0.252: Solid line calculated results, circles measurements. Froude number 0.988: Dashed line calculated results, squares measurements.

Several parameters can be used to characterize the surface signature during the interaction of a vortex ring with the free surface. Perhaps the simplest measure of the strength of the interaction is the surface elevation at the center. Figure 4 is a plot of the normalized maximum elevation at the center,  $h/R$ , as a function of Froude number,  $\Gamma/(g R^3)^{1/2}$ , for all the cases tested in the

laboratory. The straight line in this plot has slope 2, the expected scaling behavior derived from considerations of momentum balance of the vortical flow and the surface deformation.

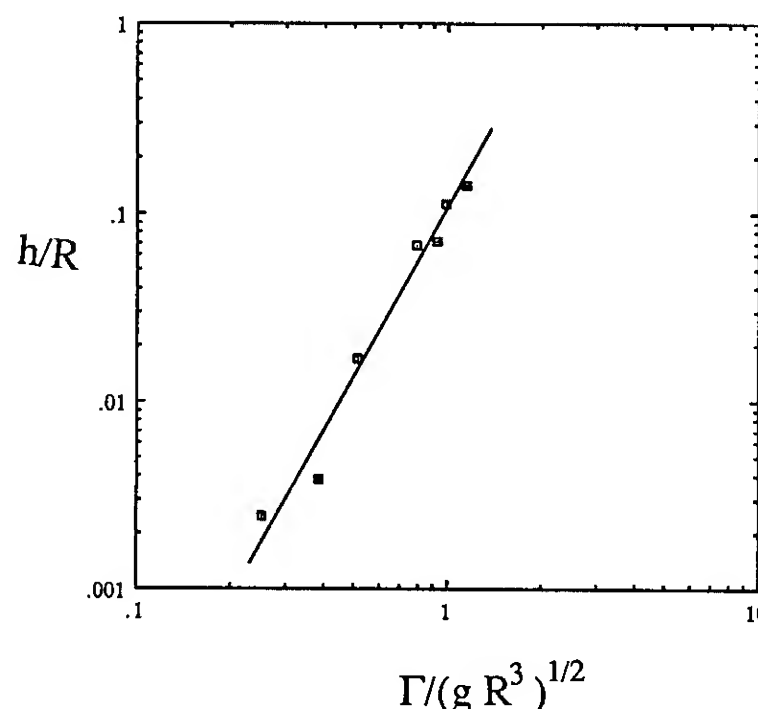


Figure 4. Normalized maximum surface elevation at the centerline as a function of Froude number. Only experimental results are presented.

The surface signature during the interaction was obtained from the numerical simulations. Figure 5 is a plot of the instantaneous surface shape for the case  $Fr = 0.252$  at nondimensional time  $t\Gamma/R^2 = 14.16$ . Note that the vertical axis is stretched by a factor of ten compared to the horizontal axis. The surface features in this plot are in good qualitative agreement with the shadowgraph flow visualization picture of the surface shown in Figure 2a. The dark band in the photograph corresponds to the surface depression at  $r/R \approx 3.0$ . The bright regions next to the dark band in the photograph correspond to the surface rise at either side of the depression.

More detailed comparisons between the measured and calculated results is presented in Figures 6 and 7 for Froude numbers of 0.252 and 0.988 respectively. In both Figures we plot various measures of the position of the vortices and associated surface features as a function of time. The solid lines are the calculated location of the vortex core. The open circles are the measured location of the cores determined from the hydrogen bubbles flow visualization. The broken line is the radial location of the maximum surface depression from the numerical simulations. The cross symbols are the measured location of the dark band in the shadowgraph images.

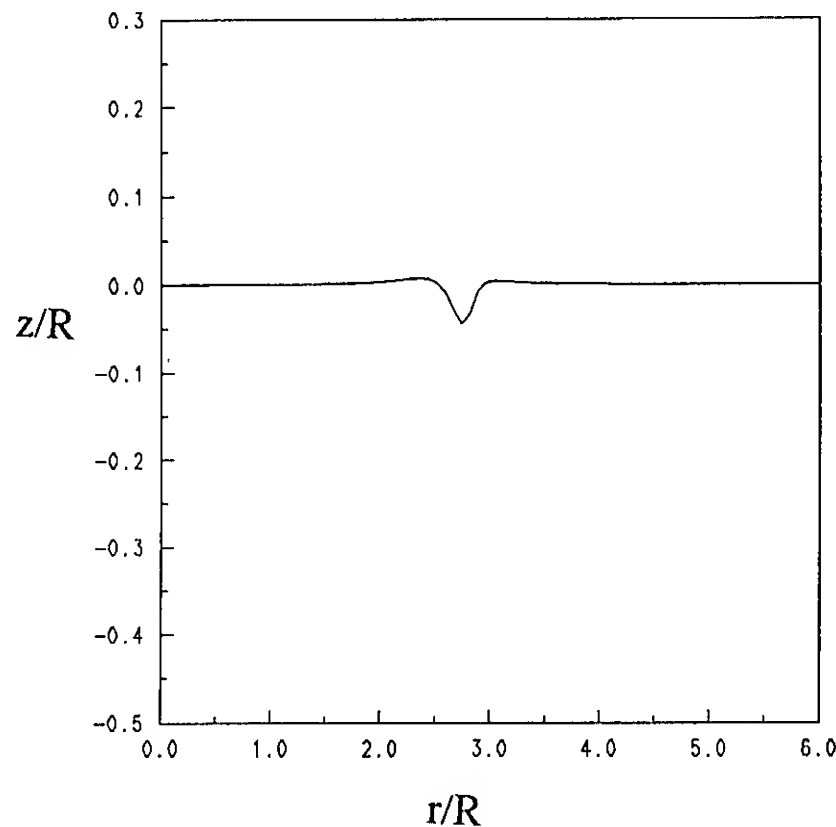


Figure 5. Calculated free surface shape for Froude number 0.252.

The results at low Froude number, Figure 6, show good agreement between the numerical calculation and the measurements. The agreement is excellent for the distance

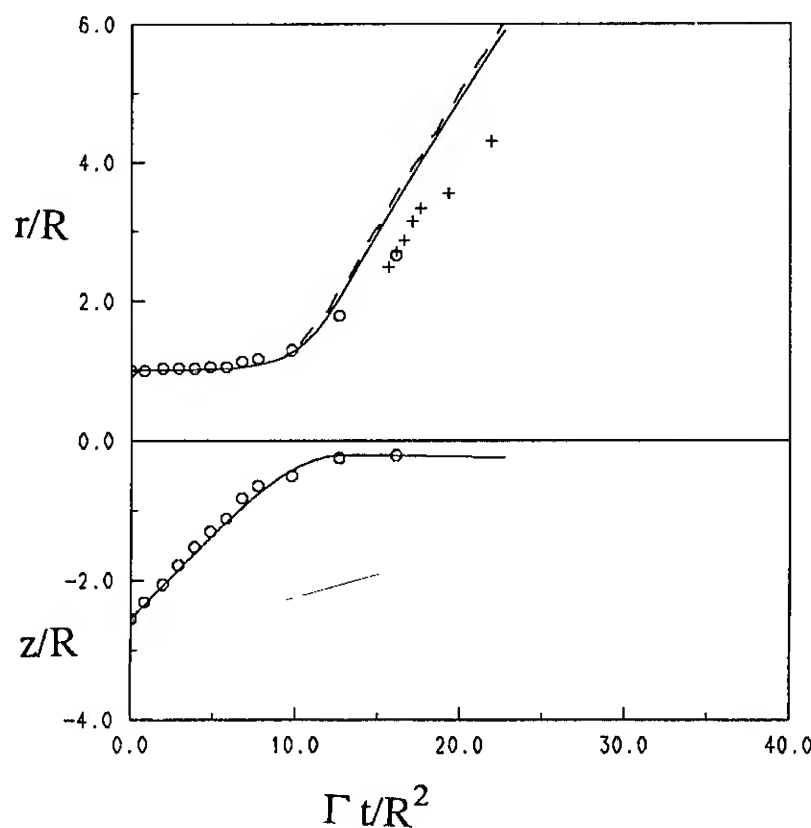


Figure 6. Temporal evolution of various flow parameters at a Froude number of 0.252. Solid line calculated core location. Dashed line radial location of minimum surface depression. Circles measured core location. Crosses radial location of dark band.

to the free surface. The calculation show that the location of the maximum depression moves outwards ahead of the core. The calculated speed of this outward motion is in good agreement with the measured value. Although there are discrepancies in the absolute location of the core. At later times, however, ( $\Gamma t/R^2 > 15$ ) there appears to be a change in the measured core trajectory.

The results at high Froude number, Figure 7, show significant discrepancies between the calculated and measured results. Again there is excellent agreement between the calculations and the measurements for the distance to the free surface. The evolution of the radial location of the core is in good agreement up to  $\Gamma t/R^2 \approx 12$ . After that time the measurements show a slower outward motion of the vortex core compared to the calculations. The reason for this discrepancy is the three-dimensional instability observed in the flow visualization study. Before the instability the outward motion of the core results from the induced velocity field caused by the image vorticity above the free surface. This induced motion is well characterized by the axisymmetric vortex filament model used in the numerical calculations. As three-dimensional motions develop after the instability, vortex lines break and connect to the free surface, a phenomenon discussed in more detail later, thus destroying the axial coherence of the vorticity distribution. These vortex patches attached to the free surface determine the speed of the outward motion of the core after the three-dimensional instability.

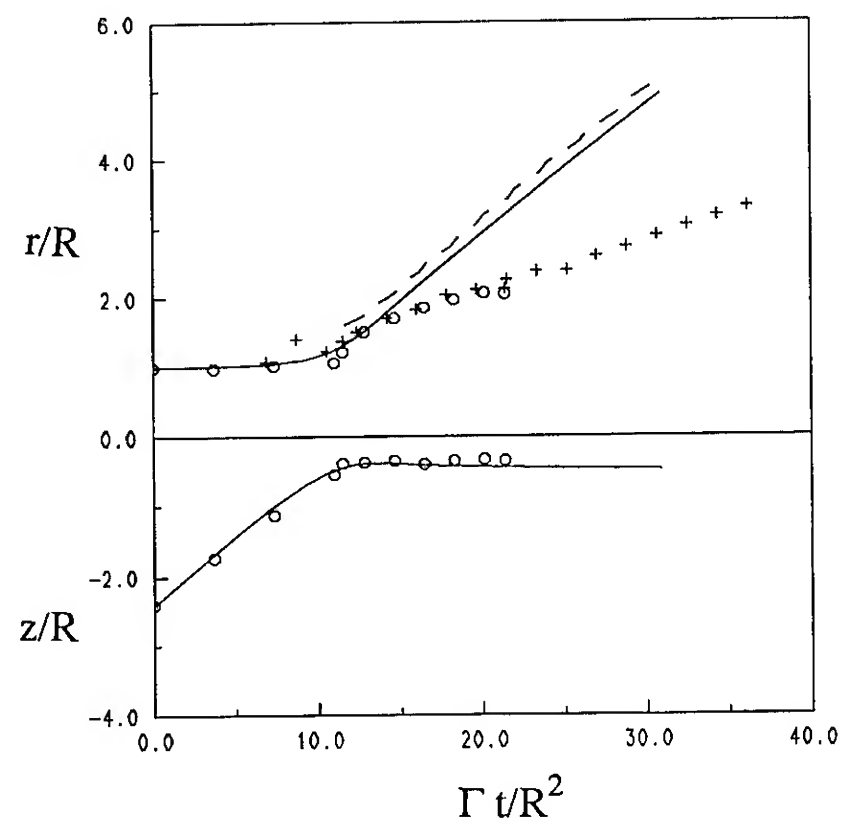


Figure 7. Temporal evolution of various flow parameters at a Froude number of 0.988. For key to the symbols see caption of Figure 6.



## INTERACTION AT INCLINED INCIDENCE

Investigations on the interaction of a turbulent jet with the free surface<sup>9</sup> revealed the development of characteristic features on the free surface consisting of dark dimples associated with vortex lines terminating at the free surface. It was also observed that vortical structures in the near field of the jet were directly responsible for the formation of the dimples. Bernal and Kwon<sup>10</sup> experimented with vortex rings moving parallel

to the surface. These experiments demonstrated that surface dimples result from vortex lines breaking and reconnecting with the free surface. To further examine this phenomenon a systematic investigation on the interaction of a vortex ring, at an inclined incidence to the free surface, was undertaken (see Figure 1b).

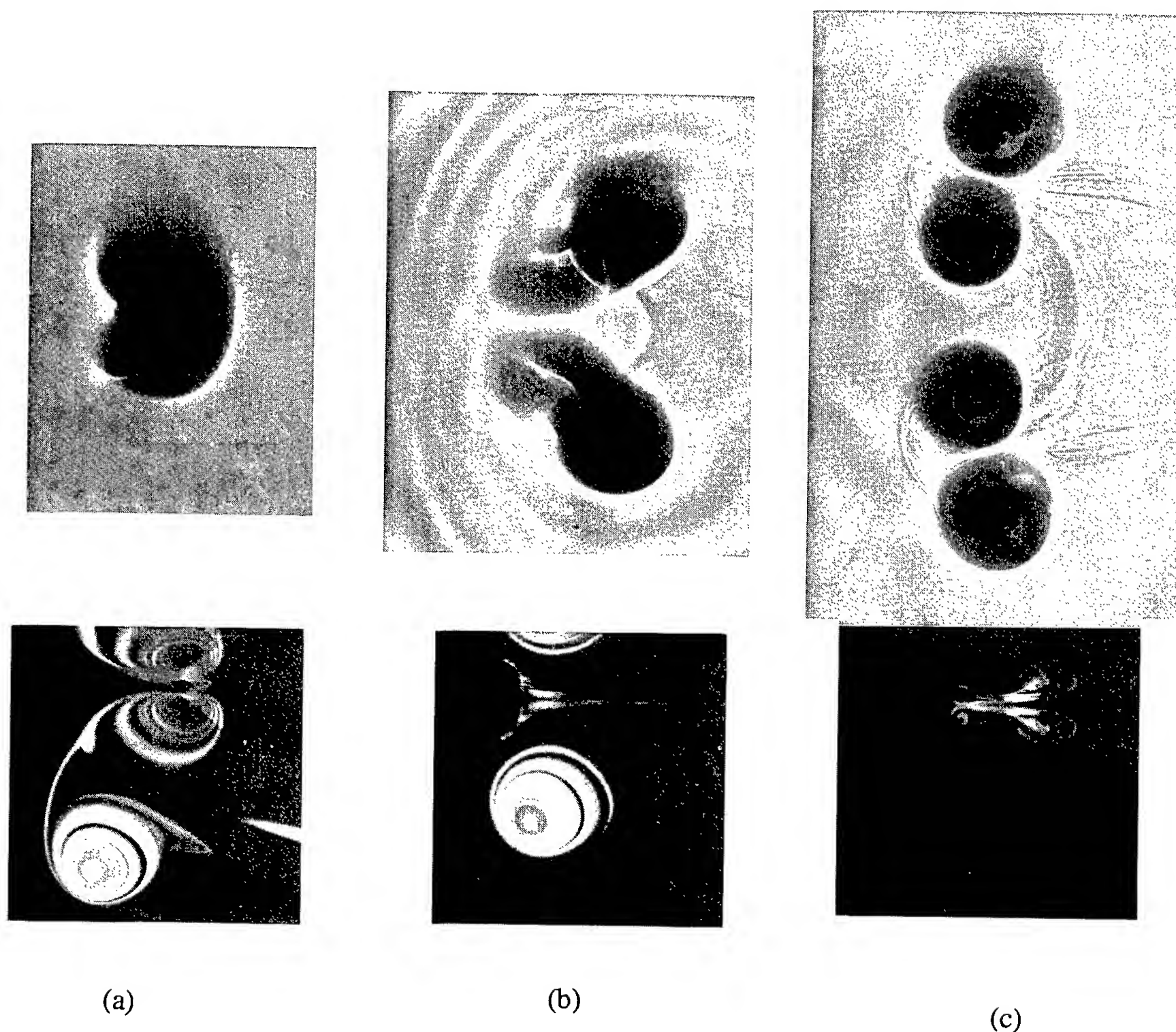


Figure 8. Flow visualization pictures of the interaction of a vortex ring with a clean free surface at a Reynolds number of 5,000 and incidence angle of  $20^\circ$ . Shadowgraph visualizations of the surface are shown on top and Cross-section views at the bottom. In each photograph the vortex motion is from right to left. (a)  $\Gamma t/R^2 = 18$ . (b)  $\Gamma t/R^2 = 26$ . (c)  $\Gamma t/R^2 = 43$ .

In considering these flow processes at a free surface the role of surface contamination is an important parameter. The flow visualization results by Bernal, Hirsa, Kwon and Willmarth<sup>17</sup> showed that vorticity generation at the free surface can alter the evolution of the subsurface flow. The study of this interaction in the more complicated case of inclined incidence was another motivation for the present study.

The experiments were conducted in the free surface water tank described by Bernal and Madnia<sup>9</sup>. Several modifications were added to help control contamination of the free surface. A stand-up drain pipe was installed, and a continuous current of water was allowed to flow into the facility to remove surface contaminants before they could have accumulated on the free surface. During the actual tests the water current was temporarily halted and the remaining turbulence in the tank was allowed to dissipate before generating the vortex rings. This procedure resulted in highly reproducible results for a clean free surface.

A vortex ring generator having a 2.5 cm nozzle exit diameter was used in all the experiments at inclined incidence. A short duration water pulse is allowed to flow out of the generator to produce the vortex rings. A pressurized tank and a solenoid valve are used to control the speed and duration of the water pulse. A detailed study was conducted to determine the operating characteristics of the vortex ring generator. These as well other information on the operation of the vortex ring generator can be found in Kwon<sup>11</sup>. The flow field and surface signature was documented by Laser Induced Fluorescence (LIF) flow visualization of the symmetry plane and by shadowgraph visualization of the free surface.

#### Interaction with a clean free surface

Shown in Figure 8 are flow visualization pictures of the interaction at an incidence angle of 20°. On top are the shadowgraph images of the free surfaces, at the bottom are LIF cross-sections through the symmetry plane. The vortex ring motion is from left to right. The flow conditions were Reynolds number  $\Gamma/\nu = 5,000$  and the Froude number  $\Gamma/(gR^3)^{1/2} = 0.81$ . These photographs show the three stages of the interaction process. The first photographs at  $\Gamma t/R^2 = 18$ , Figure 8a, show the upper vortex core interacting with the free surface which causes a surface depression. The second set of photographs obtained at  $\Gamma t/R^2 = 26$ , Figure 8b, show a single vortex core in the cross-section while the surface signature shows two dimples on the surface at either side of the symmetry plane. These features indicate that the vortex lines in the ring have opened-up and are now attached to the surface at the dimples. The shadowgraph image also shows that surface waves were generated during the vortex line breaking and reconnection process. At a later time (Figure 8c,  $\Gamma t/R^2 = 43$ ) the flow visualization of the cross-section shows little evidence of the vortex ring core while the

surface shadowgraph shows four dimples on the surface. The top pair propagates away from the lower pair in time. Each individual pair of dimples represents the surface signature of a half vortex ring with vortex lines beginning and terminating at the free surface.

Flow visualization studies were conducted to determine the effect of Reynolds number and incidence angle on the interaction. The results are summarized in Figure 9. Vortex line breaking and reconnection of the top and bottom parts of the ring were found for a large range of Reynolds numbers (from 2,000 to 7,000) and incidence angles in the range between 10° and 30°. At a Reynolds number of 5,000 the vortex line breaking and reconnection of the lower part of the core was observed for angles up to 45°. Small variations were observed within this range of parameters in the sense that the half-vortex rings would propagate at different angles after the interaction, and in some cases they will move along converging paths, interact with each other again and form a single open ring.

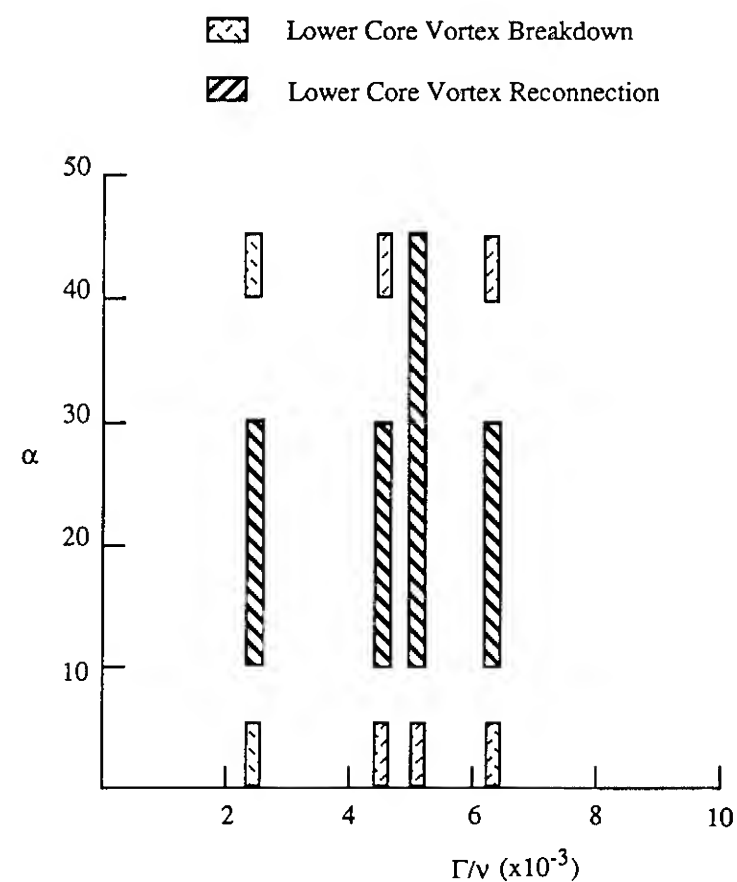


Figure 9. Observed interaction outcome as a function of vortex ring Reynolds number and incidence angle.

For vortex rings formed at conditions outside this region, the vortex lines of the upper core break and reconnect to the surface as in the other cases. But when the bottom core reached the surface the vortical region broke down into smaller scale vortical structures.



The vortex line breaking and reconnection process can be quantified by a characteristic time,  $t_r$ . This reconnection time was defined in the experiments as the elapsed time between the time when the vortex outline in the LIF image first reaches the surface and the time when the dimples on the surface are first observed. Measurements were conducted of the reconnection time of the upper vortex core at several conditions. The results are shown in Figure 10 where the reconnection time nondimensionalized by the circulation and the core diameter,  $\delta$ , is plotted as a function of the Reynolds number for different incidence angles. The results show that the normalized reconnection time is independent of the Reynolds number, suggesting that the breaking of vortex lines is by and large an inviscid process. There is a systematic reduction of the normalized reconnection time as the incidence angle is increased suggesting a strong dependence on the details of the vortex line topology as they approach the surface.

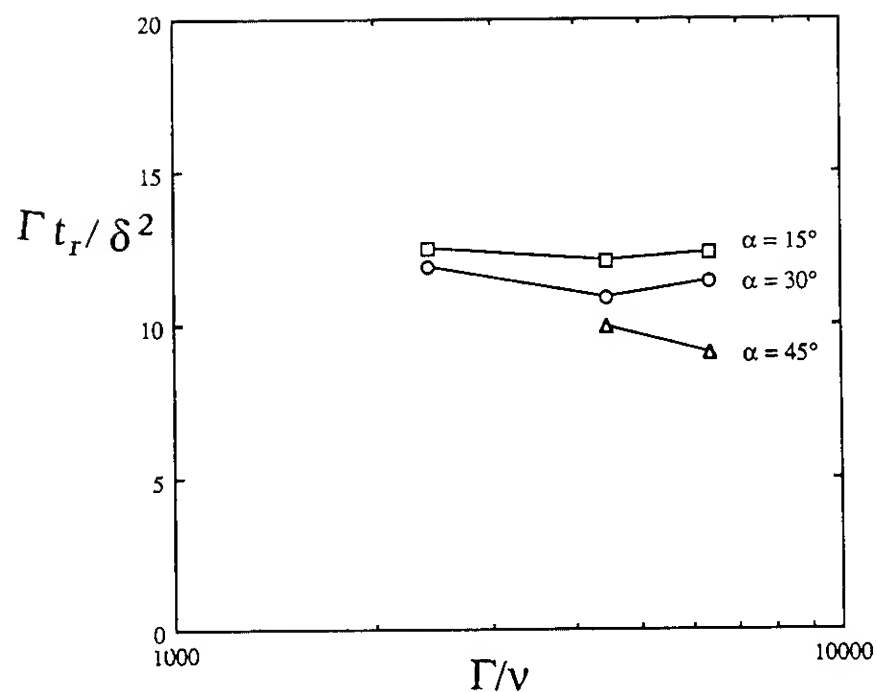


Figure 10. Effect of vortex ring Reynolds number and incidence angle on vortex line reconnection time.

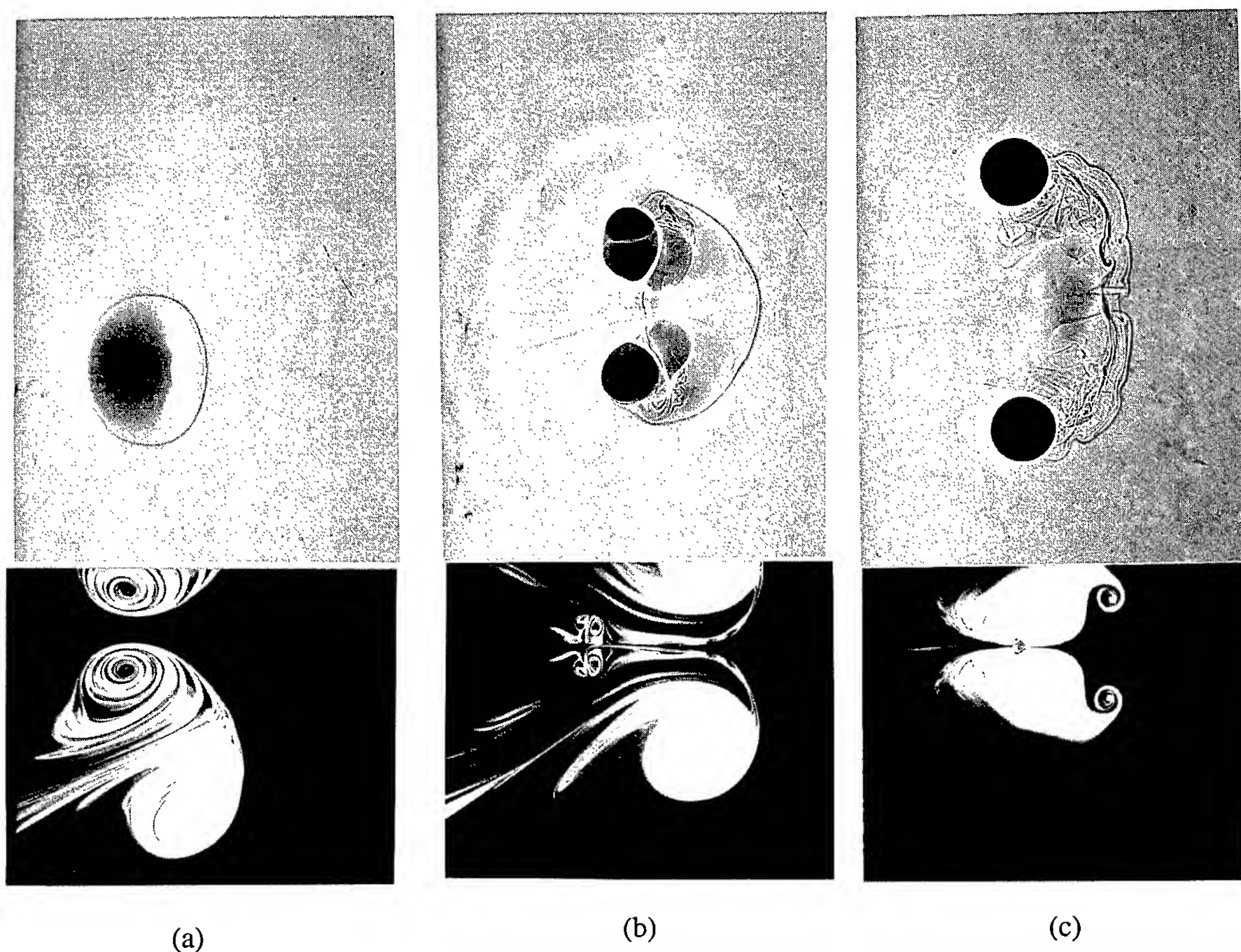


Figure 11. Flow visualization photographs of the interaction of a vortex ring with a contaminated surface at a Reynolds number of 5,000, incidence angle of  $20^\circ$  and surface pressure of 12.7 dynes/cm. Shadowgraph visualizations of the surface are shown on top and Cross-section views at the bottom. In each photograph the vortex motion is from left to right. (a)  $\Gamma t / R^2 = 42$ . (b)  $\Gamma t / R^2 = 53$ . (c)  $\Gamma t / R^2 = 65$ .

The flow visualization at a nondimensional time  $\Gamma t/R = 53$  shown in Figure 11b reveals the formation of a pair of counter rotating vortices trailing behind the lower core. This small pair of vortices is the remanence of the upper vortex core and the opposite sign vorticity generated by surface tension effects at the contaminated surface. The shadowgraph image of the surface shows the dimples due to the reconnection of the top vortex core with the surface and the waves generated in the process of reconnection. The shadowgraph image also shows a distinct Reynolds ridge moving ahead of the reconnected vortex cores.

At a later time,  $\Gamma t/R^2 = 65$  Figure 11c, the cross section view still shows evidence of the counter rotating vortex pair at the surface which has now been entrained by the lower vortex core. Also a large secondary vortex has formed ahead of the lower vortex core. The induced velocity field of the secondary vortex tends to stop the motion of the lower vortex core towards the surface. The surface signature in this case show well defined circular dimples as well as a highly distorted Reynolds ridge.

These flow visualization results illustrate the effect that surface active agents have on the dynamics of vorticity near a free surface. The effect vary depending on the local details of the flow. For the upper core the surfactant does not suppress the vortex line breaking and reconnection process. This is consistent with the observed Reynolds number independence of the reconnection time. In contrast the lower core dynamics is strongly influenced by the presence of surface active agents. As the lower core region approaches the free surface secondary vorticity generated at the surface by surfactant action accumulates in a secondary vortex. The velocity field induced by the secondary vortex causes rebounding of the core and prevents vortex line breaking at the surface.

#### ACKNOWLEDGEMENTS

This research was sponsored by the Office of Naval Research, Contract no. N000184-86-K-0684 under the U.R.I. Program for Ship Hydrodynamics.

#### REFERENCES

1. Sarpkaya, T. & Henderson, Jr., D.O. "Free surface scars and striations due to trailing vortices generated by a submerged lifting surface," AIAA paper 85-0445, 1986.
2. Willmarth, W.W., Tryggvason, G., Hirsa, A. & Yu, D. "Vortex pair generation and interaction with a free surface," Physics of Fluids A, vol 1, no 2, Feb. 1989, pp 170-172.
3. Sarpkaya, T., Elnitsky II, J., & Leeker Jr., R.E., "Wake of a vortex pair on the free surface," Proc. 17th Symposium on Naval Hydrodynamics, The Hague, The Netherlands, 1989.
4. Tryggvason, G., "Deformation of a free surface as a result of vortical flows," Physics of Fluids, Vol. 31, No. 5, May 1988, pp. 955-957.
5. Telste, J.H., "Potential flow about two counter-rotating vortices approaching a free surface," J Fluid Mech. vol 201, pp 259-278, 1989.
6. Marcus, D.L., "The interaction between a pair of counter-rotating vortices and a free boundary," PhD Thesis, The University of California at Berkeley, 1988.
7. Yu, D. & Tryggvason, G., "The free surface signature of unsteady two-dimensional flows," Submitted to J Fluid Mech., 1989
8. Hirsa, A., "An experimental investigation of vortex pair interaction with a clean or contaminated free surface," PhD Thesis, The University of Michigan, 1990.
9. Bernal, L.P. & Madnia, K., "Interaction of a turbulent round jet with the free surface," Proc. 17th Symposium on Naval Hydrodynamics, The Hague, The Netherlands, 1989.
10. Bernal, L.P. & Kwon, J.T., "Vortex ring dynamics at a free surface," Physics of Fluids A, vol 1, no 3, March 1989, pp 449-451.
11. Kwon, J.T., "Experimental study of vortex ring interaction with a free surface," PhD Thesis, The University of Michigan, 1989.
12. Davies, J.T., "The effect of surface films in damping eddies at a free surface of a turbulent liquid," Proc. Royal Soc. London A, vol 290, pp 515-526, 1966.
13. Davies, J.T. & Driscoll, J.P. Eddies at free surfaces simulated by pulses of water," Industrial and Eng. Chemistry Fundamentals, vol 13, pp 105-109, 1974.
14. Barker, S.J. & Crow, S.C., "The motion of two-dimensional vortex pair in a ground effect," J Fluid Mech. vol 82, pp 659-671, 1977.
15. Saffman, P.G., "The approach of a vortex pair to a plane surface in inviscid fluid," J Fluid Mech. vol 82, pp 659-671, 1977.
16. Peace, A.J. & Riley, N., "A viscous vortex pair in ground effect," J Fluid Mech. vol 125, pp 187-202, 1983.
17. Bernal, L.P., Hirsa, A., Kwon, J.T. & Willmarth, W.W., "On the interaction of vortex ring and pairs with a free surface for varying amounts of surface active agent," Physics of Fluids A, vol 1, no 12, Dec 1989, pp 2001-2004.
18. Dahm, W.J.A., Scheil, C.M. and Tryggvason, G., "Dynamics of vortex interaction with a density interface," J Fluid Mech. vol 205, pp 1-43, 1989.
19. Scott, J.C., "Flow beneath a stagnant film on water: the Reynolds ridge," J Fluid Mech. vol 69, pp 339-351, 1975.
20. Song, M., Bernal, L.P., and Tryggvason, G., to be submitted to Physics of Fluids A, 1990.

## DISCUSSION

Daniel Marcus  
Lawrence Livermore National Laboratory, USA

What is the effect of changing the ratio of core radius to ring radius on the reconnection event?

## AUTHORS' REPLY

We have only limited amount of data on the effect of core radius or ring radius on the reconnection event. The data presented in Figure 10 shows that the vortex reconnection time when nondimensionalized by core parameters is approximately independent of the Reynolds number. For these data, the change in Reynolds number is accompanied by a change of the ratio of core radius to ring radius. Kwon (1989) estimates the values of this parameter for the cases plotted in Figure 10. The values changed from a minimum value of 0.23 at the low Reynolds number case to a maximum value of 0.39 at the largest Reynolds number case. On the basis of this evidence, it appears that the nondimensional reconnection time is also independent of the ratio of core radius to ring radius.

## DISCUSSION

Theodore Y. Wu  
California Institute of Technology, USA

The authors deserve our warm thanks for the very enlightening report on their investigations of this fascinating subject. In view of Helmholtz's theorem that no vortex filaments can terminate in the midst of a fluid (or fluids), I wonder if the authors have investigated the vortical flow induced in the air by the submerged vortices that have opened up at the interface. I further wonder if such more complete vortex systems may have a bearing on the secondary vortices sequentially generated in the course of the vortex bifurcation.

## AUTHORS' REPLY

We would like to thank Professor Wu for his kind remarks. Yes, Helmholtz's theorem requires that vortex lines with a component normal to the free surface continue in the air above the free surface. We have not attempted to measure or in any way characterize the air motion above the free surface during the interaction. Elucidation of the topology of the vortex lines in air is a challenging problem. The Reynolds number for the air flow is one order of magnitude lower than for the water flow and consequently the air vortices are expected to dissipate more rapidly. In any case, these induced vortices in air or other weak air flow disturbances above the surface do not significantly influence the vortex reconnection process because of the large density ratio. Free surface dynamics, including contamination effects, dominate the interaction process.

## DISCUSSION

Richard Yue  
Massachusetts Institute of Technology, USA

In your work, the induced velocity on the surface is a known function (of space and time) since the influence of the free surface on the vortex pair is not considered. This is consistent with the assumption of deep submergence. In this context it seems that the present problem can be addressed by simply considering the dispersion relationship in terms of the known surface advection which can be applied directly to a wave spectrum.

## AUTHORS' REPLY

Although the induced velocity on the surface is a known function of space and time, a solution method based solely on the spectral variation due to this known surface current requires an additional assumption. This assumption is that the variation in surface current be slowly varying in time and space with respect to the length and time scales of the ambient waves. The ambient wavelengths here is allowed to be of the same order of magnitude as the vortex pair separation and depth. The problem is therefore transient in nature rather than quasi-steady as would be assumed in the direct modification of the dispersion relationship. The transient problem is handled in a straightforward manner using the simulation technique. In the limit of small waves under the influence of large scale vortices, such as in the ship example at the end of the paper, the direct method suggested will likely give reasonable agreement.

## Submerged Vortex Pair Influence on Ambient Free Surface Waves

S. Fish (David Taylor Research Center, USA)  
C. von Kerczek (University of Maryland, USA)

### ABSTRACT

This paper examines how free surface gravity waves travelling over a fluid are modified by the presence of a submerged pair of vortex singularities. Greater attention has recently been focused on the problem of vortex flows near a free surface due to its possible importance in determining the influence of vortical ship wakes on radar images of the ocean surface. Although much research has concentrated on studying vortices near a still free surface, a theory for vortical influence on ambient free surface waves has not been addressed. Initial steps in uncovering the subtleties of the ambient wave modification by submerged vortices are taken utilizing first order free surface boundary conditions to demonstrate the importance of the vortex-induced surface current in the interaction of vortices with ambient waves. A parametric study is then conducted showing that the relative strength of the vortices and their geometric configurations are more important in characterizing the form of surface modification than the relative phase or steepness of the ambient waves. And finally, analysis of simulation data is performed indicating how a vortex pair ship wake model can contribute to the observed dark centerline wakes in radar images of ships at sea.

### INTRODUCTION

Research interest in the behavior of vortex structures near a free surface has recently been revived by the detection of dark regions in radar images of the sea surface. The significance of these long narrow dark streaks is their coincidence with the centerline wake regions of ships travelling on the sea surface at the time of radar exposure. For this reason, they are generally referred to as *dark centerlines*. Examples and details on the radar operation and image processing can be found in Lyden, et al.<sup>1</sup> and Peltzer et al.<sup>2</sup>. Although the cause of the dark centerlines is not well understood, there is widespread agreement that the lower energy radar return in this region is a result of the elimination of surface waves

normally responsible for constructive interference of the reflected radar signal. Constructive interference occurs when the component of the surface wavenumber vector in the "look" direction of the radar satisfies the following expression (Wright<sup>3</sup>):

$$k_w = 2 k_r \sin(\theta) \quad (1)$$

where:  $k_w = 2\pi/\lambda_w$  = surface wavenumber  
 $k_r = 2\pi/\lambda_r$  = radar wavenumber  
 $\lambda$  = wavelength  
 $\theta$  = vertical incidence angle of the radar  
(normal to the free surface:  $\theta=0^\circ$ )

Waves satisfying this criterion, termed Bragg scattering waves, are typically wind generated, and form the background signal return level in SAR images. Dark centerlines in the radar images of moving ships at sea suggest the reduction or elimination of these Bragg waves in the ship wake.

The elimination of these Bragg waves and the long term maintenance of a Bragg-free region in the wake is the subject of intense research in several hydrodynamic fields, from surfactant distribution to nonlinear ship wave generation. It is likely that many of these hydrodynamic processes are combining to produce the dark centerlines and that their relative importance depends on the ambient environmental conditions. The process being studied here is the effect of the large scale rotations generated in the ship wake on the ambient waves present in the background of the radar image. These longitudinal vortex-like motions in the ship wake have been measured (Lindenmuth<sup>4</sup>) and calculated (Griffin et al.<sup>5</sup>) for a variety of ships and are illustrated in figure 1. The origin of this vorticity is the overall boundary layer of the ship and occurs in slight variations regardless of propulsion configuration. The weaker persistence of these vortices in the wake cannot, by itself, account for the length of the dark centerline but may contribute to both the initial Bragg wave elimination and help sustain the other processes (such as surfactant redistribution) in the far wake. The presence of ambient waves in the real ocean



environment therefore indicates the need to determine how waves may be modified by the wake itself. This work will concentrate on wave modification by the large scale wake vorticity just described.

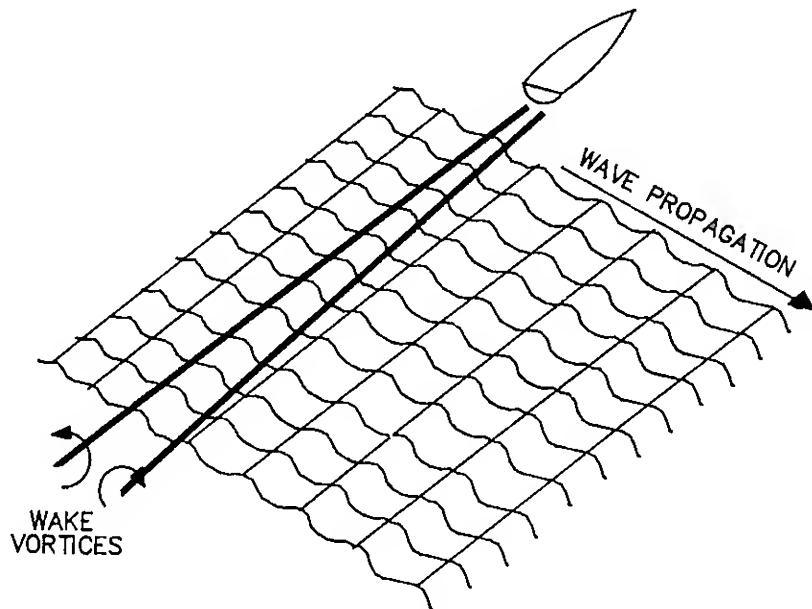


Fig. 1 Ship Wake Vortex Model with Ambient Waves

Prior studies of vortex-free surface interactions focused on the dynamics of an initially flat free surface under the influence of the vortex pair. This problem is relevant only under the limited conditions of a glassy smooth sea surface. The more common wind-generated ambient wave background is of concern here. In this case, the important phenomenon is the modification of the ambient Bragg scattering waves by vortices of relatively weak strength. The term "weak" here refers to circulation strength and speed of the vortex relative to the gravitational forces on the free surface. Weak vortices are representative of the large scale flow measurements in the far wake, and result in minimal vertical surface deflections, and no wave breaking. It will be shown that a first order formulation of the free surface boundary condition retains the dominant nonlinear surface characteristics without the additional computational difficulties associated with nonlinear surface modelling. Linearization of the free surface also allows simulation of simple monochromatic ambient waves. The alteration of these simple waveforms by submerged vortices can therefore be easily identified both visually and using spectral analysis. Because Bragg waves for typical radar wavelengths are much shorter than the depth of the modelled wake vortices, their inviscid influence on the vortex paths is negligible and will be ignored in this study. The resulting paths of the vortex pair correspond to the paths for a flat, rigid free surface. Simulations of the two dimensional vortex pair near a free surface with monochromatic ambient waves are used here to determine which parameters of the governing equations are dominant. The Froude number and initial vortex positions are shown to play the most important roles in modifying ambient waves. Other

parameters, such as the ambient wave steepness and relative phase that result from the analytic study as independent quantities, play secondary roles, as might be expected from linear theory.

In addition, spectral analysis is used in a form which extracts characteristics in the surface similar to the radar imaging process. This analysis shows that submerged vortices can give images with darker center regions where the ambient waves undergo the modification. This analysis will be performed on a vortex pair with parameters derived from typical ship operating characteristics.

## PROBLEM FORMULATION AND SOLUTION METHOD

In developing a solution technique for the vortex/ambient wave interaction problem, one would like to start with the simplest model possible while retaining the most significant flow interaction terms. The model used here follows the classical assumptions of inviscid, incompressible flow without surface tension. In addition, the three dimensional ship wake will be considered as a quasi-two dimensional (2-D) flow. See figure 2. This modelling hypothesis assumes that velocity gradients in the axial direction are sufficiently small to permit 2-D flow realizations in a plane perpendicular to the ship track to be integrated in time to represent the three dimensional problem. The constant ship speed may then be used to transform time data into axial distance behind the ship.

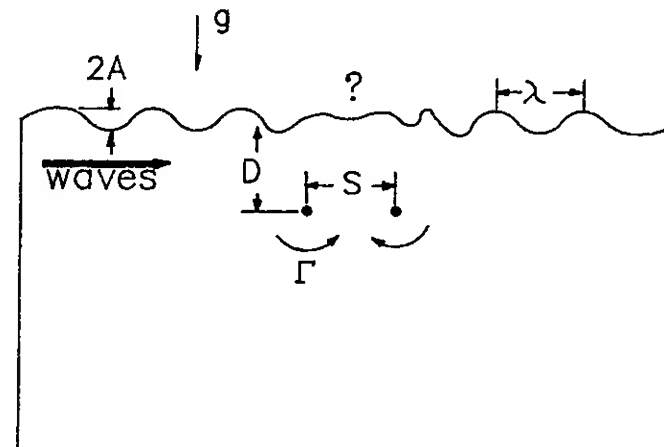


Fig. 2 2-Dimensional Flow Model

Because simple sinusoidal ambient waves are desired for the interaction problem, a linearized approach is formulated with the small perturbation parameter,  $\epsilon$ , defined as follows:

$$\epsilon = \frac{\Gamma}{\sqrt{gD^3}} \quad (2)$$

where  $D$  is vortex depth, and  $g$  the gravitational acceleration. Although  $\epsilon$  represents the traditional

form of Froude number governing the flow when no ambient waves are present, the use of "Froude number" in this paper will refer to another parameter, defined later, which the reader will find more intuitive for cases including ambient waves. Nevertheless, the value of  $\epsilon$  will be kept small since this is representative of the "weak" large scale vortical motion in the ship wake.

Following a standard perturbation theory and using a zeroth order solution of the vortex near a rigid surface (corresponding to  $\epsilon$  approaching 0), one can derive the following boundary conditions for the free surface. (See Fish<sup>6</sup> or Fish and von Kerczek<sup>7</sup> for details.)

Dynamic:

$$\phi_t + 0.5\phi_x^2 + \frac{\eta}{\epsilon} = 0 \quad (3)$$

Kinematic:

$$-\phi_y + \eta_t + \phi_{0x}\eta_x - \eta\phi_{0yy} = 0 \quad (4)$$

where:

$$\phi = \phi_0 + \epsilon\phi_1$$

$$\eta = \eta_0 + \epsilon\eta_1$$

It should be noted here that these equations include the first order Taylor series expansion of each term about its evaluation on the still water level (corresponding to the rigid surface boundary). Note also that the  $0.5\phi_x^2$  term in the dynamic boundary condition and the  $\phi_{0x}\eta_x$  term in the kinematic boundary condition represent the influence of induced surface currents on the modification of ambient waves. In particular, the  $\phi_{0x}\eta_x$  term provides a direct coupling of the vortex induced surface current and the ambient wave slope. These terms are excluded in the classical free surface linearizations utilizing the quiescent zero<sup>th</sup> order base state.

For the problem here, the ambient waves are propagated from the side of the 2-D domain as shown in figure 2. These waves represent ambient waves moving transverse to the ship track. Because of the quasi-2-D nature of the ship wake model, modelling waves propagating in directions much different from this lateral condition should not be assumed practical.

The solution method used to march through the 2D computations utilizes the widely used Boundary Integral Technique (BIT) of Trygvasson<sup>8</sup>, Telste<sup>9</sup> and others. The BIT utilizes the Cauchy Integral Theorem to describe potential flows such as this one by the values of the potential and stream function on the boundaries of the fluid domain.

$$\int_{\Omega} \frac{\beta}{z-z_0} dz + i\alpha_0\beta(z_0,t) = 0 \quad (5)$$

where:

$$\beta = \phi + i\psi$$

$\phi$  = velocity potential

$\psi$  = stream function

$\alpha_0$  = exterior angle between boundary tangents on either side of  $z_0$

The boundary is discretized for numerical integration assuming a continuous linear variation in potential and stream function over each element. In the present study, the boundaries are composed of the free surface, two vertical side walls and a flat bottom. At each time step Cauchy's Integral Theorem is used to determine the equilibrium unknown  $\phi_i$  or  $\psi_i$  on a boundary element in which the corresponding  $\psi_i$  or  $\phi_i$  is prescribed. This is achieved by solving the set of simultaneous equations resulting from the application of equation 5 to the node point,  $z_{0i}$ , of each element of the boundary.

The prescribed values of  $\psi$  and  $\phi$  for the next time step are determined as follows. First, the  $\phi_i$  distribution over the free surface elements is obtained by integrating the dynamic free surface boundary condition.

$$\phi(t+\Delta t) = \phi(t) + \Delta t (0.5\phi_{0x}^2 + \phi_{0x}\phi_{1x} + \frac{\eta}{\epsilon}) \quad (6)$$

$\eta_i$  on the free surface is also updated by integrating the kinematic boundary condition.

$$\eta(t+\Delta t) = \eta(t) + \Delta t (\phi_y - \phi_{0x}\eta_x + \eta\phi_{0yy}) \quad (7)$$

Then the new distribution of  $\psi_{\text{wall}}$  on the side and bottom boundaries is prescribed by the undisturbed deep water ambient wave stream function.

$$\psi_{\text{wall}}(x_i, t+\Delta t) = gA/\omega \cos(\omega(t+\Delta t) - kx_i) \quad (8)$$

where:

$$k = 2\pi/\lambda \quad \omega = \sqrt{gk}$$

A comparison of calculation methods for the surface disturbance caused by a single vortex moving at constant speed below the free surface is given in figure 3. One can see that the method used here compares very well with the fully nonlinear calculations of Telste<sup>9</sup> while calculations utilizing the classical zero flow base state for linearization are in error.

In determining the relative importance of the additional terms in equations 3 and 4 with respect to the classical linearized form, equivalent simulations were conducted with each term deleted. It was found in this study that the terms containing  $\phi_{0x}$ , representing the induced surface current from the vortices were significant contributors to the solution. The  $\eta\phi_{0yy}$  value remained small. In addition, the cross term  $\phi_{0x}\phi_{1x}$  provides a direct interaction term between the ambient waves (whose potential will be contained in  $\phi_1$  and the submerged vortices). Without this term calculations were almost equivalent



to the superposition of independent calculations of the vortices and waves. Figures 4a and 4b show the influence of the induced current terms on the ambient wave modification. This figure shows free surface profiles at discrete time intervals corresponding to the period of the ambient wave,  $T$ , which is propagating from left to right. A counter rotating pair is positioned in the center region as shown in figure 2. The details of the flow parameters will be described further in the next section.

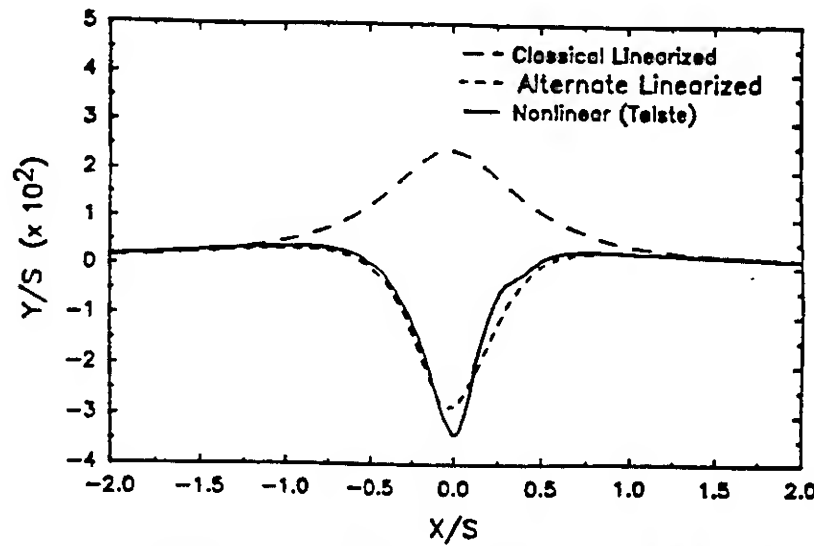


Fig. 3 Free Surface Profiles Above Single Vortex  $\epsilon = 0.5$

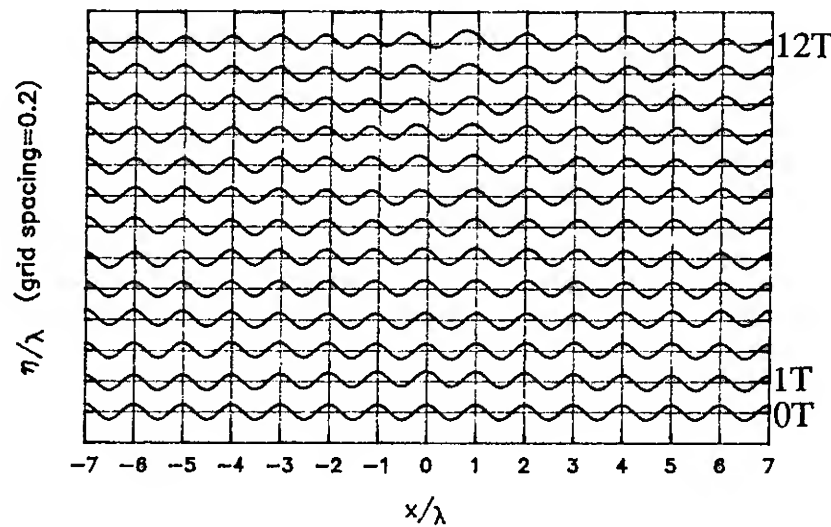


Fig. 4a Surface Profiles with Vortex Pair: Classical Linearization

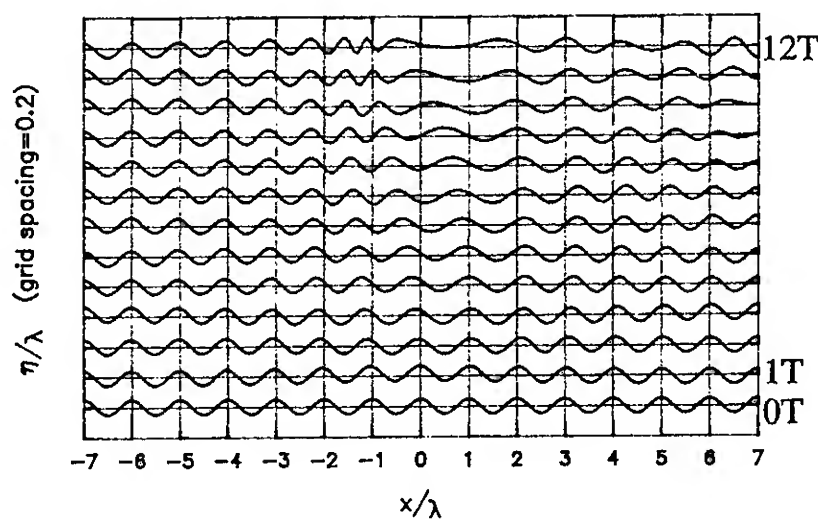


Fig. 4b Surface Profiles with Vortex Pair: First Order Theory with Induced Current Terms

## NONDIMENSIONAL PARAMETER IDENTIFICATION

When ambient waves are included in the vortex/free surface problem, the characteristic length scale should correspond to the ambient wavelength. This wavelength is of primary concern since eventually it will be this scale which determines the character of radar return from the free surface. The problem therefore is nondimensionalized as follows: (where ' indicates a dimensional quantity)

$$\begin{aligned} x &= x'/\lambda & y &= y'/\lambda & \eta &= \eta'/\lambda \\ t &= t'\lambda^2/\Gamma & \phi &= \phi'/\Gamma \end{aligned} \quad (9)$$

The governing inputs to the problem are  $\Gamma$ ,  $g$ ,  $A$ ,  $S$ ,  $D$ , and  $\lambda$ . Dimensional analysis reduces these six variables to four parameters. The choice of parameter definitions must be made with care to allow meaningful conclusions to be drawn. The ambient waves, for instance, are described by their steepness,  $A/\lambda$ .

Since the paths taken by the vortices will be defined by their "rigid wall" paths and therefore are known a-priori, one choice for a parameter would be the ratio of the initial separation distance to initial depth,  $S/D$ . Small values of  $S/D$  indicate that the vortex pair is initiated at greater depth than separation, and will initially propagate upwards toward the free surface. Large values of  $S/D$  represent a vortex pair which is widely separated and will move parallel to the free surface under the primary influence of their image vortices above the free surface. One then needs to define either  $S/\lambda$  or  $D/\lambda$  as the other parameter relating the vortex geometric configuration to the ambient wavelength. Most of the cases studied here are for small values of  $S/D$ , giving a minimum depth achievable by the vortex of approximately  $S/2$ . Since this will correspond to the highest value of induced surface current by the vortices,  $S/\lambda$  was chosen as the second parameter.

The last parameter gives the relative scales of the vortex strength to the wave velocity, and is commonly called the Froude number. The Froude number for this problem can be defined in several ways depending on one's choice of length scale. Previous works without ambient waves have utilized the initial vortex separation following the definition  $F = \epsilon$  of equation (2). Since it has been shown that the induced surface current has a dominant influence on the modification of waves, it would appear prudent to define a Froude number based on the ratio of this induced current and the group velocity of the ambient waves. The maximum induced velocity (including image vortex above free surface) is given by:

$$v_i = 2\Gamma/\pi S \quad \text{which occurs at } D = S/2 \quad (10)$$

and occurs after the vortices have approached the free surface and separated. The deep water group velocity for the ambient waves is

$$V_g = 0.5 \sqrt{\frac{g\lambda}{2\pi}} \quad (11)$$

The ratio  $V_i/V_g$  will be used as the Froude number,  $F$ , and can therefore be formed as shown below.

$$\frac{V_i}{V_g} = \frac{\frac{4\Gamma}{\pi S}}{\sqrt{\frac{g\lambda}{2\pi}}} = \frac{4\sqrt{2}}{\sqrt{\pi}} \frac{\Gamma}{S\sqrt{g\lambda}} \quad (12)$$

$$\text{with } \frac{\Gamma}{S\sqrt{g\lambda}} = \sqrt{\frac{S}{\lambda}} \frac{\Gamma}{\sqrt{gS^3}} = \sqrt{Q} F \quad (13)$$

$$F = \Gamma/(gS^3)^{1/2} \quad P = A/\lambda \quad Q = S/\lambda \quad R = S/D$$

where  $\Gamma$  is the vortex circulation,  $S$  is the initial vortex pair separation,  $D$  is the initial vortex pair depth,  $\lambda$  is the ambient wavelength, and  $A$  is the ambient wave amplitude. Substituting these relations into the previously defined ALM boundary conditions gives the following results:

Dynamic:

$$\phi_t = -\phi_{0x}^2/2 - \phi_{0x}\phi_{1x} - \eta/(F^2 Q^3) \quad (14)$$

Kinematic:

$$\eta_t = \phi_y + \eta\phi_{0y} - \phi_{0x}\eta_x \quad (15)$$

The corresponding deepwater wave potential using the above nondimensional parameters takes the form:

$$\phi_w = P/(F Q^{3/2} (2\pi)^{1/2}) e^{2\pi y} \sin [2\pi x - (2\pi)^{1/2} t/(F Q^{3/2})] \quad (16)$$

The vortex potential is also nondimensionalized and given below in complex form:

$$\beta_0 = \phi_0 + i\psi_0 = i^{-1} \ln [(z-z_1)/(z-z_2)] - i^{-1} \ln [(z-z_1^*)/(z-z_2^*)] \quad (17)$$

where the "\*" character represents the complex conjugate.

## FROUDE NUMBER VARIATION

The examination of Froude number influences will consist of flow simulations with the vortices started at a relatively deep position ( $S/D=1/3$ ). This value of  $S/D$  was chosen to minimize surface disturbances associated with the transients of the vortices' impulsive start. The ambient wave modifications would therefore be associated predominantly with the velocity field generated by the slowly moving vortices rather than the initial condition wave motion generated by the vortices.  $S/D=1/3$  also corresponds well with the experimental studies of Willmarth et.al.<sup>10</sup>.  $S/\lambda$  is set to 1 to equate Froude numbers based on different length scales. The resulting surface profiles for  $F$  ranging between 0.1 and 0.6 are shown in figures 5 to 9. Since the time scale of modification is much slower at  $F=0.1$ , the profiles shown in figure 5 coincide with  $2T$  intervals rather than the  $1T$  intervals used at the other Froude numbers. The vortex path is shown in figure 10. The surface modification in these profiles involves a stretching of waves in the center region above the vortices at later times. The ambient waves also appear to be shortened somewhat on the left or "windward" side due to the opposite directions of  $v_i$  and  $v_g$ . The wave shortening on the right or "leeward" side is much less pronounced since  $v_i$  and  $v_g$  are in the same direction.

The most obvious effect of varying  $F$  in these cases is the change in time scale for the surface disturbance to develop. The occurrence of ambient wave modification at earlier times at higher  $F$  is due primarily to the increase in relative speed of the vortex pair moving towards the surface. To minimize this attribute, surface wave profiles can be compared between different  $F$  cases when the vortex pairs are at common positions. Two common positions are labeled "A" and "B" in figure 10. The corresponding profiles from each  $F$  are collected and shown in expanded vertical scale in figures 11 and 12. Case "A" corresponds to a moderately deep vortex pair. Only the higher  $F$  cases corresponding to relatively stronger vortices have an influence at this depth, verifying the notion that stronger vortices will influence the surface from greater depths.

A more subtle and interesting difference is observed as the vortex pair draws near the surface at position "B". Here one notices the lengthening of residual ambient waves in the central region above the vortices. This increase in residual wave length is presumably caused by the higher tangential velocity gradients at the surface in cases where  $F$  is increased. The width of the disturbed region above the vortex pair does not depend heavily on the value of  $F$ . Figure 13 shows the vortex-induced current for condition B without waves. For any threshold value of  $v_i/v_g$ , one would expect from this figure that increasing  $F$  would cause a greater increase in the affected region width than the simulations actually

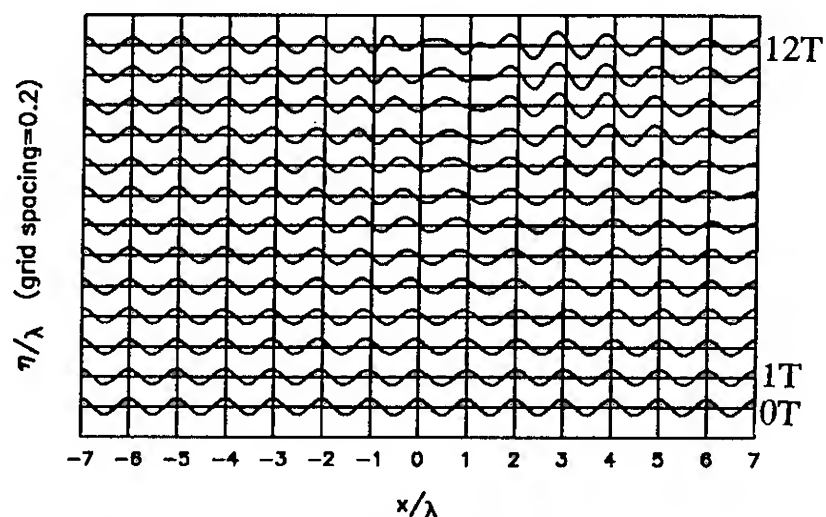


Fig. 5  $V_i/V_g$  Variation:  $V_i/V_g = 0.1$

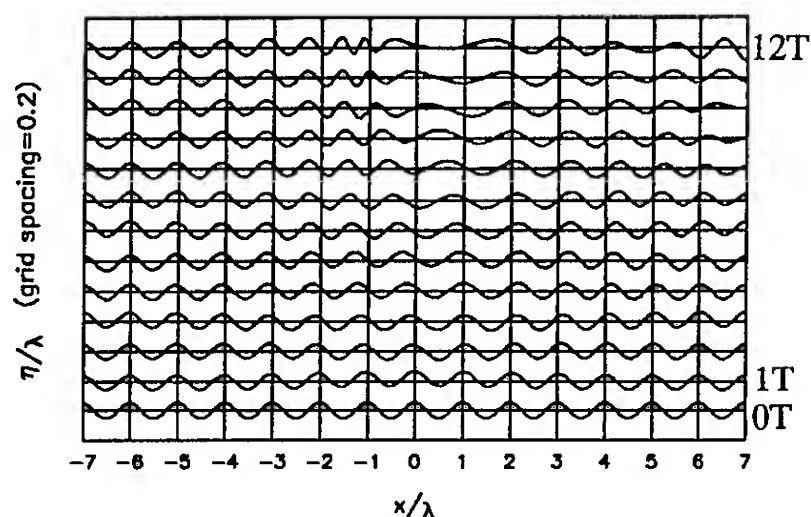


Fig. 6  $V_i/V_g$  Variation:  $V_i/V_g = 0.2$

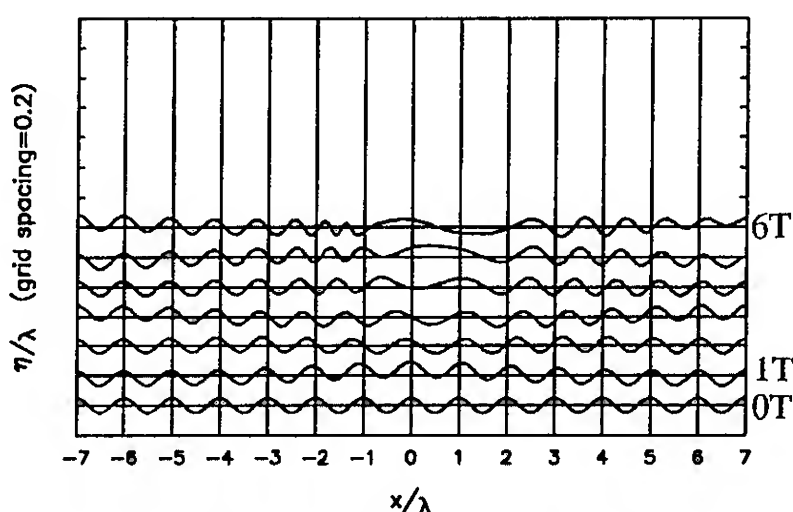


Fig. 7  $V_i/V_g$  Variation:  $V_i/V_g = 0.4$

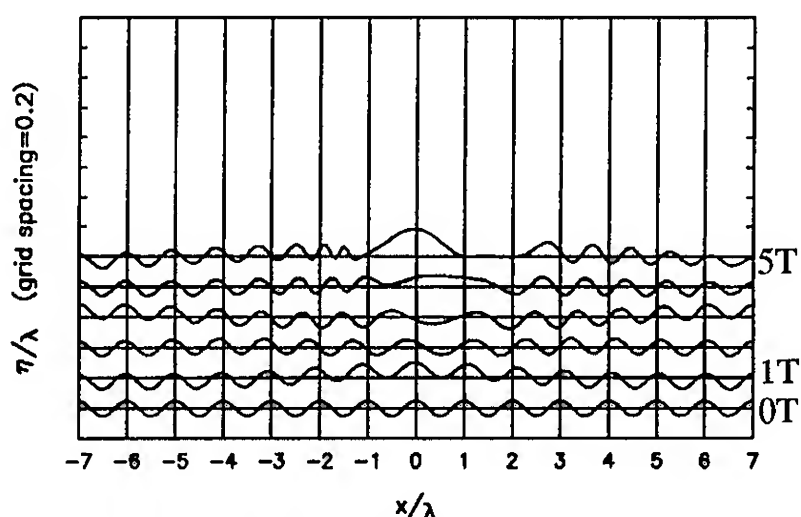


Fig. 8  $V_i/V_g$  Variation:  $V_i/V_g = 0.5$

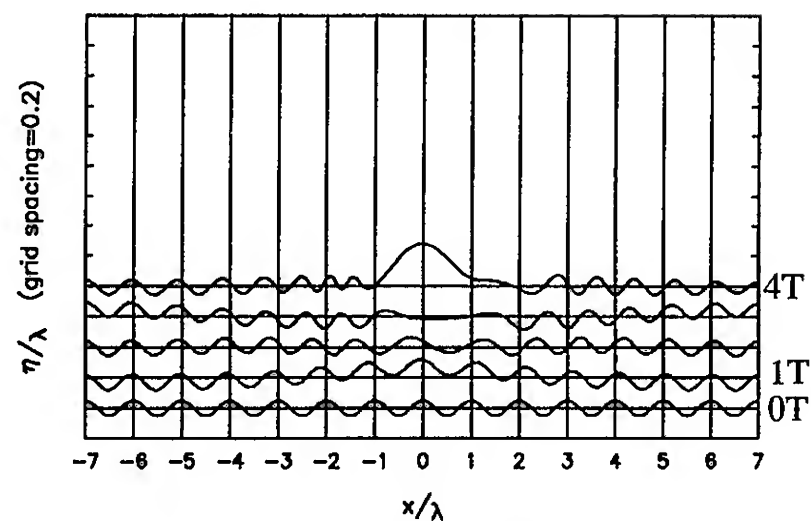


Fig. 9  $V_i/V_g$  Variation:  $V_i/V_g = 0.6$

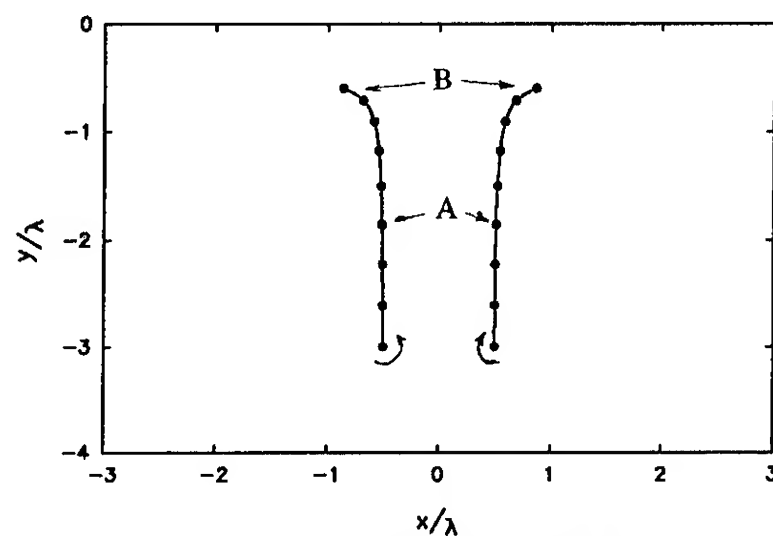


Fig. 10  $V_i/V_g$  Variation: Vortex Paths

show in figure 4b. The reduced dependency of affected region width on  $F$  suggests that the time scale of the free surface interaction is relatively short, and that using slowly varying current distribution theories such as the *conservation of wave action* is inadequate for treatment of problems of this type. This further emphasizes the inherent transient nature of the wave modification by vortices of the scale used to model ship wakes.

An additional note on the variation of  $F$  is the transition occurring around values of 0.5 of the surface disturbance directly above the vortex pair. At values above 0.5, the creation of a center "hump" appears similar to center humps calculated by Telste<sup>9</sup> at higher Froude numbers without ambient waves. It should be noted that in this case the vortices have not deviated from their rigid wall paths. This indicates a transition Froude number value of 0.5 above which the vortex pair begins dominating the surface profile.

#### INITIAL GEOMETRIC CONDITIONS

The initial position of the vortex pair is equally important to its strength in defining the form of ambient wave modification. As noted previously, the ratio of induced surface velocity to ambient wave group velocity is highly dependent on the depth of the vortex. Time scales for the vortex pair to approach the surface from large depths is also obviously dependent on the initial depth and separation distance.

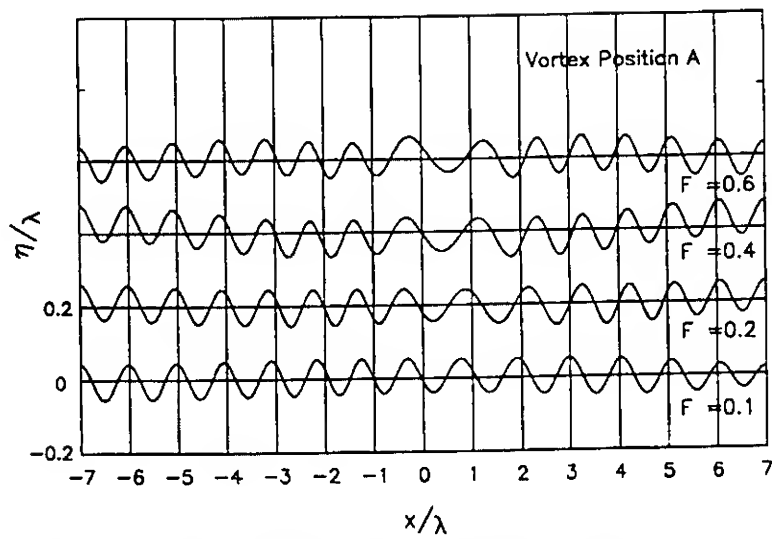


Fig. 11  $V_i/V_g$  Variation: Position "A",  $F=V_i/V_g$

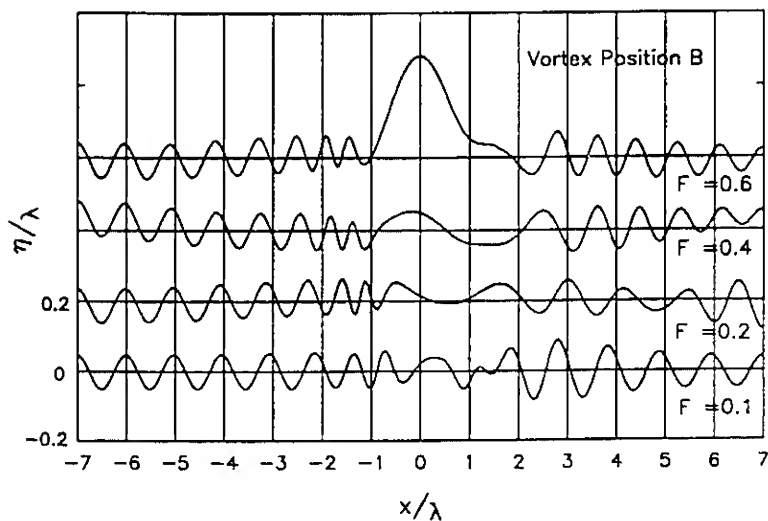


Fig. 12  $V_i/V_g$  Variation: Position "B",  $F=V_i/V_g$

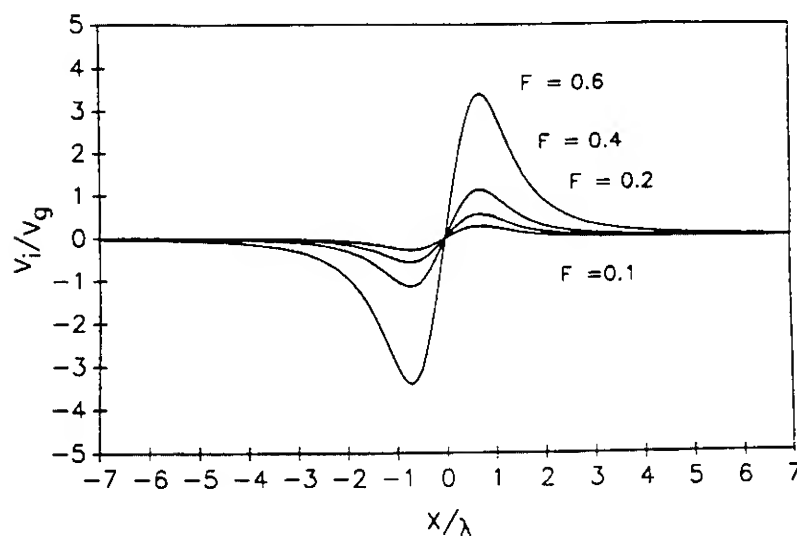


Fig. 13  $V_i/V_g$  Variation: Induced Current from Position "B"

The position of the vortex pair can be identified by two parameters. One parameter has been chosen as  $S/D$  specifying the relative position of the vortex on its prescribed path. The particular path desired may then be specified by designating a value for either  $S$  or  $D$ .

#### $S/D$ Variation

The influence of starting at various points on a given path will be examined first. The controlling parameter in this case is  $S/D$ , which determines the initial point on the path. Three values of  $S/D$  are examined at various stages of the path corresponding

to: deep ( $S/D=0.5$ ), turning ( $S/D=2$ ), and shallow ( $S/D=6$ ). As shown earlier, the direction of motion of the vortex pair is quite different in each of these cases. The value of  $F$  used in these cases was set to 0.125, and the common path chosen corresponded to a final submergence depth of the vortices of  $D_{\text{final}}=\lambda$ . Figures 14 to 16 show the resulting profiles and figure 17 shows the corresponding trajectories of the vortex pair.

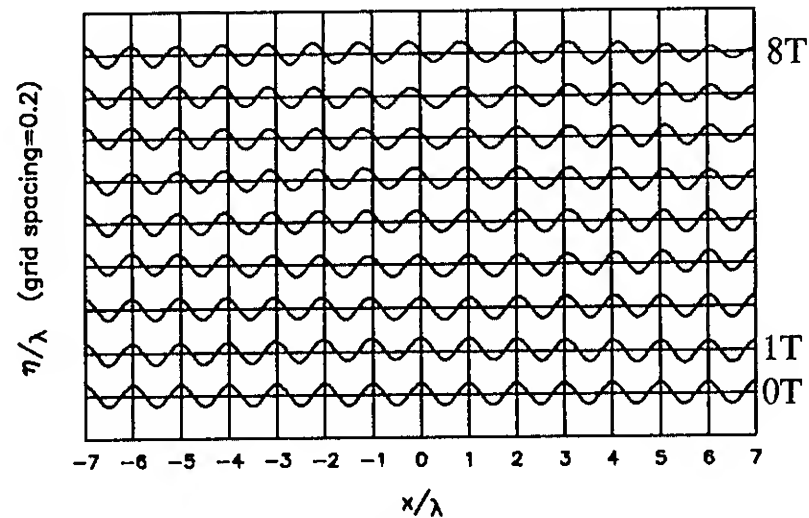


Fig. 14  $S/D$  Variation:  $S/D = 0.5$

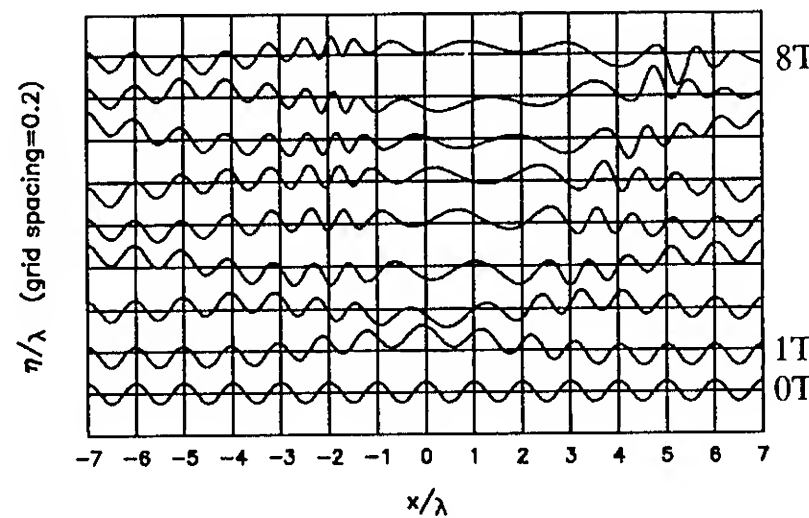


Fig. 15  $S/D$  Variation:  $S/D = 2.0$

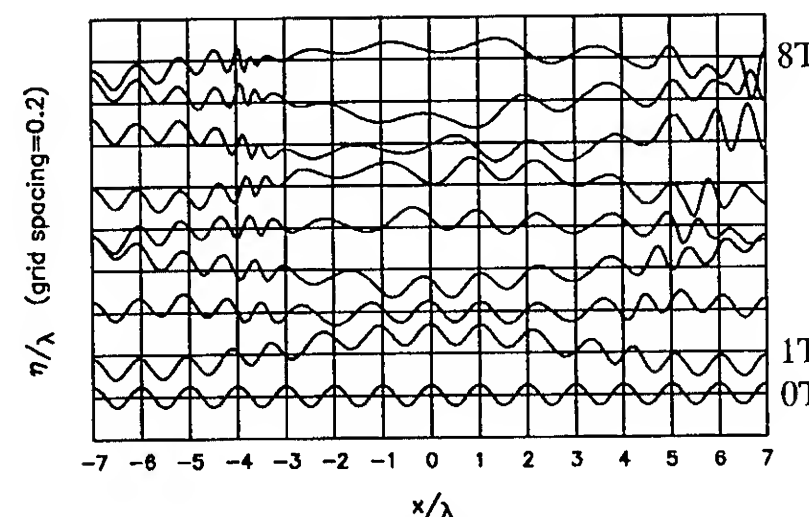


Fig. 16  $S/D$  Variation:  $S/D = 6.0$

In these figures one can see the influence of the instantaneous vortex pair depth on the surface wave modification. In the case of  $S/D=0.5$ , the surface is modified only by a slight shifting in the waves caused by the small vortex-induced surface

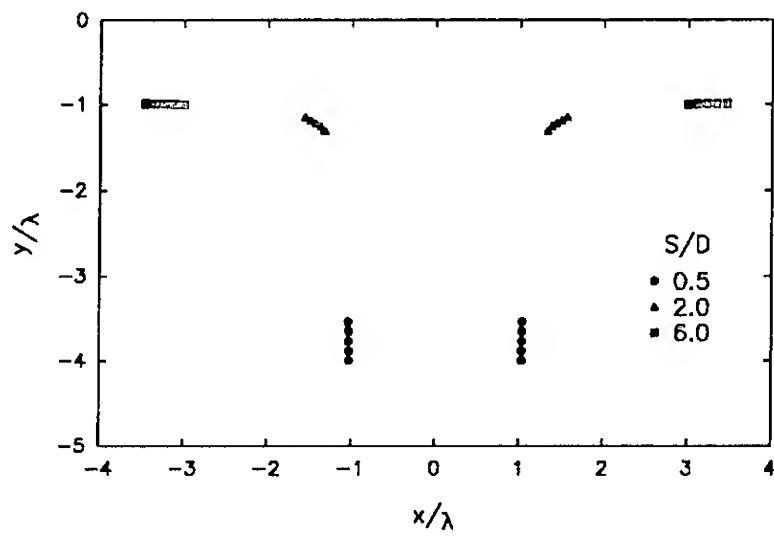


Fig. 17 S/D Variation: Vortex Paths

current. This wave alteration is also noticed to be almost symmetric about the line of symmetry for the vortex paths. This indicates little net exchange of energy between the vortices and the waves as they pass through. As the depth is decreased, the vortex induced surface current grows to the value of the group velocity of the ambient waves, and essentially stops the transfer of ambient wave energy from left to right. Two important processes occur which deserve further attention. First, the ambient waves are shortened as they enter the region of influence of the vortex pair by the opposing induced current. The resultant decrease in ambient wavelength is accompanied by a decrease in the absolute group velocity of the waves. The result of this process, is that ambient waves of higher speed may be halted by vortices of smaller magnitude than that predicted from  $v_i/v_g=1$ .

#### S/λ Variation

As mentioned in the S/D section above, initial vortex pair location is important in examining the influences on ambient surface waves. In addition to specifying the portion of the path that the pair will be started on, a particular path must be chosen. The parameter  $S/\lambda$  is used as a path selection parameter for its role in scaling the vortex path geometry to the ambient wavelength. Three values of  $S/\lambda$  were simulated with a constant value of  $S/D=6$ .  $S/\lambda$  values were set to 3.0, 4.5, and 6.0. The upper limit on  $S/\lambda$

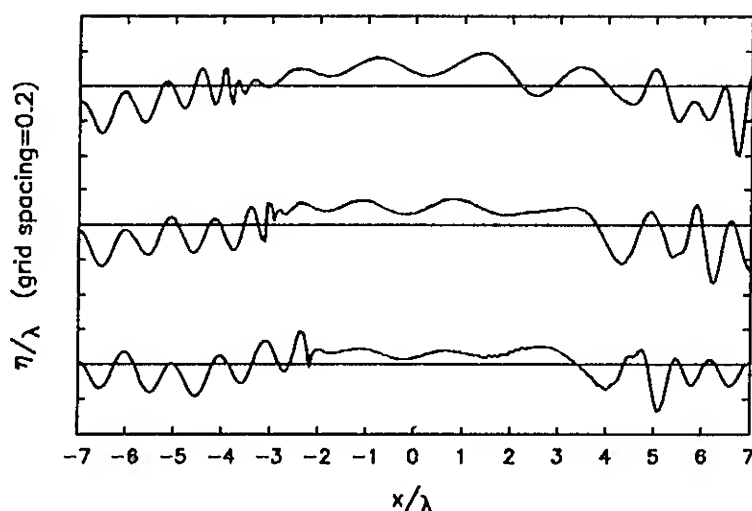


Fig. 18 S/λ Variation: Final Profiles t=8T

is caused by the size limitation of the computational domain, and the influence of partial wave reflections on the right hand boundary.  $F$  varied between 0.06 and 0.125 to preserve a  $v_i/v_g$  at the surface of 0.5. The surface profiles after  $8T$  for each condition are shown in figure 18. Note the growth in modified wave region size as  $S/\lambda$  is increased.

An additional process observed in the simulations is the dynamics of waves caught in the central influence region during the initial motion of the vortex pair. These surviving center waves may be leftover from the initial ambient wave profile in this region in the shorter time scales. These left over waves are found in greater numbers as  $S/\lambda$  is increased, as shown in figure 18. In the cases shown, a wave blocking action is rapidly generated due to a relatively large value of  $v_i/v_g$ . Wave energy may also propagate into the center region when the vortex pairs are initialized at low values of  $S/D$ . This energy propagation is facilitated by the canceling influence of the induced tangential velocity from each of the counter rotating submerged vortices at low values of  $S/D$ . The evolution of these center waves is particularly complex in cases of moderate  $S/D$ . Initial waves in this region are typically stretched by the surface current gradient. The resulting increase in wavelength gives rise to an increase in phase and group velocity. Because the gravity wave dispersion relation specifies that longer waves move at higher velocity, the central region may be evacuated over a shorter time than that predicted by ambient wave group velocity. Simulation results were not carried far enough in time to show complete smoothing of the central region due to the influence of partial wave reflection from the right side boundary. Larger surface grids and greater computer times will therefore be necessary to validate this hypothesis.

#### WAVE STEEPNESS AND PHASE VARIATION

The wave steepness and phase with respect to the vortex pair are additional parameters which result from the problem formulation and enter the calculations through the initial boundary condition on the free surface and the time varying stream function prescribed on the side boundaries. Simulation results show no significant influence of these parameters on the form of the interaction. In the case of wave steepness, the waves and their modification can be linearly scaled with  $A/\lambda$  for values less than 1/10 corresponding to the linearized ambient waves being described. The relative phase of the ambient wave was also found to have no effect on the general form of the wave modification at the  $S/\lambda$  values studied here.



## SPECTRAL ANALYSIS

In order to make the previous findings useful in the study of real ocean flows, a method of analysis must be developed which illuminates the impact of wave modification on radar images. It was shown in the introduction how the reflected radar intensity is proportional to the amount of Bragg waves present in the region being illuminated by the radar. This intensity is usually expressed as the *backscattering cross section* per unit surface area,  $\sigma_0$ . This cross section is derived by Valenzuela<sup>11</sup> in the well known Bragg scattering expression:

$$\sigma_0 = 4\pi k_r^4 \cos^4 \theta F(\theta) M(2k_r \sin \theta) \quad (18)$$

where:  $k_r$  = radar wavenumber and  $\theta$  = vertical incidence angle of radar. Here  $F(\theta)$  is a scattering coefficient dependant on the radar polarization and incidence angle, and  $M()$  is the component of the wave spectra corresponding to the Bragg condition. Remember, from the introduction, that the Bragg condition is satisfied when  $k_w$  (surface wavenumber component in the look direction of the radar) is equal to the argument of  $M()$  in the equation above. If  $\theta$  and  $k_w$  are known constants, then  $\sigma_0$  is proportional to  $M()$ . This property indicates that a relative variation in radar backscatter over different sections of the water surface can be determined by the variations in the Bragg wave spectral component among the respective surface sections. Estimates of the relative radar intensity image can therefore be compiled by performing finite Fourier transforms of the surface elevation over regions corresponding in size to the resolution cell size of the radar. This will be performed here by sweeping a window across the simulated surface data and calculating the finite Fourier transform at various window positions. The Fourier transform component corresponding to the Bragg waves in each window position is then assigned to the midpoint location of the window. The resulting distribution of Bragg wave components over the surface is then contour plotted for comparison with SAR imagery.

### Method

The finite Fourier transform used to determine the Bragg wave spectral content in a data window is given by:

$$Y(k, L) = \int_{-L/2}^{L/2} \eta(x) e^{-i2\pi kx} dx \quad (19)$$

where  $L$  is the window width. The application of this equation to discrete data can be performed using an algorithm known as the Fast Fourier Transform, or FFT. This common method is described in detail by

Bendat and Piersol<sup>12</sup>. The FFT output coefficients are complex in form providing phase information for each wavenumber component. Since this phase was shown to be unimportant in the previous chapter, the absolute magnitude of each wavenumber component is formed from the modulus of the real and imaginary parts:

$$M(k) = (Y_{\text{real}}^2(k) + Y_{\text{imag}}^2(k))^{1/2} \quad (20)$$

where:  $FFT(k)$  is an output coefficient.

Before applying the scanning FFT window to simulation results, several comments must be made here to avoid misinterpretation of the method. The regions used in computation of the spectra will be overlapped here because of the finite extent of the surface domain and the desire to have moderate sized surface patches. If the patches are allowed to be too small, the resolution of low wavenumber components decreases, resulting in undistinguishable movements of wave energy among the wavenumbers of concern. This overlapping is not representative of radar imaging, and therefore the results must not be considered direct simulation of radar operation. The general trends in the resultant component levels in the Bragg wavenumber range are believed to be somewhat representative of results obtained with radar processing.

### Application to Ship Wake

The case examined using this technique is a simulation approximating the wake velocities from a twin screw destroyer calculated by Sween<sup>13</sup>. It should be noted that in simulating the full ship case, the grid resolution was lowered considerably by constraints in available computer memory. The grid density is 32 points per ambient wavelength. The ambient wavelength is set to 25 cm and corresponds to the Bragg scattering wavelength for an "L band" SAR operating at an incidence angle of 30 degrees. The initial vortex separation and depth are 5 m and 2 m respectively. Gravitational acceleration is equal to  $9.8 \text{ m/s}^2$ , and the ambient wave amplitude is set to 2.5 cm. The vortex circulation strength,  $\Gamma$ , is chosen to give approximately the same maximum surface current reported by Sween<sup>13</sup> for the given depth of submergence. The resulting  $\Gamma$  value was 1.0. The simulation domain extended to  $\pm 6.25 \text{ m}$  in the  $x$  direction with a depth of 12.5 m. The simulation was carried out for 8 periods of the ambient wave (3.2 seconds) and the resultant profiles at each half period are shown in figure 19. The corresponding downstream distance spanned by the simulation is 25 m for a ship speed of 15 knots.

The FFT window size was chosen to be 2 m wide, which is typical of SAR resolution cell dimensions. The resultant spectral resolution is  $3.14/\text{cm}$  in wavenumber giving components at wavelengths of 22 cm, 25 cm, and 28 cm. The



consecutive FFT windows were overlapped in the analysis by  $3\lambda$ . This overlap gives denser data for examining the variations in Bragg component, though only non-overlapping sections would be directly comparable to typical radar imaging techniques. The Bragg component of each spectrum is assigned to the location of the FFT window center. The resulting contour plot of the magnitude of the Bragg component versus space and time is given in figure 20. This plot indicates a reduction in Bragg wave component in the center region as time progresses. In order to understand the energy flow path in this region, figure 21 is constructed. This figure shows the progression of the spectra as the window is traversed across the contour plot at the 2 second time frame. The thick line indicates the wavenumber associated with the Bragg wavelength. Figure 21 illuminates the shift in wave energy to lower wavenumbers in the center region. Since these wavenumber components do not satisfy the Bragg scattering criterion, the resultant received energy at the radar is decreased. This phenomenon of wavenumber shifting due to induced surface currents appears to produce a weaker radar return signal in the region between the vortices. In the ocean, the wave field can be described by the superposition of many wavelength waves. Pierson-Moskowitz spectral models of the sea show a decreasing level of energy as wavenumber is increased in the range of the L Band Bragg scattering waves. The implication of this is that though higher wavenumber (shorter) waves will be stretched into the Bragg wavelength, their original energy is lower. Thus one would expect that a larger amount of energy was shifted out of the Bragg sensitivity window than was being shifted in. The inclusion of these higher wavenumbers would however, decrease the magnitude of variation in  $M()$  shown in figure 20. The importance of this action is that it produces the proper trend in the surface response in the wake region of a ship and may be a significant contributor to the overall signature production process for the dark centerline wake.

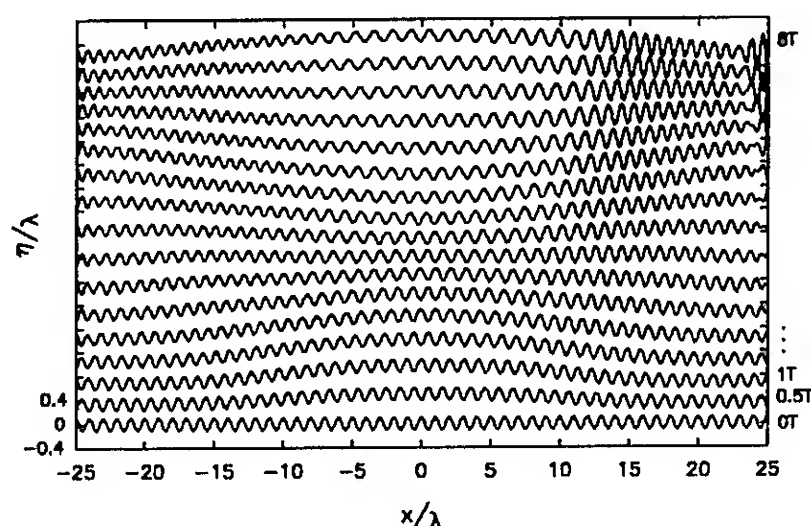


Fig. 19 Ship Wake Simulated Surface Profiles

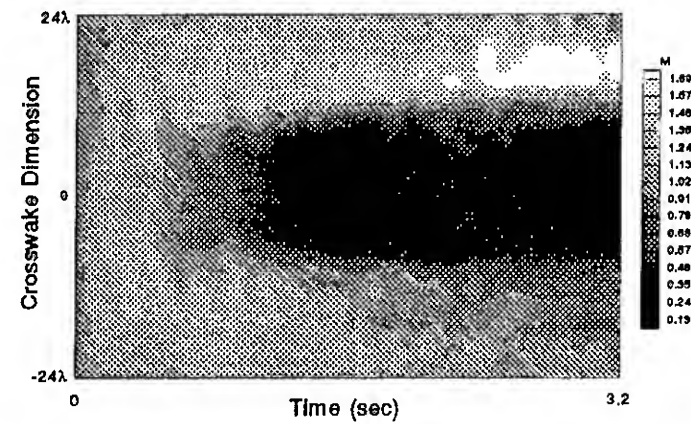


Fig. 20 Contours of Bragg Wave Content

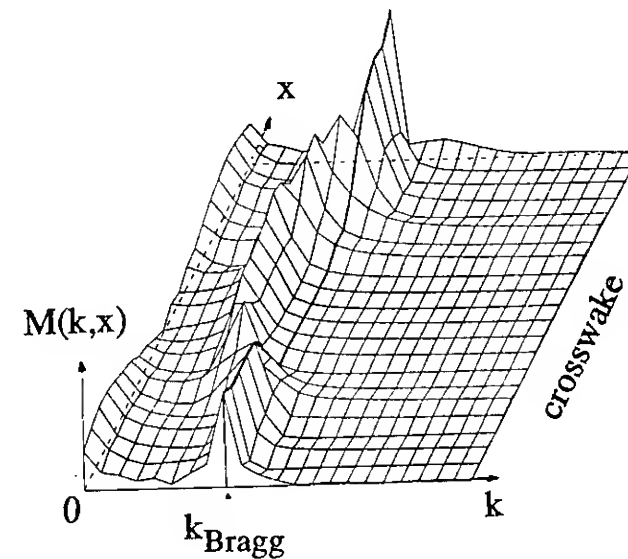


Fig. 21 Crosswake Variation in Wave Spectra,  $t=2$  sec

## SUMMARY

The modification of surface waves by submerged vortices has been explored here in a straightforward progression from analytical examination through numerical simulation of a simple vortex ambient wave model. The motivation for study of this problem is the determination of ship wake impacts on synthetic aperture radar images showing dark centerline regions behind ships moving at sea. This process has led to several discoveries in the nature of the interaction process between vortices and ambient waves.

A perturbation analysis of the free surface boundary conditions about the zero Froude number base state shows that additional terms (not found in the classical free surface linearization for small amplitude waves) are needed to describe the first order interaction of vortices with the free surface. These terms show the importance of the vortex induced surface current on the modification of ambient waves. Example simulations show that neglect of these induced current terms give much smaller modification of surface waves.

The simulation program has been used to examine the specific flow configuration of a vortex pair impulsively started below a free surface containing a sinusoidal ambient wave train. This examination determines which parameters are

significant in determining the form of the ambient wave modification. It is found that the Froude number of the vortices and their position relative both to each other and the free surface play the dominant roles in modifying ambient waves. The ambient wave steepness and initial relative phase with respect to the vortices have only secondary influence in the surface modification.

The simulation is then extended to represent the simple twin vortex wake model of a generic ship wake. The results of this simulation are analyzed using a scanning Fast Fourier Transform window on the surface to obtain spatial distributions of the spectral content of the surface. These spatial distributions are filtered to extract the Bragg scattering wave component and contour plotted. The resulting image shows that the current induced shift in wave energy to longer wavelengths can produce an effect consistent with the observed dark centerline wake regions of moving ships in radar images.

#### ACKNOWLEDGEMENT

This work was sponsored by the ONT Independent Research Program administered by the David Taylor Research Center.

#### REFERENCES

1. Lyden, J., D. Lyzenga, R. Shuchman, and E. Kasischke, "Analysis of Narrow Ship Wakes in Georgia Strait SAR Data", ERIM report 155900-20-T, 1985, Ann Arbor, MI.
2. Peltzer, R., and W. Garrett and P. Smith, "A Remote Sensing Study of a Surface Ship Wake", International Journal of Remote Sensing, vol 8, no. 5, 1987, pp. 689-704.
3. Wright, J.W., "Backscattering from Capillary Waves with Application to Sea Clutter", IEEE Transactions, AP-14, 1966, pp. 749-754.
4. Lindenmuth, B., private communication; data from model experiments at DTRC, Aug. 1986.
5. Griffin, O.M. and G.A. Keramidas, T.F. Sween, and H.T. Wang, "Ocean and Ship Wave Modification by a Surface Wake Flow Pattern", NRL Mem. report # 6094, 1988.
6. Fish, S., "Ambient Free Surface Wave Modification by a Submerged Vortex Pair", PhD Thesis, 1989, Univ. of Maryland.
7. Fish, S. and C. von Kerczek, "Development of First Order Free Surface Boundary Conditions for Vortical Flows", *being submitted to ASME J. of Appl. Mech.*
8. Tryggvason, G., "Deformation of a Free Surface as a Result of Vortical Flows", Physics of Fluids, Vol. 31, No. 5, 1988, pp. 955.
9. Telste, J.G., "Potential Flow About Two Counter-Rotating Vortices Approaching a Free Surface", Journal of Fluid Mechanics, Vol 201, 1989.
10. Willmarth, W.W. and G. Tryggvason and A. Hirs and D. Yu, "Vortex Pair Generation and Interaction with a Free Surface", Physics of Fluids A, Vol 1, Feb. 1989, pp. 170-172.
11. Valenzuela, G.R., "Theories for the Interaction of Electromagnetic and Ocean Waves - a Review", Boundary Layer Meteorology, Vol 13, 1978, pp. 61-85.
12. Bendat, J.S., and A.G. Piersol, Random Data: Analysis and Measurement Procedures, Wiley Interscience, New York, 1971, pp. 252-253 and pp. 299-309.
13. Sween, T., "Numerical Simulations of the Wake Downstream of a Twin-Screw Destroyer Model", NRL Mem. report # 6131, 1987.

## Scarred and Striated Signature of a Vortex Pair on the Free Surface

T. Sarpkaya, P.B. Suthon (Naval Postgraduate School, USA)

### ABSTRACT

This paper describes a numerical and experimental study of three-dimensional flow structures (striations, whirls, and scars) resulting from the interaction of a pair of ascending vortices with the free surface. The characteristics of the flow features at the scar-striation interface (a constellation of whirls or coherent vortical structures, thought to be the boundaries of the dark narrow radar images), are investigated through the use of an infra-red camera, flow visualization, an image analysis system, and the vortex-element method. The results have shown that the striations are a consequence of the short wavelength instability, inherent to the vortex pair itself, and the whirls result from the interaction of striations with the surface vorticity ( $\Delta\omega = 2\mathbf{q}\kappa$ , twice the tangential velocity times the curvature of the intersection of the free surface with the plane normal to it). The whirlmerging leads to an up-cascading process in size and energy in fewer vortices while the total energy decreases rapidly.

### INTRODUCTION

Just a narrow patch of darkness, bounded by two bright lines, provides the impetus for this investigation partly because it is seen in the synthetic aperture radar (SAR) images of a ship's wake, partly because it extends many miles directly in the ship's track, partly because the reasons for its existence have not yet been explained, and partly because the surface footprints of subsurface phenomena can give trace of the generating bodies. This is the basis of the current intense interest in the interaction of internal waves, wakes, and vortices with the free surface.

A few facts are known about the SAR images: Their physics is elusive; they are by no means easily accessible to precise measurement; they are not related, at least directly, to the Kelvin wake; they do not reflect the incident electro-magnetic waves back to the source (negative spectral perturbation); and they can bifurcate. Various proposals have been advanced to provide a feasible explanation of the dark band: Interaction of the wake of a vortex pair with the free surface; turbulence and surface mean flow resulting from the ship's motion; redistribution of surface impurities by large-scale vortical motions (as in Langmuir circulations [1] and Reynolds ridges [2]); entrained air in the wake; bubble scavenging of surface and subsurface surfactant materials; interaction of Kelvin waves, ambient waves, and momentum wake; generation of vorticity-retaining inverse bubbles and drops by a Kelvin-Helmholtz instability [3], just to name a few of the existing proposals. Each model attempts to provide a more feasible explanation of the dark narrow band seen in the SAR images.

As far as the footprints of a vortex pair on the free surface are concerned, the original observations leading to the present study may be summarized as follows. When a trailing vortex pair, generated by a lifting foil, rises toward the free surface, with or without mutual induction instability and/or vortex breakdown, the vortices and/or the crude vortex rings give rise to surface disturbances (whirls, scars, and striations). These were first reported by Sarpkaya and Henderson [4, 5] and Sarpkaya [6, 7]. The striations are essentially three-dimensional free-surface disturbances (which appear as ridges as shown in Figs. 1 and 2), normal to the direction of the motion of the lifting

---

Prof. Turgut Sarpkaya and LT Peter B. Suthon, Mechanical Engineering, Code: ME,  
Naval Postgraduate School, Monterey, California 93943-5000 U.S.A.



surface, and come into existence when the vortex pair is at a distance equal to about one initial vortex separation from the free surface. The scars are small free-surface depressions, comprised of many randomly distributed whirls, and come into existence towards the end of the pure striation phase, as in Fig. 2, and when the vortices are at a distance equal to about sixty percent of the initial vortex separation from the free surface (Fig. 3). When the vortices migrate large distances upward, the vortex pair usually undergoes both short-wavelength and long-wavelength sinusoidal instability (Fig. 4) and often breaks up into isolated rings (Fig. 5), (for additional details see, e.g., Sarpkaya [8]).

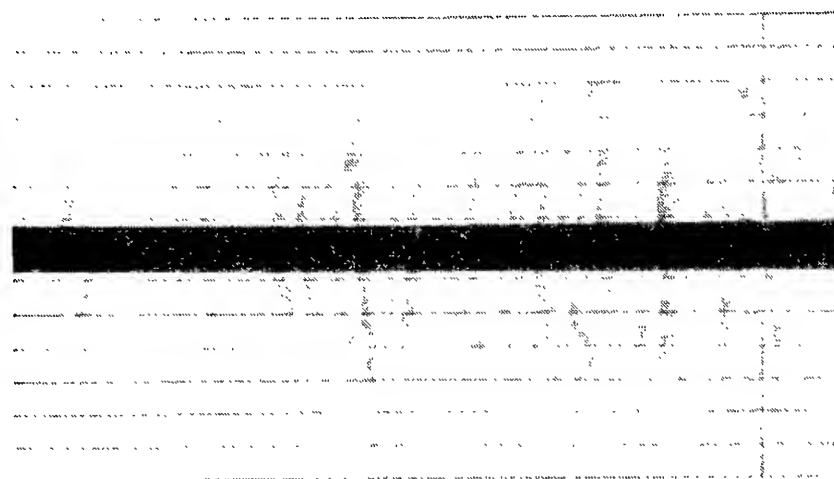


Fig. 1 Appearance of striations

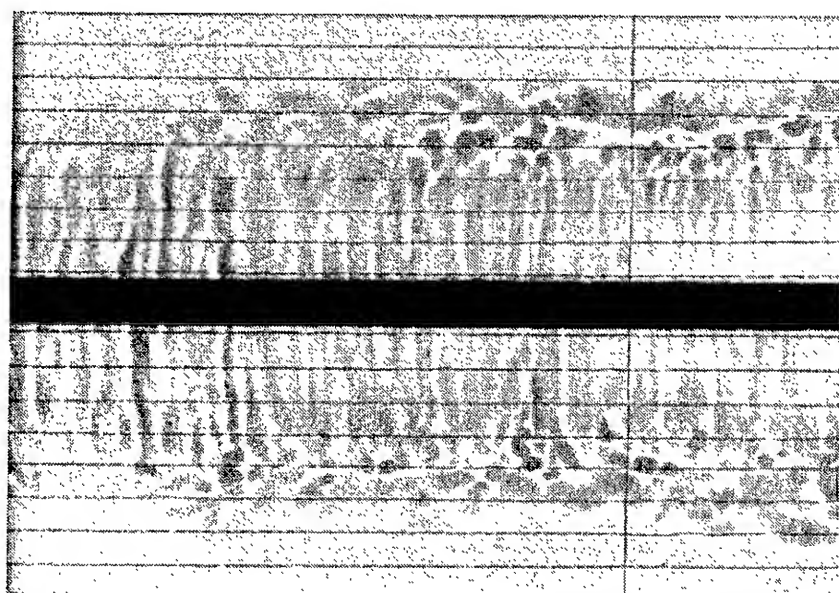


Fig. 2 Transition from striations to scars

Sarpkaya and Henderson's [5] and Sarpkaya's [6] theoretical models of the scar cross-section created by the trailing vortices was based on the classical solution of Lamb [9], assuming the vortices to be two-dimensional and the free surface to be a rigid plane. For small Froude numbers  $Fr (= V_0/\sqrt{gb_0})$ , where  $V_0$  is the initial mutual induction velocity of the vortex pair), the vortices follow the simple path described by Lamb's potential-flow solution, the free surface remains fairly flat, and each scar front

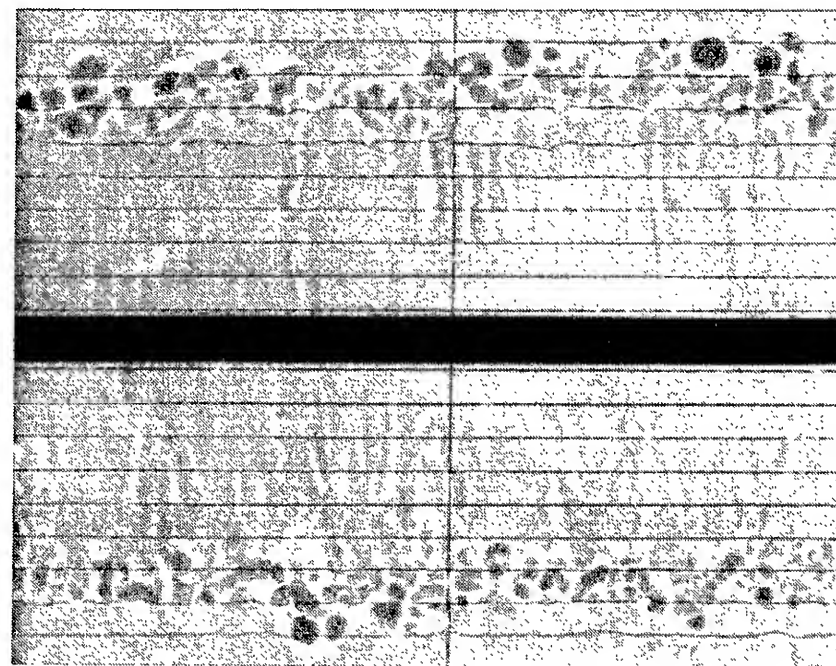


Fig. 3 Evolution of scars and whirls

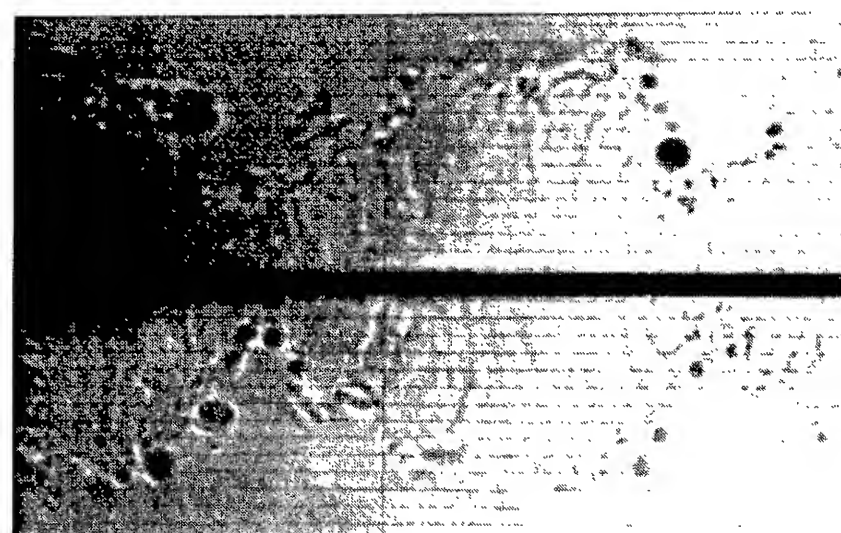


Fig. 4 Onset of long wave instability



Fig. 5 Single inclined rising ring

approximately coincides with the stagnation point on the Kelvin oval, formed by one of the pair of the trailing vortices and its image, as shown by Sarpkaya and Henderson [4-7]. For Froude numbers larger than about 0.15, not only the deformation of the free surface but also the nonlinear interaction

between the said deformation and the motion of the vortices become significant. The vortices follow Lamb's solution only during the early stages of their rise. Subsequently, they exhibit paths of varying degrees of complexity, depending on  $Fr$  and the Reynolds number  $Re$  (see, e.g., Fig. 6 for  $Fr = 0.6$  and  $Re \approx 4000$ , reproduced from Leeker's thesis [10]). Here the vortex paths rise vertically upward and, instead of moving away from the center, move initially toward the center line as the vortex is drawn up into the domed area underneath the free surface (Fig. 7). Occasionally, the path of the approximate center of a vortex forms a loop as seen in Fig. 6. It is not clear whether this is due to three-dimensional instabilities along the axis of the vortex, or due to the formation of the "wall vortex", observed by Yamada and Honda [11], or due to the successive 'rebounding' of the decaying turbulent vortex (for rebounding in general, see, e.g., Peace and Riley [12]).

Even though it was fully realized at the outset that the problem ultimately to be solved is the understanding of the three-dimensional nature of the phenomenon, the relative ease of the two dimensional counterpart has attracted the immediate attention of experimentalists and numerical analysts alike (e.g., Sarpkaya et al. [13] Dahm et al. [14], Willmarth et al. [15], Marcus [16], Marcus and Berger [17], Tryggvason [18], Telste [19]) and Ohring and Lugt [20], just to name a few). Most of the numerical simulations dealt with the inviscid, two-dimensional interaction between a pair of counter-rotating line vortices and a free, initially planar, surface. In these calculations the critical time at which the numerical instability manifests itself does not correspond to the instability of the free surface or to its extremum position. The calculations of Ohring and Lugt are for a two-dimensional laminar flow at relatively small Reynolds numbers ( $Re = V_0 b_0 / \nu = 10$  and  $50$ ). Recently, Marcus [21] calculated the deformation of a density interface for  $Fr = 1.125$ ,  $Re = 500$ , and a density ratio of 5:1 using a second-order finite-difference projection method for the full variable-density (i.e., without invoking the Boussinesq approximation). The resolution of fine structure in the flow is obtained through the use of higher-order Godunov methods in evaluating the nonlinear advective terms. Figure 8 shows sample vorticity and density plots (reproduced here with permission from the original color plots).

Even though some insight has been gained through the use of two-dimensional

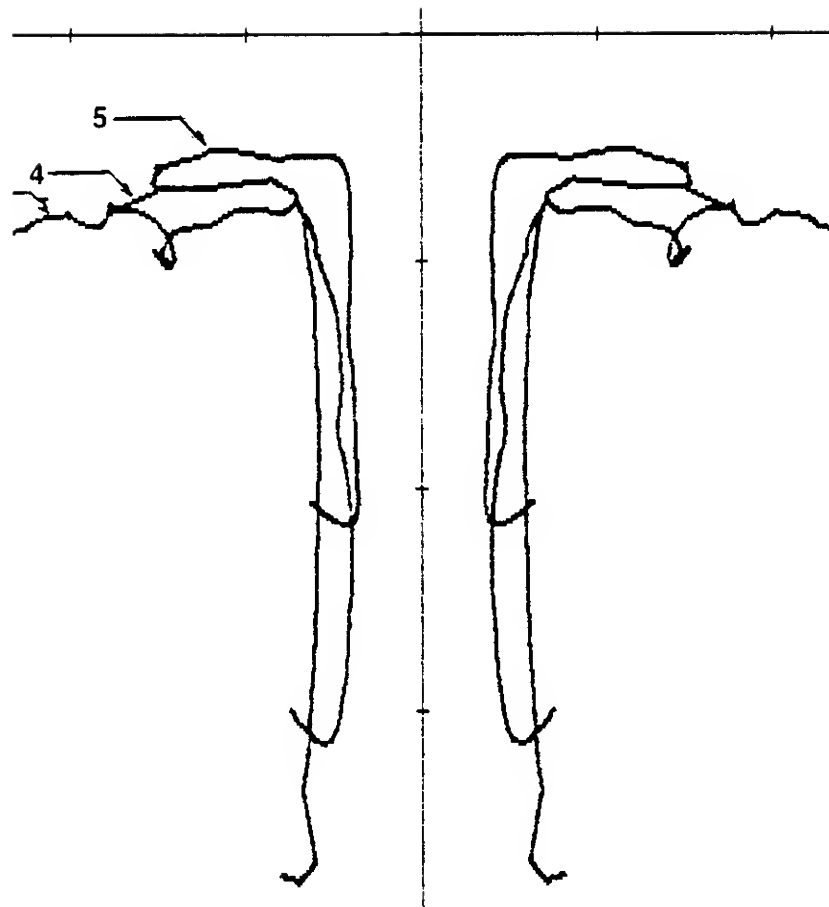


Fig. 6 Sample vortex-center paths

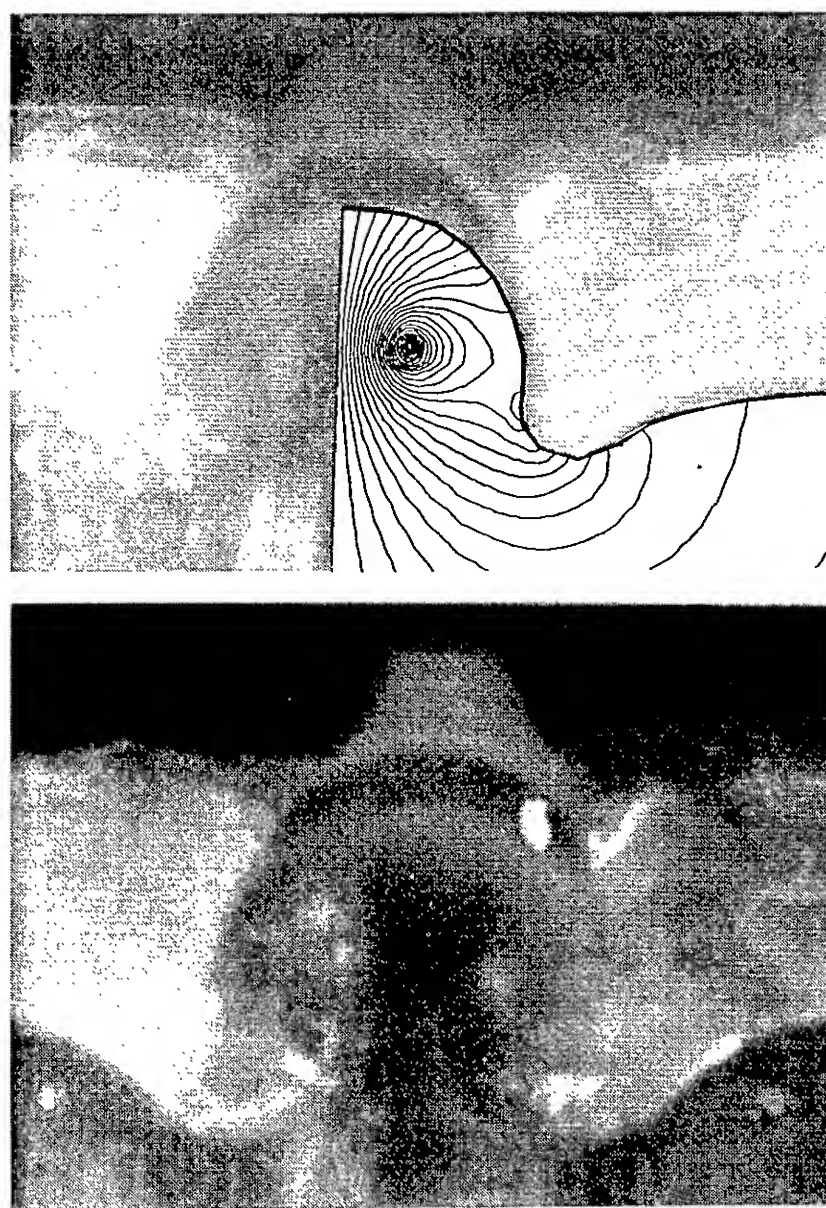


Fig. 7 Sample scar cross sections

viscous- or inviscid-flow numerical models, the results are not likely to lead to the understanding of the physics of the dark narrow images. Observations and measurements strongly suggest that the three-

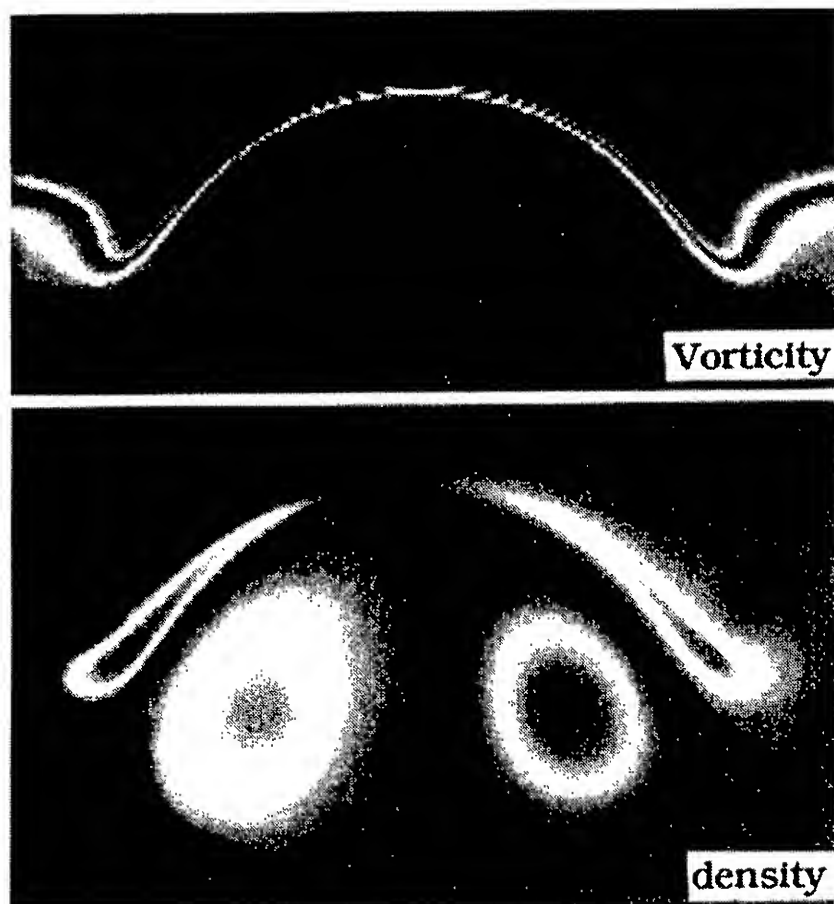


Fig. 8 Vorticity and density contours, (from Marcus [21] with permission)

dimensionality of the phenomenon is essential to the existence and longevity of the scars and striations.

The three-dimensional instability of an initially parallel vortex pair has attracted great attention because of its importance in the understanding of the demise mechanisms of aircraft trailing vortices. Crow [22] was the first to show that both symmetric and asymmetric modes of instability will develop on the vortices due to the mutual inductance of the sinusoidally perturbed pair. Figure 9, adopted from Widnall [23], shows Crow's stability diagram for the vortex pair. The shaded areas show the stability regions. The solid curve shows the wave-

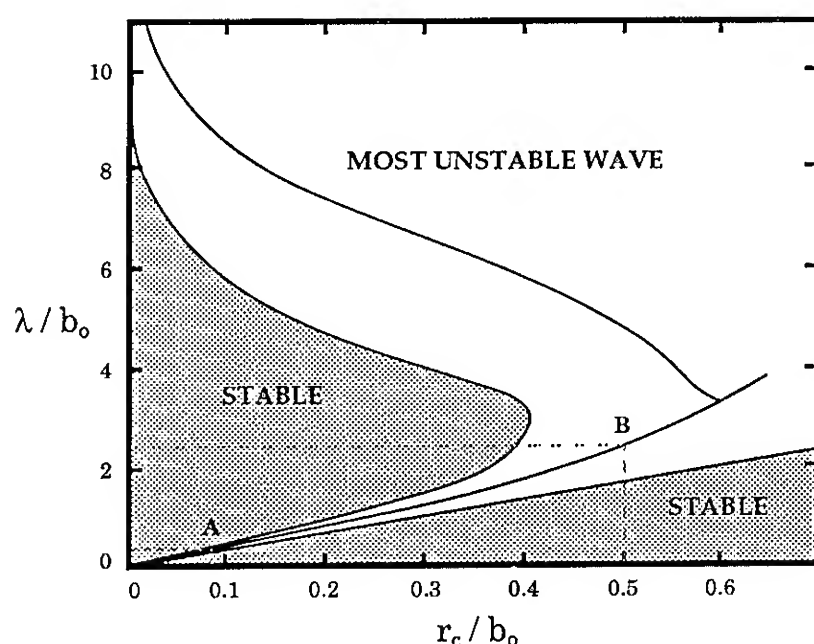


Fig. 9 Stability diagram for a vortex pair

lengths of maximum amplification for each  $r_c/b_0$ . The upper curve shows the most unstable long wave and the lower curve shows the most unstable short wave. The preferred mode of instability at the longest wavelength is  $8.6b_0$ . The wave number  $\beta$  for the short wavelength instability varies from about 4 to 17, corresponding to wavelengths of  $\lambda = 0.37b_0$  to  $1.57b_0$ .

It is in view of the foregoing that it was decided to generate nearly two-dimensional vortex pairs at relatively large Froude numbers, rather than inclined trailing vortices at relatively small Froude numbers, and to construct a numerical model of the three-dimensional surface structures. Such an effort is complicated by the difficulty and expense of quantitative measurements, image analysis, and high-resolution numerical simulations. Some of the experimental difficulties stem from the occurrence of Helmholtz instability during the roll-up of the vortex sheets, the short-wavelength and the long-wavelength instabilities of the vortex pair, turbulent diffusion of the trailing vortices, and the unknown (and perhaps unknowable) physical condition of the liquid surface. Some of the numerical problems stem from the difficulty of prescribing the initial conditions, including the free-surface characteristics, the three-dimensional nature of the resulting surface disturbances, and the stochastic nature of the whirl constellation.

## EXPERIMENTAL PROCEDURES

Experiments were conducted in three different water basins. The first was a long towing tank. It was used previously for the exploration of the characteristics of scars and striations resulting from the trailing vortices generated by lifting bodies (Sarpkaya and Johnson [24], Sarpkaya et al. [13]). The second, a multipurpose basin, was used for the study of the scar cross section in a two-dimensional mode (Sarpkaya et al. [13]) either through the use of counter-rotating plates or through the use of a streamlined nozzle, mounted on top of a piston chamber. The third water basin was constructed partway through the current investigation when it was realized that the existing basins were insufficient for the type and scope of experiments desired. It was built three times wider than the second tank and allowed the generation of two-dimensional Kelvin ovals (with aspect ratios as large as 18) and the study of two counter-rotating stationary circulations at prescribed depths below the free surface, through the use of two counter-rotating



cylinders of identical diameter and angular velocity.

The test tanks were covered with plywood and the water was recirculated continuously prior to each experiment in order to protect the free surface from airborne contaminants. Nevertheless, the tanks may have had a contaminated free surface with a surface viscosity larger than the corresponding bulk viscosity. The average value and/or the spatial distribution of the surface tension ultimately produced are not easy to quantify. The surface tension always exists at a free surface (due to intermolecular cohesive forces) regardless of whether the interface is contaminated or not by agents foreign to either fluid. Surface tension can affect the motion of the free surface partly by imposing a tangential pressure gradient as a result of spatial variations of the curvature of the air-water interface and partly by applying a tangential stress to the liquid beneath as a result of the variations of the surface tension along the interface, brought about by the gradients of surfactant concentration and temperature. The effects of viscosity, curvature, surface-velocity, and surface-tension appear to play significant roles in the creation of the surface vorticity and the evolution of surface signatures.

Experimental data were collected using the same equipment regardless of which basin the experiments were conducted in. Two video-recorder systems were used, one with a black-and-white video camera and the other with a color video camera. The output signal of each camera was sent to a screen date/timer before it is recorder on a videotape. The black-and-white camera was used primarily with the shadowgraph technique (for optimum contrast and clarity of the shadows of the surface disturbances), and the color camera was used primarily for the recording of the striations, visualized through the use of various fluorescent dyes (introduced into the Kelvin oval at the nozzle exit, not onto the free surface). In addition, two still cameras were used for the recording of streaklines through the use of surface markers. Thermal-imaging was conducted using an infra-red camera which sent a video signal to a date/timer and then to a videocassette recorder.

The video-screen images of whirls, scars, and striations were tracked through the use of a digital image processing system and the data were transferred to a computer for flow structure and motion recognition in whirl constellation (for additional details, see Leeker [10]). The stored data could be manipulated to generate detailed informa-

tion on whirl centers, number of whirls per reference area, angular velocities as function of whirl radius, whirl-migration velocity, whirl-whirl interaction (fusing and cancellation, etc). All of the experiments cited above were repeated at least twice to assure that the results could be reproduced within reasonable experimental errors. The experimental data corresponding to the earlier stages of the motion were used to prescribe the initial conditions in the numerical calculations. The data at later times were used for comparison with the numerical predictions at the corresponding times.

## NUMERICAL SIMULATION

Following extensive observations and measurements, the vortex dynamics or the vortex-element method (see, e.g., Sarpkaya [25]) was used to simulate the phenomenon. In doing so, the most important flow features to be reproduced by this or any other model were identified and a numerical code, with very little or no sensitivity to the perturbations in the input parameters, was developed. The model is idealized enough for simple calculation but realistic enough to be interesting.

The initial separation  $b_0$  of the vortex pair was chosen as the reference length; the mutual-induction velocity  $V_0$  of the vortex pair as the reference velocity;  $b_0/V_0$  as the reference time, and the initial strength  $\Gamma_0$  of a vortex as the reference vortex strength. The equations describing the motion were non-dimensionalized through the use of the characteristic parameters  $b_0$ ,  $V_0$ ,  $b_0/V_0$ , and  $\Gamma_0$  where  $V_0 = \Gamma_0 / (2\pi b_0)$ .

The numerical model simulates the mutual interaction of the whirls on the free surface, beginning with their creation, through the use of the vortex-element method. The results of the previous investigations (Sarpkaya et al. [6]), and the experimental results obtained in this investigation helped to define the parameters necessary for the construction of the numerical model. As shown in Fig. 10, the position of the inboard edge of the scar band is denoted by  $\mathbf{s}$ , the width of the scar band by  $\mathbf{w}$ , the average spacing of whirls in the longitudinal direction (a measure of whirl population density per unit length) by  $\mathbf{c}$ , and the horizontal component of the convection velocity of one of the vortices in the original vortex pair by  $\mathbf{V}_b$ . It has been shown previously that the scars are slaved to and transported by the vortices [4-7].

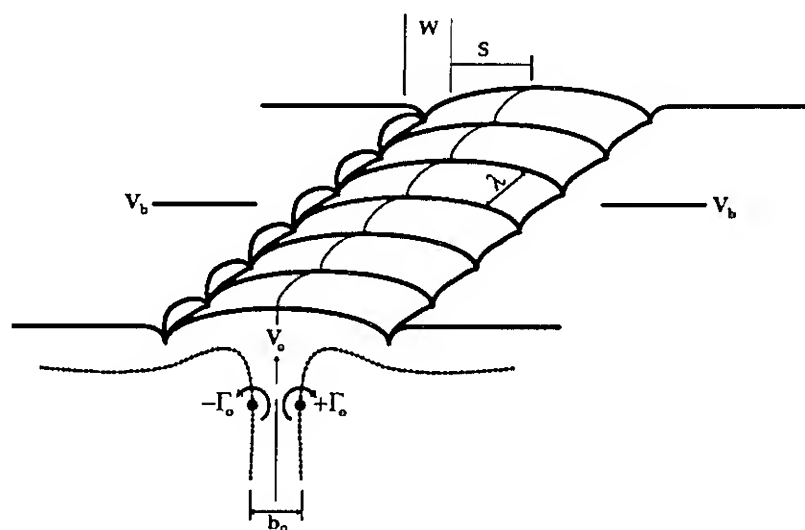


Fig. 10 Schematic of scars and striations

A right-handed coordinate system has been defined in the complex plane where the real  $x$ -axis is parallel to the scars and the  $y$ -axis is perpendicular to the scar bands. Ideally, the length of the scar band should extend from  $-\infty$  to  $+\infty$ . However, this is not numerically possible. Instead, a finite scar length  $L$ , defined by  $L = c [N_w]$  and extending from  $(-L/2, y)$  to  $(L/2, y)$ , is used.  $N_w$  is the number of whirls in each scar band.

The whirl strength is given by

$$\Gamma_w = 2\pi r_c V_t = 2\pi r_c^2 \omega \quad (1)$$

where  $r_c$  is the core radius and the tangential velocity at the core boundary is  $V_t = r_c \omega$ . The normalized, time-averaged, angular velocity  $\omega$  of each whirl core, for a large number of whirls, was determined from the image analysis and was found to vary from about 0.6 to 1.2, the majority of the data falling closer to unity. The core radius was then calculated from

$$r_c = \sqrt{\frac{\Gamma_w}{2\pi}} \quad (2)$$

where now  $\omega$  is assigned approximately the size- and time-averaged value of unity.

The numerical analysis began by randomly placing the whirls into two parallel scar bands,

$$z = \left[ \text{Rnd}_1 L - \frac{L}{2} \right] + i \text{Rnd}_2 w \quad (3)$$

where  $z$  is the position of the whirl center and  $\text{Rnd}_1$  and  $\text{Rnd}_2$  are random numbers (independently seeded) with a uniform distribution from 0.0 to 1.0, inclusive. Each whirl is also assigned a vortex strength in a random manner,

$$\Gamma_w = (\text{Rnd}_3 \Gamma_m) (-1)^{\text{Rnd}_4} \quad (4)$$

where  $\Gamma_w$  is the strength of a whirl,  $\Gamma_m$  is the mean absolute value of the strengths of all whirls,  $\text{Rnd}_3$  is a random number from a standard normal distribution (with a mean of  $\Gamma_m$  and a standard deviation one-quarter the expected range of the whirl strengths), and  $\text{Rnd}_4$  is a random integer from 1 to 10, inclusive.

It has been customary to amalgamate two or more vortices into a single vortex, placed at their center of vorticity, (see, e.g., Sarpkaya [25]), when their cores touch, or are less than a prescribed critical distance  $\epsilon$ , or overlap by a prescribed amount. Like-signed whirls merge into a larger whirl. Oppositely signed whirls are merged into a smaller whirl, to mimic the cancellation of oppositely signed vorticity (thought to be the major mechanism of enhanced energy dissipation in turbulent flow). If the resulting whirl strength is below a prescribed minimum ( $\gamma_{\min}$ ), the whirl is removed from the scar. The amalgamation process does not conserve total vorticity nor is the linear or angular momentum conserved due to the merging of oppositely-signed whirls and the removal of weak whirls. Nevertheless, the conservation of these quantities is not considered important for a number of reasons. First, the purpose of the simulation is not an exact treatment of the viscous diffusion although the removal of very small whirls do in fact accomplish this purpose indirectly. Second, the random nature of the distribution has far greater effect on the mutual interaction of the whirls than the occasional amalgamation of the whirls. Third, the calculations with different ranges of the fundamental parameters, such as the whirl density, minimum survival strength ( $\gamma_{\min}$ ), amalgamation distance, etc., have shown that the fundamental nature of the randomly distributed vortices within a narrow band is to self-limit the amalgamation process and to reduce the effect of the imposed perturbations (for sensitivity analysis) on the resulting characteristics of the scar band.

For an incremental time step  $\Delta t$ , the mutual induction velocity of each whirl is calculated using a cutoff scheme similar to that first proposed by Rosenhead [26]

$$\frac{\Delta z}{\Delta t} = u - iv = \sum_k \frac{i\Gamma_k}{2\pi(z - z_k)} \left( \frac{|z - z_k|^2}{|z - z_k|^2 + \delta^2} \right) \quad (5)$$

The cutoff parameter  $\delta$  was taken to be proportional to the sum of the core sizes on the basis of past experience [25]. Each whirl is moved to a new position, after the calculation of the induction velocity, using

$$z_{t+\Delta t} = z_t + \left[ u + i(v + V_b) \right] \Delta t \quad (6)$$

The whirl-energy density or the specific energy in the system is estimated through the use of

$$E \propto \sum_k (V_t)_k^2 \propto \sum_k \Gamma_k \omega_k \quad (7)$$

The diffusion of vorticity due to viscosity is introduced artificially by reducing the strength of each whirl either through the use of a Gaussian vorticity distribution or through the use of a simple percentage, (e.g., 0.5 percent per time step), in a manner similar to that done previously by others (for details see, e.g., Sarpkaya [25]). The artificial reduction of circulation is justified on the grounds that it accounts for the three-dimensional deformation of vortex filaments, for the cross-diffusion of oppositely-signed vorticity, and for the observed fact that the strength of the vortices continues to decrease with time or downstream distance. Numerical experiments did not show a significant dependence on the type and magnitude of the circulation reduction (0.5 % to 1% per time step).

A few additional features of the model need to be explained. These concern the creation of the whirls, sensitivity analysis, and the selection of the numerical parameters ( $\mathbf{c}$ ,  $\mathbf{s}_0$ ,  $\mathbf{w}$ ,  $\Gamma_m$ ,  $\delta$ ,  $\epsilon$ ,  $\mathbf{N}_w$ ,  $\Delta t$ , and  $\gamma_{\min}$ ). Whirls were created at a particular time in the initial stages of the scar formation in accordance with the observed characteristics of the whirl population. The sensitivity of the predictions of the later stages of the scar motion to the parameters involved in the simulation was examined with great care. Accordingly, every significant parameter involved in the calculations was varied within reasonable limits. For example,  $\mathbf{c}$  was varied by 100 percent and  $\mathbf{w}$  was varied from zero to 0.4. The other parameters, such as  $\Gamma_m$ ,  $\delta$ ,  $\epsilon$ ,  $\mathbf{N}_w$ ,  $\Delta t$ ,  $\gamma_{\min}$ , were varied by at least 100 percent.. The initial inboard position of the scar front  $\mathbf{s}_0$  was kept at the experimentally-observed value of 1.6 at the corresponding time and was not varied further since it naturally increased as a function of time and since it influenced only indirectly the mutual interaction of the two scar

strips. Several runs were made with identical sets of parameters, changing only the seeding of the random numbers involved, in order to ascertain that the insensitivity of the results and basic conclusions to the variation of the parameters selected was not a consequence of the use of a particular set of random numbers. In fact, the randomization was performed by the computer using the system clock time at the commencement of each run. Several plots were created at regular intervals during the execution of the numerical simulation, carried out to times corresponding to the disappearance of the surface structures, in order to compare the predicted results with those obtained experimentally.

## DISCUSSION OF RESULTS

### Physical Experiments

A careful frame-by-frame analysis of the video recordings of literally hundreds of test runs has shown that the sloping of the vortex pair relative to the free surface or the generation of vortices by a lifting surface is not necessary for the creation of scars and striations. Nearly identical surface signatures can be produced through the use of an initially horizontal vortex pair. Figure 11 and many others like it have shown clearly that the three-dimensional instability leading to striations do not originate at the free

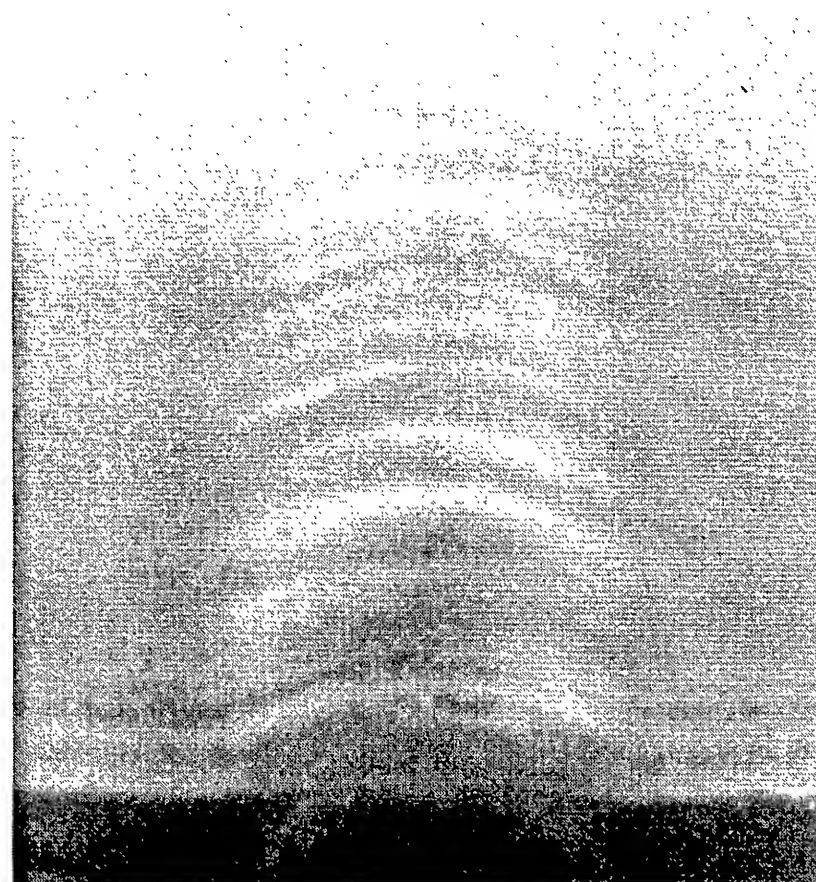


Fig. 11 Inception of short wavelength in stability on a Kelvin oval below the free surface



surface but rather on the Kelvin oval, long before the latter 'sees' the free surface. Subsequently, the free surface interacts with and is modified by the instability brought to it by the Kelvin oval (see Figs. 12-15), i.e., the striations (nearly uniform corrugations, at least at their inception) are a manifestation of the short wavelength instability of the vortex pair. The flow features on the scar front (Figs. 13-15) are clearly identifiable and show the creation of whirls. Figure 16 shows the whirls and the whirl pairs (Kelvin-oval like structures at the free surface), resulting from a pair of trailing vortices. The only contribution of the sloping of

the trailing vortices is the divergence of the scar lines (the V-shaped footprints) and the fact that the striations come into existence sequentially rather than simultaneously.

As noted previously, the wave number  $\beta$  for the short wavelength instability varies from about 4 to 17, corresponding to wavelengths of  $\lambda = 0.37b_0$  to  $1.57b_0$ . The wavelength  $\lambda$  of the striations has been deduced

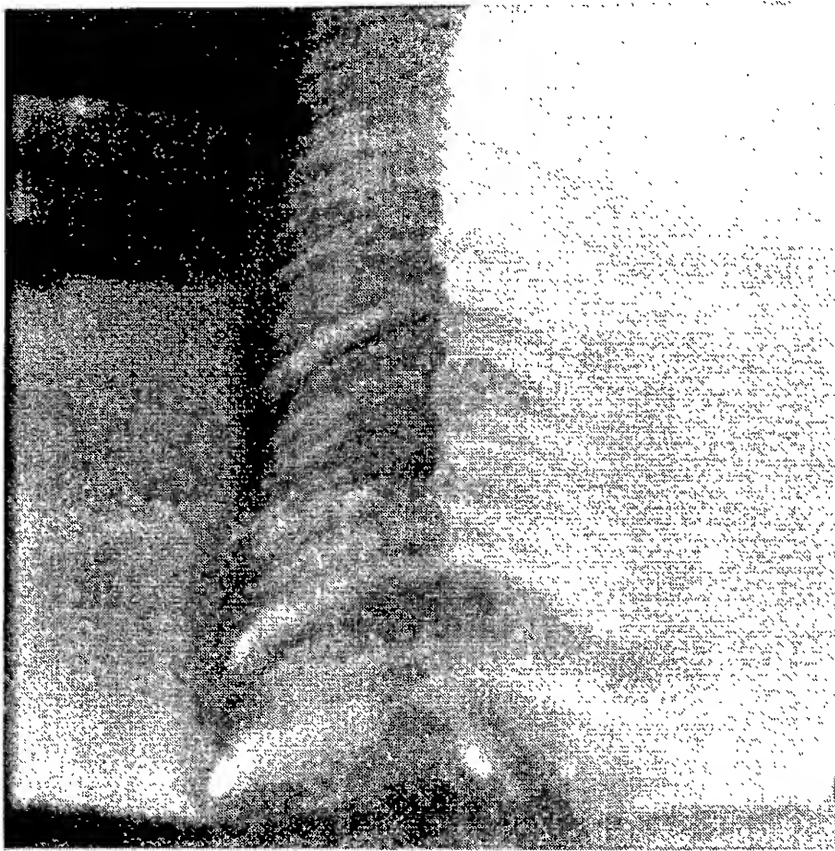


Fig. 12 Rise of corrugated vortex dome

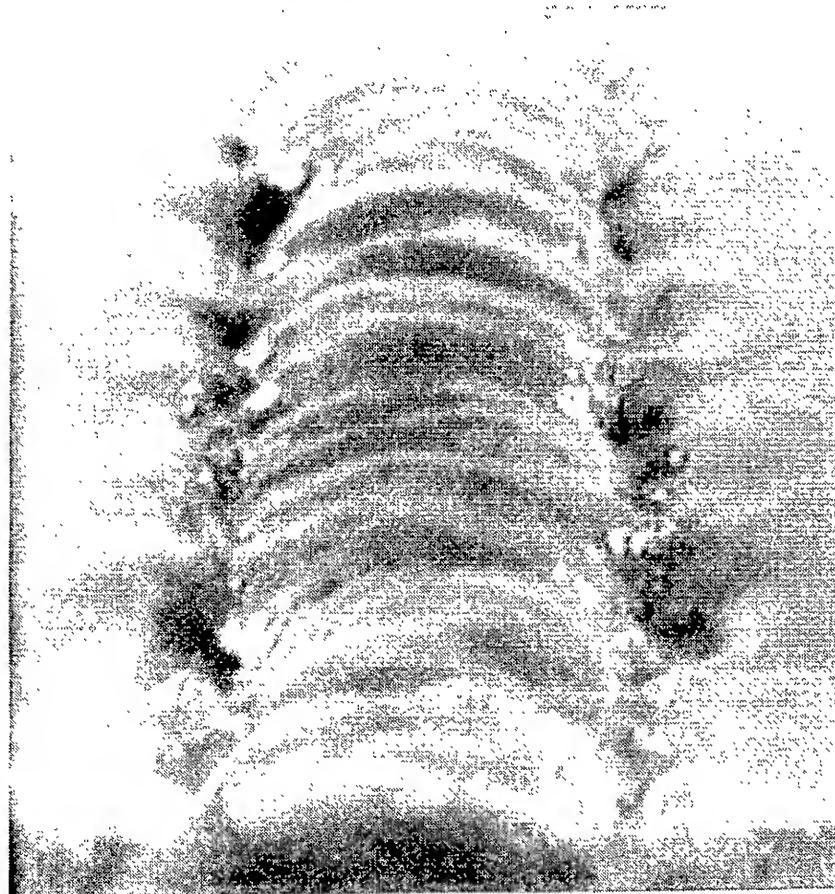


Fig. 13 Formation of scars and whirls

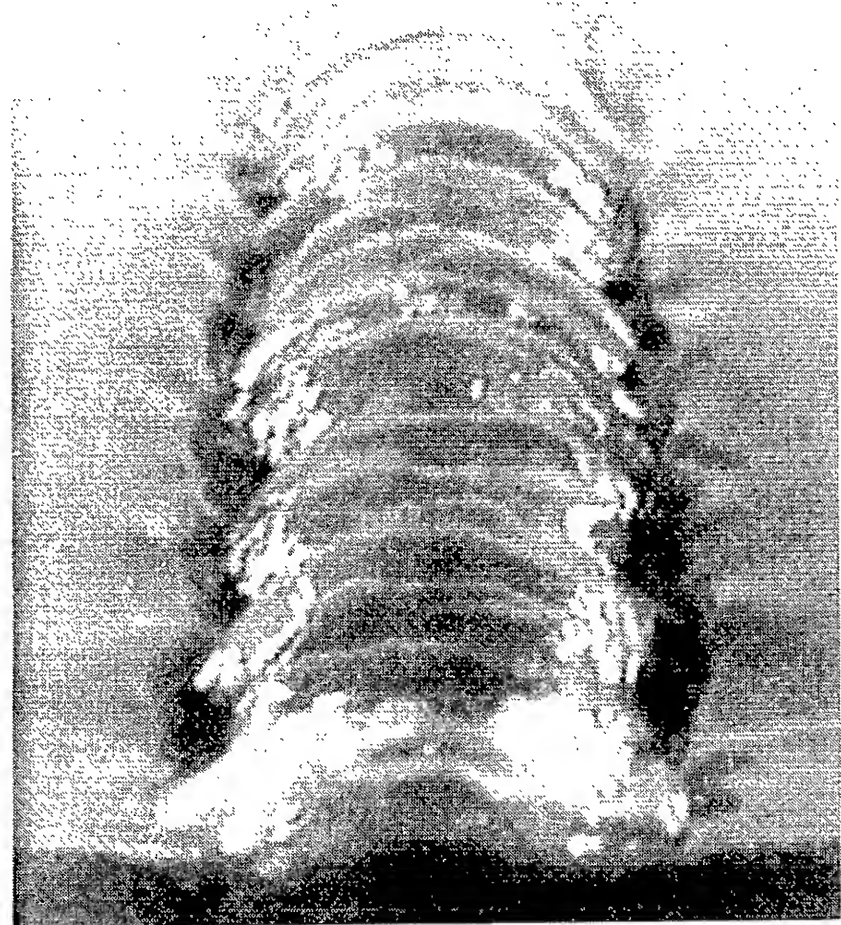


Fig. 14 Intensification of scars

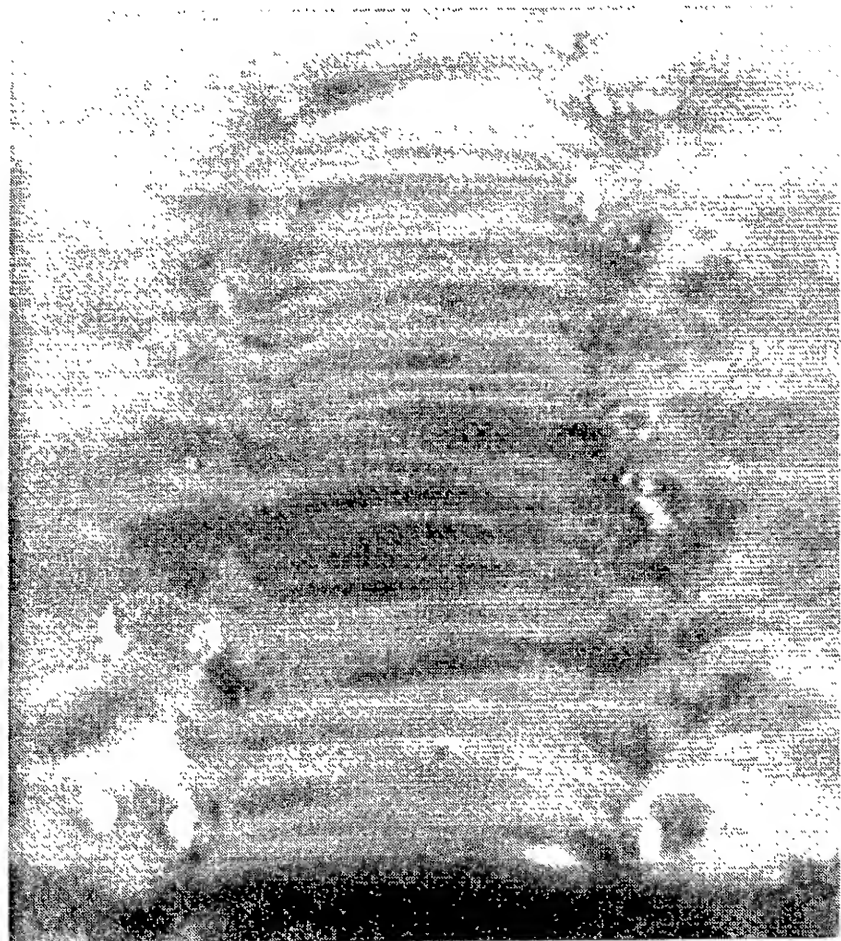


Fig. 15 Later stages of scar formation



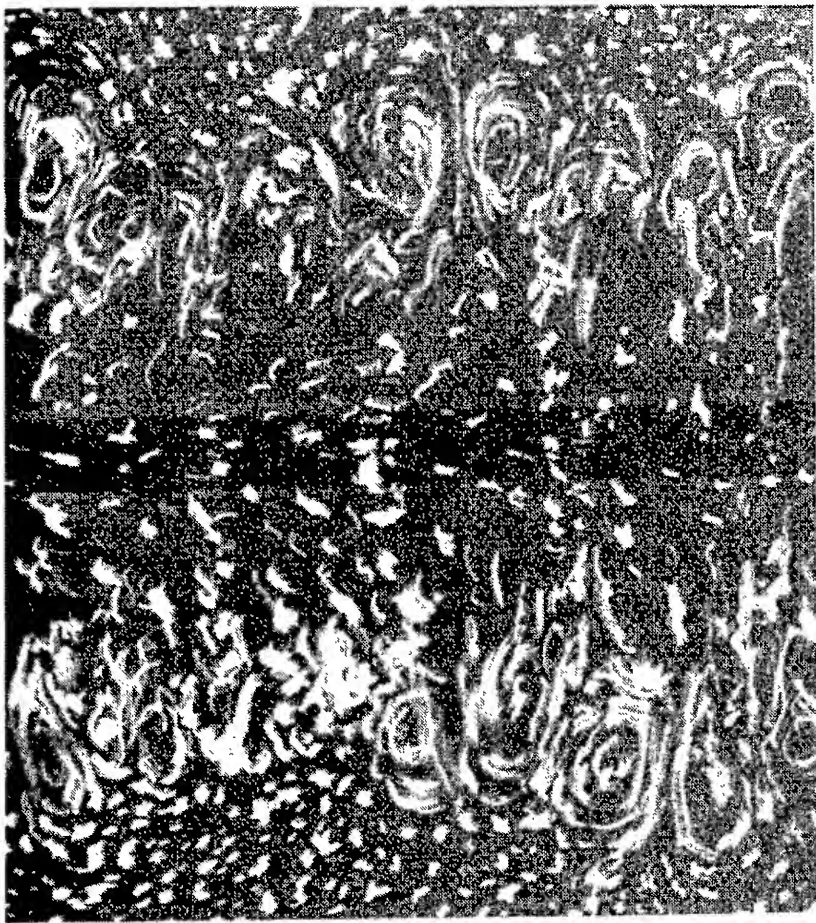


Fig. 16 Whirl formation in scars

from numerous runs as a function of the initial spacing of the main vortex pair. The histograms of the striation wavelength have shown that  $\lambda/b_0$  varies from about 0.75 to 1.25, depending primarily on the initial roll-up of the vortex sheets as dictated by the Froude number. As far as a vortex pair in an infinite homogeneous medium is concerned, the striational instability corresponds to the short wavelength instability (see Fig. 9).

The interaction of a 'corrugated' Kelvin oval with the free surface under the influence of gravitational, centrifugal, and surface tension effects is anything but simple. The surface acquires space and time dependent curvature and velocity and produces vorticity even in the absence of surface tension or surface contamination. This vorticity is  $\Delta\omega = 2q\kappa$ , twice the tangential surface velocity times the surface curvature [27]. The surface velocities are induced partly by the motion of scars and striations and partly by the vortex pair. The surface vorticity is largest at the scar-striation intersection because this is where the curvature and the surface velocities are largest. Consequently, the scars are the regions where the surface vorticity is most likely to be converted into whirls with vertical axes. Thus, what begins as a short wavelength instability quickly degenerates into a far more complex three-dimensional free-surface phenomenon (Figs. 14-15) with its own source and mechanism of vorticity generation. The unsteady motion of the striations (particularly those of the ends where strongest *surface-tension concentration* and whipping action occurs)

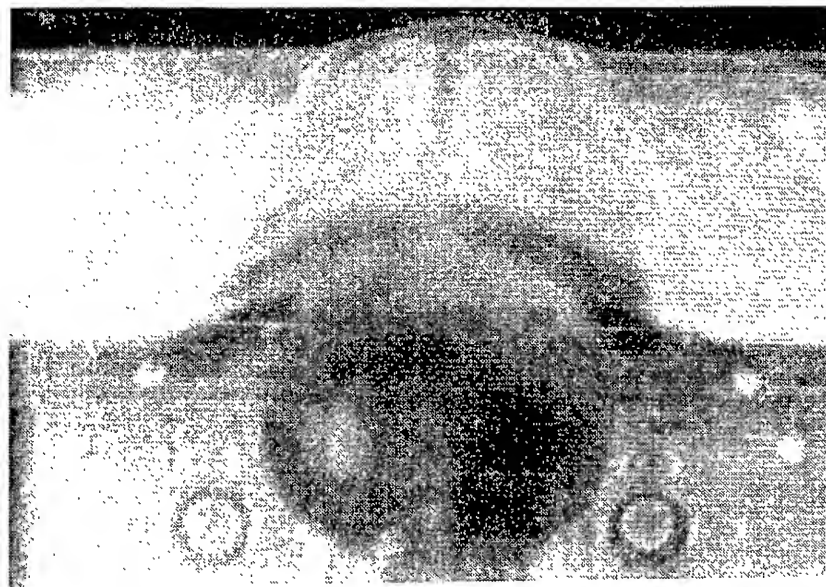


Fig. 17 An additional sample of Kelvin oval free-surface interaction



Fig. 18 Vortex dome for  $Fr = 1.125$

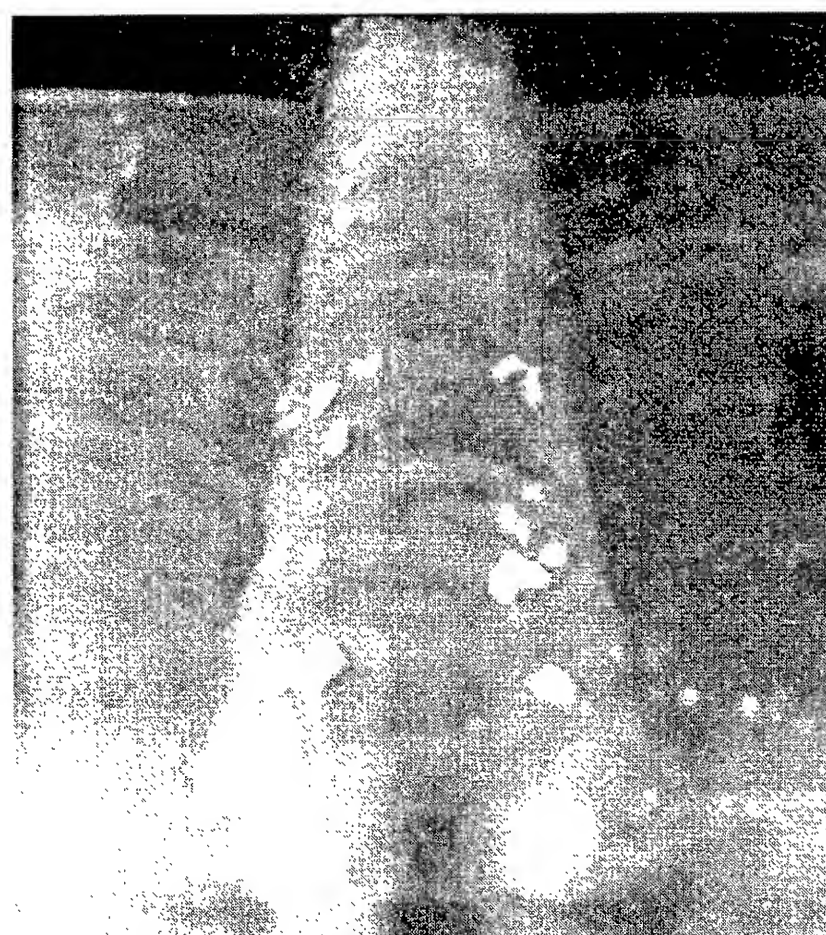


Fig. 19 Rapid increase of the striations

provide the stroke necessary to concentrate the surface vorticity into whirls. The hypothesis of vorticity transport to the free surface from the main vortex pair is not necessary simply because the free surface acquires its own curvature and surface velocity even if it were initially flat and free of vorticity. Figures 17 through 19 show additional samples of the evolution of Kelvin oval, striations, and scars at a Froude number close to unity.

Experiments with rotating cylinders have shown that even at fairly low angular velocities and at fairly large depths of immersion (as much as  $1.5D$  below the free surface), the rotation of the cylinders give rise to striations and whirls. Figure 20 shows the evolution of a whirl and its neighborhood during a time interval of 0.25 seconds. It is clear that neither a trailing vortex pair nor a nearly two-dimensional Kelvin oval, neither a contaminated free surface nor a Reynolds ridge is necessary to create scars and striations. The mere presence of two counter-rotating circulations near a free surface (with curvature and velocity) is sufficient to create all the phenomena observed in other scar experiments. There is, obviously, much more to be explored. The only purpose of reference to rotating-cylinder experiments at this time is to point out that conjectures regarding surface contamination and Reynolds ridge are not necessary. There are, obviously, some fundamental differences as well as strong similarities between the classical Taylor instability, the striational instability, resulting from the counter-rotation of two cylinder, and the three-dimensional instability observed in the actual vortex experiments. These will be explored in some detail in future studies.

The sequence of events emerging from the experimental observations and measurements may be summarized as follows:

- Vortex pair and Kelvin oval;**
- Short wavelength instability;**
- Interaction with the free surface;**
- Formation of striations, leading to:**  
*3-D curvature, Surface velocity, and;*  
*Dividing and pairing of striations;*
- Surface vorticity, mostly near the scars;**
- Gravitational, centrifugal and surface-tension effects;**
- Formation of whirls, whirl pairing, and cascading of vorticity;**
- Self-limiting amalgamation process;**
- Dissipation of whirls.**

As the Kelvin oval rises, the spiralling vortex sheets in each vortex undergo Helmholtz and, subsequently, Rayleigh instability and, eventually, degenerate into turbulent motion. The distance travelled by the oval more or less determines the sequence of events. In the present experiments the said distance to the free surface has been kept below  $6b_0$  in order to obtain a clearly defined oval near the free surface. The vorticity is initially confined to the Kelvin oval and the motion outside it is irrotational. With the passage of time, the vorticity diffuses over a wider area and some vorticity gets annihilated in the overlapping regions of oppositely-signed vorticity. The distance between the vortices during the initial period of rise of the Kelvin oval remains fairly constant but the core radius and, hence,  $r_c/b_0$  increases due to diffusion. As the short wavelength instability begins to grow, the initial value of  $\lambda/b_0$  in Figure 9 is in the order of unity. Had the cores touched,  $\lambda/b_0$  would have been as large as 2.45 (point B in Figure 9). However, the vortex cores do not grow to such large sizes, not at least during the short period of migration of the Kelvin oval toward the free surface. Once the vortices begin to diverge,

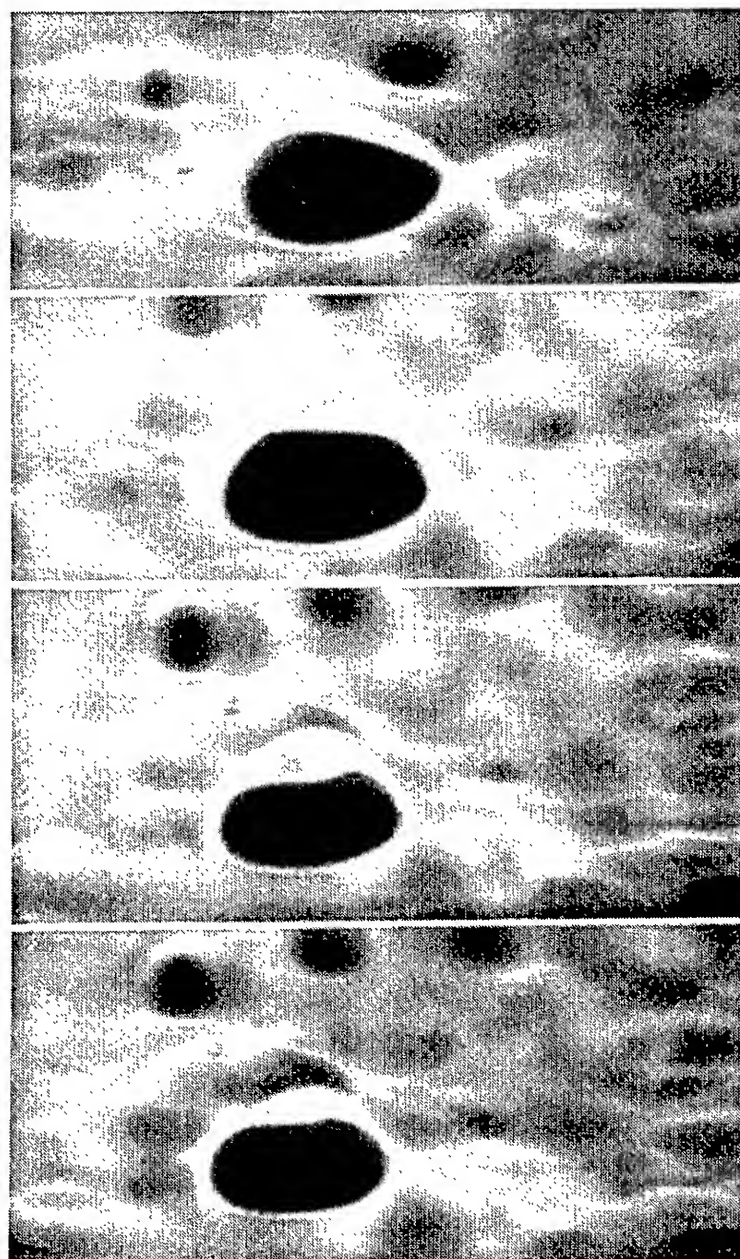


Fig. 20 Evolution of a single whirl in 0.25 s.



as in the case of parallel line vortices approaching a rigid plane, the distance between them increases. This decreases the mutual interaction of the vortices and the relative wavelength  $\lambda/b_0$  decreases. It is not, therefore, surprising to see that the striations multiply quickly and concentrate in the regions directly above the vortices and adjacent to the scars (see Figs. 13-15). The dividing and pairing of the striations are accompanied by the stroking and meandering of the ends (a fishtail-like motion) of the striations. It is this action that is thought to be responsible for the reconstitution of the surface vorticity into numerous, randomly-sized, randomly-shaped, and randomly-distributed whirls.

A number of whirls in close proximity to each other may give rise to a number of complex interactions, such as, amalgamation, annihilation (at least partially), or pairing for a brief period and then re-separation. Thus, it is clear that the interaction of three-dimensional whirls, penetrating only a short distance into the fluid, is not a simple matter and needs further study through the inclusion of viscous effects. The amalgamation as well as annihilation is particularly strong during the formation period of the scars. The amalgamation amounts to cascading of circulation into larger vortices and hence to their longer life-span. It is this process and the generation of surface vorticity that are thought to be responsible for the longevity of the SAR images. Evidently, some sort of regeneration process is necessary without violating the principles of conservation of energy and circulation. One could interpret this whirl-growth phenomenon as an indication of an inverted energy cascade. However, the total internal energy decreases in spite of the growth in size of a number of whirls. This completes the observed as well as perceived evolution of the surface signatures. It will be interesting to discover as to how the scar band, comprised of whirls, tend to increase the radar return in order to provide bright lines in the SAR images.

### Numerical Experiments

Figures 21a through 21c show at  $s_0/b_0 = 1.6$  (where time is taken to be  $\tau = 0$ ), the position of the whirls, the streamlines (with respect to a coordinate system moving with the scars), and the streamlines (with respect to a fixed coordinate system). The size of the whirls is drawn proportional to the square root of their strength. A solid circle denotes clockwise circulation and a hollow circle indicates counter-clockwise circulation. Figures 22a through 22c show

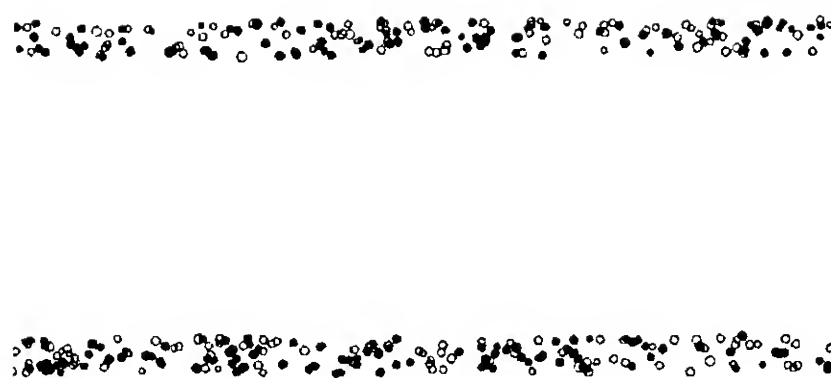


Fig. 21a Initial whirl distribution on scars

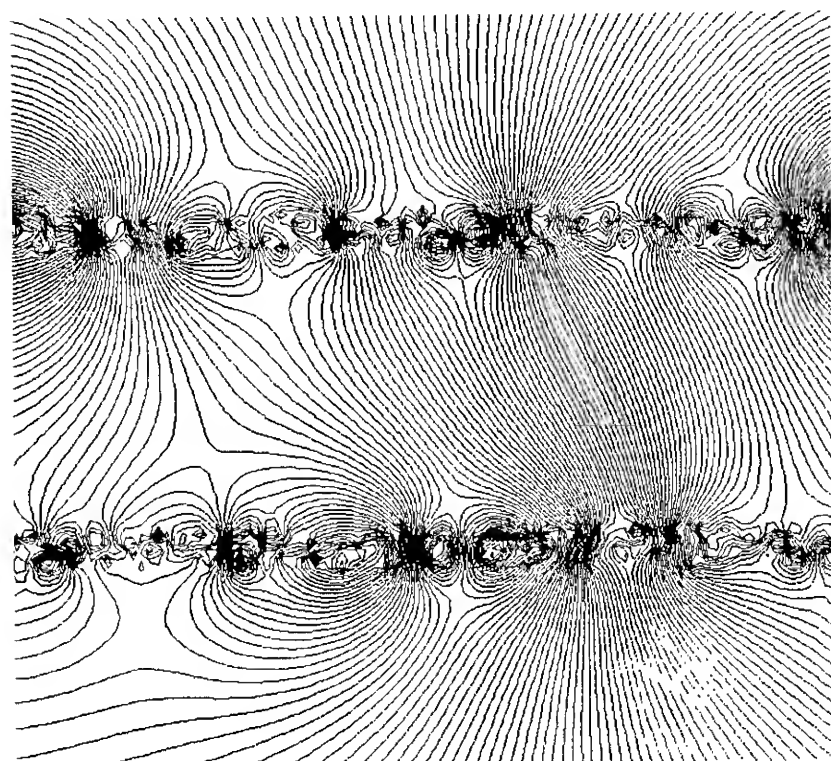


Fig. 21b Streamlines at  $\tau = 0$  (comoving with the scars)

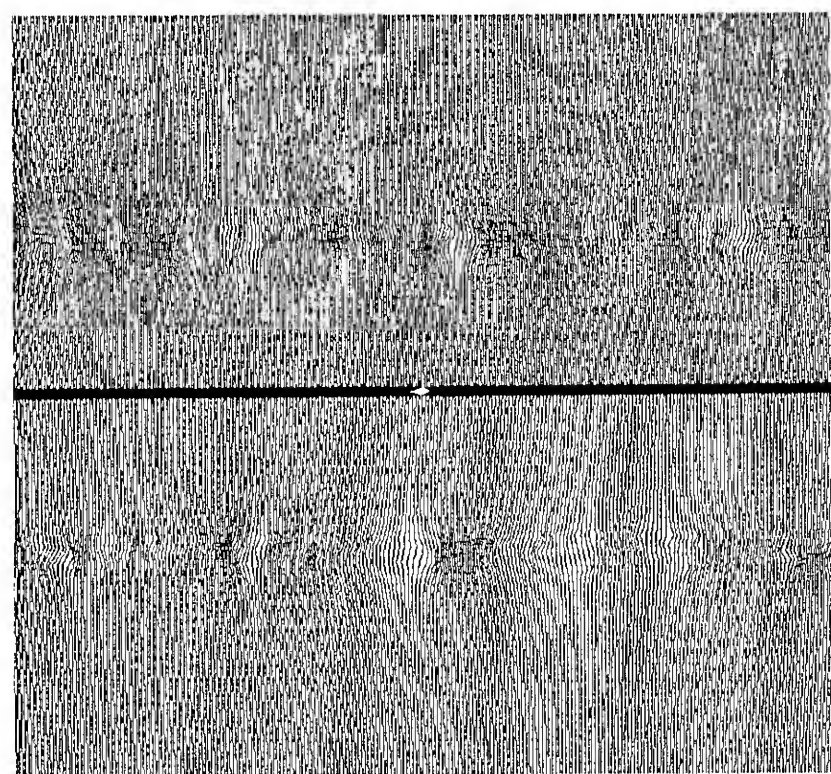


Fig. 21c Streamlines at  $\tau = 0$  (relative to a fixed coordinate system)

the corresponding plots at  $\tau = 1.6$ . Thus, it is seen that the whirls amalgamate as time increases. Figures 21c and 22c show that

the wide region between the scar bands is fairly calm whereas the scar bands are a constellation of depressions created by the whirls. Additional facts emerging from these figures are as follows: The width of the scar band increases naturally partly because of the transport velocity imposed on them by the main vortex pair and partly because of the mutual-induction of the whirls. It is rather remarkable that the band essentially retains its identity (eventually, a long wave instability is seen to develop). What is more remarkable is the fact that the calculated mean scar-separation, for the example shown here, is within 3 percent of that measured at the corresponding times.

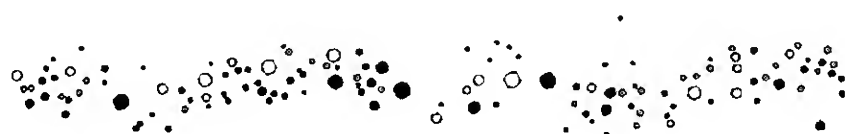
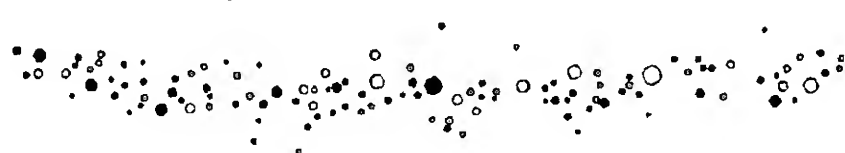


Fig. 22a Predicted whirl distribution on scars at  $\tau = 1.6$

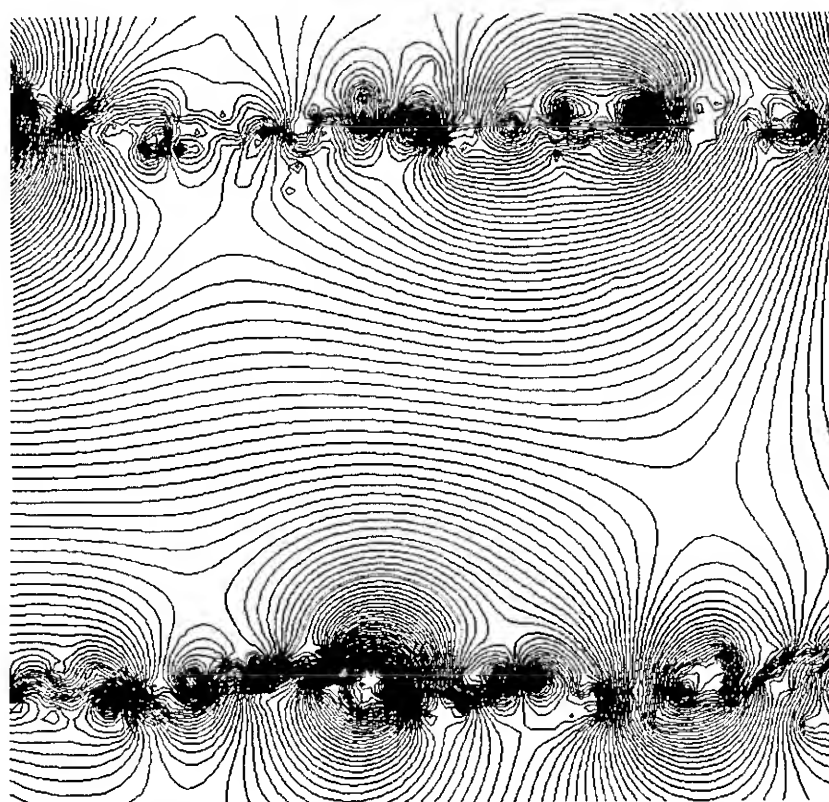


Fig. 22b Predicted Streamlines at  $\tau = 1.6$  (comoving with the scars)

Figure 23 shows a sample plot of the path lines of a number of particles initially situated along a line on the scar.

Typical whirl strength distribution is shown in Fig. 24. Clearly, the total strength of the whirl system decreases with time. However, the amalgamation process does lead to a set of larger whirls. The increase of the number of large structures slows down or stops after a short time period. In other words, the whirl system reaches an equilibrium.

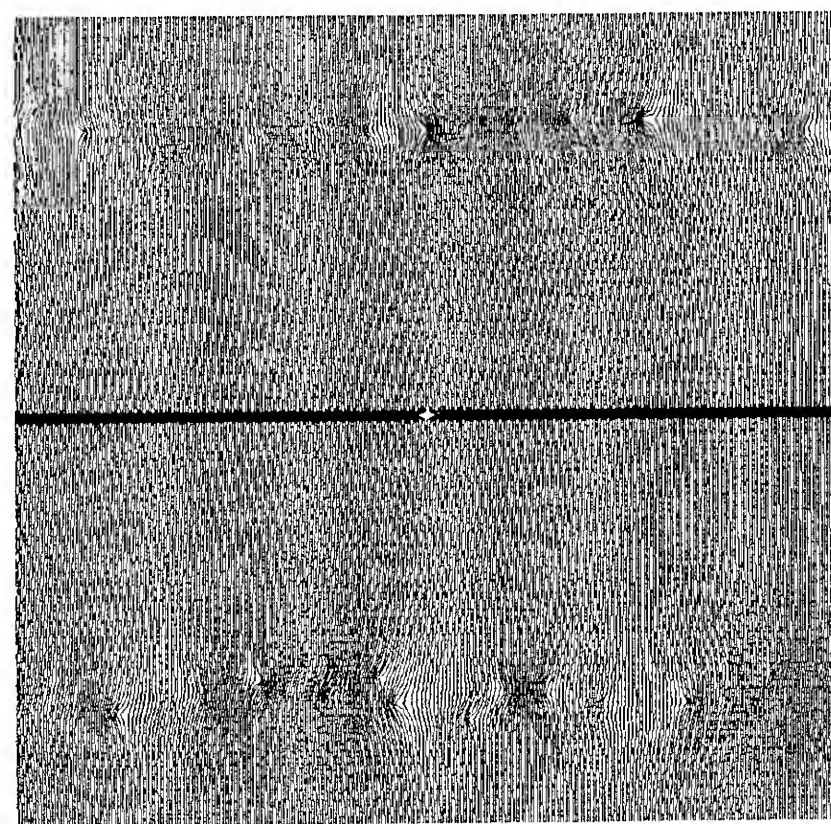


Fig. 22c Predicted streamlines at  $\tau = 1.6$  (relative to a fixed coordinate system)

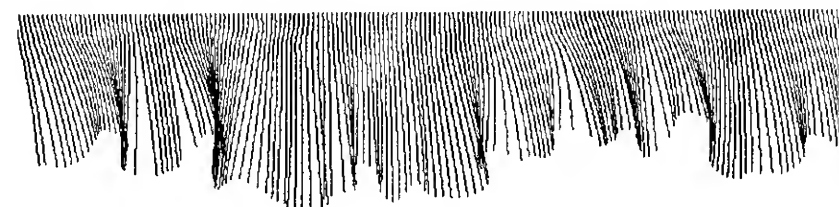
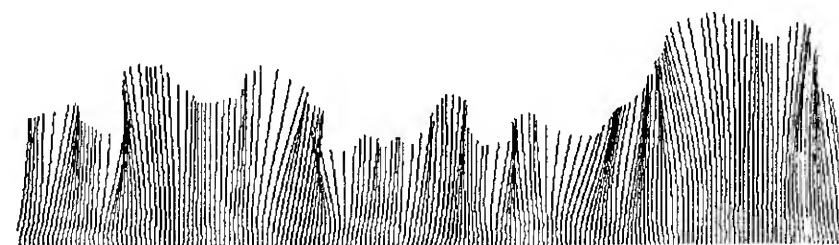


Fig. 23 Marker path lines on scars at  $\tau = 2$

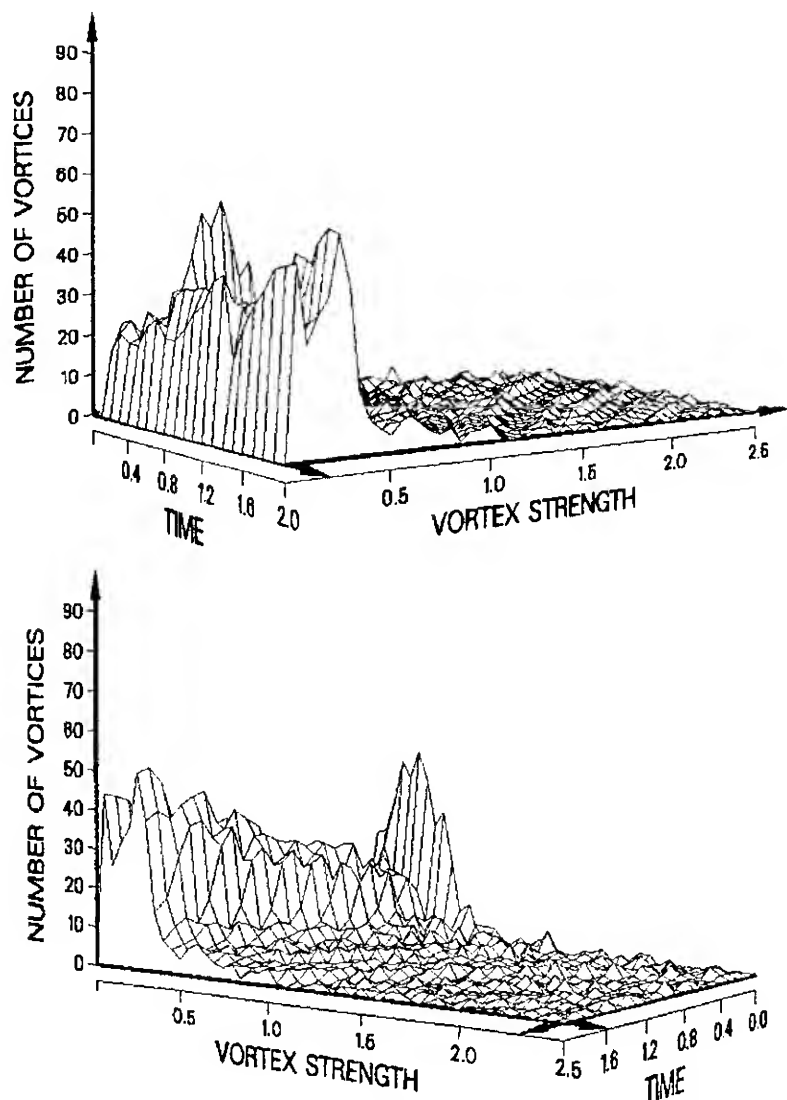


Fig. 24 Whirl strength distribution

Clearly, the whirl-whirl interaction should contribute most significantly to the evolution of the initial distribution, and such events should occur only if the number of whirls is high enough. In the present calculations the whirl population has been doubled several times to explore this very question. Furthermore, numerical experiments were carried out with different random-number seedings to ascertain that the results concerning the energy-density distribution and the cascading of the energy did not depend on either the number of the whirls or on their statistical distribution. It has been found that the population density and the number of random samplings are sufficiently large to arrive at statistically meaningful conclusions. The time variations of the distributions, therefore, allow one to estimate whether whirl-whirl interactions are important. The results presented above show that the shift in the size distribution toward larger structures and the concentration of energy in these structures are an important ingredient of the scar formation and scar life-span.

The numerically-simulated scars were intentionally started parallel, with no further intrusion into their evolution in succeeding steps. As described above, the scars evolved, remaining essentially parallel, with the superposition of a long wavelength sinusoidal

instability as seen in Fig. 22a. At no time did the scar fronts exhibit a V-shaped divergence as observed in the SAR images. This was entirely expected because it is the continuous creation and upwash of the trailing vortices that give rise to the V-shaped scar bands with an included angle of  $2\alpha$  [where  $\alpha$  is  $\arctan(V_0/U)$ ]. It was deemed necessary to apply the numerical model to the trailing vortex case with a few minor differences, partly to further substantiate the predictions of the model and partly to observe the similarities or differences between the measurements and calculations. Figure 25

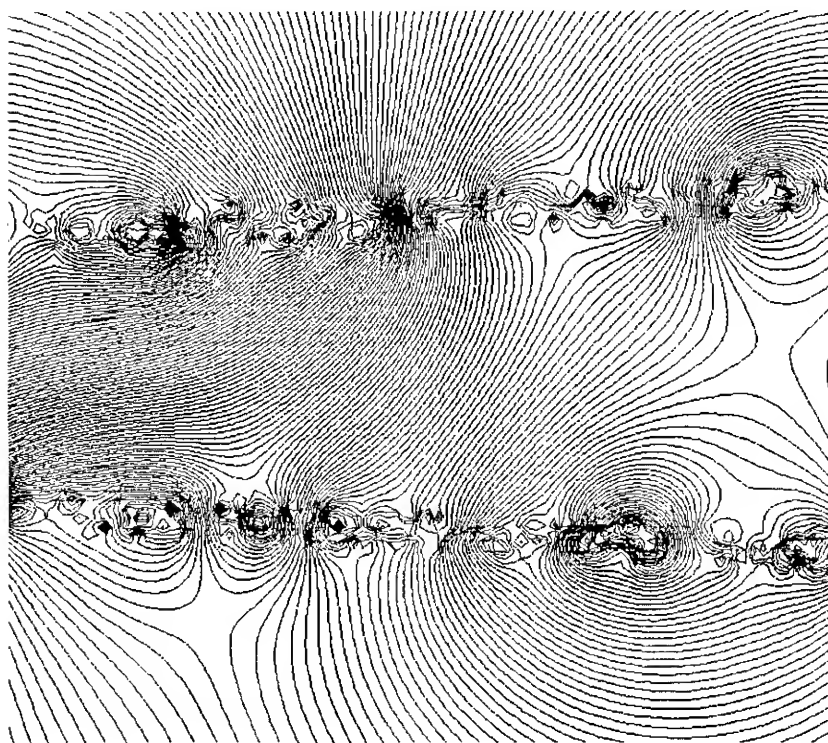


Fig. 25 V-shaped scar streamlines at  $\tau = 0$  (comoving with the scars)

shows the instantaneous streamlines at  $\tau = 0$ , as they would be seen by an observer moving with the scars, and Fig. 26 shows at  $\tau = 0-1.2$ , the instantaneous streamlines as they would be seen by an observer fixed to the coordinate system. Finally, Figures 27a and 27b show a comparison of the experimental and numerical results. One half of these figures represent the numerical results and the other half the experimental results. A comparison of the two halves show the remarkable similarity between the observations and predictions at the corresponding times.

## V. CONCLUSIONS

The numerical and experimental results presented herein warranted the following conclusions:

1. The sloping of the vortex pair (as in the case of trailing vortices) is not necessary to produce surface signatures or footprints of vortex wakes in the form of scars and stri-



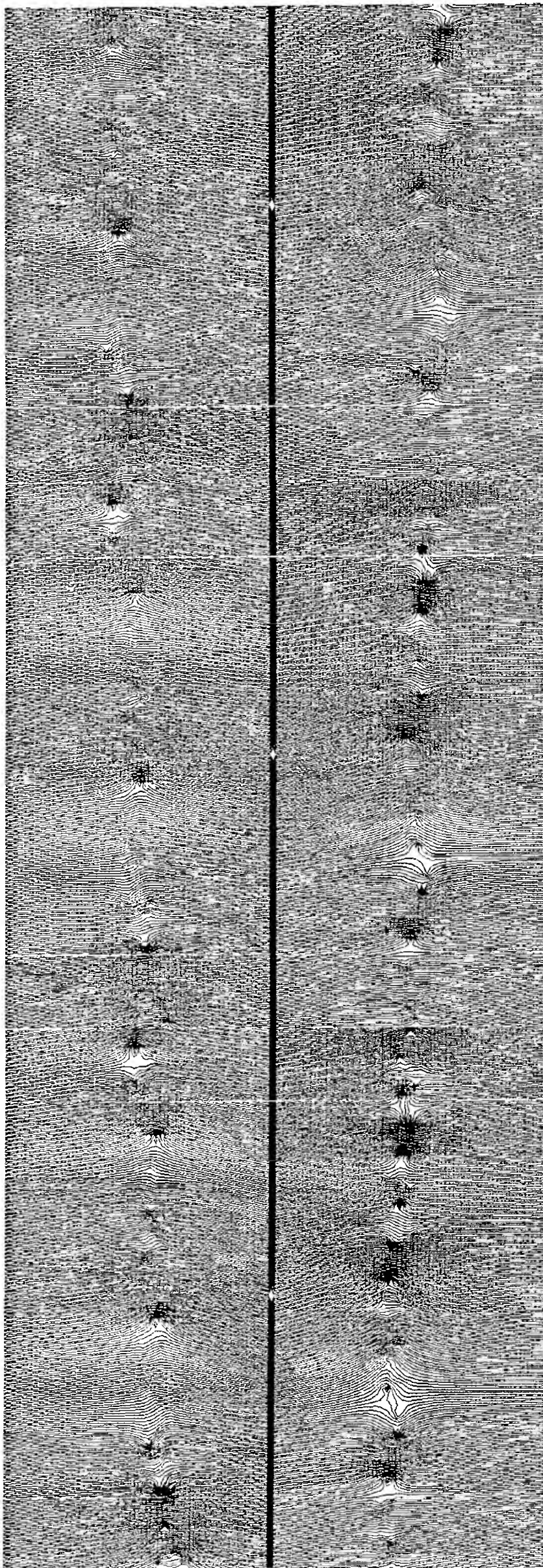


Fig. 26 Growth of a V-shaped scar in time and space

ations. An initially two-dimensional vortex pair yields similar structures.

2. A fully submerged vortex pair is subject to both long- and short-wavelength instabilities. The latter is particularly prevalent when the former is suppressed. The experiments have revealed their existence and the role played by them in the generation of striations.

3. The short-wavelength instability has a wavelength in the order of unity, compared with the initial spacing of the main vortex pair. The wavelength decreases as the vortex spacing increases.

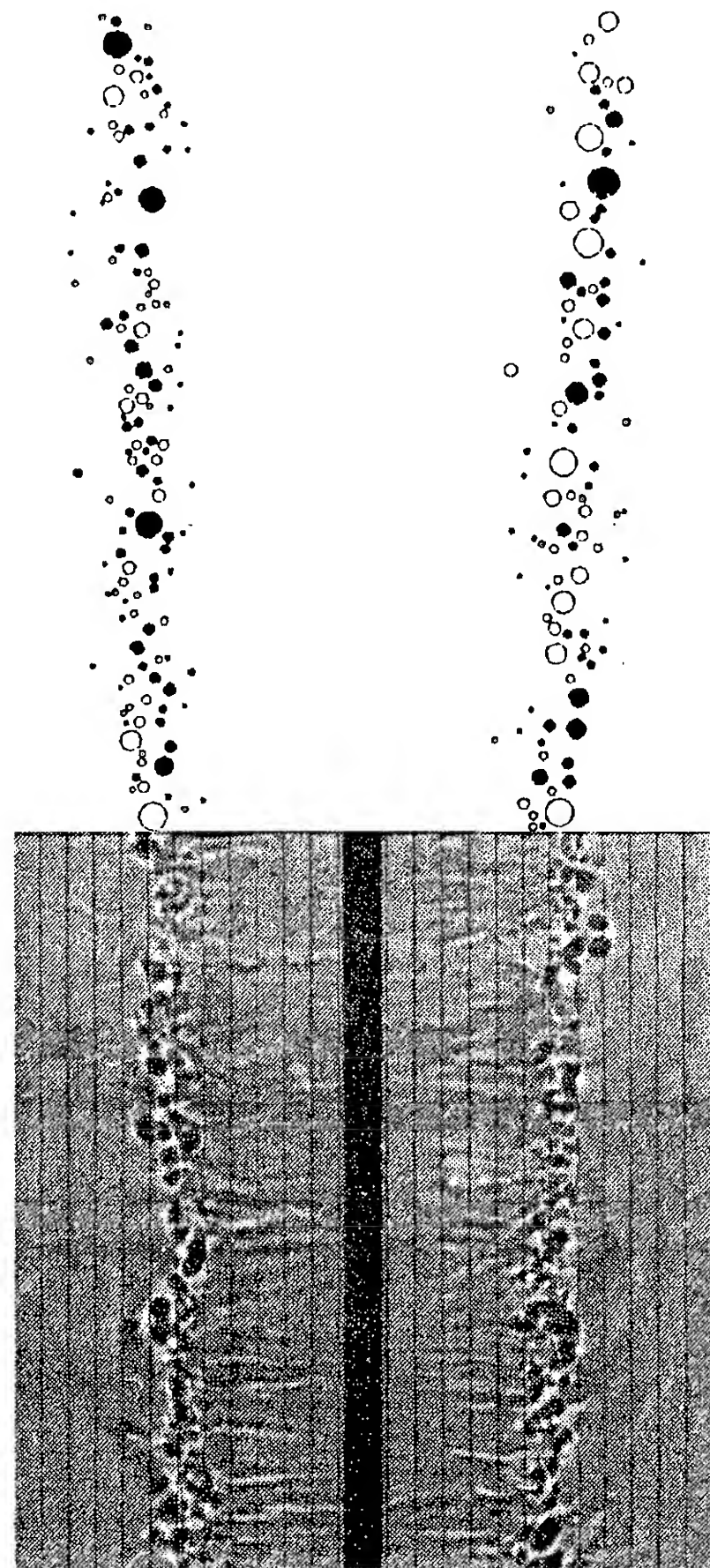


Fig. 27a Comparison of measured and predicted V-shaped scars (No. 1)

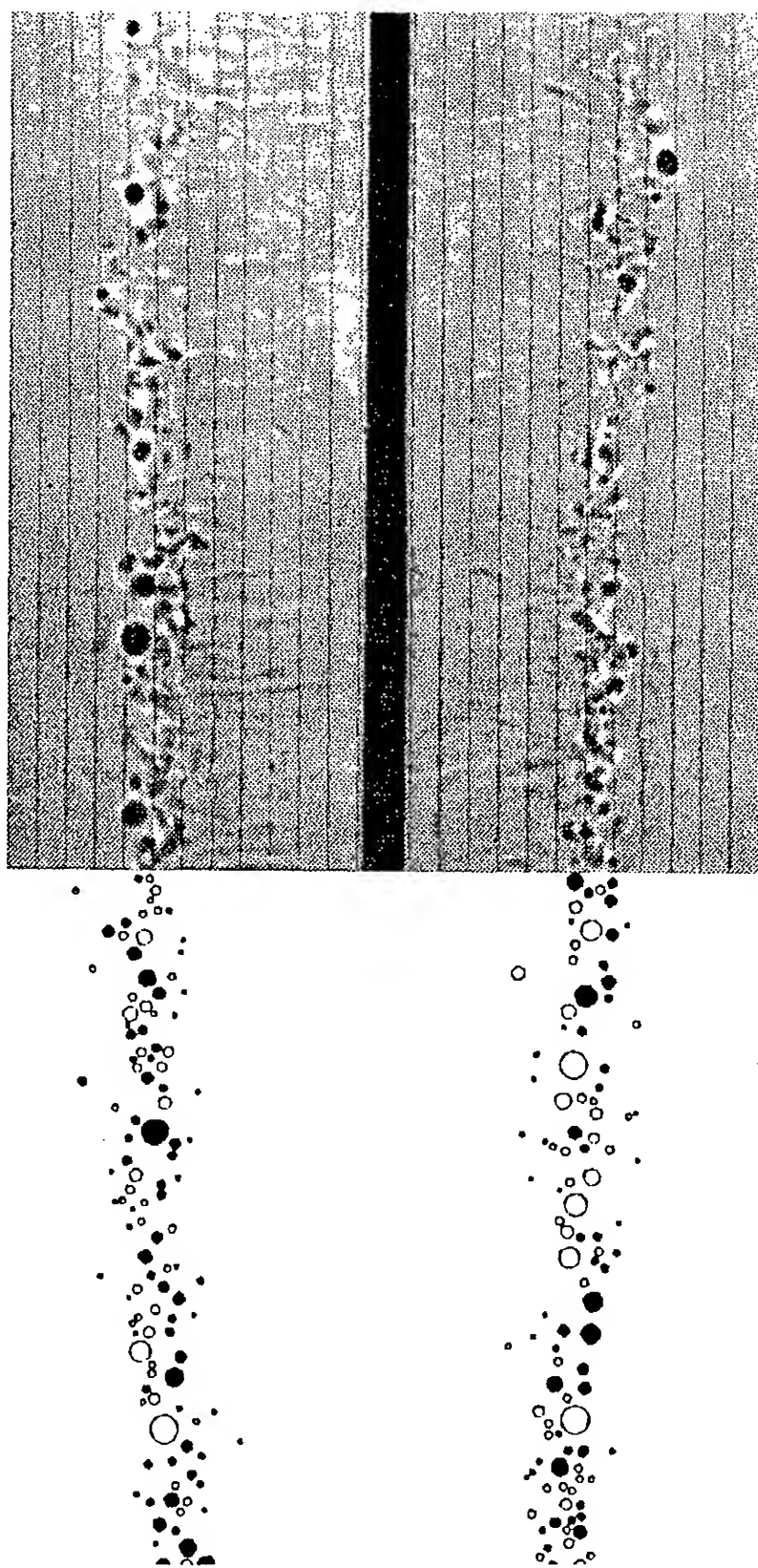


Fig. 27b Comparison of measured and predicted V-shaped scars (No 2)

4. The short wavelength instability leads to striations, surface curvature, surface velocity, and surface vorticity. The strongest surface-tension concentration occurs near the tips of the striations. Consequently, these are the regions where the new whirls are created through the use of the surface vorticity. This type of whirl formation appears to be unique to the scar generation.

5. The scar and striation generation may be affected by the degree of surface contamination. However, the changes in surface tension and surface elasticity brought about by contamination, beyond that due to intermolecular cohesive forces, are neither necessary nor sufficient for the creation of striations and scars.

The most indispensable ingredients for the generation of whirls are the viscosity of fluid, generation of surface vorticity due to surface curvature, and the unstable motion of the ends of whirls. Also, it is equally important to note that the so-called Reynolds ridge is akin to but not related to the scar formation. The Reynolds ridges do not give rise to whirls.

6. The numerical simulation of the phenomenon through the use of vortex dynamics or vortex element method has shown that all of the fundamental characteristics of the scar evolution (e.g., the preservation of scar-band width, whirl distribution, whirl-whirl interaction, energy cascading, mutual annihilation of whirls, self-limiting amalgamation, etc.) are faithfully reproduced.

7. Among the numerous mechanisms proposed to explain the physics of the SAR images, the hypothesis of the interaction of a vortex pair with the free surface emerges as the most viable one in view of the observations and measurements made and the conclusions arrived at in this investigation.

8. The above conclusions are further vindicated by the experiments carried out with two rotating cylinders. The analogy between the two types of circulatory motions need to be further explored, partly because such experiments will provide an excellent opportunity to discover many new and interesting vortex patterns and partly because they will lead to the closer examination of the similarities between the striations, whirls, and scars generated by the two types of circulations.

#### ACKNOWLEDGMENTS

The authors wish to express their sincere appreciation to the Office of Naval Research and the Naval Postgraduate School for the support of the investigation. The project was monitored by Dr. Edwin P. Rood.

#### REFERENCES

1. Langmuir, I., "Surface Motion of Water Induced by Wind," *Science*, Vol. 87, 1938, pp. 119-123.
2. Scott, J. C., "Flow Beneath a Stagnant Film on Water, The Reynolds Ridge," *Journal of Fluid Mechanics*, Vol. 116, 1982, pp. 283-296.
3. Furey, R. J., "Hydrodynamic Stability and Vorticity in a Ship-Model Wake," Research and Development Report No. DTRC-90/005, 1990, David Taylor Research Center, Bethesda, Maryland.



4. Sarpkaya, T. and Henderson, D. O., "Surface Disturbances due to Trailing Vortices," Naval Postgraduate School Technical Report No. NPS-69-84-004, 1984, Monterey, CA.
5. Sarpkaya, T., and Henderson, D., "Surface Scars and Striations," AIAA Paper No. 85-0445, 1985.
6. Sarpkaya, T., 1985, "Surface Signatures of Trailing Vortices and Large Scale Instabilities," *Proceedings of the Colloquium on Vortex Breakdown* (Sonderforschungsbereich 25), University of Aachen, 1985, pp. 145-187.
7. Sarpkaya, T., "Trailing-Vortex Wakes on the Free Surface," *Proceedings of the 16th Symposium on Naval Hydrodynamics*, National Academy Press, 1986, pp. 38-50.
8. Sarpkaya, T., "Trailing Vortices in Homogeneous and Density Stratified Media," *Journal of Fluid Mechanics*, Vol. 136, 1983, pp. 85-109.
9. Lamb, H. (Sir), *Hydrodynamics*, Dover Publications, (6th ed.), 1945, pp. 221-224.
10. Leeker, R. E., Jr., "Free Surface Scars due to a Vortex Pair," M.S. Thesis, Naval Postgraduate School, Monterey, CA., March 1988.
11. Yamada, H. and Honda, Y., "Wall Vortex Induced by and Moving with a Confined Vortex Pair," *Physics of Fluids A*, Vol. 1, No. 7, 1989, pp. 1280-1282.
12. Peace, A. J. and Riley, N., "A Viscous Vortex Pair in Ground Effect," *Journal of Fluid Mechanics*, Vol. 129, 1983, pp. 409-426.
13. Sarpkaya, T., Elnitsky, J., and Leeker, R. E., 1988, "Wake of a Vortex Pair on the Free Surface," *Proc. Seventeenth Symposium on Naval Hydrodynamics*, National Academy Press, Washington, D. C., pp. 53-60.
14. Dahm, W. J. A., Scheil, C. M., Tryggvason, G., "Dynamics of Vortex Interaction with a Density Interface," Report No. MSM-8707646-88-01, The Univ. of Michigan.
15. Willmarth, W. W., Tryggvason, G., Hirsa, A., and Yu, D., "Vortex Pair Generation and Interaction with a Free Surface," *Physics of Fluids*, Vol. A1, 1989, pp. 170-172.
16. Marcus, D. L., "The Interaction Between a Pair of Counter-Rotating Vortices and a Free Boundary," Ph. D. thesis, UC Berkeley, 1988.
17. Marcus, D. L., and Berger, S. A., 1989, "The Interaction Between a Counter-Rotating Vortex Pair in Vertical Ascent and a Free Surface," *Physics of Fluids*, A-1, Vol. 12, pp. 1988-2000.
18. Tryggvason, G., "Deformation of a Free Surface as a Result of Vortical Flows," *Physics of Fluids*, Vol. 31, 1988, pp. 955-957.
19. Telste, J. G., "Potential Flow about Two Counter-Rotating Vortices Approaching a Free Surface," *Journal of Fluid Mechanics*, Vol. 201, pp. 259-278, 1989.
20. Ohring, S., and Lugt, H. J., 1989, Two Counter-Rotating Vortices Approaching a Free Surface in a Viscous Fluid, Research and Development Report No. DTRC-89/013, David Taylor Research Center, Bethesda, Maryland.
21. Marcus, D. L., (Private communication), March 1990.
22. Crow, S. C., "Stability Theory for a Pair of Trailing Vortices," *AIAA Journal*, Vol. 8, No. 12, 1970, pp. 2172-2179.
23. Widnall, S. E., "The Structure and Dynamics of Vortex Filaments," *Ann. Rev. Fluid Mech.*, Vol. 7, 1975, pp. 141-165.
24. Sarpkaya, T., and Johnson, S., K., "Trailing Vortices in Stratified Fluids," Technical Report No. NPS-69-82-003, 1982, Naval Postgraduate School, Monterey, California.
25. Sarpkaya, T., "Computational Methods with Vortices—1988 Freeman Scholar Lecture," *Journal of Fluids Engineering, Transactions of ASME*, Vol. 111, No. 1, 1989, pp. 5-52.
26. Rosenhead, L., "The Spread of Vorticity in the Wake Behind a Cylinder," *Proc. Roy. Soc., Ser. A*, Vol. 127, 1930, pp. 590-612.
27. Batchelor, G. K., *An Introduction to Fluid Dynamics*, Camb. Univ. Press, 1967.



## DISCUSSION

Owen M. Griffin  
Naval Research Laboratory, USA

In your introductory remarks you noted that the surface disturbances and effects are caused by shed vortices which accompany the passage of a submerged body. There is equal, if not more, interest in the wake of a surface ship in terms of the persistent synthetic aperture radar (SAR) signature produced by the ship's passage. Can you comment upon the possible importance of the vortex-free surface interactions discussed in your paper as they might apply to the remotely sensed surface ship wake?

## AUTHORS' REPLY

As I have noted in the Introduction of the written version of the paper, "Just a narrow patch of darkness, bounded by two bright lines, provides the impetus for this investigation partly because it is seen in the synthetic aperture radar (SAR) images of a ship's wake, partly because it extends many miles directly in the ship's track, ...." Dr. Griffin is of course correct in reinforcing this fact. My introductory remarks at the oral presentation of the paper were confined to ascending heterostrophic vortices, generated by submerged bodies, primarily because of the mechanism with which the vortices were created in our experiments. I should have pointed out that a well-known example of such a SAR image is that of the wake of the surface ship USS Quapaw.

As far as the possible importance of the vortex/free-surface interactions discussed in the paper to the understanding of the mechanisms leading to the SAR images of surface ship wakes is concerned, the current state of the understanding of either phenomena does not allow one to explain the physics of what relationship could scars and striations have with the SAR images. Among the many proposals made, one that appeals this writer most is the interaction of the vortical fluid motions generated by the boundary layers and propellers of the ship with the free surface. However, such an interaction is not as simple and as relatively clean as that of ascending vortices because of intense turbulence (patches and parcels of vorticity of many scales and intensities) and air-water mixture accompanying the ship's wake. The development of a U-shaped vortex wrapping around the outside of the main vortex core (discussed in 1985 in author's Ref[6]), restructuring of vorticity in the wake, the reverse energy cascading, and the self-limiting growth of the surface whirls (all discussed in the present paper) may go long ways towards establishing a relationship between the scars and striations generated by ascending heterostrophic vortices and the SAR images of ship wakes. It is also possible that the real fall-out benefits of the investigation will be in yet-unthought-of areas of experimental and computational fluid dynamics. The investigation has just begun.

# Measurement and Computations of Vortex Pair Interaction with a Clean or Contaminated Free Surface

A. Hirs, G. Tryggvason, J. Abdollahi-Alibeik, W.W. Willmarth  
(The University of Michigan, USA)

Observations of surface deformations produced by the interaction of trailing vortices with a free surface, behind a submerged delta wing at negative angle of attack, were described by Sarpkaya and Henderson (1985). The flow field during the laminar interaction with the free surface is studied experimentally using a pair of vertically oriented, computer controlled, counter rotating flaps to generate laminar vortex pairs with the same Reynolds number and Froude number as the trailing vortices. Numerical computations in two-dimensions, flow visualization (laser induced fluorescence and shadowgraph) and particle image velocimetry (PIV) with known surfactants on the surface show that surface contamination has a significant influence on the flow field and surface motion during the interaction. New vorticity produced on either side of the vortex pair when the surface is contaminated initially forms a Reynolds ridge, (the surface signature at the leading edge of a subsurface boundary layer), and then the new vorticity beneath the contaminated surface rolls up to form secondary vortices outboard of the original vortices and with opposite sign. The secondary vortices cause the original vortex pair to rebound from the free surface.

## INTRODUCTION

Synthetic aperture radar images made at high altitudes show that a ship produces a long, narrow signature on the surface in the wake that is detectable long after the passage of the ship (Munk et al. 1987). Since the wake directly behind a ship contains vortical structures produced by the hull and the propeller blades which interact with the surface, it appears that an explanation of the surface signature in the wake will require a fundamental understanding of the interaction of vorticity with the free surface.

When a pair of counter rotating vortices in an ideal fluid approach a flat surface the velocity field due to the image vortices will cause them to diverge (Lamb 1932). Since the motion of each vortex is a result of the velocity induced by the other vortex as well as the image vortices, the diverging vortices ultimately move along straight lines parallel to the flat surface. When the viscosity of the fluid

is considered, the flow field will be different owing to the diffusion of the initial vorticity and the additional no slip boundary condition at the flat surface. The observed surface features produced by the wake of a submerged delta wing at a negative angle of attack, as originally described by Sarpkaya and Henderson (1985), are sketched in Figure 1.

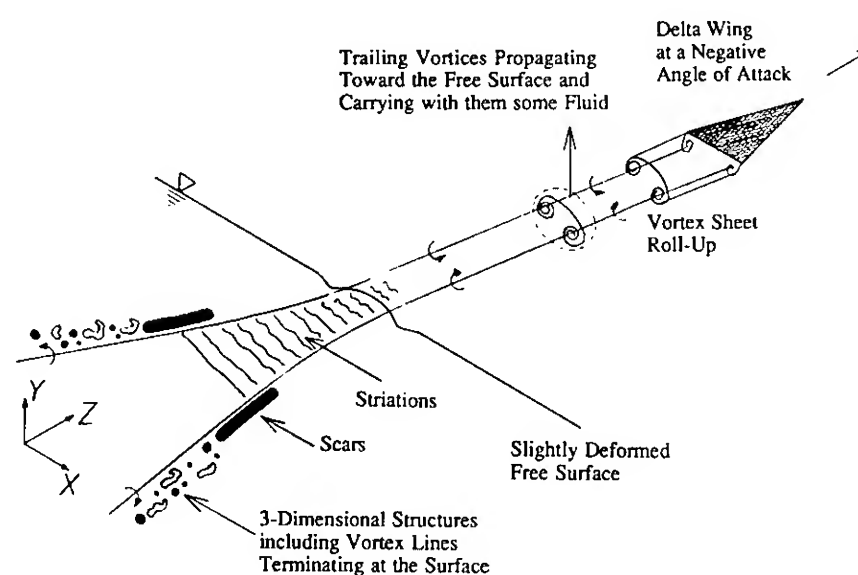


Figure 1 Surface deformations resulting from the trailing vortices interacting with a free surface.

The subsurface flow field associated with many of the surface features that they described are not yet understood. There are also numerous other experimental and theoretical studies of the interaction of vortex pairs with solid and free surfaces. A survey of the literature for many of these studies has been made by Hirs (1990).

From the literature it is clear that the interaction of vorticity with a free surface is a very complex problem. The flow may or may not be turbulent and one must consider the Reynolds number. In addition, the momentum of the vortex pair may be great enough to cause vertical displacement of the free surface with rebounding of the vortex pair during the interaction, as Tryggvason has shown through numerical computations [see Willmarth et al. (1989)] and one must consider the Froude number. Finally, it has become apparent (as will be demonstrated in this paper) that an understanding of the interaction of vortex pairs with a free surface at low

521

A. Hirs Department of Mechanical Engineering, Aeronautical Engineering and Mechanics, Rensselaer Polytechnic Institute, Troy NY 12180 U.S.A.

G. Tryggvason and J. Abdollahi-Alibeik Department of Mechanical Engineering and Applied Mechanics, The University of Michigan, Ann Arbor MI 48109 U.S.A.

W. W. Willmarth Department of Aerospace Engineering, The University of Michigan, Ann Arbor MI 48109 U.S.A.

Froude and Reynolds numbers requires that one also must consider the effect of a dimensionless number representing the ratio of the viscous force tangential to the free surface to the tangential surface force exerted by a surface film with a gradient in concentration. When surface contaminating films are not present on the free surface (which in nature is a very rare condition) the basic interaction, at low Froude numbers and for a laminar flow, is approximately similar to the flow that would be observed for an inviscid fluid with a flat surface. However, clean surfaces are a rarity and varying amounts of surface film contaminants are usually present on the surface. When present, as will be shown, surface contaminants can completely change the nature of the flow field during the later stages of the interaction of vortex pairs with the surface.

Initial experiments were made with a small delta wing, similar to the one used by Sarpkaya and Henderson (1985), which was towed beneath and parallel to the surface at negative angle of attack. The flow beneath the surface was observed using a fluorescent dye (Fluorescein) injected at the trailing edge of the wing and illuminated from below the surface by a thin sheet of laser light normal to the surface and to the towing direction. These flow visualization experiments were in general agreement with the results described by Sarpkaya and Henderson (1985).

In addition to observations of the wake cross-section, we observed the motion of the surface with the aid of particles placed on the surface after the wing had passed. We found that as the vortex pair approached the surface the particles on the center line of the wake were swept to either side by the upwelling of fluid carried with the vortex pair. We also discovered that the surface motion was not consistent because the velocity and amount of surface motion observed on either side of the wake was dependent upon the type of particles used as passive markers. In one case, punched circles (chaff) from oiled, paper computer tape placed on the surface after the wing were completely motionless. However, a few pieces of chaff that were completely wet and had sunk slightly below the surface were observed to be moving outward from the wake center line while the drier pieces of chaff just above them and floating on the surface were stationary.

After these initial observations, the status of the project was discussed with personnel of the Naval Research Laboratory and the Office of Naval Research. We were alerted to the possibility that surfactants could be present in the Ann Arbor city water used to fill our small towing tank. Jack Kaiser of the Naval Research Laboratory offered to measure the surface tension of our water and found severe surface contamination of the Ann Arbor tap water. He suggested that we investigate methods to clean the water in our tow tank water and referred us to the papers of Scott (1975 and 1982). Scott (1975) describes methods to prepare clean water for fluid mechanical experiments with an uncontaminated surface. In the other paper, Scott (1982), experimental measurements are described of the boundary layer flow beneath a contaminated surface in which the convection of surface contaminants is blocked by a barrier which penetrates below the surface. A steady state boundary layer is formed as a result of a balance between viscous shear forces in the viscous flow beneath the surface and the force produced by gradients in the surface tension which are a result of surface active agent concentration gradients in the blocked film of surface active agent. At the leading edge of the contaminated surface, where the surface tension begins to decrease, there is a rapid

variation in height of the surface which appears as an easily observable ridge. The ridge is formed when the upstream flow, with high surface tension, first encounters the contaminated surface which has a considerably lower surface tension. The upstream fluid is rapidly decelerated as a result of the upstream "pull" of the clean oncoming flow with a rapid increase and then decrease in surface elevation.

At this initial stage of the investigation it was apparent that a study of the interaction of vorticity with a free surface would require both experimental measurements of the flow field and numerical computations of the velocity, vorticity and displacement of the fluid particles in the wake flow field. Experimental measurements of the flow field in the wake of the delta wing would require many measurements for a large number of runs in the tow tank facility.

To reduce the time and labor required for the experimental and numerical investigation of the wake flow field, the flow in the wake was approximated by a two-dimensional vortex pair propagating toward and interacting with a free surface. In the experiments the flow field of a laminar vortex pair was produced by a vortex pair generator designed for this investigation. In the numerical computations the time dependent, two-dimensional flow resulting when two line vortices were placed at an initial position beneath the surface was calculated. The line vortices were approximated by two blobs of vorticity, with opposite sign. Both a clean free surface and a free surface contaminated by various known amounts of surface active agents were studied in the experiments and in the numerical computations.

In the paper we first present a description of the flow visualization experiments and the quantitative measurements that we have made which serve to outline many fundamental aspects of the problem. This is followed by a description of the numerical computations for vortex blobs interacting with clean and contaminated free surfaces at low Froude and Reynolds numbers. The numerical computations allow the study, at little cost in time and labor, of the effect of many different parameters on the flow variables during the interaction of vorticity with the free surface.

## EXPERIMENTS

### 1) Vortex pair Generation

The vortex pair generator used for the experiments was designed to produce a two-dimensional pair of counter rotating vortices that propagate upward toward the free surface. A pair of initially vertical flaps, see Figure 2, which were driven by a computer controlled stepping motor were rotated toward each other to produce a pair of vortices without any measurable effect on the free surface caused by the flap motion. The velocity induced by the vorticity in the vortex pair causes the pair to propagate upwards as the flaps close. The flow field produced by the flaps was found to be uniform along the span. This vortex generation scheme also produced little interference between the flaps and the newly formed vortex pair. As the vortices form, the inward rotation of the flaps allows the vorticity to roll up and entrain additional fluid as required for the formation of the Kelvin oval associated with the vortex pair. The Kelvin oval is the oval region bounded by a closed streamline around the vortex pair which can be observed in frame of reference moving with the vortex pair. The triangle formed by the flaps after they are closed had an apex angle of less than  $74^\circ$ . See Hirs (1990) for further information on the

vortex pair generator.

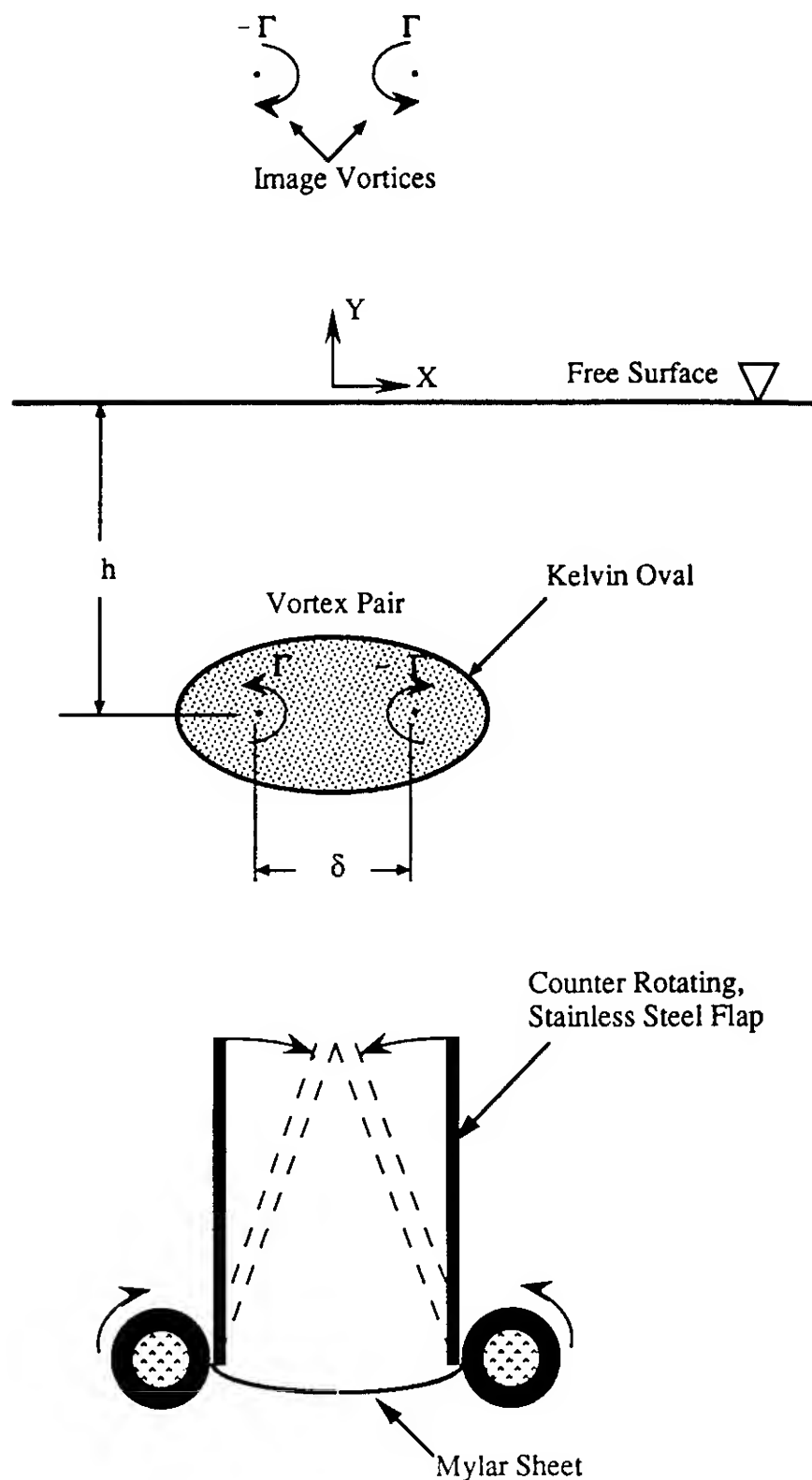


Figure 2 Schematic of the vortex pair approaching a free surface.

The dimensions of the vortex pair generator were chosen so that the vortex pair would have a Reynolds number,  $Re$ , and Froude number,  $Fr$ , matching the vortex pair produced in the wake of the delta wing. The Reynolds number of the vortex pair is defined by:

$$Re \equiv \frac{\Gamma}{\nu} \quad (1)$$

where  $\Gamma$  is the circulation about one of the vortices and  $\nu$  is the kinematic viscosity. The Froude number of the vortex pair is defined by:

$$Fr \equiv \frac{\Gamma}{\sqrt{g \delta_0^3}} \quad (2)$$

where  $g$  is the gravitational acceleration and  $\delta_0$  is the vortex pair separation when the vortices are far beneath the surface.

## 2) Flow Field of the Vortex Pair

Observations, using laser induced fluorescence (LIF), of a cross-section of the flow field when vortex pairs interact with the free surface were made for a number of different strength vortex pairs generated with the flaps and for various degrees of surface contamination. The dye used was fluorescein which was injected with a syringe fitted with a slender plastic tube into the water between and around the flaps before flap motion was initiated. The laser light sheet was less than 1 mm thick and illuminated the flow field above the flaps from one side, see Hirs (1990) for further information.

As described in the introduction, our initial measurements with the delta wing and a contaminated surface demonstrated conclusively that the motion of the surface was inhibited if the surface was contaminated. During the experiments with the vortex pair generated with the flaps the free surface with an area of approximately one half square meter above the vortex generator was cleaned for at least one hour by means of a drain pipe and a fan blowing air toward the drain prior to the first experiment each day. After each vortex pair was generated, the free surface was cleaned first for a minimum of 5 minutes by surface draining with the fan on, then the fan was turned off and the surface drain was continued for at least another 5 minutes. The surface drain was then stopped and the free surface was undisturbed for a minimum of 5 minutes to allow the surface currents to completely decay before the next run.

To illustrate the typical flow phenomena observed for low Froude number vortex pairs of various strengths a set of (LIF) photographs of a the flow produced for a typical vortex pair ( $Re=12,400$  and  $Fr=0.217$ ) interacting with the free surface with and without surfactant added on the surface is shown in Figure 3. The photographs on the left, labeled (A), are for a relatively clean free surface with no oleyl alcohol added. The photographs on the right, labeled (B), are for an initially clean free surface with  $1.06 \times 10^{-7} \text{ (cm}^3/\text{cm}^2\text{)}$  of oleyl alcohol spread on the surface before the vortex pairs were generated. Hirs (1990) contains a complete description of the method used to determine the surface concentration of the oleyl alcohol. From the concentration and using the state relationship for oleyl alcohol, see Hirs (1990) Figure 4.5, the initial surface pressure  $\pi \equiv \sigma_0 - \sigma$  (the difference between the surface tension,  $\sigma_0$ , of the clean and the surface tension,  $\sigma$ , of the contaminated free surface was approximately 2.5 dynes/cm).

For the vortex pairs shown in Figure 3, the tips of the flaps (when vertical) were at a depth of 21 (cm). The average velocity and spacing of the vortices when the pairs were well below the surface was  $v_{p0} = 2.36$  (cm/sec) and  $\delta_0 = 6.93$  (cm/sec). A dimensionless time  $\tau^*$  was defined as:

$$\tau^* = \frac{t - t_1}{\delta_0 / v_{p0}} \quad (3)$$

where  $t$  is the time since the start of the flap motion and,  $t_1 = 7.55$  (sec), is the time elapsed from the start of the



flap motion until the time the vortices are at a depth equal to the vortex pair separation after roll-up. Thus,  $\delta_0 / v_{p0}$ , is the time it takes the vortex pair to propagate a distance equal to their separation, when they are far from the free surface. The circulation,  $\Gamma$ , and the Froude number,  $Fr$ , for the vortex pairs produced in the experiments was estimated using an inviscid point vortex model. The model treats each of the vortices as a point vortex and consists of two point vortices and the two image vortices associated with the original vortices when they are in the proximity of a free surface. Lamb (1932) describes the trajectory of a vortex pair approaching a flat wall in inviscid fluid. Using the trajectory equations and observations of the position, spacing and velocity of the vortex pairs, the apparent circulation of the vortex pairs was estimated. This is equivalent to assuming an inviscid vortex pair with  $Fr=0$ , approaching a free surface.

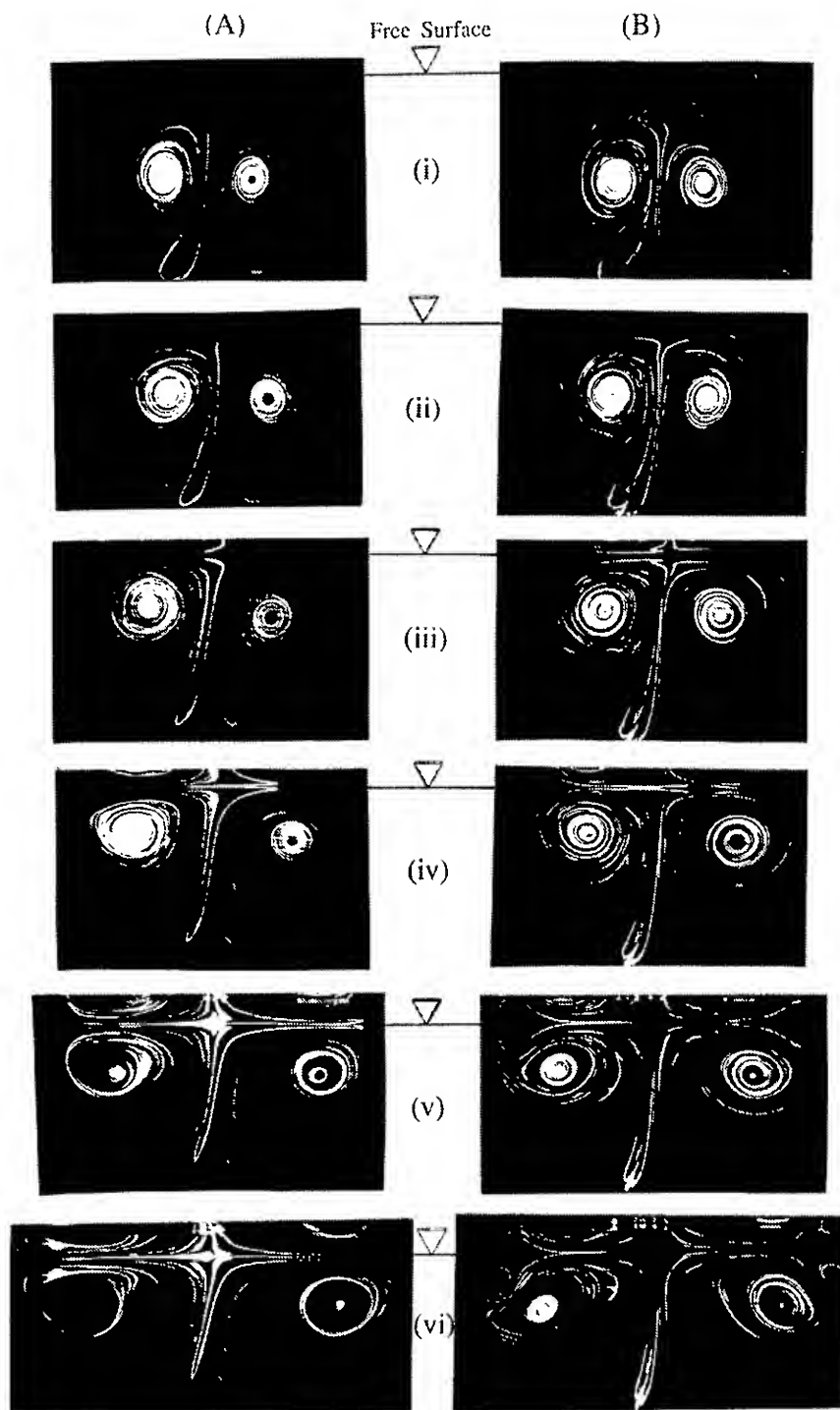


Figure 3 LIF photograph of a vortex pair interacting with a free surface with: (A) no surfactant added & (B) with oleyl alcohol added with surface pressure of 2.5 (dynes/cm); initial vortex pair separation  $\delta_0=6.93$  (cm) and propagation speed  $v_{p0}=2.36$  (cm/sec),  $Re=12,400$  and  $Fr=0.217$  (scale: 1 cm on the photograph = 8.4 cm in the flow field). The dimensionless times are: (i)  $\tau^* = 0.59$ , (ii)  $\tau^* = 0.93$ , (iii)  $\tau^* = 1.27$ , (iv)  $\tau^* = 1.61$ , (v)  $\tau^* = 1.95$ , and (vi)  $\tau^* = 2.29$ .

Figure 3 (i) shows the vortex pair approaching the free surface. The dimensionless time  $\tau^*$  is 0.59. The vortices have started to move apart and no difference is apparent between the case without oleyl alcohol (A), and the case with oleyl alcohol (B). The subsequent photographs, (ii) to (vi), show the vortex pair at equal  $\tau^*$  intervals of 0.34. The mirror image that appears on the upper portion of each photograph is due to total internal reflection at the free surface. Location of the free surface was determined in each photograph by drawing a bisector through the symmetrical image.

There is little visible difference in the flow field between the case (A), and case (B) up to the time  $\tau^*=1.61$ . At  $\tau^*=1.61$ , Figure 3 (iv) shows a marked difference between the two cases. In the case where oleyl alcohol is added, the streamlines near the free surface appear to diverge from the free surface whereas in the case with no oleyl alcohol the streamlines near the free surface stay close to the surface. By  $\tau^*=1.95$ , Figure 3 (v) shows that a secondary vortex is being formed for the case (B), but in case (A) no secondary vorticity is formed. In the last Figure 3 (vi), a pair of secondary vortices are visible in the case (B) with oleyl alcohol which drastically alter the path of the primary vortices as they begin to rebound from the free surface. The case without oleyl alcohol shows no sign of secondary vorticity formation or rebounding of the primary vortices.

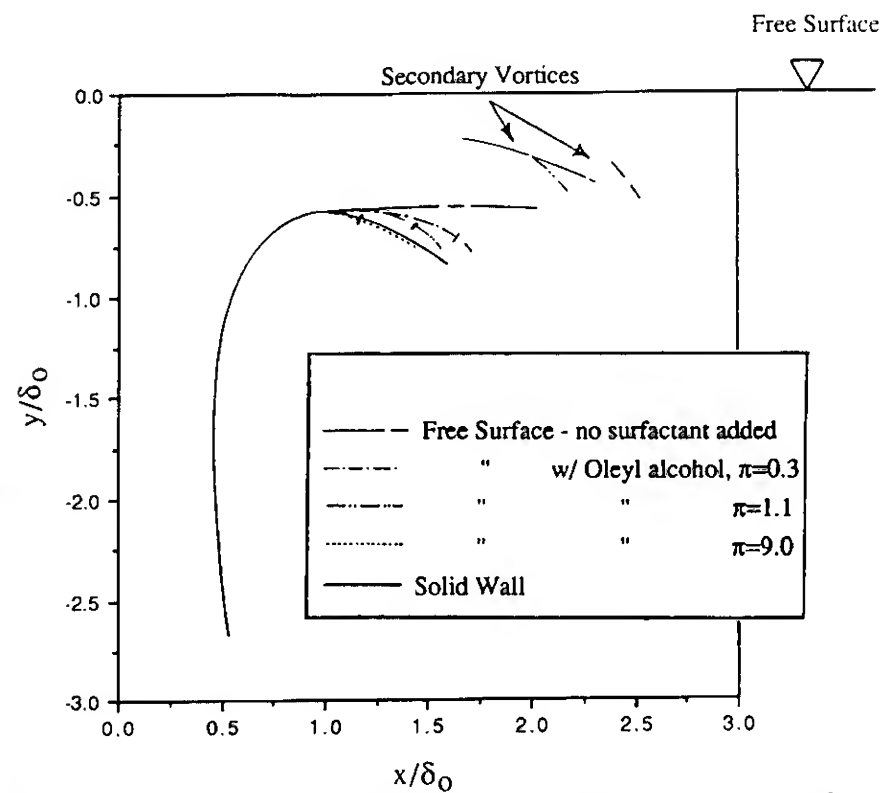


Figure 4 Average trajectory of the apparent center of the (right) vortex during the interaction of the vortex pair with a solid wall and a free surface with various amounts of oleyl alcohol whose surface pressure is denoted by  $\pi$ .  $Re=12,400$  and  $Fr=0.217$ . A tick mark on the primary vortex trajectory indicates the position of the primary vortex at the beginning of the secondary vortex trajectory. The time at the beginning and the end of each primary and secondary vortex trajectory is as follows:

no surfactant;  $-1.55 \leq \tau^* \leq 2.19$ , not formed:  
 $\pi = 0.3$ ;  $-1.55 \leq \tau^* \leq 2.19$ ,  $1.85 \leq \tau^* \leq 2.19$ :  
 $\pi = 1.1$ ;  $-1.55 \leq \tau^* \leq 1.85$ ,  $1.51 \leq \tau^* \leq 1.85$ :  
 $\pi = 9.0$ ;  $-1.55 \leq \tau^* \leq 1.51$ , Turbulent:  
Solid Wall,  $-1.55 \leq \tau^* \leq 1.85$ ;  $1.17 \leq \tau^* \leq 1.85$ .



### 3) Vortex Pair Trajectories

Figure 4 shows the trajectories of the apparent center of the right vortex for various surface conditions for vortex pairs with,  $Re=12,400$  and  $Fr=0.217$ . Also plotted, are the apparent center of the secondary vortex which is produced outboard of the right vortex. The five primary vortex trajectories overlap in the beginning, but diverge at later times during the interaction. The primary vortex trajectories all begin at  $\tau^* = -1.55$ . The time at the end of each primary vortex trajectory is given in the caption along with the time at the beginning and the end of secondary vortex trajectories. The secondary vortex for the case with the largest surface pressure, 9.0 (dynes/cm), rapidly became turbulent and no distinct vortex center could be observed. A tick mark on each of the primary vortex trajectories indicates the position of the primary vortex at the time of formation of the secondary vortex. Turbulence in the primary vortex was first observed at time,  $\tau^* = 2.19 (\pm 0.24)$  for all the surface conditions tested.

The trajectories plotted in Figure 4 show that when oleyl alcohol is present on the free surface, the trajectory of the primary vortex departs from the trajectory for the case with no surfactant. From these trajectories it is apparent that the greater the surface pressure, the greater the amount of rebounding of the primary vortex from the free surface. When the surface pressure is as high as 9.0 (dynes/cm), the vortex trajectory is very similar to that for vortex interaction with a solid wall.

### 4) Particle Image Velocimetry Measurements

In order to provide quantitative data for the phenomena observed and results obtained using flow visualization the entire velocity field in the cross section was measured for a vortex pair at  $Re=12,400$  and  $Fr=0.217$  using a particle image velocimetry (PIV) technique. The method we used is one of the variations of double-pulse velocimetry used in the past fifteen years, as described in Stetson (1975), Lauterborn and Vogel (1984), and Dudderar et al. (1986). From a double-exposed transparent photograph of a seeded flow, the velocity at each point in the flow is deduced by measuring the displacement of the seeding particles during the time between two exposures. In the present study, a pulsed copper vapor laser was used to illuminate a thin cross-section of the vortex pair flow field. The Young's fringe method was chosen to determine the particle displacements and direction of displacement. The magnitude of the velocity was determined from the displacement divided by the time between the two exposures. The flow direction was obtained by inspection of the velocity magnitude data. The system and method we used to interrogate double exposure photographs of the particle images was developed by L. P. Bernal and is described by Kwon (1989). This system consists of a Helium-Neon laser, a set of mirrors, a transform lens, a beam stopper, a video camera with a pair of imaging lenses and a Gould model FD 5000 image analysis system controlled by a Zeos model 286 personal computer. Some time was spent learning how to seed the flow. After a number of trials the seeding particles selected for PIV measurements were 12 to 50 microns particles of titanium dioxide in the rutile crystalline form and 50 to 100 micron diameter micro-balloons. Micro-balloons are hollow glass bubbles with specific gravity of less than one which tend to migrate inward toward the

core of the vortices while the much heavier titanium dioxide particles migrate away from the vortex core. The fluid in the vicinity of the flaps was seeded with both glass micro-balloons and titanium dioxide particles and titanium dioxide particles were also continuously deposited on the free surface.

Figure 5 shows the velocity vector field of the vortex pair for  $Re=12,400$  and  $Fr=0.217$  as it approaches a clean surface at time  $\tau^* = 0.49$ .

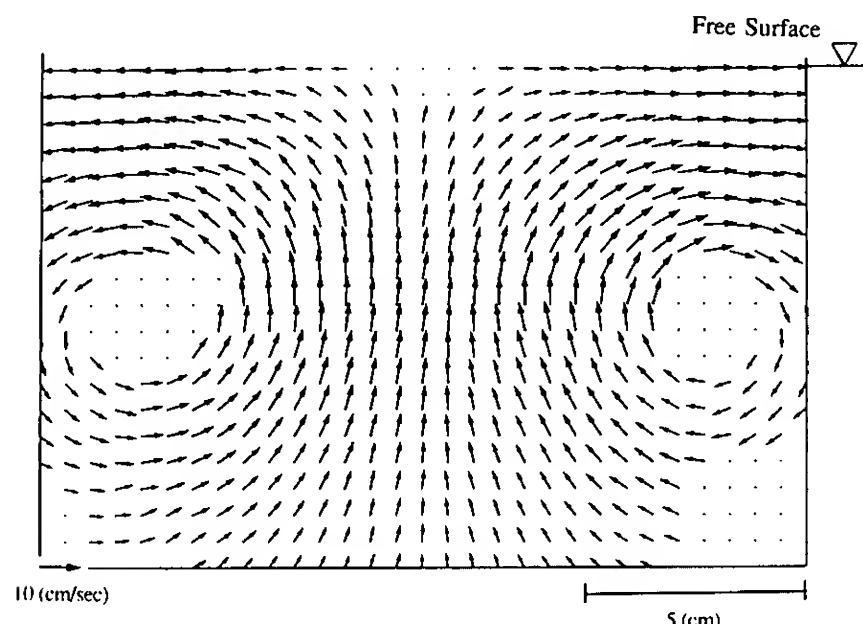


Figure 5 Vortex pair velocity field during the interaction with a free surface with no surfactant added;  $\tau^* = 0.49$ ,  $Re=12,400$  and  $Fr=0.217$ .

The non-zero velocities on the top of the figure show that the free surface is adequately clean and free to move. The lack of data near the center of the vortices is primarily due to the limits in the spatial resolution of the interrogation system. Inadequate seeding is responsible for the missing data near the lower part of the figure. The dynamic range of the interrogation system limits the lowest velocity that could be measured. The flow on the plane of symmetry at the free surface resembles a stagnation region of very low velocity. As a result, the spacing between the Young's fringes is too large to measure. PIV images at later times with a clean surface were also obtained and there was no sign of the development of secondary vorticity near the free surface.

From the PIV data the contours of constant vorticity in the primary vortices were determined. The circulation for each side of the vortex pair was also calculated using a line integral around a square contour surrounding the vortex core. The magnitude of circulation for each vortex was found to be 145.9 ( $\text{cm}^2/\text{sec}$ ). A few of the vorticity contour lines extended outside the domain of the calculation. This implies that the total circulation for each vortex is slightly more than the 145.9 ( $\text{cm}^2/\text{sec}$ ) measured. In contrast, the apparent circulation, i.e. the circulation based on the measured propagation speed and spacing of the vortex pair and using a point vortex model, was found to be 124 ( $\text{cm}^2/\text{sec}$ ).

In marked contrast to the flow with a clean free surface, Figure 6 shows the velocity vector field of the left primary vortex and the secondary vortex developed outboard of the left primary vortex at a time  $\tau^* = 1.54$ , when the free surface is contaminated with oleyl alcohol with a surface pressure of 9.0 (dynes/cm).

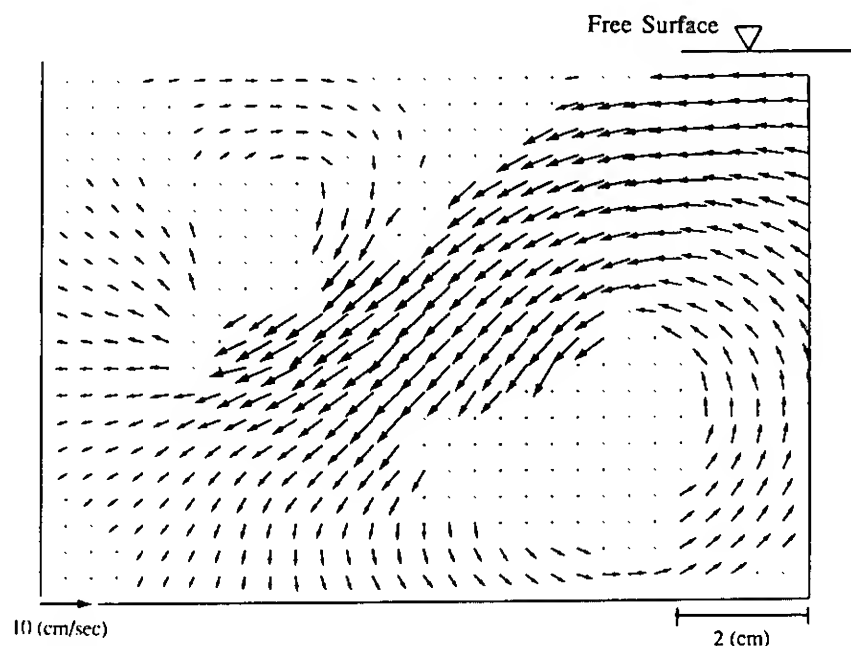


Figure 6 Velocity field for the left vortex interacting with a free surface with oleyl alcohol with  $\pi=9.0$  (dynes/cm); the right edge of the figure is 7.7 (cm, actual) from the centerline;  $\tau^*=1.54$ ,  $Re=12,400$  and  $Fr=0.217$ .

The circulation around the secondary vortices in this PIV vector plot was calculated and found to be approximately  $-45 \text{ (cm}^2\text{/sec)}$ , opposite to and approximately 30% of the circulation in the primary vortex. This clearly illustrates the fact that surface contamination can lead to the generation of new vorticity during interaction of vorticity with the free surface.

#### 5) Free Surface Signatures of a Vortex Pair

The Froude number for the vortex pairs in these experiments was not large enough to cause appreciable wave generation when the vortex pairs interact with the free surface. However, a variety of slight surface deformations were observed that were associated with the velocity and pressure field of the primary, secondary and any other vorticity produced by the vortex pair. These surface deformations were visually observed using the shadowgraph method. The shadowgraph system used in the experiments with the vortex pair generator was very simple, a mercury vapor light source beneath the glass bottom tank containing the vortex pair generator and a white cloth screen 6 X 2 feet mounted 3 feet above the free surface. The image on the screen was recorded on video tape using the video camera and recorder. The shadowgraph effect is a result of the refraction of light by the free surface. When an approximately parallel beam of light passes upward from water to air normal to the surface, a depression of the surface will result in the light rays diverging and an upward displacement of the free surface will cause the light rays to converge. The screen placed above the free surface will then show surface depressions as darker regions and elevations of surface as brighter regions.

The vortex pair with  $Re=18,700$  and  $Fr=0.277$  produced a surface signature which from our observations of the signatures of various strength vortex pairs (at low Froude number) contains the typical phenomena observed with weaker and stronger vortex pairs before transition to turbulent flow occurs. The surface signature for the right half of a clean surface above a vortex pair is shown in Figure 7.

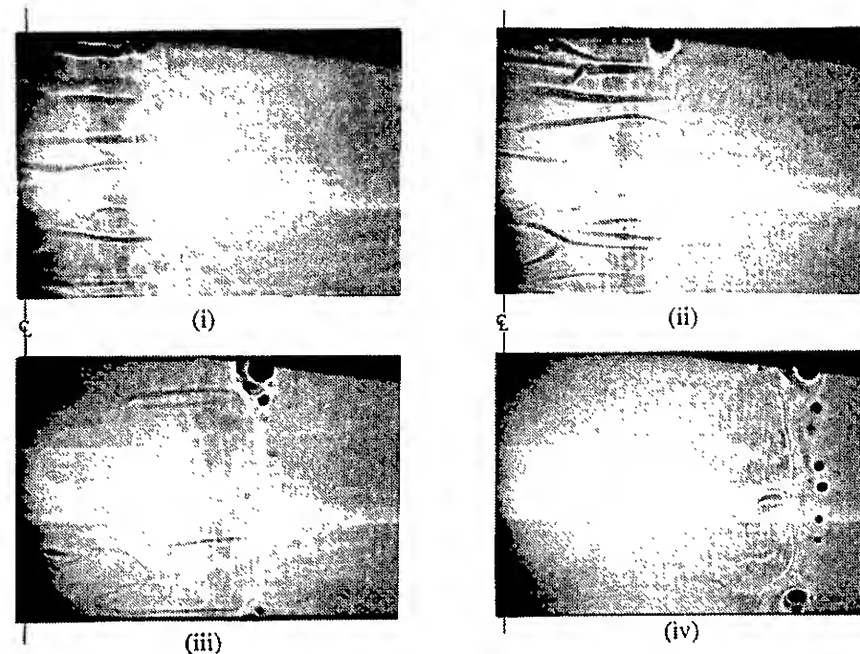


Figure 7 Shadowgraph view (of the right half) of the free surface during the interaction of a vortex pair with a free surface with no surfactant added;  $Re=18,700$  and  $Fr=0.277$  (scale: 1 cm on the photograph = 10.0 cm on the surface).

The first observable features are the striations that were first described by Sarpkaya and Henderson (1985). Using LIF and other techniques to observe the flow beneath the surface we have determined that the striations are caused by spanwise vorticity which is stretched in the upwelling flow field of the primary vortex pair, see Hirs (1990). A paper describing and summarizing these observations of the flow field of the striations is in preparation. The first photograph in Figure 7, (i), is at time  $\tau^*=0.79$ . The striations, observed to produce narrow dark strips of surface depression, are clearly visible in this photograph. A surface depression which is wider than and normal to the striation depressions can be observed directly above the right hand primary vortex. Just outboard of this depression the initial formation of a Reynolds ridge can be observed (an undulating, narrow, line bright on the left and dark on the right) which becomes stronger in the following photographs, (ii) through (iv). The photograph (ii), taken at  $\tau^*=1.16$ , shows the striations and the Reynolds ridge as well as a surface dimple, a dark region at the top of the photograph. This dimple is caused by a vortex line terminating at the free surface. A similar dimple occurred on the bottom but does not appear in this photograph. The vortex induced at the end wall (see Yamada and Honda 1989) is thought to be responsible for this phenomenon. The third photograph (iii), taken at  $\tau^*=1.90$ , shows that the Reynolds ridge has been convected to the right. A few striations are still visible in this photograph. Adjacent to the large dimple near the top of the photograph, a series of smaller dimples appear in this picture. The last photograph (iv), shows the Reynolds ridge which by this time has moved very much to the right. The photograph was taken at  $\tau^*=2.63$ . There are some last remnants of the striations visible to the left of the Reynolds ridge. The dimples are more numerous by this time. It should be noted that the small dimples all appear on the outboard, i.e. on the contaminated side of the Reynolds ridge.

The surface deformations on the right side of the same vortex pair formed when a small amount of oleyl alcohol, surface pressure of 0.3 (dynes/cm), is present on the free surface are shown in Figure 8.

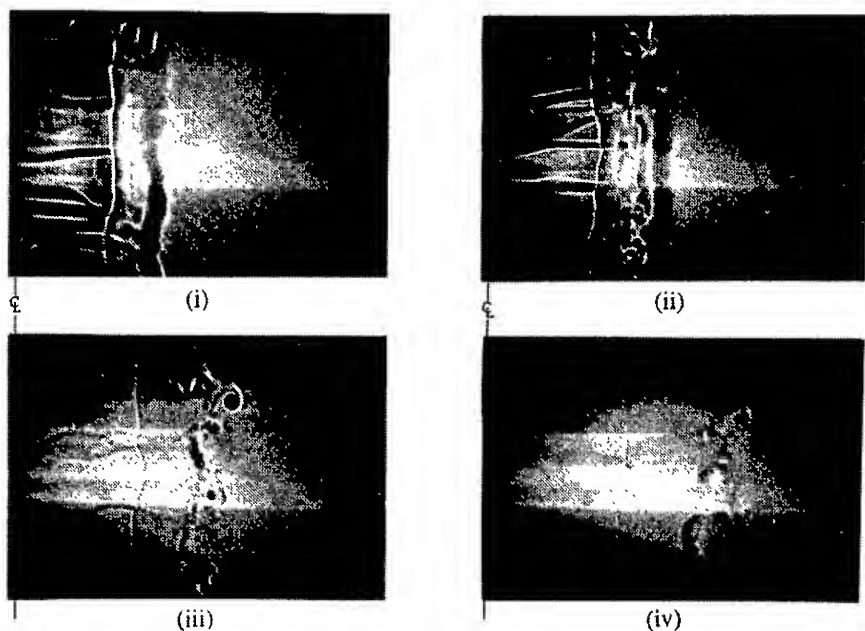


Figure 8 Shadowgraph view (of the right half) of the free surface during the interaction of a vortex pair with a free surface with oleyl alcohol with  $\pi=0.3$  (dynes/cm);  $Re=18,700$  and  $Fr=0.277$  (scale: 1 cm on the photograph = 10.0 cm on the surface).

The first photograph, (i), at  $\tau^*=0.79$ , shows the striations, an intense, narrow bright and dark wavy line, the Reynolds ridge, and two wide depressions (which will be referred to as scars) parallel to the Reynolds ridge and to the primary vortex. The weaker depression is formed to the left of the Reynolds ridge (above the primary vortex) and a stronger one just to the right of the Reynolds ridge (above the secondary vortex). The next photograph, (ii), at  $\tau^*=1.16$ , shows that the Reynolds ridge has moved slightly to the right. The striations are still visible in this photograph. A series of surface deformations, primarily depressions, are visible between the two scars. The next photograph, (iii), shows the effect of three-dimensional structures along with vortex lines terminating at the free surface (dimples) to the right outboard) of the Reynolds ridge. The last photograph, (iv), at  $\tau^*=2.63$  again shows the surface signatures of the three-dimensional structures which have been onvected to the right. The Reynolds ridge, which did not move very much since the last photograph appears to be less intense at this time.

Figure 9 is for the same vortex pair ( $Re=18,700$  and  $Fr=0.277$ ) as the previous two figures but with a higher concentration of oleyl alcohol. For this case, enough oleyl alcohol was spread on the surface to saturate it so that the surface pressure was equal to the saturation pressure which for oleyl alcohol is approximately 31.5 (dynes/cm). The striations and the scars are visible in this photograph. The photograph shows that no Reynolds ridge is formed. The scar above the secondary vortex observed out board of the primary vortex is more intense than the previous cases.

## NUMERICAL COMPUTATIONS

### 1) Problem Formulation and Numerical Method

The flow is assumed to be viscous, and confined to two dimensions. In addition to the assumption of two-dimensionality, the major limitation is that the free surface is assumed to remain flat for all times. This limits the results presented here to relatively low Froude numbers. However, these are the cases most frequently

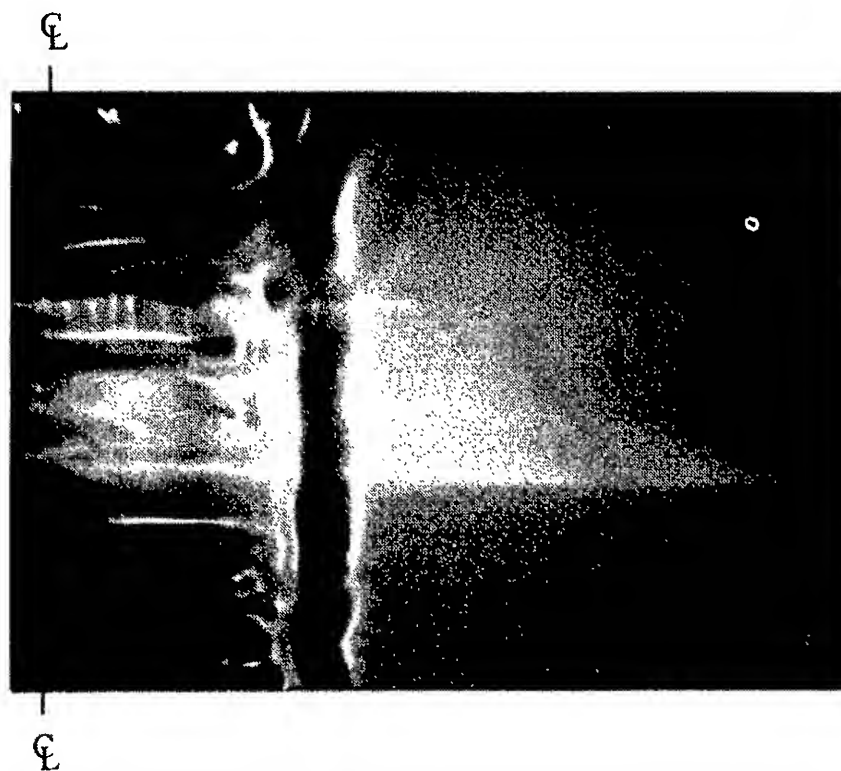


Figure 9 Shadowgraph view of the free surface showing the scar during the interaction of a vortex pair with the free surface with  $\pi=31$  (dynes/cm);  $\tau^*=0.79$ ,  $\Gamma=187$  ( $\text{cm}^2/\text{sec}$ ) ( $Re=18,700$ ),  $Fr=0.277$ ; (scale: 1 cm on the photograph = 4.0 cm on the surface).

studied experimentally, and since the surface deformations are observed to be small the limitation is not as severe as might be thought. In order to avoid any arbitrary modeling of inflow and outflow boundaries we simply take the flow domain to be periodic in the horizontal direction, and to have a flat full slip bottom. The effects of this limited domain size is discussed below in section 2). The flow is governed by the Navier-Stokes equation, which in vorticity form can be written,

$$\partial\omega/\partial t + J(\psi, \omega) = \frac{1}{Re} \nabla^2(\omega) \quad (4)$$

where  $J(\psi, \omega) = (\partial\psi/\partial y)(\partial\omega/\partial x) - (\partial\psi/\partial x)(\partial\omega/\partial y)$ , and a Poisson equation relating the stream function to the vorticity

$$\nabla^2(\psi) = -\omega \quad (5)$$

Here the Reynolds number is defined as  $Re = \Gamma/\nu$ .

The free surface boundary condition is very important for the present investigation. Surface contaminants are known to have an effect on the motion of vortices. In a previous investigation Davies (1966) described the damping of turbulent eddies at a free surface and later Davies and Driscoll (1974) experimented with ejecting pulses of colored water towards a free surface, specifically addressing the rate of surface renewal and they found that the spreading of colored water at the free surface is reduced considerably for contaminated surfaces. Their simple visualization technique did not allow a clear explanation of the mechanism responsible for this behavior. The explanation for rebounding from a free surface is clear from recent experiments of Bernal et. al. (1989) who investigated collision of both vortex rings and two-dimensional vortex pairs with a free surface. They observed (as did Davies and Driscoll) that surface contamination led to considerable differences in the vortex motion itself. Using LIF for flow visualization they found that the surface motion induced by vorticity



approaching a contaminated free surface generated an uneven distribution of surface contaminant that in turn caused a shear stress at the surface, thereby generating vorticity with sign opposite to the initial vorticity. The generation of vorticity at a contaminated surface appears to be a primary effect of the surface contaminants since for contaminated surfaces the behavior is similar to vortices encountering a rigid wall.

For the numerical computations the boundary condition at the surface requires knowledge of the surface contaminant which is assumed to be conserved, leading to a hyperbolic conservation equation

$$\partial c / \partial t + \partial (u_s c) / \partial x = 0 \quad (6)$$

Here  $u_s$  is the horizontal velocity at the surface. Notice that since the surface divergence of  $u_s$  is in general not zero and depends on  $c$ , this equation allows for the possibility of "contamination shocks" (that is the development of a discontinuity in  $c$ ). The surface contaminant affects the flow field through shear stresses induced by variations in the surface tension. At the free surface, surface tension gradients induce a shear given by

$$\tau = \partial \sigma / \partial x \quad (7)$$

Since the surface is flat the vorticity at the surface is  $\omega_s = \partial u / \partial y$ . The surface tension depends on the amount of contaminant,  $\sigma = \sigma(c)$ , and the boundary conditions for the vorticity, at the surface, is therefore

$$\omega = \mu^{-1} (\partial \sigma / \partial c) \partial c / \partial x \quad (8)$$

The quantity  $\epsilon = c_0 (\partial \sigma / \partial c)$  is usually called the elasticity of the surface. If the contamination,  $c$ , is nondimensionalized by its initial value,  $c_0$ , and the vorticity is as before, we end up with the boundary condition  $\omega_s = C \partial c / \partial x$  in nondimensional units, where

$$C = [L / (\Gamma \mu)] c_0 (\partial \sigma / \partial c) \quad (9)$$

The flow is therefore governed by the parameters  $Re$  and  $C$  as well as the initial vorticity configuration. The dimensionless variables used for the computations were, the dimensionless time  $= t \Gamma / L^2$ , and the dimensionless distances,  $x/L$  and  $y/L$ . Where  $\Gamma$  is the circulation and  $L$  is the half width of the computational box. To solve these equations numerically we have used a rather standard finite difference approximations. Equation (4) is integrated by an explicit second order predictor-corrector method in time, and the spatial discretization is done with second order centered-differences. For the Jacobian,  $J(x,y)$ , Arakawa's conservative stencil is used. The Poisson equation is solved with a fast solver (HWCRT form FISHPACK). For the contaminant we also use a second order predictor corrector in time, and second order differences in space. For stability an artificial viscosity term is added on the right hand side of (6) with viscosity that is small everywhere except where the contaminant value changes rapidly. The surface velocity is found by a one sided, second order differentiation of the stream function. Several of our results have been checked for convergence by repeating the calculation using a different resolution.

## 2) Results and Parameter Studies

Most of our computations have been done for the case of a two dimensional vortex pair colliding head on with the top surface. Since the problem is symmetric about the centerline it is sufficient to calculate only one of the vortices and use symmetry boundary conditions. The central question that we are addressing is how the contaminants on the surface affect the evolution of the vorticity, and how it differs from the case when the free surface is clean. In Figure 10, for  $Re = 2000$ , we show the evolution of the flow produced by two blobs of primary vorticity with opposite sign, with an initial spatial distribution proportional to  $r \exp(-ar^2)$  where  $r$  is the distance from the center of each blob. The boundary conditions on the top surface are, (a) a stress free boundary (also called a full slip boundary) and (b) a contaminated top surface with  $C = 2$ . The right hand vortex is initially half way between the top and bottom boundary, and the first frame is at the time the motion begins. There is no boundary layer for the full slip surface. A slight boundary layer (not visible at the initial time,  $t = t_1$ ) is formed beneath the contaminated surface an instant after the motion begins. In the second frame the upward motion of the vortex has ended, and, due to the image vorticity above the free surface, it is now moving outward. The boundary layer in (b) has grown considerably, and it is clear that separation is about to take place. In the third frame the vortex in (a) continues its outward motion along the full slip boundaries, but in (b) the boundary layer has separated and formed a secondary vortex that deflects the path of the primary vortex away from the surface. This evolution continues in the fourth frame, the vortex in (a) moves out along the wall, but in (b) the primary vortex has moved further away from the wall under the influence of the secondary vortex. At the same time the stronger primary vortex swings the secondary vortex around so it is now almost below the primary one, and thus induces an inward motion. Viscosity now has visible effect on the evolution, the maximum vorticity of both the single vortex in (a), as well as in (b) has decreased compared with the previous frames. In the last frame the vortex in (a) has encountered the outer boundaries of the computational box, and is starting to move downward along the outer wall, and in (b) the primary vortex is actually moving upward again as well as inward. Perhaps the most striking feature of the above sequence is the similarity between the results for the contaminated surface case (b) and results of calculations (not shown in this paper) for the case of a "no slip" rigid wall. The flow field, primary vortex motion and secondary vortex motion for case (b) and the "no slip" wall case are very similar.

The rebounding of the primary vortex for the contaminated top surface in (b) is obviously due to the uneven distribution of the contaminant produced after the motion begins. This distribution is shown in Figure 11, at times corresponding to those in Figure 10. In (a) the contaminant is passive, and is simply advected with the flow and this does not lead to any shear stresses on the fluid at the boundaries, as mentioned above. As the vortex collides with the surface the contaminant is swept outward, depleting the region between and above the vortices of contaminant and accumulating it outward of the vortices. This contaminant peak is then pushed outward. Since the computational box is of finite width, the contaminant eventually reaches large values at the

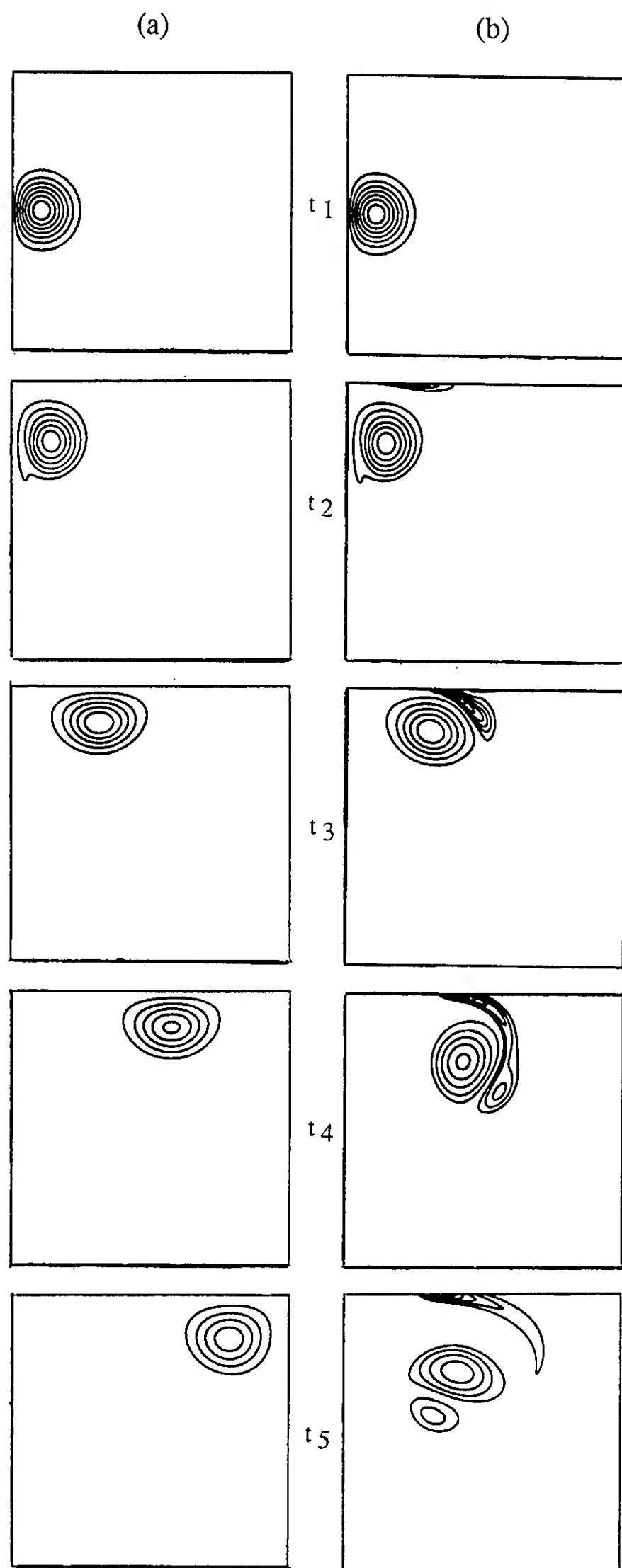


Figure 10 Computational results showing contours of constant vorticity on the right side of a vortex pair approaching the free surface for a clean surface (a),  $C = 0$  and a contaminated surface (b),  $C = 2$ .  $Re = 2000$ . The dimensionless time is zero at the top of the Figure and increases in increments of 0.7 dimensionless time units.

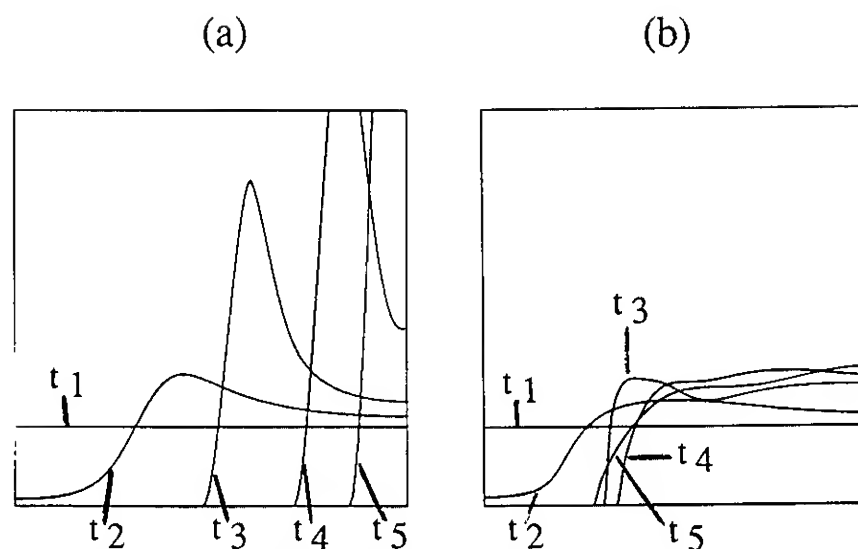


Figure 11 Contamination profiles for the computations shown in Figure 10. Full slip case is (a) and the  $C = 2$  case is (b). The time between the profiles is the same as in Figure 10 and the profiles all become steeper with time except for the last profile for the case  $C = 2$ .

outer side of the box in the down welling region. Although the finite box size obviously has effects on the final profile, the maximum contamination peak increases rapidly even before the side effects become significant, since the outward velocity decreases outboard of the vortex. In the second frame, (b),  $C = 2$ , as in Figure 10. Now the uneven contaminant distribution creates shear stresses on the top surface that opposes the outward motion due to the vortices. This balance---outward motion due to the vortices, and inward motion due to the uneven contaminant distribution---eventually slows down the spreading of the clean region above the vortices. The shear stresses due to the contaminants create vorticity that eventually separates and causes the primary vortex to rebound. As the vortices rebound their effect on the surface diminishes, and the contamination "shock" that separates the clean and contaminated surface starts to move inward again. In Figure 11 at time  $t_5$  the inward motion has just started. The large accumulation of contaminants, seen for the "full slip" case does not take place in the contaminated surface case although the contamination profile behind the shock equilibrates with time. We have made computations for larger values of  $C$  and find that the restoring effect of the contaminants is much stronger. As a result for  $C = 10$ , only a small clean region forms on the surface between the primary vortices. The vortices then move outboard of the shock, and as they pass under and rebound the "hole" closes rapidly. For the case with  $C = 50$  the vortices only cause a small initial dimple in the contamination profile which disappears rapidly as the vortices move outward. Perhaps the most noticeable feature of the contamination profiles is how different they are when compared to the similarity of the vorticity distributions which the contamination has created. Except for the completely stress free boundary a secondary vortex is formed and the primary vortex rebounds, even though in some cases a clean region is formed, and in others the contaminant distribution is hardly changed at all. The only difference in the vorticity distribution is that the boundary layer at the top starts further away from the center when a clean region is formed.

The above runs have all been done in a relatively small computational domain. To assess the influence of the boundaries on the evolution we have repeated one of



the runs with,  $C = 2$ , in a domain that is twice as wide. The vorticity distribution appeared almost identical, and only for the latest times were there any significant differences in the contamination profiles. The primary difference was that the value of the contamination concentration was slightly higher behind the shock for the shorter box, and as a result the shock moved slightly faster to close the hole in the contamination profile after the vortices had rebounded. We therefore feel rather confident that boundary effects are of minimal significance.

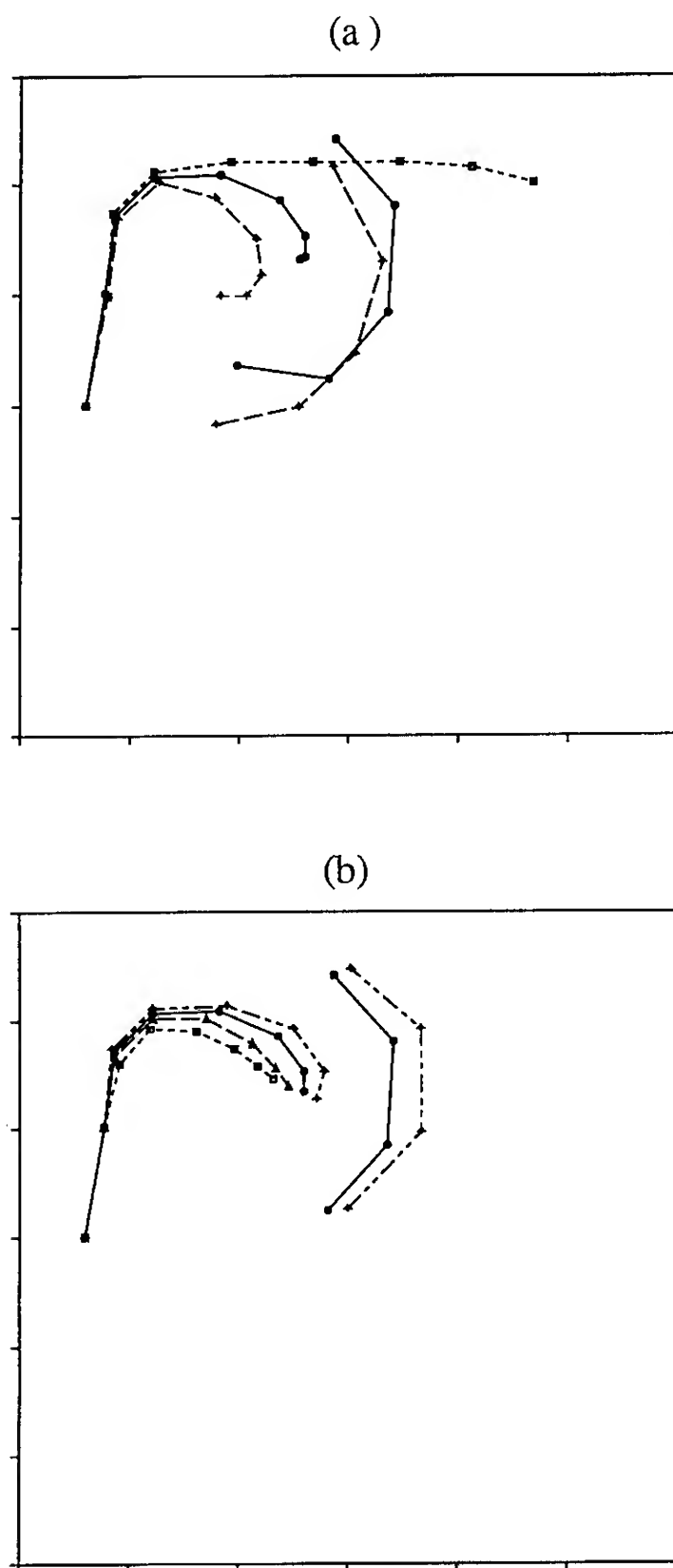


Figure 12 The paths of the primary and secondary vortices. In (a), the full slip case with no secondary vortex is a dotted line, the solid line is for  $C = 2$  and the dashed line is the solid wall case. The two large radius curves are the secondary vortex paths. In (b), the primary and secondary vortex paths for increasing Reynolds numbers of 500, 1000, 2000, & 4000 are shown for contaminated surface with,  $C = 2$ . There are no secondary vortices for  $Re = 500$  and 1000. For  $Re = 2000$  and 4000 the secondary vortex paths have a large radius of curvature as the Reynolds number increases.

To efficiently display the similarities and differences in the flow fields caused by the surface boundary condition and/or Reynolds number, we plot in Figure 12 (a), the path of the primary vortices and secondary vortices, at  $Re = 2000$ , for the no-stress case, for a contaminated surface with  $C = 2$  and for the rigid boundary case. For the no-stress case there is no secondary vortex and no rebounding. The slight downturn in the primary vortex trajectory is caused by the proximity of the right hand boundary. For the contaminated surface and for the rigid wall there is a secondary vortex and there is rebounding of the primary vortex.

In Figure 12 (b) the paths of the primary and secondary vortices are shown for a contaminated surface with  $C = 2$  at various Reynolds numbers of 500, 1000, 2000, and 4000. At the higher Reynolds numbers the diffusion of vorticity is less rapid in comparison to convection. This results in greater outboard motion of the primary and secondary vortices as the Reynolds number increases.

## CONCLUSIONS

- Experiments and numerical computations for vorticity interaction with a free surface show good qualitative agreement.
- Surface contamination, in the experiments and computations, was found to have a strong influence on the nature of the interaction of the vortex pair (or the trailing vortices) in both the surface deformations and the flow field below the surface.
- During interaction of a vortex pair (or trailing vortices) with a contaminated free surface, shear stress produced at the free surface causes the production of vorticity. This vorticity can roll-up into a pair of secondary vortices with sign opposite to the adjacent primary vortex. This alters the trajectory of the original vortices.
- A Reynolds ridge is formed as a result of the interaction of vortex pair (or the trailing vortices) with a slightly contaminated free surface.
- The strong scar (surface depression) was found to be caused by secondary vortices formed when a surfactant was present on the surface.
- The circulation of the secondary vortex produced as a result of the vortex pair interacting with a free surface with surfactant was found to be about one third of the circulation of the primary vortex.

## REFERENCES

- Davies, J. T., 1966 The effect of surface films in damping eddies at a free surface of a turbulent liquid. *Proc. Royal Soc. London A* **290**, 515-526.
- Davies, J. T. & Driscoll, J. P., 1974 Eddies at free surfaces, simulated by pulses of water. *Industrial and Engr. Chemistry Fundamentals* **13**, 105-109.

Dudderar, T. D., Meynart, R., & Simpkins, P. G., 1986 Laser speckle velocimetry. *The Tenth U. S. National Congress of Appl. Mech.*, The Univ. of Texas at Austin.

Hirsa, A., 1990 An Experimental Investigation of Vortex Pair Interaction with a Clean or Contaminated Free Surface. PhD. Thesis, *Dept. of Aerospace Engr. The University of Michigan*.

Kwon, J. T., 1989 Experimental study of vortex ring interaction with a free surface. PhD. Thesis, *Dept. of Aerospace Engr. The University of Michigan*.

Lamb, H., 1932 *Hydrodynamics* 6th ed. Cambridge University Press.

Lauterborn, W., & Vogel, A., 1984 Modern optical techniques in fluid mechanics. *Ann. Rev. Fluid Mech.*, **16**, 223-244.

Sarpkaya, T. & Henderson Jr., D. O., 1985 Free surface scars and striations due to trailing vortices generated by a submerged lifting surface. AIAA paper no. 85-0445, *AIAA 23rd Aerospace sciences meeting*, Jan. '85 Reno, Nevada.

Scott, J. C., 1982 Flow beneath a stagnant film on water: the Reynolds Ridge. *J. Fluid Mech.* **116**, 283-296.

Scott, J. C., 1975 The preparation of water for surface clean fluid mechanics. *J. Fluid Mech.* **69** pt. 2, 339-351.

Stetson, K. A., 1975 A review of speckle photography and interferometry. *Optical Engr.* **14** (5), 482-489.

Willmarth, W. W., Tryggvason, G., Hirsa, A., & Yu, D., 1989 Vortex pair generation and interaction with a free surface. *Phys. Fluids A* **1** (2), 170-172.

Yamada, H. & Honda, Y., 1989 Wall vortex induced by and moving with a confined vortex pair. *Phys. Fluids A* **1** (7), 1280-1282.

## DISCUSSION

Targut Sarpkaya  
Naval Postgraduate School, USA

Contrary to authors' arguments, contamination does not change the physics of the phenomena. Authors' use of low speeds and scales in their model overly accentuated the effect of surface tension and hence the Weber number. They could have minimized the said effects at relatively larger Froude numbers and thereby gained a clearer understanding of the physics of the phenomenon. As I have shown in my papers, variations in contamination at higher Froude numbers (relatively lower numbers) did not alter the fundamental character of the scars and striations. In ocean environments, the vortex motion and the turbulent wake is such that the relative significance of Weber number is not exaggerated.

## AUTHORS' REPLY

In the near-wake of large, high speed ships, it is possible to encounter very energetic, high Froude number vortices which try to "leap out" of the surface. For such high Froude number vortices, it is true that the effect of surface contamination might not be as great as it is for vortices with lower Froude number. On the other hand, in the far-wake of ships, which are observed in the SAR images, the turbulence is decaying and the Froude number for the eddies is relatively small and therefore surface contamination plays an important role in the interaction of the eddies with the free surface.

## DISCUSSION

Hyong-Tae Kim  
The University of Iowa, USA (Korea)

1. Besides the secondary vortices identified in your measurement of the velocity for the case of the contaminated surface, could you really resolve the free-surface boundary layer in the measurement?
2. Could you tell how this vortex pair model is related with the persistent trace on the ocean surface of the ship wake?

## AUTHORS' REPLY

1. The measurements which we made using PIV do not resolve the velocity within the free surface boundary layer. For that information we have to rely on our results from full Navier-Stokes simulations. Information on the finer scales of flow obtained from the computations should be reliable since the agreement on large scale comparisons to the laboratory measurements is very good and the flow is relatively laminar.

2. Although there are vortex pair-like structures in the wake of ships (e.g., bilge vortices and propeller vortices), an exact comparison between the vortex pair flow and the actual ship wake is not possible and in fact is not intended. The vortex pair offers a simple flow which can be studied in order to provide insight into the nonlinear ship wake problem. For example, the mass transport to the surface by a vortex pair and the important effects of surface contamination on this transport process shows the role surfactants can play in the wake of a ship in the ocean.

# Hydrodynamics of Ship Wake Surfactant Films

R. Peltzer<sup>1</sup>, J.H. Milgram<sup>2</sup>, R. Skop<sup>3</sup>, J. Kaiser<sup>1</sup>, O. Griffin<sup>1</sup>, W. Barger<sup>1</sup>

(<sup>1</sup>Naval Research Laboratory, USA)

(<sup>2</sup>Massachusetts Institute of Technology, USA)

(<sup>3</sup>University of Miami, USA)

## ABSTRACT

When compacted at the free-surface, surface-active materials have very strong wave damping properties. Careful measurements are required to characterize these physical effects. Prior to a Field Experiment in January 1989, we refined the spreading oil technique, developed by Adam in 1937 to characterize the physical properties of a surfactant film, so as to provide the necessary spatial resolution to identify fine structure in the surface tension gradients on the surface generated by the passage of a ship. We present an in-depth look at the measurements of the cross-wake surface tension distributions that were obtained during the Field Experiment for a Navy ship at 25 knots. These cross-wake surface tension profiles, together with the film pressure-area and elasticity data also presented, allow us for the first time to realistically calculate the changes in wave energy due to these surfactants for a given radar wavelength band. To accomplish these calculations we have developed a computer model which uses the time series of surface tension together with the film pressure-area and elasticity data from the Langmuir trough and the wind velocity and direction as input to generate cross-wake profiles or two-dimensional maps of wave energy decay for a given radar wavelength. In this paper we describe the development of this model and present some results of wave energy decay for a given radar wavelength obtained with the model and compare these results to aircraft SAR intensity measurements obtained during the run.

## NOMENCLATURE

$A$	free surface area of surfactant film
$a$	surface wave height
$c$	wave phase speed
$\vec{c}_g, c_g$	(vector) group velocity of a wave
$dw'/dz$	vertical derivative, RMS turbulent vertical velocity
$D$	ship draft
$E$	energy density spectrum
$E_a$	ambient spectral level outside the wake
$E_s$	surface elasticity
$F$	force on Wilhelmy plate exerted by liquid
$g$	gravitational acceleration
$H$	depth below the free surface
$h$	definition, $h = \frac{E_s k^2}{\rho g + \alpha k^2}$
$k$	wavenumber

$L, L_{WL}$	ship length, waterline length
$L_t$	length of the zone of ship-affected turbulence
$L_{wp}$	length of Wilhelmy plate in contact with liquid
$L_{WW}$	length of the white water wake
$n$	logarithmic slope of pressure-area curve
$n$	propeller revolutions per second (Figure 1)
$S_{AW}$	surface tension force at the air-water interface
$S_{AO}$	surface tension force at the air-oil interface
$S_{OW}$	surface tension force at the oil-water interface
$S_w$	wave energy growth due to wind energy input
$S_{nl}$	wave energy growth due to nonlinear interactions
$S_t$	wave energy decay due to turbulence
$S_s$	wave energy decay due to surfactant damping
$t$	time
$u_*$	friction velocity of the wind
$u_{10}$	ten meter wind speed
$V, V_s$	ship speed
$W$	wake width
$x$	downstream distance
$\alpha$	surface tension of clean water
$\beta_1$	wind induced wave growth rate
$\beta_2$	wind induced wave growth rate
$\beta_s$	wave decay rate due to surfactant damping
$\beta_w$	wind induced wave growth rate
$\gamma$	wave growth rate from nonlinear interactions
$\eta$	definition, $\eta = (gk + \frac{\alpha}{\rho} k^3)^{1/2}$
$\theta$	angle between wave and wind direction
$\nu$	kinematic viscosity of seawater
$\Pi$	surface film pressure
$\pi$	3.14159.....
$\rho$	density of seawater
$\sigma$	radian wave frequency
$\tau_{meas}$	measured surface tension
$\phi$	definition, $\phi = \frac{\nu k^2}{\sigma}$

## 1.0 INTRODUCTION

One prominent feature of the wake of a surface ship is a long narrow region of relatively calm water behind the ship that is characterized by the absence of short wavelength waves. This region is commonly referred to as the "dead" water or centerline wake region. It is usually several ship beams in width and persists for many ship lengths behind the ship. This region of relatively low radar backscatter is the most consistently seen wake manifestation in synthetic aperture radar (SAR) images of ship wakes on the ocean surface. Another feature in the SAR images of ship wakes is

the appearance of dark lines aligned at some narrow angle to the ship's path that sometimes outline this centerline wake region far behind the ship. Surface tension changes caused by the presence of surface-active films that have been concentrated at the edges of the centerline wake by the passage of the ship have been suggested as one of the physical mechanisms responsible for these SAR image features. Surfactant films strongly affect the propagation of short gravity and capillary waves which interact with electromagnetic waves at both radar and visible wavelengths. Surface tension and surface elasticity are the two major physical properties of surfactant films which contribute to short wave damping.

To investigate the physical origin of these SAR image features, a small, towable, instrumented catamaran was built and deployed by NRL scientists to measure the cross-wake surface tension distribution after the ships passage. This instrument package was named the Surface Tension Measuring System (STEMS). The device measures surface tension by dropping a sequence of calibrated spreading oils along a straight line on the water surface and recording their behavior with a video camera. Each individual oil represents one surface tension value so that if one oil spreads and the next one does not, then the surface tension is bracketed between the two values.

Surface elasticity cannot be measured in situ by the spreading oil technique. Therefore, 1-liter water samples were collected for later measurements in a Langmuir trough. Surface elasticity is defined as the product of film area times the slope of the pressure-area curve at the corresponding value of the film area as measured in the trough. The surface elasticity distribution can then be calculated from the resulting pressure-area curve together with the ambient surface tension distribution measured using STEMS. Coupling the surface tension measurements made by STEMS to the determination of the pressure-area curves has for the first time allowed us to infer elasticity distributions for ocean

water and to realistically calculate the changes in wave amplitude due to these surfactants.

In this paper we describe the STEMS device and give examples of the results that were obtained during its deployment in an extensive Field Experiment that was conducted in the vicinity of Santa Cruz Island, California in January, 1989 to study surfactant films. Previous to this experiment, in situ surface tension data have never been measured to the resolution in surface tension obtained or with such fine spatial resolution. The NRL data from the experiment show that these surface active films play a significant and sometimes dominant role in the formation of the two SAR image features of ship wakes. We also present an overview of the chemical and physical properties of surface active materials and the techniques used to measure and determine their physical properties when they adsorb at the air-water interface.

## 2.0 BACKGROUND

### 2.1 Description of the Ship Wake

In this section we will describe the wake of a surface ship from a perspective corresponding to the large-scale physical phenomena that are observed both visually and by means of remote sensing systems. A schematic of a surface ship wake is illustrated in Figure 1. The wake is composed of white water, viscous wake, propeller wake, and Kelvin wake. The white water generally originates at the bow, is reinforced at the stern, and extends aft of the ship for a few ship lengths. The viscous wake extends many ship lengths aft from the stern of the ship and incorporates the flow moving in the direction of the ship's travel due to the viscous drag, as well as large-scale vortical flows and turbulence. Embedded within the viscous wake is the propeller outflow or propeller wake. Superimposed over this is the classical Kelvin wave pattern or Kelvin wake. The Kelvin wake is also the source

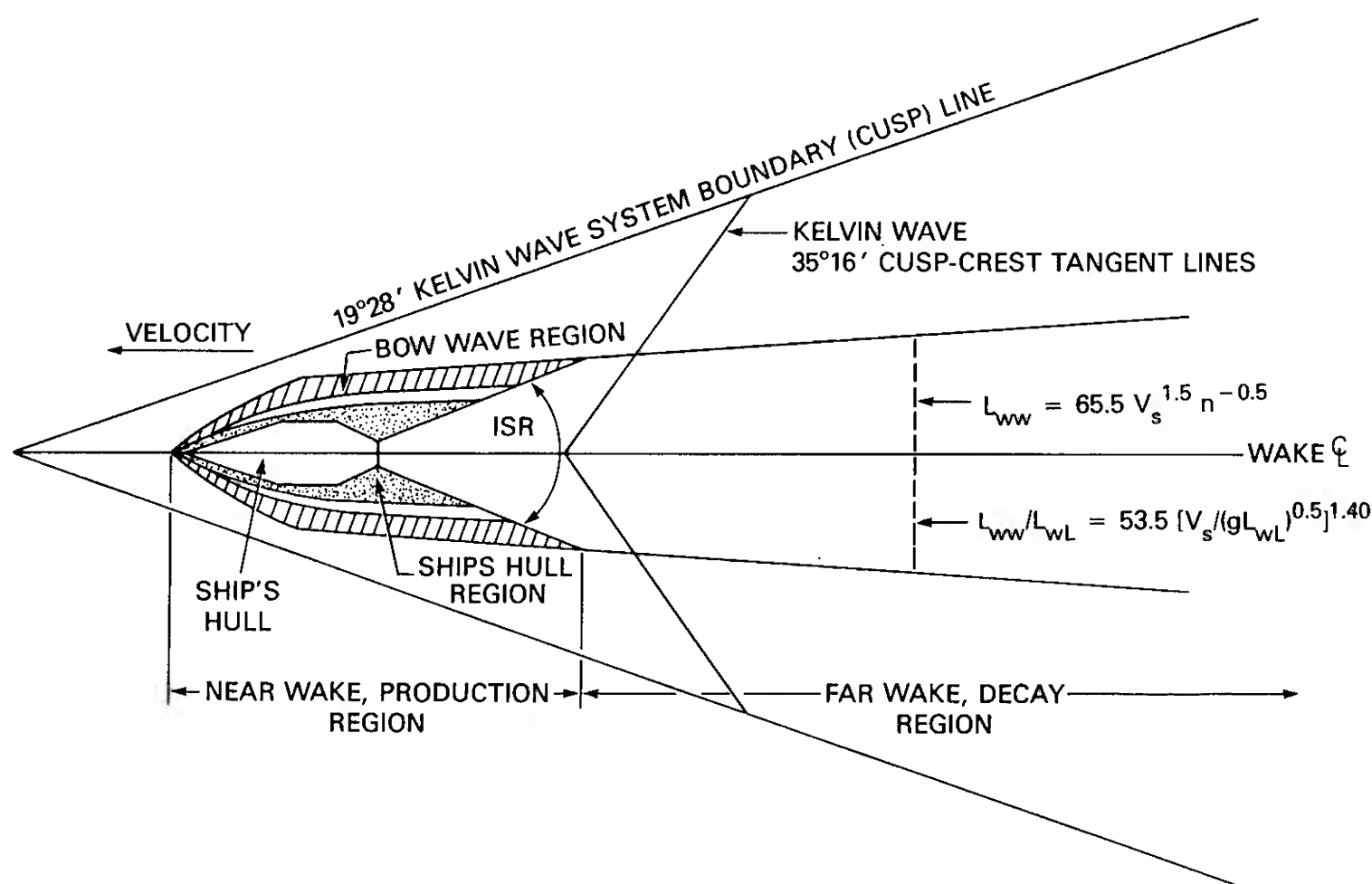


Figure 1. Schematic of a surface ship wake

of many of the viscous wake manifestations. It is in fact the breaking bow and stern waves from the Kelvin wave system which contribute significantly to the white water regions at the bow and stern. These wake manifestations lie upon the ambient seaway made up of swell, wind waves, and short gravity and capillary waves; all of which confuses the picture even more.

It is often useful to draw an imaginary ellipse, extending several ship beams ahead of and off to each side of the ship and a ship length or so aft of the ship, around the ship. We call the region internal to the ellipse the near wake and the region external to the ellipse the far wake. The near wake can be thought of as the region where surface foam, subsurface bubbles, and strong turbulence is generated. It is also where the most rapid decay of these features occurs. In the near wake, the initial region of the viscous and propeller wakes is a region of high angular divergence (initial spreading region, ISR) of foamy, turbulent, white water directly aft of the ship's stern, generally outlined by what appears to be a spilling-type breaking wave. There are two additional sources of highly energetic white water in the near wake. The bow wave that is generated by the ship's motion breaks, producing white water and turbulence when the wave steepness  $ak$  ( $a$  = wave amplitude and  $k$  = wavenumber), is greater than  $ak = 0.30$  (Ramberg and Griffin 1987). The region adjacent to the ship's hull produces foam, bubbles and turbulence because of the frictional drag forces at the surface of the hull.

The far wake is that region where the variations are relatively slow i.e., where the foam, viscous, propeller, turbulence and vortical features of the wake decay slowly and steadily and where the surface roughness and thermal characteristics gradually return to those of the surrounding ambient surface. Measurements have shown that thermal and subsurface bubble wakes can persist for an hour or more after the passage of a ship (National Defense Research Committee 1969).

Under moderate to high wind conditions ( $u_{10} > 3$  m/s), the ambient surface is sufficiently rough so that, visually, the surface in the far wake appears smooth relative to the surrounding surface. Recent high altitude photographs released by NASA show that the centerline wake can be observed as far back as 100 km behind a ship. Centerline wakes are visible in SAR imagery as a dark narrow line along the ship's track when the surface is sufficiently rough to yield a measurable background return. Centerline wakes, in addition to various other wake features are also visible in SEASAT SAR imagery up to 15 km aft of the ship (Lyden et al. 1988, Vesecky and Stewart 1982). Observations of the dark centerline return in many wake images show that this region is generally significantly greater than the ship's beam in extent. The width of the dark centerline corresponds very well with the width of the region over which there are breaking bow and stern waves, waves from the Kelvin wave system.

The Kelvin wave system's  $19^\circ 28'$  boundary lines (cusp lines) and  $35^\circ 16'$  cusp-crest tangent lines are illustrated in the figure. The apex of the boundary lines is always forward of the bow (Newman 1970). The transverse and divergent wave crests are visible optically for many ship lengths astern and to either side of the ship's path. The shorter, steeper divergent waves tend to be emphasized in aerial photographs. Under moderate to high wind conditions the transverse and cusp waves appear in SAR images of the surface because

these waves modulate the existing field of ambient Bragg waves (Lyden et al. 1988).

The persistence of surface foam in the far wake depends on the time it takes for the bubbles to break after they reach the surface. The major factors that increase the stability of a bubble at the surface are increasing salinity (Peltzer and Griffin 1988), decreasing water temperature (Miyake and Abe 1948), increased surface viscosity (Kitchener and Cooper 1957), and the presence of organic surface active materials which modify the surface rheology (Adamson 1976). A recent photographic analysis by Peltzer (1984) developed empirical relations for the length of the foamy white-water region. These empirical relations are shown in the figure and indicate that the length of the white water region is a function of the Froude number.

## 2.2 Surface-Active Materials

The surface-active (surfactant) materials that are found in all natural water bodies are chemicals which are by-products of plant and animal life. The term surfactant means that the long-chain (10 to 1000's) carbon polar-organic chemicals which constitute these materials have a natural affinity for the free surface of the water in which they reside. Typically the molecules have an acid, alcohol, ketone or other water-soluble radical on one end, which makes that end of the molecule hydrophilic. The opposite end is very similar to a pure hydrocarbon, which is insoluble in water and is hydrophobic. Because of the polar nature of these substances, when they reach the water surface they find a preferred state in which the hydrophobic end of the molecule removes itself (sticks out) from the water, and this reduces the Gibbs free energy of the water-surfactant system. The lower free energy of the system requires energy to be put back into the system to force the surfactants back into the bulk water. Wind stress is the primary mechanism to do this.

As the surfactants adsorb on the surface, they reduce the surface tension and increase the two-dimensional elastic modulus of the surface. A small increase in the surface concentration of the materials at the interface can lead to significant capillary and small surface-gravity wave ( $\leq 20$  cm) damping because the film viscously retards the very-small-scale velocity field just under the interface. When these areas become large enough they alter the appearance of the sea surface being observed by remote sensing instruments. In light to moderate winds ( $u_{10} < 3$  m/sec) these surfactant films are highly persistent. The films can reduce the radar cross-section of the surface by as much as 15 dB depending on the concentration and elastic properties of the film and the radar wavelength.

Films can become concentrated enough to attenuate surface waves when they are compacted by horizontal convergences due to current field variations at the ocean surface. The currents which are most likely to compact the surfactant films within a ship's wake are the transverse currents generated by flow around the hull or currents associated with the breaking bow and stern waves. Surfactant material can also be rapidly transported to the water surface by adsorption at the air/water interface of rising bubbles generated by air entrainment around the ship's hull, in the breaking bow and stern waves and, in the wake flow. As these bubbles burst when they reach the air/water interface, the material is merged with that already adsorbed on the water



surface (Skop, Brown and Lindsley, 1989). These bubbles are also concentrated by the horizontal convergences in the wake flow behind the ship; this is an additional mechanism which should enhance surfactant concentrations in the surface convergence zones.

Measurements and observations of the wakes of large ships (Kaiser et al., 1988) show the most persistent wake feature to be a pair of bands of compacted surfactant material aligned with the ship track along the edges of the turbulent wake. The bands are typically one to several meters wide and show a pronounced depression in surface tension. The surface tension in the core of the wake generally has the same value as the ambient water. Photographs suggest that the surfactant material is being organized into these bands by rising bubbles generated in the breaking bow wave which scour the surfactants from the water column. Bubbles are additionally important because they have been observed to persist for an hour or more in a ship's wake. Since these bubbles presumably transport surfactants to the surface during this time, they may contribute substantially to the long persistence of the dark centerline wake signature.

Remote sensing of these ship-generated surfactant bands with a SAR depends on the interaction of the electromagnetic waves with the Bragg-resonant short waves in the region of the bands. The viscous properties of the surfactant films in these bands attenuate the short waves and also block their formation or reformation by wind. The damping of these short waves reduces the Bragg scattering in the films compared to that of the surrounding clean water and the film bands appear dark in SAR images. Laboratory experiments

(Garrett 1967) have shown that surface-active materials attenuate capillary waves through viscous damping at the surface. Full-scale experiments (Huhnerfuss et al. 1981) have demonstrated that slicks of surface-active materials attenuate Bragg waves in the X- and L- SAR wavelength bands by 40 to 60 percent. Since the magnitude of the backscattered radiation from the surface is proportional to the amplitude squared of the Bragg scatterers, this attenuation results in a significant reduction of the backscattered radiation.

An example of the reduced return from these ship-generated slick bands is shown in Figure 2a (Ochadlick, et al. 1990). The measurements were made near the Chesapeake Light Tower by the NADC SAR during the SAXON 88 experiment. Note the remarkable similarity between the ship wakes and ambient features (mesoscale circulation patterns highlighted by surfactant film bands) in the SAR image and the similar features in the photographic image (Figure 2b) of the Mediterranean Sea taken from the Space Shuttle Challenger by Scully-Power in 1984 (Scully Power, 1986). The photograph was taken into the sunglint pattern which is produced on the water surface by those wave facets which are oriented with respect to the surface to produce specular reflections of the sun. In this case, the long persistent ship wakes appear as bright, double bands with a darker area between the bands. Both of these images are approximately 10 km wide and 42 km long. These concentrated films affect the wake surface because they influence the transfer of energy and momentum from the wind to the wave field and inhibit wave formation (Barger et al. 1974).

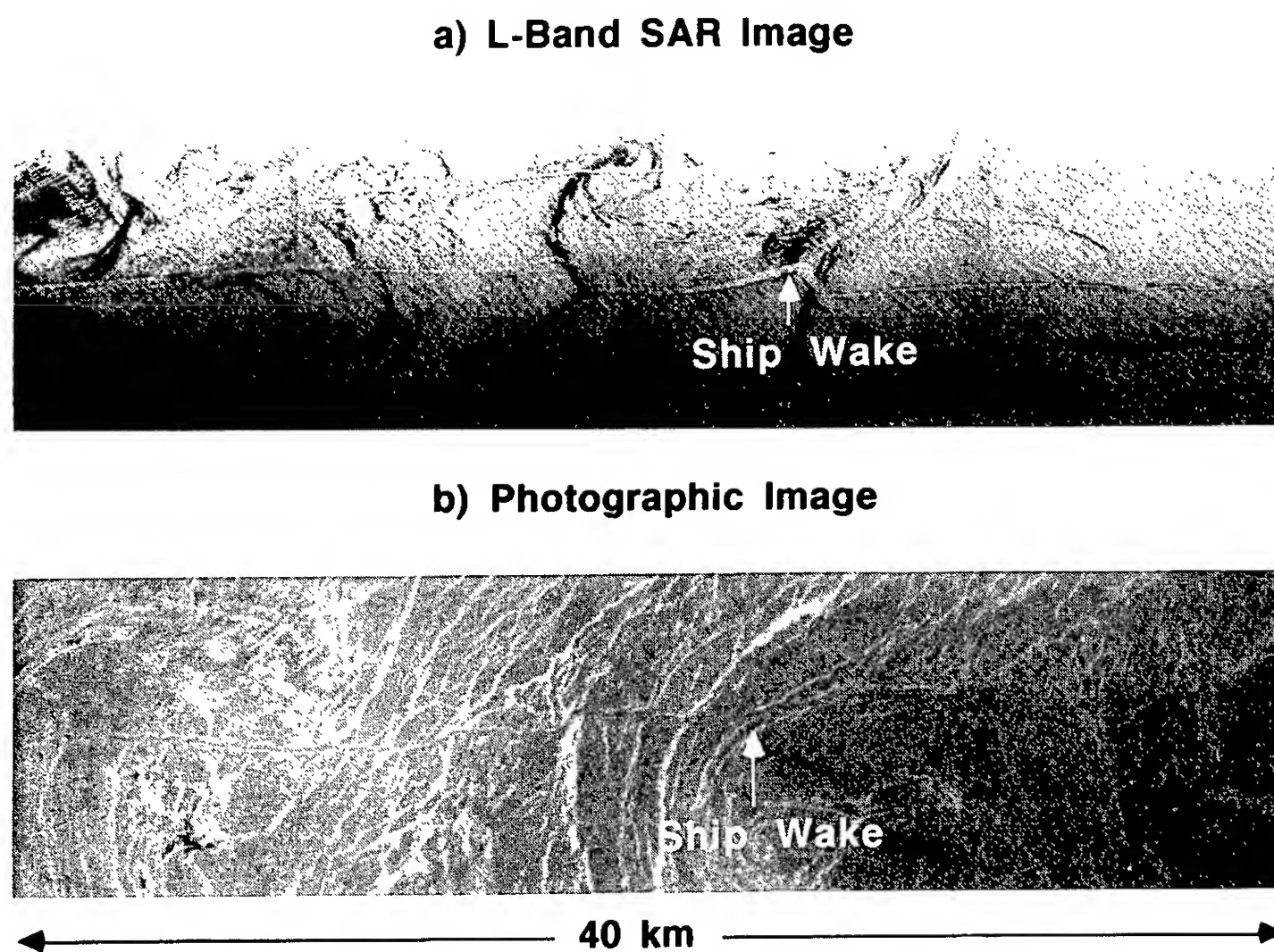
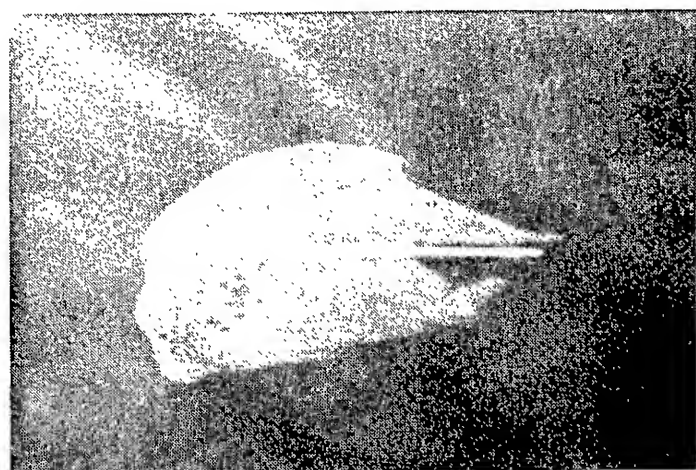


Figure 2. Airborne SAR and photographic images of ship-generated surfactant bands

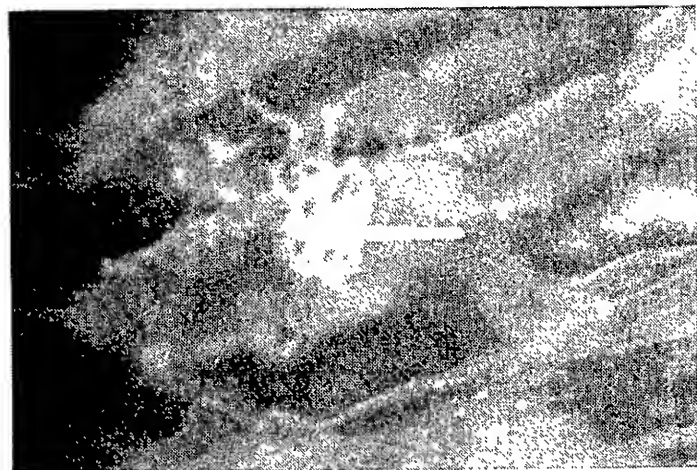
### 3.0 SURFACTANT MEASUREMENTS

#### 3.1 Surface Tension Measurement by Spreading Oils

Several techniques have been proposed to measure the mechanical properties of ocean surfactant films in situ (e.g., capillary wave damping, laser second-harmonic generation, and spreading oils), but only the use of spreading oils has been successful thus far. Adam (1937) was the first to use a series of buoyant calibrated oils to determine the surface tension of sea water in situ. More recently this technique has been described by Garrett and Duce (1980). When several oils are dropped onto the surface of the sea where a film of surface-active material may or may not be present, some will spread while others will not, and therefore the surface tension of the sea at the test point can be bracketed between the calibrated values of any two oils in the set. Figure 3 illustrates (a) a spreading oil and (b) a non-spreading oil on the water surface. The straight white lines are toothpicks that were used to apply the oils to the surface. The resolution of the surface tension measurements depends on the differences in the calibrated values of the test oils. The oils must also be dispensed rapidly and close together to identify fine structure in the surface tension gradients. For the Field Experiment we refined this technique to provide the necessary spatial resolution and prepared a set of twenty three spreading oils to cover the surface tension range from 44 to 73 mN/m. The preparation and calibration of these oils and the principle by which these oils work is described below.



a) Spreading Oil



b) Non-Spreading Oil

Figure 3. Video image of the spreading oil distribution

The spreading oils were made from a pure non-spreading paraffin oil into which precisely controlled trace quantities of a pure surface-active compound, dodecanol, were dissolved. Different batches of commercially available paraffin oil already contain traces of surface-active components, so each set of spreading oils must be calibrated – they cannot be made reliably by following the recipe employed for an earlier set. Calibrations were carried out using the Langmuir trough facility of the NRL Chemistry Division and can be more easily discussed in terms of film pressures. Film pressure ( $\Pi$ ) is defined as the difference in surface tension calculated by subtracting the surface tension of water covered by a film ( $\tau_{meas}$ ) from the surface tension of clean water ( $\alpha$ ), or  $\Pi = \alpha - \tau_{meas}$ .

The surface tension (and therefore the film pressure) was varied in the Langmuir trough instrument by compressing or expanding a monolayer film of oleyl alcohol surrounding the oil to be calibrated. The plateau film pressure (at which the oil drop had expanded to a thin disc that could be varied in diameter by expanding or compressing the monolayer while still maintaining a constant film pressure) was the assigned equilibrium spreading pressure (ESP) of the oil. For oil drops of approximately 20 mg the diameter was approximately 3 cm at the ESP.

The principle by which these oils work is illustrated in Figure 4.  $S_{AW}$  is the surface tension at the air-water interface,  $S_{AO}$  is the surface tension at the air-oil interface, and  $S_{OW}$  is the oil-water interfacial tension. Since  $S_{AO}$  and  $S_{OW}$  are reduced by adding a surface-active compound to the paraffin oil, a series of oils with varying spreading characteristics can be prepared. If  $S_{AW} > (S_{AO}\cos A + S_{OW}\cos B)$  the oil will spread. Organic surface-active films on water will reduce  $S_{AW}$ . As the oil becomes thinner by spreading, both  $\cos A$  and  $\cos B$  approach the value of 1 and the force balance required for continued spreading becomes  $S_{AW} > (S_{AO} + S_{OW})$ . When the colorless oil spreads to a thickness in the 500 to 700 nanometer range, interference colors can be observed visually from a distance. To make a measurement, oils with progressively higher concentrations of dodecanol are dropped onto the surface until one is observed to spread.

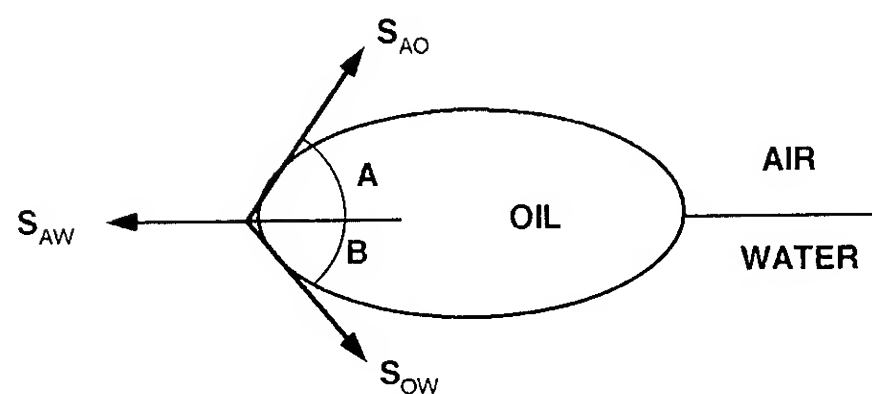


Figure 4. Balance of forces acting on an oil drop

The resolution of the measurement in surface tension depends on the ambient surface tension. Table 1 gives the spreading pressures for the twenty three oils used in the Field Experiment. The resolution is nominally the difference in pressure between adjacent oils, which is tabulated in Column Three of Table 1. Note that at high surface tensions (near

the clean water values) the resolution is nearly 0.16 mN/m, but reduces to several mN/m at very low surface tensions. The spreading pressures were intentionally graduated this way to optimize the resolution of the measurement to the physical processes involved.

Oil Number	Surface Tension	Difference
1	73.03	.16
2	72.87	.15
3	72.72	.16
4	72.56	.16
5	72.40	.14
6	72.26	.18
7	72.08	.16
8	71.92	.16
9	71.76	.13
10	71.63	.28
11	71.35	.34
12	71.01	.17
13	70.84	.31
14	70.53	.53
15	70.00	.67
16	69.33	.62
17	68.71	2.09
18	66.62	1.99
19	64.63	2.64
20	61.99	1.17
21	60.82	7.42
22	53.40	8.85
23	44.55	

TABLE 1. SPREADING OILS

### 3.2 Determination of Film Elasticity

The important property of a surfactant film which governs the wave damping is its elasticity ( $E_s$ ). However, we did not measure this in situ, but determined it indirectly as follows.

We collected samples of water during the Field Experiment and then transported them back to NRL for measurement in the Chemistry Division's Langmuir trough. The bottles were chemically cleaned, one liter reagent bottles containing a residual amount of triple-distilled water. The bottles were drained, flushed several times with the sea water to be sampled from a depth of 0.25 to 0.5 meters, and then filled. This was done by lowering the bottles over the side of the host research vessel R/V Garnet Banks. The samples were then treated with 10  $\mu$ l of a sodium azide solution to kill any life in the sample, thus "freezing" the chemical composition of the surfactants. The bottle was then sealed and stored in a cool, dark place until measurements were made in the Langmuir trough.

The measurement in the Langmuir trough consists of determining the pressure-area relationship for the surfactant, from which its elastic properties are calculated. This procedure is described in detail by Barger and Means (1985) and outlined here. The surfactant material in the sample adsorbs to the surface in a few hours and forms a thin film. The free surface area ( $A$ ) containing the film is decreased slowly by moving a barrier along the surface as the surface tension ( $\tau_{meas}$ ) is measured with a Wilhelmy plate (Barger and Means 1985). The Wilhelmy plate technique uses a flame-cleaned thin platinum plate which is over the filmed water surface. It is carefully and slowly brought into contact with the film and a meniscus forms which then exerts a downward force  $F$  on the plate equal to  $2\tau_{meas}L_{wp}$ , where  $L_{wp}$  is the length of the plate in contact with the liquid (buoyancy and plate-effects are ignored here). The surface tension is  $\tau_{meas} = F/2L_{wp}$ . In the actual procedure the force is measured with a strain gauge and the system carefully calibrated against known liquids. This procedure generates the function  $\tau(A)$ . The measured surface tension  $\tau_{meas}$  is related to the underlying clean water surface tension ( $\alpha$ ) and the pressure ( $\Pi$ ) exerted by the surfactant film by the relation

$$\tau_{meas} = \alpha - \Pi. \quad (1)$$

The elasticity of the film is defined as

$$E_s = -A \frac{d\Pi}{dA}. \quad (2)$$

Thus, by taking the negative of the logarithmic slope of the  $\Pi(A)$  curve measured in the Langmuir trough we obtain the function  $E_s(A)$ . From the measured  $\Pi(A)$  relation we then obtain

$$E_s = E_s(\Pi), \quad (3)$$

since both  $E_s(A)$  and  $\Pi(A)$  are single valued over the range of values of  $\Pi$  encountered in the Field Experiment (0 to 30 mN/m).

In order to determine the elasticity  $E_s$  by this method we make the assumption that the surfactant material adsorbing at the water sample in the laboratory has the same physical properties as that which had adsorbed on the sea surface. Treating the samples with sodium azide solution is intended to help insure this process. Very recent tests by W. Barger (private communication, 1990) suggest that samples collected and measured within one hour give the same results as samples stored for months. Hundreds of film samples collected by various techniques, including screens and rotating glass drums which sample a layer on the order of microns near the surface, have shown remarkably similar pressure-area relations (Barger and Means, 1985; Barger et al., 1988). In addition, surface chemists define the reciprocal of the elasticity as the coefficient of compressibility. Compressibility measurements for fifty two film samples from Atlantic surface, bulk and deep water and Chesapeake Bay water are reported in Barger and Means (1985) and also show remarkable similarities in behavior.

However, there is the possibility that mechanical and chemical reactions occur on the ocean surface which may alter the mechanical properties of the surfactant film. The two most likely possibilities are photo-chemical reactions due to the ultraviolet component of the solar spectrum and working of the film due to the continual compaction and expansion



caused by the passage of surface waves. Furthermore, in calm conditions the surface constituents may not have the same relative concentrations as those in the sampled water column. Presently there is little or no evidence to address these issues, so we are reasonably confident in the relationship given by equation (3) to determine the elasticity of films on the the ocean surface.

### 3.3 STEMS (Surface Tension Measuring System) Description

#### 3.3.1 Deployment and Operation

STEMS is a catamaran which is towed from the host vessel (R/V Garnet Banks, an ex-Navy YTB class tug) from a boom (6 m long) off the forward port side of the vessel. A photograph of STEMS is shown in Figure 5. It is 2 m wide, 3 m long, and weighs 135 kg (300 lbs). Figure 6 shows the towing configuration employed in the Field Experiment. STEMS needs to be outside of any disturbance created by the host vessel, so it has a movable rudder to control its distance away from the towing vessel. In all cases it must sample an undisturbed water surface. Maximum tow speed depends on sea conditions and wind, but generally a tow speed of 0.5 m/sec (1 kt) was found to give reliable performance of STEMS. During the operation we positioned the R/V Garnet Banks either north or south of the wake produced by the passing target ship, about 100 to 200 meters off-track before the scheduled start of the individual test runs. As the target approached, we moved up on its track and towed STEMS across the wake, intending to follow the serpentine pattern shown in Figure 7. Our tow speed was about 0.5 m/sec, so that in the time allocated for each run (approximately 50 minutes) we could only make three to four wake crossings. If the sea became too rough, turbulence and splashing within STEMS made observation of the spreading oil behavior difficult to impossible.

The device measures the surface tension in situ by dropping any twenty two of the twenty three calibrated spreading oils on the water surface from twenty two individually regulated channels. The spreading behavior of the oils (whether they do or don't spread) is recorded with a video camera system. Each oil represents one surface tension value, so if one oil spreads and the next one does not, the in situ surface tension is bracketed between the values of the two spreading oils. In some cases a drop of oil will neither spread nor not spread, but it will oscillate instead. Presumably its spreading pressure is almost exactly the value of the surfactant film and the oscillation occurs because the ambient surface tension oscillates about a mean value due to alternate surface compactions and expansions induced by the passage of surface waves. The dropping of each individual oil is controlled from the ship and a permanent video record of its spreading behavior is obtained for later analysis. In addition to being recorded on VHS video tapes, the STEMS data were monitored in real time with the operator annotating the videos with verbal comments on the audio track. A second video system was placed on a mast above the bridge to monitor STEMS and to record the general environmental conditions encountered. In addition, an audio cassette record was made from the bridge describing various facets of the operation, the environmental conditions, when STEMS entered a slick, and other pertinent test information.

#### Surface Tension Measurement System (STEMS)

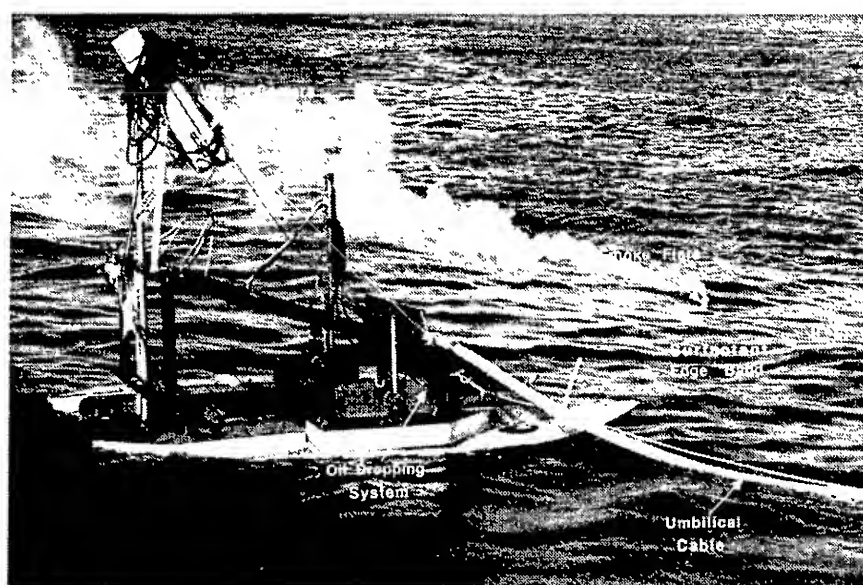


Figure 5. Photograph of the STEMS

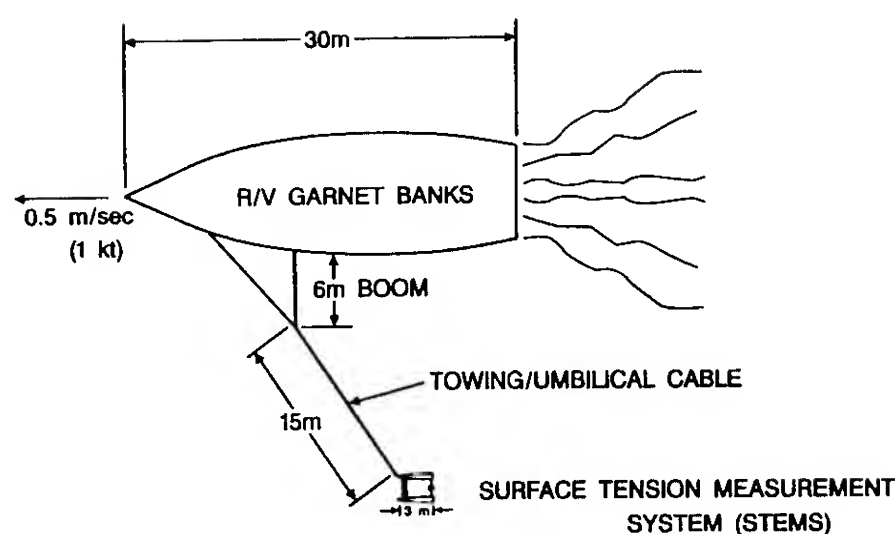


Figure 6. STEMS towing configuration

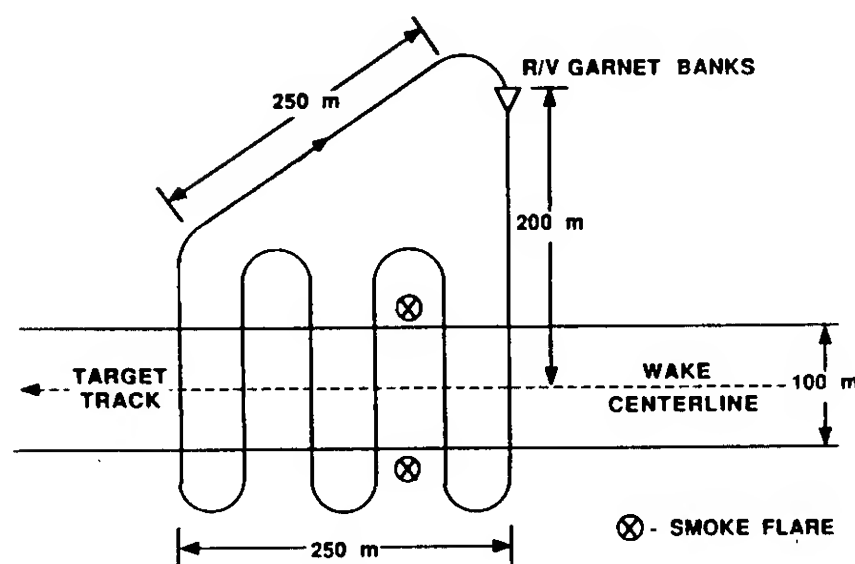


Figure 7. STEMS wake crossing pattern

#### 3.3.2 Data Resolution and Quality

One reading of surface tension was typically obtained every one to two seconds when the winds were under 5.5 m/sec, and less frequently for higher wind speeds. This gave a cross-wake resolution of 0.5 to 1.0 m in the lighter-wind runs. The down-wake resolution was highly variable

but averaged 50 m. The resolution in surface tension varied from 0.16 mN/m to a few mN/m based on the differences in spreading pressures of the oils (see Table 1). Through the first nine days of the Field Experiment (Jan. 23rd to Jan. 30th), the oil number in the table corresponded directly to the channel number on the STEMS. Channels 5 and 8 did not work throughout the entire test and channel 22 worked only on the final two days of the Field Experiment (Jan. 31st and Feb 1st). Oil 23 was used on the final day of the test (Feb. 1st) in place of oil 1. It was unfortunate that oils 22 and 23 were not working or available during most of the Field Experiment because we could not establish the maximum value of the surface tension decrease in certain regions of both the ship generated and ambient surfactant bands. If we assume that the physical properties of the compacted surfactant material in the bands were similar throughout the Field Experiment, we know that the maximum surface tension decrease in the bands varied between our measured value of 11.3 mN/m and some value greater than 27.2 mN/m. There were regions where oils 21, 22 and 23 did not spread when they were used on the final day (Feb. 1st) of the Field Experiment and in addition, oils 21 and 22 did not spread during portions of the measurements on Jan. 31st. All of the film pressure - area curves we have examined so far (1/26, 1/28, 1/29) have similar characteristics, which suggests that the physical properties of the surfactant films are indeed similar on a day to day basis. Furthermore, measurements of surface film pressures of surface-active organic matter generated by marine phytoplankton typically range between 20 mN/m and 30 mN/m (Frew et al., 1990). Considering all of the above, we can confidently assume that the maximum surface film pressure in the film bands varied somewhere between 11.3 mN/m and 30 mN/m.

### 3.4 Results of the Surface Tension Measurements

The STEMS data processing consists of playing back the video tapes several times and recording the spreading behavior of each oil. In this manner the dividing line between spread and non-spread is determined as a function of time on the video. Readings are made each second. The time series of surface tension is then input to a computer together with the film pressure-area and elasticity data from the Langmuir trough. Also, wave damping coefficients (as a function of elasticity for a given surface wavelength) can be calculated. Finally cross-wake profiles or two-dimensional maps of surface tension, film pressure, elasticity and wave damping can be generated for a given surface wavelength. We include here for each of the wake crossings, the measured surface tension profiles across the wake. The corresponding film pressure profiles can be calculated using equation (1) with  $\alpha$  taken as the surface tension measured in the clean water well outside of the wake. The film pressure directly relates our field measurements to the laboratory-determined elasticity. The wake widths were determined by multiplying the speed of the towed STEMS platform by the total time it took the STEMS to cross the wake.

Surface tension measurements were obtained during the 25 knot run along three wake crossings centered at 3735 m, 11978 m and 21316 meters aft of the ship. These surface tension distributions are shown in Figure 8. All crossings are plotted so that the water south of the wake (0.0 m) is at the left of the figure. The wake edges are defined as the lo-

cation of the edge of the outermost foam bands in the video record made by the STEMS as it crossed the wake and/or the region corresponding directly to the sudden decrease (or increase) in surface tension measured by the STEMS as it entered (or exited) these outermost surfactant bands. Regions of decreased surface tension relative to the ambient value are caused by increased film pressure of a compacted surfactant in those regions. Each of the three crossings has two edge bands of compacted film as well as one or more additional bands between the edge bands. From this data alone it is not clear whether these inner bands persist, but rather move around, or appear and disappear. The two outermost bands were visible to the eye as slicks, whereas this was not generally true for the inner bands. Since the surface is already smooth in the centerline region of the turbulent wake, the visibility of these inner bands will be limited. In addition, the surfactant films will not allow the wind waves to regrow in these regions and will limit the regrowth throughout the entire centerline wake region. The outer bands are visible because of the contrast between the ambient surface where small waves are present and the smooth surface where the small waves have been damped by the compacted surfactant material. The surface tension in the core of the wake has the same value as the ambient (away from the wake).

As was discussed in Section 3.3.2, we were not able to measure the minimum surface tension value in certain regions of the crossings. For the crossings shown in Figure 8 we have assigned an arbitrary value of 60.0 mN/m to those regions where oil 21 did not spread. This value is only slightly less than the measured value of 60.82 mN/m associated with oil 21 which did not spread.

## 4.0 MODEL DEVELOPMENT, CALCULATIONS AND COMPARISONS WITH MEASUREMENTS

### 4.1 The Energy Balance Equation

To examine the short wave field in the wake of a surface ship, we have developed a model based on the spectral energy balance equation

$$\frac{\partial E(\vec{k})}{\partial t} + \vec{c}_g(\vec{k}) \cdot \nabla E(\vec{k}) = S_w(\vec{k}) + S_{nl}(\vec{k}) - S_t(\vec{k}) - S_s(\vec{k}) \quad (4)$$

where  $E$  is the energy density spectrum,  $\vec{k}$  is the circular wave number vector,  $t$  is time and  $\vec{c}_g(\vec{k})$  is the group velocity vector for the spectral component and the  $S$ 's are the energy source terms for the spectral component at the wave number  $\vec{k}$ .

$S_w$  and  $S_{nl}$  represent the rates of energy input to the waves from, respectively, the wind and wave-wave nonlinear interactions.  $S_t$  is the rate of energy dissipation due to the interactions of the waves with turbulence.  $S_s$  is the direct rate of energy dissipation due to viscosity which can be influenced by the effect of surface film elasticity on the free surface boundary layer.

The energy balance in the form of equation (4) neglects wave scattering by turbulence and wave diffraction by mean flows. These effects are insignificant compared to the other



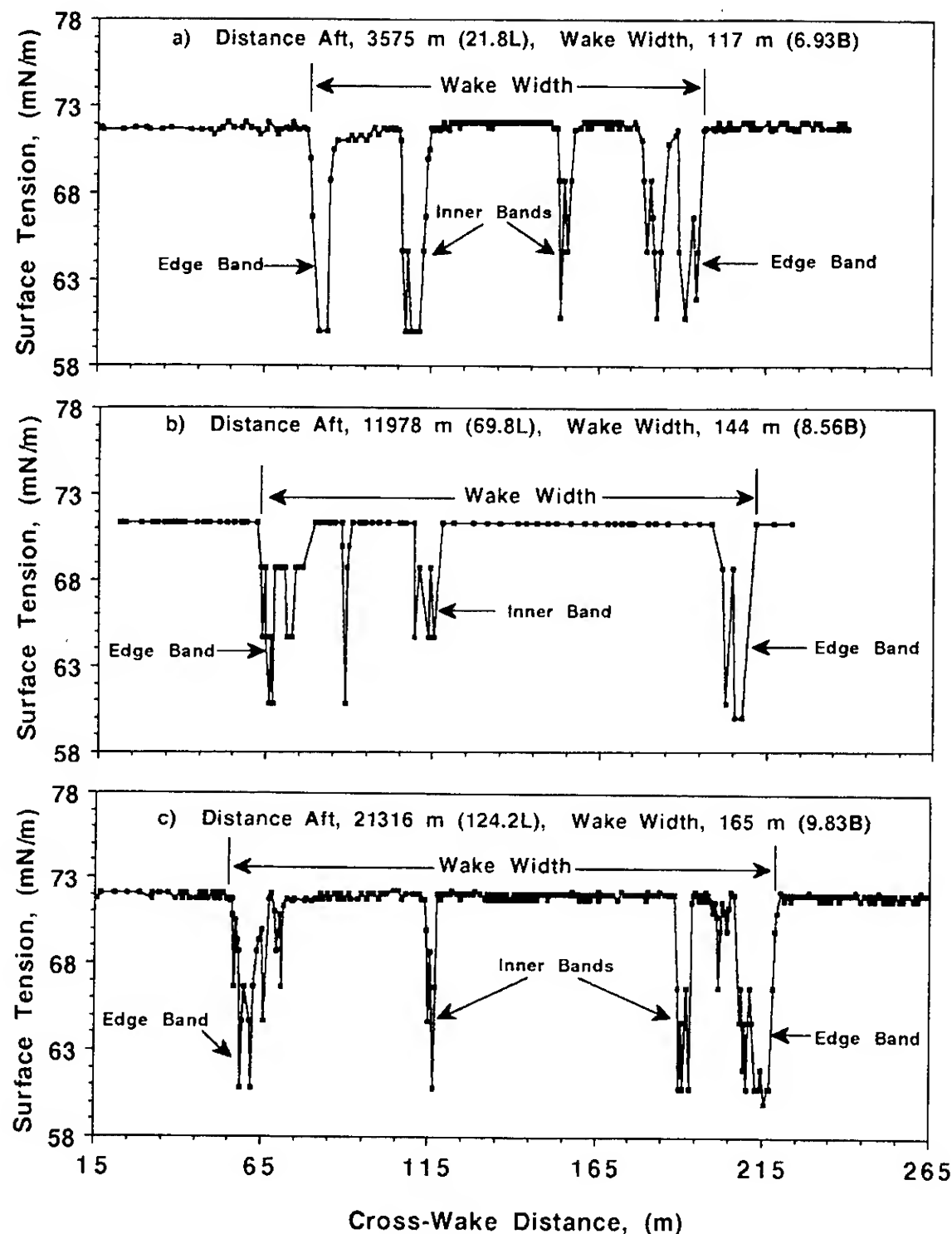


Figure 8. Measured cross-wake surface tension distributions

source terms except in the first few ship lengths of the wake (near field region), when estimated from the scattering theory of Phillips (1958) and the analysis of diffraction by ship wake flows by Skop et al. (1990).

At the present time little is known about relationships between the four source terms on the right hand side of equation (4) and oceanic conditions, either in or out of ship wakes, for the short waves associated with radar backscattering. For this reason, we cannot make a precise comparison between radar measurements and the predicted wave energy distribution. Instead, we shall compare radar measurements with predictions from equation (4) using plausible formulations for the source terms based on what is currently known about them. The resulting qualitative agreement between radar measurements and the calculated wave energy distribution, including its sensitivity to variations in the source term formulations, will indicate the important hydrodynamic effects leading to the short wave calming in ship wakes. Taking this approach, we now explain the formulations we have used for the source terms.

#### 4.1.1 Wind Energy Input to Short Waves

Wind induced growth of short waves was determined by Plant (1982) on the basis of available experimental data. He expressed the growth rate,  $\beta_w(\sigma)$ , of a spectral component with circular frequency  $\sigma$  as:

$$\beta_w = (0.04 \pm 0.02)\sigma(u_*/c)^2 \cos\theta. \quad (5)$$

Here  $u_*$  is the friction velocity of the wind,  $c$  is the phase velocity of the wave component and  $\theta$  is the angle between the wind and the direction of wave propagation. Since the data used by Plant includes damping from viscosity, the growth due to wind alone should be slightly larger than his estimate. Therefore, we will use 0.05 for the numerical coefficient which is slightly above the median, but still in Plant's range. Under typical conditions,  $u_*$  is related to the ten meter wind speed  $u_{10}$  by:

$$u_* = u_{10}/30. \quad (6)$$

Useful information on wind energy input in addition to equation (5) is provided by the studies of Mitsuyasu and Honda (1982). They found that when the water surface was calmed, interestingly achieved with a surfactant, the friction velocity was reduced to less than  $u_{10}/30$ . Changing from a naturally wind roughened surface to a nearly calm surface reduced the friction velocity by roughly 14 percent. If the formulation of equation (5) applies, this reduces the spectral growth by thirty percent.

To account for the reduction in growth rate when the waves are calmed, rather than using  $S_w = \beta_w E$ , we approximate  $S_w$  as:

$$S_w = (\beta_1 + \beta_2 \frac{E}{E_a}) E, \quad (7)$$

where  $E_a$  is the ambient spectral level outside the wake, and

$$\beta_1 + \beta_2 = 0.05 \sigma(u_*/c)^2 \cos \theta. \quad (8)$$

For our subsequent "base case" calculations, we shall take  $\beta_2 = \beta_1/2$ . This corresponds to a 33 percent reduction in the energy growth rate from the wind if the waves were completely calmed.

The short waves which are attenuated in the ship wakes have wavenumbers and frequencies several times that of the spectral peak. On the other hand, the available data used by Plant in developing equation (5) are based on wave frequencies close to the spectral peak. The validity of the formulation for frequencies much higher than the spectral peak is unknown. However, it is the best information presently available and that is why we have used it, modified by the reduction due to surface smoothness. We shall include the base case of  $\beta_2 = 0$  in our subsequent calculations to demonstrate the effect of neglecting the reduction in growth rate due to smoothness.

#### 4.1.2 Nonlinear Energy Transfer to Short Waves

The present state of the art in estimating nonlinear energy transfer is the resonant interaction theory of Hasselmann (1962). This is a perturbation based theory that includes Taylor series expansions about the mean free surface elevation. As a result, when short waves have lengths that are small in comparison to the long wave amplitudes, the range of use of the series covers many short wavelengths. The validity of the existing theory for this situation is uncertain and is an area of active fundamental research at this time. Nevertheless, with nothing more certain or better available at this time, we have applied a computer code based on the Hasselmann theory to the range of frequencies from very small to those responsible for L-band radar backscattering. Heretofore, application of the Hasselmann theory has not included these short, high-frequency waves.

Figure 9 shows the computed nonlinear energy transfer rate to waves propagating in the wind direction as a function of wave frequency for a Jonswap spectrum corresponding to a wind speed of 6.2 m/s (12 knots at a height of 10 meters). The figure also shows the wind energy input rate as a function of the theory according to Plant (1982). For the frequency range corresponding to L-band scattering, the nonlinear energy transfer rate is roughly 20 percent of the wind energy input rate.

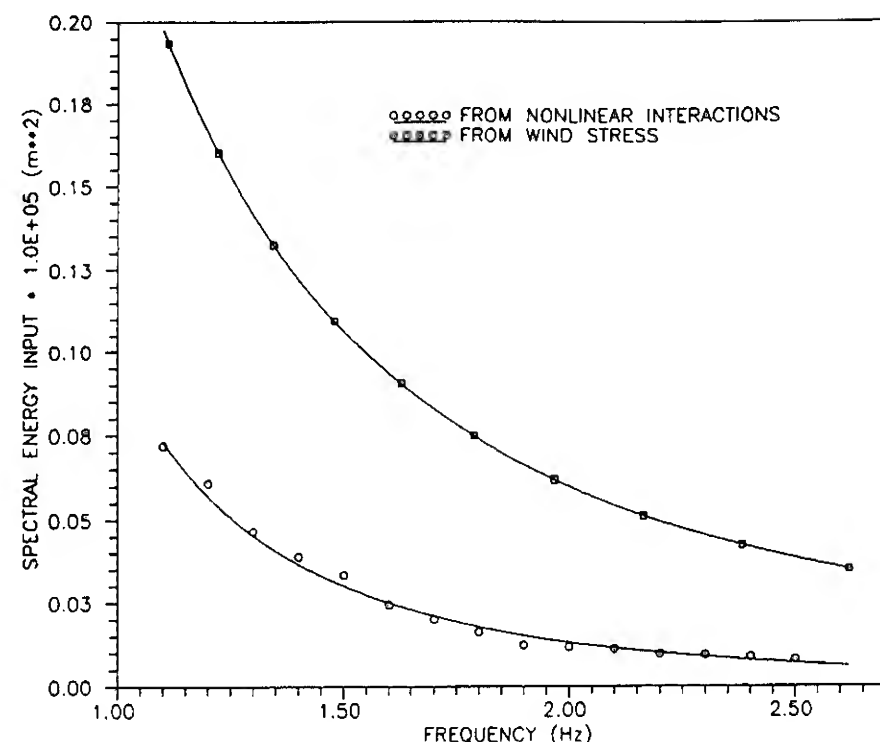


Figure 9. Computed energy transfer to short waves from the wind and nonlinear interactions

Although knowledge of nonlinear energy input to waves much shorter than the spectral peak wavelength in equilibrium conditions is scanty, even less is known about it for the non-equilibrium condition of attenuated and regrowing short waves in a ship wake. To deal with this uncertainty here, we will take two steps:

1. Set the nonlinear energy input to 20 percent of the wind energy input for our "base case" calculations,

$$S_{nl} = \gamma E \quad (9a)$$

$$\gamma = 0.20(\beta_1 + \beta_2 \frac{E}{E_a}). \quad (9b)$$

2. Perform calculations with other values of  $\gamma$  to determine both the effect of the uncertainty and the order-of-magnitude of the influence of the nonlinear energy transfer on the short wave energy distribution through the wake.

#### 4.1.3 Short Wave Energy Dissipation Due to Turbulence

The primary mechanism for wave energy dissipation by turbulence in non-breaking wave conditions is thought to be downward convection of wave energy by the vertical velocity components of the turbulence. Kitaigorodskii and Lumley (1983) derived a mathematical relationship, based on this concept, between the dissipation rate and the correlation between the vertical turbulence velocity and the square of the fluid velocity due to the waves. However, as far as we know, this correlation has never been measured either in or out of a ship wake. Thus, we are directed to an alternative approach for estimating the downward convection of wave energy by turbulence.

Olmez and Milgram (1989) measured the dissipation of short waves due to turbulence generated by a submerged oscillating grid in a laboratory tank. Using the concept of the downward convection of wave energy, they developed the following order-of-magnitude formula for  $S_t$ :

$$S_t = \frac{(dw'/dz)}{(2\pi)^{1/2}} E = 0.4(dw'/dz)E, \quad (10)$$

where  $dw'/dz$  is the rate of increase of the RMS vertical turbulence velocity near the water surface.  $w'$  is presumed to be zero at the surface.

To use equation 10, the RMS vertical turbulence velocity,  $w'$ , must be estimated. Kitaigorodskii et al., (1983) have estimated this velocity component from measurements made in Lake Ontario. Their shallowest measurement location was 0.3 meters beneath the surface where both  $w'$  and the RMS horizontal velocity,  $u'$ , were roughly  $u_{10}/120$ .  $u_{10}$  is the wind speed at a height of ten meters. The turbulent velocity was estimated by subtracting the vertical wave velocity, inferred from the measured wave elevation, from the measured total velocity. We note nearly all errors in the estimate of wave velocity will lead to over estimates of  $w'$ .

Brumley and Jirka (1987) studied the influence of a free surface on otherwise homogeneous turbulence. Parameters of the horizontal turbulence velocity were altered slightly whereas parameters of the vertical velocity were strongly altered in a layer having a depth about equal to the integral length scale of the horizontal turbulence. The vertical RMS velocity and integral length scale were nearly zero at the free surface and increased to values comparable to those of the horizontal turbulence at the bottom of the layer.

The functional form of  $w'$  versus depth is uncertain. The Brumley and Jirka data show a linear dependence for the upper 2 percent changing to a  $(\text{depth})^{1/3}$  dependence over the lower 95 percent. McDougal (1979) measured the effect of a rigid lid on otherwise homogeneous turbulence. His results were similar to those of Brumley and Jirka, except the increase of  $w'$  with depth was nearly linear over a depth equal to the integral length scale of the horizontal turbulence. Hunt and Graham (1978) have shown theoretically and numerically that the form of  $w'$  versus depth depends on details of the turbulence spectrum.

For our purposes here, we will make the approximation that  $w'$  increases linearly from zero at the surface to  $u_{10}/120$  at a depth  $H$  (which we shall take to be 0.3 meters),

$$dw'/dz = u_{10}/(120H), \quad (11)$$

outside the wake.

The only wake turbulence measurements available to us are those taken in model tests and provided to us by W. Lindenmuth (private communication, 1990). Very strong turbulence just behind the ship model decayed such that at a distance of ten ship beams aft of the stern,  $u'$  was approximately  $0.02V$  in the near surface region, where  $V$  is the ship speed. The depth of the zone of influence of the free surface on the vertical turbulence velocity was about one-eighth of the ship draft ( $D/8$ ). Further aft, the turbulent velocities became too small to reliably measure with the laser doppler anemometer being used. We need to couple Lindenmuth's measurements with our measurements of wake widths and known features of turbulent wakes in general.

Under the assumption of self-similar velocity profiles and eddy viscosities, a round drag wake grows asymptotically as  $W \sim x^{1/3}$ , where  $W$  is the width and  $x$  is the downstream distance. A wake with zero net axial momentum grows as  $W \sim x^{1/5}$  (Birkhoff and Zarantonello 1957). Because of the low Froude numbers of wakes further aft than

one ship length, they are expected to behave globally in the same fashion as round wakes. If all of the hull drag were due to skin friction, this drag would be exactly balanced by the propeller thrust and the wake as a whole would have zero axial momentum. Because of the energy radiated by the ship-generated waves, the wake has net momentum flux directed aft with a magnitude equal to the wave drag. However, for the ship parameters and speeds of interest here, the skin friction drag is larger than the wave drag so we expect the far wake behavior to be more like a zero-momentum wake than a drag wake or a jet. This expectation is justified by the measured widths of the zone of wake-modified surface tensions. Figure 10 shows these measured widths (corresponding to Figure 8) as well as the following equation which fits the data well:

$$W(x) = 22.9(x + 0.4B)^{1/5}, \quad (12)$$

where  $W$ ,  $x$ , and the ship beam  $B$  are measured in meters. For the ship that generated the data for Figures 8 and 10 the beam  $B = 16.75$  meters.

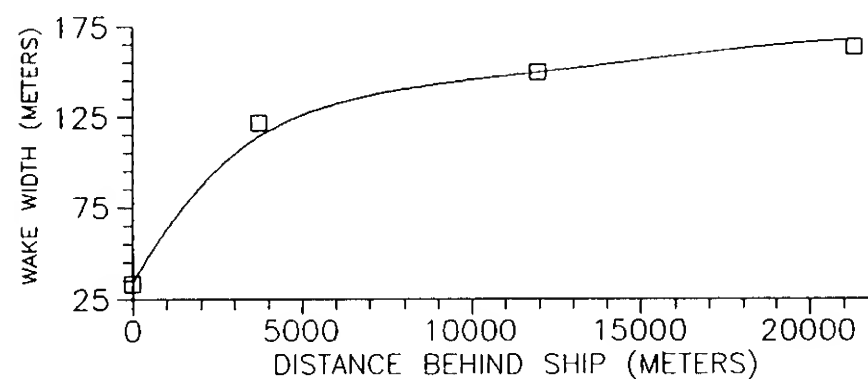


Figure 10. Measured and theoretical wake widths

For a self-similar zero-momentum wake, all velocities behave asymptotically as  $x^{-4/5}$ , so with  $u' = 0.02V$  ten ship beams aft of the ship, we model  $u'$  over the entire wake as:

$$u'(x) = 0.02V \left( \frac{10.4B}{x + 0.4B} \right)^{4/5}. \quad (13)$$

Then,  $dw'/dz$  is approximated as

$$dw'/dz = 0.02 \frac{V}{(D/8)} \left( \frac{10.4B}{x + 0.4B} \right)^{4/5}, \quad (14)$$

inside the wake. Equation 14 neglects the variation in turbulence across the wake. Also, this equation is used in our model only when the turbulence gradient exceeds the ambient level given by equation (11). Setting the two expressions equal yields the length  $L_t$  of the zone of ship-affected turbulence as:

$$L_t = 418B \left( \frac{H}{D} \frac{V}{u_{10}} \right)^{5/4} - 0.4B. \quad (15)$$

#### 4.1.4 Dissipation of Energy Due to the Presence of a Surfactant Film

The damping of surface waves in clean water is well known to have a  $1/e$  time of  $1/(2\nu k^2)$  where  $\nu$  is the kinematic viscosity and  $k$  is the wavenumber (Lamb 1945). The  $1/e$  times are about 4500 seconds for 30 cm waves responsi-

ble for L-band Bragg scattering, 32 seconds for 5 cm waves associated with C-band scattering and 5 seconds for 2 cm waves associated with X-band scattering. These decay rates are typically small in comparison to growth rates (equation 5) due to modest winds.

What is less well known, is that elastic surface films can dramatically increase the viscous damping rates of short waves. In the absence of a surface film, the requirement of zero shear on the surface leads to a very weak surface boundary layer with similarly weak damping. In the presence of an elastic film, however, a much stronger boundary layer with increased damping can be necessary to provide a shear stress equal to the gradient of the surface tension.

A thorough study of the wave damping due to a laminar boundary layer beneath an elastic surface film was conducted by Dorrestein (1951). His results can be written as:

$$S_s = \beta_s E \quad (16a)$$

where

$$\beta_s = \frac{\eta \left[ 4\phi - \frac{4\phi h}{\sqrt{2\phi}} + \frac{h^2}{\sqrt{2\phi}} \right]}{\left[ \left( 1 - \frac{h}{\sqrt{2\phi}} \right)^2 + \left( \frac{h}{\sqrt{2\phi}} \right)^2 \right]}, \quad (16b)$$

with

$$\eta = (gk + \frac{\alpha}{\rho} k^3)^{1/2}, \quad \phi = \frac{\nu k^2}{\eta}, \quad h = \frac{E_s k^2}{\rho g + \alpha k^2}. \quad (16c)$$

Here  $g = 980 \text{ cm/s}^2$  is the gravitational acceleration,  $\rho = 1.02 \text{ gm/cm}^3$  is the density of seawater,  $\nu = 0.01 \text{ cm}^2/\text{s}$  is the kinematic viscosity of seawater,  $\alpha = 73 \text{ mN/m}$  is the nominal surface tension at the air/seawater interface,  $E_s$  (in mN/m) is the film elasticity and  $k$  is the wavenumber of the wave.

Figure 11 illustrates the rate of decay of capillary-gravity waves on the free surface due to the presence of a surfactant film based on the studies of Dorrestein. The wavelength range in the figure covers the Ka- to L-Band range in SAR operating frequencies. Plotted are a family of curves showing the ratio of the wave energy after one wavelength of propagation in the surfactant film band to the energy at the beginning of the cycle for surfaces films with different physical or elastic properties. In addition, the two limiting cases, a clean free surface where only the viscosity of the fluid is responsible for wave damping and a surface covered by an infinitely stiff, incompressible film are also included. The figure shows that the presence of a surfactant film greatly increases the rate of decay of capillary-gravity waves less than 20 cm in wavelength. Note also that a small change in surface elasticity can result in a significant change in capillary and small surface gravity wave damping for a given wavelength.

We close this subsection by noting that in the presence of a turbulent free surface boundary layer, the actual surfactant-induced wave damping could be different than predicted by Dorrestein's laminar analysis. However, it seems likely that the effect of turbulence would be small here, on the basis of the vanishing vertical turbulence velocity at the free surface found by Brumley and Jirka (1987) and the very small depth,  $O(\nu/\sigma)$ , of the wave-induced laminar surface boundary layer.

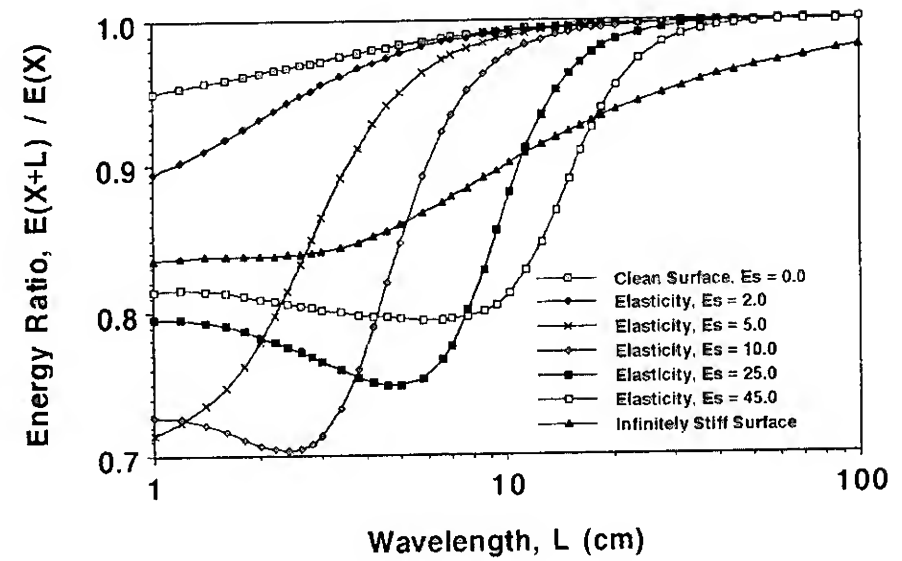


Figure 11. Wave energy decay in a surfactant film

## 4.2 Data and Conditions Used for the Model Computations

Calculations were carried out using data that were obtained in the wake of a Navy ship at a speed of 12.9 m/s (25 kt) on January 28th, 1989. The Navy ship reported a wind speed of 5 knots whereas the R/V Sea Tech reported wind speeds varying between 7 and 9 knots while in the wake. These vessels reported disparate and varying wind directions with angles between 30 and 90 degrees with respect to the cross-wake direction. We cannot fully resolve the disagreement over the wind speed. However, the direction of the short waves is clearly visible on a videotape made from the R/V Garnet Banks during the surface tension measurements. This direction is about 50 degrees with respect to the cross-wake direction.

The uncertainty of the actual wind speed is unfortunate for the modelling of L-band Bragg scattering waves. For these, the model growth rate terms from the wind and nonlinear interactions have the same order of magnitude as the dissipation terms from turbulence, viscosity and surfactants. Thus the L-band waves can be modelled as growing or decaying, depending on the chosen wind speed within the reported range. The same difficulty applies to C- and X-band waves in the first few ship lengths of the wake. However, it is not severe in the far field at C- and X-band because there, for all the reported wind speeds, these waves grow outside the surfactant bands and decay in the strong surfactant bands.

We will use a wind speed of 7 knots at an angle of 50 degrees from the cross-wake direction in our model calculations here. However, we must point out that if 9 knots were chosen very little wave attenuation would be predicted in the wake for L-band waves, and if 5 knots were chosen the waves would be predicted to decay, even outside the wake.

The SAR image with which model calculations will be compared was made from an aircraft flying parallel to the wake. Thus the predominant Bragg scattering waves to which the SAR is most sensitive propagate directly across the wake. For our estimated wind direction, the value of  $\theta$  to be used in Equation 5 is 50 degrees.

Surface tension measurements were obtained along three wake crossings centered at 3735 m, 11978 m and 21316 meters aft of the ship. These surface tension distributions are shown in Figure 8. Regions of decreased surface tension



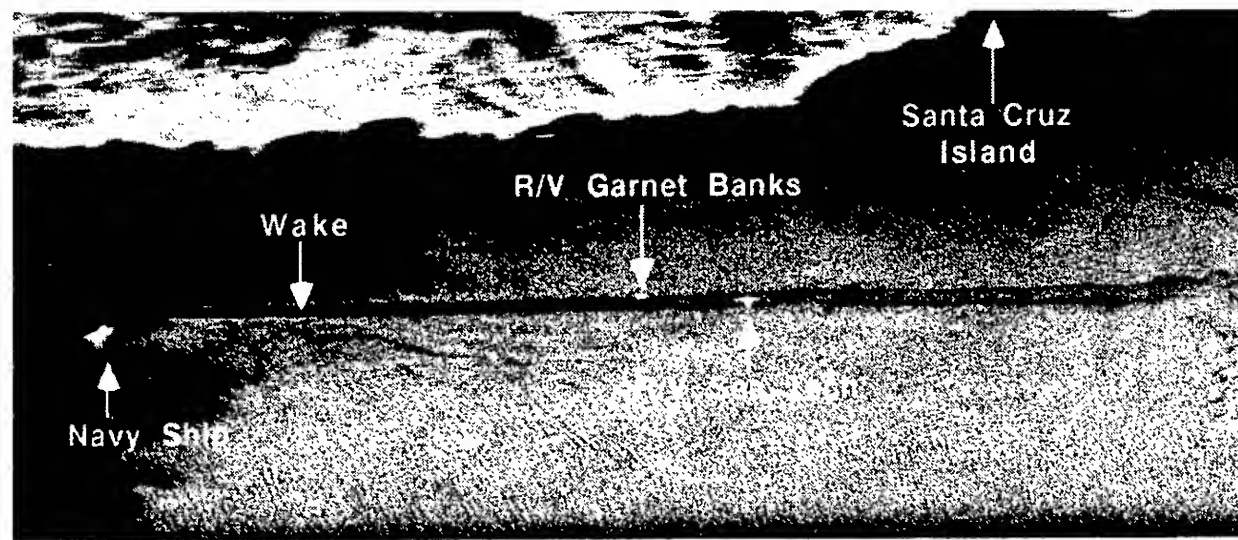


Figure 12. L-band SAR image of the Navy ship wake (courtesy of J. Lyden, ERIM)

relative to the ambient value are caused by increased film pressure of a compacted surfactant in those regions. Each of the three crossings has two edge bands of compacted film as well as one or more additional bands between the edge bands.

Figure 12 is an L-band SAR image of the Navy ship wake obtained from an aircraft during the same time that the surface tension measurements in the ship wake were being made by STEMS as it was towed across the wake by the R/V Garnet Banks. C- and X-band data were also obtained simultaneously by the multi-band aircraft SAR. We will compare the multiband SAR backscatter intensity data with model calculations using the surface tension data from the 3735 m cut and film elasticity values calculated from the pressure-area curve of the water sample obtained prior to the 25 knot run as input to the model.

The film pressure - area curve for the surfactant material is needed to relate the film elasticity  $E_s$  to the measured surface tension. A subsurface water sample was collected prior to the 25 knot run for later film pressure versus area measurements in the Chemistry Division at NRL. The results of these measurements, plotted as the natural logarithm of the film pressure (in mN/m) versus the natural logarithm of the surface area (in  $\text{cm}^2$ ), are shown in Figure 13. These data have been fitted with three straight line segments so that for each portion of the fitted curve we have

$$\Pi = CA^n, \quad (17)$$

where  $n$  is the slope of the portion and  $C$  is a characteristic constant of that portion of the curve. Then, from equation (2), we find that

$$E_s = -n\Pi \quad (18)$$

or, specifically from the three segment fit in Figure 13,

$$E_s = \begin{cases} 0.0 & \Pi \leq 0.20, \\ 5.21\Pi & 0.20 < \Pi < 4.42, \\ 2.90\Pi & 4.42 \leq \Pi \leq 8.58, \\ 1.27\Pi & \Pi > 8.58. \end{cases} \quad (19)$$

As was noted in section 3.2, we make the assumption that the surfactant material adsorbing at the water surface in the laboratory sample has the same physical properties as that which had adsorbed on the sea surface during the test. It is quite possible that the film elasticity determined from

the subsurface water sample is not exactly representative of the film elasticity of the material in the surfactant bands. Nevertheless, the value of the film pressure at each location across the wake used in equation (19) to determine the cross-wake elasticity distribution used in the energy calculations is that measured by STEMS.

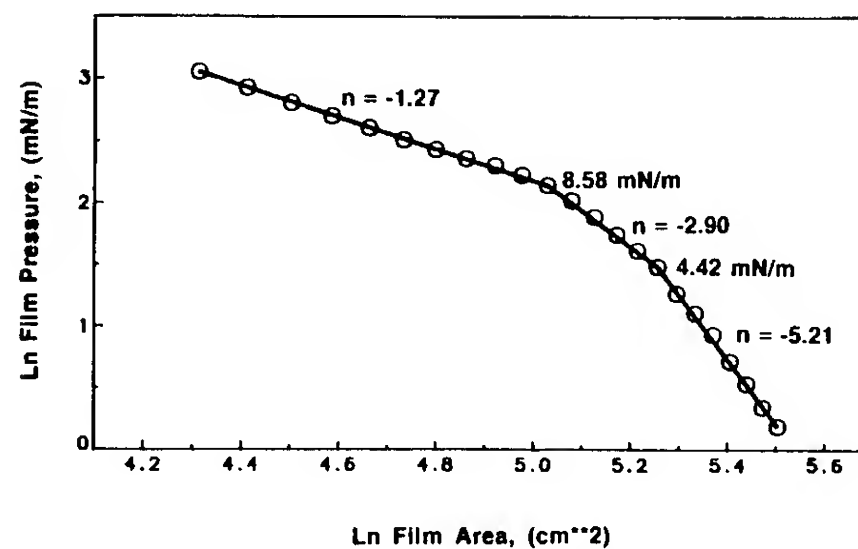


Figure 13. Measured surfactant film pressure-area curve

It is very difficult to nearly impossible to determine the exact composition of the material in the surfactant film bands measured during the January Field Experiment. There are literally hundreds of different materials present in these film bands. Surface chemists (Frew et al., 1990, Barger and Means, 1985) agree that the major constituents of these film bands are relatively soluble, highly oxygenated and condensed, but poorly defined polymeric materials of high molecular weight. However, it is not the composition of the material in the bands that is important, but rather the effects of physical properties of the material on the ambient wave field. A small change in surface elasticity will lead to significant changes in capillary and small surface gravity wave damping. Given the relative similarity in the pressure-area curves of the water samples obtained during the Field Experiment with hundreds of samples obtained from varied locations throughout the major oceans (Frew, 1990, Barger and Means, 1985; Barger et al., 1988) we feel confident that the physical properties of the films present during the Field Experiment are representative of many films throughout the major oceans. To properly char-



acterize and measure the physical properties of surfactants that are important for wave damping studies, controlled natural surfactant materials must be developed by extracting the material from natural seawater samples. Comparing the physical properties of these extracted films, which we now know the concentration of, with untreated seawater samples will provide some insight into the concentration of the materials in the untreated samples.

Surface tensions throughout the wake, for use in the model computations, are found by interpolating between measurements on the wake cuts. This requires an estimated surface distribution on a wake cut at the ship stern. For this, we have hypothesized two eight meter wide edge bands whose centers are spaced two ship beams apart. The surface tension used in the bands is 12 mN/m which is the lowest value we measured in the actual cuts.

When integrating the energy balance equation, the results at each time step must be restrained to prescribed upper and lower limits. The upper limit is the ambient energy level outside the wake. For the lower limit we have used 20 percent of the ambient inasmuch as this is the typical reduction in wave energy level we measured directly in wakes during the experiments.

The initial condition we used for the model computations has the energy reduced to 20 percent of the ambient level at the ship stern over a distance of one ship beam. The initial energy is taken as linearly rising from this depressed level back to the ambient level on each side of the ship over a distance of one-half a ship beam, thus making the entire depressed zone two ship beams wide.

#### 4.3 Computations and Comparisons With Measurements

Results of calculations for the spectral energy ratio ( $E/E_a$ ) along the SAR look direction at a center distance of 3735 m aft of the Navy ship are shown in Figures 14, 15 and 16. This is the distance of our closest wake crossing measurements for which the surface tension distribution is also shown in the figures. The results are expressed in dB down from the ambient,  $[10\log_{10}(E/E_a)]$ . For these calculations we have used 60.0 mN/m for the value of surface tension in the regions where oil 21 did not spread and we do not know the lower surface tension limit (see Section 3.3.2). The results are shown for three wavelengths: 15.9 cm, 3.6 cm and 2.0 cm which correspond to the L-, C- and X-band wave-

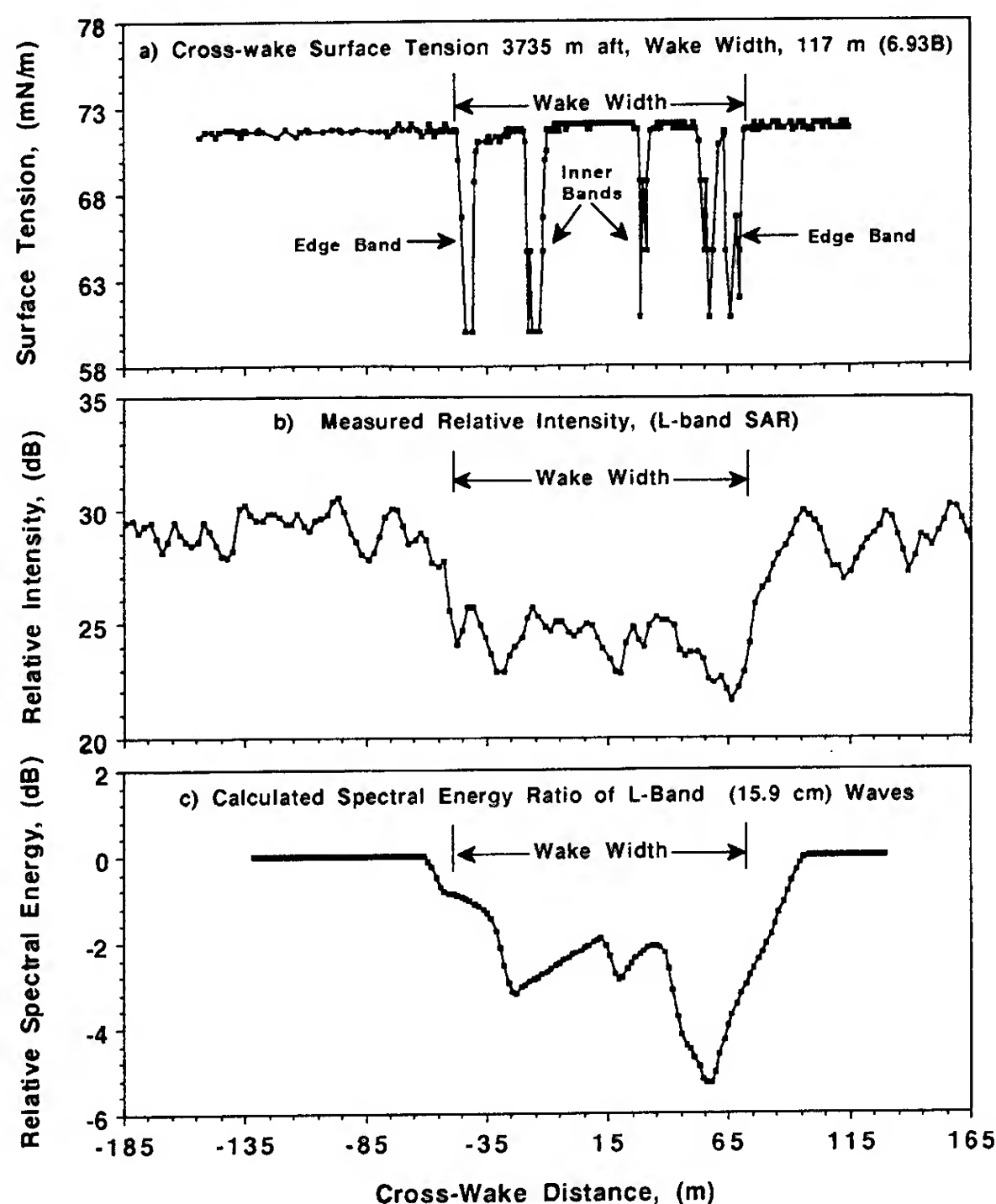


Figure 14. Calculated spectral energy ratio of L-band waves together with the measured cross-wake surface tension and SAR intensity distributions 3735 m aft of the ship

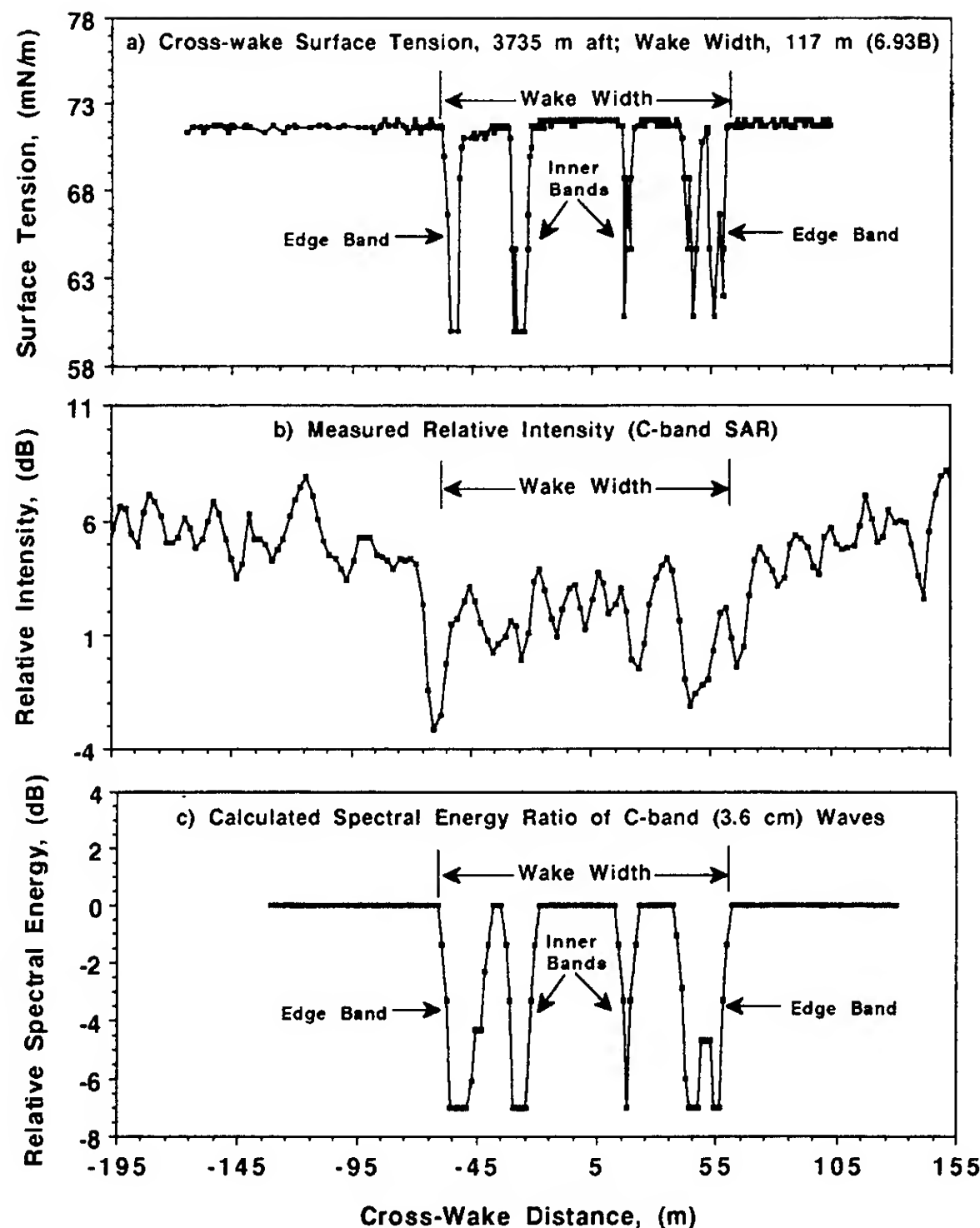


Figure 15. Calculated spectral energy ratio of C-band waves together with the measured cross-wake surface tension and SAR intensity distributions 3735 m aft of the ship

lengths at the incidence angle of 52 degrees used for SAR images of this experimental run. The measured SAR cross-sections at 3735 m aft are also shown in the figures. The SAR intensity data shown are averaged longitudinally over a length of 100 meters. The X-band signal to noise ratio was near unity for this run, so that any direct comparison with the data may be subject to some error.

The mathematical model predicts L-band waves have not recovered to ambient levels and are attenuated across the entire wake. Conversely, the C- and X-band waves are predicted to have recovered to ambient levels except in and immediately downwind of zones of compressed surface films. These findings are consistent with the SAR measurements at the same location shown in the figures. The L-band SAR data shows the full width attenuation and several of its variations in intensity across the wake can be visually "matched up" with spectral energy variations in the mathematical predictions. Correlations between the regions of the largest backscatter intensity reduction in the SAR data and the regions of lowest surface tension are evident in the C- and X-band data as well. The reductions in image intensity in

these regions are about 6 dB at L-band and 5 dB at C-band. Corresponding attenuations predicted by the mathematical model are about 5 dB at L-band and 7 dB at C- and X-band. The latter value is set by the arbitrary minimum energy level of 20 percent of the ambient level used for the computations.

As is predicted by the mathematical model, the C- and X-band SAR data show backscatter intensity in the wake to be nearly at ambient levels except in isolated regions whose locations are in reasonable correspondence with zones of measured surfactant concentration.

#### 4.4 Influence of Variations in Model Input Parameters

Because of uncertainties about the accuracy of some of the formulations used for the source terms in the energy balance equation, a study of the influence of variations in the source terms should be done. Although a complete study of this type cannot be included in this paper, we will show the influences of a few variations. The effects of source term variations on the wake 3735 meters and further aft will be

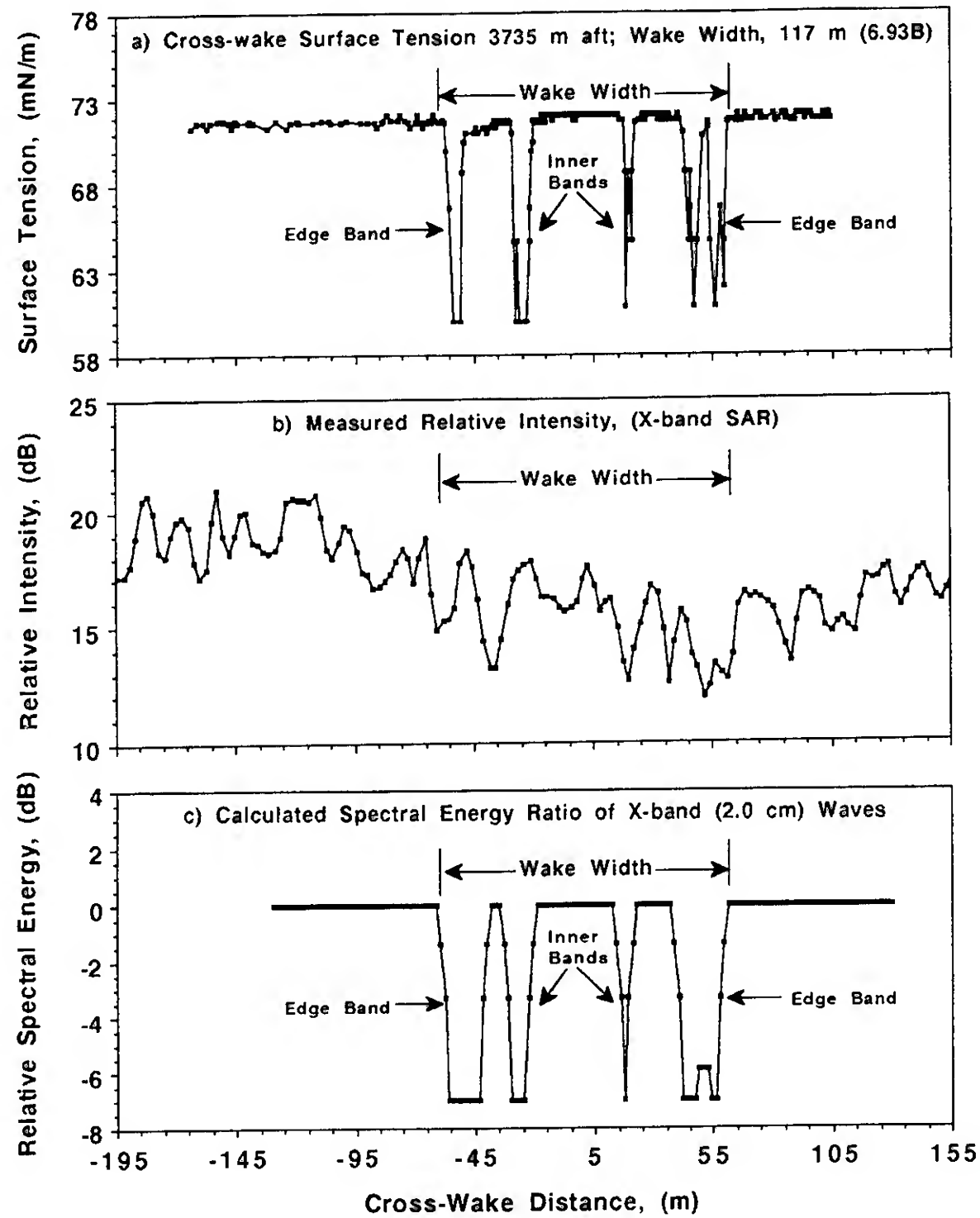


Figure 16. Calculated spectral energy ratio of X-band waves together with the measured cross-wake surface tension and SAR intensity distributions 3735 m aft of the ship

most pronounced for L-band waves since the others have regrown to the ambient level except in the surfactant bands. We will compare results with source term variations with the base case L-band results shown in Figure 14.

Figure 17 shows the predicted L-band energy distribution 3735 meters aft when the wave energy decay rate due to turbulence in the ambient sea is reduced to seventy-five percent of the value used to produce Figure 14. This changes the decay rate in the wake because the ship-induced turbulent decay is taken as diminishing with distance aft (equations 10 and 14) until it becomes equal to the ambient level. The effect of the modest reduction in decay from turbulence is strong with significant wave attenuation remaining only in the regions of strong surfactant concentration on the down-wind side of the wake instead of all across the wake as in the base case.

Figure 18 shows the effect of raising the energy input due to nonlinear interactions by fifty percent. Comparison with Figure 14 shows the significant change that can be caused by such an increase in the energy transfer from nonlinear interactions.

As was discussed in Section 3.3.2, we were not able to determine the maximum value of the surface tension decrease in the regions where oil 21 did not spread. For the original model calculations shown in Figure 14, we used 60.0 mN/m as the surface tension in these regions. It is entirely possible that that surface tension value could have been as low as 42.0 mN/m. Figure 19 shows the effect of decreasing the surface tension value in these regions to 42.0 mN/m. 42.0 mN/m is the lower limit on the surface tension value that can be associated with the compacted surfactant material at the surface during the Field Experiment. Decreasing the surface tension increases the surfactant damping in these regions. Comparing the two figures shows that the possible variation in surfactant damping is shown to have a marked effect on the L-band wave energy levels.

Figure 20 shows the results of eliminating the effect of the reduction in wind growth rate due to surface smoothness. For this computation, The wind energy input rate was set to:

$$S_w = 0.05\sigma(u_*/c)^2 E \cos\theta. \quad (20)$$

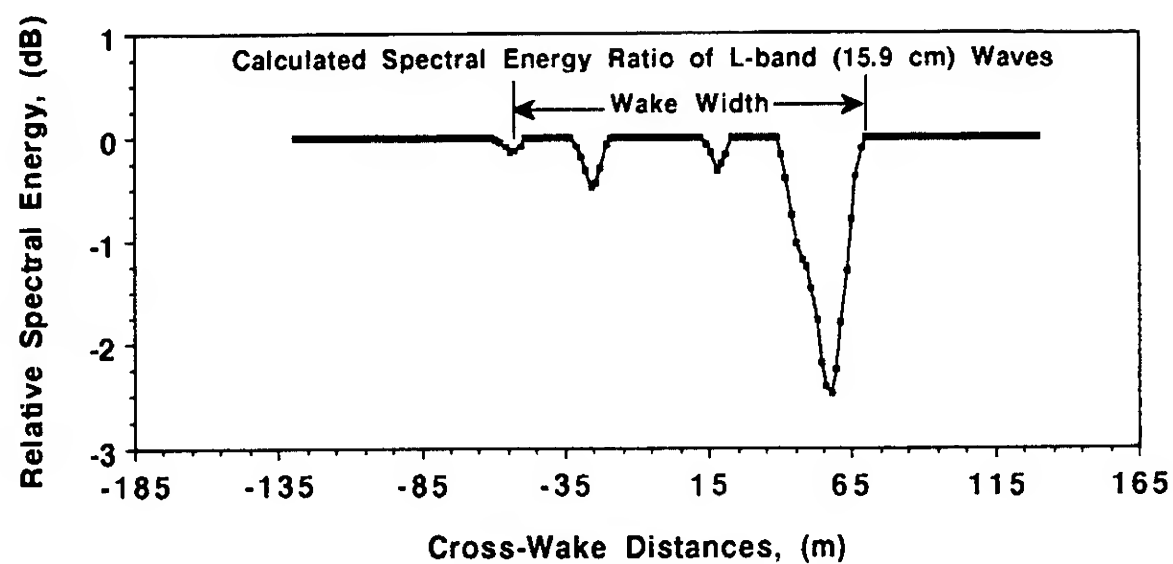


Figure 17. Calculated spectral energy ratio of L-band waves when the ambient turbulence level is reduced by seventy-five percent

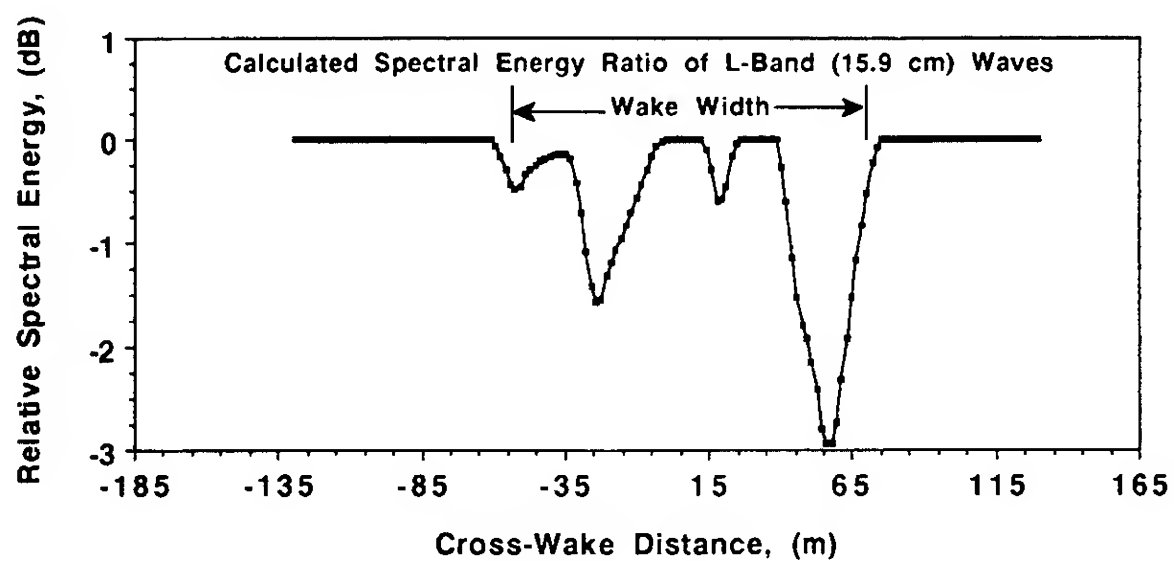


Figure 18. Calculated spectral energy ratio of L-band waves when the energy input due to nonlinear interactions is increased by fifty percent

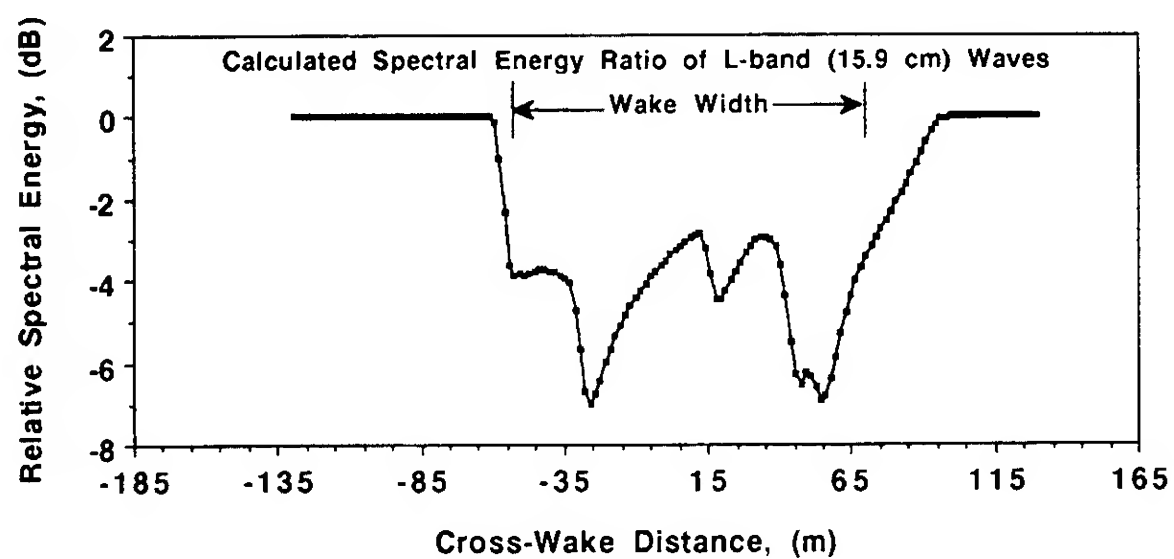


Figure 19. Calculated spectral energy ratio of L-band waves when the surfactant damping is increased

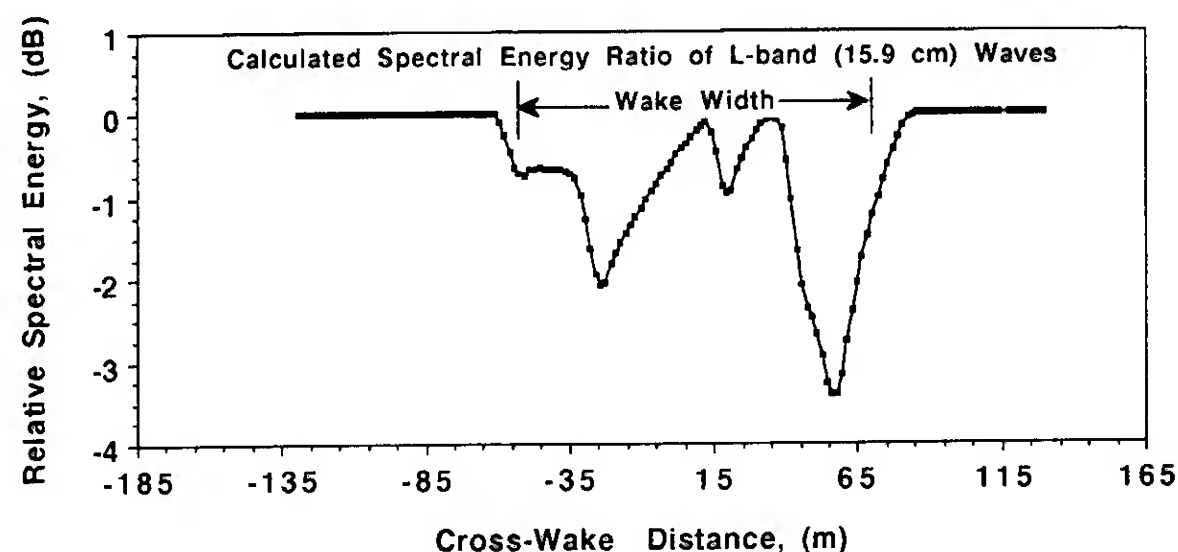


Figure 20. Calculated spectral energy ratio of L-band waves when the reduction in wind growth rate due to surface smoothness is removed

Comparing Figure 20 with Figure 14 shows that, at least at the 3735 meter location, the effect of this variation in wind energy input is clearly observable.

Although a much more complete sensitivity study should be done in the future, the above examples clearly show that distributions of short waves in wakes are sensitive to all of the terms in the energy balance equation. However, it is because of the surfactant effects alone that attenuation can persist into the very far wake. The other attenuating effects and the energy input effects, at least to the extent that we presently understand them, would lead to wave regrowth to ambient levels in the very far wake if surface film concentration did not persist into this region. This is probably why SAR centerline images do not persist into the very far wake when the sea is rough. The mixing associated with wave breaking eliminates the bands of ship-induced surfactant concentration in that situation.

## 5.0 SUMMARY AND CONCLUSIONS

Previous to this experiment in situ surface tension data have never been measured to the resolution in surface tension obtained or with such a fine spatial resolution. Coupling these measurements to the determination of the pressure-area curves has for the first time allowed us to infer film elasticity distributions for ocean water and to realistically calculate the changes in wave amplitude due to the presence of these surfactants.

The major process by which surfactants affect synthetic aperture radar (SAR) or other radar images of the ocean surface is through wave damping, and two important variables in this process are the Bragg scattering wave number (if the incidence angle is not too large or small) and the surface film elasticity as determined above. It is apparent from our measurements, calculations, and comparisons with observations that surfactant films play an important role in the formation and persistence of the centerline wake region. The role is probably dominant in the far wake. In the near and intermediate wake regions other influences on wave energy cannot be neglected.

All of the ship wakes we have analyzed from the Field Experiment have exhibited a banded structure for many kilometers downstream. Even in one run in which the wind speed was 9 m/sec the bands were measured at distances

nearly 20 km behind the target vessel. In lighter wind cases bands were easily detected more than one hour late (equivalent to 35 to 40 km behind the target). The width of the wake slowly grew in time as indicated in Figures 8 and 10. From our limited data analysis so far, we cannot reach any conclusions about the dependence of these ship-generated surfactant film bands on environmental parameters (wind speed and direction, ambient surfactant concentration) and ship operating characteristics (hull form, speed, number of propellers). However, we conclude that continued analysis of the remaining data will allow us to determine the effects of both environmental and ship operating parameters on the origin and downstream persistence of these ship wake surfactant bands.

As our sensitivity studies have shown, variations in each of the source terms in the model (within our present knowledge of what we can reasonably expect their variations to be) have a strong effect on the L-band calculations. This points out the need to learn more about these source terms.

Within the present model, the approximations for wind wave regeneration and nonlinear energy transfer are both subject to limited data on which to base the approximations. Here again, both a careful analysis of available information and additional laboratory experiments are indicated in order to resolve the uncertainties which still remain after this "first look" analysis. In particular, existing theories and experiments apply to wave frequencies up to twice that of the spectral peak. On the other hand, radar scattering waves have frequencies about ten times that of the spectral peak. That is why new experiments are needed.

Finally, wave damping by turbulence in ship wakes is the least understood of all the source terms. Our knowledge of wave damping by turbulence is very limited. Our knowledge of the amount of turbulence that actually exists in the wake more than a few ship lengths downstream is non-existent. Like all the other uncertainties, this one can only be fully resolved by careful experiments focused on the hydrodynamics in question.

## ACKNOWLEDGEMENT

This work was sponsored by the Ship Wake Consortium and by the Surface Ship Wake Detection Program of the Applied Research and Technology Directorate (Code 12) of the Office of Naval Research.



## 6.0 REFERENCES

- Adam, N.K., "A Rapid Method for Determining the Lowering of Tension of Exposed Water Surfaces, with Some Observations on the Surface Tension of the Sea and Inland Waters," *Proceedings of the Royal Society of London, Series B*, Vol. 122, 1937, pp. 134-139.
- Adamson, A.Q., *Physical Chemistry of Surfaces*, Third Edition (New York: John Wiley), 1976.
- Barger, W.R., Daniel, W.H., and Garrett, W.D., "Surface Chemical Properties of Banded Sea Slicks," *Deep-Sea Res.*, Vol. 21, 1974, pp. 83-89.
- Barger, W.R. and Means, J.C., "Clues to the Structure of Marine Organic Material From the Study of Physical Properties of Surface Films," in *Marine and Estuarine Geochemistry*, A. C. Sigleo and A. Hattori, eds., Lewis Publishers, Chelsea, MI, 1985, pp. 44-67.
- Barger, W. R., Kaiser, J.A.C. and Klusty, M.A., "Physical Effects of Sea Surface Microlayer Films Collected From the Coastal Waters of Maine, Virginia and Bermuda," *EOS, Trans., AGU*, Vol. 69, No. 44, 1988, pp. 1095.
- Birkhoff, G. and Zarantonello, E.H., *Jets, Wakes and Cavities*, Academic Press, New York, 1957.
- Brumley, B.H. and Jirka, G.H., "Near Surface Turbulence in a Grid-Stirred Tank," *J. Fluid Mech.*, Vol. 183, 1987, pp. 235-263.
- Dorrestein, R., "General Linearized Theory of the Effect of Surface Films on Water Ripples," *Proceedings of the Amsterdam Academy of Science*, Vol. 54, 1951, pp. 260-350.
- Frew, N.M., Goldman, J.C., Dennett, M.R. and Johnson, A.S., "Impact of Phytoplankton-Generated Surfactants on Air-Sea Gas Exchange," *J. Geophys. Res.*, Vol. 95, No. C3, 1990, 3337-3352.
- Garrett, W.D., "Damping of Capillary Waves at the Air-Sea Interface by Oceanic Surface-Active Material," *J. Mar. Res.*, Vol. 25, 1967, pp. 279-291.
- Garrett, W.D. and Duce, R.A., "Surface Microlayer Samplers," in *Air-Sea Interaction Instruments and Methods*, F. Dobson, L. Hasse and R. Davis (eds.), Plenum Press: New York, 1980, pp. 471-490.
- Hasselmann, K., "On the Nonlinear Energy Transfer in a Gravity Wave Spectrum, 1. General Theory," *J. Fluid Mech.*, Vol. 12, 1962, pp. 481-500.
- Huhnerfuss, H., Alpers, W., Jones, W.L., Lange, P.A., and Richter, K., "The Damping of Ocean Surface Waves by a Monomolecular Film Measured by Wave Staffs and Microwave Radars," *J. Geophys. Res.*, Vol. 86, No. C1, 1981, pp. 429-438.
- Hunt, J.C.R. and Graham, J.M.R., "Free Stream Turbulence Near Plane Boundaries," *J. Fluid Mech.*, Vol. 84, 1978, pp. 209-235.
- Kaiser, J.A.C., Ramberg, S.E., Peltzer, R.D., Andrews M.D. and Garrett, W.D., "Wakex 86, A Ship Wake/Films Exploratory Experiment," *NRL Memo. Rep.* 6270, 1988.
- Kitaigorodskii, S.A. and Lumley, J.L., "Wave-Turbulence Interactions in the Upper Ocean, Part I. The Energy Balance of the Interacting Fields of Surface Wind Waves and Wind-Induced Three-Dimensional Turbulence," *J. Phys. Oceanogr.*, Vol. 13, 1983, pp. 1977-1987.
- Kitaigorodskii, S.A., Donelan, M.A., Lumley, J.L. and Teray, E.A., "Wave-Turbulence Interactions in the Upper Ocean, Part II. Statistical Characteristics of Wave and Turbulent Components of the Random Velocity Field in the Marine Surface Layer," *J. Phys. Oceanogr.*, Vol. 13, 1983, pp. 1988-1998.
- Kitchener, J.A. and Cooper, C.F., "Current Concepts in the Theory of Foaming," *Q. Rev.*, Vol. 13, 1957, pp. 71-97.
- Lamb, H., *Hydrodynamics*, Dover: New York, 631, 1945.
- Lyden, J.D., Hammond, R.R., Lyzenga, D.R. and Shuchman, R.A., "Synthetic Aperture Radar Imaging of Surface Ship Wakes," *J. Geophys. Res.*, Vol. 93, No. C10, 1988, pp. 12293-12303.
- McDougall, T.J., "Measurements of Turbulence in a Zero-Mean-Shear Mixed Layer," *J. Fluid Mech.*, Vol. 94, 1979, pp. 409-431.
- Mitsuyasu, H. and Honda, T., "Wind-Induced Growth of Water Waves," *J. Fluid Mech.*, Vol. 123, 1982, pp. 425-442.
- Miyake, Y. and Abe, T., "A Study on the Foaming of Sea Water," *J. Mar. Res.*, Vol. 7, No. 2, 1948, pp. 67-73.
- National Defense Research Committee Division 6, Physics of Sound in the Sea, Part IV — Acoustic Properties of Wakes. Summary of Technical Report Vol. 8, 1946, reprinted as NAVMAT Report P-9675, 1969.
- Newman, J.N., "Recent Research on Ship Wakes," 8th Symposium on Naval Hydrodynamics: Hydrodynamics in the Ocean Environment (Arlington, Virginia: Office of Naval Research, Department of the Navy), 1970, pp. 519-545.
- Ochadlick, A.R. Jr., Schmidt, W.A. and Cho, P., "Quantitative Stability of Slicks Observed With the NADC SAR During SAXON," *Naval Air Development Center Tech. Memo. SAXON/CLT*, 1990.
- Olmez, H. and Milgram, J.H., "Attenuation of Water Waves by Turbulence," *MIT Dept. Ocean Eng. Rep.*, 1989.
- Peltzer, R.D., "White-Water Wake Characteristics of Surface Vessels," *NRL Memo. Rep.* 5335, 1984.

Peltzer, R.D. and Griffin, O.M., "Stability of a Three-Dimensional Foam Layer in Sea Water," J. Geophys. Res., Vol. 93, No. C9, 1988, pp. 10804-10812.

Phillips, O.M., "The Scattering of Gravity Waves by Turbulence," J. Fluid Mech., Vol. 5, No. 12, 1958, pp. 177-192.

Plant, W.J., "A Relationship Between Wind Stress and Wave Slope," J. Geophys. Res., Vol. 87, No. C3, 1982, pp. 1961-1967.

Ramberg, S.E. and Griffin, O.M., "Laboratory Study of Steep and Breaking Deep Water Waves," Proc. ASCE, J. Waterways, Port, Coastal and Ocean Eng., Vol. 113, No. 5, 1987, pp. 493-506.

Scully-Power, P., "Navy Oceanographer Shuttle Observations STS41-G," Naval Underwater Systems Center, NUSC Tech. Doc. 7611, 1986.

Skop, R.A., Brown, J.W. and Lindsley, W.G., "Bubble Transport of Surface-Active Organic Compounds in Seawater: Initial Measurements and Results," Rosenstiel School of Marine and Atmospheric Science, U. of Miami, Rep. RSMAS-TR89-003, 1989.

Skop, R.A., Griffin, O.M., and Leipold, Y., "Modification of Directional Wave Number Spectra by Currents in the Wake of a Surface Ship," J. Ship Res., Vol. 34, 1990, pp. 69-78.

Vesecky, J.F. and Stewart, R.H., 1982, "The Observation of Ocean Surface Phenomena Using Imagery From the SEASAT Synthetic Aperture Radar: An Assessment," J. Geophys. Res., Vol. 87, No. C5, 1982, pp. 3397-3430.

# Three-Dimensional Instability Modes of the Wake Far Behind a Ship

G. Triantafyllou (Massachusetts Institute of Technology, USA)

## 1 Abstract

The three-dimensional linear stability of the viscous wake far behind a ship is investigated. The Euler equations are linearized around the time-average flow in the wake, and the stability problem is formulated as an eigenvalue problem for waves travelling parallel to the course of the ship. It is shown that the complex phase velocity of the unstable waves satisfies Howard's semi-circle theorem. For a self-similar velocity profile, a numerical solution is obtained by expanding the perturbation pressure in a Fourier series and solving a set of simultaneous ordinary differential equations. It is found that the wake becomes unstable in its antisymmetric pressure mode for a range of wavenumbers less than a "cut-off" value. In the zero Froude number limit, the frequency and phase-velocity of the unstable gravity waves are determined entirely by the characteristics of the shear flow in the wake, a fact allowing the derivation of a simple approximation for the eigenvalues and eigenvectors. As the Froude number is increased, the growth-rates of the unstable waves, and the "cut-off" value are reduced, indicating a stabilizing effect on this mode. In the infinite Froude number limit the wake becomes unstable in a different mode. The wake does not exhibit self-excited behaviour, because the instability of the shear flow is of the convective type at all Froude numbers. External noise, like ambient waves in the ocean, can drive the wake instability producing spatially growing waves. The free-surface manifestation of the spatially unstable waves exhibits a characteristic staggered pattern of alternating "hills" and "valleys".

## 2 Introduction

The best known feature of the flow behind a ship is the Kelvin wave pattern. The Kelvin wave pattern has been extensively studied, because it is a very significant source of ship resistance at high speeds. The viscous wake of the ship has received much less attention, since it is assumed that it is for most ships thin, and its influence on the wavemaking of the ship has routinely been neglected, with some notable exceptions (Tatinclaux, 1970, Peregrine, 1971). In recent years, however, the viscous wake of the ship has attracted a considerable amount of attention, both as a basic fluid mechanical problem, and in connection with the problem of wake imaging. As aerial pictures of the ocean have revealed, viscous wakes of ships are visible at very large distances behind the ship (see, among others, Peltzer et al., 1978, Milgram, 1988, and Skop et al., 1990). Thus, the viscous wake, even though relatively thin, leaves a very persistent "trace" on the ocean surface, and offers an effective means of ship detection. The problem has several different aspects, including the backscatter of electromagnetic waves from the ocean surface (Valenzuela, 1978), and is currently extensively studied.

From the fluid mechanics point of view, which is mainly of interest in the present paper, investigations of the interaction of vortical flows with a free surface have revealed several interesting

new properties: Benney and Chow, 1986, Sarpkaya, 1986, Lugt, 1987, Oikawa et al., 1987, Tryggvason, 1988, Willmarth et al., 1989, Bernal and Kwon, 1989, Triantafyllou and Dimas, 1989, Liepmann, 1990. The basic hydrodynamics of wake/free surface interactions are not understood well enough yet to provide a full description of the complex phenomena involved, nor an explanation of the aforementioned persistence of ship wakes. A solution of the problem from first principles, through direct simulation of the Navier-Stokes equations, is still impossible, owing to the combined complexity provided by the very high value of the Reynolds numbers of ships, typically  $10^9$ , and the presence of a moving boundary, the free surface, which renders the computational domain time-dependent. It appears therefore that the problem has to be approached in successive stages.

In this paper a specific aspect of the wake/free surface interaction is addressed, namely the linear hydrodynamic stability of wake, seen as a three-dimensional shear flow. It has been well known that in supercritical transitions, linear theory can determine whether a certain flow state is unstable or not. In recent years, it has become increasingly clear that linear theory can also provide a good description of the "shape" of the unsteady flow patterns that result from the instability, whereas the amplitude of the patterns is determined by non-linear effects. (See for instance Koch, 1985, Triantafyllou et al., 1986, Triantafyllou et al., 1987, Chomaz et al., 1988, Unal and Rockwell, 1988, Karniadakis and Triantafyllou, 1989, Hanneman and Oertel, 1989, Triantafyllou and Karniadakis, 1990). Linear theory has thus become a very useful conceptual tool in interpreting the physics of unsteady viscous flows. A fundamental concept in the linear instability theory in media that are unbounded in the direction of propagation of the instability waves is the distinction between absolute and convective instabilities (see the review article by Bers, 1983). Absolutely unstable flows are *self-excited*, and a localized perturbation leads to growing motions at any fixed location in space. Convectively unstable flows on the other hand remain steady in a noise-free environment, because all localized perturbations are convected away. It is interesting to investigate to what extent these concepts can elucidate the problem of shear flow/free surface interaction.

For the two-dimensional wake/free surface interaction problem, it has been recently shown (Triantafyllou & Dimas, 1989) that the vicinity of a free surface drastically alters the instability properties of two-dimensional shear flows, and renders an absolutely unstable flow convectively unstable. As a result, high Reynolds number wakes of floating objects remain steady at low Froude numbers, and have the form of steady recirculating flows. Few things have been known for the considerably more complex three-dimensional problem, studied here. We consider the space-time evolution of perturbations around the mean flow in the wake. The perturbations have the form of waves that propagate parallel to the course of the ship, and have an eigenfunction type of dependence in the other two directions. The presence of the free

surface is acknowledged through the kinematic and the dynamic boundary conditions. An eigenvalue problem is thus obtained for the frequency which depends parametrically on the Froude number of the flow. The eigenvalues and eigenvectors are solved for numerically. From the computed eigenvectors, the shape of the free-surface manifestations of the instability waves is determined. The issues that are of interest here are: (i) The shape of the unsteady patterns that result from the wake/free surface interaction, and (ii) Whether these patterns can be self-excited (which, as mentioned before, is related to the absolute versus convective instability distinctions).

### 3 Three-dimensional shear flow/free surface interactions

In this section we discuss the formulation of the shear flow/free surface interaction problem in general. Let  $x, y, z$  be a system of coordinates, with the  $x$ -axis parallel to the direction of the flow, the  $z$ -axis parallel and opposite to the direction of gravity, and the  $y$ -axis perpendicular to the other two. The unit vectors along the  $x, y, z$  axes are  $i, j, k$  respectively (figure 1). For the problem of interest here, the frame of reference is fixed with respect to the ship.

We assume that all velocities have been non-dimensionalized with respect to some reference velocity  $U_\infty$ , (in this case the speed of the ship), the pressure with respect to  $\rho U_\infty^2$  ( $\rho$  is the density), and all lengths with respect to the width  $b$  of the wake. Consistent with this non-dimensionalization, the acceleration of gravity  $g$  is replaced by  $1/F^2$ , where  $F$  is the Froude number of the flow, defined as  $F = U_\infty / \sqrt{gb}$ .

The non-dimensional Euler equations, linearized around a parallel flow  $U(y, z)$ , can be written as follows (Drazin and Howard, 1966):

$$\left(\frac{\partial}{\partial t} + U \frac{\partial}{\partial x}\right) u + v \nabla U + \frac{\partial p}{\partial x} = 0 \quad (1)$$

$$\left(\frac{\partial}{\partial t} + U \frac{\partial}{\partial x}\right) v + \nabla p = 0$$

where  $u$  is the component of the perturbation velocity parallel to the  $x$ -axis,  $v = (v, w)$  is the projection of the perturbation velocity vector in the  $y, z$  plane, and  $p$  is the perturbation pressure field; also,  $\nabla = (\partial/\partial y, \partial/\partial z)$ . In equation (1)  $p$  is the *dynamic* pressure, i.e. the total pressure  $p$  minus the hydrostatic:  $p = p + F^{-2}z$ . The incompressibility condition requires that the perturbation velocity has to be divergence-free:

$$\frac{\partial u}{\partial x} + \nabla v = 0 \quad (2)$$

At the free surface we have the kinematic and dynamic conditions for the free-surface elevation  $\eta(x, y, t)$ . They can be written as follows:

$$\left(\frac{\partial \eta}{\partial t} + U \frac{\partial \eta}{\partial x}\right) = v k = w \quad (3)$$

$$p = F^{-2} \eta \quad (4)$$

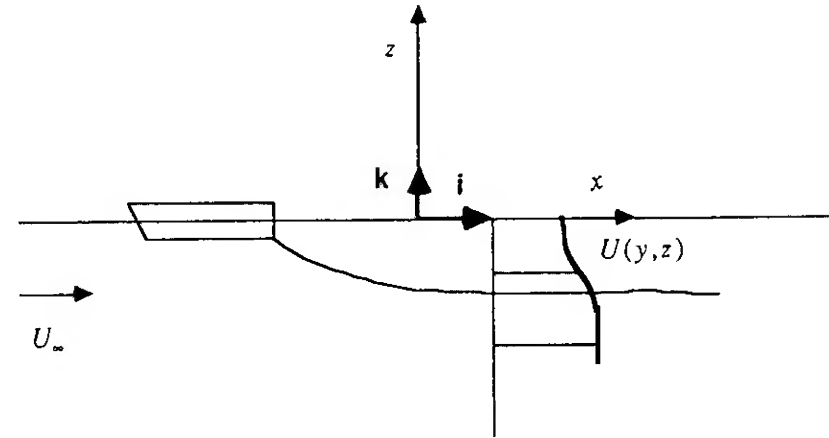


Figure 1 : Definition sketch.

From the momentum equation in the  $z$ -direction (the second of (1)), we have that:

$$\left(\frac{\partial w}{\partial t} + U \frac{\partial w}{\partial x}\right) = -\frac{\partial p}{\partial z} \quad (5)$$

We use (5) to eliminate  $w$  from (3), in order to combine the two boundary conditions into a single condition for the pressure:

$$F^2 \left(\frac{\partial}{\partial t} + U \frac{\partial}{\partial x}\right)^2 p + \frac{\partial p}{\partial z} = 0 \quad (6)$$

The dispersion relation of the flow can now be obtained by considering wavy perturbations, i.e. by setting  $u, v, w, p$  into the momentum and continuity equations proportional to  $\exp(i(kx - \omega t))$ , where  $\omega$  is the frequency and  $k$  the wavenumber. Then the momentum equations (1) become:

$$i(kU - \omega)u + v \nabla U + i k p = 0 \quad (7)$$

$$i(kU - \omega)v + \nabla p = 0$$

The incompressibility condition for the perturbation velocity  $v = (u, v, w)$  is written as:

$$i k u + \nabla v = 0 \quad (8)$$

The boundary condition (6) at the free surface is written as:

$$F^2 (kU - \omega)^2 p - \frac{\partial p}{\partial z} = 0 \quad (9)$$

We also impose the condition that the perturbation decays far outside the wake, i.e.  $u, v, w, p \rightarrow 0$  when  $\sqrt{y^2 + z^2} \rightarrow \infty$ .

We have used for notational simplicity in (7), (8), (9) the same symbols for the perturbation quantities in the frequency and in the time-domain; this does not cause confusion since we will work mainly in the frequency domain.

We multiply the first of (7) by  $ik$ , operate on the second of (7) with  $\nabla$ , add the two, and use the incompressibility condition (8) to obtain a single second-order partial differential equation for the dynamic pressure  $p$ :

$$(kU - \omega)(\nabla^2 p - k^2 p) - 2k \nabla p \nabla U = 0 \quad (10)$$

Equation (10) subject to the boundary condition (9) plus the condition  $p \rightarrow 0$  for  $|y|, |z| \rightarrow \infty$  defines an eigenvalue problem for  $\omega$ , which depends parametrically on the Froude number. If for some range of real wavenumbers complex frequencies with positive imaginary parts exist, the flow is unstable. In fact, since the flow is inviscid, complex eigenvalues appear in conjugate pairs, corresponding to one growing and one decaying mode. Finally, when the flow is uniform, i.e.  $dU/dr=0$ , the basic equation (10) reduces to Laplace's equation, and from the free surface boundary condition the classical dispersion relation for deep water waves is recovered.

We will now show that Howard's semi-circle theorem is valid for the complex eigenvalues. To this purpose, we first recast the basic equation (10) into the following form:

$$\nabla \left( \frac{\nabla p}{(U-c)^2} \right) - k^2 \frac{p}{(U-c)^2} = 0 \quad (11)$$

where  $c=\omega/k$  is the phase velocity of the wave. We multiply (11) by the complex conjugate of  $p$ ,  $p^*$  and integrate along the  $y, z$  plane. This gives:

$$\int_A dy dz (p^* \nabla \left( \frac{\nabla p}{(U-c)^2} \right) - k^2 \frac{|p|^2}{(U-c)^2}) = 0 \quad (12)$$

Since unstable waves have complex phase velocity,  $U-c$  does not vanish anywhere in the flow field, and the integral in (12) converges. For the first term of the integrand we write:

$$p^* \nabla \left( \frac{\nabla p}{(U-c)^2} \right) = \nabla \left( \frac{p^* \nabla p}{(U-c)^2} \right) - \frac{\nabla p^* \nabla p}{(U-c)^2} \quad (13)$$

We substitute into (12), and apply the divergence theorem for the integral of the first term.

$$\int_A dy dz \nabla \left( \frac{p^* \nabla p}{(U-c)^2} \right) = \int_S dl \mathbf{n} \frac{p^* \nabla p}{(U-c)^2} \quad (14)$$

where  $S$  represents the boundary of the domain  $A$ , consisting of the free-surface and a line at infinity (figure 2), and  $\mathbf{n}$  is the outward pointing unit vector. We use the boundary condition at the free surface, and that  $p$  tends to zero at infinity to obtain:

$$\begin{aligned} \int_A dy dz (U-c)^2 (|\nabla p|^2 + k^2 |p|^2) |U-c|^{-4} = \\ = k^2 F^2 \int_{-\infty}^{\infty} dy |p(y, 0)|^2 \end{aligned} \quad (15)$$

With  $c=c_r+ic_i$ ,  $|c_i|>0$ , we can separate the real and imaginary parts of (15) as follows:

$$\begin{aligned} \int_A dy dz ((U-c_r)^2 - c_i^2) Q = \\ = k^2 F^2 \int_{-\infty}^{\infty} dy |p(y, 0)|^2 \end{aligned} \quad (16)$$

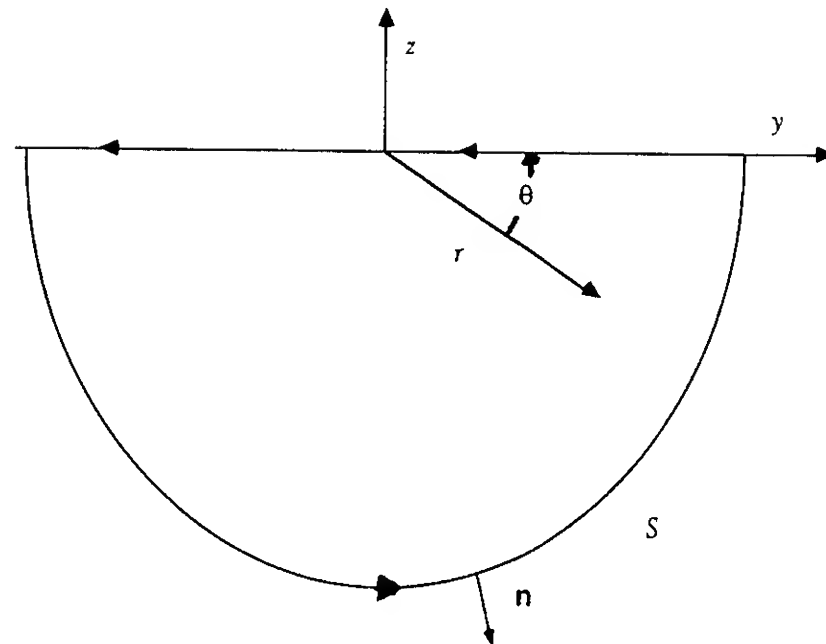


Figure 2 : Integration contour in the  $y, z$  plane.

$$\int_A dy dz (U-c_r) Q = 0 \quad (17)$$

where  $Q$  stands for:

$$Q = (|\nabla p|^2 + k^2 |p|^2) |U-c|^{-4} \geq 0 \quad (18)$$

Also, following Howard, 1961, we note that, if  $U_{min}, U_{max}$  denote, respectively, the minimum and maximum velocity in the flow field, we have:

$$\int_A dy dz (U-U_{min})(U-U_{max}) Q \leq 0 \quad (19)$$

We use (16), (17) to eliminate the integrals  $\int U^2 Q$ ,  $\int U Q$  from the left side of (19). This yields:

$$\begin{aligned} 0 \geq \int_A dy dz (U-U_{min})(U-U_{max}) Q &= \int_A dy dz \times \\ &((c_r^2 + c_i^2) - (U_{min} + U_{max})c_r + U_{min}U_{max}) Q + \\ &+ k^2 F^2 \int_{-\infty}^{\infty} dy |p(y, 0)|^2 \geq \\ &\geq \int_A dy dz \left( \left( c_r - \frac{U_{min} + U_{max}}{2} \right)^2 + c_i^2 - \right. \\ &\left. - \left( \frac{U_{min} - U_{max}}{2} \right)^2 \right) Q \end{aligned} \quad (20)$$

which implies, since  $Q$  is positive, that:

$$\left( c_r - \frac{U_{min} + U_{max}}{2} \right)^2 + c_i^2 - \left( \frac{U_{min} - U_{max}}{2} \right)^2 \leq 0 \quad (21)$$

Equation (21) is Howard's semi-circle theorem (Howard, 1961, Drazin and Howard, 1966), for the three-dimensional shear-flow free surface interaction; it states that the vector  $c_r, c_i$  lies within a



circle with center at the average of the maximum and minimum of the velocity, and radius half their difference. Equation (21) generalizes an earlier result by Yih, 1972 for the instability of two-dimensional shear flows with a free-surface.

Before proceeding with the instability of the wake, it is useful to discuss briefly the zero and infinite Froude number limits of the formulation. In the former the free surface condition is reduced to  $\partial p / \partial z = 0$ , whereas in the latter to  $p = 0$ . It is reasonable to assume that on the free surface  $\partial U / \partial z = 0$ . In this case, we can define the "double-flow" in the whole space through the extension  $U(y, z) = U(y, -z)$ . Then the zero Froude number limit corresponds to an instability mode with pressure that is symmetric around the  $z=0$  plane in the unbounded fluid, and the infinite Froude number limit to a mode with pressure that is antisymmetric around  $z=0$ . In two-dimensional flows, for instance, the zero Froude number limit corresponds to the "varicose" mode in unbounded fluid, and the infinite Froude number limit to the "sinuous" mode. For wake flows, the first is convectively unstable, and the second absolutely unstable. The instability properties of the wake as a function of the Froude number give a smooth transition from the one limit to the other (Triantafyllou and Dimas, 1989).

#### 4 Instability of the far wake

Far behind the ship, where the effects of the details of the ship hull form have diffused, we assume that the average flow has become self-similar, independent of the angle  $\theta = \arctan(z/y)$  in the  $y, z$  plane. We consider, in other words, a time-average velocity of the form  $U = U(r)$ . The reasoning behind this assumption is that, at low Froude numbers, the time-average flow can be approximated by half of that behind the "double-body", (a fictitious object that is twice the submerged part of the ship), which far behind the object asymptotically tends to acquire an axisymmetric form. This assumption is supported by the numerical computations of Swean, 1987, who computed the *steady* flow past a ship using the parabolized Navier-Stokes equations, and a  $K-\epsilon$  model of turbulence. Swean's results suggest that indeed the steady flow tends to become self-similar; his computational results show good agreement with the experimental results of Mitra et al., 1985, and Mitra et al., 1986.

Because of the self-similarity assumption, it seems natural to work in polar coordinates. Equation (10) for the perturbation  $p(r, \theta)$  is written in polar coordinates as follows:

$$(kU - \omega) \left( \frac{\partial^2 p}{\partial r^2} + \frac{1}{r} \frac{\partial p}{\partial r} + \frac{1}{r^2} \frac{\partial^2 p}{\partial \theta^2} - k^2 p \right) - 2k \frac{dU}{dr} \frac{\partial p}{\partial r} = 0 \quad (22)$$

defined for  $r \geq 0$ ,  $-\pi < \theta < 0$ . For the boundary conditions on the free surface, we note that on  $\theta = 0, -\pi$ , we have:

$$\cos(\theta) \frac{\partial}{\partial z} = \frac{\partial}{r \partial \theta} \quad (23)$$

Consequently, the boundary condition on the free surface becomes:

$$\cos(\theta) (kU - \omega)^2 F^2 p - \frac{1}{r} \frac{\partial p}{\partial \theta} = 0 \quad \text{on } \theta = 0, -\pi \quad (24)$$

Finally, we impose the condition that far from the wake the perturbation vanishes, i.e.

$$p(r, \theta) \rightarrow 0 \quad r \rightarrow \infty \quad (25)$$

Equations (22), (24), (25) define for any given  $k$  an eigenvalue problem for the frequency  $\omega$ ; that is to say, they constitute the dispersion relation for gravity waves propagating above the wake of the ship.

#### 5 Fourier Series Solution

Because of the linearity of the problem, and the symmetry of the average flow  $U(r)$  around the plane  $y = 0$ , an arbitrary perturbation can be decomposed into two parts: One in which the pressure is *anti-symmetric* around  $y = 0$ , referred to as Mode I, and one in which the pressure is *symmetric* around  $y = 0$ , referred to as Mode II. Thus, given that the free surface elevation is proportional to the value of the dynamic perturbation pressure there, Mode I disturbs the free surface in an antisymmetric manner around  $y = 0$ , whereas Mode II disturbs the free surface in a symmetric manner (figure 3). The fact that the two modes are separable facilitates the numerical solution of the problem.

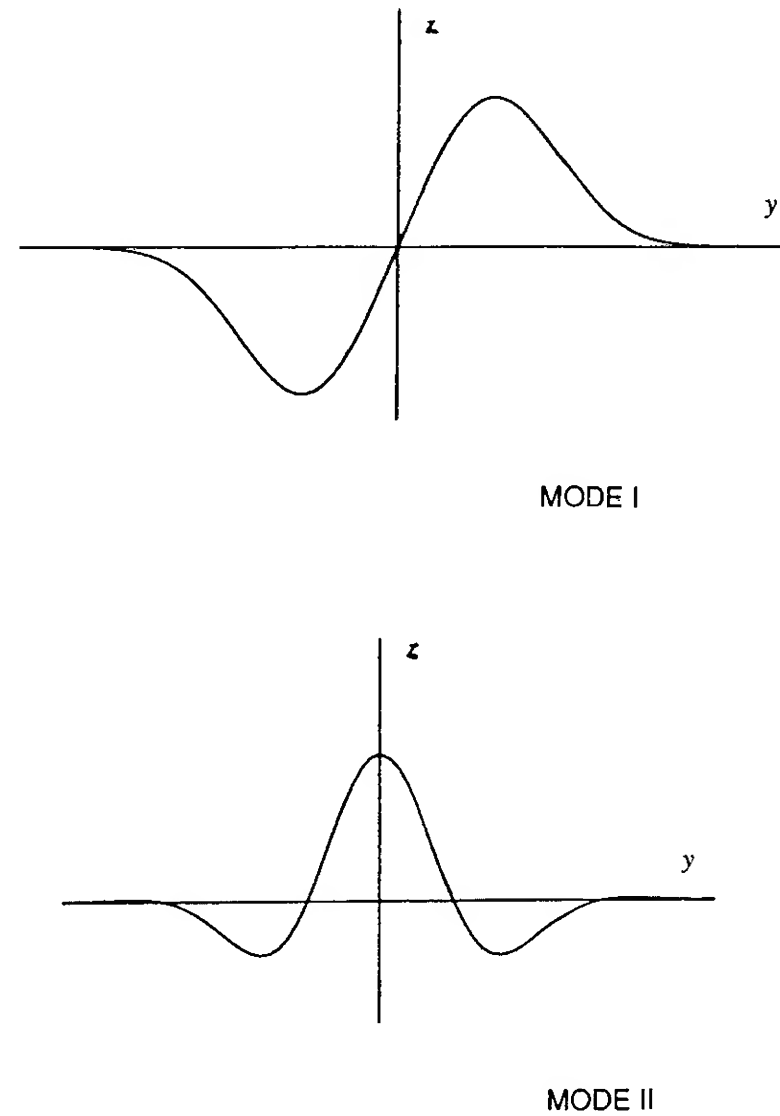


Figure 3 : Free surface elevation for Mode I (antisymmetric), and Mode II (symmetric).

##### 5.1 Mode I

We start with mode I, which satisfies the following symmetry relations:

$$p(r, -\pi) = -p(r, 0) \quad (26)$$

$$\frac{\partial p}{\partial \theta}(r, -\pi) = \frac{\partial p}{\partial \theta}(r, 0)$$

Since the initial flow is independent of the angle  $\theta$ , it is convenient to expand  $p(r, \theta)$  in a cosine-series in the interval  $-\pi \leq \theta \leq 0$ . In accordance with the antisymmetric character of Mode I, the Fourier series will contain odd-order coefficients only. Direct substitution of a Fourier series in the basic partial differential equation (22) is not applicable, because, for non-zero values of the Froude number,  $p$  satisfies a mixed boundary condition on the free surface, and its Fourier series can not be differentiated twice.

We thus make the following substitution:

$$p(r, \theta) = q(r, \theta) + \frac{\partial p}{\partial \theta}(r, 0) \left(\theta + \frac{\pi}{2}\right) \quad (27)$$

or, after using the free surface boundary condition (24):

$$p(r, \theta) = q(r, \theta) + G(r) \left(\theta + \frac{\pi}{2}\right) \quad (28)$$

where  $G(r)$  is defined by:

$$G(r) = F^2 r (kU - \omega)^2 p(r, 0) \quad (29)$$

The new variable  $q(r, \theta)$  satisfies the following conditions at  $\theta = 0, -\pi$ :

$$\frac{\partial q}{\partial \theta}(r, 0) = \frac{\partial q}{\partial \theta}(r, -\pi) = 0 \quad (30)$$

The function  $\theta + \pi/2$  is antisymmetric around the  $y=0$  plane. Consequently, the new variable  $q$  can be expanded in a cosine Fourier series containing odd terms only. The Fourier series is twice differentiable with respect to  $\theta$  because of the boundary conditions (30). We write for  $q$ :

$$q(r, \theta) = \sum_{n=1}^{\infty} q_n(r) \cos(n\theta) \quad (31)$$

Where in (31) it is implied that the summation is carried over all odd  $n$  only. The same convention applies for the rest of the section too. The coefficients  $q_n(r)$  of the Fourier series in (31) are given by:

$$q_n(r) = \frac{2}{\pi} \int_{-\pi}^0 q(r, \theta) \cos(n\theta) d\theta \quad (32)$$

In order to obtain the differential equations satisfied by the coefficients  $q_n$ , we substitute (28) into (10) and use the finite Fourier transform method, i.e. we multiply both sides of (10) by  $\cos(n\theta)$ , and integrate with respect to  $\theta$  from  $-\pi$  to 0. In an unbounded fluid this procedure yields an infinite set of *uncoupled* ordinary differential equations for  $q_n(r)$ , completely equivalent to those obtained for the perturbation velocity by Batchelor and Gill, 1962. In the problem considered here, however, owing to the presence of the free surface, the equations for the coefficients of the Fourier series are coupled, as follows:

$$\begin{aligned} (kU - \omega) \left( L_0 q_n - \frac{n^2}{r^2} q_n + \frac{4}{\pi n^2} L_0 G \right) - \\ - 2k \frac{dU}{dr} \left( \frac{dq_n}{dr} + \frac{4}{\pi n^2} \frac{dG}{dr} \right) = 0 \end{aligned} \quad (33)$$

where in (33)  $L_0$  stands for the following operator:

$$L_0 = \frac{d^2}{dr^2} + \frac{1}{r} \frac{d}{dr} - k^2 \quad (34)$$

In the derivation of (33) the following result has been used:

$$\int_{-\pi}^0 d\theta \left(\theta + \frac{\pi}{2}\right) \cos(n\theta) = \frac{1 - (-1)^n}{n^2} \quad (35)$$

We also need to express  $G$  in terms of the Fourier coefficients  $q_n$ . This can be done by substituting (31) into (28) and the result into (29); we obtain:

$$G = F^2 r (kU - \omega)^2 \left( \sum_n q_n + \frac{\pi}{2} G \right) \quad (36)$$

or, after solving with respect to  $G$ :

$$G = \frac{F^2 r (kU - \omega)^2}{1 - (\pi/2) F^2 r (kU - \omega)^2} \sum_n q_n \quad (37)$$

Equation (37) expresses  $G(r)$  in terms of  $q_n(r)$ , but is not very appropriate for the numerical solution of the problem, since it depends non-linearly on the frequency  $\omega$ . In order to obtain relations between the unknown variables that are linear in  $\omega$ , we introduce an auxiliary unknown function  $H(r)$  defined as follows:

$$H = F(kU - \omega) p(r, 0) \quad (38)$$

Now equation (36) can be replaced by the following pair of coupled equations:

$$H = F(kU - \omega) \left( \sum_n q_n + \frac{\pi}{2} G \right) \quad (39)$$

$$G = F(kU - \omega) r H \quad (40)$$

Also, because of the antisymmetry of the free surface elevation around the plane  $y=0$ , we have the following condition for the coefficients of the Fourier series:

$$q_n(r=0) = G(r=0) = 0, \quad n = 1, 3, \dots \quad (41)$$

Equations (39), (40), and (33), subject to the conditions (41), and that the unknown functions  $H(r), G(r), q_n(r)$   $n = 1, 3, 5, \dots$  vanish as  $r \rightarrow \infty$ , define for a given  $k$  an eigenvalue problem that depends linearly on the eigenvalue  $\omega$ . Consequently, if we truncate the domain to  $0 \leq r \leq R$ , and use finite-differences to approximate the derivatives in (33) at specified points  $r_i, i = 1, 2, \dots, N$ , the discretized versions of equations (39), (40) and (33) define a generalized algebraic eigenvalue problem for  $\omega$ . The latter can be solved using a standard Q-Z algorithm.

## 5.2 Mode II

Mode II satisfies the following symmetry relations:

$$p(r, 0) = p(r, -\pi) \quad (42)$$

$$\frac{\partial p}{\partial \theta}(r, 0) = -\frac{\partial p}{\partial \theta}(r, -\pi)$$

The eigenvalue problem for Mode II can thus be formulated in a similar manner as for Mode I, with the important difference that the Fourier series has to be chosen in a way that is compatible with the symmetry conditions (42).

We thus use the following substitution (instead of (28)):

$$p(r, \theta) = q(r, \theta) + \frac{1}{\pi} \frac{\partial p}{\partial \theta}(r, 0) \left(\theta + \frac{\pi}{2}\right)^2 \quad (43)$$

As with Mode I, the derivative of  $q(r, \theta)$  satisfies the boundary conditions (30), and can be expanded in a cosine Fourier series:

$$q(r, \theta) = \frac{1}{2} q_0(r) + \sum_n q_n(r) \cos(n\theta) \quad (44)$$

where the coefficients  $q_n$  are given by (32), and the summation in (43) is carried now over all *even*  $n$  only. We substitute (43) into (10), and apply the finite Fourier transform technique, noting that for  $n$  even:

$$\int_{-\pi}^0 \left(\theta + \frac{\pi}{2}\right)^2 \cos(n\theta) d\theta = \frac{2\pi}{n^2} \quad (45)$$

Using the same procedure as for Mode I we obtain the following equations:

$$H = F(kU - \omega) \left( \frac{1}{2} q_0 + \sum_n q_n + \frac{\pi}{4} G \right) \quad (46)$$

$$G = F(kU - \omega) r H \quad (47)$$

for  $n=2, 4, \dots$  we have :

$$(kU - \omega) \left( L_0 q_n - \frac{n^2}{r^2} q_n + \frac{4}{\pi n^2} L_0 G \right) - \quad (48)$$

$$-2k \frac{dU}{dr} \left( \frac{dq_n}{dr} + \frac{4}{\pi n^2} \frac{dG}{dr} \right) = 0$$

whereas for  $n=0$  we have:

$$\begin{aligned} (kU - \omega) \left( L_0 q_0 + \frac{\pi}{6} L_0 G + \frac{4}{\pi} \frac{G}{r^2} \right) - 2k \frac{dU}{dr} \left( \frac{dq_0}{dr} + \right. \\ \left. + \frac{\pi}{6} \frac{dG}{dr} \right) = 0 \end{aligned} \quad (49)$$

in equations (47), (48), and (49)  $G(r) = F^2 r (kU - \omega)^2 p(r, 0)$ , and  $L_0$  is defined as before by equation (34). Finally, instead of (41), we have that the slope of the unknowns vanishes at  $r=0$ :

$$\frac{dq_n}{dr}(r=0) = \frac{dG}{dr}(r=0) = 0 \quad n=0, 2, 4, \dots \quad (50)$$

and that the unknown functions  $H(r)$ ,  $G(r)$ , and  $q_n(r)$ ,  $n=0, 2, \dots$  vanish as  $r \rightarrow \infty$ .

## 6 Numerical results

In order to solve for  $\omega$  as a function of  $k$ , we truncate the Fourier series for  $q(r, \theta)$  after  $M$  terms, and use a finite-difference scheme to discretize the ordinary differential equations on a grid that has  $N$  points. We then form a compound eigenvector  $\mathbf{X}$  of order  $(M+2) \times N$  as follows: The first  $N$  positions of the eigenvector are occupied by the values of  $H(r)$  at the  $N$  discretization points  $r_i$ ,  $i=1, 2, \dots, N$ , the next  $N$  positions by the values of  $G(r)$ , the next  $N$  positions by the values of  $q_1(r)$ , and so on; finally, the last  $N$  positions are occupied by the values of  $q_M(r)$  at the discretization points. The discretized equations can then be combined into a single matrix equation of the form:

$$\mathbf{A} \cdot \mathbf{X} = \omega \mathbf{B} \cdot \mathbf{X} \quad (51)$$

where  $\mathbf{A}, \mathbf{B}$  are compound matrices of order  $((M+2)N) \times ((M+2)N)$ .

In general, depending on the value of  $M$  which is required for the convergence of the Fourier series, the order of the eigenvalue problem can become quite high, and require enormous amounts of computation (the number of operations is of order  $(M+2)^3 N^3$ ). We note however that the coefficients of the Fourier series are not directly coupled with each other, but, indirectly, through the variable  $G$ , which is of order  $F^2$ . As a result, for low values of the Froude number  $F$ , which are mainly of interest here, the coupling between the coefficients  $q_n$  is very weak. This, combined with the fact that for  $F=0$  only the  $n=1$  mode is unstable, allows an accurate representation of the Fourier series using only a low number of terms. The decomposition of the pressure field into modes I and II proves quite helpful in that respect too, since, say for mode I, truncating the series at the  $(2M+1)$ -th term requires the use of  $M$  coefficients in the Fourier series. For the finite difference grid, the domain was truncated at  $R=6$ , and  $N=80$  grid points were used in a second-order finite difference scheme. At the two ends of the interval all perturbation quantities were set equal to zero.

The free surface elevation  $A(r)$  can easily be determined from the computed values of  $H(r)$ , which occupy the first  $N$  positions of the compound eigenvector  $\mathbf{x}$ , as follows:

$$A = F^2 p(r, 0) = \frac{F H(r)}{(kU(r) - \omega)} \quad (52)$$

For a self-similar average flow, the following non-dimensional velocity distribution can be used:

$$U(r) = 1 - u_m \exp(-\alpha r^2) \quad (53)$$

where  $u_m, \alpha$  are constants. In this paper the values  $u_m = 0.368$ ,  $\alpha = 0.89$  were used. Those are the values for the self-similar profile measured by Ogata and Sato, 1966, far behind an axisymmetric body in unbounded fluid. The numerical results obtained using (53) are discussed in the next two subsections. We only discuss Mode I, since Mode II was found for this velocity profile to be stable. For velocity profiles with larger velocity deficits, both modes can become unstable.

## 6.1 Form of the instability waves

When the Froude number is equal to zero, the Fourier coefficients become *uncoupled*, i.e. each one represents a different wave, and only the  $n=1$  coefficient represents an unstable wave. The eigenvalue problem is therefore identical with the one in infinite fluid, which is unstable, with the maximum amplification occurring for a wavenumber equal to 0.55, and giving a complex frequency (0.4524, 0.0172). The variation of the amplitude of the first coefficient as a function of  $r$  is shown in figure 4a (semi-log scale). Subsequently, a finite value of the Froude number was used, using three terms in the Fourier expansion:  $n=1, n=3, n=5$ . The series was thus truncated at the seventh term. The variation of the amplitude of the three coefficients  $q_n$  as a function of  $r$  is shown in figure 4b. The first coefficient is indistinguishable from the one found in the  $F=0$  case. The other two coefficients are extremely small; the maximum value of the  $n=3$  coefficient is for example about  $10^{-4}$  times smaller than the  $n=1$ . The Fourier series can accurately be represented using the  $n=1$  term only, as further attested by the fact that the complex frequency has changed by less than one per cent from its  $F=0$  value. As the Froude number is further increased, the importance of the other terms is gradually increased. At  $F=1.5$  the computation was repeated using five terms ( $n=1, 3, 5, 7, 9$ ). The maximum value of the  $n=3$  term is now about  $10^{-3}$  times smaller than that of the first (figure 4c). The complex frequency has changed somewhat, to a value (0.4526, 0.0166); the real part has thus changed by less than one per cent, whereas the imaginary part has been reduced by four per cent. This implies that increasing the Froude number has a stabilizing effect on Mode I. At  $F=2.5$  the  $n=3$  term is still considerably more than  $10^{-2}$  times smaller than the first. The contribution of the Fourier coefficients with  $n > 1$  is more visible in the far field. The complex frequency has changed to the value (0.4527, 0.0155), showing a decrease in the growth-rate of about eight per cent from the  $F=0$  value.

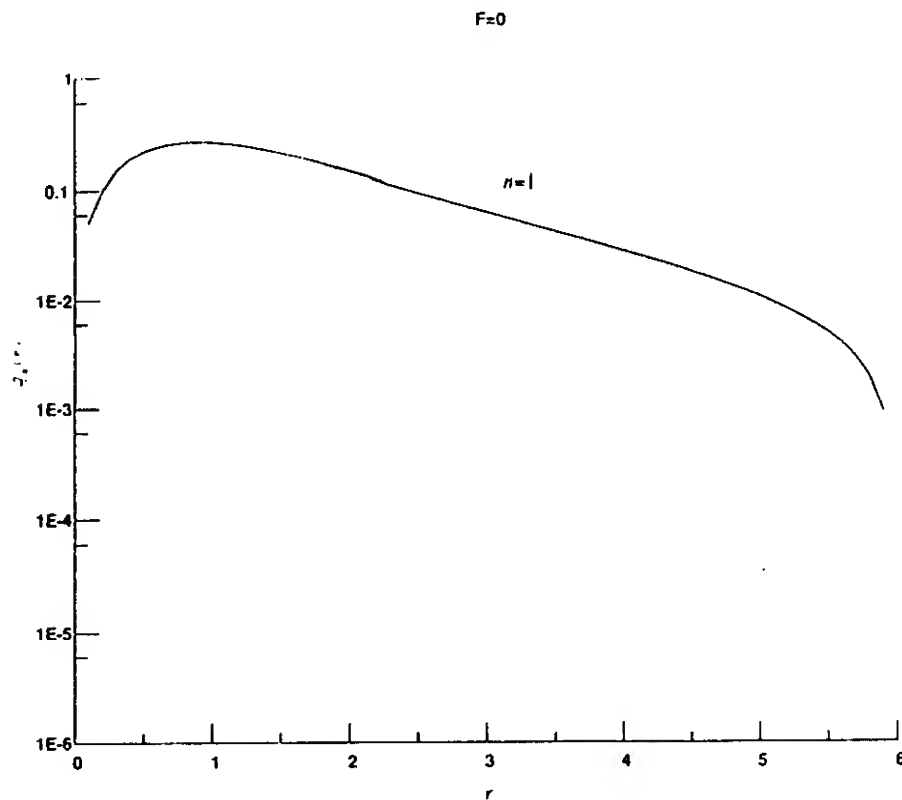


Figure 4a : Variation of the amplitude of the most unstable pressure eigenmode with  $r$  for zero Froude number (semi-log scale).

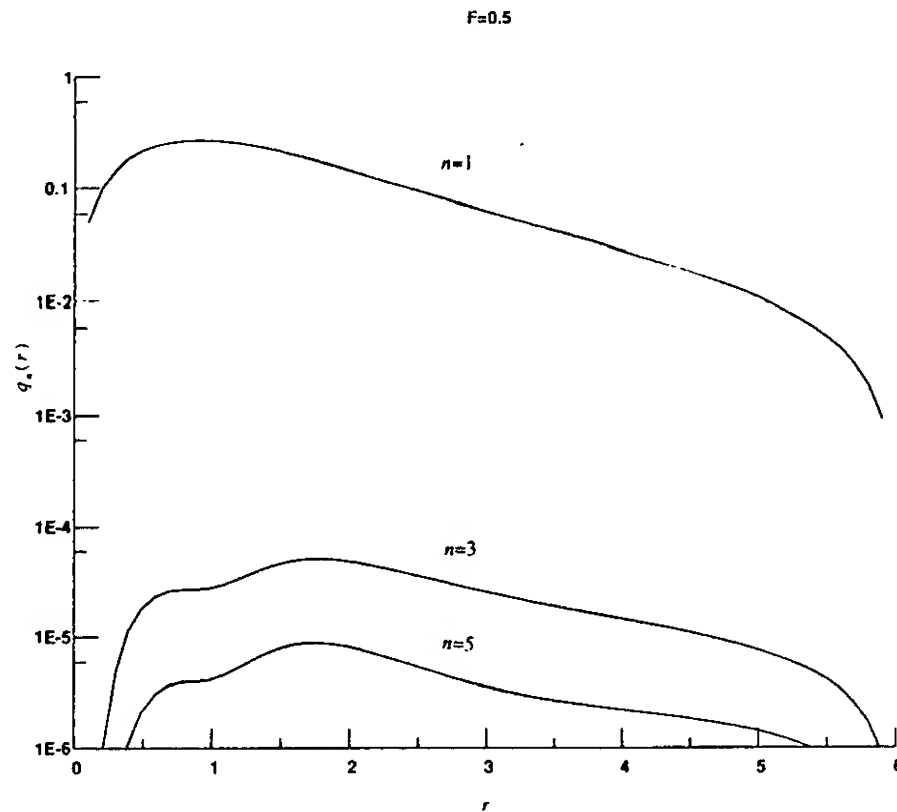


Figure 4b : Variation of the amplitude of the Fourier coefficients  $n=1, 3, 5$  with  $r$  for the most unstable wave at  $F=0.5$  (semi-log scale).

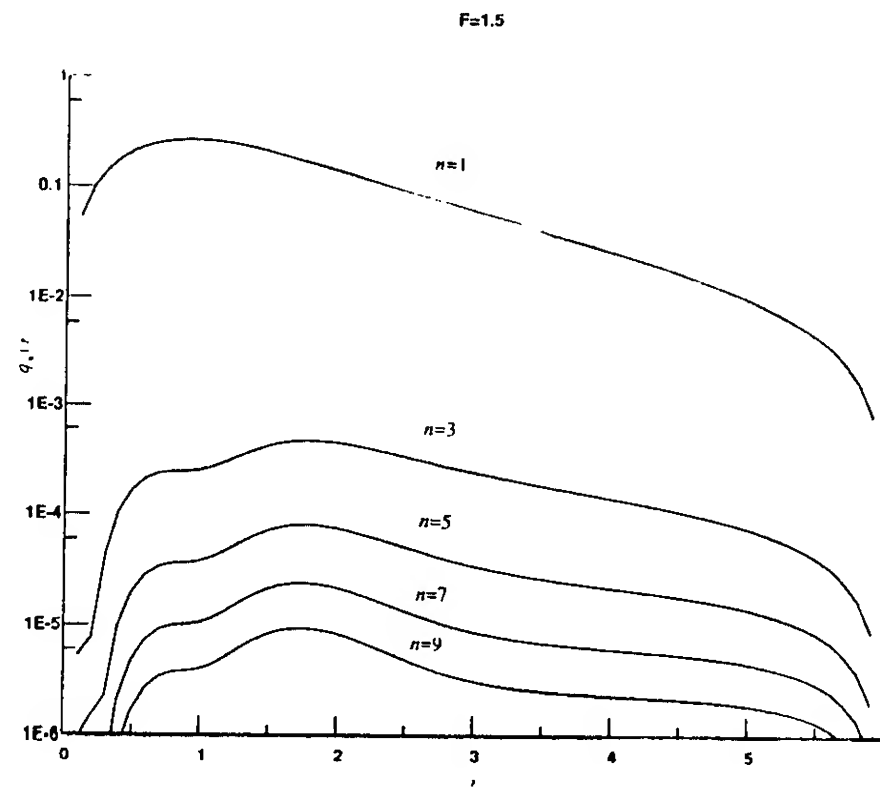


Figure 4c : Variation of the amplitude of the Fourier coefficients  $n=1, 3, 5, 7, 9$  with  $r$  for the most unstable wave  $F=1.5$  (semi-log scale).

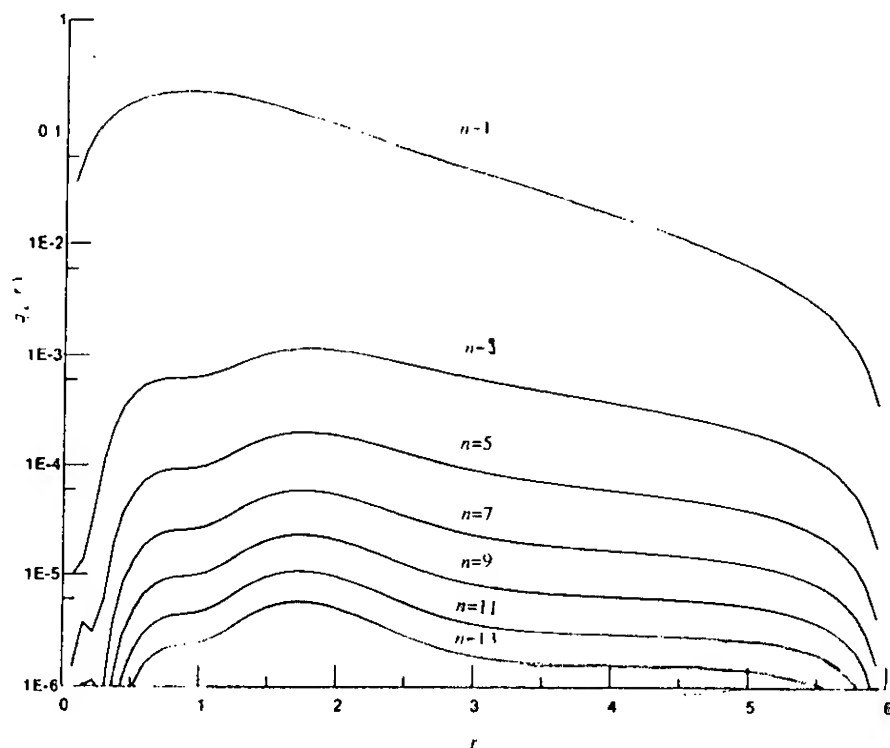


Figure 4d : Variation of the amplitude of the Fourier coefficients  $n=1, 3, 5, 7, 9, 11, 13$  with  $r$  for the most unstable wave at  $F=2.5$  (semi-log scale).

A common feature of figures 4a-4d, where the Froude number is not too high, is that there is a wide separation in magnitude between the  $n=1$  and the subsequent coefficients. For large  $n$ , the Fourier series converges faster than  $n^{-3}$ ; this can be seen in figure 4e, where the Fourier coefficients for  $F=2.5$  have been multiplied by  $n^3$  and replotted as a function of  $r$  in a linear scale. In fact equations (33), (34) suggest that, with the exception of the region around  $r=0$ , the convergence is like  $n^{-4}$ . The convergence rate is therefore algebraic, and we can safely say that the main advantage in using the Fourier series expansion, as opposed to a direct numerical solution of (10), lies in the wide separation in magnitude between the first and the subsequent Fourier coefficients, which allows an accurate representation of the series using very few coefficients.

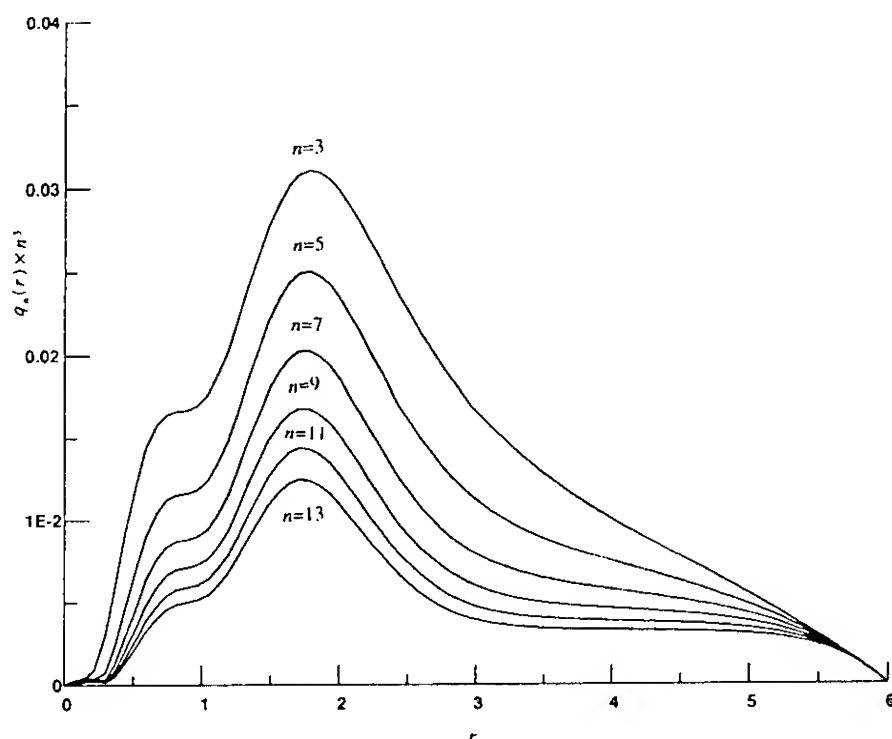


Figure 4e : Plot of  $q_n \times n^3$ ,  $n=3, 5, 7, 9, 11, 13$  as a function of  $r$ , for the same wave as in figure 4d, exhibiting a convergence rate faster than  $n^{-3}$ .

The variation of the free surface displacement generated by the most unstable wave along an  $x = \text{constant}$  plane as a function of the coordinate  $y$  is shown in figure 5a for Froude number equal to 0.5. (Only the part  $0 < y < \infty$  is shown). The free surface elevation basically follows the  $F=0$  pressure eigenmode and decays exponentially with the distance  $y$  far from the region where shear is present. The phase of the free surface elevation of the same eigenmode is shown in figure 5b (again only the part  $0 < y < \infty$  is shown). The free surface elevation in the middle of the wake, where the fluid velocity is reduced, lags behind the elevation outside the wake, where the fluid velocity has its free-stream value. This is basically the variation of the phase of the pressure eigenmode for zero Froude number. As the Froude number is increased, the free surface elevation is also increased, proportionally to the square of the Froude number. The shape of the elevation changes however by very little, owing to the aforementioned separation in magnitude between the  $n=1$  and the subsequent Fourier coefficients. It is only after  $F=2.5$  that the latter become significant enough to start altering the shape of the elevation. This can be seen in figure 6a, where the free surface elevation divided by the square of the Froude number is plotted as a function of  $r$  for  $F=0.5, 1.5, 2.5$ . The effect of the Froude number is more visible in the phase of the free surface elevation (figure 6b).

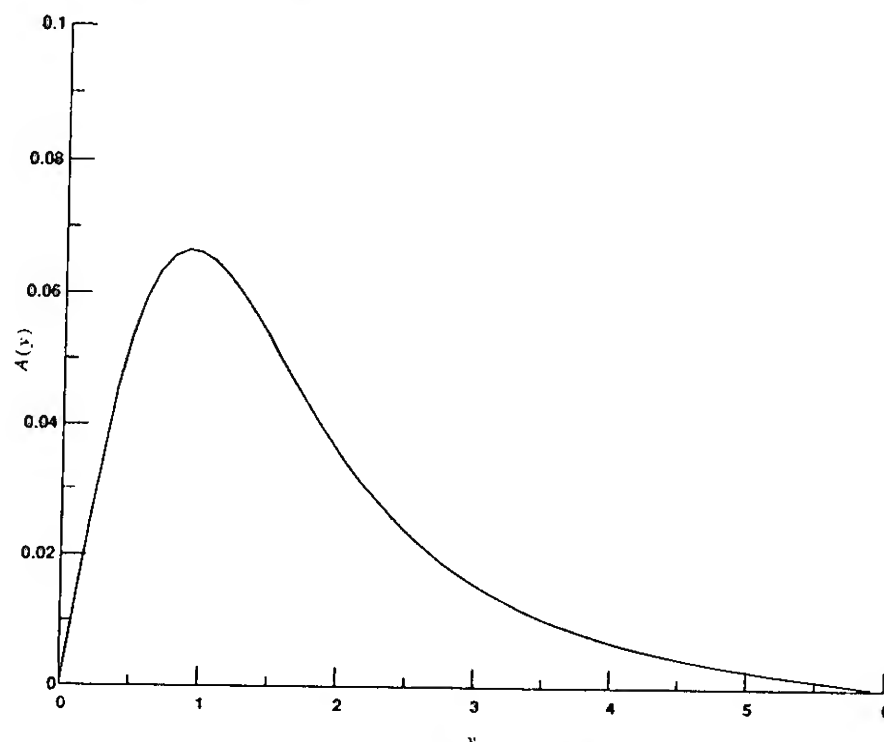


Figure 5a : Amplitude of the free surface elevation as a function of  $y$ , for the most unstable wave at  $F=0.5$ .

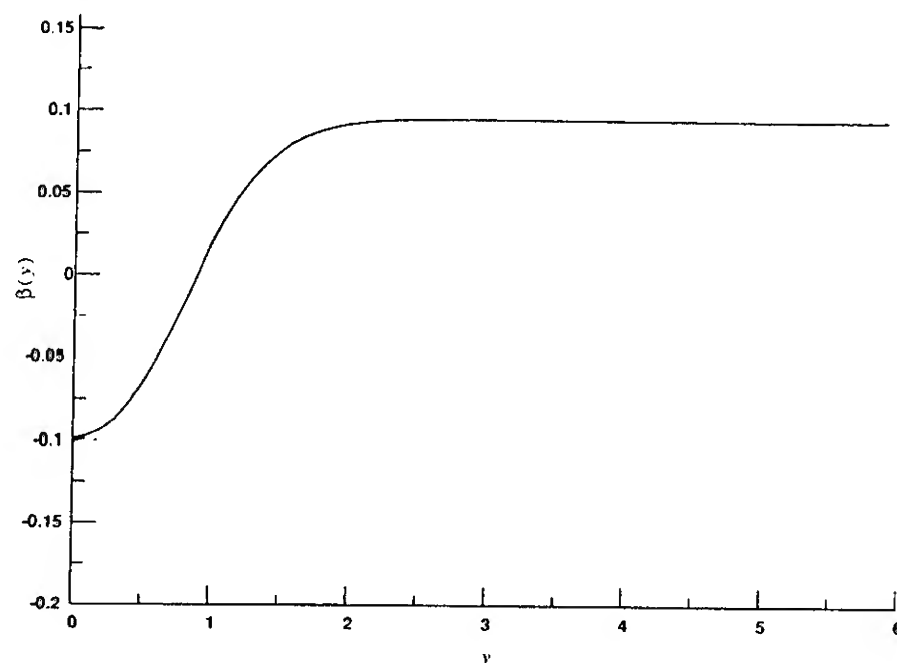


Figure 5b : Phase of the free surface elevation as a function of  $y$ , for the most unstable wave at  $F=0.5$ .



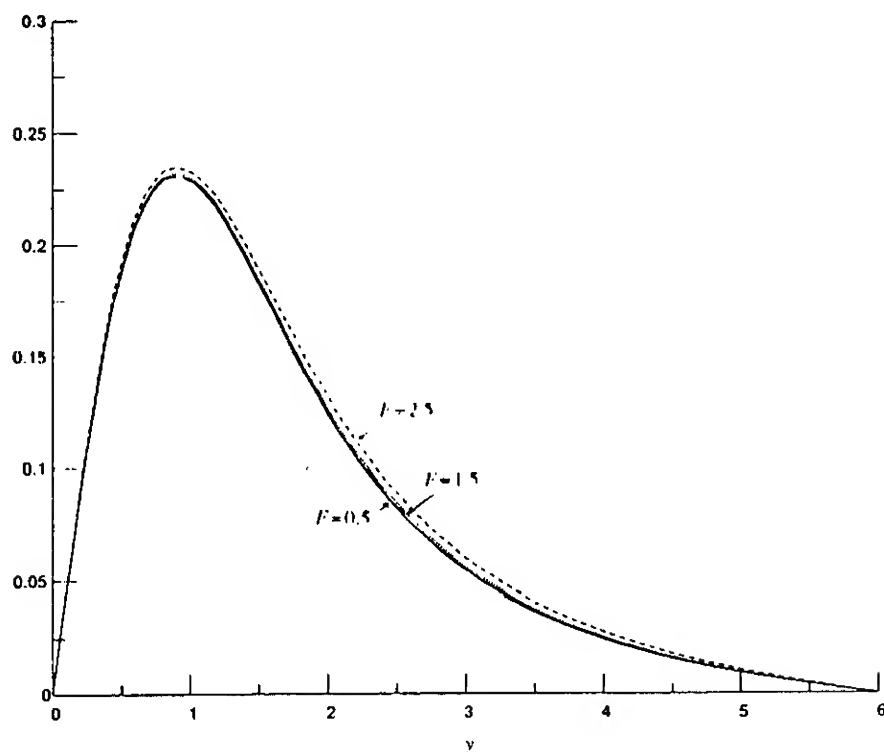


Figure 6a : Amplitude of the free surface elevation as a function of  $y$  for  $F=0.5, 1.5, 2.5$ .

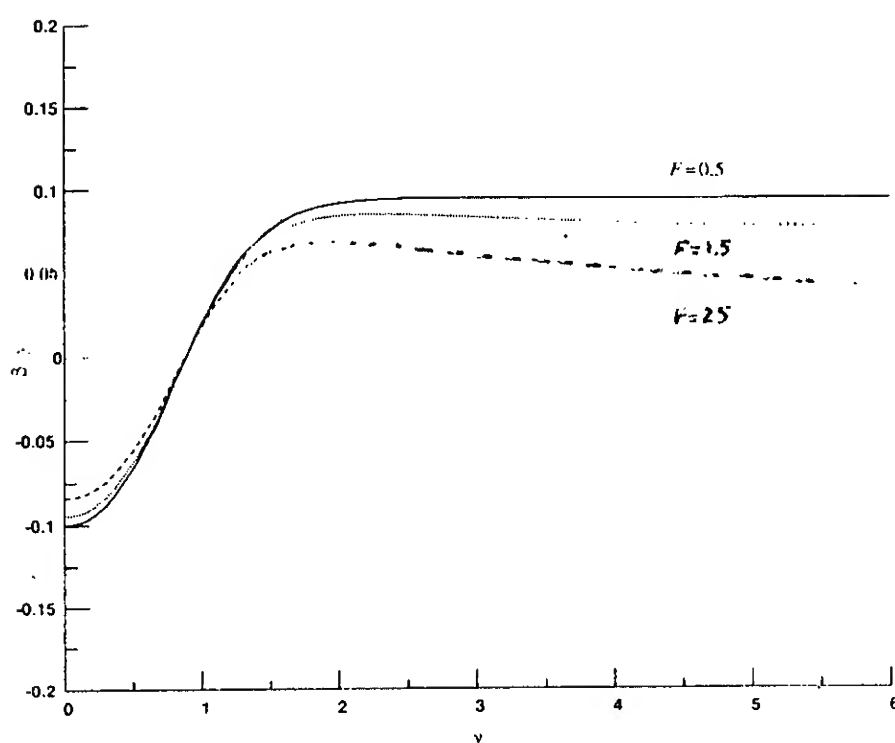


Figure 6b : Phase of the free surface elevation as a function of  $y$  for  $F=0.5, 1.5, 2.5$ .

As discussed above, the growth-rate of the unstable waves is consistently decreased as the Froude number is increased, showing that the latter has a stabilizing effect. This can be seen in figure 7, where the whole unstable frequency range has been plotted for three different values of the Froude number,  $F=0, 0.5, 1.5$ . The cut-off frequency, marking transition from stable to unstable waves is reduced as the Froude number is increased, and the growth-rates of the unstable waves are also decreased. Increasing the Froude number causes therefore a, slow, but clear, "shrinking" of the unstable wave range. At the cutoff frequency, the frequencies of the growing and the decaying mode coalesce. Consequently, the condition  $\partial D / \partial \omega = 0$  is satisfied there, where  $D(\omega, k; F) = 0$  denotes the dispersion relation of the flow at Froude number  $F$ . This condition is typical of the onset of instability in non-dissipative media.

Finally, in the infinite Froude number limit there is a symmetric mode that becomes unstable. More specifically, when  $F = \infty$ , the boundary condition on the free surface becomes  $p = 0$ . Then an exact solution of the problem is given by:

$$p(r, \theta) = q_1(r) \sin(\theta) \quad (54)$$

where  $q_1(r)$  is the pressure eigenmode in the zero Froude number case. The frequency of (54) is the same as the  $F=0$ . The fact that the  $F = \infty$  mode is just the  $F=0$  mode rotated by  $\pi/2$  in the  $y, z$  plane is due to the axisymmetry of the basic flow. In a non-axisymmetric flow the two limits will be different.

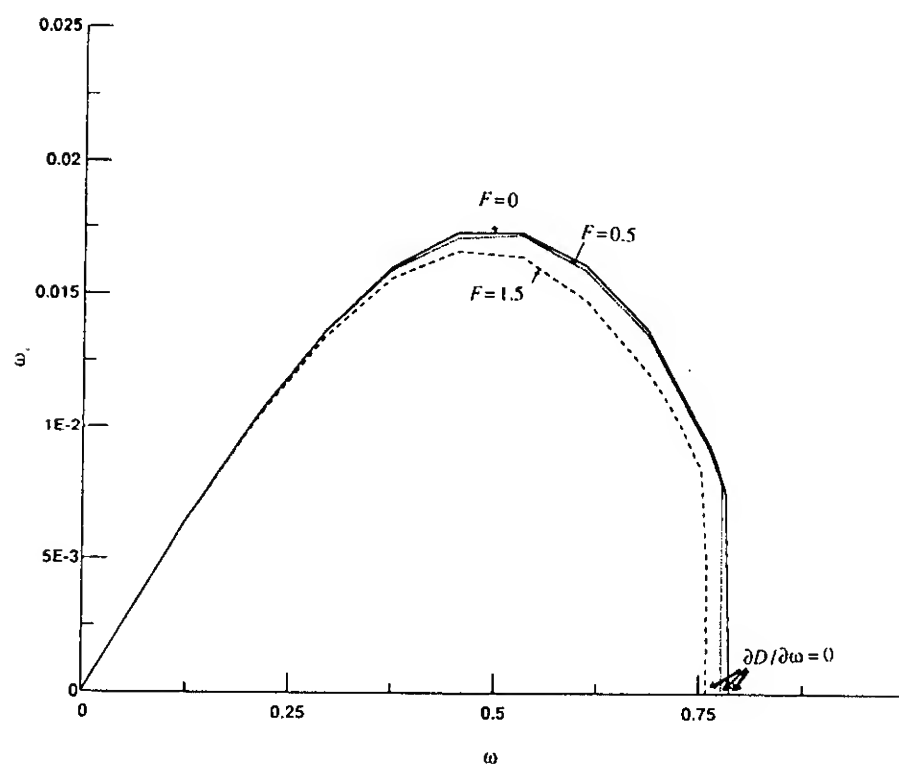


Figure 7 : Growth-rate as a function of frequency in the unstable wave range, for  $F=0, 0.5, 1.5$ . (Note, that at the "cut-off" point  $\partial D / \partial \omega = 0$ ).

## 6.2 Spatial instability

The physical character of the wake instability was determined next, i.e. whether it is of the absolute or of the convective type. As mentioned before, if mapping of the  $k$ -real axis through the dispersion relation into the  $\omega$ -plane yields frequencies with positive imaginary parts, the flow is unstable. This was done in the previous subsection, where an unstable wavenumber range was found, by solving the dispersion relation with respect to the frequency. In order to distinguish whether this instability is absolute, or convective, the "pinching" double roots (Bers, 1983) of the dispersion relation have to be determined. More specifically, one has to determine a complex pair  $(\omega_0, k_0)$  that satisfies:

$$D(\omega_0, k_0; F) = \frac{\partial D}{\partial k}(\omega_0, k_0; F) = 0 \quad (55)$$

plus the "pinching" requirement, stating that the double root should be formed from the coalescing of a right-travelling with a left-travelling wave. Then it can be shown (Bers, 1983) that, if the imaginary part of  $\omega_0$  is positive, any localized perturbation leads to

a growing motion at any location in space, and the instability is termed absolute; if the imaginary part of  $\omega_0$  is negative, any localized perturbation will be convected away in finite time, leading to decaying motions at any fixed location in space; the instability is then termed convective.

It can be further shown that, if the instability is absolute, the long-time response of the flow develops a normal-mode with a characteristic frequency and wavenumber. After non-linearities saturate the growth of the linear instability, the flow settles into a self-sustained oscillation at approximately this frequency and wavenumber. Absolutely unstable media are for this reason called "oscillators". Convective instabilities are on the other hand very receptive to persistent external excitations: There exists a range of excitation frequencies which lead to asymptotic states that are oscillatory in time and grow in space along the direction of propagation of the instability waves. Convectively unstable flows are thus characterized as "amplifiers". This distinction is fundamental in discussing the spontaneous appearance of unsteady patterns in viscous flows.

The double roots were determined using the procedure suggested in Triantafyllou et al., 1986, and Triantafyllou et al., 1987, in which the complex wavenumber plane is mapped through the dispersion relation into the complex frequency plane; the pinch-point type of double roots are located from the local angle-doubling property of the map. This procedure is particularly appropriate for the present problem, where it is possible to solve for  $\omega$  as a function of  $k$ , in the manner described before, but in general it is extremely difficult to do it the other way around. That the so determined double roots are of the "pinch-point" type can be verified from the fact that there is only one unstable branch of the  $\omega(k)$  function (Triantafyllou et al., 1987).

For the velocity profile (53) the instability was found to be convective at all Froude numbers. This is due to the fact that the instability is convective when the Froude number is equal to zero, which is the most unstable case. The presence of flow reversal is required to produce an absolute instability in the self-similar wake, but such a velocity profile can not exist far behind the ship. We note that, if such a profile were present, it would remain absolutely unstable for low Froude numbers.

Since the flow is convectively unstable, the question of spatial instability to an excitation periodic in time is very important. The spatially unstable waves for this problem can be determined using an iterative procedure: A complex wavenumber is assumed, the frequency is determined by solving the eigenvalue problem as explained in the previous section, and then a new guess is made until a wave with complex wavenumber and real frequency is obtained. That the complex wavenumber corresponds to a growing, as opposed to an evanescent, mode can be verified again from the fact that only one unstable mode exists for real  $k$ . For Froude number equal to 0.5, the absolute value of the growth-rate of the spatial mode as a function of frequency is shown in figure 8. (The growth-rates are actually negative, showing that the wave are amplified as  $x \rightarrow \infty$ ). The most amplified spatial mode has complex wavenumber (0.65, -0.02217) and real frequency 0.5306. The real parts of its frequency and wavenumber differ thus somewhat from those of the most amplified temporal mode. The variation of the amplitudes of the Fourier coefficients of the spatially unstable mode as a function of  $r$  is shown in figure 9. The amplitude and phase of the free surface elevation are shown in figures 10a, and 10b respectively. The more clear difference between the spatially unstable mode and the temporal modes discussed before can be seen in the variation of the phase with the distance from the wake axis. Figure 10b shows that a phase-lag is present in the spatial mode over a larger distance than in the temporal mode, which implies that the wavecrests of the spatial mode will be more curved.

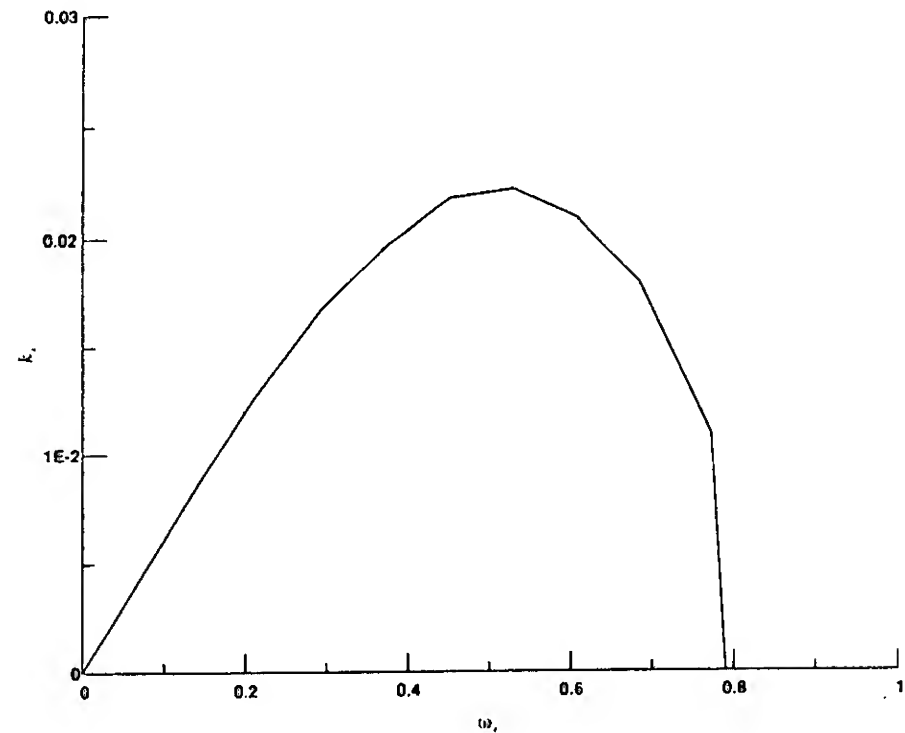


Figure 8 : Absolute value of the spatial growth-rate as a function of frequency for  $F=0.5$ .

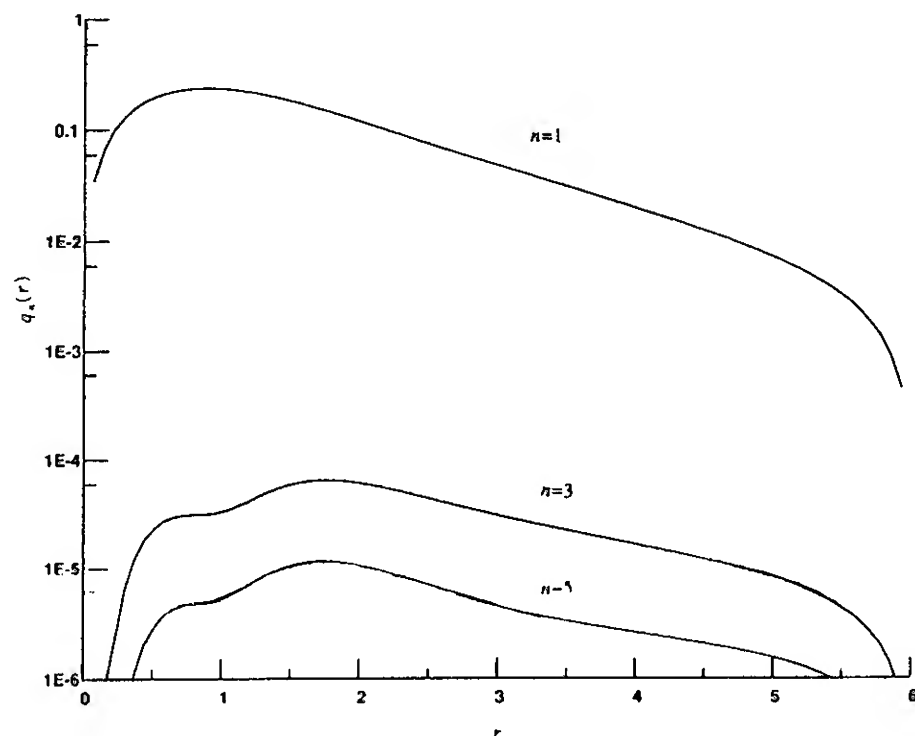


Figure 9 : Variation of the amplitude of the Fourier coefficients  $n = 1, 3, 5$  with  $r$  for the most unstable spatial mode at  $F=0.5$  (semi-log scale).

Given the convective character of the wake instability, it is the spatial modes that are the physically significant ones. It is therefore interesting to obtain a visual picture of how their free surface manifestation can be expected to look like. A perspective view of the free surface elevation caused by the most amplified spatial mode at Froude number  $F=0.5$  is shown in figure 11. The plot has been constructed in a frame of reference that moves with the phase velocity of the wave. In this frame of reference the wave appears stationary in time, and its spatial growth can be seen more clearly. The free surface elevation thus consists of two parallel series of alternating hills and valleys the height of which increases exponentially with  $x$ . The wave grows indefinitely according to linear theory, but in reality the growth will be eventually saturated by non-linear effects, unless the free surface wave breaks before that.

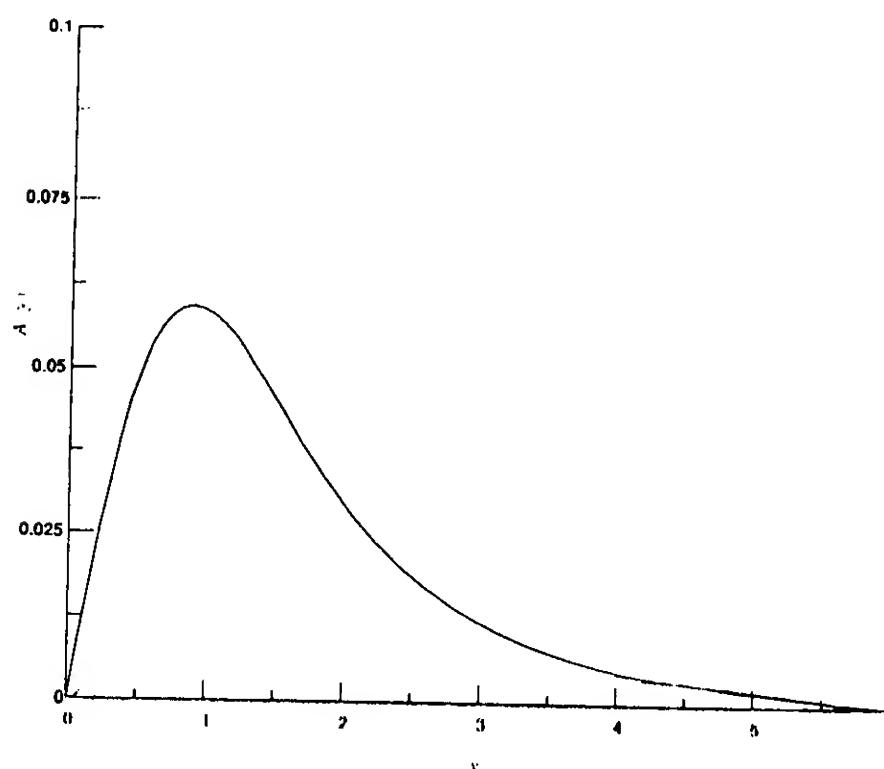


Figure 10a : Amplitude of the free surface elevation as a function of  $y$ , for the most unstable spatial mode at  $F=0.5$ .

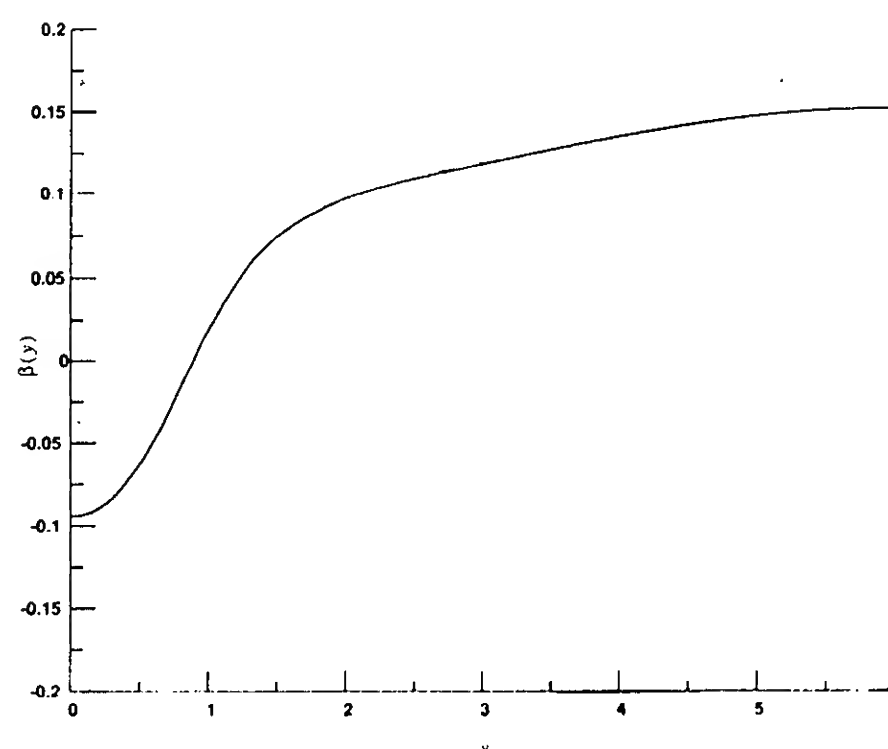


Figure 10b : Phase of the free surface elevation as a function of  $y$ , for the most unstable spatial mode at  $F=0.5$ .

Finally, it should be mentioned that we have investigated the presence and form of spatially unstable modes in the wake of the ship, without discussing the mechanics of excitation of these modes by ambient waves. This is a subject that little is known about, and will probably attract attention in the near future. A related problem is the response of the wake to excitations in the stable wavenumber range: An incident harmonic wave will be then partly reflected and partly transmitted when it meets the region of shear flow, whereas a stable wave will be excited above the wake. It will be interesting to determine the reflected and transmitted waves in relation to the energy carried by the wave propagating above the shear flow. A study of the stable response of the wake to water waves will complement the results presented here.

## 7 Conclusions

The instability of the wake behind a ship has been investigated numerically. The main outcome of this investigation is that the unstable waves are antisymmetric about the centerplane of the wake. The free surface manifestation of the instability wave develops a pattern consisting of two parallel series of alternating "hills" and "valleys". An interesting observation is that, at low Froude numbers, the frequency and phase velocity of the instability waves is controlled by the characteristics of the shear flow in the wake, and is practically the same as in the  $F=0$  case. This allows the derivation of a very simple approximation for the unstable modes, as follows: We first solve for the eigenvalue  $\omega$  and eigenvector  $q_1(r)$  for  $F=0$ ; this requires the numerical solution of only an  $N \times N$  eigenvalue problem. Then, for low  $F$ , the unstable eigenmode of the same flow with a free surface can be approximated by the first term of the Fourier series:

$$p(r, \theta) = q_1(r) \cos(\theta) + \frac{F^2 r (kU - \omega)^2 q_1(r)}{1 - (\pi/2) F^2 r (kU - \omega)^2} \left( \theta + \frac{\pi}{2} \right) \quad (56)$$

Equation (56) satisfies exactly the linearized boundary conditions at the free surface, (as in fact will any truncated series for  $q$  in (28)), and approximately the basic partial differential equation (10). Equation (56) becomes asymptotically exact as the Froude number tends to zero.

The fact that the instability of the wake is convective, implies that unstable wavepackets are convected with the mean flow, and the flow can not be self-excited. Even a convectively unstable flow can, however, be driven by background noise, to generate a spatially growing response. For the wake/free surface interaction problem, a source of persistent "noise" is provided by the ambient waves, which are almost always present in the ocean. Thus, if the frequencies of the ambient waves cover the range of spatial instability, they can excite waves that grow in the streamwise direction. The vortices that are formed by this noise-driven instability can cause a local mixing in that part of the wake where shear exists, creating a region of fluid with somewhat different properties than the surrounding fluid (e.g. lower temperature, since cooler fluid from below has been brought upwards). This region, which has a width roughly equal to the width of the wake, can therefore become visible to scientific instruments and the human eye. The formation of such a region might account for the observation that ship wakes remain visible long after the passage of the ship, when all hydrodynamic disturbances have presumably been dissipated.

## ACKNOWLEDGEMENTS

Most computations were performed using the Cray-2 of the MITSF. This work is supported by the Office of Naval Research, under Contracts N00014-87-K-0356 and N00014-90-J1312, and the National Oceanic and Atmospheric Administration, under Sea-Grant Contract NA86AA-D-SG089.

## 8 References

1. Batchelor, G.K. and Gill, A.E., 1962, *J. Fluid Mech.*, **14**, p. 529.
2. Benney, D.J., and Chow, K., 1986, *Stud. Appl. Math.*, **74**, p. 227.
3. Bernal, L.P., and Kwon, J.T., 1989, *Phys. Fluids A*, **1**, p. 449.

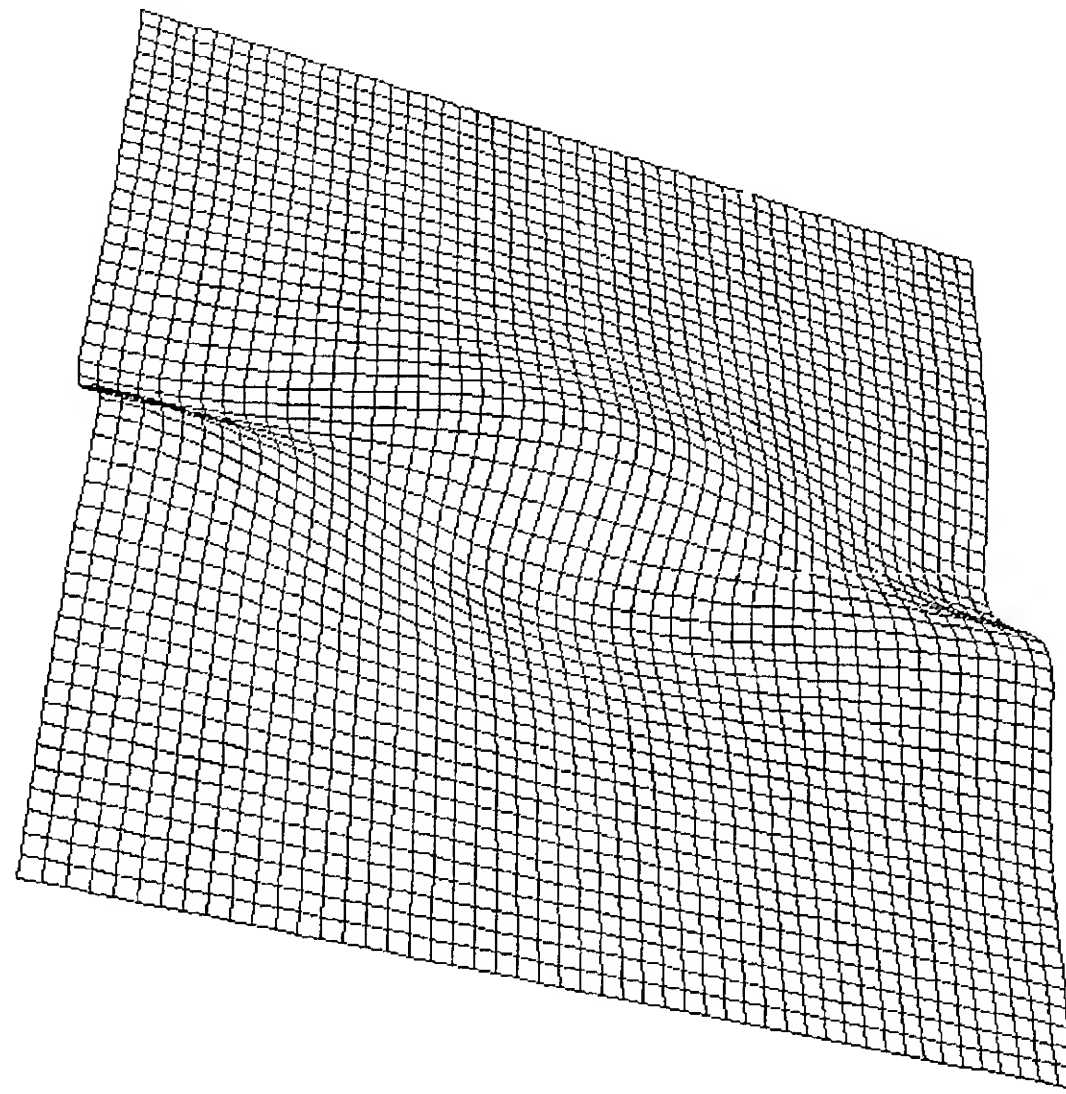


Figure 11 : Perspective view of the spatially amplified wave.

4. Bers, A., 1983, in *Handbook of Plasma Physics*, M.N. Rosenbluth and R.Z. Sagdeev, gen. eds., vol.1, Ch 3.2, North Holland.
5. Chomaz, J.M., Huerre, P., and Redekopp, L.G., 1988, *Phys. Rev. Lett.*, **60**, p. 25.
6. Drazin, P.G., and Howard, L.N., 1966, in *Advances in Applied Mechanics*, **7**, p. 1.
7. Hanneman, K., and Oertel, H., 1989, *J. Fluid Mech.*, **199**, p. 55.
8. Howard, L.N., 1961, *J. Fluid Mech.*, **10**, p. 509.
9. Karniadakis, G.E., and Triantafyllou, G.S., 1989, *J. Fluid Mech.*, **199**, p. 441.
10. Koch, W., 1985, *J. Sound Vibr.*, **99**, p. 53.
11. Liepmann, D., 1990, *Phd Thesis*, University of California San Diego, La Jolla, California.
12. Lugt, H.J., 1987, *Phys. Fluids*, **30**, p. 3647.
13. Milgram, J.H., 1988, *J. Ship Res.*, **32**(1), p. 54.
14. Mitra, P.S., Neu, W.L. and Schetz, J.A., 1985, VPI-aero-146, Virginia Polytechnic Institute and State University.
15. Mitra, P.S., Neu, W.L. and Schetz, J.A., 1986, VPI-aero-153, Virginia Polytechnic Institute and State University.
16. Oikawa, M., Chow, K., and Benney, D.J., 1987, *Stud. Appl. Math.*, **76**, p. 69.
17. Peltzer, R.D., Garret, W.D., and Smith, P.A., 1978, *Int. J. Remote Sensing*, **8**, p. 689.
18. Peregrine D.H., 1971, *J. Fluid Mech.*, **49**, p. 253.
19. Sarpkaya, T., 1986, *Proceedings, 16-th Symposium on Naval Hydrodynamics*, Berkeley, California, p. 38.
20. Sato, H., and Okada, O., 1966, *J. Fluid Mech.*, **26**, p. 237.
21. Skop, A.R., Griffin, O.M., and Leipold, Y., 1990, *J. Ship Res.*, **34**(1), p. 69.
22. Swann, T.F. 1987, NRL Memorandum Report 6075.
23. Tatinclaux, J.C. 1970, *J. Ship Res.*, **14**, p. 84.
24. Triantafyllou, G.S., and Dimas, A.A., 1989, *Phys. Fluids A*, **1**, p. 1813.
25. Triantafyllou, G.S., and Karniadakis, G.E., 1990, *Phys. Fluids A*, **2**, p. 653.
26. Triantafyllou, G.S., Kupfer, K., Bers A., 1987, *Phys. Rev. Letters*, **59**, p. 1914.
27. Triantafyllou, G.S., Triantafyllou, M.S., Chrysostomidis, C., 1986, *J. Fluid Mech.*, **170**, p. 461.
28. Tryggvason, G. 1988, *Phys. Fluids*, **31**, p. 955.
29. Unal, M., and Rockwell, D., 1988, *J. Fluid Mech.*, **190**, p. 419.
30. Valenzuela, G.R., 1978, *Boundary Layer Meteorology*, **13**, p. 61.
31. Willmarth, W.W., Tryggvason, G., Hirs, A., and Yu, D., 1989, *Phys. Fluids A*, **1**, p. 170.
32. Yih, C.S., 1972, *J. Fluid Mech.*, **51**, p. 209.

## DISCUSSION

John P. McHugh

The University of New Hampshire, USA

I have recently considered very similar problems as in this paper, and I have a comment and a question. The comment is that the reduction of the quadratic eigenvalue problem to a linear eigenvalue problem may be accomplished another way. Instead of your analytical version (Eq. 38, p. 55), you can create a matrix version of the quadratic problem:  $[A\lambda + B\lambda + C](y) = 0$ . Then use  $Z = \lambda y$  in the first two terms. The question concerns neutral modes. Did you find any neutral modes where the wavespeed is outside the range of velocity of the primary hull? I have found such waves in similar cases.

## AUTHORS' REPLY

First, regarding the comment, the proposed alternative linearization of the eigenvalue problem seems equivalent with what I have done. I believe that the treatment I have presented is closer to the physics of the problem, but the final choice is probably a matter of preference. I am not familiar with the work of the discussor, and as he gives no specific reference for his work, I cannot make a more detailed comparison. Regarding the question, I have determined the neutrally stable modes of this problem for various Froude numbers by considering the limit of the unstable modes as their growth-rate goes to zero (see Figure 7). The phase velocities of these modes are inside the range of velocity of the basic flow. In fact, from Howard's theorem, it is straightforward to see that in the limit as the growth-rate of the unstable wave tends to zero the phase velocity has to remain within the range of the basic flow. Consequently, I do not see how in the similar problem that the discussor has considered that the phase velocity of neutrally stable modes can possibly lie outside this range. I would like to thank Prof. McHugh for his interest and comments.

## DISCUSSION

Ali H. Nayfeh

Virginia Polytechnic Institute and State University, USA

The results presented in the paper show a weak influence of the Froude number on the growth-rates and bandwidth of unstable disturbances, contrary to the known results about the influence of the Mach number on the stability of compressible boundary layer. Are these results due to neglecting the influence of the Froude number on the mean-flow profile  $U(y,z)$ ?

## AUTHORS' REPLY

Increase of the Froude number clearly results in a reduction of the growth-rates and of the unstable wavenumber range, and, in the infinite Froude number limit, Mode I gets stabilized. Overall, therefore, the influence of the Froude number cannot be considered weak. The influence is weak only for low Froude numbers, a result that simply reflects the physics of the problem: at low Froude numbers, the presence of the free surface reduces the motion of the fluid in the vertical direction. As a result, the motion of the fluid is confined mostly in the horizontal direction, and the free surface is merely deformed to accommodate the non-uniform pressure caused by the fluid motions. This behavior does not change until the Froude number becomes high enough for the free surface to behave like an almost perfectly compliant boundary, and accounts for the weak influence of the Froude number on the instability mode. I believe, therefore, for low Froude numbers, the weak influence of the Froude number on the instability is a realistic result. I do agree, however, that, above some value of the Froude number, the average flow itself might start to change significantly in a manner that would accelerate the stabilization. There are no data available, to my knowledge, as to what that value may be; existing steady computations of the wake behind a ship (Ref. 22) show a velocity profile similar to the one used in this paper. I would like to thank Prof. Nayfeh for his interest and comments.



# Ship Internal Waves in a Shallow Thermocline: The Supersonic Case

M. Tulin (University of California, Santa Barbara, USA)

T. Miloh (Tel Aviv University, Israel)

## ABSTRACT

We develop a general theory of ship internal waves in a thermocline of moderate thickness below a well mixed upper layer, when the ship is traveling faster than the fastest internal waves. This theory provides both the kinematical pattern earlier discussed by Keller and Munk, and also the amplitude of the internal waves (the deflection of the top of the thermocline) in terms of the spectral amplitude function generated by the ship.

The wave far field consists of an inner and outer wake. In the inner wake, near the track of the ship, each phase line originates in a cusp, periodically spaced on the track, with a time interval corresponding to the average Vaisalla-Brunt period of the water in the thermocline. The inner wake is created by the high frequency content of the disturbance. In the outer wake, further downstream, each phase line approaches the Mach angle,  $\sin^{-1}(1/F)$ , defined by the densimetric Froude number corresponding to the depth of the thermocline and the density jump across it. The kinematical wave field near the limiting Mach line (the outer field) is independent of the thermocline thickness. The distance between the dominant wave crests in the outer wake corresponds to  $(kh)$  of order one.

The spectral amplitude function is given in terms of two factors, one depending on the thermocline but not the ship, and another depending on the ship, Froude number, and the thermocline. The latter is shown to be related to the wave disturbance just behind the ship in its near field.

An asymptotic non-linear theory is developed for the calculation of the near field around the ship. For supersonic speeds the field equation is hyperbolic and can be solved numerically by the method of characteristics. Calculations show the development of a narrow wake immediately behind the ship, consisting of three lobes, a central lobe of elevation and two side lobes of depression.

The amplitude spectrum is concentrated in the region  $0 < kh < 2-3$ . This coincides with the wavenumbers most prevalent in the outer wake in the region of interest and helps to explain why internal waves are so readily made by ships traveling at supersonic speed in shallow thermoclines.

## INTRODUCTION

At a previous Symposium on Naval Hydrodynamics (Miloh and Tulin, 1988), we have presented a non-linear theory of internal waves made by surface ships in the transonic region,  $F = O(1)$ , with particular reference to early studies of "deadwater" (Ekman, 1904). Here  $F$  is the ratio of ship speed to the speed of longest internal waves,  $c^*$ .

Here we consider the case of internal waves made by ships traveling over stratified water in the supersonic case,  $F > 1$ . Since values of  $c^*$  in nature lie in the range 20-70 cm/sec, while ship speeds are normally an order of magnitude larger, we are especially interested in the hypersonic case,  $F \gg 1$ .

Our interest in this problem has been created originally by the fact that ships at sea are known sometimes to leave behind them narrow V wakes of great length (measured in kilometers), detectable by remote sensing radar, (Hughes, 1986). The circumstances of occurrence and the hydrodynamic mechanism of their origin remains unknown. The angles of the V wake are sufficiently small (normally less than  $10^\circ$ ), however, to be consistent with the notion that they are surface manifestations of a pattern of limiting thermoclineal waves propagating at speeds close to the so-called Mach angle,  $\alpha = \sin^{-1}(1/F)$ . Such a pattern, including waves internal to the V have been theoretically predicted using ray kinematical considerations by Keller and Munk (1970) and by Yih (1990). An

adequate theory of such ship waves, connecting their amplitude distributions with the parameters of the problem, and taking adequate recognition of non-linear effects remains absent, however.

Heightened interest in the problem is caused by recent field research conducted by a team led by the Royal Aircraft Establishment Space Division (Farnborough, UK) recently reported at a Workshop held at Farnborough under the aegis of the British Remote Sensing Society (Workshop Proceedings, 1990). The RAE team has systematically measured in the water, internal wave wakes produced by a number of ships traveling over shallow thermoclines with a depth of the order of the ship draft as well as above water, visual, and radar signatures due to the internal waves. It is noteworthy that in these careful scientific studies, no above water V-wake signatures have yet been observed except those which originate with the internal waves.

Excepting the kinematical studies mentioned above, almost all of the previously published work on ship internal waves is concerned with the description of singularities (Green's functions) in a two-layered fluid [Stretensky (1959), Uspenskii (1959), Hudimac (1961), Crapper (1967), Miles (1971)]; Sabuncu (1961) applied the source singularity to the derivation of a theory for the interfacial wave resistance of a thin ship, *à la* Michell, and carried out some calculations. Unpublished work on internal waves due to ships has been carried out and presented in unclassified contractor reports: (Munk, et al., 1968); (Holliday, 1981). These have resulted in algorithms for computation.

Our interest is in providing an adequate mathematical analysis and concurrent description of the wake. Our ultimate practical interest is in predicting the long internal waves propagating away from the track of the ship and comprising a dominant pattern near the limiting Mach angle.

## THEORETICAL DEVELOPMENT: THE LINEAR FAR FIELD

### General Theory

We assume a mixed upper layer depth,  $h$ , and wish to calculate the wavy displacement at that depth. The approach of Havelock, introduced for the prediction of the Kelvin wave pattern of a ship, is generalized. It involves synthesizing the far field as a summation of waves propagating in the ship direction and at all angles,  $\theta$ , to that direction within a sector,  $\pm \pi/2$ . The amplitude of the

individual waves is given by  $a^*(\theta)d\theta$ , and the wave amplitude at any point  $(x,y;z=-h)$  is given by,

$$\eta(x,y) = R \left\{ \int_{-\pi/2}^{+\pi/2} a^*(\theta) e^{ik[x \cos \theta - y \sin \theta]} d\theta \right\} \quad (1)$$

The wave number,  $k$ , for each wave element is not arbitrary, but corresponds to the phase velocity,  $c$ , which on account for stationarity, is simply related to  $\theta$ :

$$c = c_0 \cos \theta \quad (2)$$

where  $c_0$  is the ship speed; therefore  $k = k(\theta)$ . The relationship between  $k$  and  $c$  follows from the dispersion relation  $\omega = \omega(k)$ , where  $c = \omega/k$ . These relations alone, allow the determination of the asymptotic wave pattern due to a steady disturbance propagating in the general medium defined by  $\omega(k)$ . If the disturbance is located at  $(x,y) = 0$  and the coordinates  $(x,y)$  are replaced by polar coordinates  $(r,\beta)$ , see Figure 1, then:

$$\eta(x,\beta) = R \left\{ \int_{-\pi/2}^{+\pi/2} a^*(\theta) \exp[ix \cdot g(\theta,\beta)] d\theta \right\} \quad (3)$$

where

$$g(\theta,\beta) = k[\cos \theta - \tan \beta \sin \theta] \quad (4)$$

For large values of  $x$ , the stationary phase solution of (3) is given by:

$$\eta(x,\beta) = R \left\{ \frac{a^*(\theta_s) \sqrt{2\pi}}{\sqrt{x |g''(\theta_s)|}} \exp\{ix \cdot g(\theta_s) + \text{sgn}[g''(\theta_s)] \cdot \pi/4\} + O(1/x) \right\} \quad (5)$$

where  $dg/d\theta = g'(\theta_s) = 0$ , the stationary phase condition. This corresponds to:

$$\tan \beta = y/x = \frac{c_g/c_0 \cdot \sin \theta_s}{1 - c_g/c_0 \cdot \cos \theta_s} \quad (6)$$

where  $c_g/c_0$  is evaluated at  $\theta_s$  and where  $c_g$ , the group velocity, is given by  $c_g = d\omega/dk$ . This same result, (6), can be readily obtained by geometrical construction, Figure 1. The shape of the phase lines follows from (6) and from the relation (see Figure 1):

$$dy/dx = \cot \theta_s \quad (7)$$

which allows the elimination of  $\theta_s$  in (6) and (7). This first order system requires an initial condition  $y(x_n) = 0$  which defines the  $n$ th phase line. This condition follows from consideration of the wave along the track; using (1):

$$\eta(x,0) = R \left\{ \int_{-\pi/2}^{+\pi/2} a^*(\theta) e^{ikx \cos \theta} d\theta \right\} \\ = R \left\{ \int_{-\pi/2}^{+\pi/2} a^*(\theta) e^{i \left( \frac{\omega^* x}{c_0} \right)} d\theta \right\} \quad (8)$$

where we have used  $c = c_0 \cos \theta$  and  $\omega/k = c$ , and where  $\omega^*$  corresponds to the frequency of waves on the track of the ship ( $\beta = 0$ ). We are entitled to shift the origin of this far field result corresponding to a given value of  $\eta(0,0)$ . Here we take  $\eta(0,0) = 0$ , since no internal waves are generated ahead of the ship in the supersonic case. In addition we expect the first wave at the ship to be given a net initial downward impetus due to the early action of the bow of the ship. Therefore we replace  $ie^{i(\omega^* x/c_0)}$  by  $ie^{i(\omega^* x_n/c_0)}$ . The values of  $x_n$  corresponding to crests in  $\eta(x,0)$  behind the ships are therefore given by:

$$x_n = c_0/\omega^* [2\pi n - \pi/2] \quad n=1,2,\dots \quad (9)$$

Therefore phase lines originate at intervals of  $2\pi c_0/\omega^*$  along the track.

This completes the general theory. It remains to specify the dispersion relation.

For a shallow thermocline of moderate thickness in very deep water, a useful approximation for the dispersion relation has been given by Phillips (1977; pg. 213)

$$\omega^2 = gk \frac{\Delta \rho}{\rho} \{1 + k\epsilon + \coth(kh)\}^{-1} \quad (10)$$

see Figure 2 for definitions of  $h$ ,  $\epsilon$ , and  $\Delta \rho/\rho$ . The corresponding asymptotic limits are:

$$\begin{array}{ccccccc} \omega & c & c_g & c_g(c) & & & \\ (kh) \rightarrow 0 & c^* k \left[1 - \frac{kh}{2}\right] & c^* \left[1 - \frac{kh}{2}\right] & c^* [1 - kh] & c_g = 2c - c^* & & \end{array} \quad (11)$$

$$\begin{array}{ccccccc} (kh) \rightarrow \infty & \omega^* [1 - 1/(k\epsilon)] & \omega^*/k & \omega^*/\epsilon k^2 & c_g = c^2/\omega^* \epsilon & & \end{array} \quad (12)$$

where the longest wave speed,  $c^*$ , and the maximum frequency,  $\omega^*$ , are:

$$c^* = \left( \frac{\Delta \rho}{\rho} gh \right)^{1/2} ; \quad \omega^* = \left( \frac{\Delta \rho}{\rho} g/\epsilon \right)^{1/2} \quad (13)$$

Since the local Brunt-Vaisalla frequency is,  $\omega_{BV}^2 = g \frac{\partial \rho / \partial z}{\rho}$ , the average of  $\omega_{BV}$  over the thermocline is  $\omega^*$ .

Note that the long wave limit is independent of the thermocline thickness,  $\epsilon$ , while the short wave limit is independent of the thermocline depth.

### The Hypersonic Case: Wave Patterns

In the hypersonic case,  $c/c_0 = \cos \theta \ll 1$ , so that  $\sin \theta \approx 1$ . Then, (6) and (7) simplify to:

$$F \gg 1: \quad y/x \sim c_g/c_0 ; \quad dy/dx \sim c/c_0 \quad (14)$$

Therefore the shortest and slowest waves are found near the track of the ship ( $y/x \rightarrow 0$ ), the inner wake, and the longest waves near the Mach line,  $y^*/x = 1/F$ , the outer wake. Using  $c_g = c_g(c)$ , (12) and (11), the asymptotic shape of the phase lines in the inner and outer wakes may be calculated (upperbranch):

Outer wake

$$\frac{2d(y-y^*)}{dx} = \frac{(y-y^*)}{x}; \quad y = \frac{x}{F} - \sqrt{Kx}; \\ \frac{dy}{dx} \xrightarrow{x \rightarrow \infty} \frac{1}{F} \quad (15)$$

where  $K$  is a constant depending on the phase.

Inner wake

$$\frac{dy}{dx} = \left[ \frac{\omega^* \epsilon}{c_0} \right]^{1/2} \sqrt{\frac{y}{x}} ; \quad y = \left[ \frac{\omega^* \epsilon}{c_0} \right] \cdot \left[ \sqrt{x} - \sqrt{x_n} \right]^2 ; \\ \frac{y}{x_n} \xrightarrow{x \rightarrow x_n} \frac{1}{4} \left[ \frac{\omega^* \epsilon}{c_0} \right] \left[ \frac{x - x_n}{x_n} \right]^2 \quad (16)$$

Therefore the phase lines are cusped at their origin ( $x_n$ ), with a curvature,  $d^2y/dx^2 = [\omega^* \epsilon/c_0] / [2x_n]$ , and are straight in the outer field with a slope,  $dy/dx \sim 1/F$ . According to these relations, it is only necessary to know

$c_0, x_n, y'(x \rightarrow \infty); y''(x_n)$ , in order to determine the oceanographic variables,  $\epsilon, h$ , and  $\Delta\rho/\rho$ . Therefore, in cases where ship internal wave patterns are visible from above, oceanographic surveys of shallow thermocline characteristics may be made by remote observation.

We have calculated numerically the crest lines for a range of  $F$  and  $\epsilon/h$ , using the eqns. (6), (7) and (10), see Figure 3. These in general, closely resemble the observations in Loch Linnie. We also show corresponding values of  $(kh)$ , Figure 4.

The crest lines provide a good kinematical description of the wave field. For example, the wave lengths are given by the normal distance between crest lines.

#### Hypersonic Case: Amplitude

It is useful to express the amplitude, (5), in terms of the amplitude spectrum in wavenumber space,  $A^*(k)$ , where:

$$a^*(\theta) = A^* dk/d\theta = A^*(k) [kc_0/(c - c_g)] \quad (17)$$

Then (5) can be put in the following useful form:

$$\frac{\eta(x, y)}{h} = R \left\{ \left( \frac{A^*(k)}{h^2} \right) \cdot B(x/h; \epsilon/h; n) \cdot \exp \left[ i(kx) \left( \frac{c - c_g}{c_0} \right) + \text{sgn} \bar{\omega}'' \cdot \frac{\pi}{4} \right] \right\} \quad (18)$$

where,

$$B(x/h; \epsilon/h; n) = \left[ \frac{2\pi F}{(x/h) |\bar{\omega}''|} \right]^{1/2} \quad (19)$$

$$\bar{\omega}'' = d^2(\omega h / c^*) / d(kh)^2$$

and where we have used the following results in (5):

$$d^2 g / d\theta^2 = \frac{k^2 c_0}{(c_g - c)^2} \cdot \frac{d^2 \omega}{dk^2} + O(1/F^3) \quad (20)$$

The amplitude at each point in the field is seen to be given by the product of two factors, one involving  $A^*$  depends on the ship and must be separately calculated, while the other,  $B/\sqrt{F}$ , depending on the thermocline and position in the wake, is independent of the ship. The amplitude factor  $B$  may therefore be computed along each

phase line.

In the outer wake ( $kh \rightarrow 0$ ), the amplitude (18) simplifies,  $\bar{\omega}'' = -1$ , and the amplitude on a cut at a fixed value of  $x = x^*$  is:

$$\frac{\eta(y^* - y; x^*)}{h} = R \left\{ \frac{A^*(k)}{h^2} \left[ \frac{2\pi F}{x^*/h} \right]^{1/2} \cdot \exp \left\{ i \left( \frac{F}{2x^*/h} \right) \left[ \frac{y^* - y}{h} \right]^2 - \frac{\pi}{4} \right\} \right\} \quad (21)$$

where  $(x^*, y^*)$  lie on the limiting ray,  $y^*/x^* = 1/F$ . The wavenumber,  $k$ , in  $A^*(k)$  is given by:

$$(kh) = \left[ \frac{y^* - y}{y^*} \right] \quad (22)$$

The outer wake amplitude for a cut at a fixed value of  $y = y^*$  is, correspondingly:

$$\frac{\eta(x - x^*; y^*)}{h} = R \left\{ \frac{A^*(k)}{h^2} \left[ \frac{2\pi}{y^*/h} \right]^{1/2} \cdot \exp \left\{ i \left( \frac{1}{2F^2 y^*/h} \right) \left[ \frac{x - x^*}{h} \right]^2 - \frac{\pi}{4} \right\} \right\} \quad (23)$$

and,

$$(kh) = \left[ \frac{x - x^*}{x^*} \right] \quad (24)$$

This is the waveprofile seen by a wave staff as the ship passes in a straight line alongside. It is significant that the outer wake in the far field is independent of the thermocline thickness,  $\epsilon/h$ , although it is necessary to move very far downstream (beyond  $x/h = O(10^3)$ ) to enter the far wake ( $kh \rightarrow 0$ ), see Figure 4. In a very significant region,  $100 < x/h < 500$ , the waves are only moderately long,  $kh = O(1)$ , on the leading crest.

#### The Waveform Amplitude Factor, $B(x/h; \epsilon/h; n)$

This factor has been computed along the first and second crest lines for values  $x/h$  out to 600, Figure 5. At the origin of the phase lines (cusps),  $B$  becomes unbounded since:

$$\lim_{x \rightarrow x_n} \left( \frac{x_n}{h} \left| \frac{\omega}{\omega} \right| \right)^{1/2} = \frac{1}{2F(2\pi n - \pi/2)} \left( \frac{\varepsilon}{h} \right)^{1/4} \left[ \frac{x - x_n}{h} \right]^{3/2} \quad (25)$$

However,  $B$  decreases rapidly along the crest line leaving the cusp, and for  $F = 0(10)$ ,  $\varepsilon/h = 0(1)$ , then  $B \approx 0(1)$  when  $((x-x_n)/h)$  becomes larger than about 3. It then decreases slowly with distance downstream, remaining  $0(1)$  out to  $x/h = 600$ . In the outer wake, far downstream, it decreases as  $(x/h)^{-1/2}$ , see (21).

#### The Shipform Amplitude Factor, $A^*(kh;F)$

The shipform amplitude factor will determine the order of magnitude of the interfacial wave in a large part of the wake. It can be related to the narrow interfacial wave disturbance in the region near, but behind the ship,  $\eta_n$ , before dispersion has created the kinematical patterns previously discussed.

If we take  $x'$  as the origin of the wave wake, then it follows from (1) and (17):

$$\frac{\eta(x';y)}{h} = R \int_{-\infty}^{+\infty} \frac{A^*(k)}{h^2} e^{-i(kh)(y/h)} d(kh) \quad (26)$$

The Fourier Integral Theorem then allows determination of  $A^*(k)$  in terms of  $\eta(x';y)$ :

$$\frac{A^*(k)}{h^2} = \frac{1}{2\pi} \int_{-\infty}^{+\infty} \frac{\eta(x';y)}{h} e^{i(kh)(y/h)} d(y/h) \quad (27)$$

where on account of symmetry the exponential function can be replaced by the cosine.

#### The Nearfield Wave Disturbance, $\eta_n(x',y)$

As the ship passes over the thermocline, it deforms into a surface having the impression of the ship's form. The thermoclineal water closest to the ship's track is pressed largely downward under the ship at the bow and back up again at the stern. Water sufficiently far from the ship's track will be pressed largely to the side around the ship as it slides forward. The relative effect of the thermocline on the fluid displacement near the hull is  $O[(\Delta\rho/\rho)(gL/c_0^2)]$ , where  $L$  is the ship length. When this quantity is much smaller than unity, then the flow field about the ship may be represented to first order, neglecting the presence of the thermocline, by a potential  $\phi_0 + c_0 x$ ,

which can be approximated by the double hull potential flow.

One of the consequences of the ship's motion is to cause a pressure field in the thermocline, generated partly by dynamic and mostly by hydrostatic effects due to inclination of the isopycnics from the horizontal. The component of pressure gradient,  $\nabla p_0$ , normal to the density gradient,  $\nabla \rho$ , in the thermocline, generates vorticity there with its direction normal to both  $\nabla p_0$  and  $\nabla \rho$ ; Bjerknes law prevails. This vorticity generates a flow field on either side of the thermocline (the Biot-Savart Law prevails), which can be described by  $\tilde{\phi}^{(i)}$ , where  $i$  is an index locating the flow above or below the thermocline. The total potential in the flow field outside the thermocline is therefore:  $\bar{\phi}_0 + c_0 x + \tilde{\phi}$ . When  $\bar{\phi}_0$  is the double model disturbance, it is localized near the ship. Upstream  $\tilde{\phi}$  vanishes as the thermocline has not seen the effect of the ship. Around the bow, at hypersonic speeds, outgoing waves of depression propagate sideways, and under the stern, these are joined by outgoing waves of elevation. These tend to cancel each other, except that they are separated due to the time interval involved in their generation. A residual signature results centered on the track not far behind the ship, which has an upward lobe in the center, and two lobes of depression on either side. The entire wave wake downstream will find its origin in this residual nearfield wake. Examples of the near field wave patterns just described, are shown in Figures 6 and 7.

The most rigorous way to carry out the calculation of  $\tilde{\phi}$  is through strictly numerical means, without further approximation; this is not simple and involves its own problems.

As a simpler, and for us, more feasible alternative, we have derived an asymptotic, non-linear theory (long waves and sharp thermoclines) and we have solved the resulting second order PDE numerically in the dispersion-free limit. The justification for these approximations in the near field is that our interest settles on long waves near the leading characteristic (which are most visible in the experiments). As these become dispersion free in the long wave limit, it seems justifiable to neglect dispersion for their calculation in the near field. They then propagate away from the ship track as acoustic waves would.

In the hypersonic case, our PDE is normally hyperbolic and may therefore be both accurately and quickly solved numerically using the method of characteristics (a particular forward marching procedure). The equation is [here,  $c^{*2} = (\Delta\rho/\rho)g(h-\eta)$ ]:



$$\begin{aligned}
& [c^{*2} - c_0^2 - 2c_0\bar{\phi}_{0x} - 2c_0\tilde{\phi}_x]\tilde{\phi}_{xx} - [2c_0(\bar{\phi}_{0y} + \tilde{\phi}_y)]\tilde{\phi}_{xy} \\
& + [c^{*2} - \tilde{\phi}_y\bar{\phi}_{0y} - (\tilde{\phi}_y)^2]\tilde{\phi}_{yy} \\
& - [c_0\bar{\phi}_{0xx}]\tilde{\phi}_x - [c_0\bar{\phi}_{0xy}]\tilde{\phi}_y - \underline{c_0^2 h H^{(2)}(\nabla_h^2 \tilde{\phi}_{xx})} \\
& = \frac{\nabla \rho}{\rho} c_0 \frac{\partial}{\partial x} (p_0 / \rho)
\end{aligned} \quad (28)$$

where the underlined term,

$$H^{(2)}[\nabla_h^2 \tilde{\phi}_{xx}] = \frac{1}{2\pi} \int_{-\infty}^{+\infty} \int_{-\infty}^{+\infty} \frac{[\nabla_h^2 \tilde{\phi}_{xx}(x', y')]}{\sqrt{(x-x')^2 + (y-y')^2}} dx' dy' \quad (29)$$

represents the effects of dispersion, and where the RHS is the forcing term due to the ship's pressure field. The disturbance field due to the ship without the thermocline,  $\bar{\phi}_0 = \phi_0 - c_0 x$ , appears in the coefficients of the PDE and represents convective effects of the ship's field, which may not necessarily be neglected for small  $c^*$ . In the field near the ship, we assume that we may neglect dispersive effects (the underlined term, [29]), as they are weak for long waves and will require some time (distance aft) to be effective. The potential,  $\tilde{\phi}$ , in (28) represents the flow field in the upper mixed layer, and, from it, the elevation of the top of the thermocline may be calculated. Some examples of the calculated thermocline deflections due to the passage of a semi-submerged spheroid (representing a ship) are shown as Figure 6. Transverse cuts through the wake reveal the emergence of the triple-lobe pattern at a certain distance,  $x'$ , behind the middle of the ship. This pattern,  $\eta(x', y)$  from which the amplitude function,  $A^*(k)$ , may be calculated is shown as Figure 7 in a particular case.

#### Amplitude Results

The shipform amplitude function,  $A^*(k)$ , has been calculated from Equation (27), using the triple-lobed wake pattern  $\eta(x', y)$ . Results for three Froude numbers are shown, Figure 8, all for a semi-submerged spheroid, whose draft is 90% of the mixed layer thickness, and 9% of its own length.

The peaks of this spectral function are seen to vary inversely with Froude number, and shift to higher values of  $(kh)$  with increasing Froude number. The spectral content is seen to become small for  $(kh) > 2-3$ . Since  $B(kh)$  becomes very large for large values of  $kh$  (the inner wake), the calculation of the wake wave amplitudes there

requires a separate calculation of  $A^*(kh)$  for large wavenumbers; we have not given it here.

The resulting wave amplitude,  $(\eta/h)$ , along the crest lines are exactly the product  $(A^*/h^2) \cdot B$ . The variation of  $(\eta/h)$  along these lines is shown as Figure 9. The peak values are shown to vary only slowly from one crest line to another; typical peak values are  $5 \times 10^{-2}$ . The declines for the smallest values of  $x/h$  are due to the corresponding decline in  $A^*$ . The region in the immediate vicinity of the Mach line requires further study, as the method of stationary phase used in the integration fails there.

#### DISCUSSION AND SUMMARY

The linear theory presented here is comprehensive in that it provides for both the calculation of the kinematical field and the wave elevations starting from a single relation, eq. (1). It then provides separate algorithms for the calculation of the phase lines in space and for the wave amplitudes on these lines. A necessary input is the dispersion relation,  $\omega(k)$ , which depends on the thermocline shape. The determination of  $\omega(k)$  is a separate problem, for which theory has long existed. In this paper we took a simple model of the thermocline and an appropriate approximate to its dispersion relation, due to Phillips.

The amplitude is represented in this theory by the product of two factors. One,  $B(kh)$ , represents kinematical effects and depends on  $\omega(k)$ , but not on the ship. The other,  $A^*(kh)$ , depends on both the thermocline, and the ship; it may be determined from the near field wave wake behind the ship. The latter requires a separate theory and calculation, an example of which we have provided.

The specific calculations shown here reveal that the spectral content due to the ships disturbance (for the thermocline depth  $h$  about equal to the ship draft,  $D$ ), is concentrated in wavenumbers,  $kh$ , between 0 and (2-3), with a peak at about  $(kh) = 1$ , Figure 8. At the same time, the wavenumbers on the first few phase lines in the outer wake are also in this range, Figure 4. It is this particular "coincidence" which result in measurable internal wave patterns for large distances downstream under circumstances which prevail at Loch Linnie, for example. We do not believe that this "coincidence" depends critically on the shape of the ship, or the shape of the thermocline, or the hypersonic Froude number, although the non-dimensional magnitude of the wave elevation will clearly decay as the thermocline depth,  $h$ , increases beyond the draft of the ship.

Peak wave amplitudes,  $\eta/h$ , of the order  $5 \times 10^{-2}$  are typical for the cases considered, and these values are reached at substantial distances behind the ship, see Figure 9. The peak values do not vary much from crest to crest.

This theory does not take any account of non-linear effects. We have studied these separately and derived an evolution equation for the outer wake, allowing for soliton generation. Although solitons of depression traveling ahead of the leading Mach line are, in principal, possible, they require a significantly large initial disturbance; their generation is enhanced by very shallow thermoclines ( $h \ll D$ ). It is unlikely that they can be generated under conditions which prevail at Loch Linnhe.

It would be highly desirable to have available systematic model scale measurements of internal wave wakes for validation of theory such as we have presented here.

#### ACKNOWLEDGEMENTS

The first author is grateful to Dr. Dennis Holliday of RDA and to Dr. Brian Barber of RAE for many useful discussions. The authors are also very grateful to Mrs. Pei Wang Yao and Mr. Yi Tao Yao of the Ocean Engineering Laboratory at UCSB for their invaluable help, especially in carrying out numerical calculations.

This work was partially supported by the Office of Naval Research Ocean Technology Division and that support is very gratefully acknowledged.

#### REFERENCES

Crapper, G.D., "Ship Waves in a Stratified Ocean," *J. Fluid Mech.*, Vol. 29 (1967), p. 667.  
 Ekman, V.W., "On Dead Water: The Norwegian North Polar Expedition 1893-1896," Vol. V, Ch. XV (1904), Christiania.

Holliday, D., "Internal Wave Wake of a Ship," RDA-TR-118100-001, R&D Associates, 1981.

Hudimac, A.A., "Ship Waves in Stratified Ocean," *J. Fluid Mech.*, Vol. 10 (1961), p. 229.

Hughes, B.A., "Surface Wave Wakes and Internal Wave Wakes Produced by Surface Ships," Proceedings of the 15th Symposium on Naval Hydrodynamics, National Academy Press, 1986.

Keller, J.B. and Munk, W.H., "Internal Wave Wakes of a Body in a Stratified Fluid," *Physics of Fluids*, Vol. 13 (1970), p. 1425.

Miles, J.W., "Internal Waves Generated by a Horizontally Moving Source," *J. of Geophys. Fluid Mech.*, Vol. 2 (1971), p. 63.

Miloh, T. and Tulin, M.P., "A Theory of Dead Water Phenomena," Proceedings of the 17th Symposium on Naval Hydrodynamics, National Academy Press, 1988.

Munk, W.H., et. al., "Generation and Airborne Detection of Internal Waves from an Object Moving through a Stratified Ocean," JASON Study S-334, IDA, 1969.

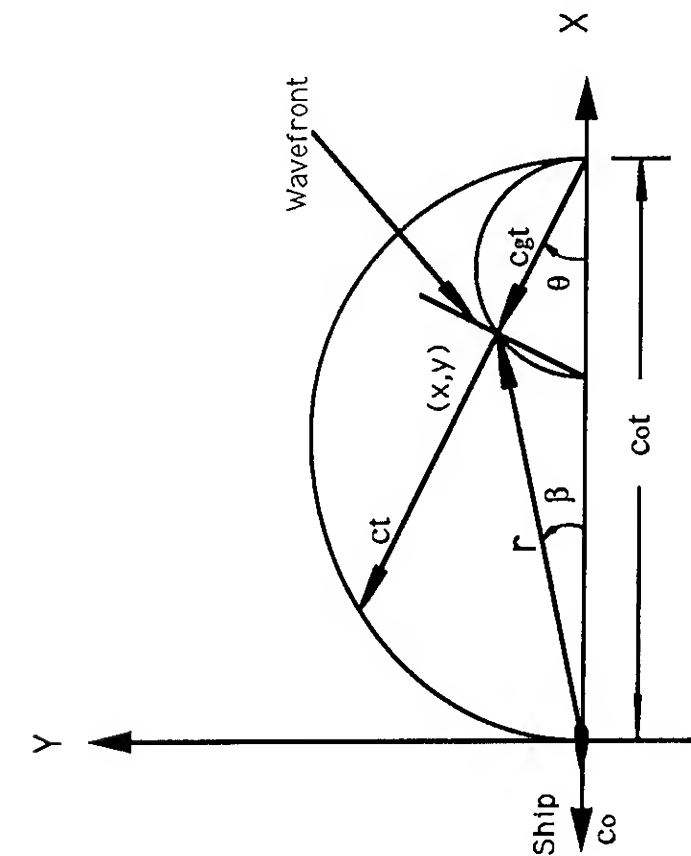
Phillips, O.M., The Dynamics of the Upper Ocean, Cambridge University Press, 1977.

Sabuncu, T., "The Theoretical Wave Resistance of a Ship Travelling Under Interfacial Wave Conditions," Norwegian Ship-Model Experiment Tank, Trondheim Pub. No. 63 (1961).

Stretenski, L.N., "Wave Resistance of a Ship in the Presence of Internal Waves," *Izv. Akad Nauk SSSR, Otd. Tekhn. Nauk. Mekh., Mashinostr.* (1959), p. 56.

Uspenski, P.N., "On the Wave Resistance of a Ship in the Presence of Internal Waves Under Conditions of Finite Depth," *Trudy. Morsk Gidrofiz. Inst.*, Vol. 18 (1959), p. 68.

Yih, C.S., "Patterns of Ship Waves," Engineering Science, Fluid Dynamics, World Scientific Publishers, 1990.



$$y = (C_g t) \sin \theta ; \quad x = C_0 t - (C_g t) \cos \theta$$

$$\frac{y}{x} = \tan \beta = \frac{C_g \sin \theta}{C_0 - C_g \cos \theta}$$

$$\frac{dy}{dx} = \tan \theta$$

**Figure 1.** Wavefront Geometrical Construction

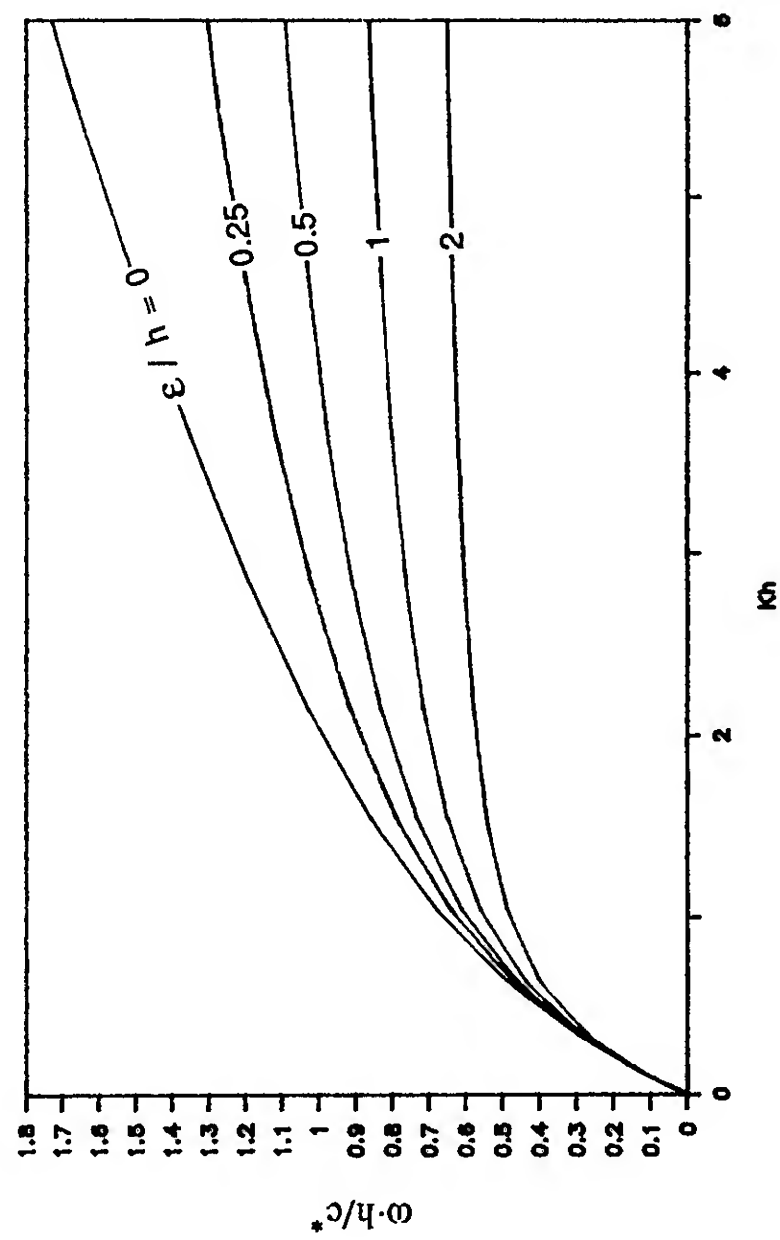
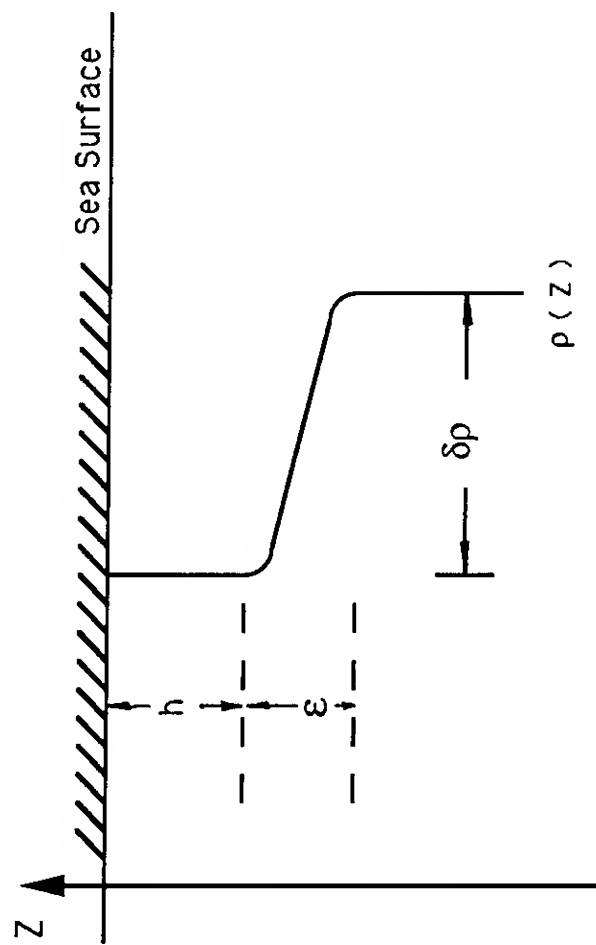


**Figure 2.** Dispersion Relation for Thickened Thermocline Beneath Mixed Layer

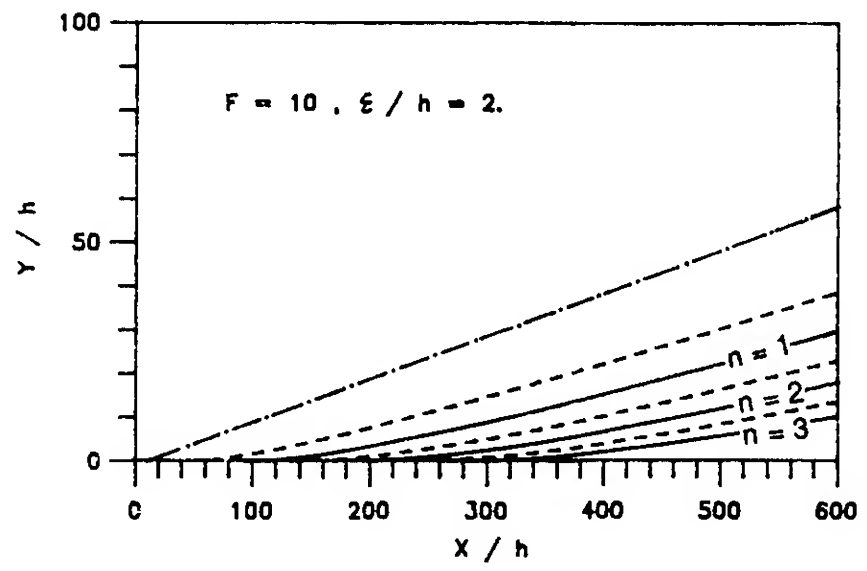
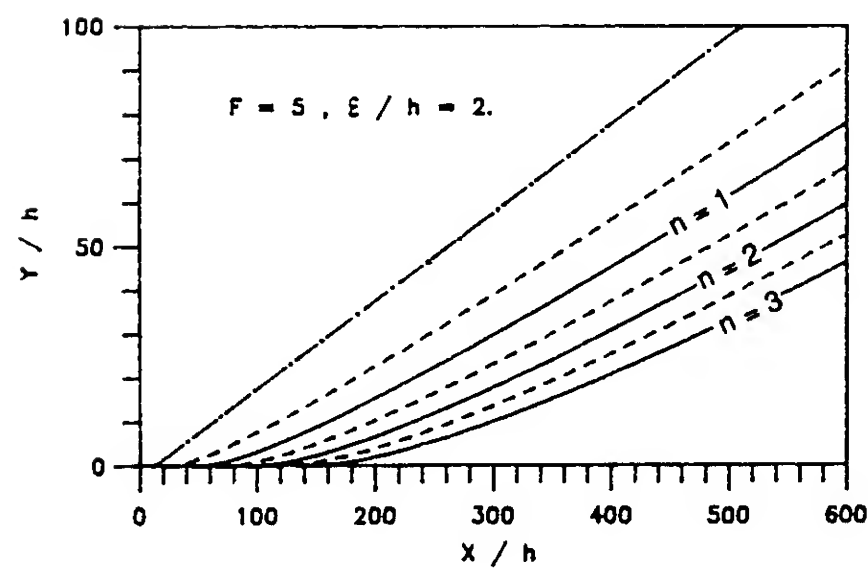
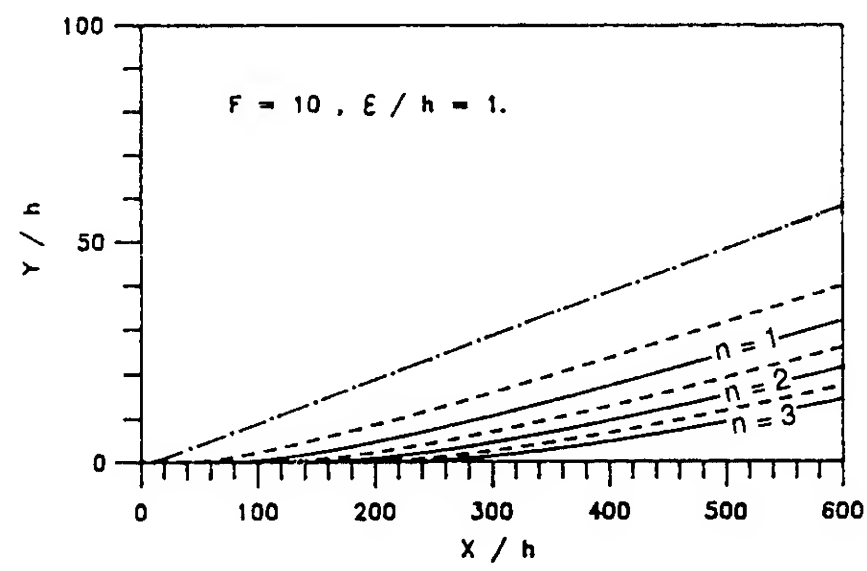
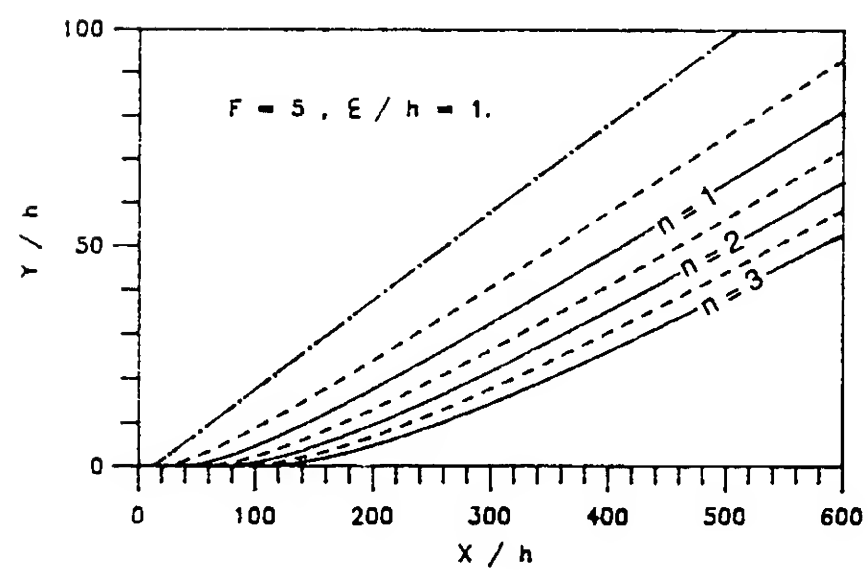
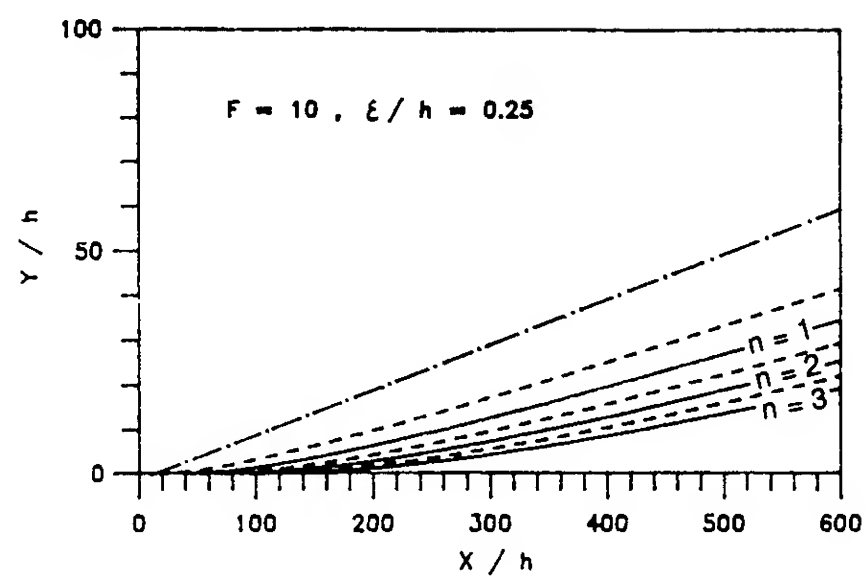
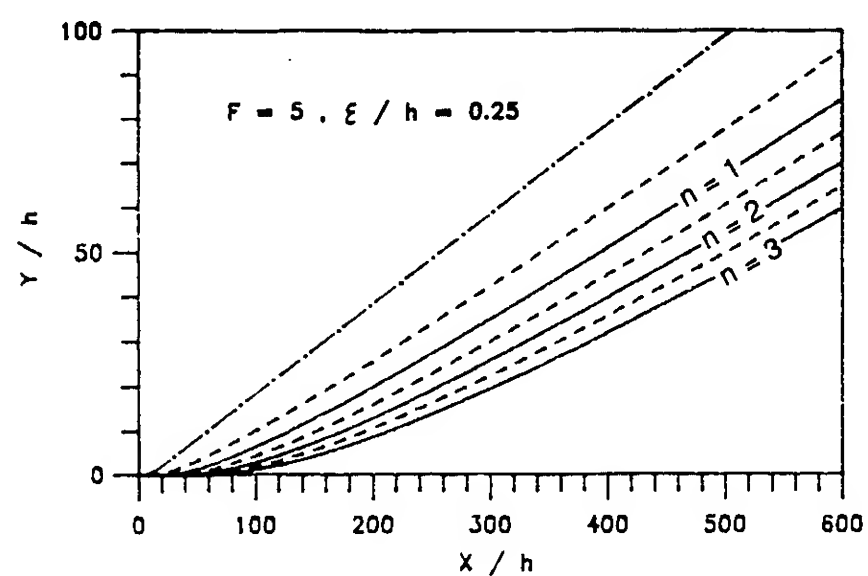


**Figure 3.** Internal Wave Crest Lines ( solid ) & Trough Lines ( dashed ), and Mach Line ( dashdot )

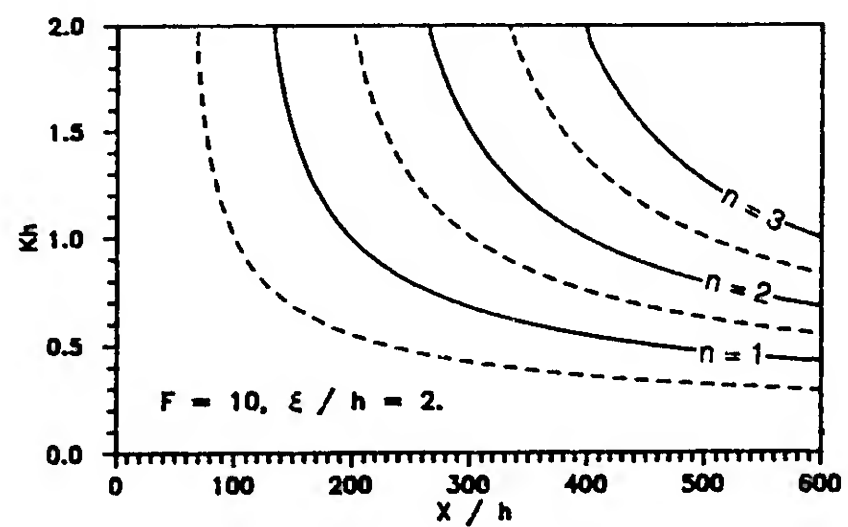
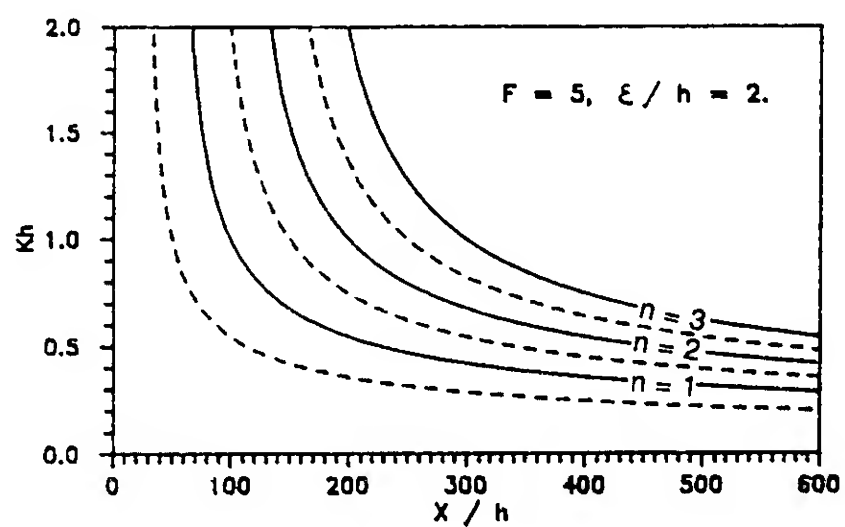
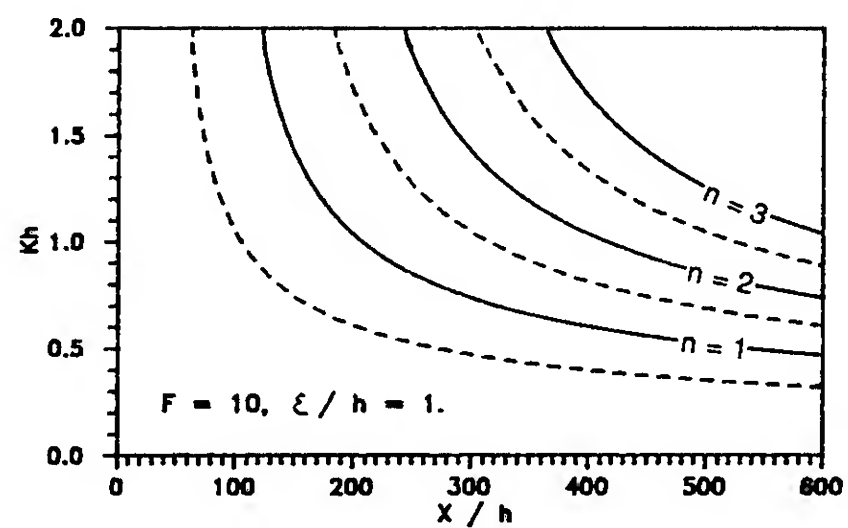
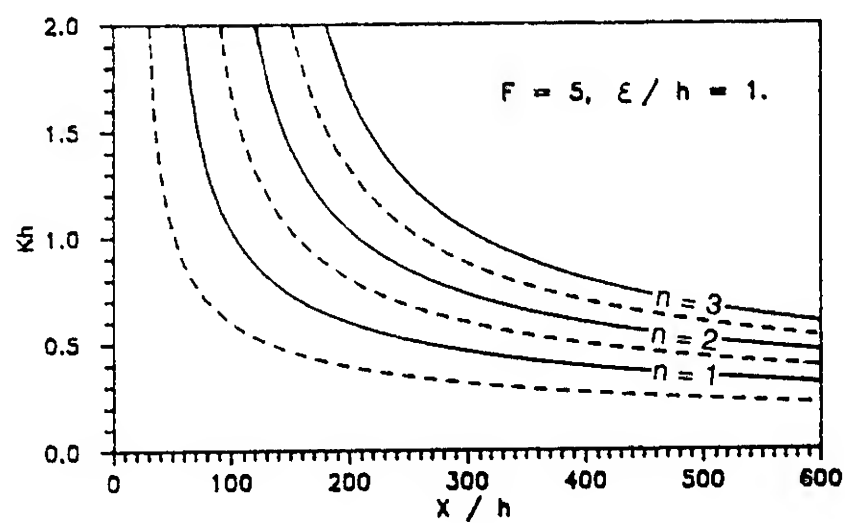
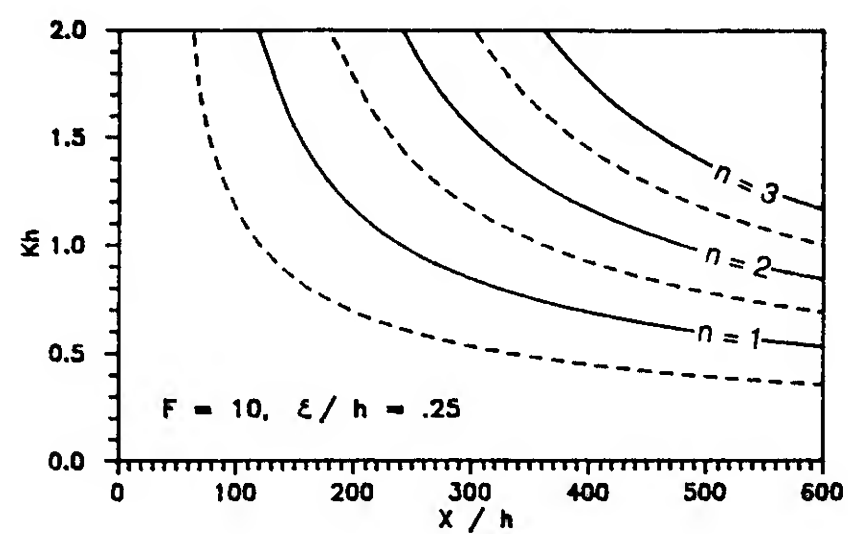
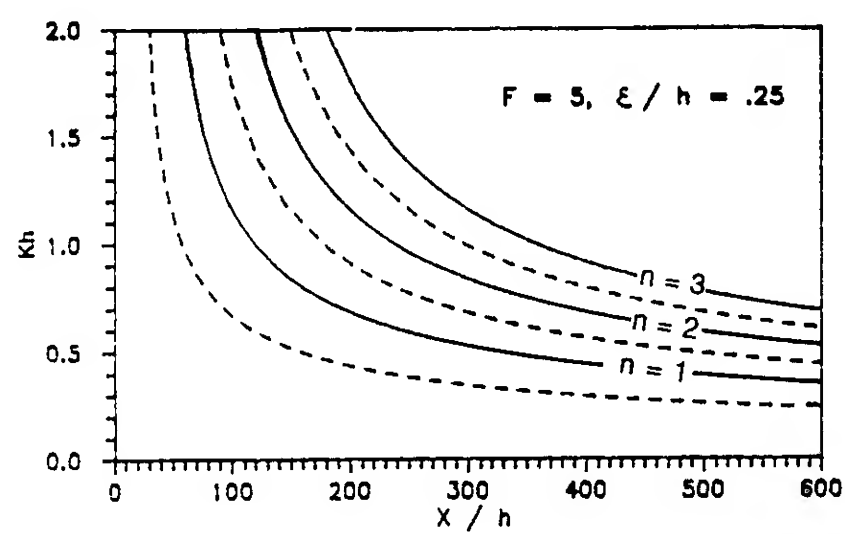


**Figure 4.** Wave Numbers Along Crest Lines ( solid ) & Trough Lines ( dashed )



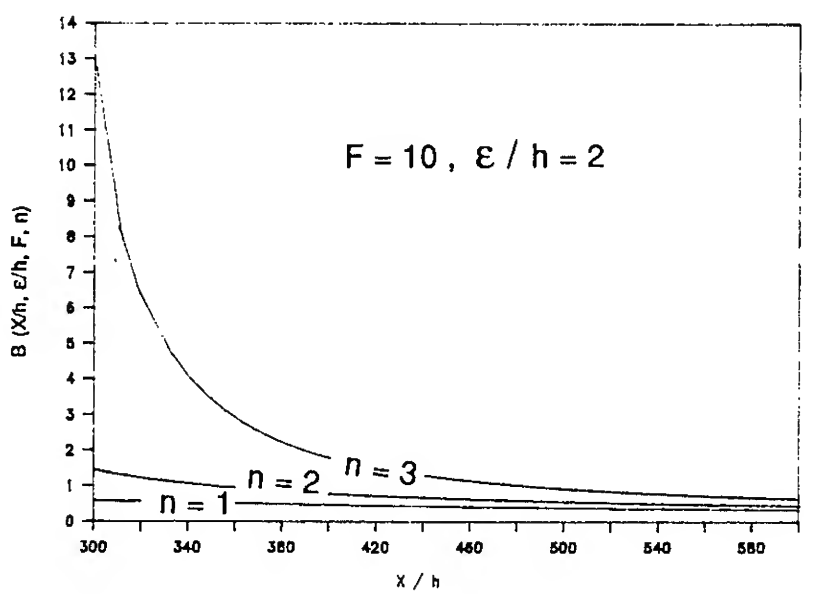
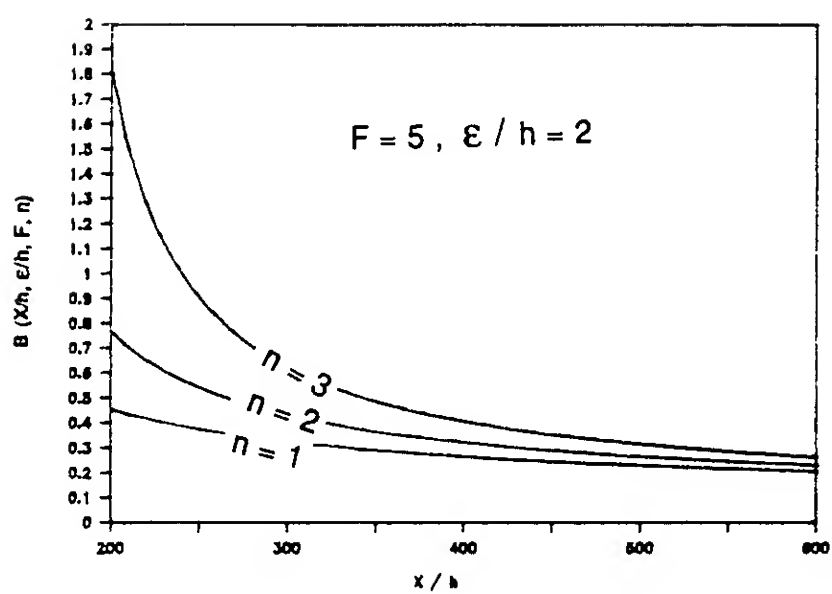
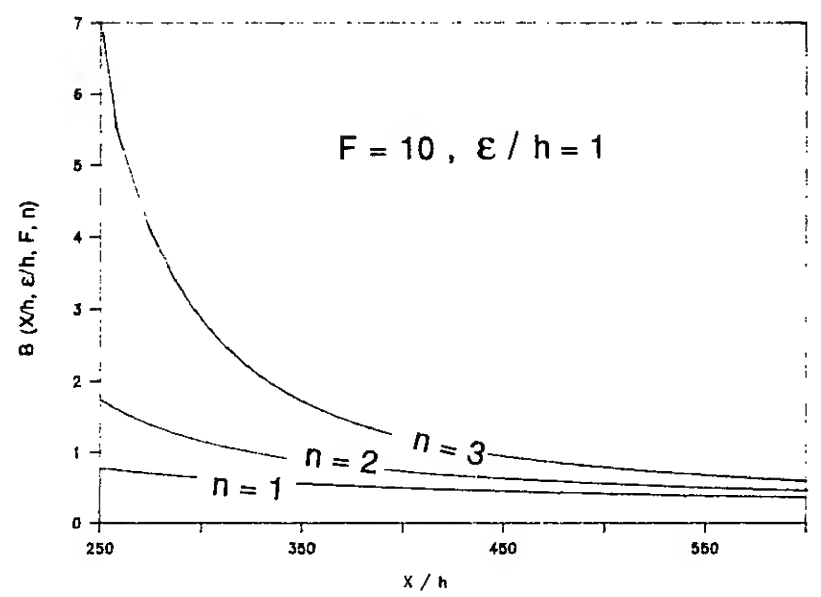
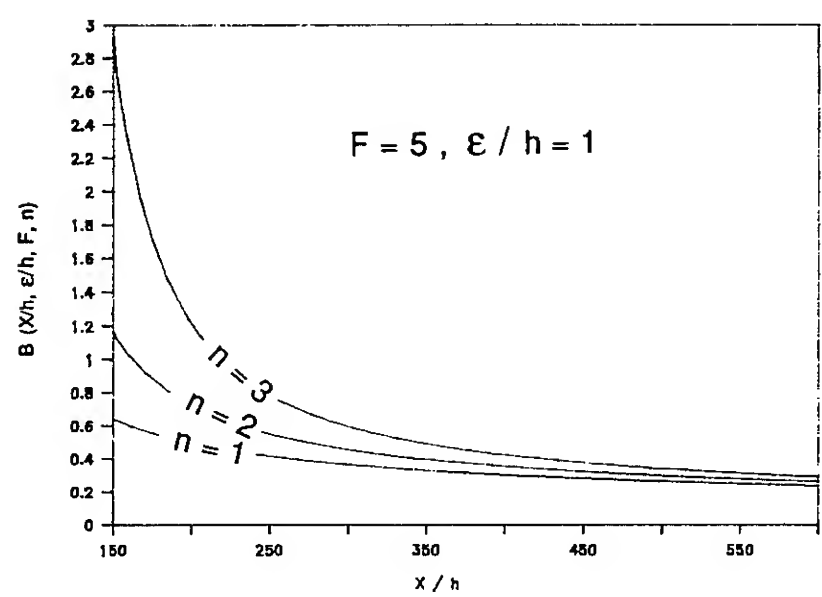
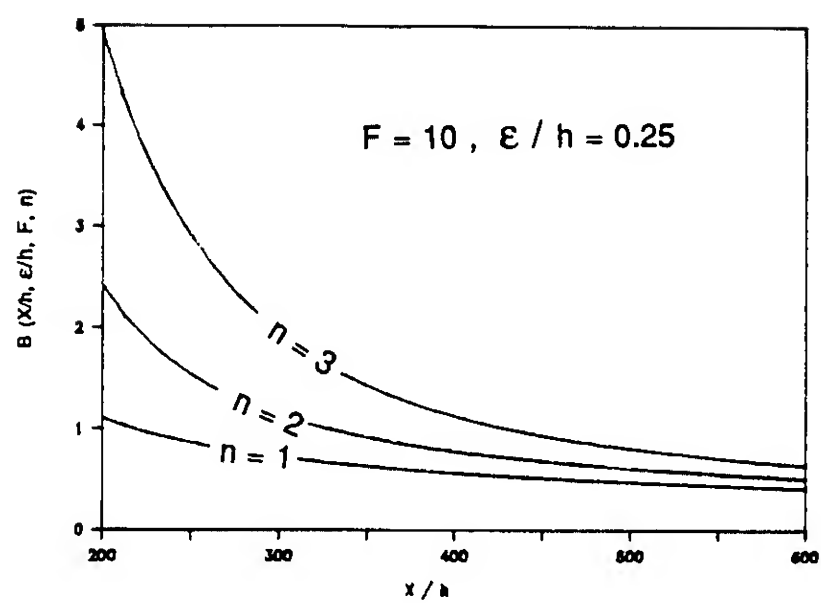
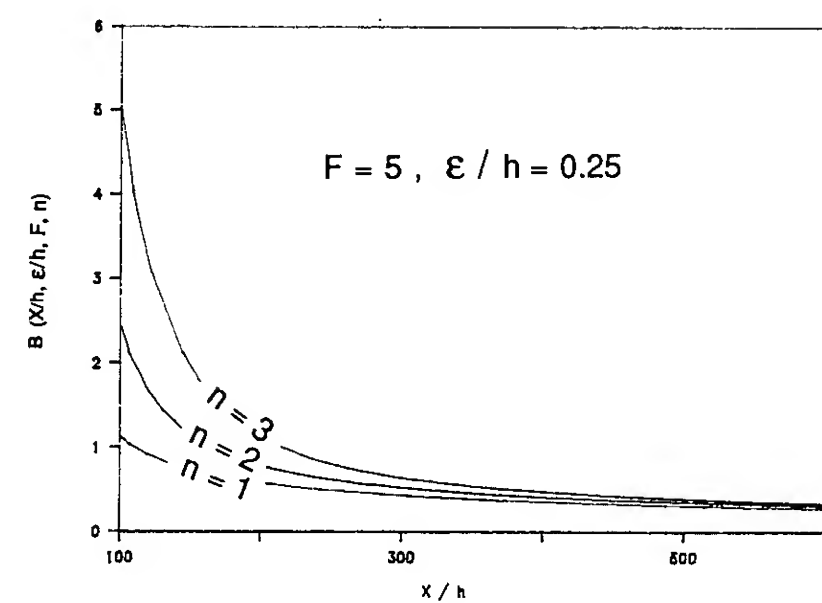
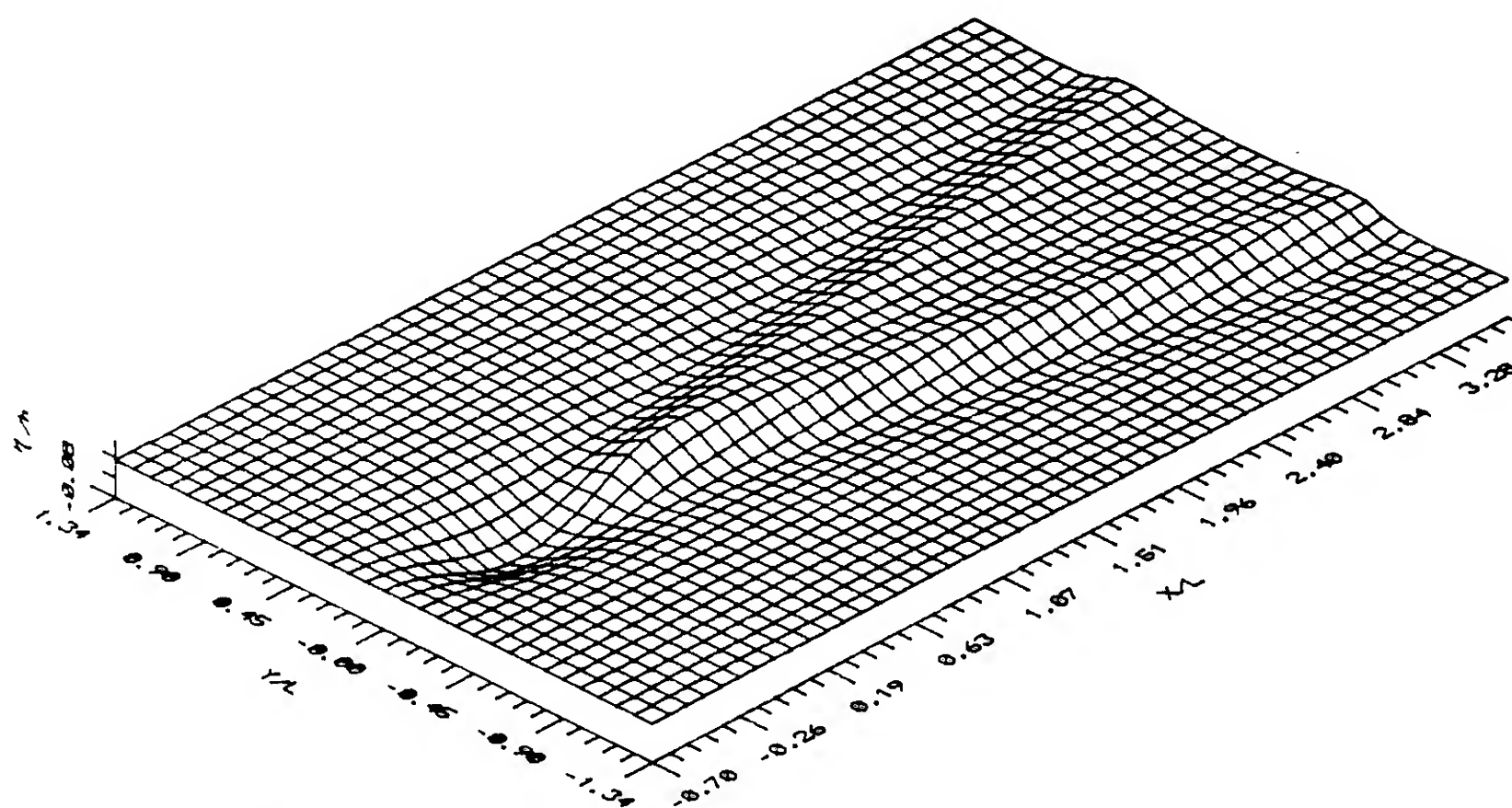
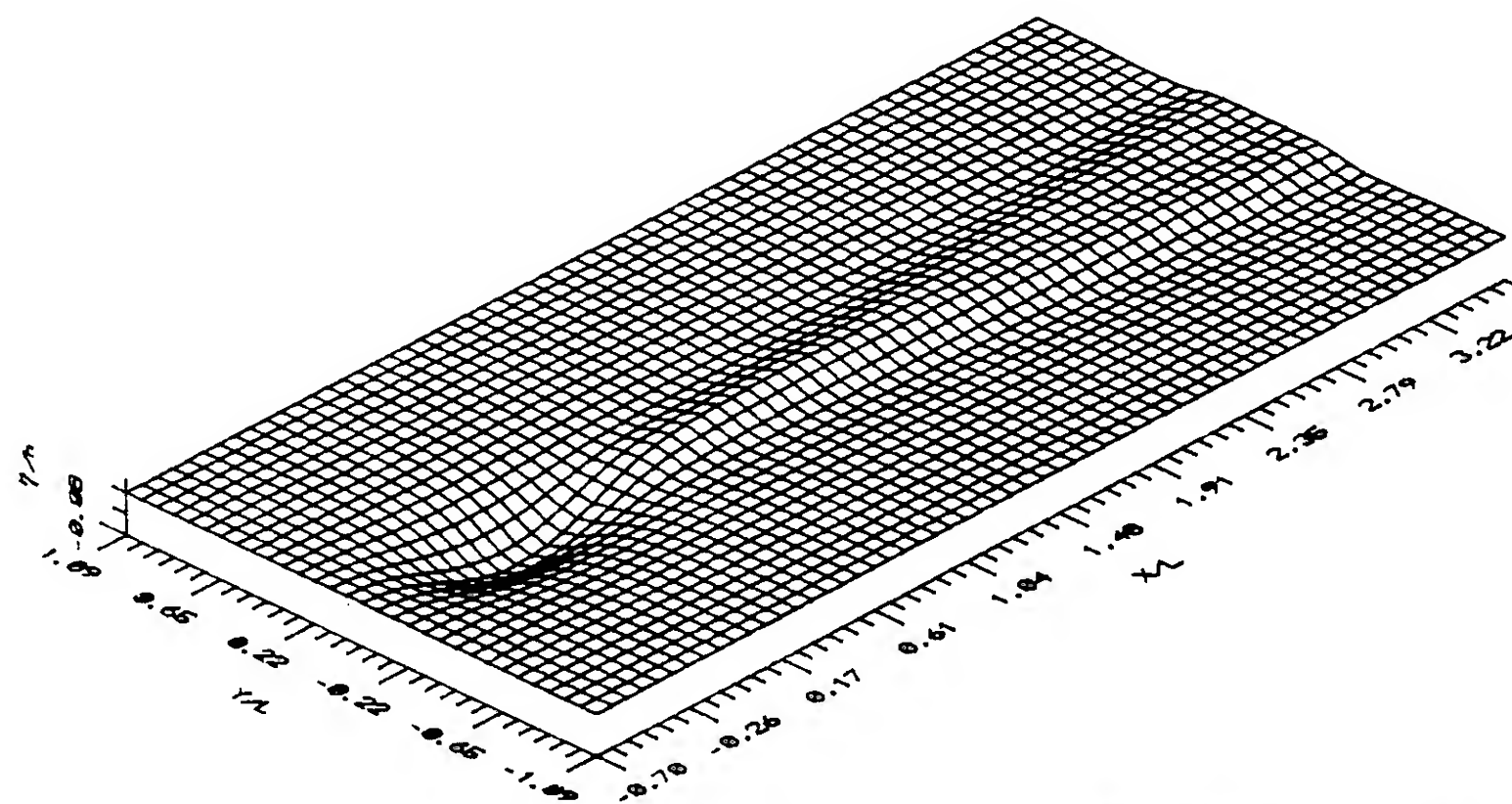


**Figure 5.** Waveform Amplitude Factor

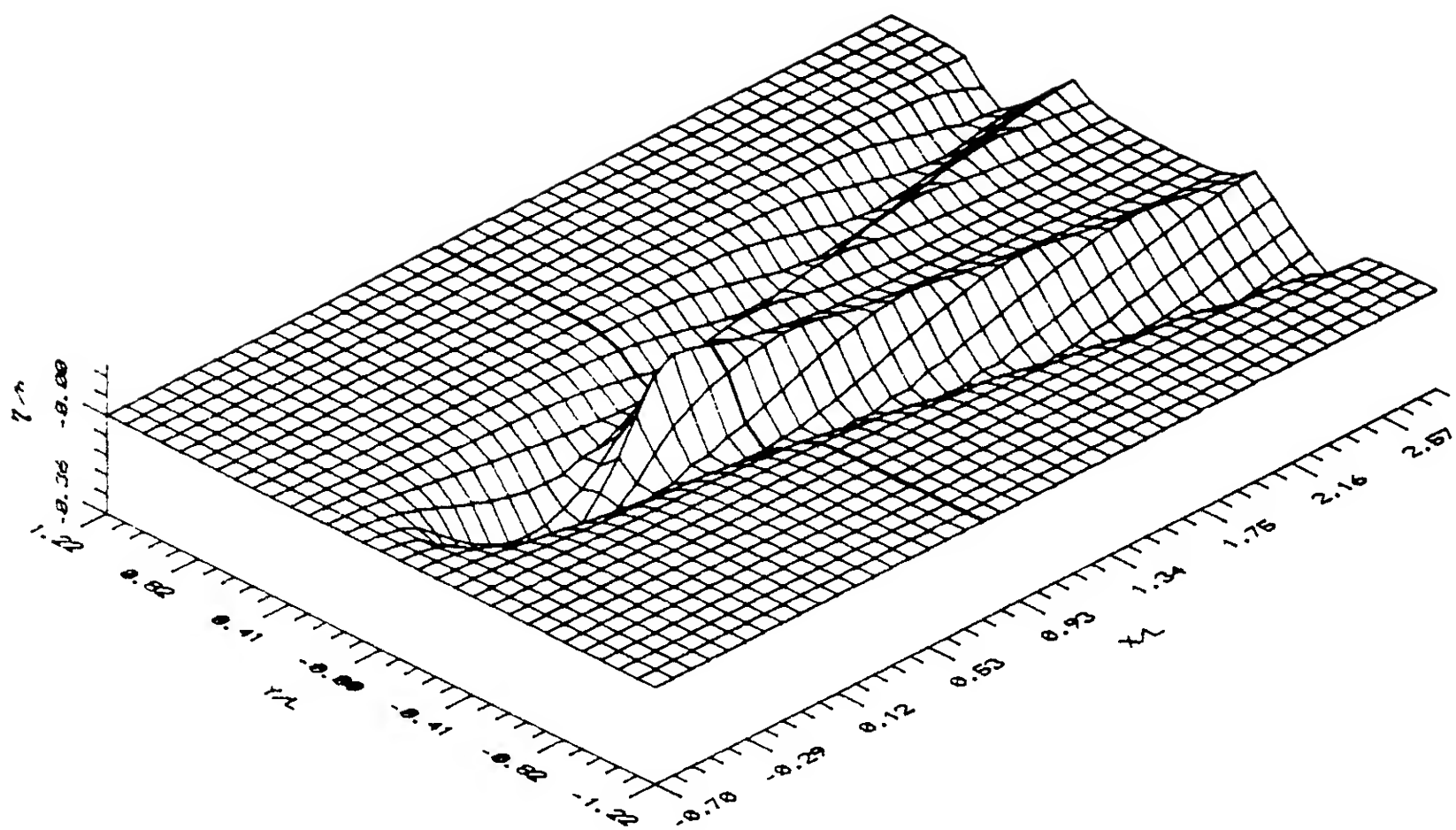


INTERNAL WAVE (  $F=5$ ,  $D/h=0.45$ ,  $L/h=5$ ,  $\eta(\text{MIN.})/h=-.0778$ ,  $\eta(\text{MAX.})/h=.0383$  )

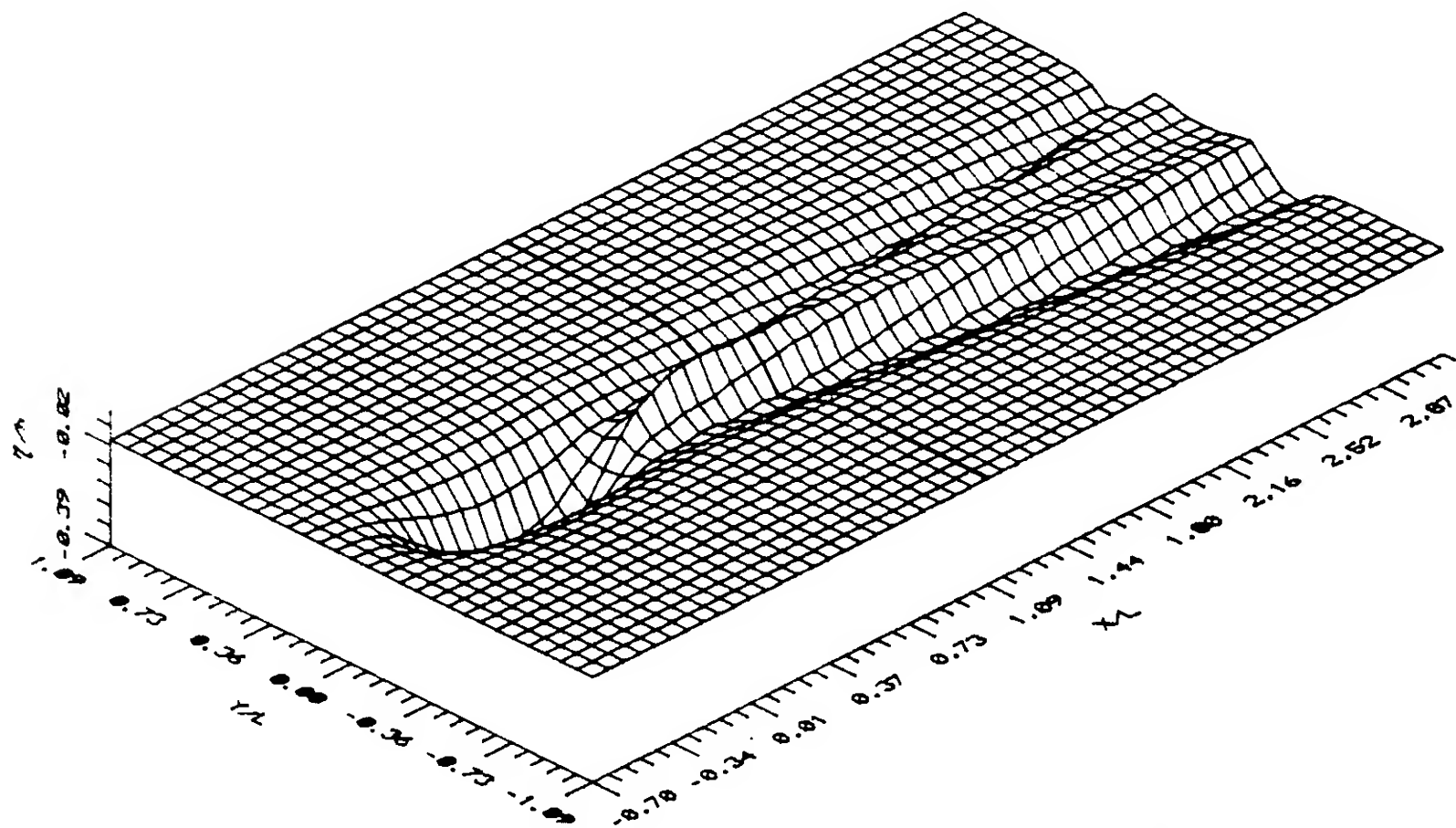


INTERNAL WAVE (  $F=10$ ,  $D/h=0.45$ ,  $L/h=5$ ,  $\eta(\text{MIN.})/h=-.0818$ ,  $\eta(\text{MAX.})/h=.0255$  )

**Figure 6(a).** Thermocline Displacement Patterns ( Near Field )



INTERNAL WAVE (  $F=5$ ,  $D/h=0.9$ ,  $L/h=10$ ,  $\eta(\text{MIN.})/h=-.3574$ ,  $\eta(\text{MAX.})/h=.1800$  )



INTERNAL WAVE (  $F=10$ ,  $D/h=0.9$ ,  $L/h=10$ ,  $\eta(\text{MIN.})/h=-.3905$ ,  $\eta(\text{MAX.})/h=.1070$  )

**Figure 6(b).** Thermocline Displacement Patterns ( Near Field )

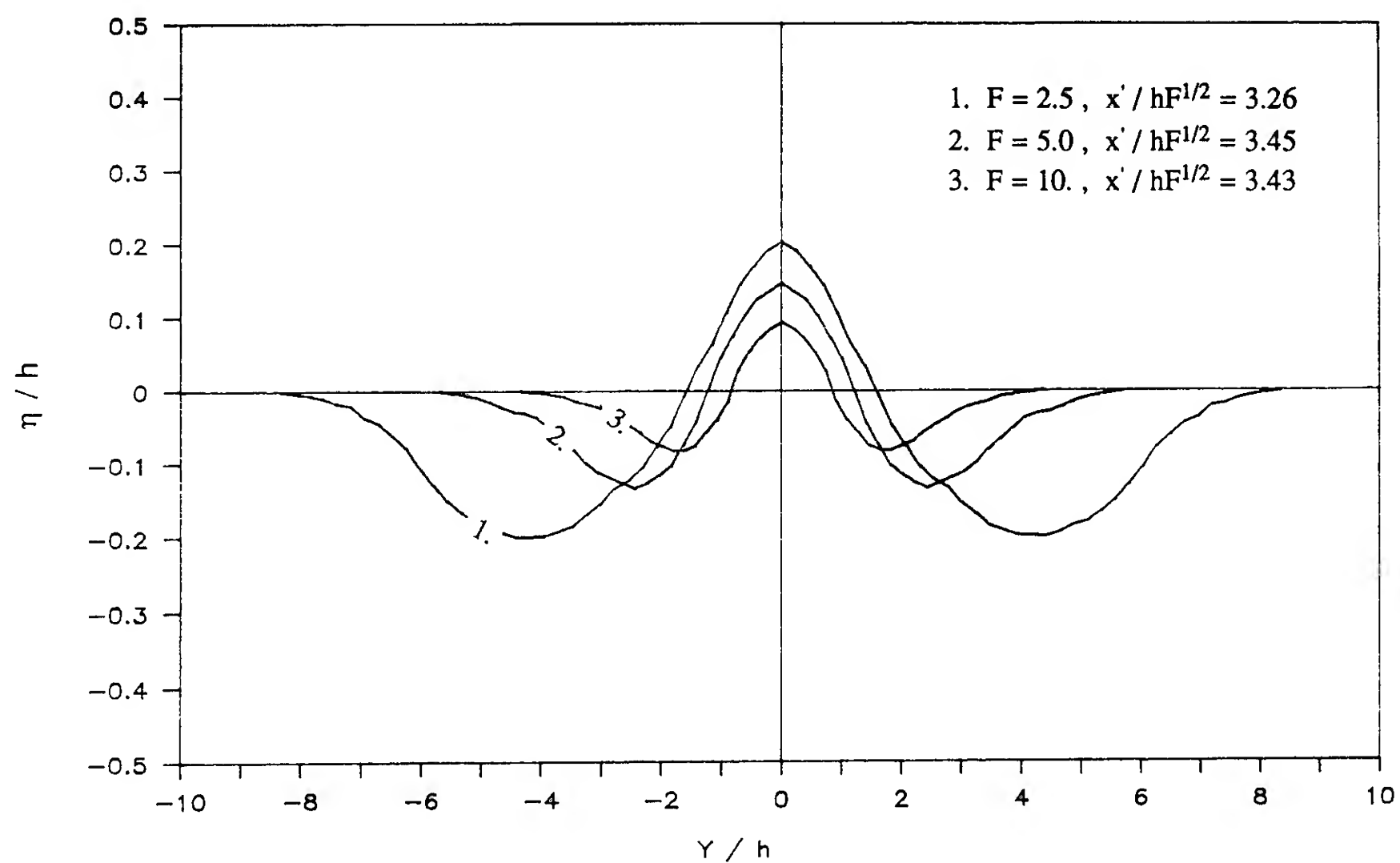


**Figure 7.** Near Field Wake Patterns

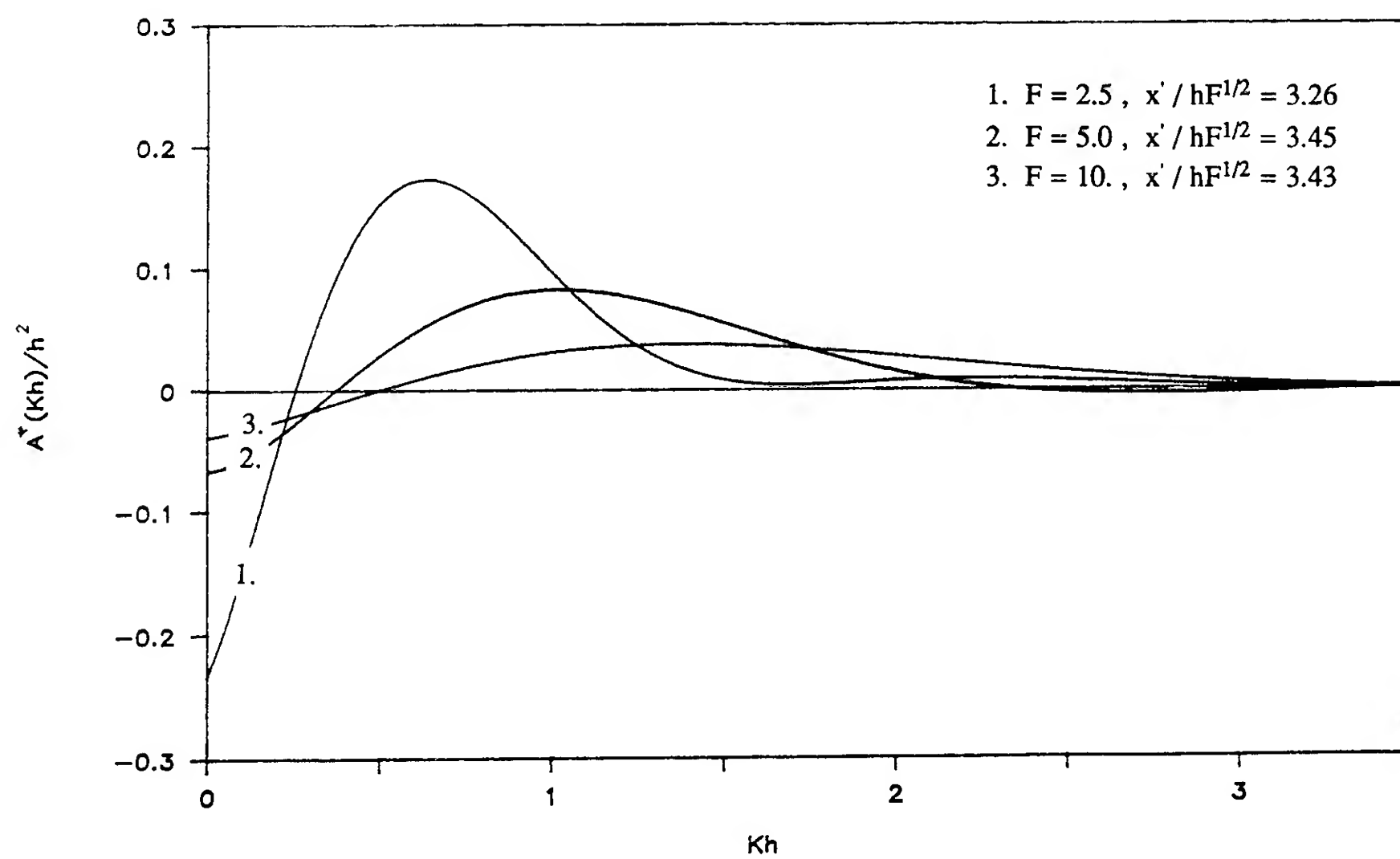


**Figure 8.** Shipform Amplitude Factor

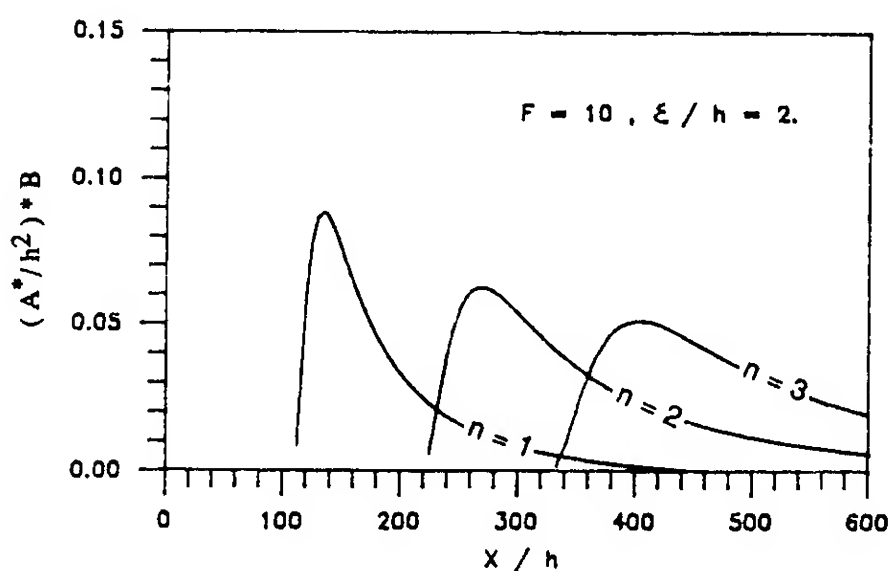
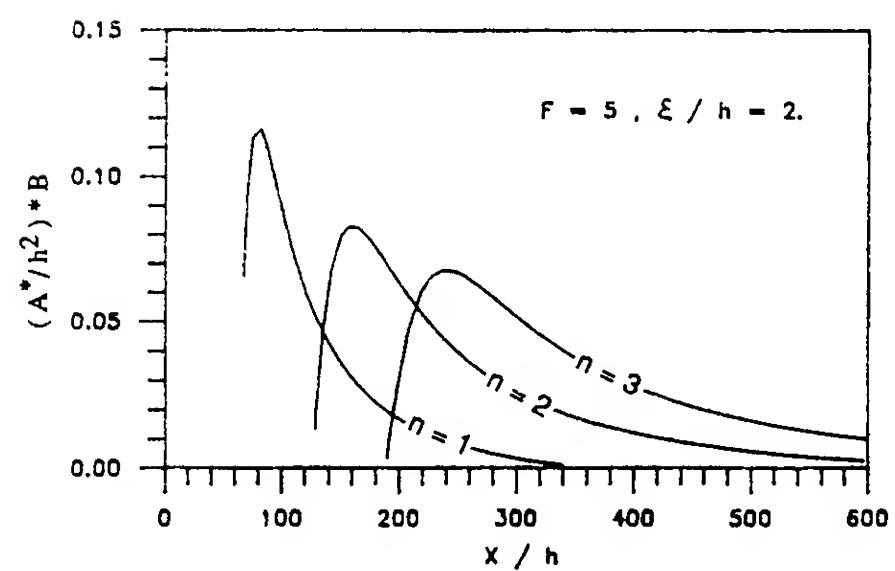
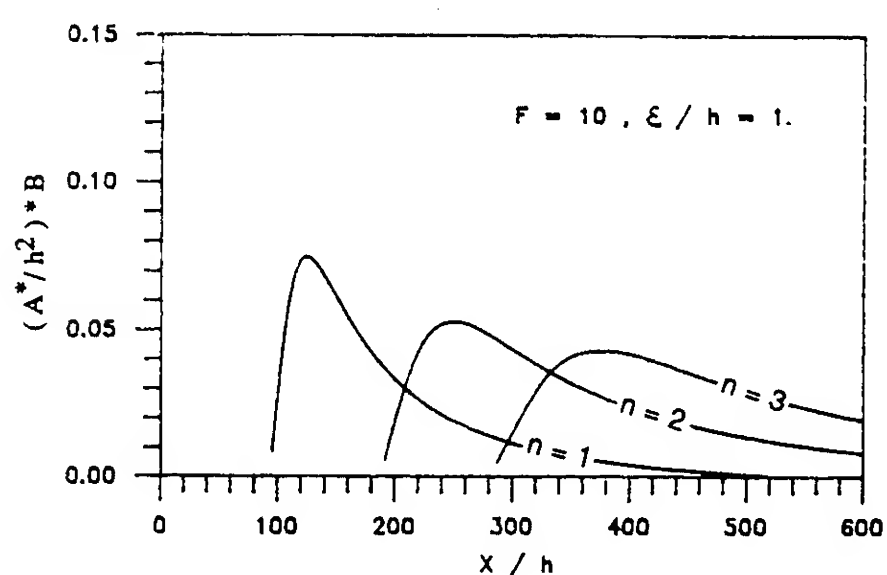
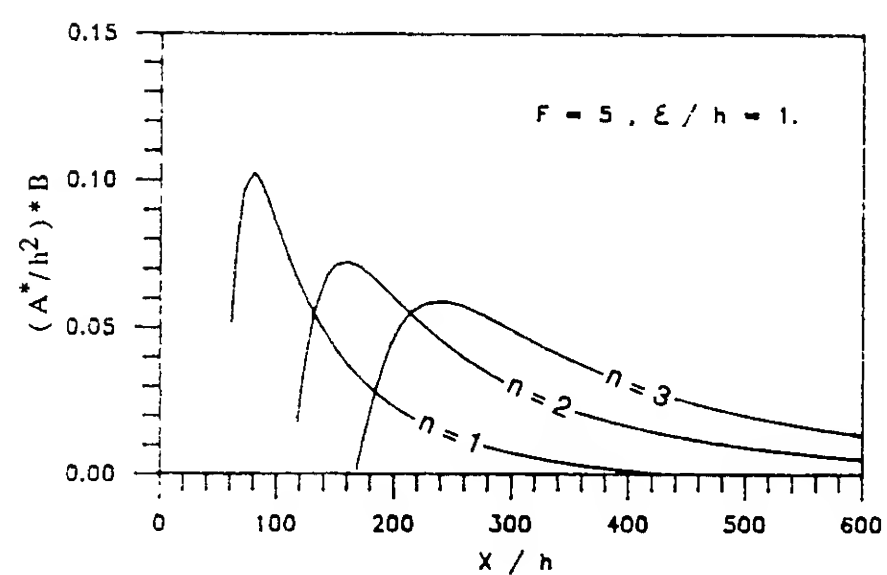
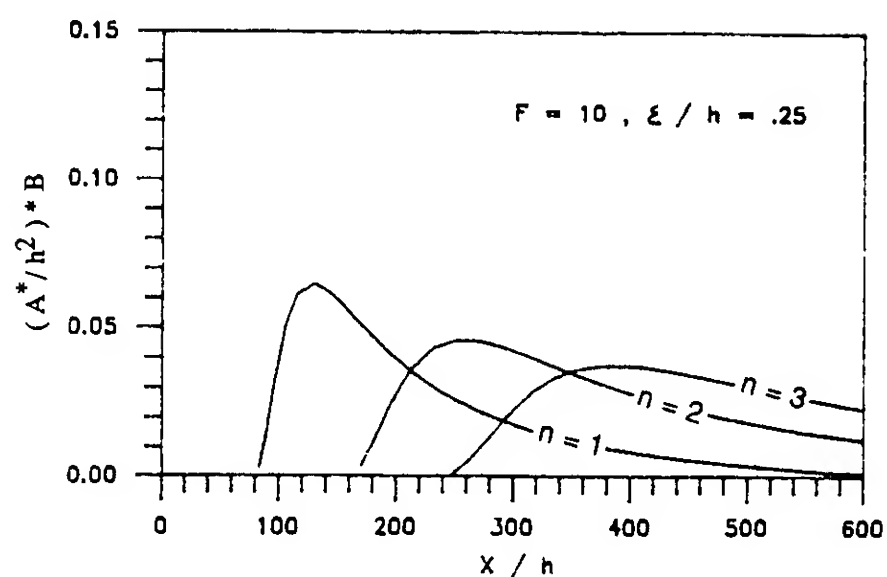
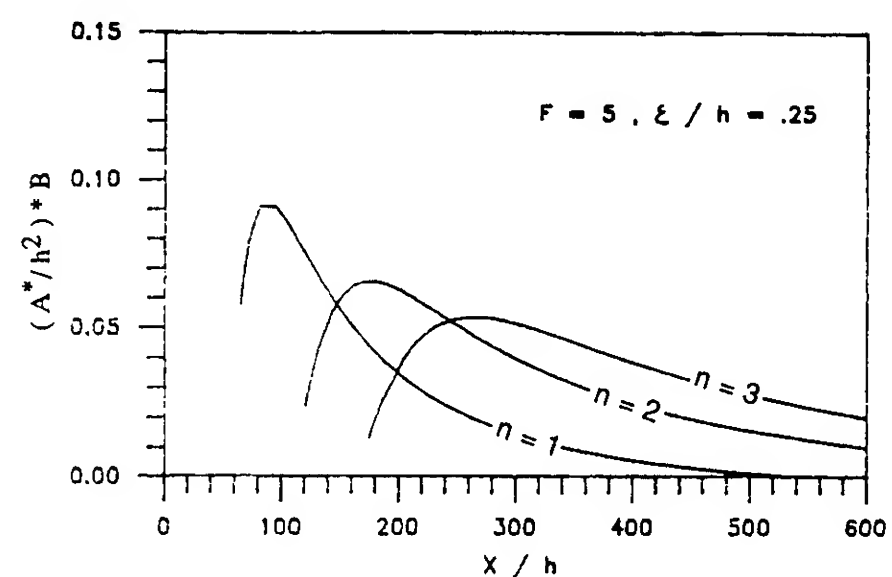


**Figure 9.** Crestline Wave Amplitudes



**Session VII**  
**Propeller/Hull/Appendage Interactions**

# On the Optimization, Including Viscosity Effects, of Ship Screw Propellers with Optional End Plates

K. de Jong (University of Groningen, The Netherlands)

## ABSTRACT

For ship screw propellers an optimization theory is discussed, that can be applied to propellers with and without end plates. The method differs from the classical optimization in that for the derivation of the optimum circulation distributions the sum of kinetic and viscous energy loss of the propeller is minimized instead of kinetic energy loss only. A criterion for the risk of cavitation, a simple strength model and an optional nonlinear correction are incorporated in the optimization method. Hydrodynamically favourable planform shapes of screw blades and end plates are discussed. Numerical results of optimum screws are given, including a comparison between the application of different types of end plates. It is shown under what circumstances and to what extent the theory predicts a higher optimum efficiency for propellers with certain types of end plates than for propellers that have no end plates.

This paper is a summary of [1], in which some topics are treated at greater length and in which more numerical results are given.

## 1. INTRODUCTION

In [2] the design of a model screw propeller with end plates is discussed, and results of experiments are given. These results are promising for the end plate concept. In this paper we want to obtain a better insight into the circumstances under which optimum propellers with end plates can have a higher efficiency than optimum propellers without end plates. In the classical optimization theory for ship screw propellers, as used for instance in [2], [3], [4] and [5], when the propeller reference surfaces are given the optimum circulation distributions are determined by solving a variational problem such that the kinetic energy loss of the propeller is a minimum. A major subject in this paper will be an optimization theory in which in the variational problem the *sum of kinetic and viscous energy loss* is minimized. In this paper we will speak of the latter optimization theory as "*optimization including viscosity*".

Bearing in mind the results of [3] we confine ourselves to propellers with zero rake and with end plate planforms lying in a circular cylinder. Furthermore, for reasons of simplicity, we restrict ourselves to propellers with homogeneous inflow.

Viscous energy loss depends mainly on the distributions of chord length and of maximum profile thickness along the spans of screw blades and, if it does apply, of the end plates. When we want the risk of cavitation to be approximately equal along all spanwise stages of blades and end plates of a screw propeller, the distributions of chord length and maximum profile thickness can not be chosen arbitrarily. Therefore in section 3 we will introduce a criterion for the risk of cavitation, being a relation between circulation, chord length and maximum profile thickness, depending on some parameters. That the cavitation criterion can be satisfied for a "two-sided" end plate, is discussed in section 4 by explaining the concept of an end plate consisting of two "shifted" parts. The required strength of the propeller also puts constraints upon the distributions of chord length and maximum profile thickness. Therefore an approximative strength calculation is embedded in the optimization method, as is explained in [1].

The relation associated with our cavitation criterion, makes the viscous energy loss of a screw propeller depend in essence only on the circulation distributions of the screw, see section 5. Because it is evident that also the kinetic energy loss depends on the circulation distributions, we are able to formulate in section 6 a variational problem for the minimization of the sum of kinetic and viscous energy loss, which both can now be considered as functionals of the circulation distributions. The optimization including viscosity seems to be important especially when propellers with end plates are optimized. This we expect because end plates have the effect of relatively increasing the circulation and chord length at large radii with respect to a propeller without end plates, while at large radii the viscous energy loss becomes important. Also for lightly loaded propellers which have a relatively large viscous energy loss the optimization including viscosity seems useful.

For more heavily loaded propellers the kinetic loss becomes predominant, while the prediction of the kinetic loss for higher loadings is more uncertain because of the nonlinear character of the problem. Therefore we made a rough attempt to correct the linear theory by iteratively adapting the advance ratio of our vortex wake.

Some design requirements, hydrodynamical aspects, strength aspects, aspects of the viscous energy loss, our cavitation criterion and our nonlinear correction

are combined in an iterative numerical optimization method which is outlined in section 7. The iterative numerical method delivers, when some design choices are put into it, optimum distributions of circulation, chord length and maximum profile thickness along the spans of blades and end plates. Moreover it delivers the chordwise pressure jump distributions. Some aspects of the influence of the shape of the leading and trailing edges of the screw blades and end plates, on the design of screw propellers by lifting surface theory are discussed in section 4. Hence the obtained results from the theory and numerical method, can be used as input for a lifting surface computer program, by which the full geometry of the considered propellers can be calculated.

Some conclusions from the numerical results given in sections 8 and 9 are as follows. Combination of the iterative numerical method with the optimization including viscosity gives somewhat different optimum distributions of circulation, chord length and maximum profile thickness along blades and end plates than combination with the classical optimization gives. However the predicted optimum propeller efficiency by the two methods is much the same for most propellers.

Our nonlinear correction changes the optimum propellers to a rather large extent, but the same trends are visible as in the linearized case. For instance the gain in efficiency caused by application of end plates to a propeller does not differ so much when instead of the linear theory the nonlinear theory is used.

In large areas of application, the methods predict a gain in efficiency caused by application of end plates. However there are areas for which the allowance of end plates can not increase the propeller efficiency, for instance when the diameter or the rotational velocity of the screw are prescribed to be sufficiently large.

As another conclusion we mention here that our "two-sided shifted" end plate has a noticeably higher efficiency than the two-sided symmetrical end plate which is used in [2].

## 2. PRELIMINARIES

In Figure 1 the planforms of a screw blade with an end plate, consisting of two shifted parts, are depicted in a cartesian frame  $(x, y, z)$ . The cylindrical

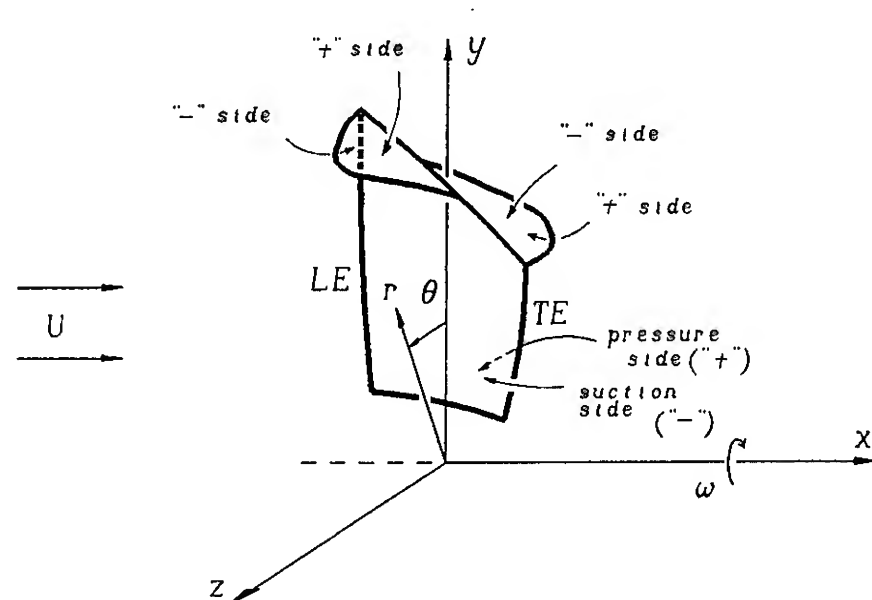


Fig. 1 Planforms of a screw blade with a "two-sided" end plate.

coordinates  $(x, r, \theta)$  are such that in the  $yz$ -plane the angle  $\theta$  vanishes at the positive  $y$ -axis and increases towards the positive  $z$ -axis. The screw has a rotational velocity  $\omega > 0$  (rad/sec) around the  $x$ -axis in the negative  $\theta$ -direction. There is an incoming homogeneous flow  $U$  in the positive  $x$ -direction.

In our model we neglect the influence of the ship and of the hub, hence we consider freely moving screw blades. The reason for the neglect of the hub is that then in the optimum case the circulation vanishes at the root of the blade, and it seems reasonable that when such a blade is mounted to a hub of finite length, no strong hub vortex will occur. A more fundamental approach for the hub of finite length is given in [6]. The blade and end plate are situated in a close neighbourhood of their planforms, which are parts of the corresponding reference surfaces. The reference surface  $H_b$  of the blade is

$$H_b : \theta = \omega x / (U + v_x), \quad r_h \leq r \leq r_p, \quad -\infty \leq x \leq \infty, \quad (1)$$

where  $r_h$  is the hub radius,  $r_p$  the blade tip radius and  $v_x$  is a corrective velocity which is used for approximating nonlinear effects and which will be discussed later on. In case we take  $v_x = 0$  we have the linearized theory. From (1) it follows that the screws we will consider have no rake. The reason is that we can not expect a worthwhile gain in the optimum efficiency by the application of a nonzero rake angle, as is shown in [3] by symmetry considerations and also by numerical calculations.

The end plate is mounted to the tip of the blade. If it is a two-sided end plate, one part of the end plate is at the pressure side ( $p$ ) of the blade, the other one is at the suction side ( $s$ ). The reference surfaces  $H_p$  and  $H_s$  of these two end plate parts are

$$H_p : \theta = \omega x / (U + v_x) + \tilde{\theta}, \quad r = r_p, \quad \theta_p \leq \tilde{\theta} \leq 0, \quad -\infty \leq x \leq \infty, \quad (2)$$

$$H_s : \theta = \omega x / (U + v_x) + \tilde{\theta}, \quad r = r_p, \quad 0 \leq \tilde{\theta} \leq \theta_s, \quad -\infty \leq x \leq \infty, \quad (3)$$

respectively. The angles  $\theta_p$  and  $\theta_s$  determine the span of the two end plate parts. We take  $H_p$  and  $H_s$  as parts of the cylinder  $r = r_p$ , because in [3] it is shown numerically that reference surfaces which do not coincide with this cylinder, yield lower quality numbers than those which are part of it, when the propeller radius, which is the greatest distance of points of the reference surfaces to the  $x$ -axis, is preserved. Hence the propeller radius in the following equals the already introduced  $r_p$ .

Figure 2 gives the expanded planform  $P_b$  of a blade and the developed planforms  $P_p$  and  $P_s$  of two end plate parts at pressure and suction side. To identify spanwise positions at the end plate the length parameters  $\sigma_p$  and  $\sigma_s$  are used. They are in the reference surfaces  $H_p$  and  $H_s$  and perpendicular to the family of helices (2) and (3). At the helix passing through the point  $R, (x, r, \theta) = (0, r_p, 0)$ , the parameters  $\sigma_p$  and  $\sigma_s$  vanish and they increase towards the end plate tips up to the end values  $\sigma_{p,e}$  and  $\sigma_{s,e}$ , respectively. For the sake of a consistent notation we use, in addition to the radius parameter  $r$ , the length parameter  $\sigma_b$  to identify spanwise positions at the blade planform. We take  $\sigma_b = 0$  for  $r = r_h$  and  $\sigma_b = \sigma_{b,e} = r_p - r_h$  for  $r = r_p$ .

In chordwise directions we introduce the length parameters  $\chi_i$ , increasing from the leading edge  $LE$  to the trailing edge  $TE$ , along the helices of the

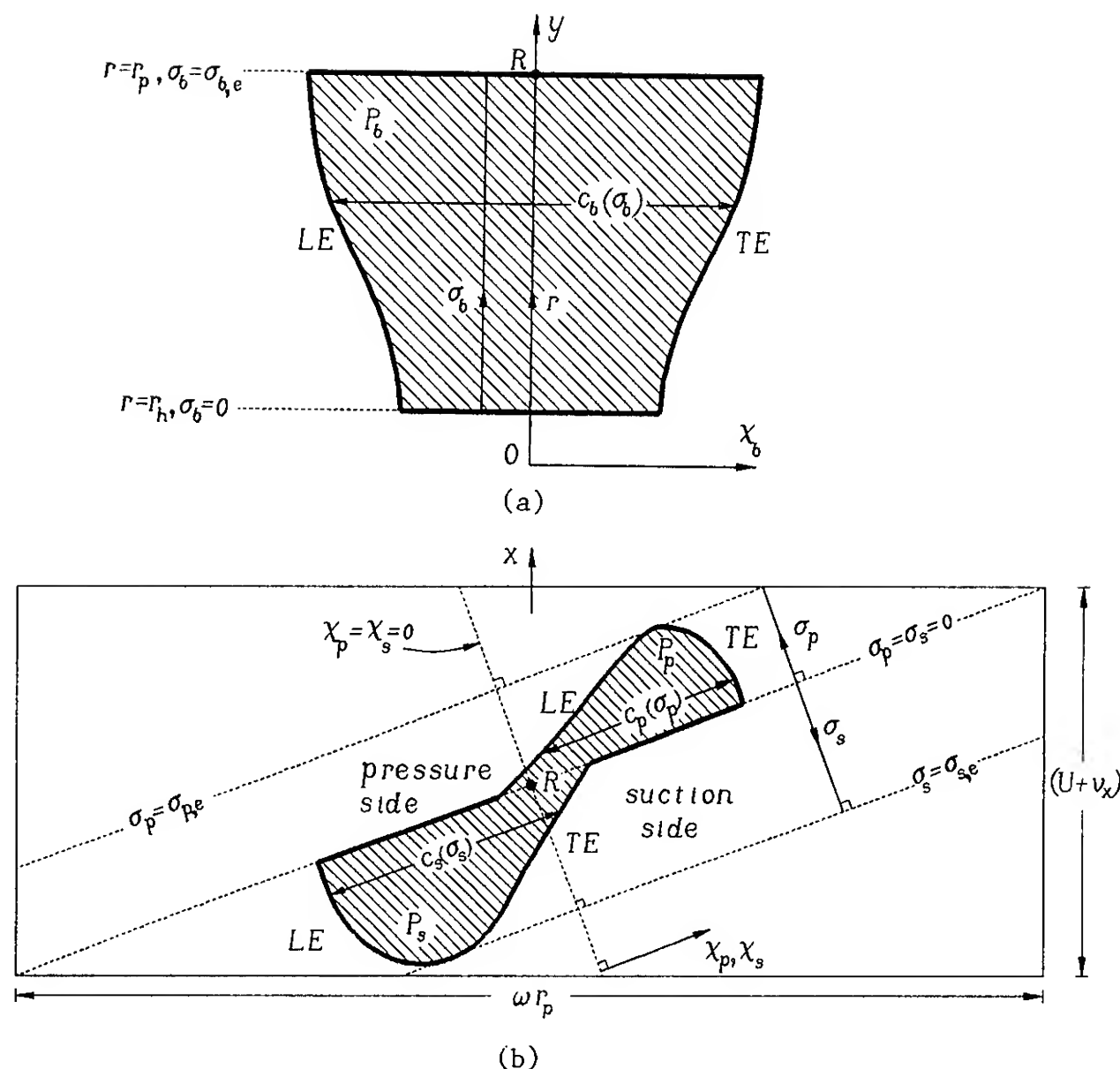


Fig. 2 Impression of planforms  
(a) Expanded planform  $P_b$  of blade  
(b) Developed planforms  $P_p$  and  $P_s$  of end plate at radius  $r=r_p$

reference surfaces  $H_i$ , ( $i=b, p, s$ ). In  $H_b$  the parameter  $\chi_b$  vanishes at the  $y$ -axis. In  $H_i$ , ( $i=p, s$ ), we reckon  $\chi_i$  zero at the line which is orthogonal to the helices of  $H_i$  and which passes through the point  $R$  at the  $y$ -axis.

Chord lengths at blade and end plate are denoted by  $c_i(\sigma_i)$ , while the maximum thickness distributions of the profiles are denoted by  $t_i(\sigma_i)$ , ( $i=b, p, s$ ). The quotient  $t_i(\sigma_i)/c_i(\sigma_i)$  is called the thickness ratio. Each reference surface  $H_i$ , ( $i=b, p, s$ ), has two sides, a "+" side and "-" side, which are defined as follows. At  $H_b$  the "+" side corresponds to the pressure side of the screw blade. At  $H_p$  the "+" side is the side facing smaller radii, while at  $H_s$  the "+" side is the side facing larger radii. The "-" sides are the opposite ones. See Figure 1.

Although in Figure 1 for simplicity a one-bladed screw is drawn, we will consider in the following  $Z$ -bladed screws with  $Z > 1$ . The blades and end plates of a  $Z$ -bladed screw all have the same geometry and are equally spaced. This means we have  $Z$  sets of planforms  $P_b$ ,  $P_p$  and  $P_s$ , each set rotated with respect to a neighbouring set over an angle  $2\pi/Z$  radians around the  $x$ -axis. The use of a second subindex  $j$ , ( $j=1, \dots, Z$ ), refers to the specific number of a blade. For instance for the  $Z$ -bladed propeller the reference surfaces are denoted by  $H_{i,j}$ , ( $i=b, p, s$ ;  $j=1, \dots, Z$ ).

We shall make use of the expanded blade area ratio  $A_e/A_0$  given by

$$A_e/A_0 = \frac{Z}{\pi r_p^2} \int_{r_h}^{r_p} c_b(r) dr = \frac{Z}{\pi r_p^2} \int_0^{\sigma_{b,e}} c_b(\sigma_b) d\sigma_b \quad (4)$$

The outer circular cylinder ( $r=r_p$ ) is partly covered by the reference surfaces  $H_{p,j}$  and  $H_{s,j}$ , ( $j=1, \dots, Z$ ), of the end plate parts. The ratio of covering  $k$  is defined by

$$k = Z(\theta_s - \theta_p) / (2\pi) \quad (5)$$

We only consider screws with  $k$  in the range  $0 \leq k \leq 1$ , because from the potential theoretic point of view  $k > 1$  yields the same efficiency as  $k=1$  while the viscous resistance of the end plate only increases. Splitting  $k$  in the contributions of the pressure sides and of the suction sides, we define

$$k_p = -Z\theta_p/(2\pi) \quad , \quad k_s = Z\theta_s/(2\pi) \quad , \quad k_p + k_s = k \quad (6)$$

### 3. RELATION BETWEEN CIRCULATION, CHORD LENGTH AND MAXIMUM PROFILE THICKNESS

In this section we assume the chordwise pressure jump distribution along a profile of a blade or end plate to be prescribed. In design methods often pressure jump distributions are encountered of the type given in Figure 3.

The parameter  $\chi_i$  is the length parameter in chordwise direction and  $c_i = c_i(\sigma_i)$  is the chord length of the wing section at the spanwise position  $\sigma_i$  of the planform  $P_i$ . Furthermore we denote by

$$[p_i]^\pm(\sigma_i, \chi_i) = p_i^+(\sigma_i, \chi_i) - p_i^-(\sigma_i, \chi_i) \quad , \quad (i=b, p, s) \quad (7)$$

the pressure jump between the "+" and "-" side of a wing section per unit of length in the chordwise  $\chi_i$  direction. The parameters  $\alpha_i = \alpha_i(\sigma_i)$  and  $\beta_i = \beta_i(\sigma_i)$  determine the shape of  $[p_i]_{-}^{+}$ , they are taken in the range  $0 \leq \alpha_i \leq \beta_i \leq 1$ .

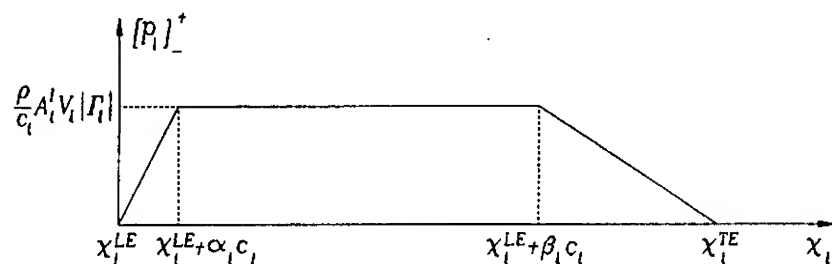


Fig. 3 Prescribed chordwise pressure jump distribution of a wing section,  $0 \leq \alpha_i \leq \beta_i \leq 1$ .

A wing section (profile) at the radial position  $r$  has the velocity  $V_i = V_i(\sigma_i)$  with respect to the water

$$V_i(\sigma_i) = ((\omega r)^2 + (U + v_x)^2)^{1/2}, \quad (8)$$

where the corrective velocity  $v_x$  will be discussed later on. At the end plate we have  $r = r_p$ , hence  $V_i(\sigma_i) = V_b(\sigma_{b,e})$  for all values of  $\sigma_i$ , ( $i = p, s$ ).

To create the pressure difference over a planform we assume that the planforms and the reference surfaces downstream of the trailing edges of the planforms are covered with vorticity. To represent the thickness of the blades and end plates we assume an appropriate distribution of sources and sinks over the planforms. The vorticity  $\vec{\gamma}_i(\sigma_i, \chi_i)$  has two components. The free vorticity, denoted by  $\gamma_i^f(\sigma_i, \chi_i)$ , is the component in the helicoidal  $\chi_i$ -direction, hence it does not deliver a lift. It is reckoned positive with a "right hand screw" in the positive direction of the length parameter  $\chi_i$ . The bound vorticity, denoted by  $\gamma_i^b(\sigma_i, \chi_i)$ , is the component perpendicular to the helices in a planform  $P_i$ , hence it is the pressure jump generating component. The sign of  $\gamma_i^b$  is taken equal to the sign of the corresponding pressure jump  $[p_i]_{-}^{+}$ . Both components  $\gamma_i^f$  and  $\gamma_i^b$  are taken per unit of length in their perpendicular directions in the reference surfaces. Note that these perpendicular directions at  $H_b$  are not the coordinate directions of the  $(\sigma_b, \chi_b)$  system, which is not orthogonal. At the reference surfaces  $H_p$  and  $H_s$  belonging to the end plate however the perpendicular directions are the same as the coordinate directions  $(\sigma_i, \chi_i)$ , ( $i = p, s$ ). We remark that we call free vorticity that component of the vorticity which does not give rise to a pressure jump, even when it is situated at the planform of blade or end plate.

In our theory the picture of the chordwise pressure jump along a wing section (Figure 3) is proportional to the picture of the bound vorticity  $\gamma_i^b(\sigma_i, \chi_i)$ . Hence the prescribed pressure jump distribution determines how the circulation  $\Gamma_i = \Gamma_i(\sigma_i)$  around a profile is distributed as bound vorticity  $\gamma_i^b(\sigma_i, \chi_i)$  along the chord. This means that when  $\Gamma_i(\sigma_i)$  and  $\alpha_i(\sigma_i)$  and  $\beta_i(\sigma_i)$  are fixed for a specific wing section (that is  $i$  and  $\sigma_i$  are specified), the pressure jump is inversely proportional to the chord length  $c_i(\sigma_i)$ , hence

$$\max_{0 \leq \chi_i \leq c_i} |[p_i]_{-}^{+}(\sigma_i, \chi_i)| = \rho A_i^I(\sigma_i) V_i(\sigma_i) |\Gamma_i(\sigma_i)| / c_i(\sigma_i), \quad (9)$$

where  $\rho$  is the fluid density and where the constant  $A_i^I(\sigma_i)$  equals

$$A_i^I(\sigma_i) = 2 / (1 + \beta_i(\sigma_i) - \alpha_i(\sigma_i)) \quad (10)$$

In agreement with the sign definition of  $\gamma_i^f$  and  $\gamma_i^b$ , the circulation  $\Gamma_i(\sigma_i)$  is taken positive with a "right-hand screw" in the positive direction of the length parameter  $\sigma_i$ .

The actual pressure at pressure and suction side of a wing (in our case a wing can be a screw blade as well as an end plate part) also depends on the thickness distribution of the wing. For instance, consider a two dimensional flow around a symmetrical profile with zero angle of attack. The fluid flow at infinity is the uniform parallel flow  $V_i(\sigma_i)$ . When the thickness ratio  $t_i(\sigma_i)/c_i(\sigma_i)$  is sufficiently small, the greatest drop of pressure is quadratic in  $V_i(\sigma_i)$  and about proportional to the thickness ratio. Therefore, omitting terms which are of quadratic or higher order in the thickness ratio, we can write

$$p_i^{min}(\sigma_i) - p_\infty = -\rho A_i^{II}(\sigma_i) V_i^2(\sigma_i) \frac{t_i(\sigma_i)}{c_i(\sigma_i)}, \quad (11)$$

where  $p_\infty$  is the ambient pressure (pressure at infinity),  $p_i^{min}(\sigma_i)$  the minimum pressure at the profile, and  $A_i^{II}(\sigma_i)$  a section constant depending on the type of thickness distribution of the profile. For simplicity we have neglected the influence of the variable static pressure, and therefore we consider a constant ambient pressure  $p_\infty$ .

For our propeller optimization method we want to have at our disposal an easy to handle criterion which yields an estimate of the greatest drop of pressure at the suction side of a wing. Therefore we simply superimpose half the pressure jump which was prescribed, and the greatest pressure fall due to thickness derived from the two dimensional consideration. We obtain

$$p_i^{min}(\sigma_i) - p_\infty = \rho \left( \frac{1}{2} A_i^I(\sigma_i) \frac{V_i(\sigma_i) |\Gamma_i(\sigma_i)|}{c_i(\sigma_i)} + A_i^{II}(\sigma_i) \frac{V_i^2(\sigma_i) t_i(\sigma_i)}{c_i(\sigma_i)} \right), \quad (12)$$

where  $A_i^I(\sigma_i)$  is given in (10). In (12) we have assumed that at the spanwise stage  $\sigma_i$  the minimum pressure due to thickness occurs in the range  $\chi_i^{LE} + \alpha_i c_i \leq \chi_i \leq \chi_i^{LE} + \beta_i c_i$ .

We want to consider screw propellers which concur to the desire to spread evenly the cavitation danger over all values of  $\sigma_i$  ( $i = b, p, s$ ), at the propeller. This means we want  $p_i^{min}(\sigma_i)$  for all values of  $i$  and of  $\sigma_i$  to be a constant, denoted by  $p^{min}$ . Then we find by solving (12) with respect to the chord length a relation between the chord length  $c_i(\sigma_i)$  and the circulation  $\Gamma_i(\sigma_i)$ , depending on the minimum pressure level  $p^{min}$ , on the relative velocity  $V_i(\sigma_i)$  of the wing section and on the maximum thickness  $t_i(\sigma_i)$ .

Because a real screw blade at its root is mounted to a hub, this relation can not be satisfied everywhere along the blade. Strength requirements of the propeller are such that for small radii  $r$  the chord length has to be larger than the one following from (12). Otherwise, the thickness ratio  $t_i/c_i$  in the neighbourhood of the hub, where in this theory  $\Gamma_b$  tends to zero, would become too large. Therefore for the screw blade we make



use of an adequate weight function  $w_b = w_b(\sigma_b)$  and we suggest the following relation between circulation and chord length

$$c_i(\sigma_i) = B w_i \left\{ \frac{1}{2} A_i^I V_i |\Gamma_i| + A_i^{II} V_i^2 t_i \right\}, \quad (i = b, p, s), \quad w_i \geq 1, \quad (13)$$

where we introduced the constant  $B$  defined by

$$B = \rho / (p^{min} - p_\infty). \quad (14)$$

If we had considered a variable static pressure and hence a variable ambient pressure  $p_\infty$ , then from the for cavitation most dangerous vertical upward position of a screw blade, we could derive that it is better to use functions  $B_i = B_i(\sigma_i)$  instead of the constant  $B$ . However, as remarked, for simplicity this is not considered.

The way in which we choose the weight function  $w_b = w_b(\sigma_b)$  is a subject which is discussed in [1]. It is taken into account in the optimization method, which determines among others the functions  $\Gamma_i = \Gamma_i(\sigma_i)$  and  $t_i = t_i(\sigma_i)$ , ( $i = b, p, s$ ), occurring in relation (13), and its choice has an influence on the determination of these functions. In relation (13) we also introduced for the end plate the weight functions  $w_p = w_p(\sigma_p)$  and  $w_s = w_s(\sigma_s)$ . We introduced the weight functions  $w_i$  as a tool which can be of use in the optimization method, to give weight not only to the constraint related to the cavitation danger, but also to constraints concerning hydrodynamics, strength and other aspects, see [1].

#### 4. DISTRIBUTION OF VORTICITY AT THE REFERENCE SURFACES

We assumed already that the vorticity belonging to the lifting surfaces of blades and end plates, is lying at the planforms  $P_i$ , (Figure 2). Because the vorticity field is free of divergence, we can define at each planform  $P_i$  and its corresponding reference surface  $H_i$  a "vorticity stream function"  $\Psi_i = \Psi_i(\sigma_i, \chi_i)$ , ( $i = b, p, s$ ). The meaning of such a stream function is the following. For two points  $(\sigma_i, \chi_i)$  and  $(\tilde{\sigma}_i, \tilde{\chi}_i)$ , both situated at  $H_i$ , we have

$$\Psi_i(\tilde{\sigma}_i, \tilde{\chi}_i) - \Psi_i(\sigma_i, \chi_i) = \int_{(\sigma_i, \chi_i)}^{(\tilde{\sigma}_i, \tilde{\chi}_i)} \gamma_n ds, \quad (i = b, p, s), \quad (15)$$

where  $\gamma_n$  is the component of the vorticity  $\vec{\gamma}_i$  perpendicular to the line element  $ds$  of an arbitrary line connecting the two points.

The leading edges,  $\chi_i = \chi_i^{LE}(\sigma_i)$ , of the planforms  $P_i$  are "stream lines" of the vorticity field. Upstream of the planforms, ( $\chi_i < \chi_i^{LE}$ ), there is no vorticity. Hence we can choose

$$\Psi_i(\sigma_i, \chi_i) \equiv 0, \quad \chi_i \leq \chi_i^{LE}(\sigma_i), \quad (i = b, p, s). \quad (16)$$

The circulation  $\Gamma_i = \Gamma_i(\sigma_i)$  at spanwise stage  $\sigma_i$  is distributed as bound vorticity  $\gamma_i^b$  along the chord

$$\Gamma_i(\sigma_i) = \int_{\chi_i^{LE}(\sigma_i)}^{\chi_i^{TE}(\sigma_i)} \gamma_i^b(\sigma_i, \chi_i) d\chi_i, \quad 0 \leq \sigma_i \leq \sigma_{i,e}, \quad (17)$$

where the bound vorticity distribution  $\gamma_i^b$  is

proportional to the chordwise pressure jump distribution  $[p_i]^+$ , see Figure 3.

When at the blades and end plates the distribution of circulation  $\Gamma_i(\sigma_i)$  and of chord length  $c_i(\sigma_i)$  and the chordwise pressure jump distributions are given, then the shape of the leading edge determines how the vorticity is spread over the planforms. Namely at all spanwise stages  $\sigma_i$  of the reference surfaces we can calculate, from the now known bound vorticity  $\gamma_i^b(\sigma_i, \chi_i)$ , the vorticity stream function  $\Psi_i(\sigma_i, \chi_i)$  for the values  $\chi_i > \chi_i^{LE}$  by the special case of (15)

$$\Psi_i(\sigma_i, \chi_i) = \int_{\chi_i^{LE}(\sigma_i)}^{\chi_i} \gamma_i^b(\sigma_i, \tilde{\chi}_i) d\tilde{\chi}_i, \quad \chi_i > \chi_i^{LE}(\sigma_i), \quad (18)$$

where we used that  $\Psi_i$  is taken zero at the leading edge, see (16). By (15)–(18) the stream functions  $\Psi_i$  are uniquely determined at the two-sided infinitely long reference surfaces. Because of the preservation of the vorticity stream we obtain a picture of the vorticity lines by plotting the level lines of the functions  $\Psi_i$ .

In the case when an end plate is mounted to the tip of the screw blade we discuss the important issue of how to convey adequately the vorticity of the screw blade to the end plate. It is desirable that the vorticity at the lifting surfaces and the trailing vorticity do not induce too large (or theoretically infinite) velocities at the lifting surfaces themselves. Otherwise, from the view point of the vortex theory, the desired propeller could not or only unrealistically be constructed using a lifting surface theory.

A first consequence of the above is that in the vortex model of the screw, it is desirable that no concentrated vortex line segment occurs at the propeller, because, following the law of Biot and Savart, such segment would induce at the propeller velocities which are inversely proportional to the distance from the segment. The possible occurrence and the avoidance of such a singularity will be discussed later on.

A second consequence is that discontinuities in the strength of the vortex sheets, inducing infinite velocities at the planforms, have to be avoided as much as possible. We illustrate this point as follows. Consider, (Figure 4), in the half planes  $I$  and  $II$ , two vortex sheets of constant finite strength  $\gamma_I$  and  $\gamma_{II}$  respectively, with  $\gamma_I \neq \gamma_{II}$ . The vorticity is parallel to the straight line  $l$ , at which the two sheets are connected.

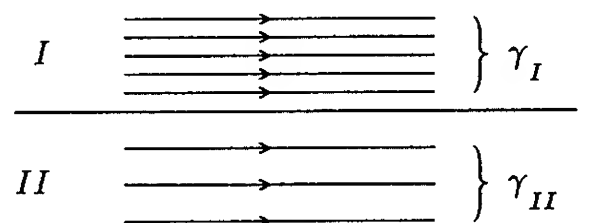


Fig. 4 Discontinuity at the connection line  $l$  of two vortex sheets with constant strengths  $\gamma_I$  and  $\gamma_{II}$  respectively, when  $\gamma_I \neq \gamma_{II}$ .

The induced velocity at the sheets is infinite at the

line  $l$  according to a singularity which is logarithmic in the distance to the line  $l$ . This second consequence implies for instance that at leading and trailing edges of a planform  $P_i$  the induced velocity would be infinite, when we had chosen  $\alpha_i=0$  and  $\beta_i=1$  in the chordwise bound vorticity distribution given in Figure 3. Hence from this point of view values of  $\alpha_i$  and  $\beta_i$  with  $\alpha_i>0$  and  $\beta_i<1$  are to be preferred.

To illustrate some basic ideas we direct our attention in the remainder of this section to a screw with a two-sided end plate of which both end plate parts have equal span  $\sigma_{p,e}=\sigma_{s,e}$  or  $k_p=k_s$ . When the functions  $\Gamma_b$ ,  $c_b$ ,  $\alpha_b$  and  $\beta_b$  are given as in Figure 5(a), (b) and (c) respectively, we can draw pictures of the vorticity field in the expanded screw blade planform by using (15)–(18). In Figure 5(d), (e) and (f) for different choices of leading edges of the screw blade, results are drawn.

We remark that the motivation for the choice of the shape of the functions  $\Gamma_b$ ,  $c_b$ ,  $\alpha_b$  and  $\beta_b$  is given

in later sections. By  $\Delta\Psi_i$ , ( $i=b,p,s$ ), we denote the difference in the stream function  $\Psi_i$  between the leading edge and the nearest depicted vorticity line and between each two depicted neighbouring vorticity lines. We must realize that the density of the vorticity lines in Figure 5(d), (e) and (f) is not an exact picture of the density of the vorticity lines in space, because the surface  $H_b$  is not flat and even not developable. However a good insight can be obtained in this way.

For the three types of considered screw blade planforms it is seen that at the blade tip there are ranges of  $\chi_b$  in which the free vorticity strength  $\gamma_b^f$  does not vanish

$$\gamma_b^f(\sigma_{b,e}, \chi_b) \neq 0, \quad \chi_b^{LE} \leq \chi_b \leq \chi_b^{TE} \quad (19)$$

Because for  $\sigma_b > \sigma_{b,e}$ , hence at the radially lengthened blade planform  $P_b$ , we know that there is no vorticity, and hence  $\gamma_b^f=0$  for  $\sigma_b > \sigma_{b,e}$ , we conclude that a

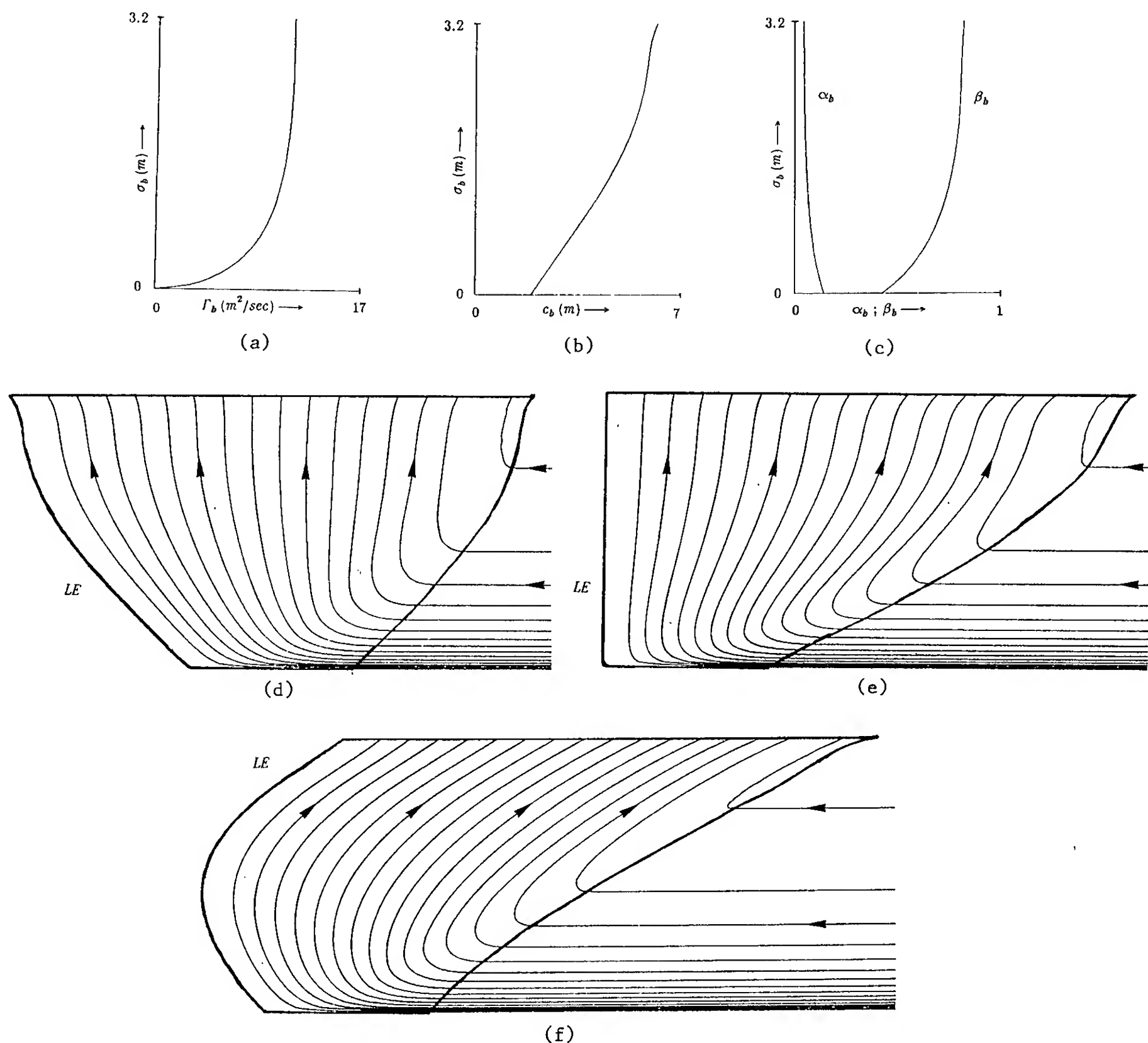


Fig. 5 Vorticity distributions at three different, expanded screw blade planforms  $P_b$  of a propeller with end plates;  $\Delta\Psi_b=0.7 \text{ m}^2/\text{sec}$ .

discontinuity arises of the type given in Figure 4. It is observed that this type of discontinuity is less strongly in the case of Figure 5(d) than in the case of Figures 5(e) and (f).

Now we come to the question as to what kind of two-sided end plates have to be mounted to screw blades whose planforms are for instance as depicted in Figure 5. In order to avoid the creation of a concentrated vortex line segment at the junction of blade and end plate planforms, it is necessary to choose the bound vorticity of the end plate parts such that at the line  $\sigma_p = \sigma_s = 0$ , hence at the roots of these parts, their sum equals the bound vorticity at the tip of the screw blade

$$\gamma_p^b(0, \chi_p) + \gamma_s^b(0, \chi_s) = \gamma_b^b(\sigma_{b,e}, \chi_b) \quad ,$$

$$\chi_b^{LE}(\sigma_{b,e}) \leq \chi_b = \chi_p = \chi_s \leq \chi_b^{TE}(\sigma_{b,e}) \quad . \quad (20)$$

A first idea would be to choose an end plate which is symmetric with respect to the blade tip, and which

satisfies

$$\alpha_p(0) = \alpha_s(0) = \alpha_b(\sigma_{b,e}) \quad , \quad \beta_p(0) = \beta_s(0) = \beta_b(\sigma_{b,e}) \quad . \quad (21)$$

An end plate of this kind was used for a model screw propeller as discussed in [2]. An example of such an end plate is given in Figure 17. For this type of end plate we have no concentrated vortex line segment at the junction of blade and end plate and because the free vorticity at the two symmetric end plate parts is of equal strength at their connection, also there exists no discontinuity in the vorticity field of the type of Figure 4. Aside we remark that experiments in a cavitation tunnel showed that the more or less concentrated blade tip vortex, which normally arises for propellers without end plates that have a square root singularity in the circulation distribution at the blade tip (see for instance Figure 14) could not be made visible for the model screw propeller with this type of end plates. The reason is that the trailing vorticity is spread over the trailing edge of the end

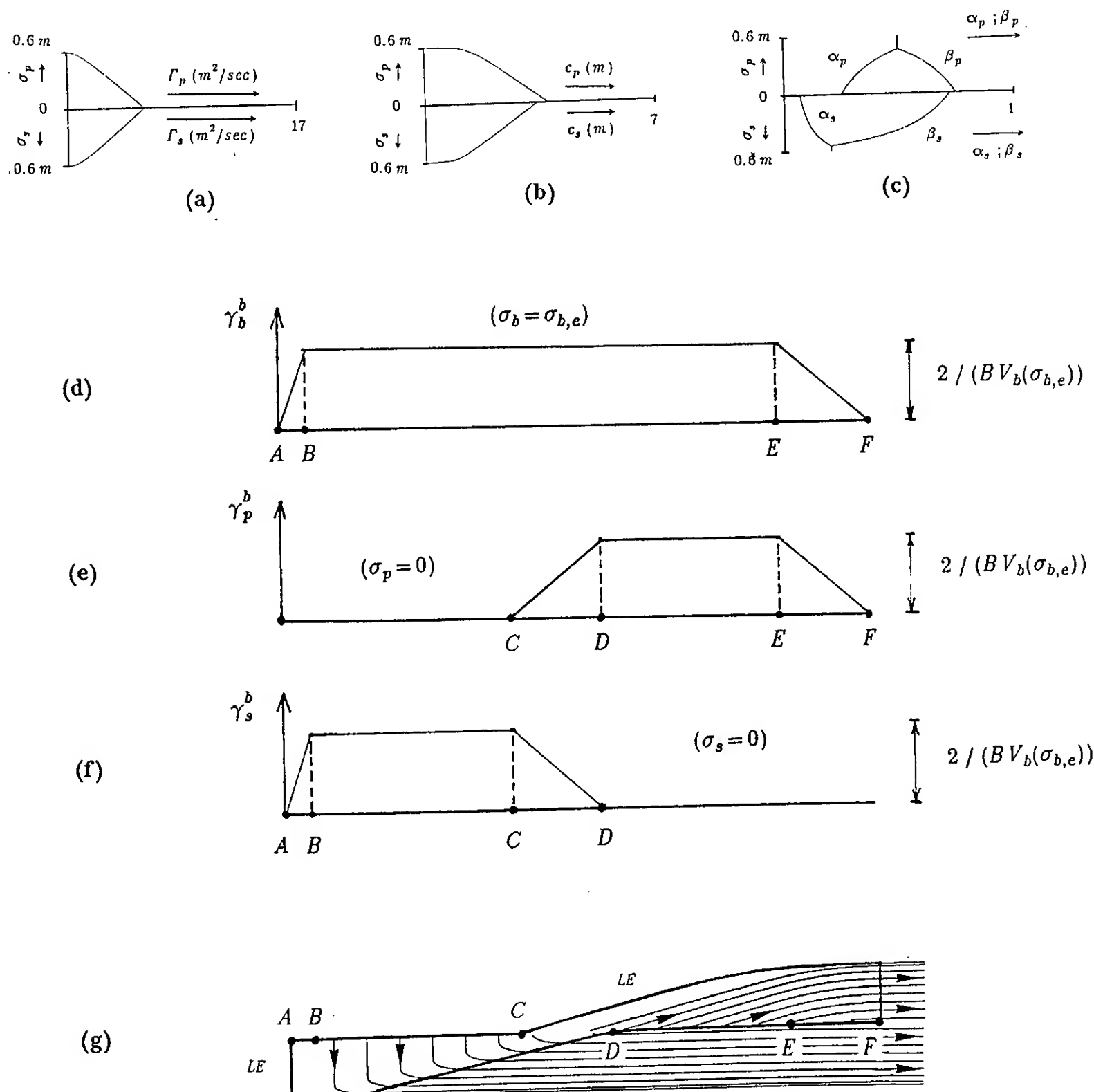


Fig. 6 Vorticity distribution belonging to a two-sided end plate with planforms which are relatively shifted with respect to each other;  $\Delta\psi_p = \Delta\psi_s = 0.7 \text{ m}^2/\text{sec}$ .

plate, compare Figures 14 and 17.

However a disadvantage of the above end plate is that its chord lengths are relatively too large compared with the chord length of the screw blade. Since only half of the circulation of the blade tip is conveyed to each end plate part, in relation with the avoidance of cavitation only about half of the chord length of the blade tip would suffice for the chord lengths at the roots of the end plate halves, see relation (13). Obviously, shorter chord lengths will cause smaller viscous losses, and minimization of the viscous loss especially is important for the end plates, because they have a relatively large velocity with respect to the water. This will be discussed now.

For simplicity we choose in first instance chord lengths based on relation (13) without taking into account the thickness. Furthermore at the end plate near the blade tip ( $0 \leq \sigma_i \leq \varepsilon$ ), we take the weight functions  $w_i(\sigma_i)$ , ( $i=p, s$ ), identically equal to one. Hence near the blade tip we take chord lengths of the end plate which are proportional to the circulation

$$c_i(\sigma_i) = \frac{1}{2} B V_b(\sigma_{b,e}) A_i^I(\sigma_i) \Gamma_i(\sigma_i) \quad , \quad 0 \leq \sigma_i \leq \varepsilon \quad , \quad (i=p, s) \quad . \quad (22)$$

This means that the chordwise maximum value of  $\gamma_i^b$  at the end plate ( $i=p, s$ ) for not too large values of  $\sigma_i$  equals  $2 / (B V_b(\sigma_{b,e}))$ .

In order to avoid concentrated vortices at the roots of the end plate parts we choose pressure jump distributions, satisfying relation (20) and we choose planforms of the end plate which are relatively shifted with respect to each other, see Figure 6.

In this figure for the "two-sided shifted" end plate the leading edge of the anterior planform and the trailing edge of the posterior planform are taken locally perpendicular to the tip of the blade planform (Figure 6(g)). Furthermore the functions  $\alpha_i = \alpha_i(\sigma_i)$  and  $\beta_i = \beta_i(\sigma_i)$ , ( $i=p, s$ ), at the end plate are such that the line segments along the chords where the bound vorticity is increasing ( $\chi_i^{LE} \leq \chi_i \leq \chi_i^{LE} + \alpha_i c_i$ ) and decreasing ( $\chi_i^{LE} + \beta_i c_i \leq \chi_i \leq \chi_i^{TE}$ ) are, for sufficiently small values of  $\sigma_i$ , line segments of constant length.

With the foregoing choices and assumptions it is not difficult to show (see [1]) that the free vorticity at the end plate planforms is of equal strength at the connection line  $AF$  (Figure 6(g)) of the end plate parts

$$\gamma_p^f(0, \chi_p) \equiv \gamma_s^f(0, \chi_s) \quad , \quad \chi_b^{LE}(\sigma_{b,e}) = \chi_s^{LE}(0) \leq \chi_p = \chi_s \quad . \quad (23)$$

The bound vorticity components  $\gamma_i^b$ , ( $i=p, s$ ), do not induce infinite velocities at  $AF$  as can be checked easily by the law of Biot and Savart. Hence in total the induced velocity field at the end plate planforms has no singularity.

With respect to the above mentioned aspects of the vorticity field, it does not matter whether the anterior and posterior end plate planforms are taken at the suction and pressure side of a screw blade respectively, as is done in Figure 6(g), or vice versa. However, from the view point of the strength of the propeller, it is slightly favourable that the anterior planform is situated at the suction side of the blade and the posterior planform at the pressure side, as is shown in [1].

When the thickness effect is included in relation (13), there will arise different chord lengths, and the vorticity field of Figure 6(g) can be disturbed somewhat. However it is always possible to

adjust the free vorticity strength  $\gamma_i^f$ , ( $i=p, s$ ), of the anterior and posterior end plate planforms at the line  $AF$  by altering the angle under which the leading edge of the anterior planform cuts  $AF$ , and the trailing edge of the posterior planform cuts  $AF$ . In this way the differences in the free vorticity strength between both sides of the line  $l$  can be made zero or sufficiently small, such that at  $AF$  no or only weak singularities of the induced velocity field are left.

It is seen from Figures 17 and 6 that we made the two end plate parts cooperate in trying to avoid possible singularities. For a one-sided end plate, ( $k_p=0, k_s \neq 0$  or  $k_p \neq 0, k_s=0$ ), this cooperation can not be achieved. There always the nonzero free vorticity at the end plate root adjoins a region without free vorticity.

## 5. ENERGY LOSS AND THRUST

In this section energy losses are considered. For the approximation of the kinetic energy loss, caused by the induced drag, we use the theory of a propeller in an ideal frictionless fluid. To find an approximation of the viscous drag of the propeller we apply a correction to the theory by using a resistance formula that includes the influence of the thickness of the profiles. In this way we have assumed that kinetic and viscous losses can be treated separately.

From the trailing edges of blades and end plates free vortex sheets are formed, which in our theory consist of helicoidal vorticity lines. At the points of the trailing edges the velocity of such a vorticity line consists in first instance of the velocity  $U$  in the positive  $x$ -direction. Furthermore it consists of velocity induced by the free vortex sheets themselves and by the presence of screw blades and end plates. The latter action can be represented by appropriate vorticity distributions and source-sink distributions. Especially when the screw is delivering higher thrusts the induced velocities relatively gain importance, because of the stronger vorticity in that case.

For the calculation of the lost kinetic energy it is necessary to know the shape of the free vortex sheets. In order to calculate the lost kinetic energy per unit of time, we continue the vortex lines until infinity downstream with the velocity they have when they are created. Using for this velocity only the axial component  $U$ , the approximation of the kinetic energy is appropriate only for lightly or moderately loaded propellers. In our approximation of the kinetic energy loss we shall add to the axial velocity component  $U$  an extra axial term  $v_x$  which is assumed to be constant all over the trailing edges. This velocity  $v_x$  will be chosen to increase in one way or another with increasing thrust  $T$ , as we will discuss in section 7. It reflects to some extent non-linear effects of the flow.

We consider infinitely far downstream of the propeller, vortex sheets which are located at the reference surfaces  $H_{i,j}$ , ( $i=b, p, s$ ;  $j=1, \dots, Z$ ), defined in section 2, with a suitable value of  $v_x \neq 0$ . This helicoidal continuation is not the actual wake of a screw propeller, however we hope that the kinetic energy loss per unit of time  $E_{kin}$  can be approximated in this way better than by taking  $v_x=0$ , which yields the strictly linear theory. We find

$$E_{kin} = \frac{1}{2} \rho \int_{x=const.}^{\substack{x=const. \\ +U+v_x}} \int \int |\text{grad} \Phi(x, y, z)|^2 dx dy dz, \quad (24)$$

where  $\Phi = \Phi(x, y, z)$  is the velocity potential of the trailing vorticity lying in the two-sided infinitely long reference surfaces  $H_{i,j}$  ( $i = b, p, s$ ;  $j = 1, \dots, Z$ ). It is a straightforward task to reduce equation (24) to

$$E_{kin}(\Gamma_i) = -\frac{1}{2} \rho Z \left( \int_0^{\sigma_{b,e}} \frac{\partial \Phi}{\partial n_b} \Gamma_b(\sigma_b) V_b(\sigma_b) d\sigma_b + \sum_{i=p,s} \int_0^{\sigma_{i,e}} \frac{\partial \Phi}{\partial n_i} \Gamma_i(\sigma_i) d\sigma_i \right), \quad (25)$$

where  $\vec{n}_i$  ( $i = b, p, s$ ) is the unit normal at the reference surfaces  $H_{i,1}$ , directed from the "-" to the "+" side.

When the screw blades and the end plates move through the water, frictional forces arise. Consider across a wing from leading to trailing edge an elementary wing strip of width  $d\sigma_i$ . The strip has the chord length  $c_i(\sigma_i)$  and maximum thickness  $t_i(\sigma_i)$  and is moving with relative velocity  $V_i(\sigma_i)$  through the water. For the resultant viscous force  $dF_i^{visc}(\sigma_i)$  on the strip we use the formula

$$dF_i^{visc}(\sigma_i) = \frac{1}{2} \rho C_i^D(\sigma_i) V_i^2(\sigma_i) c_i(\sigma_i) d\sigma_i, \quad (26)$$

where the section drag coefficient  $C_i^D(\sigma_i)$  is defined by

$$C_i^D(\sigma_i) = 2 C_i^F(\sigma_i) \left( 1 + A_i^{III}(\sigma_i) t_i(\sigma_i) / c_i(\sigma_i) \right). \quad (27)$$

In expression (27) there occurs the skin friction drag coefficient  $C_i^F(\sigma_i)$ , for which we take

$$C_i^F(\sigma_i) = 0.075 (\log \text{Rey}_i(\sigma_i) - 2)^{-2}. \quad (28)$$

The constant  $A_i^{III}(\sigma_i)$  in a section depends on the location of maximum thickness of the wing section. For instance for sections with maximum thickness located at or near 30% of the chord,  $A_i^{III}$  can approximately be taken as 2.0, however for sections where this location is at 40 or 50% of the chord, the value 1.2 will be more appropriate, see [7]. The local Reynolds number  $\text{Rey}_i(\sigma_i)$  is taken as

$$\text{Rey}_i(\sigma_i) = V_i(\sigma_i) c_i(\sigma_i) / \nu, \quad (29)$$

with in the denominator the kinematic viscosity of water  $\nu = 1.2 \cdot 10^{-6} \text{ m}^2/\text{sec}$ . The approximative formula (26) should not be used for  $\text{Rey}_i$  below  $5 \cdot 10^5$ . Further we remark that the drag coefficient  $C_i^D$ , (27), depends on the lift coefficient  $C_i^L$  of the wing section, in that at higher lift coefficients, a greater part of the drag is contributed by pressure or form drag resulting from separation of the flow from the profile. See for instance [8]. One can think for example, for some types of profiles, of the "bucket-shaped" drag minimum of the function  $C_i^D = C_i^D(C_i^L)$ . For simplicity we did not include this effect in (27), however in the iteration method that we discuss in section 7, one can account for this influence on  $C_i^D$  in step 5 of the iteration scheme of Figure 7.

The work done by the frictional forces causes energy loss. This energy loss per unit of time we

denote by  $E_{visc}$ . Denoting the contribution of the wing strip to this energy by  $dE_i^{visc}(\sigma_i)$ , we have

$$dE_i^{visc}(\sigma_i) = V_i(\sigma_i) dF_i^{visc}(\sigma_i), \quad (i = b, p, s). \quad (30)$$

Using (26) and (27), choosing the chord length  $c_i = c_i(\sigma_i)$  according to relation (13), and taking the sum of the contributions of all  $Z$  blades and end plates, we can write  $E_{visc}$  as a function of the circulation distributions  $\Gamma_i$ , ( $i = b, p, s$ ),

$$E_{visc}(\Gamma_i) = \rho Z \sum_{i=b,p,s} \left( 2 \int_0^{\sigma_{i,e}} C_i^F A_i^{III} V_i^3 t_i d\sigma_i + B \int_0^{\sigma_{i,e}} C_i^F V_i^4 w_i \left\{ \frac{1}{2} A_i^I |\Gamma_i| + A_i^{II} V_i t_i \right\} d\sigma_i \right). \quad (31)$$

The dependence of  $E_{visc}$  on the circulation distributions is a complicated one, when we realize that the skin friction drag coefficient  $C_i^F$  depends via the Reynolds number  $\text{Rey}_i$  and the chord length  $c_i$  on the circulation  $\Gamma_i$ , see formulae (28), (29) and (13).

The component of the frictional forces in the direction of the screw axis counteracts the propeller thrust. Using (26) and again relation (13) we find the resultant thrust deduction  $T_{visc}$  due to viscosity

$$T_{visc}(\Gamma_i) = \rho(U + v_x) Z \sum_{i=b,p,s} \left( \int_0^{\sigma_{i,e}} C_i^F A_i^{III} V_i t_i d\sigma_i + B \int_0^{\sigma_{i,e}} C_i^F V_i^2 w_i \left\{ \frac{1}{2} A_i^I |\Gamma_i| + A_i^{II} V_i t_i \right\} d\sigma_i \right). \quad (32)$$

For the potential theoretical thrust  $T_{pot}$  we take

$$T_{pot} = \rho \omega Z \int_0^{\sigma_{b,e}} \tau(\sigma_b) \Gamma_b(\sigma_b) d\sigma_b, \quad (33)$$

whereby the thrust  $T$  becomes

$$T = T_{pot} - T_{visc}. \quad (34)$$

Finally we remark that in the approximation of the viscous energy loss  $E_{visc}$  and of the thrust deduction due to viscosity  $T_{visc}$  we have neglected the positive or negative interference drag produced in the corners of the blade-end plate junctions. The interference drag is caused by the interaction of the boundary layers of blades and end plates and it depends among others on the thickness ratios  $t_i/c_i$  and on the lift coefficient  $C_L$  of the wing sections near the junction.

## 6. FORMULATION AND SOLUTION OF A VARIATIONAL PROBLEM

In our screw propeller model the energy-balance equation reads

$$Q(\Gamma_i) \omega = (T_{pot}(\Gamma_i) - T_{visc}(\Gamma_i)) U + E_{kin}(\Gamma_i) + E_{visc}(\Gamma_i), \quad (35)$$

where  $Q(\Gamma_i)$  is the torque about the propeller axis and  $T_{pot}$ ,  $T_{visc}$ ,  $E_{kin}$  and  $E_{visc}$ , as functions of the



circulation distributions  $\Gamma_i$ , are given in (33), (32), (25) and (31) respectively. Evidently it is demanded that  $T_{pot}(\Gamma_i) > T_{visc}(\Gamma_i)$ . For the propeller efficiency  $\eta$  we have

$$\eta = \frac{\text{useful work}}{\text{total work}} = \frac{(T_{pot}(\Gamma_i) - T_{visc}(\Gamma_i)) U}{Q(\Gamma_i) \omega} \quad (36)$$

In this section we assume  $r_h/r_p$ ,  $U$ ,  $v_x$ ,  $Z$ ,  $r_p$ ,  $\omega$ ,  $k_p$  and  $k_s$  to be given, that is the geometry of the reference surfaces is given. We minimize the sum of the kinetic and viscous losses,  $(E_{kin} + E_{visc})$ , under a number of constraints. One constraint is that a prescribed thrust  $\bar{T}$  has to be delivered

$$T_{pot}(\Gamma_i) - T_{visc}(\Gamma_i) = \bar{T} \quad (37)$$

Notice that when we place a bar on top of a symbol, we want to stress the fact that the variable in question is prescribed.

Another constraint is that the distribution of circulation and of the chord length along the span of blades and end plates has to be such that the danger of cavitation is about the same for blades and end plates. It can be demanded that along the spans of blades and end plates the chordwise minimum pressure at the suction side of blade or end plate equals a prescribed minimum pressure level  $p^{min} = \bar{p}^{min}$ , or equivalently  $B = \bar{B}$ , see (14). Instead of this last condition, another one can be required, namely that the screw has a specific blade area ratio  $A_e/A_0$ , (4). Thus we formulate two problems.

**Problem I:** We assume  $T = \bar{T}$  and  $B = \bar{B}$  to be prescribed. Then we want to find the optimum circulation distributions  $\Gamma_i^{opt}$  ( $i = b, p, s$ ), belonging to the given quantities, from which follow automatically the optimum chord length distributions  $c_i^{opt}$  by relation (13). Hence for  $\Gamma_i^{opt}$  we require the efficiency  $\eta$ , (36), to be maximum and therefore  $(E_{kin}(\Gamma_i^{opt}) + E_{visc}(\Gamma_i^{opt}))$  to be minimum, under the constraint that  $\Gamma_i^{opt}$  satisfies (37). Then the blade area ratio  $A_e/A_0$  follows from the optimum chord length distributions  $c_b^{opt}$  by formula (4).

**Problem II:** We assume the thrust  $T = \bar{T}$  and the blade area ratio  $A_e/A_0 = \bar{A}_e/\bar{A}_0$  to be prescribed. Then it is possible to calculate the corresponding minimum pressure level  $p^{min}$  in the optimum case. We remark that problem II can be important for the purpose of tuning the constant  $\bar{B}$  in our cavitation criterion on the basis of existing screw propeller designs, for which the blade areas are known.

For both problems we consider the functional  $J = J(\Gamma_i)$  given by

$$J(\Gamma_i) = E_{kin}(\Gamma_i) + E_{visc}(\Gamma_i) - \lambda (T_{pot}(\Gamma_i) - T_{visc}(\Gamma_i) - \bar{T}) \quad (38)$$

$(i = b, p, s)$  ,

where  $\lambda$  is a Lagrange multiplier.

For a functional  $J = J(\Gamma_i)$ , ( $i = b, p, s$ ), we denote the Gâteaux-variation at  $\Gamma_i$  with respect to a set of perturbational functions  $h_i$ , ( $i = b, p, s$ ), by  $\delta J(\Gamma_i; h_i)$ . The Gâteaux-variation, also called the first variation, is given by

$$\delta J(\Gamma_i; h_i) = \lim_{\varepsilon \rightarrow 0} (J(\Gamma_i + \varepsilon h_i) - J(\Gamma_i)) / \varepsilon \quad (39)$$

provided that the limit exists.

Here we remark that in our model  $\Gamma_i^{opt}$  vanishes automatically at the root and the tip of the blade when

the screw propeller has no end plates (ratio of covering  $k = 0$ ). Otherwise a concentrated hub vortex or tip vortex would arise which theoretically gives an infinite energy loss. For the same reason, when the screw propeller does have end plates,  $\Gamma_i^{opt}$  has to vanish at the end plate tips when  $0 < k < 1$ . For  $k = 1$  we could add a constant circulation to the end plates, whereby concentrated free vortex line segments of finite length are allowed to arise which connect the neighbouring end plate tips.

A necessary condition for the optimum is that at  $\Gamma_i^{opt}$  the first variation of  $J$ , (38), vanishes for all admissible  $h_i$ , that is

$$\delta J(\Gamma_i^{opt}; h_i) = 0 \quad (40)$$

for all sets of functions  $h_i$ , ( $i = b, p, s$ ), satisfying  $h_b(0) = h_b(\sigma_{b,e}) = 0$  (screw without end plates),  $h_b(0) = h_i(\sigma_{i,e}) = 0$  ( $i = p, s$ ; screw with end plates,  $k < 1$ ).

We derive from the demand (40) the following conditions

$$H_b : \frac{\partial \Phi}{\partial n_b} = \lambda \left\{ -\frac{\omega r(\sigma_b)}{V_b} + \frac{B \Gamma_b}{|\Gamma_b|} (U + v_x) C_b^F V_b w_b A_b^I \right\} + \frac{1}{2} \frac{B \Gamma_b}{|\Gamma_b|} C_b^F V_b^3 w_b A_b^I \quad (41)$$

$$H_i : \frac{\partial \Phi}{\partial n_i} = \lambda \left\{ \frac{B \Gamma_i}{|\Gamma_i|} (U + v_x) C_i^F V_i w_i A_i^I \right\} + \frac{1}{2} \frac{B \Gamma_i}{|\Gamma_i|} C_i^F V_i^3 w_i A_i^I \quad (42)$$

$(i = p, s)$

In deriving (41) and (42) for the determination of the first variations of  $E_{visc}$  and  $T_{visc}$  we have considered in first instance the skin friction drag coefficient  $C_i^F$  to be independent of  $\Gamma_i$ . Remember that  $C_i^F$  depends on  $\Gamma_i$ , see the remark below formula (31). The influence of  $\Gamma_i$  on  $C_i^F$  is not included in the first variation. Because in this way we do not derive the exact first variations of  $E_{visc}$  and  $T_{visc}$ , the exact first variation of the functional  $J$  will not become precisely zero. This neglect does not have much effect on the results of our optimization method. Calculations by the optimization method with the use of a constant Reynolds number instead of with variable Reynolds numbers  $Re_{y_i} = Re_{y_i}(\sigma_i)$ , ( $i = b, p, s$ ), showed that the optimum circulation distributions  $\Gamma_i^{opt}$  remained practically unchanged.

To obtain the optimum potential satisfying (41) and (42) we make a further assumption. We assume that the optimum circulation distributions  $\Gamma_i(\sigma_i)$  are positive, except possibly in the start and end values  $\sigma_i = 0$  and  $\sigma_i = \sigma_{i,e}$  where they are allowed to vanish. Then we can replace in (41) and (42) the factor  $\Gamma_i/|\Gamma_i|$ , ( $i = b, p, s$ ), by the value one. Anyway, when we have obtained a solution, it can be checked whether indeed the optimum circulation distributions satisfy our assumption.

The vorticity of the screw propeller is free of divergence. Therefore, for the optimum potential  $\Phi$ , we have the extra condition that the total circulation around the free vortex sheets has to vanish. We introduce three potentials  $\Phi_1$ ,  $\Phi_2$  and  $\Phi_3$  satisfying

$$\left( \frac{\partial^2}{\partial x^2} + \frac{\partial^2}{\partial y^2} + \frac{\partial^2}{\partial z^2} \right) \Phi_i = 0 \quad (i = 1, 2, 3) \quad (43)$$

$$\Phi = \lambda (\Phi_1 + B \Phi_2) + B \Phi_3 \quad (44)$$

To satisfy the condition of vanishing total circulation around the free vortex sheets, we require each of the three potentials to be uniquely valued in the whole space, their boundary conditions are

$$H_b : \frac{\partial \Phi_1}{\partial n_b} = -\frac{\omega r(\sigma_b)}{V_b}, \quad H_i : \frac{\partial \Phi_1}{\partial n_i} = 0, \quad (45)$$

$i=p,s$

$$H_i : \frac{\partial \Phi_2}{\partial n_i} = \frac{1}{2} (U + v_x) C_i^F V_i w_i A_i^I, \quad (46)$$

$(i=b,p,s)$

$$H_i : \frac{\partial \Phi_3}{\partial n_i} = \frac{1}{2} C_i^F V_i^3 w_i A_i^I, \quad (47)$$

$(i=b,p,s)$

where the potential  $\Phi_1$  is the optimum potential belonging to the optimization in which only kinetic energy loss is minimized.

For the boundary value problems (45), (46) and (47) some properties of the corresponding free vorticity strength in the reference surfaces  $H_i$ ,  $(i=b,p,s)$ , infinitely far behind the propeller are discussed in [1]. These properties are necessary to formulate wellposed systems of singular integral equations which are equivalent to the boundary value problems and which can be solved numerically by a collocation method analogous to [3].

In the beginning of this section we formulated two problems, *problem I* and *problem II*, to be solved. Assuming we have solved numerically the circulation distributions  $[\Phi_1]^+(\sigma_i)$ ,  $[\Phi_2]^+(\sigma_i)$  and  $[\Phi_3]^+(\sigma_i)$ ,  $(i=b,p,s)$ , we now explain how the resulting optimum circulation distributions

$$\Gamma_i^{opt}(\sigma_i) = \lambda \{ [\Phi_1]^+(\sigma_i) + B [\Phi_2]^+(\sigma_i) \} + B [\Phi_3]^+(\sigma_i), \quad (48)$$

are obtained for each of the two problems.

In the case of *problem I* where we have a prescribed minimum pressure level  $p^{min} = \bar{p}^{min}$  we know by formula (14) the value of  $B = \bar{B}$  in (44). Then the Lagrange multiplier  $\lambda$  can be solved from the prescribed thrust  $T = \bar{T}$  by substituting (44) in (34) with the use of (32), (33) and relation (13). We find

$$\lambda = \frac{\bar{T}/(\rho Z) + \bar{K} - \bar{B} \bar{J}(\Phi_3)}{\bar{J}(\Phi_1 + \bar{B} \Phi_2)}, \quad (49)$$

where  $\bar{K}$  and  $\bar{J}(\phi)$  are given by

$$\bar{K} = (U + v_x) \sum_{i=p,s} \int_0^{\sigma_i^e} C_i^F V_i t_i (A_i^{III} + \bar{B} V_i^2 w_i A_i^{II}) d\sigma_i, \quad (50)$$

$$\bar{J}(\phi) = \int_0^{\sigma_b^e} \{ \omega r - \frac{1}{2} \bar{B} (U + v_x) C_i^F V_i^2 w_i A_i^I \} [\phi]^+ d\sigma_b - \frac{1}{2} \bar{B} (U + v_x) \sum_{i=p,s} \int_0^{\sigma_i^e} C_i^F V_i^2 w_i A_i^I [\phi]^+ d\sigma_i. \quad (51)$$

For *Problem II* we have to solve  $\lambda$  and  $B$  from the prescribed thrust  $T = \bar{T}$  and the prescribed blade area ratio  $A_e/A_0 = \bar{A}_e/\bar{A}_0$ . This gives us two equations for the unknowns  $\lambda$  and  $B$ , one by substituting (44) in (34), the other by substituting (44) in (4), using for the chord length relation (13). The more complicated formulae that arise for the solution of  $\lambda$  and  $B$  are skipped

here, but are given in [1].

## 7. ITERATIVE DETERMINATION OF SOME DESIGN REQUIREMENTS

In this section we discuss how some design parameters and functions, occurring in the solution of the variational problem discussed in section 6, are iteratively determined.

When  $r_h/r_p$ ,  $U$ ,  $Z$ ,  $r_p$ ,  $\omega$ ,  $k_p$ ,  $k_s$ ,  $T = \bar{T}$  and  $(B = \bar{B}$  or  $A_e/A_0 = \bar{A}_e/\bar{A}_0)$  are given, an iteration method can be carried out according to the scheme given in Figure 7.

Prescribed quantities:

$r_h/r_p$ ,  $U$ ,  $Z$ ,  $r_p$ ,  $\omega$ ,  $k_p$ ,  $k_s$ ,  $T = \bar{T}$ ,  
*Problem I*:  $B = \bar{B}$ ,  
*Problem II*:  $A_e/A_0 = \bar{A}_e/\bar{A}_0$ .

Iteration scheme:

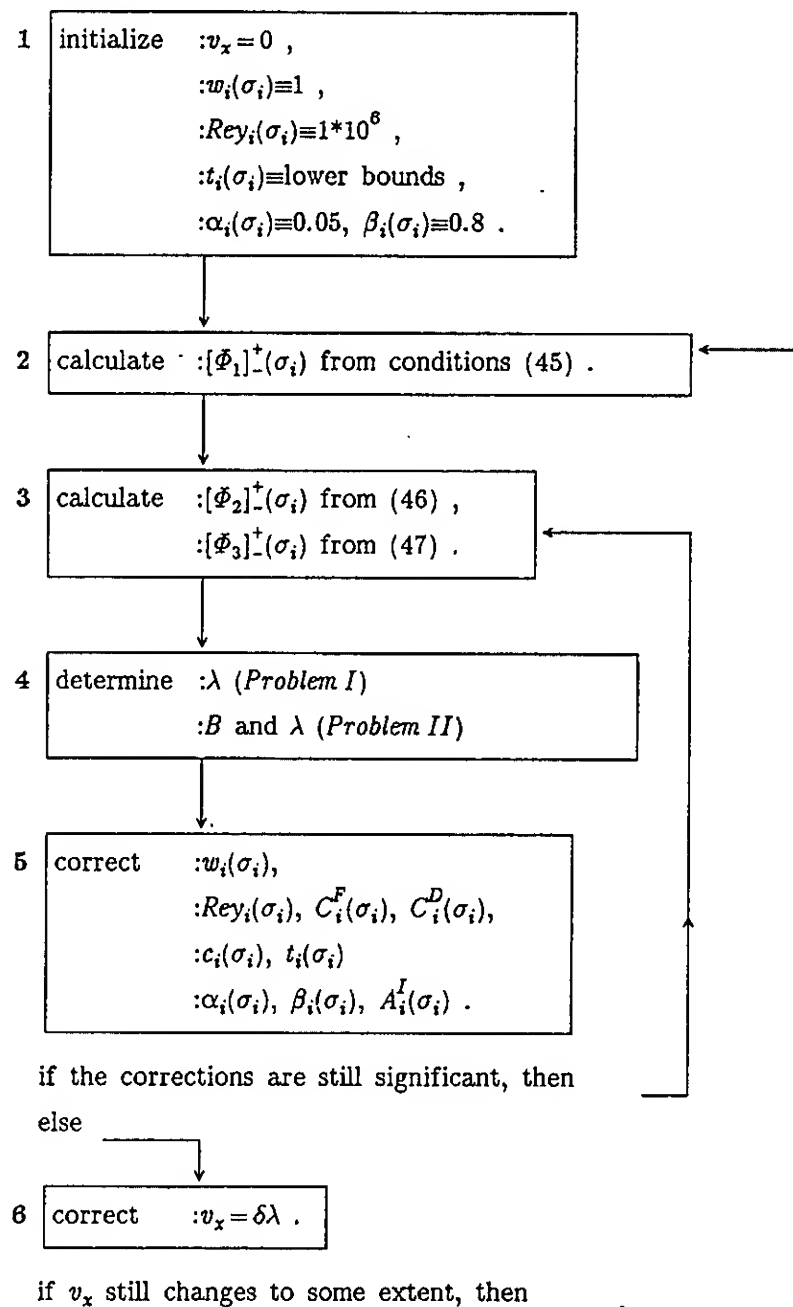


Fig. 7 Iteration scheme for the optimization including viscosity when the given quantities are prescribed.

In the initialization step 1 of the iteration we introduced lower bounds for the maximum thickness distributions  $t_i = t_i(\sigma_i)$ . As the lower bound at the screw blade we take  $2 r_p f_{th}$ , where we introduced the

thickness factor  $f_{th}$ . At an end plate part we choose as lower bound for the maximum profile thickness distribution, a tapered distribution from  $t_i(0) = 2\tau_p f_{th}$  at the end plate root to  $t_i(\sigma_{i,e}) = \tau_p f_{th}$  at the end plate tip, ( $i=p,s$ ). Thus the use of the lower bound in particular results in a nonzero thickness at the free ending tips of blades and end plates and according to relation (13) also in a nonzero chord length there. In the calculations used in this paper we have used the value  $f_{th} = 0.0035$ , see (52).

For the calculations in step 2 and step 3 of the iteration we use the collocation method described in [3]. When we want to apply only the linearized theory, then in the iteration we keep  $v_x$  equal to zero, and hence leave the outer loop undone.

Step 4 is the determination of the Lagrange multiplier  $\lambda$  from (49) (Problem I), or of  $\lambda$  and the constant  $B$  belonging to our cavitation criterion from more complicated algebraic formulas (Problem II), see [1].

In step 5 the occurring functions are adapted according to some design aspects, which are discussed more closely in [1]. For instance a strength calculation based upon simple beam theory is incorporated in this step. In the strength calculation the considered force fields acting on the beams representing the screw blades and end plates, are the potential theoretically induced lift forces, the centrifugal forces and the viscous forces. Another adaptation concerns appropriate choices from a hydrodynamical point of view of the functions  $\alpha_i = \alpha_i(\sigma_i)$  and  $\beta_i = \beta_i(\sigma_i)$ . For some different types of screw propellers values of the occurring functions which are eventually found using our iteration method, are given in Figures 14-17.

Finally in step 6 we want the velocity  $v_x$  to be such that it equals the Lagrange multiplier  $\lambda$ , multiplied by a factor  $\delta$  with  $\delta \approx 1/2$ . The reason that we take  $v_x = \delta\lambda$ , is that in the linearized lifting line theory where only kinetic energy loss is minimized, the induced backwards translational velocity of the vortex sheets infinitely far behind a propeller, equals the Lagrange multiplier  $\lambda$ . Then in the neighbourhood of the blades and end plates of the propeller the induced velocity is about  $1/2\lambda$  in the positive  $x$ -direction. For higher thrusts the optimization including viscosity, resembles the kinetic optimization more, because in that case the kinetic loss becomes relatively more important than the viscous loss. Therefore we expect that the corrective velocity  $v_x = \delta\lambda$ , which has a greater influence for higher thrusts, will be useful of the optimization including viscosity also.

Here we emphasize that it is not claimed that the use of the corrective velocity  $v_x$  gives an exact result for the kinetic energy loss for higher thrusts. We did not take into account the vortex sheet deformation, and the induced velocity by the vorticity and the source-sink distributions representing blades and end plates. However the influence of the trailing vorticity, which delivers a substantial part of the induced velocities, is possibly treated more realistic than in the pure linearized theory.

## 8. SOME ASPECTS OF THE OPTIMIZATION METHOD

### Preliminary choices

In this section we first make choices of some design parameters and functions that are kept the same for the calculations in this paper. Of course these

particular choices are not essential for our optimization method. We take

$$\begin{aligned} \rho &= \rho_{seawater} = 1023 \text{ kg/m}^3, \quad \rho_{screw} = 7650 \text{ kg/m}^3, \\ r_h/r_p &= 0.2, \quad U = 6 \text{ m/sec}, \quad (\overline{t/c})_h = 0.2, \\ \overline{\alpha_b(\frac{2}{3}\sigma_{b,e})} &= 0.05, \quad \overline{\beta_b(\frac{2}{3}\sigma_{b,e})} = 0.8, \\ f_{th} &= 0.0035, \quad \overline{S^{per}} = 5.6 \cdot 10^7 \text{ N/m}^2, \\ \text{for Problem I : } \overline{B} &= 0.024 \text{ sec}^2/\text{m}^2, \end{aligned} \quad (52)$$

where  $\overline{S^{per}}$  is the prescribed permissible stress level for use in the strength calculation. The density of the material of the screw  $\rho_{screw}$  and the prescribed permissible stress level  $\overline{S^{per}}$  are chosen corresponding to the material cunial bronze.  $\overline{S^{per}}$  is based on load variations of 50 %.

We choose for blades and end plates chordwise thickness distributions belonging to the NACA 16-series sections (see for instance [8]), which for ship screw blades are commonly used.

The location of maximum thickness of the section is at 50% of the chord length from the leading edge, so that for the constant  $A_i^{III}(\sigma_i)$ , introduced in the section drag coefficient  $C_i^D(\sigma_i)$ , (27), we will choose the value 1.2. The symmetrical section at zero lift has its minimum pressure located at 60% of the chord from the leading edge, and from the "basic thickness forms" tables given in [8] it can be derived that the constant  $A_i^{II}(\sigma_i)$ , introduced in relation (13) can approximately be taken as 1.25.

When, in our calculations, propellers with end plates are considered, we assume the two-sided shifted end plate with the anterior end plate part located at the suction side of the screw blade, unless we explicitly state that another type of end plate is considered.

### Comparison with the classical optimization

In the classical screw propeller optimization, as used for instance in [2], [3], [4] and [5], circulation distributions are derived from a minimization of only the kinetic energy loss  $E_{kin}$  of a screw propeller under the constraint that the potential theoretical thrust  $T_{pot}$  equals a prescribed thrust  $\overline{T}$ . Hence in the classical theory instead of our functional  $J = J(\Gamma_i)$ , (38), the functional  $J_{clas} = J_{clas}(\Gamma_i)$  given by

$$J_{clas}(\Gamma_i) = E_{kin}(\Gamma_i) - \mu (T_{pot}(\Gamma_i) - \overline{T}), \quad (i=b,p,s), \quad (53)$$

is considered, where  $\mu$  is the Lagrange multiplier. By demanding the first variation of  $J_{clas}(\Gamma_i)$  to vanish we obtain the conditions

$$H_b: \frac{\partial \Phi}{\partial n_b} = -\mu \frac{\omega r(\sigma_b)}{V_b}, \quad H_i: \frac{\partial \Phi}{\partial n_i} = 0, \quad (i=p,s), \quad (54)$$

in analogy with the derivation of (41) and (42). We put

$$\Phi = \mu \Phi_1, \quad (55)$$

so that  $\Phi_1$  is the potential already introduced in relation (44), and which was solved from condition (45).

We want to obtain a comparison between the

optimization including viscosity and the classical optimization. Therefore we use for the classical theory the relation between circulation and chord length which is explained in section 3 and we derive our design requirements by using the iteration scheme discussed in section 7. For the classical optimization as well as for our optimization including viscosity we solve *problem I*, hence with a prescribed thrust  $T=\bar{T}$  and a prescribed value  $B=\bar{B}$ . Then we derive the value of the Lagrange multiplier  $\mu$  from the condition

$$T_{pot} - T_{visc} = \bar{T} \quad (56)$$

which, for a fair comparison, contains the thrust deduction  $T_{visc}$  due to viscosity. Analogous to the derivation in section 6 we find from (56) that  $\mu$  can be solved from

$$\mu = \frac{\bar{T} / (\rho Z) + \tilde{K}}{\tilde{J}(\phi_1)} \quad (57)$$

with  $\tilde{K}$  and  $\tilde{J}(\phi)$  given in (50) and (51) respectively.

Now we give some numerical results of the comparison between the optimization including viscosity and the classical optimization theory. Note that, strictly speaking, we do not make a comparison with the exact classical theory, because we make the comparison with the classical theory embedded in our numerical iteration method, in which we incorporated various nonclassical aspects. In both theories we use the linearized versions ( $v_x=0$ ), and we solve *Problem I* introduced in section 6. We consider propellers satisfying

$$Z=3 \quad , \quad r_p=4m \quad , \quad \omega=6 \text{ rad/sec} \quad , \quad (58)$$

for a case without end plates ( $k=0$ ) and a case with end plates ( $k=2k_p=2k_s=0.5$ ). Results are given in Table 1 for three different values of the prescribed thrust  $T=\bar{T}$  for which the dimensionless thrust coefficient  $C_T$  defined by

$$C_T = T / (\frac{1}{2} \rho U^2 \pi r_p^2) \quad , \quad (59)$$

attains the values 1, 2 and 3. We remark that, for the optimization including viscosity as well as for the classical optimization, for the efficiency  $\eta$  we used relation (36).

Table 1 Comparison between optimization including viscosity and classical optimization for propellers without end plates ( $k=0$ ) and propellers with end plates ( $k=2k_p=2k_s=0.5$ ); linear theory ( $v_x=0$ ).

$k$	$E_{kin} (10^6 \text{ Nm/sec})$			$E_{visc} (10^5 \text{ Nm/sec})$			$\eta (\%)$			optimization
0	2.369	9.445	21.23	2.871	4.552	6.114	67.65	52.87	43.27	incl. visc.
	2.368	9.444	21.23	2.895	4.569	6.129	67.64	52.87	43.27	classical
0.5	1.932	7.644	17.16	4.640	7.447	10.02	69.86	56.97	47.85	incl. visc.
	1.915	7.631	17.14	4.888	7.630	10.17	69.79	56.95	47.84	classical
	1	2	3	1	2	3	1	2	3	

$C_T \longrightarrow$

From Table 1 it is seen that in the classical theory the kinetic energy loss is slightly smaller than in our theory, however the sum of kinetic and viscous loss is larger, resulting in a lower efficiency.

To obtain some insight into how the difference between optimization including viscosity and classical optimization affects in our theory the corresponding screw propellers, we give in Figure 8 for the propellers of Table 1 with  $k=0.5$  the corresponding circulation distributions.

It is seen from these figures that in the linearized theory for the optimization including viscosity there occur somewhat smaller values of circulation at large radii than for the classical optimization. Smaller values of circulation in our theory imply smaller values of chord length, see relation (13). Obviously the cause of the occurrence at large radii of smaller chord length for the optimization including viscosity, is that at large radii the relative velocity of the wing sections is large and therefore the viscous energy loss is

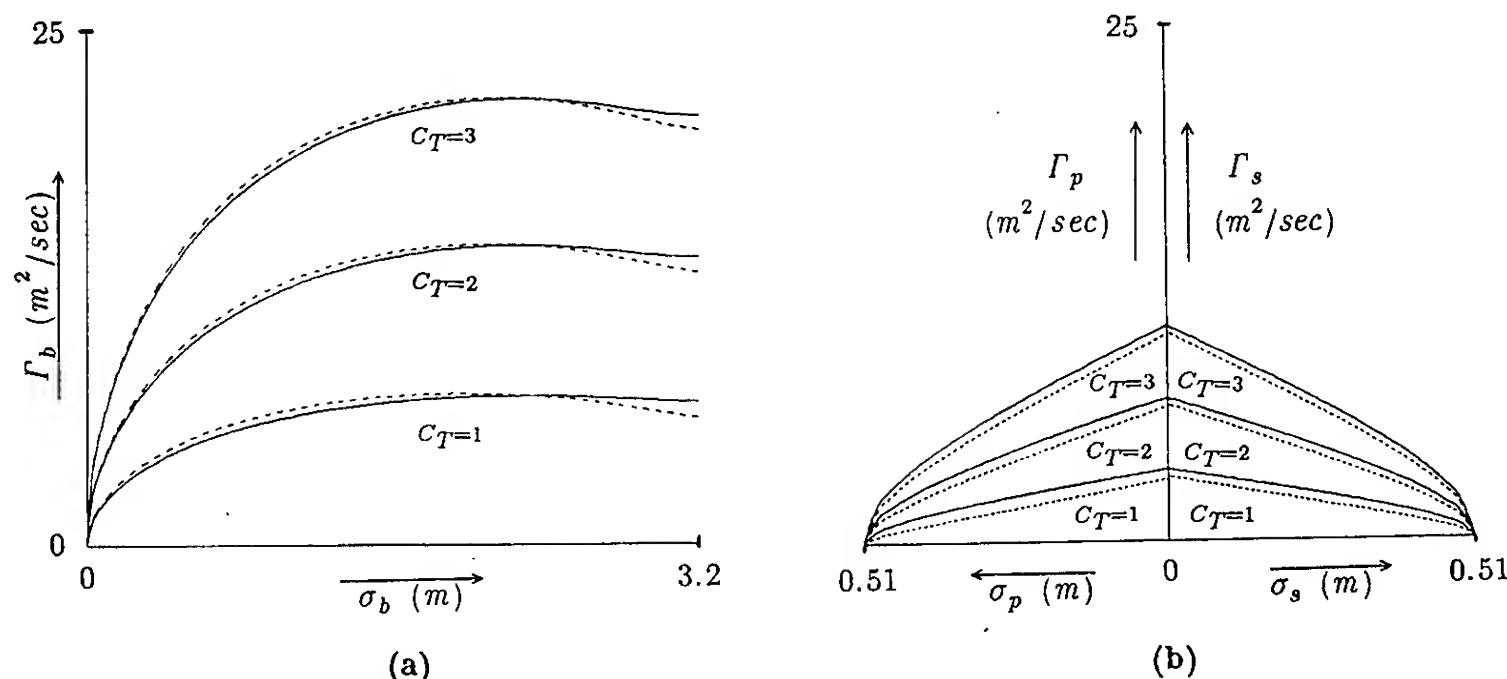


Fig. 8 Distributions of circulation  $\Gamma_i$  ( $i=b, p, s$ ) of screw propellers with end plates ( $k=2k_p=2k_s=0.5$ ); linearized theory ( $v_x=0$ )  
 ————— classical optimization  
 - - - - - optimization including viscosity



relatively important there, while the classical optimization does not worry about large chord lengths. This also explains why the difference between classical optimization and optimization including viscosity is greater for propellers with end plates than for propellers without end plates, see Table 1.

Since kinetic energy loss becomes relatively more important for propellers with higher loadings, the difference in the results obtained from the two optimization methods is relatively smaller for larger values of the thrust coefficient  $C_T$  than for smaller values of  $C_T$ , as can be seen from Table 1 and Figure 8. Summarizing we can state that the results of both optimization theories differ only slightly.

#### When no solution is found

In section 6 in the paragraph following relation (42) we have assumed that our circulation distributions are positive along all spans and therefore we replaced the quotients  $\Gamma_i(\sigma_i)/|\Gamma_i(\sigma_i)|$ , ( $i=b,p,s$ ) by the value one. When the circulation distributions are numerically calculated we can verify whether this assumption is correct.

For *problem I* and *problem II* there exists a region in the  $(\omega, r_p, k)$ -space, for which our formulation of the variational problem does not lead to a solution of the optimization including viscosity. This appears for large values of  $\omega$ ,  $r_p$  and  $k$ . For these cases we numerically find only circulation distributions which change sign along the span of a screw blade or end plate, and which therefore are not solutions of our problem. For instance for a screw propeller without end plates ( $k=0$ ) the numerically calculated circulation distributions along the screw blade can be as in Figure 9. It is understandable that this type of circulation distribution is found, because since the quotient  $\Gamma_i(\sigma_i)/|\Gamma_i(\sigma_i)|$  has unjustly been taken equal to one, at the spanwise stages of negative circulation  $\Gamma_b$  there can occur viscous energy gain  $E_{visc}$  and thrust production  $T_{visc}$  due to viscosity, instead of viscous energy loss and thrust deduction due to viscosity.

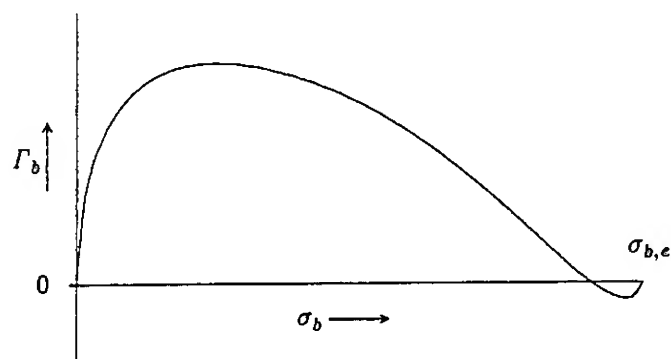


Fig. 9 Example of circulation distribution of a screw propeller without end plates, that is found when the assumption  $\Gamma_i(\sigma_i)/|\Gamma_i(\sigma_i)| = 1$  is incorrect.

It seems that, to solve this problem, another variational approach for the optimization, including viscosity effects, has to be undertaken. In this paper this will not be carried out and in section 9 we will designate the regions in which our optimization method does not give a solution. Fortunately it seems that the relevant optima are found in those regions where our method does give a solution.

## 9. SOME RESULTS OF OPTIMIZATION

### Efficiency $\eta$ as a function of $T$ , $Z$ , $\omega$ , $r_p$ and $k$ in some theories

To obtain some feeling for the dependency of the efficiency  $\eta$  on the various parameters we have drawn in this section for some cases pictures with level lines of the optimum efficiency  $\eta$ . As for all calculations in this paper, we made choices from (52).

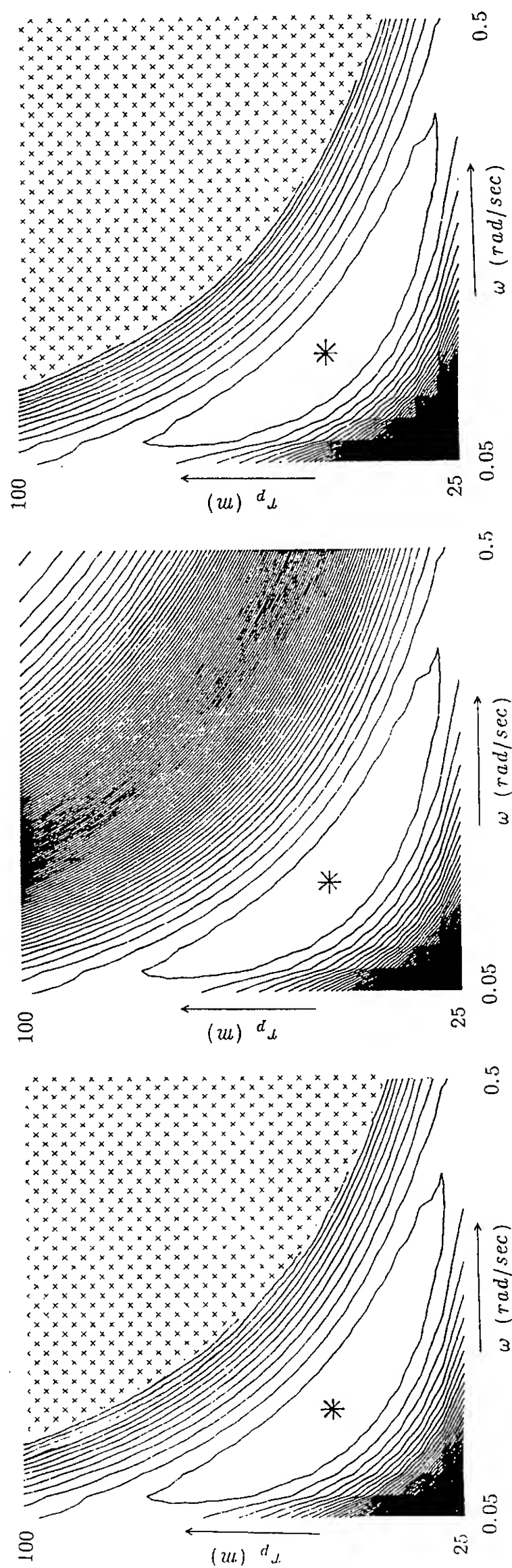
The equiefficiency lines are constructed by calculating on equidistant  $21 \times 21$  grids of  $(\omega, r_p)$ ,  $(\omega, k)$  or  $(r_p, k)$  values, propellers which all are optimized by one of the methods discussed in this paper. Although in reality the level lines of the propeller efficiency are smooth lines, they are sometimes drawn less smoothly. This is due to the discretization on the equidistant grids. The efficiency  $\eta$  as a function of two considered variables in each picture has not more than one local extreme. The location at which the absolute maximum of the efficiency is attained is designated by an asterisk \* in the corresponding pictures. In the pictures on the  $(\omega, k)$  and  $(r_p, k)$  grids we have designated by the little ball ● the location of the maximum efficiency  $\eta$  of an optimum screw propeller without end plates ( $k=0$ ). Notice that the propellers \* and ● are in a sense optima of optimum propellers, because all the propellers for which the equiefficiency lines are drawn have optimum distributions of circulation, chord length and the other relevant functions occurring in our model. By  $\Delta\eta$  we denote the difference in the efficiency  $\eta$  between propeller \* and its nearest level line and between each two neighbouring level lines, so that from the value of  $\eta$  at the point \* the efficiency  $\eta$  at each depicted level line can be derived.

In the pictures the ratio of covering  $k$  is chosen in the range  $0 \leq k \leq 1$  and the ranges of  $\omega$  and  $r_p$  are chosen such that the pictures contain the optima for the screws without end plates and, if it does apply, for the screws with end plates. Some data about the optima are given in the tables included in the figures. For the pictures belonging to the optimization including viscosity, the cross hatched regions in the upper right parts of the pictures are the regions in which our formulation of the variational problem does not lead to a solution of the optimization, a problem which we mentioned at the end of section 8.

Figure 10 contains the optimum efficiency of screw propellers without end plates ( $k=0$ ) as a function of the rotational velocity  $\omega$  and of the propeller radius  $r_p$ . In Figure 11 the optimum efficiency as a function of  $\omega$  and the ratio of covering  $k$  is given, when the propeller radius  $r_p$  is fixed. Figure 12 contains for a fixed value of  $\omega$  the level lines of the optimum efficiency as a function of  $r_p$  and  $k$ .

In the Figures 10–12, pictures (a) are the results of the optimization including viscosity in the linearized case ( $v_x=0$ ), pictures (b) of the classical linearized optimization adapted to our situation (see section 8), and pictures (c) of the optimization including viscosity in the nonlinear case ( $v_x=\frac{1}{2}\lambda$ ). For the screws that have end plates in Figures 11 and 12, we have chosen two-sided shifted end plates with the same ratio of covering at pressure and suction sides of the screw blades, that is with  $k_p=k_s=\frac{1}{2}k$ . The planform of the anterior end plate part is taken at the suction side of the screw blade and the posterior part at the pressure side, as is drawn for instance in Figure 6(g).





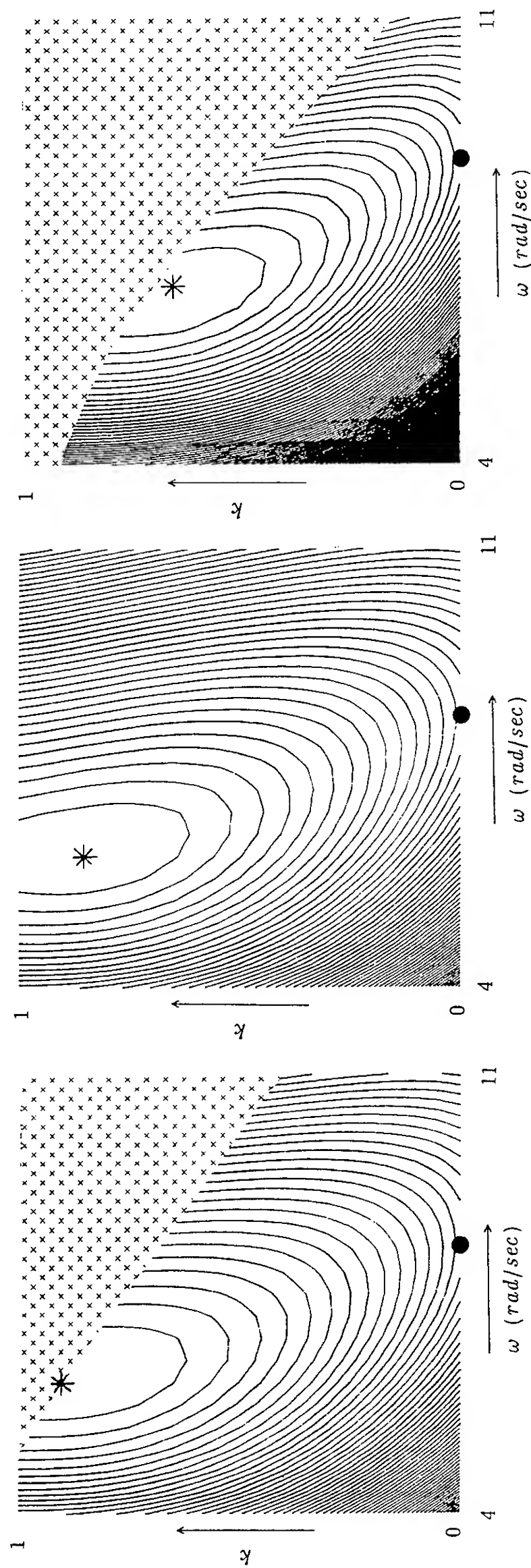
(a) optimization including viscosity, linear theory ( $v_x = 0$ )

(b) classical optimization, linear theory ( $v_x = 0$ )

(c) optimization including viscosity, nonlinear theory ( $v_x = \frac{1}{2}\lambda$ )

Figure	screw	$\omega$	$r_p$	$v_x$	$A_c/A_0$	$E_{kin}$	$E_{visc}$	$\eta$
10(a)	*	0.163	47.5	0.000	0.041	0.262	0.447	94.4
10(b)	*	0.163	47.5	0.000	0.041	0.262	0.447	94.4
10(c)	*	0.163	47.5	0.152	0.042	0.266	0.472	94.2
		$\frac{rad}{sec}$	$m$	$m/sec$		$10^6 \frac{Nm}{sec}$	$10^6 \frac{Nm}{sec}$	%

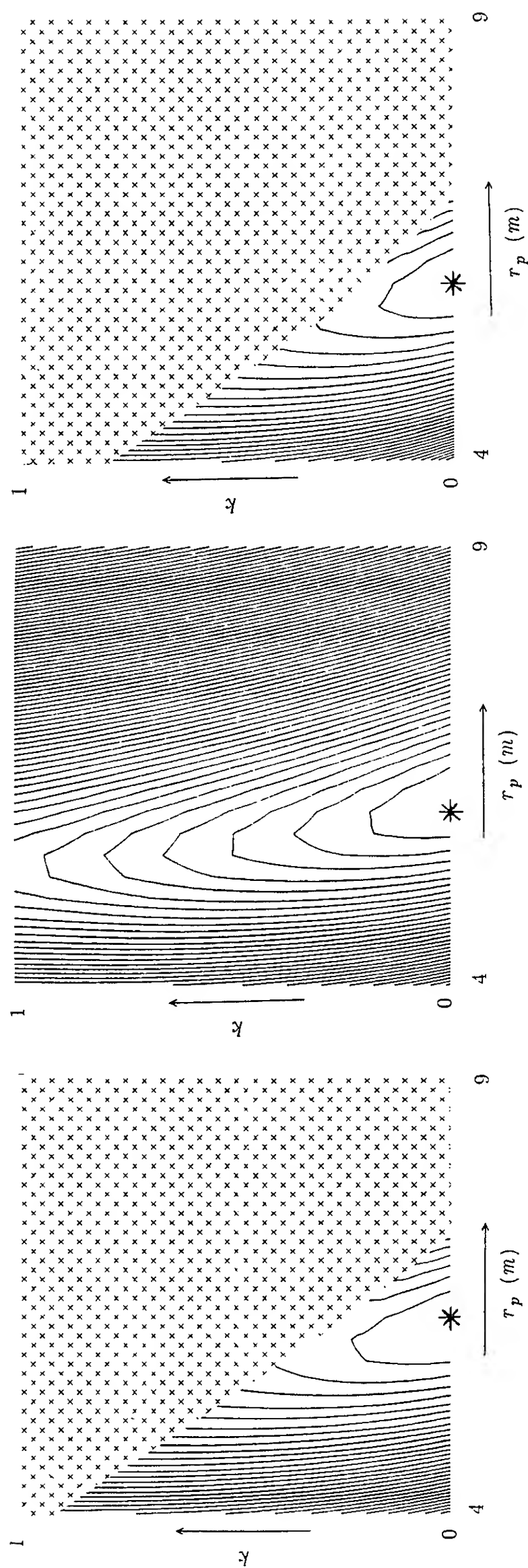
Fig. 10 Level lines of efficiency  $\eta$  as a function of the rotational velocity  $\omega$  and the propeller radius  $r_p$ ; screw propellers without end plates,  $k = k_p = k_s = 0$ ;  $Z = 3$ ,  $T = 2 \cdot 10^6 N$ ;  $\Delta\eta = 1.0\%$ .



(a) optimization including viscosity, linear theory ( $v_x = 0$ ) (b) classical optimization, linear theory ( $v_x = 0$ ) (c) optimization including viscosity, nonlinear theory ( $v_x = 1/2 \lambda$ )

Figure	screw	$\omega$	$k$	$v_x$	$A_e/A_0$	$E_{km}$	$E_{visc}$	$\eta$	$\eta(*)-\eta(\bullet)$
11 (a)	*	6.1	0.90	0.000	0.789	8.437	1.011	56.0	2.9
	•	8.2	0.00	0.000	0.815	9.459	1.156	53.1	
11 (b)	*	6.1	0.85	0.000	0.793	8.419	1.045	55.9	2.8
	•	8.2	0.00	0.000	0.818	9.452	1.169	53.1	
11 (c)	*	6.8	0.65	3.562	0.891	6.504	1.704	59.4	2.3
	•	8.9	0.00	3.940	0.897	7.270	1.750	57.1	
		$\frac{rad}{sec}$		$\frac{m}{sec}$		$10^6 \frac{Nm}{sec}$	$10^6 \frac{Nm}{sec}$	%	%

Fig. 11 Level lines of efficiency  $\eta$  as a function of the rotational velocity  $\omega$  and the ratio of covering  $k = 2k_p = 2k_s$ , when the propeller radius is fixed,  $r_p = 4 m$ ;  $Z = 3$ ,  $T = 2 \cdot 10^6 N$ ;  $\Delta\eta = 0.2 \%$ .



(a) optimization including viscosity, linear theory ( $v_x = 0$ )

(b) classical optimization, linear theory ( $v_x = 0$ )

(c) optimization including viscosity, nonlinear theory ( $v_x = \frac{1}{2}\lambda$ )

Figure	screw	$r_p$	$k$	$v_x$	$A_e/A_0$	$E_{kin}$	$E_{visc}$	$\eta$
12 (a)	*	6.25	0.00	0.000	0.479	3.747	2.344	66.3
12 (b)	*	6.00	0.00	0.000	0.499	4.076	2.059	66.2
12 (c)	*	6.00	0.00	2.044	0.508	3.519	2.150	67.9
		$m$		$m/sec$		$10^6 Nm/sec$	$10^6 Nm/sec$	%

Fig. 12 Level lines of efficiency  $\eta$  as a function of the propeller radius  $r_p$  and the ratio of covering  $k = 2k_p = 2k_g$ , when the rotational velocity of the screw is fixed,  $\omega = 6 \text{ rad/sec}$ ;  $Z = 3$ ,  $T = 2 \cdot 10^3 \text{ N}$ ;  $\Delta\eta = 0.5\%$ .

From Figures 10-12 we conclude that, in the regions where the optimization including viscosity gives an answer, the efficiency obtained by the optimization including viscosity is quite the same as the efficiency obtained by the classical optimization. The nonlinear  $v_x$ -correction of Figure 10(c) gives values which differ not much from the values of the linear theories of Figures 10(a) and (b). The reason is that the propellers have very large propeller radii  $r_p$  ( $25 m \leq r_p \leq 100 m$ ). Then the considered propellers are lightly loaded ( $0.0035 \leq C_T \leq 0.055$ ), so that the  $v_x$ -correction becomes very small, for instance in Figure 10(c) we have  $v_x(*) = 0.152 m/sec$ . In the heavier loaded cases of Figures 11 and 12 the nonlinear  $v_x$ -correction does change the efficiency. However the same tendencies are found in the linear and nonlinear case, and the values of  $\omega$ ,  $r_p$  and  $k$  belonging to the optima \* and • do not differ that much in the linear and nonlinear case.

Figure 10 shows that for the propellers without end plates ( $k = k_p = k_s = 0$ ) the absolute maximum in the optimum efficiency occurs for a very large propeller radius  $r_p$  together with a very small rotational velocity  $\omega$ . It goes without saying that the propellers in Figure 10 are unrealistic for a practical application. In fact the figure demonstrates that in practice propellers are far from the theoretically ideal situation and there will always exist certain constraints on the propeller diameter and rotational velocity.

In Figure 11 we examine the more realistic situation of propellers with a fixed propeller radius,  $r_p = 4 m$ . In this figure it is seen that in a large range of the rotational velocity optimum propellers with end plates are better than optimum propellers without end plates. The best propeller with end plates (\*) has a smaller rotational velocity than the best propeller without end plates (•). Evidently this is because the end plate propeller can have at a smaller rotational velocity the same kinetic energy loss as a propeller without end plates at a larger rotational velocity, while because of the increased viscous resistance the end plate propeller feels more content with a smaller rotational velocity. From the table in Figure 11 it is seen that the nonlinear correction predicts a gain in efficiency between the two optima \* and • of the same order as in the linear cases.

In practice it can be important to optimize propellers with a fixed value of the rotational velocity, because of the given characteristics of a ship's motor. Therefore in Figure 12 we have drawn the equiefficiency lines for a fixed value of the rotational velocity,  $\omega = 6 rad/sec$ . The best propellers in Figure 12, designated by the asterisk \*, do not have an end plate, that is  $k(*) = 0$ . When the propeller radius  $r_p$  is smaller than the optimum propeller radius  $r_p(*)$ , optimum end plate propellers have a higher efficiency than optimum propellers without end plates, while the opposite is true when the propeller radius  $r_p$  is larger than  $r_p(*)$ .

The results we have given depend on some choices we made. For instance the choice of  $\bar{B}$ , see (52), has influence on the cavitation danger, on the blade area ratio  $A_e/A_0$  and on the viscous energy loss  $E_{visc}$  of the propeller. Furthermore the number of screw blades  $Z$  and the thrust  $T$  have influence on the efficiency. To illustrate the effect of the two last mentioned variables we have given in Tables 2 and 3, related to the case of Figure 11(a), results for some different values of the thrust  $T$  and of the number of screw

blades  $Z$ . From now on we only show the results of the linear theory because the calculations are less time consuming and because we have seen that the gain in efficiency  $\eta(*) - \eta(\bullet)$  caused by the application of end plates does not differ so much between the linear and nonlinear case. However for an actual screw propeller design the use of the  $v_x$ -correction may be helpful.

**Table 2** Influence of the demanded thrust  $T$ ;  $r_p = 4 m$ ,  $Z = 3$ ,  $k = 2k_p = 2k_s$ ; optimization including viscosity, linear theory ( $v_x = 0$ ).

screw	$\omega$	$k$	$A_e/A_0$	$E_{kin}$	$E_{visc}$	$\eta$	$\eta(*) - \eta(\bullet)$	$\frac{\eta(*) - \eta(\bullet)}{\eta(\bullet)}$	$T$
*	5.05	0.80	0.461	2.284	0.399	69.1	2.5	3.8	1
•	6.80	0.00	0.464	2.583	0.429	66.6			
*	6.10	0.90	0.789	8.437	1.011	56.0	2.9	5.5	2
•	8.20	0.00	0.815	9.459	1.156	53.1			
*	7.15	0.85	1.112	18.17	1.921	47.3	2.9	6.5	3
•	9.25	0.00	1.160	20.32	2.181	44.4			
	rad/sec			$10^6 Nm/sec$	$10^6 Nm/sec$	%	%	%	$10^6 N$

**Table 3** Influence of the number of screw blades  $Z$ ;  $r_p = 4 m$ ,  $T = 2 \cdot 10^6 N$ ,  $k = 2k_p = 2k_s$ ; optimization including viscosity, linear theory ( $v_x = 0$ ).

screw	$\omega$	$k$	$A_e/A_0$	$E_{kin}$	$E_{visc}$	$\eta$	$\eta(*) - \eta(\bullet)$	$\frac{\eta(*) - \eta(\bullet)}{\eta(\bullet)}$	$Z$
*	6.45	0.85	0.742	8.646	1.241	54.8	3.8	7.5	2
•	9.25	0.00	0.769	10.12	1.423	51.0			
*	6.10	0.90	0.789	8.437	1.011	56.0	2.9	5.5	3
•	8.20	0.00	0.815	9.459	1.156	53.1			
*	6.10	0.85	0.837	8.315	0.961	56.4	2.3	4.3	4
•	7.85	0.00	0.870	9.042	1.140	54.1			
	rad/sec			$10^6 Nm/sec$	$10^6 Nm/sec$	%	%	%	

Table 2 shows for  $Z = 3$  the influence of the thrust  $T$ , and Table 3 shows for  $T = 2 \cdot 10^6 N$  the influence of the number of screw blades  $Z$ . It is concluded that the relative gain in efficiency  $(\eta(*) - \eta(\bullet))/\eta(\bullet)$  increases when the number of screw blades  $Z$  decreases, or when the thrust  $T$  increases. This is a logical conclusion because end plates can help to decrease the relatively large kinetic energy loss which occurs for screw propellers which are heavily loaded or have a small number of screw blades.

#### On the influence of the type of end plate planform

Here we compare the application of some different types of end plate planforms. We will consider optimum situations corresponding to the situation of Figure 11(a), that is with

$$r_p = 4 m, \quad T = 2 \cdot 10^6 N, \quad Z = 3, \quad (60)$$

and with the "optimization including viscosity" in the linear theory ( $v_x = 0$ ). In Figure 11(a) we had chosen two-sided shifted end plates with  $k_p = k_s = \frac{1}{2}k$  and with the anterior end plate part at the suction side of the screw blade. In addition we will now investigate a one-sided end plate and a two-sided symmetrical end plate, see Table 4.

For leading and trailing edges and the chord lengths of the two-sided symmetrical end plate we make the choice as in Figure 13, hence with a circular shaped leading edge and a straight trailing edge.

These choices are rather arbitrary, because we only want to realize chord lengths which are roughly twice as large as those of the two-sided shifted end

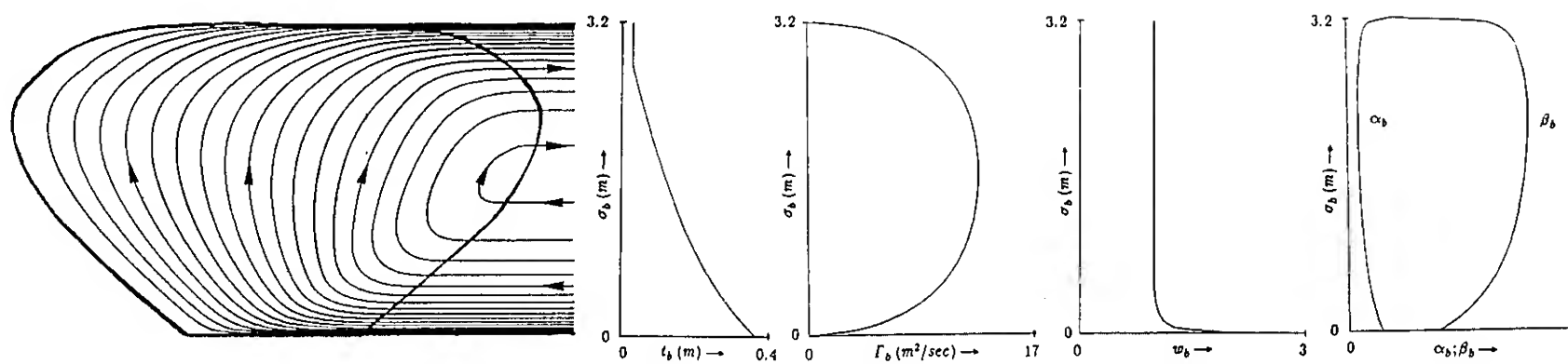


Fig. 14 The optimum propeller • of Figure 11(a); without end plates;  $\Delta\psi_b = 0.7 \text{ m}^2/\text{sec}$ .

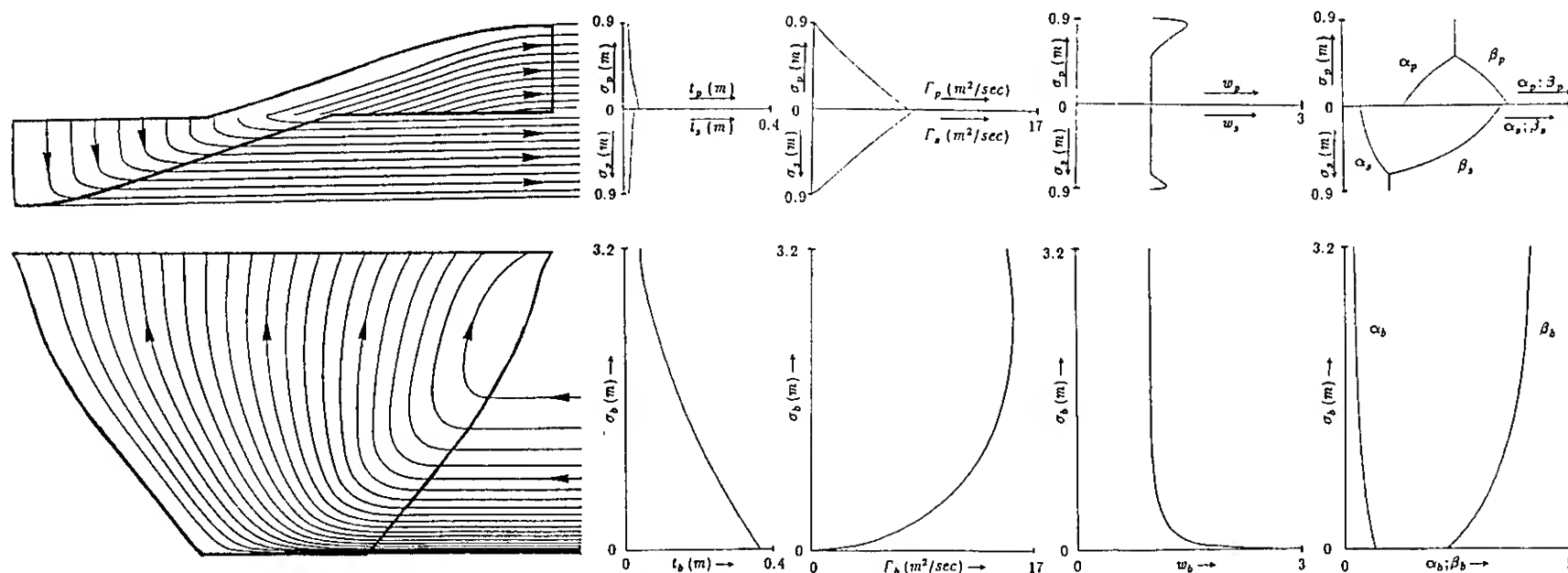


Fig. 15 The optimum propeller \* of Figure 11(a); two-sided shifted end plates; anterior end plate parts at suction sides of screw blades;  $\Delta\psi_b = \Delta\psi_p = \Delta\psi_s = 0.7 \text{ m}^2/\text{sec}$ .

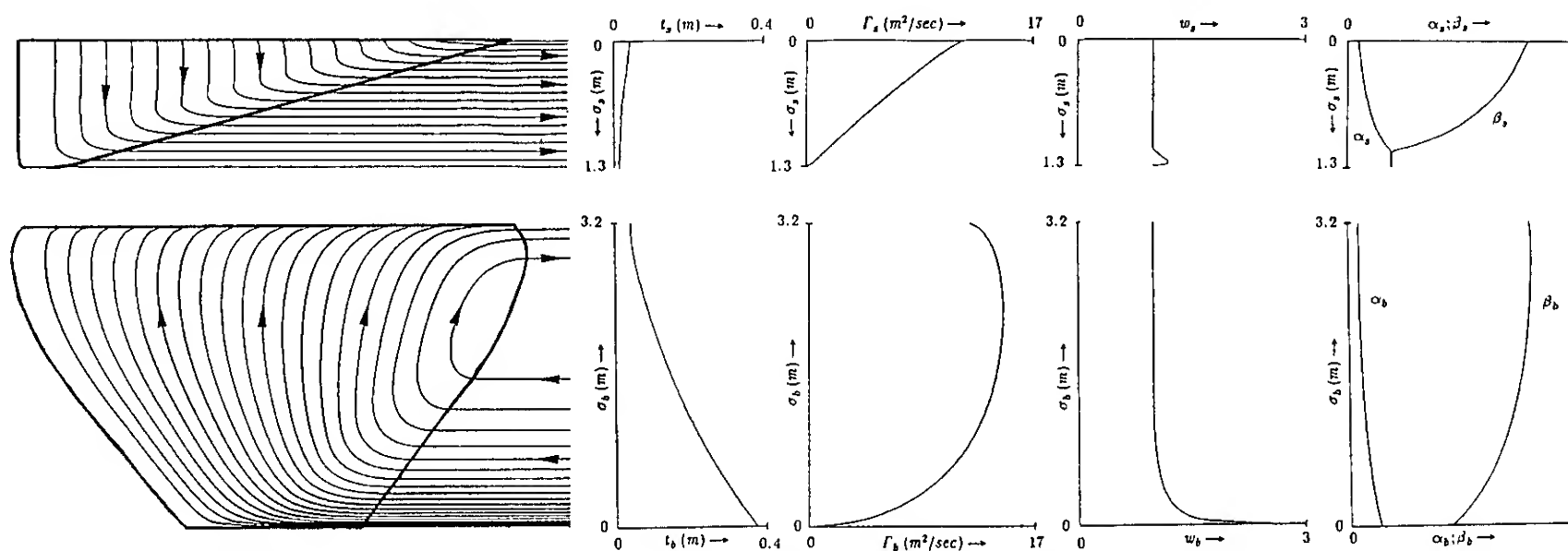


Fig. 16 The optimum propeller \* of Table 4 with one-sided end plates at suction sides of screw blades;  $\Delta\psi_b = \Delta\psi_s = 0.7 \text{ m}^2/\text{sec}$ .

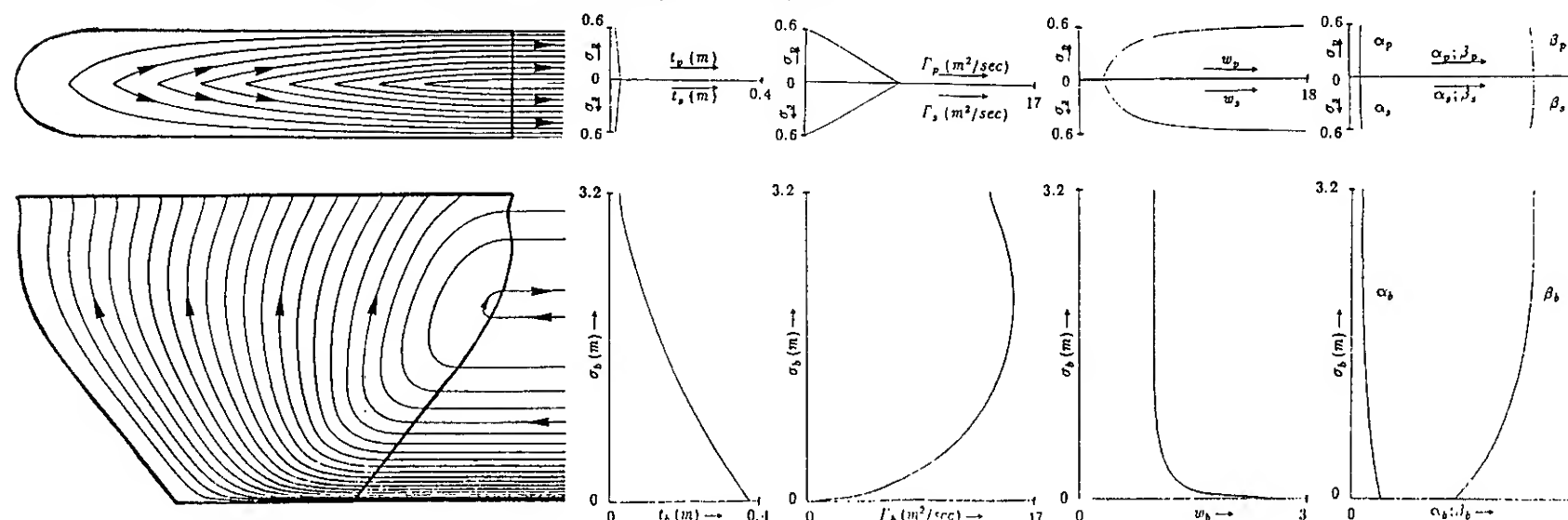


Fig. 17 The optimum propeller \* of Table 4 with two-sided symmetrical end plates;  $\Delta\psi_b = \Delta\psi_p = \Delta\psi_s = 0.7 \text{ m}^2/\text{sec}$ .



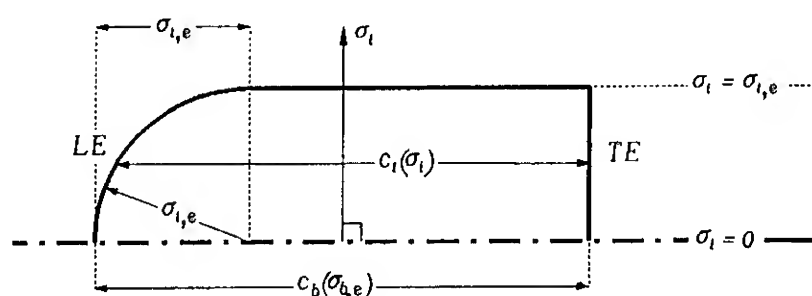


Fig.13 Leading and trailing edge and corresponding chord lengths of our two-sided symmetrical end plate planform;  $k_p = k_s = \frac{1}{2}k$ ;  $i = p, s$ .

plate. Assuming the span of an end plate part to be smaller than the chord length of the screw blade tip, the chord lengths of the two-sided symmetrical end plate are

$$c_i(\sigma_i) = c_b(\sigma_{b,e}) + (\sigma_{i,e}^2 - \sigma_i^2)^{1/2} - \sigma_{i,e}, \quad 0 \leq \sigma_i \leq \sigma_{i,e}, \quad (61)$$

$$(\sigma_{i,e} \leq c_b(\sigma_{b,e}); i = p, s)$$

To account for the difference in chord length distribution we make use of our weight functions  $w_i$  belonging to the end plate, ( $i = p, s$ ). In our optimization method each time we iteratively correct these weight functions such that the desired chord lengths (61) result.

Table 4 Influence of the type of end plate planform for screws satisfying (60); screw \* of Figure 11(a) with two-sided shifted end plates; screw with one-sided end plates at suction sides of screw blades ( $k = k_s$ ;  $k_p = 0$ ); screw with two-sided symmetrical end plates of Figure 13 ( $k = 2k_p = 2k_s$ ).

screw	$\omega$	$k$	$A_e/A_0$	$E_{kin}$	$E_{visc}$	$\eta$	$\eta(*) - \eta(\bullet)$	end plate
*	6.10	0.90	0.789	8.437	1.011	56.0	2.9	two-sided, shifted
●	8.20	0.00	0.815	9.459	1.156	53.1		
*	6.45	0.70	0.802	8.443	1.137	55.6	2.5	one-sided
●	8.20	0.00	0.815	9.459	1.156	53.1		
*	6.10	0.55	0.780	8.857	1.126	54.6	1.5	two-sided, symmetrical
●	8.20	0.00	0.815	9.459	1.156	53.1		
	rad/sec			$10^6 Nm/sec$	$10^6 Nm/sec$	%	%	

The results of Figure 11(a) and Table 4 show some clear and understandable tendencies. Under the considered circumstances the best optimum propellers ordered with respect to decreasing efficiency  $\eta$  are as follows. First the propeller with the two-sided shifted end plate, \* of Figure 11(a), second the propeller with the one-sided end plate \* of Table 4, third the propeller with the two-sided symmetrical end plate \* of Table 4, and finally the propeller without end plates, ● of Figure 11(a). That the application of a one-sided end plate appears to be somewhat less favourable than the application of a two-sided shifted end plate, was already predicted from some approximate considerations given in [3].

To obtain some insight into the underlying propellers we have drawn in Figures 14–17 some results of the optimum propellers occurring in the Figure 11(a) and Table 4, at the optimum values of  $\omega$  and  $k$ . In these figures we have chosen the leading and trailing edges of the screw blades symmetrically with respect to the

blade generator line, which is the line segment  $r_h \leq r \leq r_p$  at the  $y$ -axis.

About the Figures 14–17 we mention some points. First one can clearly observe the more or less concentrated vorticity strength near the tip of the screw blade without end plates (Figure 14), while for the screw propellers with end plates (Figures 15–17) the trailing vorticity of the propeller tip is coming off more spread along the trailing edges of the end plate parts.

Second the considered propellers with end plates have relatively more circulation along the screw blades than the considered propeller without end plates has. This is because the propellers with end plates have a smaller rotational velocity  $\omega$  than the propeller without end plates has, while the demanded thrust is the same for all propellers.

Finally we remark that it is seen from Figure 15 that the end plate part at the pressure side is somewhat thicker than the end plate part at the suction side. The cause is the counteraction and reinforcement respectively of the centrifugal and potential theoretical forces at the end plate parts at the suction and pressure side of the screw blade, so that by the use of the strength calculation different maximum thickness distributions  $t_i = t_i(\sigma_i)$  are required for the two end plate parts, see [1].

#### ACKNOWLEDGEMENTS

The author is indebted to Prof. Dr. J.A. Sparenberg for many valuable discussions. This research is sponsored by the Technology Foundation STW in The Netherlands under grant GWI 55.0819. A budget for calculations on a super computer was provided by the foundation SURF from the fund NFS.

#### REFERENCES

- [1] de Jong, K., "On the Optimization, Including Viscosity Effects, of Ship Screw Propellers with Optional End Plates", *International Shipbuilding Progress*, to be published.
- [2] Sparenberg, J.A. and de Vries, J., "An Optimum Screw Propeller with End Plates", *International Shipbuilding Progress*, Vol. 34, 1987, pp 124–133.
- [3] de Jong, K. and Sparenberg, J.A., "On the Influence of Choice of Generator Lines on the Optimum Efficiency of Screw Propellers", *Journal of Ship Research*, June 1990.
- [4] Betz, A., "Schrauben Propeller mit geringstem Energieverlust", *Klg. Ges. d. Wiss. Nachrichten, Math-Phys.*, Heft 2, 1919.
- [5] Goldstein, S., "On the Vortex Theory of Screw Propellers", *Proc. Royal Society London*, Vol. CXXIII, 1929.
- [6] Braam, H., "Optimum Screw Propellers with a Large Hub of Finite Downstream Length", *International Shipbuilding Progress*, Vol. 31, 1984, pp 231–238.
- [7] Hoerner, S.F., "Fluid-Dynamic Drag", Published by the author, LCCN 57-13009, USA, 1958.
- [8] Abbot, I.H., and von Doenhoff, A.E., "Theory of Wing Sections", Dover Publications, 1959.

## DISCUSSION

William B. Coney  
Bolt, Beranek and Newman, Inc., USA

I wish to commend the author on his extension of classical optimization theory to include viscous losses. Several comments regarding the linearized approach are in order. End plates can effect propeller efficiency in two ways. The first, well described here, can be readily obtained under linear theory. The second effect a propeller forces comes from the axisymmetric, or near, loading on the end plates. It perhaps can be more easily seen in the aductor disk model for a ducted propeller in which efficiency gains arise which are associated with the percentage of the total thrust which is carried on the duct. Since the examples presented seem to be for fairly heavily loaded propellers, could the author comment on this? Also, can the theory presented here be extended to the wave adapted case in which the inflow is not uniform?

## AUTHORS' REPLY

The first question concerns the fact that in the paper some results are presented for fairly heavily loaded screw propellers while the theory in the first instance is only a linearized one. As described in the paper there is included in the optimization model a more or less nonlinear effect, the so-called  $v_x$ -correction. However, this correction is only an approximate way to account for the complicated nonlinear character of the problem. From Figures 11 and 12 it is seen that although the nonlinear  $v_x$ -correction gives results which differ from the results of the linear theory; the same tendencies arise in the linear and nonlinear theories. Thus, it is hoped that the linearized optimization theory also for more heavily loaded propellers gives some information about the influence of end plates.

The author agrees that thorough future research on nonlinear effects is important for the understanding of propellers with end plates of the type discussed, but he also believes that understanding of the phenomena observed by application of linearized theory is an essential first step.

Regarding the second question as to whether the theory can be extended to the wake adapted case, I would like to refer to [9]. In that paper Klaren and Sparenberg incorporated in the linearized classical optimization theory for propellers with end plates, a method to deal with inhomogeneous inflow. It is possible to extend also the "optimization including viscosity" discussed in the present paper to the case of inhomogeneous inflow by using their method. This can be done for the cases with and without the nonlinear  $v_x$ -correction.

[9] Karen, L. and Sparenberg, J.A. "On Optimum Screw Propellers with End Plates, Inhomogeneous Inflow". *Journal of Ship Research*, Vol. 25, No. 4., Dec. 1981, pp. 252-263.

## DISCUSSION

Philippe Genoux  
Bassin d'Essais des Carènes, France

How do your computations compare to experiments if there were any?

## AUTHORS' REPLY

Some information about experimental work connected to the theoretical and numerical work carried out at the Department of Mathematics of the University of Groningen is given now. So far, experiments have been performed only on one propeller with end plates, namely the one designed by Sparenberg and de Vries, see [2]. It concerns a model screw propeller with end plates of the "two-sided symmetrical" type, an example of which is given in Figure 17. A disadvantage of that propeller model is that the theories used for optimization and for lifting surface design were linearized theories. This might be a reason that in the experiments the propeller model in the design conditions turned out not to deliver the thrust which was prescribed for the design. Another disadvantage is that the optimization theory used in the design was not as detailed as the optimization method described in the present paper. Furthermore, Table 4 illustrates that the used type of end plate planforms is not the most ideal for obtaining high efficiency. As explained in the present paper, application of "two-sided shifted" end plate planforms is expected to give higher efficiency.

Despite these drawbacks, the experiments with the model screw propeller revealed some promising features. It turned out that tip vortices could not be made visible, which is an indication that the basic principle of minimizing kinetic energy loss seems to work. Indeed, open water tests showed that the efficiency of the propeller with end plates for larger thrusts was significantly better than the efficiency of a corresponding B-screw propeller, even though it concerned model scale experiments, see [2]. Moreover the absence of tip vortices means that carefully designing propellers with end plates can probably help to reduce propeller noise. Application of types of end plate planforms that have relatively larger surface areas will presumably yield relatively higher noise reduction at the price of lower efficiency.

To fulfill the need for further experiments with improved propeller designs with end plates, at the time of this writing this reply the geometry is calculated for a propeller model meant to be tested at MARIN in The Netherlands. In this new design we hope to diminish the shortcomings of the linearized theory by making use of the nonlinear  $v_x$ -correction in the optimization process as well as in the lifting surface design theory. Moreover, the end plates will be of the two-sided shifted type and the optimization process will be based upon the one described in the present paper.

The author wishes to thank the discussers for their contributions.

# **Steady and Unsteady Characteristics of a Propeller Operating in a Non-Uniform Wake: Comparisons Between Theory and Experiments**

F. Genoux, R. Baubeau (Bassin d'Essais des Carènes, France)

A. Bruere, M. DuPont

(Office National des Etudes et Recherches Aéronautiques, France)

## **ABSTRACT**

The predictions of the steady and unsteady characteristics of a propeller operating in a non-uniform wake has been a task of R&D for the past decades, seeking to meet the increasingly demanding requirements of acoustical discretion in the design of propellers for ships.

The present paper exposes the latest work conducted at the Bassin d'Essais des Carènes in the theoretical and numerical fields to produce a numerical code able to answer this need, as well as the results issued from an original technology developed at ONERA to give access to the fluctuating pressure field on a blade. The code issued from these efforts is based on a linearized lifting surface theory and is fitted for low and moderate loadings. Its originality lies in its ability to solve either the inverse problem or the analysis one with the same numerical schemes. Its formulation is adequate for the computation of both steady and unsteady characteristics of a propeller operating in a non-uniform incoming flow.

The convergence tests are commented to give an idea of the robustness of the code. The numerical results are compared to experimental data available in the open literature and to measurements derived from experiments conducted with the technology of thin film pressure transducers.

## **INTRODUCTION**

The prediction of the steady and unsteady characteristics of a propeller operating in a non-uniform wake aims to meet the increasingly demand-

ing requirements of acoustical discretion in the design of propellers for ships. These predictions rely on both theoretical and numerical developments able to match the designer's need for a reliable and accurate tool. The validation of the approach requires extensive and accurate experimental data, thus motivating highly complex and heavy tests. From a designer stand-point, the knowledge of steady and unsteady loadings is needed to compute the levels of fluctuating forces transmitted to ship through the shafts and the hull, and thus to optimize the dimensioning of shaft supports and bearings for fatigue. A good prediction of radiated noise induced by the propeller as well as the evaluation of unsteady cavitation are also conditioned by an accurate computation of fluctuating pressure fields on propeller blades. Despite the clear need for predictive tools, the progress have been slowed for a long time due to the lack of computational power and the release of new generation computers during the two last decades have certainly contributed to the improvements in the area of propeller computing.

Although an extensive review of all the theoretical and experimental works conducted on the prediction of steady and unsteady characteristics of propellers is out of the scope of the present paper, it is interesting to underline the main steps in both theories and documented experiments in the development of tools for the computation of unsteady loadings. The first consistent and pertinent tools from an engineering point of view were based on lifting line method, ranging from quasi-steady approach (1, 2, 3) to two-dimensional unsteady method (4, 5, 6). Some refinements were brought by combining quasi-steady approach and two-dimensional unsteady method (7). The limita-

tions of these methods are precisely identified - a good review of their failures can be found in the reference (8). Theoretical attempts (9), using matched asymptotic method, have been made to solve the most obvious and severe restrictions, such as neglecting three-dimensional effects - span, skew.

Despite the save of computational time in comparison to heavier methods, the remaining inaccuracies - specially for low Expanded Area Ratio propellers - as well as the increasing computational power of computers have motivated the development of new codes based on linearized lifting surface theory. The reference (10) summarizes the different steps taken in that direction for the last twenty years. The codes developed within this theory lead to a clear improvement of the accuracy and reliability of the numerical results (11). From a designer's stand-point, the use of the linearized lifting surface theory to solve the inverse problem - computing a propeller geometry meeting propulsive requirements - is proposed in (12), where the presence of an axisymmetric body is taken in account.

As opposed to the important number of theoretical efforts, there are very few well documented experiments in the open litterature. Therefore, the possibilities of validation are limited and numerous numerical results are compared to the measurements referenced in (8) and (13) published in 1968, more than twenty years ago. This is partly due to the difficulties of gathering all the data needed for a reliable validation. Besides the access to the fluctuating forces transmitted to the shaft, one has to accurately measure the flow field feeding the propeller in its presence, and determine a proper procedure to deduce the effects of the suction from the wake inhomogeneities. Furthermore, there is no experimental data in the open litterature that is known delivering information on fluctuating pressures at the blade surface of a propeller. The lack of adequate sensors fulfilling the requirements for such measurements has clearly limited the knowledge of pressure fluctuations related to a propeller to measurements on adjacent walls.

Unfortunately, no unified tool based on the linearized lifting surface theory was available to allow the computation of both steady and unsteady

characteristics of a propeller operating in a non-uniform flow, within the solving of the inverse problem or of the direct one. The present paper exposes the latest work conducted at Bassin d'Essais des Carènes de Paris in the theoretical and numerical fields to develop a numerical code able to eliminate some of the previously mentioned restrictions, as well as the experimental results obtained in its facilities from an original technology developed at the Office National d'Etudes et de Recherches Aérospatiales aimed at giving access to the fluctuating pressure field on a blade. The numerical results are compared to experimental data found in the open litterature and to the ones obtained at Bassin d'Essais des Carènes. The experiments are documented as carefully as possible to allow comparison.

## MODEL AND SOLUTION PROCEDURE

The numerical code is based on a linearized lifting surface theory and is fitted for low and moderate loadings. The starting core was developed in the late seventies and limited to the solving of the inverse problem (12). Implemented at Bassin d'Essais des Carènes, the code has gone through many evolutions and is now stabilized in its mature form.

Its originality lies in its ability to solve the inverse problem - determination of pitch and camber laws for a given shaft power - as well as the direct analysis - computation of thrust and torque for a given geometry - within the same formulation. Such a feature allows the validation of the code used in its inverse mode - the important mode for the designer - by checking the accuracy of the results computed in its direct mode on geometries of reference propellers.

The code has been extended to permit the calculation of unsteady forces due to the interactions of a propeller with a non-uniform steady incoming flow. This calculation remains possible in both inverse and direct modes, thus allowing skew optimisation in the design process.

The Figure 1 shows the geometry of the problem. The propeller, which is represented by its geometry  $H$ , operates behind an axisymmetric body  $C$  whose geometry is given by the equation of its meridian. The body's advance speed,

$V_s$ , is supposed constant and the single screw propeller rotates at a constant rotation speed  $n$ . The plane of reference used to describe the propeller geometry is named  $\Pi$ . The helicoids emitted by the blades are noted  $\Sigma$ .

In both inverse and direct modes, the diameter,  $D$ , of the propeller, its number of blades,  $Z$ , the spanwise laws of skew, rake, maximum thickness and chord length, as well as the chordwise law of thickness are given. The spanwise pitch and camber laws and the chordwise camber laws are known in the direct mode and are unknown in the inverse mode. The effective wake is supposed to be known in the propeller plane.

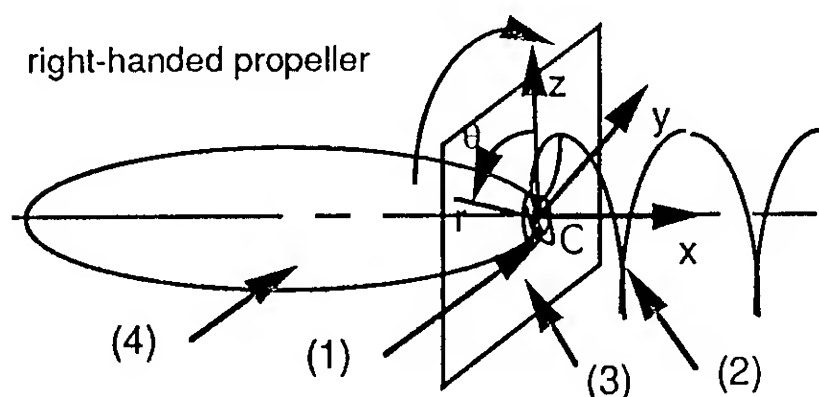


Fig. 1 Geometry of the problem  
(1) Propeller H  
(2) Helicoids  $\Sigma$   
(3) propeller plane  $\Pi$   
(4) Body C

The geometry of the propeller H is described in the system of polar coordinates of axis the body axis. Following ITTC standards, one defines a right hand orthogonal system of cartesian coordinates with the origin O coinciding with the centre of the propeller. The longitudinal axis  $x$  coincides with the body axis, positive downstream; the transverse axis, positive part; the third axis  $z$  positive upward. One uses a cylindrical system with origin O and longitudinal axis  $x$ .

The effective wake field is described by the three components,  $V_r$ ,  $V_\theta$ ,  $V_x$ , of the velocity vector,  $\underline{V}(r, \theta)$ , in the propeller plane, written in cylindrical coordinates. The three components are known by their harmonical amplitudes,  $A_{i,k}$ , and phases  $\phi_{i,k}$ , for  $k$  varying from 0 to infinity:

$$V_i = V_s \left\{ \sum_{k=0}^{\infty} A_{i,k}(r) \cos[k\theta + \phi_{i,k}] \right\} \quad (1)$$

The fluid is assumed to be incompressible and the flow irrotational. No presence of cavitation is considered within this work. Therefore, the absolute velocity field derives from a potential  $\Phi$ , which satisfies the Laplace equation:

$$\Delta \Phi = 0 \quad (2)$$

Steady case

In the steady case, the only amplitudes of velocity components that are not equal to zero are  $A_{r,0}$  and  $A_{x,0}$ . The phases  $\phi_{i,0}$  are equal to zero.

The absolute potential  $\Phi$  can be split in two terms:

$$\Phi(r, \theta, x) = V_s x + \phi(r', \theta', x) \quad (3)$$

where the first term takes in account the body advance velocity and the second term is the relative velocity potential written in the polar coordinate system,  $(O, r', \theta', x)$ , rotating with the propeller.

The boundary conditions are written on the body C and on the propeller, H, including its hub. If  $\underline{n}$  is the normal to the boundary, these conditions can be written as:

- on the body C :

$$\frac{\underline{\nabla} \Phi \cdot \underline{n}}{2\pi n R} = \lambda_s \underline{i} \cdot \underline{n} \quad (4)$$

where  $\lambda_s$  is the advance ratio of the propeller,

- on the propeller H:

$$\frac{\underline{\nabla} \Phi^\pm \cdot \underline{n}}{2\pi n R} = \frac{\partial \eta^\pm}{\partial \theta} + (\beta - B) \sqrt{(\xi^2 + A_{x,0}^2(r) \lambda_s^2)} \quad (5)$$

where  $\eta^-$  and  $\eta^+$  are the positions of back and face of the blade sections at the reduced radius,  $\xi$ ,



$V_s$ , is supposed constant and the single screw propeller rotates at a constant rotation speed  $n$ . The plane of reference used to describe the propeller geometry is named  $\Pi$ . The helicoids emitted by the blades are noted  $\Sigma$ .

In both inverse and direct modes, the diameter,  $D$ , of the propeller, its number of blades,  $Z$ , the spanwise laws of skew, rake, maximum thickness and chord length, as well as the chordwise law of thickness are given. The spanwise pitch and camber laws and the chordwise camber laws are known in the direct mode and are unknown in the inverse mode. The effective wake is supposed to be known in the propeller plane.

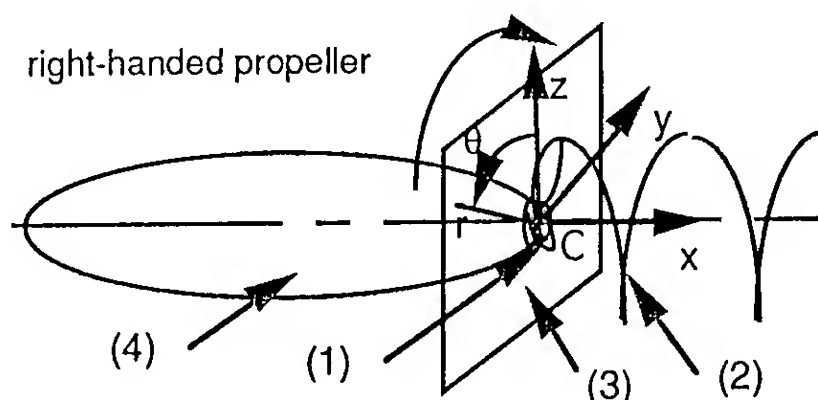


Fig. 1 Geometry of the problem  
(1) Propeller H  
(2) Helicoids  $\Sigma$   
(3) propeller plane  $\Pi$   
(4) Body C

The geometry of the propeller H is described in the system of polar coordinates of axis the body axis. Following ITTC standards, one defines a right hand orthogonal system of cartesian coordinates with the origin O coinciding with the centre of the propeller. The longitudinal axis  $x$  coincides with the body axis, positive downstream; the transverse axis, positive part; the third axis  $z$  positive upward. One uses a cylindrical system with origin O and longitudinal axis  $x$ .

The effective wake field is described by the three components,  $V_r$ ,  $V_\theta$ ,  $V_x$ , of the velocity vector,  $\underline{V}(r, \theta)$ , in the propeller plane, written in cylindrical coordinates. The three components are known by their harmonical amplitudes,  $A_{i,k}$ , and phases  $\phi_{i,k}$ , for  $k$  varying from 0 to infinity:

$$V_i = V_s \left\{ \sum_{k=0}^{\infty} A_{i,k}(r) \cos[k\theta + \phi_{i,k}] \right\} \quad (1)$$

The fluid is assumed to be incompressible and the flow irrotational. No presence of cavitation is considered within this work. Therefore, the absolute velocity field derives from a potential  $\Phi$ , which satisfies the Laplace equation:

$$\Delta \Phi = 0 \quad (2)$$

Steady case

In the steady case, the only amplitudes of velocity components that are not equal to zero are  $A_{r,0}$  and  $A_{x,0}$ . The phases  $\phi_{i,0}$ , are equal to zero.

The absolute potential  $\Phi$  can be split in two terms:

$$\Phi(r, \theta, x) = V_s x + \phi(r', \theta', x) \quad (3)$$

where the first term takes in account the body advance velocity and the second term is the relative velocity potential written in the polar coordinate system,  $(O, r', \theta', x)$ , rotating with the propeller.

The boundary conditions are written on the body C and on the propeller, H, including its hub. If  $\underline{n}$  is the normal to the boundary, these conditions can be written as:

- on the body C :

$$\frac{\nabla \Phi \cdot \underline{n}}{2\pi n R} = \lambda_s \underline{i} \cdot \underline{n} \quad (4)$$

where  $\lambda_s$  is the advance ratio of the propeller,

- on the propeller H:

$$\frac{\nabla \Phi^\pm \cdot \underline{n}}{2\pi n R} = \frac{\partial \eta^\pm}{\partial \theta} + (\beta - B) \sqrt{(\xi^2 + A_{x,0}^2(r) \lambda_s^2)} \quad (5)$$

where  $\eta^-$  and  $\eta^+$  are the positions of back and face of the blade sections at the reduced radius,  $\xi$ ,

duced by the interactions between the propeller and the hull. It can be split into two terms:

- $q_1$  strength of the source due to the sources distributed on the projected propeller  $H'$ ,
- $q_2$  strength of the source due to the doublets distributed on the projected propeller  $H'$  and the helicoids  $\Sigma$ .

The intensity of sources located on the projected propeller  $H'$  is directly related to the thickness law of the blade profile at the considered radius, according to the relation:

$$\left( \frac{q}{2\pi n R} \right)_M = \frac{\left( \frac{\partial(\eta^+ - \eta^-)}{\partial\theta} \right)_M}{R} \quad (10)$$

It should be underlined that it is not necessary to compute the strength of the source induced by the flow around the body without the propeller.

The use of equation (8) and the Kutta-Joukowski condition allow to derive the equation relating camber, pitch and source strength:

$$\begin{aligned} & \frac{V_s}{\omega R} \begin{pmatrix} A_{r,0}(r) \\ 0 \\ A_{x,0}(r) \end{pmatrix} \cdot \underline{\Omega}_M \\ & - \frac{1}{4\pi} \iint_C \frac{\Delta q_P}{\omega R} \nabla \left[ \frac{1}{|PM|} \right] \cdot \underline{\Omega}_M dS_P \\ & - \frac{1}{4\pi} \iint_{H'} \frac{q_P}{\omega R} \nabla \left[ \frac{1}{|PM|} \right] \cdot \underline{\Omega}_M dS_P \\ & - \frac{1}{4\pi} \iint_{H'} \frac{\delta\phi_P R}{\omega R^2} \nabla \left[ \frac{\underline{n}_P \cdot \underline{PM}}{|PM|^3} \right] \cdot \underline{\Omega}_M dS_P \\ & - \frac{1}{4\pi} \iint_{\Sigma} \frac{\delta\phi_{Tr. Ed.} R}{\omega R^2} \nabla \left[ \frac{\underline{n}_P \cdot \underline{PM}}{|PM|^3} \right] \cdot \underline{\Omega}_M dS_P \\ & = \frac{\left( \frac{\partial\eta^+ + \partial\eta^-}{\partial\theta} \right)_M}{2R} \\ & + \left( (\beta - B) \sqrt{\xi^2 + A_{x,0}(r)^2 \lambda_s^2} \right)_M \end{aligned} \quad (11)$$

In the direct problem, the unknowns  $\delta\phi$  and  $\delta\phi_{Tr. Ed.}$  can be directly computed from the known values of pitch and camber.

In the inverse problem, the designer chooses the normalized circulation law and the performances - either thrust or torque to be by the propeller. Thus, the circulation law is defined with an unknown multiplicative constant  $\Gamma_{max}$ .

In both modes, the discretization of the equation (11) produces a linear system with a predominantly diagonal matrix. The resolution of the system does not raise any particular difficulty. The forces are computed using the Joukowski theorem.

In the inverse mode, the shock-free entrance condition suppresses the suction force at the leading edge of profiles. The integration of forces and moments produces a second degree equation with the unknown  $\Gamma_{max}$ . Reference (12) details the approach.

In the direct mode, the leading edge suction force has to be taken in account and is calculated with the method described in (14) and (15).

The suction effects due to the potential effects of the propeller on the body can be computed by integrating the efforts on its surface. These efforts are directly calculated using Lagally theorem.

At last, the linearization of the equations with respect to  $\lambda_s$  allows to compute the performances at off-design conditions close to the design point.

Unsteady case

In the presence of non-uniformities in the flow feeding the propeller, the wake field velocity vector can be split into two parts:

$$V_i(r, \theta) = V_s A_{i, \alpha}(r) + \tilde{V}_i(r, \theta) \quad (12)$$

with:

$$\tilde{V}_i(r, \theta) = V_s \sum_{k=1}^{\infty} A_{i, k}(r) \cos[k\theta + \varphi_{i, k}] \quad (13)$$

where  $\tilde{V}_i$  are the three components of the velocity fluctuations encountered by the propeller blades during the rotation.

Besides, it is assumed that the geometry of the helicoids,  $\Sigma$ , is not affected by the inhomogeneities of the incoming flow. Therefore, the solution of the potential is split into three terms:

$$\Phi = V_S x + \phi(r', \theta', x) + \tilde{\phi}(r', \theta', x) \quad (14)$$

With the mentioned assumption, the linearization of the problem eases considerably its solving, for the two first terms are solution of the steady problem. As a further simplification, the unsteady interactions between the propeller and the body are neglected and the indetermination between sources and doublets is solved by assuming that the fluctuations of potential are only related to the doublets.

Thus, the only boundary condition remaining applies to the projected propeller surface,  $H'$ :

$$\frac{\nabla \tilde{\phi}^\pm \cdot \underline{n}}{2\pi n R} = 0 \quad (15)$$

The integral equation associated to the problem is:

$$\begin{aligned} & \frac{1}{\omega R} \begin{pmatrix} \tilde{V}_r(r, \theta_k) \\ \tilde{V}_\theta(r, \theta_k) \\ \tilde{V}_x(r, \theta_k) \end{pmatrix} \cdot \underline{n}_M \\ & - \frac{1}{4\pi} \iint_{H'} \frac{\tilde{\delta\phi}_P}{\omega R^2} \underline{\nabla} \left[ \frac{\underline{n}_P \cdot \underline{PM}}{|\underline{PM}|^3} \right] \cdot \underline{n}_M dS_P \\ & - \frac{1}{4\pi} \iint_{\Sigma} \frac{\tilde{\delta\phi}_P}{\omega R^2} \underline{\nabla} \left[ \frac{\underline{n}_P \cdot \underline{PM}}{|\underline{PM}|^3} \right] \cdot \underline{n}_M dS_P \\ & = 0 \end{aligned} \quad (16)$$

The angle  $\theta_k$  is the sum of the angle due to the propeller rotation and the phase shift from blade to blade. Thus, it is time dependent:

$$\theta_k = 2\pi \left( nt - \frac{(k-1)}{Z} \right) \quad (17)$$

The Kutta-Joukowski is implicitly satisfied at the trailing edge of the blades but, in the unsteady case, the value of the potential jump,  $\tilde{\delta\phi}$ , is not uniform on the helicoids  $\Sigma$  and is not constant in time at the trailing edges of the blades.

To solve the problem raised by the time-dependency of the potential, the following procedure has been implemented:

- the value of the doublet associated to the jump of potential  $\tilde{\delta\phi}$  at the trailing edge at a given time is obtained from the integral equation (16),
- the doublet element associated to the potential jump is convected downstream on the helicoid at a speed equal to the steady component of the local at-infinity velocity,
- the computation is actually conducted on the first blade only, due to the blade-to-blade periodicity of the solution. Nevertheless, the other blades are taken in account in the calculation,
- the computation, which can be seen as a transient approach, is stopped when the periodicity of the unsteady circulation is achieved.

#### Numerical procedure

The mesh used to solve the problems is based on a collocation method described in (14) and (15). This method allows to use non-planar surface elements which are required to get accurate results in the case of highly skewed propellers.

In the unsteady case, the calculation of the unsteady pressures is required. Thus, the time derivative of the potential is deduced from the analytical computation of the potential. Special care is to be taken for the doublet locations in the vicinity of the trailing edge. Therefore, second degree doublets have been used to insure the continuity of doublet intensity and of its first derivative at the borders of the panels adjacent to the trailing edge. Moreover, the time-step is chosen according to the Shannon rule to allow consistent harmonical analysis. The numerical tests show that high enough discretizations in space and time give good stability of the results.

## COMPARISON TO BOSWELL EXPERIMENTS

This section presents and comments the numerical results when simulating the experiments referenced in (8) and (13). These experiments consisted in measuring the characteristics of a series of three-blade propellers in open water conditions and behind two wake screens - a three-cycle wake screen and a four-cycle screen. Four propellers were designed with the same diameter, thrust, speed of advance and rotational speed. The first three propellers have different Expanded Aspect Ratio: 0.3 for the Propeller NRSDC N° 4132, 0.6 for Propeller NRSDC N° 4118 and 1.2 for Propeller NRSDC N° 4133. The fourth propeller, Propeller NRSDC N° 4143 has a highly skew of 120° and an Expanded Aspect Ratio of 0.6. In the trials behind the wake screens, besides the monitoring of fluctuating resulting forces and moments, the measurements included averaged thrust and torque measurements and the wake surveys.

The computations were made on an ALLIANT FX-80 machine equipped with 8 processors and 256 Mbytes of RAM. Both open water and behind wake generators conditions were numerically tested. In the open water tests, the design point plus two off-design points were computed. The mesh used in all cases was 11 points spanwise and 15 points chordwise. The durations of each case were in the order of 5 mn CPU for the steady cases and 3 mn CPU for the unsteady cases.

Figures 2, 3, 4 and 5 show the comparison between computational and experimental results in the open water case. The thrust and torque coefficients are plotted versus the advance coefficient. These variables are defined as:

$$\begin{aligned} KT_0 &= \frac{T}{\rho n^2 D^4} \\ KQ_0 &= \frac{Q}{\rho n^2 D^5} \\ J_0 &= \frac{V_0}{n D} \end{aligned} \quad (18)$$

The analysis of the curves shows a satisfactory agreement between computation and measurement for the four tested propellers. The worst results are found with the smallest EAR propeller while

the highly skewed propeller's performances are well predicted. For all propellers, the computed slopes of thrust and torque coefficients curves versus advance coefficient are very close to the experimental ones on a reasonably wide range of advance coefficient.

Figures 6 and 7 show the comparisons between computations and experiments in the unsteady cases. As in reference (13), only the non-skewed propellers have been represented. The fluctuating force and torque coefficients are defined as:

$$\begin{aligned} K\tilde{T}_i &= \frac{\tilde{T}_{i,Z}}{\rho n^2 D^4} \text{ for } i = x, y, z \\ K\tilde{Q}_i &= \frac{\tilde{Q}_{i,Z}}{\rho n^2 D^5} \text{ for } i = x, y, z \end{aligned} \quad (19)$$

where  $\tilde{T}_{i,Z}$  and  $\tilde{Q}_{i,Z}$ ,  $i = x, y, z$  are respectively the axial, horizontal and vertical components of the force and moment fluctuating at the blade rate frequency of the propeller.

The results obtained in the two experimental configurations - three-cycle and four-cycle wake screens are gathered on these two figures. The three-cycle screen generates the axial fluctuating force and torque, while the four-cycle screen generates the fluctuating transverse forces and bending moments.

With figure 6, one can see that the axial forces are well predicted. On the other hand, the transverse forces seem to be overestimated by the computation although the trend of the coefficients with EAR is respected. Figure 7 shows that the predictions of fluctuating moments are good in amplitude as well as in trend versus EAR.

## BASSIN D'ESSAIS DES CARENES EXPERIMENTS

In the prediction of unsteady efforts, one of the expected advantage of the linearized lifting surface methods over lifting line theories is to give access to the fluctuating force amplitudes as well to the fluctuating pressure field with a better accuracy. This last hope is a requirement for a better computation of sheet cavitation in non-uniform

flow conditions. The lack of experimental data allowing the validation motivated new experiments consisting in equipping a propeller with pressure thin film transducers.

#### Thin film pressure transducer technology

The objective of the thin film pressure transducers is to give accurate measurements of the fluctuating pressures at specified points located on the surface of a propeller blade with the smallest alterations of the flow around the profiles. Besides, the sensitive part of the captor has to be as small as possible. To meet these requirements, a new kind of transducers -thin film pressure transducers - have been developed (16).

#### Principle

The pressure gauge uses capacitive variations. The sensitive element is made of a flexible dielectric foil metallised on both sides, thus forming a capacitor (see figure 8).

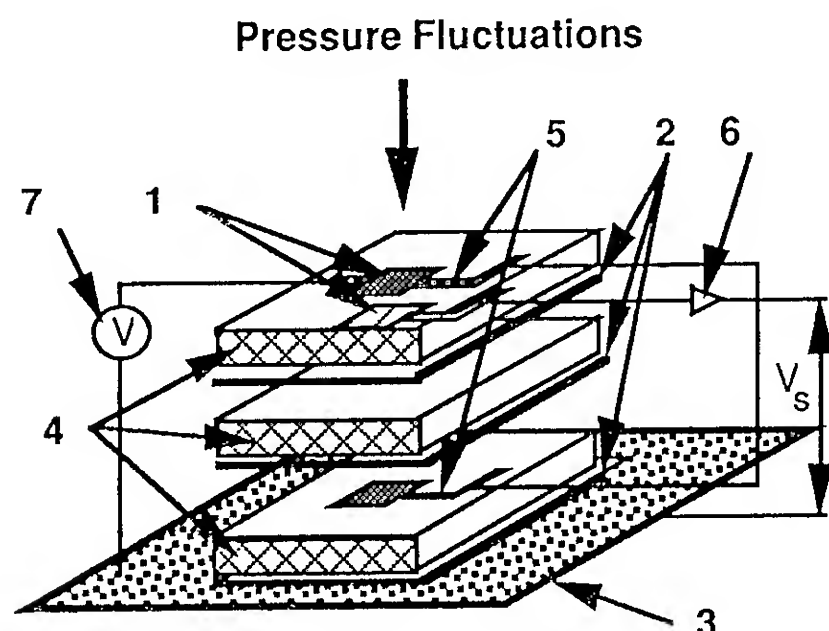


Fig. 8 View of pressure thin film transducer

- (1) Sensitive electrodes
- (2) Glue layers
- (3) Profile
- (4) Dielectric sheets
- (5) Guard ring electrodes
- (6) Preamplifier
- (7) Polarisation source

The thickness of the dielectric foil varies under the action of a pressure fluctuation. That produces a relative variation of the capacitance which is linearly proportional to the pressure fluctuation.

The coefficient relating the pressure fluctuations to the capacitance variations is directly related to the mechanic characteristics of the foil - Elastic modulus and Poisson coefficient. The variation of capacitance is transformed into a voltage variation using a polarisation source  $V$  connected to the first electrode of the sensitive element and to the preamplifier connected to the second electrode. Thus, the output voltage  $V_s$  is proportional to the pressure fluctuation.

In order to reduce the leakage effects on the sensor sensitivity, guard rings are mounted on both sides of the sensitive connection, which links the sensitive electrode to the input of the preamplifier. The guard rings are driven by the output voltage of the preamplifier whose gain is one. Therefore, no current flows through the sensitive electrode into guard electrode capacitor and the leakage capacitors are completely cancelled.

The basic transducer is composed of three 12.5  $\mu\text{m}$  thick dielectric sheets made of Kapton:

- the first sheet contains the connections, the upper and lower sensitive electrodes, the upper guard ring,
- the second sheet isolates electrically the lower sensitive electrode and the lower guard,
- the third sheet contains the lower part of the guard ring.

The electrodes and the connections are manufactured by metal vacuum deposit which is 0.2  $\mu\text{m}$  thick. The three sheets are bonded together and at the profile surface with 3 to 5  $\mu\text{m}$  glue layers.

On  $\varnothing$  0.30 m propellers, 3 to 6 transducers can be mounted on the same blade in the vicinity of high curvature area such as leading edge. The integration on the blade itself is done using bonding technique and does not require special equipment. The preamplifiers are located as close as possible to the transducer, in the blade root. From the preamplifier exit, the signal is sent through coaxial cables to a rotating electronics feeding a slip ring. The same ring is used to bring the DC power to the preamplifier(s) and the probes. Underwater experiments require special water leakproof caution. A fourth 50  $\mu\text{m}$  dielectric sheet made of Kapton metallised on one side is bonded on the three other ones. A special epoxy paint is coated all over the blade surface. Experience shows that the life time of the transducers is more than a month,



even in deep water.

### Performances

The main specifications of thin film pressure transducers, given under a 100 V polarisation level, are:

- sensitivity:  $2.5 \cdot 10^{-8}$  V/Pa
- frequency range: 1 to  $10^5$  Hz
- detectivity at 1 kHz:  $2 \text{ Pa/Hz}^{1/2}$
- sensitive standard area: 4 mm x 6 mm
- thickness<sup>1</sup>: 170  $\mu\text{m}$
- temperature range accepted: 0°C to 60°C

The microelectronics volume required to mount the microelectronics associated to three preamplifiers is less than 10 mm x 7 mm x 1.7 mm

### Experimental program

The experimental program focused on the measurement of fluctuating pressures on the blades of a skewed seven-blade propeller operating in the wake of a submarine model. It also included the wake survey by Laser Doppler Velocimeter. The LDV used at Bassin d'Essais des Carènes gives access to the three components of the velocity field in the propeller plane.

The propeller was equipped with six thin film pressure transducers, three on the back and three on the face. They were located mid-chord at three different radii, respectively 0.5R, 0.7R and 0.9R. The model was mounted under the platform of the towing tank Bassin III (length 220 m) and driven at constant speeds. All the presented tests were done at the same advance coefficient,  $J_s$ , equal to 0.63.

Pressure signals were monitored, processed and stored. A fast Fourier analysis was applied after several successive acquisitions to improve the signal to noise ratio and to check the stationnarity of the signal. With a power spectral-type analysis, the pressure levels for the harmonics at the Shaft Rate frequency were extracted.

Tables I, II and III give all the informations relative to the geometries of both the propeller BA N° 2515 and the model. The symbols used are the ones recommended by the ITTC. The back and face

coordinates are given in the usual frame in percentage of the projected chord length on the blade mean line.

The harmonical content measured by LDV is given in Tables IV, V and VI, which contain the eleven first harmonical half amplitudes and phases for ten dimensionalized radii ranging from 0.0265 m to 0.1165 m and for the axial, orthoradial and radial components of the velocity vector. The coefficients  $A_{i,k}$  introduced in formula (13) are obtained for k ranging from 1 to 11 by multiplying by 0.002 the values read in the tables. The coefficients  $A_{x,0}$  are given in Table I.

The experimental measurements are presented in Table VII. The eight first harmonics at the Shaft Rate frequency are given for three model speeds that were selected during the tests. The reference is 1  $\mu\text{Pa}$  at 0 dB.

### Numerical results

The computations were conducted with the code tested on the Boswell experiments. Figure 9 shows the results obtained in the steady case (harmonic 0 of the wake only) and the unsteady case (complete wake) when the propeller operates in the model wake. The reference advance coefficient is taken at the design point, i.e.  $J_s$  equal to 0.63. There is a good agreement between calculations and measurements.

Figures 10 and 11 give the amplitudes of the harmonics of fluctuating forces and moments acting on one blade. No dynamical balance allowed a comparison to experiments.

The pressure calculated versus time on the mesh points, analysed with a fast Fourier algorithm at the Shaft Rate frequency, and finally interpolated at the locations of the transducers. Table VIII gives the power pressure levels in dB computed at the model speed of 1 m/s.

### Discussion

The fluctuating pressure induced by the flow inhomogeneities can be written as:

<sup>1</sup> including the waterproof protection

$$p = \sum_{k=1}^{\infty} \tilde{p}_k e^{j 2\pi k n t} \quad (20)$$

where the coefficients  $\tilde{p}_k$  are complex numbers containing amplitude and phase informations for the harmonical order  $k$ . The power spectrum analysis gives the coefficients  $\pi_k$  versus  $k$ , related to the complex  $\tilde{p}_k$  according to:

$$\pi_k = \left( \frac{\tilde{p}_k \tilde{p}_k^*}{2} \right)^{1/2} \quad (21)$$

where  $\tilde{p}_k^*$  is the conjugate of  $\tilde{p}_k$ .

One introduces a pressure coefficient at the harmonical order  $k$  defined as:

$$K_{p,k} = 20 \log \pi_k - 40 \log V_s \quad (22)$$

where the coefficients  $\pi_k$  are the values coming from either the experiment -Table VII - or the computation - Table VIII.

Assuming that the wake harmonical content is not affected by Reynolds effects, one finds that the pressure coefficients should remain constant except the harmonic 1 which is affected by Froude effects. Unfortunately, the analysis of the experimental data shows that the coefficients  $K_{p,i}$  are far from being constant. These discrepancies can be attributed to the weak signal-to-noise ratio obtained at the velocity of 1 m/s besides the Reynolds and Froude effects affecting the wake content. Nevertheless, it should be underlined that experiments conducted on that model geometry in various test facilities - wind tunnel and towing tank - did not show a strong influence of the Reynolds number on the wake harmonical content.

For these reasons, only values of pressure coefficients obtained at the two highest model speeds have been averaged. This operation was also applied to the harmonic SR1 despite the preceding remark. Figures 12 to 17 show the comparisons between the calculated and averaged pressure coefficients. The analysis of the results underlines a good agreement between computation

and experiment. The only problems encountered are mainly for the harmonic 1 and, on figure 17, for the harmonic 5. The discrepancies for harmonic 1 can be associated to the absence of correction for the immersion variations in the averaging of pressure coefficients measured at different velocities. For the second problem, there is no clear explanation: the experiment as well as the computation can be suspected at this stage.

Nevertheless, it should be underlined that these results are quite encouraging. The differences between calculations and experiments are in most cases less than 3 dB. Such results are accurate enough to allow noise radiation prevision and give credit to the results obtained for the amplitude of fluctuating forces and moments.

## CONCLUSIONS

The code that was developed at Bassin d'Essais des Carènes offers a good reliability, partly due to the use of new collocation techniques insuring the consistency of the method. The comparisons to experiments found in the open literature and to measurements realized at Bassin are quite rewarding, both in steady and unsteady operating conditions.

Nevertheless, as a dampening to this optimism, it should be remembered that a difference of 6 dB on levels is associated to a ratio of 100% on the linear values. Further experimental tests are underway to increase the base of experimental data. Specifically, measurements will be carried out in the vicinity of the leading edge and LDV acquisitions have already been realized in a plane adjacent to a propeller operating in a non-uniform flow. Such measurements are required to confirm the absence of propeller influence on the wake harmonical content.

As future possible developements, the method has the potential to take in account the unsteadiness of the flow due to the presence of low frequency turbulent structures in the wake. Besides, prediction of fluctuating sheet cavitation seems to be feasible because of the confidence in the accuracy of computed pressure field.

## REFERENCES

- (1) Lewis, F. M., Tachmindji, A. J., "Propeller Forces Exciting Hull Vibrations," Transactions of SNAME, Vol. 62, 1954
- (2) Ritger, P. D., Breslin, J. P., "A Theory for the Quasi-Steady and Unsteady Thrust and Torque of a Propeller in a Ship Wake," Experimental Towing Tank Report 686, Jul 1958, Stevens Institute of Technology, Hoboken, New Jersey, USA
- (3) MacCarthy, J. H., "On the Calculation of Thrust and torque Fluctuations of Propellers in Nonuniform Wake Flow," Report 1533, Oct 1961, Naval Ship Research and Development Center, Washington, D.C., USA
- (4) Lewis, F. M., "Propeller Vibration Forces," Transactions of SNAME, Vol. 71, 1963
- (5) Sears, W. R., "Some Aspects of Nonstationary Airfoil Theory and its Pactical Application," Journal of Aeronautical Sciences, Vol. 8, N° 3, Jan. 1941
- (6) Sevik, M., "Measurements of Unsteady Thrust in Turbomachinery," American Society of Mechanical Engineers, Paper 64-FE-15, Mar. 1964
- (7) Krohn, J. K., "Numerical and Experimental Investigations on the Dependence of Transverse Force and Bending Moment Fluctuations on the Blade Area Ratio of Five-Bladed Ship Propellers," Proceedings of the Fourth Symposium on Naval Hydrodynamics, Office of Naval Research, Aug. 1962
- (8) Denny, S.B., "Cavitation and Open-Water Performances Tests of a Series of Propellers Designed by Lifting-Surface Methods," Report 2878, Sept. 1968, Naval Ship Research and Development Center, Washington, D.C., USA.
- (9) Guermond, J.-L., "Théorie Asymptotique Instationnaire de la ligne Portante. Application à l'Hélice Marine en Sillage Non Uniforme," Thèse de Docteur-Ingénieur, 1985, Université Pierre et Marie Curie, Paris, France
- (10) Kerwin, J. E., "Marine Propellers," Annual Review of Fluid Mechanics, Vol. 18, 1986, pp. 367-403.
- (11) Kerwin, J. E., "Prediction of Steady and Unsteady Marine Propeller Performance by Numerical Lifting-Surface Theory," Transactions of the Society of Naval Architects and Marine Engineers, Vol. 86, 1978, pp. 218-253.
- (12) Luu, T. S., Dulieu, A., "Calcul de l'Hélice Fonctionnant en Arrière d'un Corps à Symétrie Axiale," Proceedings of Association Technique Maritime et Aéronautique, 1977, pp. 301-317.
- (13) Boswell, R.J., Miller, M.L., "Unsteady Propeller Loading-Measurement, Correlation with Theory, and Parametric Study," Report 2625, Oct. 1968, Naval Ship Research and Development Center, Washington, D.C., USA
- (14) Guermond, J.-L., "About Collocation Methods for Marine Propeller Design," Proceeding of Propeller '88 Symposium, Paper N°8, Sept. 88
- (15) Guermond, J.-L., "Collocation methods and lifting-surfaces," European Journal of Mechanics, B/Fluids, Vol 8, n°4, 1989, pp. 283-305
- (16) Portat, M., Bruere, A., Godefroy, J.-C., Helias F., "ONERA developed thin film transducers and their applications," Proceedings of Sensors Symposium, Jan. 1982

Fig. 2 Propeller NSRDC N° 4118  
Open water results

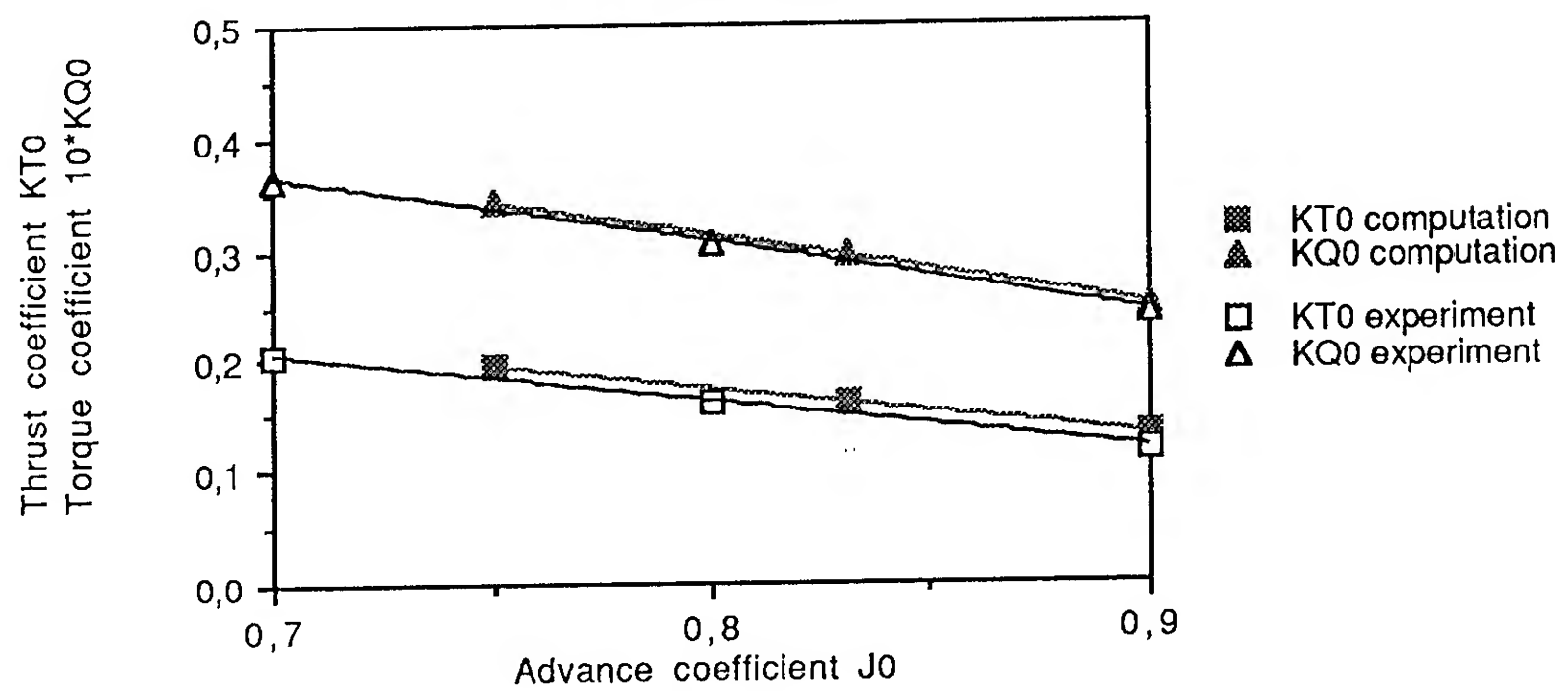


Fig. 3 Propeller NSRDC N° 4132  
Open water results

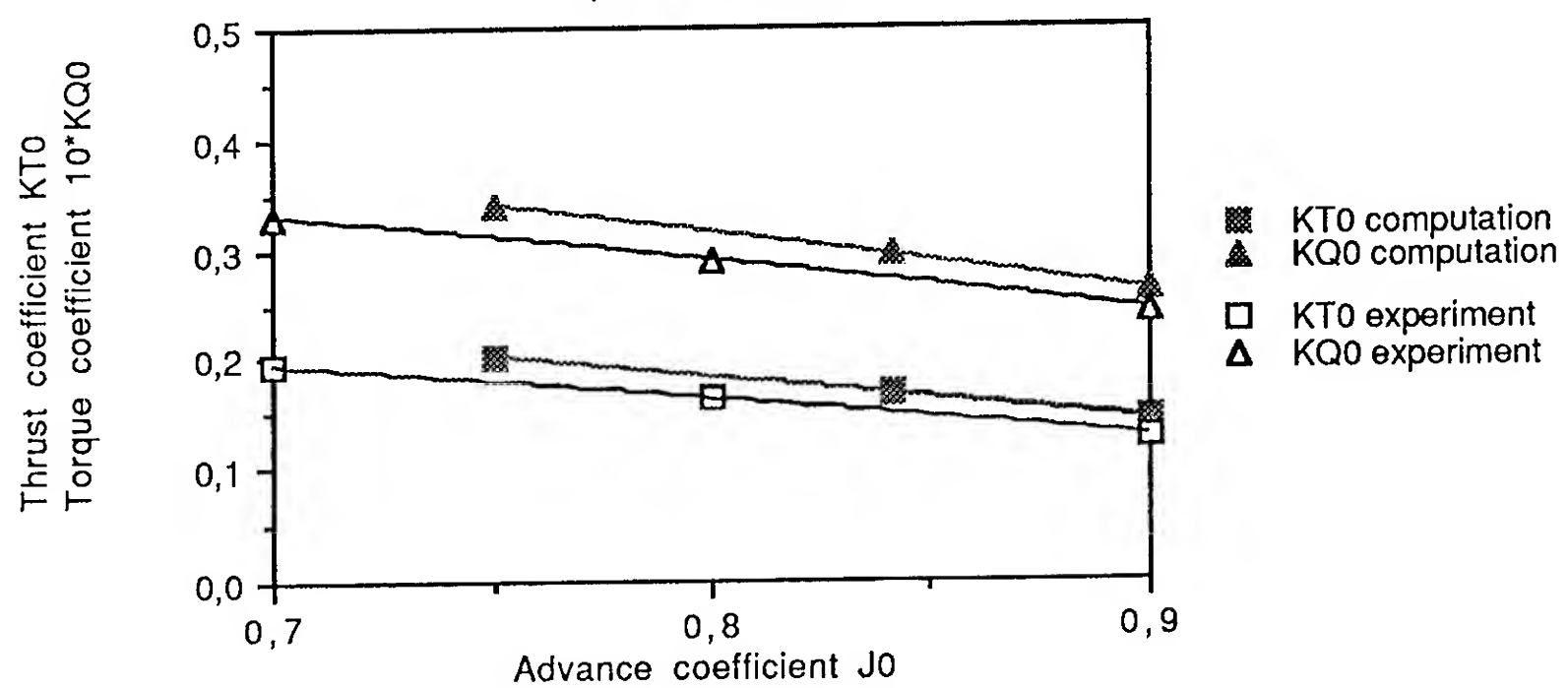


Fig. 4 Propeller NSRDC N° 4133  
Open water results

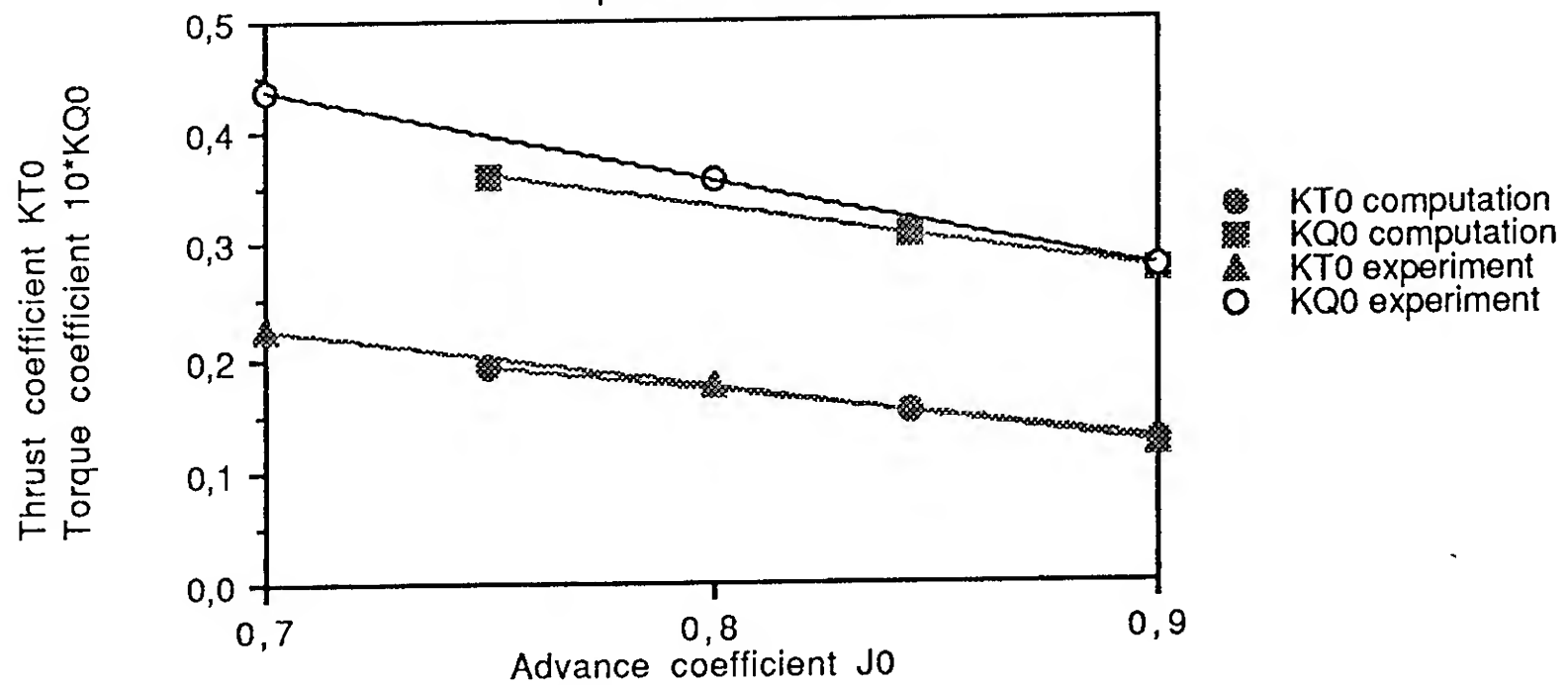


Fig. 5 Propeller NSRDC N° 4143  
Open water results

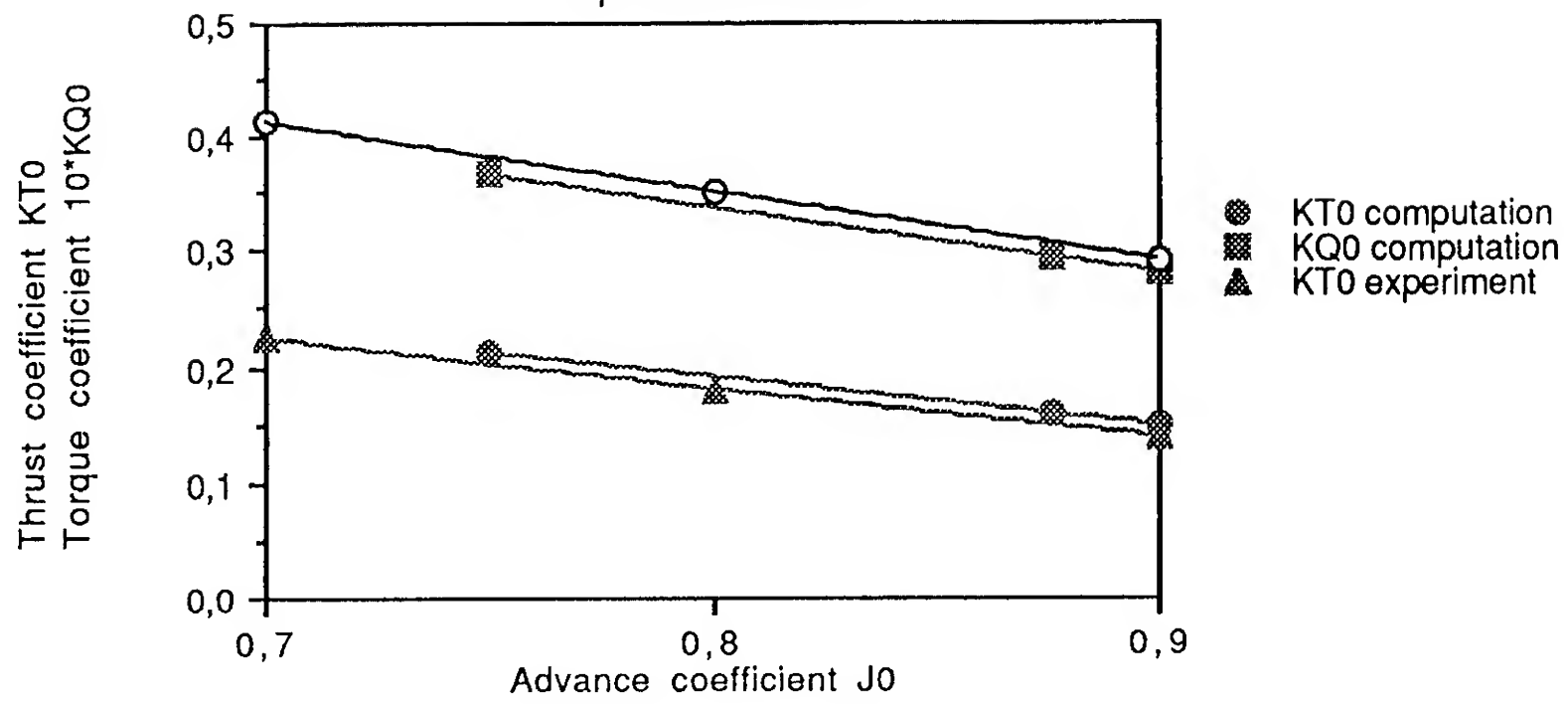


Fig. 6 Boswell experiments  
Fluctuating forces

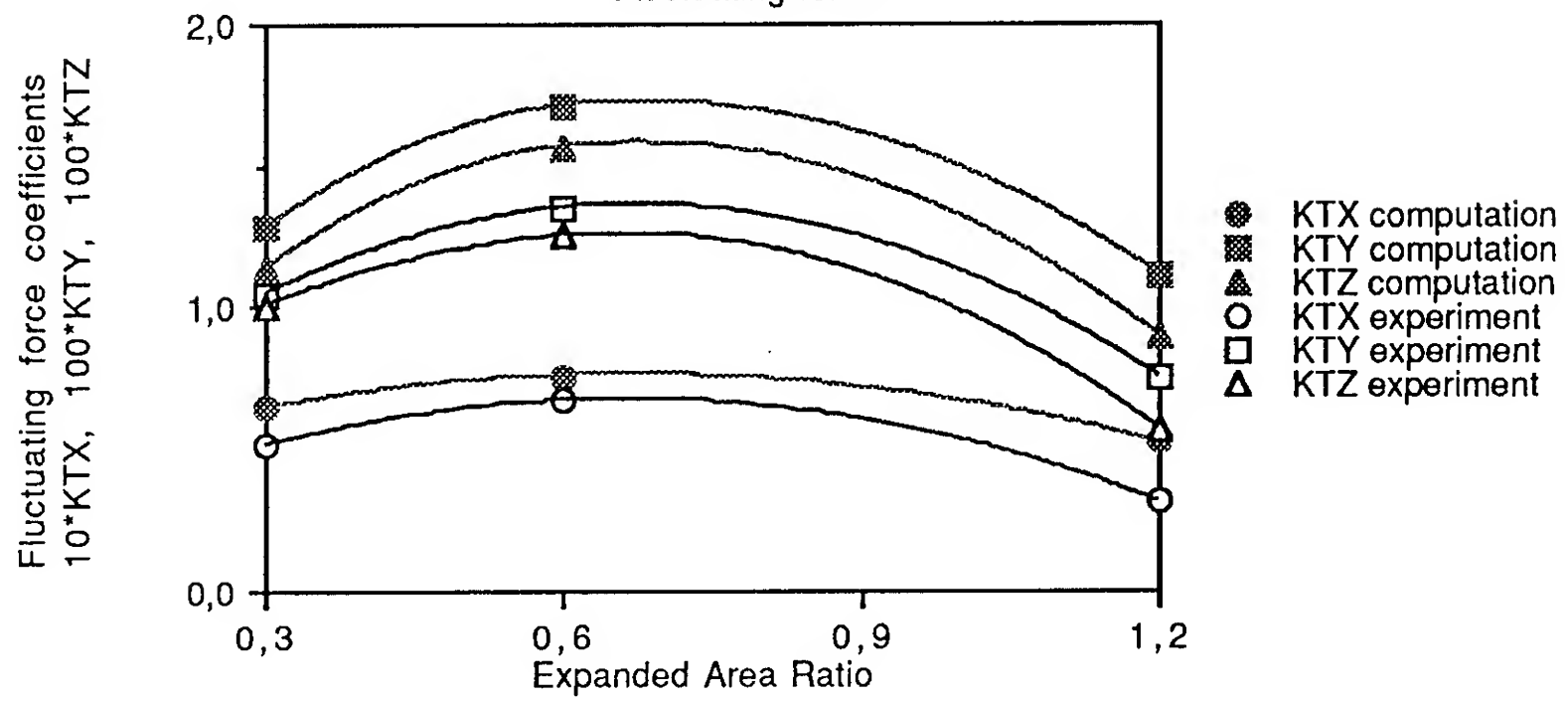


Fig. 7 Boswell experiments  
Fluctuating moments

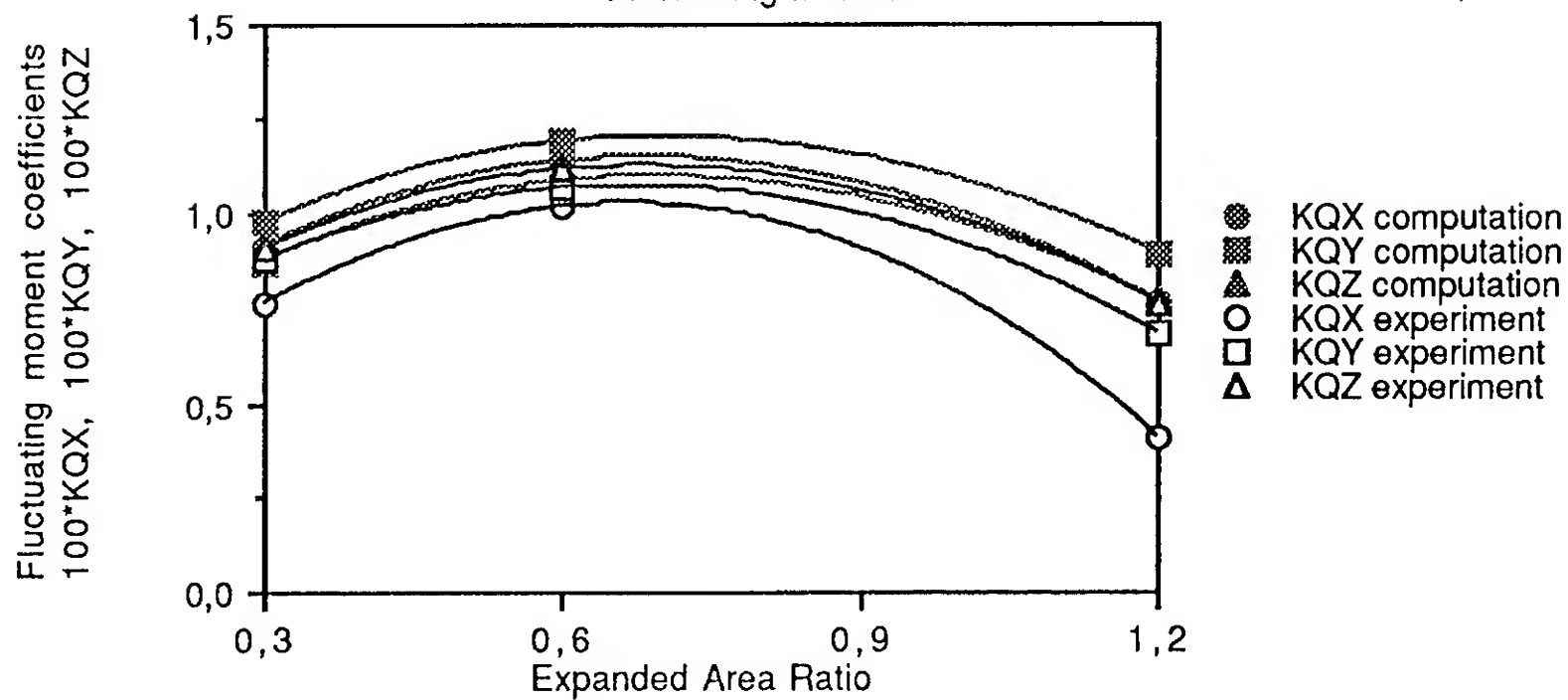




Fig. 9 Propeller BA N° 2515  
Behind model results

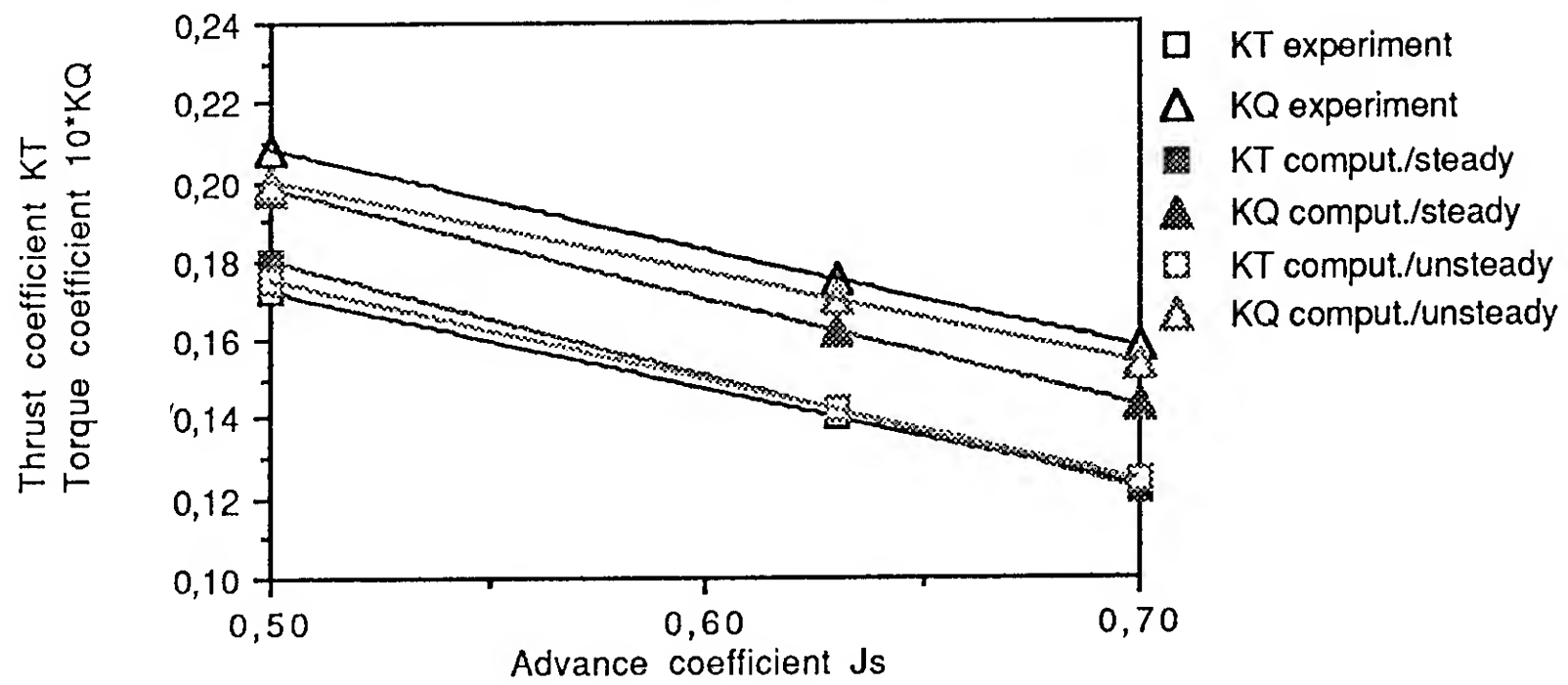


Fig. 10 Propeller BA N° 2515  
Fluctuating forces acting on one blade

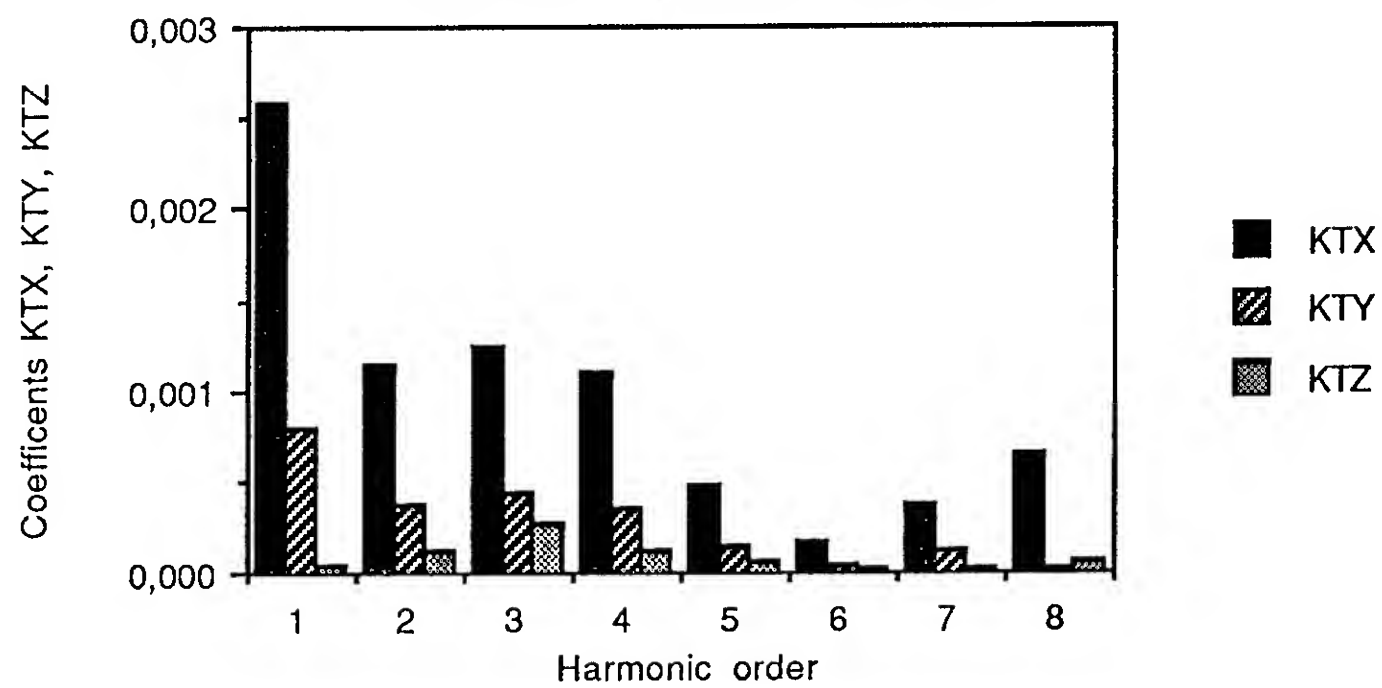


Fig. 11 Propeller BA N° 2515  
Fluctuating moments acting on one blade

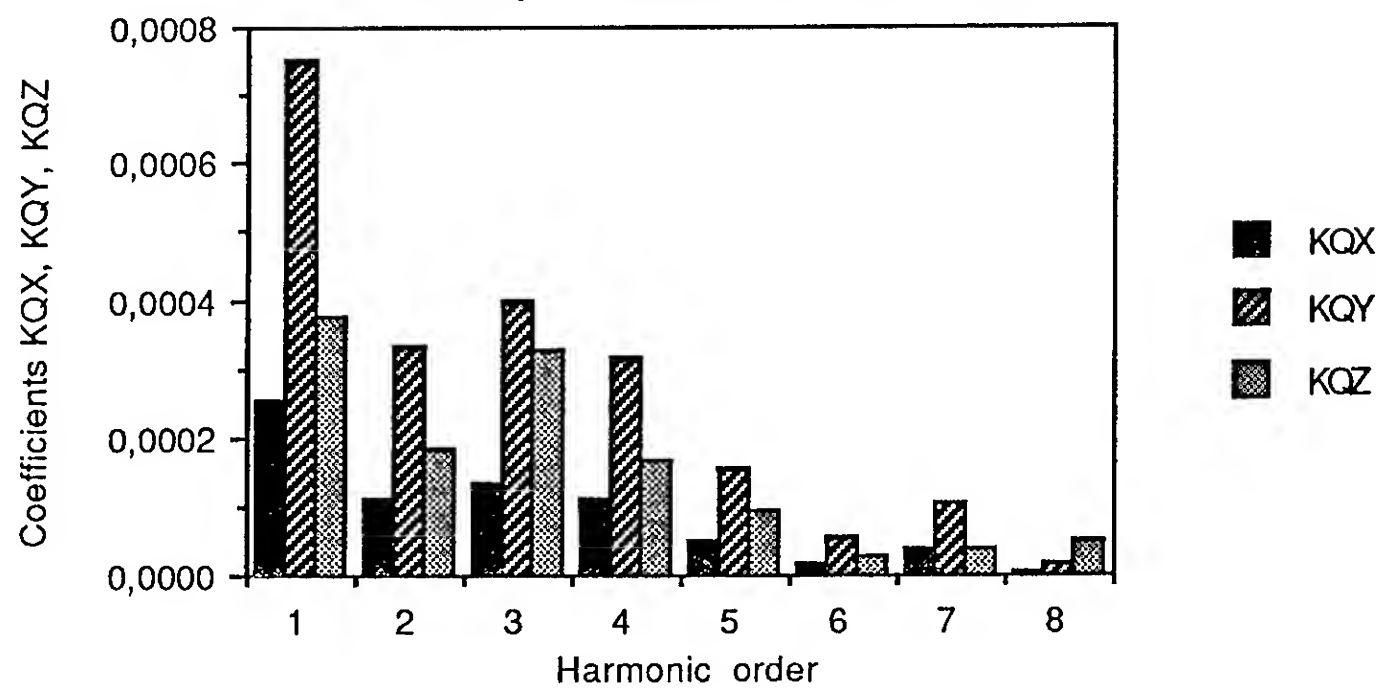


Fig. 12 Propeller BA N° 2515  
0.5R - Back - Midchord

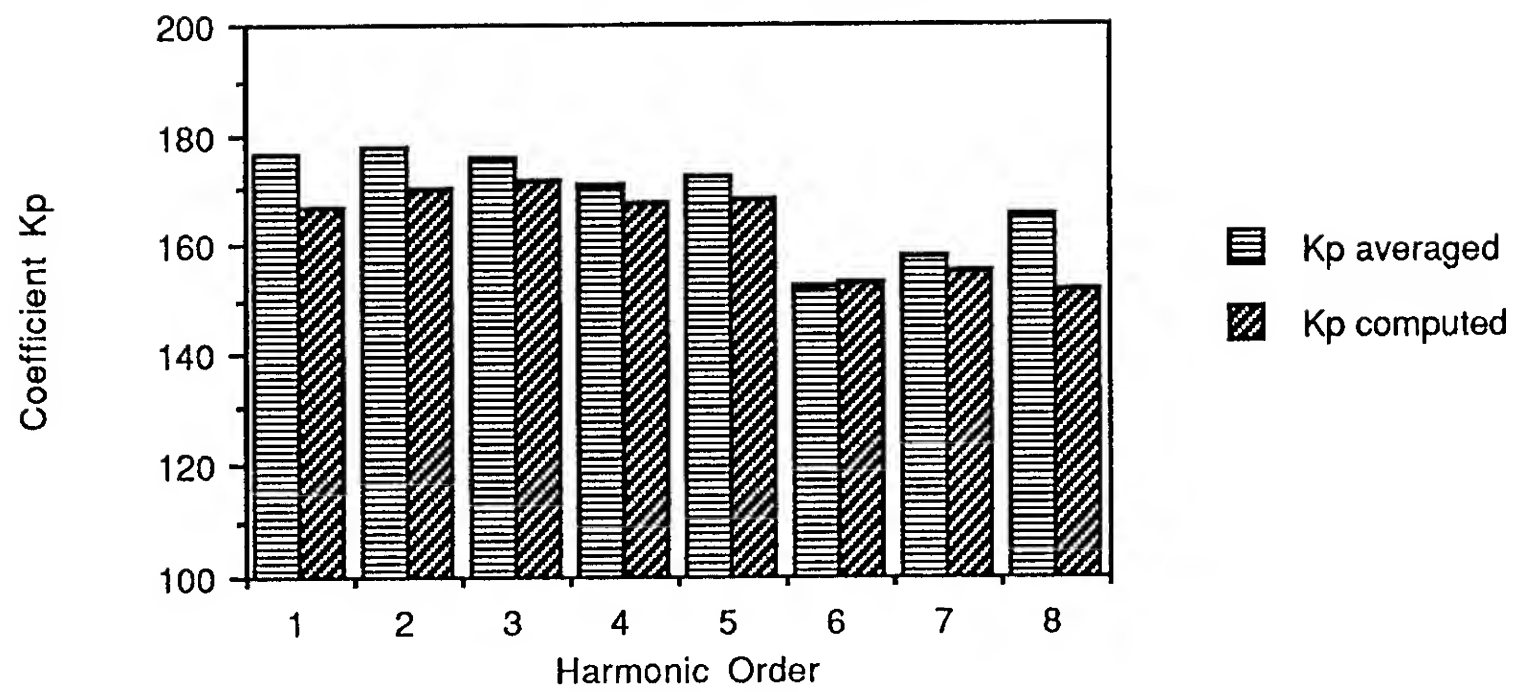


Fig. 13 Propeller BA N° 2515  
0.5R - Face - Midchord

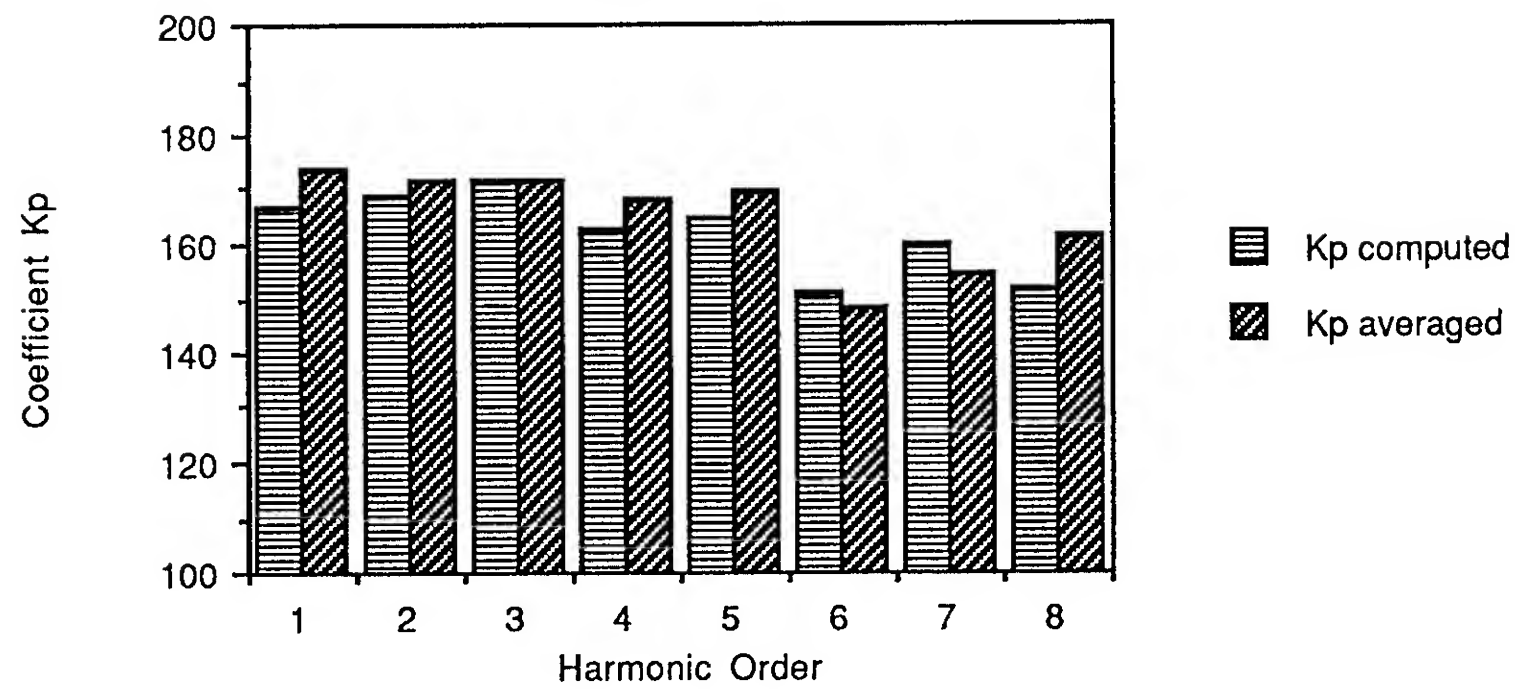


Fig. 14 Propeller BA N° 2515  
0.7R - Back - Midchord

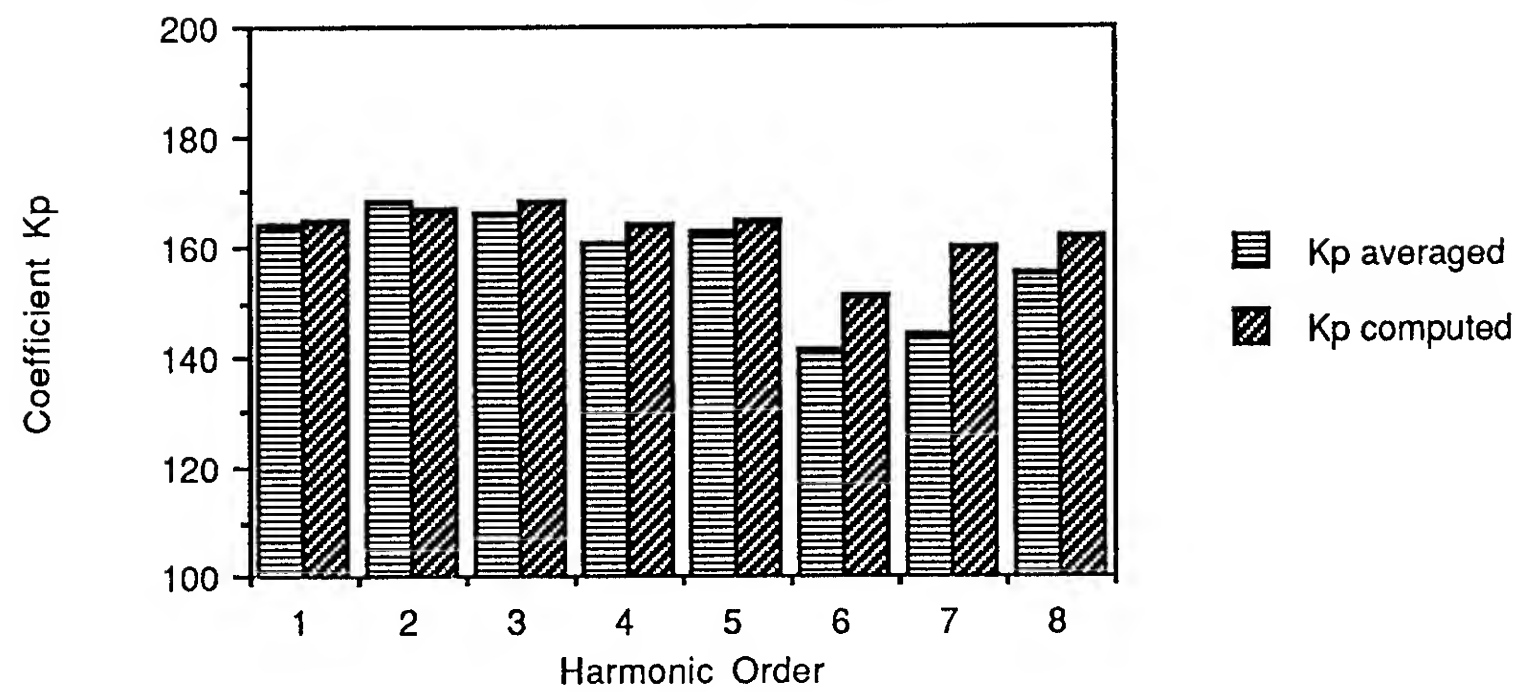


Fig. 15 Propeller BA N° 2515  
0.7R - Face - Midchord

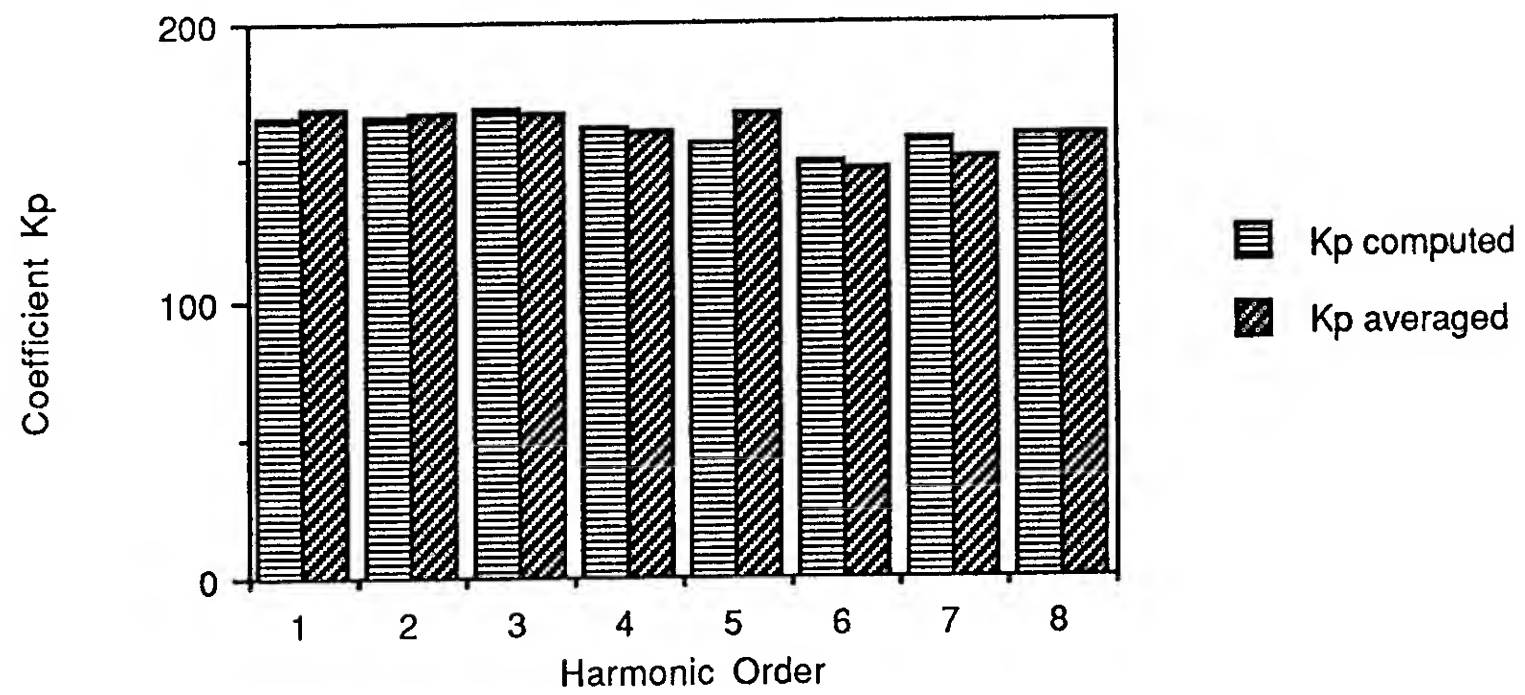


Fig. 16 Propeller BA N° 2515  
0.9R - Back - Midchord

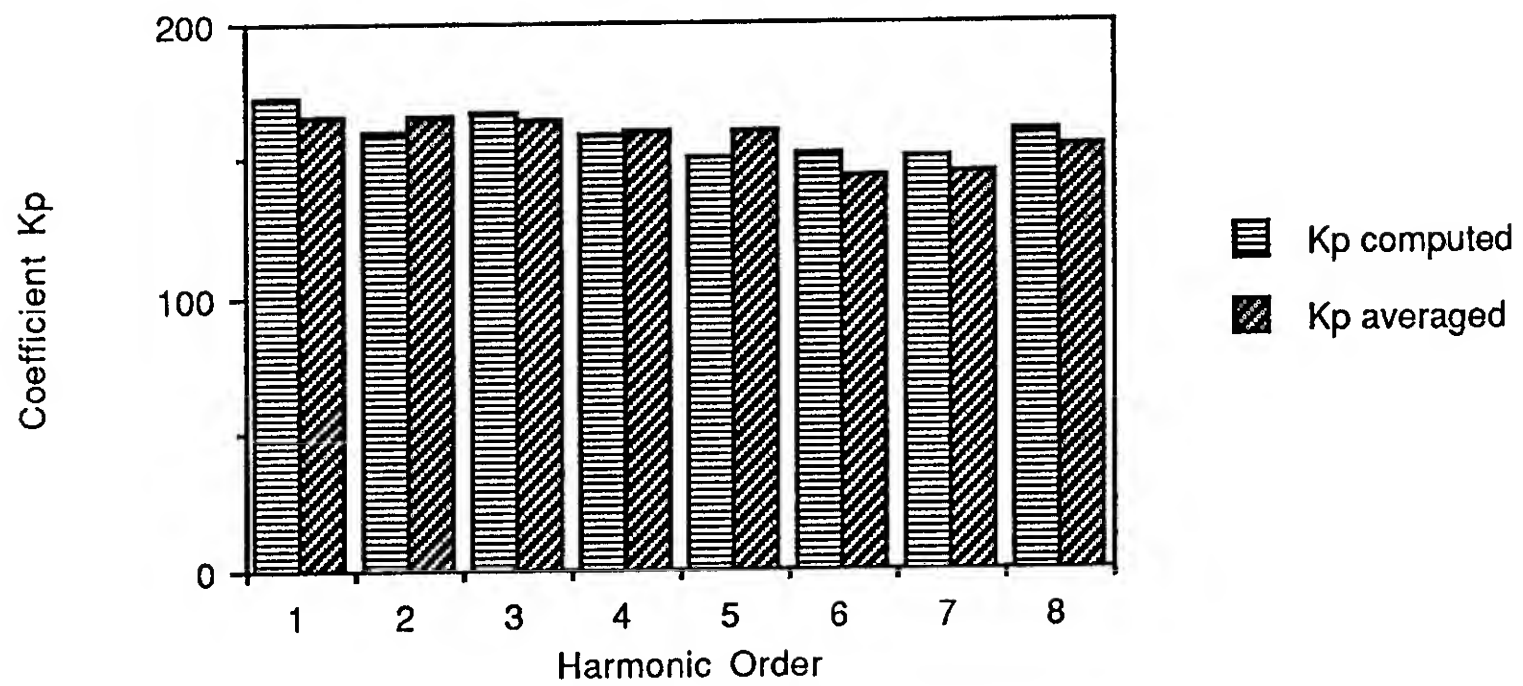


Fig. 17 Propeller BA N° 2515  
0.9R - Face - Midchord

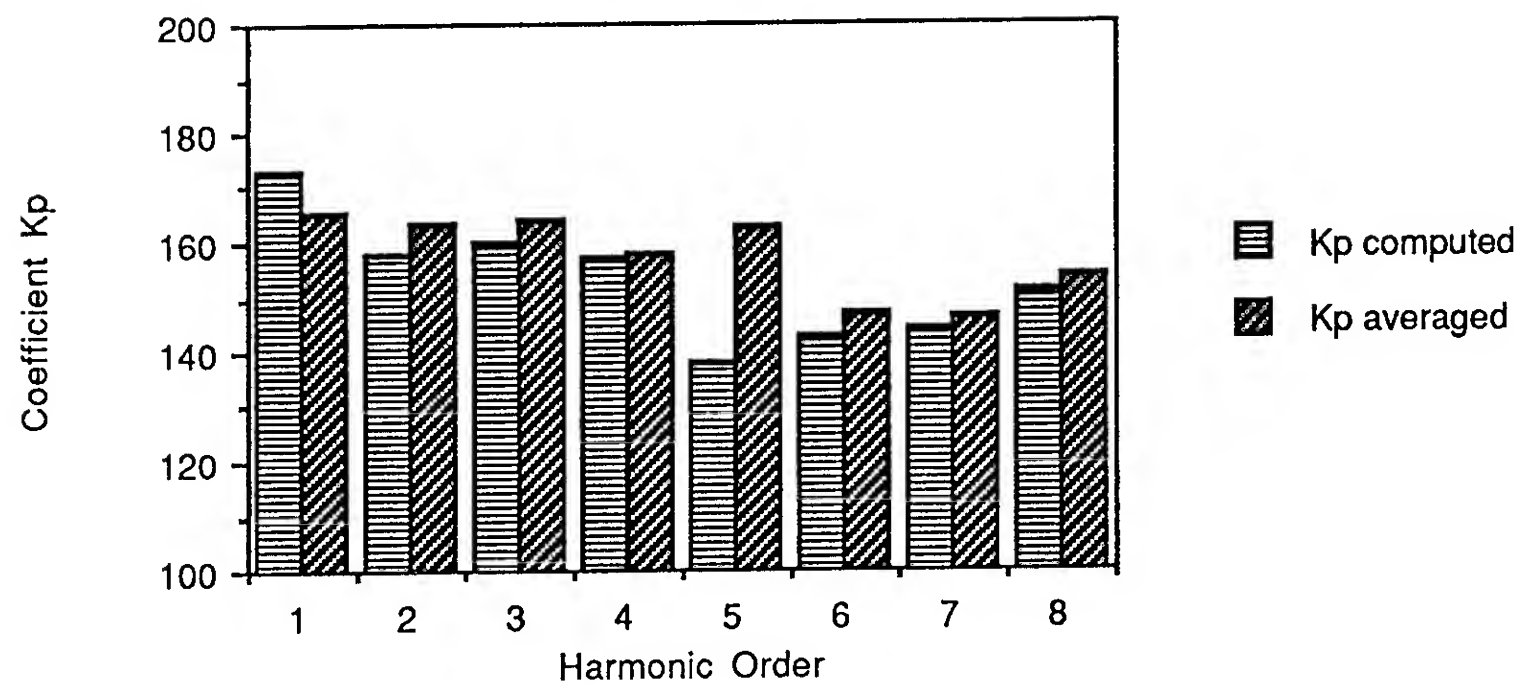


Table I - Propeller BA N° 2515 and model geometries

Propeller BA N° 2515 geometry

Diameter D = 0.235 m

Hub diameter d = 0,047 m

Number of blades Z = 7

Right-handed

$\xi$	C/D	H/D	$\theta_S$	$i_T$	100*Re/C	ds/dx	$A_{x,0}$
0.200	0.1603	0.2960	0.0000	0.000	4.7203	0.0105	0.4183
0.250	0.1702	0.3801	0.8673	0.0019	3.8411	0.0334	0.4289
0.300	0.1799	0.4698	2.7244	0.0060	3.1369	0.0587	0.4376
0.350	0.1900	0.5515	4.7791	0.0110	2.5618	0.0805	0.4513
0.400	0.2007	0.6158	7.1098	0.0172	2.0907	0.0950	0.4714
0.450	0.2110	0.6617	9.7462	0.0248	1.7157	0.1006	0.4883
0.500	0.2195	0.6924	12.6561	0.0333	1.4238	0.0974	0.5016
0.550	0.2257	0.7108	15.7396	0.0423	1.1871	0.0891	0.5220
0.600	0.2300	0.7198	18.8603	0.0513	0.9809	0.0818	0.5566
0.650	0.2323	0.7209	22.0084	0.0603	0.7993	0.0772	0.6033
0.700	0.2322	0.7150	25.2566	0.0693	0.6431	0.0736	0.6364
0.750	0.2284	0.7019	28.6280	0.0781	0.5086	0.0691	0.6513
0.800	0.2189	0.6808	32.0666	0.0863	0.3967	0.0638	0.6754
0.850	0.2009	0.6490	35.3733	0.0931	0.3188	0.0629	0.7074
0.900	0.1702	0.6014	38.7550	0.0976	0.2470	0.0479	0.7315
0.950	0.1274	0.5306	42.4303	0.0993	0.2136	0.0082	0.7535
0.975	0.0931	0.4826	44.0882	0.0980	0.2200	0.0055	0.7657
1.000	0.0429	0.4270	45.4417	0.0946	0.2466	0.0299	0.7774

$\xi$  is the reduced radius,  $r/R$

C is the chord length

H is the geometrical pitch,

$\theta_S$  is the skew angle expressed in °,

$i_T$  is the total axial displacement. Rake is considered positive downstream,

Re is the curvature radius of the blade at the leading edge,

ds/dx is the slope of the mean camber line versus the profile mean line at the leading edge

Model geometry

Model length  $L_M = 6.9$  m

Model Midsection diameter  $D_M = 0.625$  m

The meridian equation is given as:

if  $0 < x \leq 0.045914 L_M$ , then  $r / R_M = 5.7532 \cdot x$

if  $0.045914 < x \leq 0.40171$ , then  $r / R_M = Y_{aft}((x-0.005439) \cdot 0.6/0.39627)$

if  $0.40171 < x \leq 0.73582$ , then  $r / R_M = 1$ .

if  $0.73582 < x \leq 1$ , then  $r / R_M = Y_{fore}((x-0.33955) \cdot 0.6/0.66045)$

where x is the longitudinal axis described in the paper and  $Y_{aft}$  and  $Y_{fore}$  are functions of x defined by:

$Y_{aft} = x \cdot \sqrt{23.9927 - 91.82582 \cdot x + 161.51997 \cdot x^2 - 140.33319 \cdot x^3 + 46.64635 \cdot x^4}$

$Y_{fore} = x \cdot \sqrt{6.44272 + 12.57402 \cdot x - 68.57971 \cdot x^2 + 81.66653 \cdot x^3 + 32.10355 \cdot x^4}$

Table II - PROPELLER BA N° 2515 - Face coordinates, in mm

Nota: all the cotations given in Table II are to be multiplied by -1.

$\xi$	1.25	2.50	5.00	10.00	20.00	30.00	40.00	50.00	60.00	70.00	80.00	90.00	95.00	100.00
0.2000	1.17	1.56	2.16	2.95	4.06	4.68	4.99	5.00	4.68	4.07	3.09	1.97	1.09	0.33
0.2500	1.09	1.47	1.98	2.76	3.77	4.34	4.62	4.62	4.32	3.75	2.84	1.82	1.01	0.32
0.3000	1.02	1.38	1.85	2.55	3.47	3.98	4.23	4.22	3.94	3.41	2.58	1.67	0.92	0.31
0.3500	0.95	1.28	1.72	2.35	3.16	3.61	3.83	3.81	3.55	3.07	2.32	1.51	0.83	0.29
0.4000	0.89	1.20	1.59	2.16	2.87	3.25	3.43	3.41	3.17	2.74	2.07	1.36	0.75	0.28
0.4500	0.84	1.12	1.48	1.98	2.60	2.92	3.06	3.03	2.82	2.43	1.84	1.22	0.67	0.27
0.5000	0.79	1.04	1.37	1.82	2.36	2.63	2.75	2.71	2.51	2.17	1.64	1.10	0.61	0.25
0.5500	0.74	0.97	1.26	1.67	2.15	2.38	2.47	2.44	2.26	1.95	1.47	0.99	0.55	0.24
0.6000	0.68	0.89	1.16	1.52	1.94	2.14	2.22	2.18	2.02	1.74	1.32	0.89	0.50	0.22
0.6500	0.62	0.81	1.05	1.37	1.73	1.90	1.96	1.93	1.78	1.54	1.16	0.80	0.44	0.20
0.7000	0.56	0.73	0.93	1.21	1.52	1.66	1.71	1.68	1.55	1.34	1.01	0.70	0.39	0.18
0.7500	0.49	0.64	0.81	1.05	1.31	1.43	1.47	1.44	1.32	1.14	0.87	0.60	0.34	0.16
0.8000	0.42	0.54	0.69	0.88	1.10	1.20	1.23	1.20	1.10	0.96	0.73	0.50	0.28	0.13
0.8500	0.35	0.45	0.57	0.73	0.90	0.98	1.00	0.98	0.90	0.78	0.59	0.41	0.23	0.11
0.9000	0.26	0.33	0.42	0.55	0.69	0.74	0.77	0.75	0.69	0.60	0.46	0.31	0.18	0.08
0.9500	0.18	0.23	0.30	0.38	0.49	0.53	0.55	0.55	0.51	0.44	0.33	0.22	0.13	0.05
0.9750	0.14	0.18	0.23	0.30	0.39	0.43	0.45	0.45	0.42	0.36	0.27	0.18	0.10	0.04
1.0000	0.07	0.09	0.12	0.17	0.23	0.26	0.28	0.28	0.26	0.23	0.17	0.11	0.06	0.02



Table III - PROPELLER BA N° 2515 - Back coordinates, in mm

$\xi$	1.25	2.50	5.00	10.00	20.00	30.00	40.00	50.00	60.00	70.00	80.00	90.00	95.00	100.00
0.2000	1.21	1.62	2.20	3.08	4.22	4.90	5.24	5.26	4.93	4.29	3.26	2.09	1.15	0.33
0.2500	1.18	1.58	2.15	3.01	4.15	4.82	5.17	5.18	4.87	4.24	3.23	2.06	1.14	0.32
0.3000	1.15	1.53	2.09	2.95	4.08	4.76	5.10	5.13	4.83	4.21	3.21	2.04	1.13	0.31
0.3500	1.11	1.49	2.04	2.89	4.03	4.71	5.06	5.09	4.80	4.19	3.19	2.02	1.11	0.29
0.4000	1.08	1.44	1.98	2.83	3.98	4.66	5.02	5.06	4.77	4.17	3.18	2.00	1.10	0.28
0.4500	1.03	1.39	1.92	2.76	3.91	4.60	4.96	5.01	4.72	4.13	3.14	1.98	1.09	0.27
0.5000	0.98	1.33	1.84	2.66	3.79	4.48	4.84	4.89	4.61	4.03	3.07	1.92	1.06	0.25
0.5500	0.92	1.25	1.75	2.53	3.62	4.29	4.64	4.69	4.43	3.87	2.95	1.84	1.01	0.24
0.6000	0.85	1.17	1.63	2.37	3.40	4.04	4.37	4.42	4.18	3.65	2.78	1.73	0.95	0.22
0.6500	0.78	1.07	1.50	2.19	3.14	3.73	4.05	4.10	3.87	3.38	2.57	1.60	0.88	0.20
0.7000	0.70	0.96	1.35	1.98	2.85	3.39	3.69	3.73	3.52	3.08	2.34	1.45	0.80	0.18
0.7500	0.61	0.84	1.19	1.75	2.52	3.01	3.27	3.31	3.13	3.73	2.07	1.28	0.70	0.16
0.8000	0.52	0.72	1.02	1.49	2.16	2.58	2.80	2.84	2.68	2.34	1.78	1.10	0.60	0.13
0.8500	0.43	0.59	0.83	1.23	1.79	2.13	2.31	2.34	2.22	1.93	1.47	1.91	0.50	0.11
0.9000	0.32	0.44	0.63	0.92	1.33	1.59	1.72	1.75	1.65	1.44	1.09	0.68	0.37	0.08
0.9500	0.20	0.28	0.40	0.59	0.85	1.01	1.10	1.10	1.04	0.91	0.70	0.43	0.23	0.05
0.9750	0.15	0.20	0.28	0.41	0.59	0.70	0.76	0.76	0.72	0.63	0.48	0.30	0.16	0.04
1.0000	0.08	0.11	0.14	0.20	0.28	0.33	0.36	0.36	0.34	0.29	0.22	0.14	0.08	0.02

Table IV - Half-amplitudes and phases of axial velocity harmonics (values of half-amplitudes to be multiplied by  $10^{-3}$ )

r, m	1	2	3	4	5	6	7	8	9	10	11
0.0265	7.53 0°	3.69 0°	9.34 180°	22.02 0°	10.19 180°	2.89 0°	2.32 0°	4.17 180°	1.22 0°	1.28 0°	3.39 180°
0.0365	1.22 180°	14.88 0°	5.30 180°	21.56 0°	11.09 180°	4.08 180°	4.65 0°	4.16 180°	2.63 0°	4.05 0°	3.43 180°
0.0465	10.42 180°	13.82 0°	7.07 180°	21.12 0°	8.23 180°	1.67 180°	6.58 0°	1.92 180°	5.03 0°	0.22 0°	3.30 0°
0.0565	9.40 180°	9.26 0°	4.95 180°	16.06 0°	9.26 180°	1.26 0°	1.23 0°	1.20 0°	1.75 180°	0.45 0°	0.43 0°
0.0665	9.97 180°	10.06 0°	2.13 180°	2.63 0°	4.07 180°	1.21 0°	0.47 0°	4.52 180°	4.29 180°	3.27 0°	1.04 0°
0.0765	15.79 180°	8.80 0°	8.64 180°	0.93 180°	12.03 180°	1.48 0°	5.39 0°	10.71 180°	5.33 0°	4.05 0°	0.06 180°
0.0865	13.08 180°	14.13 0°	3.66 180°	2.80 0°	7.13 180°	4.48 180°	11.17 180°	14.61 180°	0.76 0°	0.53 0°	3.86 0°
0.0965	12.02 180°	5.71 0°	7.37 180°	5.39 180°	3.11 180°	5.79 180°	7.35 180°	10.59 180°	4.13 180°	9.31 0°	0.01 0°
0.1065	16.17 180°	7.89 0°	11.55 180°	7.54 180°	3.82 180°	3.87 180°	6.14 0°	7.71 180°	2.00 180°	7.06 0°	1.48 0°
0.1165	15.93 180°	7.58 0°	11.48 180°	5.33 180°	2.47 180°	4.73 180°	4.79 0°	8.65 180°	0.57 180°	7.07 0°	1.90 0°

Table V - Half-Amplitudes and phases of orthoradial velocity harmonics (values of half-amplitudes to be multiplied by  $10^{-3}$ )

$r, m$	1	2	3	4	5	6	7	8	9	10	11
0.0265	57.58 -90°	53.78 90°	25.80 -90°	71.60 90°	47.18 -90°	1.62 -90°	62.63 -90°	17.26 90°	14.94 90°	34.37 90°	14.07 -90°
0.0365	34.81 -90°	4.11 -90°	1.16 90°	5.95 -90°	2.94 -90°	2.41 90°	13.41 -90°	18.73 90°	3.16 -90°	6.14 -90°	6.70 -90°
0.0465	36.22 -90°	2.48 90°	20.79 -90°	5.71 90°	0.87 90°	4.98 90°	13.61 -90°	0.73 90°	15.06 -90°	3.14 90°	3.23 -90°
0.0565	46.45 -90°	43.89 90°	43.69 -90°	19.79 90°	36.85 -90°	5.01 90°	5.56 -90°	7.88 90°	16.21 -90°	7.36 90°	25.29 -90°
0.0665	68.21 -90°	15.81 90°	39.58 -90°	23.51 90°	6.04 -90°	3.75 90°	10.20 -90°	9.04 -90°	2.82 -90°	8.69 90°	24.52 -90°
0.0765	54.51 -90°	41.46 90°	58.97 -90°	41.50 90°	25.06 -90°	7.52 90°	19.97 -90°	9.09 90°	8.60 -90°	0.80 -90°	8.69 -90°
0.0865	52.10 -90°	31.84 90°	36.75 -90°	15.82 90°	12.35 -90°	2.48 90°	18.65 -90°	1.25 -90°	16.25 -90°	11.83 90°	11.78 -90°
0.0965	71.95 -90°	7.69 -90°	60.42 -90°	36.76 90°	6.10 -90°	12.47 90°	18.92 -90°	7.52 90°	14.18 -90°	11.71 -90°	20.59 -90°
0.1065	82.61 -90°	49.37 90°	71.80 -90°	25.91 90°	1.90 90°	1.75 90°	6.51 90°	1.65 90°	9.81 -90°	3.13 -90°	11.29 -90°
0.1165	73.33 -90°	19.65 90°	52.13 -90°	54.21 90°	14.50 -90°	9.04 90°	26.74 -90°	1.33 90°	14.94 -90°	1.73 90°	13.53 -90°

Table VI - Half-Amplitudes and phases of radial velocity harmonics (values of half-amplitudes to be multiplied by  $10^{-3}$ )

$r, m$	1	2	3	4	5	6	7	8	9	10	11
0.0265	10.77 180°	27.53 0°	7.17 0°	3.30 0°	11.04 0°	4.13 0°	25.19 180°	3.44 180°	5.86 0°	16.94 180°	13.14 180°
0.0365	13.71 0°	0.14 0°	14.25 180°	3.78 180°	30.00 0°	18.34 0°	28.12 180°	12.09 180°	10.48 180°	19.09 180°	2.63 0°
0.0465	7.98 0°	11.50 0°	16.97 180°	2.79 180°	31.87 0°	1.83 180°	26.49 180°	5.73 0°	3.04 180°	13.40 180°	0.17 0°
0.0565	14.67 0°	21.18 0°	14.90 180°	1.45 180°	17.27 0°	12.22 180°	29.42 180°	1.27 180°	9.29 0°	7.21 180°	12.95 180°
0.0665	38.13 0°	8.29 0°	55.32 180°	26.94 180°	20.29 0°	18.64 0°	15.28 180°	0.38 0°	4.41 0°	25.71 180°	14.66 0°
0.0765	23.63 0°	15.40 0°	30.38 180°	7.15 180°	21.46 0°	11.00 180°	25.47 180°	18.30 0°	2.53 180°	7.78 180°	0.43 180°
0.0865	41.08 0°	23.03 0°	50.60 180°	21.77 180°	23.05 0°	14.22 0°	28.00 180°	14.85 0°	16.87 180°	2.98 180°	7.09 180°
0.0965	34.97 0°	11.16 0°	64.09 180°	33.76 180°	31.61 0°	25.16 0°	9.78 180°	10.25 0°	2.78 180°	3.62 180°	11.66 180°
0.1065	45.71 0°	27.76 0°	87.47 180°	6.65 0°	17.41 0°	2.25 180°	12.32 0°	20.69 180°	21.01 180°	12.64 180°	4.84 180°
0.1165	16.48 0°	19.06 0°	37.72 180°	3.30 180°	29.15 0°	1.71 0°	32.69 180°	2.29 0°	12.72 180°	8.99 180°	8.25 180°

Table VII - Experimental measurements of pressure fluctuation levels,  $\pi_k$ , in dB - Propeller BA N° 2515

Experimental measurements on back

$\xi$	model speed	SR1	SR2	SR3	SR4	SR5	SR6	SR7	SR8
0.5	1 m/s	179	179	172	164	168	152	148	155
	2 m/s	187	187	186	180	180	164	167	175
	3 m/s	190	193	190	185	188	165	173	180
0.7	1 m/s	177	177	168	160	166	151	154	154
	2 m/s	181	185	184	178	179	161	158	172
	3 m/s	179	182	179	174	178	153	162	169
0.9	1 m/s	171	173	165	154	156	158	159	146
	2 m/s	178	177	177	172	170	155	155	168
	3 m/s	184	185	181	178	180	164	166	172

Experimental measurements on face

$\xi$	model speed	SR1	SR2	SR3	SR4	SR5	SR6	SR7	SR8
0.5	1 m/s	186	177	176	165	172	155	163	160
	2 m/s	187	184	184	180	181	163	166	175
	3 m/s	191	190	190	187	189	165	174	179
0.7	1 m/s	182	172	170	168	157	156	154	150
	2 m/s	181	179	180	172	178	158	161	170
	3 m/s	186	186	186	180	186	165	171	177
0.9	1 m/s	182	166	166	155	165	158	158	152
	2 m/s	180	177	178	170	175	159	158	168
	3 m/s	182	181	181	177	181	166	165	171



Table VIII - Computed pressure fluctuations levels,  $\pi_K$ , in dB  
Propeller BA 2515

Numerical results at model speed of 1 m/s									
$\xi$		SR1	SR2	SR3	SR4	SR5	SR6	SR7	SR8
0.5	back	167	170	172	168	168	153	155	152
	face	167	169	172	163	165	151	160	152
0.7	back	165	167	168	164	165	151	160	162
	face	165	166	168	162	156	149	157	158
0.9	back	173	160	167	158	150	152	150	160
	face	173	158	160	157	138	143	144	151

## DISCUSSION

Hajime Maruo  
University of California at Santa Barbara, USA

The most important feature of the unsteady propeller characteristics is the change of efficiency when the propeller is operating in the non-uniform wake. It is expressed by the relative rotative efficiency. It is widely recognized that the relative rotative efficiency is lightly higher than one. Another feature of unsteady characteristics is the phase shift of the fluctuating thrust and torque. This is due to the term associated with  $\partial\phi/\partial t$  in the pressure equation. In the present paper, data concerning the above quantity are not given. The computation of a propeller characteristics, when the propeller is operating in circumferentially varying wake, has been carried out by us several years ago (15th ONR Symposium, Hamburg, 1984). According to our experience, the simple linearized lifting surface theory is not able to provide results which show satisfactory agreement with experiment, and the nonlinear deformation of the trailing vortex sheet in the slip stream must be taken into account.

## AUTHORS' REPLY

The following Table gives the values of the steady components  $\tilde{T}_{i,0}$  and  $\tilde{Q}_{i,0}$ ,  $i = x, y, z$  resulting from the interactions between the propeller N° 2525 and the non-uniform wake at the nominal design point  $J$ , equal to 0.63. Fig. 9 shows the comparison between the axial thrust and torque  $\tilde{T}_{x,0}$  and  $\tilde{Q}_{x,0}$ , and the thrust and the torque computed in the uniform wake which nevertheless takes in account the radial gradient of axial velocities.

	x	y	z
$\tilde{T}_{i,0}$	0.142	0.0019	0.0021
$10*\tilde{Q}_{i,0}$	0.170	0.0133	0.0257

In our opinion, the relative rotative efficiency is not affected as much by the circumferential non-uniformities as by the radial gradient of axial velocity field. In the ideal case of a purely axisymmetric body ending with a large aft conicity angle, the relative rotative efficiency would be substantial while, in the absence of fins, rudders, ..., the unsteady periodical efforts would remain null.

In regard to the question relative to phase shift, it appeared that phases are not important to know with accuracy in terms of their practical meaning. Therefore, the results are not given.

At last, a theory mixing linearized lifting surface and nonlinear deformation of vortex sheddings, as suggested by the discussion, does not seem consistent. Moreover, the theory developed in the present paper gives numerical results in good agreement with the experimental measures available at the present time, thus, no extension in the suggested direction has been considered.

# Navier-Stokes Analysis of Turbulent Boundary Layer and Wake for Two-Dimensional Lifting Bodies

P. Nguyen, J. Gorski (David Taylor Research Center, USA)

## ABSTRACT

Navier-Stokes calculations were performed on two 2-D lifting foils which have been tested in a wind tunnel. In the experiment, the angles of attack for the two foils were set up to yield approximately the same lift at a Reynolds number of  $2.25 \times 10^6$  (based on chord). One foil has a thicker trailing edge than the other, and has mild flow separation on the last 4% chord of the suction side. The flow solver, called the David Taylor Navier-Stokes (DTNS) code, is formulated with artificial compressibility and upwind differencing. The Launder-Spalding  $k-\epsilon$  turbulence model is used. Predictions of the turbulent flow quantities of the boundary layer and wake are compared with the experimental data for both foils. These predictions, including flow separation location, agree reasonably well with the data. After these validation predictions, the Navier-Stokes analysis method and a design technique based on conformal mapping are combined to develop new 2-D foil sections. Since the turbulent kinetic energy is the dynamic pressure, and the Reynolds shear stresses are related to the turbulence production, these quantities are used to develop new 2-D sections with desirable turbulent boundary layer characteristics. The characteristics of one new section are presented as results of the new foil design process.

## INTRODUCTION

In this paper, with the aid of a Navier-Stokes (N-S) analysis method we explore the potential of tailored blade

sections instead of standard NACA sections for optimisation of propeller performance. Propeller designers normally use sections with NACA 16 or NACA 66 thickness distributions and an  $a=0.8$  meanline. Due to recent improvement in computational capability, it is now feasible to shape the section to achieve a specific design goal, whether it be maximizing efficiency, minimizing cavitation, or boundary layer control. Also, for some applications, it is desirable to maximize the section thickness without degrading the propeller performance by massive flow separation. The motivation for this N-S analysis is due to the experimental results of Gershfeld et al. [1], and Huang et al. [2], which have shown that the pressure spectra on the trailing edge are related to the turbulent flow characteristics in the near-wake region. The turbulent flow data in Ref. [2] are used for validation of the N-S analysis. This paper presents the validation results, and the calculated flow characteristics for a new section developed with the aid of the N-S analysis.

The mean momentum balance for viscous flow at high Reynolds number yields the time-averaged N-S equations. The full N-S formulation is used here as separated flow is analyzed. There are two fundamental difficulties in using the N-S equations to predict the flows: 1) numerical instability due to the convection terms, and 2) modelling of turbulence. The instability problem has been attacked by various numerical techniques such as 1) central differencing with artificial damping [3], and 2) upwind differencing with Total

Variational Diminishing (TVD) schemes [4]. These techniques, however, only address the mean flow. The nonlinearity of the fluctuating flow yields turbulence, which is a more challenging problem.

Little progress has been made in the development of a general theory for complex turbulent flows [5]. Most of the fundamental understanding of turbulent flow has been acquired through experimentation, and just recently through direct numerical simulation. In practice, turbulence models have evolved from the simple mixing-length models, to the more physically realistic models such as Mean Vorticity and Covariance [6]. Most turbulence models are based on the eddy-viscosity concept which, although not very rigorous, has been widely used since it was proposed. The turbulence models used in this paper are based on this approach.

#### OUTLINE OF ANALYTICAL METHOD

The objective is to maximize the thickness of a 2-D lifting foil and to reduce trailing edge turbulent kinetic energy without incurring significant flow separation. This is achieved by control of the turbulent boundary layer and wake characteristics through careful shaping of the 2-D section. The N-S analysis is used in the last stage of a foil design process to calculate the turbulent flow characteristics. The design parameters are the turbulent kinetic energy, and the turbulent shear stress.

There are two steps in obtaining a N-S solution: 1) geometry preparation, including grid generation, and 2) flow calculation. For this study, the grid generation is based on the work of Coleman [7], which uses partial differential equations to define a body-fitted grid. Here, a multi-zone grid is used for better control of the grid structure, which is especially useful when combined with a multi-zone flow code such as the David Taylor Navier-Stokes (DTNS) code developed by Gorski [8]. For a high Reynolds number flow (greater than  $10^6$ ) the first grid point should be as close as  $10^{-5}$  chord length away from the body, approximately  $y^+$  of 5, so that the sub-layer can be resolved. Fig. 1 shows a 3-zone grid used for computing the flow over a foil with Reynolds number of  $5 \times 10^6$ . The flow

calculation steps are described in the following sections.

#### Navier-Stokes Equations

Using the idea of artificial compressibility developed by Chorin [9] allows the N-S equations for an incompressible fluid, in cartesian coordinates, to be written in the following conservative form:

$$\frac{\partial q}{\partial t} + \frac{\partial(f_1 + g_1)}{\partial x} + \frac{\partial(f_2 + g_2)}{\partial y} = 0 \quad (1)$$

where the subset

$$\frac{\partial q}{\partial t} + \frac{\partial f_1}{\partial x} + \frac{\partial f_2}{\partial y} = 0 \quad (2)$$

constitutes the corresponding inviscid flow equations. For 2-D flow, the dependent variable  $q$  and the inviscid fluxes  $f_1$  and  $f_2$  are given by:

$$q = \begin{bmatrix} p/\beta \\ u \\ v \end{bmatrix}, f_1 = \begin{bmatrix} u \\ u^2 + p \\ uv \end{bmatrix}, f_2 = \begin{bmatrix} v \\ uv \\ v^2 + p \end{bmatrix}$$

where  $p$  is pressure, and  $u$  and  $v$  are the cartesian velocity components in the  $x$  and  $y$  directions, respectively. The term  $p/\beta$  is the pseudocompressibility which should approach zero as the solution converges.  $\beta$  controls the convergence rate of the scheme with a value of 1 being used for the present calculations. The viscous "fluxes"  $g_1$  and  $g_2$  are given by:

$$g_1 = \frac{1}{R_e} \begin{bmatrix} 0 \\ \mu \frac{\partial u}{\partial x} \\ \mu \frac{\partial v}{\partial x} \end{bmatrix}, g_2 = \frac{1}{R_e} \begin{bmatrix} 0 \\ \mu \frac{\partial u}{\partial y} \\ \mu \frac{\partial v}{\partial y} \end{bmatrix}$$

where  $R_e$  is the Reynolds number and  $\mu$  is the molecular viscosity. The equations (1) and (2) form a hyperbolic system which can be marched in time using implicit techniques.

#### $k-\epsilon$ Equations

The  $k-\epsilon$  model used here is developed by Launder and Spalding [10]. The model equations already have a time derivative term and can be written in a form similar to the N-S equations (1).

$$\frac{\partial q_k}{\partial t} + \frac{\partial(f_{k1} + g_{k1})}{\partial x} + \frac{\partial(f_{k2} + g_{k2})}{\partial y} + S = 0 \quad (3)$$

where

$$q_k = \begin{bmatrix} k \\ \epsilon \end{bmatrix}, f_{k1} = \begin{bmatrix} uk \\ u\epsilon \end{bmatrix}, f_{k2} = \begin{bmatrix} vk \\ v\epsilon \end{bmatrix}$$

$$g_{k1} = \frac{1}{R_e} \begin{bmatrix} \mu_k \frac{\partial k}{\partial x} \\ \mu_\epsilon \frac{\partial \epsilon}{\partial x} \end{bmatrix}, g_{k2} = \frac{1}{R_e} \begin{bmatrix} \mu_k \frac{\partial k}{\partial y} \\ \mu_\epsilon \frac{\partial \epsilon}{\partial y} \end{bmatrix}$$

$$S = \frac{1}{R_e} \begin{bmatrix} P - \epsilon R_e \\ C_1 \frac{\epsilon}{k} P - C_2 \frac{\epsilon^2}{k} R_e \end{bmatrix},$$

and

$$\mu_k = (\mu + \mu_t/\sigma_k), \mu_\epsilon = (\mu + \mu_t/\sigma_\epsilon)$$

where  $k$  is turbulent kinetic energy,  $\epsilon$  is turbulent dissipation, and  $\mu_t$  is the eddy viscosity.  $P$  represents the production of kinetic energy and the following form of it is used here:

$$P = \mu_t(u_y^2 + v_x^2 + 2u_y v_x)$$

Here  $f_{k1}$  and  $f_{k2}$  are convective terms and  $g_{k1}$  and  $g_{k2}$  are viscous diffusion terms.  $S$  is a source term added to the equations which models the production and dissipation of turbulent kinetic energy.

The  $k-\epsilon$  model still employs the eddy viscosity/diffusivity concept as it relates eddy viscosity to the kinetic energy and dissipation by

$$\mu_t = C_\mu \frac{k^2}{\epsilon} R_e \quad (4)$$

This eddy viscosity is then used to create an effective viscosity  $(\mu + \mu_t)$  which replaces  $\mu$  in the N-S equations (1). To implement the above turbulence model the following constants are specified as given in Ref. [10]:  $\sigma_k = 1.0$ ,  $\sigma_\epsilon = 1.3$ ,  $C_1 = 1.44$ ,  $C_2 = 1.92$ , and  $C_\mu = 0.09$ .

Because the N-S and  $k-\epsilon$  equations are similar the same numerical technique has been used for both sets of equations.

#### Solution Procedure

The N-S and the  $k-\epsilon$  equations contain both first derivative convective terms and second derivative viscous terms. The viscous terms are numerically well-behaved terms and central differencing is used. An upwind differenced TVD scheme was used for differencing the convective part of the

equations. This upwind differenced scheme gives third-order accuracy without any artificial dissipation terms being added to the equations. Details of how this discretization method is applied to the N-S equations for incompressible flows can be found in Gorski [8].

The equations are solved in an implicit coupled manner using approximate factorization. The implicit sides of the equations (the sides in which the values at the grid points are unknown) are discretized with a first-order accurate upwind scheme for the convective terms. This creates a diagonally dominant system which requires the inversion of block tri-diagonal matrices. The implicit sides of the equations are only first-order accurate but the final converged solution has the higher order of accuracy of the explicit sides of the equations (the sides in which the values at the grid points are known already).

An important quality of any scheme is its convergence rate. The diagonal dominance of the present method allows large time steps to be used for fast convergence. A spatially varying time step was also implemented but not used in this case.

The solution starts with initial estimates for the kinetic energy and dissipation fields. Here, a calculation with the Baldwin-Lomax [11] turbulence model provides the estimates. The N-S equations and the  $k-\epsilon$  model equations are iterated in pseudo-time until convergence is obtained. The N-S equations are solved to the wall with proper no-slip boundary conditions for all cases. With the Baldwin-Lomax turbulence model, the Van Driest mixing-length model takes care of the near-wall region. The  $k-\epsilon$  model however needs approximation as the flow physics in the near-wall sublayer ( $y^+ \leq 15$ ) is not well represented by the standard  $k-\epsilon$  equations. This DTNS code has a novel near-wall calculation technique [12] in which the N-S equations are solved to the wall, but near-wall empirical algebraic equations are used to calculate the kinetic energy and dissipation in this region.



## RESULTS AND DISCUSSION

The experimental data [2] for two 2-dimensional lifting foils are used as benchmarks for the N-S analysis. Both foils have an  $a=0.8$  meanline and NACA 16 Type II thickness distribution. These foils are plotted in Figs. 2.a and 3.b. The thick foil (also referred to as T1) has additional thickness from the midchord to the trailing edge as compared to the thin foil (also referred to as TN0). The wedge angle at the trailing edge of the TN0 foil is approximately 20 deg. That angle for the T1 foil is about 45 deg which results in a bevel shape on the suction side. The geometrical details are carefully documented in Ref. [2].

### Precision of Validation Data and Accuracy of Calculations

The data from Ref. [2] include: surface pressure distribution, wake mean velocity profiles, and turbulence characteristics such as Reynolds stresses, and power spectral density. Surface pressures were measured with a scanning valve system and a precision pressure transducer. Repeated measurements of the streamwise and normal velocity components yielded precision within 1% of the measured free-stream velocity at any position. And, the precision of the measured turbulence intensities and Reynolds shear stress was within 5% of the maximum measured values of a given wake profile. Wall shear stress measurement across the span, and hot-film measurement across the wake indicated that the mean flow approximates a 2-dimensional flow field well. Since the acoustic measurements of Ref. [1] were also performed with exactly the same foil models and set-up, the models had to be located with the aft 1/3 foil sticking outside of the test tunnel. Later pressure measurements in free 2-D jet agreed with the earlier measurements at most positions. The geometrical angle of attack for both foils was set at 0.68 deg. Due to the effect of the 2-D jet configuration on the foils, the corresponding free-field angles of attack were calculated in Ref. [2] to be -1.01 deg for foil TN0, and -1.54 deg for T1 foil. To calculate these angles, iterations were performed on the free-field lift coefficient using the free 2-D jet correction formula of Rae and

Pope [13] and the boundary layer program of Cebeci et al. [14]. All experimental measurements were reported without any "correction". The above free-field angles of attack were used only for analytical calculations to compare with the data.

For the N-S calculations, several grid sizes were used to establish computational accuracy. First of all, the boundaries were established by preliminary calculations to be at least 9 to 10 chord lengths upstream and normal to the foil so that free-stream condition applies. And the downstream boundary was set at 10 chords from the trailing edge to assume negligible streamwise gradients there. With the wake streamwise grid fixed at 40 points, different grid sizes were used: 121x40, 121x60, 181x60, 211x60, and 241x60. Convergence of the calculation with respect to the grid was established when the foil surface pressures changes within 0.2% of the free-stream pressure.

### Validation Results

The bench-mark cases were simulated as free-field 2-D flows with the following conditions:

- Reynolds number =  $2.25 \times 10^6$
- The angles of attack used were the same as the "corrected angles" used for boundary layer calculations in Ref. [2] (-1.01 deg for foil TN0, and -1.54 deg for foil T1).
- A 3-zone C-grid was used with 241 points around the body and 60 points normal to the body. The upstream boundary is 14 chord lengths from the leading edge. Top and bottom boundaries are 10 chords from the body. The downstream boundary is 10 chords from the trailing edge.
- The first grid point normal to body located at the trailing edge region is about  $1.4 \times 10^{-5}$  chord away which translates to  $y^+ \leq 5$ .
- The first axial grid point in the wake is  $1.5 \times 10^{-4}$  chord from the trailing edge which is about the same as the value used in Ref. [15] to resolve the streamwise gradient of mean velocity near the trailing edge.

Figs. 2.a and 2.b show the computed and measured pressure distributions for the TN0 foil, and the T1 foil, respectively. The

calculated pressure distributions are in reasonable agreement with the experimental data of Ref. [2], more so for the thin trailing edge foil than for the thick one. Note that the predicted loading for foil T1 is higher than the data (see Fig. 2.b), especially in the aft region. Therefore, the 2-D jet correction to the angles of attack may not be adequate. Several different angles of attack were tried for both foils and the resulting pressure distributions were not any better. One of the reasons for the discrepancy between the calculations and the data may be due to the wall effect. The foil chord length is 0.9144 m (3 ft), and the walls are about 2.667 chords away from the foil. And according to Rae and Pope [13], the wall/chord ratio should be at least 4 so that the measured lift coefficient is negligibly different from the free-field value. How the 2-D jet arrangement affects the foil surface pressure distribution is unknown. Also, recall in the previous section that the foils were set-up to be 2/3 in the tunnel test section and 1/3 outside. It is probable that this arrangement changes the pressure field of the foils more than the usual free 2-D jet arrangement. No rigorous reason can be found at this time to explain the above discrepancy. Other than the calculated pressure, the calculated flow separation location for the thick foil agrees well with the experimental value, which is around 96% chord on the suction side.

Figs. 3.a and 3.b show good match between the computed and measured velocity vectors for foil TN0, and foil T1, respectively. This match is relatively better than that of the foil surface pressure distribution. A possible explanation is that the surface pressure is more sensitive than the boundary layer flow, and the presumed wall effect is not significant for the boundary layer development. These velocity vectors are in the near-wake region, from 2% to 10% chord length downstream of the trailing edge. The wake deficit for the thick foil is larger than that for the thin foil. The thick foil also shows larger normal velocity component than the thin foil, which is due to the flow separation on the suction side of the thick foil. This flow separation, even though very mild, results in a recirculating region which the N-S code does not calcu-

late very well as seen in Fig. 3.b for the  $x/C=1.02$  station. A possible reason is that in the turbulence models local isotropy is assumed, i.e. all three velocity components contribute equally to the turbulent kinetic energy. This assumption is not met when there is flow separation. Further downstream in the wake, however, the calculated velocity vectors agree well with the data.

The N-S calculations of the turbulent kinetic energy  $k$  also match the data reasonably well. Figs. 4.a and 4.b show the calculated and measured  $k$  for the TN0 foil, and the T1 foil, respectively. The data are actually approximated because the  $z$ -component was not measured and only the  $x$ - and  $y$ - components were obtained from Huang et al. in Ref. [2]. According to the boundary layer data of Klebanoff [16], the  $z$ -component can be assumed to be approximately equal to the average of the  $x$ -component and the  $y$ -component. For the TN0 foil, the N-S calculation tends to over-predict  $k$  on the suction side consistently for all three wake stations. The pressure side, which looks almost flat, has better agreement. Therefore, this observation could signal that the turbulence models do not work well with a highly curved wall or large adverse pressure gradient. For the thick T1 foil, the mild flow separation on the suction side causes large over-prediction of the data for the wake station closest to the trailing edge,  $x/C=1.02$ . Further downstream in the wake, however, the calculated  $k$  agrees relatively better with the data. As discussed earlier in the previous paragraph for the velocity profiles, this observation could mean that the turbulence models do not work well even for mild flow separation. Also, this observation illustrates the elliptic nature of the N-S simulation, i.e. errors upstream do not necessarily propagate downstream and increase as seen in the boundary layer simulation in Ref. [2].

The N-S calculations of the Reynolds shear stress  $\overline{uv}$  also match the data reasonably well. Figs. 5.a and 5.b show the calculated and measured  $\overline{uv}$  for foil TNO, and foil T1, respectively. The magnitude of  $\overline{uv}$  is slightly over-predicted on the suction side for the TN0 foil. But the distribution shape is well predicted for both foils, i.e. the cal-

culated locations of the two extrema of  $\overline{uv}$  agree well with the data. This could be because the modelled  $\overline{uv}$  term is proportional to the local velocity gradient which is predicted very well. Again, we observe that the pressure side is predicted better than the suction side because it is almost flat. Also, the data for foil T1 in the closest wake station  $x/C=1.02$  are over-predicted due to the mild flow separation on the suction side. Both of these observations correlate with the previous ones for the velocity vectors and the turbulent kinetic energy.

#### Application of N-S Analysis to Section Design

With this successful validation of the N-S analysis, we can have confidence in using such a tool to develop new section shapes. Here, the design goal is to maximize the thickness of the section without too much flow separation. The baseline section, from an existing design, has an  $a=0.8$  meanline and a NACA 16 thickness distribution with thickness of 17.16 % chord and camber of 4.79 % chord. The design lift coefficient is approximately 0.68. For this study, the chosen Reynolds number is  $5 \times 10^6$  to match the conditions for 1/4-scale tests of naval propellers. The new section, shown in Fig. 6, is initially designed with the conformal mapping technique of Eppler-Somers [17]. The design approach is: 1) move the minimum pressure on the suction side further upstream, 2) start recovering the pressure with a steep gradient because the boundary layer is still strong after the minimum pressure point, and 3) decrease the adverse pressure gradient as the trailing edge is approached to avoid flow separation. After the initial design, a thin section is produced which has the three features stated above. As the desired pressure distribution is not input to this Eppler-Somers code, a final design is not easily obtained at this step. Also, the conformal mapping technique is based on the potential flow model and therefore can not account for the thickness effect accurately. The N-S analysis is used iteratively to obtain the final design. Two parameters are used in the iteration with the N-S analysis: thickness, and angle of attack. For simplicity, thin airfoil theory is used to calculate the "camber-versus-lift-coefficient" behavior of the new section. The criterion

for the final design is "no-separation" in the  $\pm 4$  deg around the design angle of attack with the thickness as high as possible. The  $\pm 4$  deg range is normally the fluctuation of angle of attack that a propeller section sees in straight-ahead operation.

After some iterations with the N-S analysis, the final design is produced, with the pressure distribution at design angle of attack (2.5 deg) shown in Fig. 6. The lift coefficient from this pressure distribution is approximately 0.68, the same as the baseline. The desirable characteristics for the boundary layer development are presented in this pressure distribution. Maximum suction peak is around 50% chord on the suction side; steep pressure recovery follows immediately, then the gradient becomes milder to minimize flow separation as the trailing edge is approached. Also, the pressure side distribution is rather flat over most of the surface; this should reduce the turbulent kinetic energy. The velocity vector plot in Fig. 7 shows attached flow on both the pressure side and suction side at design angle of attack. This attached flow field of the new section produces lower turbulent kinetic energy as seen in Fig. 8.a, and lower Reynolds shear stress as seen in Fig. 8.b when compared to the baseline section. This trend is more pronounced for the suction side than the pressure side. At this design lift for the baseline foil, the N-S analysis indicates some flow separation on the suction side which accounts for the high turbulence activity. And the pressure side of the new section has low turbulence activity because the pressure distribution there is almost flat over the entire surface. An undesirable feature of this new section is the thin trailing edge. This could prove harmful when structural analysis is performed even though care is taken during the designing to ensure minimum loading in that region. More details of the design process, and the comparison between the new section and the baseline can be found in Ref. [18].

#### CONCLUSIONS

In this paper, a N-S analysis is performed on the turbulent boundary layer and wake flows over lifting surfaces. This

analysis is performed as bench-mark calculations for 2 airfoils at high Reynolds number for which turbulent flow data are available. Overall agreement between data and calculations is reasonably good. There is a better match of the mean velocity than the turbulence stresses. A possible reason for this is the inability of the turbulence model to simulate accurately flows with strong adverse pressure gradient or flow separation. Since the normal stress data from Refs. [2,14] show that the streamwise turbulence intensity  $\overline{uu}$  is significantly larger (up to a factor of 2) than the transverse component  $\overline{vv}$ , assumptions of local isotropy should be reconsidered.

A new 2-dimensional airfoil section is developed by combining a conformal mapping technique with an iterative N-S analysis. Results show that the new section has better boundary layer characteristics, for the same lift coefficient, than the baseline. Since the design goal is to maximize thickness with minimum flow separation, this new section is not recommended for other applications in which high thickness is not needed. This particular new section will certainly have poor cavitation performance. Nevertheless, this paper illustrates that N-S analysis is very useful in guiding 2-D section design. The N-S analysis, however, can only give insight about the magnitude and the spatial distribution of the mean flow, and Reynolds stresses. The spectral behavior is entirely unknown. Until better turbulence models, numerical techniques, and computers become more easily accessible, the N-S analysis should only be used for final design fine-tuning or off-design predictions as done in this case. From the results, further work is recommended to: 1) simulate the wall in the N-S calculation of the same 2-dimensional foils to establish the significance of the wall effect; 2) develop a new section with thicker trailing edge; 3) develop a series of new sections with different locations of the minimum pressure point on the suction side and experimentally evaluate them in the same manner as in Refs. [1,2]; and 4) concentrate on the development of turbulence models that can calculate more accurately turbulent flows with strong adverse pressure gradient, and even separation.

## ACKNOWLEDGMENT

The authors would like to thank Drs. Tommy Huang, Pat Purtell, and Yu-Tai Lee (DTRC) for making available the validation data, and Dr. Rod Coleman (DTRC) for the mesh generation code. The guidance and support of Dr. Frank Peterson (DTRC) for the New Section work is much appreciated. And the New Section work is supported by the Office of Naval Technology under work unit number 1-1506-060-34 for FY-90.

## REFERENCES

1. Gershfeld, J., W.K. Blake, C.W. Kinsley, "Trailing Edge Flows and Aerodynamic Sound," AIAA, ASME, ASCE, SIAM, APS 1st National Fluid Dynamics Congress, Cincinnati, Ohio, paper 88-3826-CP, July 1988.
2. Huang, T.T., L.P. Purtell and Y.T. Lee, "Turbulence Characteristics of Trailing-Edge Flows on Thick and Thin Hydrofoils," presented at the 4th Symposium of Numerical and Physical Aspects of Aerodynamics Flows, CSU Long Beach, CA, Jan 16-19, 1989.
3. Sung, C.-H., "An Explicit Runge-Kutta Method for 3-D Turbulent Incompressible Flows," DTNSRDC/SHD Report 1244-01, July 1987.
4. Harten, A., "High Resolution Schemes for Hyperbolic Conservation Laws," J. Comp. Phys., Vol. 49, pp. 357-393, 1983.
5. Tennekes, H. and Lumley, J.L. 1972. A First Course in Turbulence. MIT Press, Cambridge, MA.
6. Bernard, P. S. and Berger B.S., "A Method for Computing Three-Dimensional Turbulent Flows," SIAM J. Appl. Math., Vol. 42, 1982, pp. 453-470.
7. Coleman, R.M., "Inmesh: An Interactive Program for Numerical Grid Generation," DTNSRDC-85/054, 1985.
8. Gorski, J.J., "Solutions of the Incompressible Navier-Stokes Equations Using an Upwind Differenced TVD Scheme," 11th Int. Conf. on Num.



Methods in Fluid Dynamics, Williamsburg, Va., Jul 1988.

9. Chorin, A.J. "A Numerical Method for Solving Incompressible Viscous Flow Problems," J. Comp. Phys., Vol. 2, pp. 12-26, 1967.

10. Launder, B.E. and Spalding, D.B., "The Numerical Computation of Turbulent Flows," Computer Methods in Applied Mechanics and Engineering, Vol. 3, pp. 269-89, 1974.

11. Baldwin, B.S. and Lomax, H., "Thin Layer Approximation and Algebraic Model for Separated Turbulent Flows," AIAA 16th Aerospace Sciences Meeting, Huntsville, Al., Jan. 1978.

12. Gorski, J.J., "A New Near-Wall Formulation for the k-e Equations of Turbulence," AIAA Paper 86-0556, 1986.

13. Rae, W.H., Jr., and A. Pope, Low-Speed Wind Tunnel Testing, John Wiley & Sons, New York, 1984, p.361.

14. Cebeci, T., R.W. Clark, K.C. Chang, N.D. Halsey and K. Lee, "Airfoils with Separation and the Resulting Wakes," Jou. Fluid Mech., Vol. 163, 1986, pp.323-47.

15. Mehta, U., K.C. Chang, and T. Cebeci, "A Comparison of Interactive Boundary-Layer and Thin Layer Navier-Stokes Procedures," Num. and Phys. Aspects of Aero. Flows III, Chapter 11, p. 198, 1985.

16. Klebanoff, P., "Characteristics of Turbulence in a Boundary-Layer with Zero Pressure Gradient," NACA TN 3178, 1954.

17. Eppler, R. and Somers, D.M., "Low Speed Airfoil Design and Analysis," Advanced Technology Airfoil Research Conference, Langley Research Center, NASA, Hampton, Va., Mar 1978.

18. Nguyen, P.N., "A Design Method for Boundary-Layer Control of 2-D Lifting Surfaces," DTRC/SHD 1262-04, 1990 (in review).



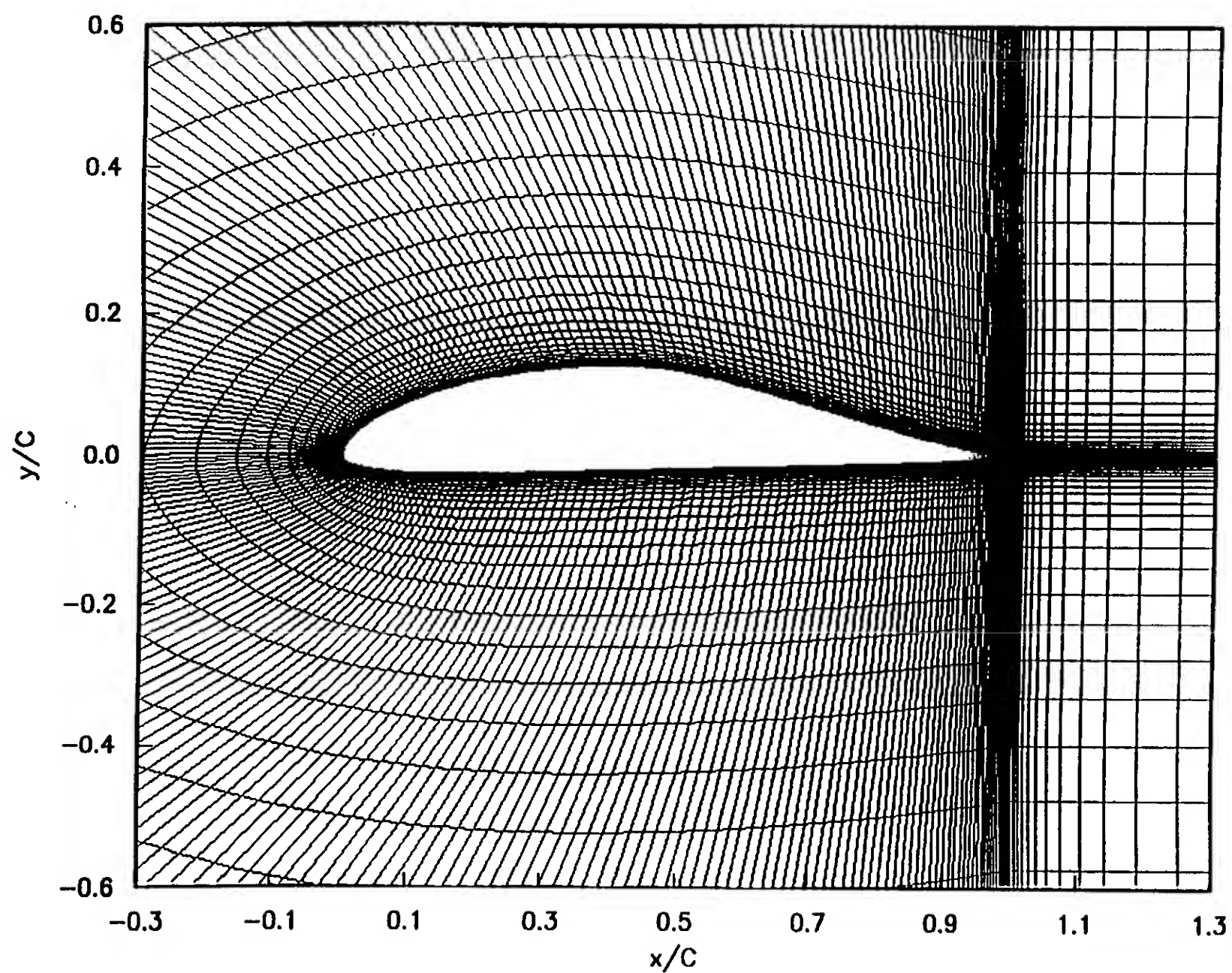


Figure 1. C-type grid with 3-zone structure for a lifting surface

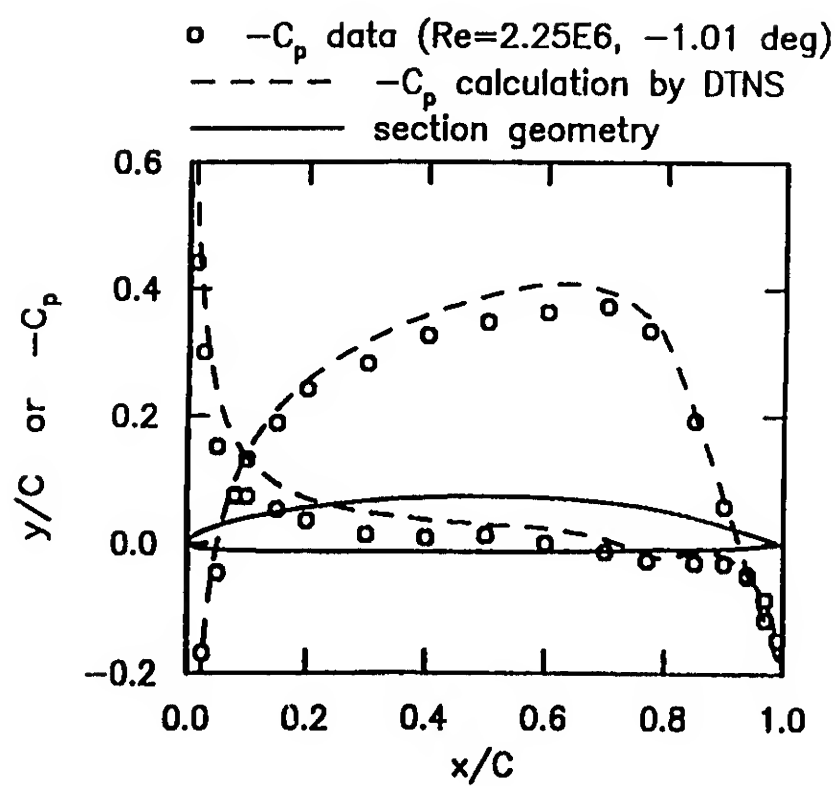


Figure 2.a) Pressure distribution for the thin section (data from Ref. 2)

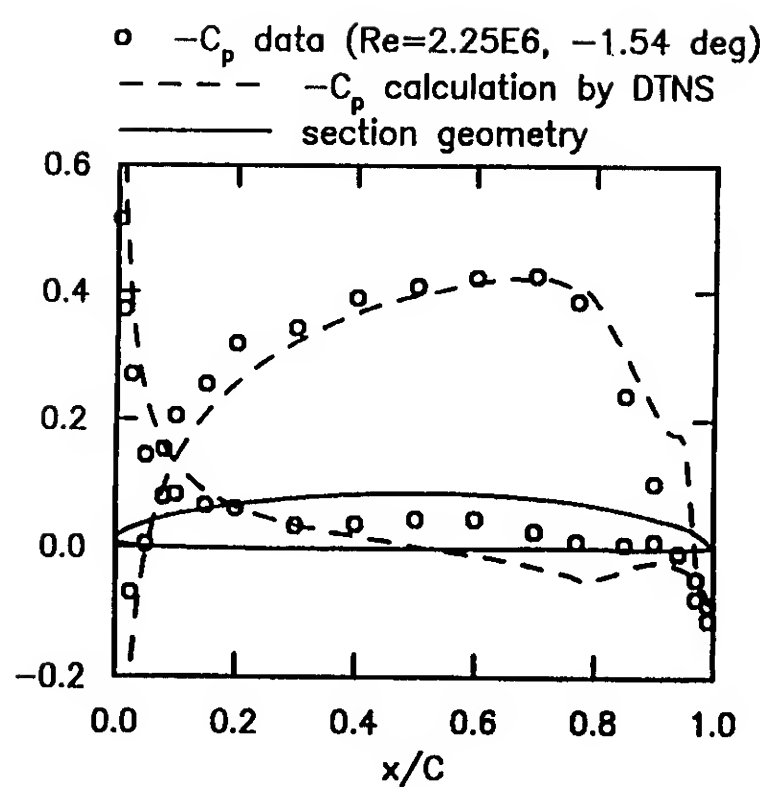


Figure 2.b) Pressure distribution for the thick section (data from Ref. 2)

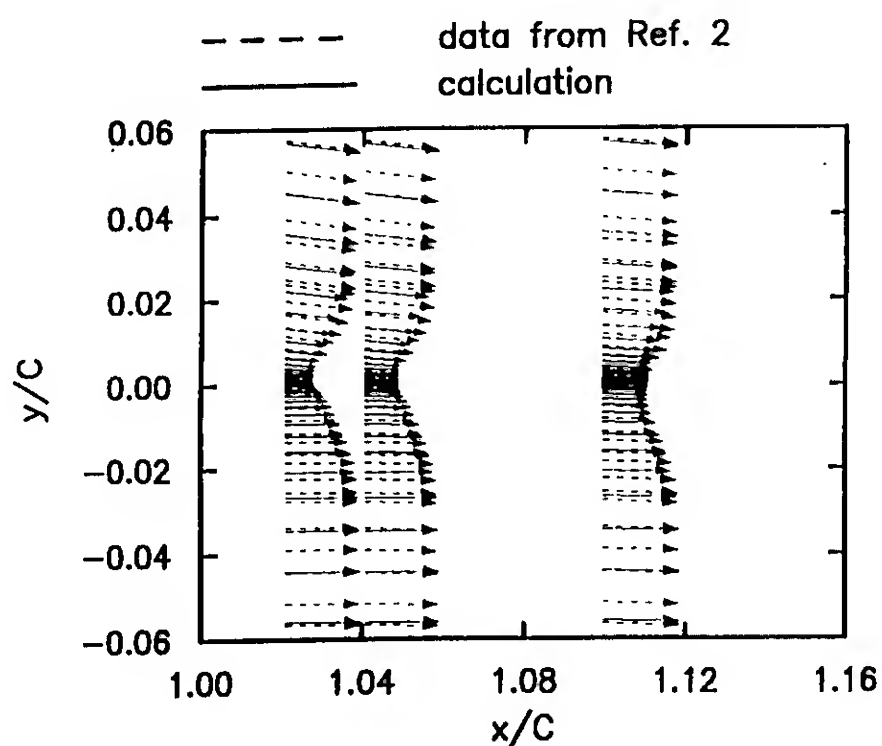


Figure 3.a) Velocity vector data and DTNS calculations for the thin section

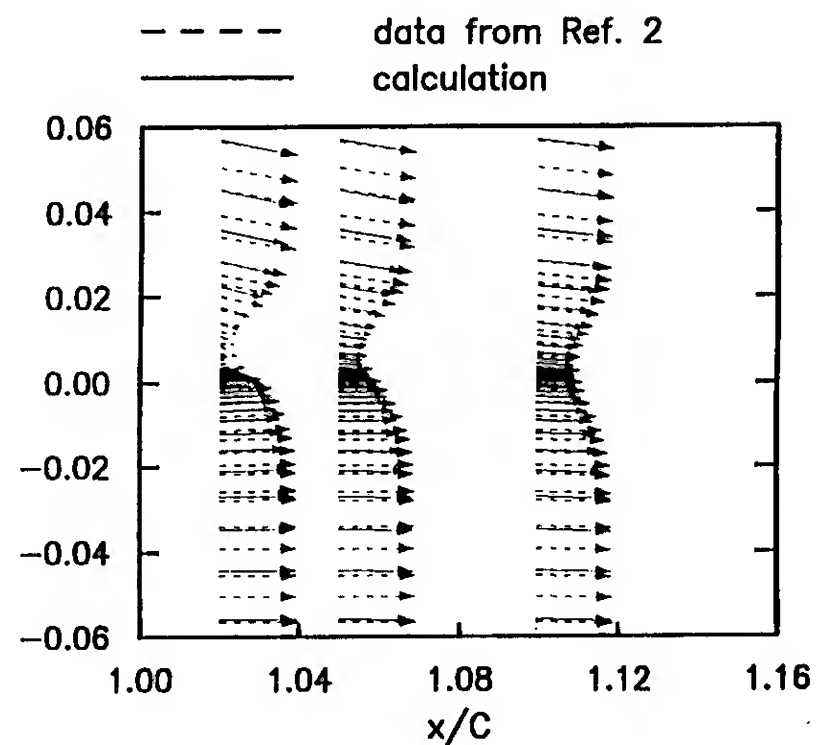


Figure 3.b) Velocity vector data and DTNS calculations for the thick section

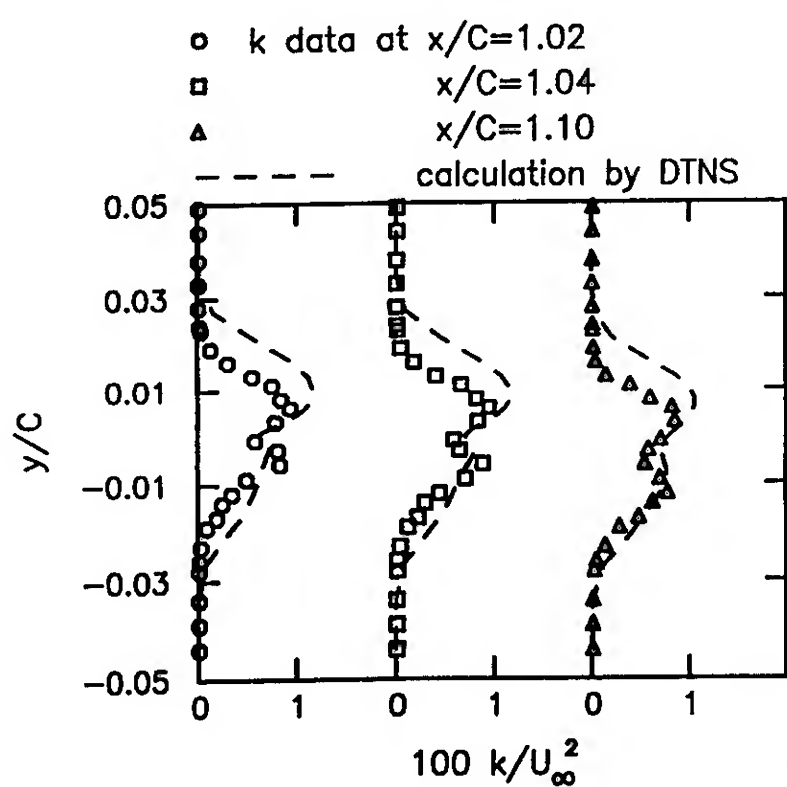


Figure 4.a) Profiles of turbulent kinetic energy for the thin section (data from Ref. 2)

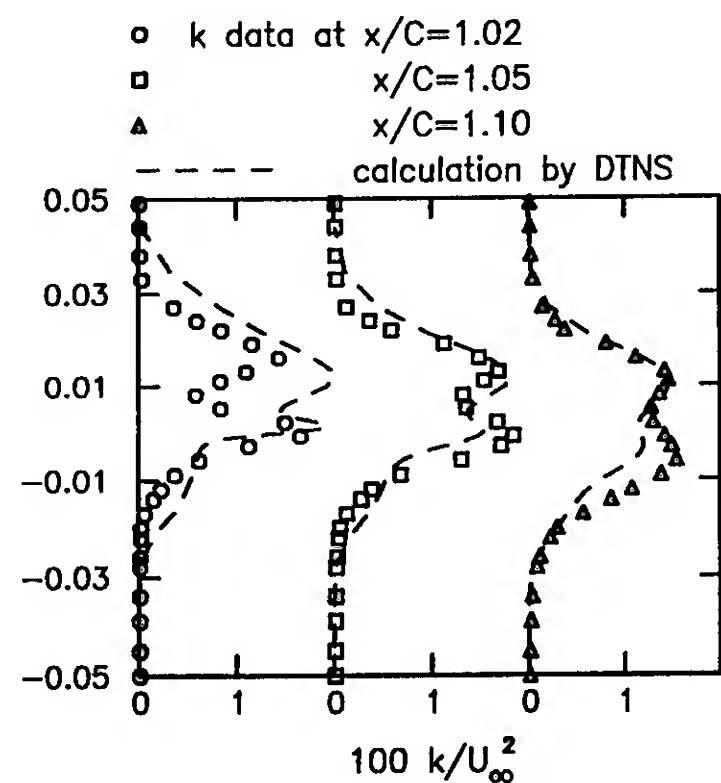


Figure 4.b) Profiles of turbulent kinetic energy for the thick section (data from Ref. 2)

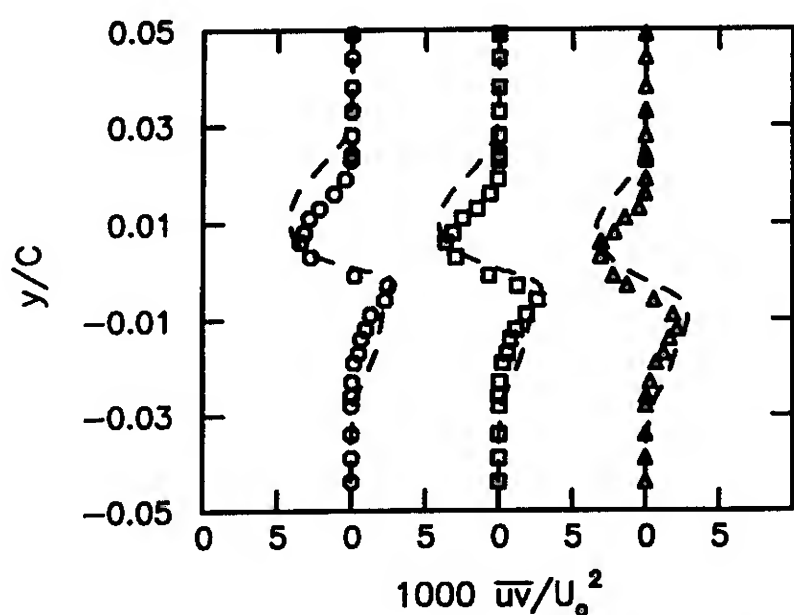


Figure 5.a) Profiles of Reynolds shear stress for the thin section (legend in Fig. 4.a)

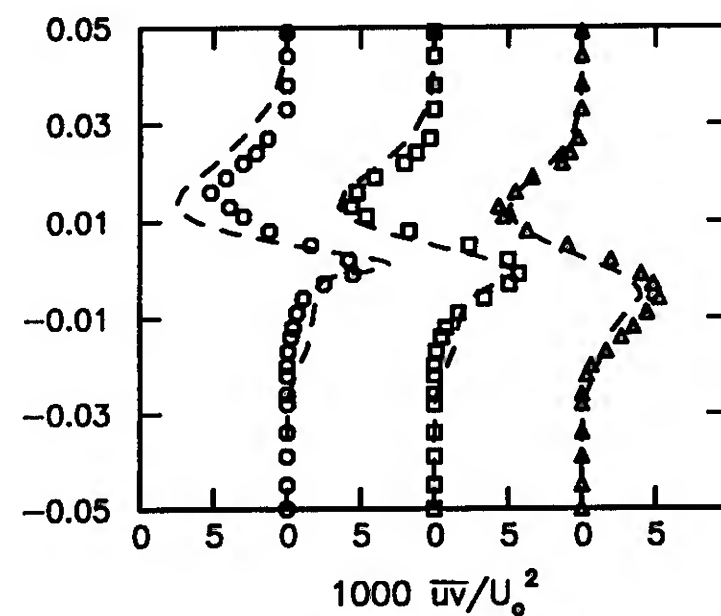


Figure 5.b) Profiles of Reynolds shear stress for the thick section (legend in Fig. 4.b)

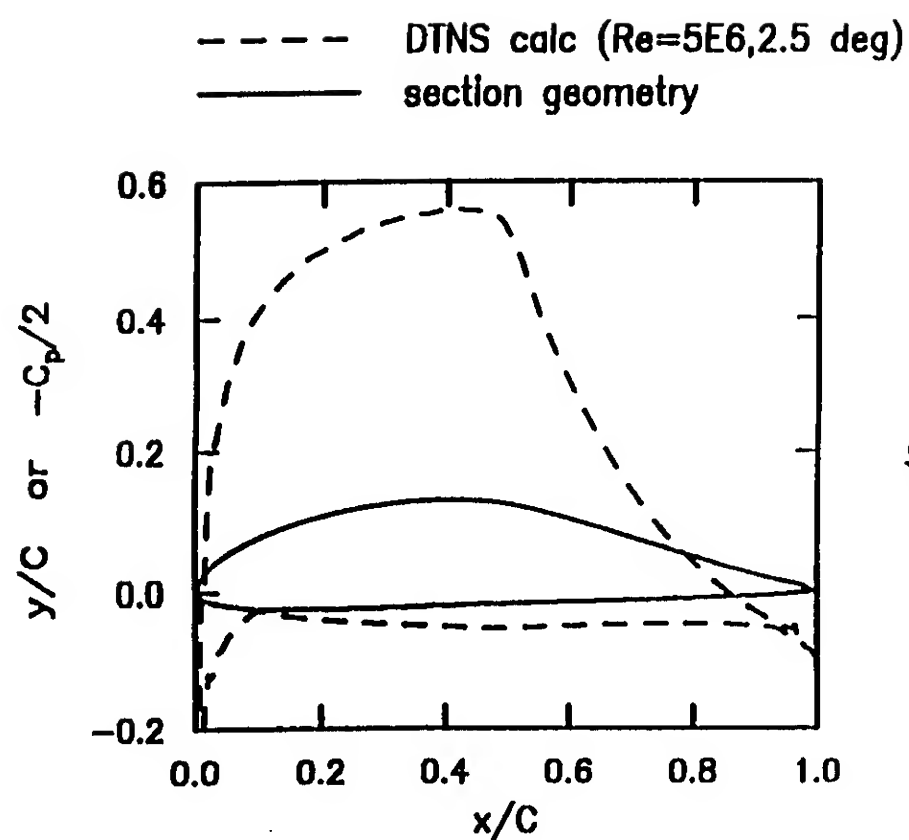


Figure 6. Pressure distribution for the new section

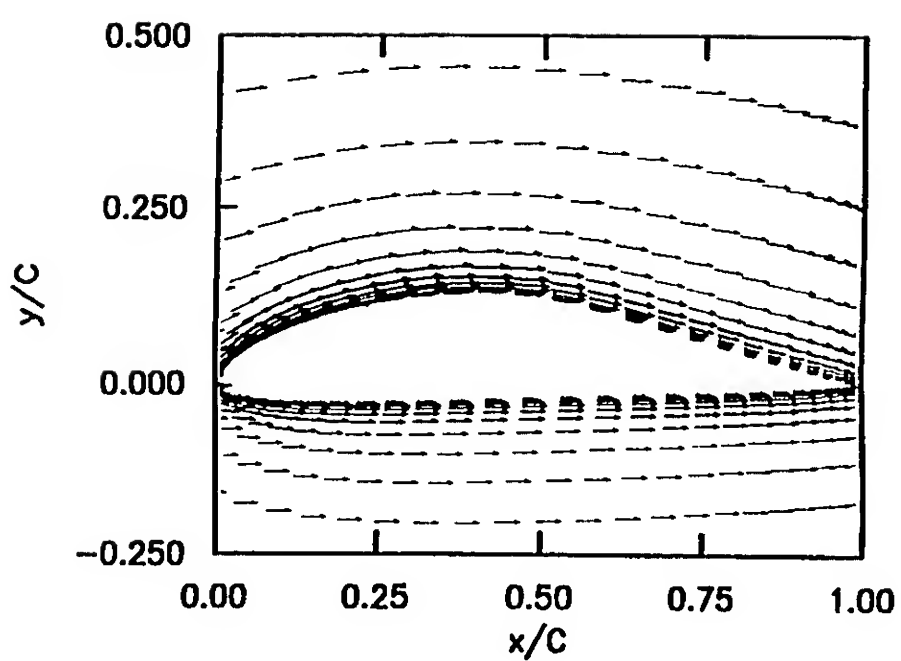


Figure 7. Velocity vector calculations for the new section

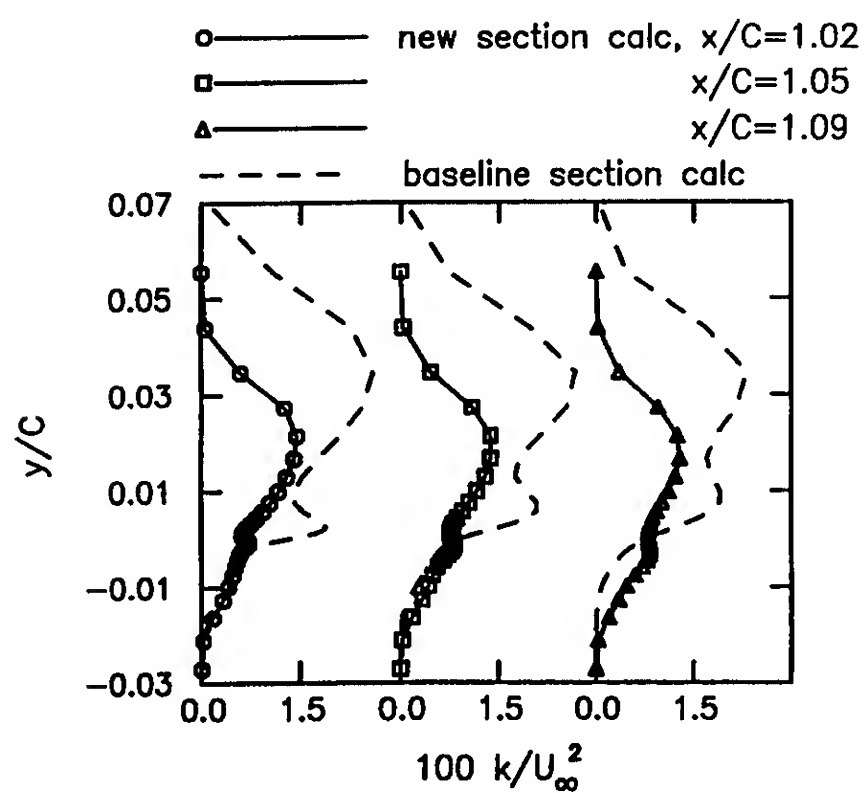


Figure 8.a) Profiles of turbulent kinetic energy for the baseline and the new section

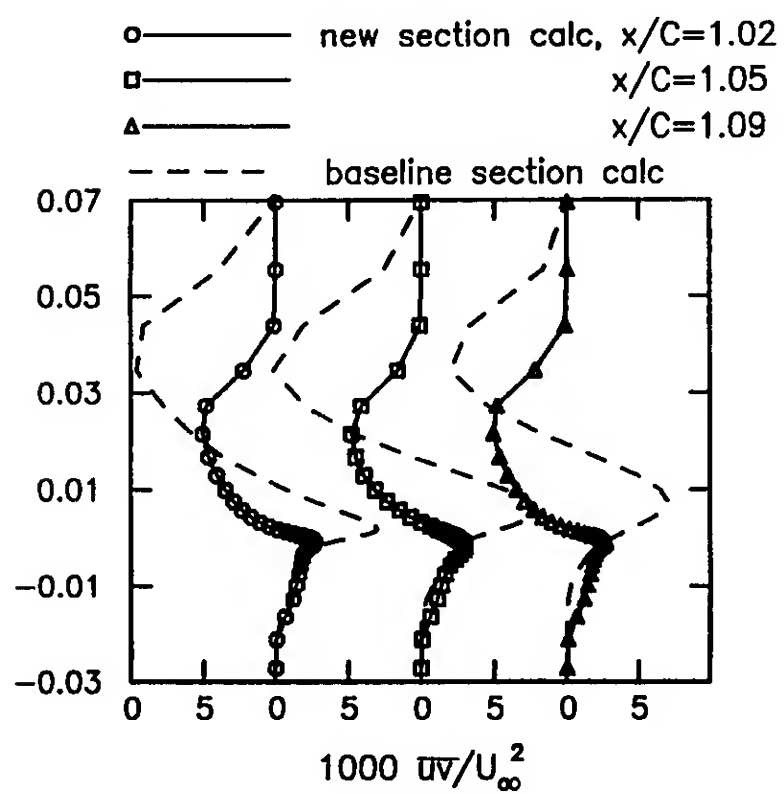


Figure 8.b) Profiles of Reynolds shear stress for the baseline and the new section

## DISCUSSION

Wolfgang Faller  
Sulzer Escher Wyss, Germany

For your comparison between experiment and 2-D N-S calculation, the computational domain used is infinite. Would a closer modelling of the actual experimental configuration improve the correlation, e.g.,  $C_p$  distribution and B.L. development?

## AUTHORS' REPLY

Modelling of the foil and wall configuration would possibly lead to better match of the bench-mark calculations to the hydrodynamics data. Plan is underway to implement a grid structure necessary for this study.

## DISCUSSION

Ali H. Nayfeh  
Virginia Polytechnic Institute and State University, USA

1. How sensitive is the pressure distribution of the new section to variation in the angle of attack? 2. How sensitive is the designed shape to the turbulence model? 3. How much is the drag reduced by the new section?

## AUTHORS' REPLY

1. The new section does not have flow separation in the  $\pm 4$  deg. range around the design angle of attack. 2. Preliminary study indicates that the flow solution converges to approximately the same pressure distribution for both the Baldwin-Lomax and the k- $\epsilon$  turbulence models. 3. Drag is not computed in this study as the current project focuses on the turbulence activity. The drag of the new section is included in the plan for future investigation.

## DISCUSSION

Philippe Genoux  
Bassin d'Essais des Carènes, France

1. Is your model able to take in account turbulent levels of the incoming flow? 2. What would become of the turbulent energy levels when the profile is placed in incoming flow?

## AUTHORS' REPLY

1. The code currently does not have a model for the free-stream turbulence. 2. When placed in flow with free-stream turbulence, the turbulent kinetic energy level of the new section would likely increase (as compared to incoming flow without turbulence). The redistribution and the magnitude of the increase in turbulence energy would need to be calculated with a proper turbulence model.

## DISCUSSION

Hyoung-Tae Kim  
The University of Iowa, USA (Korea)

First, I want to know if there is any reason not to show the distribution of the shear stress on the surface of the foil section? Secondly, I want to point out that the "low turbulence activity" simulated in the computation doesn't necessarily mean the new foil section has a lower drag than the baseline section.

## AUTHORS' REPLY

The study focuses on the turbulence activity in the near-wake region of lifting surfaces. The drag itself is, however, included in the plan for future investigation. The authors agree with the discussor on his second point. No claim is made about drag reduction in the paper. The resistance of the new section to flow separation only provides for higher lift at the same angle of attack as the baseline section. And the low turbulence activity provides for lower fluctuating pressure on the trailing edge of the section.

# A Three-Dimensional Theory for the Design Problem of Propeller Ducts in a Shear Flow

J. Falcao de Campos

(Maritime Research Institute Netherlands, The Netherlands)

## ABSTRACT

A linearised theory of the three-dimensional steady interaction between a ducted propeller system and a radially and circumferentially sheared axial onset flow is presented. Following duct lifting surface theory the duct is modelled by a distribution of pressure dipoles and sources on a reference cylinder to represent the effects of loading and thickness. An actuator disk model is used to represent the effects of propeller loading. An integral equation for the pressure disturbance is derived which may be applied to treat both the effects of loading and thickness. The potential and shear interaction components of the disturbance pressure are treated separately and a computational scheme is applied to solve the integral equation for the interaction pressure. The results of sample calculations for the effects of duct loading in axisymmetric and non-axisymmetric wakes are presented and discussed.

## NOMENCLATURE

$A_{mn}, B_{mn}$	- Functions of shear parameters
$a, b$	- Shear parameters
$c$	- Duct semichord
$(\vec{e}_x, \vec{e}_y, \vec{e}_z)$	- Unit vectors, Cartesian coordinates
$(\vec{e}_x, \vec{e}_r, \vec{e}_\theta)$	- Unit vectors, cylindrical coordinates
$F_m$	- Fourier integral in the downwash calculation
$\vec{F}$	- External force field
$f$	- Duct camber
$G_{mn}$	- Kernel function
$\bar{G}_{mnij}, G_{mnij}$	- Matrix elements
$G_{11}, G_{12}, G_{21}, G_{22}$	- Functions in degenerate kernel function
$H(x)$	- Heaviside unit step function
$h_1, h_2, h_3, h_4$	- Functions of shear parameters for duct loading and thickness

$I_m, K_m$	- Modified Bessel functions of order $m$
$i$	- $\sqrt{-1}$ , index of radial node
$i_1, i_2, i_p, k_p$	- Functions of shear parameters for propeller loading
$j$	- index of radial node
$k$	- Parameter in x-wise Fourier transform
$L(\omega)$	- Function in downwash calculation
$P( \eta )$	- Downwash kernel function
$p, \tilde{p}$	- Pressure, respectively its x-wise Fourier transform
$\Delta p, \Delta \tilde{p}$	- Strength of pressure dipole, respectively its x-wise Fourier transform
$Q_{m+1/2}$	- Legendre function of second kind and half order
$q$	- Strength of source distribution
$R$	- Radius, distance between two joints
$\bar{r}$	- Transformed radius
$S$	- Right-hand side of Poisson-type equation
$T$	- Function of source distribution
$t$	- Duct thickness
$\vec{U}, U$	- Undisturbed axial velocity, respectively its modulus
$U_0$	- Reference velocity
$U_1, U_2, U_3, U_4$	- Parameters in analytical defined wake
$\vec{u}$	- Disturbance velocity
$(u, v, w)$	- Axial, radial and circumferential components of disturbance velocity
$\vec{V}$	- Fluid velocity
$V_m^{(0)}$	- Influence function for radial downwash velocity on the duct
$\bar{v}$	- Average radial velocity induced on the duct
$\Delta v$	- Radial velocity jump on the duct
$(x, y, z)$	- Cartesian coordinates
$(x, r, \theta), (\xi, \sigma, \phi)$	- Cylindrical coordinates

J.A.C. Falcão de Campos, MARIN, P.O. Box 28, 6700 AA Wageningen, The Netherlands



$\alpha$	- Conical angle
$\Delta$	- Expansion rate
$\delta(x)$	- Dirac delta function
$\varepsilon$	- Small parameter
$\eta$	- Normalised axial distance on the duct
$\lambda$	- Parameter of x-wise Fourier transform
$\rho$	- Fluid density
$T$	- Integral operator
$\tau, \nu$	- Integration volumes
$\psi$	- Right-hand side of integral equation
$\omega$	- Argument of Legendre functions

#### Subscripts

d	- Refers to duct
m, n	- Index of circumferential harmonics
p	- Refers to propeller
t	- transverse component

#### Superscripts

(0)	- Refers to potential, induction part
(1)	- Refers to shear interaction part

## 1. INTRODUCTION

Ducted propellers are a well-established means of ship propulsion. It is well-known, [1] that the use of a ducted propeller with an accelerating type of duct improves the efficiency of the propulsor in case of heavy loading. Also the use of a decelerating type of duct may be beneficial to reduce the risk of cavitation of the propeller. A large number of conventional duct designs, which have been most successfully applied in practice [2]-[1], are axisymmetric but the application of non-axisymmetric ducts has also been subject to investigation both experimentally [1] and theoretically [3]-[4]. These ducts have been applied to reduce the non-uniformity of the inflow to the propeller in the ship's wake leading to improved performance from the point of view of efficiency, cavitation and vibrations.

For the design of ducted propellers a number of analytical tools have become available along the years. Early ducted propeller theories [5]-[6] were based on linearised annular airfoil theory for the singularity representations of the effects of duct loading and thickness, in combination either with an infinite blade number model (actuator disk) or with a finite bladed lifting line model of the propeller. An extensive review of these theories was made by Weissinger and Maass in ref. [7]. It is interesting to notice that the truly inverse methods published to date for designing axisymmetric propeller ducts are based on these theories. The methods determine the duct geometry (in the presence of a time averaged propeller induced velocity field) for

specified duct pressure distribution [8] or given load and thickness distributions [9]. These methods suffer from the drawback that it is not possible to guarantee a priori that the given pressure or load distribution will lead to an acceptable duct geometric shape. Nevertheless, those inverse methods were of great assistance in designing famous ducted propeller systematic series, such as the ones published in references [1] and [10]. Often the final duct shapes needed to be modified to meet practical requirements.

Following the developments in the numerical methods for the calculation of potential flow on lifting bodies, methods for the hydrodynamic analysis of ducted propellers evolved to a greater degree of sophistication. More accurate panel representations of the duct geometry have been employed for axisymmetric flow [11] and, more recently, for three-dimensional flow [12]-[13]. These last methods for steady three-dimensional analysis have concentrated on the complex interaction between propeller and duct in uniform inflow by incorporating lifting surface or panel representations of the propeller blades. Also complete unsteady potential flow analysis [14] of the ducted propeller system has been attempted.

The methods mentioned previously are restricted to potential flows. In reality the ducted propeller operates in the highly non-uniform flow endowed with vorticity in the ship's wake and the interaction with this flow is an important field of research in propulsor design. In dealing with this problem the potential flow methods have retained completely their usefulness through the introduction of the concept of the effective onset velocity, which is defined as the total velocity minus the potential velocity induced by the propulsor. The effective onset velocity has to be computed by some (viscous or inviscid) rotational model for the propulsor-hull interaction. Examples of the inviscid approach to the computation of the effective velocity for conventional propellers in axisymmetric flow can be found in [15]-[17].

There is a considerable amount of references in the turbomachinery literature dealing with the problem of solving approximate forms of the Euler equations for determining the inviscid disturbance flow to parallel shear flows, as can be found in the survey given by Hawthorne [18]. In particular, the large shear - small disturbance approximation, applied along the lines set in the classical works of Kármán and Tsien [19] for a lifting line and of Lighthill [20] for a simple source, have been used to fundamentally study the effects of shear in the flow around aerodynamic shapes [21]-[22], including the annular airfoil [23]-[24]. For an infinitely bladed propeller, modelled by an actuator disk, the same approach has been followed to investigate the effects of shear in the incoming flow in the axisymmetric case [25]-[26], plane flow [27] and three-dimensional flow

[28]. The latter reference includes the effects of shear of a radially and circumferentially varying axial inflow to the actuator disk and incorporates some non-linear terms in the equations of motion adequate for extending the method for heavier loadings.

For ducted propellers the effects of shear have been investigated in [11] using a numerical vortex panel method in axisymmetric flow. Recently, Lee [29]-[30] presented a linearised analysis of the ducted propeller system in axisymmetric shear flow suitable for solving the duct design problem in the presence of the propeller. He showed that the shear significantly affects not only the duct camber and ideal angle of attack but also the duct induced velocity at the propeller.

The objective of the present paper is to present a three-dimensional theoretical analysis of the steady interaction between a ducted propeller and a radially and circumferentially sheared axial inflow. Consistent with the steady flow assumption, an infinitely bladed propeller (actuator disk) is considered. Although not strictly necessary to the analysis, an axisymmetric loading over the propeller disk will be assumed in this paper for simplicity. The duct loading and thickness may vary in the circumferential direction. The theory may be used in the analysis of a ducted propeller with a given duct shape but it will be most readily applied (non-iteratively) in the inverse mode i.e. to determine the duct section camber and angle of attack for given thickness and loading distributions.

As in the method followed by Lee [29] in the axisymmetric case, the analysis developed herein approaches the solution of the problem from the theory of the Poisson equation to derive a system of coupled integral equations for the disturbance pressure harmonics. However, some essential differences with the formulation used by Lee are noteworthy: First, a single type of integral equation in the disturbance pressure is used throughout, encompassing both the effects of loading and thickness. Second, by separating shear interaction effects from induction effects, the method recovers the potential formulation of the duct lifting surface theory, see for instance [6], [31]-[33], and actuator disk theory [34], while, at the same time, the presence of any singularities of the pressure field are removed from the problem for the interaction with shear.

The paper is organised as follows: In section 2 the theoretical analysis is presented. Section 3 deals with the numerical procedures employed so far to solve the integral equation and compute the velocity field. In section 4 the results of sample calculations illustrating the effects of shear in the velocity field due to a non-symmetric duct in a wake field are presented and discussed. The paper closes with some remarks regarding the basic limitations of the method and its further development.

## 2. THEORETICAL ANALYSIS

### 2.1. Equations of Motion for General Steady Disturbances to a Shear Flow

We start by deriving the linearised Euler equations for the steady flow of an inviscid and incompressible fluid in the presence of an external force field. Anticipating the use of sources and sinks to represent thickness effects, we will assume the rate of expansion to be zero except at the points where such singularities will be present.

The continuity equation for an incompressible fluid reads, see for instance ref. [35]:

$$\nabla \cdot \vec{V} = \Delta, \quad (1)$$

where  $\vec{V}$  is the fluid velocity and  $\Delta$  is the local rate of expansion.

The Euler equations for the steady flow of an incompressible ideal fluid are

$$(\vec{V} \cdot \nabla) \vec{V} + \nabla \left( \frac{p}{\rho} \right) = \frac{\vec{F}}{\rho}, \quad (2)$$

where  $p$  is the pressure,  $\rho$  the fluid density and  $\vec{F}$  the external force field per unit volume.

We introduce a Cartesian coordinate system  $(x, y, z)$ , with unit vectors  $(\vec{e}_x, \vec{e}_y, \vec{e}_z)$  and a cylindrical coordinate system with unit vectors  $(\vec{e}_r, \vec{e}_\theta, \vec{e}_z)$ , Fig. 1. We consider a radially and circumferentially non-uniform axial flow  $\vec{U}(r, \theta)$ , independent of the axial coordinate, to be disturbed by the presence of the ducted propeller. Let  $\vec{u}$  denote the disturbance velocity so that the fluid velocity may be written as

$$\vec{V}(x, r, \theta) = U(r, \theta) \vec{e}_x + \vec{u}(x, r, \theta). \quad (3)$$

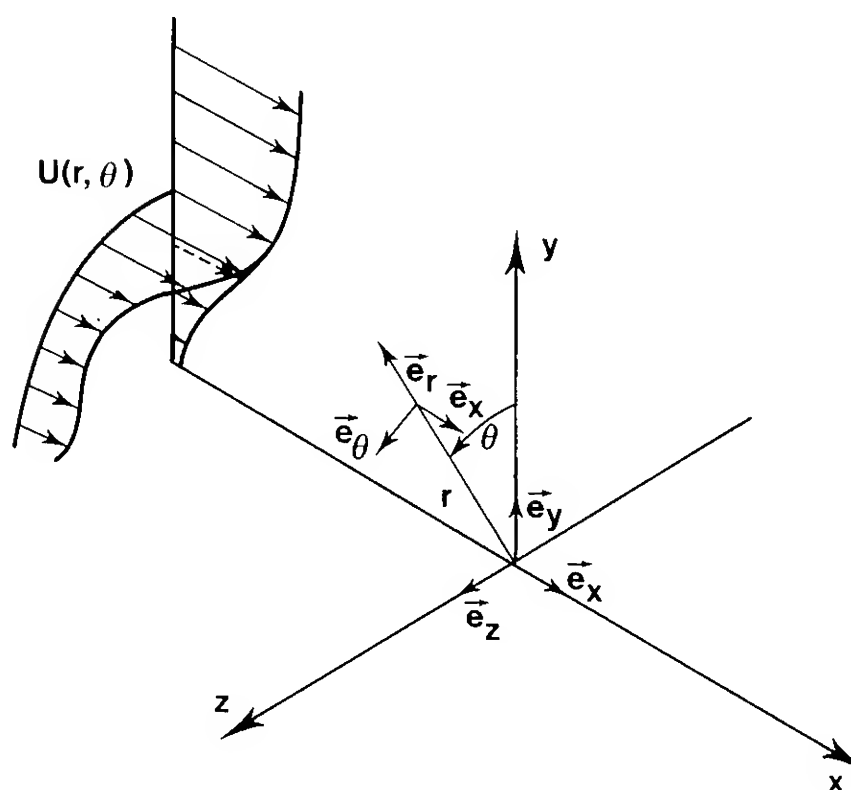


Fig. 1. Coordinate system and axial inflow.

The equations of motion (2) may be linearised by assuming the disturbance velocity to be small, say of  $O(\varepsilon)$ , in comparison with the undisturbed velocity  $\vec{U}=0(1)$ . Substituting eq. (3)<sub>2</sub> into (2) and neglecting squared terms of  $O(\varepsilon^2)$  in the disturbance velocities we obtain

$$U \frac{\partial \vec{u}}{\partial x} + (\vec{u} \cdot \nabla)(U \vec{e}_x) + \nabla \left( \frac{P}{\rho} \right) = \frac{\vec{F}}{\rho}, \quad (4)$$

since  $(U \vec{e}_x \cdot \nabla)(U \vec{e}_x) = U \partial(U \vec{e}_x)/\partial x = 0$ .

We further decompose the disturbance velocity into its axial and transverse components

$$\vec{u} = u \vec{e}_x + \vec{u}_t, \quad (5)$$

with  $\vec{u}_t = -\vec{e}_x \times (\vec{e}_x \times \vec{u}) = v \vec{e}_r + w \vec{e}_\theta$ . With (5) we find that

$$\begin{aligned} (\vec{u} \cdot \nabla)(U \vec{e}_x) &= u \frac{\partial}{\partial x} (U \vec{e}_x) + (\vec{u}_t \cdot \nabla)(U \vec{e}_x) = \\ &= \vec{e}_x (\vec{u}_t \cdot \nabla U) \end{aligned}$$

and (4) may be written in the form

$$U \frac{\partial \vec{u}}{\partial x} + \vec{e}_x (\vec{u}_t \cdot \nabla U) + \nabla \left( \frac{P}{\rho} \right) = \frac{\vec{F}}{\rho}. \quad (6)$$

Taking the divergence of (6) and using (1) we obtain

$$\nabla^2 \left( \frac{P}{\rho} \right) + 2 \frac{\partial}{\partial x} (\vec{u}_t \cdot \nabla U) = \nabla \cdot \left( \frac{\vec{F}}{\rho} \right) - U \frac{\partial \Delta}{\partial x}. \quad (7)$$

We may eliminate the transverse velocity component  $\vec{u}_t$  between (6) and (7) to obtain a single equation for the pressure. To do so we first take the transverse vector component of (6)

$$U \frac{\partial \vec{u}_t}{\partial x} + \nabla_t \left( \frac{P}{\rho} \right) = \frac{\vec{F}_t}{\rho}, \quad (8)$$

where  $\nabla_t \equiv -\vec{e}_x \times (\vec{e}_x \times \nabla)$  is the gradient operator in the transverse plane, and substitute (8) into (7) to obtain

$$\begin{aligned} \nabla^2 \left( \frac{P}{\rho} \right) + \frac{2}{U} \left[ \nabla_t U \cdot \nabla_t \left( \frac{P}{\rho} \right) \right] &= \\ = \nabla \cdot \left( \frac{\vec{F}}{\rho} \right) - \frac{2}{U} \left( \frac{\vec{F}_t}{\rho} \cdot \nabla_t U \right) - U \frac{\partial \Delta}{\partial x}. \end{aligned} \quad (9)$$

Equation (9) is a linear partial differential equation for the pressure disturbance which needs to be solved for given  $U$ ,  $\vec{F}$  and  $\Delta$  distributions.

## 2.2. Ducted Propeller Model

Let us consider now the specific form of the right-hand side of eq. (9) for the external force fields  $\vec{F}$  representing the duct and propeller loadings and for the rate of expansion field  $\Delta$  representing the duct thickness in the linearised theory. We note that, since  $\vec{U}=0(1)$ , from eq. (9) we will require  $\vec{F}=0(\varepsilon)$  and  $\Delta=0(\varepsilon)$ . Denoting by  $S(x, r, \theta)$  the right-hand side of eq. (9) (multiplied by  $\rho$ ), we obtain in cylindrical coordinates:

$$\begin{aligned} S(x, r, \theta) &= \frac{\partial F_x}{\partial x} + \frac{1}{r} \frac{\partial(r F_r)}{\partial r} + \frac{1}{r} \frac{\partial F_\theta}{\partial \theta} \\ &\quad - \frac{2}{U} \left( F_r \frac{\partial U}{\partial r} + \frac{F_\theta}{r} \frac{\partial U}{\partial \theta} \right) - \rho U \frac{\partial \Delta}{\partial x}. \end{aligned} \quad (10)$$

Consistent with the linearisation applied to the Euler equations, we will place the force field singularities and the rate of expansion singularities (sources) producing the disturbance velocities, on a reference surface aligned with the undisturbed flow  $\vec{U}$ . In the present ducted propeller application we choose the reference surface to be a cylinder of constant radius and chord.

We represent the duct loading by a radially directed force field  $\vec{F}=(0, F_r, 0)$  distributed on a cylinder of radius  $R_d$  and chord  $2c$ , extending from  $x=-c$  to  $x=+c$ , Fig. 2, in the form:

$$F_r = \Delta p_d(x, \theta) [H(x+c) - H(x-c)] \delta(r - R_d), \quad (11)$$

where  $H(x)$  is the Heaviside unit step function,  $H(x)=0$  if  $x<0$ ,  $H(x)=1$  if  $x>0$ , and  $\delta(x)$  is the Dirac delta function. Substituting eq. (11) into eq. (10) we obtain

$$\begin{aligned} S(x, r, \theta) &= \\ &= \Delta p_d(x, \theta) [H(x+c) - H(x-c)] \\ &\quad \left[ \left( \frac{1}{r} - \frac{2}{U} \frac{\partial U}{\partial r} \right) \delta(r - R_d) + \delta'(r - R_d) \right]. \end{aligned} \quad (12)$$

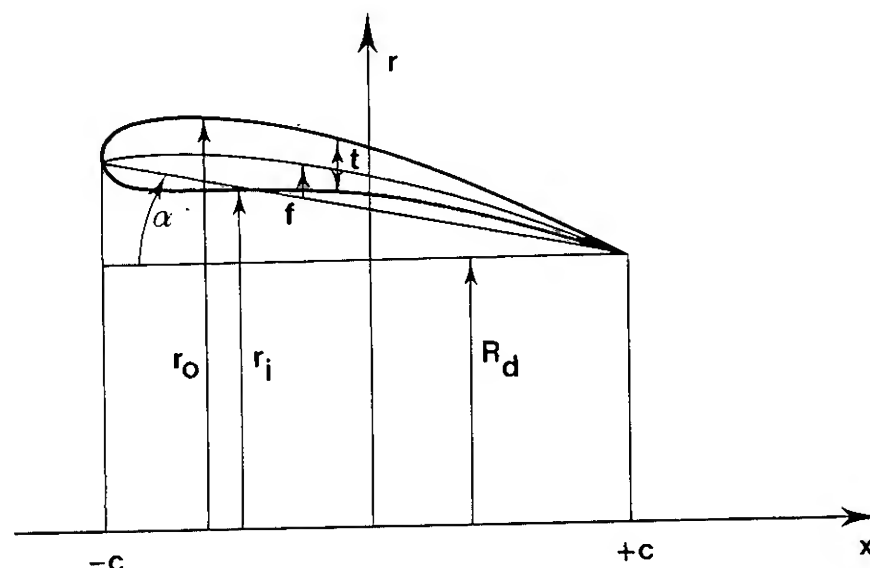


Fig. 2. Duct geometry conventions

It is seen from equations (9) and (12) that the duct loading is represented by a distribution of pressure dipoles of strength  $\Delta p_d(x, \theta)$  on the reference cylinder.

The duct thickness is represented by a source distribution  $q(x, \theta)$  on the reference cylinder. The rate of expansion becomes

$$\Delta(x, r, \theta) = q(x, \theta) [H(x+c) - H(x-c)] \delta(r-R_d). \quad (13)$$

Substitution of eq. (13) into (10) yields

$$S(x, r, \theta) = -\rho U \frac{\partial}{\partial x} \left\{ q(x, \theta) [H(x+c) - H(x-c)] \right\} \delta(r-R_d). \quad (14)$$

The propeller loading is assumed axisymmetric over the propeller disk. Neglecting the radial and circumferential components, the force field is assumed to be of the form  $\vec{F} = (F_x, 0, 0)$ , with

$$F_x(x, r) = \Delta p_p(r) \delta(x-x_p), \quad r < R_p, \quad (15)$$

where  $\Delta p_p(r)$  is the radial distribution of propeller loading,  $x_p$  the axial coordinate of the propeller plane and  $R_p$  the propeller radius. In this case the function  $S$  takes the form

$$S(x, r) = \Delta p_p(r) \delta'(x-x_p). \quad (16)$$

The expression (16) provides the usual representation of the force field associated with the actuator disk as a distribution of pressure dipoles on the disk.

### 2.3. Formulation of the Integral Equation

#### 2.3.1. Derivation of Kernel Function

By application of Green's third identity we may transform the Poisson-type eq. (9) into an integral equation for the pressure disturbance. We first note that the function  $S$  is only different from zero in a bounded region of space. Assuming the pressure disturbance to vanish at infinity to sufficient order, eq. (9) can be recast in the form (using cylindrical coordinates):

$$p(x, r, \theta) + \frac{1}{2\pi} \int_V \frac{1}{U} \left[ \frac{\partial U}{\partial \sigma} \frac{\partial p}{\partial \sigma} + \left( \frac{1}{\sigma} \frac{\partial U}{\partial \phi} \right) \left( \frac{1}{\sigma} \frac{\partial p}{\partial \phi} \right) \right] \frac{1}{R} d\tau = -\frac{1}{4\pi} \int_V \frac{S(\xi, \sigma, \phi)}{R} d\tau, \quad (17)$$

where  $R$  is the distance of the field point  $(x, r, \theta)$  to the integration point  $(\xi, \sigma, \phi)$

$$R = [(x-\xi)^2 + r^2 + \sigma^2 - 2r\sigma \cos(\theta-\phi)]^{1/2} \quad (18)$$

and  $d\tau = \sigma d\xi d\sigma d\phi$ . In eq. (17) the integrations are to be carried out over the whole region of space  $v$  extending to infinity.

The integral eq. (17) can be reduced by the use of Fourier transforms to a system of coupled one-dimensional integral equations for the pressure disturbance harmonics. To perform such reduction we represent the pressure field by a double Fourier expansion in the axial and circumferential coordinates as follows:

$$p(x, r, \theta) = \frac{1}{2\pi} \sum_{n=-\infty}^{\infty} e^{in\theta} \int_{-\infty}^{\infty} \tilde{p}_n(r; \lambda) e^{i\lambda x} d\lambda, \quad (19)$$

with inverse<sup>1)</sup>

$$\tilde{p}_n(r; \lambda) = \frac{1}{2\pi} \int_0^{2\pi} \int_{-\infty}^{\infty} p(x, r, \theta) e^{-i(\lambda x + n\theta)} dx d\theta. \quad (20)$$

The "source" potential  $1/R$  given by eq. (18) admits the expansion

$$\frac{1}{R} = \frac{1}{\pi} \sum_{m=-\infty}^{\infty} e^{im(\theta-\phi)} \int_{-\infty}^{\infty} I_k^{(m)}(r, \sigma; k) e^{ik(x-\xi)} dk, \quad (21)$$

with

$$I_k^{(m)}(r, \sigma; k) = \begin{cases} I_m(|k|r) K_m(|k|\sigma), & r < \sigma \\ K_m(|k|r) I_m(|k|\sigma), & r > \sigma \end{cases}, \quad (22)$$

where  $I_m$  and  $K_m$  are the modified Bessel functions of order  $m$ .

We introduce the notation

$$a(r, \theta) = \frac{1}{U} \frac{\partial U}{\partial r}, \quad b(r, \theta) = \frac{1}{U} \frac{1}{r} \frac{\partial U}{\partial \theta} \quad (23)$$

1. The following convention was adopted in defining Fourier transforms:

$$\tilde{f}(\lambda) = \int_{-\infty}^{\infty} f(x) e^{-i\lambda x} dx$$

$$\text{with inverse } f(x) = \frac{1}{2\pi} \int_{-\infty}^{\infty} \tilde{f}(\lambda) e^{i\lambda x} d\lambda$$

$$\text{for a continuous F.T.; } f(\theta) = \sum_{n=-\infty}^{\infty} f_n e^{in\theta}$$

$$\text{with inverse } f_n = \frac{1}{2\pi} \int_0^{2\pi} f(\theta) e^{-in\theta} d\theta$$

for a discrete Fourier series.

and we expand  $a(r, \theta)$  and  $b(r, \theta)$  in Fourier series

$$a(r, \theta) = \sum_{n=-\infty}^{\infty} a_n(r) e^{in\theta}, \quad (24)$$

$$b(r, \theta) = \sum_{n=-\infty}^{\infty} b_n(r) e^{in\theta},$$

with

$$a_n(r) = \frac{1}{2\pi} \int_0^{2\pi} a(r, \theta) e^{-in\theta} d\theta, \quad (25)$$

$$b_n(r) = \frac{1}{2\pi} \int_0^{2\pi} b(r, \theta) e^{-in\theta} d\theta.$$

Substituting eq. (19) and eqs. (21)-(23) into the first integral of (17) and carrying out the integration in  $\sigma$  we obtain

$$\begin{aligned} & \int_V \left( a \frac{\partial p}{\partial \sigma} + \frac{b}{\sigma} \frac{\partial p}{\partial \phi} \right) \frac{1}{R} d\tau = \\ & = \frac{1}{\pi} \sum_{m=-\infty}^{\infty} e^{im\theta} \int_{-\infty}^{\infty} dk e^{ikx} \int_0^{\infty} d\sigma \sigma I_k^{(m)}(r, \sigma; k) \\ & \times \int_{-\infty}^{\infty} d\lambda \sum_{n=-\infty}^{\infty} \left[ a_{m-n}(\sigma) \tilde{p}'_n(\sigma; \lambda) + \right. \\ & \left. \frac{in}{\sigma} b_{m-n}(\sigma) \tilde{p}_n(\sigma) \right] \int_{-\infty}^{\infty} d\xi e^{i(\lambda-k)\xi}, \quad (26) \end{aligned}$$

where  $\tilde{p}'_n = d\tilde{p}_n/d\sigma$ . By noting that

$$\delta(\lambda-k) = \frac{1}{2\pi} \int_{-\infty}^{\infty} e^{i(\lambda-k)\xi} d\xi, \quad (27)$$

the integration in  $\lambda$  can be carried out to give the integral, the value

$$\begin{aligned} & \sum_{m=-\infty}^{\infty} e^{im\theta} \int_{-\infty}^{\infty} dk e^{ikx} 2 \sum_{n=-\infty}^{\infty} \int_0^{\infty} d\sigma I_k^{(m)}(r, \sigma; k) \\ & \left[ \sigma a_{m-n}(\sigma) \tilde{p}'_n(\sigma; k) + in b_{m-n}(\sigma) \tilde{p}_n(\sigma; k) \right]. \quad (28) \end{aligned}$$

The integral involving  $\tilde{p}'_n$  can be further reduced by partial integration. Evaluating the derivatives of the terms involving the Bessel functions we finally obtain

$$\begin{aligned} & \int_V \left( a \frac{\partial p}{\partial \sigma} + \frac{b}{\sigma} \frac{\partial p}{\partial \phi} \right) \frac{1}{R} d\tau = \\ & = - \sum_{m=-\infty}^{\infty} e^{im\theta} \int_0^{\infty} d\lambda e^{i\lambda x} \\ & \times \sum_{n=-\infty}^{\infty} \int_0^{\infty} G_{mn}(r, \sigma; \lambda) \tilde{p}_n(\sigma; \lambda) d\sigma, \quad (29) \end{aligned}$$

with

$$G_{mn}(r, \sigma; \lambda) = \begin{cases} 2 K_m(|\lambda|r) [A_{mn}(\sigma) I_m(|\lambda|\sigma) + \\ B_{mn}(\sigma)|\lambda| I_{m-1}(|\lambda|\sigma)] , & r > \sigma \\ 2 I_m(|\lambda|r) [A_{mn}(\sigma) K_m(|\lambda|\sigma) - \\ B_{mn}(\sigma)|\lambda| K_{m-1}(|\lambda|\sigma)] , & r < \sigma \end{cases} \quad (30)$$

and

$$\begin{aligned} A_{mn}(\sigma) &= (1-|m|) a_{m-n}(\sigma) + \\ &\sigma a'_{m-n}(\sigma) - in b_{m-n}(\sigma), \quad (31) \end{aligned}$$

$$B_{mn}(\sigma) = \sigma a_{m-n}(\sigma).$$

In eq. (31) the prime denotes differentiation with respect to the function argument. We note that the kernel function  $G_{mn}(r, \sigma; \lambda)$  has a discontinuity at  $r=\sigma$  given by

$$\begin{aligned} & - 2B_{m-n}(r)|\lambda| \left[ I_m(|\lambda|r) K_{m-1}(|\lambda|r) + \right. \\ & \left. I_{m-1}(|\lambda|r) K_m(|\lambda|r) \right] = - 2a_{m-n}(r). \quad (32) \end{aligned}$$

### 2.3.2. Duct Loading

The right-hand side of eq. (17) for the effect of duct loading may be reduced in a similar way. We assume the duct loading to be represented by the double Fourier expansion

$$\Delta p_d(x, \theta) = \frac{1}{2\pi} \sum_{n=-\infty}^{\infty} e^{in\theta} \int_{-\infty}^{\infty} \Delta \tilde{p}_d(\lambda) e^{i\lambda x} d\lambda, \quad (33)$$

with inverse

$$\Delta \tilde{p}_d(\lambda) = \frac{1}{2\pi} \int_0^{2\pi} \int_{-c}^c \Delta p_d(x, \theta) e^{-i(n\theta + \lambda x)} dx d\theta. \quad (34)$$

Substituting eqs. (33), (12) and (21) in (17) we obtain, after carrying out the integrations in  $\sigma$ ,  $\phi$  and  $\xi$ ,

$$\begin{aligned} & \int_V \frac{S(\xi, \sigma, \phi)}{R} d\tau = \\ & = - 2 \sum_{m=-\infty}^{\infty} e^{im\theta} \int_{-\infty}^{\infty} d\lambda e^{i\lambda x} \\ & \times \left[ R_d I K_{\sigma}^{(m)}(r, R_d; \lambda) \Delta \tilde{p}_d(\lambda) + \right. \\ & \left. 2R_d I K^{(m)}(r, R_d; \lambda) \sum_{n=-\infty}^{\infty} a_{m-n}(R_d) \Delta \tilde{p}_d(\lambda) \right]. \quad (35) \end{aligned}$$



In eq. (35) we have used  $IK_{\sigma}^{(m)}(r, \sigma; \lambda)$  to denote

$$IK_{\sigma}^{(m)}(r, \sigma; \lambda) = \begin{cases} |\lambda| I_m(|\lambda|r) K'_m(|\lambda|\sigma), & r < \sigma \\ |\lambda| K_m(|\lambda|r) I'_m(|\lambda|\sigma), & r > \sigma \end{cases} \quad (36)$$

### 2.3.3. Duct Thickness

In the case of duct thickness, inserting (14) and (21) into the right-hand side of eq. (17), we obtain

$$\begin{aligned} \int_v \frac{S(\xi, \sigma, \phi)}{R} d\tau = \\ = -\frac{\rho}{\pi} \sum_{m=-\infty}^{\infty} e^{im\theta} \int_{-\infty}^{\infty} d\xi \int_0^{\infty} d\sigma \sigma \\ \int_{-\infty}^{\infty} dk IK^{(m)}(r, \sigma; k) e^{ik(x-\xi)} \delta(\sigma - R_d) \\ \frac{\partial}{\partial \xi} \left\{ [H(\xi+c) - H(\xi-c)] \int_0^{2\pi} U(\sigma, \phi) q(\xi, \phi) e^{-im\phi} d\phi \right\} d\phi. \end{aligned} \quad (37)$$

Introducing the function

$$T_m(\xi, \sigma) = \frac{1}{2\pi} \int_0^{2\pi} U(\sigma, \phi) q(\xi, \phi) e^{-im\phi} d\phi, \quad (38)$$

and carrying out the integration in  $\sigma$  we have for the integral (37)

$$\begin{aligned} -2\rho \sum_{m=-\infty}^{\infty} e^{im\theta} R_d \int_{-\infty}^{\infty} d\lambda IK^{(m)}(r, R_d; \lambda) \\ \times \int_{-\infty}^{\infty} d\xi e^{i\lambda(x-\xi)} \frac{d}{d\xi} \{T_m(\xi, R_d) [H(\xi+c) - H(\xi-c)]\}. \end{aligned} \quad (39)$$

In the previous expression the integration in  $\xi$  may be performed by introducing the Fourier expansion

$$\tilde{T}_m(\lambda) = \int_{-c}^c T_m(\xi, R_d) e^{-i\lambda\xi} d\xi \quad (40)$$

to yield

$$\begin{aligned} \int_v \frac{S(\xi, \sigma, \phi)}{R} d\tau = -2 \sum_{m=-\infty}^{\infty} e^{im\theta} \int_{-\infty}^{\infty} d\lambda e^{i\lambda x} \\ \times i\rho\lambda R_d IK^{(m)}(r, R_d; \lambda) \tilde{T}_m(\lambda). \end{aligned} \quad (41)$$

### 2.3.4. Propeller Loading

With the propeller loading given by eq. (15), the right-hand side of eq. (17) is reduced in the same way as the previous cases. The integral is

$$\begin{aligned} \int_v \frac{S(\xi, \sigma, \phi)}{R} d\tau = \\ = \frac{1}{\pi} \int_{-\infty}^{\infty} d\xi \int_0^R d\sigma \sigma \int_0^{2\pi} d\phi \sum_{m=-\infty}^{\infty} e^{im(\theta-\phi)} \\ \int_{-\infty}^{\infty} dk IK^{(m)}(r, \sigma; k) e^{ik(x-\xi)} \Delta p_p(\sigma) \delta'(\xi - x_p). \end{aligned} \quad (42)$$

Since the load distribution is assumed independent of  $\phi$ , the integration in  $\phi$  gives

$$\int_0^{2\pi} e^{-im\phi} d\phi = 2\pi \delta_{m0}, \quad (43)$$

where  $\delta_{mn}$  is the Kronecker delta, and, hence, the integral becomes

$$\begin{aligned} \int_v \frac{S(\xi, \sigma, \phi)}{R} d\tau = \\ = 2 \sum_{m=-\infty}^{\infty} e^{im\theta} \int_{-\infty}^{\infty} dk \int_0^R d\sigma IK^{(0)}(r, \sigma; k) \\ \sigma \Delta p_p(\sigma) \int_{-\infty}^{\infty} e^{ik(x-\xi)} \delta'(\xi - x_p) d\xi \\ = 2 \sum_{m=-\infty}^{\infty} e^{im\theta} \int_{-\infty}^{\infty} d\lambda e^{i\lambda x} \\ \times i\lambda e^{-i\lambda x_p} \int_0^R IK^{(0)}(r, \sigma; \lambda) \Delta p_p(\sigma) \sigma d\sigma. \end{aligned} \quad (44)$$

### 2.3.5. Integral equation

Gathering the previous results expressed by eqs. (29), (35), (41) and (44), by equating the corresponding harmonics of the left and right-hand sides of eq. (17) we may write (symbolically) the integral equation in the form

$$\tilde{p}_m - T \tilde{p}_n = \tilde{\psi}_m, \quad (45)$$

with the operator  $T$  defined by

$$T \tilde{p}_n = \sum_{m=-\infty}^{\infty} \int_0^{\infty} G_{mn}(r, \sigma; \lambda) \tilde{p}_n(\sigma; \lambda) d\sigma \quad (46)$$

The function  $\tilde{\psi}_m$  takes different forms for the effects of duct loading, thickness and propeller loading. In the case of duct loading it is given by

$$\begin{aligned}
\tilde{\psi}_m(r; \lambda) &= \\
&= R_d IK_{\sigma}^{(m)}(r, R_d; \lambda) \Delta \tilde{p}_d(\lambda) + \\
&2R_d IK^{(m)}(r, R_d; \lambda) \sum_{n=-\infty}^{\infty} a_{m-n}(R_d) \Delta \tilde{p}_{dn}(\lambda).
\end{aligned} \quad (47)$$

It is easily seen from the properties of the modified Bessel functions that  $\tilde{\psi}_m(r; \lambda)$  is discontinuous at the duct reference cylinder  $r=R_d$ . The discontinuity amounts to the (Fourier transformed) pressure jump on the duct, i.e. the strength of the pressure dipole  $\Delta \tilde{p}_d(\lambda)$ .

In the case of duct thickness, eq. (41), the function takes the form

$$\tilde{\psi}_m(r; \lambda) = i\rho\lambda R_d IK^{(m)}(r, R_d; \lambda) \tilde{T}_m(\lambda). \quad (48)$$

It is also seen that this function is continuous at  $r=R_d$  but has discontinuous first derivatives at that radius.

Finally, in the case of propeller loading, the function  $\tilde{\psi}_m$  is

$$\begin{aligned}
\tilde{\psi}_m(r; \lambda) &= \\
&= -i\lambda e^{-i\lambda x_p} \int_0^R IK^{(0)}(r, \sigma; \lambda) \Delta p_p(\sigma) \sigma d\sigma,
\end{aligned} \quad (49)$$

which is a continuous function of the radius with continuous first derivatives.

The eq. (45) constitutes an infinite system of one-dimensional integral equations, with a discontinuous kernel, for the disturbance pressure harmonics. At this stage it should be remarked that, as shown in the classical work in shear flow problems [19], [20], the advantage of having introduced the x-wise Fourier Transform is to reduce the three-dimensional problem to a set of decoupled two-dimensional problems, each one for a single value of the parameter  $\lambda$  in eq. (45). However, it should be noted that, in the case of a circumferentially sheared inflow, the circumferential pressure harmonics do not decouple. In fact, they are coupled through the harmonics of the shear parameters, as shown by the form of the integral operator in eq. (46).

We would like also to stress that the integral operator  $T$  is a function of the shear parameters  $a$  and  $b$  only, being independent of duct loading, thickness or propeller loading, which affect only the right-hand side of eq. (45).

#### 2.4. Separation of Potential and Interaction Effects

The numerical approach to the solution of the integral equation (45) has to be done with

care. First, the kernel  $G_{mn}$  is discontinuous at  $r=\sigma$ , as given in (32). This may not constitute a major problem since a number of numerical techniques are available to handle this type of kernel, as it may be found, for instance, in ref. [36]. Second, the right-hand side of eq. (45) is either discontinuous at  $r=R_d$ , as in the case of duct loading, or has the discontinuity in its first derivative, as in the case of duct thickness. The integral equation (45) is of the second kind and this means that the solution will inherit the discontinuous behaviour at  $r=R_d$ . This fact has major consequences for the computation of the velocity field because, as shown in the next section, differentiation of the pressure in the radial direction is required to derive the radial velocity component from the radial momentum equation.

In the pursuit of an accurate numerical solution of the integral equation (45) and of an accurate computation of the associated velocity field, it is quite natural to distinguish two contributions to the pressure field, respectively the potential pressure  $p^{(0)}$ , which satisfies the Poisson equation (9) in the absence of shear,  $\nabla_t U=0$ , and the interaction pressure  $p^{(1)}$  which satisfies the remaining part of the equation (9). For the transformed equation (45) in Fourier space this means that

$$\tilde{p}_m = \tilde{p}_m^{(0)} + \tilde{p}_m^{(1)}, \quad (50)$$

with

$$\tilde{p}_m^{(0)} = \tilde{\psi}_m^{(0)} \quad (51)$$

and

$$\tilde{p}_m^{(1)} - T \tilde{p}_m^{(1)} = \tilde{\psi}_m^{(1)} + T \tilde{\psi}_m^{(0)}. \quad (52)$$

In eqs. (51) and (52) we have decomposed the right-hand side into a shear-independent term  $\tilde{\psi}_m^{(0)}$  and a shear-dependent term  $\tilde{\psi}_m^{(1)}$ . In the case of duct loading we have

$$\tilde{\psi}_m^{(0)} = R_d IK_{\sigma}^{(m)}(r, R_d; \lambda) \Delta \tilde{p}_d(\lambda) \quad (53)$$

and

$$\tilde{\psi}_m^{(1)} = 2R_d IK^{(m)}(r, R_d; \lambda) \sum_{n=-\infty}^{\infty} a_{m-n}(R_d) \Delta \tilde{p}_{dn}(\lambda). \quad (54)$$

In the cases of duct thickness and propeller loading the shear-dependent term  $\tilde{\psi}_m^{(1)}$  is inexistent and  $\tilde{\psi}_m^{(0)}$  is given by eqs. (48) and (49), respectively.

The potential flow problem eq. (51) for the duct loading and thickness leads to the formulation of the duct lifting surface theory. Solution of the loading (vortex distribution) and thickness (source distribution) problems has been given in refs. [6], [31], [32], where expressions can be found for the evaluation of the radial velocity (downwash) at the duct reference cylinder. Expressions for the duct induced axial and tangential velocities are also given in ref. [6]. We will discuss briefly the solution of this problem in the section devoted to the computation of the velocity field.

The solution of the shear interaction problem eq. (52) requires the computation in the right-hand side of eq. (52) of the term  $T \tilde{\psi}_m^{(0)}$ . A straightforward computation allows this term to be expressed in terms of functions which can be easily evaluated numerically. The results of these computations for all cases are given in the Appendix A. It may be readily verified using the expressions of the Appendix A that the right-hand side of eq. (52) in the cases of duct loading and thickness is continuous and has continuous first derivatives at  $r=R_d$ , a property which is shared by the solution  $\tilde{p}_m^{(1)}$  of the shear interaction problem.

## 2.5. Velocity Field

In accordance with the decomposition of the pressure field into its potential and interaction parts, we write for the disturbance velocity

$$\vec{u} = \vec{u}^{(0)} + \vec{u}^{(1)}, \quad (55)$$

where  $\vec{u}^{(0)}$  is the velocity associated with the potential pressure  $p^{(0)}$ , which we call the induction velocity, and  $\vec{u}^{(1)}$  is the shear interaction velocity.

By definition  $\vec{u}^{(0)}$  satisfies eq. (1) and the momentum equation

$$U \frac{\partial \vec{u}^{(0)}}{\partial x} + \nabla \left( \frac{p^{(0)}}{\rho} \right) = \frac{\vec{F}}{\rho}, \quad (56)$$

while  $\vec{u}^{(1)}$  is a solenoidal velocity field

$$\nabla \cdot \vec{u}^{(1)} = 0, \quad (57)$$

satisfying

$$U \frac{\partial \vec{u}^{(1)}}{\partial x} + \vec{e}_x \left[ (\vec{u}_t^{(0)} + \vec{u}_t^{(1)}) \cdot \nabla U \right] + \nabla \left( \frac{p^{(1)}}{\rho} \right) = 0. \quad (58)$$

If the pressure fields  $p^{(0)}$  and  $p^{(1)}$  are known, respectively from eq. (51) and the solution of eq. (52), the velocity fields  $\vec{u}^{(0)}$  and  $\vec{u}^{(1)}$  can be evaluated by integrating eqs.

(56) and (58). We note that, in using (58) for the determination of the interaction velocity, the potential part of the solution affects the radial and tangential components of the interaction velocity only through the interaction pressure  $p^{(1)}$ . For the axial velocity component, however, there is an additional term  $\vec{u}_t^{(0)} \cdot \nabla U$  coupling the two problems and this requires the calculation of the induction velocity  $\vec{u}_t^{(0)}$  first.

Integrating eq. (56) from  $x=-\infty$  to  $x$ , we obtain for the induction velocity components

$$u^{(0)} = - \frac{p^{(0)}}{\rho U} + \frac{1}{U} \int_{-\infty}^x \frac{F_x}{\rho} d\xi, \quad (59)$$

$$v^{(0)} = - \frac{1}{U} \int_{-\infty}^x \frac{\partial}{\partial r} \left( \frac{p^{(0)}}{\rho} \right) d\xi + \frac{1}{U} \int_{-\infty}^x \frac{F_r}{\rho} d\xi, \quad (60)$$

$$w^{(0)} = - \frac{1}{U} \int_{-\infty}^x \frac{1}{r} \frac{\partial}{\partial \theta} \left( \frac{p^{(0)}}{\rho} \right) d\xi. \quad (61)$$

In writing eq. (59) to (61) we have made use of the fact that the velocity  $\vec{u}^{(0)}$  and the disturbance pressure  $p^{(0)}$  vanish at infinity upstream,  $x=-\infty$ .

In the cases of duct loading and thickness,  $F_x=0$  and the evaluation of the axial and tangential velocity components  $u^{(0)}$  and  $u^{(1)}$  do not pose particular problems. They can be computed from the inverse Fourier transform of  $\tilde{\psi}_m^{(0)}$ , attention being paid to the calculation on both sides of the duct reference cylinder  $r=R_d \pm 0$ . However, in the evaluation of the radial velocity component from eq. (60) special care has to be taken in carrying out the required differentiation and integration at  $r=R_d$ . Such evaluation constitutes the subject of duct lifting surface theory dealing with the evaluation of the Cauchy singularity in the kernel function for the radial downwash. The solution of this problem can be found in refs. [6], [31]-[33] and will not be treated in detail here. In Appendix B the relevant expressions are collected for the case of duct loading, together with an outline of their derivation from the present formulation.

In the case of propeller loading  $F_x=0$  and with  $F_x$  given by eq. (15), we obtain for the axial component

$$\begin{aligned} u^{(0)} &= - \frac{p^{(0)}}{\rho U} + \frac{\Delta p_p(r)}{\rho U} H(x-x_p), \quad r < R_p \\ &= - \frac{p^{(0)}}{\rho U}, \quad r > R_p \end{aligned} \quad (62)$$

the well-known result from actuator disk theory.

For the interaction velocity  $\vec{u}^{(1)}$ , integration of eq. (58) from  $x=-\infty$  to  $x$  yields

$$u^{(1)} = -\frac{p^{(1)}}{\rho U} - a \int_{-\infty}^x (v^{(0)} + v^{(1)}) d\xi - b \int_{-\infty}^x (w^{(0)} + w^{(1)}) d\xi, \quad (63)$$

$$v^{(1)} = -\frac{1}{U} \int_{-\infty}^x \frac{\partial}{\partial r} \left( \frac{p^{(1)}}{\rho} \right) d\xi, \quad (64)$$

$$w^{(1)} = -\frac{1}{U} \int_{-\infty}^x \frac{1}{r} \frac{\partial}{\partial \theta} \left( \frac{p^{(1)}}{\rho} \right) d\xi, \quad (65)$$

with the definition (23) of  $a$  and  $b$ . Again, in deriving (63) to (65) we have made use of the fact that the interaction pressure and velocities vanish at infinity upstream. In eqs. (63)-(65), which hold for the cases of loading and thickness we have been considering,  $v^{(1)}$  and  $w^{(1)}$  have to be evaluated first from the interaction pressure;  $u^{(1)}$  is then computed from eq. (63) with known values of  $v^{(0)}$ ,  $v^{(1)}$ ,  $w^{(0)}$  and  $w^{(1)}$ .

## 2.6. Duct Boundary Conditions

We describe the duct surface by specifying the deviations of the outer and inner surfaces from the reference cylinder due to the conical angle, camber and thickness distributions of the duct sections, Fig. 2. The outer and inner surfaces may be given by the expression

$$r(x, \theta) = R_d - \alpha(\theta)(x-c) + f(x, \theta) \pm \frac{1}{2} t(x, \theta), \quad -c \leq x \leq c, \quad (66)$$

where  $\alpha(\theta)$  is the conical angle,  $f(x, \theta)$  is the camber distribution, satisfying

$$f(-c, \theta) = f(c, \theta) = 0, \quad (67)$$

and  $t(x, \theta)$  is the thickness distribution. In eq. (66) the plus and minus signs apply to the duct outer and inner surfaces, respectively. The conical angle  $\alpha(\theta)$  is defined positive as shown in Fig. 2. The duct surface may be described by the equation

$$F_d(x, r, \theta) = r - R_d + \alpha(\theta)(x-c) - f(x, \theta) \mp \frac{1}{2} t(x, \theta) = 0. \quad (68)$$

The unit vector normal to the surface may be expressed as  $\nabla F_d / |\nabla F_d|$ . The kinematic boundary condition on the duct surface reads

$$(\vec{V} \cdot \nabla F_d) / |\nabla F_d| = 0, \quad (69)$$

which can be written, using eq. (68),

$$(U+u) \left[ \alpha(\theta) - \frac{\partial f}{\partial x} \pm \frac{1}{2} \frac{\partial t}{\partial x} \right] + v + \frac{w}{r} \left[ \alpha'(\theta)(x-c) - \frac{\partial f}{\partial \theta} \pm \frac{1}{2} \frac{\partial t}{\partial \theta} \right] = 0. \quad (70)$$

The first order approximation to (70) is

$$v(x, R_d \pm 0, \theta) = U(R_d, \theta) \left[ -\alpha(\theta) + \frac{\partial f}{\partial x} \pm \frac{1}{2} \frac{\partial t}{\partial x} \right]. \quad (71)$$

Writing

$$v(x, R_d \pm 0, \theta) = \bar{v}(x, R_d, \theta) \pm \frac{1}{2} \Delta v(x, R_d, \theta), \quad (72)$$

where  $\bar{v}(x, R_d, \theta)$  is the average radial velocity at  $r=R_d$  between the outer and the inner surfaces and  $\Delta v(x, R_d, \theta)$  is the radial velocity jump, we conclude from (71) and (72) that

$$\Delta v(x, R_d, \theta) = U(R_d, \theta) \frac{\partial t}{\partial x}, \quad (73)$$

which gives to the first order the strength of the source distribution

$$q(x, \theta) = U(R_d, \theta) \frac{\partial t}{\partial x}. \quad (74)$$

From eq. (71) we derive also to first order

$$\frac{\partial f}{\partial x} - \alpha(\theta) = \frac{\bar{v}(x, R_d, \theta)}{U(R_d, \theta)}. \quad (75)$$

Integrating (75) and using (67), we obtain

$$\alpha(\theta) = -\frac{1}{2c} \int_{-c}^c \frac{\bar{v}}{U} dx \quad (76)$$

and

$$f(x, \theta) = \alpha(x+c) + \int_{-c}^x \frac{\bar{v}}{U} d\xi. \quad (77)$$

It is well-known that the use of the first order boundary condition (71) can be rather crude for design purposes at increasing loadings, since the perturbation velocities will no longer be small compared with the undisturbed velocity  $U(R_d, \theta)$ . A simple refinement to eq. (75) can be used if we neglect the contribution of the circumferential velocity  $w$  to the component of the velocity  $\vec{V}$  normal to the surface in eq. (70). If, in addition, we retain the first order approximation to the source distribution (74), we obtain

$$\frac{\partial f}{\partial x} - \alpha = \frac{\bar{v}}{U+u}, \quad (78)$$

which includes the axial perturbation velocity in the calculation of the conical angle and camber distributions.

### 3. NUMERICAL SOLUTION PROCEDURE

For the purposes of numerical analysis a dimensionless form of the equations is used. The duct radius  $R_d$  is taken as reference length, velocities are made dimensionless by a reference velocity  $U_0$ , taken here as the (finite) asymptotic value of the velocity  $U$  at large radii, and pressures are made dimensionless by  $\rho U_0^2$ .

To solve numerically the integral equation (52) we first apply a transformation to the radial coordinate  $\bar{r} = \bar{r}(r)$  which maps the integration interval  $(0, \infty)$  onto the interval  $(0, 1)$ . Various possibilities exist to choose such transformation, but we have applied a simple exponential transformation defined by

$$\bar{r} = 1 - \exp(-\bar{a}r), \quad (79)$$

with the constant  $\bar{a} = \ln(1/2)$  chosen as to map the duct radius  $r=1$  to  $\bar{r}=0.5$ . The integral equation is solved by a quadrature method using the trapezoidal rule. Introducing the equidistant nodes

$$\bar{r}_i = (i-1)/(NR-1), \quad i=1, \dots, NR, \quad (80)$$

the integral in eq. (46) evaluated at the node  $i$  is approximated by (omitting the parameter  $\lambda$  for simplicity)

$$\begin{aligned} & \int_0^1 \bar{G}_{mn}(\bar{r}_i, \bar{\sigma}) \tilde{p}_n(\bar{\sigma}) d\bar{\sigma} = \\ & = 2 G_{11i} \sum_{j=1}^i w_{ij}^{(1)} \bar{G}_{12j} \tilde{p}_{nj} + \\ & \quad 2 G_{21i} \sum_{j=1}^{NR} w_{ij}^{(2)} \bar{G}_{22j} \tilde{p}_{nj}, \end{aligned} \quad (81)$$

with

$$\begin{aligned} G_{11i} &= K_m(|\lambda| r_i), \quad G_{21i} = I_m(|\lambda| r_i), \\ G_{12j} &= [A_{mn}(r_j) I_m(|\lambda| r_j) + \\ & \quad B_{mn}(r_j) |\lambda| I_{m-1}(|\lambda| r_j)] (dr/d\bar{r})_j \\ G_{22j} &= [A_{mn}(r_j) K_m(|\lambda| r_j) - \\ & \quad B_{mn}(r_j) |\lambda| K_{m-1}(|\lambda| r_j)] (dr/d\bar{r})_j, \end{aligned} \quad (82)$$

$w_{ij}^{(1)}$  and  $w_{ij}^{(2)}$  being the weights of trapezoidal rule. For the first  $N+1$  harmonics of the disturbance pressure, the discretized form of the left-hand side of equation (52) reads

$$\tilde{p}_{mi}^{(1)} - (T \tilde{p}_n^{(1)})_{mi} = \sum_{n=-N}^N \sum_{j=1}^{NR} G_{mnij} \tilde{p}_{nj}, \quad (83)$$

with

$$G_{mnij} = \bar{G}_{mnij} \quad \text{for } m \neq n \text{ or } i \neq j$$

$$G_{mmii} = 1 - \bar{G}_{mmii},$$

$$\bar{G}_{mnij} = \begin{cases} 2 G_{11i} \bar{G}_{12j} w_{ij}^{(1)}, & j < i, \\ 2(G_{11i} \bar{G}_{12i} w_{ii}^{(1)} + G_{21i} \bar{G}_{22i} w_{ii}^{(2)}), & j = i, \\ 2 G_{21i} G_{22j} w_{ij}^{(2)}, & j > i. \end{cases} \quad (84)$$

With the mapping (79) and the equidistant node distribution an equal number of nodes are placed inside and outside the duct. The mapping ensures a larger concentration of nodes near the axis  $r=0$ , where the Bessel functions  $K_m$  are rapidly varying. To achieve an acceptable accuracy near  $r=0$  and at large radii exponential scaling of the Bessel functions is applied. The integrals appearing on the right-hand side of equation (52) (see Appendix A) are evaluated by trapezoidal integration using the same set of nodes (80).

The system of equations is solved in sequence for the set of values of the parameter  $\lambda$  coinciding with the nodes of Laguerre integration in the interval  $(0, \infty)$  which is used for inverting the pressure x-wise Fourier Transform. A LU factorization of the matrix is carried out for each value of  $\lambda$ , and then used to obtain the solution vectors for the different right-hand sides (47), (48) and (49).

With the interaction pressure obtained from the inversion of the double Fourier Transform (20) at a specified number of axial planes, the interaction velocity field is computed with the eqs. (63)-(65). The integrals are computed by trapezoidal integration. Central differencing is applied to evaluate the radial and circumferential derivatives.

### 4. RESULTS OF SAMPLE CALCULATIONS

To illustrate the effects of shear a number of sample calculations were carried out for an analytically defined wake field. Here we will only discuss the results concerning the effects of duct loading on the velocity field.

The wake field chosen is a sinusoidal perturbation superposed to the axisymmetric wake field used by Lee in ref. [30]. It is defined by the expression

$$U(r, \theta) = 1 - U_1 e^{-U_2 r^2} (1 - U_3 r^2 \sin^2 U_4 \theta). \quad (85)$$



With  $U_1=0.72$ ,  $U_2=1.70$  and  $U_3=0$  we recover the axisymmetric wake of Lee. For the wake field (85) the functions  $A_{mn}$  and  $B_{mn}$  approach zero at the axis sufficiently fast to ensure a zero value of the element  $G_{22j}$  at the axis,  $j=1$ .

In all the calculations a chord/diameter ratio  $c/R_d=0.5$  has been chosen. In general the duct loading and thickness distributions are specified by a sum of chordwise modes which are used in the solution of the duct lifting surface problem. In the present application we have chosen the NACA  $a=0.8$  chordwise loading, which is constant from the leading edge to 0.8 of the chord and decreases linearly to zero from 0.8 of the chord to the trailing edge. The Kutta condition of zero loading at the trailing edge is automatically satisfied by this load distribution. The duct loading is expressed in terms of the duct section lift coefficient defined by

$$C_L = \frac{L}{\frac{1}{2}\rho U_0^2 (2c)} = \frac{1}{-1} \int \Delta p_d dx \quad (86)$$

Since the theory is linear, the disturbance pressure and velocities are proportional to the loading coefficient  $C_L$ , and the results hold for an arbitrary loading. The results are presented for a considerably high duct loading and a strongly sheared inflow which may be considered as representatives of a typical ducted propeller application. In such cases the disturbance velocity is no longer small in comparison with the velocity of the incoming flow. Of course the assumption of small disturbance velocities does not hold in such cases and non-linear effects will certainly affect (in an unknown manner) the accuracy of the predictions. In any event, the results are easily scaled to smaller loadings.

To examine the convergence of the numerical solution of the integral equation a computation for axisymmetric flow was carried out first for a section lift coefficient  $C_L=0.9$ . Fig. 3 shows the convergence of the interaction pressure at the duct inlet plane  $x=-0.5$  with the number of radial nodes. The convergence of the Fourier inversion procedure was checked by performing the calculations with 7 and 15 nodes of the Laguerre integration, the results remaining unchanged. It can be seen that with a number of 65 nodes the solution coincides with the solution with 129 nodes except near the axis  $r=0$ . It must be remarked that none of these solutions accurately satisfy the condition of a zero radial derivative at the axis, as shown in the enlarged view of the region near the axis in Fig. 4, although with increasing number of nodes the numerical error decreases. This was to be expected since, with the present quadrature solution method, the condition is not enforced explicitly and, therefore, the accuracy of the solution will depend on the discretization error of the integrals appearing both on the

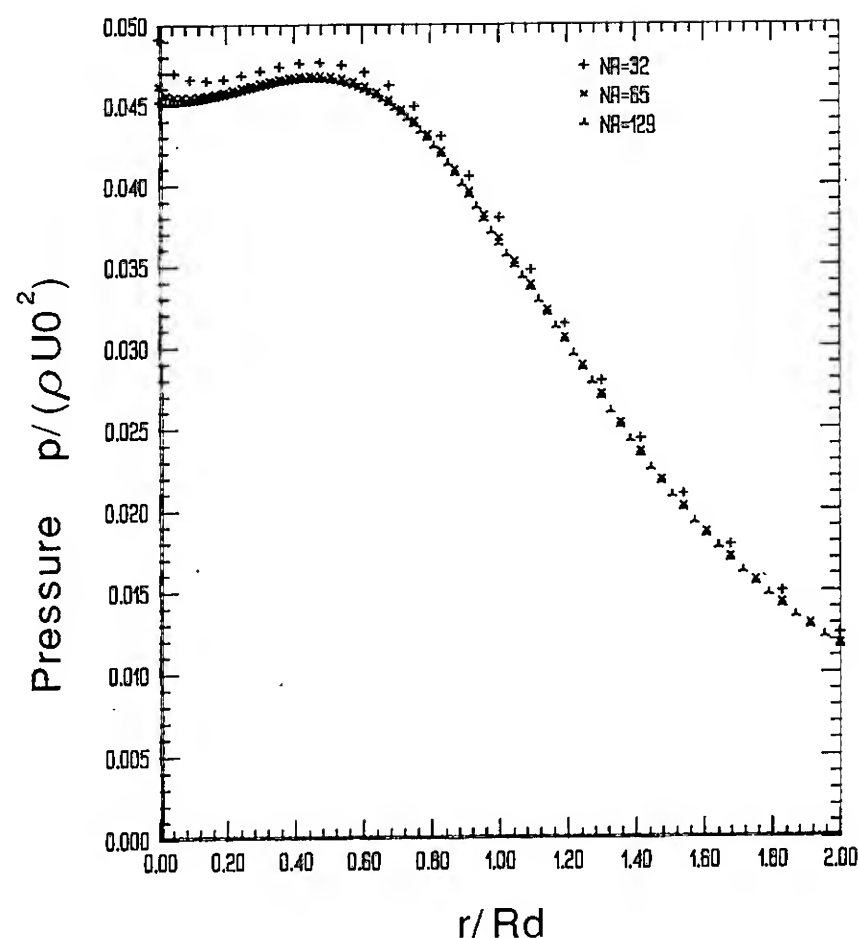


Fig. 3. Convergence of interaction pressure at  $x=-0.5$  with the number of radial nodes. Axisymmetric flow.  $c/R_d=0.5$ ,  $a=0.8$ ,  $C_L=0.9$ .

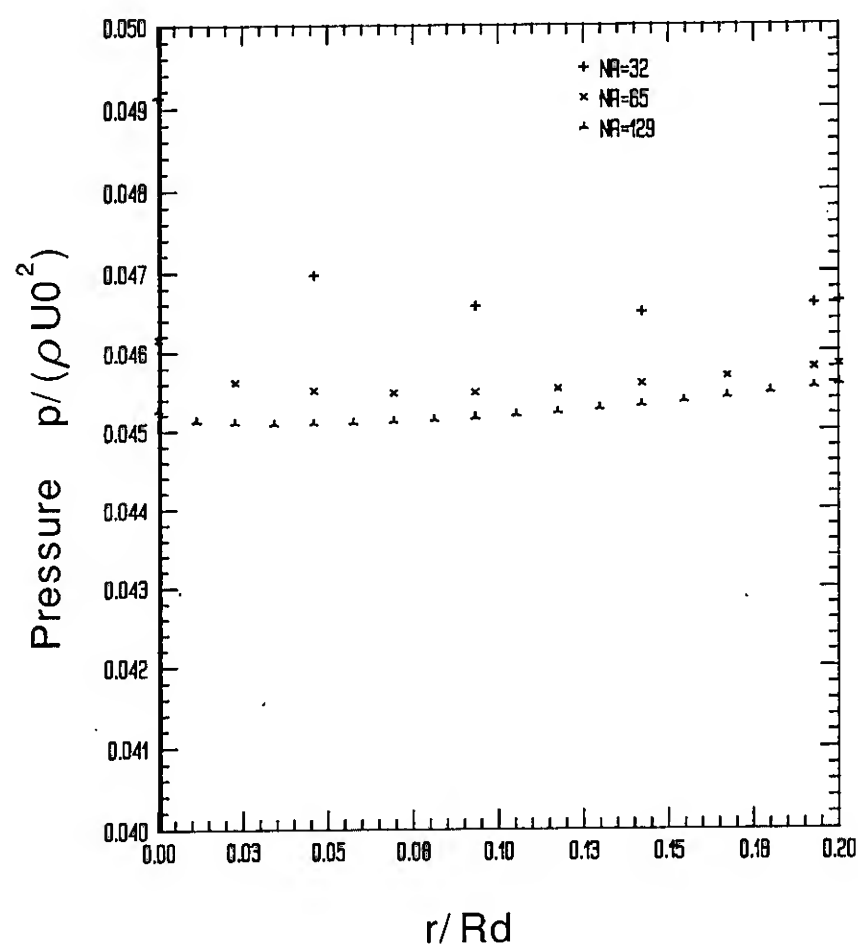


Fig. 4. Detail of computed interaction pressure near the axis at  $x=-0.5$  for different number of radial nodes. Axisymmetric flow.  $c/R_d=0.5$ ,  $a=0.8$ ,  $C_L=0.9$ .

left and right-hand sides of the integral equation. It should also be noted that the numerical solution exhibits the expected degree of smoothness at the duct radius  $r=1$ . We insist in the importance of obtaining a smooth pressure distribution since the velocity field is derived from it by numerical differentiation.

The radial component of the interaction velocity on different planes is shown in Fig. 5 for the solution with 65 nodes. The interaction radial velocity is rather small. In Fig. 6 the axial velocity distribution due to the effect of the duct loading inside and outside the duct is shown for this case. The velocity distribution of the oncoming flow is also shown in this figure. The induction velocity is simply the potential flow velocity in uniform flow divided by the local inflow velocity. This of course produces the large velocities close to the symmetry axis. The interaction velocity is negative and corrects to a certain extent this extreme behaviour. Nevertheless, for this strongly sheared inflow and, in contrast with the uniform flow case, the present method predicts in shear flow an increase to the axis of the disturbance velocity due to the duct. Again near the axis the interaction velocity and thus, the disturbance velocity due to the duct is influenced by the local error in the pressure distribution.

As a second application we considered a non-axisymmetric wake field defined by (85) with  $U_1=0.72$ ,  $U_2=1.70$ ,  $U_3=2.0$  and  $U_4=0.5$ . The

wake field is shown in Fig. 7. At all radii the velocity is lowest at  $\theta=0$ . (say the upper part of the propeller plane) and highest at  $\theta=180$  deg. (the lower part of the propeller plane). To examine the capability of the duct to change this incoming velocity, two types of duct loading were considered: an axisymmetric loading with the section lift coefficient  $C_L=0.9$ , as in the previous axisymmetric case, and an asymmetric loading defined by  $C_L = C_{L0} + \Delta C_L \cos \theta$ , with  $\Delta C_L = 0.15C_{L0}$ ; this corresponds to a 30% variation of duct section loading around the circumference, the highest loading being placed where the incoming velocities are lowest and vice versa. The same chord-diameter ratio  $c/R_d=0.5$  and the same chordwise load distribution are assumed. The integral equation was solved using a number of 65 radial nodes, for 7 nodes of the Laguerre integration. A number of 3 circumferential harmonics was sufficient to carry out the solution in the present case. The induction, interaction and the total disturbance axial velocities at  $x=0$  inside the duct are shown, respectively in Figs. 8, 9 and 10 for the duct with axisymmetric loading. Similar results are shown in Figs. 11, 12 and 13 for the case of asymmetric duct loading.

In the case of axisymmetric loading opposite tendencies are found for the inner radii up to about 0.5 and the outer radii. For the outer radii the total disturbance velocities are lower at  $\theta=180$  deg., where the incoming

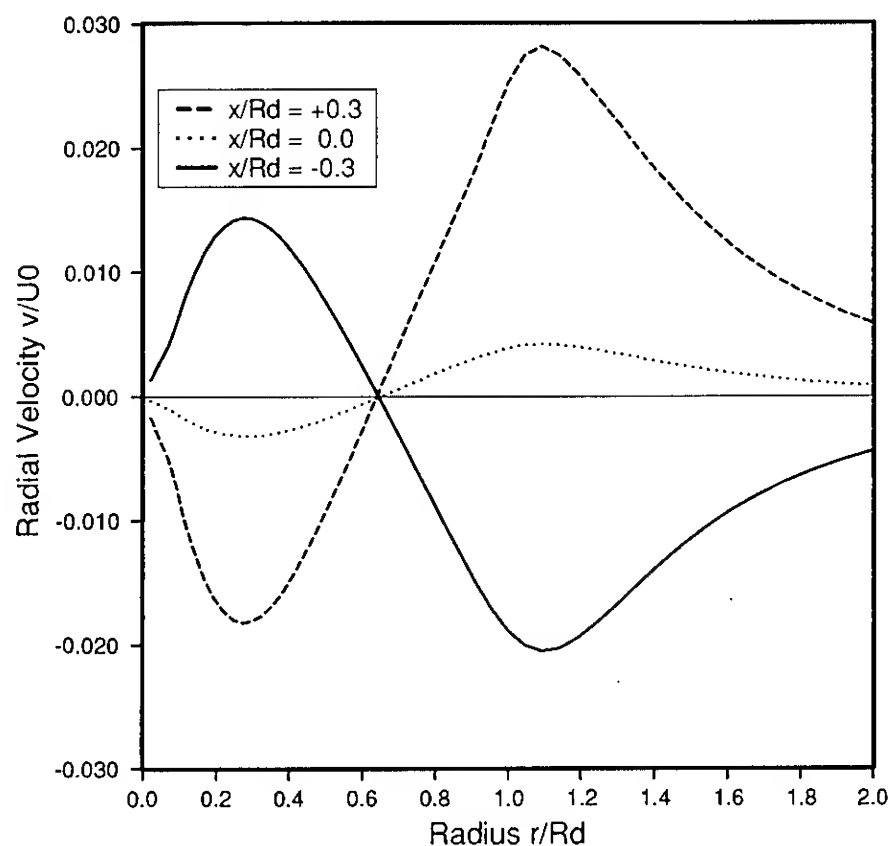


Fig. 5. Interaction radial velocity due to duct loading. Axisymmetric flow.  $c/R_d=0.5$ ,  $a=0.8$ ,  $C_L=0.9$ .

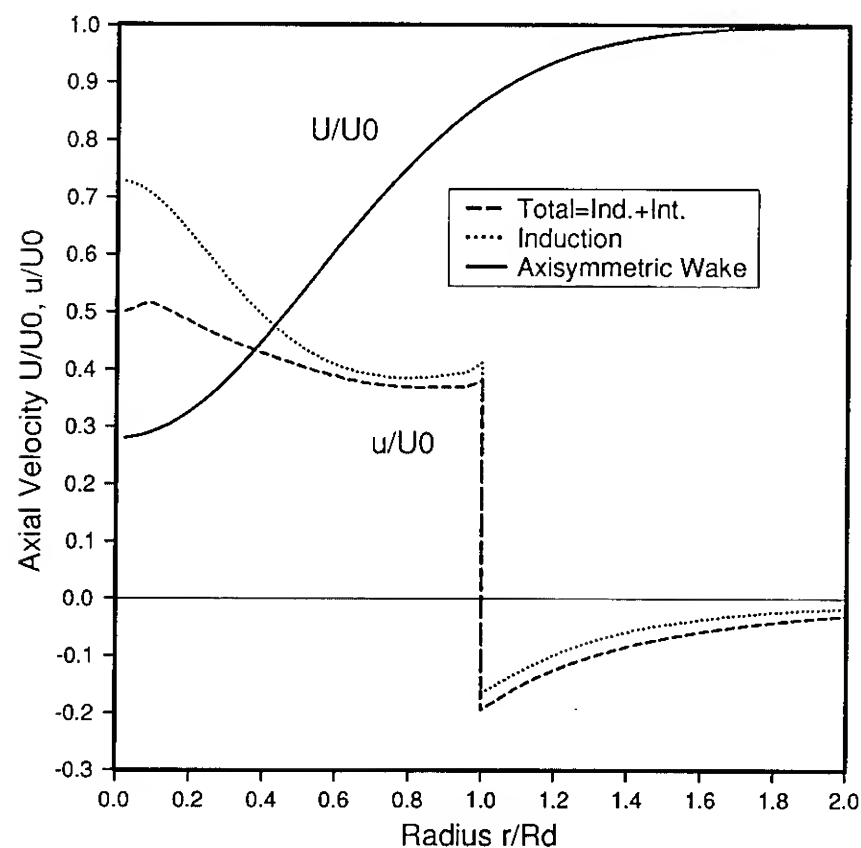


Fig. 6. Axial velocity due to duct loading at  $x=0$ . Axisymmetric flow.  $c/R_d=0.5$ ,  $a=0.8$ ,  $C_L=0.9$ .

velocity is large while for the inner radii large velocities are found at that angular position. This is caused by the large positive interaction velocity calculated for the smaller radii, see Fig. 9 for  $r/R_d=0.30$ . The dominant term in eq. (63) is the second term which couples the negative radial velocities with a large positive value of the shear parameter  $a$  (note that for this wake field this parameter is larger than on the base axisymmetric wake). For the outer radii the interaction velocities are very small, and the total disturbance velocities are dominated by the induction part.

In the case of asymmetric loading the induction part shows a more pronounced variation, Fig. 11, as expected from the duct load variation. The level of interaction velocities decreases considerably at the inner radii, as shown in Fig. 12, especially at the angular position  $\theta=180$  deg, where the local duct loading is lowest. The interaction velocities at the outer radii remain small. Still an increase of the total disturbance velocity to the axis is found in this case, Fig. 13. Clearly, an important result of practical interest is the better capability of the second duct with asymmetric loading to make the incoming flow more uniform.

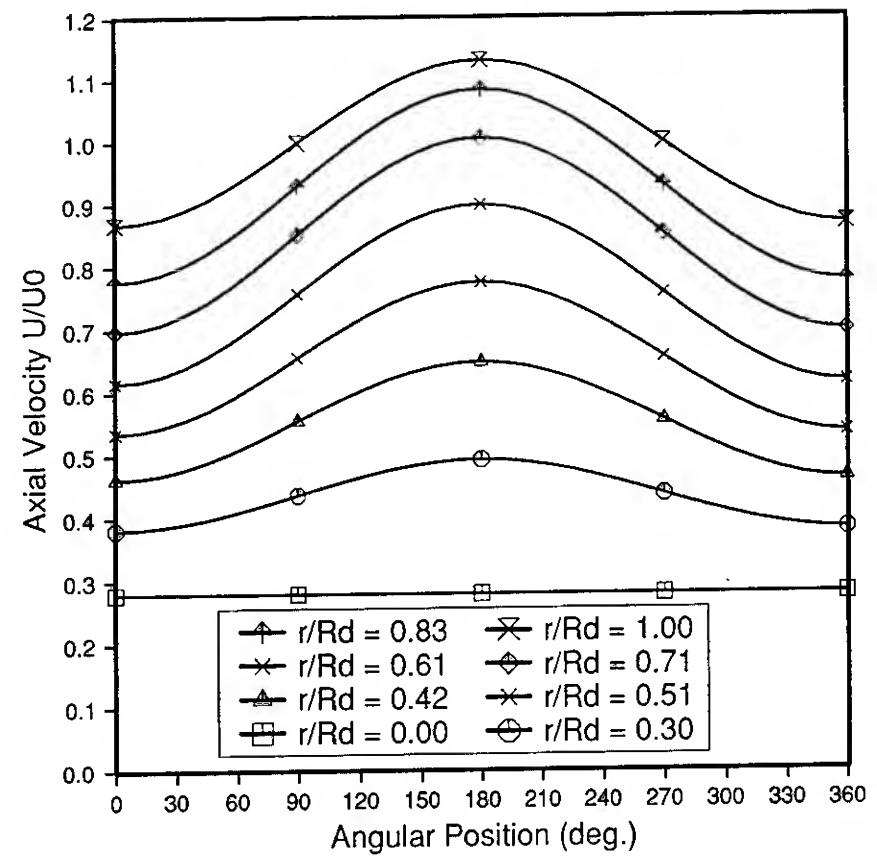


Fig. 7. Axial velocity of non-axisymmetric wake field. Eq. (85) with  $U_1=0.72$ ,  $U_2=1.7$ ,  $U_3=2$ ,  $U_4=0.5$ .

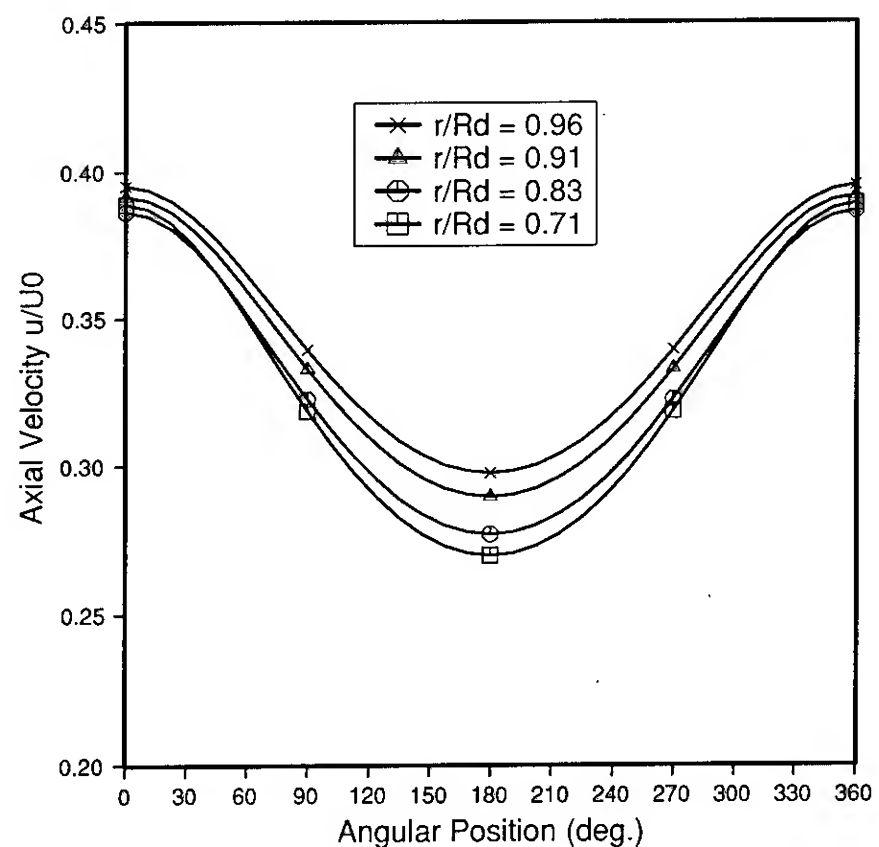
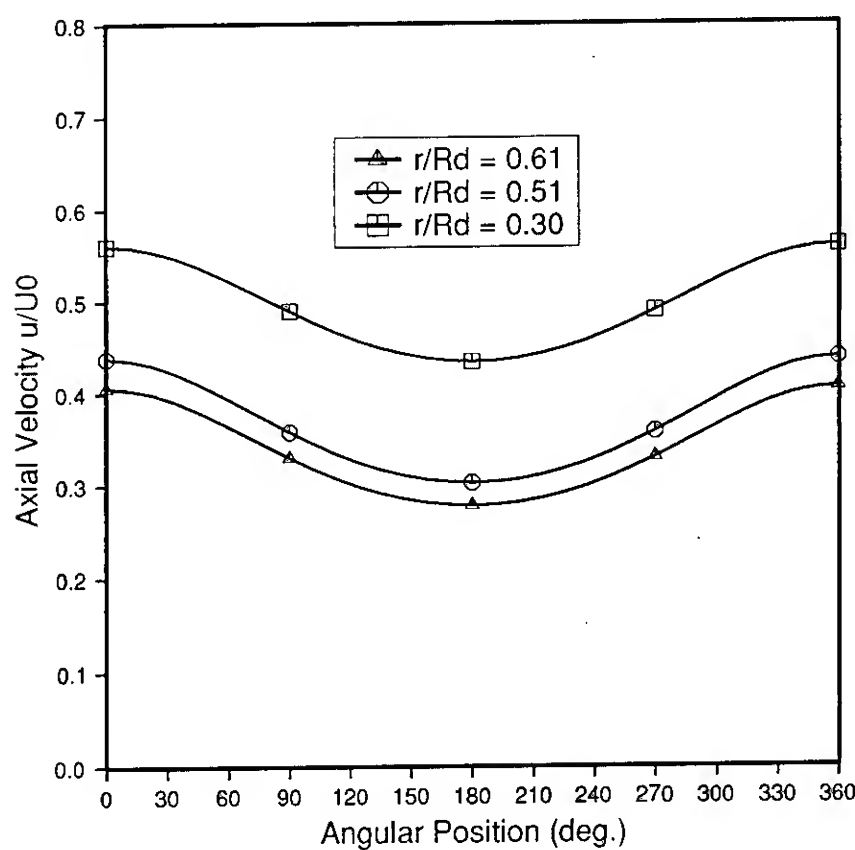


Fig. 8. Induction part of the axial velocity due to duct loading at  $x=0$ . Non-axisymmetric wake. Axisymmetric duct loading.  $c/R_d=0.5$ ,  $a=0.8$ ,  $C_L=0.9$ .

## 5. SUMMARY AND CONCLUSION

A linearised analysis of the three-dimensional steady interaction between a ducted propeller system, modelled by a suitably chosen external force field and source distribution, and a non-axisymmetric sheared axial onset flow has been given. The basic assumption of the theory is that the disturbance velocities should remain small compared with the velocity of the onset flow. Consistent with this assumption, linearised boundary conditions are applied on the duct surface. As a consequence of the linearisation the effects of duct loading and thickness and propeller loading can be treated separately and superposed.

For the three-dimensional problem a formulation in terms of the pressure seems an obvious choice and a linear integral equation has been derived for the disturbance pressure, which can be applied to describe both loading and thickness effects. By separating the potential pressure from the interaction pressure, the integral equation governing the interaction part may be in principle solved with great accuracy using suitable numerical procedures. The solution of the potential part and, more specifically, the computation of the corresponding induced velocity field can be obtained from the results of duct lifting surface theory.

As it stands, the analysis may be applied to solve the design problem of a duct in the ship's nominal axial wake field in the presence of the propeller. This requires the specification of the duct loading and thickness distributions, both circumferentially and

chordwise, and the propeller radial load distribution. The computation of the disturbance velocities on the duct reference cylinder enables the determination of the duct camber and conical angle distributions. Due to the non-linear character of the interaction thrust forces between duct and propeller some iteration will be required to meet given duct and propeller thrust values.

A computational scheme has been developed to solve the integral equation and evaluate the velocity field. The scheme has been applied to investigate the influence of shear on the velocity field due to the effects of duct loading for axisymmetric and non-axisymmetric wake fields. Relatively low computational costs are associated with the utilisation of the scheme when compared with a more direct numerical approach to the solution of the problem.

Although the present results have not yet been validated by a proper comparison with other calculation methods or experimental data, the following conclusions may be drawn from the results of the sample calculations presented in this paper:

- The effects of shear on the disturbance velocity inside the duct are found to be rather significant for the strongly sheared wake fields used in the calculations. Both for the axisymmetric wake and the non-axisymmetric wake fields, the axial disturbance velocity distribution considerably differs from the distribution in uniform flow.
- For the axisymmetric case a disturbance velocity distribution increasing to the symmetry axis is found as a result of the effect of shear. Also for the non-axisymmetric

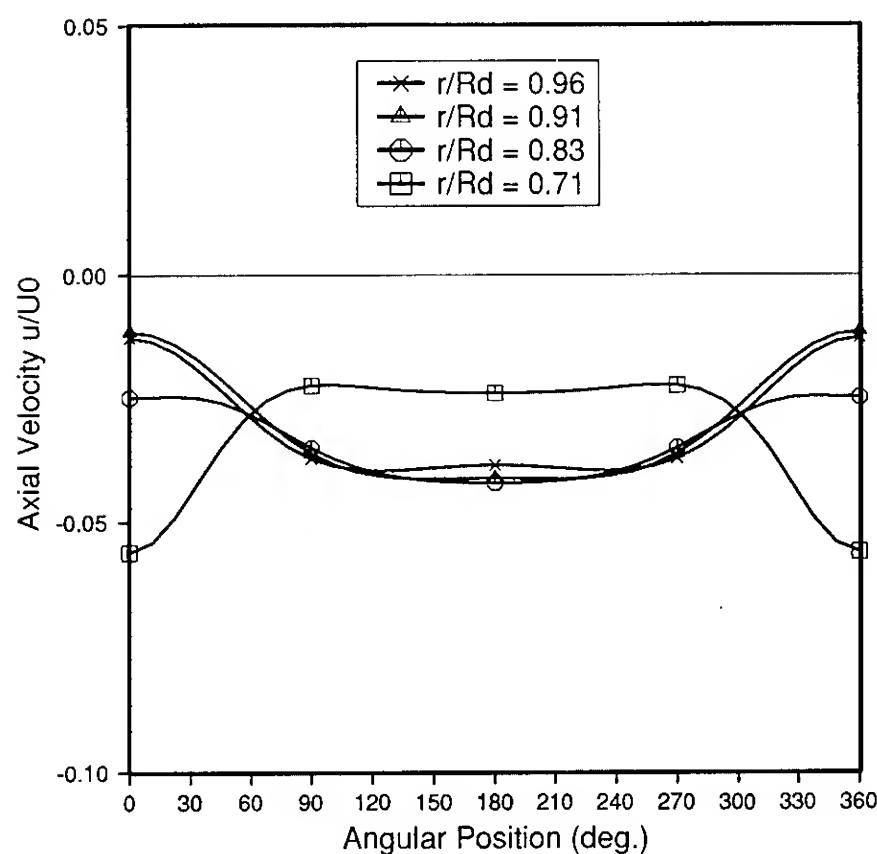
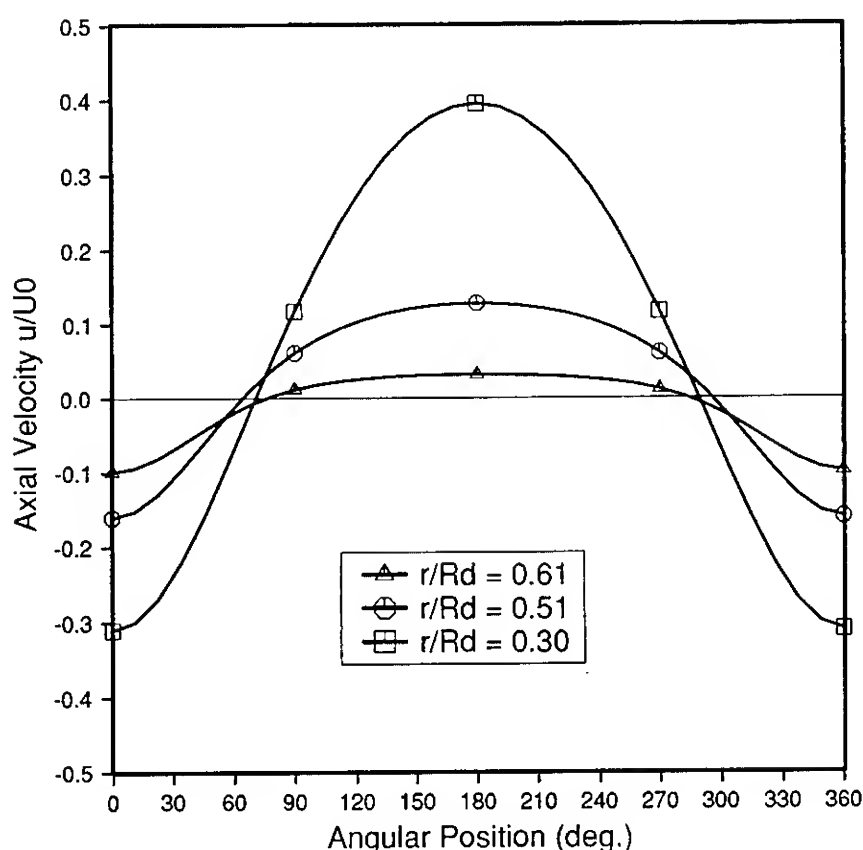


Fig. 9. Shear interaction part of the axial velocity due to duct loading at  $x=0$ . Non-axisymmetric wake. Axisymmetric duct loading.  $c/R_d=0.5$ ,  $a=0.8$ ,  $C_L=0.9$ .

wake the effects of shear considerably affect the disturbance velocity distribution both radially and circumferentially at the inner radii up to  $r/R_d=0.5$ . For the outer radii the effects of shear become much smaller.

- A large effect on the disturbance velocities on the inner radii arising from the effects of shear, is found if the duct circumferential load distribution is changed.

The foregoing results certainly indicate the need for pursuing the development of a model for the interaction between the propeller, duct and wake field, if the design of wake-adapted ducts using design criteria for flow rectification is aimed at. At present, work on this linearised model will concentrate on the application of the method to duct design including the effect of duct thickness and propeller loading. In addition, steps to validate the numerical results of the model will be undertaken.

#### REFERENCES

1. Oosterveld, M.W.C., "Wake Adapted Ducted Propellers," Doctor's Thesis, Netherlands Ship Model Basin Publ. No. 345, 1970, Wageningen, The Netherlands.
2. Van Manen, J.D., and Oosterveld, M.W.C., "Analysis of Ducted Propeller Design," *Transactions of the Society of Naval Architects and Marine Engineers*, Vol. 74, 1966, pp. 522-562.
3. Turbal, V.K., "Theoretical Solution of the Problem on the Action of a Non-Axisymmetrical Ducted Propeller System in a Non-Uniform Flow," *Proceedings of the Symposium on Ducted Propellers*, The Royal Institution of Naval Architects, 1973, pp. 11-19.
4. George, M.F., "Linearised Theory Applied to Annular Aerofoils of Non-Axisymmetrical Shape in a Non-Uniform Flow," *Transactions of the Royal Institution of Naval Architects*, Vol. 120, 1977, pp. 201-210.
5. Dickmann, H.E., and Weissinger, J., "Beitrag zur Theorie optimaler Düsenschrauben (Kortdüsen)," *Jahrbuch Schiffbautechnischen Gesellschaft*, Band 49, 1955, pp. 253-305.
6. Morgan, W.B., "Theory of the Annular Airfoil and Ducted Propeller," *Fourth Symposium on Naval Hydrodynamics*, Office of Naval Research, ACR-92, 1962, pp. 151-197.
7. Weissinger, J., and Maass, D., "Theory of the Ducted Propeller - A Review," *Seventh Symposium on Naval Hydrodynamics*, Office of Naval Research, DR-148, 1968, pp. 1209-1264.
8. Morgan, W.B., "Some Results From the Inverse Problem of the Annular Airfoil and Ducted Propeller," *Journal of Ship Research*, Vol. 13, No. 1, March 1969, pp. 40-52.
9. Dyne, G., "A Method for the Design of Ducted Propellers in a Uniform Flow," Publ. No. 62 of the Swedish State Shipbuilding Experimental Tank, 1967, Göteborg, Sweden.
10. Dyne, G., "An Experimental Verification of a Design Method for Ducted Propellers," Publ. No. 63 of the Swedish State Shipbuilding Experimental Tank, 1968.
11. Falcão de Campos, J.A.C., "On the Calculation of Ducted Propeller Performance in Axisymmetric Flows," Doctor's Thesis, Netherlands Ship Model Basin Publ. No. 696, 1983, Wageningen, The Netherlands.
12. Kerwin, J.E., Kinnas, S.A., Lee, J.-T. and Shih, W.-Z., "A Surface Panel Method for the Hydrodynamic Analysis of Ducted Propellers," *Transactions of the Society of Naval Architects and Marine Engineers*, Vol. 95, 1987, pp. 93-122.

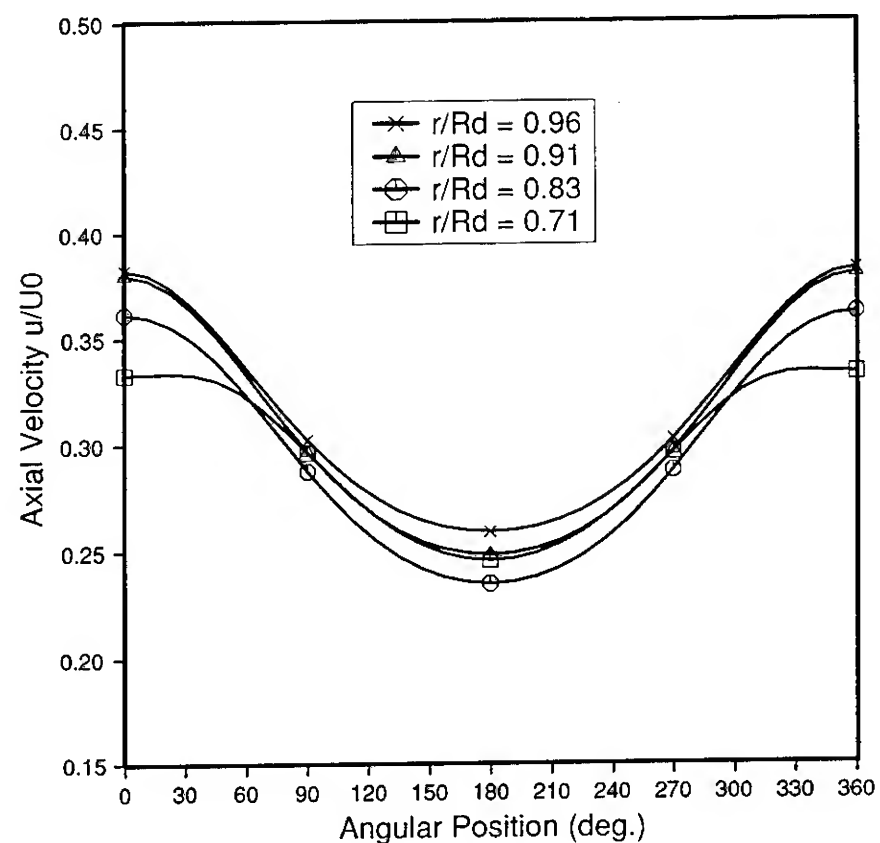
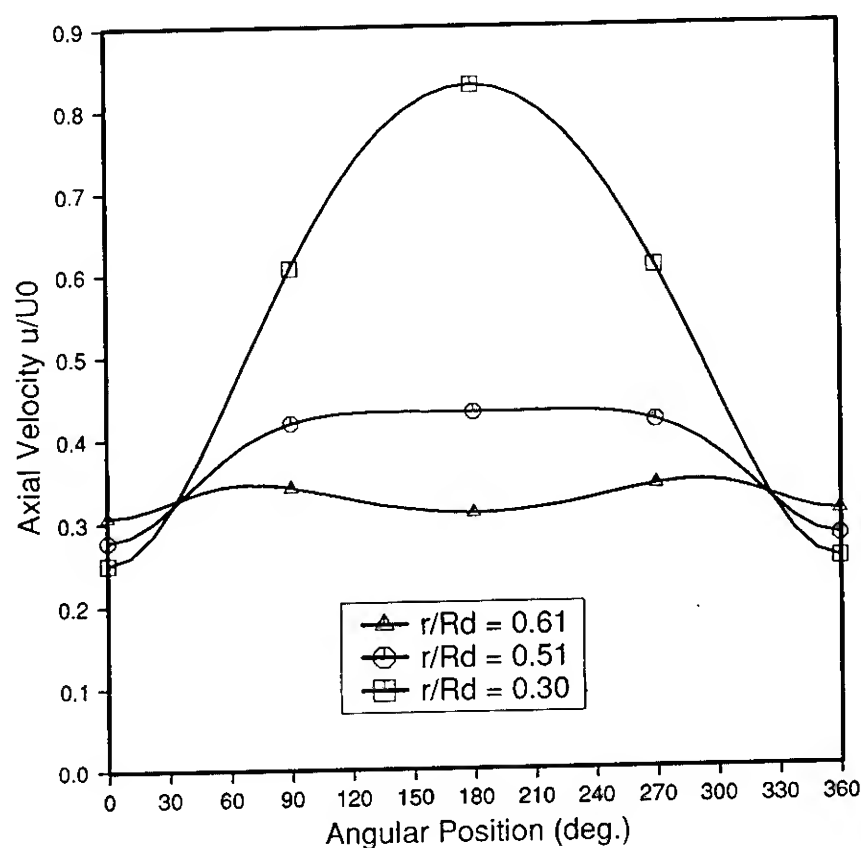


Fig. 10. Total disturbance axial velocity due to duct loading at  $x=0$ .  
Non-axisymmetric wake. Axisymmetric duct loading.  $c/R_d=0.5$ ,  $a=0.8$ ,  $C_L=0.9$ .



13. Kinnas, S.A. and Coney, W.B., "A Systematic Method for the Design of Ducted Propellers," Fourth International Symposium on Practical Design of Ships and Mobile Units, 1989, Varna, Bulgaria.
14. Feng, J. and Dong, S., "A Panel Method for the Prediction of Unsteady Hydrodynamic Performance of the Ducted Propeller with a Finite Number of Blades," Proceedings of the International Symposium on Propeller and Cavitation, 1986, Wuxi, China.
15. Huang, T.T., Wang, H.T., Santelli, N. and Groves, N.C., "Propeller/Stern Boundary Layer Interaction on Axisymmetric Bodies: Theory and Experiments," DTNSRDC Report 76-0113, Dec. 1976.
16. Huang, T.T. and Groves, N.C., "Effective wake: Theory and Experiment," Thirteenth Symposium on Naval Hydrodynamics, The Shipbuilding Research Association of Japan, 1980, pp. 651-673.
17. Dyne, G., "A Note on the Design of Wake Adapted Propellers," Journal of Ship Research, Vol. 24, No. 4, 1980, pp. 227-231.
18. Hawthorne, W.R., "On the Theory of Shear Flow," Gas Turbine Laboratory Report No. 88, Oct. 1966, Massachusetts Institute of Technology, Cambridge, Massachusetts.
19. Von Kármán, T. and Tsien, H.S., "Lifting-line Theory for a Wing in Nonuniform Flow," Quarterly of Applied Mathematics, Vol. 3, 1945, pp. 1-11.
20. Lighthill, M.J., "The Fundamental Solution for Small Steady Three-dimensional Disturbances to a Two-dimensional Parallel Shear Flow," Journal of Fluid Mechanics, Vol. 3, 1957, pp. 113-144.
21. Weissinger, J., "Linearisierte Profiltheorie bei ungleichförmiger Anströmung," Acta Mechanica 10, 1970, pp. 207-228.
22. Weissinger, J., "Linearisierte Profiltheorie bei ungleichförmiger Anströmung. Teil II: Schlanke Profile," Acta Mechanica 13, 1972, pp. 133-154.
23. Weissinger, J. and Overlach, B., "Grundlagen zu einer Theorie des Ringflügels in axialsymmetrischer Scherströmung," ZAMM 55, 1975, pp. 413-421.
24. Overlach, B., "Linearisierte Theorie der axialsymmetrischen Strömung um Ringflügel bei ungleichförmiger Anströmung," Dissertation, 1974, Karlsruhe.
25. Goodman, T.R., "Momentum Theory of a Propeller in a Shear Flow," Journal of Ship Research, Vol. 23, No. 4, Dec. 1979, pp. 242-252.
26. Falcão de Campos, J.A.C. and Van Gent, W., "Effective Wake of an Open Propeller in Axisymmetric Shear Flow," Netherlands Ship Model Basin Report No. 50030-3-SR, May 1981.
27. Van der Vegt, J.J.W., "Actuator Disk in a Two-Dimensional Non-Uniform Flow," International Shipbuilding Progress, Vol. 30, No. 348, Aug. 1983, pp. 158-178.
28. Van Gent, W., "A Model of Propeller - Ship Wake Interaction," Proceedings of the International Symposium on Propeller and Cavitation, 1986, Wuxi, China.
29. Lee, H., "Ducted Ship Propellers in Radially Sheared Flows," Ph.D. Thesis, Stevens Institute of Technology, 1985.
30. Lee, H., "Effects of Radially Sheared Inflow on the Design of Propeller Ducts," Third International Symposium on Practical Design of Ships and Mobile Units, 1987, Trondheim, Norway.
31. Weissinger, J., "Zur Aerodynamik des Ringflügels I. Die Druckverteilung dünner, fast drehsymmetrischer Ringflügel in Unterschallströmung," D.V.L. Bericht Nr. 2, 1955.

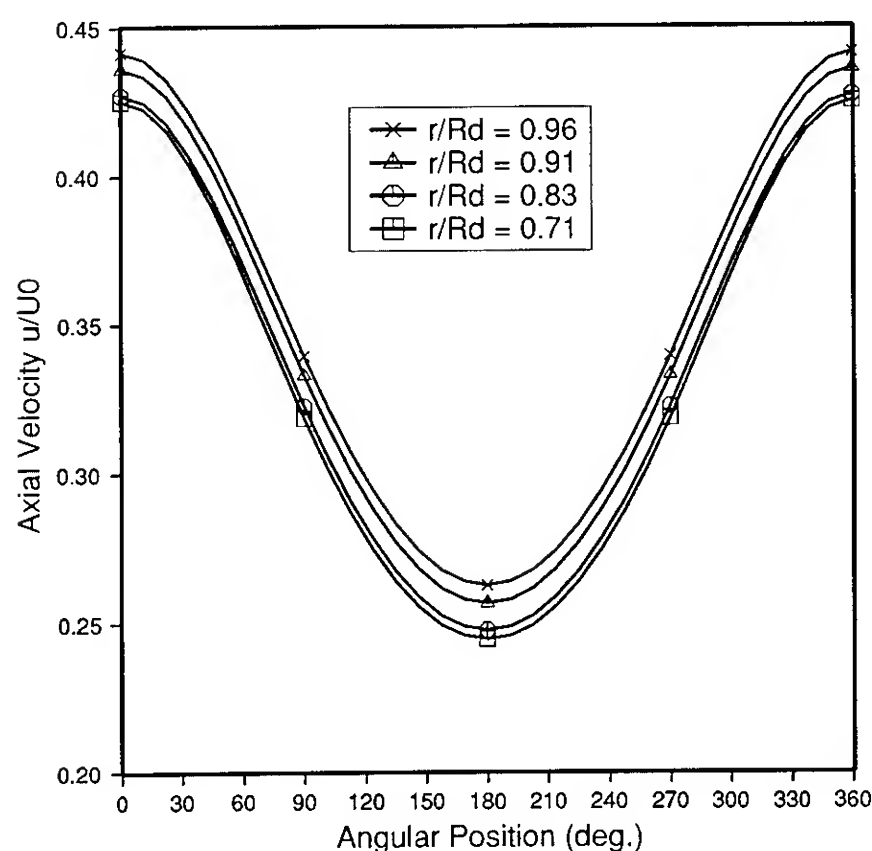
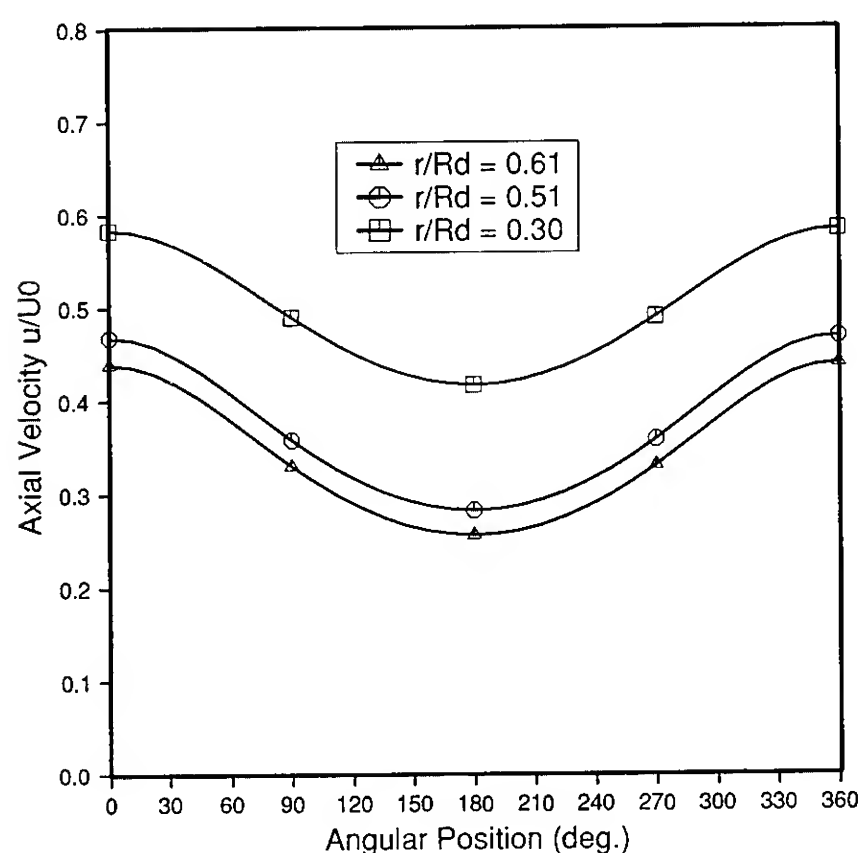


Fig. 11. Induction part of the axial velocity due to duct loading at  $x=0$ .  
Non-axisymmetric wake. Asymmetric duct loading.  $c/R_d=0.5$ ,  $a=0.8$ ,  $C_{L0}=0.9$ .

32. Weissinger, J., "Zur Aerodynamik des Ringflügels III. Der Einfluss der Profildicke," D.V.L. Bericht Nr. 42, 1957.
33. Ordway, D.E., Sluyter, M.M. and Sonnerup, B.O.U., "Three-Dimensional Theory of Ducted-Propellers," TAR-TR-602, Aug. 1960, Therm Advanced Research, Ithaca 1, New York.
34. Hough, G.R., and Ordway, D.E., "The Generalized Actuator Disk," *Developments in Theoretical and Applied Mechanics*, Vol. II, Pergamon Press, Oxford [etc.], 1965, pp. 317-336.

35. Batchelor, G.K., *An Introduction to Fluid Dynamics*, Cambridge University Press, Cambridge, 1967.
36. Baker, C.T.H., *The Numerical Treatment of Integral Equations*, Clarendon Press, Oxford, 1977, pp. 375.
37. Erdélyi, A., ed., *Tables of Integral Transforms*, Vol. 1, McGraw-Hill, New York, 1954, pp. 106.

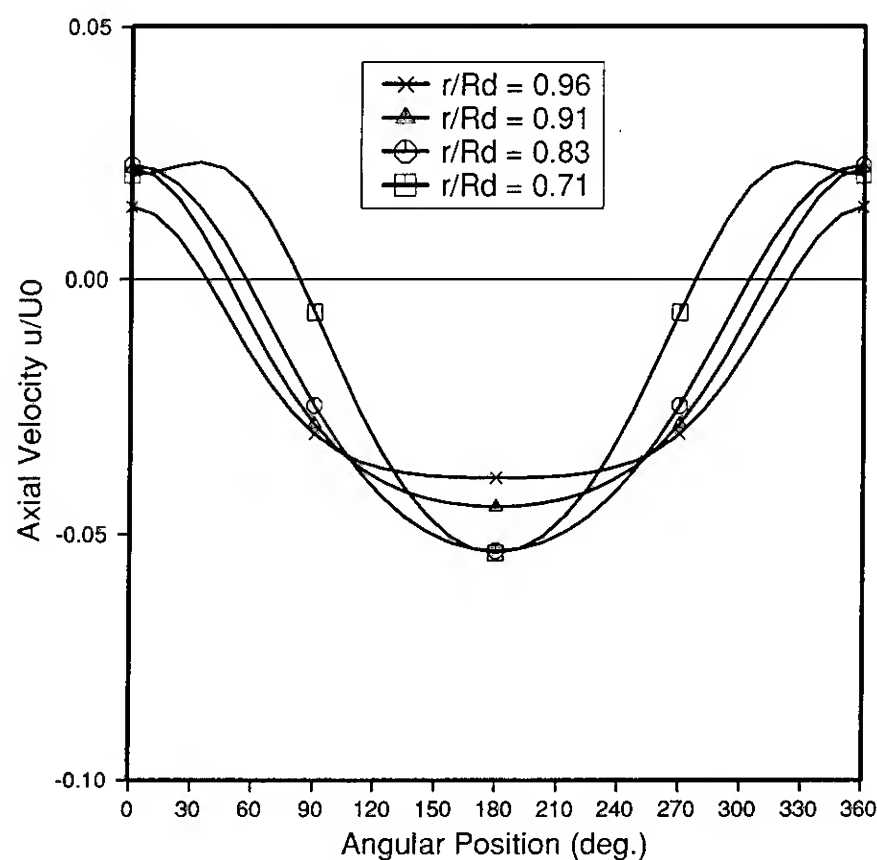
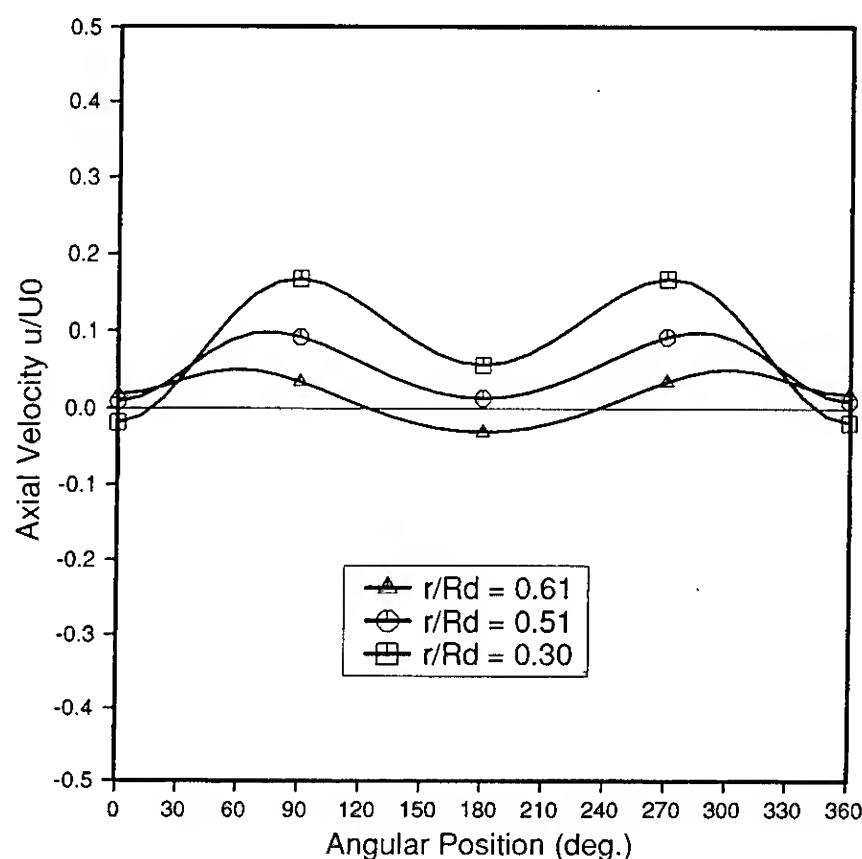


Fig. 12. Shear interaction part of the axial velocity due to duct loading at  $x=0$ . Non-axisymmetric wake. Asymmetric duct loading.  $c/R_d=0.5$ ,  $a=0.8$ ,  $C_{Lo}=0.9$ .

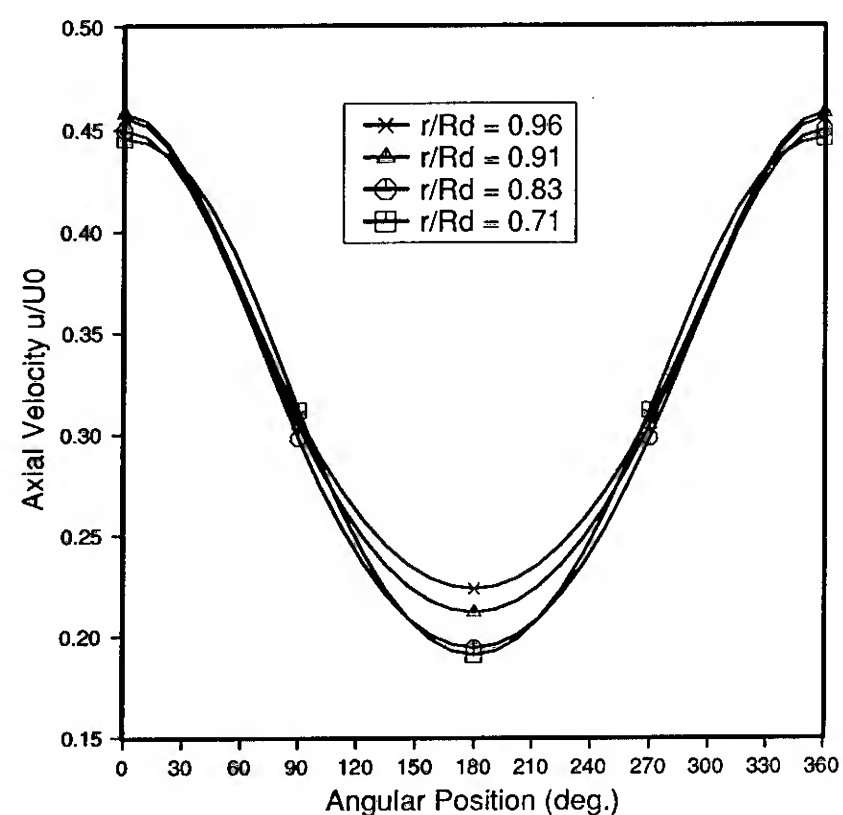
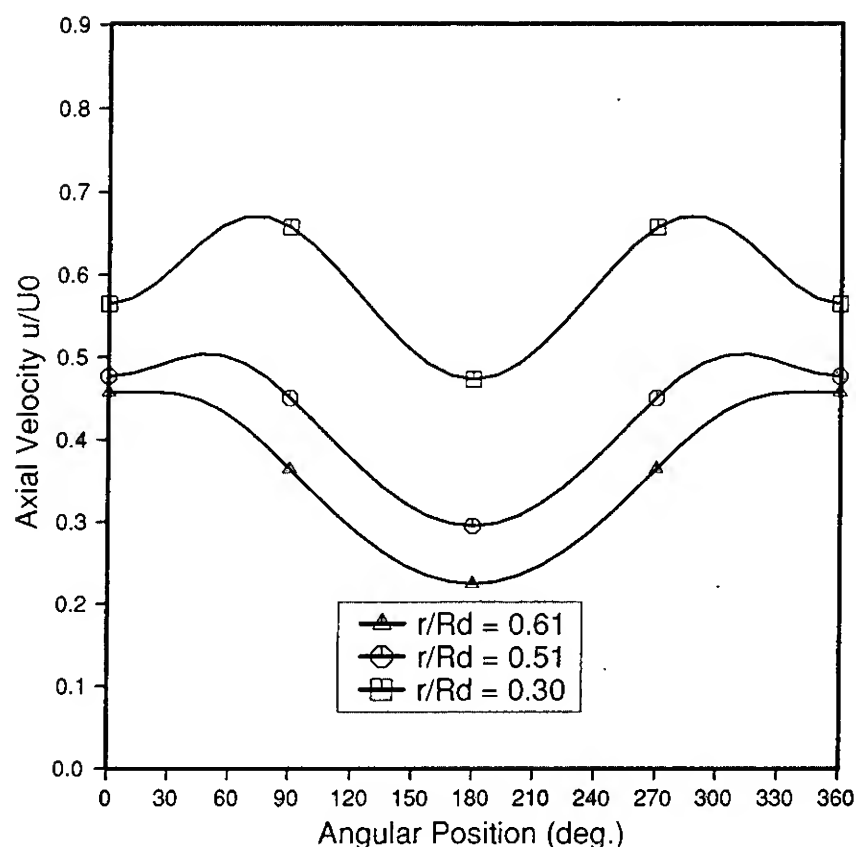


Fig. 13. Total disturbance axial velocity due to duct loading at  $x=0$ . Non-axisymmetric wake. Asymmetric duct loading.  $c/R_d=0.5$ ,  $a=0.8$ ,  $C_{Lo}=0.9$ .

# APPENDIX A

## Shear-Dependent Pressure Disturbance

Term  $T \tilde{\psi}_n^{(0)}$

### Duct Loading

The term is

$$T \tilde{\psi}_n^{(0)} = R_d \sum_{n=-\infty}^{\infty} G_{d_{mn}}^{(L)}(r; \lambda) \Delta \tilde{p}_{d_n}(\lambda) \quad (87)$$

with

$$G_{d_{mn}}^{(L)}(r; \lambda) = 2 |\lambda| K_n'(|\lambda| R_d) [K_m(|\lambda| r) h_1(r) + I_m(|\lambda| r) h_2(r)] + 2 |\lambda| I_n'(|\lambda| R_d) I_m(|\lambda| r) h_4(R_d), \quad r < R_d, \quad (88)$$

$$G_{d_{mn}}^{(L)}(r; \lambda) = 2 |\lambda| K_n'(|\lambda| R_d) K_m(|\lambda| r) h_1(R_d) + 2 |\lambda| I_n'(|\lambda| R_d) [K_m(|\lambda| r) h_3(r) + I_m(|\lambda| r) h_4(r)], \quad r > R_d, \quad (89)$$

with

$$h_1(r) = \int_0^r G_{12}(\sigma) I_n(|\lambda| \sigma) d\sigma, \quad (90)$$

$$h_2(r) = \int_r^{R_d} G_{22}(\sigma) I_n(|\lambda| \sigma) d\sigma, \quad (91)$$

$$h_3(r) = \int_{R_d}^r G_{12}(\sigma) K_n(|\lambda| \sigma) d\sigma, \quad (92)$$

$$h_4(r) = \int_r^{\infty} G_{22}(\sigma) K_n(|\lambda| \sigma) d\sigma. \quad (93)$$

and

$$G_{12}(r) = A_{mn}(r) I_m(|\lambda| r) + B_{mn}(r) |\lambda| I_{m-1}(|\lambda| r), \quad (94)$$

$$G_{22}(r) = A_{mn}(r) K_m(|\lambda| r) - B_{mn}(r) |\lambda| K_{m-1}(|\lambda| r). \quad (95)$$

### Duct Thickness

$$T \tilde{\psi}_n^{(0)} = i \rho \lambda R_d \sum_{n=-\infty}^{\infty} G_{d_{mn}}^{(T)}(r; \lambda) \tilde{T}_n(\lambda) \quad (96)$$

where

$$G_{d_{mn}}^{(T)}(r; \lambda) = 2 K_n(|\lambda| R_d) [K_m(|\lambda| r) h_1(r) + I_m(|\lambda| r) h_2(r)] + 2 I_n(|\lambda| R_d) I_m(|\lambda| r) h_4(R_d), \quad r < R_d, \quad (97)$$

$$G_{d_{mn}}^{(T)}(r; \lambda) = 2 K_n(|\lambda| R_d) K_m(|\lambda| r) h_1(R_d) + 2 I_n(|\lambda| R_d) [K_m(|\lambda| r) h_3(r) + I_m(|\lambda| r) h_4(r)], \quad r > R_d. \quad (98)$$

### Propeller Loading

$$T \tilde{\psi}_o^{(0)} = -i \lambda e^{-i \lambda x_p} G_{p_m}^{(L)}(r; \lambda) \quad (99)$$

with

$$G_{p_m}^{(L)}(r; \lambda) = 2 K_m(|\lambda| r) i_1(r) + 2 I_m(|\lambda| r) i_2(r) + 2 I_m(|\lambda| r) \times i_p(R_p) \int_{R_p}^{\infty} G_{22}(\sigma) K_o(|\lambda| \sigma) d\sigma, \quad r < R_p, \quad (100)$$

$$G_{p_m}^{(L)}(r; \lambda) = 2 K_m(|\lambda| r) [i_1(R_p) + i_p(R_p) \int_{R_p}^r G_{12}(\sigma) K_o(|\lambda| \sigma) d\sigma] + 2 I_m(|\lambda| r) \times i_p(R_p) \int_r^{\infty} G_{22}(\sigma) K_o(|\lambda| \sigma) d\sigma, \quad r > R_p, \quad (101)$$

where

$$i_1(r) = \int_0^r G_{12}(\sigma) [K_o(|\lambda| \sigma) i_p(\sigma) + I_o(|\lambda| \sigma) k_p(\sigma)] d\sigma, \quad r \leq R_p, \quad (102)$$

$$i_2(r) = \int_r^{R_p} G_{22}(\sigma) [K_o(|\lambda| \sigma) i_p(\sigma) + I_o(|\lambda| \sigma) k_p(\sigma)] d\sigma, \quad r \leq R_p, \quad (103)$$

and

$$i_p(r) = \int_0^r I_o(|\lambda| \sigma) \Delta p_p(\sigma) \sigma d\sigma, \quad (104)$$

$$k_p(r) = \int_r^{R_p} K_o(|\lambda| \sigma) \Delta p_p(\sigma) \sigma d\sigma. \quad (105)$$

## APPENDIX B

Radial Downwash  $v^{(0)}$  Due To Duct Loading

The radial momentum equation is

$$U \frac{\partial v^{(0)}}{\partial x} = - \frac{1}{\rho} \frac{\partial p^{(0)}}{\partial r} + \frac{\Delta p_d}{\rho} [H(x+c)-H(x-c)] \delta(r-R_d). \quad (106)$$

Taking Fourier transforms we obtain

$$i\lambda \rho U \tilde{v}^{(0)} = \sum_{m=-\infty}^{\infty} e^{im\theta} \left[ - \frac{\partial \tilde{\psi}_m^{(0)}}{\partial r} + \Delta \tilde{p}_{dm}(\lambda) \delta(r-R_d) \right]. \quad (107)$$

Evaluating the derivative in eq. (107) with (53) we obtain

$$i\lambda \rho U \tilde{v}^{(0)} = - \sum_{m=-\infty}^{\infty} e^{im\theta} \frac{1}{2} R_d \lambda^2 \Delta \tilde{p}_{dm}(\lambda) \times [I'_m(|\lambda|R_d) K'_m(|\lambda|R_d) + K'_m(|\lambda|R_d) I'_m(|\lambda|R_d)]. \quad (108)$$

At the duct  $r=R_d$  we obtain, after inverting the Fourier transforms  $\tilde{v}^{(0)}$  and  $\Delta \tilde{p}_{dm}$ ,

$$v^{(0)}(x, R_d, \theta) = - \frac{1}{4\pi \rho U} \sum_{m=-\infty}^{\infty} e^{im\theta} \left[ \frac{1}{2} R_d \int_{-c}^c \Delta p_{dm}(\xi) d\xi \times \int_{-\infty}^{\infty} \lambda IK_{(m-1)}^{(m+1)}(|\lambda|R_d) e^{i\lambda(x-\xi)} d\lambda \right], \quad (109)$$

with

$$IK_{(m-1)}^{(m+1)} = (I_{m+1} + I_{m-1})(K_m + K_{m-1}). \quad (110)$$

In terms of non-dimensional velocities and pressures

$$v^{(0)}(x, R_d, \theta) = \frac{1}{U} \sum_{m=-\infty}^{\infty} V_m^{(0)}(x, R_d) e^{im\theta}, \quad (111)$$

with

$$V_m^{(0)} = \frac{1}{4\pi} \frac{c}{R_d} \int_{-1}^1 \Delta p_{dm}(\xi) F_m(\eta) d\xi, \quad (112)$$

where

$$F_m(\eta) = - \frac{i}{2} \int_{-\infty}^{\infty} \lambda IK_{(m-1)}^{(m+1)}(|\lambda|) e^{i\lambda\eta} d\lambda \quad (113)$$

and

$$\eta = \frac{c}{R_d} (x-\xi). \quad (114)$$

The Fourier integral (113) can be written in the form

$$F_m(\eta) = \int_0^{\infty} \lambda IK_{(m-1)}^{(m+1)}(\lambda) \sin(\lambda\eta) d\lambda \quad (115)$$

and may be evaluated in terms of the Legendre functions of second kind and its derivatives. Using the results for the Fourier transforms of the modified Bessel functions [37] it may be shown that

$$F_m(\eta) = 2 \frac{P_m(|\eta|)}{\eta} + m\pi, \quad (116)$$

with

$$P_m(|\eta|) = \frac{\eta^2}{2} [(m-1)Q'_{m+1/2}(\omega) - (m+1)Q'_{m-3/2}(\omega) + 2m\eta^2 L_m(\omega)], \quad (117)$$

where  $L_m(\omega)$  is given by the recurrence relation

$$L_m(\omega) = L_{m-1}(\omega) - \frac{1}{2} [Q'_{m-1/2}(\omega) + Q'_{m-3/2}(\omega)], \quad m \geq 2, \quad (118)$$

$$L_0(\omega) = 0,$$

$$L_1(\omega) = - \frac{1}{2} [Q'_{-1/2}(\omega) + Q'_{1/2}(\omega)], \quad (119)$$

and

$$\omega = 1 + \frac{\eta^2}{2}. \quad (120)$$

With eq. (116), eq. (112) becomes

$$V_m^{(0)}(x, R_d) = \frac{1}{2\pi} \frac{c}{R_d} \left[ \int_{-1}^1 \frac{P_m(|\eta|)}{\eta} \Delta p_{dm}(\xi) d\xi + m \frac{\pi}{2} \int_{-1}^1 \Delta p_{dm}(\xi) d\xi \right]. \quad (121)$$

Since  $Q'_{m+1/2}(\omega) = -\eta^2 + O(\ln|\eta|)$  for small values of  $\eta$ ,  $P(0) = 1$  and the first integral in eqs. (3-36)<sup>m</sup> has a Cauchy singularity. The result (121) agrees with the result given by Weissinger in ref. [31]. Further reduction of eq. (121) including the treatment of the Cauchy singularity can be found in the original reference.

## DISCUSSION

Ali H. Nayfeh  
Virginia Polytechnic Institute and State University, USA

The convergence problem near the axis may be alleviated if one uses an analytical rather than a numerical solution there. Such a procedure was used by Nayfeh, Kaiser, and co-workers in the seventies to treat acoustic waves propagating in circular ducts. The results were published in the *AIAA Journal*, *Journal of Sound and Vibration*, and the *Journal of the Acoustical Society of America*.

## AUTHORS' REPLY

The author thanks Prof. Nayfeh for pointing out the possibility of using an analytical solution in the vicinity of the axis. Indeed, see for instance references [1] and [2]; the form of the solution near the axis is determined by the potential part of the solution, even in the absence of a uniform flow core and certainly in the case of bounded shear parameters  $a$  and  $b$  at the axis. In this case, the analytical solution for each circumferential pressure harmonic behaves like the modified Bessel function  $I_m$  multiplied by a constant. Its asymptotic behavior for small arguments can then be used to determine the constant by collocation of the integral equation (45) at a point off the center line but sufficiently close to it.

[1] Eversman, W., "Effect of Boundary Layer on the Transmission and Attenuation of Sound in an Acoustically Treated Circular Duct," *Journal of the Acoustical Society of America*, Vol. 49, No. 5, 1971, pp. 1372-1380.

[2] Nayfeh, A. H., Kaiser, J. E. and Telionis, D. P., "Acoustics of Aircraft Engine-Duct Systems," *AIAA Journal*, Vol. 13, No. 2, 1975, pp. 130-153.

## DISCUSSION

William B. Morgan  
David Taylor Research Center, USA

This is a very interesting paper on the design problem of ducted propellers. I have a question concerning the optimum ducted propeller in a shear flow. Can you say anything about how to calculate the optimum ducted propeller considering both the optimum propeller and the optimum duct shape in a shear flow?

## AUTHORS' REPLY

Dr. Morgan raises the question of how to optimize both the propeller and the duct in a shear flow. Although the interaction with shear covers only a particular aspect of the propulsor-hull interaction, the question may be addressed without considering in detail the shear producing mechanism which is the presence of the ship's hull with its boundary layer and wake. From an untheoretical point of view, it would be interesting to know for a given sheared inflow velocity field what are the load distributions on the duct reference cylinder and on the propeller disk which minimize the kinetic energy of the fluid left far behind the ducted propeller system and which satisfy a given thrust constraint. Such optimization would lead to the ducted propeller loading for maximum recover of the kinetic energy of the fluid present in the sheared incoming flow. The formulation of such optimization problem has not been attempted. From a more practical point of view, the present model may be conceivably used to determine the duct shape for maximum attainable rectification of the inflow to the propeller, for given propeller radial load distribution in a given wake field. This is a desirable feature from the standpoint of avoiding cavitation on the propeller blades which may also lead to efficiency improvement.



# A Potential Based Panel Method for the Unsteady Flow Around Open and Ducted Propellers

S. Kinnas, C.-Y. Hsin, D. Keenan  
(Massachusetts Institute of Technology, USA)

## Abstract

The unsteady flow around an open marine propeller subject to a spatially nonuniform inflow is analyzed by utilizing a time marching potential based panel method. An efficient algorithm is implemented in order to ensure an explicit Kutta condition (i.e. pressure equality) at the blade trailing edge at each time step. The numerical method is shown to be very robust for a *broad range* of reduced frequencies as well as *consistent* with known analytic solutions and with an existing unsteady lifting surface method.

A hybrid panel method is developed for the analysis of the unsteady flow around ducted propellers. It combines an unsteady lifting surface method for the propeller with a potential based panel method for the duct. The propeller is essentially treated with an existing time marching vortex lattice scheme which has been developed for open propellers, with the effects of the duct being accounted for via the *generalized images* of the propeller singularities with respect to the duct. The proposed method is shown to be appropriate for treating unsteady ducted propeller flows in a computationally efficient and robust manner, especially when a given ducted propeller geometry must be analyzed for various inflow conditions.

## 1 Introduction

In most marine applications the propeller is subject to severe non-axisymmetric wakes produced from the boundary layer of the vehicle. Therefore unsteady marine propeller flows are a very important aspect of the overall propeller / hull hydrodynamic analysis problem.

One of the important steps in determining the complete propeller/wake interaction, is the analysis of the unsteady flow around a propeller in the presence of a prescribed spatially nonuniform inflow. Accurate predictions of the unsteady pressure distributions on the blade, especially at the blade leading edge and tip, are crucial in determining cavitation inception, unsteady boundary layer separation as well as leading-edge vor-

tex separation.

Numerical lifting surface methods have been extensively applied for the analysis of unsteady propeller flows. One of the first investigators to formulate the unsteady propeller lifting surface problem in terms of the acceleration potential was Hanaoka [7,8]. The acceleration potential formulation was implemented, in terms of finite number of chordwise modes, by Tsakonas et al. [32,31]. More recently, the unsteady vortex lattice technique was employed by Kerwin and C.S. Lee [17]. The unsteady vortex lattice technique was extended by Keenan [14] to include unsteady vortex wake relaxation. A review of the different steady and unsteady lifting surface methods as applied to marine propellers has been given by Kerwin [16].

One of the major drawbacks of the lifting surface methods though, is their inherent failure at the blade leading edge and tip where the blade thickness effects are substantial. On the other hand, panel methods have been applied for the analysis of the steady flow around marine propellers, including the hub by, among others, Hess and Valarezo [10], Kerwin, Kinnas, J.T. Lee and Shih (who also included the duct) [18] and Hoshino [12]. The first of those methods employs a source based formulation [9], and the other two employ a potential based formulation [27].

Panel methods were first extended to treat unsteady flows around two dimensional hydrofoils by Giesing [4], who employed a source based formulation, and then by Basu and Hancock [1] who employed a surface vorticity formulation but also allowed for wake relaxation. More recently, panel methods have been extended to treat the unsteady flow around helicopter blades by Maskew [25] and by Morino, Kaprielian and Sipicic [26], with emphasis given to the evolution of the rotor free wakes.

In the present work, a time marching potential based panel method is developed for the analysis of the unsteady flow around marine propellers, with emphasis on the accurate predictions of unsteady blade pressures and forces for a large range of blade rate harmonics. A computationally efficient explicit pressure Kutta condition is implemented in the panel method in order to ensure pressure equality at the blade trailing edge at

each time step. The numerics of the panel method are shown to be *robust* with respect to the size of the time step and the number of panels on the blade for a broad range of reduced frequencies. The numerical method is also shown to be consistent with existing analytic solutions as well as with an unsteady lifting surface method.

Finally, a hybrid lifting surface / potential based panel method is developed for the analysis of unsteady flows around ducted propellers. The propeller is treated with a time marching vortex lattice method, with the effects of the duct being accounted for via the generalized images of the singularities representing the propeller and its trailing wake with respect to the duct.

The generalized image idea was first applied to the analysis of the flow around a propeller in the presence of a duct by Kinnas and Coney [21]. The propeller was modelled in lifting line theory by using a finite number of semi-infinite helical vortex horseshoes. The effect of the duct on the propeller was accounted for via the generalized images of the horseshoes with respect to the duct. The flow field of the generalized image of each horseshoe was computed by solving for the non-axisymmetric potential around the duct in the presence of the horseshoe.

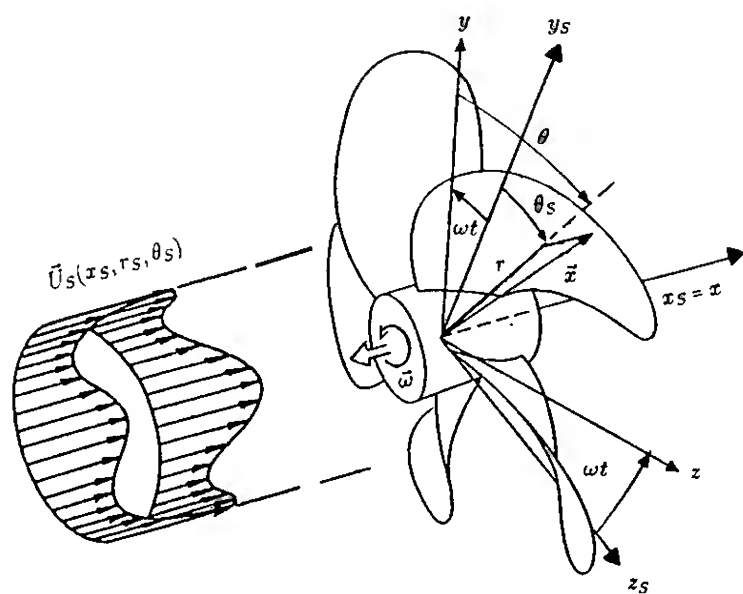


Figure 1: The propeller in a spatially nonuniform inflow.

## 2 The Unsteady Panel Method for Open Propellers

### 2.1 Formulation

Consider a propeller subject to a spatially nonuniform inflow  $\vec{U}_S(x_S, r_S, \theta_S)$ , as shown in Figure 1. The inflow is taken with respect to the absolute (ship fixed) system of cylindrical coordinates  $x_S, r_S, \theta_S$ . The flow around the propeller will be analyzed with respect to the propeller fixed system  $(x, y, z)$ , also shown in Figure 1. If the propeller rotates with angular velocity  $-\vec{\omega}$  (i.e. right-handed), then the inflow relative to the propeller,  $\vec{U}_{in}$ , will be time dependent and given as

$$\vec{U}_{in}(x, y, z, t) = \vec{U}_S(x, r, \theta - \omega t) + \vec{\omega} \times \vec{x}, \quad (1)$$

where  $r = \sqrt{y^2 + z^2}$ ,  $\theta = \arctan(z/y)$  and  $\vec{x} = (x, y, z)$ .

We assume at this point, that the interaction between the propeller and the inflow is inviscid and irrotational<sup>1</sup>. Then, the time dependent total flow velocity relative to the propeller fixed system,  $\vec{q}(x, y, z, t)$ , can be written in terms of the perturbation potential,  $\phi(x, y, z, t)$ , as follows:

$$\vec{q}(x, y, z, t) = \vec{U}_{in}(x, y, z, t) + \nabla \phi(x, y, z, t). \quad (2)$$

By applying Green's formula for  $\phi(x, y, z, t)$  at any time  $t$ , we will get the following integral equation for the perturbation potential  $\phi_p$  at every point  $p$  on the propeller blade surface  $S_P$ :

$$2\pi\phi_p = \int_{S_P} \left[ \phi_q \frac{\partial G(p; q)}{\partial n_q} - G(p; q) \frac{\partial \phi_q}{\partial n_q} \right] dS + \int_{S_W} \Delta \phi(r_q, \theta_q, t) \frac{\partial G(p; q)}{\partial n_q} dS, \quad (3)$$

with the subscript  $q$  corresponding to the variable point in the integrations;  $\vec{n}$  is the unit vector normal to the propeller surface or to the wake surface,  $\Delta \phi$  is the potential jump across the wake sheet, and  $G(p; q)$  is the Green's function. In the case of unbounded three dimensional fluid domain,  $G$  is given as

$$G(p; q) = \frac{1}{R(p; q)}, \quad (4)$$

with  $R(p; q)$  being the distance between points  $p$  and  $q$ .

Equation (3) expresses the potential on the propeller blade as the superposition of the potentials induced by a continuous source distribution,  $G$ , on the propeller surface,  $S_P$ , and a continuous dipole distribution,  $\partial G / \partial n$ , on the propeller surface  $S_P$  and its wake  $S_W$ . The strength of the source distribution is given, via the kinematic boundary condition, as

$$\frac{\partial \phi_q}{\partial n_q} = -\vec{U}_{in}(x_q, y_q, z_q, t) \cdot \vec{n}_q \quad (5)$$

where  $x_q, y_q, z_q$  are the coordinates of point  $q$  with respect to the propeller fixed system.

The strength of the dipole distribution is unknown and equal to the perturbation potential on the propeller or to the potential jump in the wake. The dipole strengths will be determined by inverting integral equation (3).

The position of the trailing wake,  $S_W$ , is assumed to be invariant with time and taken to be the same as that corresponding to the circumferentially averaged inflow [5]. The dipole strength  $\Delta \phi(r, \theta, t)$  in the wake, is convected along the assumed wake model with angular

<sup>1</sup>This is equivalent to assuming that  $\vec{U}_S$  is the *effective* wake.

speed  $\omega$ , in order to ensure that the pressure jump in the wake is equal to zero, i.e.,

$$\begin{aligned}\Delta\phi(r, \theta, t) &= \Delta\phi\left(r, \theta_T(r), t - \frac{\theta - \theta_T(r)}{\omega}\right) = \\ &= \Delta\phi_T\left(r, t - \frac{\theta - \theta_T(r)}{\omega}\right); t \geq \frac{\theta - \theta_T(r)}{\omega} \\ \Delta\phi(r, \theta, t) &= \Delta\phi^S(r); t < \frac{\theta - \theta_T(r)}{\omega}\end{aligned}\quad (6)$$

where  $r, \theta$  are the cylindrical coordinates of the wake surface,  $S_W$ , and  $\theta_T(r)$  is the  $\theta$  coordinate of the propeller blade trailing edge at radius  $r$ .  $\Delta\phi^S(r)$  is the steady flow potential jump in the wake when the propeller is subject to the circumferentially averaged inflow. For  $t < 0$  we assume that the propeller is subject to the circumferentially averaged inflow. The unsteady inflow is "turned on" at  $t = 0$ .

The value of the dipole strength,  $\Delta\phi_T(r, t)$ , at the trailing edge of the blade at time  $t$ , will be given by

$$\Delta\phi_T(r, t) = \phi_T^+(r, t) - \phi_T^-(r, t) = \Gamma(r, t) \quad (7)$$

where  $\phi_T^+(r, t)$  and  $\phi_T^-(r, t)$  are the values of the potential at the upper (suction side) and lower (pressure side) blade trailing edge, respectively, at time  $t$ . The difference in those potentials is also equal to the circulation  $\Gamma$  at time  $t$  around the blade section at radius  $r$ . The condition (7) is equivalent to requiring the shed vorticity from the blade trailing edge to be proportional to the time rate of change of the circulation around the blade.

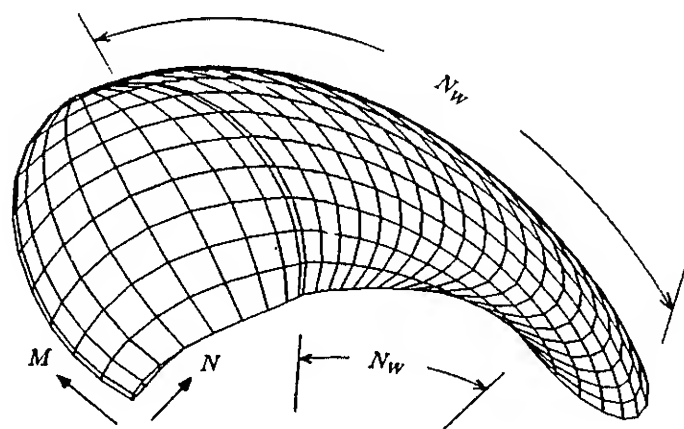


Figure 2: Panel arrangement for a propeller blade and its wake,  $N = 20$ ,  $M = 10$ ,  $\Delta\theta_W = 6^\circ$ .

## 2.2 Numerical Implementation

Equation (3) is a Fredholm integral equation of the second kind with respect to  $\phi_p$ . To solve this equation numerically, we discretize the propeller and wake surface into quadrilateral panels. A typical panel arrangement for a propeller and its wake is shown in Figure 2. The propeller blade panel arrangement is identical to that used in the steady propeller panel method [24]. The time domain is also discretized into equal time intervals  $\Delta t$ . The panels in the wake start from the blade trailing

edge and their edges are located on the prescribed wake surface at equal angular spacing  $\Delta\theta_W$ , which is related to the time step  $\Delta t$  as follows:

$$\Delta\theta_W = \omega\Delta t. \quad (8)$$

On each of the quadrilateral panels, the dipole or source distributions are approximated by constant strength distributions. The discretized version of the integral equation (3) is applied at the centroids of each of the propeller panels and at each time step  $n = t/\Delta t$ . This renders the following system of linear equations:

$$\begin{aligned}&\sum_{K=1}^{N_B} \sum_{j=1}^{N_P} a_{i,j}^K \phi_j^K(n) + \sum_{K=1}^{N_B} \sum_{m=1}^M \sum_{l=1}^{N_W} W_{i,m,l}^K \Delta\phi_{m,l}^K(n) \\ &= \sum_{K=1}^{N_B} \sum_{j=1}^{N_P} b_{i,j}^K \sigma_j^K(n); \quad i = 1, N_P \times N_B\end{aligned}\quad (9)$$

where  $N_B$  is the number of blades, and for each blade,  $N$  is the number of chordwise panels.  $M$  is the number of spanwise panels,  $N_P = N \times M$  is the total number of panels and  $N_W$  is the number of chordwise panels in the wake.

The influence coefficients  $a_{i,j}^K$  and  $b_{i,j}^K$  are defined as the potentials induced at panel  $i$  by unit (constant) strength dipole and source distributions, respectively, located at panel  $j$  on blade  $K$ . The wake influence coefficients  $W_{i,m,l}^K$  are defined similarly. The shape of the surface bounded by the edges of each panel (nonplanar in general), is approximated by a hyperboloidal surface and the corresponding influence coefficients are evaluated by using analytical expressions [27], [28], [13]. The use of hyperboloidal surface panels instead of planar panels, has been found crucial for the consistency and convergence of the steady flow propeller panel method [24], especially, when applied to extreme propeller geometries (i.e. high skew and twist) [13]. A similar conclusion has also been reached by Hoshino [12].

The source strength  $\sigma_j^K(n)$  is defined from equation (5) as

$$\sigma_j^K(n) = -\vec{U}_{in}(x_j^K, y_j^K, z_j^K, n\Delta t) \cdot \vec{n}_j^K \quad (10)$$

with  $x_j^K, y_j^K, z_j^K$  being the coordinates of the centroid of panel  $j$  on blade  $K$  and  $\vec{n}_j^K$  being the unit vector normal to that panel.

The terms in equation (9) can be regrouped as (the superscript 1, which denotes the key blade, is omitted):

$$\sum_{j=1}^{N_P} a_{i,j} \phi_j(n) + \sum_{m=1}^M \sum_{l=1}^{N_W} W_{i,m,l} \Delta\phi_{m,l}(n) = RHS_i(n); \quad i = 1, N_P \quad (11)$$

where

$$\begin{aligned}RHS_i(n) &= \sum_{K=2}^{N_B} \sum_{j=1}^{N_P} b_{i,j}^K \sigma_j^K(n) - \sum_{K=2}^{N_B} \sum_{j=1}^{N_P} a_{i,j}^K \phi_j^K(n) \\ &- \sum_{K=2}^{N_B} \sum_{m=1}^M \sum_{l=1}^{N_W} W_{i,m,l}^K \Delta\phi_{m,l}^K(n) - \sum_{m=1}^M \sum_{l=2}^{N_W} W_{i,m,l} \Delta\phi_{m,l}(n).\end{aligned}\quad (12)$$

The system of equations (11) must be solved at each time step  $n$  with respect to the potentials on the key blade,  $K = 1$ . The potentials on the other blades ( $K > 2$ ) and their wakes, which appear on the right-hand side of equation (11), are taken equal to those on the key blade at an earlier time step, when the blade  $K$  was at the place of the key blade. This scheme, already used in an unsteady propeller lifting surface vortex lattice method [19], is essentially an iterative method of solving the system of equations (9) in order to determine the steady state oscillatory solution for a given inflow. The solution, in most cases, was found to converge after three propeller revolutions. Solving equation (11) instead of equation 9 requires the inversion of a much smaller matrix and thus reduces substantially the computing time. It also requires less computer storage, since only the solution for the key blade, rather than for all blades, needs to be stored at each time step.

The values of  $\Delta\phi_{m,l}(n)$  for  $l > 2$  (i.e. for all panels in the wake, except those next to the trailing edge) are determined from the discretized form of equation (6):

$$\begin{aligned}\Delta\phi_{m,l}(n) &= \Delta\phi_{m,1}(n-l+1); \quad l \geq 2, \quad n \geq l, \\ \Delta\phi_{m,l}(n) &= \Delta\phi_m^S; \quad l \geq 2, \quad n < l.\end{aligned}\quad (13)$$

On the other hand, the value of the potential  $\Delta\phi_{m,1}$ , at the first wake panel may be given, by using equation (7), as

$$\Delta\phi_{m,1} = \frac{\Gamma_m(n) + \Gamma_m(n-1)}{2} \quad (14)$$

with  $\Gamma_m(n)$  denoting the circulation around the blade strip  $m$  at time step  $n$ .

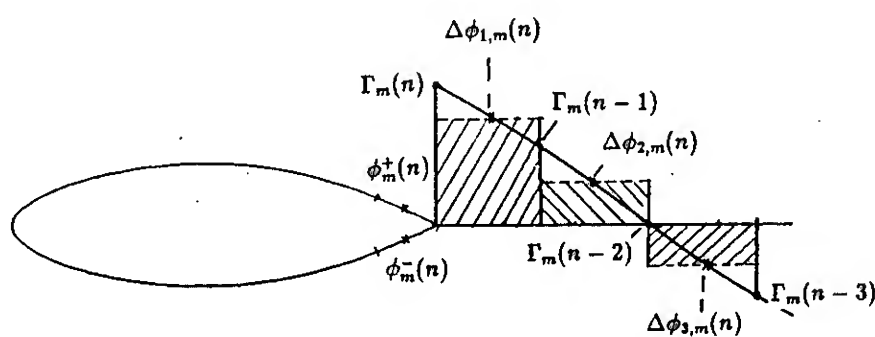


Figure 3: Expanded view of the dipole distribution in the wake of blade strip  $m$ .

In deriving equations (13) and (14), the continuous dipole distribution over each wake panel is approximated by a constant distribution with strength equal to the mean value of the potentials at the edges of the panel, as shown in Figure 3.

Numerically,  $\Gamma_m(n)$  is approximated by

$$\Gamma_m(n) = \phi_m^+(n) - \phi_m^-(n) \quad (15)$$

where  $\phi_m^+$  and  $\phi_m^-$  are the potentials at the upper and lower trailing edge panel, respectively, at blade strip  $m$ .

Equation (15) is an extension of Morino's Kutta con-

dition in steady flow [27], though different from the unsteady Kutta condition employed by Morino et. al. in [26].

The right-hand side of equation (15) approximates the jump in the potential at the trailing edge with the difference of the potentials at the trailing edge control points on the blade, as shown in Figure 3. An improvement on this approximation will be presented in the next section.

By substituting equations (15) and (14) into equation (11) we end up with a linear system of equations with respect to the unknown potentials  $\phi_j(n)$  on the key blade. This system of equations is inverted at each time  $n$ .

A modification on the previously presented numerical scheme has been implemented, in which the dipole sheet on the first wake panel is approximated by a linear instead of a constant distribution. As will be described in section 2.5, that modification is necessary to make the results of the unsteady panel method practically insensitive to the size of the time step. In that case, the system of equations (11) will be modified to be

$$\sum_{j=1}^{N_P} a_{i,j} \phi_j(n) + \sum_{m=1}^M T_{i,m}^L \Gamma_m(n) = \overline{RHS}_i(n), \quad i = 1, N_P, \quad (16)$$

with

$$\overline{RHS}_i(n) = RHS_i(n) - T_{i,m}^R \Gamma_m(n-1); \quad i = 1, N_P \quad (17)$$

and where  $T^L$  ( $T^R$ ) are the influence coefficients of a linear dipole distribution (in the chordwise direction) with unit value at the left - i.e. trailing edge - (right) edge and zero value at the right (left) edge. Substituting equation (15) in equation (16) we end up, at each time step, with a system of  $N_P$  linear equations with respect to the  $N_P$  unknown potentials on the panels of the key blade.

Equation (16) can also be written in the following matrix form

$$[A][\phi] + [T][\Gamma] = [RHS] \quad (18)$$

with  $[A]$ ,  $[\phi]$  and  $[T]$  being the matrices of  $a_{i,j}$ 's,  $\phi_j(n)$ 's and  $T_{i,m}^L$ 's, respectively, and

$$\begin{aligned}[\Gamma] &= [\Gamma_1(n), \dots, \Gamma_M(n)]^T, \\ [RHS] &= [\overline{RHS}_1(n), \dots, \overline{RHS}_{N_P}(n)]^T.\end{aligned}\quad (19)$$

## 2.3 Unsteady Pressures and Forces on the Blade

The pressure,  $p$ , at every point  $\vec{x}$  on the blade and for each time step  $n$  is computed from the potentials on the blade by applying the unsteady flow Bernoulli's equation with respect to the propeller system:

$$\frac{p}{\rho} + \frac{1}{2}q^2 + \frac{\partial\phi}{\partial t} = \frac{p_\infty}{\rho} + \frac{1}{2}q_\infty^2 \quad (20)$$

where  $\rho$  is the density of the fluid,  $q$  is the magnitude of the total surface velocity with respect to the propeller system at point  $\vec{x}$  and time step  $n$ ,  $p_\infty$  and  $q_\infty$  are the pressure and the magnitude of the velocity of the unperturbed flow, with respect to the propeller system, respectively.

The surface velocity  $q$  is computed in terms of the derivatives of the perturbation potentials on the blade surface, in the same way as in the steady flow panel method [18]. The  $\partial\phi/\partial t$  term in equation (20) is computed numerically, by implementing a backward finite difference – second order accurate – scheme with respect to time [13].

The inviscid unsteady forces acting on each propeller blade are computed by integrating the unsteady pressure distributions on the surface of the blade.

## 2.4 The Unsteady Pressure Kutta Condition and the Base Problems

In the steady flow panel method for propellers and ducts [18], it was found that the numerical Kutta condition (15) [27] was not sufficient and an iterative scheme was developed in order to modify the solution and ensure pressure equality at the trailing edge.

An explicit pressure Kutta condition was also found to be required in the unsteady panel method. For example, in Figure 4 the unsteady pressure distributions before and after applying the iterative pressure condition, are shown for the N4118 propeller in the wake field described in section 2.5.2. The iterative method to ensure pressure equality at the trailing edge, is described next.

The pressure difference,  $\Delta p_m$ , at the trailing edge of each blade strip  $m$ , is defined as

$$\Delta p_m(n) = p_m^+(n) - p_m^-(n) \quad (21)$$

with  $p_m^+$  and  $p_m^-$  being the pressures at the upper and lower trailing edge, respectively.

We call  $\phi_j^*$  and  $\Gamma_m^*$  the potentials and the circulations, respectively, which satisfy equation 18 and which, in addition, produce a zero pressure difference (within a desired tolerance) at the blade trailing edge. That is,

$$[A][\phi^*] + [T][\Gamma^*] = [RHS], \quad (22)$$

and

$$\Delta p_m^*(n) = 0; \quad m = 1, M. \quad (23)$$

Because of the nonlinear dependence of  $\Delta p_m^*$  on  $\phi^*$ , an iterative method is used in solving the system of equations (22) and (23) with respect to the unknown  $\phi_j^*$ 's and  $\Gamma_m^*$ 's. The following  $M$ -dimensional Newton-Raphson scheme is employed in order to determine the circulations  $\Gamma_m^*$ 's:

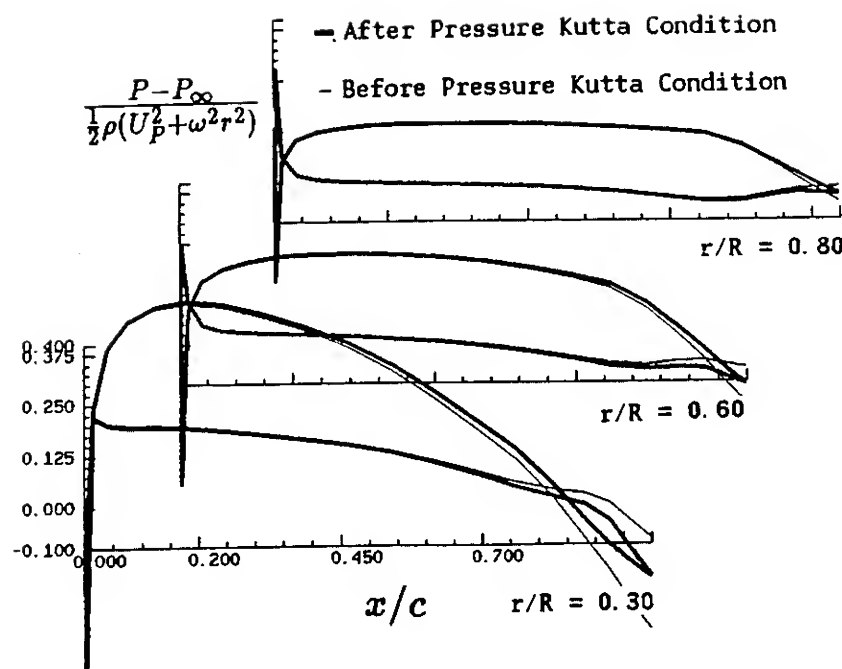


Figure 4: Pressure distributions vs. chordwise location at different propeller radii,  $r/R$ , for the N4118 propeller at blade angle  $\theta_S = 300^\circ$ .  $J_P = 0.833$ ,  $u_g = 0.2$ . Before and After applying an iterative pressure Kutta condition.

$$[\Gamma^*]^{(k+1)} = [\Gamma^*]^{(k)} - [J^{(k)}]^{-1}[\Delta p^*]^{(k)} \quad (24)$$

where  $k$  denotes the iteration number and  $[\Delta p^*]^{(k)}$  are the pressure differences which correspond to the solution  $[\phi^*]^{(k)}$  of the system of linear equations

$$[A][\phi^*]^{(k)} = [RHS] - [T][\Gamma^*]^{(k)}. \quad (25)$$

The first iteration ( $k = 1$ ) is taken equal to the solution when the Kutta condition (15) is applied as

$$\begin{aligned} [\phi^*]^{(1)} &= [\phi], \\ [\Gamma^*]^{(1)} &= [\Gamma]. \end{aligned} \quad (26)$$

In equation (24) the elements of the Jacobian matrix  $[J^{(k)}]$  are defined as

$$J_{i,j}^{(k)} = \frac{\partial \Delta p_i^*(k)}{\partial \Gamma_j^*(k)}. \quad (27)$$

The derivatives in equation (27) are determined numerically in a similar way as described in [18].

The present iterative scheme has been found to converge rapidly (in 3 to 4 iterations). This would require solving, for each time step, the system of equations (25) as many times as the number of iterations. As a result the already considerable computing time<sup>2</sup> would be increased approximately by a factor equal to the number of iterations, since a substantial part of the total computing time is devoted in inverting the system of equations 22. Instead of inverting the system of equations 25 at each time step, the following technique of base problems is developed and implemented:

<sup>2</sup>For a discretization with  $N = 40$  and  $M = 20$  the computing time on an IRIS 4D/25 TG is approximately equal to four hours.



First, the observation is made that for each time step the matrix  $[RHS]$  is identical in equations (22) and (25). Thus, subtracting equations 25 from 22 we get

$$[A] [\phi^{*(k)} - [\phi]] = -[T] [\Gamma^{*(k)} - [\Gamma]]. \quad (28)$$

By defining

$$\begin{aligned} [\delta\phi] &= [\phi^{*(k)} - [\phi]], \\ [\delta\Gamma] &= [\Gamma^{*(k)} - [\Gamma]] \end{aligned} \quad (29)$$

equation (28) can then be written as

$$[A][\delta\phi] = -[T][\delta\Gamma]. \quad (30)$$

At this point, we define the base potentials,  $[\Phi]^m$ , which correspond to the system of equations (30), and which are the solutions to the base problems

$$[A][\Phi]^m = -[T][B]^m, \quad m = 1, M, \quad (31)$$

where

$$[B]^m = [B_1 = 0, B_2 = 0, \dots, B_m = 1, \dots, B_M = 0]^T. \quad (32)$$

Physically, the base potentials  $[\Phi]^m$  correspond to the potentials on the propeller blade, when there is *no inflow* and the potential jumps are equal to zero in all the wake panels except the first panel in the wake at blade strip  $m$ , in which there is a linear dipole distribution with potential equal to unity at the left (trailing edge) end, and equal to zero at the right end. The base problem is also shown schematically in Figure 5. Notice that the base solutions depend only on the propeller discretization and that they are independent of the propeller inflow and the time step  $n$ .

Due to the linear character of the system of equations (30), the solution,  $[\delta\phi]$ , can then be expressed as a linear superposition of the base potentials

$$[\delta\phi] = \sum_{m=1}^M \delta\Gamma_m [\Phi]^m, \quad (33)$$

and by using the definitions (29), the solution to the system of equations (25) is expressed as:

$$[\phi^{*(k)}] = [\phi] + \sum_{m=1}^M (\Gamma_m^{*(k)} - \Gamma_m) [\Phi]^m. \quad (34)$$

In conclusion, by employing the previously described technique of the *base problems*, we avoid solving the system of equations (25) for each Kutta condition iteration and at each time step. Instead, we express the solution to equations (25) in terms of the base potentials. The base potentials are determined before the unsteady solution process starts, by solving the system of equations (31) as many times as the number of the spanwise blade sections  $M$ , which is *far less* than the number of times the system of equations (22) is solved. As a result the

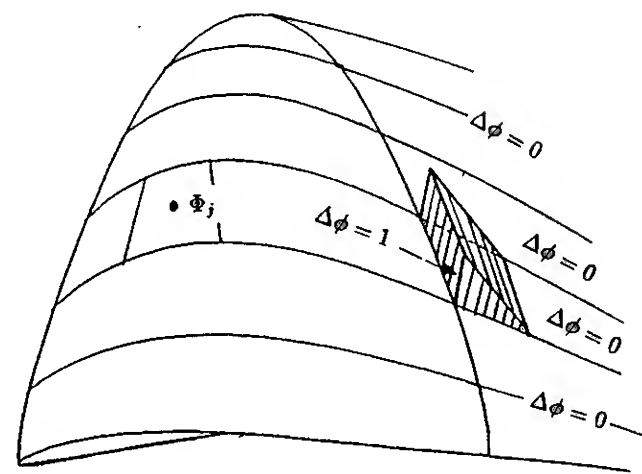


Figure 5: Definition of the base problem at blade strip  $m$ .

increase in the total computing time, when the present iterative pressure Kutta condition is applied, is insignificant.

## 2.5 Numerical Validation of the Unsteady Panel Method

In this section, the convergence of the results from different applications of the present unsteady flow panel method is investigated by varying the main discretization parameters. In addition, the consistency of the results from the presented panel method versus analytical or numerical results from lifting surface theory is investigated. Due to the facts that potential based panel methods cannot treat zero thickness wings (equation (3) degenerates to an identity for zero thickness) and that lifting surface theory is exact only for zero thickness, a direct comparison of the presented method with lifting surface theory is not possible. Instead, the following *consistency test* has been proposed by Kinnas [20].

The unsteady panel method is applied on a series of wings (or propellers) with identical mean camber surfaces but with thickness distributions scaled from an original distribution by a (non-zero) uniform factor. The resulting spanwise circulation distributions are extrapolated to zero thickness and then compared with the results from applying an unsteady lifting surface method to the zero thickness wing (or propeller) from the above series. When applying the consistency test for several wings and propellers in steady flow it has been found that the effect of thickness on the spanwise circulation distribution is almost linear with thickness for a large range of thicknesses [20], [13], and thus linear extrapolation with thickness of the results from the panel method is employed.

In the next two sections the convergence and consistency of the unsteady panel method is investigated first when applied to two dimensional hydrofoils and then to propellers.

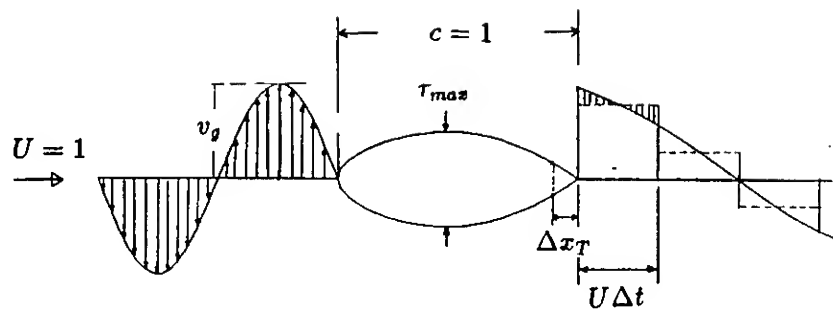


Figure 6: Two dimensional symmetric foil subject to a sinusoidal gust

### 2.5.1 Sinusoidal Gust in Two Dimensions

The two dimensional version of the presented method is applied on several symmetric modified NACA66 forms [3] with chord  $c = 1$  and various maximum thicknesses  $\tau_{max}$ . The foils are subject to a sinusoidal gust normal to their chord, of amplitude  $v_g = 0.2$  and of frequency  $\omega$ . The gust is carried downstream by a uniform flow  $U = 1$  and reaches the leading edge of the foil at time  $t = 0$ , as shown in Figure 6. The vorticity shed from the foil is positioned along the trailing edge bisector line. The reduced frequency of the gust is defined as usual as

$$k = \frac{\omega c}{2U}. \quad (35)$$

First, the sensitivity of the method to the size of the time step,  $\Delta t$ , is investigated, when a constant strength dipole distribution is utilized in the first wake panel. The results, shown in Figure 7, appear to be very dependent on the ratio of the length of the first wake panel  $U\Delta t$  to the length of the trailing edge panel  $\Delta x_T$ . Dependency on the time step is a very undesirable characteristic of any unsteady panel method, especially if the method is expected to be able to handle low as well as high frequency components of the incoming flow.

However, when the first panel in the wake is treated with a linear rather than constant dipole distribution, as described in section 2.2, the results, shown in Figure 8, become independent of the time step. Replacing the rest of the constant strength panels in the wake with linear was found to have no significant effect on the results. The poor performance of the constant wake dipole panel is attributed to the fact that the potentials induced on the trailing edge panels by the *saw-tooth* dipole distribution on the first wake panel, shown shaded in Figure 6, are not negligible. Those saw-tooth induced potentials become larger, the larger the ratio of the first wake panel to the trailing edge panel, and the larger the slope of the dipole distribution at the trailing edge (i.e. frequency) are.

Due to the previous investigation, a linear dipole distribution is always employed in the first wake panel in the unsteady panel method for hydrofoils as well as propellers.

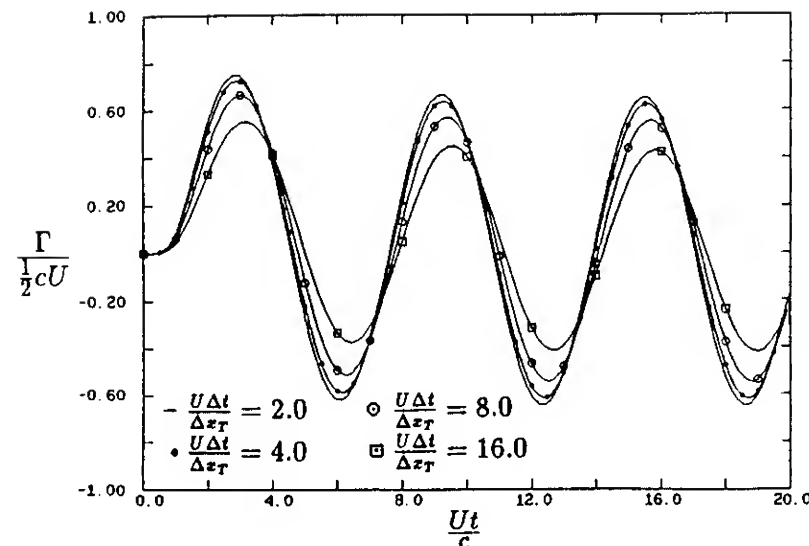


Figure 7: Convergence with time step size. *Constant dipole distribution* on the first wake panel. Modified NACA66 form with 10% thickness to chord ratio. Sinusoidal transverse gust with amplitude  $v_g = 0.2$  and reduced frequency  $k = 0.5$ . Number of panels on the foil  $N = 40$ .

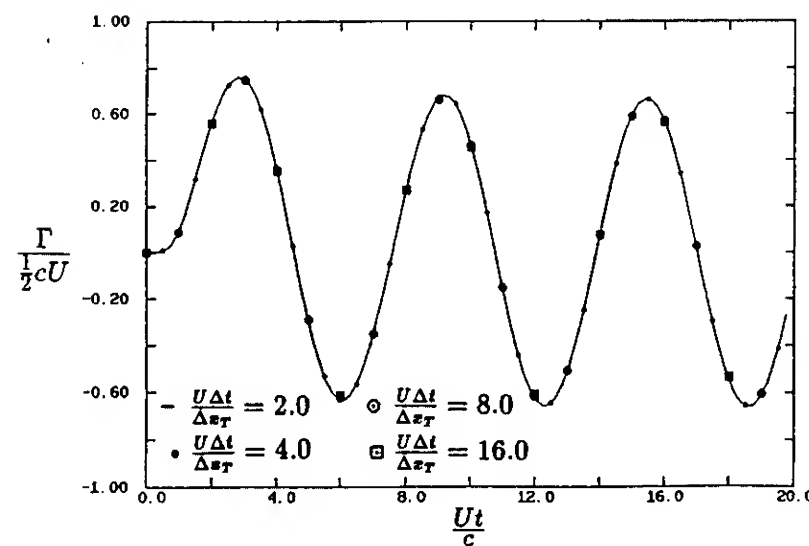


Figure 8: Convergence with time step size. *Linear dipole distribution* on the first wake panel. Modified NACA66 form with 10% thickness to chord ratio. Sinusoidal transverse gust with amplitude  $v_g = 0.2$  and reduced frequency  $k = 0.5$ . Number of panel on the foil  $N = 40$ .

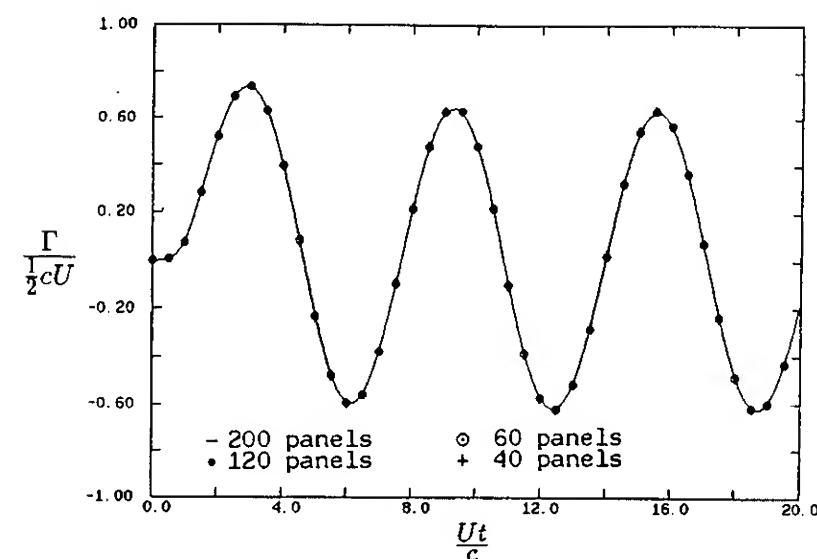


Figure 9: Convergence with number of panels on the hydrofoil. *Low frequency case*. Modified NACA66 form with 10% thickness to chord ratio. Sinusoidal transverse gust with amplitude  $v_g = 0.2$  and reduced frequency  $k = 0.5$ .

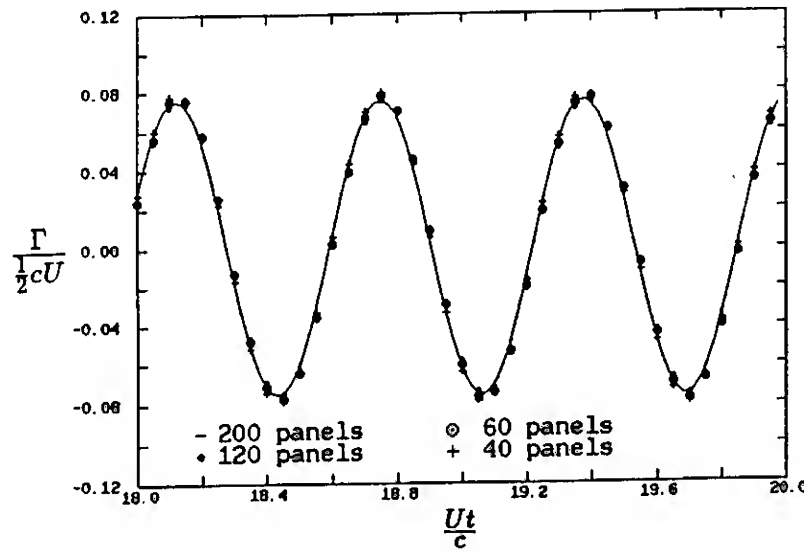


Figure 10: Convergence with number of panels on the hydrofoil. *High frequency case*. Modified NACA 66 form with 10% thickness to chord ratio. Sinusoidal transverse gust with amplitude  $v_g = 0.2$  and reduced frequency  $k = 5$ .

The convergence with number of panels on the foil,  $N$ , is then shown in Figures 9 and 10 for a low and a high reduced frequency, respectively. The convergence appears to be very good.

Finally, in order to compare the results from the panel method with the analytic results for a flat plate in a sinusoidal gust – the well known Sears problem [29] – the consistency test, as described in the beginning of this section, is applied. The unsteady panel method is applied to three foils with  $\tau_{max} = 0.05, 0.1$  and  $0.2$ . The results (in this case the time history of the circulation around the foil), appear to be linear in thickness and thus, are linearly extrapolated to zero thickness and compared against the steady state analytic circulation of a flat plate in a gust. The comparisons are shown in Figures 11 and 12 for a low and a high reduced frequency. In both those cases, the consistency test appears to be valid, within acceptable accuracy<sup>3</sup>.

The analytic complex circulation,  $\tilde{\Gamma}$ , with respect to

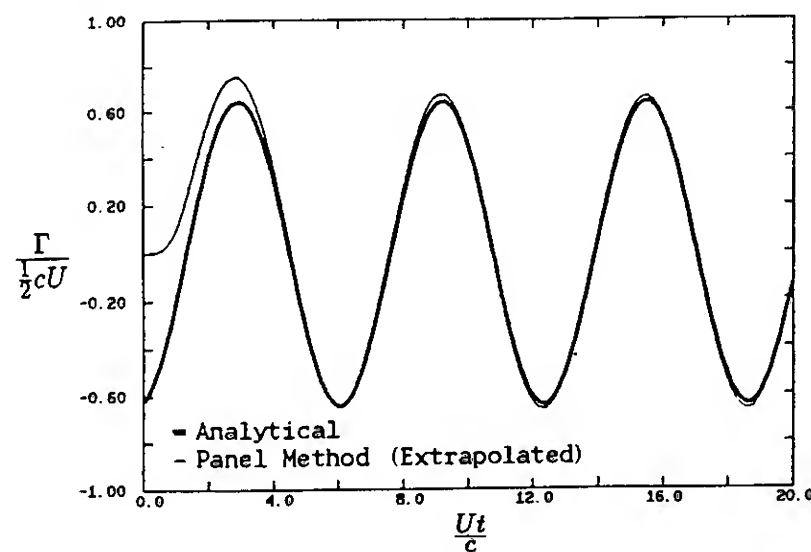


Figure 11: Consistency test of unsteady panel method with analytic result - *Low frequency*. Sinusoidal transverse gust with amplitude  $v_g = 0.2$  and reduced frequency  $k = 0.5$ .

<sup>3</sup>Only the steady state numerical circulation should be compared to the analytical.

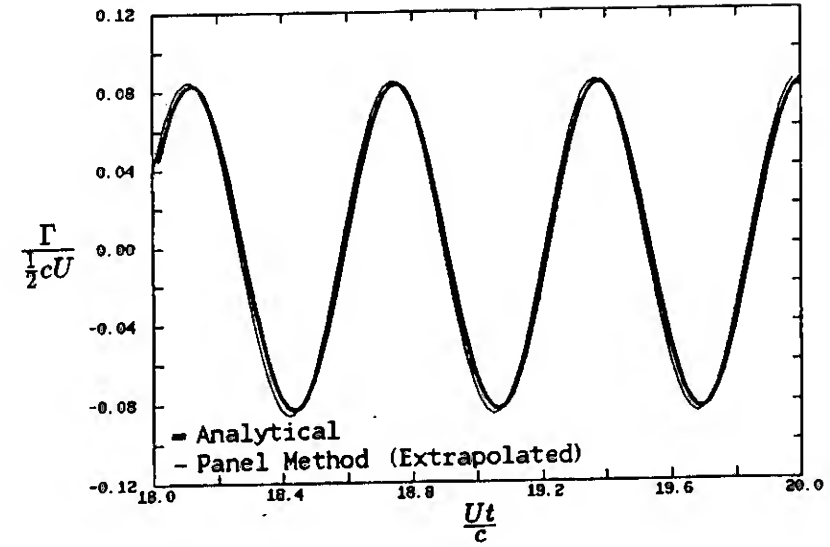


Figure 12: Consistency test of unsteady panel method with analytic result - *High frequency*. Sinusoidal transverse gust with amplitude  $v_g = 0.2$  and reduced frequency  $k = 5$ .

the leading edge, for the flat plate in a sinusoidal gust is

$$\frac{\tilde{\Gamma}}{2\pi c v_g} = \frac{e^{-2ik} J_0(k) - i J_1(k)}{\pi k H_0(k) - i H_1(k)} \quad (36)$$

where  $J_0, J_1$  and  $H_0, H_1$  are the Bessel and Hankel functions, respectively, and  $i = \sqrt{-1}$ .

## 2.5.2 The Propeller in Nonuniform Inflow

The unsteady panel method is applied to the *DTRC N4118* propeller, of which the geometry is given in [2]. The incoming wake is assumed to be axial, with a once per revolution circumferential variation:

$$U_{Sx} = U_P(1 + u_g \cos \theta_S) \quad (37)$$

with  $U_P$  being the circumferentially averaged inflow and  $u_g$  the amplitude of the wake variation, taken equal to 0.2.

The advance coefficient, defined as  $J_P = 2\pi U_P / (\omega D)$ , with  $D$  being the diameter of the propeller, is taken equal to 0.833.

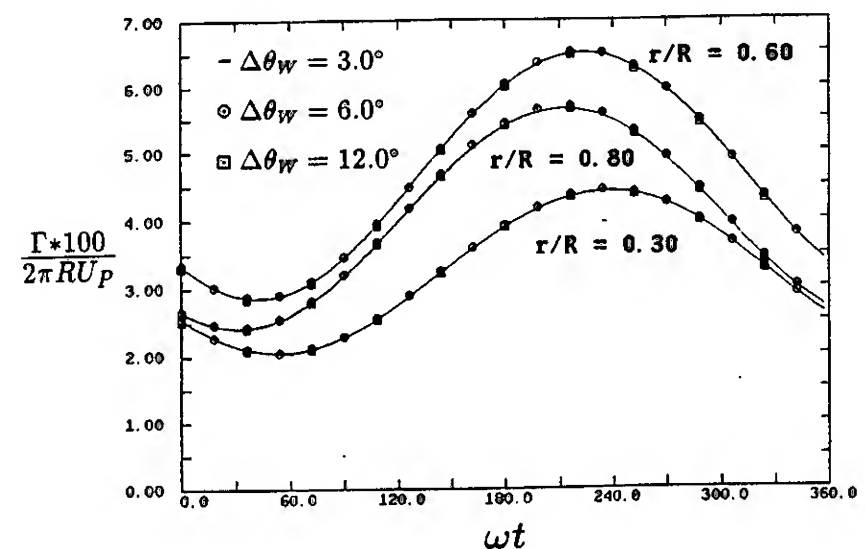


Figure 13: Convergence of the unsteady propeller panel method with time step size. Circulation vs. blade angle at different propeller radii,  $r/R$ , for the *N4118* propeller.  $J_P = 0.833, u_g = 0.2$ .

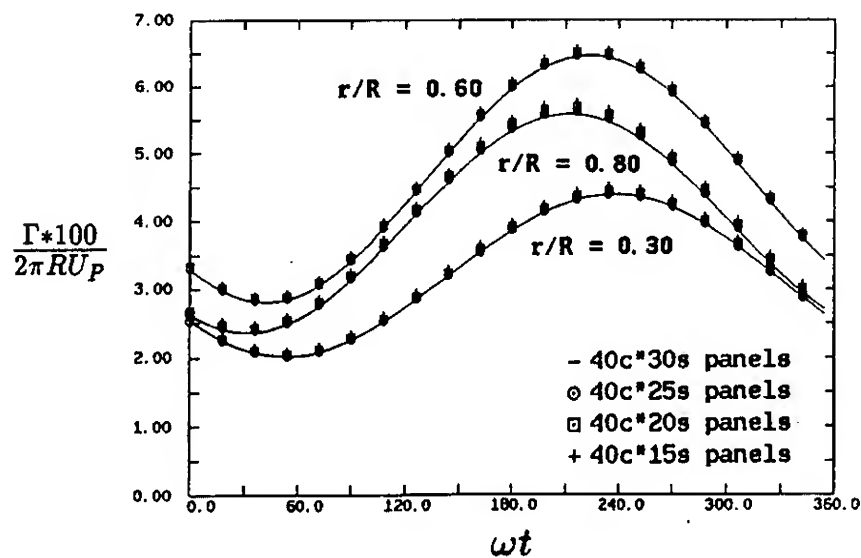


Figure 14: Convergence of the unsteady propeller panel method with chordwise number of panels. Circulation vs. blade angle at different propeller radii,  $r/R$ , for the N4118 propeller.  $J_P = 0.833$ ,  $u_g = 0.2$ .

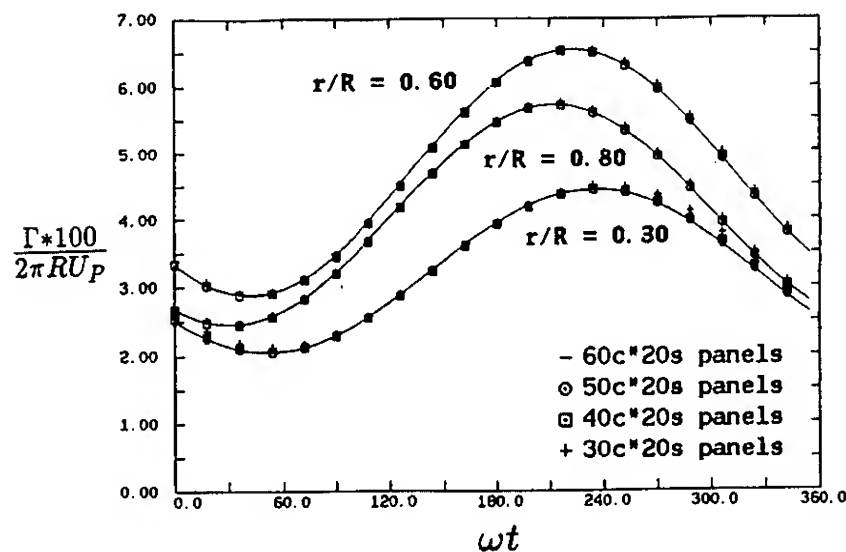


Figure 15: Convergence of the unsteady propeller panel method with spanwise number of panels. Circulation vs. blade angle at different propeller radii,  $r/R$ , for the N4118 propeller.  $J_P = 0.833$ ,  $u_g = 0.2$ .

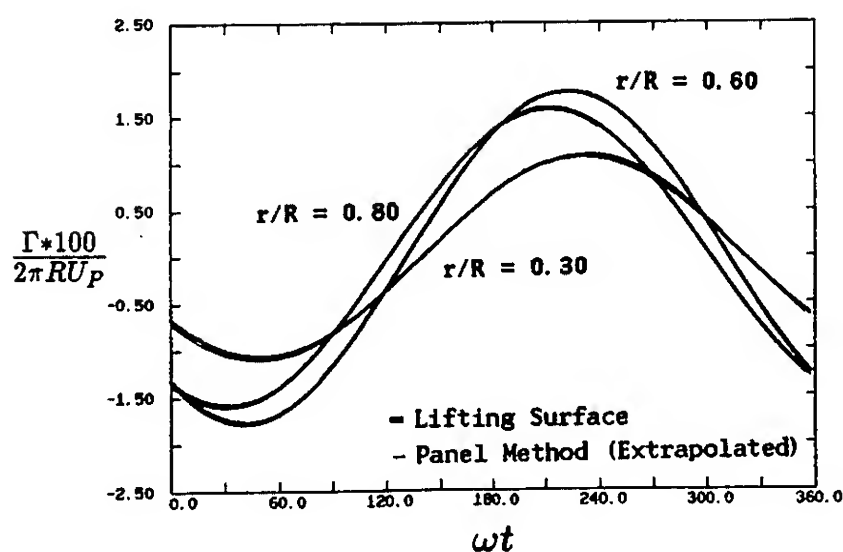


Figure 16: Consistency test of the unsteady propeller panel method with the unsteady lifting surface method. Circulation vs. blade angle at different propeller radii,  $r/R$ , for the N4118 propeller.  $J_P = 0.833$ ,  $u_g = 0.2$ .

The convergence of the results for this case is investigated by varying the time step size, the chordwise and the spanwise number of panels. The results are shown in Figures 13, 14 and 15, respectively. The convergence with all those parameters is shown to be very good.

Finally, the consistency test for the unsteady panel method versus the unsteady lifting surface method [14], is applied for the N4118 propeller. The linearly extrapolated results from the panel method and those from the lifting surface method are in very good agreement, as shown in Figure 16.

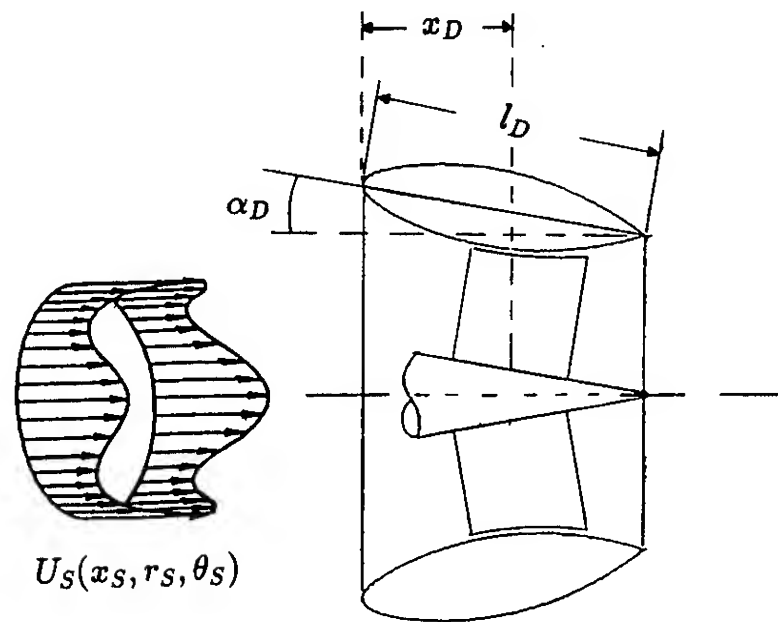


Figure 17: Ducted propeller in spatially nonuniform inflow.

### 3 The Unsteady Panel Method for Ducted Propellers

#### 3.1 Formulation

Consider now, a ducted propeller, shown in Figure 17, subject to the spatially nonuniform inflow  $\vec{U}_s(x_s, r_s, \theta_s)$  with respect to the ship fixed system as described in Section 2.1. The duct is defined by its chord length,  $l_D$ , the thickness and camber distributions of its meridional section, the angle of attack,  $\alpha_D$ , and, the axial distance,  $x_D$ , of its leading edge from the midpoint of the propeller at the hub section.

The formulation of the unsteady ducted propeller flow problem is identical to that in the case of open propellers, which was described in Section 2.1. The perturbation potential,  $\phi$ , is again determined by using Green's formula, equation (3). Both the propeller and duct surfaces must be panelled and unsteady wakes must be shed from the trailing edges of the propeller blades and duct. In the present work, we model the duct with a potential based panel method and the propeller with a lifting surface vortex lattice method which will be described in Section 4. A typical arrangement of panels on the duct, the propeller and their trailing wakes is shown in Figure 18.

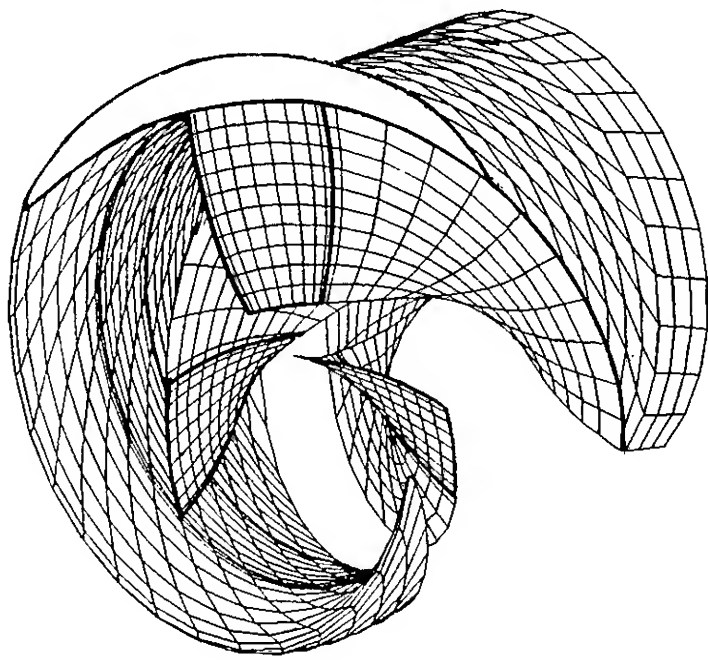


Figure 18: Panel arrangement of the duct, propeller and their trailing wakes in unsteady flow. Only half of the duct panels are shown.

One way of analyzing the unsteady flow around the ducted propeller is by treating the duct and propeller as one body and by employing a time marching scheme similar to that described in Section 2.2. Instead, in the present work, we only treat the propeller with a time marching lifting surface scheme with the effects of the duct on the unsteady propeller flowfield being accounted for via the generalized images of the propeller singularities with respect to the duct. Some of the advantages of the latter versus the former scheme will be outlined later in this section.

It is well known that the potential flow around a body in the presence of an infinite wall, can be modelled with singularities distributed on the surface of the body, as if the flow domain were unbounded, with the effects of the wall being accounted for via the images of the singularities with respect to the wall. The generalized image idea, as introduced by Kinnas and Coney [21], is an extension of the classical image idea for the case that the infinite wall is a generally shaped body, for example a duct. The flow field of the generalized image of a singularity (i.e. source, vortex or dipole) with respect to a generally shaped body  $A$ , is defined as the modification to the flow field of the singularity due to the presence of body  $A$ . In mathematical terms, as described in the next section, the combined flow field due to the singularity and its *generalized image* with respect to a body  $A$ , consists the modified Green's function which satisfies the boundary conditions on  $A$ . A similar idea has been applied in analyzing the flow around a body in the presence of a free surface, where the modified Green's function is required to satisfy the free surface condition [22].

The implementation of the generalized image idea in the analysis of the unsteady flow around ducted pro-

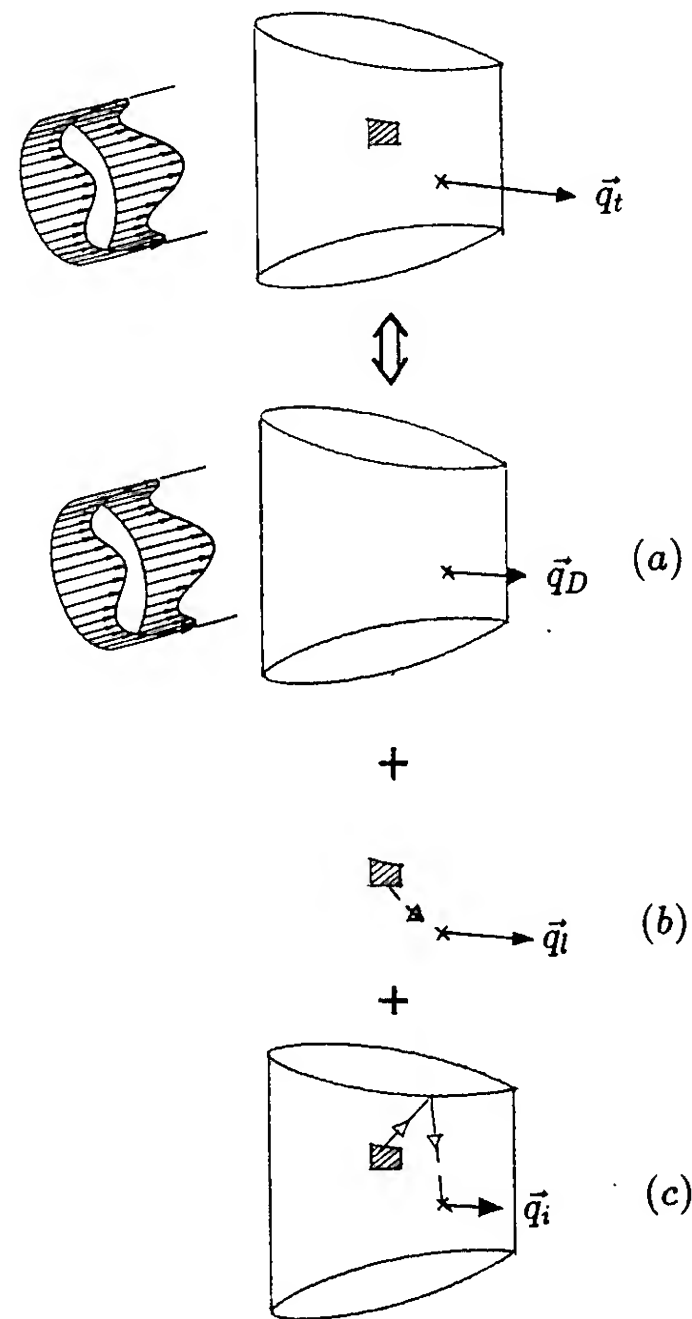


Figure 19: Decomposition of the flow field around a duct and the propeller vortex loops, subject to a spatially nonuniform inflow.

pellers consists of the following steps, which are also shown schematically in Figure 19:

**Step 1** Solve for the flow around the duct (without the propeller) subject to the nonuniform inflow  $\vec{U}_S(x_S, r_S, \theta_S)$ , by using a potential based panel method [18]. The resulting flow field is in general non-axisymmetric, but steady with respect to the ship fixed system. The total velocity,  $\vec{q}_D$ , is computed at the propeller control points.

**Step 2a** For each unit strength vortex loop on the propeller key blade and its trailing wake, the generalized image flow field is computed. This is achieved by solving for the non-axisymmetric potential on the duct in the presence of that loop and in *zero inflow*, by applying a potential based panel method [21]. The same panel arrangement on the duct is used as in Step 1, thus avoiding re-computing the duct to duct influence coefficients



for each vortex loop.

**Step 2b** The velocities,  $\vec{q}_i$ , induced by the generalized image of each of the unit strength vortex loops at the propeller control points are computed and stored.

**Step 3** The unsteady propeller lifting surface method, described in Section 4, is then applied as if the propeller was open, but with the following modifications in order to take into account the duct:

- The propeller inflow is taken equal to  $\vec{q}_D$ , as computed in Step 1.
- The propeller to propeller influence coefficients, velocities  $\vec{q}_i$ , are modified by adding to them the corresponding generalized image influence coefficients,  $\vec{q}_i$ , which were computed in Step 2b.

Steps 2a and 2b consume the largest and Step 3 the smallest part of the total computing time. If the same ducted propeller must be analyzed for different inflows, Steps 1 and 3 must be repeated, but Steps 2a and 2b, which depend on the duct and propeller geometry but not on the inflow, must not, as long as the generalized image influence coefficients have been stored. Thus, the same configuration can be analyzed for different inflow conditions, rather quickly, after the first condition has been analyzed.

The matrices that have to be inverted for each vortex loop in Step 2a are identical, and the corresponding right-hand sides are *independent* from each other. This makes Steps 2a and 2b amenable to parallel processing. This would not be feasible, if the duct and propeller were treated with a time marching scheme, since the right-hand sides at each time step are *not* independent from each other.

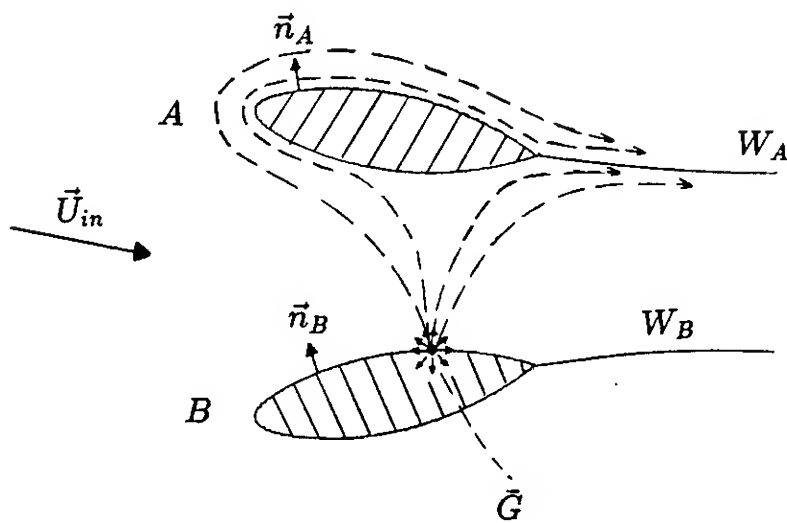


Figure 20: Potential flow around bodies  $A$  and  $B$ . The flow field due to the modified source  $\tilde{G} = G + G_i$  is shown with dashed lines.

### 3.2 The Generalized Image Model

A mathematical justification behind the generalized image model is given in this section. We consider two bodies  $A$  and  $B$  subject to a general inflow  $\vec{U}_{in}$  as shown in Figure 20. Assume that the flow around  $A$  and  $B$  is lifting and that the geometry of their trailing wakes  $W_A$  and  $W_B$ , respectively, is known.

The flow can be analyzed by considering bodies  $A$  and  $B$  as one and proceed in the usual way by applying Green's formula, equation (3), with respect to the perturbation potential  $\phi$  on  $A$  or  $B$ :

$$\begin{aligned} 2\pi\phi = & \int_{S_A} \phi \frac{\partial G}{\partial n_B} dS + \int_{S_B} \phi \frac{\partial G}{\partial n_A} dS \\ & + \int_{W_A} (\Delta\phi)^A \frac{\partial G}{\partial n_{W_A}} dS + \int_{W_B} (\Delta\phi)^B \frac{\partial G}{\partial n_{W_B}} dS \\ & - \int_{S_A} G(-\vec{U}_{in} \cdot \vec{n}_A) dS - \int_{S_B} G(-\vec{U}_{in} \cdot \vec{n}_B) dS \end{aligned} \quad (38)$$

where  $G$  is the infinite fluid domain Green's function, defined by equation (4),  $S_A$  and  $S_B$  are the surfaces of bodies  $A$  and  $B$ ,  $\vec{n}_A$  and  $\vec{n}_B$  are the normals on the bodies  $A$  and  $B$ , respectively,  $\vec{n}_{W_A}$  and  $\vec{n}_{W_B}$  are the normals on the wake surfaces  $W_A$  and  $W_B$ , respectively,  $(\Delta\phi)^A$  and  $(\Delta\phi)^B$  are the jumps in the potential across the wake sheets  $W_A$  and  $W_B$ , respectively.

An alternative way of formulating Green's formula on  $B$ , in the presence of  $A$ , can be found by introducing the Green's function  $\tilde{G}$  which satisfies

$$\begin{aligned} \nabla^2 \tilde{G}(p; q) = & -4\pi\delta(x_p - x_q)\delta(y_p - y_q)\delta(z_p - z_q) \\ & \text{outside } A \end{aligned} \quad (39)$$

with  $\delta$  being the *delta* function and,  $(x_p, y_p, z_p)$  and  $(x_q, y_q, z_q)$  being the cartesian coordinates of points  $p$  and  $q$ , respectively. Also

$$\frac{\partial \tilde{G}}{\partial n_A} = 0, \quad \text{on } A, \quad (40)$$

$$\tilde{G}(p; q) \rightarrow 0 \quad \text{as } p \rightarrow \infty, \quad (41)$$

$$\nabla \tilde{G} = \text{finite at the trailing edge of } A. \quad (42)$$

Physically,  $\tilde{G}(p; q)$  corresponds to the potential due to a point source of strength  $-4\pi$ , placed at  $q$ , in the presence of body  $A$ , as shown in Figure 20. Notice that  $\tilde{G}$  must satisfy the Kutta condition (42) at the trailing edge of  $A$ .

It can easily be shown that  $\tilde{G}$  satisfies

$$2\pi\tilde{G}(p; q) - \int_{S_A} \tilde{G}(p; q) \frac{\partial G}{\partial n_A} dS = \int_{W_A} (\Delta\tilde{G})^A \frac{\partial G}{\partial n_{W_A}} dS + 4\pi G(p; q) \quad (43)$$

for  $p \in A$ .  $G$  is the infinite domain Green's function. The jump of the potential  $(\Delta\tilde{G})^A$  in the wake of  $A$  is set equal to the difference of the potentials at the trailing edge of  $A$  in order for the Kutta condition (42) to be satisfied.

The function  $\tilde{G}$  will be given in the fluid domain as

$$\tilde{G}(p; q) = G(p; q) + \frac{1}{4\pi} \left[ \int_{S_A} \tilde{G} \frac{\partial G}{\partial n_A} dS + \int_{W_A} (\Delta\tilde{G})^A \frac{\partial G}{\partial n_{W_A}} dS \right] \quad (44)$$

for points  $p$  outside body  $A$ .

By defining

$$G_i(p; q) = \frac{1}{4\pi} \left[ \int_{S_A} \tilde{G} \frac{\partial G}{\partial n_A} dS + \int_{W_A} (\Delta\tilde{G})^A \frac{\partial G}{\partial n_{W_A}} dS \right] \quad (45)$$

$\tilde{G}$  can then be expressed as

$$\tilde{G}(p; q) = G(p; q) + G_i(p; q). \quad (46)$$

$G_i$  is the modification to the infinite fluid domain Green's function due to the presence of body  $A$ . We call  $G_i$  the generalized image of the source  $G$  with respect to body  $A$ . In the case the body  $A$  is an infinite wall then  $G_i$  is identical to the actual image of  $G$  with respect to the wall.

It can be shown that the perturbation potential,  $\phi$ , in the presence of both  $A$  and  $B$  can then be expressed as

$$\phi = \phi_A + \tilde{\phi}_B \quad (47)$$

where  $\phi_A$  is the perturbation potential outside  $A$  in the presence of the flow field  $\vec{U}_{in}$  but in the absence of body  $B$ , and  $\tilde{\phi}_B$  is the perturbation potential on  $B$  in the presence of the flow field  $\vec{U}_{in} + \nabla\phi_A$ . The potentials  $\phi_A$  and  $\tilde{\phi}_B$  satisfy the following equations:

$$2\pi\phi_A = \int_{S_A} \phi_A \frac{\partial G}{\partial n_A} dS + \int_{W_A} (\Delta\phi_A) \frac{\partial G}{\partial n_{W_A}} dS - \int_{S_A} G(-\vec{U}_{in} \cdot \vec{n}_A) dS \quad \text{on } A; \quad (48)$$

$$2\pi\tilde{\phi}_B = \int_{S_B} \tilde{\phi}_B \frac{\partial \tilde{G}}{\partial n_B} dS + \int_{W_B} (\Delta\tilde{\phi}_B) \frac{\partial \tilde{G}}{\partial n_{W_B}} dS - \int_{S_B} \tilde{G}(-\vec{U}_{in} \cdot \vec{n}_B - \frac{\partial \phi_A}{\partial n_A}) dS \quad \text{on } B. \quad (49)$$

The physical meaning behind equation (47) is that the flow in the presence of bodies  $A$  and  $B$  can be decomposed into two parts:

- The flow around body  $A$  in the presence of the incoming flow  $\vec{U}_{in}$ .
- The flow around body  $B$  in the presence of the modified flow field resulting from the previous step. The potential  $\tilde{\phi}_B$  can be expressed as the superposition of distributions of modified sources  $\tilde{G}$  and modified dipoles  $\frac{\partial \tilde{G}}{\partial n_B}$  on body  $B$  and its wake.

The modified dipole  $\frac{\partial \tilde{G}}{\partial n_B}$  can easily be shown, by using equations (40) and (42), that satisfies the kinematic boundary condition and the Kutta condition on  $A$ . Physically, the modified dipole consists of the infinite fluid domain dipole and its generalized image with respect to body  $A$ .

It is obvious that the role of bodies  $A$  and  $B$  in the decomposition, equation (47), is interchangeable.

The special case of  $A$  being the *duct* and  $B$  being the *propeller*, has been utilized in analyzing a ducted propeller in a spatially nonuniform flow, as described in Section 3.1.

## 4 Unsteady Lifting Surface Theory for Ducted Propellers

The panel method for ducts described earlier has been combined with a lifting surface representation of the enclosed propeller to permit time-domain solution for unsteady blade forces. We describe here the formulation of the propeller boundary value problem, the method by which forces are obtained and review the convergence behavior of the model. Some findings based on the application of the code are given in the next section.

### 4.1 Formulation

Keenan [14] has shown that the vortex lattice lifting surface representation of the propeller blades described here follows naturally from the potential-based method described in Section 2. Differentiating equation (3) to obtain the perturbation velocity at the field point  $\mathbf{x}$  and then passing to the limit of vanishing blade (and wake sheet) thickness one finds

$$\begin{aligned} \int_{S_P} \mu(\xi) \mathbf{n}(\mathbf{x}) \cdot \left[ \nabla_x(\mathbf{n}(\xi)) \cdot \nabla_\xi \frac{1}{|\mathbf{x} - \xi|} \right] d\sigma = \\ - \int_{S_W} \mu_W(\xi) \mathbf{n}(\mathbf{x}) \cdot \left[ \nabla_x(\mathbf{n}(\xi)) \cdot \nabla_\xi \frac{1}{|\mathbf{x} - \xi|} \right] d\sigma \\ - 2\pi \mathbf{n}(\mathbf{x}) \cdot \mathbf{v}_1(\mathbf{x}). \end{aligned} \quad (50)$$

This is an expression for the velocity normal to the blade at point  $\mathbf{x}$  due to a distribution of dipoles of unknown strength  $\mu$  on the blade surfaces  $S_P$  and known  $\mu_W$  on the wake surfaces  $S_W$ . The dipole strength in the wake,  $\mu_W$ , is known from the history of blade circulation.

We require that

$$\mathbf{v}_1 \cdot \mathbf{n} = (\mathbf{U} - \mathbf{v}_2) \cdot \mathbf{n} \quad \text{on } S_P, \quad (51)$$

$$\mathbf{v}_1 \rightarrow 0 \quad \text{at infinity} \quad (52)$$

where  $\mathbf{v}_1$  is the perturbation due to the propeller and wake sheets,  $\mathbf{v}_2$  is the background velocity and  $\mathbf{U}$  is the velocity of the body itself. The total fluid velocity is  $\mathbf{V} = \mathbf{v}_1 + \mathbf{v}_2$ .

There are two integrals in equation (50); one,  $I_P$ , over  $S_P$  and one,  $I_W$ , over  $S_W$ . The discretization is the same for both so we consider only  $I_P$ , namely

$$I_P = \int_{S_P} \mu(\boldsymbol{\xi}) \mathbf{n}(\mathbf{x}) \cdot \left[ \nabla_{\mathbf{x}}(\mathbf{n}(\boldsymbol{\xi}) \cdot \nabla_{\boldsymbol{\xi}} \frac{1}{|\mathbf{x} - \boldsymbol{\xi}|}) \right] d\sigma. \quad (53)$$

The surface  $S_P$  is divided into quadrilateral panels whose vertices are placed on the camber surface of the blade as described later. Within each panel, the dipole strength  $\mu$  is assumed constant. Thus  $I_P$  is approximated as

$$I_P = \sum_i \mu_i \int_{S_i} \mathbf{n}(\mathbf{x}) \cdot \left[ \nabla_{\mathbf{x}}(\mathbf{n}(\boldsymbol{\xi}) \cdot \nabla_{\boldsymbol{\xi}} \frac{1}{|\mathbf{x} - \boldsymbol{\xi}|}) \right] d\sigma. \quad (54)$$

The surface  $S_P$  is replaced by the collection of panels  $S_i$ . Two problems arise at this point. The required integrals are hyper-singular and must be performed on arbitrarily curved surfaces  $S_i$ . By recalling the equivalence between a constant strength dipole patch and a vortex loop around its perimeter (see, *e.g.*, [24]) one can escape these difficulties. One then can write the discrete form of  $I_P$  as

$$I_P = \sum_i \mu_i \mathbf{n}(\mathbf{x}) \cdot \left[ \oint \frac{\mathbf{x} - \boldsymbol{\xi}}{|\mathbf{x} - \boldsymbol{\xi}|^3} \times d\mathbf{l} \right]. \quad (55)$$

The integral on  $S_i$  is replaced with a simple application of Biot-Savart's law for the straight vortex segments bounding each panel.

The arrangement of the panelling on the blades is shown in Figure 21. The spacing follows the so-called quasi-continuous method (QCM) described by Lan [23] and greatly enhances the method's ability to capture the square root like behavior near the blade edges as compared to classical vortex lattice methods (VLM). This arrangement of panels is often referred to as "co-sine spacing". QCM has the added benefit over VLM of placing panels closer to the edges of the blade, thus increasing resolution. For a ducted propeller, the spanwise panelling is modified. The typical ducted propeller will not exhibit square-root-like behavior of the spanwise loading near the tip (unless there is a large tip gap) so QCM spacing is inappropriate in the spanwise direction. Figure 21 shows the uniform spacing used in the spanwise direction for duct-fitted propellers. The tangency boundary condition on the blades is satisfied by collocation at control points given by QCM.

The geometry of the wake sheets is prescribed. The angular extent of the panels is equal to that swept out by the blade in one time step except that the wake panel adjoining the trailing edge is one quarter this size.

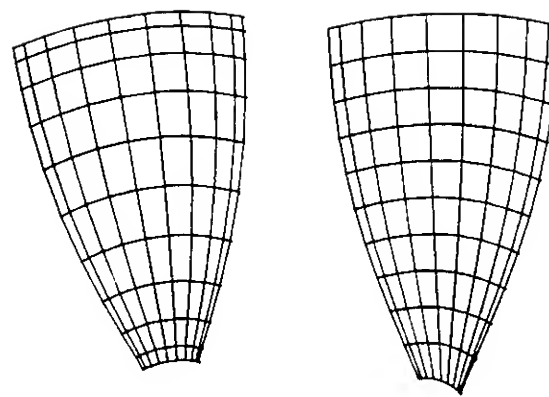


Figure 21: Typical blade panellings. On the left, following Lan's Quasi-Continuous Method. On the right, using uniform spacing spanwise as for a ducted propeller. On the right, sections near the root have been trimmed to fit a tapered hub.

The discretization of equation (50) is described more fully in [14]. Eventually, it leads to the linear system

$$\begin{aligned} \sum_{k=1}^K \sum_{m=1}^M \sum_{n=1}^N a_{i,n,m,k} \Gamma_{n,m,k}^S = \\ - \sum_{k=1}^K \sum_{m=1}^M \sum_{n=2}^{N_w} a_{i,n,m,k}^w \mu W_{n,m,k} \\ - \mathbf{n}_i \cdot \mathbf{v}_1(\mathbf{x}_i). \end{aligned} \quad (56)$$

Each  $a_{i,n,m,k}$  is the influence at control point  $i$  due to the  $(n,m)^{th}$  unit strength dipole panel/vortex loop *plus its exact image in the duct*. Having computed these matrix elements, it is left to solve for the  $\Gamma^S$ 's which are simply the jumps in dipole strength going from one panel to its neighbor along a chordwise strip.

With

$$b_i = - \sum_{k=1}^K \sum_{m=1}^M \sum_{n=2}^{N_w} a_{i,n,m,k}^w \mu W_{n,m,k} - \mathbf{n}_i \cdot \mathbf{v}_1(\mathbf{x}_i). \quad (57)$$

one can recast equation (56) into the form

$$\begin{pmatrix} (\mathbf{A}_{11}) & \dots & (\mathbf{A}_{1K}) \\ \vdots & \ddots & \vdots \\ (\mathbf{A}_{K1}) & \dots & (\mathbf{A}_{KK}) \end{pmatrix} \begin{pmatrix} (\boldsymbol{\Gamma}_1^S) \\ \vdots \\ (\boldsymbol{\Gamma}_K^S) \end{pmatrix} = \begin{pmatrix} (\mathbf{b}_1) \\ \vdots \\ (\mathbf{b}_K) \end{pmatrix}. \quad (58)$$

Each block in the matrix corresponds to the influence of one blade on another. Suppose that the matrix is separated so that only the diagonal blocks appear on the left side. Then equation (58) breaks down into the following series of  $K$  sub-equations:

$$(\mathbf{A}_{kk}) (\boldsymbol{\Gamma}_k^S) = (\mathbf{b}_k) - \sum_{i=1}^K (\mathbf{A}_{ki}) (\boldsymbol{\Gamma}_i^S), \quad k = 1, 2, \dots, K. \quad (59)$$

The form of equation (59) hints at a substantial computational savings. If the  $\boldsymbol{\Gamma}^S$ 's appearing on the right side were known the matrix solution could be reduced from an  $(N \times M \times K)^2$  effort to  $K \times (N \times M)^2$ . Fortunately, for a normal propeller, the blade-to-blade influence rep-

resented by the summation on the right is small. This circumstance permits use of a block Gauss-Seidel iterative solution, thus:

$$(\mathbf{A}_{kk})(\boldsymbol{\Gamma}_k^S)^{(n+1)} = (\mathbf{b}_k) - \sum_{i=1}^{k-1} (\mathbf{A}_{ki})(\boldsymbol{\Gamma}_i^S)^{(n+1)} - \sum_{i=k+1}^K (\mathbf{A}_{ki})(\boldsymbol{\Gamma}_i^S)^{(n)}, \quad k = 1, 2, \dots, K. \quad (60)$$

The superscripts in parentheses indicate the iteration level. The iteration continues until the desired tolerance for  $\boldsymbol{\Gamma}^S$  is achieved.

The speed-up over direct solution of the full matrix equation is, in fact, even greater than suggested above. Each  $(\mathbf{A}_{ij})$  is constant in time (by virtue of the placement of the 1<sup>st</sup> shed vortex, cf.[14]) so an *LU* decomposition may be performed once at the beginning of the calculation. Only back-substitution is required at each time step thereafter. For normal propellers, a further advantage accrues from the fact that each blade is the same shape. That means that each  $(\mathbf{A}_{kk})$  is the same — only one block needs to be decomposed. The resulting scheme is very fast. Computation of the right-hand-side vector  $\mathbf{b}$  takes far longer than does extracting  $\boldsymbol{\Gamma}^S$  once  $\mathbf{b}$  is known.

## 4.2 Forces on the propeller

Once the discrete vortex strengths are known, the blade forces may be calculated. Previous implementations of vortex lattice lifting surface models have obtained blade forces from the “rotating bedspring” analogy (a term coined by J. E. Kerwin) [5,11,17]. In that approach, one imagines the lifting surface to be *replaced* by the array of singularities. The forces computed are those arising from the application of Joukowski’s rule to each vortex segment using velocities evaluated at the vortex segment (usually on its midpoint). Guermond [6] has correctly criticized this approach. Its fault lies in the fact that velocities calculated on the body anywhere away from the control points do not satisfy the kinematic boundary condition (51). Kerwin [15] has observed that while the leading edge suction acts principally at the first vortex, its effect is distributed over the entire chord. Thus, moments will be incorrect even if total forces are accurate.

Two alternative methods of calculating force distributions may be suggested as being correct. One may interpolate the velocities, correctly computed at the control points, to the vortex elements or one may evaluate vorticity at the control points. The latter approach is taken here. Also, rather than apply the Joukowski rule, local pressures will be evaluated. This is seen as a convenience since one often requires surface pressures anyway for additional studies.

### 4.2.1 Blade surface pressures

To obtain surface pressures we employ Bernoulli’s equation in the form

$$p - p_a = \frac{1}{2}\rho(\mathbf{V}_\infty \cdot \mathbf{V}_\infty - \mathbf{V} \cdot \mathbf{V} - 2\frac{\partial\phi}{\partial t}) \quad (61)$$

where  $p_a$  is the ambient pressure far enough upstream so that  $\partial\phi/\partial t$  may be assumed small,  $\mathbf{V}_\infty$  is the total fluid velocity at the same location and  $\mathbf{V}$  is the total fluid velocity at the point of interest. This differs from the normal Bernoulli equation derived for unsteady, purely potential flow in that the velocities involved are not merely  $\nabla\phi$  but include the contribution from the rotational background flow. Equation (61) also differs from Bernoulli’s equation for steady rotational flow because of the  $\partial\phi/\partial t$  term. A more expansive discussion of this point can be found in [14].

Having solved equation (50), the velocities at the control points on the blade are immediately available as

$$\mathbf{V}^M(\mathbf{x}_i) = \mathbf{v}_2 - \frac{1}{2\pi} \sum_{k=1}^K \sum_{m=1}^M \left[ \sum_{n=1}^N \mathbf{v}_{i,n,m,k}^a \boldsymbol{\Gamma}_{n,m,k}^S + \sum_{n=1}^{N_w} \mathbf{v}_{i,n,m,k}^{aw} \boldsymbol{\Gamma}_{n,m,k}^W \right] \quad (62)$$

where  $\mathbf{v}_{i,n,m,k}^a$ ,  $\mathbf{v}_{i,n,m,k}^{aw}$  are the *vector* influences at  $\mathbf{x}_i$  of the unit strength vortex loops. The velocity on the left is written as  $\mathbf{V}^M$  to emphasize that it is the mean velocity at the control point. There is also a local jump in velocity caused by the local vortex density  $\gamma_{n,m,k}$  which is

$$\begin{aligned} 2\Delta\mathbf{v}_{n,m,k} &= \boldsymbol{\gamma}_{n,m,k} \times \mathbf{n}_{n,m,k} \\ &= \nabla_{S_P} \mu_{n,m,k} \end{aligned} \quad (63)$$

so that  $\mathbf{V}^\pm = \mathbf{V}^M \pm \Delta\mathbf{v}$  on the suction/pressure sides.

Equation (61) also includes the term  $\partial\phi/\partial t$  which must be evaluated for unsteady flows. Unsteady in this sense refers to the ship-fixed, inertial coordinates so, in this model, propellers operating in axisymmetric inflows are unsteady. This term can be written as

$$\frac{\partial\phi}{\partial t} = r\Omega u_t + \frac{\partial\phi}{\partial\tau} \Big|_t. \quad (64)$$

The quantity  $u_t$  is the tangential velocity induced by the singularities on the propeller and wake sheets and  $\Omega$  is the shaft angular velocity. The second term on the right is the potential change at the blade-fixed point of interest.

It turns out that this last term can be related simply to the circulation around that portion of the blade forward of the control point[14]. In discretized form, it is:

$$\frac{\partial(\phi^+ - \phi^-)}{\partial t} \approx \sum_{j=1}^n \frac{\partial\Gamma_j^S}{\partial t}, \quad (65)$$

the sum being from the leading edge to the  $n^{\text{th}}$  panel along the chord. Thus, the pressure jump across the blade  $S_P$  is

$$p^+ - p^- \approx \rho \left( \mathbf{V}^M \cdot \Delta\mathbf{v} + \frac{\partial}{\partial t} (\phi^+ - \phi^-) \right). \quad (66)$$

assuming  $p_\infty^+ = p_\infty^-$  and that the vorticity in the back-

ground is weak. The pressure jumps are combined with the corresponding directed panel area to obtain an incremental force  $\Delta \mathbf{F}$  which acts at the control point.

#### 4.2.2 Leading Edge Suction

As a consequence of idealizing the propeller blades as zero thickness surfaces we introduce a singularity in pressure at the leading edge. This gives rise to the well known leading edge suction force. Derivations of this force may be found in many classical references. One such is by Milne-Thomson [30]. The leading edge suction force  $\mathbf{F}_S$  is

$$\mathbf{F}_S = -\frac{1}{4}\pi\rho C_S^2 \mathbf{i} \quad (67)$$

where

$$C_S = \lim_{s \rightarrow 0} \sqrt{s} \gamma(s) \cdot \mathbf{l} \quad (68)$$

and  $\mathbf{l}$  is a unit vector directed towards the tip along the leading edge,  $\mathbf{i}$  is directed streamwise normal to the leading edge and lying in the surface  $S_P$ . The quantity  $s$  is the arc length from the leading edge measured along a curve on  $S_P$  in the  $\mathbf{i}$  direction;  $\gamma$  is the vortex density on  $S_P$ .

Lan showed in his analysis of the QCM that the value of  $C_S$  could be obtained directly by computing the downwash at the leading edge. In this work, a direct application of the limit process expressed in equation (68) is employed instead.

To evaluate the limit, the vorticity  $\gamma$  is calculated at the control points along a streamwise strip. At each control point, we set  $\gamma_n = \gamma_n \cdot \mathbf{l}$ . Now, apart from a factor related to the leading edge sweep, we have a sequence in  $n$ ,

$$C_{S_n} = \sqrt{s_n} \gamma_n, \quad (69)$$

which must be evaluated for  $n \rightarrow 0$ . This requires extrapolation since the quantities called for are only known inboard of the leading edge. The extrapolation can be made reliable if it is assumed that  $\gamma$  may be expressed as

$$\gamma(s) = \frac{1}{\sqrt{s}} P(s) \quad (70)$$

where  $P(s)$  is a polynomial to any degree in  $s$ . If this is the case, the slope of the curve  $\sqrt{s}\gamma$  vanishes at the leading edge. The assumption is not very restrictive. It is true for a flat plate and for parabolic camber. It strictly fails for NACA  $a$ -series loadings but these are mathematical idealizations, requiring a logarithmic singularity in camber at the leading edge. The loading actually achieved is probably closer to something expressible by (70). This approach is computationally effective in that it obtains  $C_S$  directly from already known quantities: no additional influence coefficients need be calculated.

### 4.3 Results

After the duct and propeller panelling is specified the

duct problem is solved for each panel on the propeller and wake sheets in turn. This gives the duct contribution to the propeller panel Green's functions. The remainder of the code is virtually the same as for an open propeller except that the influence coefficients in the matrix include the image effects. The time-domain solver then proceeds just as fast for the ducted problem as for an open propeller.

Test Propeller R4-55

meanline:  $a = 0.8$

thickness form: NACA66

r/R	P/D	rake	skew	c/D	t/c	t/D
0.182	1.423	0.000	0.000	0.179	0.018	0.039
0.300	1.402	0.000	0.000	0.208	0.020	0.031
0.400	1.389	0.000	0.000	0.232	0.022	0.023
0.500	1.380	0.000	0.000	0.254	0.023	0.016
0.600	1.379	0.000	0.000	0.273	0.023	0.015
0.700	1.386	0.000	0.000	0.288	0.023	0.015
0.800	1.408	0.000	0.000	0.299	0.020	0.015
0.900	1.446	0.000	0.000	0.306	0.014	0.015
0.950	1.472	0.000	0.000	0.308	0.009	0.015
1.000	1.502	0.000	0.000	0.309	0.005	0.015

Test Duct

$l_D = R$   $\alpha_D = 0^\circ$

$t/l_D = 0.10$  NACA66

Table 1

As long as the panelling of the duct, propeller or wake is not changed, one may run the time-domain solver repeatedly for various inflow configurations *without returning to the duct presolver*. Thus one may amortize the presolver overhead according to the number of inflow cases one considers.

We have tested the code for a simple propeller/duct combination described in Table 1. In Figure 22 we show the spanwise distribution of circulation for uniform flow at a nominal advance coefficient of  $J = 1.0$ . Three curves are presented for various panellings of the duct and propeller combination. The  $6 \times 5$  curve has six panels over the span of the propeller, five over the chord. The duct has 24 panels circumferentially and 40 around the chord. The curves labelled  $10 \times 5$  and  $10 \times 10$  have

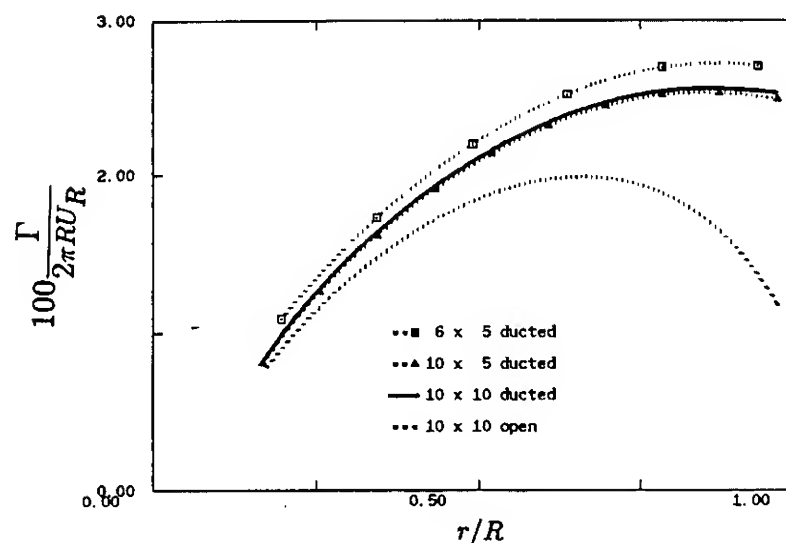


Figure 22: Convergence of spanwise distribution of circulation with propeller and duct panelling.



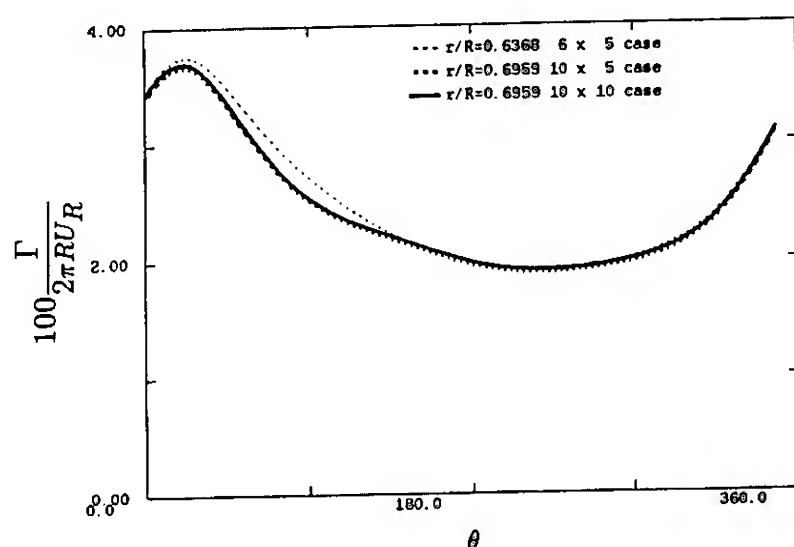


Figure 23: Convergence of unsteady circulation for the ducted propeller.

40 panels circumferentially on the duct. For comparison, we include a fourth curve which is for the same propeller but without a duct. All have twelve streamwise along the propeller wake corresponding to 30 time steps per revolution. Predictions of steady  $\Gamma$  agree well with corresponding results from the code based on the work of Kerwin *et. al.* [18].

To study the unsteady behavior we ran the same three cases in the artificial inflow given by

$$V_x(\theta) = 1 - c \left( \frac{1}{\left(\frac{\theta}{\pi}\right)^2 + \varepsilon} - \frac{1}{1 + \varepsilon} \right) - b$$

$$\begin{aligned} V_r &= 0 \\ V_t &= 0 \end{aligned} \quad (71)$$

where

$$\begin{aligned} c &= a\varepsilon(1 + \varepsilon) \\ b &= a\varepsilon - a\varepsilon^{1/2}(1 + \varepsilon)\arctan \varepsilon^{-1/2}. \end{aligned} \quad (72)$$

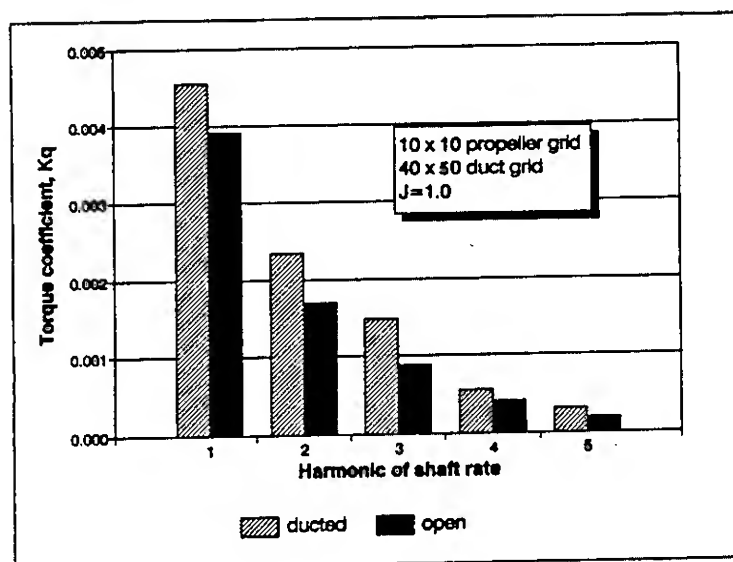


Figure 24: Unsteady torque computed directly for the ducted propeller and inferred from an open propeller case.

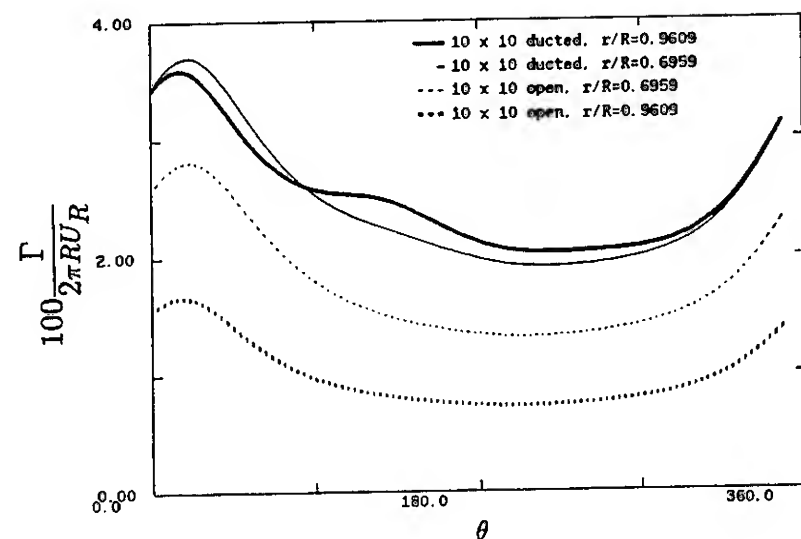


Figure 25: Unsteady circulation for ducted and open propeller.

The quantities  $a$  and  $\varepsilon$  permit adjustment of the depth of the wake defect and its width, respectively. Here they are set to  $a = 0.5$  and  $\varepsilon = 0.05$ . The result is a wake with a 50% defect at zero degrees and has a volumetric mean velocity of unity.

Figure 23 shows unsteady circulation near  $0.7R$  as a function of shaft rotation angle for the three ducted cases presented above. Notice convergence appears to be very rapid. The lifting surface code used in this model generally gives very good convergence behavior for circulation both spatially and temporally. We find here that the ducted case is nearly as well behaved once the duct is sufficiently resolved circumferentially.

Finally, to examine the effect the duct has on the unsteady forces we look at Figure 24 which compares the  $10 \times 10$  ducted propeller case with a run using the same propeller without the duct. For the unducted propeller we include the augment to the steady flow which the duct produces; only the panel image effects are turned

off. Given only an open propeller code one might imagine taking this latter approach to get unsteady forces on a ducted propeller. As the figure shows, one would underpredict unsteady torque by a significant fraction. Thrust behaves similarly. Figure 25 compares circulation for these same runs at two radii. Near  $0.7R$ , the curves for the open and ducted cases are, apart from the expected mean offset, essentially the same. However, the curves near  $0.96R$  show significantly different behavior. Thus, the sectional forces can be expected to show even greater divergence in their spectra than do the global forces shown above.

## 5 Conclusions

A time marching potential based panel method was presented for the analysis of the unsteady flow around open marine propellers subject to spatially nonuniform inflows. An efficient algorithm is implemented in order to ensure an explicit Kutta condition (*i.e.* pressure equality) at the blade trailing edge at each time step. The

numerics of the method are shown to be very robust for a broad range of reduced frequencies. The method is also shown to be consistent with known analytic solutions as well as with an existing unsteady lifting surface method. The method provides the user with accurate unsteady pressure distributions which may be coupled with a viscous / inviscid interaction scheme to predict unsteady boundary layer separation and / or leading edge separation.

A hybrid panel method is also developed for the analysis of the unsteady flow around ducted propellers. The method combines an unsteady lifting surface method for the propeller with a potential based panel method for the duct. The propeller is treated with a time marching vortex lattice scheme as if the propeller were open. The effects of the duct on the propeller are included via the modified inflow which is due to the presence of the duct (in the absence of the propeller) and via generalized images for the propeller and its trailing wake. The proposed method is shown to be appropriate for treating unsteady ducted propeller flows in a computationally efficient and robust manner, especially when a given ducted propeller geometry must be analyzed for various inflow conditions.

## 6 Acknowledgments

Support for this research was provided by the MIT Sea Grant College Program and the David Taylor Research Center, Department of the Navy, Grant Number NA86AA-D-SG089, and by the Office of Naval Research Contracts N00014-89-J-3194 and N00014-87-K-0422. The authors would like to thank Professor Justin E. Kerwin of the Department of Ocean Engineering at MIT for his valuable comments and suggestions during the course of this work, and also Lisa Shields, a former graduate student in the Department of Ocean Engineering, for her help during the initial development of the unsteady ducted propeller computer codes.

## References

- [1] B.C. Basu and G.J. Hancock. The unsteady motion of a two-dimensional aerofoil in incompressible inviscid flow. *Journal of Fluid Mechanics*, Vol. 87:pp 159-178, 1978.
- [2] R.J. Boswell and M.L. Miller. *Unsteady Propeller Loading - Measurement, Correlation, with Theory and Parametric Study*. Technical Report DTNSRDC 2625, DTNSRDC, October 1968.
- [3] T. Brockett. *Minimum Pressure Envelopes for Modified NACA-66 Sections with NACA  $a=0.8$  Camber and Buships Type I and Type II Sections*. Report 1780, DTNSRDC, Teddington, England, Feb 1966.
- [4] Joseph P. Giesing. Nonlinear two-dimensional unsteady potential flow with lift. *J. Aircraft*, 5(2), Mar-Apr. 1968.
- [5] D.S. Greeley and J.E. Kerwin. Numerical methods for propeller design and analysis in steady flow. *Trans. SNAME*, vol 90, 1982.
- [6] J. L. Guermond. About collocation methods for marine propeller design. In *Propellers '88*, 1988.
- [7] T. Hanaoka. Hydrodynamics of an oscillating screw propeller. In *Proc. 4th Symp. Nav. Hydrodyn.*, Natl. Acad. Press, 1962.
- [8] T. Hanaoka. *Numerical Lifting Surface Theory of a Screw Propeller in Non-uniform Flow (Part 1: Fundamental Theory)*. Technical Report 6(5):1-14, Ship Res. Inst., Tokyo, 1969.
- [9] J. L. Hess. *Calculation of Potential flow About Arbitrary Three-Dimensional Lifting Bodies*. Technical Report MDC J5679-01, McDonnell Douglas, October 1972.
- [10] J. L. Hess and Walter O. Valarezo. Calculation of steady flow about propellers by means of a surface panel method. In *23rd Aerospace Sciences Meeting*, AIAA, Reno, Nevada, January 1985.
- [11] T. Hoshino. Application of quasi - continuous method to unsteady propeller lifting surface problems. *J. Soc. Nav. Arch. Japan*, 158, 1985.
- [12] T. Hoshino. Hydrodynamic analysis of propellers in steady flow using a surface panel method. In *Proceedings of the Spring Meeting*, The Society of Naval Architects of Japan, May 1989.
- [13] Ching-Yeh Hsin. *Development and Analysis of Unsteady Propeller Panel Method*. PhD thesis, Department of Ocean Engineering, MIT, 1990. Under preparation.
- [14] D. P. Keenan. *Marine Propellers in Unsteady flow*. PhD thesis, Massachusetts Institute of Technology, May 1989.
- [15] J. E. Kerwin. Private communication.
- [16] J. E. Kerwin. Marine propellers. *Annual Review of Fluid Mechanics*, 18:367-403, 1986.
- [17] J. E. Kerwin and C. S. Lee. Prediction of steady and unsteady marine propeller performance by numerical lifting-surface theory. *SNAME Transactions*, 86, 1978.
- [18] J.E. Kerwin, S.A. Kinnas, J-T Lee, and W-Z Shih. A surface panel method for the hydrodynamic analysis of ducted propellers. *Trans. SNAME*, 95, 1987.

- [19] Kerwin, J.E. and C-S Lee. Prediction of steady and unsteady marine propeller performance by numerical lifting-surface theory. *Trans. SNAME*, vol 86, 1978.
- [20] S.A. Kinnas. A General Theory for the Coupling Between Thickness and Loading for Wings and Propeller. Submitted for Publication, June 1990.
- [21] Spyros A. Kinnas and William B. Coney. On the optimum ducted propeller loading. In *Proceedings of the Propellers '88 Symposium*, SNAME, Virginia Beach, VA, September 1988.
- [22] F.T. Korsmeyer, C.H. Lee, J.N. Newman, and P.D. Scalvounos. The analysis of wave effects on tension-leg platforms. In *OMAE '88 Conference*, 1988.
- [23] C. E. Lan. A quasi-vortex-lattice method in thin wing theory. *Journal of Aircraft*, 11(9), September 1974.
- [24] J. T. Lee. *A potential based panel method for the analysis of marine propellers in steady flow*. Technical Report 87-13, Dept. of Ocean Engineering, Massachusetts Institute of Technology, July 1987.
- [25] Brian Maskew. Influence of rotor blade tip shape on tip vortex shedding – an unsteady inviscid analysis. In *Proceedings of 36th Annual AHS Forum*, 1980.
- [26] Luigi Morino, Zaven Jr. Kaprielian, and Slobodan R. Sipicic. *Free Wake Aerodynamic Analysis of Helicopter Rotors*. Technical Report CN. DAAG29-80-C-0016, U.S. Army Research Office, May 1983.
- [27] Luigi Morino and Ching-Chiang Kuo. Subsonic potential aerodynamic for complex configurations : a general theory. *AIAA Journal*, vol 12(no 2):pp 191-197, February 1974.
- [28] J.N. Newman. Distributions of sources and normal dipoles over a quadrilateral panel. *Journal of Engineering Mathematics*, vol 20:pp 113-126, 1986.
- [29] William R. Sears. Some aspects of non-stationary airfoil theory and its practical application. *Journal of the Aeronautical Sciences*, vol. 8(No. 2), 1941.
- [30] L. M. Milne - Thomson. *Theoretical Aerodynamics*. Dover, fourth edition, 1966.
- [31] S. Tsakonas, W.R. Jacobs, and M.R. Ali. An exact linear lifting-surface theory for a marine propeller in a nonuniform flow field. *Journal of Ship Research*, vol. 17(No. 4):pp 196-207, Dec. 1973.
- [32] S. Tsakonas, W.R. Jacobs, and P.H. Rank. Unsteady propeller lifting-surface theory with finite number of chordwise modes. *Journal of Ship Research*, vol. 12(No. 1):pp 14-45, 1968.

## DISCUSSION

Jinzhang Feng  
Pennsylvania State University, USA (China)

1. Regarding the implementation of Kutta C.D., an analytical expression of Eq. 27 can easily be formulated. In fact, such an expression has been successfully used in a 3-D panel code developed at Penn. State. Why the authors chose to use a numerical approach to determine the Jacobin, which is inevitably more expensive, at least in terms of CPU time?

2. Theoretically, when using the generalized image model, the immense numerical effort needed to evaluate the modified Green function  $\hat{G}$  may well surpass any likely advantage in solving the potential at a later stage after  $\hat{G}$  is known. More important, I think, any simplified model derived as a result of employ such  $\hat{G}$  can be equivalently established with the original Green Function. Would the authors explain their consideration of using such a procedure?

3. A non-uniform inflow for propeller is usually rotational. The inflow vortex will redistribute when propeller disturbance is introduced. Further, wake vortex shed from the blade trailing edge might deform, including rolling up as one often sees in a similar two dimensional lifting flow. Why is it important to use an unsteady approach to tackle the problem if the vortex transportation feature cannot be accounted for properly? Would it not be easier, for example, just to use a quasi-steady approach to attempt the problem?

## AUTHORS' REPLY

On the implementation of the iterative pressure Kutta condition: to determine the elements of the Jacobin matrix (Eq. 27), we evaluate the derivatives involved numerically by perturbing the circulation distribution at each strip by a small amount and then computing its effect on the pressure difference at the trailing edge of all strips (the details are described in [18]). This operation involves only differentiations of potentials to find pressures, and thus requires very minimal CPU time, especially as compared to the CPU time required to solve for the propeller potentials at each time step. The discussor mentions an alternative method to determine the elements of the Jacobin matrix, but he does not give a reference and thus we cannot assess the validity of his approach for our problem.

On the use of the generalized image model: as described in Section 3.1 of the paper, the generalized image of each unit strength vortex loop on the propeller or on its wake corresponds to the solution on the duct in the presence of that vortex loop and in zero inflow. Thus, the generalized image coefficients depend only on the geometry of the duct and propeller and do not need to be recomputed for each time step in the propeller solution or for a different inflow. The primary reasons for selecting the generalized image technique as opposed to a direct duct and propeller time marching solver are mentioned in Section 3.1. They are as follows: (1) the same geometry can be run with considerably less CPU time for different inflows and, (2) the computations of the generalized images of each propeller vortex loop are independent of each other and can be performed very quickly on a parallel processing computer.

On his suggestion to use a quasi-steady technique instead of our fully unsteady method: it is well established in the hydrodynamic community that the quasi-steady theory fails in predicting unsteady forces on propellers, especially at blade rate (for example look at Fig. 15 of [16]). We prefer to be systematic in accounting for each of the effects (e.g., potential flow effect, effective wake effect). At present, we have developed a computationally reliable method to account for the potential flow effect. We plan to couple our method with a Euler solver in determining the effective wake contribution resulting from the vorticity transport Mr. Feng mentions.

## DISCUSSION

Ali H. Nayfeh  
Virginia Polytechnic Institute and State University, USA

It would be very useful to compare your results with the detailed experimental results of D. Telionis and co-workers and the panel results D.T. Mook and co-workers for the case of sinusoidal gust in two dimensions. D.T. Mook, A.H. Nayfeh, and co-workers developed steady and unsteady discrete and continuous vortex methods for lifting surface and rotor blades at high angles of attack, including interference effects. They used a Kutta condition that does not require iteration. The results were published in the AIAA Journal of Aircraft.

## AUTHORS' REPLY

On comparing the results of our method in two dimensions against existing experiments: this is something that we plan to do in the near future, though not before we include the tunnel wall effects as well as the unsteady boundary layer effects. The primary goal of the research reported in the paper was to produce a boundary element method (BEM) for the unsteady potential flow around hydrofoils or propellers, which method would be accurate, robust, and consistent for a broad range of reduced frequencies. We will perform an experiment at the MIT water tunnel on a two dimensional hydrofoil subject to a sinusoidal gust in reduced frequencies ( $k=10$ ) which are closer to propeller applications than those used in previous experiments. We also plan to compare our results to this experiment.

On the application of an iterative pressure Kutta condition: it has been found to be necessary when applying velocity based BEM formulations (Hess[9]) and more recently when applying potential based BEM formulations (Kerwin, Kinnas, Lee & Shih [18]). However, when a lifting surface (zero thickness) vortex lattice technique, such as that of Mook & Nayfeh, is applied, then the Kutta condition is equivalent to requiring the bound vorticity at the trailing edge to be equal to zero (which can be imposed either explicitly or implicitly) and thus an iterative condition is not needed (for example look in Kerwin & Lee[18]).

# **A Navier-Stokes Solution of Hull-Ring Wing-Thruster Interaction**

C.-I. Yang (David Taylor Research Center, USA)

P. Hartwich, P. Sundaram, (NASA Langley Research Center, USA)

## **ABSTRACT**

Navier-Stokes simulations of high Reynolds number flow around an axisymmetric body supported in a water tunnel were made. The numerical method is based on a finite-differencing high resolution second-order accurate implicit upwind scheme. Four different configurations were investigated, these are, 1. barebody, 2. body with an operating propeller, 3. body with a ring wing and 4. body with a ring wing and an operating propeller. Pressure and velocity components near the stern region were obtained computationally and are shown to compare favorably with the experimental data. The method correctly predicts the existence and extent of stern flow separation for the barebody and the absence of flow separation for the three other configurations with ring wing and/or propeller.

## **I. INTRODUCTION**

It has been known in marine propulsion technology that certain advantages can be achieved by properly integrating a ring wing and the propeller. With a ring wing that accelerates the flow the efficiency of the propeller remains more or less at a constant level over a wider range of advance ratios. With a ring wing that decelerates the flow, the inception of cavitation on the propeller can be delayed. In order to take advantage of the ring wing to obtain the desirable benefit, a clear understanding of the role it plays is important. Thorough water tunnel experiments and reliable numerical simulations serve as complementary approaches to gain understanding.

By combining the body, ring wing and propeller, appropriate configurations can be generated for water tunnel experiments, and the influence of each individual component can be isolated. The configurations studied here are 1. barebody, 2. body with an operating propeller, 3. body with a ring wing and 4. body with a ring wing and an operating propeller. Data collected from the water tunnel tests included the velocity components around the afterbody and the pressure on the stern. The data show the degree of inter-

action at the given operating conditions and serve as benchmarks for evaluating the present numerical simulations.

One important parameter in hull-propulsor interaction is the thrust deduction coefficient  $t$ , which signifies the drag augmentation due to the interaction. In the past, inviscid methods [1,2] have been successful in computing the coefficient  $t$ . The methods become somewhat inadequate in a situation where the propulsor unit is imbedded in the stern boundary layer where the viscous effect plays a dominating role. Efforts have been made to address the problem; in particular, Falcão de Campos [3] presented an inviscid approach to calculate the flow on the stern with and without propulsor based on the Euler equation of motion and Huang et al [4] developed a numerical technique to study the interaction between a propeller and unseparated viscous stern boundary layer. To further enhance the ability to predict the effect of hull-propulsor interaction, a Navier-Stokes type viscous analysis is needed. This is particular true when barebody flow separation may occur. Previously, Haussling et al [5] performed extensive numerical simulations of viscous flow about bodies with appendages using a Navier-Stokes solver. Here a three-dimensional incompressible Navier-Stokes solver is used to simulate the flow around a compound propulsor unit on an axisymmetric body supported in a water tunnel with a square cross-section. The solver is based on a high resolution second-order accurate implicit upwind scheme [6,7]. The propeller effect is simulated by imbedding body forces in a disk located at the propeller plane [8,9]. The experimental data were used to validate the Navier-Stokes solver.

## **II. DESCRIPTION OF EXPERIMENTS**

The test body is axisymmetric with a length of 139.12 cm and a maximum diameter of 24 cm. Its radius offsets,  $y$ , as a function of axial length,  $x$ , are given in cm units by:



for  $0.00 \leq x \leq 24.00$   
 $y = [12.0^2 - (12.0 - x/2)^2]^{1/2}$   
for  $24.00 \leq x \leq 97.81$   
 $y = 12$   
for  $97.81 \leq x \leq 115.84$   
 $y = [42.67^2 - (x - 97.81)^2]^{1/2} - 30.67$   
for  $115.84 \leq x \leq 129.17$   
 $y = (133.0 - x) \tan 25^\circ$   
for  $129.17 \leq x \leq 131.93$   
 $y = -0.0214x + 4.554$   
for  $131.93 \leq x \leq 139.12$   
 $y = -0.0310x^2 + 8.162x - 535.51$

The ring wing has a NACA 4415 profile section with a  $5^\circ$  angle of attack; its chord length is 5.3 cm. The diameter of ring wing measured at its trailing edge is 16 cm; its trailing edge is located at 129.7 cm from the nose of the body. The propeller has four blades with a diameter of 15.71 cm and was driven from behind with a Z-drive propelling device. The device consists of a tapered forebody, a cylindrical mid-body and an elliptical afterbody. The length of the device is about 85 cm and the diameter of midbody is about 10 cm. The propeller plane is located at 135 cm from the nose. The water tunnel in which the experiments were conducted has a square cross-section with round corners and its dimensions are 90 cm  $\times$  90 cm. The model/tunnel blockage ratio is about 5.6 percent. The body was supported from the ceiling of the water tunnel with two struts located at  $x = 14.0$  cm and  $x = 64.0$  cm from the nose. A schematic sketch is shown in Fig. 1; the propeller drive is not included. The geometric tolerances are less than 0.5 mm. The reference length is chosen to be 133.0 cm.

Experiments were conducted at a Reynolds number of  $6 \times 10^6$  (based on reference length 133.0 cm). The flow measurements were carried out on lines lying on the horizontal plane and perpendicular to the center line. The pressures on the body surface were measured by means of transducers and all signals could be reproduced satisfactorily within 1.0 percent. For the flow measurements, the standard deviation of all signals varied between 0.1 and 2.0 percent.

### III. DESCRIPTION OF NUMERICAL PROCEDURE

Using Chorin's artificial compressibility formulation, the incompressible Navier-Stokes equations are written in conservation law form for three-dimensional flow as [10]

$$\mathbf{Q}_t + (\mathbf{E}^* - \mathbf{E}_v)_x + (\mathbf{F}^* - \mathbf{F}_v)_y + (\mathbf{G}^* - \mathbf{G}_v)_z = 0 \quad (1)$$

where the dependent variable vector

$$\mathbf{Q} = (p, u, v, w)^T$$

represents the pressure and velocity components in a Cartesian coordinate system  $(x, y, z)$ . The inviscid flux vectors  $\mathbf{E}^*, \mathbf{F}^*, \mathbf{G}^*$  and the viscous shear flux vectors  $\mathbf{E}_v, \mathbf{F}_v, \mathbf{G}_v$  are given by

$$\begin{aligned} \mathbf{E}^* &= (\beta u, u^2 + p, uv, uw)^T \\ \mathbf{F}^* &= (\beta v, uv, v^2 + p, vw)^T \\ \mathbf{G}^* &= (\beta w, uw, vw, w^2 + p)^T \\ \mathbf{E}_v &= Re^{-1}(0, \tau_{xx}, \tau_{xy}, \tau_{xz})^T \\ \mathbf{F}_v &= Re^{-1}(0, \tau_{yx}, \tau_{yy}, \tau_{yz})^T \\ \mathbf{G}_v &= Re^{-1}(0, \tau_{zx}, \tau_{zy}, \tau_{zz})^T \end{aligned} \quad (2)$$

The coordinates  $x, y, z$  are scaled with an appropriate characteristic length scale  $L$ . The velocity components  $u, v, w$  are nondimensionalized with respect to the free stream velocity  $V_\infty$ , while the normalized pressure is defined as  $p = (P - P_\infty)/\rho V_\infty^2$ . The kinematic viscosity  $\nu$  is assumed to be constant, and the Reynolds number is defined as  $Re = \frac{V_\infty L}{\nu}$ . The artificial compressibility parameter  $\beta$  monitors the error associated with the addition of the unsteady pressure term  $\frac{\partial p}{\partial t}$  in the continuity equation which is needed for coupling the mass and momentum equations in order to make the system hyperbolic.

Equations (1) can be transferred to a curvilinear, body-fitted coordinates system  $(\zeta, \xi, \eta)$  through a coordinate transformation of the form

$$\zeta = \zeta(x, y, z), \quad \xi = \xi(x, y, z) \quad \text{and} \quad \eta = \eta(x, y, z)$$

Eq. (1) becomes

$$(\mathbf{Q}/J)_t + (\mathbf{E} - \mathbf{E}_v)_\zeta + (\mathbf{F} - \mathbf{F}_v)_\xi + (\mathbf{G} - \mathbf{G}_v)_\eta = 0 \quad (3)$$

with

$$(\mathbf{E}, \mathbf{F}, \mathbf{G})^T = [\mathbf{T}] (\mathbf{E}^*, \mathbf{F}^*, \mathbf{G}^*)^T$$

and

$$(\mathbf{E}_v, \mathbf{F}_v, \mathbf{G}_v)^T = [\mathbf{T}] (\mathbf{E}_v^*, \mathbf{F}_v^*, \mathbf{G}_v^*)^T$$

, where

$$[\mathbf{T}] = \begin{bmatrix} \zeta_x & \zeta_y & \zeta_z \\ \xi_x & \xi_y & \xi_z \\ \eta_x & \eta_y & \eta_z \end{bmatrix}$$

and the Jacobian of the coordinate transformation is given by

$$J^{-1} = \det \begin{bmatrix} x_\zeta & y_\zeta & z_\zeta \\ x_\xi & y_\xi & z_\xi \\ x_\eta & y_\eta & z_\eta \end{bmatrix}$$

The Cartesian derivatives of the shear fluxes are obtained by expanding them using chain rule expansions in the  $\zeta, \xi$ , and  $\eta$  directions.

Defining computational cells with their centroids at  $l = \frac{\theta}{\Delta\theta}$  ( $\theta$  is  $\zeta, \xi$ , or  $\eta$ ) and their cell interfaces at  $l \pm 1/2$ , the backward Euler time differencing of the three-dimensional conservation form is



$$\frac{\Delta \mathbf{Q}^n}{\Delta t} = - [\Delta_\zeta(\mathbf{E}^{n+1} - \mathbf{E}_v^{n+1}) + \Delta_\xi(\mathbf{F}^{n+1} - \mathbf{F}_v^{n+1}) + \Delta_\eta(\mathbf{G}^{n+1} - \mathbf{G}_v^{n+1})] \quad (3)$$

where  $\Delta t$  is the time step,  $\Delta \mathbf{Q}^n = \mathbf{Q}^{n+1} - \mathbf{Q}^n$  and  $\Delta_l(\ ) = [(\ )_{l+1/2} - (\ )_{l-1/2}]/\Delta\theta$ . Superscript denotes the time level at which the variables are evaluated.

Linearizing Eq. (3) about time level  $n$ , we obtain

$$\begin{aligned} & \left[ \frac{\mathbf{I}}{\Delta t J} + \left( \frac{\partial \mathbf{E}^n}{\partial \mathbf{Q}} - \frac{\partial \mathbf{E}_v^n}{\partial \mathbf{Q}} \right) \Delta_\zeta + \left( \frac{\partial \mathbf{F}^n}{\partial \mathbf{Q}} - \frac{\partial \mathbf{F}_v^n}{\partial \mathbf{Q}} \right) \Delta_\xi \right. \\ & \left. + \left( \frac{\partial \mathbf{G}^n}{\partial \mathbf{Q}} - \frac{\partial \mathbf{G}_v^n}{\partial \mathbf{Q}} \right) \Delta_\eta \right] \Delta \mathbf{Q}^n \\ & = - [\Delta_\zeta(\mathbf{E}^n - \mathbf{F}_v^n) + \Delta_\xi(\mathbf{F}^n - \mathbf{F}_v^n) + \Delta_\eta(\mathbf{G}^n - \mathbf{G}_v^n)] \end{aligned} \quad (4)$$

where  $\mathbf{I}$  is the identity matrix.

The left hand side is the implicit part and the right hand side is the explicit part of the formulation. The explicit part is the spatial derivatives in Eq. 2 evaluated at the known time level  $n$ ; its value diminishes as the steady state solution is approached. Hence, it is also called the residual. The  $L_2$  norm of the residual is often used as a measure of convergence of a solution. Letting the flux Jacobians  $\mathbf{A}$ ,  $\mathbf{B}$  and  $\mathbf{C}$  be defined as follow

$$\mathbf{A} \equiv \frac{\partial \mathbf{E}^n}{\partial \mathbf{Q}}, \quad \mathbf{B} \equiv \frac{\partial \mathbf{F}^n}{\partial \mathbf{Q}}, \quad \mathbf{C} \equiv \frac{\partial \mathbf{G}^n}{\partial \mathbf{Q}},$$

discretize the inviscid and viscous fluxes according to upwind differencing scheme and central differencing scheme respectively in  $\zeta$ ,  $\xi$  and  $\eta$  coordinate direction independently and then assemble them together. Equation (4) becomes

$$\begin{aligned} & \left[ \left( \frac{\mathbf{I}}{\Delta t J} \right) \right. \\ & - (\mathbf{A}^- + \mathbf{X})_{i+\frac{1}{2}} \Delta_{i+\frac{1}{2}} + (\mathbf{A}^+ + \mathbf{X})_{i-\frac{1}{2}} \Delta_{i-\frac{1}{2}} \\ & - (\mathbf{B}^- + \mathbf{Y})_{j+\frac{1}{2}} \Delta_{j+\frac{1}{2}} + (\mathbf{B}^+ + \mathbf{Y})_{j-\frac{1}{2}} \Delta_{j-\frac{1}{2}} \\ & \left. - (\mathbf{C}^- + \mathbf{Z})_{k+\frac{1}{2}} \Delta_{k+\frac{1}{2}} + (\mathbf{C}^+ + \mathbf{Z})_{k-\frac{1}{2}} \Delta_{k-\frac{1}{2}} \right]^n \Delta \mathbf{Q}^n \\ & = -RES(\mathbf{Q}^n) \end{aligned} \quad (5)$$

where  $i, j$ , and  $k$  are spatial indices associated with the  $\xi$ ,  $\eta$  and  $\zeta$  coordinate direction.  $\mathbf{A}^\pm, \mathbf{B}^\pm$  and  $\mathbf{C}^\pm$  are flux matrices split from the flux Jacobians  $\mathbf{A}, \mathbf{B}$  and  $\mathbf{C}$  according to the signs of their eigenvalues. The residual  $RES(\mathbf{Q}^n)$  is evaluated with a TVD technique together with Roe's [11] flux-difference splitting scheme, the discretization is third-order accurate. Conventional second-order central differencing is applied to obtain the viscous flux matrices  $\mathbf{X}, \mathbf{Y}$  and  $\mathbf{Z}$ . Equation(5) is solved by an implicit hybrid algorithm, where a symmetric planar Gauss-Seidel relax-

ation is used in the streamwise direction  $\zeta$  in combination with approximate factorization in the remaining two coordinate directions  $\xi$  and  $\eta$ . It is used to avoid the  $\Delta t^3$  spatial splitting error incurred in fully three-dimensional approximate factorization methods. This scheme is unconditionally stable for linear systems and offers the advantage of being completely vectorizable like a conventional three-dimensional approximate factorization algorithm. As a result, Eq. (5) becomes

$$\begin{aligned} & [\mathbf{M} - (\mathbf{B}^- + \mathbf{Y})_{j+\frac{1}{2}} \Delta_{j+\frac{1}{2}} + (\mathbf{B}^+ + \mathbf{Y})_{j-\frac{1}{2}} \Delta_{j-\frac{1}{2}}] \Delta \hat{\mathbf{Q}} \\ & = -RES(\mathbf{Q}^n, \mathbf{Q}^{n+1}) \\ & [\mathbf{M} - (\mathbf{C}^- + \mathbf{Z})_{k+\frac{1}{2}} \Delta_{k+\frac{1}{2}} + (\mathbf{C}^+ + \mathbf{Z})_{k-\frac{1}{2}} \Delta_{k-\frac{1}{2}}] \Delta \mathbf{Q}^n \\ & = \mathbf{M} \Delta \hat{\mathbf{Q}} \end{aligned} \quad (6)$$

$$\mathbf{Q}^{n+1} = \mathbf{Q}^n + \Delta \mathbf{Q}^n$$

with

$$\mathbf{M} = \left[ \frac{\mathbf{I}}{\Delta t J} + (\mathbf{A}^- + \mathbf{X})_{i+\frac{1}{2}} + (\mathbf{A}^+ + \mathbf{X})_{i-\frac{1}{2}} \right],$$

and the residual on the RHS indicates the nonlinear updating of the residual by using  $\mathbf{Q}^{n+1}$  whenever it becomes available while sweeping in the  $\zeta$  direction back and forth through the computational domain.

For laminar flow computations the coefficient of molecular viscosity  $\mu = \mu_l$  is obtained from Sutherland's law. Turbulence is simulated using the Baldwin-Lomax algebraic turbulence model[12]. For turbulent flow laminar viscosity coefficients are replaced by

$$\mu = \mu_l + \mu_t$$

The turbulent viscosity coefficient  $\mu_t$  is computed by using the isotropic, two-layer Cebeci type algebraic eddy-viscosity model as reported by Baldwin-Lomax. Modifications proposed by Degani and Schiff [13] and Hartwich and Hull [14] were implemented.

#### IV. DESCRIPTION OF BODY FORCE PROPELLER MODEL

The principle of the body force model is to introduce the body force terms into the Navier-Stokes equation to include the effects of the propeller. The essential parameters that define the propeller effects are the thrust coefficient  $C_T$ , the torque coefficient  $C_Q$ , the advance coefficient  $J$  and the radial circulation distribution  $G(r)$ . The same parameters were used to define the body force for the propeller model. The thrust and torque coefficients are defined as follow:

$$C_T = \frac{T}{\frac{1}{2} \rho V^2 \frac{\pi}{4} D^2}, \quad C_Q = \frac{Q}{\frac{1}{2} \rho V^2 \frac{\pi}{4} D^3}$$

where  $T$  and  $Q$  are thrust and torque, respectively.  $D$  is the diameter of the propeller. The axial and circumferential body force per unit volume are obtained from

the following equations:

$$fb_x = \frac{C_T R_p^2 G(r)}{4\Delta X \int_{R_h}^{R_p} G(r) r dr}$$

$$fb_\theta = \frac{C_Q R_p^3 G(r)}{2r\Delta X \int_{R_h}^{R_p} G(r) r dr}$$

where  $fb_x$  and  $fb_\theta$  are the body forces per unit volume in the axial and circumferential directions, respectively,  $R_h$  and  $R_p$  are the radii of propeller hub and blade tip, respectively, and  $\Delta X$  is the thickness of the disk. The computed body forces are then incorporated into the right hand side of Eq. 5 and form a part of the residual. Only a slight modification to the flow solver is needed to accommodate the body force type propeller model and there is no need for special gridding.

In reality, the blade circulation distribution  $G(r)$  depends upon the inflow at the propeller plane which in turn is influenced by the blade circulation. This mutual dependency implies that the body forces  $fb_x$  and  $fb_\theta$  which are functions of  $G(r)$  should be obtained by an iterative procedure. To complete this procedure, knowledge of propeller-induced axial and tangential velocities,  $u_a$  and  $u_t$  is needed. A propeller program based on the vortex-lattice lifting-surface method developed by Greeley and Kerwin [15] can be used for this purpose. The iterative procedure can be described as follow:

1. Calculate the nominal inflow with the Navier-Stokes solver.
2. Obtain the circulation distribution  $G(r)$ , the induced-velocities  $u_a$  and  $u_t$ , the thrust and torque coefficients  $C_T$  and  $C_Q$  by using the calculated nominal inflow as input to the propeller program [15].
3. Compute the body forces  $fb_x$  and  $fb_\theta$  by using the calculated circulation distribution  $G(r)$ , thrust and torque coefficients  $C_T$  and  $C_Q$ .
4. Obtain the total velocities at the propeller plane by using the Navier-Stokes solver with the information obtained in step 3.
5. Compute the effective wake by subtracting the propeller-induced velocities obtained in step 2 from the total velocities obtained in step 4.
6. Obtain an updated circulation distribution, propeller-induced velocities, and thrust and torque coefficients by using the newly computed effective wake as input to the propeller program.
7. Repeat the process from step 1 to step 6 until the total velocities, the body forces and the propeller-induced velocities are unchanged.

It has been shown that this procedure converged after two iterations [8]. For the purpose of illustration, the results presented in following are obtained by using measured thrust and torque without any iteration. In spite of its simplicity, it was able to predict the flow

pattern around the propeller disk and the stern region rather accurately [8,9].

## V. GRID GENERATION

Based on the configuration shown in Fig. 1, which models the experimental setup described in Section II above, a 180° sector of the tunnel needs to be modelled in order to resolve the effect on flow due to the supporting struts. This requires a large amount of grid points and extensive computational resources. After one computation for the barebody configuration, it was found that the struts produced an influence around and directly behind them with no significant effect on the horizontal plane on which measurements were made. Therefore, the struts were eliminated allowing the numerical simulations to be performed accurately in a 90° sector of the tunnel. Also included, due to its proximity to the stern, is the propeller drive.

To include the ring wing geometry, two block  $C-O$  type grids were generated. The grid points were matched at the branch cut that separated the two blocks. Computations were performed on a CRAY-YMP machine which has eight processors. Computational efforts on the two blocks can be performed on two processors simultaneously. For the purpose of synchronization between the processors, it is more efficient if the number of computations is the same for each block. For this reason, each block has the same number of grid points. The grid system was generated by a transfinite interpolation technique. Several grid systems with different number of grid and distributions had been generated and were used for computations on barebody configuration in order to investigate the relationship between the convergence and grid density and distribution. The grid systems examined include 1. a two block  $25 \times 49 \times 110$  ( $r, \theta, x$ ) grids, 2. a two block  $25 \times 25 \times 90$  grids and 3. a two block  $25 \times 13 \times 98$  grids. Grid points were clustered near the boundaries such as tunnel wall and body and ring wing surfaces where the viscous effect dominates. The minimum spacing normal to the body surface for the three grid systems mentioned above is  $5.0 \times 10^{-4}$ . The differences between the solutions based on the grid system 1 and 3 are about two percent which is within the reported experimental accuracy. The results presented below are based on a two block  $25 \times 13 \times 98$  ( $r, \theta, x$ ) coarse grid system. Convergence is achieved when the  $L_2$  normal of all residuals is reduced by three order of magnitude with CFL=10. Computational CPU time is 40  $\mu$ sec per node per iteration. For each computation, over 500 iterations were carried out to ensure convergence.

## VI. BOUNDARY CONDITIONS

On the solid boundaries such as surfaces of tunnel wall, ring wing, body and propeller drive the no-slip condition is applied, in addition, the normal gradient

of the pressure is assumed to be zero. Freestream condition is applied as inflow condition. Zero-order extrapolation is used to obtain the outflow conditions.

During the computation process, the variables on the branch cut that separates the two blocks are not computed. At the end of each iteration, these variables are updated by averaging the values at the adjacent grid points from each block. The averaging process is linear. The updated values are then used as boundary conditions for both blocks for the next iteration.

## VII. RESULTS AND DISCUSSIONS

The four configurations that were investigated are 1. flow over the barebody, 2. flow over the body with an operating propeller, 3. flow over the body with a ring wing and 4. flow over the body with a ring wing and an operating propeller. Computational results are presented in the form of velocity profiles and pressure contours in the stern region; they are compared with available experimental data. In addition, to facilitate the flow visualization and discussion, computed particle trace are also included. The length scale was normalized with reference length  $L = 133\text{cm}$ .

### Case 1. Flow over the Barebody

In this test case, the configuration is simple but the flow is rather interesting. At a Reynolds number of  $6.0 \times 10^6$ , flow separation was observed in the stern region. Figure 2 shows the velocity vectors in the stern region from both computation and experiment. The correlation is good except at the axial location  $X/L = 0.89$  where the experiment shows a somewhat fuller profile near the body. Figure 3 shows the particle traces and clearly depicts the separation bubble. The predicted separation location is about 1.5 cm (1.13 percent of body length) ahead of where it was observed experimentally. Figure 3 also indicates that the size of the bubble is predicted correctly. Figure 4 shows the predicted and measured pressure distributions on the surface of the stern. The surface pressure begins to recover as the flow passes the shoulder of the afterbody at  $X/L = 0.78$ . The recovery levels off where flow separation takes place. Figure 5 shows the pressure contours in the stern region.

### Case 2. Flow over the Body with an Operating Propeller

In this test case, the propeller was operating at  $J = 0.47$  and  $V = 4\text{m/s}$ ;  $C_T$  and  $C_Q$  were measured as 2.052 and 0.247, respectively. To apply the body force propeller model, the circulation  $G(r)$  was assumed to be distributed over the disk according to:

$$G(r) = r(1 - r)^{1/2}$$

with  $r = (y - y_{hub})/(R_p - y_{hub})$ . The propeller was located at  $X/L = 1.015$ .

Figure 6 shows the comparison of predicted and measured velocity vectors in the stern region. The prediction confirms that the separation bubble is removed due to the propeller suction. Experimental data indicate stronger downward radial velocities at all four stations. In addition, at axial locations  $X/L = 0.89$  and  $X/L = 0.93$  the predicted velocity profiles are less full than those that were measured near the body. It is found from computations that the predictions behind the propeller are sensitive to the circulation distribution over the propeller disk and the axial locations at which the predictions are made. Figure 7 shows the particle traces, indicating that flow contraction takes place immediately in front of and behind the propeller disk. Figure 8 shows the predicted and measured pressure distributions on the surface of the stern. The difference between the pressures presented in Fig. 8 and Fig. 4 gives the amount of the pressure drag on the barebody due to propeller action. The added drag constitutes the major part of the thrust deduction fraction ( $t$ ). The agreement between prediction and measurement is very good. This is an indication that thrust deduction ( $1 - t$ ) can be predicted correctly with this numerical method. Figure 9 shows the pressure contours in the stern region; the pressure jump across the propeller plane is clear.

### Case 3. Flow over the Body with a Ring Wing

An intended function of the ring wing was to accelerate the flow and produce thrust. It was also expected that the flow separation over the stern would be removed once the ring wing was in place. Figure 10 shows the velocity vectors in the stern region from both computation and experiment. In comparison with Fig. 2, it can be seen that the ring wing achieved its function in accelerating the flow and removing the stern separation. The predicted and the measured velocity vectors are in good agreement. Due to lack of details, the experimental data failed to resolve the wake structure behind the ring wing. Figure 11 shows the particle traces and there is no detectable flow separation on the surface of either the body or the ring wing. Figure 12 shows the pressure on the stern surface. Note that the predicted surface pressure immediately upstream of the ring wing's leading edge at  $X/L = 0.93$  is somewhat higher than that measured. Figure 13 shows the pressure contours in the stern region. Clearly shown are the locations of the pressure and suction peaks on the ring wing surface.

#### Case 4. Flow over the Body with a Ring Wing and an Operating Propeller

In this test case, the propeller was operating at  $J = 0.47$  and  $V = 4m/s$ ;  $C_T$  and  $C_Q$  were measured as 2.081 and 0.250, respectively, and are about 2 percent higher than those shown in Case 2. Figure 14 shows the comparison of predicted and measured velocity vectors in the stern region. The agreement is quite good. Figure 15 shows the particle traces. It can be seen that flow is accelerated as it passes the ring wing and is contracted as it passes the propeller disk. Figure 16 shows the pressure on the stern surface. The discrepancy between the predicted and measured pressure immediately upstream of the ring wing at  $X/L = 0.93$  as discussed in Case 3 is present here also. The difference between the pressures presented in Fig. 16 and Fig. 12 gives the amount of the pressure drag on the body due to the propeller action, the agreement between the prediction and measurement is very good, despite the discrepancy mentioned above. Figure 17 shows the pressure contours in the stern region.

#### VIII. CONCLUSION

A numerical method based on a finite-differencing high resolution second-order accurate implicit upwind scheme was used to discretize the three-dimensional Navier-Stokes equations. Simulations of flow over an axisymmetric body with a compound propulsor supported in a square water tunnel were performed. A body force type propeller model was used to simulate the propeller action. Results indicate that this numerical method is effective and accurate. Observed flow phenomena such as separation, acceleration and contraction were realistically predicted. The pressure drags due to propeller action were computed correctly. A ring wing may affect the circulation distribution on the propeller, depending on its proximity to the propeller. In order to improve the predictions further, an iterative procedure described in section IV will be explored in a future study.

#### ACKNOWLEDGEMENT

This study was supported by The Office of Naval Technology under David Taylor Research Center Work Unit 1-1506-060-40. The computing time of CRAY-YMP was provided generously by NASA Ames Numerical Aerodynamic Simulation (NAS) Program. The experimental data presented in this paper are of foreign origin, obtained via informal correspondence.

#### REFERENCES

1. Wald, Q., "Performance of a Propeller in a Wake and the Interaction of Propeller and Hull", *Journal of Ship Research*, Vol 9, no. 1, Jun. 1965, pp1-8.
2. Beveridge, J.L., "Analytical Prediction of Thrust Deduction for Submersibles and Surface Ships", *Journal of Ship Research*, Vol. 13, no. 4, Dec. 1969, pp. 258-271
3. Falcão de Campos, J.A.C., "On the Calculation of Ducted Propeller Performance in Axisymmetric Flows", Technical Report 696, Netherlands Ship Model Basin, Wageningen, The Netherlands, 1983
4. Huang, T. T., Wang, H. T., Santelli, N., Groves, N. C., "Propeller/Stern/Boundary Layer Interaction on Axisymmetric Bodies, Theory and Experiment", DTRC Report 76-0113, 1976.
5. Haussling, H.J., Gorski, J.J., Coleman, R., "Computation of Incompressible Fluid Flow about Bodies with Appendages", Presented at International Seminar on Supercomputing in Fluid Flow, Lowell, Massachusetts, 3-5 Oct. 1989.
6. Hartwich, P.-M., Hsu, C. H., "High Resolution Upwind Schemes for the Three-Dimensional, Incompressible Navier-Stokes Equations", *AIAA Journal*, Vol. 26, No. 11, Nov. 1988, pp 1321-1328.
7. Hartwich, P.-M., Hsu, C. H. and Liu, C.H., "Vectorizable Implicit Algorithms for the Flux-Difference Split, Three-Dimensional, Incompressible Navier-Stokes Equations", *ASME Journal of Fluids Engineering*, Vol. 110, No. 3, Sept. 1988, pp 297-305.
8. Stern, F., Kim, H.T., Patel, V.C., Chen, H.C., "A Viscous Flow Approach to the Computation of Propeller-Hull Interaction", *Journal of Ship Research*, Vol.32, No. 4, Dec. 1988, pp 246-262.
9. Yang, C-I, Hartwich, P.-M., Sundaram, P., "Numerical Simulation of Three-Dimensional Viscous Flow around a Submersible Body", *The Proceedings Fifth International Conference on Numerical Ship Hydrodynamics*, Sept. 25-28 1989, Hiroshima, Japan.
10. Chorin, A. J., "A Numerical Method for Solving Incompressible Viscous Flow Problems", *Journal of Computational Physics*, Vol. 2, No. 1, Aug. 1967, pp 12-26.
11. Roe, P.L., "Approximate Riemann Solvers, Parameter Vectors, and Difference Schemes", *Journal of Computational Physics*, Vol. 43, No. 2, Oct. 1981, pp 357-372.

12. Baldwin, B.S., Lomax, H., "Thin Layer Approximation and Algebraic Model for Separated Turbulent Flows", AIAA Paper 78-257 Jan. 1978.
13. Degani, D., Schiff, L.B., "Computation of Turbulent Supersonic Flows around Pointed Bodies Having Crossflow Separation", Journal of Computational Physics, Vol. 66, No. 1, Sept. 1986, pp 173-196.
14. Hartwich, P-M., Hall R.M., "Navier-Stokes Solutions for Vortical Flows over a Tangent-Ogive Cylinder", AIAA Paper No. 89-0337, Jan. 1989
15. Greeley, D.S., Kerwin, J.E., "Numerical Methods for Propeller Design and Analysis in Steady Flow", Trans. SNAME, Vol. 90, 1982, pp. 415-453.

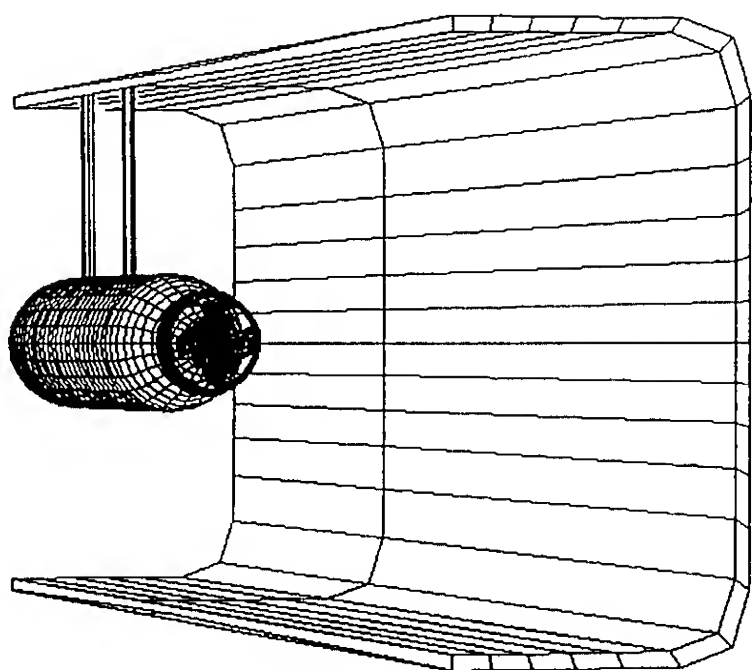


Figure 1. Schematic Sketch of Test Configuration

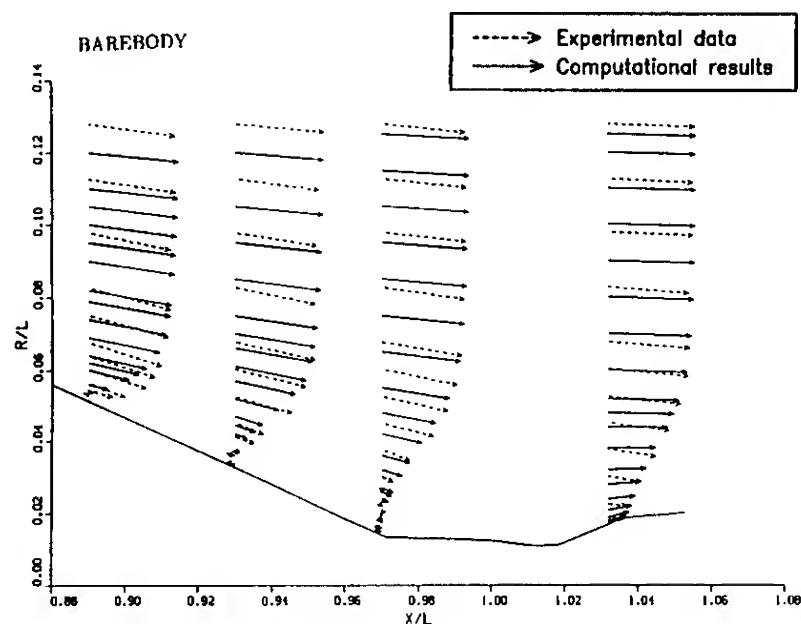


Figure 2. Velocity Vectors in Stern Region for Case 1

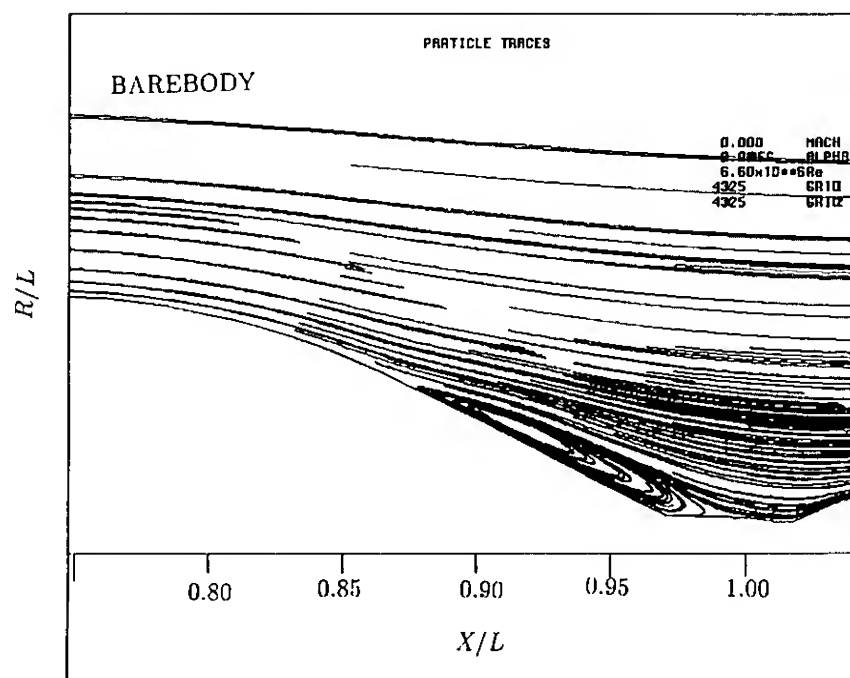


Figure 3. Particle Traces for Case 1

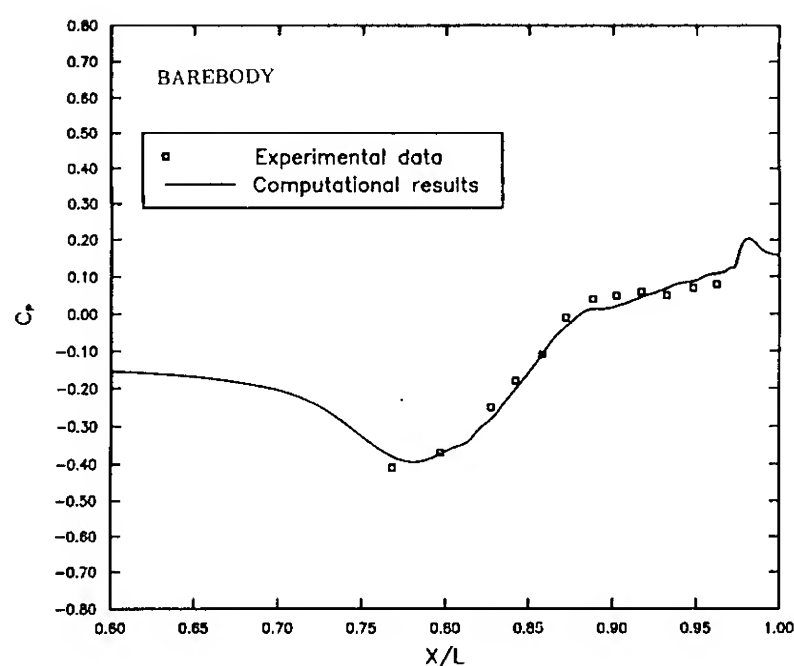


Figure 4. Pressure Distribution on Stern Surface for Case 1

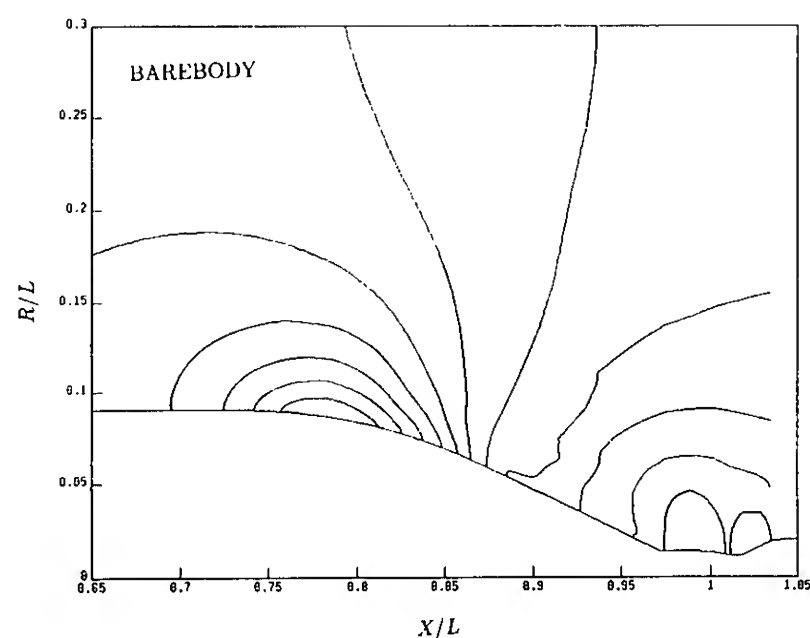


Figure 5. Pressure contours in Stern Region for Case 1



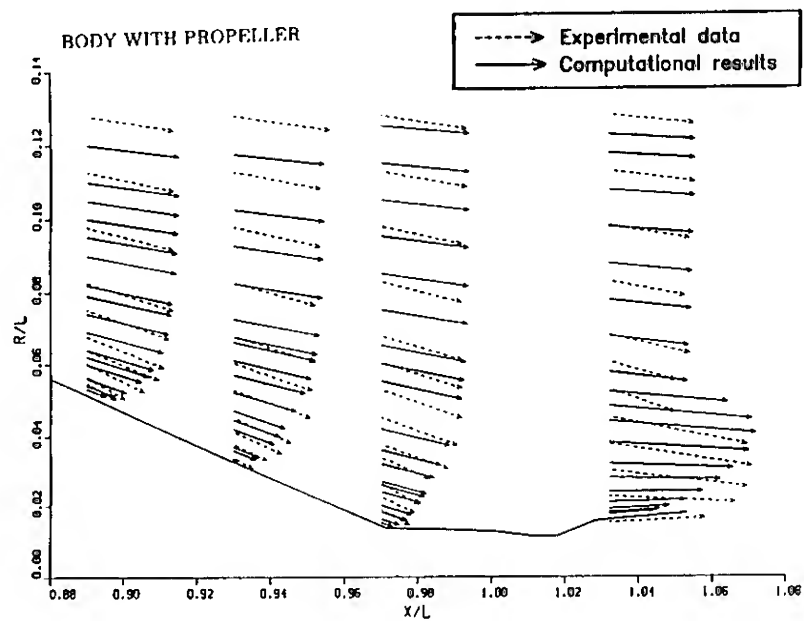


Figure 6. Velocity Vectors in Stern Region for Case 2

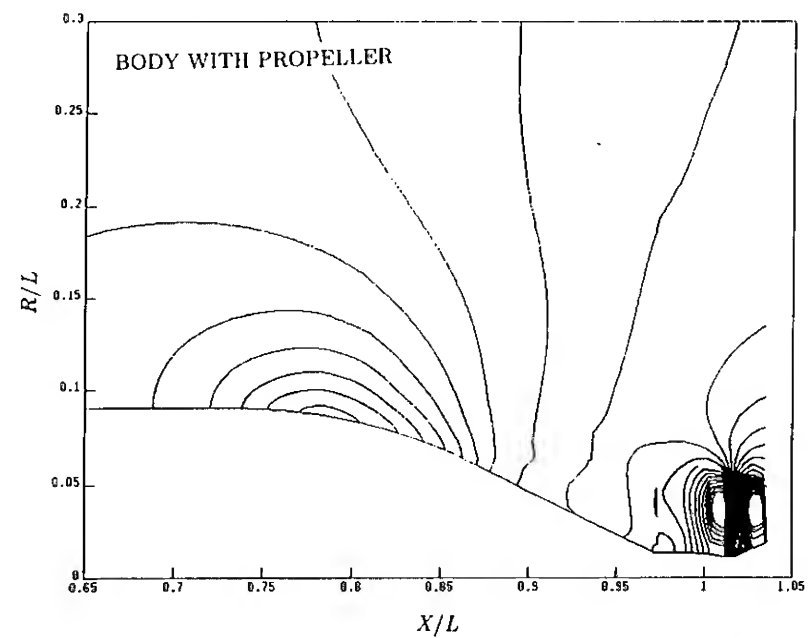


Figure 9. Pressure contours in Stern Region for Case 2

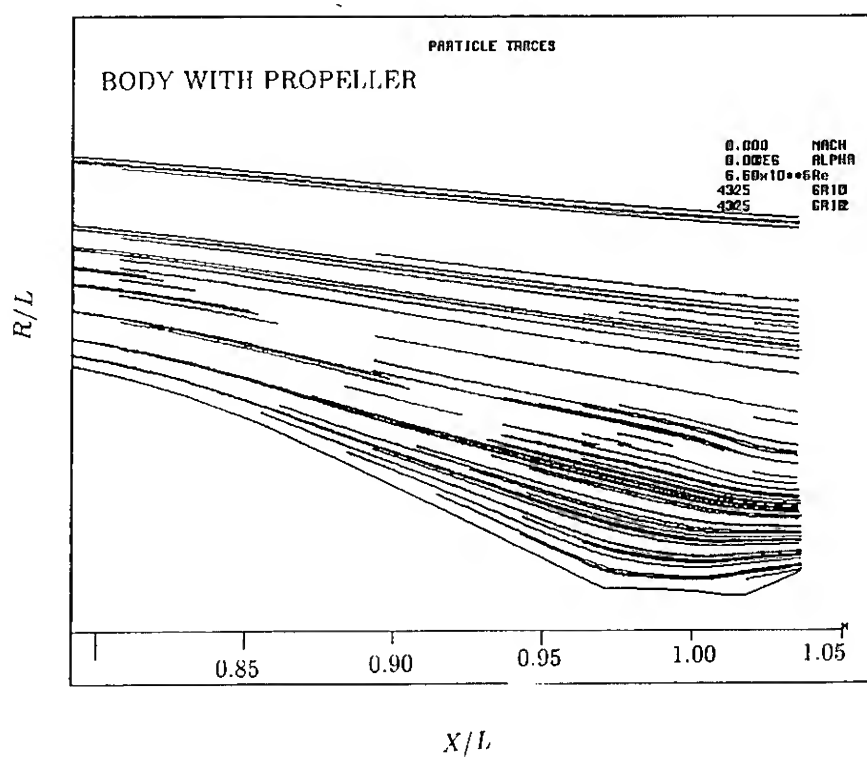


Figure 7. Particle Traces for Case 2

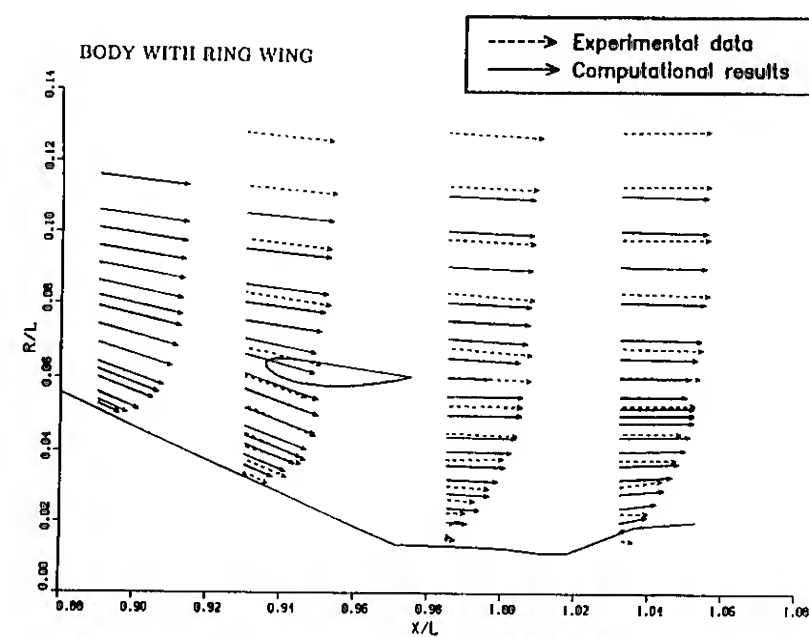


Figure 10. Velocity Vectors in Stern Region for Case 3

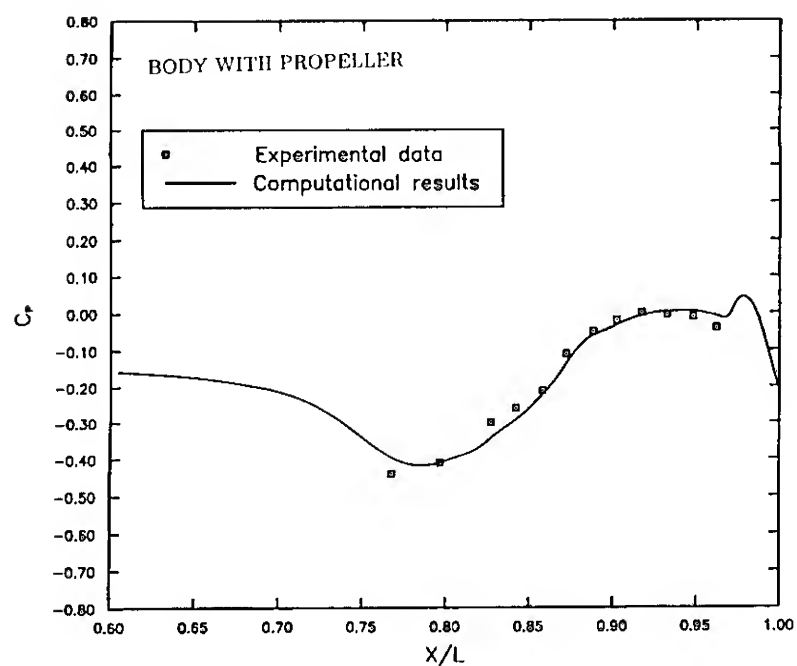


Figure 8. Pressure Distribution on Stern Surface for Case 2

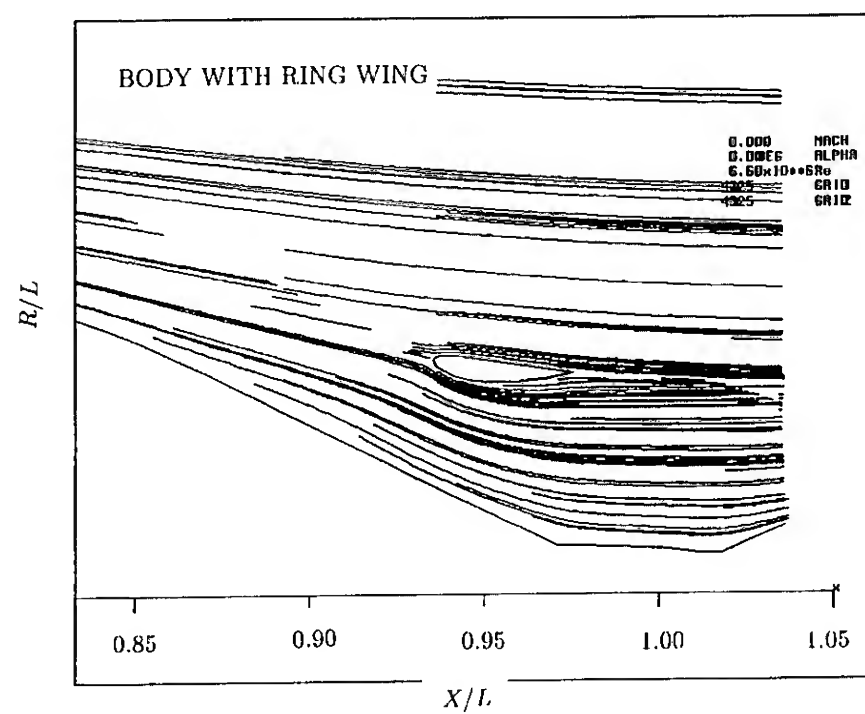


Figure 11. Particle Traces for Case 3



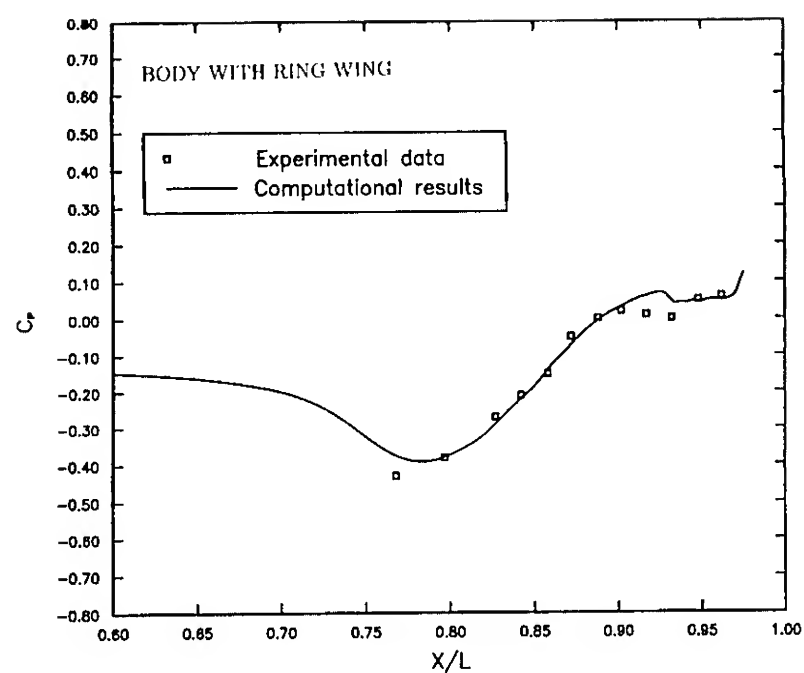


Figure 12. Pressure Distribution on Stern Surface for Case 3

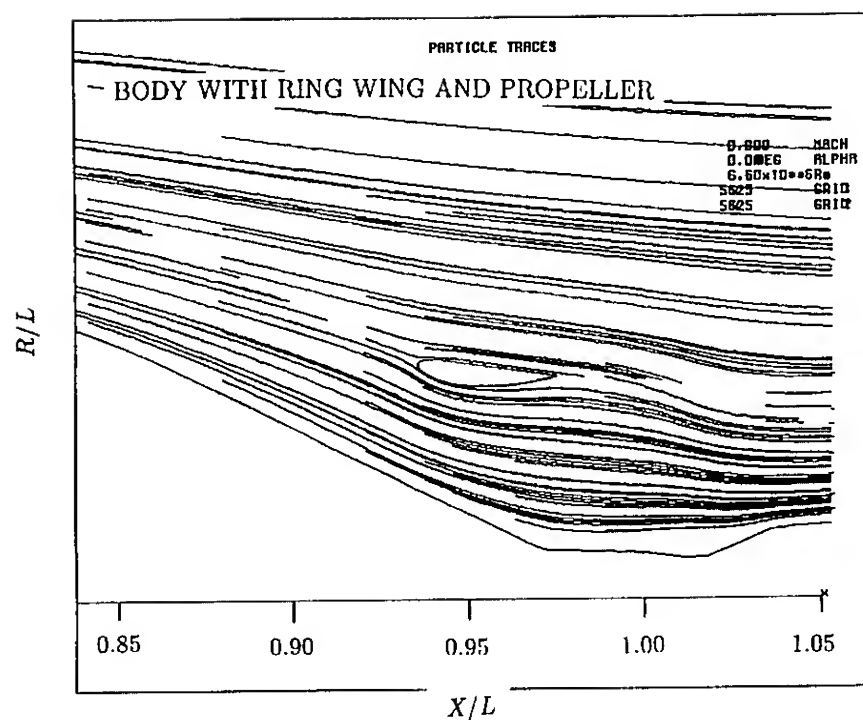


Figure 15. Particle Traces for Case 4

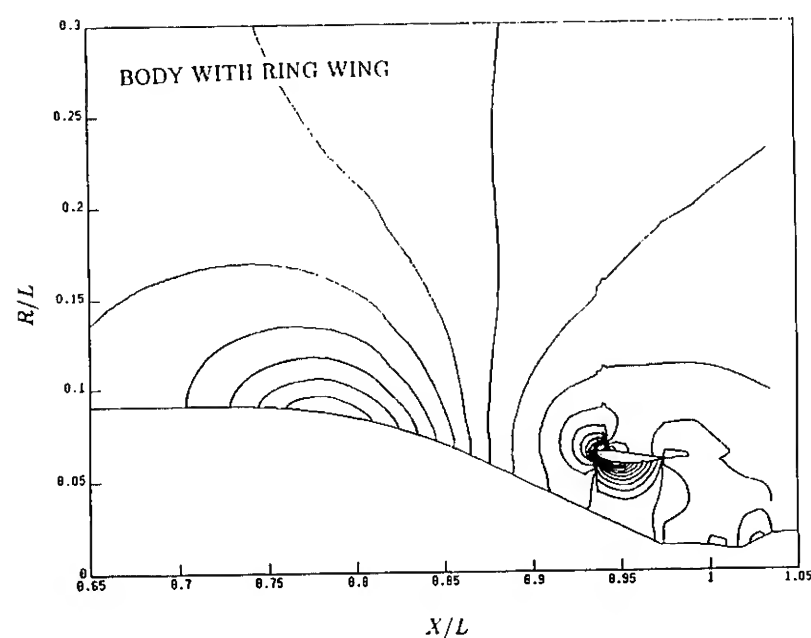


Figure 13. Pressure contours in Stern Region for Case 3

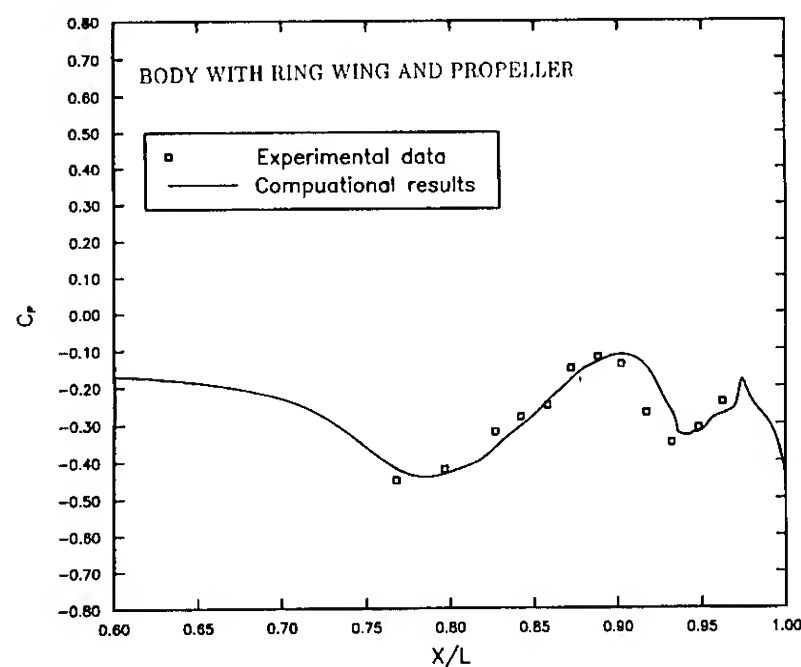


Figure 16. Pressure Distribution on Stern Surface for Case 4

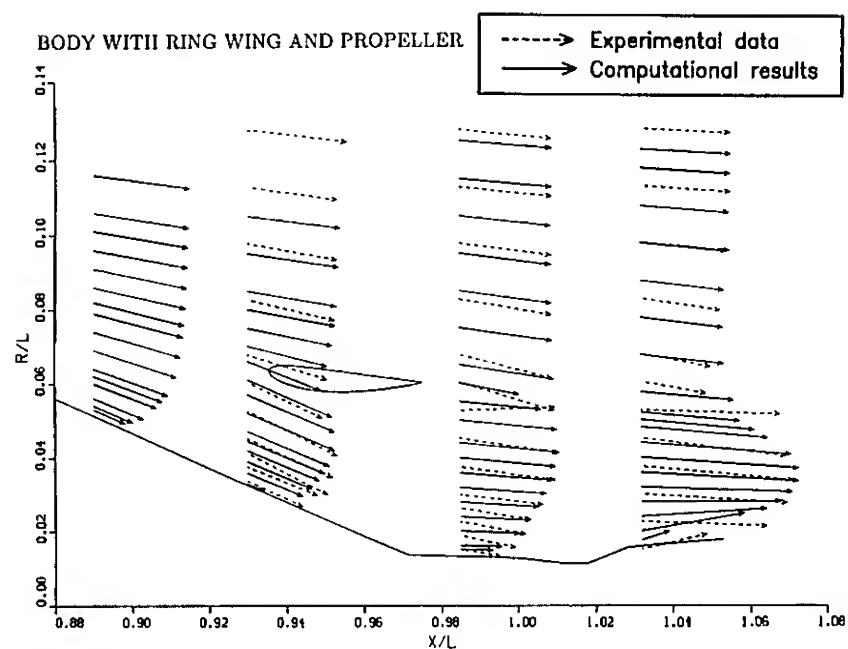


Figure 14. Velocity Vectors at Stern Region for Case 4

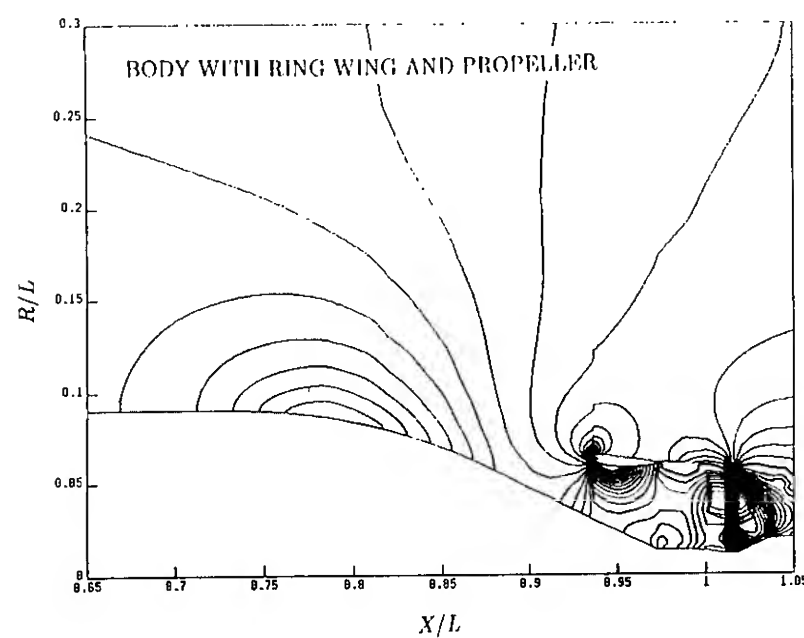


Figure 17. Pressure contours in Stern Region for Case 4

## DISCUSSION

Philippe Genoux  
Bassin d'Essais des Carènes, France

It is well known that Navier Stokes solvers may have difficulties at high Reynolds numbers. How does your code behave at full scale Reynolds numbers?

## AUTHORS' REPLY

The differencing scheme presented in this paper is based on hyperbolic formulation, assuming that at high Reynolds numbers the behavior of Navier-Stokes equations becomes hyperbolic-like. At present, the solver has been used to simulate flow at Reynolds number  $15 \times 10^6$ . The agreement between computation and experiment is good. No convergence problem was experienced.

## DISCUSSION

Fred Stern  
The University of Iowa, USA

The results presented display some interesting features for a ducted propulsor; however, it would be of greater interest if the authors would include the propulsor-hull interaction, i.e., make full use of the viscous-flow approach to propulsor-hull interaction and demonstrated in Reference [8].

## AUTHORS' REPLY

We appreciate Prof. Stern's comments and suggestions. We are using the method described in Reference [8] for our future work.

**Session VIII**  
**Viscous Effects**

# An Interactive Approach for Calculating Ship Boundary Layers and Wakes for Nonzero Froude Number

Y. Tahara, F. Stern

(Iowa Institute of Hydraulic Research, The University of Iowa, USA)

B. Rosen (South Bay Simulations Inc., USA)

## ABSTRACT

An interactive approach is set forth for calculating ship boundary layers and wakes for nonzero Froude number. The Reynolds-averaged Navier-Stokes equations are solved using a small domain with edge conditions matched with those from a source-doublet-Dawson method solved using the displacement body. An overview is given of both the viscous- and inviscid-flow methods, including their treatments of the free-surface boundary conditions and interaction procedures. Results are presented for the Wigley hull, including comparisons for zero and nonzero Froude number and with available experimental data and the inviscid-flow results, which validate the overall approach and enable an evaluation of the wave-boundary layer and wake interaction.

## NOMENCLATURE

$A_\phi, B_\phi, \text{etc.}$	coefficients in transport equations
$A_{ij}, B_{ij}, a_j, b_{jk}$	influence coefficients
$b_j^i$	geometric tensor
$C_D, C_P, C_U, C_{nb}$	finite-analytic coefficients (nb = NE, NW, SE, etc.)
$C_f$	friction coefficient ( $= 2\tau_w/\rho U_0^2$ )
$C_p$	pressure coefficient
$C_R$	residuary-resistance coefficient ( $= 2R/\rho S U_0^2$ )
$Fr$	Froude number ( $= U_0/\sqrt{gL}$ )
$g_{ij}$	conjugate metric tensor in general curvilinear coordinates $\xi^i$
$k$	turbulent kinetic energy
$L$	characteristic (ship) length
$\mathbf{n}$	normal unit vector
$\hat{p}$	piezometric pressure
$R$	residuary resistance
$Re$	Reynolds number ( $= U_0 L/\nu$ )
$S$	wetted surface area
$S_b, S_e, \text{etc.}$	boundaries of the solution domain
$S_\phi, S$	source functions
$t$	time; arclength in tangential direction
$\mathbf{t}$	tangent unit vector
$U, V, W$	velocity components in cylindrical polar coordinates
$U_x, V_y, W_z$	velocity components in Cartesian coordinates
$U_c$	wake centerline velocity

$U_0$	characteristic (freestream) velocity
$U_\tau$	wall-shear velocity ( $= \sqrt{\tau_w/\rho}$ )
$\bar{u}\bar{u}, \bar{v}\bar{v}, \text{etc.}$	Reynolds stresses
$x, y, z$	Cartesian coordinates
$x, r, \theta$	cylindrical polar coordinates
$x^+, y^+, z^+$	dimensionless distances ( $= U_\tau x/\nu$ , etc.)
$\delta^*$	displacement thickness
$\epsilon$	rate of turbulent energy dissipation
$\eta$	free-surface elevation
$\mu$	dipole strength
$\nu$	kinematic viscosity
$\nu_t$	eddy viscosity
$\xi, \eta, \zeta$	body-fitted coordinates
$\rho$	density
$\sigma$	source strength
$\tau$	time increment
$\tau_{ij}, \tau_{ij}^*$	fluid- and external-stress tensors
$\tau_w$	wall-shear stress
$\phi$	transport quantities ( $U, V, W, k, \epsilon$ ); velocity potential

## Subscripts

$e$	edge value
$o$	freestream or zero Fr value
$p$	inviscid-flow value

## INTRODUCTION

The interaction between the wavemaking of a ship and its boundary layer and wake is a classic and important problem in ship hydrodynamics. Initially, the interest was primarily with viscous effects on wave resistance and propulsive performance due to the lack of Reynolds number ( $Re$ ) similarity in model tests. More recently, also of interest are the wave-boundary layer and wake interaction effects on the details of ship wakes and wave patterns due to the advent of satellite remote sensing. The present study is central to the aforementioned problems, i.e., it concerns the development of an interactive approach for calculating ship boundary layers and wakes for nonzero Froude number ( $Fr$ ). Thus, both the effects of wavemaking on the boundary layer and wake and, vice versa, the effects of the boundary layer and wake on wavemaking are included in the theory, although the focus here is somewhat more on the former.

Historically, inviscid-flow methods have been used to calculate wavemaking and viscous-flow methods the boundary layer and wake, in both cases, without accounting for the interaction. Recent work on wavemaking has focused on the solution of the so-called Neumann-Kelvin problem using both Rankine- and Havelock-source approaches. Methods implementing these approaches were recently competitively evaluated and ranked by comparing their results with towing-tank experimental data [1]. In general, the methods underpredicted the amplitude of the divergent bow waves, were lacking in high wave-number detail in the vicinity of the bow-wave cusp line, and overpredicted the amplitudes of the waves close to the stern. These difficulties were primarily attributed to nonlinear and viscous effects. The methods using the Havelock-source approach generally outperformed those using the Rankine-source approach, except with regard to the near-field results (i.e., within one beam length of the model) for which one of the latter methods [2] was found to be far superior.

Considerable effort has been put forth in the development of viscous-flow methods for ship boundary layers and wakes. Initially, three-dimensional integral and differential boundary-layer equation methods were developed; however, these were found to be inapplicable near the stern and in the wake. More recently, efforts have been directed towards the development of Navier-Stokes (NS) and Reynolds-averaged Navier-Stokes (RANS) equation methods; hereafter both of these will simply be referred to as RANS equation methods. At present, the status of these methods is such that practical ship geometries can be considered, including complexities such as appendages and propellers. Comparisons with experimental data indicate that many features of the flow are adequately simulated; however, turbulence modeling and grid generation appear to be pacesetting issues with regard to future developments (see, e.g., the review by Patel [3] and the Proceedings of the 5th International Conference on Numerical Ship Hydrodynamics [4]).

Relatively little work has been done on the interaction between wavemaking and boundary layer and wake. Most studies have focused separately on either the effects of viscosity on wavemaking or the effects of wavemaking (i.e., waves) on the boundary layer and wake. Professor Landweber and his students have both demonstrated experimentally the dependence of wave resistance on viscosity and shown computationally that by including the effects of viscosity in inviscid-flow calculations of wave resistance better agreement with experimental data is obtained (most recently, [5]). Such effects have been confirmed by others, including other more detailed aspects of the flow field such as surface-pressure distributions and wave profiles and patterns [6].

Most studies concerning the effects of waves on boundary layer and wake have been of an approximate nature utilizing integral methods and assuming small-crossflow conditions (see Stern [7] for a more complete review, including references). In [7,8], experiment and theory are combined to study the fundamental aspects of the problem utilizing a unique, simple model and computational geometry, which enabled the isolation and identification of certain important features of the wave-induced effects. In particular, the variations of the wave-induced piezometric-pressure gradients are shown to cause acceleration and deceleration phases of the

streamwise velocity component and alternating direction of the crossflow, which results in large oscillations of the displacement thickness and wall-shear stress as compared to the no-wave condition. For the relatively simple geometry studied, first-order boundary-layer calculations with a symmetry-condition approximation for the free-surface boundary conditions were shown to be satisfactory; however, extensions of the computational approach for practical geometries were not successful [9].

Miyata et al. [10] and Hino [11] have pursued a comprehensive approach to the present problem in which the NS equations (sub-grid scale and Reynolds averaged, respectively) are solved using a large domain with approximate free-surface boundary conditions. In both cases, the basic algorithms closely follow those of MAC [12] and SUMMAC [13]. However, [10] uses a time-dependent free-surface conforming grid, whereas [11] uses a fixed grid which does not conform to the free surface. The results from both approaches are promising, but, thus far, have had difficulties in accurately resolving the boundary-layer and wake regions and, in the case of [10], have been limited to low  $Re$ .

The present interactive approach is also comprehensive. Two of the leading inviscid- [2] and viscous-flow [14] methods are modified and extended for interactive calculations for ship boundary layers and wakes for nonzero  $Fr$ . The interaction procedures are based on extensions of those developed by one of the authors for zero  $Fr$  [15]. The work of [7,8,15] is precursory to the present study. Also, it should be mentioned that the present study is part of a large project concerning free-surface effects on boundary layers and wakes. Some of the related studies under this project will be referenced later.

In the following, an overview is given of both the viscous- and inviscid-flow methods, with particular emphasis on their treatments of the free-surface boundary conditions and the interaction procedures. Results are presented for the Wigley hull, including comparisons for zero and nonzero  $Fr$  and with available experimental data and inviscid-flow results, which validate the overall approach and enable an evaluation of the wave-boundary layer and wake interaction. In the presentation of the computational methods and results and discussions to follow, variables are either defined in the text or in the NOMENCLATURE and are nondimensionalized using the ship length  $L$ , freestream velocity  $U_0$ , and fluid density  $\rho$ .

## COMPUTATIONAL METHODS

Consider the flow past a ship-like body, moving steadily at velocity  $U_0$ , and intersecting the free surface of an incompressible viscous fluid. As depicted in figure 1, the flow field can be divided into four regions in each of which different or no approximations can be made to the governing RANS equations: region 1 is the inviscid flow; region 2 is the bow flow; region 3 is the thin boundary layer; and region 4 is the thick boundary layer and wake. The resulting equations for regions 1 and 3 and their interaction (or lack of one) are well known. Relatively little is known about region 2. Recent experiments concerning scale effects on near-field wave patterns have indicated a  $Re$  dependency for the bow wave both in amplitude and divergence angle [16]; however, this aspect of the problem is deferred for later study. Herein, we are primarily concerned with the flow

in region 4 and its interaction with that in region 1. As discussed earlier, the description of the flow in region 4 requires the solution of the complete RANS equations (or, in the absence of flow reversal, the so-called partially-parabolic RANS equations, however, this simplification will not be considered here).

There are two possible approaches to the solution of the RANS equations: a global approach, in which one set of governing equations appropriate for both the inviscid- and viscous-flow regions are solved using a large solution domain so as to capture the viscous-inviscid interaction; and an interactive approach, in which different sets of governing equations are used for each region and the complete solution obtained through the use of an interaction law, i.e., patching or matching conditions. Both approaches are depicted in figure 1. The former approach is somewhat more rigorous because it does not rely on the patching conditions that usually involve approximations. Nonetheless, for a variety of reasons, both types of approaches are of interest. In [15], both approaches were evaluated for zero Fr by comparing interactive and large-domain solutions for axisymmetric and simple three-dimensional bodies using the same numerical techniques and algorithms and turbulence model. It is shown that both approaches yield satisfactory results, although the interaction solutions appear to be computationally more efficient. As mentioned earlier, the present study utilizes the interactive approach. This takes advantage of the latest developments in both the inviscid- and viscous-flow technologies; however, a large-domain solution for the present problem is also of interest and a comparative evaluation as was done previously for zero Fr is planned for study under the present project for nonzero Fr.

### Viscous-Inviscid Interaction

Referring to figure 1, there are two primary differences between the interactive and large-domain approaches with regard to the solution of the RANS equations: (1) the size of the solution domain, i.e., the placement of the outer boundary  $S_o$ ; and (2) the boundary (i.e., edge) conditions specified thereon. For the large-domain solution, uniform-flow and wave-radiation conditions are appropriate, whereas the interaction solution requires the specification of the match boundary (i.e.,  $S_o$ ) as well as an interaction law, and also a method for calculating the inviscid flow.

In the present study, solutions were obtained with the match boundary at about  $2\delta$ , where  $\delta$  is the boundary-layer and wake thickness. The interaction law is based on the concept of displacement thickness  $\delta^*$ . A three-dimensional  $\delta^*$  for a thick boundary layer and wake can be defined unambiguously by the two requirements that it be a stream surface of the inviscid flow continued from outside the boundary layer and wake and that the inviscid-flow discharge between this surface and any stream surface exterior to the boundary layer and wake be equal to the actual discharge between the body and wake centerplane and the latter stream surface. A method for implementing this definition for practical geometries is presently under development [17]; however, in lieu of this, an approximate definition is used in which two-dimensional definitions for  $\delta^*$ , i.e.

$$\delta^* = \int_0^\delta \left(1 - \frac{U}{U_p}\right) dr \quad (1)$$

for the keelplane and waterplane at each station are connected by a second order polynomial.

In summary, the inviscid-flow solution is obtained for the displacement body  $\delta^*$ . This solution then provides the boundary conditions for the viscous-flow solution, i.e.

$$\begin{aligned} U(S_o) = U_p(S_o) = U_e \quad W(S_o) = W_p(S_o) = W_e \\ p(S_o) = p_p(S_o) = p_e \end{aligned} \quad (2)$$

Because  $\delta^*$  and  $V_p(S_o)$  are not known a priori, an initial guess must be provided and the complete solution obtained by iteratively updating the viscous- and inviscid-flow solutions until the patching conditions (1) and (2) are satisfied.

### Viscous Flow

The viscous flow is calculated using the large-domain method of Patel et al. [14], modified and extended for interactive calculations and to include free-surface boundary conditions. The details of the basic method are provided by [14]. Herein, an overview is given as an aid in understanding the present modifications and extensions.

### Equations and Coordinate System

The RANS equations are written in the physical domain using cylindrical coordinates  $(x, r, \theta)$  as follows:

$$\frac{\partial U}{\partial x} + \frac{1}{r} \frac{\partial}{\partial r} (rV) + \frac{1}{r} \frac{\partial W}{\partial \theta} = 0 \quad (3)$$

$$\begin{aligned} \frac{DU}{Dt} = - \frac{\partial}{\partial x} (\beta + \overline{uu}) - \frac{\partial}{\partial r} (\overline{uv}) - \frac{1}{r} \frac{\partial}{\partial \theta} (\overline{uw}) \\ - \frac{\overline{uv}}{r} + \frac{1}{Re} \nabla^2 U \end{aligned} \quad (4)$$

$$\begin{aligned} \frac{DV}{Dt} - \frac{W^2}{r} = - \frac{\partial}{\partial x} (\overline{uv}) - \frac{\partial}{\partial r} (\beta + \overline{vv}) - \frac{1}{r} \frac{\partial}{\partial \theta} (\overline{vw}) \\ - \frac{1}{r} (\overline{vv} - \overline{ww}) + \frac{1}{Re} \left( \nabla^2 V - \frac{2}{r^2} \frac{\partial W}{\partial \theta} - \frac{V}{r^2} \right) \end{aligned} \quad (5)$$

$$\begin{aligned} \frac{DW}{Dt} + \frac{VW}{r} = - \frac{\partial}{\partial x} (\overline{uw}) - \frac{\partial}{\partial r} (\overline{vw}) \\ - \frac{1}{r} \frac{\partial}{\partial \theta} (\beta + \overline{ww}) - \frac{2}{r} (\overline{vw}) + \frac{1}{Re} \left( \nabla^2 W \right. \\ \left. + \frac{2}{r^2} \frac{\partial V}{\partial \theta} - \frac{W}{r^2} \right) \end{aligned} \quad (6)$$

with



$$\frac{D}{Dt} = \frac{\partial}{\partial t} + U \frac{\partial}{\partial x} + V \frac{\partial}{\partial r} + \frac{W}{r} \frac{\partial}{\partial \theta}$$

$$\text{and } \nabla^2 = \frac{\partial^2}{\partial x^2} + \frac{\partial^2}{\partial r^2} + \frac{1}{r} \frac{\partial}{\partial r} + \frac{1}{r^2} \frac{\partial^2}{\partial \theta^2}$$

Closure of the RANS equations is attained through the use of the standard  $k$ - $\epsilon$  turbulence model without modifications for free-surface effects. The limited experimental data available for surface-piercing bodies [18] indicate that, near a free surface, the normal component of turbulence is damped and the longitudinal and transverse components are increased. This effect has also been observed in open-channel flow [19] and in recent measurements for free-surface effects on the wake of a submerged flat plate [20] and a plane jet [21]. Such a turbulence structure cannot, in fact, be simulated with an isotropic eddy viscosity turbulence model like the present one; however, this aspect of the problem is deferred for later study.

In the standard  $k$ - $\epsilon$  turbulence model, each Reynolds stress is related to the corresponding mean rate of strain by the isotropic eddy viscosity  $\nu_t$  as follows:

$$\begin{aligned} -\overline{uv} &= \nu_t \left( \frac{\partial U}{\partial r} + \frac{\partial V}{\partial x} \right) & -\overline{uw} &= \nu_t \left( \frac{1}{r} \frac{\partial U}{\partial \theta} + \frac{\partial W}{\partial x} \right) \\ -\overline{vw} &= \nu_t \left( \frac{1}{r} \frac{\partial V}{\partial \theta} + \frac{\partial W}{\partial r} - \frac{W}{r} \right) \\ -\overline{uu} &= \nu_t \left( 2 \frac{\partial U}{\partial x} \right) - \frac{2}{3} k & -\overline{vv} &= \nu_t \left( 2 \frac{\partial V}{\partial r} \right) - \frac{2}{3} k \\ -\overline{ww} &= \nu_t \left( \frac{2}{r} \frac{\partial W}{\partial \theta} + 2 \frac{V}{r} \right) - \frac{2}{3} k \end{aligned} \quad (7)$$

$\nu_t$  is defined in terms of the turbulent kinetic energy  $k$  and its rate of dissipation  $\epsilon$  by

$$\nu_t = C_\mu \frac{k^2}{\epsilon} \quad (8)$$

where  $C_\mu$  is a model constant and  $k$  and  $\epsilon$  are governed by the modeled transport equations

$$\begin{aligned} \frac{Dk}{Dt} &= \frac{\partial}{\partial x} \left( \frac{1}{R_k} \frac{\partial k}{\partial x} \right) \\ &+ \frac{1}{r} \frac{\partial}{\partial r} \left( \frac{1}{R_k} r \frac{\partial k}{\partial r} \right) + \frac{1}{r^2} \frac{\partial}{\partial \theta} \left( \frac{1}{R_k} \frac{\partial k}{\partial \theta} \right) + G - \epsilon \end{aligned} \quad (9)$$

$$\begin{aligned} \frac{D\epsilon}{Dt} &= \frac{\partial}{\partial x} \left( \frac{1}{R_\epsilon} \frac{\partial \epsilon}{\partial x} \right) + \frac{1}{r} \frac{\partial}{\partial r} \left( \frac{1}{R_\epsilon} r \frac{\partial \epsilon}{\partial r} \right) \\ &+ \frac{1}{r^2} \frac{\partial}{\partial \theta} \left( \frac{1}{R_\epsilon} \frac{\partial \epsilon}{\partial \theta} \right) + C_{\epsilon 1} \frac{\epsilon}{k} G - C_{\epsilon 2} \frac{\epsilon^2}{k} \end{aligned} \quad (10)$$

$G$  is the turbulence generation term

$$G = \nu_t \left\{ 2 \left[ \left( \frac{\partial U}{\partial x} \right)^2 + \left( \frac{\partial V}{\partial r} \right)^2 + \left( \frac{1}{r} \frac{\partial W}{\partial \theta} + \frac{V}{r} \right)^2 \right] \right.$$

$$\left. + \left( \frac{\partial U}{\partial r} + \frac{\partial V}{\partial x} \right)^2 + \left( \frac{1}{r} \frac{\partial U}{\partial \theta} + \frac{\partial W}{\partial x} \right)^2 + \left( \frac{1}{r} \frac{\partial V}{\partial \theta} + \frac{\partial W}{\partial r} - \frac{W}{r} \right)^2 \right\} \quad (11)$$

The effective Reynolds number  $R_\phi$  is defined as

$$\frac{1}{R_\phi} = \frac{1}{Re} + \frac{\nu_t}{\sigma_\phi} \quad (12)$$

in which  $\phi = k$  for the  $k$ -equation (9) and  $\phi = \epsilon$  for the  $\epsilon$ -equation (10). The model constants are:  $C_\mu = .09$ ,  $C_{\epsilon 1} = 1.44$ ,  $C_{\epsilon 2} = 1.92$ ,  $\sigma_U = \sigma_V = \sigma_W = \sigma_k = 1$ ,  $\sigma_\epsilon = 1.3$ .

The governing equations (3) through (12) are transformed into nonorthogonal curvilinear coordinates such that the computational domain forms a simple rectangular parallelepiped with equal grid spacing. The transformation is a partial one since it involves the coordinates only and not the velocity components ( $U, V, W$ ). The transformation is accomplished through the use of the expression for the divergence and "chain-rule" definitions of the gradient and Laplacian operators, which relate the orthogonal curvilinear coordinates  $x^i = (x, r, \theta)$  to the nonorthogonal curvilinear coordinates  $\xi^i = (\xi, \eta, \zeta)$ . In this manner, the governing equations (3) through (12) can be rewritten in the following form of the continuity and convective-transport equations

$$\begin{aligned} \frac{\partial}{\partial \xi} (b_1^1 U + b_2^1 V + b_3^1 W) + \frac{\partial}{\partial \eta} (b_1^2 U + b_2^2 V + b_3^2 W) \\ + \frac{\partial}{\partial \zeta} (b_1^3 U + b_2^3 V + b_3^3 W) = 0 \end{aligned} \quad (13)$$

$$\begin{aligned} g_{11} \frac{\partial^2 \phi}{\partial \xi^2} + g_{22} \frac{\partial^2 \phi}{\partial \eta^2} + g_{33} \frac{\partial^2 \phi}{\partial \zeta^2} = 2A_\phi \frac{\partial \phi}{\partial \zeta} \\ + 2B_\phi \frac{\partial \phi}{\partial \eta} + 2C_\phi \frac{\partial \phi}{\partial \xi} + R_\phi \frac{\partial \phi}{\partial t} + S_\phi \end{aligned} \quad (14)$$

#### Discretization and Velocity-Pressure Coupling

The convective-transport equations (14) are reduced to algebraic form through the use of a revised and simplified version of the finite-analytic method. In this method, equations (14) are linearized in each local rectangular numerical element,  $\Delta \xi = \Delta \eta = \Delta \zeta = 1$ , by evaluating the coefficients and source functions at the interior node  $P$  and transformed again into a normalized form by a simple coordinate stretching. An analytic solution is derived by decomposing the normalized equation into one- and two-dimensional partial-differential equations. The solution to the former is readily obtained. The solution to the latter is obtained by the method of separation of variables with specified boundary functions. As a result, a twelve-point finite-analytic formula for unsteady, three-dimensional, elliptic equations is obtained in the form

$$\phi_P = \frac{1}{1 + C_P[C_U + C_D + \frac{R}{\tau}]} \left\{ \sum_{n=1}^8 C_{nb} \phi_{nb} + C_P(C_U \phi_U + C_D \phi_D + \frac{R}{\tau} \phi_P^{n-1} - S) \right\} \quad (15)$$

It is seen that  $\phi_P$  depends on all eight neighboring nodal values in the crossplane as well as the values at the upstream and downstream nodes  $\phi_U$  and  $\phi_D$ , and the values at the previous time step  $\phi_P^{n-1}$ . For large values of the cell  $Re$ , equation (15) reduces to the partially-parabolic formulation which was used previously in other applications. Since equations (15) are implicit, both in space and time, at the current crossplane of calculation, their assembly for all elements results in a set of simultaneous algebraic equations. If the pressure field is known, these equations can be solved by the method of lines. However, since the pressure field is unknown, it must be determined such that the continuity equation is also satisfied.

The coupling of the velocity and pressure fields is accomplished through the use of a two-step iterative procedure involving the continuity equation based on the SIMPLER algorithm. In the first step, the solution to the momentum equations for a guessed pressure field is corrected at each crossplane such that continuity is satisfied. However, in general, the corrected velocities are no longer a consistent solution to the momentum equations for the guessed  $\hat{p}$ . Thus, the pressure field must also be corrected. In the second step, the pressure field is updated again through the use of the continuity equation. This is done after a complete solution to the velocity field has been obtained for all crossplanes. Repeated global iterations are thus required in order to obtain a converged solution. The procedure is facilitated through the use of a staggered grid. Both the pressure-correction and pressure equations are derived in a similar manner by substituting equation (15) for  $(U, V, W)$  into the discretized form of the continuity equation (13) and representing the pressure-gradient terms by finite differences.

### Solution Domain and Boundary Conditions

The solution domain is shown in figure 1. In terms of the notation of figure 1, the boundary conditions on each of the boundaries are as follows. On the inlet plane  $S_i$ , the initial conditions for  $\phi$  are specified from simple flat-plate and the inviscid-flow solutions. On the body surface  $S_b$ , a two-point wall-function approach is used. On the symmetry plane  $S_k$ , the conditions imposed are  $\partial(U, V, \hat{p}, k, \epsilon)/\partial\theta = W = 0$ . On the exit plane  $S_e$ , axial diffusion is negligible so that the exit conditions used are  $\partial^2\phi/\partial x^2 = 0$ , and a zero-gradient condition is used for  $\hat{p}$ . On the outer boundary  $S_o$ , the edge conditions are specified according to (2), i.e.,  $(U, W, \hat{p}) = (U_e, W_e, \hat{p}_e)$  and  $\partial(k, \epsilon)/\partial r = 0$ , where  $(U_e, W_e, \hat{p}_e)$  are obtained from the inviscid-flow solution evaluated at the match boundary  $S_o$ .

On the free-surface  $S_\eta$  (or simply  $\eta$ ), there are two boundary conditions, i.e.

$$\mathbf{V} \cdot \mathbf{n} = 0 \quad (16)$$

and

$$\tau_{ij} n_j = \tau_{ij}^* n_j \quad (17)$$

where  $\mathbf{n}$  is the unit normal vector to the free surface and  $\tau_{ij}$  and  $\tau_{ij}^*$  are the fluid- and external-stress tensors, respectively, the latter, for convenience, including surface tension. The kinematic boundary condition expresses the requirement that  $\eta$  is a stream surface and the dynamic boundary condition that the normal and tangential stresses are continuous across it. Note that  $\eta$  itself is unknown and must be determined as part of the solution. In addition, boundary conditions are required for the turbulence parameters,  $k$  and  $\epsilon$ ; however, at present, these are not well established.

In the present study, the following approximations were made in employing (16) and (17): (a) the external stress and surface tension were neglected; (b) the normal viscous stress and both the normal and tangential Reynolds stresses were neglected; (c) the curvature of the free surface was assumed small and the tangential gradients of the normal velocity components were neglected in the tangential stresses; and (d) the wave elevation was assumed small such that both (16) and (17) were represented by first-order Taylor series expansions about the mean wave-elevation surface (i.e., the water-plane  $S_w$ ). Subject to these approximations, (16) and (17) reduce to the following:

$$(U_x \eta_x + V_y \eta_y - W_z) \Big|_{S_w} = 0 \quad (18)$$

$$\hat{p}(S_w) = \eta / Fr^2 - \eta \frac{\partial \hat{p}}{\partial z} \Big|_{S_w} \quad (19)$$

$$\frac{\partial(V, k, \epsilon)}{\partial \theta} \Big|_{S_w} = 0 \quad (20)$$

where Cartesian coordinates  $(x, y, z)$  have been used in (18) and (19). Conditions (18) through (20) were implemented numerically as follows. The kinematic condition (18) was used to solve for the unknown free-surface elevation  $\eta$  by expressing the derivatives in finite-difference form and  $\eta$  in terms of its difference from an assumed (or previous) value. A backward difference was used for the  $x$ -derivative, a central difference for the  $y$ -derivative, and the inviscid-flow  $\eta_p$  was used as an initial guess. The dynamic conditions, (19) and (20), were used in conjunction with the solution for  $\eta$  in solving the pressure and momentum and turbulence model equations, respectively. Backward differences were used for the  $z$ - and  $\theta$ -derivatives.

### Inviscid Flow

The inviscid flow is calculated using the method of Rosen [2], i.e., the SPLASH computer code. The method is an extended version of the basic panel method of Maskew [22,23] originally developed for the prediction of subsonic aerodynamic flows about arbitrary configurations, modified to include the presence of a free surface and gravity waves both for submerged and surface-piercing bodies. As is the case with the basic

method, lifting surfaces and their associated wake treatments as well as wall boundaries are included; however, the present overview and calculations are for nonlifting unbounded flow (see [24] for SPLASH results for lifting flow). The details of the basic method are provided by [22,23]. Herein, an overview is given as an aid in understanding the extensions for the inclusion of the free surface and gravity waves and the present interaction calculations.

The flow is assumed irrotational such that the governing differential equation is the Laplace equation

$$\nabla^2 \phi = 0 \quad (21)$$

where  $\phi$  is the external perturbation velocity potential, i.e.

$$\mathbf{V}_p = U_o \mathbf{x} + \nabla \phi \quad (22)$$

A solution for  $\phi$  may be obtained by defining also an internal perturbation potential  $\phi_I$  and applying Green's theorem to both the inner and outer regions and combining the resulting expressions to obtain

$$\phi = - \int_{S_b} \left\{ \mu \frac{\partial}{\partial n_Q} \left( \frac{1}{R_{PQ}} \right) + \frac{\sigma}{R_{PQ}} \right\} dS \quad (23)$$

where  $R_{PQ}$  is the distance from the surface point  $Q$  to the field point  $P$  and  $\mu = \phi_I - \phi$  and  $\sigma = \partial(\phi - \phi_I)/\partial n_Q$  are the dipole and source strengths, respectively. In [22], the nature of solutions to (23) is investigated for two different specifications for  $\phi_I$ , i.e.,  $\phi_I = 0$  and  $U_o x$ . In both cases, (23) is solved for the surface potential (i.e.,  $\phi(S_b)$ ) by representing the body by flat quadrilateral panels over which  $\mu$  and  $\sigma$  are assumed constant and utilizing the far-field  $\phi \rightarrow 0$  and body  $\partial\phi/\partial n = -U_o n_x$  boundary conditions. The zero internal perturbation potential formulation ( $\phi_I = 0$ ) is shown to produce "results of comparable accuracy to those from higher-order methods for the same density of control points." In this case, the velocity normal to the external surface  $V_n$  is

$$V_n = U_o n_x + \partial\phi/\partial n = U_o n_x + \sigma \quad (24)$$

and, the velocity tangent to the external surface  $V_t$  is

$$V_t = U_o t_x + \partial\phi/\partial t = U_o t_x - \partial\mu/\partial t \quad (25)$$

where  $t_x$  is the x-component of a tangent vector and  $t$  is arclength in a tangential direction. For solid surfaces,  $V_n$  is usually zero, but it may be a specified nonzero value to simulate body motion, boundary-layer growth, inflow and outflow, control-surface deflection, etc. Hence, in the basic method, (24) is used to evaluate the source strengths directly. The corresponding doublet strengths are then given by solution of the discretized form of (23). Values of  $V_t$  are subsequently computed using (25) with a central difference for the  $t$ -derivative. It should be recognized that the so-called zero internal perturbation formulation is, in fact, equivalent to methods based on Green's third formula applied directly to the external perturbation potential (e.g., [25]).

In the SPLASH code, the internal zero-perturbation boundary condition is satisfied not only inside the submerged portion of the configuration, but also on the "other side" of a finite portion of the free surface. Both are represented by source-doublet singularity panels and flow leakage from one side of the free-surface to the other, at the free-surface outer boundary, is assumed to be negligible. This assumption is valid if the outer boundary of the free surface is sufficiently far from the configuration, and if wave disturbances are eliminated before reaching the free-surface outer boundary. In this case, the discretized form of (23) is

$$\phi_i = \sum_{s_b + S_w} A_{ij} \mu_j + \sum_{s_b + S_w} B_{ij} \sigma_j = 0 \quad (26)$$

The free-surface shape is determined by representing the undisturbed free surface by panels, whereupon free-surface boundary conditions linearized with respect to zero  $Fr$  are imposed [26]. The zero  $Fr$  velocities,  $U_o$ ,  $V_o$ , and  $W_o$ , are obtained by first considering all free-surface panels as solid and fixed (in contrast to a traditional approach which employs the double panel or image model). The nonzero  $Fr$  velocities are then expressed as small increments to those for zero  $Fr$ . The velocities tangent and normal to a free-surface panel are, respectively

$$U_x \approx U_o + \Delta U \quad V_y \approx V_o + \Delta V \quad (27)$$

and

$$V_n \approx W_z \approx W_o + \Delta W \approx \Delta W \quad (28)$$

since  $W_o = 0$  for a free-surface panel. Through Bernoulli's equation, the pressure on free-surface panels is a function of local velocity, and is approximated by retaining only first-order incremental velocity terms

$$\begin{aligned} \hat{p} &= \frac{1}{2} \left\{ 1 - (U_x^2 + V_y^2 + W_z^2) \right\} \\ &\approx \frac{1}{2} \left\{ 1 - (U_o^2 + V_o^2) \right\} - \left\{ U_o \Delta U + V_o \Delta V \right\} \\ &\approx \frac{1}{2} \left\{ 1 - (U_o^2 + V_o^2) \right\} - \left\{ U_o (U_x - U_o) \right. \\ &\quad \left. + V_o (V_y - V_o) \right\} \end{aligned} \quad (29)$$

Free-surface boundary conditions are linearized in a similar manner, retaining only first-order incremental velocity and surface-elevation terms. The kinematic free-surface boundary condition (18) is approximated by

$$W_z = V_n \approx U_o \eta_x + V_o \eta_y \approx (U_o^2 + V_o^2)^{1/2} \eta_{s_o} \quad (30)$$

where the subscript  $s_o$  denotes differentiation along a zero  $Fr$  streamline. The dynamic free-surface boundary condition (19), after differentiation along  $s_o$ , and substituting for  $\eta_{s_o}$  from (30), becomes

$$\frac{\partial \hat{p}}{\partial s_o} \approx \frac{1}{Fr^2} \frac{V_n}{(U_o^2 + V_o^2)^{1/2}} \quad (31)$$

A five-point backward difference is used in the  $\xi$  and  $\eta$  directions, and the free-surface grid metrics, are used to compute the pressure gradient

$$\frac{\partial \hat{p}}{\partial s_o} = \frac{U_o \frac{\partial \hat{p}}{\partial x} + V_o \frac{\partial \hat{p}}{\partial y}}{(U_o^2 + V_o^2)^{1/2}}$$

$$= \frac{U_o \left( \frac{\partial \hat{p}}{\partial \xi} \frac{\partial \xi}{\partial x} + \frac{\partial \hat{p}}{\partial \eta} \frac{\partial \eta}{\partial x} \right) + V_o \left( \frac{\partial \hat{p}}{\partial \xi} \frac{\partial \xi}{\partial y} + \frac{\partial \hat{p}}{\partial \eta} \frac{\partial \eta}{\partial y} \right)}{(U_o^2 + V_o^2)^{1/2}} \quad (32)$$

The pressure-gradient algorithm is structured to permit the use of any blocked free-surface grid arrangement. Also, using less than a five-point backward difference tends to dampen wave amplitudes. This wave-damping mechanism is employed on panels near the outer boundary of the finite free-surface model, so that wave disturbances are eliminated before reaching the free-surface outer boundary.

At this point, a sufficient number of linear dependencies have been established to permit the elimination of the unknown free-surface source strengths in (26), i.e., (24) relates source strength to panel normal velocity, (31) relates free-surface panel normal velocity to streamwise pressure gradient, (32) with backward differences relates streamwise pressure gradient to free-surface pressures, (29) relates free-surface pressure to free-surface panel tangential velocities, (25) relates panel tangential velocities to the local surface gradient of doublet strength, and central differences relate the local surface gradient of doublet strength to doublet strengths. Hence, free-surface source strengths can be expressed as a linear combination of free-surface doublet strengths, i.e.

$$\sigma_j = a_j + \sum_{S_w} b_{jk} \mu_k \quad (33)$$

Substituting for  $\sigma_j$  from (33) into (26) yields

$$\phi_i = \sum_{S_b + S_w} A_{ij} \mu_j + \sum_{S_b} B_{ij} \sigma_j$$

$$+ \sum_{S_w} B_{ij} \left( a_j + \sum_{S_w} b_{jk} \mu_k \right) \quad (34)$$

With free-surface source strengths eliminated, and source strengths on the solid body evaluated directly, solution of (34) yields the corresponding doublet strengths. The free-surface source strengths are then given by (33), and (24) and (25) are used to compute the resulting velocities on both body and free-surface panels. Pressures on free-surface panels are given by (29). A similar linearized formula is used for pressures acting on body panels, and configuration forces and moments are obtained by panel pressure integration.

For interactive calculations, the SPLASH code calculates the inviscid free-surface flow about the equivalent displacement body resulting from the previous

viscous calculation. For this purpose, the equivalent displacement body is treated as a solid fixed surface. The inviscid flow velocities required for the next viscous flow calculation, at off-body points on the viscous grid outer boundary  $S_o$ , are obtained using the computed source-doublet solution and velocity influence coefficients. A sub-panel velocity influence-coefficient algorithm was developed which utilizes a bilinear variation of source and doublet strength across each panel. The continuous variation of source and doublet strength on each panel, and across panel edges, enhances the accuracy of off-body velocity calculations at points close to any body and/or free-surface panels.

## WIGLEY HULL GEOMETRY AND EXPERIMENTAL INFORMATION

The Wigley parabolic hull was selected for the initial calculations since the geometry is relatively simple and it has been used in many previous computational and experimental studies. In particular, it is one of the two hulls, the other being the Series 60  $C_B = .6$  ship model, selected by the Cooperative Experimental Program (CEP) of the Resistance and Flow Committee of the International Towing Tank Conference [27] for which extensive global (total, wave pattern, and viscous resistance, mean sinkage and trim, and wave profiles on the hull) and local (hull pressure and wall shear-stress distributions and velocity and turbulence fields) measurements were reported. It was for these same reasons that the Wigley hull was selected as the first test case of the basic viscous-flow method [14], including comparisons with some of the zero Fr data of the CEP. Herein, comparisons are made for zero Fr with this same data and for nonzero Fr with the appropriate data of the CEP. As will be shown later, the nonzero Fr data is not as complete or of the same quality as that for zero Fr, which was the motivation for a related experimental study for the Series 60  $C_B = .6$  ship model [28] for which calculations and comparisons are in progress. However, the comparisons are still useful in order to validate the present interactive approach and display the shortcomings of both the computations and experiments.

The coordinates of the Wigley hull are given by

$$y = \frac{B}{2} \{ 4x(1-x) \} \{ 1 - (z/d)^2 \} \quad (35)$$

where  $B = .1$  and  $d = .0625$ . Waterplane and typical crossplane views are shown in figure 2.

## RESULTS

In the following, first, the computational grids (figures 2 and 3) and conditions are described. Then, some example results are presented and discussed for zero Fr, followed by those for nonzero Fr, including wherever possible comparisons with available experimental data, and, in the latter case, with inviscid-flow results. The convergence history of the pressure is shown in figure 4. Figure 5 provides a comparison of the large-domain and interactive solutions. The free-surface perspective view and contours, wave profile, and surface-pressure profiles and contours are shown in figures 6 through 10, respectively. The axial-velocity contours, crossplane-velocity vectors, and pressure, axial-vorticity, and turbulent kinetic energy contours for several representative stations are shown in figures 11 through 13. Lastly, the velocity, pressure, and turbulent



kinetic energy profiles for similar stations are shown in figures 14 through 16. On the figures and in the discussions, the terminology "interactive" refers to results from both the interactive viscous and displacement-body inviscid solutions. When the distinction is not obvious it will be made. The terminology "inviscid" or "bare-body" refers to the noninteractive inviscid solution.

### Computational Grids and Conditions

The viscous-flow computational grid was obtained using the technique of generating body-fitted coordinates through the solution of elliptic partial differential equations. Because of the simplicity of the present geometry, it is possible to specify the axial  $f^1$  and circumferential  $f^3$  control functions as, respectively, only functions of  $\xi$  and  $\zeta$ ; however, in order to accurately satisfy the body-surface boundary condition and resolve the viscous flow,  $f^2 = f^2(\xi, \eta, \zeta)$ . Partial views of the grids used in the calculations are shown in figures 2a,b for a longitudinal plane and typical body and wake cross-planes, respectively. Initially, a large-domain grid was generated. Subsequently, a small-domain grid was obtained by simply deleting that portion of the large-domain grid that lay beyond about  $r > .2$ . The outer boundary for the small-domain grid is shown by the dashed line in figure 2. For the large-domain grid, the inlet, exit, and outer boundaries are located at  $x = (.296, 4.524)$  and  $r = 1$ , respectively. The first grid point off the body surface is located in the range  $90 < y^+ < 250$ . 50 axial, 30 radial, and 15 circumferential grid points were used. As already indicated, the small-domain grid was similar, except 21 radial grid points were used. In summary, the total number of grid points for the large- and small-domain calculations are 22,500 and 15,750, respectively.

The inviscid-flow displacement-body and free-surface panelization is shown in figure 3. 423 panels are distributed over the displacement body and 546 over the free surface for a total number of 969 panels. The panelization covers an area corresponding to 1 ship length upstream of the bow, 1.5 ship lengths in the transverse direction, and 3 ship lengths downstream of the stern. This panel arrangement was judged optimum based on panelization dependency tests [16].

The conditions for the calculations are as follows:  $L = 1$ ;  $U_0 = 1$ ;  $Re = 4.5 \times 10^6$ ;  $Fr = 0$  and  $.316$ ; and on the inlet plane the average values for  $\delta$  and  $U_\tau$  are  $.0033$  and  $.0455$ , respectively. These conditions were selected to correspond as closely as possible to those of the experiments of the CEP with which comparisons will be made [5,29,30].

Initially, large-domain calculations were performed for zero Fr. A zero-pressure initial condition was used and the values for the time  $\alpha_t$ , pressure  $\alpha_p$ , and transport quantity  $\alpha_\phi$  (where  $\phi = k$  and  $\epsilon$ ) underrelaxation factors and total number of global iterations were  $.05$  and  $200$ , respectively. Next, small-domain calculations were performed, first for zero Fr, and then for nonzero Fr. For zero Fr, the interaction calculations were started with a zero-pressure initial condition and freestream edge conditions ( $U_e = 1, W_e = p_e = 0$ ). After 200 global iterations, the edge conditions were updated using the latest values of displacement thickness. Subsequently, the edge conditions were updated every 200 global iterations until convergence was achieved, which took three updates. For nonzero

Fr, the calculations were started with the zero Fr solution as the initial condition and with nonzero Fr edge conditions obtained utilizing the zero Fr displacement body. This solution converged in 200 global iterations. Most of the results to be presented are for this case; however, some limited results will be shown in which the nonzero Fr edge conditions were obtained using an updated nonzero Fr displacement body. The values for  $\alpha_t$ ,  $\alpha_p$ , and  $\alpha_\phi$  (where  $\phi = k$  and  $\epsilon$ ) used for the small-domain calculations were the same as those for the large-domain calculations; however, for nonzero Fr, in addition, a value of  $.01$  was used for  $\alpha_\phi$  (where  $\phi = U$ ) for grid nodes near the outer boundary. The  $\partial\phi/\partial z$  term in (19) was found to have a small influence and was neglected in many of the calculations; however, this may be due, in part, to the present grid resolution. The calculations were performed on the Naval Research Laboratory CRAY XMP-24 supercomputer. The CPU time required for the calculations was about 17 minutes for 200 global iterations for the viscous-flow code and 1 minute for the inviscid-flow code.

Extensive grid dependency and convergence checks were not carried out since these had been done previously both for the basic viscous-flow method [14] and for other applications. However, some calculations were performed using both coarser and finer grids. These converged, respectively, more rapidly and slower than the present solution. Qualitatively the solutions were very similar to the present one, but with reduced and somewhat increased resolution, respectively. The convergence criterion was that the change in solution be less than about  $.05\%$  for all variables. Usually the solutions were carried out at least 50 global iterations beyond meeting this criterion. Figure 4 provides the convergence history for the pressure and is typical of the results for all the variables. In figure 4, the abscissa is the global iteration number  $it$  and the ordinate is the residual  $R(it)$ , which is defined as follows:

$$R(it) = \frac{\sum_{i=1}^{imax} |p(it-1) - p(it)|}{\sum_{i=1}^{imax} |p(itl)|} \quad (36)$$

where  $itl$  and  $imax$  are the total number of iterations and grid points, respectively. Referring to figure 4, global iterations 1 - 200 correspond to the final iterations of the zero Fr solution and global iterations 200 - 400 to those for the nonzero Fr solution.

### Zero Fr

Figure 5 provides a comparison of the zero Fr large-domain and interactive solutions and experimental data. The two solutions are nearly identical and show good agreement with the data, which validates the present interactive approach. The agreement with the data for the large-domain case is, of course, not surprising since this was already established in [14] for a similar grid and conditions, i.e., the present zero Fr solution is essentially the same as that of [14]. Some additional aspects of the zero Fr solution are displayed in figures 11 through 15 for later comparison with the nonzero Fr solution. Reference [14] provides detailed discussion of the zero Fr solution, including comparisons with the available experimental data. In summary, there is a downward flow on the forebody and an upward flow on the afterbody in response to the external-flow pressure gradients. The boundary layer and wake remain thin and attached and the viscous-inviscid interaction is weak;

however, on the forebody, the boundary layer is relatively thicker near the keel than the waterplane, whereas the reverse holds true on the afterbody and in the near wake. The stern vortex is very weak. In the intermediate and far wake, the flow becomes axisymmetric. As indicated in figures 5 and 14 through 16, the agreement between the calculations and data is quite good; however, there are some important differences, which are primarily attributed to the deficiencies of the standard  $k-\epsilon$  turbulence model with wall functions. In particular, the axial velocity and turbulent kinetic energy are overpredicted near the stern and there is a more rapid recovery in the wake.

### Nonzero Fr

Figure 5 also includes nonzero Fr results for comparison. On the waterplane, the surface and wake centerplane pressure displays very dramatic differences, the wall-shear velocity shows similar trends, but with reduced magnitude, and the wake centerplane velocity indicates faster recovery in the intermediate and far wake. As will be shown later, the first closely follows the wave profile, the second is due to an increase in boundary-layer thickness near the waterplane for the nonzero Fr case, and the third can be explained by the wave-induced pressure gradients. On the keel, all three of these quantities are nearly the same as for zero Fr.

The free-surface perspective views (figure 6) and contours (figure 7) vividly display the complex wave pattern consisting of both diverging and transverse wave systems. The bow and stern wave systems are seen to initiate with crests and the shoulder systems initiate with troughs, which conforms to the usual pattern described for this type of hull form. Very apparent is the reduced amplitude of the stern waves for the interactive as compared to the inviscid solution. Also, the diverging wave system is more pronounced and at a smaller angle with respect to the centerplane. Note that the axial and transverse wave-induced pressure gradients can be discerned from these figures, but with an appropriate phase shift, i.e., increasing and decreasing wave elevations imply, respectively, adverse and favorable gradients. The wave profile along the hull is shown in figure 8, which, in this case, includes experimental data for comparison. On the forebody, the two solutions are nearly identical and underpredict the amplitude of the bow-wave crest and the first trough. On the afterbody, the interactive solution indicates larger values than the inviscid solution, with the data in between the two. The wave profile for the nonzero Fr displacement body (figure 3b) is also shown in figure 8. The differences are minimal on the forebody, whereas, they are significant on the afterbody and depart from the data. It appears that the present simple definition (1) is insufficient for "wavy" displacement bodies.

The surface-pressure profiles (figure 9) show similar tendencies as just discussed with regard to the wave profile. On the forebody, the two solutions are nearly identical, but, in this case, in very close agreement with the data. The pressure on the forebody shown by the dashed line is that obtained from the inviscid displacement-body solution. On the afterbody, here again, the interactive solution indicates larger values than the inviscid solution, with the data in between the two. The wave-induced effects are seen to diminish with increasing depth and the agreement between the two solutions and the data on the afterbody shows

improvement. The surface-pressure contours (figure 10) graphically display the differences between the two solutions and the data. Note that the axial and vertical surface-pressure gradients can be discerned from these figures, i.e., increasing and decreasing pressure imply, respectively, adverse and favorable gradients. The larger wave elevation and pressure on the afterbody for the interactive solution results in the closed contours near the stern displayed in figure 10b. As already mentioned, the viscous-inviscid interaction is weak for the Wigley hull, which is the reason that the inviscid and viscous pressure distributions are quite similar. However, it appears that the interaction is greater for nonzero as compared to zero Fr.

Figures 11 through 13 show the detailed results for several representative stations, i.e.,  $x = .506, .904$ , and  $1.112$ , although the discussion to follow is based on the complete results at all stations. Note that for zero Fr the upper boundary shown is the waterplane, whereas for nonzero Fr, it is the predicted free surface. Also, the axial-velocity, -vorticity, and turbulent kinetic energy contours are not shown for the inviscid solution since, in the former case, their values are all very close to 1 and, in the latter two cases, they are, of course, zero. Solid curves indicate clockwise vorticity.

On the forebody (figure 11), the boundary layer is thin such that many aspects of the solutions are similar; however, there are some important differences. The nonzero Fr pressure fields show local and global effects of the free surface, i.e., near the free surface, regions of high and low pressure coincide with wave crests and troughs, respectively, and at larger depths, the contours are parallel to the free surface. Also, for nonzero Fr, the crossplane-velocity vectors are considerably larger, especially for the interactive solution. The inviscid solution clearly lacks detail near the hull surface. The extent of the axial vorticity is increased for nonzero Fr and is locally influenced by the free surface. In both cases, as expected, the direction of rotation is mostly anticlockwise.

On the afterbody (figure 12), almost all aspects of the solutions show significant differences. The boundary layer is thicker near the waterplane for nonzero as compared to zero Fr. This behavior begins at  $x \approx .825$ , which coincides with a region of adverse axial wave-induced pressure gradient (see figure 7). The differences for the pressure field and axial-vorticity contours are similar as described for the forebody; however, in the case of the crossplane-velocity vectors, there is an additional difference that near the free surface the interactive solution displays downward flow. This is consistent with the fact that the free-surface elevation is above the waterplane and the pressure is generally higher near the free surface than it is at larger depths, i.e.,  $\eta > 0$  and  $\partial\phi/\partial z < 0$ . Note that, as expected, in both cases, the direction of rotation for the axial-vorticity is mostly clockwise. The turbulent kinetic energy contours are nearly the same for both Fr.

In the wake (figure 13), the solutions continue to show significant differences. Initially, the low-velocity region diffuses somewhat and covers a larger depthwise region; then, for  $x > 1.2$ , recovers quite rapidly. A similar behavior was noted earlier for the wake centerline velocity for  $x > 1.2$ , both of which, as already mentioned, are consistent with the wave pattern. The zero Fr pressure field is nearly axisymmetric and fully



recovered by the exit plane. The nonzero Fr pressure field continues to show free-surface effects, i.e., the contours are parallel to the free surface, but also fully recovered by the exit plane. Note the considerably larger wave elevation near the wake centerplane for the inviscid as compared to the interactive solution, which was pointed out earlier with regard to figures 6 and 7. Here again, the crossplane-velocity vectors are larger for nonzero as compared to zero Fr, especially near the wake centerplane for the interactive solution. The interactive and inviscid solutions display differences near the free surface, which appear to be consistent with the differences in their predicted wave patterns. The zero Fr axial vorticity decays fairly rapidly, whereas, for nonzero Fr, the decay is slow with a layer of nonzero vorticity persisting near the free surface all the way to the exit plane. The turbulent kinetic energy contours are similar for both Fr, but recover faster for the nonzero case.

Figures 14 through 16 show the velocity, pressure, and turbulent kinetic energy profiles for similar stations as for figures 11 through 13, i.e.,  $x = .5, .9$ , and  $1.1$ . Also, included are both zero and nonzero Fr experimental data. At the largest two depths,  $z = .05$  and  $.0625$ , data for both Fr are available, whereas, at the waterplane,  $z = 0$ , only zero Fr data are available. At the intermediate depths, data are available for both Fr, but for different  $z$  values. Since the interest here is primarily nonzero Fr and the zero Fr data and comparisons were already displayed in [14], only nonzero Fr data are shown for  $z = .0125, .025$ , and  $.0375$ . For zero Fr, a corrected pressure is also shown which includes a constant ( $= -.03$ ) reference-pressure correction as described in [14]. Turbulent kinetic energy data are only available for zero Fr.

At  $x = .5$ , consistent with previous discussions the differences between the two solutions are quite small and the agreement with the zero Fr data is good. However, the nonzero Fr data show some unexpected differences. In particular, the axial-velocity profile has a laminar appearance and the boundary-layer thickness is relatively large, the vertical velocity is upward, and the pressure shows considerable scatter. It is pointed out in [5] that the pressure-measurement error was appreciable.

At  $x = .9$  and  $1.1$ , here again, consistent with previous discussions the differences between the two solutions are significant and the agreement between the zero Fr solution and data is good, except for the aforementioned discrepancies. The nonzero Fr solution shows larger axial velocities than the measurements for the inner part of the profiles. Here again, the measured profiles have a laminar appearance and the boundary layer is thick. However, no doubt, a part of the difference is due to the calculations, i.e., as is the case for zero Fr, due to deficiencies of the  $k-\epsilon$  turbulence model an overprediction of the velocity near the wall and wake centerplane is expected. The transverse velocity is small and with similar trends for both calculations and measurements. The calculations indicate downward vertical velocities near the free surface and upward values for the midgirth region and near the keel. The agreement with the data near the keel is satisfactory, but in the midgirth region and near the free surface the data display greater upward flow than the calculations. In the wake, the nonzero Fr data show surprisingly small vertical velocities near the wake centerplane. Here again, the nonzero Fr pressure data shows considerable scatter

and is difficult to compare with the calculations. Consistent with earlier discussions the turbulent kinetic energy profiles are nearly the same for both Fr.

Lastly, Table 1 provides a comparison of the calculated pressure-resistance coefficient and experimental values of the residuary-resistance (i.e., total - frictional) coefficient. The experimental values cover a range of  $Re$ , including the present value, and clearly show a dependency on  $Re$ . Interestingly, the inviscid result compares well with the data at the highest  $Re$ , whereas the interactive result is close to that that the data implies at the present  $Re$ .

## WAVE-BOUNDARY LAYER AND WAKE INTERACTION

The comparisons of the zero and nonzero Fr interactive and inviscid-flow results with experimental data enables an evaluation of the wave-boundary layer and wake interaction. Very significant differences are observed between the zero and nonzero Fr interactive results due to the presence of the free surface and gravity waves. In fact, the flow field is completely altered. Most of the differences were explicable in terms of the differences between the zero and nonzero Fr surface-pressure distributions and, in the latter case, the additional pressure gradients at the free surface associated with the wave pattern. The viscous-inviscid interaction appears to be greater for nonzero as compared to zero Fr. It should be mentioned that other factors undoubtedly have important influences, e.g., wave-induced separation, which are not included in the present theory.

The interactive and inviscid nonzero Fr solutions also indicate very significant differences. The inviscid solution clearly lacks "real-fluid effects." The viscous flow close to the hull and wake centerplane is clearly not accurately resolved. The interactive solution shows an increased response to pressure gradients as compared to the inviscid solution, especially in regions of low velocity. Also, the inviscid solution overpredicts the pressure recovery at the stern and the stern-wave amplitudes.

## CONCLUDING REMARKS

The present work demonstrates for the first time the feasibility of an interactive approach for calculating ship boundary layers and wakes for nonzero Fr. The results presented for the Wigley hull are very encouraging. In fact, in many respects, the present results appear to be superior to the only other solutions of this type available, i.e., [10,11]. This is true both with regard to the resolution of the boundary-layer and wake regions and the wave field. Furthermore, it appears that the present interactive approach is considerably more computationally efficient than the large-domain approaches of [10,11]. This is consistent with the previous finding for zero Fr [15]. However, a complete evaluation of the present method was not possible. In the former case, due to the limited available experimental data. As mentioned earlier, a related experimental study for the Series 60  $C_B = .6$  ship model [28] was recently completed for which extensive measurements were made at both low and high Fr for which calculations and comparisons are in progress. In the latter case, due to the considerable differences in numerical techniques and algorithms and turbulence models between the present methods and those of

[10,11]. As mentioned earlier, the pursuit of a large-domain approach to the present problem is also of interest and will enable such an evaluation.

Finally, some of the issues that need to be addressed while further developing and validating the present approach are as follows: further assessment of the most appropriate free-surface boundary conditions; improved definition and construction of displacement bodies; the inclusion and resolution of the bow-flow region; extensions for lifting flow; and the ever present problem of grid generation and turbulence modeling. Also, of interest is the inclusion of nonlinear effects in the inviscid-flow code.

## ACKNOWLEDGEMENTS

This research was sponsored by the Office of Naval Research under Contract N00014-88-K-0113 under the administration of Dr. E.P. Rood whose support and helpful technical discussions are greatly appreciated.

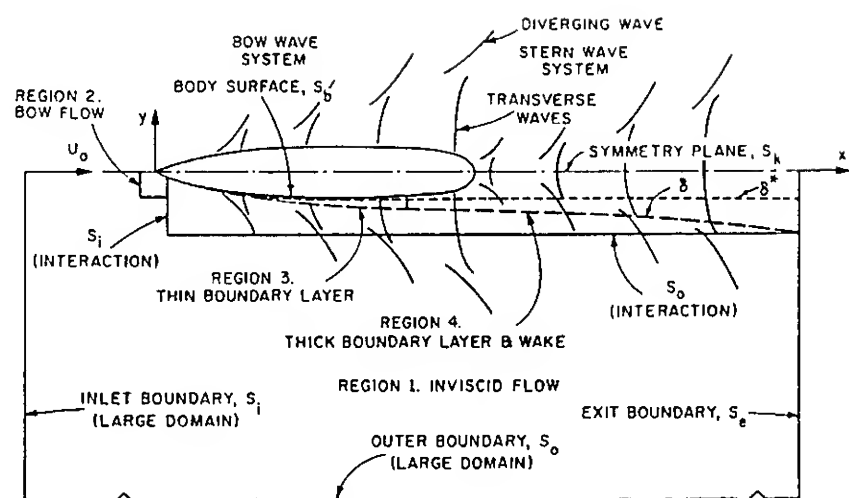
## REFERENCES

1. Lindenmuth, W., Ratcliffe, T.J., and Reed, A.M., "Comparative Accuracy of Numerical Kelvin Wake Code Predictions - "Wake-Off", DTRC/SHD-1260-1, 1988.
2. Rosen, B., "SPLASH Free-Surface Code: Theoretical/Numerical Formulation," South Bay Simulations Inc., Babylon, NY, 1989 (proprietary report).
3. Patel, V.C., "Ship Stern and Wake Flows: Status of Experiment and Theory," Proc. 17th Office of Naval Research Symposium on Naval Hydrodynamics, The Hague, 1988, pp. 217-240.
4. Proc. 5th International Conference on Numerical Ship Hydrodynamics, Hiroshima, 1989.
5. Shahshahan, A., "Effects of Viscosity on Wavemaking Resistance of a Ship Model," Ph.D. Thesis, The University of Iowa, Iowa City, IA, 1985.
6. Ikehata, M. and Tahara, Y., "Influence of Boundary Layer and Wake on Free Surface Flow around a Ship Model," J. Society of Naval Architects of Japan, Vol. 161, 1987, pp. 49-57 (in Japanese).
7. Stern, F., "Effects of Waves on the Boundary Layer of a Surface-Piercing Body," J. of Ship Research, Vol. 30, No. 4, 1986, pp. 256-274.
8. Stern, F., Hwang, W.S., and Jaw, S.Y., "Effects of Waves on the Boundary Layer of a Surface-Piercing Flat Plate: Experiment and Theory," J. of Ship Research, Vol. 33, No. 1, 1989, pp. 63-80.
9. Stern, F., "Influence of Waves on the Boundary Layer of a Surface-Piercing Body," Proc. 4th International Conference on Numerical Ship Hydrodynamics, Washington, D.C., 1985, pp. 383-406.
10. Miyata, H., Sato, T., and Baba, N., "Difference Solution of a Viscous Flow with Free-Surface Wave about an Advancing Ship," J. of Computational Physics, Vol. 72, No. 2, 1987, pp. 393-421.
11. Hino, T., "Computation of a Free Surface Flow around an Advancing Ship by the Navier-Stokes Equations," Proc. 5th International Conference on Numerical Ship Hydrodynamics, Hiroshima, 1989.
12. Harlow, F.H. and Welch, J.E., "Numerical Calculation of Time-Dependent Viscous Flow of a Fluid with Free Surface," The Physics of Fluids, Vol. 8, 1965, pp. 2182-2189.
13. Chan, R.K.C. and Street, R.L., "A Computer Study of Finite-Amplitude Water Waves," J. of Computational Physics, Vol. 6, 1970, pp. 68-94.
14. Patel, V.C., Chen, H.C. and Ju, S., "Ship Stern and Wake Flows: Solutions of the Fully-Elliptic Reynolds-Averaged Navier-Stokes Equations and Comparisons with Experiments," Iowa Institute of Hydraulic Research, The University of Iowa, IHR Report No. 323, 1988; also J. of Computational Physics, Vol. 88, No. 2, June 1990, pp. 305-336.
15. Stern, F., Yoo, S.Y. and Patel, V.C., "Interactive and Large Domain Solutions of Higher-Order Viscous-Flow Equations," AIAA Journal, Vol. 26, No. 9, 1988, pp. 1052-1060.
16. Longo, J., "Scale Effects on Near-Field Wave Patterns," M.S. Thesis, The University of Iowa, Iowa City, IA, 1990.
17. Black, R., "Definition of Three-Dimensional Displacement Thickness Appropriate for Ship Boundary Layers and Wakes," M.S. Thesis, The University of Iowa, Iowa City, IA, expected 1991.
18. Hotta, T. and Hatano, S., "Turbulence Measurements in the Wake of a Tanker Model on and under the Free Surface," Fall Meeting of the Society of Naval Architects of Japan, 1983.
19. Rodi, W., "Turbulence Model and Their Application in Hydraulics," Presented at the IAHR Section on Fundamentals of Division II: Experimental and Mathematical Fluid Dynamics, 1980.
20. Swean, T.F. and Peltzer, R.D., "Free Surface Effects on the Wake of a Flat Plate," NRL Memo Report 5426, Naval Research Laboratory, Washington D.C., 1984.
21. Ramberg, S.E., Swean, T.F., and Plesniak, M.W., "Turbulence Near a Free Surface in a Plane Jet," NRL Memo Report 6367, Naval Research Laboratory, Washington D.C., 1989.
22. Maskew, B., "Prediction of Subsonic Aerodynamic Characteristics: A Case for Low-Order Panel Methods," Journal of Aircraft, Vol. 19, No. 2, 1982, pp. 157-163.

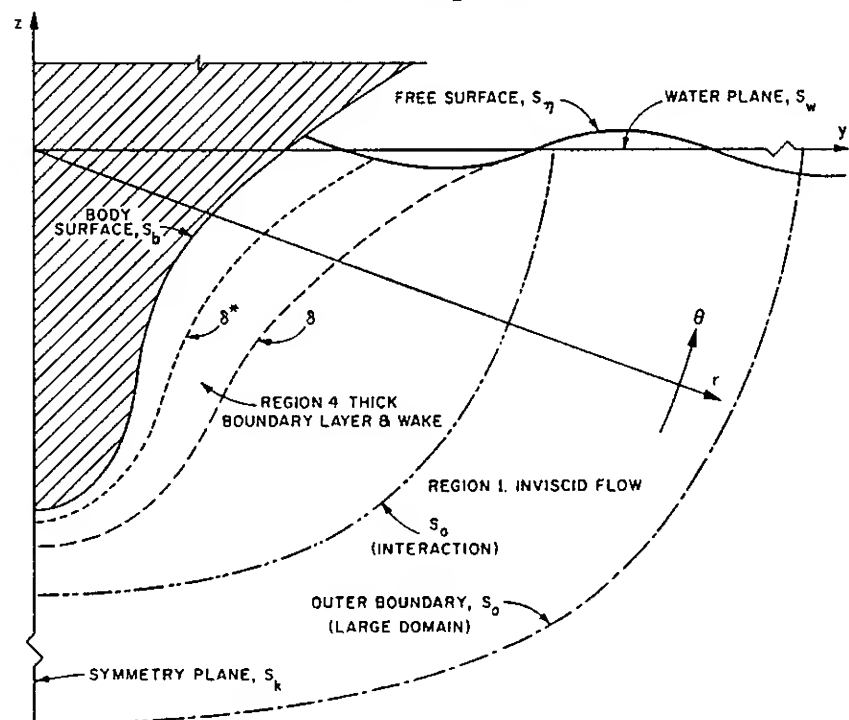
23. Maskew, B., "A Computer Program for Calculating the Non-Linear Aerodynamic Characteristics of Arbitrary Configurations," NASA CR-166476, 1982.
24. Boppe, C.W., Rosen, B.S., Laiosa, J.P., and Chance, B., Jr., "Stars & Stripes '87: Computational Flow Simulations for Hydrodynamic Design," The Eighth Chesapeake Sailing Yacht Symposium, Annapolis, MD., 1987.
25. Stern, F., "Comparison of Computational and Experimental Unsteady Cavitation on a Pitching Foil, ASME J. Fluids Eng., Vol. 111, 1989, pp. 290-299.
26. Dawson, C.W., "A Practical Computer Method for Solving Ship-Wave Problems," Proc. 2nd International Conference on Numerical Ship Hydrodynamics, Berkeley, CA., 1977, pp. 30-38.
27. "Report of the Resistance and Flow Committee," Proc. 18th Int. Towing Tank Conf., Kobe, Japan, 1987, pp. 47-92.
28. Toda, Y., Stern, F., and Longo, J., "Mean-Flow Measurements in the Boundary Layer and Wake and Wave Field of a Series 60  $C_B = .6$  Ship Model for Froude Numbers .16 and .316," Iowa Institute of Hydraulic Research, The University of Iowa, IIHR Report No. xxx, 1990 (in preparation).
29. Sarda, O.P., "Turbulent Flow Past Ship Hulls - An Experimental and Computational Study," Ph.D. Thesis, The University of Iowa, Iowa City, IA., 1986.
30. Kajatani, H., Miyata, H., Ikehata, M., Tanaka, H., Adachi, H., Namimatsu, M., and Ogiwara, S., "The Summary of the Cooperative Experiment on Wigley Parabolic Model in Japan," Proc. 2nd DTNSRDC Workshop on Ship Wave-Resistance Computations, 1983, pp. 5-35.

Table 1. Residuary-Resistance Coefficients

	L(m)	T(°C)	$U_0$ (m/s)	Fr	Re	$C_R$
Experiment IHI	6	12.8	2.423	0.316	$11.9 \times 10^6$	$1.803 \times 10^{-3}$
Experiment SRI	4	10.6	1.978	0.316	6.14	1.998
Experiment UT	2.5	17.3	1.564	0.316	3.6	1.866
Inviscid	--	--	--	0.316	--	1.79
Interactive	--	--	--	0.316	$4.5 \times 10^6$	1.92

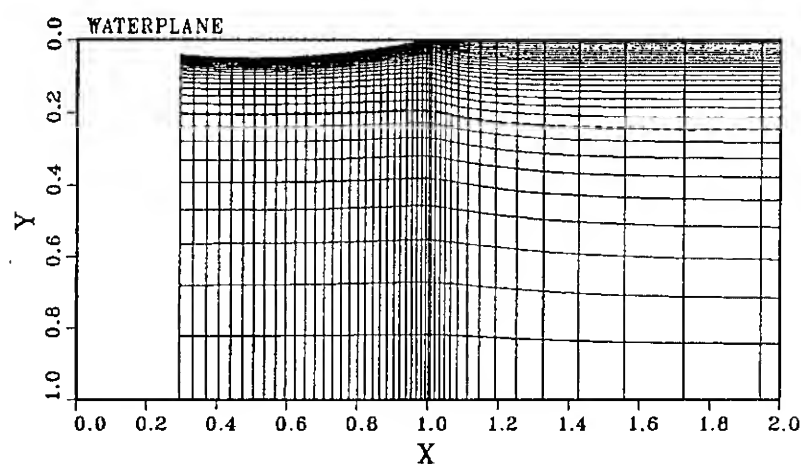


(a) (x,y) plane

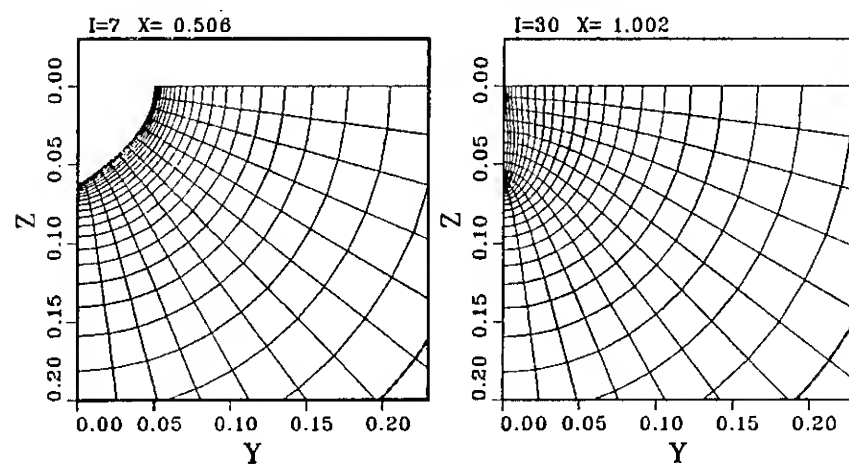


(b) (y,z) plane

Figure 1. Definition sketch of flow-field regions and solution domains.



(a) longitudinal plane



(b) body and wake crossplanes

Figure 2. Computational grid.

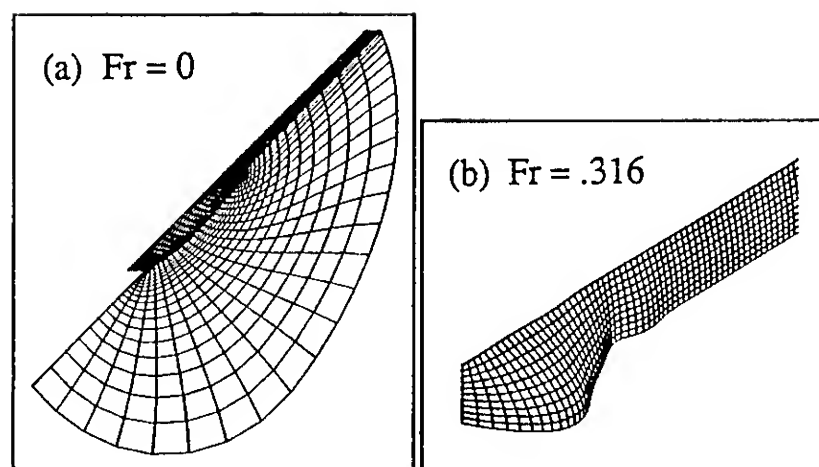


Figure 3. Displacement bodies.

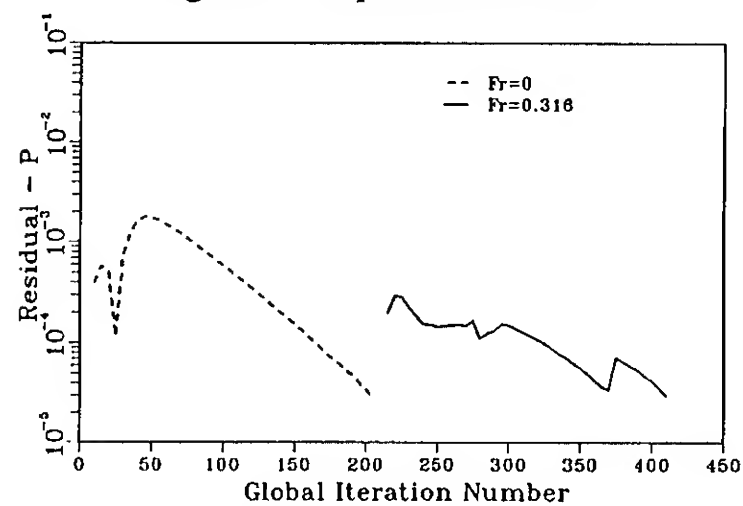


Figure 4. Convergence history.

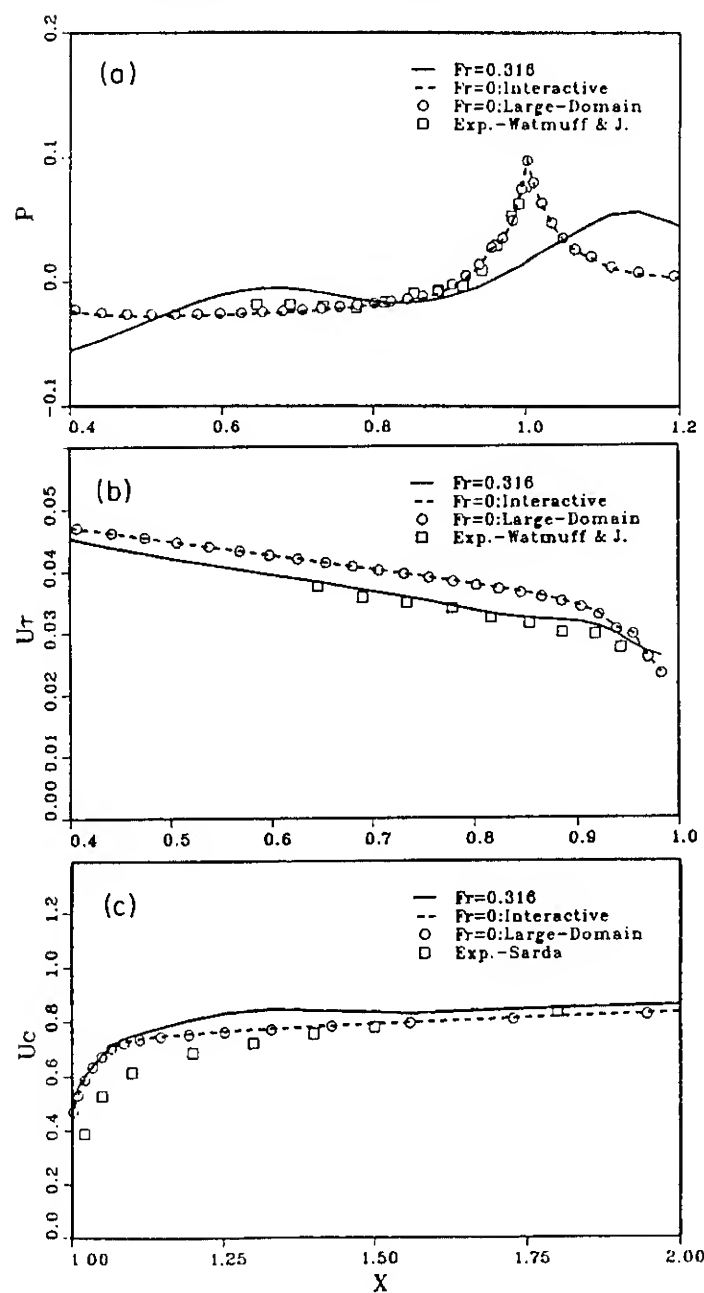


Figure 5. Comparison of interactive and large-domain solutions for the waterplane: (a) surface and wake centerplane pressure; (b) wall-shear velocity; and (c) wake centerplane velocity.

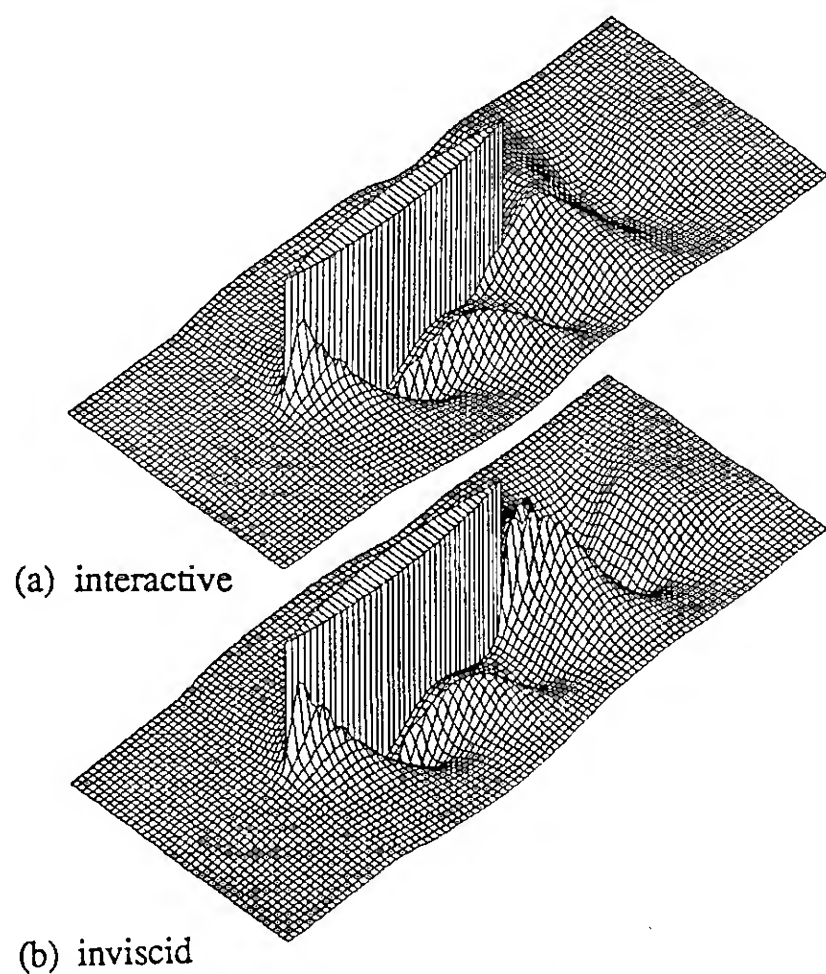


Figure 6. Free-surface perspective view.

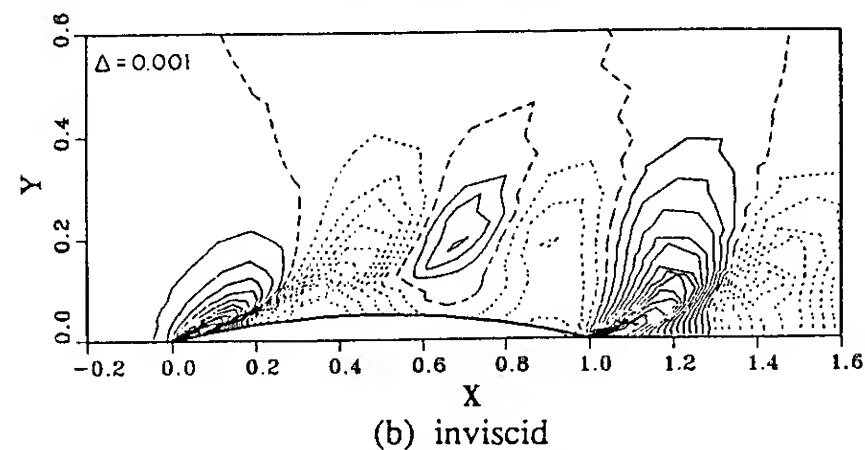
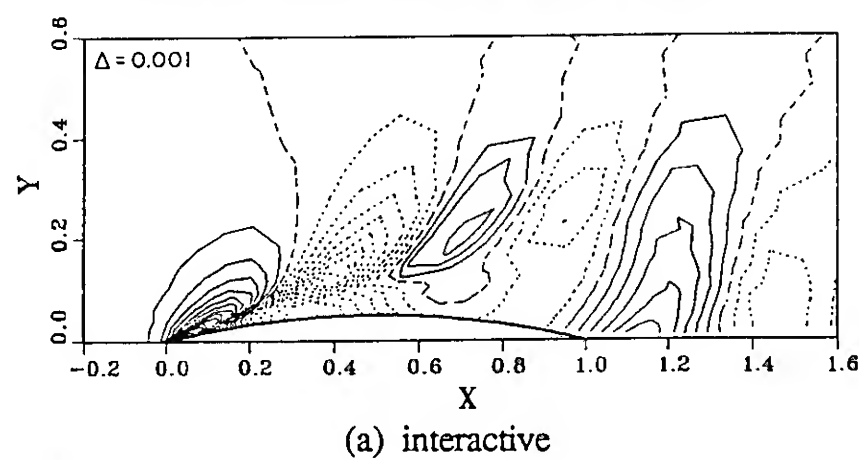


Figure 7. Free-surface contours.

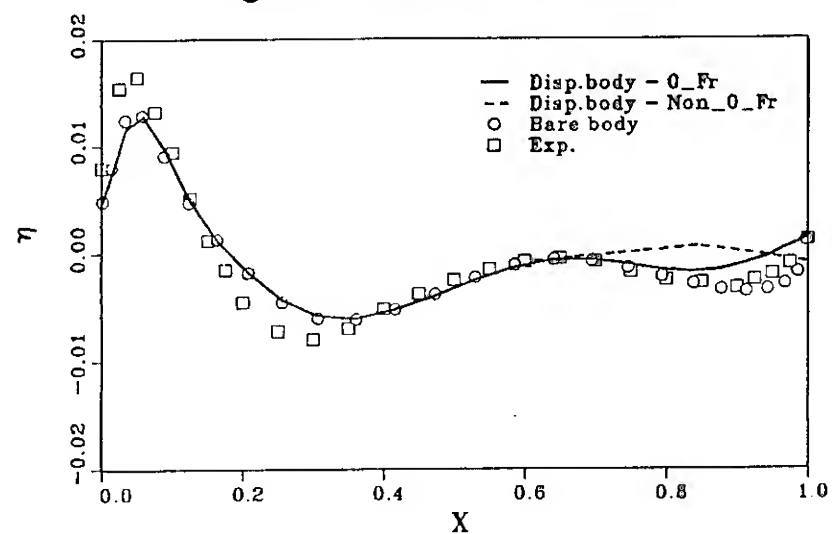


Figure 8. Wave profile.

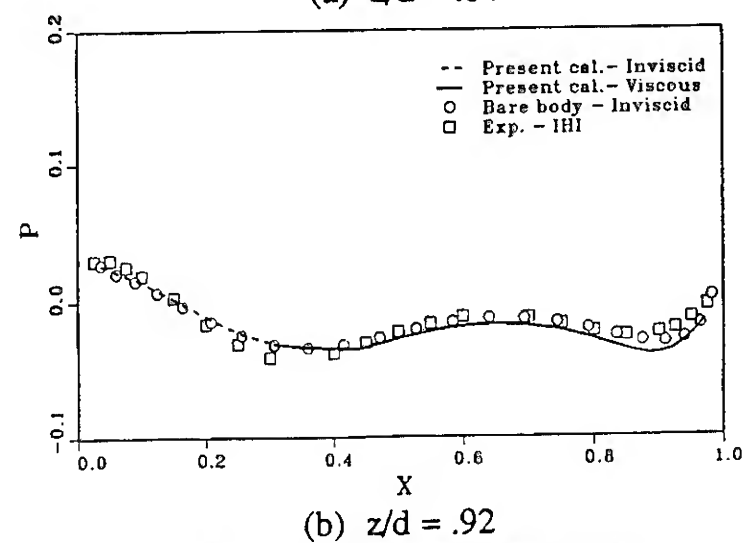
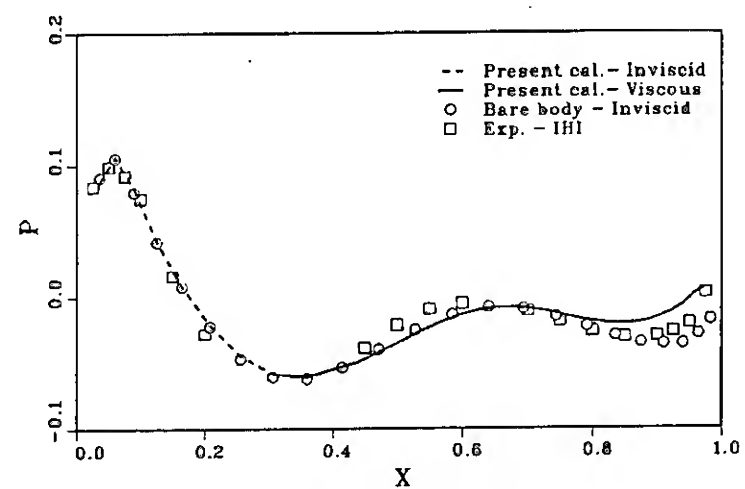


Figure 9. Surface-pressure profiles

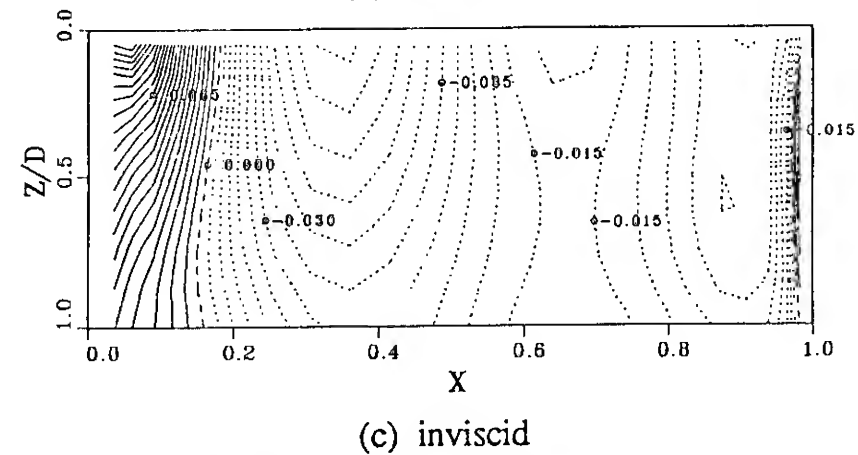
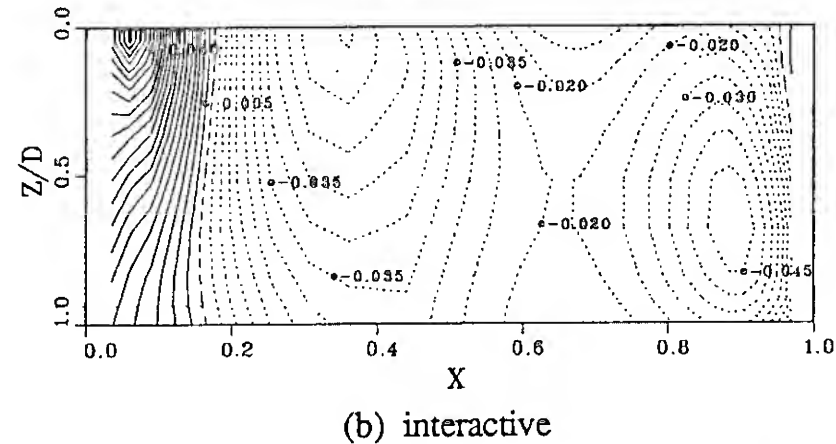
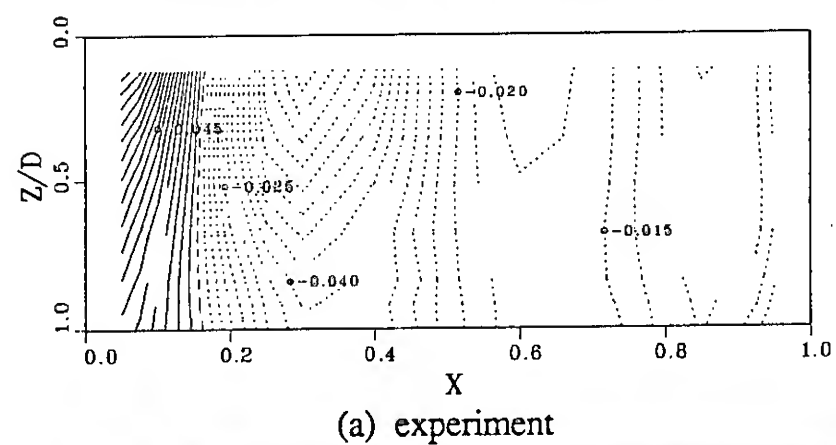


Figure 10. Surface-pressure contours.



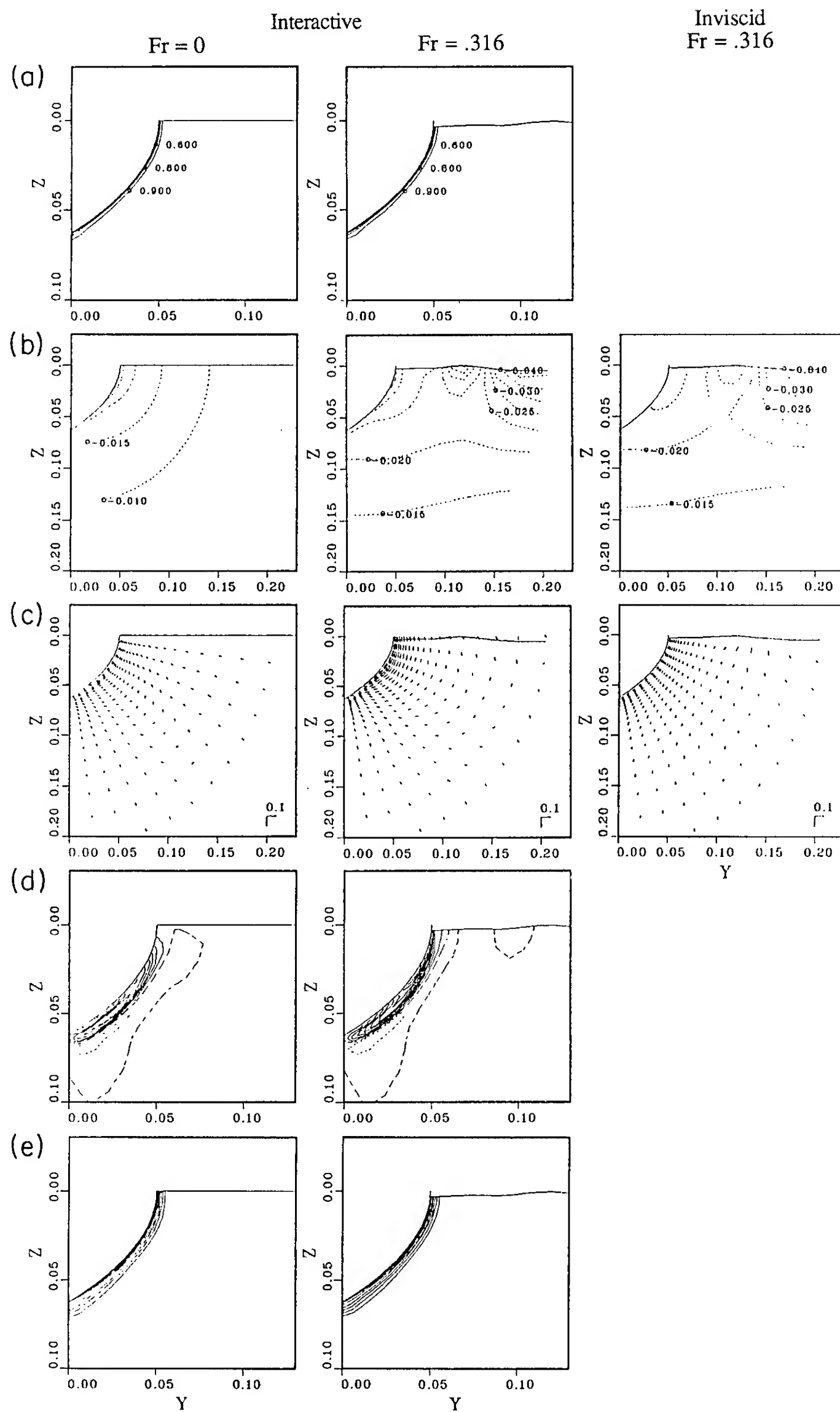


Figure 11. Comparison of solutions at  $x = .506$ : (a) axial-velocity contours; (b) pressure contours; (c) crossplane-velocity vectors; (d) axial-vorticity contours; and (e) turbulent kinetic energy contours.



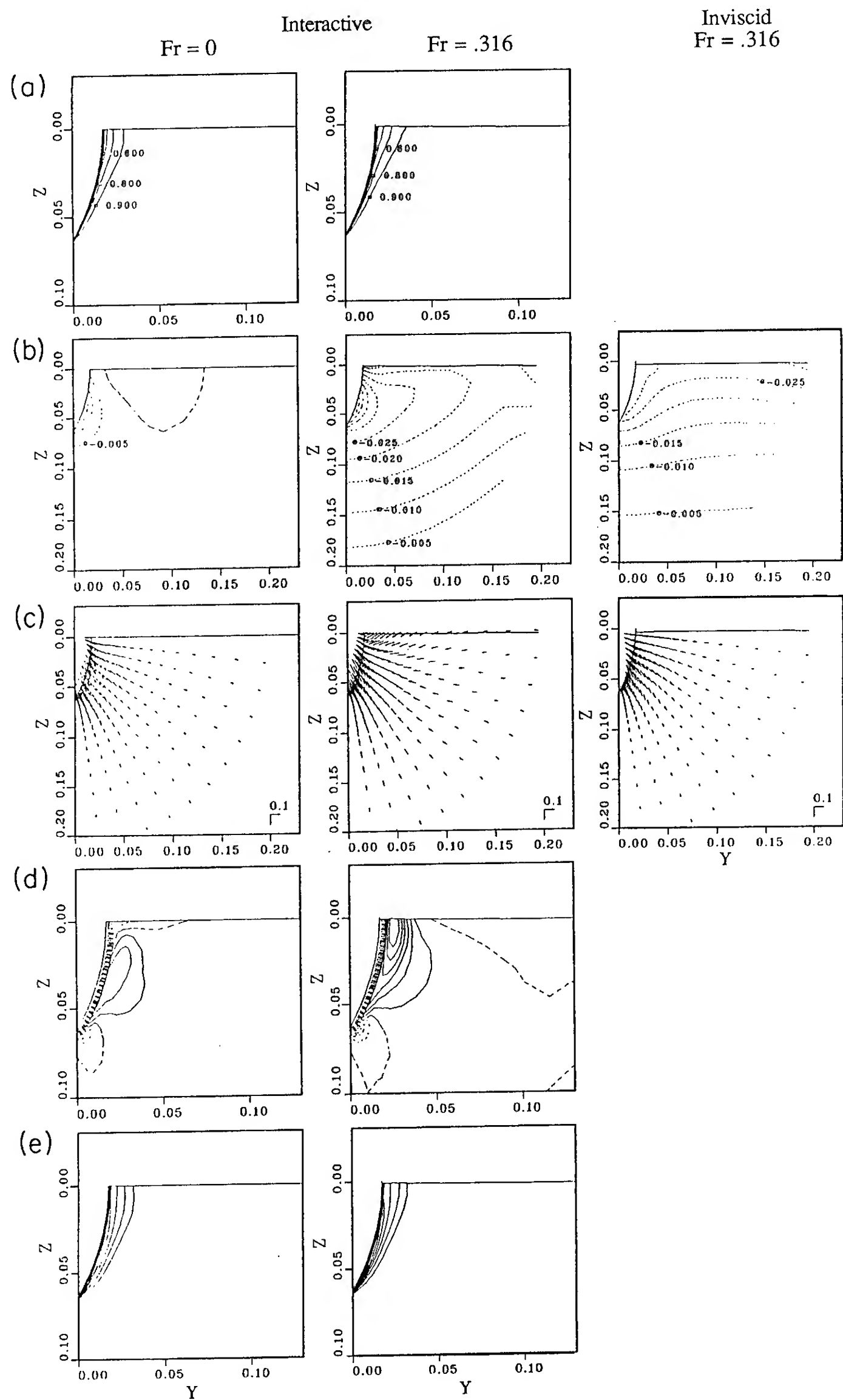


Figure 12. Comparison of solutions for  $x = .904$ : (a) axial-velocity contours; (b) pressure contours; (c) crossplane-velocity vectors; (d) axial-vorticity contours; and (e) turbulent kinetic energy contours.

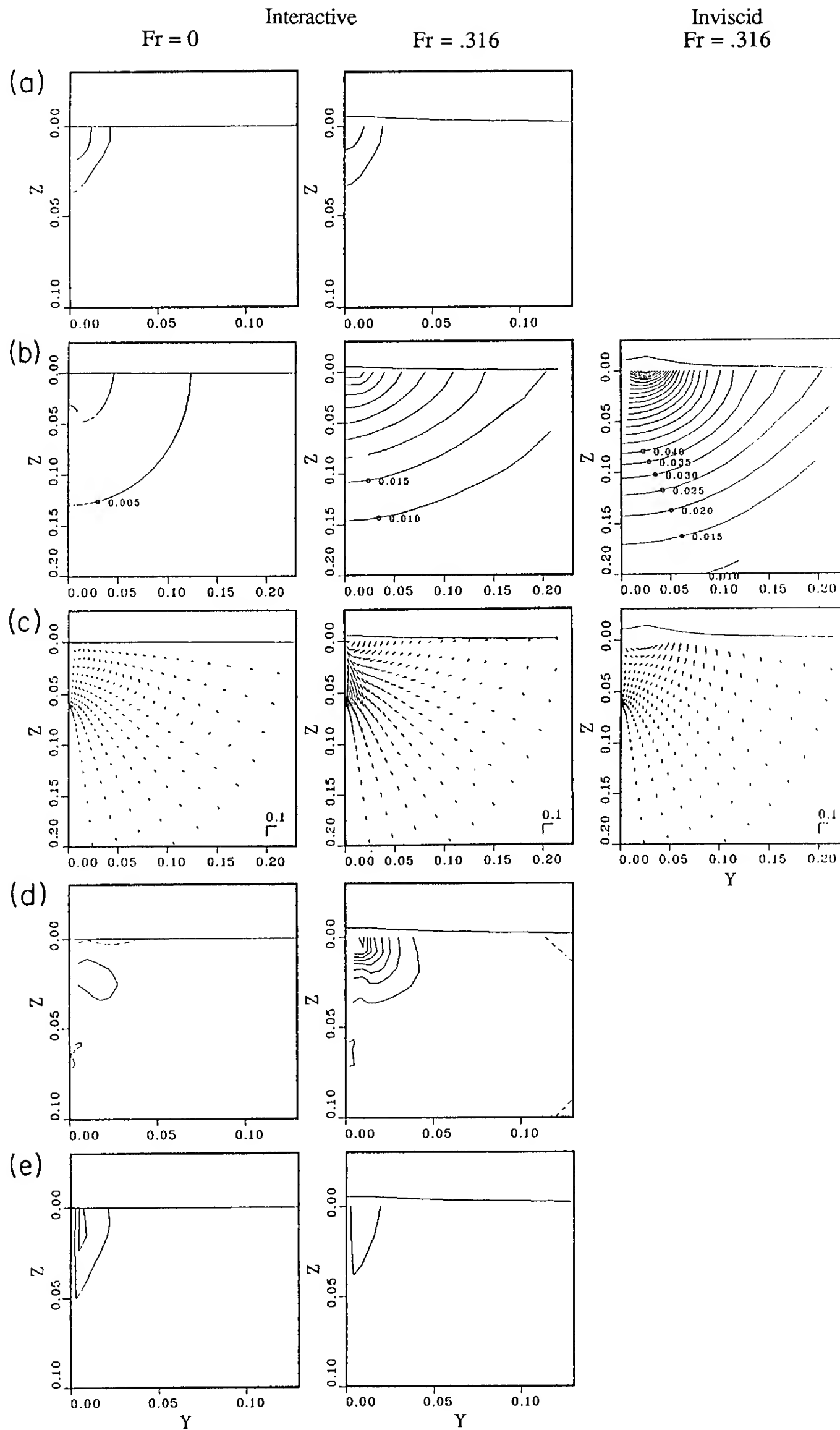


Figure 13. Comparison of solutions for  $x = .112$ : (a) axial-velocity contours; (b) pressure contours; (c) crossplane-velocity vectors; (d) axial-vorticity contours; and (e) turbulent kinetic energy contours.

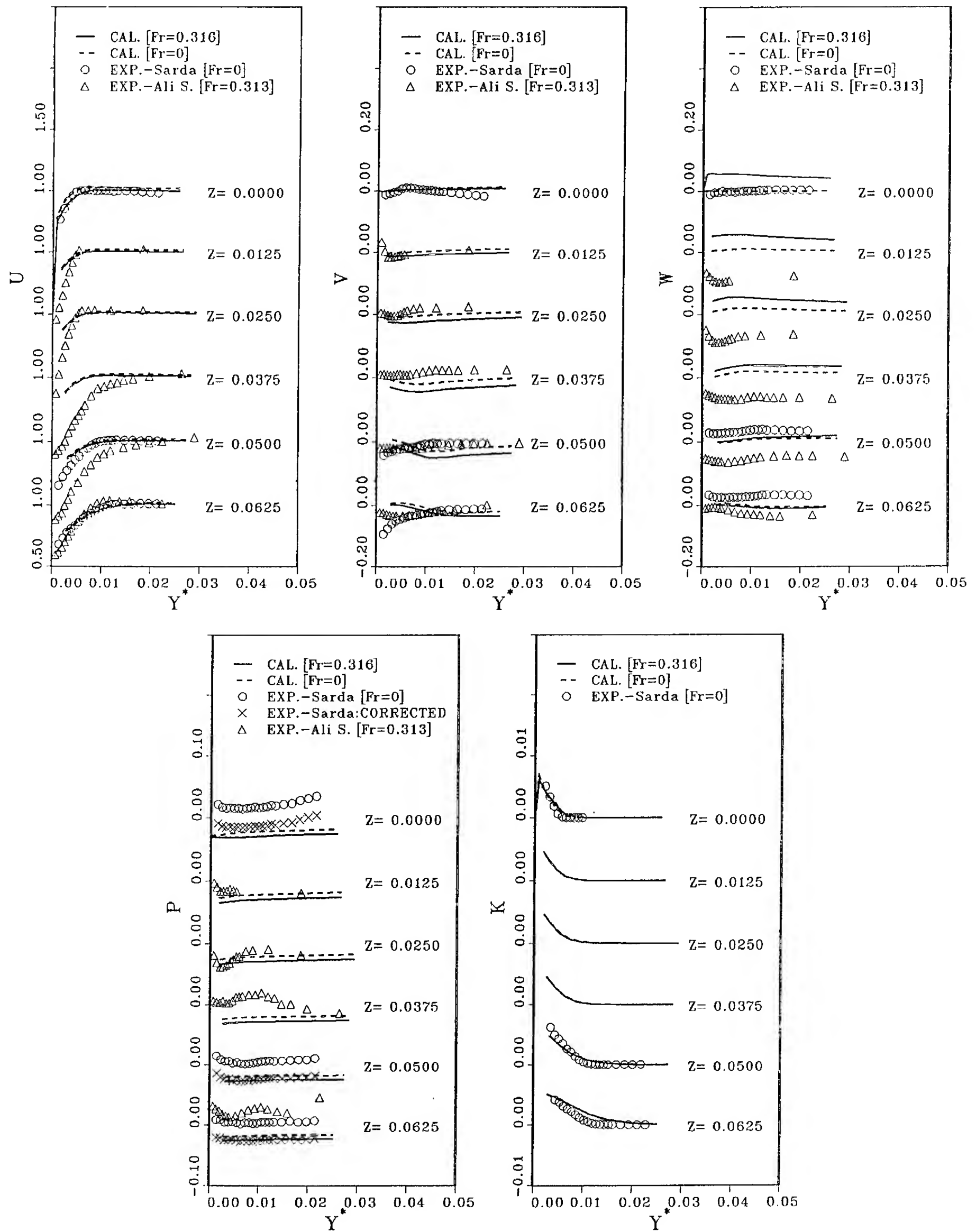


Figure 14. Velocity, pressure, and turbulent kinetic energy profiles at  $x = .5$ .

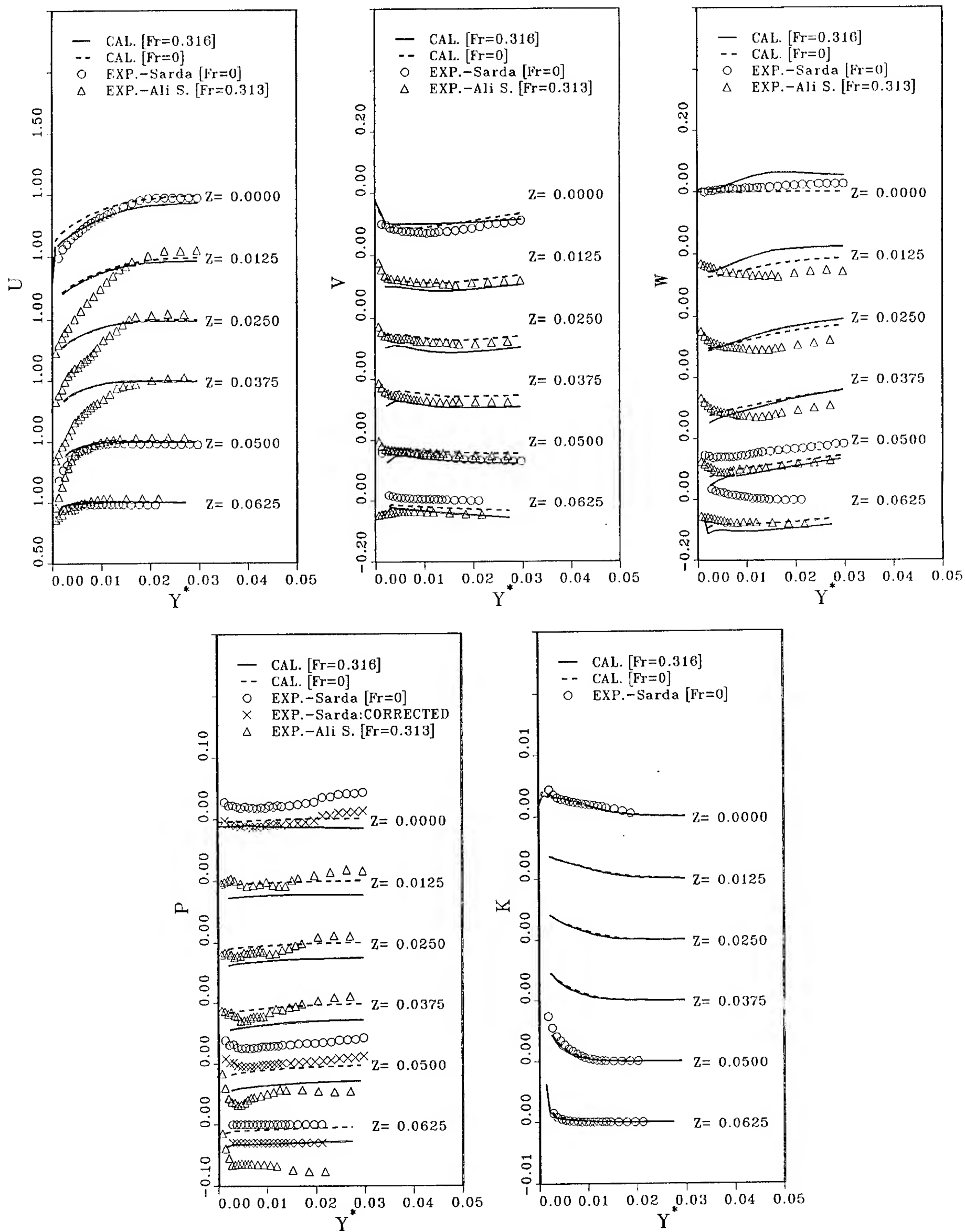


Figure 15. Velocity, pressure, and turbulent kinetic energy profiles at  $x = .9$ .

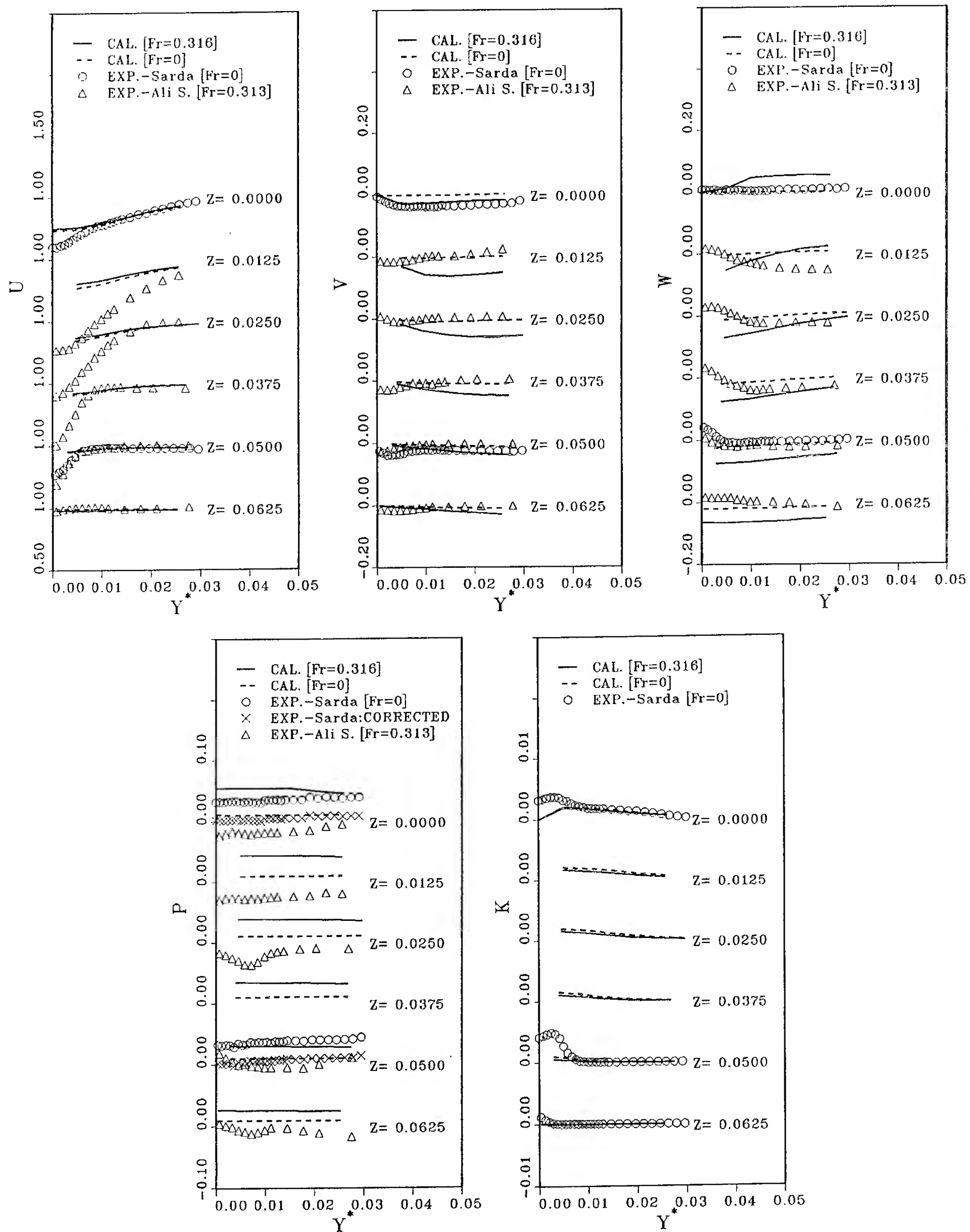


Figure 16. Velocity, pressure, and turbulent kinetic energy profiles at  $x = 1.1$ .



## DISCUSSION

Kuniharu Nakatake  
Kyushu University, Japan

I appreciate your interesting paper. In your calculation, the flow field and pressure distribution around wave surface are not taken into account. If you distribute source panel on the calculated wave surface and determine its strength from the kinematic condition on the wave surface, you may obtain more plausible results. This is possible in the linearized framework.

## AUTHORS' REPLY

We agree that a higher-order treatment of the free-surface boundary conditions would be preferable. We hope to make progress in this area in the future.

## DISCUSSION

Hoyte Raven  
Maritime Research Institute Netherlands, The Netherlands

This valuable paper addresses the difficult problem of prescribing free-surface boundary conditions inside the viscous domain. The authors solve the wave elevation from integration of the kinematic condition, and thus from the velocities at the undisturbed free surface. Prescribing boundary conditions for these velocities here is, therefore, critical. If I understand it correctly, in (20) not only the stresses but also the associated strain rates have been neglected, which are of leading order in the wake elevation. This is not a definite solution of course. What alternatives for the free-surface condition do you consider?

## AUTHORS' REPLY

The approximations (a) through (d) utilized in deriving equations (18) through (20) have been clearly stated in the text, and therefore do not require further explanation. An alternative treatment of the free-surface boundary conditions within the present overall framework is to retain more terms in the approximations (a) through (c) and higher-order terms in approximation (d).

## DISCUSSION

William B. Morgan  
David Taylor Research Center, USA

In the authors' presentation of their problem they stated that they were using an "Unsteady RANS Code using a  $k-\epsilon$  turbulence model." I believe this statement is inconsistent in that a RANS Code with a  $k-\epsilon$  model cannot be unsteady. I can understand attempting to use this code in a "quasi-steady" sense, but I believe it is not applicable to the unsteady problem. Would the authors please comment?

## AUTHORS' REPLY

Although not discussed in the present paper, we recognize the limitations of the  $k-\epsilon$  turbulence model with regard to simulating unsteady flow. Issues concerning this point were discussed in one of our earlier papers on another topic [31]. In our presentation, we only wished to emphasize the general capability of the IIHR basic viscous-flow method for unsteady flow notwithstanding the limitations of current turbulence models for such applications.

[31] Stern, F., Kim, H.T., Patel, V.C., and Chen, H.C., "A Viscous-Flow Approach to the Computation of Propeller-Hull Interaction," *Journal of Ship Research*, Vol. 32, No. 4, December 1988, pp. 246-262.

## DISCUSSION

Kazuhiro Mori  
Hiroshima University, Japan

1. It must be important to be of the same order in approximations when the viscous effects are taken into account in the free-surface computation. From this standpoint of view, the use of the displacement thickness method is not consistent where the thickness is calculated exactly. This may be crucial when the 3-D separation is dominant. My suggestion is that the viscous flow should be taken into account as the double model flow directly in the inviscid computation.

2. According to our computation and experiment, the separation of the flow at stern is much affected by the bow wave system. This means that we should not expect precise discussions on the interaction between the viscosity and the free surface by the iterative procedure as done in the present study.

## AUTHORS' REPLY

We are not clear as to the precise meaning of your questions; however, we would like to point out that viscous effects have been included directly in the inviscid-flow computation through the use of the displacement body. As discussed in the text, the limitations of this approach are not yet known. The present results are encouraging, but a complete evaluation requires further validation through comparisons with experimental data and a large-domain approach. Work along these lines is in progress.

We thank both the oral and written discussers of our paper for their pertinent remarks.

# Viscous Flow Past a Ship in a Cross Current

V.C. Patel, S. Ju, J.M. Lew

(Iowa Institute of Hydraulic Research, The University of Iowa, USA)

## ABSTRACT

A numerical method for the solution of the Reynolds-averaged Navier-Stokes equations is used to calculate the viscous flow over the stern of a ship in a cross current, i.e., a ship in yaw. The solutions are started with assumed initial conditions downstream of the bow. The numerical results are compared with the limited data that are available. Although the calculations are successful in describing the port-starboard flow asymmetry and vortex formation, the solutions indicate a need for a better resolution of the bow flow.

## INTRODUCTION

Patel, Chen and Ju (1988, 1990) have recently developed a numerical method for the solution of the Reynolds-averaged Navier-Stokes (RANS) equations and applied it to study the flow around ship hulls under the assumptions that the ship is symmetric about the vertical centerplane, and is advancing in a straight course in a calm sea. To the authors' knowledge, all viscous-flow calculations for ship hulls performed over the years with different methods have been made with these restrictions (see Patel, 1988, for a review). In this paper, extension and application of the numerical method of Patel et al. to asymmetric flow around the stern of a symmetric ship advancing in a straight course in a cross current, as depicted in Figure 1, are considered. This problem is equivalent to a ship in a uniform stream at an angle of yaw. From a basic fluid-flow perspective, this situation is more general than that of a body of revolution at incidence, which has been studied experimentally and numerically in many investigations (see, for example, Patel and Baek, 1985). We now have a more complex body at incidence. The resulting flow also bears some resemblance to the flow around a turning ship. A study of the flow around a ship in a cross current is thus of practical interest and also of value in further developing the capabilities of modern numerical methods.

Before describing the extension of the method, it is useful to make two important observations with regard to the present work. First, as in the previous work, we will be concerned with the flow downstream of some section in the middle body of the ship. This implies that there is some uncertainty in the establishment of proper initial conditions which reflect the flow over the bow. Secondly, experimental information on the viscous flow past a ship in yaw is limited and, therefore, the success of the method cannot be ascertained with confidence.

## CALCULATION OF ASYMMETRIC FLOWS

A detailed description of the basic numerical method and its applications to symmetric flows about double models, i.e., with the water and keel planes treated as planes of symmetry, is given in Patel, Chen and Ju (1988, 1990). The modifications in the method and the associated computer programs to calculate the flow around a ship double model at an angle of yaw are relatively minor. The main changes are concerned with the size and shape of the computational domain, the initial conditions, and the boundary conditions. These are outlined below.

As shown in Figure 1, a positive value of yaw angle  $\alpha$  is used to represent a cross current from the port side. A cylindrical  $(x, r, \theta)$  coordinate system in the physical plane is used for the velocity components. For the symmetric-flow calculations presented in Patel et al. (1988, 1990), the solution domain in the transverse plane was  $(0^\circ \leq \theta \leq 90^\circ)$ , i.e., it extended from the keel plane,  $\theta = 0^\circ$ , to the water plane,  $\theta = 90^\circ$ . Plane-of-symmetry conditions were applied on these planes.

For the current application, the required solution domain is  $(-90^\circ \leq \theta \leq 90^\circ)$ , and plane-of-symmetry conditions are applied on the water plane at  $\theta = -90^\circ$  and  $\theta = 90^\circ$ , on the port and starboard (or, windward and lee) sides, respectively. The outer boundary of the solution domain is located farther than before, at  $r = 2.0$ , i.e., it is a cylindrical boundary, two ship lengths in radius. The number of grid points in the radial direction is increased to 40 to accommodate the more severe variations of flow quantities in that direction. The locations of the transverse sections ( $x = \text{constant}$ ) and the number of grid points in the axial direction are the same as before ( $= 50$ ). The number of grid lines in the circumferential direction was increased to 27. Thus, the present calculations have been performed with a  $50 \times 40 \times 27$  grid, which is close to the finest that could be accommodated on a CRAY XMP/48 supercomputer.

At the outer boundary of the solution domain, uniform-stream conditions, i.e.,  $U_x = U_0 \cos \alpha$ ,  $U_r = U_0 \sin \alpha \sin \theta$ ,  $U_\theta = U_0 \sin \alpha \cos \theta$ , are imposed. The calculations were started downstream from the bow, with the most upstream transverse section located at  $x = 0.3$ . The profiles used at this section were generated in a similar manner to that described in Patel, Chen and Ju (1990). Briefly, it involves prescription of a girthwise distribution of the boundary-layer thickness  $\delta$ , the friction coefficient  $C_f (=$

<sup>1</sup> Presently Manager of Technical Research Center, Daewoo Shipbuilding & Heavy Machinery Ltd., Korea.

<sup>2</sup> Visiting Professor from Chungnam National University, Daejeon, Korea.

$2U_\tau^2$ , where  $U_\tau$  is the friction velocity), and the velocity at the edge of the boundary layer  $U_\delta$ . These are used, together with the law of the wall and the law of the wake, to generate the profiles of the longitudinal velocity  $U_x$  inside the boundary layer, and the reduction from  $U_\delta$  to unity in the inviscid flow is assumed to take place as  $r^{-2}$ . Uniform stream conditions are specified beyond a distance of five boundary-layer thickness from the hull. In the first instance,  $U_r$  and  $U_\theta$  components are determined by interpolation in the boundary-layer profiles and the known conditions at the wall and in the uniform stream, and  $k$  and  $\epsilon$  are obtained from correlations for a flat-plate boundary layer. As the solution progresses, the values of  $U_r$ ,  $U_\theta$ ,  $k$  and  $\epsilon$  within the boundary layer are updated by scaling those calculated at the first downstream station. This process is continued only for the first 20 global sweeps, and then the initial profiles are fixed. This procedure for the generation of the initial conditions does not affect the principal quantity, i.e., the axial velocity profile. However, it ensures that the subsequent solution is carried out with initial profiles of transverse velocity components and turbulence parameters which are compatible with the governing equations. In the present calculations, the girthwise distribution of the boundary-layer thickness and friction velocity were assumed to be the same as those in the symmetric (zero yaw) case but the velocity at the edge of the boundary layer was prescribed from an inviscid solution. This is obviously an approximation and the resulting initial conditions do not properly reflect all of the flow phenomena that may occur over the bow, particularly at an angle of yaw.

In the calculations at nonzero yaw angles, some difficulties were encountered in the application of the boundary conditions in the ship centerplane and at the exit plane. As noted in Patel, Chen and Ju (1988), for the symmetric-flow calculations with  $\alpha = 0$ , the ship centerplane was extended as a false wake plane, and the condition of symmetry,  $U_\theta = 0$ , was applied on it. Also, along the wake centerline,  $r = 0$ , the conditions  $U_r = U_\theta = 0$  were implicitly imposed. In the present application, the false wake plane is no longer a plane of flow symmetry although it is a plane of symmetry for the numerical grid. Also,  $U_r$  and  $U_\theta$  do not vanish along  $r = 0$ . In fact,  $U_r$  and  $U_\theta$  change rapidly near the singular point  $r = 0$  in the grid. These points are no longer calculated directly in the extended method. Because we are now considering a half plane of  $-90^\circ \leq \theta \leq 90^\circ$ , there are no explicit boundary conditions to be satisfied at the false wake plane. However, because of the rapid changes occurring in the velocity components in cylindrical coordinates near the singular point  $r = 0$ , increased accuracy and stability of the solution procedure was obtained by interpolating in these components in Cartesian coordinates, and then transforming back to the cylindrical coordinates.

Finally, at the downstream (exit) boundary, the conditions  $p_{x'} = 0$  and  $(U_x, U_r, U_\theta, k, \epsilon)_{x'x'} = 0$  are imposed, where  $x'$  denotes the direction of the uniform stream. This requires complicated interpolations near the exit plane as  $x'$  is different from the ship axis  $x$ . All values required in the exit plane were extrapolated linearly in the  $x$  direction first and then shifted by the amount of  $(x_f - x_{f-1}) \tan \alpha$  in the  $r$  direction, where  $x_f$  and  $x_{f-1}$  denote, respectively, the  $x$  coordinates at the last and the next to last axial stations.

## RESULTS

With the modifications described above, the numerical method was employed to calculate the flow around double

models of the HSVA Tanker (Wieghardt, 1982) and the SR107 Bulk Carrier (Okajima et al., 1985). The hull shapes are shown in Figure 2. Comparisons between calculations and experiments for both hulls with symmetric flow, at zero yaw, were presented and discussed in Patel et al. (1988, 1990). There is no experimental information with asymmetric flow around the HSVA Tanker but some measurements at  $\alpha = 5^\circ$  and  $10^\circ$  have been reported by Nishio et al. (1988) for the SR107. In the presentation of the results all quantities are made dimensionless by the reference velocity  $U_0$  and the ship length  $L$ .

Figures 3 and 4 provide an overview of the effects of yaw angle on the HSVA Tanker at  $Re = 5 \times 10^6$ . The limiting, or wall streamlines determined from the calculated friction vectors on the hull are shown in Figure 3. The port and starboard asymmetry is very clearly seen. The regions of strong streamline convergence are those where the pressure and the friction coefficients assume low values. These are also the regions which are readily identified in surface flow-visualizations using such techniques as oil flow, wool tufts, and dye injection.

Figure 4 shows the velocity field at a section near the stern,  $x/L = 0.9$ . In general, the effect of the cross current is to drive the flow from the port to the starboard side. This produces a thinning of the boundary layer on the port side and a thickening on the starboard side. The secondary motion at this section reveals reversals in direction that are characteristic of converging limiting streamlines and vortex formation. They are also associated with a local decrease in the wall shear stress and thickening of the viscous layer. These flow features are particularly difficult to handle in space-marching numerical methods usually employed for the solution of the three-dimensional boundary-layer equations. Here they are predicted without any special treatment.

The general features of these and other results presented below are qualitatively similar to those observed on a body of revolution at angles of attack. However, subtle differences arise in the shapes of the distributions and in the magnitudes of the pressure and friction coefficients due to the present three-dimensional geometry and, in particular, due to the rapid changes in this geometry at the stern.

The remaining results pertain to the SR107 hull. In this case, comparisons are made between the calculations and experimental data at  $\alpha = 10^\circ$  and  $Re = 2.7 \times 10^6$ . We examine the velocity field as well as the contours of the axial component of vorticity,  $\omega_x$ , in the format presented by Nishio et al. (1988). Figures 5, 6 and 7, show the results at three sections,  $x/L = 0.5, 0.7$  and  $0.9$ , respectively.

From Figure 5 it is clear that the effect of the cross current is to thin the boundary layer on the port side and thicken it on the starboard side. A vortex is observed around the turn of the bilge, particularly in the experiment. In general, at this section the calculations reproduce the overall trends but differ in intensity. For example, the measured secondary motion and axial vorticity are both stronger than predicted, and Figure 5(c) indicates some difference in the location of the vortex. It is possible that better agreement between measurements and calculations can be secured, at least in some respects, by adjustment of the initial conditions at  $x/L = 0.3$ . An alternative, of course, is to include the bow in the calculations. We shall return to this later.

At the next axial station,  $x/L = 0.7$ , the results are similar to those at the previous section. Figure 6(b) again indicates that the secondary motion observed in the experiment was considerably stronger than is calculated although there is good correspondence in the extent over which axial vorticity is found. The calculations fail to reproduce a detached core of high axial vorticity.

At the last section where measurements were made,  $x/L = 0.9$ , Figure 7 shows continued qualitative agreement between the calculations and data but somewhat greater differences in the details. The dual vortex structure indicated by the experiments is perplexing because it gives the appearance of vortex shedding and yet such a phenomenon, even if it were present, could not have been captured by the simple pressure probes employed for the measurements. The calculations also do not produce the high levels of axial vorticity observed in the experiments. Be that as it may, Figure 7(c) shows that the calculations are successful in identifying the region over which there is significant axial vorticity.

Although the calculations were continued well into the wake, there is no data to gauge their success. An interesting feature of the calculated wake is that the longitudinal vorticity (secondary motion) is destroyed rather rapidly although a measurable axial velocity defect persists for large distances.

## DISCUSSION

This first attempt to calculate the viscous flow over a ship in a cross current is regarded only as a partial success because it has raised a number of issues which need further investigation. Among these, the most important is the problem of specifying realistic initial conditions at the upstream station. Numerical experiments performed with different initial conditions during the course of this work indicated that the strength and location of the vortices on the lee side depended rather markedly on the initial conditions. For this reason, it was decided to present results obtained with the same initial conditions as those used earlier and found satisfactory for the zero-yaw case. Of course, calculations can be performed for the inviscid flow and the boundary layer over the bow to determine these conditions in a systematic way. But, it is possible that even these will fail if, as the results from the present calculations indicate, a vortex is formed well ahead of midships. In fact, the likelihood of vortices arising near the bow is greatly increased for a full hull form, and with a bulbous bow, at angles of yaw. Thus, it appears that the problem of initial conditions may have to be addressed, in the final analysis, by extending the full Navier-Stokes type of solutions to include the complete ship. At model scale, this would also require a careful treatment of transition or tripping devices.

The failure of the calculations to reproduce the observed high levels of axial vorticity in well defined cores is another feature brought forth by this investigation. The differences between calculations and experiment arise as early as midships and continue over the stern. It is possible that this is due, at least in part, to the use of the wall-functions approach in the turbulence model. In this approach, the flow near the wall is not explicitly calculated, and therefore, flow features arising from a roll up of the near-wall layer, such as vortex formation, are unlikely to be resolved in detail. A near-wall turbulence model, along with integration of the equations of motion up to the

wall, are needed to obtain an adequate resolution of these features.

Finally, it should be noted that the present calculations were carried out for a ship in a uniform stream (in unrestricted waters) whereas the experiments on the SR107 were conducted on a double model in a wind tunnel. The effects of tunnel blockage, which increases when the model is mounted at an angle of yaw, remain to be explored.

## CONCLUDING REMARKS

Calculations of the flow past a ship in a cross current, presented here, have served to illustrate not only the capabilities of the numerical method employed but also the additional complexities that arise in real-life situations. The asymmetries in the stern flow, resulting from asymmetric stern shapes, cross currents, or maneuvers, are obviously of interest in the design of propulsors and appendages, and in the prediction of hull vibration. The present calculations represent a first step in the development of numerical methods capable of addressing these issues in a comprehensive and realistic manner.

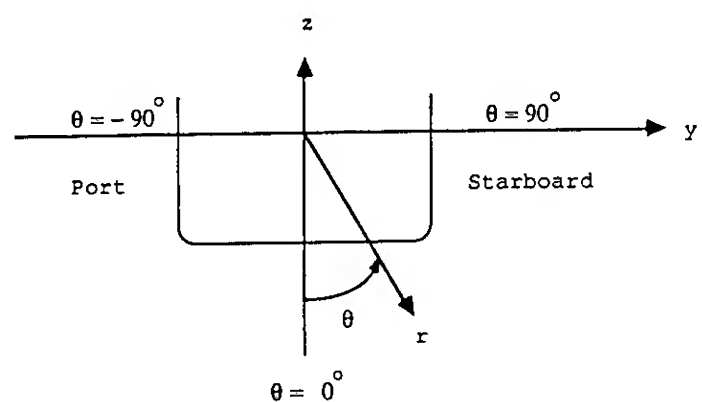
## ACKNOWLEDGEMENTS

This research was partially sponsored by the Office of Naval Research, first under the Accelerated Research Initiative (Special Focus) Program in Ship Hydrodynamics, Contract N00014-83-K-0136, and then under Contract N00014-88-K-0001. The calculations reported here were performed on the CRAY X/MP-24 supercomputer of the Naval Research Laboratory, and on the CRAY X/MP-48 machine of the National Center for Supercomputing Applications at Urbana-Champaign.

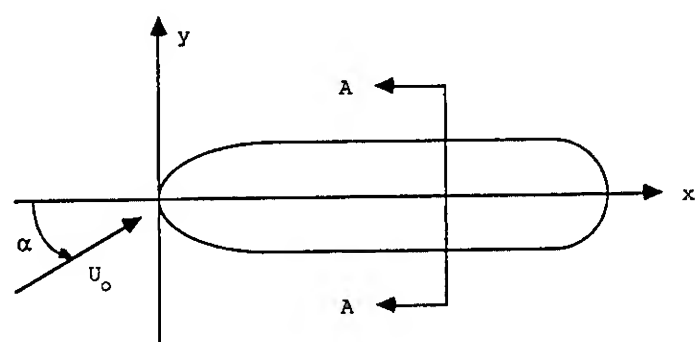
## REFERENCES

- Nishio, S., Tanaka, I., and Ueda, H. (1988), "Study on Separated Flow around Ships at Incidence," J. Kansai Soc. Nav. Architects, Japan, Vol. 210, pp. 9-17.
- Okajima, R., Toda, Y., and Suzuki, T. (1985), "On a Stern Flow Field with Bildge Vortices," J. Kansai Soc. Nav. Architects, Japan, Vol. 197, pp. 87-95.
- Patel, V.C. (1988), "Ship Stern and Wake Flows: Status of Experiment and Theory," Proc. 17th ONR Sym. Naval Hydrodyn., The Hague, The Netherlands, pp. 217-240.
- Patel, V.C. and Baek, J.H. (1985), "Boundary Layers and Separation on a Spheroid at Incidence," AIAA Journal, Vol. 23, pp. 55-63.
- Patel, V.C., Chen, H.C. and Ju, S. (1988), "Ship Stern and Wake Flows: Solutions of the Fully-Elliptic Reynolds-Averaged Navier-Stokes Equations and Comparisons with Experiments," Iowa Inst. Hydraulic Research, Uni. Iowa, IHR Report No. 323.
- Patel, V.C., Chen, H.C., and Ju, S. (1990), "Computations of Ship Stern and Wake Flow and Comparisons with Experiment," J. Ship Research, to appear.
- Wieghardt, K. (1982), "Kinematics of Ship Wake Flow, The Seventh David W. Taylor Lecture," DTNSRDC-81/093. See also Z. Flugwiss Weltraumforsch., Vol. 7, pp. 149-158.



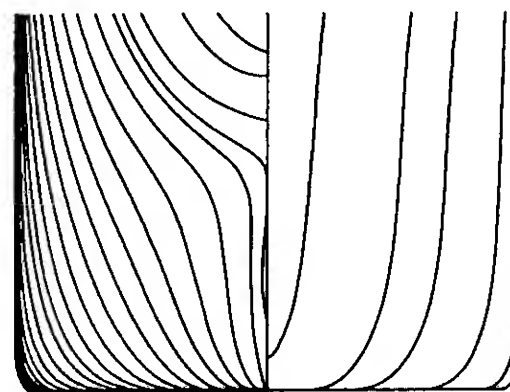


(a) transverse section A-A

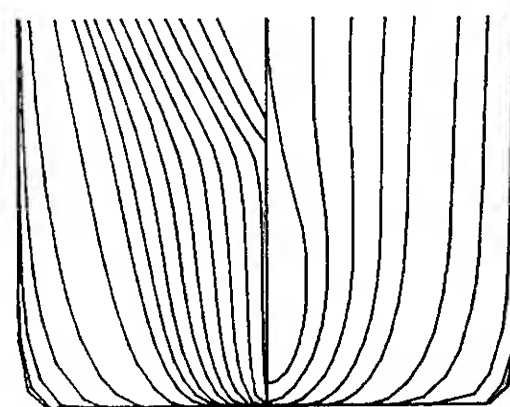


(b) waterplane

Figure 1. Ship in a cross current; notation

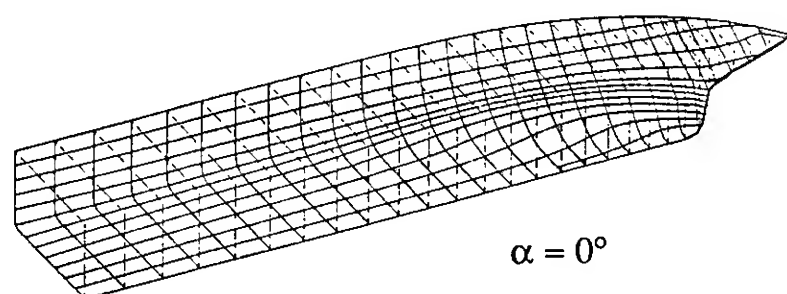


(a) HSVA Tanker

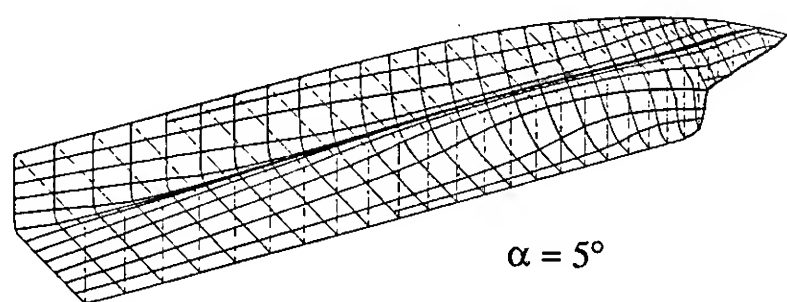


(b) SR107 Bulk Carrier

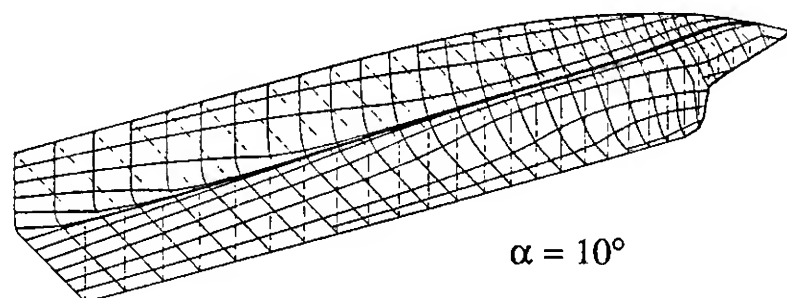
Figure 2. Hull shapes



$\alpha = 0^\circ$

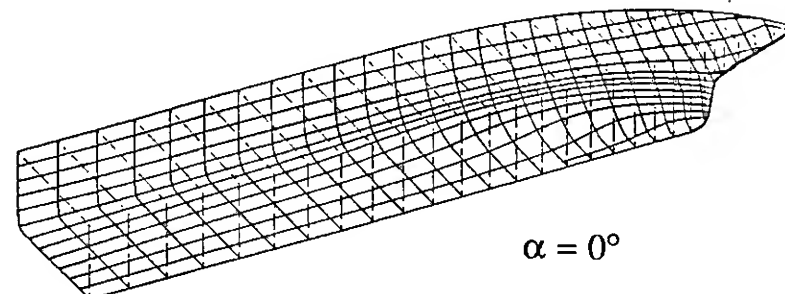


$\alpha = 5^\circ$

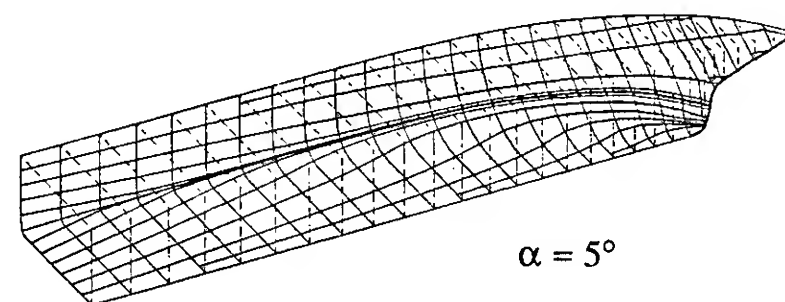


$\alpha = 10^\circ$

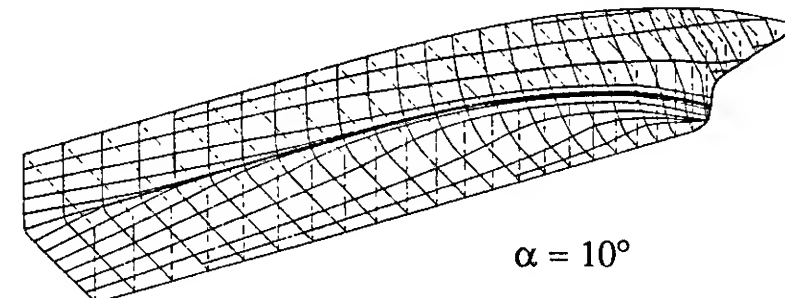
(a) port



$\alpha = 0^\circ$



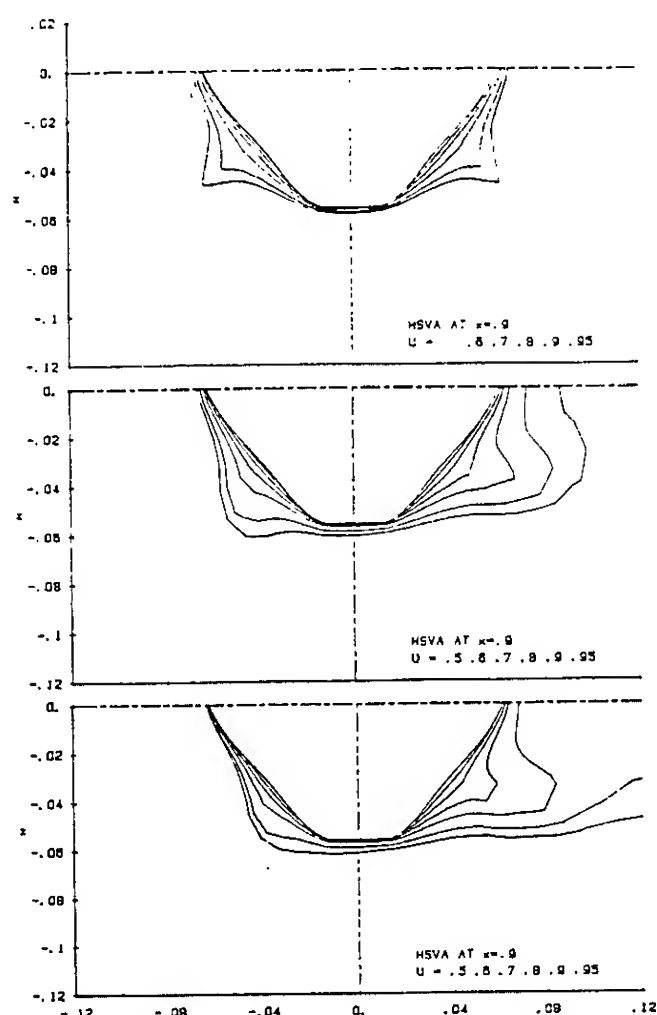
$\alpha = 5^\circ$



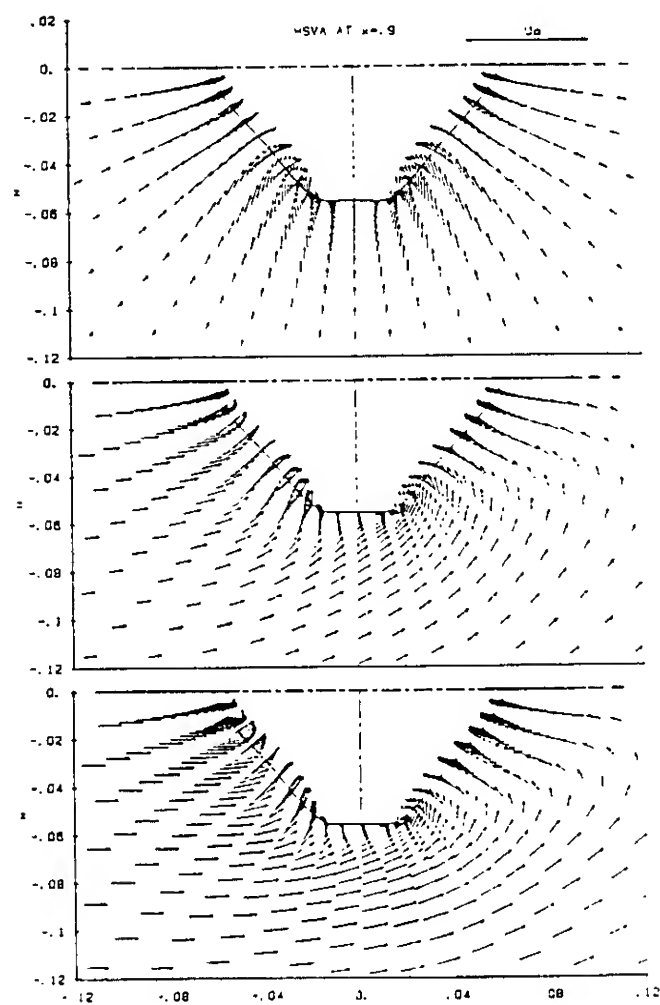
$\alpha = 10^\circ$

(b) starboard

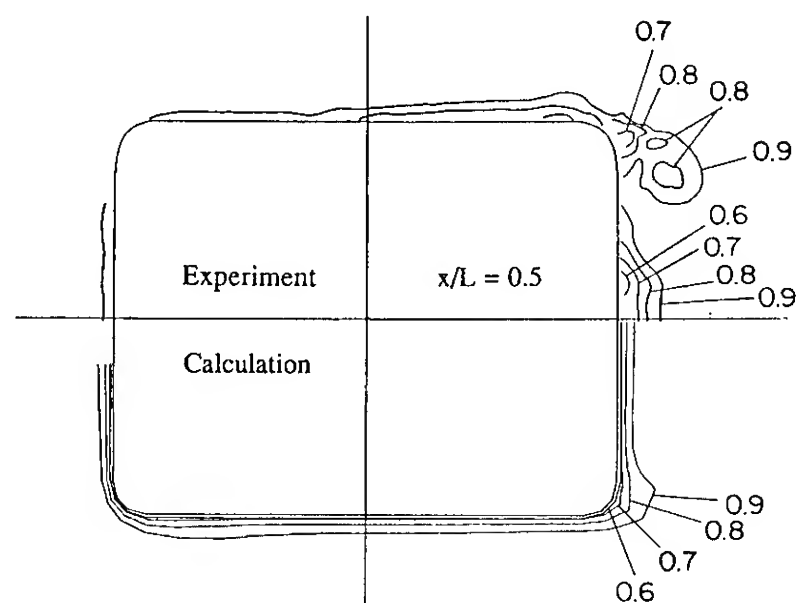
Figure 3. Surface streamlines, HSVA Tanker



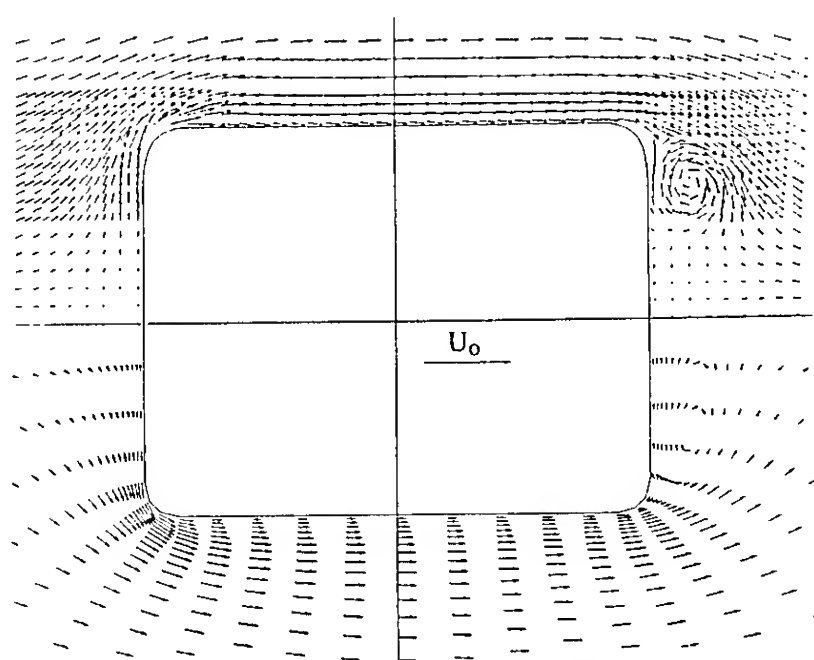
(a) Axial velocity



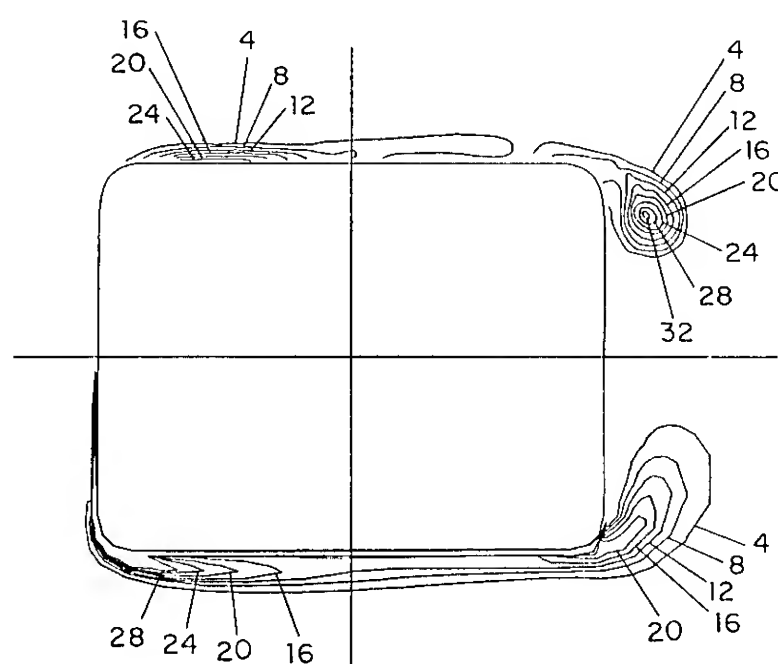
(b) Transverse velocity



(a) Axial velocity



(b) Transverse velocity

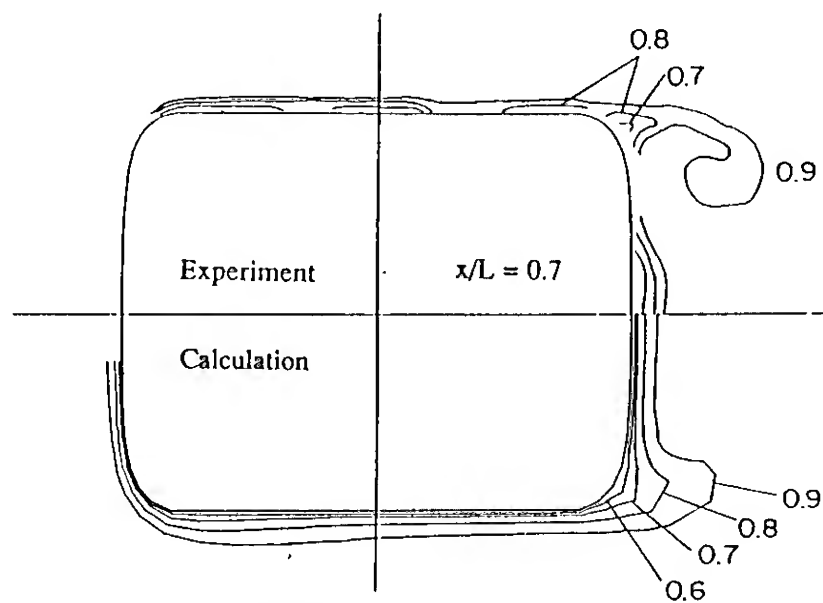


(c) Axial vorticity

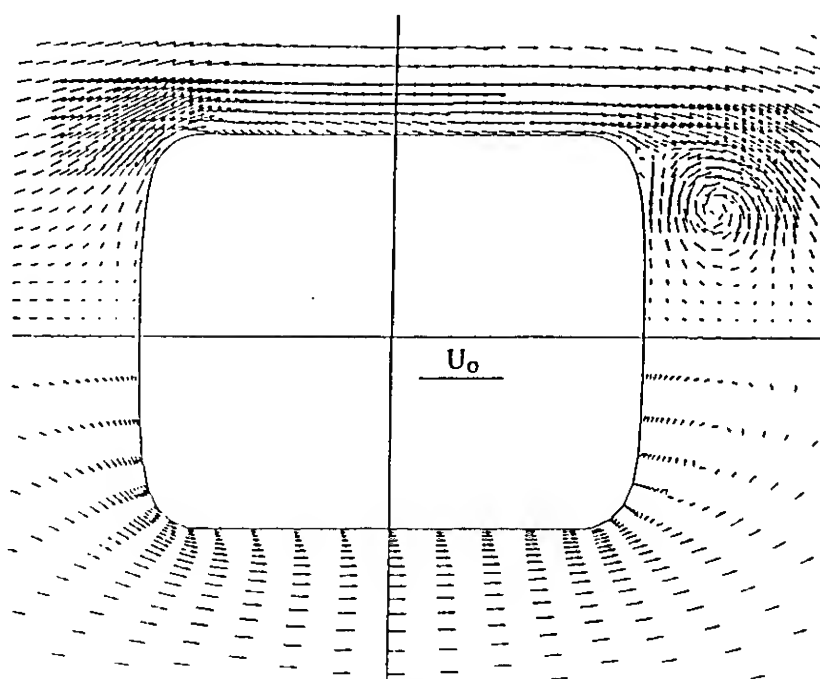
Figure 4. Velocity field on HSVA tanker at transverse section  $x/L = 0.9$

Figure 5. Velocity field and axial vorticity on SR107 at  $x/L = 0.5$

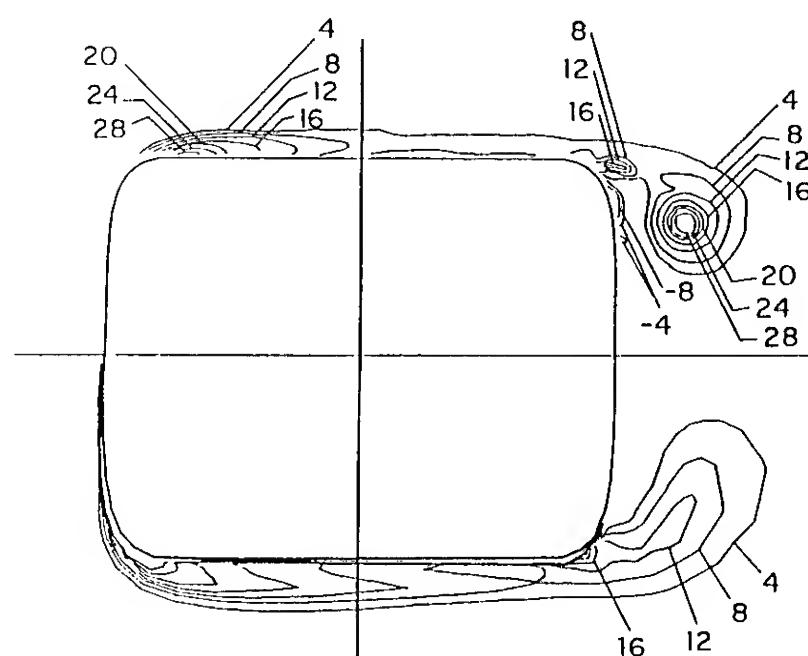




(a) Axial velocity

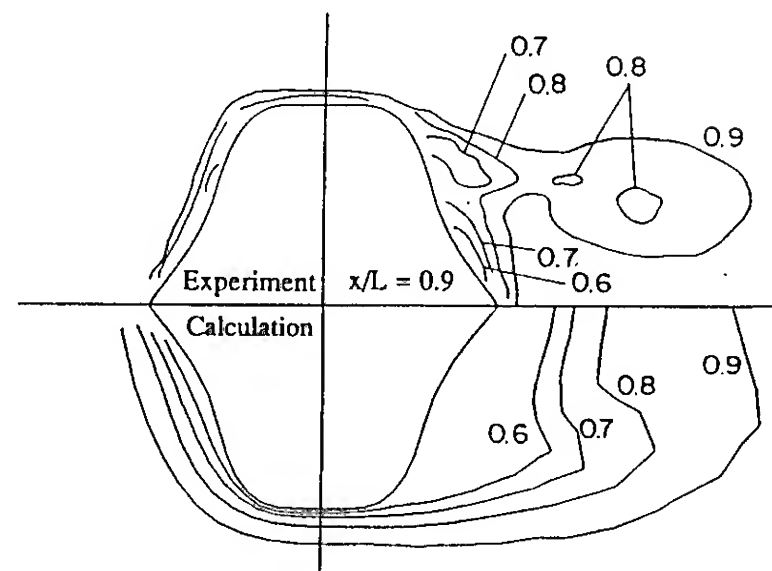


(b) Transverse velocity

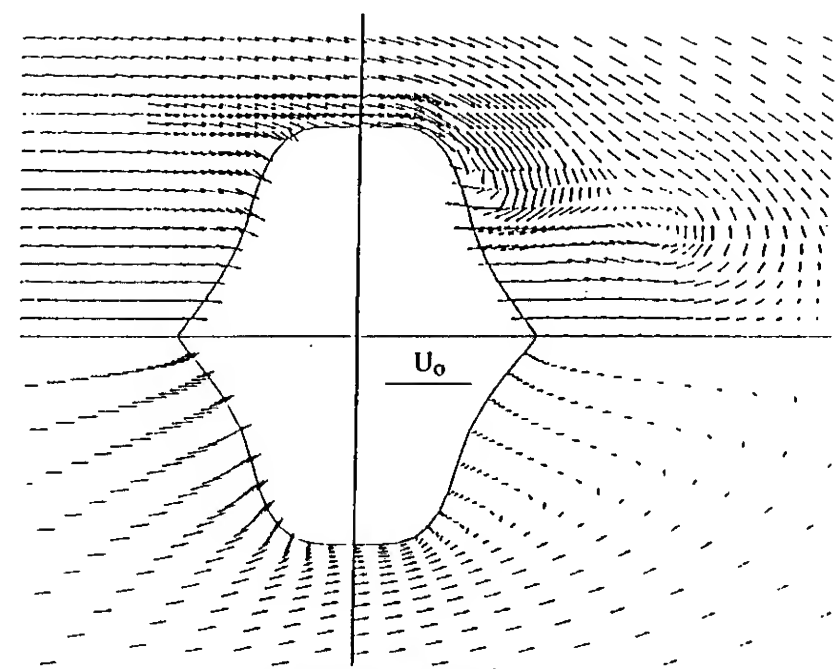


(c) Axial vorticity

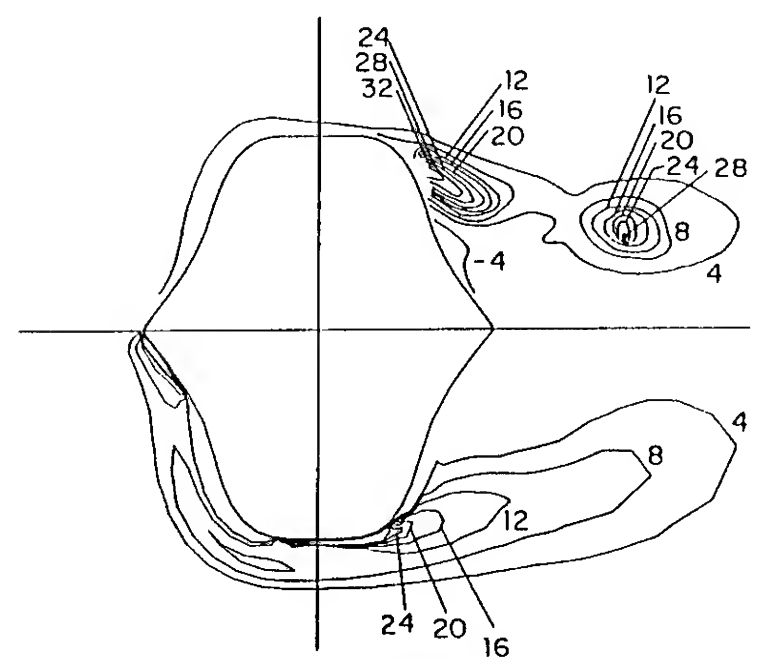
Figure 6. Velocity field and axial vorticity on SR107 at  $x/L = 0.7$



(a) Axial velocity



(b) Transverse velocity



(c) Axial vorticity

Figure 7. Velocity field and axial vorticity on SR107 at  $x/L = 0.9$

# A Numerical Study of Three-Dimensional Viscous Interactions of Vortices with a Free Surface

D. Dommermuth (Science Applications International Corporation, USA)

D. Yue (Massachusetts Institute of Technology, USA)

## ABSTRACT

We develop semi-implicit and explicit numerical methods for the *direct* simulation of the three-dimensional Navier-Stokes equations with a free surface. The efficiency of a novel multigrid flow solver permits the simulation of three-dimensional flows with free surfaces at low Reynolds and Froude numbers. The numerical schemes are used to study vortex rings and tubes interacting with walls and free surfaces.

In the case of vortex rings interacting with a no-slip wall our observations of the formation of secondary and tertiary vortex rings agree qualitatively with experimental measurements. When a free surface is present, the results are sensitive to the Froude number. For sufficiently low Froude numbers, the free surface behaves like a free-slip wall, which agrees qualitatively with experimental observations of vortex rings interacting with clean free surfaces. At intermediate Froude numbers, the normal incidence of a vortex ring with a clean free surface results in the formation of secondary vortex rings.

Numerical studies of vortex tubes interacting with free surfaces show two possible mechanisms for the reconnection of vorticity with a free surface including primary and secondary vorticity reconnections. One type of primary vorticity reconnection should result in a cusp pattern on the free surface and secondary vorticity reconnections should manifest themselves as paired dimples on the free surface. The essential stages of the reconnection of secondary vorticity with the free surface are as follows: generation of helical vortex sheets by the primary vortex tube, stripping of the helical vortex sheets due to self-induced straining flows, attachment of the helical vortex sheets to the separated

free-surface boundary layer, wrapping of U-shaped vortices around the primary vortex tube, feeding of boundary-layer vorticity into the U-vortices, and reconnection of U-vortices with the free surface. We provide evidence which suggests that the striations that may be observed on the free-surface above a pair of trailing tip vortices are caused by helical vorticity.

## 1 Introduction

In the field of free-surface hydrodynamics few things are as complex as the wave and viscous wakes of ships. Consider the region downstream of a moving ship where the steady wave pattern of Kelvin waves is located. This wave pattern is composed of two wave systems which move steadily with the ship: the transverse and diverging waves. The transverse waves are normal to the ship track, and the diverging waves obliquely intersect the ship track. These two wave systems are bounded by the cusp line which occurs at an angle of about  $\pm 19.5^\circ$  off the ship track. Most of the steady waves disperse linearly, but if the conditions are right, rays of the diverging waves that are inside of the cusp lines may evolve into solitons (Brown, *et al*, 1988).

In addition to the Kelvin waves, there is also a small sector centered near the ship track that contains short unsteady waves. Some possible sources of these short unsteady waves include breaking waves and turbulence generation near the ship. Munk, *et al*, (1987) hypothesize that Bragg scatter from these short unsteady waves is responsible for the narrow V-shaped features that are observed in Synthetic Aperture Radar (SAR) images of ship wakes in very calm seas. The viscous turbulent wake, which is also located near the ship track,

has a thrust component that is associated with the propeller(s) and a drag component that is due to the ship hull. Axial vortices that are generated in the bow region (Baba, 1969; Mori, 1984; and Takekuma & Eggers, 1984)) and helical vortices that are shed by the propeller (Kerwin, 1986) are embedded in the turbulent wake. Field observations of ships suggests that bubbles rising through the turbulent wake transport surfactant material to the free-surface (Kaiser, *et al*, 1986). These bubbles appear to be entrained by the bow wave, but other sources include propeller cavitation. Slicks consisting of compacted surfactant material form on each side of the ship track possibly due to the action of vortices moving surface water away from the viscous wake's center. These slicks damp capillary and gravity-capillary waves that cross the ship track (Dorrestein, 1951) and may contribute to the persistent centerline feature that is observed in SAR images (Lyden, *et al*, 1988). Clearly, ship wakes are very complex, and there are many mechanisms that affect direct and remote observations of ship wakes.

Faced with such a diversity of phenomena, we have chosen to focus on a very specialized portion of the problem. Specifically, we are interested in modeling the viscous interaction of vorticity with a free surface. Vortices may generate and modulate short unsteady surface waves and thus affect the observable features. Two sources of vortical flows include turbulent bow-wave breaking (Baba, 1969) and lifting devices (propellers, rudders, & hydrofoils). In addition, coherent vortical structures may also occur in the viscous turbulent wake (Brown & Roshko, 1974, and Roshko, 1954). The three-dimensional interactions of these flow fields with the free surface are very complicated, but it is our hope that simple models will provide much needed insight. Some simple models of the large-scale vortical flows that occur in ship wakes include two-dimensional vortex pairs, ring vortices, and three-dimensional vortex tubes. Even these simple models are so complicated that they challenge our basic understanding of vortex interactions with free surfaces.

As an initial step toward understanding the interactions of ship-scale vortices with a free surface, we consider the direct simulation of the Navier-Stokes equations with a free surface at a finite Froude number. Although the Reynolds numbers that we are able to simulate so far are considerably be-

low those observed in reality, our three-dimensional method is capable of modeling physical phenomena that are simply not possible using inviscid approaches. A notable example is the reconnection of vortex tubes, which is an inherently viscous phenomena. Moreover, extensions to our method may eventually allow us to study the effects of turbulence, air entrainment, and surfactants.

We can partially classify vortical flows near a free-surface in terms of Reynolds, Froude, and Weber numbers. As our velocity scale, we use the centerline velocity of a vortex pair,  $U_c = 2\Gamma/\pi s$ , where  $\Gamma$  is the circulation and  $s$  is the span. In correspondence with this velocity, the length scale is the half span,  $L = s/2$ , and for ring vortices the ring radius is used. Based on these scales, the Reynolds number is  $Re = \Gamma/\pi\nu$ , where  $\nu$  is the kinematic viscosity; the Froude number is  $Fr = \Gamma/\pi g^{1/2}(s/2)^{3/2}$ , where  $g$  is gravity; and the Weber number is  $We = 2\rho\Gamma^2/\pi^2 sT$ , where  $\rho$  is the fluid density and  $T$  is the surface tension. Although surface contamination plays a very important role in the interaction of vorticity with free surfaces, this effect is difficult to quantify and model, and has not been considered so far in the present simulations. We note that the hydrodynamics of ship-scale surfactant films are discussed by Peltzer, *et al*, (1990) in this proceedings. In addition, Hirs, *et al*'s (1990) experimental and numerical studies of two-dimensional vortex pairs, which also appears in this proceedings, provides a preliminary model of surfactant films.

As preparation for our literature review of vortices interacting with free surfaces, we also discuss the related problems of vortex interactions with no-slip walls and the stability and reconnection of vortex tubes. We conclude our introductory section with a review of numerical methods for simulating the incompressible Navier-Stokes equations. In Sec. 2 we provide the mathematical formulation for describing the viscous interactions of three-dimensional vortices with free surfaces, and in Sec. 3 we discuss the numerical implementations of our theory. In Sec. 4 we apply our numerical methods to three problems: 1) ring vortex interactions with a wall, 2) ring vortex interactions with a free surface, and 3) vortex tube interactions with a free surface. In Sec. 5 we discuss the long-term directions and promise of this line of research.

## 1.1 Interaction of Vortices with Walls

Harvey & Perry's (1971) studies of a wingtip vortex near a wall confirm observations of aircraft vortices bouncing off the ground. They argue that the rebound effect may be attributed to unsteady boundary-layer separation and the formation of secondary vortices. Their experimental measurements show that motion of a vortex moving parallel to a wall may be stopped or even reversed due to viscous and inviscid interactions. Inviscid effects alone are ruled out by Saffman (1978), who proves that a vortex pair normally incident to a wall in an inviscid fluid will monotonically approach the wall and then separate apart due to the velocity induced by themselves and their images. Walker's (1978) two-dimensional computations show that explosive boundary-layer growth is possible, but his boundary-layer theory is not capable of modeling the formation of secondary vortices. Peace & Riley's (1983) two-dimensional Navier-Stokes simulations show substantial growth of the boundary layer, but their Reynolds numbers ( $Re = O(10)$ ) are too low for secondary vortex formation to occur.

Walker, *et al*'s (1986) studies of vortex rings normally incident to a wall exhibit many of the same phenomena as two-dimensional vortices. An important difference is that ring vortices may stretch. According to inviscid theory, a ring vortex approaching a wall will expand radially outward and the diameter of its core will decrease. However, the experimental results of Walker, *et al*, and others (see Cerra & Smith, 1983) show much more complexity including boundary-layer separation, secondary and tertiary vortex formation, rebounding, azimuthal instabilities, and transition to turbulence. For  $Re \leq 250$ , no secondary vortices are observed and the primary vortex rapidly diffuses while being held fixed against the wall. Flow separation and secondary vortex formation occur for  $Re > 250$ . For  $Re \geq 3000$ , Walker, *et al*, have difficulties producing laminar vortex rings. They also perform boundary-layer calculations which once again show explosive growth of the boundary layer, but fail to predict the formation of secondary and tertiary vortices.

As a prelude to our study of vortex ring interactions with a free-surface, we have chosen to simulate the interactions of a vortex ring with a wall because Walker, *et al*'s (1986) documentation permits

qualitative validation of our Navier-Stokes computer code. In addition, the comparisons between vortex ring interactions with walls and free surfaces are very useful. Our numerical simulations for the wall case show the formation of secondary and tertiary vortex rings. In fact, the primary vortex ring is wrapped in a sheath of counter-sign vorticity. Initially, a sharp gradient, which diffuses with time, exists between the primary vortex and the shed vortices. Despite the appearance of rapid dissipation, however, the kinetic energy of these no-slip wall simulations does not decrease significantly more rapidly than our simulations with a free-slip wall.

## 1.2 Stability and Reconnection of Vortex Tubes

Spreiter & Sacks (1951) show that the trailing wake shed from an elliptically loaded wing will roll up into a pair of trailing vortices. The span of the trailing vortices in terms of the original span of the foil ( $L_s$ ) is  $s = \pi L_s/4$ , and the core radius, assuming constant strength, is  $r_c = 0.0985s$ . This trailing vortex pair is unstable to sinusoidal disturbances along the length of the tube (Crow, 1970). The wavelength of the instabilities ( $\lambda_{crow}$ ) in terms of the span are  $\lambda_{crow} \approx 8.6s$ , and the e-folding time of the instability is  $t_{crow} = 1.21T_i$ , where  $T_i = 2\pi s^2/\Gamma$  is the time it takes the vortices to move one span length due to their own induction.

Leonard (1985) indicates that large changes in the curvature of a vortex tube may lead to the rapid formation of helical vortex lines and even vortex breakdown. The exponential growth of helical vorticity is related to unstable perturbations of the vortex core in the presence of straining fields. The two-dimensional numerical simulations of Dritschel (1989) suggest that in addition to causing the initial instability, the straining flows may also strip the helical vortices away from the primary vortex. According to Leonard's (1985) review, once the helical vortices are formed, the axial flows that are induced by the helical vortices may tend to straighten the primary vortex tube.

As Crow (1970) notes, trailing vortex tubes that have gone unstable may eventually join to form crude vortex rings in the late stages of the instability. This process of reconnection is also observed in the vortex ring experiments of Kambe



& Takao (1971), Fohl & Turner (1975), Oshima & Asaka (1977), Schatzle (1987), and Oshima & Izutsu (1988). The observations in these experiments seem to indicate that vortex reconnection takes place as a result of cancellation of vorticity as two oppositely signed vortex tubes intersect. Melander & Hussain's (1988) cut-and-connect model of vortex reconnection (1988), which is based on spectral simulations of anti-parallel vortex tubes, describes vortex reconnection in three stages:

1. *Inviscid induction.* Self-induced velocities cause the vortex cores to approach each other and form a contact zone. The vortex cores flatten and stretch to form a dipole cross-section.
2. *Bridging.* Vorticity is annihilated in the contact zone and bridges of cross-linked vortex lines form at both ends of the contact zone. The bridges are orthogonal to the positions the vortex tubes had prior to contact.
3. *Threading.* Remnants of the original vortex tubes form between the bridges as the vortex tubes pull apart.

Numerical studies of vortex ring reconnections include Winckelmans & Leonard's (1989) vorton method, Chamberlain & Liu's (1985) finite-difference methods, and Kida, Takaoka, & Hussain's (1989) three-dimensional spectral methods. A notable feature of Chamberlain & Liu's finite-difference scheme is their use of multi-pole expansions to specify a radiation condition.

According to Helmholtz theorems vortex filaments cannot begin or end within a fluid (inviscid or viscous) because the vorticity field is solenoidal. In addition Kelvin's circulation theorem states that vortex filaments move as material lines and cannot be broken in an inviscid fluid. As a result vortex reconnection is an inherently viscous phenomenon. Siggia & Pumir's (1987) analysis of vortex filaments suggests that reconnection should take place on viscous time scales, as one might expect. However, Meiron, *et al*, (1989) provide numerical and theoretical evidence that the reconnection process occurs on nearly convective time scales. Their arguments are supported by Kwon's (1989) experimental studies of vortex rings connecting with free surfaces which show no time dependence as a function of Reynolds number.

The experiments of Sarpkaya & Henderson (1984) and Sarpkaya (1986) indicate that Crow instabilities can develop in the trailing wakes of deeply submerged hydrofoils. Our own Navier-Stokes simulations of a sinusoidally perturbed vortex tube moving parallel to a free surface show that reconnection of the primary vortex tube with the free surface is possible even if the computational domain is too short to permit Crow instability to occur. Based on the experimental evidence, we may speculate that the preferred wavelength of primary vortex reconnection corresponds to a Crow instability, but as shown by our own numerical simulations Crow instabilities are not a necessary condition for the connection of primary vorticity with the free surface.

Our numerical simulations also indicate that the generation of helical vorticity plays an essential role in the reconnection of secondary vorticity with the free-surface. Instabilities in the primary vortex tube appear to be the source of helical vorticity. Once the helical vorticity is formed it merges with the secondary vorticity that is separated from the free-surface boundary layer by the primary vortex tube. This merging process eventually leads to the formation of U-shaped vortices that are wrapped around the primary vortex tube. The U-vortices may connect with the free surface at their bases or tips.

### 1.3 Interaction of Vortices with Free-Surfaces

Madnia & Bernal's (1989) experimental studies of jet flows interacting with free surfaces show that the interactions of vorticity with the free surface may generate short unsteady waves. They find that surface waves are generated as vortical structures in the jet approach the free surface. Far downstream the surface motions are caused by large-scale vortical structures interacting directly with free surface. They also observe that vortex lines connecting with the free surface are common far downstream. The early development of the near-surface jet itself is studied experimentally by Liepmann (1990). During the transition phase from laminar to turbulent flow, submerged and near-surface jets convert azimuthal vorticity (vortical rings) into streamwise vorticity. His experiments show that the presence of a free surface accelerates the formation of streamwise vorticity.

Sarpkaya, *et al*, (1988) use experiments and numerical simulations to study the normal incidence of a two-dimensional vortex pair with the free surface. A novel counter-rotating plate arrangement is used during the experiments to generate vortex pairs. For their numerical simulations the vortex pair is modeled using two point vortices and line vortices are used to model the free surface. Numerical results and experiments are presented for two Froude numbers,  $F_r = 6.4$  &  $2.8$ . The Reynolds numbers are not provided. For low Froude numbers ( $F_r < 0.8$ ), the experiments indicate that the free-surface acts like a free-slip wall, and the vortex centers spread apart. A scar (a dip in the free-surface elevation) appears in front of each vortex and moves with the vortex. At higher Froude numbers, both experiments and simulations show that a hump of fluid rises above the vortex pair. The vortex pair subsequently spreads apart before diffusing due to turbulence.

Telste's (1989) numerical studies of the interaction of two point vortices with a free surface suggest that vortices translating beneath a free surface will not generate significant wavetrains at low Froude numbers,  $F_r < 0.5$ . For higher Froude numbers Telste's results indicate that wave breaking may inhibit the outward expansion of the vortex pair. For  $F_r \approx 6.4$  the point vortices entrain themselves in a hump of fluid that is located entirely above the mean position of free surface. Telste's numerical simulations indicate that the hump would eventually collapse on top of itself. For an intermediate Froude number ( $F_r \approx 2.0$ ), steep wave troughs form on each side of a small hump of fluid. The curvature of the wave troughs is so high that wave breaking appears to be imminent.

Willmarth, *et al*, (1989) also study the normal incidence of a two-dimensional vortex pair with a free surface. They compare experimental results to the predictions of an inviscid theory which uses dipole sheets to represent the free surface and the vortex pair. They report their Froude number as  $F_r = 2.2$ , and we estimate their Reynolds and Weber numbers as  $Re \approx 5,600$  and  $We \approx 60$ . As the Kelvin oval (the volume of fluid entrained by the vortex pair) rises upward, the free surface forms an upwelling that is centered above the vortices. Two sharp troughs form at the edges of the upwelling. The vortex pair rises slightly into the upwelling and then sinks as the upwelling springs back. Yu & Tryggvason (1990), call this phenomena, which de-

pends on the Froude number, an inviscid rebounding effect. Although the flow field induced by the vortex pair becomes turbulent during the experiment, Willmarth, *et al*, do not report observing the formation of secondary vortices.

Ohring & Lugts' (1989) numerical studies of the viscous interactions of two-dimensional vortex pairs with a free surface indicate that secondary vortices form at low Froude numbers. They use the method of artificial compressibility with a generalized coordinate system to solve the Navier-Stokes equations. They consider two cases with very low Reynolds numbers ( $Re < 20$ ) and intermediate Froude numbers ( $F_r \approx 0.3$  &  $1.0$ ). Surface tension effects are not modeled, but exact boundary conditions on the free surface are otherwise specified. For the high Froude number result, the vortex pair entrains itself in the upwelling, and a patch of counter-sign vorticity develops at the base of the upwelling where there is high curvature. At the low Froude number, the height of the upwelling is significantly reduced and the vortex pair splits apart upon impact with the free surface. Secondary vortices form and partially wrap themselves around the primary vortex, but the Reynolds number is so low that the vortices lose too much energy for significant inviscid interactions to take place.

The normal and oblique incidence of vortex rings with a free surface has been studied experimentally by Kwon (1989). Kwon generates laminar vortex rings with Reynolds numbers,  $600 \leq Re \leq 3200$ , and Froude numbers,  $0.14 \leq F_r \leq 0.32$ . We estimate that his Weber numbers are  $0.5 \leq We \leq 5$ . Kwon documents single and double reconnections at oblique angles of incidence. According to Kwon the reconnection time depends on the angle of incidence but not the Reynolds number.

The experiments of Sarpkaya & Henderson (1984) (see also Sarpkaya, 1986) show that trailing vortices shed by wings may interact with free surfaces to form striations and scars. The striations occur during the initial phases of the interaction and are normal to the wing's track. The scar features form after the striations, and they are parallel to the wing's track. The scars appear to be localized free-surface disturbances which move with the vortices. The early development of the scars is similar to the free-surface upwellings and the steep wave troughs that have been already discussed. In the later stages of the flow, dimples form in the scar region due to normal vorticity connecting with the



free surface. They observe that Crow instabilities can occur for deeply submerged wings, which often leads to the connection of vortices with the free surface and a crescent shaped disturbance on the free surface. The nondimensional parameters (in our notation) which characterize their experiments are as follows:  $7,000 \leq R_e \leq 21,000$  and  $0.3 \leq F_r \leq 1$ . Based on this data, we also estimate that  $10 \leq W_e \leq 100$ . In this parameter regime, Sarpkaya (1986) states that the free-surface signatures are not sensitive to changes in the Reynolds and Froude numbers. Sarpkaya claims further that the influence of capillary waves on his free-surface signatures is very small, although no experimental evidence is offered.

In contrast to the results of Sarpkaya's experiments, Bernal, *et al*, (1989) and Kwon (1989) report that the presence of surface active agents on free surfaces strongly influences the interaction of ring vortices with free surfaces. They find that the motions of a vortex ring normally incident to a contaminated free surface are similar to the motions caused by a no-slip wall. Secondary and tertiary vortices are shed, and the primary vortex rebounds. For a cleaner free surface they find that the shed vortices are weaker and the radial expansion of the primary vortex is greater. They report  $R_e \approx 1200$  and  $F_r \approx 0.09$ , and we estimate  $W_e \approx 0.9$ . These physical parameters are less than Sarpkaya's (1986) and may explain why Sarpkaya's observations differ from Bernal, *et al*, in regard to the influence of surface contamination on surface signatures. Bernal, *et al*, (1989), also report preliminary experiments with delta wings towed beneath a free surface. They observe what appears to be a Reynolds ridge, which is the flow region beneath a stagnant film on the water surface (see Scott, 1982). According to them, the scar features that are observed by Sarpkaya may in fact be Reynolds ridges. Interestingly, Grosenbaugh & Yueng (1988) report that surface contamination strongly influences the onset of turbulence in the bow waves of model ships. They describe a stagnant zone which causes the free surface to separate farther upstream than it would in the absence of surface contamination. This description fits Scott's definition of a Reynolds ridge.

As one example of the range of scales that are possible for full-scale ships, consider a lightly-loaded foil traveling slightly below and parallel to the free surface. For negative lift, the trail-

ing tip vortices will rise upward. We assume a long span,  $s=O(10\text{m})$  and a low circulation,  $\Gamma = O(1\text{m}^2/\text{s})$ . In our notation we have then relatively high Reynolds numbers ( $R_e \approx 10^5$ ), low Froude numbers ( $F_r \approx 10^{-2}$ ), and high Weber numbers ( $W_e \approx 10^3$ ). This parameter regime is far outside the numerical simulations and laboratory experiments that we have reviewed in this section. The impact of this mismatch is not clear. We note that our own numerical simulations of vortex interactions with a free surface are near the appropriate Froude numbers, but our Reynolds numbers ( $R_e = O(10^3)$ ) are too low. Hopefully, the three-dimensional flow phenomena that we observe at these low Reynolds numbers capture some of the important features of flows at much higher Reynolds numbers. We emphasize that inviscid approximations are inadequate because the salient features of vortex interactions with a free surface such as boundary-layer formation and vortex reconnections are fundamentally viscous.

Having noted these limitations, we now proceed to summarize the free-surface phenomena that we observe in our direct numerical simulations of the Navier-Stokes equations. Our numerical studies of vortex rings interacting with a free surface show that secondary vortex rings may be torn away from the free-surface boundary layer at intermediate Froude numbers, and at lower Froude numbers the free surface acts like a free-slip wall. Our numerical simulations at low Froude numbers agree qualitatively with the vortex ring experiments of Bernal, *et al*, (1989) and Kwon (1989). Our studies of vortex tubes illustrate two possible mechanisms for the reconnection of vorticity with a free surface including primary and secondary vorticity reconnections. The free-surface signatures of these two mechanisms are distinctly different. One type of primary vorticity reconnection should result in a cusp pattern on the free surface, and secondary vorticity reconnection should manifest itself as paired dimples on the free surface. These numerical experiments show that the generation of helical vortices is an initial stage in the reconnection of the secondary vorticity with the free surface, and our simulations also suggest that the striations that may be observed in the wakes of trailing tip vortices are caused by the interaction of the helical vorticity with the free-surface boundary layer.

## 1.4 Numerical Methods

A very general method for the direct simulation of the incompressible Navier-Stokes equations with free-surface effects is the MAC (Marker-And-Cell) method (see Hirt, *et al*, 1975). MAC methods are distinguished from other numerical methods by their technique for solving for the pressure, treatment of the convective terms, formulation on a staggered grid, and capability for particle tracing. MAC methods enforce mass conservation by solving a Poisson equation for the pressure. The MAC equation for the pressure retains temporal and spatial derivatives of the dilation term ( $\nabla \cdot \vec{u}$ ) to inhibit the growth of numerical errors, and the convective terms in the momentum equations are calculated using a combination of upwinding and central differencing. The MAC time integrator without the upwinded terms is similar to the explicit FTCS (Forward Time Central Space) method (Roache, 1976).

As evidenced by the application of the MAC technique to a wide range of problems including nonlinear ship wave problems (see Miyata & Nishimura, 1985), the MAC method is useful for determining qualitative features of very complicated free-surface flows. For simple geometries the high accuracy of spectral methods relative to finite-difference methods has proven to be very desirable. A good example is Orszag & Patterson's (1972) direct simulation of homogeneous and isotropic turbulence using Fourier series. In theory Patera's (1984) spectral element method allows complex geometric modeling with spectral accuracy, but in practice general three-dimensional problems have not been very accommodating. As a result, low-order finite-difference methods with high resolution appear at this moment to be more robust than spectral methods.

The MAC and FTCS methods are subject to stringent stability criteria because of their use of explicit time integrators, and as a result, several semi-implicit schemes have been proposed for overcoming this deficiency, including SIMPLE (Patankar & Spalding, 1972), SIMPLER (Patankar, 1981), PISO (Issa, 1985), and the Finite-Analytic method (Chen & Chen, 1982). These four methods solve the momentum equations for the velocities and the Poisson equation for the pressure separately, and iterations are used to strongly couple the velocities with the pressures. An interest-

ing feature of Chen & Chen's method is their use of locally analytic solutions to solve the Navier-Stokes equations. They claim that this technique gives superior modeling of the convective terms without incurring a numerical diffusion penalty. However, the Finite-Analytic method requires significantly more memory without improving the second-order spatial accuracy of more conventional finite-difference methods.

In contrast to these iterative solution procedures, Kim & Moin's (1985) fractional step method uses only one iteration to couple the velocity field with the pressure field to maintain a divergence-free flow. Note that Kim & Moin, just like Ghia, *et al*, (1977), use Neumann boundary conditions in the Poisson equation for the pressure, and as a result, they must satisfy a numerical solvability condition. Kim & Moin are able to achieve second-order accuracy in time by using an explicit Adams-Bashforth scheme for the convective terms and an implicit Crank-Nicholson scheme for the viscous terms. Although Kim & Moin's hybrid time-integrator eliminates time-step restrictions due to viscosity, their numerical scheme must still meet a Courant condition because of their explicit treatment of the convective terms.

A fully-implicit scheme has been devised by Hartwich & Hsu (1988) who uses Chorin's (1967) artificial compressibility method as a framework. Chorin's method inserts a time-dependent pressure term in the mass-conservation equations, and as the solution nears steady-state, the pressure term drops out. This artifice permits the use of advanced compressible flow techniques (*e.g.*, Warming & Beam, 1978). In addition, the technique can be generalized to time-dependent problems. Other researchers including Brandt & Dinari (1977), Fuchs & Zhao (1984), Vanka (1986), and Thompson & Ferziger (1989) solve the incompressible equations implicitly. Typically, these implicit primitive-variable solution schemes use block Gauss-Seidel iterations to drive the divergence to zero, and multigrid methods are used to accelerate the solution procedure. The block in lieu of point Gauss-Seidel solvers are necessary because the finite-difference approximations to the mass-conservation equation are not diagonally dominant.

So far we have limited our discussions to the primitive-variable formulation of the Navier-Stokes equations. The widespread use of vorticity formu-

lations also warrant a discussion. More comprehensive reviews of vortex methods can be found in Saffman & Baker (1979) and Leonard (1980 & 1985). There are two main vorticity formulations: vortex element methods which use line and sheet singularities and finite-difference approximations of the vorticity-stream function equations. Vortex element methods are ideally suited for simulating small regions of rotational flow such as isolated vortex tubes (Leonard, 1985) and sharp density interfaces (Dahm, Scheil, & Tryggvason, 1989). Generally, large core deformations and viscous phenomena are not modeled well by three-dimensional vortex element methods, but Winckelmans & Leonard (1989) have developed a vorton (vortex sticks) method to study the initial stages of vortex reconnection. Finite-difference approximations to the vorticity-stream function equations do allow large core deformations with strong viscous interactions, but boundary conditions other than free-slip boundary conditions are difficult to implement in three dimensions. We note that vortex methods are continually being improved and their range of application will certainly increase with time.

Regardless of what formulation is used to simulate the incompressible Navier-Stokes equations, implicit schemes are traditionally used for rapidly attaining steady-state solutions and explicit schemes for simulating time-dependent flows. Explicit schemes are not used to reach steady state because they require too many time steps, and implicit schemes are not used for time-dependent problems because they are computationally more intensive and the time steps are so small based on accuracy considerations that stability is often not a problem for explicit schemes. In some special cases of time-dependent flows, such as creeping flows and capillary waves, implicit schemes are used because the stability limits of explicit schemes are too restrictive.

In this paper, we present a second-order explicit method and a first-order semi-implicit method for solving the three-dimensional Navier-Stokes equations in primitive-variable form with and without free surfaces. The unconditional stability of the semi-implicit scheme is useful for obtaining steady-state solutions, and the accuracy of the explicit scheme is desirable for time-domain problems. In both numerical schemes the effects of numerical viscosity are reduced to a minimum by

using central differencing. The nonlinear momentum equations in the implicit scheme are solved using Newton-Raphson linearization and multigrid iteration. We also use multigrid iteration to solve the Poisson equations for the pressures in both time-stepping procedures. The convergence properties of the numerical schemes are demonstrated for three test problems: (1) the axisymmetric stagnation flow against a wall, (2) the viscous attenuation of an axisymmetric standing wave, and (3) the translation and diffusion of a two-dimensional vortex. The numerical schemes are used to study several physical problems including vortex rings and tubes impacting walls and free surfaces.

## 2 Mathematical Formulation

### 2.1 Field Equations

We consider the unsteady incompressible viscous flow of a Newtonian fluid under a free surface. For an isotropic and homogeneous fluid, the Navier-Stokes equations for conservation of momentum have the form:

$$\vec{u}_t + (\vec{u} \cdot \nabla) \vec{u} = -\nabla p + \frac{1}{Re} \nabla^2 \vec{u}, \quad (1)$$

where  $\vec{u} = \vec{u}(x, y, z, t) = (u, v, w)$  is a three-dimensional vector field. Note that the momentum equations have been normalized based on a length scale  $L$  and a velocity scale  $U$ .  $Re = UL/\nu$  is the Reynolds number where  $\nu$  is the kinematic viscosity. In addition, we have defined  $p$  as the hydrodynamic pressure:

$$p = P - \frac{1}{Fr^2} z, \quad (2)$$

where  $P$  is the total pressure which is equal to the sum of the hydrodynamic plus hydrostatic pressures. The pressure terms are normalized by  $\rho U^2$  where  $\rho$  is the density.  $Fr^2 = U^2/gL$  is the Froude number. The vertical coordinate  $z$  is positive upward, and the origin is located at the mean free surface. The dynamic pressure may be interpreted as a Lagrange multiplier which projects the velocity field onto a divergence-free field as expressed by the mass-conservation equation:

$$\nabla \cdot \vec{u} = 0. \quad (3)$$

The pressure field itself does not require boundary conditions or initial conditions, but a well-posed initial-boundary-value problem does require these conditions for the velocities. Note, however, that the field equations and boundary conditions for the velocity field can be used to deduce the initial pressure and the behavior of the pressure near the boundaries. For example, the divergence of the momentum equations (eqts. 1) used in combination with the mass-conservation equation (eqt. 3) may be used to derive a useful Poisson equation for the pressure. This equation expressed in indicial notation is as follows:

$$\nabla^2 p = -\frac{\partial u_j}{\partial x_i} \frac{\partial u_i}{\partial x_j} . \quad (4)$$

Similarly, the momentum equations may also be used to prescribe the normal derivative of the pressure on the boundaries of the fluid. Thus, according to the divergence theorem the pressure is subject to the following solvability condition:

$$\int_S \frac{\partial p}{\partial n} = - \int_V \frac{\partial u_j}{\partial x_i} \frac{\partial u_i}{\partial x_j} , \quad (5)$$

where  $V$  is a volume of fluid,  $S$  is the surface bounding the volume, and  $n$  is the unit outward-pointing normal on that surface.

For the velocities, we are required to specify the initial velocity field:

$$\vec{u} = \vec{u}_o(x, y, z) \quad \text{at } t = 0 . \quad (6)$$

According to Helmholtz's theorem, we can express this initial vector velocity field  $\vec{u}_o$  in terms of scalar  $\phi_o$  and vector  $\vec{\psi}_o = (\psi_x, \psi_y, \psi_z)_o$  velocity potentials:

$$\vec{u}_o = \nabla \phi_o + \nabla \times \vec{\psi}_o . \quad (7)$$

The initial velocity field, like the time-dependent velocity field, is required to be solenoidal. Therefore, we can show that by taking the divergence of equation (7) that  $\phi_o$  satisfies Laplace's equation:

$$\nabla^2 \phi_o = 0 . \quad (8)$$

Here,  $\phi_o$  may represent the effects of currents, the disturbances of surface-piercing and submerged bodies, etc. A similar Poisson equation is satisfied

by the vector potential  $\vec{\psi}_o$  in terms of the initial vorticity field  $\vec{\omega}_o$ :

$$\nabla^2 \vec{\psi}_o = -\vec{\omega}_o , \quad (9)$$

where  $\vec{\omega} = (\omega_x, \omega_y, \omega_z)$  may be expressed in terms of the curl of the velocity field at any instant of time:

$$\vec{\omega} = \nabla \times \vec{u} . \quad (10)$$

Based on this definition, the vorticity field is itself a solenoidal quantity. In addition to posing initial conditions for the velocity field, we must also specify boundary conditions as discussed in the following sections.

## 2.2 Linearized Free-Surface Boundary Conditions

Let the free surface elevation be given by  $\eta(x, y, t)$ . We posit the presence of a viscous free-surface boundary layer scaled by  $\delta = O(R_e^{-1/2})$ . We obtain a linearization of the free-surface boundary conditions by assuming small surface slopes, i.e.,  $\eta_x$  &  $\eta_y = O(\epsilon) \ll 1$ , and consequently  $\eta$  is much smaller than the other length scales of the flow including  $\delta$ . Under these assumptions, the exact (nonlinear) field equations are still valid outside the boundary layer, but the nonlinear kinematic and dynamic free-surface boundary conditions (Wehausen & Laitone, 1960) reduce to:

$$\begin{aligned} u_z &= 0 \\ v_z &= 0 \\ -p + \frac{1}{F_r^2} \eta &= \frac{1}{W_e} (\eta_{xx} + \eta_{yy}) \end{aligned} \quad (11)$$

$$\eta_t + u\eta_x + v\eta_y = w , \quad (12)$$

where  $W_e = \rho U^2 L / T$  is the Weber number,  $\rho$  is the water density, and  $T$  is the surface tension, and the conditions are applied on  $z=0$ . The first set of equations (11) state that the shear stresses and normal stresses are zero on the free surface. Note that the kinematic free-surface condition (12) is still nonlinear in the flow variables and is obtained without otherwise requiring that the velocities be small.



### 2.3 Free-slip Wall Boundary Conditions

We next consider the case of a free-slip wall. This type of boundary condition is useful for imposing symmetry boundary conditions and modeling free-surfaces at low Froude numbers. By definition the tangential stresses and the normal flux are zero on a free-slip boundary. Therefore, the boundary conditions for the velocity on a free-slip plane at  $z = 0$  are:

$$u_z = 0, \quad v_z = 0, \quad \text{and} \quad w = 0, \quad (13)$$

where the first two equations give zero tangential stresses and the third equation states that there is no flux across the plane  $z = 0$ .

These boundary conditions for the velocities enable us to deduce the behavior on the free-slip wall of the pressure and vorticity, and also the initial conditions for the scalar and vector velocity potentials. For example, upon substitution of the boundary conditions (13) into the  $z$ -component of (1), we can show that  $p_z = 0$ , where the  $z$ -derivative of (3) has been used to eliminate the  $w_{zz} = 0$  term. Similar arguments may be used to show that the vorticity vector is always normal to a free-slip wall,  $\vec{\omega} = (0, 0, \omega_z)$  on  $z = 0$ . Finally, in regard to the initial conditions, we can derive the following relations for the vector velocity potential on the free-slip plane  $z = 0$ :

$$(\psi_x)_o = 0, \quad (\psi_y)_o = 0, \quad \frac{\partial(\psi_z)_o}{\partial z} = 0, \\ \text{and} \quad \nabla^2 \vec{\psi}_o = -(0, 0, (\omega_z)_o), \quad (14)$$

where we have assumed that the scalar velocity potential is initially zero,  $\phi_o = 0$ .

### 2.4 No-slip Wall Boundary Conditions

On a no-slip wall the velocity is zero:

$$\vec{u} = 0. \quad (15)$$

In general, the shear stresses are nonzero and as a result, boundary-layer formation and flow separation are possible. Certainly, the flow field near a no-slip wall is more complex than that for a free-slip wall, but it is still possible to deduce the behav-

ior of certain flow quantities near the wall. For example, suppose that a no-slip wall is located on the boundary  $z = 0$ , then the no-slip boundary conditions (15) and the mass-conservation equation (3) may be used to show  $w_z = 0$ . Also, substitution of the no-slip conditions into the  $z$ -component of momentum (1), gives the normal derivative of the dynamic pressure:

$$p_z = \frac{1}{R_e} w_{zz}. \quad (16)$$

A similar procedure may be used to show that the source term is zero in the Poisson equation for the pressure (4). Unlike a free-slip wall, the vorticity vector must be parallel to a no-slip wall,  $\vec{\omega} = (\omega_x, \omega_y, 0)$  on  $z = 0$ , and as a result a vortex tube cannot terminate normal to a no-slip wall. For a no-slip wall it is difficult to pose unique initial conditions and boundary conditions that are physically meaningful for the vector velocity potential. One method for eliminating this problem is to let the velocity be prescribed by free-slip boundary conditions at time  $t = 0$ , and then at time  $t = 0+$  set all velocity components equal to zero. As a result, a sheet of vorticity is instantaneously formed on the no-slip wall.

### 2.5 Conservation of Energy

The vector product of the velocity with the momentum equations (1) integrated over the fluid volume gives a formula for the conservation of energy, and the transport theorem in conjunction with divergence theorem may be used to simplify the resulting equations. In indicial notation the equation is as follows:

$$\frac{d}{dt} \int_V \frac{u_i u_i}{2} = \\ \int_S n_j u_i \left[ -p \delta_{ij} + \frac{1}{R_e} \left( \frac{\partial u_i}{\partial x_j} + \frac{\partial u_j}{\partial x_i} \right) \right] \\ - \frac{1}{R_e} \int_V \left( \frac{\partial u_i}{\partial x_j} + \frac{\partial u_j}{\partial x_i} \right) \frac{\partial u_i}{\partial x_j}, \quad (17)$$

where the first term represents the change in kinetic energy integrated over the material volume of the fluid ( $V$ ), the second term represents the work done by the stresses on the fluid boundaries ( $S$ ), and the last term equals the energy that is dissipated. ( $\delta_{ij}$  denotes the Kroenecker delta function.)

Note that the stresses do not do any work on slip and no-slip walls. Upon substitution of the exact free-surface boundary conditions into this energy equation, we may derive the following formula:

$$\begin{aligned} \frac{d}{dt} \int_V \frac{u_i u_i}{2} + \frac{1}{2F_r^2} \frac{d}{dt} \int_{S_f} \eta^2 = \\ - \frac{1}{We} \int_{S_f} \eta \left( \frac{1}{R_1} + \frac{1}{R_2} \right) \\ - \frac{1}{Re} \int_V \left( \frac{\partial u_i}{\partial x_j} + \frac{\partial u_j}{\partial x_i} \right) \frac{\partial u_i}{\partial x_j}, \end{aligned} \quad (18)$$

where the first term represents the change in kinetic energy, the second term the change in potential energy, the third term the work done by surface tension, and the last term the dissipated energy.  $S_f$  is the projection of the free-surface onto the  $xy$ -plane and  $R_1$  and  $R_2$  are the principal radii of curvature. Note that we have assumed that the work done by the stresses on all other boundaries besides the free surface is zero. If the free-surface elevation and slope are small, then the volume integrals are evaluated below the mean waterline ( $z = 0$ ) and the principal radii of curvature terms simplify to  $-(\eta_{xx} + \eta_{yy})$ .

### 3 Numerical Formulation

In this section we derive semi-implicit and explicit finite-difference schemes for direct simulation of the three-dimensional Navier-Stokes equations at low Reynolds numbers. (See Appendix A for an outline of the axisymmetric formulation.) We show how the initial velocity field is set up, and demonstrate the implementation of periodic, slip, no-slip, and free-surface boundary conditions. For periodic and/or wall boundary conditions a solvability condition for the pressure is also implemented. We then discuss the vectorization of a multigrid solution technique for solving the field equations. We conclude the numerical formulation section with stability analyses and validation studies. The validation studies include numerical simulations of axisymmetric stagnation flows, attenuation of axisymmetric standing waves, and translation and diffusion of two-dimensional vortices.

#### 3.1 A Semi-Implicit Time-stepping Scheme

We derive here a first-order semi-implicit scheme for solving the Navier-Stokes equations. The basic concept of our scheme is based on the PISO scheme (Issa, 1985) which updates the velocities independently of the pressure. We use Newton-Raphson iteration to solve the nonlinear Navier-Stokes equations, and we assume that the velocities for each implicit time step are equal to some known estimates plus some small corrections. Let superscript  $( )^n$  denote the  $n$ -th time step, and consider the perturbations of the velocities at the  $(n+1)$ -th time step as follows:

$$\begin{aligned} u^{n+1} &= U + \tilde{u} \\ v^{n+1} &= V + \tilde{v} \\ w^{n+1} &= W + \tilde{w}, \end{aligned} \quad (19)$$

where  $(u, v, w)^{n+1}$  are the unknown velocities at the next time step,  $(U, V, W)$  are the known estimates, and  $(\tilde{u}, \tilde{v}, \tilde{w})$  are the unknown errors. Note that for a fully-implicit scheme the hydrodynamic pressure would be expanded in a similar way. For our semi-implicit scheme the hydrodynamic pressure is always known in terms of the most recent estimate of  $(u, v, w)^{n+1}$ . In (19) we continuously update  $(u, v, w)^{n+1}$  until the desired accuracy has been achieved. First we estimate the fluid velocity at the  $(n+1)$ -th time step by letting  $(U, V, W) = (u, v, w)^n$ , and then we find the error terms,  $(\tilde{u}, \tilde{v}, \tilde{w})$ . Our improved estimate of the velocities is given as  $(u, v, w)^{n+1} = (U, V, W) + (\tilde{u}, \tilde{v}, \tilde{w})$  and the new pressure can be calculated based on these updated velocities. The Newton-Raphson iterations can stop at this point if the errors are small enough, or they may continue by letting  $(U, V, W)$  equal our new estimate of  $(u, v, w)^{n+1}$ , etc. Generally, only one to two iterations are necessary because the Newton-Raphson procedure has quadratic convergence.

Upon substitution of the perturbation expansions (19) into the momentum equations (1) and elimination of quadratic error terms, we derive the following set of linearized equations:

$$\begin{aligned} \tilde{u}_t + 2(\tilde{u}U)_x + (\tilde{u}V)_y + (U\tilde{v})_y + (\tilde{u}W)_z \\ + (U\tilde{w})_z - \frac{1}{Re} \nabla^2 \tilde{u} = U_{res} \end{aligned}$$



$$\begin{aligned} \tilde{v}_t + (\tilde{u}V)_x + (U\tilde{v})_x + 2(\tilde{v}V)_y + (\tilde{v}W)_z \\ + (V\tilde{w})_z - \frac{1}{R_e} \nabla^2 \tilde{v} = V_{res} \end{aligned} \quad (20)$$

$$\begin{aligned} \tilde{w}_t + (\tilde{u}W)_x + (U\tilde{w})_x + (\tilde{v}W)_y + (V\tilde{w})_y \\ + 2(\tilde{w}W)_z - \frac{1}{R_e} \nabla^2 \tilde{w} = W_{res}, \end{aligned}$$

where the unknown error terms are grouped on the left-hand side and  $(U_{res}, V_{res}, W_{res})$  is the known residual error vector given below:

$$\begin{aligned} U_{res} &= -U_t - (UU)_x \\ &\quad - (UV)_y - (UW)_z - p_x + \frac{1}{R_e} \nabla^2 U \\ V_{res} &= -V_t - (UV)_x \\ &\quad - (VV)_y - (VW)_z - p_y + \frac{1}{R_e} \nabla^2 V \\ W_{res} &= -W_t - (UW)_x \\ &\quad - (VW)_y - (WW)_z - p_z + \frac{1}{R_e} \nabla^2 W. \end{aligned} \quad (21)$$

In these equations for the residual errors, the hydrodynamic pressure is expressed in terms of the most recent estimate of  $(u, v, w)^{n+1}$ . Note that the equations for the error terms (20) and the residual errors (21) are expressed in conservation forms.

We solve the set of equations (20) and (21) for  $(\tilde{u}, \tilde{v}, \tilde{w})$  by using finite differencing. Let  $(\Delta x, \Delta y, \Delta z)$  be the unstaggered grid spacing along the  $x, y$ , and  $z$ -axes respectively, and let  $\Delta t$  be the time step. Also, let subscript  $(i, j, k)$  denote the indices of the grid points along the  $x, y$ , and  $z$ -axes respectively. We define the following finite-difference formulas:

$$\begin{aligned} \delta_x^+ F &= \frac{F_{i,j,k} - F_{i-1,j,k}}{\Delta x} \\ \delta_x^- F &= \frac{F_{i+1,j,k} - F_{i,j,k}}{\Delta x} \\ \delta_x^c F &= \frac{F_{i+1,j,k} - F_{i-1,j,k}}{2\Delta x} \\ \tilde{\nabla}^2 F &= \frac{F_{i+1,j,k} - 2F_{i,j,k} + F_{i-1,j,k}}{(\Delta x)^2} \\ &\quad + \frac{F_{i,j+1,k} - 2F_{i,j,k} + F_{i,j-1,k}}{(\Delta y)^2} \\ &\quad + \frac{F_{i,j,k+1} - 2F_{i,j,k} + F_{i,j,k-1}}{(\Delta z)^2}, \end{aligned} \quad (22)$$

where the first two difference formulas are first-order one-sided formulas for  $\partial/\partial x$ , the third formula is a second-order centered formula for  $\partial/\partial x$ , and the last formula is a second-order centered formula for the Laplacian operator. Similar formulas are written for the partial derivatives with respect to  $y$  and  $z$ .

We use upwind differencing in (20) to ensure diagonal dominance, and we use central differencing in (21) to reduce the effects of numerical damping. Since the final converged solution for  $(u, v, w)^{n+1}$  is central differenced, we are able to realize the efficiency of first-order upwind differencing without the numerical damping and the accuracy of second-order central differencing without the slow convergence.

We illustrate how to upwind a single convective term:

$$\begin{aligned} (\tilde{u}V)_y &= \frac{1}{2}(\tilde{u}(V + |V|))_y + \frac{1}{2}(\tilde{u}(V - |V|))_y \\ (\tilde{u}V)_y &\simeq \frac{\delta_y^+}{2}(\tilde{u}(V + |V|)) + \frac{\delta_y^-}{2}(\tilde{u}(V - |V|)) \\ (\tilde{u}V)_y &\simeq \frac{(\tilde{u}(V - |V|))_{i,j+1,k}}{2\Delta y} + \frac{(\tilde{u}|V|)_{i,j,k}}{\Delta y} \\ &\quad - \frac{(\tilde{u}(V + |V|))_{i,j-1,k}}{2\Delta y}. \end{aligned}$$

This upwinding scheme always contributes a positive element to the diagonal of the equation system. We use this upwinding procedure to discretize (20) as follows:

$$\begin{aligned} \frac{\tilde{u}_{i,j,k}}{\Delta t} + \delta_x^+ [\tilde{u}(U + |U|)] + \delta_x^- [\tilde{u}(U - |U|)] \\ + \frac{\delta_y^+}{2} [\tilde{u}(V + |V|)] + \frac{\delta_y^-}{2} [\tilde{u}(V - |V|)] \\ + \frac{\delta_y^+}{2} [\tilde{v}(U + |U|)] + \frac{\delta_y^-}{2} [\tilde{v}(U - |U|)] \\ + \frac{\delta_z^+}{2} [\tilde{u}(W + |W|)] + \frac{\delta_z^-}{2} [\tilde{u}(W - |W|)] \\ + \frac{\delta_z^+}{2} [\tilde{w}(U + |U|)] + \frac{\delta_z^-}{2} [\tilde{w}(U - |U|)] \\ - \frac{1}{R_e} \tilde{\nabla}^2 \tilde{u} = U_{res_{ijk}} \\ \frac{\tilde{v}_{i,j,k}}{\Delta t} + \frac{\delta_x^+}{2} [\tilde{u}(V + |V|)] + \frac{\delta_x^-}{2} [\tilde{u}(V - |V|)] \\ + \frac{\delta_x^+}{2} [\tilde{v}(U + |U|)] + \frac{\delta_x^-}{2} [\tilde{v}(U - |U|)] \end{aligned}$$

$$\begin{aligned}
& +\delta_y^+[\tilde{v}(V+|V|)] + \delta_y^-[\tilde{v}(V-|V|)] \\
& +\frac{\delta_z^+}{2}[\tilde{v}(W+|W|)] + \frac{\delta_z^-}{2}[\tilde{v}(W-|W|)] \quad (23) \\
& +\frac{\delta_z^+}{2}[\tilde{w}(V+|V|)] + \frac{\delta_z^-}{2}[\tilde{w}(V-|V|)] \\
& -\frac{1}{R_e}\tilde{\nabla}^2\tilde{v} = V_{res_{ijk}}
\end{aligned}$$

$$\begin{aligned}
& \frac{\tilde{w}_{i,j,k}}{\Delta t} + \frac{\delta_x^+}{2}[\tilde{u}(W+|W|)] + \frac{\delta_x^-}{2}[\tilde{u}(W-|W|)] \\
& +\frac{\delta_x^+}{2}[\tilde{w}(U+|U|)] + \frac{\delta_x^-}{2}[\tilde{w}(U-|U|)] \\
& +\frac{\delta_y^+}{2}[\tilde{v}(W+|W|)] + \frac{\delta_y^-}{2}[\tilde{v}(W-|W|)] \\
& +\frac{\delta_y^+}{2}[\tilde{w}(V+|V|)] + \frac{\delta_y^-}{2}[\tilde{w}(V-|V|)] \\
& +\delta_z^+[\tilde{w}(W+|W|)] + \delta_z^-[\tilde{w}(W-|W|)] \\
& -\frac{1}{R_e}\tilde{\nabla}^2\tilde{w} = W_{res_{ijk}} ,
\end{aligned}$$

where a first-order Euler scheme is used to approximate the time derivative terms. Note that by definition there are no errors in the velocities at the  $n$ -th time step, and so only one term is required to approximate each time derivative of  $(\tilde{u}_{i,j,k}, \tilde{v}_{i,j,k}, \tilde{w}_{i,j,k})$ . As pointed out earlier, the convective terms are upwinded in (23) to ensure the diagonal dominance of the equation system.

The discretized forms for (21) are given by:

$$\begin{aligned}
U_{res_{ijk}} &= -\frac{(U_{i,j,k} - u_{i,j,k}^n)}{\Delta t} - \delta_x^c(UU) \\
& -\delta_y^c(UV) - \delta_z^c(UW) - \delta_x^c p + \frac{1}{R_e}\tilde{\nabla}^2\tilde{U} \\
V_{res_{ijk}} &= -\frac{(V_{i,j,k} - v_{i,j,k}^n)}{\Delta t} - \delta_x^c(UV) \\
& -\delta_y^c(VV) - \delta_z^c(VW) - \delta_y^c p + \frac{1}{R_e}\tilde{\nabla}^2\tilde{V} \quad (24) \\
W_{res_{ijk}} &= -\frac{(W_{i,j,k} - w_{i,j,k}^n)}{\Delta t} - \delta_x^c(UW) \\
& -\delta_y^c(VW) - \delta_z^c(WW) - \delta_z^c p + \frac{1}{R_e}\tilde{\nabla}^2\tilde{W} ,
\end{aligned}$$

where once again, a first-order Euler scheme is used for the time-derivative terms.

The system of equations (23) and (24) are solved using Gauss-Seidel iteration. A good initial guess of the error terms may be obtained by ignoring all of the off-diagonal terms as illustrated below:

$$\begin{aligned}
\tilde{u}_{ijk} &= \frac{\Delta t U_{res_{ijk}}}{d_{ijk}^u} \\
\tilde{v}_{ijk} &= \frac{\Delta t V_{res_{ijk}}}{d_{ijk}^v} \\
\tilde{w}_{ijk} &= \frac{\Delta t W_{res_{ijk}}}{d_{ijk}^w} \\
d_{ijk}^u &= 1 + 2\frac{\Delta t|U_{ijk}|}{\Delta x} + \frac{\Delta t|V_{ijk}|}{\Delta y} + \frac{\Delta t|W_{ijk}|}{\Delta z} \\
& + \frac{2\Delta t}{R_e}\left(\frac{1}{(\Delta x)^2} + \frac{1}{(\Delta y)^2} + \frac{1}{(\Delta z)^2}\right) \\
d_{ijk}^v &= 1 + \frac{\Delta t|U_{ijk}|}{\Delta x} + 2\frac{\Delta t|V_{ijk}|}{\Delta y} + \frac{\Delta t|W_{ijk}|}{\Delta z} \\
& + \frac{2\Delta t}{R_e}\left(\frac{1}{(\Delta x)^2} + \frac{1}{(\Delta y)^2} + \frac{1}{(\Delta z)^2}\right) \\
d_{ijk}^w &= 1 + \frac{\Delta t|U_{ijk}|}{\Delta x} + \frac{\Delta t|V_{ijk}|}{\Delta y} + 2\frac{\Delta t|W_{ijk}|}{\Delta z} \\
& + \frac{2\Delta t}{R_e}\left(\frac{1}{(\Delta x)^2} + \frac{1}{(\Delta y)^2} + \frac{1}{(\Delta z)^2}\right) .
\end{aligned} \quad (25)$$

We observe that the FTCS scheme is recovered if all the  $\Delta t$  terms are eliminated in the denominators of (25) and if only one Newton-Raphson iteration is used. Also, if the time step is small enough such that the diffusion terms are much less than one,

$$\frac{2\Delta t}{R_e}\left(\frac{1}{(\Delta x)^2} + \frac{1}{(\Delta y)^2} + \frac{1}{(\Delta z)^2}\right) \ll 1 ,$$

the system of equations (23) and (24) are parabolic and Gauss-Seidel iteration may be used to efficiently solve the equations. For larger time steps, however, the diffusion terms dominate, the system of equations are elliptic, and multigrid iteration is much more effective. Finally, if the diffusion terms dominate and if the grid spacing along one or two axes is much smaller than the spacings along the other axes, the system of equations are anisotropic and a line Gauss-Seidel solver should be used in conjunction with a multigrid solver.

After solving (23) and (24), we first update the velocities  $(u, v, w)^{n+1} = (U, V, W) + (\tilde{u}, \tilde{v}, \tilde{w})$ , then reassign the approximate solutions  $(U, V, W) = (u, v, w)^{n+1}$ , and finally update the pressure. The Poisson equation for the pressure (4) must be discretized carefully because numerical errors may otherwise accumulate and cause the solution to diverge. In particular, in the analytic derivation of

the Poisson equation, we neglected functions of the velocity dilation term ( $\nabla \cdot \bar{u}$ ) which may differ from zero in our numerical calculations. Thus, for the numerical implementation of our implicit scheme we retain the time derivative of the dilation term which is a function of the  $n$ -th time step. Functions of the dilation term at the  $(n+1)$ -th time step are set equal to zero so that mass conservation will be satisfied. Our discrete equation for the pressure is:

$$\begin{aligned} \tilde{\nabla}^2 p^{n+1} = & + \frac{1}{\Delta t} (\delta_x^c u^n + \delta_y^c v^n + \delta_z^c w^n) \\ & + 2(\delta_x^c u^{n+1} \delta_y^c v^{n+1} + \delta_x^c u^{n+1} \delta_z^c w^{n+1} \\ & + \delta_y^c v^{n+1} \delta_z^c w^{n+1} - \delta_y^c u^{n+1} \delta_x^c v^{n+1} \\ & - \delta_z^c u^{n+1} \delta_x^c w^{n+1} - \delta_z^c v^{n+1} \delta_y^c w^{n+1}). \end{aligned} \quad (26)$$

We solve this elliptic equation by using a combination of Gauss-Seidel and multigrid iteration. Once the pressure has been updated, the Newton-Raphson iteration may continue to reduce the residual errors or the solution scheme may progress to the next time step. The stability and accuracy of this numerical scheme are discussed later.

### 3.2 An Explicit Time-stepping Scheme

We derive here the second-order extension of the FTCS method. The time integrator uses a two-stage modified Euler method. The first stage is a standard Euler step:

$$\begin{aligned} \bar{u}_{i,j,k} &= u_{i,j,k}^n + \Delta t f_{i,j,k}^u \\ \bar{v}_{i,j,k} &= v_{i,j,k}^n + \Delta t f_{i,j,k}^v \\ \bar{w}_{i,j,k} &= w_{i,j,k}^n + \Delta t f_{i,j,k}^w, \end{aligned} \quad (27)$$

where the forcing terms are defined by:

$$\begin{aligned} f_{i,j,k}^u &= -\delta_x^c(uu)^n - \delta_y^c(uv)^n - \delta_z^c(uw)^n \\ &\quad - \delta_x^c p^n + \frac{1}{R_e} \tilde{\nabla}^2 u^n \\ f_{i,j,k}^v &= -\delta_x^c(uv)^n - \delta_y^c(vv)^n - \delta_z^c(vw)^n \\ &\quad - \delta_y^c p^n + \frac{1}{R_e} \tilde{\nabla}^2 v^n \\ f_{i,j,k}^w &= -\delta_x^c(uw)^n - \delta_y^c(vw)^n - \delta_z^c(ww)^n \end{aligned} \quad (28)$$

$$-\delta_z^c p^n + \frac{1}{R_e} \tilde{\nabla}^2 w^n.$$

We observe that the convective terms and the diffusion terms are all central differenced. Next we calculate the hydrodynamic pressure as a function of this first estimate of the velocities at the next time step:

$$\begin{aligned} \tilde{\nabla}^2 \bar{p} = & + \frac{1}{\Delta t} (\delta_x^c \bar{u}^n + \delta_y^c \bar{v}^n + \delta_z^c \bar{w}^n) \\ & + 2(\delta_x^c \bar{u} \delta_y^c \bar{v} + \delta_x^c \bar{u} \delta_z^c \bar{w} \\ & + \delta_y^c \bar{v} \delta_z^c \bar{w} - \delta_y^c \bar{u} \delta_x^c \bar{v} \\ & - \delta_z^c \bar{u} \delta_x^c \bar{w} - \delta_z^c \bar{v} \delta_y^c \bar{w}), \end{aligned} \quad (29)$$

This equation for the pressure is the same as that for the implicit scheme (Eq. 26). Upon solving this equation, we proceed to the second stage:

$$\begin{aligned} u_{i,j,k}^{n+1} &= u_{i,j,k}^n + \frac{\Delta t}{2} (f_{i,j,k}^u + \bar{f}_{i,j,k}^u) \\ v_{i,j,k}^{n+1} &= v_{i,j,k}^n + \frac{\Delta t}{2} (f_{i,j,k}^v + \bar{f}_{i,j,k}^v) \\ w_{i,j,k}^{n+1} &= w_{i,j,k}^n + \frac{\Delta t}{2} (f_{i,j,k}^w + \bar{f}_{i,j,k}^w), \end{aligned} \quad (30)$$

where the second-stage forcing terms are defined by:

$$\begin{aligned} \bar{f}_{i,j,k}^u &= -\delta_x^c(\bar{u}\bar{u}) - \delta_y^c(\bar{u}\bar{v}) - \delta_z^c(\bar{u}\bar{w}) \\ &\quad - \delta_x^c \bar{p} + \frac{1}{R_e} \tilde{\nabla}^2 \bar{u} \\ \bar{f}_{i,j,k}^v &= -\delta_x^c(\bar{u}\bar{v}) - \delta_y^c(\bar{v}\bar{v}) - \delta_z^c(\bar{v}\bar{w}) \\ &\quad - \delta_y^c \bar{p} + \frac{1}{R_e} \tilde{\nabla}^2 \bar{v} \\ \bar{f}_{i,j,k}^w &= -\delta_x^c(\bar{u}\bar{w}) - \delta_y^c(\bar{v}\bar{w}) - \delta_z^c(\bar{w}\bar{w}) \\ &\quad - \delta_z^c \bar{p} + \frac{1}{R_e} \tilde{\nabla}^2 \bar{w} \end{aligned} \quad (31)$$

This two stage process gives a second-order accurate estimate of the velocities at the next time step. We conclude the algorithm by updating the pressure field:

$$\tilde{\nabla}^2 p^{n+1} = + \frac{1}{\Delta t} (\delta_x^c u^n + \delta_y^c v^n + \delta_z^c w^n) \quad (32)$$

$$\begin{aligned}
& +2(\delta_x^c u^{n+1} \delta_y^c v^{n+1} + \delta_x^c u^{n+1} \delta_z^c w^{n+1} \\
& + \delta_y^c v^{n+1} \delta_z^c w^{n+1} - \delta_y^c u^{n+1} \delta_x^c v^{n+1} \\
& - \delta_z^c u^{n+1} \delta_x^c w^{n+1} - \delta_z^c v^{n+1} \delta_y^c w^{n+1}) .
\end{aligned}$$

The procedure repeats for the next time step. The stability and accuracy of the above algorithm is discussed later.

### 3.3 Numerical Solution of the Initial Conditions

According to Helmholtz theorem, the initial velocity field may be expressed in terms of scalar and vector velocity potentials (Eq. 7). The vortex problems that interest us most in this paper are completely specified by the vector velocity potentials. The finite-difference forms of the Poisson equations for the vector velocity potentials (see Eq. 9) are:

$$\begin{aligned}
\tilde{\nabla}^2 \psi_{x_o} &= -(\omega_{x_o})_{i,j,k} \\
\tilde{\nabla}^2 \psi_{y_o} &= -(\omega_{y_o})_{i,j,k} \\
\tilde{\nabla}^2 \psi_{z_o} &= -(\omega_{z_o})_{i,j,k} ,
\end{aligned} \tag{33}$$

where  $(\vec{\omega}_o)_{i,j,k}$  is the discrete sampling of the initial vorticity field which is prescribed. Upon solving (33) for the potentials, we use a discrete form of Helmholtz theorem to calculate the initial velocities:

$$\begin{aligned}
(u_o)_{i,j,k} &= \delta_y^c \psi_{z_o} - \delta_z^c \psi_{y_o} \\
(v_o)_{i,j,k} &= -\delta_x^c \psi_{z_o} + \delta_z^c \psi_{x_o} \\
(w_o)_{i,j,k} &= \delta_x^c \psi_{y_o} - \delta_y^c \psi_{x_o} .
\end{aligned} \tag{34}$$

Formally, the initial vorticity field prescribed in (33) should be solenoidal, but in practice an initial vorticity field which is not necessarily solenoidal may be used. The primitive variable formulation allows this flexibility because any vector field for the initial vorticity will lead to a solenoidal velocity field due to the Helmholtz decomposition. In fact, the vorticity field that is recalculated based on the definition of vorticity (10) is also solenoidal.

### 3.4 Numerical Implementation of the Boundary Conditions

Our numerical simulations use periodic, free-slip, no-slip, and free-surface boundary conditions. To illustrate how these boundary conditions are implemented, we assume that one of these types of boundary conditions is imposed on the plane  $z=0$ . Let indices  $(i, j, K)$  denote a grid point on  $z=0$ , and  $(i, j, K+1)$  an imaginary set of grid points above the plane  $z=0$ . The grid points on the  $k$ -axis are ordered  $k = 1, 2, \dots, K$ . For Dirichlet boundary conditions the field equations are never evaluated on  $z = 0$  and no special treatment is required for the field equations. For periodic and Neumann boundary conditions, expressions for the imaginary set of grid points in terms of real grid points are formulated and substituted into the field equations.

#### 3.4.1 Periodic Boundary Conditions

The field equations for the velocities, pressures, and stream functions are evaluated at the grid level  $(i, j, K)$ , and the centered difference operators (22) are functions of the imaginary set of grid points. We impose periodic boundary conditions by setting the imaginary grid points at the grid level  $(i, j, K+1)$  equal to the grid points at the first grid level  $(i, j, 1)$ . Similarly, we set the imaginary grid points at  $(i, j, 0)$  equal to the grid points at  $(i, j, K)$ . This algorithm gives second-order spatial approximations to the field equations without adversely affecting vectorization (see Appendix B).

#### 3.4.2 Free-Slip Boundary Conditions

As shown in Sec. 2.3, the horizontal velocities  $(u, v)$  and the hydrodynamic pressure  $p$  are even functions about  $z=0$ , the vertical velocity  $w$  is an odd function, and  $w=0$  on the wall. These relations may be used to assign the flow quantities at the imaginary set of grid points in terms of the same quantities at interior grid points:

$$\begin{aligned}
u_{i,j,K+1} &= u_{i,j,K-1} \\
v_{i,j,K+1} &= v_{i,j,K-1} \\
w_{i,j,K+1} &= -w_{i,j,K-1} \\
p_{i,j,K+1} &= p_{i,j,K-1} .
\end{aligned} \tag{35}$$

At the  $(i, j, K)$  grid level, these relations are back substituted into the horizontal components of the momentum equations and the Poisson equation for the pressure. The resulting finite-difference approximations are second-order accurate. The value and behavior of the velocities on the free-slip plane are used to assign the boundary values and behavior of the vector velocity potentials. For example, setting  $\psi_{x_o}=0$  and  $\psi_{y_o}=0$  on  $z=0$  ensures that the no-flux condition is met. In addition we assume that  $\psi_{x_o}$  and  $\psi_{y_o}$  are odd functions about the free-slip plane, and assign  $\psi_{z_o}$  to be even ( $\partial\psi_{z_o}/\partial z = 0$ ). At the  $(i, j, K)$  level these relations are substituted into the  $\psi_{z_o}$ -Poisson equation (33) and the discrete velocity calculations (34). This form of the vector velocity potentials ensures that the horizontal velocities  $(u, v)$  are even functions on the free-slip plane.

### 3.4.3 No-Slip Boundary Conditions

Free-slip boundary conditions are used to set up the initial conditions at time  $t = 0$ , and at time  $t = 0^+$  we set  $\vec{u} = 0$  on the no-slip wall. As a result, a sheet of vorticity is instantaneously formed on the no-slip wall. In our simulations of vortex rings impacting the wall, the rings are initially far enough away from the wall such that the strength of the vorticity on wall is less than one percent of the core strength. As shown in Sec. 2.4, the source term in the Poisson equation for the pressure is zero on a no-slip wall. For our numerical simulations we also set the time derivative of the dilation term equal to zero. The fact that  $w_z = 0$  on the no-slip wall is used together with the Neumann boundary condition for the pressure (16) to assign the pressure at the imaginary grid point  $(p_{i,j,K+1})$ :

$$p_{i,j,K+1} = p_{i,j,K-1} + \frac{4}{\Delta z R_e} w_{i,j,K-1} . \quad (36)$$

This equation is then substituted into the 7-point star for the Laplace operator in (26, 29, or 32). In the multigrid solution of the pressure we find it convenient to store the inhomogeneous velocity term  $(w_{i,j,K-1})$  in the vector used for the source strengths (see Appendix B).

### 3.4.4 Free-Surface Boundary Conditions

Again, free-slip boundary conditions are used to assign the initial velocity field. Dirichlet conditions are specified for the hydrodynamic pressure since the pressure is known in terms of the free-surface elevation (see Eq. 11). The kinematic condition for the free-surface elevation (12) may be evaluated either implicitly or explicitly. As an example, for the first-stage of our explicit scheme, we use:

$$\bar{\eta}_{i,j} = \eta_{i,j}^n + \Delta t f_{i,j}^n \quad (37)$$

$$f_{i,j}^n = w_{i,j,K}^n - u_{i,j,K}^n \delta_x^c \eta^n - v_{i,j,K}^n \delta_y^c \eta^n .$$

The evaluation of the momentum equations on the free surface depends on the imaginary grid points. Since the horizontal velocities are even functions about the free-surface (see Eq. 11), they are assigned using our free-slip wall method. The mass-conservation equation (3) is used to evaluate the vertical velocity at an imaginary grid point in terms of real quantities:

$$w_{i,j,K+1} = w_{i,j,K-1} - 2\Delta z \delta_x^c u - 2\Delta z \delta_y^c v . \quad (38)$$

Finally, the  $z$ -derivative of the pressure in the momentum equations is evaluated using a 3-point one-sided difference scheme:

$$p_z = \frac{1}{2\Delta z} (3p_{i,j,K} - 4p_{i,j,K-1} + p_{i,j,K-2}) . \quad (39)$$

This implementation of the free-surface conditions gives second-order spatial accuracy. In addition, the compact nature of the scheme does not affect the vectorization of either the semi-implicit or the explicit time integrators.

### 3.5 Solvability Condition for the Pressure

As noted in Sec. 2, a solvability condition must be satisfied for the pressure if Neumann or periodic boundary conditions are specified on all of the boundaries. The numerical implementation of this integral constraint is discussed by Ghia, *et al*, (1977), which we extend to a multigrid solver. Let

$\sigma_{i,j,k}$  represent the source term in the discretized Poisson equation (see Eqs. 26, 29, or 32), and let  $\mathcal{E}$  be the error of the integral constraint normalized by the fluid volume  $V$ . We use trapezoidal rule to evaluate the error:

$$\mathcal{E} = \frac{1}{V} \left( \sum_{i,j,k} \Delta v \delta_v \sigma_{i,j,k} - \sum_{i,j,k} \Delta s \delta_s \left( \frac{\partial p}{\partial n} \right)_{i,j,k} \right), \quad (40)$$

where  $\Delta v = \Delta x \Delta y \Delta z$  and  $\Delta s = \Delta x \Delta y$ ,  $\Delta x \Delta z$ , or  $\Delta y \Delta z$ ;  $\delta_v = 1, 1/2, 1/4$ , or  $1/8$  if the grid point is respectively in the volume, on a side, edge, or corner of the computational domain; and similarly,  $\delta_s = 1, 1/2$ , or  $1/4$  depending on whether the grid point is on a side, edge, or corner respectively. Let  $\hat{\sigma}_{i,j,k}$  represent a source strength which satisfies the integral constraint, then one possible solution for  $\hat{\sigma}_{i,j,k}$  is simply:

$$\hat{\sigma}_{i,j,k} = \sigma_{i,j,k} - \mathcal{E}. \quad (41)$$

These modified source strengths  $\hat{\sigma}_{i,j,k}$  are used instead of the original source strengths  $\sigma_{i,j,k}$  in the discrete Poisson equations for the pressure. We emphasize that the discrete Laplacian operator with all Neumann or Periodic boundary conditions is still singular, but  $\hat{\sigma}_{i,j,k}$  is in the same solution space as the generalized inverse. As a result, a point Gauss-Seidel scheme will converge to an optimum solution for the pressure. Note that trapezoidal rule is used to evaluate the integral constraint because the trapezoidal rule is the adjoint of central differencing. Other numerical integration schemes, even more accurate numerical integrators, will reduce the accuracy of the pressure solution. We also note that the numerical implementation of the integral constraint has to be applied at each level of a multigrid method, not just the level of the finest grid.

### 3.6 Multigrid Solutions of the Field Equations

The efficiency of our Navier-Stokes' codes is due to multigrid solution techniques. Multigrid is used to solve the momentum equations in the implicit time-stepping scheme (23), the Poisson equations

for the stream functions (33), and the Poisson equations for the pressure (26, 29, and 32). One obvious advantage of the multigrid method is that the convergence speed does not deteriorate as grid resolution increases in contrast to conventional iterative techniques such as Jacobi or Gauss-Seidel (Hackbusch, 1985). Indeed, the multigrid convergence rate and memory requirements, which are directly proportional to the number of unknowns, are ideally suited for three-dimensional solutions of the Navier-Stokes equations. Multigrid uses fine grids to reduce the high wavenumber errors and coarse grids to reduce the low wavenumber errors. This interplay of fine and coarse grids is easily coded using recursive languages like PASCAL; however, FORTRAN can mimic recursive algorithms by using array pointers in subroutine calling arguments. We provide a multigrid FORTRAN code for solving the hydrodynamic pressure in Appendix B.

### 3.7 Convergence Tests and Error Analyses

In this section we establish the stability and convergence properties of our implicit and explicit time-stepping procedures. We consider three test cases: the axisymmetric stagnation problem, translation and diffusion of two-dimensional vortices, and attenuation of axisymmetric standing waves. The axisymmetric stagnation flow problem illustrates the rapid convergence to steady state of our implicit scheme. In addition, we show the spatial accuracy of our numerical scheme as a function of grid Reynolds number. The numerical simulations of two-dimensional vortices orbiting in a box test the temporal and spatial accuracy of our vortex formulations. Finally, numerical simulations of the attenuation of axisymmetric standing waves validates the formulation of the free-surface boundary conditions for low Reynolds numbers and small wave amplitudes.

#### 3.7.1 Implicit Scheme for the Steady-State Problems

Except for the treatment of the pressure, our semi-implicit scheme is directly related to the Briley-McDonald (1973) method for the compressible Navier-Stokes equations. Both schemes are first-order accurate in time and second-order accurate in space. A linearized stability analysis shows that



both schemes are unconditionally stable. The main difference is that instead of a block-tridiagonal solver, we use a multigrid solver for the momentum equations.

As a test of our semi-implicit scheme, we consider the axisymmetric stagnation flow problem for which an exact solution to the Navier-Stokes equations is known (Schlichting, 1968). We let  $v$  and  $w$  respectively denote the radial ( $r$ ) and axial ( $z$ ) velocities. The problem is normalized by a length  $L=1$  and the velocity at infinity  $U_o = w(r=1, z=-\infty)=1$ . Two sets of results, one using an axisymmetric version of our scheme (see Appendix A) and one using the full three-dimensional formulation (without assuming axisymmetry) are provided. The computations are performed with known Dirichlet conditions on the boundaries and zero initial interior velocity, and the iterations are continued until the maximum change in the velocity between iterations is less than a tolerance of  $\tau_o=10^{-6}$ . For both computer codes the parameters which control the number of sweeps over the finest grid level are as follows: number of Newton-Raphson iterations,  $N_{newt}=1$ ; number of multigrid iterations,  $N_{mult}=6$ ; number of Gauss-Seidel iterations,  $N_{gaus}=6$ ; and number of Jacobi iterations,  $N_{jaco}=2$ . (For all our numerical studies, the number of Jacobi iterations is always fixed at  $N_{jaco}=2$ .) We use a constant grid spacing with  $\Delta=2^{-5}$ , where  $\Delta = \Delta r = \Delta z$  is the grid size. The computational domain has unit height and unit radius (or half-width), and the time step is  $\Delta t=1$ . To minimize initial transients and to improve convergence, the viscosity is decreased linearly from an initial value of  $\nu_o=1$  to the prescribed value after  $N_{ramp}=5$  time steps.

Figures (1) show the maximum absolute error in the velocities  $v$  and  $w$  as a function of grid Reynolds number  $R_\Delta = U_o \Delta / \nu$ . The plots measure the resolution of the wall boundary layer as  $R_\Delta$  increases. The axisymmetric code performs slightly better than the three-dimensional code possibly because the three-dimensional computational domain is larger than the axisymmetric domain by a factor of  $\sqrt{2}$ . The errors for both methods diminish rapidly as  $R_\Delta$  decreases below  $\sim 2$ . For  $R_\Delta \sim 1$  the maximum normalized error is  $O(10^{-3})$ .

To evaluate the efficiency of these codes, and as a guide to later computations, we seek the optimal set of computational parameters (as a func-

tion of  $R_\Delta$ ) for minimum total operations. In the interest of economy, only the axisymmetric code is used with the expectation that results for the three-dimensional code will be similar. To facilitate comparison for these multigrid computations, we define a measure of the number of operations  $N_{oper}$  to be the equivalent number of Gauss-Seidel sweeps over the finest grid level for the entire set of unknowns ( $v, w, p$ ). Table (1) shows partial results (near the optimums) of an extensive validation study. Note that when a ramp down of the viscosity is not applied ( $N_{ramp}=0$ ), the solution may diverge even though the implicit scheme is unconditionally stable.

Finally, we show the performance of the multigrid scheme as a function of the number of grid points. This is shown in Figure (2) for the case  $R_\Delta=1$  with the *optimal* parameters  $N_{newt}=1$ ,  $N_{mult}=2$ ,  $N_{gaus}=1$ ,  $\Delta t=.5$ , and  $N_{ramp}=4$ , and keeping the same tolerance of  $\tau_o=10^{-6}$ . The number of grid points  $N_{tot}$  is increased by uniformly decreasing the grid size and keeping the same domain dimensions. Note that the log-log plot of  $N_{oper}$  versus  $N_{tot}$  has an average slope of  $\sim 0.3$ . This indicates that the rate of convergence of the multigrid solver is only slightly slower than a linear function of the number of unknowns.

### 3.7.2 The Explicit Scheme for Unsteady Problems

For the time-dependent problems, we use a second-order predictor-corrector (Runge-Kutta) method for time integration and centered differences for the spatial derivatives. Our principal concerns here are first stability and second accuracy of the time integration.

The linearized stability analysis of the Navier-Stokes equations is usually performed by assuming periodic boundary conditions, ignoring the (linear) pressure gradient terms, and linearizing the convective terms to obtain the linear advective-diffusion equation:

$$\vec{u}_t + \vec{U} \cdot \nabla \vec{u} = \nu \nabla^2 \vec{u} ,$$

where  $\vec{U}$  is assumed to be constant and prescribed. For one-dimensional problems, the stability criteria for the (first-order) forward-time centered-space (FTCS) scheme is well known (*e.g.*, Roach, 1976):

$$\beta_x^2 \leq 2\alpha_x \leq 1, \quad (42)$$

where  $\alpha_x = \nu \Delta t / \Delta x^2$  and  $\beta_x = U \Delta t / \Delta x$ . For more spatial dimensions and higher-order time integrations, the generalization is in principle straightforward but algebraically quite complicated. For two dimensions, a generalization of the following form has often been suggested and used (Fromm, 1964; Miyata & Nishimura, 1985):

$$(\beta_x + \beta_y)^2 \leq 2(\alpha_x + \alpha_y) \leq 1, \quad (43)$$

which can be derived by essentially letting  $\Delta x = \Delta y$  and assuming equal phases in the two dimensions. Unfortunately, (43) is neither necessary nor sufficient for stability in general. The latter being obvious since (43) does not even guarantee the one-dimensional condition (42).

By not assuming equal phases, the correct analysis is more involved and the final results can be summarized as follows. Without loss of generality, we assume  $U \neq 0$  and define  $\gamma = V/U$ . For simplicity we denote the left inequality of (42) applied to  $x$  and  $y$  by  $I_x$  and  $I_y$  respectively, the right inequality of (43) as II, and the phrase 'necessary and sufficient for stability' by 'iff'. For  $\gamma \leq \sqrt{2} - 1$ : II is iff for  $R_x = U \Delta x / \nu \leq 2\sqrt{2}$  and  $I_x$  is iff otherwise. The symmetric case is for  $\gamma \geq (\sqrt{2} - 1)^{-1}$ : II is iff for  $R_x \leq 2\sqrt{2}/\gamma$  and  $I_y$  is iff otherwise. For intermediate values of  $\sqrt{2} - 1 \leq \gamma \leq (\sqrt{2} - 1)^{-1}$ , II is again iff for  $R_x \leq 4/(1 + \gamma)$ . For  $R_x > 4/(1 + \gamma)$ , the results depend on whether  $\gamma$  is greater or less than 1. For  $\gamma <, > 1$ ,  $I_x, I_y$  eventually become established as iff for large  $R_x$ , while for  $\gamma = 1$ ,  $I_x, I_y$  are never sufficient. The overall solution is rather complicated and is depicted graphically in Figures (3) where the relevant quantities involved in the inequalities (eqts. 42 & 43) evaluated at the maximum  $\Delta t$  for stability are plotted as a function of  $R_x$ , for three values of  $\gamma = .7, 1.0$ , and  $1.4$ .

For the second-order Runge-Kutta scheme in time, the resulting (complex) amplification factor is simply:

$$G = 1 + f + f^2/2, \quad (44)$$

where  $f$  is the amplification factor for the first-order (FTCS) difference scheme. The analysis is somewhat more involved but qualitatively unchanged. In practice, the maximum value of  $\Delta t$  is computed

numerically using the best estimates for  $\vec{U}$ . In view of the linearization, the elimination of the (linear) pressure term, and the simplified boundary conditions in the stability analysis, more conservative values for the time step are often found necessary in actual computations.

We now turn to the accuracy of our second-order (Runge-Kutta) explicit scheme. We consider two problems for which analytic solutions (for the idealized cases) exist. The first problem is the decay of a two-dimensional rectilinear Gaussian vortex tube. Since the free decay of this vortex in an unbounded domain is relatively trivial and does not involve the nonlinear convective terms, we consider instead the vortex tube placed asymmetrically inside a rectangular domain. Free-slip conditions are applied on the boundaries of the domain. Because of the presence of the image vortices, the tube orbits within the box. The core vorticity should, however, decay at a rate close to that for unbounded domain, at least for small core sizes compared to the dimension of the domain.

Specifically, we consider a  $4 \times 4$  box with a Gaussian vortex of core radius  $r_c = 0.5$  placed initially one unit inboard of a side's midpoint. The initial circulation of the vortex is  $\Gamma = \pi$ . Equal grid spacings with  $\Delta x = \Delta y = 4/2^5$  are used, and a grid Reynolds number,  $R_\Delta = U_o \Delta x / \nu$  with  $U_o \equiv 1$  is again defined. Figures (4) plot, as functions of  $R_\Delta$ , the relative error in the maximum vorticity,  $|\omega_{max} - \omega_{exa}|/\omega_{exa}$ , where  $\omega_{max}$  is the maximum calculated value for the vorticity and  $\omega_{exa} = \Gamma/(\pi(r_c^2 + 4\nu t))$  is the analytic value in an unbounded domain. The errors are plotted at two times,  $t=1$  and  $10$ . The corresponding relative error in conservation of total energy are shown in Figures (5). Three time step sizes,  $\Delta t = .01, .02$  and  $.05$  are considered for which the minimum  $R_\Delta$  for stability are respectively  $R_\Delta = .32, .64$ , and  $1.6$ .

As seen in Figure (4a) the peak errors in the vorticity occur at  $R_\Delta = 2$  for  $t=1$ . However, the energy at this point (5a) is well conserved probably due to the conservation-law form we use to formulate the Navier-Stokes equations. Here, we have defined the relative error in the energy conservation formula as  $\epsilon_c = |E(t) - E(0) + D(t)|/E(0)$ , where  $E(t)$  is the kinetic energy and  $D(t)$  is the energy that is dissipated (the Reynolds number term in Eq. 17 integrated over time). For grid resolutions lower than  $R_\Delta \geq 2$ , one expects an increase in error due to oscillations (Roach, 1976), this is indicated in

both our steady-state and unsteady calculations. The errors, however, are not intolerable and may at times even decrease as  $R_\Delta$  increases above two.

Finally, we consider a time-dependent problem with a free surface. We study the decrease in wave amplitude due to viscous dissipation of an axisymmetric standing wave in a cylindrical basin. For simplicity, we choose the tank radius and the tank depth  $R_t = D_t = 1$  and the standing wave period  $T = 1$ . For this axisymmetric problem, we use a  $2^6 \times 2^6$  grid, and  $\Delta t = .005$ . The Froude number is fixed at  $F_r = .5$  and consistent with the free-surface linearization, a relatively small wave slope of  $A(0)k = .1$ , where  $k = j_{1,0} \approx 3.832$  is the wavenumber corresponding to the first-mode standing wave, and  $A(t)$  is the (centerline) wave amplitude. The analytic solution for this problem is  $dA_{exa}/dt = \exp(-2\nu k^2 t)$  (Lamb, 1932). For comparison, we integrate for one wave period ( $t = T$ ) and compute the relative errors,  $\epsilon_1 = |A(T) - A_{exa}(T)|/A(0)$  and  $\epsilon_2 = |A(T) - A_{exa}(T)|/(A(0) - A_{exa}(T))$ , as functions of the grid Reynolds number  $R_\Delta = R_t^2/\nu T$ . These results are shown in Figure (6). The relative errors are all less than four percent. For  $R_\Delta > 4$  the relative errors increase due to low damping at low spatial resolutions. For  $R_\Delta < 4$  the errors increase as the diffusion stability boundary is neared.

## 4 Numerical Studies

The present numerical methods are used to study ring vortices and vortex tubes impinging on walls and free surfaces. The vortex ring studies are performed using an axisymmetric version of the program (see Appendix A). For the vortex tube studies the full three-dimensional code is used. Schematic pictures illustrating the axisymmetric ring vortex and the three-dimensional vortex tube simulations are given in Figures (7) and (8) respectively. The actual physical and numerical parameters used in the simulations are provided in three tables: Table (2) for ring vortices interacting with walls, Table (3) for ring vortices interacting with free surfaces, and Table (4) for vortex tubes interacting with walls and free surfaces. In later discussions of the numerical results the figure headings refer to the detailed information that is provided in the tables.

### 4.1 Ring Vortices Impinging on Walls and Free-Surfaces

We study the normal incidence of vortex rings with no-slip walls, free-slip walls, and free surfaces. For the no-slip wall cases the radial expansions of the primary vortex rings are stopped by the growth of the boundary layer on the wall. As in the experiments of Walker, *et al*, (1987) with a solid wall, we too observe that at sufficiently high Reynolds numbers, secondary and tertiary vortex rings are separated from the boundary-layer on the wall. In addition, our numerical simulations show that these secondary and tertiary vortices form their own boundary layers on the wall as they are pinched off from the wall. Once they are formed, the secondary and tertiary vortices are wrapped around the primary vortex. In the later stages of the flow, the secondary vortex is thrust through the center of the primary vortex ring whereupon it merges with the wall boundary layer.

Similarly, when the wall is replaced by a free surface, our numerical simulations show that secondary vortex rings are shed from the surface at intermediate Froude numbers ( $F_r^2 > .25$ ). At lower Froude numbers, free surfaces appear to behave like free-slip walls. The ring expands radially outward, the core diameter is reduced due to stretching and the ring cross-section develops a distinctive head and tail shape. These low Froude number results agree qualitatively with the observations of Bernal, *et al*, (1989) and Kwon (1989) for vortex rings interacting with a clean free surface.

These conclusions regarding the interactions of vortex rings with walls and free surfaces are based on the analyses of 12 numerical simulations. For these computations, a Gaussian core distribution is used to specify the initial vorticity field of the vortex ring:

$$\omega_o = \omega_c \exp\left(-\frac{(r - r_o)^2 + (z - z_o)^2}{r_c^2}\right), \quad (45)$$

where  $\omega_c$  is the peak vorticity,  $(r_o, z_o)$  denotes the center of the core, and  $r_c$  is the core radius. We also assign an *image* vortex about the centerline in order to make the initial vorticity field solenoidal. The Reynolds and Froude numbers are based on the length scale  $r_o = 1$  and a centerline velocity scale  $U_c \equiv \Gamma/(\pi r_o) = 1$ . The Reynolds numbers vary from 200 to 400, and the Froude numbers are

less than one. The vortex rings we choose to simulate are thick with a core to ring radii ratio of  $1/2$ . As indicated in Figure (7) and Tables (2) and (3), the initial conditions are set up so that the vortex ring rises up towards the wall or the free surface and then spreads out. Free-slip boundary conditions are imposed on the remaining boundaries of the cylindrical domain. The numerical parameters which control the number of solution iterations over the grid are chosen so that the average divergence over the grid points is maintained to within a tolerance of  $10^{-6}$ .

Figures (9 & 10) compare the trajectories of ring vortices interacting with free-slip and no-slip walls. The vortex cores are initially circular in both simulations in accordance with the choice of Gaussian core distributions. The vortex cores then evolve into elongated shapes reminiscent of Norbury's (1973) steadily translating family of vortex-ring solutions. When the vortex rings are within one ring radius of the wall, the two numerical simulations begin to differ. The most striking difference is that the vortex ring continues to expand radially in the free-slip wall case, whereas in the no-slip wall case the vortex ring is stopped at about  $r \approx 2.25$  due to a boundary layer forming on the wall. The final positions of the vortex core in the no-slip wall case agree qualitatively with the vortex ring experiments of Walker, *et al*, (1987) who observed radial expansions of  $r \approx 2$ . Also in agreement with experiments, our numerical simulation shows that the ring vortex rebounds from the no-slip wall. In the free-slip wall case, as the ring expands radially outward, the core diameter is reduced due to stretching and the core's appearance develops a distinctive head and tail shape. This shape of the vortex core agrees qualitatively with the very initial stages of the experiments of Bernal, *et al*, (1989) for vortex rings interacting with a clean free surface. Shariff, *et al*'s (1989) inviscid studies also show the development of such head and tail shapes. As an aside, they find that the deformations of the vortex core in the free-slip wall case are primarily responsible for the noise that is generated in the head-on collision of two vortex rings.

Figures (11, 12, & 13) show several stages in the interaction of a ring vortex with a no-slip wall. As illustrated in Figure (11) the boundary-layer has just separated from the wall due to the adverse pressure gradient formed by the primary vortex ring. Here, we refer to the original vortex ring as

the primary vortex ring, and any vortex rings that are ejected from the boundary layer of the primary vortex as secondary and tertiary vortex rings depending on when they are formed. The secondary and tertiary vortex rings have a sense of rotation that is opposite to the primary vortex ring, but as we observe in Figure (11), the separated vorticity may itself form a boundary layer which has the same rotation as the primary vortex. This formation of multiple boundary layers appears not to have been observed in laboratory studies of vortex rings.

We note that the secondary vorticity induces a velocity on the primary vortex which causes the rebounding that is observed in experiments (see Fig. 10). At this Reynolds number of  $Re = 400$ , the primary vortex ring is sufficiently strong to pinch off the boundary-layer vorticity as illustrated in Figure (12) to form a secondary vortex ring. This secondary vortex ring orbits the primary vortex ring due to the velocities induced by the primary vortex on the secondary vortex ring. In addition, we observe that boundary-layer vorticity is being wrapped around the primary vortex ring such that a tertiary vortex may form as shown in Figure (13). Here the secondary vortex ring has been thrust through the core of the primary ring where it merges with the boundary-layer vorticity. The formation of secondary and tertiary vortex rings has been observed in the experiments of Walker, *et al*, (1987). Unlike the boundary-layer theory they use, however, the present direct simulations of the Navier-Stokes equations permit the actual modeling of the secondary and tertiary vortex rings.

In Figure (14) we show how well energy is conserved by our numerical simulations. Observe that the kinetic energy is reduced to about 10% of its initial value in the no-slip simulation and 30% of its initial value in the free-slip simulation due to diffusion. (Note that the duration of the free-slip simulation is less than that for the no-slip wall because we have stopped the former before the vortex ring hit the outer boundary.) In both numerical simulations the energy is conserved to within 2%. Interestingly, the rates at which the kinetic energies are dissipated are only slightly different between the two simulations. In fact, if the free-slip simulation were continued further, the energies of the two cases may become close again. We hope to investigate this phenomenon in a future paper.

In Figure (15) we compare high and low resolu-



tion simulations of a vortex ring interacting with a no-slip wall. The high resolution simulation is twice as dense as the low resolution run. The agreement that exists between the two simulations indicates that we have adequate resolution of the wall boundary-layer, where the peak vorticity magnitude reaches a value five times greater than its initial value in the primary vortex ring.

In Figures (16) we report results for the normal incidence of a vortex ring with a clean free-surface at a low Froude number of  $F_r^2 = .125$ . Figure (16a) plots the free-surface elevations, and Figure (16b) plots the motion of a single contour of vorticity. For this numerical simulation, the mean free-surface elevation is not always correctly predicted to be zero. For time  $t \leq 5$  the spurious mean free-surface elevation is less than 10% of the peak free-surface elevation, and for  $t > 5$  the mean free-surface elevation is the same magnitude as the peak elevation. We note that the free-surface disturbances are quite small, and in fact the attenuation of the kinetic and potential energies are conserved to within 5%. The results we present in Figure (16a) have the mean free-surface elevation subtracted out so that we may focus on the features in the free-surface elevation that we believe are correctly predicted. Observe that the evolution of the vortex core at this low Froude number is very similar to the free-slip case shown in Figure (9). The most significant difference is that the tail is now slightly longer.

The plots of the free-surface elevations indicate that a wave trough is located above the low pressure region in the vortex core and a wave crest near the front of the core where the pressures are highest. The free-surface elevation decreases in amplitude as the disturbance moves radially outward due to mass conservation, but no waves appear to radiate away from the vortex ring. The wave troughs that travel with the vortex ring are similar to the free-surface depressions observed in the vortex-pair experiments of Willmarth, *et al*, (1988) and Sarpkaya, *et al*, (1988).

In Figures (17, 18, & 19) we report results for the normal incidence of a vortex ring with a clean free-surface at an intermediate Froude number. The magnitudes of the predicted free-surface elevations are beyond the restrictions imposed by the approximations used to derive the linearized free-surface boundary conditions (11 & 12), but the gross features of the flow should be valid. For this numerical

simulation, the attenuation of the kinetic and potential energies are conserved to within 15%, which is not unacceptable for the present purposes. We observe in Figure (17a) that the free-surface elevation reaches a maximum height above the center of the vortex ring that is about half the initial core radius, but once again no waves appear to radiate away from the vortex ring. From Figure (17b) the motion of the core is similar to the case of the no-slip wall (see Fig. 10). This is especially clear in Figures (18 & 19), where we observe the secondary and tertiary vortex rings shed by the free surface. These numerical simulations show that vortex shedding can occur at intermediate Froude numbers even if the free surface is clean.

#### 4.2 Three-dimensional Vortex Tubes Impinging on Walls and Free Surfaces

In this section we study the interaction of vortex tubes with no-slip walls and free surfaces. Specifically, we model two problems: (1) the interaction of a pair of trailing tip vortices with boundaries, and (2) the horizontal translation of a vortex tube slightly submerged below a free surface. As observed by Sarpkaya (1986), an interesting aspect of these problems is the reconnection of the vortex tubes with the boundaries. Our numerical simulations illustrate two possible mechanisms for the reconnection process: (1) reconnection of the primary vortex tube; and (2) reconnection of the secondary vorticity that is generated in the free-surface boundary layer and swept up by the primary vortex.

We hypothesize that reconnection of the primary vortex tubes may occur for deeply submerged trailing vortices that have enough time to develop large undulations prior to their impact with the free surface. The connection process of the primary vortex with the free surface is similar to the formation of crude vortex rings that is observed in the far wakes of aircraft (see Crow, 1970). Instead of the trailing vortex connecting with its neighbor, however, in the present case, the trailing vortex connects with its *image* above the free surface. A unique characteristic of the primary vortex reconnection is the cusp pattern that is traced by the normal vorticity on the free-surface. If the trailing vortices are very deeply submerged, they may connect with each other prior to contact with the free surface



and the vortex reconnection with the free surface would be different.

Two sources of boundary-layer vorticity which may connect with the free surface include shear stresses induced by surfactants and variations in the free-surface elevation at high Froude numbers. Thick sheets of helical vorticity spiral off the primary vortex and unevenly pull at the free-surface boundary-layer in the axial direction. The origin of the sheets of helical vorticity appears to be the result of a helical instability that is initiated by large changes in curvature along the axis of the primary vortex tube. Self-induced straining flows may help to strip the tightly wound helical vortices off of the primary vortex tube.

Figure (20) provides a schematic of the helical vorticity spiraling off of the primary vortex tube. As the helical vortices are swept around the primary vortex, they attach themselves to the free-surface boundary layer. The free-surface boundary-layer separates in front of the primary vortex tube and the helical vortex sheets evolve into narrow ridges of cross-axis vorticity that are wrapped around the primary vortex and ride on top of the secondary-vorticity that is shed by the boundary layer. The separated boundary-layer feeds into the undersides of the ridges, and the ridges swell into U-shaped vortices as shown in Figure (21). The bases of the U-shaped vortices are located close to the free surface in the region where the free-surface boundary-layer separates. The bases are either free or anchored in the secondary vorticity depending on their energy level, and the undersides of the tips of the U-vortices are anchored in the secondary boundary-layer vorticity that is wrapped around the primary vortex. The vortex lines enter the tip of one leg of the U-shape, move down to the base of the U-shape, and exit the tip of the other leg. The U-vortices are large in size at their bases, and the diameters of the legs of the U-vortices become slightly smaller near the tips possibly due to stretching around the primary vortex. The orientation of the U-vortices permits reconnection of normal vorticity with the free surface at the bases of U-vortices and the tips of the legs. We conjecture that reconnection may take place as the bases of the U-vortices open up when they come into contact with the free surface. If our conjecture is correct, the reconnection of the bases of the U-vortices with the free surface should manifest itself as a pair of closely spaced dimples on the free sur-

face, and these dimples should appear on the outboard side of the primary vortex. Similarly, if the primary vortex is sufficiently strong, the two tips of the U-vortices may be wrapped into contact with the free surface. As a result, we may expect more reconnections in the region where the tips of the U-vortices feed into the secondary vorticity shed by the boundary layer. The reconnection of the two tips should also manifest itself as one or two pairs of dimples on the free surface, but the tip dimples will most likely be inboard of the dimples formed by the bases of the U-vortices. In addition, the tip dimples may be smaller than the dimples formed by the thicker bases of the U-vortices.

Our conclusions regarding the interactions of vortex tubes with free surfaces are based on analyses of 7 three-dimensional numerical simulations. The geometry definitions are provided in Figure (8), and the numerical parameters of the simulations are provided in Table (4). A Gaussian core distribution is used to specify the initial vorticity field as follows:

$$\begin{aligned}
 (\omega_y)_o &= \omega_c \exp\left(-\frac{(x - x_{cen})^2 + (z - z_{cen})^2}{r_c^2}\right) \\
 x_{cen} &= x_o + x_{amp} \cos\left(\frac{\pi}{W_t} y\right) \\
 z_{cen} &= z_o + z_{amp} \cos\left(\frac{\pi}{W_t} y\right), \quad (46)
 \end{aligned}$$

where  $\omega_c$  is the peak vorticity,  $(x_o, z_o)$  denotes the mean position of the core center in the  $xz$ -plane,  $(x_{amp}, z_{amp})$  are sinusoidal perturbations applied to the core position,  $W_t$  is the width of the tank, and  $r_c$  is the core radius. We use free-slip boundary conditions on the bottom of the computational domain and on the walls in the  $xz$ -planes. For the first six of the simulations we use free-slip boundary conditions also on the  $yz$ -planes, and for the seventh run we use periodic boundary conditions along the  $x$ -axis. On the top boundary either no-slip or free-surface boundary conditions are employed.

As indicated in Figure (8) and Table (4), the initial conditions for the first six vortex tube studies are meant to simulate the rise of a pair of trailing vortices up towards either a wall or free surface. For these six simulations we assign 3 image vortices in the lower corner of the computational domain where the tubes are initially located. The

final computer run is meant to simulate a vortex tube that has risen to the free surface with a large sinusoidal disturbance along its length. For this simulation we assign an image vortex above the free surface, and use periodic boundary conditions along the  $x$ -axis to allow the vortex tube to translate parallel to the free surface.

For all the computer simulations, the Reynolds and Froude numbers are based on the mean half span  $s/2 = 1$  and centerline velocity scales  $U_c \equiv 2\Gamma/(\pi s) = 1$ . The Reynolds numbers vary from 200 to 400, and the Froude numbers vary from 0 to 4. Note that the core radii are very thick for three of the simulations ( $r_c=0.5$ ), but the other computer runs have more realistic core radii of  $r_c=0.25$ . For these simulations we choose to focus on the reconnection process itself and not the mechanism by which the vortex tube becomes initially disturbed. As a result, we use a width for the computational domain that is too short to permit Crow instability. As before, the numerical parameters which control the number of solution iterations over the grid have been chosen such that the average divergence over all the grid points is less than a tolerance of  $10^{-6}$ . A typical three-dimensional simulation consisting of  $65^3$  grid points and 3,000 time steps takes about 3 hours on a Cray Y-MP.

Figure (22) shows the cusp pattern that is formed on the free surface by the reconnection of primary vorticity with the free surface at a low Froude number. A single vortex tube with a sinusoidal perturbation is initially submerged slightly below a free surface. The actual physical and numerical parameters are provided in Run 7 of Table (4). The portion of the vortex tube that is closest to the free surface connects with the free surface. At this low Froude number ( $F_r^2 = .25$ ), the free surface acts like a free-slip wall, and the image of the vortex tube above the free surface induces high horizontal velocities in the region where the primary vortex tube is connecting with the free surface. The connector region moves faster than the deeply submerged portions of the primary vortex tube so that as the vortex tube breaks apart, a cusp pattern is formed. Although we are actually plotting the normal vorticity on the free surface in Figure (22), the free-surface elevations are directly related to the normal vorticity according to the solution of Rankine's combine vortex (Streeter, 1948). Thus, we may expect to see a pair of shallow dimples on the free surface that split apart as the primary vortex

tube connects with the free surface. In fact, this phenomenon is observed in our numerical results, but the free-surface elevation is contaminated by initial transients. For this numerical simulation the attenuation of the kinetic and potential energies is conserved to within 2% relative to the initial energy.

Figures (23a-e) show the evolution of the primary vortex tube as it reconnects with the free surface. Figure (23a) shows the vortex tube a short time after the numerical simulation began. The isolated structures that are not attached to the vortex tube are remnants of helical vorticity that have been torn off of the vortex tube. Typically, these remnants have very little kinetic energy relative to the vortex tube. In Figures (23b & c) we see that one end of the vortex tube has developed a head and tail shape that is very similar to the shape formed as a vortex ring approaches a free-slip wall (see Fig. 9). This phenomenon has also been observed by Stanaway, *et al*, (1988). When we consider the vortex tube and its image above the free surface as one unit, we realize that the head and tail feature forms a dipole as pointed out by Melander & Hussain (1988). The next phase of the reconnection process is known as bridging in the notation of Melander & Hussain. During this phase, which is illustrated in Figure (23d), vortex lines connect with the free surface in the head region of the dipole. The flat section of the tail in Figure (23d) is composed of vorticity that is normal to the symmetry (free-slip) boundary in the  $yz$ -plane and parallel to the free surface in the  $xy$ -plane. Similarly, the bridge, which is the raised cylinder on top of the flat tail, is composed of vorticity normal to the free surface and parallel to the symmetry boundary in the  $yz$ -plane. Since vorticity can only be normal to a free-slip plane, the bridge does not touch the  $yz$ -plane and the tail does not touch the free surface. This explains the slot above the flat tail and the gap on the side of the bridge. In Figure (23e) the reconnection with the free surface is complete, and one end of the vortex tube is connected to the free surface and the other end of the vortex tube is connected to the symmetry boundary in the back of the computational domain on the  $yz$ -plane.

Hirsa, *et al*'s (1990) measurements and two-dimensional computations indicate that the interactions of a vortex pair with a contaminated free-surface are similar to those for a no-slip wall. This

provides the motivation for us to consider the simulation of the interactions of a pair of trailing tip vortices with a no-slip wall because such simulations should allow us to understand the most important features of vortex tube interactions with contaminated free surfaces. Thus we consider a deeply submerged vortex tube with centerplane symmetry to model the rise of a trailing vortex pair toward a no-slip wall as illustrated in Figure (8). The initial position of the vortex tube is perturbed sinusoidally according to Equation (46). The Reynolds number is  $Re = 400$ , and we choose a initial core radius  $r_c = .25$ , which according to Spreiter & Sacks (1951) is the right order of magnitude for an elliptically loaded wing with span  $s = 2$ . The other physical and numerical parameters are provided in Run 3 of Table (4).

Figures (24a-g) show the interactions of the vortex tube with the no-slip wall. We plot a single isosurface of three relevant quantities at different instants of time: the magnitude of the helical vorticity ( $\sqrt{\omega_x^2 + \omega_z^2} = 0.5$ ), the magnitude of the axial vorticity ( $|\omega_y| = 0.5$ ), and the magnitude of the total vorticity ( $|\vec{\omega}| = 0.5$ ).

Figure (24a) shows the initial unwinding of the helical vorticity. An outer sheet of helical vorticity covers an inner sheet. At earlier time steps, which correspond to the onset of a helical instability, the sheets of helical vorticity are very tightly wound around the primary vortex tube. Dritschel's (1989) two-dimensional simulations suggest that self-induced straining flows may strip the helical vortices away from the primary vortex. The plot of the axial vorticity in Figure (24a) indicates that the initial perturbations in the primary vortex tube have been eliminated. According to Leonard (1985) the axial flows that are induced by the helical vortices may cause this straightening of the primary vortex. We see that the formation of the wall boundary-layer is also visible in the plot of the axial vorticity. The plot of total vorticity in Figure (24a) shows how the helical vortex sheets wrap around the primary vortex tube.

Figures (24b) show more unraveling of the helical vortex sheets from the primary vortex tube. As the helical sheets unravel they sometimes attach themselves perpendicularly to the symmetry boundary on the centerplane. Figures (24b) also show that the boundary layer on the wall is being affected by flow fields induced by the helical vortices. Note that the helical vortex sheets have become slightly

narrower relative to the preceding figure.

In Figure (24c) the helical vortex sheets have merged with the wall boundary layer, which has separated from the wall. The attachment of the helical vortex sheets to the wall boundary layer is a very important mechanism for increasing the low kinetic energy of the helical vortices. We base this conclusion on our free-surface simulations which show that the helical vortices rapidly diffuse if no energy is fed into them. In contrast, the no-slip wall simulations indicate that the helical vortices gain energy from the wall boundary layer.

Figures (24d) show that one sheet of the helical vorticity has evolved into a narrow ridge of cross-axis vorticity that is wrapped around the base of the primary vortex tube. On the other hand, portions of the top sheet of helical vorticity appear to be weakening. A slot has opened up between the narrow ridge and the symmetry boundary because the cross-axis vorticity is parallel to the symmetry boundary and cannot connect with the symmetry boundary. However, the secondary vorticity near the base of the ridge is normal to the symmetry boundary, and connection with the symmetry boundary occurs. The plot of axial vorticity in Figure (24d) shows another boundary layer forming behind the separated secondary vorticity. The separated secondary vorticity also induces a velocity on the primary vortex core that causes a rebound. This phenomenon is more clearly seen from other perspectives (not shown).

Figures (24e) show more growth of the ridge at the base of the primary vortex, and the cross-axis vorticity at the top of the primary vortex appears to be strengthening. The boundary layer that is generated by the shed secondary vorticity is clearly visible in Figures (24e). A curved sheath of secondary vorticity is being wrapped around the primary vortex.

Figures (24f) show two distinctive ridges of cross-axis vorticity wrapped around the primary vortex tube. The plot of axial vorticity shows that a fat secondary vortex is beginning to form at the top of the vortex tube. At the bottom of the vortex tube, a filament of secondary vorticity has broken away from the sheath of secondary vorticity that is wrapping around the primary vortex. The plot of total vorticity in Figure (24f) illustrates that the vortex lines move down the sheath of secondary vorticity, feed into the ridge of cross-axis vorticity

from underneath, move parallel along the ridge of cross-axis vorticity, and exit through the filament of secondary vorticity.

Figures (24g) show that the ridges have swelled into tubes of cross-axis vorticity. As illustrated in the plot of axial vorticity, the secondary vortex is clearly attached to the sheath of secondary vorticity, whereas the filament of axial vorticity at the base of the tube hangs free. In Figure (25) the image of the  $|\vec{\omega}|=0.5$  isosurface of vorticity is reflected about its midspan to emphasize the structure of the U-shaped vortex tubes that are wrapped around the primary vortex.

Although our no-slip wall simulations do not permit the connection of normal vorticity with the wall, we can speculate as to how normal vorticity would connect with a contaminated free surface. As illustrated in Figures (24g & 25), the tips of the U-shaped vortex tubes are wrapped around the primary vortex to the point where contact may occur with the free surface. In addition, as the secondary vorticity is wrapped around the primary vortex core, the velocities induced by the secondary vorticity on the primary vortex can cause the primary vortex to collide with the wall again. This reasoning is supported by the two-dimensional simulations of vortex pairs by Orlandi (1990), which show multiple rebounds of the primary vortex and multiple ejections of secondary vorticity. The same flow field which causes the primary vortex to impact the wall a second time should also propel the U-vortices against the free surface. Once the U-vortices are near the free surface, the bases of the U-vortices can open up to form two closely-spaced dimples on the outboard side of the primary vortex. Similarly, the tips of the U-vortices, where they connect with sheath of secondary vorticity, can also open up, and they too will form two pairs of closely-spaced dimples on the free surface.

In Figure (26) we show how well energy is conserved for the no-slip wall case. We observe that the kinetic energy is reduced to about 50% of its initial value, and the attenuation of the kinetic energy is conserved to within 3% relative to its initial value. As mentioned earlier, the average divergence over all the grid points is maintained to within a tolerance of  $10^{-6}$ . This evidence together with earlier validation studies confirm the reliability of the numerical simulation.

As already shown in Figures (24a-c), the longitu-

dinal structure of the helical vorticity involves inner and outer sheets of vorticity that are tucked inside of each other. These sheets of helical vorticity would tug at the free-surface boundary layer in both directions along the axis of the primary vortex tube. Figures (27a-c) show the cross-track vorticity evaluated on a no-slip wall at different instants of time. These figures show a banded structure, especially when one considers the symmetry conditions that are imposed at the ends of the  $y$ -axis. Our numerical simulations of vortex tubes interacting with clean free surfaces at low Froude numbers also develop helical vortices, but the free surface does not form any striations (banded structures). This suggests that the striations that are observed in laboratory experiments (see Sarpkaya & Henderson, 1984; and Sarpkaya, 1986) are probably the result of helical vorticity interacting with a contaminated free surface. We hypothesize that a trailing vortex pair sweeps the free surface clean of surfactants at different rates in the central region of the vortex pair due to the influence of axial flows induced by the helical vorticity. As a result, the concentration levels of the surfactants will have a banded structure that is normal to the track of the trailing vortices. Furthermore, we expect this sweeping phenomenon to be strongest during the initial interactions of the vortex pair with the free surface because the helical vorticity is strongest at that moment. This conjecture regarding the strength is supported by the sequence of contour plots we provide in Figures (27a-c), which show that the cross-track vorticity attenuates with time due to viscous effects. In addition, we may also expect to see dimples at the ends of the striations because the helical vortex sheets ultimately lead to the reconnection of normal vorticity with the free surface.

In summary, we believe that the essential stages of the reconnection of secondary vorticity with the free surface are as follows:

- Generation of helical vortex sheets by the primary vortex tube due to the onset of a helical instability.
- Stripping of the helical vortex sheets due to self-induced straining flows.
- Attachment of the helical vortex sheets to the separated free-surface boundary layer.
- Wrapping of U-shaped vortices around the pri-



mary vortex tube.

- Feeding of boundary-layer vorticity into the U-vortices.
- Reconnection of the tips of the U-vortices with the free surface as the primary vortex wraps the tips of the U-shaped vortices into contact with the free surface.
- Reconnection of the bases of the U-vortices with the free surface as the primary vortex tube collides with the wall a second time after the first rebound and carries the U-vortices into contact with the free surface.

We have also shown evidence which suggests that striations that may be observed on the free surface above a pair of trailing tip vortices are caused by helical vorticity.

## 5 Conclusions

We have developed numerical methods for the direct simulation of the three-dimensional Navier-Stokes equations with a free surface. These time-dependent simulations are feasible due to the small memory requirements and vectorized solution capabilities of a unique application of multigrid finite-difference methods. The numerical schemes have been used to investigate the interactions of ring vortices and vortex tubes with walls and free surfaces.

In the case of vortex rings interacting with walls, our numerical simulations, which show the formation of secondary and tertiary vortex rings, agree qualitatively with experiments. In addition, we show that secondary and tertiary vortex rings generate their own boundary layers, a phenomenon that has apparently not been observed in experiments. Similarly, secondary vortex rings are also shed by clean free surfaces at intermediate Froude numbers. At lower Froude numbers, free surfaces appear to behave like free-slip walls so that as the ring expands outward radially, the core diameter is reduced due to stretching and the core appearance develops a distinctive head and tail shape. These low Froude number results also agree qualitatively with experimental measurements of vortex rings interacting with clean free surfaces.

Our numerical studies of vortex tubes interacting with the free surface show that primary and secondary vorticity may connect with the free surface. The free-surface signatures of these two mechanisms are distinctly different. One type of primary vortex reconnection forms a cusp pattern on the free surface, and secondary vorticity reconnection should appear as paired dimples on the free surface. The essential aspects of the reconnection of secondary vorticity with the free surface include the generation of U-shaped vortices by helical vorticity shed from the primary vortex tube, the wrapping of the U-shaped vortices around the primary vortex tube, and the reconnection of the bases and tips of the U-shaped vortices with the free surface. We also provide evidence which suggests that free-surface striations observed above a pair of trailing tip vortices are caused by helical vorticity emanating from the primary vortex tube.

There are many questions that need answering and problems that need resolving as we continue our efforts to develop computational models for three-dimensional viscous flows involving a free surface. Some of the more immediate issues that need to be addressed are:

- *Experimental validations.* Until recently the technology did not exist for quantitative comparisons between numerical simulations and experimental measurements of time-dependent viscous flows. There have, however, been significant recent advances in both these fields. In the area of flow visualization, three-dimensional graphical techniques are helping us to understand numerical simulations of complex flows (Schiavone & Papathomas, 1990) heretofore not easy to comprehend. Similar advances have also occurred in the laboratory. A noteworthy example is Willert & Gharib's (1990) Digital Particle Image Velocimetry (DPIV) which allows the analysis of temporal evolutions of two-dimensional cuts of low speed flows. One application of the DPIV technology is the specification of initial conditions for vortex ring simulations. For example, the use of DPIV measurements as input to numerical models would allow detailed comparisons between theories and experiments. Validation studies of this sort should result in rapid progress in the understanding of viscous free-surface flows.



- *Radiation conditions.* Wave reflections contaminate the present simulations of a vortex tube moving parallel to a free surface, and in addition the vortex tube has strong interactions with its own images. In order to alleviate these problems, possible solutions include the implementation of far-field matching boundaries to eliminate wave reflections (Dommermuth & Yue, 1987), and the use of multi-pole expansions to eliminate the effects of images (*e.g.*, Chamberlain & Liu, 1985).
- *Nonlinear free-surface boundary conditions.* Our present method assumes that the amplitude of the free-surface is smaller than the thickness of the boundary layer. This assumption is no longer valid at higher Reynolds numbers and moderate Froude numbers. Fully-nonlinear free-surface boundary conditions would remove this restriction, but their implementation will at least require the use of an adaptive grid (*e.g.*, Thompson & Ferziger, 1989).
- *Surfactants.* In the open ocean, surfactants inhibit the generation of short waves by wind, and in the absence of wind the damping of short waves increases if surfactants are present (see Dorrestein, 1951). In ship wakes, slicks consisting of compacted surfactant material form on either side of the ship track possibly due to the action of vortices moving surface water away from the wake center (see Kaiser, *et al.*, 1986). These slicks damp capillary and gravity-capillary waves crossing the ship wake. In addition, experiments of Bernal, *et al.*, (1989) show that the interaction of vortices with these slicks may lead to the formation of secondary vorticity. A linear stability analysis of surface-tension effects indicates that limitations on time-step size would be too restrictive for explicit schemes. The situation does not improve with the addition of surfactants since the gradients of surface-tension must be balanced by viscous stresses within the free-surface boundary layer. We anticipate that a fully-implicit time-stepping scheme will be required.
- *Free-surface turbulence.* Even without the additional complexity of a free surface, Frisch & Orszag (1990) note that the study of turbulence continues to pose unique challenges

that are no less formidable than those occurring in post-Newtonian physics. Some of the unique aspects of free-surface turbulence are illustrated by the entrainment of air due to breaking waves and the exchange of energy at the air-water interface (Bonmarin, 1989). Solutions to these problems will certainly require major developments in turbulence theories and models currently being developed for unbounded and wall-bounded flows.

In view of these formidable challenges, the present work represents only a modest first step toward what we believe will be a most exciting and fruitful journey.

**Acknowledgements:** This research is financially supported by the Office of Naval Research. Much of this work is based on the multigrid research of DGD which is supported by ONR Code 1215 (contract N00014-90-C-0027). DKPY is supported by ONR Code 11 (contract N00014-90-J-1158). Although the majority of DGD's research in the viscous flow area is a personal endeavor, he is grateful to Science Applications International Corporation (SAIC) for their understanding and partial financial support. Most of the reported computations have been performed on the Cray Research, Inc., Cray-2S through a grant from the Industry, Science, and Technology Department. Some computations have also been performed on the NSF Pittsburgh Supercomputer Center Cray Y-MP. We thank the members of the Naval Hydrodynamics Division at SAIC for their encouragement and support. In particular, we are grateful to R.E. Hall, G.E. Innis, D. Liepmann, and D.J. Loeser for their fruitful interactions, and we especially thank J.C. Talcott for his graphics expertise.

## REFERENCES

- Baba, E. (1969). A new component of viscous resistance of ships. *J. Soc. Naval Arch. Japan*, 125, 23-34.
- Bernal, L.P., Hirsa, A., Kwon, J.T., & Willmarth, W.W. (1989). On the interaction of vortex rings and pairs with a free surface for varying amounts of surface active agent. *Phys. Fluids*, A 1 (12), 2001-2004.
- Bonmarin, P. (1989). Geometric properties of deep-water breaking waves. *J. Fluid Mech.*, 209, 405-433.
- Brandt, A. & Dinar, N. (1977). Multigrid solution to elliptic flow problems. In *Numerical methods in Partial Differential Equations* (ed. S.V. Parter), Academic Press, 53-147.

- Briley, W.R. & McDonald, H. (1973). Solution of the three-dimensional compressible Navier-Stokes equations by an implicit technique, *Proc. Fourth Int. Conf. Num. Methods Fluid Dyn.*, Boulder, Colorado, *Lecture Notes in Physics*, 35, Springer-Verlag, 105-110.
- Brown, E.D., Buchsbaum, S.B., Hall, R.E., Penhune, J.P., Schmitt, K.F., Watson, K.M., & Wyatt, D.C. (1988). Observations of a nonlinear solitary wave packet in the Kelvin Wake of a Ship. *J. Fluid Mech.*, 204, 263-293.
- Brown, G.L. & Roshko, A. (1974). On density effects and large structures in turbulent mixing layers. *J. Fluid Mech.*, 64, 775-816.
- Cerra, A.W. & Smith, C.R. (1983). Experimental observations of vortex ring interaction with the fluid adjacent to a surface. *Dept. of Mech. Eng. and Mechanics, Lehigh University*, Report FM-4.
- Chamberlain, J.P. & Liu, C.H. (1985). Navier-Stokes calculations for unsteady three-dimensional vortical flows in unbounded domains. *AIAA J.*, 23: 868-874.
- Chen, C.-J. & Chen, H.-C. (1982). The finite analytic method. *Iowa Institute of Hydraulic Research*, Report No. 232-IV.
- Chorin, A.J. (1967). A numerical method for solving incompressible viscous flow problems. *J. Comp. Phys.*, 2: 12-26.
- Crow, S. (1970). Stability theory for a pair of trailing vortices *AIAA J.*, 8: 2172-2179.
- Dahm, W.J.A., Scheil, C.M., & Tryggvason, G. (1989). Dynamics of vortex interaction with a density interface. *J. Fluid Mech.*, 205, 1-43.
- Dommermuth, D.G. & Yue, D.K.P. (1987). Numerical simulations of nonlinear axisymmetric flows with a free surface. *J. Fluid Mech.*, 178: 195-219.
- Dorrestein, R. (1951). General linearized theory of the effect of surface films on water ripples. I & II. In *Proc. Amsterdam Acad. of Sci.*, 54, 260-272, 350-356.
- Dritschel, D.G. (1989). Strain-induced vortex stripping. In *Mathematical Aspects of Vortex Dynamics* (ed. R.E. Caflisch), SIAM, 107-119.
- Fohl, T. & Turner, J.S. (1975). Colliding vortex rings. *Phys. Fluids*, 18: 433-436.
- Frisch, U. & Orszag, S.A. (1990). Turbulence: challenges for theory and experiment. *Physics Today*, January, 24-32.
- Fromm, J. (1964). The time dependent flow of an incompressible viscous fluid. *Meth. in Comp. Phys.*, 3: 345-383.
- Fuchs, L. & Zhao, H.-S. (1984). Solution of three-dimensional viscous incompressible flows by a multi-grid method. *Int. J. Numer. Meth. Fluids*, 4: 539-555.
- Ghia, K.N., Hankey, W.L., & Hodge, J.K. (1977). Study of incompressible Navier-Stokes equations in primitive variables. In *3rd Comp. Fluid Dyn. Conf.*, AIAA, 156-167.
- Grosenbaugh, M.A. & Yeung, R.W. (1988). Nonlinear bow flows - an experimental and theoretical investigation. In *Proc. 17th Symp. on Naval Hydro.*, The Hague, 49-67.
- Hackbusch, W. (1985). *Multi-grid methods and applications* Springer-Verlag.
- Hartwich, P.-M. & Hsu, C.-H. (1988). High resolution upwind schemes for the three-dimensional, incompressible Navier-Stokes equations. *AIAA J.*, 26
- Harvey, J.K. & Perry, F.J. (1971). Flowfield produced by trailing vortices in the vicinity of the ground. *AIAA J.* 15: 250-260.
- Hirsa, A., Tryggvason, G., Abdollahi-Alibeik, J., & Willmarth, W.W. (1990). Measurement and computations of vortex pair interaction with a clean or contaminated free surface. In *Proc. 18th Symp. on Naval Hydro.*, Ann Arbor, To appear.
- Hirt, C.W., Nichols, B.D., & Romero, N.C. (1975). SOLA-A numerical solution algorithm for transient fluid flows. *Los Alamos Scientific Lab.*, Report No. LA-5852.
- Issa, R.I. (1985). Solution of the implicitly discretized fluid flow equations by operator-splitting. *J. Comp. Phys.*, 62: 40-65.
- Kaiser, J.A.C., Garrett, W.D., Ramberg, S.E., Peltzer, R.D., & Andrews, M.D. (1986). WAKEX 86: A ship wake/films exploratory experiment. Naval Research Laboratory, NRL memorandum Report 6270.
- Kambe, T. & Takao, T. (1971). Motion of distorted vortex rings. *J. Phys. Soc. Japan*, 31 (2), 591-599.
- Kerwin, J.E. (1986). Marine propellers. *Ann. Rev. Fluid Mech.*, 18, 367-403.
- Kida, S., Takaoka, M., & Hussain, F. (1989). Reconnection of two vortex rings. *Phys. Fluids*, A 1 (4): 630-632.
- Kim, J. & Moin, P. (1985). Application of a fractional-step method to incompressible Navier-Stokes equations. *J. Comp. Phys.*, 59: 308-323.
- Kwon, J.T. (1989). Experimental study of vortex ring interaction with a free surface. Ph.D. thesis, University of Michigan, Dept. of Aero. Eng.
- Lamb, H. (1932). *Hydrodynamics*, Dover Publications.
- Leonard, A. (1980). Vortex methods for flow simulation. *J. Comp. Phys.* 37, 289-335.
- Leonard, A. (1985). Computing three-dimensional incompressible flows with vortex elements. *Ann. Rev. Fluid Mech.* 17, 523-559.
- Liepmann, D. (1990). Ph.D. thesis, University of California, San Diego, Dept. of App. Mech.
- Lyden, J.D., Hammond, R.R., Lyzenga, D.R., & Shuchman, R.A. (1988). Synthetic aperture radar imaging of surface ship wakes. *J. of Geophys. Res.*, 93 (C10), 12,293-12,303.
- Madnia, K. & Bernal, L.P. (1989). Interaction of a turbulent round jet with the free surface. *The University*

- of Michigan Prog. in Ship Hydro., Report No. 89-05.
- Meiron, D.I., Shelly, M.J., Ashurst, W.T., & Orszag, S.A. (1989). Numerical studies of vortex reconnection. In *Mathematical Aspects of Vortex Dynamics* (ed. R.E. Caflisch), SIAM, 183-194.
- Melander, M.V. & Hussain, F. (1988). Cut-and-connect of two antiparallel vortex tubes. In *Studying turbulence using numerical simulation databases - II: proceedings of the 1988 summer program*, Center for Turbulence Research, NASA Ames Research Center & Stanford University, Report CTR-S88.
- Miyata, H. & Nishimura, S. (1985). Finite-difference simulation of nonlinear ship waves. *J. Fluid Mech.*, **157**: 327-357.
- Mori, K. (1984). Necklace vortex and bow wave around blunt bodies. In *Proc. 15th Symp. on Naval Hydro., Hamburg*, 303-317.
- Munk, W.H., Scully-Power, P., & Zachariasen, F. (1987). The Bakerian Lecture, 1986. Ships from space. *Proc. R. Soc. Lond., A* **412**, 231-254.
- Norbury, J. (1973). A family of steady vortex rings. *J. Fluid Mech.*, **57**, 417-431.
- Ohring, S. & Lugt, H.J. (1989). Two counter-rotating vortices approaching a free surface in a viscous fluid. *David Taylor Research Center*, Report No. DTRC-89/013.
- Ohsima, Y. & Asaka, S. (1977). Interaction of two vortex rings along parallel axes in air. *J. Phys. Soc. Japan*, **42** (2), 708-713.
- Ohsima, Y. & Izutsu, N. (1988). Cross-linking of two vortex rings. *Phys. Fluids*, **31** (9), 2401-2403.
- Orlandi, P. (1990). Vortex dipole rebound from a wall. *Phys. Fluids A*, **2** (8), 1429-1436.
- Orszag, S.A. & Patterson, G.S. (1972). Numerical simulation of three-dimensional homogeneous isotropic turbulence. *Phys. Rev. Lett.* **28**, 76-79.
- Patankar, S.V. & Spalding, D.B. (1972). A calculation procedure for heat, mass, and momentum transfer in three-dimensional parabolic flows. *Int. J. Heat Mass Trans.*, **15**: 1787-1806.
- Patankar, S.V. (1981). A calculation procedure for two-dimensional elliptic situations. *Numer. Heat Trans.*, **4**: 409-425.
- Patera, A.T. (1984). A spectral element method for fluid dynamics: laminar flow in a channel expansion. *J. Comp. Phys.* **54**, 468-488.
- Peace, A.J. & Riley, N. (1983). A viscous vortex pair in ground effect. *J. Fluid Mech.*, **129**: 409-426.
- Peltzer, R., J. Kaiser, O. Griffin, W. Barger, & Skop, R. (1990). Hydrodynamics of ship wake surfactant films. In *Proc. 18th Symp. on Naval Hydro., Ann Arbor*, To appear.
- Roache, P.J. (1976). *Computational fluid dynamics*. Hermosa.
- Roshko, A. (1954). Structure of turbulent shear flows: a new look. *AIAA J.*, **14**, 1349-1457.
- Saffman, P.G. (1978). The approach of a vortex pair to a plane surface in inviscid fluid. *J. Fluid Mech.*, **92**, 497-503.
- Saffman, P.G. & Baker G.R. (1979). Vortex interactions *Ann. Rev. Fluid Mech.* **11**, 95-122.
- Sarpkaya, T., & Henderson, D.O. (1984). Surface disturbances due to trailing vortices, *Naval Postgraduate School, Monterey, CA*, Technical Report No. NPS-6984004.
- Sarpkaya, T. (1986). Trailing-vortex wakes on the free surface. In *Proc. 16th Symp. on Naval Hydro., Berkeley*, 38-50.
- Sarpkaya, T., Elnitsky, J., & Leeker, R.E. (1988). Wake of a vortex pair on the free surface. In *Proc. 17th Symp. on Naval Hydro., The Hague*, 47-54.
- Schatzle, P.R. (1987). An experimental study of fusion of vortex rings. Ph.D. thesis, California Institute of Technology.
- Scott, J.C. (1982). Flow beneath a stagnate film on water: The Reynolds ridge. *J. Fluid Mech.*, **116**, 283-296.
- Schlichting, H. (1968). *Boundary-layer theory*, McGraw-Hill.
- Schiavone, J.A. & Papathomas, T.V. (1990). Visualizing meteorological data. *Bulletin of the Amer. Meteorological Soc.* **71** (7), 1012-1020.
- Shariff, K., Leonard, A., & Ferziger, J.H. (1989). Dynamics of a class of vortex rings. *Ames Research Center, Moffet Field, CA*, NASA Technical Memorandum 102257.
- Siggia, E.D. & Pumir, A. (1987). Vortex dynamics and the existence of solutions to the Navier-Stokes equations. *Phys. Fluids*, **30**, 1606-1626.
- Spreiter, J.R. & Sacks, A.H. (1951). The rolling up of the trailing vortex sheet and its effect on the downwash behind wings. *J. Aero. Sci.*, **18**: 21-32.
- Stanaway, S., Shariff, K., & Hussain, F. (1989). Head-on collision of viscous vortex rings. In *Studying turbulence using numerical simulation databases - II: proceedings of the 1988 summer program*, Center for Turbulence Research, NASA Ames Research Center & Stanford University, Report CTR-S88.
- Streeter, V.L. (1948). *Fluid dynamics*, McGraw-Hill.
- Takekuma, K. & Eggers, K. (1984). Effect of bow shapes on the free-surface shear flow. In *Proc. 15th Symp. on Naval Hydro., Hamburg*.
- Telste, J.G. (1989). Potential flow about two counter-rotating vortices approaching a free surface. *J. Fluid Mech.*, **201**:
- Thompson, M.C. & Ferziger, J.H. (1989). An adaptive multigrid technique for the incompressible Navier-Stokes equations. *J. Comp. Phys.*, **82**: 94-121.

Vanka, S.P. (1986). Block-implicit multigrid solution of Navier-Stokes equations in primitive variables. *J. Comp. Phys.*, 65: 138-158.

Walker, J.D.A. (1978). The boundary layer due to a rectilinear vortex. *Proc. R. Soc. Lond. A* 359. 167-188.

Walker, J.D.A., Smith, C.R., Cerra, A.W., & Doligalski, T.L. (1987). The impact of a vortex ring on a wall. *J. Fluid Mech.* 181. 99-140.

Warming, R.F. & Beam, R.M. (1978). On the construction and application of implicit factored schemes for conservation laws. *SIAM-AMS proc.*, 11: 85-129.

Wehausen, J.V. & Laitone, E.V. (1960). Surface waves. *Handbuch der Physik*, 9: 446-778. Springer.

Willert, C.E. & Gharib, M. (1990). Digital particle image velocimetry applied to an evolving vortex ring. To appear in *Exp. in Fluids*.

Willmarth, W.W., Tryggvason, G., Hirs, A., & Yu, D. (1988). Vortex pair generation and interaction with a free surface. *Phys. Fluids*, A 1 (20), 170-172.

Winckelmans, G., & Leonard, A. (1989). Numerical studies of vortex reconnection. In *Mathematical Aspects of Vortex Dynamics* (ed. R.E. Caflisch), SIAM, 25-35.

Yu, D. & Tryggvason, G. (1990). The surface signature of unsteady, two-dimensional vortex flows. *Submitted for publication*.

## Appendix A: Axisymmetric Flow Equations

Our studies of vortex rings interacting with walls and free-surfaces are based on an axisymmetric formulation. We summarize the basic equations in this appendix. The finite-difference forms of these equations are directly related to our full three-dimensional formulation. Let  $v$  and  $w$  respectively denote the radial ( $r$ ) and axial ( $z$ ) velocities, then the axisymmetric momentum equations for  $r > 0$  are:

$$\begin{aligned} w_t + (ww)_z + (vw)_r + \frac{vw}{r} = \\ -p_z + \frac{1}{Re}(w_{zz} + w_{rr} + \frac{w_r}{r}) \\ v_t + (vw)_z + (vv)_r + \frac{v^2}{r} = \\ -p_r + \frac{1}{Re}(v_{zz} + v_{rr} + \frac{v_r}{r} - \frac{v}{r^2}) . \end{aligned} \quad (47)$$

For  $r = 0$  the radial velocity is zero,  $v = 0$ , and we

use the following limiting form for the axial momentum:

$$w_t + (ww)_z + 2(vw)_r = -p_z + \frac{1}{Re}(w_{zz} + 2w_{rr}) .$$

Similarly, the equations for mass conservation are:

$$\begin{aligned} w_z + v_r + \frac{v}{r} &= 0 \quad \text{for } r > 0 \\ w_z + 2v_r &= 0 \quad \text{for } r = 0 . \end{aligned} \quad (48)$$

The gradient of the momentum equations (47) gives a Poisson equation for the pressure:

$$\begin{aligned} p_{zz} + p_{rr} + \frac{p_r}{r} = \\ -w_z w_z - 2v_z w_r - v_r v_r - \frac{v^2}{r^2} \quad \text{for } r > 0 \\ p_{zz} + 2p_{rr} = \\ -w_z w_z - 2v_z w_r - 2v_r v_r \quad \text{for } r = 0 . \end{aligned} \quad (49)$$

If the thickness of the free-surface boundary layer is greater than the amplitude of the free-surface elevation, then the linearized free-surface boundary conditions for axisymmetric flow are:

$$\begin{aligned} v_z &= 0 \quad \text{for } r \geq 0 \\ \eta_t + v\eta_r &= w \quad \text{for } r \geq 0 \\ -p + \frac{1}{F_r^2}\eta &= \frac{1}{We}(\eta_{rr} + \frac{\eta_r}{r}) \quad \text{for } r > 0 \\ -p + \frac{1}{F_r^2}\eta &= \frac{2}{We}\eta_{rr} \quad \text{for } r = 0 . \end{aligned} \quad (50)$$

We use the following stream function formulation to calculate the initial velocity field for  $r > 0$ :

$$\begin{aligned} w = \frac{\psi_r}{r}, \quad v = -\frac{\psi_z}{r}, \quad \omega_o = v_z - w_r, \\ \text{and } \psi_{zz} + \psi_{rr} - \frac{\psi_r}{r} = -r\omega_o . \end{aligned} \quad (51)$$

On  $r = 0$ , the limiting forms are  $v = 0$ ,  $\omega_o = 0$ ,  $\psi = 0$ , and  $w = \psi_{rr}$ .



The conservation of energy equation with a linearized surface-tension term is as follows:

$$\begin{aligned} \frac{1}{2} \frac{d}{dt} \int_V r (w^2 + v^2) + \frac{1}{2F_r^2} \frac{d}{dt} \int_{S_f} r \eta^2 = \\ \frac{1}{We} \int_{S_f} r \eta_t (\eta_{rr} + \frac{\eta_r}{r}) \\ - \frac{1}{Re} \int_V r [2(w_z^2 + v_r^2 + \frac{v^2}{r^2}) + (v_z + w_r)^2] . \quad (52) \end{aligned}$$

## Appendix B: Multigrid solution of the hydrodynamic pressure

Consider the following segment of code which is written in quasi-FORTRAN to illustrate a typical multigrid solution of the hydrodynamic pressure:

```
CALL SOURCE
IF(WALL PROBLEM) CALL FEASIBLE
IF(FREE-SURFACE) CALL SURFACE_PRESSURE
DO WHILE MULTIGRID
DO WHILE FINE-TO-COARSE GRID
CALL SOLVE_PRESSURE
CALL RESTRICTION
IF(WALL PROBLEM) CALL FEASIBLE
ENDDO
DO WHILE COARSE-TO-FINE GRID
CALL PROLONGATION
CALL MINUS
ENDDO
ENDDO
CALL SOLVE_PRESSURE
```

Subroutine SOURCE assigns the source term in the Poisson equation for pressure (see Eqs. 26, 29, and 32), and subroutine FEASIBLE makes the source term compatible with pure Neumann boundary conditions based on (40) and (41). Since free-surface problems involve mixed Dirichlet and Neumann boundary conditions, subroutine FEASIBLE is not called, but instead subroutine SURFACE\_PRESSURE is used to assign the pressure on the free-surface (Eqs. 11 and 12).

Upon completion of subroutines SOURCE, FEASIBLE, and SURFACE\_PRESSURE, we implement a V-cycle multigrid algorithm using an unstaggered grid with uniform mesh coarsening. At the finest grid level the number of grid points along the x-, y-, and z-axes are respectively  $I_{max} = 2^{i_{pow}} + 1$ ,

$J_{max} = 2^{j_{pow}} + 1$ , and  $K_{max} = 2^{k_{pow}} + 1$ . The total number of grid points is  $N_{tot} = I_{max} \times J_{max} \times K_{max}$ , and the next finest grid level has about 1/8 the number of grid points, and the coarsest grid level has  $3 \times 3 \times 3 = 27$  grid points. The total number of grid levels is equal to the maximum of  $i_{pow}$ ,  $j_{pow}$ , and  $k_{pow}$ .

The fine-to-coarse grid iterations start with a call to subroutine SOLVE\_PRESSURE which uses a vectorized Gauss-Seidel smoother with checkerboard ordering followed by two iterations of vectorized Jacobi iteration. Upon completion of the Jacobi iterations, SOLVE\_PRESSURE also calculates the residual error. The calling arguments of SOLVE\_PRESSURE include vectors to store at all grid levels the pressure solutions, the source terms, and the residual errors. As a result, each vector requires approximately  $(1 + 1/8 + 1/64 + \dots)N_{tot} = 8N_{tot}/7$  storage locations. An array pointer is used to position each vector at the correct grid level in the calling arguments of SOLVE\_PRESSURE. The pressure solver is discussed in more detail in the next paragraph.

Subroutine RESTRICTOR uses a 27-point restrictor to calculate the source terms at the next coarser grid level based on the residual errors at the current grid level. The 27-point restrictor is calculated in three sweeps over the i, j, and k grid lines using a vectorized 3-point restrictor:  $\frac{1}{4}(1, 2, 1)$ . If a wall problem is being solved, subroutine FEASIBLE is called to make the source terms realizable at each of the coarse grid levels. The fine-to-coarse grid iterations continue until the coarsest grid level is reached, and then the coarse-to-fine grid iterations begin.

Subroutine PROLONGATION uses 27-point prolongation to interpolate the solutions of the coarse grid equations onto the next finer grid. The 27-point prolongation is calculated in three sweeps over the grid lines using a vectorized piecewise linear interpolation. Subroutine MINUS corrects the solutions at the finer grid levels by using the interpolated data from coarser grid levels. The coarse-to-fine grid iterations continue until the finest grid level is reached. At this point the V-cycles may stop if the residual errors are small enough; otherwise we start another V-cycle. We conclude the multigrid iterations with a post-smoothing step represented by a call to SOLVE\_PRESSURE.



The Gauss-Seidel smoother in SOLVEPRESSURE is by far the most computationally intensive portion of the multigrid scheme. In addition, the Gauss-Seidel smoother also has to be very general because it must work on all grid levels. Consider the following FORTRAN code for the Poisson solver with Neumann (wall) boundary conditions:

```

1. DX2= 1.0/(DX*DX)
2. DY2= 1.0/(DY*DY)
3. DZ2= 1.0/(DZ*DZ)
4. FAC=-0.5/(DX2+DY2+DZ2)
5. DO 10 IGAUS=1,ITER
6. DO 10 ITYPE=1,27
7. CALL INDICE(LEVEL,ITYPE,IBEG,IEND)
8. CALL JUMPER(ITYPE,ISKIP,JSKIP,
  1          KSKIP,MOVE)
9. DO 10 IVECT=1,2
10. CALL DOCRAY(IGAUS,IVECT,IBEG,IEND,
  1          ISTAR,IFINI,ISTEP)
11. CDIR$ IVDEP
12. DO 10 I=ISTAR,IFINI,ISTEP
13. IC=IPOINT(I)
14. PNEW(IC)=
  1 -(DX2*(PNEW(IC+MOVE(2))
  2      +PNEW(IC+MOVE(1)))
  3 +DY2*(PNEW(IC+MOVE(4))
  4      +PNEW(IC+MOVE(3)))
  5 +DZ2*(PNEW(IC+MOVE(6))
  6      +PNEW(IC+MOVE(5)))
  7 -PSOU(IC))*FAC
15. 10 CONTINUE

```

Lines 1 through 3 calculate off-diagonal elements in the linear system of equations. DX, DY, and DZ are the grid spacings, which depend on grid level, along the x-, y-, and z-axes respectively. FAC is the inverse of the diagonal element. The outer-most DO-loop at line 5 controls the number (ITER) of Gauss-Seidel iterations. The second DO-loop at line 6 sweeps over the 27 different portions of the computational domain: 1 set of interior grid points, 6 sets of side grid points, 12 sets of edge grid points, and 8 sets of corner grid points.

Subroutine INDICE returns two pointers (IBEG & IEND) that describe where grid points are stored in a pointer array IPOINT as a function of grid level (LEVEL) and the type of boundary (ITYPE). Subroutine JUMPER describes how off-diagonal elements are related to the diagonal elements as a function of boundary type.

The arguments of JUMPER include skip parameters which depend on the grid level. If the pressure is stored i-indices first, j-indices second, and k-indices last, then ISKIP=1, JSKIP= $I_{max}$ , and KSKIP= $I_{max} \times J_{max}$  at the finest grid level. Subroutine JUMPER returns a 6-integer array named MOVE which stores the skip parameters along the i-, j-, and k-axes. For the interior points, MOVE(1)=-ISKIP, MOVE(2)=ISKIP, MOVE(3)=-JSKIP, MOVE(4)=JSKIP, MOVE(5)=-KSKIP, and MOVE(6)=KSKIP. Suppose the grid points are on the  $i=1$  side boundary, and on this boundary we specify free-slip boundary conditions for the pressure. We pretend that a fictitious set of grid points exists at  $i=-1$ , and we set these grid points equal to the grid points at  $i=2$ . This is a second-order difference formula which can be implemented by setting MOVE(1)=ISKIP (note the positive sign).

The pointer array IPOINT stores grid points sequentially as a function of the boundary type and grid level. For example, for the interior points at the finest grid level, we make the following assignments:

```

IBEG=1
IEND=0
DO 10 K=2,KMAX-1
KC=(K-1)*KSKIP
DO 10 J=2,JMAX-1
JC=(J-1)*JSKIP+KC
DO 10 I=2,IMAX-1
IC=I+JC
IEND=IEND+1
IPOINT(IEND)=IC
10 CONTINUE

```

Based on this type of ordering of IPOINT, the DO-loop at line 9 can set up a chequer-board ordering of the Gauss-Seidel solver. Subroutine DOCRAY controls sweeps over the odd or even grid points in the forward or backward direction as a function of IGAUS and IVECT. The table below summarizes what DOCRAY returns as values for ISTAR, IFINI, and ISTEP:

IGAUS	IVECT	ISTAR	IFINI	ISTEP
odd	1	IBEG	IEND	2
odd	2	IBEG+1	IEND	2
even	1	IEND	IBEG	-2
even	2	IEND-1	IBEG	-2

Line 11 is a CRAY directive which specifies that the inner-most DO-loop vectorizes. The inner-most DO-loop implements Gauss-Seidel iteration using a 7-point star for the Laplace operator. The diagonal element is IC, and the assignments of the off-diagonal elements are controlled by MOVE. PNEW stores the pressures, and PSOU stores the source terms. Note that PSOU may also be used to store inhomogeneous Neumann boundary conditions. The inner DO-loop vectorizes because ISTEP=2 ensures that no diagonal element is a function of another diagonal element until the DO-loop is exited. As a result, half of the interior grid points vectorize in the Gauss-Seidel solver.

The residual error that is associated with this vectorizing scheme has some high wavenumber content due to the alternating sweeps over the grid. As a result, the multigrid scheme will diverge unless measures are taken to smooth the residual error. We perform this additional smoothing by using two Jacobi iterations in addition to the Gauss-Seidel iterations. Jacobi algorithms vectorize without using chequer-board ordering, but their smoothing rate is slower than vectorized Gauss-Seidel and they require one additional vector for storage. However, as it turns out, we also need an additional vector to store the residual errors which we calculate after the Jacobi iterations are complete. We emphasize that the residual errors are calculated after the Jacobi iterations and not during the Jacobi iterations in order to provide the smoothest residual errors and the fastest convergence of the multigrid scheme.

$R_\Delta$	$N_{newt}$	$N_{mult}$	$N_{gaus}$	$\Delta t$	$N_{ramp}$	$N_{time}$	$N_{oper}$
1.0	1	2	1	.5	4	24	218
	1	2	1	.5	2	24	218
	1	2	1	.5	1	24	218
	1	2	1	.5	0	*	*
	1	2	1	.25	0	*	*
	1	2	1	.2	0	46	408
	1	2	1	.1	0	65	572
	1	2	1	.75	4	26	235
	1	2	1	1.0	4	28	253
	1	2	1	.25	4	33	296
	1	2	2	.5	4	24	278
	1	2	2	.25	4	32	365
	1	2	2	1.0	4	26	299
	1	2	3	.5	4	24	337
	1	2	3	1.0	4	25	350
	1	2	4	1.0	4	24	396
	1	1	1	1.0	4	225	1175
	1	1	2	.5	4	44	288
	1	1	2	1.0	4	50	326
	1	3	4	1.0	4	23	550
	1	3	8	1.0	4	23	893
	2	2	2	1.0	4	16	365
	2	3	8	1.0	4	16	1217
2.0	1	2	1	.75	4	32	287
	1	2	1	.75	2	32	287
	1	2	1	.75	1	36	322
	1	2	1	.75	0	*	*
	1	2	1	.01	0	*	*
	1	2	1	.005	0	710	6135
	1	2	1	.5	4	33	296
	1	2	1	.5	2	32	287
	1	2	1	.5	1	36	322
	1	2	1	.5	0	*	*
	1	2	1	1.0	4	34	304
	1	2	2	.5	4	33	376
	1	2	3	.5	4	34	469
	1	3	1	.5	4	34	426
	1	1	1	.5	4	258	1347
	2	2	1	.5	4	25	442
	2	1	1	.5	4	60	630

Table 1: *Convergence of implicit scheme to steady-state.*

The grid Reynolds number is denoted by  $R_\Delta$ , and the time step is  $\Delta t$ . The number of Newton-Raphson iterations, multigrid iterations, and Gauss-Seidel iterations are respectively  $N_{newt}$ ,  $N_{mult}$ , and  $N_{gaus}$ . The number of time steps and sweeps over the finest grid level are respectively  $N_{time}$  and  $N_{oper}$ . The number of time steps required to ramp down the initial viscosity to the prescribed viscosity is  $N_{ramp}$ . The initial viscosity is  $\nu_o = 1$  for all cases. Most of the solutions have converged to a tolerance  $\tau_o = 10^{-6}$ . Solutions that have diverged are denoted by an asterisk (\*).

Item	Run 1	Run 2	Run 3	Run 4	Run 5	Run 6
Code?	exp.	exp.	imp.	imp.	exp.	exp.
B.C.?	no	no	no	no	no	slip
$R_e$	400	400	400	400	400	400
$r_c$	0.5	0.5	0.5	0.5	0.5	0.5
$\omega_c$	-4	-4	-4	-4	-4	-4
$r_o$	1	1	1	1	1	1
$z_o$	-3	-3	-3	-3	-3	-3
$R_t$	4	4	4	4	6	6
$D_t$	4	4	4	4	6	6
$\Delta t$	0.005	0.0025	0.005	0.0025	0.0025	0.0025
$N_{time}$	3000	8000	3000	6000	6000	6000
$N_{newt}$	-	-	1	1	-	-
$N_{mult}$	2	2	2	2	2	2
$N_{gaus}$	5	8	5	8	8	8
$I_{max}$	129	257	129	257	257	257
$K_{max}$	129	257	129	257	257	257

Table 2: Data for ring vortices impinging on a wall.

The 'Code' item indicates whether the explicit (exp.) or semi-implicit (imp.) computer codes had been used to perform the calculation. The 'B.C.' item indicates whether a no-slip (no) or slip (slip) boundary condition is used on the wall at  $z = 0$ .  $R_e = \Gamma/(\pi \nu)$  is the Reynolds number. The initial core radius and peak vorticity are denoted by  $r_c$  and  $\omega_c$ . The vortex core is centered at  $(r_o, z_o)$ . The radius and depth of the tank are respectively  $R_t$  and  $D_t$ . The time step is  $\Delta t$ . The number of time steps, Newton-Raphson iterations for the implicit scheme, multigrid iterations, and Gauss-Seidel iterations are respectively denoted by  $N_{time}$ ,  $N_{newt}$ ,  $N_{mult}$ , and  $N_{gaus}$ . The number of grid points along the  $r$ - and  $z$ -axes are respectively  $I_{max}$  and  $K_{max}$ .

Item	Run 1	Run 2	Run 3	Run 4	Run 5	Run 6
$R_e$	400	400	400	200	200	200
$F_r^2$	0.5	0.25	0.125	0.5	0.25	0.125
$r_c$	0.5	0.5	0.5	0.5	0.5	0.5
$\omega_c$	-4	-4	-4	-4	-4	-4
$r_o$	1	1	1	1	1	1
$z_o$	-3	-3	-3	-3	-3	-3
$R_t$	6	6	6	6	6	6
$D_t$	4	4	4	4	4	4
$\Delta t$	0.0025	0.0025	0.0025	0.0025	0.0025	0.0025
$N_{time}$	6000	6000	6000	6000	6000	6000
$N_{mult}$	2	2	2	2	2	2
$N_{gaus}$	8	8	8	8	8	8
$I_{max}$	257	257	257	257	257	257
$K_{max}$	257	257	257	257	257	257

Table 3: Data for ring vortices impinging on a free-surface.

Most of the entries in this table are defined in Table (2), except for the Froude number  $F_r = \Gamma/(\pi g^{1/2} (r_o)^{3/2})$ .

Item	Run 1	Run 2	Run 3	Run 4	Run 5	Run 6	Run 7
B.C.?	noslp	noslp	noslp	free	free	free	free
$R_e$	200	200	400	200	200	400	200
$F_r^2$	0	0	0	0.25	0.25	0.25	0.25
$r_c$	0.5	0.25	0.25	0.5	0.25	0.25	0.5
$\omega_c$	4	16	16	4	16	16	4
$x_o$	1	1	1	1	1	1	2
$z_o$	-3	-3	-3	-3	-3	-3	-1
$x_{amp}$	-0.25	-0.25	-0.25	-0.25	-0.25	-0.25	-0.5
$z_{amp}$	-0.25	-0.25	-0.25	-0.25	-0.25	-0.25	-0.5
$L_t$	4	4	4	4	4	4	4
$W_t$	4	4	4	4	4	4	4
$D_t$	4	4	4	4	4	4	4
$\Delta t$	0.005	0.005	0.005	0.005	0.005	0.005	0.005
$N_{time}$	3000	3000	4000	3000	3000	3000	3000
$N_{mult}$	4	4	4	4	4	4	4
$N_{gaus}$	8	8	8	8	8	8	8
$I_{max}$	65	65	65	65	65	65	65
$J_{max}$	65	65	65	65	65	65	65
$K_{max}$	65	65	65	65	65	65	65

Table 4: *Data for vortex tubes impinging on walls and free surfaces.*

Runs 1 thru 6 use free-slip boundary conditions on the vertical walls, and Run 7 uses periodic boundary conditions along the  $x$ -axis. The axes of the vortex tubes are aligned with the  $y$ -axis. The 'B.C.' item indicates whether a no-slip (noslp) or free-surface (free) boundary condition is used on the wall at  $z = 0$ . The Reynolds number is denoted by  $R_e$  and the Froude number is  $F_r$ . The initial core radius and peak vorticity are denoted by  $r_c$  and  $\omega_c$ . The mean position of the vortex core is centered at  $(x_o, z_o)$ . The initial amplitudes of the sinusoidal perturbations in the core's position are  $x_{amp}$  and  $z_{amp}$ . The length ( $x$ ), width ( $y$ ), and depth ( $z$ ) of the tank are respectively  $L_t$ ,  $W_t$ , and  $D_t$ . The time step is  $\Delta t$ . The number of time steps, multigrid iterations, and Gauss-Seidel iterations are respectively denoted by  $N_{time}$ ,  $N_{mult}$ , and  $N_{gaus}$ . The number of grid points along the  $x$ -,  $y$ -, and  $z$ -axes are respectively  $I_{max}$ ,  $J_{max}$ , and  $K_{max}$ .



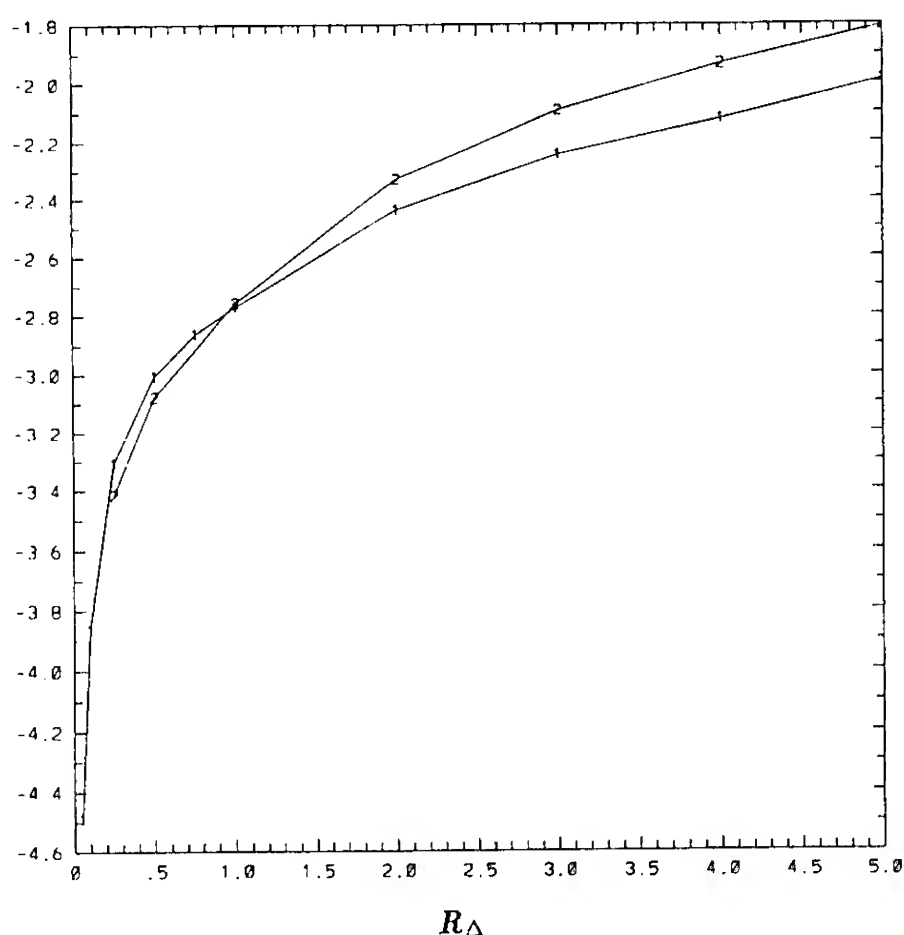


Figure 1a: Radial velocity.

Figure 1: The spatial accuracy as a function of grid Reynolds number for a jet impinging a wall. The  $\log_{10}$  maximum absolute errors in the (a) radial and (b) axial velocities are plotted versus grid Reynolds number ( $R_{\Delta}$ ) for axisymmetric (— 1 —) and three-dimensional (— 2 —) results.

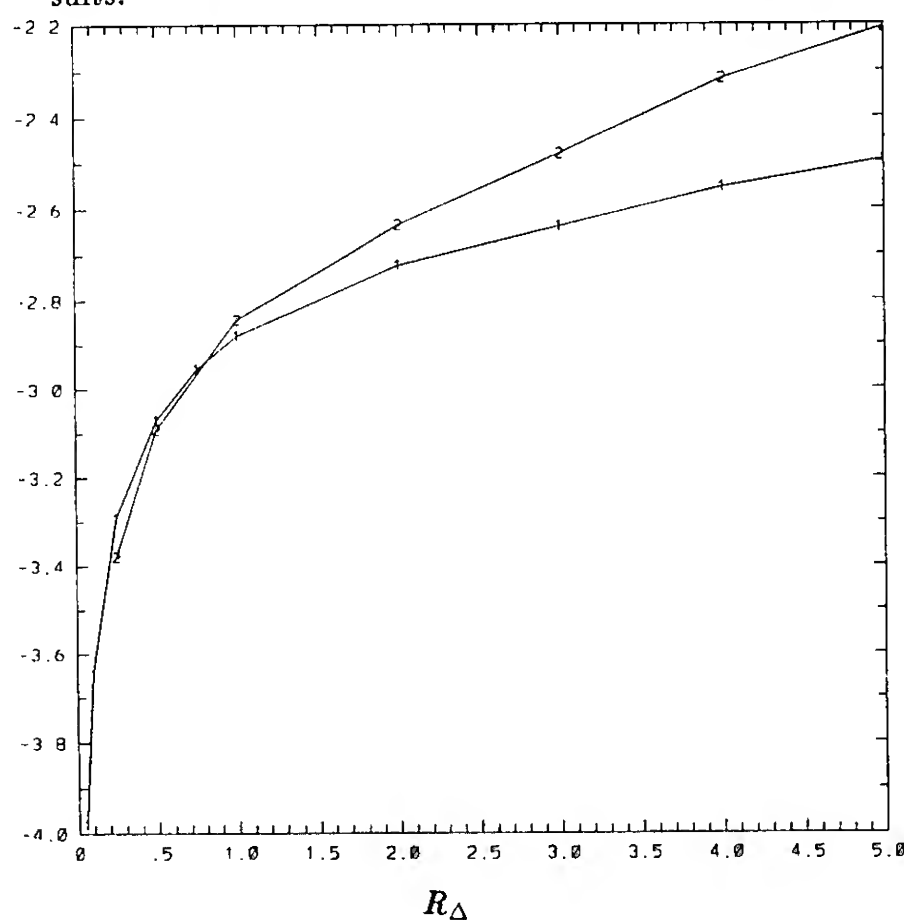


Figure 1b: Axial velocity.

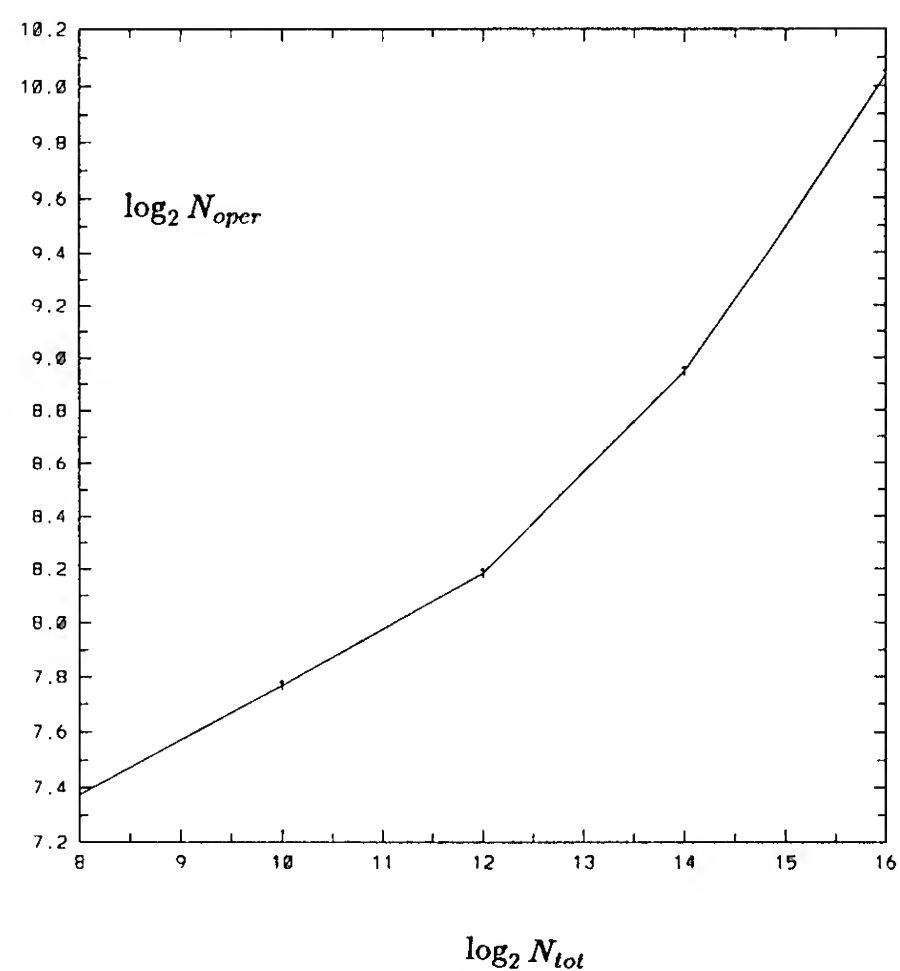


Figure 2: The performance of multigrid scheme as a function of the number of grid points for a jet impinging a wall. The  $\log_2$  of the normalized number of operations ( $N_{oper}$ ) is plotted versus the  $\log_2$  of the number of grid points ( $N_{tot}$ ).

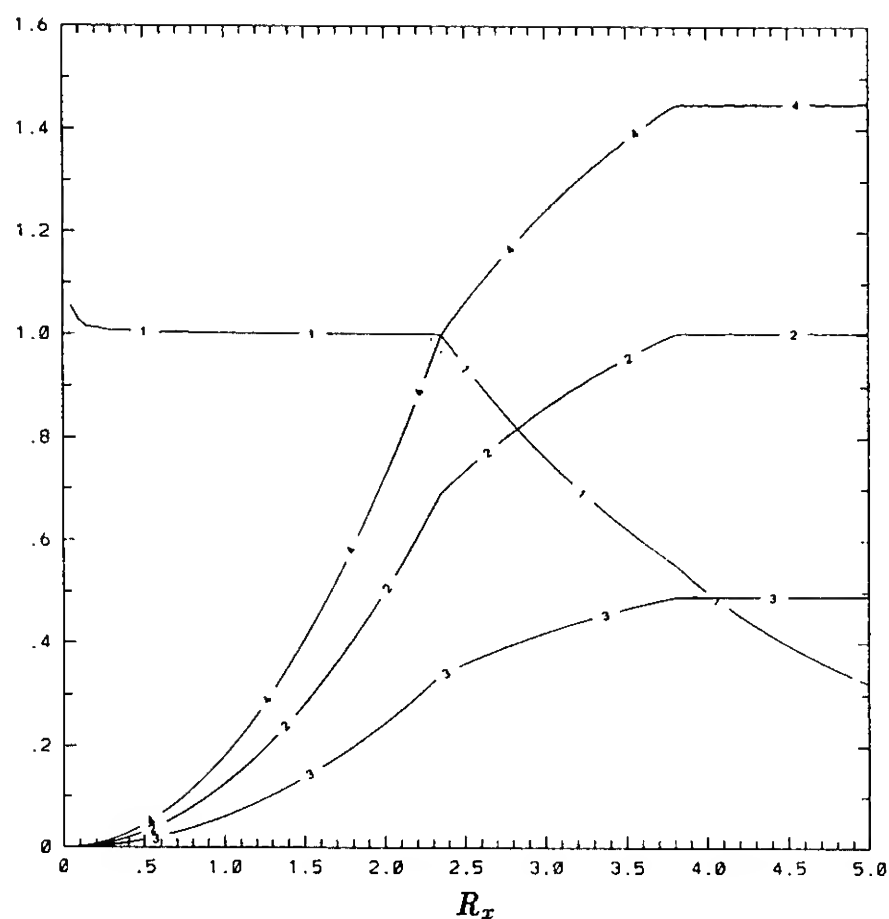


Figure 3a:  $\gamma = 0.7$ .

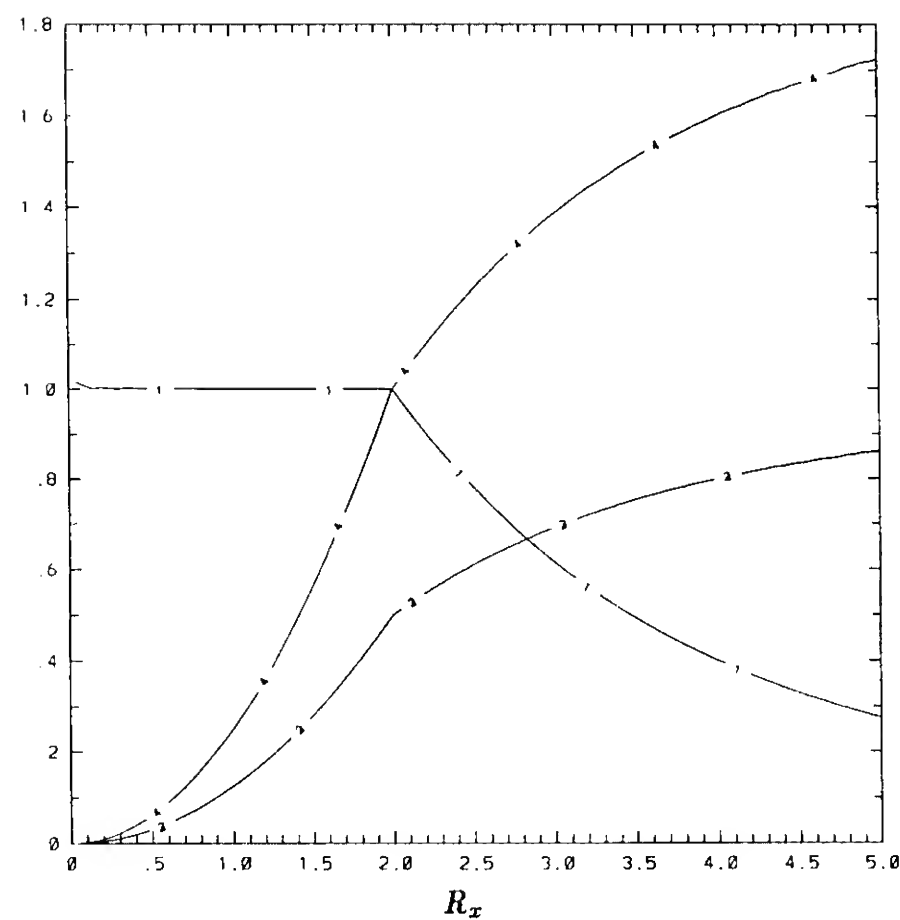


Figure 3b:  $\gamma = 1.0$ .

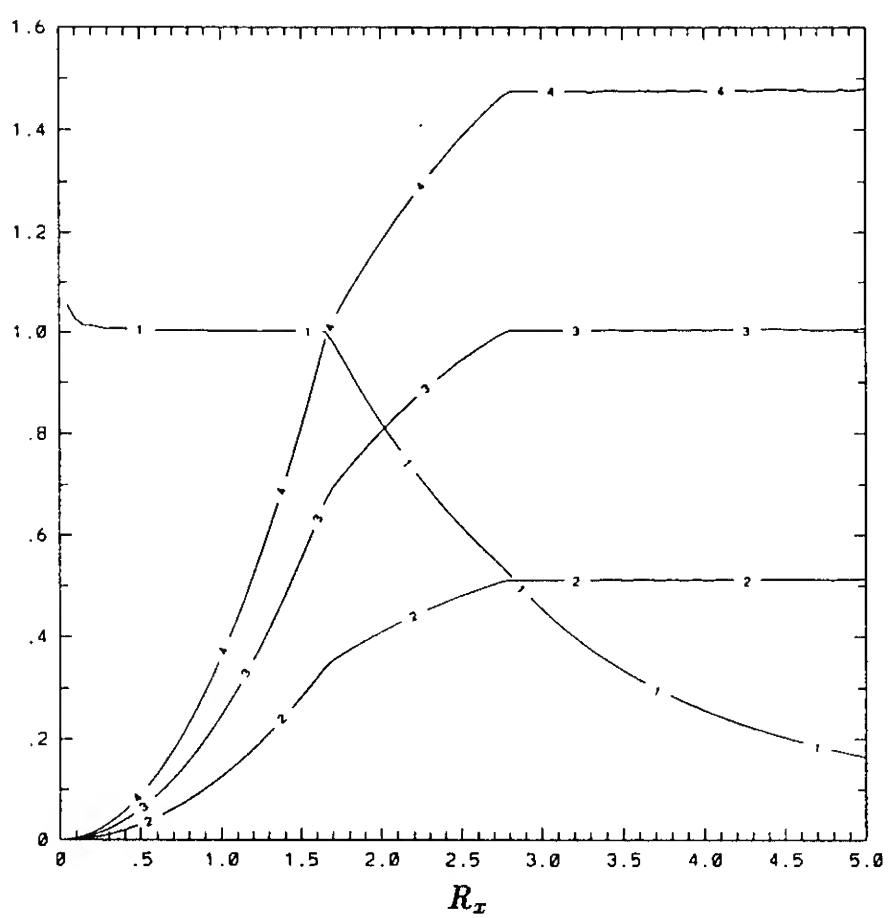


Figure 3c:  $\gamma = 1.4$ .

Figure 3: The values of stability parameters at the maximum allowable time step as a function of grid Reynolds number for a FTCS scheme in two dimensions. The parameters are labeled as follows: (— 1 —) denotes  $2(\alpha_x + \alpha_y)$ ; (— 2 —) denotes  $\beta_x^2/(2\alpha_x)$ ; (— 3 —) denotes  $\beta_y^2/(2\alpha_y)$ ; and (— 4 —) denotes  $(\beta_x + \beta_y)^2/(2(\alpha_x + \alpha_y))$ . The results are plotted for different velocity ratios ( $\gamma$ ): (a)  $\gamma = 0.7$ , (b)  $\gamma = 1.0$ , and (c)  $\gamma = 1.4$ .

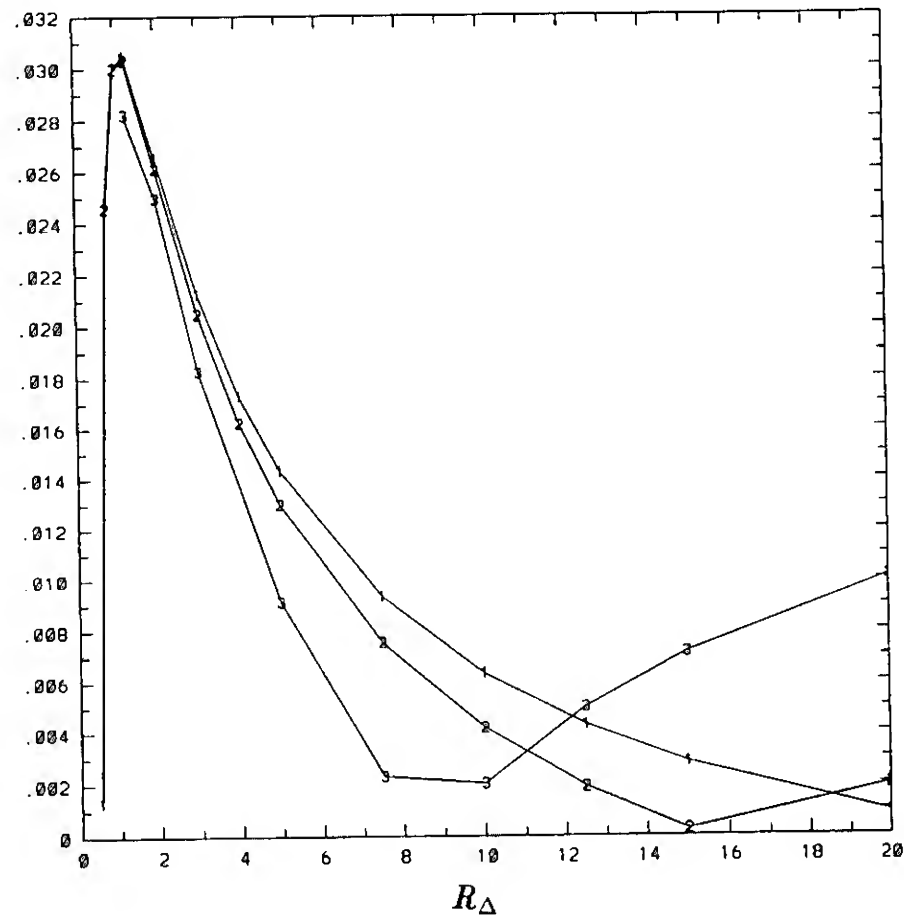


Figure 4a:  $T = 1$ .

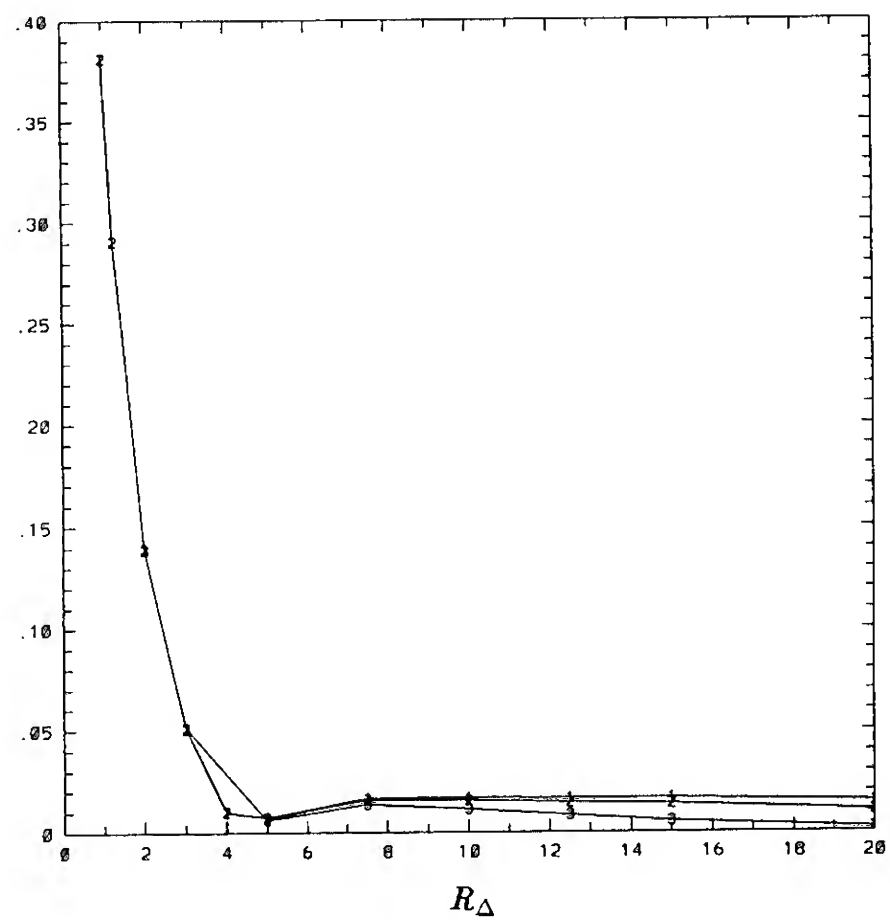


Figure 4b:  $T = 10$ .

Figure 4: The relative error in the maximum vorticity as a function of grid Reynolds number for a Gaussian vortex core orbiting a box. The results are plotted for  $\Delta t = 0.01$  (— 1 —) ;  $\Delta t = 0.02$  (— 2 —) ; and  $\Delta t = 0.05$  (— 3 —) .

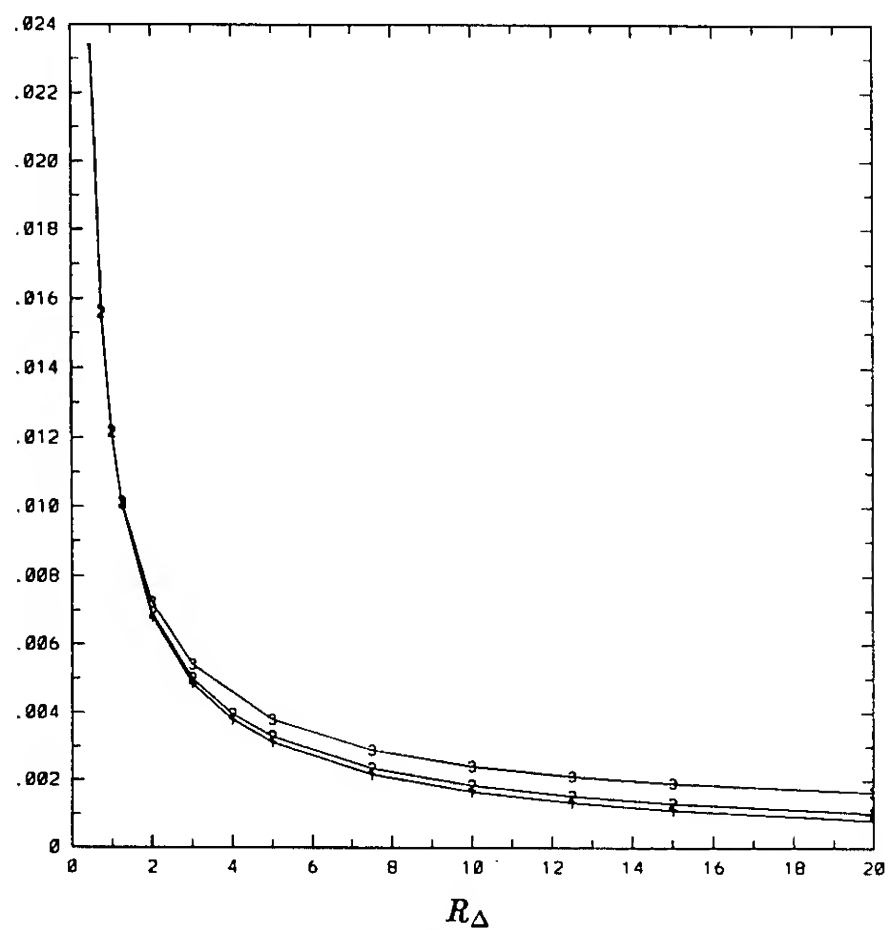


Figure 5a:  $T = 1$ .

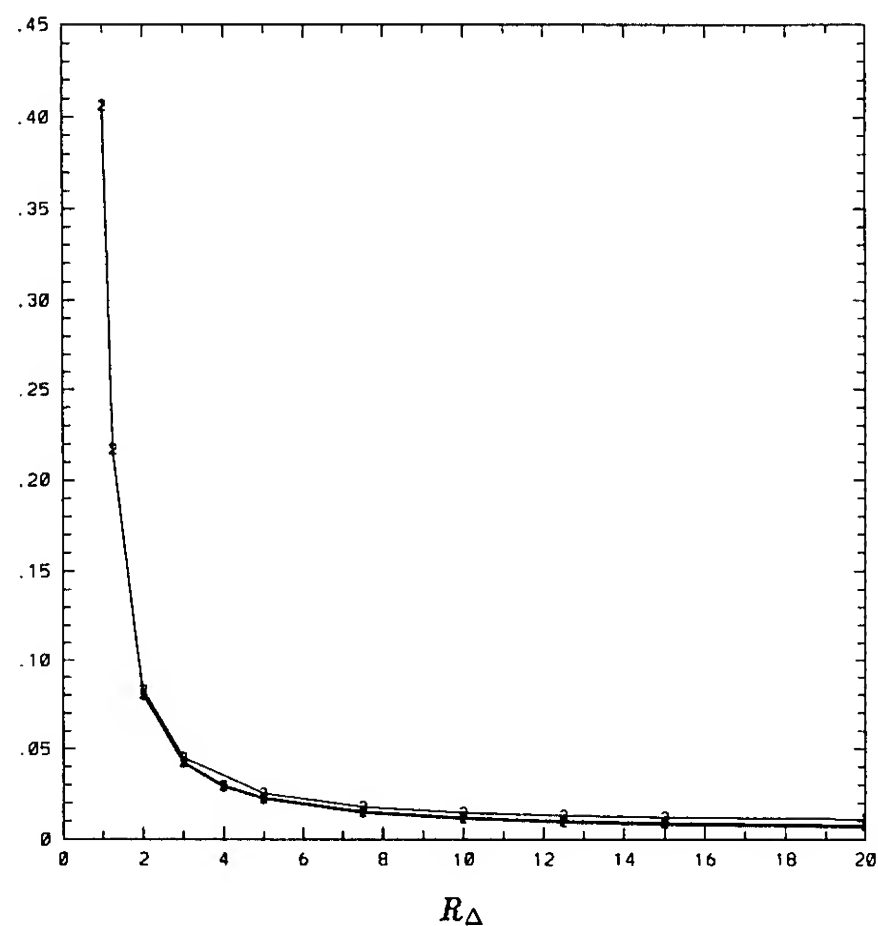


Figure 5b:  $T = 10$ .

Figure 5: The relative error in an energy conservation law as a function of grid Reynolds number for a Gaussian vortex core orbiting a box. The results are plotted for  $\Delta t = 0.01$  (— 1 —) ;  $\Delta t = 0.02$  (— 2 —) ; and  $\Delta t = 0.05$  (— 3 —) .

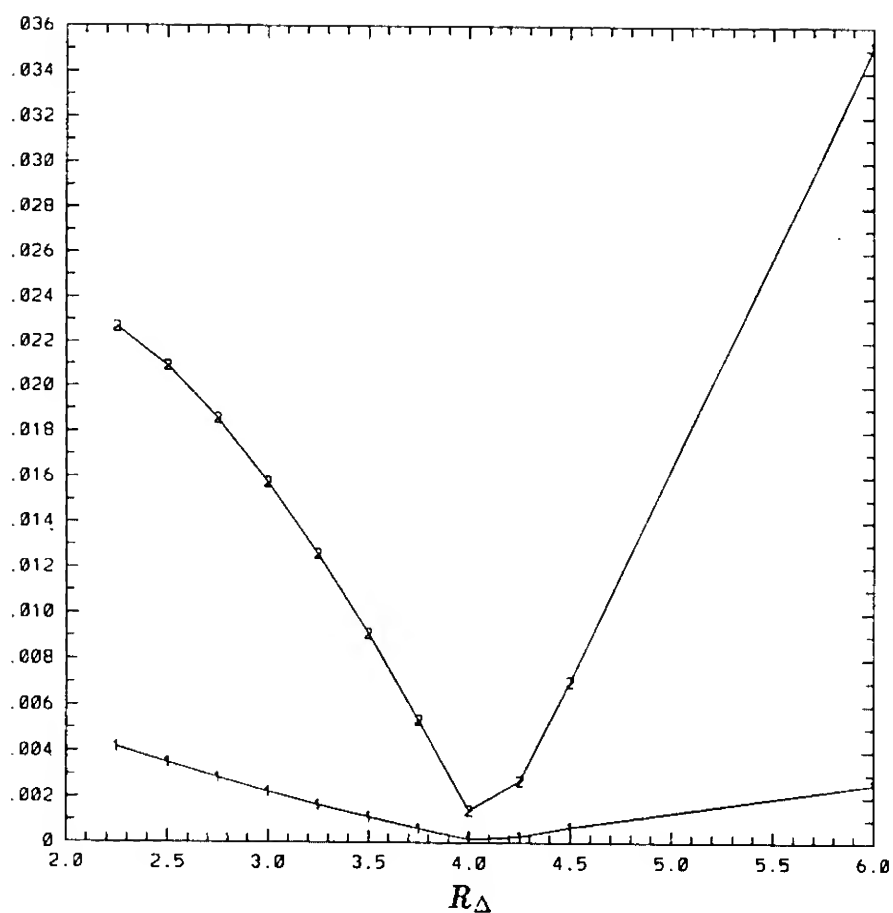


Figure 6: The relative error in the wave amplitude as a function of grid Reynolds number for an attenuating axisymmetric standing wave. The relative errors  $\epsilon_1$  (— 1 —) and  $\epsilon_2$  (— 2 —) are defined in the text.

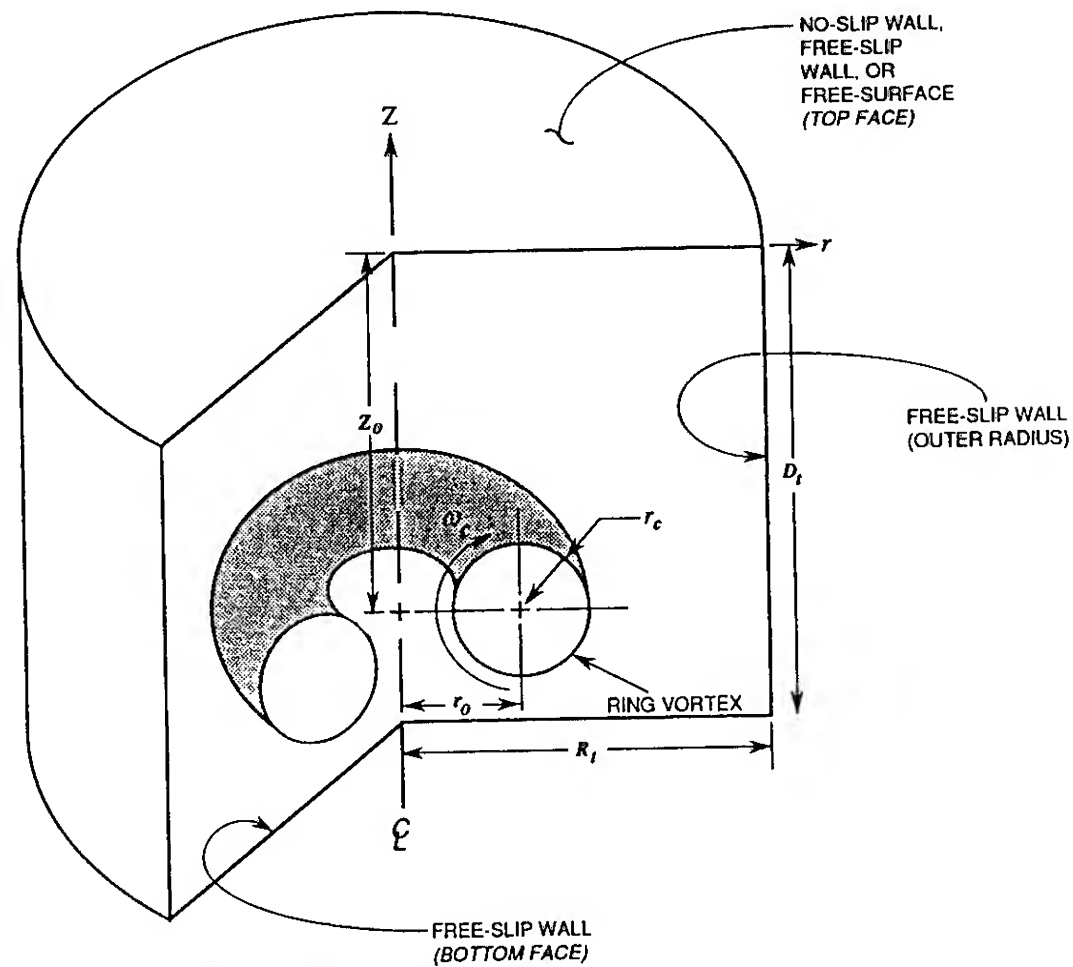


Figure 7: *The numerical simulation of a vortex ring impinging a boundary.* The initial core radius and peak vorticity are denoted by  $r_c$  and  $\omega_c$ . The vortex core is centered at  $(r_o, z_o)$ . The radius and depth of the tank are respectively  $R_t$  and  $D_t$ .

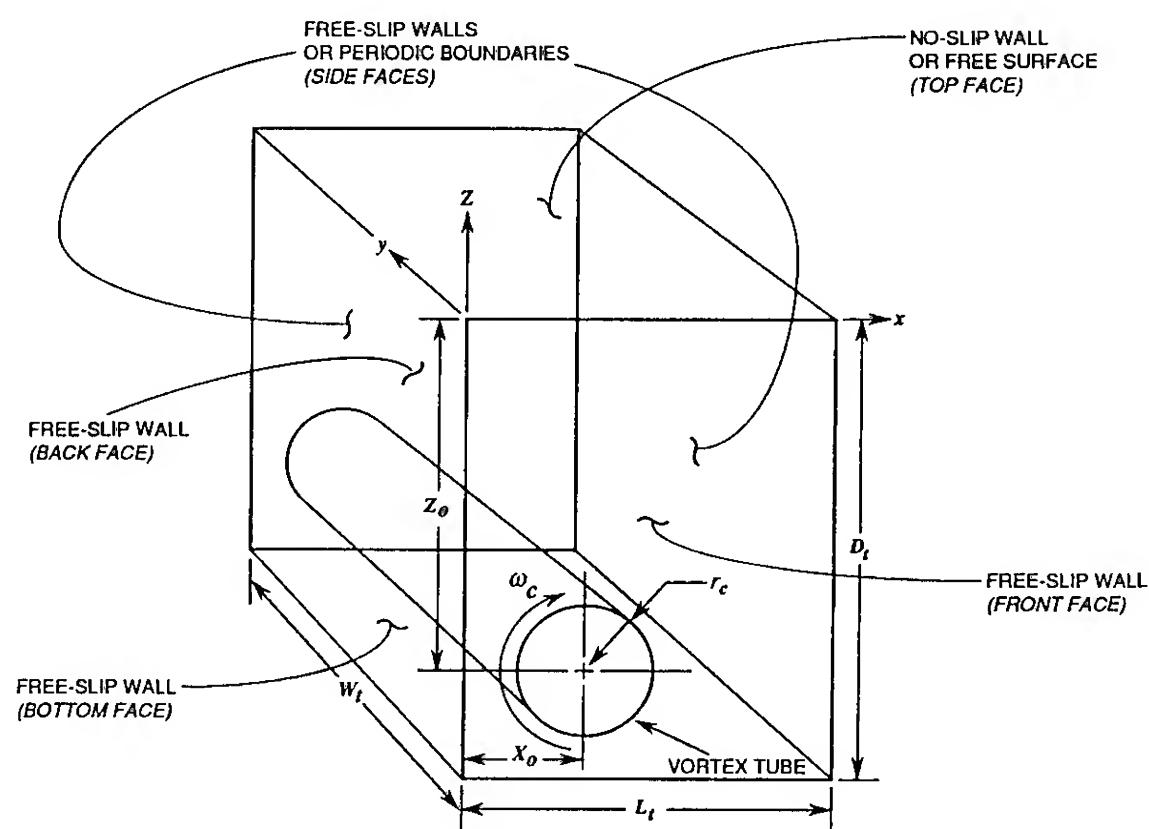


Figure 8: *The numerical simulation of a vortex tube impinging a boundary.* The initial core radius and peak vorticity are denoted by  $r_c$  and  $\omega_c$ . The mean position of the vortex core is centered at  $(x_o, z_o)$ . The length ( $x$ ), width ( $y$ ), and depth ( $z$ ) of the tank are respectively  $L_t$ ,  $W_t$ , and  $D_t$ .



Figure 9: *A ring vortex impinging a free-slip wall.* The  $\omega=-1$  contours of the primary vortex core are plotted at different instants of time:  $t=0, 2, 4, 6, 8, 10, 12, \& 14$ . The ring vortex starts at the bottom of the figure and expands radially outward. The numerical parameters for this run are provided in Run 6 of Table (2).

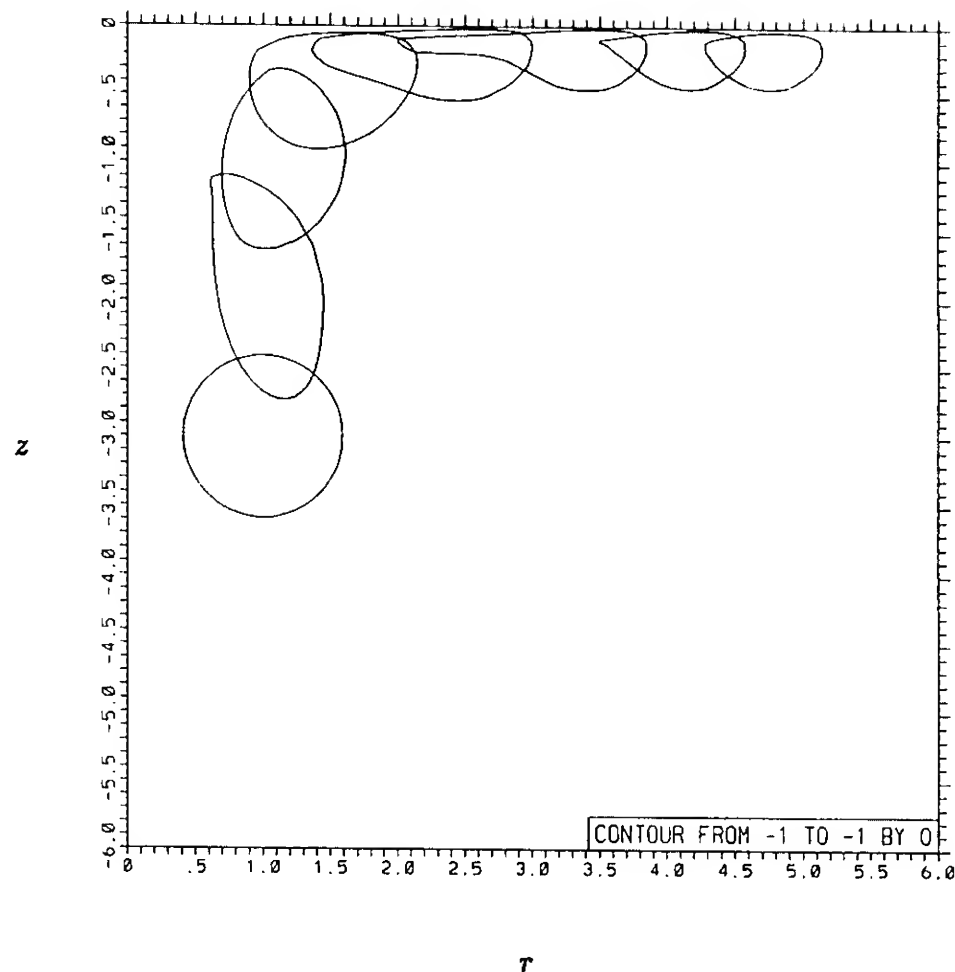
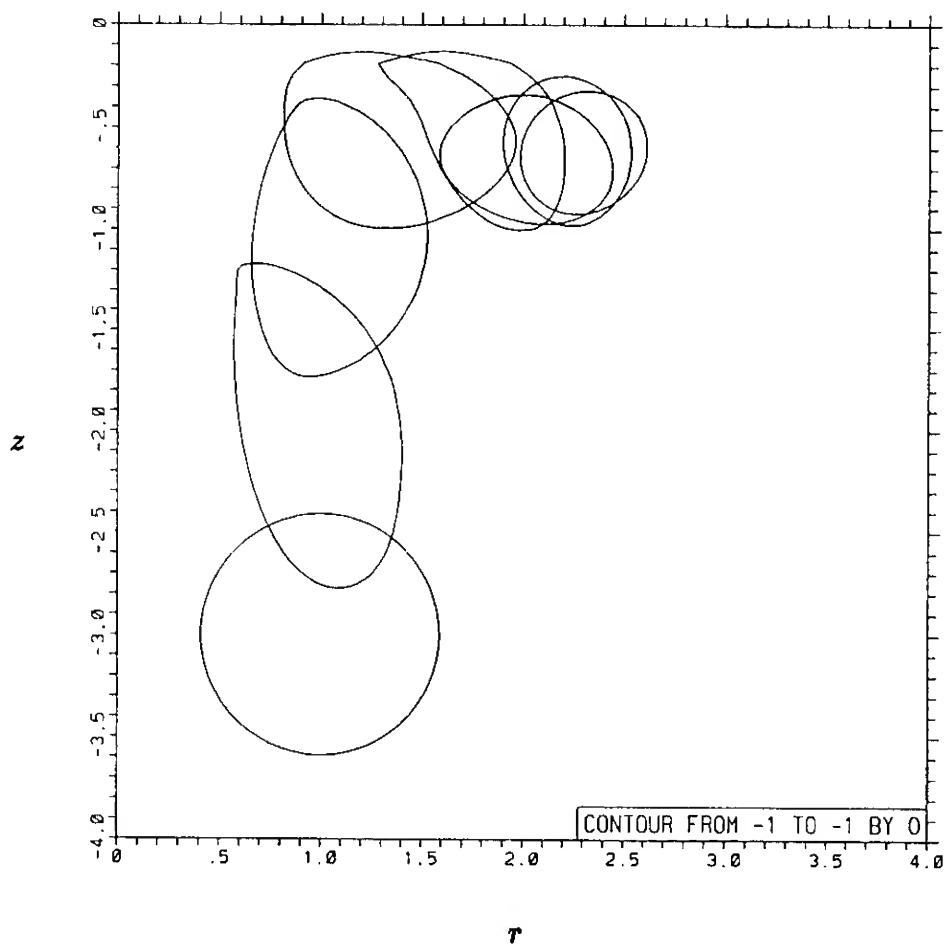


Figure 10: *A ring vortex impinging a no-slip wall.* The  $\omega=-1$  contours of the primary vortex core are plotted at different instants of time:  $t=0, 2, 4, 6, 8, 12, 16, \& 20$ . The ring vortex starts at the bottom of the figure and expands radially outward up to  $r \approx 2.25$ . The numerical parameters for this run are provided in Run 2 of Table (2).



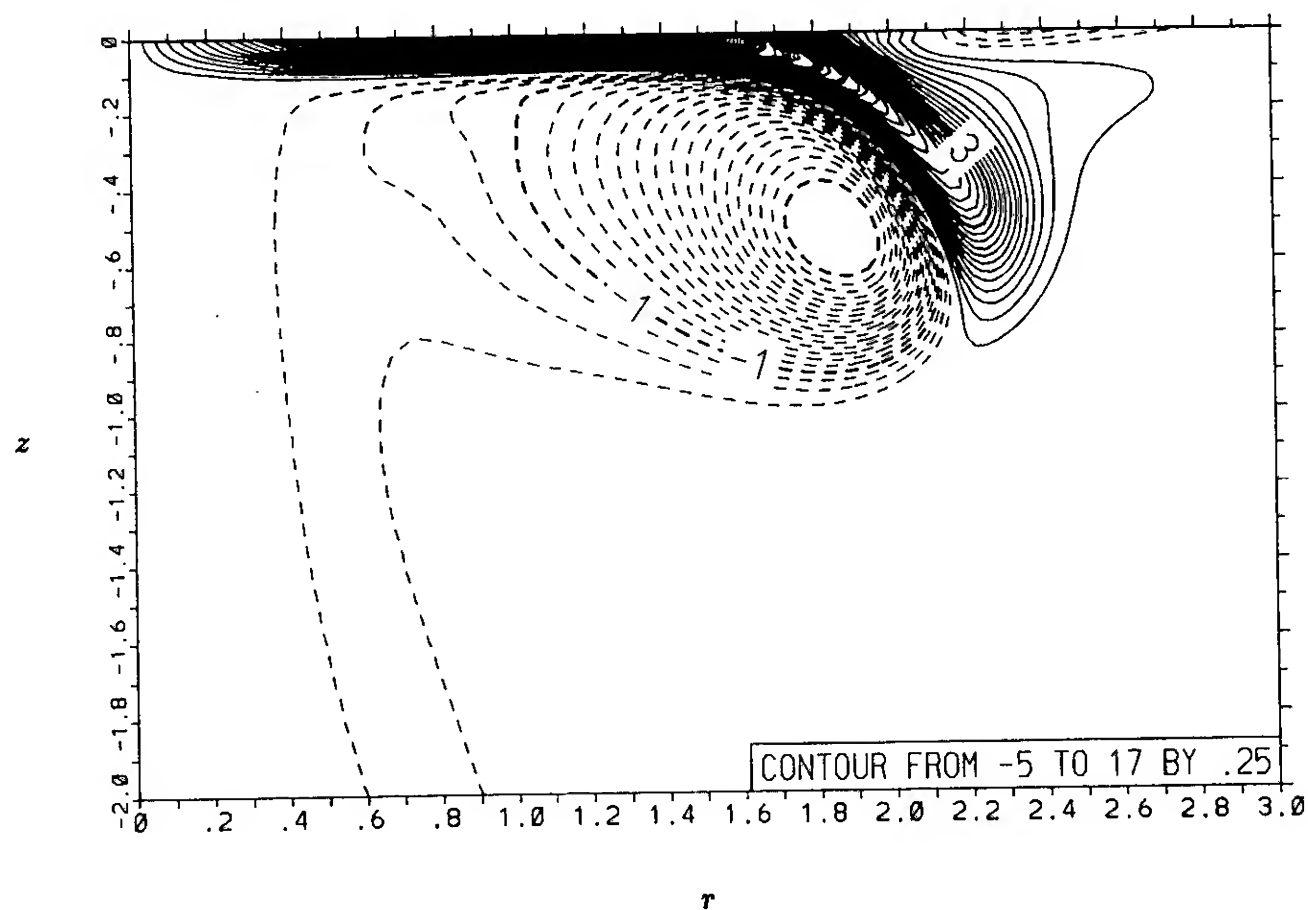
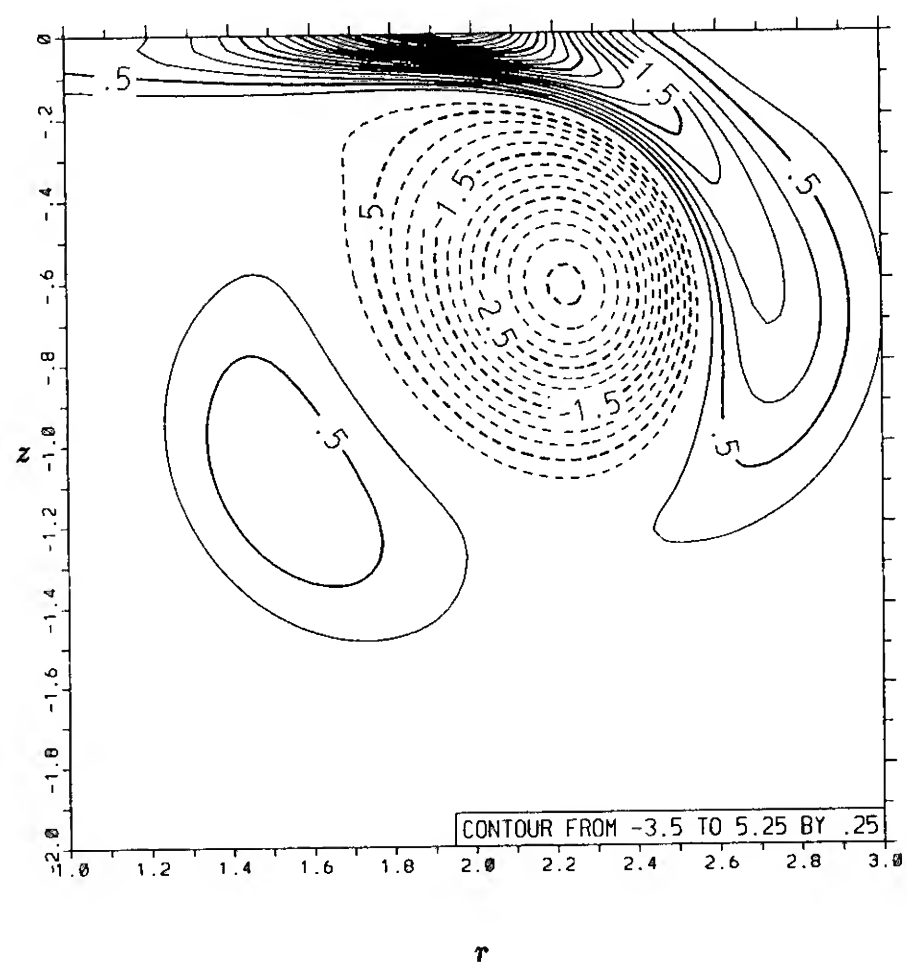


Figure 11: *The boundary-layer separation due to a ring vortex interacting with a no-slip wall. The solid and dashed contour lines represent positive and negative vorticity respectively at time  $t=7$ . Note that only a small portion of the computational domain is plotted. The numerical parameters for this run are provided in Run 2 of Table (2).*

Figure 12: *The orbit of a secondary vortex ring. The solid and dashed contour lines represent positive and negative vorticity respectively at time  $t=15$ . Note that only a small portion of the computational domain is plotted. The numerical parameters for this run are provided in Run 2 of Table (2).*



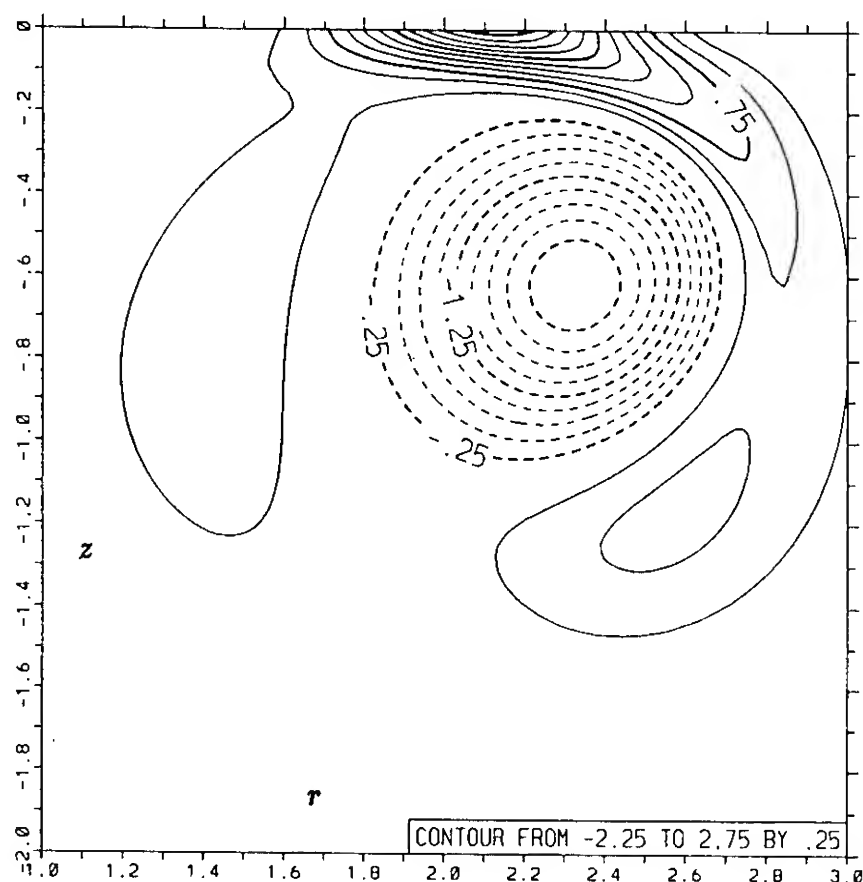


Figure 13: *The formation of a tertiary vortex ring.* The solid and dashed contour lines represent positive and negative vorticity respectively at time  $t=20$ . Note that only a small portion of the computational domain is plotted. The numerical parameters for this run are provided in Run 2 of Table (2).

Figure 14: *The energy conservation for ring vortices impinging on no-slip and free-slip walls as a function of time.* The kinetic energy  $E(t)$  is compared to the energy that is dissipated  $D(t)$  (the Reynolds number term in eqt. (18) integrated over time). The results are plotted as follows: (— 1 —) denotes  $E(t)/E(0)$  for the no-slip case, (— 2 —) denotes  $(E(0) + D(t))/E(0)$  for the no-slip case, (— 3 —) denotes  $E(t)/E(0)$  for the free-slip case, and (— 4 —) denotes  $(E(0) + D(t))/E(0)$  for the free-slip case. The numerical parameters for these runs are provided in Runs 2 & 6 of Table (2).

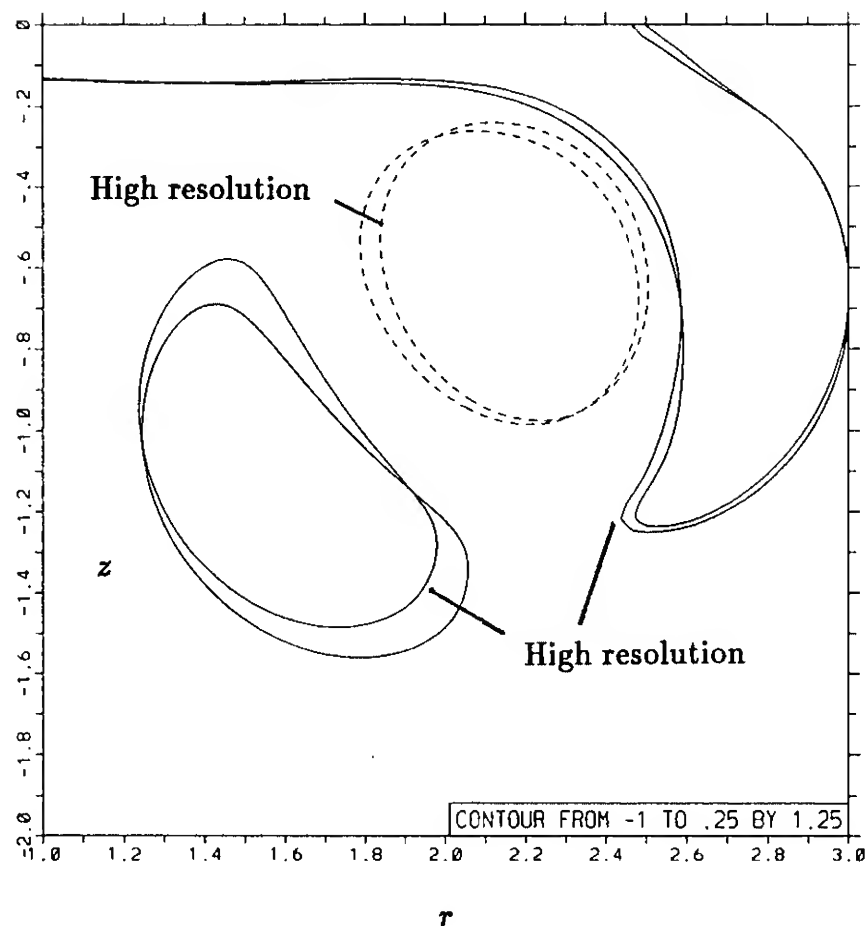
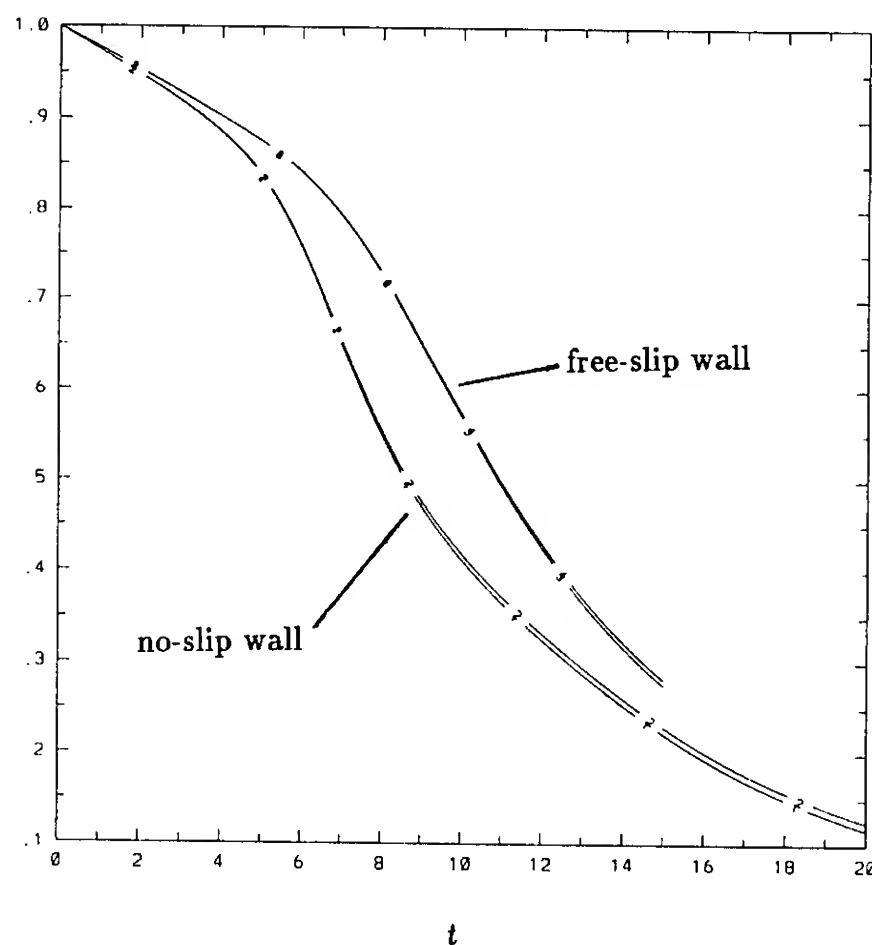


Figure 15: *A comparison of low and high resolution simulations of a ring vortex interacting with a no-slip wall.* The solid and dashed contour lines correspond to  $\omega = .25$  and the dashed contour lines correspond to  $\omega = -1$  at time  $t=15$ . Note that only a small portion of the computational domain is plotted. The numerical parameters for these runs are provided in Runs 1 & 2 of Table (2).

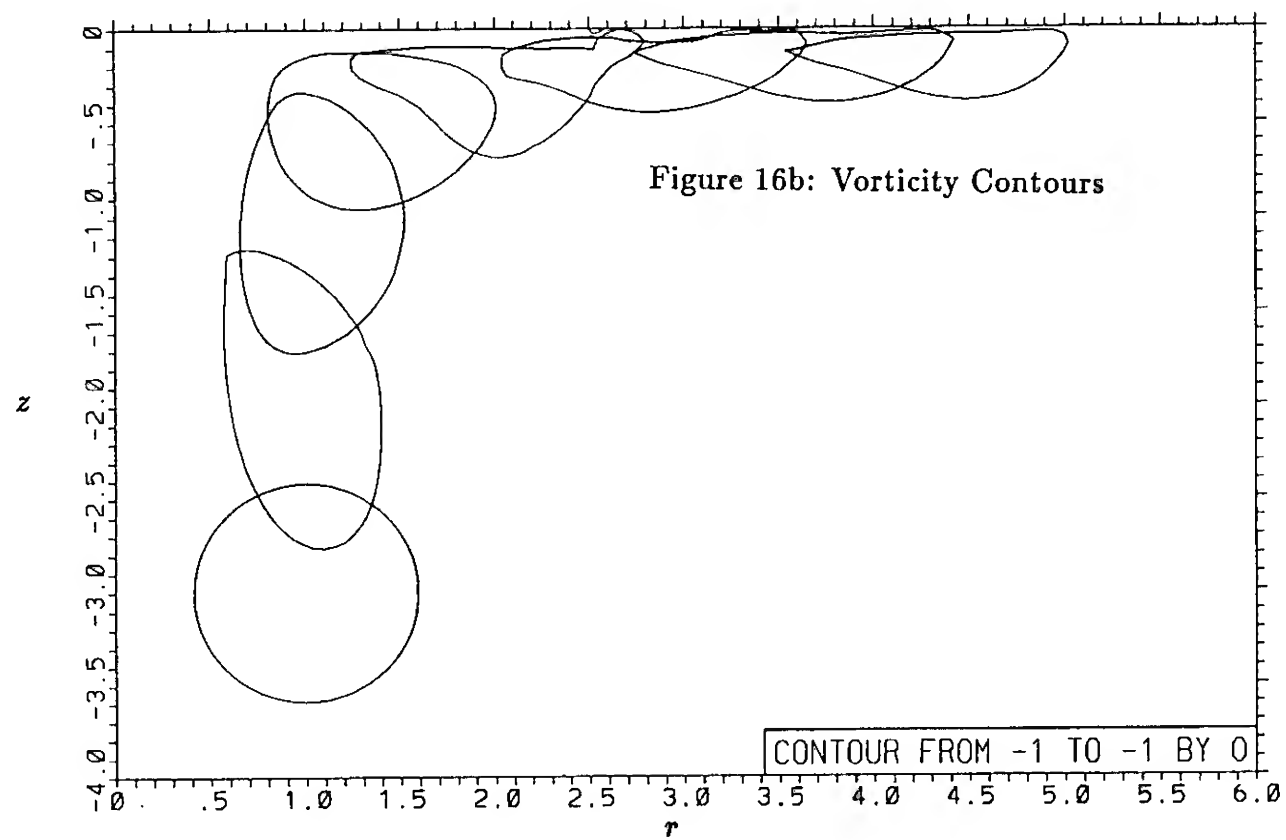
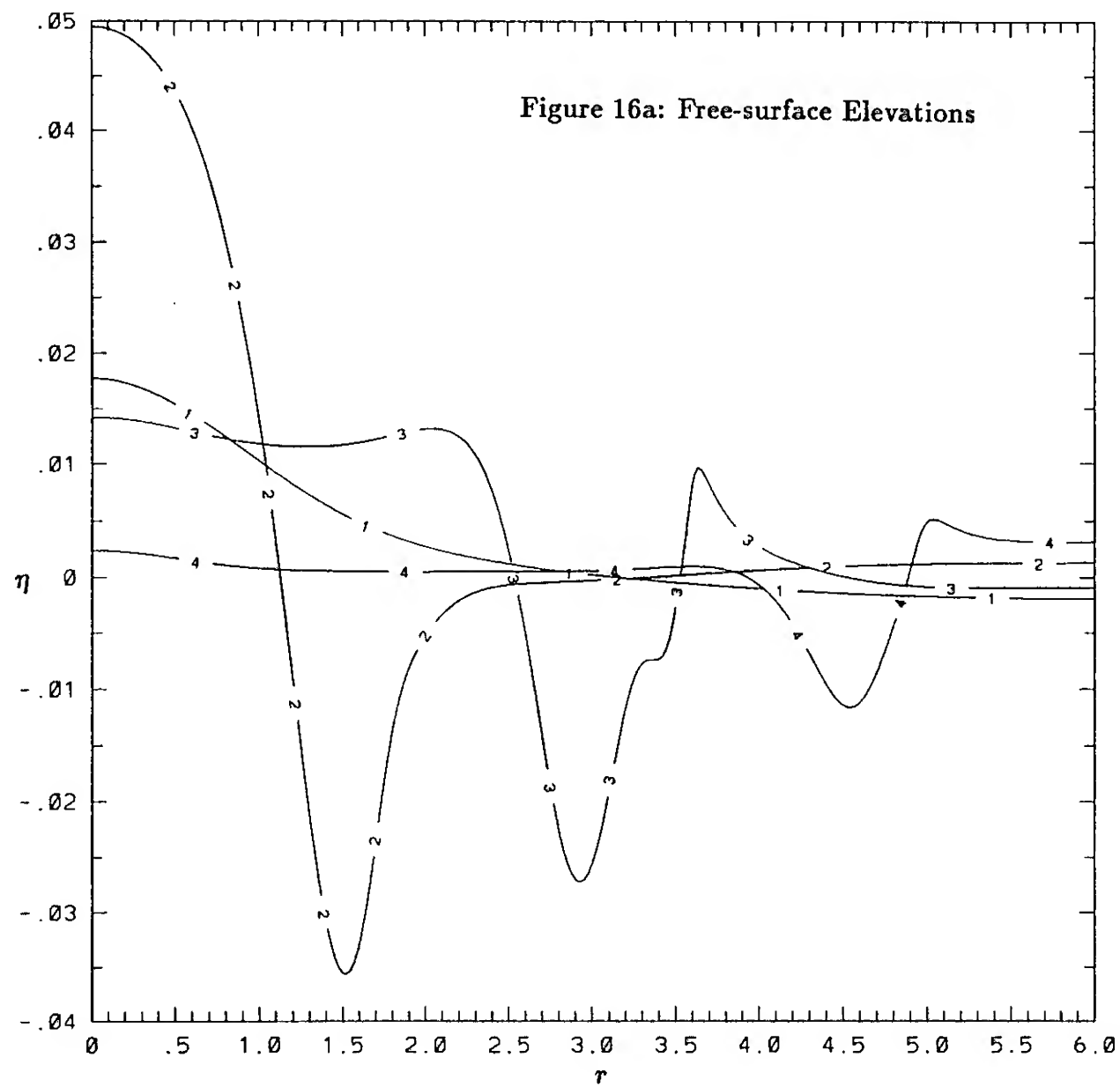


Figure 16: A ring vortex interacting with a free surface at a low Froude number. Part (a) plots the free-surface elevation as a function of the radial coordinate at times  $t=2, 6, 10$ , &  $14$ . Part (b) plots  $\omega = -1$  contours at times  $t=0, 2, 4, 6, 8, 10, 12$ , &  $14$ . The ring vortex starts at the bottom of Part (b) and expands radially outward. The numerical parameters for this run are provided in Run 3 of Table (3).

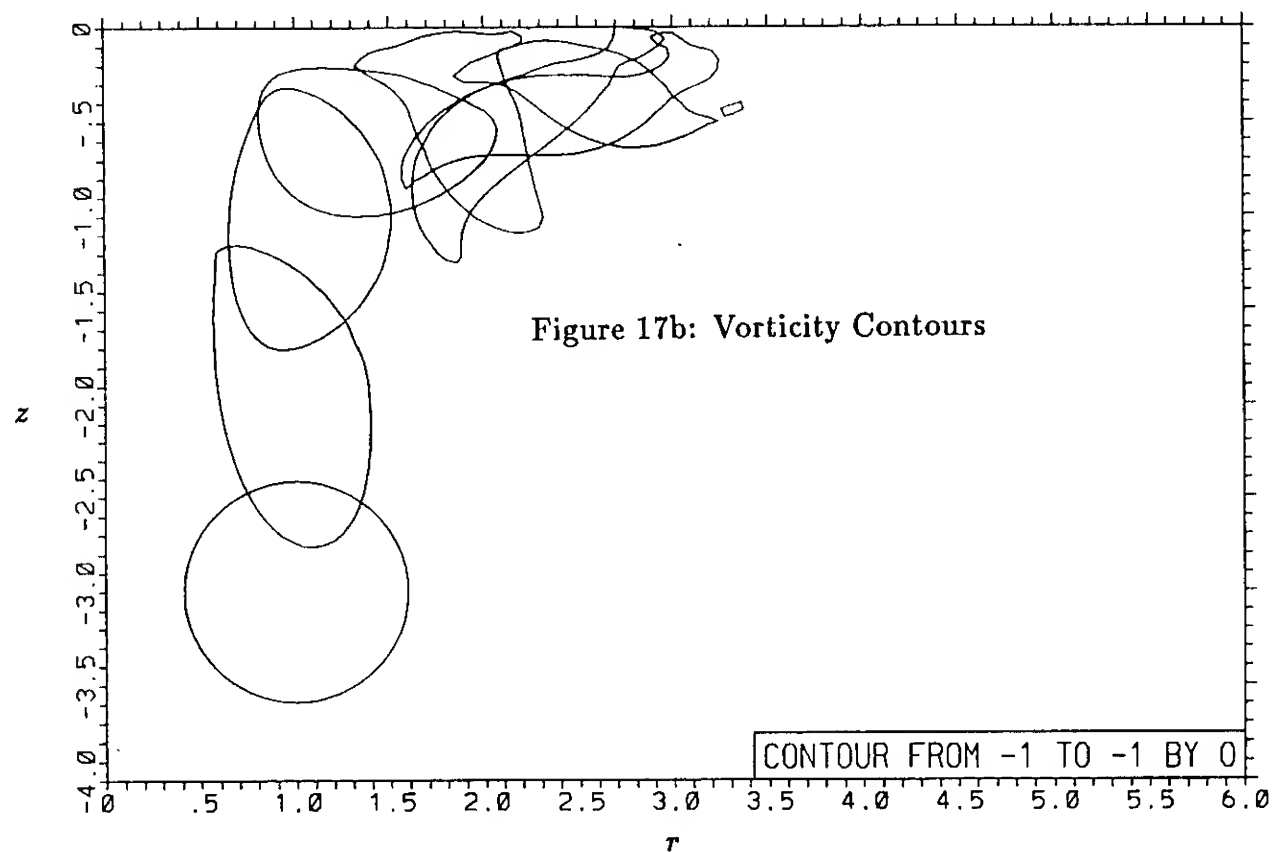
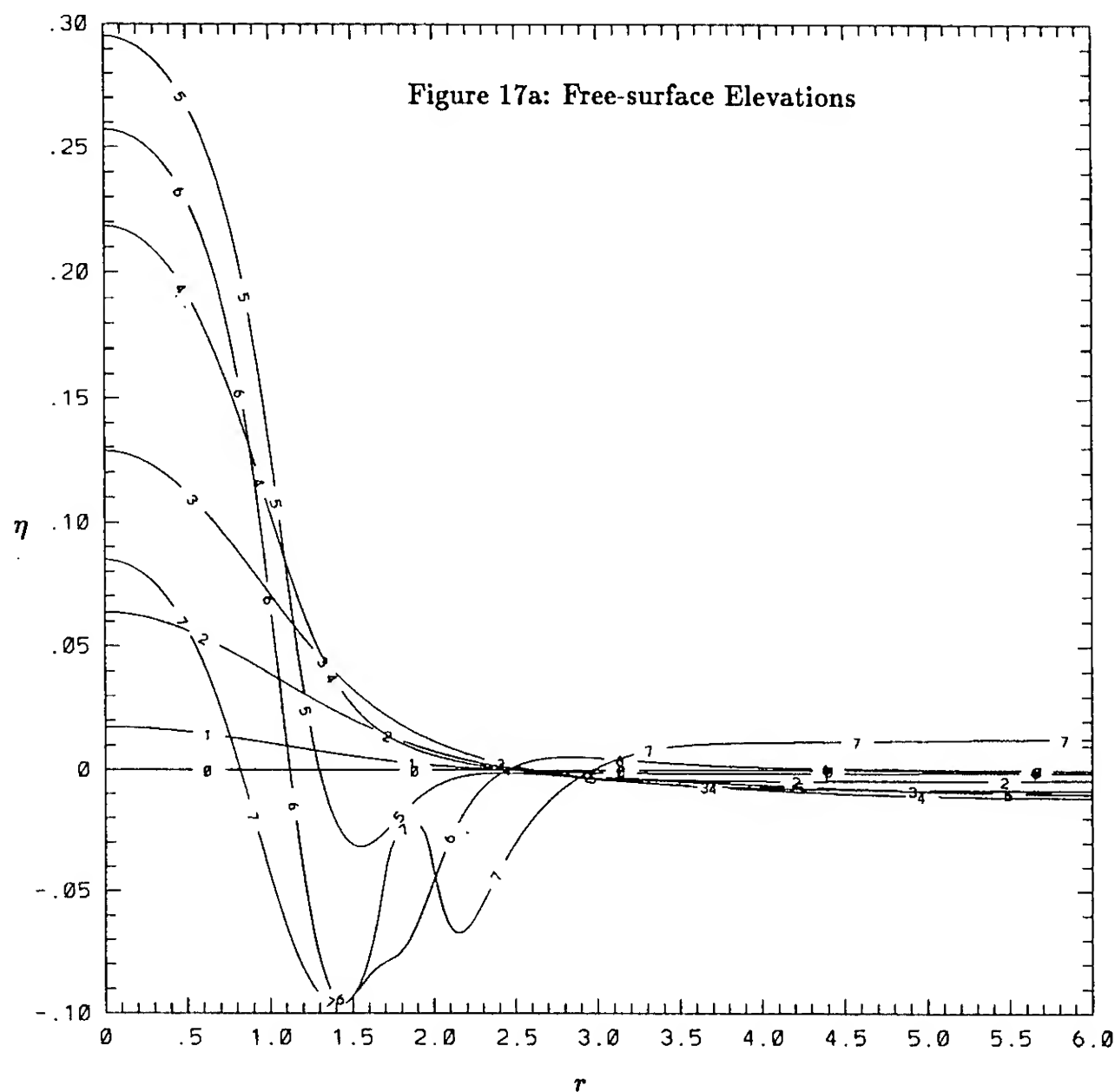


Figure 17: A ring vortex interacting with a free surface at an intermediate Froude number. Part (a) plots the free-surface elevation as a function of the radial coordinate at times  $t=0, 1, 2, 3, 4, 5, 6$ , &  $7$ . Part (b) plots  $\omega = -1$  contours at times  $t=0, 2, 4, 6, 8, 10, 12$ , &  $14$ . The ring vortex starts at the bottom of Part (b) and expands radially outward up to  $r \approx 2.25$ . The numerical parameters for this run are provided in Run 1 of Table (3).



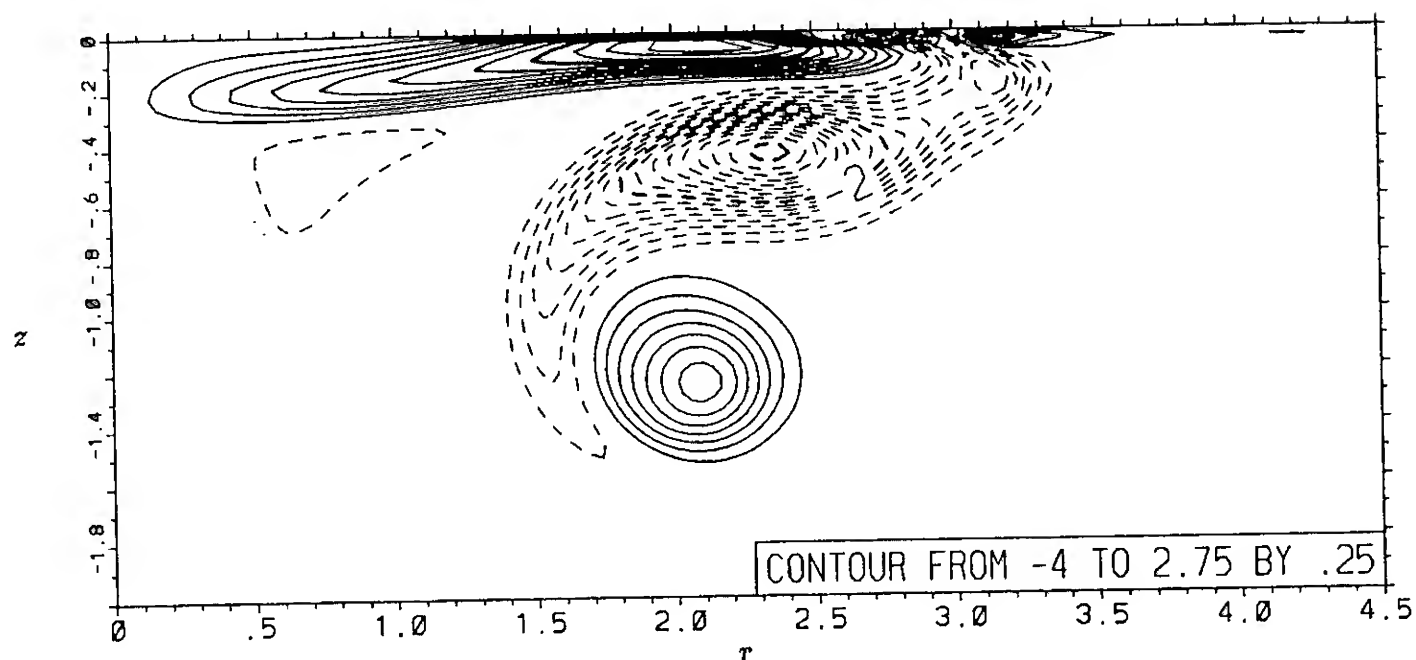


Figure 18: *The orbit of a secondary vortex ring that is shed by a free surface at an intermediate Froude number. The solid and dashed contour lines represent positive and negative vorticity respectively at time  $t=12$ . Note that only a small portion of the computational domain is plotted. The numerical parameters for this run are provided in Run 1 of Table (3).*

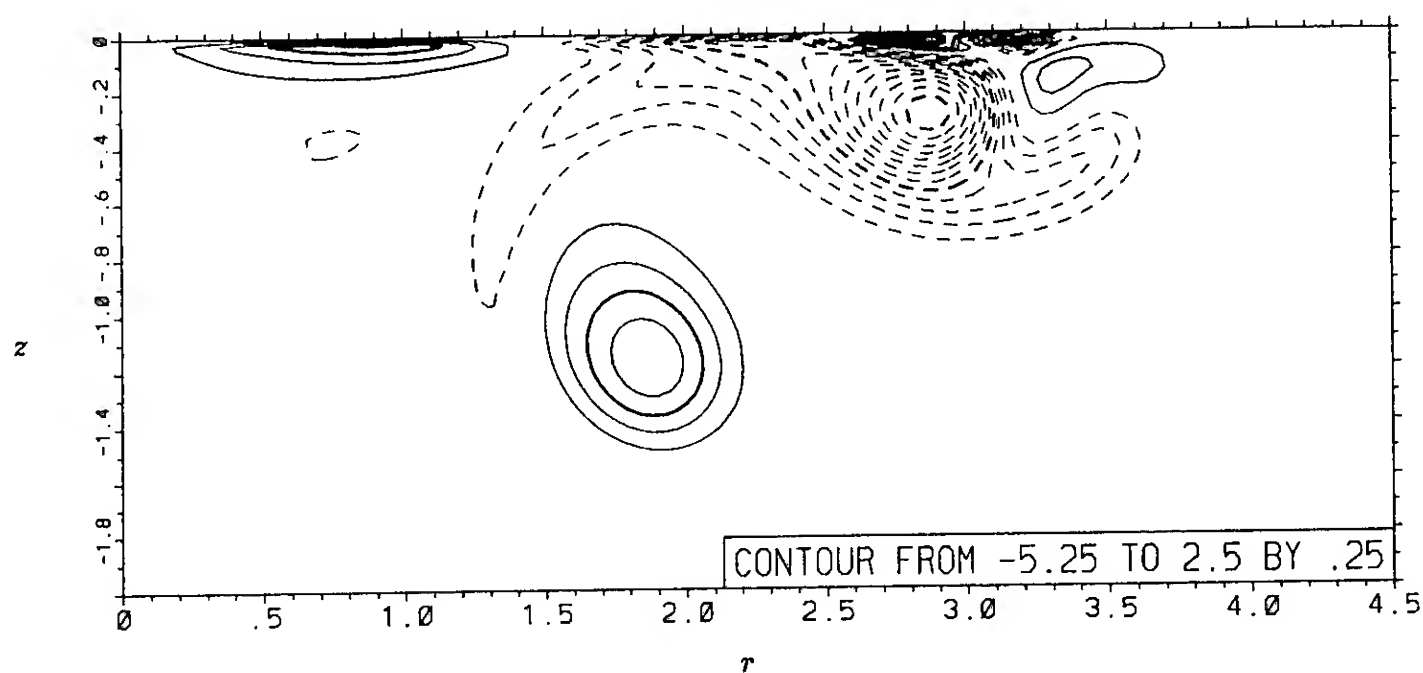


Figure 19: *The shedding of a tertiary vortex ring by a free surface at an intermediate Froude number. The solid and dashed contour lines represent positive and negative vorticity respectively at time  $t=15$ . Note that only a small portion of the computational domain is plotted. The numerical parameters for this run are provided in Run 1 of Table (3).*

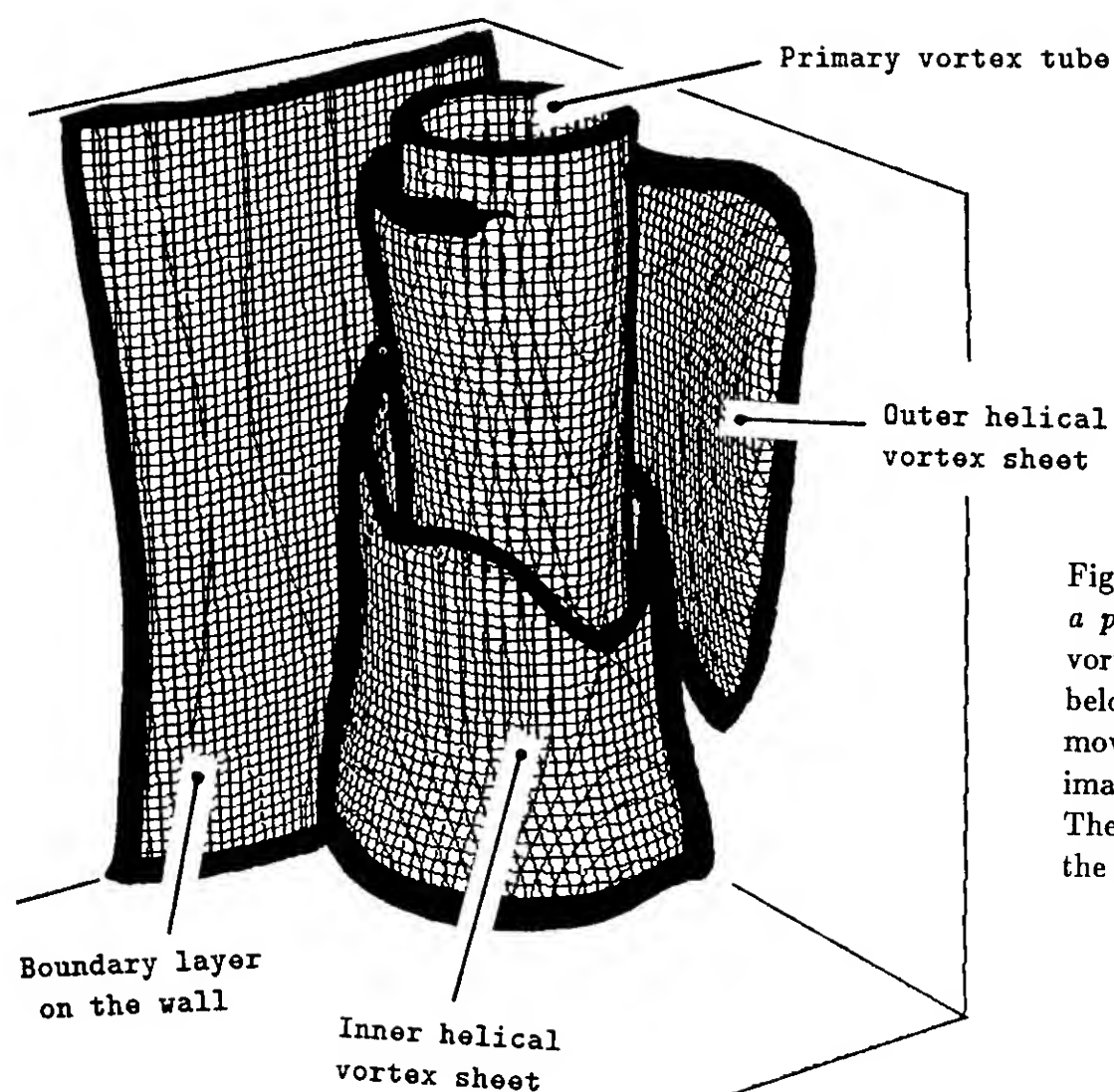


Figure 20: *The winding of helical vorticity around a primary vortex tube. A constant isosurface of vorticity magnitude is shown. The view is from below a no-slip wall, and the primary vortex is moving into and to the left of the page due to its images across the centerplane and above the wall. The neighboring vortex that is on the right side of the page is not shown.*

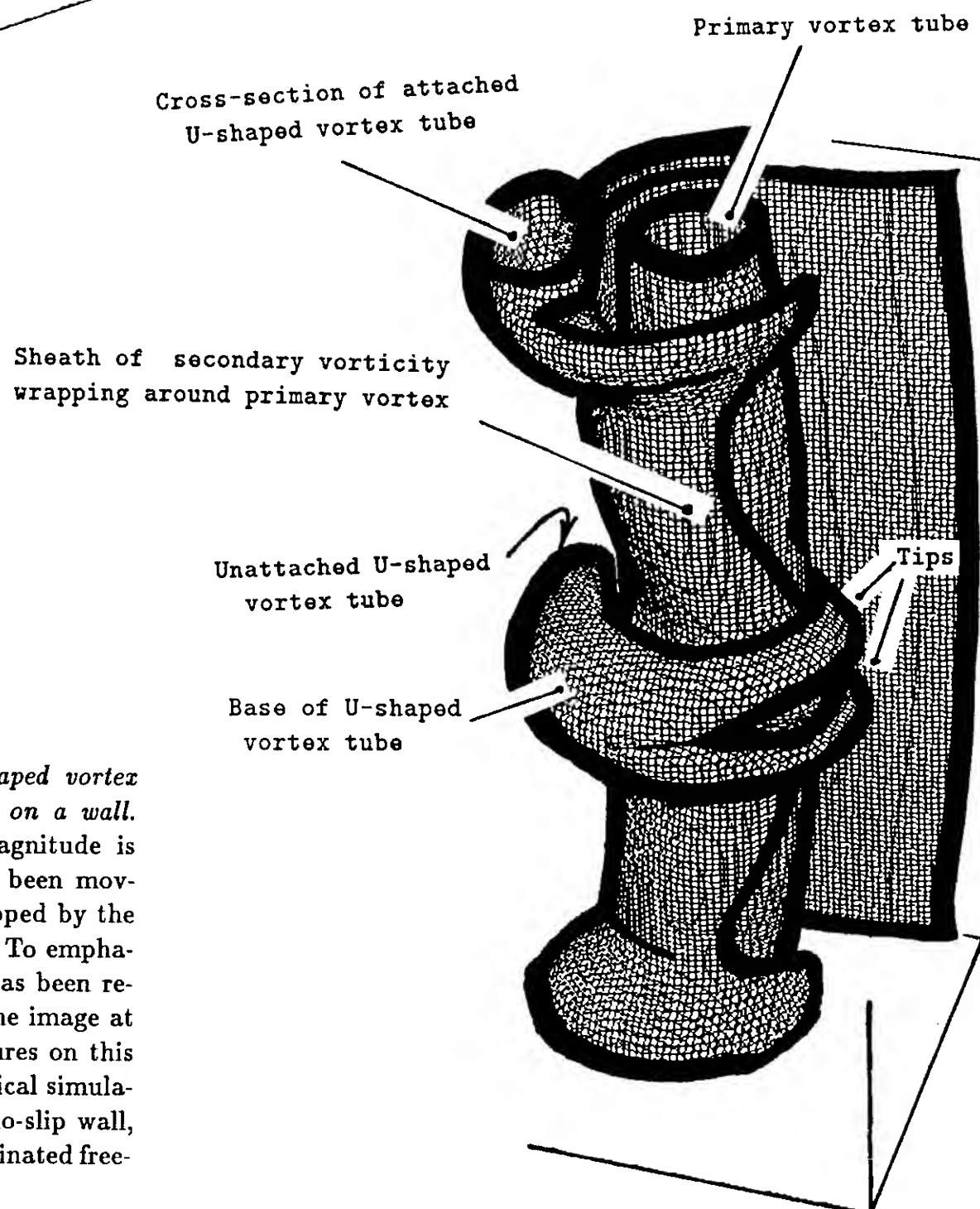


Figure 21: *The attachment of U-shaped vortex tubes to the separated boundary-layer on a wall. A constant isosurface of vorticity magnitude is shown. The primary vortex tube had been moving from right to left before being stopped by the separated boundary-layer on the wall. To emphasize the U-shaped feature this image has been reflected about its midspan relative to the image at the top of the page. Although the figures on this page have been adapted from a numerical simulation of a vortex tube impinging on a no-slip wall, we expect similar behavior for a contaminated free-surface.*

Figure 22: The free-surface cusp pattern formed by the reconnection of primary vorticity with a free surface. The  $\omega_z = \pm 1$  contours of primary vorticity on the free surface are plotted at different instants of time:  $t=8, 9, 10, 11, 12, 13, 14$ , &  $15$ . The submerged portion of the primary vortex tube is moving from left to right across the page. To emphasize the cusp pattern this image has been reflected across the symmetry boundary at  $y = 4$ . The numerical parameters for this run are provided in Run 7 of Table (4).

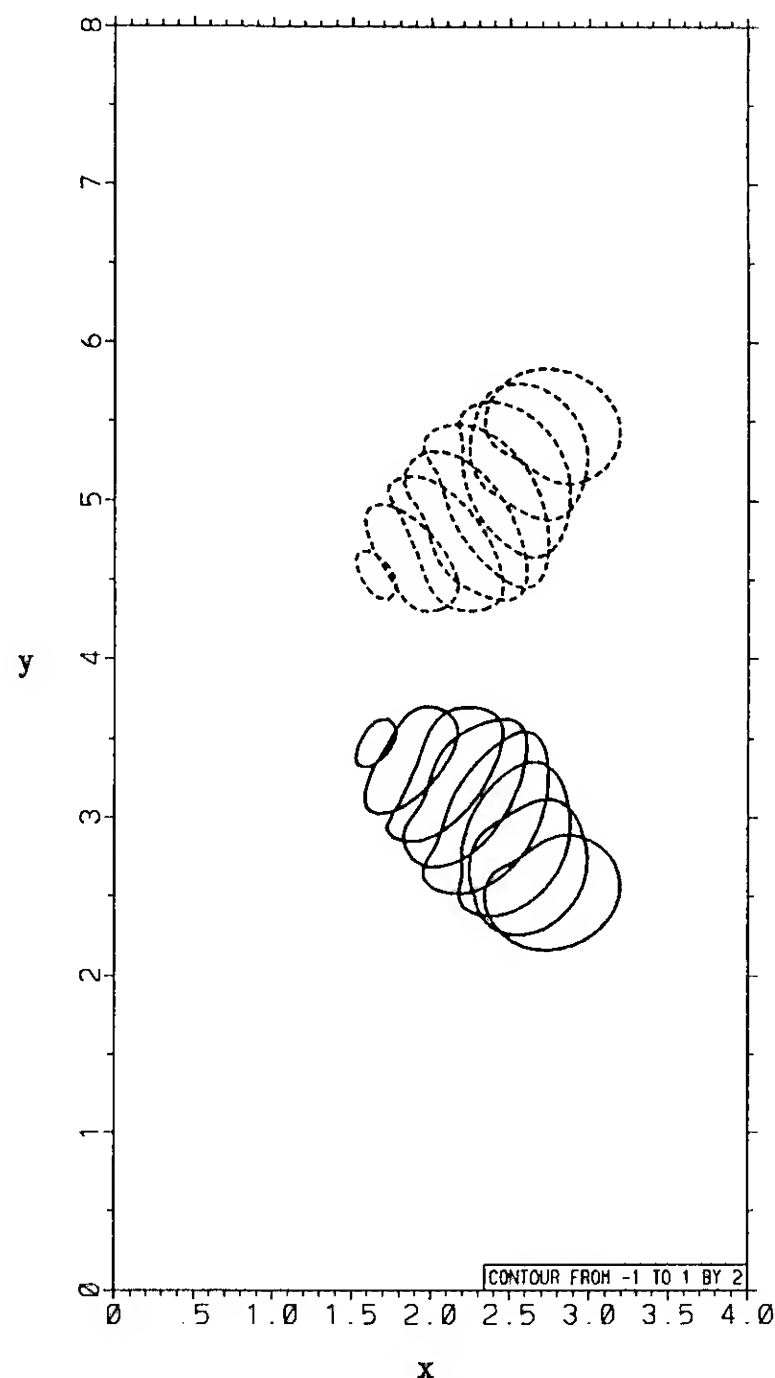


Figure 23: The evolution of a vortex tube traveling slightly submerged below a free-surface. The  $|\vec{\omega}| = 1.25$  isosurface of the primary vortex core is plotted at different instants of time: (a)  $t=2.5$ , (b)  $t=5$ , (c)  $t=7.5$ , (d)  $t=10$ , & (e)  $t=15$ . The view is looking down on the free surface, and the vortex tubes are moving from right to left due to their images above the free surface. The computational domain has been doubled in length to avoid confusion as portions of the vortex tube enter and exit the periodic boundaries at the left and right sides of the page. The geometry triad is in a submerged corner of the computational domain. The numerical parameters for this run are provided in Run 7 of Table (4).

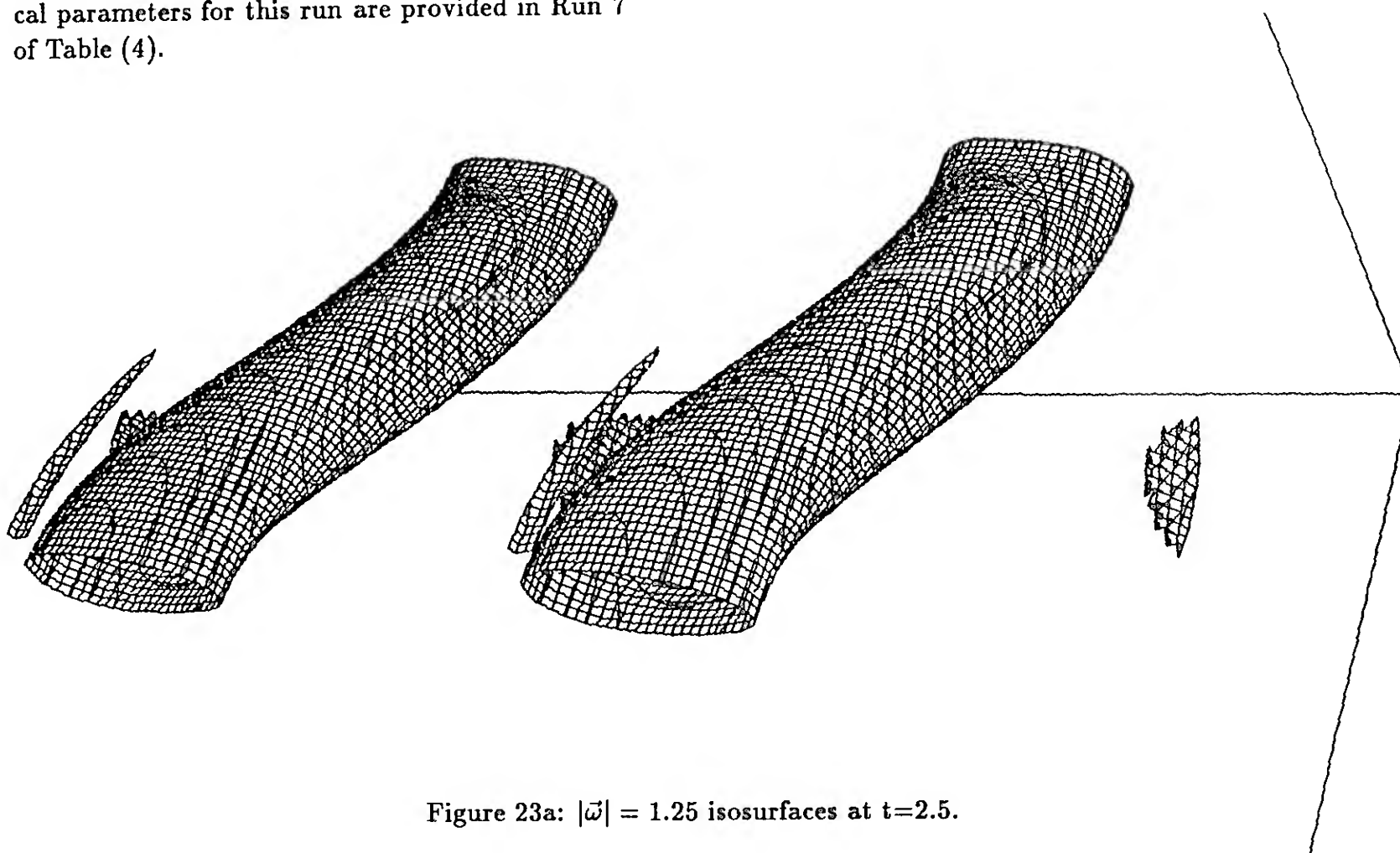


Figure 23a:  $|\vec{\omega}| = 1.25$  isosurfaces at  $t=2.5$ .

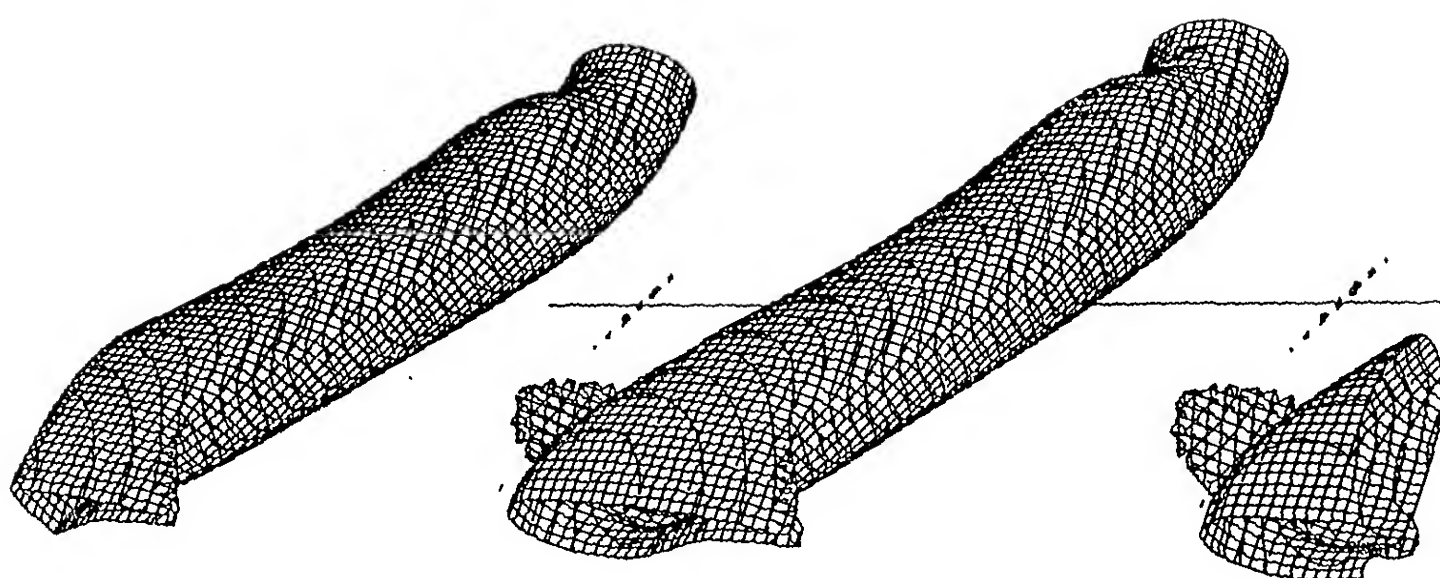


Figure 23b:  $|\vec{\omega}| = 1.25$  isosurfaces at  $t=5$ .

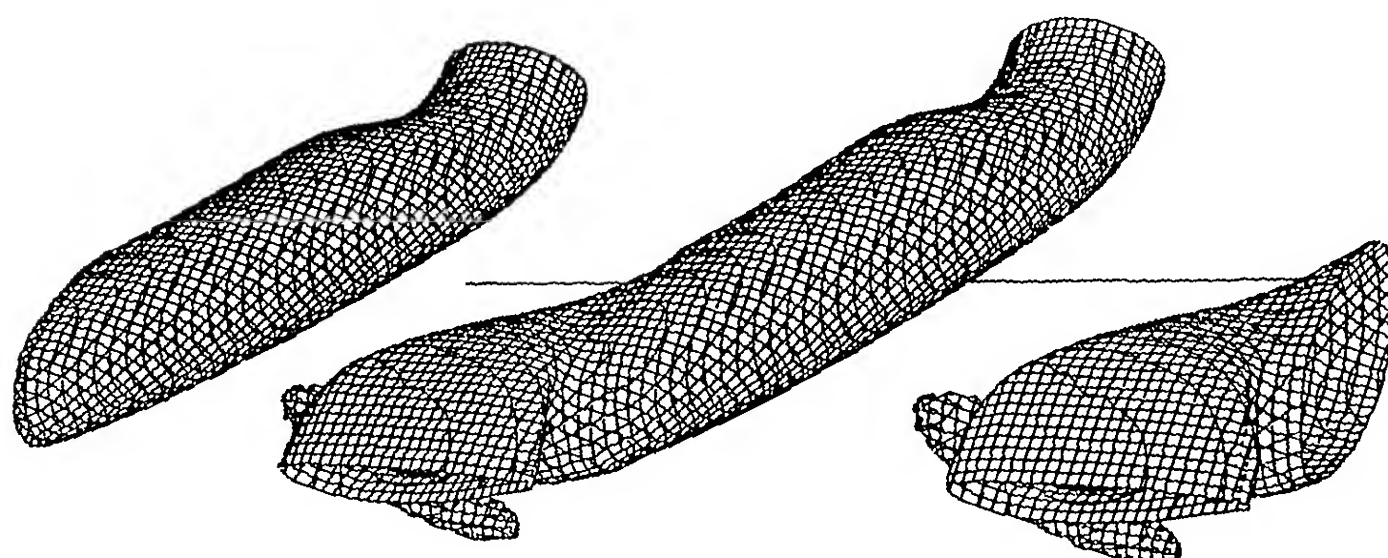


Figure 23c:  $|\vec{\omega}| = 1.25$  isosurfaces at  $t=7.5$ .

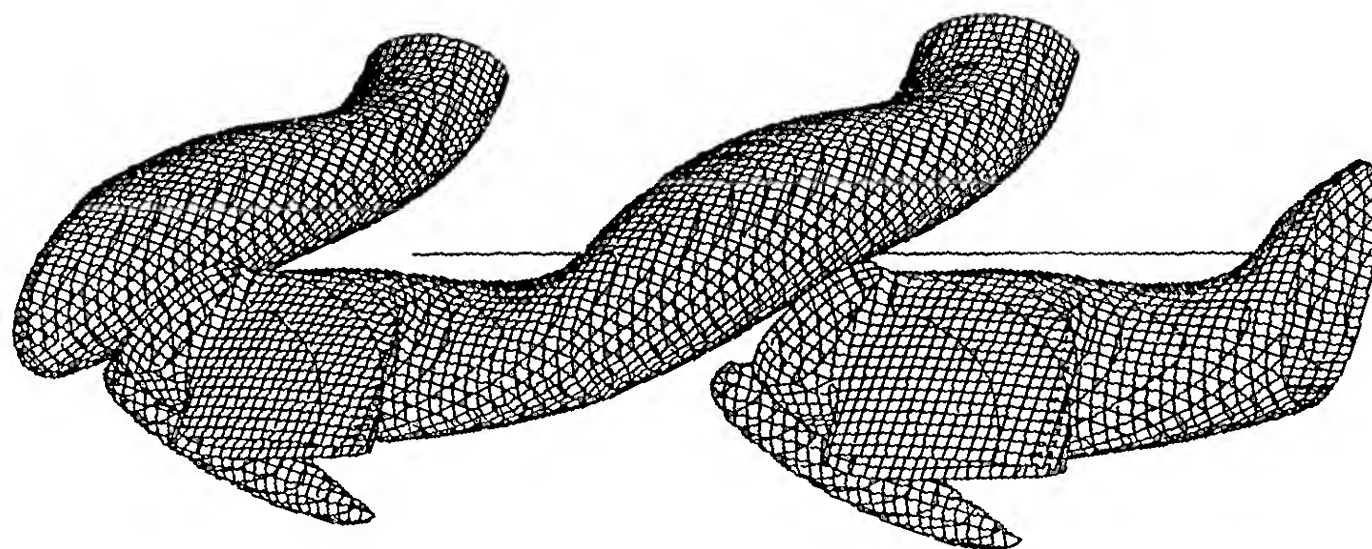


Figure 23d:  $|\bar{\omega}| = 1.25$  isosurfaces at  $t=10$ .

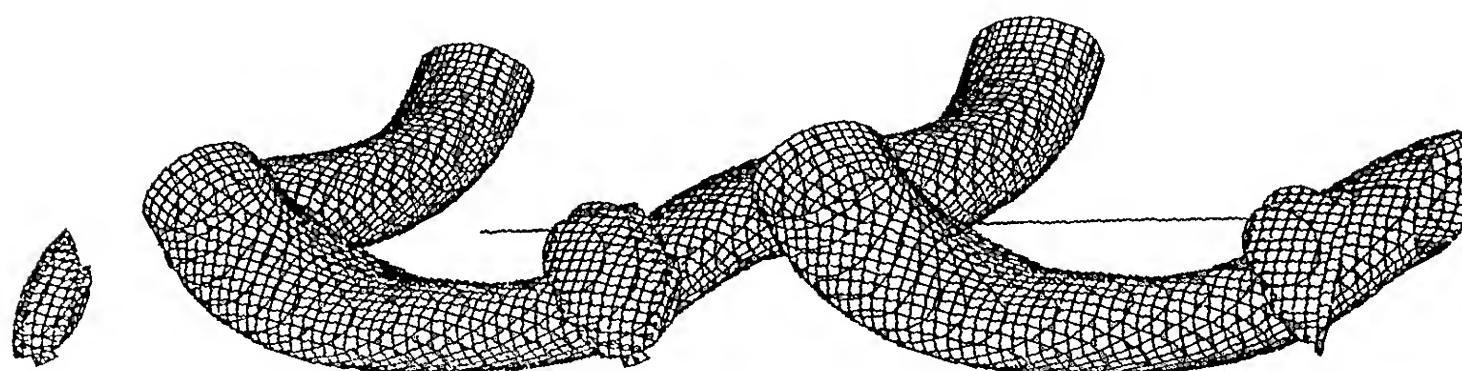


Figure 23e:  $|\bar{\omega}| = 1.25$  isosurfaces at  $t=15$ .



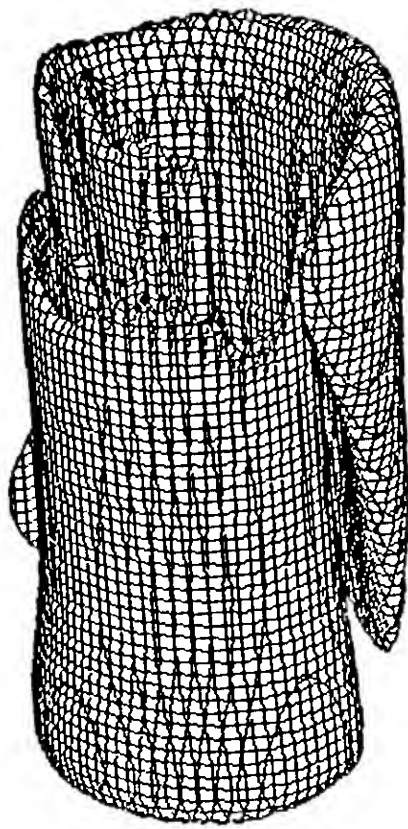


Figure 24a:  $\sqrt{\omega_x^2 + \omega_z^2} = 0.5$  isosurfaces at  $t=5$ .

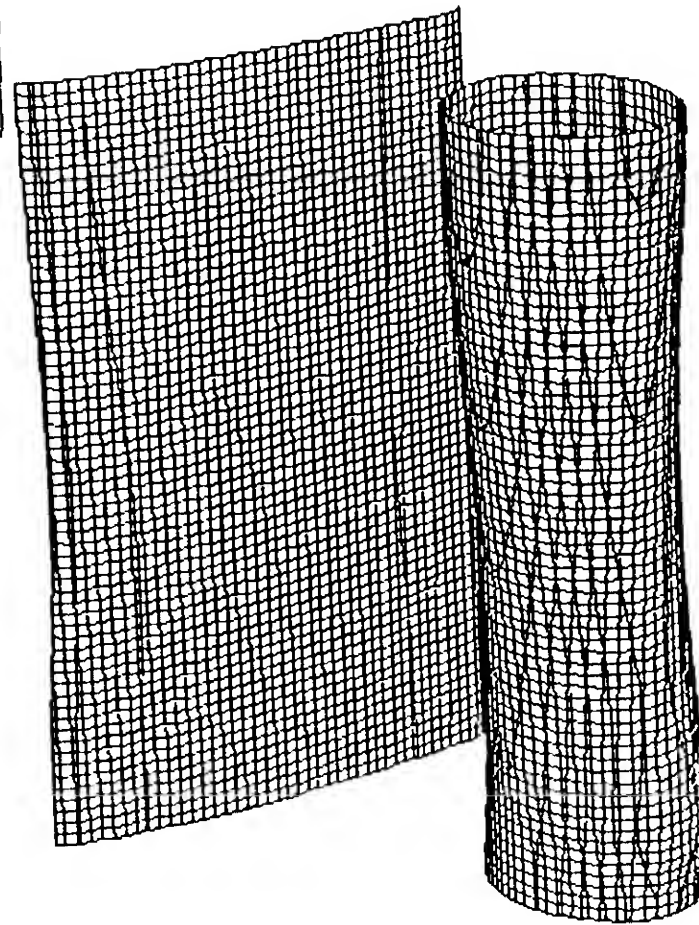


Figure 24a:  $|\omega_y| = 0.5$  isosurfaces at  $t=5$ .

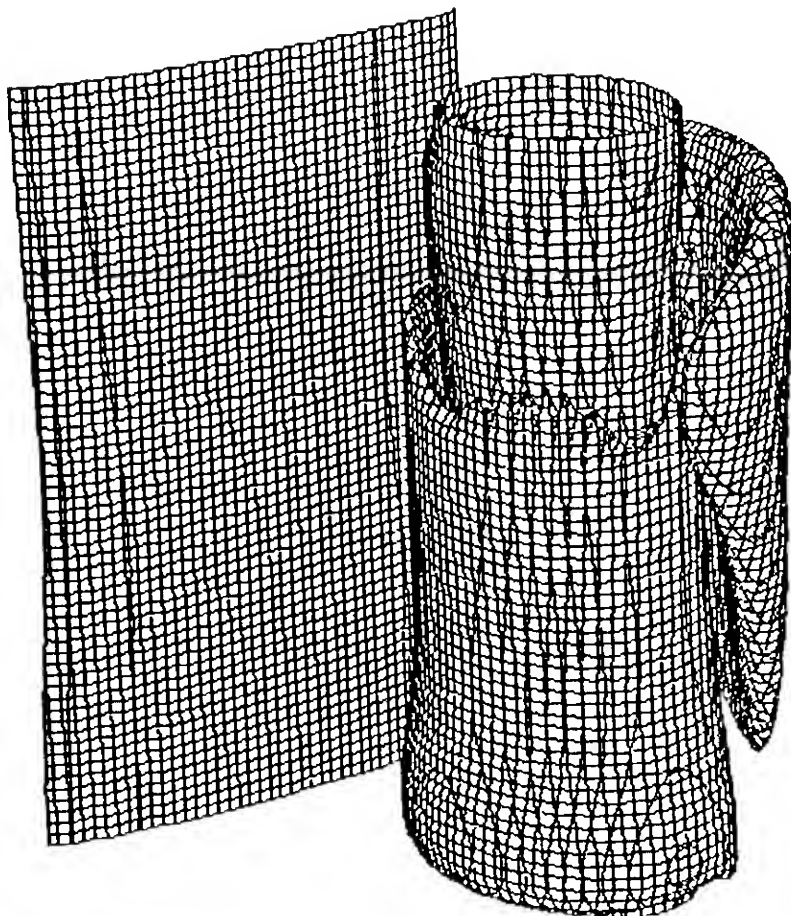


Figure 24a:  $|\vec{\omega}| = 0.5$  isosurfaces at  $t=5$ .

Figure 24: The interactions of a vortex tube with a no-slip wall. The  $\sqrt{\omega_x^2 + \omega_z^2} = 0.5$  (helical vorticity),  $|\omega_y| = 0.5$  (axial vorticity), and  $|\vec{\omega}| = 0.5$  (total vorticity) isosurfaces are plotted at different instants of time: (a)  $t=5$ , (b)  $t=7.5$ , (c)  $t=10$ , (d)  $t=12.5$ , (e)  $t=15$ , (f)  $t=17.5$ , & (g)  $t=20$ . The view is from below a no-slip wall, and the primary vortex is moving into and to the left of the page due to its images across the centerplane and above the wall. The geometry triad is in a submerged corner on the centerplane of the computational domain. Note that the perspective in Part (g) is slightly different from Parts (a)-(f). The numerical parameters for this run are provided in Run 3 of Table (4).

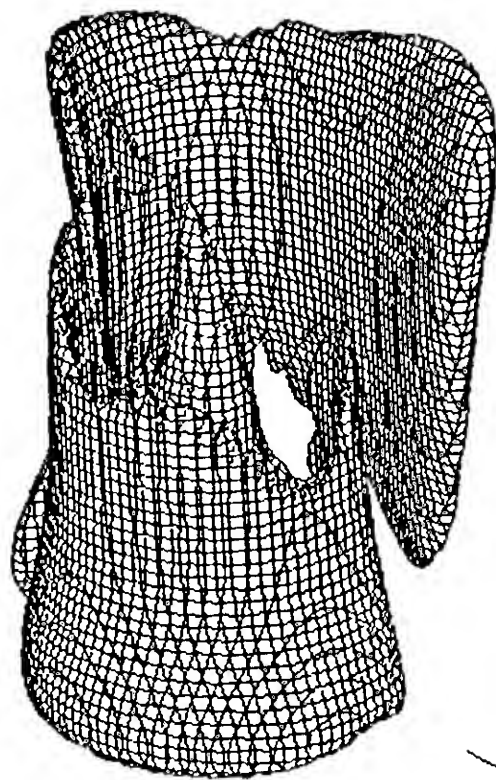


Figure 24b:  $\sqrt{\omega_x^2 + \omega_z^2} = 0.5$  isosurfaces at  $t = 7.5$ .

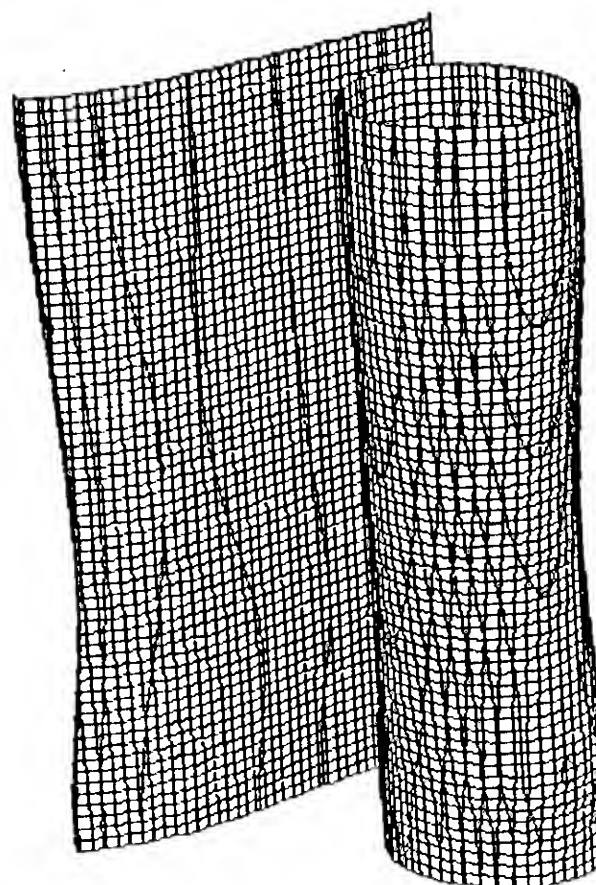


Figure 24b:  $|\omega_y| = 0.5$  isosurfaces at  $t = 7.5$ .

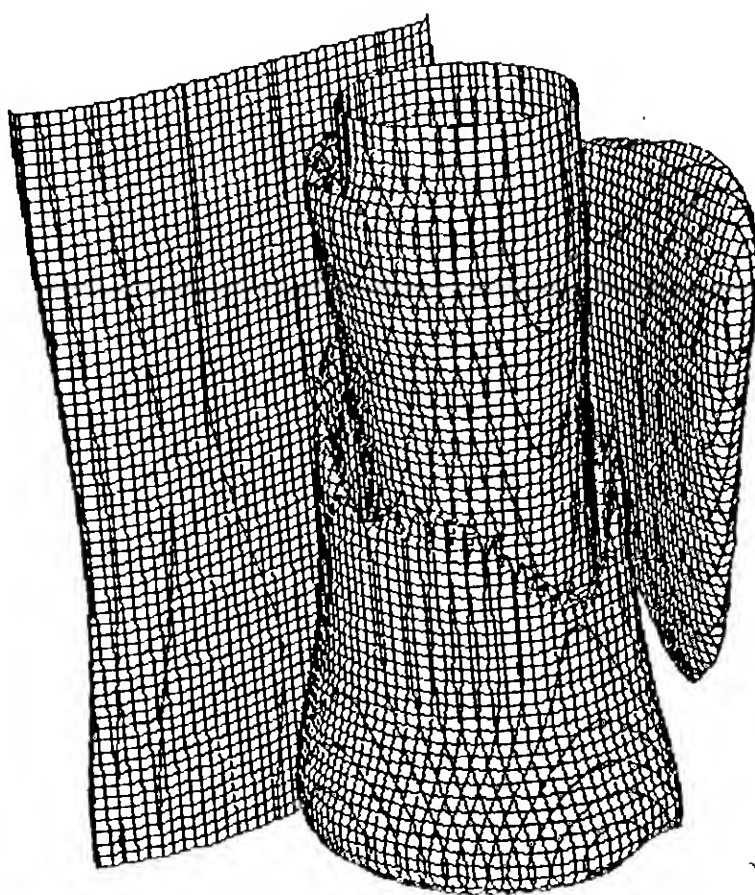


Figure 24b:  $|\vec{\omega}| = 0.5$  isosurfaces at  $t = 7.5$ .

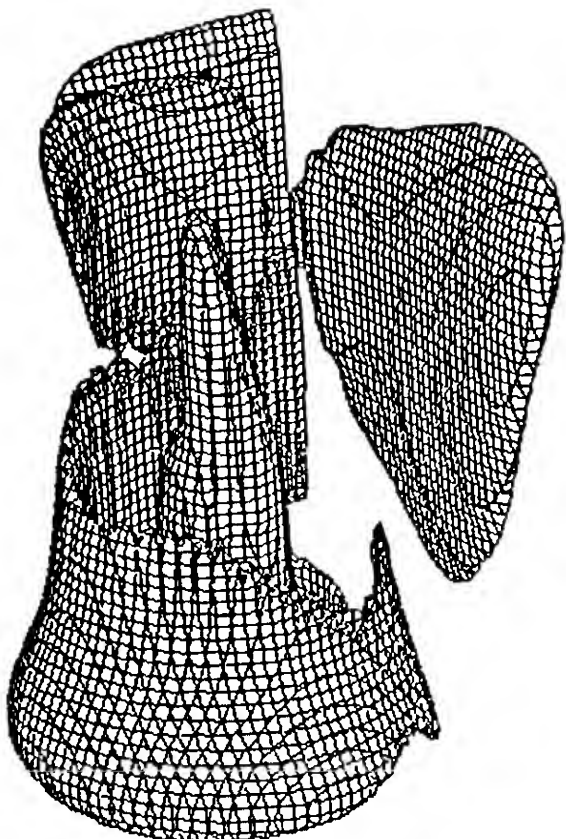


Figure 24c:  $\sqrt{\omega_x^2 + \omega_z^2} = 0.5$  isosurfaces at  $t=10$ .

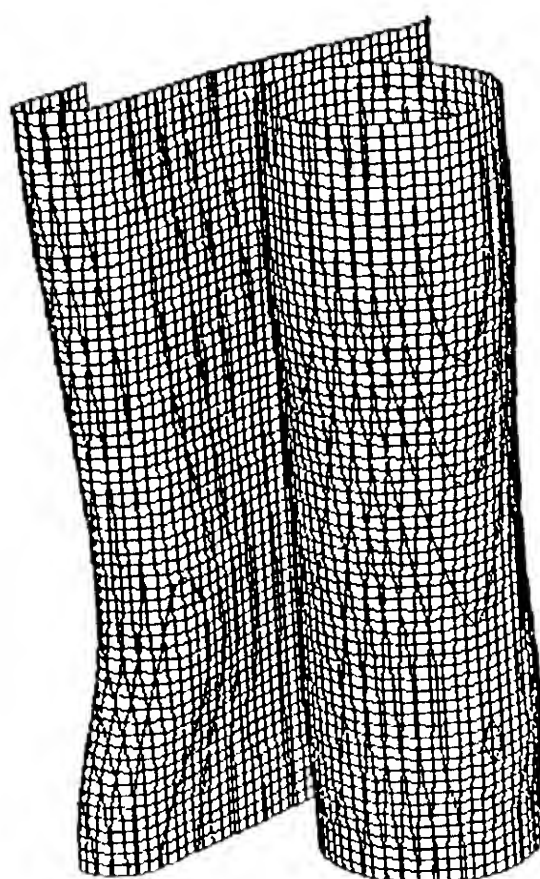


Figure 24c:  $|\omega_y| = 0.5$  isosurfaces at  $t=10$ .

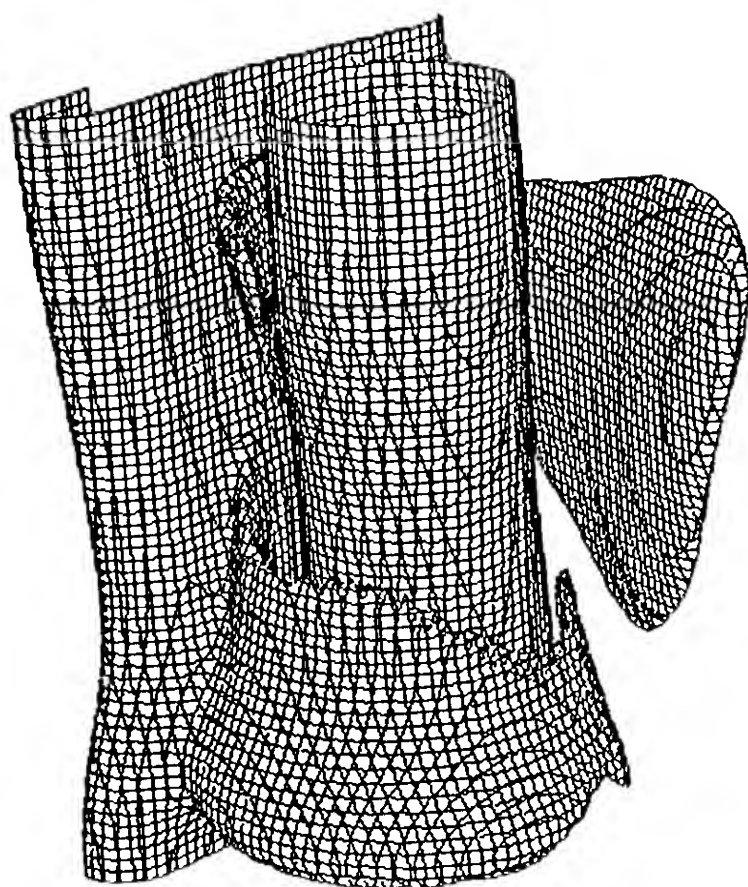


Figure 24c:  $|\omega| = 0.5$  isosurfaces at  $t=10$ .

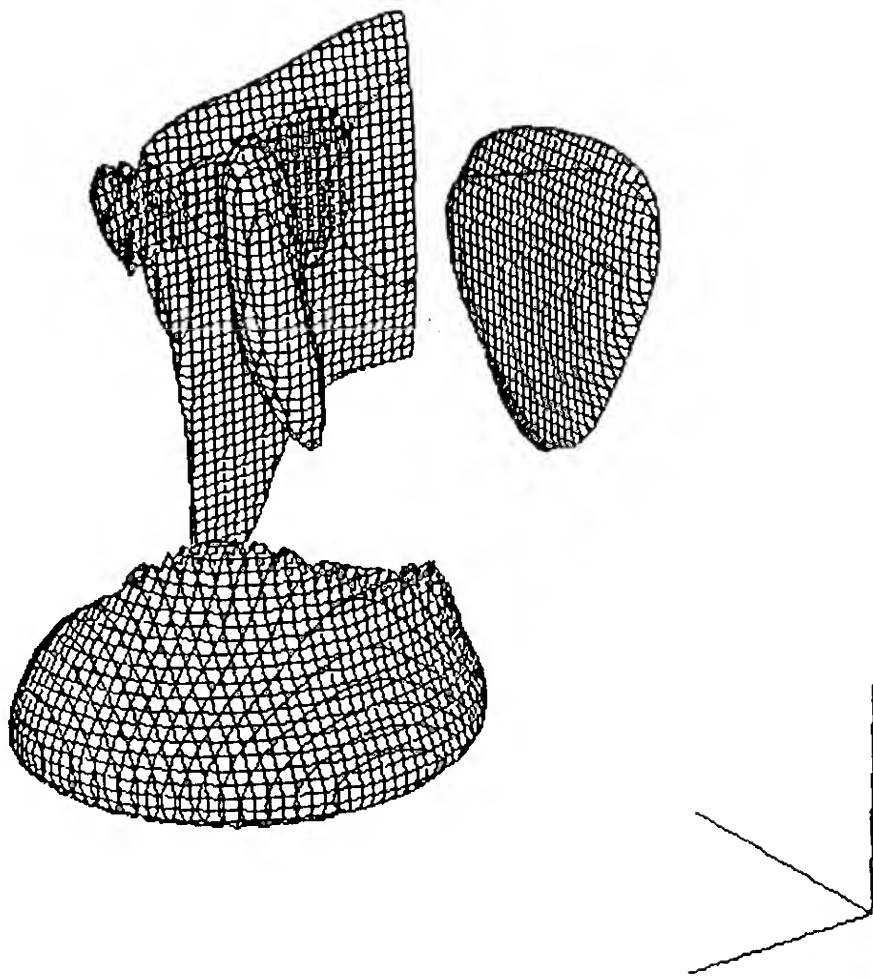


Figure 24d:  $\sqrt{\omega_x^2 + \omega_z^2} = 0.5$  isosurfaces at  $t=12.5$ .



Figure 24d:  $|\omega_y| = 0.5$  isosurfaces at  $t=12.5$ .

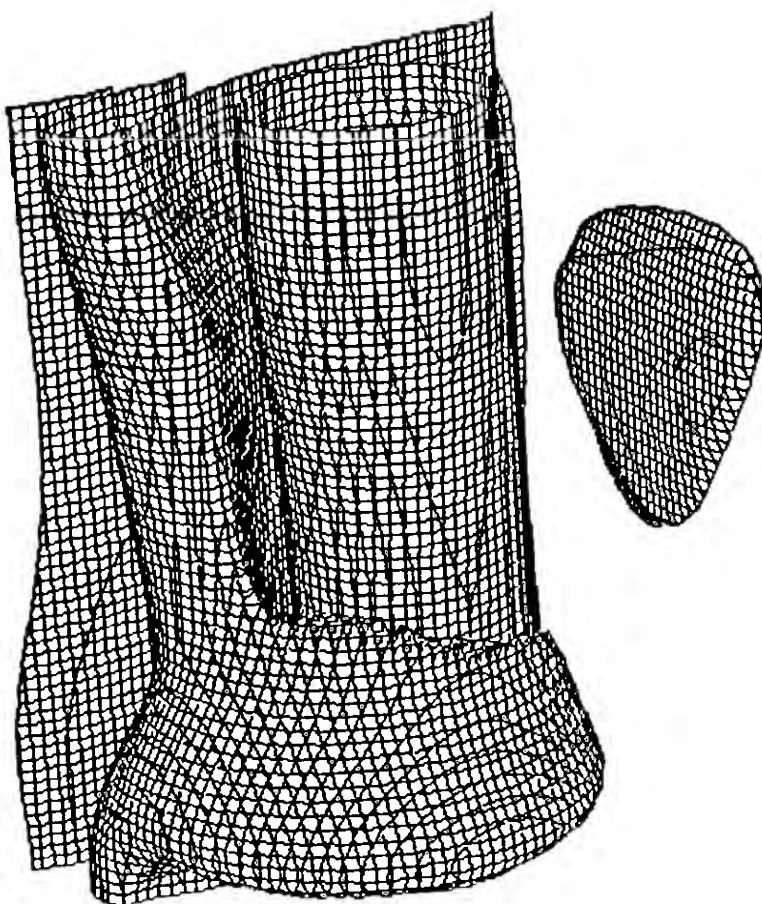


Figure 24d:  $|\vec{\omega}| = 0.5$  isosurfaces at  $t=12.5$ .



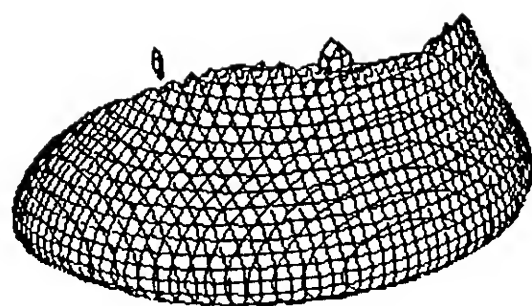
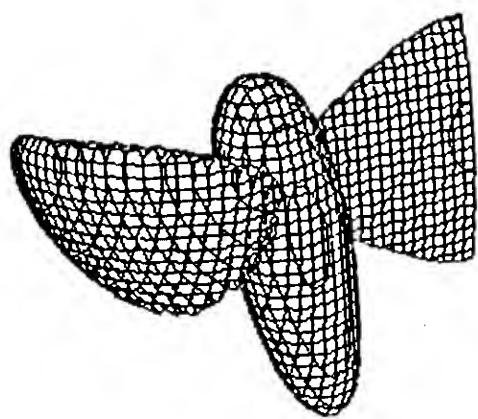


Figure 24e:  $\sqrt{\omega_x^2 + \omega_z^2} = 0.5$  isosurfaces at  $t=15$ .

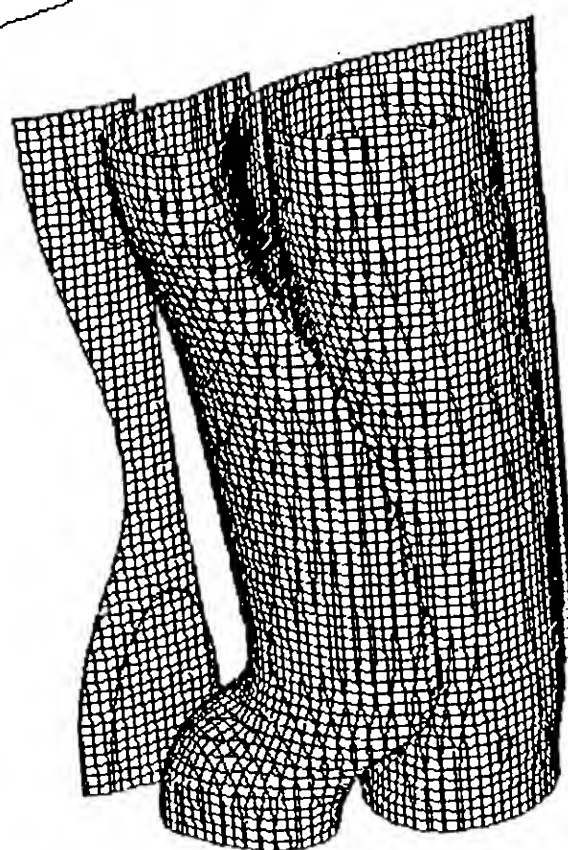


Figure 24e:  $|\omega_y| = 0.5$  isosurfaces at  $t=15$ .

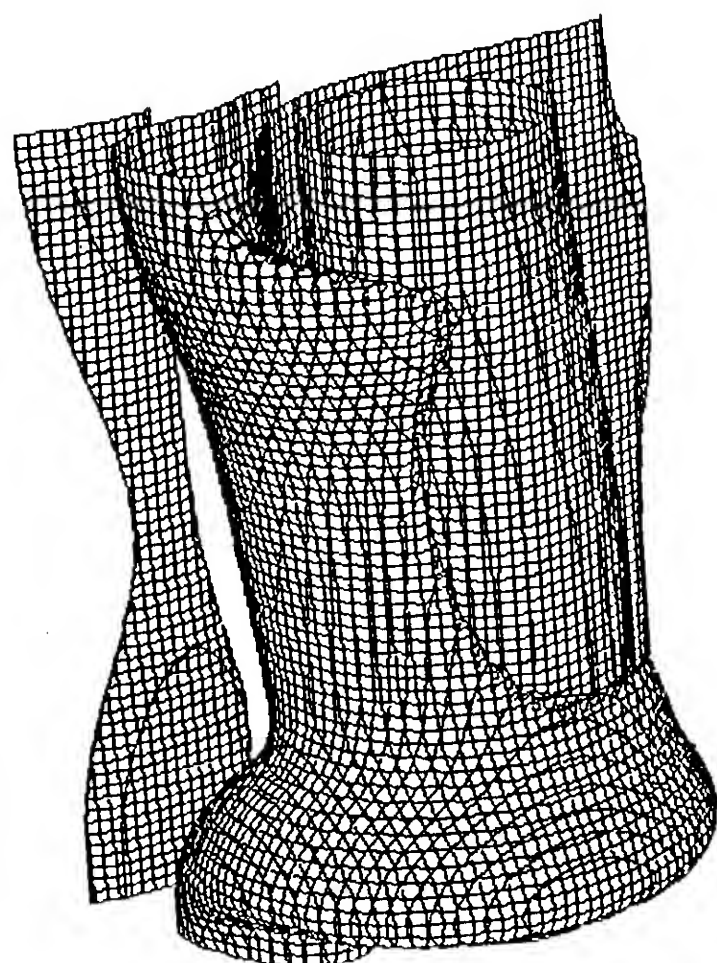


Figure 24e:  $|\vec{\omega}| = 0.5$  isosurfaces at  $t=15$ .



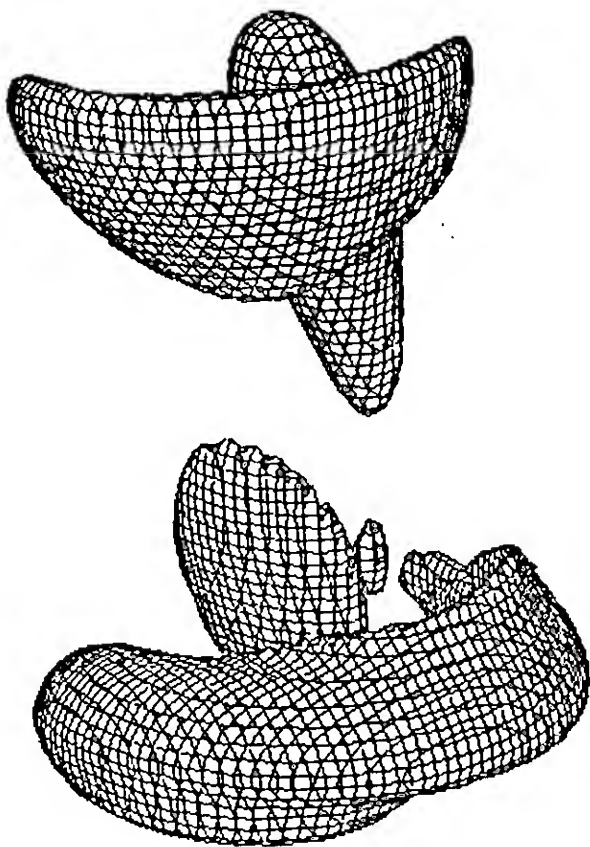


Figure 24f:  $\sqrt{\omega_x^2 + \omega_z^2} = 0.5$  isosurfaces at  $t=17.5$ .

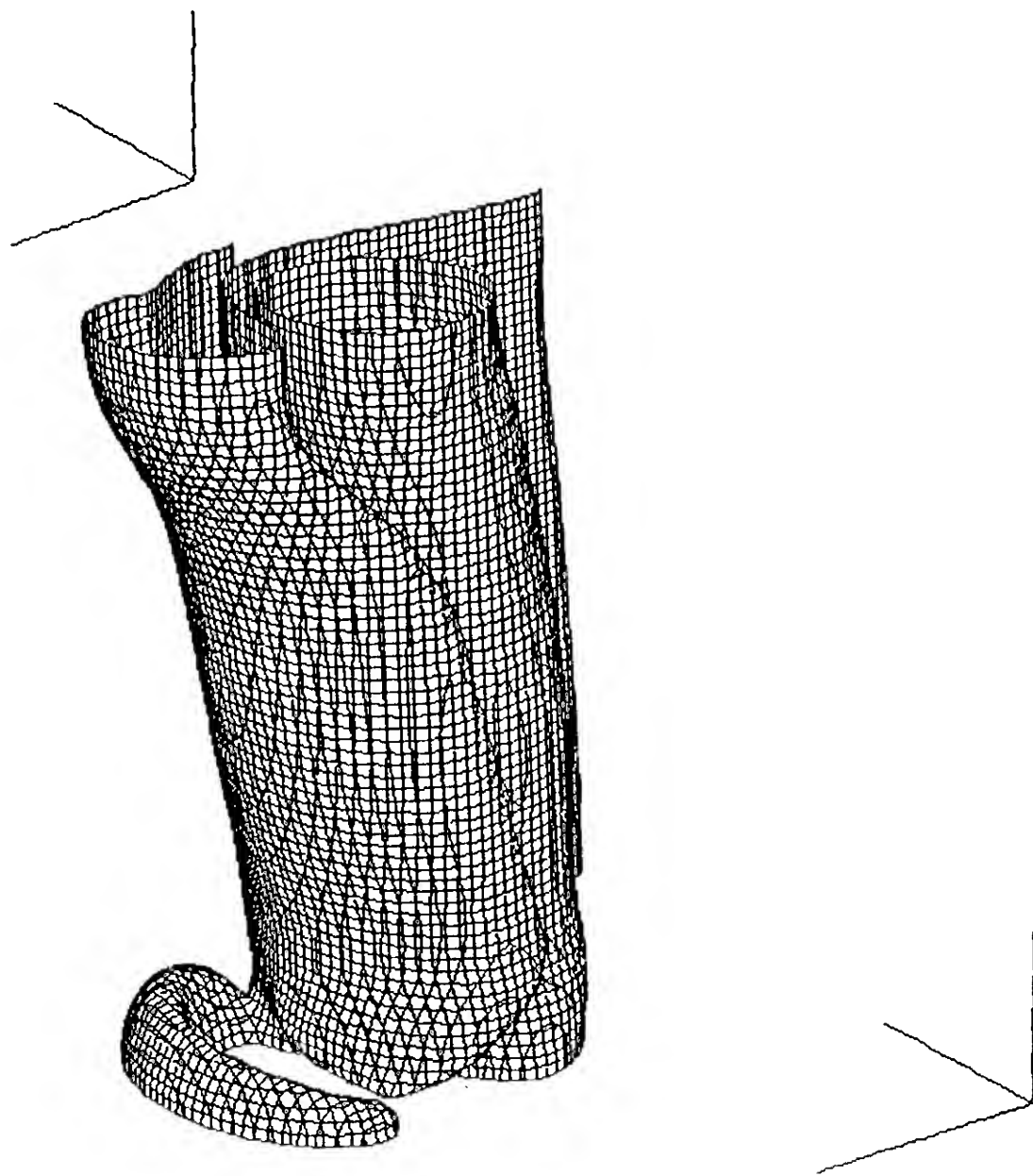


Figure 24f:  $|\omega_y| = 0.5$  isosurfaces at  $t=17.5$ .

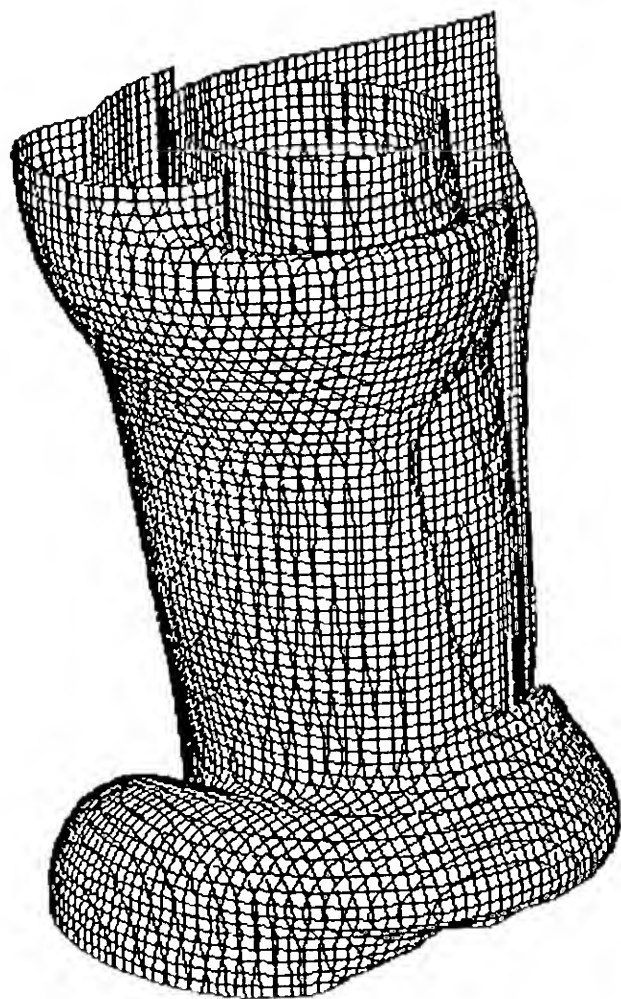


Figure 24f:  $|\vec{\omega}| = 0.5$  isosurfaces at  $t=17.5$ .

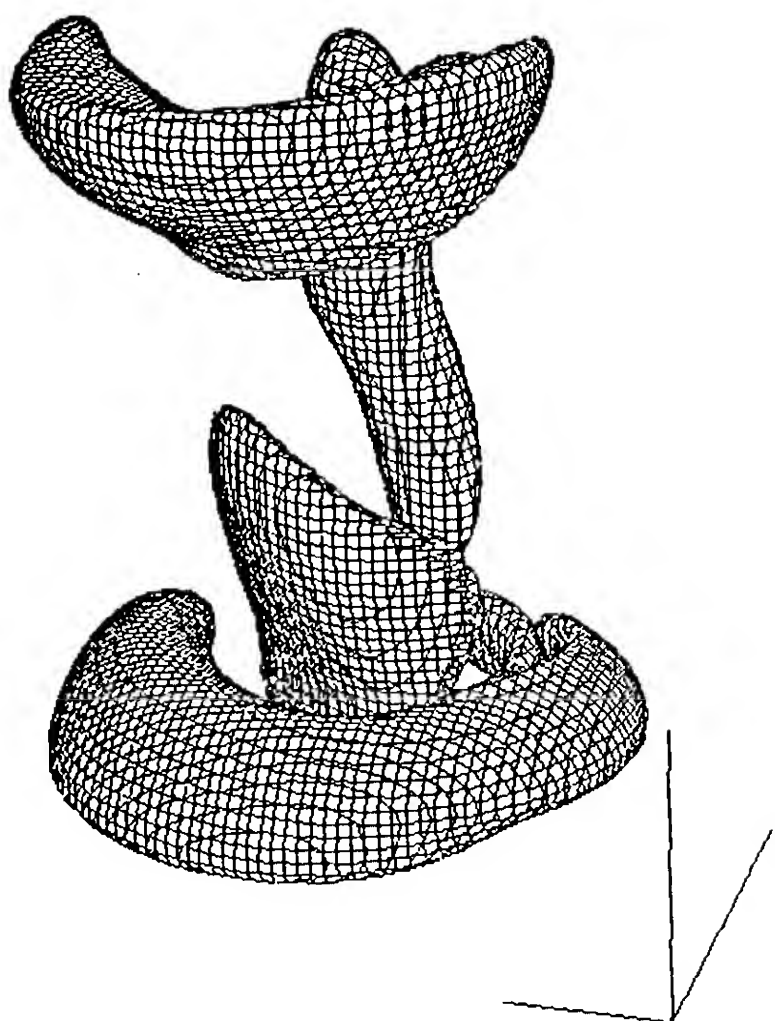


Figure 24g:  $\sqrt{\omega_x^2 + \omega_z^2} = 0.5$  isosurfaces at  $t=20$ .

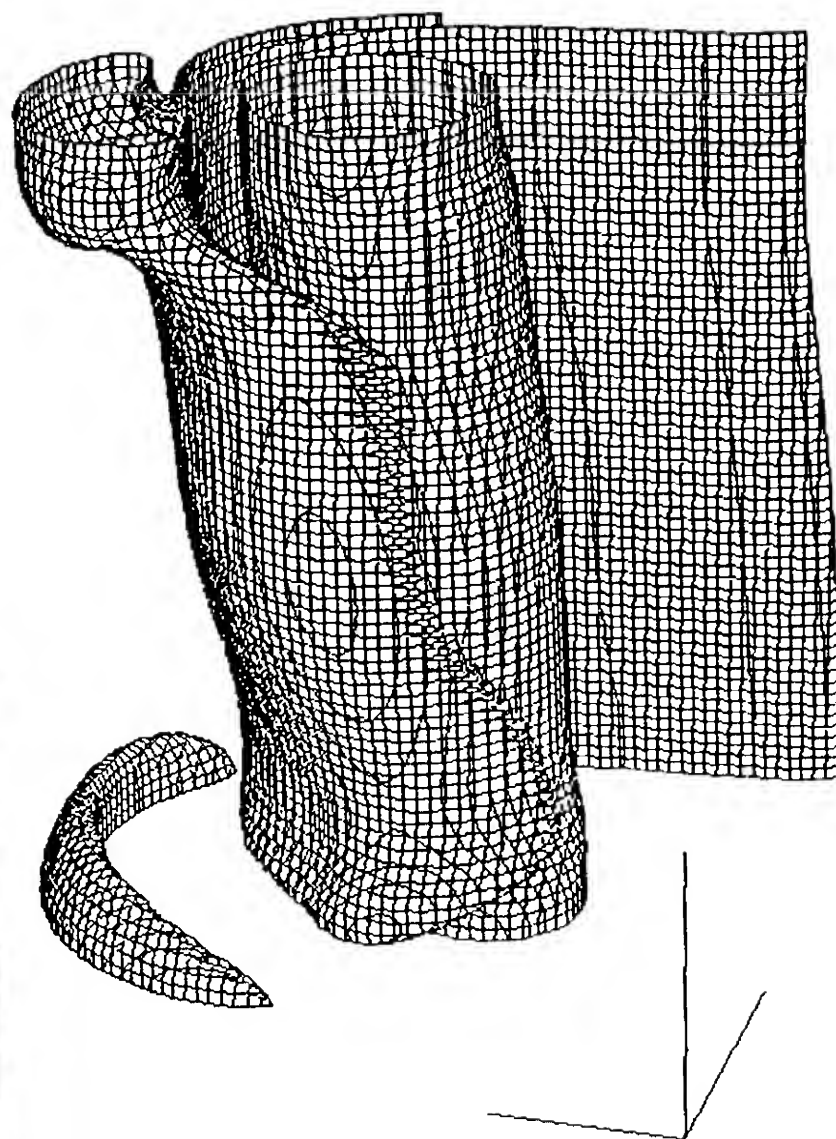


Figure 24g:  $|\omega_y| = 0.5$  isosurfaces at  $t=20$ .

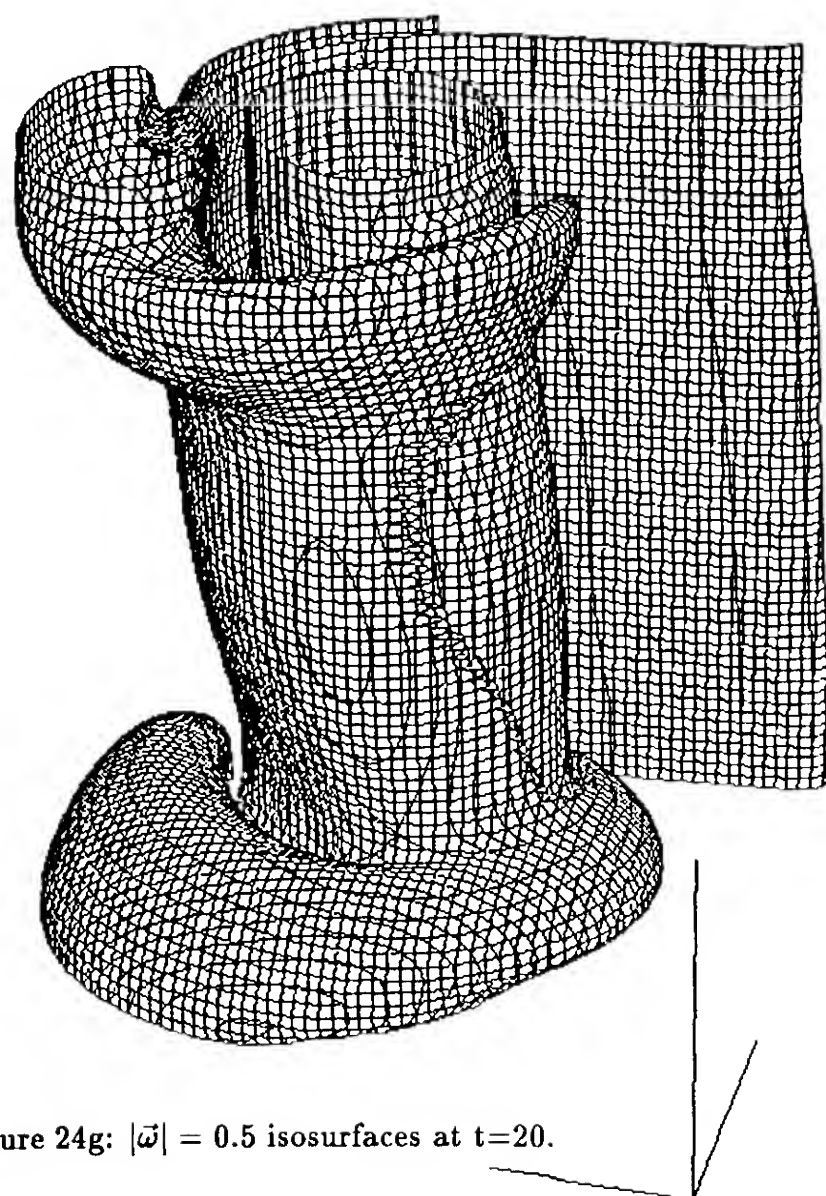


Figure 24g:  $|\vec{\omega}| = 0.5$  isosurfaces at  $t=20$ .

Figure 25: The wrapping of U-shaped vortex tubes around the primary vortex tube. The  $|\bar{\omega}| = 0.5$  iso-surface of vorticity is plotted at time  $t=20$ . To emphasize the U-shaped feature this image has been reflected about its midspan relative to the images appearing in Figures (24). The numerical parameters for this run are provided in Run 3 of Table (4).

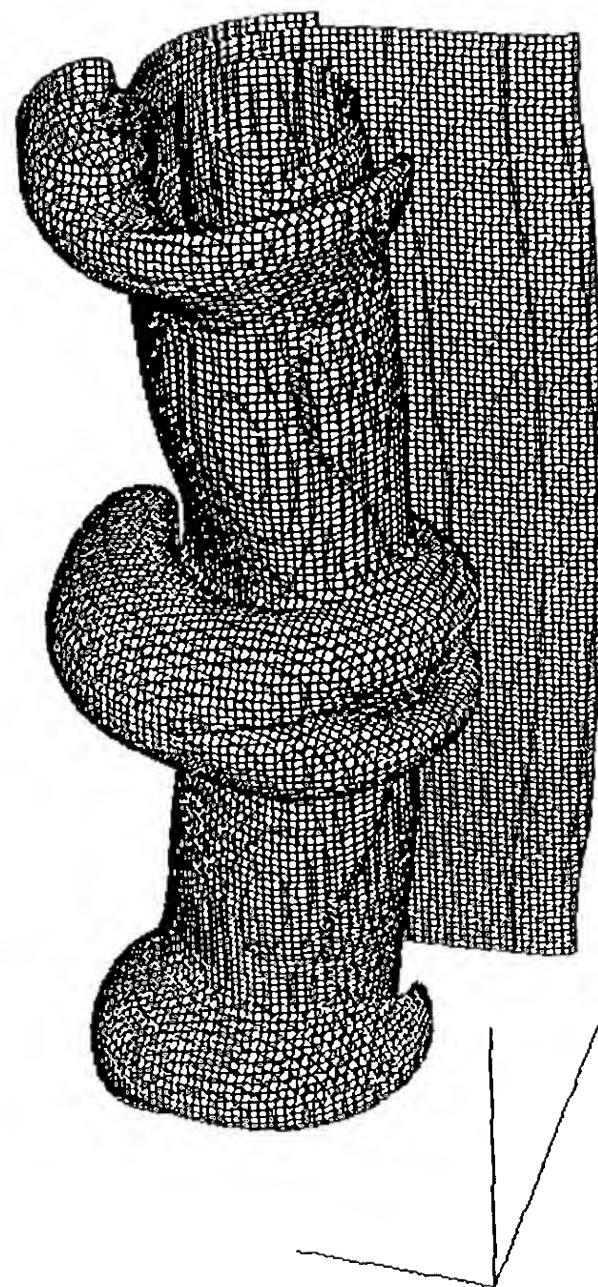
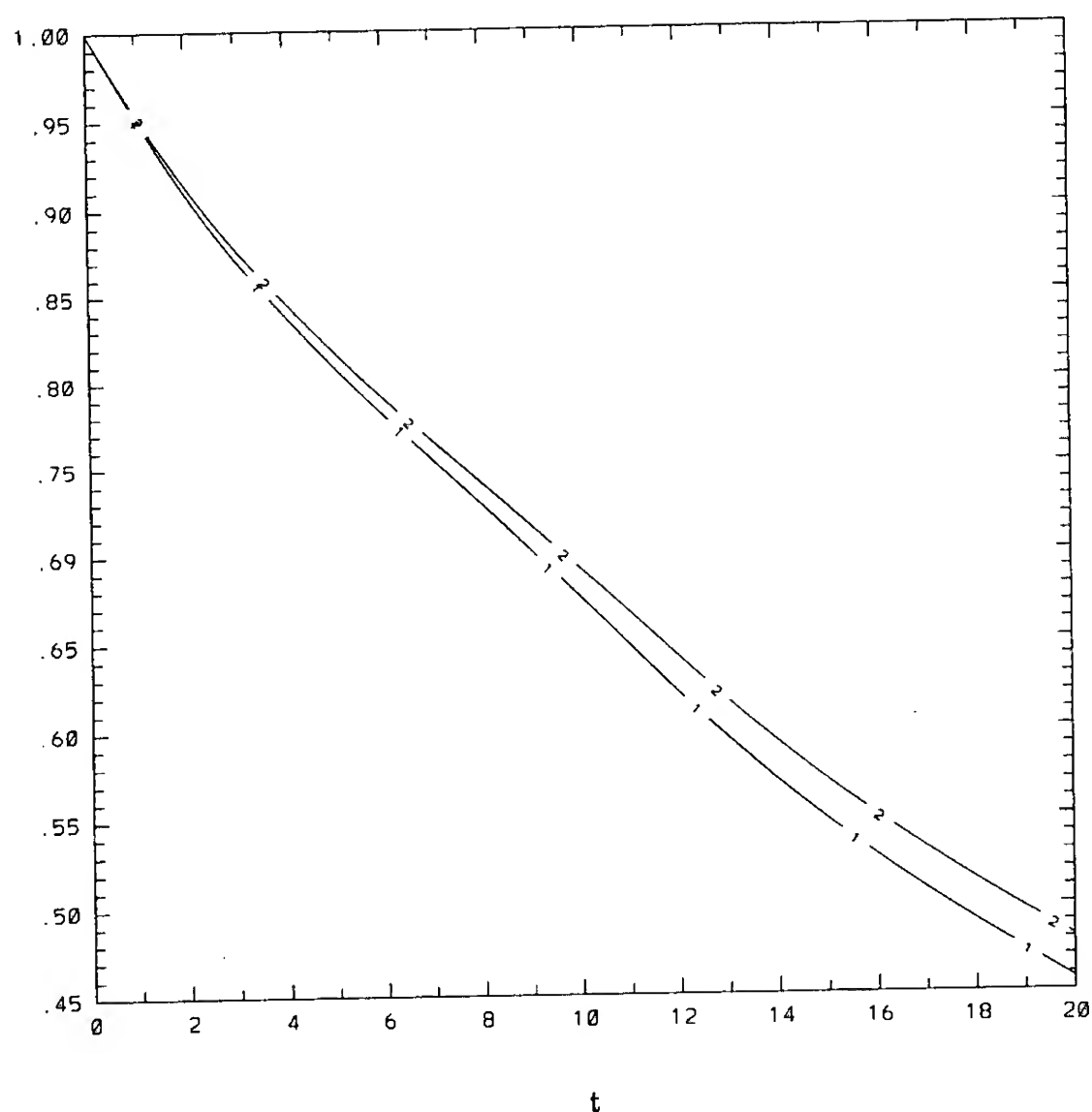


Figure 26: The conservation of energy for a three-dimensional vortex tube interacting with a no-slip wall as a function of time. The kinetic energy  $E(t)$  is compared to the energy that is dissipated  $D(t)$  (the Reynolds number term in eqt. (18) integrated over time). The results are plotted as follows: (— 1 —) denotes  $E(t)/E(0)$  and (— 2 —) denotes  $(E(0) + D(t))/E(0)$ . The numerical parameters for this run are provided in Run 3 of Table (4).



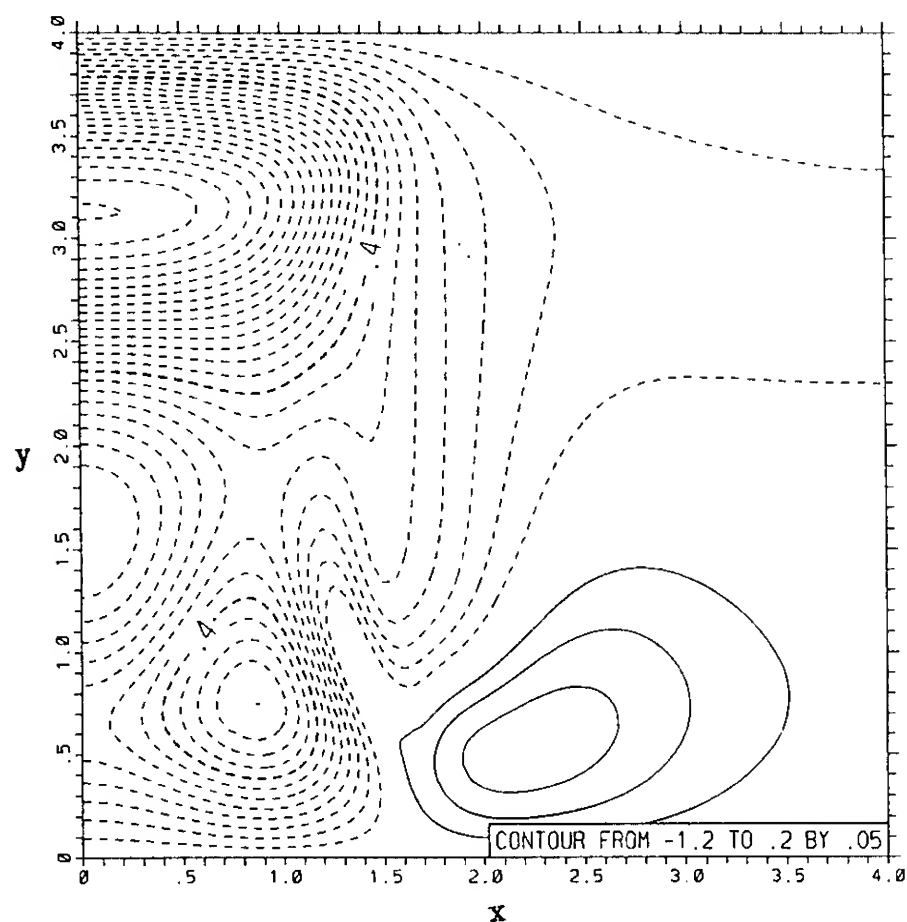


Figure 27a:  $t=10$ .

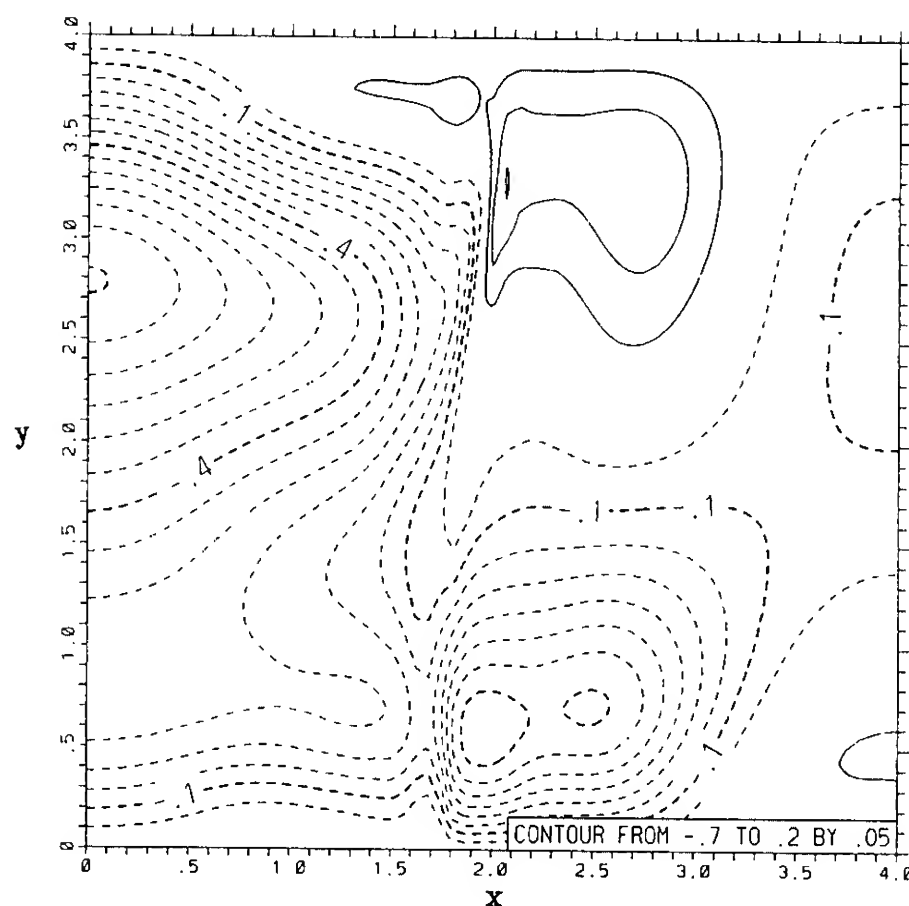


Figure 27b:  $t=15$ .

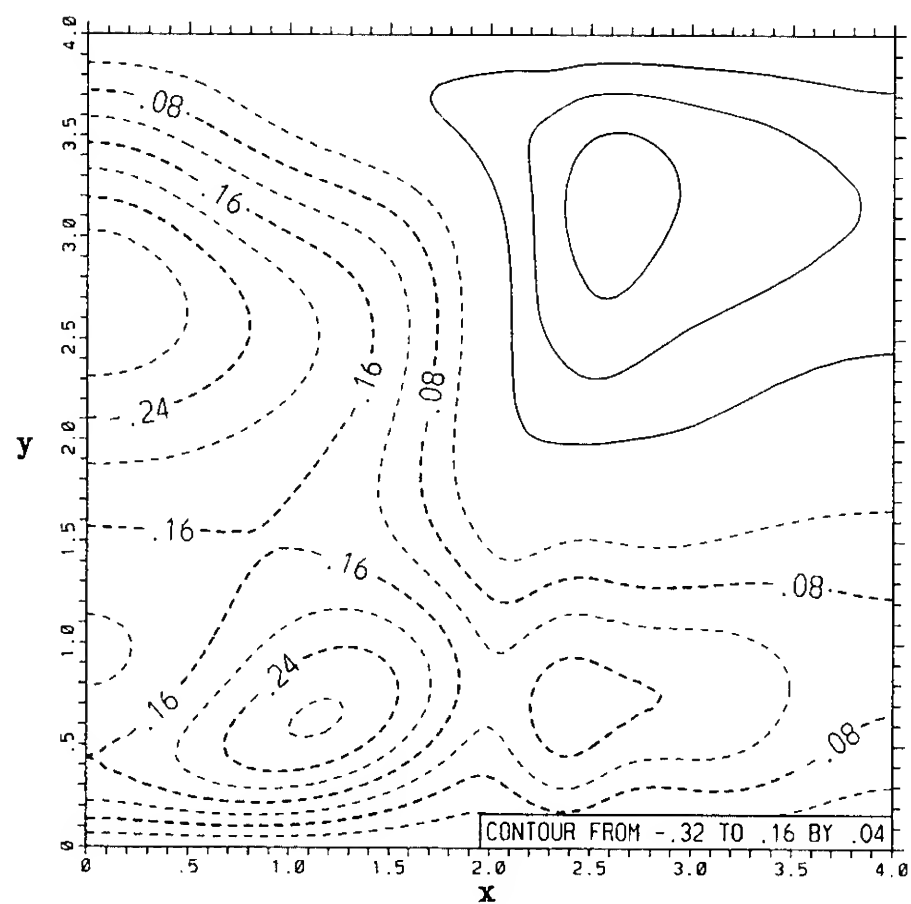


Figure 27c:  $t=20$ .

Figure 27: *The helical vorticity evaluated on the wall.* The contours of  $\omega_x$  on the wall are plotted for different instants of time: (a)  $t=10$ , (b)  $t=15$ , and (c)  $t=20$ . Observe that the features are oriented normal to the axis of the primary vortex tube which is parallel to the  $y$ -axis. The numerical parameters for this run are provided in Run 3 of Table (4).

## DISCUSSION

P. Ananthakrishnan  
University of California at Berkeley, USA (India)

My question/remark is regarding the results corresponding to the interactions due to a vortex ring that is normally incident on the free surface. According to Song, et al (in M. Song, N. Kachman, J.T. Kwon, L.P. Bernal, and G. Tryggvason, "Vortex Ring Interaction with a Free Surface," preprint, 18th Symp. on Naval Hydro.), a dip on the free surface right above the vortex core, which moves radially outward as the vortex ring stretches at the free surface, is observed. They also observe three-dimensional small scale motions and propagating waves at higher Froude numbers. But your results (Fig. 17) show a rise in wave elevation at the axis of symmetry that is comparable in magnitude to the surface depression. Could you comment on the possible reasons for the difference between the observed and computed results?

## AUTHORS' REPLY

Relative to Song, et al's, (1990) experiments, our numerical axisymmetric results are valid for much higher Froude numbers. Even so, we also predict the free-surface depression that occurs above the vortex core as is evident in our Fig. (16). In regard to the small-scale three-dimensional features that are observed in experiments, we believe that some of these features may be explained in terms of U-vortices. For example, Fig. (2b) of Song, et al's (1990) paper shows a U-shaped feature wrapped around the primary vortex tube. The base of the U is on the inside of the ring vortex. Both these features are consistent with the U-vortex phenomena as explained in our paper

## DISCUSSION

Ronald W. Yeung  
University of California at Berkeley, USA

In your results corresponding to Fig. (16) and Fig. (17), you have mentioned the existence of a non-zero mean wave elevation, which you artificially subtract off to obtain presented results. The non-zero mean implies that mass is not conserved; I was wondering if the authors can shed some light on the source of this trouble?

## AUTHORS' REPLY

For our linearized free-surface boundary conditions, the free-surface elevation is much smaller than the boundary-layer thickness ( $\eta \ll \delta$ ). The Froude and Reynolds numbers that are illustrated in Figs. (16 & 17) push the limits of this theory so that an interesting physical regime could be investigated. Fully-nonlinear free-surface boundary conditions would eliminate the problem with mass conservation.

## DISCUSSION

Fred Stern  
The University of Iowa, USA

The authors should not use the terminology "direct simulation" to refer to their solutions of the unsteady Navier-Stokes equations for low Reynolds numbers (i.e., laminar flow). Generally, this terminology has become synonymous with the direct simulation of turbulence through extremely high-resolution solutions of the unsteady Navier-Stokes equations for relative high Reynolds numbers as opposed to the use of the Reynolds-averaged Navier-Stokes equations. Would the authors please specifically point out the novel aspects of their method since most aspects appear to be familiar. In fact, this should be the focus of the discussion on the numerical formulation which is too long and often confusing.

The real value of this work is in the use of such numerical methods for free-surface flows and, in particular, the applications chosen for study. The authors appear to have captured many of the observed phenomena although I have not been able to decipher all that they have from the figures. The free-surface boundary conditions used appear to be identical to those used in my paper. Essentially, these are inviscid approximations in which the viscous-stress conditions are neglected, or if you like, only satisfied to a very low order. It would appear then that many of the observed phenomena are pressure-driven. Also, some of the vorticity in the calculations near the free surface may be erroneous due to these approximations. Would the authors please comment on these points?

## AUTHORS' REPLY

We agree that "laminar flow simulation" is more appropriate terminology than "direct simulations." Both our semi-implicit and explicit schemes use unique fully-vectorized multi-grid methods to solve the unsteady three-dimensional Navier-Stokes equations at low Reynolds numbers with and without free surfaces. Our linearized free-surface boundary conditions are derived from the exact normal and tangential stress conditions and the exact kinematic free surface condition subject to our assumption of small free-surface slopes. The range of validity of these free-surface boundary conditions are discussed in our paper and in our answer to Professor Yeung's question. A curved free surface, just like the afterbody of a bluff object, may have unfavorable pressure gradients that lead to flow separation.



# On the Numerical Solution of the Total Ship Resistance Problem under a Predetermined Free Surface

G. Tzabiras, T. Loukakis, G. Garofallidis  
(National Technical University of Athens, Greece)

## ABSTRACT

The free surface around a ship model moving at constant speed was determined experimentally. The resistance components of the model were computed numerically by solving the Reynolds equations beneath the predetermined free surface. The calculations were made using the finite volume approach and the partially parabolic procedure. The standard  $k-\epsilon$  turbulence model was used for the Reynolds stresses. Calculated and measured values for the total resistance have been compared and the applicability of the method is discussed.

## NOMENCLATURE

$A_i$	finite difference coefficients
$C(\Phi)$	convection term of $\Phi$
$C_p$	pressure coefficient
$C_f$	skin friction coefficient
$G$	generation term of $k$
$g$	gravitational acceleration
$h_i$	metrics
$h$	vertical distance
$k_{ij}$	curvature tensor
$k$	turbulence kinetic energy
$e_{ij}$	deformation tensor
$P$	pressure
$P^*$	pressure ( $P + \rho gh$ )
$R_F$	frictional resistance
$R_P$	pressure resistance
$R_T$	total resistance
$u_i$	velocity components
$x_i$	curvilinear co-ordinates
$S_\Phi$	source terms

## Greek symbols

$\epsilon$	dissipation of $k$
$\mu$	fluid viscosity
$\mu_t$	eddy viscosity
$\mu_e$	effective viscosity
$\rho$	fluid density
$\sigma_{ij}$	stress tensor
$\Phi$	variable

## INTRODUCTION

The degree of accuracy at which a physical problem should be solved depends, obviously, on the application of the solution. In this respect, in ship design and construction, the most important problem pertaining to hydrodynamics is the accurate prediction of the ship speed and the corresponding propeller revolutions and shaft horsepower. This is because these quantities are specified in the contract of a newbuilding and the shipyard has to pay penalties if the ship propulsion performance is found inferior during the ship delivery trials.

Therefore, the efforts of untold numbers of marine hydrodynamicists and mathematicians during the last century or so to solve analytically the ship propulsion problem have been well directed. However, and from the practical point of view, these efforts have been largely unsuccessful. Thus, in current engineering practice, only the prediction of the propeller performance in a prescribed wake field is thought to be trustworthy enough to be actually used on a routine basis. The prediction of pressures and shear stresses around the hull of a ship, moving at constant speed in calm water, remains an elusive goal. The same is true for the wake field behind the hull and for the propeller hull form interactions. This state of the art is especially bothersome if the availability of virtually unlimited computational power is taken into account.

On the other hand, more difficult but less important problems, from the point of view of contractual obligations, such as the dynamic behaviour of the ship in waves can be and are successfully treated using simple theories of moderate accuracy.

The simplest of the yet unsolved problems in ship hydrodynamics is that of the ship resistance in calm water and at constant speed. In this case it is the belief of the authors, that for the vast majority of practical applications this problem should be treated from the beginning as a viscous flow problem. That is, it is believed that the incomplete modeling of the flow as inviscid, in order to obtain the wavemaking resistance separately, will not lead to a successful solution of the real life problem.

Dept. of NAME, NTUA, 42, 28th Oktovriou Str., Athens 10682, GREECE

In recent years the availability of computer codes solving the complete Reynolds equations and of powerful computers has yielded promising results in the case of computing the flow field around three dimensional, shiplike bodies in the absence of a free surface. A recent survey of this area of research is presented by Patel (1). But even for this simplified case some problems seem to remain as can be deduced from the scarcity of computations for the high Reynolds numbers of the ship scale (2). Very recently, results have been presented for the solution of the complete problem of a ship moving in a viscous fluid, e.g. Hino (3). Although the results presented seem reasonable when compared to experimental values, no result for the ship resistance is given. Moreover, the method does not seem at this stage to include the computation of the equilibrium position of the ship under way. That is the ship is assumed to move at its static equilibrium position, which is a common assumption when trying to solve the ship resistance problem. However, as it is well known from experimental results, the dynamic equilibrium position is an important factor for the determination of the ship resistance, for a ship moving at constant speed and weight.

From this discussion, one might conclude that, although many steps have been made towards the prediction of the ship resistance, no practical solution of the problem is in sight. This conclusion is strengthened by the fact that no model of turbulence, required for the Reynolds equations, has been derived with free surface flows in mind.

In view of the above it was decided that a meaningful intermediate step, in the long route necessary before ship resistance can be analytically computed, was to remove as many uncertainties as possible and to treat a simpler case with the method described in (4). Thus, a three meter model of a liner ship was tested in a Towing Tank and its dynamic equilibrium position as well as the wave pattern around it were measured together with its total resistance. In this manner, and looking at the ship from below, the actual solid and liquid boundaries for the flow were determined. It was then straightforward to run the NTUA viscous flow computer code for this prescribed fluid region, applying appropriate conditions at the boundaries and obtain the total ship resistance, as the sum of the pressure and the wall shear stress forces.

The viscous flow computer code of NTUA uses the standard  $k-\epsilon$  turbulence model which has been applied with relative success but it is unknown if it is valid near a free surface. For axisymmetric fully submerged bodies, the method gives good pressure predictions and a small overestimation of the velocities (5). The integrated results, that is the force predictions, are good. For double hull ship forms, the method gives again good results for pressures and wall shear stresses although it overestimates the velocities in some areas (2). However, when the method was used to obtain the integrated resistance force for the case of a landing ship running at a low Froude number, the computed results seemed to overpredict the measured resistance by almost 7% (6).

The results of the present research effort, which is modest in scope as it is unsponsored, can be of value since they focus on the capabilities of the numerical solution of the viscous flow problem in a predetermined domain.

As will be seen in the sequel, the analytical prediction of the total ship resistance, although reasonable, does not compare well with the experimental value. Therefore, more research is necessary as will be explained in the conclusions. For this reason, the idea of using the predetermined free surface to compute the ship resistance for the Reynolds number of the full size ship was abandoned as premature.

## DESCRIPTION OF THE EXPERIMENTS

The 1:50 scale model of a liner ship was selected for the purposes of the investigation. This model had been tested previously at the Towing Tank of N.T.U.A. For the same ship, another model at a 1:30 scale had been tested at N.T.U.A. and a third model, at a 1:22.43 scale at the Bulgarian Ship Hydrodynamics Center. Thus, enough data were available for the determination of the form factor according to the ITTC methods and definitions.

The principal characteristics of the 1:50 model are shown below and the body plan of the model is shown in Fig.1.

Length on Waterline	$L_{WL} = 3.083 \text{ m}$
Beam	$B = 0.429 \text{ m}$
Draught	$T = 0.179 \text{ m}$
Block Coefficient	$C_B = 0.575$
Prismatic Coefficient	$C_p = 0.601$
Midship section Coefficient	$C_M = 0.956$
Wetted Surface	$S = 1.694 \text{ m}^2$
Displacement	$\Delta = 133 \text{ kp}$

The dimensions of the Towing Tank are 90mx4.65mx3.0m.

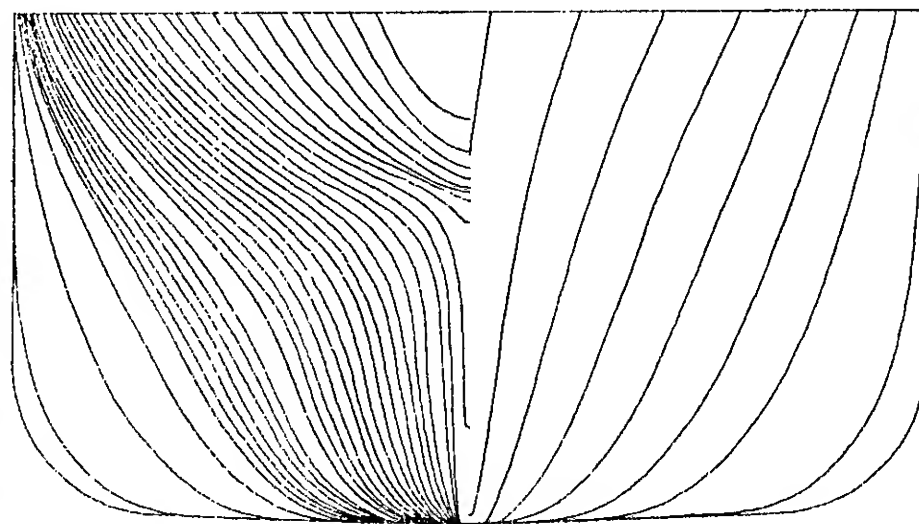


Figure 1. The body plan of the model.

## Resistance Measurements

The model was attached to a dynamometer-heave rod-pitch bearing assembly, which can measure the model resistance, parallel sinkage and running trim as the model is towed at constant speed.

The model was tested repeatedly at a speed of 1.346 m/sec., which corresponds to a Froude Number of 0.245. At this speed and for a water temperature of 22°C, the measured resistance and parallel sinkage were:

Speed	Resistance	Parallel Sinkage
1.346 (m/s)	0.682 (kp)	0.6 (cm)

The measured value of running trim was practically zero.

With regard to the resistance measurements in particular and the test conditions in general, two remarks are in order. Firstly, the blockage effect on this model is negligible, about 0.4% when expressed as a speed correction and secondly that, although the model speed is quite constant, the resistance force is not. This can be explained by the fact that resistance measurements are obtained by measuring the deflection of an elastic member connecting the model to the towing carriage. During the run this spring - mass system can be excited to oscillate along the longitudinal axis of the model. For the particular model, an analysis of the time history of the resistance force during a typical 30 seconds run showed an oscillation of approximately  $\pm 10\%$  about the mean value. However, since the actual longitudinal deflections of the system are extremely small, the oscillation of the model is not expected to affect the steady wave pattern.

## Form Factor Determination

During previous tests with the 1:50 and 1:30 scale models, it has been determined that the value of the form factor for this hull form is 0.14. That is the total viscous resistance is  $C_v = 1.14C_F$ , where  $C_F$  is the frictional resistance of a flat plate according to the ITTC 1957 formulation.

The same value for the 1:22.43 scale model is 0.16. Needless to say that the ITTC method for determining these form factors is approximate, as one tries to establish visually at what speed the wavemaking resistance practically disappears and what is the corresponding model resistance, at a low speed region around  $Fr.No = 0.12$ , where the experimental results show no negligible scatter.

## Measurements of the Steady Wave Pattern

The wavy free surface necessary for the numerical calculations was obtained in a mixed manner. Different methods were used for the intersection of the free surface and the hull surface, for the wave region near the hull surface and for the wave region away from the hull surface.

## Measurements of the Free Surface-Hull Intersection

An auxiliary grid was painted on the surface of the model about the waterline. The dimensions of the grid were 1cm for the waterlines and 2cm for the transverse sections. It was then tried to determine the intersection photographically. The resolution of this procedure was not satisfactory, in particular near the bow where the measurements are most important. The required intersection was finally obtained by scratching several points at the side of the model during the run and then taking the model out of the water and drawing a faired line through these points.

## Measurement of the Wave Region Near the Hull Surface

This region was defined to extend from the centerline of the model to a distance of 38.9cm sideways. It is reminded here that the maximum half breadth of the model is 21.45cm. For this region the wave pattern was obtained using photogrammetric methods. The methodology applied and the results obtained have been described in (7) and will only briefly be discussed here.

Two non-metric motor driven cameras, Hasselblad EL/M with normal angle lenses of 80mm principal distance, were used. The cameras were positioned on a rigid base, which could slide along a specially constructed guiding rail bolted on the towing bridge. In this way the relative position of the cameras remained undisturbed and the coverage of the ship model with stereoscopic models became possible. The two cameras were electronically synchronised and a powerful flash was attached to the system in order to take care of the poor lighting conditions under the bridge. The cameras were positioned approximately 200mm apart, at a distance of 1m from the waterline and with an inclination of approximately 35 grad. In this way a favourable base-to-distance ratio was ensured, while at the same time maximum possible coverage of the object was obtained.

The problem of providing detail points on the water surface was solved by spraying, just before the shutters were fired, yellow paper-tape punch of 1mm diameter on the water surface. For the basic control of the orientations, an aluminum bar bearing two retro-targets at a distance of 283mm was hung on the model. The stereoscopic models were levelled, by taking two pairs of pictures, one at rest and one underway for each case. Nine pairs of stereoscopic models were taken in order to cover the whole length of the model and the necessary area behind it.

The photogrammetric processing of the photography was carried out on a ZEISS Stereocard G2 connected via a DIREC 1 unit to a desk top computer. Analytical processing of the stereocard data was used. An accuracy of about 1mm for the wave heights can be obtained using this method.

### Measurement of the Wave Region Away from the Hull Surface

The wave region extending from a distance of 38.9cm from the centerline of the model to a distance of 218.9cm was covered by taking 95 longitudinal cuts of the wave surface. The longitudinal cuts were obtained by the repeated use of commercially available wave monitors of the resistance type. A specially constructed overhang beam was used for the attachment of five wave monitors at predetermined distances from the centerline of the tank. The probes were stationary and they were recording the wave elevation as the model was passing by. One probe was always positioned at a distance of 28.9cm from the centerline and it was used to "align" the other probes longitudinally.

Thus, four longitudinal cuts were obtained per run and 24 runs were necessary to obtain 96 longitudinal cuts. The alignment of the wave cuts was based on the crest of the first wave of the 28.9 cm cut. The same point was used to align the whole system of the longitudinal cuts to the model using the results of the stereoscopic model of the bow region. An additional cut at a distance of 33.9 cm was used to check the results of the photogrammetric procedure. The details of the longitudinal cut measurements are given in (8).

The accuracy of the wire probe measurements is of the order of one millimeter, on the basis of their static calibration curves. How this accuracy is affected during dynamic measurements is not known.

### Analytical Determination of Transverse Cuts of the Wave Pattern

Based on the model speed and the frequency at which the probe signals were digitized, a minimum distance of 1.034 cm between successive transverse cuts could be used to determine the free surface in the outer field. Since the measured points near the hull were located at random, an interpolation procedure was firstly applied to estimate the wave elevation in the inner field, on the transverse cuts determined at the outer field. Actually, all points within a bandwidth of 1.034 cm were used to determine the wave contour on the mid-plane of the band. Finally, a second order smoothing method was used to generate the waveform in the combined inner and outer field domain of each transverse cut, as shown in Fig.2. In this manner 300 transverse cuts were generated along the ship length, of which 150 were used for the numerical computations.

### DESCRIPTION OF THE NUMERICAL METHOD

#### The co-ordinate system

The transport equations describing the flow around the ship are solved numerically in the physical space. The calculation domain consists of transverse sections and on each section a

curvilinear orthogonal grid is created using the method of singular distributions, as described in the sequel. In Fig. 2 eight orthogonal curvilinear meshes are shown at various sections along the ship model and the wake. The boundary S (Fig. 2a) is the model section contour and the boundary W is the free surface intersection with the corresponding transverse plane.

The generation of an orthogonal grid in the 2D domain defined by the boundaries N,S, E, W shown in Fig. 2a is based on the incompressible potential flow solution (9). A singularity distribution on the four boundaries is assumed, i.e., a source distribution on boundaries N, S and an eddy distribution on E. and W. Using rectilinear elements, the unknown distributions are calculated to satisfy the boundary conditions of a potential function  $\Phi$ , that is

$$\frac{\partial \Phi}{\partial n} \Big|_{N,S} = 0, \quad \frac{\partial \Phi}{\partial s} \Big|_{E,W} = 0$$

where  $n$  is the normal direction on N or S contours and  $s$  the direction tangential to E or W boundaries. After the element source or eddy distributions are computed, the grid nodes can be specified as intersections of equi-potential and equi-stream function lines, following the iterative procedure described in (9).

The velocity components and the other flow variables refer to local orthogonal curvilinear co-ordinate systems coinciding in two dimensions with the grid lines  $x_1 = \text{const}$  and  $x_2 = \text{const}$ , while their third direction  $x_3$  is always parallel to the ship longitudinal axis. These systems vary, in general, along the ship as the geometry of the frames and the free surface changes. It should be noticed here that the co-ordinate system is always orthogonal, while the numerical grid is non-orthogonal in the  $x_3$  - direction.

### The Governing Equations

In a local orthogonal curvilinear co-ordinate system, described as above, with metrics  $h_1, h_2, h_3=1$  and curvatures  $k_{12}, k_{21}$ , the time averaged Navier-Stokes (Reynolds) equations can be written as in (10) :

$u_1$ -momentum

$$C(u_1) = -\frac{1}{h_1} \frac{\partial p^*}{\partial x_1} + \rho u_2^2 k_{21} - \rho u_1 u_2 k_{12} + (\sigma_{11} - \sigma_{22}) k_{21} + 2\sigma_{12} k_{12} + \frac{1}{h_1} \frac{\partial \sigma_{11}}{\partial x_1} + \frac{1}{h_2} \frac{\partial \sigma_{12}}{\partial x_2} + \frac{1}{h_3} \frac{\partial \sigma_{13}}{\partial x_3}$$

$u_2$ -momentum

$$C(u_2) = -\frac{1}{h_2} \frac{\partial p^*}{\partial x_2} + \rho u_1^2 k_{12} - \rho u_1 u_2 k_{21} + (\sigma_{22} - \sigma_{11}) k_{12} + 2k_{21} \sigma_{12} + \frac{1}{h_2} \frac{\partial \sigma_{22}}{\partial x_2} + \frac{1}{h_1} \frac{\partial \sigma_{12}}{\partial x_1} + \frac{1}{h_3} \frac{\partial \sigma_{23}}{\partial x_3}$$



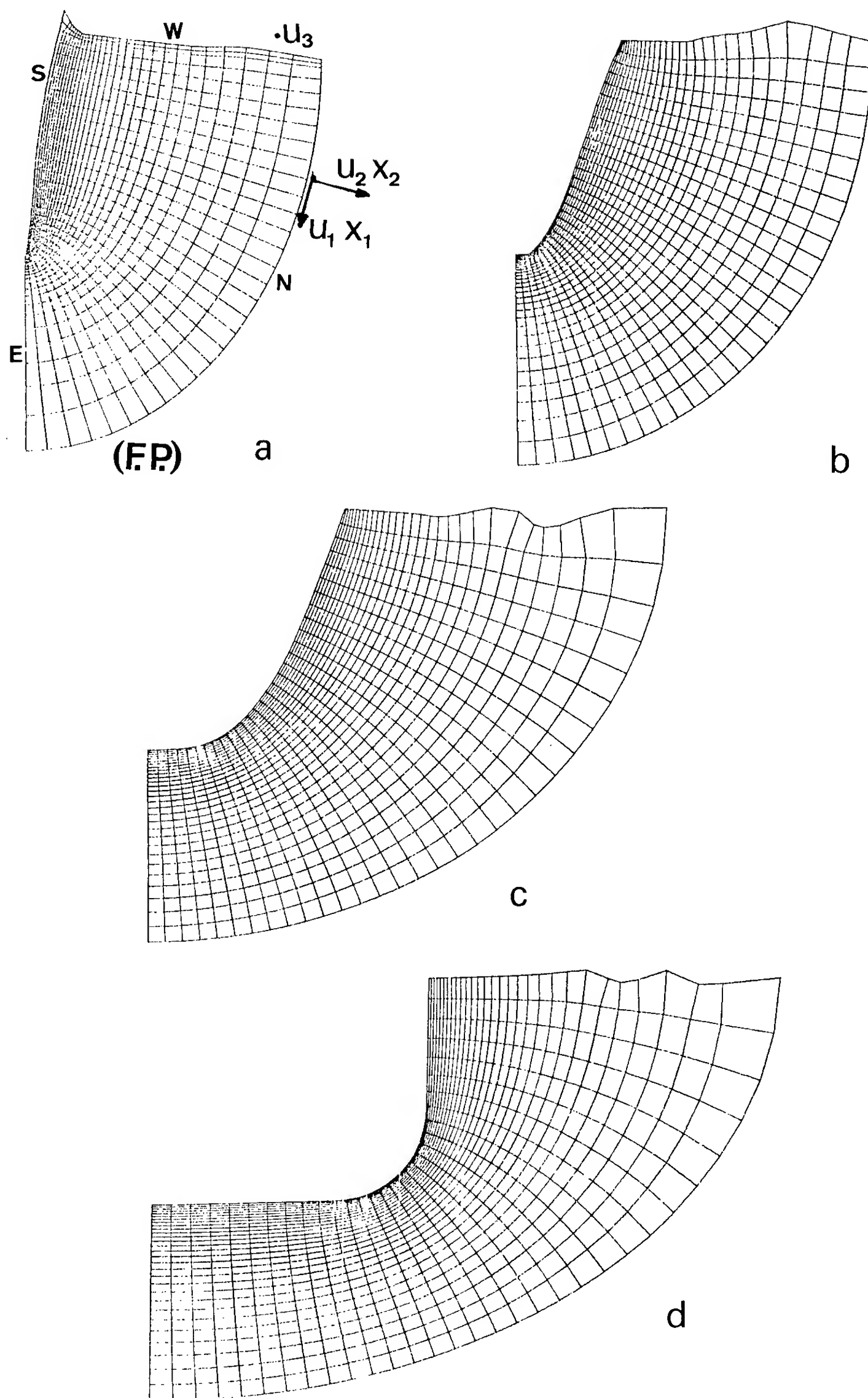


Figure 2. Orthogonal curvilinear grids along the domain.



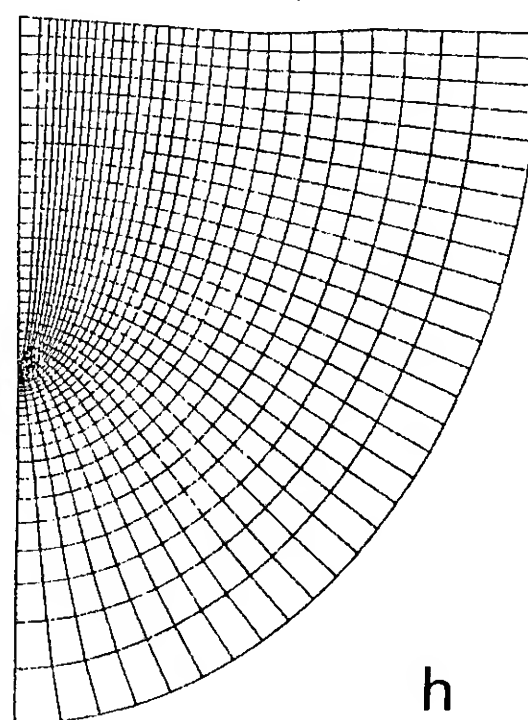
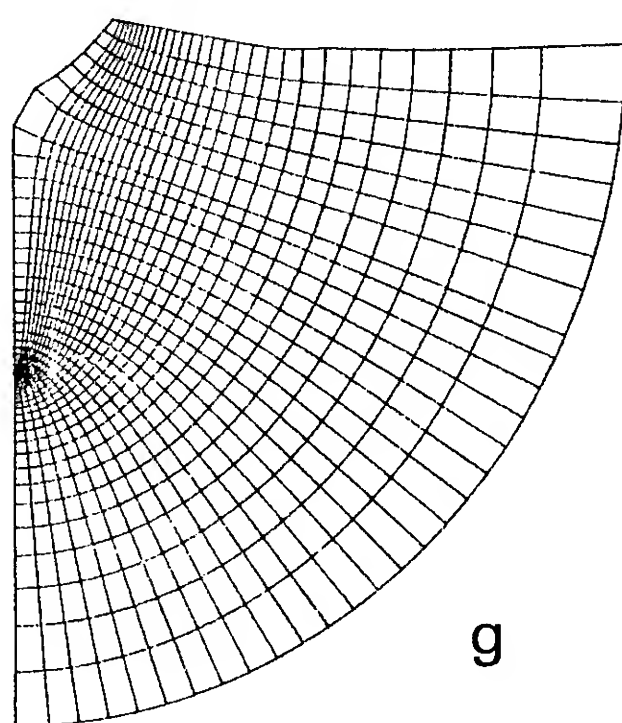
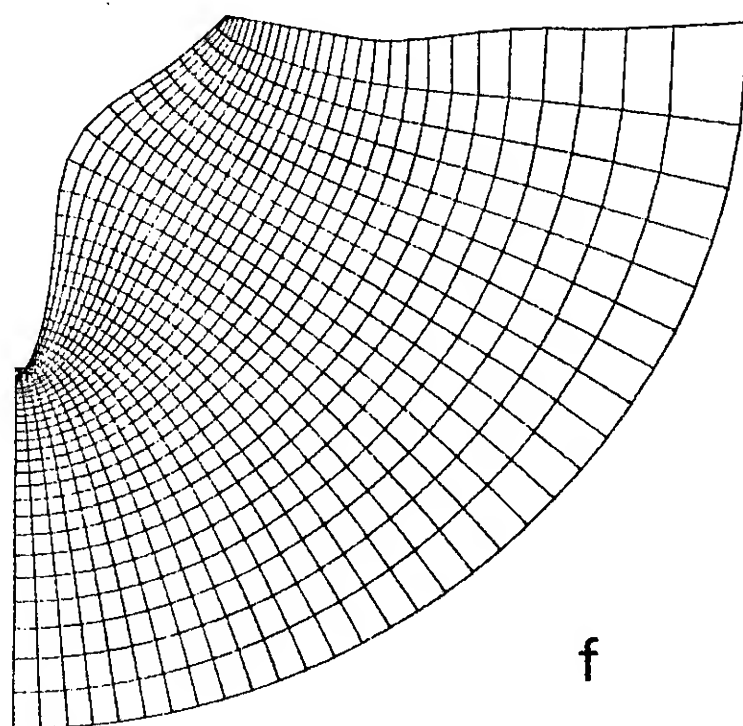
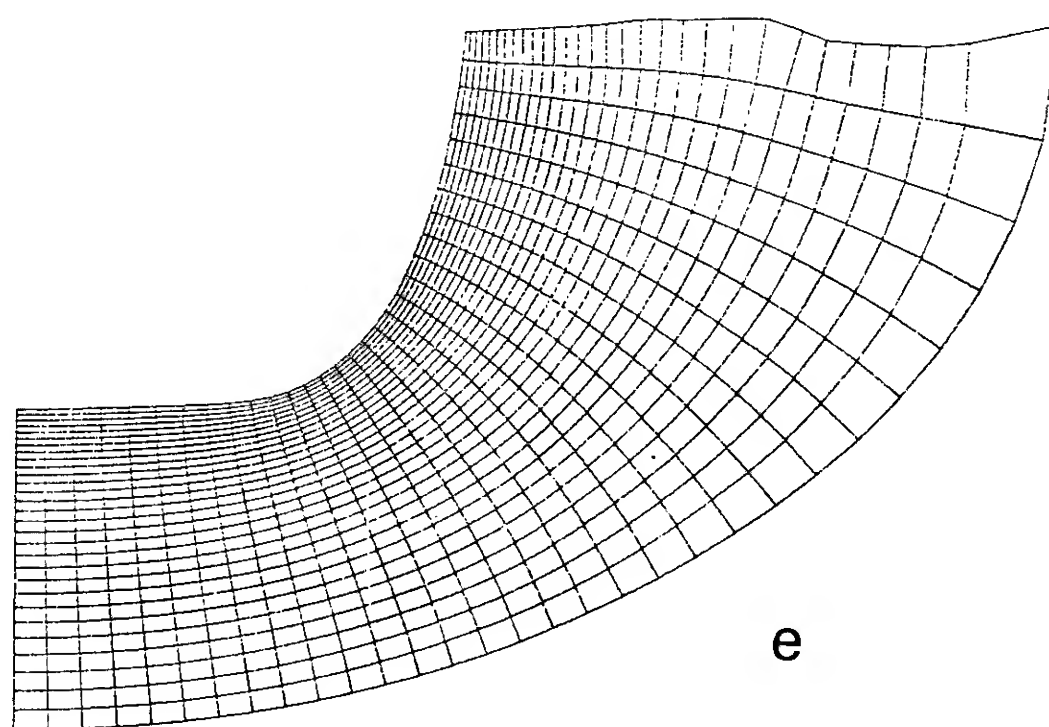


Figure 2. (Continued)

$u_3$  momentum

$$C(u_3) = -\frac{1}{h_3} \frac{\partial p^*}{\partial x_3} + k_{12}(\sigma_{13} + \sigma_{23}) + \frac{1}{h_3} \frac{\partial \sigma_{33}}{\partial x_3} + \frac{1}{h_2} \frac{\partial \sigma_{23}}{\partial x_2} + \frac{1}{h_1} \frac{\partial \sigma_{13}}{\partial x_1} \quad (1)$$

where  $C(u_i)$  shows the convection terms, i.e.:

$$C(u_i) = \frac{\rho}{h_1 h_2} \left[ \frac{\partial h_2 u_1 u_i}{\partial x_1} + \frac{\partial h_1 u_2 u_i}{\partial x_2} \right] + \rho \frac{\partial u_i u_i}{\partial x_3} \quad (2)$$

and the stress tensor  $\sigma_{ij}$  includes the viscous stresses and the double velocity correlations. The components of  $\sigma_{ij}$  are expressed as :

$$\begin{aligned} \sigma_{11} &= 2\mu_e \left[ \frac{1}{h_1} \frac{\partial u_1}{\partial x_1} + u_2 k_{12} \right] = \mu_e \cdot e_{11} \\ \sigma_{22} &= 2\mu_e \left[ \frac{1}{h_2} \frac{\partial u_2}{\partial x_2} + u_1 k_{21} \right] = \mu_e \cdot e_{22} \\ \sigma_{33} &= 2\mu_e \frac{\partial u_3}{\partial x_3} = \mu_e e_{33} \\ \sigma_{12} &= \mu_e \left[ \frac{1}{h_1} \frac{\partial u_2}{\partial x_1} + \frac{1}{h_2} \frac{\partial u_1}{\partial x_2} - u_2 k_{21} - u_1 k_{12} \right] = \mu_e e_{12} \\ \sigma_{13} &= \mu_e \left[ \frac{1}{h_1} \frac{\partial u_3}{\partial x_3} + \frac{\partial u_1}{\partial x_3} \right] = \mu_e e_{13} \\ \sigma_{23} &= \mu_e \left[ \frac{1}{h_2} \frac{\partial u_3}{\partial x_2} + \frac{\partial u_2}{\partial x_3} \right] = \mu_e e_{23} \end{aligned} \quad (3)$$

The value of  $p^*$  appearing on the right hand side of momentum equations (1) is equal to  $p + \rho gh$ , where  $h$  is the vertical distance from a fixed level.

The effective viscosity  $\mu_e$  in expressions (3) is calculated according to the standard  $k$ - $\epsilon$  turbulence model (11) as follows:

$$\mu_e = \mu + \mu_t = \mu + 0.09 \rho k^2 / \epsilon \quad (4)$$

where  $\mu_t$  is the eddy viscosity,  $k$  the turbulence kinetic energy and  $\epsilon$  its dissipation rate. The values of  $k$  and  $\epsilon$  are determined by solving two more differential equations, which in the orthogonal curvilinear system under consideration are written as:

$k$ -equation

$$C(k) = \frac{1}{h_1 h_2} \left[ \frac{\partial}{\partial x_1} \left( \mu_t \frac{h_2}{h_1} \frac{\partial k}{\partial x_1} \right) + \frac{\partial}{\partial x_2} \left( \mu_t \frac{h_1}{h_2} \frac{\partial k}{\partial x_2} \right) \right] + \frac{\partial}{\partial x_3} \left( \mu_t \frac{\partial k}{\partial x_3} \right) + G - \rho \epsilon$$

$\epsilon$  - equation

$$C(\epsilon) = \frac{1}{h_1 h_2} \left[ \frac{\partial}{\partial x_1} \left( \frac{\mu_t}{\sigma_\epsilon} \frac{h_2}{h_1} \frac{\partial \epsilon}{\partial x_1} \right) + \frac{\partial}{\partial x_2} \left( \frac{\mu_t}{\sigma_\epsilon} \frac{h_1}{h_2} \frac{\partial \epsilon}{\partial x_2} \right) \right] + \frac{\partial}{\partial x_3} \left( \frac{\mu_t}{\sigma_\epsilon} \frac{\partial \epsilon}{\partial x_3} \right) + 1.44 G \frac{\epsilon}{k} - 1.92 \rho \frac{\epsilon^2}{k} \quad (5)$$

where  $\sigma_\epsilon = 1.3$  and the generation term  $G$  is expanded as:

$$G = \frac{1}{2} \mu_t \left[ e_{11}^2 + e_{22}^2 + e_{33}^2 + 2(e_{12}^2 + e_{23}^2 + e_{13}^2) \right]$$

The Reynolds equations (1) as well as the turbulence model equations (5) are discretized according to the finite volume approach using a staggered node arrangement (10). The resulting algebraic equations have the general form

$$A_p \Phi_p = \sum_1^6 A_i \Phi_i + S_\Phi \quad (6)$$

where  $\Phi_p$  stands for the velocity components, the turbulence kinetic energy and its dissipation rate and  $\Phi_i$  are the values at the neighbouring nodes of  $P$ . Central differences are used to model  $A_i$  along  $x_1$  and  $x_2$  directions while the corresponding coefficients on upstream and downstream planes are calculated by the hybrid scheme (12).

### Boundary Conditions

The boundaries of the calculation domain shown in Figs. 2a and 3 are the inlet  $U$  and outlet  $D$  planes, the external boundary  $N$ , the solid surface  $S$ , the free surface  $W$  and the flow symmetry plane  $E$ . The elliptic form of equations (6) requires specification of boundary conditions (Dirichlet or Neumann type) on each of these boundaries.

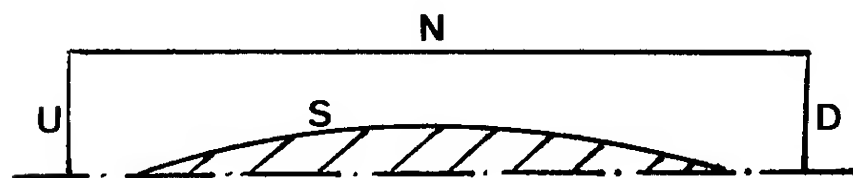


Figure 3. Definition of boundaries.

At the inlet plane U and external boundary N the values of the velocity components  $u_1$ ,  $u_2$ ,  $u_3$  and the pressure are calculated by the potential flow solution under the predetermined free surface. The latter is performed by the classical Hess and Smith method (13). The ship hull and the free surface are covered by quadrilateral panels. Once the wave elevations are a priori known, the source distribution on each panel is calculated by satisfying the unique boundary condition  $u_n=0$ , where  $n$  is the normal to the hull or the free surface. The panel arrangement on the free surface region which has been used for the computations is shown in Fig.4. The external NP and the upstream UP boundaries of this region are located in the undisturbed free surface part in order to avoid as far as possible errors due to end effects (14). It should be noticed here that the external boundary N for the viscous flow calculations is almost five times closer to the ship hull than NP and, therefore, it is expected that the calculation of the velocity components at N will not be practically affected by the aforementioned effects. A total of 1400 panels has been used to model the ship hull and 2000 panels to model the free surface. These numbers refer to the one half of the whole domain, since the flow has one symmetry plane. At the same boundaries U and N the values of  $k$  and  $\epsilon$  are assumed to be equal to zero. For viscous flow computations the inlet plane was placed at  $x = -0.2$  m and the external boundary almost 25 cm (in the mean) apart from the solid surface.

Neglecting surface tension, the dynamic boundary condition on the free surface can be written as  $\sigma_n - p = \tau = 0$ , where  $\sigma_n$  and  $\tau$  are the normal and the shear stresses respectively. It is easy to show that these conditions, together with the elimination of the convective terms on the free surface (due to the kinematic condition) result in the application of Neumann type boundary conditions for the  $u_2$  and  $u_3$  velocity components on the W-boundary (Fig.5). The same conditions are assumed to hold for  $k$  and  $\epsilon$  (i.e.  $\partial k / \partial n = \partial \epsilon / \partial n = 0$ ), while the normal to the surface  $u_1$ -component is set equal to zero.

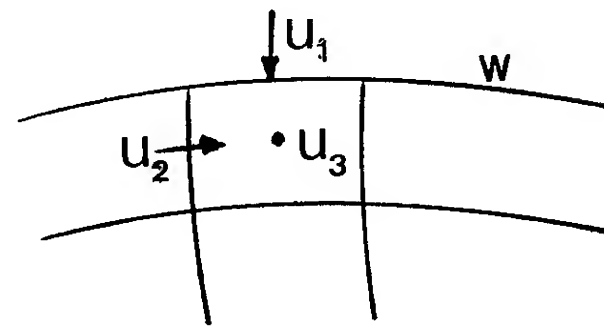


Figure 5. The free surface boundary.

The wall function method (10), (11) has been employed to model the flow characteristics near the solid boundary. The values of  $y^+$  ranged between 30 and 180 in any case.

On the symmetry plane the following conditions are valid:

$$u_2 = 0, \quad \frac{\partial \Phi}{\partial x_2} = 0, \quad \Phi = u_1, u_3, k, \epsilon$$

Finally, at the outlet plane D the flow is assumed to be fully developed, corresponding to the application of Neumann conditions for each variable. This plane was placed at  $x = 3.6$  m.

### The Solution Procedure

The solution of the transport equations (6) together with the determination of the pressure are made according to the partially parabolic algorithm (15). An initial guess of the pressure field is made, based on the calculated pressure values at the external boundary N. Then the solution proceeds by solving the momentum, pressure correction and  $k$ - $\epsilon$  equations in each transverse section successively. The pressure is corrected according to the SIMPLE (16) algorithm so that continuity is satisfied in each cell of the domain. Once the free surface is known, a Dirichlet-type boundary condition for the pressure correction cannot be applied at this boundary, since it leads to overdetermination of the problem and prevents the satisfaction of the continuity equation in the adjacent to the surface cells.

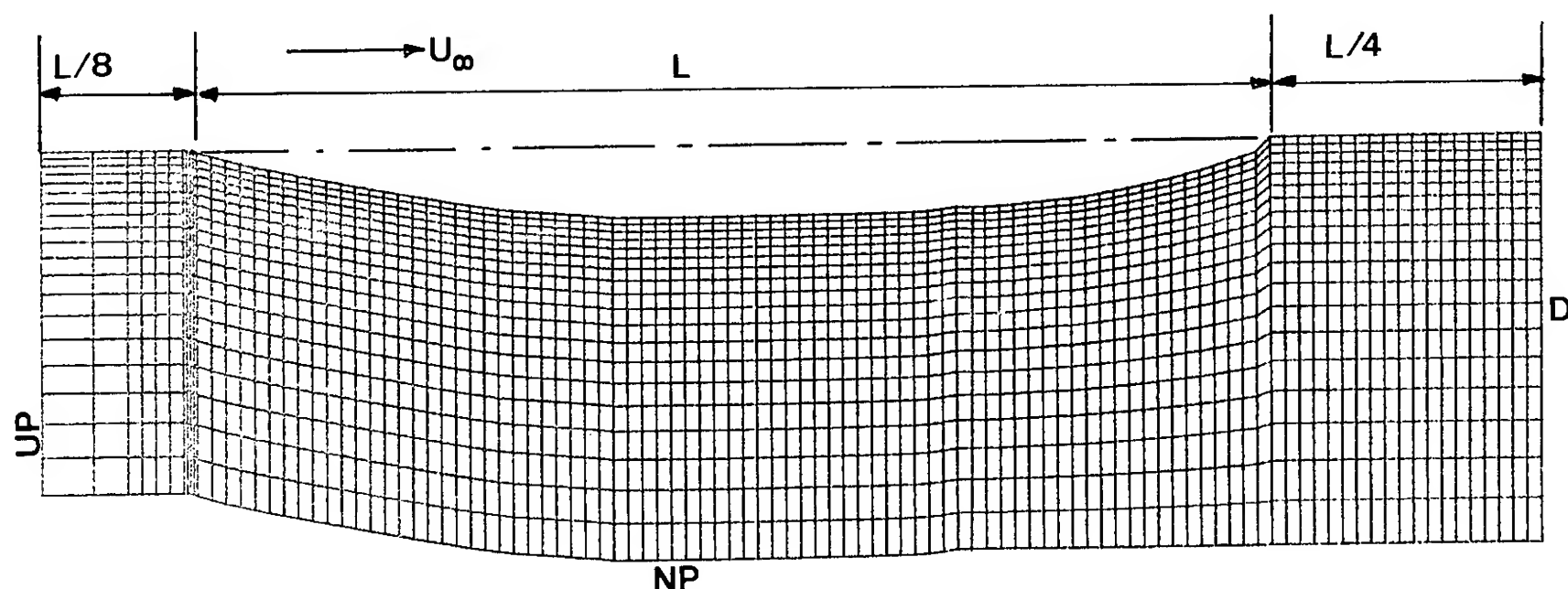


Figure 4. The free surface panel arrangement.

During the application of the partially parabolic algorithm only two-dimensional in-core storage is essentially needed for the various geometrical and flow parameters and, therefore, fine grids can be used. The upstream and downstream values of different variables are constant when calculations are performed at a certain station. After the solution for every section of the domain is obtained, a sweep is completed and the calculations start again. Several sweeps are needed until both the velocity and the pressure field converge.

The use of an orthogonal grid in two dimensions proved to be quite successful with respect to convergence. This is due to the rather simple way that velocity corrections are coupled to changes of the corresponding pressure gradients, the latter being of crucial importance when the SIMPLE approach is followed.

It has been found that relatively high underrelaxation factors can be used for the solution of the momentum and  $k-\epsilon$  equations even if only one SIMPLE step is performed in each station. Underrelaxation, necessary to obtain convergent solutions, is applied for every variable as:

$$\Phi = r\Phi_n + (1 - r)\Phi_o$$

where  $r$  is the underrelaxation factor (constant throughout the calculation domain),  $\Phi_n$  the solution of (6) and  $\Phi_o$  the previous value of the variable.

A 178 x 32 x 31 grid was used for the computations in any case, where 178 is the number of transverse sections, 32 the nodes girthwise and 31 along a normal. Constant underrelaxation factors equal to 0.5 were applied for all variables except the pressure correction for which the value of  $r = 0.3$  was adopted. Convergence was achieved in 400 single-step sweeps of the domain.

## RESULTS AND DISCUSSION

As mentioned earlier, the predetermined boundary used for the computer runs consisted of the measured wave pattern plus the actual wetted surface of the hull. In this case the model sustained a parallel sinkage of 6 mm but no running trim. As a first result it should be mentioned that the numerical calculations under the aforementioned boundary exhibited good behaviour, i.e. they converged always. The running time for the computations was about 24 hours on a 2.6 Mflops workstation for the grid described in the previous section. The corresponding time for the potential flow calculations was one hour for 3500 elements on the same machine.

In order to gain some more insight in the relative magnitudes of the different components of ship resistance, it was decided to obtain similar results for a double model of the tested hull, even keeled but with the draught increased by 6 mm (3.35%). This reasonable choice turned out to be very meaningful from the point of view of the wetted surface. That is whereas the static

equilibrium wetted surface of the model was 1.694 m<sup>2</sup>, the wetted surface underway was 1.738 m<sup>2</sup>, that is increased by 2.6%, and the wetted surface of the double model was 1.734 m<sup>2</sup>, very close to the actual wetted surface. In addition, the pressure resistance of the potential flow for the actual wetted surface and the measured wave pattern was computed.

Because of the differences in the wetted surface, it was decided to present all calculated and measured resistance values in terms of force (kp), and not in the form of non-dimensional coefficients. The results of calculations and measurements are shown in Table 1, whereas the non-dimensional, integrated resistance force along the length of the ship are shown in Figs 6 and 7. In both the Table and the Figures the subscripts T, F & P correspond to the total force, the shear stress component and the pressure component respectively. This rule does not apply to the  $R_F$  value computed from the experimental results, which is thought to contain both the shear stress and the viscous pressure component of the resistance. This value of  $R_F$  was computed on the basis of the ITTC friction line and a form factor of 1.14 determined from the experiments.

Case	$R_T$ (kp)	$R_F$ (kp)	$R_P$ (kp)
Calculated for actual free surface	0.766	0.604	0.162
Calculated for double model	0.694	0.572	0.122
Calculated for potential flow & actual free surface			0.128
Measured $R_T$ & Calculated $R_F$ on the basis of form factor method	0.682	0.596	

Table 1. Comparison of resistance componets.

From the contents of Table 1, it can be concluded that the method used overpredicts the resistance. This is obvious from the double model calculations which yield a total resistance value slightly higher than the experimental one, which contains a wavemaking resistance component. The same trend has been noticed in previous calculations for another ship shown in (6). In the present case the overprediction for the total resistance is 12.5%, which renders the use of the results doubtful for practical applications.



There are however some useful conclusions to be drawn from the contents of Table 1 and Figs 6 and 7. Firstly, if the difference between the calculated total resistance for the ship and the double model is taken to represent the wavemaking resistance, its value is  $R_w = 0.766 - 0.694 = 0.072$  kp. This is significantly smaller than the wavemaking (or pressure) solution. If one then adds this value to the experimentally determined  $R_F$  of 0.596, a value of  $R_T = 0.668$  is obtained, which is very close to the experimental value. Secondly, the value of  $R_F$  along the length of the model is slightly different for the actual free surface and the double model, as the shape of the free surface seems to increase the shear flow resistance. And, finally, that the accuracy of the computations at the aftermost part of the ship for the pressure component of the resistance is very important due to the large slope of the curves, just before the final result is obtained.

From the point of view now of possible improvements of the calculation procedure, there are at least two areas which can lower the predicted value of the resistance. The first such area is connected with an artificial blockage effect, which is inserted to the procedure by imposing the potential flow velocities as boundary conditions relatively close to the surface of the body. Obviously, this is done to reduce the time of computations and our experience (2) shows that if this effect is eliminated, the predicted value of the resistance will be reduced by 2-3%. The second area of possible improvements is of a more fundamental nature as it questions the accuracy of the wall function approach in turbulent flow calculations. As it has been shown in (17) and (18), if a direct solution of the Reynolds equations is used all the way up to the solid boundary, better values for the wall shear stresses are predicted. Unpublished results of NTUA indicate that in this case a reduction of the frictional resistance by 5.5% is obtained for the aft part of a tanker hull. Unfortunately, this improvement is accompanied by a 25% increase in computing time.

Nevertheless the up to now discussion of the results should also be seen in the light of the unavoidable shortcomings of any such experimental-numerical investigation. In this respect, the authors cannot guarantee the degree of accuracy of the free surface measurements and subsequent interpolation. Also, no attempt was made to achieve a grid independent solution, although the grid is fine enough according to our experience, but not necessarily so in the aftermost part of the hull surface.

Finally, we recall the discussion made in the introduction about the shortcomings of the  $k-\epsilon$  turbulence model, which need to be further investigated.

## ACKNOWLEDGMENTS

The authors would like to thank Dr. D. Lyrides for the careful measurements of the free surface, while he was carrying out his Diploma Thesis. Many thanks to our colleagues from the Laboratory of Photogrammetry for their companion measurements of the free surface near the model. Finally, we appreciate the help of Dr. S. Voutsinas and Dr. Y. Glekas for the analytical determination of the free surface.

## REFERENCES

1. Patel, V.C., "Ship Stern and Wake Flows : Status of Experiment and Theory", Proceedings of 17th ONR Symposium on Naval Hydrodynamics, The Hague, 1988.
2. Tzabiras, G.D. and Loukakis, T.A., "On the Numerical Solution of the Turbulent Flow-Field past Double Ship Hulls at Low and High Reynolds Numbers", Proceedings of 5th International Conference on Numerical Ship Hydrodynamics, Hiroshima, 1989, pp. 395-408.
3. Hino, T., "Computation of a Free Surface around an Advancing Ship by the Navier-Stokes Equations", Proceedings of 5th International Conference on Numerical Ship Hydrodynamics, Hiroshima, 1989, pp. 69-83.
4. Tzabiras, G.D., "On the Calculation of the 3-D Reynolds Stress Tensor by two Algorithms", Proceedings of 2nd International Symposium on Ship Viscous Resistance, Göteborg, 1985.
5. Tzabiras, G., Hytopoulos, F. and Nassos, G., "On the Numerical Calculation of the Turbulent Flow-Field around Bodies of Revolution at Zero Incidence", Proceedings of Marine and Offshore Computer Applications Conference, Southampton, 1988, pp. 31-47.
6. Tzabiras, G.D. and Loukakis, T.A., "Reynolds Number Effect on the Resistance Components of 3D Bodies", Proceedings of 18th I.T.T.C., vol.2, 1987, pp 70-71.
7. Georgopoulos, A., Ioannidis, C., Potsiou, C. and Badekas, J., "Photogrammetric Wave Profile Determination", Proceedings of XVI ISPRS Congress, vol. 27, part V.II, commission 5, Qyoto, 1988.
8. Lyridis, D.B., "Experimental and Numerical Investigation of the Wave Pattern around a Ship Moving with Cosntant Speed", Diploma Thesis, Dept. of N.A.M.E., N.T.U.A., 1987.
9. Tzabiras, G., Vafiadou, M. and Nassos, G., "A Numerical Method for the Generation of 2-D Orthogonal Curvilinear Grids", Proceedings of 1st Conference on Numerical Grid Generation in Computational Fluid Dynamics, 1986, pp. 183-195.
10. Tzabiras, G.D., "Numerical and Experimental Investigation of the Turbulent Flow-Field at the Stern of Double Ship Hulls", Ph.D. Thesis, N.T.U.A., 1984.
11. Launder, B.E. and Spalding, D.B., "The Numerical Computation of Turbulent Flows", Computer Methods in Applied Mechanics and Engineering, vol. 3(3), 1974, pp. 269-289.



12. Spalding, D.B., "A Novel Finite-Difference Formulation for Different Expressions Involving both First and Second Derivatives", Int. J. of Numerical Methods in Engineering, vol.4, 1972, pp. 551-559.
13. Hess, J.L. and Smith, A.M.O., "Calculation of Potential Flow about Arbitrary Bodies", Progress in Aeronautical Sciences, vol.8, 1966, pp. 1-138.
14. Kim, K.J., "Ship Flow Calculations and Resistance Minimization", Ph. D. Thesis, Chalmers University of Technology, 1989.
15. Pratap, V.S. and Spalding D.B., "Numerical Computations of the Flow in Curved Ducts", Aeronautical Quarterly, vol. 26, 1975, pp. 219-232.
16. Patankar, S.V. and Spalding, D.B., "A Calculation Procedure for Heat, Mass and Momentum Transfer in 3D Parabolic Flows", Int. J. of Heat and Mass Transfer, vol.15, 1972, pp. 1787-1806.
17. Chen, H.C. and Patel, V.C., "Practical Near-Wall Turbulence Models for Complex Flows Including Separation", Proceedings of AIAA 19th Fluid Dynamics, Plasma Dynamics and Lasers Conference, Honolulu, 1987.
18. Tzabiras, G.D., "A Numerical Investigation of the Turbulent Flow-Field at the Stern of a Body of Revolution", J. of Applied Mathematical Modelling, vol.11, 1987, pp. 45-61.

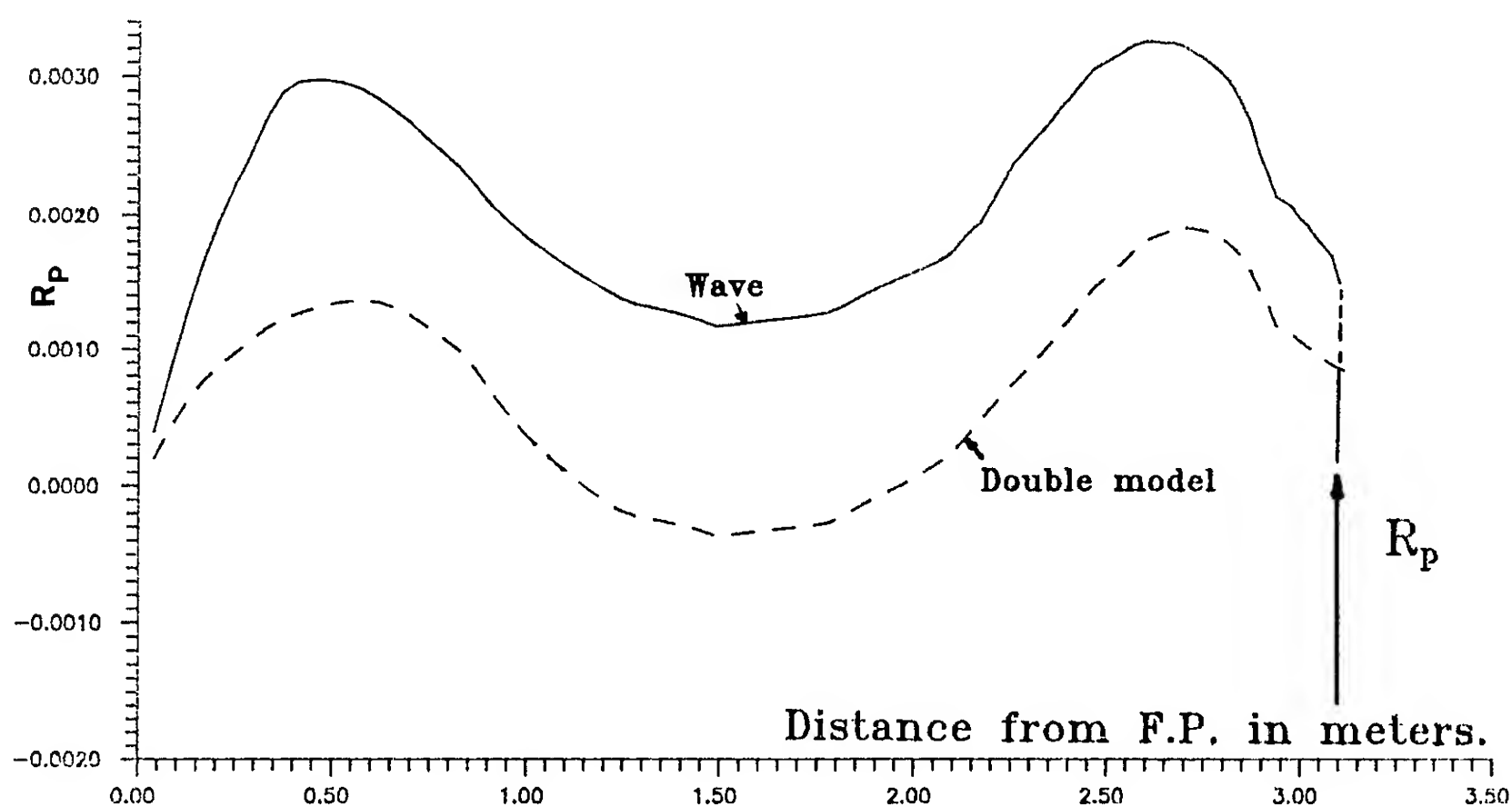


Figure 6. Non-dimensional integrated pressure force.

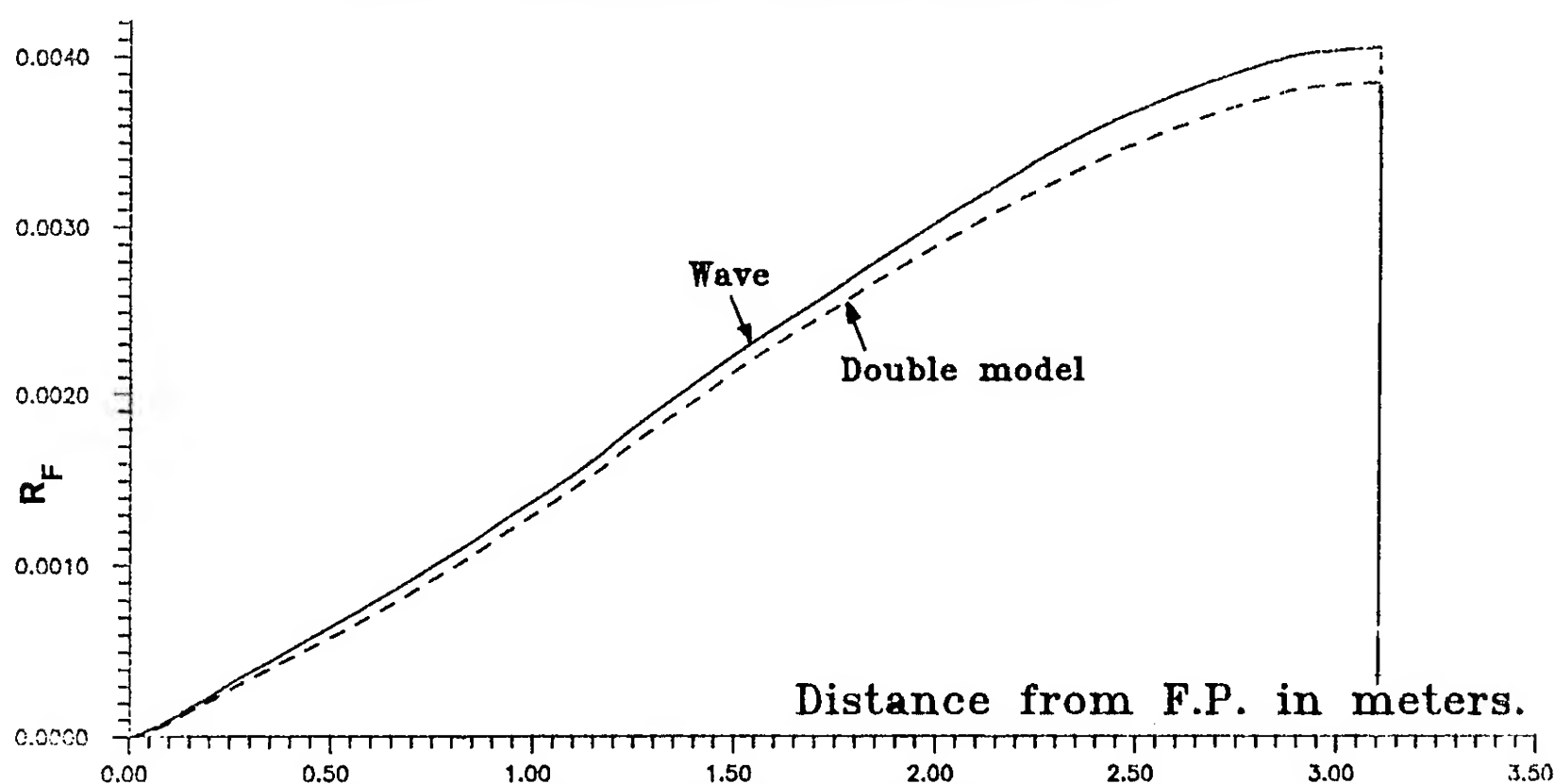


Figure 7. Non-dimensional integrated frictional force.

# **The Calculations of Fluid Actions on Arbitrary Shaped Submerged Bodies Using Viscous Boundary Elements**

W. Price, M. Tan (Brunel University, United Kingdom)

## **ABSTRACT**

A time dependent viscous boundary element method is developed to calculate the unsteady fluid forces acting on a rigid body moving in a stationary, unbounded, incompressible viscous fluid. The theoretical approach presented is analogous to a potential flow singularity distribution panel method. Here the singularity is replaced by a time dependent fundamental solution derived from a modified Oseen equation developed through an integral equation formulation involving convolution time integrations. Analytical expressions are given for the unsteady and steady state fundamental solutions appropriate to two- and three-dimensional fluid-structure interaction problems.

By distributing the viscous panels over the wetted surface of the body and into the fluid domain, a numerical scheme of study is devised to solve the non-linear time dependent integral equations. To illustrate the method, preliminary results are presented of the unsteady and steady state fluid actions and flow fields associated with arbitrary shaped, submerged bodies moving through prescribed manoeuvres.

## **INTRODUCTION**

When a rigid body departs from steady motion in a straight line the surrounding fluid exerts a resultant force and a resultant moment about the centre of gravity of the body as a consequence of the disturbance. In manoeuvring and control studies the variations of fluid actions to disturbances (i.e. displacement, velocity, acceleration), referred to as slow motion derivatives[1-3], are required when assessing the stability and manoeuvring characteristics of ships, submarines and submersibles.

It is usual to describe the behaviour of a manoeuvring body[1-3] with reference to an orthogonal axis system,  $Oxyz$  say, fixed to the body. For example, in many typical problems it is appropriate to let  $O$  coincide with the centre of gravity of the body, the axis  $Ox$  to lie in the longitudinal plane of symmetry, the axes  $Oy$  and  $Oz$  to point to starboard and vertically downwards respectively. It is with reference to a body fixed axis system that derivative data are measured. These are obtained from oblique tow, rotating arm and planar motion mechanism (PMM) oscillatory model experiments.

In the steady state oblique tow and rotating arm tests, velocity and angular velocity derivatives are measured. For example, for a body towed at constant forward speed

$U$  and at a heading or drift angle  $\beta$  to the tank's centreline, the variation of the transverse body force  $Y$  in the  $Oy$  direction to drift angle may be derived and hence the slow motion sway velocity derivative  $Y_v$  deduced, since the parasitic sway velocity  $v \sim -U\beta$ .

Although the PMM oscillatory test was specifically designed to obtain acceleration derivatives[1-3], both velocity and acceleration data are derived. In these experiments, the towed model travels along a prescribed path and is forced to oscillate with fixed amplitude and frequency. By repeating the test at different frequencies, an analysis of the measured in-phase and quadrature forces allows the derivative data to be estimated.

The experimental procedures and analysis methods adopted in the steady state and oscillatory tests are fully described in the literature[3-6] and therefore a description of their details is omitted here.

The theoretical prediction of derivative data has achieved limited success[7-11]. Potential flow theory allows certain flow parameters (i.e. wavemaking resistance, ship hydrodynamic coefficients, etc) to be determined and in general, the predictions confirm the qualitative and quantitative trends observed from experiments. However, where viscous effects dominate (i.e. resistance, etc), confidence in theoretical predictions is greatly reduced. Thus acceleration derivative data evaluated by potential flow methods (strip theory, panel distribution methods, etc) have provided comparable predictions with experimental data but velocity derivative predictions are not totally satisfactory because of the influence of the viscous flow component to the fluid actions.

To overcome this problem, in previous investigations[12,13] we described a hybrid analytical-numerical method to model the viscous nature of the steady fluid flow arising in fluid-structure interactions. This approach is based on an analytically defined viscous panel element distribution to evaluate the steady fluid actions associated with two- and three-dimensional arbitrary shaped bodies in an unbounded, incompressible, viscous flow. That is, the singularity panel distribution over the body's wetted surface area used in the potential flow analysis is replaced in the viscous flow problem by a distribution of analytically defined viscous panel elements of unknown strength extending over the body's wetted surface area and into the wake. Thus many of the techniques successfully developed for the potential flow calculations can, after suitable modifications, be used again in the prediction of the viscous fluid action components.

In these steady flow studies, the analytically defined fundamental solution adopted to describe the viscous element was derived from a modified Oseen's equation. This was chosen because Oseen's equation and Navier-Stokes' equation are qualitatively similar, so that solutions of the former are expected to yield qualitative information about solutions of Navier-Stokes equation for all Reynolds number. In reality, however, steady flow around a body exists only in the small Reynolds number flow regimes and it becomes academic (though remaining of great interest) to extend the investigation into the high Reynolds number flows where unsteady influences dominate.

The previous investigations showed that by distributing viscous boundary panels over the wetted body's surface only an Oseen flow-linearised model was created, whereas distributing panels over the body's surface and into the wake a non-linear convective model resulted. The method could be readily applied to describe the forces acting on bodies of arbitrary shape, the flow field around such bodies and it was suitable to use in multi-body structure - fluid interaction problems, e.g. the flow around clusters of cylinders such as occur in a cross-section of a leg of a lattice jack-up structure. Further, after checks on convergence of solution, panel distribution idealisations etc. of the numerical procedures, in low Reynolds number flows  $Re < 100$  theoretical predictions of the fluid actions and experimental data [14,15] showed good agreement and for higher Reynolds number flows ( $Re < 10^3$ ) the results confirm the qualitative and quantitative trends observed by others [16,17]. In comparison with the non-linear model, the linear model overestimates the values of the fluid actions. The global solutions (i.e. pressure distribution, fluid actions, etc) derived by the non-linear model are relatively insensitive to panel distribution, idealisation etc., allowing simplifications in the numerical procedures; however, the evaluation of a detailed flow velocity field is more sensitive to idealisation and the wake fluid domain must be modelled to allow for the complete formation of the vortex wake pattern.

Building on these previous studies, here we present a viscous boundary element panel distribution method to evaluate the unsteady fluid actions experienced by two- and three-dimensional arbitrary shaped bodies moving in a stationary, unbounded, incompressible viscous fluid. The final objective of this study is to describe the fluid actions on a rigid body undergoing a prescribed, though arbitrary, manoeuvre, e.g. a sequence of commands involving an acceleration, constant forward speed, a deceleration etc., rather than an oscillatory motion or steady state condition. For this reason the problem is described in a body fixed frame of reference and an integral equation formulation derived involving convolution time integrations. The analytically defined time dependent fundamental solution or oseenlet adopted to describe the viscous element is derived from a modified time dependent Oseen's equation. The numerical scheme of studies devised previously for the steady state problem are adapted for this unsteady problem and preliminary findings are presented of the fluid actions and flow fields associated with a two-dimensional circular cylinder moving through prescribed manoeuvres.

## EQUATIONS OF MOTION

In a body fixed coordinate system translating with velocity  $-\mathbf{u}(t)$ ,  $[\mathbf{u}(0) = 0]$ , the flow of an incompressible fluid of constant viscosity described by Navier-Stokes' equations, expressed in terms of non-dimensional Oseen variables, are given in the form

$$\frac{\partial \mathbf{V}}{\partial t} + (\mathbf{V} \cdot \nabla) \mathbf{V} = \nabla^2 \mathbf{V} - \nabla p + \mathbf{f} + \dot{\mathbf{u}} \quad (1)$$

$$\nabla \cdot \mathbf{V} = 0 = \text{div } \mathbf{V} \quad (2)$$

where  $\mathbf{V}$ ,  $p$ ,  $\mathbf{f}$  represent non-dimensional expressions for the fluid flow velocity, pressure in the fluid and external or body force respectively. The corresponding dimensional quantities, denoted by a prime, are

$$\mathbf{V}' = \bar{U} \mathbf{V}, \quad \mathbf{U}' = \bar{U} \mathbf{U}, \quad p' = \rho' \bar{U}^2 p, \quad \mathbf{f}' = (Re \bar{U}^2 / L') \mathbf{f},$$

$$\xi' = (L'/Re) \xi, \quad t' = (L'/Re \bar{U}) t, \quad \nabla' = (Re/L') \nabla,$$

$$\partial/\partial t' = (Re \bar{U}/L') \partial/\partial t,$$

where  $L'$  and  $\bar{U}$  denote characteristic length and velocity parameters respectively,  $\rho'$  represents the fluid density,  $\xi'$ ,  $\xi$  denote spatial variables and the Reynolds number  $Re = \bar{U} L' / \nu'$  where  $\nu'$  represents the kinematic viscous coefficient.

Letting  $\mathbf{V} = \mathbf{U} + \mathbf{v}$ , where  $\mathbf{U}$  denotes a constant velocity, it follows from equations (1) and (2) that the pressure  $p$  and velocity  $\mathbf{v}$  satisfy the equations

$$\left. \begin{aligned} \dot{\mathbf{v}} + (\mathbf{U} + \mathbf{v}) \cdot \nabla \mathbf{v} &= \nabla^2 \mathbf{v} - \nabla p + \mathbf{f} + \dot{\mathbf{u}} \\ \nabla \cdot \mathbf{v} &= 0 \end{aligned} \right\} \quad (3)$$

where an overdot denotes differentiation with respect to time.

This equation of motion is non-linear, but by invoking the usual assumptions, Oseen's equation is obtained in the form

$$\dot{\mathbf{v}} + \mathbf{U} \cdot \nabla \mathbf{v} = \nabla^2 \mathbf{v} - \nabla p + \mathbf{f} + \dot{\mathbf{u}}, \quad (4)$$

$$\nabla \cdot \mathbf{v} = 0 \quad (5)$$

subject to the initial time condition  $\mathbf{v}(\xi, 0) = -\mathbf{U}$ .

## INTEGRAL EQUATION FORMULATION

Before transforming the Navier-Stokes' equations of motion described in equation (3) into an integral equation using Gaussian integral formulae, let us introduce the linear, time dependent Oseen matrix operator

$$\Theta = \begin{bmatrix} \mathbf{I} (\partial/\partial t + \mathbf{U} \cdot \nabla - \nabla^2) - \nabla \nabla & \nabla \\ \nabla & 0 \end{bmatrix} \quad (6)$$

and its linear adjoint time dependent operator

$$\Theta^* = \begin{bmatrix} \mathbf{I} (\partial/\partial t - \mathbf{U} \cdot \nabla - \nabla^2) - \nabla \nabla & -\nabla \\ -\nabla & 0 \end{bmatrix}. \quad (7)$$

Here  $\mathbf{I}$  denotes the unit matrix,  $\mathbf{U} = (U, V, W)$  and these operators are applicable to either two- or three-dimensional problems. Continuing this use of matrix and tensor notation we may define

$$\mathbf{V} = \begin{bmatrix} \mathbf{v} \\ p \end{bmatrix}, \quad \mathbf{F} = \begin{bmatrix} \mathbf{f} + \dot{\mathbf{u}} - \nabla \cdot (\mathbf{v} \mathbf{v}) \\ 0 \end{bmatrix}$$

$$\mathbf{V}_s^* = \begin{bmatrix} \mathbf{v}_s^* \\ p_s^* \end{bmatrix}, \quad \mathbf{F}_s^* = \begin{bmatrix} \mathbf{f}_s^* \\ 0 \end{bmatrix} \quad (8)$$

and the components

$$\left. \begin{aligned} p_{lj} &= -p\delta_{lj} + v_{lj} + v_{j,l}, \\ p_{slj}^* &= p_s^* \delta_{lj} + v_{slj}^* + v_{sj,l}^* \end{aligned} \right\} \quad (9)$$

In these expressions  $v_{lj} = \partial v_l / \partial x_j$ ,  $v_{slj}^* = \partial v_{sl}^* / \partial x_j$ , etc. and the subscripts  $s, l, j$ , etc. take values 1,2 in a two-dimensional problem and values 1,2,3 in a three-dimensional problem.

This notation allows the Navier-Stokes' equations to be written as

$$\Theta \cdot \mathbf{V} = \mathbf{F} \quad (10)$$

in which the non-linear convective term is included in  $\mathbf{F}$ .

By introducing a convolution integration over the time domain  $0^- \leq \tau \leq t$  and using Gaussian integral formulae we find that a Green's function identity can be constructed. That is

$$\begin{aligned} & \int_{0^-}^t d\tau \int_{\Omega} \{ \mathbf{V}^T(\mathbf{x}, t-\tau) \cdot \Theta^* \cdot \mathbf{V}_s^*(\mathbf{x}, \tau) - \mathbf{V}_s^{*T}(\mathbf{x}, t-\tau) \cdot \Theta \cdot \mathbf{V}(\mathbf{x}, \tau) \} d\Omega \\ &= \int_{\Omega} \{ \mathbf{V}^T \cdot \Theta^* \cdot \mathbf{V}_s^* - \mathbf{V}_s^{*T} \cdot \Theta \cdot \mathbf{V} \} d\Omega \\ &= \int_{\Sigma} \{ \mathbf{v}_{sj}^* \cdot (\mathbf{R}_j - \mathbf{U} \cdot \mathbf{n} v_j) - v_j \cdot \mathbf{R}_{sj}^* \} d\Sigma \\ &\quad - \int_{\Omega} \{ \mathbf{v}_{sj}^*(\mathbf{x}, 0^-) v_j(\mathbf{x}, t) + U_j v_{sj}^*(\mathbf{x}, t) \} d\Omega \end{aligned} \quad (11)$$

where

$$\mathbf{R}_j = p_{ij} \mathbf{n}_i = (-p\delta_{ij} + v_{ij} + v_{j,i}) \mathbf{n}_i \quad (12)$$

denotes the force component in the  $j$ th direction and

$$\mathbf{R}_{sj}^* = p_{sij}^* \mathbf{n}_i \quad (13)$$

where  $\mathbf{n}_i$  is redefined as the  $i$ th component of the unit normal vector at the boundary surface  $\Sigma$  pointing into the fluid domain  $\Omega$ . In equation (11), the surface  $\Sigma$  encloses the domain  $\Omega$ , the superscript  $T$  denotes a transposed matrix, a summation convention holds i.e.

$$U_j n_j = \sum_{j=1}^3 U_j n_j = \mathbf{U} \cdot \mathbf{n}$$

etc, and the multiplication symbol  $*$  implies a convolution operation (e.g.  $a * b = b * a$ ).

Now the function  $\mathbf{V}_s^*$  is an undefined vector which we are at liberty to choose. We shall make this the time dependent fundamental solution of the linear adjoint Oseen operator subject to a unit impulsive loading in the  $j$ th direction acting at the position  $\xi = \mathbf{x}$ , i.e. where the field point  $\xi$  coincides with the source point,  $\mathbf{x}$ . That is  $\mathbf{V}_s^*$  satisfies the equations

$$\left. \begin{aligned} \Theta^* \cdot \mathbf{V}_s^* &= \mathbf{F}_s^* && \text{in } \Omega \\ \mathbf{V}_s^* &\rightarrow 0 && \text{at infinity} \end{aligned} \right\} \quad (14)$$

together with the imposed initial condition  $\mathbf{v}_{sj}^*(\mathbf{x}, 0) = 0$ .

Here the  $j$ th component of the external impulsive force  $\mathbf{F}_s^*$  is given by  $f_{sj}^* = \delta_{sj} \Delta(\xi - \mathbf{x}) \delta(t)$ , such that

$$\int_{\Omega} \mathbf{V}^T \cdot \Theta^* \cdot \mathbf{V}_s^* d\Omega = C(\xi) v_s(\xi, t) \quad (15)$$

where  $C(\xi) = 0, 0.5$  or  $1$  depending on  $\xi \notin (\Omega \cup \Sigma)$ ,  $\xi \in \Sigma$  or  $\xi \in \Omega$  respectively.

Substituting equation (15) into equation (11) and using equations (8) and (10) we find that the integral equation becomes,

$$\begin{aligned} C(\xi) v_s(\xi, t) &= \int_{\Sigma} \{ \mathbf{v}_{sj}^* \cdot (\mathbf{R}_j - v_j \mathbf{U} \cdot \mathbf{n}) - v_j \cdot \mathbf{R}_{sj}^* \} d\Sigma \\ &\quad + \int_{\Omega} \mathbf{v}_{sj}^* \cdot (\dot{\mathbf{u}}_j - v_k v_{j,k}) d\Omega - \int_{\Omega} U_j v_{sj}^* d\Omega \end{aligned} \quad (16)$$

assuming a zero body force i.e.  $\mathbf{f} = 0$ .

## FUNDAMENTAL SOLUTIONS OR OSEENLETS

### TIME DEPENDENT SOLUTIONS

Analogous to the steady state solutions ( $\dot{\mathbf{v}} = 0$ ) derived previously[12,13], the time dependent fundamental solutions or oseenlets satisfy the equations

$$\left. \begin{aligned} \dot{\mathbf{v}}_{sj}^* - \mathbf{U} \cdot \nabla \mathbf{v}_{sj}^* &= \nabla^2 \mathbf{v}_{sj}^* + p_{s,j}^* + \delta_{sj} \Delta(\xi - \mathbf{x}) \delta(t) \\ \mathbf{v}_{sj,j}^* &= 0 \\ \mathbf{v}_{sj}^*(\xi, 0^-) &= 0 \end{aligned} \right\} \quad (17)$$

A solution to these equations can be derived using Laplace (L) and Fourier (F) transforms. That is, let  $\gamma$  and  $\lambda$  denote the Laplace and Fourier transform parameters respectively and an application of the sequence of operations  $LF()$  to the previous equations gives

$$\begin{aligned} \gamma \mathbf{v}_{sj}^* + i\lambda \cdot \mathbf{U} \mathbf{v}_{sj}^* &= -\lambda^2 \mathbf{v}_{sj}^* - i\lambda_j p_s^* + \{ \delta_{sj} e^{i\lambda \cdot \mathbf{x}} / (2\pi)^{n/2} \} \\ \lambda_j \mathbf{v}_{sj}^* &= 0 \end{aligned}$$

where  $i = \sqrt{-1}$ ,  $n = 2$  for a two-dimensional flow problem ( $s = 1, 2 = j$ ) and  $n = 3$ , for the three-dimensional case ( $s = 1, 2, 3 = j$ ).

From these equations it follows that

$$p_s^* = - (i\lambda_s / \lambda^2) e^{i\lambda \cdot \mathbf{x}} / (2\pi)^{n/2}$$

and

$$\mathbf{v}_{sj}^* = \left( \delta_{sj} - \frac{\lambda_s \lambda_j}{\lambda^2} \right) e^{i\lambda \cdot \mathbf{x}} / (2\pi)^{n/2} [\gamma + i\lambda \cdot \mathbf{U} + \lambda^2].$$

By reversing the transform operations, we obtain[18]

$$F(p_s^*) = L^{-1} \{ LF(p_s^*) \} = -i (\lambda_s / \lambda^2) e^{i\lambda \cdot \mathbf{x}} \delta(t) / (2\pi)^{n/2},$$

$$F(\mathbf{v}_{sj}^*) = \left( \delta_{sj} - \frac{\lambda_s \lambda_j}{\lambda^2} \right) e^{i\lambda \cdot \mathbf{x}} e^{-(\lambda^2 + i\lambda \cdot \mathbf{U})t} / (2\pi)^{n/2}$$

or

$$p_s^* = \frac{\delta(t)}{(2\pi)^n} \left[ \int_{-\infty}^{\infty} \frac{e^{i\lambda \cdot r}}{\lambda^2} d\lambda \right]_{,s}, \quad r = \xi - x \quad (18)$$

and

$$v_{sj}^* = \frac{\delta_{sj}}{(2\pi)^n} \int_{-\infty}^{\infty} e^{-\{\lambda^2 t + i\lambda \cdot (r + Ut)\}} d\lambda + \frac{1}{(2\pi)^n} \left[ \int_{-\infty}^{\infty} \frac{e^{-\{\lambda^2 t + i\lambda \cdot (r + Ut)\}}}{\lambda^2} d\lambda \right]_{,sj} \quad (19)$$

### Three Dimensional Solution (n = 3)

For a three dimensional fluid-structure interaction flow problem involving a field point  $\xi$  and a source point  $x$ , such that the distance  $r = |\xi - x|$  and  $r_s$  ( $s = 1, 2, 3$ ) denotes the  $s$ th component of  $r$ , the time dependent fundamental solution is

$$p_s^* = \frac{\delta(t)}{4\pi} \left[ 1/r \right]_{,s} \quad (20)$$

$$v_{sj}^* = \frac{\delta_{sj}}{(4\pi t)^{3/2}} e^{-(r+Ut)^2/4t} + \frac{1}{4\pi} \left[ \frac{1 - \text{erfc} \{ |r+Ut|/2\sqrt{t} \}}{|r+Ut|} \right]_{,sj} \quad (21)$$

where the complementary error function,

$$\text{erfc}(x) = \frac{2}{\sqrt{\pi}} \int_x^{\infty} e^{-t^2} dt$$

and  $s = 1, 2, 3 = j$ .

### Two Dimensional Solution (n = 2)

The appropriate fundamental solution for this case is

$$p_s^* = \frac{\delta(t)}{2\pi} \left[ \ln 1/r \right]_{,s} \quad (22)$$

$$v_{sj}^* = \frac{\delta_{sj}}{4\pi t} e^{-(r+Ut)^2/4t} + \frac{1}{2\pi} \left[ \ln (1/|r+Ut|) - \frac{1}{2} E_1 \{ (r+Ut)^2/4t \} \right]_{,sj} \quad (23)$$

$$= \frac{1}{4\pi t} \left\{ \delta_{sj} - \frac{(r_s + U_s t)(r_j + U_j t)}{(r + Ut)^2} \right\} e^{-(r+Ut)^2/4t} - \frac{\{1 - e^{-(r+Ut)^2/4t}\}}{2\pi (r + Ut)^2} \left\{ \delta_{sj} - \frac{2(r_s + U_s t)(r_j + U_j t)}{(r + Ut)^2} \right\} \quad (24)$$

where  $E_1\{\}$  denotes the exponential integral function [18]

$$E_1\{x\} = \int_x^{\infty} \frac{e^{-t}}{t} dt, \quad |\arg(x)| < \pi$$

and  $s = 1, 2, = j$ .

Note that when  $U = 0$ , these solutions give the equivalent Stokeslet solutions.

Further, the vorticity field distribution in  $v_{sj}^*$  is given by

$$\omega_{sj} = e_{jkl} v_{sl,k}^*$$

where

$$e_{jkl} = 0 \quad \text{if } j = k \text{ or } k = l \text{ or } j = l$$

$$e_{123} = e_{231} = e_{312} = 1$$

and  $e_{132} = e_{213} = e_{321} = -1$ .

That is,

$$\omega_{s3} = -e_{3ks} \left\{ (r_k + U_k t) / 8\pi t^2 \right\} e^{-(r+Ut)^2/4t}$$

with

$$\omega_{13} = \left\{ (r_2 + U_2 t) / 8\pi t^2 \right\} e^{-(r+Ut)^2/4t}$$

$$\omega_{23} = - \left\{ (r_1 + U_1 t) / 8\pi t^2 \right\} e^{-(r+Ut)^2/4t}$$

When  $U = i$  and the source point is at the origin  $\xi = 0$ , it follows that

$$\omega_{13} = (y/8\pi t^2) e^{-(x^2 + y^2 + 2xt + t^2)/4t}$$

$$\omega_{23} = - \left\{ (x+t) / 8\pi t^2 \right\} e^{-(x^2 + y^2 + 2xt + t^2)/4t}$$

such that the maximum value of  $\omega_{13}$  occurs on  $\{x = -t, y = (2t)^{1/2}\}$  and for  $\omega_{23}$  on  $\{x = -t + (2t)^{1/2}, y = 0\}$ .

### STEADY STATE SOLUTIONS

The steady state fundamental solution or oseenlet ( $\dot{v} = 0$ ) can be obtained by integrating the time dependent solutions over the entire time range, i.e.  $0 \leq t \leq \infty$  or by repeating a similar analysis to the one described previously in the space domain only [12,13]. It can be shown that both approaches produce the same steady state fundamental solutions.

### Three Dimensional Solution ( $s = 1, 2, 3 = j = k$ )

The appropriate fundamental solution for this case is

$$p_s^* = -r_s / 4\pi r^3, \quad (25)$$

$$v_{sj}^* = \frac{\delta_{sj}}{4\pi r} e^{-(U \cdot r + r)/2} - \frac{1}{4\pi} \left[ \ln (U \cdot r + r) + E_1 \{ (U \cdot r + r)/2 \} \right]_{,sj}$$

$$= \frac{1}{4\pi} e^{-(U \cdot r + r)/2} \left\{ \frac{\delta_{sj}}{r} - \frac{(U_s + r_s/r)(U_j + r_j/r)}{2(U \cdot r + r)} \right\}$$



$$-\frac{\{1-e^{-(U \cdot r + r)/2}\}}{4\pi(U \cdot r + r)} \left\{ \frac{\delta_{sj}}{r} - \frac{r_s r_j}{r^3} - \frac{(U_s + r_s/r)(U_j + r_j/r)}{U \cdot r + r} \right\} \quad (26)$$

The vorticity distribution is given by

$$\omega_{sj} = \frac{e_{skj}}{8\pi r^3} \{2r_k + r(U_k r + r_k)\} e^{-(U \cdot r + r)/2}$$

where  $e_{skj}$  is defined previously.

When  $r \rightarrow 0$ , the velocity solution reduces to

$$v_{sj}^* = \frac{1}{8\pi r} \left( \delta_{sj} + \frac{r_s r_j}{2} \right),$$

corresponding to the equivalent Stokes flow solution and when  $r \rightarrow \infty$  we have

$$v_{sj}^* \rightarrow \begin{cases} 0 & (1/r^2) & \text{outside the wake region,} \\ 0 & (1/r) & \text{inside the wake region.} \end{cases}$$

### Two Dimensional Solution ( $s = 1, 2 = j = k$ )

The oscelet solution takes the form

$$p_s^* = -r_s / 2\pi r^2, \quad (27)$$

$$v_{sj}^* = \frac{\delta_{sj}}{2\pi} e^{-U \cdot r/2} K_0(r/2)$$

$$+ \frac{1}{2\pi} \left[ U \cdot r e^{-U \cdot r/2} K_0(r/2) + U \cdot r \ln r - r e^{-U \cdot r/2} K_1(r/2) \right. \\ \left. - \frac{(U \times r)^2}{r} \int_0^{r/2} K_0(\mu) e^{-(U \cdot r)\mu/r} d\mu \right]_{,sj}$$

$$= \frac{\delta_{sj}}{4\pi} e^{-U \cdot r/2} K_0(r/2)$$

$$+ \left\{ \frac{U_s r_j + U_j r_s - U \cdot r \delta_{sj}}{2\pi r^2} \right\} \{1 - 0.5r e^{-U \cdot r/2} K_1(r/2)\} \quad (28)$$

where  $K_0, K_1$  are modified Bessel functions of the zero and first order[18]. When  $U = (1, 0, 0)$ , this solution agrees with the form presented by Bessho[19] using an alternative approach.

When  $r \rightarrow 0$ , the previous solution reduces to

$$v_{sj}^* = \frac{1}{4\pi} \left( -\delta_{sj} \ln r + \frac{r_s r_j}{r} \right)$$

and for  $r \rightarrow \infty$ , we have

$$v_{sj}^* \rightarrow \begin{cases} 0 & (1/r) & \text{outside the wake region,} \\ 0 & (1/r^{1/2}) & \text{inside the wake region.} \end{cases}$$

In this case, the vorticity distribution is described by the expression

$$\omega_{s3} = \frac{e_{sk3}}{4\pi} \left\{ U_k K_0(r/2) + \frac{r_k}{r} K_1(r/2) \right\} e^{-U \cdot r/2}.$$

### MODIFIED INTEGRAL EQUATIONS

Using the fundamental solutions derived in the previous section, the integral equation described in equation (16) can be written in alternative forms.

For the submerged body, the surface boundary  $\Sigma$  ( $=\Sigma_\infty - \Sigma_b$ ) consists of the body boundary  $\Sigma_b$  and an outer boundary  $\Sigma_\infty$  at infinity. It can be shown that

(i) on  $\Sigma_\infty$ ,  $R_j$  is constant,  $v_j = u_j - U_j$  and

$$v_j^* \int_{\Sigma_\infty} R_{sj}^* d\Sigma = -(u_s - U_s)/n,$$

$$\int_{\Sigma_\infty} v_{sj}^* (R_j - v_j U \cdot n) d\Sigma = 0,$$

where  $n = 2, 3$  for two- and three-dimensional problems respectively.

(ii) on  $\Sigma_b$ ,  $v_j = -U_j$  and

$$\int_{\Sigma_b} v_j^* R_{sj}^* d\Sigma \\ = \{1 - C(\xi)\} U_s - \int_{\Omega_b} U_j^* \dot{v}_{sj}^* d\Omega + \int_{\Sigma_b} U_j^* v_{sj}^* U \cdot n d\Sigma$$

and,

$$\int_{\Omega_b} U_j^* \dot{v}_{sj}^* d\Omega + \int_{\Omega} U_j^* v_{sj}^* d\Omega \\ = \int_{\Sigma_\infty} U \cdot r_0 v_{sj}^* n_j d\Sigma = (n-1) U_s/n$$

$$\int_{\Omega} v_{sj}^* \dot{u}_j d\Omega = \int_{\Sigma_\infty} v_{sj}^* \dot{u} \cdot r_0 n_j d\Sigma - \int_{\Sigma_b} v_{sj}^* \dot{u} \cdot r_0 n_j d\Sigma \\ = (n-1) U_s/n - \int_{\Sigma_b} v_{sj}^* \dot{u} \cdot r_0 n_j d\Sigma$$

where  $r_0 = x - y$  and  $y$  is any point in the domain and  $\Omega_b$  denotes the internal volume of the body.

The substitution of these expressions into equation (16) gives the integral equation relationships,

$$C(\xi) v_s(\xi, t) = u_s - C(\xi) U_s - \int_{\Sigma_b} v_{sj}^* (R_j + \dot{u} \cdot r_0 n_j) d\Sigma \\ - \int_{\Omega} v_{sj}^* (v_k v_{j,k}) d\Omega,$$

or

$$C(\xi) v_s(\xi, t) = u_s - C(\xi) U_s - \int_{\Sigma_b} v_{sj}^* (R_j + \dot{u} \cdot r_0 n_j - U_j U \cdot n) d\Sigma \\ + \int_{\Omega} v_{sj,k}^* (v_k v_j) d\Omega \quad (29)$$

or

$$C(\xi) v_s(\xi, t) = u_s - C(\xi) U_s - \int_{\Sigma} v_{sj}^* (R_j + \dot{u} \cdot r_0 n_j - 0.5 U^2 n_j) d\Sigma \\ + \int_{\Omega} v_{sj}^* (v \times \omega)_j d\Omega$$

where  $\omega$  represents the vorticity of the flow.

The basic unknowns in these formulations are the fluid velocity  $\mathbf{v}$  and fluid force  $\mathbf{R}$  which can be determined directly from the discretised forms of these equations. In fact, although the details of the terms in these equations differ from those occurring in the steady state problem, the general method of solution adopted in the latter can be suitably modified to solve the present integral equations.

Further, since  $\dot{\mathbf{u}}, \mathbf{r}_0, \mathbf{U}$  and  $\mathbf{n}$  are all prescribed quantities we may treat  $\mathbf{X}_j = \mathbf{R}_j + \dot{\mathbf{u}} \cdot \mathbf{r}_0 \mathbf{n}_j - \mathbf{U}_j \mathbf{U} \cdot \mathbf{n}$  in equation (29) as the unknown and this integral equation reduces to

$$C(\xi) \mathbf{v}_s(\xi, t) = \mathbf{u}_s - C(\xi) \mathbf{U}_s - \int_{\Sigma_b} \mathbf{X}_j * \mathbf{v}_{sj}^* d\Sigma + \int_{\Omega} (\mathbf{v}_k \mathbf{v}_j) * \mathbf{v}_{sj,k}^* d\Omega. \quad (30)$$

## NUMERICAL SCHEME

By discretising the continuous integral equation expressed in equation (29 or 30), the unknown  $\mathbf{X}$  (or  $\mathbf{R}$ ) and  $\mathbf{v}$  can be determined. Apart from the additional complication of the convolution time integral, the approach adopted here is similar to the one developed previously to evaluate solutions of the steady state flow problem[12,13]. That is, in the spatial idealisation, the body boundary  $\Sigma_b$  and fluid domain  $\Omega$  are discretised into  $m_b$  elemental surface panels and  $m_d$  elemental surface panels or volumes respectively and to assume that the unknowns satisfy prescribed distributions. Integrations are performed over each idealised element and the integral equation transformed into a set of simultaneous algebraic equations from which the unknowns on each panel and in each volume (or panel) are determined. Thus equation (30) can be written as

$$C(\xi) \mathbf{v}_s(\xi, t) = \mathbf{u}_s(t) - C(\xi) \mathbf{U}_s - \sum_{m=1}^{m_b} \mathbf{X}_j^{(m)} * \int_{\Sigma_b^{(m)}} \mathbf{v}_{sj}^* d\Sigma + \sum_{m=1}^{m_d} (\mathbf{v}_k \mathbf{v}_j)^{(m)} * \int_{\Omega^{(m)}} \mathbf{v}_{sj,k}^* d\Omega = \mathbf{u}_s(t) - C(\xi) \mathbf{U}_s - \sum_{m=1}^{m_b} \mathbf{X}_j^{(m)} * \int_{\Sigma_b^{(m)}} \mathbf{v}_{sj}^* d\Sigma + \sum_{m=1}^{m_d} (\mathbf{v}_k \mathbf{v}_j)^{(m)} * \int_{\Sigma\Omega^{(m)}} \mathbf{v}_{sj}^* \mathbf{n}_k d\Sigma \quad (31)$$

where  $\Sigma\Omega^{(m)}$  denotes the boundary of the  $m$ th fluid domain panel. As can be seen, this expression involves an integration of the time dependent fundamental solution over defined surface boundaries and this can be represented analytically, as shown in the appendix.

Following previously described procedures[12], the continuous integral equation represented by the discretised form of equation (31) can be expressed at each time step by general matrix equations written in the form

$$\left. \begin{aligned} -\mathbf{A} \mathbf{X} + \mathbf{B} + \mathbf{C}(\mathbf{V}) &= \mathbf{0} \\ -\mathbf{V} - \mathbf{A}' \mathbf{X} + \mathbf{B}' + \mathbf{C}'(\mathbf{V}) &= \mathbf{0} \end{aligned} \right\} \quad (32)$$

where  $\mathbf{X}$  and  $\mathbf{V}$  are the unknowns to be solved. Although the individual descriptions of the matrices,  $\mathbf{A}, \mathbf{A}', \mathbf{B}, \mathbf{B}', \mathbf{C}, \mathbf{C}'$  are omitted, the matrices  $\mathbf{A}, \mathbf{A}'$  consist of linear elements,  $\mathbf{B}$  contains linear and non-linear (i.e. products of terms) elements whilst  $\mathbf{B}', \mathbf{C}, \mathbf{C}'$  represent totally non-linear expressions in the unknown  $\mathbf{V}$ .

In the steady state case, when the Reynolds number  $Re \ll 1$ , the non-linear contributions are negligible and can be ignored. Thus the unknowns  $\mathbf{X}$  and  $\mathbf{V}$  are obtained by direct solution from equation (32). When  $Re \sim 1$  and the non-linear contributions retained, a simple iterative scheme can be devised but when the Reynolds number is large, a more refined iterative scheme is required. This is based on the Levenberg-Marquardt algorithm[12,20-22] which is a hybrid algorithm combining Newton's iteration method and the method of steepest descent.

## COMPUTATIONS

### STEADY STATE PREDICTIONS ( $\dot{\mathbf{v}} = \mathbf{0}$ )

Since details of the steady state calculations are described elsewhere[12,13], they are omitted here and the example included serves to illustrate the method.

For a cylinder of diameter  $D' (=2A')$ , figure 1 illustrates the variation of the drag coefficient  $C_d (=Force/0.5\rho U^2 D')$  with Reynolds number  $Re$ . Presented are predictions derived from an oseen flow-linearised model and a non-linear convective model as well as experimental results[14]. As can be seen, the linear results overestimate the other two data sets, with the non-linear results showing the better agreement with the experimental data.

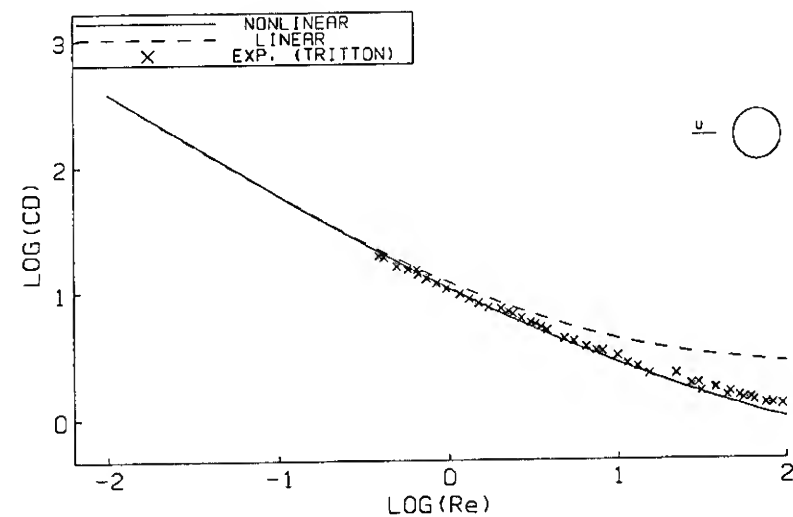


Figure 1 A comparison between measured[14] and calculated (i.e. linear and non-linear flow models) steady state drag coefficient data  $C_d$  for a circular cylinder in uniform flows.

In the linear model, the cylinder's surface was idealised by a distribution of 100 equally spaced viscous boundary elements though it was shown that a 10 element distribution produced similar convergent solutions and both sets of numerical results compared very well with Oseen's theoretical prediction as given by Lamb[23,  $Re \leq 1$ ]. Further, in the limit  $Re \rightarrow \infty$ ,  $C_d \rightarrow 2.28$  again indicating an overestimation of the experimental data.

In the non-linear model, 100 equally spaced elements were distributed over the cylinder's surface as well as a similar number over an imposed surrounding outer boundary six diameters ( $R=6D$ ) away from the surface. The enclosed fluid domain was idealised by 400 panels with the distribution showing a greater density near the cylinder and decreasing radially. Figure 2 shows the computed flow field around the cylinder ( $Re = 200$ ) with the vortex wake pattern clearly defined.



Figure 2 Computed Oseen flow field around a circular cylinder,  $Re=200$ .

This investigation showed that calculations of the fluid actions, pressure distributions over the cylinder's surface etc. are satisfactorily determined by the non-linear convective model and the global solutions are relatively insensitive to the mathematical model and idealisation. However, calculations of the flow velocity field are far more sensitive to idealisation and the truncation distance  $R$  of the surrounding outer fluid domain boundary. The latter must be placed at a sufficient distance from the cylinder to allow for the complete generation of the vortex wake pattern. Therefore, if information on fluid actions is required only, a much reduced computational model can be adopted, significantly decreasing the computational effort with a relatively small numerical error introduced if the truncation distance  $R$  is taken to be some value  $R > 2D$  (say).

#### NONSTEADY PREDICTIONS ( $\dot{\psi} = 0$ )

##### Oseen Flow-Linearised Model

A linearised mathematical model can be developed if the time dependent fundamental solutions are distributed only over the cylinder's surface. The convolution time integration is retained in the modified integral equation of equation (29) but the troublesome non-linear convective contribution is discarded.

For the time history predictions presented in figure 3, the cylinder's surface was idealised by a distribution of 40 equally spaced viscous boundary elements each containing at its centre a time dependent oseenlet. The component velocities  $u_1, u_2$  defined in the body frame of reference are shown in figure 3(a). That is, the motion in the longitudinal direction of the body (i.e. surge,  $u_1$ ) shows the body accelerating to a fixed speed, remaining steady until it experiences a slight blip before returning to the previous steady condition. At the same time, in the transverse direction the sway component  $u_2$  is sinusoidal. This simple example serves to demonstrate the arbitrarily selected motions (e.g. a prescribed manoeuvre) which can be introduced into the mathematical model without difficulty, though it bears a similarity to a PMM test procedure.

The time histories of the drag coefficient  $Cd_x (=R_1)$  shown in figures 3(b-d) follow the variations of the motion  $u_1(t)$  in each of the Reynolds number flows  $Re = 2, 40, 200$ . At each transition the coefficient exhibits an over- or undershoot tendency whereas the transverse force coefficient  $Cd_y (=R_2)$  retains the oscillatory behaviour of the prescribed motion input but with a phase shift depending on Reynolds number.

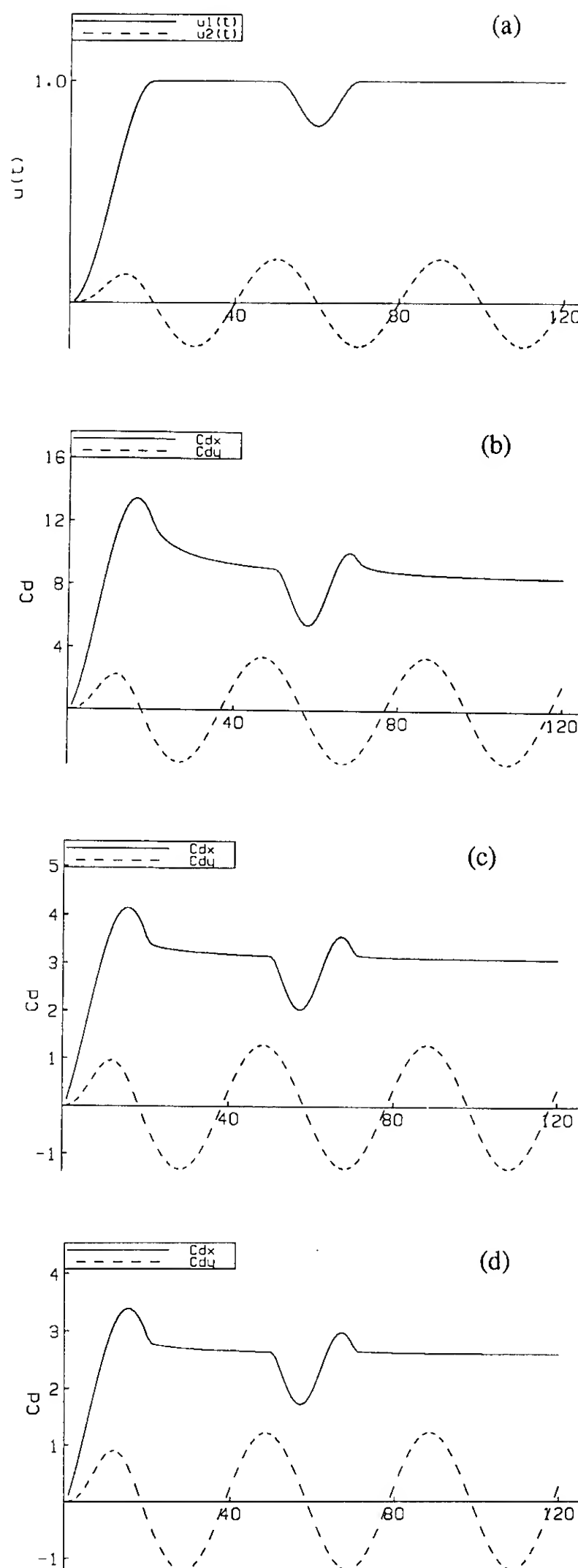


Figure 3 The time histories of the prescribed manoeuvre of the circular cylinder and the associated calculated Oseen drag coefficient  $Cd_x$  and sway transverse force coefficient  $Cd_y$  for different Reynolds number flows. The abscissa denotes the number of time intervals passed into the calculation.

(a) the surge  $u_1(t)$  and sway  $u_2(t)$  motions, (b)  $Re=2$ , (c)  $Re=40$ , (d)  $Re=200$ .

Figure 4 illustrates a series of snapshots of the flow field behind the cylinder observed from a fixed reference position. This sequence of frames at 10, 20, 30,..., 120 times the time interval increment clearly shows the vortex wake forming and decaying behind the cylinder as it undergoes the prescribed manoeuvre shown in figure 3a. The continuous line behind the cylinder indicates the path of the cylinder, in a flow field associated with a Reynolds number  $Re = 40$ .

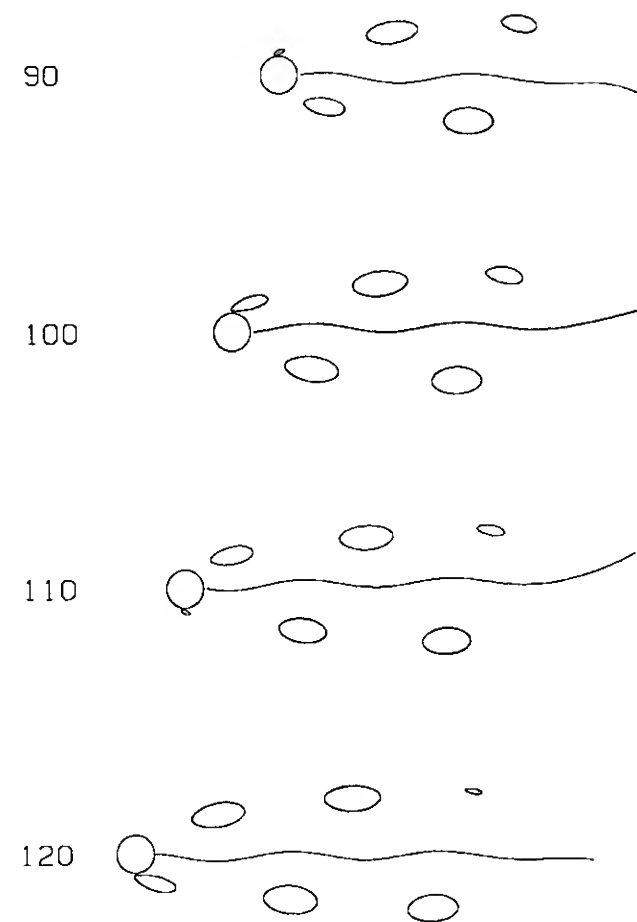
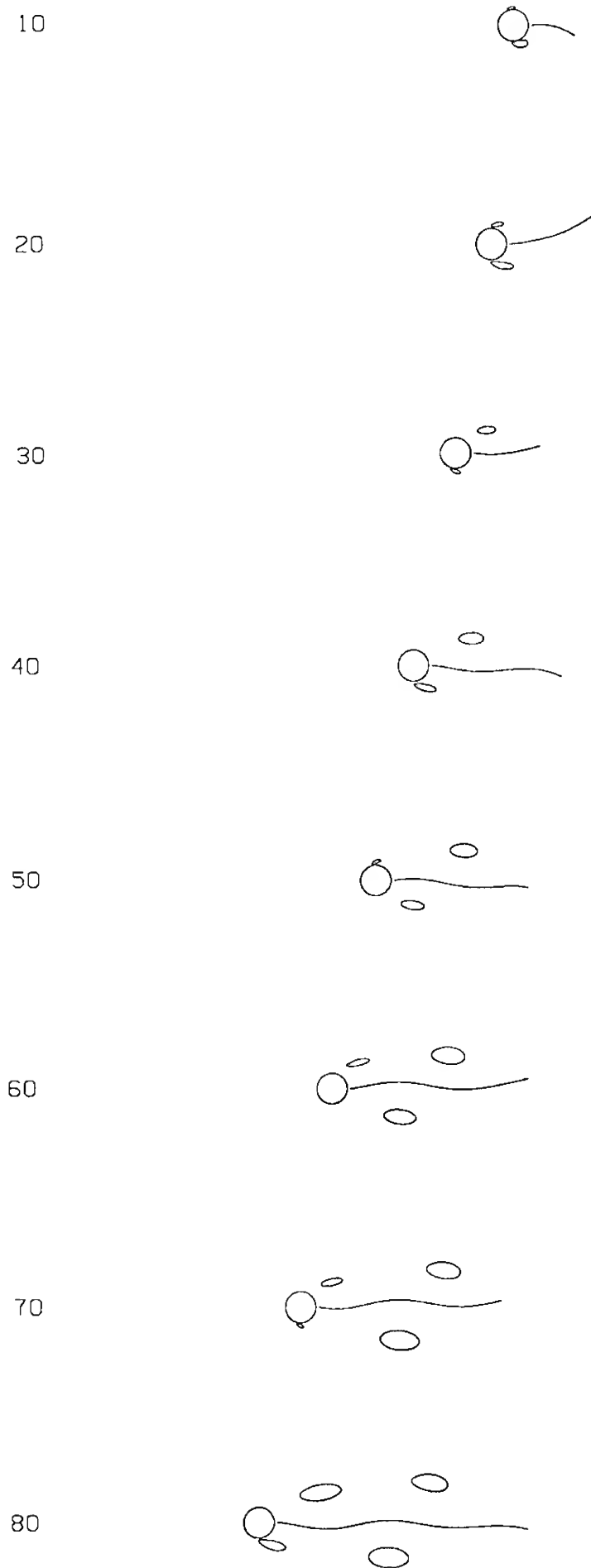


Figure 4 A sequence of snapshot frames at 10, 20, ..., 120 times the time interval increment illustrating the formation of the vortex wake behind the cylinder associated with the calculation  $Re=40$  in figure 3.

In both the steady and unsteady oseen flow calculations, no difficulties were encountered in the numerical scheme of study for any chosen value of Reynolds number (e.g.  $10^m$ , etc). However, it must be emphasised that from the evidence available the results derived from this linearised model are expected to overestimate the experimental data and, as we shall further show, the results obtained from the non-linear convective model.

#### Non-linear Convective Model

In the results presented in figure 5, the non-linear convective term in the modified integral equation, i.e. equations (29,30), is included in the numerical scheme of study. To do so requires distributing viscous panel elements into the fluid domain and this greatly increases the computational effort needed to provide solutions. In fact, this necessitates the full solution of the non-linear, coupled matrix equations in equation (32) whereas the oseen flow solutions are obtained from a much simpler linear matrix model [12,13].

The cylinder's surface was again idealised by a distribution of 40 equally spaced viscous boundary elements, each containing a time dependent oseenlet and in a similar procedure to the equivalent steady state calculations, 400 panels were distributed into the fluid domain contained within an imposed surrounding outer boundary at  $R = 6D$  (say). The prescribed manoeuvre displayed in figure 3(a) was again chosen and figures 5(a-c) show the calculated force coefficient components as a function of the number of time step intervals and Reynolds number  $Re = 2, 40, 100$ . It is seen that these time histories show similar trends to the equivalent linear predictions in figures 3(b-d) following the variations of the

input parasitic motions but, in comparison with the linear findings, their values are reduced. Note, however, the oscillatory variation now evident in the  $Cd_x$  time record created by the oscillatory sway motion. This again illustrates the influence of the non-linear convective term in the mathematical model.

Figure 6 shows a limited sequence of pictures illustrating the creation and decay of the vortex wake flow field around the cylinder as seen by a fixed observer.

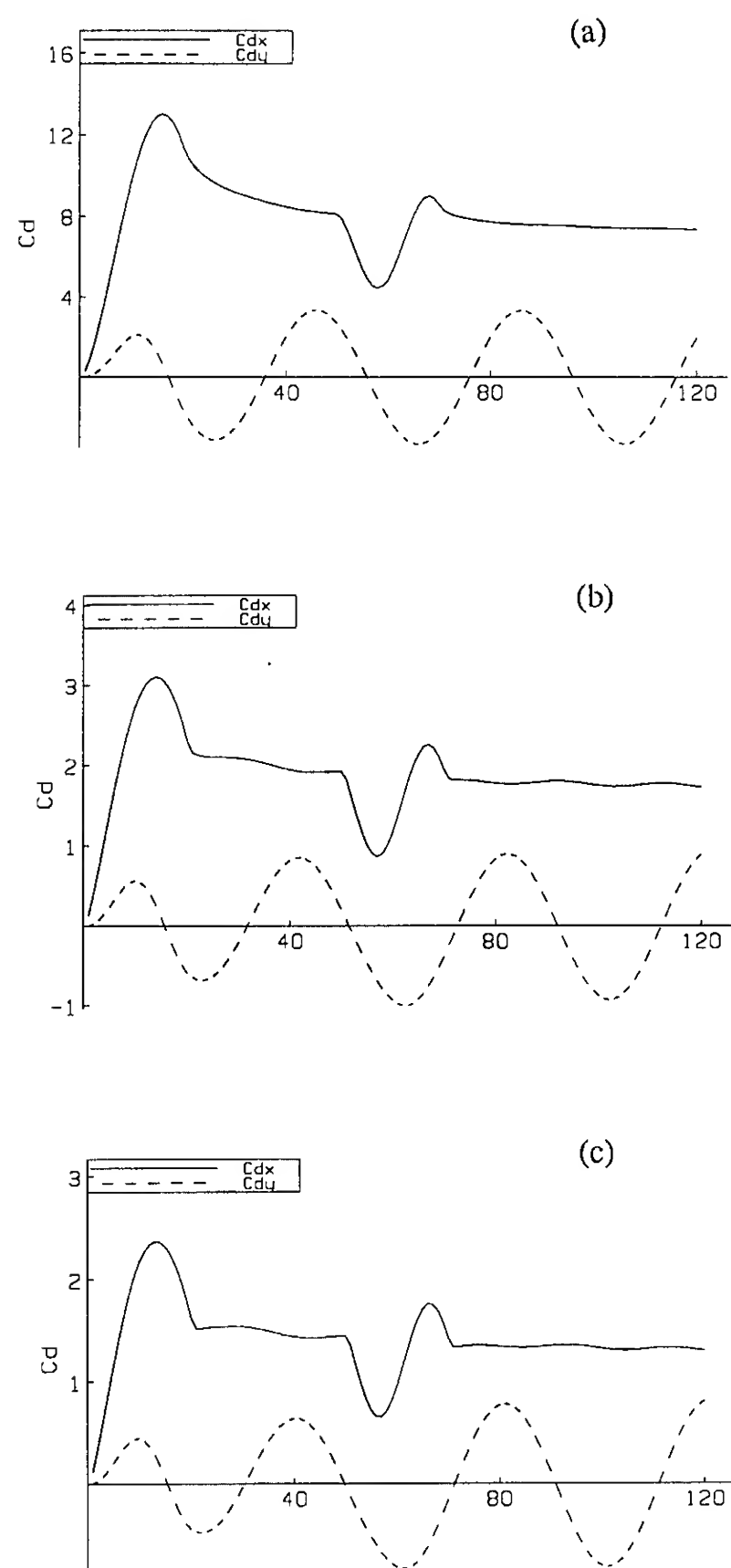
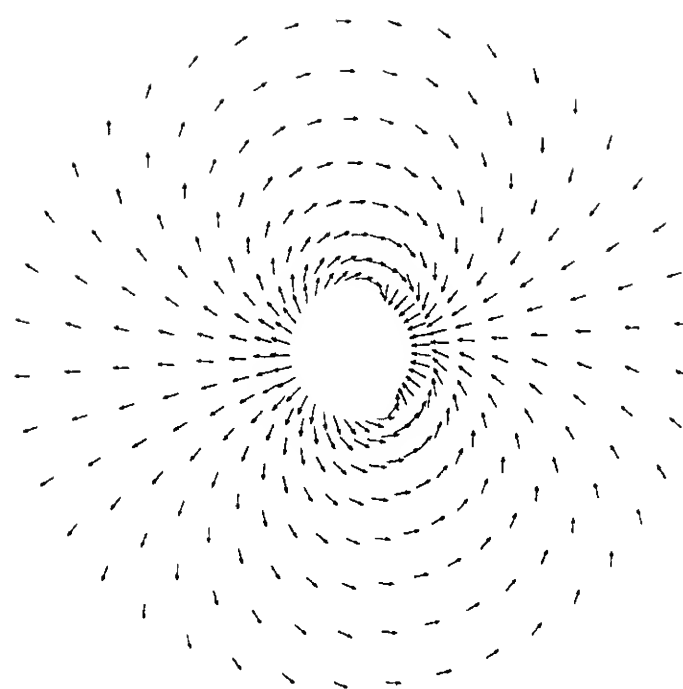
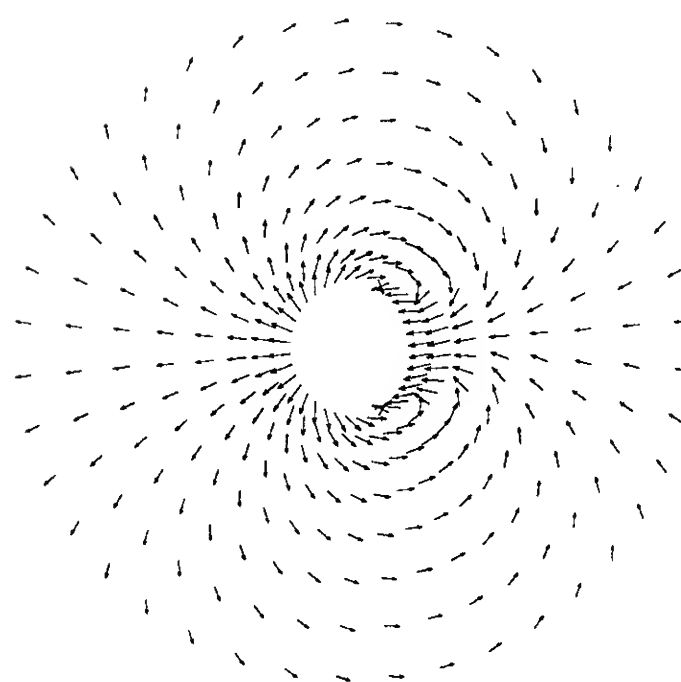


Figure 5 For the manoeuvre illustrated in figure 3(a), this figure shows the associated drag coefficient  $Cd_x$  and sway transverse force coefficient  $Cd_y$  for different Reynolds number flows calculated from the non-linear convective model. The abscissa denotes the number of time interval increments passed into the simulation.

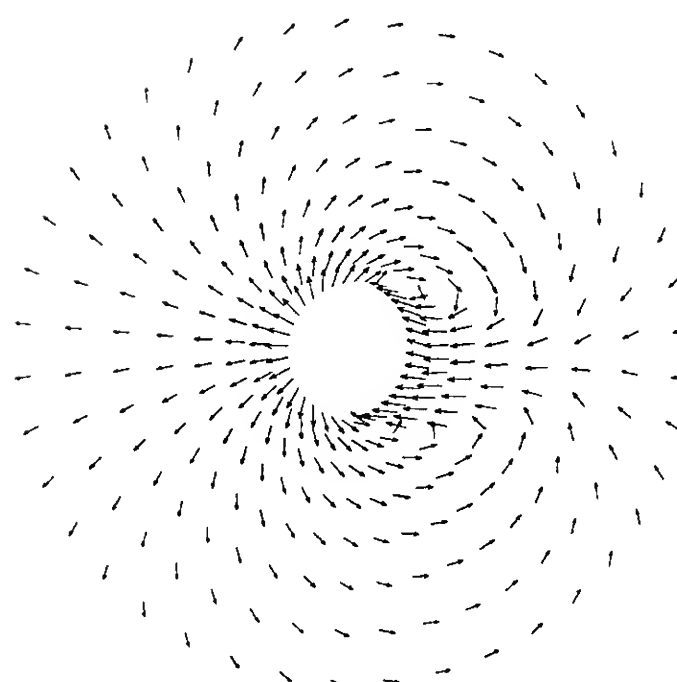
(a)  $Re=2$ , (b)  $Re=40$ , (c)  $Re=100$ .



10

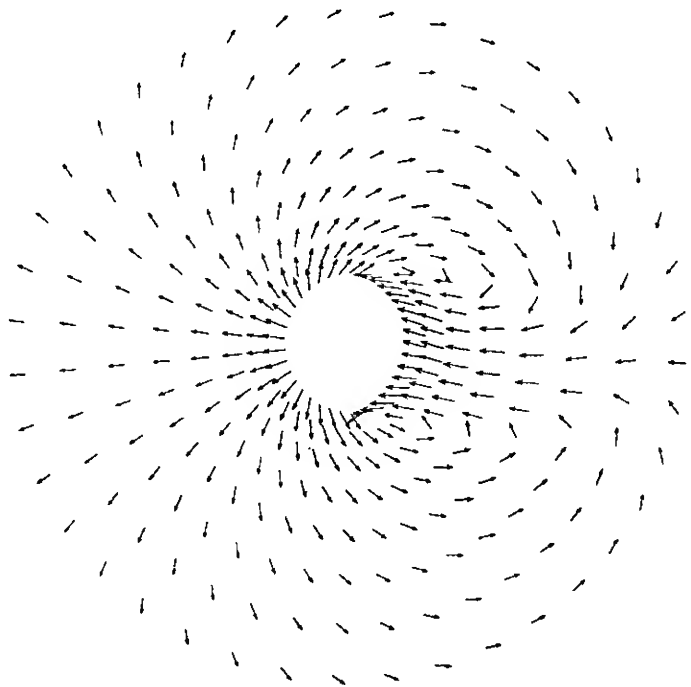


20

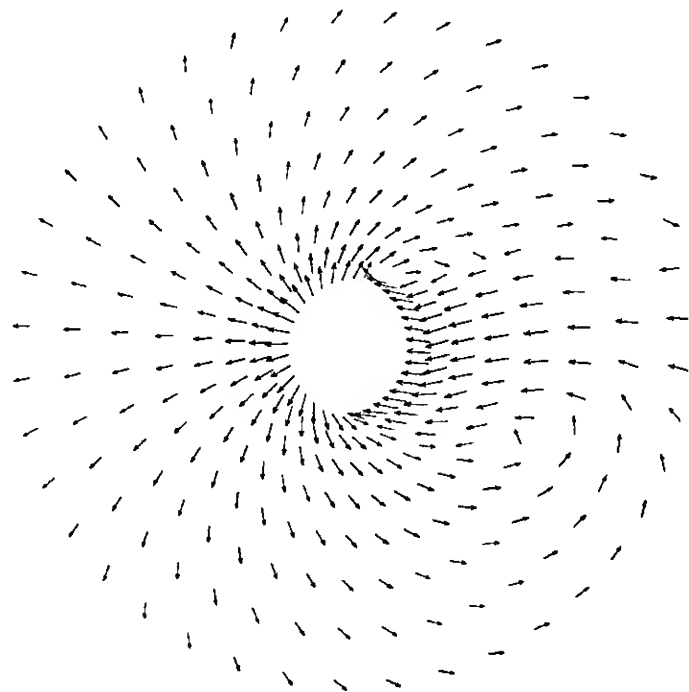


30

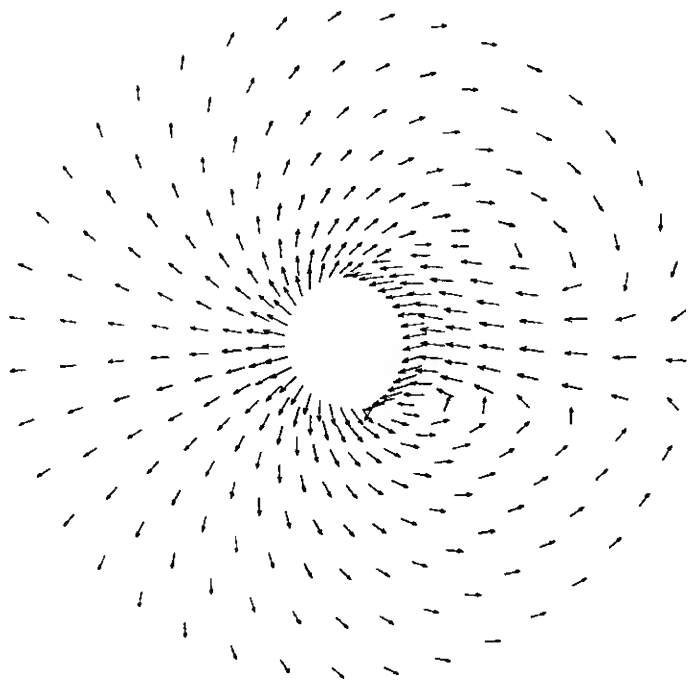




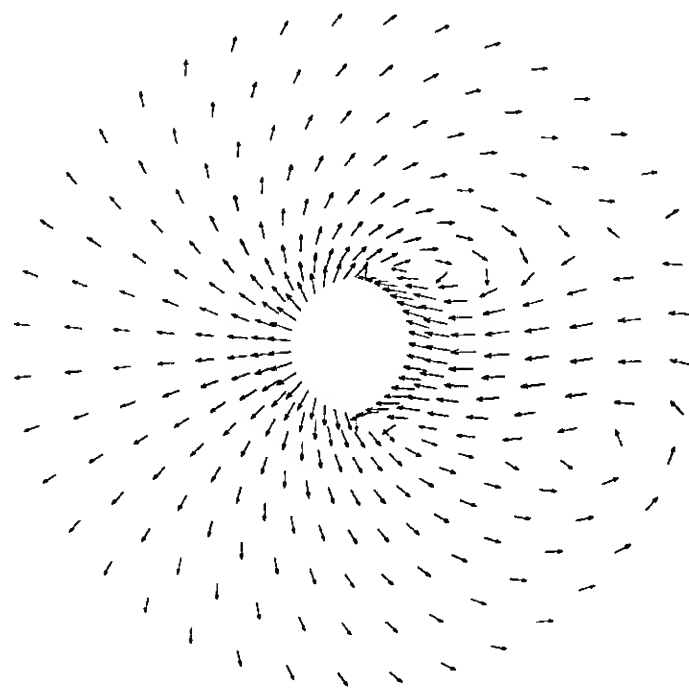
40



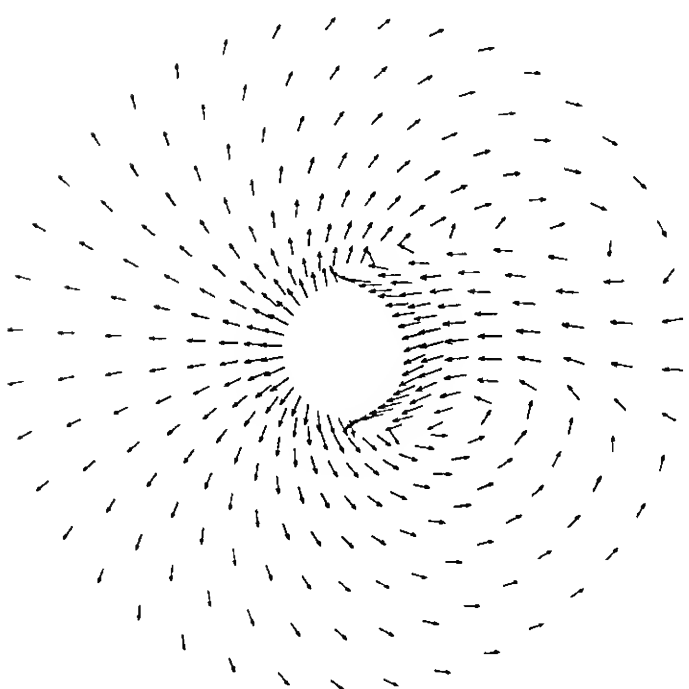
70



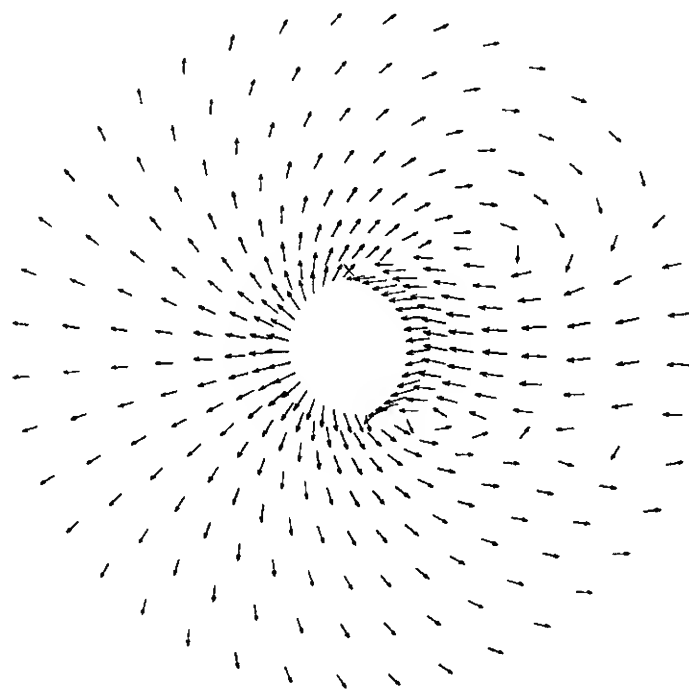
50



80



60



90

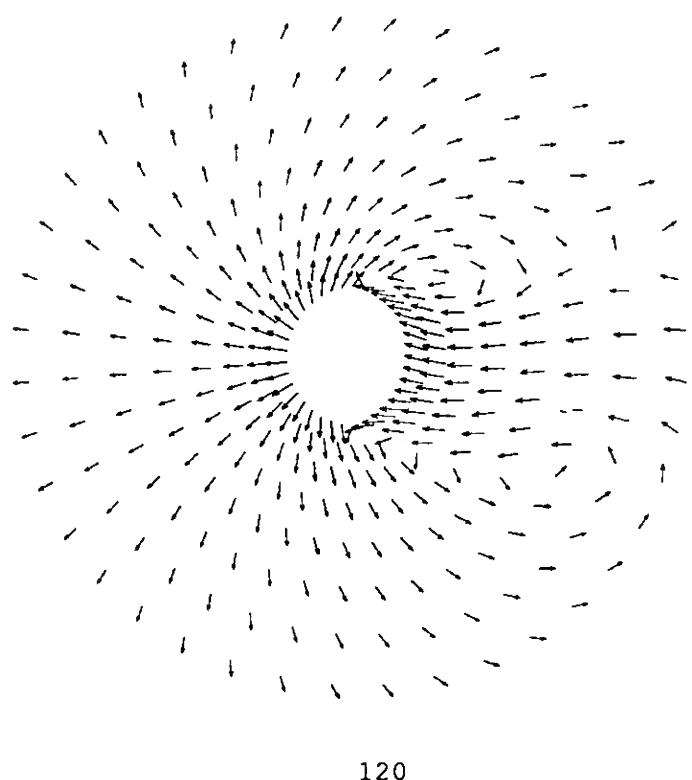
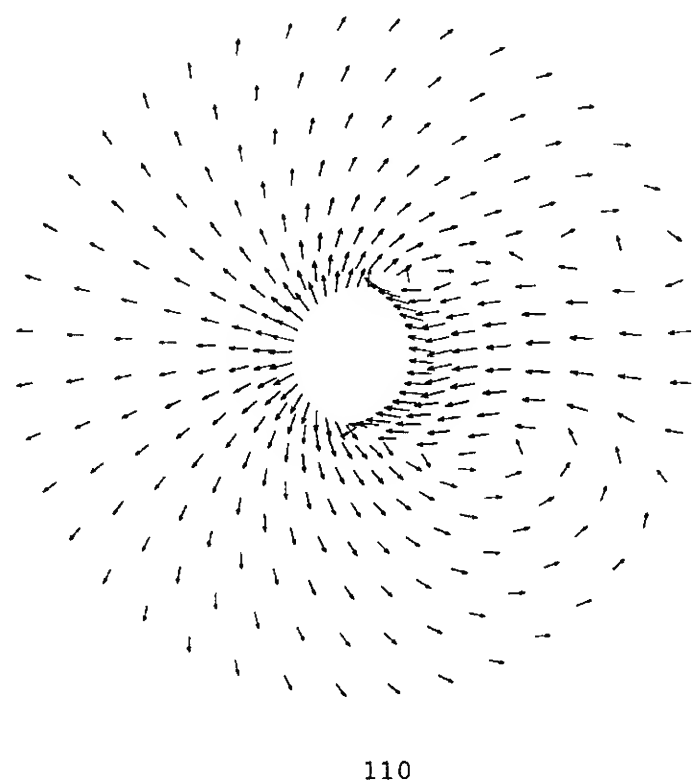
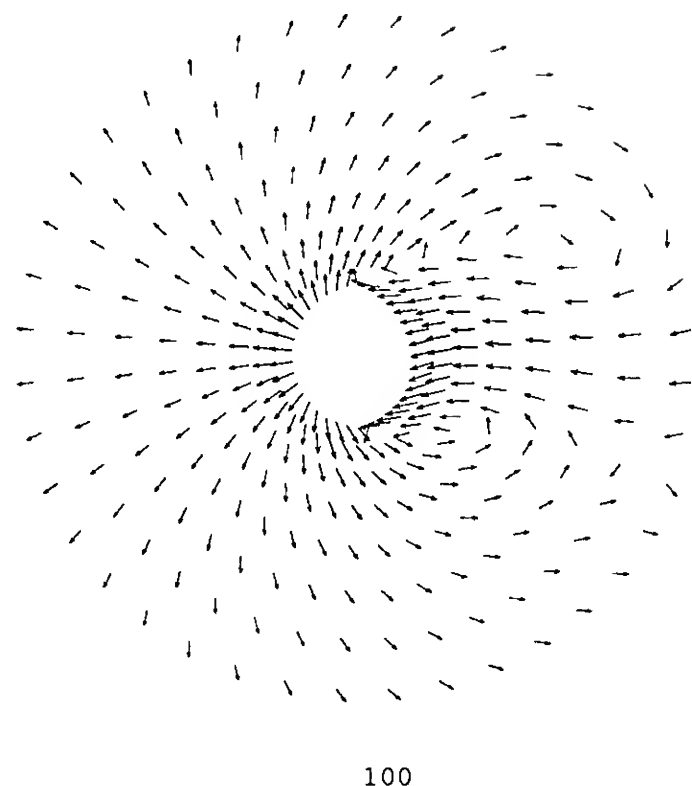


Figure 6 A sequence of snapshot frames at 10, 20, ..., 120 times the time interval increment showing the generation and decay of the vortex wake behind the circular cylinder associated with the calculation  $Re=100$  in figure 5(c) and also figure 3(a).

## CONCLUSIONS

The hybrid analytical and numerical viscous boundary element approach using time dependent oseenlets described herein, allows the predictions of the fluid actions and flow fields associated with arbitrary shaped bodies moving in a prescribed manoeuvre in an incompressible, viscous fluid. Although the method is demonstrated using a two-dimensional simple shaped body, the concepts introduced remain valid when tackling three-dimensional fluid-structure problems. However, in the latter, the presentation of information - especially a description of the flow field - becomes more difficult and the computational effort greatly increases.

The Oseen flow-linearised model produces over-estimates of the fluid actions and flow fields but it is easy to apply and, since it provides a 'broad brush' picture of the fluid-structure interactions, in engineering terms, it produces a reasonable first insight and solution to the problem.

The non-linear convective model is computationally more time consuming though the evaluation of the fluid actions is obtained from a relatively robust numerical scheme of study. However, because of the sensitivity of the flow field calculation to panel idealisation, truncation distance etc., the preliminary calculations presented serve to illustrate the applicability of the viscous boundary element approach to evaluate the time dependent fluid actions and flow fields associated with bodies manoeuvring in an incompressible, viscous fluid.

## ACKNOWLEDGEMENT

We gratefully acknowledge the support of the Science Engineering Research Council, the Ministry of Defence Procurement Executive and the encouragement of the staff at Admiralty Research Establishment (Haslar). We are indebted to Mrs Christa Steele for her typing (and retyping) of this manuscript.

## REFERENCES

1. Duncan, W.J., The Principles of the Control and Stability of Aircraft, Cambridge University Press, Cambridge, 1952.
2. Etkin, B., The Dynamics of Flight, Wiley, New York, 1959.
3. Mandel, P., "Ship Maneuvering and Control," Principles of Naval Architecture, (ed.J.P.Comstock), Society of Naval Architects and Marine Engineers, New York, 1967, pp. 463-606.
4. Bishop, R.E.D., Burcher, R.K. and Price, W.G., "The Uses of Functional Analysis in Ship Dynamics," Proceedings of The Royal Society London, Vol. A332, 1973, pp. 23-35.
5. Bishop, R.E.D., Burcher, R.K. and Price, W.G., "Application of Functional Analysis to Oscillatory Ship Model Testing," Proceedings of The Royal Society London, Vol. A332, 1973, pp. 37-49.

6. Booth, T.B. and Bishop, R.E.D., "The Planar Motion Mechanism," Admiralty Experiment Works, Haslar, 1973.
7. Burcher, R.K., "Developments in Ship Manoeuvrability," Transactions Royal Institution of Naval Architects, Vol. 114, 1972, pp. 1-32.
8. Clarke, D., "A Two-Dimensional Strip Method for Surface Ship Hull Derivatives : Comparison of Theory with Experiments on a Segmented Tanker Model," Journal Mechanical Engineering Science, Vol. 14, 1972, pp. 53-61.
9. Mikelis, N.E. and Price, W.G., "Calculation of Hydrodynamic Coefficients for a Body Manoeuvring in Restricted Waters Using a Three-Dimensional Method," Transactions Royal Institution of Naval Architects, Vol. 123, 1981, pp. 209-216.
10. Mikelis, N.E. and Price, W.G., "Calculations of Acceleration Coefficients and Correction Factors Associated with Ship Manoeuvring in Restricted Water : Comparison between Theory and Experiments," Transactions Royal Institution of Naval Architects, Vol. 123, 1981, pp. 217-232.
11. Price, W.G. and Tan, M., "A Preliminary Investigation into the Forces Acting on Submerged Body Appendages," Proceedings of the Conference on Ship Manoeuvrability, Prediction and Achievement, The Royal Institution of Naval Architects, 1987, paper 13.
12. Price, W.G. and Tan, M., "The Evaluation of Steady State Flow Parameters Around Arbitrarily Shaped Bodies Using Viscous Boundary Elements," Report 1/89, 1989, Department of Mechanical Engineering, Brunel University.
13. Price, W.G. and Tan, M., "The Evaluation of Steady Fluid Forces on Single and Multiple Bodies in Low Speed Flows Using Viscous Boundary Elements," International Union of Theoretical and Applied Mechanics Symposium on The Dynamics of Marine Vehicles and Structures in Waves, June 1990, Brunel University, (Also Elsevier Press, 1991).
14. Tritton, D.J., "Experiments on the Flow Past a Circular Cylinder at Low Reynolds Number," Journal Fluid Mechanics, Vol. 6, 1960, pp. 547-567.
15. Thom, A., "The Flow Past Circular Cylinders at Low Speeds," Proceedings of The Royal Society London, Vol. A141, 1933, pp.651-669.
16. Fornberg, B., "A Numerical Study of Steady Viscous Flow Past a Circular Cylinder," Journal Fluid Mechanics, Vol. 98, 1980, pp. 819-855.
17. Fornberg, B., "Steady Viscous Flow Past a Circular Cylinder up to Reynolds Number 600," Journal Computational Physics, Vol. 61, 1985, pp.297-320.
18. Abramowitz, M. and Stegun, I.A., ed., Handbook of Mathematical Functions, Dover, New York, 1972.
19. Bessho, M., "Study of Viscous Flow by Oseen's Scheme, (Two Dimensional Steady Flow)," Journal Society of Naval Architects Japan, Vol. 156, 1984, pp.37-49.
20. Levenberg, M., "A Method for the Solution of Certain Non-linear Problems in Least Squares," Quarterly Journal of Applied Mathematics, Vol. 2, 1944, pp.164-168.
21. Marquardt, D.W., "An Algorithm for Least Squares Estimation of Non-linear Parameters," Journal of Industrial Applied Mathematics, Vol. 11, 1963, pp. 651-661.
22. Twizell, E.H., "Numerical Methods, with Applications in the Biomedical Sciences," Ellis Horwood and John Wiley, Chichester, 1988.
23. Lamb, H., "Hydrodynamics," (6th ed.), Cambridge University Press, Cambridge, 1932.

## APPENDIX

Before writing equation (31) in matrix form, we need to integrate the time dependent fundamental solution over an elemental surface panel or volume. For the two dimensional problem under discussion this may be achieved as follows.

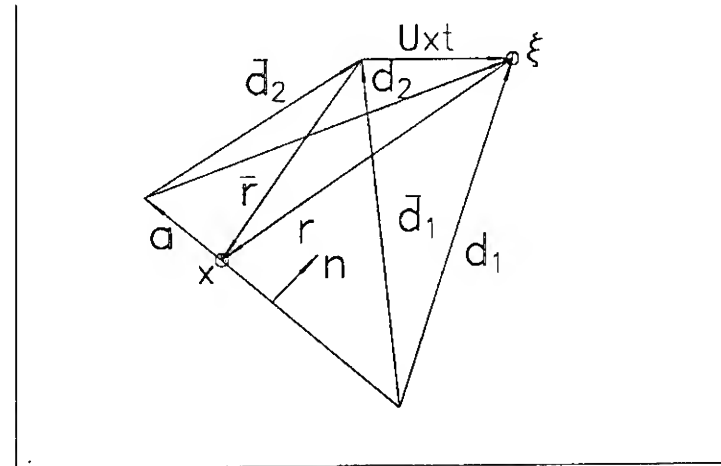


Figure 7 Schematic illustration of the panel, field point, etc. and symbol definitions.

Figure 7 illustrates a panel with end points (1,2) lying in the direction of  $\mathbf{a}$  and  $\xi$  is a field point connected to the source point  $\mathbf{x}$  on the panel by the vector  $\mathbf{r} = \mathbf{x} - \xi$ . The vectors  $\mathbf{d}_1, \mathbf{d}_2$  are as shown and the unit normal  $\mathbf{n}$  points out of the panel. If we let

$$\bar{\mathbf{r}} = \mathbf{r} + \mathbf{U}t, \quad \bar{\mathbf{d}}_1 = \mathbf{d}_1 - \mathbf{U}t, \quad \bar{\mathbf{d}}_2 = \mathbf{d}_2 - \mathbf{U}t$$

then

$$\bar{\mathbf{r}} = 2(\bar{\beta} \mathbf{a}_0 - \bar{\epsilon} \mathbf{n}), \quad \bar{\beta} \in [-\bar{\sigma}_1, -\bar{\sigma}_2]$$

where

$$\mathbf{a}_0 = \mathbf{a}/|\mathbf{a}|, \quad \bar{\epsilon} = 0.5 \bar{\mathbf{d}}_1 \cdot \mathbf{n} = 0.5 \bar{\mathbf{d}}_2 \cdot \mathbf{n},$$

$$\bar{\sigma}_1 = 0.5 \bar{\mathbf{d}}_1 \cdot \mathbf{a}_0, \quad \bar{\sigma}_2 = 0.5 \bar{\mathbf{d}}_2 \cdot \mathbf{a}_0$$

and

$$d\Sigma = 2d\bar{\beta}, \quad \bar{r}^2 = 4(\bar{\beta}^2 + \bar{\epsilon}^2), \quad d\bar{r}^2 = 8\bar{\beta}d\bar{\beta}$$

Because

$$2\mathbf{r}_i \mathbf{r}_j - \delta_{ij} \bar{r}^2 = (\mathbf{n} \mathbf{n} - \mathbf{a}_0 \mathbf{a}_0)(8\bar{\epsilon}^2 - \bar{r}^2)d\bar{\beta} - (\mathbf{a}_0 \mathbf{n} + \mathbf{n} \mathbf{a}_0)\bar{\epsilon} d\bar{r}^2$$

and

$$\frac{d}{d\bar{\beta}} \left( \frac{\bar{\beta}}{\bar{r}^2} \right) = (8\bar{\epsilon}^2 - \bar{r}^2)/\bar{r}^4$$

it follows that

$$\frac{d}{d\bar{\beta}} \left\{ (\mathbf{n} \mathbf{n} - \mathbf{a}_0 \mathbf{a}_0) \frac{\bar{\beta}}{\bar{r}^2} + (\mathbf{a}_0 \mathbf{n} + \mathbf{n} \mathbf{a}_0) \frac{\bar{\epsilon}}{\bar{r}^2} \right\} = \left( \frac{-\delta}{\bar{r}^2} + \frac{2\bar{r}\bar{r}}{\bar{r}^4} \right)$$

where  $\mathbf{n} \mathbf{n}$  etc denotes a (2 x 2) matrix in this two-dimensional problem. Further, since

$$\delta - \frac{\bar{\mathbf{r}} \bar{\mathbf{r}}}{\bar{r}^2} + (\mathbf{a}_0 \mathbf{a}_0 - \mathbf{n} \mathbf{n}) \frac{4\bar{\beta}^2}{\bar{r}^2} - (\mathbf{a}_0 \mathbf{n} + \mathbf{n} \mathbf{a}_0) \frac{4\bar{\epsilon} \bar{\beta}}{\bar{r}^2} = \delta - \mathbf{n} \mathbf{n} = \mathbf{a}_0 \mathbf{a}_0,$$

$$\int_{\bar{\sigma}_1}^{\bar{\sigma}_2} \frac{e^{-\bar{r}^2/4t}}{t} d\bar{\beta}$$

$$= 0.5(\pi/t)^{1/2} e^{-(\mathbf{n} \cdot \bar{\mathbf{d}}_1)^2/4t} [\text{erf}(\mathbf{a}_0 \cdot \bar{\mathbf{d}}_1/2t^{1/2}) - \text{erf}(\mathbf{a}_0 \cdot \bar{\mathbf{d}}_2/2t^{1/2})]$$

then the surface integral involving the two-dimensional, time dependent oseenlet is given by the analytical expression

$$2\pi \int v_{sj}^* d\Sigma = \int_{\bar{\sigma}_1}^{\bar{\sigma}_2} \left\{ \frac{1}{t} \left( \delta - \frac{\bar{\mathbf{r}} \bar{\mathbf{r}}}{\bar{r}^2} \right) e^{-\bar{r}^2/4t} + 2 \left( \frac{-\delta}{\bar{r}^2} + \frac{2 \bar{\mathbf{r}} \bar{\mathbf{r}}}{\bar{r}^4} \right) (1 - e^{-\bar{r}^2/4t}) \right\} d\bar{\beta}$$

$$= \left[ \frac{2\bar{\beta}}{\bar{r}^2} (\mathbf{n} \mathbf{n} - \mathbf{a}_0 \mathbf{a}_0) + \frac{2\bar{\epsilon}}{\bar{r}^2} (\mathbf{a}_0 \mathbf{n} + \mathbf{n} \mathbf{a}_0) \right] (1 - e^{-\bar{r}^2/4t}) \Big|_{\bar{\sigma}_1}^{\bar{\sigma}_2}$$

$$+ \int_{\bar{\sigma}_1}^{\bar{\sigma}_2} \frac{e^{-\bar{r}^2/4t}}{t} \left\{ \delta - \frac{\bar{\mathbf{r}} \bar{\mathbf{r}}}{\bar{r}^2} + (\mathbf{a}_0 \mathbf{a}_0 - \mathbf{n} \mathbf{n}) \frac{4\bar{\beta}^2}{\bar{r}^2} - (\mathbf{a}_0 \mathbf{n} + \mathbf{n} \mathbf{a}_0) \frac{4\bar{\epsilon} \bar{\beta}}{\bar{r}^2} \right\} d\bar{\beta}$$

$$= 0.5(\pi/t)^{1/2} e^{-(\mathbf{n} \cdot \bar{\mathbf{d}}_1)^2/4t} \left\{ \text{erf}(\mathbf{a}_0 \cdot \bar{\mathbf{d}}_1/2t^{1/2}) - \text{erf}(\mathbf{a}_0 \cdot \bar{\mathbf{d}}_2/2t^{1/2}) \right\} \mathbf{a}_0 \mathbf{a}_0$$

$$+ (\mathbf{a}_0 \mathbf{a}_0 - \mathbf{n} \mathbf{n}) \left\{ \frac{\mathbf{a}_0 \cdot \bar{\mathbf{d}}_2}{\bar{\mathbf{d}}_2^2} (1 - e^{-\bar{\mathbf{d}}_2^2/4t}) - \frac{\mathbf{a}_0 \cdot \bar{\mathbf{d}}_1}{\bar{\mathbf{d}}_1^2} (1 - e^{-\bar{\mathbf{d}}_1^2/4t}) \right\}$$

$$+ (\mathbf{a}_0 \mathbf{n} + \mathbf{n} \mathbf{a}_0) \left\{ \frac{\mathbf{n} \cdot \bar{\mathbf{d}}_2}{\bar{\mathbf{d}}_2^2} (1 - e^{-\bar{\mathbf{d}}_2^2/4t}) - \frac{\mathbf{n} \cdot \bar{\mathbf{d}}_1}{\bar{\mathbf{d}}_1^2} (1 - e^{-\bar{\mathbf{d}}_1^2/4t}) \right\}$$

Although this is an unwieldy analytical expression, it avoids the numerical integration of the oseenlet over the surface panel but, unfortunately, its form does not readily permit the convolution integration to be reduced to analytical expressions.

## DISCUSSION

Gerard Fridsma  
General Dynamics, USA

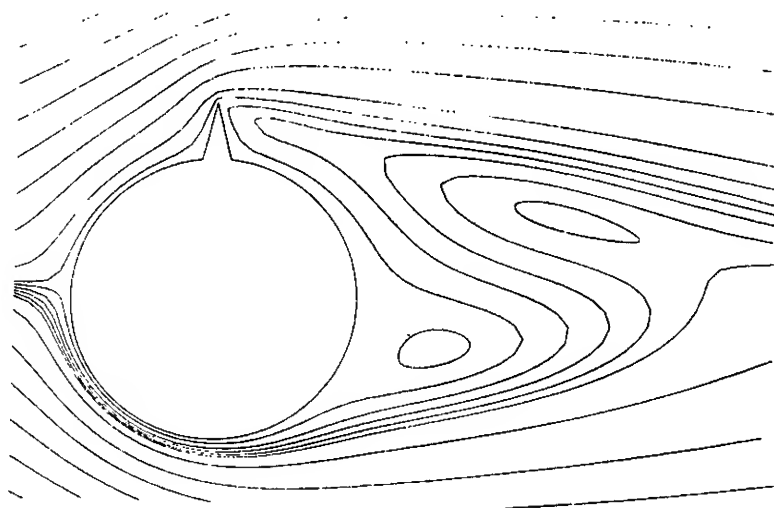
The statement was made about the importance of Reynolds number on model testing of submerged bodies. While indeed answers are being obtained on the testing tunnel and towing tank, these are of a qualitative nature to understand the nature of the flow and production of loads. For small cross-flow angles (yaw), the loads are linear and not Reynolds number dependent in this range. As one goes to higher cross-flows (yaw angles from  $10^\circ$  to  $20^\circ$ ), vortices are generated from the hull which create serious nonlinearities in the trends of the loads. These must be dealt with for a full maneuvering submerged body which means Reynolds number must be dealt with, since separation and vortex generation is very much dependent on  $Re$ .

## AUTHORS' REPLY

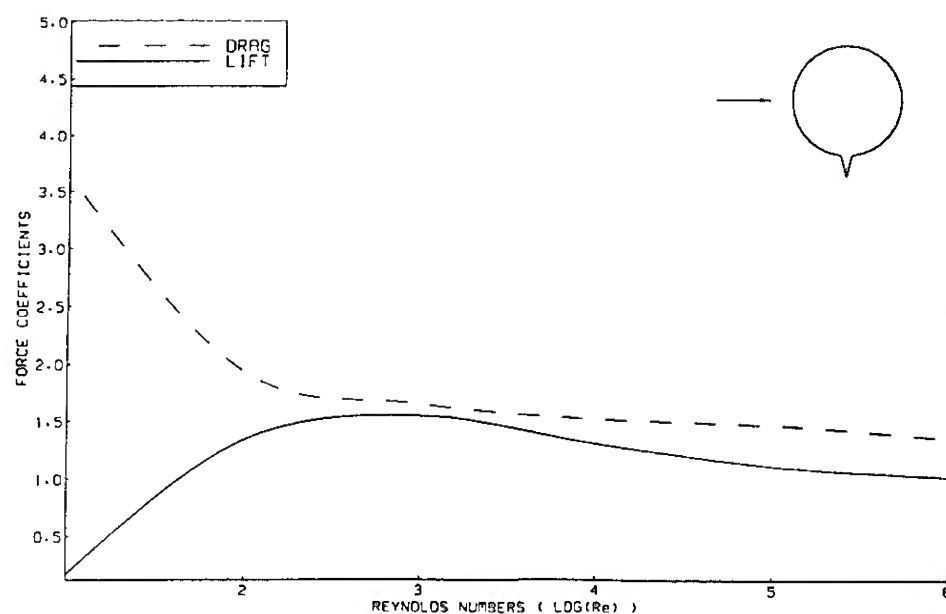
We thank Mr. Fridsma for his contribution to this paper and we agree with his overall observations.

Our comments relating to a submarine hull were based on steady state calculations performed on a two-dimensional cross-section with sail plane or fin. This was simply idealized by a circular cylinder and appendage as illustrated in the following figures. These also display the steady flow field around the section and show the variation of the steady drag and lift coefficients with Reynolds number. In the region  $Re < 10^3$  (say) the curves tend to flatten indicating that large changes in the Reynolds number produce relatively small changes in these steady forces. These preliminary findings may provide a simple explanation why model scale and full scale submarine experiments produce a measure of correlation even though true scaling is impossible to apply in practice.

Although a free running or towed model is geometrically scaled correctly, it must be of a size to contain the instrumentation measurement packages and not too large for the towing tank or maneuvering basin. Thus constant Reynolds number and viscosity coefficient imply that the model's forward speed must be set at  $U_m = (L_{FS}/L_m) U_{FS}$ , where subscript FS denotes full scale value. Practically, in a towing tank, this relationship is impossible to fulfill and so a model forward speed is chosen as high as safe powering allows within the confines of the test facility. Thus the Reynolds number for the model and full scale differ, but if both experiments are performed at Reynolds numbers lying within the flat portion of the drag and lift curves, then it can be expected that steady state predictions for model and full scale would display reasonable correlation. In fact, from the values of the steady state forces at the appropriate Reynolds numbers for a model and full scale submarine a simple correction factor could be deduced and incorporated into maneuvering prediction mathematical models.



The calculated fluid flow field around a body appendage configuration ( $Re=10$ ).



The calculated variation in the lift and drag coefficients with Reynolds number.



# The Flow Past a Wing-Body Junction - An Experimental Evaluation of Turbulence Models

W. Devenport, R. Simpson  
(Virginia Polytechnic Institute and State University, USA)

## ABSTRACT

Detailed three-component LDV measurements have been made in the flow of a turbulent boundary layer past an idealized wing-body junction. These measurements, which show great variety and three-dimensionality in the vortex-dominated turbulence structure of this flow, are here used to evaluate a number of turbulence models. Many of these models require or imply a relationship between the angles of the turbulence shear-stress and mean-velocity vectors. In the present flow these angles are not only different but do not follow any simple relationship. To predict the shear-stress angle, accurate modeling of the full shear-stress transport equations is clearly needed. In particular, new models based on measurements are needed for the pressure-strain term. The ability of six turbulence models to predict the magnitude of the shear-stress vector from the mean-velocity and/or turbulence kinetic energy is examined. Among the best are the Cebeci-Smith and algebraic-stress models. Other models, particularly the Johnson-King, are not well suited to this vortical flow.

## INTRODUCTION

This paper follows several (Devenport and Simpson, 1986, 1987, 1988a, 1988b, 1988c, 1990a) in which we have presented detailed velocity measurements made in the flow of a turbulent boundary layer around the nose of a wing-body junction. The purposes of this paper are; (i) to briefly review these measurements, (ii) to present new measurements made around the rest of the junction, and (iii) to use the whole data set to evaluate the usefulness and generality of a variety of turbulence models and modelling parameters.

For a review of other experimental work on wing-body junction flows see Devenport and Simpson (1990a).

## EQUIPMENT

Only abbreviated descriptions are given here; for complete details see Devenport and Simpson (1990b).

### The Wing and Wind Tunnel

The wing (figure 1) is cylindrical, has a maximum thickness (T) of 71.7mm, a chord of 305mm and a span of 229mm. In cross section its shape (figure 2) consists of a 3:2 elliptical nose

(major axis aligned with the chord) and a NACA 0020 tail joined at the maximum thickness. Trips are attached to both sides of the wing to ensure steady and fixed transition.

The wing is mounted at zero sweep and incidence at the center of the flat 0.91-m wide test wall of the Virginia Tech Boundary Layer Tunnel, forming the junction. In the absence of the wing this tunnel produces a flow of zero streamwise pressure gradient, consisting of a closely uniform (to within 1%) low turbulence (0.2%) free stream and an equilibrium two-dimensional turbulent boundary layer (see Ahn (1986)) on the test wall. With the wing in place, inserts attached to the wind tunnel side walls are used to minimize blockage-induced pressure gradients.

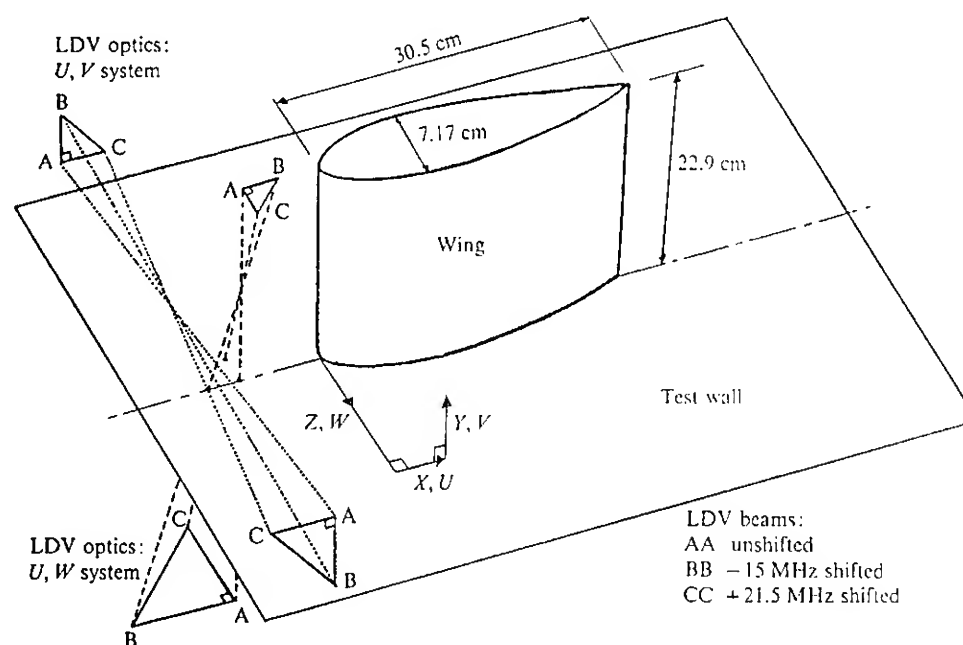


Figure 1. Perspective view of the wing-body junction.

### Laser Doppler Velocimeter (LDV)

A 3-component LDV was used to measure detailed profiles of mean-velocity and turbulence quantities in 6 planes surrounding the wing. These planes (numbered 1,3,4,5,8, and 10 for organizational reasons) are illustrated in figure 2.

The LDV has three sets of sending optics, two of which are shown schematically in figure 1.

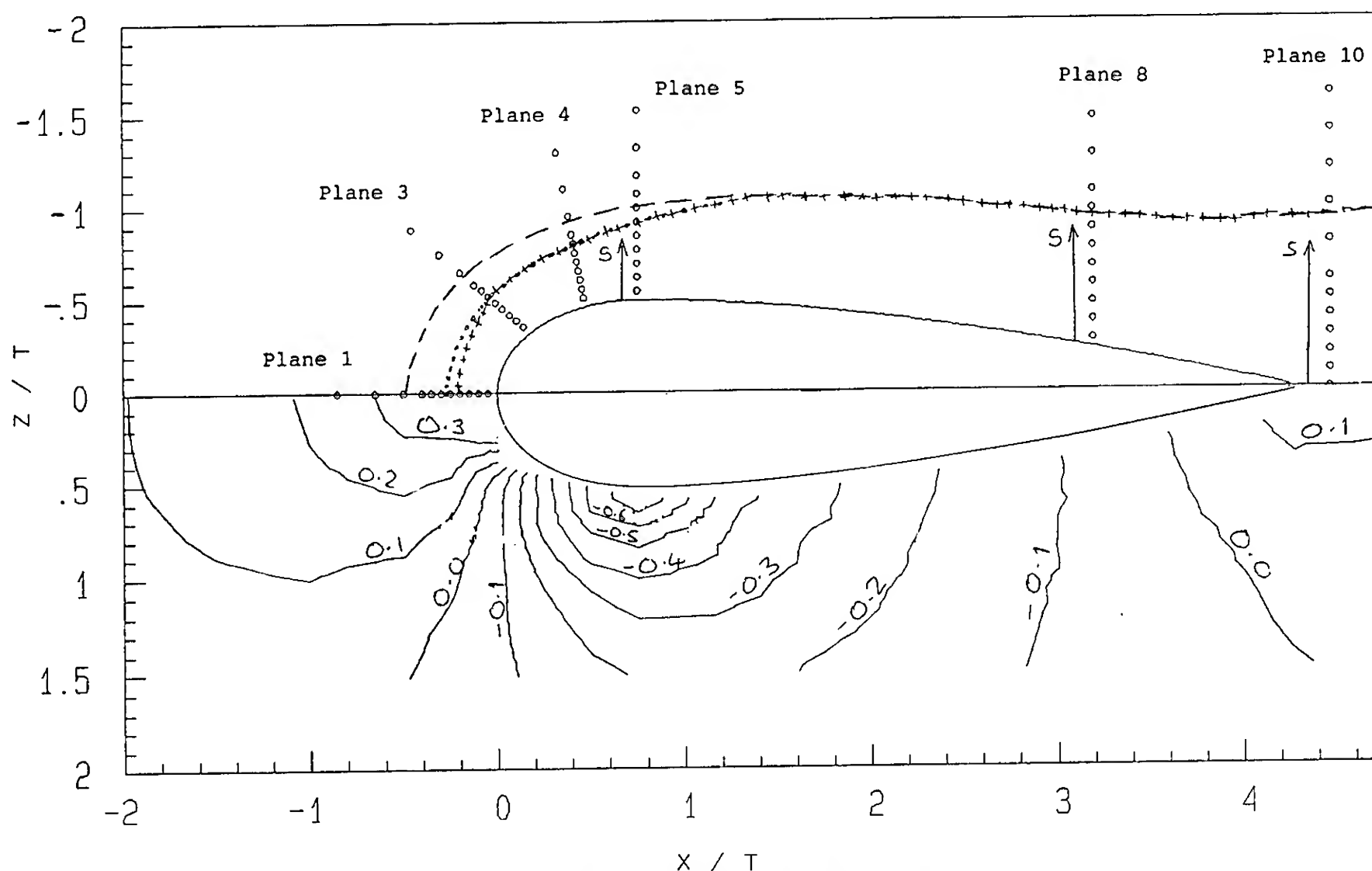


Figure 2. Contours of mean-surface pressure coefficient  $C_p$  on the wall surrounding the wing; o - locations of LDV profiles, --- line of separation, ..... line of low shear, +++ locus of peak turbulence kinetic energy in the vortex.

Each set produces an arrangement of beams sensitive to a different pair of velocity components and their associated Reynolds shear stress. Only one set is used at a time. The flow is seeded using dioctyl phthalate smoke (typical particle diameter 1 micron). Light scattered from the measurement volume is focussed onto the pinhole of a single photomultiplier tube. Data are obtained from the photomultiplier signal using either fast sweep rate sampling spectrum analysis (see Simpson and Barr, 1975) or a DANTEC 55N10 Burst Spectrum Analyzer. Velocity statistics are obtained by time (not particle) averaging and thus should be free of bias.

Measurements presented here have been corrected, where necessary, for velocity gradient broadening and finite transit time broadening using the techniques described by Durst et al. (1981). Uncertainty estimates for 95% confidence limits are listed in table 1.

Quantity	Uncertainty
Mean velocity	$\pm 0.03 U_{ref}$
Turbulence kinetic energy, $k$	$\pm 0.00026 U_{ref}^2$
Turbulence shear-stress $-uv$	$\pm 0.00033 U_{ref}^2$
Turbulence shear-stress $-vw$	$\pm 0.00027 U_{ref}^2$
Turbulence shear-stress magnitude	$\pm 0.00033 U_{ref}^2$

Table 1 Typical uncertainties in LDV measurements. 95% confidence limits.

#### COORDINATE SYSTEMS, TEST CONDITIONS

Most results and discussion will use the lab fixed coordinate system  $X, Y, Z$  and  $U, V, W$  centered at the intersection of the wing leading edge and wall (figure 1).  $X$  is measured downstream from the leading edge,  $Y$  normal to the wall and  $Z$  completes a right-handed system. In presenting LDV measurements the additional coordinate  $S$  will be used.  $S$  is measured along any of the LDV measurement planes from the wing surface or flow centerline, as shown in figure 2. In discussing turbulence models and parameters other coordinate systems will be used, distinguished by subscripts. Subscripts 'f', 's' and 'g' refer to coordinates fixed in the local free-stream direction, the local mean-flow direction and the local direction of the mean-velocity gradient vector, respectively. In calculating these directions  $V$  component velocities will be ignored. In all coordinate systems, upper case and lower case symbols will be used to denote the mean and fluctuating components of velocity respectively.

Distances will in general be non-dimensionalized on the maximum thickness of the wing ( $T$ ), velocities on the undisturbed approach free-stream velocity,  $U_{ref}$ . Under nominal test conditions the momentum thickness Reynolds number of the approach boundary layer, measured in the plane of symmetry  $2.15T$  upstream of the wing leading edge, was 6700, corresponding to a total boundary layer thickness  $\delta$  of 36mm ( $.50T$ ) and  $U_{ref}$  of 27 m/s.

## EXPERIMENTAL RESULTS

Figure 2 shows contours of mean surface pressure coefficient  $C_p$  (based on undisturbed free-stream conditions) and principle features of an oil-flow visualization performed on the wall surrounding the wing. Figures 3 and 4 show mean-velocity vectors and contours of turbulence kinetic energy  $k/U_{ref}^2$  measured in planes 1 through 10. The mean-velocity vectors represent components normal to the centerline of the horseshoe vortex defined as the locus of peak turbulence kinetic energy (see figure 2). Other projections of the mean-velocity field (e.g. normal to the wing, parallel to the measurement planes) do not clearly show the secondary-flow velocities associated with the vortex. Note that the measurements presented here in planes 1, 3 and 4 have previously been published by Devenport and Simpson (1987, 1988a, 1988b and 1990a).

This flow is dominated by the pressure field produced by the wing and the velocity field generated by the horseshoe vortex that is wrapped around the junction between the wing and wall. In the plane of symmetry upstream of the wing (plane 1) the oncoming boundary layer experiences an adverse pressure gradient that causes it to separate  $0.47T$  upstream of the leading edge (figure 2). The separation region formed (figure 3(a)) is dominated by the recirculation associated with the horseshoe vortex. This roughly elliptical structure, centered at  $X/T = -.2$ ,  $Y/T = .05$ , generates an intense backflow by reversing fluid impinging on the leading edge of the wing. The backflow reaches a maximum mean velocity of  $-0.48U_{ref}$  and then decelerates, giving the appearance of reattachment between  $X/T = -.25$  and  $-.3$ . Reattachment, however, does not occur as a thin region of weak reversed flow is sustained adjacent to the wall. This region is then all that remains of the backflow upstream to the separation point. The near reattachment of the backflow produces a distinct line in the surface oil-flow visualization known as the line of low shear (figure 2).

In the vicinity of the horseshoe vortex the turbulence stresses (and thus the turbulence kinetic energy) become very large reaching values an order of magnitude greater than in the approach boundary layer (figure 4(a)). These large stresses are associated with bimodal (double-peaked) histograms of velocity fluctuations like those shown in figure 5, and are produced by intense low-frequency bistable unsteadiness in the structure of the vortex. This unsteadiness is a result of the turbulent/non-turbulent intermittency of fluid entrained into the corner between the wing and wall (Devenport and Simpson (1990a)).

Moving out of the plane of symmetry, fluid experiences a strong favorable pressure gradient (figure 2) that accelerates it as it moves around the nose. Close to the wing in planes 3, 4 and 5 this acceleration, acting in concert with the rotational motion of the vortex (which here is bringing low-turbulence high-momentum fluid from the free-stream down close to the wall), locally relaminarizes the boundary layer (Devenport and Simpson (1988b and c)). Turbulence shear stresses in this region are therefore much smaller than elsewhere. Turbulence kinetic energy (figures 4(b), (c) and (d)) is also reduced. Although the intensity of turbulent fluctuations in the vicinity of the vortex falls in the favorable pressure gradient the peak values of turbulence kinetic energy remain many times those in the surrounding boundary layer because of the bimodal unsteadiness. Bimodal histograms are seen in the vicinity of the vortex in planes 3, 4 and 5 (figures 4(b), 4(c) and 4(d)). Despite the favorable pressure gradient the vortex clearly grows in this region moving away from the wall and the wing (figures 3 and 4). (Projected onto

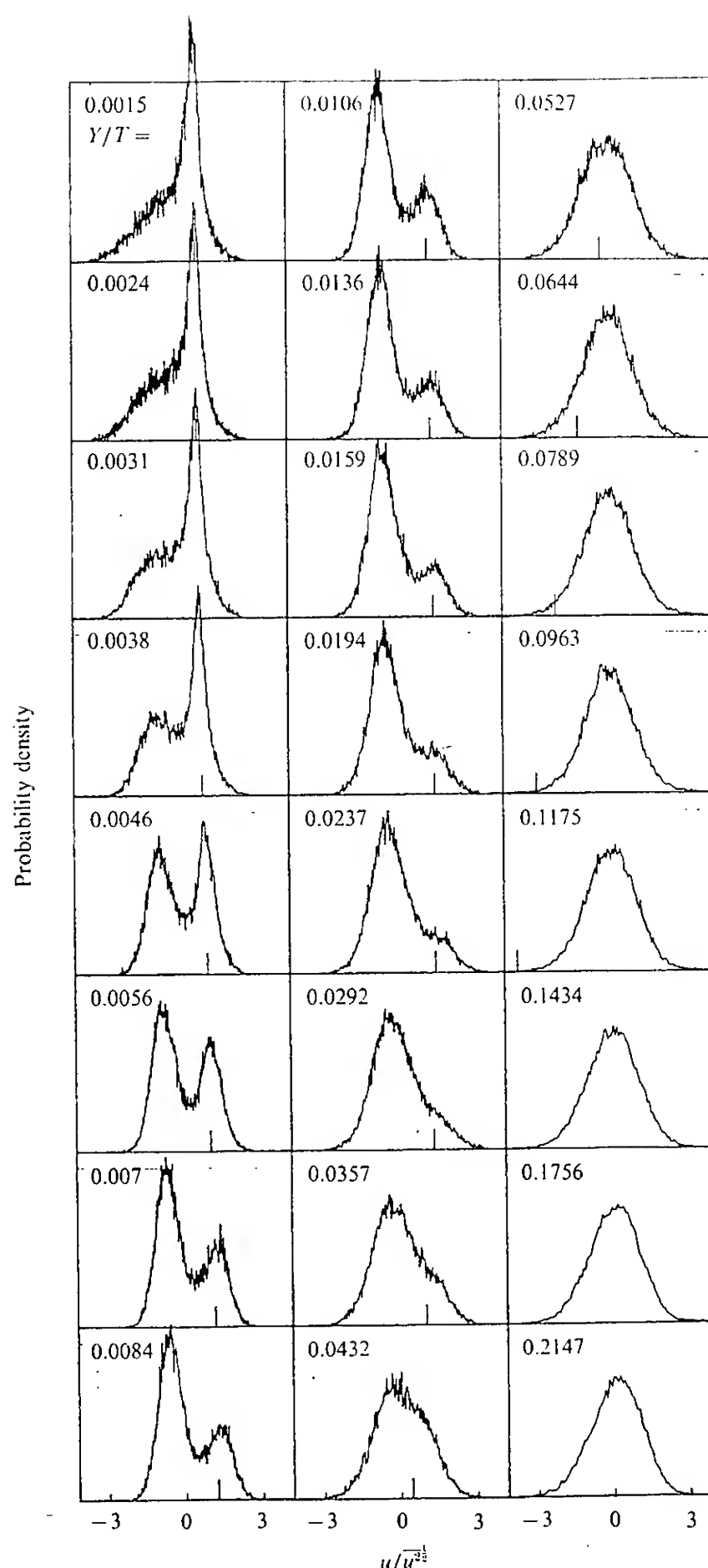
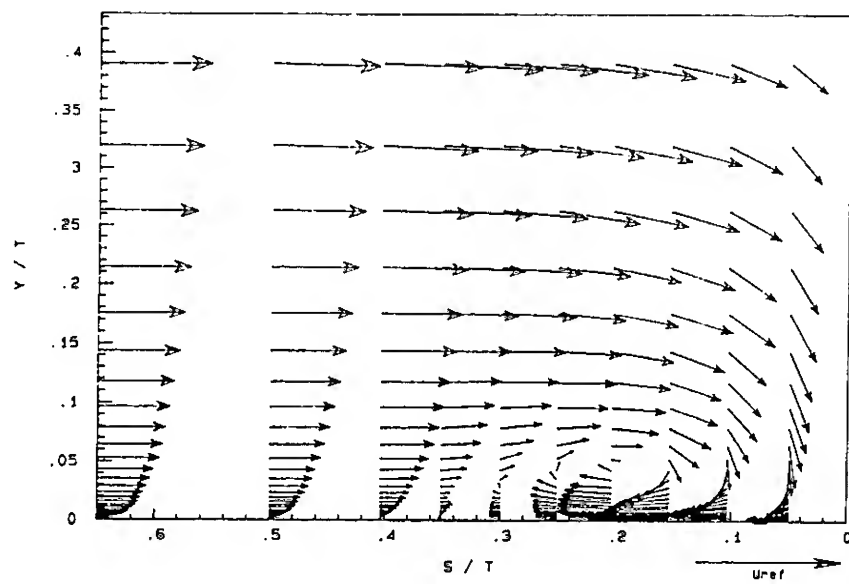


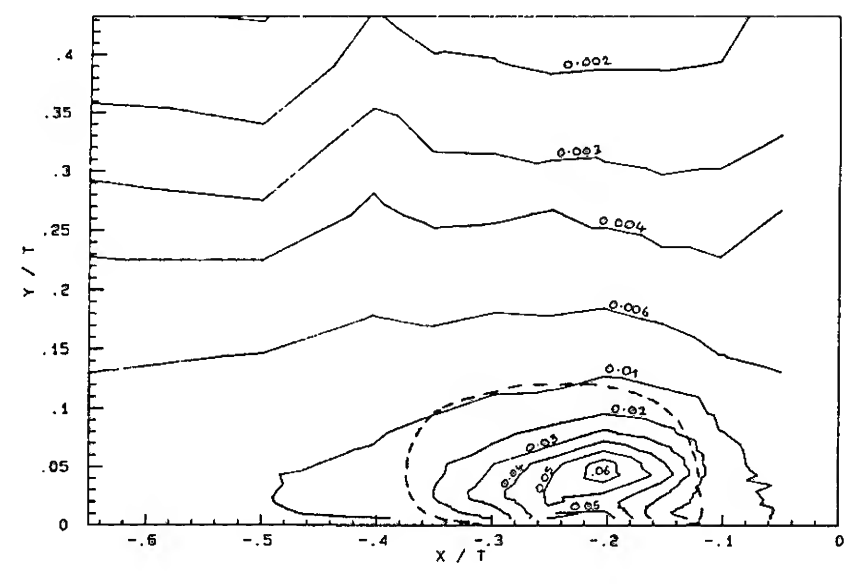
Figure 5. Histograms of U-component velocity fluctuations measured at  $X/T = -.2$  in plane 1.

the wall the centerline of the vortex fairly closely follows the line of low shear, see figure 2.) In addition mean secondary flow velocities fall by a factor of about 2 between planes 1 and 5 (figure 3).

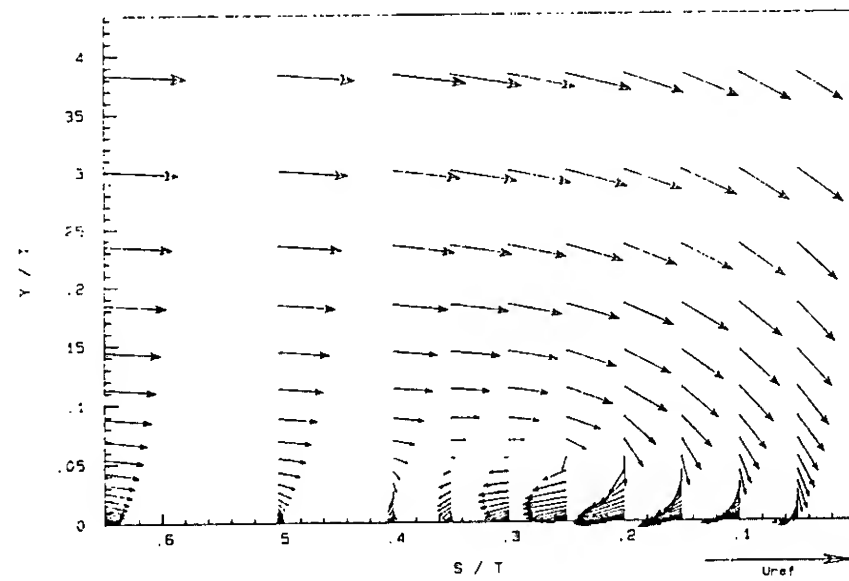
Downstream of the maximum thickness this flow is subjected to an adverse pressure gradient (figure 2) that appears to cause rapid growth in the vortex and a dissipation of the bimodal unsteadiness. (Note the change in scales between different parts of figures 3 and 4.) Bimodal histograms were not observed in planes 8 and 10 and peak turbulence kinetic energies are much lower here than upstream. Secondary-flow velocities, which are also reduced in the adverse pressure gradient, become much more difficult to



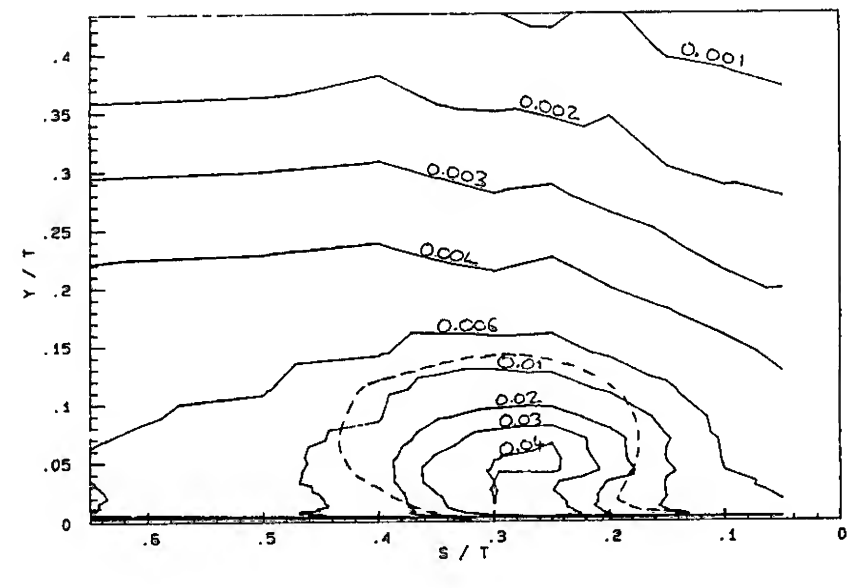
(a) Plane 1



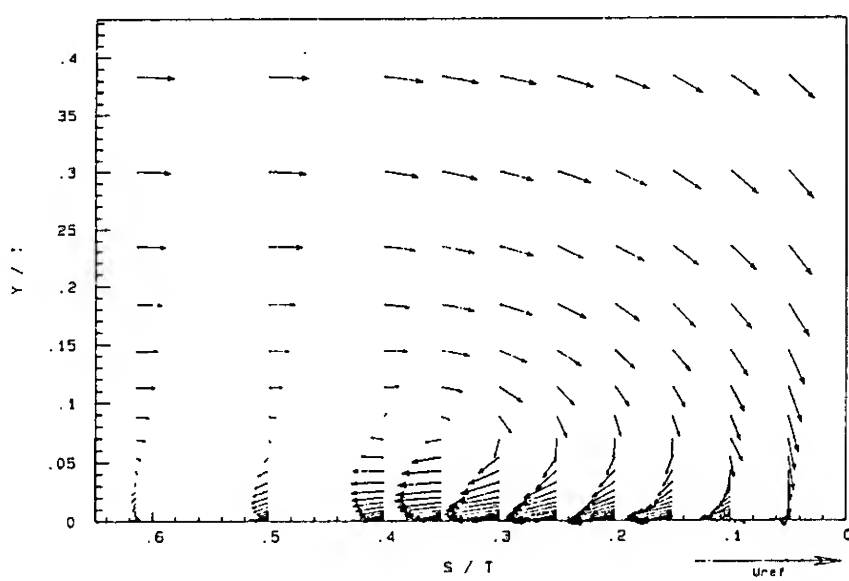
(a) Plane 1



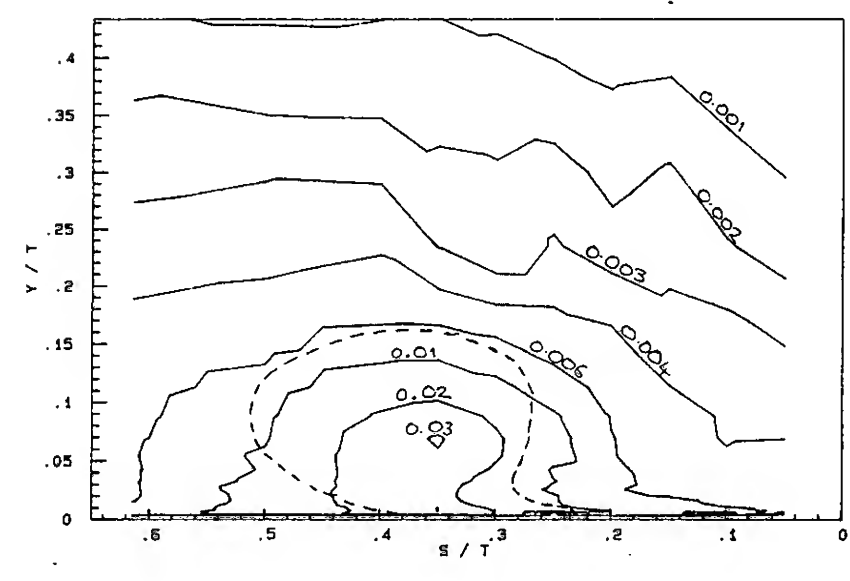
(b) Plane 3



(b) Plane 3



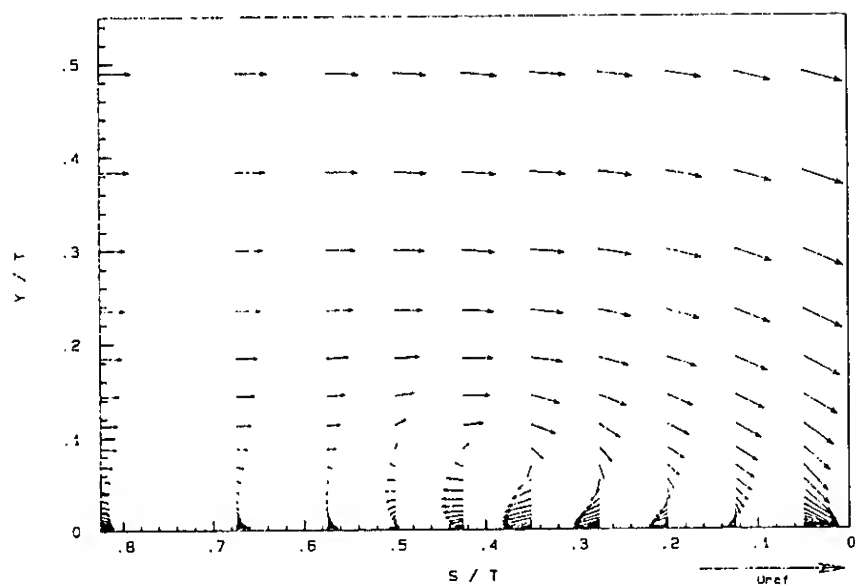
(c) Plane 4



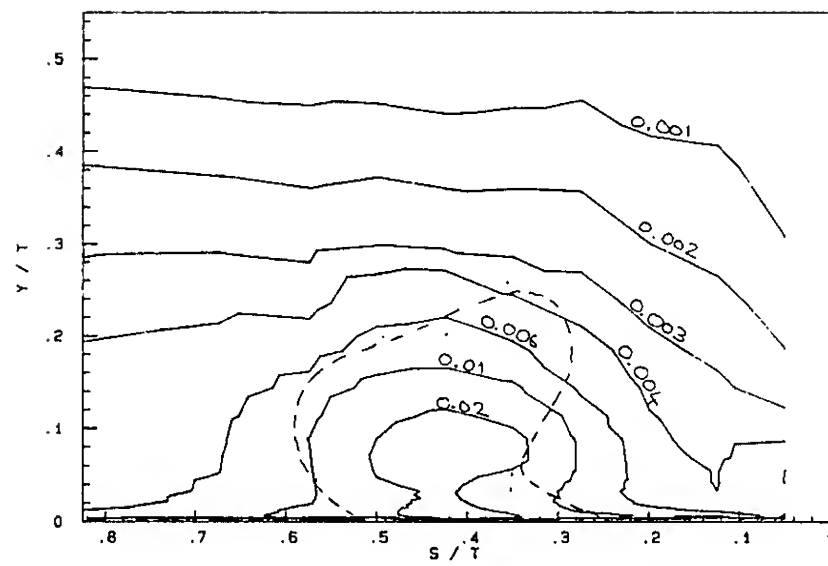
(c) Plane 4

Figure 3. Mean secondary flow field generated by the vortex.

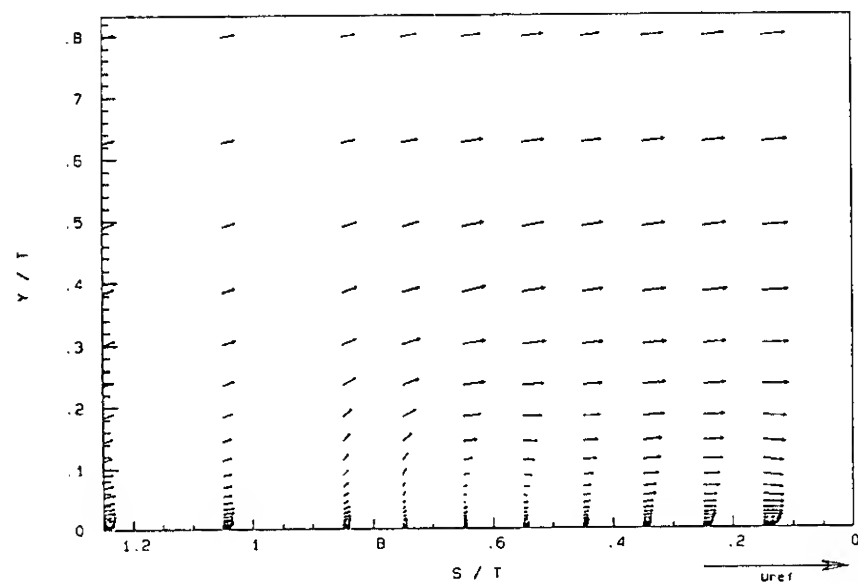
Figure 4. Contours of turbulence kinetic energy  $k/U_{ref}^2$  in the vicinity of the vortex. Dotted lines enclose the regions in which bimodal histograms are observed



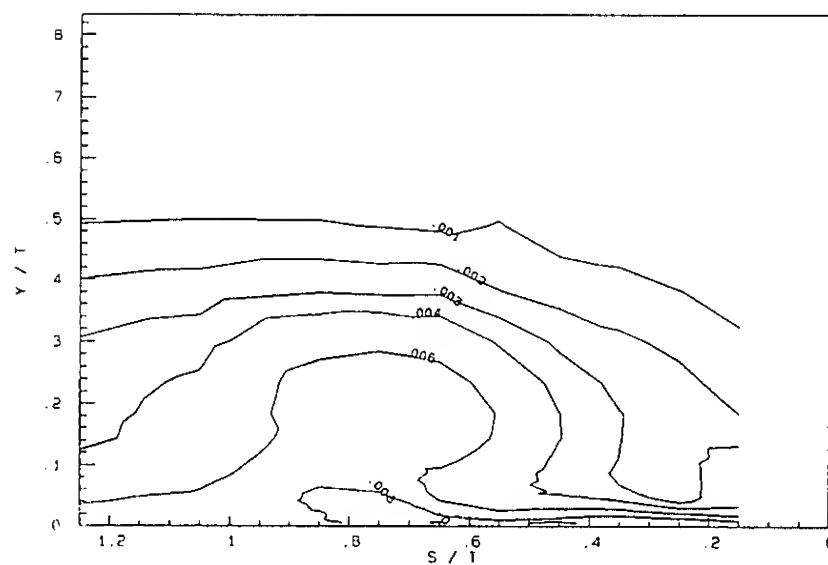
(d) Plane 5



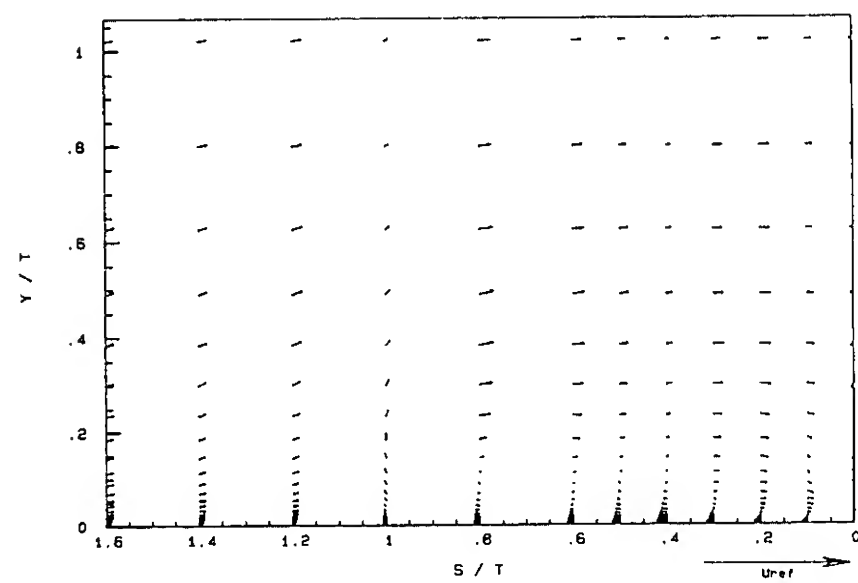
(d) Plane 5



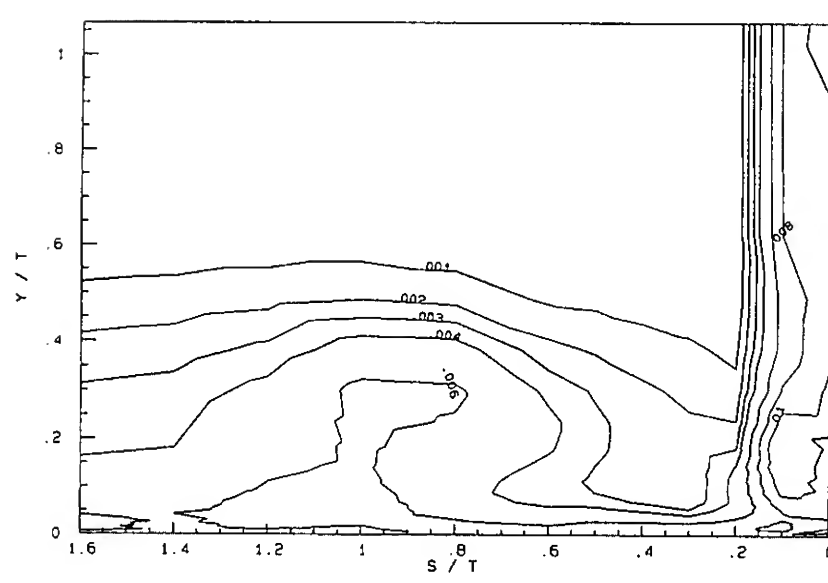
(e) Plane 8



(e) Plane 8



(f) Plane 10



(f) Plane 10

Figure 3. Mean secondary flow field generated by the vortex.

Figure 4. Contours of turbulence kinetic energy  $k/U_{ref}^2$  in the vicinity of the vortex. Dotted lines enclose the regions in which bimodal histograms are observed



distinguish from the rest of the mean-velocity field (figures 3(e) and (f)). Despite these changes the region between the vortex and the wing remains one of low turbulence shear-stresses because of the free-stream fluid entrained here by the vortex.

Figures 3 and 4 represent only a fraction of the mean-velocity and turbulence information we have collected. All mean-velocity and Reynolds stress components, some triple products and histograms of fluctuations in all three components have been measured at over 1400 points in this flow. The quantity of experimental data and the variety of turbulence structure in this flow make it, in our opinion, ideal for testing the generality and therefore usefulness of turbulence models.

## EVALUATION OF TURBULENCE MODELS

### General Remarks

Before evaluating the validity of turbulence models it is appropriate to discuss the relationship between the turbulent shear stress and velocity gradient directions since many models use or imply such a relationship. The shear-stress and velocity-gradient vectors are defined as having components  $-\overline{uv}$ ,  $-\overline{vw}$  and  $\partial U/\partial Y$ ,  $\partial W/\partial Y$  in the X and Z directions respectively. Their directions are given by the angles,

$$\alpha_t = \tan^{-1}\left(\frac{-\overline{vw}}{-\overline{uv}}\right) \quad \text{and} \quad \alpha_g = \tan^{-1}\left(\frac{\partial W/\partial Y}{\partial U/\partial Y}\right) \quad (1)$$

Most often the shear-stress and velocity gradient angles are assumed to be the same, i.e.

$$\frac{-\overline{vw}}{-\overline{uv}} = \frac{\partial W/\partial Y}{\partial U/\partial Y} \quad \text{or} \quad \frac{-\overline{uv}}{\partial U/\partial Y} = \frac{-\overline{vw}}{\partial W/\partial Y} \quad (2)$$

As shown this implies that the streamwise and cross-flow eddy viscosities are the same. Although this is ideal for converting turbulence models designed for two-dimensional flows to three dimensions, it is not supported by the present or past experiments (see Johnston (1970), van den Berg and Elsenaar (1972), Fernholz (1981) and others). Figure 6 shows a plot of spanwise vs. streamwise eddy viscosity for all points inside the boundary layer in planes 3 through 10. Points outside the line of separation, where the direct effects of the horseshoe vortex and its bimodal unsteadiness are much smaller, are plotted with different symbols to those inside. In neither region does there appear to be any significant correlation between these two parameters.

A possible improvement has been suggested by Rotta (1977) who derives an alternative relationship between the eddy viscosities using the transport equations for the shear stresses approximated for thin shear layers,

$$\frac{D(-\overline{uv})}{Dt} = -\overline{v^2} \frac{\partial U}{\partial Y} - \frac{p'}{\rho} \left( \frac{\partial u}{\partial Y} + \frac{\partial v}{\partial X} \right) + \frac{\partial}{\partial y} \left( \frac{p'u}{\rho} + \overline{uv^2} \right) \quad (3)$$

$$\frac{D(-\overline{vw})}{Dt} = -\overline{v^2} \frac{\partial W}{\partial Y} - \frac{p'}{\rho} \left( \frac{\partial w}{\partial Y} + \frac{\partial v}{\partial Z} \right) + \frac{\partial}{\partial y} \left( \frac{p'w}{\rho} + \overline{wv^2} \right) \quad (4)$$

The terms from left to right represent convection, production, pressure strain and diffusion. By substituting the Poisson equation for the fluctuating pressure  $p'$  it can be shown that the pressure strain is composed of two terms, the first  $\Phi_1$  is associated with the interaction of the mean strain and fluctuating velocities and the second  $\Phi_2$  with the interaction of the fluctuating velocities alone.  $\Phi_2$  is usually

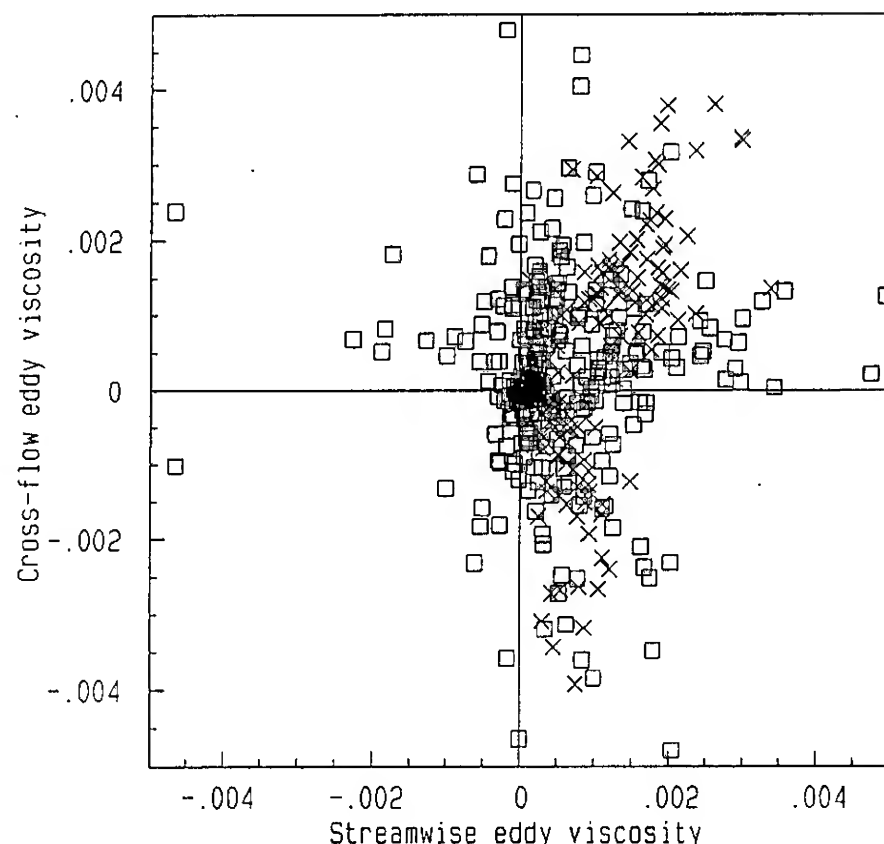


Figure 6. Spanwise vs. streamwise eddy viscosity in local mean flow coordinates for all measurement points inside the boundary layer ( $\sqrt{u^2}/U > 5\%$ ). Squares represent points inside the line of separation.

approximated by the shear stress itself multiplied by a factor related to the turbulence kinetic energy (see Rodi (1984)), that factor being the same in both equations. Rotta approximated  $\Phi_1$  using the Poisson equation for the pressure fluctuation  $p'$  and by assuming local symmetry in the turbulence structure. Neglecting convection and diffusion, which can be shown to be higher order terms for thin shear layers, and dividing equation (2) by equation (1), he then obtained the expression,

$$\tan(\alpha_t - \alpha) = T \tan(\alpha_g - \alpha) \quad (5)$$

or  $\frac{-\overline{vw_s}}{\partial W_s/\partial Y} = T \frac{-\overline{uv_s}}{\partial U_s/\partial Y}$

i.e. the cross-flow eddy viscosity is an empirical constant  $T$  times the spanwise eddy viscosity, in local flow coordinates. Unfortunately, as can be seen from figure 6 this equation is no more valid than equation (2) in the present flow. This result is confirmed by figure 7 in which values of  $T$  deduced from these measurements are plotted together as a histogram. This shows a large spread with  $T$  varying over a range of at least  $\pm 2$ .

We have tested a number of other hypothetical relationships between the shear-stress and velocity gradient angles also without success. These have included a relationship between  $\alpha_t - \alpha_g$  and the local cross-flow velocity  $W_t/U_e$ , one between the spanwise and streamwise eddy viscosities, and one between  $\alpha_t$  and  $\alpha_g$  based on van den Berg's (1982) hypothesis.

There are two principle reasons for the failure of the above concepts. The first becomes apparent if we transform the problem to coordinates based on the direction of the local mean velocity gradient vector (subscript 'g'). In this system the cross-flow shear stress exactly represents the lag or lead of the angle of the shear stress vector over that of the velocity gradient vector, i.e.

$$\frac{-\overline{vw_g}}{-\overline{uv_g}} = \tan(\alpha_t - \alpha_g) \quad (6)$$

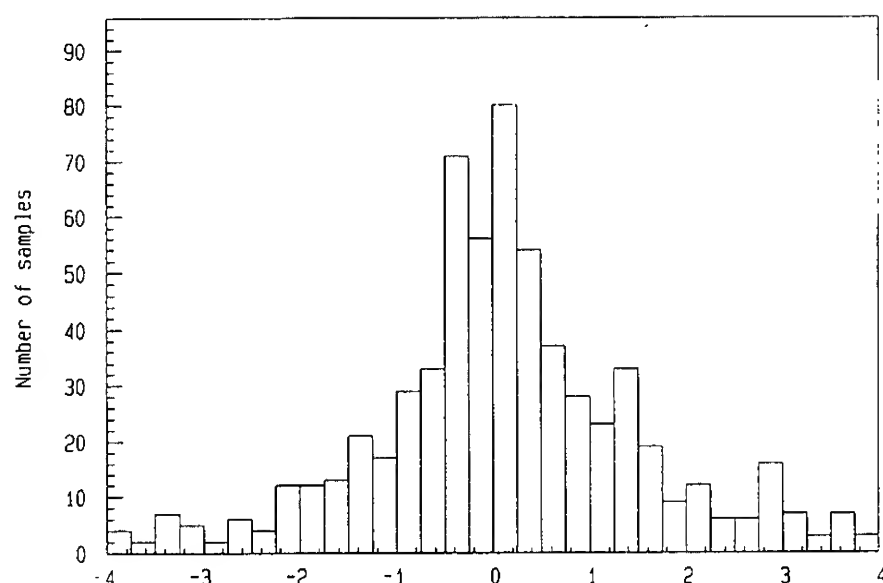


Figure 7. Histogram of values of Rotta's T parameter compiled from all-measurement points inside the boundary layer ( $\sqrt{u^2}/U > 5\%$ ).

Also in this system, however, the transport equation for the cross-flow stress (equation (4)) loses the term  $v^2 \partial W / \partial Y$  since by definition  $\partial W / \partial Y$  is zero. The cross-flow stress and the lag of the shear-stress vector are therefore determined entirely by the unknown pressure strain and the neglected convection and diffusion terms which, in the absence of  $v^2 \partial W / \partial Y$  are likely to be important. The second reason for the failure is the way in which the pressure strain terms are usually modelled. It is simple to show that (without the boundary-layer approximation) the pressure strain and pressure diffusion can be combined into a single term with the form,

$$-v \frac{\partial p'}{\partial X} + u \frac{\partial p'}{\partial Y} \quad (7)$$

in the  $\overline{uv}$  transport equation, and

$$-v \frac{\partial p'}{\partial Z} + w \frac{\partial p'}{\partial Y} \quad (8)$$

in the  $\overline{vw}$  transport equation. These terms obviously cannot be modelled by substituting for  $\partial p' / \partial X$ ,  $\partial p' / \partial Y$  and  $\partial p' / \partial Z$  from the Navier-Stokes equations or an approximation to them (as done by van den Berg (1982)) since this will lead to an identity or an expression of the error in the approximation. By the same argument, substituting for  $p'$  using the Poisson equation (which is just the Navier-Stokes rearranged) or an approximation (as is done in effect by Rotta (1977)) must also eventually lead to an identity or an expression of the error in the approximation. Neither of these approaches are therefore valid.

The pressure strain terms can in general only be modelled by substituting different moments of Navier-Stokes equations and/or by using information derived from experiments. In our opinion only the latter approach is likely to prove successful since higher moments of the Navier-Stokes will only introduce more unknowns. Careful experiments in which the pressure strain terms are (presumably) measured by difference are therefore needed.

#### Turbulence models

In this section the assumptions of several prescribed eddy viscosity models, the  $k-\epsilon$  model, an algebraic-stress model and Bradshaw's (1971) model are tested. For each model, predictions of the magnitude of the shear-stress vector from the

measured mean-velocity or turbulence kinetic energy distributions are compared with measurements. For models that use the eddy-viscosity  $\nu_t$  the shear-stress magnitude is assumed to be given by

$$\frac{|\tau|}{\rho} = (\overline{uv^2} + \overline{vw^2})^{\frac{1}{2}} = \nu_t \left[ \left( \frac{\partial U}{\partial Y} \right)^2 + \left( \frac{\partial W}{\partial Y} \right)^2 \right]^{\frac{1}{2}} \quad (9)$$

i.e. the cross-flow and streamwise eddy viscosities are assumed equal. Although the results of the previous section show that this is not the case, there appears to be no better alternative. Since skin-friction data are not yet available for the present flow the wall treatments employed by most of the models are not tested and are ignored in the following discussion. Comparisons with experimental data do not include points in the near-wall region  $Y/T < .02$  ( $y^+$  less than about 120).

The authors concede that several of the models examined here were never intended for use in flows as complex as this one. However, they, or models like them, are often used in complex flows. It is therefore important that their limitations be known.

In the first and simplest turbulence model considered here the eddy viscosity is prescribed as a function of  $Y$  entirely in terms of mixing length ' $l$ ',

$$\begin{aligned} l &= \kappa Y & Y/\delta < \lambda/\kappa \\ l &= \lambda \delta & Y/\delta \geq \lambda/\kappa \end{aligned} \quad (10)$$

where the eddy viscosity is given by

$$\nu_t = l^2 \left[ \left( \frac{\partial U}{\partial Y} \right)^2 + \left( \frac{\partial W}{\partial Y} \right)^2 \right]^{\frac{1}{2}} \quad (11)$$

$\lambda$  and  $\kappa$  are empirical constants and  $\delta$  is the boundary-layer thickness. From two-dimensional test calculations Patankar and Spalding (1970) suggest  $\lambda = .09$  and  $\kappa$  (the von Karman constant) = .435.

The Cebeci-Smith and Johnston-King turbulence models, described for three-dimensional flows by Abid (1988), are variations on this basic form. The Cebeci-Smith model is described by the relations

$$\nu_t = \nu_{t_0} (1 - \exp(-\nu_{t_i}/\nu_{t_0})) \quad (12)$$

where

$$\begin{aligned} \nu_{t_i} &= l^2 \left[ \left( \frac{\partial U}{\partial Y} \right)^2 + \left( \frac{\partial W}{\partial Y} \right)^2 \right]^{\frac{1}{2}} \\ l &= \kappa Y, & \kappa &= .4 \end{aligned} \quad (13)$$

and

$$\nu_{t_0} = 0.0168 \gamma_k \int_0^\delta (Q_0 - Q) dy \quad (14)$$

$$\gamma_k = [1 + 5.5 \left( \frac{Y}{\delta} \right)^6]^{-1} \quad (15)$$

$$Q = \sqrt{U^2 + W^2} : Q_0 = Q|_{Y=0} \quad (16)$$

the principal difference with the basic model being the explicit prescription of the eddy viscosity in the outer region in terms of the Klebanoff intermittency function  $\gamma_k$  and the use of a smoothing function between the inner and outer regions. The Johnston-King model uses the same smoothing function but defines

$$v_{t_i} = l \left( \frac{\tau_m}{\rho} \right)^{\frac{1}{2}} \quad (17)$$

$$l = \kappa Y, \quad \kappa = .4$$

and

$$v_{t_o} = 0.0168 \sigma \gamma_k \int_0^{\delta} (\rho_o - \rho) dy \quad (18)$$

where

$$\frac{\tau_m}{\rho} = (\overline{uv^2} + \overline{vw^2})^{\frac{1}{2}} \quad (19)$$

the maximum turbulence shear stress in the profile. The Johnson-King model was originally designed for two-dimensional adverse pressure gradient and separated boundary layers in which the maximum shear stress appears to be an appropriate scaling parameter. In the turbulence model  $\tau_m$  is determined from a differential transport equation. The parameter  $\sigma$  is chosen so that the equation

$$\frac{\tau_m}{\rho} = v_t \left[ \left( \frac{\partial U}{\partial Y} \right)^2 + \left( \frac{\partial W}{\partial Y} \right)^2 \right]^{\frac{1}{2}} \quad (20)$$

is satisfied at the location of maximum shear stress in each profile. This requires an iterative procedure.

The above three models were used to calculate the turbulence shear-stress magnitude from the measured mean-velocity field. In the case of the Johnson-King model the maximum shear stress and its location were also provided from the experimental data.

The  $k$ - $\epsilon$  model is one of the most widely used in calculating two-and three-dimensional turbulent flows. Coupled with the wall treatment of Chen and Patel (1988) it has been used by Deng (1990) to calculate the flow past a wing-body junction very similar to that studied in the present experiments. The  $k$ - $\epsilon$  model defines the eddy viscosity in terms of the turbulence kinetic energy  $k$  and the dissipation  $\epsilon$ ,

$$v_t = C_\mu \frac{k^2}{\epsilon} \quad (21)$$

$k$  and  $\epsilon$  are determined from approximate transport equations (see Rodi (1984) or Abid and Schmitt (1984)),

$$\frac{Dk}{Dt} = -\overline{uv} \frac{\partial U}{\partial Y} - \overline{vw} \frac{\partial W}{\partial Y} - \epsilon + \frac{\partial}{\partial Y} \left[ \left( v + \frac{v_t}{\sigma_k} \right) \frac{\partial k}{\partial Y} \right] \quad (22)$$

$$\frac{D\epsilon}{Dt} = -C_{\epsilon_1} \frac{\epsilon}{k} (\overline{uv} \frac{\partial U}{\partial Y} + \overline{vw} \frac{\partial W}{\partial Y}) - C_{\epsilon_2} \frac{\epsilon^2}{k} + \frac{\partial}{\partial Y} \left[ \left( v + \frac{v_t}{\sigma_\epsilon} \right) \frac{\partial \epsilon}{\partial Y} \right] \quad (23)$$

The empirical constants are usually given the values,

$$C_\mu = 0.09, \quad \sigma_k = 1, \quad C_{\epsilon_1} = 1.57, \quad C_{\epsilon_2} = 2.0, \quad \sigma_\epsilon = 1.3 \quad (24)$$

The  $\epsilon$  equation could not be tested using the present measurements. The  $k$  equation was tested by substituting the eddy-viscosity and the velocity gradients for the Reynolds stresses and substituting equation (21) for the dissipation.

This gives,

$$\frac{Dk}{Dt} = v_t \left[ \left( \frac{\partial U}{\partial Y} \right)^2 + \left( \frac{\partial W}{\partial Y} \right)^2 \right] - \frac{C_\mu k^2}{v_t} + \frac{\partial}{\partial Y} \left[ \left( v + \frac{v_t}{\sigma_k} \right) \frac{\partial k}{\partial Y} \right] \quad (25)$$

Using the measured distributions of  $k$  and the mean-velocity gradients this equation was solved iteratively for  $v_t$ . Initial and boundary values for  $v_t$  required for this calculation were determined from the measurements. Convection of  $k$  normal to the LDV measurement planes was ignored in this calculation since it could not be deduced from the measurements. This term was almost certainly negligible at most points.

The algebraic stress model uses transport equations for  $k$  and  $\epsilon$  similar to those above. However, instead of relating the turbulent stresses to  $k$  and  $\epsilon$  through an eddy viscosity, algebraic equations for the individual stresses are used. These are derived from the full (differential) stress transport equations by assuming, among other things, that the convection and diffusion of the individual stresses is proportional to that of  $k$ . The algebraic stress equations, written in standard tensor notation in their full form (Rodi (1984), Abid and Schmitt (1984)), are

$$\overline{u_i u_j} = \frac{2}{3} \delta_{ij} k + \frac{(1-\gamma) \left( \frac{P_{ij}}{\epsilon} - \frac{2}{3} \delta_{ij} \frac{P}{\epsilon} \right) + \Phi_{ijw}/\epsilon}{C_1 + P/\epsilon - 1} k \quad (26)$$

where  $P_{ij}$  is the production of  $\overline{u_i u_j}$ ,  $P$  is the production of  $k$ ,  $\delta_{ij}$  is 1 if  $i=j$  and zero otherwise, and  $\Phi_{ijw}$  is a component of the pressure-strain correlation that accounts for wall proximity effects.  $\Phi_{ijw}$  is an algebraic function of only  $k$ ,  $\epsilon$ ,  $Y$  and the stresses themselves (see Abid and Schmitt (1984)). The following values for the empirical constants, suggested by Abid and Schmitt (1984) and Launder (1982), were used

$$\gamma = 0.55, \quad C_1 = 2.2, \quad C'_1 = 0.5, \quad C'_2 = 0.3 \quad (27)$$

$C'_1$  and  $C'_2$  appearing in the equations for  $\Phi_{ijw}$ . Equation (26), together with the definition of  $k$ , give seven algebraic equations for the six Reynolds stresses and  $\epsilon$  in terms of  $k$  and the mean-velocity field. If the latter are provided from experimental data then the stresses and  $\epsilon$  can be deduced. This requires an iterative Newton-Raphson procedure since the equations are non-linear. Combining  $uv$  and  $vw$  then gives the magnitude of the shear stress. In performing this calculation production terms associated with gradients of  $V$  and  $W$  normal to the measurement planes were ignored since they could not be obtained from the measurements. These terms were almost certainly negligible at most points. Note that equation (26) does not involve boundary layer approximations. Without these the algebraic stress model can, at least in theory, predict a lag or lead in the angle of the turbulence shear-stress vector.

Bradshaw's (1971) turbulence model for three-dimensional boundary layers uses approximate differential transport equations for  $uv$  and  $vw$ . These are derived by analogy with the transport equation for  $k$  assuming a simple constant of proportionality between  $k$  and the shear-stress magnitude,

$$a_1 = \frac{(\overline{uv^2} + \overline{vw^2})^{\frac{1}{2}}}{2k} \quad (28)$$

By analogy with two-dimensional flows Bradshaw suggests a value of 0.15 for  $a_1$ . Bradshaw's model was tested simply by multiplying measured values of  $k$  by 0.15 to obtain estimates of the shear stress magnitude.

## Results

Results for the turbulence model calculations are presented in figures 8 and 9. Figures 8(a) through 8(i) show measured and computed contours of shear-stress magnitude in plane 8 located towards the trailing edge of the wing (figure 2). Because of space limitations detailed comparisons in other planes are not presented. However, figures 9(b) through 9(i) show, for each turbulence model, histograms of the ratio of computed to measured shear-stress magnitude compiled from data in all planes. For reference figure 9(a) shows a probable histogram of experimental error in the measured values of the shear-stress deduced from uncertainty estimates. Note that figures 9(a) through 9(g) do not contain data from close to the wall ( $Y/T < .02$ ) or from in the free stream ( $Vu^2/U < 5\%$ ).

Of the prescribed eddy-viscosity models (figures 8 and 9 (b) through (e)) the Cebeci-Smith appears to be the best. Although there are some obvious qualitative differences in the shapes of the measured and computed shear-stress contours in plane 8 (compare figures 8(a) and (d)) these do not represent large quantitative differences at most points. In other planes there are some large differences, however, as indicated by the histogram in figure 9(d). According to this histogram the r.m.s. error in predictions with the Cebeci-Smith model is about 70% while the mean error is only +3%.

Clearly the worst of these three models is the Johnson-King which produces an unrealistic shear-stress field in the vortex (figure 8(e)). This model fails because the eddy viscosity distribution it prescribes depends not just on the peak shear-stress magnitude but also, implicitly, on the distance from the wall at which it occurs. Moving across plane 8, or any other plane through the vortex, the peak jumps from the near-wall region to the center of the vortex producing a sudden and unrealistic change in the prescribed eddy-viscosity profile. There are also problems with the smoothing function used in this model, equation (12). This function requires  $v_t < v_{tj}$  at the maximum shear-stress location, a condition not always met near the center of the vortex. Note that the histogram of calculated to measured shear-stress magnitude for the Johnson-King model (figure 9(e)) is misleading since it, and the mean and r.m.s. errors stated on it, do not include many points where the computed shear-stress magnitude exceeded 4 times that measured. Also, the peak near 1 in this histogram does not necessarily represent any accuracy in the model since the maximum shear-stress magnitude and its location were provided to the model from the experimental data. The model is therefore bound to produce accurate estimates of the shear-stress magnitude at and near this point.

Although the shear-stress magnitude distributions produced by the basic mixing length model of equations (10) and (11) appear qualitatively realistic (figure 8(b)), the histogram in this case (figure 9(b)) shows large quantitative discrepancies (mean and r.m.s. errors +57% and 97% respectively). A detailed comparison with the measurements shows that most of the larger discrepancies occur in the near-wall region where the mixing length is prescribed as a linear function of  $Y$  with slope  $\kappa = 0.435$  (equation (10)). This suggests that a different value of  $\kappa$  might improve the predictions. Figures 8(c) and 9(c) show that some improvement is achieved by optimizing this constant to 0.3. The

r.m.s. error with  $\kappa = 0.3$  is still 86% however.

Unlike the above models the  $k-\epsilon$ , algebraic stress and Bradshaw's (1971) model were given the measured distribution of turbulence kinetic energy from which to calculate the shear-stress magnitude. It is surprising then that these models appear to perform little better (see figures 8 and 9 (f) through (i)).

The  $k-\epsilon$  model does not accurately reproduce the features of the shear-stress field in plane 8 (figure 8(f)), the vortex being much flatter and the point of maximum shear-stress magnitude occurring much closer to the wing than in the measurements. As indicated by the histogram (figure 9(f)) the  $k-\epsilon$  model also does poorly in the other planes, the mean and r.m.s. errors in its predictions being +58% and 83% respectively.

Bradshaw's model produces slightly better qualitative agreement in plane 8 but over estimates the shear-stress magnitude at most locations (figure 8(h)). This model seems unable to account for the low shear stress levels in the region adjacent to the wing where the vortex is bringing low-turbulence fluid down close to the wall. As shown by the histogram (figure 9(h)) the shear-stress magnitude is also over-predicted in other planes, the mean and r.m.s. errors being +63% and 72% respectively. These errors can be reduced somewhat by optimizing the value of  $a$ , (see figures 8(i) and 9(i)). A value of 0.11 seems to best suit the present data set reducing the r.m.s. error to 68%. Much of this remaining error results from over-estimation of the shear stress magnitude in the low turbulence region between the vortex and wing, which still persists.

The algebraic stress model, perhaps the best of these three, produces the most realistic shear-stress contours in plane 8 (figure 8(g)) especially away from the wall. Overall comparisons with shear-stress measurements in other planes (figure 9(g)) give mean and r.m.s. errors of +12% and 75%. Theoretically, at least, the algebraic stress model is capable of predicting leads and lags in the angle of the shear-stress vector relative to the mean-velocity gradient vector. As shown in figure 10, lag angle predictions appear much smaller than, and largely uncorrelated with, measured angles.

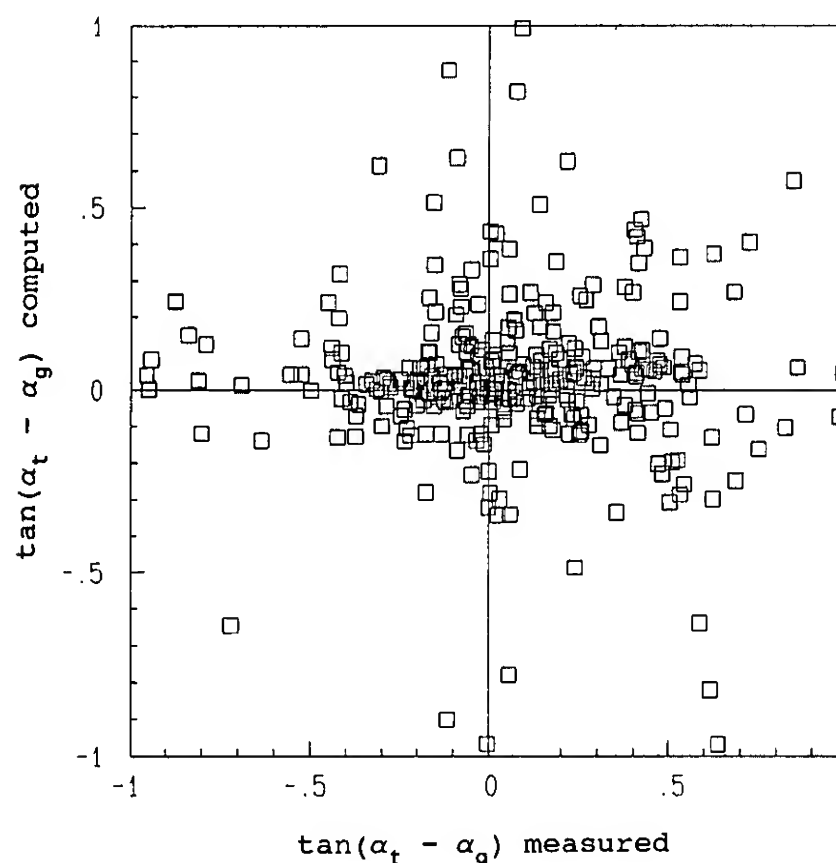
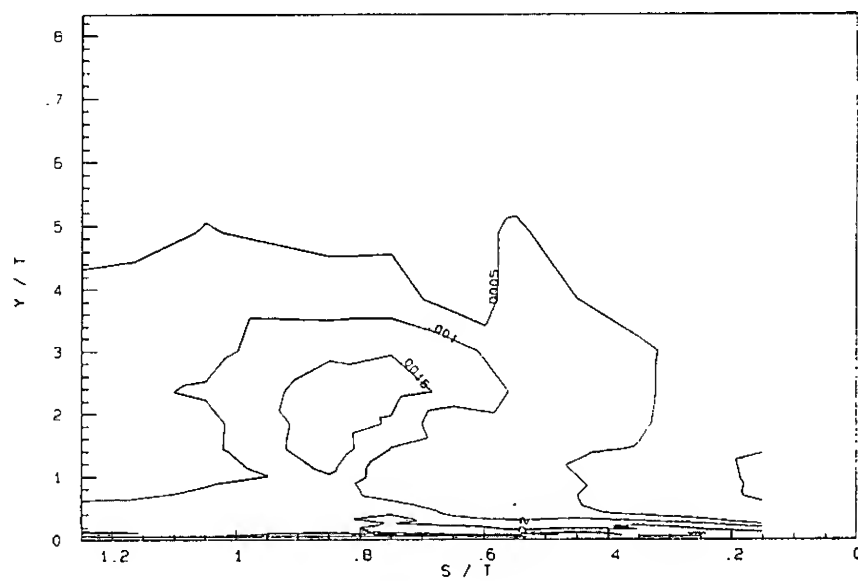
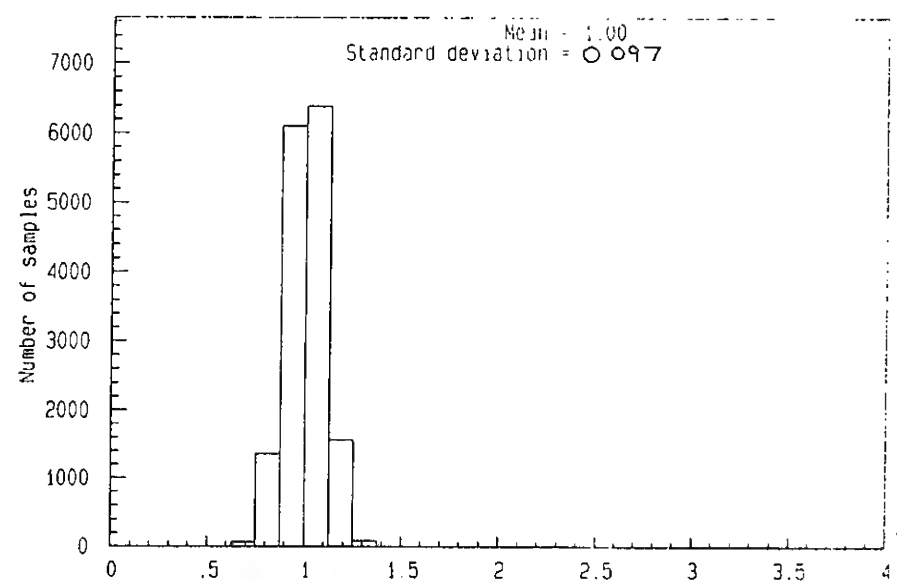


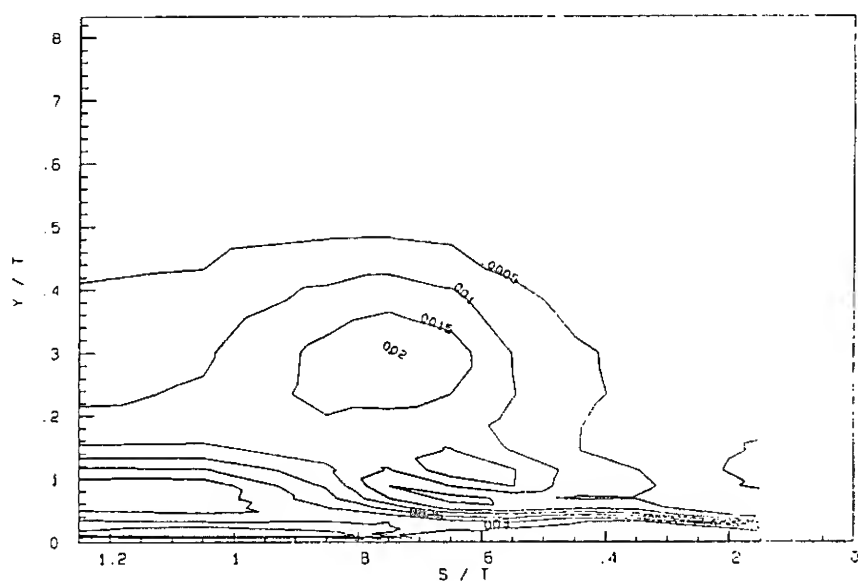
Figure 10. Comparison of angles between the turbulence shear-stress and mean-velocity gradient vectors measured and computed using the algebraic stress model.



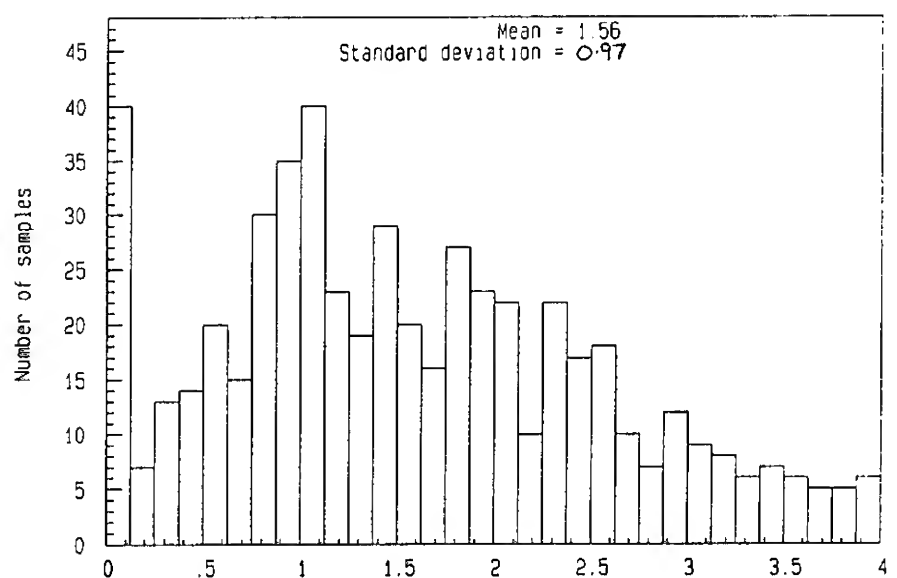
(a) Measurements



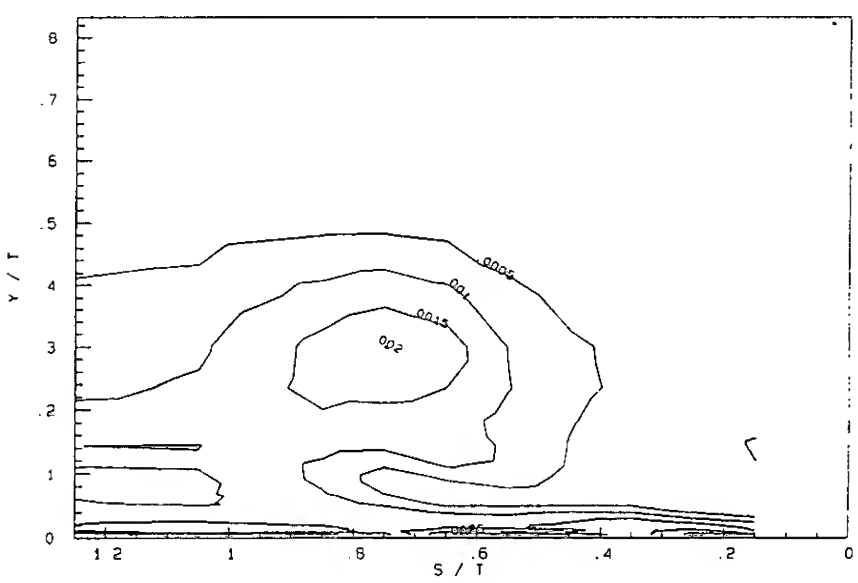
(a) Probable histogram of error in shear-stress magnitude measurements.



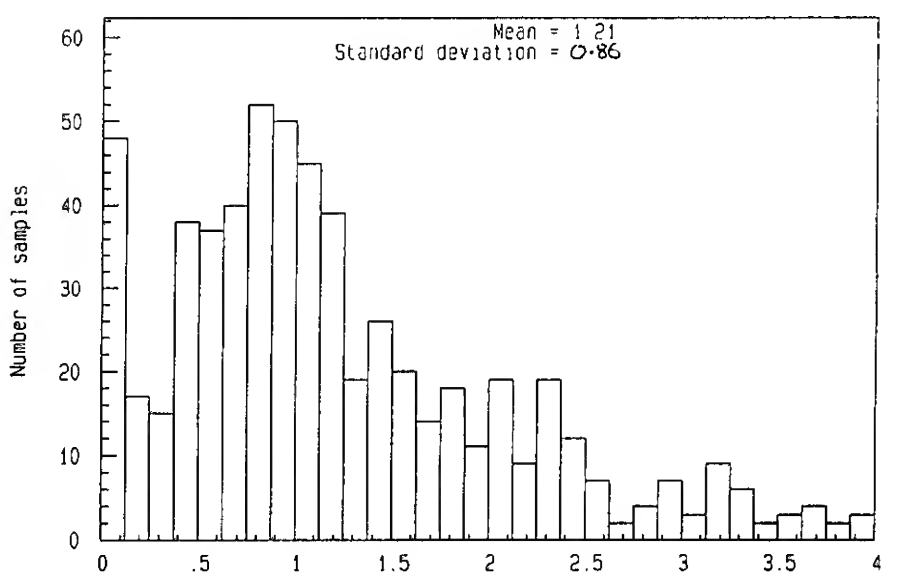
(b) Basic mixing-length model  $\kappa = .435$



(b) Basic mixing-length model  $\kappa = .435$



(c) Basic mixing-length model  $\kappa = .3$

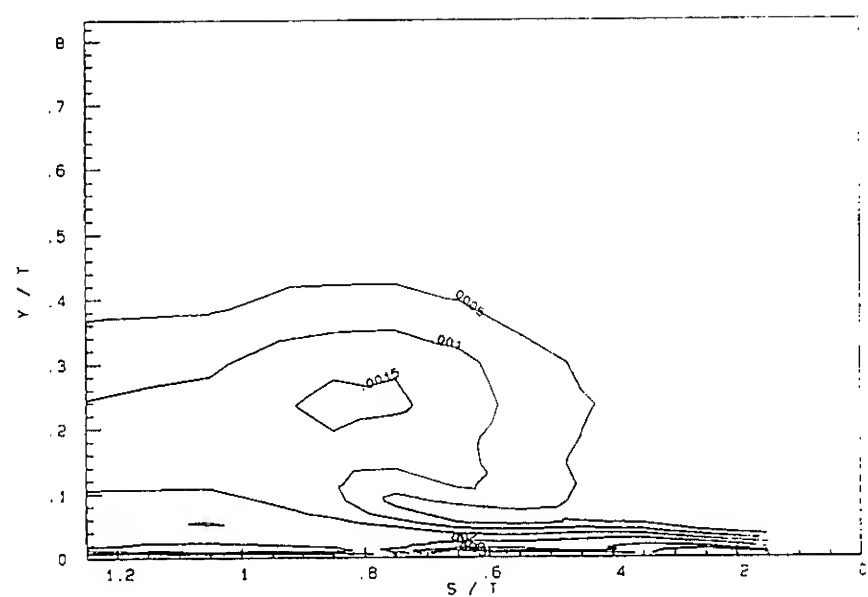


(c) Basic mixing-length model  $\kappa = .3$

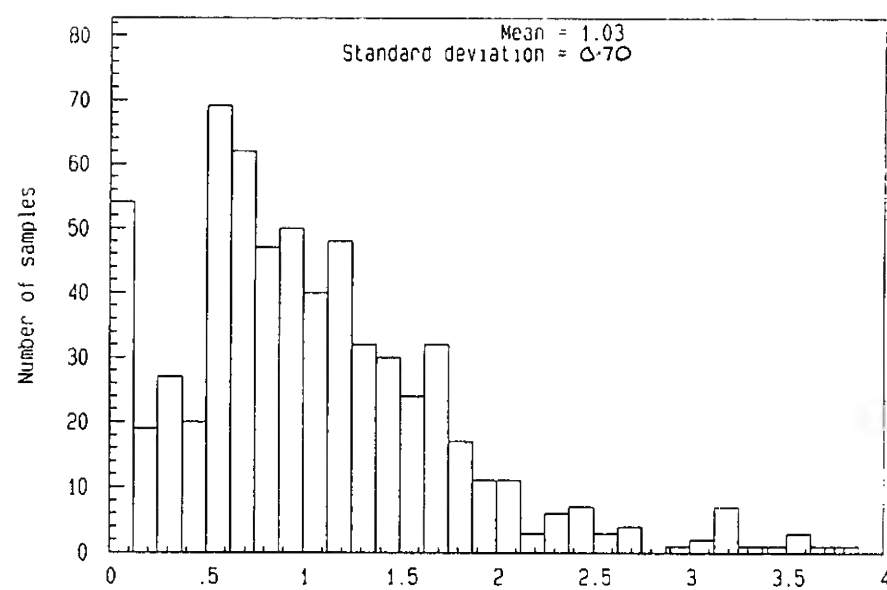
Figure 8. Contours of measured and computed turbulence shear-stress magnitude  $\sqrt{(uv^2 + vw^2)}/U_{ref}^2$  in plane 8.

Figure 9. Histograms of the ratio of computed to measured turbulence shear stress magnitude compiled from comparisons at points inside the boundary layer ( $\sqrt{vu^2}/U > 5\%$ ) but outside the near-wall region ( $Y/T > .02$ ).

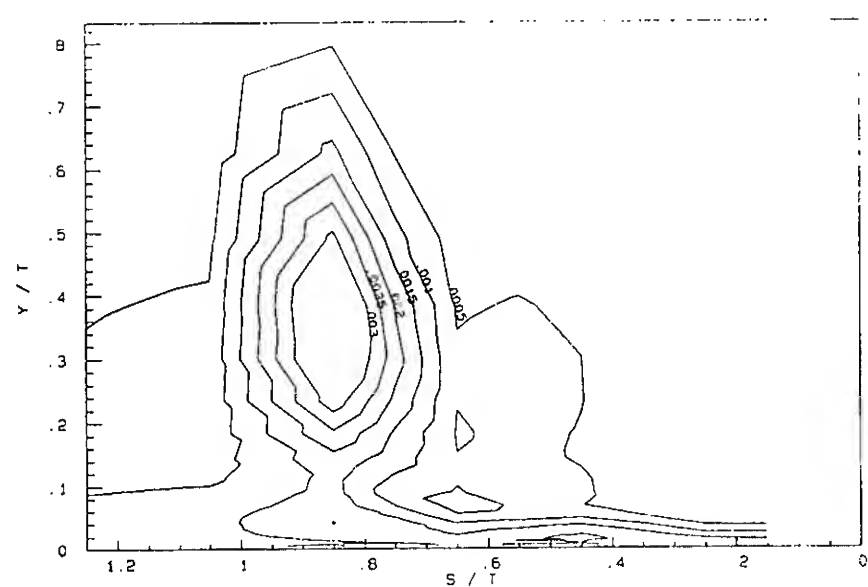




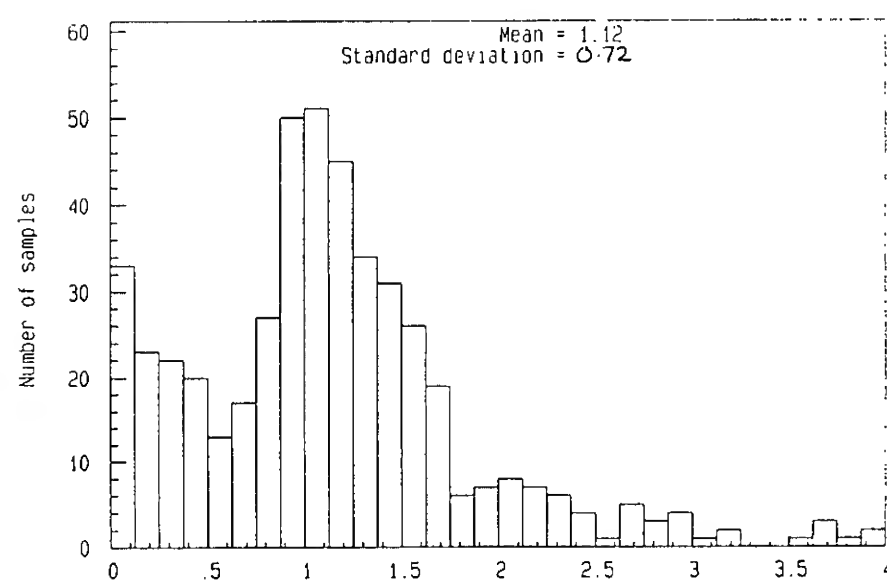
(d) Cebeci Smith model



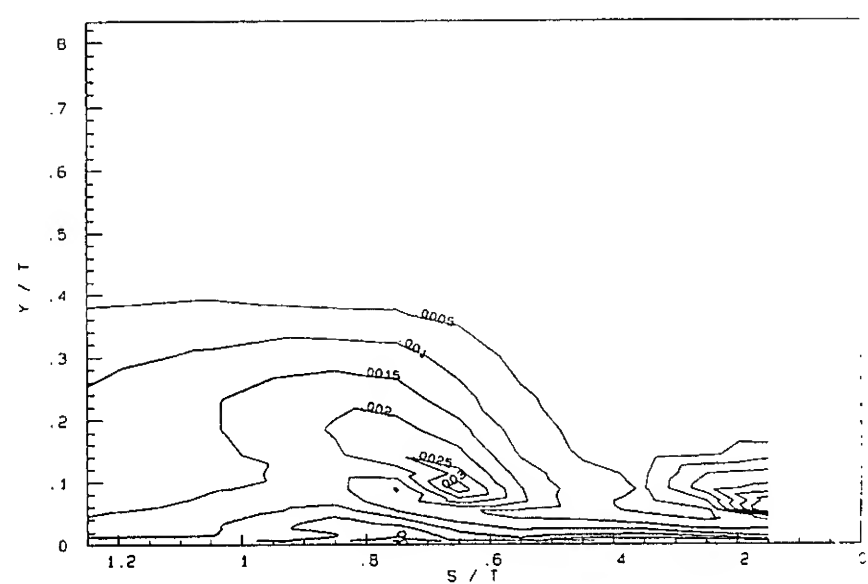
(d) Cebeci Smith model



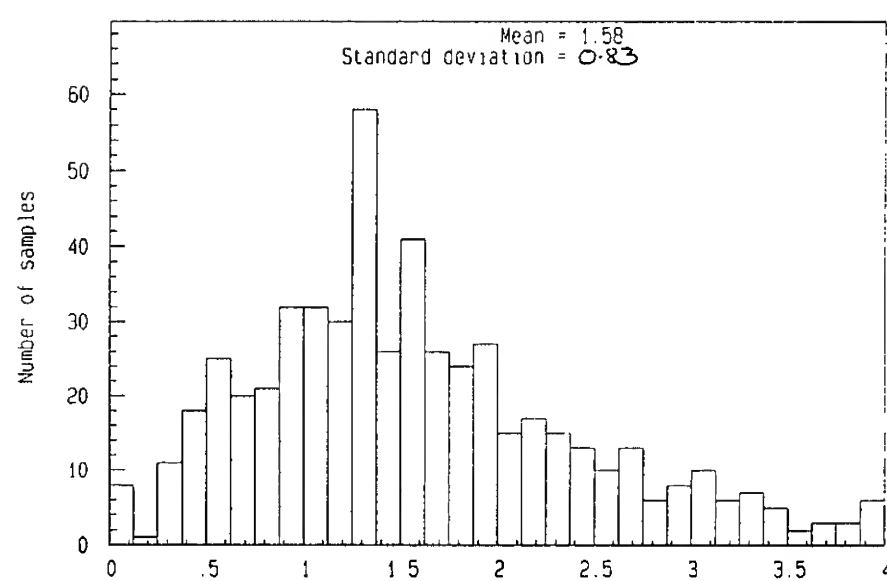
(e) Johnson-King model



(e) Johnson-King model



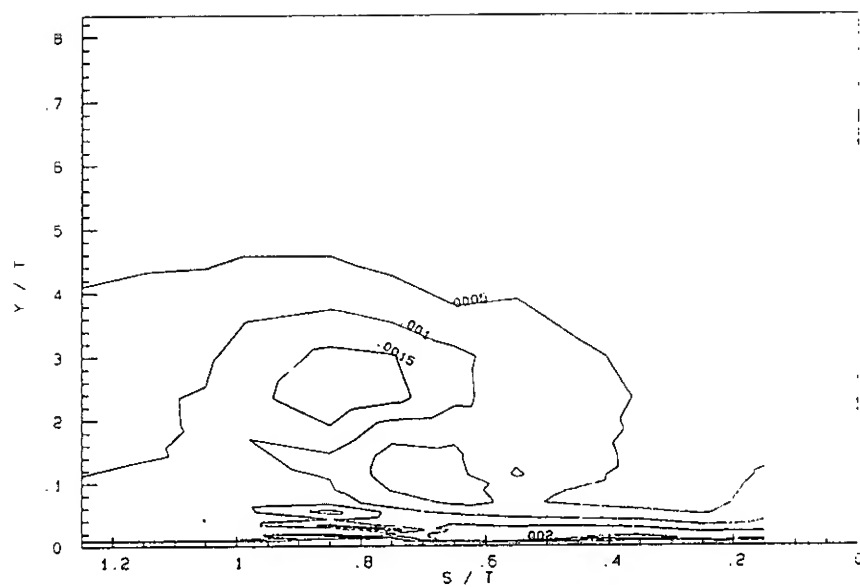
(f) k-epsilon model



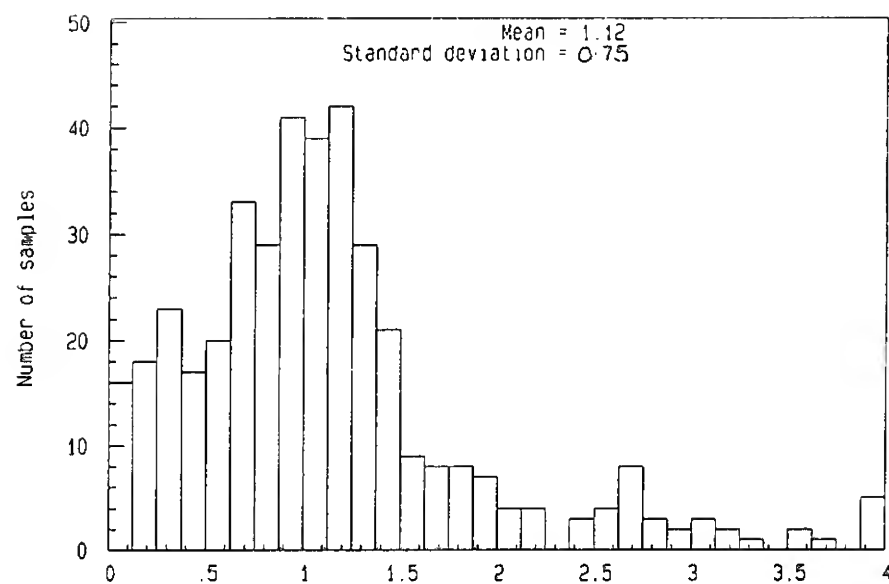
(f) k-epsilon model

Figure 8. Contours of measured and computed turbulence shear-stress magnitude  $\sqrt{(uv^2 + vw^2)}/U_{ref}^2$  in plane 8.

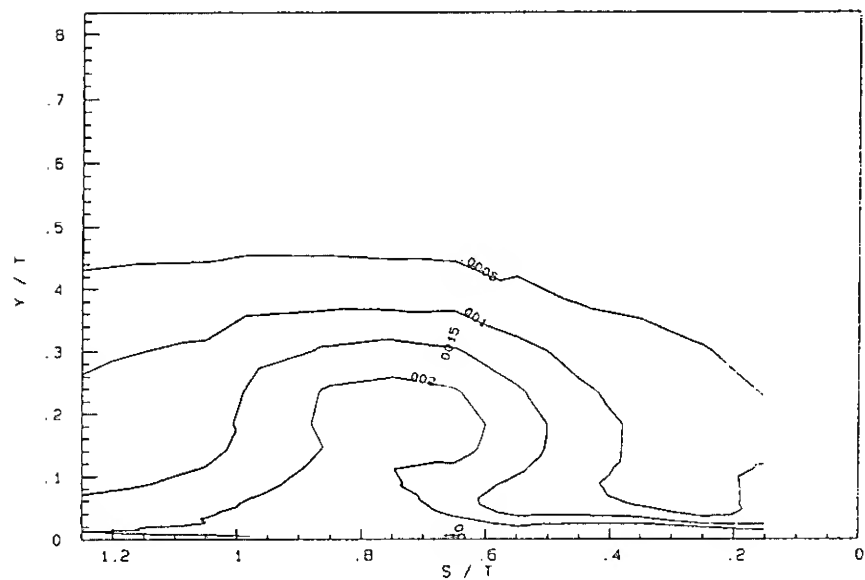
Figure 9. Histograms of the ratio of computed to measured turbulence shear stress magnitude compiled from comparisons at points inside the boundary layer ( $\sqrt{vu^2}/U > 5\%$ ) but outside the near-wall region ( $Y/T > .02$ ).



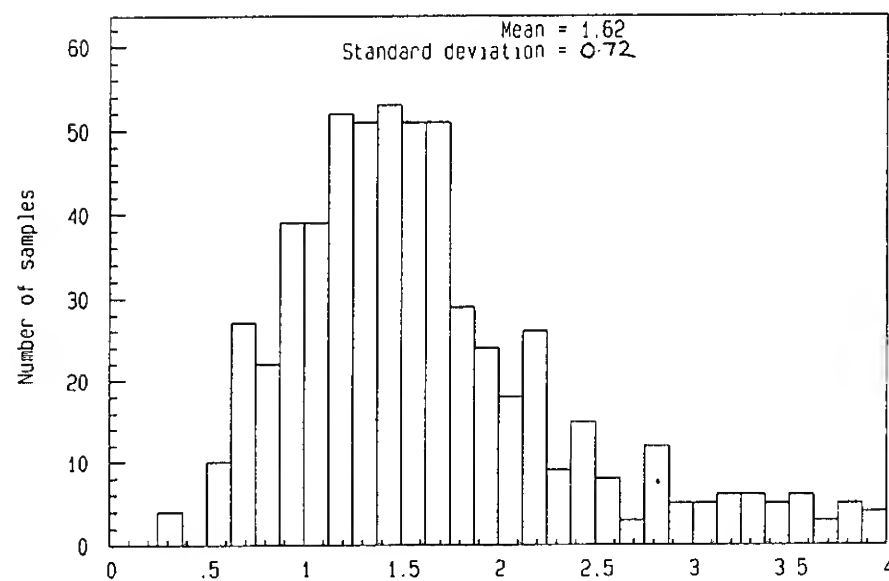
(g) Algebraic stress model



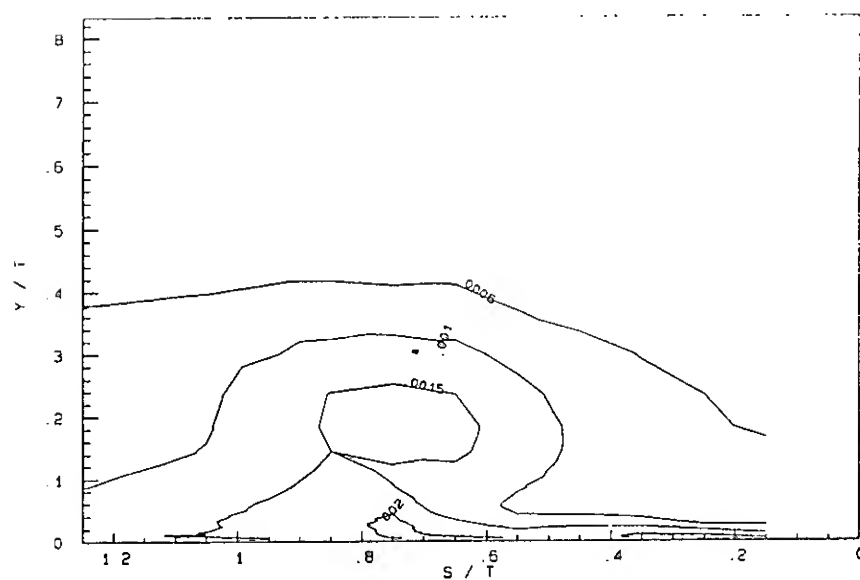
(g) Algebraic stress model



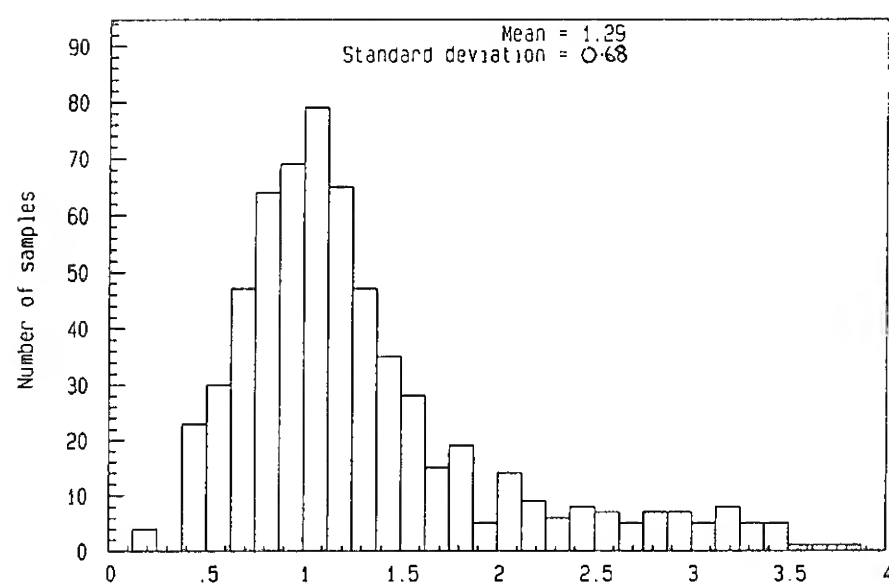
(h) Bradshaw's (1971) model,  $a_1 = .15$ .



(h) Bradshaw's (1971) model,  $a_1 = .15$ .



(i) Bradshaw's (1971) model,  $a_1 = .11$ .



(i) Bradshaw's (1971) model,  $a_1 = .11$ .

Figure 8. Contours of measured and computed turbulence shear-stress magnitude  $\sqrt{(uv^2 + vw^2)}/U_{ref}^2$  in plane 8.

Figure 9. Histograms of the ratio of computed to measured turbulence shear stress magnitude compiled from comparisons at points inside the boundary layer ( $\sqrt{v^2}/U > 5\%$ ) but outside the near-wall region ( $Y/T > .02$ ).

In summary, it appears that more complex turbulence models do not necessarily do better than simpler ones. It could be argued that, out of the 6 models tested here, the Cebeci Smith is the best. Despite the fact that the Cebeci Smith uses a prescribed eddy viscosity profile intended for much simpler flows than the present, its predictions of shear-stress magnitude from the mean-velocity field alone are on the whole better than those of the more complex models. This implies, contrary to conventional thinking, that the more complex models are no more general.

## CONCLUSIONS

New velocity measurements, made in the flow past a wing body junction, have been presented. Combined with earlier results these show the formation and development of the horseshoe vortex and its three-dimensional turbulence structure around the entire wing.

A number of turbulence models have been examined using these data. Many of these models require or imply a relationship between the angles of the turbulence shear-stress and mean-velocity vectors. In the present flow these angles are not only different but do not follow any simple relationship. To predict the shear-stress angle, accurate modeling of the full shear-stress transport equations is clearly needed. In particular, new models based on measurements are needed for the pressure-strain term.

The assumptions of several prescribed eddy viscosity models, the  $k-\epsilon$  model, an algebraic-stress model and Bradshaw's (1971) model have been tested. For each model, predictions of the magnitude of the shear-stress vector from the measured mean-velocity or turbulence kinetic energy distributions were compared with measurements. The Cebeci-Smith eddy-viscosity model is among the best. The algebraic stress and Bradshaw's model also do well but appear to gain little from their relative complexity. Other models, particularly the Johnson-King, are not well suited to this vortical flow.

All the experimental data presented and referred to here is available in tables and on magnetic disc from the authors.

## ACKNOWLEDGEMENTS

The authors would like to thank Dr. S. Olcmen and Mr. A. Obst for their help in taking some of the above measurements. This work was sponsored by NAVSEA through NSWC contract N00014-87-K-0421.

## REFERENCES

- Abid R, 1988, "Extension of the Johnson-King turbulence model to the 3-D flows", AIAA paper 88-0223, 26th Aerospace Sciences Meeting, Reno, Nevada, January 11-14.
- Abid R and Schmitt R, 1984, "Critical examination of turbulence models for a separated three dimensional turbulent boundary layer", *Rech. Aerosp.*, No 6.
- Ahn S, 1986, "Unsteady Features of Turbulent Boundary Layers", M.S. Thesis, Dept. of Aerospace and Ocean Engineering, VPI&SU.
- Bradshaw PP, 1971, "Calculation of three-dimensional turbulent boundary layers", *Journal of Fluid Mechanics*, vol.46, p.417-445.
- Chen H C and Patel V C, 1988, "Near-wall turbulence models for complex flows including separation", *AIAA Journal*, vol. 26, p.641-648.
- Deng G, 1989, "Resolution des equations Navier Stokes tridimensionnelles. Application au calcul d'un raccord plaque plane-alle", PhD thesis, Universite de Nantes, France.
- Devenport W J and Simpson R L, 1990a, "Time-dependent and time-averaged turbulence structure near the nose of an wing-body junction", *Journal of Fluid Mechanics*, vol. 210, pp 23-55.
- Devenport W J and Simpson R L, 1990b, "An experimental investigation of the flow past an idealized wing-body junction: preliminary data report", AOE Dept., VPI&SU.
- Devenport W J and Simpson R L, 1988a, "The turbulence structure near an appendage-body junction", 17th Symposium on Naval Hydrodynamics, The Hague, The Netherlands.
- Devenport W J and Simpson R L, 1988b, "LDV measurements in the flow past a wing-body junction", 4th International Symposium on Applications of Laser Anemometry to Fluid Mechanics, Lisbon, Portugal.
- Devenport W J and Simpson R L, 1988c, "Time-dependent structure in wing-body junction flows", *Turbulent Shear Flows 6*, Springer Verlag.
- Devenport W J and Simpson R L, 1987, "Turbulence structure near the nose of a wing-body junction", AIAA paper 87-1310, AIAA 19th Fluid Dynamics, Plasma Dynamics and Lasers Conference, Honolulu, Hawaii.
- Devenport W J and Simpson R L, 1986, "Some time-dependent features of turbulent appendage-body juncture flows", 16th Symposium on Naval Hydrodynamics, Berkeley, California.
- Durst F, Melling and Whitelaw J H, 1981, *Principles and Practice of Laser Doppler Anemometry*, NY: Academic Press.
- Fernholz H H and Vagt J D, 1981, "Turbulence measurements in an adverse pressure gradient three dimensional turbulent boundary layer along a circular cylinder", *Journal of Fluid Mechanics*, vol. 111, p233.
- Johnston J P, 1970, "Measurements in a three-dimensional turbulent boundary layer induced by a swept forward-facing step", *Journal of Fluid Mechanics*, vol. 42, p823.
- Launder B E, 1982, "A generalized algebraic stress transport hypothesis", *AIAA Journal*, vol. 20, p. 436-437.
- Patankar S V and Spalding D B, 1970, *Heat and Mass Transfer in Boundary Layers*, Second edition, Intertext, London.
- Rodi W, 1984, *Turbulence Models and Their Application in Hydraulics - A State of the Art Review*, Second Edition, IAHR, Delft, The Netherlands.
- Rotta J C, 1977, "A family of turbulence models for three-dimensional thin shear layers", Symposium on Turbulent Shear Flows, University Park, PA.
- Simpson R L and Barr P W, 1975, "Laser Doppler Velocimeter Signal Processing Using Sampling Spectrum Analysis", *Rev. Sci. Inst.*, 46, pp. 835-837.
- van den Berg B, 1982, "Some notes on three-dimensional turbulent boundary-layer data and turbulence modelling", *Three-Dimensional Turbulent Boundary Layers*, p. 1-18, Springer.

van den Berg B and Elsenaar A, 1972, "Measurements in a three-dimensional incompressible turbulent boundary layer in an adverse pressure gradient under infinite swept wing conditions", NLR-TR-72092U.

## DISCUSSION

Fred Stern  
The University of Iowa, USA

Is there a reason that the Baldwin-Lomax turbulence model was not chosen for evaluation? As I'm sure you are aware, this model is the workhorse of the aerospace industry and also used extensively by the Navy laboratories and others. Also, was it possible through the comparisons to reach any conclusion with regard to the quasi-steady assumption, which is made in most current turbulence models?

## AUTHORS' REPLY

The Baldwin-Lomax model is identical to the Cebeci-Smith model in the inner region of an attached two-dimensional turbulent boundary layer. The form of the outer region model is also identical to the Cebeci-Smith model, with the differing length scales. Stock and Haase, *AIAA Journal*, Vol. 27, pp. 5-14, 1989, show that the Cebeci-Smith model performs better than the Baldwin-Lomax model for the two-dimensional flows tested.

## SYMPOSIUM ATTENDEES

### Belgium

V. Ferdinande  
State University of Ghent

### Canada

S. Calisal  
University of British Columbia  
J. Chuang  
Technical University of Nova Scotia  
D. Murdey  
Institute for Marine Dynamics

### China

Forng-Chen Chiu  
National Taiwan University  
Shean-Kwang Chou  
National Taiwan University  
Shi-Tang Dong  
China Ship Scientific Research Center  
Ya-Jung Lee  
National Taiwan University  
Sheng-Shen Yu  
China Ship Scientific Research Center  
Zhen-Quan Zhou  
China Ship Scientific Research Center

### Denmark

J. Petersen  
The Technical University of Denmark

### France

R. Baubeau  
Bassin d'Essais des Carènes  
A. Cariou  
Chantiers de L'Atlantique  
R. Cointe  
Bassin d'Essais des Carènes  
J.C. Dern  
Bassin d'Essais des Carènes  
M. Dupont  
ONERA  
P. Ferrant  
Sirehna S.A.  
P. Genoux  
Bassin d'Essais des Carènes  
B. King  
Bassin d'Essais des Carènes  
J.P. LeGoff  
Sirehna S.A.  
C. Monod  
ONERA  
M.P. Tramoni  
Institut Français du Pétrole

### Germany

V. Bertram  
University of Hamburg  
W. Faller  
Solzer-Escher Wyss GmbH Ravensburg  
B. Remmers  
Kempf & Remmers GmbH  
S. Sharma  
University Duisburg  
H.D. Stinzing  
Versuchsanstalt für Wasserbau und Schiffbau

### Greece

D. Garofallidis  
National Technical University of Athens

### Italy

L. Accardo  
Italian Navy Ship Design Committee  
G. Bailo  
Italian Navy Ship Design Committee  
A. Cardo  
University of Trieste  
C.M. Casciola  
INSEAN  
P. Cassella  
Università di Napoli  
A. Francescutto  
University of Trieste  
R. Piva  
Università di Roma  
A. Scamardella  
Università di Napoli

### Japan

A. Fujii  
Mitsui Engineering & Shipbuilding Co., Ltd.  
T. Hoshino  
Mitsubishi Heavy Industries, Ltd.  
Seung-Hyun Kwag  
Hiroshima University  
Kazu-hiro Mori  
Hiroshima University  
K. Nakatake  
Kyushu University  
M. Ohkusu  
Kyushu University  
S. Takezawa  
Yokohama National University  
M. Takki  
Hiroshima University  
T. Terao  
Society of Naval Architects  
Y. Toda  
Osaka University



### Korea

Kwang June Bai  
Seoul National University  
Gun il Choi  
Seoul National University  
Hang Shoon Choi  
Seoul National University  
Jong Heal Hwang  
Seoul National University  
Chang-Gu Kang  
Korea Research Institute of Ships & Ocean Engineering  
Do Young Kim  
Seoul National University  
Jang Whan Kim  
Seoul National University  
Choung Mook Lee  
Pohang Institute of Science and Technology

### The Netherlands

K. de Jong  
University of Groningen  
J. de Vries  
University of Groningen  
J. Falcao de Campos  
Maritime Research Institute Netherlands  
M. Oosterveld  
Maritime Research Institute Netherlands  
H. Raven  
Maritime Research Institute Netherlands  
J. Sparenberg  
University of Groningen  
E.F.G. van Daalen  
Maritime Research Institute Netherlands  
C. Van Der Stoep  
Technical University Delft  
G. Van Oortmerssen  
Maritime Research Institute Netherlands

### Norway

J. Brembo  
Veritas Sesam Systems A.S.  
O. Faltinsen  
Norwegian Institute of Technology  
T. Vinje  
Norwegian Contractors

### Spain

J. Alaez  
Canal de Experiencias Hidrodinamicas  
A. Baquero  
Canal de Experiencias Hidrodinamicas

### Sweden

P. Andersson  
Royal Institute of Technology  
N.A. Petersson  
Royal Institute of Technology  
O. Rutgersson  
SSPA Maritime Consulting AB  
W. Van Berlekom  
SSPA Maritime Consulting AB

### United Kingdom

M. Downie  
The University of Newcastle-upon-Tyne  
J.M.R. Graham  
Imperial College  
W.G. Price  
Brunel University  
Mingyi Tan  
Brunel University  
P. Wilson  
University of Southampton  
G.X. Wu  
University College London

### United States

J. Abdollahi-Alibeik  
The University of Michigan  
P. Ananthakrishnan  
University of California, Berkeley  
D. Anthony  
The University of Michigan  
F. Ashcroft  
The University of Michigan  
Yeong Soo Bae  
The University of Michigan  
R. Beck  
The University of Michigan  
L. Bernal  
The University of Michigan  
R. Black  
The University of Iowa  
C. Brennen  
California Institute of Technology  
Yusong Cao  
The University of Michigan  
S. Ceccio  
The University of Michigan  
P. Chang, III  
David Taylor Research Center  
Liyong Chen  
The University of Michigan  
Jung-Eun Choi  
The University of Iowa  
Jin-Sug Chung  
The University of Michigan  
Kyung-Nam Chung  
The University of Iowa  
S. Cole  
Rensselaer Polytechnic Institute  
W. Coney  
Bolt Beranek and Newman, Inc.  
R. Couch  
The University of Michigan  
D. Cusanelli  
David Taylor Research Center  
D. Delisi  
Northwest Research Associates, Inc.  
W. Devenport  
Virginia Polytechnic Institute and State University  
D. Dommermuth  
Science Applications International Corporation  
J. Falzarano  
The University of Michigan  
J. Fein  
Office of Naval Research  
Jinzhong Feng  
Pennsylvania State University  
S. Fish  
David Taylor Research Center

## United States

G. Fridsma  
General Dynamics/Electric Boat Division  
Shiyuan Gou  
The University of Michigan  
O. Griffin  
Naval Research Laboratory  
R. Hall  
Science Applications International Corporation  
Soon Hung Han  
The University of Michigan  
A. Hirs  
Rensselaer Polytechnic Institute  
Ching-Yeh Hsin  
Massachusetts Institute of Technology  
Ching-Jer Huang  
The University of Iowa  
T. Huang  
Naval Civil Engineering Laboratory  
Jin Huh  
The University of Michigan  
L. Hunt  
National Research Council  
T. Johnson  
The University of Iowa  
V. Johnson  
The University of Michigan  
Sang Joo  
Northwestern University  
N. Kachman  
The University of Michigan  
Byungsik Kang  
The University of Michigan  
P. Kaplan  
Hydromechanics, Inc.  
K. Kelly  
The University of Michigan  
G. Keramidas  
Naval Research Laboratory  
Hung Tao Kim  
The University of Iowa  
Nan-Chui Kim  
The University of Michigan  
Sung-Eun Kim  
The University of Iowa  
Yoon Ho Kim  
David Taylor Research Center  
S. Kinnas  
Massachusetts Institute of Technology  
J. Kuhn  
Science Applications International Corporation  
Han-Hsiung Kuo  
General Dynamics/Electric Boat Division  
C. Lai  
The University of Michigan  
K. Lawrenson  
The University of Michigan  
Jae-Moon Lew  
The University of Iowa  
S. Liapis  
Virginia Polytechnic Institute and State University  
Woei-Min Lin  
Science Applications International Corporation  
T. Lucas  
University of North Carolina, Charlotte  
A. Magee  
The University of Michigan  
D. Marcus  
Lawrence Livermore National Laboratory  
H. Maruo  
University of California, Santa Barbara

## United States

B. Maskew  
Analytical Methods, Inc.  
J. McCarthy  
David Taylor Research Center  
W. McCreight  
David Taylor Research Center  
J. McHugh  
University of New Hampshire  
G. Meadows  
The University of Michigan  
L. Miller  
The University of Michigan  
W. Miller  
U.S. Navy  
W. Morgan  
David Taylor Research Center  
D. Nakos  
Massachusetts Institute of Technology  
A. Nayfeh  
Virginia Polytechnic Institute and State University  
J.N. Newman  
Massachusetts Institute of Technology  
Phuc Nguyen  
David Taylor Research Center  
F. Noblesse  
David Taylor Research Center  
J. O'Dea  
U.S. Naval Academy  
T.F. Ogilvie  
Massachusetts Institute of Technology  
Jong-Hwan Park  
The University of Michigan  
M. Parsons  
The University of Michigan  
R. Peltzer  
Naval Research Laboratory  
M. Perlin  
The University of Michigan  
L.P. Purtell  
David Taylor Research Center  
A. Reed  
David Taylor Research Center  
E. Rood  
Office of Naval Research  
I. Sahin  
Western Michigan University  
T. Sarpkaya  
Naval Postgraduate School  
D. Savitsky  
Stevens Institute of Technology  
J. Scherer  
The University of Michigan  
W. Schultz  
The University of Michigan  
P. Slavounos  
Massachusetts Institute of Technology  
C. Scragg  
Science Applications International Corporation  
A. Sirviente  
The University of Iowa  
R. Skop  
University of Miami  
T. Smith  
David Taylor Research Center  
W. Smith  
Atlantic Research Corporation  
M. Song  
The University of Michigan  
F. Stern  
The University of Iowa

United States

Y. Tahara  
The University of Iowa

J. Telste  
David Taylor Research Center

K. Thiagarajan  
The University of Michigan

G. Triantafyllou  
The Benjamin Levich Institute

A. Troesch  
The University of Michigan

M. Tulin  
University of California, Santa Barbara

Suak-Ho Van  
The University of Iowa

J.M. Vandenbroeck  
The University of Wisconsin

D. Walker  
The University of Michigan

W. Webster  
University of California, Berkeley

J. Wehausen  
University of California, Berkeley

J. White  
U.S. Coast Guard

K. Williams  
University of California, Santa Barbara

W. Willmarth  
The University of Michigan

E. Wright  
The University of Michigan

T. Wu  
California Institute of Technology

Hongbo Xu  
Massachusetts Institute of Technology

C.I. Yang  
David Taylor Research Center

G. Yates  
California Institute of Technology

R. Yeung  
University of California, Berkeley

Joon-Yong Yoon  
The University of Iowa

D. Yue  
Massachusetts Institute of Technology

PLEASE CHECK THE APPROPRIATE BLOCK BELOW:

-AO # M97-12-6 350

☒ 1 copies are being forwarded. Indicate whether Statement A, B, C, D, E, F, or X applies.

☒ DISTRIBUTION STATEMENT A: Per Dixie Gordon  
APPROVED FOR PUBLIC RELEASE: DISTRIBUTION IS UNLIMITED

☐ DISTRIBUTION STATEMENT B:  
DISTRIBUTION AUTHORIZED TO U.S. GOVERNMENT AGENCIES ONLY; (Indicate Reason and Date). OTHER REQUESTS FOR THIS DOCUMENT SHALL BE REFERRED TO (Indicate Controlling DoD Office).

☐ DISTRIBUTION STATEMENT C:  
DISTRIBUTION AUTHORIZED TO U.S. GOVERNMENT AGENCIES AND THEIR CONTRACTORS; (Indicate Reason and Date). OTHER REQUESTS FOR THIS DOCUMENT SHALL BE REFERRED TO (Indicate Controlling DoD Office).

☐ DISTRIBUTION STATEMENT D:  
DISTRIBUTION AUTHORIZED TO DoD AND U.S. DoD CONTRACTORS ONLY; (Indicate Reason and Date). OTHER REQUESTS SHALL BE REFERRED TO (Indicate Controlling DoD Office).

☐ DISTRIBUTION STATEMENT E:  
DISTRIBUTION AUTHORIZED TO DoD COMPONENTS ONLY; (Indicate Reason and Date). OTHER REQUESTS SHALL BE REFERRED TO (Indicate Controlling DoD Office).

☐ DISTRIBUTION STATEMENT F:  
FURTHER DISSEMINATION ONLY AS DIRECTED BY (Indicate Controlling DoD Office and Date) or HIGHER DoD AUTHORITY.

☐ DISTRIBUTION STATEMENT X:  
DISTRIBUTION AUTHORIZED TO U.S. GOVERNMENT AGENCIES AND PRIVATE INDIVIDUALS OR ENTERPRISES ELIGIBLE TO OBTAIN EXPORT-CONTROLLED TECHNICAL DATA IN ACCORDANCE WITH DoD DIRECTIVE 5230.25, WITHHOLDING OF UNCLASSIFIED TECHNICAL DATA FROM PUBLIC DISCLOSURE, 6 Nov 1984 (Indicate date of determination). CONTROLLING DoD OFFICE IS (Indicate Controlling DoD Office).

☐ This document was previously forwarded to DTIC on \_\_\_\_\_ (date) and the AD number is \_\_\_\_\_.

☐ In accordance with provisions of DoD instructions, the document requested is not supplied because:

☐ It will be published at a later date. (Enter approximate date, if known).

☐ Other. (Give Reason)

DoD Directive 5230.24, "Distribution Statements on Technical Documents," 18 Mar 87, contains seven distribution statements, as described briefly above. Technical Documents must be assigned distribution statements. 18th Symposium

Pat Maubey per  
Dixie Gordon  
Authorized Signature/Date

DIXIE GORDON  
Print or Type Name  
(202) 334-3523  
Telephone Number

19970924 049